CLINICAL ULTRASOUND

PAUL L. ALLAN • GRANT M. BAXTER • MICHAEL J. WESTON

VOLUME ONE

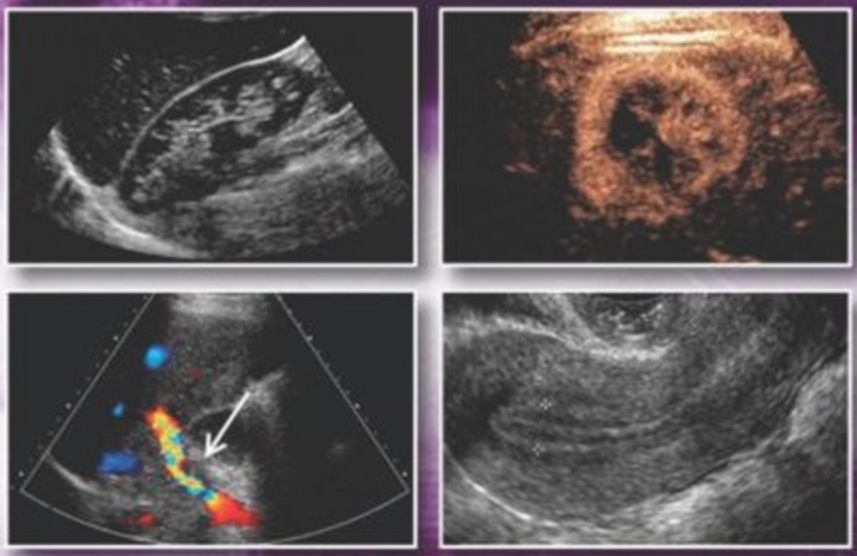

THIRD EDITION

CHURCHILL LIVINGSTONE ELSEVIER

CLINICAL ULTRASOUND

Commissioning Editor: Michael Houston
Development Editor: Ben Davie
Editorial Assistant: Rachael Harrison/Kirsten Lowson
Project Manager: Elouise Ball
Design: Charles Gray
Illustration Manager: Gillian Richards
Illustrator: Amanda Williams
Marketing Manager (UK/USA): Gaynor Jones/Tracie Pasker

CLINICAL ULTRASOUND

THIRD EDITION

Edited by

Paul L. Allan BSc MBChB DMRD FRCR FRCPE
Consultant Radiologist
Department of Radiology
Royal Infirmary
Edinburgh, UK

Grant M. Baxter MBChB FRCR
Consultant Radiologist
Department of Radiology
Western Infirmary
Glasgow, UK

Michael J. Weston MBChB MRCP FRCR
Consultant Radiologist
Department of Radiology
St James's University Hospital
Leeds, UK

Section Editors

Ian Beggs MBChB FRCR
Consultant Musculoskeletal Radiologist
Department of Radiology
The Royal Infirmary of Edinburgh
Edinburgh, UK

Norman McDicken BSc PhD FIPEM
Emeritus Professor
Medical Physics
Edinburgh University
Edinburgh, UK

David W. Pilling MBChB DCH DMRD FRCR FRCPCH
Consultant Paediatric Radiologist
Department of Radiology
Royal Liverpool Children's Hospital Alder Hey
Liverpool, UK

CHURCHILL LIVINGSTONE
ELSEVIER

CHURCHILL
LIVINGSTONE
ELSEVIER

First edition 1993
Second edition 2001
Third edition 2011

Notices
Knowledge and best practice in this field are constantly changing. As new research and experience broaden our understanding, changes in research methods, professional practices, or medical treatment may become necessary. Practitioners and researchers must always rely on their own experience and knowledge in evaluating and using any information, methods, compounds, or experiments described herein. In using such information or methods they should be mindful of their own safety and the safety of others, including parties for whom they have a professional responsibility.

With respect to any drug or pharmaceutical products identified, readers are advised to check the most current information provided (i) on procedures featured or (ii) by the manufacturer of each product to be administered, to verify the recommended dose or formula, the method and duration of administration, and contraindications. It is the responsibility of practitioners, relying on their own experience and knowledge of their patients, to make diagnoses, to determine dosages and the best treatment for each individual patient, and to take all appropriate safety precautions.

To the fullest extent of the law, neither the Publisher nor the authors, contributors, or editors, assume any liability for any injury and/or damage to persons or property as a matter of products liability, negligence or otherwise, or from any use or operation of any methods, products, instructions, or ideas contained in the material herein.

ISBN: 978-0-7020-3131-1

British Library Cataloguing in Publication Data
A catalogue record for this book is available from the British Library

Library of Congress Cataloging in Publication Data
A catalog record for this book is available from the Library of Congress

Printed in China
Last digit is the print number: 9 8 7 6 5 4 3 2 1

PREFACE

Ultrasound remains one of the most frequently used and valuable modalities for imaging and guiding interventional procedures. The number of ultrasound examinations carried out world-wide continues to increase and the global sales of ultrasound equipment, both new and refurbished, is increasing at some 3-5% each year. The flexibility, ease of use, range of applications and relatively low cost of the equipment make ultrasound an important investigative imaging tool.

The first and second editions of this book, edited by David Cosgrove, Keith Dewbury, Hylton Meire and Pat Farrant, were a great success, providing information and advice across the full range of diagnostic ultrasound. They were essential reading for those training in ultrasound and a source of information for many sonographers and sonologists across the world.

Techniques, hardware and data processing have all evolved and progressed at a rapid rate since the second edition of this book was published in 2001. As a result of these developments, ultrasound equipment is now available in more sizes, specifications and complexity than ever before and this has enabled many different types of clinician to use ultrasound in particular niche areas, in addition to the more general imaging function that it has always provided.

The chapters in the two volumes of this book cover all aspects of general ultrasound, as well as more specialised areas such as peripheral vascular and ophthalmic ultrasound. Some areas, such as musculoskeletal ultrasound, have developed into major applications of ultrasound and this is now essential to the management of patients with a wide variety of muscle and joint disorders. There has therefore been a significant enhancement of the coverage of these areas in this new edition.

Conversely, detailed fetal and maternal obstetric scanning in the mid and final trimesters has followed cardiac echography into a separate sphere of expertise. There are many excellent text books dealing with these aspects, therefore, the editors felt that a comprehensive review of obstetric scanning was best left to these volumes. However, first trimester problems will still be seen by sonographers undertaking general scanning so an account of these is included in this book.

The potential applications of echo enhancing agents, or microbubbles, have developed and changed significantly since the publication of the second edition of this book. Originally developed to rescue inadequate Doppler examinations, interesting properties of these agents have led to potential uses delivering drugs and genes.

The editors of the third edition of Clinical Ultrasound are extremely grateful to the many experts in their particular fields of ultrasound who have contributed the authoritative, comprehensive and informative chapters that make up this book. In particular, our thanks go to Ian Beggs, David Pilling and Norman McDicken, who were responsible for coordinating the musculoskeletal, paediatric and physics sections of the book. We are also very grateful to Michael Houston, Ben Davie and all the other staff at Elsevier who have worked on the many aspects of publication between the first outline discussions and the final published product.

Paul Allan
Grant Baxter
Michael Weston

Volume 1

LIST OF CONTRIBUTORS

Laurence J. Abernethy MD FRCR
Consultant Paediatric Radiologist
Department of Radiology
Royal Liverpool Children's Hospital,
Alder Hey
Liverpool, UK

Paul L. Allan BSc MBChB DMRD FRCR FRCPE
Consultant Radiologist
Department of Radiology
Royal Infirmary
Edinburgh, UK

Georgina M. Allen BM MRCGP DCH MFSEM MRCP FRCR
Consultant Radiologist
Radiology Department
University Hospitals Birmingham
Birmingham University
Birmingham, UK

Zahir Amin MBBS MRCP MD FRCR
Consultant Radiologist
Department of Radiology
University College London Hospitals
London, UK

Tom Anderson MSc
Senior Research Fellow
Medical Physics
University of Edinburgh
Edinburgh, UK

Grant M. Baxter MBChB FRCR
Consultant Radiologist
Department of Radiology
Western Infirmary
Glasgow, UK

Ian Beggs FRCR
Consultant Musculoskeletal Radiologist
Department of Radiology
The Royal Infirmary of Edinburgh
Edinburgh, UK

Stefano Bianchi MD
Director
CIM SA
Cabinet Imagerie Médicale
Geneva, Switzerland

Gerd Bodner MD
Professor of Radiology
Specialist Medical Centre
Gibraltar

Michael J. Bradley MBChB DMRD FRCR
Honorary Clinical Lecturer, Bristol University
Lecturer, University of the West of England
Consultant Radiologist
Department of Radiology
Southmead
Westbury-on-Trym, Bristol, UK

David J. Breen MRCP FRCR
Consultant Abdominal Radiologist
Department of Radiology
Southampton University Hospitals
Southampton, UK

Robert S.D. Campbell MBChB DMRD FRCR
Consultant in Musculoskeletal Radiology
Department of Radiology
Royal Liverpool University Hospital
Liverpool, UK

Orlando Catalano MD
Assistant
Department of Radiology
Pascale Institute
Naples, Italy

Dania Cioni MD
Assistant Professor of Radiology
Division of Diagnostic Imaging and Intervention
Department of Liver Transplantation, Hepatology, and Infectious Diseases
University of Pisa
Pisa, Italy

Anne Marie Coady MRCP FRCR
Consultant Radiologist
Head of Obstetric and Gynecologic Ultrasound
Ultrasound Department
Hull and East Yorkshire Women and Children's Hospital
Hull, UK

Dennis L. Cochlin MBBCh FRCR
Consultant Radiologist
Division of Radiology
University Hospital of Wales
Cardiff, UK

David O. Cosgrove MA MSc FRCP FRCR
Emeritus Professor
Imaging Sciences Department
Hammersmith Hospital
Imperial College
London, UK

Neil J.A. Cozens MBChB DMRD FRCR
Consultant Radiologist
Derby Hospitals NHS Foundation Trust
Derbyshire Royal Infirmary
Derby, UK

Laura Crocetti MD PhD
Assistant Professor of Radiology
Division of Diagnostic Imaging and Intervention
Department of Liver Transplantation, Hepatology, and Infectious Diseases
University of Pisa
Pisa, Italy

Colin R. Deane PhD MIPEM
Clinical Scientist
Vascular Laboratory
Department of Medical Engineering and Physics
King's College Hospital
London, UK

Diane DeFriend BSc MBChB FRCR
Consultant Radiologist
Imaging Directorate
Derriford Hospital
Plymouth, UK

Clotilde Della Pina MD PhD
Consultant Radiologist
Division of Diagnostic Imaging and Intervention
Department of Liver Transplantation, Hepatology, and Infectious Diseases
University of Pisa
Pisa, Italy

Keith Dewbury BSc MBBS FRCR
Consultant Radiologist and Senior Lecturer
Department of Clinical Radiology (Ultrasound)
Southampton General Hospital
University of Southampton
Southampton, UK

Rob Dineen MRCP FRCR PhD
Clinical Associate Professor
Honorary Consultant Neuroradiologist
Academic Radiology
University of Nottingham
Nottingham, UK

Ferdinando Draghi
Fondazione IRCCS Policlinico S. Matteo
Università degli Studi Istituto di Radiologia
Pavia, Italy

Francis A. Duck PhD DSc
Medical Physicist
Department of Medical Physics and Bioengineering
Royal United Hospital
Bath, UK

Anthony J. Edey BMedSci MRCP FRCR
Specialist Registrar
Department of Radiology
King's College Hospital
London, UK

Simon T. Elliott MBChB FRCR
Consultant Radiologist
Radiology Department
Freeman Hospital
Newcastle-upon-Tyne, UK

Andrew J. Evans MRCP FRCR
Professor of Breast Imaging
Centre for Oncology & Molecular Medicine
Division of Medical Sciences
University of Dundee
Ninewells Hospital & Medical School
Dundee

John A. Fielding MD FRCR FRCP(Edin)
Consultant Radiologist
Department of Radiology
Royal Shrewsbury Hospital NHS Trust
Shrewsbury, UK

Simon J. Freeman MBBS MRCP FRCR
Consultant Radiologist
Department of Radiology
Derriford Hospital
Plymouth, UK

Fergus V. Gleeson MBBS FRCR
Consultant Radiologist
Department of Radiology
The Churchill Hospital
Headington, Oxford, UK

David E. Goss PhD MIPEM
Clinical Scientist
Vascular Laboratory
Department of Medical Engineering and Physics
King's College Hospital
London, UK

Andrew J. Grainger MRCP FRCR
Consultant Musculoskeletal Radiologist
Department of Radiology
Leeds Teaching Hospitals
Leeds, UK

Timothy Hartshorne AVS
Vascular Technologist
Department of Surgery
Leicester Royal Infirmary
Leicester, UK

Christopher J. Harvey BSc(Hons) MBBS MRCP FRCR
Consultant Radiologist
Honorary Senior Lecturer, Imperial College
Department of Imaging
Hammersmith Hospital
London, UK

Jeremiah C. Healy MA MB BChir MRCP FRCR
Consultant Musculoskeletal Radiologist
Honorary Senior Lecturer, Imperial College
Department of Radiology
Chelsea and Westminster Hospital
London, UK

Tracey Hughes MB, BCh, BAO, BA, MRCP, FRCR
Consultant Radiologist
Radiology Department
Queen Elizabeth Hospital
Gateshead, UK

Scott Inglis BSc MSc PhD MIPEM CSci
Senior Clinical Scientist
Department of Medical Physics
NHS Lothian / University of Edinburgh
The Royal Infirmary of Edinburgh
Edinburgh, UK

Jonathan J. James FRCR
Consultant Radiologist
Nottingham Breast Institute
Nottingham City Hospital
Nottingham, UK

Tim Jaspan MBChB BSc FRCR FRCP
Consultant Paediatric Neuroradiologist
Imaging Centre
University Hospital
Queen's Medical Centre
Nottingham, UK

Steven J. Kennish MBChB, MRCS(Ed) FRCR
Specialist Registrar in Radiology
St James University Hospital
Leeds, UK

Stephen R. Killick MD FRCOG FFSRH
Professor of Reproductive Medicine and Surgery
University of Hull and Hull York Medical School (HYMS)
Women and Children's Hospital
Hull, UK

Caren J. Landes MBChB MRCPCH FRCR
Consultant Paediatric Radiologist
Radiology Department
Alder Hey Children's NHS Foundation Trust
Liverpool, UK

Edward Y. Lee MD MPH
Assistant Professor of Radiology
Department of Radiology and
Department of Medicine
Pulmonary Division
Children's Hospital Boston and Harvard Medical School
Boston, MA, USA

Justin C. Lee BSc MBBS MRCS FRCR
Consultant Musculoskeletal Radiologist
Department of Radiology
Chelsea and Westminster Hospital
London, UK

Edward Leen MB MD FRCR
Professor of Radiology
MRC Clinical Sciences Centre
Faculty of Medicine
Imperial College London
Hammersmith Hospital
London, UK

Riccardo Lencioni MD
Associate Professor of Radiology
Director, Division of Diagnostic and Intervention
Department of Liver Transplantation, Hepatology, and Infectious Diseases
University of Pisa
Pisa, Italy

Adrian Kuok Pheng Lim MD FRCR
Consultant Radiologist
Honorary Senior Lecturer, Imperial College
Imaging Department
Charing Cross Hospital
London, UK

Gavin Low MBChB MRCS FRCR
Assistant Professor
Department of Radiology & Diagnostic Imaging
University of Alberta Hospital
Edmonton, AB, Canada

Gurdeep S. Mann MBChB MRCP(UK) FRCR
Consultant Radiologist
Department of Radiology
Royal Liverpool Children's Hospital, Alder Hey
Liverpool, UK

Kevin Martin BSc PhD FIPEM
Consultant Clinical Scientist
Department of Medical Physics
Leicester Royal Infirmary
Leicester, UK

Carlo Martinoli MD
Associate Professor of Radiology
Radiologia – DISC. Università di Genova
Genoa, Italy

Catherine L. McCarthy MBChB FRCR
Consultant Musculoskeletal Radiologist
Department of Radiology
Nuffield Orthopaedic Centre NHS Trust
Headington, Oxford, UK

Norman McDicken BSc PhD
Emeritus Professor
Medical Physics
Edinburgh University
Edinburgh, UK

Eugene G. McNally MB BCh BAO FRCPI FRCR
Consultant Musculoskeletal Radiologist
Department of Radiology
Nuffield Orthopaedic Centre NHS Trust
Headington, Oxford, UK

Carmel M. Moran PhD FIPEM
Reader in Medical Physics
Centre for Cardiovascular Sciences
University of Edinburgh
Queens Medical Research Institute
Edinburgh, UK

Philip J. O'Connor MRCP FRCR
Consultant Musculoskeletal Radiologist
Department of Radiology
Leeds Teaching Hospitals
Leeds, UK

Simon Ostlere FRCR
Consultant Musculoskeletal Radiologist
Department of Radiology
Nuffield Orthopaedic Centre NHS Trust
Headington, Oxford, UK

Uday Patel MBChB MRCP FRCR
Consultant Radiologist
Department of Radiology
St George's Hospital and Medical School
London, UK

James M. Pilcher MSc MRCP FRCR
Consultant Radiologist and Clinical Lead of Adult Ultrasound
Department of Radiology
St George's Hospital
London, UK

David W. Pilling MBChB DCH DMRD FRCR FRCPCH
Consultant Paediatric Radiologist
Department of Radiology
Royal Liverpool Children's Hospital, Alder Hey
Liverpool, UK

John N. Plevris MD DM PhD FRCP(E)
Consultant Gastroenterologist & Reader (hon)
Centre for Liver & Digestive Disorders
The Royal Infirmary of Edinburgh;
University of Edinburgh Medical School
Edinburgh, UK

Najib M. Rahman BM BCh MA(Oxon) MRCP
MRC Training Fellow
Specialist Registrar in Respiratory Medicine
Oxford Centre for Respiratory Medicine
Churchill Hospital
Headington, Oxford, UK

Rhian Rhys MBBCh FRCS(Otol) FRCR
Consultant Radiologist
Department of Radiology
Royal Glamorgan Hospital
Llantrisant, Cardiff, UK

Jonathan L. Richenberg MA MRCP FRCR
Consultant Uroradiologist and Honorary Senior Lecturer
Department of Radiology
Brighton and Sussex University Hospitals NHS Trust
Brighton, East Sussex, UK

Philip Robinson MBChB MRCP FRCR
Consultant Musculoskeletal Radiologist
Department of Radiology
Chapel Allerton Hospital
Leeds Teaching Hospitals
Leeds, UK

Peter Rodgers MBBS FRCR
Consultant Radiologist
Leicester Royal Infirmary
University Hospitals of Leicester NHS Trust
Leicester, UK

Elizabeth E. Rutherford BMedSci MBBS MRCS FRCR
Consultant Radiologist
Department of Ultrasound
Southampton General Hospital
Southampton, UK

Suzanne M. Ryan MD MRCP(Ireland) FRCR
Consultant Radiologist
Department of Radiology
King's College Hospital
London, UK

Maria E.K. Sellars
King's College Hospital
London, UK

Paul S. Sidhu BSc MBBS MRCP FRCR DTMBH
Consultant Radiologist and Senior Lecturer
Department of Radiology
King's College Hospital
London, UK

Marilyn J. Siegel MD
Professor of Radiology and Pediatrics
Mallinckrodt Institute of Radiology
Washington University School of Medicine
St Louis, MO, USA

Rakesh Sinha MBBS MD FRCR FICR
Consultant Radiologist and Assistant Professor
Department of Clinical Radiology
Warwick Hospital Foundation Trust and Warwick Medical School
Warwick, UK

Jane A. Smith MPhil DMU DCRR
Consultant Sonographer
Ultrasound Department
St James's University Hospital
Leeds, UK

Hazel C. Starritt PhD FIPEM
Medical Physicist
Medical Physics and Bioengineering
Royal United Hospital
Bath, UK

Brian Stedman BSc FRCR FRCS
Consultant Abdominal and Interventional Radiologist
Department of Radiology
Southampton University Hospitals NHS Trust
Southampton, UK

Alberto Tagliafico MD
Staff Radiologist
Department of Radiology
University of Genoa
Genoa, Italy

James Teh BSc MBBS MRCP FRCR
Consultant Musculoskeletal Radiologist
Department of Radiology
Nuffield Orthopaedic Centre NHS Trust
Headington, Oxford, UK

Tze Min Wah MBChB FRCR
Consultant Radiologist and Lead for Percutaneous Tumour Ablation Program
Department of Radiology
Leeds Teaching Hospital NHS Trust
Leeds, UK

Joanna M. Wardlaw MB ChB (Hons) FRCP FRCR MD FMedSci
Professor of Applied Neuroimaging and Honorary Consultant Neuroradiologist
University of Edinburgh and NHS Lothian
Director, Scottish Imaging Network, A Platform for Scientific Excellence (SINAPSE) Collaboration
Division of Clinical Neurosciences
Western General Hospital
Edinburgh, UK

Michael J. Weston MBChB MRCP FRCR
Consultant Radiologist
Department of Radiology
St James's University Hospital
Leeds, UK

C. Jason Wilkins MA MRCP FRCR
Consultant Radiologist
Department of Radiology
King's College Hospital
London, UK

Helen Williams MRCP FRCR
Consultant Paediatric Radiologist
Radiology Department
Birmingham Children's Hospital
Birmingham, UK

David J. Wilson MBBS BSc FRSEM FRCP FRCR
Consultant Musculoskeletal Radiologist
Department of Radiology
Nuffield Orthopaedic Centre NHS Trust
Headington, Oxford, UK

CHAPTER

40 The abdominal aorta and inferior vena cava

Tim Hartshorne

INTRODUCTION

The aorta is the largest artery in the body and is divided into thoracic and abdominal sections. The abdominal aorta is smaller in diameter than the thoracic segment and has major branches supplying blood to the abdominal viscera. Distally, it bifurcates into the iliac arteries to supply the pelvis and legs. The main pathologies that affect the abdominal aorta are aneurysms and atherosclerotic disease. Rupture of an aortic aneurysm is normally fatal and accounts for approximately 9000–15000 deaths in the USA annually.[1,2] Ultrasound is the simplest and most cost-effective method of imaging the aorta but its accuracy in identifying the level of major branches, including the renal arteries, is less reliable than other imaging technologies such as computed tomography (CT) and magnetic resonance imaging (MRI).[3] With increasing use of endovascular grafts to repair aortic aneurysms, vascular surgeons require detailed information from CT or MRI regarding the morphology of the aorta before proceeding to elective surgery.[4] The use of ultrasound has now shifted towards aneurysm detection within abdominal aortic aneurysm (AAA) screening and surveillance programmes and, to an increasing extent, the surveillance of endovascular aortic aneurysm repair. Additionally, ultrasound can be used as a non-invasive technique for imaging the inferior vena cava (IVC).

ANATOMY OF THE ABDOMINAL AORTA

The abdominal aorta commences at the level of the diaphragm, where it enters through the aortic hiatus and lies just in front of the spine. It descends slightly to the left of the midline to the level of the fourth lumbar vertebra, where it divides into the left and right common iliac arteries. The IVC lies to the right of the aorta and can be easily distinguished as it has a thinner wall and is often seen as an oval or flattened shape when imaged in transverse section. The aorta tapers slightly as it descends through the retroperitoneum and branches are given off to the abdominal viscera. The anatomy of the aorta and its branches is shown in Figure 40.1. Branches of the aorta that can be identified with ultrasound include the coeliac axis and superior mesenteric artery (SMA), together with the renal arteries. The inferior mesenteric artery (IMA) is less frequently seen, especially if an aneurysm is present. Accessory renal arteries are often missed with ultrasound, this being one of the reasons why alternative imaging is required before planning aneurysm repair.[3]

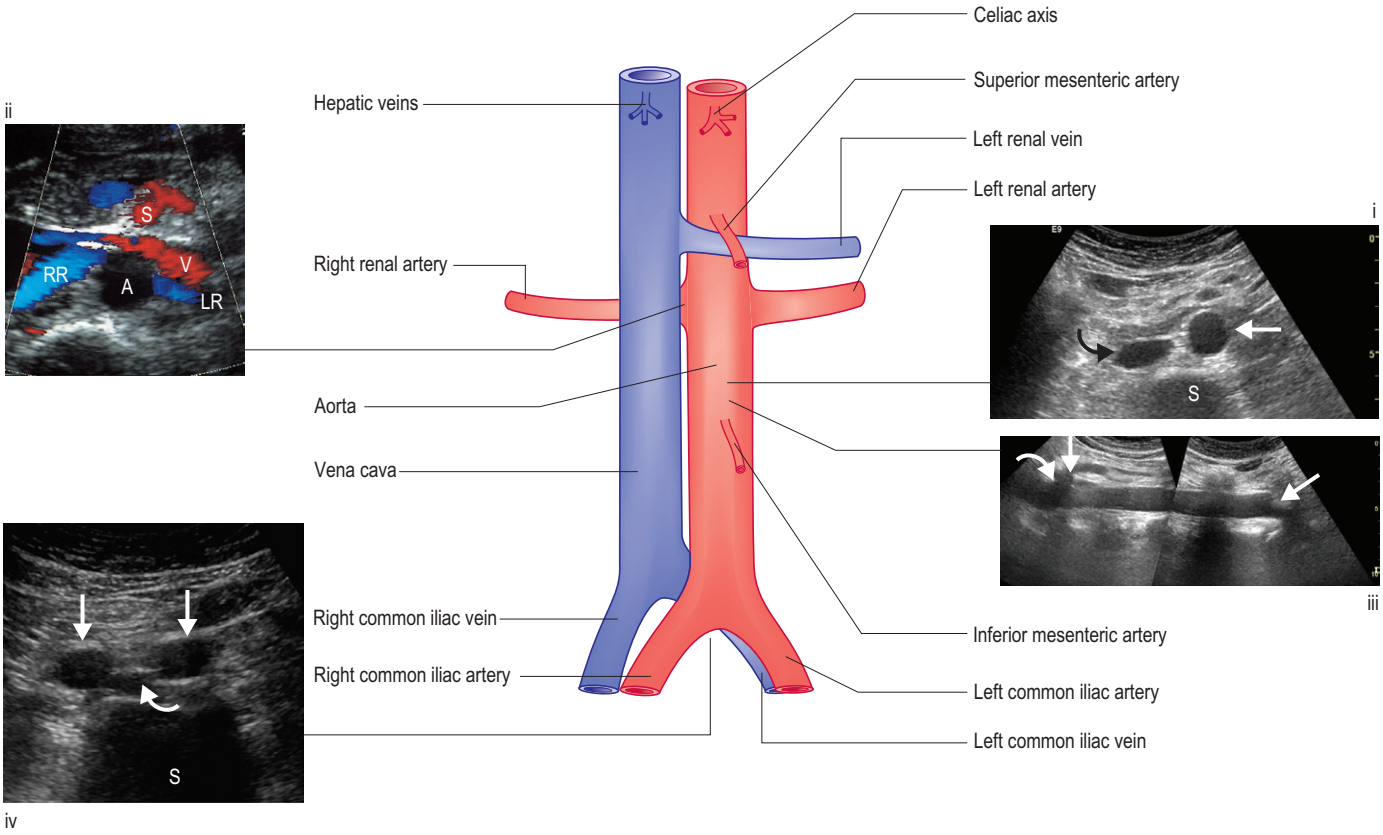

Figure 40.1 The anatomy of the abdominal aorta and IVC with corresponding ultrasound images. i: Transverse section of the mid-aorta (straight arrow), and IVC (curved arrow), lying anterior to the spine (S). **ii:** Transverse image of the aorta (A) showing the right (RR) and left (LR) renal arteries. The superior mesenteric artery is seen (S), with a section of the left renal vein (V) (reproduced with permission from Thrush A, Hartshorne T. Peripheral Vascular Ultrasound. How, why and when. 2nd edition. Churchill Livingstone, 2005). **iii:** A longitudinal extended image of the aorta showing the origins to coeliac axis (curved arrow), and SMA (straight arrow). The level of the aortic bifurcation is shown by the arrowhead. **iv:** Transverse image just below the aortic bifurcation showing the proximal common iliac arteries (straight arrows). A segment of the left common iliac vein is visible (curved arrow), with the lumber spine (S) seen below.

AORTIC DIAMETER AND AORTIC ANEURYSM

There is no absolute consensus as to what value constitutes the upper limit of normal aortic diameter or at what threshold the aorta is considered aneurysmal.[5] Some authors suggest the diameter of the normal aorta is also dependent on age, sex and body size.[6] An Ad Hoc Committee on Reporting Standards on arterial aneurysms[7] suggested that the normal diameter of the abdominal aorta is between 1.4 and 2.5 cm and that an aneurysm is present when the aorta exceeds 3 cm in diameter or where there is a permanent localised dilatation of at least 50% compared to the normal expected diameter. Other definitions have used the ratio of the diameter of a dilatation compared to the expected diameter of an adjacent segment.[8] A summary of recommendations is shown in Table 40.1.

A population-based study using MRI to define variations in aortic dimension in 70-year-old men and women, suggested that for men, the dividing line between a normal infrarenal aorta and an aneurysm is 3.0 cm.[9] The corresponding dividing line for women was 2.7 cm. Importantly, an aortic diameter of 3 cm is also the threshold used to indicate the presence of an AAA adopted by the US Preventive Services Task Force and the UK aortic aneurysm screening programmes.[10,11] This, however, leaves some patients in a potential 'grey zone' with aortic diameters of 2.6–2.9 cm. At this diameter the aorta would be considered ectatic or mildly dilated. If there is a family history of AAA-related disease, or if the patient is <65 years, it has been suggested that a further ultrasound scan be performed within 5 years to ensure that an aneurysm is not developing.[5]

Table 40.1 Suggested definitions of normal aortic diameter and thresholds to indicate AAA

Author	Normal diameter	AAA indicated
Sterpetti[8]		≥1.5 times suprarenal diameter
Johnston[7]	1.4–2.5 cm	≥3 cm or ≥50% localised dilatation
Wanhainen[9]		Men ≥ 3 cm Women ≥ 2.7 cm

BACKGROUND AND CAUSES OF ABDOMINAL AORTIC ANEURYSMS

The prevalence of aortic aneurysms found in population-based screening studies is approximately 4–9% for men and 1% for women.[12–17] Almost all aneurysms occur in later life after 50 years.[18] Abdominal aortic aneurysms are six times more likely to occur in men than in women.[19] They are also up to four times more likely to

Summary of the risk factors associated with aortic aneurysm

- Age (>50 years)
- Male sex
- History of smoking
- High mean blood pressure
- Family history
- Hypercholesterolaemia

occur in first-degree male relatives of patients with aneurysms.[20] To date there is not a clear understanding as to why aneurysms develop but it is thought to involve the destruction of structural matrix proteins in the aortic wall due to increased local proteolytic enzymes capable of degrading elastic fibres as well as interstitial collagens.[21] The risk factors associated with aortic aneurysm are summarised above, but the main modifiable risk factor is smoking.

Some aneurysms exhibit inflammatory changes in the wall with thickened adventitia and perianeurysmal fibrosis, which may adhere to surrounding structures such as the IVC, ureters and duodenum. Approximately 2.5–5% of patients undergoing aneurysm repair have clinical features of inflammation.[22,23] Ureteral displacement or obstruction is also more prevalent, compared to non-inflammatory aneurysms.

Aortic aneurysms can become infected and these are termed mycotic aneurysms. Mycotic aneurysms can also occur in other arteries, especially the common femoral arteries.[24] Potential sources of infection include systemic infections, malignancy and sepsis from cardiac infections, such as bacterial endocarditis. Mycotic aneurysms are often saccular in shape and can expand rapidly. They may be associated with perivascular inflammation. In rare cases primary infection of the aorta may be the cause of the aneurysm.

Some aortic aneurysms are associated with less common disorders such as Ehlers–Danlos and Marfan syndromes.

ANEURYSM SHAPES AND TYPES

Aneurysms vary considerably in shape and size (Fig. 40.2). Most aneurysms are fusiform in shape and there is uniform dilation across the entire cross-section of the vessel (Fig. 40.2Ai and B). Approximately 95% of aneurysms of the abdominal aorta are infrarenal[25] and have a variable distance between the renal arteries and the start of the aneurysm sac – the neck of the aneurysm. As the aorta dilates, it also tends to increase in length; this can result in tortuosity that often shifts the aorta to the left of the midline (Fig. 40.2Aii) or deflects it in an anterior direction. Saccular aneurysms exhibit a typical localised bulging of the wall (Fig. 40.2Aiii and C). Dissecting aneurysms occur following disruption of the intimal lining of the vessel, allowing blood to enter the subintimal space resulting in the stripping of the intima from the artery wall. If the dissection is partial, large amounts of thrombus may be seen in the subintimal space (Fig. 40.2Avi). If there is a complete dissection, a false lumen is created and the dissected layer of intima may be seen flapping freely in time with arterial pulsation (Fig. 40.2Avii). In rare instances, two aneurysmal dilations may be seen along the length of the abdominal aorta, separated by a relatively normal segment of the aorta, which gives rise to a classic 'dumbbell' shape when viewed in longitudinal section (Fig. 40.2Aviii and D). False aneurysms of the aorta are infrequent and they are usually associated with trauma or a leak from a failed graft anastomosis after open repair. Thoracic aneurysms can extend to the abdominal aorta.

Aortic aneurysm risks, size and symptoms

The primary complication of abdominal aortic aneurysm is rupture, which in the majority of cases (60–80%) leads to rapid death, and even patients who reach hospital alive may not survive.[26–28] The risk of rupture is related to aortic diameter and increases with size. One study demonstrated that the annual rates of rupture of aneurysms measuring 5.5–5.9 cm, 6–6.9 cm and ≥7 cm were 9%, 10% and 33%, respectively.[29] The United Kingdom Small Aneurysm Trial Participants (UKSAT) and the Aneurysm Detection and Management (ADAM) Veterans Affairs Cooperative Study Group in the USA each compared the outcomes of surveillance to the outcomes from surgery for infrarenal aneurysms measuring 4–5.4 cm in diameter.[30,31] They found that the mean risk of rupture of aneurysms measuring 4–5.5 cm was approximately 1% per annum and that there was no overall survival benefit in offering early surgery compared to surveillance for this group. This was confirmed at 12-year follow-up by UKSAT.[32] The 30-day operative mortality rates for UKSAT and ADAM were 5.4% and 2.1%, respectively, and are in line with other published studies.[33–35] These trials indicated that abdominal aneurysms can be safely kept under surveillance until they measure 5.5 cm in diameter.[36] Above 5.5 cm the decision to undertake surgery will depend not only on the size of the aneurysm but also on the general health of the patient. There is evidence that the rupture rate of small aneurysms in women may be higher than men but there is no clear consensus for offering surgery to women at diameters <5.5 cm, or whether to include women in aneurysm screening programmes.[10,37–39] Interest has also focused on the outcome of endovascular repair of small aneurysms of the abdominal aorta versus surveillance and the results of current trials should be available in the near future.[40]

The growth rate of an aneurysm is broadly related to its size but not all aneurysms of a similar size will grow at the same rate and some may demonstrate a 'growth spurt'. For aneurysms measuring 4.0–5.4 cm in UKSAT the growth rate was 0.33 cm per year.[30] However, larger aneurysms >6 cm in diameter can expand by as much as 7–8 mm annually.[41] Smaller aneurysms (3–4 cm diameter) may grow only 1–2 mm annually.[42] It is therefore important that operators working in an aneurysm surveillance programme are regularly assessed and measurements audited to ensure consistency, as patients may be scanned by a number of different operators.

The symptoms associated with aneurysm leakage or rupture include back or abdominal pain and acute shock. Ultrasound can be used to confirm the diagnosis in the emergency room and many emergency physicians are now trained to undertake ultrasound scanning of the aorta as an extension of Focused Assessment with Sonography in Trauma (FAST).[43–45] The concept is to rapidly identify an aneurysm in a collapsed or unstable patient with abdominal or back pain. If an aneurysm is confirmed, the patient can be taken to theatre immediately. However, CT scanning is the gold standard for detecting a ruptured or leaking aneurysm and if the patient is stable, they should undergo a rapid CT scan.

Other risks related to abdominal aneurysms are distal embolism of thrombus from the aneurysm sac to the lower limbs. For this reason, the possibility of an aortic or popliteal artery aneurysm should be considered in a patient presenting with embolic changes in the foot or toes, especially in the absence of cardiac arrhythmia.

Renal symptoms can occur due to compression of the ureters (frequently the left side) leading to hydronephrosis.

ULTRASOUND SURVEILLANCE PROGRAMMES

The majority of abdominal aneurysms are asymptomatic and discovered incidentally during medical examination by palpation or by imaging investigations.[46,47] Analysis of the results from several

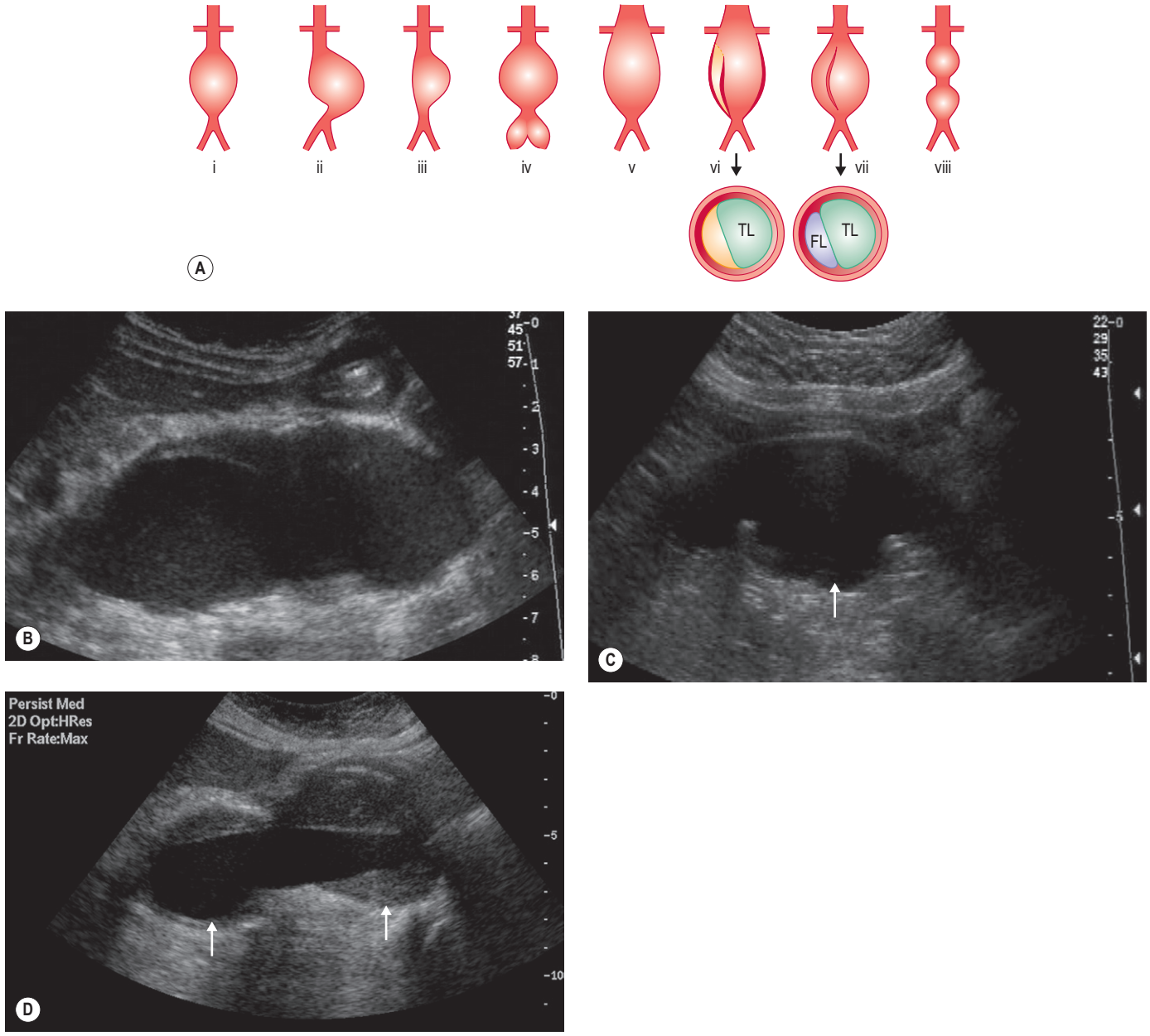

Figure 40.2 Shapes and types of abdominal aortic aneurysms. A: Diagrams showing the different types of aneurysm: **i:** Fusiform infrarenal aortic aneurysm. **ii:** Tortuous elongated aortic aneurysm with the sac shifted to the left of the midline. **iii:** Saccular aortic aneurysm. **iv:** Infrarenal aortic aneurysm extending into the iliac arteries. **v:** Suprarenal aortic aneurysm involving the renal arteries. **vi:** Dissecting aortic aneurysm with a tear between the intima and media allowing blood into the subintimal space where it has thrombosed. **vii:** Dissecting aortic aneurysm in which the intima or media has fully dissected, creating a false flow lumen. **viii:** Double aneurysm of the aorta producing a 'dumb-bell appearance'. TL, true lumen; FL, false lumen. **B:** A longitudinal image of a fusiform aneurysm. **C:** An image of a saccular aneurysm showing a localised dilatation of the posterior wall (arrow). **D:** Ultrasound image of a 'dumb bell' aneurysm (arrows).

large trials confirms that population-based screening for men aged 65–75 years reduces aneurysm-related mortality.[48,49] Ultrasound can detect almost all abdominal aneurysms and when screening is combined with elective surgery, the mortality associated with the disease is almost halved.[50] If a patient has an aorta measuring <2.5 cm in diameter at the age of 65 years, the chances of developing an aneurysm within their lifetime are low. In the USA, the Preventive Services Task Force and a consortium of leading professional organisations recommend one-time screening with abdominal ultrasound for all men aged 65–74 years who have ever smoked.[10] In the UK, a national screening programme has been implemented and will offer one-off screening to all men aged 65 by 2012. The recommendations for the NHS Abdominal Aortic Aneurysm Screening Programme in England are shown in Table 40.2.[11]

An example of a local screening programme

The protocol below has been used by the Leicester Vascular Unit and is included as an example of a local screening programme, including surveillance of iliac artery aneurysms.

Aorta diameter	Follow-up and comments
<2.5 cm	No further follow-up
<4 cm	Yearly
4–4.9 cm	6-monthly*
5–5.4 cm	3-monthly*
≥5.5 cm	Refer to vascular surgeon

AAA growth rates	Action
>5 mm in 6 months	Refer to vascular surgeon
>1 cm in 1 year	Refer to vascular surgeon

**If the patient complains of abdominal tenderness or back pain during the examination, advice is sought.*

Iliac artery diameter	Action
>2 cm	1 year
2.5–3 cm	6-month follow-up
>3 cm	Refer to vascular consultant

Table 40.2 Surveillance intervals for patients with AAA *NHS AAA screening programme*

Aortic diameter	Follow-up interval and comments
3.0–4.4 cm	1 year
4.5–5.4 cm	3 months
≥5.5 cm	Refer to vascular surgeon

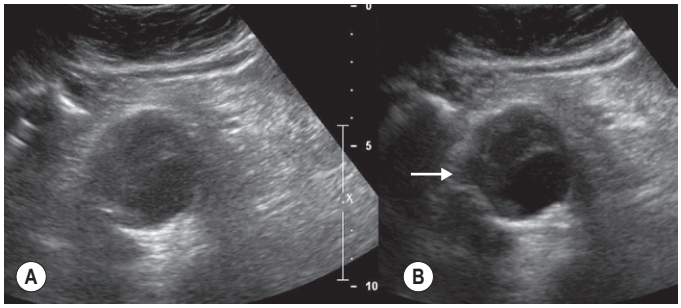

Figure 40.3 Harmonic and compound imaging. A: Standard image of a small AAA. **B:** The use of harmonic imaging has improved the image. Note in this example, there appears to be a small localised dilation of the wall (arrow).

DUPLEX SCANNING OF ABDOMINAL AORTIC ANEURYSMS

Objectives of the scan and patient preparation

No special preparation is required, although some units use bowel preparation to improve visualisation of the aorta; however, for screening scans this is rarely necessary. The patient should lie supine with the head supported on a pillow. Sometimes the patient may have to roll on to one side (decubitus position) to try and shift obscuring bowel or gas. The ultrasound system should be configured for an aortic investigation or, a general abdominal examination set-up with an appropriate scan depth. A low-frequency broadband curvilinear array transducer is the most suitable probe for this investigation. Harmonic and compound imaging can improve the image quality (Fig. 40.3).

The aorta is identified by starting with the transducer in a transverse image plane, approximately 3–4 cm above the umbilicus (Fig. 40.4Ai). The aorta is then imaged in transverse section throughout its visible length from the upper abdomen above the coeliac axis, or SMA, to the aortic bifurcation. It is normally apparent if an aneurysm is present. The liver can act as a useful window to visualise the aorta in the region of the coeliac axis but views are sometimes either poor or completely inadequate (Fig. 40.4Aii).

The abdominal aorta is then imaged in a longitudinal or sagittal plane from the midline along its length to the aortic bifurcation and the maximum diameter recorded (Fig. 40.4Aiii). The measurement of diameter in the longitudinal plane is often more accurate as it is possible to avoid obliquity.

The aorta is next viewed from a coronal scan plane throughout its length in a longitudinal view to obtain more accurate measurements of the lateral diameter of the aorta (side to side) (Fig. 40.4Aiv).

It is good practice to assess the proximal iliac arteries in transverse and longitudinal scan planes to exclude an isolated iliac artery aneurysm or to define the lower limit of an aneurysm if it extends into the iliac arteries (Fig. 40.4Av and B). Some protocols also require a scan of the kidneys to exclude hydronephrosis secondary to ureteric obstruction by the aneurysm.

For screening scans the key measurement is the maximum diameter of the aorta, which ideally can be made in the sagittal and coronal planes. The shape of the aneurysm and features such as tortuosity or dissection should be documented.

Normal appearance

A normal aorta will measure less than 2.5 cm at its maximum diameter (Fig. 40.1); there is usually slight tapering of the abdominal aorta from top to bottom and in the longitudinal plane the aorta is sometimes seen to curve gently as it lies on the lumbar spine. The lumbar spine is usually visible behind the aorta and there is sometimes retroperitoneal tissue between the posterior wall of the aorta and the spine; this can cause confusion when attempting to identify the position of the back wall of the aorta, especially when scanning in a longitudinal plane, as a number of echo boundaries may be visible (Fig. 40.5). In these circumstances, turning to a transverse section may be of value as the overall circular shape of the aorta can be more readily appreciated.

Abnormal appearance

With an aneurysm, the aorta is abnormally enlarged to more than 3 cm in diameter (Fig. 40.6). Mildly dilated or ectatic aortas will measure 2.6–2.9 cm. The length of the aneurysm can vary and may involve only the distal segment of the aorta to the bifurcation, or a more substantial length, up to the whole of the visible abdominal aorta. Thrombus may be imaged as concentric layers within the

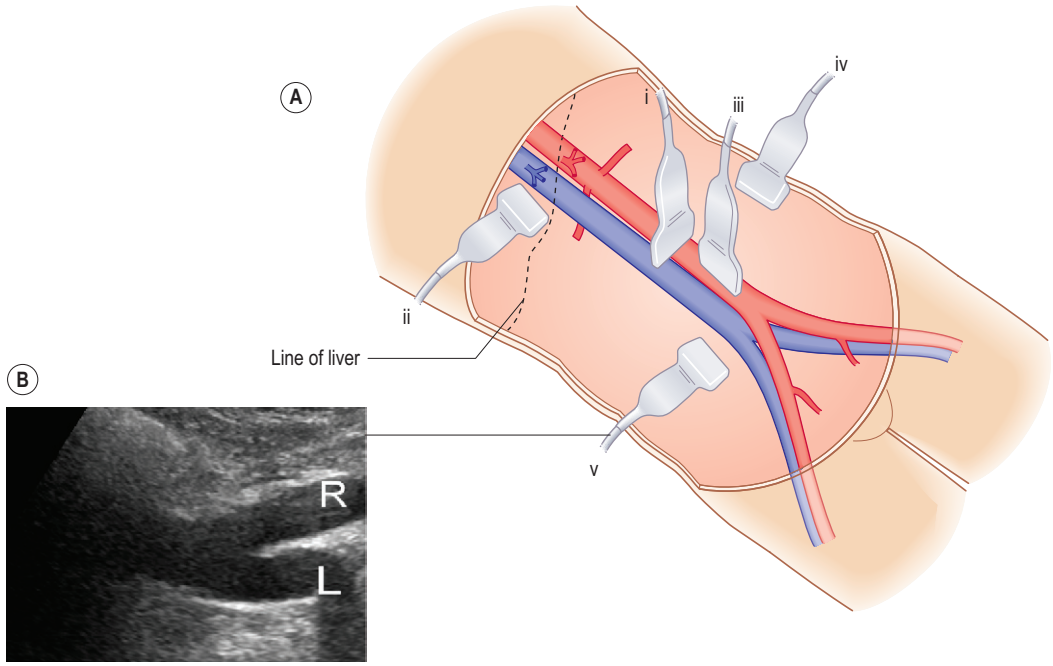

Figure 40.4 Transducer positions for imaging the aorta and IVC (A). i: Transverse image of the mid-aorta and IVC. **ii:** Imaging through the liver to identify the proximal aorta and IVC. **iii:** Sagittal image of the aorta. **iv:** Coronal imaging plane. **v:** Imaging the aortic bifurcation in longitudinal plane from a right oblique position enables both common iliac arteries to be seen in the same image. **B:** Ultrasound image at position **v** to show the aortic bifurcation and the right (R) and left (L) proximal common iliac arteries.

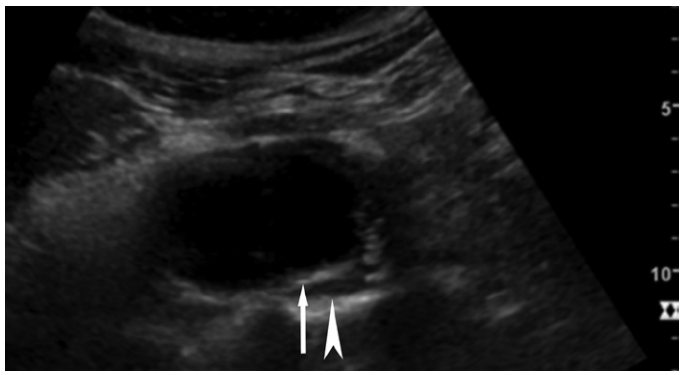

Figure 40.5 Localising the posterior wall of the aorta. The posterior wall of the aorta (arrow) can sometimes be difficult to clearly define as shown in this image. It may be mistaken for the anterior margin of the spine (arrowhead). Turning into a transverse plane may give a better appreciation of the boundary.

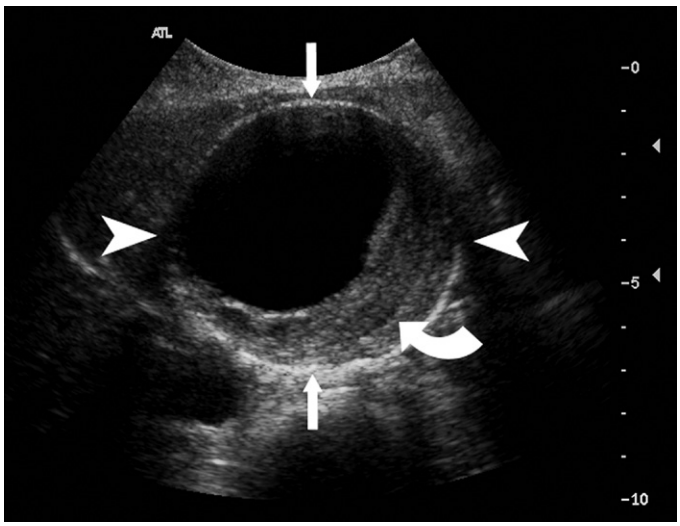

Figure 40.6 Abdominal aortic aneurysm, transverse section. Thrombus is seen within the sac (curved arrow). The position for measuring the anteroposterior diameter from outer wall to outer wall is shown by the arrows. Note that an attempt to measure the transverse diameter (arrowheads) would not be accurate as the aortic walls lie parallel to the ultrasound beam and are not clearly defined.

Scanning AAAs. A summary of the key features that may be required in a report

- Maximum diameter of the aneurysm.
- What is its shape (fusiform, saccular etc.)?
- Can the extent or length be defined (infrarenal, suprarenal, or involving the aortic bifurcation and/or iliac arteries)?
- Does the sac contain a large amount of thrombus?
- Is there tortuosity?
- Other relevant features: dissection, mobile flaps, inflammation.
- Any limitations of the scan, stating clearly what measurements were made and from what positions. Measurement can be ambiguously reported and the overall length of an aneurysm may be mistakenly interpreted as its diameter.

Note: for screening scans, only the diameter is necessary.

lumen which have differing degrees of echogenicity, depending on its age and degree of organisation. Localised liquefaction of the thrombus can occur and appears as hypoechoic areas within the thrombus. This appearance can be confused with a dissection, although there is usually a thick layer of thrombus separating the liquefied region from the patent lumen (Fig. 40.7). It is sometimes possible to see a mobile flap of thrombus or intima moving in time with arterial pulsation (Fig. 40.8).

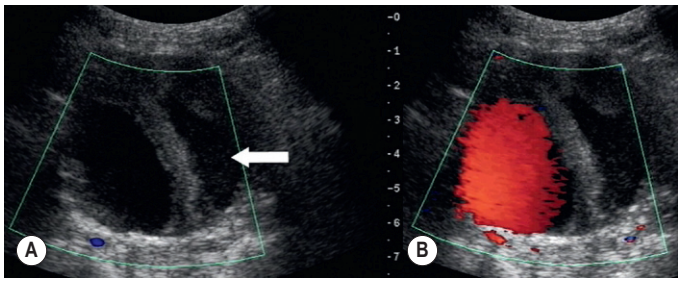

Figure 40.7 Thrombus liquefaction. A: The B-mode image suggests a possible dissection of the aorta (arrow). **B:** Colour Doppler demonstrates no flow within this region which represents an area of thrombus liquefaction.

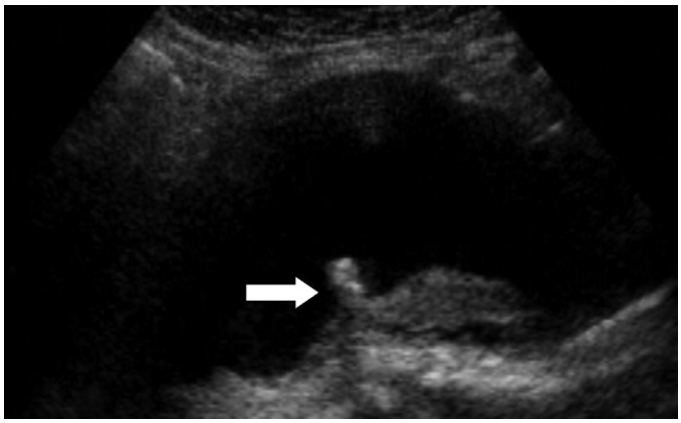

Figure 40.8 Adherent thrombus. The patient presented with embolic changes in his feet. Imaging of the aorta demonstrated a mobile area of thrombus (arrow) moving with arterial pulsation. This was thought to be the likely source of the emboli as other causes had been excluded.

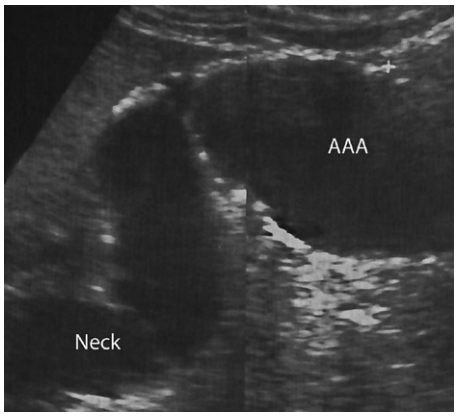

Figure 40.9 Tortuosity of the aneurysm neck. Marked tortuosity is seen in the neck of an aortic aneurysm, giving rise to a 'swan neck' appearance (reproduced with permission from Zwiebel W and Pellerito J. Introduction to Vascular Ultrasonography, 5th edition. Saunders, 2005).

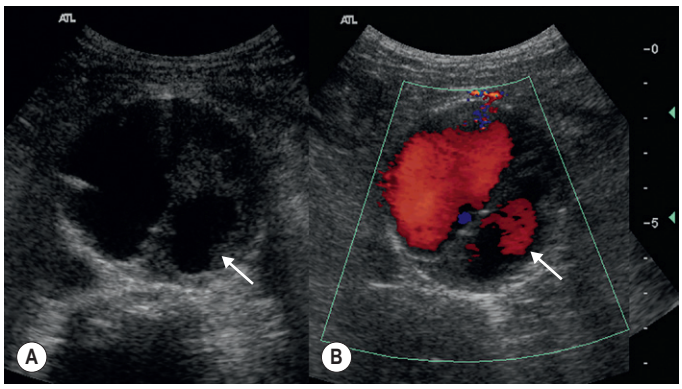

Figure 40.10 Aortic dissection. A: Transverse image of an aortic dissection (arrow) that has occurred in an abdominal aortic aneurysm. **B:** Colour Doppler demonstrates flow in the false lumen (arrow).

The shape of an aneurysm can vary, as shown in Fig. 40.2A. As the aorta dilates it can also elongate, resulting in kinking of the posterior wall, especially at the level of the proximal neck, which may be mistaken for an atherosclerotic stenosis. The aneurysm may deflect in an anterior direction with tortuosity of the proximal segment of the abdominal aorta, sometimes described as a 'swan neck' appearance (Fig. 40.9). It can be very difficult to demonstrate the level of the renal arteries in these circumstances.

A partial intimal tear may be undetected, as blood that has leaked into the wall may be mistaken for mural thrombus. In a full dissection, flow will be observed in the false lumen, which is separated from the true lumen by a flap of intima and, sometimes, the media of the arterial wall (Fig. 40.10).

Inflammatory aneurysms demonstrate a hypoechoic area of ill-defined inflammatory tissue and fibrosis surrounding the aorta. However, this appearance can be confused with the presence of para-aortic lymph nodes. Mycotic aneurysms often have a saccular appearance, which may be associated with an area of adjacent fluid.

Many iliac artery aneurysms are seen as an extension of aortic aneurysms but occasionally an isolated iliac aneurysm may be seen with a relatively normal section of iliac artery proximal to the aneurysm (Fig. 40.11).

The ultrasound diagnosis of a leaking aneurysm is extremely difficult, although it is sometimes possible to identify fresh blood or haematoma as hypoechoic or anechoic areas associated with the aneurysm in the retroperitoneal space (Fig. 40.12). Other imaging techniques, such as CT and MRI, are better suited for excluding leaking aneurysms, providing the patient is in a stable condition. In some instances, aneurysms can rupture into the duodenum or the inferior vena cava producing aorto-enteric or aorto-caval fistulae.

Variability of measurement between ultrasound and CT

It is not uncommon to find variation in the reported diameter of an aneurysm of the abdominal aorta on CT and ultrasound. The maximum diameter is consistently larger when measured by CT compared to that measured on ultrasound.[51,52] One possible reason for this may be that in CT the maximal diameter is measured in any direction, whereas in ultrasound it is often only the anteroposterior dimension that is measured. This is why it is good practice to obtain a lateral diameter from a coronal scan plane. A second possible reason is that the aneurysm may be angled in relation to the scan plane and CT will obtain an oblique diameter, although modern data reformatting techniques should avoid this discrepancy. With ultrasound it is possible to orientate the scan plane to avoid oblique/elliptical measurements (Fig. 40.13).

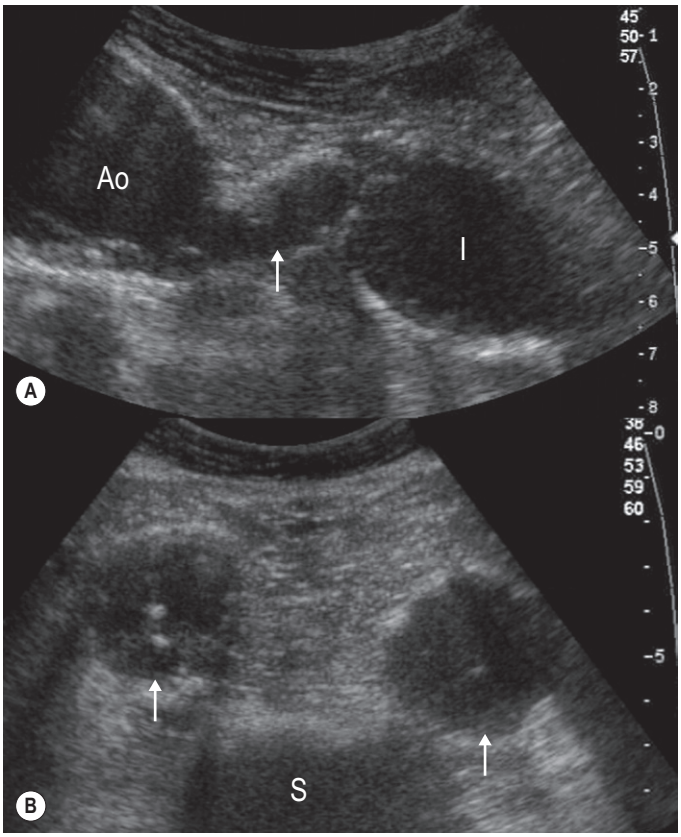

Figure 40.11 Iliac artery aneurysms. A: Longitudinal view of an aortic aneurysm (Ao) and a common iliac artery aneurysm (I), separated by a relatively normal segment of proximal common iliac artery (arrow). **B:** Transverse image of large left and right common iliac artery aneurysms (arrows). S, spine.

Measurement of aneurysm size

For aneurysm screening programmes, the maximum diameter is the only measurement that is required. Most studies have recommended measurement of the anteroposterior diameter from outer wall to outer wall (Fig. 40.6), which is similar to the measurement on a CT image.[30,34,53] Measurements of the aortic diameter are generally more accurate in a longitudinal plane as it is possible to correct for obliquity of the course of the vessel (Figs 40.13 and 40.14). In order to find the maximum diameter in the longitudinal plane, the transducer should be swept across the aorta from one side to the other until the widest point is seen and a number of measurements then made. Ultrasound measurements of the transverse diameter of the aneurysm can be prone to error as the lateral vessel walls are parallel to the ultrasound beam and are therefore not well defined, as shown in Figures 40.3 and 40.6.[54] The lateral, side-to-side diameter of the aorta is most accurately measured from a coronal position (Fig. 40.14). Again, it is possible to correct for obliquity in this plane.

Distance between the renal arteries and aneurysm sac (neck length)

It can be difficult to see if an aneurysm is juxta- or suprarenal in the transverse plane as the renal arteries can be difficult to visualise, especially in obese patients.[55] The technique is shown in Figure 40.15. If the renal arteries are difficult to image, the origin of the SMA is a useful landmark as the renal arteries usually lie within 2 cm of the SMA origin.[56] If the aneurysm starts below this level, it is unlikely to involve the renal arteries. However, a potential pitfall occurs if there are accessory or polar renal vessels arising distal to the main renal artery, as these are not easily seen with ultrasound.

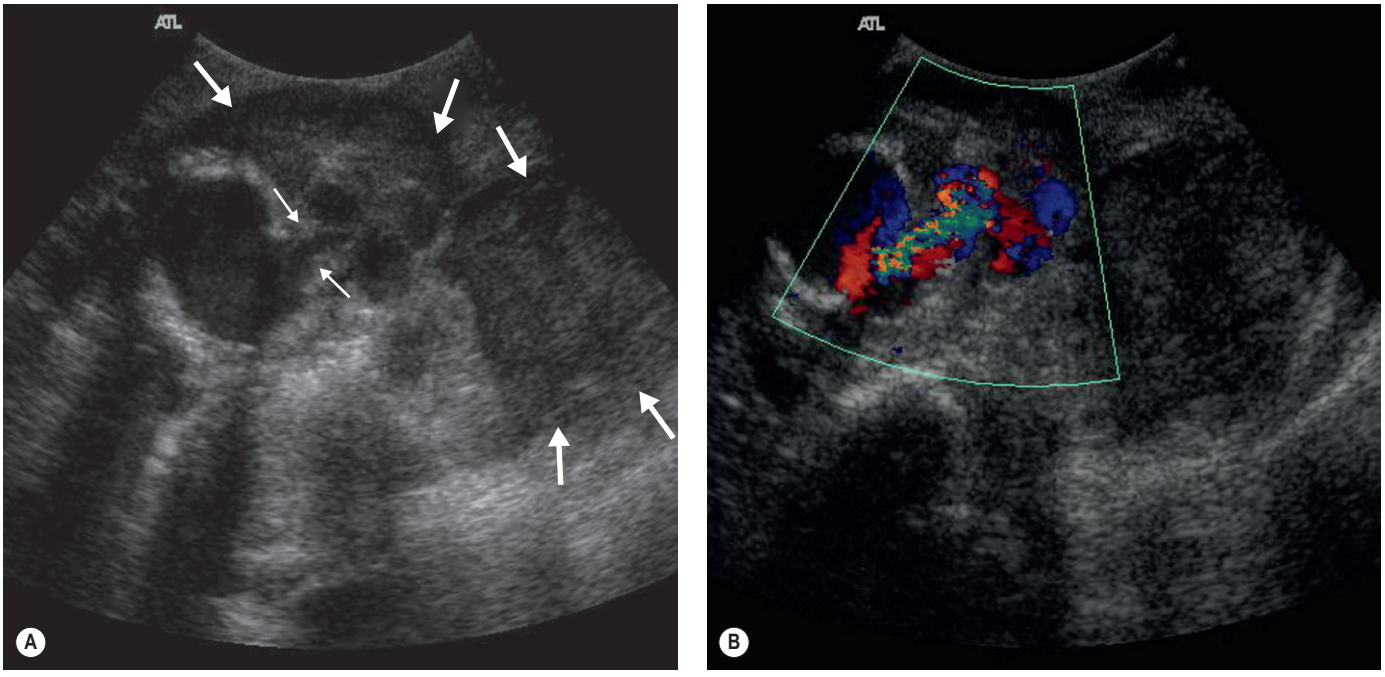

Figure 40.12 Ruptured abdominal aortic aneurysm. A: An aneurysm has ruptured into the left retroperitoneal space (small arrows). The haematoma (large arrows) is seen adjacent to the aorta. **B:** Colour Doppler shows flow through the defect in the aorta into the patent component of a false aneurysm.

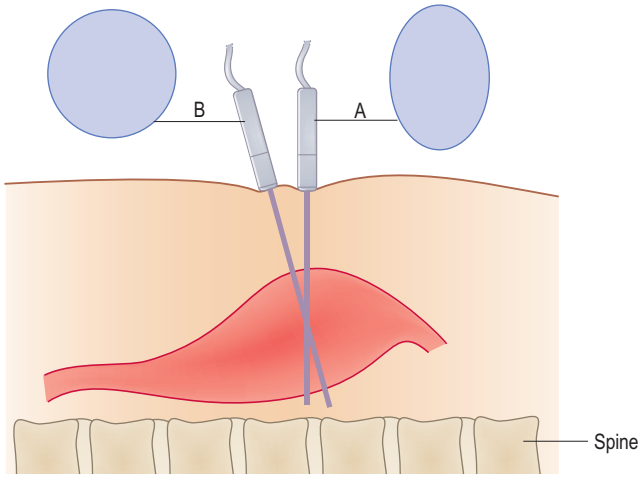

Figure 40.13 Measuring the true anteroposterior diameter. The aorta is deflecting in an anterior direction, therefore scanning in a transverse plane along line A will result in an oblique/elliptical image of the aorta, resulting in overestimation of the diameter. The transducer should be tilted to measure the correct diameter along the direction of line B (modified from Thrush A, Hartshorne T. Peripheral Vascular Ultrasound. How, why and when. 2nd edition. Churchill Livingstone, 2005).

Limitations and pitfalls

Apart from the limitations discussed above, the main problem for ultrasound assessment of an aneurysm is inadequate views due to bowel gas. A potential error can occur if an oblique measurement of a tortuous vessel is misinterpreted as the diameter. Another pitfall is to mistake the lumbar spine for an aneurysm (Fig. 40.16). This normally occurs when non-trained or occasional operators perform the scan in unsupervised or non-accredited centres.

TREATMENT FOR AORTIC ANEURYSM

Open repair

Open surgical repair of aortic aneurysms involves using straight tube grafts or bifurcating grafts if the aneurysm extends into the iliac arteries. The graft is sutured into position and the sac closed around the graft. Postoperatively, patients normally spend at least a day in intensive care and usually leave hospital 10–14 days after surgery. The elective mortality rate for open repair is in the region of 5%; suprarenal aneurysms have a higher rate of perioperative and postoperative complications.

Endovascular repair

Endovascular aneurysm repair was first described in the early 1990s.[57] The latest generation of commercially available grafts are made of synthetic material such as Dacron and polytetrafluoroethylene (PTFE), supported on an expandable metal framework of nitinol or stainless steel to prevent kinks and twisting. Bifurcating grafts are the most commonly deployed devices (Fig. 40.17A). The graft consists of the main body and one complete limb together with a short stump for the second limb. The graft is introduced via an arteriotomy made in the femoral artery and deployed in the aorta to exclude flow into the aneurysm sac. The second limb is delivered

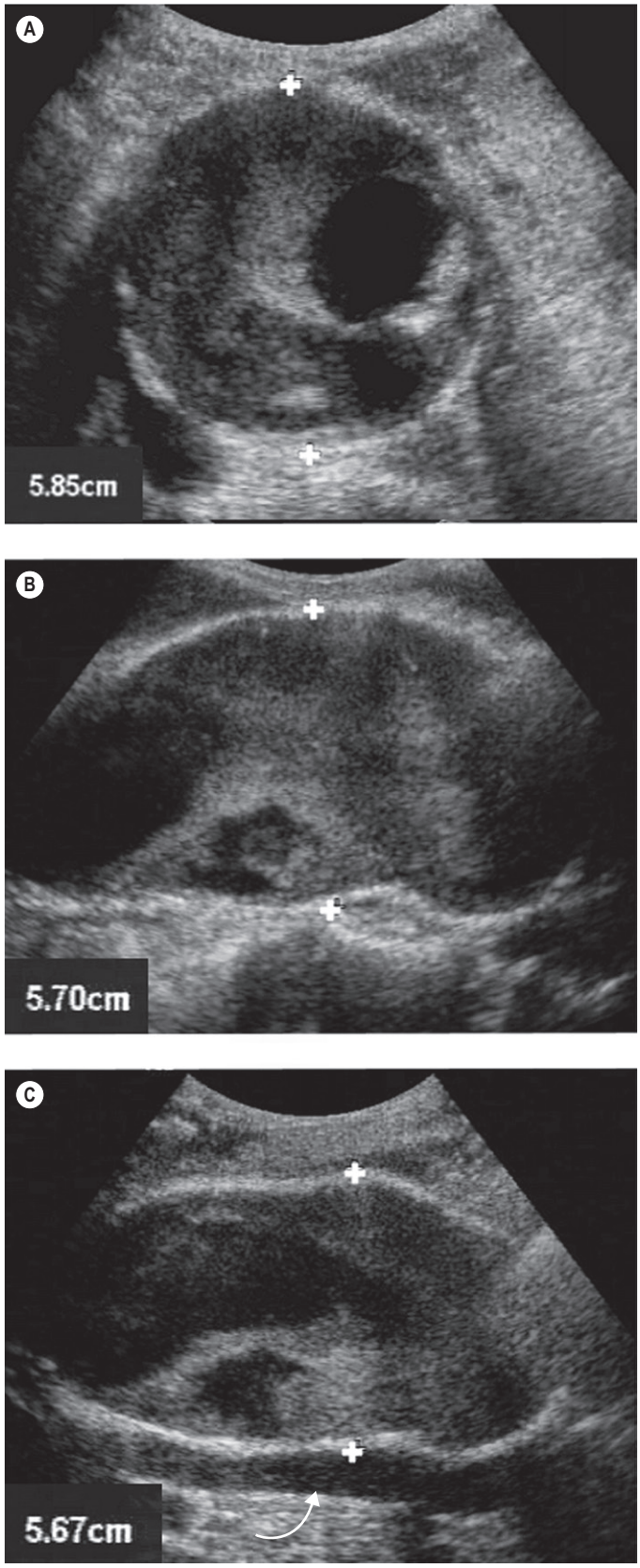

Figure 40.14 Three views of an aneurysm. A: Transverse image. The anteroposterior (AP) diameter is measured from the outer wall to the outer wall (callipers). **B:** A sagittal image, demonstrating the calliper positions to measure the aneurysm in this plane. **C:** A coronal image. The IVC is shown by the curved arrow. (Reproduced with permission from Thrush A, Hartshorne T. Peripheral Vascular Ultrasound. How, why and when. 3rd edition. Churchill Livingstone, 2009.)

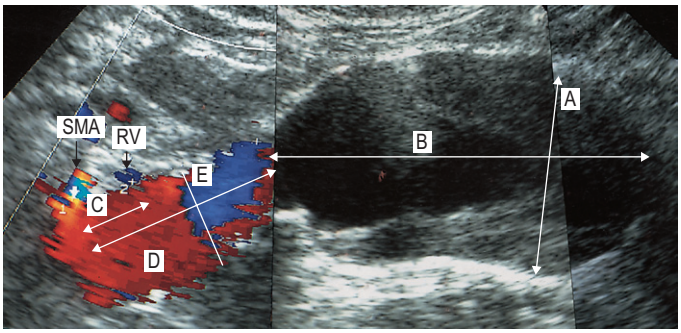

Figure 40.15 Measurement of the length of the proximal neck of an aneurysm. The SMA origin acts as a useful landmark as the renal arteries normally lie within 2 cm of its origin (line C). If the aneurysm starts below this level, the renal arteries are unlikely to be involved. However, accessory or polar vessels may arise from the sac. The left renal vein (RV) can be seen in cross-section as it passes over the anterior wall of the aorta (reproduced with permission from Thrush A, Hartshorne T. Peripheral Vascular Ultrasound. How, why and when. 2nd edition. Churchill Livingstone, 2005).

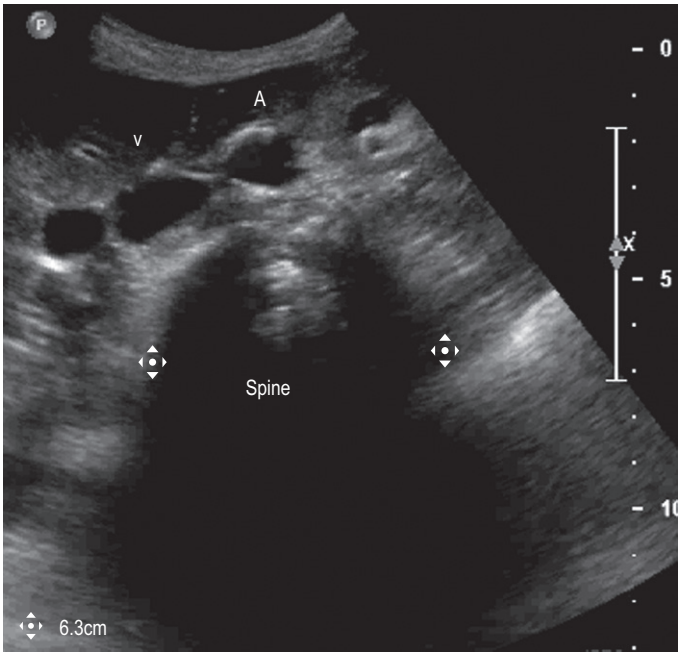

Figure 40.16 Mistaking the spine for an aneurysm. In this image from a thin patient, the image depth has been set too deep and the lumber spine (Spine) mistaken for the aorta (A). The IVC is also visible (V).

separately via the contralateral common femoral artery and located appropriately into the main graft. As the devices are modular, it is possible to add extensions to the limbs to exclude iliac artery aneurysms. The use of fenestrated grafts that can be deployed across the renal arteries can overcome the problem of treating juxta- or suprarenal aneurysms. Aorto-uni-iliac systems can be deployed in situations where one of the iliac arteries is diseased, occluded, excessively tortuous or aneurysmal. Plugs or occluder devices are used to prevent back flow into the aorta through the bypassed iliac artery (Fig. 40.17B).

Not all aneurysms are suitable for endovascular repair. This can be due to aneurysm tortuosity, excessive proximal neck diameter, limited proximal neck length, or severe iliac disease preventing access. Postoperative recovery is usually very quick following endovascular repair, with patients being discharged within 2–4 days. The Endovascular Aneurysm Repair Trial 1 (EVAR 1) reported a reduction of two-thirds in 30-day postoperative mortality compared to open repair.[58]

Complications of endovascular aneurysm repair

Although endovascular repair is less traumatic for the patient, the EVAR 1 trial also found that by 4 years, 40% of patients who had undergone endovascular repair had suffered a complication and that 20% had required reintervention, including the correction of endoleaks. An endoleak is defined as persistent blood flow outside the graft and within the aneurysm sac.[59–64] The classification of endoleaks is shown in Table 40.3 and a diagrammatic representation is shown in Figure 40.18 with a CT image of an endoleak. In the presence of an endoleak or other graft-related complication in which the aneurysm sac has not been fully excluded, the aneurysm sac can continue to expand and ultimately rupture, although the risk is relatively low at approximately 1% and approximately half the patients survive the rupture.[61–63] It is recommended that patients should undergo surveillance to detect endoleaks or other complications so that they can be managed and corrected in a timely manner.[64] Current evidence suggests that type I and III endoleaks may be more closely linked with rupture than type II leaks, although type II leaks have also been associated with rupture, especially if there has been continued growth in sac size.[63,65] Type I and III endoleaks can be treated by insertion of further covered stents or collars. Significant type II leaks can be embolised if they are accessible via catheter angiography.

Other graft complications are shown in Table 40.4 but not all of these can be monitored or surveyed with ultrasound.

ULTRASOUND SURVEILLANCE OF ENDOVASCULAR ANEURYSM REPAIR

The primary role of surveillance following endovascular aneurysm repair is the detection and grading of endoleaks. Duplex ultrasound is a useful method of detecting endoleaks following endovascular repair and can complement CT in surveillance programmes.[66–68] Whilst studies indicate that ultrasound is not as sensitive as CT for identifying endoleaks, it has good specificity and in particular is able to detect almost all type I leaks, which are more clinically important. An example of a surveillance protocol for endovascular aneurysm repair patients is shown in Table 40.5. Apart from cost-effectiveness and convenience, another major advantage of ultrasound is that the patient is exposed to fewer CT scans and associated contrast injections over the surveillance period. Improved endoleak detection has been reported with the injection of ultrasound-enhancing contrast agents although a second bolus of contrast or continuous infusion may be required to image the whole sac.[69,70]

Practical scanning of EVAR grafts

It is important to optimise the scanner controls so that the system is sensitive for detecting low-velocity flow. The colour image may be noisy with flash artefacts and bowel movement but without careful optimisation it is possible to miss endoleaks. Ultrasound images of EVAR grafts, endoleaks and other graft-related complications are shown in Figures 40.19 and 40.20.

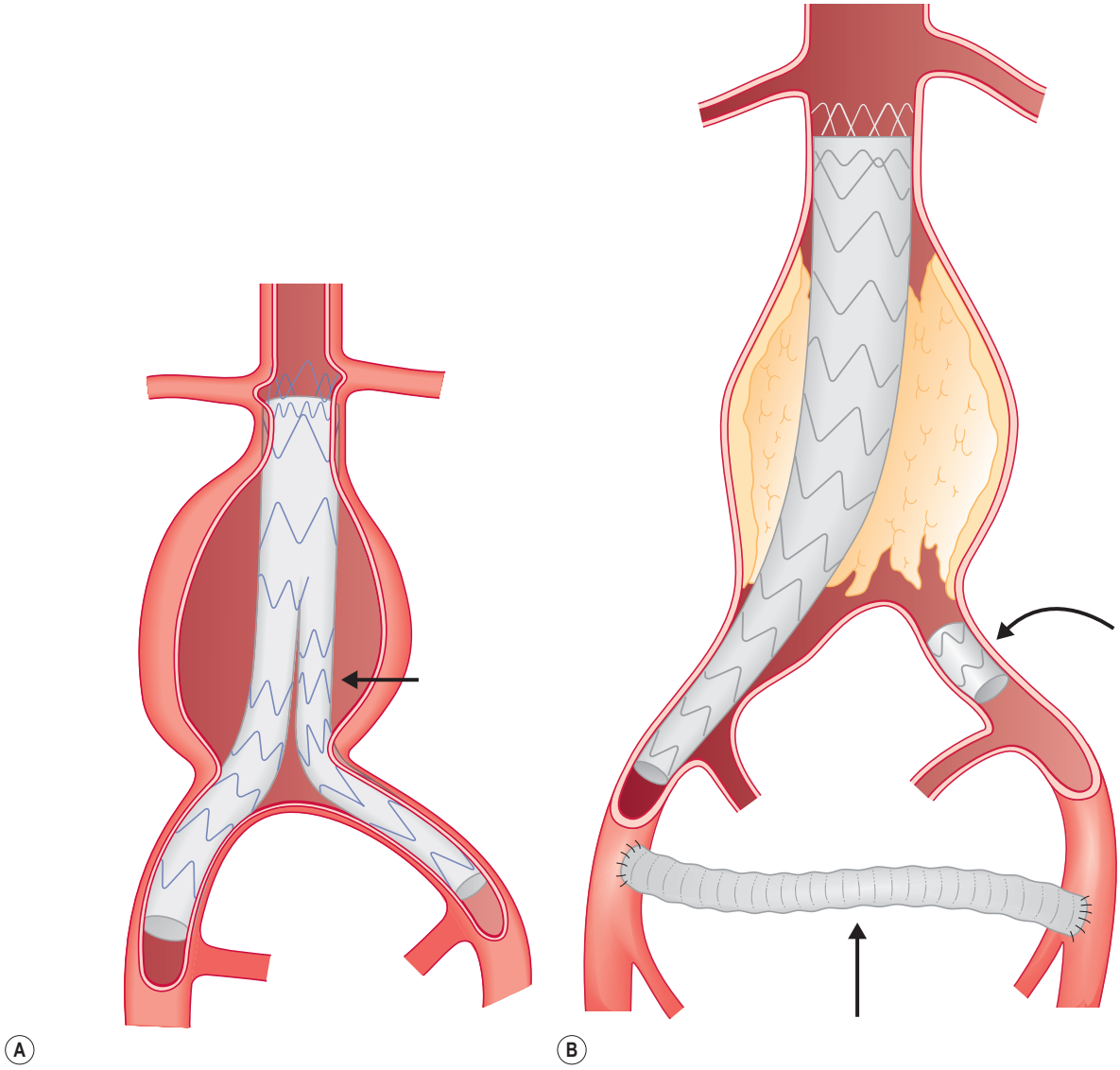

Figure 40.17 Images of EVAR grafts. A: A bifurcating system. The position of the modular limb is shown (arrow). **B:** An aorto-uni-iliac system. In this example an occluder or plug has been deployed in the common iliac artery to prevent back flow into the aneurysm sac (curved arrow). A femoro-femoral crossover graft provides flow to the contralateral leg (straight arrow). (Images modified from Thrush A, Hartshorne T. Peripheral Vascular Ultrasound. How, why and when. 3rd edition. Churchill Livingstone, 2009.)

Table 40.3 Classification of endoleaks

Type Ia and Ib: Attachment site leaks. These occur at the proximal (Ia) or distal attachment sites (Ib) when there is an inadequate seal between the device and the aortic or iliac artery wall, respectively. Colour flow imaging demonstrates evidence of flow, often in the form of a jet at the point of the leak, filling part of the aneurysm sac (Fig. 40.20A). The amount of flow in the sac can be variable and may involve a large volume. **Type Ic** occur when there is a leak around an iliac occluder plug (Fig. 40.17B).

Type II: Collateral endoleaks involve some filling of the sac via lumbar vessels or the inferior mesenteric artery or accessory renal arteries (Fig. 40.20B and C). Type IIA are simple to-and-fro single branch leaks (Fig. 40.22A). Type IIB leaks represent flow through the sac with two patent vessels (Fig. 40.22B).

Type III: Leaks between the modular limb and main body of the graft or tears in the graft. This type of leak is rare.

Type IV: Thought to occur due to graft porosity or 'sweating' of graft material, leading to progressive increase in sac size within the first month. It is not possible to image this type of leak in real-time, but serial surveillance scans may show a progressive increase in the diameter of the aneurysm sac. This type of leak is thought to be less common in the new generation of grafts.

Endotension has been classed as a fifth type of leak. This is described as a persistent or recurrent pressurisation of the sac without a visualised endoleak. This can lead to expansion of the sac and potential rupture. The causes of endotension are uncertain. In practice, some cases of endotension could be due to a very small, undetected endoleak.

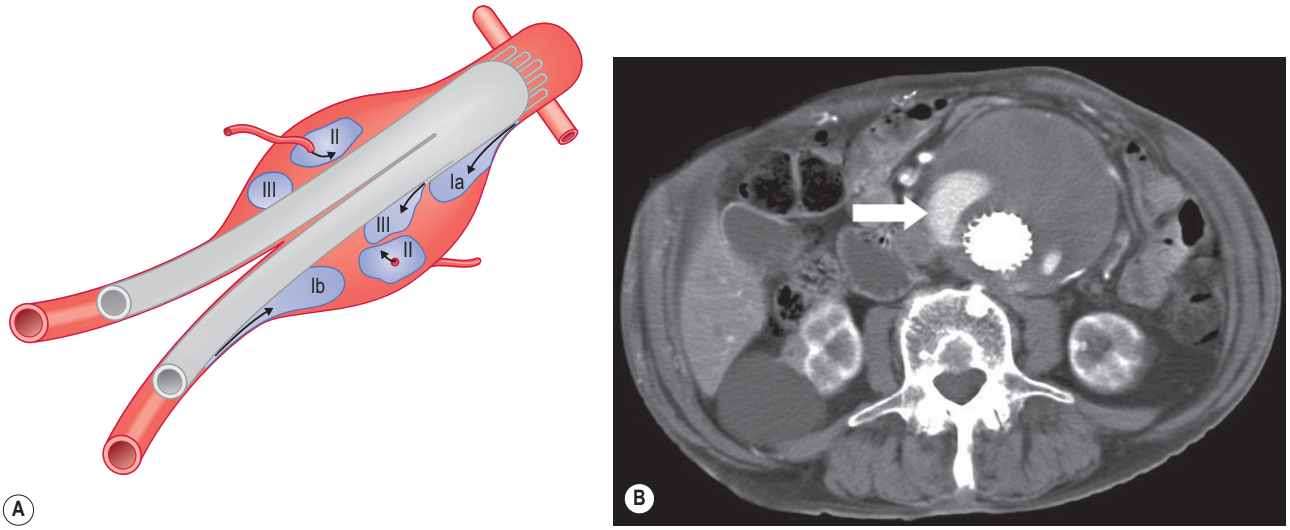

Figure 40.18 Endoleaks after endovascular aneurysm repair. A: Diagram of different types of endoleaks. Type Ia and 1b, attachment site leak, Type II, collateral endoleaks from the inferior mesenteric artery or lumbar vessels. Type III, failure of modular limb seal or graft fabric. Type IV, endoleaks due to porous/leaky graft material, are not demonstrated in this diagram (modified from Thrush A, Hartshorne T. Peripheral Vascular Ultrasound. How, why and when. 2nd edition. Churchill Livingstone, 2005). **B:** CT scan of an endoleak (arrow).

Table 40.4 Other EVAR device related complications

Complication	Comment
Graft limb occlusion or stenosis	Easy to assess with ultrasound (Fig. 40.20E)
Graft migration	Difficult to assess with ultrasound unless there has been a significant migration (Fig. 40.20D)
Stent strut fracture leading to structural failure	Assessed with plain films

Table 40.5 A suggested surveillance protocol for the surveillance of EVAR patients

Time	Scan type	Comment
Pre discharge from hospital	Duplex	Bowel gas can be a problem
1 month	Duplex[a]	
3 months	CT	
6 months	Duplex[a]	
9 months	Duplex[a]	
1 year	CT	
Then 6-monthly	Duplex[a]	CT if significant problem detected

[a]*If there is an increase in sac size ≥0.5 cm the responsible clinician should be alerted and alternative imaging such as CT may be required.*

Scanning technique

1. Start the scan in a transverse section in the middle of the sac using B-mode imaging alone. For bifurcating devices, it is usual to see the two limbs, which usually lie adjacent to each other (Fig. 40.19C); they may be seen to spiral around each other as the probe is moved down the sac. If poor images are obtained, the patient may need to be scanned in a lateral decubitus position.
2. The graft is followed up the sac in transverse section. For bifurcating devices, the bifurcation of the graft should be identified (Fig. 40.19B). The upper body of the graft and the native aorta at the level of the renal arteries should be examined.
3. The graft is then followed distally to the aortic bifurcation and iliac arteries, especially if iliac aneurysms have been excluded by the graft. Anechoic areas in the aneurysm sac should be identified and should be scrutinised carefully with colour Doppler imaging to exclude leakage.
4. The aorta is imaged in longitudinal section and any abnormal features identified, particularly any evidence of device migration (Fig. 40.20D).

Optimisation of scanner controls to detect endoleaks

- Set pulse repetition frequency (PRF) or colour scale to 1–1.5 kHz.
- Increase colour sensitivity/gain.
- Set wall filter to a minimum level.
- Use write zoom to image the area of interest to maintain frame rate.
- Apply some tilt of the transducer if imaging in transverse section to obtain a Doppler angle to the aorta.

5. The aorta is then scanned in transverse section using colour Doppler imaging. There should be colour filling within the graft but no flow visible in the sac outside the device (Fig. 40.19F). The transducer should be tilted with respect to the graft to maximise the Doppler angle and colour signal (Fig. 40.21). If the neck of the aneurysm is clearly visible, the proximal neck diameter should be measured to monitor any increase in size due to progression of aneurysmal disease.

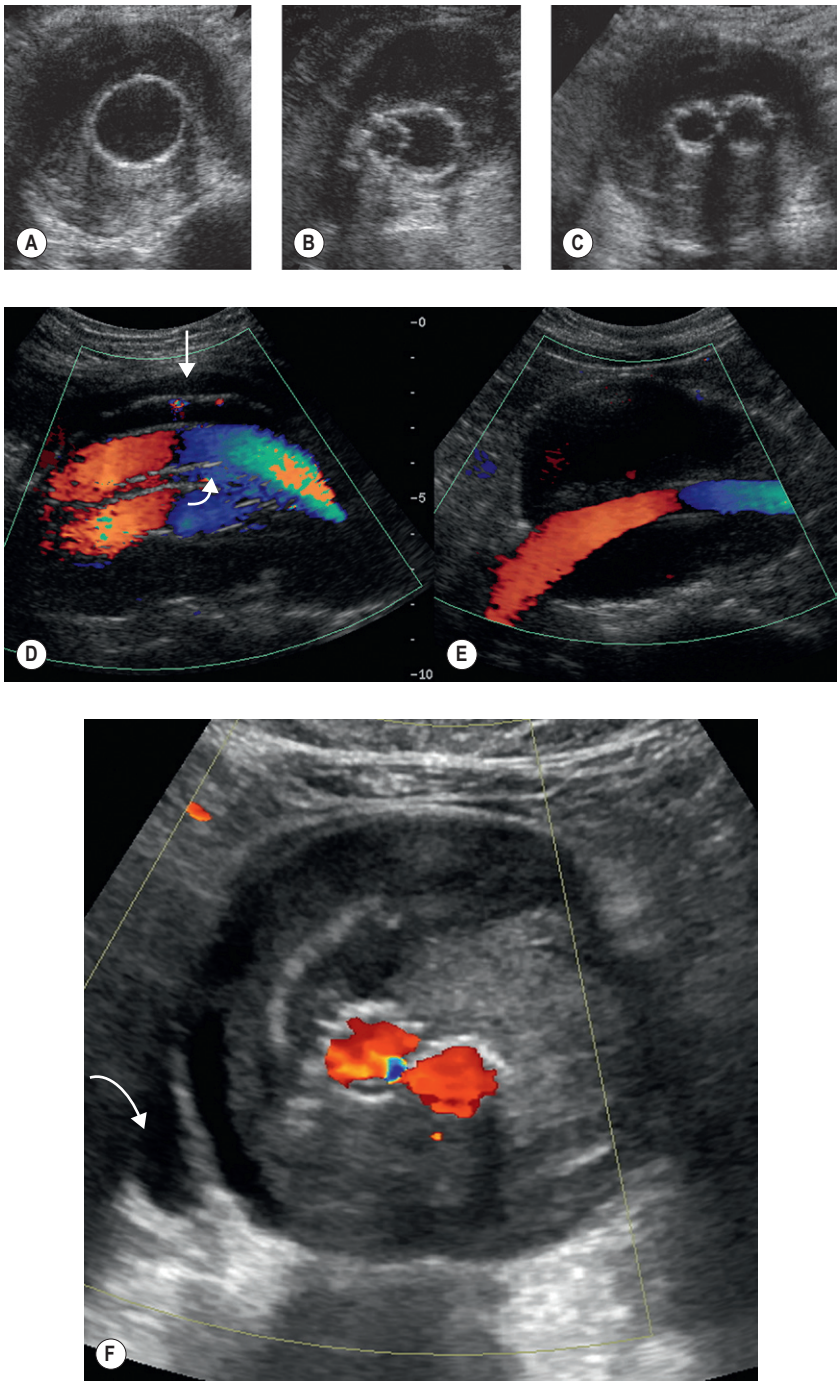

Figure 40.19 **Images of a successfully deployed EVAR graft. A:** Transverse image of the main body. **B:** Transverse image at the device bifurcation. **C:** Transverse image showing both graft limbs. **D:** Longitudinal image showing the graft limbs lying on top of each other but in many cases they lie side by side, as shown in example **C**. Note that mirroring artefact can sometimes be seen below the strongly reflecting graft walls, as shown by the curved arrow. This aneurysm also had an inflammatory component, as demonstrated by the outer cuff (straight arrow). **E:** Longitudinal colour Doppler image of an aorto-uni-iliac device. **F:** Transverse colour image of an EVAR graft. The IVC is visible (curved arrow).

6. Colour Doppler imaging in longitudinal section using sagittal and coronal planes is used to examine flow through the device and to identify any areas of flow disturbance, stenosis or occlusion that could be caused by kinking of the graft, especially in relation to the limbs of the graft as they run into the common iliac arteries, or at the distal attachment sites (Fig. 40.19D). Spectral Doppler is used to assess the flow in the graft limbs and any abnormal areas shown on the colour Doppler image.
7. The maximum diameter of the aneurysm sac should be recorded in transverse, longitudinal and coronal planes, so that changes in size can be assessed on serial scans.
8. For aorto-uni-iliac devices, it is especially important to ensure that there is no flow in the contralateral occluded common iliac artery that might be leaking back into the sac around any occluder devices or plugs (Fig. 40.17B). Flow in associated iliofemoral or femoro-femoral crossover grafts should also be assessed.

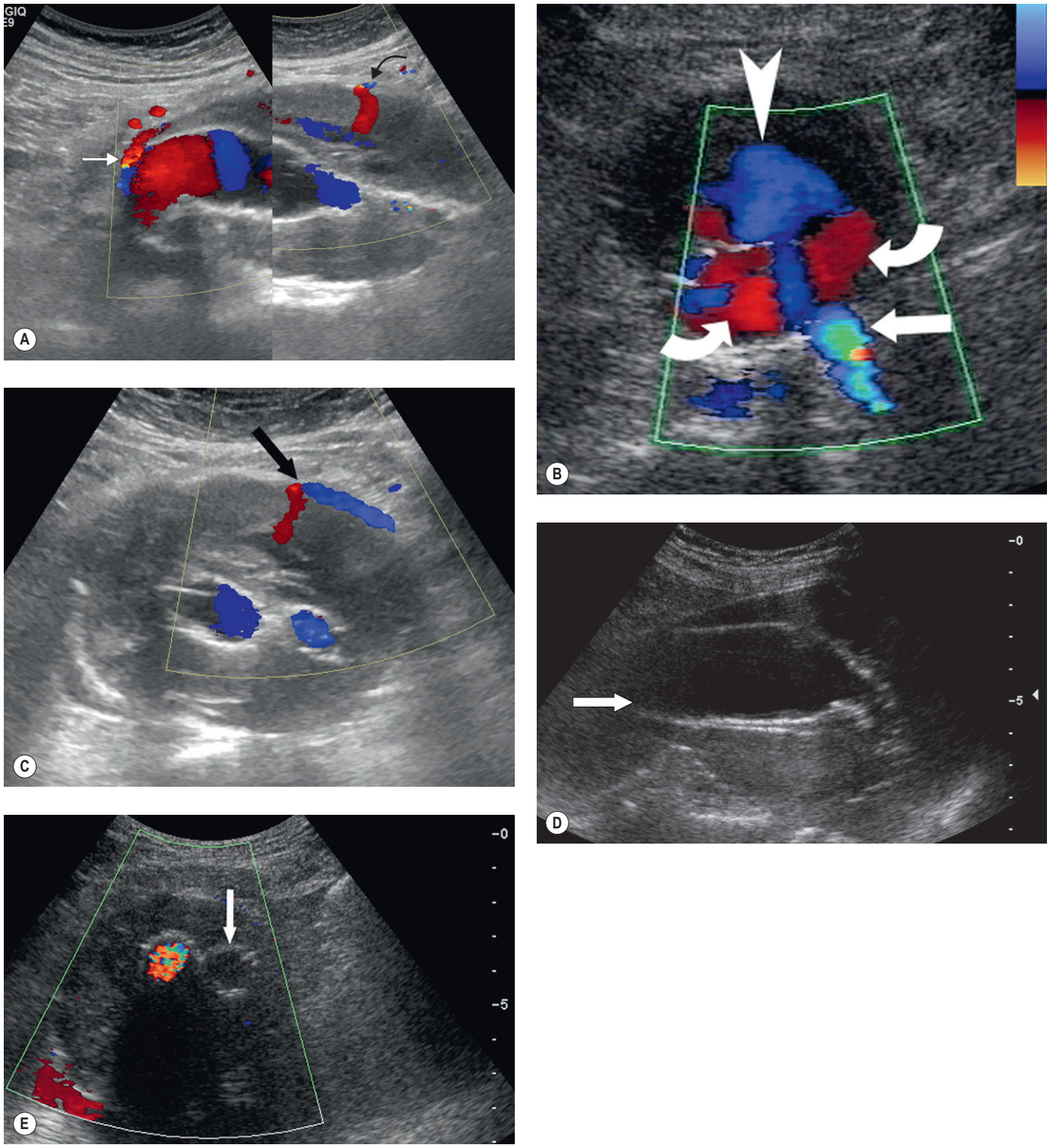

Figure 40.20 **Types of endoleak and graft complications. A:** Conjoined longitudinal image showing a type Ia endoleak (arrow) from the proximal end of the graft and exiting through the IMA (curved arrow). **B:** Transverse image of a type II endoleak demonstrating perfusion of the sac (arrowhead) via a patent lumbar artery (straight arrow). The two graft iliac limbs are demonstrated by the curved arrows. **C:** Transverse image of a small type II endoleak from the inferior mesenteric artery (arrow). **D:** An example of graft migration. The proximal end of the graft (arrow) is now in the sac and is not making contact with the posterior aortic wall. **E:** The left graft limb (arrow) has occluded as no flow is demonstrated. It is important to optimise the image as shown in Figure 40.21 before reporting this finding.

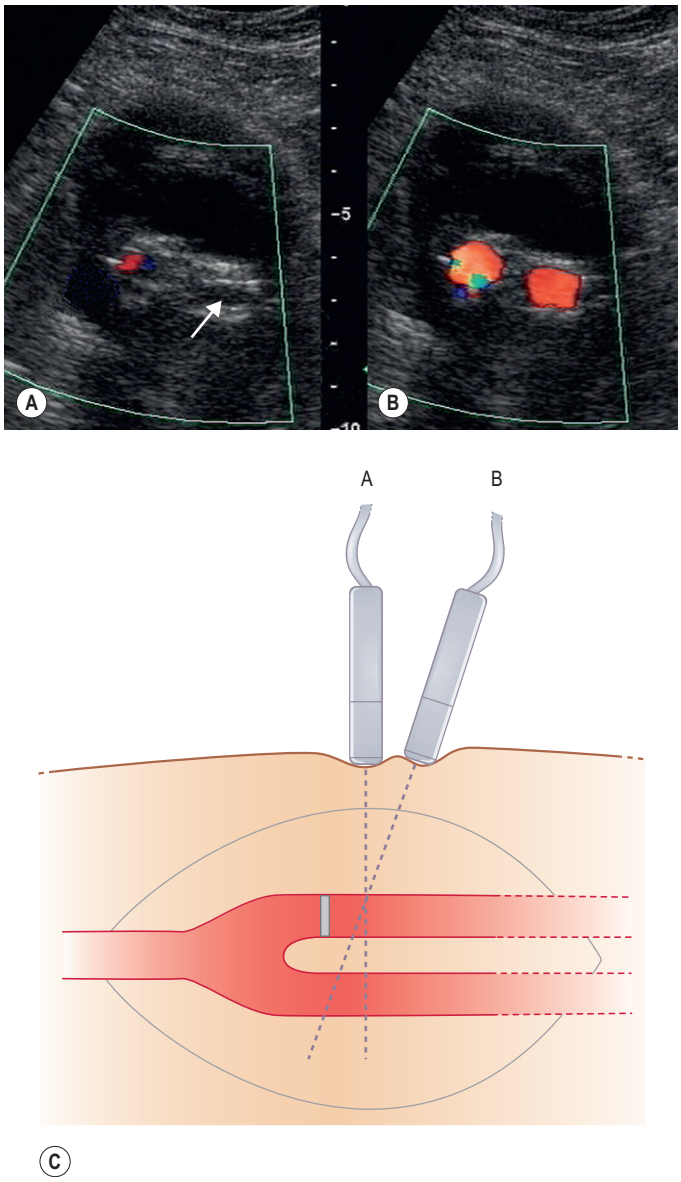

Figure 40.21 Colour Doppler and endoleaks. A: In order to demonstrate flow in the graft or detect an endoleak in the transverse plane, it is usually necessary to tilt the transducer from position (A) to (B) as shown in diagram (C), so that the angle of insonation is <90° relative to the device and sac. In position A, flow cannot be seen in the left graft limb arrow. Optimum imaging in plane B demonstrates flow in both limbs but no evidence of endoleak.

Limitations and pitfalls

The main limitation for ultrasound is inadequate visualisation of the sac and graft due to obscuring bowel gas or obesity. The graft material is a strongly reflecting boundary and mirroring artefacts may be seen behind the graft material, which may be mistaken for an endoleak (Fig. 40.19D). To clarify this situation, the aorta should be assessed from a number of different angles to see if any suspected leak remains in the same position with respect to the graft.

Doppler flow patterns and endoleaks

It is possible to observe different spectral Doppler waveform patterns associated with endoleaks.[71,72]

Firstly, to-and-fro spectral waveforms, similar to the type seen in a false aneurysm (Fig. 40.22A), can be observed when there is only one point of communication into the aneurysm sac. This pattern is often recorded in type II branch leaks but can occur in both type I and type III leaks. The colour Doppler image often shows forward and reverse flow across the entry point in the systolic and diastolic phases, respectively. It has been suggested that this type of endoleak is more likely to thrombose spontaneously. As a personal observation the timing of the onset of the systolic phase in type II endoleaks, adjacent to the entry point, may be slightly out of phase with the systolic pulse in the graft, as shown in Figure 40.23.

Secondly, it is possible for both an entry point and an exit point to be present, so that there is net flow across the sac (Fig. 40.22B). Colour and spectral Doppler can be used to determine the flow direction; for example, if it is from the inferior mesenteric artery to a lumbar artery or vice versa (Fig. 40.22B). It has been speculated that these leaks are less likely to spontaneously thrombose, especially if there is high velocity within the leak (>100 cm/s).[72]

Long-term surveillance and sac size

Normally, in the absence of any significant complications, many aneurysm sacs slowly shrink in size and can eventually disappear altogether. Some sacs remain a similar size to the original aneurysm. Increasing sac size is more commonly associated with an endoleak.[73] If a number of sonographers are involved in the surveillance programme, it is important that they all follow the same protocol for measuring the maximum diameter of the sac size, otherwise significant discrepancies could be recorded between sequential scans.

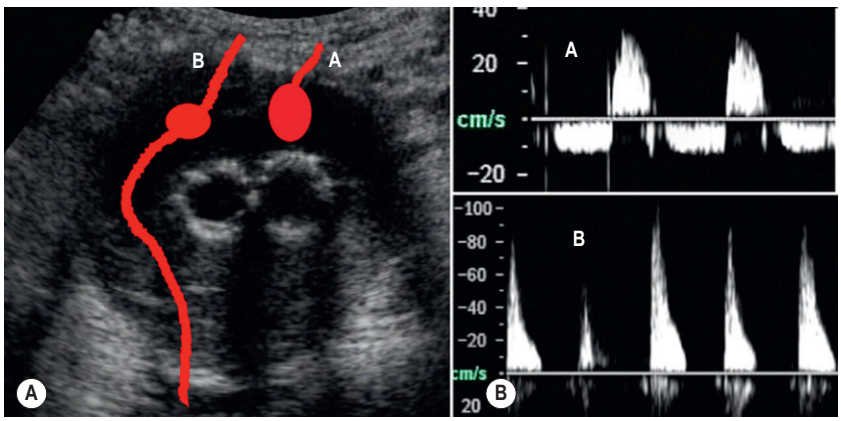

Figure 40.22 Collateral endoleaks. It is possible to observe different spectral flow patterns associated with endoleaks. In example **A**, there is blind ending in the sac and a to-and-fro waveform similar to the type associated with false aneurysms is seen. In example **B**, there are separate entry and exit points and the Doppler waveform demonstrates net flow from a lumbar artery to the inferior mesenteric artery.

ATHEROSCLEROSIS

The aorta can become severely diseased and narrowed by atherosclerotic plaque, resulting in lower limb ischaemic symptoms. The commonest site for narrowing is in the distal aorta, often in association with proximal common iliac disease. In some cases a long segment of the aorta can be involved. The end stage of disease is severe calcification or occlusion. Aortic disease can involve the origins of the renal and mesenteric vessels; renal artery narrowing often results in hypertension or reduced kidney function. Disease of the splanchnic arteries can lead to mesenteric angina after eating or bowel ischaemia.

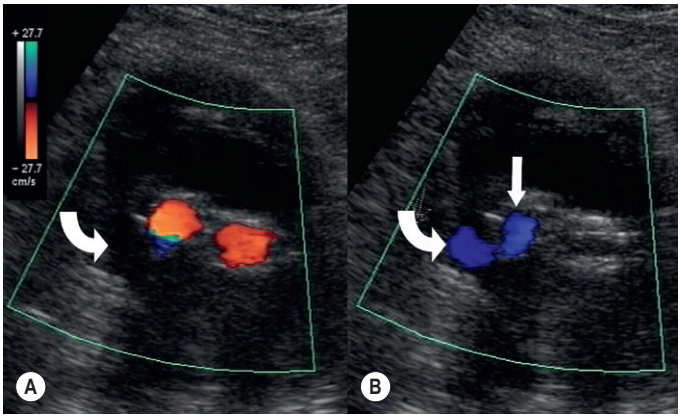

Figure 40.23 Delayed endoleak flow. An example of a time delay between the onset of systole in a small type II endoleak. **A:** There is no filling of the leak (curved arrow) but flow is clearly seen in the two graft limbs. **B:** A few frames later, the onset of systole is seen in the endoleak but evidence of reverse flow is seen in the right graft limb (straight arrow) during the onset of diastole.

Waveform appearance

The suprarenal aortic spectral waveform demonstrates a rapid systolic upstroke and a degree of forward flow during diastole due to perfusion of the kidneys from the upper aorta. The infrarenal waveform usually has a reverse flow component during the diastolic phase, similar to that seen in the iliac vessels, and a biphasic or even triphasic flow pattern may be observed as seen in the lower limbs at rest (Fig. 40.24). The peak systolic velocity recorded in the aorta of individuals aged approximately 60 years has been reported as 45 ± 13 cm/s.[74]

Imaging, signs and grading

Aortoiliac disease should be suspected if an abnormal arterial Doppler waveform is recorded from the common femoral artery, typically demonstrating increased systolic rise time (Fig. 40.25). In the majority of cases this is due to iliac artery disease. However, the iliac arteries should be imaged to the level of the aortic bifurcation even in the presence of more distal iliac disease as aortic disease may still be present. Longitudinal scanning with colour Doppler imaging is the easiest way of identifying flow disturbance, or colour aliasing that might indicate disease. Spectral Doppler using angles of ≤60° is used to grade the stenosis. Pre-stenosis and maximum intra-stenotic peak systolic velocities should be recorded and the peak systolic velocity ratio (PSV ratio) calculated. In the absence of any specific guidelines for grading aortic disease, a doubling of peak systolic velocity is normally indicative of a significant haemodynamic disturbance, especially if this is associated with post-stenotic turbulence or waveform damping.[75]

Aortic occlusion

Aortic occlusion is relatively rare and normally results in lower limb ischaemia with severe claudication but it can be difficult to diagnose. The occlusion usually starts at the distal aorta but in some

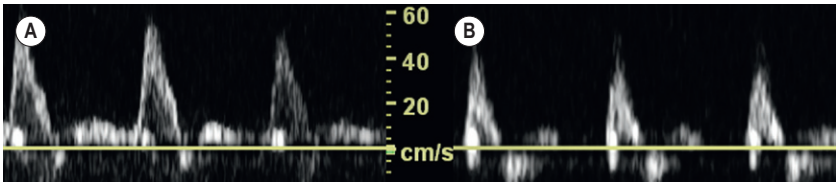

Figure 40.24 The spectral waveform in the abdominal aorta. A: The spectral Doppler waveform from the aorta proximal to the renal arteries, exhibiting forward diastolic flow. **B:** Aortic waveform towards the bifurcation demonstrating triphasic flow.

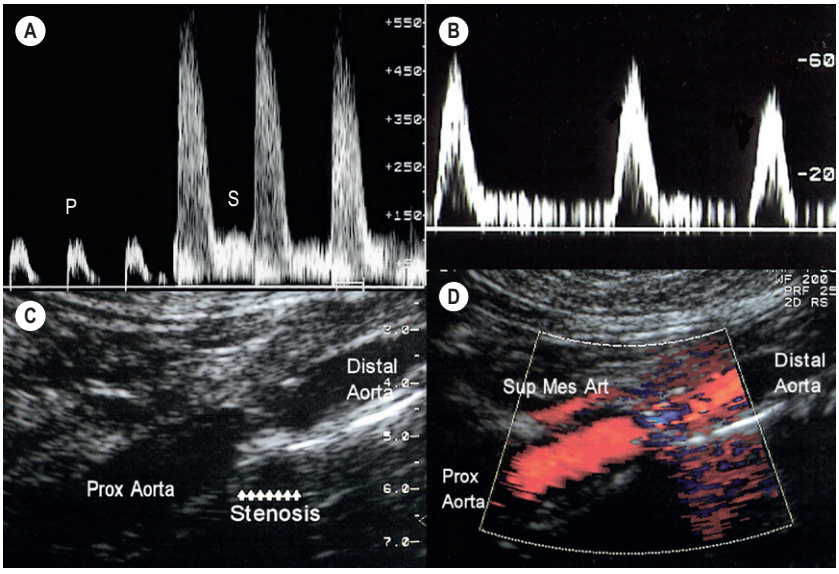

Figure 40.25 A severe stenosis of the aorta. **A:** Doppler waveforms just proximal (P) and across the stenosis (S) are shown and indicate a significant haemodynamic stenosis with a PSV ratio of >4. **B:** An abnormal damped Doppler waveform was recorded in the common femoral artery. **C:** B-mode imaging demonstrates echogenic plaque in the aorta (arrows). **D:** Colour Doppler imaging shows marked flow disturbance and aliasing across the stenosis.

cases it can start just below the renal arteries. On the B-mode image the aorta is visible but it is difficult to demonstrate a normal colour Doppler signal.

A potential pitfall is to misdiagnose a distal occlusion as a more extensive proximal occlusion because the overall flow in the still patent upper/mid aorta may be very slow with a partially reverberant waveform; this may be missed unless the colour and spectral Doppler settings are optimised to detect low velocity flow by reducing the colour scale and wall filter. Imaging in cross-section with some transducer angle tilt can be useful to obtain a sufficient Doppler angle to enable demonstration of flow.

AORTIC DISSECTION

Dissection of the abdominal aorta nearly always results from the extension of a dissection of the thoracic aorta extending into the abdomen (Fig. 40.26). Rarely, it may originate in the abdominal aorta, or result from trauma. The aorta is usually dilated to some extent but dissection can occur in the presence of a normal-calibre aorta. The flap may be visible depending on its orientation in relation to the ultrasound beam and if a dissection is suspected the aorta should be examined from several different approaches in an effort to show the flap. Spectral and colour Doppler will show the presence and character of any flow in the true and false lumens and, even if a flap is not visible, the different flows in the two channels may be apparent on Doppler; reversed flow may be seen in the non-dominant channel due to compression in systole (Fig. 40.26B); if one of the channels is thrombosed then the appearances can be a little confusing. Doppler can also be used to assess blood flow in the major branches supplying the bowel, liver, kidneys and lower limbs, which may be supplied from either the true or the false lumen.[76] Colour Doppler, power Doppler and B-flow imaging have all been shown to be of value in the diagnosis and assessment of aortic dissection.[77]

THE SPLANCHNIC ARTERIES

The bowel in the abdomen is supplied primarily by the three splanchnic arteries: the coeliac axis, the superior mesenteric artery and the inferior mesenteric artery. The coeliac axis and the origin of the superior mesenteric artery are visible in most patients unless obscured by bowel gas, or marked obesity (Fig. 40.27). Gentle pressure with the transducer may help disperse bowel gas sufficiently to visualise the arteries. The inferior mesenteric artery can be more difficult to identify and is best sought by scanning transversely down the lower aorta above the bifurcation until the relatively small inferior mesenteric artery is seen coming off the anterior margin of the aorta and passing down and away to the left (Fig. 40.28).

Normal blood flow in the coeliac and superior mesenteric arteries varies depending on whether the patient is fasting or has recently eaten. In the fasting state there is relatively low diastolic flow but following food the level of diastolic flow increases as the enteric vascular bed opens up and the resistance to blood flow decreases (Fig. 40.29).

Stenosis

The main indication for assessing the splanchnic arteries is the investigation of patients for possible intestinal ischaemia. Stenoses in the coeliac axis and superior mesenteric arteries usually occur in the proximal 1–2 cm at their origins; colour Doppler helps identify areas of abnormal flow in relation to the arteries or a visible tissue bruit secondary to a stenosis (Fig. 40.30). However, care must be taken in the interpretation of the colour Doppler signal from the proximal arteries as they leave the aorta because they are angled towards the transducer on the anterior abdominal wall and therefore generate a relatively high Doppler shift on the colour scale, which may be mistakenly identified as representing a stenosis. The

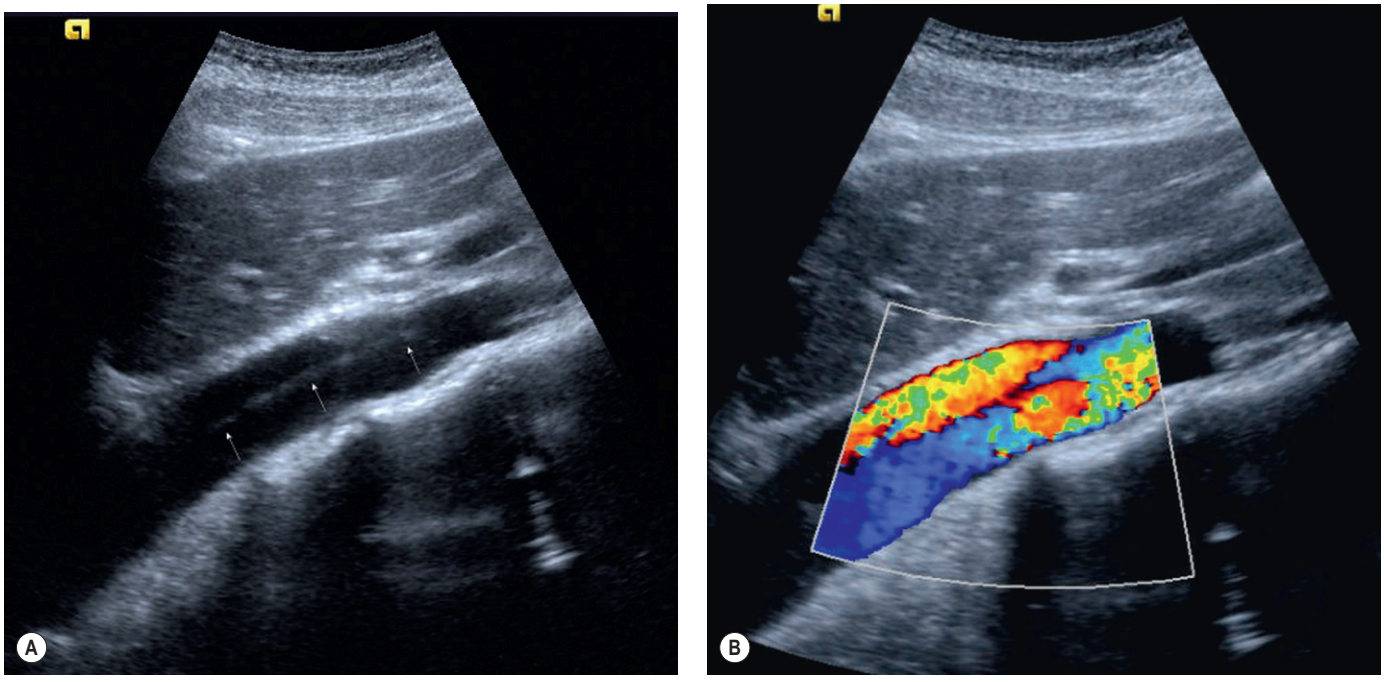

Figure 40.26 Dissection of the abdominal aorta. A: Real-time scan showing dissection flap in the lumen of the upper abdominal aorta behind the left liver. **B:** Colour Doppler image from the same segment of aorta showing the bidirectional flow on either side of the flap.

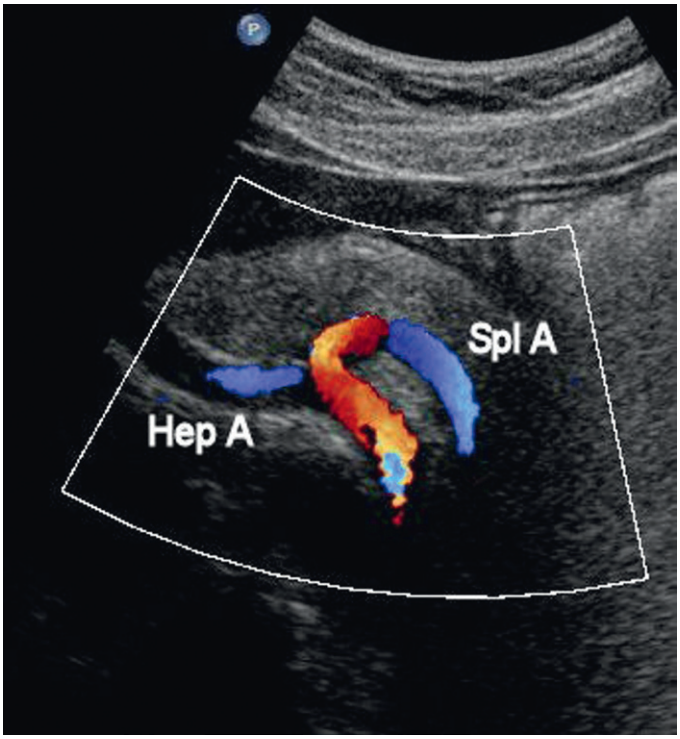

Figure 40.27 The coeliac axis. Transverse view of the coeliac axis showing the splenic and hepatic arteries.

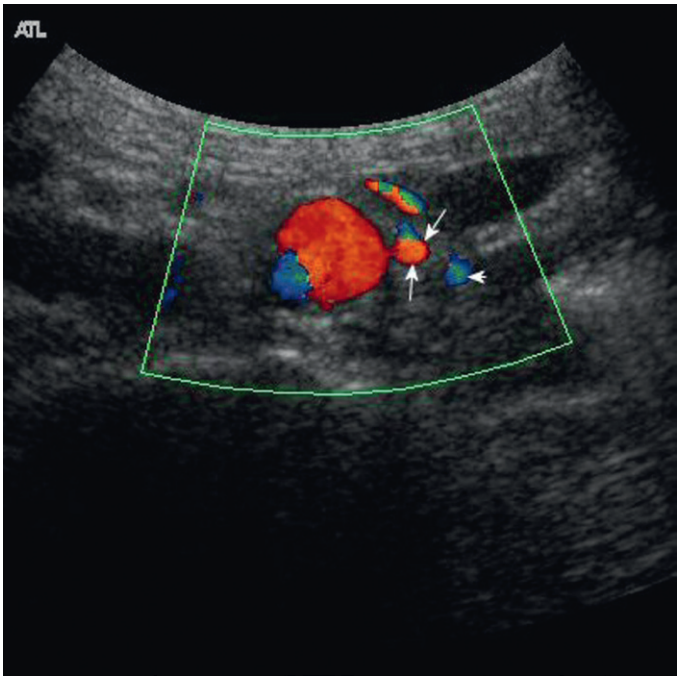

Figure 40.28 The inferior mesenteric artery. Transverse scan showing the inferior mesenteric artery beside the lower aorta (arrows); the inferior mesenteric vein is alongside (arrowhead).

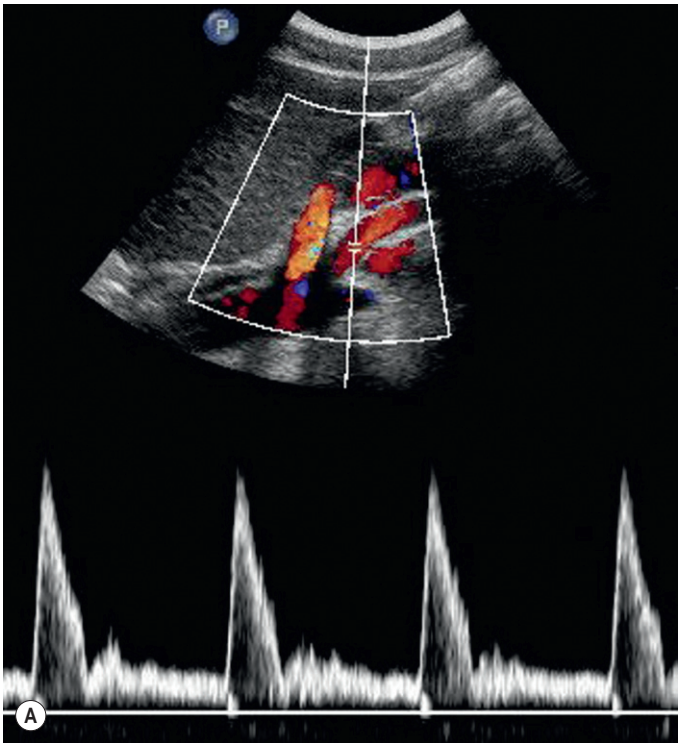

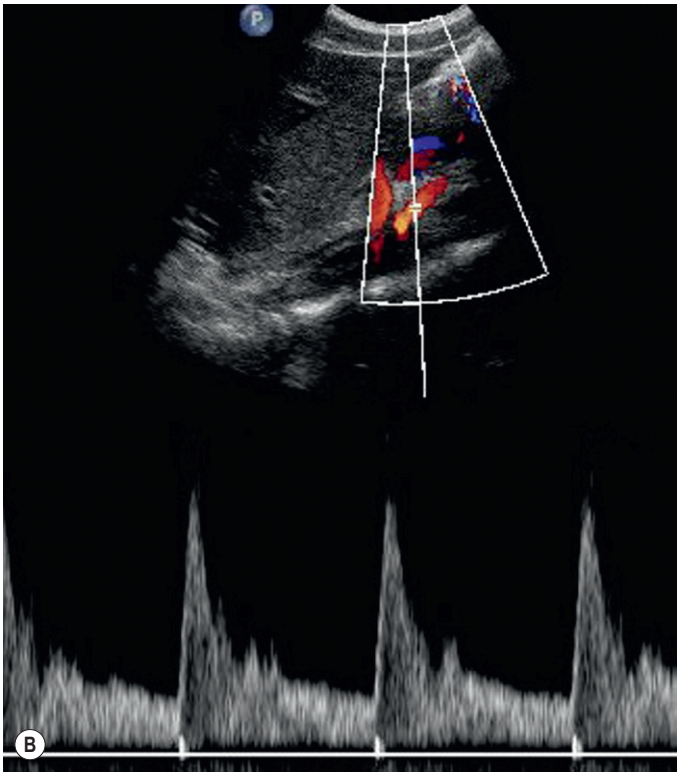

Figure 40.29 Superior mesenteric artery blood flow. A: In the preprandial state the diastolic flow is relatively low. **B:** Following food, diastolic flow has increased.

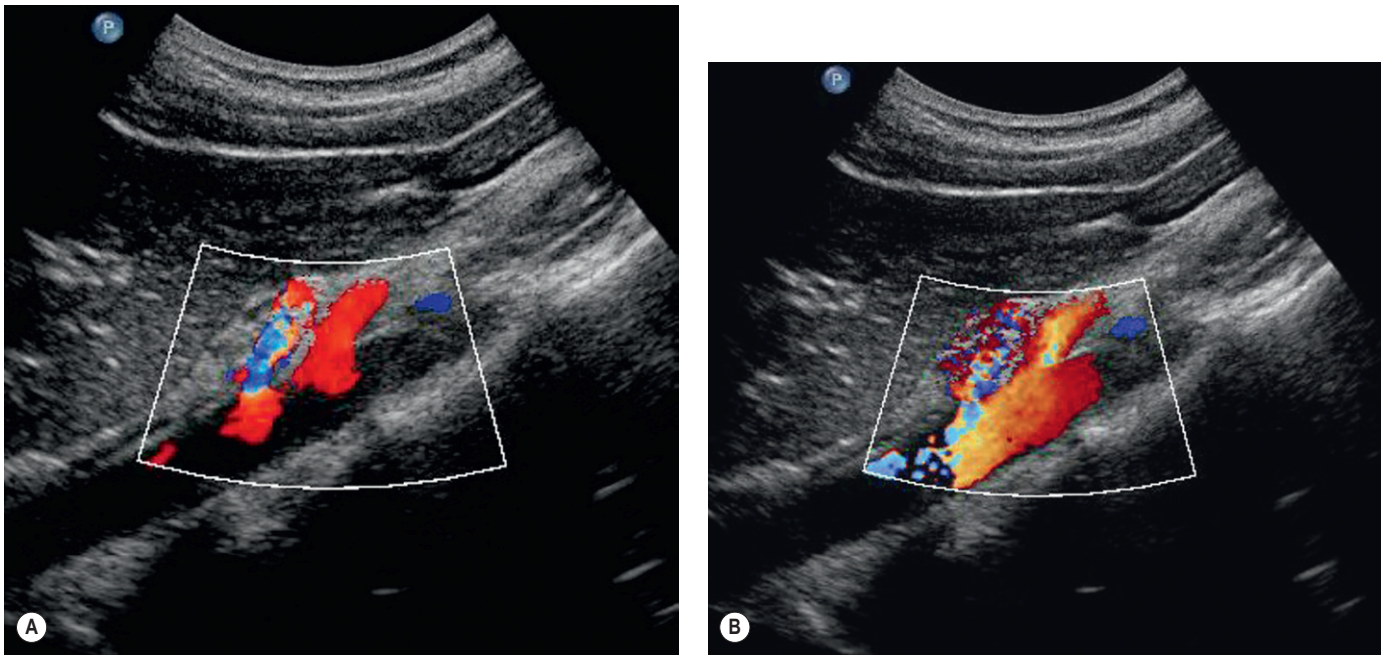

Figure 40.30 Coeliac axis stenosis. A: Colour Doppler shows aliasing at the origin of the coeliac axis. **B:** A tissue bruit is seen at the site of the stenosis during peak systole.

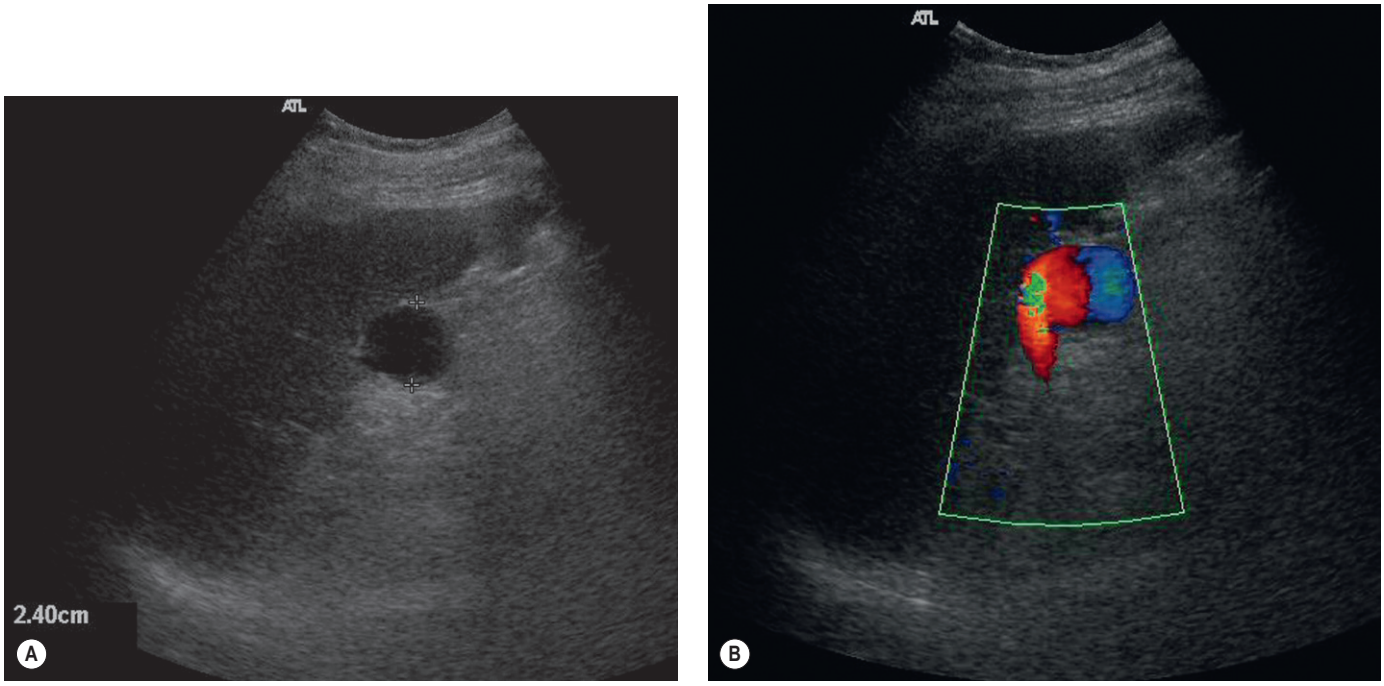

Figure 40.31 Splenic artery aneurysm. A: A 2.4 cm anechoic area adjacent to the spleen. **B:** Colour Doppler shows flow in an aneurysm.

presence of a tissue bruit is therefore a useful secondary sign of a significant stenosis. Peak systolic velocities greater than 3 m/s and an end-diastolic velocity of 0.45 m/s in the superior mesenteric artery correlate with >50% diameter stenosis.[78] Equivalent velocities for the coeliac axis are a peak systolic velocity of 2 m/s and an end-diastolic velocity of 0.55 cm/s. The splanchnic circulation can produce multiple collateral channels to bypass arterial stenosis, so at least two of the three main arteries should be compromised with either severe stenosis or occlusion before symptoms of significant ischaemia appear. Retrograde flow to the coeliac axis from the superior mesenteric artery is highly predictive of significant coeliac stenosis.

Aneurysms

Aneurysms can develop in these arteries, usually the splenic artery (Fig. 40.31) in association with acute pancreatitis or the hepatic

artery following liver transplantation. Trauma and biopsy can also give rise to aneurysms in these vessels.

THE INFERIOR VENA CAVA

Anatomy and flow patterns

The IVC is formed by the confluence of the left and right common iliac veins at about the level of the fifth lumbar vertebra. It lies to the right of the aorta and anterior to the right aspect of the spine. In its upper abdominal segment it runs in a groove on the posterior aspect of the liver and is separated from the aorta by the right crus of the diaphragm before piercing the diaphragm at the level of the eighth thoracic vertebra. Anatomical variations occur but many are rare.[79,80] The most common variations occur below the level of the renal veins and involve transposition or duplication of the IVC, resulting in a left-sided vena cava or double inferior venae cavae where the common iliac veins do not join but continue superiorly as paired vessels with the left component joining the right side at the level of the left renal vein (Fig. 40.32).

The size of the IVC can change significantly in response to a variety of factors outlined in Table 40.6. In particular, diameter changes with respiration can be observed owing to changes in intrathoracic and abdominal pressure. During inspiration venous return is increased as blood is sucked into the chest by the negative intrathoracic pressure and the abdominal cava is compressed by the increased intra-abdominal pressure resulting from the descent of the diaphragm; the diameter of the IVC therefore reduces during inspiration. Conversely, during expiration the intrathoracic pressure increases, thereby slowing blood flow into the chest, and the intra-abdominal pressure reduces as the diaphragm ascends, resulting in the caval diameter increasing. In addition, changes in right atrial pressure secondary to normal cardiac activity or disease will affect flow and the size of the inferior vena cava. The flow patterns recorded in the IVC are normally phasic with respiration and with a pulsatile element superimposed due to reflected right atrial pressure waves (Fig. 40.33). These features are generally more pronounced in the proximal IVC. Changes in the variation of the caval diameter have been correlated with blood loss[81] and the state of dehydration/fluid overload, in trauma and renal replacement therapy patients.[82]

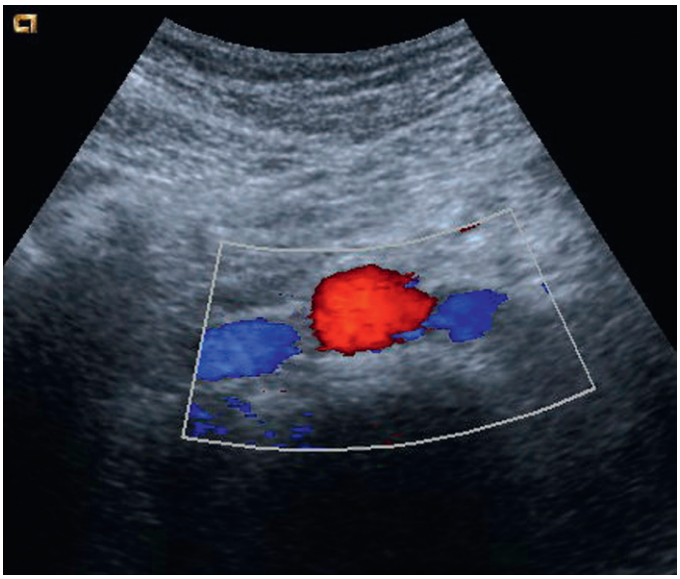

Figure 40.32 Dual caval segments. Two caval segments (blue) are seen on either side of the lower abdominal aorta (red).

Objectives of the scan and scanning technique

The primary reason for imaging the IVC is to assess its patency and to detect intraluminal obstruction such as thrombus, or extraluminal compression caused by tumours or other masses. The technique for imaging the IVC is similar to that described for the aorta. The intrahepatic and upper segment can be visualised by using the liver as an acoustic window (Fig. 40.34). Imaging of the distal segment of the IVC may be improved by rolling the patient into a left lateral decubitus position. To obtain adequate colour Doppler images and spectral Doppler recordings, the inferior cava is best imaged in longitudinal section, although transverse imaging will be required to image the renal veins as they drain to the cava.

Abnormal findings

Thrombosis

Thrombosis can occur due to propagation of deep vein thrombosis from the lower extremity veins or pelvis. The thrombus may be anechoic if very fresh or exhibit a moderate degree of echogenicity if more than a few weeks old. The thrombus may be completely occlusive or partially obstructing the IVC (Fig. 40.35). Colour Doppler imaging can be useful for identifying any residual patent lumen. Often, the thrombus does not extend above the level of the renal veins as the high inflow from these veins prevents propagation. Acute caval obstruction normally results in bilateral lower limb oedema within hours and the skin in the legs may develop a bluish tinge.[83] If the common femoral veins are patent, they often exhibit a non-phasic continuous low velocity flow pattern as blood will have to drain through collateral channels in the abdomen.

Table 40.6 The IVC can vary in diameter due to a number of factors

Increased diameter	Decreased diameter
Deep expiration	Deep inspiration
Fluid overload	Dehydration/Hypovolaemia
Proximal obstruction	Intra-abdominal mass, e.g. tumour, AAA
Congestive cardiac failure	

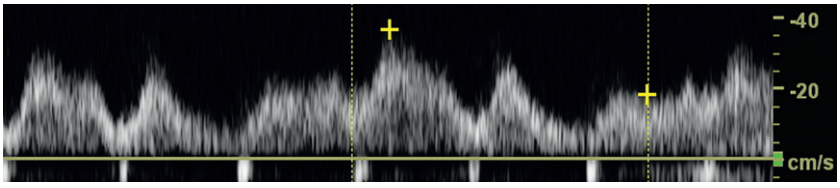

Figure 40.33 Normal inferior vena cava waveform. Spectral Doppler flow patterns from the IVC demonstrate variations in flow due to respiration and cardiac activity.

Tumour obstruction

Obstruction of the inferior vena cava can occur from extension of tumour thrombus in the renal veins due to renal cell carcinoma, or hepatic veins due to hepatocellular carcinoma or hepatoblastoma (Fig. 40.36).[84] Intraluminal tumour thrombus is reasonably echogenic and evidence of flow or small vessels may be seen within the thrombus with colour Doppler imaging.[85] Intracaval tumour may

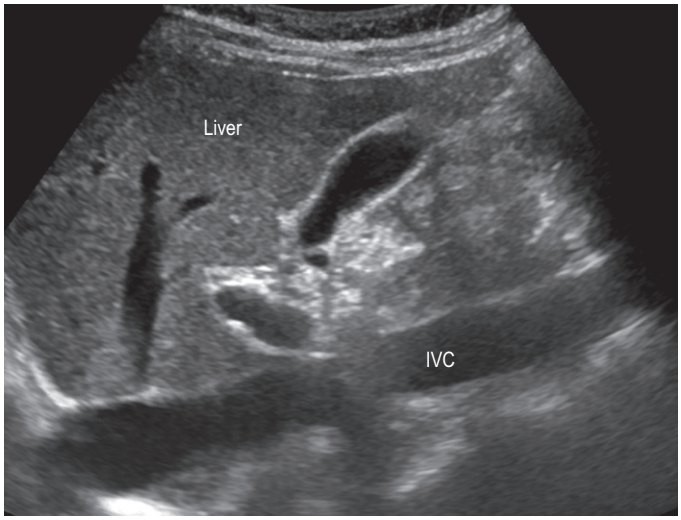

Figure 40.34 The upper cava seen through the liver. The liver can act as a window to image the intrahepatic segment of the IVC, as shown from the position in Figure 40.4Aii.

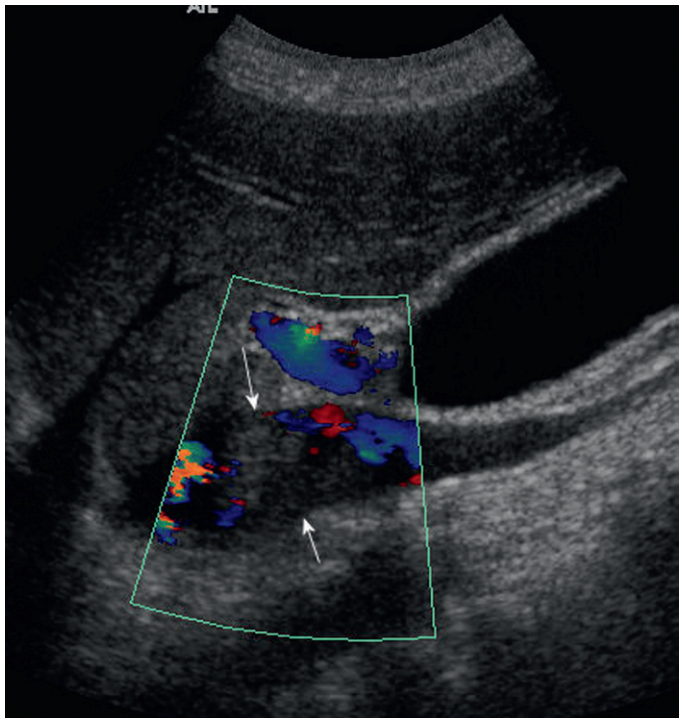

Figure 40.36 Tumour thrombus in the inferior vena cava. Tumour thrombus from a renal cell carcinoma distending the upper inferior vena cava (arrows).

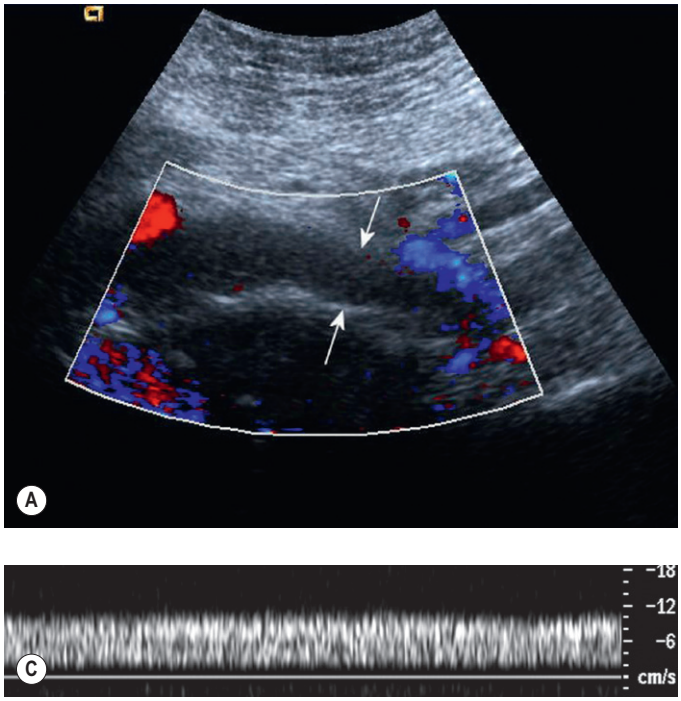

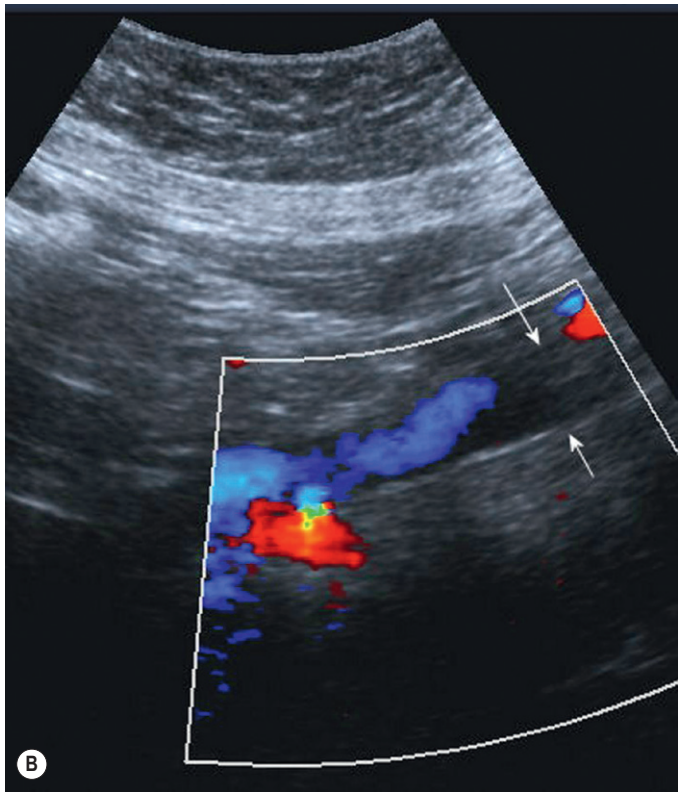

Figure 40.35 Caval thrombosis and femoral Doppler waveform. A: Colour Doppler image of the lower inferior vena cava showing no evidence of flow in the cava, which is distended by thrombus (arrows). **B:** The upper end of the thrombus (arrows) with blood flow demonstrated above it. **C:** An abnormal waveform recorded in the common femoral vein in a different patient showing continuous flow with a loss of phasicity due to proximal vein obstruction.

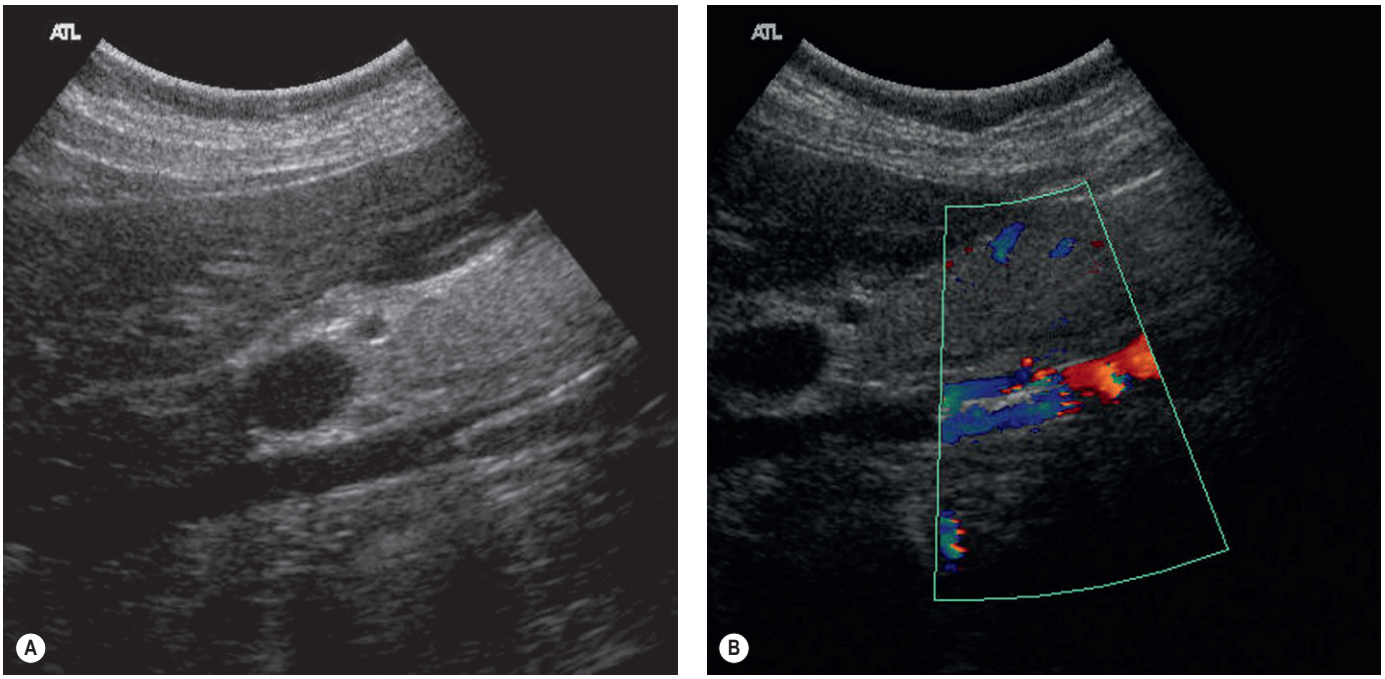

Figure 40.37 Caval filter. A: An IVC filter in the inferior cava. **B:** Colour Doppler showing patency of the cava at the level of the filter.

extend above the diaphragm and into the atrium, which has implications for planning treatment.[86]

External compression of the inferior vena cava can be due to a number of causes including adjacent tumours, such as renal and adrenal neoplasms, pancreatic tumours, large aortic aneurysms, enlarged retroperitoneal lymph nodes and retroperitoneal haematoma. Tumours arising from the wall of the IVC are rare and are mainly due to leiomyosarcomas.[83]

Caval filters

Caval filters are deployed in the IVC to capture or prevent embolisation of clot from the pelvis and lower limbs to the pulmonary circulation.[87,88] They are normally positioned below the renal veins. The filters are echogenic and usually visible with ultrasound (Fig. 40.37). Ultrasound can be used to assess the inferior vena cava prior to insertion of the filter to ensure that it is patent and that there is no free-floating thrombus present that could be dislodged during the procedure. Following insertion, ultrasound can be used to assess the patency of the filter or extension of thrombus above it. Breakage of filter struts is difficult to demonstrate with ultrasound and a plain film is more useful.

Liver transplantation

Following liver transplantation the cava should be assessed to ensure satisfactory flow. The appearances will depend on the type of anastomosis performed. In the past, the segment of donor cava attached to the new liver replaced the equivalent segment of native cava, which had been removed with the diseased liver. Many surgeons now perform a 'piggyback' technique, where the native cava is left in place, the inferior end of the donor caval segment is oversewn and the upper end anastomosed to the native cava with an end-to-side anastomosis. This results in a postoperative appearance which can be confusing if it is not recognised, as there will appear to be two cavae associated with the transplanted liver (Fig. 40.38).

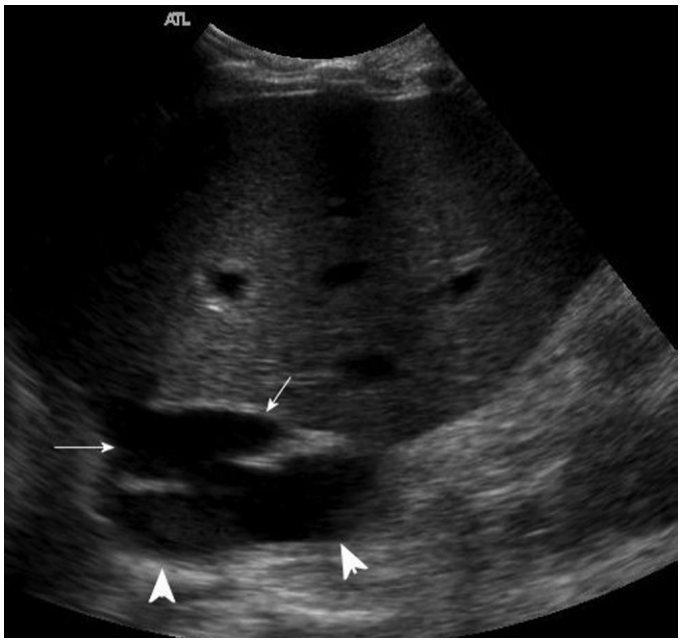

Figure 40.38 Liver transplantation. Dual segment of inferior vena cava following a 'piggyback' transplantation procedure. The donor cava lies superiorly (arrows) and the native cava more posteriorly (arrowheads).

Other postoperative problems which may occur in relation to the cava following transplantation include compression, if the new liver is relatively large; distortion of the cava may also occur if there is relative twisting of the caval channel as a result of fitting the donor liver into the native abdomen. In the longer term stenosis may develop at the sites of anastomosis. Liver transplantation is covered further in Chapter 13.

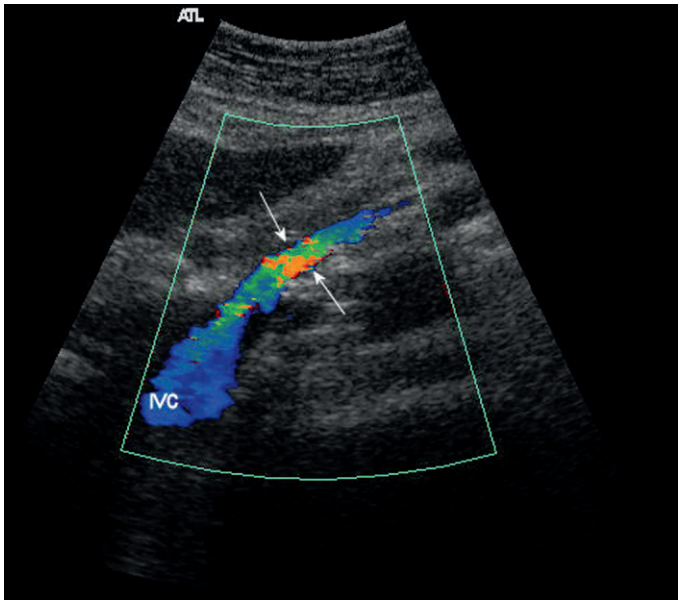

Figure 40.39 Portacaval anastomosis. Colour Doppler image of a surgical portacaval shunt. The portal vein (arrows) has been anastomosed to the inferior vena cava (IVC).

Fistulae

Fistulae involving the cava may rarely occur spontaneously, often secondary to an aortic aneurysm, or they may be surgically created, as is the case with portacaval shunts. In cases of aortocaval fistulae, colour Doppler may show a visible tissue bruit with pulsatile flow in the cava above the level of the fistula; sometimes the fistula itself is difficult to identify. Surgical portacaval shunts are usually side-to-side shunts in the upper abdomen at the level where the proximal main portal vein passes close in front of the cava (Fig. 40.39). A tissue bruit may be apparent and the shunt is more easily identified if the liver can be used as a window through to the point of anastomosis; turning the patient up onto the left side may facilitate visualisation. However, these are rarely performed now, having been replaced by transjugular intrahepatic portosystemic shunts (TIPS); see Chapter 12.

REFERENCES

1. Gillum RF. Epidemiology of aortic aneurysm in the United States. J Clin Epidemiol 1995;48:1289–1298.
2. National Centre for Health Statistics. Deaths, percent of total deaths and death rates for the 15 leading causes of death: United States and each state, 2000. Atlanta, GA: CDC/NCHS, National Vital Statistics System; 2001.
3. Gomes MN, Choyke PL. Pre-operative evaluation of abdominal aortic aneurysms: ultrasound or computed tomography? J Cardiovasc Surg 1987;28:159–166.
4. Parker MV, O'Donnell SD, Audrey MC, et al. What imaging studies are necessary for abdominal aortic endograft sizing? A prospective blinded study using conventional computed tomography, aortography, and three-dimensional computed tomography. J Vasc Surg 2005;4:199–205.
5. Wanhainen A. How to define an abdominal aortic aneurysm – influence on epidemiology and clinical practice. Scand J Surg 2008;97:105–109.
6. Sonesson B, Länne T, Hansen F, et al. Infrarenal aortic diameter in the healthy person. Eur J Vasc Surg 1994;8: 89–95.
7. Johnston KW, Rutherford RB, Tilson MD, et al. Suggested standards for reporting on arterial aneurysms. Subcommittee on Reporting Standards for Arterial Aneurysms, Ad Hoc Committee on Reporting Standards, Society for Vascular Surgery and North American Chapter, International Society for Cardiovascular Surgery. J Vasc Surg 1991;13:452–458.
8. Sterpetti AV, Schultz RD, Feldhaus RJ, et al. Factors influencing enlargement rate of small abdominal aortic aneurysms. J Surg Res 1987;43:211–219.
9. Wanhainen A, Themundo R, Ahlström H, et al. Thoracic and abdominal aortic dimensions in 70-year old men and women. A population-based whole-body magnetic resonance imaging (MRI) study. J Vasc Surg 2008;47:504–512.
10. US Preventive Services Task Force. Screening for abdominal aortic aneurysm: recommendation statement. Ann Intern Med 2005;142:198–202.
11. National Screening Programme for Abdominal Aortic Aneurysm. Department of Health; 2008: website at http://aaa.screening.nhs.uk/.
12. Bengtsson H, Bergqvist D, Ekberg O, et al. A population based screening of abdominal aortic aneurysms (AAA). Eur J Vasc Surg 1991;5:53–57.
13. Cosford PA, Leng GC. Screening for abdominal aortic aneurysm. Cochrane Database of Systematic Reviews 2007, Issue 2. Art. No.: CD002945. DOI: 10.1002/14651858.CD002945.pub2.
14. Lindholt JS, Henneberg EW, Fasting H, et al. Mass or high-risk screening for abdominal aortic aneurysm. Br J Surg 1997;84:40–42.
15. Morris GE, Hubbard CS, Quick CR. An abdominal aortic aneurysm screening programme for all males over the age of 50 years. Eur J Vasc Surg 1994;8:156–160.
16. Simoni G, Pastorino C, Perrone R, et al. Screening for abdominal aortic aneurysms and associated risk factors in a general population. Eur J Vasc Endovasc Surg 1995;10:207–210.
17. Smith FC, Grimshaw GM, Paterson IS, et al. Ultrasonographic screening for abdominal aortic aneurysm in an urban community. Br J Surg 1993;80:1406–1409.
18. Bengtsson H, Sonesson B, Bergqvist D. Incidence and prevalence of abdominal aortic aneurysms, estimated by necropsy studies and population screening by ultrasound. Ann NY Acad Sci 1996;800:1–24.
19. Scott RA, Bridgewater SG, Ashton HA. Randomized clinical trial of screening for abdominal aortic aneurysm in women. Br J Surg 2002;89:283–285.
20. Adams DC, Tulloh BR, Galloway SW, et al. Familial abdominal aortic aneurysm: prevalence and implications for screening. Eur J Vasc Surg 1993;7:709–712.
21. Wassef M, Baxter BT, Chisholm RL, et al. Pathogenesis of abdominal aortic aneurysms: a multidisciplinary research program supported by the National Heart, Lung, Blood Institute. J Vasc Surg 2001;34: 730–738.
22. Dalainas I, Nano G, Ranucci M, et al. Inflammatory abdominal aortic aneurysms. A 20-year experience. J Cardiovasc Surg (Torino) 2007;48:305–308.
23. Pennell RC, Hollier LH, Lie JT, et al. Inflammatory abdominal aortic aneurysms: a thirty-year review. J Vasc Surg 1985;2:859–869.
24. Lee WK, Mossop PJ, Little AF, et al. Infected (mycotic) aneurysms: spectrum of imaging appearances and management. Radiographics 2008;28:1853–1868.
25. Stonebridge PA, Ruckley CV. Abdominal aortic aneurysms. In: Tooke JE, Lowe DO, editors. A Textbook of Vascular Medicine. London: Arnold; 1996. p. 176–190.
26. Johansson G, Swedenborg J. Ruptured abdominal aortic aneurysms: a study of incidence and mortality. Br J Surg 1986;73:101–103.
27. Johansen K, Kohler TR, Nicholls SC, et al. Ruptured abdominal aortic aneurysm: the Harborview experience. J Vasc Surg 1991;13:240–247.
28. Bradbury AW, Makhdoomi KR, Adam DJ, et al. Twelve-year experience of the management of ruptured abdominal aortic aneurysm. Br J Surg 1997;84:1705–1707.
29. Lederle FA, Johnson GR, Wilson SE, et al. Rupture rate of large abdominal aortic aneurysms in patients refusing or unfit for elective repair. JAMA 2002;287:2968–2972.
30. The UK Small Aneurysm Trial Participants. Mortality results for randomised controlled trial of early elective surgery or ultrasonographic surveillance for small abdominal aortic aneurysms. Lancet 1998;352:1649–1655.
31. Lederle FA, Wilson SE, Johnson GR. Immediate repair compared with surveillance of small abdominal aortic aneurysms. N Engl J Med 2002;346:1437–1444.
32. Powell JT, Brown LC, Forbes JF, et al. Final 12-year follow-up of surgery versus surveillance in the UK Small Aneurysm Trial. Br J Surg 2007;94:702–708.
33. Heller JA, Weinberg A, Arons R, et al. Two decades of abdominal aortic aneurysm repair: have we made any progress? J Vasc Surg 2000;32:1091–1100.

34. Huber TS, Wang JG, Derrow AE, et al. Experience in the United States with intact abdominal aortic aneurysm repair. J Vasc Surg 2001; 33:304–311.
35. Dimick JB, Stanley JC, Axelrod DA, et al. Variation in death rate after abdominal aortic aneurysmectomy in the United States: impact of hospital volume, gender, and age. Ann Surg 2002;235:579–585.
36. Ballard DJ, Filardo G, Fowkes G, et al. Surgery for small asymptomatic abdominal aortic aneurysms. Cochrane Database Syst Rev 2008; Oct 8 (4). http://www.cochrane.org/reviews/en/ab001835.html.
37. Brown LC, Powell JT. Risk factors for aneurysm rupture in patients kept under ultrasound surveillance. UK Small Aneurysm Trial Participants. Ann Surg 1999;230:289–296; discussion 296–729.
38. Lederle FA. Should abdominal aortic aneurysm be managed differently in women? Scand J Surg 2008;97:125–127.
39. Kent KC, Zwolak RM, Jaff MR, et al. Screening for abdominal aortic aneurysm: a consensus statement. J Vasc Surg 2004;39:267–269.
40. Cao P. Comparison of surveillance vs Aortic Endografting for Small Aneurysm Repair (CAESAR) trial: study design and progress. Eur J Vasc Endovasc Surg 2005;30:245–251.
41. Grimshaw GM, Thompson JM, Hamer JD. A statistical analysis of the growth of small abdominal aortic aneurysms. Eur J Vasc Surg 1994;8:741–746.
42. Santilli SM, Littooy FN, Cambria RA, et al. Expansion rates and outcomes for the 3.0-cm to the 3.9-cm infrarenal abdominal aortic aneurysm. J Vasc Surg 2002;35:666–671.
43. Kuhn M, Bonnin RL, Davey MJ. Emergency department ultrasound scanning for abdominal aortic aneurysm: accessible, accurate, and advantageous. Ann Emerg Med 2000;36:219–223.
44. Moore CL, Holliday RS, Hwang JQ, et al. Screening for abdominal aortic aneurysm in asymptomatic at-risk patients using emergency ultrasound. Am J Emerg Med 2008;26:883–887.
45. Mackway-Jones K. Towards evidence based emergency medicine: Best BETs from the Manchester Royal Infirmary. Emerg Med J 2008; 26:57.
46. Akkersdijk GJ, Puylaert JB, de Vries AC. Abdominal aortic aneurysm as an incidental finding in abdominal ultrasonography. Br J Surg 1991;78:1261–1263.
47. Lederle FA, Simel DL. The rational clinical examination. Does this patient have abdominal aortic aneurysm? JAMA 1999;281:77–82.
48. Ashton HA, Buxton MJ, Day NE, et al. The Multicentre Aneurysm Screening Study (MASS) into the effect of abdominal aortic aneurysm screening on mortality in men: a randomised controlled trial. Lancet 2002;360:1531–1539.
49. Fleming C, Whitlock EP, Beil TL, et al. Screening for abdominal aortic aneurysm: a best-evidence systematic review for the US Preventive Services Task Force. Ann Intern Med 2005;142:203–211.
50. Kim LG, Scott AP, Ashton HA, et al. A sustained mortality benefit from screening for abdominal aortic aneurysm. Ann Intern Med 2007;146:699–706.
51. Sprouse LR 2nd, Meier GH 3rd, Lesar CJ, et al. Comparison of abdominal aortic aneurysm diameter measurements obtained with ultrasound and computed tomography: Is there a difference? J Vasc Surg 2003;38:466–471; discussion 471–472.
52. Sprouse LR 2nd, Meier GH 3rd, Parent FN, et al. Is ultrasound more accurate than axial computed tomography for determination of maximal abdominal aortic aneurysm diameter? Eur J Vasc Endovasc Surg 2004;28:28–35.
53. Zwiebel WJ. Ultrasound assessment of the aorta, iliac arteries and inferior vena cava. In: Zwiebel WJ, Pellerito JS, editors. Introduction to Vascular Ultrasonography. Philadelphia: Elsevier Saunders; 2005. p. 529–552.
54. Evans JA, Hoskins PR. Quality assurance. In: Hoskins P, Thrush A, Martin K, Whittingham T, editors. Diagnostic ultrasound. London: Greenwich Medical Media; 2002. p. 165–178.
55. Vowden P, Wilkinson D, Ausobsky JR, et al. A comparison of three imaging techniques in the assessment of an abdominal aortic aneurysm. J Cardiovasc Surg (Torino) 1989;30:891–896.
56. Hanley M, Ryley NG, Lewis P, et al. Can duplex accurately assess the relationship between the renal arteries and an abdominal aortic aneurysm using the superior mesenteric artery as a fixed point? J Vasc Technol 2000;25:97–101.
57. Parodi JC, Palmaz JC, Barone HD. Transfemoral intraluminal graft implantation for abdominal aortic aneurysms. Ann Vasc Surg 1991;5:491–499.
58. EVAR trial participants. Endovascular repair versus open repair in patients with abdominal aortic aneurysm (EVAR trial 1): randomised controlled trial. Lancet 2005;365:2179–2186.
59. White GH, Yu W, May J, et al. Endoleaks as a complication of endoluminal grafting of abdominal aortic aneurysms: classification, incidence, diagnosis, and management. J Endovasc Surg 1997;4:152–168.
60. White GH, May J, Waugh RC, et al. Type III and type IV endoleak: towards a complete definition of blood flow in the sac after endoluminal AAA repair. J Endovasc Surg 1998;5:305–309.
61. Veith FJ, Baum RA, Ohki T, et al. Nature and significance of endoleaks and endotension: summary of opinions expressed at an international conference. J Vasc Surg 2002;3(5):1029–1035.
62. van Marrewijk C, Buth J, Harris PL, et al. Significance of endoleaks after endovascular repair of abdominal aortic aneurysms: The EUROSTAR experience. J Vasc Surg 2002;35:461–473.
63. Schlosser FJ, Gusberg RJ, Dardik A, et al. Aneurysm rupture after EVAR: Can the ultimate failure be predicted? Eur J Vasc Surg 2009;37:15–22.
64. National Institute for Health and Clinical Excellence. IPG 163. Stent-graft placement in abdominal aortic aneurysm-guidance. 2006; http://guidance.nice.org.uk/IPG163.
65. van Marrewijk CJ, Fransen G, Laheij RJ, et al EUROSTAR Collaborators. Is a type II endoleak after EVAR a harbinger of risk? Causes and outcome of open conversion and aneurysm rupture during follow-up. Eur J Vasc Endovasc Surg 2004;27:128–137.
66. Sandford RM, Bown MJ, Fishwick G, et al. Duplex ultrasound is reliable in the detection of endoleak following endovascular aneurysm repair. Eur J Vasc Endovasc Surg 2006;32: 537–541.
67. Stavropoulos SW, Charagundla SR. Imaging techniques for detection and management of endoleaks after endovascular aortic aneurysm repair. Radiology 2007;243:641–655.
68. Manning BJ, O'Neill SM, Haider SN, et al. Duplex ultrasound in aneurysm surveillance following endovascular aneurysm repair: a comparison with computed tomography aortography. J Vasc Surg 2009;49: 60–65.
69. Napoli V, Bargellini I, Sardella SG, et al. Abdominal aortic aneurysm: contrast-enhanced US for missed endoleaks after endoluminal repair. Radiology 2004;233:217–225.
70. Henao EA, Hodge MD, Felkai DD, et al. Contrast-enhanced Duplex surveillance after endovascular abdominal aortic aneurysm repair: improved efficacy using a continuous infusion technique. J Vasc Surg 2006;43:259–264; discussion 264.
71. Parent FN, Meier GH, Godziachvili V, et al. The incidence and natural history of type I and II endoleak: a 5-year follow-up assessment with color duplex ultrasound scan. J Vasc Surg 2002;35:474–481.
72. Arko FR, Filis KA, Siedel SA. Intrasac flow velocities predict sealing of type II endoleaks after endovascular abdominal aortic aneurysm repair. J Vasc Surg 2003;37:8–15.
73. Fairman RM, Nolte L, Snyder SA, et al. Factors predictive of early or late aneurysm sac size change following endovascular repair. J Vasc Surg 2006;43:649–656.
74. Fraser KH, Meagher S, Blake JR, et al. Characterization of an abdominal aortic velocity waveform in patients with abdominal aortic aneurysm. Ultrasound Med Biol 2008;34:73–80.
75. Cossman DV, Ellison JE, Wagner WH, et al. Comparison of contrast arteriography to arterial mapping with color-flow duplex imaging in the lower extremities. J Vasc Surg 1989;10:522–528; discussion 528–529.
76. Thomas EA, Dubbins PA. Duplex ultrasound of the abdominal aorta – a neglected tool in aortic dissection. Clin Radiol 1990;42:330–334.
77. Clevert DA, Rupp N, Reiser M, et al. Improved diagnosis of vascular dissection by ultrasound B-flow: a comparison with color-coded Doppler and power Doppler sonography. Eur Radiol 2005;15:342–347.
78. Zwolak RM, Fillinger MF, Walsh DB, et al. Mesenteric and celiac duplex scanning: a validation study. J Vasc Surg 1998;27(6):1078–1087.
79. Mozes G, Gloviczki P. Venous embryology and anatomy. In: Bergan J, editor. The vein book. San Diego, CA: Elsevier Academic Press; 2007. p. 15–25.
80. Bass JE, Redwine MD, Kramer LA, et al. Spectrum of congenital anomalies of the inferior vena cava: cross-sectional imaging findings. Radiographics 2000;20:639–652.
81. Lyon M, Blaivas M, Brannam L. Sonographic measurement of the inferior vena cava as a marker of blood loss. Am J Emerg Med 2005; 23:45–50.
82. Mandelbaum A, Ritz E. Vena cava diameter measurement for estimation of dry weight in haemodialysis patients. Nephrol Dial Transplant 1996;11(Suppl 2):24–27.
83. Browse NL, Burnand KG, Irvine AT, Wilson NM. Diseases of the veins. London: Arnold; 1999.

84. Kandpal H, Sharma R, Gamangatti S, et al. Imaging the inferior vena cava: a road less traveled. Radiographics 2008;28:669–689.
85. Hübsch P, Schurawitzki H, Susani M, et al. Color Doppler imaging of inferior vena cava: identification of tumor thrombus. J Ultrasound Med 1992;11:639–645.
86. Guinan P, Sobin LH, Algaba F, et al. TNM staging of renal cell carcinoma: Workgroup No. 3. Union International Contre le Cancer (UICC) and the American Joint Committee on Cancer (AJCC). Cancer 1997;80:992–993.
87. Kazmers A, Groehn H, Meeker C. Duplex examination of the inferior vena cava. Am Surg 2000;66:986–989.
88. AbuRahma F. Permanent vena cava filters: Indications, filter types and results. In: Bergan J, editor. The vein book. San Diego, CA: Elsevier Academic Press; 2007. p. 417–433.

CHAPTER

41

The abdominal wall, peritoneum and retroperitoneum

Michael J. Bradley and David O. Cosgrove

ABDOMINAL WALL

Ultrasound of the anterior abdominal wall is most often performed either to ascertain the nature of a painful symptom/tender area or in the evaluation of a palpable mass. Ultrasound lends itself well to this task as it is possible to locate painful/tender sites and correlate the symptoms with the anatomy. The excellent soft tissue contrast resolution can demonstrate the palpable mass, not only delineating its anatomical features but also its internal echo structure, which may often achieve a specific diagnosis.

Ultrasound technique

No specific patient preparation is required. A high-frequency (10–14 MHz or greater), high-resolution probe is required including the capability for Doppler imaging. A lower-frequency curvilinear probe may be useful occasionally in the obese patient. The patient should be in a relaxed supine position but a variety of coughing, straining and Valsalva manoeuvres are required to create a dynamic image. Similarly raising the head from the pillow or asking the patient to distend the abdomen may create suitable muscle contraction. The sonographer should apply light probe pressure on the skin so as not to compress any superficial lesion. Deeper palpation may be required, particularly in the obese. Panoramic ultrasound imaging, if available, is useful to display a larger footprint image and to appreciate features such as rectus abdominis divarication.

Anatomy of the anterior abdominal wall

The principal components of the anterior abdominal wall are listed in Table 41.1. The paired parallel rectus abdominis muscles extend from the lower rib cage, xiphisternum and sternum to the distal insertion over the pubic rami and symphysis pubis. The fascial condensation, the linea alba, joins them in the midline (Figs 41.1 and 41.2). The oblique muscles and transversalis extend from the iliac blade laterally to merge with the rectus sheath which extends around the rectus abdominis muscle. The inguinal ligament extends from the anterior superior iliac spine to the pubic tubercle. Deep to this ligament is the neurovascular bundle, femoral artery, vein and nerve. The femoral canal lies on the medial aspect of the femoral vessels with the pectineus muscle posteriorly (Figs 41.3 and 41.4).

Pathological conditions affecting the anterior abdominal wall

The sonographer should visualise all incisions and scars prior to scanning and enquire as to their nature. Laparoscopy scars may be small and relatively obscure, particularly around the umbilicus. Normal mature scars when scanned in the transverse plane to the scar appear as a linear hypoechoic band extending from the skin into the subcutaneous fat.[1] Immature scars are more easily seen as there may be surrounding oedema or fluid/haematoma within the plane of the scar. Keloid scars may be recognised as thickening in the skin but also as thickening in the subcutaneous component. Open wounds should be scanned using probe protection to avoid contamination. Penetrating injuries can be evaluated with ultrasound to assess peritoneal injury with stab or gunshot wounds[2] but computed tomography (CT) may be the preferred imaging modality for this indication.

Infections

Fresh wounds or surgical incisions show surrounding oedema but the presence of cellulitis may suggest a significant wound infection. Oedematous subcutaneous fat is usually hyperechoic, losing its normal hypoechogenicity and stromal architecture. Cellulitis is seen when there are oedematous islands of fat surrounded by hypoechoic areas, sometimes consisting of frank fluid. Note should be made of any gas microbubbles which may alert the clinician to gas-forming organisms or necrotising fasciitis[3,4] (Fig. 41.5).

Abscesses are diagnosed when there is a localised fluid collection. They often show increased blood flow in the surrounding tissues on colour Doppler. The abscess can contain gas microbubbles and often has surrounding oedema or cellulitis. These collections can be internally septated. Needle aspiration may be diagnostic and therapeutic as well as allowing microbiological study of the specimen. Ultrasound should assess the abscess size, loculation and involvement of other structures as well as the presence of any foreign body material.

A stitch granuloma usually presents with localised pain but may have changes of frank infection or abscess formation around it. It may cause a palpable lump. The stitch itself is linear, or curvilinear and hyperechoic with the granulomatous reaction apparent as an irregular surrounding hypoechoic area. Doppler is usually unhelpful. The presence of these ultrasound appearances is significant if the area is directly tender to finger point pressure. If surgical treatment is intended then ultrasound-guided localising wire placement is often helpful to the surgeon preoperatively.

Table 41.1 The principal components of the anterior abdominal wall

Skin
Subcutaneous fat
Deep fascia
Muscles:
- rectus abdominis
- internal and external oblique laterally
- transversalis, lying deep to the obliques

Peritoneum
Inguinal ligament and canal
Femoral canal

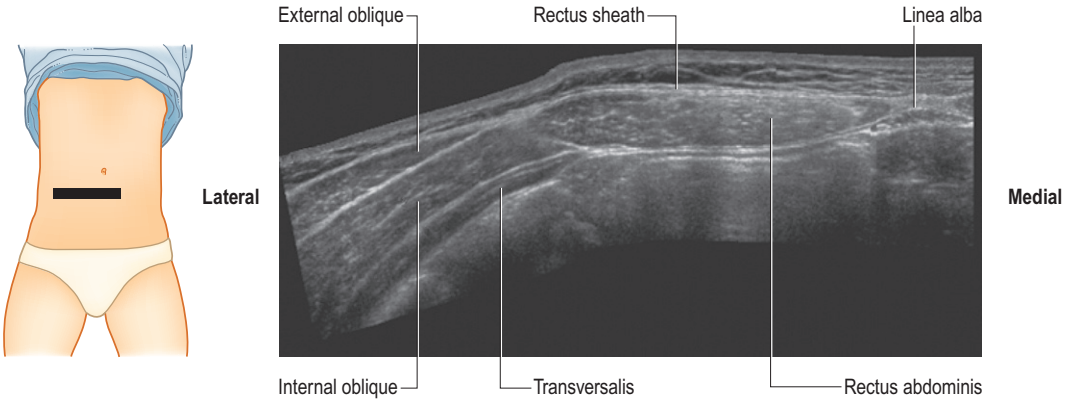

Figure 41.1 Transverse panoramic scan of the anterior abdominal wall.

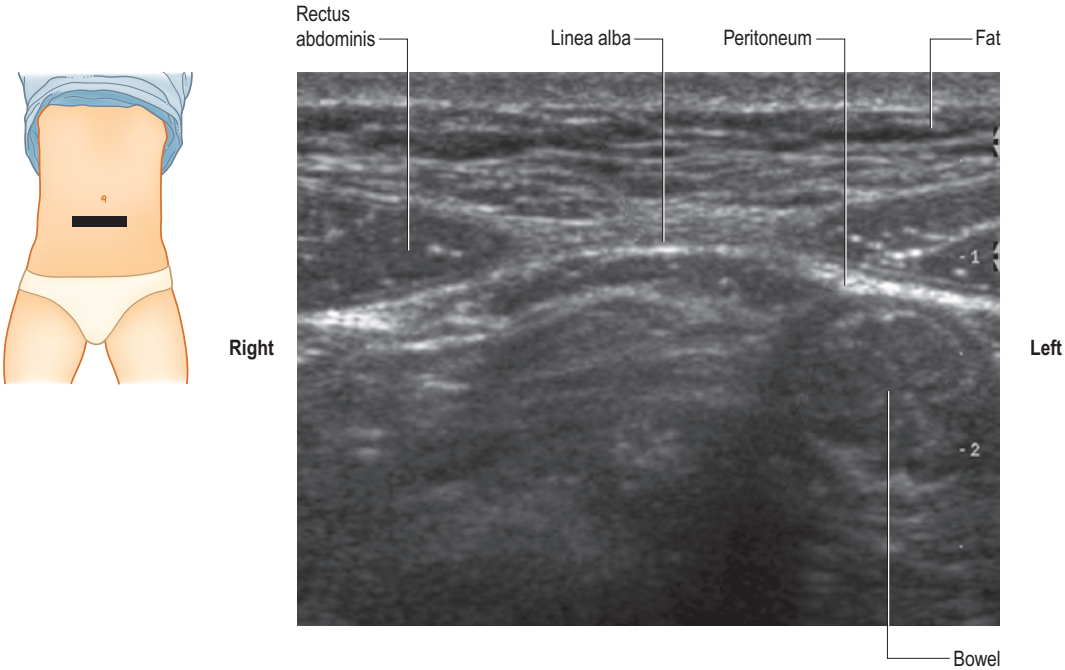

Figure 41.2 Transverse midline scan of the anterior abdominal wall.

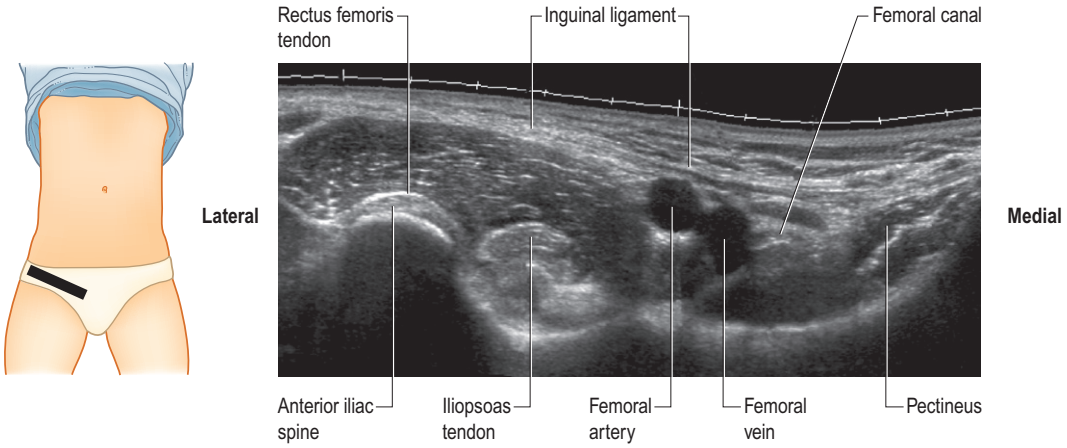

Figure 41.3 Transverse panoramic scan of the inguinal ligament.

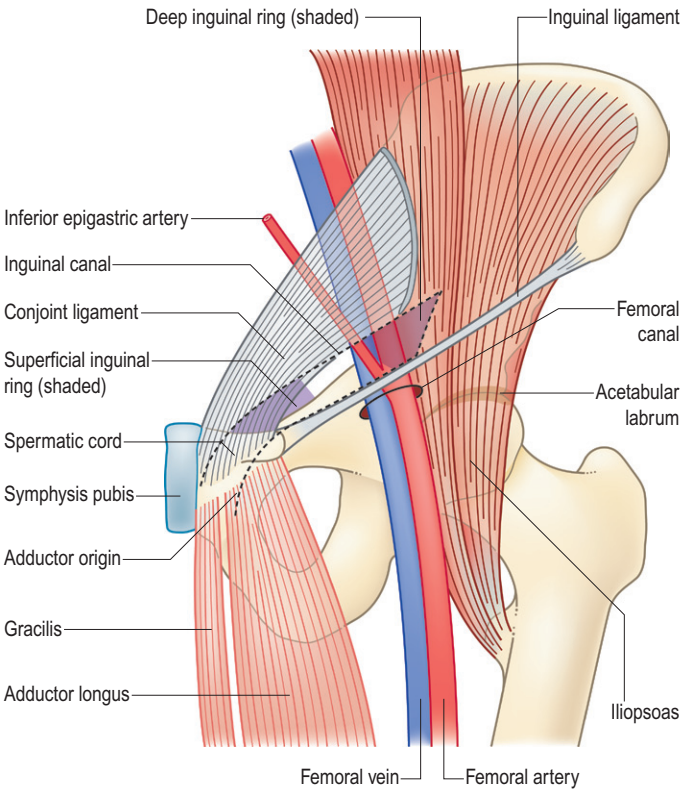

Figure 41.4 The relationships around the inguinal ligament in the coronal plane. (Modified from Bradley M and O'Donnell P, Atlas of Musculoskeletal Ultrasound Anatomy, 2nd edition. 2010 Cambridge University Press.)

An abscess may also occur due to haematogenous spread, or secondary to a necrotic lymph node. TB abscesses typically show marked surrounding oedema and should be considered if there is evidence of tuberculous infection elsewhere in the chest, abdomen or skeleton.[5,6]

Musculo-cutaneous flaps

Surgeons may create vascularised flaps for a variety of procedures, commonly for breast reconstruction and other plastic surgery procedures. Ultrasound monitoring can be useful, particularly using Doppler to evaluate the vascular anatomy before and after flap creation.[7]

Divarication of the rectus muscles

The paired rectus abdominis muscles normally lie parallel to each other with their medial borders 1–2 cm apart and separated by the midline linea alba. Divarication may be a congenital abnormality or may be acquired following pregnancy or abdominal surgery. The muscles lie further apart with an enlongated linea alba which may bow in shape on straining. A linea alba width larger than 3 cm is usually diagnostic but may be better appreciated using a transverse panoramic image.[8] It may involve the whole length of the muscle but may be focal, in either the supra- or infra-umbilical regions.

An everted xiphisternum may present as a palpable mass which may be tender. Ultrasound shows a superficially curved but normal xiphisternum which feels hard on palpation.[3]

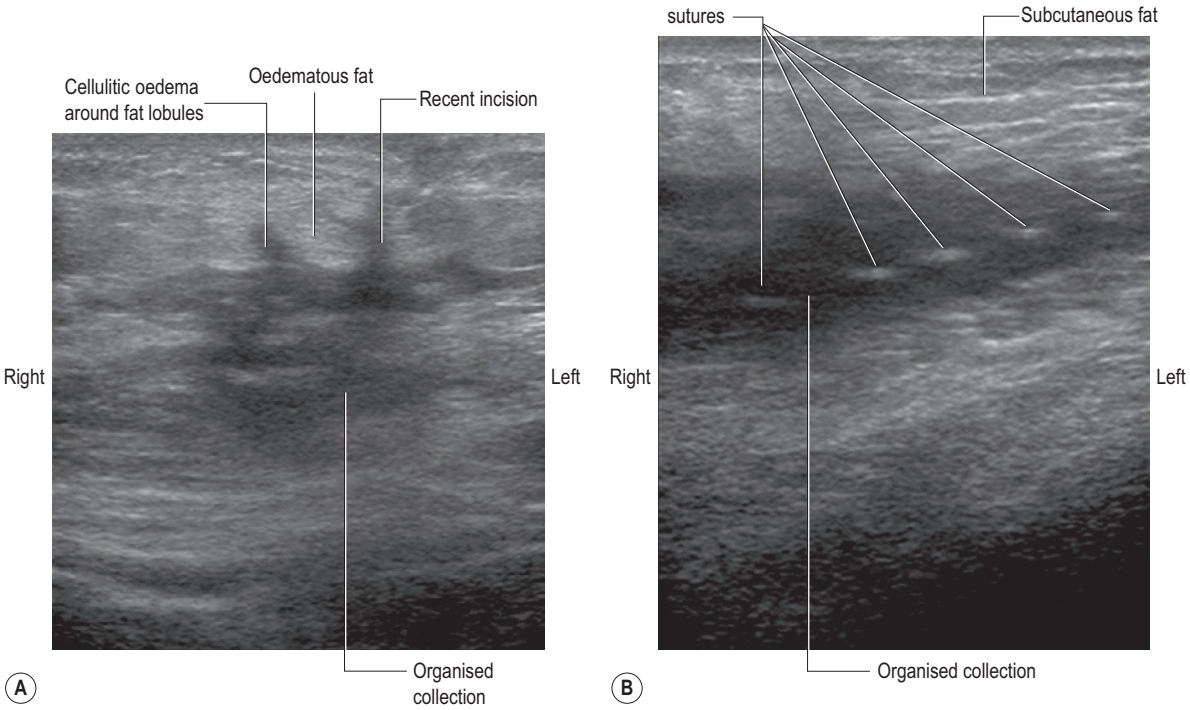

Figure 41.5 Infection. A: Transverse scan through incision showing cellulitis in the recent incision due to infection. **B:** Organised collection around suture material which may be focus for infection.

Trauma

A haematoma may be caused by blunt trauma or after a lifting/stretching injury. It may be seen also in non-trauma patients who have a bleeding diathesis or who are being treated with anticoagulants.[9–11] Ultrasound is used to describe its size and position and to evaluate any underlying muscle tear. Hyper-acute haematomas appear hyperechoic; acute haematomas are hypoechoic and, over several weeks, they organise and eventually liquefy.[12] Haematoma aspiration should only be considered for the liquefied stage to aid resolution, otherwise there is an increased risk of introducing infection. Liquefaction is best assessed by ballotting the haematoma during scanning or using probe compression to see the fluid moving or visualising compression.

Muscle tears are most frequently seen in the rectus abdominis muscles and rarely in the oblique muscles. Acute muscle tears form hypoechoic linear areas in the muscle or tendon with varying degrees of associated haematoma or oedema. A localised area of muscle oedema may reflect a muscle strain rather than a full tear of muscle fibres. Chronic tears with scarring and fibrosis are more difficult to demonstrate with ultrasound but may be seen as areas of hyperechogenicity within the muscle. Musculotendinous injuries may be seen involving the insertions of sartorius or rectus femoris in the region of the anterior iliac spines of the pelvis. Other tendinopathies may be seen, particularly involving the adductor tendon insertions, and these may produce symptoms similar to a hernia.

Hernias

Hernias occur when there is a fascial or muscular defect in the abdominal wall which allows intra-abdominal contents to extend into the defect. The main types of hernia affecting the anterior abdominal wall are given in Table 41.2. The contents of a hernia are often peritoneal or mesenteric fat, or it may contain bowel. Fat is clearly identified as hypoechoic, heterogeneous compressible material, whilst bowel may be appreciated on identification of the bowel wall, particularly when the segment of bowel contains fluid and/or gas. Bowel typically shows peristaltic movement unless it is incarcerated and irreducible. The sonographer needs to perform a variety of Valsalva techniques to contract the abdominal wall muscles to exaggerate the hernia protrusion and to induce movement of the hernia sac and contents. If no hernia is found with the patient supine, the scan should be completed with the patient standing; this may show hernia not seen in the supine position. Three-dimensional (3D) sonography can be more successful for small hernias.[13]

Table 41.2 The principal types of hernia affecting the anterior abdominal wall

1. Inguinal
2. Femoral
3. Umbilical/para-umbilical
4. Incisional
5. Epigastric
6. Spigelian
7. Lumbar
8. Sportsman's hernia

A hernia consists of three parts – the sac itself, its contents and covering (Fig. 41.6). The sac is a diverticulum of the peritoneum. The coverings are derived from the layers of the abdominal wall through which the sac extends. The contents are usually fat or bowel but have occasionally been described to contain any of the abdominal or pelvic organs.[14] The sonographer may visualise any or all of these three components.

The sonographer generally studies the static ultrasound features of the hernia sac and contents but also needs to assess whether the hernia is reducible where the hernia and its contents can be pushed back through the defect using palpation or probe pressure. Most hernias are reducible and this helps to differentiate a hernia from fatty tumours, which are not reducible. A hernia may pose a diagnostic dilemma when it is incarcerated and not reducible as the

dynamic features are much less apparent. Strangulation occurs when the vascular supply to the incarcerated bowel or other content is impaired; necrosis and gangrene of the contents can ensue.[15] A strangulated hernia presents as a painful, often red and hot swelling. The sonographer needs to be aware that there is normally fat visible in the inguinal canal which moves on dynamic ultrasound. Normal canal fat moves along the canal but is not reducible.

The commonest hernias are inguinal (73%), femoral (17%) and umbilical (8.5%). These figures do not include iatrogenic incisional hernias.[14] The diagnosis of a hernia is often apparent clinically and ultrasound is reserved for those patients in whom the clinical features are non-specific and further information is required to diagnose the 'occult' hernia.[16–18]

Types of hernia

- Reducible – a simple hernia can be pushed back through the defect using palpation or probe pressure.
- Incarcerated – the hernia is non-reducible and contains viable content.
- Strangulated – the bowel is vascularly impaired and may become necrotic or perforate.

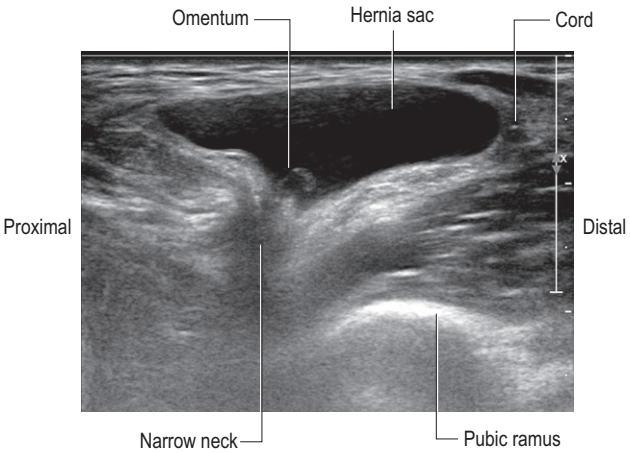

Figure 41.6 Longitudinal scan of the superficial ring showing hernia sac containing omentum.

Inguinal hernia

The superficial inguinal ring is a small aperture in the external oblique aponeurosis just cranial to the pubic tubercle and the medial end of the inguinal ligament (Fig. 41.7). The deep inguinal ring is a U-shaped evagination of the transversalis fascia, cranial to the inguinal ligament and midway between the symphysis pubis and the anterior superior iliac spine (Fig. 41.8). The inguinal canal passes between the deep and superficial rings. In males it contains the spermatic cord, the ilio-inguinal nerve and the genital branch of the genitofemoral nerve. In the female the round ligament replaces the spermatic cord.

The anterior wall of the inguinal canal is formed by the aponeurosis of the external oblique and in its lateral part by the muscular fibres of the internal oblique. The posterior wall is formed by the transversalis fascia and more medially by the conjoint tendon. Components of the internal oblique and transversalis muscles passing towards the conjoint tendon lie superiorly. The inguinal ligament lies inferiorly.

Inguinal hernias are divided into direct and indirect hernias. Ultrasound is recognised as a reproducible and highly accurate method for diagnosing inguinal hernias.[19–24]

Indirect inguinal hernias

These account for about 85% of inguinal hernias. An indirect inguinal hernia arises from the deep ring and extends inferomedially. Larger hernias extend through the superficial ring and into the scrotum or labia. The hernia arises lateral to the inferior epigastric vessels[25] and the cough impulse is directed inferomedially along the inguinal canal towards the superficial ring (Fig. 41.9). It needs to be differentiated from a hydrocele, spermatocele, undescended testis, lipoma of the cord or hydrocele of the canal of Nuck in females (Fig. 41.10). These are differentiated largely on the basis of their echo characteristics as to whether they are solid or liquid. A lipoma can be difficult to differentiate from fat in a hernia. Normal fat in the inguinal canal moves but does not reduce. Similarly a lipoma does not reduce. Occasionally a hernia sac is seen without apparent content but dynamic imaging will usually demonstrate content, differentiating it from a hydrocele[26] (Fig. 41.11).

Direct inguinal hernia

This type of hernia accounts for some 15% of inguinal hernias. It is due to a defect in the transversalis fascia in the posterior wall of the inguinal canal. Ultrasound demonstrates the hernia arising medial to the inferior epigastric artery and moving towards the footprint

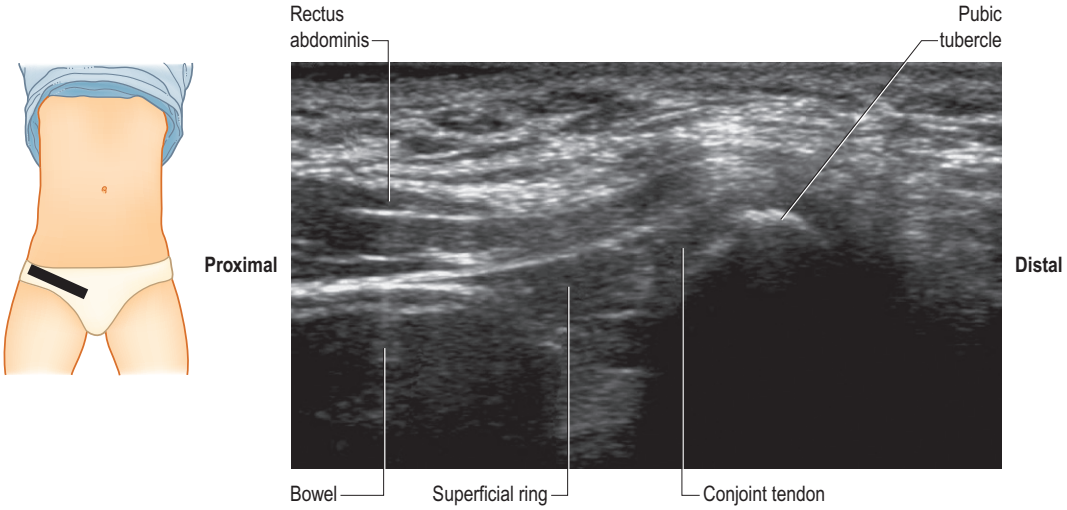

Figure 41.7 Longitudinal scan of the superficial ring in the inguinal canal.

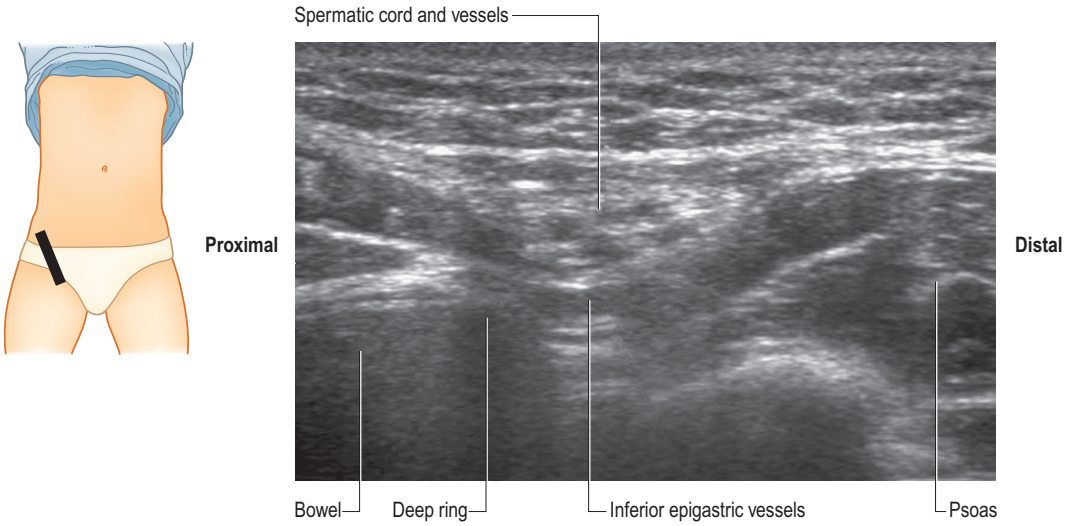

Figure 41.8 Longitudinal scan, oblique, of the deep inguinal ring.

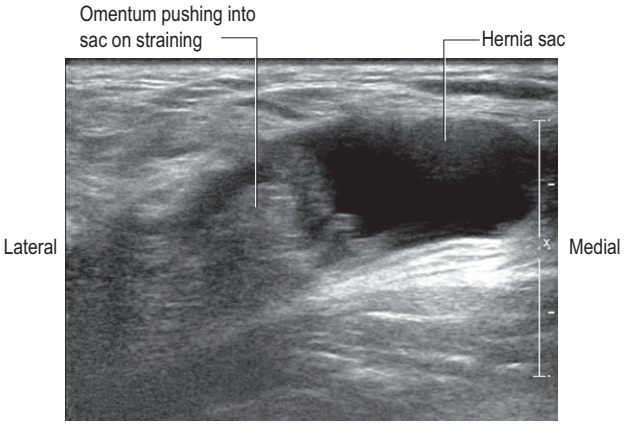

Figure 41.9 Longitudinal scan, oblique, of indirect inguinal hernia – direction of movement along the canal.

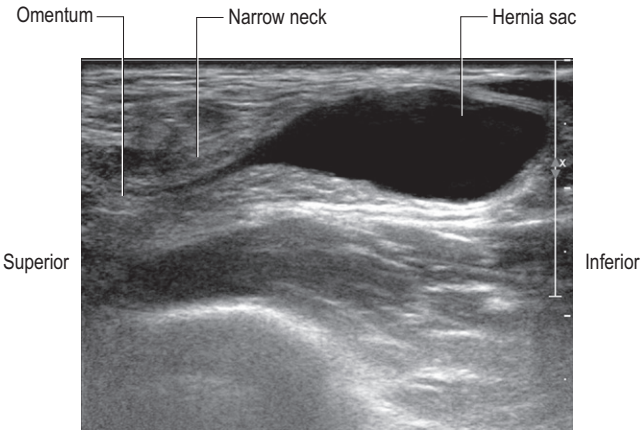

Figure 41.11 Longitudinal scan of the femoral hernia sac with narrow neck. Omentum protrudes through the neck on dynamic imaging.

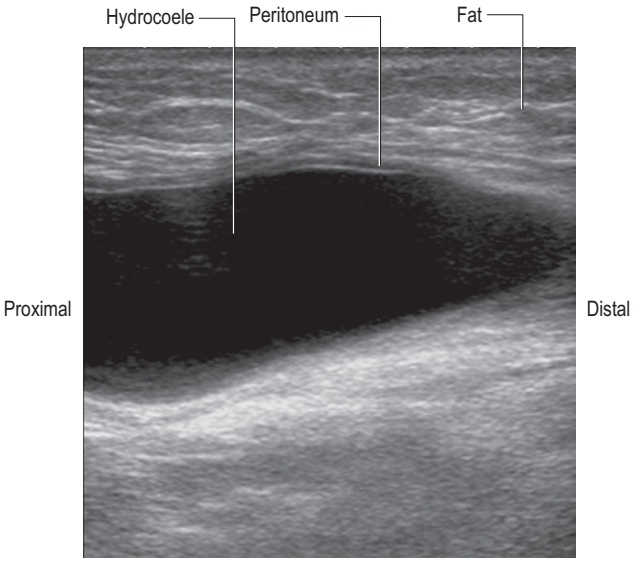

Figure 41.10 Hydrocele in the inguinal canal.

of the transducer on straining. It extends into the superficial ring (Fig. 41.12).

It is possible for both direct and indirect types of hernia to be present simultaneously and so careful scanning of both the deep and superficial rings is required to ensure the optimum surgical approach.

Femoral hernia

Femoral hernias account for 20% of hernias in women and 5% of hernias in men. The femoral canal is the most medial component of the femoral sheath. It extends from the femoral ring to the saphenous opening below. It contains fat, lymph vessels and lymph nodes (Fig. 41.13). Anteriorly lies the inguinal ligament with the ileopectineal ligament, pubic bone and pectineus muscle lying posteriorly. The lacunar ligament lies medially and the common femoral vein forms the lateral boundary of the canal.

The sonographer should identify the femoral canal between the long saphenous vein inferiorly and the inguinal ligament superoanteriorly. The common femoral vein is lateral. The cough impulse due to a hernia generally shows a narrow neck both transversely and longitudinally (Fig. 41.11). This and the reducible movement clearly defines it from a simple fatty bulge on straining. It should

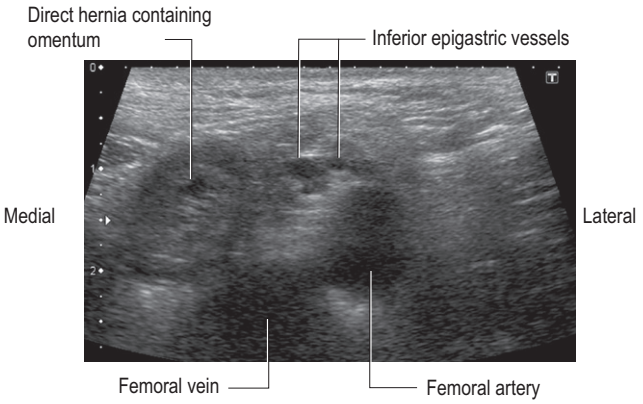

Figure 41.12 Transverse scan, left, inguinal canal direct hernia.

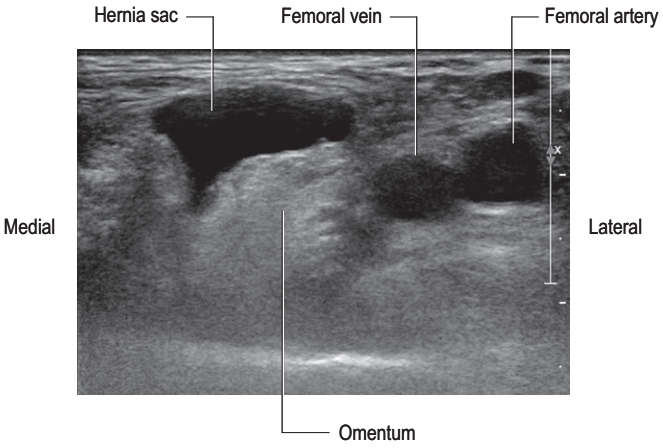

Figure 41.13 Transverse scan, left, femoral hernia.

be differentiated from a direct inguinal hernia by its relation to the inguinal ligament and pubic tubercle (Fig. 41.13). Other lumps in this area to be differentiated from a femoral hernia are: a saphenous varix, lymph nodes, a lipoma, an aneurysm or pseudo-aneurysm and a hydrocele.

Umbilical and para-umbilical hernia

An umbilical hernia extends through the umbilicus centrally whilst the para-umbilical hernia is eccentric, usually above the umbilicus but occasionally below. The hernia defect extends through the linea alba in the midline but the patient often notices a more lateral lump depending on its size. The cough impulse is often satisfactory to demonstrate movement but otherwise asking the patient to distend the abdomen or raising the head off the couch may be necessary to elicit movement in the hernia.

Incisional hernia

This is seen when there is disruption of the deeper layers of the abdominal wall after an incision. Postoperative collections may suggest some dehiscence and ultrasound is helpful in the exclusion of a hernia. It may often occur in the obese or those with chronic cough or straining. The scar is best scanned through its transverse plane to identify complications such as fluid, stitches or hernia. Dynamic ultrasound rapidly demonstrates the hernia extending into the scar (cough impulse).

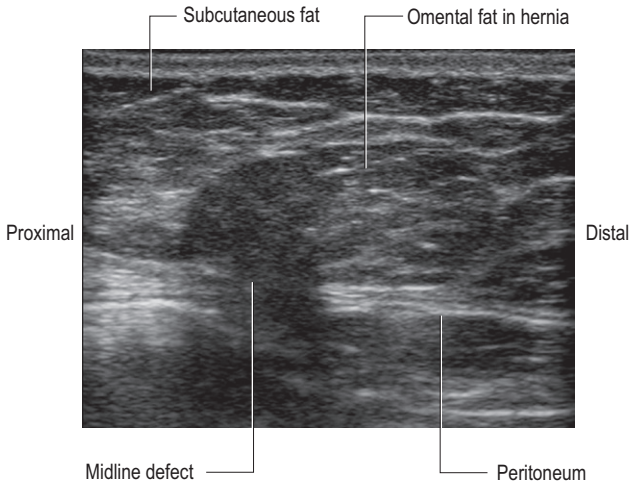

Figure 41.14 Longitudinal scan of an epigastric hernia containing omental fat.

Epigastric hernia

An epigastric hernia occurs when there is a defect in the linea alba anywhere from the xiphisternum to the umbilicus. The defect is often small and may only be appreciated with careful scanning with good dynamic imaging (Fig. 41.14). It typically contains a small amount of the preperitoneal fat but can be large enough to contain bowel. They are often best appreciated in the transverse plane. Care should be taken to delineate multiple hernias as failure to appreciate these may result in apparent early surgical failure or re-occurrence. Documentation of the defect size and position is useful information for the surgeon, allowing efficient location of the hernia at surgery and preoperative consideration of the type of repair. These hernias may coexist with divarication of the recti (Fig. 41.15).

Spigelian hernia

This hernia extends through the spigelian fascia, between the transversalis and the rectus abdominis muscles.[27] It is typically at the level of the umbilicus or inferior to it. It is usually best seen on ultrasound during a straining manoeuvre and usually contains bowel. Larger ones protrude laterally over the internal oblique muscle. The sonographer should scan both sides of the abdomen for comparison so as not to overcall the normal anatomical bulging in this area. Incarceration is a greater risk in this type of hernia but the ultrasound transducer can often be used to reduce the hernia.[28]

Lumbar hernia

Lumbar hernias typically extend through the inferior lumbar triangle, which is bounded inferiorly by the iliac crest, laterally by the external oblique muscle and medially by latissimus dorsi. Incisional lumbar hernias develop typically after renal surgical interventions. The rare superior lumbar triangle types occur between the twelfth rib, sacrospinous muscle and internal oblique muscles.

The rare obturator hernia which extends through the obturator canal is more likely to be diagnosed on CT. It is covered by pectineus and so is not readily seen on ultrasound but may be seen with a lower-frequency probe.

Sportsman's hernia

This is not a true hernia and may be a difficult ultrasound and clinical diagnosis.[29] They occur in sports enthusiasts, more frequently in males who perform pivoting, kicking and turning such as soccer

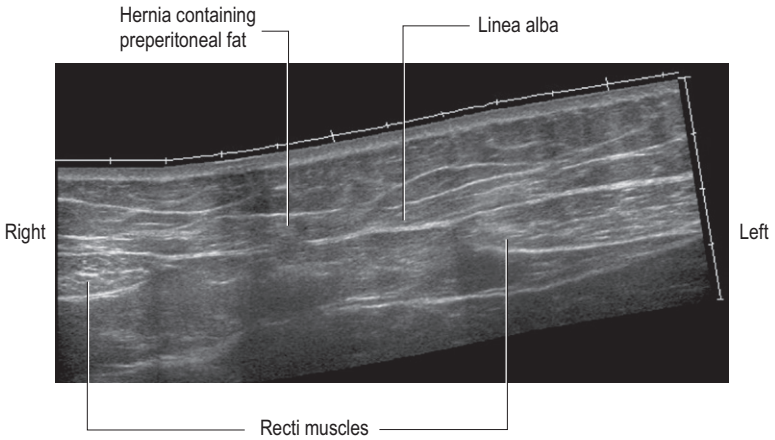

Figure 41.15 Transverse panoramic scan showing divarication of the rectus muscles with small midline hernia.

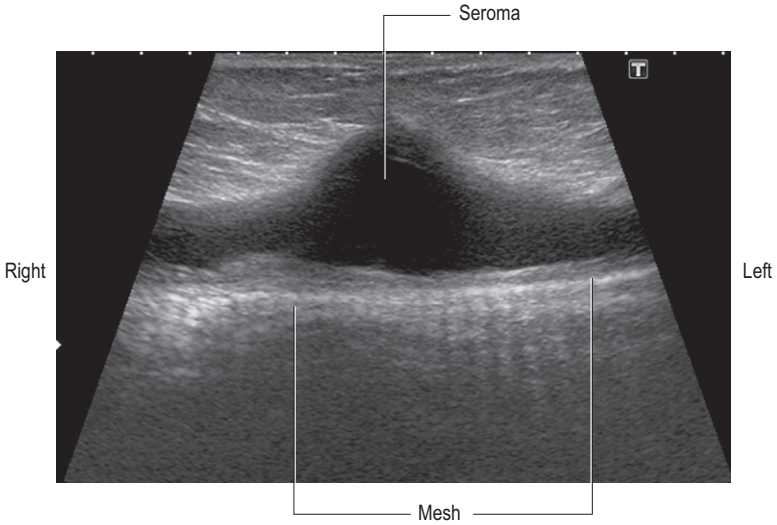

Figure 41.16 Postoperative hernia. Transverse scan of anterior abdominal wall showing mesh with overlying seroma.

players or in ice hockey.[30] It is likely to be caused by weakening of the posterior wall of the inguinal canal from excessive or repetitive shearing forces during poorly balanced hip adduction and abdominal wall muscle activity. Clinical and imaging diagnosis is difficult; management of this condition may be conservative or surgical.[31] Ultrasound findings of local posterior wall bulging on straining adjacent to the superficial ring can be normal as well as being seen in the sportsman's hernia. A tender focal bulge during straining, particularly if it is asymmetrical, is a little more specific for this diagnosis but more studies are needed.[30]

The postoperative hernia

Mesh repairs are most likely to be performed either using a large sheet or a small plug. Plugs can be difficult to visualise, usually seen as an irregular area of increased echogenicity with acoustic shadowing over the deep or superficial ring. A mesh sheet is well visualised as a linear sheet of hyperechoic foci with acoustic shadowing. Ultrasound scans are performed in the postoperative period for assessment of pain or of a recurrent lump in order to differentiate between a recurrent hernia or other mesh complications. Recurrent hernias appear at the margin where the mesh has become detached; in the inguinal canal this is most commonly along its inferomedial border.

Mesh complications include infection, seromas, haematomas, detachment or fibrosis causing pain (Fig. 41.16). Seromas are not uncommon and are usually best left to resolve. Fibrosis is shown after several months as marked areas of reduced echogenicity around the mesh, often with acoustic shadowing. Transducer pressure reproduces the symptoms of pain/tenderness. Detachment of the mesh is seen when the normally flat mesh edge is curled over at one or more borders; this is more apparent in the presence of a seroma (Fig. 41.17). An enterocutaneous fistula is a rare complication of hernia surgery.[32]

Hernias can also occur around stomal sites.[33] Ultrasound may be best performed with the stomal bag removed and direct scanning using a transducer cover. Alternatively an impermeable barrier, such as cling film, over the stoma can be used,

Masses and cysts affecting the anterior abdominal wall and groin

Haematomas and infective lesions of the abdominal wall have already been discussed. The commonest masses seen are lipomas, hydroceles and varices. The lipoma can occur anywhere in the anterior abdominal wall, but most commonly in the subcutaneous compartment. Lipomas of the cord also occur in the inguinal canal[34] and have the typical ultrasound appearances of a lipoma, with hypoechoic septated fat (Fig. 41.18). The lipoma is soft and mobile in the canal and straining can make it move down the canal with retraction on relaxation. However, it does not reduce through the deep or superficial ring, differentiating it from a hernia. Lipomas of the cord can undergo sarcomatous change, but this is very rare.

Varices may arise from the long saphenous vein. It is compressible and shows flow on colour Doppler unless it is thrombosed. A hydrocele is a collection of fluid in the inguinal canal which can

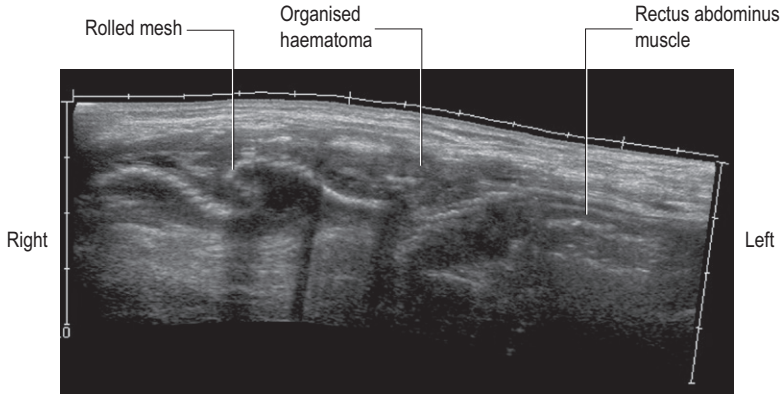

Figure 41.17 Postoperative hernia. Transverse panoramic scan of detached mesh in anterior abdominal wall.

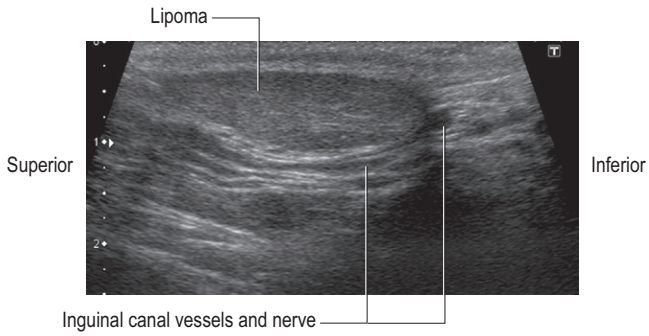

Figure 41.18 Lipoma of the cord.

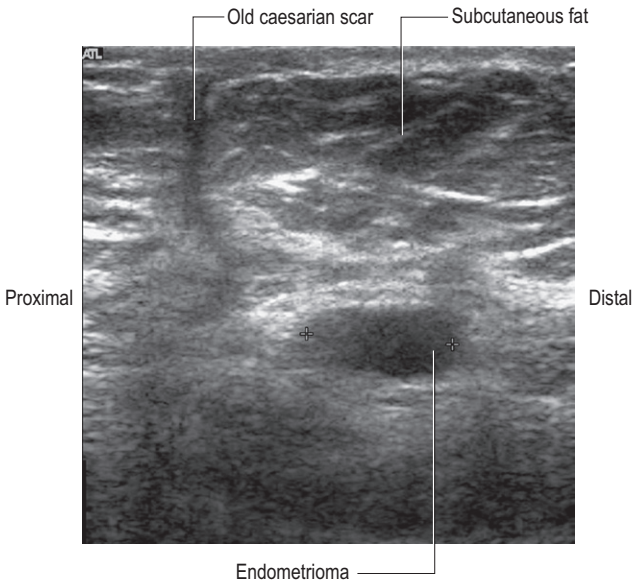

Figure 41.19 Endometrioma. Longitudinal scan of lower anterior abdominal wall showing an ovoid hypoechoic mass due to an endometrioma.

connect with the scrotum. In women the hydrocele forms in the canal of Nuck around the round ligament.[35] It is differentiated from a hernia sac by a negative cough impulse and the lack of extension through the deep ring.

Most solid lesions are hypoechoic. A hard, heterogeneous and irregular mass with abnormal vessels seen on colour Doppler are features of malignancy. A metastasis may appear in the umbilicus or para-umbilical region and is sometimes known as Sister Joseph's nodule. This is usually secondary to tumours of the stomach, colon or an ovary. Metastases from breast tumours may also occur.[36] Primary tumours are rare but show similar features.[37] They are most commonly seen in the groin or around the rectus abdominis muscle. A sarcoma is typically ill defined, heterogeneous, solid, with abnormal vasculature on Doppler, but these features are not specific. Liposarcomas are the most common primary tumour but synovial sarcomas, leiomyosarcomas, malignant fibrous histocytomas, fibrosarcomas and undifferentiated sarcomas have all been described.[17,37] Abdominal wall fibromatosis can appear similarly heterogeneous and ill defined but differs from malignancy in that few or no vessels are seen on Doppler. The hypoechogenicity is marked and may cause acoustic shadowing. These lesions are very hard and non-deformable on probe pressure.

An endometrioma is also a firm or hard hypoechoic mass but usually better defined than malignant tumours. It is often Doppler negative. An endometrioma may be very tender to palpation (Fig. 41.19). A history of pain or lump varying in size with the menstrual cycle may be obtained.[38–40]

Desmoid tumours are usually seen in or around the rectus abdominis muscle but otherwise they show the non-specific ultrasound features of a well-defined solid mass (Fig. 41.20). Epidermoid cysts are described as a hypoechoic mass with internal echogenicity from keratin materials.[37] Other benign tumours include leiomyomas,[41] dermoid cysts[42] and lymphangiomas.[43]

Masses and cysts affecting the anterior abdominal wall and groin

- Haematoma
- Endometrioma
- Abscess
- Stitch granuloma
- Undescended testis
- Cystic lesions
  - Cyst in the canal of Nuck
  - Hydrocele
  - Varix
  - Aneurysm/pseudo-aneurysm
  - Urachal cyst
- Benign tumours
  - Lipoma
  - Desmoid
  - Fibromatosis
- Malignant tumours
  - Sarcoma
  - Metastases

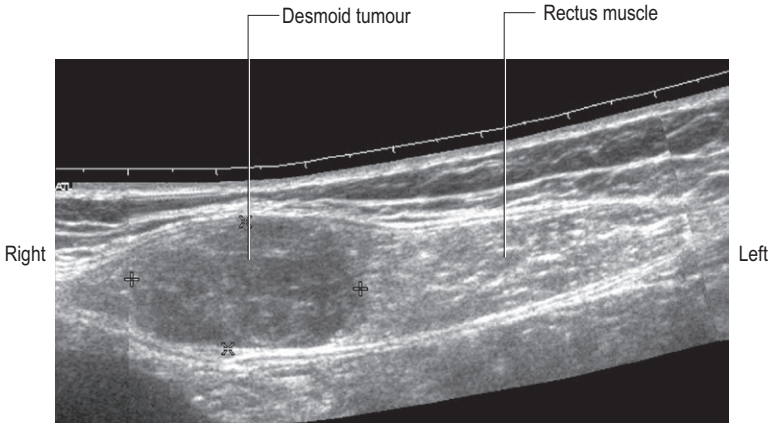

Figure 41.20 Desmoid tumour. Transverse panoramic scan of a rectus abdominis mass due to a desmoid tumour.

In cryptorchidism an undescended testicle cannot be palpated in the scrotum. Ultrasound shows the affected testis as an ovoid hypoechoic solid lesion often in the inguinal canal, usually smaller than a normal testicle. There is a slightly increased incidence of testicular neoplasia, which may be seen as a heterogeneous echo pattern with abnormal vessels on colour Doppler.[44] In some cases the testis may be highly retractile and ascend up into the groin towards the inguinal canal.

Urachal cysts are rare and are seen between the umbilicus and bladder. They are usually anechoic but may contain echoes.[45,46]

A pseudo-aneurysm is a localised fluid-filled collection containing swirling blood on real-time or colour Doppler imaging. It is related to recent vascular access.[3] True aneurysms of the common femoral artery may also be seen in the groin.

Nerve entrapment

Nerve entrapment can cause groin pain.[47] Single or multiple small tears in the external oblique aponeurosis adjacent to the ilio-hypogastric and ilio-inguinal nerves have been described as a cause of referred pain to the groin. These tears are usually not identified on ultrasound but the nerves can be seen and finger point palpation during scanning may elicit the trigger point pain. Occasionally the nerve may show localised oedema or thickening, confirming a tunnel compression. An ultrasound-guided nerve block can be diagnostic.

PERITONEUM

Anatomy

The abdominal cavity is lined by a thin peritoneal membrane which lies deep to the transversalis fascia on the anterior abdominal wall and anterior to the retroperitoneal fascia on the posterior wall. The elongation, convolutions, rotations and glandular outpouchings from the embryological gastrointestinal tract result in the many loops of bowel and digestive glands that project into the abdominal cavity. All are covered by the peritoneal membrane, which they have evaginated. Where the evagination is most marked, organs such as bowel are suspended from the posterior abdominal wall by a mesentery. Where there is less evagination, organs are directly attached to the abdominal wall, an example being the bare area of the liver. Some gastrointestinal structures remain retroperitoneal, such as the pancreas and the ascending and descending colon (see below). Knowledge of the anatomy of the peritoneal cavity, its mesenteries and ligaments is important for the proper understanding of the development and spread of pathology within the peritoneal cavity.[48]

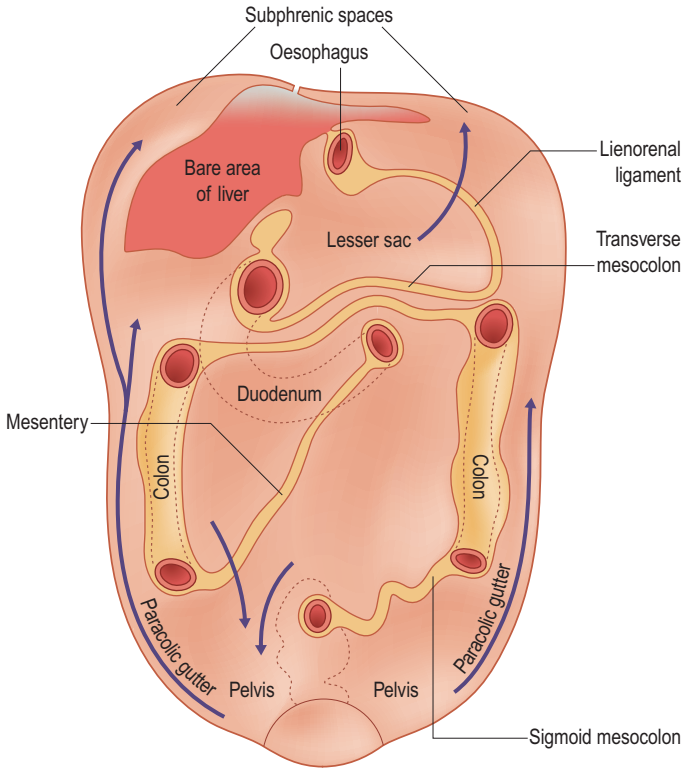

Figure 41.21 The peritoneal cavity. The pathways along which infections tend to track are indicated in this diagram of the peritoneum. The commonest origins for infections are the pelvis and from the lower bowel and appendix.

The peritoneal cavity is a potential space and the peritoneum is so thin that it can only be demonstrated on ultrasound in the presence of ascites, which allows the identification of many of the mesenteric and ligamentary layers and of the potential spaces.[2] The peritoneal reflections and mesenteric attachments determine the routes of spread of intraperitoneal fluid and serve as boundaries for its compartments (Fig. 41.21). The transverse mesocolon, the mesentery of the transverse colon, divides the abdominal cavity into supra- and infra-mesocolic compartments. The root of the small bowel mesentery further divides the lower compartment into two unequal infra-mesocolic spaces.[49] Although the transverse

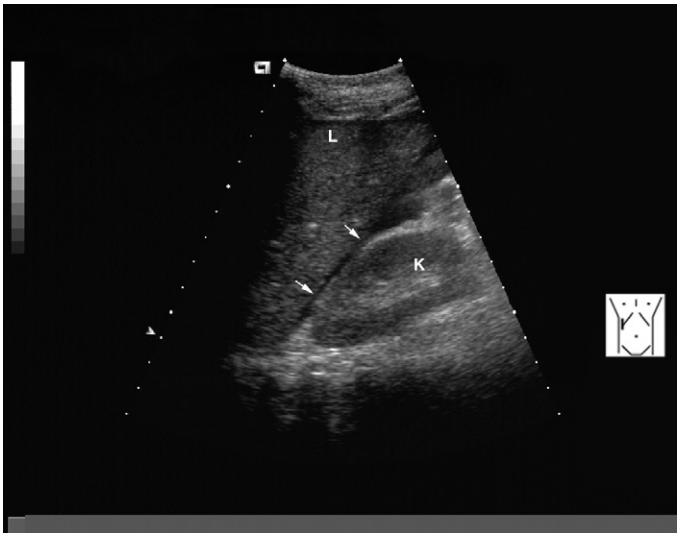

Figure 41.22 Ascites. Fluid has collected in Morison's pouch (arrows). K, kidney; L, liver.

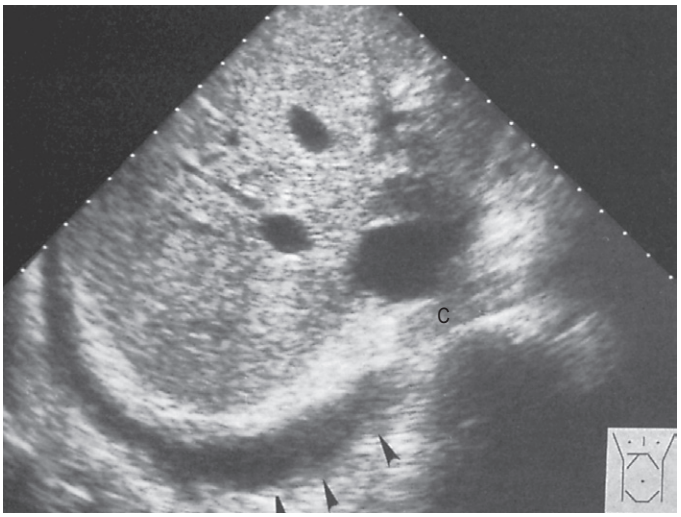

Figure 41.24 Pleural fluid. Extension of pleural fluid (arrowheads) posterior and medial to the bare area of the liver, displacing the crus (C) of the diaphragm to the right and the inferior vena cava anteriorly.

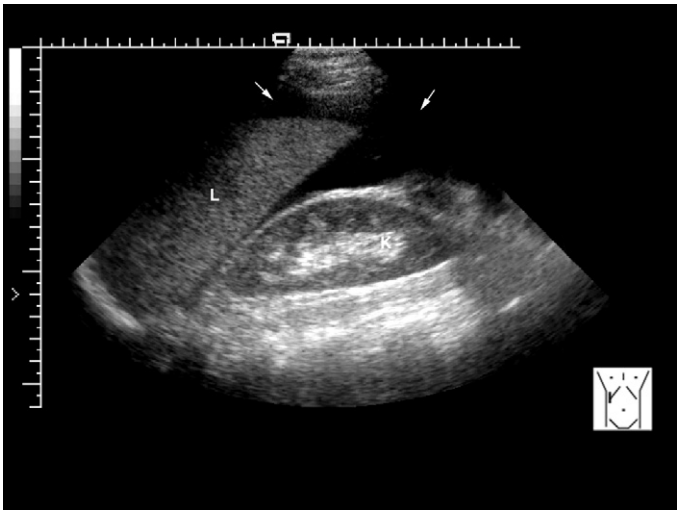

Figure 41.23 Gross ascites. Fluid is demonstrated in Morison's pouch and widely in the peritoneum (arrows). K, kidney; L, liver.

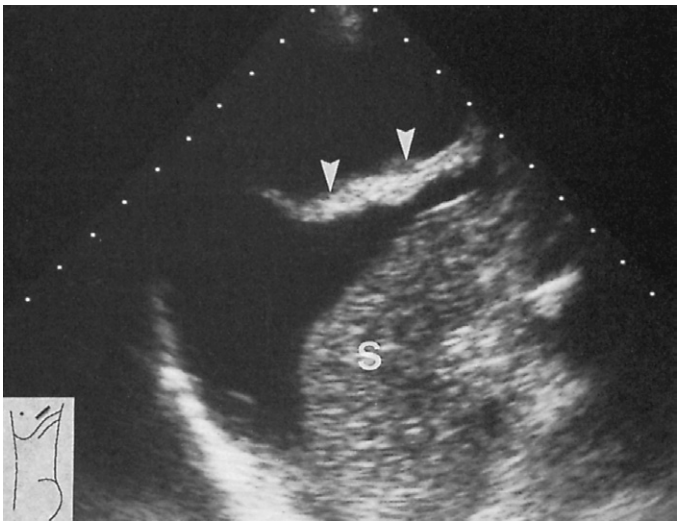

Figure 41.25 The phrenolienal ligament is seen as a thick, highly reflective band (arrowheads). S, spleen.

mesocolon may occasionally be demonstrated on ultrasound, neither it nor the root of the small bowel mesentery is usually seen, even in the presence of ascites, largely because of their situation posterior to multiple bowel loops, which usually contain some gas.

The supra- and infra-mesocolic spaces communicate via the paracolic gutters on the posterior abdominal wall, bounded medially by the ascending and descending colons. The right paracolic gutter is continuous with the right subhepatic space and its posterior extension, the hepatorenal fossa (Morison's pouch) and, further superiorly, the right subphrenic space (Figs 41.22 and 41.23). The posterior aspect of a portion of the right lobe of the liver is in direct relationship with the diaphragm without intervening peritoneum (the bare area). If fluid is displayed posterior to the liver in this region it must be located within the pleural space; this sign may therefore help to differentiate pleural from peritoneal fluid (Fig. 41.24).[50] The falciform ligament separates the right and left subphrenic and subhepatic spaces. It appears as a thin strip between two fluid-containing areas. On the left the phrenocolic ligament fixes the splenic flexure of the colon to the left hemidiaphragm, thereby partially obstructing communication between the left paracolic gutter and the left perisplenic space. This ligament may be identified above the upper pole of the spleen as a linear strip (Fig. 41.25).

The lesser omentum represents the mesentery of the stomach and, with the gastrocolic, splenogastric and splenopancreatic ligaments, delineates the lesser sac. Of these, only the lesser omentum is regularly visualised (in the presence of ascites), but its free edge is identified by the position of the portal vein and the common bile duct (Fig. 41.26). The separation of fluid layers between the lesser sac and the rest of the peritoneal cavity has been named the 'butterfly wings' sign by Weill[51] (Fig. 41.27). However, the compartmentalisation of the lesser sac is so effective that pathologies arising elsewhere in the peritoneal cavity rarely involve it, and vice versa, with the exception of simple ascites, which fills every part of the peritoneal cavity.

In the lower abdomen both infra-mesocolic spaces communicate with the pelvis, but the right is directly continuous with the pelvic cavity. In general, therefore, intraperitoneal spread occurs more commonly from pathology on the right than on the left side of the

pelvis. The peritoneum is reflected over the dome of the bladder, the anterior and posterior surface of the uterus and the superior portion of the rectum (Fig. 41.28A). The peritoneal reflection over the fallopian tubes, the broad ligament, may be demonstrated in the presence of ascites (Fig. 41.28B). In men there is a single potential space for fluid collection, the rectovesical pouch, whereas in women there are two, the uterovesical pouch and the pouch of Douglas between the uterus and the rectum.

These anatomical features determine the route of spread of abdominal fluid, infections and tumours. Spread from the pelvis along the right paracolic gutter to the perihepatic spaces is the most common route, but anatomical variations, incompleteness of ligamentous obstacles and the presence of postoperative or postinfective adhesions may alter the pattern of spread.

Scanning technique

Ultrasound examination of the peritoneal cavity requires a meticulous and flexible approach.[52,53] Pathology affecting the peritoneal cavity may be inflammatory or neoplastic, but the examination is aimed primarily at the detection of intra-abdominal fluid. If fluid collections are to be localised accurately, the anatomical basis of the spread within the abdomen needs to be fully understood, ultrasonic windows need to be appreciated, and the limitations of the ultrasound technique must be accepted.[54,55] Free fluid within the abdomen is easily detected: it collects in the most dependent portions, and in the supine position this is Morison's pouch (Fig. 41.29) or the pouch of Douglas or rectovesical pouch (Fig. 41.30). The detection of loculated fluid, particularly intra-abdominal abscesses, however, requires an approach designed to examine the likely sites of collection. Thus the right subphrenic and perihepatic spaces should be examined with the patient in the supine and left posterior oblique positions using the liver as an acoustic window, including scanning intercostally to obtain access to the right hemidiaphragm. A similar approach is used for the left upper quadrant and perisplenic regions, with the patient in the right posterior oblique and supine positions. The paracolic gutters are examined by placing the transducer on the flanks, and the pelvis can be imaged either using a filled urinary bladder as an acoustic window or transvaginally.

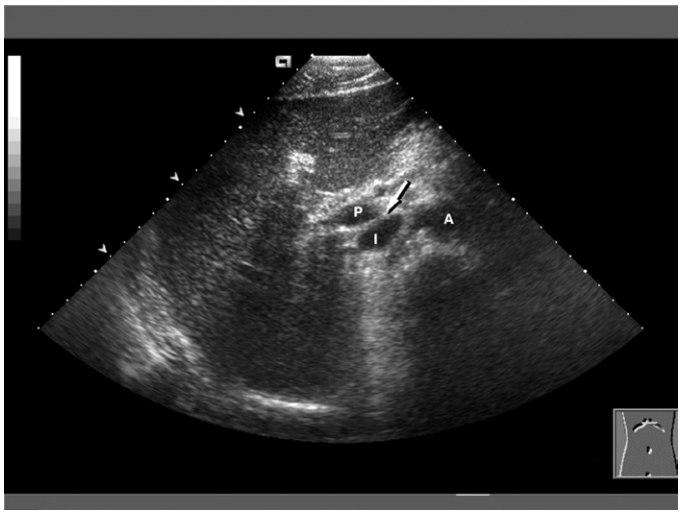

Figure 41.26 The free edge of the lesser sac. The opening to the lesser sac (arrow) lies between the portal vein and the inferior vena cava. P, portal vein; I, inferior vena cava; A, aorta.

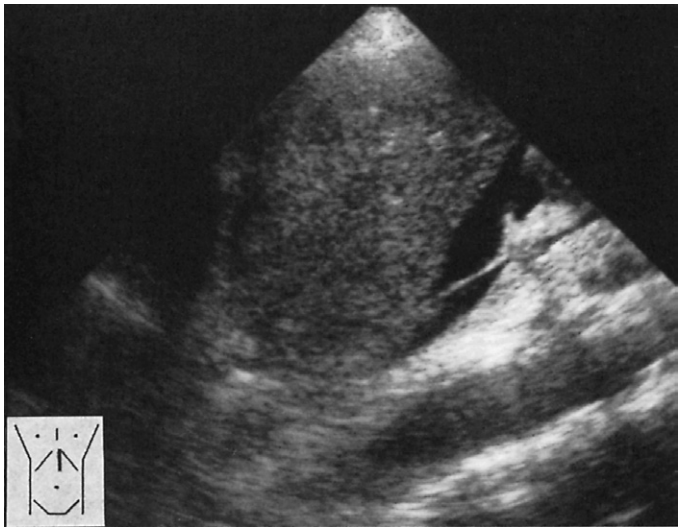

Figure 41.27 Fluid in the lesser sac separated from fluid elsewhere in the peritoneum by the lesser omentum. This appearance has been described as 'butterfly wings'.

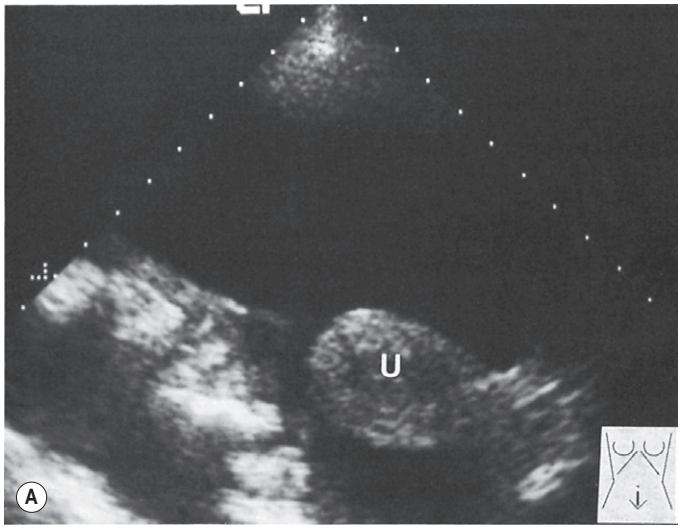

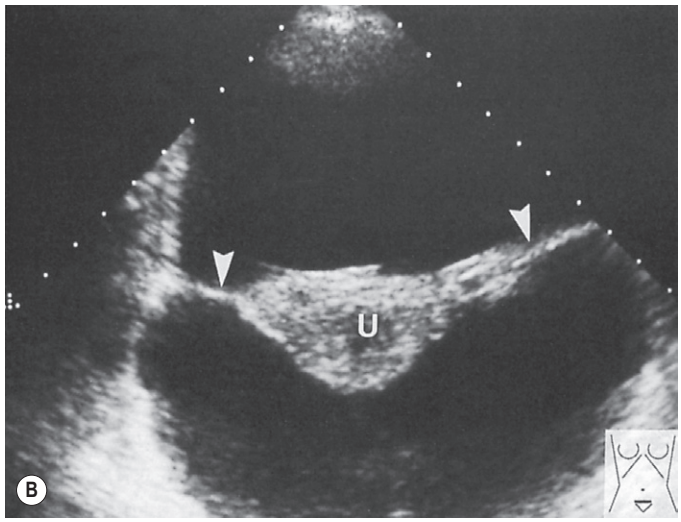

Figure 41.28 Pelvic ascites. A: In longitudinal section the ascites surrounds the fundus of the uterus (U). **B:** In transverse section the broad ligaments (arrowheads) are clearly shown.

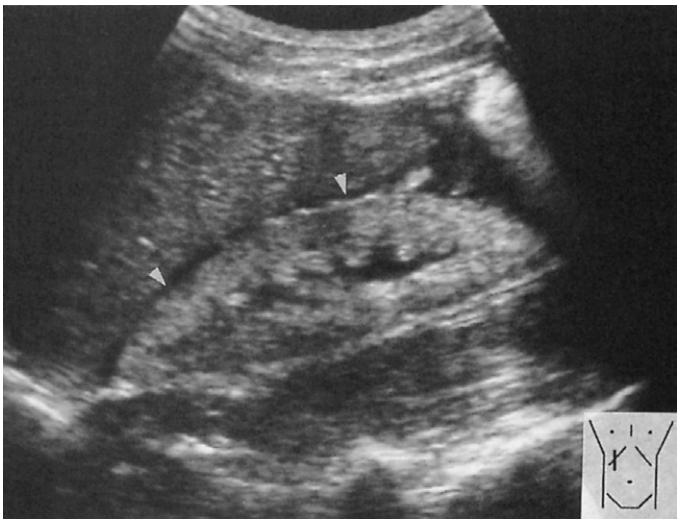

Figure 41.29 Fluid in Morison's pouch. A small amount of free fluid is present in Morison's pouch (arrowheads) in this patient with renal failure secondary to glomerulonephritis. Note the highly reflective kidney.

Fluid collections loculated in the mid-abdomen (interloop collections) are the most difficult to demonstrate with ultrasound as they are easily confused with bowel loops or obscured by the gas they contain.

Ascites

Ultrasound is an extremely sensitive technique for the detection of free fluid within the peritoneum: although as little as 10 mL of fluid has been shown to be detectable in the pouch of Douglas and Morison's pouch in experimental studies,[52,56] it is probable that several hundred millilitres must be present for routine clinical detection. Typically ascitic fluid is echo-free, moves within the peritoneal cavity with change in patient position or compression by the transducer, and allows gas-containing bowel loops to float within it (Fig. 41.31). The fluid tends to collect in the most dependent positions. Rotating the patient to a right decubitus position facilitates the demonstration of small amounts of fluid in Morison's pouch. However, if only a very small quantity of ascites is present it may spread across the surface of a large organ, producing a thin film over the lower or lateral border of the liver (Fig. 41.32).

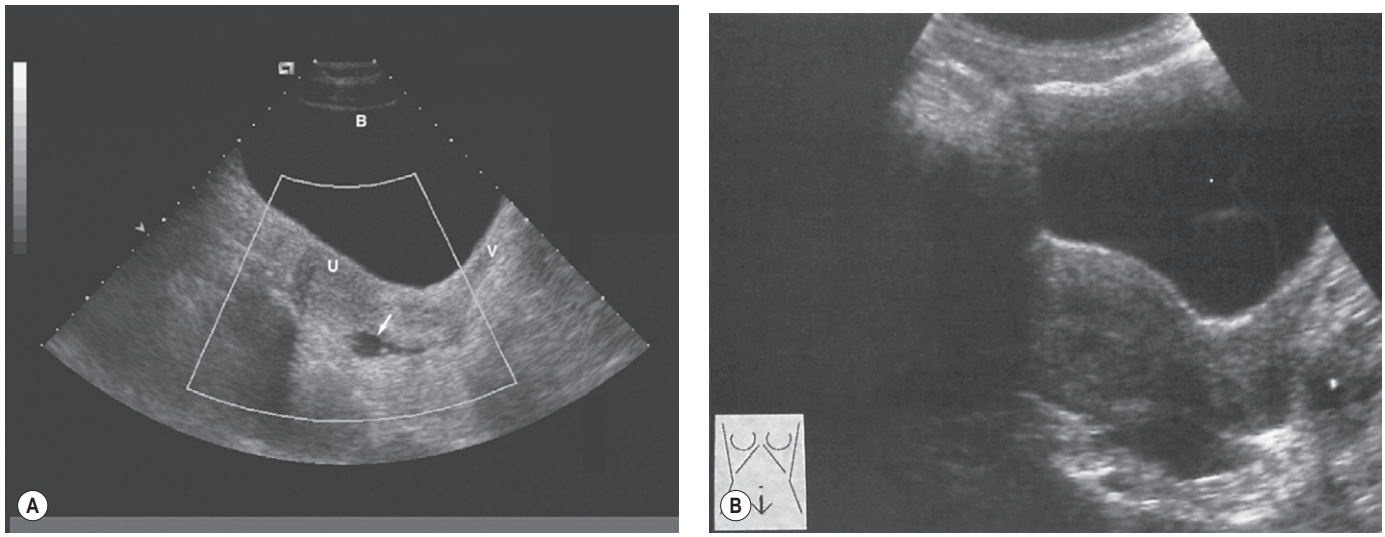

Figure 41.30 Fluid in the pouch of Douglas. A trace of free fluid (arrow) lies behind the body and cervix of the uterus. Its sharp inferior limit indicates that it is peritoneal fluid rather than a collection, which would have rounded margins. It contains a small amount of debris. B, bladder; U, uterus; V, vagina.

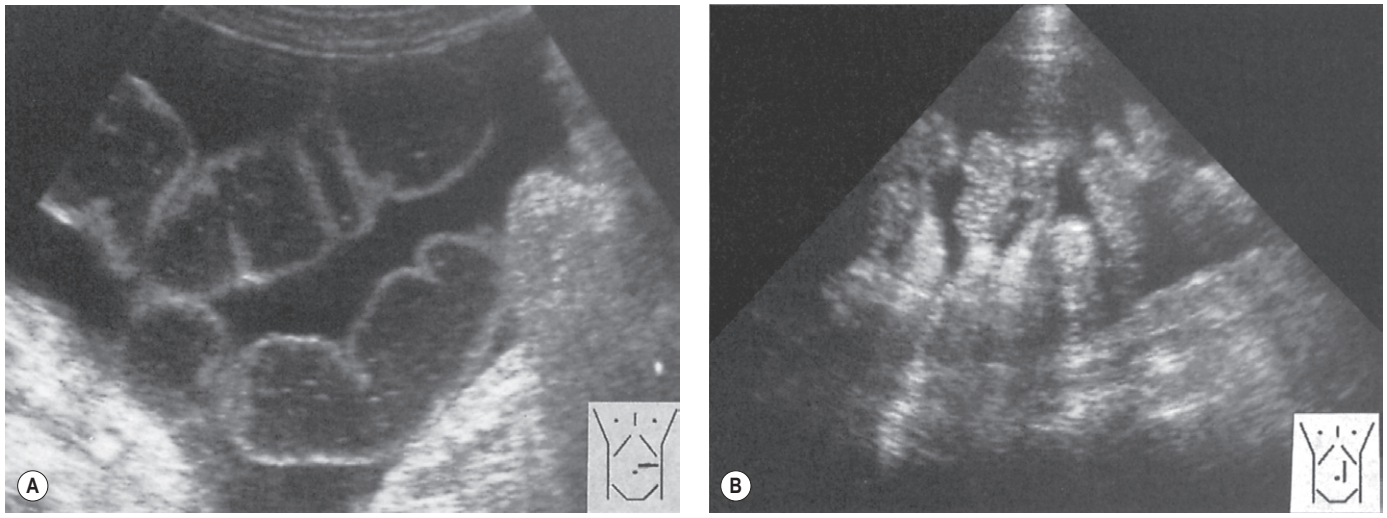

Figure 41.31 Bowel loops in ascites. A: Scan of the mid-abdomen in a patient with ascites, showing multiple dilated loops of floating bowel. **B:** Scan in the mid-abdomen showing loops of bowel in ascites. The mesenteric attachments are well seen in this case.

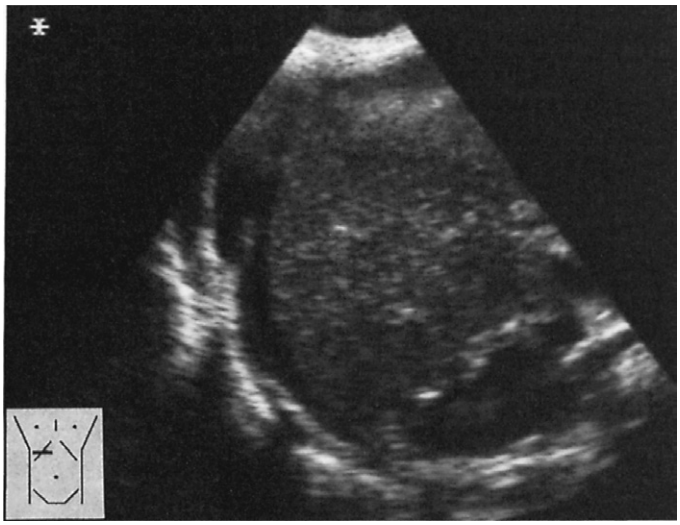

Figure 41.32 Subtle ascites. A thin layer of ascitic fluid is shown over the surface of the liver.

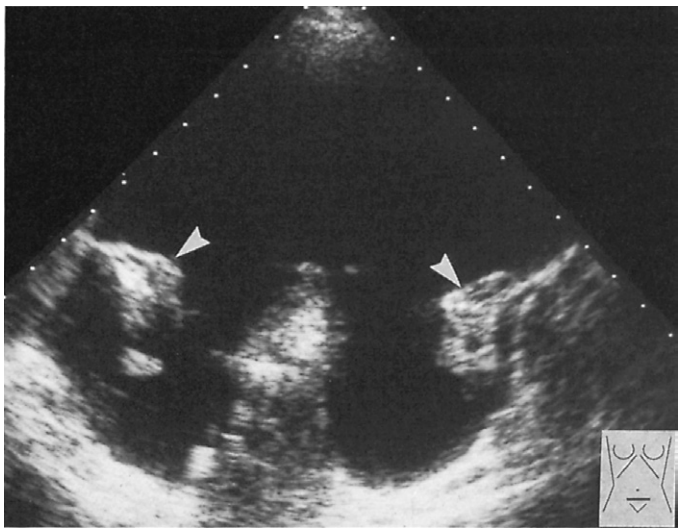

Figure 41.33 Ovaries outlined by ascites. The normal ovaries are shown situated on the lateral pelvic walls (arrowheads), outlined by ascitic fluid.

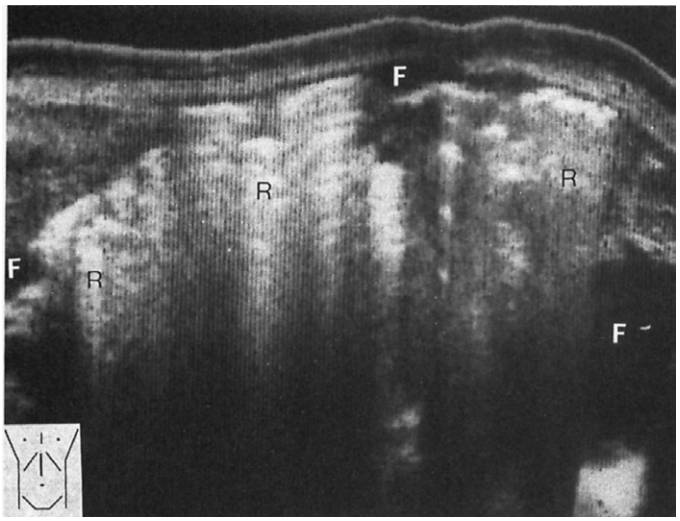

Figure 41.34 Central abdominal bowel loops in ascites. The retroperitoneal structures are obscured by multiple loops of gas-containing bowel that float to the anterior abdominal wall and produce distal reverberation artefacts (R). Loculated ascitic fluid is noted (F).

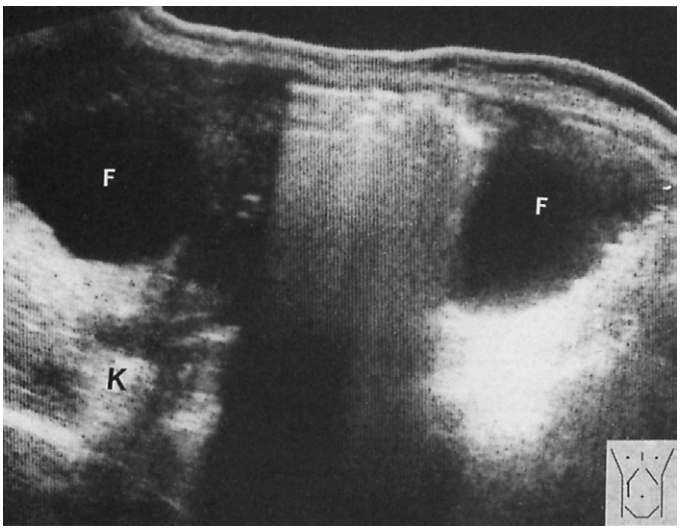

Figure 41.35 Loculated ascites. Scan through the right abdomen showing partially loculated ascitic fluid (F). The loculated fluid in the right upper quadrant produces acoustic enhancement, obscuring the margins of the right kidney (K).

Careful scanning is required to elicit the subtle signs of small amounts of fluid.

The presence of ascites can improve the demonstration of many intra-abdominal structures (such as the peritoneal reflections and ligaments), though other features may be less well seen.[49] Whereas the female pelvic organs may be clearly outlined by ascitic fluid (Figs 41.28 and 41.33), the para-aortic regions and other retroperitoneal structures may become obscured by gas-containing bowel that floats towards the midline (Fig. 41.34). In some cases scanning through the flanks or changing the patient's position improves visualisation of retroperitoneal structures, but in many cases the patient must be re-examined after paracentesis for an adequate study. Furthermore, ascites alters the appearances of some intra-abdominal organs on ultrasound. The right kidney may appear to be abnormally reflective as a result of increased through-transmission of ultrasound through non-attenuating fluid (Fig. 41.35): care must be taken not to confuse this artefactual appearance with a true increase in reflectivity caused by diffuse parenchymal renal disease.[57] Tense ascites pushes bowel to the middle of the abdomen, giving a classic appearance that helps the differentiation between ascites and a large cystic tumour (Figs 41.34 and 41.35).

Thickening of the gallbladder wall is a leading feature of acute cholecystitis (see Chapter 14), but thickening also occurs in a number of other conditions, including ascites.[58] The cause here is still a matter of debate: it may result from hypoalbuminaemia[59] or represent an artefact arising from the layer of ascites adjacent to the gallbladder, although a study in patients on peritoneal dialysis in situ did not substantiate this.[60] In patients with malignant ascites the gallbladder wall is only thickened when the serum albumin is decreased (Fig. 41.36).[61]

Occasionally it is difficult to differentiate between pleural and peritoneal fluid, especially when it is loculated. Features implying intrathoracic fluid are lateral displacement of the right crus of the diaphragm, anterior displacement of the inferior vena cava, and fluid immediately superior to the bare area of the liver (Fig. 41.24).[50]

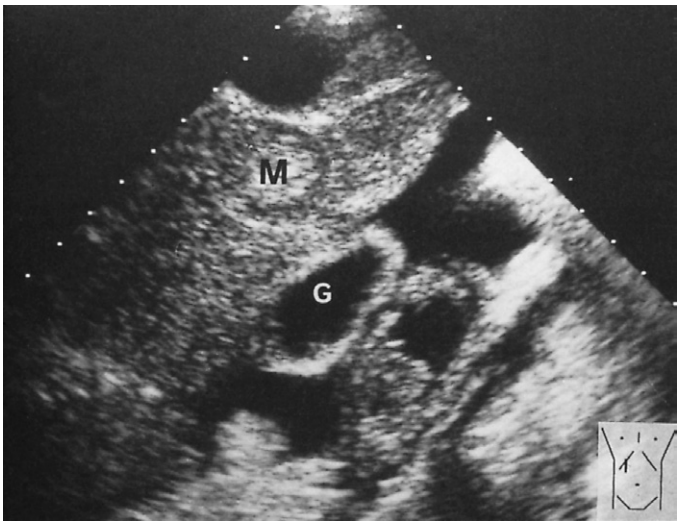

Figure 41.36 Thickened gallbladder wall in ascites. There is free fluid in the right upper quadrant in this scan. There is a metastasis in the liver (M) and thickening of the wall of the gallbladder (G).

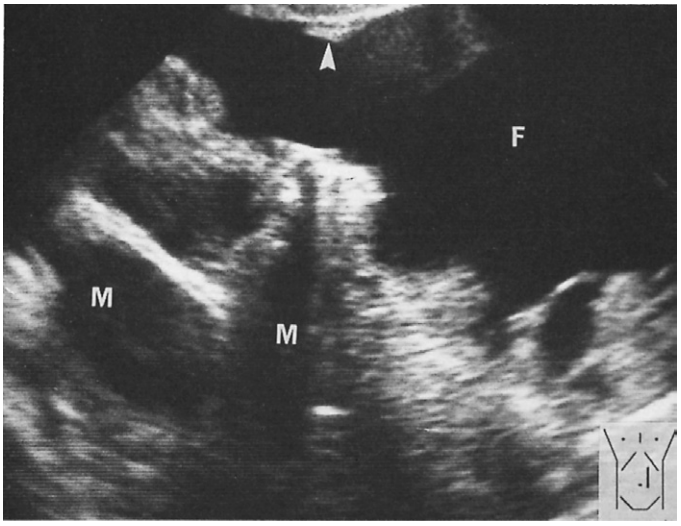

Figure 41.38 Malignant ascites. Ascitic fluid is demonstrated (F) but the bowel loops are matted against the posterior abdominal wall by the thickened mesentery (M). There is a small peritoneal deposit (arrowhead).

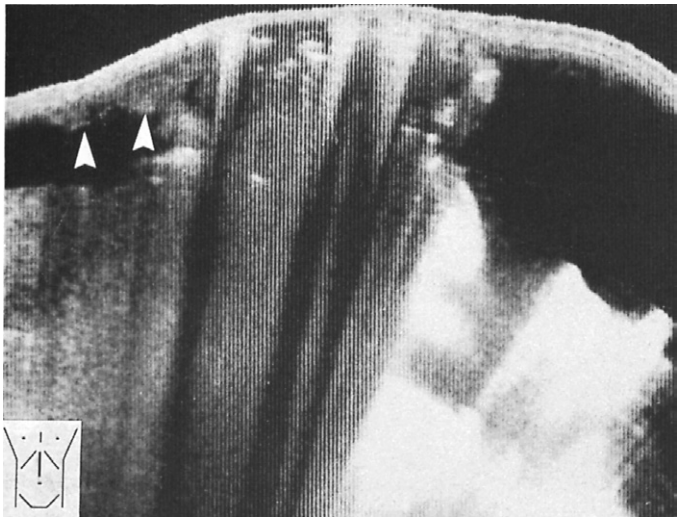

Figure 41.37 Malignant ascites. There is loculated ascitic fluid and some tethering of bowel to the anterior abdominal wall; other gas-containing loops do not float freely. Peritoneal deposits are present (arrowheads).

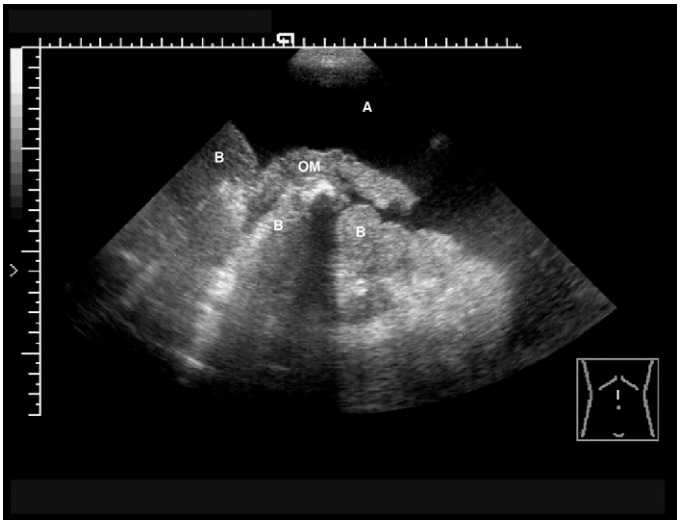

Figure 41.39 Thickened omentum. The thickened omentum is surrounded by ascites in this patient with peritoneal tumour spread. The bowel loops are attached posteriorly. A, ascites; B, bowel loops; OM, omentum.

If the layers of the diaphragmatic muscle can be demonstrated, the level of the fluid can be ascertained.

In uncomplicated ascites, the fluid is freely mobile within the peritoneal cavity, allowing gas-containing bowel loops to float to the anterior abdominal wall. In complicated ascites (either infected or malignant) the fluid may become loculated and the bowel tethered to the abdominal wall (Fig. 41.37), with a thickened mesentery (Figs 41.38 and 41.39) and diminished or abolished peristalsis.[62] Thickening of the mesentery may follow malignant infiltration of the mesenteric root, and peritoneal seedlings can sometimes be demonstrated (Figs 41.37 and 41.38), though usually they are too small to be resolved by ultrasound, even when high-resolution transducers are used.

Uncomplicated ascitic fluid is echo-free and produces increased through-transmission of sound. In malignant or infected ascites the fluid frequently contains blood or pus, which produces mobile echoes (Fig. 41.40).[62] Septa within the fluid are typically seen in infection, especially tuberculosis (Fig. 41.41), but also occur in malignancy (Fig. 41.42). In the extreme form, pseudomyxomatous peritonitis, the entire cavity is filled with innumerable cystic spaces ranging from a few millimetres to several centimetres in diameter (Fig. 41.43).[63,64]

Occasionally it is possible to demonstrate the primary cause of the ascites, such as an ovarian carcinoma or metastatic disease within the liver (Fig. 41.44), thus allowing a confident diagnosis of the cause and nature of the ascitic fluid. The assessment of ancillary findings often allows differentiation of benign from malignant or complicated ascites. However, there are certain caveats. In the presence of severe hypoalbuminaemia, gallbladder wall thickening may be seen in both malignant and benign ascites. Gallbladder wall thickening and ascites are also frequently combined in severe acute hepatitis. Similarly, there may be difficulty with diagnosis when transudative ascites is associated with pre-existing bowel adhesions.

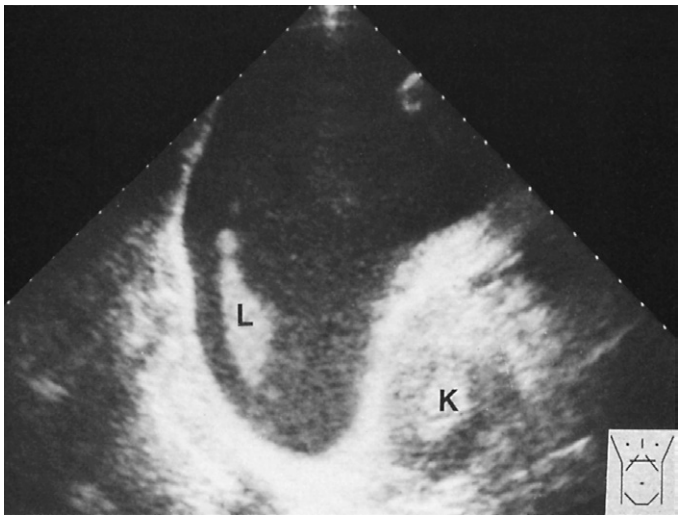

Figure 41.40 Haemorrhagic malignant ascites. The inferior margin of the right lobe of the liver (L) and the right kidney (K) are seen. However, there is extensive intraperitoneal fluid which contains multiple low-level echoes. These appearances are characteristic of haemorrhagic ascites consistent with malignancy.

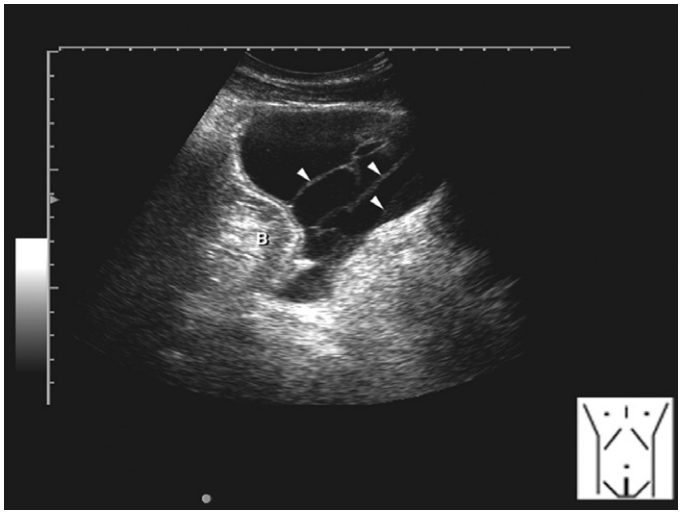

Figure 41.41 Tuberculous peritonitis. Marked stranding is present within the ascites (arrowheads). Bowel loops have become attached to the posterior abdominal wall. B, bowel.

Paracentesis

Traditionally paracentesis has been performed via the insertion of a trocar and cannula in the left lower quadrant. However, the clinical diagnosis of ascites is unreliable and, although in gross ascites fluid is almost invariably present in the left lower quadrant, this may not be the safest site for drainage, as frequently bowel loops interpose between the anterior abdominal wall and the fluid collection in this location. Ultrasound-planned or -guided paracentesis is safer and more reliable: fluid can almost always be obtained.[65]

Intra-abdominal abscess

Despite advances in medical and surgical management there remains a significant morbidity and mortality from intra-abdominal abscess.[66,67] Symptoms and signs are often non-specific, and this is particularly true of postoperative abscesses.

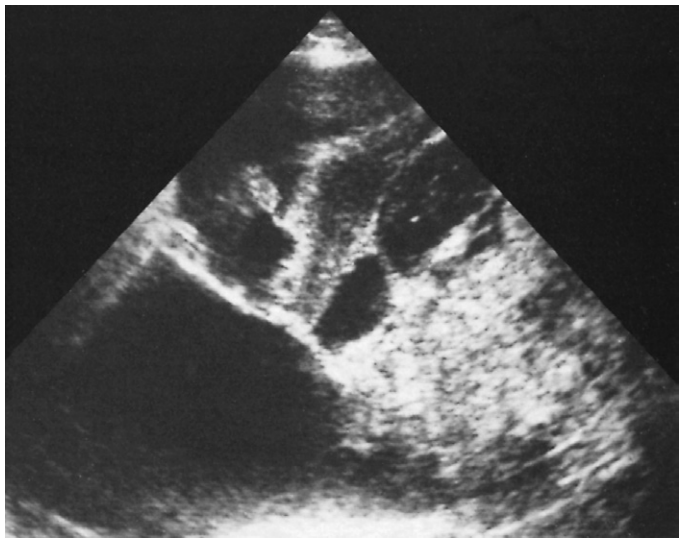

Figure 41.42 Septa in malignant ascites.

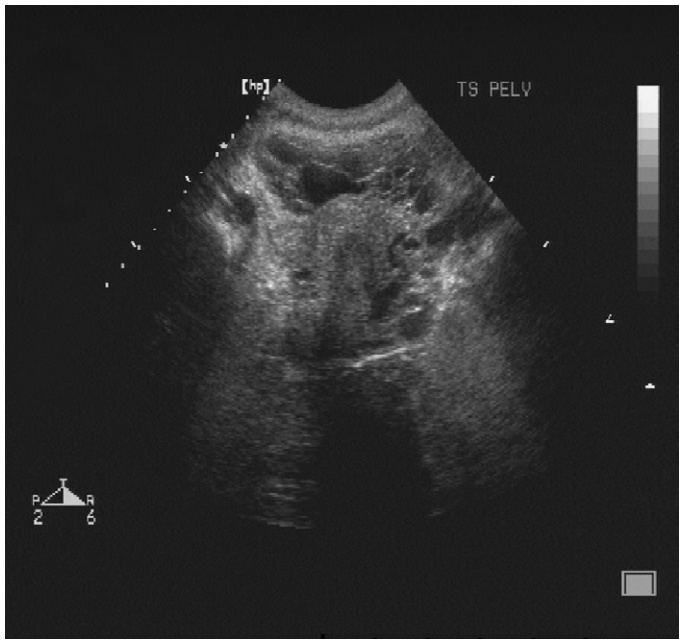

Figure 41.43 Pseudomyxoma peritonei. Multiple septations and loculations (arrows) are seen within the intraperitoneal fluid in this patient with an ovarian carcinoma. Strictly, the term pseudomyxoma peritonei applies to non-malignant aetiologies (mostly following a ruptured mucinous appendicitis), but it is often loosely applied to any multicystic peritoneal condition.

Early diagnosis and effective treatment are important in the management of abscesses.[68–70] Ultrasound can play a role in both, but should not be considered in isolation. No single method of investigation is ideal. The sensitivity and specificity of CT, for example, is better than ultrasound in isolation. Isotope-labelled leukocyte studies are also sensitive in the detection of intra-abdominal abscess, but its specificity is low. Moreover, isotope imaging cannot be used as a guide for needle aspiration or catheter drainage, so this limits its role in management. The higher cost of CT, its use of ionising radiation and the need to transport the patient to the CT unit are significant factors. Ultrasound is relatively cheap, almost universally available and mobile, making it suitable for the examination even of a very sick patient in the intensive care unit.

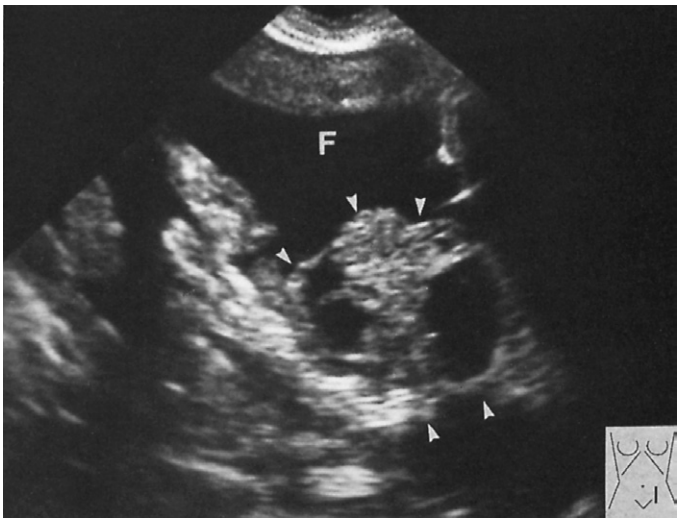

Figure 41.44 Malignant ascites. Ascitic fluid (F) is noted in the pelvis in this patient with an empty bladder. A complex mass (arrowheads) replaces the left ovary.

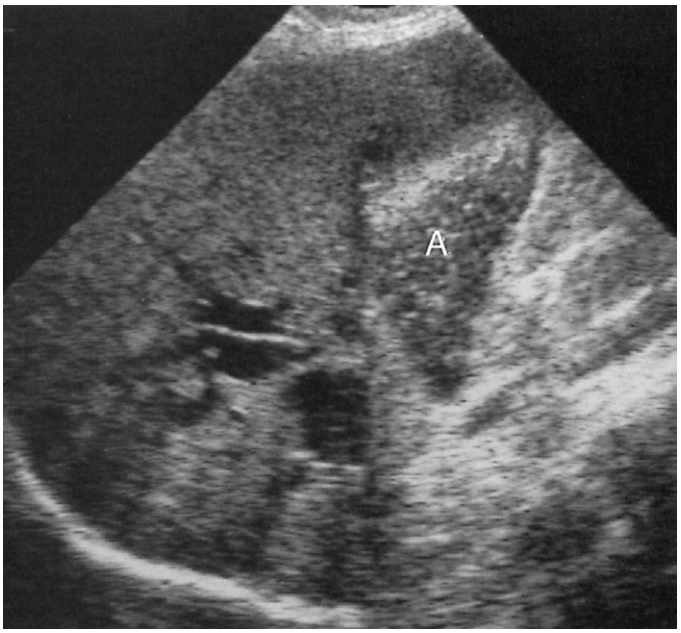

Figure 41.45 Right subhepatic abscess. An abscess cavity (A) is shown in Morison's pouch. This is predominantly echo-free with distal enhancement, and contains a few low-level echoes.

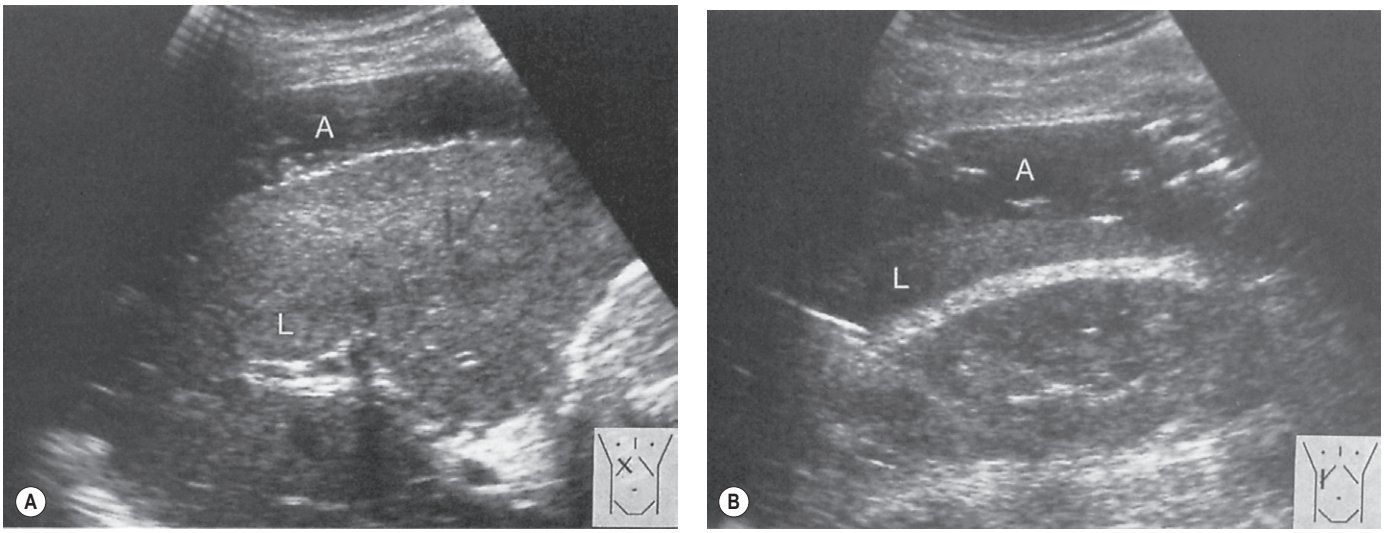

Figure 41.46 Right subphrenic abscess. A: A fluid space with low level echoes (A) is interposed between the diaphragm and the liver (L). **B:** A longitudinal scan further laterally shows highly reflective echoes from gas within the fluid.

Examination of the patient with a suspected intra-abdominal abscess requires a careful approach.[54,55] The examination is often limited by poor access owing to abdominal wounds, dressings and drainage tubes. The examination should first be directed towards any suspected abscess site, suggested by symptoms, signs or radiological features, such as an elevated hemidiaphragm on a chest X-ray. If there are no such localising features a systematic examination of the various common sites for abscess collection must be made. The sub- and perihepatic regions are examined, using the liver as an acoustic window with the patient in the supine and left posterior oblique positions (Figs 41.45 and 41.46). The left perisplenic region is examined using the spleen as a window in the supine and right posterior oblique positions. Care must be taken not to confuse a fluid-filled stomach or the left lobe of the liver with an abscess cavity.[54,71] The paracolic gutters are assessed with the patient supine; it is sometimes helpful to tilt the bed head-down in order to improve imaging of the upper abdominal organs. Pelvic scanning is best with a distended urinary bladder, which may have to be filled via a catheter if inadequate visualisation of the pelvis is achieved; transvaginal scanning does not require a filled bladder and gives higher-resolution images. Postoperative scanning is often severely hindered by traditional wound dressings: surgeons should be encouraged to use spray-on dressings to improve ultrasound access.

The operator must be conscious of the potential for auto- and cross-infection from open abdominal wounds throughout the examination.[72,73] Scrupulous cleaning and disinfection of the equipment (as well as of the operator's hands) before and after the examination is extremely important; the use of a sheath or other cover on the transducer should be considered to reduce the risk of cross-infection.

There is no unique appearance of an abscess on ultrasound. The abscess cavity may appear echo-free, thereby mimicking a cyst; it may have low-level echoes with an irregular margin (Fig. 41.47); or it may contain clumps of solid material within a predominantly fluid cavity. Occasionally, strong echoes from particles within the fluid may suggest a solid mass (Fig. 41.45). Gas within an abscess can produce a confusing picture which may be indistinguishable from adjacent bowel and thus render the abscess invisible to ultrasound (Fig. 41.48).[74] Free intraperitoneal gas may be encountered in perforation of a viscus such as the duodenum, when it has been described as collecting preferentially in the region of the ligamentum teres.[75]

Potential sites of abscesses

- Subphrenic
- Subhepatic
- Lesser sac
- Paracolic gutters
- Pelvis
- Interloop collections
- Paravertebral
- Psoas

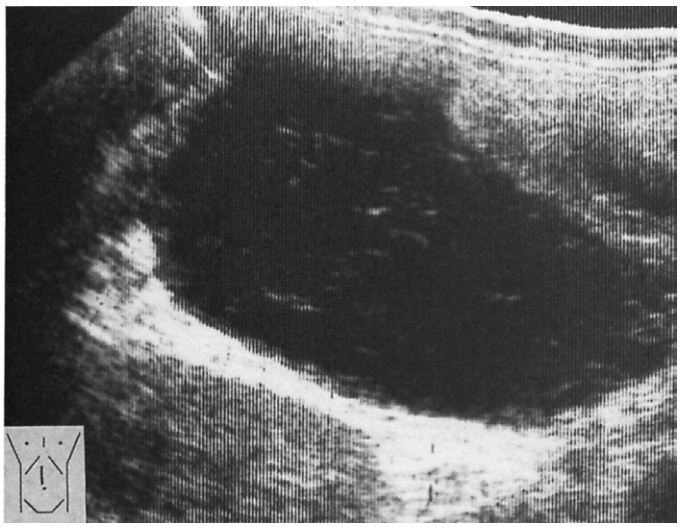

Figure 41.47 Abdominal abscess. Large irregular fluid collection in the mid-abdomen communicating with the subcutaneous tissues and containing scattered low-level echoes.

Percutaneous aspiration and drainage

Because of the high morbidity of reoperation for intra-abdominal abscess[76] there is increasing interest in percutaneous needle aspiration and catheter drainage (see Chapter 43)[68,77–81] This provides the opportunity for microbiological analysis of the aspirate to assist with the choice of antibiotics and to direct management; this is particularly important as fungal abscesses respond poorly to percutaneous drainage.[82]

Whereas the fine needle used for aspiration can safely traverse bowel loops, the insertion of a catheter necessitates a bowel-free pathway. The type of procedure chosen depends upon the size of the abscess and its position. Lesions smaller than 6 cm in diameter can usually be successfully aspirated with an 18G needle under direct ultrasound control; in one series, a success rate of greater than 95% was recorded. Larger abscesses, which are often more complex, require catheter insertion and yield poorer results, with success rates around 70% (which compares well with operative intervention and certainly shortens hospital stay). When a catheter must be inserted, planning the route for the guide needle generally requires CT to ensure that intervening gut is avoided. Fistulae require excision rather than drainage, and this diagnosis should be excluded by X-ray contrast studies.

Although ultrasound is valuable in the investigation and management of suspected intra-abdominal abscesses, optimum management should follow a diagnostic algorithm. For patients too sick to be moved from intensive care, ultrasound is the only imaging technique available for investigation and aspiration or drainage of an abscess at the bedside, and this can be life-saving. If there are clinical features or radiological signs pointing to a specific site for an abscess collection, ultrasound is the most cost-effective investigation. However, when the site of abscess is not clear (e.g. a fever of unknown origin), a radiolabelled leukocyte study or abdominal CT scan should be used.

Other fluid collections

Lymphoceles, haematomas and urinomas can all be demonstrated by ultrasound, but their sonographic appearances are variable, so

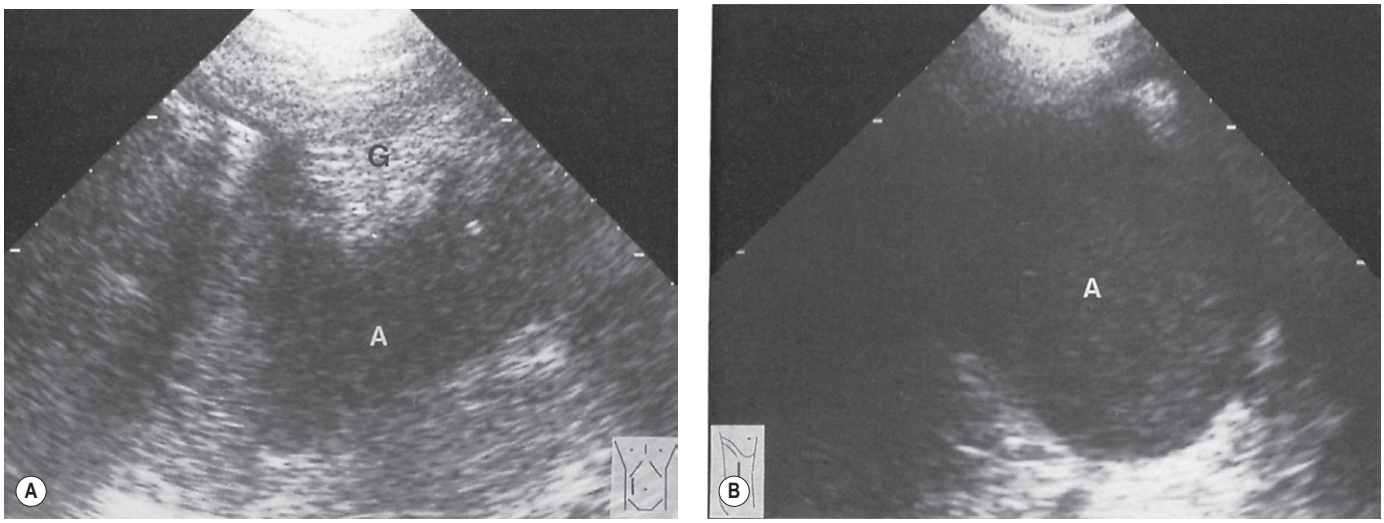

Figure 41.48 Gas within an abdominal abscess. A: Much of the abscess cavity (A) in the mid-abdomen is obscured by superficially located gas (G). **B:** Scanning the abscess from a lateral approach the gas is avoided and the abscess cavity (A) can be identified.

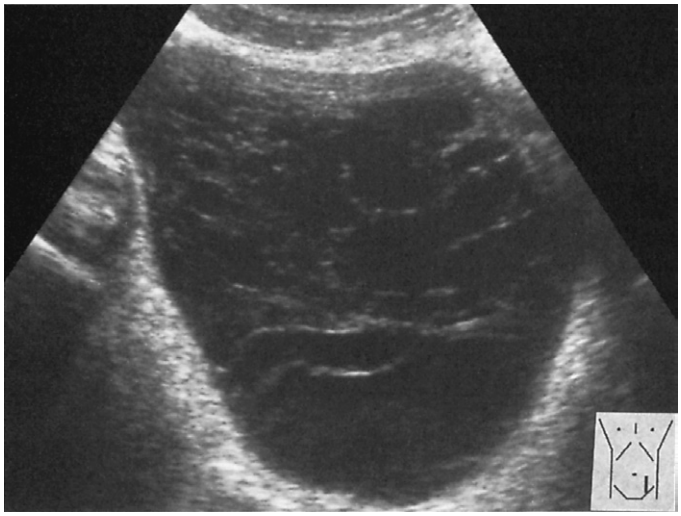

Figure 41.49 Septated fluid collection in the left iliac fossa. This septated appearance is said to be characteristic of a lymphocele, but this was in fact a haematoma.

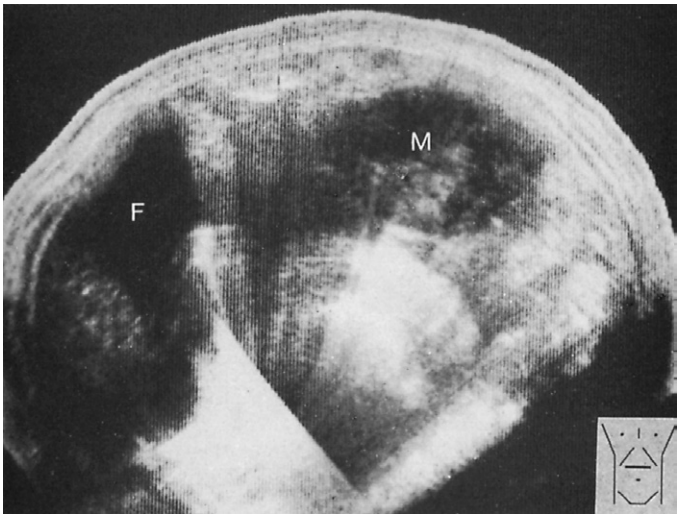

Figure 41.50 Large mesenteric metastasis. A large mass is seen in the central abdomen (M) in a patient with ascites (F).

that the nature of the collection cannot be determined by ultrasound alone.[50] The examination should be directed towards the site of trauma, bearing in mind, as always, that fluids tend to collect in the most dependent portion of the peritoneum. In vitro, blood clots change with time: initially echo-free, they develop reflective regions with clot retraction. However, the variations in the rate of this process mean that the ultrasound appearances are not very reliable for estimating the age of the haematoma. Ultrasound is widely used to direct the tapping of peritoneal fluid in blunt abdominal trauma (FAST: focused assessment with sonograpy for trauma): if the fluid is bloodstained, further investigation for ruptured viscera is required (usually either CT or laparoscopy or laparotomy), whereas a negative scan or aspiration of clear fluid supports conservative management.[83] However, in a proportion of cases rupture is not accompanied by peritoneal bleeding, and so follow-up ultrasound scans should be considered in 'negative' cases.[84]

Lymphoceles are frequently septated, but septa can also occur in haematomas and in abscesses (Fig. 41.49). Echogenic fluid within lymphoceles is suggestive of infection. As in abdominal abscesses, percutaneous aspiration is an important diagnostic technique and may be an alternative to surgical management.

Miscellaneous pathologies

Duplication cysts

Small bowel duplication cysts are rare but generally have the characteristic appearances of cysts. If they contain echogenic fluid they may be confused with other causes of intra-abdominal fluid collection. Bowel loops are displaced around the cyst and may partially or completely obscure it.

Mesenteric and peritoneal tumours

The difficulties of imaging peritoneal seedlings in intra-abdominal metastatic disease have already been described. Occasionally large peritoneal deposits can be seen, particularly those in the mesentery (Fig. 41.50). They are usually solid, but may contain areas of necrosis with irregular cystic regions. Adjacent bowel loops are stretched around the mass in a similar fashion to duplication cysts.

Peritoneal metastases

Peritoneal spread of malignancies is not uncommon and is a particular feature of ovarian carcinoma (in which it receives its own staging classification) (Fig. 41.51). Intra-abdominal lymphoma is usually manifest as enlargement of the para-aortic and paracaval nodes, typically with a rounded shape and effacement of the vascular hilum. Assessment of the extent of nodal and extranodal disease is important in the staging of lymphomas: extension into the root of the mesentery is particularly important, as it represents a more advanced disease stage. These appearances have been described as the 'sandwich sign', with lymph node infiltration sandwiching the vessels of the mesentery (Fig. 41.52). Occasionally on ultrasound this sign can be mimicked by the presence of large amounts of fat in the mesentery, but generally fat tends to be more reflective than lymphomatous tissue.

RETROPERITONEUM

Anatomy

The retroperitoneum is that part of the abdomen which is bounded anteriorly by the posterior parietal peritoneum, posteriorly by the transversalis fascia and laterally by the latero-conal ligaments (Fig. 41.53). It is largest posteriorly but continues anteriorly as the properitoneal fat compartment, and extends from the pelvic brim inferiorly to the diaphragm superiorly. The retroperitoneum contains the adrenals, kidneys and ureters, the duodenal loop and the pancreas, the great vessels with their branches and associated lymph node chains, and the ascending and descending portions of the colon, including the caecum. It can be divided into three distinct compartments by the fascial planes it contains: these constrain the distribution of reteroperitoneal collections such as pseudocysts, haematomas and abscesses, and so an understanding of their arrangement has practical diagnostic value.

The anterior pararenal space lies between the posterior parietal peritoneum and the anterior renal fascia; the latero-conal ligament lies laterally, blending with the parietal peritoneum anteriorly. The space is continuous across the midline and contains the pancreas, the duodenum, the ascending and descending colon, the caecum, and also the appendix when it lies in a retrocaecal position.

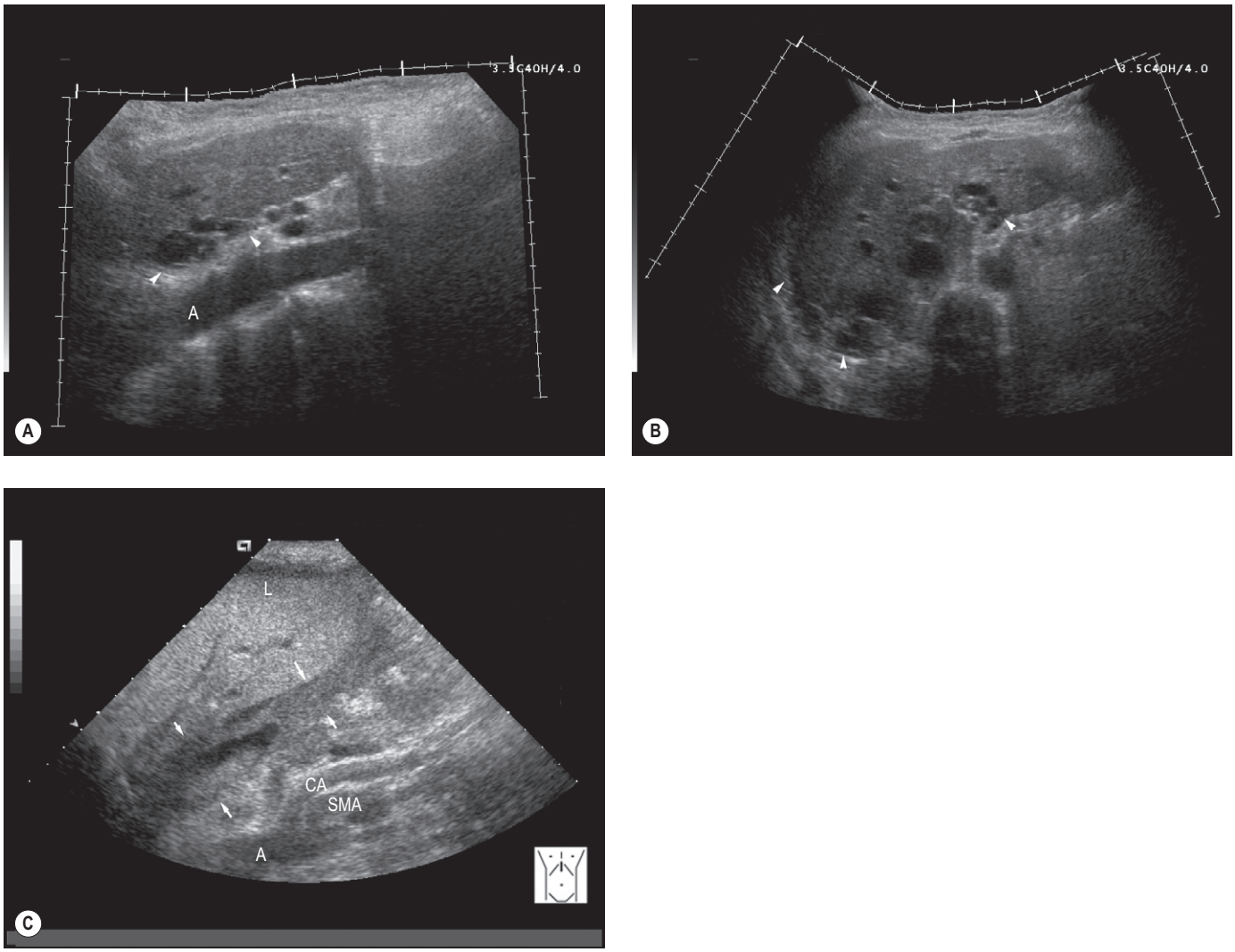

Figure 41.51 Peritoneal tumour. A: Cystic masses (arrowheads) lie posterior to the liver in this patient with trans-coelomic spread of an ovarian cancer (extended field-of-view scan). **B:** Transverse scan in the same patient showing tumour (arrowheads) over the right lobe of the liver. **C:** In another patient, also with an ovarian carcinoma, the peritoneal spread is more solid in consistency (arrows). A, aorta; CA, coeliac axis; SMA, superior mesenteric artery.

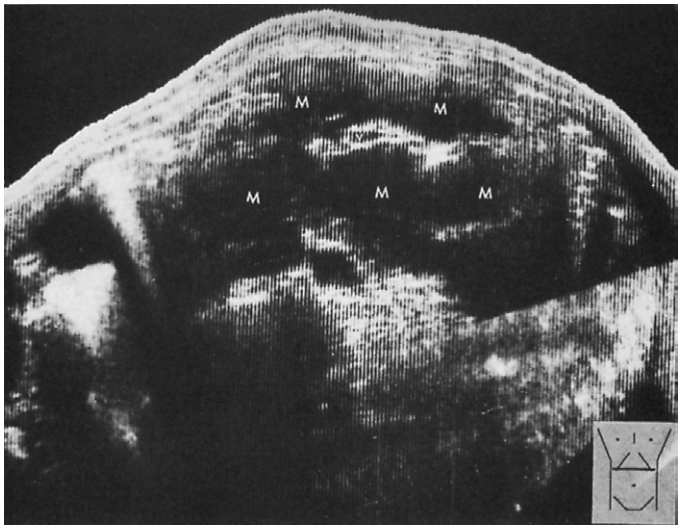

Figure 41.52 The 'sandwich sign'. Multiple lymph node masses (M) envelop the mesenteric vessels, producing a sandwich effect.

The perirenal space is confined by the anterior and posterior renal fasciae, which fuse laterally to form the latero-conal ligament. The precise site at which this blends with the renal fascia varies widely. The posterior renal fascia (Gerota's fascia) is generally thicker than the anterior and has at least two layers, the anterior of which is continuous with the anterior renal fascia whereas the posterior layer continues into the latero-conal ligament. Superiorly the layers fuse above the adrenals and attach to the diaphragm. Inferiorly the renal fasciae extend into the pelvis, where they thin out so that the anterior and posterior pararenal spaces communicate in the iliac fossae. The fascial layers consist of dense connective tissue which blends with the connective tissue enveloping the aorta, the inferior vena cava (IVC) and the roots of the superior mesenteric vessels. The perirenal space contains the kidneys, adrenals, fat and blood vessels.

The posterior pararenal space lies between the posterior renal and latero-conal ligaments anteriorly and the transversalis fascia posteriorly. Its medial border is formed by the psoas major and quadratus lumborum muscles. Laterally it communicates with the properitoneal fat compartment (flank stripe). It contains only fat.[85–88]

All the compartments of the retroperitoneal space contain varying amounts of adipose tissue, depending on body habitus, but the right anterior and both posterior pararenal spaces are usually thin compartments.

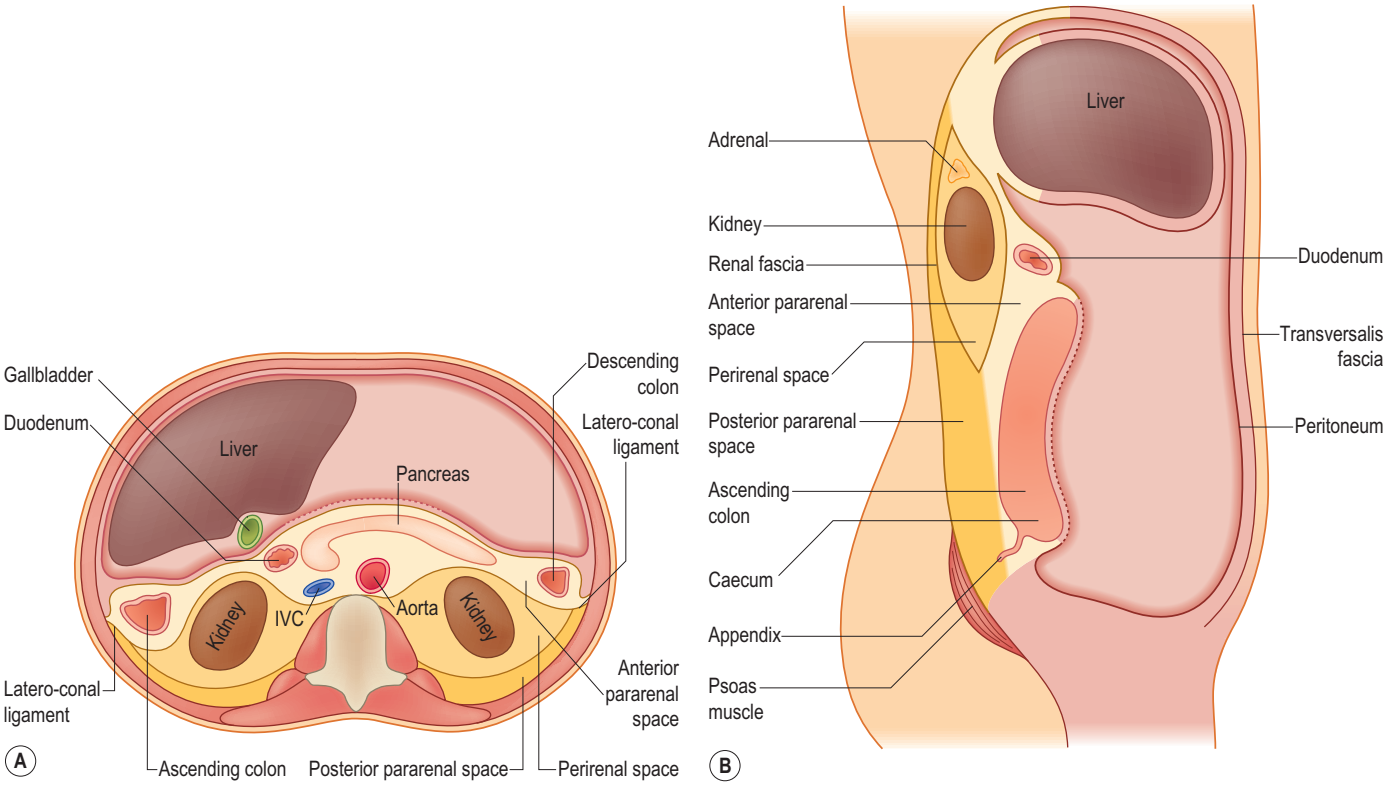

Figure 41.53 The retroperitoneal spaces. Diagrammatic sections through the kidneys; **A:** transverse, **B:** parasagittal, to show the perirenal and pararenal spaces and the latero-conal ligaments. IVC, inferior vena cava. (Reproduced with permission of Springer-Verlag from Meyer, MA. Dynamic radiology of the abdomen. Normal and pathologic anatomy, 3rd edn. New York: Springer-Verlag, 2000.)

The diaphragmatic crura extend inferiorly as tendinous fibres that attach to the vertebrae and their transverse processes down as far as L3 on the right and L1 on the left. The right crus is more prominent and usually more lobular than the left. It is bounded by the IVC anterolaterally, and by the right adrenal gland and the right lobe of the liver posterolaterally. Its fibres diverge as they ascend: the lateral fibres insert on the central tendon of the diaphragm and the medial fibres ascend on the left side of the oesophageal hiatus, decussating with those of the left crus in front of the abdominal aorta. On parasagittal scans the right crus can be seen as a longitudinal echo-poor structure immediately posterior to the IVC or, to the left of the midline, anterior to the aorta. The intra-abdominal portion of the oesophagus begins at the cephalic end of the right crus. The left crus ascends along the anterior lumbar vertebral bodies and inserts into the central tendon of the diaphragm. It is closely related to the adrenal gland, the splenic vessels and the oesophagogastric junction. Occasionally the medial fibres of the left crus cross the aorta and run toward the IVC.

The right crus is more readily seen on ultrasound than the left, though both may be apparent on transverse scans.[89] The prevertebral spaces at the level of the crura contain the aorta, nerves, portions of the azygos venous system, lymph nodes and the cisterna chyli.

Scanning techniques and general appearances

Using transverse and longitudinal scans, the superior reaches of the retroperitoneum are well seen because the liver and spleen can be used as acoustic windows. Little if any patient preparation is required for retroperitoneal ultrasound: fasting for 12 hours beforehand may reduce gas, but is not always necessary. Parenteral fluid or fluid enemas may occasionally be helpful, and the use of pharmaceutical gas-displacing liquids ('contrast agents') improves visualisation.[90] Barium studies should be performed after rather than immediately before an ultrasound because barium is a strong reflector.

The diaphragmatic crura, pancreas, kidneys, duodenum, psoas muscles and prevertebral vessels are all detectable and, in the lower abdomen, the iliopsoas, quadratus lumborum and the prevertebral vessels can be visualised when scanning conditions are favourable. Oblique coronal views are a valuable addition to the standard views in visualising the retroperitoneum, particularly for the great vessels.[91–93] They are best performed from the right flank with the patient in a left posterior oblique position so that the right lobe of the liver and the right kidney move antero-inferiorly and act as acoustic windows. At the same time, fatty tissue and gas-filled bowel loops move anteriorly, facilitating acoustic access posterior to them. Similarly, scans can be performed from the left flank in the right posterior oblique position, but these are usually less successful than on the right, where a better window is provided by the liver.

Using oblique coronal views the proximal renal arteries can be demonstrated in up to 90% of patients, though success is lower in the presence of an aortic aneurysm (presumably because of the anatomical distortion it causes[91]), and the proximal portions of the common iliac arteries can be seen in 80% of patients. An anomalous (e.g. circumaortic) or duplicated vena cava can be displayed in sagittal or oblique coronal scans.

The general fat in the retroperitoneum is moderately reflective and this increases the contrast with the echo-poor lumina of vessels and ducts. Occasionally, however, the fat is relatively echo-poor and its appearance as unexpectedly dark tissue, often with a striated structure from the fascial layers within it, can be confusing, creating the false impression of retroperitoneal pathology such as an infiltrating tumour. This is most often encountered in neonates (where it may be so echo-poor as to suggest fluid) and in the obese (Fig. 41.54).

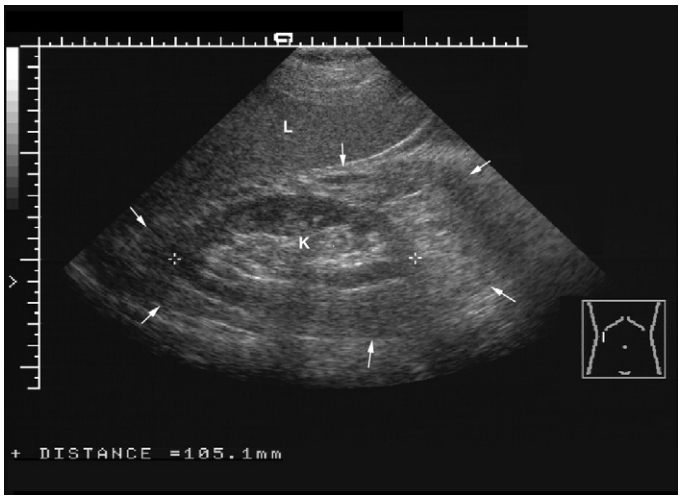

Figure 41.54 Retroperitoneal fat. Retroperitoneal fat is usually moderately reflective but can be confusingly echo-poor. In this obese patient the echo-poor fat around the right kidney (arrows) suggested an infiltrating malignancy: CT revealed low-density tissue in the retroperitoneum and around the gallbladder. K, kidney; L, liver.

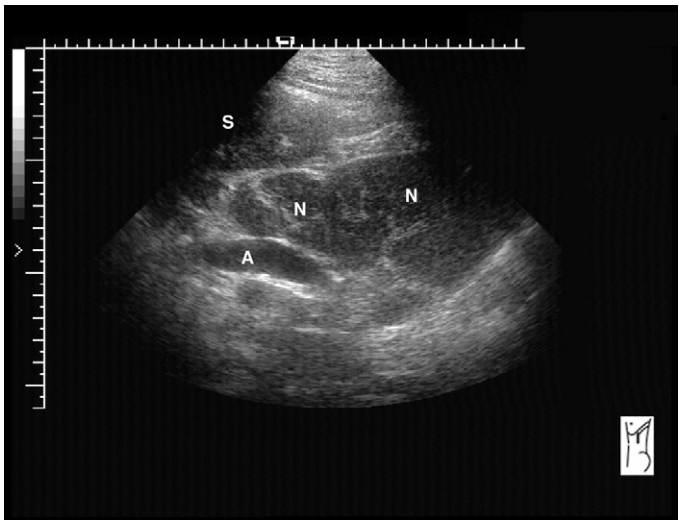

Figure 41.55 Retroperitoneal lymphadenopathy. A large lobulated mass of confluent lymph nodes is seen in this left coronal section in a patient with abdominal Hodgkin's disease. A, aorta; N, nodes; S, spleen.

In easy-to-scan subjects, normal retroperitoneal nodes are sometimes identified. These are bean-shaped, less than 1 cm in length, and their hila can be demonstrated with a careful search as a reflective strip extending part-way into the echo-poor parenchyma.[94] On colour Doppler a vessel may be found in the hilum but there should be no vessels perforating the convexity of the node – this and a spherical shape suggest malignant involvement. Enlarged posterior abdominal lymph nodes can be detected with an accuracy, sensitivity and specificity of around 90% and their oval or rounded shapes permit differentiation from the para-aortic vessels[87] (Fig. 41.55).

Retroperitoneal tumours

Most retroperitoneal tumours arise in the kidneys (see Chapter 23), adrenals (see Chapter 33) or pancreas (see Chapter 16). Of the remainder, primary retroperitoneal tumours other than lymphomas are uncommon.[95,96] Approximately 80% are malignant.[97,98] Most retroperitoneal tumours in the adult are mesenchymal in origin (Table 41.3), the three commonest being liposarcoma, leiomyosarcoma and malignant fibrohistiocytoma.[99] Metastatic disease in the retroperitoneum is usually recurrence of a urological or gynaecological tumour.

Retroperitoneal tumours

- Lipoma
- Tumours of the kidney, adrenals and pancreas
- Lymphoma
- Neurogenic tumours including schwannoma and paraganglioma
- Phaeochromocytoma (extra-adrenal)
- Haemangiopericytoma
- Malignant fibrohistiocytoma
- Sarcoma
- Rhabdomyosarcoma (tends to occur in children)
- Neuroblastoma (tends to occur in children)
- Ganglioneuroblastoma (tends to occur in children)
- Teratoma (tends to occur in children)

Clinically, retroperitoneal tumours are insidious in onset with few early manifestations, so that they reach a large size by the time of diagnosis: in 80% of cases they are large enough to be palpable (Table 41.4). Abdominal pain is the commonest presentation, probably attributable to bowel and renal tract obstruction. Surgery offers the best hope of cure as there is limited response to radiotherapy or chemotherapy. However, most are invasive and cannot be resected completely, so the prognosis is poor.[100,101]

Although it is not always possible to confirm the retroperitoneal origin of the tumour with ultrasound, some characteristic features may be helpful in locating their origin. Anterior displacement of the pancreas, kidneys, great vessels, or the ascending or descending colon is highly suggestive of a retroperitoneal lesion (Fig. 41.56). Encasement of retroperitoneal structures such as the aorta, IVC, renal vessels, kidney and pancreas, and compression of the iliopsoas or quadratus lumborum muscles are also typical features (Fig. 41.57).

The histology of the tumour cannot be determined from the ultrasound appearances, though in some cases there are features suggestive of a specific diagnosis. Many retroperitoneal tumours are large (particularly haemangiopericytomas), but functioning tumours (e.g. extra-adrenal phaeochromocytoma) and those associated with disease elsewhere (e.g. a schwannoma in a patient with neurofibromatosis) may be small at diagnosis. Neurogenic tumours are generally paravertebral in position, whereas those of sympathetic nerve origin tend to lie in the para-aortic region. Extra-adrenal phaeochromocytomas or paragangliomas often arise in the organs of Zuckerkandl, which are usually found below the renal hilum, or at the origin of the inferior mesenteric artery. Teratomas typically involve the sacrococcygeal area, whereas malignant fibrohistiocytomas typically lie very close to the kidney (nephrectomy is needed in 50% of cases).[102] The patient's age may also provide a clue to the tumour type: rhabdomyosarcomas, neuroblastomas, ganglioneuroblastomas and teratomas tend to occur in children, whereas malignant fibrohistiocytomas are the commonest retroperitoneal soft tissue sarcoma of late adult life.

The ultrasound appearances are very variable, with strongly and poorly reflective or mixed tumours all occurring, both with and without anechoic zones from necrosis. Tumours with a uniform cell type and a paucity of connective tissue and fat have fewer internal echoes, so that they produce lesions that are echo-poor or nearly anechoic, as is typical of malignant schwannomas and fibrohistiocytomas. A highly reflective tumour suggests a liposarcoma, although this feature may be absent when the tumour is poorly differentiated.[103] The reflectivity of lipomas varies from highly intense to weak, depending on the content and distribution of fat

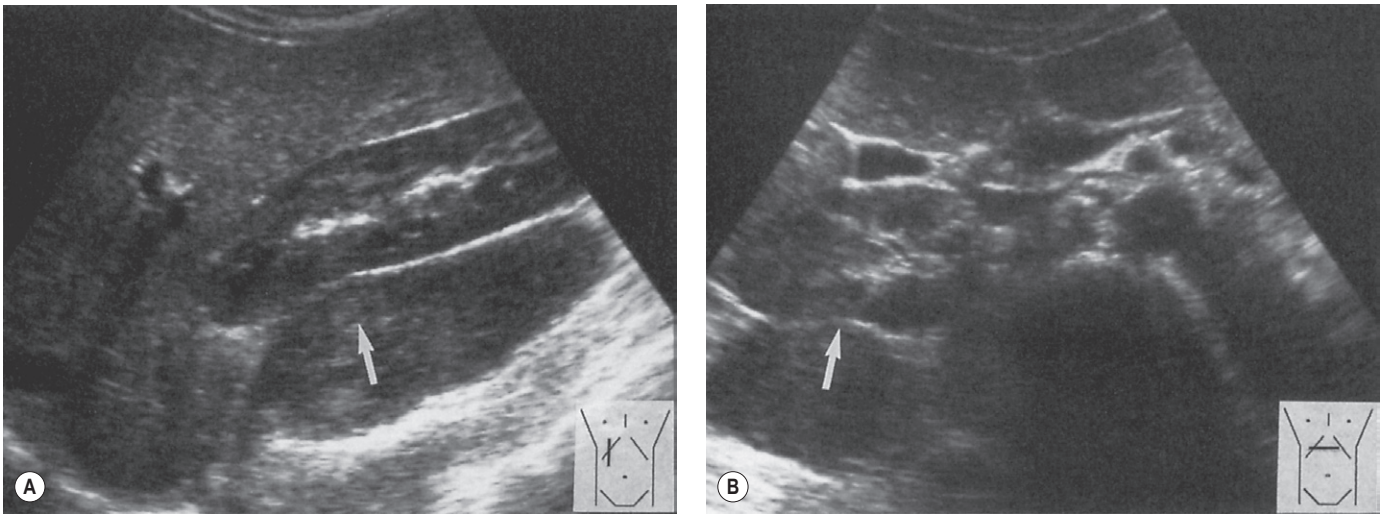

Figure 41.56 Retroperitoneal sarcoma. Longitudinal right parasagittal **(A)** and transverse **(B)** sections of a retroperitoneal mass elevating the right kidney (arrow). The uniform echotexture is typical of a sarcoma.

Table 41.3 Classification of retroperitoneal tumours[96]

	Malignant	Benign
Mesenchymal	Liposarcoma Leiomyosarcoma Rhabdomyosarcoma Fibrosarcoma Malignant fibrous histiocytoma	Lipoma Leiomyoma Rhabdomyoma Fibroma, fibromatosis
Vascular	Haemangiopericytoma Angiosarcoma Lymphangiosarcoma	(Haemangioma) (Lymphangioma)
Neurogenic	Malignant schwannoma Neurofibroma	Neurolemmoma
Tumours of sympathetic nerve origin	Neuroblastoma Ganglioneuroblastoma Malignant paraganglioma Extra-adrenal phaeochromocytoma	Ganglioneuroma Paraganglioneuroma
Germ cell tumours	Malignant teratoma Embryonal carcinoma Seminoma*	Benign teratoma

**Occasionally arises in the retroperitoneal space as a primary tumour.*
Very rare lesions are bracketed.

Table 41.4 Presenting features of retroperitoneal tumours[98]

Feature	Frequency (%)
Abdominal pain	88
Fatigue	44
Weight loss	32
Anorexia	24
Fever	20
Radiating nerve root pain	16
Back pain	12

and fibrous tissue (Fig. 41.58). Vascular tumours such as haemangiopericytomas are also reflective, presumably because of the abundant interfaces produced by the multiple vessel walls.[104]

A solid mass of mixed reflectivity with an echo-poor centre suggests a sarcoma, as these rapidly progressive tumours tend to outgrow their blood supply, causing central necrosis with haemorrhage. This is particularly true of leiomyosarcomas.

Teratomas have a characteristically heterogeneous mixed echo pattern with solid areas, calcification (50%) and cystic spaces (76%) (similar to ovarian teratomas). They occur in female infants under 6 months of age, with a second peak in incidence in young men. However, the latter are more likely to represent metastases from a testicular primary, and so the testes should also be scanned. Contrary to early reports, it is not possible to distinguish benign from malignant teratomas on the basis of whether they are predominantly cystic or solid.[105]

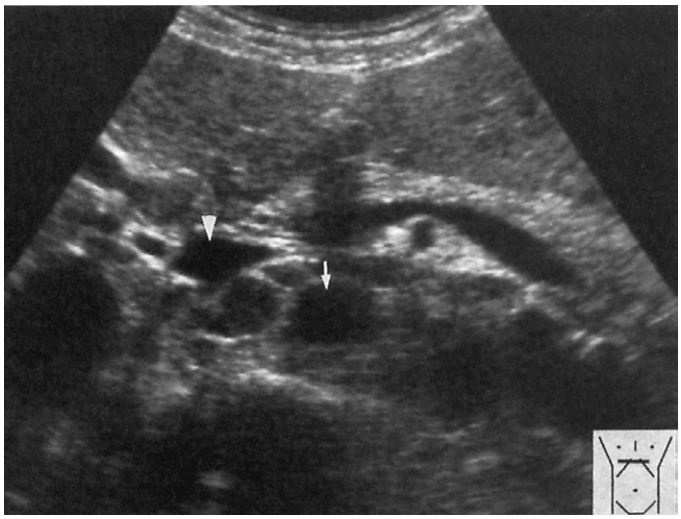

Figure 41.57 Retroperitoneal tumour encasing the aorta. Numerous retroperitoneal masses are seen surrounding the aorta (arrow) and elevating the inferior vena cava (arrowhead).

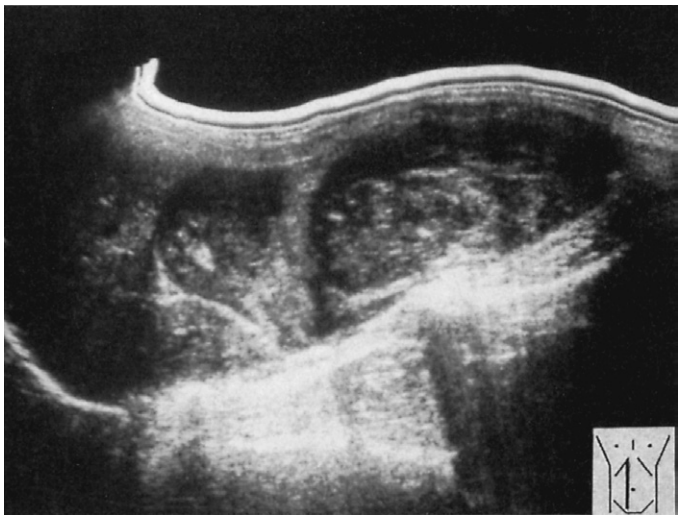

Figure 41.58 Liposarcoma. The strong echoes that are typical of a liposarcoma are attributable to the admixture of fatty and watery soft tissue elements; for this reason, only well-differentiated tumours (i.e. those that retain the ability to form fat) have this appearance.

The benign or malignant nature of any retroperitoneal tumour cannot be reliably determined on ultrasound. A smooth, round, well demarcated cystic mass may be benign or malignant; however, an irregular lesion is more likely to be malignant, benign fibromatosis being an exception as it may be very irregular and show features of muscle invasion.

Retroperitoneal cysts

Primary retroperitoneal cysts are rare. They include simple inclusion cysts (teratomatous cysts) and cysts arising from embryonic gastrointestinal and genitourinary tract rests (e.g. Wolffian or Müllerian duct remnants). They may also be lymphatic, parasitic, traumatic or inflammatory, and are usually asymptomatic, being discovered incidentally on routine physical examinations as a soft, non-tender abdominal mass, or detected on an abdominal X-ray because of calcification in their wall.

Retroperitoneal cysts meet the usual ultrasound criteria for simple cysts: they are smooth-walled and echo-free, with increased through-transmission of sound (Fig. 41.59).[50,106,107] The absence of internal echoes helps distinguish them from abscesses, haematomas and complex cysts such as dermoids or hydatids, although a lymphangioma may consist of multiseptated cysts.[108] The history helps distinguish cysts from lymphoceles or urinomas, which are usually postoperative or follow an episode of ureteric obstruction.

The recommended treatment for retroperitoneal cysts is surgical removal, as they tend to recur after simple aspiration.

Retroperitoneal fluid collections

Retroperitoneal fluid collections tend to spread along the path of least resistance, namely between the fascial planes. Although occasionally more than one compartment is involved, or the fascia is destroyed by the disease process (e.g. in trauma), the fluid can generally be localised to a specific compartment, allowing its source to be deduced from anatomical considerations (see Fig. 41.53 and Table 41.5).[86]

Although ultrasound is reliable in detecting retroperitoneal collections it is often unhelpful in distinguishing between the types of collection, so that needle aspiration is an integral part of the examination. Subsequently ultrasound may be used to establish therapeutic drainage and to follow the progress of the lesion. Scans performed with the patient supine allow comparison between the two sides, but gas often obscures the views in this position and coronal decubitus and prone views (both transverse and longitudinal) may be more helpful.

Retroperitoneal abscesses are most commonly complications of surgery or extensions from renal, spinal or paraspinal infections (Fig. 41.60). Less often they follow septicaemia, trauma, or the perforation of an abdominal viscus such as the colon, appendix or duodenum. They often involve the psoas muscles (psoas abscess) and the perirenal spaces.[95] As elsewhere, abscesses typically have thick irregular walls, septa, layering of internal debris and, occasionally, contain diagnostic gas bubbles which may be observed floating upwards (Fig. 41.61). Large pockets of gas, although uncommon, may completely obscure views of the abscess so, where there is a clinical suspicion of a retroperitoneal abscess but a negative ultrasound, a CT scan should be performed. Gas may leak into the retroperitoneal space from a perforated viscus (typically the duodenum), where it obscures the right kidney.[109]

The psoas muscles are a relatively frequent site for abscess formation, tuberculosis being a common aetiology, but may also follow appendicitis, perirenal pathology and non-tuberculous bacterial spondylitis (Fig. 41.61). Clinically there is unilateral flank, hip or back pain, which is aggravated by hip extension. There may be a palpable and tender abdominal mass (particularly in children) or sometimes a lump in the anterior upper thigh. Typically there is fever, leukocytosis and a raised ESR. The radiograph may show bone destruction but this is a late and inconstant finding. Ultrasound reveals the psoas outline to be enlarged and rounded. The size and extent of the abscess can be assessed as well as its relationship to adjacent structures, particularly the kidneys and blood vessels. The muscle itself may be echo-poor if the infection has spread diffusely, or may contain a localised fluid collection.

The right anterior pararenal space and the anterior perirenal fascia may become thickened and reflective as a result of extension of inflammation from retroperitoneal organs into the pararenal space. Although this is typical of acute pancreatitis, it has also been reported in association with acute cholecystitis and acute appendicitis.[95,110]

Retroperitoneal haematomas are not uncommon, especially in anticoagulated patients and those with bleeding diatheses, and in leaking abdominal aortic aneurysms (Fig. 41.62). Haematomas in the perirenal space most often follow renal trauma, whereas those

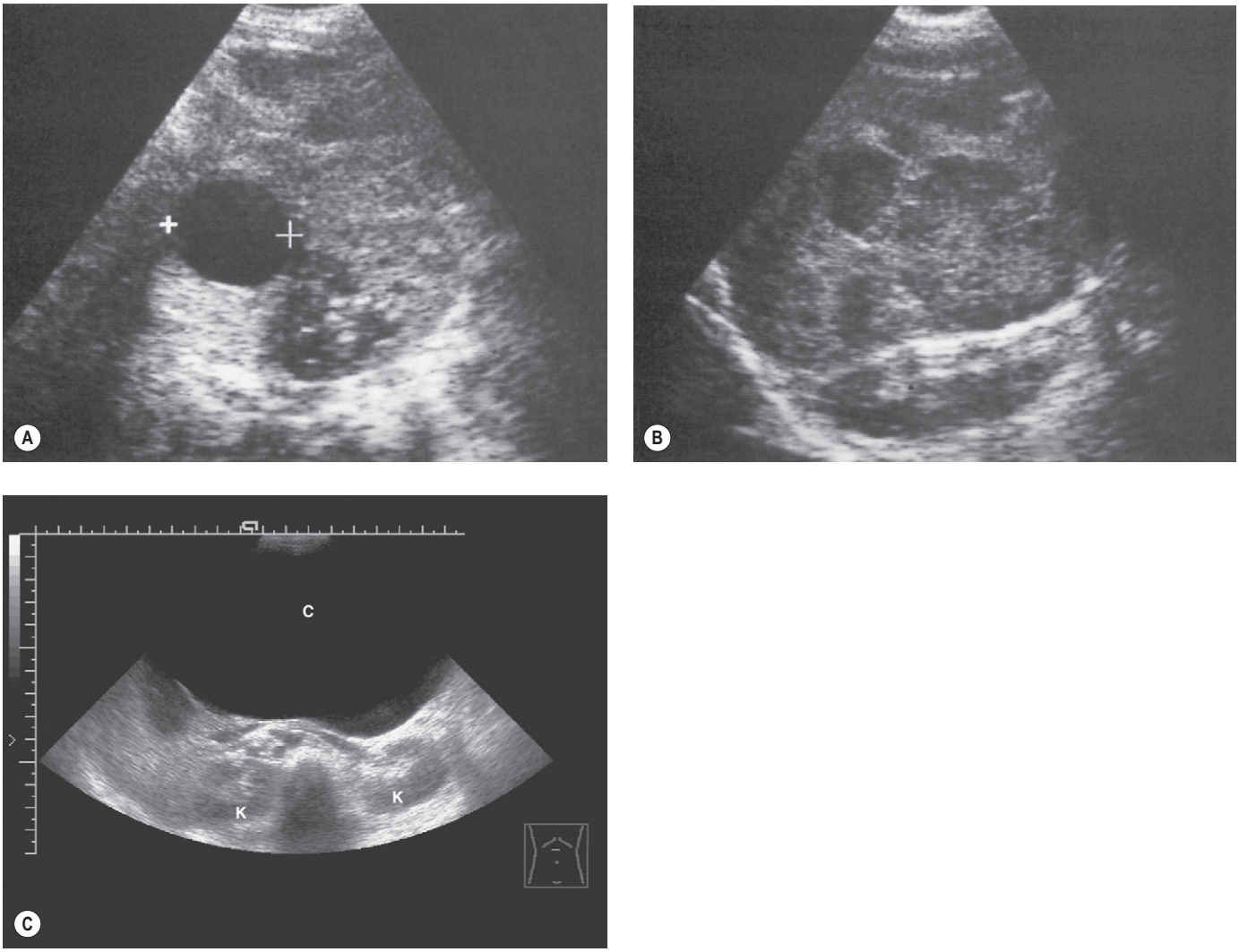

Figure 41.59 Retroperitoneal cysts. A: A large cyst compressing the viscera posteriorly is seen in this transverse section through the epigastrium. The patient presented with abdominal swelling and a retroperitoneal cyst was removed at surgery. **B:** Transverse scan through a left intercostal space in a 4-month-old with a congenital retroperitoneal cyst. The distinction from a pancreatic cyst cannot be made on imaging, but at laparotomy the clear fluid that was aspirated had a very low amylase level. **C:** Scan through the liver showing multiple echo-poor lesions which were haemangioendotheliomas; the purpose of the laparotomy was to tie off the hepatic artery. The discovery of one developmental anomaly should prompt a careful search for others. C, cyst; K, kidney.

Table 41.5 Features of retroperitoneal collections

Compartment	Direction of movement	Renal displacement	Likely source
Perirenal	Dorsolateral to lower renal pole	Anteromedial and superior	Intrarenal infection Urine leak (hydronephrosis)
Posterior pararenal	Inferolaterally parallel to psoas	Anterior and Superior	Retroperitoneal haemorrhage (bleeding diathesis, anticoagulant therapy)
Anterior pararenal	Bulges anteriorly into peritoneal cavity, displacing small bowel loops	Superior ± lateral (anterior or descending anterolaterally)	Exudates from lesions of colon, pancreas, duodenum, bile ducts, appendix or trauma Haemorrhage from rupture of splenic or hepatic artery aneurysm

in the posterior pararenal space or psoas muscle are more likely to occur spontaneously. There is a spectrum of ultrasound appearances: very fresh haematomas may be anechoic and thus difficult to differentiate from simple retroperitoneal fluid collections. A more chronic haematoma often develops complex multiseptate cystic spaces containing reflective material, which may layer and move with changes in the patient's position. Diffusely infiltrating haematomas may be very poorly defined in shape and size. A chronic haematoma may become so well organised that it cannot be distinguished from a solid mass; it may also calcify.

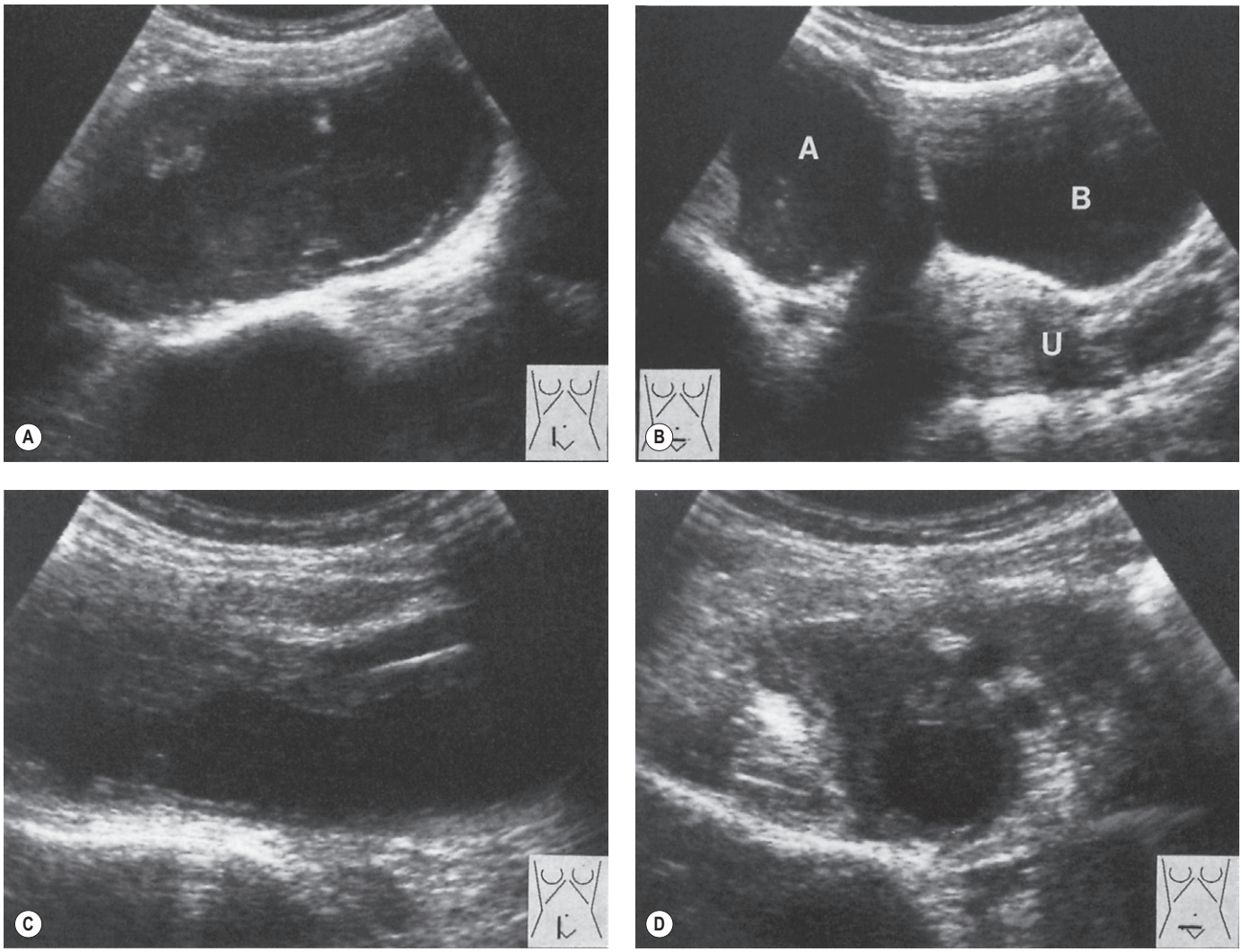

Figure 41.60 **Psoas abscess. A:** Longitudinal and **B:** transverse section in the right iliac fossa. The abscess (A) is seen as a complex of fluid spaces, many with internal echoes, extending into the false pelvis. *Mycobacteria* were cultured and antituberculous drugs started. B, bladder; U, uterus. **C:** Longitudinal and **D:** transverse sections in similar positions 1 month later. The changes of organisation are seen with an increase in the solid elements.

The psoas muscle is a particular site for spontaneous retroperitoneal haemorrhage in haemophiliacs. Pain and stiffness in the flank, hip or groin are typical presenting symptoms, and flexion deformities of the hip may follow iliopsoas spasm. Large psoas haematomas may cause anorexia, constipation, fever, leukocytosis, dysuria and frequency (from pressure on the bladder), and may even mimic acute appendicitis or ureteric colic.[111] Femoral nerve entrapment can cause loss of sensation on the anterior surface of the thigh and, more seriously, paralysis of the quadriceps muscles. Early diagnosis of a psoas haematoma is particularly important in haemophiliacs as prompt treatment with factor VIII prevents femoral nerve damage. In addition to infection and haematoma, the differential diagnosis of psoas muscle enlargement includes invasion by retroperitoneal tumour and hemihypertrophy (occasionally also seen as a normal variant in young Caribbean males, when it is typically bilaterally symmetrical). It must also be differentiated from adjacent lymphadenopathy.

Urinomas and lymphoceles are mainly postoperative complications, although a urinoma may also result from urinary extravasation following ureteric obstruction (see Chapter 22). Both appear as anechoic fluid spaces on ultrasound. Urinomas track along the perirenal space, following the line of the ureter, where they often produce a pattern of multiple layers representing the fluid separating the peri-ureteric tissues, whereas lymphoceles are more typically seen in the pelvis following renal transplantation (see Chapter 28) or pelvic lymphadenectomy.

Retroperitoneal fibrosis

Retroperitoneal fibrosis is a proliferation of fibrous tissue generally confined to the central and paravertebral regions of the retroperitoneum in the perirenal space between the renal hila and the dome of the bladder.[112–115] It is typically thickest immediately anterior to the sacrum and lower lumbar spine. Rarely, extension into the mediastinum, porta hepatis and mesentery has been reported;[116] infiltration of the small bowel, uterus, vagina, bladder and rectum is also recognised.[117,118] The tissue is sharply delineated but not encapsulated. It tends to envelop rather than displace adjacent structures, such as the ureters, blood and lymphatic vessels and, rarely, bowel loops. Approximately 70% of cases are idiopathic,[114]

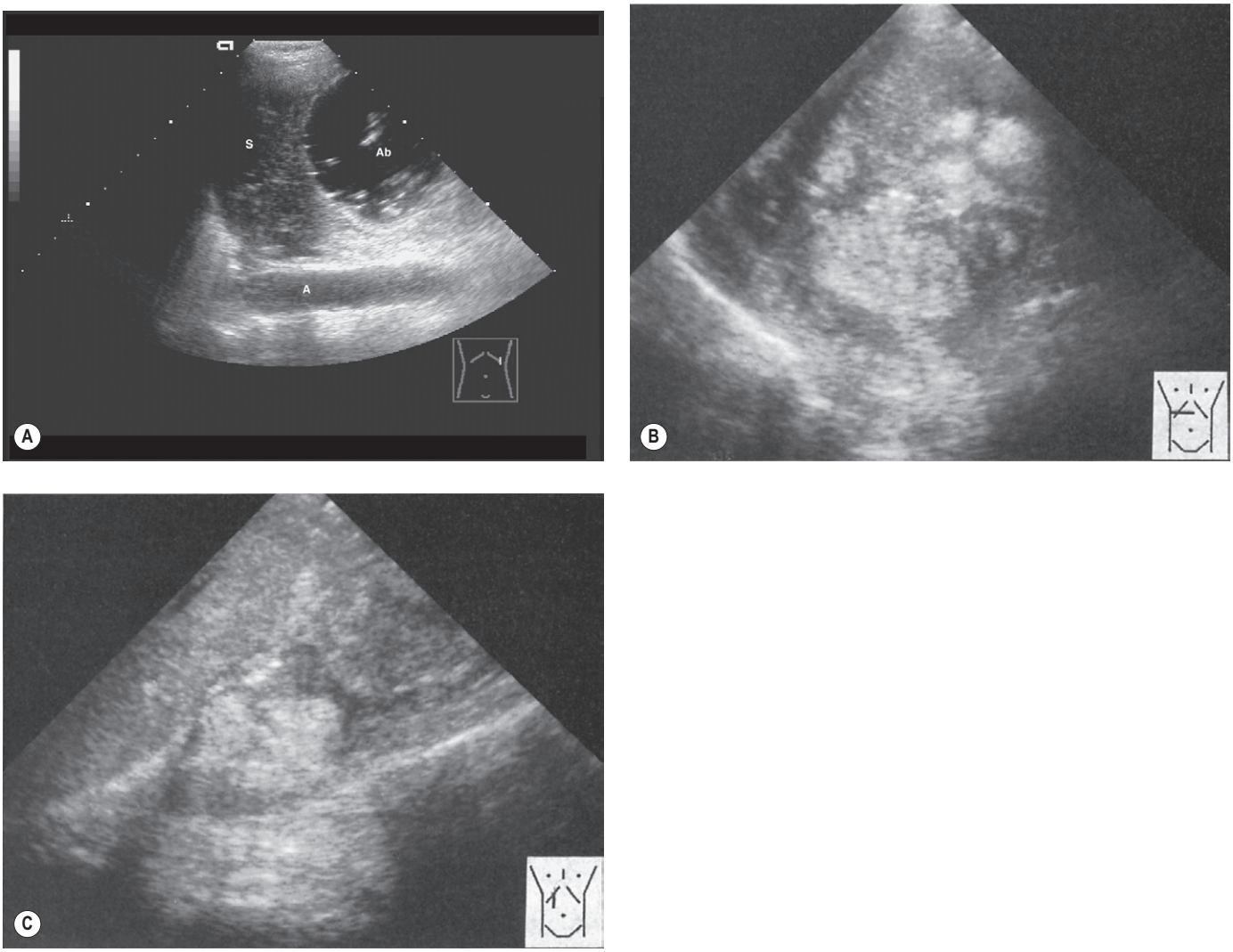

Figure 41.61 **Retroperitoneal abscess. A:** A postoperative collection lying below the spleen in this left coronal section was considered suspicious for an abscess because of the intensely reflective mobile foci it contained. It was treated by guided drainage. In another case of an abscess that followed a nephrectomy, **(B)** transverse and **(C)** longitudinal sections in the right upper quadrant show a generally reflective mass that could be mistaken as a solid lesion. The intense echoes are due to multiple minute gas bubbles in the purulent fluid. A, aorta; Ab, abscess; S, spleen.

whereas others are associated with drugs (notably methysergide), inflammation, infection, trauma, retroperitoneal haemorrhage, and both primary and metastatic tumours. The rare association with Riedel's thyroiditis, sclerosing cholangitis and pseudo-tumour of the orbit suggests an immune basis in some cases. The incidence peaks in the fifth or sixth decade and it is commoner in males (2:1).

The insidious onset and progressive nature of the fibrosis make it difficult to diagnose. Presentation tends to be delayed until ureteric or vascular obstruction occurs. Symptoms are often vague and the clinical features are generally non-specific: patients present with abdominal or flank pain and tenderness, weight loss, anorexia, malaise, hypertension and renal failure. There may be scrotal or leg oedema from lymphatic obstruction. A palpable abdominal or rectal mass is found in approximately 30%.[119] Laboratory investigations are also non-specific, with anaemia, raised inflammatory markers and hypoalbuminaemia.

Ultrasound reveals a pre-aortic mass that is echo-poor, presumably because of its homogeneous consistency, extending beyond the limits of the aorta (Fig. 41.63). It may be bulky, with an ill-defined irregular margin, or form a flat plaque with smooth margins. Adjacent solid organs such as the kidney may be displaced. Typically the plaque extends below the aortic bifurcation and across the pelvic brim.

The classic diagnostic triad of urographic findings in retroperitoneal fibrosis (upper tract dilatation with narrowed and medially deviated ureters) is not entirely reliable: occasionally there is no hydronephrosis, and medial deviation of the ureters may be a normal variant,[112] so that further imaging is required when retroperitoneal fibrosis is suspected. CT is the investigation of choice to delineate the extent of the disease and to detect minimal or localised areas of fibrosis.[120] However, there is a role for ultrasound in follow-up, particularly in assessing the associated hydronephrosis. It may not always be possible to distinguish retroperitoneal fibrosis from other retroperitoneal masses such as lymphoma, sarcoma or haematoma. A needle biopsy, which can be performed under ultrasound guidance, is often needed.

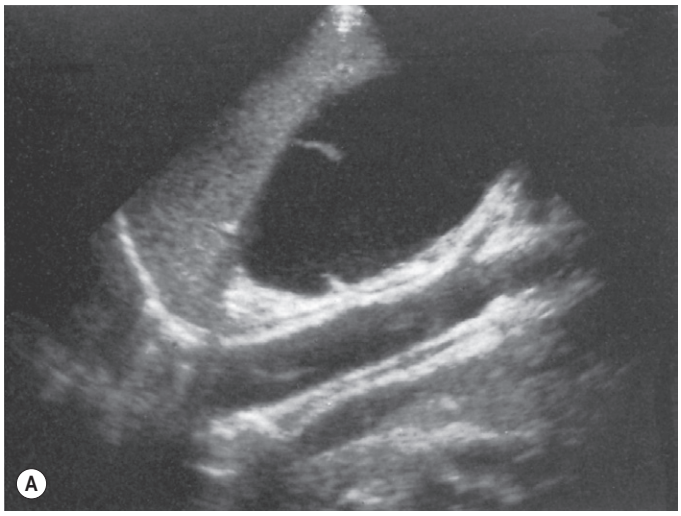

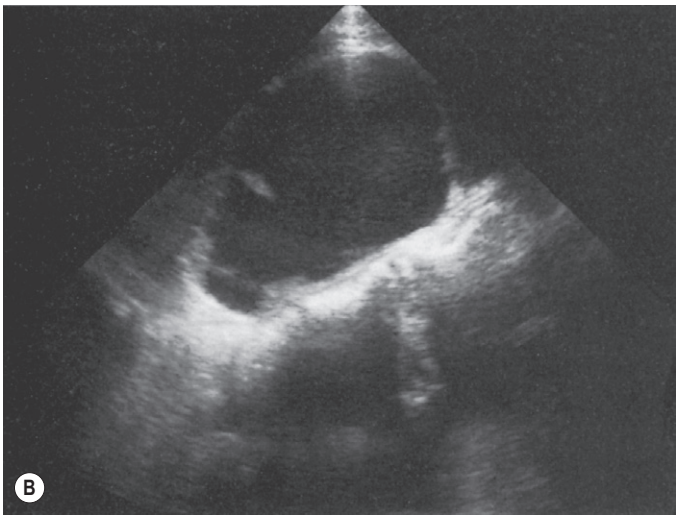

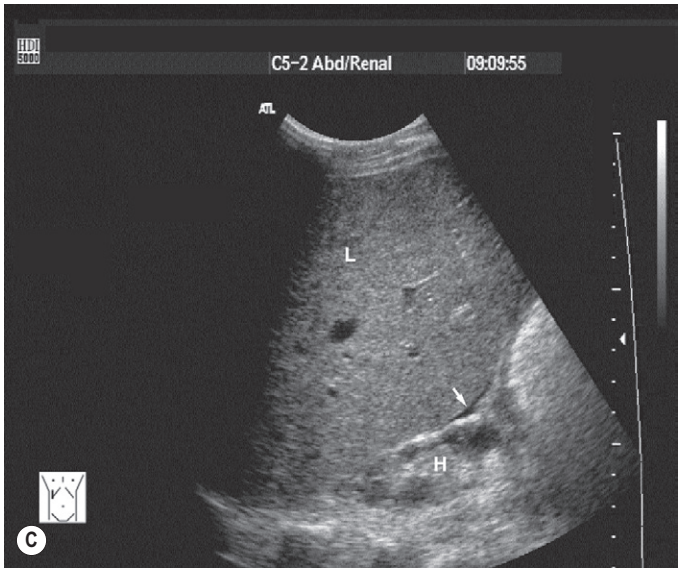

Figure 41.62 Retroperitoneal haematoma. A and B: Left coronal sections showing two views of a well-demarcated collection in the left para-aortic position. Note the low-level internal echoes and the septa. The bleed in this patient was from retroperitoneal metastases from a malignant melanoma. **C:** Right longitudinal section showing a post-adrenalectomy haematoma in the right adrenal bed. The relatively high level of echoes suggests organisation. Note also the trace of ascites (arrow). H, haematoma; L, liver.

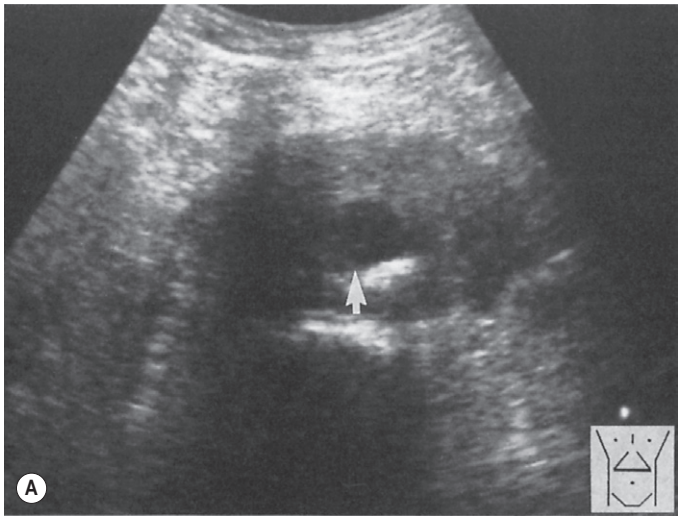

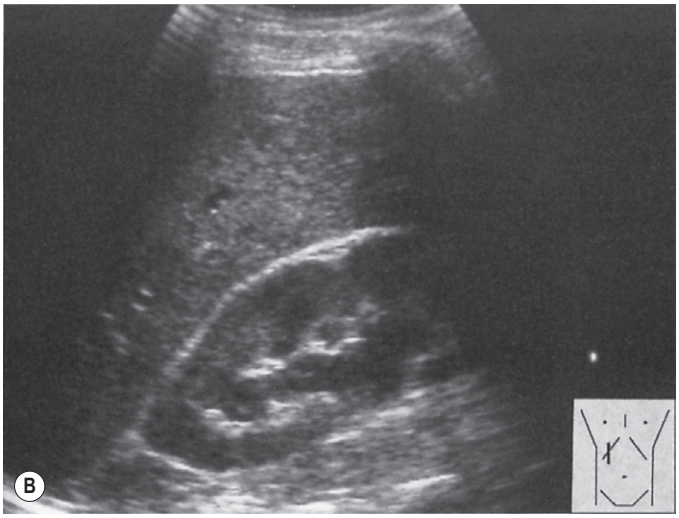

Figure 41.63 Retroperitoneal fibrosis. A: Transverse section across the aorta (arrow) showing the echo-poor cuff of fibrous tissue which is thicker anteriorly. **B:** Right longitudinal section through the kidney showing the hydronephrosis.

REFERENCES

1. Kenny IJ. Early phase wound healing by primary intention as shown by ultrasonography. J Wound Care 1998;7:222–224.
2. Fry WR, Smith RS, Schneider JJ, Organ CH Jr. Ultrasonographic examination of wound tracts. Arch Surg 1995;130:605–607.
3. Gokhale S. Sonography in identification of abdominal wall lesions presenting as palpable masses. J Ultrasound Med 2006;25(9): 1199–1209.
4. Hanif MA, Bradley MJ. Sonographic findings of necrotizing fasciitis in the breast. J Clin Ultrasound 2008;36(8):517–519.
5. Dhar AM, Bhargav SK, Bankata S. Isolated abdominal parietal cold abscess diagnosed on ultrasound. Indian J Radiol Imaging 1999;9:165.
6. Taylor RH, McNicol MW. Ultrasound in the diagnosis of two unusual tuberculous abscesses. Br J Surg 1980;67:556.
7. Pacifici A, Tinti A, Flamini FO, et al. Colour flow duplex scanning: an accurate, non-invasive technique for preoperative evaluation of the vascular supply of the rectus abdominis myocutaneous flap. Scand J Plastic Reconstruc Surg Hand Surg 1995;29:319–324.
8. Krombach GA, Truong S, Staatz G, et al. Panorama ultrasonography of the abdominal wall for delineation of the anatomy and diagnosis of pathological findings. Rofo Fortschr Geb Rontgenstr Neuen Bildgeb Verfahr 2001;173(8):714–719.
9. Kaftori JK, Rosenberger A, Pollack S, Fish J. Rectus sheath hematoma: ultrasonographic diagnosis. AJR Am J Roentgenol 1977;128:281.
10. Cervantes J, Sanchez-Cortazar J, Ponte RJ, Manzo M. Ultrasound diagnosis of rectus sheath hematoma. Am Surg 1983;49:542.
11. Guivarch M, Boeuf B. Hematomes des muscles droits de l'abdomen: vingt-sept observations. Presse Med 1988;17:1845.
12. Van den Berg JC, Rutten MJ, de Valois JC, et al. Masses and pain in the groin: a review of imaging findings. Eur Radiol 1998;8:911–921.
13. Gokhale S. Three dimensional sonography of muscle hernias. J Ultrasound Med 2007;26(2):239–242.
14. Bailey & Love's Short practice of surgery. London: HK Lewis & Co Ltd.
15. Rettenbacher T, Hollerweger A, Macheiner P, et al. Abdominal wall hernias: cross-sectional imaging signs of incarceration determined with sonography. AJR Am J Roentgenol 2001;177(5):1061–1066.
16. Young J, Gilbert AI, Graham MF. The use of ultrasound in the diagnosis of abdominal wall hernias. Hernia 2007;11(4):347–351.
17. Bradley M, Morgan J, Pentlow B, Roe A. The positive predictive value of diagnostic ultrasound for occult herniae. Ann R Coll Surg Engl 2006;88(2):165–167.
18. Koehler RH. Diagnosing the occult contralateral inguinal hernia. Surg Endosc 2002;16(3):512–520.
19. Bradley M, Morgan D, Pentlow B, Roe A. The groin hernia – an ultrasound diagnosis? Ann R Coll Surg Engl 2003;85(3):178–180.
20. Chen KC, Chu CC, Chou TY, Wu CJ. Ultrasonography for inguinal hernias in boys. J Pediatr Surg 1998;33(12):1784–1787.
21. Robinson P, Hensor E, Lansdown MJ. Inguinofemoral hernia: accuracy of sonography in patients with indeterminate clinical features. AJR Am J Roentgenol 2006;187(5):1168–1178.
22. Lilly MC, Arregui ME. Ultrasound of the inguinal floor for evaluation of hernias. Surg Endosc 2002;16(4):659–662.
23. Kervancioglu R, Bayram MM, Ertaskin I, Ozkur A. Ultrasonographic evaluation of bilateral groins in children with unilateral inguinal hernia. Acta Radiol 2000;41(6):653–657.
24. Jamadar DA, Jacobson JA, Morag Y, et al. Sonography of inguinal region hernias. AJR Am J Roentgenol 2006;187(1):185–190.
25. Zhang GQ, Sugiyama M, Hagi H, et al. Groin hernias in adults: value of color Doppler sonography in their classification. J Clin Ultrasound 2001;29(8):429–434.
26. Jamadar DA, Jacobson JA, Morag Y, et al. Characteristic locations of inguinal region and anterior abdominal wall hernias: sonographic appearances and identification of clinical pitfalls. AJR Am J Roentgenol 2007;188(5):1356–1364.
27. Malik KA, Chopra P. Spigelian hernia: a rarity. J Pak Med Assoc 2006;56(9):417–419.
28. Torzilli G, De Fabbro D, Felisi R, et al. Ultrasound guided reduction of an incarcerated Spigelian hernia. Ultrasound Med Biol 2001;27(8):1133–1135.
29. Fon LJ, Spence RA. Sportsman's hernia. Br J Surg 2000;87(5):545–552.
30. Caudill PH, Nyland JA, Smith CE, et al. Sports hernias: a systematic literature review. Br J Sports Med 2008; Jul 4.
31. Diesen DL, Pappas TN. Sports hernias. Adv Surg 2007;41:177–187.
32. Jamadar DA, Jacobson JA, Girish G, et al. Abdominal wall hernia mesh repair: sonography of mesh and common complications. J Ultrasound Med 2008;27(6):907–917.
33. Cingi A, Solmaz A, Attaallah W, et al. Enterostomy closure site hernias: a clinical and ultrasonographic evaluation. Hernia 2008;12(4):401–405.
34. Lilly MC, Arregui ME. Lipomas of the cord and round ligament. Ann Surg. 2002;235(4):586–590.
35. Safak AA, Erdogmus B, Yazici B, Gokgoz AT. Hydrocele of the canal of Nuck: sonographic and MRI appearances. J Clin Ultrasound 2007;35(9):531–532.
36. Yang DM, Kim HC, Lim JW, et al. Sonographic findings of groin masses. J Ultrasound Med 2007;26(5):605–614.
37. Lipset RE, Kirpekar M, Cooke KS, Abiri MM. US case of the day: myxoid liposarcoma of the spermatic cord. Radiographics 1997;17:1316–1318.
38. Patterson GK, Winburn GB. Abdominal wall endometriosis: a report of eight cases. Am Surg 1999;65:36–39.
39. Francica G, Giardiello C, Angelone G, et al. Abdominal wall endometriomas near caesarean delivery scars: sonographic and color Doppler findings in a series of 12 patients. J Ultrasound Med 2003;22:1041–1047.
40. Hensen JH, Van Breda Vriesman AC, Puylaert JB. Abdominal wall endometriosis: clinical presentation and imaging features with emphasis on sonography. AJR Am J Roentgenol 2006;186:616–620.
41. Sakai N, Yamada T, Muratama T, Asao T. Leiomyoma of the spermatic cord extending along the vas deferens. Hinyokika Kiyo 1998;44:121–123.
42. Wegner HE, Herbst H, Dieckmann KP. Paratesticular epidermoid cyst and ipsilateral spermatic cord dermoid cyst: case report and discussion of pathogenesis, diagnosis and treatment. J Urol 1994;152:2101–2103.
43. Jung JL, Abouelfadel Z, Straub P. Cystic lymphangioma of the spermatic cord: report of a new case. Prog Urol 1996;6:948–949.
44. Shadbolt CL, Heinze SB, Dietrich RB. Imaging of groin masses: inguinal anatomy and pathologic conditions revisited. Radiographics 2001;21 Spec No: S261–S271.
45. Cappele O, Sibert L, Descargues J, et al. A study of the anatomic features of the duct of the urachus. Surg Radiol Anat 2001;23:229–235.
46. Yu JS, Kim KW, Lee HJ, et al. Urachal remnant diseases: spectrum of CT and US findings. Radiographics 2001;21:451–461.
47. Ziprin P, Williams P, Foster ME. External oblique aponeurosis nerve entrapment as a cause of groin pain in the athlete. Br J Surg 1999;86(4):566–568.
48. Meyer MA. Dynamic radiology of the abdomen. Normal and pathologic anatomy. 3rd ed. New York: Springer Verlag; 2000.
49. Weill F, Watrin J, Rohmer P, et al. Ultrasound and CT of peritoneal recesses and ligaments: a pictorial essay. Ultrasound Med Biol 1986;12:977.
50. Halvorsen RA, Thompson WM. Ascites or pleural effusion? CT and ultrasound differentiation. Crit Rev Diagn Imag 1986;26:201.
51. Weill F, Perriguey G, Belloir A, et al. Ultrasonic anatomical study of the lesser omental sac: a pictorial essay. Eur J Radiol 1983;2:143.
52. Gerzof SG, Oates ME. Imaging techniques for infections in the surgical patient. Surg Infect 1968;68:147.
53. Forsby J, Henriksson L. Detectability of intraperitoneal fluid by ultrasonography. Acta Radiol Diagn 1984;25:375.
54. Dubbins PA, Kurtz AB. Intraabdominal fluid collections. In: Goldberg BB, ed. Abdominal Ultrasonography. New York: Wiley; 1984.
55. Baker ME, Blinder RA, Rice RP. Diagnostic imaging of abdominal fluid collections and abscesses. Crit Rev Diagn Imag 1986;25:233.
56. Paajanen H, Lahti P, Nordback I. Sensitivity of transabdominal ultrasonography in detection of intraperitoneal fluid in humans. Eur Radiol 1999;9:1423–1425.
57. Fontaine S, Lafortune M, Breton G, et al. Ascites as a cause of hyperechogenic kidneys. J Clin Ultrasound 1985;13:633.
58. Sanders RC. The significance of sonographic gallbladder wall thickening. J Clin Ultrasound 1980;8:143.
59. Fiske CE, Laing FC, Brown TW. Ultrasonographic evidence of gallbladder wall thickening in association with hypoalbuminemia. Radiology 1980;135:713.
60. Kaftori JK, Pery M, Green J, et al. Thickness of the gallbladder wall in patients with hypoalbuminemia: a sonographic study of patients on peritoneal dialysis. AJR Am J Roentgenol 1987;148:1117.
61. Tsujimoto T, Miyamoto T, Tada T. Differentiation of benign from malignant ascites by sonographic evaluation of gallbladder wall. Radiology 1985;157:503.
62. Edell SL, Gefter WB. Ultrasonic differentiation of type of ascitic fluid. AJR Am J Roentgenol 1979;133:111.
63. Merrit CB, Williams SM. Ultrasound findings in a patient with

pseudomyxoma peritonei. J Clin Ultrasound 1978;6:417.
64. Matsumi H, Kozuma S, Osuga Y, et al. Ultrasound imaging of pseudomyxoma peritonei with numerous vesicles in ascitic fluid [letter]. Ultrasound Obstet Gynecol 1999;13:378–379.
65. Bard C, Lafortune M, Breton G. Ascites: ultrasound guidance or blind paracentesis. Can Med Assoc J 1986;135:209.
66. Lurie K, Plzak L, Deveney CW. Intraabdominal abscess in the 1980s. Surg Clin North Am 1988;67:621.
67. Witzigmann H, Geissler F, Uhlmann D, et al. Intra-abdominal abscess. Chirurgie 1998;69:813–820.
68. Casola G, Vansonnenberg E. Diagnosis and percutaneous drainage of abdominal abscesses. Clin Gastroenterol 1985;14:469.
69. Joseph AE. Imaging of abdominal abscesses. BMJ 1985;291:1447.
70. Dobrin PB, Heer Gully P, Greenlee HB, et al. Radiologic diagnosis of an intra-abdominal abscess. Arch Surg 1986;121:41.
71. Crivello MS, Peterson IM, Austin RM. Left lobe of the liver mimicking perisplenic collection. J Clin Ultrasound 1986;14:697.
72. Ohara T, Itoh Y, Itoh K. Ultrasound instruments as possible vectors of staphylococcal infection. J Hosp Infect 1998;40:73–77.
73. Tesch C, Froschle G. Sonography machines as a source of infection [letter; comment]. AJR Am J Roentgenol 1997;168:567–568.
74. Kressel HY, Filly RA. Ultrasonographic appearance of gas-containing abscesses in the abdomen. AJR Am J Roentgenol 1978;130:71.
75. Patel S, Gopichandran T. Ultrasound evidence of gas in the fissure for the ligamentum teres: a sign of perforated duodenal ulcer. Br J Radiol 1999;72:901–902.
76. Butler JA, Huang J, Wilson SE. Repeated laparotomy for postoperative intra-abdominal sepsis: an analysis of outcome predictors. Arch Surg 1987;122:702.
77. Walters R, Herman CM, Neff R, et al. Percutaneous drainage of abscesses in the postoperative abdomen that is difficult to explore. Am J Surg 1985;149:623.
78. Brooke Jeffrey R, Wing VW, Laing FC. Real-time sonographic monitoring of percutaneous abscess drainage. AJR Am J Roentgenol 1985;144:469–470.
79. Worthen NJ, Gunning JE. Percutaneous drainage of pelvic abscesses: management of the tubo-ovarian abscess. J Ultrasound Med 1986;5:551–556.
80. Cadotte RN, Rankin RN. Percutaneous drainage and aspiration of fluid collections: emphasis on pancreatic collections and transplant patients. J Can Assoc Radiol 1988;39:121.
81. Pruett TL, Rotstein OD, Crass J. Percutaneous aspiration and drainage for suspected abdominal infection. Surgery 1984;96:731.
82. Jansen M, Truong SN, Sparenberg P, et al. Ultrasound-controlled, percutaneous drainage: a safe and simple method for treatment of intra-abdominal abscesses. Langenbecks Arch Chir 1997;114:1205–1206.
83. Rozycki G. Abdominal ultrasonography in trauma. Surg Clin North Am 1995;75:175–191.
84. Shanmuganathan K, Mirvis S, Sherbourne C, et al. Hemoperitoneum as the sole indicator of abdominal visceral injuries: a potential limitation of screening abdominal US for trauma. Radiology 1999;212:423–430.
85. Belli AM, Joseph AE. The renal rind sign: a new ultrasound indication of inflammatory disease in the abdomen. Br J Radiol 1988;61:806–810.
86. Meyers MA, Whalen JP, Peele K. Radiological features of extraperitoneal effusions. Radiology 1972;104:249–257.
87. Raptopoulos V, Kleinman PK, Marks S, et al. Renal fascial pathway: posterior extension of pancreatic effusions within the anterior pararenal space. Radiology 1986;158:367–374.
88. Raskin M. Combination of CT and ultrasound in the examination of the retroperitoneum and pelvis. Crit Rev Diag Imag 1980;13:173–228.
89. Callen PW, Filly RA, Sarti DA, Sample WF. Ultrasonography of the diaphragmatic crura. Radiology 1979;130:721–724.
90. Lev-Toaff A, Goldberg B. Gastrointestinal ultrasound contrast. In: Ultrasound contrast agents. London: Martin Dunitz; 1997.
91. Pardes JG, Auh YH, Kneeland JB. The oblique coronal view in sonography of the retroperitoneum. AJR Am J Roentgenol 1985;144:1241–1247.
92. Creagh-Barry M, Adam EJ, Joseph AE. The value of oblique scans in the ultrasonic examination of the abdominal aorta. Clin Radiol 1986;37:239–241.
93. Grunebaum M, Ziv N, Kornreich L. The sonographic evaluation of the great vessels' interspace in the pediatric retroperitoneum. Pediatr Radiol 1986;16:384–387.
94. Dietrich CF, Zeuzem S, Caspary WF, Wehrmann T. Ultrasound lymph node imaging in the abdomen and retroperitoneum of healthy probands. Ultraschall Med 1998;19:265–269.
95. Koenigsberg M, et al. Sonographic evaluation of the retroperitoneum. Semin Ultrasound 1982;3:79–95.
96. Yeh HC. Adrenal gland and non-renal retroperitoneum. Urol Radiol 1987;9:127–140.
97. Felix EL, Wood DK, Das Gupta TK. Tumours of the retroperitoneum. Curr Probl Cancer 1981;6:3–47.
98. Jacobsen S, Juul-Jorgensen P. Primary retroperitoneal tumours. Acta Chir Scand 1974;140:498–500.
99. Davidson AJ, Hartman DS. Imaging strategies for tumors of the kidney, adrenal gland, and retroperitoneum. Cancer 1987;37:151–164.
100. Kryger-Baggesen N, Kjaergaard J, Sehested M. Nonchromaffin paraganglionoma of the retroperitoneum. J Urol 1985;134:536–537.
101. Goldman SM, Davidson AJ, Neal J. Retroperitoneal and pelvic haemangiopericytomas: clinical, radiologic and pathologic correlation. Radiology 1988;168:13–17.
102. Goldman SM, Hartman DS, Weiss SW. The varied radiographic manifestations of retroperitoneal malignant fibrous histiocytoma revealed through 27 cases. J Urol 1986;135:33–38.
103. Skaane P. The right iliac fossa features of a large retroperitoneal liposarcoma. Fortschr Rontgenstr 1986;145:351–353.
104. Bertolotto M, Cittadini G Jr, Crespi G, et al. Hemangiopericytoma of the greater omentum: US and CT appearance. Eur Radiol 1996;6:454–456.
105. Davidson AJ, Hartman DS, Goldman SM. Mature teratoma of the retroperitoneum. Radiologic, pathologic and clinical correlation. Radiology 1990;172:421–425.
106. Derchi LE. Rizzatto G, Banderali A, et al. Sonographic appearance of primary retroperitoneal cysts, J Ultrasound Med 1989;8:381–384.
107. Kehagias DT, Karvounis EE, Fotopoulos A, Gouliamos AD. Retroperitoneal mucinous cystadenoma. Eur J Obstet Gynecol Reprod Biol 1999;82:213–215.
108. Davidson AJ, Hartman DS. Lymphangioma of the retroperitoneum: CT and sonographic characteristic. Radiology 1990;175:507–510.
109. McWilliams RG, Blakeborough A, Johnson MI, Weston M. Case report: The 'veiled right kidney sign' – an ultrasound finding in retroperitoneal perforation of the duodenum. Br J Radiol 1996;69:1061–1063.
110. Hoddick W, Jeffrey RB, Goldberg HI, et al. CT and sonography of severe renal and perirenal infections. AJR Am J Roentgenol 1983;140:517–520.
111. Kumari S, Pillari G, Phillips G, Pochachaczevsky R. Fluid collections of the psoas in children. Semin Ultrasound 1982;3:139–155.
112. Fagan CJ, Amparo EG, Davis M. Retroperitoneal fibrosis. Semin Ultrasound 1982;3:123–138.
113. Sanders RC, Duffy T, McLoughlin MG, Walsh PC. Sonography in the diagnosis of retroperitoneal fibrosis. J Urol 1977;118:944–946.
114. Gilkeson GS, Allen NB. Retroperitoneal fibrosis. A true connective tissue disease. Rheum Dis Clin North Am 1996;22:23–38.
115. Kottra JJ, Dunnick NR. Retroperitoneal fibrosis. Radiol Clin North Am 1996;34:1259–1275.
116. Arger PH, Stolz JL, Miller WT. Retroperitoneal fibrosis: an analysis of the clinical spectrum and roentgenographic signs. AJR Am J Roentgenol 1973;119:812–821.
117. Coleman PK. Radiologic/pathologic correlation conference. Case 15: abdominal mass in a 73 year old man. Appl Radiol 1980;12:121–126.
118. Kittredge RD, Nash AD. The many facets of sclerosing fibrosis. AJR Am J Roentgenol 1974;122:288.
119. Fagan CJ, Larrieu AJ, Amparo EG. Retroperitoneal fibrosis: ultrasound and CT features. AJR Am J Roentgenol 1979;133:239–243.
120. Brooks AP. Computed tomography of idiopathic retroperitoneal fibrosis ('periaortitis'): variants, variations, patterns and pitfalls. Clin Radiol 1990;4:75.

CHAPTER

42

Abdominal trauma

Orlando Catalano

INTRODUCTION

Patient history, physical examination and laboratory data are important but not reliable in predicting the presence and severity of injuries in abdominal trauma. Diagnostic imaging has permitted a dramatic change in the management and outcome of the trauma patient over the past three decades. Adequate detection and grading of injuries has reduced the number of unnecessary laparotomies and allowed an appropriate choice between surgical and non-surgical treatment. Exploratory laparotomy, which was almost the rule till thirty years ago, is now a selective, therapeutic laparotomy, used only in 6% of blunt abdominal trauma (BAT) cases.

In European and Asian countries, ultrasound (US) has been employed in trauma imaging since the late 1970s.[1] Thanks to improvements in scanners and probes, US has been used to screen trauma patients and to monitor injury evolution in those managed conservatively. In North American institutions, the potential of US has been neglected for a long time.[2] Only at the beginning of the 1990s, did some authors start using US, although in the modified version of Focused Assessment of Sonography for Trauma (FAST). FAST is a technique employed mostly by emergency physicians, to rule out peritoneal fluid (as an indirect sign of solid organ injury) in a patient with abdominal trauma. It is the non-invasive substitute for diagnostic peritoneal lavage (DPL), allowing quantification of the fluid.[3–6] In this chapter, the term 'ultrasound' will be used when referring to a complete US examination (targeting both fluid and solid organs). This is what we like to call 'full potential' US. The acronym 'FAST' will be employed only when specifically referring to this simplified, fluid-targeted triage modality.

SCANNING METHODOLOGY

FAST

In the beginning, the FAST procedure was used only to explore Morison's hepatorenal recess, the most dependent area of the peritoneal cavity in the supine patient. This was achieved by using longitudinal scans with the patient in the Trendelenburg position.[7] Nevertheless, clinicians performing FAST soon felt the need to include other peritoneal spaces, being dependent or closer to the bleeding site. Some authors[8] advocate four points to be systematically explored, still using mostly longitudinal scans: epigastrium, right and left hypochondrium, and pelvis. McGahan et al.[9,10] categorised a five-point survey: right upper quadrant including the hepatorenal fossa, left upper quadrant including the perisplenic area, left and right paracolic gutter, and pelvis. This multifocal system proved to be more effective than limiting the procedure to Morison's pouch.[11] Some authors[12,13] include the pericardium, in addition to the right and left subphrenic space, the subhepatic space, and the pelvis. Other authors[14] described a six-point scan, with views of the subxiphoid area, suprapubic area, right and left abdominal quadrant, and right and left pelvic quadrant. Finally other groups[15] evaluated seven areas to rule out intraperitoneal and retroperitoneal fluid (upper quadrants, renal fossae, paracolic gutters, and pelvis). In some institutions, the so called 'extended FAST' is performed, to include the chest and consequently rule out pleural effusion and pneumothorax[16] (Figs 42.1 and 42.2). Whichever study protocol is employed, the tendency is to standardise the FAST exploration by defining a precise number of well-defined views.

Some groups performing FAST scans, especially those with a radiological background, have progressively modified their scanning technique.[2,10,17–20] These groups have started to use a more complete abdominal exploration, including organ parenchyma, although this is still far from the 'full potential' technique we will describe below. Most non-radiological groups limit their approach to the FAST technique, often performed with small, portable scanners during the initial emergency room assessment of the patient or even during pre-hospital retrieval.[21] In Europe, till recently, trauma US has been mostly performed by radiologists, both in the imaging department and in the emergency room.[22] In the USA, the trauma US studies are usually carried out by sonographers, with

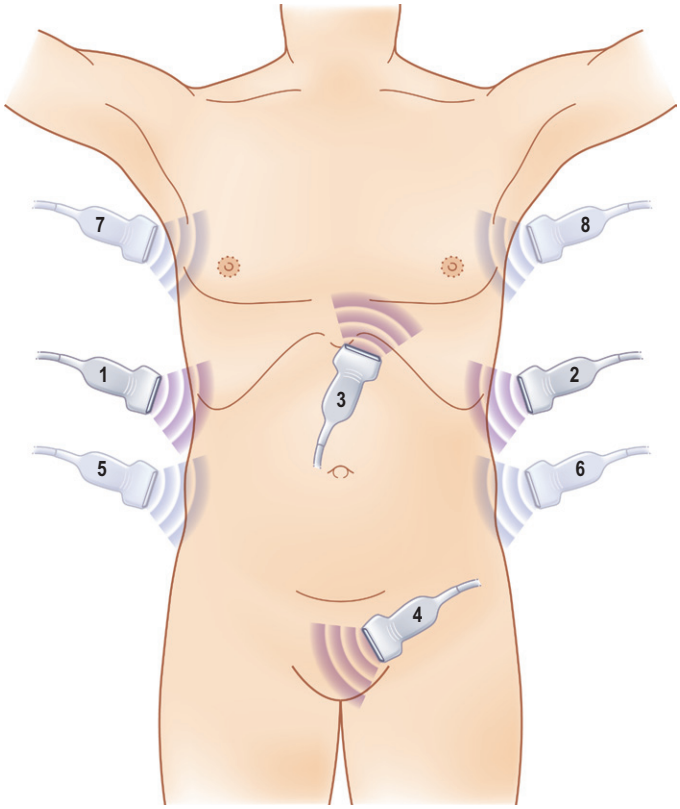

Figure 42.1 Placement of ultrasound probes during FAST and extended FAST technique. 1: Right hypochondrium (Morison's pouch). 2: Left hypochondrium. 3: Pericardium. 4: Pelvis (retrovesical space). 5: Right renal fossa. 6: Left renal fossa. 7: Right chest base. 8: Left chest base.

Role of imaging in assessing abdominal trauma

- Imaging plays a major role in the assessment of the trauma patient, since clinical and laboratory indicators can be inconstant and non-specific.
- Imaging has greatly reduced the number of exploratory laparotomies.
- Imaging is employed to:
  1. detect the injuries on admission
  2. characterise lesion type, size and grade
  3. choose the most appropriate treatment
  4. establish the appropriate timing for all therapeutic steps
  5. understand the dynamics of the trauma
  6. identify underlying non-traumatic abnormalities
  7. monitor conservative treatment
  8. detect the post-traumatic and post-therapeutic, early and late complications.
- The main imaging modalities currently employed are Focused Assessment of Sonography for Trauma (FAST), 'full potential' US, and contrast-enhanced CT.
- Diagnostic peritoneal lavage (DPL) and X-ray diagnostic modalities such as urography, gastrointestinal tract studies and angiography have lost their role.

the direct or indirect supervision of a radiologist.[2,14,15,18,20] FAST has achieved a rapid acceptance among emergency doctors, who now perform FAST scans themselves.

Sensitivity for detecting and quantifying the peritoneal fluid depends on operator experience. If training is minimal, moderate, or considerable, the sensitivity is respectively 45%, 87%, and 100% for an effusion smaller than 1000 mL and 38%, 63%, and 90% for an amount smaller than 250 mL.[23] In a case series collected over 19 months, 67% of the false negative results happened during the first 3 months.[14] Hence, some suggest at least 200 supervised exams are needed to achieve an adequate diagnostic capability[24] while others believe that 10 studies are enough.[25] Since it is common experience that a large amount of free peritoneal fluid is easily recognisable, an adequately trained physician or nurse should be able to identify this without significant false negatives (or false positives).

FAST

- FAST is a fluid-targeted sonographic study, intended as a quick and non-invasive substitute for DPL.
- FAST is used in the pre-hospital and in-hospital triage of trauma patients, to rule out a haemoperitoneum.
- FAST protocols include a variable number of systematic views employed to explore the main, dependent peritoneal spaces. Some protocols also include views for the pericardial and/or pleural space.
- FAST has shown 57–85% sensitivity, a 96–99% specificity, a 80–96% positive predictive value, a 96–97% positive predictive value, and a 90–96% accuracy.
- FAST is extremely useful in the subject with haemodynamic instability but its role in the stable patient is questionable.

'Full potential' US

As an alternative to FAST scan, 'full potential' US consists of a complete (although frequently rapid) exploration of all abdominal spaces and organs, without predefined 'points of view', to detect both haemoperitoneum and parenchymal injuries. Advocates of the 'full potential' scan highlight the ability of US to decrease the number of unnecessary computed tomography (CT) studies, whilst aware of the lower sensitivity of US compared to CT in the detection of organ trauma,. To perform a 'full potential' US study, the operator must be skilled in all the techniques of modern, state-of-art scanners. These include selective use of superficial transducers, harmonic imaging, power Doppler mode and US contrast media.

Superficial, high-frequency transducers (7.5 MHz) allow, at least in children and slim adults, a better visualisation of parenchyma than standard abdominal probes.[26] These transducers should be employed whenever possible, both to identify minimal effusions, especially around the liver apex and the lower splenic pole, and to recognise parenchymal injuries, at least in the most superficial part of the spleen and kidneys (Figs 42.3 and 42.4). Pneumoperitoneum and pneumothorax can be found with high-frequency probes.

Tissue harmonic imaging offers greater resolution and tissue contrast in comparison with the fundamental mode. Tissue harmonics have proved useful in the assessment of parenchymal injuries, especially in obese subjects. It improves the recognition of free peritoneal fluid.[27]

The use of the colour Doppler and especially of the power Doppler mode, both unenhanced and contrast-enhanced, can be helpful.[28] Power Doppler can identify cases with total or near total organ devascularisation, as may happen in splenic or renal trauma. By using both abdominal and superficial probes, power Doppler may help in detecting significant defects within the vascular map of an organ (Fig. 42.5).

Contrast-specific, greyscale US (CEUS) increases the conspicuity of organ injuries with a closer morphological correlation with CT.[29,30] Subtle findings at baseline US become clearer after contrast injection and active contrast extravasation, an indicator of active bleeding, can be detected. US contrast media are very well tolerated, do not require fasting or laboratory tests, can be used in the unstable patient or the patient with renal failure, and their injection

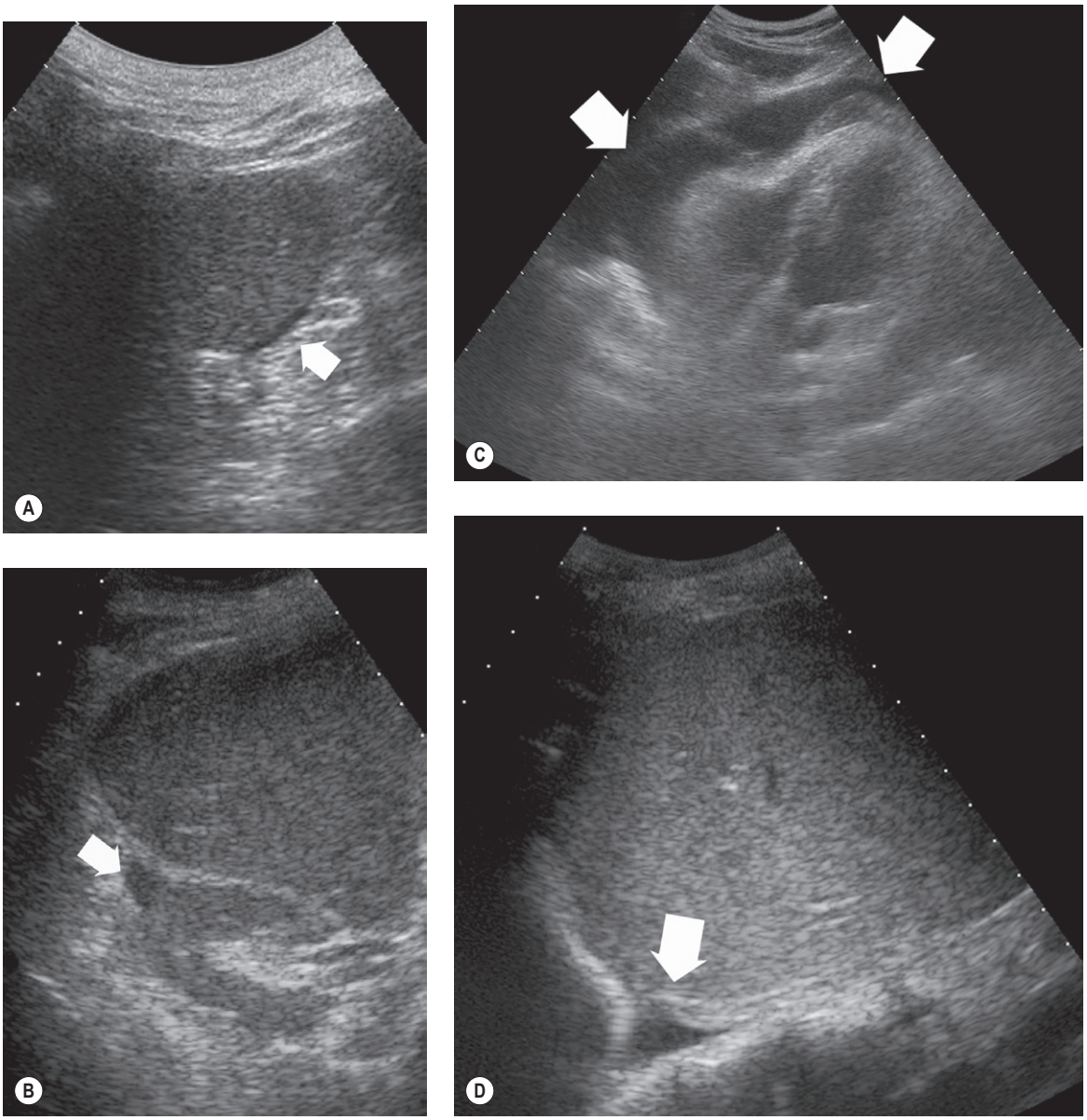

Figure 42.2 Small amounts of free fluid recognisable during FAST and extended FAST exploration. **A:** Intraperitoneal, perisplenic fluid (arrow). **B:** Retroperitoneal, perirenal fluid (arrow). **C:** Pericardial fluid (arrows). **D:** Right-sided pleural fluid (arrow).

can be repeated. Contrast enhancement of abdominal parenchyma lasts long enough (up to 4–5 minutes) to allow an adequate exploration of the whole abdomen. The kidneys have the most early and transient enhancement while the spleen is inhomogeneous at the beginning and then becomes persistently and homogeneously enhanced. Hence, the examination protocol may consist of a single contrast bolus exploring first the kidneys, then the liver, and finally the spleen, or it may be split into two injections, one for the right kidney and the liver and the second for the left kidney and the spleen.

A typical 'full potential' US scan for BAT starts with the abdominal transducer on the left side. Subcostal and intercostal scans are taken to explore the left kidney and left retroperitoneal area, the spleen and perisplenic spaces, the left hemidiaphragm and the left chest base. A very posterior view of the spleen may be particularly useful and a cooperative patient will be asked to move their left side slightly out of the bed. The colour Doppler mode during renal scans will rule out a severe shattering or a total devascularisation from renal pedicle avulsion. Next, transverse scans are taken at the level of the epigastrium, to explore the left liver lobe, the pancreas, the lesser omental cavity and, by angling the probe cephalad, the pericardium. Next, the right side is scanned, to explore the right kidney (also with a rapid colour Doppler view), right retroperitoneal space, right liver lobe, right perihepatic spaces and right chest base. Anterior and lateral views taken at subcostal and intercostal level are all useful. Finally the exploration is moved to the pelvis, searching for free fluid around the bladder and posterior to the uterus, by using longitudinal and transverse scans. A longitudinal view searching for fluid between the vesical dome and the intestinal loops is particularly helpful. Bladder distension with retrograde fluid filling can help to maximise the acoustic window but usually is not necessary.

Whenever possible, a slight rotation of the patient on the left and right sides (if spine injuries have already been excluded or are not suspected!) is useful. Nevertheless, a good US exploration can be obtained in a constantly supine subject. Additionally, whenever achievable, patient deep inspiration is helpful to scan the subphrenic areas. Limiting factors include obesity, inability to cooperate with breathing and decubitus variation, subcutaneous emphysema, pneumothorax and wounds.

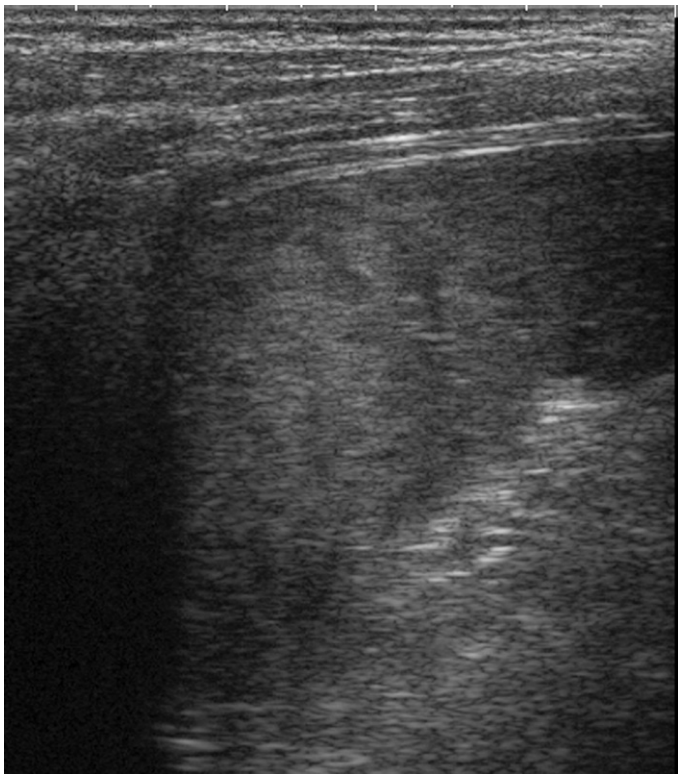

Figure 42.3 Paediatric splenic injury imaged with superficial transducer.

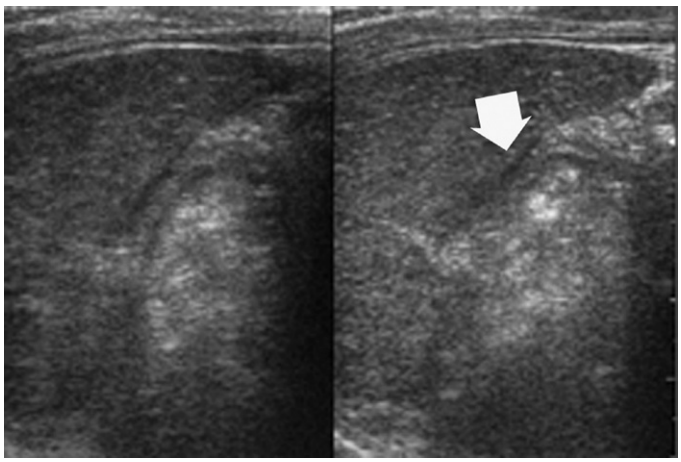

Figure 42.4 Minimal amount of perisplenic fluid (arrow) in a child, shown with a superficial transducer.

When there is enough time, this systematic exploration should be completed by a rapid scan using the superficial transducer. This is used to search for peritoneal fluid around the caecum, around the lower splenic pole and around the right liver lobe apex and to evaluate the near-field part of abdominal parenchyma, especially the spleen and kidneys.

FAST versus 'full potential' US

The key problem of the FAST scan is its application in haemodynamically stable patients.[31] This population represents the vast majority of the wide spectrum of injured people seen daily in an emergency centre. Stable patients should be evaluated carefully, not just to recognise a haemoperitoneum but also to identify organ injuries. Additionally, in a stable patient the recognition of presence or absence of free fluid has a smaller value as a stand-alone practice. Contrast-enhanced CT, especially with modern multidetector scanners, is the most accurate imaging modality in the assessment of traumatic lesions but the practice of CT scanning all subjects is debatable, especially those with a low pre-test probability of injury. It is necessary to have a pre-CT filter, other than clinic-laboratory data, patient observation, DPL or FAST findings. This presently can be obtained only by the 'full potential' US scan.[31]

FAST has a 57–85% sensitivity, a 96–99% specificity, a 80–96% positive predictive value, a 96–97% positive predictive value and a 90–96% accuracy in the detection of abdominal trauma through the recognition of the free peritoneal fluid.[32–34] In 2.5–7% of cases, the FAST result is indeterminate, especially because of obesity.[35,36] FAST is falsely negative in 17–29% of cases when compared with CT.[37–39] In children, compared with CT, sensitivity is 30–59%, specificity 79–100%, negative predictive value 75–82% and accuracy 76–91%.[20,32,40,41]

False negative FAST may be due to errors of interpretation, when fluid is present but not recognised. However, the major risk arises when haemoperitoneum is absent but a parenchymal injury is present.[20,37,39,42] In CT series, a solid or hollow viscus injury not combined with peritoneal fluid was found in 29–34% of all cases, in 11% of liver injuries and in 12% of splenic injuries.[38,39,42,43] In 25–37% of injured children there is no fluid associated with traumatic lesions.[35,44] In sonographic series, 12% of isolated spleen

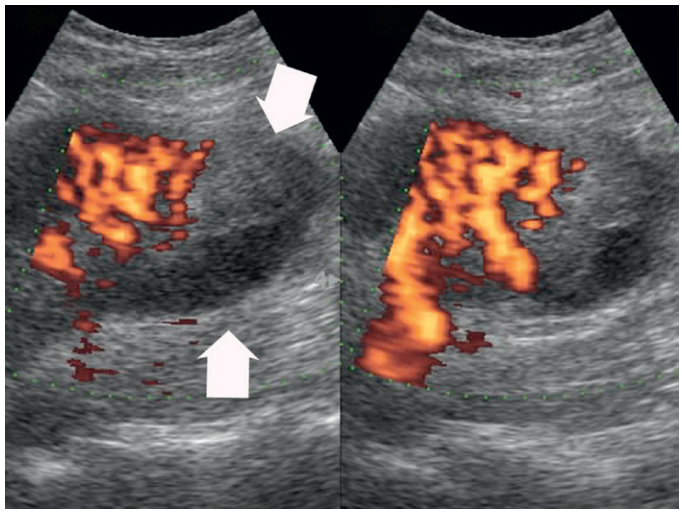

Figure 42.5 Renal injury as depicted using power Doppler US. The lower renal pole (arrows) is inhomogeneous, with a subcapsular collection and with an evident colour signal defect.

Full potential' US

- 'Full potential' US is intended as an accurate and complete sonographic exploration of abdominal organs (direct injury detection) and peritoneal spaces (indirect injury detection).
- Tissue harmonic imaging can improve the detection of both peritoneal fluid and parenchymal lesions.
- High-frequency transducers can improve the examination of superficial organs or organ portions and should be used routinely in children and slim adults.
- Colour and power Doppler can help recognise parenchymal injuries.
- Contrast-enhanced US (CEUS) is more accurate than US and almost as accurate as CT in recognising solid organ injuries. It may also show contrast extravasation as a sign of active bleeding.

lesions, 5% of liver lesions and 15% of isolated liver lesions did not show a haemoperitoneum.[45,46] The idea that an injury without combined effusion is usually a low-grade one, which if overlooked would not compromise patient management, is not always correct. In 10–17% of cases of organ trauma without free fluid, the injury required invasive treatment.[39,43] These published data demonstrate the need to examine both the abdominal organs and the peritoneal spaces, so that trauma will be recognised from free fluid or from organ changes.

A secondary reason to search for organ injury without limiting the US search to fluid is the possibility of a pre-existing effusion, for example due to ovulation, ascites, peritoneal dialysis or DPL. Theoretically these circumstances may lead to an unnecessary CT study or even laparotomy, while a US study negative for organ injury will help to correctly assess the patient.[18,46]

'Full potential' US versus CT

CT is the main imaging tool in the assessment of the polytrauma victim (i.e. a person with multiple potentially fatal injuries to more than one body region, with a suspected Injury Severity Score >14).[16] Individuals who have experienced a high-to-intermediate energy impact should be imaged principally with contrast-enhanced, whole-body CT. This is the only imaging modality able to examine the multisystem effects of trauma, detecting and grading the head, chest, abdomen and axis injury.

US has the advantages of being simple, rapid, non-invasive, scarcely interfering with resuscitation manoeuvres (just overhead lighting attenuation), transportable (admissions area, bedside, operating room, CT room, etc.), repeatable (the 'two-hour later' scan), and cheap. US is very sensitive for minimal amounts of free fluid and may allow the imaging of very fat subjects who do not fit into the CT gantry (although the sonographic exploration of these patients will be difficult). The limitations include a limited or impossible examination of some organs and structures (deep splenic pole, posterior segments of the right liver lobe, kidneys, hollow viscera); a limited accuracy in the direct demonstration of organ injures (low lesion-to-parenchyma contrast gradient); a limited accuracy for detecting retroperitoneal blood; patient body habitus (obesity); poor cooperation (difficult deep inspiration or side turning in subjects with diminished level of consciousness), and a dependence on the operator (need for training in trauma imaging and 24-hour presence on site).[10,42] US has a limited accuracy in directly depicting hypovolaemic shock signs and vascular injuries and is unable to recognise ongoing bleeding.

Complete US has shown a 41–95% sensitivity, a 94–100% specificity, a 95–99% accuracy, a 61–87% positive predictive value and a 62–99% negative predictive value.[17–19,22,42] False negative results from complete US were 28% in one series[42] while liver-related false negative in another series were 28%.[45] In two series,[18,19] 11–33% of false negatives required a laparotomy while in another series[9] the false negative results did not have any relevant consequences. The most pessimistic of these studies, although not confirmed by our own experience, might lead to trauma US being abandoned for the stable patient.[42,43,47] However, these not always excellent US results should prompt us to work to improve its performance.[31]

Clinical and laboratory parameters have been developed to indicate whether further work-up is needed with a negative US result. Subjects with pulmonary contusion, haemothorax, pneumothorax, rib fractures (from the sixth to the twelfth, especially on the left side), dorsal and especially lumbar vertebral fractures, pelvic ring fractures, macrohaematuria or unexplained hypertransaminasaemia (AST value >360 IU/L)[15,48] should undergo CT scan even if the US result (or more so, if the FAST result) is negative. Arguably, if these indicators are identified before the US study is performed, patients should go directly to CT. Conversely, in the absence of these indicators, the probability of a false negative US is very low.[15]

In the USA, where CT scanners are widely available, CT is commonly regarded as almost the only imaging tool.[49] In Europe, even acknowledging the superiority of CT imaging, primary CT is used mostly for (stable) patients suspected of severe, high-energy, multitrauma. In the remaining cases, with a lower clinical suspicion or with a low-energy/localised trauma mechanism, US is employed together with clinical and laboratory parameters to initially screen the patient. CT is limited to cases found to be positive, inconclusive or discrepant at initial work-up. A diagnostic algorithm heavily based on CT carries lower diagnostic and malpractice risks, shorter hospitalisation time, and lower dependence on the operator and patient body habitus. Alternatively, if the institutional protocol relies more on primary US, there will be lower costs, lower risks related to iodinated contrast media, and lower patient exposure to radiation.

Although a negative CT scan leads to a more rapid patient discharge, an alternative may consist of observation of the patient with the eventual repetition of a US study (the 'two hours later' scan). After an accurate, 'full potential' US study, a repeated US scan carried out a couple of hours later allows definitive exclusion of significant injuries. This is the most reasonable choice in low-risk, fertile women when the only finding at initial US is a limited amount of pelvic fluid.

CEUS versus US and CT

CEUS is more sensitive than US and it is almost as sensitive as CT in the detection of solid organ injury in BAT. It allows a more accurate assessment of solid organ lesions in comparison with baseline US: very subtle injuries become sharply demarcated, due to the intense enhancement of the surrounding normal parenchyma. Additionally, CEUS can demonstrate changes not recognisable with US, such as post-traumatic infarction and contrast extravasation (Fig. 42.6). The spread of contrast-enhanced blood out of vessels into parenchyma, peritoneal cavity, or retroperitoneum, is considered a CT indicator of failing conservative management of an

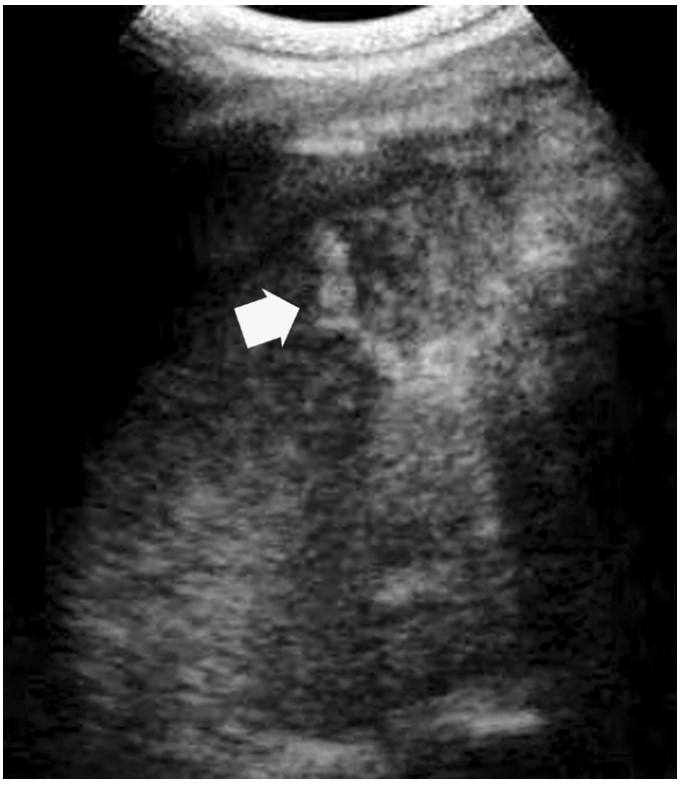

Figure 42.6 Contrast medium extravasation (arrow) as an indicator of active bleeding from spleen trauma.

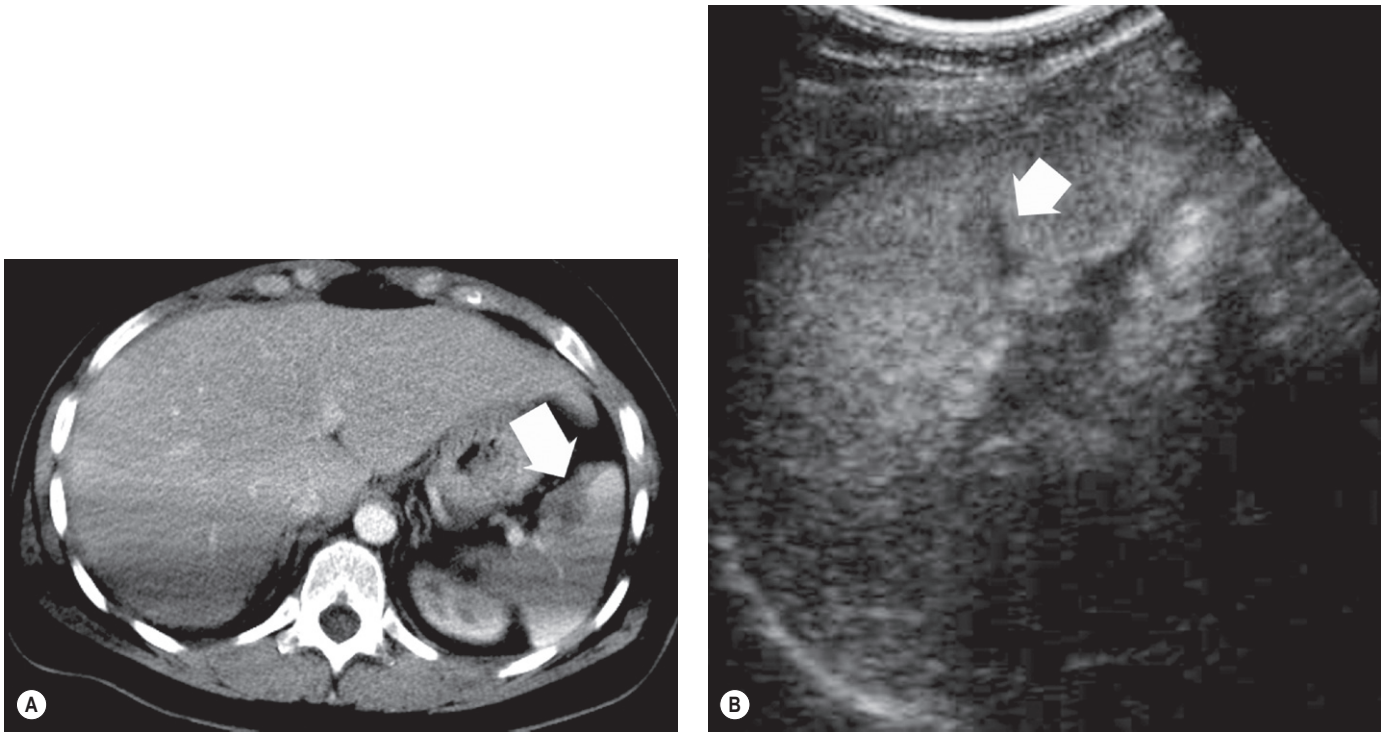

Figure 42.7 CEUS versus CT. A: A CT scan shows irregularity of the spleen (arrow) but beam hardening artefacts partially obscure the organ analysis. **B:** CEUS clearly shows the splenic laceration (arrow).

injury. The potential to detect this finding with CEUS opens new perspectives during the initial assessment and follow-up of the trauma patient.[50]

Contrast enhancement may overcome some intrinsic limitations of US and increase its diagnostic role. Consequently, the number of CT studies may be decreased. CT is the most effective modality in the trauma victim imaging, with a mean room time that is similar to that of US plus CEUS. In many trauma centres, CT scanners are sited inside the emergency room, minimising patient transport and speeding work-up. Nevertheless, CEUS may play a role in several clinical scenarios, such as unstable patient imaging, bed-side examination, isolated moderate-energy abdominal or flank trauma assessment (sport or horse-riding accidents, falls, minor bicycle accidents, etc.), and monitoring conservatively treated injuries. CEUS can be used when contrast-enhanced CT is contraindicated, or when it has failed or is unclear: not infrequently, emergency CT scans of trauma patients can show motion or positioning artefacts and CEUS may be used to better assess some unclear finding (Fig. 42.7).

CEUS may allow further evaluation of subtle parenchymal abnormalities shown by baseline US, to rule out injuries, or to diagnose a non-traumatic change, for example haemangiomas simulating traumatic lesions on baseline US. Operator confidence in affirming or excluding the presence of a traumatic injury is boosted by CEUS. A larger use of CEUS may reduce observation time for patients with a negative baseline US, decreasing the number of repeat US examinations and expediting patient discharge. CEUS may permit imaging of patients not ideal for contrast-enhanced CT such as children and pregnant women. Several published series demonstrate that US plus CEUS allows a confident exclusion of significant abdominal injuries. Hence, many patients may be discharged, after a period of observation, without being submitted to CT.[29,30]

Follow-up during non-operative trauma treatment is probably the main future application of CEUS, although there is no published report on cost-effectiveness. In patients where the injury has already been detected and graded by CT, use of CEUS may significantly decrease the number of follow-up CT examinations.

US limitations such as obesity or difficulty in exploring deeply located areas are usually not improved by contrast medium and CEUS should not be used to overcome these limitations. Current CEUS systems have some specific drawbacks, such as loss of spatial resolution and overall image quality, and difficulty in assessing deep regions such as the right liver lobe posterior aspect (especially in patients with steatosis or fibrosis), the subphrenic spleen parenchyma, and the kidneys (especially in fat individuals).

FREE PERITONEAL FLUID

Peritoneal fluid mostly collects in dependent spaces, particularly Morison's hepatorenal recess and the median pelvic space (retrovesical in males and retrouterine in females). It was believed that Morison's recess was the first site where fluid collected, away from the injury site, but this is not true. A CT series[51] has shown the right anterior subphrenic space can be involved alone; this site is less ideal for US than CT detection, especially in patients unable to breathe deeply. The anatomical distribution of peritoneal fluid depends on the location of bleeding, on the anatomy of the various supramesocolic and inframesocolic spaces in the supine patient (dependent or non-dependent), and on the anatomical pathways of spread (easier diffusion along the right paracolic gutter than along the left, oblique orientation of the mesenteric root toward the right iliac fossa, and so on).[52] As the volume of free fluid increases, fluid will be seen conforming to the various dependent spaces and anechoic triangles will be noted between the bowel loops. Next, fluid will surround the mesenteric folds and loops, allowing their distinct depiction. With massive haemoperitoneum, all abdominal hollow and solid organs will be seen floating in the fluid.[2]

The knowledge of distribution patterns can be helpful in the search for the injured organ. In adults, it has been shown[46] that an effusion in the left upper quadrant, in both upper quadrants, or diffuse suggests a splenic injury, whilst an effusion in the right upper quadrant (alone or combined with inframesocolic fluid)

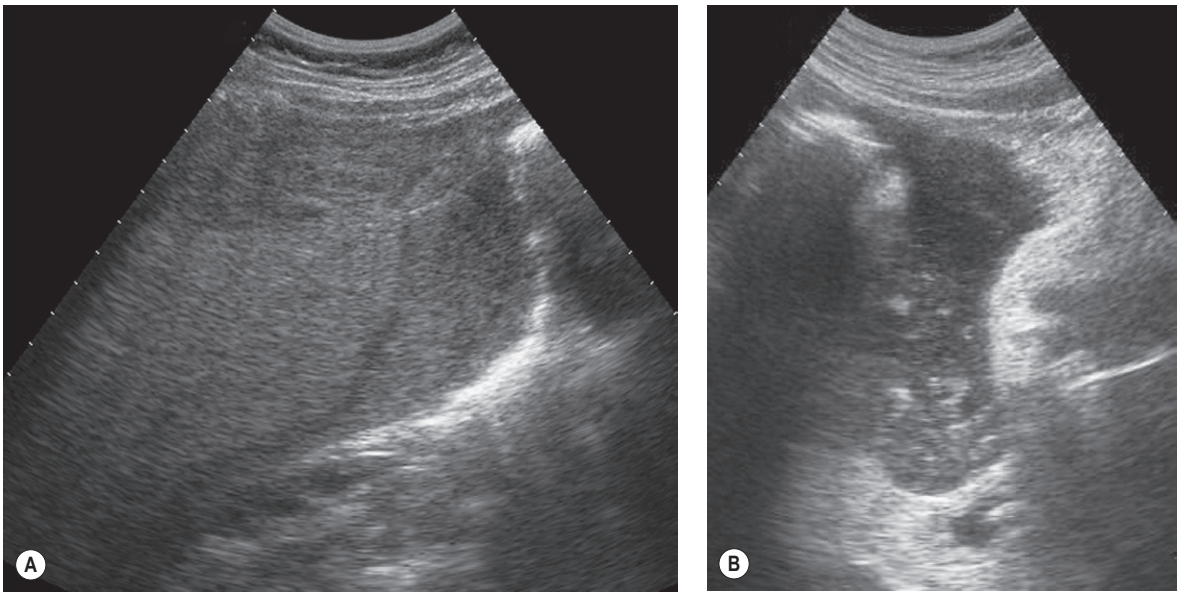

Figure 42.8 Slowly developing haemoperitoneum. A: Diffuse, inhomogeneous, hyperechoic fluid around the right liver lobe apex. **B:** Clots within the pelvic fluid.

usually indicates hepatic trauma. In intestinal injury, the fluid is distributed randomly, while in extraperitoneal trauma the fluid remains accumulated locally. In children, it seems that the pelvic spaces are always the main site of accumulation, aside from the location of the bleeding source.[53] The presence of fluid around the liver seems to be a predictor of the need of laparotomy, while fluid elsewhere and not in the perihepatic space seems to correlate better with a successful non-operative management.

A problem arises when US detects only a small peritoneal effusion in the absence of parenchymal injuries: decision making should be done case by case, considering the clinical and laboratory findings.[54] In women of childbearing age, it is very probable that fluid limited to the pouch of Douglas is due to ovulation. Nevertheless, it is important to be certain of the non-traumatic nature. Our approach is to carefully scan the other peritoneal spaces in search of even minimal amounts of fluid. Frequently we scan the pericaecal area with a high-resolution transducer: if there is no fluid around the caecum it becomes almost certain that the fluid in the pouch of Douglas is ovulatory. Repeating the US a couple of hours later or obtaining a CT or a CEUS scan is frequently necessary. If the fluid amount is significant, the fluid involves some extrapelvic space, or the woman is not of reproductive age (or she is pregnant or has previously undergone oophorectomy), immediate further imaging is mandatory. In children, a small amount of pelvic fluid can be physiological, in all ages and in both sexes.[55] Care should be taken not to automatically consider a small fluid collection, recognisable in up to 7% of asymptomatic children, as a sign of trauma.

An attempt to quantify the fluid should be made. This is because the amount of blood frequently correlates with the probability of a severe parenchymal injury and hence with prognosis (although the decision to surgically treat the patient should not be based only on fluid amount). Secondly, careful reporting of the number of peritoneal spaces involved and a tentative quantification of the fluid may help to compare serial US examinations. Several scoring systems have been proposed. These include the arithmetic addition of the number of positive peritoneal spaces,[56] the arithmetic addition of the number of peritoneal spaces with a fluid layer thicker than 2 mm,[57] the addition of the thickness (in centimetres) of the collections in a five-space exploration,[58] the anteroposterior thickness (in centimetres) of the largest collection plus one point for each additional positive space.[59] Probably, since the amount of fluid is directly related to the number of peritoneal spaces involved, all quantification methods are equally valid. Nevertheless, these scores are not easy to use and have scarcely entered clinical practice. Surgeons prefer fluid amounts expressed in millilitres, instead of an absolute score. We try to subjectively quantify the overall amount of fluid expressing it in millilitres in our reports. Correlating the amount of effusion recognised with US and the amount of blood aspirated during the subsequent surgical operation, we have built a personal, totally subjective, quantification parameter to which we refer.

The sensitivity of US for free peritoneal fluid is commonly regarded as very high, comparable if not superior to that of CT. We believe that both techniques are highly sensitive but that US can detect minimal amounts of fluid around abdominal organs, which may be missed by CT because of volume averaging artefact (reduced but still present with multislice scanners). In clinical series[7,9] the reported sensitivity of US for peritoneal fluid is 63–98%, specificity 94–100%, positive predictive value 86–100%, negative predictive value 85–95% and overall accuracy 85–95%. Experimentally, the US sensitivity reported by evaluating women who had had hysterosalpingography (about 10 mL of contrast medium) and subjects submitted to herniography (about 50 mL of contrast medium) has been 71% for the former group and 100% for the latter.[52] By examining the pelvis of a subject who has undergone DPL, it has been shown that a moderate amount of fluid (mean volume 100 mL) is needed for detection with US.[60] In another study[61] evaluating Morison's pouch during fluid infusion for DPL (in the Trendelenburg position), only 10% of participants were able to recognise a volume lower than 400 mL while the mean volume identified was 619 mL.

In most trauma patients evaluated acutely, the US appearance of intraperitoneal, unclotted blood is that of a homogeneous or near homogeneous anechoic effusion, indistinguishable from ascites. The fluid is freely distributed, without septation or loculation, although sometimes small, low-level echoes are recognisable. When bleeding has been very fast and intense and is still active, or when the haemorrhage has developed over many hours from a small source, other features can be identified. These include clots floating within the fluid, layered clots adjacent to the injured organ or within a dependent recess, and echoic debris in the dependent peritoneal spaces (Fig. 42.8). The echogenicity of the extravasated blood depends on the pre-trauma haematocrit, the bleeding speed, the time interval between trauma and US, and finally the proximity of the scanned area to the bleeding source. While free fresh blood is anechoic, its echogenicity increases in the areas where it clots into a haematoma. This particularly happens in proximity to the bleeding site, where the clotted blood may form a hyperechoic deposit.

This 'sentinel clot' is useful to draw the operator's attention to that specific anatomical area.

Care should be taken to identify anechoic areas within an injured organ. These small areas may indicate the site of active bleeding within a parenchymal laceration or may correspond to an arterial pseudo-aneurysm developed after the trauma.[62] Since both these conditions require immediate treatment, colour Doppler should be used to rule out a vascular nature of any abnormal anechoic image.

Peritoneal fluid

- US is extremely sensitive for free peritoneal fluid, being comparable to CT. Specificity is lower than that from CT.
- Peritoneal fluid initially fills the most dependent peritoneal recesses (Morison's pouch and pelvic median space) and then extends to the other spaces, between bowel loops and around solid organs.
- The following should be assessed:
  1. Is there free peritoneal fluid?
  2. Where is it distributed? How many peritoneal spaces are involved? Which is the space with the largest collection?
  3. What is the overall amount of fluid?
  4. Is it really blood or is it something else?
  5. Where is the bleeding site?
  6. Is the bleeding still ongoing?

LIVER TRAUMA

General considerations

Hepatic injuries represent 3–10% of all abdominal traumas, being less frequent than splenic ones. Recognition of liver trauma is important when it is deeply located, near vascular structures. Damage to major portal branches, main hepatic veins, or the retrohepatic inferior vena cava may cause a severe loss of blood and may be very difficult to manage. However, in most cases, the main vascular structures are preserved, and the bleeding, being mostly venous, is less dramatic than in the mostly arterial-related splenic trauma.

The bleeding from a liver injury is usually into the peritoneal cavity, resulting in a haemoperitoneum. A lesion at the dorsal aspect of the liver dome may also cause a retroperitoneal haemorrhage due to the liver bare area, where there is direct contact between the parenchyma and the right anterior pararenal space.

Clinical findings include right upper quadrant pain, right shoulder pain (uncommon) and hypotension (only in the case of extrahepatic bleeding). In biliary peritonitis, guarding, tenderness and ileus develop but this is not an early phase occurrence.

Severe liver injuries still carry a high mortality. This is due to dramatic haemorrhage developing with involvement of great hepatic and perihepatic vessels. Later complications developing in major liver injury, such as large bilomas, abscesses or pseudoaneurysms, may cause morbidity and mortality and prolonged hospitalisation.

With the exception of high-grade injuries, most liver trauma is managed conservatively. In both children and adults, monitoring, blood transfusion and percutaneous or intra-arterial treatment of complications allows avoidance of surgery.

Mechanisms of injury and classification

It is generally believed that a greater energy transfer is necessary to produce an injury in the liver than in the spleen. The intrahepatic vessels, especially the hepatic veins, represent points of decreased resistance and frequently lacerations follow the vascular planes or extend to vessel walls.

The most commonly involved liver area is the right lobe, particularly its posterior segments: this is not the easiest area to explore sonographically, especially in a patient unable to inspire deeply. Left lobe lesions are less common but tend to be deeper within the liver. An extension to the capsular surface causes greater bleeding than in cases without involvement of the capsule.

Up to 77–90% of liver trauma is combined with injury of other structures. Specifically, in a right-sided impact, injuries to right kidney, right adrenal, right hemidiaphragm, right base of the chest (pleura and lung) and right ribs can occur. In a frontal impact, injury to the duodenum, pancreatic head, vertebrae and left liver lobe can coexist. There is a greater probability of combined lesions of the pancreas and small bowel in liver trauma compared to splenic trauma.

The grading scale most commonly used for liver trauma is that from the American Association for the Surgery of Trauma (AAST).[63] This scale includes six levels of injury severity (Table 42.1). The extent and depth of the lesions must be precisely measured and this is not possible with US. The objective of performing a US study is only to detect a liver injury and to tentatively recognise the kind of lesion. Distinguishing between contusion (focal injury without macroscopic parenchymal interruption), laceration (focal

Table 42.1 Liver injury scale. The score must be advanced by one level for multiple injuries up to grade III (data from *Journal of Trauma* 38:323, 1995)[63]

Grade	Type of injury	Description of injury
I	Haematoma	Subcapsular, <10% surface area
	Laceration	Capsular tear, <1 cm parenchymal depth
II	Haematoma	Subcapsular, 10–50% surface area; intraparenchymal <10 cm in diameter
	Laceration	Capsular tear 1–3 parenchymal depth, <10 cm in length
III	Haematoma	Subcapsular, >50% surface area of ruptured subcapsular or parenchymal haematoma; intraparenchymal haematoma >10 cm or expanding
	Laceration	>3 cm parenchymal depth
IV	Laceration	Parenchymal disruption involving 25–75% hepatic lobe or 1–3 Couinaud's segments
V	Laceration	Parenchymal disruption involving >75% of hepatic lobe or >3 Couinaud's segments within a single lobe
	Vascular	Juxtahepatic venous injuries; i.e. retrohepatic vena cava/central major hepatic veins
VI	Vascular	Hepatic avulsion

parenchymal interruption) and lacero-contusion (focal interruption within a larger area of contusive inhomogeneity) is difficult. Very complex lacerations, with eventual fragmentation of the organ, can occur but are not specifically recognisable with US. The same applies to fractures (a full-thickness laceration extending from one liver surface to the other). The term 'fracture' should not be used to generically describe a laceration or a deep laceration. A rare kind of fracture is polar avulsion, where the apex of the right or most frequently of the left lobe is detached from the organ. In infarction, there is no specific injury within the parenchyma but its vascular supply has been involved. The term 'rupture' should probably be avoided in reports as it is potentially confusing. Some surgeons consider rupture to be any grade of liver injury combined with peritoneal fluid, some an injury extending to the liver capsule, while others consider it to be a very complex and severe parenchymal injury with or without haemoperitoneum.

US findings

Liver injury tends to be associated with a lower amount of peritoneal fluid in comparison with spleen injury. Liver injuries, even of a significant grade, may develop in the absence of a significant, concomitant haemoperitoneum, at least initially.

In the acute phase, liver contusions, haematomas and localised lacerations all appear as subtle and ill-defined hyperechoic regions within liver parenchyma[16] (Figs 42.9 and 42.10). Lacerations, the most common type of liver lesion, tend to appear as linear, branching or stellate areas. However, appearances are very variable, ranging from hypoechoic to hyperechoic, and this contributes to the difficulty even for the expert operator to detect an acute liver trauma with US. Additionally, focal or diffuse steatosis, spared non-steatotic areas and focal lesions such as haemangiomas may complicate the detection and characterisation of hepatic injuries.

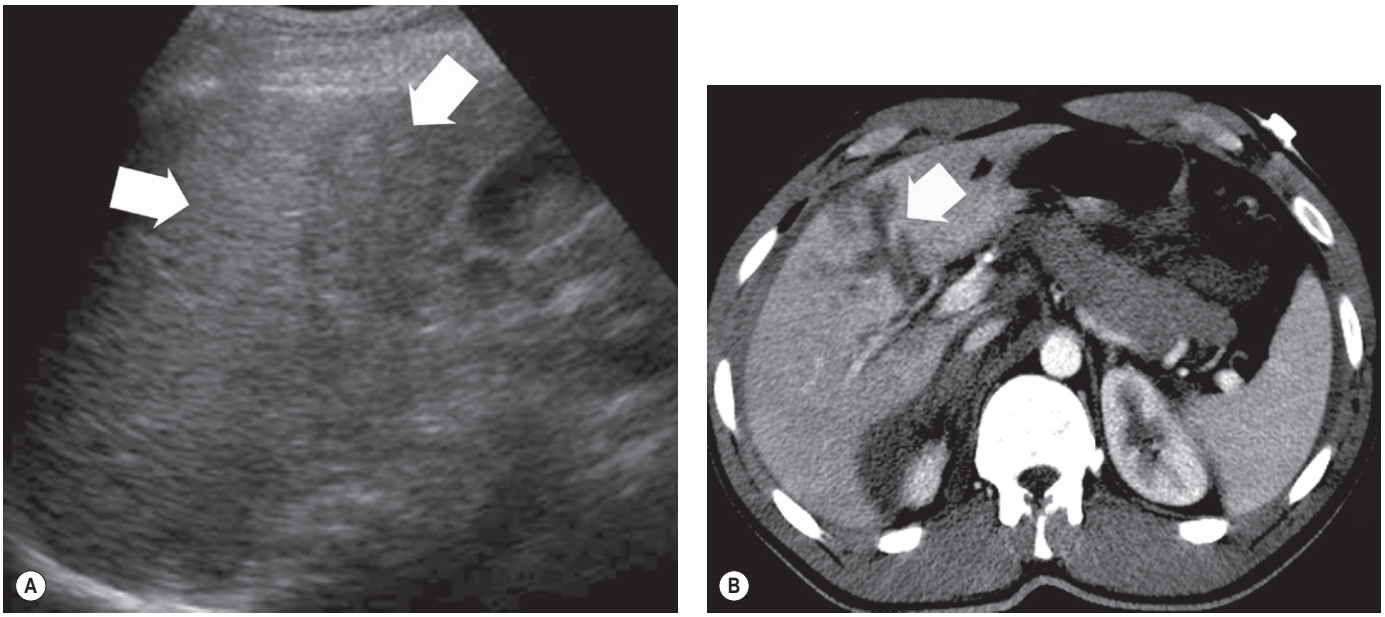

Figure 42.9 Liver injury. A: Subtle inhomogeneity of the hepatic echotexture (arrows). **B:** CT scan demonstration of the liver laceration (arrow).

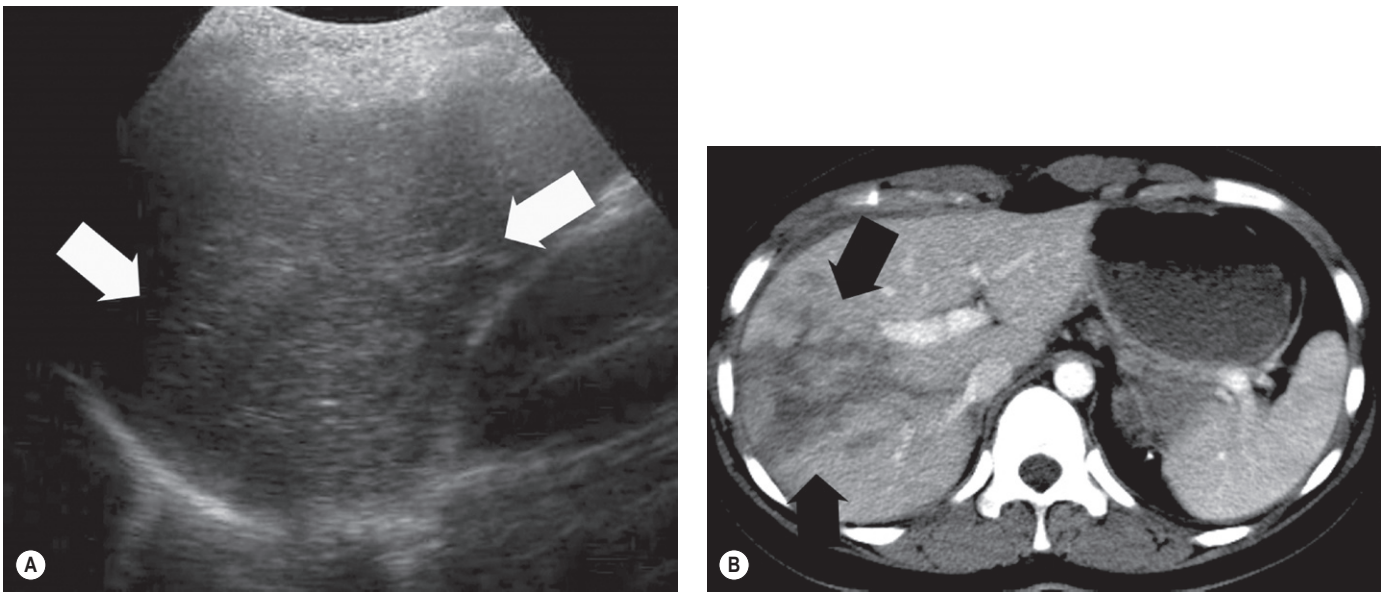

Figure 42.10 Liver injury. A: Subtle inhomogeneity of the hepatic echotexture (arrows). **B:** CT scan demonstration of liver lacerations (arrows).

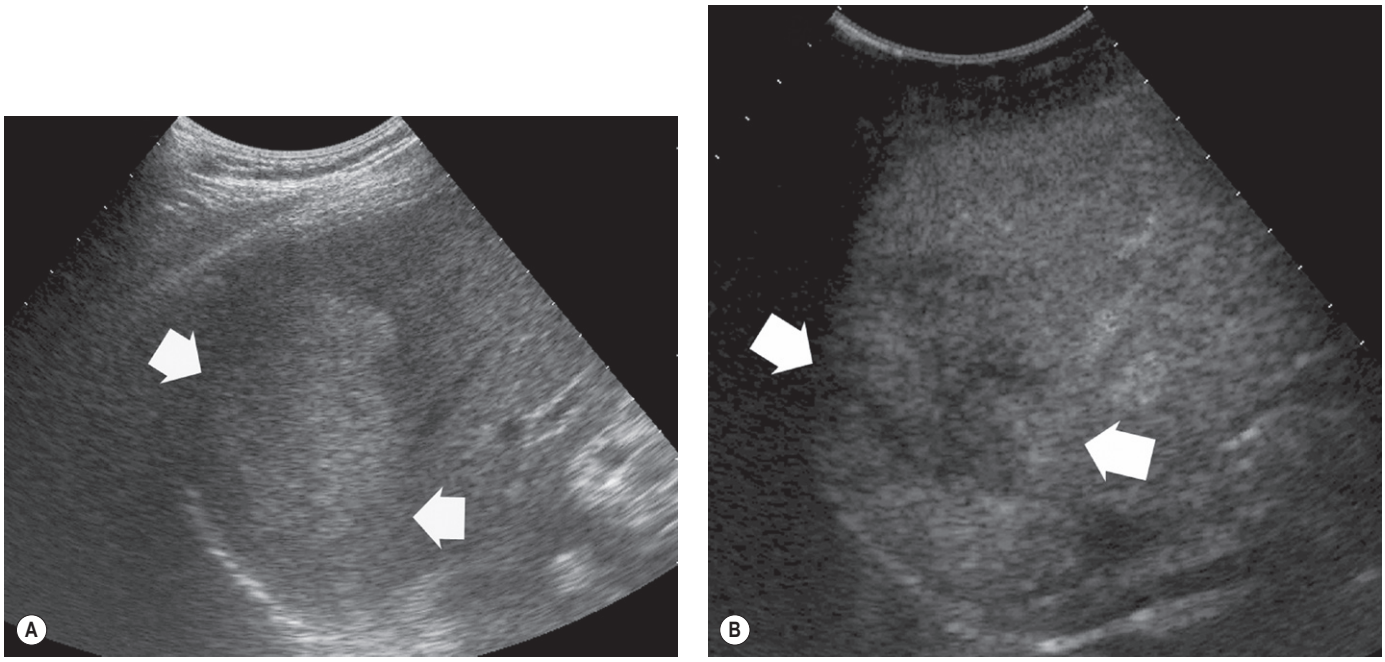

Figure 42.11 Hyperechoic, haemangioma-like hepatic injury as shown by **(A)** US (arrows). **B:** CEUS demonstrates an inhomogeneous and ill-defined non-enhancing area (arrows).

Subcapsular haematomas appear as peripheral, lenticular collections, with the thin echoic delimitation of the hepatic capsule externally and with the flattened contour of the parenchyma internally. Subcapsular haematomas are mostly recognised around the right or left lobe apex, compressing the adjacent tissue. Very large, burst injuries may be identified as diffuse disruption of normal texture and vascularisation. One or more small anechoic, pseudocavitary foci can appear internal to the injury in the case of brisk bleeding or pseudo-aneurysm formation: these images will reflect the exact point of contrast extravasation found at CT or CEUS imaging. Periportal tracking, a common CT finding around the enhanced portal branches, is rarely recognised with US. Occasionally, a thin hypoechoic halo around hilar vessels can be identified.

Real-time CEUS can directly demonstrate parenchymal injuries, as non-enhancing defects within the enhanced normal tissue.[30,64] Contusion appears as an area of subtle hypoechogenicity (Fig. 42.11). Lacerations will appear as clear, hypoechoic, linear bands, usually oriented perpendicularly with respect to liver surface. A haematoma is recognisable as an inhomogeneous, non-enhancing area without enhanced vessels internally. All these lesions become more evident as the portal-sinusoidal phase replaces the arterial one. CEUS can detect findings unrecognisable with conventional US, such as infarcts, perilesional reactive hyperaemia and contrast medium extravasation. Recognition of contrast extravasation is very important since it indicates the presence of ongoing haemorrhage and need for invasive treatment. Contrast extravasation appears as a pooling or as a jet of hyperechoic material outside the vessels, within the liver parenchyma or the peritoneal cavity.

SPLEEN TRAUMA

General considerations

The spleen is the most frequently injured abdominal organ, being involved in 25–60% of adults with intra-abdominal trauma.[65] Damage to the spleen is important because it is the most vascular body organ and as bleeding is mostly arterial, it can produce a lethal haemoperitoneum. Unlike the liver, haemorrhage from splenic trauma is always within the peritoneal cavity.

Symptoms include left upper quadrant pain, left shoulder pain (uncommon), abdominal distension, and hypotension (intraperitoneal bleeding).

Splenic trauma is managed conservatively in a growing number of cases, particularly in childhood. Unlike the liver, splenic injuries may worsen during the hours or days following trauma and should be observed very carefully. 'Delayed rupture', developing after a 48-hour asymptomatic period, is described; however, a spleen that is not damaged cannot develop an injury after a delay. If the organ is intact, an injury having been ruled out by an adequate CT study, it is not necessary to re-evaluate the patient. Nevertheless, it is possible that a delayed 'rupture' will develop, if a lesion is overlooked at initial imaging work-up or if a patient does not present to the emergency room at the time of initial injury. In 1–20% of cases, an asymptomatic trauma will become evident 48 hours or more after the impact. Mostly, this is due to the delayed rupture of a traumatic intrasplenic pseudo-aneurysm or to the secondary development of a haemoperitoneum in a patient with a progressively growing, subcapsular haematoma.

Mechanisms of injury and classification

Splenic trauma occurs with liver trauma in 18–48% of cases and with left-sided renal trauma in 10% of cases. Other frequently combined injury sites are the left adrenal, the pancreatic body and tail, the stomach, the left hemidiaphragm, the vertebrae, and the left thoracic base. Left lower ribs are involved in up to 25% of cases of splenic trauma. Abnormal or slightly enlarged spleens are the most easily injured (Fig. 42.12).

The AAST scale is the grading system most commonly employed.[63] It considers five levels of severity and the final score is advanced by one level for multiple injuries up to grade III (Table 42.2). Splenic lesions considered include haematomas (subcapsular or intraparenchymal), contusive, lacerative, or lacero-contusive areas, and infarctions. Distinguishing between a contusion, a laceration and a lacero-contusion is difficult. It is important to distinguish between a superficial injury and a deep injury and especially between a

Table 42.2 Spleen injury scale. The score is advanced by one level for multiple injuries up to grade III (data from *Journal of Trauma* 38:323, 1995)[63]

Grade	Injury type	Description of injury
I	Haematoma	Subcapsular, <10% surface area
	Laceration	Capsular tear, <1 cm parenchymal depth
II	Haematoma	Subcapsular, 10–50% surface area; intraparenchymal, <5 cm in diameter
	Laceration	Capsular tear, 1–3 cm parenchymal depth that does not involve a trabecular vessel
III	Haematoma	Subcapsular, >50% surface area or expanding; ruptured subcapsular or parenchymal haematoma; intraparenchymal haematoma ≥5 cm or expanding
	Laceration	>3 cm parenchymal depth or involving trabecular vessels
IV	Laceration	Laceration involving segmental or hilar vessels producing major devascularisation (>25% of spleen)
V	Laceration	Completely shattered spleen
	Vascular	Hilar vascular injury which devascularises spleen

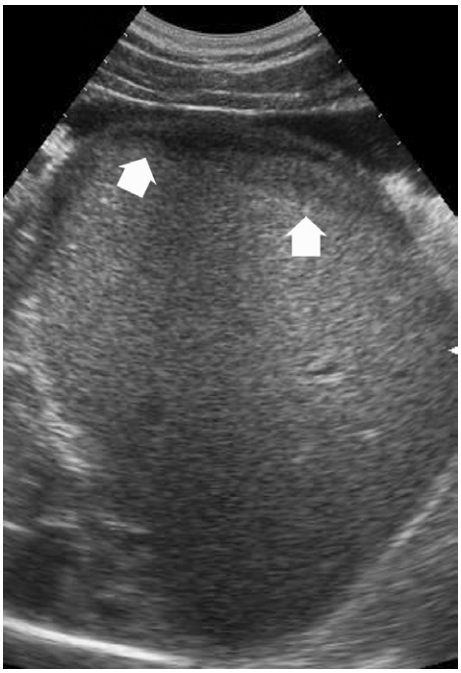

Figure 42.12 Subcapsular haematoma (arrows) and perisplenic fluid in a subject with lymphomatous splenomegaly who had sustained a minor left flank trauma.

perihilar and a polar injury: perihilar lesions involve larger vessels and cause more bleeding than the polar lesions. Very complex lacerations, with eventual fragmentation of the organ or with a complete fracture, are also possible but not specifically distinguishable with US. Infarction may be partial or total. The term 'rupture' should be avoided for the same reasons of confusion as in the liver.

US findings

As the spleen is under the left hypochondrium and lung base, US examination can be difficult, particularly looking at the deep pole. Additionally, rib shadowing may reduce organ visibility.

Splenic haematomas and localised lacerations appear as hyperechoic regions within the normal parenchyma. These lesions can be irregular or linear in configuration. With colour Doppler, no signal is seen internally.[65] Intrasplenic haematomas may also be hypoechoic or even anechoic, with a slightly increased through-transmission.

Subcapsular haematomas appear as regularly shaped, crescentic, often hypoechoic collections close to the splenic margin. The underlying parenchymal contour is flattened and compressed due to the mass effect. Hence, a smooth collection conforming to the organ margin indicates a subcapsular bleed. In comparison, extracapsular blood is usually shaped more irregularly. Although mass effect is produced in both cases, subcapsular blood is more likely to compress the organ shape.

Global injuries may be identified as diffuse disruption of the normal parenchymal texture and vascularisation, with combined hypoechoic and hyperechoic spotty areas (Fig. 42.13). It should be noted that the extent and conspicuity of the splenic changes at US does not correlate with injury severity.

Single or multiple infarctions may occur as a result of damage to arterial branches. Their size and distribution are directly related to the level of vascular compromise. Infarcts are typically wedge-shaped, with the apex towards the hilum. This is in contrast to haematoma, which shows a more irregular and complex shape and distribution. Colour Doppler will fail to identify internal flow.

The CEUS findings in splenic trauma are similar to those described above for the liver. The conspicuity of traumatic lesions increases from the arterial to the venous phase of contrast medium circulation.

RENAL TRAUMA

General considerations

The kidney is involved in 8–10% of cases of abdominal trauma in the adult.[66] In children, the prevalence of renal injury is higher. Blunt trauma accounts for 80–90% of cases, with no side preference. Penetrating injuries are more frequent on the left side, especially in the case of stab wound. Bilateral trauma is infrequent but possible.

Isolated renal trauma is classified as a major injury in only 2% of cases. Combined trauma (75% of blunt renal injuries and 80% of penetrating renal injuries) carries a greater severity. Right renal injury is mostly combined with trauma to the liver, right ribs, and vertebrae while left renal injury is mostly found in combination with splenic trauma or with left rib or lumbar vertebrae fracture.

Gross haematuria is a very important indicator for urinary tract trauma (severe renal injury in 25% of the cases), although it can be absent in 30% of patients with renal pedicle injury. Microhaematuria is less specific, since renal injury is identified in only 1–2% of these patients. Other clinical findings include back, flank or abdominal pain and shock.

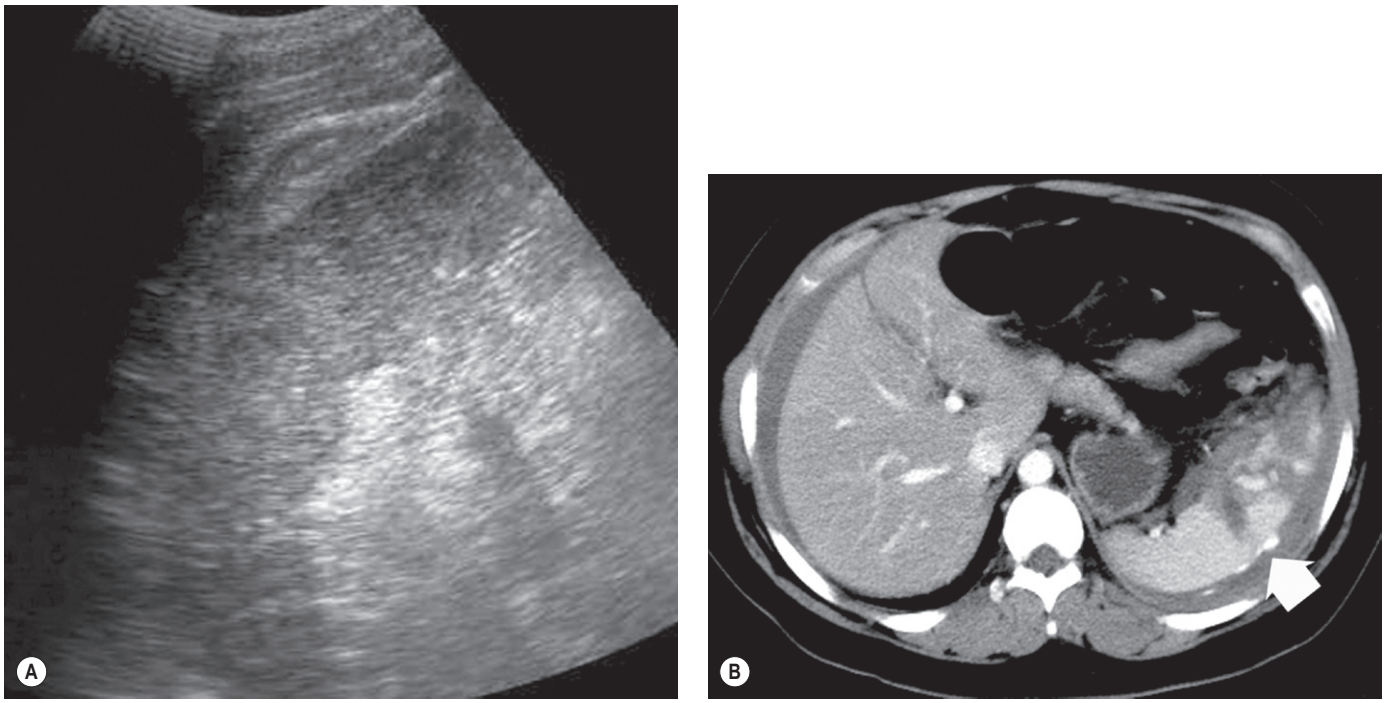

Figure 42.13 Splenic injury. A: Diffusely inhomogeneous spleen with perisplenic clots and fluid. **B:** Diffuse shattering of the spleen on the CT scan with evidence of contrast extravasation (arrow).

Table 42.3 Kidney injury scale. The score is advanced by one grade for bilateral injuries up to grade III (data from *Journal of Trauma* 29:1664, 1989)[67]

Grade	Type of injury	Description of injury
I	Contusion	Microscopic or gross haematuria, urological studies normal
	Haematoma	Subcapsular, non-expanding without parenchymal laceration
II	Haematoma	Non-expanding perirenal haematoma confirmed to renal retroperitoneum
	Laceration	<1.0 cm parenchymal depth of renal cortex without urinary extravasation
III	Laceration	<1.0 cm parenchymal depth of renal cortex without collecting system rupture or urinary extravasation
IV	Laceration	Parenchymal laceration extending through renal cortex, medulla and collecting system
	Vascular	Main renal artery or vein injury with contained haemorrhage
V	Laceration	Completely shattered kidney
	Vascular	Avulsion of renal hilum which devascularises kidney

Bleeding can be into the retroperitoneal spaces and/or into the collecting system. The lack of direct intraperitoneal bleeding and the presence of septa within the perinephric space explain why blood loss is usually less severe and rapid than in liver or splenic trauma.

Modern work-up for renal trauma no longer relies on urography and angiography. It is based on US and contrast-enhanced CT (including excretory phase scans).

Mechanisms of injury and classification

Unlike other organs, the kidney is primarily fixed by its vascular pedicle. Consequently, both horizontal and vertical forces, especially from acceleration and deceleration, may produce a tear of the vascular supply. It is not uncommon for the injured kidney to be also an abnormal one: an occult abnormality is present in 15–35% of paediatric and in about 4% of adult renal traumas. Horseshoe kidney, ectopic kidney, malrotated kidney or enlarged kidney (cysts, polycystic disease, hydronephrosis, etc.) all carry a greater risk of injury.

The AAST injury scale for the kidney includes five progressive grades (Table 42.3).[67] Renal trauma may involve the parenchyma itself, the pyelo-calyceal structures and the vascular pedicle. Parenchymal injuries include contusion, haematoma (parenchymal or subcapsular) and laceration (partial or complete, with fracture or with shattering). Parenchymal lesions that reach the medulla and calyces cause urinary leakage. Lesions of the upper urinary tract include calyceal injury, pelvic injury and the dramatic pyelo-ureteral junction avulsion. These injuries may produce a perirenal urinoma or accumulation of blood clots within the lumen (eventually leading to hydronephrosis). Vascular injuries may involve the renal artery and/or renal vein and may consist of laceration with retroperitoneal bleeding, intimal tear with dissection, thrombosis, pseudo-aneurysm formation and arteriovenous fistula formation; the kidney may consequently undergo ischaemia, segmental infarction or total infarction. Small, subsegmental infarctions have a limited relevance but a total infarction may lead to irreversible loss of renal function.

Four categories of injury can be considered. Category 1 includes minor cortical contusion, subcapsular haematoma, minor laceration with limited perirenal haematoma, and small cortical infarct. Category 2 includes major laceration with medullary extension (involving the calyces or not) and segmental infarction. Category 3 includes multiple renal lacerations and vascular pedicle injury. Category 4 is the pelvic junction avulsion.[66] Clearly, this classification cannot be based on US findings alone and requires a targeted CT study.

With the exception of very severe injuries (5–10% of cases), involving the renal vascular pedicle or the pyelo-ureteral junction, initial conservative management is normal. This applies most to minor injuries (70–85% of cases) and also to intermediate injuries (10–30% of cases). Blunt renal trauma requires surgery in no more than 5% of cases while penetrating trauma needs surgery in 52% of cases.

US findings

The use of US in renal trauma is difficult for two main reasons. First, the kidney is more deeply located within the abdomen compared to the spleen and liver, and its visualisation can be difficult or incomplete; the left kidney can be particularly difficult to see because of superimposition of bowel gas and because the splenic acoustic window is smaller than the hepatic one. Secondly, isolated renal injuries are only rarely associated with intraperitoneal fluid whilst retroperitoneal haemorrhage can be detected with US only if it is large and in a favourable site. US has a limited accuracy in the direct detection of renal injuries, with a reported 22% overall sensitivity and a 60% sensitivity in the subset of patients with severe injury.[68]

The involved kidney can be modified in shape and size. Focal deformities and areas of enlargement of the kidney are frequent, especially in the case of subcapsular collections or of severe, full-thickness injuries. Echogenic clots may distend the urinary tract and cause hydronephrosis. Contusions may be undetectable or only identified as a subtle area of increased echogenicity; this is particularly true in the first hours. Colour Doppler may recognise an area of decreased flow signal but this finding can be misleading, with risk of false positive diagnoses. Subcapsular collection may occur immediately or develop after some hours, as a consequence of blood filtration from intraparenchymal injuries; frequently US fails to recognise the associated intraparenchymal injury. This needs CEUS or CT for demonstration. In severe parenchymal injuries with multiple areas of combined contusion, laceration and devascularisation, US will demonstrate perirenal collections, ill-defined renal borders and loss of normal renal echotexture (Figs 42.14 and 42.15). Nevertheless,

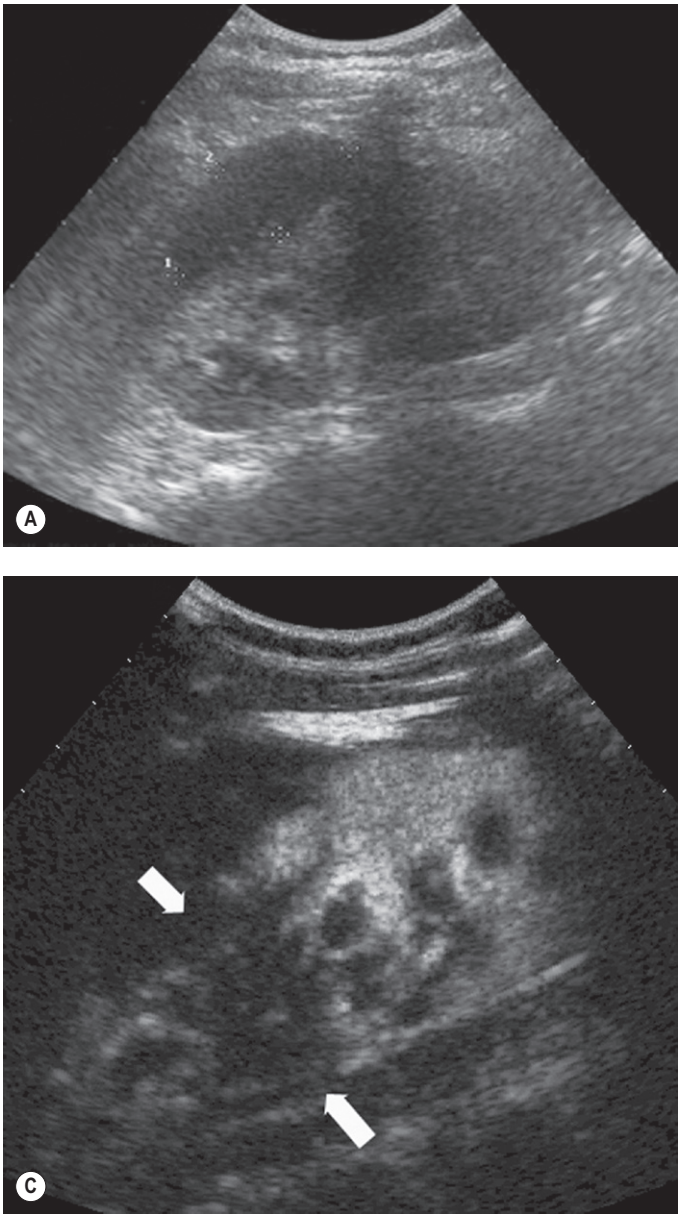

Figure 42.14 Renal injury. A: US image shows a subcapsular haematoma (callipers). **B:** Directional power Doppler image confirms the collection (arrow) but also shows a colour defect with the renal upper third. **C:** CEUS directly depicts the enhancing defect due to renal laceration (arrows).

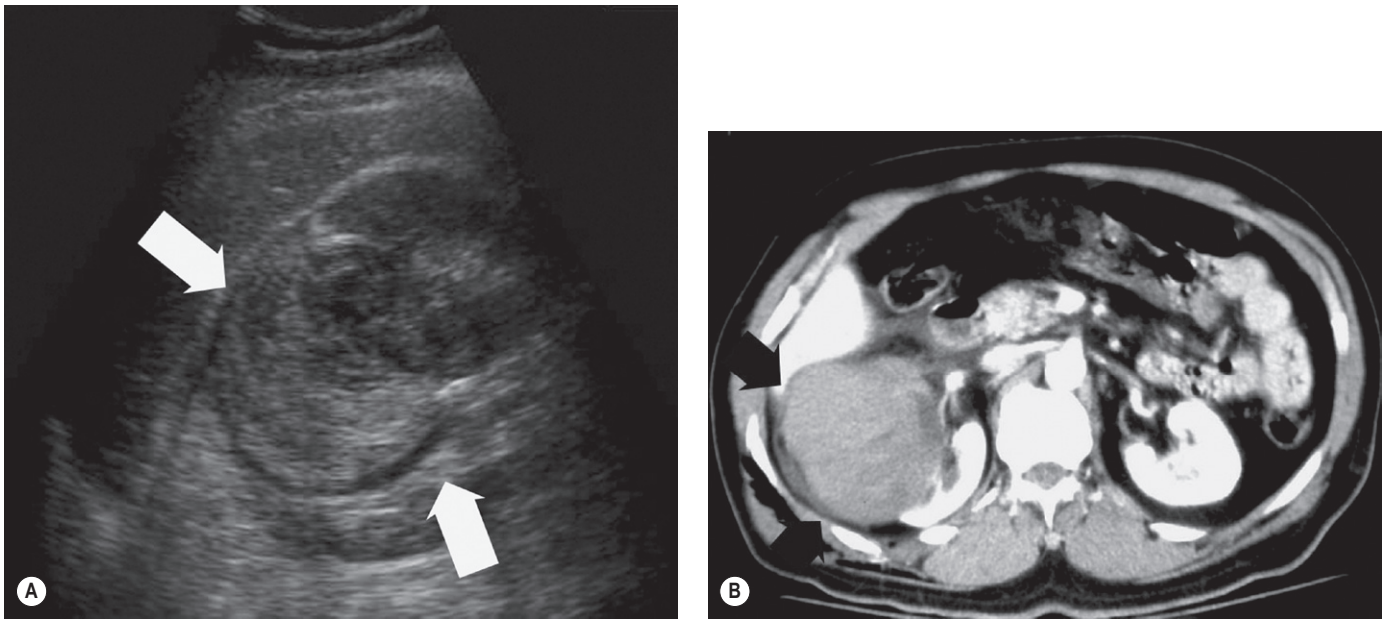

Figure 42.15 Renal injury. A: The US scan shows a large, echoic, and inhomogeneous haematoma (arrows). **B:** The CT scan confirms the right renal haematoma (arrows).

US versus CT in assessing parenchymal injuries

- US is less sensitive than CT for parenchymal injuries though the specificity is comparable.
- Parenchymal injuries can be barely recognisable on US in the first hours after the trauma. Usually, CT depicts injuries with a greater conspicuity.
- The main organ injuries are contusion, laceration, intraparenchymal haematoma and subcapsular haematoma.
- The US appearance of parenchymal injuries is variable. The lesion can be mostly hyperechoic, mostly hypoechoic, or can have a mixed texture.
- Parenchymal changes at US examination may not correlate with the grade of the injury and CT is necessary for trauma staging and decision making.

only CT will demonstrate the real severity of the injury, accurately demonstrating the vascular and pyelo-calyceal involvement. Perirenal collections after renal trauma can be due to blood or urine. In pyelo-ureteral avulsion the collection is usually recognisable medially, along the psoas muscle border, and colour Doppler will demonstrate the unilateral absence of a uretero-vesical jet.

The CEUS appearance of renal trauma is similar to that described for the liver (see previously).[30] Nevertheless, given the rather transient nature of the renal enhancement, the first two minutes from contrast injection are most important for injury detection. Furthermore, the 'blood pool' US contrast media, unlike the radiographic ones, are not excreted in the urine and so contrast leakage from injured calyces and pelvis cannot be shown.

OTHER INJURY SITES

Injury to the **gallbladder** is uncommon, accounting for 2–8% of all blunt abdominal visceral injuries. Isolated injury is rare. A compression mechanism may cause gallbladder injury, resulting in haemorrhage (especially in the case of cystic artery involvement) and bile peritonitis. US will show a distended or collapsed viscus, with thickened walls and pericholecystic effusion. Direct visualisation of the parietal laceration is rare.

Pancreatic injuries are uncommon, representing 1–12% of intra-abdominal trauma lesions.[16] Nevertheless, these lesions are important because they carry a significant morbidity and mortality (up to 20%) and because their recognition is frequently delayed, especially when the retroperitoneal portions of the gland are involved. The duodenum and the main pancreatic ducts can be damaged. Increased amylase and lipase levels will be identified. Pancreatic lesions are difficult to identify with US, especially in the acute phase, and direct recognition of pancreatic contusion and partial laceration is ineffective. Occasionally, a perivascular hypoechoic halo, a crescent fluid collection between the stomach and pancreas, or a complex, mass-like tissue around the gland will be identified. US can demonstrate post-traumatic pseudocyst formation and pancreatitis.

Bowel injury is difficult to identify and often recognised only after a delay. An intestinal injury (1% of injuries in BAT) should be suspected in every patient with a significant amount of peritoneal fluid and no evidence of parenchymal trauma. Direct US findings eventually include focal, usually circumferential bowel wall thickening, pneumoperitoneum and loculated peritoneal fluid[16] (Fig. 42.16).

Bladder lesions are usually identified with CT, following contrast opacification. In an intraperitoneal rupture of the bladder, the urine collects within the pelvic spaces but the amount depends on the degree of pre-trauma distension of the bladder. Transcatheter retrograde filling of the bladder will increase the peritoneal fluid. Extraperitoneal rupture of the bladder does not cause peritoneal fluid and may be overlooked. Pelvic ring fractures are a very important risk factor.

Direct detection of post-traumatic **diaphragmatic** defects is possible but difficult. The hyperechoic, curvilinear band of the hemidiaphragm will be seen focally interrupted. The injury may sometimes be indirectly highlighted by the herniation of intra-abdominal contents into the thoracic cavity.

PITFALLS

Blood clot may mask the presence of an intra-abdominal haemorrhage. The echogenicity of clotted blood and its eventual isoechogenicity with adjacent parenchyma, makes it more difficult to detect.[49]

The contour of an organ, especially the spleen and left kidney, may mimic a traumatic injury. This also applies to the hyperechoic incisures and clefts of the splenic surface, to the hepatic round ligament, and to the hyperechoic diaphragmatic slips seen at level of the hepatic surface (Fig. 42.17). Knowledge of these normal variants is usually sufficient to avoid an interpretative mistake. It is of note that splenic clefts are generally located along the median aspect of the organ while lacerations typically involve the lateral surface.

A long left liver lobe, partially encircling the spleen below the diaphragm, may mimic a subcapsular or a perisplenic haematoma, as the liver is less echoic than the spleen (Fig. 42.18). By scanning the left hypochondrium from an anterior view it will be possible to see the left lobe reaching the spleen.

Non-traumatic lesions may simulate traumatic injuries, such as medium to large liver haemangiomas, especially if they are inhomogeneous and only slightly more echoic than the surrounding parenchyma. Subcapsular fibrosis of the spleen, a rare occurrence consisting of a thin layer of abnormal tissue along the splenic margin, may simulate a haematoma.

Enlargement of the spleen during follow-up may indicate an intraparenchymal injury but may also reflect the return to the normal state of the organ after vasoconstriction.

Some CEUS pitfalls have also been reported.[29,30] During the early enhancing phase the splenic parenchyma may appear inhomogeneous (a finding similar to the well-known zebra pattern of dynamic CT and MRI). The transient nature of these pseudo-lesions allows the differentiation from true injuries, which persist and become more evident over time.

At 2–3 minutes from the contrast injection, the densely enhanced superficial portion of the spleen may cause transient obscuration of deeply located portions. Enhanced parenchymal arteries may mimic intrasplenic contrast extravasation and vice versa. Contrast medium extravasation should be differentiated from other causes of focal hyperechogenicity, including calcifications, enhanced pseudo-aneurysms, enhanced normal vessels and viable tissue within injured parenchymal areas. A contrast extravasation may be overlooked if the specific area is not adequately scanned or if it is scanned during the venous phase.[50]

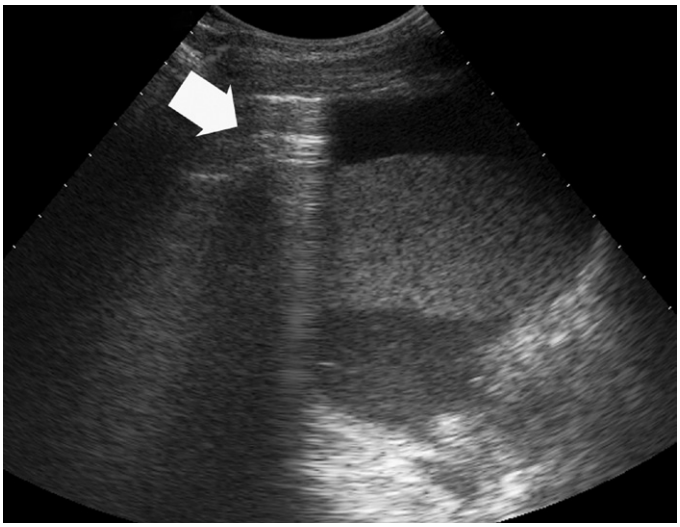

Figure 42.16 Pneumoperitoneum in a patient with stomach laceration. The US image depicts the perihepatic fluid and the free air-related artefacts (arrow).

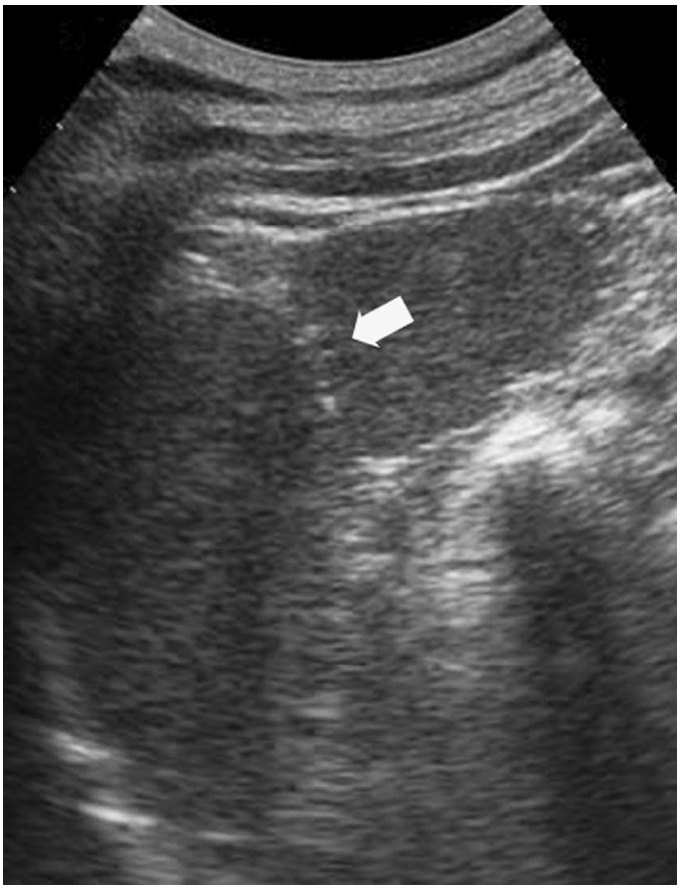

Figure 42.17 A hyperechoic band within the spleen (arrow) mimics laceration.

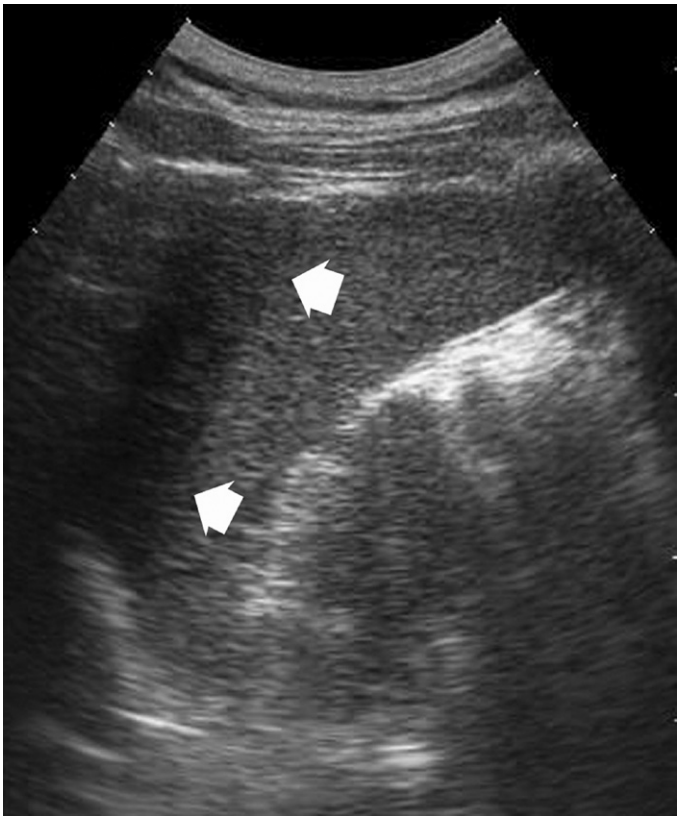

Figure 42.18 A large left liver lobe encircles the spleen and simulates a subcapsular haematoma (arrows).

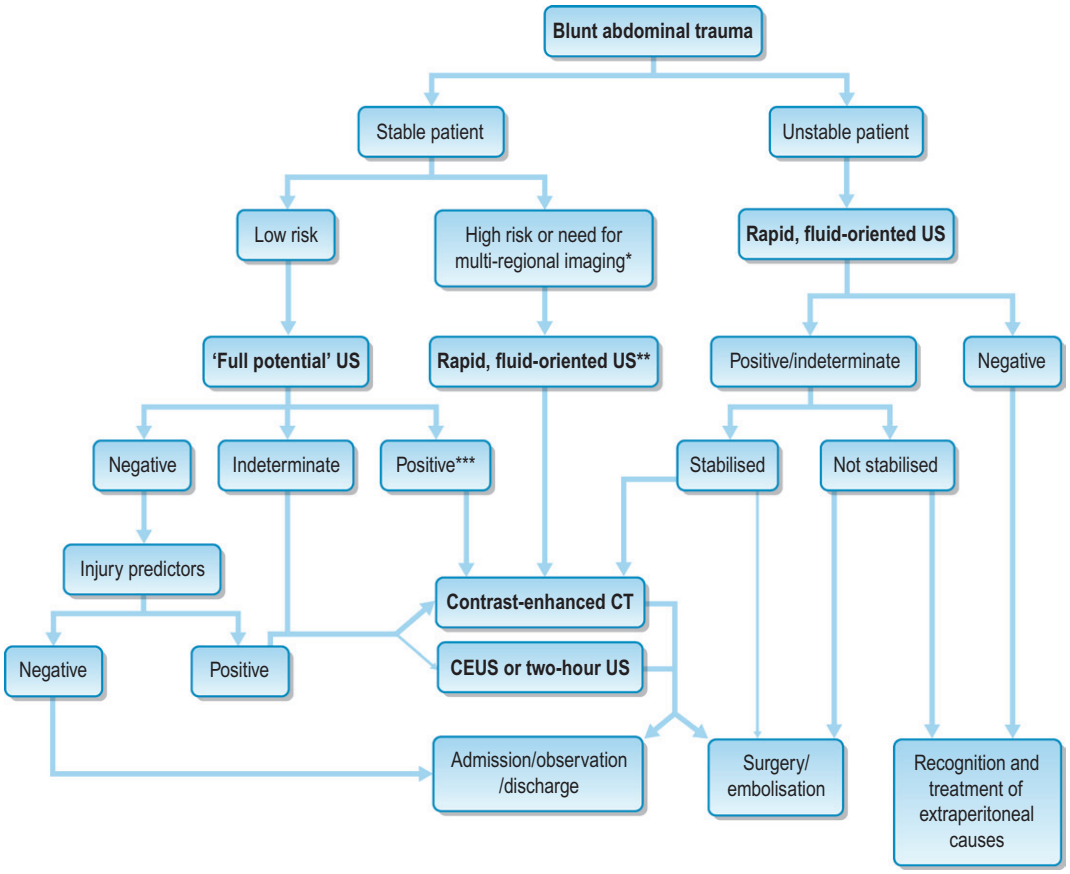

Figure 42.19 Algorithm for the diagnostic management of the stable and unstable trauma patient. *In selected cases the polytrauma patient may initially undergo unenhanced head and cervical spine CT, chest film and abdominal US. **Not always needed. ***In selected cases the patient may go directly to surgery.

THE UNSTABLE TRAUMA PATIENT

A rapid US scan (FAST) is very important in the initial assessment of hypotensive subjects, in the Advanced Trauma Life Support (ATLS) protocol. Injured patients with systolic blood pressure lower than 90 mmHg on arrival need very prompt assessment and treatment. The main question is: is the hypotension due to a severe intraperitoneal bleed or to other causes (blood loss, intrathoracic or retroperitoneal bleeding, bony and muscular haemorrhage)? US has proven effective in detecting intraperitoneal fluid in subjects with out-of-hospital or emergency room hypotension, with an 83% sensitivity.[69,70] In a retrospective study on 128 hypotensive patients US showed an 85% sensitivity for detection of any injuries, a 97% sensitivity for surgical injuries and a 100% sensitivity for fatal injuries. It showed that in this subset of the trauma population, a negative FAST scan virtually excludes a surgical injury while a positive FAST indicates a surgical injury in 64% of cases.[71]

Hypotensive patients are usually considered not stable enough to undergo CT scanning. There is no standard definition on fitness to undergo CT, and judgement is made by the trauma team based on various institutional and individual factors. Stabilisation is usually attempted prior to CT, allowing US to be performed during resuscitation manoeuvres.

US may fail to detect minor abdominal injuries but this will not modify the immediate management of a hypotensive patient. Hypotensive patients with a negative US scan will be further evaluated, once they have been stabilised, to search for a cause of the hypotension: appropriate investigations will be expedited while, at the same time, unnecessary, catastrophic emergency laparotomy is avoided.

If US is positive and the patient cannot be stabilised, surgery should be performed immediately, without the need for CT. If US is positive but the subject can be stabilised, an attempt to perform CT should still be done[33,59,71] (Fig. 42.19).

The potential role of CEUS in the unstable trauma patient is intriguing but it has not been adequately investigated yet.

PENETRATING TRAUMA

Penetrating abdominal trauma is usually the result of stab or gunshot wounds. A variety of trauma patterns may arise, depending on the type, entrance site, direction and penetration depth of the traumatic agent. Unlike the blunt trauma patient, most individuals with a non-superficial penetrating injury, especially in the case of gunshot wounds, will undergo surgery. Another specific aspect is the high incidence of hollow viscera injury (especially the small bowel) in comparison with blunt trauma. Gunshot wounds frequently involve multiple organs while stab wounds are often isolated, especially if the wound is limited to the back or flank.

US examination of a patient with a penetrating torso trauma may be technically more difficult than in the case of a blunt trauma. In a prospective study on 75 patients with stab or gunshot wounds FAST showed a 46% sensitivity and a 94% specificity, being useful only with a positive result.[72] In the unstable patient with a FAST scan positive for pleural, pericardial or peritoneal fluid, surgery should be performed immediately. In the normotensive patient with positive FAST/US, a CT study should be obtained to accurately detect and stage the lesions, although the US recognition of peritoneal fluid is an adequate indicator of peritoneal violation and consequent need for surgery. Finally, in the stable patient with a negative FAST or US, the decision to take a CT scan should be taken case by case.

FOLLOW-UP OF ABDOMINAL TRAUMA

Non-operative management of patients with BAT is being employed with growing frequency and success rates. This is especially true in the child, where surgeons particularly try to avoid splenectomy because of the current understanding of the splenic role in the immunity process and of the potential risk of severe infections (including overwhelming post-splenectomy sepsis). It has been shown that mortality rate, morbidity rates, days of hospital stay, incidence of complications, and need for blood transfusion are not higher in patients managed conservatively than in those treated surgically. Currently up to 90% of spleen traumas in children and up to 50% of spleen traumas in adults are managed conservatively.

The probability of success in conservative management of liver and spleen trauma seems to correlate with the amount of haemoperitoneum, as well as clinical and laboratory data.[58,73,74] The decision to operate should not be based solely on a large amount of fluid. The most important aspects to consider for liver trauma include haemodynamic stability, limited amount of haemoperitoneum (<500 mL) and limited severity of liver trauma (intrahepatic haematoma or laceration, unilobar fracture, absence of devitalised tissue). Secondary aspects include absence of peritoneal signs, adequate quality of CT scans, high radiologist expertise, availability of intensive care monitoring, rapid accessibility of the operating room and absence of surgical injuries in other organs (particularly absence of hollow viscera trauma).[74] Non-operative management can be catastrophic if the patient is not selected adequately.

Management guidelines include serial vital signs, physical findings and laboratory values. Worsening of any of these parameters indicates the need for imaging assessment. The modality to be employed, US or CT, is different in various institutions and the exact timing is unclear. There is a need to avoid an unnecessary number of imaging studies, especially when using CT and in children.

In a study of 25 patients with hepatic trauma successfully treated conservatively[75] interval US agreed with CT in 92% of the cases, being adequate to detect or exclude complications, especially in low-grade liver injury. In patients with high-grade injury US may be an adjunct to follow-up CT. Although no series has yet investigated the possibilities of CEUS in the follow-up of known injuries, it is reasonable to hypothesise that this technique may play a significant role. CEUS correlates better than US with the

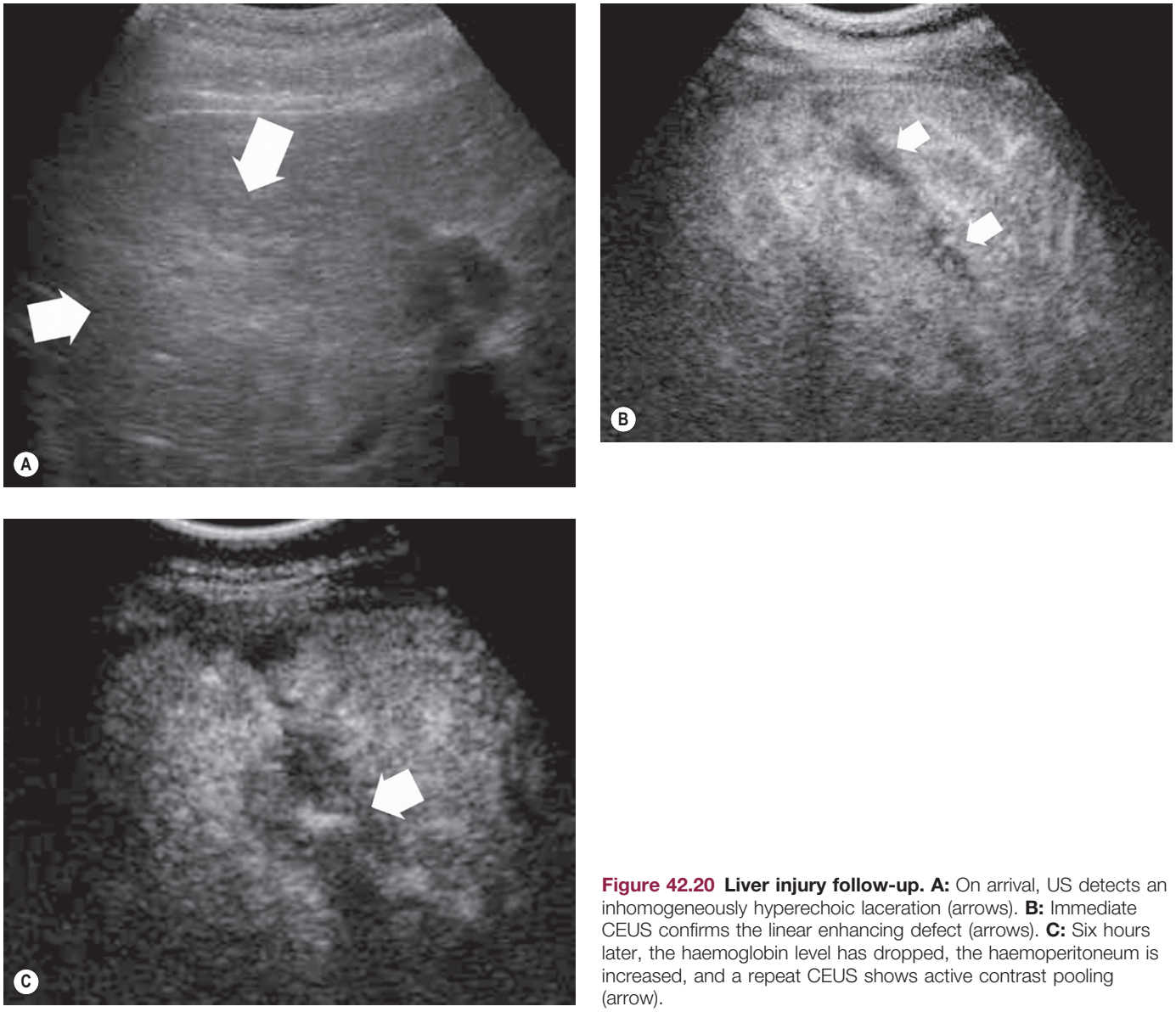

Figure 42.20 Liver injury follow-up. A: On arrival, US detects an inhomogeneously hyperechoic laceration (arrows). **B:** Immediate CEUS confirms the linear enhancing defect (arrows). **C:** Six hours later, the haemoglobin level has dropped, the haemoperitoneum is increased, and a repeat CEUS shows active contrast pooling (arrow).

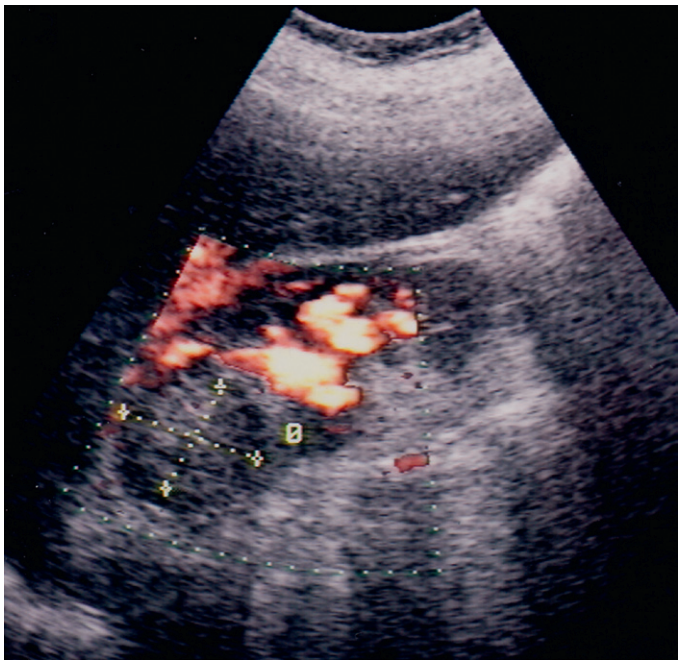

Figure 42.21 Kidney trauma follow-up. The power Doppler image obtained 6 days after a renal trauma managed conservatively identified an inhomogeneous, hyperechoic injury and a clear defect in colour map (callipers).

CT appearance of the lesion and can demonstrate accurately its changes in shape and size, also detecting active bleeding and pseudo-aneurysm formation. When CT has accurately detected, located and graded the abdominal injuries, CEUS can be employed for their monitoring. This would decrease the number of follow-up CT studies.

A follow-up examination should look for development of peritoneal fluid or changes in quantity. Peritoneal fluid recovers more quickly than the parenchymal injuries. Failure of reabsorption should raise the suspicion of ongoing, low-flow bleeding or non-haemorrhagic nature of the fluid. Recurrent major bleeding from a parenchymal injury usually occurs within the first days after the trauma (Fig. 42.20). Delayed bleeding, occurring weeks or months after the event, is uncommon.

The changes in size, shape and structure of the organ injuries should also be noted (Fig. 42.21). The extent of the injury tends to decrease significantly during the first 48 hours, because of the diminished oedematous component. Parenchymal lesions, especially liver ones, tend to become hypoechoic or even anechoic (cystic-like) during the first week and appear progressively more sharply demarcated from the surrounding normal tissue. An early and rapid increase of the fluid component within an injury should alert the operator for ongoing haemorrhage. The usual course of intraparenchymal haematomas is to contract and then liquefy. Haematomas may heal completely, evolve into a pseudocyst, or result in scarring of variable echogenicity. With time, a subcapsular haematoma may show peripheral or internal calcification.[65] Liver lacerations may persist for several months. Splenic injuries recover more rapidly: in 2–3 weeks the injury may become difficult to detect, owing to filling with granulation tissue.

Complications are mostly encountered during the first month after trauma. They include infection of a previously sterile, intraparenchymal or periparenchymal collection (haematoma, biloma, urinoma), pseudocyst formation (particularly at the level of the spleen), biliary or pancreatic fistulas, infarction and infected infarction, development of arterial pseudo-aneurysm (with eventual haemorrhage), arteriovenous fistulas (especially in the kidney) or venous thrombosis.

REFERENCES

1. Asher WM, Parvin S, Virgiglio RW, et al. Echographic evaluation of splenic injury after blunt trauma. Radiology 1976;118:411–415.
2. McKenney KL. Role of US in the diagnosis of intrabdominal catastrophes. Radiographics 1999;19:1332–1339.
3. McKenney M, Lentz K, Nunez D, et al. Can ultrasound replace peritoneal lavage in the assessment of blunt trauma? J Trauma 1994;37:439–441.
4. Chambers JA, Pilbrow WJ. Ultrasound in abdominal trauma: an alternative to peritoneal lavage. Arch Emerg Med 1988;5:26–33.
5. Kimura A, Otsuka T. Emergency center ultrasonography in the evaluation of hemoperitoneum: a prospective study. J Trauma 1991;31:20–23.
6. Lentz KA, McKenney MG, Nunez DB, et al. Evaluating BAT: role for ultrasonography. J Ultrasound Med 1996;15:447–451.
7. Jehle D, Guarino J, Karamanoukian H. Emergency department ultrasound in the evaluation of BAT. Am J Emerg Med 1993;11:342–346.
8. Rothlin MA, Naef R, Amgwerd M, et al. Ultrasound in blunt abdominal and thoracic trauma. J Trauma 1993;34:488–495.
9. McGahan JP, Rose J, Coates TL, et al. Use of ultrasonography in the patient with acute abdominal trauma. J Ultrasound Med 1997;16:653–662.
10. McGahan JP, Wang L, Richards JR Focused abdominal US for trauma. Radiographics 2001;21:S191-S199.
11. Ma OJ, Kefer MP, Mateer JR, et al. Evaluation of hemoperitoneum using a single- vs multiple-view ultrasonographic examination. Acad Emerg Med 1995;2:581–586.
12. Rozycki GS, Ballard RB, Feliciano DV, et al. Surgeon-performed ultrasound for the assessment of truncal injuries: lessons learned from 1540 patients. Ann Surg 1998;228:557–567.
13. Bahner D, Blaivas M, Cohen HL, et al. AIUM practice guideline for the performance of the focused assessment with sonography for trauma (FAST) examination. J Ultrasound Med 2008;27:313–318.
14. Nunes LW, Simmons S, Hallowell MJ, et al. Diagnostic performance of trauma US in identifying abdominal or pelvic free fluid and serious abdominal or pelvic injury. Acad Radiol 2001;8:128–136.
15. Sirlin CB, Brown MA, Deutsch R, et al. Screening US for BAT: objective predictors of false-negative findings and missed injury. Radiology 2003;229:766–774.
16. Körner M, Krötz MM, Degenhart C, et al. Current role of emergency US in patients with major trauma. Radiographics 2008;28:225–244.
17. Yoshii H, Sato M, Yamamoto S, et al. Usefulness and limitations of ultrasonography in the initial evaluation of BAT. J Trauma 1998;45:45–51.
18. Brown MA, Casola G, Sirlin CB, et al. BAT: screening US in 2,693 patients. Radiology 2001;218:352–358.
19. Dolich MO, McKenney MG, Varela JE, et al. 2,576 ultrasounds for BAT. J Trauma 2001;50:108–112.
20. Richards JR, Knopf NA, Wang L, et al. BAT in children: evaluation with emergency US. Radiology 2002;222:749–754.
21. Mazur SM, Pearce A, Alfred S, et al. The F.A.S.T.E.R. Focused assessment by sonography in trauma during emergency retrieval: a feasibility study. Injury 2008;39:512–518.
22. Bode PJ, Edwards MJ, Kruit MC, et al. Sonography in a clinical algorithm for early evaluation of 1671 patients with BAT. AJR Am J Roentgenol 1999;172:905–911.
23. Gracias VH, Frankel HL, Gupta R, et al. Defining the learning curvature of the focused abdominal sonogram for trauma (FAST) examination: implications for credentialing. Am Surg 2001;67:364–368.
24. Scalea TM, Rodriguez A, Chiu WC, et al. Focused assessment with sonography for trauma (FAST): results from an international consensus conference. J Trauma 1999;46:466–472.
25. Shackford SR, Rogers FB, Osler TM, et al. Focused abdominal sonogram for trauma: the learning curve of nonradiologist clinicians in detecting hemoperitoneum. J Trauma 1999;46:553–564.
26. Stengel D, Bauwens K, Sehouli J, et al. Discriminatory power of 3.5 MHz convex and 7.5 MHz linear ultrasound probes for the imaging of traumatic splenic lesions: a feasibility study. J Trauma 2001;51:37–43.
27. Blaivas M, DeBehnke D, Sierzenski PR, et al. Tissue harmonic imaging improves organ visualization in trauma ultrasound when compared to standard ultrasound mode. Acad Emerg Med 2002;9:48–53.
28. Nilsson A, Loren I, Nirhov N, et al. Power Doppler ultrasonography: alternative to computed tomography in abdominal trauma patients. J Ultrasound Med 1999;18:669–672.

29. Catalano O, Lobianco R, Sandomenico F, et al. Splenic trauma: evaluation with contrast-specific sonography and a second-generation contrast medium: preliminary experience. J Ultrasound Med 2003;22:467–477.
30. Valentino M, Serra C, Pavlica P, et al. Contrast-enhanced ultrasound for BAT. Semin Ultrasound CT MR 2007;28:130–140.
31. Catalano O, Siani A. Focused assessment with sonography for trauma (FAST): what it is, how it is carried out, and why we disagree. Radiol Med 2004;108:443–453.
32. Mutabagani KH, Coley BD, Zumberge N, et al. Preliminary experience with focused abdominal sonography for trauma (FAST) in children: is it useful? J Pediatr Surg 1999;34:48–52.
33. Lee BC, Ormsby EL, McGahan JP, et al. The utility of sonography for the triage of BAT patients to exploratory laparotomy. AJR Am J Roentgenol 2007;188:415–421.
34. Kirkpatrick AW, Simons RK, Brown R, et al. The hand-held FAST: experience with hand-held trauma sonography in a level-I urban trauma center. Injury 2002;33:303–308.
35. Boulanger BR, Brenneman FD, Kirkpatrick AW. The indeterminate abdominal sonogram in multisystem blunt trauma. J Trauma 1998;45:52–56.
36. Lingawi SS, Buckley AR. Focused abdominal US in patients with trauma. Radiology 2000;217:426–429.
37. Abu-Zidan FM, Sheikh M, Jadallah F, et al. BAT: comparison of ultrasonography and computed tomography in a district general hospital. Australas Radiol 1999;43:440–443.
38. Chiu WC, Cushing BM, Rodriguez A, et al. Abdominal injuries without hemoperitoneum: a potential limitation of focused abdominal sonography for trauma (FAST). J Trauma 1997;42:617–623.
39. Shanmuganathan K, Mirvis SE, Sherbourne CD, et al. Hemoperitoneum as the sole indicator of abdominal visceral injuries: a potential limitation for screening abdominal US for trauma. Radiology 1999;212:423–430.
40. Benya EC, Lim-Dunham JE, Landrum O, et al. Abdominal sonography in examination of children with BAT. AJR Am J Roentgenol 2000;174:1613–1616.
41. Emery KH, McAneney CM, Racadio JM, et al. Absent peritoneal fluid on screening trauma ultrasonography in children: a prospective comparison with computed tomography. J Pediatr Surg 2001;36:565–569.
42. Poletti P-A, Kinkel K, Vermeulen B, et al. BAT: should US be used to detect both free fluid and organ injuries? Radiology 2003;227:95–103.
43. Ochsner MG, Knudson MM, Pachter HL, et al. Significance of minimal or no intraperitoneal visible on CT scan associated with blunt liver and splenic injuries: a multicenter analysis. J Trauma 2000;49:505–510.
44. Taylor GA, Sivit CJ. Posttraumatic peritoneal fluid: is it a reliable indicator of intraabdominal injury in children? J Pediatr Surg 1995;30:1644–1648.
45. Richards JR, McGahan JP, Pali MJ, et al. Sonographic detection of blunt hepatic trauma: hemoperitoneum and parenchymal patterns of injury. J Trauma 1999;47:1092–1097.
46. Sirlin CB, Casola G, Brown MA, et al. Patterns of fluid accumulation on screening ultrasonography for BAT. Comparison with site of injury. J Ultrasound Med 2001;20:351–357.
47. Poletti P-A, Wintermark M, Schnyder P, et al. Traumatic injuries: role of imaging in the management of polytrauma victim (conservative expectation). Eur Radiol 2002;12:969–978.
48. Ballard RB, Rozycki GS, Newman PG, et al. An algorithm to reduce the incidence of false-negative FAST examinations in patients at high risk for occult injury. Focused Assessment for the sonography examination of the trauma patient. J Am Coll Surg 1999;189:145–150.
49. McGahan JP, Richards J, Gillen M. The focused abdominal sonography for trauma scan. Pearls and pitfalls. J Ultrasound Med 2002;21:789–800.
50. Catalano O, Sandomenico F, Mattace Raso M, et al. Real-time, contrast-enhanced sonography: a new tool for detecting active bleeding. J Trauma 2005;59:933–939.
51. Srinualnad N, Dixon AK. Right anterior subphrenic space: an important site for the early detection of intraperitoneal fluid on abdominal CT. Abdom Imaging 1999;24:614–617.
52. Paajanen H, Lahti P, Nordback I. Sensitivity of transabdominal ultrasonography in detection of intraperitoneal fluid in humans. J Trauma 1999;9:1423–1425.
53. Nance ML, Mahboubi S, Wickstrom M, et al. Pattern of abdominal free fluid following isolated blunt spleen or liver injury in the pediatric patient. J Trauma 2002;52:85–87.
54. Sirlin CB, Casola G, Brown MA, et al. US of BAT: importance of free pelvic fluid in woman of reproductive age. Radiology 2001;219:229–235.
55. Rathaus V, Grunebaum M, Konen O, et al. Minimal pelvic fluid in asymptomatic children. The value of sonographic finding. J Ultrasound Med 2003;22:13–17.
56. Sirlin CB, Casola G, Brown MA, et al. Quantification of fluid on screening ultrasonography for BAT: a simple scoring system to predict severity of injury. J Ultrasound Med 2001;20:359–364.
57. Huang MS, Liu M, Wu JK, et al. Ultrasonography for the evaluation of hemoperitoneum during resuscitation: a simple scoring system. J Trauma 1994;36:173–177.
58. Ma OJ, Kefer MP, Stevison KF, et al. Operative versus nonoperative management of BAT: role of ultrasound-measured intraperitoneal fluid levels. Am J Emerg Med 2001;19:284–286.
59. McKenney KL, McKenney MG, Cohn SM, et al. Hemoperitoneum score helps determine need for therapeutic laparotomy. J Trauma 2001;50:650–654.
60. Von Kuenssberg Jehle D, Stiller G, Wagner D. Sensitivity in detecting free intraperitoneal fluid with the pelvic views of the FAST exam. Am J Emerg Med 2003;21:476–478.
61. Branney SW, Wolfe RE, Moore EE, et al. Quantitative sensitivity of ultrasound in detecting free intraperitoneal fluid. J Trauma 1995;39:375–380.
62. Fitoz S, Atasoy C, Dusunceli E, et al. Post-traumatic intrasplenic pseudoaneurysms with delayed rupture: color Doppler sonographic and CT findings. J Clin Ultrasound 2001;29:102–104.
63. Moore EE, Cogbill TH, Jurkovich MD, et al. Organ injury scaling: spleen and liver (1994 revision). J Trauma 1995;38:323.
64. Catalano O, Lobianco R, Mattace Raso M, et al. Blunt hepatic trauma: evaluation with contrast-enhanced sonography: sonographic findings and clinical application. J Ultrasound Med 2005;24:299–310.
65. Doody O, Lyburn D, Geoghegan T, et al. Blunt trauma of the spleen: ultrasonographic findings. Clin Radiol 2005;60:968–976.
66. Kawashima A, Sandler CM, Corl FM, et al. Imaging of renal trauma: a comprehensive review. Radiographics 2001;21:557–574.
67. Moore EE, Shackford SR, Pachter HL, et al. Organ injury scaling – spleen, liver and kidney. J Trauma 1989;29:1664.
68. McGahan JP, Richards JR, Jones CD, et al. Use of ultrasonography in the patient with acute renal trauma. J Ultrasound Med 1999;18: 207–213.
69. Holmes JF, Harris D, Battistella FD. Performance of abdominal ultrasonography in blunt trauma patients with out-of-hospital or emergency department hypotension. Ann Emerg Med 2004;43:354–361.
70. Wherrett LJ, Boulanger BR, McLellan BA, et al. Hypotension after BAT: the role of emergent abdominal sonography in surgical triage. J Trauma 1996;41:815–820.
71. Farahmand N, Sirlin CB, Brown MA, et al. Hypotensive patients with BAT: performance of screening US. Radiology 2005;235:436–443.
72. Udobi KF, Rodriguez A, Chiu WC, et al. Role of ultrasonography in penetrating abdominal trauma: a prospective clinical study. J Trauma 2001;50:475–479.
73. Ong AW, McKenney MG, McKenney KA, et al. Predicting the need for laparotomy in pediatric trauma patients on the basis of the ultrasound score. J Trauma 2003;54:503–508.
74. Peitzman AB, Heil B, Rivera L, et al. Blunt splenic injury in adults: multi-institutional study of the eastern association for the surgery of trauma. J Trauma 2000;49:177–187.
75. Chiu WC, Wong-You-Cheong JJ, Rodriguez A, et al. Ultrasonography for interval assessment in the nonoperative management of hepatic trauma. Ann Surg 2005;71:841–846.

CHAPTER

43 Interventional ultrasound in the abdomen

Elizabeth E. Rutherford, Brian Stedman and David J. Breen

INTRODUCTION

Image-guided abdominal percutaneous interventional procedures have increased in popularity over the past couple of decades as they are less invasive than their surgical alternatives, are generally more cost-effective and have a high diagnostic accuracy.[1,2] Many abdominal biopsies, drainage and ablation procedures can be performed under computed tomography (CT) or ultrasound guidance according to user preference and experience but ultrasound has the advantages of being comparatively inexpensive, portable and does not involve exposure to ionising radiation. Often ultrasound-guided procedures are less time-intensive than those performed under CT guidance and hence can be more cost-effective.[3] Use of colour Doppler imaging enables assessment of the overall vascularity of a mass or lesion and allows identification of blood vessels along the proposed course of the biopsy needle or drainage catheter.[4] Ultrasound-guided interventional procedures have a learning curve and there is no substitute for breadth and depth of experience in performing them.

General principles of ultrasound-guided abdominal interventional procedures (biopsy, drainage and ablation) will be covered in this chapter; other individual chapters will discuss organ-specific procedures in more depth.

PRINCIPLES OF BIOPSY/FNA TECHNIQUES

Ultrasound-guided percutaneous biopsy and fine-needle aspiration (FNA) cytology are invaluable techniques that have many applications in the abdomen. Technological advances in ultrasound platforms and software in addition to biopsy needle design have resulted in ultrasound-guided biopsy being considered an accurate, safe and widely accessible technique. Ultrasound allows real-time visualisation of the needle, which is particularly advantageous over other imaging modalities such as CT, when performing biopsies of organs such as the liver where the length of time the biopsy needle remains within liver parenchyma should be minimised to reduce the risk of haemorrhagic complications. In addition, it allows an angled approach that may be more challenging at CT imaging.

Patient selection/preparation

The decision to proceed to biopsy or drainage should be made with the clinical team responsible for the patient's overall care. The benefits of confirming a suspected diagnosis, or of a therapeutic procedure need to be evaluated against the inherent risks of the procedure.

Ultrasound-guided procedures are usually performed under local anaesthesia and patient cooperation is paramount. If the patient is unable or unlikely to be able to cooperate with breathing instructions during the needle pass then the procedure and indications must be reassessed. Occasionally sedation or general anaesthesia is required and this is often the case in the paediatric setting.

Before a biopsy is performed, the coagulation status (a recent INR and platelet count) should be examined. When clotting is deranged, alternative methods of obtaining tissue can be sought or the coagulopathy corrected.

It is important to consider the transient nature of platelets or fresh frozen plasma (FFP) replacement and to optimise the timing of the procedure to obtain maximum benefit. These patients are likely to have an increased post-procedural bleeding incidence and may require extended or overnight observations.

Similarly, vascular lesions are at increased risk of post-procedural haemorrhage and this may necessitate the need for peripheral venous access and the availability of cross-matched blood prior to the procedure.

Biopsy of an organ with an obstructed drainage system represents an increased risk for post-procedural complications and attempts should be made to decompress a system prior to biopsy (e.g. biliary drainage via percutaneous transhepatic cholangiogram).

Pre-procedural assessment

The pre-procedural assessment should aim to reduce the risk of procedural complications by optimising the patient's physiology and identifying contraindications. For elective procedures, the patient requires skilled clinical assessment by the operator or a senior radiology nurse before the planned biopsy. The evaluation determines if a day case procedure is appropriate in the light of the patient's fitness and home circumstances. It will also identify any contraindications and pre-procedural requirements prior to admission and allow the patient time to see the unit and discuss the procedure and the post-procedural care. Patient information leaflets should be available for all common procedures and should be posted to the patient prior to the pre-assessment visit. This will help inform the consent process and should allay any anxiety and uncertainty.

Anxious patients or those with previous experience of painful biopsy procedures may require a pre-biopsy anxiolytic or prophylactic analgesia. Following the biopsy the patient should be advised of the routine nature of the post-procedural observations and given comprehensive aftercare advice and relevant contact numbers. Patients should be told how and when they will receive their results and a follow-up outpatient clinic appointment organised prior to discharge.

FNA versus core biopsy

Fine-needle aspiration (FNA) provides a sample of cells for cytological analysis using a small calibre needle (20–25G). Generally no information on tissue architecture is obtained, although small calibre needles are occasionally used to obtain a core of tissue by fine-needle aspiration biopsy (FNAB). Core biopsy using larger calibre needles (14–19G) provides more structural information, which may be necessary for the histological diagnosis of both benign and malignant lesions.[5,6] Both sampling methods have their advantages and limitations and the decision as to which sampling method to use depends on many factors.

Smaller calibre needles are useful where a deep mass lies posterior to a loop of bowel, which may have to be punctured to gain access. As a general rule, the smaller the calibre of the needle, the less the risk of infection as a result of bowel puncture. Similarly, where a deep lesion lies close to critical structures (e.g. a pancreatic mass encasing the superior mesenteric vessels, or a central liver lesion abutting the vena cava), core biopsy may be deemed too hazardous but FNA could be performed as an alternative with minimal risk of vascular injury. In addition to the reduced risk of iatrogenic injury, FNA is generally quicker to perform and may therefore be useful in very frail or unwell patients who are unable to tolerate a biopsy procedure. FNA has the added advantage of being safe to perform in an outpatient setting. Cytological slides can be prepared and examined immediately to assess for adequacy and formal reports can be issued rapidly if required. The processing of an FNA specimen is also less expensive than for a core biopsy.

When performing FNA procedures, the local availability and expertise of cytologists is a consideration. Also the degree of confidence in cytological diagnosis will vary according to the indication: for example, the diagnosis of recurrent malignancy can be more easily made on a cytological sample if previous tumour tissue has been obtained for comparison. For a new diagnosis of primary malignancy, however, a larger sample of tissue is often required and therefore core biopsy is generally preferred over FNA cytology. This is particularly important where different subtypes of malignancy exist, such as with lymphomas, and accurate histological typing is necessary to plan treatment. Other conditions requiring histological confirmation include diffuse liver disease such as cirrhosis and renal parenchymal disease such as glomerulonephritis. However, FNA cytology allows better assessment of cellular detail, especially for small-cell tumours with fragile cells that are easily crushed during sectioning.

Most studies have shown core biopsy to be more sensitive than FNA in the diagnosis of suspected intra-abdominal tumours.[7,8] A combination of core biopsy and FNA has, however, been found to improve diagnostic sensitivity.[9]

Needle types used for fine-needle aspiration

Needles vary in calibre (Table 43.1), tip design and length and there are a wide range of different products available from which to choose. Cytological samples are usually taken with small calibre needles (20–25G), although when a larger calibre needle is used for a core biopsy, a slide may also be prepared by pressing the core obtained onto a glass slide, to provide an additional cytological smear which can be used to give a more rapid result if required.

Different lengths of small calibre needle are available and the needle should be carefully selected according to the depth and size of lesion to be sampled (Fig. 43.1). For abdominal aspirations, the target will often be deeply situated and a spinal needle with a stylet, or another stylet needle is often used. The presence of a stylet within the needle helps to avoid contamination of the needle lumen with blood or tissue before it reaches its target. When using very fine needles, a stylet also aids insertion by stiffening the needle, which may otherwise bend and deviate from its course.

Needle and catheter size standards

Catheters

- The French catheter scale (Fr) was devised by Joseph-Frédéric-Benoît Charrière, a maker of surgical instruments in Paris in the nineteenth century.
- The symbol used is sometimes Ch instead of Fr.
- The external diameter of the catheter approximates to the Fr number divided by 3; e.g. a 12Fr catheter has an external diameter of 4 mm.

Needles

- The Stubs Iron Wire Gauge (SWG) was devised by Peter Stubs in the nineteenth century to measure the size of wires being manufactured in Birmingham, UK.
- The diameter of the needle (in inches) approximates to the reciprocal of the SWG number; e.g. a 20G needle has a diameter of one-twentieth of an inch (0.05 in).

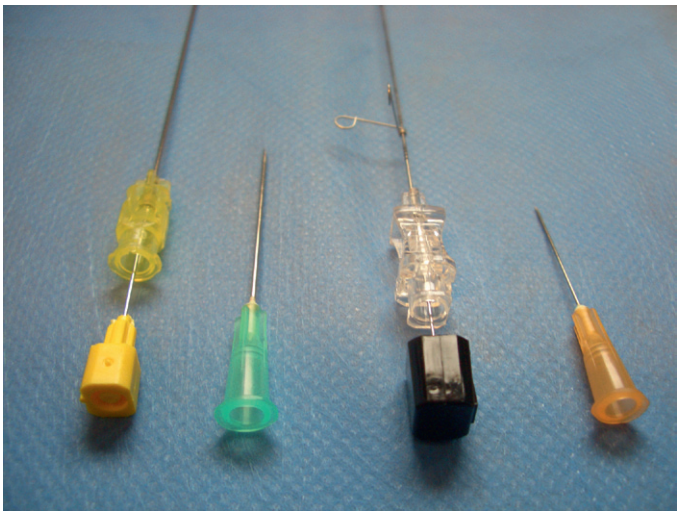

Figure 43.1 FNA needle types. The type of needle used for FNA procedures should be selected according to the size of the target lesion and depth from the skin. Longer needles incorporate a stylet. From left to right: 20G spinal needle, 21G needle, 22G Chiba needle, 25G needle.

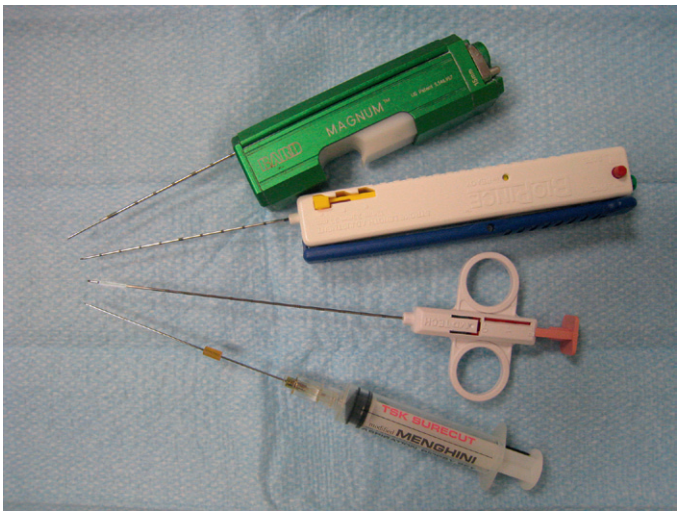

Figure 43.2 Core biopsy instruments from top to bottom: fully automated metal biopsy gun, fully automated disposable biopsy device, semi-automated disposable biopsy device, Menghini technique biopsy needle.

Table 43.1 Needle sizes: gauges of needles frequently used in abdominal interventional procedures, with their actual diameter (mm)

Needle gauge	Diameter (mm)
22G	0.72
21G	0.82
19G	1.10
18G	1.26
16G	1.67
14G	2.13

Various FNA techniques have been described but the method used is generally a matter of personal preference. FNA can be performed using the needle alone: a rapid 'jiggling' motion with simultaneous rotation of the needle hub draws cellular material up into the needle lumen by capillary action. Alternatively a syringe (e.g. 20 mL) may be attached to the needle and suction applied. There are also aspiration handles available that can be attached to the syringe to aid the process.

Needle types used for core biopsy

For core biopsy, larger calibre cutting needles are employed (normally 16–18G for abdominal biopsies) (Fig. 43.2). The size of biopsy needle chosen depends on the organ being targeted and may also vary according to the number of samples being obtained. For example, for a routine 'background' liver biopsy, a single pass is usually sufficient and so a larger (e.g. 16G) biopsy needle may be chosen. If the operator anticipates that several cores will need to be obtained, for example in the case of malignancy with focal lesions, then an 18G needle may be a more appropriate choice to reduce the risk of bleeding complications as a result of multiple punctures through the liver capsule. The shape of the tissue core obtained varies according to the design of the chamber within the biopsy needle; various manufacturers have designed biopsy instruments which optimise the volume of tissue obtained for a given needle gauge.

Menghini technique biopsy needles

Needles of this type are now rarely used for ultrasound-guided biopsy procedures. They are based on the Menghini principle in which the needle, stylet and syringe form a single unit. The stylet is attached to the plunger of the syringe and as the plunger is retracted, it moves up into the needle lumen, revealing the cutting needle tip. A locking device retains the plunger in the retracted position to maintain the negative pressure when the needle is advanced. When the needle is subsequently removed, the tissue core remains in the distal portion of the needle because of the stylet. The most commonly used size for abdominal biopsies is 21G (0.8 mm).

Manual sheathed biopsy needles

These needles have a biopsy chamber that can be opened and closed. After insertion to the correct depth, the needle is opened by advancing its inner portion so that the surrounding tissue falls into the biopsy chamber. As the outer part of the needle is advanced with the inner part fixed, the tissue in the chamber is cut by the sharp edge of the outer needle. The closed needle can then be removed with the tissue core in the chamber. This type of needle requires two hands to operate and so is not ideal for ultrasound-guided procedures; it is now rarely used.

Semi-automated sheathed biopsy needles

Some biopsy instruments allow placement of the central stylet and its sampling notch at the exact position required and then fire the cutting sheath over the stylet (Fig. 43.3). There is therefore no additional forward excursion of the needle upon firing the gun, so minimising potential damage to adjacent structures. This is useful in the case of small lesions or those adjacent to critical structures such as large veins. A disadvantage is that when the target tissue is fibrous or very firm in texture, it may be difficult to manually advance the cutting needle through the lesion. This is often overcome by the use of spring-loaded fully automated devices that provide more forward force to advance the needle into the target organ or tissue.

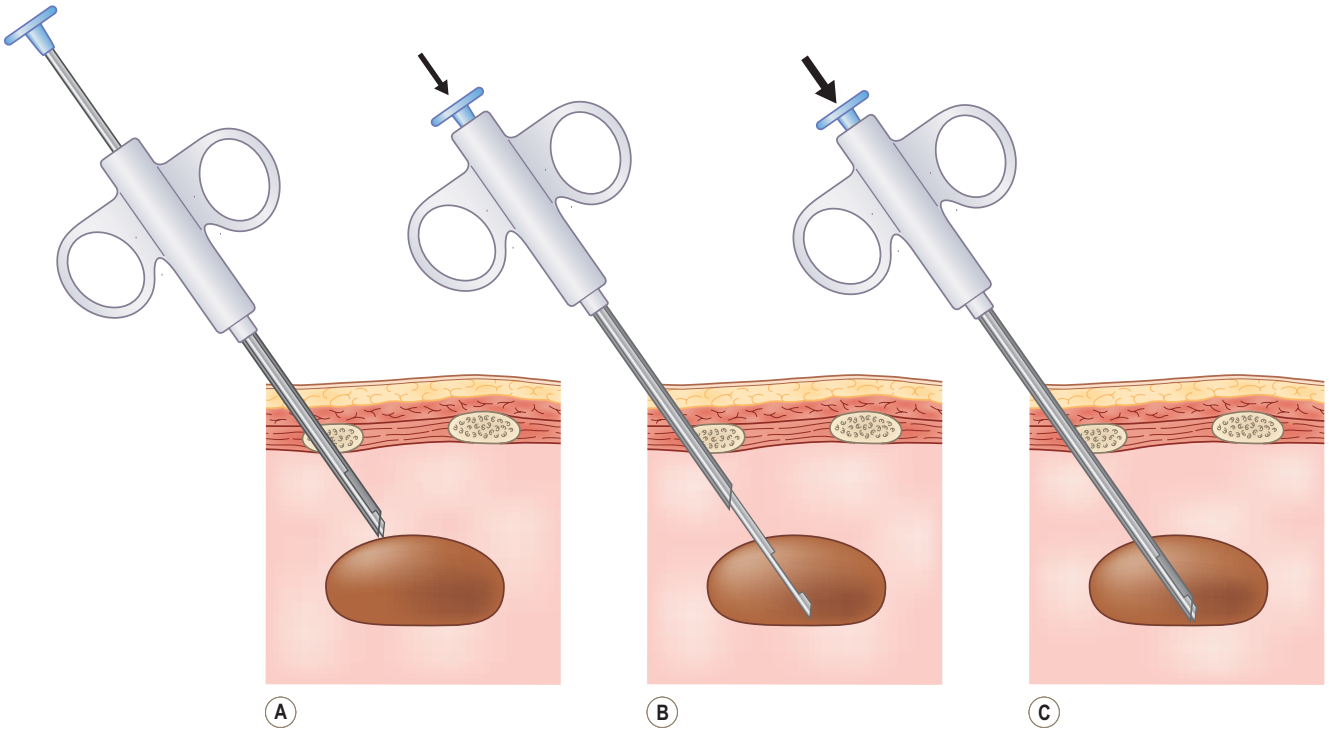

Figure 43.3 Mechanism of action of semi-automated biopsy instrument. A: The biopsy instrument is 'primed' prior to insertion under ultrasound guidance. Most disposable instruments offer the option of 1 or 2 cm core lengths. The biopsy needle is slowly advanced to the edge of the target lesion. **B:** The central stylet is then slowly advanced through the lesion whilst keeping the remainder of the instrument still. The notch can usually be visualised easily and so the operator can confirm that the target tissue will fall within the biopsy specimen. **C:** Once the operator is satisfied with the position of the central stylet/notch, the instrument is 'fired' by further firm forward pressure on the 'plunger', which rapidly advances the outer cutting sheath over the central stylet and samples a core of tissue.

Fully automated sheathed biopsy needles

Automated, spring-loaded biopsy instruments are popular. These can take the form of metal biopsy guns, which are designed for use with disposable biopsy needles of different gauges, or fully disposable integrated plastic biopsy devices, which have a similar mechanism of action. Whilst the disposable devices are more expensive, they avoid the difficulties associated with sterilisation of the metal biopsy guns. Fully automated biopsy instruments fire both a central stylet and cutting sheath in a rapid forward motion such that the tissue core is obtained at a preset distance (e.g. 2 cm) ahead of the visualised needle tip. Many of the instruments offer a choice of a 1 cm or 2 cm throw depending on the size of target lesion or organ. This mechanism of action means that the operator needs to pay careful attention to the size of the lesion to be biopsied relative to the throw of the biopsy needle. Often the needle tip can be positioned at the superficial margin of the target lesion to avoid injury to adjacent organs. Some disposable devices have a dual action which allows an almost simultaneous advance of both components, as described above but, alternatively, they can be inserted with the inner specimen chamber extended, so that it can be positioned across the lesion under ultrasound control before the outer sheath is activated to cut off the sample.

Coaxial technique

Most abdominal biopsies are performed by making one or more passes into an organ or mass with a single biopsy needle. Occasionally it may be helpful to employ a coaxial system whereby a coaxial needle is guided to the region of interest, the central stylet is removed and then a smaller calibre biopsy needle is inserted through the coaxial needle several times to obtain the required number of cores. This has the advantage of allowing several samples to be taken without re-puncturing the superficial soft tissues or organ capsule, so reducing risk of haemorrhage and time taken to target the lesion/organ.[9] The coaxial needle can be angled between samples to increase the volume of tissue sampled. Whilst this technique may be useful for ultrasound-guided biopsy of deep structures such as retroperitoneal lymph nodes, in practice, it is more commonly employed during CT-guided biopsy, particularly for lung lesions, where minimising the number of passes through the pleura and lung parenchyma reduces the risk of pneumothorax. A disadvantage is that the calibre of coaxial needle has to be larger than that of the biopsy needle, increasing the overall size of the needle track, with a possible increased risk of bleeding complications and damage to adjacent tissues.

Needle tip visualisation

Optimising visualisation of the needle tip is a key factor in the success of biopsy and drainage procedures performed under ultrasound guidance. Imaging of the needle shaft and tip can, however, be technically difficult, particularly during procedures that target deep structures, or in obese patients. The needle tip is more easily visualised in cystic structures, fluid collections or relatively

hypoechoic organs such as the kidney or liver but can be difficult to localise in more reflective tissues. The needle and sampling groove are better seen in superficial biopsies, such as breast or neck masses, when the needle shaft is at right angles to the ultrasound beam. In most abdominal biopsies, the needle shaft is angling away from transducer, making accurate localisation more difficult.

Several aspects of needle design may aid visualisation. Roughening the outer surface of the distal end of needles improves visualisation by increasing the scatter of the ultrasound beam[10] and this technique is often employed in the manufacture of modern biopsy needles (Fig. 43.4). Other methods that have been reported to increase the reflectivity of the needle include coating them with a porous polymer, which traps microscopic air bubbles, so increasing beam reflection[11] or embedding a polymer in the needle tip, which acts as a passive acoustic electrical transducer.[12] Larger calibre needles are usually more easily visualised than those of smaller calibre and this may be a factor when deciding on the gauge of needle to use. By turning the needle so that the bevel faces upwards, the conspicuity of the needle tip is increased.

Figure 43.4 Tip of a typical biopsy needle in the closed and open positions. Note how there is a short section of the distal needle shaft, close to the tip, which appears 'roughened'. This design feature increases scatter of the ultrasound beam and hence improves needle tip visualisation. With the biopsy needle in the open position, the 'gate' or 'notch' where the core biopsy sample will lie is clearly visible.

The most frequent error seen amongst novices at freehand ultrasound intervention is lack of proper alignment of the needle and transducer (Fig. 43.5). It is imperative that the needle and ultrasound beam are aligned in the same plane for accurate visualisation of the needle tip. If the needle is proving difficult to visualise, the alignment of the needle with the transducer is the first thing that should be checked. Even if the needle passes through the skin at a point aligned with the centre of the transducer, it may be angled away from the centre plane and this should be checked by the operator and corrected if necessary. There are also various 'tricks' that can be employed by the operator to improve needle tip visualisation. Where a co-axial system is being used, retracting the central stylet a few millimetres and moving it in and out rapidly improves conspicuity with minimal tissue trauma.[13] 'Jiggling' the needle during insertion can aid visualisation by alerting the operator to movement around the needle tip. Sometimes injecting a tiny amount of local anaesthetic, saline or even air may help to accurately locate the tip of the needle although care must be taken not to introduce too much air, as this can obscure the view. It is important to choose the correct transducer for the individual procedure being performed and the focal zone should be adjusted to the near field to optimise needle tip visualisation. It is also helpful to minimise the field of view to exclude extraneous anatomy and allow the needle to traverse at least one-third of the image.[2] The use of colour Doppler imaging has also been suggested as a tool for improving detection of the needle tip due to the colour disturbance produced by manipulation of needles or catheters.[4] Patient movement can also hinder needle tip visualisation; this can often be reduced by explaining the importance of keeping still to the patient before the

Aiding needle tip visualisation

- Explanation of need to keep still to reduce patient movement.
- Use appropriate transducer.
- Consider larger needle.
- Bevel of needle held uppermost.
- Ensure correct alignment of needle and transducer.
- Optimise focal zone and field of view.
- 'Jiggle' needle or move stylet in and out.
- Inject small amount of anaesthetic/saline.
- Needle guides may help.

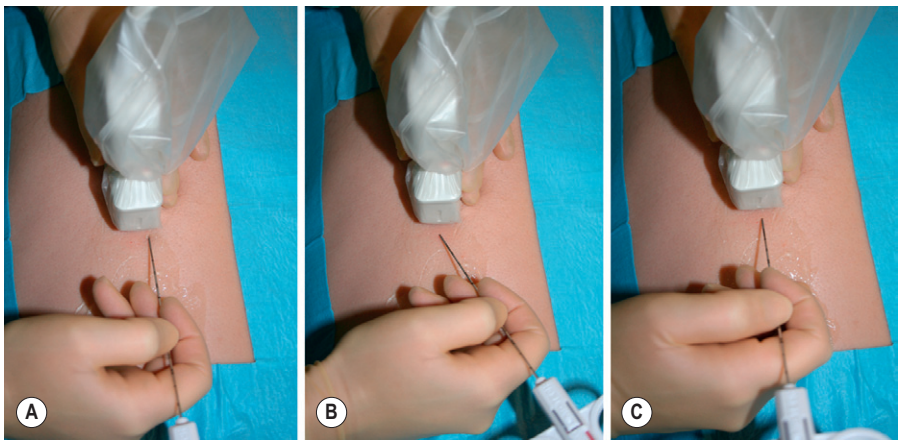

Figure 43.5 Incorrect and correct alignment of transducer and needle. A: *Incorrect alignment* – the biopsy needle is off centre with respect to the transducer. **B:** *Incorrect alignment* – although the biopsy needle is correctly positioned with respect to the centre of the transducer, it is angled away from the plane of the beam such that the tip will not be visualised. These types of errors are best appreciated by looking along the line of the transducer or directly from above it; otherwise parallax error may result in an inaccurate assessment of transducer and needle alignment. **C:** *Correct alignment* – the biopsy needle is centred with respect to the transducer and is angled along the plane of the beam to optimise needle visualisation.

Figure 43.6 The majority of needle guides are disposable, or have a disposable component which clips onto the relevant transducer over the top of the probe cover. This needle guide that clips onto an endocavity transducer can be used for procedures such as prostate biopsy or drainage of deep collections via a transrectal approach.

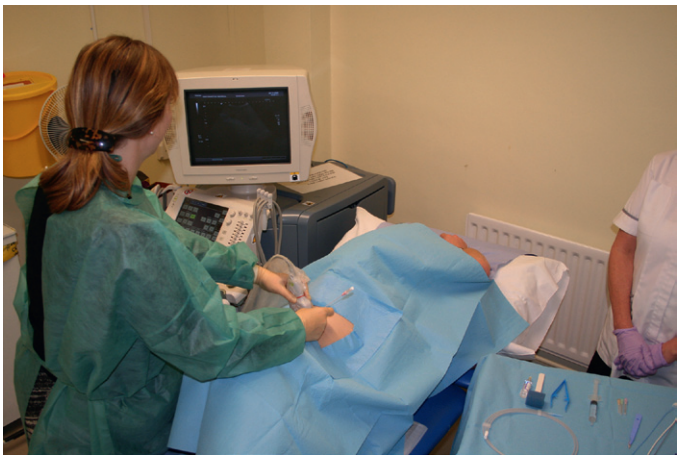

Figure 43.7 Room set-up for a typical interventional ultrasound procedure. It is important that the operator, biopsy/drainage site and screen are in alignment to facilitate the procedure. Everything required during the procedure (sharps disposal, waste bin, needles, catheters etc.) should be within easy reach and a trained assistant should be available in the room. Table position and height should be adjusted to suit the individual operator.

procedure and ensuring adequate local anaesthesia has been administered. There is no substitute for practice in ultrasound-guided procedures and it is often helpful to use a biopsy phantom in order to hone the necessary hand–eye coordination skills for ultrasound intervention.[14]

Needle guides on the transducer control the path of the needle, restricting the needle's course to a predetermined path in the image plane, which is projected onto the screen, so allowing rapid visualisation and accurate placement of the needle tip. Most guides are in the form of attachments, which are clipped onto normal transducers; they may be disposable or require sterilisation. Their use is generally a matter of personal preference although they are particularly useful for biopsy/drainage of deep structures or for endocavity procedures such as prostate biopsy (Fig. 43.6). There are many different commercially available needle guidance systems. Many of these guides allow a preselected angle of the guide relative to the ultrasound transducer. Guides are available with different calibre canals to accommodate different sizes of needles. The canal should be at least 3 cm long as this prevents the needle from deviating during the procedure. Many radiologists prefer a freehand approach to needle insertion and lesion targeting as it allows for fine adjustments to be made during the procedure, to compensate for patient movement or altered position of bowel.

Targeting an area for biopsy or drainage may occasionally be performed in combination with other imaging modalities such as CT or fluoroscopy. This combined approach is useful during procedures such as nephrostomies. Software is becoming available which allows fusion of CT or magnetic resonance (MR) data with the ultrasound image to aid in guidance when lesions are difficult to identify on ultrasound alone.

Procedural planning and ergonomics

It is important to scan the patient carefully and spend some time planning any intervention in terms of patient positioning and access route, before commencing local anaesthetic injection. This will facilitate the procedure and minimise the time taken performing the subsequent biopsy or drain insertion.

It is necessary to consider probe shape and frequency, in addition to the depth and angle of needle insertion required. If additional imaging has been performed, e.g. CT, then it is helpful to have the imaging to hand for reference when planning and performing a subsequent ultrasound-guided procedure. It is useful to be able to perform FNAs and operate a core biopsy instrument with either hand, as there are occasions when the location of the target tissue makes it awkward to perform the procedure with the needle in the operator's dominant hand. Newer ultrasound platforms have a flat screen which can be moved into alignment with the patient and operator so that the operator does not have to turn to visualise the screen, as any such movement may cause inadvertent needle or probe movement resulting in misalignment and loss of needle tip visualisation. It is also vital to have the bed or trolley at the correct height for the person performing the procedure and the patient should be turned and moved to the edge of the bed to avoid the operator having to lean too far over them. Optimising room set-up in this way improves overall procedural efficiency (Fig. 43.7).

The exact site to be sampled within the target tissue also requires consideration. Some lesions such as squamous cell metastases tend to be centrally necrotic and so it is important to plan a needle trajectory through the periphery of the lesion to obtain useful tissue for histological analysis. The degree of vascularity of a lesion may be variable and colour Doppler imaging will help the operator avoid major vessels within a lesion or organ.

Ultrasound has the advantage of portability and so procedures may be performed on wards, intensive care units or in a theatre or emergency department setting if required. It is, however, important to consider the requirements of an individual procedure carefully before commencing and ensure that all the necessary equipment and assistance is available. Ideally, an interventional ultrasound room should be equipped with a sink, sharps disposal bin, biopsy trolley and be in close proximity to resuscitation facilities. If patients are admitted for day case biopsies through a dedicated day case unit, this should be located close to the ultrasound room and trained assistants and nurses should be available to assist with the biopsy procedure itself and subsequently monitor the patient according to procedure-specific protocols.

Specimen handling

Having obtained a tissue sample, it is important to maximise the diagnostic value by carefully handling the sample and providing clear clinical and anatomical information for the pathologist. Specimen handling is simplified by the presence of an assistant; however, every effort should be made to minimise the risk of needle stick injuries. The preparation of high quality slides requires the presence of a cytopathology technician. If this facility is not available, advice on fixation methods and slide preparation should be sought from the local department.

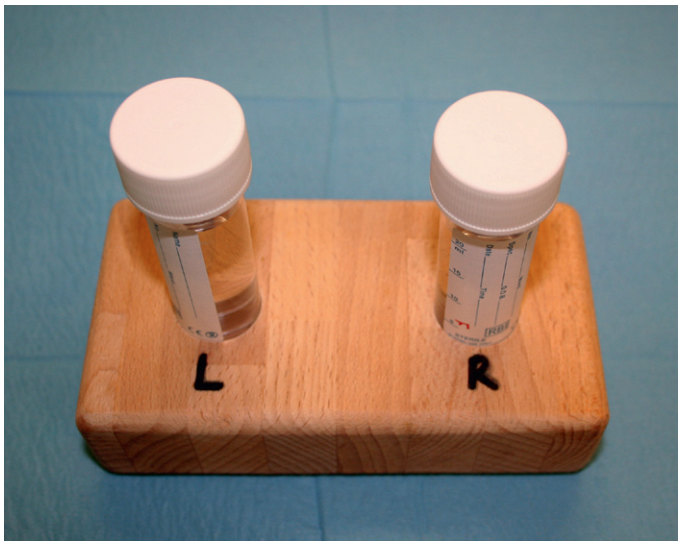

Figure 43.8 Wooden stand designed to contain two specimen pots so that core biopsies from the prostate can easily be placed into the correct pot according to the lobe of the prostate from which they were taken. By securing specimen pots in a stand, rather than an assistant holding them when the core of tissue is removed from the biopsy needle, the risk of needle stick injury is greatly reduced.

Following core biopsy the needle should be placed within formalin and the needle gate opened according to the manufacturer's instructions. Specimen pots should be securely fixed within a stand and should not be held by an assistant (Fig. 43.8). The needle may require gentle agitation to release the sample but efforts should be made not to damage the tissue sample. Occasionally a second needle is required to help remove the tissue from the biopsy needle. After the biopsy has been performed, the sample should be carefully evaluated under a bright light to assess for sample adequacy. Soft tissue is seen to sink while fat floats to the surface.

Post-procedural care

Good post-procedural care reduces the morbidity associated with percutaneous biopsies and interventions by identifying complications early and instigating the appropriate management. Immediate post-procedural scanning has a low sensitivity and specificity for identifying complications. The majority of complications become evident during the early post-procedural period; it is for this reason that the patient should be closely observed to a standard protocol in a dedicated nursing unit. Patients are best observed in the peri-procedural period within a day care unit in the radiology department. This allows for the operator to easily assess all patients and when pain or observations warrant, arrange for a repeat ultrasound or CT assessment. Post-procedural pain is a common finding and usually responds to simple non-steroidal analgesia (e.g. diclofenac 100 mg suppository) and reassurance. If opiate analgesia is required the patient should be reviewed to assess for early evidence of hypovolaemia. Standard procedure-specific post-biopsy observation sheets should be used and clearly highlight the management of suspected complications.

Safety/Complications

Ideally biopsy procedures should be performed on a morning list. This is particularly important for day case procedures to enable observation of the patient for the appropriate length of time prior to discharge. It also allows any complications to be identified and managed whilst the maximum numbers of staff are on duty and whilst interventional rooms are running. There is an argument that biopsy procedures should only be performed in a unit where any associated complications can be definitively managed to avoid the need for patient transfer with the associated delays that ensue. For the purposes of clinical governance, those performing biopsy or drainage procedures should audit their complication rates and monitor their success rate of biopsies in terms of the percentage of biopsy procedures resulting in sufficient material for histological evaluation.

Complications are specific to the organ/lesion undergoing biopsy or to the type of drainage procedure being performed. Complications will also be higher in those patients who have co-morbidity and in whom clotting studies are abnormal. Targeting of lesions that are deeper is also more likely to result in iatrogenic injury to adjacent structures due to poor visualisation of the needle tip.

Haemorrhage is the most common major complication after biopsy procedures. If there is clinical suspicion regarding haemorrhage, ultrasound may be employed to assess for the presence of free fluid but false negative scans may result from the fact that acute haemorrhage can be isoechoic to the surrounding organs. CT imaging is therefore preferable, provided that the patient is stable. Haemorrhage can also occur as a result of drain placement due either to injury to vessels along the course of the drain at the time of placement, or to subsequent erosion of adjacent vessels by the drain over a period of time. Other major complications as a result of ultrasound-guided abdominal intervention include infection (wound infection, deeper abscess formation or peritonitis), bile leak and pneumothorax. Following drainage of intra-abdominal abscesses, rigors may occur, although the incidence is less than 5% and is usually avoided by appropriate use of antibiotic prophylaxis.

Minor complications include post-procedural pain and vasovagal reactions as well as complications specific to individual procedures such as self-limiting haematuria after renal or prostate biopsy.

Track seeding

Needle track seeding as a result of abdominal biopsy has been reported from a number of different tumour sites including pancreas, prostate, liver, kidney and retroperitoneum.[15–19] It is a rare complication with rates of 0.0002% to 0.00005% reported for FNA biopsy.[20,21] For biopsy of hepatocellular carcinoma using 18–20G needles, however, track seeding rates of up to 3% have been reported.[22] A recent review of 41 papers revealed a median risk of tumour seeding from percutaneous biopsy of hepatocellular carcinoma of 2.29% (range 0–11%).[23] As a result of the risk of seeding of hepatocellular carcinoma along biopsy tracks, it is generally recommended that diagnosis be achieved by non-invasive means and that core biopsy be reserved for cases not amenable to surgical resection.[24]

PRINCIPLES OF DRAINAGE TECHNIQUES

Diagnostic aspiration versus drainage

Ultrasound-guided aspiration of fluid collections to obtain a diagnostic sample, or more frequently for therapeutic drainage, has become an essential service for the acute management of surgical and medical patients. With improvements in the equipment and technique the vast majority of fluid collections can now be managed with appropriately sized and sited catheters; however, success depends on an understanding of a few key concepts. The initial assessment of the fluid collection along with an understanding of the overall management plan for the patient is essential before embarking on any intervention.

Pre-procedural assessment

As with biopsies, careful consideration must be given to the reasons for percutaneous drainage of a collection and a risk/benefits assessment made, preferably in discussion with the clinical team looking after the patient. The nature of the collection, its location in relation to surrounding structures, potential access routes, the type and the number of drains to be used must all be considered. If an infected collection is considered likely and the patient is not already on antibiotics, then broad spectrum antibiotic cover should be arranged.

The nature of the collection

Ultrasound is an accurate method for the assessment of the internal complexity and viscosity of a fluid collection. The initial assessment should involve the use of colour Doppler to prevent the inadvertent drainage of an aneurysm, followed by characterisation of the fluid component to determine needle and drain type and approach (Table 43.2, Fig. 43.9).

As fine-bore 21G or 22G needles are flexible, a generous skin incision is required to prevent the needle bending and deviating. If no fluid is aspirated with a 21G needle, a repeat puncture with an 18G needle should be attempted. If this fails, the collection should be re-examined to exclude a necrotic tumour, for which ultrasound-guided biopsy would be more appropriate.

When draining complex collections, it is important to scan the collection carefully and scrutinise any other available imaging (e.g. CT) in order to establish whether multiple collections are likely to connect and hence whether insertion of a single drain or multiple drains is appropriate. The choice of drain insertion site should also depend on the most dependent part of the collection, comfort for the patient (ideally a drain should not be placed where a patient will sit or lie on it) and ease of drain emptying if required.

Drain types (Fig. 43.10)

Drainage catheters are produced in a wide range of sizes (Table 43.3) but the ability of a catheter to drain viscous fluids and particulate debris is determined by two limiting factors, namely the side hole size and the end connector type of the catheter. Many commercially available 8–14Fr drains have the same sized side holes, providing little advantage to larger drains of this type. Large-bore 16Fr and 18Fr drains are available with Luer lock type ends. These are often attached to a three-way tap, completely negating the advantage of a large drain as the internal diameter of the standard three-way tap ranges from 1.27 to 1.52 mm, which is much smaller than the internal diameter of the 8Fr catheter (1.68 mm).[25] If large-bore drains are to be used, a bladder catheter type connection is preferable as these can be flushed using a bladder syringe and allow large particulate debris to drain.

Locking drains

Fine-bore drainage tubes (5–7Fr) are usually unlocked. However, from 7Fr to 16Fr the option of a locking loop is often incorporated to improve anchorage and reduce the possibility of inadvertent drain removal. The locking pigtail is usually tensioned with a thread that is then captured within a locking mechanism within the hub. While the various mechanisms are different they can usually be released by cutting off the hub well away from the skin entry site. Locked drains reduce accidental removal rates but are more expensive and often require removal within the radiology department.

Sump drains

Sump drains have a second smaller lumen through which air can pass to prevent a cavity from collapsing around the catheter tip. This channel can also be used for irrigation of viscous collections. These drains are advocated for peritoneal collections although the advantage over a conventional 10–12Fr locked drain is debatable. They can be used to replace smaller drains if collections fail to resolve.

Side holes

Most polyurethane drains have the side holes along the inside of the pigtail. Biliary drains have further holes along the shaft of the drain for a variable length. When planning drainage procedures it is important to assess the need for extra side holes along the shaft. If required these can be tailor-made using a scalpel. Extreme caution is required not to weaken the drain or damage the locking thread within the tube. Extra holes can be cut in larger drains by kinking the drain and cutting across the corner (Fig. 43.11).

Drain placement

There are a large number of indications for ultrasound-guided drain placement in the abdomen and pelvis ranging from drainage of a complex solid organ abscess to drainage of large volume simple ascites. Drainage procedures may be employed as a definitive treatment or as a temporising measure in a patient unfit for general anaesthetic. It is important to ensure that the appropriate equipment is to hand before starting a procedure, for example checking that the correct size guidewire is available for the selected aspiration needle and drainage catheter and giving consideration to any alternative equipment that may be useful, depending on how the procedure evolves. By scanning collections prior to drainage, it is possible to predict what type of material is contained within them (see above); however, it is always advisable to aspirate some of the collection before making a final decision as to what type and calibre of drain to insert, as some collections can be deceptively viscous. If the aspirated fluid appears non-infected and it can easily be

Table 43.2 The nature of the collection: initial ultrasound characterisation of the fluid collection is helpful in determining the most appropriate type and size of needle and drainage catheter

Ultrasound appearance	Likely fluid	Needle type/gauge (G)	Drain
Anechoic (Fig. 43.9A)	Clear thin	21G for diagnostic aspiration	5–8Fr pigtail drain
Scattered echoes (Fig. 43.9B)	Turbid fluid – pus	18–19G cannula needle	8–10Fr pigtail drain
Extensive echoes (Fig. 43.9C)	Thick pus – haematoma	18G cannula needle	12–16Fr pigtail or sump drain
Semi-solid collection (Fig. 43.9D)	Phlegmon, necrotic tissue or haematoma	18G (may be unable to aspirate)	Large-bore drain 14–28Fr

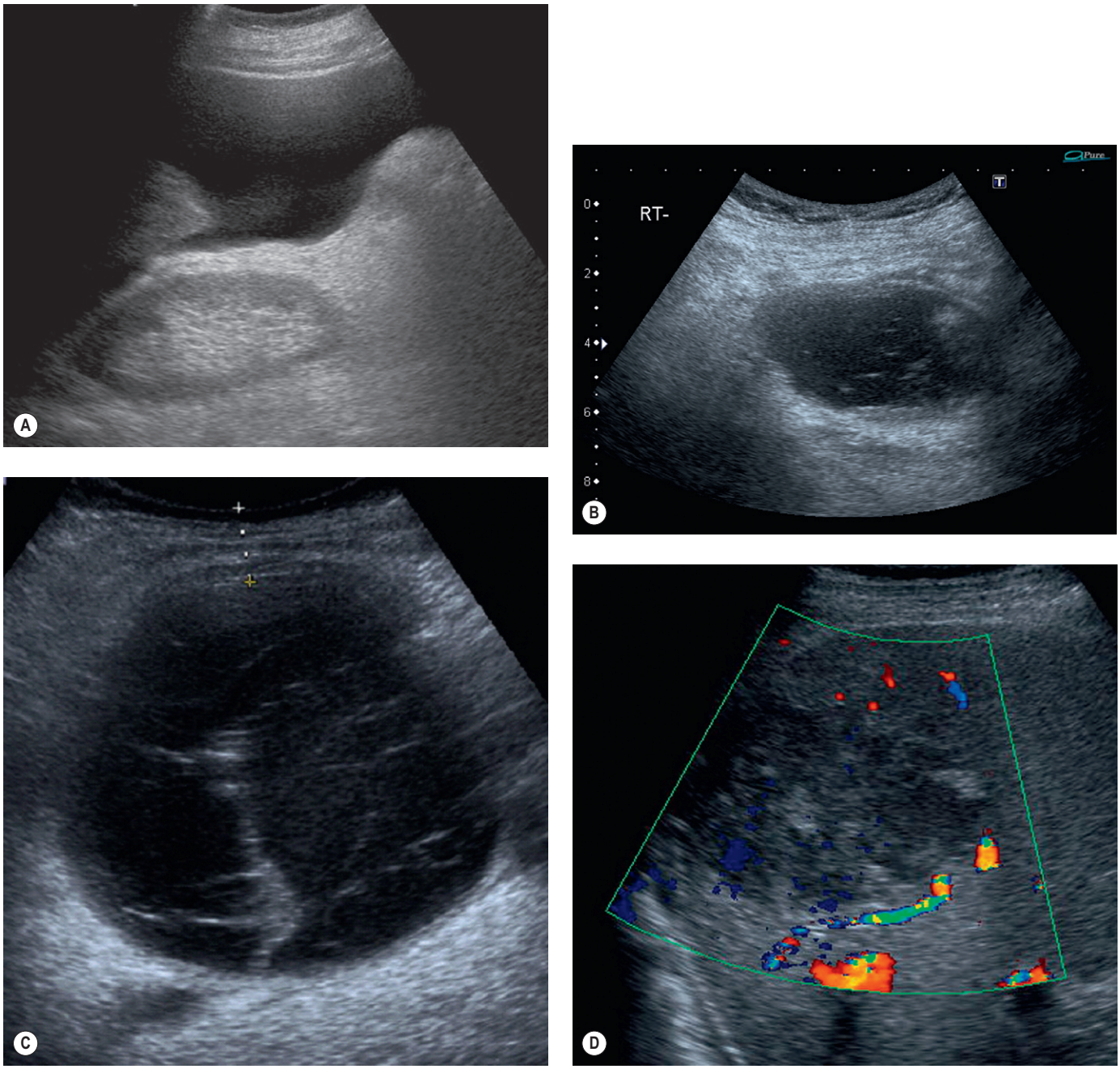

Figure 43.9 **Assessing the nature of a fluid collection. A:** Longitudinal ultrasound image in right upper quadrant – simple (anechoic) ascites, amenable to drainage with a 5–8Fr pigtail catheter. **B:** A post-appendicectomy collection in the right iliac fossa – note there are scattered low-level echoes indicating the presence of turbid fluid or pus. An 8–10Fr drain would be suitable for draining this type of collection. **C:** Left upper quadrant collection in a patient with pancreatitis. Note the degree of complexity and internal echoes, which indicate thicker pus (or haematoma). Collections with this appearance usually require a 12–16Fr drain or sump drain. **D:** A liver abscess – note the heterogeneous and more solid appearance but with some distal acoustic enhancement. Collections such as this require a larger-bore drain (14–28Fr).

aspirated to dryness, then it may not be necessary to go on to drain insertion. If, however, pus is obtained, then only a small amount should be aspirated to maximise the size of the residual collection, which aids subsequent drain placement.

Interventional ultrasound procedures should be performed using sterile technique. Disposable plastic probe covers are commonly used as they avoid the difficulties of sterilising ultrasound transducers themselves. Enough gel should be placed inside the probe cover so as not to allow air to degrade image quality and sterile gel is then used as a coupling agent.

Trocar technique

This is a single-step technique utilising a drainage catheter which fits over a stiffening cannula which in turn contains a central sharp stylet. The three-part drainage assembly is inserted directly into the centre of the collection and then the central stylet is withdrawn and if fluid is successfully aspirated, the drainage catheter is advanced over the stiffening cannula. This method is quick to perform and may be suitable for large superficial collections such as large volume ascites.

Seldinger technique

A 16G or 18G vascular access needle, or similar, is used for the initial puncture and aspiration of the collection. A standard 18G vascular access needle allows the passage of a standard guidewire (0.035 or 0.038 inches); the guidewire should have a long flexible tip to allow it to coil within the collection and it should be longer than the drain. For small or challengingly located collections, the initial puncture may be made with a 21G needle from a proprietary access set, which takes an 0.018 guidewire and allows exchanges up to 0.035. When the main guidewire is established in the collection, the needle is removed over the guidewire and exchanged for dilators, which widen the track to an appropriate size for the required drain. A drainage catheter/stiffening cannula assembly (without a sharp central stylet) is then passed over the guidewire into the collection. The guidewire and stiffening cannula are then removed at the same time as the drainage catheter is advanced (Fig. 43.12). Confirmation of drain position can be achieved with post-procedural ultrasound scanning if required and if difficult to visualise, colour Doppler imaging during aspiration may improve conspicuity. If the drainage is potentially less than straightforward, it is of value to carry out the procedure in a fluoroscopy room, where screening and contrast enhancement can be used in addition to ultrasound to position guidewires and drainage catheters.

Following placement of a drainage catheter, the collection should be aspirated straight away as drains may soon block or become dislodged. Samples can then be sent for microbiological or biochemical analysis as required. Once the collection is fully aspirated, it is good practice to flush an abscess cavity with saline to ensure that as much debris as possible is cleared.

Drain fixation

It is important that the drain is placed in a practical and comfortable position. The drain should be securely fixed to minimise the risk of accidental displacement either using a propriety adhesive anchoring system (Fig. 43.13) or suturing the drain to the skin. If the drain is attached to a drainage bag this should also be carefully secured. Locked drainage catheters can be placed directly into stoma bags and this reduces the risk of accidental displacement.

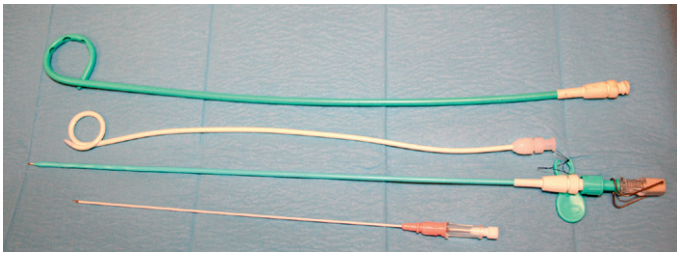

Figure 43.10 A selection of drainage catheters. Note the variation in calibre, length, end connector type and side hole configuration. Many drains incorporate a pigtail loop at the catheter tip and may also have a locking thread mechanism.

Post-procedural care

To gain maximum benefit from a drainage catheter the interventional radiologist needs to maintain ownership of the patient and should routinely review the patient on the ward, which should have experience in dealing with patients who have percutaneous drains. Many drainage catheters benefit from irrigation with 10–15 mL normal saline 2–3 times daily but this volume may be increased in certain clinical situations (turbid or semisolid collections). If the clinical response is slow the abscess should be re-imaged with a view to possible further drain insertions or 'up-sizing' the initial drain. Occasionally 'tubograms' can be useful to identify fistulous communications or to allow for fluoroscopically guided repositioning of a drain within a complex collection. The decision to remove a drain should be taken in the context of the patient's recovery. Repeat imaging is not required prior to drain removal in systemically well patients with normalisation of the white cell count and a drainage output of less than 15 mL per day. More complex collections may require imaging review prior to removal. Most drains can be simply withdrawn without the need for 'shortening', a practice often used for surgical drains. Locked drains should be removed with fluoroscopic assistance if there is any resistance or pain following initial attempts at drain removal. Occasionally guidewire manipulation is required to release the locking loop.

Cyst ablation

When large cysts within the abdomen or pelvis become symptomatic, ultrasound-guided drainage may be considered. Simple aspiration may relieve symptoms temporarily but often cyst fluid

Drain removal – endpoints

- Drainage less than 15 mL/day.
- Resolution of sepsis and normalisation of appetite.
- Reduction or normalisation of white cell count.
- Reduction or resolution of collection on repeat imaging.

Table 43.3 Drain sizes: commonly used drainage catheter sizes (French gauge), with their actual diameter (mm) and relative cross-sectional luminal size

Catheter size 'French'	Diameter (mm)	Relative internal lumen
6	2.0	
8	2.7	
10	3.3	
12	4.0	
14	4.7	
18	6.0	
24	8.0	

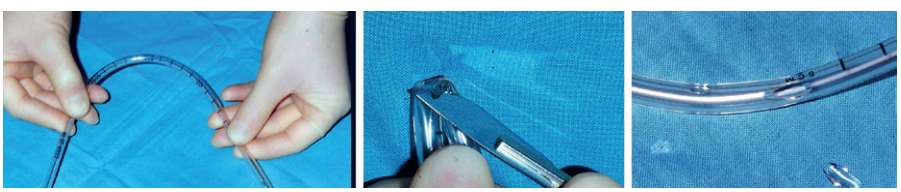

Figure 43.11 Cutting extra side holes in a large-bore drain. The drain is kinked and then using a sharp blade, extra side holes can be cut across the corner but extreme care must be taken not to weaken the drain by cutting too large a hole or to damage the locking thread if present.

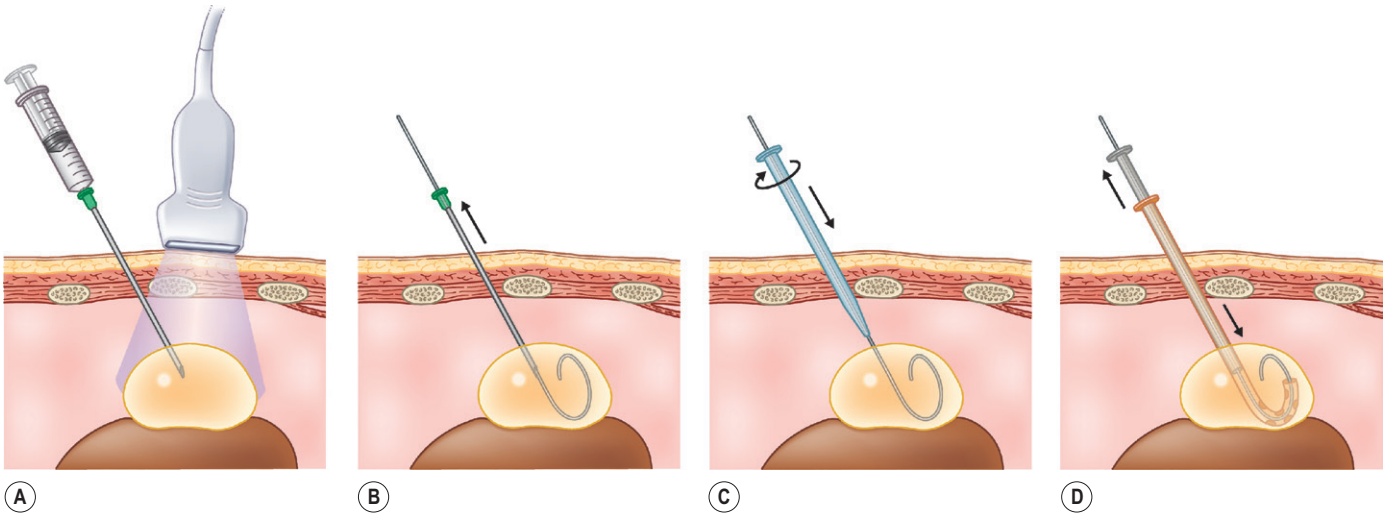

Figure 43.12 The Seldinger technique for drainage catheter insertion. A: Under ultrasound guidance, a vascular access needle is inserted into the collection, with a 10 mL syringe attached. Fluid is then aspirated to confirm correct positioning and to assess the nature of the collection. **B:** A guidewire is then inserted through the needle, such that the flexible end is coiled within the collection, whilst ensuring that the remaining visible guidewire is significantly longer than the drain to be inserted. The vascular access needle is then removed over the guidewire, taking care not to dislodge the guidewire in the process. **C:** If the track requires dilatation (depending on the size of drain to be inserted), a series of plastic dilators may be passed over the guidewire to facilitate subsequent drain insertion. Gently twisting the dilator whilst advancing forward through the abdominal/chest wall aids insertion. The dilator is exchanged for the drain together with the central stiffening cannula (but without the central sharp stylet if one is provided in the drain pack). The drain may also require a twisting action to aid insertion through muscles and fascia. **D:** When the tip of the drainage catheter assembly is within the collection, the central stiffening cannula is held still and the drainage catheter is gently advanced further over the guidewire into the collection. The guidewire and stiffening cannula are then removed together, taking care not to dislodge the drain. As soon as the guidewire is removed, the 'pigtail' of the drain will form and can be locked if necessary.

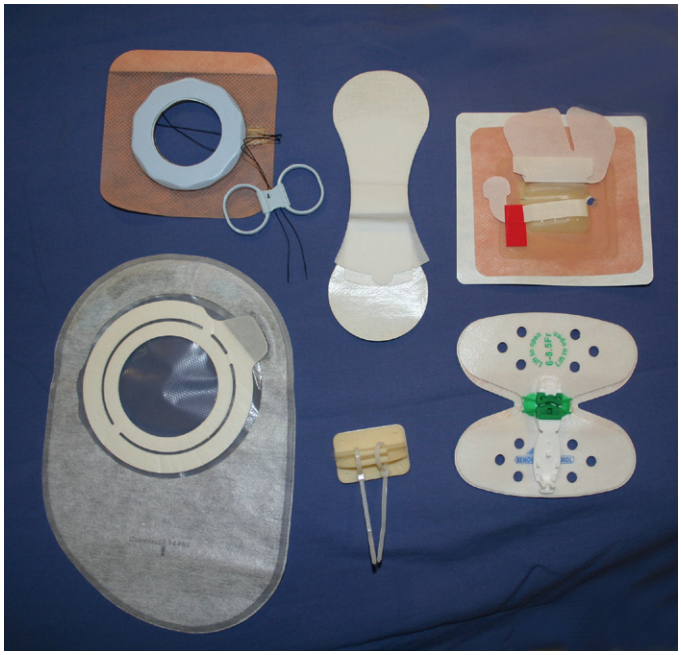

Figure 43.13 A selection of drainage bags and fixation devices. It is important to secure the drain before the patient is moved from the ultrasound table and to inform the patient and nursing staff of the mechanism of drain fixation and whether or not it is locked.

reaccumulates and hence subsequent sclerosis of the cyst can be performed to reduce the risk of recurrence. Although various substances have been used as sclerosing agents for cyst ablation, including tetracycline and talc, 95% ethanol is the most widely utilised. Prior to any cyst ablation procedure, lack of communication with other structures should be established (e.g. by contrast injection and fluoroscopy), as inadvertent alcohol injection into the renal collecting system or biliary tract could have disastrous consequences. The procedure involves initial aspiration of cyst fluid, usually via a small drain (5–8Fr) followed immediately by injection of sclerosant into the cyst cavity. If alcohol is used, the addition of local anaesthetic may be beneficial as patients sometimes experience burning pain as a result of the alcohol injection. With the drain still in situ, the patient is asked to slowly roll to either side over a 20-minute period to allow the sclerosant to coat the entire cyst cavity. After this time, the alcohol is aspirated and the drain removed. If the cyst is large the drain may be left in situ to facilitate further treatments, if these are considered likely to be necessary. High success rates for ablation of renal cysts[26] and hepatic cysts have been reported.[27] Occasionally patients with large benign ovarian cysts benefit from ultrasound-guided transvaginal aspiration.[28] However, care must be taken to confidently exclude malignancy prior to the procedure.

PRINCIPLES OF TUMOUR ABLATION

Advances in diagnostic imaging are significantly improving the detection and confirmation of smaller tumours in different organ systems. The identification of these small malignancies is causing a management dilemma as it is increasingly difficult to justify major surgery for small lesions in an often elderly patient population. This in turn has driven the evolution of less invasive techniques such as image-guided tumour ablation. Image guidance is central to tumour ablation and ultrasound plays a key role in such treatments for small volume, solid organ and abdominal disease. Ablative techniques within specific organ systems are also dealt with under separate chapter headings so this section will deal with the general principles of image-guided ablation (IGA). Lung tumour ablation will not be addressed here, as this is largely a CT-guided technique.

Image-guided ablation is easy in concept but more difficult in practice if oncological outcomes from standard resective surgery are to be matched. Undoubtedly the improved spatial and contrast resolution of modern imaging has enabled the accurate confirmation of disease in the liver and kidneys in the 10–30 mm range. This imaging achievement has brought small volume disease within the scope of image-guided ablation. In-situ thermal ablation must be achieved without significant injury to adjacent organ structures. It needs to be monitored both during the procedure for the purposes of determining accurate thermal ablative volumes and in post-procedural follow-up to ensure that the tumour target has been destroyed without complications or adjacent injury. In involving ultrasound as a key image-guidance tool this discussion will centre around liver and renal tumour ablation but the general principles can be applied to focal nodal, adrenal, lung and bone disease (although specifics of the latter are not detailed in this chapter).

There are three key areas to address in achieving safe and effective ablation. The practitioner must have a clear understanding of all three areas and how they can best be modified in an individual tumour and patient to achieve an optimal outcome that is at least equivalent to that achieved with traditional surgical resection.

Ablative energy

In undertaking an ablative procedure the operator must have a firm understanding of the biophysical principles of the ablative energy they are to use. Most ablative techniques employ thermal injury to achieve coagulative tissue necrosis through heat deposition; however, the volume of ablation achieved is modified in vivo by local tissue interactions, which affect how well the thermal energy is propagated, and by heat loss, which is related to tissue-mediated cooling by virtue of local perfusion or 'heat sumping' arising from blood flow in adjacent vessels. Some techniques such as radio-frequency ablation are highly reliant on conductive heating of the tissues at anything more than a few millimetres from the probe tip and the operator must be cognisant of these limitations in planning a tumour ablation. The key target for the operator is complete treatment of the tumour and it should be self-evident that this will require a complex, global, 360° treatment margin. Usually the more central tumour neovascularity is highly susceptible to thermal ablation, with subtotal treatments and marginal recurrences occurring because of sublethal temperatures towards the tumour margin. It is striking that targeted tumour ablation in the abdominal viscera has been evolving over the last two decades and this slow development testifies to the difficulties of adequate thermal ablation in vivo, for the reasons outlined above.

Ablative techniques

Radio-frequency

This technique has evolved rapidly in recent years and now represents the most widely used ablative energy. Monopolar radio-frequency ablation (RFA) involves the application of high-frequency alternating current (at approximately 460–500 kHz) to the target tissue through a needle-like probe. The technique can be likened to large volume electrocautery with the induction of heat around the uninsulated probe tip through 'radio-frequency' agitation of polarised water molecules causing localised frictional heating. Large dispersive electrodes are attached to the patient's trunk or thighs and the concentration of current flux around the probe tip results in irreversible cell damage (coagulative necrosis) at temperatures between 55°C and 110°C. If temperatures of 60°C and 100°C can be maintained throughout the treatment volume for more than a few minutes, cell death occurs.[29,30]

Basic single needle applicators have been modified to achieve useful and reproducible 3–5 cm spheres of tissue destruction within a clinically relevant time frame of 15–20 minutes. This has been achieved by 'clustering' needles on a single hand piece or in multipolar arrays or through expandable, 'multi-tined' needle arrays (Fig. 43.14).

Cryoablation

This thermal ablative energy has been in variable use for a few decades but only recently has there been renewed interest in this technique as a result of the introduction of narrow gauge (17G) argon cryoprobes (rather than the previous larger nitrogen probes), so enabling a percutaneous treatment approach (Fig. 43.15). Given current technology, multiple parallel probes still need to be placed in the target (approximately three to four probes to obtain a reliable 3 cm sphere of confluent tissue destruction) under imaging guidance. Cryoablation uses multiple 'freeze–thaw' cycles (usually two) to incur adequate tissue injury and the 'cell kill' line is usually defined by the −20°C to −40°C isotherm. Clearly, as with other thermal techniques, the cyto-destructive, 'treatment front' fades into sublethal temperatures but it is believed that the −20°C isotherm lies within a few millimetres of the advancing 'iceball' edge (depending on the organ environment). Uniquely and significantly,

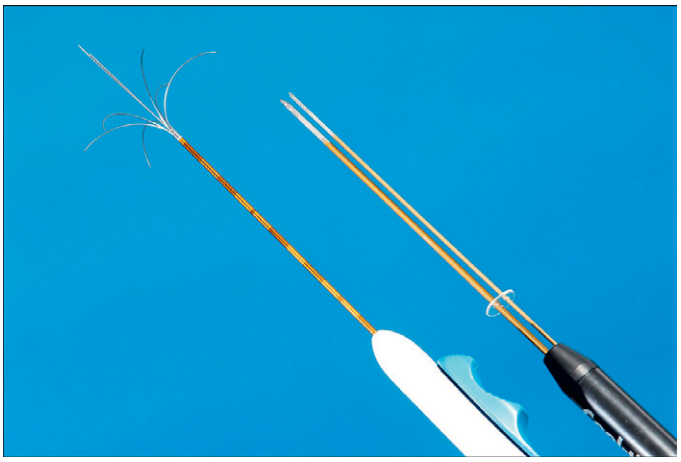

Figure 43.14 Examples of common radio-frequency probe configurations. By clustering the monopolar RF probe tips, the volume of ablation is compounded. Similarly the expandable probe is gradually deployed through the tumour mass to achieve 'cytoablative' temperatures from the inside outwards.

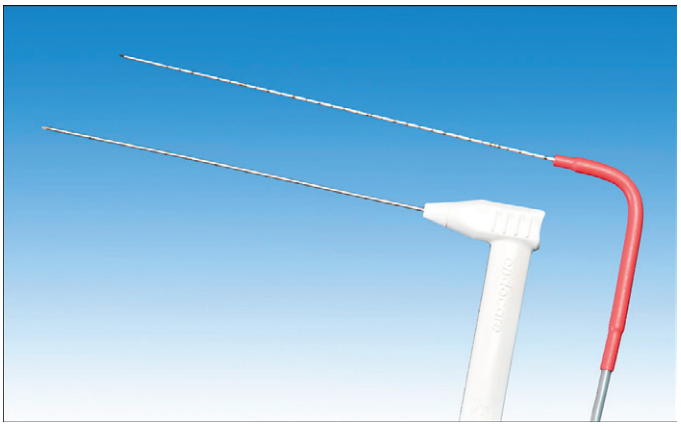

Figure 43.15 Examples of argon cryoprobes. In order to achieve a clinically useful therapeutic 'iceball' multiple probes are placed around the tumour, as a rule, usually 1 cm in from the tumour margin and 15–20 mm apart.

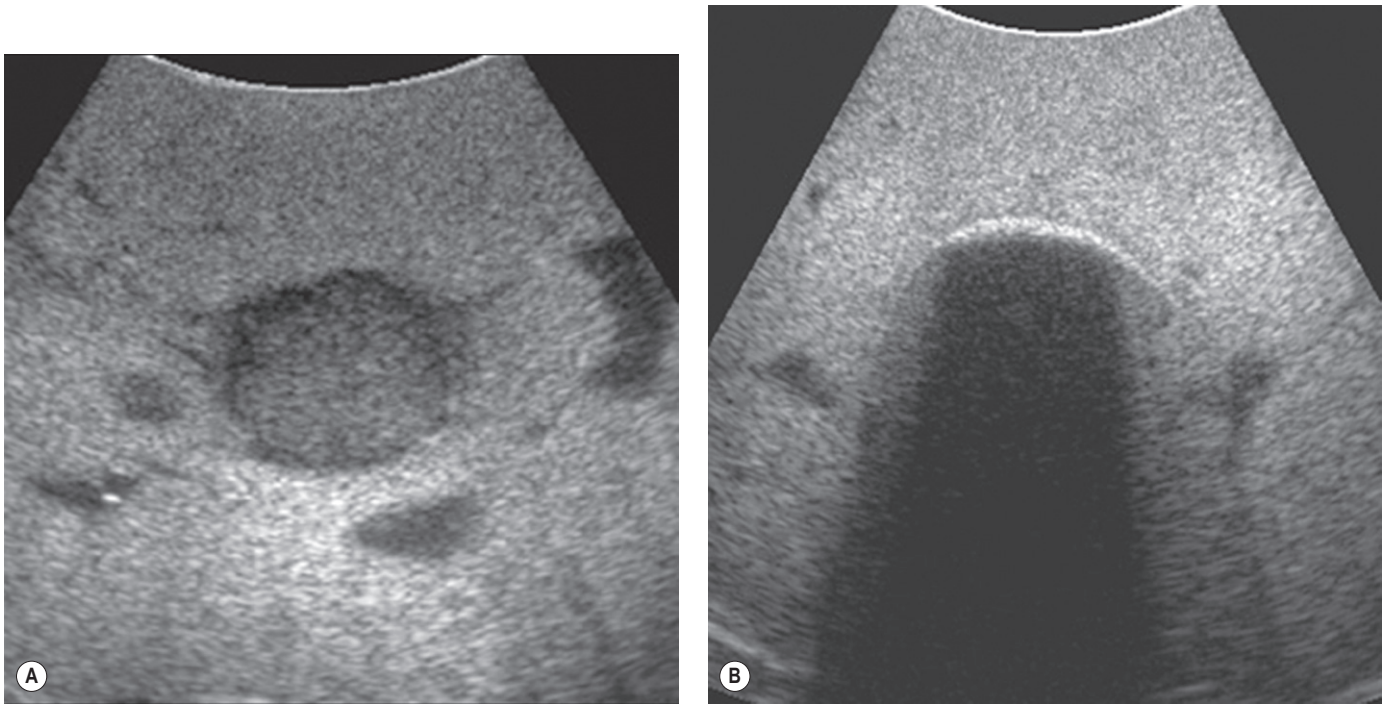

Figure 43.16 Cryoablation. A: Ultrasound of colorectal liver metastasis suitable for cryoablation at just 3 cm. **B:** The engulfing 'iceball' casts a dense specular reflection at its leading edge, obscuring global appreciation of the target lesion during treatment. Cryoablation within radiology departments is therefore often combined with CT or MR guidance for fuller appreciation of the evolving iceball. (Images courtesy of Fred Lee Jr MD, University of Wisconsin, Madison.)

the iceball itself is readily resolved by ultrasound (Fig. 43.16), CT or MR.

The mechanism of cryoablative cell death appears to be multifactorial.[31] Rapid intra-and extracellular ice formation injures the cell membrane and intracellular organelles and slower extracellular ice formation causes osmotic dehydration and perforation of cells, particularly towards the edge of the 'cryo-lesion'. The thermal injury is compounded by small vessel thrombosis and vascular injury as well as possible 'immuno-sensitisation' of the treated tissue. Importantly cryoablation may achieve a better-defined treatment margin than RFA with less of trailing thermal profile towards the edge of the treatment zone.

Microwave

Microwave radiation lies close to radio-frequency radiation in the electromagnetic spectrum, with operating frequencies in the 900–2450 MHz range. Water molecules are intrinsically polar in terms of charge distribution and when subjected to oscillating microwave radiation they rapidly vibrate within the field. Water molecules are relatively 'free' to do so but the phase of the oscillating water molecule lags behind the applied microwave (MW) field and results in localised heating ('lossy dielectrics'). Microwave ablation achieves larger, more effective areas of lethal heating than RFA as it actively heats up to 2 cm from probe and is therefore less subject to tissue-mediated cooling.[32]

Microwave energy is applied through single or grouped arrangements of needle-like applicators. By tuning these probes to 915 MHz, optimal soft tissue heating is achieved in less time with larger ablation zones, along with thrombosis of small to moderate calibre vessels when compared with radio-frequency ablation.[33]

However, microwaves, like radio-frequency ablation, induce considerable 'outgassing' during the procedure and peri-procedural monitoring of the treatment zone remains problematic.

Focused ultrasound

This topic will be reviewed under prostate ablation in the genitourinary section of this text and is only briefly reviewed here. Focused ultrasound achieves small focal areas of thermal tissue destruction by means of focusing sound energy in the 1 MHz range using an extracorporeal acoustic lens. This technique has the clear advantage of being non-invasive but to date only achieves small ovoid ablations of approximately 12 × 3 mm (i.e. 'rice grain'-sized lesions). These foci must be 'stacked' together to achieve clinically useful confluent areas of tissue destruction. The procedure is therefore still time-intensive and limited by inadequate acoustic access to permit wide aperture systems, besides the problems of accurate respiratory gating for the purposes of targeting. As a result, clinical and oncological applications remain largely confined to transrectal prostate ablation and central devascularisation of uterine fibroids.[34]

Interstitial laser photocoagulation

Interstitial laser photocoagulation (ILP) was developed in the 1980s and its use has been reported in the successful treatment of liver metastases.[35] However, its clinical applicability has remained compromised by the need to place multiple fibres to create even modestly sized treatment zones.

Alcohol ablation

Ultrasound-guided instillation of absolute alcohol remains a valid ablation technique for small nodular hepatomas of less than 20 mm. Many practitioners feel that in lesions any larger than this its distribution is unreliable due to tumour heterogeneity and intratumoral septa. As a result there is often an unacceptable local tumour recurrence rate in hepatomas any greater than 20 mm in diameter. Due to unreliable intratumoral distribution it has largely been

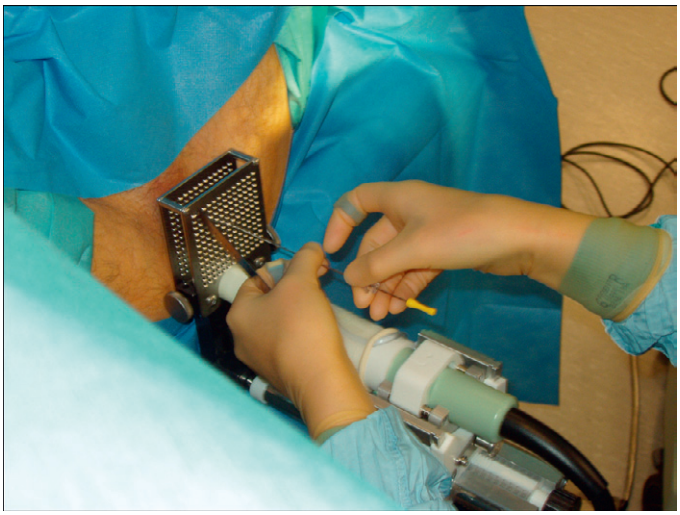

Figure 43.17 Prostate brachytherapy. Under transrectal ultrasound guidance the needle sources are placed according to the perineal guidance template for optimal conformal dosing. (Image courtesy of Dr Catherine Heath and Dr James Smart, Southampton University Hospitals.)

replaced by techniques such as radio-frequency ablation in many centres. On occasion it can be useful for small focal ablations alongside critical structures as an adjunct to radio-frequency ablation.

Brachytherapy

This essentially ablative technique permits the long-term delivery of low-dose and optimally conformed radiotherapy.[36] It is used in the treatment of localised, intraglandular prostatic carcinoma. Loose or stranded iodine-125 or rarely palladium-103 seeds are implanted through needles which are placed using a transperineal template under transrectal ultrasound guidance (Fig. 43.17).

Image guidance

Interestingly this remains one of the most significant limiting factors in the delivery of adequate and accurate image-guided ablation. Image guidance can be subdivided into procedural targeting, peri-procedural monitoring and post-procedural imaging follow-up.

Procedural targeting

With current ablative technologies, most appropriate tumour targets are in the 10–40 mm diameter size range. It is essential that they are readily visualised in all three dimensions. This author (DB) almost always sees patients 1 week before an ablation procedure for the purposes of radiology review, ultrasound assessment and consent. This outpatient assessment allows the operator to confirm adequate visualisation of the entire lesion and to notionally plan a treatment approach via an intercostal, subcostal or oblique approach using single or multiple probe placements, patient positioning, together with other aspects relating to the procedure. Such pre-planning is essential to the success of the procedure. The imaging technique must be able to assess the deep aspect of the tumour mass so that the posterior interface between tumour and parenchyma can be addressed at the initial probe placement. Similarly, when multiple tumours are to be treated, it is often advisable to target the smaller, less visible lesions at the outset of the procedure.

It should be self-evident to most practising radiologists that small lesions easily appreciated on a portal venous phase CT study may be considerably less apparent at unenhanced CT or ultrasound. Some practitioners will assist image guidance by placing a metallic embolisation coil close to a target tumour, thereby easing visualisation via another approach.

In routine practice this author (DB) uses a combination of real-time ultrasound guidance for optimal depth of probe placement and dispersal before secondary CT confirmation. CT can then be used for additional manoeuvres such as 5% dextrose 'hydrodissection' to displace adjacent bowel. On occasion ultrasound visualisation is compromised and some manufacturers have moved to address this by combining ultrasound and CT on a single display platform (Fig. 43.18). The position of an ultrasound probe can be defined within a radio-frequency space around the patient and a volume of previously acquired CT data is then displayed corresponding to the plane of the real-time ultrasound image. This permits the dual display of the real-time ultrasound image and cold CT data in any plane and considerably addresses the limitations of either modality alone.

Peri-procedural monitoring

Intra-procedural confirmation of treatment adequacy remains problematic. Visualisation of tumours during radio-frequency and microwave ablation procedures is severely compromised by 'outgassing' from the treated lesion (Fig. 43.19). A number of authors have reported the potential of peri-procedural contrast-enhanced ultrasound[37] or MR-thermometry.[38] In current practice experience has taught most ablationists how much energy needs to be deposited at a particular site to achieve the desired treatment volume. It remains clear, however, that over-treatment in relation to the in-vivo treatment claims and guidelines from probe manufacturers is still required to achieve adequate treatment volumes.

Cryoablation induces a perceivable iceball which can be readily visualised by many imaging techniques (Figs 43.16 and 43.20). This is an undoubted and uniquely advantageous feature of cryoablation. However, as illustrated in Figure 43.16, the specular reflection of ultrasound at the leading edge of the iceball can confound global target visualisation, which may be better achieved by CT (Fig. 43.20) or MR. Importantly the distribution of the apparent 'iceball' should not be confused with the ultimate, lethal cryoablation zone which may lie some millimetres deep to the advancing margin of the iceball.

Post-procedural imaging

To date, the ultimate ablation zone achieved by a treatment has largely been determined by contrast-enhanced imaging techniques, taking non-enhancement as a surrogate marker of tumour ablation. Whilst immediate post-procedural, contrast-enhanced CT, for example, can be undertaken, this author (DB) believes that the ablation zone matures and becomes much better defined 1–2 weeks after treatment. If a contrast-enhanced technique is employed, it is important to be aware that degraded blood products within the treated zone may cause spurious central high attenuation on CT and that, in the acute phase (up to 3 months), there is considerable relative arterialisation in the penumbra of the ablation zone. These features should not be misinterpreted as residual enhancing disease (Fig. 43.21).

While no consensus exists regarding the follow-up scheduling for various malignancies this should be guided by the natural history of the treated tumour. Most protocols advocate early imaging at 3 months and then every 6 months. Clearly, however, an under-treated colorectal metastasis can be expected to develop local recurrence earlier than a subtotally treated indolent carcinoid deposit. Solbiati et al. reported the follow-up of 117 patients with 179 colorectal metastases and noted that 54 of 70 (70%) local recurrences were apparent within 6 months of the initial treatment.[39]

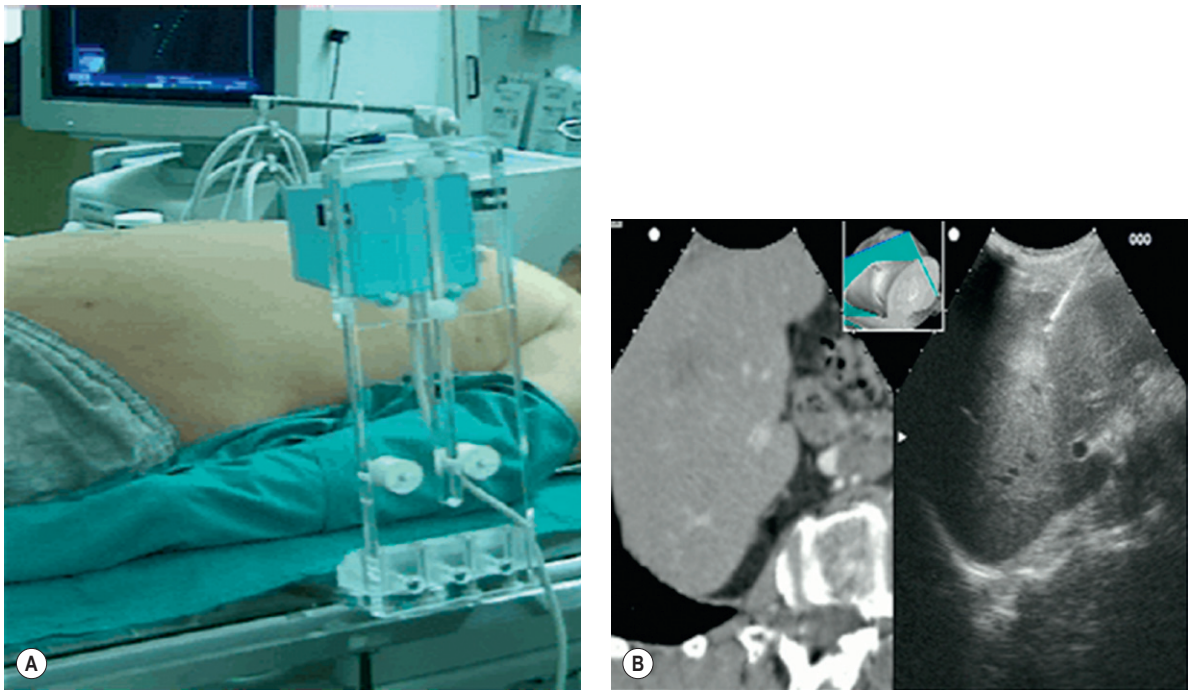

Figure 43.18 Simultaneous combined or fusion CT-US imaging ('Real time virtual sonography', Hitachi Medical Systems Ltd). **A:** The RF frame around the patient's abdomen permits the 'toggling' of the volumetric CT dataset and US images in 3D space. **B:** The 'cold' CT dataset is then displayed simultaneously alongside the live US image. This helps to overcome some of the weaknesses of either imaging modality alone.

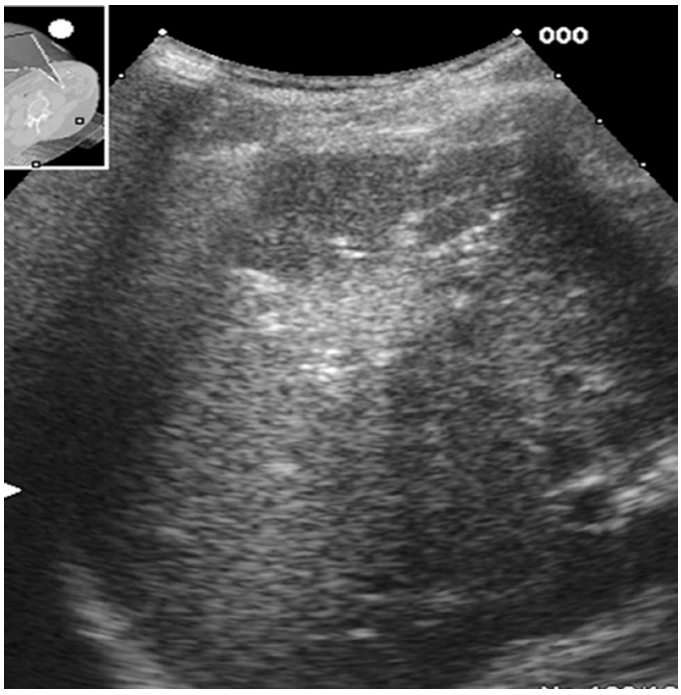

Figure 43.19 A small liver metastasis undergoing ultrasound-monitored RFA. The considerable 'outgassing' of the lesion under treatment obscures the target and provides little useful intra-procedural information.

Tumour pathophysiology and its modification

As noted previously, this chapter aims to discuss principles of tumour ablation and as such will not go into the specifics of tumour ablation in each organ system. Those undertaking ablation of any individual tumour do, however, need to be aware of how the parenchyma adjacent to a tumour, or the organ environment in which the tumour resides, will modify the ablation achieved. For example, it is evident that an exophytic renal tumour largely surrounded by perirenal fat is far more amenable to complete ablation than a central and often perivascular renal tumour of the same size.[40,41] The improved current flux density within the tumour and relative insulating effect of the perirenal fat, together with the absence of adjacent vessels and well-perfused parenchyma, all compound to enhance the ablation of the pedunculated lesion.

Tumoral perfusion itself and perfusion-mediated cooling by the adjacent parenchyma can also limit the efficacy of radio-frequency ablation.[42] As a result, temporary inflow occlusion of both the liver and kidney has been advocated as a method to improve treatment volumes during radio-frequency ablation and to reduce the risk of perivascular tumour sparing and thereby subsequent recurrence. Use of this approach has declined in recent years as more adequate ablation zones have been achieved through device improvements.

There is, however, a very real and evolving place for combined approaches to tumour ablation. Tumour ablation is most commonly combined with particulate embolisation, thereby diminishing tumour perfusion and enhancing treatment volumes. More recently, ablation has been combined with chemoembolisation with a view to enhancing the efficacy of both techniques. In particular, it has recently been advocated that drug-eluting beads should be used for

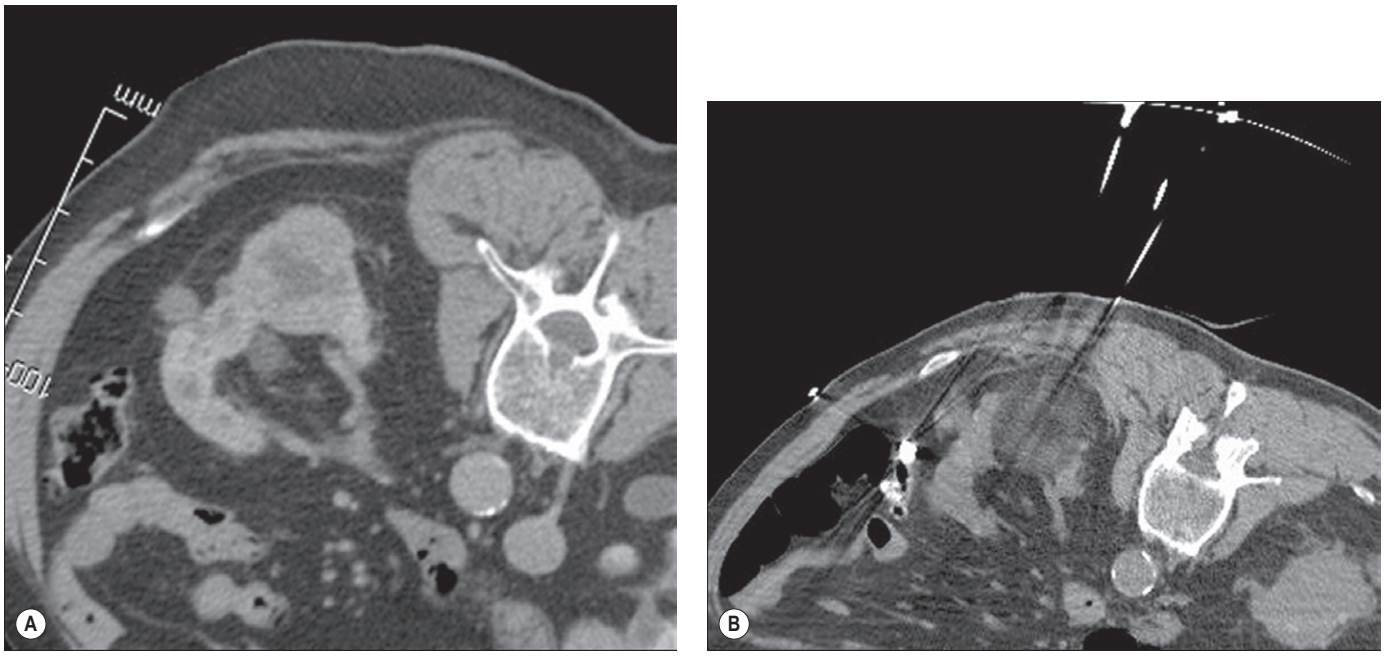

Figure 43.20 CT-monitored cryoablation of left renal tumour in prone-oblique position. **A:** Contrast-enhanced CT of renal tumour. **B:** The iceball must clearly subsume the tumour by 5 or more millimetres.

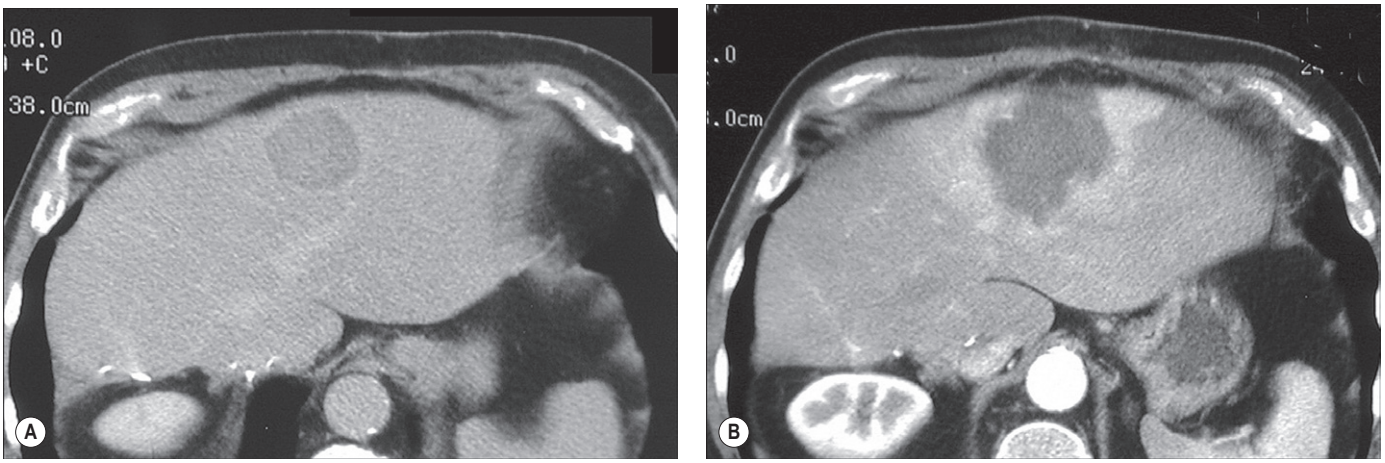

Figure 43.21 Post-procedural imaging. A: A cholangio-hepatocellular carcinoma in a remnant left hemi-liver following previous right lobar resection. **B:** A late arterial venous phase CT image of ablated tumour 10 days after RFA treatment. Note the adjacent relative arterialisation of the liver parenchyma and patchy central higher attenuation material, probably reflecting degraded blood products. If the lesion declares a crisp margin and slowly involutes over the next 6 months this will confirm a complete treatment.

chemoembolisation of moderate volume hepatocellular carcinomas within 24 hours of ablation, with the aim of delivering a maximal dose of chemoembolic agent to the penumbra of the treatment zone.[43] Similarly, it would appear that tumours may be treated by systemic chemotherapeutic agents for the purposes of enhanced focal ablation. One study[44] showed that pre-treatment of a mouse renal tumour model with the anti-angiogenic drug sorafenib reduced microvascular density and significantly increased ablation volumes.

The tumour setting can also be manipulated so that an aggressive and thereby adequate ablation procedure can be undertaken. Renal tumour ablation, for example, may be compromised by the close approach of adjacent bowel, risking thermal injury to the gut, or other viscera. In practice these structures can be displaced from the renal area using 5% dextrose instilled retroperitoneally in typical volumes of 100–500 mL – 'hydrodissection' (Fig. 43.22) or by using air, or balloons, to separate organs. These techniques can be modified in a number of organ settings to permit an adequate and complete procedure.

Tumour ablation technique

Careful and effective image-guided tumour ablation is a major intervention, which is considerably easier in concept than in practice. Case selection is critical and with regard to individual organ systems the reader should consult the relevant chapters. Broadly, and given current ablative device capabilities, ablation can be offered to treat renal carcinomas of less than 4 cm. Hepatocellular carcinomas, if discrete and preferably encapsulated, can be treated up to 5 cm in diameter but at the upper end of this range treatment is usually in conjunction with chemoembolisation. Outcome data for colorectal[39] and to a lesser extent neuroendocrine metastases suggest that current ablative techniques should be restricted to

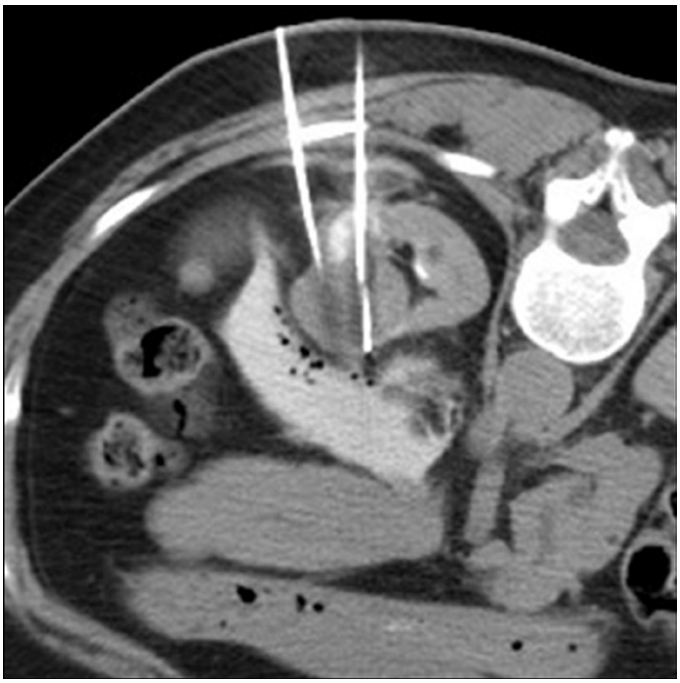

Figure 43.22 A renal tumour undergoing ultrasound and CT-guided ablation. The close proximity of adjacent pancreatic tail necessitated its displacement by injection of 5% dextrose and contrast. This is seen as a high-attenuation fluid crescent within the anterior pararenal space.

Case selection for image-guided ablation (IGA)

- Understand the natural history of the disease and relative merits of alternative treatments.
- If multidisciplinary discussion refers for IGA, confirm up-to-date imaging and amenability for ablation.
- See the patient in an outpatient setting, assess the target tumour by ultrasound and consent appropriately.
- Careful case selection is critical to procedural outcomes.

Image-guided ablation: procedural considerations

- Seek formal anaesthetic assistance.
- Pre-plan treatment approach.
- Plan to treat thoroughly so as to achieve complete ablation.
- Careful, critical follow-up imaging is essential.

lesions of less than 25 and 30 mm respectively. Microwave ablation may be set to overcome some of the treatment limitations of radio-frequency ablation of metastases within the liver but substantive outcome data are awaited.

Following appropriate case selection in the multidisciplinary team setting, it is essential that these patients are reviewed as outpatients. This permits the interventionist to review the up-to-date radiology and assess the target lesion(s) at outpatient ultrasound for the purposes of treatment planning. The small chemo-modulated colorectal metastasis that was easily identified at portal venous phase CT may be considerably more difficult to resolve with ultrasound or unenhanced CT fluoroscopy. Contrast-enhanced ultrasound (CEUS) undoubtedly has a role to play in confirming the site and position of a lesion but the operator needs to consider the limited temporal window that CEUS allows for careful probe placement. This outpatient visit allows the operator to plan an approach and thereby appropriately position the patient at the time of the procedure. At the same visit the drug history should be reviewed to take into account any anticoagulant or antiplatelet therapy.

This author (DB) most commonly utilises a combination of real-time ultrasound guidance and CT to check probe positioning relative to bowel etc. Most of these procedures need to be carried out under general anaesthesia or intravenous sedation/anaesthesia administered by an anaesthetist. Effective, complete procedures, which often require adjunctive manoeuvres such as hydrodissection, can take up to 2 hours. It is advisable that all practitioners wishing to undertake ablations routinely and aiming to treat anything but the smallest lesions seek out formal anaesthetic assistance for these procedures.

All but the smallest lesions require a number of overlapping ablations and in this respect if a tumour is asymmetric or ovoid it is often best to pass the ablation device along the long axis of the tumour, permitting overlapping treatment 'stations' as the device is pulled back. With regard to device placement relative to the tumour, straightforward longitudinal devices should be placed across the lesion but the deployment pattern of expandable devices needs to be taken into account if the subsequent ablation zone is to encompass satisfactorily the target tumour. As a rule, where multiple tumours are being targeted at a single session, it is often better to target and treat the smaller more obscure lesions at the outset.

Most modern radio-frequency devices have a 'track ablation' mode and it is common practice to thoroughly ablate the track during device withdrawal, thereby reducing the risk of track seeding. All patients undergoing abdominal ablation procedures require careful post-procedural observation for potential haemorrhage, or peritonism, given the small risk of occult gut perforation (<1%). Most visceral ablations are well tolerated with limited post-procedural discomfort that can be treated with simple oral analgesia. On occasion adjacent injury of the diaphragm and abdominal wall may require opiate analgesia.

Safety/Complications

Adequate and complete visceral tumour ablations are major interventions with a risk of significant injury. These procedures must be carefully planned and executed with a view to complete tumour ablation. However, all the published data indicate a low complication rate for image-guided ablation.

In the liver the largest reported experience to date remains that of the Italian Collaborative Group:[45] 2320 patients (3554 tumours, size: 3.1 cm ± 1.1 cm (SD)) were treated between 1995 and 2001 in 41 centres using similar radio-frequency ablation protocols. Of these, 1620 were cases of hepatocellular carcinoma in the setting of chronic liver disease and 683 patients had metastatic disease, mostly colorectal carcinoma. When considering these results the currently quoted 0.5–4% mortality and 16–35% major complication rate of surgical liver resection needs to be taken into account. Mortality in the early image-guided ablation experience of the Italian Collaborative Group Study was 0.25% (6 patients). Two of the deaths were attributed to faecal peritonitis as a result of thermal colonic injury. Thermal injury with central biliary stricturing was implicated in another death. A superficial hepatoma ruptured following treatment, causing massive intraperitoneal haemorrhage and subsequent hepatic coma. Two further deaths were reported, although the exact cause of these remains unclear.

In consenting for abdominal visceral ablation the author (DB) usually quotes a 1% risk of haemorrhage requiring embolisation, a 0.5% risk of full thickness thermal gut injury and a risk of pain, abscess formation or subtotal treatment at around 5–10%. Obviously the latter is amenable to further ablation for treatment completion. Careful case selection and meticulous image-guided technique will reduce the risk of all of the above.

REFERENCES

1. Bret PM, Fond A, Casola G, et al. Abdominal lesions: a prospective study of clinical efficacy of percutaneous fine-needle biopsy. Radiology 1986;159:345–346.
2. Dodd III GD, Esola CC, Memel DS, et al. Sonography: the undiscovered jewel of interventional radiology. Radiographics 1996;16:1271–1288.
3. Sheafor DH, Paulson EK, Simmons CM, et al. Abdominal percutaneous interventional procedures: comparison of CT and US guidance. Radiology 1998;207:705–710.
4. Longo JM, Bilbao JI, Barettino MD, et al. Percutaneous vascular and nonvascular puncture under US guidance: role of color Doppler imaging. Radiographics 1994;14:959–972.
5. Haaga JR, LiPuma JP, Bryan PJ, et al. Clinical comparison of small and large calibre cutting needles for biopsy. Radiology 1983;146:665–667.
6. Pagani JJ. Biopsy of focal hepatic lesions. Comparison of 18 and 22 gauge needles. Radiology 1983;147:673–675.
7. Nyman RS, Cappelen-Smith J, Brismar J, et al. Yield and complications in ultrasound-guided biopsy of abdominal lesions. Comparison of fine needle aspiration biopsy and 1.2mm needle core biopsy using an automated gun. Acta Radiol 1995;36:485–490.
8. Moulton JS, Moore PT. Coaxial percutaneous biopsy technique with automated biopsy devices: value in improving accuracy and negative predictive value. Radiology 1993;186:515–522.
9. Stewart CJR, Coldewey J, Stewart IS. Comparison of fine needle aspiration cytology and needle core biopsy in the diagnosis of radiologically detected abdominal lesions. J Clin Pathol 2002;55:93–97.
10. McGahan JP. Laboratory assessment of ultrasonic needle and catheter visualization. J Ultrasound Med 1986;5:373–377.
11. Bergin D, Pappas JN, Hwang JJ, et al. Echogenic polymer coating: does it improve needle visualization in sonographically guided biopsy? AJR Am J Roentgenol 2002;178:1188–1190.
12. Winsberg F, Mitty HA, Shapiro RS, Yeh H. Use of an acoustic transponder for US visualization of biopsy needles. Radiology 1991;180:877–878.
13. Bisceglia M, Matalon TAS, Silver B. The pump maneuver: an atraumatic adjunct to enhance ultrasound needle tip localization. Radiology 1990;176:867–868.
14. McNamara Jr MP, McNamara ME. Preparation of a homemade ultrasound biopsy phantom. J Clin Ultrasound 1989;17:456–458.
15. Bergenfeldt M, Genell S, Lindholm K, et al. Needle-tract seeding after percutaneous fine-needle biopsy of pancreatic carcinoma. Case report. Acta Chir Scand 1988;154:77–79.
16. Greenstein A, Merimsky E, Baratz M, et al. Late appearance of perineal implantation of prostatic carcinoma after perineal needle biopsy. Urology 1989;33:59–60.
17. Onodera H, Oikawa M, Abe M, et al. Cutaneous seeding of hepatocellular carcinoma after fine-needle aspiration biopsy. J Ultrasound Med 1987;6:273–275.
18. Kiser GC, Totonchy M, Barry JM. Needle tract seeding after percutaneous renal adenocarcinoma aspiration. J Urol 1986;136: 1292–1293.
19. Hidai H, Sakuramoto T, Miura T, et al. Needle tract seeding following puncture of retroperitoneal liposarcoma. Eur Urol 1983;9:368–369.
20. Livraghi T, Damascelli B, Lombardi C, et al. Risk in fine-needle abdominal biopsy. J Clin Ultrasound 1983;11:77–81.
21. Smith EH. The hazards of fine needle aspiration biopsy. Ultrasound Med Biol 1984;10:629–634.
22. Chapoutot C, Perney P, Fabre D, et al. Needle-tract seeding after ultrasound-guided puncture of hepatocellular carcinoma. A study of 150 patients. Gastroenterol Clin Biol 1999;23:552–556.
23. Stigliano R, Marelli L, Yu D, et al. Seeding following percutaneous diagnostic and therapeutic approaches for hepatocellular carcinoma. What is the risk and the outcome? Seeding risk for percutaneous approach of HCC. Cancer Treat Rev 2007;33(5):437–447.
24. John TG, Garden OJ. Needle track seeding of primary and secondary liver carcinoma after percutaneous liver biopsy. HPB Surgery 1993;6:199–204.
25. Macha DB, Thomas J, Nelson RC. Pigtail catheters used for percutaneous fluid drainage: comparison of performance characteristics. Radiology 2006;238(3):1057–1063.
26. Fontana D, Porpiglia F, Morra I, et al. Treatment of simple renal cysts by percutaneous drainage with three repeated alcohol injections. Urology 1999;53:904–907.
27. Van Sonnenberg E, Wroblicka JT, D'Agostino HB, et al. Symptomatic hepatic cysts: percutaneous drainage and sclerosis. Radiology 1994;190:387–392.
28. Troiano RN, Taylor KJ. Sonographically guided therapeutic aspiration of benign-appearing ovarian cysts and endometriomas. AJR Am J Roentgenol 1998;171:1601–1605.
29. Gazelle GS, Goldberg SN, Solbiati L, Lirvaghi T. Tumour ablation with radiofrequency energy. Radiology 2000;217:633–646.
30. Goldberg SN, Gazelle GS, Mueller PR. Thermal ablation therapy for focal malignancy: a unified approach to underlying principles, techniques and diagnostic imaging guidance. AJR Am J Roentgenol 2000;174:323–331.
31. Hoffman NE, Bischof JC. The cryobiology of cryosurgical injury. Urology 2002;60(Suppl. 2A):40–49.
32. Simon CJ, Dupuy DE, Mayo-Smith WW. Microwave ablation: principles and applications. Radiographics 2005;25:S69–S83.
33. Wright AS, Sampson LA, Warner TF, et al. Radiofrequency versus microwave ablation in a hepatic porcine model. Radiology 2005;236:132–139.
34. Dubinsky TJ, Cuevas C, Dighe MK, et al. High intensity focused ultrasound: current potential and oncologic applications. AJR Am J Roentgenol 2008;190:191–199.
35. Vogl TJ, Stroud R, Eichler K, et al. Colorectal carcinoma metastases in liver: laser-induced interstitial thermotherapy: local tumour control rate and survival data. Radiology 2003;230:450–458.
36. Heysek RV. Modern brachytherapy for treatment of prostate cancer. Cancer Control 2007;14:238–243.
37. Johnson DB, Duchene DA, Taylor GD, Cadeddu JA. Contrast-enhanced ultrasound monitoring of radiofrequency ablation. J Urol 2004;171(Suppl.)509:A1929.
38. Botnar RM, Steiner P, Dubno B, et al. Temperature quantification using proton frequency shift technique: in vitro and in vivo validation in an open 0.5 Tesla interventional MR scanner during RF ablation. J Magn Reson Imaging 2001;13(3):437–444.
39. Solbiati L, Livraghi T, Goldberg SN, et al. Percutaneous radio-frequency ablation of hepatic metastases from colorectal cancer: long term results in 117 patients. Radiology 2001;221:159–166.
40. Gervais DA, McGovern FJ, Arellano RS, et al. Radiofrequency ablation of renal cell carcinoma: Part 1, indications, results and role in patient management over a 6-year period and ablation of 100 tumours. AJR Am J Roentgenol 2005;185:64–71.
41. Gervais DA, Arellano RS, McGovern FJ, et al. Radiofrequency ablation of renal cell carcinoma: Part 2, lessons learned with ablation of 100 tumours. AJR Am J Roentgenol 2005;185:72–80.
42. Patterson EJ, Scudamore CH, Owen DA, et al. Radiofrequency ablation of porcine liver in vivo: effects of blood flow and treatment time on lesion size. Ann Surg 1998;227(4):559–565.
43. Lencioni R, Crocetti L, Petrozzi P, et al. Doxorubicin-eluting bead-enhanced radiofrequency ablation of hepatocellular carcinoma: a pilot clinical study. J Hepatol 2008;49:217–222.
44. Hakime A, Hines-Peralta A, Peddi H, et al. Combination of radiofrequency ablation with antiangiogenic therapy for tumour ablation. Radiology 2007;244:464–470.
45. Livraghi T, Solbiati L, Meloni MF, et al. Treatment of focal liver tumors with percutaneous radio-frequency ablation: complications encountered in a multicenter study. Radiology 2003;226:441–451.

CHAPTER

44 Thyroid and parathyroid

Neil Cozens

THYROID

Introduction

High-resolution ultrasound is the ideal imaging modality for evaluation of the thyroid gland due to its superficial location, homogeneous texture, clearly defined surrounding structures and anatomical landmarks. Colour and power Doppler examination are also facilitated by the combination of superficial location and relatively profuse normal vascularity.

The importance of nuclear medicine imaging of the thyroid in the initial evaluation of nodules and differentiation of benign from malignant disease has diminished in direct proportion to the increasing role of ultrasound over recent years. Given the current importance of ultrasound for evaluation of thyroid abnormalities, it is easy to forget that just over two decades have elapsed since original papers correlated gross pathology with corresponding ultrasound findings in cadaveric specimens.[1] Computed tomography (CT), magnetic resonance imaging (MRI) and more recently positron emission tomography (PET/CT) each have relatively small but invaluable roles to play in thyroid imaging. It seems likely that the utility and application of PET/CT in particular may increase in future, particularly in the management of patients with proven thyroid malignancy. However, due to the combination of anatomical factors, relative availability, cost and lack of ionising radiation exposure, ultrasound is likely to remain the imaging modality of choice for the primary evaluation of thyroid nodules for the foreseeable future, particularly as it also facilitates swift and accurate needle localisation for fine-needle aspiration (FNA) cytology.

Anatomy and scanning techniques

Scanning technique

High-frequency linear transducers demonstrate the thyroid in high resolution, but lower-frequency (e.g. 5 MHz) linear transducers may be needed for obese patients or those with limited neck extension. The thyroid and adjacent structures, including all nodal regions, carotid artery and jugular vein, strap muscles, trachea and oesophagus, are scanned initially in the transverse, then in longitudinal planes. Hyperextension of the neck facilitates optimal visualisation; swallowing may also improve visualisation of the lower poles.

Anatomy

The thyroid lies in the anterior neck between the level of the fifth cervical and the first thoracic vertebrae, with two lateral lobes, joined by the isthmus, bridging the underlying trachea. The essential ultrasound anatomy is best appreciated in the axial anatomical figure and ultrasound images (Figs 44.1–44.3). Further detailed anatomical delineation is superbly covered in the recent ultrasound anatomy text by Ahuja and Antonio.[2] The oesophagus and recurrent laryngeal nerve can often be appreciated lying deep to the thyroid; the former more often on the left side, the latter in the trachea-oesophageal groove. The internal jugular veins show significant asymmetry in approximately two-thirds of people, with the right jugular vein larger in two-thirds of these.

The size and shape of the thyroid varies, often being thinner and more elongated in slim subjects. The normal, healthy, euthyroid adult gland volume is approximately 10–12 mL. It is uniformly more echogenic than the sternomastoid muscle, and similar in

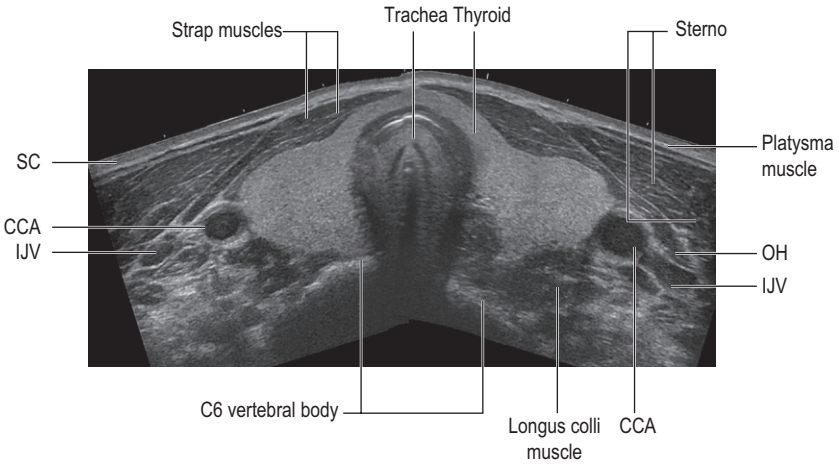

Figure 44.1 Axial panoramic ultrasound of the thyroid and adjacent anatomy. SC, subcutaneous tissue; Sterno, sternomastoid muscle; OH, omohyoid muscle; IJV, internal jugular vein; T. thyroid; CCA, common carotid artery.

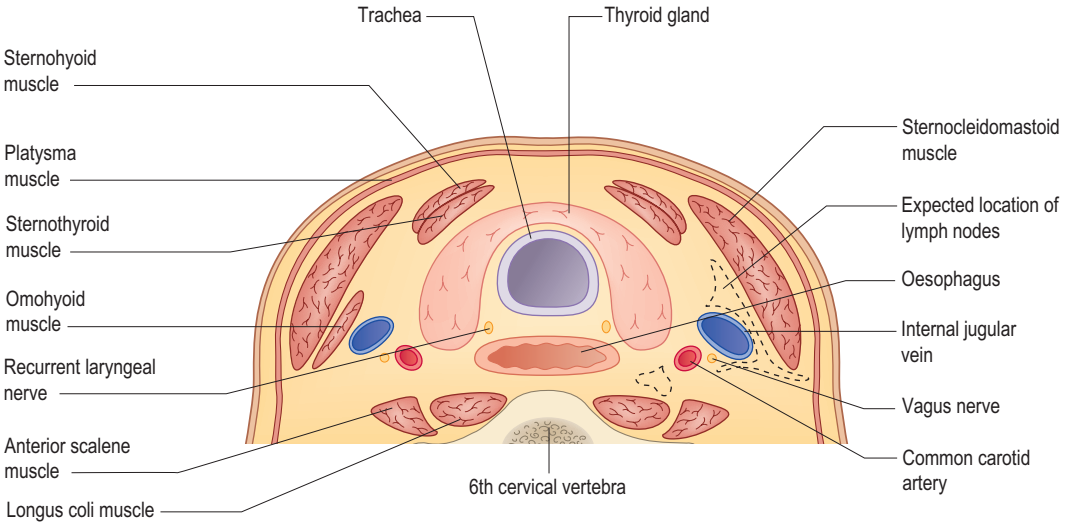

Figure 44.2 Axial diagrammatic section of thyroid and anterior neck at the level of C6. Fat predominantly fills in the 'gaps' between labelled structures; it is variable in echogenicity and semi-fluid at body temperature.

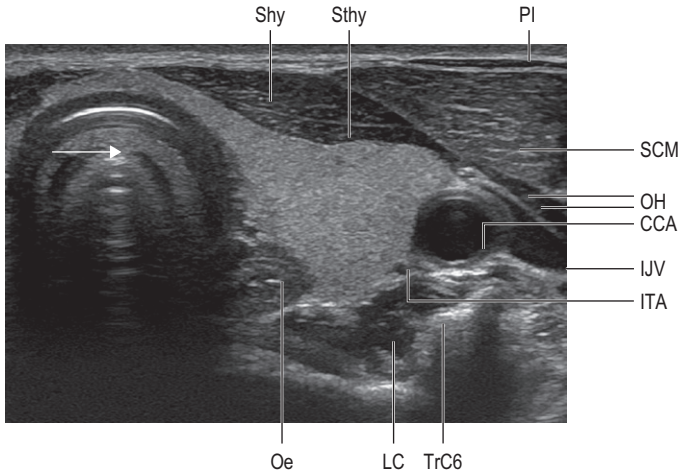

Figure 44.3 Axial ultrasound of the left lobe of thyroid and relevant anatomy. Shy, sternohyoid muscle; Sthy, sternothyroid muscle; PI, platysma muscle; SCM, sternocleidomastoid muscle; OH, omohyoid muscle; CCA, common carotid artery; IJV, internal jugular vein; ITA, inferior thyroid artesy; TrC6 transverse process of C6 vertebra; Oe, oesophagus; Tr, trachea.

echogenicity to the adult submandibular salivary gland (but more echogenic than the paediatric submandibular gland). The maximal anteroposterior diameter of the normal thyroid is approximately 2 cm.

Although relatively infrequently appreciated during ultrasound examinations (10–40%), due to its small anteroposterior thickness, the pyramidal lobe is best considered as a normal component of the thyroid rather than a 'congenital abnormality'. It is most frequently appreciated on ultrasound in children, becoming less readily visualised with increasing age. It is demonstrable in 55–65% of cadaveric[3] and surgical thyroidectomy[4] dissection specimens, more commonly left-sided than central or right-sided.

Embryology

An appreciation of the embryological development of the thyroid and parathyroid glands facilitates comprehension of some of the various anatomical and pathological processes affecting these glands.

The thyroid gland is the first endocrine organ to develop in the embryo (starting day 24); it develops from an outgrowth of the pharyngeal endoderm in the midline between the first and second branchial arches (i.e. from the first pharyngeal pouch). By 7 weeks gestation, the thyroid has migrated from its initial location in the

developing tongue base, to lie in its final anatomical site and has also developed both lobes and isthmus. It remains connected to the tongue base by a narrow tube, the thyroglossal duct, which usually closes completely by week 10. The foramen caecum in the tongue base is the residue of the opening of the upper thyroglossal duct. The pyramidal lobe of thyroid represents the persistence of the inferior end of the thyroglossal duct; it may be attached to the hyoid bone or may be incorporated into a thyroglossal duct cyst. Parafollicular thyroid ('C') cells are derived from a combination of cells migrating from the neural crest and a fifth pharyngeal pouch structure, the ultimobranchial body. These fuse with the embryonic thyroid gland, disseminating cells within it which will later secrete calcitonin.

Clinically relevant consequences of this embryology include:

- Ectopic or aberrant position of thyroid tissue can occur anywhere along the track of descent of the thyroid (most commonly in the tongue base), often associated with hypothyroidism functionally.
- Accessory thyroid tissue can also occur, arising from remnants of the thyroglossal duct. Whilst this tissue may be physiologically active, it would rarely maintain euthyroid status if the thyroid is excised totally.
- Incomplete involution of the thyroglossal duct can lead to a thyroglossal duct cyst, most commonly at or around the level of the hyoid bone. Extending the ultrasound examination towards the tongue base can alert the surgeon to the extent of surgery required, reducing the likelihood of incomplete excision and postoperative fistula or cyst recurrence.
- Residual thyroid tissue in the inferior thyroglossal duct produces the pyramidal lobe.
- Parafollicular cells: the precursors of medullary carcinoma.
- Congenital pyriform sinus fistula: recurrent neck 'abscesses' usually left-sided, from the third or fourth branchial pouch fistula.

Nodular disease and tumours

Generic ultrasound features of thyroid nodules

Thyroid nodules are very common. Their prevalence varies between series, but approximately 4–8% of adults have a clinically palpable nodule, and prevalence rates of 10–41% at ultrasound examination and at least 50% by pathological examination at autopsy have been cited.[5–7] Their apparent prevalence has increased as the sensitivity and resolution of ultrasound technology increased. Thyroid nodules are more common in women and also increase in frequency with advancing age.[8]

Unfortunately, one of the major challenges of thyroid ultrasound is the overlap in appearances between benign and malignant nodules;[9] varying combinations of these features can strongly influence the likelihood of benignity or malignancy within individual nodules and help to guide further management. These features help to select the choice of nodules to undergo ultrasound-guided fine-needle aspiration (FNA) for cytological evaluation.

General features more commonly associated with malignant nodules are: marked hypoechogenicity, calcification (particularly microcalcification), spiculated margins and a taller-than-wide shape. Conversely, relatively benign features are isoechogenicity, predominantly cystic appearance (particularly spongiform) and comet tail signs.

Nodule size

As an independent factor, nodule size is not helpful for predicting or excluding malignancy. The practice of selecting the largest nodule in a multinodular goitre probably arose from the clinicians or pathologists performing unguided FNA from the most readily palpable (and therefore easiest) nodule. The choice of nodule for FNA should be based upon the ultrasound characteristics rather than nodule size.[10,11] Smaller malignant thyroid nodules do, however, generally exhibit a better prognosis than larger primary lesions.[12]

Solitary versus multiple nodules (Fig. 44.4)

Multiplicity of nodules has been reported to predict benign disease in contrast to a much higher likelihood of malignancy in solitary nodules. This is perhaps historical and originated in relation to clinical palpability of nodules, which is a much less sensitive means of detecting multinodularity.

The 'solitary thyroid nodule' is often cited, particularly in endocrinological or surgical papers; it is usually a misnomer as it is used to denote a patient in whom clinical examination (by palpation alone) reveals a solitary thyroid mass. The majority of these patients actually have multiple thyroid nodules on high-resolution ultrasound examination, the largest, most superficial or prominent of which has been palpated clinically. The concept of a 'solitary thyroid nodule' is therefore relatively unhelpful and inaccurate from an ultrasound and patient management perspective. Careful differentiation between the clinically suspected solitary nodule and the more accurate solitary nodule on ultrasound examination must be made when evaluating both patients and the literature.

Whether retrospectively reviewing the presence of multinodularity in a series of proven thyroid cancers[13] or the incidence of malignant nodules in thyroid glands containing solitary or multiple nodules;[11] the risk of malignancy in a thyroid gland with multiple nodules is comparable to that in a gland with a solitary nodule.

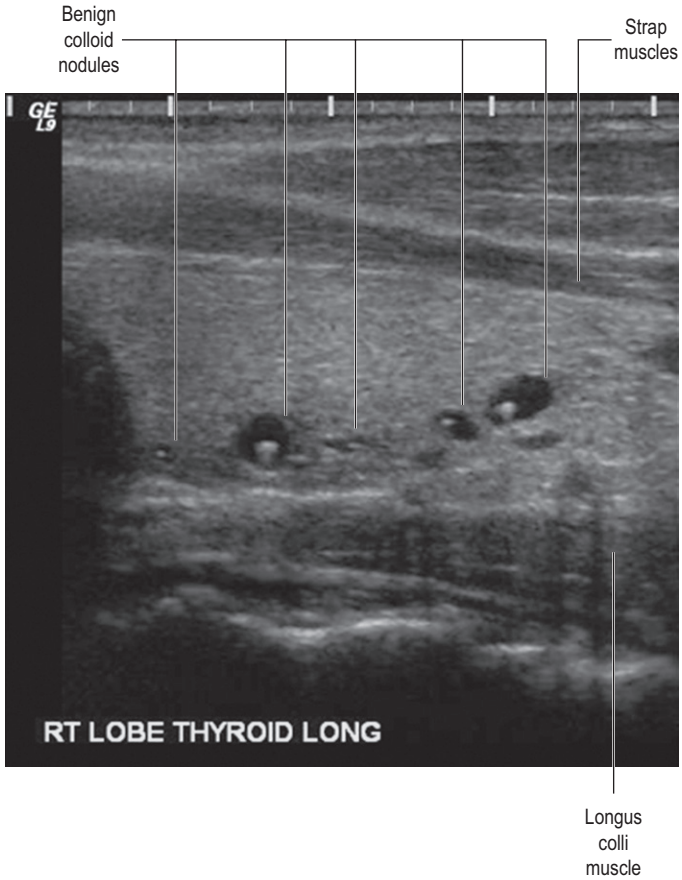

Figure 44.4 Longitudinal ultrasound of right thyroid lobe: benign colloid nodules. Multiple small predominantly cystic colloid nodules, some exhibiting comet tail signs, are typically located in the deep and inferior thyroid in early multinodular colloid change.

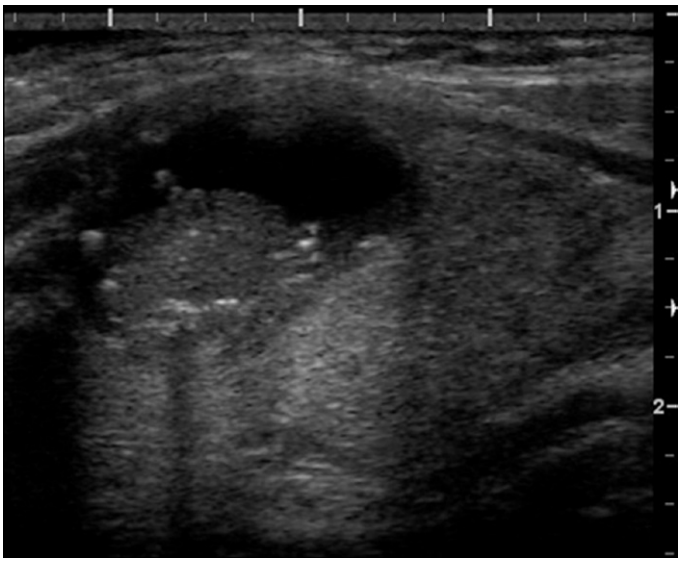

Figure 44.5 Papillary thyroid carcinoma with a cystic component. A significant cystic component at the superficial aspect of a papillary carcinoma; which also shows multifocal microcalcification.

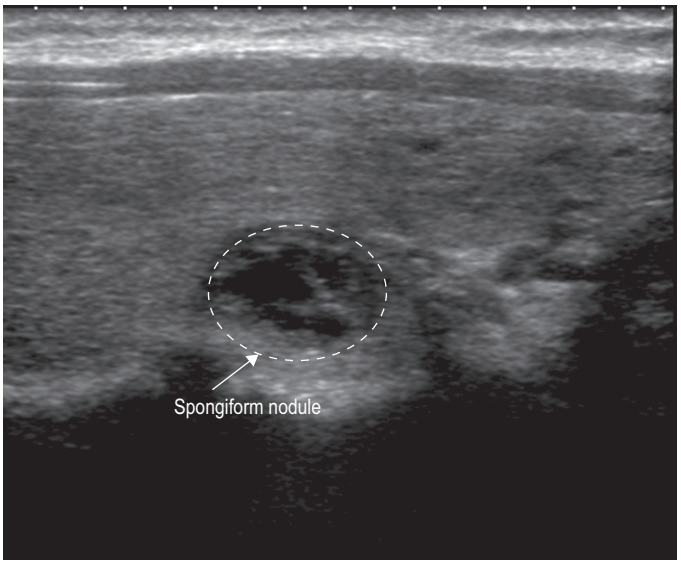

Figure 44.6 Longitudinal ultrasound showing a spongiform benign nodule.

The possibility of multifocal tumours, particularly papillary (10–20% of which are multifocal), should also be considered with multiple nodules. In patients with one or more thyroid nodules larger than 10 mm in diameter, the likelihood of thyroid cancer in each patient is independent of the number of nodules, whereas the likelihood per nodule decreases as the number of nodules increases.[14] The indications for FNA are therefore determined by the ultrasound features, not the number of nodules. When present in a multinodular gland a cancer is not always within the largest nodule. FNA of more than one nodule may be indicated in some patients.

Solid/cystic nodules

Cystic nodules are often assumed to be benign. Whilst the vast majority of cystic thyroid lesions are indeed benign colloid nodules that have undergone cystic degeneration or haemorrhage, the possibility of cystic components within tumours should also be considered. Papillary carcinomas relatively frequently (10–30%) have a small cystic component (Fig. 44.5). Rarely, they can be almost entirely cystic.[15]

True epithelial thyroid cysts are rare; intrathyroidal parathyroid cysts and intrathyroidal lymphoepithelial cysts are extremely rare.[16,17] All of these entities are benign and typically manifest as an anechoic cyst, most frequently unilocular, except the lymphoepithelial cysts. Lymphoepithelial cysts appear similar to other congenital cystic lesions within the neck, such as thyroglossal duct cysts and second branchial cleft cysts, their appearance varies from typically cystic to 'pseudo-solid'. Their diagnosis is usually only made postoperatively.

Retrospective multicentre analysis has defined a 'spongiform appearance' (the aggregation of multiple microcystic components in more than 50% of the volume of the nodule) as a highly specific (99.7%) but relatively insensitive sign of benignity.[18] It is therefore an extremely helpful ultrasound feature, if present (Fig. 44.6).

Echogenicity

Malignant thyroid nodules typically appear solid and hypoechoic compared with normal thyroid parenchyma. In combination, these two US features have a sensitivity of 87% for the detection of thyroid malignancy but a low specificity (15–27%) and a low positive predictive value[10] as this appearance is also present in the majority of benign nodules.[19]

If a thyroid nodule is markedly hypoechoic (defined as a being much less echogenic than the medium-level echogenicity of the strap muscles), the specificity for detection of malignancy is increased to 94%, but the sensitivity is reduced to 12%.[20] Marked hypoechogenicity is thus very suggestive of malignancy.

In contrast, isoechogenicity is a finding much more commonly associated with benign than malignant nodules.

Patterns of calcification

If any calcification is present in a thyroid nodule, the likelihood of malignancy is increased. Microcalcification (fine punctate calcifications, 1 mm or less in diameter, which are individually too small to induce posterior acoustic shadowing) within a predominantly solid nodule is associated with an approximately threefold increase in cancer risk and coarse calcifications are associated with a twofold increase, in comparison with predominantly solid nodules lacking any calcifications.[10] Careful subdivision of different patterns of coarse/macrocalcification demonstrates that solitary calcifications are more common in benign thyroid lesions, but no other significant differentiating features are evident.[21]

The presence of microcalcification is the most specific single sign of malignancy within a thyroid nodule, though it lacks sensitivity. However, 'microcarcinomas' (10 mm or smaller) contain microcalcification less commonly than larger carcinomas. Microcalcification is most commonly demonstrated in papillary carcinoma (25–40% of cases) and is thought to represent aggregates of psammoma bodies (Fig. 44.7).[22] As psammoma bodies measure 50–70 μm in diameter, clusters seen pathologically correlate with the 0.5–1 mm foci of microcalcification apparent at ultrasound (Fig. 44.8).

Even nodules with peripheral calcification, independent of other patient and nodule characteristics, have a significant incidence of malignancy, recently observed in 18.5% of a series of thyroid nodules with peripheral calcification.[23]

Margins

The presence of a peripheral halo of reduced echogenicity around iso- or hyperechoic nodules has been reported to be much more common in benign than malignant thyroid lesions. It was suggested that it represents either the capsule of the nodule or a combination

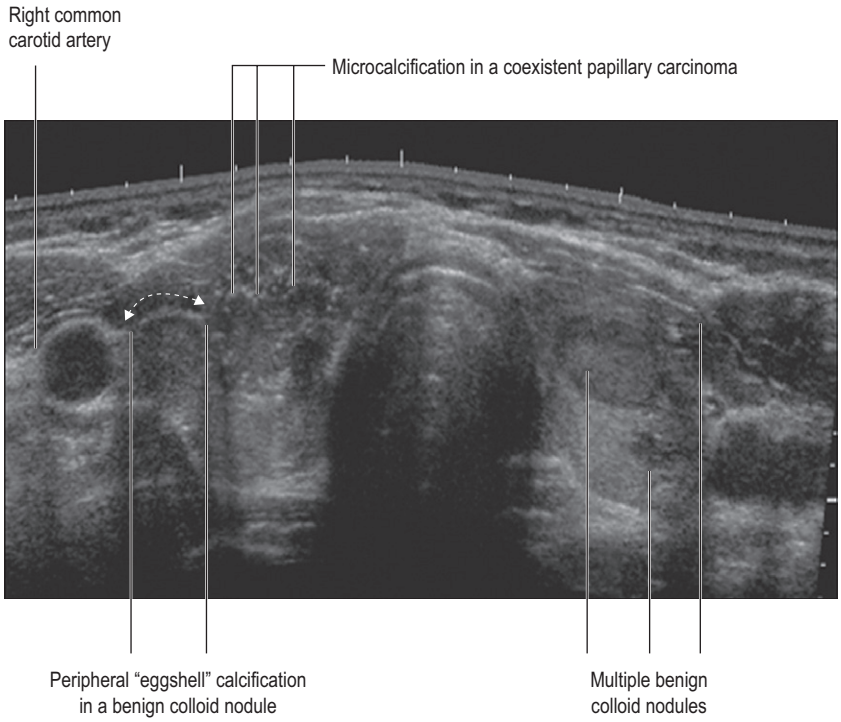

Figure 44.7 Axial panoramic ultrasound showing a multinodular thyroid with a coexistent papillary carcinoma and various patterns of calcification.

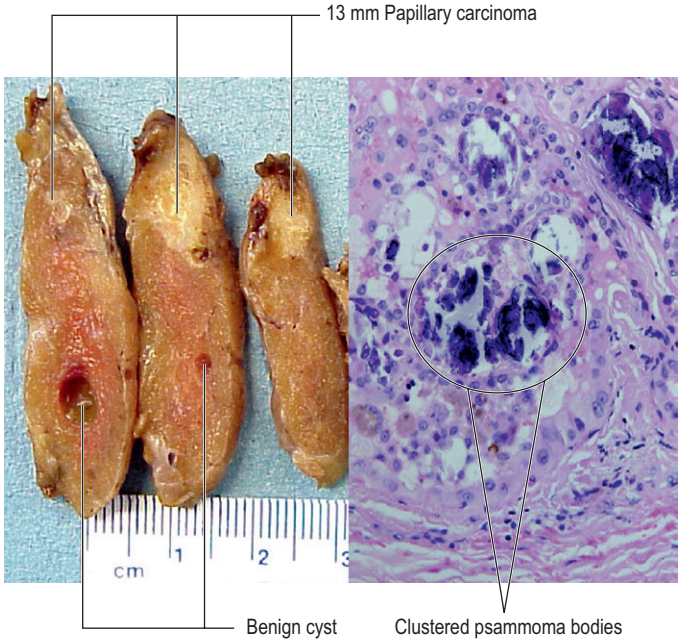

Figure 44.8 Longitudinal surgical thyroid lobe specimen with a 13 mm upper pole papillary carcinoma and benign lower pole cyst. The histological inset shows clustered psammoma bodies, correlating to the microcalcification seen at ultrasound.

of compressed thyroid tissue and vessels. If the perinodular halo was complete it predicted a higher likelihood of a benign lesion than an incomplete halo. The majority of literature evaluating this as a useful differentiating feature predates improvements in the resolution of high-frequency ultrasound; some doubt was cast on its specificity in a contemporaneous review,[24] which suggested non-specific pericapsular inflammatory infiltrate as the underlying cause of the halo.

The evaluation of nodule margins for irregularity or 'microlobulation' (the presence of many small lobules on the surface of a nodule) is potentially a more useful predictor of malignant nodules. Microlobulation is more common than an ill-defined margin in impalpable thyroid malignancy; often associated with a smaller mass and less invasive pathology.[20]

A recent review confirms that the previously cited emphasis on evaluation of the peripheral halo (and even the definition of the margins of nodules) is overstated as it is relatively unhelpful for differentiation of benign from malignant nodules.[14]

The only exception is where a hypoechoic halo coexists in thyroid nodules with peripheral 'eggshell' calcification, but no other calcifications. Disruption of this eggshell calcification may be a more sensitive predictor of malignancy than other known suspicious sonographic criteria, with similar specificity.[25]

In summary, the observation of well-defined margins, as with lesions observed in most organs, may confer an increased likelihood of benignity. In clinical practice, the detailed evaluation of the peripheral 'halo' is a relatively non-discriminatory ultrasound sign and could be omitted, unless associated with peripheral 'eggshell' type calcification.

Shape: tall versus wide

The observation that nodules in the breast that are taller than they are wide are more likely to be malignant[26] has recently been extrapolated to the thyroid. It is postulated that this phenomenon is due to the propensity for malignant nodules to grow across tissue planes, whereas benign nodules remain within normal tissue planes. Whilst this observation requires further validation, there is early evidence that if any part of a nodule is more tall than wide (defined as being greater in its anteroposterior dimension than its

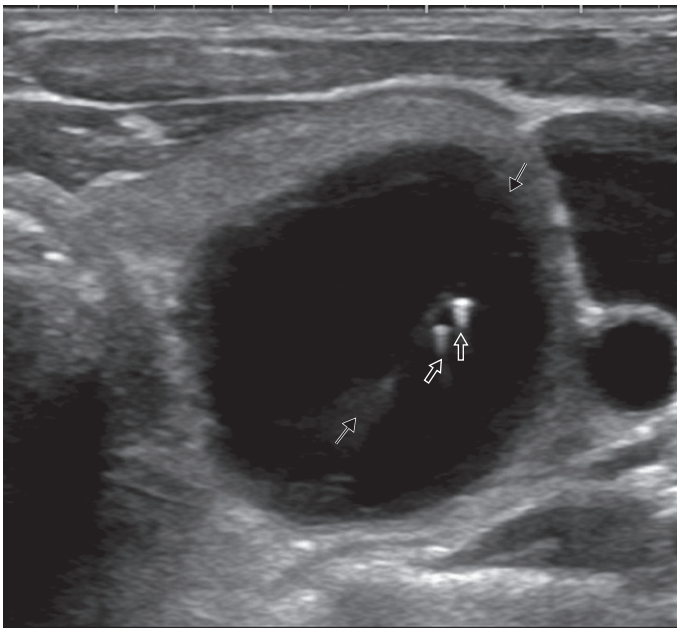

Figure 44.9 Comet tail signs (open arrows) adjacent to a septum (black arrow) within a left lobe thyroid cyst on this transverse image.

transverse dimension) this is a very specific (but not sensitive) indicator of malignancy.[18,20] If present in combination with other features suggestive of a malignant nodule it is likely that this sign will be found useful to help discriminate the more suspicious nodules from the plethora of benign thyroid nodules.[27]

Comet tail sign

A highly specific sign of benignity of a thyroid nodule is the presence of one or more 'comet tail signs';[28] it has been reported that this sign (Fig. 44.9) is pathognomonic of a benign colloid nodule, particularly within or at the periphery of cystic or partially cystic nodules.

It is sometimes difficult in clinical practice to decide definitively whether this sign is present or not. If comet tail artefacts cannot definitely be seen, tiny echoic foci must be assumed to be calcifications when considering the risk of cancer. Whilst many may indeed be due to colloid nodules it is prudent to be cautious, as comet tail signs and microcalcification have diametrically opposing implications for the likelihood of malignancy.

Colour and power Doppler

Thyroid nodules containing marked internal blood flow have an increased likelihood of malignancy compared with nodules with less internal flow. Marked internal vascularity is defined as more flow in the nodule than in the surrounding thyroid gland and more flow in the central part of the nodule than at the periphery. Whilst solid hypervascular thyroid nodules have a high likelihood of malignancy (>40%), lack of extensive vascularity cannot be used to exclude malignancy (14% of solid non-hypervascular nodules were malignant).[10,29]

Whilst the majority of reports in the literature cite the use of colour Doppler, with gain settings maximised to demonstrate slow flow, power Doppler can be substituted, particularly as quantitative indices have not added any useful additional discrimination. Colour and power Doppler are potentially useful adjuncts in the assessment of thyroid nodules (particularly in nodules smaller than 15 mm[11]) but they are not mandatory for selecting nodules to undergo FNA.

Elastography

Elastography is a new dynamic technique that combines manual transducer compression, or the electronic equivalent, with ultrasound to provide an estimation of tissue stiffness by measuring the degree of distortion of the thyroid nodule. Early reports suggest that elastography may help to differentiate malignant from benign lesions, as malignant lesions are frequently relatively harder (stiffer or less compliant) than benign nodules.[30,31] Further evaluation will assess its real efficacy and potential role as an adjunct in the management of thyroid nodules; whilst initial reports are promising, the true role and value of this technique will evolve and become evident with further research and clinical application.

Further potential variations may arise from the diversity of different interpretations of the transformation of theoretical tissue elasticity to its practical use. This may make the utility of elastography machine or manufacturer specific, at least in its early evolution.

Physical limitations to elastography include a significant fluid component or peripheral calcification within a nodule. The nodule also needs to be clearly separate from other adjacent nodules, limiting its application in multinodular goitres.

Interval growth of a nodule

Most benign thyroid nodules grow slowly over time. Therefore, slow growth of a thyroid nodule, particularly if proven benign by ultrasound-guided FNA, does not necessarily indicate a false negative initial result, or subsequent malignant transformation; it is much more likely to represent the natural history of such nodules. Approximately 90% of nodules undergo a 15% or greater increase in volume over 5 years; nodules that are predominantly cystic are less likely to enlarge than solid nodules.[32]

The exception is clinically detectable rapid growth, which most commonly occurs in anaplastic thyroid carcinoma but also may occur in lymphoma, sarcoma and occasionally, high-grade carcinoma. Anaplastic thyroid carcinoma quite commonly presents as a painful, enlarging neck mass with features of local invasion.

The dilemma of defining how much growth over what period constitutes suspicious growth has not yet been answered by research.

Ultrasound features of adjacent structures suggestive of thyroid carcinoma

Cervical lymphadenopathy

A significant minority (10–30%) of thyroid carcinomas present with an enlarged palpable lymph node rather than the primary tumour. Some primary tumours may remain occult at ultrasound examination even in the presence of local nodal metastases. These are most commonly metastases from papillary carcinomas, where nodal metastases are seen at presentation in approximately a third of cases. The distribution of the nodal metastases is most commonly pre- and paratracheal, with anterior cervical nodes along the internal jugular chain also relatively frequently involved.[33,34]

A far higher proportion of childhood papillary thyroid cancers present with nodal metastases, with 60% palpable and more proven histologically at resection in the largest series of patients under 20 years old.[35] The proportion diminishes with increasing age, but higher proportions of patients with involved nodes have been demonstrated in patients up to 40 years of age.

The characteristic ultrasound appearances of nodal metastases from thyroid tumours often resemble those of the primary tumour and are detailed under the respective features of the tumours themselves below. Whilst much less common as thyroid malignancies, anaplastic and medullary cancers, as well as thyroid lymphomas, also frequently have associated nodal metastases at presentation.

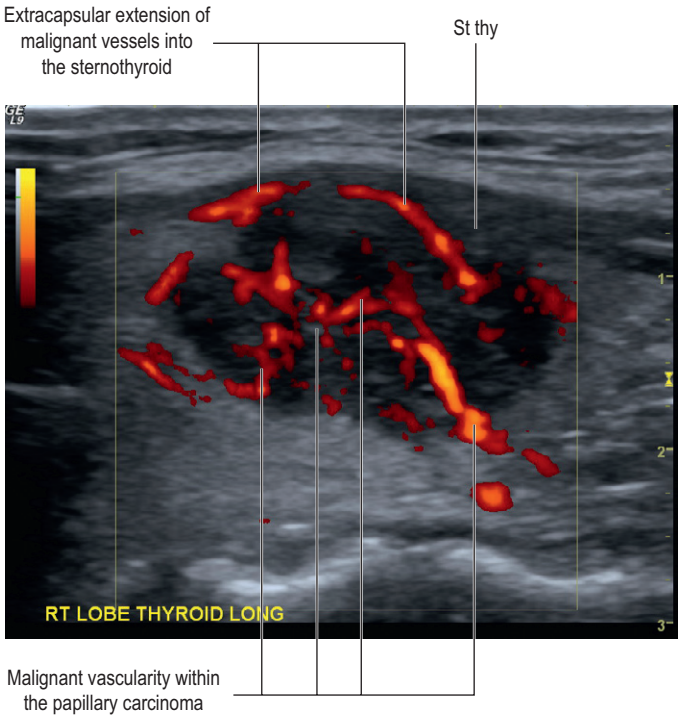

Figure 44.10 Longitudinal ultrasound showing intranodular vascularity on power Doppler examination of a papillary carcinoma. Contiguous extension of the nodule, vessels and fixation on dynamic examination (during swallowing) represents direct extracapsular tumour extension into the sternothyroid muscle. This was confirmed during surgical resection and pathological specimen examination. The preoperative recognition of extracapsular spread facilitated optimal surgical planning and management. St thy, sternothyroid muscle.

The systematic search for nodal metastases is therefore an integral and essential part of the neck ultrasound evaluation.

Spread to adjacent structures

Spread of tumour to extrathyroid tissues is a relatively uncommon manifestation of malignant thyroid nodules but prognostically very significant for the patient and critical for potential surgical planning. It most frequently occurs in anaplastic, medullary, follicular carcinomas or thyroid lymphoma.

If the normal fascial planes between the thyroid and strap muscles are lost, or the muscles have ill-defined margins, are expanded or have additional tissue within them, then this is often indicative of extracapsular spread of tumour at its superficial surface (Fig. 44.10). Neovascularity crossing the boundary between tumour and adjacent tissue on power Doppler assessment confirms invasion rather than adherence or abutting tissues.

Extension into the deep tissues can be more difficult to assess accurately, but thyroid capsular breach and invasion of the oesophagus or lateral tracheal wall can be defined on ultrasound. The combination of voice hoarseness, vocal cord palsy and deep tumour extension denotes invasion or involvement of the recurrent laryngeal nerve or, less commonly, the vagus nerve with lateral invasion.

Lateral extension can also be seen within the soft tissue planes. The common carotid artery and internal jugular vein can also be sites of potential direct invasion. Tumour thrombus can be visualised within the jugular vein; differentiation of venous thrombosis from tumour thrombus can be achieved by the demonstration of vascularity within the tumour tissue on power Doppler.

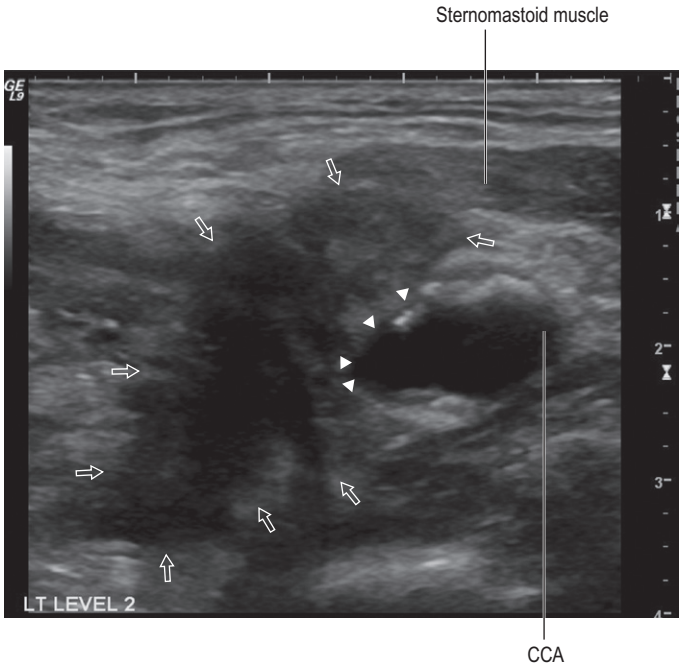

Figure 44.11 Transverse ultrasound of the distal common carotid showing involvement of the CCA medial wall (arrowheads) by an ill-defined superior extension of left lobe anaplastic thyroid carcinoma (arrows). CCA, common carotid artery.

Involvement of the common carotid often defines an inoperable tumour (Fig. 44.11).

Dynamic examination with compression or ballottement of adjacent tissues is a unique advantage of ultrasound over other imaging techniques when assessing the potential spread to adjacent tissues. If tissues and tumour can clearly be seen to move relative to one another, an operative plane can be confidently confirmed. Conversely, if dynamic examination shows definite infiltration and lack of separate movement, the affected tissue will usually require resection en bloc with the tumour. The high spatial resolution of ultrasound, in addition to its dynamic capabilities, can offer critical preoperative information that is unavailable from other modalities.

Malignant tumours

The incidence of tumours in most organs is well documented in various cancer registries. The trends in variation of incidence are also often well understood through temporal variation in risk factors. The incidence of thyroid carcinoma is an exception for a variety of reasons. This significantly influences both the imaging and management of thyroid cancer.

The incidence varies widely between geographical locations and series but the majority (60–80%) of new thyroid cancers are papillary. Less common histological types include follicular (10–20%), medullary (3–5%) and anaplastic (1–10%) cancers. Rarely, metastases, lymphoma or sarcoma present within the thyroid. The pathology and ultrasound features are specific to each histological subtype of thyroid carcinoma and are considered separately below.

Papillary carcinoma

Pathological factors

Papillary carcinoma is not only the most common thyroid malignancy overall, but it is also more frequent in younger patients and generally more common in females. The long-term prognosis is

extremely good, with most series reporting 10- and even 30-year survival rates exceeding 90%. Unusually, there is no benign counterpart of papillary cancer recognised histologically, which perhaps contributes to the generally excellent prognosis, but also contributes to some of the management dilemmas in relation to this tumour.

Surprisingly, prognosis is not adversely affected by the presence of local nodal metastases, unlike almost all other tumours. Whilst distant metastases to bone and lungs do worsen prognosis, the chance of long-term survival remains high following resection of the primary tumour, local nodal clearance and radio-iodine therapy.

Relative adverse prognostic factors include:[36]

- more advanced stage at diagnosis – particularly T3 and T4 tumours and the presence of distant metastases
- local vascular or extracapsular invasion
- poorly differentiated or diffuse sclerosing variants at histology
- elevated postoperative thyroglobulin levels (postulated to be due to otherwise occult distant metastatic disease or bulkier residual thyroid tissue, potentially impairing efficacy of radio-iodine therapy)
- male sex
- older patients.

The occurrence of incidental thyroid cancer at autopsy has been recognised for over 60 years.[37] Several autopsy studies have replicated incidences of occult thyroid cancer varying between 5% and 35.6% irrespective of geographical location. The most methodical study demonstrated the highest incidence.[38] Indeed, these authors postulated that because many of the cancers they found were both multifocal and smaller than their meticulous 2–3 mm section sample interval (67% were less than 1.0 mm), then if the glands were to be sectioned finely enough, almost every person would have foci of thyroid cancer demonstrable. Their pragmatic suggestion was that tumours less than 5 mm in size should be called 'occult papillary tumour' instead of carcinoma. The management of small papillary 'cancers' or 'micropapillary cancer' continues to provoke considerable debate and disagreement in the literature.[39]

The observed incidence of thyroid cancer has increased during recent years, best demonstrated by a thorough review of a sample of the national cancer registries in the United States.[40] Over a 30-year period, this demonstrates a 2.4-fold increase (from 3.6 to 8.7 per 100 000). Despite this increase, mortality remained stable and there was no significant change to the incidence of follicular, medullary or anaplastic cancers. Almost all of the increase was due to papillary cancer, which underwent a 2.9-fold increase. Forty-nine per cent of these papillary cancers were 1 cm or smaller and 87% were 2 cm or smaller. The observed increase in incidence was therefore due to increasing detection of 'subclinical disease', not an increase in the true occurrence of thyroid cancer. The period of this review coincided with the increasingly widespread use of ultrasound (from 1980's) and FNA (from 1990's). Advances in diagnostic techniques have increased the numbers of cancers detected in the 'subclinical reservoir'; epidemiologists have labelled this phenomenon 'overdiagnosis', most familiarly in the context of prostatic cancer.[41]

Papillary cancers are firm tumours occurring anywhere within the thyroid gland, histologically characterised by the formation of papillae and recognition of typical nuclear features. The majority are unencapsulated, though partially and fully encapsulated variants also exist. Some of these may undergo infarction, with calcification within the infarcted papillae forming psammoma bodies, the aggregation of which are evident as microcalcification at ultrasound.[22]

Ultrasound features

A spectrum of ultrasound features is possible, but typical appearances of the primary papillary carcinoma include[13,42] (Figs 44.12 and 44.13):

- Hypoechogenicity: a predominantly hypoechoic appearance is the most common feature of papillary carcinomas (75–90%).

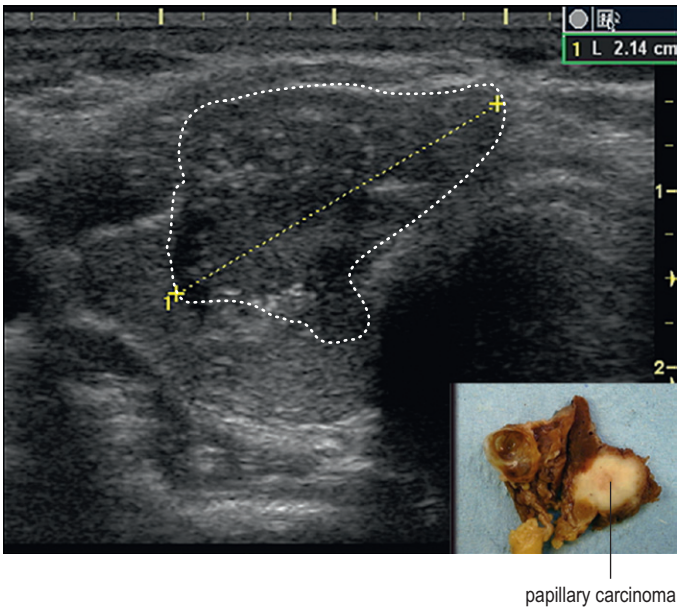

Figure 44.12 Transverse ultrasound showing a papillary carcinoma at the junction of the right lobe and isthmus. Inset shows the resected surgical specimen, demonstrating the carcinoma.

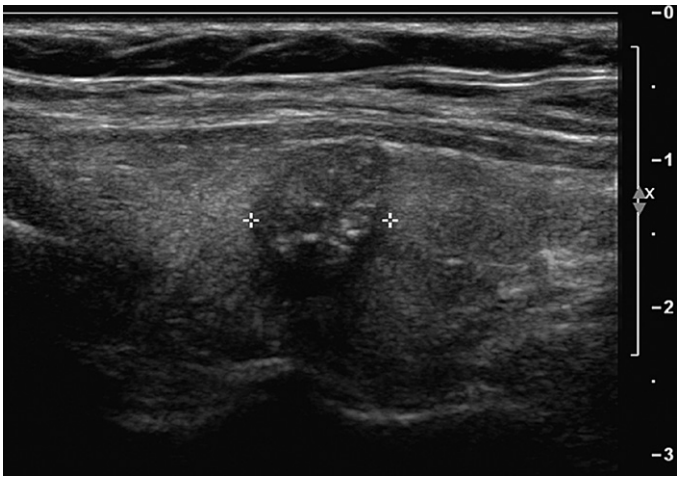

Figure 44.13 Longitudinal ultrasound showing an incidental 9 mm micropapillary thyroid carcinoma with multifocal microcalcification.

- Predominantly solid composition: however 20–30% have a variable cystic component, with almost totally cystic papillary carcinoma comprising a rare but recognised variant.[15]
- Microcalcification (25–45%): whilst highly specific for papillary tumours, it is occasionally seen (approximately 5%) in benign adenomatous nodules. Absence of visible calcification is, however, more common than microcalcification within papillary tumours but, overall, lack of calcification is much more frequently a feature of benign lesions. Coarse and rim calcification are less common and unusual in comparison to microcalcification within papillary tumours.
- Multifocal tumours: these are recognised in 10–20% of patients at ultrasound, but are even more common histologically, particularly as tiny microcarcinomas.[38]
- Hypervascular solid components: almost universal but non-specific. However, complete avascularity on appropriate

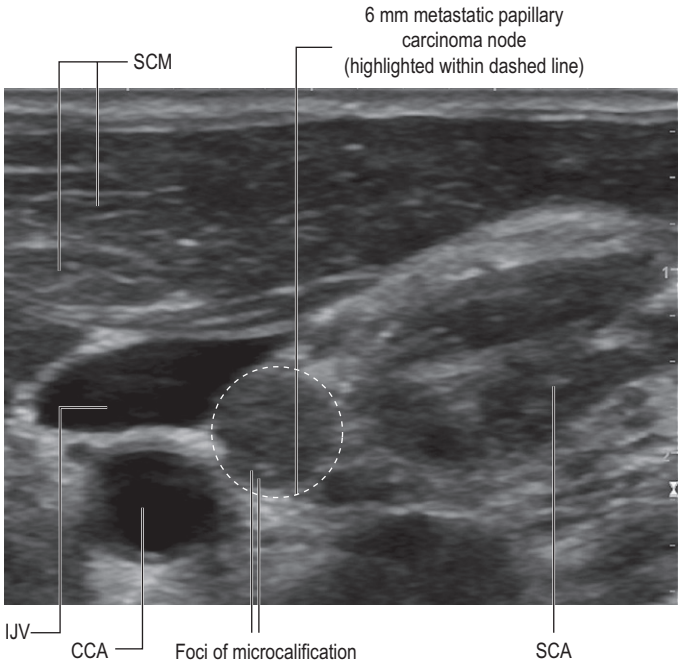

Figure 44.14 Transverse ultrasound at level IV on the left, showing a typical small (6 mm) nodal metastasis from a papillary carcinoma. It is solid, echogenic and contains foci of microcalcification, despite its size. SCA, scalenus anterior; SCM, sternocleidomastoid muscle; CCA, common carotid artery; IJV, internal jugular vein.

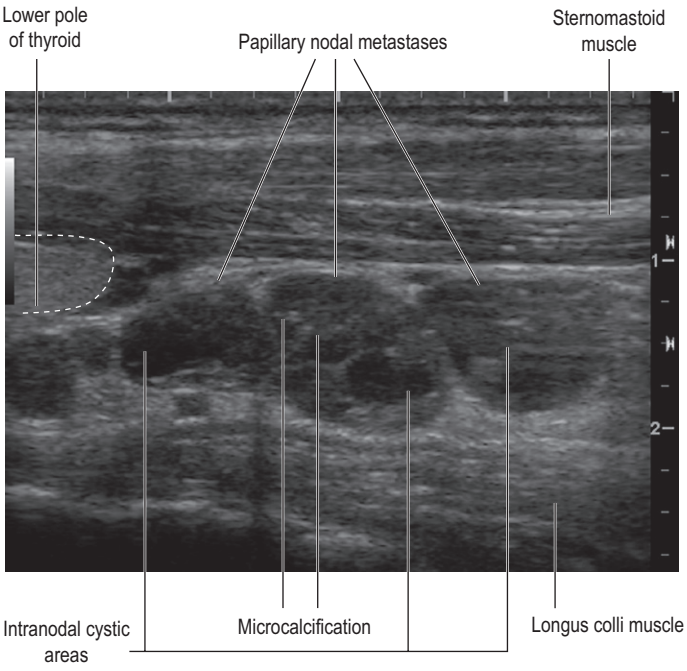

Figure 44.15 Longitudinal ultrasound showing impalpable partially cystic metastatic nodes as the only site of disease at presentation; the primary papillary carcinoma was occult.

Papillary carcinoma

- Predominantly solid composition, ill defined and hypoechoic.
- Minority have variable cystic component.
- Microcalcification; highly specific for papillary tumours.
- Multifocal tumours, particularly as tiny microcarcinomas.
- Hypervascular solid components.

Doppler examination effectively excludes the possibility of papillary carcinoma.

Metastatic local lymph nodes in papillary carcinoma frequently demonstrate typical features to suggest the underlying diagnosis[43,44] (Fig. 44.14):

- Nodal metastases are common at diagnosis (50%).
- The majority are found in the mid and lower jugular chains and ipsilateral to the primary tumour (70–85%). Whilst pre- and paratracheal nodes are also relatively common, these are often less readily visualised at ultrasound.
- Hyperechoic relative to muscle (60–80%).
- Punctate or microcalcification (50%): this tends to be restricted to the solid nodal metastases rather than those with a significant cystic component.
- Partial cystic degeneration (20–50%): this varies from small foci of cystic change to complete cavitation with no discernible residual solid component. The majority of cavitating nodes still contain internal septations or nodules (usually showing vascularity on power Doppler) and less frequently a thick outer wall (Fig. 44.15).
- Occasionally a solitary cystic metastatic node can mimic a benign cervical cyst, such as a branchial cyst, and this should be considered in its differential diagnosis, even if the primary papillary thyroid cancer is occult at presentation. These cystic nodes occur in young adults and almost all have been reported in patients under 35 years. Whilst less common in this group, the possibility of metastatic necrotic squamous carcinoma can present in an identical way and site; FNA is therefore indicated (Fig. 44.16).
- High thyroglobulin levels in the aspirated nodal cyst fluid (relative to the quoted normal laboratory blood range) may assist the discrimination of cystic nodal metastases.

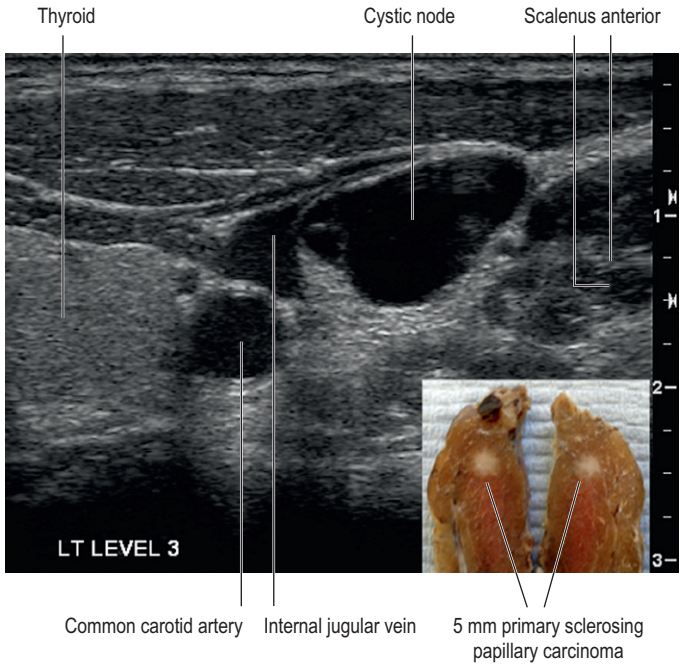

Figure 44.16 Transverse ultrasound at level III on the left, showing a solitary cystic nodal metastasis, which could be mistaken for a branchial cleft cyst. The tiny 5 mm ipsilateral upper pole primary papillary carcinoma is shown on the resected surgical specimen (inset). The diagnosis was confirmed preoperatively by thyroglobulin assay of intranodal cystic fluid obtained by fine-needle aspiration.

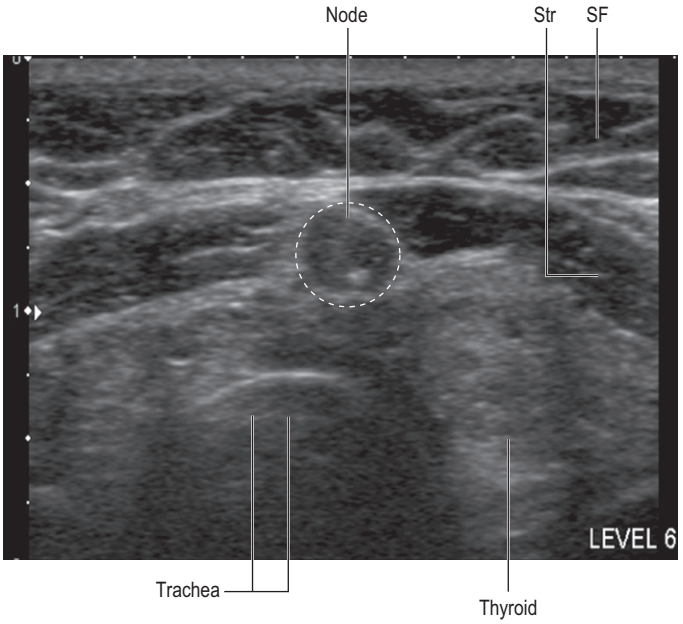

Figure 44.17 Nodal metastasis. Transverse ultrasound above the level of the thyroid isthmus, showing a solitary tiny (2 × 3 mm) pretracheal nodal metastasis from a micropapillary primary thyroid carcinoma. A tiny focus of microcalcification is evident.
SF, subcutaneous fat layer; Str, strap muscles.

Papillary carcinoma nodal metastases

- Nodal metastases common at diagnosis.
- May be the initial manifestation of disease.
- Hyperechoic relative to muscle.
- Punctate or microcalcification.
- Partial cystic degeneration.
- Occasionally a solitary cystic metastatic node can mimic a benign cervical cyst. FNA is indicated.

- Ultrasound-guided FNA (from any solid component) of a suspicious node will usually be diagnostic, irrespective of nodal size (Fig. 44.17).
- Lymph node metastases may even be the sole or initial manifestation of disease (up to 20%): occult primary tumour on ultrasound.

The possibility of recurrent tumour within the thyroid bed after total thyroidectomy for papillary carcinoma, or cervical nodal metastases can usually be demonstrated with ultrasound. Recurrent papillary carcinoma has similar features to the primary lesions. Postoperative fibrotic tissue or stitch granulomas cannot be distinguished from recurrent disease by any ultrasound features but can be readily differentiated by FNA.[45]

Follicular variant

The follicular variant of papillary carcinoma histologically shows a predominantly follicular pattern but the histological and cytological features include psammoma bodies and characteristic nuclear features. The follicular variant of papillary thyroid carcinoma can be challenging or impossible to discriminate on ultrasound as it is more likely to have relatively benign sonographic features than classical papillary thyroid carcinoma. Specifically, whilst these lesions are solid with well-defined margins, only half are hypoechoic. Microcalcification is rare, but if FNA is undertaken, most cytology results will demonstrate malignant features.[46]

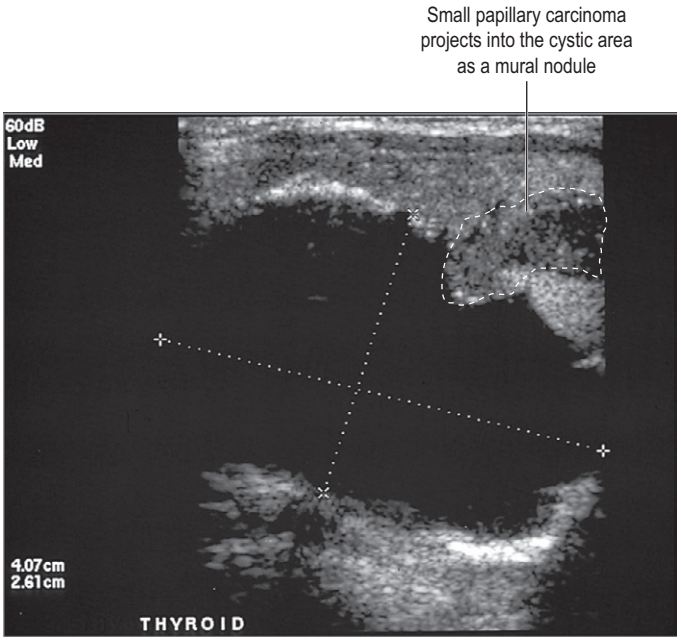

Figure 44.18 A mural nodule of tumour projects into the cystic area of a predominantly cystic variant of papillary carcinoma.

Cystic variant

Cystic papillary carcinomas (Fig. 44.18) are rare (5% or less) and may be difficult to discriminate from the extremely common benign haemorrhagic or colloid cysts. The predominantly cystic papillary carcinomas reported in the literature all had at least a small peripheral mural hypervascular solid component. Some of these mural nodules may contain foci of microcalcification. Associated cystic nodal metastases are further useful signs of this unusual entity.[15,42]

Diffuse sclerosing variant

Compared to the more common papillary carcinomas the rare variant of diffuse sclerosing papillary carcinoma occurs more frequently at a younger age and predominantly affects women. Cervical nodal and pulmonary metastases are more common and there is a smaller probability of disease-free survival on follow-up.

Histologically, there is diffuse permeative involvement of the thyroid, either unilaterally or bilaterally. Numerous psammoma bodies, marked lymphocytic infiltration, fibrosis and more frequent vascular involvement are recognised.

Ultrasound features reflect the pathological findings in the relatively small series reported.[47] The tumours are frequently large at presentation, with nodal metastases. They are solid with heterogeneous echogenicity and ill-defined margins; the most typical ultrasound sign to suggest this entity is widespread 'snowstorm' microcalcification (Fig. 44.19). If diagnosed preoperatively, appropriately aggressive surgical treatment may be indicated due to its greater malignant potential than most papillary carcinomas of the thyroid.

The recognition of diffuse microcalcification within an otherwise apparently normal thyroid should prompt FNA from the affected area in case it represents an early presentation of this diffuse sclerosing variant of papillary cancer.[48]

Follicular neoplasm

Pathological factors

Follicular neoplasms are one of the most challenging and potentially frustrating lesions to try to recognise and characterise with

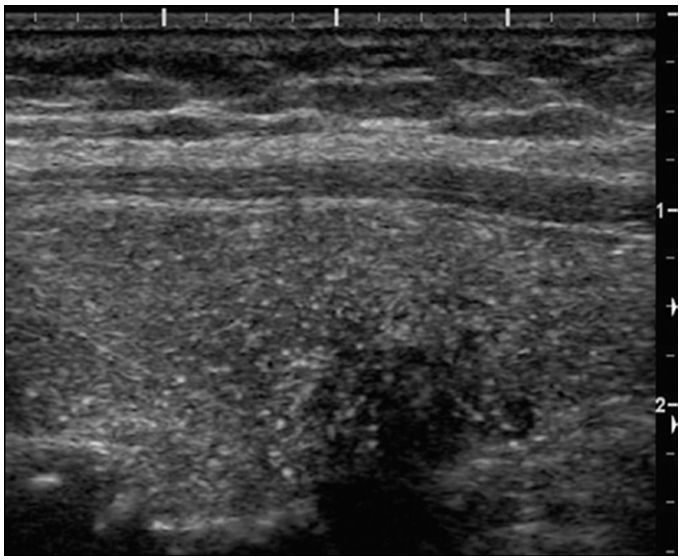

Figure 44.19 Longitudinal ultrasound showing a rare diffuse sclerosing variant of papillary carcinoma. A small (12 mm), ill-defined, low-echogenicity area and diffuse 'snowstorm' scattered throughout the rest of the lobe.

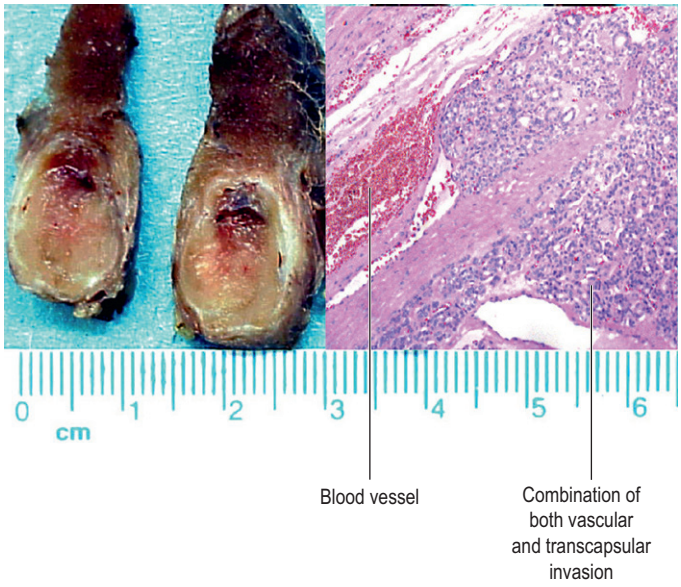

Figure 44.20 Longitudinal surgical thyroid specimen with an 18 mm lower pole circumscribed haemorrhagic follicular lesion. The histological microscopy demonstrates a carcinoma because of both vascular and transcapsular invasion.

ultrasound, or any other preoperative technique. It is impossible to separate malignant from benign follicular neoplasms by ultrasound, FNA or core biopsy. If suspected, they usually require surgical excision as the differentiation between a benign 'follicular adenoma' and a follicular carcinoma can only be made histologically. The diagnosis of malignancy depends upon unequivocal capsular invasion that penetrates the entire thickness of the capsule and/or vascular invasion, which is a more reliable sign of malignancy than capsular invasion (Fig. 44.20). To qualify as vascular invasion, the neoplastic cells should attach to the wall of a large calibre extracapsular vessel, obliterating its lumen either partially or totally.

From the definitions above it is unsurprising that the diagnosis of malignancy depends upon careful histological examination of the operative specimen, sectioning the entire nodule volume. Indeed,

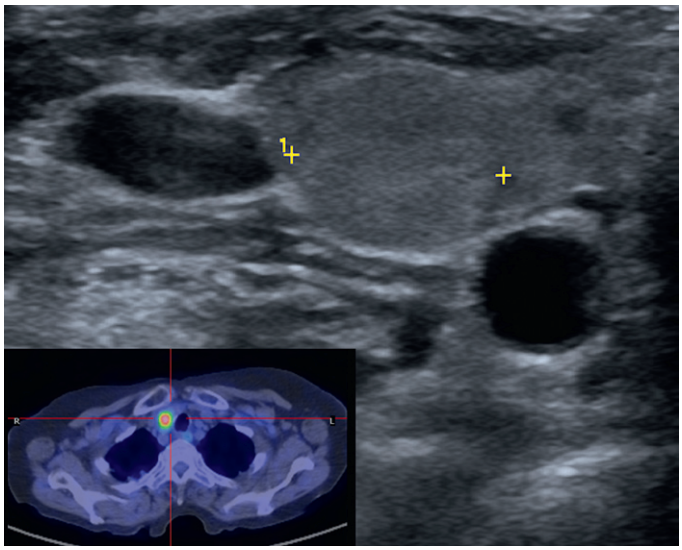

Figure 44.21 A fluorodeoxyglucose (FDG) avid follicular lesion found incidentally during a staging PET/CT examination (inset image) for lung cancer. The lesion has none of the ultrasound features of an intrathyroid metastasis. Histology showed a benign follicular lesion.

Follicular lesion

- Predominantly solid, often larger than other coexistent nodules.
- Relatively homogeneous, hyperechoic or isoechoic.
- Differentiation between benign and malignant nodules is by histological examination only.
- Cystic change is absent or relatively small.
- Calcification is unusual.
- Peripheral halo.
- Vascularity: considerable overlap between benign and malignant follicular neoplasms.
- Local nodal metastases are uncommon.
- Distant haematogenous metastases are much more common in follicular than papillary carcinomas.

minimally invasive follicular carcinoma can be demonstrated in follicular lesions in direct proportion to the thoroughness of the histological search for capsular and/or vascular invasion.

Follicular carcinomas are relatively rare thyroid cancers (less than 5%), but are much more common (20–30%) in geographical areas of iodine deficiency or endemic goitre, relative to the respective prevalence of papillary carcinoma. If dietary iodine deficiency is rectified, the incidence of follicular carcinoma reduces and papillary carcinoma increases.[49] It has also been postulated that follicular carcinoma arises from pre-existent adenomas.

Ultrasound features

The features of follicular neoplasms on ultrasound are relatively non-specific. As follicular lesions usually occur in association with other benign hyperplastic or adenomatous nodules, identification of these lesions within the background multinodular change is even more challenging.

Ultrasound features may include:

- Predominantly solid nodule, commonly considerably larger than other coexistent nodules at presentation (Figs 44.21 and 44.22).
- Relatively homogeneous and most frequently hyperechoic or isoechoic compared to thyroid parenchyma.
- Cystic change is absent or relatively minimal.

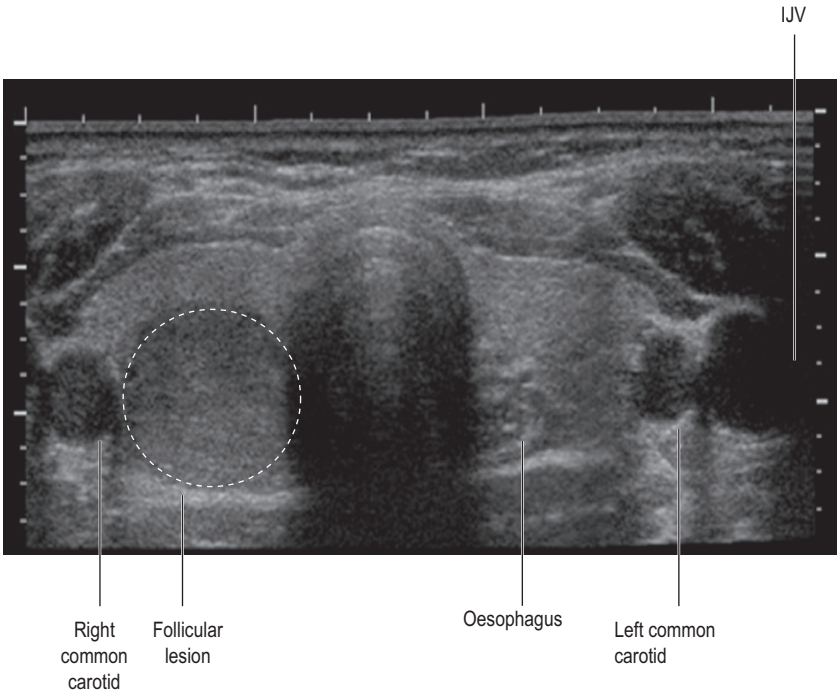

Figure 44.22 Axial panoramic thyroid ultrasound showing a right lobe follicular lesion. IJV, internal jugular vein.

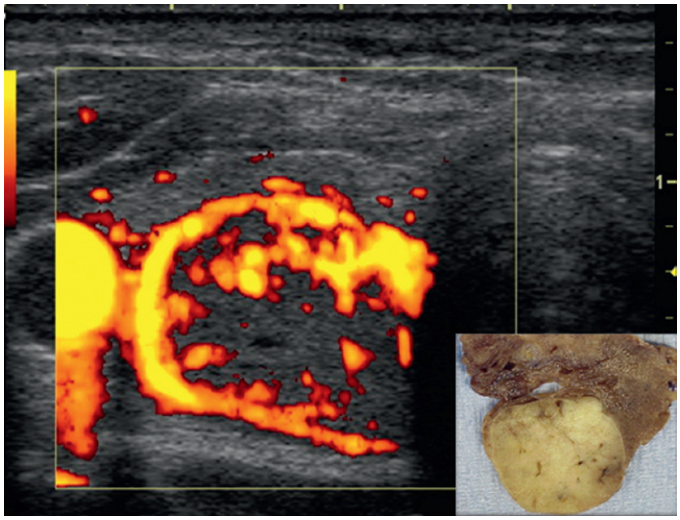

Figure 44.23 Power Doppler image of the same lesion as Figure 44.22 with inset of the surgical thyroid lobe specimen. Histologically benign.

- Calcification is unusual.
- Vascularity on power Doppler imaging is predominantly peripheral in benign follicular neoplasms (Fig. 44.23); malignant lesions have a higher intranodular vascularity. There is considerable overlap in these relatively subjective patterns of vascularity.
- Local nodal metastases are uncommon.
- Distant haematogenous metastases (skeletal, hepatic, pulmonary or cerebral) are much more common in follicular than papillary carcinomas. This is particularly prevalent in the frankly invasive form of follicular carcinoma, with extensive extracapsular and vascular invasion.

Oncocytic (Hürthle cell) neoplasms

These represent a variant of follicular neoplasms (approximately 20%) and similarly have their benign and malignant counterparts distinguishable only on histological examination. The malignant Hürthle cell tumours are a relatively aggressive subgroup of follicular carcinomas, with a greater propensity to metastatic spread and worse prognosis. Unfortunately, there are no reliable preoperative or ultrasound criteria to distinguish this malignant variant.[50]

Medullary carcinoma

Pathological and genetic factors

Medullary thyroid carcinoma (MTC) is uncommon, comprising only about 5% of all thyroid cancers. It arises from the parafollicular cells (also called 'C cells'). The C cells are found in the interstitial spaces outside the thyroid follicles in the middle to upper third of the lateral lobes. They lie next to capillaries to facilitate secretion of their hormone (calcitonin) into the bloodstream. The typical location of medullary carcinoma primary tumours reflects the maximal density of parafollicular cells as described above. Their proximity to the capillary network may also contribute to their higher rate of metastatic disease at presentation. Approximately 50% present with local cervical nodal metastases and 10–25% with distant pulmonary, hepatic or skeletal metastases.

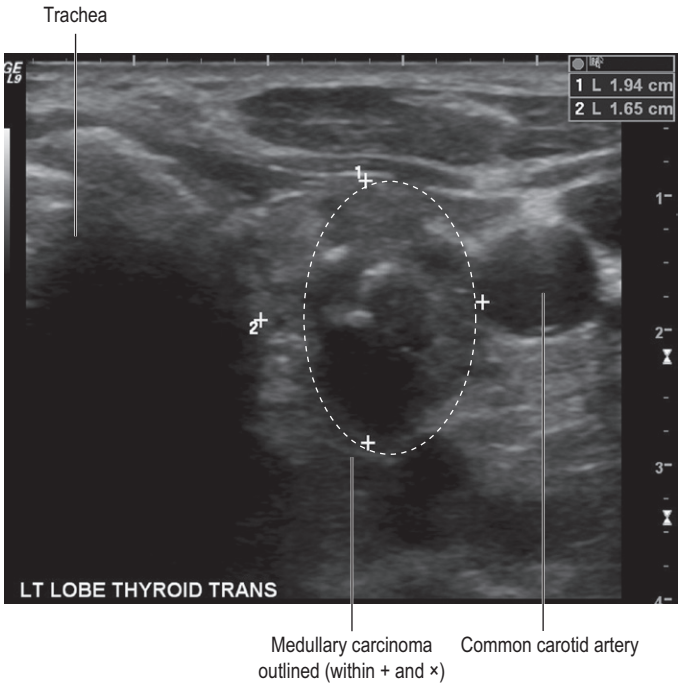

Figure 44.24 Transverse ultrasound of a medullary carcinoma in the left upper lobe of a thyroid gland. It is 'taller than wide' and contains coarser calcification than that typically associated with papillary carcinomas.

The sporadic or isolated form of the disease is most common (75%) and occurs as a typically unilateral, solitary primary lesion in patients over 40 years old. Although nodal metastases are common, it usually has a better long-term prognosis than the familial forms of the disease.

The inheritable form of medullary carcinoma may be associated with multiple endocrine neoplasia (MEN) as medullary thyroid cancer alone, or in association with phaeochromocytomas in type 2A and 2B syndromes. The inheritable forms of medullary thyroid cancer tend to be more aggressive than the sporadic cases, presenting at a much younger age (often in the teens and twenties) and before any phaeochromocytoma has developed. Type 2A multiple endocrine neoplasia can also be associated with parathyroid hyperplasia, which could be demonstrable at ultrasound. Multiple endocrine neoplasia, type 2B medullary carcinoma is the rarest form of the disease but also the most aggressive.

Whilst rare, it is crucial to diagnose familial forms of medullary thyroid carcinoma because genetic screening of family members can now be performed. The cause of type 2 multiple endocrine neoplasia syndromes is specific mutations in the '*RET* proto-oncogene', which have been localised to chromosome 10. Its inheritance is autosomal dominant with variable penetrance; as medullary thyroid cancer ultimately occurs in almost 100% of genetically predisposed individuals, prophylactic thyroidectomy can be considered before medullary carcinoma develops, thereby dramatically improving the long-term prognosis.

Ultrasound features

Typical features of medullary thyroid carcinoma:

- Solid hypoechoic mass (Fig. 44.24).
- Located in mid or superior thyroid gland if solitary and sporadic presentation.
- Familial forms more commonly show diffuse and bilateral involvement.
- Echogenic foci are very common in primary lesions (over 80%). A combination of calcification and surrounding amyloid histologically, frequently denser and coarser on ultrasound than papillary carcinoma. May exhibit posterior acoustic shadowing.
- Hypervascular (disorganised, chaotic pattern) relative to adjacent parenchyma on power Doppler; the pattern of vascularity often has a disorganised, chaotic pattern.
- Nodal metastases are hypoechoic, unlike papillary nodes, and the majority contain echogenic foci, but cystic change is much less common.
- Nodal disease within the mediastinum is more common in MTC than papillary carcinoma.
- Recurrent disease is very common postoperatively. Elevated serum calcitonin levels are a sensitive and specific marker for recurrent disease; when evident on ultrasound appears similar to the disease at initial presentation.
- FNA of the primary tumour or nodes can confirm the diagnosis. Amyloid can be detected by Congo red staining, with immunohistochemistry demonstrating calcitonin positivity.

Medullary thyroid carcinoma

- Solid hypoechoic, hypervascular mass.
- Mid or superior thyroid gland if solitary.
- Familial forms more commonly diffuse and bilateral.
- Echogenic foci are very common in primary lesions, frequently denser and coarser than papillary carcinoma.
- Nodal metastases are hypoechoic and contain echogenic foci; cystic change is uncommon. Frequently extend into mediastinum.
- Recurrent disease is very common postoperatively; serum calcitonin levels are a sensitive marker.

Anaplastic carcinoma

Pathological factors

Anaplastic thyroid carcinoma, although a rare thyroid cancer (1–5%), is extremely aggressive. It is almost invariably fatal, with survival from diagnosis measured in weeks or months, rather than years (median survival approximately 9 months). Despite its rarity, it accounts for more than half the total deaths from thyroid cancer. Recent reports showing early promise in treating radio-iodine-resistant metastatic thyroid cancer included small numbers of anaplastic cancers. This treatment is based upon angiogenesis and kinase inhibitors; it may offer some prolongation of survival in these aggressive malignancies.[51] The rarity of these aggressive cancers may mitigate some of the medico-political barriers to these treatments, which are likely to remain very expensive.

Some anaplastic cancers are considered to represent de-differentiation within previously occult, indolent papillary or follicular cancers. The diagnosis is usually evident clinically with a rapidly growing thyroid mass, presenting with pressure effects or symptoms from invasion of local structures in middle-aged to elderly patients. Differentiation from the much more treatable thyroid lymphoma is usually readily made by FNA.

Various sarcomas of the thyroid are even rarer entities. Pathologically and prognostically they behave like anaplastic carcinomas; they also share similar ultrasound features and are therefore perhaps best included in the anaplastic group.

Ultrasound features

Illustrative figures cited[52] are from a large series of this rare thyroid cancer:

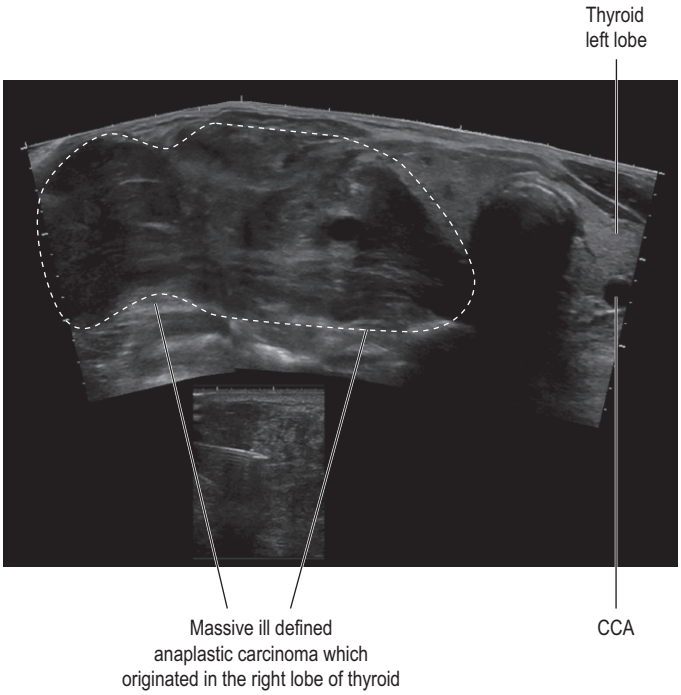

Figure 44.25 Axial panoramic thyroid ultrasound showing an anaplastic carcinoma with vascular invasion and calcification. This is typically extensive and ill defined at presentation. It encircles the right common carotid artery. Inset of diagnostic FNA from a superficial part of the primary lesion, avoiding the extensive deeper necrotic areas. CCA, common carotid artery.

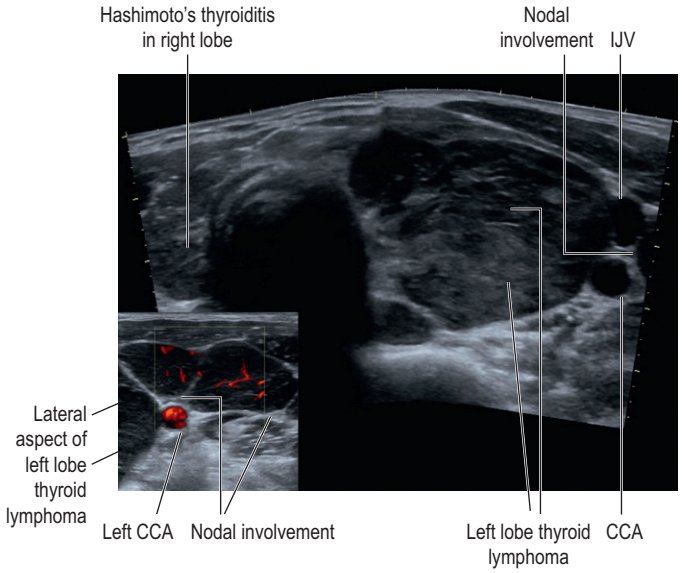

Figure 44.26 Axial panoramic thyroid ultrasound showing a left-sided thyroid lymphoma with adjacent ipsilateral nodal involvement which appears very similar to the thyroid lymphoma on ultrasound (inset). There was a long history of hypothyroidism. The appearance of the right lobe is typical of background Hashimoto's thyroiditis. CCA, common carotid artery; IJV, internal jugular vein.

Anaplastic carcinoma versus thyroid lymphoma

Anaplastic lesions have the following features on ultrasound:
- calcification – usually coarse
- heterogeneous echogenicity; both hypoechoic and ill defined
- presence of necrosis
- lymph nodes: heterogeneous, often with necrosis, compared to homogeneous and isoechoic with the thyroid mass in lymphoma.

- Diffuse hypoechoic heterogeneous mass (Fig. 44.25), which usually has ill-defined margins and involves an extensive part of the thyroid, often both lobes.
- Background nodular goitre is present in about 50%.
- Allied clinical features: recurrent laryngeal nerve palsy (37%), neck pain (50%), rapidly enlarging mass (75%), symptoms of obstruction (90%).
- Dense amorphous calcification is often associated (60%).
- Areas of necrosis are very common (80%) and should be identified and avoided at FNA.
- Regional lymphadenopathy (75%): over half of these show evidence of necrosis on ultrasound.
- Invasion of local structures: internal jugular vein or common carotid artery (50%), trachea, oesophagus, recurrent laryngeal or vagal nerves, local muscles.

Differentiation between anaplastic carcinoma and thyroid lymphoma is critical due to the potential treatment options and dramatic differences in prognosis. The main discriminatory ultrasound features of anaplastic carcinoma versus thyroid lymphoma are summarised above. Their presence is specific for anaplastic carcinoma ($p < 0.01$).[53]

Thyroid lymphoma

Pathological factors

Thyroid lymphoma is another rare (1–5%) thyroid neoplasm; within this small group, almost all patients have non-Hodgkin's lymphoma (mainly large B-cell) rather than Hodgkin's lymphoma. There is almost always previous thyroid involvement with Hashimoto's thyroiditis, although only a small minority of patients with Hashimoto's thyroiditis ever develop thyroid lymphoma., Thyroid lymphoma is more common in women, reflecting the incidence of Hashimoto's thyroiditis, and most patients are elderly (median age 60 years).

The clinical presentation is usually indistinguishable from anaplastic carcinoma with a rapidly progressive neck mass, often with compressive symptoms of dyspnoea or dysphagia, but pain is less frequently seen.

Unlike anaplastic carcinoma, thyroid lymphoma has an excellent and rapid response to chemotherapy and/or radiotherapy and therefore a much better prognosis is expected in most patients with this disorder.

Ultrasound features

- Diffuse hypoechoic homogeneous mass,[54] which may be focal or diffuse and unilateral or involving both lobes (Fig. 44.26).
- Background low echogenicity due to associated Hashimoto's thyroiditis.
- Calcification is rarely associated (under 10%).
- Necrosis is very uncommon.
- Regional lymphadenopathy is common (70%); nodes are typically homogeneous, round, hypoechoic, hypervascular and almost never contain either necrosis or calcification.
- Vascularity on Doppler is unhelpful. It may be hypovascular relative to background parenchyma, similar or chaotically hypervascular.
- Invasion of local structures is much less common than with anaplastic carcinoma; vascular invasion of the internal jugular

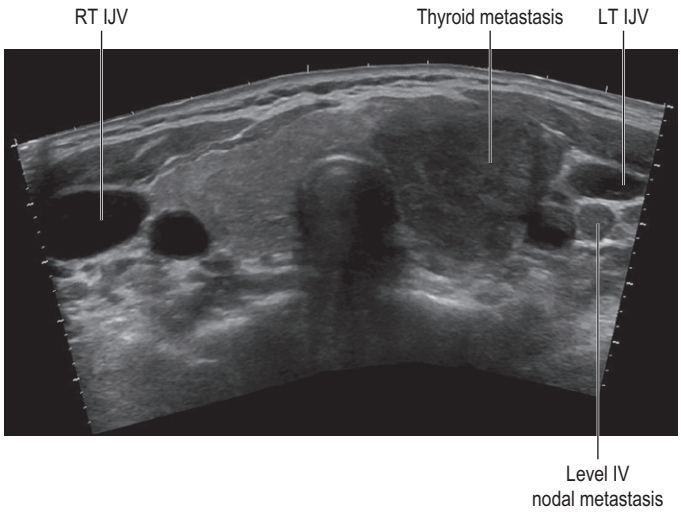

Figure 44.27 Axial panoramic thyroid ultrasound showing a large lower pole thyroid metastasis and a nodal metastasis (lateral to the common carotid artery) from an unknown primary; both were poorly differentiated adenocarcinoma on FNA. Note the incidental asymmetry of the internal jugular veins. IJV, internal jugular vein.

or common carotid may be seen in 20%. Local muscle invasion is unusual, but more common than tracheal, oesophageal, recurrent laryngeal or vagal involvement.
- Ultrasound is as effective as CT for evaluation, except for assessment of intrathoracic extension. It also facilitates optimal FNA or core biopsy guidance.[54]

Thyroid metastases

Pathological factors

Direct involvement of the thyroid from local primary tumours of the pharynx, larynx, trachea and oesophagus is also relatively unusual, occurring in advanced local disease.

Focal thyroid metastases are rarely clinically significant, occurring through haematogenous spread late in the course of the disease process in patients with disseminated malignancy. Incidental thyroid metastases are found at autopsy in approximately 10% of such patients. The commonest site of origin is melanoma, followed by breast, but lung, renal and gastrointestinal primaries also occasionally exhibit metastatic spread to the thyroid.

Ultrasound features

Metastases to the thyroid gland are usually large, predominantly solid and favour the lower poles of the gland (Fig. 44.27).

Thyroid metastases

- Solid, well defined and frequently large (Fig. 44.27).
- Predominantly in the lower pole.
- Hypoechoic, homogeneous mass.
- Diffuse involvement possible, but unusual.
- No calcification.
- Necrosis is uncommon.
- Regional lymphadenopathy is extremely common.
- Usually associated with advanced disease; haematogenous metastases elsewhere.

Thyroid incidentalomas and investigative strategies for thyroid nodules

Thyroid 'incidentalomas' are impalpable nodules discovered incidentally during imaging investigations unrelated to the thyroid and are not only being recognised increasingly frequently but cause management dilemmas when found.[55,56] Impalpable incidental nodules are demonstrated not only at ultrasound, but also with CT, MRI and latterly PET/CT (Fig. 44.21). Most are less than 1.5 cm in diameter and benign.

Consistent with the known prevalence of incidental asymptomatic papillary cancers of the thyroid,[38] it is predictable that a proportion of these incidentalomas will be malignant histologically. Whilst incidentaloma prevalence of 13% with a malignancy rate of 28.8% has been described, they were almost all small early stage papillary carcinomas.[57]

Suggested management strategies vary and no definitive agreed strategy has currently been defined. The spectrum of alternative approaches includes:

- Clinical follow-up by palpation in the absence of suspicious features or history.[58]
- Advising an immediate ultrasound examination and additional investigation as indicated; adding a standard paragraph (over 130 words long) to put the discovery and significance of thyroid incidentalomas in imaging and clinical context.[59]
- A consensus based on a combination of literature review and expert opinion for the investigative strategy of any thyroid nodules 1 cm or larger in size.[10]
- A higher index of suspicion for incidental nodules detected on PET-CT; all need ultrasound as the next investigation, with further investigation dependent upon ultrasound findings.[60]
- Consider clinical and ultrasound assessment, with FNA as appropriate, after an informed discussion with the patient.[61]
- Apply the best available ultrasound criteria to evaluate the thyroid nodule, irrespective of its initial asymptomatic presentation, and manage accordingly.[62]
- Ignore the 'misleading thyroid nodules' unless they present malignant characteristics on the initial radiological investigation that could be relevant to the patient's clinical presentation, recognising the 'inescapable responsibility' of physicians to ensure that their actions entail more good than harm.[63]
- Turning off the ultrasound machines to escape the flood of thyroid nodules[64]!

This last suggestion, far from being anti ultrasound, may prove to have a degree of merit. Just because technology and diagnostic skill can detect more and more thyroid 'cancers' at ever smaller sizes does not necessarily mean that their detection is benefiting patients. The vast majority of these impalpable cancers are papillary lesions,[40] with an excellent prognosis cited of 99% 10-year and 95% 30-year survival. Patients with an incidental nodule who are investigated and diagnosed as having cancer have to live with the psychological anxiety, daily thyroid supplementation, operative morbidity, personal insurance implications and long-term medical follow-up for a 'cancer' that was unlikely to have caused any symptoms during their lifetime. The Hippocratic principle 'to do good or to do no harm' should perhaps be considered and discussed openly both within multidisciplinary teams looking after patients who have (or may have) papillary thyroid cancers and the patients themselves. Rather than continuing to try to fine-tune diagnostic ultrasound criteria to diminish the overlap between benign and malignant features of thyroid nodules, a more pertinent research philosophy might be to focus on the small percentage of thyroid cancers that are aggressive and alter life spans. Apart from the patient-focused considerations above, conservative estimates of the economic cost of the thyroidectomies alone, for the potential pool of occult papillary cancer in the USA, exceeds 30 billion dollars.[64]

Incidental solitary nodule and fine-needle aspiration (FNA)

- Containing microcalcifications: strongly consider FNA if ≥1 cm.
- Solid (or almost entirely solid): strongly consider FNA if ≥1.5 cm.
- Coarse calcifications: strongly consider FNA if ≥1.5 cm.
- Mixed solid and cystic – consider FNA if ≥2 cm.
- Almost entirely cystic with a solid mural component: consider FNA if ≥2 cm.
- None of the above but 'substantial interval growth' (undefined): consider FNA.
- Almost entirely cystic and none of the above features: FNA probably unnecessary.

Multinodular thyroid

- Solid, unencapsulated nodules with well-defined margins; mostly isoechoic but 5% hypoechoic.
- Comet tail sign; colloid within a nodule, often adjacent to septa or peripheral.
- Early nodule formation predominantly in inferior and deep aspect of thyroid lobes.
- Cystic component very common; represents haemorrhage or colloid within the nodule. A haemorrhagic benign nodule is the commonest cause of a rapidly enlarging thyroid mass.
- Heterogeneous internal echogenicity; septa amongst mixed solid and cystic components.
- Calcification; coarse, curvilinear, peripheral or dysmorphic. Microcalcification rare.
- Vascularity; non-specific and variable.

Whilst the dilemmas above will undoubtedly provoke continuing debate and controversy, practical strategies to help us manage patients' thyroid nodules are still needed. Many algorithms and investigative strategies have been proposed.[65] Currently the best of these resulted from a multidisciplinary consensus meeting and combines a thorough literature review with 'expert opinion'. Whilst recognising the evidence in some areas is lacking, it makes management recommendations for thyroid nodules of 1 cm or larger maximum diameter, summarised according to ultrasound features demonstrated.[10]

The opinion for multiple nodules was divided but the majority of authors supported selection of FNA of one or more nodules based on the criteria above. All FNAs should unequivocally be ultrasound guided. The presence of any abnormal lymph nodes overrides the ultrasound features and should prompt FNA of the node/s and any ipsilateral thyroid nodule.

Fine-needle aspiration technique

There is unequivocal evidence that ultrasound-guided FNA is superior to clinician-obtained aspiration with guidance by palpation alone.[66,67] Techniques vary but the 'capillary technique' with no suction applied to the needle minimises the contamination of specimens by blood and produces excellent cytological samples.[68] This entails swift passage of the needle backwards and forwards within the thyroid nodule, whilst rotating the needle by its hub. The needles are designed to cleave through tissue, rather than cut and retain tissue. However, the rotation encourages clusters of cells or even tiny 'microcores' to enter the lumen, which are held there by capillary action and can be expelled either into cytology transport medium or spread onto microscope slides, dependent upon the local cytologist's preference.

A 21-gauge venepuncture needle usually provides an optimal combination of needle diameter and length for the majority of lesions. Contamination with blood can be an occasional problem with hypervascular thyroid lesions. The combination of a very swift passage within the nodule, with two or three 'rotating plunges' of the needle within the nodule over 2–3 seconds, using a 23-gauge needle, almost always facilitates a satisfactory specimen, minimising blood contamination. Smaller diameter needles can obtain satisfactory samples but have no practical advantage if the technique is optimal.

Diffuse parenchymal diseases and miscellany

Multinodular thyroid

Multiple nodules within the thyroid are often described as a 'multinodular goitre', but are extremely common within non-goitrous, normal sized glands; therefore the term 'multinodular thyroid' is more useful and appropriate. Differentiation between an adenomatous or hyperplastic nodule as recognised pathologically cannot be made on ultrasound – they represent part of the spectrum of benign thyroid nodules. It is the most common (80%) pathological condition presenting in the thyroid. Long-term follow-up of multinodular thyroid glands confirms that benign thyroid nodules remain benign for a long time:[69] 99.3% over a 10-year follow-up period.

The possibility of a thyroid carcinoma within a multinodular thyroid is one of the most difficult and contentious areas of thyroid ultrasound, with incidental cancers (predominantly papillary microcarcinoma) discovered at histological examination of otherwise benign multinodular goitres in 5–10% of cases. Although cancers were previously thought to be extremely uncommon in toxic goitres, recent evidence suggests that they are only slightly less prevalent than in non-toxic multinodular thyroid glands.[70] However, the prognosis of incidental cancer within this context is good; possible assessment strategies are discussed above.

Ultrasound features

The main features of multinodular goitres are listed above.

Thyroiditis

The description and classification of thyroiditis is very confusing in the literature.[71] This is perhaps because thyroiditis can be classified in various ways, with the same form of thyroiditis appearing under different names, descriptions or places within the classification system, depending on the method of subdivision. There are also manifestations of thyroiditis that form a spectrum, rather than specific separate entities, particularly those of an autoimmune aetiology.[72] Table 44.1 summarises the interrelated nomenclature, proposed aetiology, autoimmune association, presence of neck pain and expected radio-iodine uptake at nuclear medicine scanning. The majority of inflammatory thyroid disorders affect women much more commonly than men.

The functional presentation of thyroiditis can also cause confusion as most forms of thyroiditis can present with a patient who may be hyperthyroid, hypothyroid or euthyroid biochemically; this often depends upon the stage and activity of the disease process, which is not always evident at the time of ultrasound examination. It is also relatively unusual to have the autoimmune serology results available at the time of an initial ultrasound examination. Correlation with thyroid autoantibodies (anti-thyroid peroxidase, anti-thyroglobulin and anti-TSH receptor antibodies) is often invaluable and should be suggested if thyroiditis is suspected at ultrasound.

Conceptually, the acute inflammatory process of thyroiditis results in destruction of variable numbers of follicles, causing the

Table 44.1 Classification of thyroiditis

Histological classification	Synonyms	Eponyms	Aetiology	Neck pain	RAIU	Thyroid autoantibodies
Chronic lymphocytic	Chronic lymphocytic thyroiditis, goitrous chronic thyroiditis	Hashimoto's thyroiditis	Autoimmune (HLA-DR5)	No	Variable	Present
Subacute lymphocytic	(1) Postpartum thyroiditis (2) Sporadic painless thyroiditis		Autoimmune	No	Decreased	Present
Granulomatous	Subacute granulomatous thyroiditis	de Quervain's thyroiditis	Viral (HLA-Bw35) (drug induced)	Yes	Decreased	Absent
Microbial inflammatory	Acute suppurative thyroiditis Acute thyroiditis		Bacterial (left fourth branchial cleft anomaly)	Yes	Variable	Absent
Invasive fibrous	Chronic fibrotic	Riedel's struma, Riedel's thyroiditis	Probably primary fibrotic process	Varies	Variable	Variable

RAIU, radioactive iodine uptake at nuclear medicine scanning.

release of preformed thyroid hormone from them and thus the initial hyperthyroidism. After a variable time, as the stored thyroid hormone is depleted, the patient may pass through a transient euthyroid stage towards the hypothyroid stage of thyroiditis. The hypothyroidism may be temporary or permanent depending on the severity and underlying causative subtype of thyroiditis and the ability of the thyroid to synthesise thyroid hormone following the thyroiditis.

General ultrasound appearance of thyroiditis

Just as the acute inflammatory process of thyroiditis causes variability of thyroid function relative to the course of the inflammatory process, the ultrasound appearances are variable and alter during the thyroiditic process. In general, the inflammatory changes and oedema cause reduction in echogenicity, either in a focal, patchy or generalised distribution. If diffuse, the heterogeneous hypoechoic parenchyma is interspersed with echogenic fibrotic streaks. After the acute episode the thyroid may return to a normal appearance, remain enlarged, appear hypoechoic, appear nodular or atrophic, depending partly upon the underlying form of thyroiditis and also varying between individual patients.

Additional features of thyroiditides

Hashimoto's thyroiditis

This is the commonest chronic form of thyroiditis and cause of hypothyroidism in areas with adequate dietary iodine intake, being at least 10 times more common in women. It is strongly associated with other autoimmune conditions and predisposes to the development of thyroid lymphoma, which should be considered if there is any late growth or hypoechoic mass developing in the background of Hashimoto's.[73] FNA should be performed to confirm or exclude this diagnosis (Fig. 44.26).

In the acute situation, the thyroid is often affected heterogeneously and may show micronodularity (1–6 mm) representing areas of lymphocytic infiltration on histology. As Hashimoto's thyroiditis becomes more chronic, the thyroid is enlarged and more diffusely hypoechoic, typically with fibrous echogenic septa. Doppler shows diffuse hypervascularity within both the parenchyma and septa; this correlates with the onset of hypothyroidism. The end-stage gland appears atrophic and heterogeneous (Fig. 44.28).

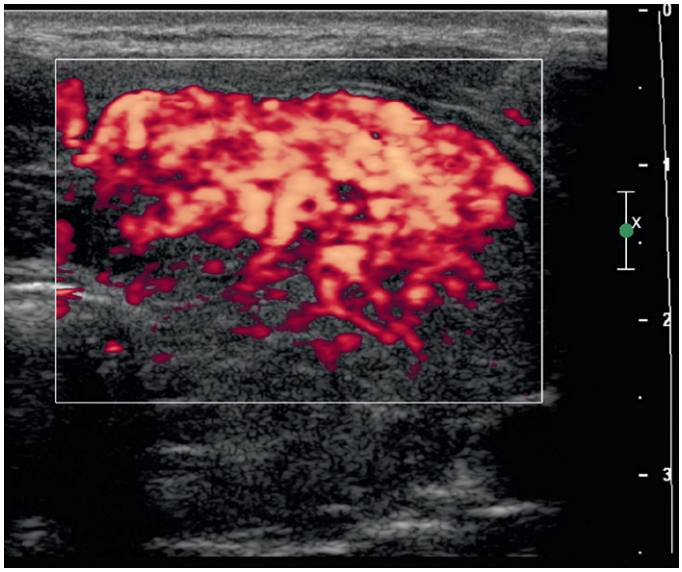

Figure 44.28 Transverse ultrasound showing Hashimoto's thyroiditis; the thyroid is diffusely enlarged and hypoechoic, with increased vascularity on this power Doppler image. This represents the early chronic stage of the disease, corresponding to the onset of hypothyroidism, but before the later thyroid atrophy.

Postpartum thyroiditis is common and presents in the first year following delivery; it can otherwise be considered to represent a variant of Hashimoto's thyroiditis.

De Quervain's subacute thyroiditis

The typical course of de Quervain's thyroiditis (also known as subacute granulomatous thyroiditis) is an acute, very painful thyroiditis following a viral illness, usually in patients with HLA-B35 antigen. This phase lasts approximately 1 month and it is usually associated with hyperthyroidism together with a transient, reactive

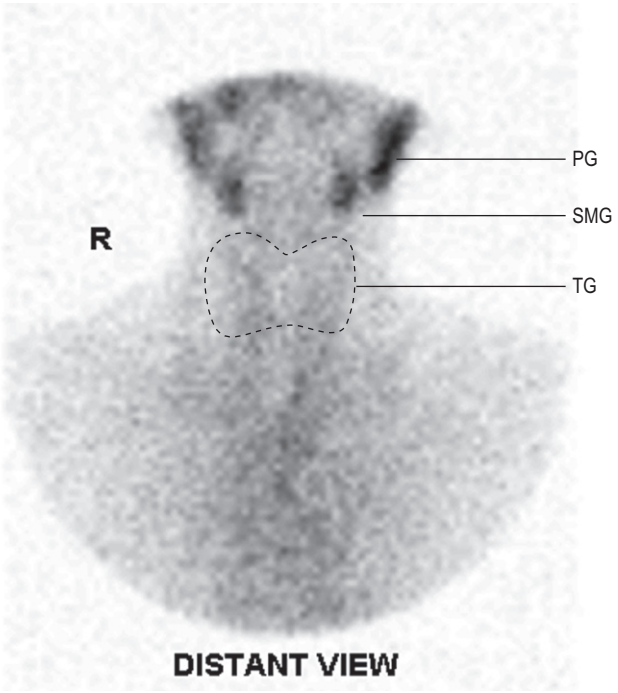

Figure 44.29 Technetium-99m pertechnetate thyroid scan showing de Quervain's thyroiditis. The normal thyroid uptake should be similar in intensity to the salivary glands (see Figure 44.33 inset), but is absent here, despite an enlarged, tender thyroid gland clinically. PG, left parotid salivary gland; SMG, left submandibular salivary gland; TG, anatomical location of thyroid gland.

rise in autoantibodies. The painful nodularity is initially subcapsular, ill-defined, hypoechoic and avascular on ultrasound (Fig. 44.29). Progression to a phase of hypothyroidism lasting 2–6 months precedes a return to euthyroid status, although a small minority of patients develop chronic hypothyroidism. The thyroid appears unilaterally or bilaterally hypoechoic in the subacute phase, when reactive local lymphadenopathy may be seen; it usually returns to a normal appearance in the longer term.

Acute suppurative thyroiditis

Involvement of the thyroid with an abscess is rare because of its thick fibrous capsule, vascularity and high iodine content. If the thyroid, or peri-thyroidal tissues, are involved with an abscess, the possibility of a fourth branchial cleft anomaly (persistent pyriform sinus–thyroid fistula) should be considered and actively excluded, otherwise recurrent future infections and inadequate surgery are likely.[74] The vast majority of these cleft anomalies are left-sided and present initially in childhood. Though rare, correct diagnosis and treatment of this entity presents an opportunity to improve dramatically the quality of future patient management. Further investigation with a gas-enhanced barium swallow or neck CT is needed to demonstrate the underlying fistula.

Riedel's thyroiditis

Riedel's thyroiditis is a rare, chronic inflammatory disease characterised by a dense fibrosis which replaces normal thyroid parenchyma. The fibrotic process invades adjacent neck structures and extends beyond the thyroid capsule; it may therefore present with hypoparathyroidism, hoarseness due to recurrent laryngeal involvement, or stridor. Differentiation from anaplastic carcinoma may be impossible on ultrasound.

PARATHYROID

Introduction

Almost invariably, the indication for imaging parathyroid glands is to localise one or more glands causing hyperparathyroidism and therefore hypercalcaemia. The necessity for preoperative localisation has been disputed. However, less invasive unilateral targeted surgery has increasingly displaced the older, traditional bilateral peri-thyroid exploration. Although time-consuming and associated with a greater incidence of complications, the more extensive exploration successfully located and removed the parathyroid in at least 90% of cases, in experienced hands. Any preoperative localisation facilitating a unilateral limited operation therefore needs a high accuracy to compete successfully.

The threshold for parathyroidectomy has also lowered during the past decade as the occult, deleterious effects of long-term hypercalcaemia on various body functions and organ systems have been increasingly recognised. The increased prevalence of routine biochemical screening for hypercalcaemia has also detected more asymptomatic hyperparathyroidism. Patients are therefore being referred earlier and many of these patients have much smaller parathyroid adenomas, which are therefore more difficult to visualise at ultrasound, despite improvements in ultrasound resolution and technology.

Embryology

As with the thyroid, an understanding of the embryological development of the parathyroid glands facilitates localisation of some of the normal anatomical variants affecting these glands.

The parathyroid glands, like the thyroid, develop from the pharyngeal endoderm, in this case the third and fourth pharyngeal pouches. Contrary to logical assumption, the inferior parathyroids develop from the dorsal aspect of the third (higher) pharyngeal pouch, with the thymus developing from its ventral aspect. They are thus also known as 'parathyroid IIIs'. The thymus migrates caudally and medially from the seventh gestational week, pulling these parathyroid IIIs with it. They then lose their connection with the thymus, usually stopping at the dorsal surface of the lower pole of the thyroid gland, outside its fibrous capsule.

The superior parathyroid glands ('parathyroid IVs') develop from the fourth pharyngeal pouch and detach from it in the seventh gestational week, attaching themselves to the thyroid as it migrates caudally. Their position is usually more constant and predictable than the inferior parathyroid glands, due to the shorter migration path. They usually lie on the dorsal surface of the thyroid, also outside its fibrous capsule but more posterior and medial than the inferior glands. It is relatively unusual for them to lie much more cephalad than the level of the thyroid isthmus.

Clinically relevant consequences of this embryology are detailed under the anatomical variations below and are relevant to both initial imaging and re-imaging of patients with recurrent hyperparathyroidism; particularly with respect to the relatively high incidence of ectopic and supernumerary glands.

Anatomy

Detailed histopathological postmortem dissection[75] demonstrates typical and less common sites for 'normal' parathyroid glands, which had a mean size of $5 \times 3 \times 1$ mm. These are not only of critical importance during surgical exploration but also for ultrasound localisation. A detailed understanding of the variety of possible anatomical sites for parathyroid glands is critical to facilitate optimal ultrasound evaluation (Fig. 44.30). Exact proportions vary between series, but typically are as listed below.

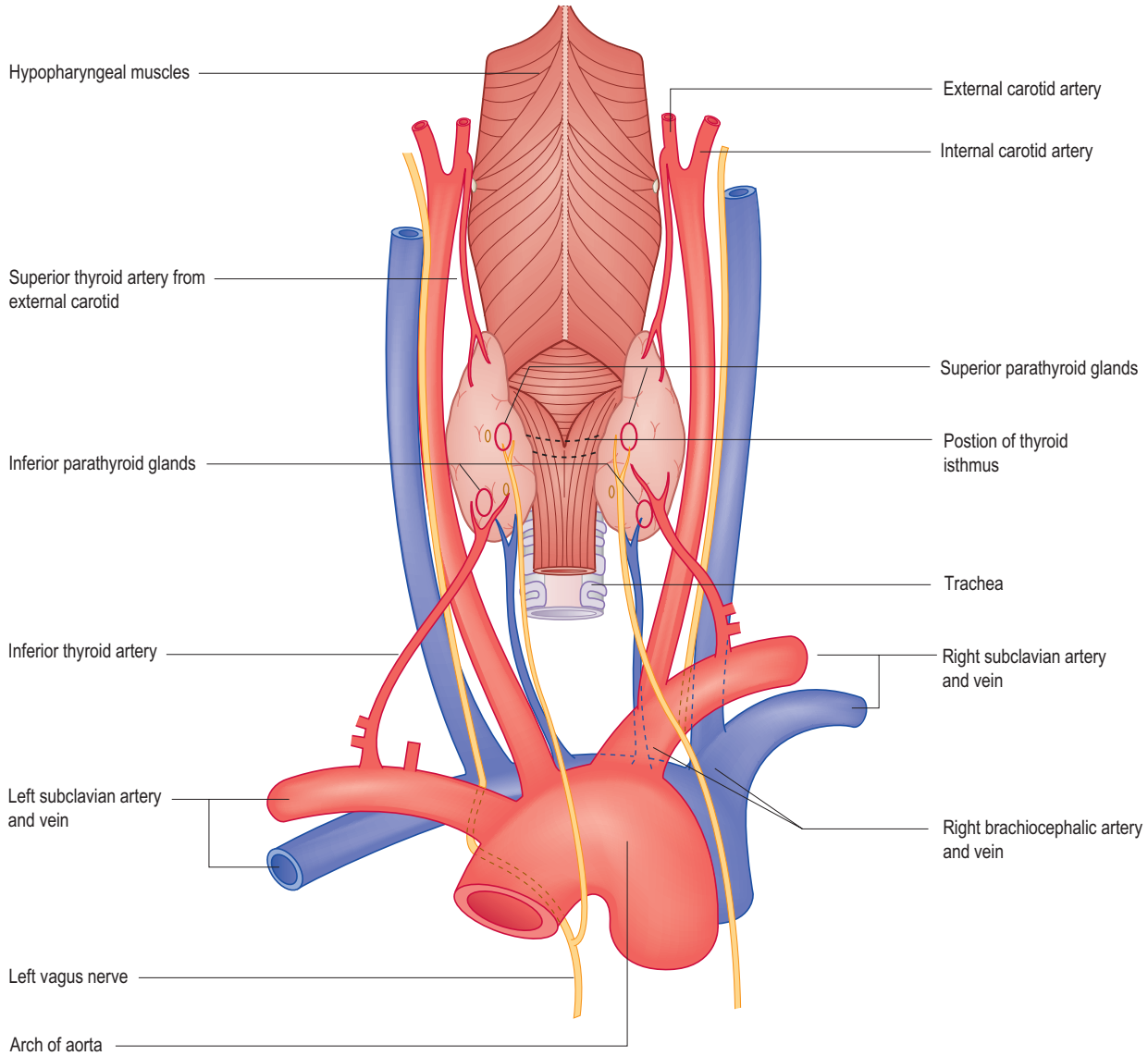

Figure 44.30 Posterior diagrammatic view of thyroid and parathyroid anatomy with adjacent vessels and nerves.

The superior parathyroid gland ('parathyroid IVs') locations:

- The cricothyroid junction (77%): intimately associated with the recurrent laryngeal nerve.
- The dorsum of the upper pole of the thyroid (22%): lying deep to the surgical capsule of the thyroid, thus remaining in this location when enlarged.
- Retropharyngeal/retroesophageal (1%): whilst rare, glands here represent a disproportionate number of 'difficult to find' parathyroid glands on imaging.

The locations of the more variable inferior parathyroids ('parathyroid IIIs'):

- At the lower pole of the thyroid (42%): either at the anterior or posterolateral surface of the lower pole of the thyroid.
- Within the 'thymic tongue' (39%): a distinct anatomical structure, extending from the lower thyroid pole to the mediastinal thymus.
- Juxtathyroidal (15%): a variable distance lateral to the lower pole of thyroid.
- 'Ectopic' (4%): within the mediastinal thymus (2%) typically 3–4 cm below sternal notch. Other rare sites include anywhere from the submandibular region, around the carotid sheath, even down to the level of the aorto-pulmonary window in the sub-thymic mediastinum.

Accessory or supernumerary parathyroid glands are found in 5–15% of individuals at autopsy. These are typically smaller than other normal glands with up to between 5 and 8 glands in total. It is presumed that these supernumerary glands result from tissue fragmentation during migration, thus they are more commonly found at parathyroid IIIs sites. This presumed aetiology is corroborated by their frequent histological association with a tiny fragment of thymic tissue.

On occasion there may be fewer than four glands (3–5% of autopsies). This may be the end result of several processes, including: failure of the primordia to differentiate into the parathyroid glands, or atrophy of one or more parathyroid glands early in development. Alternatively, failure to find one or more glands at autopsy, even when they are present, may be due to technical difficulties.

Rarely (1%), the parathyroid glands may lie in an intrathyroidal location, usually within the upper pole of the thyroid. This occurs when developing parathyroid IV tissue is trapped between the lateral and median thyroid components prior to their embryological fusion.

Parathyroid scanning techniques

The technique for scanning the parathyroid is similar to that employed for the thyroid but a knowledge of the anatomical and embryological factors described above, together with the normal variants, is critical, as parathyroid anatomy is so variable. Hyperextension of the patient's neck is essential for optimal parathyroid evaluation. Whilst high-frequency transducers also provide optimal assessment in slim patients, the routine use of a lower frequency (e.g. 5 MHz) is commended to assess deeper and lower areas of the neck, otherwise inferior gland lesions can be readily overlooked. Scanning whilst swallowing can also help to visualise low-lying inferior glands by elevating the thyroid and associated structures.

Normal parathyroid glands cannot be localised regularly with confidence at ultrasound. The majority of abnormal glands demonstrated will be hypoechoic and hypervascular on Doppler ultrasound. A polar feeding vessel is also a typical and useful observation; these are seen at the caudal part of the inferior parathyroid and cephalad part of the superior glands. Some 10–20% of parathyroid glands may be atypical in appearance; some being isoechoic to thyroid, others having variable degrees of cystic change. Calcification is relatively unusual; this is most frequently seen in carcinomas and hyperplasia due to secondary hyperparathyroidism.

Due to their location and appearance, parathyroid lesions may be readily confused with normal local anatomical structures including lymph nodes – particularly paratracheal nodes, the longus colli muscle, the oesophagus and blood vessels. Thyroid nodules can also cause confusion; indeed, patient obesity or multiple thyroid nodules are the most frequent cause of inability to delineate parathyroid lesions which would otherwise be visible at ultrasound.

As parathyroid ultrasound is usually performed as a preoperative localisation technique and surgeons often find static ultrasound images difficult to understand, meticulous reporting with reference to constant anatomical landmarks is critical. Two techniques can be of help here: storage of video clips in both transverse and longitudinal planes, showing sweeps of the adjacent normal anatomy, which can be reviewed subsequently with the surgeon. Alternatively, the patient can be re-examined with the surgeon present; immediately preoperatively. This contextualises the anatomy and is occasionally invaluable, particularly if surgical exploration has failed previously (Fig. 44.31).

The place of ultrasound and sestamibi nuclear medicine scans in the preoperative evaluation of hyperparathyroidism continues to cause controversy in the literature, but consensus gradually seems to be emerging both in the literature[76] and the author's experience that both examinations can prove invaluable to maximise both anatomical and physiological information to guide minimally invasive surgery with optimal accuracy. CT or MRI may be needed to help locate mediastinal or retrotracheal parathyroids.

Ultrasound features of parathyroid lesions

Features of parathyroid adenomas and parathyroid carcinomas on ultrasound include :

- Elliptical, low-echogenicity solid nodule; this can appear flattened when retrothyroid due to fascial planes but often appears more round if infrathyroid.
- Cystic components are relatively common, ranging from multiple small areas, to the rarer single large cyst (Fig. 44.32).
- Calcification is rare.
- 90% show an hypervascular, intraparenchymal, predominantly arterial pattern; apparently avascular adenomas on power Doppler tend to be deep and small; therefore this apparent lack of blood flow may be related to the Doppler sensitivity rather than true avascularity.
- Demonstration of dual and intrathyroid adenomas, whilst rare, will alter significantly the surgical procedure and chances of success.

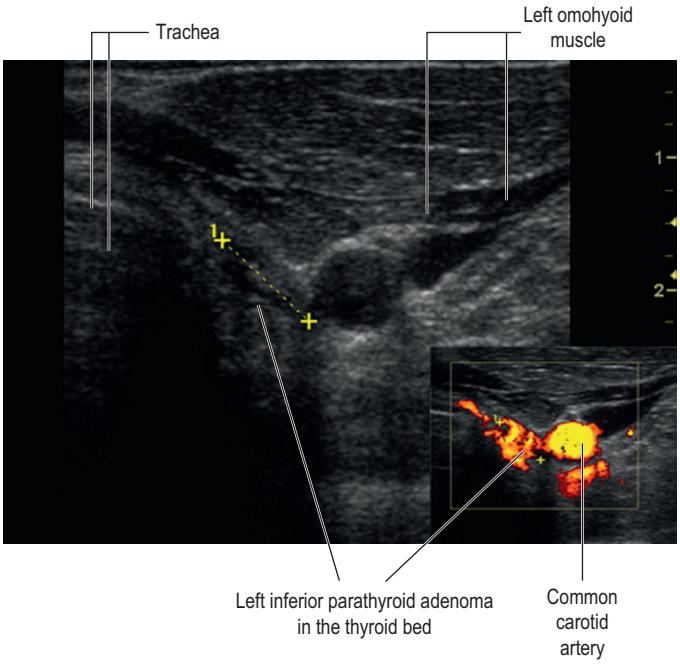

Figure 44.31 Transverse left thyroid bed ultrasound post hemithyroidectomy. Localisation of the parathyroid adenoma proved challenging (callipers) but was confirmed with the hypervascularity shown on the inset power Doppler image. The examination was performed immediately preoperatively with the surgeon present, facilitating successful resection.

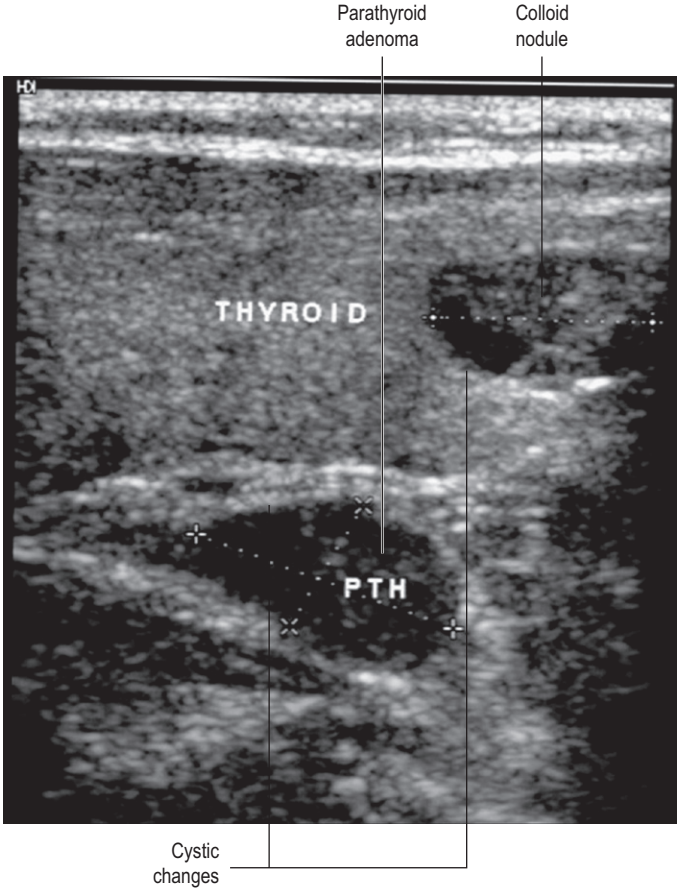

Figure 44.32 Longitudinal ultrasound showing both an inferior gland parathyroid adenoma and an adjacent benign colloid nodule in the lower pole of the thyroid. Both contain small areas of cystic change.

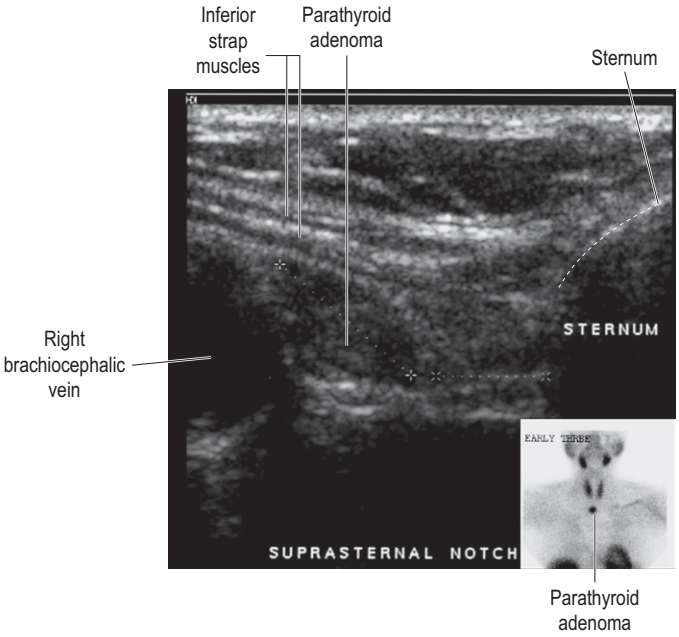

Figure 44.33 Longitudinal ultrasound showing an ectopic right inferior parathyroid adenoma, just above the suprasternal notch. Inset: comparative sestamibi scan showing normal salivary, thyroid and soft tissue uptake and the adenoma.

- Parathyroid carcinomas are a rare (1%) cause of hyperparathyroidism and cannot reliably be differentiated preoperatively. Occasionally they may be suspected due to local invasion or nodal metastases.

Secondary hyperparathyroidism is most commonly seen in patients with chronic renal failure on dialysis. Ultrasound can often demonstrate the multifocal involvement of the parathyroid glands more sensitively than sestamibi scans, helping to identify supernumerary or ectopic glands prior to surgical exploration (Fig. 44.33). Parathyroid calcification is more common in hyperplasia.

Parathyroid cysts are rare, but may be large. They are usually found within the lower cervical region (95% are located below the inferior border of thyroid), or in the superior mediastinum. They can mimic thyroid or thymic cysts.

Ethanol ablation of parathyroid lesions

The percutaneous ablation of parathyroid adenomas in patients who may have a high operative risk was first described over 20 years ago.[77] It is most frequently used in patients with secondary hyperparathyroidism.[78]

Detailed guidance has recently been developed[79] and factors to be considered include:

- The technique is suitable for ablating up to two enlarged glands, of at least 1 cm maximal length and 0.5 mL volume.
- Safe needle access with ultrasound guidance must be achievable.
- Considerable experience with ultrasound-guided needle placement is mandatory to minimise side effects.
- The most common complications are pain, haematoma and damage to the recurrent laryngeal nerve, which is often permanent. The contralateral recurrent laryngeal nerve should therefore be intact.
- Over-penetration of the parathyroid, suboptimal needle placement or over-injection of ethanol lead to extraglandular extravasation of alcohol and complications.
- The volume of alcohol injected is up to 80% of the calculated gland volume; this is injected during power or colour Doppler monitoring. Injection ceases when the volume limit is reached or intraglandular blood flow signals disappear.[80]
- Repeat injections may be needed.
- Even in experienced hands complication rates are significant; with the development of less invasive surgery, fewer alcohol ablations may be indicated.

ACKNOWLEDGEMENTS

Pathological images courtesy of Dr Ivan Robinson, Consultant Histopathologist, Derbyshire Royal Infirmary, Derby.

REFERENCES

1. Katz JF, Kane RA, Reyes J, et al. Thyroid nodules: sonographic–pathologic correlation. Radiology 1984;151:741–745.
2. Ahuja AT, Antonio GE, editors. Diagnostic and surgical imaging anatomy: ultrasound. Manitoba, Canada: Amirsys; 2007.
3. Braun EM, Windisch G, Wolf G, et al. The pyramidal lobe: clinical anatomy and its importance in thyroid surgery. Surg Radiol Anat 2007;29(1):21–27.
4. Blumberg NA. Observations on the pyramidal lobe of the thyroid gland. S Afr Med J 1981;59(26):949–950.
5. Carroll BA. Asymptomatic thyroid nodules: incidental sonographic detection. AJR Am J Roentgenol 1982;138:499–501.
6. Wiest PW, Hartshorne MF, Inskip PD, et al. Thyroid palpation versus high-resolution thyroid ultrasonography in the detection of nodules. J Ultrasound Med 1998;17:487–496.
7. Brander A, Viikinkoski P, Nickels J, Kivisaari L. Thyroid gland: US screening in a random adult population. Radiology 1991;181:683–687.
8. Bruneton JN, Balu-Maestro C, Marcy PY, et al. Very high frequency (13 MHz) ultrasonographic examination of the normal neck: detection of normal lymph nodes and thyroid nodules. J Ultrasound Med 1994;13:87–90.
9. Hoang JK, Lee WK, Lee M, et al. Sonographic features of thyroid malignancy: pearls and pitfalls. Radiographics 2007;27:847–865.
10. Frates MC, Benson CB, Charboneau JW, et al. Management of thyroid nodules detected at US: Society of Radiologists in US consensus conference statement. Radiology 2005;237:794–800.
11. Papini E, Guglielmi R, Bianchini A, et al. Risk of malignancy in nonpalpable thyroid nodules: predictive value of ultrasound and color-Doppler features. J Clin Endocrinol Metab 2002;87:1941–1946.
12. Pellegriti G, Scollo C, Lumera G, et al. Clinical behavior and outcome of papillary thyroid cancers smaller than 1.5 cm in diameter: study of 299 cases. J Clin Endocrinol Metab 2004;89(8):3713–3720.
13. Jun P, Chow LC, Jeffrey RB. The sonographic features of papillary thyroid carcinomas: pictorial essay. Ultrasound Q 2005;21:39–45.
14. Frates MC, Benson CB, Doubilet PM, et al. Prevalence and distribution of carcinoma in patients with solitary and multiple thyroid nodules on sonography. J Clin Endocrinol Metab 2006;91:3411–3417.
15. Dineen R, Robinson I, Cozens N. Sonographic features of cystic papillary carcinoma of the thyroid. Ultrasound 2005;13:186–191.
16. Ahuja AT, Chang AR, To E, et al. Intrathyroidal lymphoepithelial (branchial) cyst: sonographic features of a rare lesion. AJNR Am J Neuroradiol 2000;21:1340–1343.
17. Lee H-J, Kim E-K, Hong S. Sonographic detection of intrathyroidal branchial cleft cyst: a case report. Korean J Radiol 2006;7:149–151.
18. Moon W-J, Jung SL, Lee JH, et al. Benign and malignant thyroid nodules: US differentiation – multicenter retrospective study. Radiology 2008;247:762–770.
19. Papini E, Guglielmi R, Bianchini A, et al. Risk of malignancy in nonpalpable thyroid nodules: predictive value of ultrasound and color-Doppler features. J Clin Endocrinol Metab 2002;87(5): 1941–1946.
20. Kim EK, Park CS, Chung WY, et al. New sonographic criteria for recommending fine-needle aspiration biopsy of nonpalpable solid nodules of the thyroid. AJR Am J Roentgenol 2002;178:687–691.

21. Kim MJ, Kim E-K, Kwak JY, et al. Differentiation of thyroid nodules with macrocalcifications: role of suspicious sonographic findings. J Ultrasound Med 2008:27:1179–1184.
22. Triggiani V, Guastamacchia E, Licchelli B, Tafaro E. Microcalcifications and psammoma bodies in thyroid tumors. Thyroid 2008;18: 1017–1018.
23. Yoon DY, Lee JW, Chang SK, et al. Peripheral calcification in thyroid nodules: ultrasonographic features and prediction of malignancy. J Ultrasound Med 2007;26:1349–1355.
24. Propper RA, Skolnick ML, Weinstein BJ, Dekker A. The nonspecificity of the thyroid halo sign. J Clin Ultrasound 1980;8:129–132.
25. Kim BM, Kim MJ, Kim E-K, et al. Sonographic differentiation of thyroid nodules with eggshell calcifications. J Ultrasound Med 2008;27:1425–1430.
26. Stavros AT, Thickman D, Rapp CL, et al. Solid breast nodules: use of sonography to distinguish between benign and malignant lesions. Radiology 1995;196:123–134.
27. Cappelli C, Castellano M, Pirola I, et al. Thyroid nodule shape suggests malignancy. Eur J Endocrinol 2006;155: 27–31.
28. Ahuja A, Chick W, King W, Metreweli C. Clinical significance of the comet-tail artefact in thyroid ultrasound. J Clin Ultrasound 1996; 24:129–133.
29. Frates MC, Benson CB, Doubilet PM, et al. Can color Doppler sonography aid in the prediction of malignancy of thyroid nodules? J Ultrasound Med 2003;22:127–131.
30. Rago T, Santini F, Scutari M, et al. Elastography: new developments in ultrasound for predicting malignancy in thyroid nodules. J Clin Endocrinol Metab 2007:92:2917–2922.
31. Lyshchik A, Higashi T, Asato R, et al. Thyroid gland tumor diagnosis at US elastography. Radiology 2005:237:202–211.
32. Alexander EK, Hurwitz S, Heering JP, et al. Natural history of benign solid and cystic thyroid nodules. Ann Intern Med 2003;138(4):315–318.
33. Carcangiu ML, Zampi G, Pupi A, et al. Papillary carcinoma of the thyroid, a clinicopathologic study of 241 cases treated at the University of Florence, Italy. Cancer 1985;55:805–828.
34. Noguchi M, Kinami S, Kinoshita K, et al. Risk of bilateral cervical lymph node metastases in papillary thyroid cancer. J Surg Oncol 1993;52:155–159.
35. Frankenthaler RA, Sellin RV, Cangir A, et al. Lymph node metastasis from papillary-follicular carcinoma in young patients. Am J Surg 1990;160:341–343.
36. Lin JD, Liou MJ, Chao TC, et al. Prognostic variables of papillary and follicular thyroid carcinoma patients with lymph node metastases and without distant metastases. Endocrine-Related Cancer 1999;6:109–115.
37. VanderLaan W. The occurrence of carcinoma of the thyroid gland in autopsy material. N Engl J Med 1947;237:221–222.
38. Harach HR, Franssila KO, Wasenius VM. Occult papillary carcinoma of the thyroid: a 'normal' finding in Finland. Cancer 1985;56:531–538.
39. Roti E, Rossi R, Trasforini G, et al. Clinical and histological characteristics of papillary thyroid microcarcinoma: results of a retrospective study in 243 patients. J Clin Endocrinol Metab 2006;91:2171–2178.
40. Davies L, Welch HG. Increasing incidence of thyroid cancer in the United States, 1973–2002. JAMA 2006;295:2164–2167.
41. Etzioni R, Penson DF, Legler JM, et al. Overdiagnosis due to prostate-specific antigen screening. J Natl Cancer Inst 2002;94: 981–990.
42. Chan BK, Desser TS, McDougall IR, et al. Common and uncommon sonographic features of papillary thyroid carcinoma. J Ultrasound Med 2003;22(10):1083–1090.
43. Wunderbaldinger P, Harisinghani MG, Hahn PF, et al. Cystic lymph node metastases in papillary thyroid carcinoma. AJR Am J Roentgenol 2002;178:693–697.
44. Ahuja AT, Chow L, Chick W, et al. Metastatic cervical nodes in papillary carcinoma of the thyroid: ultrasound and histological correlation. Clin Radiol 1995;50:229–231.
45. Shin JH, Han B-K, Ko EY, Kang SS. Sonographic findings in the surgical bed after thyroidectomy: comparison of recurrent tumors and nonrecurrent lesions. J Ultrasound Med 2007;26:1359–1366.
46. Yoon JH, Kim E-K, Hong SW, et al. Sonographic features of the follicular variant of papillary thyroid carcinoma. J Ultrasound Med 2008;27:1431–1437.
47. Lee JY, Shin JH, Han BK, et al. Diffuse sclerosing variant of papillary carcinoma of the thyroid: imaging and cytologic findings. Thyroid 2007;17(6):567–573.
48. Kwak JY, Kim EK, Son EJ, et al. Papillary thyroid carcinoma manifested solely as microcalcifications on sonography. AJR Am J Roentgenol 2007;189(1):227–231.
49. Williams ED, Doniach I, Bjarnason O, Michie W. Thyroid cancer in an iodide rich area: a histopathological study. Cancer 1977;39(1): 215–222.
50. Maizlin ZV, Wiseman SM, Vora P, et al. Hürthle cell neoplasms of the thyroid sonographic appearance and histologic characteristics. J Ultrasound Med 2008;27:751–757.
51. Pfister DG, Fagin JA. Refractory Thyroid cancer: a paradigm shift in treatment is not far off (editorial). J Clin Oncol 2008;26:4701–4704.
52. Takashima S, Morimoto S, Ikezoe J, et al. CT evaluation of anaplastic thyroid carcinoma. AJR Am J Roentgenol 1990;154:1079–1085.
53. Ishikawa H, Tamaki Y, Takahashi M, et al. Comparison of primary thyroid lymphoma with anaplastic thyroid carcinoma on computed tomographic imaging. Radiat Med 2002;20(1):9–15.
54. Takashima S, Morimoto S, Ikezoe J, et al. Primary thyroid lymphoma: comparison of CT and US assessment. Radiology 1989;171:439–443.
55. Topliss D. Thyroid incidentaloma: the ignorant in pursuit of the impalpable. Clin Endocrinol (Oxf) 2004;60:18–20.
56. Ross DS. Nonpalpable thyroid nodules: managing an epidemic [editorial]. J Clin Endocrinol Metab 2002;87:1938–1940.
57. Kang HW, No JH, Chung JH, et al. Prevalence clinical and ultrasonographic characteristics of thyroid incidentalomas. Thyroid 2004;14:29–33.
58. Tan GH, Gharib H. Thyroid incidentalomas: management approaches to nonpalpable nodules discovered incidentally on thyroid imaging. Ann Intern Med 1997;126:226–231.
59. Mancuso AA. Oh #*$%#! Another pesky incidental thyroid nodule! AJNR Am J Neuroradiol 2005;26:2444–2445.
60. Kwak JY, Kim E-K, Yun M, et al. Thyroid incidentalomas identified by ^{18}F-FDG PET: sonographic correlation. AJR Am J Roentgenol 2008;191:598–603.
61. Howlett DC, Speirs A. The thyroid incidentaloma: ignore or investigate? J Ultrasound Med 2007;26:1367–1371.
62. Moon W-J, Jung SL, Lee JH, et al. Benign and malignant thyroid nodules: US differentiation – multicenter retrospective study. Radiology 2008;247(3):762–770.
63. Raymond J, Long H. Thyroid nodules and other incidentalomas: we must search for evidence and clarify our ethical priorities. AJNR Am J Neuroradiol 2006;27:1163–1164.
64. Cronan JJ. Thyroid nodules: is it time to turn off the US machines? Radiology 2008;247:602–604.
65. Cooper DS, Doherty GM, Haugen BR, et al. Management guidelines for patients with thyroid nodules and differentiated thyroid cancer. Thyroid 2006;16:109–142.
66. Danese D, Sciacchitano S, Farsetti A, et al. Diagnostic accuracy of conventional versus sonography-guided fine-needle aspiration biopsy of thyroid nodules. Thyroid 1998;8(1):15–21.
67. Gharib H, Goellner JR. Fine-needle aspiration biopsy of the thyroid: an appraisal. Ann Intern Med 1993;118:282–289.
68. Cozens NJA, Berman L. Fine needle aspiration or core biopsy? In: Ahuja AT, Evans RM, editors. Practical head and neck ultrasound. London: GMM Publisher; 2000. p. 131–147.
69. Kuma K, Matsuzuka F, Yokozawa T, et al. Fate of untreated benign thyroid nodules: results of long-term follow-up. World J Surg 1994;18:495–498.
70. Cerci C, Cerci SS, Eroglu E, et al. Thyroid cancer in toxic and non-toxic multinodular goiter. J Postgrad Med 2007;53:157–160.
71. Schubert MF, Kountz DS. Thyroiditis: a disease with many faces. Postgrad Med 1995;98:101–112.
72. Slatosky J, Shipton B, Wahba H. Thyroiditis: differential diagnosis and management. Am Fam Physician 2000;61:1047–1052, 1054.
73. Takashima S, Matsuzuka F, Nagareda T, et al. Thyroid nodules associated with Hashimoto thyroiditis: assessment with ultrasound. Radiology 1992;185:125–130.
74. Cases JA, Wenig BM, Silver CE, Surks MI. Clinical case seminar. Recurrent acute suppurative thyroiditis in an adult due to a fourth branchial pouch fistula. J Clin Endocrinol Metab 2000;85:953–956.
75. Wang C. The anatomic basis of parathyroid surgery. Ann Surg 1976;183(3):271–275.
76. Johnson NA, Tublin ME, Ogilvie JB. Parathyroid imaging: technique and role in the preoperative evaluation of primary hyperparathyroidism. AJR Am J Roentgenol 2007;188:1706–1715.
77. Solbiati L, Giangrande A, Pra LD, et al. Ultrasound-guided percutaneous fine-needle ethanol injection into parathyroid glands in secondary hyperparathyroidism. Radiology 1985;155:607–610.

78. Giangrande A, Castiglioni A, Solbiati L, Allaria P. Ultrasound guided percutaneous fine needle ethanol injection into parathyroid glands in secondary hyperparathyroidism. Nephrol Dial Transplant 1992;7:412–421.
79. Fukagawa M, Kitaoka M, Tominaga Y, et al. for the Japanese Society for Parathyroid Intervention. Guidelines for percutaneous ethanol injection therapy of the parathyroid glands in chronic dialysis patients. Nephrol Dial Transplant 2003;18(Suppl 3):iii31–iii33.
80. Kakuta T, Fukagawa M, Fujisaki T, et al. Prognosis of parathyroid function after successful percutaneous ethanol injection therapy (PEIT) guided by color Doppler flow mapping in chronic dialysis patients. Am J Kidney Dis 1999;33:1091–1099.

CHAPTER

45

Ultrasound of the neck

Rhian Rhys

Ultrasound is ideally suited for the first-line investigation of neck lumps. Clinical palpation is often non-specific and high-frequency probes give superb anatomical detail of the superficial structures of the neck. The other great advantage of ultrasound is that it is easily combined with ultrasound-guided biopsy – fine-needle aspiration (FNA) or core biopsy.

The anatomy of the neck is complex; however, a sound knowledge of normal anatomy is essential to performing ultrasound of the neck. Many neck lumps are site-specific and an awareness of the regional anatomy greatly simplifies the differential diagnosis.

High-frequency, linear probes are employed, typically 7.5–17 MHz, depending on the size of the patient's neck. A 9 MHz probe would be suitable for most adult necks, a 12 MHz probe for a child's neck or the submandibular region in a slim adult, whereas a 5 MHz probe might be required for deeper structures in a large neck such as the deep lobe of the parotid gland.

The best position for the examination is with the patient's neck extended over a pillow, with the chin in the midline (Fig. 45.1); the patient may be either supine or semi-reclined, whichever is more comfortable.

The operator's position is also important – the patient's neck should be at the same level as the operator's scanning forearm, with the shoulder abducted no more than 30° (Fig. 45.1).[1] The screen should be at eye level, with the screen and patient in an easy arc.

It is helpful to have a routine technique for scanning the neck comprehensively. This should take no longer than 10 minutes in experienced hands. A simple method for examining the neck in a series of seven sweeps is described (Fig. 45.2), which may be adapted to suit individual situations such as a restless child.

The neck is traditionally divided into anterior and posterior triangles by the sternomastoid muscle and further subdivided by the digastric and omohyoid muscles (Fig. 45.3). It is useful to be familiar with these common anatomical boundaries and the relevant anatomical areas. The 'spaces' concept, described by Harnsberger, is a very useful radiological approach to the soft tissues of the neck.[2,3]

Scanning begins in the midline submental position, and then each side of the neck is scanned in turn, ending the examination in the midline, with a sweep of the anterior neck.

1. SUBMENTAL REGION

Normal ultrasound anatomy and technique

The neck is scanned with a sweep of the transducer from the tip of the chin to the hyoid bone.

The key structure in this region is the sling-like mylohyoid muscle, attached to the hyoid in the midline and to the mandible laterally. It has a broad, free posterior border, around which wraps the submandibular gland.

The mylohyoid muscle defines the floor of mouth, separating the sublingual from the submental space (Fig. 45.4). Lesions deep to mylohyoid lie in the sublingual space, whilst a lesion superficial to

mylohyoid lies either in the submental space (midline, between the anterior bellies of digastric) or in the submandibular space (lateral to the anterior belly of digastric). This distinction is crucial to the surgical approach to these lesions – sublingual lesions are removed via an intraoral approach, whilst submental or submandibular lesions are removed via an external cervical approach. The sublingual and submandibular spaces communicate freely around the back of mylohyoid and also with the parapharyngeal space, which may be relevant when considering the possible spread of infection or malignancy.

The submental sweep starts at the point of the chin. The paired anterior bellies of the digastric muscles lie superficially in the midline. Deep to digastric, the mylohyoid muscle appears as a thin, horseshoe-shaped hypoechoic band, extending from side to side (Fig. 45.5).

The orifice of the submandibular duct in the floor of the mouth is approximately 1.5 cm deep to the anterior bellies of the digastric muscles. The duct is easily seen if there is ostial obstruction but it may also be seen in normal individuals. The lingual artery is immediately medial to the submandibular duct in the anterior floor of mouth (Fig. 45.6).

The hyoglossus muscle lies deep to and parallel to mylohyoid (Fig. 45.7) and lateral to the sublingual gland. The submandibular duct runs between hyoglossus and mylohyoid (Fig. 45.4).[4] The sublingual gland, lingual vein, and lingual and hypoglossal nerves also

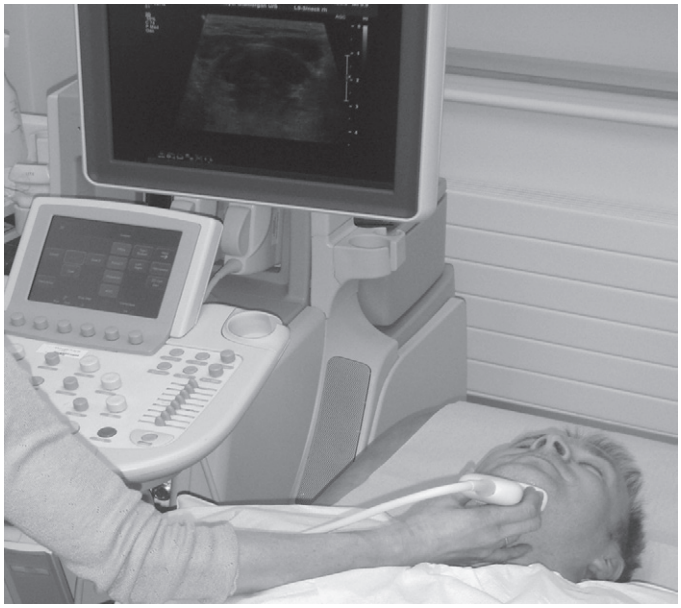

Figure 45.1 Patient position. Photograph demonstrating an ideal scanning position.

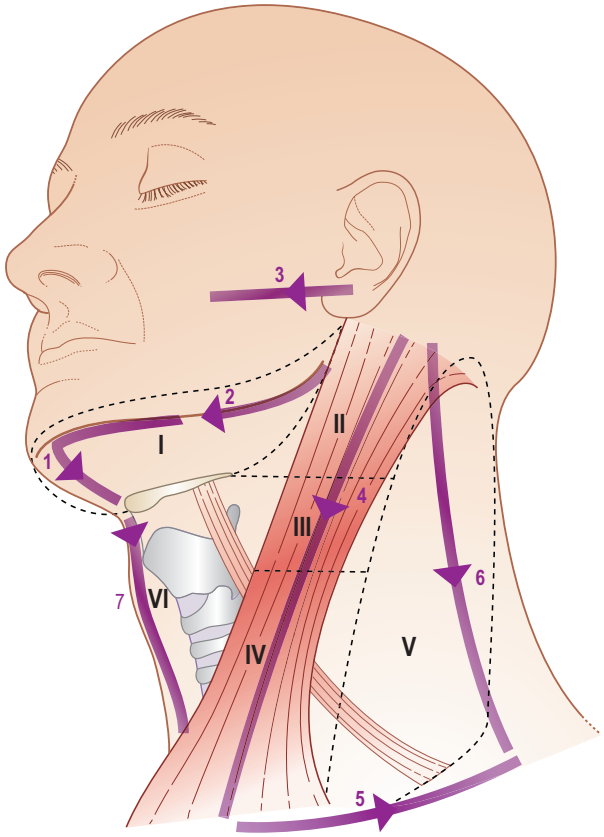

Figure 45.3 Ultrasound of the neck in seven sweeps. 1, Submental. 2, Submandibular. 3, Parotid and buccal. 4, Deep cervical chain. 5, Transverse cervical. 6, Posterior triangle. 7, Anterior cervical. (modified from Greene FL, Compton CC, Fritz AG, et al., eds. AJCC Cancer Staging Atlas. 6 edn. New York: Springer; 2006).

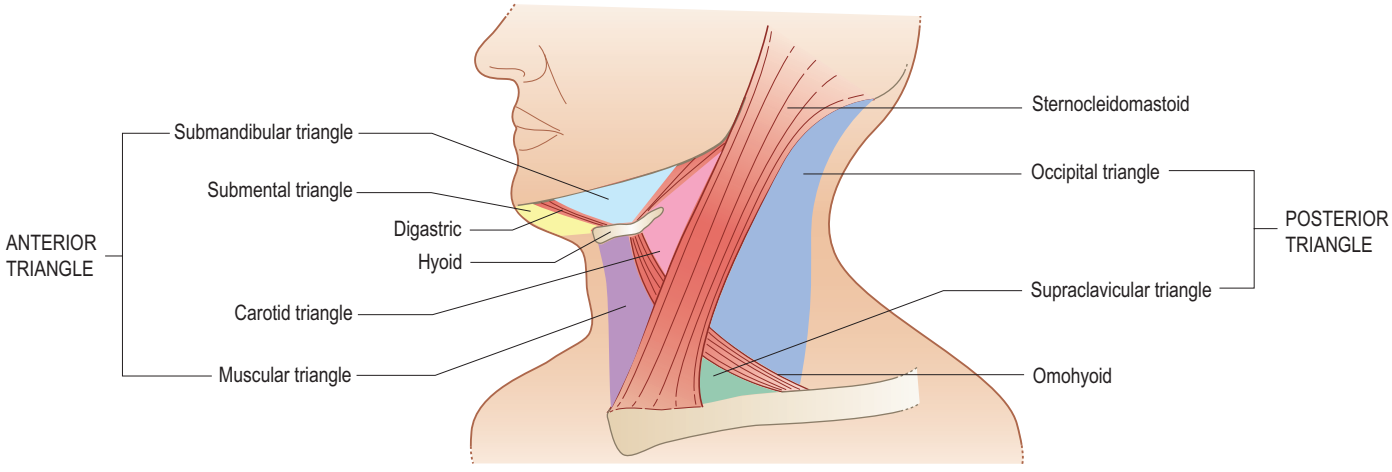

Figure 45.2 Diagram of the triangles of the neck. The standard divisions of the anatomy of the neck into anterior and posterior triangles.

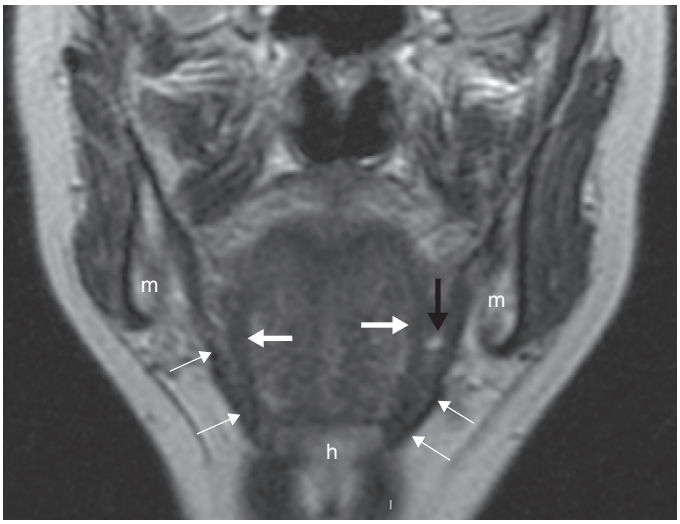

Figure 45.4 Anatomy of the floor of the mouth. Coronal T2-weighted MRI of the floor of the mouth. The sling-like mylohyoid muscle (thin arrows) separates the sublingual and submental spaces. The submandibular duct (black arrow) lies between hyoglossus (thick arrows) and mylohyoid. m, mandible; h, hyoid.

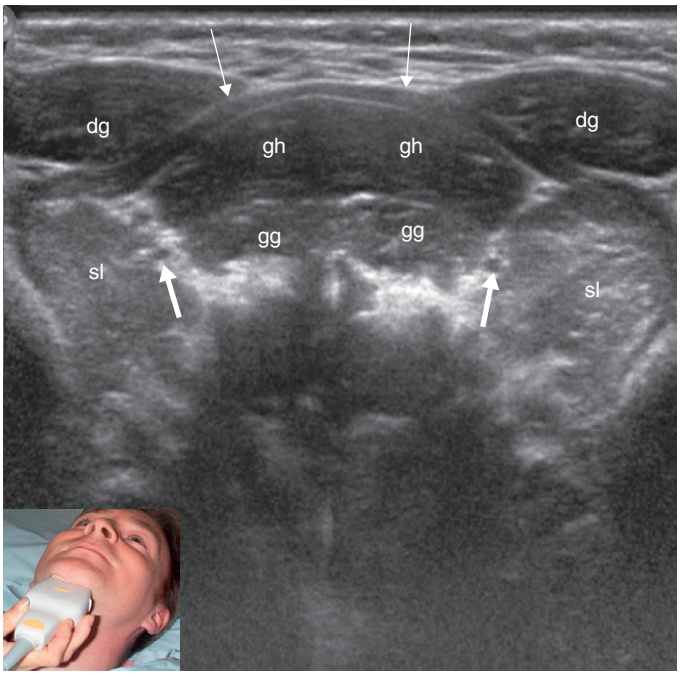

Figure 45.5 Mylohyoid muscle. Transverse submental sonogram demonstrating the mylohyoid muscle (thin arrows). The submental space lies between the anterior bellies of digastric (dg). The sublingual glands (sl) lie in the sublingual space. Thick arrows indicate lingual artery; gh, geniohyoid muscle; gg, genioglossus muscle.

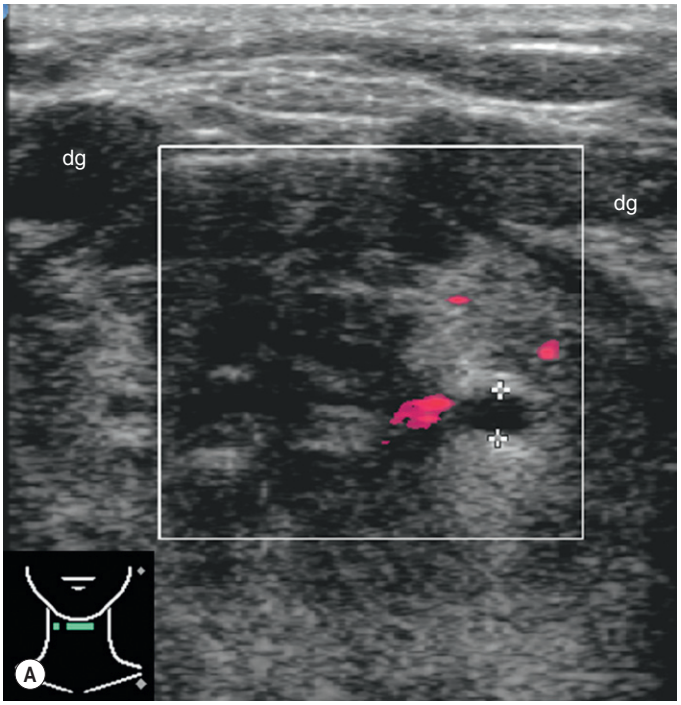

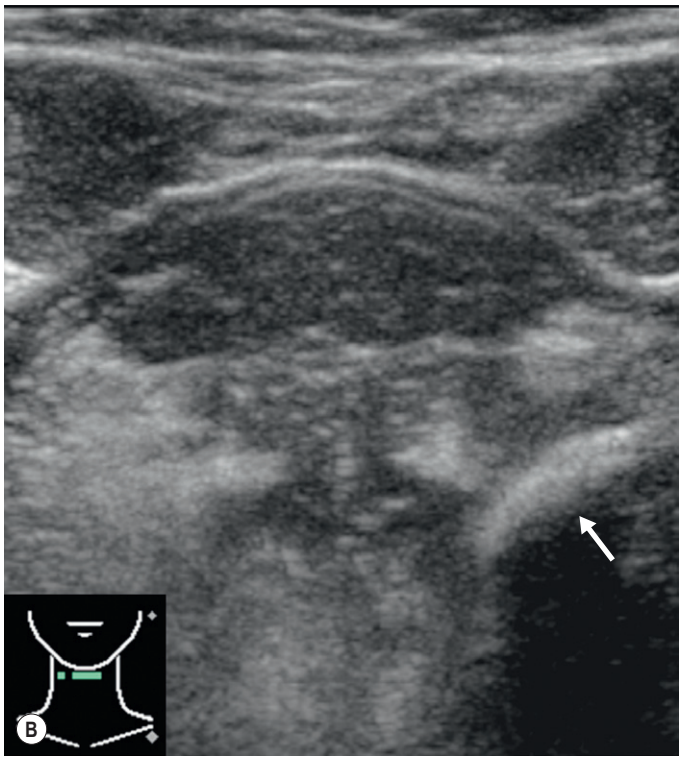

Figure 45.6 Submandibular duct. A: Transverse submental sonogram demonstrating the position of the submandibular duct (callipers), approximately 1.5 cm deep to the anterior belly of digastric (dg), adjacent to the lingual artery. **B:** Dense acoustic shadowing from a calculus in the submandibular duct (arrow).

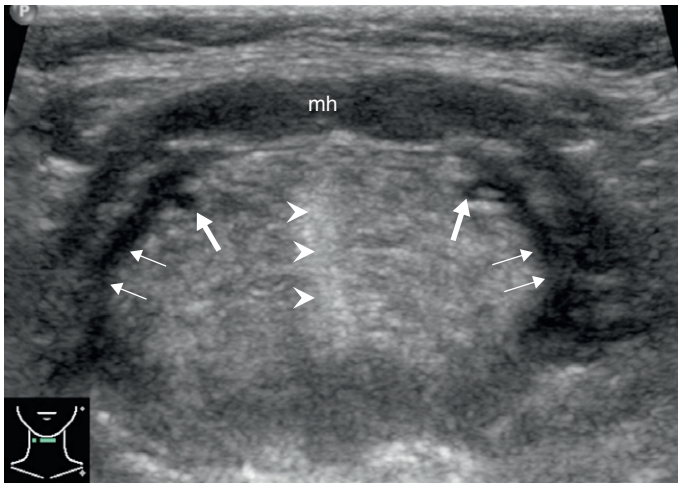

Figure 45.7 Floor of the mouth and tongue. Transverse submental sonogram, at a slightly lower level than in Figure 45.6, demonstrating the transversely orientated fibres of genioglossus, uniting at the midline raphe (arrowheads). Thin arrows indicate hyoglossus. Thick arrows, submandibular duct; mh, mylohyoid.

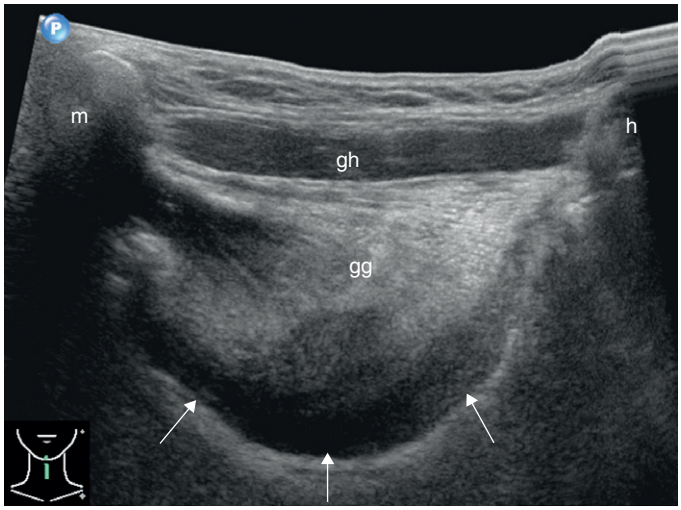

Figure 45.8 Tongue. Longitudinal panoramic sonogram of the submental region, demonstrating the dorsal surface of the tongue (arrows). gg, genioglossus; gh, geniohyoid; m, mandible; h, hyoid.

run in this space; the nerves are not resolved with ultrasound. The sublingual glands are almond-shaped, uniformly echogenic structures (Fig. 45.5), which open directly into the floor of the mouth by a series of small ducts.

The strap-like geniohyoid muscles lie in the midline; scanning more inferiorly, the transversely orientated fibres of genioglossus will be seen, uniting at the midline raphe – identified as an echogenic linear structure (Fig. 45.7). This raphe is an important landmark in staging tongue tumours; a tumour that crosses the midline will require a total glossectomy.

The sweep finishes at the hyoid bone, a horseshoe-shaped structure causing a band of focal acoustic shadowing (see Fig. 45.11). Once the hyoid bone has been identified, the submental area is then scanned longitudinally from the point of the chin to the hyoid – the fan-shaped genioglossus muscle and the mucosal surface of the dorsum of the tongue are demonstrated (Fig. 45.8). This view may be helpful in assessing the depth of tongue tumours, which is important for staging and often difficult to assess clinically.

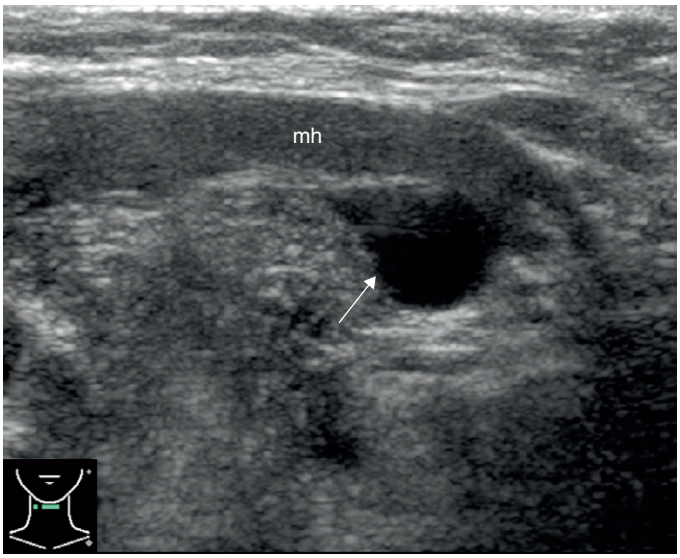

Figure 45.9 Ranula. Transverse submental sonogram, demonstrating a thin-walled anechoic ranula (arrow). mh, mylohyoid.

Pathology in the submental/sublingual region

Thyroglossal duct cyst

This is the most common midline neck mass. Fifteen per cent of thyroglossal duct cysts (TDC) occur at the level of the hyoid bone and 20% are suprahyoid – these hyoid and suprahyoid thyroglossal duct cysts are important in the differential diagnosis of a mass in the submental region. Thyroglossal duct cysts are discussed in detail later, in the section on the anterior neck.

Ranula

A **simple ranula** is a mucous retention cyst of the sublingual gland, resulting from obstruction of the duct. It is a true cyst with an epithelial lining. A ranula presents as a painless, cystic, bluish swelling in the floor of the mouth. On ultrasound, it is a well-defined, unilocular, anechoic cystic structure, situated off the midline in the sublingual space, deep to mylohyoid and related to the sublingual gland (Fig. 45.9). A ranula often splays the mylohyoid and genioglossus muscles. Its contents may become echogenic with increasing protein content or infection.

A **diving or plunging ranula** occurs when a simple ranula ruptures, forming a pseudocyst, with extravasation of saliva into the tissues of the floor of mouth. A diving ranula may present as a cervical mass, in either the submental or submandibular space, entering the neck around the posterior border of mylohyoid or via a defect in the mylohyoid muscle. A mylohyoid muscle defect has been noted in up to 77% of individuals (see Fig. 45.21).[5]

Dermoid and epidermoid cysts

Dermoid and epidermoid cysts result from sequestration of embryological ectodermal tissue. Seven percent of all epidermoid and dermoid cysts occur in the head and neck, with the lateral eyebrow being the most common location, followed by the floor of mouth.

Epidermoid cysts contain keratin and cholesterol, which derive from desquamation of the squamous epithelial lining. They contain no skin appendages.

Dermoid cysts contain skin appendages – teeth, hair and sebaceous glands. The sebaceous gland content is responsible for the fatty element.

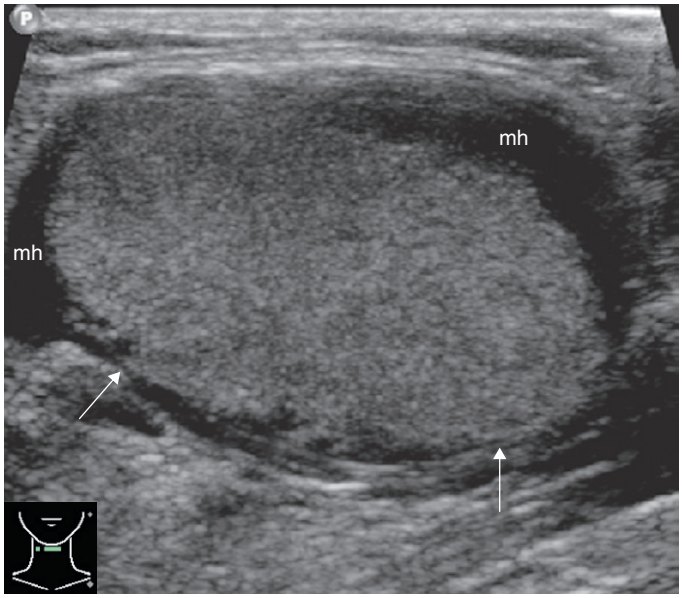

Figure 45.10 Epidermoid cyst. Transverse submental sonogram, demonstrating a midline epidermoid cyst (arrows) in the sublingual region. The cyst has a 'pseudosolid' appearance, and was avascular. mh, mylohyoid.

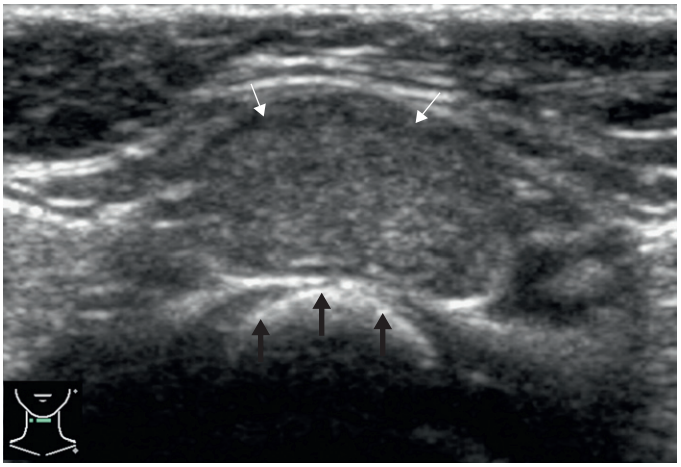

Figure 45.11 Ectopic thyroid tissue. Transverse submental sonogram demonstrating ectopic thyroid tissue (white arrows) at the level of the hyoid (black arrows). The lesion has similar appearances to the epidermoid cyst in Figure 45.10, but was vascular.

Typically, these cysts present as a midline suprahyoid mass. They are soft and often demonstrate 'retained pitting'. They are unattached to skin, and unlike thyroglossal duct cysts, are not intimately related to the hyoid, therefore do not move with tongue protrusion.

Although they are cysts, the ultrasound appearances of dermoid and epidermoid cysts are of well-defined pseudosolid lesions, containing homogeneous fine internal echoes, which vary depending on the amount of keratin (Fig. 45.10). Dermoids may have a more heterogeneous appearance; focal hyperechoic globules of fat may be seen, which correspond to the 'sack of marbles' appearance seen on computed tomography (CT) or magnetic resonance imaging (MRI).[6] Osseo-dental structures may also be seen as echogenic foci with posterior acoustic shadowing.

Most of these lesions are found in the sublingual space deep to mylohyoid and splaying the genioglossus and geniohyoid muscles. They may also present superficial to mylohyoid, in the submental or submandibular spaces. The clinical distinction between an epidermoid and a dermoid is academic; it is the location with respect to mylohyoid that is important for the surgical approach.

Pseudocystic and pseudosolid lesions

- Applying power Doppler/gentle probe pressure may cause 'swirling' of contents and is useful in differentiating pseudosolid and pseudocystic lesions.

Pseudosolid lesions
- Dermoid and epidermoid cyst
- Thyroglossal duct cyst
- Branchial cleft cyst (BCC)

Pseudocystic lesions
- Lymphoma
- Pleomorphic adenoma
- Schwannoma/neurofibroma

Ectopic thyroid tissue

Ectopic thyroid tissue is rare, the ectopic thyroid tissue may produce thyroxine, but the levels are usually subnormal. One in three patients with infantile hypothyroidism have ectopic thyroid tissue.[7]

Ninety per cent of ectopic thyroid tissue is found at the level of the base of the tongue, but it can also occur anywhere along the thyroglossal tract.[8] In 75% of cases of ectopic thyroid, no other functioning thyroid tissue exists.

The ultrasound appearances are of a well-defined, uniformly echogenic, solid, vascular mass in the sublingual or submental region (Fig. 45.11). Normal thyroid tissue in the normal location excludes ectopic thyroid tissue.[9]

Ludwig's angina

Ludwig's angina is a potentially life-threatening cellulitis of the sublingual space, leading to swelling of the tissues in the floor of the mouth. It causes elevation of the tongue, as the infection is contained by mylohyoid (Fig. 45.12), leading to upper airway obstruction. The commonest cause is dental caries, but it may also be due to sialoadenitis, the infection tracking via the submandibular duct from the submandibular gland into the sublingual space. Ultrasound may be useful in diagnosing non-dental causes and for assessing for abscess formation.

2. SUBMANDIBULAR REGION

Normal ultrasound anatomy and technique

The transducer is swept from the submental position to the angle of the mandible. The submandibular space[2] is inferolateral to mylohyoid; its principal contents are the submandibular gland and lymph nodes. It communicates freely with the submandibular space on the opposite side and also with the sublingual space around the posterior border of mylohyoid,[2,3] which can be important in relation to the spread of infection. Owing to early embryological encapsulation, the submandibular gland does not contain any lymph nodes. The submandibular nodes are located around the gland.

With the head turned laterally, the mylohyoid muscle can be followed from the submental position to its thick free posterior border,

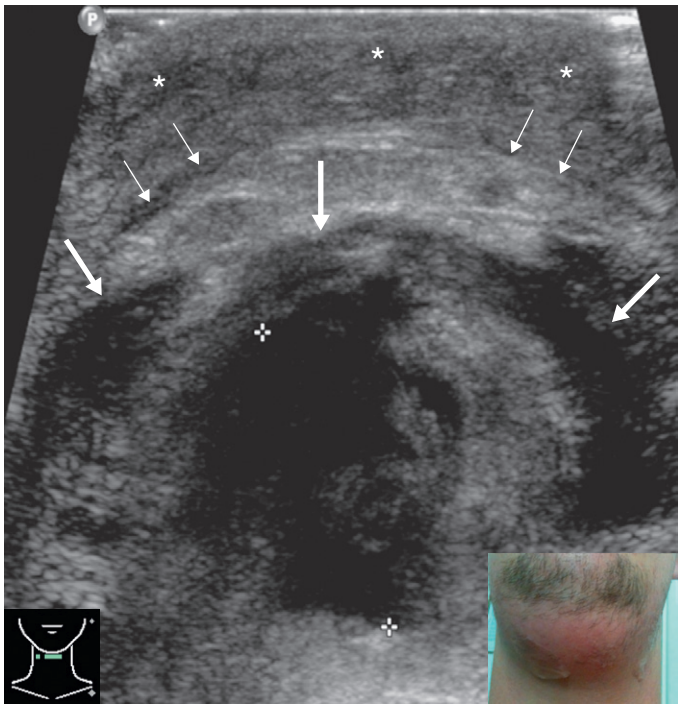

Figure 45.12 Ludwig's angina. Transverse submental sonogram, demonstrating an ill-defined abscess (callipers) deep to mylohyoid, (thick arrows) in the sublingual space, and extensive subcutaneous oedema (asterisks). Thin arrows = platysma. The patient presents with a submental swelling (photograph) and respiratory difficulties, as the oropharyngeal airway is obstructed by the elevated tongue.

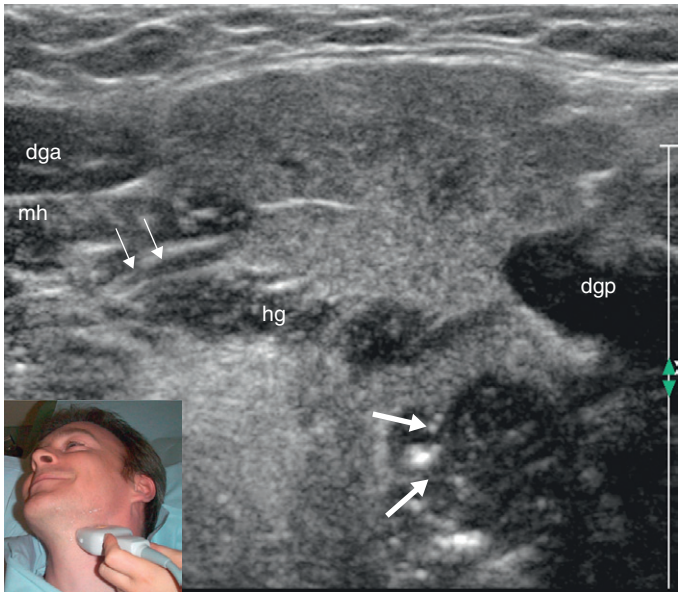

Figure 45.13 Submandibular region. Transverse sonogram of the left submandibular region. The tonsil (thick arrows) lies deep to the submandibular gland (smg). The submandibular duct (thin arrows) passes anteriorly between mylohyoid (mh) and hyoglossus (hg). dga, dgp, anterior and posterior belly of digastric.

around which the submandibular gland is wrapped. The submandibular gland is well encapsulated and uniformly echogenic, the intraglandular ductules are visible as short echogenic streaks (Fig. 45.13). The submandibular gland is a mixed serous and mucous gland, and unlike the parotid does not contain significant fat. Deep and parallel to mylohyoid, lies the hyoglossus muscle, which may

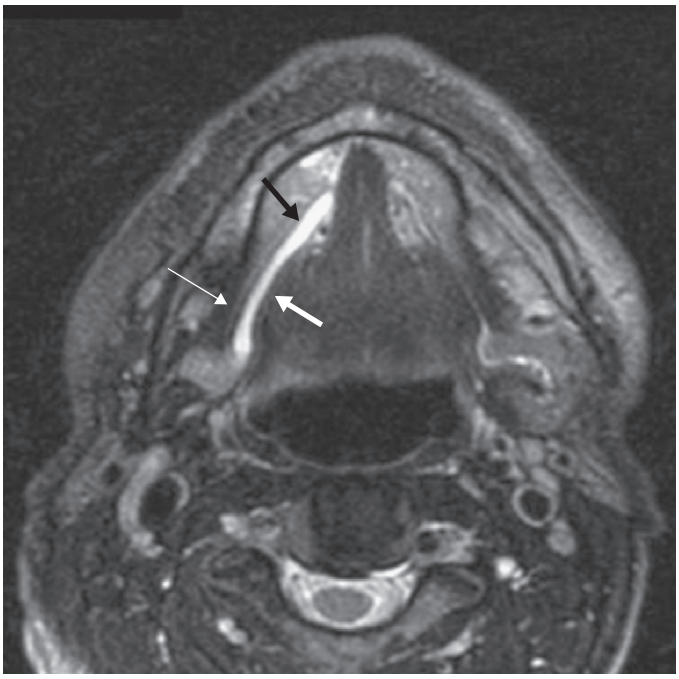

Figure 45.14 Submandibular duct. Axial T2-weighted MRI of the floor of the mouth, depicting the course of the submandibular duct (black arrow), between mylohyoid (thin arrow) and hyoglossus (thick arrow).

be identified by asking the patient to waggle their tongue (Fig. 45.14). The submandibular duct (Wharton's duct) exits medially from the hilum of the gland, hooking posteriorly around mylohyoid and then passing anteriorly between mylohyoid and hyoglossus into the floor of the mouth (Figs 45.4, 45.13, 45.14). It may be easily identified between these two muscles when obstructed, but may also be seen in normal individuals, measuring approximately 1 mm in diameter. The lingual vein also runs in the same plane and should not be mistaken for the duct. The posterior belly of digastric is posterior to the submandibular gland.

It is also useful to identify the submandibular duct in cross-section, which is best done in an oblique longitudinal plane. The probe is positioned so that it lies on a line connecting the angle of the mandible and the hyoid bone. The mylohyoid and hyoglossus muscles will be seen as a 'V'-shaped structure converging on the hyoid, in between which the submandibular duct and lingual vein can be identified in cross-section (Fig. 45.15).

The submandibular region should also be examined in longitudinal section. The anterior submandibular lymph nodes are well demonstrated in this view, tucked up under the mandible (see Fig 46.4B in Chapter 46).

Posteriorly, the tail of the parotid sometimes dips down into the submandibular space and lies adjacent to the posterior aspect of the submandibular gland (Fig. 45.16).

Pathology in the submandibular region

Most of the pathology in the submandibular region lies within the gland. The superficial location of the gland is ideal for ultrasound assessment; further cross-sectional imaging is rarely required. The vast majority of lesions are inflammatory.

Pathology in the submandibular gland

Calculi/Sialolithiasis

Calculi are far commoner in the submandibular gland (80–90%) than in the parotid (10–20%)[10] because the concentration of mucus

is higher in the submandibular gland, making the saliva more viscous. The increased viscosity and slow flow of saliva contribute to the formation of calculi. Ninety per cent of submandibular calculi are radio-opaque and are multiple in 25%[11] of patients.

An obstructed submandibular gland will be enlarged and hypoechoic with dilated ducts. The obstructed submandibular duct can be followed all the way to the floor of the mouth (Fig. 45.17). Calculi appear as hyperechoic rims with posterior acoustic shadowing. If very small, the acoustic shadowing may be difficult to appreciate and it may be helpful to turn off the compound imaging function on the ultrasound machine. Most calculi occur in Wharton's duct (85%), and commonly impact in the duct as it curves around mylohyoid.[10] Care should be taken not to mistake the greater cornu of the hyoid for a calculus in this location. Very distal calculi may be extremely difficult to demonstrate, although proximal ductal

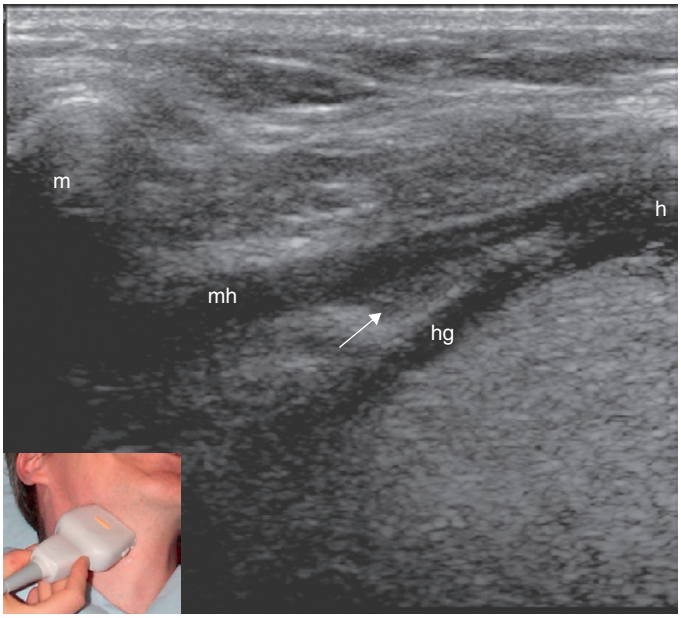

Figure 45.15 Submandibular duct. Oblique coronal sonogram of the submandibular region, demonstrating the submandibular duct in cross-section (arrow), between mylohyoid (mh) and hyoglossus (hg). h, hyoid, m, mandible.

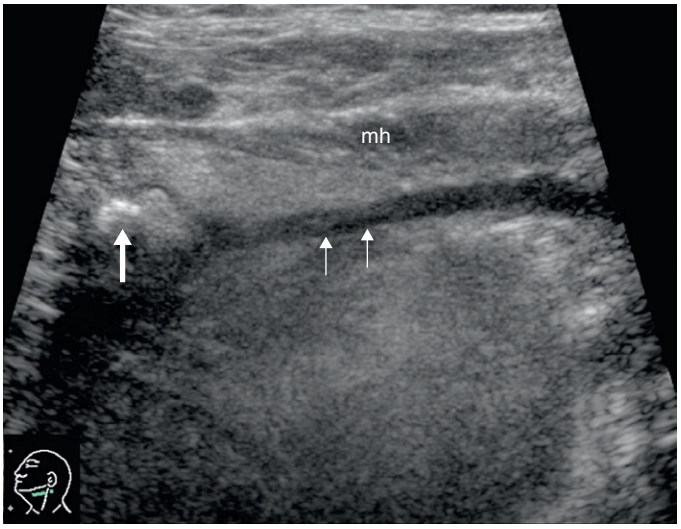

Figure 45.17 Submandibular duct calculus. Sonogram of the left submandibular duct (thin arrows), obstructed by a calculus (thick arrow). mh, mylohyoid.

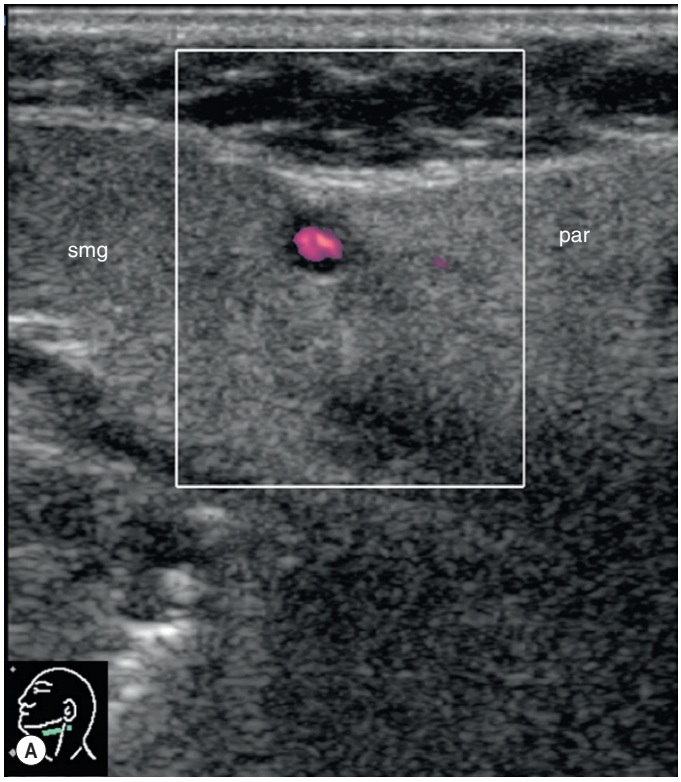

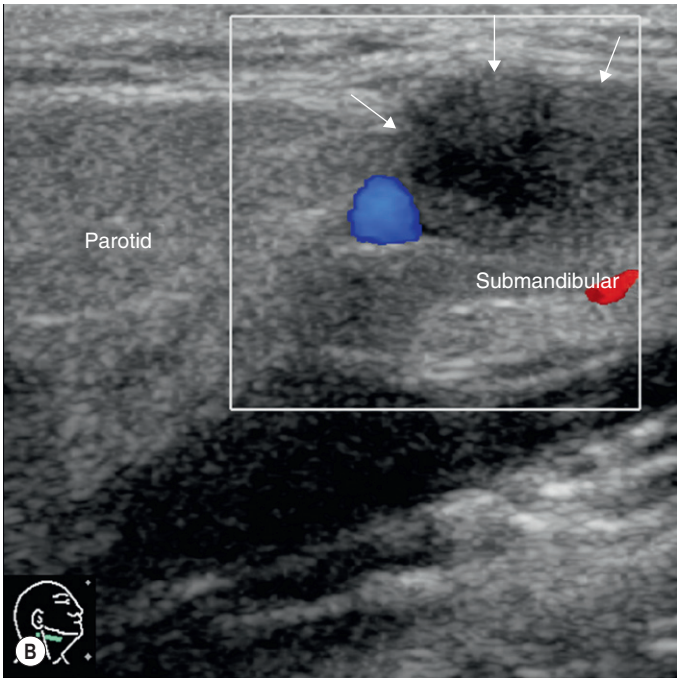

Figure 45.16 Retromandibular vein. Transverse sonograms of the submandibular region. **A:** The retromandibular vein with power Doppler lying between the submandibular gland (smg) and the parotid gland (par); the parotid gland is more echogenic than the submandibular gland. **B:** The retromandibular vein (blue) is a constant landmark, and is useful in localising this tumour (arrows) to the submandibular gland. (With thanks to Dr R. Winter for this image.)

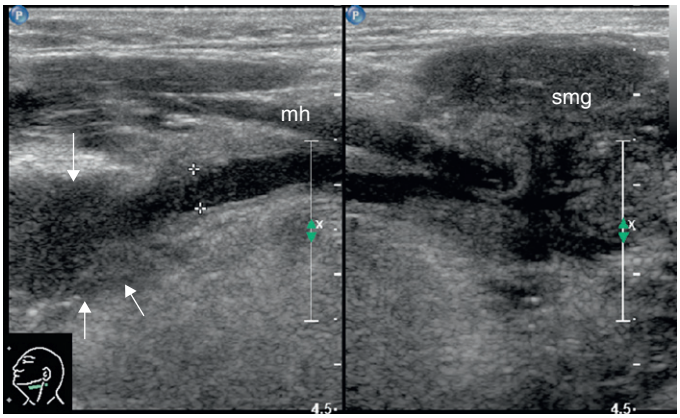

Figure 45.18 Submandibular duct obstruction by floor of mouth tumour. Transverse conjoined sonograms of the left submandibular region. The gland is obstructed by an ill-defined tumour in the floor of the mouth (arrows). callipers duct; mh, mylohyoid; smg, submandibular gland.

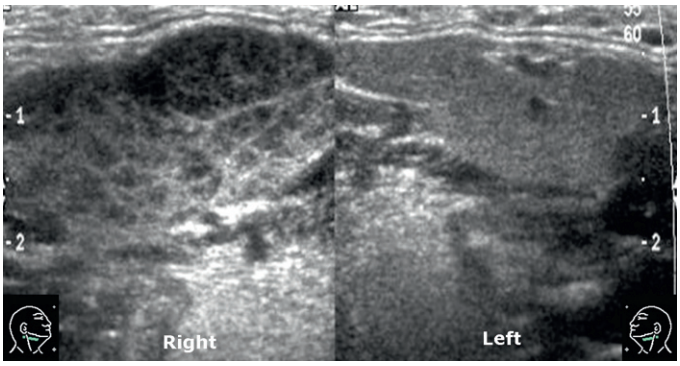

Figure 45.19 Kuttner tumour. Transverse sonograms of both submandibular regions demonstrating the characteristic 'leopardskin' appearance of a Kuttner tumour on the right, compared with the normal gland on the left.

Submandibular gland

- Adequately assessed by ultrasound, further cross-sectional imaging rarely required.
- Does not contain lymph nodes.
- Calculi are commoner than tumours.
- Greater cornu of hyoid may mimic a calculus.
- Obstructed gland and **no** calculus – always check for floor of mouth tumour.
- Tumours are more likely to be malignant.
- Kuttner tumour (benign inflammatory mass) mimics the presentation of a malignancy – 'leopard skin' appearance on US.

dilation is usually visible. These ostial calculi are usually palpable intraorally and most will be demonstrated on an intraoral radiograph. The localisation of calculi as either intraglandular or ductal is essential to plan treatment; most ductal calculi can be removed intraorally, sometimes by radiologically guided procedures. Symptomatic intraglandular calculi require removal of the gland.

Ultrasound has a high degree of accuracy (96%) for detecting calculi,[12] and it should be the first line of investigation for abnormalities in the region of the submandibular region. If the ultrasound is negative and there is a strong clinical index of suspicion, sialography should be considered.

If the submandibular gland is obstructed and there is no evidence of a calculus, it is important to examine the floor of mouth as small tumours in the floor of mouth may present with submandibular duct obstruction (Fig. 45.18).

Kuttner tumour (chronic sclerosing sialoadenitis)

This is a relatively uncommon benign inflammatory condition, virtually exclusive to the submandibular gland. The condition may be bilateral and is rarely seen in the other salivary glands. Its cause is unclear; chronic infection, disorders of secretory function and autoimmune disease have all been postulated but it probably represents the common pathological endpoint of several aetiologies. Pathologically, it is characterised by periductal sclerosis.[13] Its characteristic clinical presentation mimics a malignant neoplasm, presenting as a focal hard mass. The most typical ultrasound appearance is of multiple, small hypoechoic foci, within a heterogeneous parenchyma giving a 'leopardskin' appearance (Fig. 45.19). These appearances have been likened to 'cirrhosis' of the submandibular gland.[14] The ducts may be slightly dilated with a generalised increase in vascularity of the gland. This pattern is usually diffuse, but may also be focal.[14] Unlike in tumours, there is no displacement of vessels or ducts, both of which run through the lesion. If required, the diagnosis may be confirmed with fine-needle aspiration, although this is not usually necessary once the characteristic appearances are appreciated.

Tumours

Tumours are much less common in the submandibular gland than in the parotid gland; however, when they occur, they are more likely to be malignant (approximately 50%).

The majority will be benign pleomorphic adenomas. The commonest malignant tumour of the submandibular gland is an adenoid cystic carcinoma. Salivary tumours will be described in detail in the parotid region, where they are much more common. All submandibular masses should be sampled; two approaches are possible for obtaining a fine-needle aspiration (FNA) (Fig. 45.20). An anterior approach is the safer method, as there are no vessels, but this approach may be difficult in patients with a large chin. The posterior method is easier; however, care must be taken to avoid the retromandibular vein (Fig. 45.16).

Post-radiotherapy changes

Following radiotherapy, the submandibular gland atrophies and ceases to function. Occasionally patients with previously treated neck disease will present with a contralateral 'neck swelling' – which will be found to be a normal submandibular gland on ultrasound examination.

Pathology outside the submandibular gland (non-nodal)

Mylohyoid boutonnière

Defects in the mylohyoid muscle are very common;[5] the contents of the sublingual space may herniate through the defect into the submandibular space, presenting as a cervical mass. The herniated tissue may contain fat, vessels or portions of the sublingual gland (Fig. 45.21). If this condition is suspected on ultrasound, the herniated tissue may be made more conspicuous by asking the patient to swallow.

Diving ranula

A diving ranula occurs when a simple ranula bursts, with extravasation of saliva into the submandibular space, either around the posterior free border of mylohyoid or through a mylohyoid defect.[5]

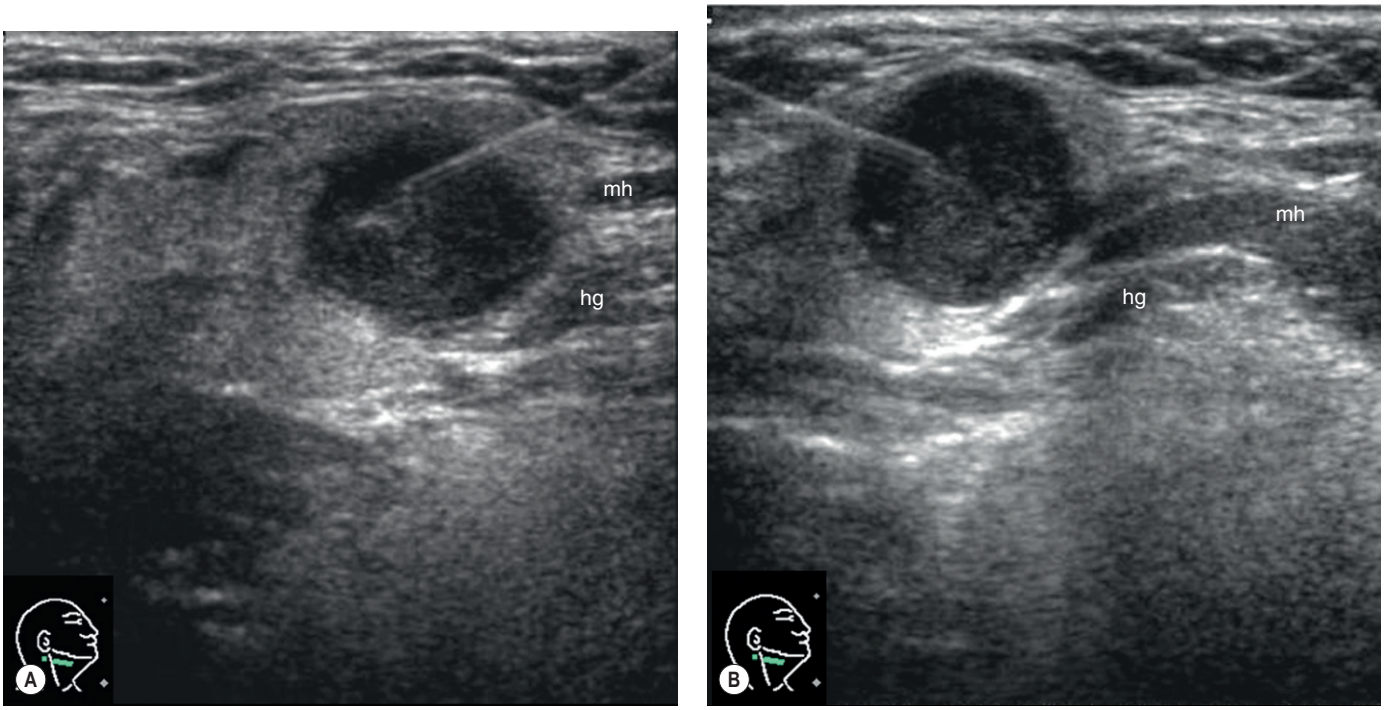

Figure 45.20 Fine-needle aspiration of submandibular gland tumour. Transverse sonogram of a pleomorphic adenoma of the right submandibular gland, demonstrating the two approaches to FNA: **A:** anterior; **B:** posterior. mh, mylohyoid; hg, hyoglossus.

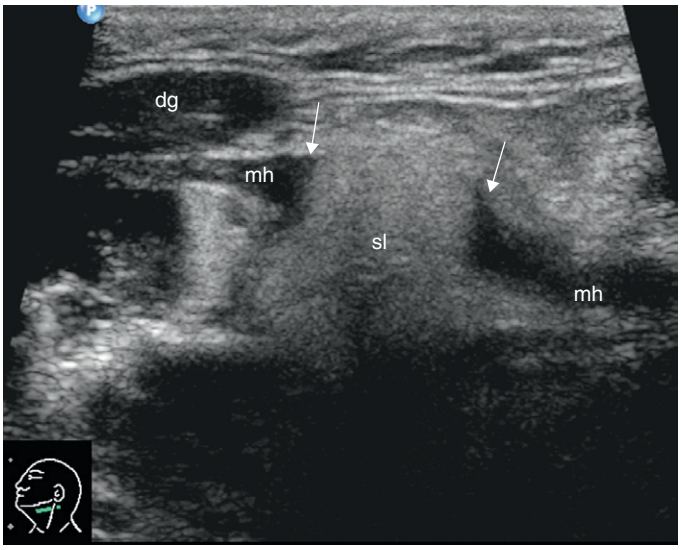

Figure 45.21 Mylohyoid boutonnière. Transverse sonogram of the left submandibular region, showing a mylohyoid boutonnière (arrows), with the sublingual gland (sl) herniating through the mylohyoid defect. mh, mylohyoid; dg, digastric.

It appears as a thin-walled anechoic cystic structure, a small extension or beak, sometimes seen extending into the sublingual space, demonstrating its site of origin.

Lymphatic malformation/lymphangioma

Lymphangiomas are benign tumours composed of lymphatic vessels. Cystic hygroma is the subtype most frequently encountered in the head and neck. It accounts for 5–6% of all benign childhood tumours, most of which are present at birth. Cystic hygroma is uncommon after the age of 2 years. The most common location for a cystic hygroma in a child is the posterior triangle; however, in adults a cystic hygroma is more commonly seen in the parotid or submandibular regions. On ultrasound these lesions are compressible, thin-walled, multiseptated cystic structures, and are almost invariably trans-spatial (see Fig. 45.36), and will usually require further cross-sectional imaging to define their full extent.

They may be removed surgically or may be injected with OK-432, an immune modulator derived from low virulent *Streptococcus pyogenes* which stimulates an inflammatory response and causes the lymphatic spaces to contract and fibrose.[15]

The most important differential diagnosis in relation to a cystic hygroma in the submandibular space is a diving ranula; the treatment of these two conditions is very different – a diving ranula requires excision of the ipsilateral sublingual gland.[16]

Lipoma

Lipomas have a characteristic appearance with a well-defined, compressible, hypoechoic mass containing linear echogenic striations, giving a feathery appearance (Fig. 45.22). The striations remain parallel to the probe, no matter in which direction the scan is performed; this feature is pathognomonic for lipomas.

3. PAROTID AND BUCCAL REGION

Normal ultrasound anatomy and technique

The parotid glands are the largest salivary glands, producing predominantly serous saliva. The probe is placed transversely, immediately below the tragus resting on the ascending ramus of the mandible. The parotid gland is visualised as a triangular wedge of soft tissue between the mastoid process posteriorly and the ramus of the mandible anteriorly (Fig. 45.23). The majority of the gland lies on the masseter muscle. The parotid gland contains abundant fat; it is homogeneously hyperechoic, more so than the submandibular gland (Fig. 45.16A). It is also prone to fatty

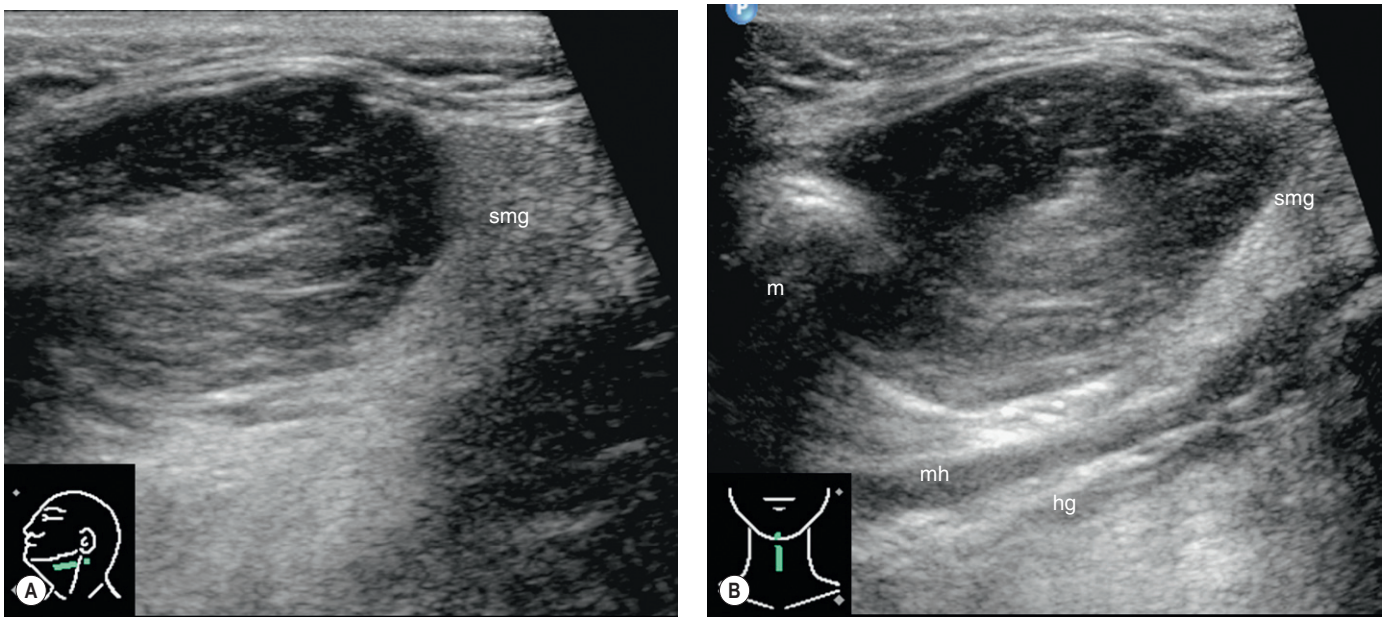

Figure 45.22 Submandibular lipoma. Transverse **(A)** and longitudinal **(B)** sonogram of a lipoma of the submandibular space (arrows), displacing the gland (smg). Lipomas have a characteristic 'feathery' echotexture, the striations remain parallel to the probe, in every direction of scanning. m, mandible; mh, mylohyoid; hg, hyoglossus.

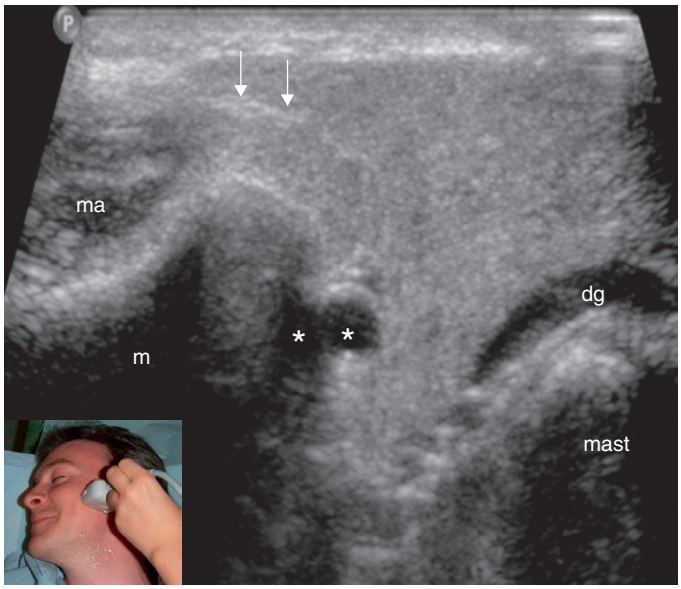

Figure 45.23 Parotid gland. Transverse sonogram of a normal left parotid gland, lying between the mastoid (mast) and the mandible (m). Stensen's duct (arrows) courses anteriorly over masseter (ma). The vessels (*) arbitrarily divide the gland into deep and superficial lobes. dg, posterior belly of digastric.

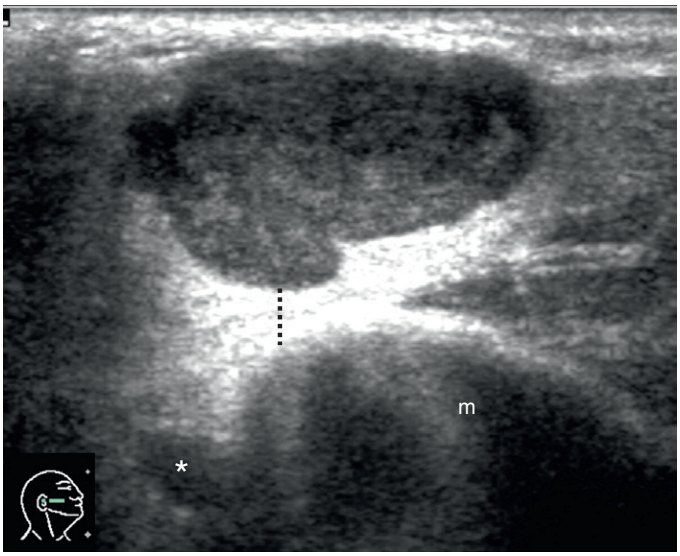

Figure 45.24 Parotid pleomorphic adenoma. Transverse sonogram of a pleomorphic adenoma of the superficial lobe of the parotid; it is useful to measure the distance of the lesion from the mandible (dashed line). *, external carotid artery; m, mandible.

infiltration, which causes a diffuse increase in echogenicity. The parotid gland is not structurally divided into deep and superficial lobes; this is an arbitrary division with respect to the plane of the facial nerve and accompanying vessels. From deep to superficial, these are the retromandibular vein, external carotid artery and facial nerve. The vessels are easily demonstrated, and may be confirmed with Doppler; although the facial nerve is not consistently resolved with ultrasound. The neurovascular plane varies considerably between patients; therefore, rather than describing a lesion as being in the deep or superficial lobe, it is more useful for the surgeon to describe the location of a lesion with respect to its relationship to the ramus of the mandible (Fig. 45.24). The deeper component of the parotid can be difficult to visualise on ultrasound as it is obscured by the mandible; this may be even more challenging in large necks. Changing the probe to a curvilinear 5 MHz probe helps in these cases. The tail of the parotid sometimes dips down into the submandibular space and abuts the posterior margin of the submandibular gland; it may therefore be difficult to localise pathology correctly. The position or displacement of the retromandibular vein is helpful as a mass lying anterior to the vein will be in the submandibular gland, whereas a lesion lying posterior to the vein will be in the parotid gland (Fig.

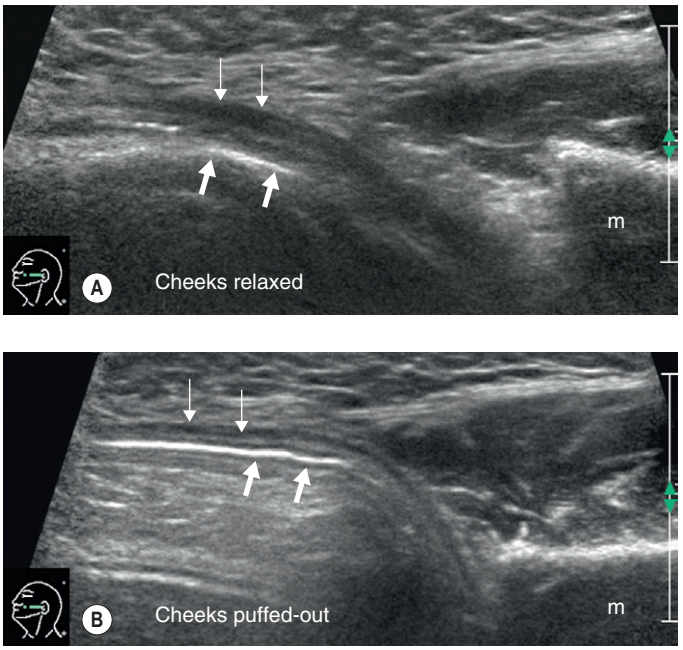

Figure 45.25 Buccal region. Transverse sonograms of the buccal region with the cheeks relaxed **(A)**. Buccinator (thin arrows) is emphasised by asking the patient to puff their cheeks out **(B)**. Thick arrows indicate buccal mucosal interface; m, mandible.

45.16A and B). A parotid tail mass must be identified as intraparotid, in order to avoid damage to the facial nerve at surgery.

Due to late embryological encapsulation the parotid gland, unlike the submandibular gland, contains lymph nodes. Lymph nodes are identified as small oval hypoechoic lesions with a linear hyperechoic hilum, usually less than 5 mm.

Stensen's duct is seen as one or two echogenic lines within the anterior aspect of the superficial lobe (Fig. 45.23), and may be followed anteriorly over the surface of the masseter before turning medially to pierce the buccinator muscle. Small segments of the intraglandular ductules are normally seen. Twenty per cent of patients have accessory parotid glands; these are usually located superior to Stensen's duct and are often bilateral. The accessory glands are elongated and narrow in shape, and have similar ultrasound characteristics to the main parotid gland.

After the parotid gland has been examined, the probe is swept in the transverse position towards the angle of the mouth in order to examine the cheek and buccal region. This region contains the distal parotid duct, buccinator muscle, the buccal fat pad and the facial artery with associated nodes. The bulky masseter muscle gives way to the thin hypoechoic stripe of the buccinator muscle; deep to this is the brightly echogenic line of the air/buccal mucosa interface, with the curvilinear hyperechoic outlines of the teeth. The buccinator muscle is well demonstrated if the patient puffs their cheeks out (Fig. 45.25). Stensen's duct passes anteriorly over the fat pad (see below), turning medially to pierce buccinator at the second upper molar. The facial artery is a constant landmark, lying immediately superficial to buccinator; this is also the location of the buccal node, which is important in cutaneous squamous cell carcinoma (SCC) and melanoma metastases (see Fig. 46.6, Chapter 46).

Pathology in the parotid region

Up to 20% of lumps clinically thought to be in the parotid gland are in fact extraparotid; correct localisation is therefore important.

Ultrasound alone is adequate in assessing the vast majority of pathology in the parotid region. However, it does not reliably assess the deep component of the gland. Any lesion in which the deep margins are not clearly defined requires further cross-sectional imaging with CT or MRI.

Features suggestive of malignancy in salivary gland tumours

- Indistinct margins
  - Locally invading
  - Deep lobe location
  - Colour Doppler: Increased internal vascularity[18]
  - Increased intratumour vascular resistance (RI >0.8, PI >1.8)[19]
  - Associated cervical lymphadenopathy
- Facial nerve palsy

Intraparotid pathology

Tumours

The parotid gland is by far the commonest site for salivary gland tumours,[17] the vast majority of which (90%) will be benign pleomorphic adenomas (60–80%) and Warthin's tumours, also known as adenolymphoma (6–10%). The ultrasound distinction between benign and malignant salivary tumours is not clear-cut. Features that should arouse suspicion of malignancy are shown in box above. Malignant lesions have indistinct margins and may show evidence of local invasion. They tend to be in deeper locations in the gland and associated cervical lymph node enlargement may be present. Colour Doppler shows increased vascularity in the mass[18] and the vascular resistance in these vessels is elevated, with a resistance index >0.8 and a pulsatility index >1.8.[19]

It is estimated that ultrasound can predict malignancy in 80–94% of cases.[20]

Ultrasound-guided FNA of all parotid masses is advised, as it increases the sensitivity of the examination significantly.

Further cross-sectional imaging, preferably with contrasted MRI, is required to assess tumours involving the deep lobe of the parotid, and any deep involvement of the parapharyngeal space and perineural spread. Further imaging is also indicated for any parotid tumour with features suspicious of malignancy or malignant cytology. Recurrent parotid tumours, whether benign or malignant, also need CT or MRI.

Salivary tumours, wherever their site of origin, have similar histology, but clinically, tumour types vary according to location. The smaller the gland, the more likely the tumour is to be malignant.

Benign tumours

Pleomorphic adenoma

The characteristic ultrasound appearance of a pleomorphic adenoma is of a well-defined, lobular, uniformly hypoechoic mass, usually in the superficial part of the gland (Fig. 45.24). The mass may demonstrate apparent distal acoustic enhancement, leading to its description as 'pseudocystic', but this phenomenon is thought to be due to compression of the gland parenchyma and ductules posterior to the tumour, rather than to increased sound transmission. Pleomorphic adenomas are usually less than 3 cm in size. As the tumour enlarges it may become atypical in appearance, with less well-defined margins, making differentiation from a malignant lesion difficult. Foci of calcification, haemorrhage and cystic change may also develop in longstanding lesions.[19]

Pleomorphic adenomas in the deep lobe are rare (less than 10%).

It is essential to remove the tumour with an intact capsule, rather than the outdated enucleation, to prevent intraoperative seeding, with late recurrence in the surgical bed. Recurrent pleomorphic adenoma characteristically has a multilobular appearance, likened to a 'bunch of grapes'[21] (Fig. 45.26).

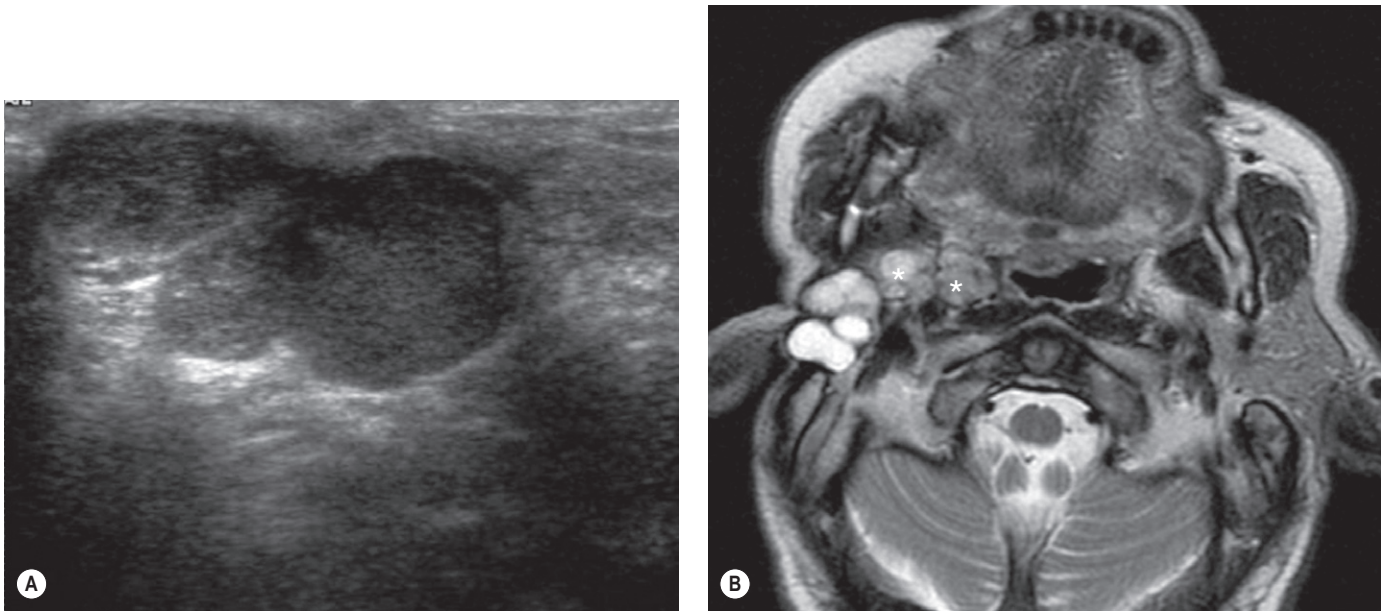

Figure 45.26 Recurrent parotid pleomorphic adenoma. A: Transverse sonogram of a recurrent parotid pleomorphic adenoma, resembling a 'bunch of grapes'. **B:** T2-weighted MRI. Further imaging is necessary to demonstrate the deep recurrence in the parapharyngeal fat space (*).

Adenolymphoma/Warthin's tumour

This is the second most common benign parotid tumour. It arises from heterotopic salivary tissue within lymph nodes, hence its almost exclusive location within the parotid gland and adjacent nodes.[10] It characteristically occurs in the tail of the parotid in elderly males, and may be bilateral in up to 15%. It may also be multifocal.

Adenolymphomas are typically well-defined, hypoechoic lesions, commonly containing cystic areas and septa (Fig. 45.27); occasionally they may be totally cystic. A fine-needle aspiration characteristically yields a much more mucoid sample than from a pleomorphic adenoma. Since these are slow-growing, benign tumours in an elderly population, cytological proof is very useful if conservative management is being considered.

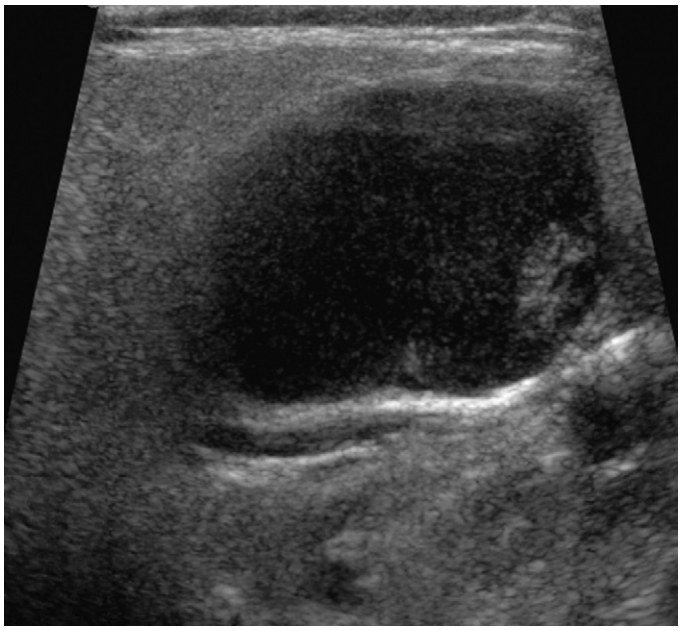

Figure 45.27 Parotid adenolymphoma. Sonogram of an adenolymphoma (Warthin's tumour) of the parotid gland. These tumours frequently have a cystic component.

Oncocytoma

This rare tumour occurs almost exclusively in the parotid gland, typically in a patient over 50 years. The ultrasound appearances are similar to those of a pleomorphic adenoma.[22]

Infantile haemangioma/congenital haemangioma

One in three children is born with a vascular birthmark;[23] the vast majority require no medical attention. Vascular anomalies may be divided into two broad categories of **malformations** and **haemangiomas**.[21] Accurate diagnosis, with reference to the correct classification system[24,25] is essential for prognosis and to allay parental anxiety. Haemangiomas are tumours, characterised by rapid postnatal proliferation, followed by slow involution over the next 1–5 years. Haemangiomas are the commonest paediatric salivary gland tumour, accounting for 90% of parotid masses in children. The typical presentation is of a soft, rapidly enlarging, unilateral, compressible swelling, appearing shortly after birth. The mass sometimes has a bluish colour, which becomes more apparent when the baby cries (Fig. 45.28).

Ultrasound demonstrates a well-defined, hypoechoic, lobular mass, containing multiple linear echogenic septa, and anechoic vascular channels. Power Doppler demonstrates the highly characteristic 'burning bush' appearance of vastly increased perfusion (Fig. 45.28). These tumours grow at a slower rate than the child, and their natural history is of spontaneous involution over 1–5 years.[23] Serial ultrasound is useful in monitoring the size of the lesion for parental reassurance. Features of venous vascular malformations are given on page 907.

Nerve sheath tumours – schwannoma, neurofibroma

These lesions are characteristically uniformly hypoechoic, with a pseudocystic appearance (see Fig. 45.47). They are ovoid in outline;

however, the characteristic 'tail', confirming their continuity with the facial nerve, is not always seen. In practice, they are difficult to distinguish from pleomorphic adenomas. A fine-needle aspiration (usually a relatively painless procedure) may be unusually painful, which is a clue to the diagnosis.

Vascular anomalies

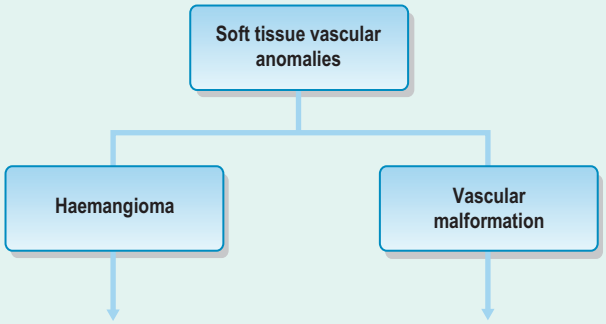

- Tumour
- Not present at birth, appear shortly after birth
- Initial rapid post natal proliferation, followed by regression over 5 years
- **Ultrasound**
  - Soft tissue mass
  - No phleboliths
  - High flow
- Do not usually require treatment, conservative management.

- Malformation secondary to error of embryonic development
- Probably present at birth, appear at puberty
- Persist through life, grow at same rate as patient
- **Ultrasound-**
  - Soft tissue mass
  - Phleboliths 20%
  - Low flow/no flow
- Treatment - sclerosant, embolisation, surgery.

Malignant tumours

Primary malignant salivary gland tumours are rare, particularly in the parotid gland – only 13% of parotid tumours are malignant, while 30% of submandibular gland tumours and 50% of palatal tumours will be malignant.[17] The ultrasound features that should arouse suspicion have already been described (Table 45.1, Fig. 45.29). There are no specific ultrasound features to distinguish one histological type from another; indeed low-grade malignant tumours often have benign appearances.

Mucoepidermoid carcinoma

This is the commonest malignant salivary gland tumour overall, and the most frequent in the parotid. It is also the commonest malignant salivary tumour of childhood.

Adenoid cystic carcinoma

This is the second commonest malignant tumour of the submandibular and minor salivary glands. It has a predilection for perineural spread and may present with pain, paraesthesia or cranial nerve palsy.

Acinic cell carcinoma

This occurs almost exclusively in the parotid gland, and is the second commonest malignant tumour of the parotid; it is also the second commonest paediatric malignant salivary tumour.[11] It arises from terminal ductules and therefore may be multifocal.

Carcinoma ex-pleomorphic adenoma

Malignant degeneration of pleomorphic adenomas increases with time and has been estimated at 9.5% in lesions present over 15

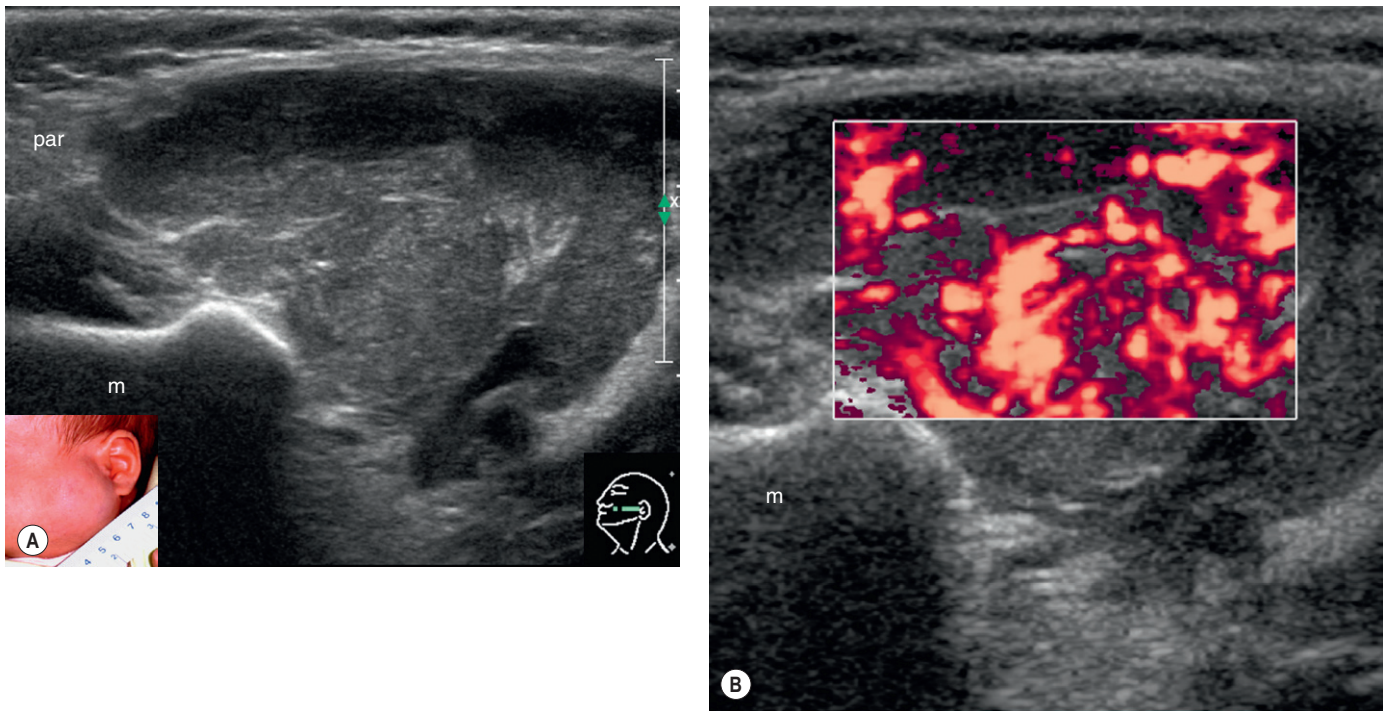

Figure 45.28 Parotid haemangioma. Transverse greyscale **(A)** and power Doppler sonograms **(B)** of a parotid haemangioma in a 2-week-old baby (see photograph) showing the characteristic vastly increased perfusion. The natural history is of spontaneous involution. m, mandible; par, parotid.

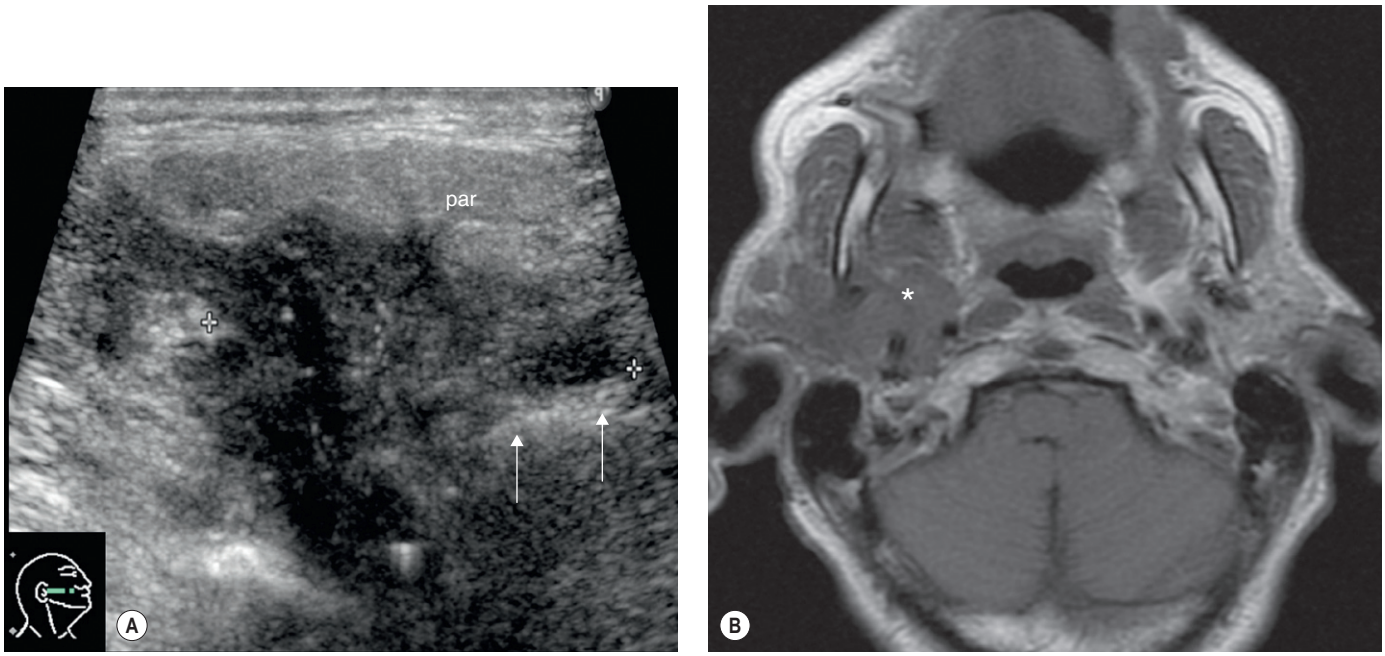

Figure 45.29 Malignant parotid neoplasm. Transverse sonogram **(A)** and T1-weighted MRI **(B)** of a malignant parotid tumour. All parotid malignancies require further cross-sectional imaging, to delineate the deep extent (*), and to assess for perineural spread. par, parotid; arrows indicate mandible.

years.[26] The classical presentation is of a recent increase in size in a longstanding parotid mass.

Metastases

Metastases may occur in the parotid gland as it contains lymph nodes. The most common metastases to the parotid nodes are from skin squamous cell carcinomas (SCC) and melanoma – 80% of head and neck melanomas and 50% of SCCs will metastasise to the parotid.[17] These are usually very well defined on ultrasound, mimicking benign lesions.

Lymphoma

Lymphoma of the salivary glands is rare; however, lymphoma is the second commonest head and neck malignancy, after squamous carcinoma. The parotid gland is the salivary gland most frequently affected in non-Hodgkin's lymphoma. It has not been established definitively whether the gland is secondarily involved from intraparotid nodes or vice versa; it is probable that both sequences of events occur.[17] The incidence of non-Hodgkin's lymphoma in patients with Sjögren's syndrome is increased 44 times.[11] Parotid involvement may be focal or diffuse. Focal disease appears as enlarged, markedly hypoechoic, reticulated intraparotid lymph nodes with an exaggerated normal pattern of vascularity (see Figs 46.16 and 46.28 in Chapter 46). Diffuse involvement has non-specific features of gland enlargement and is indistinguishable from chronic sialadenitis or granulomatous disease.

Lymphoma should always be considered in the differential diagnosis of multiple extranodal head and neck lesions, especially as the treatment is non-surgical. A core biopsy, in preference to a fine-needle aspiration, is recommended if lymphoma is suspected.

Inflammation – acute

Infection

Acute parotitis is an extremely painful condition as the parotid gland is invested with a richly innervated fascia. It is most frequently caused by the mumps virus; it occurs commonly in children and is usually bilateral, although it may be unilateral.

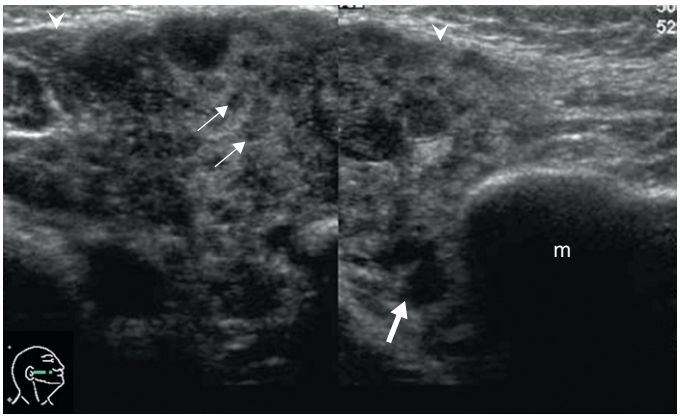

Figure 45.30 Acute parotitis and associated lymph nodes. Conjoined transverse sonograms showing acute parotitis. There are multiple hypoechoic foci of sialadenitis (thin arrows), and multiple enlarged reactive nodes (thick arrow). The capsule of the gland is tense (arrowheads). m, mandible.

Bacterial infection is usually unilateral, the commonest organism being *Staphylococcus*. The parotid gland is the commonest salivary gland to be affected by acute suppurative sialadenitis. The causes include stones, strictures and dehydration.

The acutely inflamed gland is oedematous and hypoechoic, with a convex surface. Multiple, small, rounded, non-branching, hypoechoic foci scattered diffusely throughout the gland represent areas of sialadenitis. The gland is hypervascular, with enlarged, reactive parotid nodes (Fig. 45.30). The role of ultrasound in this acute setting is to assess for abscess formation as this can be difficult to determine clinically as the gland is so tense and painful. An abscess appears as an ill-defined, hypoechoic or anechoic area, and may contain moving debris and tiny hyperechoic foci due to microbubbles of gas (Fig. 45.31). If an abscess is demonstrated, therapeutic drainage under ultrasound guidance may be performed. Ultrasound is also useful to exclude calculi as the cause of the parotitis.

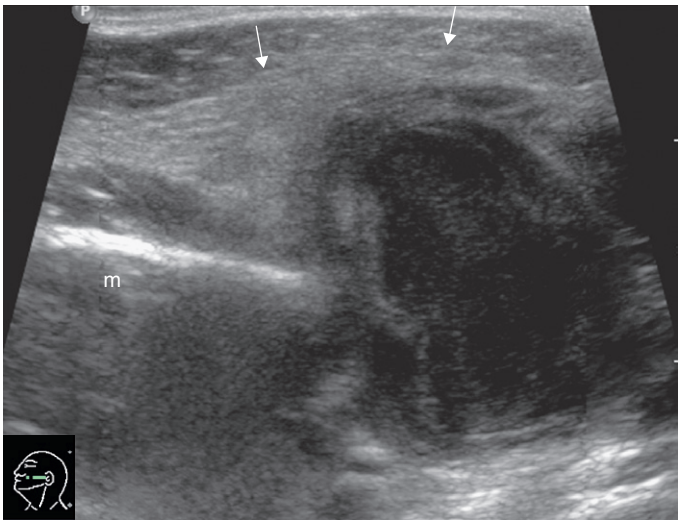

Figure 45.31 Parotid abscess. Transverse sonogram of a parotid abscess. The capsule of the gland is convex (arrows) and the margins of the abscess are ill-defined; the echogenic pus will swirl on application of power Doppler. m, mandible.

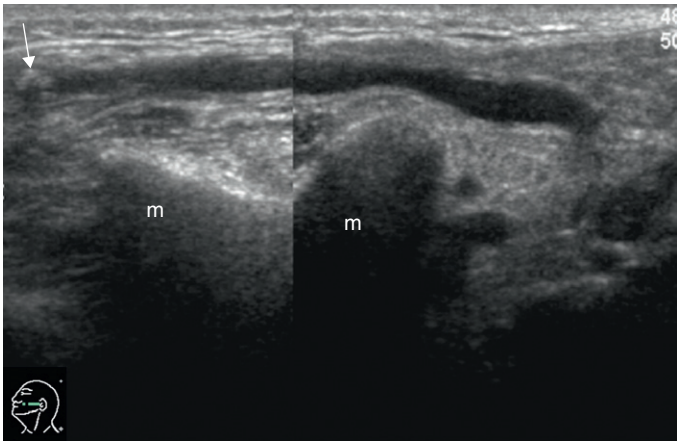

Figure 45.32 Parotid duct calculus. Conjoined transverse sonograms of a small parotid calculus (arrow) causing obstruction of Stensen's duct. m, mandible.

Calculi

Calculi are less common in the parotid gland (10–20%) than in the submandibular gland (80–90%), due to the higher serous content of the saliva. Predisposing factors for stone formation include dehydration and immunosuppression. Rarely, cystic fibrosis may present with salivary calculi.

The acutely obstructed gland is enlarged and hypoechoic, with dilation of intra- and extraglandular ducts. Calculi in Stensen's duct are easier to demonstrate than intraglandular calculi; they appear as hyperechoic 'rims' with posterior acoustic shadowing (Fig. 45.32). If the calculus is in Stensen's duct, less than 5 mm and mobile, radiologically guided extraction may be successful. A variety of catheters, balloons and baskets is available for sialoplasty and stone retrieval.

Inflammation – chronic

Chronic sialadenitis presents as intermittent salivary swelling, which may be painful and may not necessarily be related to eating. The aetiology of this condition is varied but the parenchymal appearances are similar, regardless of the cause. The parenchyma is heterogeneously hypoechoic, with multiple, non-branching, round, hypoechoic foci. The gland is small or of normal size, with no increased vascularity. The differential diagnosis for these features is wide, and includes benign lymphoepithelial lesions (BLELs) in Sjögren's syndrome, sarcoidosis, granulomatous infection, lymphoma, lymphoepithelial cysts in HIV patients (AIDS-related parotid cysts, ARPC) and recurrent juvenile parotitis.

Sjögren's syndrome

Sjögren's syndrome is an autoimmune disorder, consisting of keratoconjunctivitis sicca (dry eyes), xerostomia (dry mouth) and a connective tissue disorder which occurs almost exclusively in middle-aged women. The parotid glands are the salivary glands most frequently affected, although the submandibular glands may also be involved. In the early stages the salivary glands may appear normal. As the disease progresses, the gland enlarges due to an autoimmune sialoadenitis and non-obstructive sialectasia occurs, manifested by multiple, punctate 2–3 mm, hypoechoic foci, known as benign lymphoepithelial lesions (BLELs); these are the pathological hallmarks of autoimmune sialoadenitis. The gland is hypervascular at this stage. The punctate sialectasia progresses in some patients to larger, globular cystic spaces, associated with glandular destruction,[27] giving the pathognomonic ultrasound features of end-stage Sjögren's syndrome (Fig. 45.33). Ultrasound is useful for documenting which glands are involved and also to assess for lymphoma, which has a significantly increased incidence in patients with Sjögren's syndrome.[11] It is also useful to ultrasound the lacrimal glands, as they may show similar appearances.

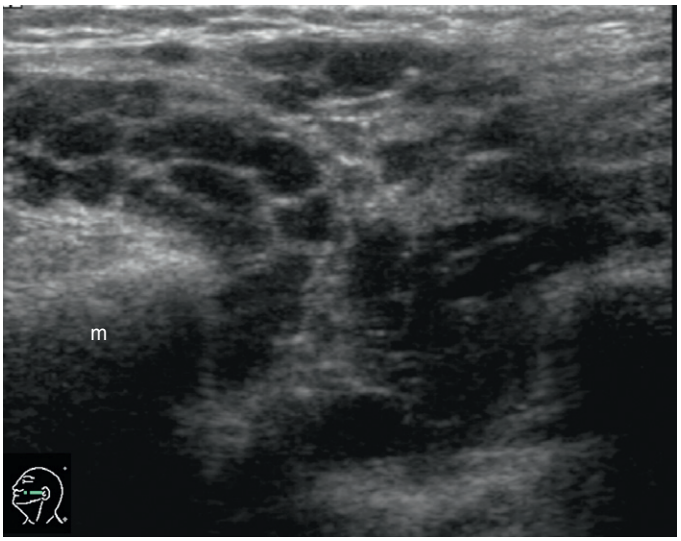

Figure 45.33 Chronic Sjögren's syndrome. Transverse sonogram of end-stage Sjögren's of the parotid gland, demonstrating multiple large cystic spaces. The gland is small and avascular. m, mandible.

Sarcoidosis

The parotid gland is affected in 6% of cases of sarcoidosis. The gland may be diffusely involved with non-specific ultrasound appearances as described above, or there may be focal enlargement of the parotid lymph nodes. Heerfordt's syndrome consists of sarcoidosis with parotid enlargement, uveitis and facial nerve palsy.

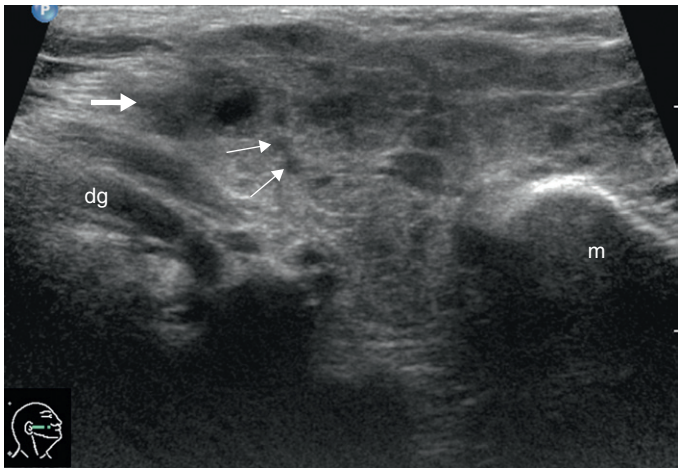

Figure 45.34 Juvenile recurrent parotitis. Transverse sonogram of juvenile recurrent parotitis. The gland is non-tender, and contains hypoechoic foci of sialadenitis (thin arrows) and reactive nodes (thick arrow). m, mandible; dg, posterior belly of digastric.

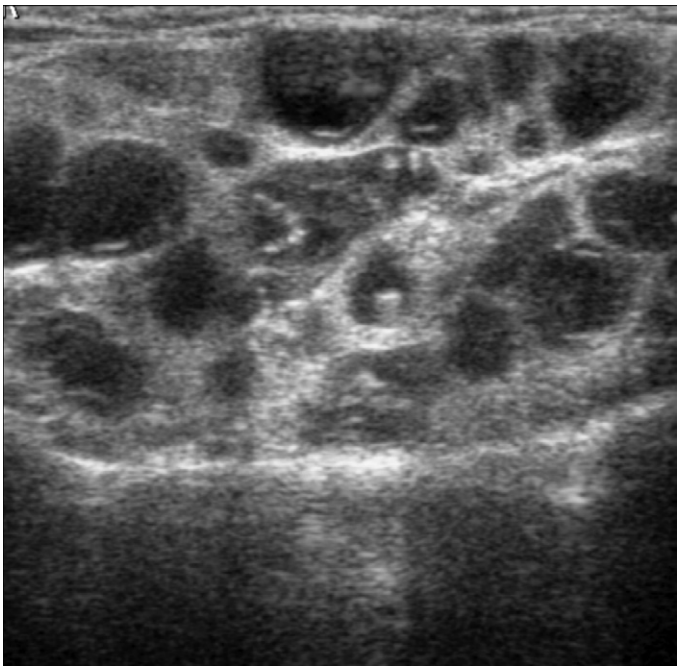

Figure 45.35 Lymphoepithelial cysts. Multiple large lymphoepithelial cysts (arrows) throughout the parotid gland in combination with reactive cervical lymphadenopathy is characteristic of AIDS-related parotid cysts (ARPC). (With thanks to Dr C. Goodwin for the image.)

Differential diagnosis of chronic sialadenitis ultrasound:
Small gland, decreased vascularity, multiple non-branching rounded hypoechoic foci

- Chronic infection – usually unilateral.
- Chronic calculus disease – usually unilateral.
- Recurrent juvenile parotitis – child.
- BLEL (benign lymphoepithelial lesion), Sjögren's syndrome – if there is a history of an autoimmune disorder.
- Sarcoidosis.
- Lymphoma.
- ARPC (AIDS-related parotid cyst) – with benign cervical lymphadenopathy.

Juvenile recurrent parotitis

This is a rare disorder of childhood characterised by repeated episodes of non-obstructive parotitis. Males are more commonly affected. The symptoms peak in the first year of school, and usually subside at puberty.[28] Its aetiology is unclear; congenital ductal malformation and immunodeficiency have been proposed. It has been suggested that children with this condition should be screened for Sjögren's syndrome and immunodeficiency, including HIV.[29] The main differential diagnosis is mumps. The ultrasound appearances are those of chronic sialadenitis and sialectasis (Fig. 45.34).

Cystic lesions

Cystic lesions of the parotid are uncommon, accounting for less than 5% of all parotid tumours. Whilst ultrasound clearly demonstrates these lesions and may suggest a specific diagnosis, the precise diagnosis relies on the pathologist. Cysts, whatever the aetiology, have similar ultrasound characteristics; they are thin-walled, well-defined, anechoic structures, with no internal vascularity. Cysts may become thick-walled and contain debris if they become infected.

True cysts (with an epithelial lining) of the salivary glands are rare; the majority occur in the parotid, and result from ductal obstruction, resulting in retention cysts. The cause of the obstruction may be calculi, strictures or a benign lymphoepithelial lesion (BLEL).

The term benign lymphoepithelial lesion refers to benign masses in the parotid gland, composed of acinar atrophy with foci of lymphoid tissue containing small islands of myoepithelial cells. These benign lymphoepithelial lesions[30] arise from the parenchyma of the gland. They are the histological hallmark of autoimmune disease of the salivary glands; however, they may also occur in the absence of autoimmune disease. Cystic change has been reported in BLELs.

A lymphoepithelial cyst (LEC) is a different entity, which arises from cystic dilation of trapped salivary tissue within intra- or periparotid lymph nodes, analogous to the development of Warthin's tumours.[31] Branchial cleft cysts are lymphoepithelial cysts and it has been suggested that first branchial cleft cysts are more likely to arise from intranodal salivary inclusion than from branchial cleft remnants.[32] Lymphoepithelial cysts may be solitary and the result of chronic infection. Multiple lymphoepithelial cysts of the parotid commonly occur with benign cervical lymphadenopathy and HIV infection (Fig. 45.35); in this situation lymphoepithelial cysts are referred to as AIDS-related parotid cysts (ARPCs). These lesions are thought to be the result of AIDS-related hyperplastic lymphadenopathy of the parotid nodes; they usually occur in the superficial lobe and vary in size from 0.5 to 5 cm. They are frequently bilateral and are more common in children.

In summary, there is considerable overlap in the pathology of cystic lesions of the parotid:

- **Congenital** causes include first branchial cleft cysts and lymphatic malformations (Fig. 45.36); in practice these are fairly easily distinguished – the former is a solitary cystic structure in or around the parotid, while the latter is a multiseptated, often trans-spatial lesion.
- **Acquired** cystic lesions may be due to chronic inflammation or autoimmune disease, may be related to HIV infection in the presence of benign cervical lymphadenopathy, or may be due to a Warthin's tumour (Fig. 45.27).

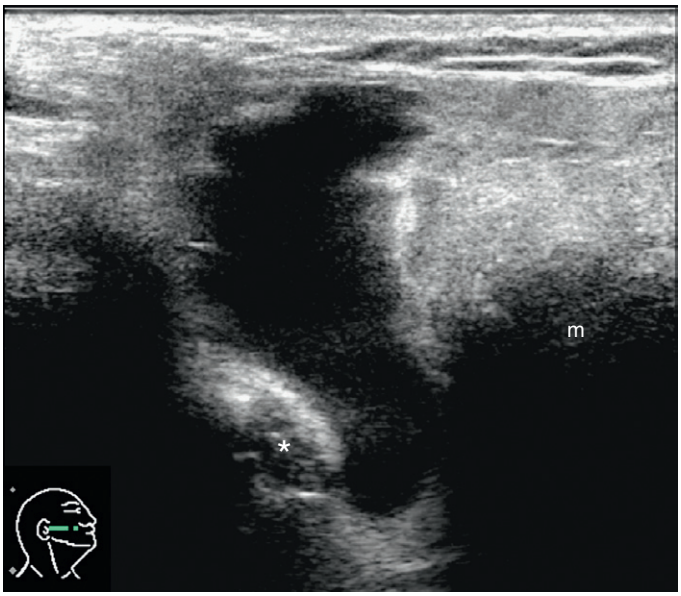

Figure 45.36 Cystic hygroma. Large solitary cystic hygroma (arrows) in the parotid gland of a young patient; these require further cross-sectional imaging, as they are almost invariably trans-spatial. *, retromandibular vein; m, mandible.

Benign lymphoepithelial lesion (BLELs) and lymphoepithelial cyst (LECs)

	BLEL	LEC
Tissue of origin	Salivary parenchyma	Lymph nodes
Associated with autoimmune disease	+++	–
Extraparotid location	No	Occasionally (Warthin's)
Association with cervical lymphadenopathy	No	+++ (AIDS-related parotid cyst – ARPC)
Multiple	✓	✓ (Warthin's)
Solitary	No	✓ Branchial cleft cyst ✓ Warthin's

Sialosis

This is non-neoplastic, non-inflammatory, chronic, recurrent swelling of the salivary glands in association with acinar hypertrophy and ductal atrophy. The condition occurs most frequently in the parotid gland, and less commonly in the submandibular and minor salivary glands. Aetiologies include nutritional deficiencies, alcoholism, anorexia or bulimia, and endocrinopathies such as diabetes.

The ultrasound findings are non-specific: the gland is enlarged; however, there are no focal lesions, nor increased blood flow. Frequently there is diffuse fatty infiltration, making visualisation difficult due to beam attenuation.

Pathology in the extraparotid/buccal space

Most of the extraparotid pathology is related to the masticator space.

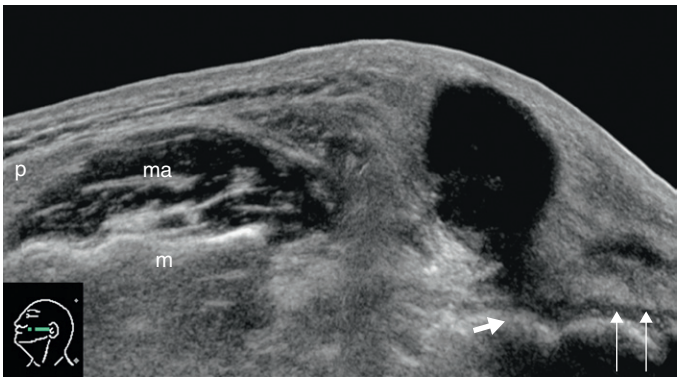

Figure 45.37 Dental abscess. Transverse panoramic sonogram of a large dental abscess in the buccal space, communicating with the tooth (thick arrow) through buccinator (thin arrows). ma, masseter; m, mandible; p, parotid.

Dental abscess

This diagnosis is usually clinically obvious, with trismus, pain and a history of recent dental problems; however, the diagnosis may be clinically unsuspected if there is no history of a recent dental extraction or if the patient is thought to be edentulous. An abscess appears as an ill-defined, hypoechoic mass within the masseter muscle or buccal space, sometimes with frank cystic change (Fig. 45.37). Periosteal reaction and fragmentation of the buccal cortex of the mandible may also be present. An abscess may be aspirated under ultrasound guidance.

Masseteric hypertrophy/bruxism

This condition is caused by teeth grinding, which is usually nocturnal. As the hypertrophy is usually unilateral, it may present as a parotid space mass. Ultrasound demonstrates an asymmetric increase in the masseter muscle; the muscle will be otherwise normal. The asymmetry may be exaggerated by asking the patient to clench their teeth. This condition may be treated conservatively with gum guards or with botulinum toxin injections.[33]

Venous vascular malformation

Venous malformations are the most common vascular malformations, 40% occurring in the head and neck. It is important to refer to the correct classification system[22,23] and to avoid false generic terms such as cavernous haemangioma, which create confusion regarding treatment and prognosis.

A venous malformation is defined as a simple malformation with low flow and an abnormal venous network. These anomalies are probably present at birth, although they do not present until adolescence or adulthood. They grow at a similar rate to the patient, and do not regress (unlike haemangiomas).[21,34] They are soft compressible lesions, often with a bluish colour, which enlarge on the Valsalva manoeuvre. They involve skin and subcutaneous tissues, as well as muscle and bone. Venous malformations are relatively easy to recognise and the radiologist plays a key role in their diagnosis. They are heterogeneous or hypoechoic lesions; anechoic channels will be seen in 50%, and 20% will have pheboliths (Fig. 45.38). Doppler demonstrates monophasic, low-velocity flow, or occasionally no flow.

Management depends on the extent of loss of function and aesthetic considerations; it involves a combination of direct sclerosant therapy and surgery. Venous vascular malformations are commonly trans-spatial, and require MRI or CT to map out their full extent before any planned intervention.

Buccal fat pad

The buccal fat pad is a roughly triangular-shaped structure, lying on buccinator, anterior to masseter. It has similar ultrasound characteristics to a lipoma: hypoechoic with multiple linear hyperechoic striations (Figs 45.39, 45.40). The buccal fat pad varies enormously in size, being largest in suckling babies, when it can be visualised sliding back and forth during feeding. It atrophies post-weaning but persists in some adults, giving rise to a buccal mass.

Pilomatrixoma

Pilomatrixoma is an unusual, slow-growing, benign tumour arising from a hair follicle. They commonly occur in the pre-auricular region. They present, usually before the age of 10 years, as hard, irregular subcutaneous nodules.[35] On ultrasound they are small, well-defined, hypoechoic, subcutaneous lesions, which occasionally contain calcium.[36]

Parotid gland

Contains lymph nodes.
Tumours are commoner than calculi.
Vast majority (90%) of tumours are benign pleomorphic adenomas.
Ultrasound differentiation of benign and malignant tumours is difficult.
US FNA: Warthin's tumours are often mucoid.
Further cross-sectional imaging required for:
- deep lobe lesions
- all malignant cytology
- recurrent pleomorphic adenomas.

Over 20% of 'parotid' masses are actually extraparotid.

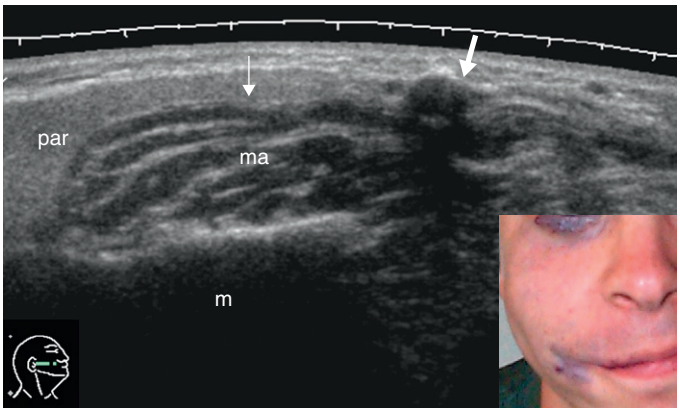

Figure 45.38 Venous vascular malformation in the masseter muscle. Panoramic transverse sonogram of a venous vascular malformation; the masseter muscle (ma) is enlarged and there is a large phlebolith (thick arrow). m, mandible; par, parotid.

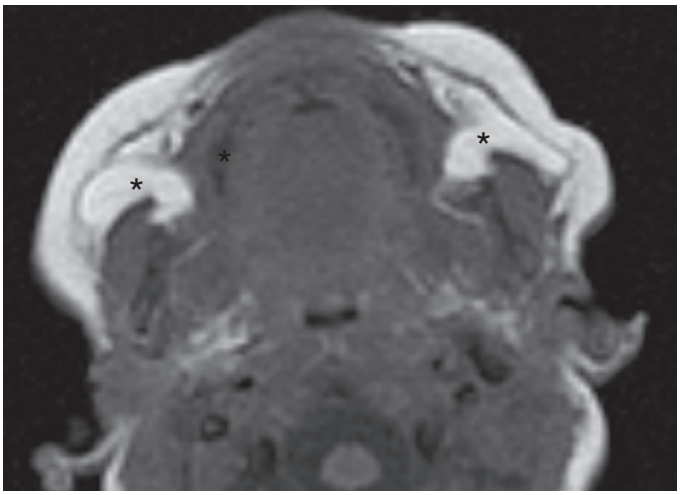

Figure 45.40 Buccal fat pad on MRI. Axial T1-weighted MRI of an infant, demonstrating the buccal fat pads (*).

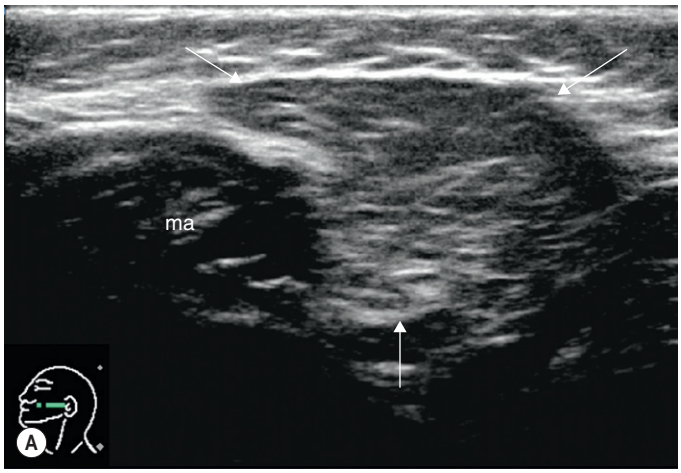

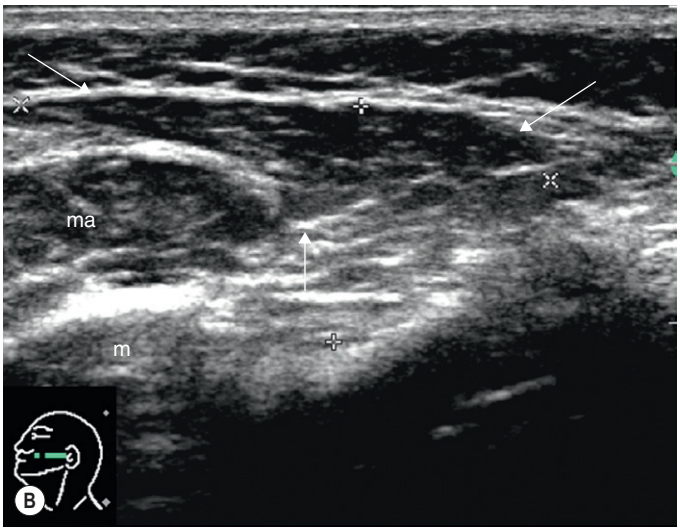

Figure 45.39 Buccal fat pad. Transverse sonograms one month apart **(A)** and **(B)**, demonstrating the involution of the buccal fat pad (arrows) over one month, following weaning, in a toddler. These may persist into adulthood, and present as a cheek mass. ma, masseter; m, mandible.

4. JUGULODIGASTRIC REGION AND DEEP CERVICAL CHAIN

Normal anatomy and ultrasound technique

Sweeping the transducer from the angle of the mandible down to the medial clavicle will show the deep cervical chain of lymph nodes, the internal jugular vein, the carotid artery and the vagus nerve. Detailed examination of the lymph nodes will be discussed in the chapter on the cervical lymph nodes (Chapter 46). For the purpose of this chapter, non-nodal pathology that is likely to be encountered in this region will be discussed.

This region is best scanned transversely, starting at the angle of the mandible and identifying the jugulodigastric node. This is the most superior node in the deep cervical chain and the largest node in the neck. Its location is constant, lying posterior to the submandibular gland, inferior to the posterior belly of digastric and superficial to the great vessels (see Fig. 46.7, Chapter 46). The long axis of the node lies obliquely, parallel to the posterior belly of digastric, rather than being orientated longitudinally, parallel to the internal jugular vein, as are the remainder of the deep cervical chain nodes. It is an ovoid, hypoechoic structure with a central linear echogenic hilum. It is the 'sentinel node' of the head and neck and may be visualised in almost all individuals. Below the jugulodigastric node, the lymph nodes are clustered around the internal jugular vein from 9 o'clock to 3 o'clock (see Fig. 46.8, Chapter 46). The vagus nerve and sympathetic chain lie between the great vessels.

Sweeping down from the jugulodigastric region to the medial clavicle, the key structure is the internal jugular vein (IJV). It is important to keep the internal jugular vein in the centre of the field of view, gently bouncing the probe intermittently on the vein, to confirm its patency. The internal jugular vein will be easily visible with the patient lying down, but will commonly be collapsed if the patient is examined sitting up. Its patency may be checked with the Valsalva manoeuvre. The vagus nerve lies deeply, between the great vessels; it is approximately 2–3 mm in transverse diameter (see Fig. 46.8, Chapter 46).

The omohyoid muscle crosses the great vessels obliquely, from anterior to posterior, marking the division between the mid and lower deep cervical chain at the level of the cricoid cartilage. It is easy to mistake this muscle for a node; scanning the muscle in longitudinal section will confirm its nature (see Fig. 46.9, Chapter 46).

Pathology in the deep cervical chain – JDG region

Branchial cleft cyst

The vast majority (95%) of branchial cleft anomalies arise from the second branchial cleft. Embryologically, the second branchial arch overgrows the second, third and fourth branchial clefts, resulting in the expansion of the second branchial cleft into an elongated common cavity: the cervical sinus of His. Incomplete closure of this sinus leads to anomalies of the second branchial cleft, which may be cysts, sinuses or fistulae. The anomalies may occur anywhere along the tract, which extends from an external opening at the anterior border of sternomastoid at the junction of its middle and lower thirds. The tract then passes superiorly, passing between the internal and external carotid arteries, to the internal opening into the tonsillar fossa. Cysts are the commonest anomaly, followed by fistulae.[37]

Second branchial cleft cysts (BCCs) have a characteristic location at the angle of the mandible, lying posterior to the submandibular gland, superficial to the great vessels and under the anterior border of sternomastoid. This location is virtually identical to the position of the jugulodigastric node, with which it may be easily confused.

Branchial cleft cyst (BCC) mimics

- Metastasis from a head and neck SCC.
- Metastasis from papillary carcinoma of the thyroid.
- Beware of making the diagnosis of a BCC in a patient older than 35–40.
- A thorough search for a possible head and neck primary, in particular the tongue, tonsil and thyroid, is indicated if the patient is older than 35–40.

Pathologically, branchial cleft cysts are lymphoepithelial cysts lined by squamous epithelium overlying lymphoid tissue, containing turbid yellowish fluid, which may contain cholesterol crystals. They usually present as a painless, fluctuant mass at the angle of the mandible, typically between the ages of 10 and 40 years. This is in contrast to branchial cleft sinuses or fistulae, which occur in the first decade.[35] The cystic mass enlarges slowly and may fluctuate in size with secondary infection, which may be associated with an upper respiratory tract infection. They may vary in size from 1 to 10 cm.

Branchial cleft cysts have a variety of sonographic appearances,[38] classically being anechoic, thin-walled and compressible, or hypoechoic with internal debris and posterior acoustic enhancement. They may occasionally have a pathognomonic beak or extension pointing medially between the internal and external carotid arteries (Fig. 45.41). They may, however, have a pseudosolid appearance, with uniform homogeneous internal echoes, which may cause an erroneous diagnosis of a solid mass (Fig. 45.42). Bouncing the probe on the lesion, or the application of power Doppler is a useful test; this causes the contents to shift and swirl, confirming its cystic nature. Ultrasound-guided fine-needle aspiration may be confirmatory, but not all the contents should be aspirated, as this will make surgical removal difficult.

As previously mentioned, the location of a BCC is almost identical to the position of the jugulodigastric node, and cystic nodal metastases from a squamous cell cancer or a papillary carcinoma of the thyroid are common and very important mimics of branchial cleft cysts (Fig. 45.43).

The diagnosis of a branchial cleft cyst is relatively easy when it occurs in a young adult, in the typical location and has the characteristics of a cystic lesion. Care should be taken in making the diagnosis of a branchial cleft cyst in a patient older than 30 years, even if cytology confirms the clinical suspicion of a branchial cleft cyst, with macrophages and cholesterol crystals. A cystic metastatic node cannot be excluded and a thorough search with a panendoscopy and biopsies should be performed in order to identify a possible occult primary tumour. Violating the neck in the presence of metastases may create ipsi- and contralateral lymphatic shunts, with the potential to upstage nodal disease.

Pathology in the deep cervical chain – below the JDG region

Most of the non-nodal pathology below the JDG node will be neurovascular in origin.

Internal jugular vein thrombosis

Internal jugular vein thrombosis, both acute and chronic, is easy to overlook on ultrasound.

Acute thrombosis mimics infection, presenting with unexplained neck swelling, tenderness and fever. The lumen of the internal jugular vein is distended by hypoechoic thrombus, with surrounding soft tissue oedema and loss of fascial planes (Figs 45.44, 45.45); attempted compression of the vein confirms the presence of a filling

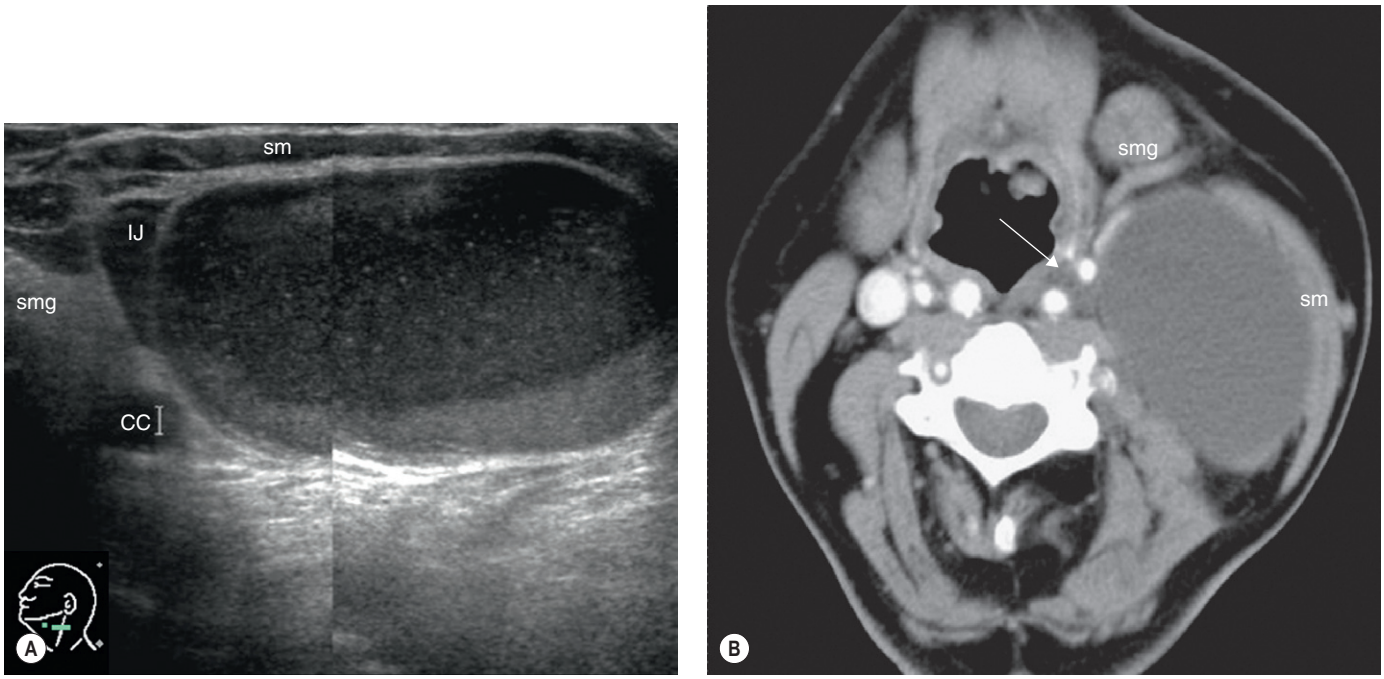

Figure 45.41 Branchial cleft cyst. Conjoined transverse sonogram **(A)** and CT scan **(B)** of a branchial cleft cyst; note the characteristic location – posterior to the submandibular gland (smg), deep to sternomastoid (sm), and superficial to the great vessels (cc, common carotid; ij, internal jugular). Occasionally a small 'beak' may be seen in between the internal and external carotid arteries (arrow).

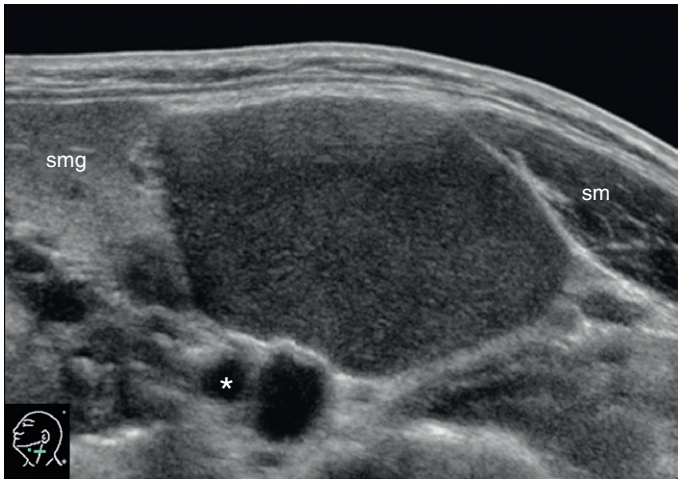

Figure 45.42 Pseudosolid appearance of a branchial cleft cyst. Transverse sonogram of a branchial cleft cyst – the lesion has a pseudosolid appearance. smg, submandibular gland; sm, sternomastoid; *, carotid artery.

defect. Other useful signs are a lack of mobile venous valves, loss of respiratory and cardiac variation and loss of distension with the Valsalva manoeuvre. Collateral veins are usually absent and the contralateral internal jugular vein may be distended.[39] A Doppler signal within the thrombus indicates tumour.

Chronic internal jugular vein thrombosis is more difficult to identify. The vein lumen is small, echogenic and non-compressible (Fig. 45.44B); collaterals will usually be present, particularly the anterior jugular vein, and the soft tissue planes will appear normal. This is a relatively common finding following a neck dissection, radiotherapy or previous central line insertion.

The most common cause of internal jugular vein thrombosis is iatrogenic intimal damage, either following internal jugular vein catheterisation or by repeated puncture by intravenous drug abusers.[40] Other causes are infective or metastatic lymphadenopathy; rarely, internal jugular vein thrombosis may be the presenting feature of an occult malignancy – Trousseau's syndrome.[41] Trousseau's syndrome is a paraneoplastic hypercoagulable state resulting in migratory thrombophlebitis. A systematic search for an occult malignancy should be guided by the patient's symptoms, the commonest associated tumours being lung, pancreas and stomach; head and neck tumours account for less than 1%.[42]

Paragangliomas/glomus tumours

Paragangliomas, also known as glomus tumours, are benign, vascular tumours arising from paraganglionic tissue in the vessel walls. They occur at various locations in the head and neck:

- Glomus jugulare: at the jugular ganglion of the vagus, at the skull base.
- Glomus vagale: at the nodose ganglion of the vagus, 1–2 cm below the skull base.
- Glomus tympanicum: around the nerves of Arnold and Jacobson in the middle ear.
- Carotid body tumour (CBT): in the carotid body, at the carotid bifurcation.

The carotid body tumour is the only one that may be reliably visualised with ultrasound. They present as painless, slow-growing, lateral neck masses. Characteristically, they will be mobile in a lateral plane but not in a vertical plane. The location of the tumour, characteristically splaying the carotid bifurcation, is the best clue to the nature of the lesion. On ultrasound, it is a well-defined, heterogeneously hypoechoic mass containing multiple anechoic foci, corresponding to blood vessels. Colour Doppler shows a highly vascular tumour with chaotic blood flow, usually coming from the external carotid artery but occasionally from the internal carotid or vertebral arteries (Fig. 45.46).

Further cross-sectional imaging is indicated in all cases of glomus tumours, to define the superior extent of the lesion with respect to the skull base and to identify further lesions; up to 10% are multiple, increasing to 30% in familial cases.[43]

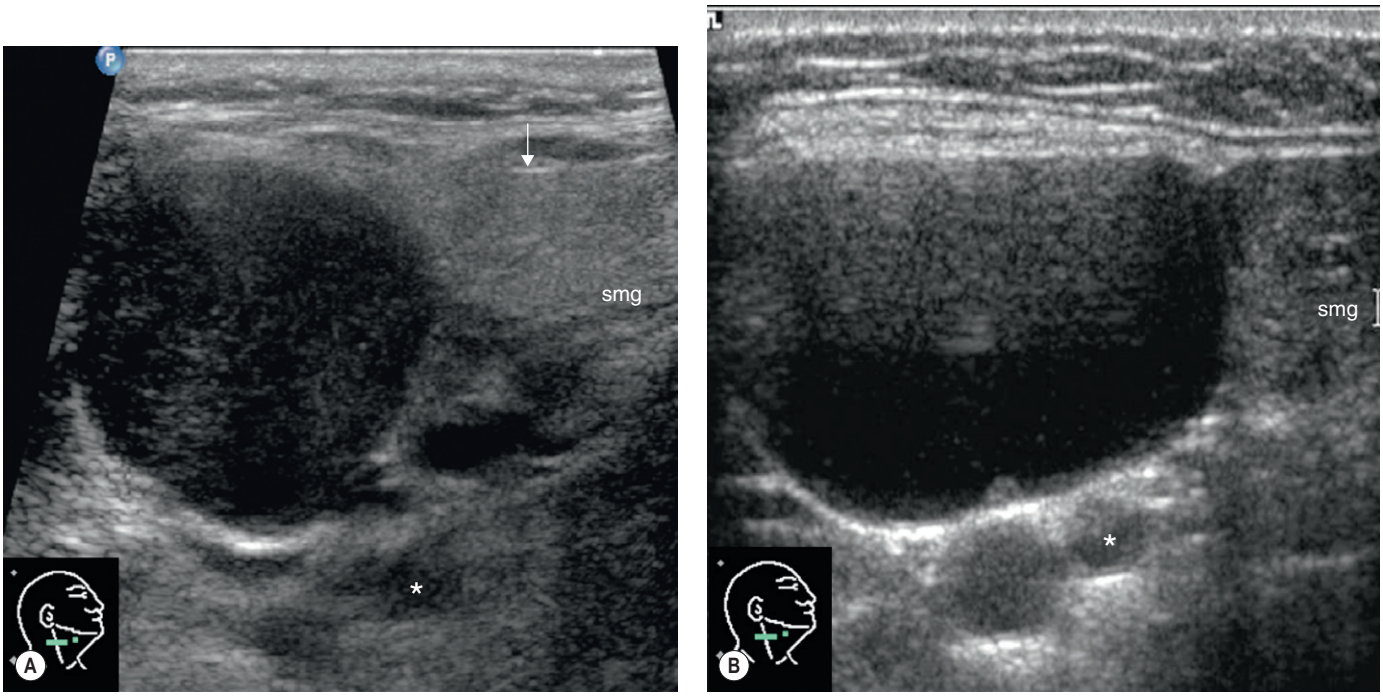

Figure 45.43 Differential diagnosis of branchial cleft cysts. Transverse sonograms of branchial cleft cyst mimicking **(A)** papillary carcinoma metastasis, **(B)** squamous cell carcinoma metastasis. Note the identical location of the jugulodigastric node and a branchial cleft cyst. smg, submandibular gland; *, carotid artery.

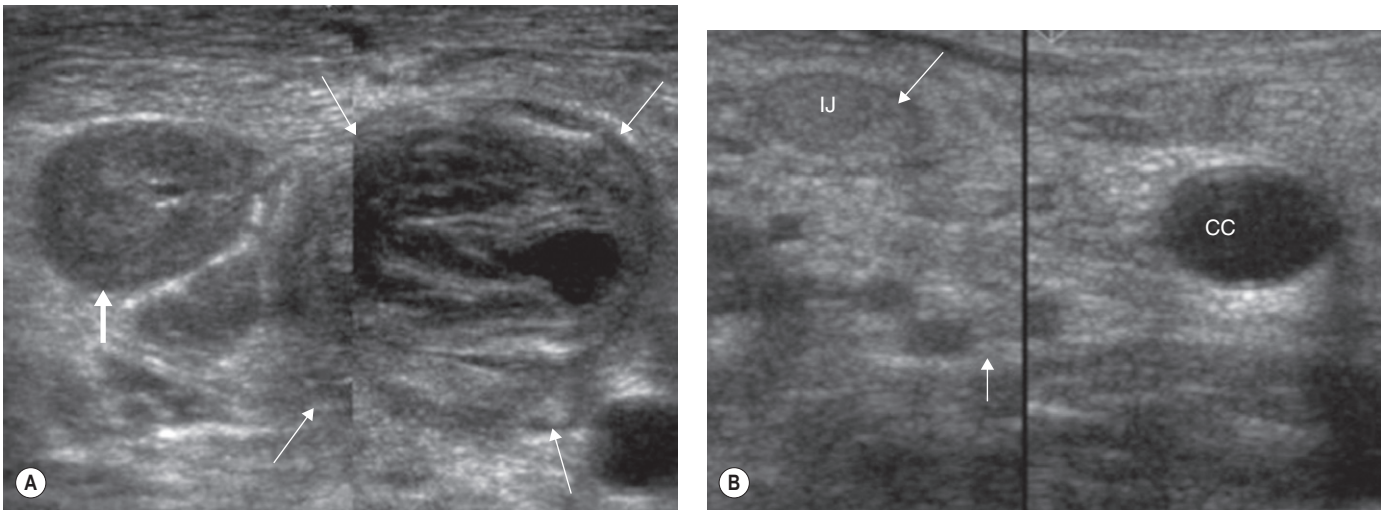

Figure 45.44 Internal jugular vein thrombosis. Conjoined transverse sonograms of acute **(A)** and chronic **(B)** internal jugular vein thrombosis (arrows) – both may be mistaken for lymph nodes (thick arrow in **A**). IJ; internal jugular vein; CC, common carotid artery.

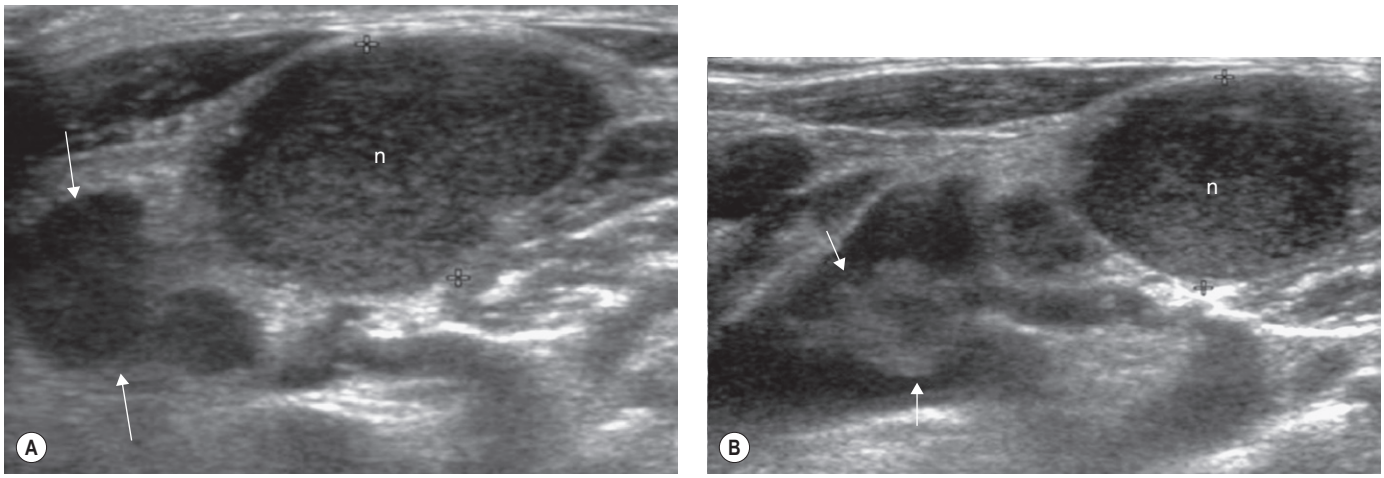

Figure 45.45 Effect of transducer pressure on internal jugular vein thrombosis. Transverse sonograms of internal jugular vein thrombosis (arrows), demonstrating how too much pressure with the transducer **(A)** may obliterate the vein, causing it to be mistaken for a node. **B:** Relaxing the pressure allows the vein and thrombus to be demonstrated. n, malignant node.

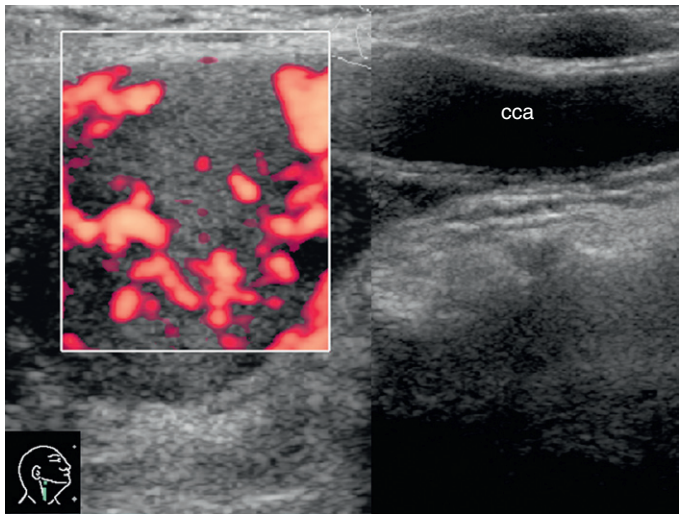

Figure 45.46 Carotid body tumour. Longitudinal conjoined sonogram of a carotid body tumour – its location at the carotid bifurcation and intense vascularity are characteristic features. cca, common carotid artery.

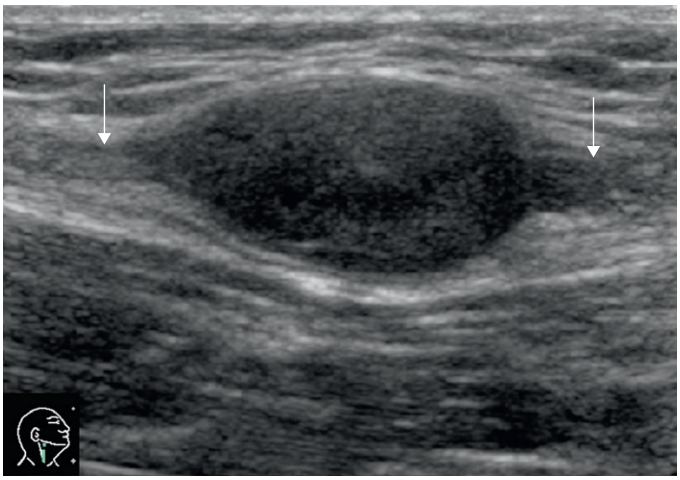

Figure 45.47 Cervical schwannoma. Longitudinal sonogram of a schwannoma in the posterior triangle – a well-defined, hypoechoic, pseudocystic lesion, with tapering ends, in continuity with the echogenic, fibrillary parent nerve (arrows).

An ectatic common carotid bifurcation is a common clinical mimic for a carotid body tumour.

Nerve sheath tumours

Peripheral nerve tumours of the neck are rare. The most common are schwannomas and neurofibromas. Clinically, they are usually mistaken for a lymph node, but they have certain characteristic sonographic features which help in differentiating them from lymph nodes.

On ultrasound, they are well-defined, ovoid, homogeneously hypoechoic nodules. The differentiating signs of a schwannoma with respect to a normal lymph node are: tapering ends, lack of an echogenic hilum and occasionally posterior acoustic enhancement, giving a pseudocystic appearance. When scanned longitudinally, the tapering ends confirm their origin from the nerve (Fig. 45.47). The parent nerve is seen as an echogenic, fibrillary structure; occasionally it may be followed around or through the lesion. Schwannomas tend to be eccentric with respect to the nerve, while neurofibromas tend to be concentric, although this relationship may be difficult to define on ultrasound.[44] These lesions are hypervascular, although not to the same extent as glomus tumours; the vascularity may be abolished by light pressure from the probe.[45]

Lymphomatous nodes may also have posterior acoustic enhancement; however, they will usually be multiple, whereas a nerve sheath tumour will be solitary.

5. SUPRACLAVICULAR FOSSA

Normal ultrasound anatomy and technique

This region is examined with the transducer positioned transversely. The transducer is swept from the medial aspect to lateral

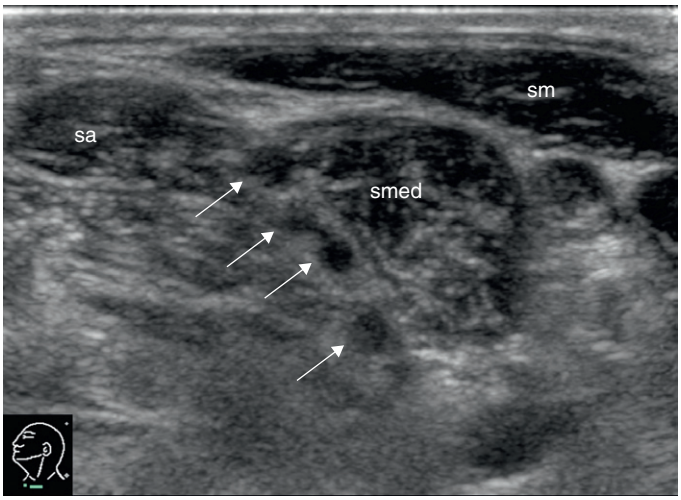

Figure 45.48 Brachial plexus roots and trunks. Transverse sonogram of the brachial plexus elements (roots and trunks), as they lie between scalenus anterior (sa) and scalenus medius (smed). sm, sternomastoid.

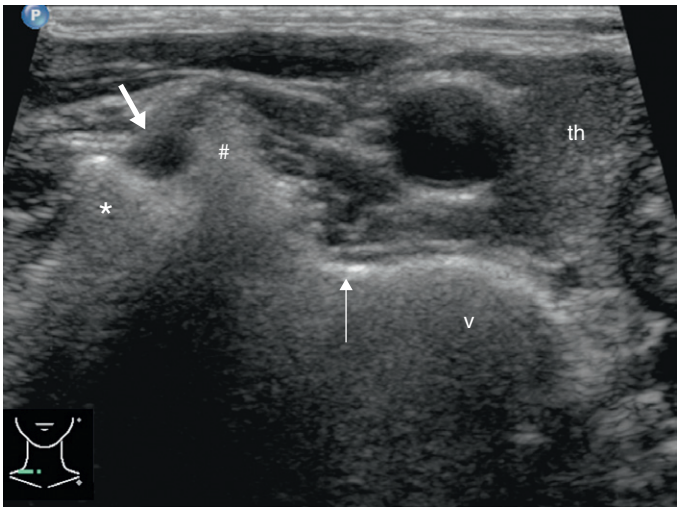

Figure 45.49 Cervical nerve root. Transverse sonogram of the right C6 nerve root (thick arrow); thin arrow indicates pedicle; #, anterior process; *, posterior process; v, vertebral body; th, thyroid.

aspect, with slight inferior angulation, along the superior margin of the clavicle. The key structure to identify is the scalenus anterior muscle with the venous structures (internal jugular vein and subclavian vein) anterior to it and the subclavian artery posteriorly. Between the scalenus anterior and scalenus medius muscles, the brachial plexus elements appear as round/ovoid hypoechoic structures, emerging from medial to lateral. There are usually three structures corresponding to the brachial plexus trunks at this level; however, depending on the angle of the probe, a combination of roots (five) and trunks (three) may be visualised (Fig. 45.48).[46]

In slim individuals and with inferior probe angulation, the brightly echogenic lung apex, sliding beneath the pleura, may be seen behind the first rib and subclavian artery.

The transverse cervical group of lymph nodes lies around the transverse cervical artery and vein as these vessels run from the costocervical trunk across the posterior triangle to the levator scapulae muscle.

Pathology in the supraclavicular fossa

Non-nodal masses of the supraclavicular fossa are rare; however, normal structures often present as 'masses'. The most common pseudo-mass in middle-aged women is fat – which is often asymmetrical.

Tortuous or prominent subclavian vessels and apical lung bullae are other pseudo-masses easily identified with ultrasound.

6. POSTERIOR TRIANGLE

Normal ultrasound anatomy and technique

The posterior triangle lies posterior to sternomastoid, bounded by trapezius posteriorly and the clavicle inferiorly; the floor is composed of a layer of muscles: scalenus anterior and scalenus medius, together with levator scapulae. It is a superficial, fat-filled space and is easily assessed in the transverse plane by a sweep from the mastoid process to the lateral clavicle/acromioclavicular joint. Within this echogenic layer of adipose tissue lie the posterior triangle chain of nodes and the spinal accessory nerve, which crosses the triangle along the line of the lymph nodes, but is not visualised on ultrasound.

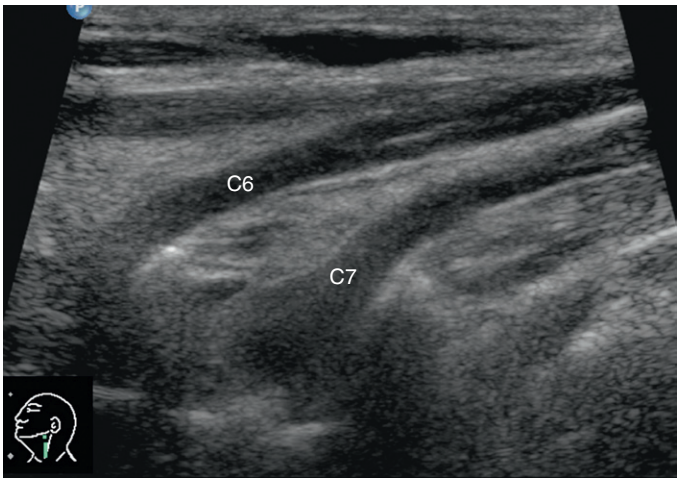

Figure 45.50 Longitudinal view of cervical nerve roots. Longitudinal sonogram of the C6 and C7 nerve roots exiting the neural foramina.

The transverse processes of the cervical vertebrae are easily seen in slim individuals and should not be mistaken for calcified lymph nodes. C3 to C6 have bifid transverse processes – the anterior tubercle may be seen immediately deep to the internal jugular vein, with the posterior tubercle posterior to it, forming an echogenic 'U'-shaped structure on transverse scanning. The 'U' shapes of the bifid transverse processes become progressively larger from C3 to C6 (Fig. 45.49), and the ovoid, hypoechoic nerve roots may be seen emerging through them to lie between scalenus anterior and scalenus medius.

C6 is easy to identify as the vertebral body lying posterior to the thyroid gland; the probe is then moved laterally to the pedicle, allowing identification of the anterior and posterior tubercles of the transverse process, with the C6 root emerging between them (Fig. 45.49). The absence of the anterior tubercle is a reliable and key anatomical landmark for C7; the roots of C8 and T1 are not consistently identified. The roots should be examined in both transverse and longitudinal planes (Fig. 45.50).[47]

Although MRI is the imaging technique of choice for the brachial plexus, ultrasound is gaining popularity as a useful adjunct to MRI

in the investigation of post-ganglionic brachial plexopathies. It is also useful for guiding local anaesthetic injections for regional blocks; it is therefore worthwhile spending time familiarising oneself with the anatomy of this region.

Pathology in the posterior triangle

Non-nodal pathology is rare – the commonest being nerve sheath tumours (Fig. 45.47).The posterior triangle is the commonest site for a cystic hygroma in children (Fig. 45.36).

7. ANTERIOR (INFRAHYOID) NECK

Normal ultrasound anatomy and technique

This final sweep starts at the hyoid bone and extends down to the suprasternal notch, in the midline. This region contains structures which may be unfamiliar on ultrasound: the larynx, trachea, hypopharynx and proximal oesophagus, as well as the pre- and paratracheal nodes (see Figs 46.11 and 46.12, Chapter 46). This region is assessed transversely for lymph nodes, supplemented by longitudinal scanning of the larynx. Although ultrasound is not the primary imaging modality for the larynx, it can provide useful and complementary information; it is therefore valuable being familiar with the normal ultrasound anatomy.[48]

The first key structure to identify in the transverse plane is the hyoid bone (Fig. 45.11), a smooth horseshoe-shaped structure, with dense posterior acoustic shadowing. The genioglossus muscle is seen immediately superior to the hyoid, fanning out into the tongue (Figs 45.7, 45.8). The valleculae are paired, mucosal pouches situated between the base of the tongue and the epiglottis; they are sometimes visualised as two short, echogenic lines parallel to the probe, just below the hyoid (Fig. 45.51). The tip of the epiglottis is seen deep to the valleculae as a single, transverse echogenic stripe parallel to the probe (Fig. 45.52). The pre-epiglottic fat lies anterior to the epiglottis, and contains uniformly fine, speckled echoes (Figs 45.53, 45.54); it is continuous with the paraglottic fat and it is a useful region to assess for submucosal spread of supraglottic tumours, as this is a clinical 'blind spot'.

The space should be assessed transversely and longitudinally; the longitudinal view is key to the delineation of thyroglossal duct cysts and their relationship to the hyoid (Fig. 45.54).

The thyroid cartilage calcifies to a variable degree; when non-calcified it is seen as a thin, hypoechoic, inverted 'v'-shaped structure in transverse section. If the thyroid cartilage is sonolucent, the mobile false and true cords may be visualised within the larynx. The false cords contain paraglottic fat and are therefore brightly echogenic, whereas the true cords are composed of muscle and are therefore hypoechoic (Fig. 45.55A and B). The arytenoid cartilages may also be visualised as small echogenic foci within the posterior aspects of the true vocal cords. This transverse view of the larynx is useful for assessing cord mobility in patients who are difficult to examine with nasendoscopy, for example children.

The echogenic paraglottic fat is an important region to identify. It is best assessed with the probe in an oblique longitudinal position

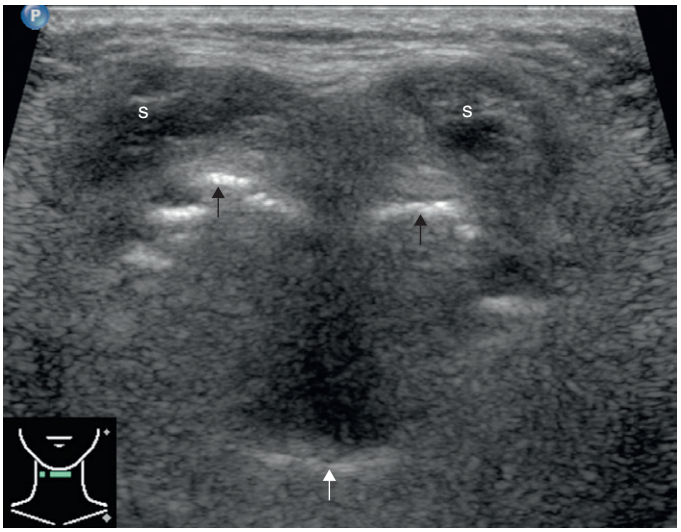

Figure 45.51 Valleculae. Transverse sonogram just below the hyoid, demonstrating the valleculae (black arrows). White arrow indicates epiglottis; s, strap muscles.

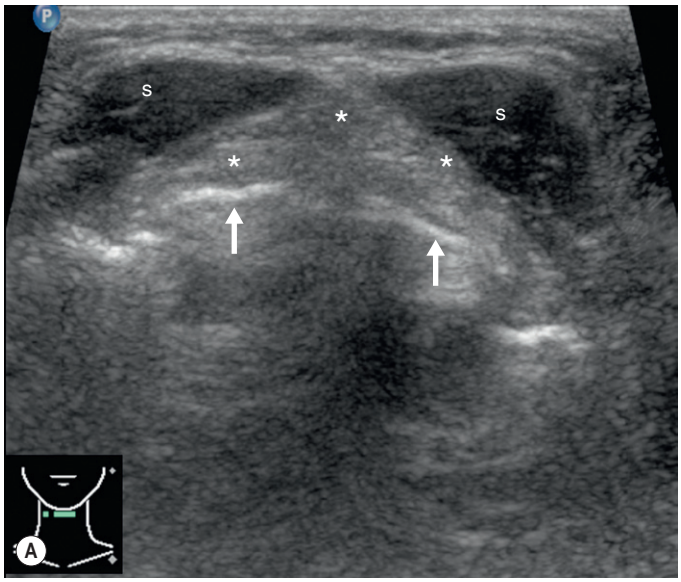

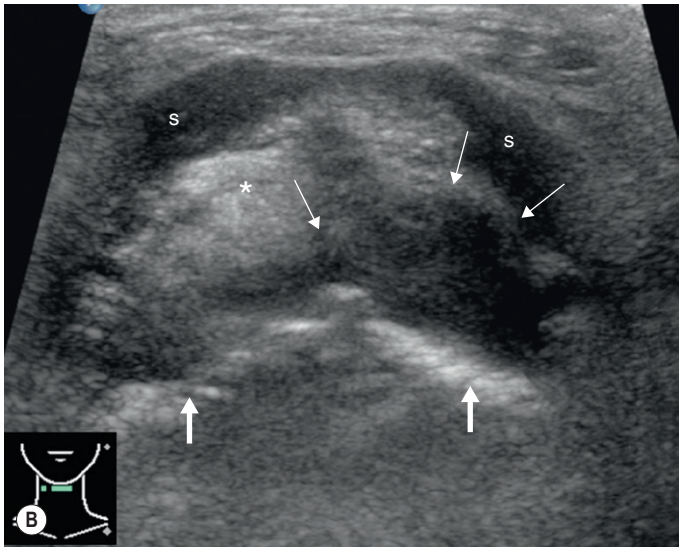

Figure 45.52 Epiglottis. Transverse sonogram at a slightly lower level than Figure 45.51 of **(A)** normal pre-epiglottic fat, and **(B)** tumour (thin arrows) in the pre-epiglottic fat. Thick arrows indicate epiglottis; *, pre-epiglottic fat; s, strap muscles.

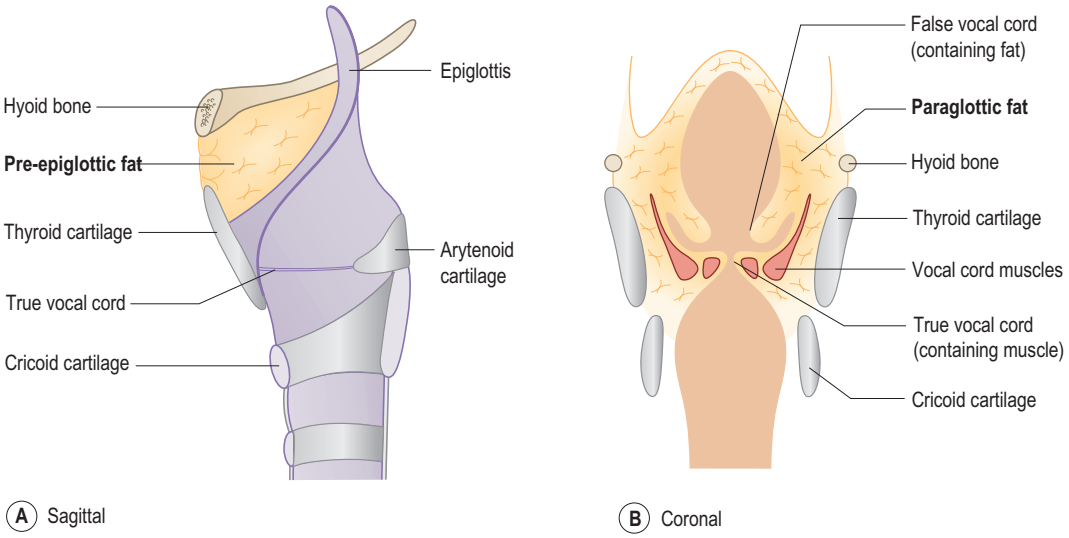

Figure 45.53 Pre-epiglottic and paraglottic fat spaces. Diagrams demonstrating the pre-epiglottic and paraglottic fat spaces. These are the site of submucosal tumour spread, and are clinical blind spots.

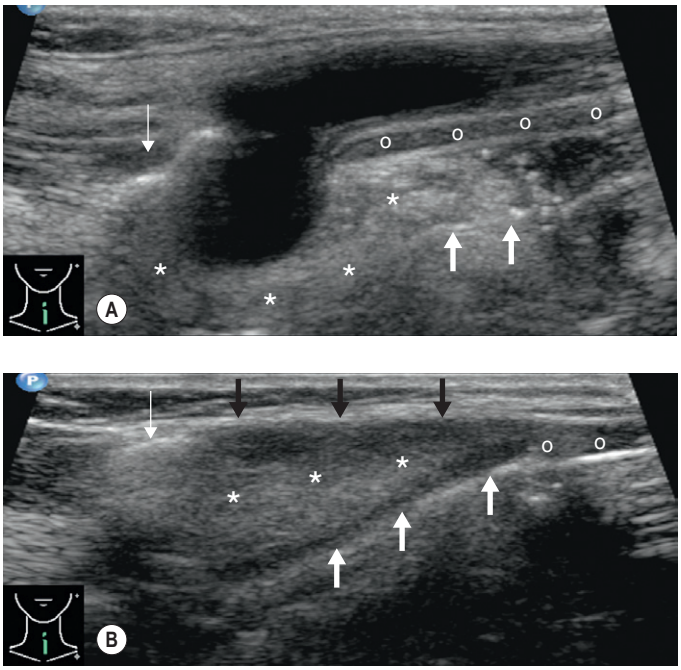

Figure 45.54 Pre-epiglottic and paraglottic fat spaces. Longitudinal midline sonograms at the infrahyoid level. **A:** Normal pre-epiglottic fat and **B:** a thyroglossal duct cyst protruding through the thyrohyoid membrane (thick black arrows), into the pre-epiglottic fat (*), which is continuous with the paraglottic fat inferiorly. Thin arrow indicates hyoid; thick arrows indicate epiglottis; o, thyroid cartilage.

(Figs 45.53, 45.56). This is another clinically invisible site of submucosal invasion from supraglottic tumours.

Thyroid cartilage invasion (denoting a T3 tumour if the inner cortex is involved, T4 if the tumour extends through the outer cortex) is often very difficult to determine clinically and radiologically, ultrasound may help in this respect.

In the transverse plane, the cricoid cartilage is seen as a bulky, smooth, hypoechoic 'mass' emerging from the posterior aspect of the upper pole of the thyroid gland; care should be taken not to mistake this for a thyroid nodule.

The trachea is seen as a series of sonolucent rings below the cricoid. Identification of these cartilaginous rings is required for safe placement of a percutaneous tracheostomy; the optimal position for the tracheostomy tube is between the first and second tracheal rings.

The postcricoid segment of the oesophagus is frequently seen posterior to the inferior pole of the thyroid gland; it is important to recognise this as a normal structure rather than mistaking it for a thyroid nodule. It has concentric hypo- and hyperechoic mural rings, corresponding to the muscle layers and the gas/mucosal interface; scanning in a longitudinal plane confirms its tubular nature. If in doubt, ask the patient to swallow and peristalsis will be observed. Tumours of the postcricoid oesophagus may also be seen (Fig. 45.57).

The normal thymus gland is sometimes visible in children, deep in the suprasternal notch. The gland has a smooth margin; the hypoechoic parenchyma has a granular texture which may show comet-tail or ring-down artefacts, giving a 'sparkly' appearance (Fig. 45.58).

Larynx

- Unfamiliar anatomy.
- Limited in heavily calcified cartilages.
- Useful for vocal cord mobility.
- Valuable in assessing submucosal spread to the pre-epiglottic and paraglottic fat spaces, as these areas are clinical blind spots.
- May be useful for assessing thyroid cartilage invasion.

Pathology in the anterior (infrahyoid neck)

Thyroglossal duct cyst (TDC)

Thyroglossal duct cyst is the most common midline neck mass and also the most common congenital neck mass.[49] Most (65%) thyroglossal duct cysts occur below the hyoid bone, 15% occur at the level of the hyoid and 20% are suprahyoid – these hyoid and suprahyoid cysts must be considered in the differential diagnosis of a mass in the submental region.

The primitive thyroid begins to develop during the third week of fetal life, descending into the anterior neck along the thyroglossal duct. The thyroglossal duct originates at the foramen caecum in the base of the tongue and descends through the floor of mouth, around

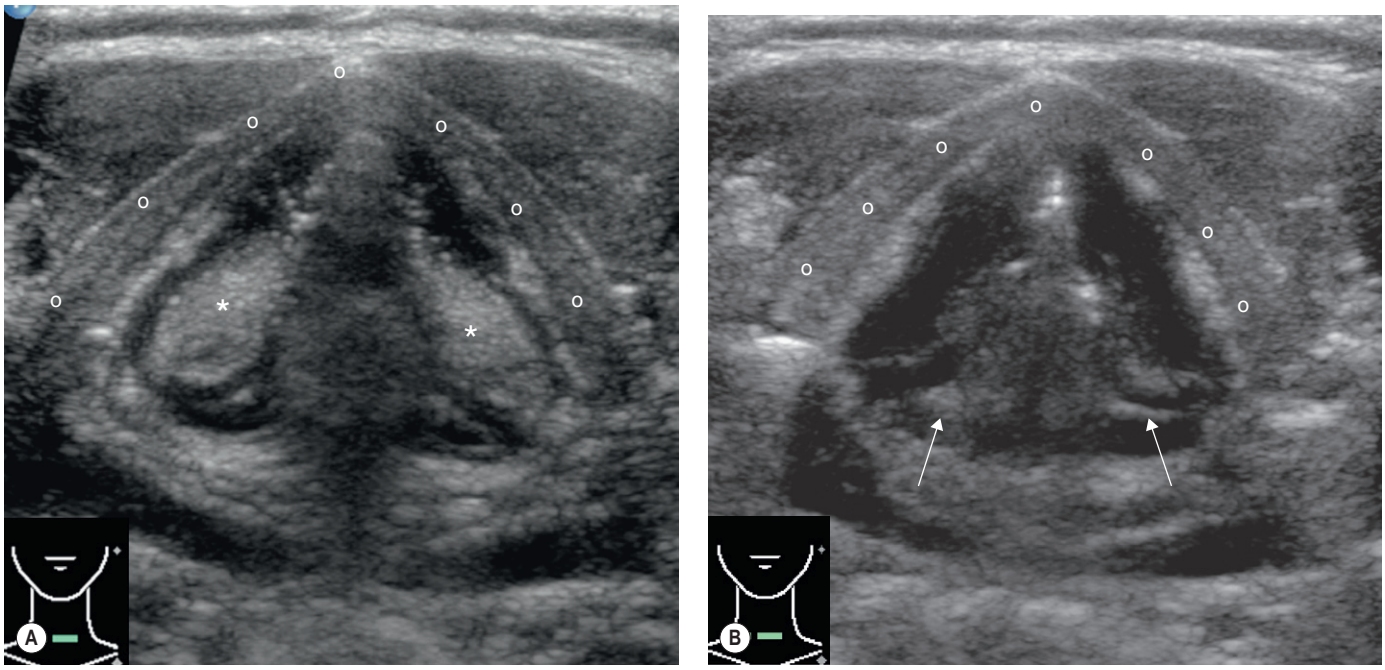

Figure 45.55 Vocal cords. Transverse sonograms at the level of the thyroid cartilage (o) showing **(A)** false vocal cords (tiny arrows) and **(B)** true vocal cords (tiny arrows). The false vocal cords are brightly echogenic as they contain paraglottic fat (*). Thick arrows indicate arytenoid cartilages.

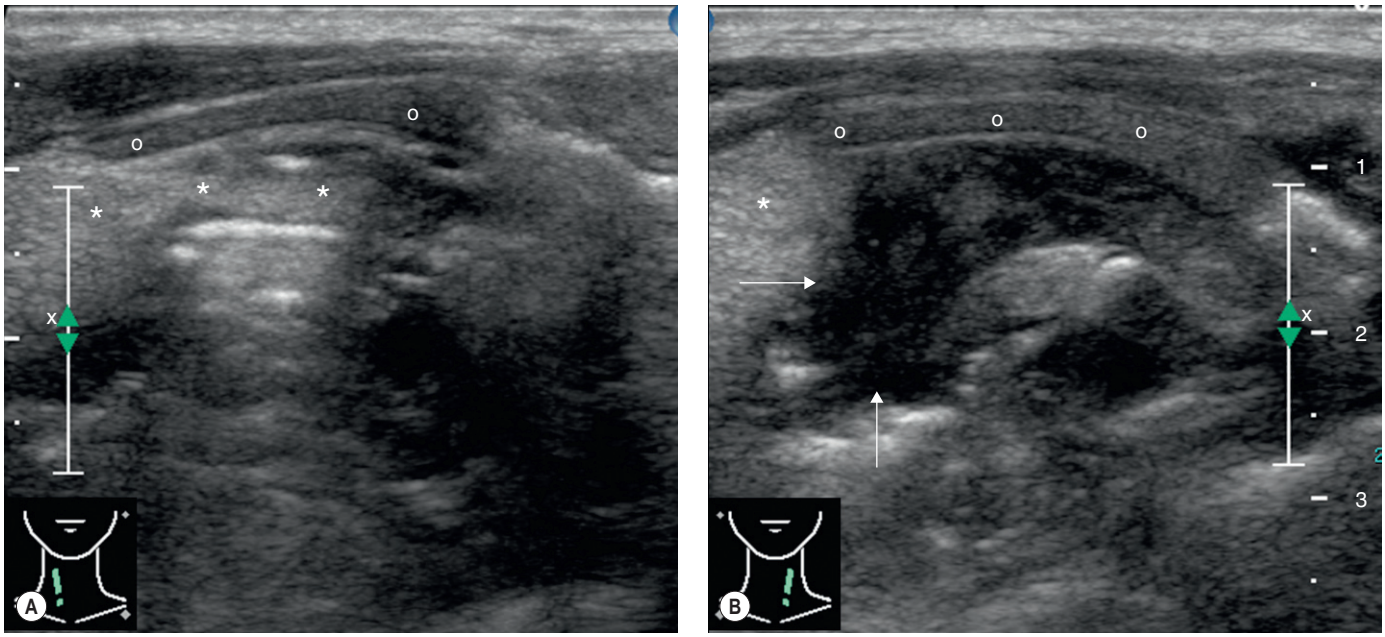

Figure 45.56 Tumour invasion into the paraglottic fat. Oblique coronal sonogram of **(A)** normal paraglottic fat (*) and **(B)** tumour invasion into the paraglottic fat (arrows) on the contralateral side. o, thyroid cartilage; *, paraglottic fat.

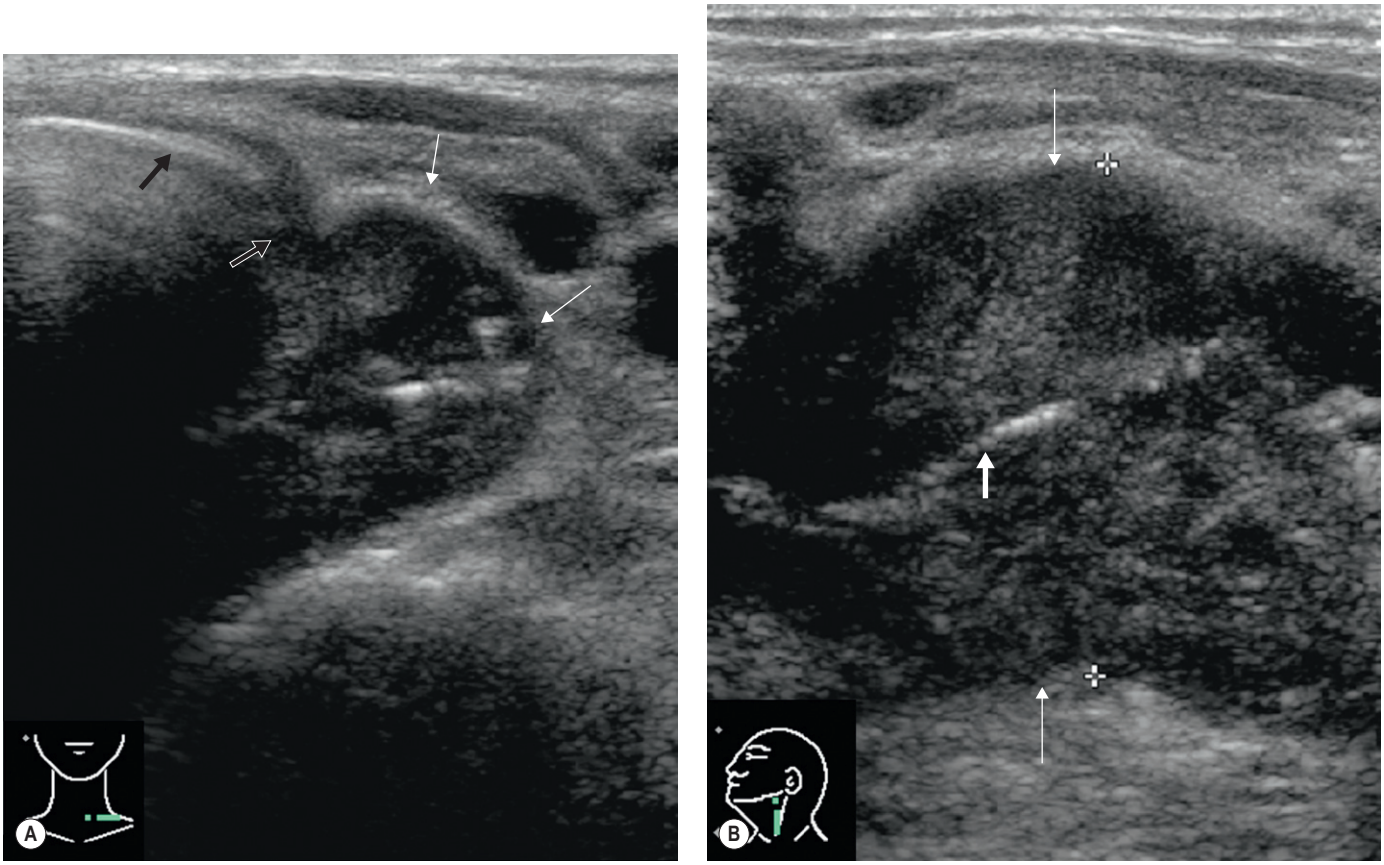

Figure 45.57 Tumour of postcricoid oesophagus. A: Transverse and **B:** longitudinal sonograms at the level of the cricoid cartilage (thick black arrows), demonstrating a postcricoid tumour (thin arrows and callipers). Thick white arrow indicates gas/mucosal interface.

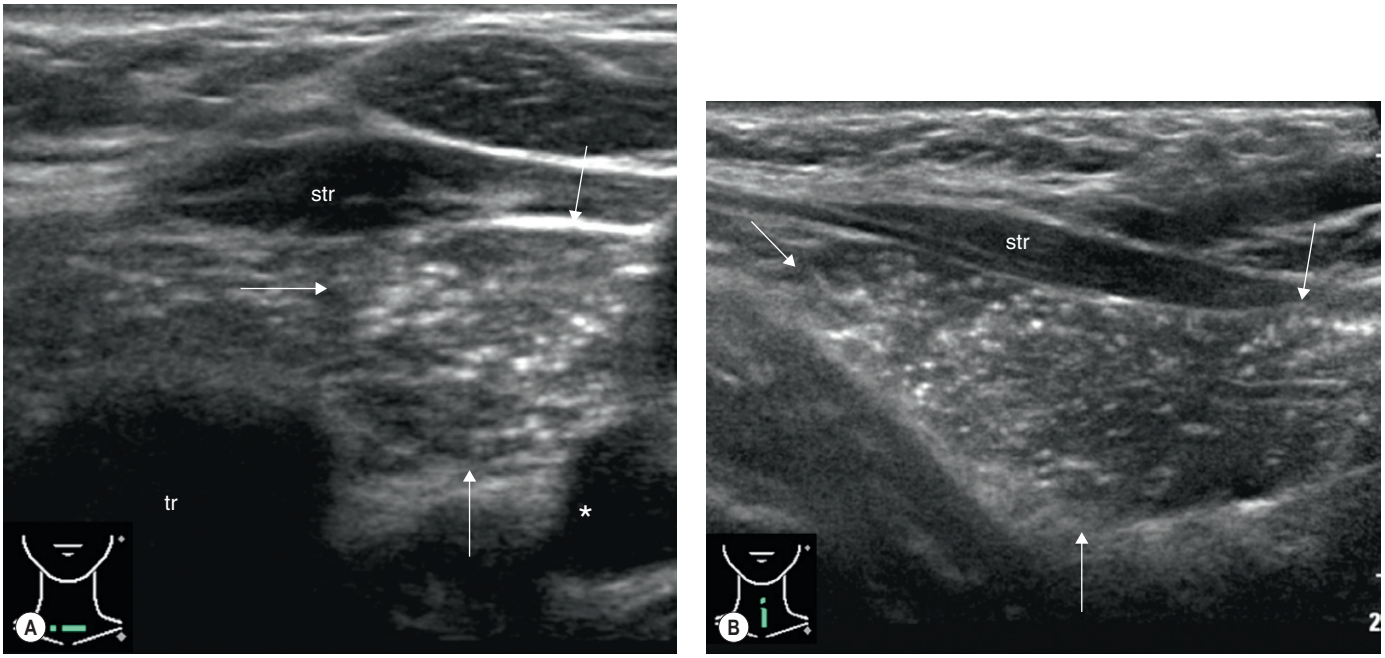

Figure 45.58 Thymus gland. Sonogram of a normal thymus gland (arrows) in the suprasternal notch. Transverse **(A)** and longitudinal **(B)** images. The gland contains multiple brightly echogenic foci with ring-down or comet-tail artefact giving a 'sparkly' appearance. tr, trachea; str, strap muscle; *, carotid artery.

or through the hyoid bone, and passes anterior to the strap muscles to the thyroid bed. Failure of involution of the thyroglossal duct at the eighth gestational week can result in congenital anomalies, such as thyroglossal duct cysts or ectopic thyroid tissue.

About 50% of patients present before the age of 10, while a second group present in young adulthood.[2] Thyroglossal duct cysts present as slowly enlarging, painless masses in the anterior neck, classically moving up and down on tongue protrusion due to their attachment to the hyoid bone. If infected they become red, indurated and painful. There is frequently a history of previous incision and drainage.

Four categories of ultrasound appearances of thyroglossal duct cysts have been described:[50]

1. Frankly cystic – anechoic with posterior acoustic enhancement.
2. Hypoechoic with internal debris.
3. Heterogeneous echo pattern, probably due to repeated infections or haemorrhage.
4. Uniformly echogenic 'pseudosolid' appearance, due to the proteinaceous content of the cyst secreted by the epithelial lining.

Most thyroglossal duct cysts are unilocular. They are intimately associated with the hyoid bone; this relationship is pathognomonic of a thyroglossal duct cyst, with the longitudinal midline image being the key view (Fig. 45.54B). The cysts may involve the pre-epiglottic space by piercing the thyrohyoid membrane. Suprahyoid thyroglossal duct cysts tend to be midline, whereas infrahyoid cysts tend to be off the midline,[51] and embedded in the strap muscles (Fig. 45.59).

All of these features may be demonstrated with ultrasound, and are useful for preoperative planning. The recommended surgery for thyroglossal duct cysts is the Sistrunk procedure in which the central portion of the hyoid bone is removed, as well as the cyst. Surgical removal is recommended following an episode of infection, as infection tends to recur.

Malignancy in a thyroglossal duct cyst is rare, the incidence being less than 1%. Papillary thyroid carcinoma is the most common malignancy and should be suspected if a solid element is noted within a thyroglossal duct cyst.

Laryngocele

Internal laryngoceles are fluid-filled structures deep to the false cords in the paraglottic space (Fig. 45.53). They may enlarge and protrude through the thyrohyoid membrane, presenting as a mass in the anterior neck which may contain gas or pus if infected. Twenty per cent of laryngoceles are secondary to a tumour obstructing the laryngeal ventricle.

Laryngeal tumours

Supraglottic tumours frequently invade the pre-epiglottic and paraglottic fat spaces; both sites are submucosal, and tumours at these sites are usually clinically invisible. Tumour is seen as a poorly defined hypoechoic mass within the echogenic fat (Figs 45.52, 45.56). Invasion through the thyroid cartilage is difficult but important to identify as it denotes a T4 tumour, which may require a laryngectomy as cartilage is relatively insensitive to radiotherapy.

Note that the pattern of spread of a postcricoid carcinoma is to spread *around* the posterior margin of the thyroid lamina rather than *through* it, as the tumour is usually confined by the superior constrictor muscle. Tumour will therefore be seen on both sides of the thyroid cartilage without direct invasion through the cartilage.

Pharyngeal pouch

A pharyngeal pouch is occasionally an incidental finding on ultrasound. It appears as a sparkling echogenic gas-containing structure, usually in the left anterior neck (Fig. 45.60). It may be mistaken for an abscess.

Chondroid tumours

These are rare tumours, accounting for less than 1% of all laryngeal tumours. They are most common in the cricoid cartilage. On ultrasound they are solid, hypoechoic lesions containing punctate foci of calcification (Fig. 45.61).

The postoperative neopharynx

Jejunal grafts and stomach pull-ups are used to reconstruct the hypopharynx following laryngectomy. As the larynx has been removed, this neopharynx is very superficial, and easily visualised in the anterior neck. The ultrasound appearances have an identical appearance to bowel elsewhere with concentric hypo- and hyperechoic mural rings. In some views these appearances may be mistaken for an abscess (Fig. 45.62).

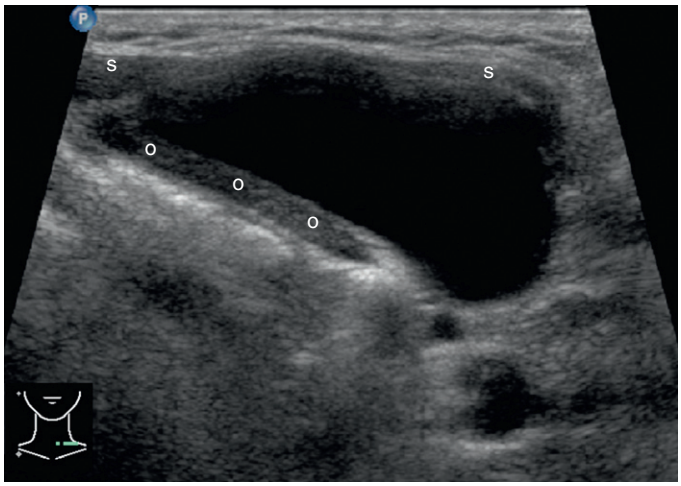

Figure 45.59 Thyroglossal duct cyst. Transverse sonogram at the level of the thyroid cartilage (o), demonstrating a thyroglossal duct cyst embedded in the strap muscles (s), just off the midline.

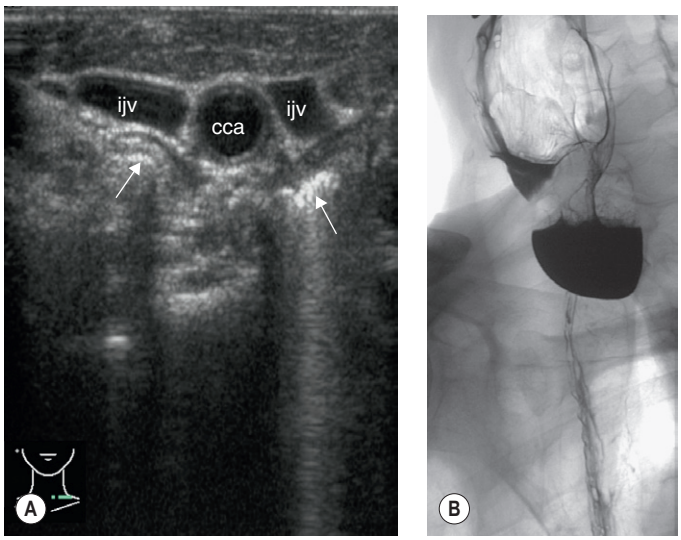

Figure 45.60 Pharyngeal pouch. Transverse sonogram at the level of the cricoid cartilage **(A)**, and a barium swallow **(B)**, demonstrating the sparking echoes of gas (arrows) within a left pharyngeal pouch. A laryngocele would have similar appearances. ijv, compressed internal jugular vein, cca, common carotid artery.

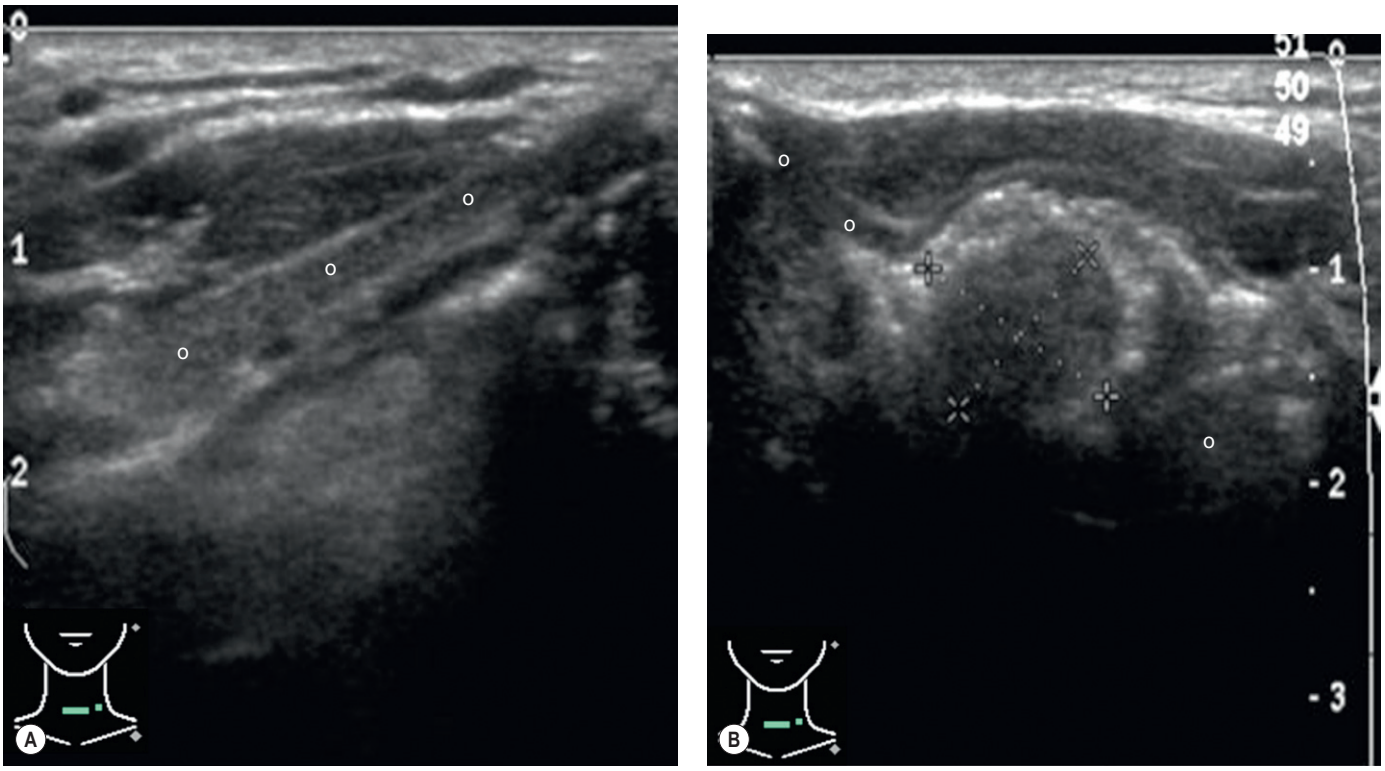

Figure 45.61 Chondroid tumour of thyroid cartilage. Transverse sonogram at the level of the thyroid cartilages (o, thyroid cartilage); **A:** normal and **B:** a chondroid lesion – a focal expansion (callipers) of the left thyroid lamina, containing calcification.

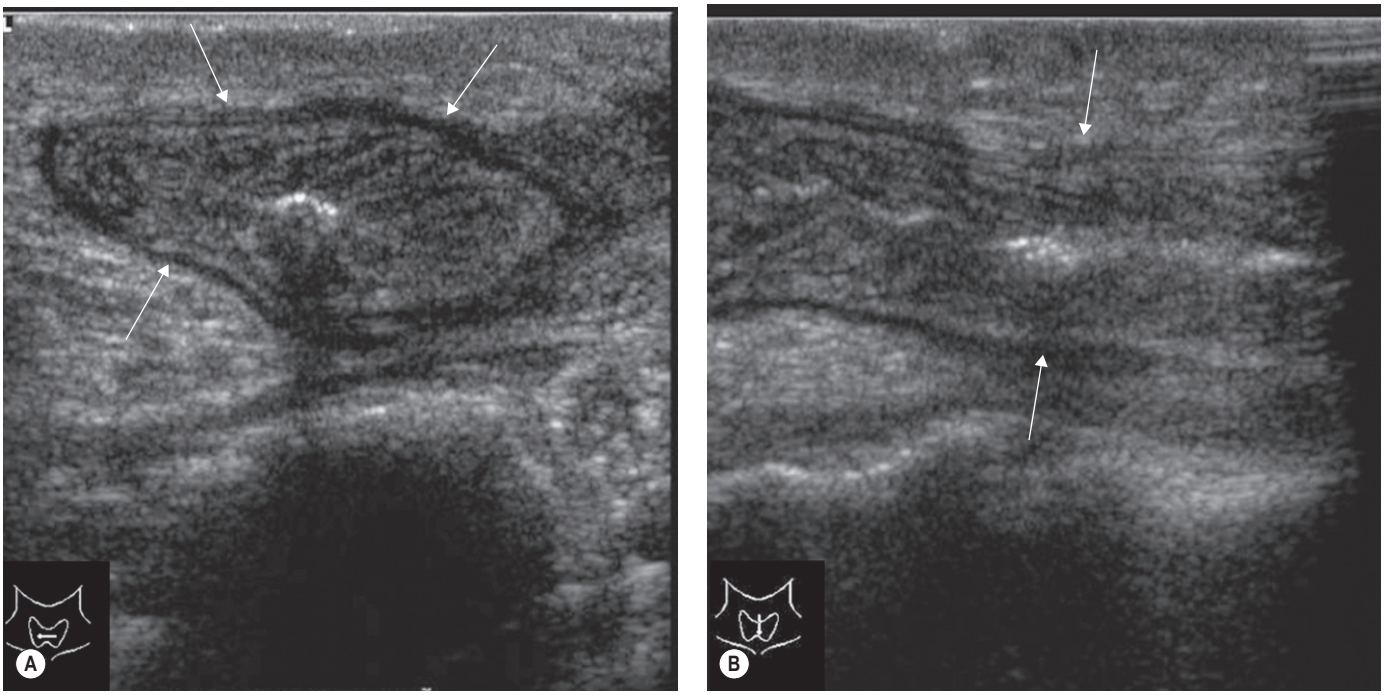

Figure 45.62 Post-laryngectomy neopharynx. (A) Transverse and **(B)** longitudinal sonograms at the level of the suprasternal notch demonstrating a jejunal pull-up (arrows); the transverse image may mimic an abscess.

REFERENCES

1. Brown G, Baker J. Work-related musculoskeletal disorders in sonographers. J Diagn Med Sonogr 2004;20(2):85.
2. Harnsberger HR. Handbook of head and neck imaging. St Louis, MO: Mosby; 1994.
3. Harnsberger HR, Hudgins PA, Wiggins RH, Davidson HC. Diagnostic imaging: head and neck. Philadelphia: Saunders; 2004:2–5.
4. Rhys R, Evans R. Sonography of the submandibular duct. Eur J Ultrasound 1998;8(3):S16 (Abstract).
5. White D, Davidson H, Harnsberger H, et al. Accessory salivary tissue in the mylohyoid boutonnière: a clinical and radiologic pseudolesion of the oral cavity. AJNR Am J Neuroradiol 2001;22(2):406–412.
6. Hunter T, Paplanus S, Chernin M, Coulthard S. Dermoid cyst of the floor of the mouth: CT appearance. AJR Am J Roentgenol 1983;141(6): 1239–1240.
7. Marinovic D, Garel C, Czernichow P, Leger J. Ultrasonographic assessment of the ectopic thyroid tissue in children with congenital hypothyroidism. Pediatr Radiol 2004;34(2):109–113.
8. Noyek A, Friedberg J. Thyroglossal duct and ectopic thyroid disorders. Otolaryngol Clin North Am 1981;14(1):187–1201.
9. Lim-Dunham J, Feinstein K, Yousefzadeh D, Ben-Ami T. Sonographic demonstration of a normal thyroid gland excludes ectopic thyroid in patients with thyroglossal duct cyst. AJR Am J Roentgenol 1995;164(6): 1489–1491.
10. Silvers A, Som P. Salivary glands. Radiol Clin North Am 1998;36(5): 941–966, vi.
11. Rabinov J. Imaging of salivary gland pathology. Radiol Clin North Am 2000;38:1047–1057, x–xi.
12. Gritzmann N. Sonography of the salivary glands. AJR Am J Roentgenol 1989;153(1):161–166.
13. Huang C, Damrose E, Bhuta S, Abemayor E. Kuttner tumor (chronic sclerosing sialadenitis). Am J Otolaryngol 2003;23(6):394–397.
14. Ahuja A, Richards P, Wong K, et al. Kuttner tumour (chronic sclerosing sialadenitis) of the submandibular gland: sonographic appearances. Ultrasound Med Biol 2003;29(7):913–919.
15. Peters DA, Courtemanche DJ, Heran MKS, et al. Treatment of cystic lymphatic vascular malformations with OK-432 sclerotherapy. Plast Reconstr Surg 2006;118(6):1441.
16. Macdonald A, Salzman K, Harnsberger H. Giant ranula of the neck: differentiation from cystic hygroma. AJNR Am J Neuroradiol 2003;24(4):757–761.
17. Eneroth C. Salivary gland tumors in the parotid gland, submandibular gland, and the palate region. Cancer 1971;27(6):1415–1418.
18. Schick S, Steiner E, Gahleitner A, Böhm P, et al. Differentiation of benign and malignant tumors of the parotid gland: value of pulsed Doppler and color Doppler sonography. Eur Radiol 1998;8(8): 1462–1467.
19. Bradley M, Durham L, Lancer J. The role of colour flow Doppler in the investigation of the salivary gland tumour. Clin Radiol 2000;55(10): 759–762.
20. Bruneton J, Mourou M. Ultrasound in salivary gland disease. ORL J Otorhinolaryngol Relat Spec 1993;55(5):284–289.
21. Som PM, Shugar JMA, Sacher M, et al. Benign and malignant parotid pleomorphic adenomas: CT and MR studies. J Comput Assist Tomogr 1988;12(1):65.
22. Bradley M. Salivary glands. In: Ahuja A, Evans R, eds. Practical head and neck ultrasound. London: Greenwich Medical Media; 2000. p. 19–33.
23. Paltiel H, Burrows P, Kozakewich H, et al. Soft-tissue vascular anomalies: utility of US for diagnosis. Radiology 2000;214(3):747–754.
24. Mulliken J, Glowacki J. Hemangiomas and vascular malformations in infants and children: a classification based on endothelial characteristics. Plast Reconstr Surg 1982;69(3):412–422.
25. Enjolras O. Classification and management of the various superficial vascular anomalies: hemangiomas and vascular malformations. J Dermatol 1997;24(11):701–710.
26. Madani G, Beale T. Tumors of the salivary glands. Semin Ultrasound CT MR 2006;27(6):452–464.
27. Bradus R, Hybarger P, Gooding G. Parotid gland: US findings in Sjögren syndrome. Work in progress. Radiology 1988;169(3): 749–751.
28. Chitre VV, Premchandra DJ. Recurrent parotitis. BMJ 1997;77(4): 359–363.
29. Bhattarai M, Wakode PT. Recurrent parotitis in children. J Ind Assoc Pediatr Surg 2006;11(4):246.
30. Godwin J. Benign lymphoepithelial lesion of the parotid gland adenolymphoma, chronic inflammation, lymphoepithelioma, lymphocytic tumor, Mikulicz disease. Cancer 1952;5(6):1089–1103.
31. Som P, Brandwein M, Silvers A. Nodal inclusion cysts of the parotid gland and parapharyngeal space: a discussion of lymphoepithelial, AIDS-related parotid, and branchial cysts, cystic Warthin's tumors, and cysts in Sjögren's syndrome. Laryngoscope 1995;105(10):1122–1128.
32. Verbin R, Barnes L. Cysts and cyst-like conditions of the oral cavity, jaws and neck. In: Barnes L, ed. Surgical pathology of the head and neck. New York: Marcel Dekker; 1985. p. 1233–1329.
33. George K, Witherow H, Marion M. Uses of botulinum toxin in maxillofacial surgery. Br J Oral Maxillofac Surg 2008;46(7):56.
34. Dubois J, Soulez G, Oliva VL, et al. Soft-tissue venous malformations in adult patients: imaging and therapeutic issues. Radiographics 2001;21:1519–1531.
35. Danielson-Cohen A, Lin S, Hughes C, et al. Head and neck pilomatrixoma in children. Arch Otolaryngol Head Neck Surg 2001;127(12):1481–1483.
36. Whittle C, Martínez W, Baldassare G, et al. [Pilomatrixoma: ultrasound diagnosis]. Rev Med Chil 2003;131(7):735–740.
37. Telander R, Deane S. Thyroglossal and branchial cleft cysts and sinuses. Surg Clin North Am 1977;57(4):779–791.
38. Ahuja A, King A, Metreweli C. Second branchial cleft cysts: variability of sonographic appearances in adult cases. AJNR Am J Neuroradiol 2000;21(2):315–319.
39. Weissleder R, Elizondo G, Stark DD. Sonographic diagnosis of subclavian and internal jugular vein thrombosis. J Ultrasound Med 1987;6:577–587.
40. Espiritu MB, Medina JE. Complications of heroin injections of the neck. Presented at the Meeting of the Middle Section of the American Laryngological, Rhinological and Otological Society, Inc., Milwaukee, WI, January 12, 1980. The Laryngoscope 1980;90(7).
41. Trousseau A. Phlegmasia alba dolens. In: Clinique medicale de l'hotel-dieu de Paris. London: New Sydenham Society; 1865. p. 94.
42. Sack GJ, Levin J, Bell W. Trousseau's syndrome and other manifestations of chronic disseminated coagulopathy in patients with neoplasms: clinical, pathophysiologic, and therapeutic features. Medicine (Baltimore) 1977;56(1):1–37.
43. Rao AB, Koeller KK, Adair CF. From the Archives of the AFIP 1. Paragangliomas of the head and neck: radiologic-pathologic correlation. Radiogaphics 1999;19:1605–1632.
44. Tsai W, Chiou H, Chou Y, et al. Differentiation between schwannomas and neurofibromas in the extremities and superficial body: the role of high-resolution and color Doppler ultrasonography. J Ultrasound Med 2008;27(2):161–166; quiz 8–9.
45. King A, Ahuja A, King W, Metreweli C. Sonography of peripheral nerve tumors of the neck. AJR Am J Roentgenol 1997;169(6): 1695–1698.
46. Cash C, Sardesai A, Berman L, et al. Spatial mapping of the brachial plexus using three-dimensional ultrasound. Br J Radiol 2005;78(936): 1086–1094.
47. Martinoli C, Bianchi S, Santacroce E, et al. Brachial plexus sonography: a technique for assessing the root level. AJR Am J Roentgenol 2002;179(3):699–702.
48. Loveday EJ. Ultrasound of the larynx. Imaging 2003;15(3):109–114.
49. Som PM. Cystic lesions of the neck. Postgrad Radiol 1987;7(21):1–236.
50. Ahuja A, King A, King W, Metreweli C. Thyroglossal duct cysts: sonographic appearances in adults. AJNR Am J Neuroradiol 1999; 20(4):579–582.
51. Telander R, Filston H. Review of head and neck lesions in infancy and childhood. Surg Clin North Am 1992;72(6):1429–1447.

CHAPTER

46

Cervical lymph nodes

Rhian Rhys

There are over 300 lymph nodes in a normal neck.[1] They may be involved with metastases, lymphoma and infection; or they may simply enlarge as a reaction to local inflammation – reactive hyperplasia.

Most of these nodes lie no more than 2–3 cm below the skin, and are easily visualised with high-frequency linear transducers (7–17 MHz). Advanced probe technology now gives spatial resolution of 0.25 mm axially and laterally, which is far superior to computed tomography (CT) and magnetic resonance imaging (MRI).

A sound knowledge of the normal ultrasound appearances and distribution of lymph nodes in the head and neck is crucial if one is to recognise and diagnose pathological changes.

STRUCTURE AND FUNCTION

It is useful to have an appreciation of the function and histology of normal nodes in order to understand their characteristic ultrasound appearances. Normal lymph nodes are flat, bean-shaped structures, 0.25–1 cm long, composed of an outer capsule, a peripheral cortex and a central medulla. The medulla is continuous with a small peripheral indentation – the hilum (Fig. 46.1).

The cortex consists of closely packed lymphoid follicles, which, when stimulated, develop foci of lymphopoiesis – the germinal centres. The medulla is composed of lymphatic sinuses, blood vessels and connective tissue. Multiple converging sinuses in the medulla form the hilum. A capsule of supporting reticular framework encircles the node, which maintains its shape; the lymphatic sinuses are simply channels within this framework, radiating from the cortex to the medulla.

Lymph enters the periphery of the node via multiple afferent lymphatic vessels and passes into the peripheral subcapsular sinus, which surrounds the node; it then passes through the radiating cortical sinuses into the medulla, leaving the node by a single efferent vessel at the hilum.[2] The main arteries and veins also enter and leave the lymph node at the hilum and spread in bundles of arterioles and venules, coursing along the longitudinal axis of the node in the medulla. The relatively avascular cortex is fed from the central medullary vessels.[3]

The ultrasound appearance of a normal node may thus be explained: the densely cellular peripheral zone appearing as the hypoechoic cortex; the parallel arrangement of the medullary sinuses acting as multiple specular reflectors, producing a hyperechoic structure termed the hilum. The hyperechoic hilum was originally thought to be due to fat;[4] however, more recent sonographic and histological correlation has confirmed that the convergence of the lymphatic sinuses is responsible for the echogenic hilum.[5]

The normal response of a lymph node to an antigenic stimulus results in an increase in its size and vascularity. Within the cortex, lymphoid follicles increase in number and develop germinal centres; within the medullary cords (which are the main site of antibody production), plasma cells increase in numbers. These changes are accompanied by a marked capillary redistribution in the cortex of the node, resulting in this normally rather avascular region becoming uniformly vascular.[3]

LYMPHATIC CIRCULATION

All the lymph ducts contain smooth muscle in their walls;[6] lymph is propelled forcefully towards the heart, via the thoracic duct on the left and the lymphatic duct on the right, which empty into the subclavian veins. Flow is directed via a series of bicuspid valves. These valves may become damaged by infection, malignancy or surgery, causing retrograde flow or shunting. This is an important point to bear in mind in the management of a neck mass that is suspected to be a malignant node. Surgical removal of the node in

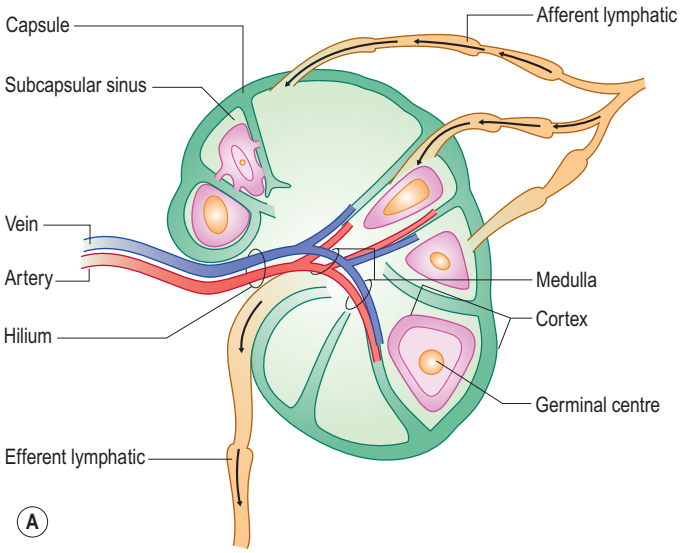

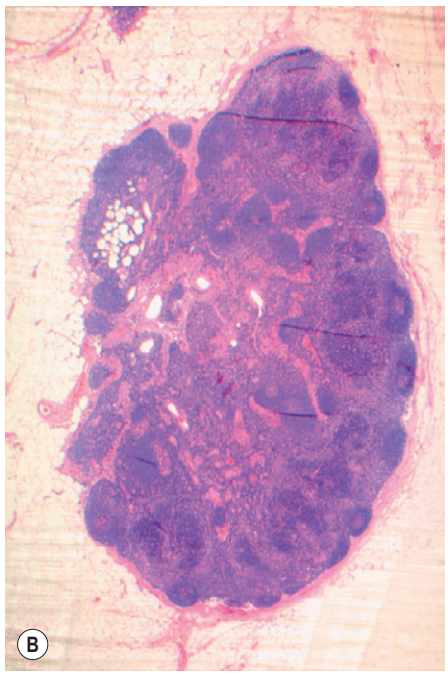

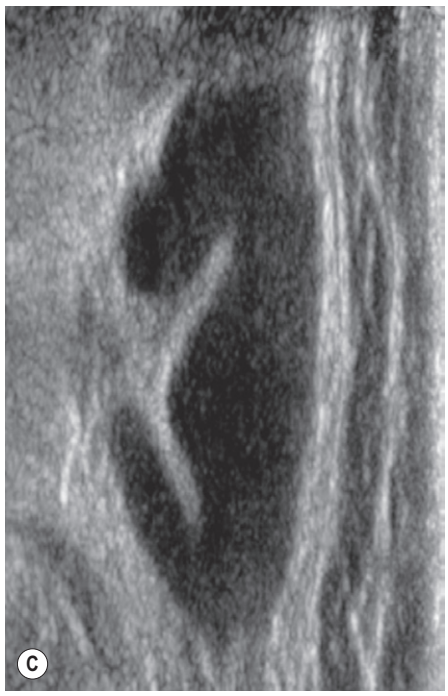

Figure 46.1 Diagram of lymph node structure (A) (modified from Evans[1]) with histological **(B)** and ultrasound **(C)** correlation. (With thanks to Dr J. Shannon for image **B**.)

isolation, for a diagnosis, should be avoided, due to the possibility of causing ipsilateral or contralateral shunting. Optimal management of these cases consists of an ultrasound-guided fine-needle aspiration (FNA) to confirm malignancy and further cross-sectional imaging with CT, MRI or positron emission tomography (PET), with panendoscopy and biopsies to identify a primary tumour. The metastatic node is then treated in continuity with the remainder of the neck nodes and the primary tumour, either surgically or with chemo-radiotherapy.

CLASSIFICATION OF CERVICAL LYMPH NODES

Many classification systems have been devised for the cervical lymph nodes, all of which are based on Rouviere's[7] original work in 1938 (Fig. 46.2A).

The most widely accepted is the clinically based American Joint Committee on Cancer (AJCC) level classification[8] (although not all nodes are included, e.g. parotid and buccal nodes) (Fig. 46.2B). Most surgeons and oncologists use this classification, and radiologists should become familiar with it. It is important that all members of the multidisciplinary team use the same system, as this simplifies accurate staging and management decisions. Som devised a classification based on CT and MRI;[9] this is compatible with the AJCC classification system. Som's classification system can be adapted for use in ultrasound (Table 46.1), with the addition of the parotid and buccal nodes and with the exception of the superior mediastinal and retropharyngeal nodes, which are inaccessible by ultrasound.

ULTRASOUND OF THE NECK NODES IN SEVEN SWEEPS

A comprehensive technique for assessing neck nodes with ultrasound using a combination of the AJCC level nomenclature and anatomical descriptions is described below (see also Fig. 45.2, Chapter 45). This scanning technique is the same as that described

Management of a malignant neck node and occult primary tumour

Management of a presumed nodal neck mass

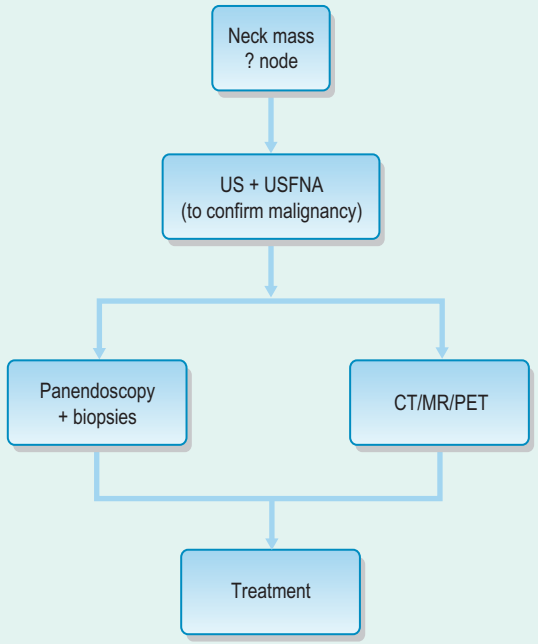

Excision of the node to obtain a diagnosis should be avoided.

in Chapter 45 ('Ultrasound of the neck'), with a series of seven sweeps, starting in the submental region and finishing in the anterior neck. The same sequence is repeated on both sides of the neck and the examination should take no longer than 10–15 minutes. For the purpose of this chapter, the relevant lymph nodes will be described for each region in relation to key anatomical structures.

1. Submental nodes (Level Ia)

With the neck extended and the chin elevated, the submental area is scanned from the tip of the chin down to the hyoid bone. The submental nodes (Ia) are located superficially, in the midline, between the anterior bellies of digastric, in the submental triangle (Fig. 46.3). These nodes may appear round. They drain the chin, lips, cheeks, floor of the mouth and the anterior tongue. Lymph drains from these nodes to the submandibular nodes and the upper deep cervical chain.

2. Submandibular nodes (Level Ib)

Turn the head to the opposite side to that being examined and sweep the transducer from the chin back to the angle of the mandible. The key structure to identify in this region is the submandibular gland, wrapped around the free posterior border of mylohyoid. The submandibular nodes (Ib) are clustered anterior and superior to the submandibular gland (Fig. 46.4). Anteriorly, the nodes are found in a small, fat-filled space, anterior to the submandibular gland and lateral to the anterior belly of digastric, in

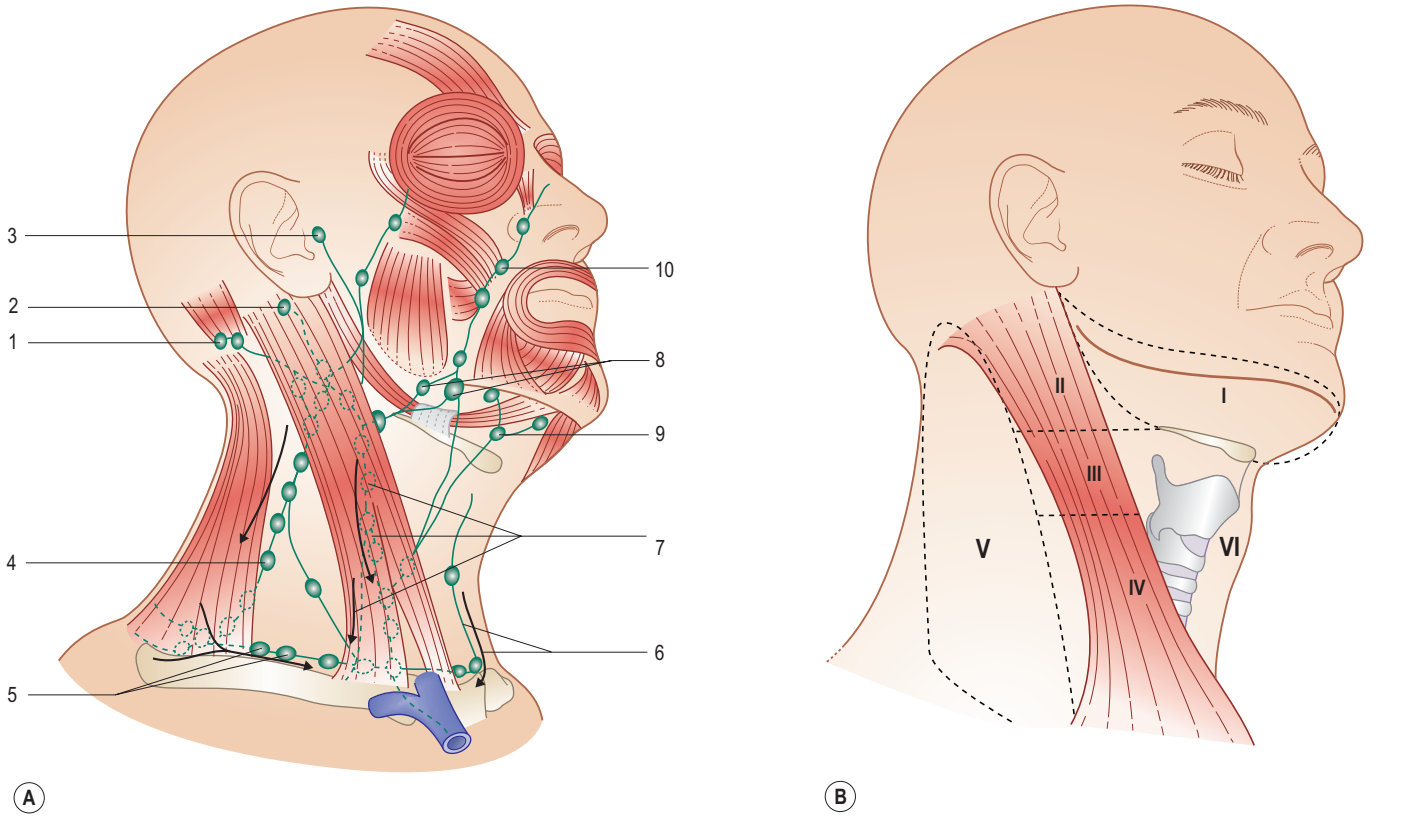

Figure 46.2 Classification. Comparison of **(A)** Rouviere's description of the lymphatic drainage of the head and neck (modified from Rouviere[7]) and **(B)** The American Joint Committee on Cancer (AJCC) level classification (modified from Greene and Compton[8]). 1, Occipital nodes. 2, Mastoid nodes. 3, Parotid nodes. 4, Spinal accessory lymphatic chain. 5, Transverse cervical lymphatic chain. 6, Anterior jugular lymphatic chain. 7, Internal jugular lymphatic chain. 8, Submaxillary lymphatic chain. 9, Submental nodes. 10, Facial node.

Table 46.1 Adaptation for ultrasound of Som's[9] imaging-based classification of neck nodes for ultrasound

Level	Name of region	Location of nodes	Ultrasound Scan Plane
I	**Submental (Ia)** **Submandibular (Ib)**	• Above hyoid bone, • Superficial to mylohyoid muscle • Anterior to submandibular gland **Ia** Between anterior bellies of digastric **Ib** Lateral to anterior belly digastric, anterior to submandibular gland	Transverse Longitudinal
II	**Jugulodigastric node &** **Upper deep cervical chain**	• From skull base to level of lower body of hyoid bone (or carotid bifurcation) • JDG posterior to submandibular gland • II-IV anterior to posterior margin of sternomastoid muscle **IIa** Inseparable from internal jugular vein, anterior, posterior, medial or lateral **IIb** Posterior to internal jugular vein, with intervening fat plane	Transverse
–	**Parotid** **Buccal**	Within the parotid fascia Adjacent to angle of mouth, on buccinator	Transverse Longitudinal
III	**Mid deep cervical chain**	• From level of hyoid to lower cricoid cartilage (or omohyoid crossing vessels) • Anterior to posterior margin of sternomastoid muscle	Transverse
IV	**Lower deep cervical chain**	• From level of lower cricoid cartilage to level of clavicle • Lateral to carotid arteries	Transverse
V	**Transverse cervical &** **Posterior triangle chain**	At or caudal to level of clavicle • Skull base to supraclavicular fossa • Posterior to posterior margin of sternomastoid muscle • Anterior to anterior margin of trapezius muscle	Transverse Transverse
VI	**Anterior cervical**	• From level of lower hyoid bone to sternal notch • Between carotid arteries	Transverse

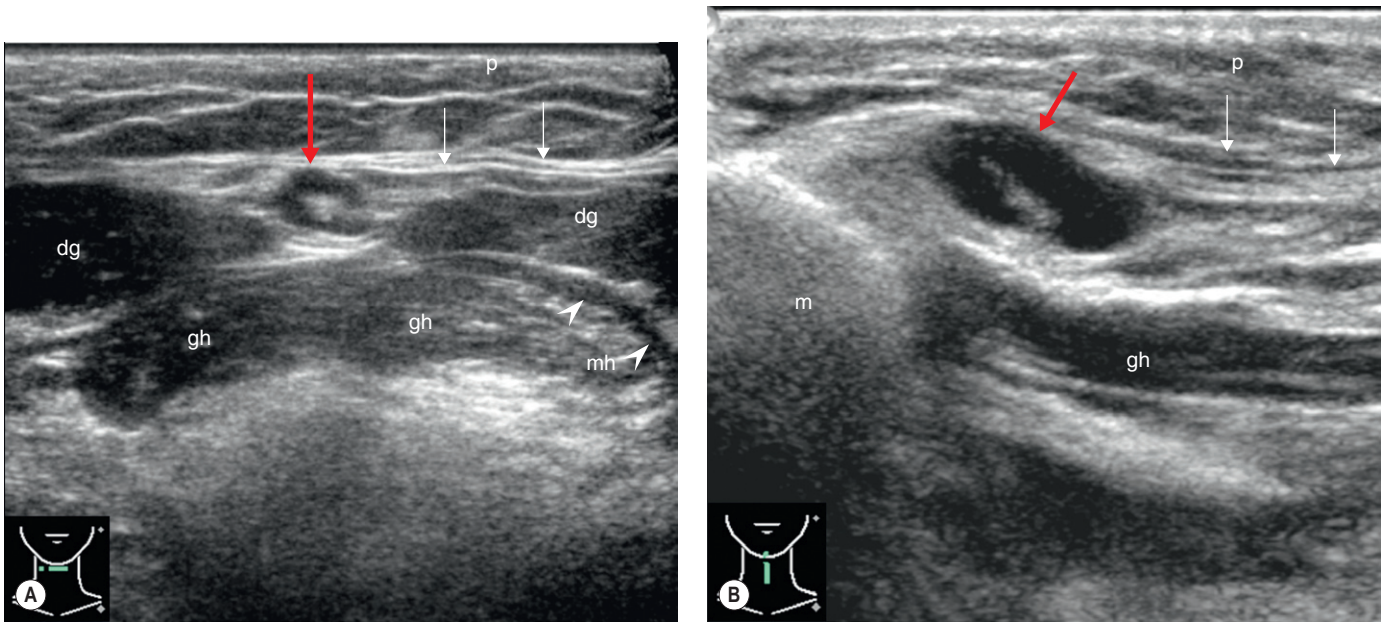

Figure 46.3 Submental ultrasound images: transverse **(A)** and longitudinal **(B)**. A Level Ia submental node (broadred red arrows) between anterior bellies of digastric (dg). mh, mylohyoid (arrowheads); gh, geniohyoid; m, mandible; p, platysma (thin arrows).

the submandibular triangle, often tucked up under the body of the mandible, and can be visualised with the scan plane parallel to the body of the mandible, angling the probe superiorly. These nodes are often better demonstrated in longitudinal section. Superiorly, the nodes are clustered around the facial artery, which can be felt pulsating as it crosses the body of the mandible.

The submandibular nodes drain the floor of mouth, anterior oral cavity and anterior face. Lymph drains from these nodes to the deep cervical chain.

There are no lymph nodes within the submandibular gland (unlike the parotid gland), due to early embryological encapsulation.

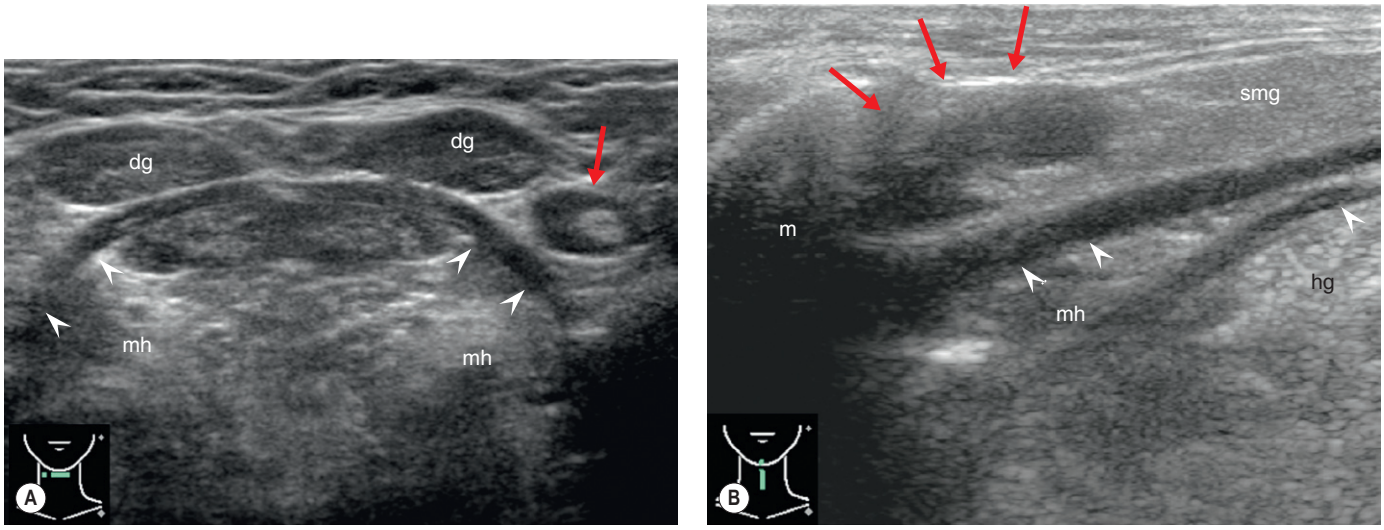

Figure 46.4 Anterior submandibular region: transverse **(A)** and longitudinal **(B)** ultrasound images. A Level Ib node (red arrows) lying lateral to the anterior belly of digastric and anterior to the submandibular gland. dg, anterior belly of digastric; mh, mylohyoid (arrowheads); hg, hyoglossus (arrowhead); m, mandible.

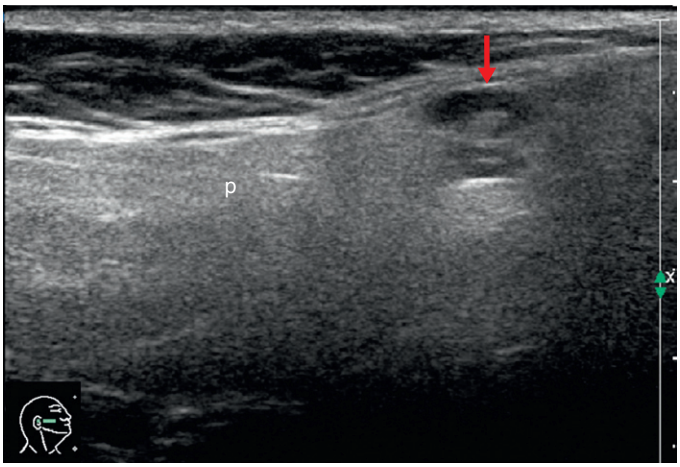

Figure 46.5 Transverse ultrasound image of the parotid gland. Parotid node (arrow) in the subcapsular region of the superficial lobe of the parotid. p, parotid.

3. Parotid and buccal region nodes (no numbered level)

The key landmarks are the mastoid tip posteriorly and the mandible anteriorly. The parotid gland is located between these two bony structures and can be seen by placing the transducer transversely, immediately beneath the tragus, resting on the ramus of the mandible. Late embryological encapsulation of the parotid gland allows the formation of an extensive lymphatic network within and around the gland. Up to 20 lymph nodes may be found in the parotid space and these may be within the gland or external to it. Intraglandular lymph nodes are situated deep within the parotid, around the retromandibular vein and the external carotid artery. Subcapsular nodes are found in the subcapsular region of the gland, commonly in the pre-tragal region anteriorly, and the tail of parotid gland posteriorly (Fig. 46.5). Extraparotid nodes may be seen in the tissues anterior to the tragus of the ear.

The parotid nodes drain the skin of lateral forehead, temple and external auditory meatus, together with the eustachian tube, posterior cheek, gums and buccal mucosa. Lymph drains from the parotid nodes to the deep cervical chain.

After examining the parotid region, the transducer is swept anteriorly, in the transverse plane, following the masseter muscle onto the buccinator muscle, which can be identified by asking the patient to puff their cheeks out. The buccal nodes, if present, are tiny nodes in the buccal fat space, superficial to buccinator, and adjacent to the facial artery (Fig. 46.6).

The buccal nodes drain the facial skin, from the upper eyelid to the upper lip and lymph drains from them to the submandibular nodes.

The most common tumours to involve the parotid and buccal nodes are squamous cell carcinomas of the scalp and malignant melanomas.[10]

4. Deep cervical/internal jugular chain (Levels II, III and IV)

This region is examined by sweeping the probe transversely from the angle of the mandible to the medial clavicle. The deep cervical chain, or internal jugular chain, is the main lymphatic drainage pathway of the neck, extending from the skull base to the supraclavicular fossa. The most superior node in this chain, the jugulodigastric node, is the largest node in the neck, often measuring up to 4 cm in length in healthy young teenagers. It is the 'sentinel node' of head and neck malignancy.

This chain, which follows the course of the internal jugular vein, is divided into upper, mid and lower regions, corresponding to Levels II, III and IV of the AJCC classification. The anatomical boundaries for each level are:

- Level II: skull base to the hyoid bone
- Level III: hyoid bone to the cricoid cartilage
- Level IV: cricoid cartilage to the clavicle.

For ultrasound purposes, as the hyoid bone and cricoid cartilage are awkward to demonstrate whilst scanning the laterally-placed deep cervical chain, the convenient landmarks are:

- Level II: posterior belly of digastric to the carotid bifurcation
- Level III: carotid bifurcation to where omohyoid crosses the great vessels
- Level IV: omohyoid to the clavicle.

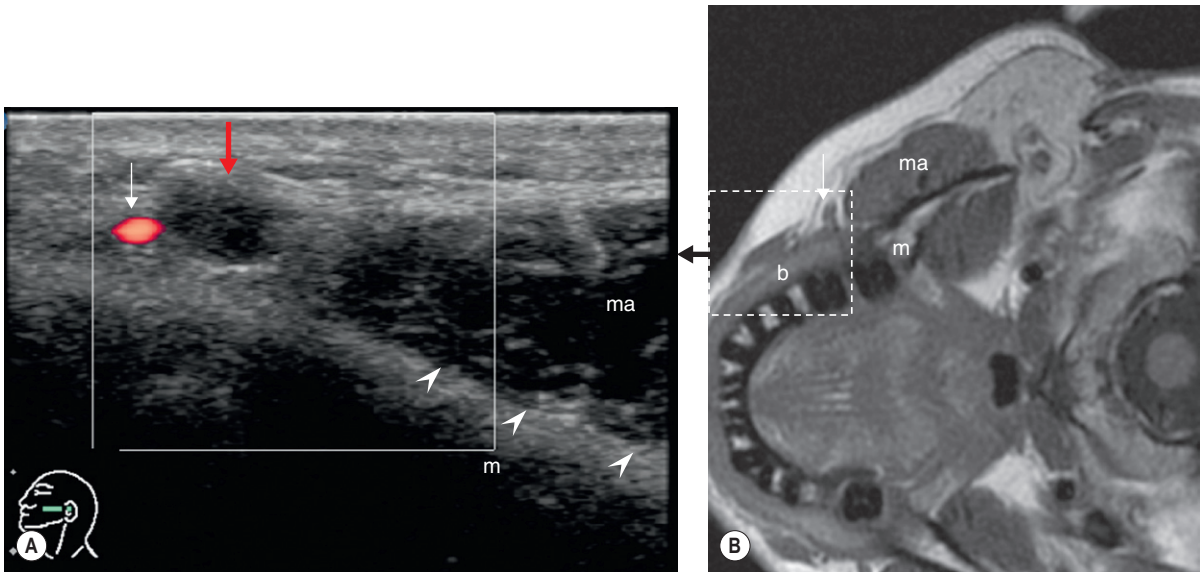

Figure 46.6 Buccal node. Transverse ultrasound image **(A)** and T1-weighted MRI image **(B)** for correlation. The buccal or facial node (red arrow) lies anterior to masseter (ma), adjacent to the facial artery in the buccal fat space (thin arrow). m, mandible (arrowheads); b, buccinator.

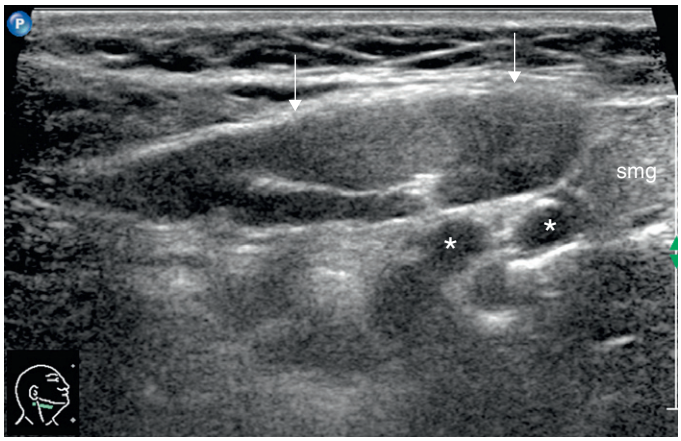

Figure 46.7 Transverse ultrasound image of the jugulodigastric node (arrows), lying posterior to the submandibular gland (smg), and superficial to the external carotid artery branches (*). Note that this position is identical to that of a branchial cleft cyst.

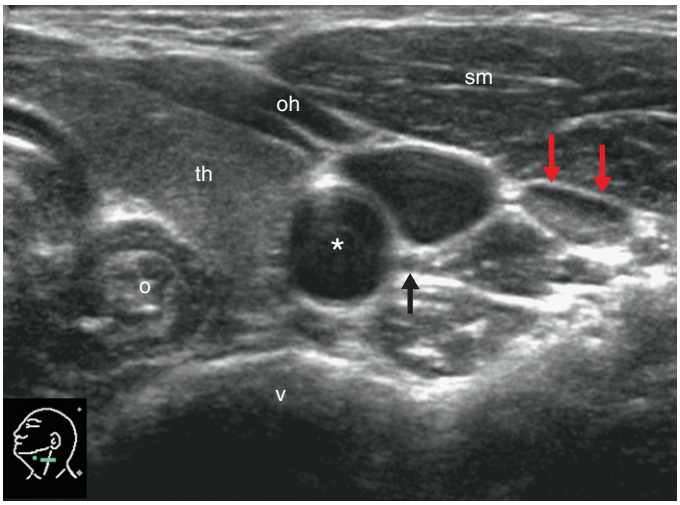

Figure 46.8 Transverse ultrasound image of a left Level III node (red arrows), deep to sternomastoid (sm) in the 3 o'clock position. Thick arrowhead indicates vagus nerve; o, oesophagus; v, vertebral body; th, thyroid; *, common carotid artery; oh, omohyoid.

Examination of this region begins by identifying the jugulodigastric node, which will be visible in virtually all patients. The transducer is placed transversely below the angle of the mandible; the jugulodigastric node lies immediately behind the submandibular gland (Fig. 46.7). It lies obliquely along the posterior belly of the digastric, and the probe is angled along the muscle to visualise the jugulodigastric node in longitudinal section. The internal jugular vein is the key structure in the examination of the deep cervical chain and it should be kept in the centre of the field of view whilst sweeping down the chain with the probe in the transverse position. Care must be taken to exert the lightest of pressure with the transducer so that the vein is not obliterated; occasional light pressure with the transducer on the internal jugular vein can be used to check compressibility and confirm its patency. If the patient is being scanned whilst sitting up, the internal jugular vein will be collapsed; its patency may be confirmed with the Valsalva manoeuvre.

In the upper deep cervical chain (Level II) on the right, nodes will be clustered around the vein from the 10 o'clock to 2 o'clock position. As the transducer is moved inferiorly, the nodes rotate laterally around the jugular vein, lying between 9 o'clock and 6 o'clock in the lower deep cervical chain. The mirror image is seen on the left (Fig. 46.8). Level II nodes are further subdivided – those that are inseparable from the internal jugular vein are termed IIa, and those that lie posterior to the internal jugular vein but separated from it by a fat plane are termed IIb.

The nodes of the deep cervical chain lie deep to sternomastoid, merging with the posterior triangle chain of nodes superiorly, and the transverse cervical chain inferiorly.

In the mid-cervical region, the omohyoid muscle crosses the deep cervical chain obliquely, demarcating Levels III from IV; this is also a surgical landmark for selective neck dissections. Take care not to mistake the muscle for a small lymph node (Fig. 46.9).

The deep cervical chain is the common final pathway for lymphatic drainage of the neck, draining submental, submandibular, parotid and retropharyngeal nodes. The deep cervical nodes drain to the thoracic duct on the left and the lymphatic duct on the right.

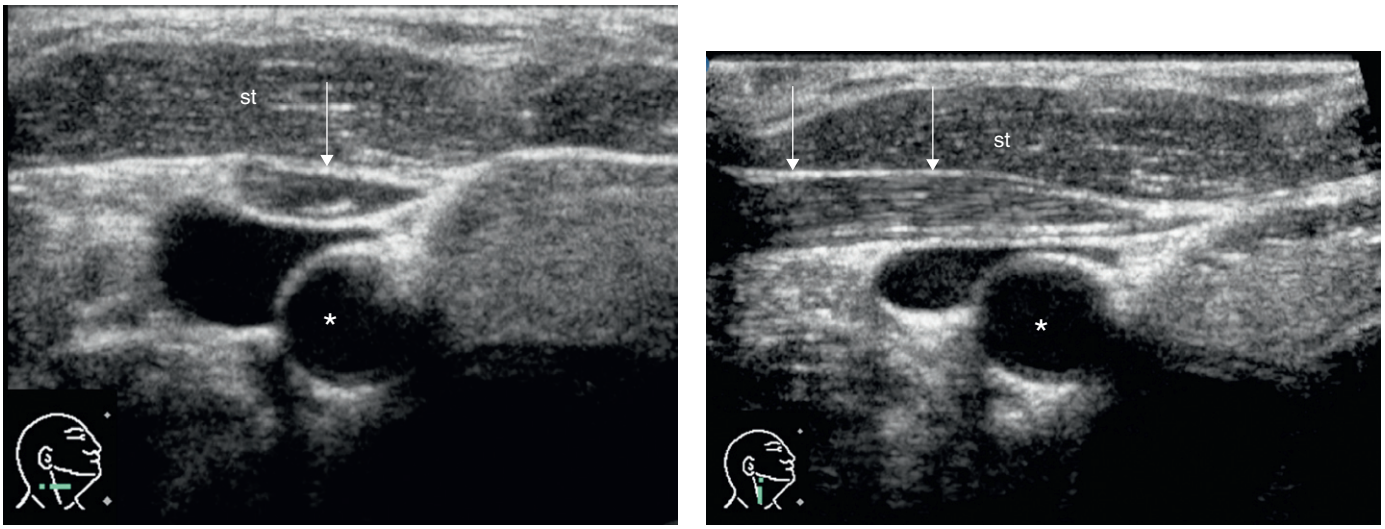

Figure 46.9 Omohyoid muscle. Transverse ultrasound image **(A)** of the right omohyoid muscle (arrow), demonstrating how it may mimic a lymph node, as it crosses the vessels, on a transverse image; this may be resolved by imaging longitudinally **(B)** (arrows). *, carotid artery; st, sternomastoid.

Scanning the deep cervical chain (Levels II, III and IV)

- Jugulodigastric node lies obliquely along posterior belly of digastric.
- Deep cervical chain (Levels II-IV) deep to sternomastoid, **lateral** to carotid artery.
- Keep internal jugular vein in middle field of view, apply intermittent pressure.
- Do not mistake the omohyoid muscle for a lymph node.
- Paratracheal chain (Level IV) **medial** to carotid artery.

5. Supraclavicular fossa/transverse cervical chain (Level V)

The transverse cervical chain of nodes joins the deep cervical and posterior triangle chains and lies superior to the subclavian vein; this chain is considered part of the posterior triangle chain (V) in the current AJCC classification. The clavicle is the key structure in this region. Scanning is carried out with the transducer positioned transversely along the superior margin of the clavicle with slight inferior angulation of the probe as it is moved from the medial end to the lateral end of the clavicle. Troisier's sign is the finding of a palpable left supraclavicular lymph node (Virchow's node); it is a sign of metastases from an upper gastrointestinal malignancy.

6. Posterior triangle (Level V)

The posterior triangle is a very superficial, fat-filled space, bordered by sternomastoid anteriorly, trapezius posteriorly and the clavicle inferiorly. The floor of the triangle is composed of muscles – scalenus anterior, medius and posterior and levator scapulae. The nodes lie in the slender, echogenic, fat stripe superficial to this carpet of muscles (Fig. 46.10). This region is scanned with the transducer positioned transversely on the mastoid process. The transducer is moved inferiorly along the posterior margin of sternomastoid to the acromioclavicular joint and the anterior border of trapezius.

Normal posterior triangle nodes are easily palpable on the surface of the muscles, and are often discovered incidentally by the patient, as they lie no more than 1–2 cm beneath the skin. Posterior triangle nodes are defined as those lying posterior to the posterior border of sternomastoid (Table 46.1); those deep to sternomastoid are in the deep cervical chain (Levels II to IV). The lymph nodes lie along the axis of the spinal accessory nerve (XI). The posterior triangle is subdivided into Va and Vb by the omohyoid muscle (see Fig. 45.2, Chapter 45).

The posterior triangle chain nodes drain the skin in the occipital and mastoid areas, the posterior scalp, the lateral neck and the postnasal space. They join with the deep cervical chain superiorly and the transverse cervical chain inferiorly. Lymph drains from the posterior triangle chain to the transverse cervical chain.

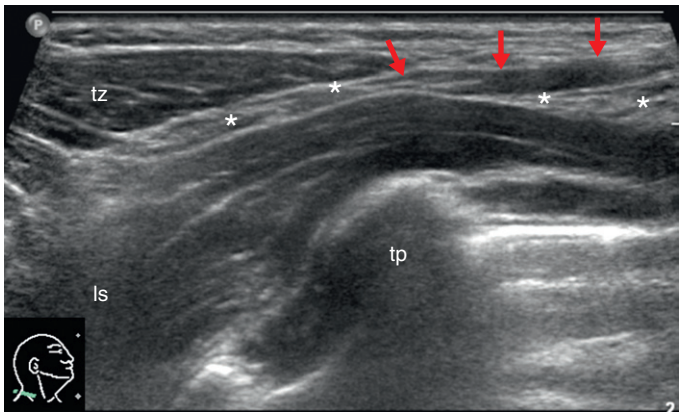

Figure 46.10 Transverse ultrasound image of the right posterior triangle. There is a tiny elongated lymph node (arrows) in the superficial fat stripe (***) anterior to trapezius (tz) and posterior to sternomastoid. Small nodes are easily palpable in this site, as they lie on the transverse processes (tp). ls, levator scapula.

7. Anterior cervical nodes (Level VI)

This group of lymph nodes is scanned in the transverse plane using a series of longitudinal midline sweeps from the hyoid down to the sternal notch. There are three subgroups of nodes within this group, the prelaryngeal, pretracheal and paratracheal nodes (Fig. 46.11). Note that Level VI nodes lie medial to the carotid artery; nodes lateral to the carotid artery lie in the deep cervical chain.

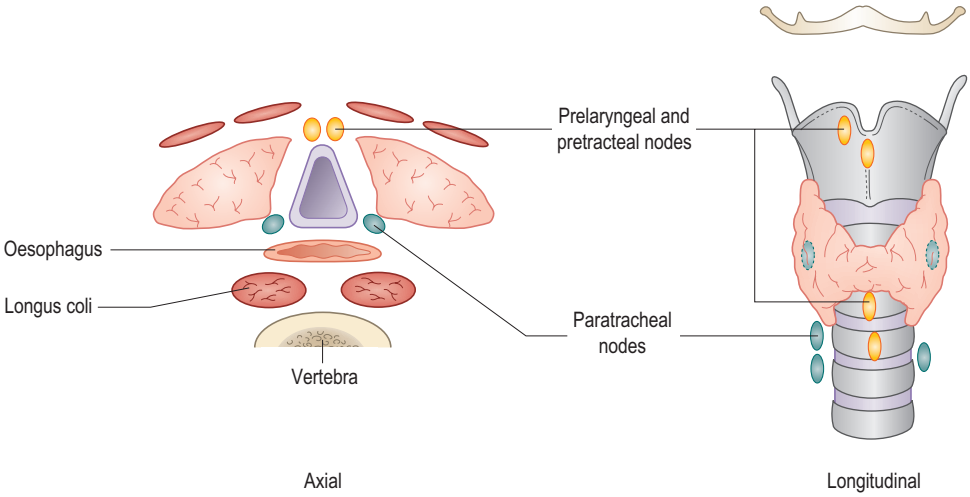

Figure 46.11 Level VI (anterior neck) nodes. The prelaryngeal and pretracheal nodes in the midline, and the deeper, laterally placed paratracheal nodes.

Prelaryngeal and pretracheal nodes

These nodes are superficially located. The prelaryngeal chain is in the midline, with the delphian node lying anterior to the cricoid cartilage. If this node is enlarged, it is an indicator of subglottic involvement in carcinoma of the larynx. The pretracheal nodes follow the course of the anterior jugular veins bilaterally. The prelaryngeal and pretracheal nodes drain the skin and muscles of the anterior neck and the thyroid gland. They drain lymph into the thoracic duct on the left and the low deep cervical chain on the right.

Paratracheal nodes

The paratracheal nodes lie more deeply and more laterally in the tracheo-oesophageal groove. They lie posterior to the thyroid and can be very difficult to image with ultrasound. If enlarged they may mimic a parathyroid adenoma (Fig. 46.12). The paratracheal nodes drain the larynx, pyriform fossae, the thyroid and the oesophagus. Lymph drains to the thoracic duct on the left and the lower deep cervical chain on the right.

Mastoid (retroauricular) and occipital nodes

These superficial nodes are not routinely examined in the seven sweeps described above; however, they should be specifically examined in cases of scalp malignancy.

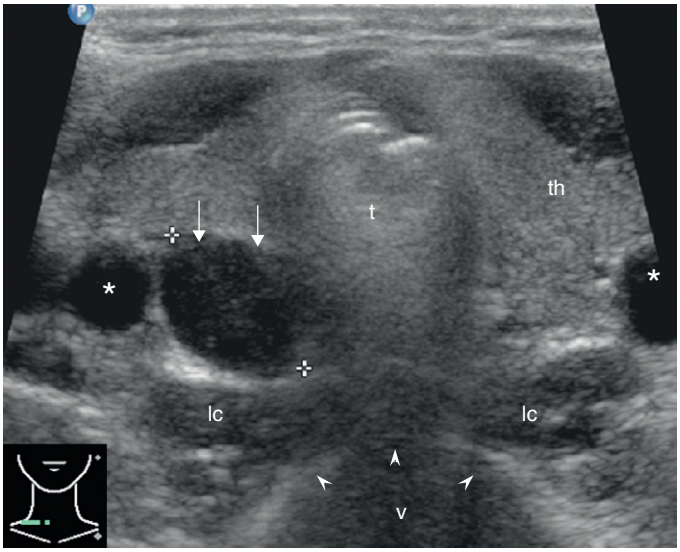

Figure 46.12 Transverse ultrasound image of a Level VI paratracheal node (arrows, callipers). A node at this site may mimic a parathyroid adenoma. th, thyroid; v, vertebral body (arrowheads); *, carotid artery; t, trachea; lc, longus colli muscles.

SIGNS USED TO ASSESS FOR MALIGNANCY

Several features may be used to try and discriminate between benign and malignant nodes; these should be used in combination, as none is of itself diagnostic. The main features to be considered are size, shape, echotexture, the appearance of the cortex and hilum, the presence of necrosis, the appearances of the nodal margin, the architecture of the vessels in the node and the location of the enlarged nodes.

Size

Size is of limited value when assessing lymph nodes for malignancy; although malignant nodes may be large, so may benign, reactive nodes. Whilst the size of a node is of limited value in differentiating benign from malignant nodes, size is important in the TNM staging of nodal disease: <3 cm being N1, 3–6 cm N2 and >6 cm N3.[8] A normal node is bean-shaped and it is not uncommon to find jugulodigastric nodes up to 4 cm long in normal healthy teenagers. When measuring nodes it is important to measure their short axis or transverse diameter, rather than the longitudinal diameter.

Practically, most nodes in the neck are assessed on transverse images (except the submandibular and submental nodes); in this plane, it is possible to measure the short axis as either the maximum axial diameter or minimum axial diameter (Fig. 46.13). There are proponents for both measurements.[11,12]

Van den Brekel[13] assessed the sensitivity and specificity of a range of cut-off measurements for minimum axial diameters, in different populations. He concluded that in patients with a known head and

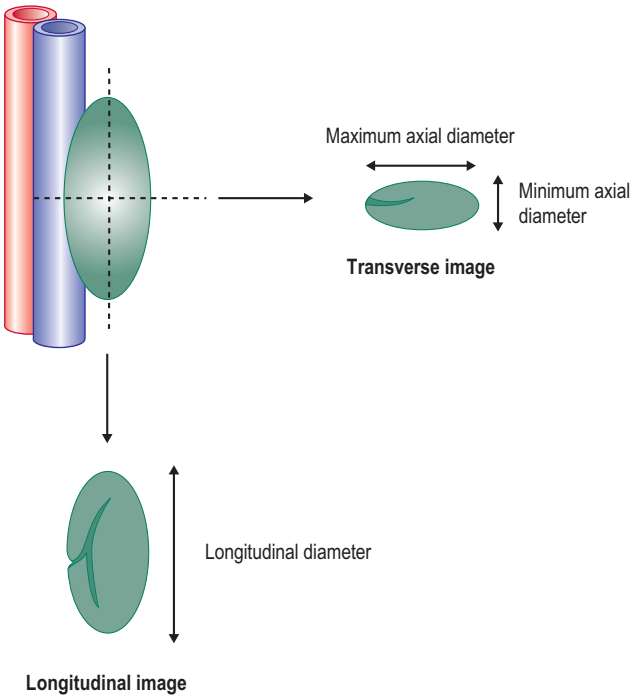

Figure 46.13 The deep cervical nodes are aligned parallel to the great vessels. When measuring nodes, the transverse diameter (short axis) should be measured, either the maximum axial or the minimum axial diameter.

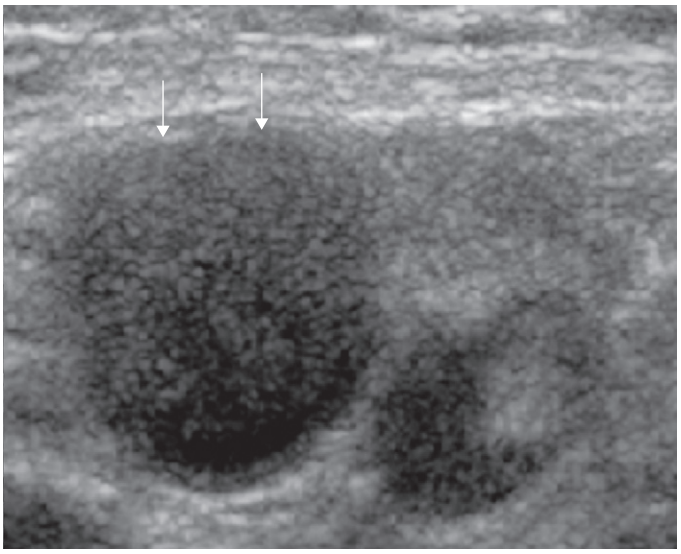

Figure 46.14 Transverse ultrasound image of two Level Ib nodes. The metastatic node (arrows) is round with no hilum, adjacent to a normal oval node, which has a hilum.

neck carcinoma and a clinically N0 neck, 7 mm minimum axial diameter was a practical cut-off for jugulodigastric nodes, and 6 mm minimum axial diameter for the remaining neck nodes. In patients with palpable metastases (N+), these criteria were 1–2 mm larger, i.e. 8–9 mm for the jugulodigastric node and 7–8 mm for the remaining neck nodes.

Nodes larger than these measurements should be considered suggestive of metastasis. Obviously, decreasing the cut-off size will increase sensitivity, but at the cost of decreased specificity. It has been estimated that it takes 1 billion malignant cells to create a mass of 1 mm^3.[14] Serial monitoring of nodal size is useful in assessing response to therapy.[15]

Shape

The shape of a lymph node is a much more reliable criterion for prediction of malignancy. A normal lymph node has a flat, bean shape. When it undergoes reactive hyperplasia, lymphopoiesis occurs, germinal centres are formed in the cortical lymphoid follicles and the number of lymphocytes in the paracortex increases. The diffuse nature of this process causes a global increase in nodal size, which tends to preserve the shape.

In metastatic disease, the processes are different – the node is focally infiltrated with malignant cells and the change in shape is not uniform. Whilst benign nodes are oval, metastatic nodes tend to be round (Fig. 46.14).

If nodal shape is expressed as a ratio of the long and short axes (L/S) then an L/S ratio of more than 2 indicates an oval shape, characteristic of a benign node, whereas a malignant node will have an L/S ratio of less than 2, indicating a round shape. This ratio was first described by Solbiati[11] and its value later confirmed by Vassallo,[16] who found that 85% of benign nodes had an L/S ratio of more than 2 (i.e. oval), and 85% of malignant nodes had an L/S ratio of less than 2 (i.e. round). Takashima[17] subsequently described the ratio of minimal axial diameter to maximal axial diameter, finding that a ratio of more than 0.55 (round) was a valid sign for predicting malignancy, achieving 80% accuracy in an N0 population, using shape as the sole criterion.

In practice, the shape of a node is easily evaluated, without resorting to measuring ratios; ultrasound has a unique advantage in this respect, as the scan plane may easily be rotated along both the long and short axis of a node. The caveat to this sign is that normal submental and submandibular nodes (Levels Ia, Ib) are often round, which should be considered when using this criterion to evaluate nodes in these regions. Lymphomatous nodes also tend to be round.[18]

Echotexture

The cortex of a normal node is uniformly hypoechoic when compared with the adjacent muscle; this feature is ascribed to its high cellular content of tightly-packed lymphoid follicles.

Lymphomatous nodes have been noted to be markedly hypoechoic, almost of fluid density with posterior acoustic enhancement (Fig. 46.15), leading to the term 'pseudocystic'.[19,20] This sign was ascribed to the increased volume of densely packed lymph follicles. With the new generation of high-resolution probes, this pseudocystic appearance is less frequently encountered. The internal architecture of the lymphomatous node may now be resolved, showing a reticulated or micronodular appearance, in many cases individual lymphoid follicles may be discerned (Fig. 46.16).[21] This appearance has been shown to correlate precisely with the hypertrophied follicles in the cortex and medulla,[5] This appearance holds true for both Hodgkin's and non-Hodgkin's lymphoma. As high-resolution probes are now widely available, these are important features to note and should prompt a core biopsy, rather than a fine-needle aspiration, for confirmation of the diagnosis.

Squamous cell cancer (SCC) metastases tend to be hypoechoic but may have a heterogeneous appearance, depending on the type of necrosis within the node (see below).

Papillary carcinoma of the thyroid metastases are usually homogeneously hyperechoic.[22] They may also contain punctate (less than 2 mm) foci of calcification (Fig. 46.17), identical to those seen in the primary thyroid tumour, which with high-resolution probes, may show posterior acoustic shadowing. These calcific foci correlate precisely with the presence of psammoma bodies; histologically, these are laminated calcific spherical bodies.

A solitary neck node may be the presenting feature of a papillary carcinoma of the thyroid. Such nodes will characteristically be

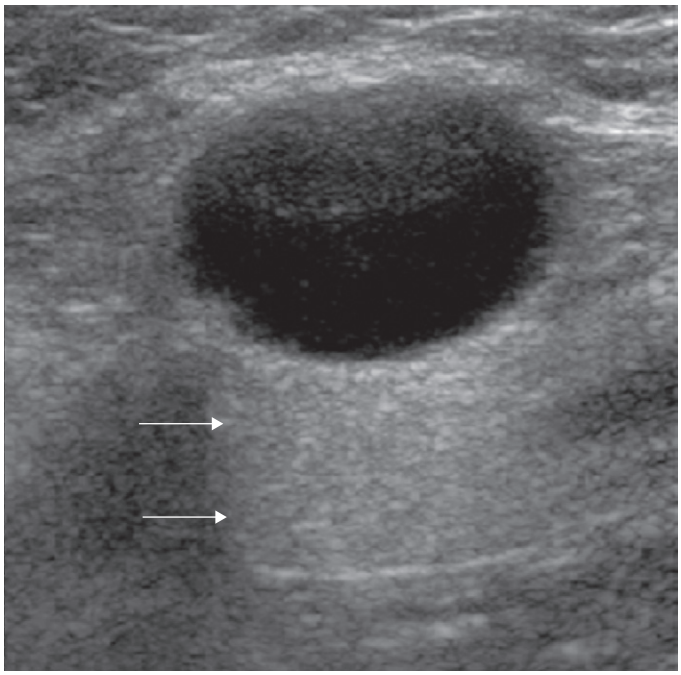

Figure 46.15 Transverse sonogram of a lymphomatous node. It is markedly hypoechoic, with posterior acoustic enhancement (arrows); the node is round, with an absent hilum.

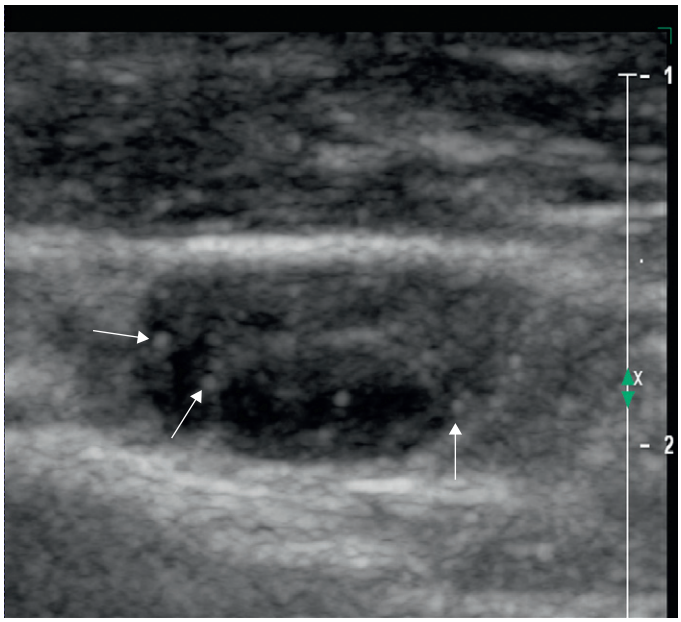

Figure 46.17 Sonogram of a metastatic node from a papillary carcinoma of the thyroid. The node contains pathognomonic flecks of microcalcification (arrows).

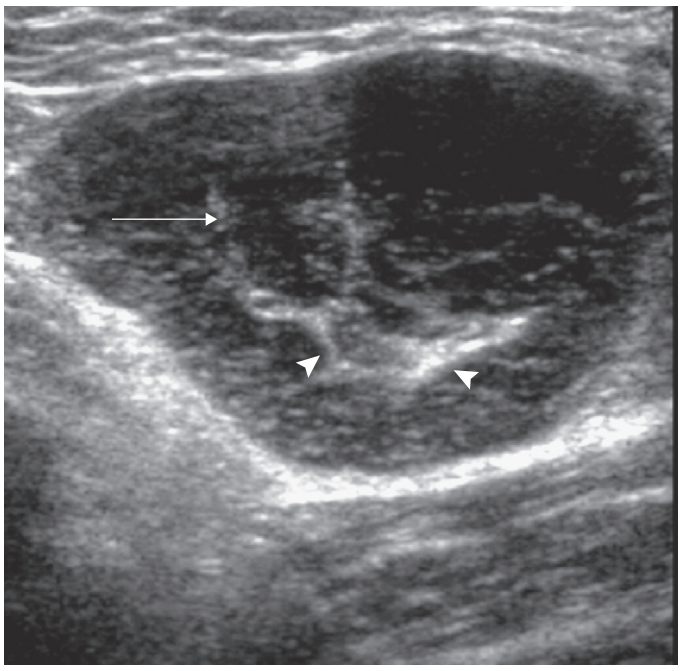

Figure 46.16 Sonogram of a lymphomatous node. The internal echotexture is reticulated, the node is round and the hilum (arrowheads) is retained. An individual lymphoid follicle is visible (arrow).

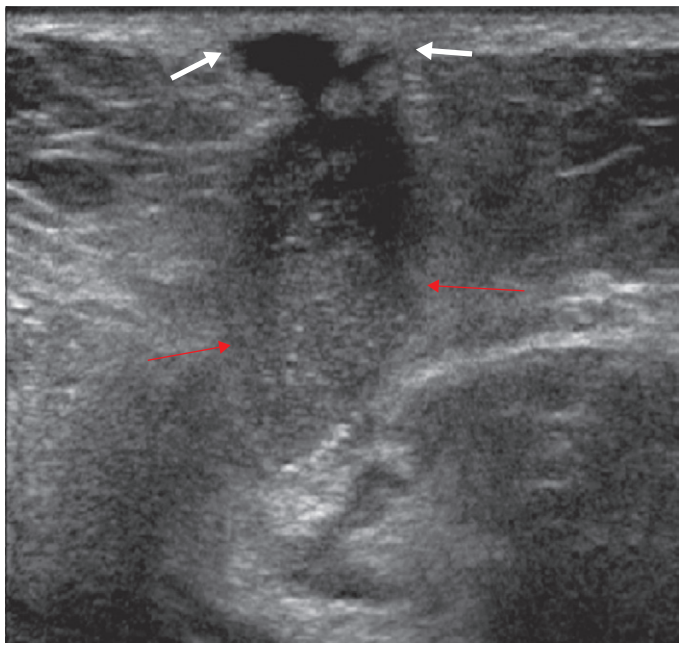

Figure 46.18 Sonogram of a suppurative node. The node is ill defined and echogenic (red arrows); applying gentle pressure with the probe causes the echogenic contents to swirl, confirming the presence of pus. The pus has burst through platysma and is presenting on the skin surface (thick arrows).

hyperechoic with punctate calcification; however, they may occasionally be entirely cystic (see below – 'Necrosis'). In both instances, a thorough examination of the thyroid is indicated.

Medullary carcinoma of the thyroid metastases also contain bright, punctate calcification, said to be slightly coarser than those in papillary carcinoma; histologically these are due to focal deposits of calcium surrounded by amyloid.[23] If a medullary carcinoma of the thyroid is suspected, the parathyroids should be reviewed for possible parathyroid adenomas, as these are an associated finding in MEN II (Sipple's syndrome).

Suppurative nodes are frequently markedly echogenic due to thick pus within them (Fig. 46.18). Bouncing the probe on the nodes, or the application of power Doppler, will show movement of the echogenic contents.

Old **tuberculous nodes** occasionally contain macrocalcification. In practice, this is easily distinguished from the microcalcification seen in papillary carcinoma of the thyroid.

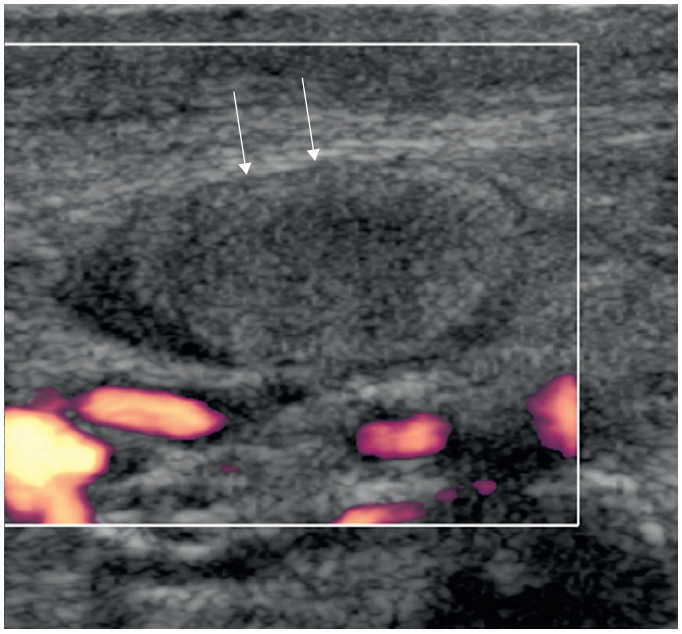

Figure 46.19 Power Doppler image of a metastatic node 3 months post treatment with radio- and chemotherapy (arrows). The node is uniformly echogenic, avascular and has no hilum.

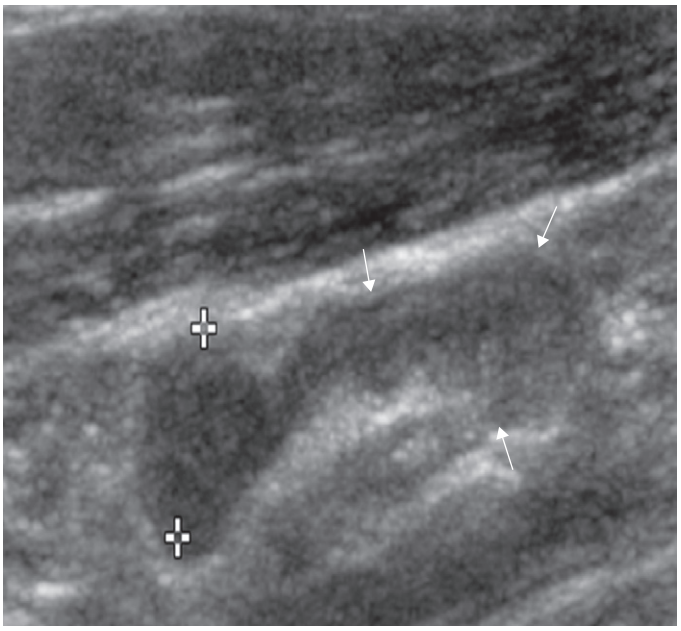

Figure 46.20 Sonogram of a node (arrows) with a small focus of eccentric cortical widening (callipers) – this node was malignant on FNA.

Following **radiotherapy**, nodes typically return to their normal size and shape approximately one year after treatment. The echogenic hilum also reverts to normal; however, the nodes tend to remain slightly more echogenic than normal nodes (Fig. 46.19); this finding is ascribed to fibrosis.[24] Post-treatment nodes (radiotherapy or chemotherapy) may also contain foci of macrocalcification.[25]

Cortex and hilum

It is useful to consider these two features together, as changes in one tend to cause reciprocal changes in the other.

An echogenic hilum is a normal sonographic feature of a lymph node; benign nodes tend to show this feature whereas malignant nodes often do not. All nodes demonstrating a hilum in Rubaltelli's[5] study, which correlated sonographic and histological findings, were benign.

Early disease, be it infection or malignancy, tends to affect the cortex initially, and later disease the hilum. Both infective and malignant disease reach the node at its periphery via multiple afferent lymphatics, which then drain into the subcapsular lymphatic channels encircling the node.

Reactive nodal disease induces a simultaneous increase in the germinal centres within the cortex, resulting in diffuse cortical widening. Malignant disease, on the other hand, causes a focal distortion in architecture, with blockage of lymphatic channels, leading to eccentric cortical widening (Fig. 46.20). Focal doubling of cortical width has been shown to be a valuable sign of malignancy; in one study, all nodes showing this feature were malignant.[16]

Continued antigenic stimulation of the node by infection stimulates the formation of additional, new germinal centres in the hilum; resulting in widening of the hilum.

The echogenic hilum may be preserved in early malignant disease if the medullary sinuses have not been sufficiently disrupted. However, continued malignant infiltration of the node will destroy the hilum and as malignant nodes increase in size, the likelihood of finding an echogenic hilum decreases. Ninety per cent of normal nodes larger than 5 mm (maximum axial diameter) will have a hilum,[26] and the absence of a hilum in larger nodes is therefore highly suspicious for malignancy. Nodes less than 5 mm (maximum axial diameter) tend not to have a discernible hilum; therefore in small nodes this sign is not a good predictor of malignancy.[26]

The hilum is usually absent in lymphomatous and tuberculous nodes. However, a hilum may remain visible, depending on the degree of distortion. Whilst preservation of the hilum is typically a feature of normal and reactive nodes, it should not be used as the sole criterion in differentiating benign from malignant nodes.

Necrosis

Necrosis may be of two types: cystic or coagulation necrosis, cystic necrosis being more common. Both may coexist in the same node and imply that there will be a poor response to radiotherapy, as the presence of necrosis indicates hypoxia.

Cystic necrosis is a highly sensitive sign of a squamous cell carcinoma metastasis in patients with head and neck cancer.[27] Squamous cell carcinoma metastases will show necrosis in virtually all nodes larger than 3 cm in greatest diameter; finding a large, non-necrotic node should therefore prompt consideration of another diagnosis such as lymphoma. Cystic necrosis appears as ill-defined, anechoic foci within a node (Fig. 46.21). The necrosis may be focal or occasionally the whole node may become cystic; this is most frequently seen in the jugulodigastric node. In patients with no known primary tumour the appearance of a cystic metastasis in the jugulodigastric node is identical to that of a branchial cleft cyst. This is a common pitfall (see Chapter 45) and the diagnosis of a branchial cleft cyst in a patient more than 30 years old should be made with care as cystic necrosis in metastases from a squamous cell carcinoma or a papillary carcinoma of the thyroid are common mimics. It is sensible to obtain cytology from these cystic lesions and to suggest a thorough ear, nose and throat examination for a possible primary head and neck tumour.

Cystic necrosis is also seen frequently in tuberculous nodes.[20,28,29]

Coagulative necrosis is less common than cystic necrosis. This type of necrosis appears as ill-defined, hyperechoic foci (Fig. 46.22). It is thought to represent fibrotic change. Coagulative necrosis should not be confused with the normal hilum; it is less echogenic than the hilum and the surrounding fat, and, unlike the hilum, is not continuous with the surrounding fat.[5]

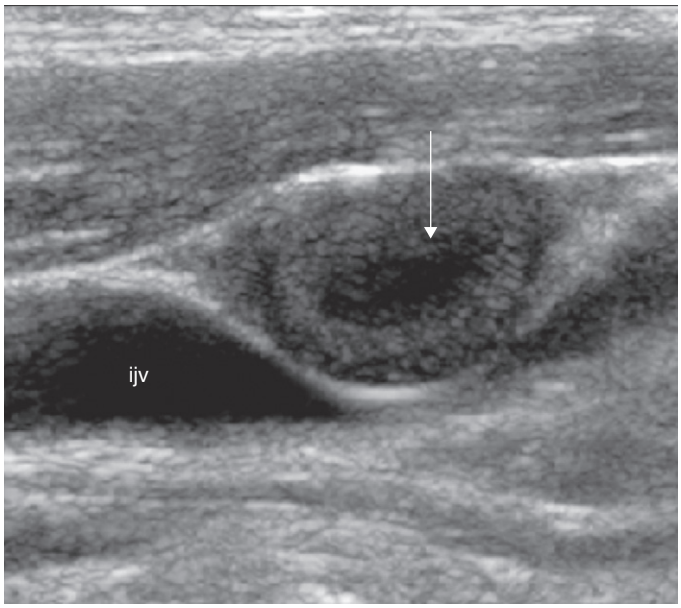

Figure 46.21 Longitudinal sonogram of a metastatic SCC node demonstrating a focus of central necrosis (arrow). ijv, internal jugular vein.

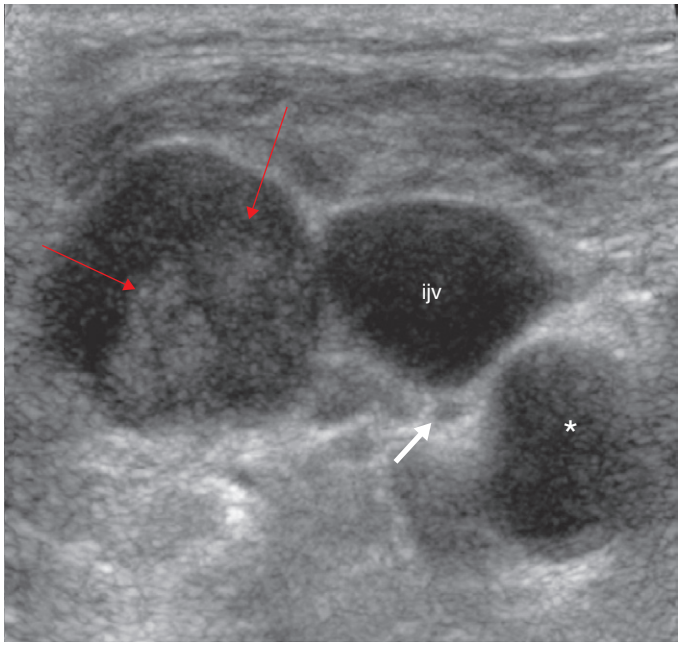

Figure 46.22 Transverse sonogram of a metastatic right Level III node demonstrating coagulative necrosis (red arrows). The necrosis is ill defined and hyperechoic, and is not continuous with the fat surrounding the node, unlike a hilum. Short arrow indicates vagus nerve; *, carotid artery; ijv, internal jugular vein.

If performing an FNA from a node containing cystic necrosis, the sample should be obtained from the solid portion of the node, as this is more likely to contain viable malignant cells. If tuberculosis is suspected, the cystic portion should be aspirated and sent for cytology as well as microbiology. Estimation of thyroglobulin levels in the nodal aspirate may also be useful to identify metastases from papillary carcinoma of the thyroid.[30]

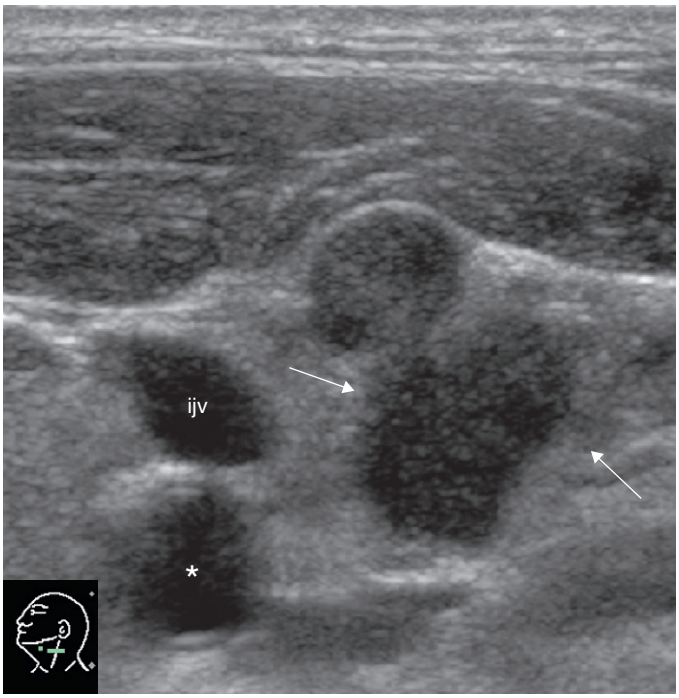

Figure 46.23 Transverse sonogram of metastatic Level III nodes demonstrating extracapsular spread. The margins of the node are irregular and ill defined (arrows). Extracapsular spread indicates a 50% decrease in overall survival. *, carotid artery; ijv, internal jugular vein.

Margins of the node

The outline of a normal node is smooth and slightly indistinct with respect to the surrounding fat.[31]

Malignant nodes, both metastatic and lymphomatous, tend to have sharp borders, thought to be due to tumour cells replacing lymphoid cells, resulting in a higher difference in acoustic impedance between the node and surrounding fatty tissues. Whilst the margin of a node does not help in differentiating absolutely between benign and malignant nodes, if a known metastatic node has ill-defined, spiculated margins, this implies extracapsular spread (Fig. 46.23), which is a grave prognostic sign for the patient, reducing the 2-year survival by 50%.[32]

Tumour may infiltrate adjacent muscle, skin and vessels. When a venous thrombosis occurs in association with metastatic nodes, the 'thrombus' should be examined for vascularity, as this indicates intravenous tumour rather than simple thrombus. Demonstration of invasion or involvement of the internal jugular vein and carotid artery by tumour is valuable preoperative information.

Acute suppurative bacterial lymphadenopathy is also ill-defined; however, the clinical presentation is different, with an acutely painful neck mass.

Tuberculous nodes demonstrate matting due to the associated perinodal inflammatory reaction (Fig. 46.24), which also causes oedema of the surrounding subcutaneous tissues and muscles.[33] It should be noted that similar features of soft tissue oedema and matting of nodes are also encountered in cervical lymph nodes following radiotherapy.

Angioarchitecture

The main artery and vein of the node enter and exit the node via the hilum and run through the middle of the node, parallel to the longitudinal axis, giving multiple side branches to the cortex and capsule. Benign and reactive nodes show this hilar pattern of vascularity on colour and power Doppler (Fig. 46.25).

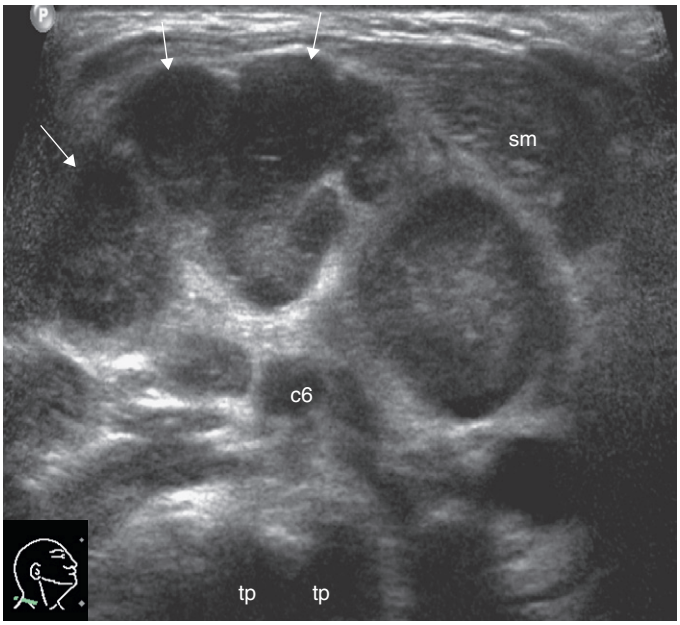

Figure 46.24 Transverse sonogram of the right posterior triangle. The nodes are matted or clumped together (arrows); note also the surrounding soft tissue oedema – both these features are characteristic of tuberculosis. sm, sternomastoid; tp, transverse process C6; C6, nerve root of C6.

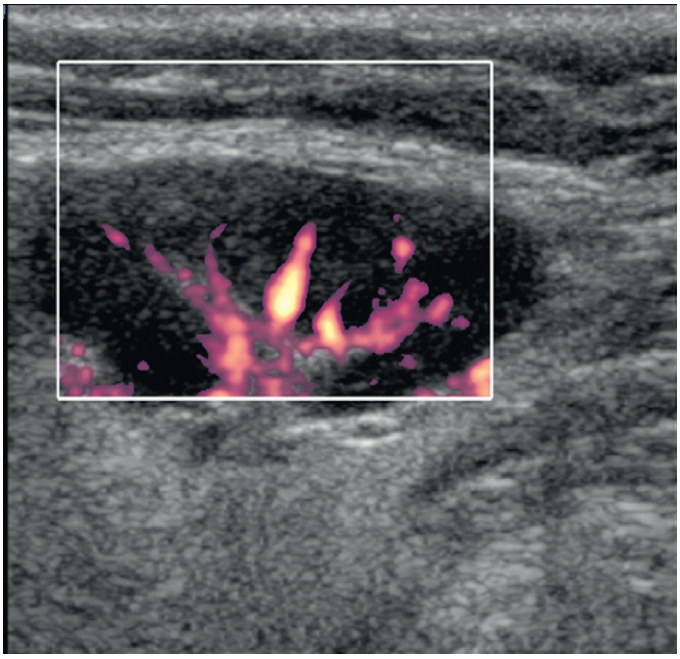

Figure 46.25 Power Doppler sonogram demonstrating a normal hilar vascular pattern. The vessels enter and exit via the hilum and are distributed along the medulla of the node; the cortex is supplied via side branches from the central hilar vessels.

The incidence of vascular signals detected within normal lymph nodes increases with the size of the nodes; 90% of nodes with a maximum axial diameter of more than 5 mm will show vascularity but nodes smaller than 5 mm may appear avascular.[26]

Colour or power Doppler may be used to assess nodal vascularity. Power Doppler is preferred as it is more sensitive to low flow and is not affected by the direction of the flow, although there is a risk of increased false positive results.[34] The parameters should be optimised for the detection of slow, small-volume flow velocities in small vessels. It is better if they are included in the programme presets, to enable a quick assessment of the vascular pattern of the node. The colour gain should be adjusted, until the first colour artefacts appear at a depth similar to the lymph node.[35]

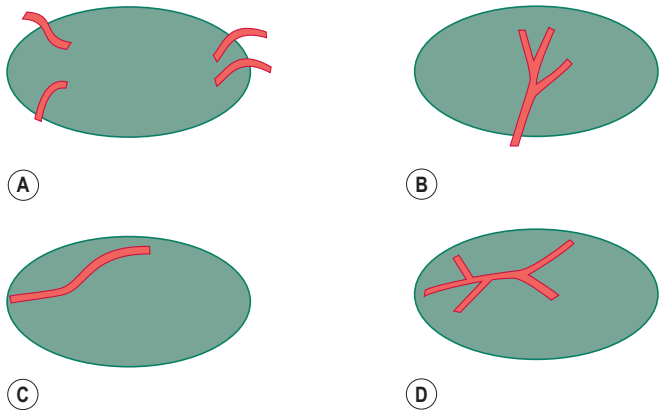

Figure 46.26 Patterns of abnormal vascularity (adapted from Tschammler et al.[35]). **A:** Subcapsular; **B:** aberrant; **C:** displaced vessels; **D:** focal perfusion defect.

Vascular characteristics of lymph nodes

Benign nodes
- Central/hilar flow
- No peripheral flow
- Small nodes may be avascular

Malignant nodes
- Peripheral subcapsular flow (also in TB)
- Perfusion defects
- Aberrant vessels

Lymphoma
- Exaggerated hilar flow

The changes in vascularity described in malignant nodes all reflect the tissue distortion caused by tumour infiltration (Figs 46.26 and 46.27). These changes include: focal perfusion defects, subcapsular vessels, aberrant vessels and displaced vessels. Focal perfusion defects and displaced vessels are caused by foci of necrosis within the node (Fig. 46.27A). Subcapsular vessels do not originate from the main central or hilar vessels (Fig. 46.27B). Aberrant vessels are defined as vessels having angles of more than 30° (usually near 90°) with the long axis of the node (Fig. 46.27C).

Tuberculous infection of a node is a great mimic of malignancy as it disrupts the nodal architecture and vascularity in a similar manner to malignancy.[18,28,29,36]

In terms of their vascularity, lymphomatous nodes demonstrate an exaggerated normal appearance with a hilar pattern of blood flow; the flow is often quite dramatic, reflecting the fact that lymphoma tends to preserve the normal nodal architecture, with minimal distortion (Fig. 46.28).

Various authors have studied the vascular resistance parameters – pulsatility index (PI) and resistive index (RI) – of benign and malignant nodes. Malignant nodes tend to have higher intranodal vascular resistance than benign nodes.[37] The resistive index and the pulsatility index are unrelated to the size of the nodes.[26] The value of these measurements in everyday clinical practice is doubtful as the assessment of the pattern of flow is far more useful and, provided the parameters are correctly set, the colour or power Doppler should only add seconds to the examination.

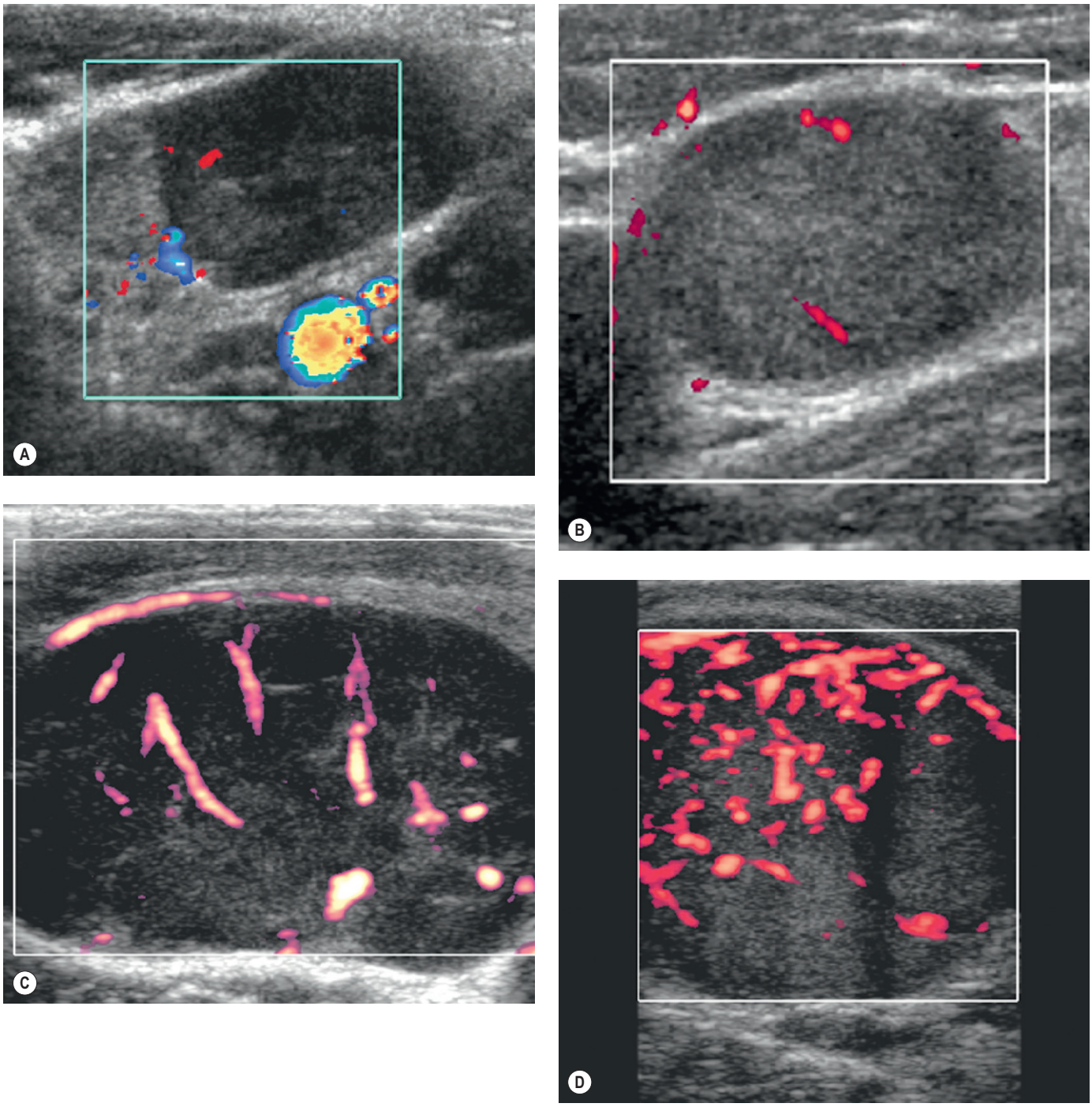

Figure 46.27 Doppler sonograms demonstrating a variety of abnormal vascular patterns in malignant nodes. **A:** Focal perfusion defect in a metastatic node with coagulative necrosis. **B:** Subcapsular vessels. **C:** Multiple aberrant vessels. **D:** Vastly increased and chaotic vascularity in a metastatic medullary carcinoma node.

Location

Cervical lymphadenopathy is a common presenting feature of metastatic disease, lymphoma and infection, including tuberculosis.

Metastases from head and neck cancers are often site-specific.[38] Oral cavity tumours tend to metastasise to the submental, submandibular and upper deep cervical chains, pharyngolaryngeal carcinomas to the deep cervical chains and nasopharyngeal cancer to the upper deep cervical chain and posterior triangle. Nodes in the supraclavicular fossa and lower posterior triangle (Level VI) point to infraclavicular primaries.

The distribution of lymphomatous nodes also seems to have a consistent pattern of submental, submandibular and upper deep cervical chain involvement.[25] Although the nodal territories involved in lymphoma are similar to those from oral cavity carcinoma metastases, these two conditions will have other distinguishing features, for example the absence of nodal necrosis in lymphoma.

Papillary carcinoma of the thyroid characteristically metastasises to the upper deep cervical chain and anterior cervical chains.

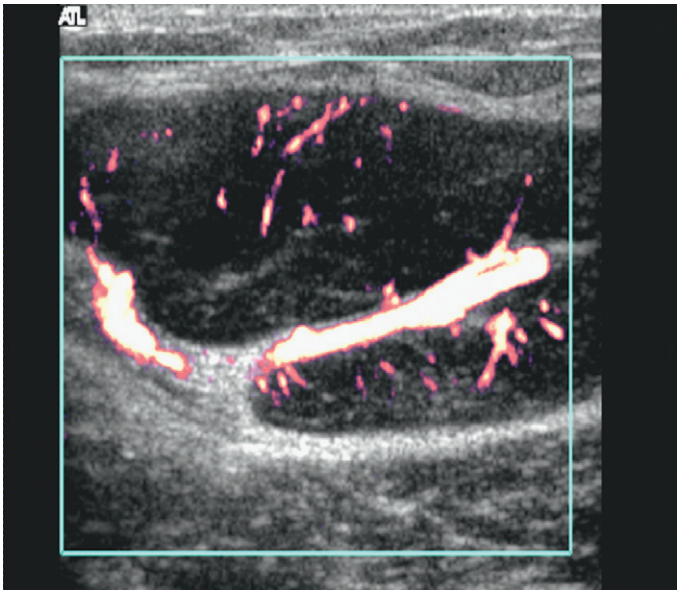

Figure 46.28 Power Doppler sonogram demonstrating an exaggerated hilar vascular pattern in a lymphomatous node.

MISCELLANEOUS CONDITIONS INVOLVING LYMPH NODES

Kimura disease

This is a rare, chronic inflammatory disease which mimics a malignancy. It is a benign entity with a good prognosis, occurring mainly in young men of Asian descent. The most common manifestation is of painless unilateral lymphadenopathy, or subcutaneous masses in the neck. Histologically the nodes are infiltrated with eosinophils, and peripheral eosinophilia is a consistent feature.[39]

On ultrasound, the nodes are round and hypoechoic, retaining their normal hila and the vascularity tends to retain a hilar pattern.[40] The affected nodes are distributed in the submental, submandibular and upper deep cervical regions. The appearances of the salivary and subcutaneous lesions are varied – the nodules being predominantly solid and hypoechoic, although they may have a cystic component.

Kikuchi disease (histiocytic necrotising lymphadenitis)

This is an uncommon cause of lymphadenitis, which may present with or without systemic symptoms. It is prevalent in Asian countries, and is generally a self-limiting disease, the lymphadenopathy resolving in 1–6 months.[41]

Sonographically, the nodes are hypoechoic, homogeneous or heterogeneous, but surrounded by hyperechoic rims. The hilum of the node and a benign vascular pattern are retained.[42] Clinically and histologically, Kikuchi disease may be mistaken for lymphoma and if it is suspected, a core biopsy should be performed.[43]

Human immunodeficiency virus (HIV)

Nodal enlargement due to HIV resembles reactive lymphadenopathy with retention of normal morphology and vascularity. In a patient with known HIV, lymphoma and tuberculosis should be included in the differential diagnosis of cervical lymphadenopathy. Cervical lymphadenopathy in association with multiple bilateral AIDS-related parotid cysts (ARPCs – see Chapter 45) suggests the diagnosis of HIV.

Sarcoidosis

Cervical lymphadenopathy may occur in association with sarcoidosis but the ultrasound features are non-specific, resembling reactive lymphadenopathy. Associated head and neck features of sarcoid include diffuse salivary gland enlargement with benign lymphoepithelial lesions (see Chapter 45), uveitis and facial palsy (Heerfordt's disease). If sarcoidosis is suspected, a core biopsy is recommended to demonstrate non-caseating granulomas.

BIOPSY TECHNIQUES

Palpation is known to be inaccurate in staging neck nodes.[44] The role of ultrasound in the assessment of cervical lymphadenopathy is well established and ultrasound-guided fine-needle aspiration cytology (US FNAC) further increases the accuracy. In the only large study comparing all five modalities – palpation, CT, MR, ultrasound and US FNAC – for staging necks the accuracy of US FNAC was significantly better, at 93%, than all the other techniques, CT, MRI and ultrasound alone having similar levels of accuracy (75–82%), whereas palpation only achieved 69% accuracy.[45]

US FNAC is useful in staging the neck in two groups of patients: those with known neck metastases (N+) and those who are clinically N0. In patients with apparently unilateral metastases particular attention should be paid to the contralateral side. Meticulous attention should also be paid to patients with limited neck disease, as there are a number of selective neck dissections that may be suitable for treatment, thereby decreasing the morbidity of the neck dissection.

US FNAC has the greatest impact in N0 necks – either by upstaging to N+, which will require further treatment with either radiotherapy or surgery, or by confirming the N0 status – enabling a watch-and-wait policy in selected cases such as a T1 oral cavity tumour.

The treatment of N0 necks is controversial. Most centres opt to treat the neck if the risk of metastases is more than 20%. It has been estimated that the risk of missing an occult metastasis with palpation is 41%, which decreases to 18% with US FNAC of the neck.[46]

All of the previously described signs help to discriminate between benign and malignant nodes; however, not one sign is absolute and the signs should be used collectively to decide whether to obtain cytology or histology for further assessment (Table 46.2). Obtaining cells or tissue is achieved by performing ultrasound-guided fine-needle aspiration (FNA) for cytology, or a core biopsy for histology. The decision whether to do an FNA or a core biopsy depends on local cytological and histopathological expertise. If cytological expertise is available, the majority of head and neck nodal samplings will be by FNA, as it is accurate, inexpensive and quick. Ultrasound-guided FNA approaches 100% specificity in head and neck cancer, as squamous cells are not normally found in lymph nodes. If repeated FNAs are negative, a core biopsy should be performed.

A core biopsy is more useful than FNA if lymphoma is suspected, as nodal architecture may be studied and flow cytometry performed. In some centres, lymphoma may be diagnosed and typed from a core biopsy alone, without resorting to an open biopsy.

The selection of the nodes to be sampled is important. For tumours close to the midline, such as small tongue tumours, with a propensity for bilateral nodal involvement, consideration should be given to sampling nodes bilaterally. In patients with known nodal metastases on one side of the neck, consideration should be given to sampling nodes on the contralateral side to exclude bilateral involvement with metastatic disease, the presence of which will have a significant effect on management.

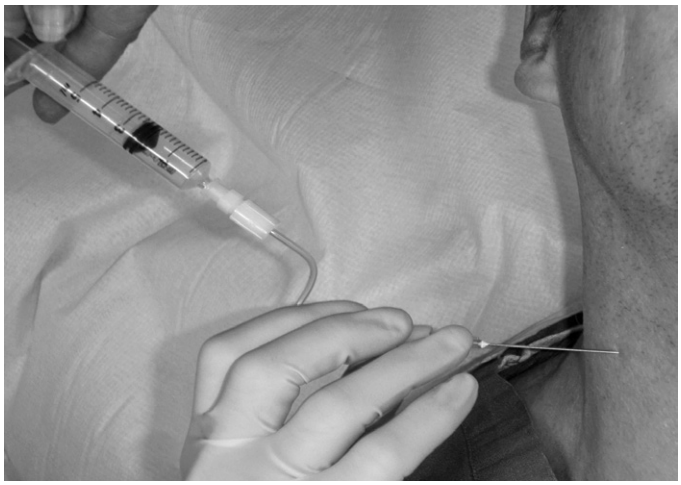

Figure 46.29 Ultrasound-guided fine-needle aspiration (FNA) technique. The operator obtains microcores of the lesion under ultrasound guidance, whilst an assistant applies 2 mL of suction.

Biopsy technique for enlarged cervical lymph nodes

General principles
- Optimal hand–needle–screen positioning.
- Probe cover.
- Biopsy along long axis of probe.

FNA
- **Either** 5 mL syringe, connecting tube and 21FG needle, 2 mL of suction by assistant **Or** capillary action (for thyroid cytology or if no assistance available for suction).
- Bevel of the needle facing transducer.
- Rotation of the needle to obtain microcores.

Core biopsy
- Rehearse firing noise with patient prior to biopsy.
- Local anaesthetic and skin incision.
- Non-advancing cutting needle 16–18FG.
- Sampling notch facing transducer.
- Fresh samples for ?lymphoma or ?infection.

Ultrasound-guided fine-needle aspiration (FNA)

The principles for successful FNA are essentially the same as those for diagnostic scanning. Ergonomic but comfortable positioning of the patient is paramount, with the operator's arm at the same level as the patient's neck, and the screen at eye-level. It may be easier to biopsy a mass in the left neck with the operator on the patient's left side. It is also very useful to develop the ability to use the aspiration/biopsy needle with both hands.

An alcohol spray to momentarily numb the skin is useful but no local anaesthetic is needed, as the anaesthetic injection is often more painful than the aspiration procedure. The exception to this rule is in children, in whom application of a local anaesthetic cream 1 hour prior to the biopsy is very helpful. A probe cover is recommended to protect the transducer, which is susceptible to damage from alcohol wipes.

A needle and syringe are the essential pieces of equipment. There are multiple possible combinations,[47] but the author's preference is for a 21G needle and 5 mL syringe. A short low-resistance connection tube between the syringe and the needle allows maximum accuracy in needle placement, enabling the operator to manipulate the needle with the index finger and thumb, whilst an assistant applies suction (Fig. 46.29). Once the needle tip is visualised within the lesion, the assistant should apply approximately 2 mL of suction using a 5 mL syringe for approximately 5 seconds, which is then released before the needle is withdrawn. If no assistance for aspiration is available, a capillary technique is recommended.[48] A needle with or without a stylet may be used. The needle is inserted into the lesion and the stylet, if used, is withdrawn; fluid, together with cells, will then migrate up the needle lumen. The capillary technique is also recommended in the thyroid, as aspiration samples obtained with suction are frequently haemorrhagic.

It is crucial to visualise the needle tip at all times when performing FNA in the head and neck in order to avoid vascular and neural structures. This is best achieved by inserting the needle along the long axis of the probe, with the bevel facing upwards. Once the target has been identified, the transducer position is fixed, whilst the needle is manipulated with the other hand along the plane of the ultrasound beam. For biopsying superficial lesions, the needle is kept as parallel to the transducer as possible to achieve maximum conspicuity of the needle. For biopsying deeper lesions, such as those in the deep lobe of the parotid, an angle of 55–60° between the needle and the probe, and a distance of 2–3 cm between the needle and the probe is optimal.[49,50]

The aim of a FNA is to obtain microcores of tissue, which is achieved by small drilling movements of the needle within the lesion. It is also useful to alter the angle of the needle within the lesion with repeated passes.

Depending on local arrangements, the sample may be directly smeared onto slides in the ultrasound department, or it may be transported in fluid to the laboratory for later preparation by the cytologist. If the sample is heavily bloodstained, the aspiration should be repeated as it is less likely that there will be sufficient tumour cells available for assessment after preparation.

Core biopsy

Core biopsy of neck masses is a safe, well-established procedure with a high diagnostic yield.[51] It is especially useful when repeated FNAs have been negative and when lymphoma is suspected. It is also useful for biopsy of thyroid lesions, as fine-needle aspiration specimens from the thyroid are often heavily contaminated with red blood cells.

The procedure requires local anaesthetic and a small skin incision. A spring-loaded biopsy needle is usually used and it is worth demonstrating the noise of the device being activated to the patient prior to the biopsy, as most head and neck biopsies occur very close to the ear. The principles of obtaining a successful core biopsy are similar to those for obtaining a fine-needle aspiration.

The essential piece of equipment is a non-advancing cutting needle, 16 or 18G. The device is inserted in the 'closed' position, to the periphery of the lesion. The inner stylet is then carefully advanced into the lesion, with the specimen notch facing upwards towards the transducer for maximum conspicuity, which allows precise positioning of the specimen notch across the region to be biopsied. On activating the device, the cutting sheath advances over the specimen notch with the inner stylet remaining stationary (Fig. 46.30).

The small cores of tissue are usually sent to the laboratory in formaldehyde. If lymphoma is suspected, it is useful to send a further fresh core kept moist with isotonic transport fluid; this can be used for flow cytometry (in order to asses whether the sample is monoclonal) and immunocytochemical analysis. Similarly, if infection is suspected, a further fresh core should be sent for microbiological assessment.

The accuracy of the pathological report on fine-needle aspiration and core biopsy specimens depends on the pathologist receiving relevant clinical information, for which a close working relationship between the radiologist and pathologist is invaluable.

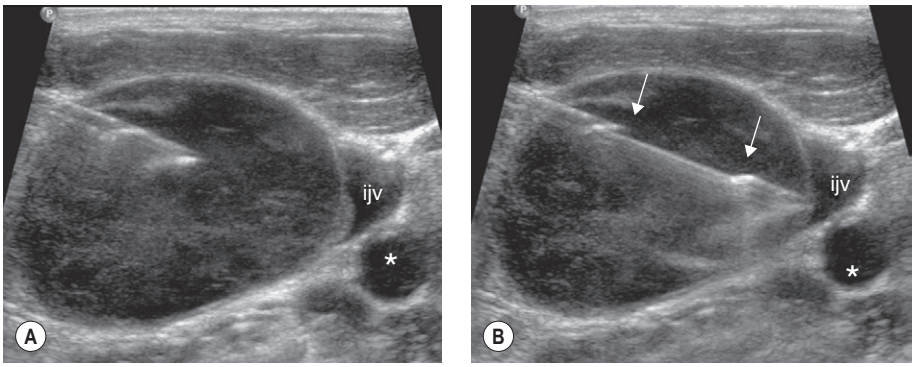

Figure 46.30 Sonograms of a core biopsy of a lymphomatous node. **A:** Non-advancing device is inserted into the node. **B:** The cutting notch (arrows) of the inner stylet is positioned across the region to be biopsied, before firing. After firing, the end of the device extends no further than the tip of the inner stylet. *, carotid artery; ijv, internal jugular vein.

Table 46.2 Signs used in assessing neck nodes with ultrasound

Sign	Value	Normal, reactive	SCC metastasis	Papillary carcinoma metastasis	Lymphoma	TB
Size (short axis)	+		>7–8 mm jugulodigastric>6–7 mm others			
Shape	+++	Flat oval (Level Ia, Ib round)	Round	Round	Round Oval	Round
Echotexture	+++	Hypoechoic	Hypoechoic	Hyperechoic microcalcification	Very hypoechoic Reticulated/ micronodular	Hypoechoic
Cortex/hilum	++	Hilum present	Absent hilum ++ Eccentric cortical hypertrophy +++	Absent hilum	Absent/present hilum	Absent hilum
Necrosis	++++	None	Cystic necrosis Coagulation	Cystic necrosis (may be totally cystic)	None	Cystic
Margins of node	+	Slightly ill defined	Sharp ill defined = extracapsular spread	Sharp	Sharp	Ill-defined Matting Surrounding soft tissue oedema
Angioarchitecture	++	Hilar pattern (>5 mm may be avascular) No peripheral flow	Peripheral vessels Aberrant vessels Perfusion defects	Peripheral vessels Aberrant vessels Perfusion defects	Exaggerated hilar pattern	Hilar pattern Peripheral vessels Perfusion defects
Location	+	No peripheral flow	Site–specific for tumour	Level II, VI	Levels I, V	IV, V
Biopsy			FNA	FNA (± thyroglobulin level)	Core: formalin + fresh	FNA Microbiology

REFERENCES

1. Evans R. Lymph nodes. In: Ahuja A, Evans R, editors. Practical head and neck ultrasound. London: Greenwich Medical Media; 2000. p. 67–83.
2. Castenholz A. Architecture of the lymph node with regard to its function. Curr Top Pathol 1990;84(Pt 1):1–32.
3. Herman P, Yamamoto I, Mellins H. Blood microcirculation in the lymph node during the primary immune response. J Exp Med 1972;136(4):697–714.
4. Marchal G, Oyen R, Verschakelen J, et al. Sonographic appearance of normal lymph nodes. J Ultrasound Med 1985;4(8):417–419.
5. Rubaltelli L, Proto E, Salmaso R, et al. Sonography of abnormal lymph nodes in vitro: correlation of sonographic and histologic findings. AJR Am J Roentgenol 1990;155(6):1241–1244.
6. Hall F. The functional anatomy of lymph nodes. In: Stansfeld A, d'Ardenne A, editors. Lymph node biopsy interpretation. London: Churchill Livingstone; 1992. p. 3–28.
7. Rouviere H. Anatomy of the human lymphatic system. Ann Arbor, MI: Edwards Brothers; 1938.
8. Greene FL, Compton C, Fritz A, editors. AJCC cancer staging atlas. 6th ed. New York: Springer; 2006.
9. Som P, Curtin H, Mancuso A. Imaging-based nodal classification for evaluation of neck metastatic adenopathy. AJR Am J Roentgenol 2000;174(3):837–844.
10. Eneroth C. Salivary gland tumors in the parotid gland, submandibular gland, and the palate region. Cancer 1971;27(6):1415–1418.
11. Solbiati LRG, Bellotti E, Montali G, et al. High-resolution sonography of cervical lymph nodes in head and neck cancers: criteria for differentiation of reactive versus malignant nodes. Radiology 1988;169(P):113(Abstract).
12. van den Brekel M, Stel H, Castelijns J, et al. Cervical lymph node metastasis: assessment of radiologic criteria. Radiology 1990;177(2):379–384.
13. van den Brekel M, Castelijns J, Snow G. The size of lymph nodes in the neck on sonograms as a radiologic criterion for

metastasis: how reliable is it? AJNR Am J Neuroradiol 1998;19(4):695–700.
14. Tannock I. Principles of cell proliferation: cell kinetics. In: De Vita VJ, editor. Principles and practice of oncology. 2nd ed. Philadelphia: Lippincott; 1988. p. 3–13.
15. Yuasa K, Kawazu T, Kunitake N, et al. Sonography for the detection of cervical lymph node metastases among patients with tongue cancer: criteria for early detection and assessment of follow-up examination intervals. AJNR Am J Neuroradiol 2000;21(6):1127–1132.
16. Vassallo P, Wernecke K, Roos N, Peters P. Differentiation of benign from malignant superficial lymphadenopathy: the role of high-resolution US. Radiology 1992;183(1):215–220.
17. Takashima S, Sone S, Nomura N, et al. Nonpalpable lymph nodes of the neck: assessment with US and US-guided fine-needle aspiration biopsy. J Clin Ultrasound 1997;25(6):283–292.
18. Ahuja A, Ying M. Sonography of neck lymph nodes. Part II: abnormal lymph nodes. Clin Radiol 2003;58(5):359–366.
19. Bruneton J, Normand F, Balu-Maestro C, et al. Lymphomatous superficial lymph nodes: US detection. Radiology 1987;165(1): 233–235.
20. Ahuja A, Ying M, Yang W, et al. The use of sonography in differentiating cervical lymphomatous lymph nodes from cervical metastatic lymph nodes. Clin Radiol 1996;51(3):186–190.
21. Ahuja A, Ying M, Yuen H, Metreweli C. 'Pseudocystic' appearance of non-Hodgkin's lymphomatous nodes: an infrequent finding with high-resolution transducers. Clin Radiol 2001;56(2):111–115.
22. Ahuja A, Chow L, Chick W, et al. Metastatic cervical nodes in papillary carcinoma of the thyroid: ultrasound and histological correlation. Clin Radiol 1995;50(4):229–231.
23. Gorman B, Charboneau J, James E, et al. Medullary thyroid carcinoma: role of high-resolution US. Radiology 1987;162(1 Pt 1):147–150.
24. Ahuja A, Leung S, Ying M, Metreweli C. Echography of metastatic nodes treated by radiotherapy. J Laryngol Otol 1999;113(11):993–998.
25. DePeña C, Van Tassel P, Lee Y. Lymphoma of the head and neck. Radiol Clin North Am 1990;28(4):723–743.
26. Ying M, Ahuja A, Brook F, Metreweli C. Vascularity and grey-scale sonographic features of normal cervical lymph nodes: variations with nodal size. Clin Radiol 2001;56(5):416–419.
27. King A, Tse G, Ahuja A, et al. Necrosis in metastatic neck nodes: diagnostic accuracy of CT, MR imaging, and US. Radiology 2004;230(3):720–726.
28. Ying M, Ahuja AT, Evans R, et al. Cervical lymphadenopathy: sonographic differentiation between tuberculous nodes and nodal metastases from non-head and neck carcinomas. J Clin Ultrasound 1998;26(8):383–389.
29. Ahuja A, Ying M, Yang WT, et al. The use of sonography in differentiating cervical lymphomatous lymph nodes from cervical metastatic lymph nodes. Clin Radiol 1996;51(3):186–190.
30. Snozek C, Chambers E, Reading C, et al. Serum thyroglobulin, high-resolution ultrasound, and lymph node thyroglobulin in diagnosis of differentiated thyroid carcinoma nodal metastases. J Clin Endocrinol Metab 2007;92(11):4278–4281.
31. Shozushima M, Suzuki M, Nakasima T, et al. Ultrasound diagnosis of lymph node metastasis in head and neck cancer. Dentomaxillofac Radiol 1990;19(4):165–170.
32. Johnson J. A surgeon looks at cervical lymph nodes. Radiology 1990;175(3):607–610.
33. Ahuja A, Ying M, Leung S, Metreweli C. The sonographic appearance and significance of cervical metastatic nodes following radiotherapy for nasopharyngaeal carcinoma. Clin Radiol 1996;51(10):698–701.
34. Tschammler A, Beer M, Hahn D. Differential diagnosis of lymphadenopathy: power Doppler vs color Doppler sonography. Eur Radiol 2002;12(7):1794–1799.
35. Tschammler A, Ott G, Schang T, et al. Lymphadenopathy: differentiation of benign from malignant disease – color Doppler US assessment of intranodal angioarchitecture. Radiology 1998;208(1):117–123.
36. Ahuja A, Ying M, Yuen YH, Metreweli C. Power Doppler sonography to differentiate tuberculous cervical lymphadenopathy from nasopharyngeal carcinoma. Am J Neuroradiol 2001;22(4):735–740.
37. Ahuja A, Ying M, Ho S, Metreweli C. Distribution of intranodal vessels in differentiating benign from metastatic neck nodes. Clin Radiol 2001;56(3):197–201.
38. Som P. Detection of metastasis in cervical lymph nodes: CT and MR criteria and differential diagnosis. AJR Am J Roentgenol 1992;158(5):961–969.
39. Kimura Disease: Differential Diagnoses and Workup [database on the Internet] 2007. Available from: http://emedicine.medscape.com/article/210752. Accessed 1 March 2009.
40. Ahuja A, Ying M, Mok J, Anil C. Gray scale and power Doppler sonography in cases of Kimura disease. AJNR Am J Neuroradiol 2001;22(3):513–517.
41. Kikuchi disease [database on the Internet] 2008. Available from: http://emedicine.medscape.com/article/210752. Accessed 1 Mar 2008.
42. Youk J, Kim E, Ko K, Kim M. Sonographic features of axillary lymphadenopathy caused by Kikuchi disease. J Ultrasound Med 2008;27(6):847–853.
43. Song JY, Cheong HJ, Kee SY, et al. Disease spectrum of cervical lymphadenitis: analysis based on ultrasound-guided core-needle gun biopsy. J Infect 2007;55(4):310–316.
44. Baatenburg de Jong R, Rongen R, Laméris J, et al. Metastatic neck disease. Palpation vs ultrasound examination. Arch Otolaryngol Head Neck Surg 1989;115(6):689–690.
45. van den Brekel M, Castelijns J, Stel H, et al. Modern imaging techniques and ultrasound-guided aspiration cytology for the assessment of neck node metastases: a prospective comparative study. Eur Arch Otorhinolaryngol 1993;250(1):11–17.
46. van den Brekel M, Castelijns J, Reitsma L, et al. Outcome of observing the N0 neck using ultrasonographic-guided cytology for follow-up. Arch Otolaryngol Head Neck Surg 1999;125(2):153–156.
47. Cozens N, Berman L. Fine-needle aspiration or core biopsy? In: Ahuja A, Evans R, editors. Practical head and neck ultrasound. London: Greenwich Medical Media; 2000. p. 131–144.
48. Robinson I, Cozens N. Does a joint ultrasound guided cytology clinic optimize the cytological evaluation of head and neck masses? Clin Radiol 1999;54(5):312–316.
49. Hopkins RE, Bradley M. In-vitro visualization of biopsy needles with ultrasound: a comparative study of standard and echogenic needles using an ultrasound phantom. Clin Radiol 2001;56(6):499–502.
50. Bradley MJ. An in-vitro study to understand successful free-hand ultrasound guided intervention. Clin Radiol 2001;56(6):495–498.
51. Screaton N, Berman L, Grant J. Head and neck lymphadenopathy: evaluation with US-guided cutting-needle biopsy. Radiology 2002;224(1):75–81.

CHAPTER

47

The eye and orbit

John A. Fielding

THE EYE

Introduction

The ultrasonic appearances of the eye and orbit closely resemble the normal anatomical structures (Fig. 47.1). The eye is the easiest object to visualise within the orbit, as its fluid content and superficial position make it ideal for ultrasound examination. Knowledge of the anatomy and the firm structural anchoring points of the vitreous, inner and middle coats of the eye enables the pathological appearances of the detached vitreous, retina and choroid to be understood. Ultrasound is the only practical method of obtaining images of the posterior segment of the eye when the light-conducting media are opaque, and is the most useful investigation prior to vitrectomy.[1,2]

The mainstays of examination are 2D real-time imaging, colour Doppler mapping and spectral Doppler.[3] The skilled operator is able to study the characteristics of the motion and topography of the pathological intraocular structures, enabling differentiation between retinal detachment and vitreous membrane, or tumour and haemorrhage. Ultrasound contributes more to tissue diagnosis than do computed tomography (CT) or magnetic resonance imaging (MRI), as they cannot scan in real-time and are not comparable with ultrasound for spatial resolution. Although combined B- and A-mode imaging is used in some centres and standardised A-scan systems provide quantitative data on intraocular echoes, they seldom yield information which usefully supplements that of the 2D image.[4]

Anatomy and ultrasound features

The eyeball

The eyeball lies in the anterior orbit, embedded in fat but separated from it by a membranous sac termed the fascia bulbi, or Tenon's capsule (Fig. 47.2). This is applied to the eyeball from attachments at the corneoscleral junction and the optic nerve. Its inner layer is thin and blends with the sclera; its outer layer is pierced by the extraocular muscle tendons, which it invests towards each muscle belly. The eyeball is composed of segments of two different-sized spheres. The transparent anterior segment forms about one-sixth of the eyeball and is part of a smaller sphere; the opaque posterior segment forms about five-sixths and is part of the larger sphere. The optic axis is a line joining the anterior pole – the central point of the anterior curvature of the eyeball – to the posterior pole, the central point of its posterior curvature. The normal axial length of the eye is 24 mm.

Sclera and cornea

The wall of the eyeball encloses the refractive media and is made of three coats (Fig. 47.3). The outer coat is tough and fibrous and comprises the sclera and cornea, which are almost avascular. The bulbar conjunctiva is attached to it by loose connective tissue. The sclera may be regarded as a cup-like expansion of the dural sheath of the optic nerve and on ultrasound images is resolvable from the inner layers of choroid and retina (Fig. 47.4). It is thicker posteriorly (1 mm) than anteriorly (0.6 mm), or at the equator (0.5 mm). The optic nerve pierces the sclera posteriorly 3 mm to the nasal side of the posterior pole and slightly above the horizontal meridian. Near the equator there are four apertures, the exit foramina of the vortex veins, one in each posterior quadrant.

The transparent cornea bulges forward from the sclera and is slightly thicker, measuring 0.9 mm at its centre and 1.2 mm at the periphery. The corneoscleral junction is circumscribed by the sinus venosus sclerae (canal of Schlemm) at the periphery of the anterior chamber. At the iridocorneal angle aqueous humour drains into the canal, which communicates with the anterior scleral veins.

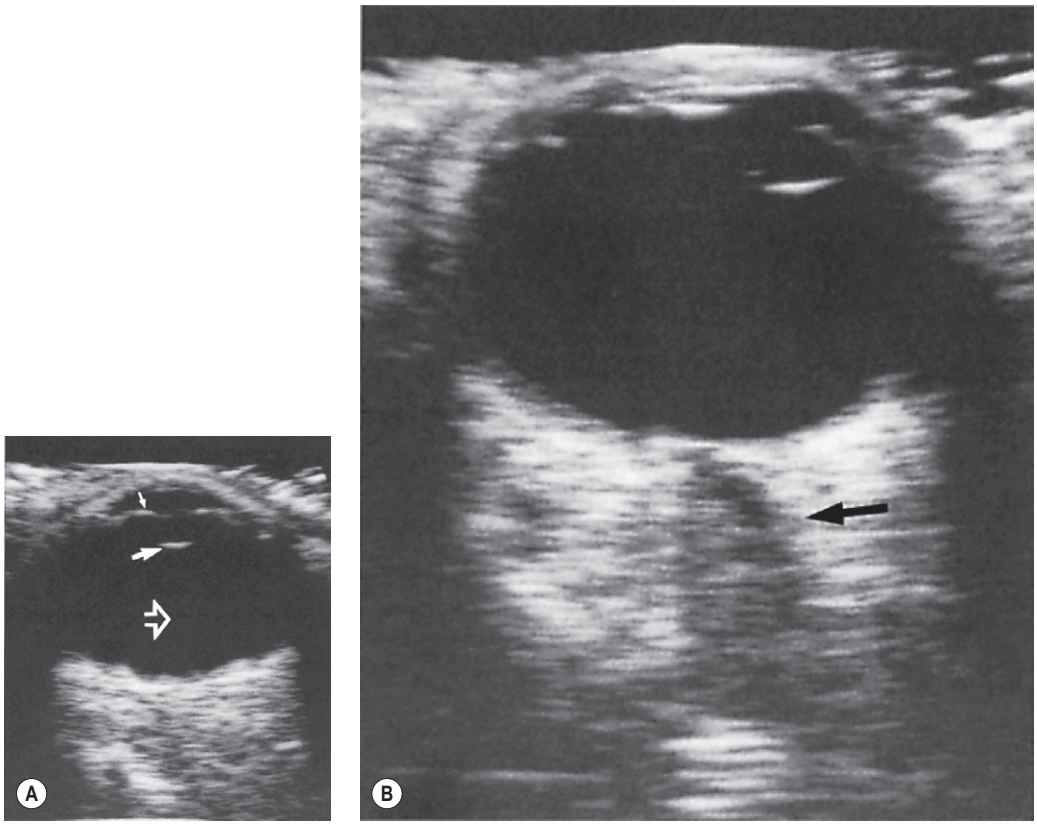

Figure 47.1 Normal eye. A: Normal eye showing iris (small arrow), posterior lens surface (arrow) and clear vitreous (open arrow). **B:** Normal eye deviated left, showing optic nerve (arrow).

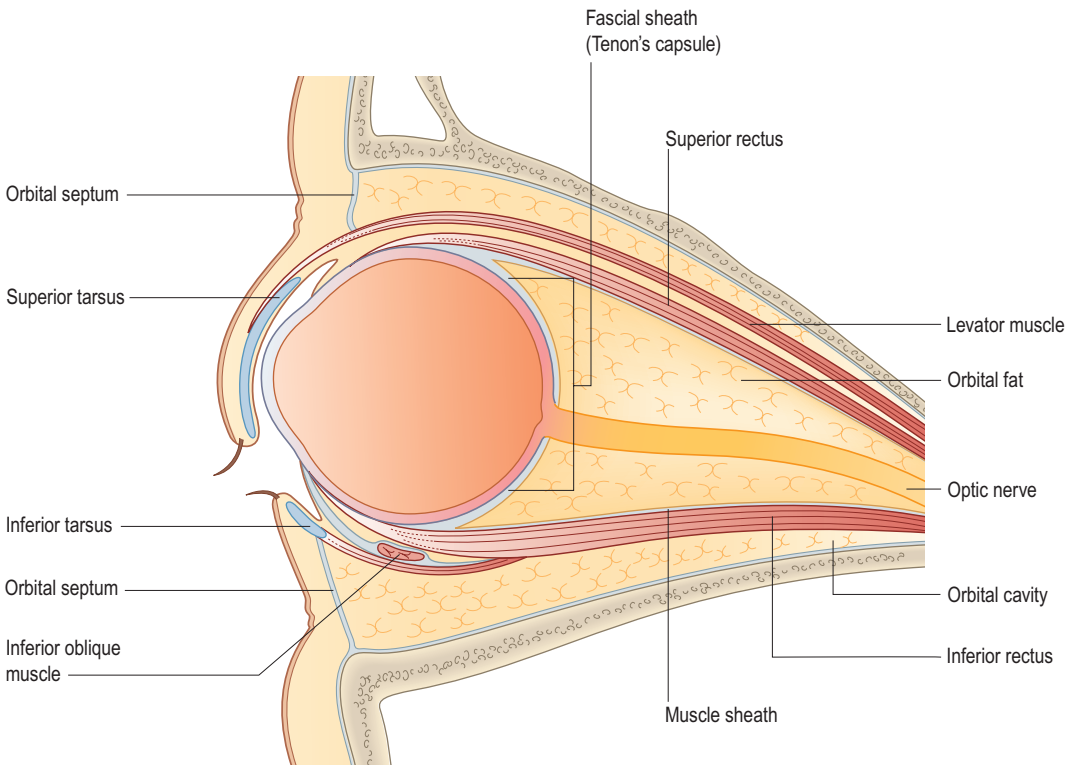

Figure 47.2 Vertical section of the eye and orbit.

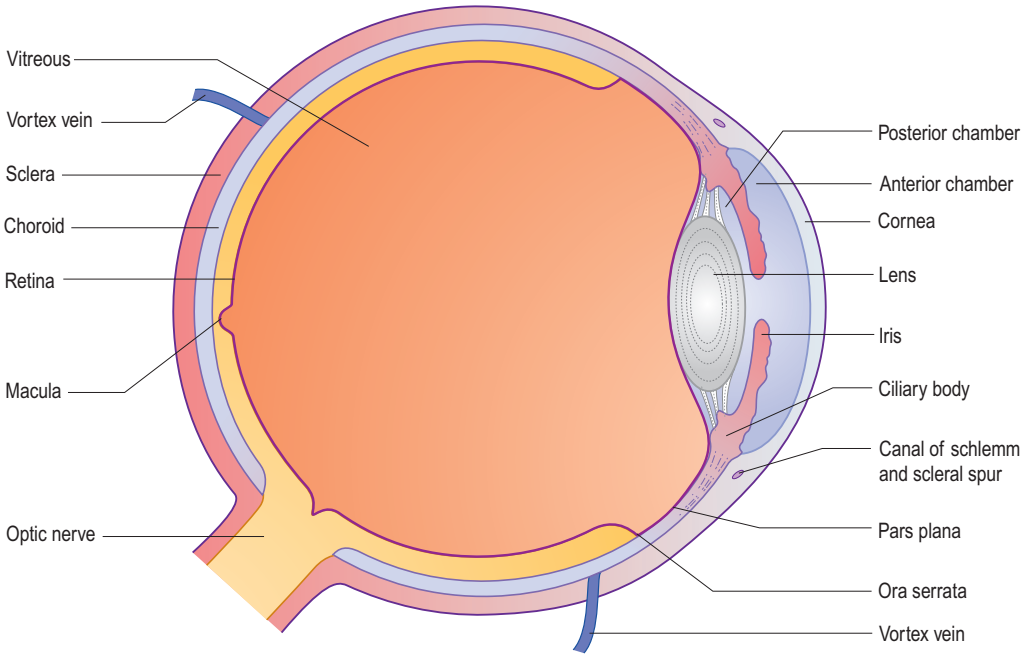

Figure 47.3 Horizontal section through eye.

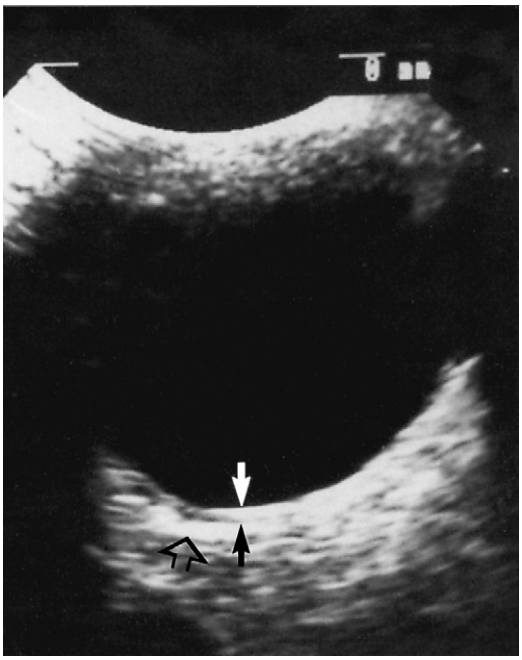

Figure 47.4 Normal retina–choroid (arrows) and sclera (open arrow).

Choroid, ciliary body and iris

The intermediate coat is a continuum of vascular tissue comprising the choroid, the ciliary body and the iris, and may be regarded as an expansion of the arachnoid and pia of the optic nerve. The choroid is a thin erectile vascular layer which may be up to 1 mm thick and is of lower reflectivity than the retina and sclera. It lines the posterior part of the sclera, from which it is separated by the suprachoroidal space, a thin connective tissue layer across which the ciliary arteries, veins and nerves pass. The choroid is firmly attached at the scleral spur and exit foramina of the vortex veins.

The ciliary body is triangular in section, being thicker in front and thinner behind. It extends from the corneoscleral junction backwards just over halfway to the equator. The scleral surface of the ciliary body contains the ciliary muscle. The iris is a contractile diaphragm up to 1 mm in thickness situated in front of the lens, obscuring the anterior lens surface on ultrasound scans. The iris partially divides the space between the cornea and lens into two sections filled with aqueous humour, the anterior and posterior chambers of the eye.

Retina

The retina is the delicate innermost nervous membrane of the eyeball and its anterior and posterior surfaces are identifiable on ultrasound examination. It may be regarded as an expansion of the neural substance of the optic nerve, whose fibres are spread out in the nervous layer of the retina. There are two layers: an outer pigmented layer attached to the choroid, and an inner neuronal layer – the retina proper – in contact with the vitreous body. Around the optic disc and at the ora serrata the retina is more firmly adherent to the choroid than elsewhere. The optic disc has a diameter of about 1.5 mm and its circumference is slightly raised. It is situated about 3 mm to the nasal side and slightly above the level of the posterior pole, and is important as the site of entry of the retinal arteries and the exit point for retinal nerves and veins. The macula is positioned 4 mm lateral to the centre of the optic disc and 1 mm inferiorly. Its central part, the fovea centralis, is a shallow depression. The macula is the area of the most acute vision, but the optic disc is insensitive to light and is known as the 'blind spot'.

During scanning the well-recognised artefacts 'Baum's bumps' are sometimes seen on the retina; they are named after the first documenter of B-scanning (Fig. 47.5). These are caused by refraction because of the increased propagation velocity of ultrasound in the lens.

Refracting media

The refracting media of the eyeball comprise the cornea, the aqueous humour, the lens and the vitreous body. The aqueous humour is a dilute saline solution secreted into the posterior chamber from the vessels of the iris and the ciliary processes. The lens is a transparent biconvex body enclosed in a transparent elastic capsule. It is 10 mm

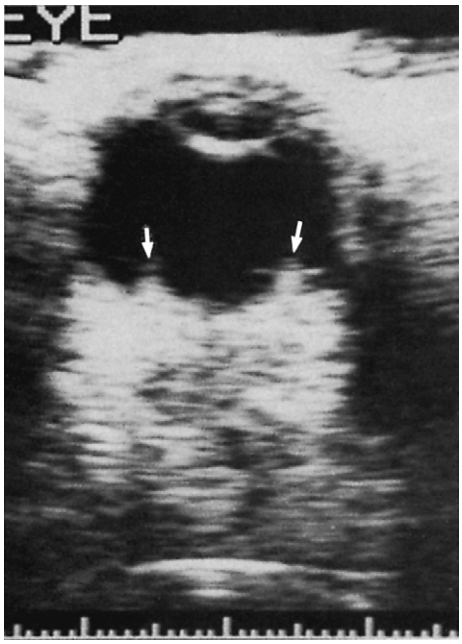

Figure 47.5 **Baum's bumps** (arrows) refraction artefact.

Attachments

- The wall of the eyeball comprises three coats: sclera, choroid, retina.
- The firm attachments of the coats and refracting media are of great relevance when understanding detachments.
- The choroid is firmly attached at the scleral spur and exit foramina of the vortex veins.
- The retina is firmly attached at the ora serrata and optic nerve head.
- The vitreous is firmly attached at the pars plana and optic disc.

in diameter and 3–4 mm thick. The interior of the normal lens is echo-free, but echoes arise from the central part of the posterior lens cortex, giving rise to a fine curved line on ultrasound images.

The suspensory ligament is a series of fibrils attached to the ciliary processes and further back to the ora serrata. Occasionally they may be seen as fine linear echoes.

The vitreous body is a transparent gel occupying the posterior four-fifths of the eyeball. It comprises a collagenous matrix containing mucopolysaccharides and water, the latter making up over 98% of the substance of the gel. It is attached to the optic disc, but more firmly at the pars plana just in front of the ora serrata. Elsewhere it lies free in contact with the retina. The normal gel is acoustically featureless, but its posterior surface is sometimes seen undulating off the retina, when scanning is performed during eye movements.

Examination technique

2D scanning

The quality of images produced by currently available general-purpose ultrasound scanners has made eye scanning a practical proposition for all departments possessing a short-focus 7.5 or 10 MHz real-time small parts probe.[5] The majority of scans illustrating this chapter were obtained with such equipment. Sector scanning is carried out with the patient lying supine, which gives stability and support to the head, making it easy for the patient to remain motionless. In this position the pull of gravity is exerted in the direction of the optic axis, enabling a detached vitreous still suspended from the vitreous base, or the sedimentation of blood, to be assessed more easily than in the erect position. Nevertheless, some operators prefer to have the patient seated. The main methods of examination are the 'contact' method, which is the routine way of examining the eye because of ease and rapidity, and the 'water-bath' method. With the contact method the probe is placed directly on the closed eyelid, with an intervening coupling gel. This is well tolerated by infants and children, as well as adults. Cineloop review is a useful record if a child cannot keep still for long. As an alternative to lid contact some purpose-built probes require direct contact with the topically anaesthetised eyeball. A stand-off facility with a small fluid-filled compartment has the advantage of improving visualisation of anterior structures, but satisfactory scans may be obtained using a thick layer of gel on the lid.[6] There is little need for the waterbath method nowadays, where the lids are retracted by a wire speculum and the eye is surrounded by a Steridrape bath containing Ringer's solution at 36°C, or an eyecup filled with methylcellulose may be used. The transducer is submerged in the fluid about 1 cm above the eye. This is the superior method for viewing anterior structures such as the vitreous base region.

Using either method, the aim is to image the globe both while static and during rapid eye movements during which the motion of intraocular structures is observed. Complete visualisation of the ocular contents is achieved by careful movement and orientation of the transducer with the eye in the primary (straight ahead) position and in all directions of gaze. The mobility of the eye enables up to 50° of movement in any direction from the primary position, and the structure of the coats of the eye (sclera, choroid and retina) resists deformation during these movements. The vitreous, however, is an elastic body which lies in free contact with the retina over most of its surface, and which may thus be distorted with each eye movement. The mobility of the pathological vitreous and retina may be observed during dynamic scanning, as may vitreoretinal adhesions. Following an ocular excursion after-movements may continue for approximately 1 second.[7] The vitreous moves as a complete body but the detached retina undulates as a membrane, unless fixed by fibrosis. Choroidal tumours appear solid and their attachment to the ocular wall is apparent; conversely, vitreous, retrohyaloid or subretinal haemorrhage may scintillate and sediment during eye movements. When vitreoretinal microsurgical techniques are being considered, information provided by these methods of scanning about the structure and mobility of the ocular contents is of great importance.

A-scan

This is carried out using the contact, the eyecup or the waterbath method, the immersion methods being preferable if measurements are to be taken (see 'Biometry' section). For diagnostic purposes the probe is positioned adjacent to the lens to avoid refraction of the ultrasound beam but for measurements the probe is positioned along the axis of the eye to produce a series of peaks corresponding with the reflecting interfaces (Fig. 47.6). The normal scan shows peak P, the main pulse, followed by peak C, the corneal reflection, which is sometimes resolved as two surfaces, the interior of the lens being echo-free. The vitreous cavity L-R is also echo-free, and the end wall spike R represents a combined reflection from the retina, choroid and sclera, with O representing orbital echoes.

Doppler

Orbital vascular disease and amaurosis fugax (transient ocular ischaemia) are intimately associated with carotid arterial atheroma and stenosis. Doppler studies can predict the degree of stenosis by demonstrating the blood flow characteristics within the carotid artery and the degree of turbulence; the flow in superficial temporal vessels; the direction of flow in supra-orbital vessels (reverse flow

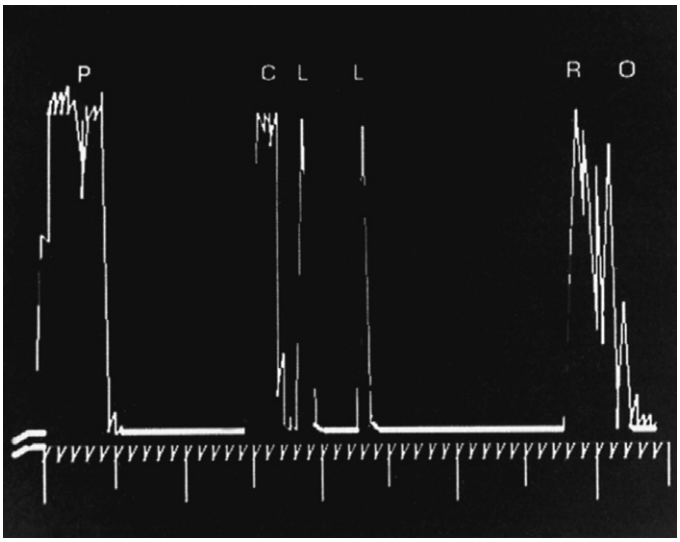

Figure 47.6 Normal A-scan. Peak P, main pulse; C, cornea; L, anterior and posterior lens surface; R, retina (end wall); O, orbital echoes.

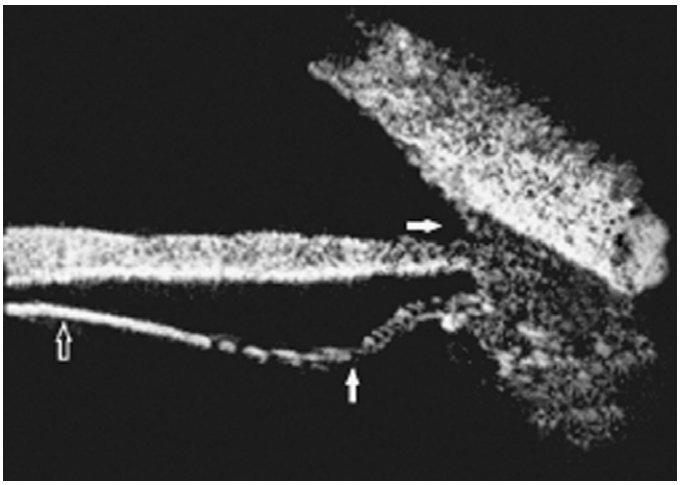

Figure 47.8 Ultrasound biomicroscope image showing anterior chamber angle (horizontal arrow), ciliary process (vertical arrow), lens (open arrow).

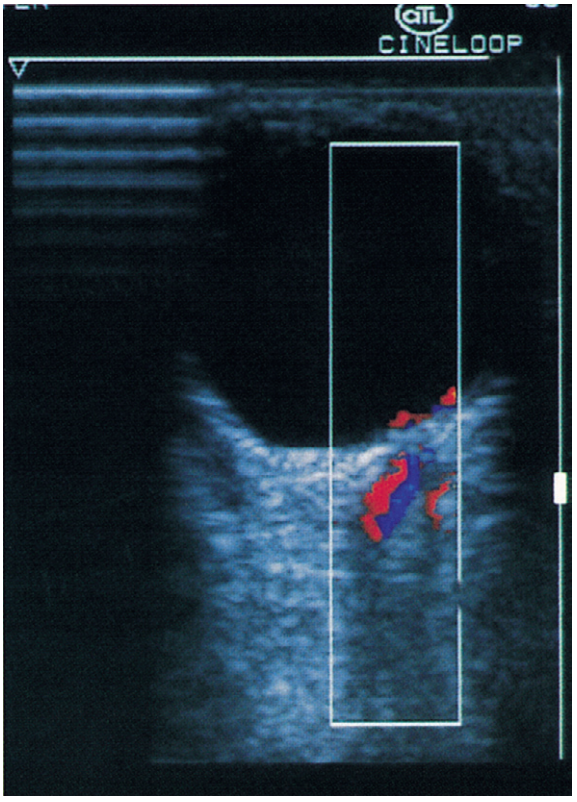

Figure 47.7 Normal central retinal vessels. Colour Doppler scan showing normal central retinal artery (red) and vein (blue).

is relevant to internal carotid disease); the presence of an anastomotic circulation;[8,9] and the time sequence in relation to these vessels.

Blood flow has also been studied in the ophthalmic artery and its branches and in pathological structures within the orbit; Doppler has also been used for quantification of vitreous mobility in posterior vitreous detachment.[10] Difficulties encountered in imaging a vessel as small as the ophthalmic artery (0.7–1.4 mm diameter) are overcome by the use of colour Doppler scanning (Fig. 47.7). Behind the globe the ophthalmic artery is frequently visualised in its usual anatomical position inferonasal to the optic nerve. The choroid receives most of the blood supply to the eye via the posterior ciliary branches of the ophthalmic artery. Examining the artery close to the globe therefore excludes blood flow to branches supplying extraocular structures, and gives an accurate estimation of blood flow to the eye itself. Changes in systemic blood pressure and intraocular pressure have a direct effect on ocular blood flow,[11] as there is no autoregulation of the choroidal vasculature. The central retinal artery and vein are even smaller vessels seen coursing along the optic nerve behind the optic disc.

Doppler technique

Doppler sampling is facilitated by the use of colour Doppler, which indicates the site of a vessel and greatly helps to position the gate. The use of a narrow gate (1.5 mm) enables the study of blood flow within small structures such as the retinal artery and vein, as well as the choroidal vessels. Spectral waveforms measured in the central retinal artery (CRA) and central retinal vein (CRV) at the optic nerve head may indicate whether arterial or venous occlusion has occurred, providing that the examination is carried out within days of the onset of symptoms.[12,13] Colour Doppler is a useful supportive method of diagnosing intraocular tumours, such as melanomas, metastases and retinoblastomas, tumour vessels showing vividly as pulsating channels or lakes of colour. Melanoma is occasionally mimicked by benign conditions such as disciform lesions, subretinal haemorrhage or choroidal folds. In this situation the demonstration of tumour vasculature by colour Doppler is a considerable aid to differential diagnosis. Colour Doppler also helps differentiate between retinal detachment (showing blood flow) and the posterior surface of the detached gel (showing no flow).[14]

Ultrasound biomicroscope

Near-field artefact hampers clear visualisation of the anterior segment in conventional scanning, unless a stand-off probe or a thick layer of gel is used. Pavlin and colleagues have developed a high-frequency (50 MHz) ultrasound biomicroscope which provides in-vivo microscopic imaging of the iris, ciliary body, anterior chamber and cornea with unparalleled detail (Fig. 47.8). This makes possible investigation of conditions of the anterior segment, such as glaucoma, iris tumours, scleral conditions and lens implantation.[15]

Indications for ultrasound examination of the eye

1. Opaque light-conducting media, making direct vision by ophthalmoscopy difficult or impossible.
2. Suspected intraocular tumour: solid lesions are readily visualised, localised and measured by ultrasound.
3. Differentiation between serous and solid retinal detachment. It is not always possible to determine ophthalmoscopically whether a detachment is concealing a tumour. The subretinal area is clearly demonstrated by ultrasound.
4. Examination of the vitreous.
5. Localisation of foreign bodies.
6. Ocular measurements (biometry, using A-scan).
7. Proptosis.
8. Doppler investigation of orbital vascular disease and tumours.

3D scanning

Three-dimensional ultrasound (3DUS) reconstruction software is available on some conventional scanners. This enables pathological structures, such as a melanoma, to be reviewed in 3D. A 3D data set is acquired which is then reconstructed into a 3D volume which may then be reviewed in any orientation (including coronal and oblique).[16] The technique may prove to be of value in evaluating ocular tumours, extrascleral extension, radioactive plaque localisation and vitreoretinal disease.

Indications

In practice patients with opaque media form the bulk of referrals, particularly those with cataracts and haemorrhages. It is not necessary to scan every patient with a cataract, but if there are concurrent symptoms, for example inflammation, pain, rapidly worsening vision, or the development of glaucoma, a scan should be performed to detect or exclude any coexistent pathology.

If vitreoretinal surgery is contemplated ultrasound assessment of the globe is essential.[1] The preoperative information required includes:

1. the state of the vitreous
2. the position and extent of any intraocular lesion visible by ultrasound
3. the condition of the retina, and particularly the macula
4. the motility of the contents of the globe, which has a direct influence on operability, and
5. the relation between the vitreous and retina, mapping out any vitreoretinal adhesions.

Pathology

Lens

Cataract

Cataracts are usually noted incidentally during scanning of the posterior segment of the opaque eye. The outline of the lens is seen particularly well if there is a senile subcapsular cataract, which leaves an outline of reflective material below the lens capsule (Fig. 47.9). An immature cataract is one in which scattered opacities are separated by clear zones, whereas a mature cataract forms a totally opaque cortex, resulting in a highly reflective lens on scanning.

Intraocular lens implant

Cataract extraction is frequently followed by intraocular lens implantation. Posterior chamber implants lie behind the iris, and anterior chamber implants in front. Artificial lenses are manufactured from plastics and show dense reverberation artefacts posteriorly (Fig. 47.10). A plane of examination to the side of the lens must therefore be sought.

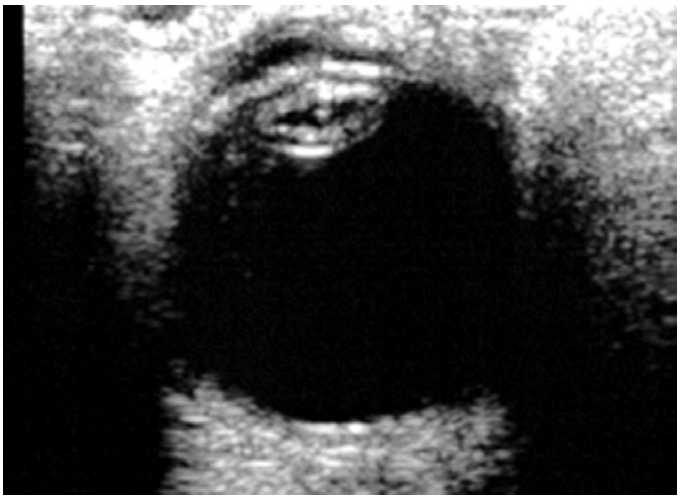

Figure 47.9 Subcapsular cataract with anterior epithelial proliferation.

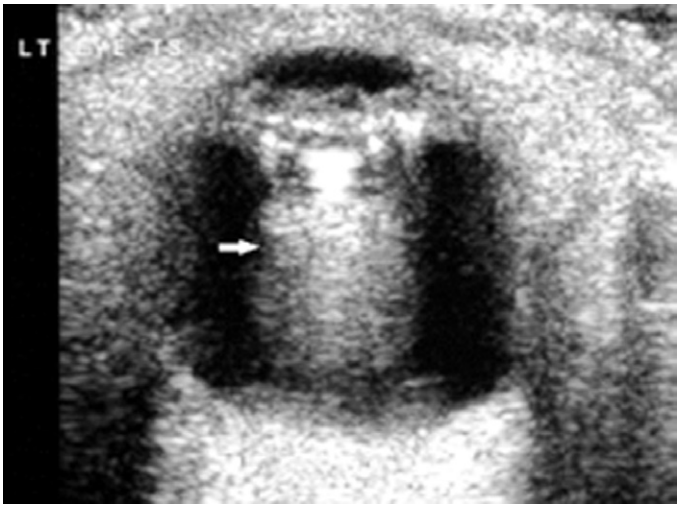

Figure 47.10 Lens implant showing reverberation artefact posteriorly (arrow).

Ectopia lentis

The non-cataractous lens is less easy to image, but it is possible to identify the ectopic lens in congenital or acquired lens dislocation. Bilateral lens subluxation in an upward direction is a feature of Marfan's syndrome, which is also a cause of retinal detachment due to retinal degeneration. Conversely, in homocystinuria the lens subluxation is typically downwards (Fig. 47.11). Glaucoma may result from pupil block, as a result of lens incarceration in the pupil, or from a total dislocation into the anterior chamber. Retinal detachment is also a complication.

Retina

Retinal detachment

Retinal detachments are divided into two main types, rhegmatogenous (arising from a break in continuity) and non-rhegmatogenous

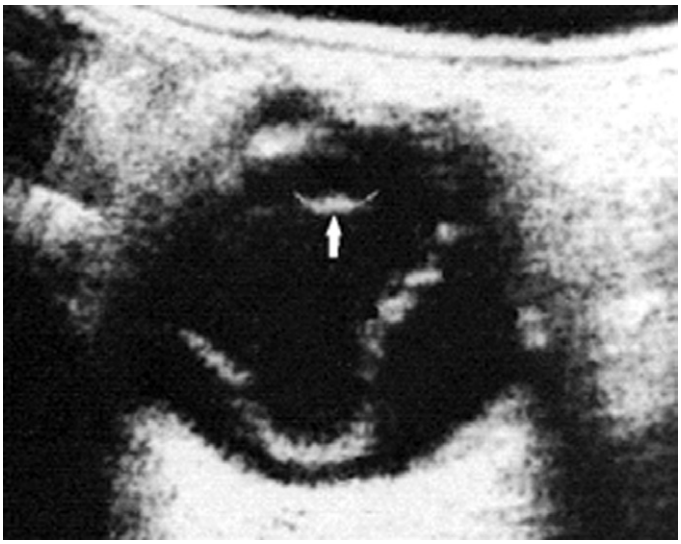

Figure 47.11 **Ectopic lens** (arrow) and retinal detachment in homocystinuria.

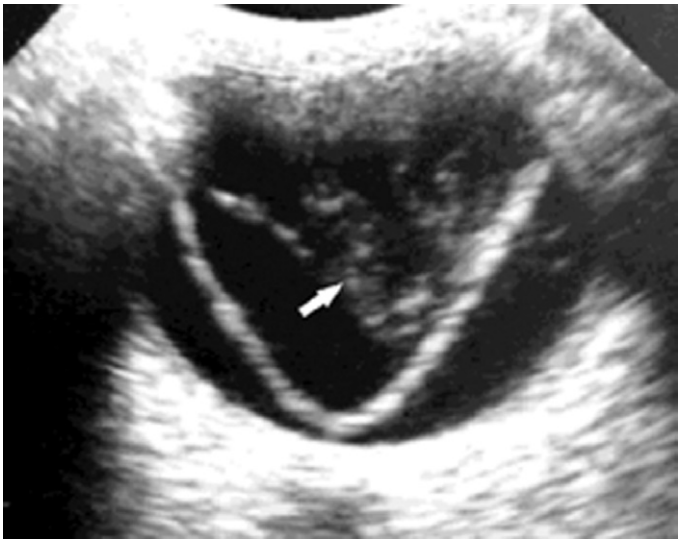

Figure 47.12 **Total retinal detachment**, firm anatomical attachment posteriorly at optic nerve head, and anteriorly at ora serrata. Vitreous collapsed (arrow). Horizontal scan.

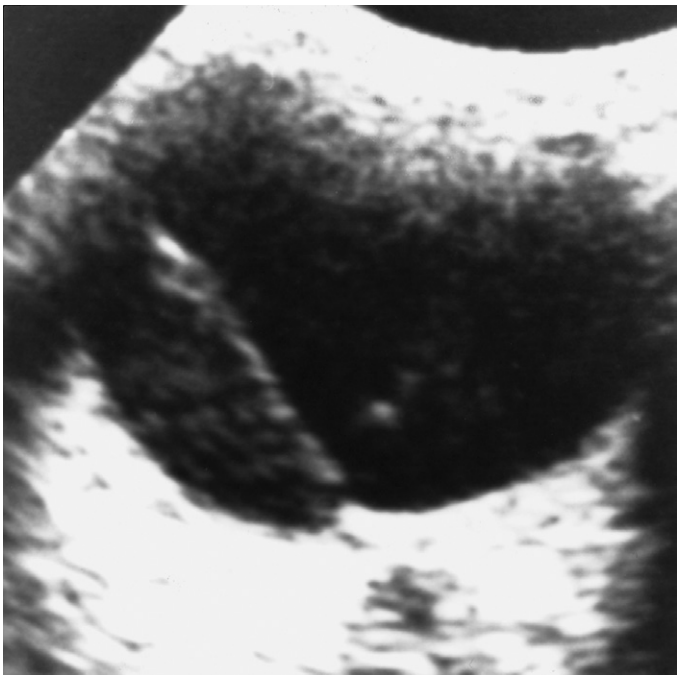

Figure 47.13 **Partial retinal detachment** with subretinal haemorrhage.

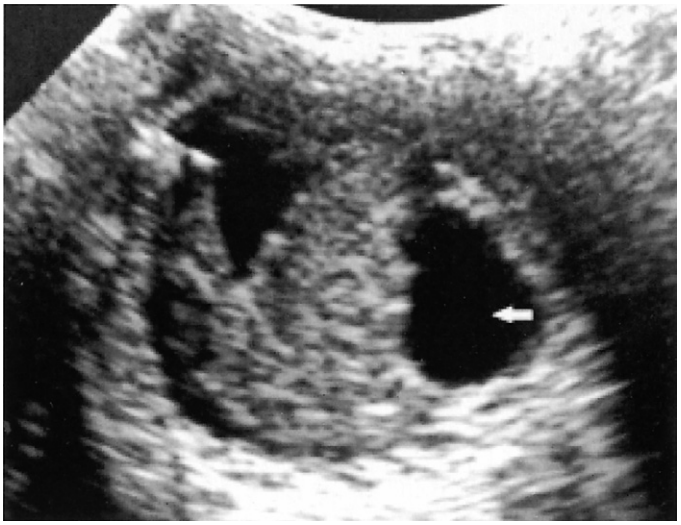

Figure 47.14 **Lacuna** (arrow) outlined by vitreous haemorrhage.

(secondary detachment). There are two main forms of non-rhegmatogenous retinal detachment: tractional and exudative.[17,18]

The firm anatomical attachments of the retina, at the ora serrata and the optic nerve head, ensure that detachment does not extend beyond these sites. A classic, total detachment therefore shows a funnel-shaped appearance (Fig. 47.12). In recent rhegmatogenous (i.e. with a retinal hole) detachment there is a sinuous or whiplash motion of the retinal leaves. Retinal mobility is less marked if the detachment is non-rhegmatogenous, shallow, partial, or if there is a large amount of subretinal fluid, causing a tense bullous detachment (Fig. 47.13). Although a minority of retinal detachments remain stationary for some years, if they are left untreated most become total and progressively immobile, owing to the development of preretinal fibrosis. The retina contracts to form a cord, stretched between the optic disc and periphery.

Rhegmatogenous retinal detachment

Retinal breaks which result in retinal detachment are caused by underlying weakness in the peripheral retina, from predisposing degeneration (for example, lattice degeneration in myopes) and vitreoretinal traction from a detached vitreous. Retinal detachment affects about 1 in 10 000 people per year, and about 10% of cases are bilateral. The fact that about 5% of the general population have retinal breaks implies that there are unknown factors associated with retinal detachment.[19]

Vitreoretinal traction

This is caused by a hypermobile degenerating vitreous. In elderly people, alterations in the micromolecular structure of the vitreous cause liquefaction of the gel (synchysis senilis), resulting in a lacuna of fluid within the gel (Fig. 47.14). Sometimes the posterior hyaloid interface becomes detached (Fig. 47.15). A hole develops in the thinned posterior vitreous cortex overlying the fovea, and synchytic

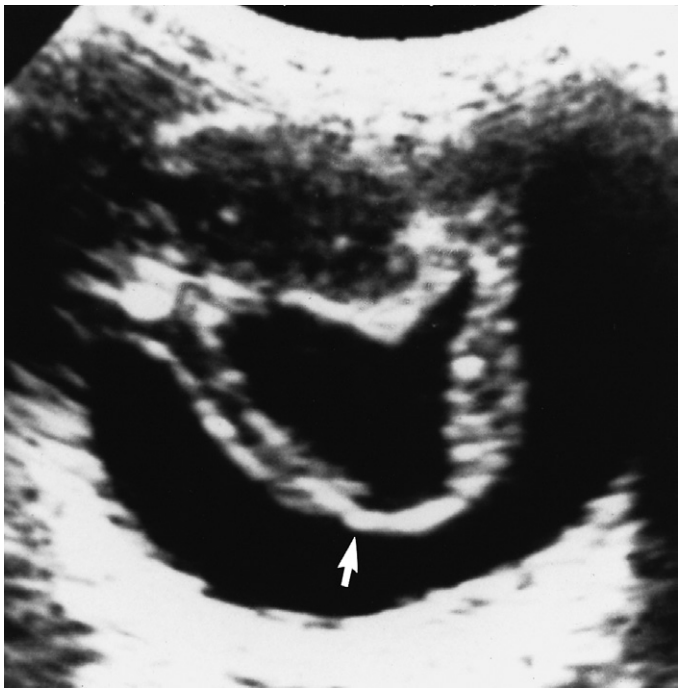

Figure 47.15 Lacuna with detached posterior hyaloid interface (arrow).

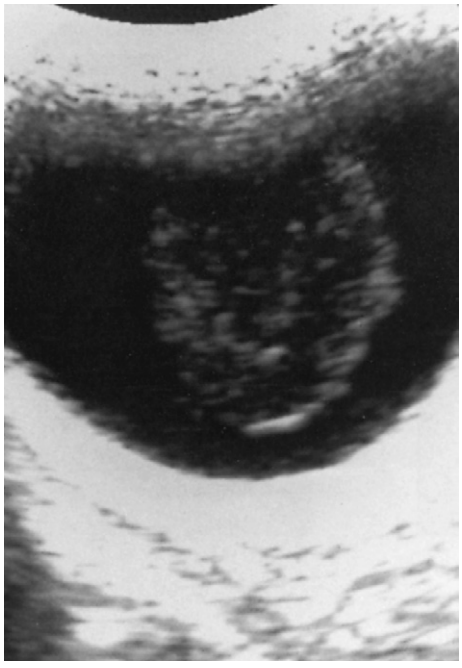

Figure 47.16 Posterior vitreous detachment.

fluid from the lacuna passes through the hole, forcibly detaching the tenuous adhesion of the posterior vitreous surface to the sensory retina, as far as the vitreous base. The vitreous gel collapses interiorly, suspended from the vitreous base, and the retrohyaloid space is occupied by synchytic fluid (Fig. 47.16). This process is termed acute rhegmatogenous posterior vitreous detachment (PVD) with collapse. As the vitreous is no longer in apposition to the sensory retina the latter is vulnerable to tractional forces exerted by any vitreoretinal adhesions. In most cases these are weak and the vitreous cortex detaches completely from the sensory retina. However, about 10% of cases develop retinal tears at sites of strong

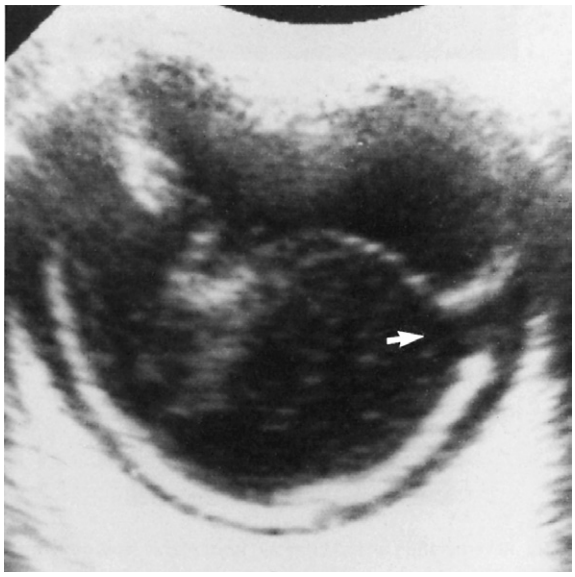

Figure 47.17 Retinal tear (arrow) and total retinal detachment.

vitreoretinal adhesions. Symptoms are usually experienced with tears due to acute posterior vitreous detachment (flashing lights, floaters), and the tears are commonly located in the upper fundus. Tears are frequently complicated by vitreous haemorrhage, which may also be caused by rupture of a peripheral retinal blood vessel. The risk of retinal detachment is high if tears are not treated by photocoagulation or cryotherapy, because retrohyaloid synchytic fluid is potentially able to enter the subretinal space. Retinal tears are small and cannot usually be identified by ultrasound. Occasionally, however, a flap of torn retina is seen protruding into the vitreous cavity (Fig. 47.17).

The aim of retinal detachment surgery is to seal the retinal break by laser or cryotherapy and to re-establish contact between the detached retina and the retinal base, in the region of the break or hole. When the hole has been sealed subretinal fluid often resorbs spontaneously. A concomitant scleral buckling technique is frequently used to appose the retinal pigment epithelium to the sensory retina, release vitreoretinal traction and increase the relative vitreous volume. This is commonly achieved with a silicone sponge explant (Fig. 47.18), which is sutured directly on to the sclera to create an 'indent'. Other methods of changing the relative volume of the vitreous to that of the vitreous cavity include 360° buckling with a circumferential strap, or intravitreal injections. Intravitreal gas injection (air, or a mixture of air and sulphur hexafluoride, which takes longer to absorb) is used to prevent hypotony following drainage of subretinal fluid, or to close a retinal tear by tamponade. Balanced salt solution is also used in hypotony, and silicone oil in eyes with complicated retinal detachments.

Proliferative vitreoretinopathy

Proliferative vitreoretinopathy (PVR) causes the progressive immobilisation of rhegmatogenous retinal detachments by the proliferation of fibroblastic membranes on the inner retinal surface (epiretinal membranes) and posterior hyaloid interface. These membranes are caused by proliferation and metaplasia of cells derived from pigment epithelium and retinal glial cells. Contraction of the membranes results in gel retraction together with retinal traction and immobilisation, but fibrosis in the gel does not always progress at the same rate as that of the epiretinal membranes. The gel may therefore remain mobile while the retina is rigid, or gel contents may show mobility when fibrotic changes are confined to the vitreous cortex. In eyes with moderate proliferative vitreoretinopathy the partially immobilised retina shows a flapping motion on dynamic scanning. Progression to massive proliferative

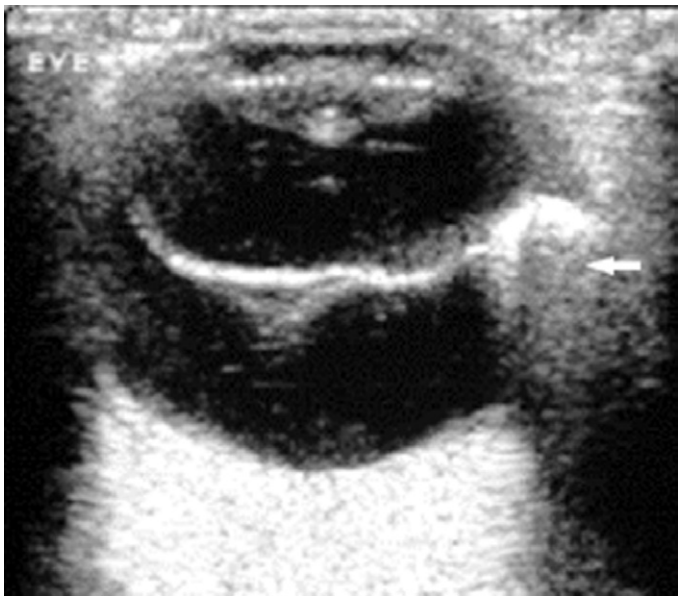

Figure 47.18 Silastic explant (arrow).

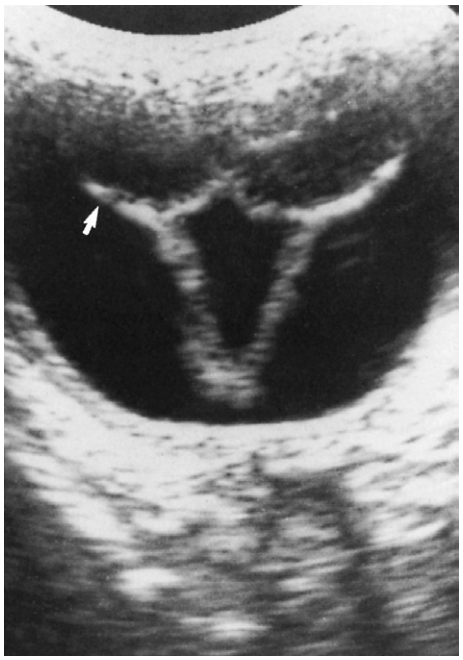

Figure 47.19 Proliferative vitreoretinopathy showing triangular retinal detachment and trans-vitreal membrane (arrow).

vitreoretinopathy is not inevitable but, if this stage is reached, scanning demonstrates a funnel-like configuration of the postequatorial retina, with shortened and thickened epiretinal fibrous tissue with a trans-vitreal membrane stretching across the anterior retina. These features produce the 'triangle sign', which is an important indicator of a poor surgical and visual prognosis (Fig. 47.19). This stage may progress further until the retinal leaves appose and fuse (Fig. 47.20).

Non-rhegmatogenous retinal detachment

In this condition there is no retinal break and the detachment is exudative or tractional.

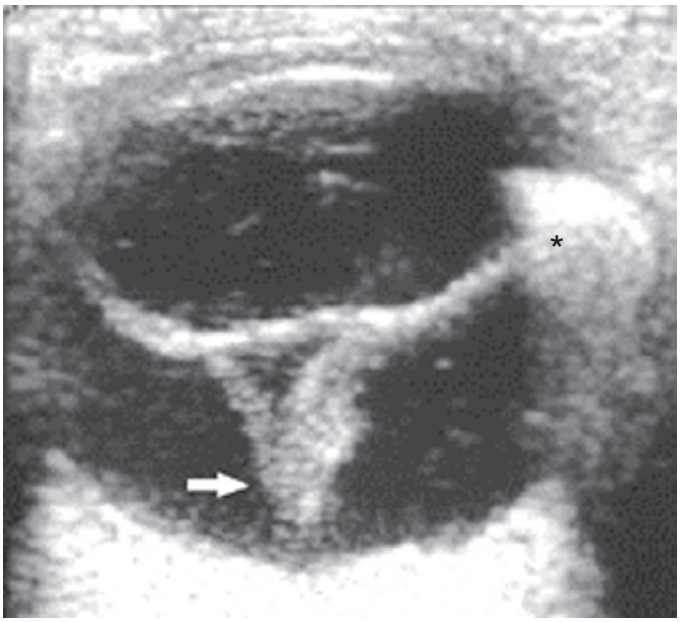

Figure 47.20 Advanced proliferative vitreoretinopathy showing centrally fused retinal leaves (arrow) and explant (*).

Choroidal detachment aetiology

- Idiopathic – uveal effusion syndrome.
- Inflammatory – uveitis, scleritis.
- Post-traumatic/surgical.
- Hypotony.
- Intraocular tumour.
- Toxic reaction to systemic medication.

Exudative (serous) retinal detachment

Subretinal fluid (SRF) from the choroid enters the subretinal space through damaged pigment epithelium caused by inflammation or tumour. In the 'uveal effusion syndrome' shifting subretinal fluid is the typical feature. Under the influence of gravity the distribution of subretinal fluid changes with alterations in eye position. In the upright position subretinal fluid accumulates under the inferior retina, but upon adopting the supine position the fluid shifts posteriorly and detaches the macula and superior retina. Dynamic scanning shows some mobility of the retina, and usually an associated anterior choroidal detachment.

Choroidal detachment

A complete choroidal detachment shows fluid in the suprachoroidal space, limited by the attachments of the choroid – anteriorly to the ciliary body and hence the scleral spur; posteriorly at the exit foramina of the vortex veins. A complete detachment, therefore, appears on scanning as a biconvex indentation of the globe (Fig. 47.21). If the vortex veins are absent or avulsed, the detachment may extend to the optic disc. Choroidal detachment in association with retinal detachment is not pathognomonic for an exudative detachment because many rhegmatogenous detachments have an associated choroidal detachment. Scanning may reveal choroidal tumour (melanoma, secondary deposit or retinoblastoma) as the cause of exudative retinal detachment, but the aetiology also includes endogenous uveitis and infection.

Traction retinal detachment

Contracting vitreoretinal membranes pull the sensory retina away from the pigment epithelium, resulting in angular immobile detachments on dynamic scanning (Fig. 47.22). Proliferative retinopathy

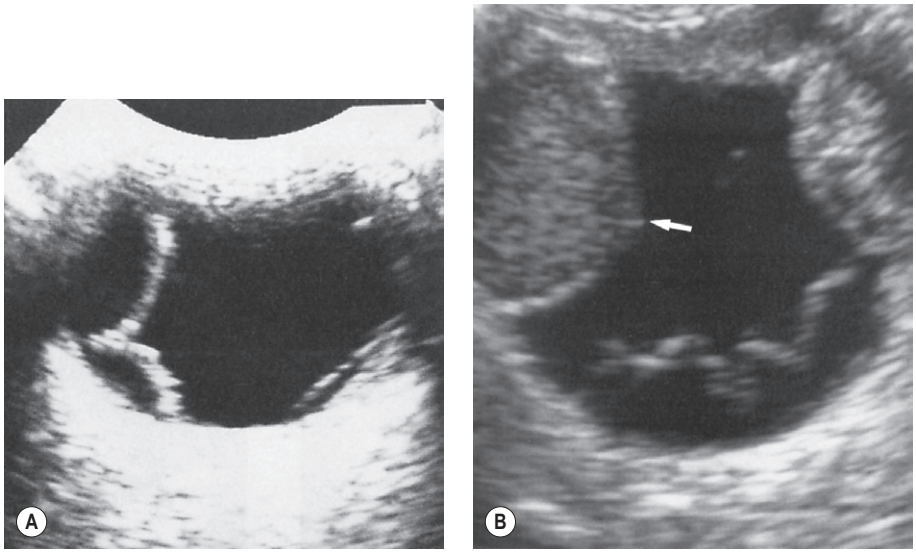

Figure 47.21 Choroidal detachment. **A:** Horizontal scan. **B:** Choroidal detachment, suprachoroidal haemorrhage (arrow).

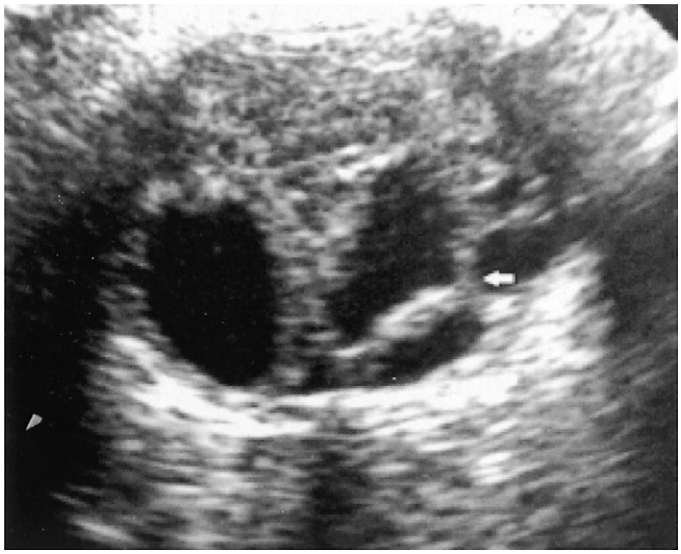

Figure 47.22 Traction retinal detachment with contracting vitreoretinal adhesion (arrow).

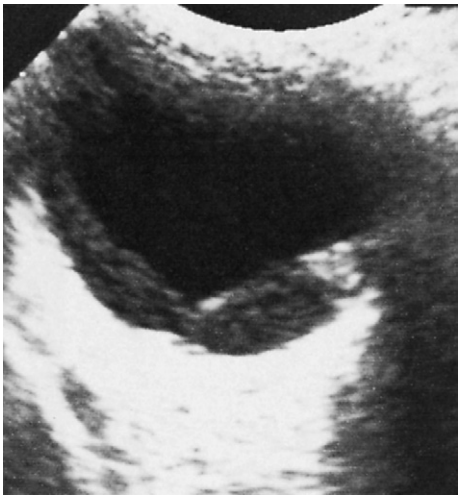

Figure 47.23 Subvitreal haemorrhage.

Conditions mimicking retinal detachment

- Vitreous membranes.
- Vitreous haemorrhage with ochre membrane.
- Incomplete posterior vitreous detachment.
- Vitreous cavities.
- Vitreous incarceration after penetrating injury.
- Kissing choroidal detachments.

and penetrating ocular trauma are the main causes. About 5% of those with diabetes are affected by proliferative diabetic retinopathy, but in juvenile-onset diabetes the risk is increased to about 60% incidence after 30 years. Neovascularisation occurs at the optic nerve head and along temporal vascular arcades, with endothelial proliferations from veins. These changes are stimulated by a biochemical mechanism residing in retinal neuronal and glial cells.[20] The new vessels project into the retrohyaloid space and are the source of fibroblasts, which in turn form fibrovascular epiretinal membranes. The membranes become attached to the vitreous, resulting in seepage of blood constituents into the gel, which degenerates and detaches. Frequently, however, detachment is incomplete owing to strong adhesions at the sites of fibrovascular proliferations. Fibrovascular membranes further develop along the surface of the partially detached vitreous. These processes are asymptomatic until haemorrhage occurs into the vitreous cavity, increasing the risk of visual loss, and are only discovered by clinical examination. Retrohyaloid (preretinal) haemorrhage is commoner than intragel haemorrhage, and usually disperses more rapidly (Fig. 47.23).

In traction retinal detachment subretinal fluid is less than in rhegmatogenous detachment and its source is unknown. The summit of the retinal elevation occurs at the site of insertion of the vitreoretinal adhesion (Fig. 47.22). Retinal breaks are absent, except when a secondary rhegmatogenous component develops, which gives the detachment some mobility on dynamic scanning.

Acquired retinoschisis

In this condition the sensory retina splits into two layers. The condition is prevalent in hypermetropes, and is present in about 5% of the population over the age of 20 years.

Initially retinoschisis affects the inferotemporal periphery of both fundi (Fig. 47.24), but the lesions may progress circumferentially to involve the whole periphery of the fundus. The usual (plexiform)

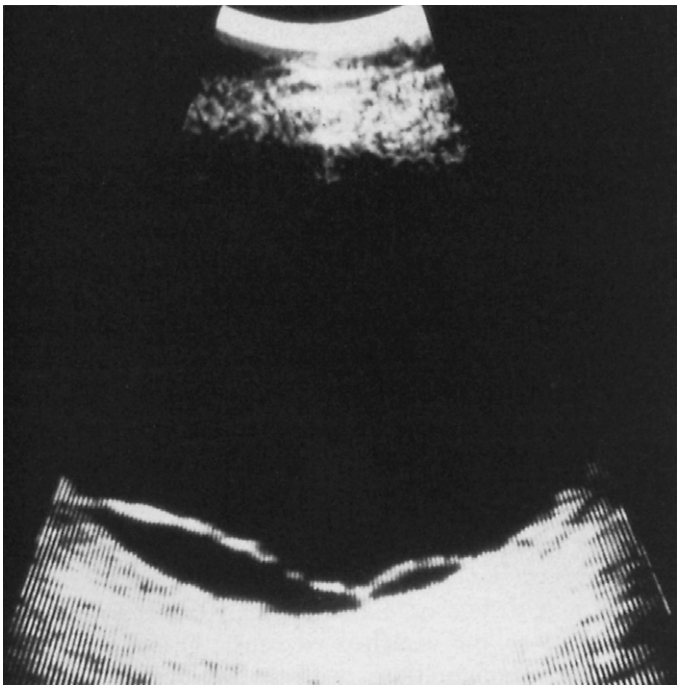

Figure 47.24 Retinoschisis.

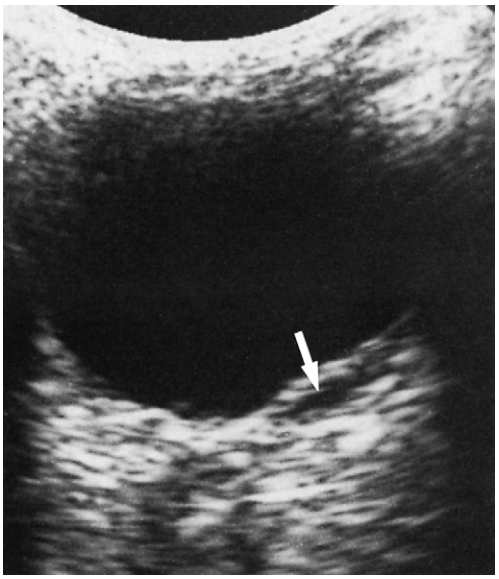

Figure 47.25 Disciform lesion (arrow), small subretinal haemorrhage.

type remains anterior to the equator, but the reticular form may progress posteriorly and encroach upon the fovea. Serial scans can check the development of this complication. Retinal detachment is a rare complication of acquired retinoschisis.

Disciform lesions

These are a manifestation of age-related macular (or paramacular) degeneration, giving rise to an elevated collection of subretinal exudate and fibrosis.

The early changes are rupture of Bruch's membrane by the penetration of a neovascular membrane derived from the choroid. The neovascular tissue may bleed or leak, producing a subretinal exudate which subsequently absorbs or heals by fibrosis. Macular degeneration is usually bilateral, but the severity and progression are often asymmetrical. Subretinal elevation caused by age-related macular degeneration may therefore mimic a choroidal tumour. On ultrasound the lesions are frequently dome-shaped, but sometimes irregular in outline with a heterogeneous appearance, ranging from low to high reflectivity. Serial scans may document a decrease in size over a period of weeks, which may be the most significant feature to differentiate a disciform lesion from a small melanoma or other tumour (Fig. 47.25). Colour Doppler imaging may be helpful in the diagnosis of lesions over 3 mm in size, if the presence of tumour vasculature is demonstrated.

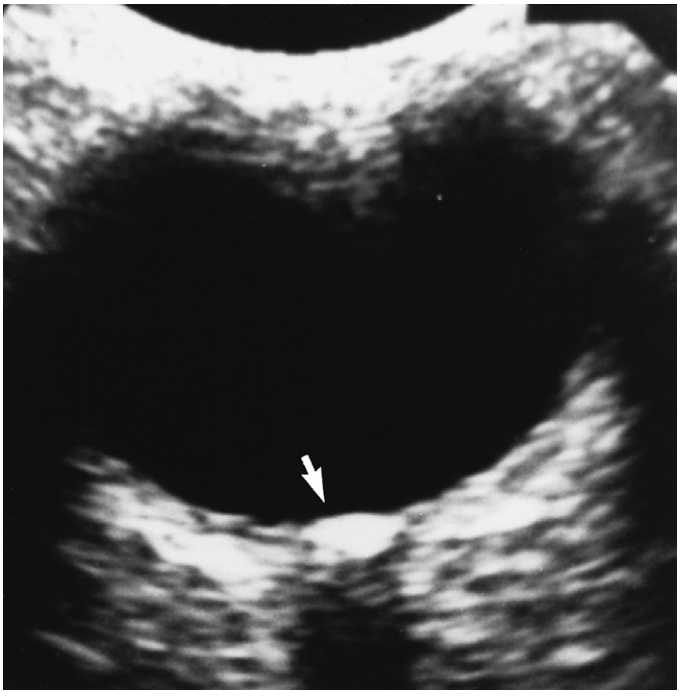

Figure 47.26 Drusen of optic nerve head (arrow).

Drusen (hyaline bodies)

These hyaline calcific deposits are seen as a congenital optic disc anomaly within the substance of the optic nerve head. They lie below the surface of the disc in children, and can be confused clinically with papilloedema, which may be investigated unnecessarily. However, early in the second decade they become visible on the surface of the optic disc as bright, pearl-like nodules. Scanning demonstrates a collection of calcific material in the optic nerve head, sometimes protruding into the vitreous and casting an acoustic shadow (Fig. 47.26). Congenital drusen usually remain asymptomatic throughout life, but occasionally cause visual impairment as a result of haemorrhage or neovascularisation.

Drusen are also a manifestation of age-related macular degeneration. Small, globular collections of hyaline material are situated between the basal lamina of retinal pigment epithelium and the inner, collagenous layer of Bruch's membrane.[21,22] They are usually distributed symmetrically at the posterior poles of both fundi, and this type is rarely visible before the age of 45 years. With advancing age they increase in size and number and secondary calcification occurs. Frequently they are localised to the macular or extramacular region, and may elevate the retina without impairing vision. Many patients with drusen have normal vision throughout life, but a significant number of elderly patients develop progressive impairment of central vision due to age-related macular degeneration.[23]

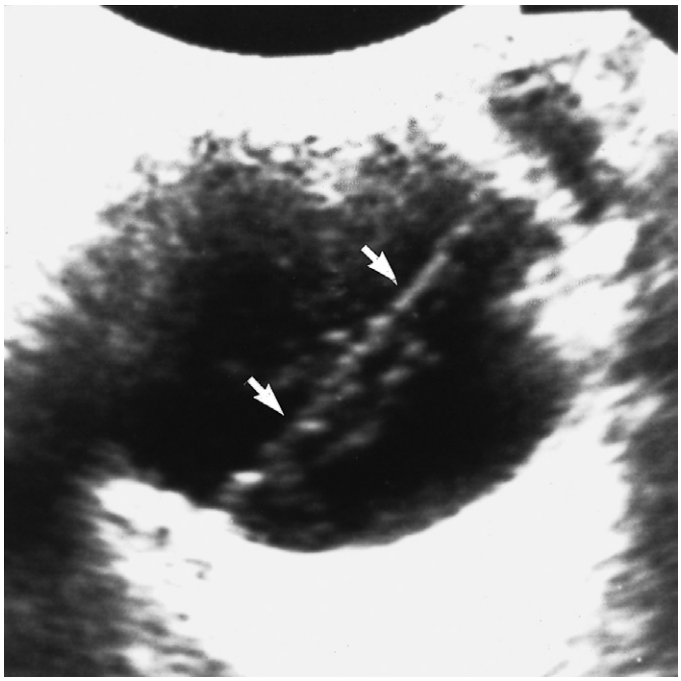

Figure 47.27 Persistent hyperplastic primary vitreous showing hyaloid artery (arrows) (eye deviated left).

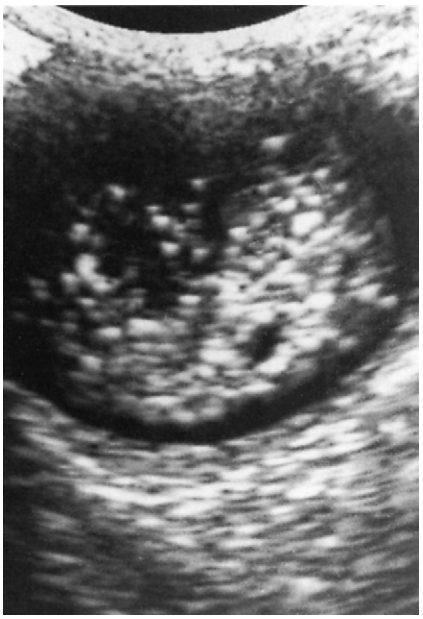

Figure 47.28 Asteroid hyalosis.

Vitreous

The structure of the normal gel renders it acoustically clear, but with careful adjustment of the scanner's sensitivity dynamic scanning demonstrates some undulations of the posterior hyaloid surface with eye movements. The posterior surface of the gel is seen transiently when correctly aligned to the incident sound. The vitreous is more easily imaged if it is occupied or surrounded by pathological material; the motion of the gel is that of a deformable, elastic mass.

Persistent hyperplastic primary vitreous

This is a serious developmental disorder of the vitreous and is a cause of leukocoria, or white pupil. Embryologically the vitreous develops from the primary vitreous, which occasionally persists in a microphthalmic eye. The more common anterior-type is characterised by the presence of a retrolental mass. In the rarer posterior type a dense membrane containing the hyaloid artery extends from the retrolental region to the optic disc (Fig. 47.27), and may be associated with retinal detachment.

Asteroid hyalosis

This is a senile degenerative disorder of unknown origin occurring in otherwise healthy eyes, and is uni-ocular in 75% of cases. Calcium soaps form asteroid bodies which are scattered through the vitreous and which remain in suspension, as there is no associated liquefaction. The calcified bodies show multiple high-amplitude echoes and demonstrate considerable after-movement on dynamic scanning (Fig. 47.28).

Synchysis scintillans

This is another degenerative condition, frequently bilateral, that occurs after long-standing uveitis or following vitreous haemorrhage. The vitreous is liquefied and contains cholesterol crystals, which sink under the action of gravity. Eye movements stir up the crystals, which are seen ophthalmoscopically as glittering particles

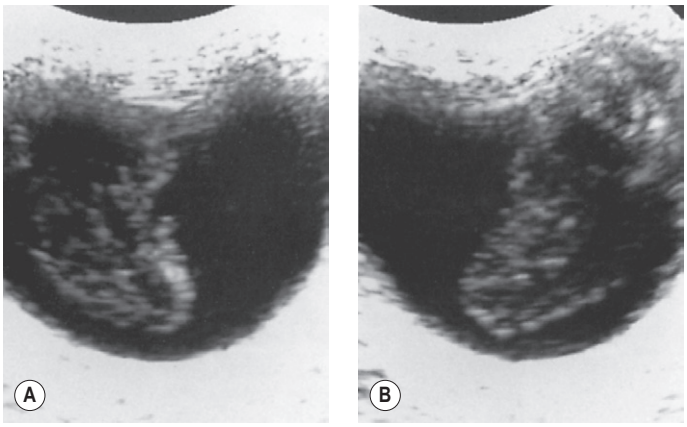

Figure 47.29 Posterior vitreous detachment. A: Eye deviated right. **B:** Eye deviated left.

and ultrasonically as multiple, high-amplitude echoes similar to asteroid hyalosis. However, the cholesterol crystals sediment, leaving an echo-free vitreous if the eye is still. Asteroid hyalosis and synchysis scintillans do not reduce visual acuity but have a striking ultrasound appearance, whereas vitreous haemorrhage reduces visual acuity but has much subtler ultrasound features.

Posterior vitreous detachment (PVD)

The mechanism of posterior vitreous detachment with collapse has been described above as the cause of acute rhegmatogenous retinal detachment. The result of synchysis senilis is a gel of reduced volume and increased mobility suspended from the vitreous base, surrounded by retrohyaloid synchytic fluid (Fig. 47.16). Most cases of synchysis senilis remain uncomplicated, and the condition is frequently seen when scanning cataractous eyes. However, if vitreous traction causes a retinal tear or avulsion of a peripheral blood vessel, intragel and retrohyaloid haemorrhage may occur. Under these circumstances dynamic scanning may demonstrate a surprisingly marked mobility and elasticity of the detached vitreous, the gel assuming mirror-image configurations when the eye is deviated to one side and then the other (Fig. 47.29). Failure to move

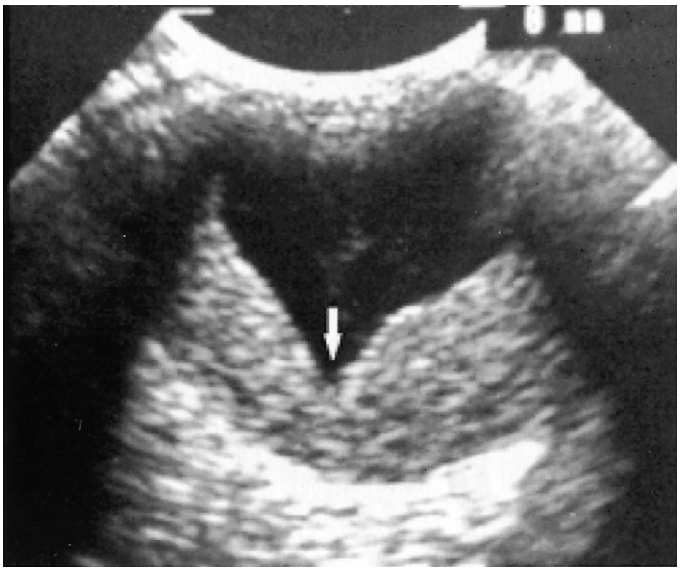

Figure 47.30 Retrohyaloid haemorrhage, vitreous attached at optic nerve head (arrow).

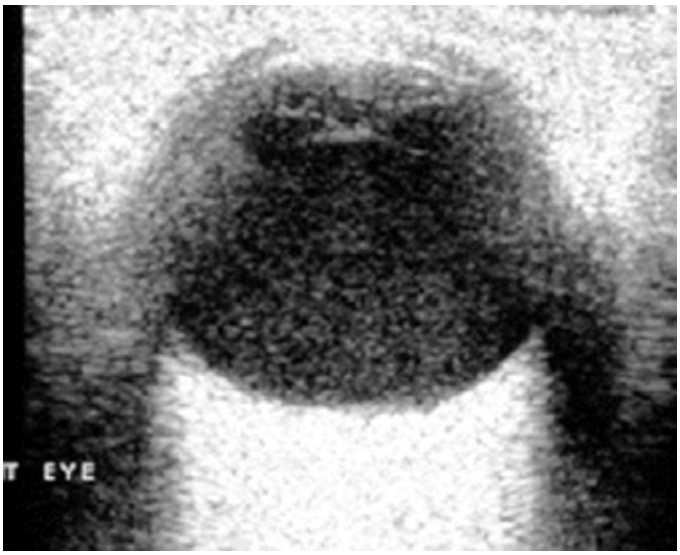

Figure 47.31 Vitreous haemorrhage.

in this way, or asymmetrical suspension, may indicate immobilisation of part of the gel by an adhesion, or restriction from a penetrating injury.[7] Retrohyaloid haemorrhage in the presence of a posterior vitreoretinal adhesion may incarcerate the gel, resulting in little mobility on dynamic scanning (Fig. 47.30).

Small haemorrhages dispersed throughout the vitreous may be difficult or impossible to demonstrate, but larger bleeds are more easily seen as widespread, low-intensity echoes with marked after-movements on dynamic scanning. In vitreous haemorrhage resulting from subarachnoid haemorrhage (Terson's syndrome) or from blunt trauma, the red blood cells sediment and compact near the posterior hyaloid surface of the detached vitreous, and scanning shows echoes of increasing intensity in the posterior gel (Fig. 47.31). Degenerating blood cells give rise to lower-level echoes and colour the posterior vitreous cortex to give the clinical feature known as 'ochre membrane'. Retrohyaloid haemorrhage may sediment to form a fluid level behind the collapsing gel.

The presence of blood has a destructive effect on gel structure, including posterior vitreous detachment, liquefaction of the gel, the formation of vitreous bands and an ochre membrane. The inflammatory response to the erythrocytes is low grade, with unphagocytosed cells remaining intact for several weeks. Fibrosis or organisation is an unusual sequel to vitreous haemorrhage, and is usually associated with severe ocular trauma or ocular disease in which vitreous haemorrhage is an incidental finding, for example diabetic proliferations or retinal vasculitis.[24]

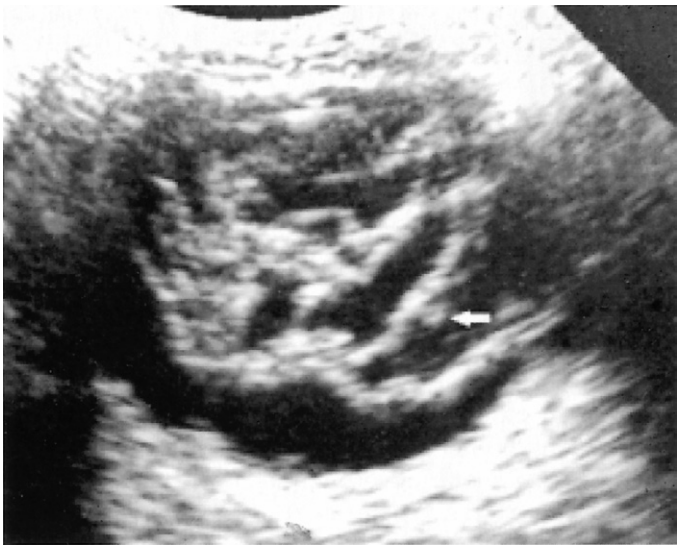

Figure 47.32 Arranged vitreous membranes (arrow).

Haemorrhage within the vitreous cavity may therefore persist for some considerable time as widely dispersed echoes in the gel or retrohyaloid space. Sometimes, however, fibrinous membranes develop, giving rise to mobile, linear structures (Fig. 47.32). This is known as 'arrangement', as true 'organisation' is not involved.[7]

Incomplete posterior vitreous detachment

In the normal eye the vitreous cortex is loosely attached to the internal limiting membrane of the sensory retina, but there are strong attachments at the vitreous base and optic disc margin. Weak attachments exist around the fovea and at the site of peripheral blood vessels. In the abnormal eye strong vitreoretinal adhesions may occur at the posterior border of retinal lattice degeneration, at congenital cystic retinal tufts, retinal pigment clumps, vitreous base anomalies, and at the impaction site of a foreign body. In diabetic patients strong adhesions are present if fibrovascular membranes form in proliferative vitreoretinopathy (Fig. 47.33). Retinal vein occlusion may result in adhesion at sites of neovascularisation at the posterior pole.[25] If vitreous haemorrhage occurs with complete posterior vitreous detachment, the likely cause is a retinal tear requiring prompt treatment. However, if haemorrhage is seen in association with a posterior vitreoretinal adhesion the likely cause is a retinal vein occlusion, and requires more prolonged assessment. Confusion may occasionally arise if a posterior vitreoretinal adhesion causes a retinal tear, or if complete posterior vitreous detachment is prevented by a strong posterior adhesion.

The moderately collapsed gel sites of vitreoretinal adhesion are not always obvious on ultrasound scanning until dynamic testing is used and positions of restricted movement identified. Similarly, fine vitreous strands, usually joining the gel mass to the posterior pole, are not seen until eye movement demonstrates gel tethering (Fig. 47.34).

The characteristic motion of vitreous and retina normally enables these structures to be distinguished. However, if the posterior hyaloid surface is thickened and attached to the optic nerve head, very careful observation during dynamic scanning may be required to differentiate the unified motion of gel mass from the membranous behaviour of a detached retina. If the vitreous contains pathological material this distinction is made easier.

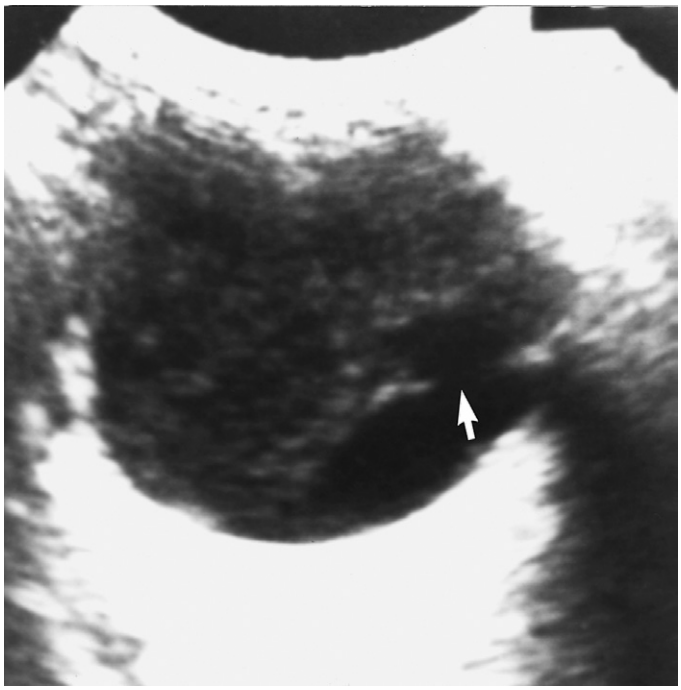

Figure 47.33 Fibrovascular vitreoretinal adhesion (arrow) with vitreous haemorrhage in a diabetic.

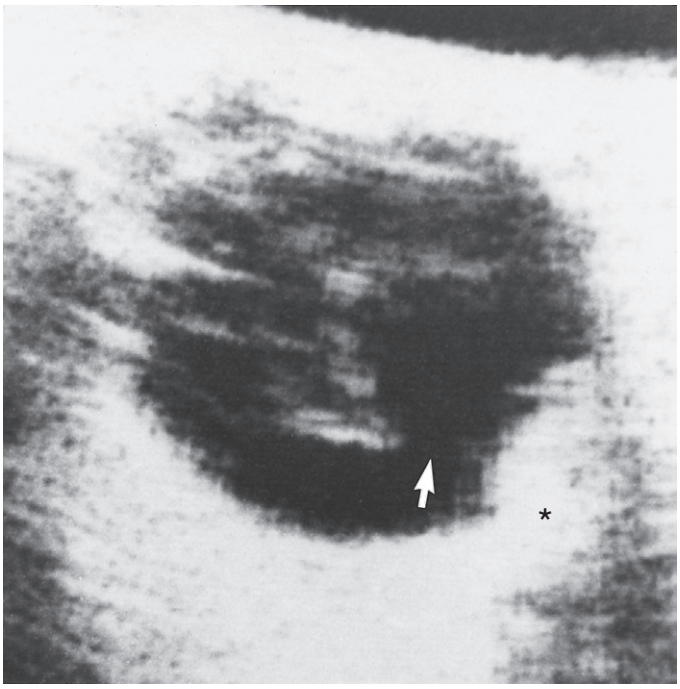

Figure 47.34 Fine vitreoretinal adhesion (arrow). Globe indented by explant (*).

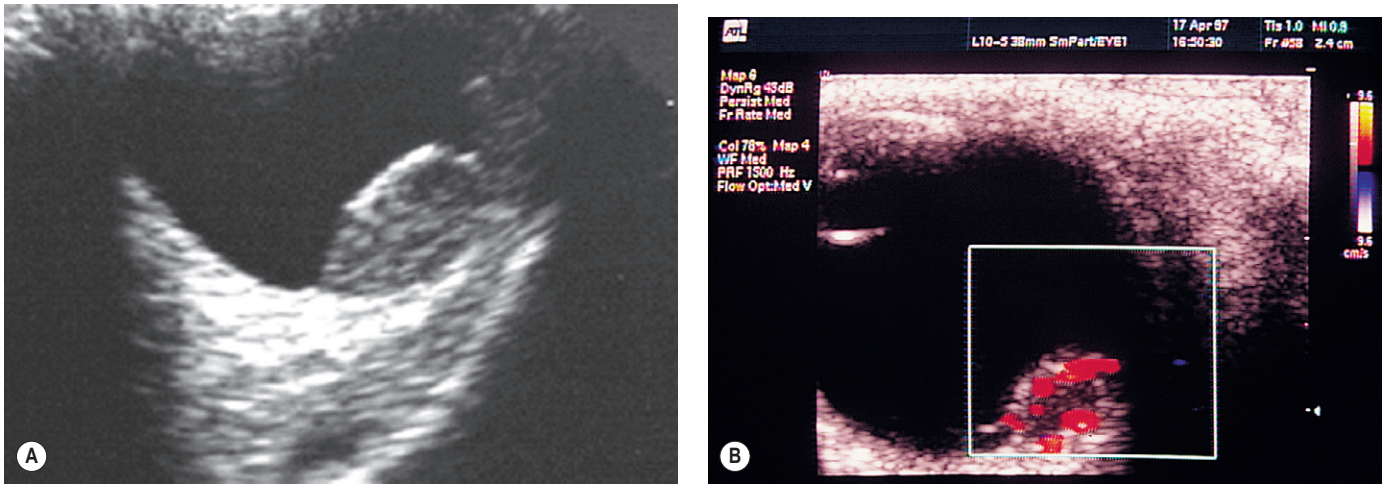

Figure 47.35 Melanoma (dome shape). A: Horizontal scan. **B:** Colour Doppler scan.

Ocular tumours

Choroidal and ciliary body melanoma

Malignant melanoma of the choroid is the commonest primary intraocular tumour in adults; 85% of ocular melanomas arise from the choroid and 15% from the ciliary body. Melanoma occurs most frequently between the ages of 50 and 60 years, and is rare below the age of 30 and above 80. The tumour is rare in blacks, but patients with ocular melanosis are at increased risk.[26] Most tumours arise posterior to the equator of the eye and are usually single and unilateral, sometimes developing from a pre-existing naevus.[27]

There has been a move away from the traditional treatment by enucleation of the eye, especially for small tumours and it is proven that there is no difference in survival rate between irradiated and enucleated patients.[28–30] A more conservative approach has given ultrasound an important role in management, particularly in eyes with hazy media, as information about the size, position, extent and growth of a tumour is readily obtained.

The ultrasound appearances of choroidal melanoma are well described.[31–34] The typical appearance is a lenticular-shaped mass deeply embedded in and arising from the choroid. The mass is usually moderately reflective and may give rise to some acoustic shadowing (Fig. 47.35). Less commonly the tumour is poorly reflective and there may be a cystic component (Fig. 47.36). An associated exudative retinal detachment may conceal an underlying melanoma from ophthalmoscopic examination, but scanning reveals the solid nature of the occult tumour (Fig. 47.37). Some melanomas have a bilobed or cottage loaf-shaped appearance, caused by waisting as they break through Bruch's membrane (Fig. 47.38). If the membrane

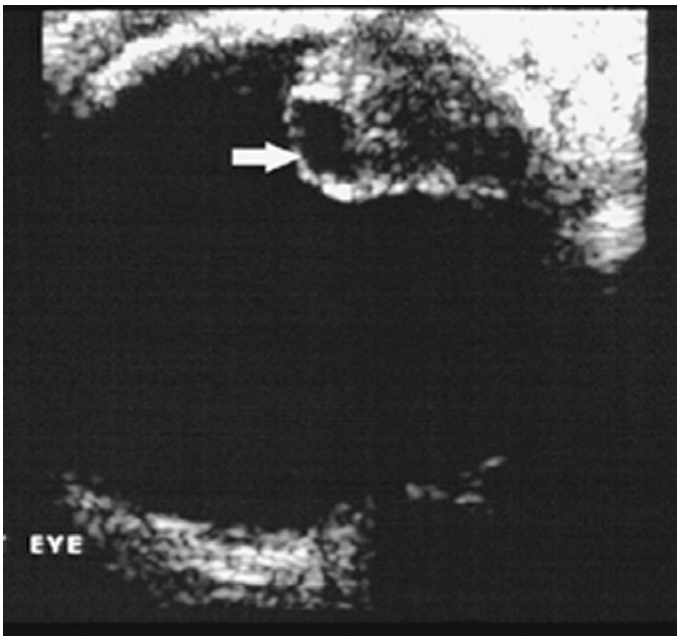

Figure 47.36 Melanoma with vacuole (arrow).

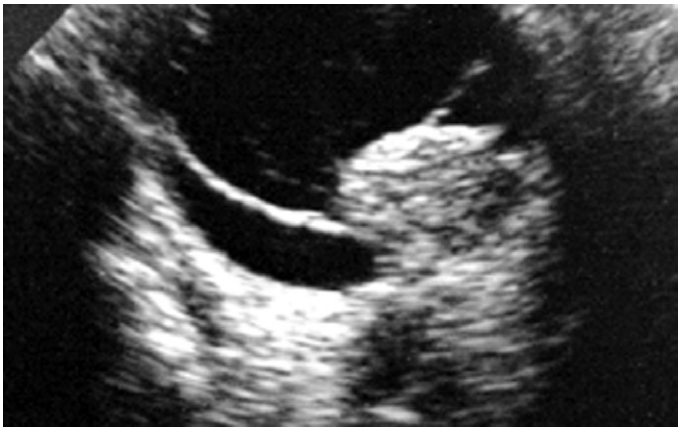

Figure 47.37 Melanoma concealed by retinal detachment.

remains intact the tumour is dome-shaped. Some tumours demonstrate choroidal excavation, in which low-amplitude tumour cell echoes replace and enlarge the choroid. Small melanomas may be relatively echo-free, making differentiation from retinal degenerative lesions difficult. However, a clue is given if the lesion is identified as lying deep in the choroid and serial examinations show growth. Colour Doppler scanning may help to differentiate melanoma from subretinal haemorrhage by demonstrating blood flow within the lesion. Tumour vessels show as pulsating channels or lakes of colour. Care must be taken so that blood flow in the overlying retina is not mistaken for tumour circulation. Not all tumours show vascularity on Doppler, especially if less than 3 mm in size. The intensifying effect of ultrasound contrast agents on the Doppler signal may prove a useful diagnostic aid in this situation.[35]

Melanoma may be complicated by subretinal or vitreous haemorrhage. The resulting ultrasound appearances are confusing, but dynamic scanning clarifies the situation. With rapid eye movements the tumour itself shows fixity to the wall of the eye, whereas subretinal haemorrhage shows some movement and sedimentation, the fluid appearing less reflective than the associated tumour (Fig. 47.39). The retina elevated over the area of haemorrhage also shows movements, as a membrane restraining a fluid collection. Bleeding into the vitreous usually causes degeneration, detachment and loss of gel volume. The resultant mobile reflective gel can be identified on dynamic scanning. Ultrasound imaging is useful in the assessment of scleral erosion and extraocular extension of a melanoma, the extraocular component showing as a poorly reflective area within the orbital fat (Fig. 47.40). However, MRI is more sensitive in the detection of extraocular growth.[36]

A wide range of therapies is now available for ocular melanoma and the information gained from ultrasound is a vital component of many therapeutic regimens. Brachytherapy with a ruthenium 106 or iodine 125 applicator is usually the first choice. Other treatments include transpupillary thermotherapy (TTT), charged particle radiotherapy, stereotactic radiotherapy and surgical resection. If local resection (choroidectomy) is to be considered several factors need to be determined, including the relationship of the tumour to the optic disc, the elevation, base diameter, presence of scleral erosion, and whether there is extraocular extension. Some centres use three-dimensional measurements of the melanoma, which correlate well with other tumour measurement techniques.[37] Observation is considered for small or asymptomatic lesions in which the diagnosis is equivocal. Melanomas less than 3 mm thick and 10 mm in diameter have an excellent prognosis and remain dormant for many years, with a low likelihood of metastasis. Radioactive plaques attached to the globe for a set period of time deliver a fixed dose of radiation.

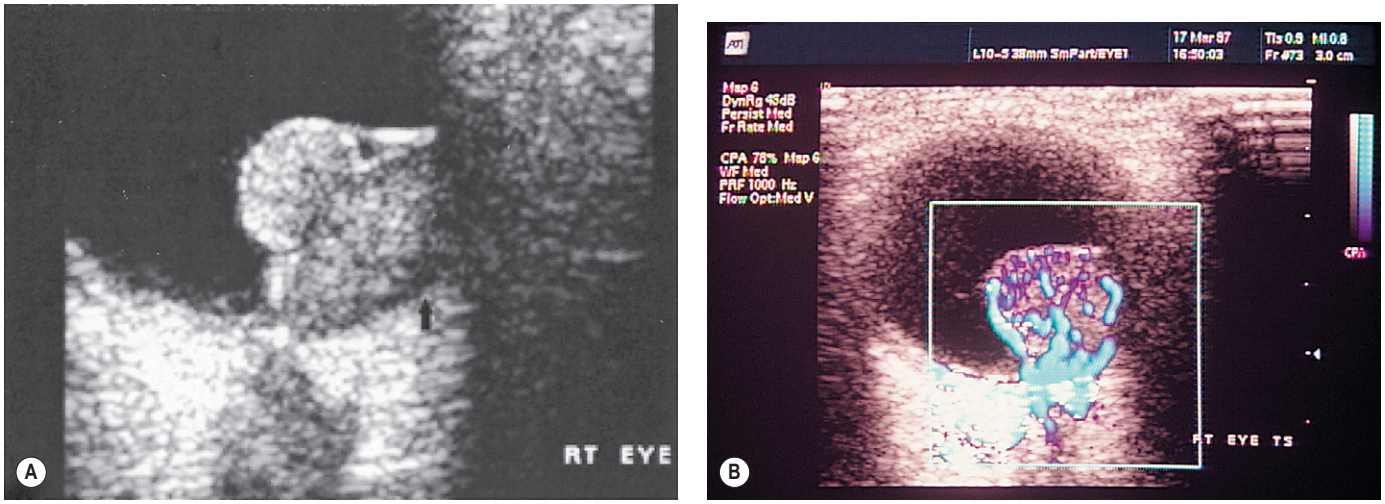

Figure 47.38 Melanoma (cottage loaf shape). A: Showing choroidal excavation (arrow). **B:** Power Doppler scan.

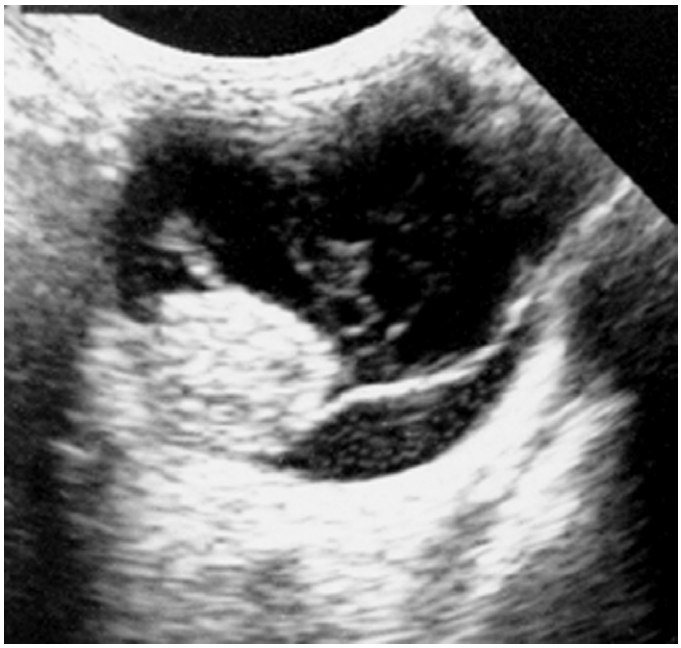

Figure 47.39 **Highly reflective melanoma** and poorly reflective subretinal haemorrhage.

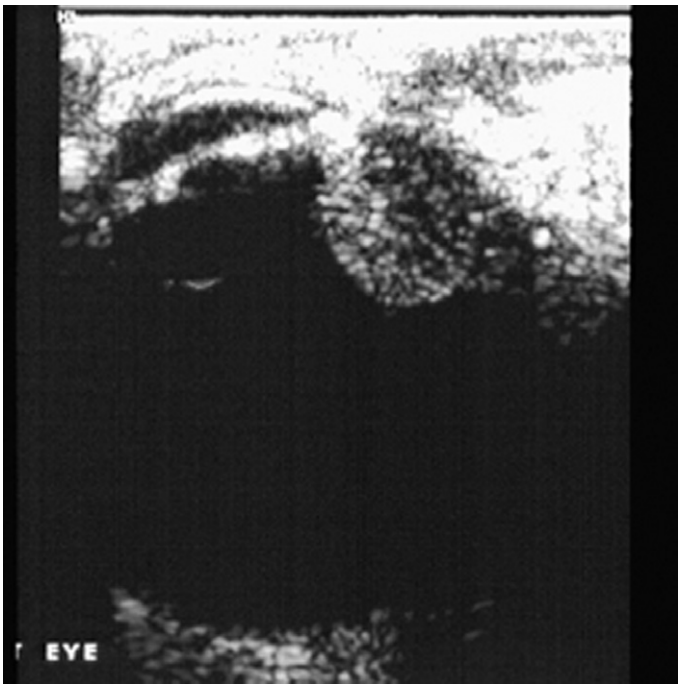

Figure 47.41 **Ciliary body melanoma.**

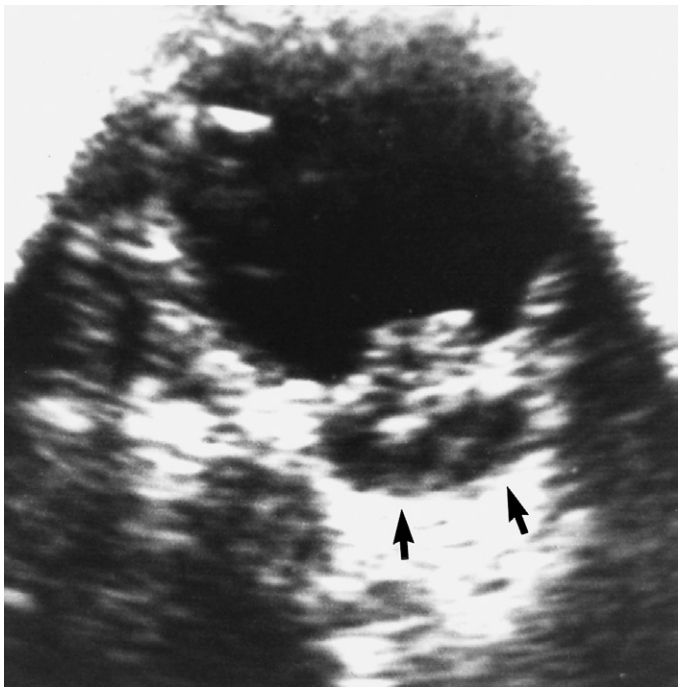

Figure 47.40 **Melanoma**, scleral erosion and extraocular extension (arrows).

Unfortunately, radiation-induced complications include retinopathy, vitreous haemorrhage and cataract. Enucleation is indicated for very large melanomas, particularly if vision has been lost. However, enucleation does not improve the prognosis in patients over 65 with slowly growing tumours and normal vision. Follow-up by Doppler is valuable in assessing the efficacy of radiotherapy, which causes flow velocities and Doppler shifts to decrease in tumour vessels, supporting the theory that radiation results in sclerosis of the supply vasculature.

Ciliary body melanomas are more difficult to see clinically than posterior tumours, unless the pupil is widely dilated. They are also less easy to image with ultrasound, particularly if small. On ultrasound scanning they are seen as solid tumours with features similar to a choroidal melanoma, and the dimensions and posterior extent should be determined (Fig. 47.41). There is also an annular form of melanoma which is differentiated from serous choroidal detachment by the fluid content of the latter. Posterior extension of ciliary body melanoma may cause retinal detachment. Pressure exerted by the tumour upon the lens may cause anterior displacement.

The diagnosis of choroidal melanoma is not always straightforward and occasionally confusion with other choroidal conditions may occur. Degenerative disease or trauma may cause choroidal defects or tears which bleed into the subretinal space. The haemorrhage is followed by neovascularisation and the formation of a fibrovascular disciform lesion. These are known as Fuchs spots, and are highly reflective but show minimal sound absorption. This condition occurs at the macula in myopic eyes and in elderly people. Disciform lesions can have an appearance indistinguishable from a small melanoma, and serial ultrasound examinations are necessary to demonstrate that the lesion is regressing or static, rather than increasing in size. Occasionally ultrasound-guided tissue biopsy is used to obtain cellular aspirates for cytological diagnosis.

Metastatic carcinoma

Choroidal metastases are commoner than primary malignancies. The most common site of the primary is the breast in females and the bronchus in males.[38,39] Less common primary sites are the testis, kidney and gastrointestinal tract. Metastases have a definite predilection for the posterior pole, and may be single or multiple. The tumours infiltrate laterally and are therefore low, undulating masses with a broad base (Fig. 47.42). Ultrasonography shows diffuse choroidal thickening. Metastases can give rise to either high- or low-amplitude echoes, and occasionally develop a globular shape which mimics amelanotic melanoma. The history gives a strong indication of the tumour's origin. Exudative retinal detachment may complicate choroidal metastases. Careful examination of the opposite eye is important, as metastases are frequently bilateral.

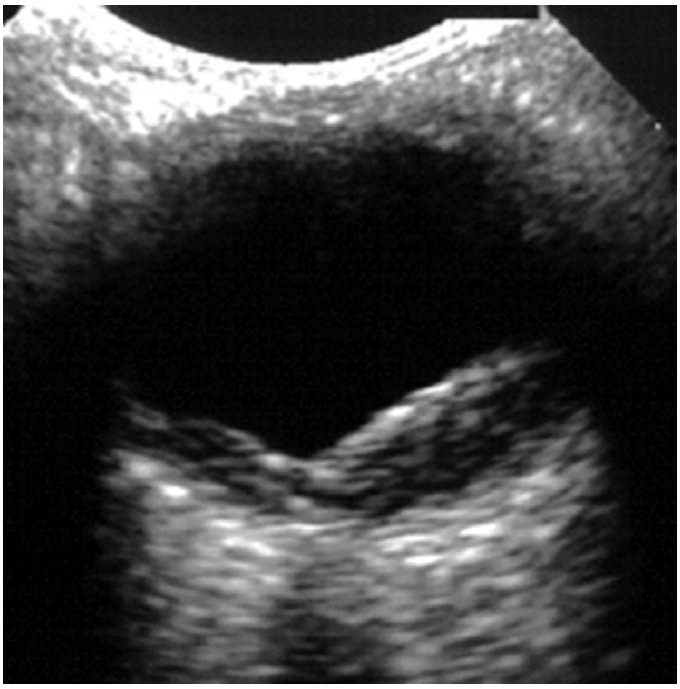

Figure 47.42 Choroidal metastasis.

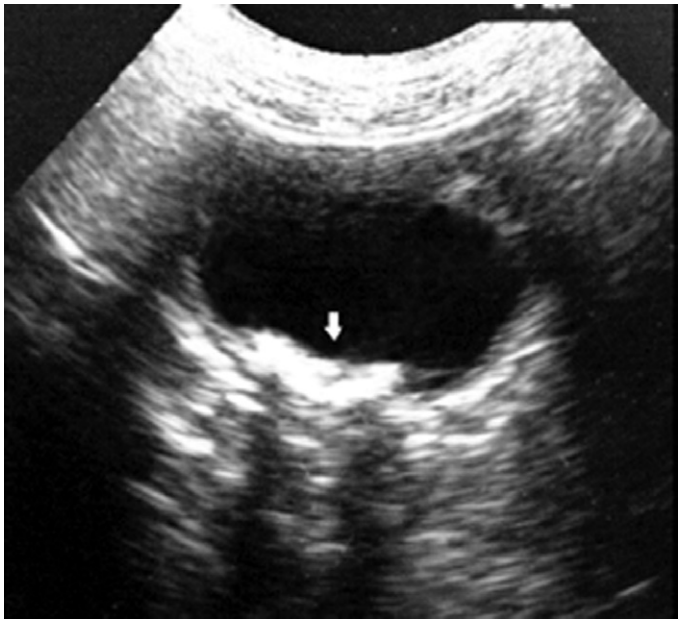

Figure 47.43 Osseous choristoma (arrow).

Osseous choristoma (choroidal osteoma)

This is a very rare benign tumour that affects young women and is sometimes bilateral.[40] It is a slightly elevated lesion with well-defined borders situated at the posterior pole or near the optic disc. Ultrasonography reveals a strongly reflective lesion, owing to bone formation, and very marked acoustic shadowing (Fig. 47.43). Confusion with drusen may arise, but the clinical features should indicate the true nature of the lesion.

Choroidal haemangioma

This is a rare congenital tumour usually presenting in adults and often associated with cutaneous angiomas or the Sturge–Weber syndrome. Typically the lesions have a low elevation with a broad base, either dome-shaped or placoid, and are situated at the posterior pole (Fig. 47.44). The tumours are composed of multiple small vascular channels and blood-filled spaces, showing high reflectivity on ultrasound. Colour Doppler scanning shows blood flow within the lesion. The scan shows a sharp anterior border but no choroidal excavation or acoustic shadowing. However, in some cases there is bone formation from metaplasia of the pigment epithelium.

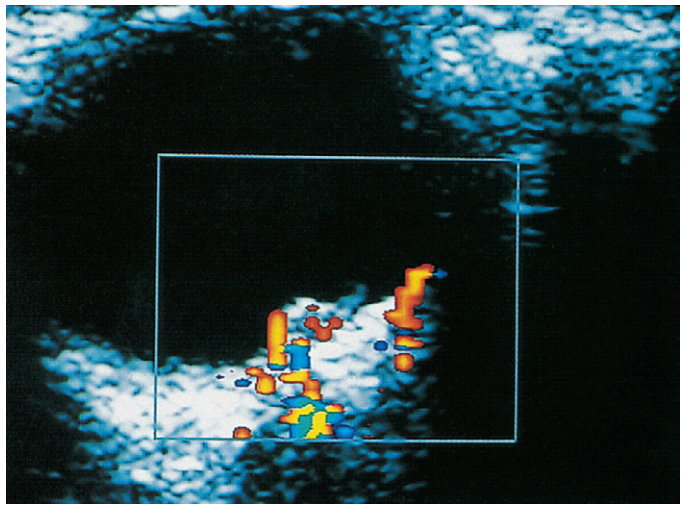

Figure 47.44 Choroidal haemangioma. Colour Doppler scan showing choroidal haemangioma.

Lesions simulating melanoma

- Metastatic carcinoma.
- Choroidal haemangioma.
- Choroidal naevus.
- Disciform lesion.
- Choroidal haemorrhage.
- Other rarer tumours.

Choroidal naevus

These are flat or slightly elevated, and usually not detectable by ultrasound. If elevated they appear highly reflective and avascular, making it impossible to differentiate from a small melanoma.

Retinoblastoma

This is the commonest primary malignant intraocular tumour of childhood, and comprises about 30% of all ocular tumours (about 40% are malignant melanomas).[41] Nevertheless, it is rare, occurring in about 1 in 20 000 live births. It arises from cells derived from the embryonic retinal epithelium of the primary optic vesicle. As modern treatments increase the survival rate the chance of hereditary transmission is increased. Retinoblastoma has the best prognosis of all childhood tumours, with over 80% survival. Both sexes are equally affected and, although initially presenting in one eye, the tumour is bilateral in about one-third of cases. Most tumours become apparent before the age of 3 years, the average age of diagnosis being 18 months. Only 6% of cases have a positive family history of retinoblastoma, and here the mode of inheritance is autosomal dominant with a high but incomplete penetrance. The remaining 94% of cases are sporadic, and of these 25% are germinal mutations able to be inherited.

Retinoblastomas normally present at a late stage with leukocoria or 'amaurotic cat's eye', but earlier stages are seen if the fundus is

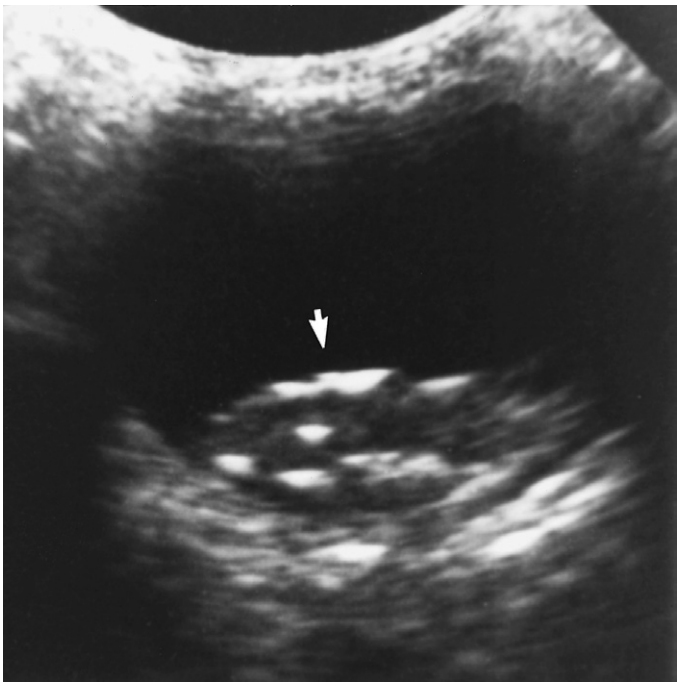

Figure 47.45 Retinoblastoma (arrow) containing calcified areas.

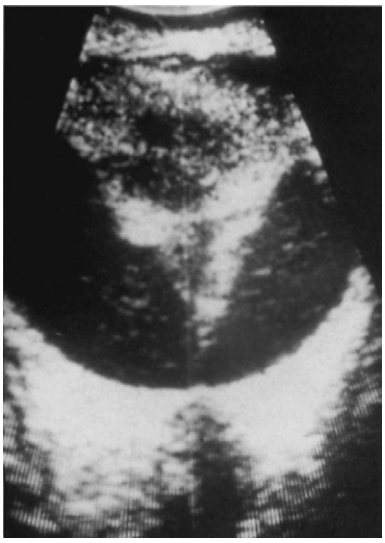

Figure 47.46 Coats' disease with retinal detachment and subretinal exudate. (Courtesy of H. Atta.)

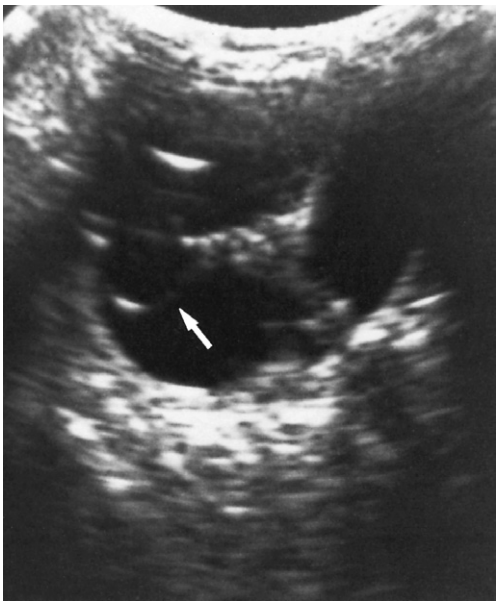

Figure 47.47 Retrolental fibroplasia with retinal loop (arrow).

being kept under observation in an at-risk patient. The endophytic varieties of tumour project from the retina into the vitreous cavity as a white or pinkish mass, and are sharply demarcated in the presence of secondary calcification. Several tumours may be present in one eye, from seedling deposits. The exophytic tumours grow in the subretinal space, causing a total retinal detachment. Ultrasound reveals the hidden tumour in this situation.

When scanning retinoblastoma, the tumour may be seen to be localised in one area of the globe, or it may be more extensive, showing confluent, random reflections even at low gain settings (Fig. 47.45). Calcium deposits may be present and are seen as highly reflective foci; they may be a helpful aid to diagnosis. The tumour outline is often irregular, and the appearance of some cystic lesions has been likened to blood clot. It is important to recognise invasion of the optic nerve, a long segment of which must be excised when the eye is enucleated. However, MRI more clearly demonstrates extraocular and optic nerve involvement, and is essential to show central nervous system spread or pineal involvement. Optic nerve involvement beyond the point of surgical transection is associated with a 65% mortality rate, but if the nerve is uninvolved the mortality rate is only about 8%.[42]

Differential diagnosis

When an infant or child presents with leukocoria, retinoblastoma is only one of several differential diagnoses to be considered. Coats' disease is the most severe form of retinal telangiectasia, and is characterised by large areas of intraretinal and subretinal exudate, progressing to retinal detachment, subretinal mass and uveitis. The mass in Coats' disease typically gives rise to lower-amplitude echoes than retinoblastoma (Fig. 47.46). The condition is uni-ocular and is commoner in boys. Although it presents in the first decade of life it usually presents at a later age than does retinoblastoma.

An opaque mass covering the posterior lens surface sometimes occurs in retrolental fibroplasia (Fig. 47.47). However, this is usually bilateral and associated with a history of prematurity and oxygen therapy. It is usually seen in normal or larger than normal sized eyes, and neovascularisation from the retinal periphery results in fibrotic changes in the anterior vitreous.

Toxocariasis, an infestation caused by ingestion of the intestinal roundworm of cats and dogs, may result in larvae travelling in the bloodstream to the eyes. Young children who eat dirt or who are in close contact with puppies are at the greatest risk of contracting the disease. In ocular toxocariasis the commonest lesions are chronic endophthalmitis, a peripheral granuloma and a posterior pole granuloma. The latter is usually between one and two disc diameters in size.

Persistent hyperplastic primary vitreous is the most serious developmental disorder of the vitreous: it is caused by failure of regression of the primary vitreous and typically occurs in a microphthalmic eye.

Causes of leukocoria

- Retinoblastoma.
- Coats' disease.
- Retinopathy of prematurity.
- Persistent hyperplastic primary vitreous.
- Toxocariasis.

Trauma

Ultrasound evaluation of the ocular contents is the best practicable method of examining the eye following major ocular trauma, as direct vision is frequently hampered by opaque media. Early assessment of intraocular damage enables vitrectomy and other microsurgical techniques to be carried out before chronic internal structural changes develop.[1]

Blunt ocular trauma causes compression of the anteroposterior diameter of the eye and corresponding expansion of the equatorial plane. The differential elasticity of the vitreous gel causes traction at the posterior aspect of the vitreous base, producing a retinal tear (dialysis). Traumatic dialyses occur in any quadrant, but are more common in the upper nasal quadrant. Many cases of trauma occur in young patients with healthy vitreous gels, with the result that progression to retinal detachment is slow, taking several months. Blows to the lateral aspect of the orbit, which strike the eye just anterior to the lateral wall, may cause rupture of the globe.

Penetrating ocular trauma involving the posterior segment results in retinal detachment in about one-fifth of cases. The detachment may be rhegmatogenous if the retina is breached by a foreign body, or tractional following vitreous incarceration in the wound.

Ultrasound findings

The lens structure is normally echo-free and therefore subluxation is difficult to evaluate. Complete dislocation is more easily demonstrated, particularly if the lens is cataractous or if the complete lens lies within an area of vitreous haemorrhage (Fig. 47.48).

Haemorrhage in the vitreous compartment may be confined to the vitreous gel, the retrohyaloid space or both. Small haemorrhages are difficult to demonstrate, but larger bleeds are easy to detect and aid the delineation of lacunae, whose formation indicates impending posterior vitreous detachment. Dynamic scanning is important in the detection of vitreoretinal adhesions, which result in traction retinal detachment and must therefore be divided during vitrectomy (Fig. 47.49). If a post-traumatic retinal detachment is left untreated proliferative vitreoretinopathy develops, resulting in the formation of epiretinal membranes and the typical triangle sign on scanning. Penetrating injuries may cause vitreous incarceration at the point of injury. This results in incomplete posterior vitreous detachment with asymmetrical suspension of the gel (Fig. 47.50).

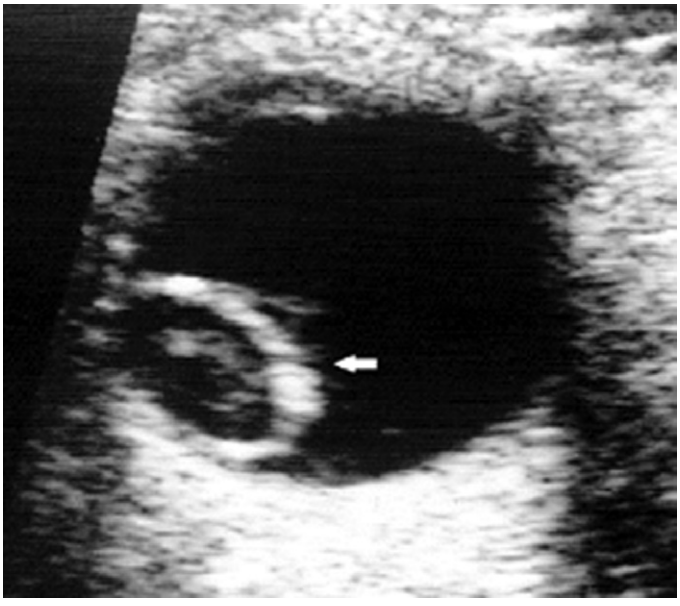

Figure 47.48 Displaced lens (arrow).

Post-traumatic retinal holes are not usually detectable by ultrasound but occasionally giant tears and dialyses may be identified (Fig. 47.51). Subretinal haemorrhage is seen as high-amplitude mobile echoes in the subretinal space, associated with retinal detachment. Penetrating injury in the region of the pars plana sometimes results in traction between the gel incarcerated at the injury site and the vitreous base, causing the ora serrata to be

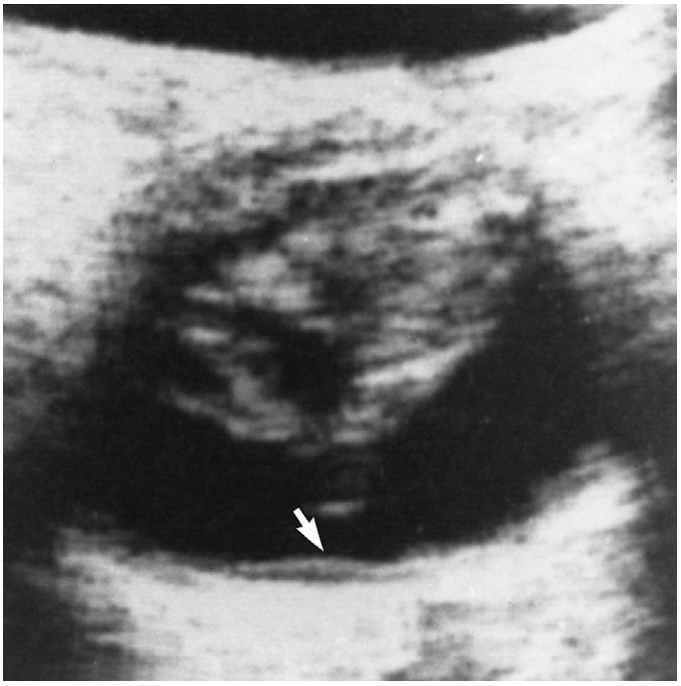

Figure 47.49 Traumatic vitreous haemorrhage and collapse, with lacuna, and vitreoretinal adhesion causing shallow traction retinal detachment (arrow).

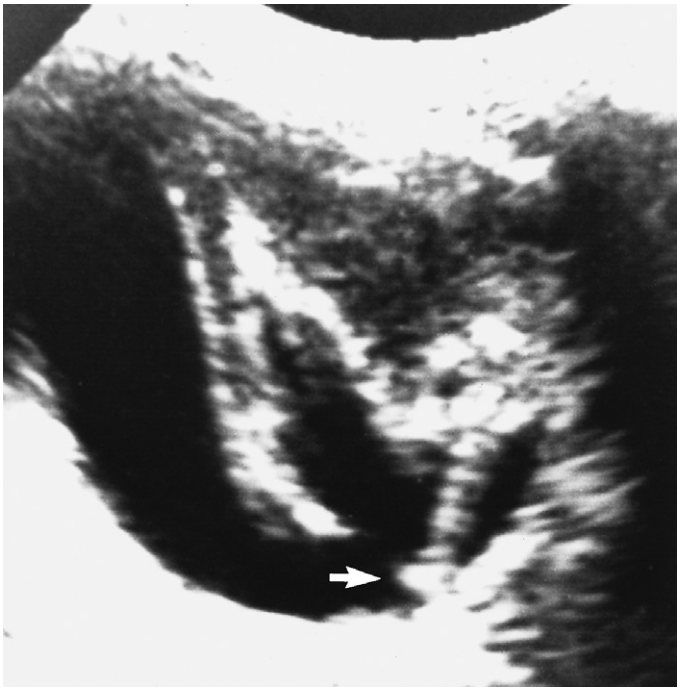

Figure 47.50 Vitreous lacerated by shotgun pellet and incarcerated into retina (arrow).

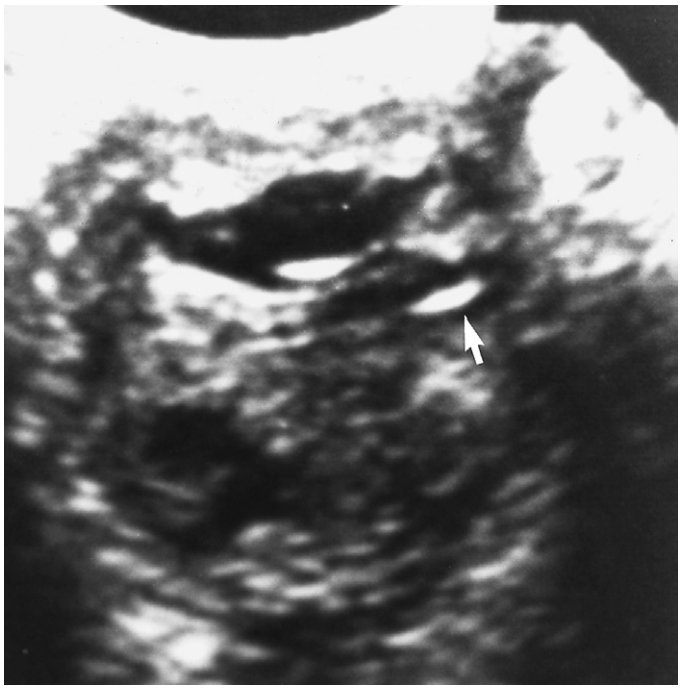

Figure 47.51 Direct blow causing extensive haemorrhage outlining lens, retinal dialysis (arrow) and rupture of globe at equator.

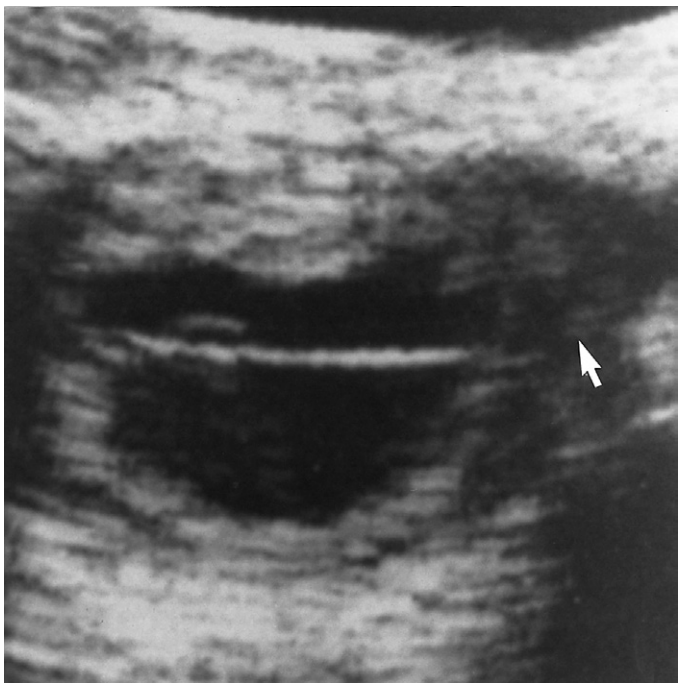

Figure 47.52 Direct blow causing intravitreal blood/fluid level, thickening of inner coats and rupture of globe (arrow).

pulled behind the lens. This is the so-called 'pursestring' retinal detachment, whose recognition is important so that surgical incision is not made into the subretinal space instead of the vitreous cavity.[7]

Rupture of the globe usually occurs in the equatorial region following an anterolateral blow (Fig. 47.52). Signs of rupture include distortion of the normal shape with loss of ocular volume, intravitreal haemorrhage and intraocular air, particularly if there is communication with an ethmoid sinus.

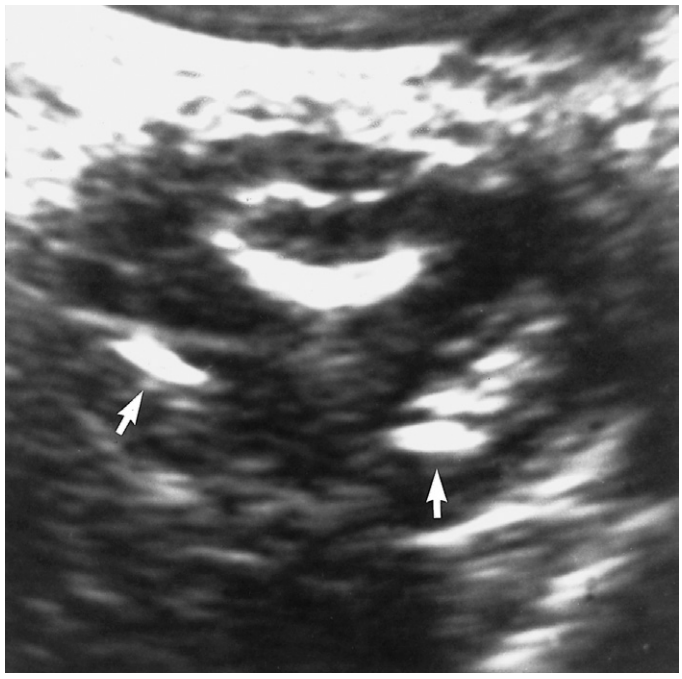

Figure 47.53 Phthisis bulbi with calcified debris (arrows).

Complications of trauma

- Hyphema.
- Cataract.
- Lens dislocation/rupture.
- Vitreous haemorrhage/track through vitreous.
- Vitreous incarceration.
- Retinal tear/dialysis.
- Posterior vitreous detachment.
- Retinal detachment.
- Haemorrhagic choroidal detachment.
- Scleral rupture.

Phthisis bulbi is an end-stage condition that follows trauma and ocular haemorrhage. The eye is blind, small, and contains extensive calcification (Fig. 47.53).

Foreign bodies

Small foreign bodies, for example metal or glass fragments travelling at high speed, cause penetrating injuries with the object retained within the globe. Most foreign bodies within the eye are detectable with ultrasound, but if the object is made of soft material, such as wood or organic matter, identification may be difficult, particularly if it is surrounded by haemorrhage.

Hard materials such as metal, glass or stone are highly reflective and therefore easier to demonstrate (Fig. 47.54). Following penetration by a foreign body a track of haemorrhage may be seen crossing the vitreous, outlining the trajectory of the object and indicating its position (Fig. 47.55). Frequently, though, intragel haemorrhage obscures the pathway. The entry or exit sites of a foreign body may cause vitreous incarceration, and some penetrating eye injuries permit the entry of air into the globe. Small spheres of intragel gas show as highly reflective spots which may be confused with foreign bodies, but the latter are usually even more highly reflective, with clear acoustic shadowing (Fig. 47.56). Gas bubbles move or rise with eye movement, and are absorbed after a day or so. However, if any doubt exists CT usually clarifies the situation. Ultrasound is able to

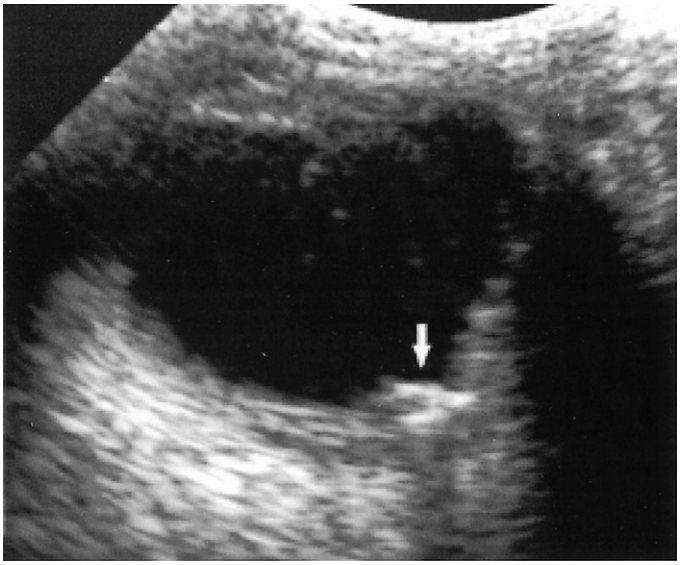

Figure 47.54 Metallic foreign body (arrow).

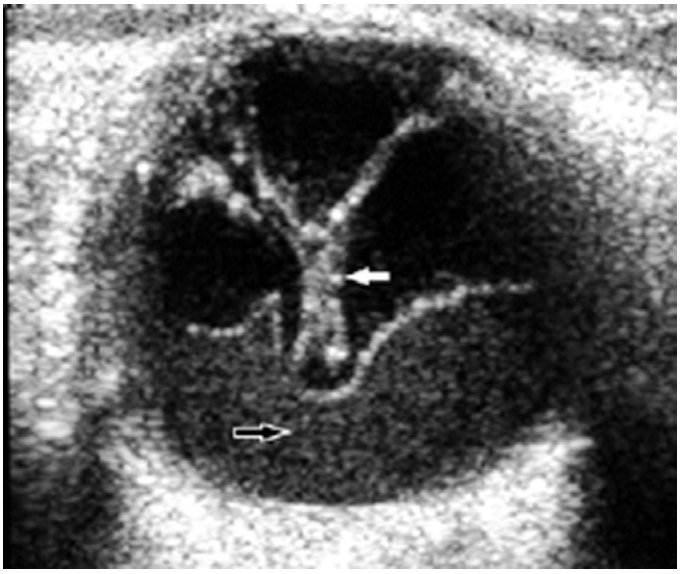

Figure 47.55 Penetrating injury with intragel haemorrhage track (white arrow), and subvitreal haemorrhage (black arrow).

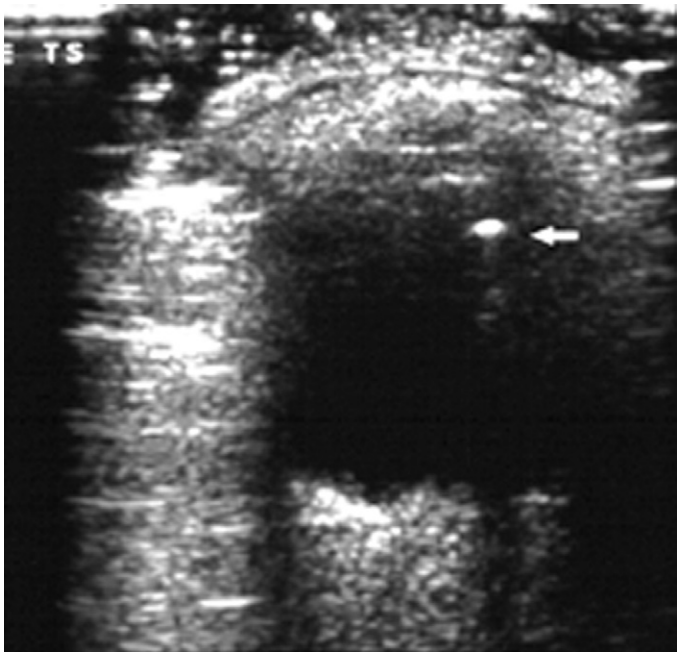

Figure 47.56 Penetrating injury with intragel haemorrhage and air bubble (arrow).

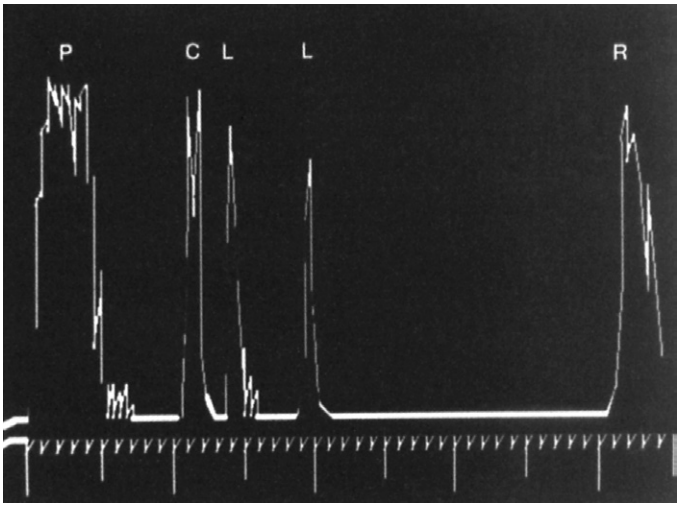

Figure 47.57 A-scan of myopic eye with increased axial length. P, main pulse; C, cornea; L, lens; R, end wall echo.

locate intraocular foreign bodies precisely prior to their removal, unless the object is very small and linear, when it may be difficult to align the beam perpendicular to the object's long axis. Because some foreign bodies may be missed with ultrasound examination it is important also to use plain radiography and CT scanning[43] but ultrasound is superior for the detection of associated intraocular abnormalities.

Biometry

Ocular measurements are carried out most accurately using A-scanning and a transducer of 10–20 MHz to ensure high resolution. A narrow beam is required as the lateral edges of a wide beam strike the curved walls of the posterior globe before the central area, resulting in an artefactually low measurement of axial length. Specially designed equipment is required for biometry. The most frequent measurements required prior to cataract surgery are the axial length of the eye and the corneal curvature, to permit calculation of the optimum focal length for intraocular lens implants. A-mode systems are specifically designed for this, calculations being performed by inbuilt computer software. The highly myopic eye has an elongated globe (pseudoproptosis), which may lead to unnecessary investigation for orbital tumour until the true nature of the problem is revealed by axial length measurement (Fig. 47.57). The measurement of axial length is also useful in monitoring congenital glaucoma and myopia. Other clinical measurements can be made, for example the thickness of the cornea, retina, choroid or sclera, and the size of intraocular tumours. Either contact or immersion techniques may be used. In the waterbath technique (for example with a small contact lens waterbath or scleral shell) the probe is 5–10 mm away from the cornea. This avoids the drawback of the contact method, which includes compression of the globe and masking of the corneal echo (see Fig. 47.6).

THE ORBIT

Introduction

MRI and CT of the retrobulbar structures have several advantages over ultrasound, including high-resolution images with thin sections, magnification techniques, and the capability for image reconstruction in multiple planes. These modalities demonstrate lesions in the posterior and apical parts of the orbit, the adjacent sinuses and intracranial structures. For these reasons MRI or CT are now the methods of choice in investigating orbital disease. Their disadvantages include the delivery of a radiation dose to the eye with CT; subtle lesions of the optic nerve are missed; and the examination may be time-consuming. Ultrasound has the advantage of rapidity and accessibility and, with its ability to identify the orbital walls, optic nerve, extraocular muscles and orbital masses, it is a useful first-line investigation in proptosis.

The aims of orbital ultrasound are the demonstration of an orbital lesion and determination of its position within the orbit. The pathological nature of the lesion may be less easy to predict as many ultrasound features are non-specific; the clinical history must therefore be taken into account. A history of other primary malignancy raises the possibility of an orbital metastasis, whereas concomitant thyroid disease suggests thyroid ophthalmopathy. A gradually developing proptosis is suggestive of a slowly growing benign tumour.

The contact method is suitable for orbital scanning and, for good penetration of the sound beam, frequencies between 5 and 10 MHz are needed. A horizontal scanning plane is more readily carried out than a vertical plane, because of the better access of the sound beam to the orbit horizontally, and interpretation is easier. A vertical scanning plane is used to examine the upper anterior orbit and inferior rectus muscle, but although modern probes may be angled in an oblique plane for examination of the lacrimal fossa, this area is more easily demonstrated on MRI.

Indications for orbital ultrasound

- Exophthalmos.
- Enophthalmos.
- Globe displacement.
- Lid abnormalities.
- Diplopia.
- Vascular lesions.
- Optic disc swelling.

Anatomy and ultrasound features

Situated behind the orbital septum, the orbit is a pear-shaped bony cavity whose stalk is the optic nerve passing through the optic canal. The medial walls of the orbits are parallel to each other and the floors nearly horizontal, but the lateral walls form a 90° angle with each other. The roof is gently concave and slopes down to the apex. The orbital opening is slightly smaller than the widest orbital diameter, which is situated 1 cm behind, providing the space for the equator of the eyeball.[44,45]

The orbital contents

The orbit contains the eyeball, the nerves to it (including the optic nerve in its bed of fat), the extrinsic muscles that move it, and the nerves and vessels that supply them (Fig. 47.58). The two eyeballs face forwards, parallel with each other. The optic nerve and ocular muscles pass anterolaterally from the apex of the orbit to their ocular attachments. The four recti arise from a tendinous ring at the apex, and broaden out to form a cone of muscles around the eyeball. Within this cone lies the fat surrounding the optic nerve, which is highly reflective and forms a triangular mass traversed by the poorly reflective optic nerve. The intraorbital part of the optic nerve is 25 mm in length, which is longer than the distance between the back of the globe to the optic foramen (18 mm). The globe may therefore be displaced forward without stretching the optic nerve, which is freely mobile with movement of the eye. Careful positioning of the probe enables the whole length of the intraorbital part of the nerve to be visualised, but in other scanning planes the nerve may be sectioned as an oval.

The orbital muscles

The ocular muscles are seen as thin, poorly reflective straps (Fig. 47.59). Their tendons are narrow anteriorly, with a more fusiform

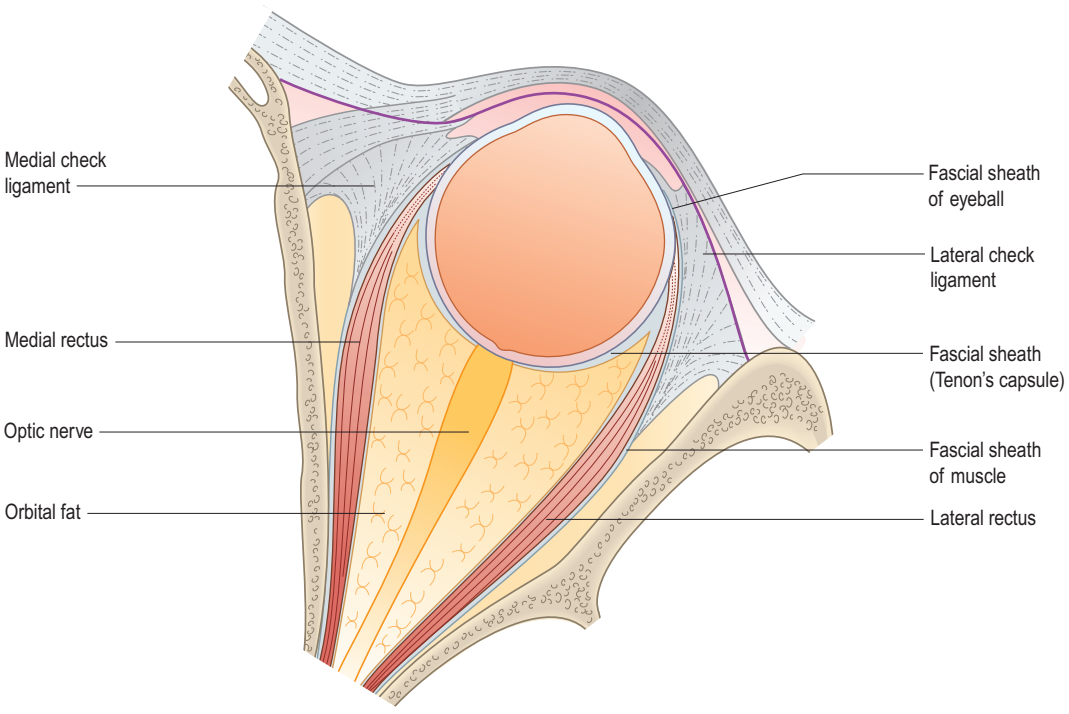

Figure 47.58 Horizontal section through eye and orbit.

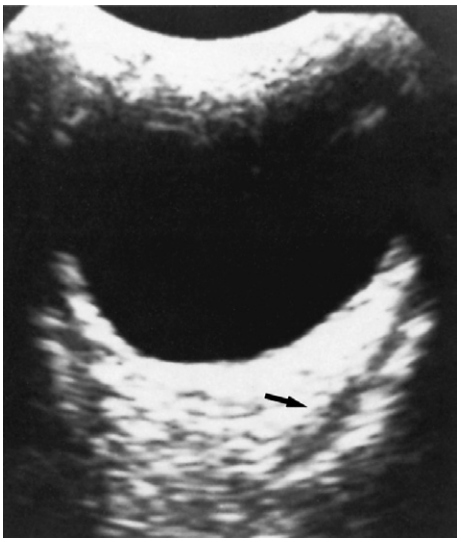

Figure 47.59 **Normal orbit**, with medial rectus and lateral rectus (arrow).

shape to the muscle belly and tapering posteriorly into the orbital apex. The medial and lateral recti are readily seen in the horizontal plane but vertical sections are required to visualise the superior and inferior muscles. The inferior oblique muscle lies inferior to the globe and is seen immediately behind it, below the macula. The superior oblique is in the upper, medial orbit and has a similar appearance to the recti.

The levator palpebrae superior muscle arises at the apex of the orbit from the roof. The thick frontal nerve lies along its upper surface. The anterior end of the muscle forms a ribbon-like tendon which is inserted into the superior tarsal plate, the skin of the upper lid and the conjunctiva.

Pathology

Thyroid ophthalmopathy

Most patients with Graves' disease develop changes of thyroid ophthalmopathy at some stage, but only 3–5% develop the sight-threatening complication of optic neuropathy, which is caused by compression of the optic nerve by the enlarged extraocular muscles. The preferred method of examination is orbital ultrasound, which is rapid, accurate and may be used harmlessly for follow-up. All the extraocular muscles may be enlarged, but the severity of involvement can be assessed by ultrasound measurements of medial rectus width,[46] which correlates well with CT measurements. Ultrasound measurements are made from horizontal scans as the subject maintains forward gaze. The upper limit of normal for the medial rectus width is 4 mm. Typically enlargement mainly affects the muscle belly, with lesser involvement of the muscle origin and insertion. Patients with ophthalmoplegia but a normal medial rectus width require assessment of the inferior rectus, which is sometimes selectively enlarged (Fig. 47.60). This muscle is more difficult to image with ultrasound and may require MR for adequate assessment.

Other features of thyroid ophthalmopathy include increased orbital fat and orbital oedema. The latter is seen as echo-poor areas within the orbital fat, sometimes with echo-free spaces, there may also be fluid within Tenon's capsule.

Inflammatory orbital disease (pseudo-tumour)

Inflammatory orbital disease is the name given to a group of relatively rare, idiopathic non-neoplastic orbital lesions, including

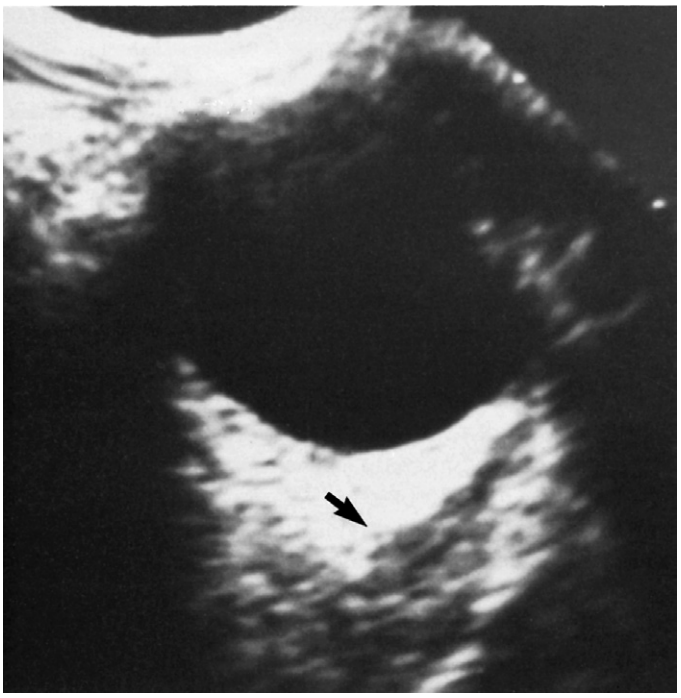

Figure 47.60 **Thyroid ophthalmopathy**, enlarged belly of inferior rectus (arrow).

myositis, dacryoadenitis, periscleritis, perineuritis and orbital pseudo-tumour. In the latter, involvement of the orbital fat predominates, causing a mottled appearance on scanning. The disease affects any or all of the soft tissue components of the orbit in any age group, but the majority are middle-aged individuals. Onset is usually acute, unilateral, and mimics the presence of an orbital tumour with proptosis, hence the term 'pseudo-tumour'. Sometimes the presence of a discrete inflammatory mass makes differentiation from a true neoplasm difficult, but pseudo-tumour usually responds well to steroid therapy. The ultrasound appearance of the mass is a poorly reflective lesion with features similar to those of a metastasis or lymphoma deposit but pseudo-tumour attenuates the sound more strongly (Fig. 47.61). Oedema of orbital fat may be present and myositis may be seen as enlargement of the whole of an extraocular muscle, including the origin and insertion, which differs from the selective muscle belly enlargement of thyroid ophthalmopathy. Oedema in the retrobulbar fascia (Tenon's capsule) tracks along the optic nerve sheath to form the 'T' sign (Fig. 47.62). In children about one-third of idiopathic pseudo-tumours are bilateral but in adults bilateral involvement raises the suspicion of systemic disease, for example lymphoma, sarcoidosis, Wegener's granulomatosis, or one of a range of autoimmune diseases. Chronic cases of inflammatory orbital disease develop a firm, fibrous stroma which replaces the orbital fat, termed sclerosing orbital pseudo-tumour.

Varices

The diagnosis of orbital varices is made by colour Doppler or by observing expansion of the blood-filled spaces while the jugular veins are compressed. This technique enables differentiation from orbital cysts, but the diagnosis is often made clinically from the sign of intermittent exophthalmos.

Arteriovenous fistula

These may develop spontaneously or after head injury, and are often not diagnosed clinically unless large. Carotico-cavernous sinus fistula and dural cavernous arteriovenous malformations are

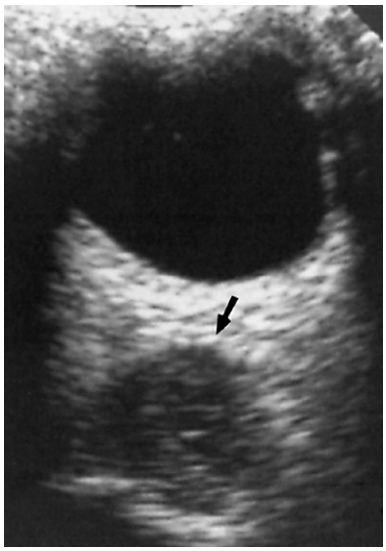

Figure 47.61 **Pseudo-tumour**, orbital mass.

readily diagnosed and monitored by colour Doppler. The superior ophthalmic vein conveys blood from the orbit posteriorly to the cavernous sinus. However, with both carotico-cavernous and dural cavernous fistulae arterial blood enters the cavernous sinus and blood flow in the superior ophthalmic vein is reversed or arterialised, resulting in proptosis with dilated conjunctival vessels. The dural fistula is a low-flow condition and colour Doppler may be the only investigation required if symptoms are mild, and can also be used to assess progression. The carotid fistula is a high-flow lesion and orbital haemodynamics can be assessed by colour Doppler prior to CT or MR angiography; colour Doppler can also be used to assess the results of therapeutic embolisation.

Orbital tumours

The ultrasound findings in a wide range of orbital malignancies are very similar. Unless there are clear indications in the clinical history as to the likely nature of the tumour the ultrasound report may have to be confined to a description of the topographical features of the lesion, and a comment on the possibility of malignancy. The demonstration of a poorly reflective, irregular orbital mass with good penetration of the sound beam is a strong indication of orbital malignancy. However, these features are not pathognomonic, as some types of pseudo-tumour and other inflammatory lesions have similar features.

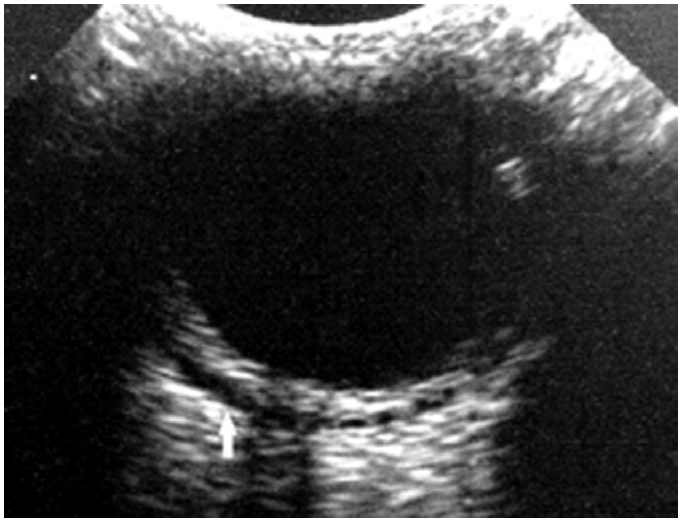

Figure 47.62 **Fluid in Tenon's capsule**, 'T' sign (arrow).

Orbital haemangioma

Cavernous haemangioma is the commonest benign orbital tumour in adults, occurring most frequently in the second to fifth decades of life, and is characterised clinically by a slowly progressive unilateral proptosis. The lesions consist of dilated endothelium-lined vascular channels surrounded by a fibrous pseudocapsule. The majority are located within the muscle cone and may occasionally compress the optic nerve but cause little proptosis.

The ultrasound appearance is that of a mass of medium to strong reflectivity with little attenuation. Doppler examination is frequently negative owing to very slow blood flow within the vascular spaces. Occasionally calcified phleboliths are seen.

In infancy, orbital haemangiomas are of the capillary type, usually presenting in the anterior orbit at birth or soon afterwards. They undergo periods of growth, then stabilisation and eventual regression, usually at about 5 years of age. Ultrasonically the lesion is less reflective than the cavernous type, because of the small vascular channels and scant stroma (Fig. 47.63). The prominent arterial supply to the lesion gives rise to good perfusion and Doppler examination usually confirms the vascular nature of the lesion.

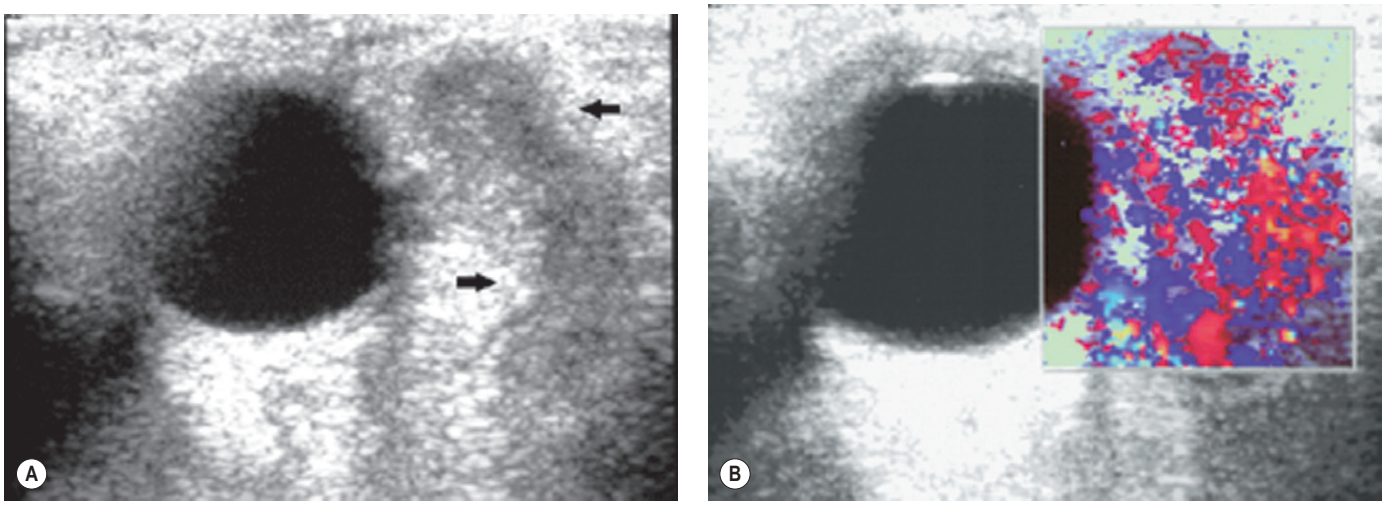

Figure 47.63 **Orbital haemangioma** (arrows). **A:** Vertical scan. **B:** Colour Doppler scan.

Rhabdomyosarcoma

This is the commonest primary malignant orbital tumour of childhood. Presentation is usually around the age of 7 years, with a rapidly progressive proptosis. The tumour arises from an extraocular muscle and may involve any part of the orbit, but usually occurs in the superonasal quadrant and appears on ultrasound as a poorly reflective mass (Fig. 47.64). Metastatic neuroblastoma should be considered as a differential diagnosis.

Lymphoproliferative disorders

These conditions usually affect patients over the age of 60 years. They may occur in any part of the orbit, are sometimes bilateral, and occasionally exclusively involve the lacrimal gland. Orbital lymphoma is usually of the non-Hodgkin's type and appears on ultrasound as an elongated oval mass, with few internal echoes and good acoustic transmission, or as a mass cupping the back of the globe (Fig. 47.65). Histological studies usually make a distinction between malignant lymphomas and inflammatory conditions but there is also an intermediate group, some of which have a benign outcome and resolve with steroid therapy, whereas others develop systemic lymphoma several years later. Thorough systemic evaluation is therefore necessary in all patients with both benign and malignant lymphoid lesions of the orbit. Ultrasound-guided biopsy is useful for the accurate retrieval of lymphoma tissue, and serial scans are helpful to demonstrate the response to therapy.

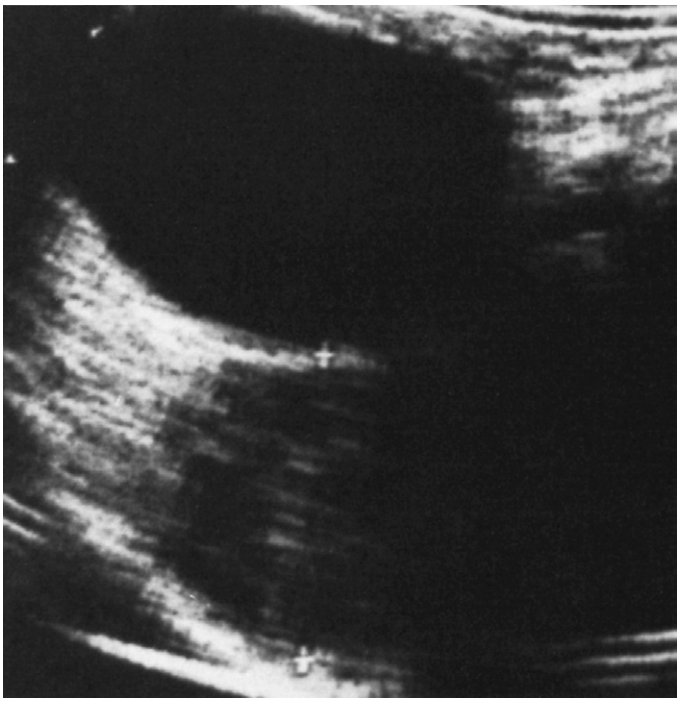

Figure 47.64 Orbital rhabdomyosarcoma.

Metastases

Orbital metastases occur in about 40% of children with neuroblastoma. Presentation is usually with rapid-onset proptosis and deposits may be bilateral. Ewing's sarcoma of bone, Wilms' tumour and leukaemia also give rise to orbital deposits.

In adults orbital metastases most commonly arise from primaries in the bronchus, breast, prostate, kidney and gastrointestinal tract (Fig. 47.66). Orbital invasion may also occur from adjacent malignancy in the paranasal sinuses (Fig. 47.67).

Optic nerve tumours

Neurilemmoma

Usually arising in the superior orbit, these rounded masses are sometimes echo-free or may contain low- to medium-amplitude echoes. They transmit sound less well than do cavernous haemangiomas (Fig. 47.68).

Glioma

This is a benign congenital hamartoma which presents between the ages of 4 and 8 years with visual loss and proptosis. Over half of these patients have neurofibromatosis. On ultrasound a fusiform or irregular expansion of the optic nerve is demonstrated, but MRI and CT are better at showing extension into the optic canal. The lesion is poorly reflective and shows poor acoustic transmission.

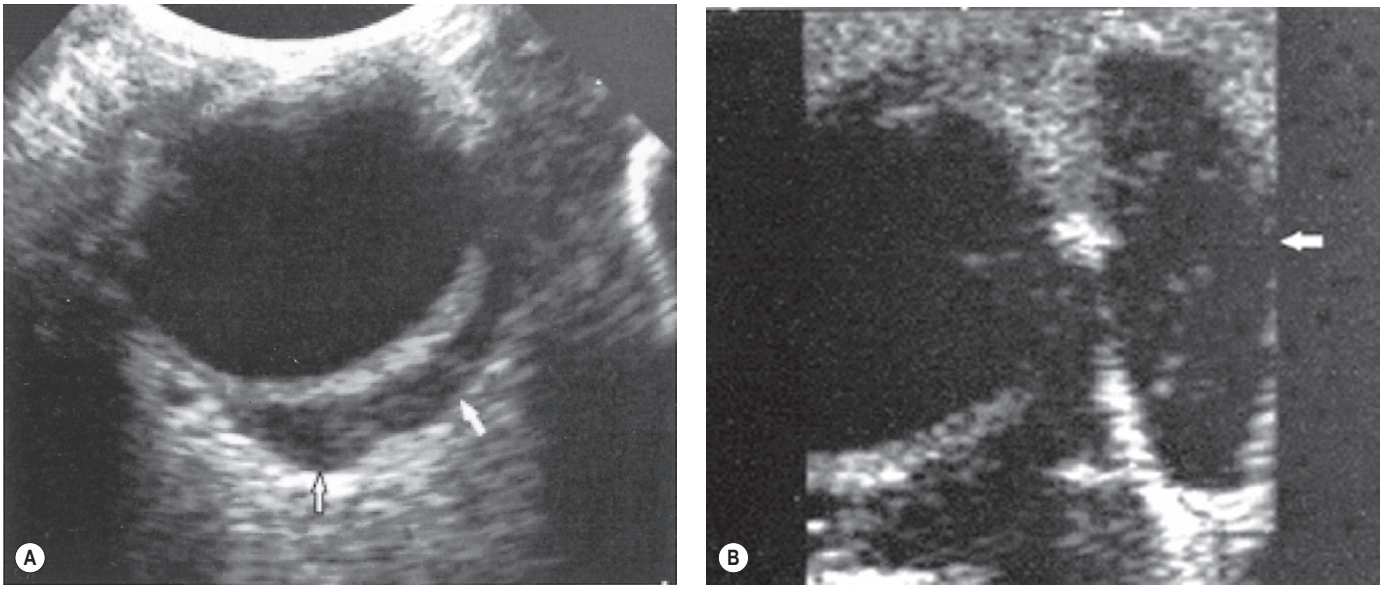

Figure 47.65 Orbital lymphoma. A: Lymphoma (arrows) cupping the globe. **B:** Lymphoma (arrow) affecting lacrimal gland. Oblique scan plane.

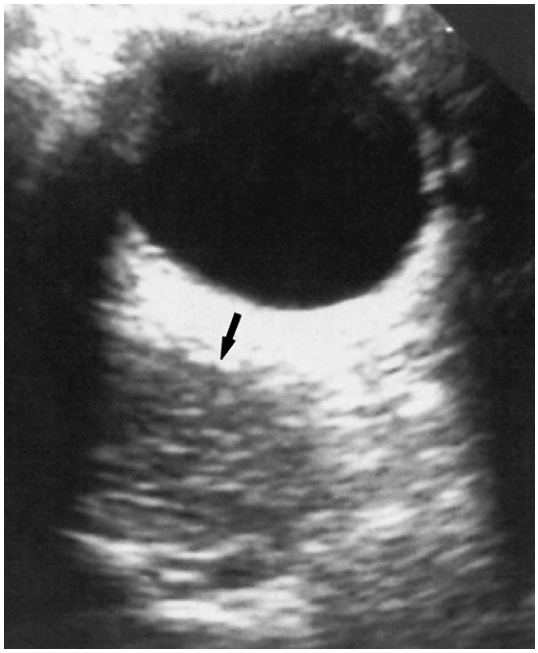

Figure 47.66 **Orbital metastasis** (arrow).

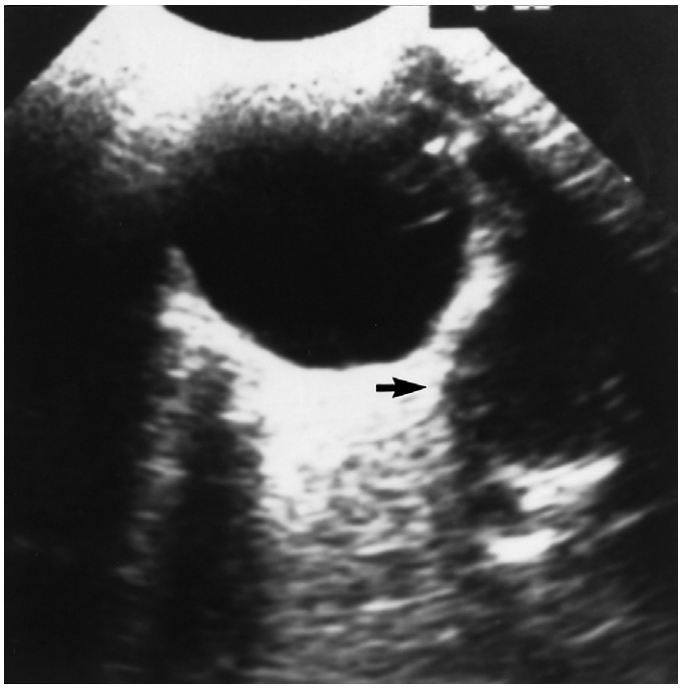

Figure 47.67 **Antral carcinoma** invading orbital floor (arrow) and elevating inferior rectus.

Neurofibromas of the optic nerve also occur in patients with neurofibromatosis.

Meningioma

Optic nerve sheath meningiomas arise from arachnoid villi and present with unilateral slowly developing impairment of vision. This results from optic nerve compression as the tumour grows within the dural sheath. When the tumour enlarges and ruptures through the dura it forms an intraconal mass, resulting in proptosis. Ultrasound shows a diffuse or focal broadening of the optic nerve,

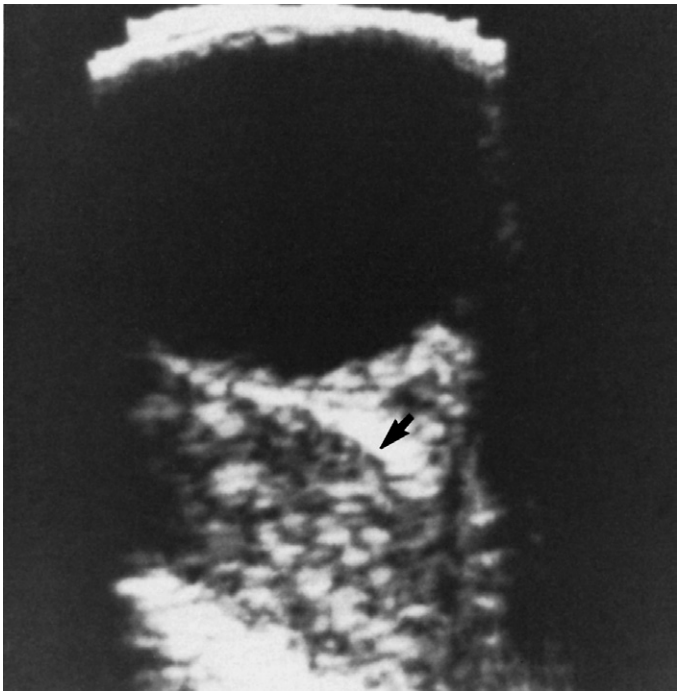

Figure 47.68 **Orbital neurilemmoma** (arrow).

sometimes giving rise to high-amplitude echoes. Meningiomas are invasive tumours, typically affecting middle-aged women. They also arise 'en plaque' in the greater and lesser wings of the sphenoid, and involve the orbit secondarily.

REFERENCES

1. Passani F, Barco L, Venturi G. Pre-vitrectomy examination of the traumatised eye. In: Hillman JS, LeMay MM, editors. Ophthalmic ultrasonography. The Hague: Martinus Nijhoff; 1983. p. 121–125.
2. Restori M, McLeod D. Ultrasound in pre-vitrectomy assessment. Trans Ophthalmol Soc UK 1977;97:232–234.
3. Fielding JA. Ocular ultrasound. Clin Radiol 1996;51:533–544.
4. McLeod D, Restori M, Wright JE. Rapid B-scanning of the vitreous. Br J Ophthalmol 1977;61:437–445.
5. Fielding JA. Imaging the eye with ultrasound. MD thesis, University of Liverpool, 1993.
6. Munk PL, Vellet AD, Lin DT-C, et al. Ultrasonographic findings in the anterior segment of the eye obtained with a non-dedicated unit. Can Assoc Radiol J 1992;43:425–430.
7. McLeod D, Restori M. Rapid B-scanning in ophthalmology. In: Barnett E, Morley P, editors. Clinical diagnostic ultrasound. Oxford: Blackwell Scientific; 1985. p. 111–120.
8. Horrocks M. The evaluation of extra-cranial cerebrovascular disease using Doppler ultrasound. MS thesis, University of London, 1982.
9. Brockenborough EC. Screening for the prevention of stroke: use of a Doppler flowmeter. Washington/Alaska Regional Medical Program; 1969.
10. Wong D, Restori M. Ultrasonic Doppler studies of the vitreous. Eye 1988;2:87–91.
11. Canning CR, Restori M. Doppler ultrasound studies of the ophthalmic artery. Eye 1988;2:92–95.
12. Williamson TH, Baxter GM, Dutton GN. Colour Doppler velocimetry of the optic nerve head in arterial occlusion. Ophthalmology 1993;100:312–317.
13. Baxter GM, Williamson TH. Colour Doppler flow imaging in central retinal vein occlusion: a new diagnostic technique? Radiology 1993;187:847–850.
14. Wong AD, Cooperberg PL, Ross WH, et al. Differentiation of detached retina and vitreous membrane with color flow Doppler. Radiology 1991;178:429–431.
15. Pavlin CJ, Easterbrook M, Harasiewicz K, et al. An ultrasound biomicroscopic analysis of angle-closure glaucoma secondary to

ciliochoroidal effusion in IgA nephropathy. Am J Ophthalmol 1993;116:341–345.
16. Finger PT. 3 Dimensional ultrasound of the eye. In: Byrne SF, Green RL, editors. Ultrasound of the eye and orbit. St Louis: Mosby; 2002. p. 236–243.
17. Foulds WS. Aetiology of retinal detachment. Trans Ophthalmol Soc UK 1975;95:118–128.
18. Schepens CL, Marden S. Data on the natural history of retinal detachment. Am J Ophthalmol 1966;61:213–226.
19. Kanski JJ. Retinal detachment. In: Kanski JJ, ed. Clinical ophthalmology, 6th edn. London: Butterworth Heinemann; 2007. p. 695–733.
20. Frank RN. On the pathogenesis of diabetic retinopathy. Ophthalmology 1984;91:626–634.
21. Kenyon KR, Maumenee AE, Ryan SJ, et al. Diffuse drusen and associated complications. Am J Ophthalmol 1985;100:119–128.
22. Ishibashi T, Patterson R, Oshnishi Y, et al. Formation of drusen in the human eye. Am J Ophthalmol 1986;101:342–353.
23. Smitty WE, Fine SL. Prognosis in patients with bilateral macular drusen. Ophthalmology 1984;91:271–277.
24. Forrester JV, Lee WR, Williamson J. The pathology of vitreous haemorrhage. Arch Ophthalmol 1978;95:703–710.
25. Hayreh SS, Podhaysky P. Ocular neovascularisation with retinal vascular occlusion. Arch Ophthalmol 1982;100:1585–1596.
26. Jakobiec FA, Levinson AW. Choroidal melanoma: aetiology and diagnosis. Clinical Modules for Ophthalmologists 1985;3:Module 5.
27. Gass JDM. Problems in the differential diagnosis of choroidal naevi and malignant melanomas. Am J Ophthalmol 1977;83:299–323.
28. Hungerford JL. Current trends in the treatment of ocular melanoma by radiotherapy. Clin Exp Ophthalmol 2003;31:8–13.
29. Damato B, Jones A. Uveal melanoma: resection techniques. Opthalmol Clin N Am 2005;18:119–128.
30. Collaborative ocular melanoma study group. The CMOS randomised trial of Iodine-125 brachytherapy for choroidal melanoma III. Initial mortality findings. CMOS Report No. 18. Arch Opthalmol 2001;119:969–982.
31. Baum G. Ultrasonic characteristics of malignant melanoma. Arch Ophthalmol 1967;78:12–15.
32. Coleman DJ, Abramson DH, Jack RL, Franzen LA. Ultrasonic diagnosis of tumours of the choroid. Arch Ophthalmol 1974;91:344–354.
33. Fuller DG, Snyder WB, Hutton WL, Vaiser A. Ultrasonographic features of choroidal malignant melanomas. Arch Ophthalmol 1979;97:1465–1472.
34. Roxburgh STD, LeMay M, Lee WR. The role of ultrasound in the investigation and management of suspected ocular melanoma. Proceedings of SIDUO VII. Documenta Ophthalmologica Proceedings Series 1980. The Hague: W Junk; 1980.
35. Lemke A-J, Hosten N, Richter M, et al. Contrast-enhanced colour Doppler sonography of uveal melanomas. J Clin Ultrasound 2001;29:205–211.
36. Recsan Z, Karlinger K, Fodor M, et al. MRI for the evaluation of scleral invasion and extrascleral extension of uveal melanomas. Clin Radiol 2002;57:371–376.
37. Romero JM, Finger, PT, Rosen RB, Iezzi R. Three-dimensional ultrasound for the measurement of choroidal melanomas. Arch Ophthalmol 2001;119:1275–1282.
38. Mewis L, Young SE. Breast carcinoma metastatic to the choroid – analysis of 67 patients. Ophthalmology 1982;89:147–151.
39. Stephens RF, Shields JA. Diagnosis and management of cancer metastatic to the uvea: a study of 70 cases. Ophthalmology 1979;86:1336–1349.
40. Cunha S L. Osseous choristoma of the choroid. Arch Ophthalmol 1984;102:1052–1054.
41. Harbour JW. What is the best treatment for retinoblastoma? Am J Ophthalmol 2004;138:471–473.
42. de Graaf P, Barkhof F, Moll AC. Retinoblastoma: MR imaging parameters in detection of tumour extent. Radiology 2005;235:1 97–207.
43. Fielding JA. The assessment of ocular injury by ultrasound. Clin Radiol 2004;59:301–312.
44. Aviv RI, Casselman J. Orbital imaging: Part 1. Normal anatomy. Clin Radiol 2005;60:279–287.
45. Aviv RI, Miszkiel K. Orbital imaging: Part 2. Intraorbital pathology. Clin Radiol 2005;60:288–307.
46. Given-Wilson R, Pope RM, Michell MJ, et al. The use of real-time orbital ultrasound in Graves' ophthalmopathy: a comparison with computed tomography. Br J Radiol 1989;62:705–709.

CHAPTER

48 Carotids, vertebrals and TCD (transcranial Doppler)

Paul L. Allan and Joanna M. Wardlaw

INTRODUCTION

One of the earliest clinical applications for Doppler ultrasound was the assessment of flow in the carotid arteries, and over the years much work has been done in this area. Ultrasound is now the initial investigation for many patients with possible carotid artery disease; it is non-invasive, relatively cheap, and fast and accurate in experienced hands, to the extent that it may be the only imaging modality that is required in many cases, including prior to endarterectomy.

INDICATIONS FOR CAROTID AND VERTEBRAL ARTERY ULTRASOUND

The main indications for carotid and vertebral artery ultrasound are to detect vascular abnormalities that may be giving rise to neurological symptoms. If a vascular abnormality, such as a significant stenosis, is demonstrated on ultrasound, then consideration can be given as to how the patient might be treated.

Ischaemic symptoms

The main symptoms of ischaemia are transient ischaemic attacks, minor strokes and amaurosis fugax. Transient ischaemic attacks (TIA) resolve within 24 hours, whereas strokes persist for more than 24 hours. The MRC European Carotid Surgery Trial (ECST)[1] and the North American Symptomatic Carotid Endarterectomy Trial (NASCET)[2] reported their results in 1991; both showed a definite benefit for patients with severe symptomatic carotid stenosis who underwent surgery. The European study showed that the risk of death or stroke related to surgery was 7.5%, but thereafter the risk of ipsilateral stroke in the surgical group was only 2.8%, compared to 16.8% for those managed conservatively. The North American study reported similar levels of benefit for surgery, although it should be noted that the two studies used different criteria for assessing stenoses on arteriograms: a European stenosis of 70% represents the same degree of stenosis as a NASCET measurement of 50%.[3] The European study also showed that there was no benefit for surgery in patients with a mild stenosis of less than 30% diameter reduction, and subsequent analysis of the ECST data showed that surgery conferred no benefit in symptomatic patients with a stenosis between 30% and 69% diameter reduction.[4] A Cochrane Review of the value of carotid endarterectomy for symptomatic carotid stenosis concluded that surgery was of benefit for patients with severe stenosis (ECST >80% or NASCET >70%) and reduced the relative risk of disabling stroke or death by 48%, with the number of patients needing to be treated to prevent a disabling stroke or death over 2–6 years of follow-up being 15. In cases with less severe stenosis (ECST 70–79%; NASCET 50–69%), there was still a benefit from surgery, with a reduction of 27% in the relative risk and a number needed to treat (NNT) of 21. These results were only applicable to surgically fit patients being operated upon in units with a surgical complication rate of <6%.[5]

A completed stroke does not normally warrant a carotid ultrasound examination, as endarterectomy will not be offered to the patient unless they make a good recovery. Occasionally younger patients with mild, resolving strokes will be offered surgery to reduce the risk of a subsequent, more severely disabling stroke.

The situation regarding asymptomatic bruits and the value of surgery is less clear cut. The Asymptomatic Carotid Artery Surgery Trial showed that there was only a 5% benefit for patients undergoing surgery who had an asymptomatic stenosis of more than 60% diameter reduction, and this only if the surgical centre had a perioperative morbidity/mortality rate of less than 3%.[6] A Cochrane

Indications for carotid and vertebral artery ultrasound

- Transient ischaemic attacks (TIA).
- Mild resolving strokes in younger patients.
- High-risk patients prior to surgery.
- Atypical, non-focal symptoms which may have a vascular aetiology.
- Post-endarterectomy.
- Pulsatile neck masses.
- Trauma or dissection.
- Screening for disease.
- Posterior fossa ischaemic symptoms.
- Vertebral artery trauma.
- Subclavian steal syndrome.

Review of carotid endarterectomy for asymptomatic carotid stenosis noted that there is only an annual risk of unheralded stroke of 1–3% in these patients but endarterectomy resulted in a 30% reduction in the risk of stroke over 3 years. However, the absolute risk reduction following surgery works out at only about 1%. These limited benefits were only relevant if the surgical complication risk is less than 3%.[7] The American Academy of Neurology has published recommendations relating to the role of carotid endarterectomy, which are based on these findings from the major trials.[8]

Several studies have looked at the role of carotid ultrasound in the management of patients with asymptomatic bruits for predicting subsequent strokes, and the results show that ultrasound confers no significant advantage in relation to predicting subsequent strokes related to the stenotic artery,[9–12] although the presence of the bruit is a sign of significant atherosclerosis.

The value of ultrasound in the assessment of patients with asymptomatic bruits will therefore depend on local clinical policy: if surgery will be offered to those with a stenosis greater than 60% diameter reduction, then carotid ultrasound is justified; if surgery is not to be offered there seems little point in performing ultrasound.

Atheroma is a generalised process and patients scheduled for surgery for vascular disease of the peripheral or coronary arteries, aortic aneurysm and other vascular disorders might be considered to be at risk from associated carotid disease. In the absence of a bruit or symptoms of carotid disease it is unlikely that they will have a significant stenosis and a carotid study is not indicated. If a bruit is present but the patient is asymptomatic it has been shown that there is no increase in risk, even if there is a haemodynamically significant stenosis,[13] although symptomatic patients with a significant stenosis should be considered for a staged, or simultaneous, endarterectomy if they are shown to have a stenosis of greater than 70% diameter reduction. However, this decision will depend on the relative urgency of the primary condition, and many centres, while taking note of the carotid disease, will proceed with the primary operation and consider subsequent endarterectomy in symptomatic patients. A review of carotid artery disease and stroke during coronary artery bypass surgery[14] noted that the overall risk of stroke following surgery was 2% and this figure had remained unchanged over the thirty years from 1970 to 2000. The review concluded that even assuming that prophylactic endarterectomy carried no additional risk, it could only ever prevent 40–50% of this small number of procedural strokes. The authors also noted that there is increasing evidence that atheroma in the ascending aorta is likely to be implicated in up to 60% of strokes related to coronary artery surgery.

Atypical symptoms

Occasionally patients may present with an unusual symptom complex which may or may not be due to carotid atheroma. Discretion in patient selection is required, but an ultrasound examination will provide a rapid assessment of the carotid arteries so that these can be ruled out as the source of the symptoms, or carotid disease identified as the cause.

Post-endarterectomy follow-up

The complications that may follow endarterectomy can be divided into three groups based on the timing in relation to surgery:

1. early occlusion in the first 24–48 hours postoperatively
2. stenosis developing over a period of 12–18 months as a result of neointimal hyperplasia
3. development of a stenosis over several years as a result of atheromatous disease progression.

Colour Doppler ultrasound provides a rapid and straightforward method for diagnosis of these complications. Routine postoperative screening of asymptomatic patients is not justified by the low diagnostic yield[15] and increased costs[16] but symptomatic patients should be assessed with ultrasound.

Pulsatile neck masses

There is a variety of causes of a pulsatile neck mass. They include tortuous or ectatic carotid arteries, aneurysm of the carotid artery, carotid bifurcation tumours and enlarged lymph nodes. Their nature can be rapidly clarified using colour Doppler ultrasound.

Carotid trauma and dissection

Dissection of a carotid artery may occur spontaneously as a result of atheroma; it may result from the extension of an aortic dissection; it can occur following hyperextension neck injuries, or as a result of iatrogenic injury following carotid catheterisation. In patients who do not require immediate treatment ultrasound provides a rapid assessment of the integrity and patency of the vessels.

Epidemiological studies

The carotids are superficial arteries that can be examined with high-resolution ultrasound. Although atheroma affects different arteries to a variable extent, changes of atheroma in the carotids will reflect the overall tendency to arteriopathy, so that they can be used as a guide to the presence and severity of atheromatous disease in an individual. An increased intima–media thickness has been shown to correlate with a higher incidence of coronary artery disease and stroke.[17–19]

Vertebral arteries

The vertebral arteries are not normally examined in isolation from the carotids, but occasionally they are the main focus of the examination, especially if the ischaemic symptoms relate to the posterior fossa or posterior cerebral artery territory, or with symptoms following cervical trauma.

ANATOMY

The carotid arteries

The common carotid artery on each side divides into the internal and external carotid arteries at the carotid bifurcation: this is usually at the level of the upper border of the laryngeal cartilage, but may vary considerably up or down the neck. The internal carotid artery is usually posterior to the external carotid artery and tends to lie a

little lateral to it.[20] The carotid bulb is seen at the origin of the internal carotid artery, and the lower cervical branches of the external carotid artery can sometimes be identified; the superior thyroid, ascending pharyngeal and lingual arteries may all arise from the external carotid artery, below, or around the level of the angle of the mandible.

The origins of the two common carotid arteries are different. On the right side the common carotid artery arises from the brachiocephalic (innominate) artery behind the sternoclavicular joint, where it can usually be examined using ultrasound. The left common carotid artery, on the other hand, arises directly from the aortic arch in the vast majority of patients, and its origin thus lies too deep in the mediastinum to be seen with ultrasound.

The vertebral arteries

The vertebral arteries arise from their respective subclavian arteries behind the medial end of the clavicle. They run backwards and upwards to enter the vertebral canal between the lateral masses of the cervical vertebrae, usually at the level of C6. They then run up the vertebral canal to the level of C2, where they exit and wind around the lateral masses of the atlas, to enter the skull through the foramen magnum. They then join together in front of the brainstem to form the basilar artery.[21]

There may be natural variation in the relative sizes of the vertebral arteries and hence their contribution to basilar artery flow; when there is a disparity of size the left artery is usually the larger of the two, and in 7–10% of individuals there are significant segments of hypoplasia, which result in the artery not being visible.[22]

TECHNIQUE

The carotid arteries

The patient lies supine, or may be semi-supine, with a pillow under the shoulders to extend the neck; the chin is turned slightly away from the side being examined in order to open up the anterior triangle. Some patients may find this position uncomfortable; sometimes it may impair cerebral circulation, and a suitable compromise position must then be sought. The highest-frequency transducer consistent with adequate penetration is used; this is normally a 7–10 MHz linear transducer although with modern equipment a 10–14 MHz transducer may provide satisfactory images. Scanning transversely up the neck from the sternoclavicular joint to the angle of the mandible from an anterolateral approach will locate the common carotid artery and identify the level of the bifurcation in the majority of patients. In patients with a high bifurcation it may be necessary to try a variety of scan planes and head positions to locate it: sometimes a posterior approach under the mastoid process is required. Areas of major calcified plaque may be identified on this initial scan.

Following the greyscale examination, colour Doppler is activated and the vessel examined again from the lower neck to the highest level visible. Colour Doppler will highlight areas of abnormal flow which require further assessment and which subsequently need to be examined with spectral Doppler in order to quantify the degree of stenosis. Colour Doppler also facilitates a quick assessment of normal flow in the artery, including the normal region of reversed flow in the carotid bulb (Fig. 48.1), thereby minimising the time required for the examination.

Technique

- Patient's neck is extended and chin turned away a little from the side being examined.
- Transverse scan up along the common carotid artery to above the carotid bifurcation.
- Identify positively the ICA and the ECA.
- If there is no significant disease take spectral Doppler velocity measurements from CCA, ICA and ECA.
- If significant disease is present make additional peak velocity measurements from area of disease.
- Longitudinal scan to assess vertebral artery.

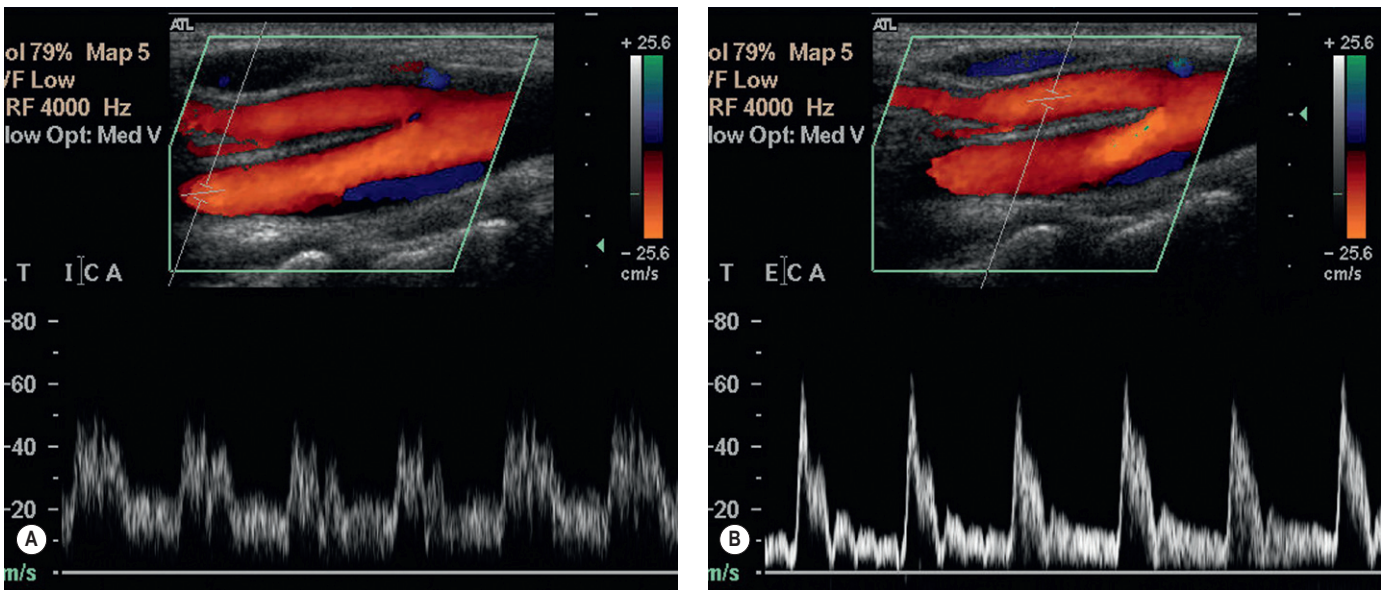

Figure 48.1 Carotid bifurcation. Longitudinal view of the carotid bifurcation showing the external carotid artery (ECA) with a branch artery at the top and the internal carotid artery (ICA) at the bottom with the carotid bulb showing normal reversed flow. **A:** Normal ICA waveform showing more marked diastolic flow compared to the ECA. **B:** Normal ECA waveform with prominent dicrotic notch and lower diastolic flow. Tapping on the superficial temporal artery as it passes over the zygoma produces the fluctuations in flow seen in the left portion of the Doppler spectral display.

Spectral Doppler is used to assess any areas of abnormal flow and to quantify the degree of stenosis. The sample volume is placed in the area of maximum colour change and the position of the maximum shift is located by visual assessment of the spectral display and by listening for the point of highest shift (not the loudest signal). If no areas of abnormal flow or significant disease are demonstrated it is customary to take velocity measurements from the common, internal and external carotid arteries, ensuring that the sample volume is positioned in the central portion of the vessel to reduce spectral broadening from the normal layer of disturbed flow adjacent to the vessel wall, and 'wall thump' from the vessel wall itself.

The bifurcation may be difficult to locate in some patients, in which case transverse scanning with colour or power Doppler may allow the two main branches to be identified as they leave the bifurcation.

It is important that the two branches of the bifurcation are identified correctly, so that any changes arising from disease are ascribed to the correct vessel. This is particularly important in the presence of moderate or marked disease which may make it difficult to distinguish between the two branches (Fig. 48.1). It is important to remember that the presence of significant disease alters the waveform criteria, which makes them less valuable for distinguishing between the internal and external carotid arteries, especially if there is 'internalisation' of the external carotid artery flow as a result of external–internal carotid artery collaterals. In these circumstances the 'temporal tap' manoeuvre is of value: tapping the superficial temporal artery as it passes over the zygomatic process will induce fluctuations in the spectral display of the external carotid artery but only minimal or no change in that of the internal carotid artery.[23] The need to assess flow in the ophthalmic arteries is less nowadays, as colour and power Doppler have improved the assessment of carotid stenosis and occlusion. However, if there is doubt as to whether a stenosis is significant, scanning the orbit may show reversal of flow in the ophthalmic artery, confirming the severity of the carotid stenosis (see 'The transorbital window' section below). In these cases it is important to scan the ophthalmic artery at the apex of the orbit, rather than the retinal artery immediately behind the eyeball, as flow in the latter will always be outwards.

With regard to the wall of the carotid artery the intimal line is best demonstrated when the ultrasound beam is orthogonal to the wall of the artery in a longitudinal plane; it is better seen on the far wall. If the intima–media thickness is to be measured, the image of the chosen area is magnified fully and the cursors placed on the luminal margin of the inner line and the inner margin of the outer line. Normal values are less than 0.8 mm (Fig. 48.2), but it should be remembered that these increase slowly with age.[24,25]

Identification of the external and internal carotid arteries

The external carotid artery

1. Lower cervical branches may be seen.
2. Lies more anteriorly and more medially.
3. Waveform characteristics:
   high resistance pattern with relatively little diastolic flow
   appears more pulsatile on colour Doppler (flashes on and off)
   dicrotic notch is more prominent.
4. Positive 'temporal tap' can be induced in the spectral display.

The internal carotid artery

1. The other branch of the bifurcation.
2. Localised widening of the bulb at the origin.
3. Posterior position and course angled posteriorly.
4. Less pulsatile waveform on colour Doppler with relatively high diastolic flow (waxes and waves).

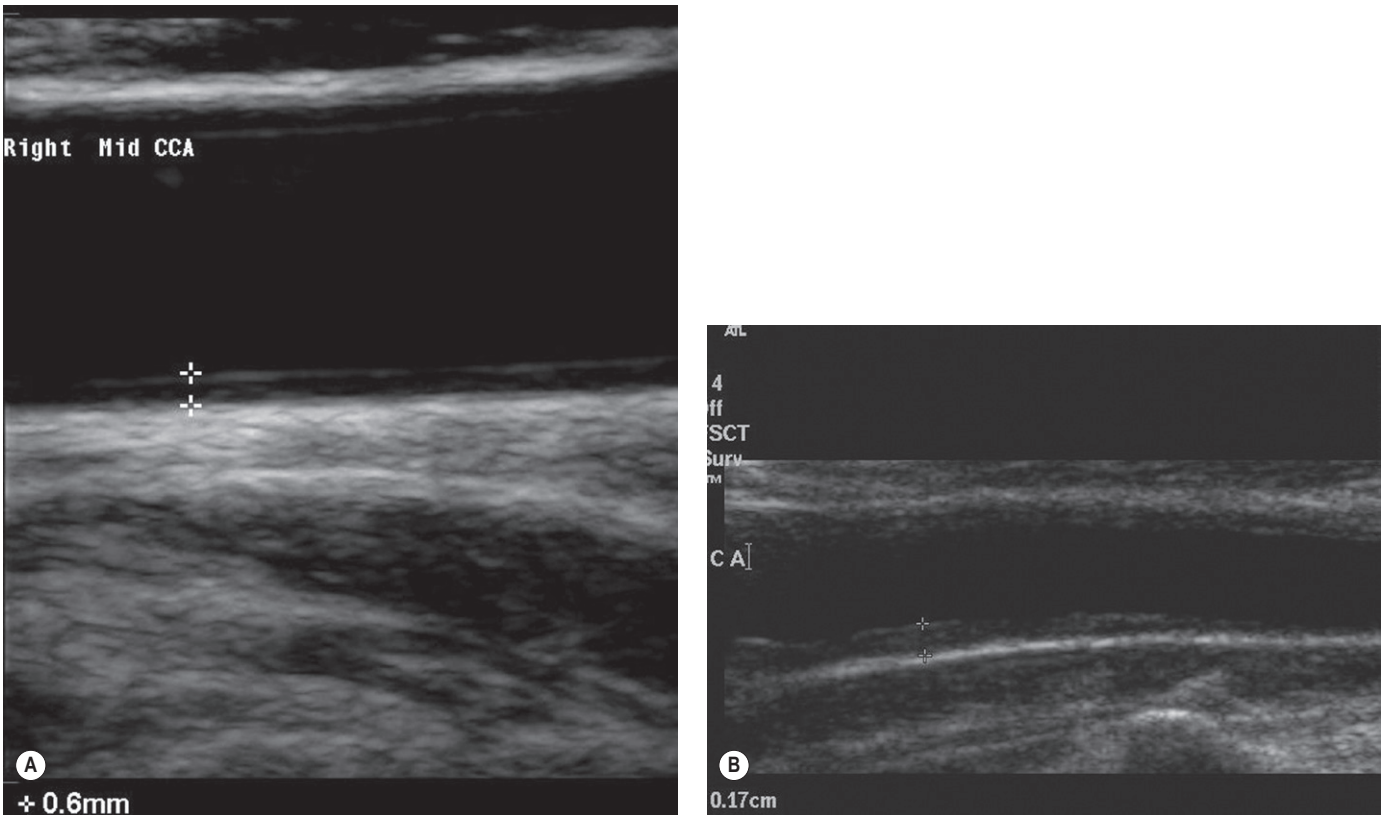

Figure 48.2 **Intima–media thickness. A:** Normal IMT measured at 0.6 mm. **B:** Thickened IMT measuring 1.7 mm.

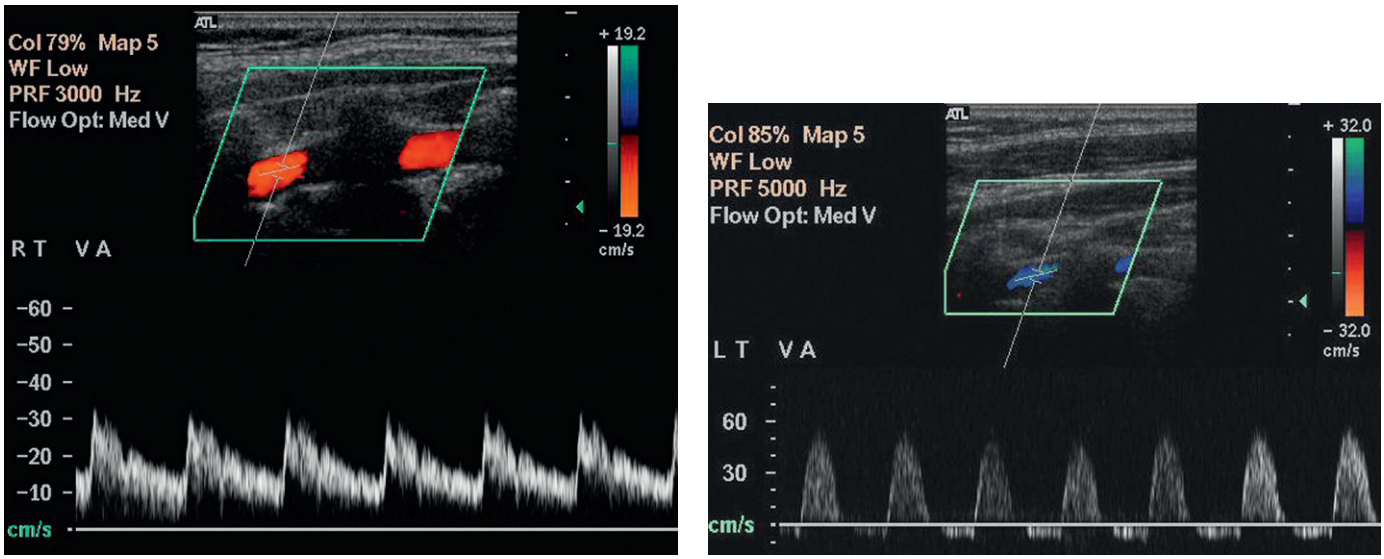

Figure 48.3 Vertebral artery. A: The vertebral artery is seen behind the acoustic shadow from the transverse process of a cervical vertebra. **B:** Reversed flow in a vertebral artery which is seen between the shadows from the cervical transverse processes.

The vertebral arteries

The vertebral arteries are located by scanning longitudinally over the common carotid artery on each side and locating the vertebral bodies. The scan plane is then rotated laterally until the gaps between the lateral masses of the cervical vertebrae are identified; the vertebral artery and vein should be visible within the vertebral artery canal through these gaps (Fig. 48.3A). Should this fail, the artery can be sought low in the neck between the vertebral column and the subclavian artery, or high in the posterior neck as it passes around the lateral mass of the atlas. If subclavian steal is suspected it is important to ensure that the colour polarity is appropriately set up; in doubtful cases reversal of flow may be provoked by asking the patient to perform some arm muscle work or by inducing reactive hyperaemia in the arm muscles by occluding the brachial artery with a blood pressure cuff for 2–3 minutes, then releasing the cuff and seeing if this unmasks a potential steal phenomenon (Fig. 48.3B).

NORMAL AND ABNORMAL FINDINGS

Colour Doppler enables the normal flow patterns in the vessel to be identified quickly. The colour may vary with the cardiac cycle but there should be no areas of persistent abnormal colour change, the presence of which indicates turbulence or an abnormal velocity, and that there is disease in the vessel. There are two main ways to quantify the severity of disease: indirectly through measurement of velocities and velocity changes in the area of the stenosis, or by direct visualisation and measurement of the stenosis itself.

Doppler criteria

The waveforms obtained from the normal internal and external carotid arteries have characteristic features. The internal carotid artery supplies the relatively low-resistance capillary bed of the cerebral circulation, and therefore there is flow throughout the cardiac cycle with appreciable end-diastolic flow (see Fig. 48.1A). The external carotid artery supplies the tissues of the face and scalp, which have a higher resistance, and there is therefore minimal or absent diastolic flow; in addition, the dicrotic notch from the closure of the aortic valve is more prominent in the external carotid waveform (Fig. 48.1B). Flow in the normal carotid arteries shows no significant turbulence except in the carotid bulb, and therefore there is a clear window under the waveform. In the normal vessels standard peak systolic velocity measurements are taken from the common carotid artery 2–3 cm below the bifurcation, from the internal carotid artery 2–3 cm above the level of the bulb (in order to allow the normal turbulence from the bulb to dissipate), and from the external carotid artery 1–2 cm above the bifurcation.

In patients with disease, Doppler waveforms are obtained from the areas of maximum velocity, as shown by colour Doppler (Fig. 48.4). The final position of the sample volume is determined by the sound of the Doppler shift as well as by the image on the screen. In the absence of colour Doppler it is necessary to reduce the size of the sample volume and move it slowly around the area of the stenosis until the maximum shift is seen on the screen and heard from the speakers, although the latter scenario is now very rare.

A variety of velocity measurements and ratios can be obtained from spectral Doppler. The most useful in practice are the peak systolic velocity (PSV), the end-diastolic velocity (EDV) and the ratio of the peak systolic velocities in the internal and common carotid arteries (IC/CC systolic ratio). The exact values for defining normality and the different degrees of stenosis quoted in the literature vary significantly; for instance, a 70% diameter reduction has been associated with peak systolic velocities of 1.3 m/s by one[26] and 2.25 m/s by another.[27] This emphasises the point that precise values vary from centre to centre and depend on a variety of factors, including the type of equipment and the specific technique employed. It is therefore important that each centre audits its results so as to define the values that work for it.

The values used by the author are shown in Table 48.1 and are based on those reported by Robinson et al.[27] and a consensus statement from the Society of Radiologists in Ultrasound.[28] It is important to remember that the peak systolic and diastolic values refer only to the internal carotid artery, not to the common or external carotids. It should also be borne in mind that physiological variations due to heart rate, cardiac output and contralateral stenosis or occlusion may affect the velocities in a vessel, potentially leading to a false diagnosis of a pathologically high velocity; these cases should be clarified by the use of the velocity ratios, as a general increase in velocity will affect flow in both the internal and common carotid arteries, whereas local internal carotid artery disease will produce a high velocity only at the site of the disease.

Table 48.1 Diagnostic criteria for Doppler diagnosis of stenoses of 50% and 70% (data from Robinson et al.[27] and Grant et al.[28])

Diameter stenosis	Peak systolic velocity ICA (m/s)	End-diastolic velocity ICA (m/s)	IC/CC systolic ratio
50%	>1.25	>0.4	>2
70%	>2.3	>1.0	>4

At very severe degrees of stenosis (greater than 90% diameter reduction) the velocity of blood flowing through the stenotic area decreases.[29] In addition, the residual lumen is very narrow, so that only a small volume of blood can pass through it, resulting in a relatively weak signal which is lower in velocity than might be expected (Fig. 48.5A). It is therefore essential that the ultrasound system is set to detect these low-velocity low-intensity signals,[30] or a false diagnosis of occlusion may be made and the patient may be denied surgery. The advent of power Doppler (Fig. 48.5B) and echo-enhancing agents has further improved the ability to detect these difficult but important lesions with ultrasound.[31,32]

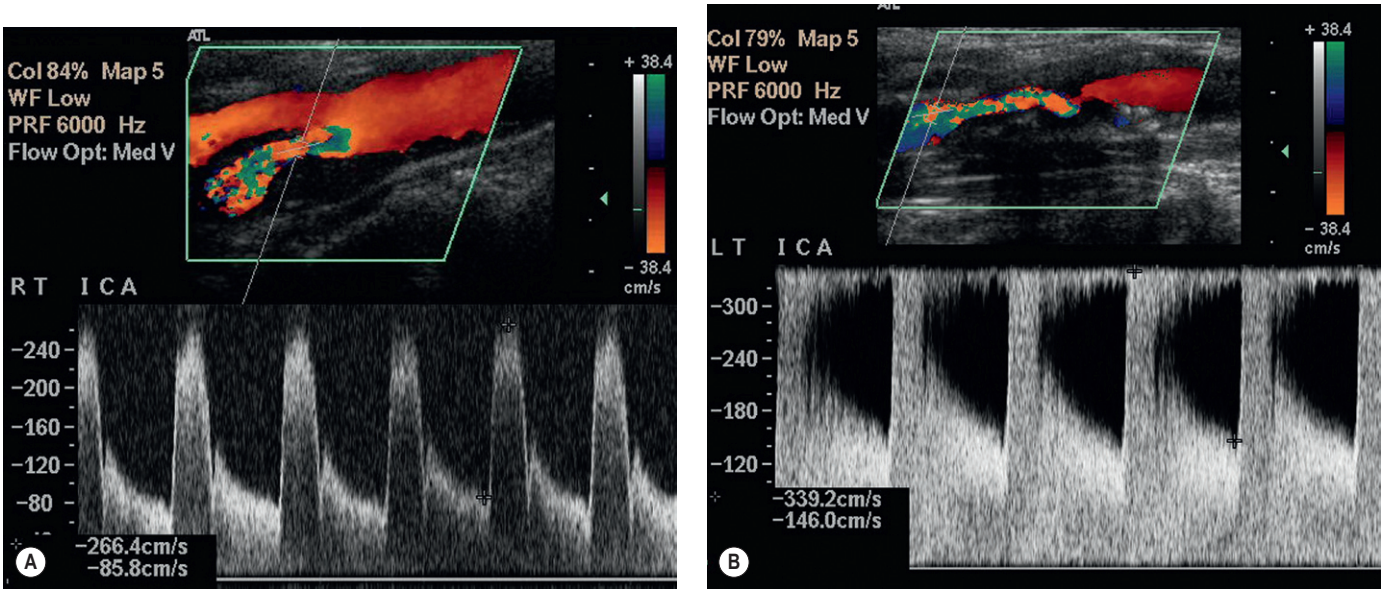

Figure 48.4 **Carotid stenosis. A:** Colour and spectral Doppler of an ICA stenosis. The colour image shows narrowing of the lumen and aliasing of the colour signal. The spectral display shows high-velocity (PSV 2.66 m/s, EDV 0.85 m/s), turbulent flow. **B:** A more severe, longer ICA stenosis with turbulent, high velocity flow (PSV 3.4 m/s, EDV 1.45 m/s).

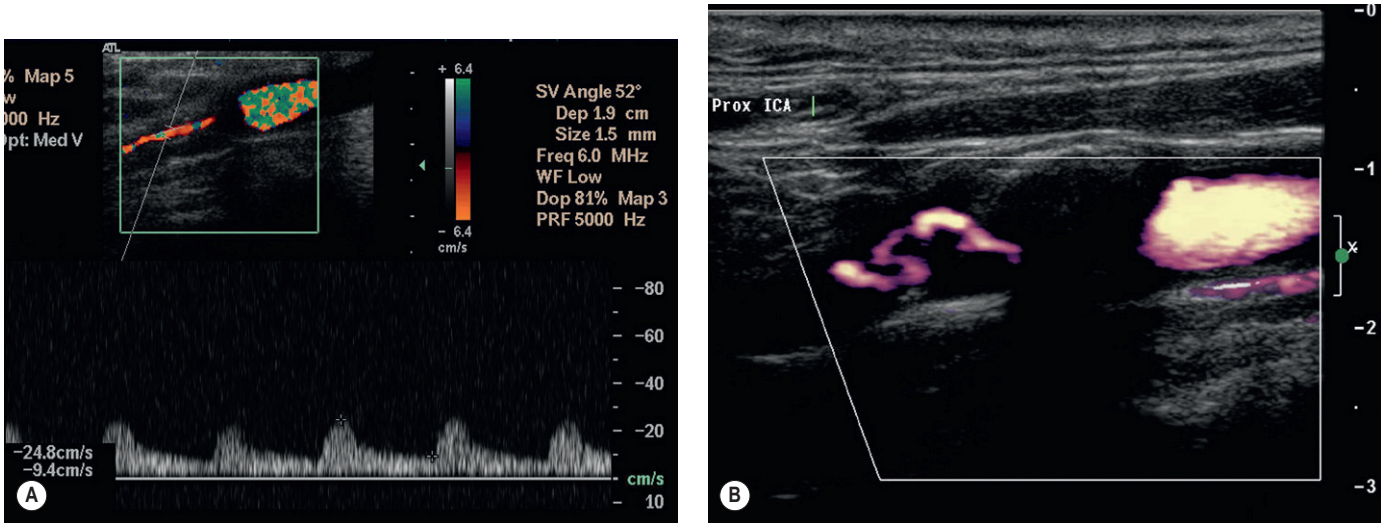

Figure 48.5 **Severe internal carotid artery stenosis. A:** Colour and spectral Doppler of a critical ICA stenosis (>90% diameter stenosis). The colour Doppler image shows a very narrow residual lumen; the spectral display shows low-velocity flow with a peak systolic velocity of 0.25 m/s. **B:** Severe stenosis with a tortuous 'string' lumen demonstrated on power Doppler.

The waveform obtained from any point in the carotid depends not only on local factors such as plaques and stenoses, but also on conditions at sites remote from the point of measurement. Proximal disease, including aortic valve abnormalities[33,34] (Fig. 48.6) or carotid origin stenoses, will affect the waveform; similarly significant distal disease in the carotid siphon can lead to increased pulsatility at proximal sites. Severe stenosis or occlusion of the contralateral carotid artery results in an increased velocity of flow in the remaining carotid, and physiological factors such as tachycardia may also produce waveform changes.

Direct measurement

If the lumen in the diseased arterial segment can be clearly seen then its calibre may be measured directly and compared to the original calibre of the vessel. Either a diameter reduction or an area reduction can be measured. The diameter reduction is a little simpler and quicker but it is necessary also to examine the vessel transversely, so that any asymmetrical distribution of plaque can be taken into account (Fig. 48.7A). The area reduction measurement takes a little longer but takes better account of the effects of asymmetrical plaques (Fig. 48.7B). It is important to define the technique used when reporting results, as a 50% diameter reduction corresponds to a 70% area reduction and there is therefore the potential for significant misunderstanding. Colour and power Doppler allow better assessment of the boundaries of the residual lumen, but care must be taken to ensure that they are set up appropriately so that a distinction between peripheral poorly reflective plaque and inadequate colour fill can be made; conversely, excessive colour gain will result in bleeding of the colour signal beyond the true lumen.

In the presence of calcified plaque or severe disease, the vessel lumen may not be seen sufficiently clearly to allow direct measurement, and the severity of the stenosis must be assessed using Doppler velocity criteria as described earlier.

Provided attention is paid to careful technique, ultrasound has proved accurate for the diagnosis of significant stenoses and occlusions. One report reviewed 16 spectral Doppler studies with 2146 Doppler/arteriogram comparisons:[35] duplex Doppler had an overall sensitivity of 96%, specificity of 86%, positive predictive

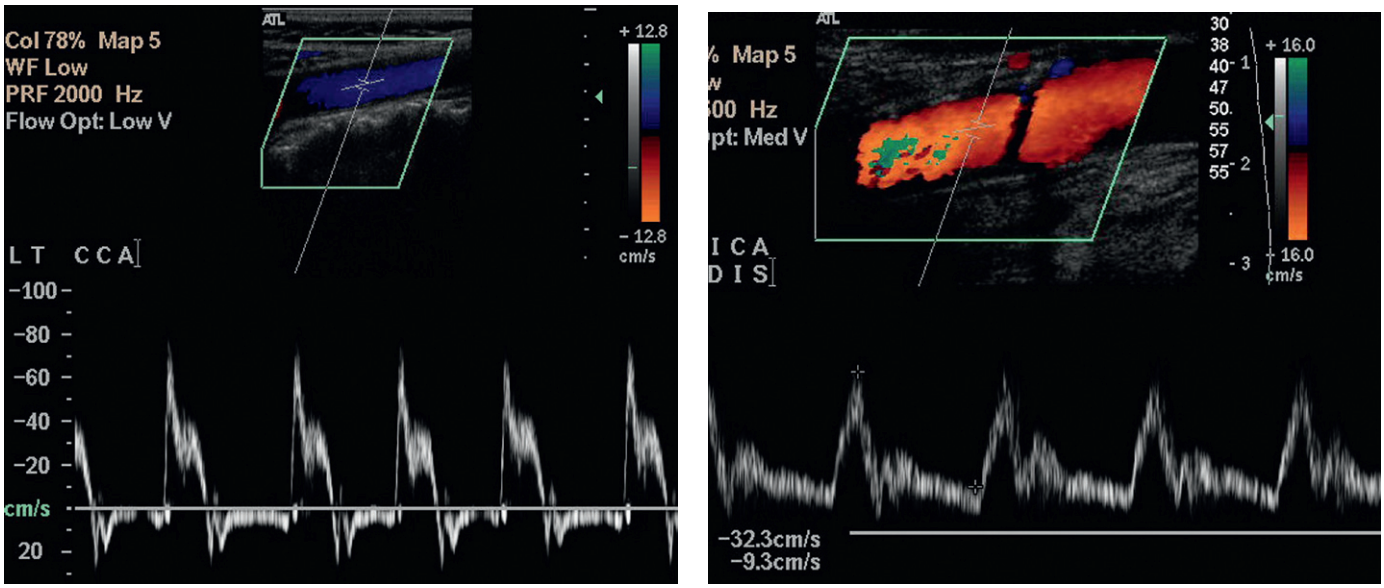

Figure 48.6 **Aortic valve disease. A:** Common carotid artery (CCA) waveform in a patient with severe aortic valve regurgitation showing reversed diastolic flow. **B:** CCA waveform in a patient with aortic valve stenosis showing slowed systolic acceleration.

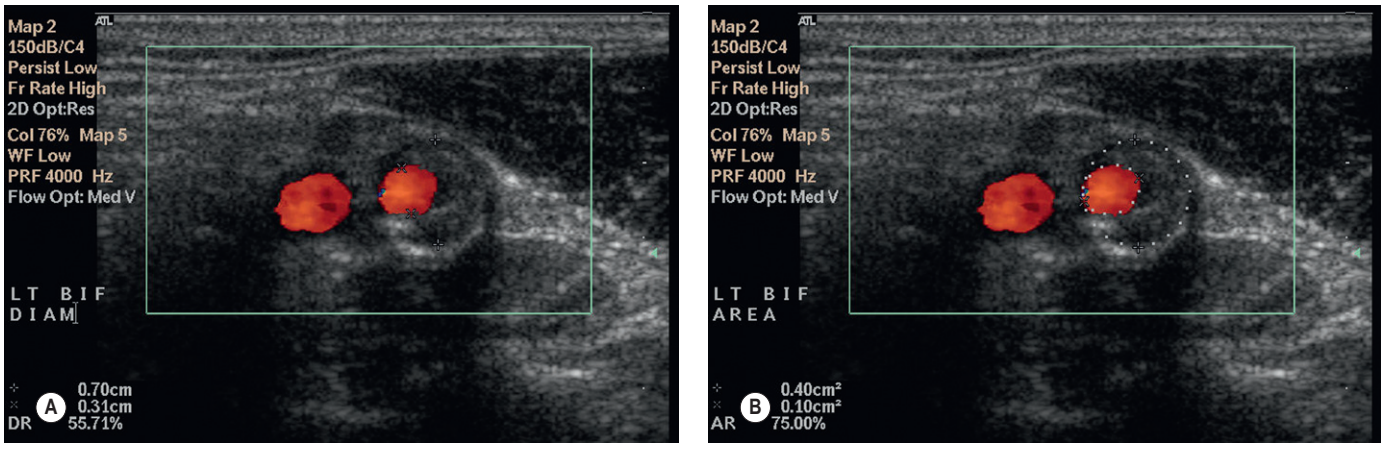

Figure 48.7 **Stenosis measurement. A:** Measurement of a stenosis using a diameter reduction ratio gives a value of 55% diameter reduction. **B:** Measurement of the same stenosis using the area reduction method gives a value of 75% area reduction.

value of 89%, negative predictive value of 94% and accuracy of 91% for the diagnosis of a diameter stenosis greater than 50%. Further studies have confirmed the value of colour Doppler with similar or better levels of accuracy, and also its value in improving diagnostic confidence, clarifying difficult situations and reducing examination times.[36] In particular, the difficult distinction between a critical stenosis and a complete occlusion can be achieved in nearly all cases with the use of colour Doppler.[37,38]

Plaque characteristics

High-resolution imaging of the carotids allows an assessment of the characteristics of the plaques in the diseased areas, and a variety of classifications of plaque morphology have been proposed. Steffen and colleagues[39] proposed a classification of four types and showed that symptoms relating to the diseased carotid artery were more common with the echo-poor types 1 and 2 (Fig. 48.8A), compared to the more reflective types 3 and 4 (Fig. 48.8B). This supports the suggestion that the softer, more friable lipid-rich plaques are more likely to suffer disruption than the firmer, more fibrotic and coherent types.

Plaques may undergo a variety of complications. Haemorrhage can occur into the plaque, leading to a sudden increase in size; the surface may be disrupted, releasing plaque contents into the bloodstream; the surface of the plaque can break down, producing an ulcer in the plaque (Fig. 48.9); and thrombus can form on this

Classification of plaque morphology (from Steffen et al.[39])

Type 1: Predominately echo-poor plaques with a thin reflective cap.
Type 2: Substantially echo-poor lesions with small areas of increased reflectivity.
Type 3: Predominately reflective lesions with small area(s) of low reflectivity of less than 25%.
Type 4: Uniformly reflective lesions.

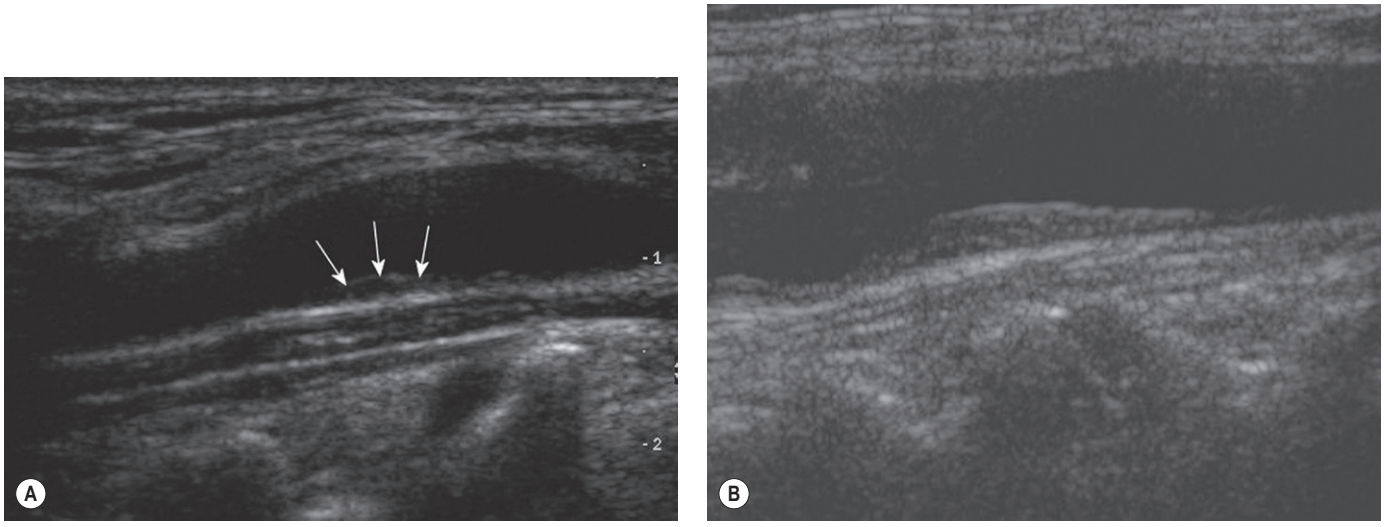

Figure 48.8 Plaques. A: A type 1 plaque with a thin reflective surface but no internal echoes (arrows). **B:** A type 4 plaque with a smooth surface and reflective internal echoes.

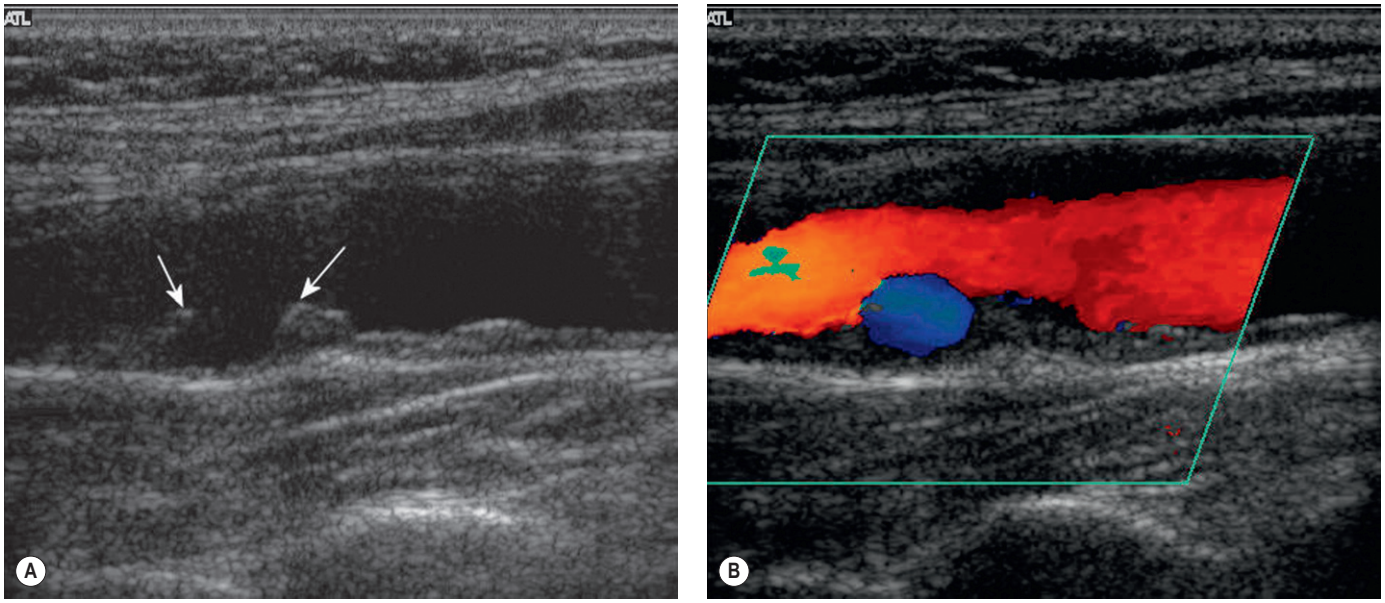

Figure 48.9 An ulcerated plaque. A: Real-time image shows an irregular defect in a partly calcified plaque (arrows). **B:** Colour Doppler shows reversed flow within the defect.

ulcerated surface, and may break off to embolise in distal arteries. Many attempts have been made to assess the ability of ultrasound to diagnose intraplaque haemorrhage or ulceration and to relate these to the risk of stroke; however, the results have not been clear and there is significant disagreement in the literature.[40] The presence of echo-poor areas in a plaque may equally be due to haemorrhage or to aggregations of lipid. Similarly, an irregular surface on a plaque may be due to ulceration or simply to an irregular but intact surface. Some plaques are seen sufficiently clearly for ulceration or adherent thrombus to be identified, and these should be noted. In many examinations this will not be the case, but a smooth, homogeneous, predominantly highly reflective plaque is less likely to be associated with symptoms, whereas an irregular, heterogeneous or echo-poor lesion is of greater concern.[41,42] In patients with more severe degrees of stenosis (>50% diameter reduction), these distinctions are more difficult to make but these larger plaques are more complex and their gross composition is similar, whether they are associated with symptoms, or not.[43]

An attempt has been made to standardise these descriptions for carotid disease in relation to ultrasound and other non-invasive modalities.[44] This proposes that lesions be described in terms of the degree of stenosis, the morphological plaque components and the surface characteristics, where these can be clearly visualised. The suggested classification is given in Table 48.2. A lesion listed as H4, S2, P2 therefore represents one that is producing a stenosis of more than 80% diameter reduction (H4), which has an irregular surface (S2) and is heterogeneous (P2).

Carotid occlusion

The distinction between a very tight stenosis and an occluded artery is important, as the former is still a candidate for surgery whereas the latter is inoperable. It is therefore essential that the ultrasound system is set to look for any residual lumen at both high and low flow settings; echo-enhancing agents can be used if there is any persisting uncertainty. In addition, colour or power Doppler may show small external carotid artery branches close to the occluded internal carotid artery, which might lead to a mistaken impression of patency if they are not recognised.[37,45]

The most common situation is occlusion of an internal carotid artery with the external and common carotid arteries remaining patent. In this circumstance only a single patent branch is apparent at the bifurcation; the occluded artery may also be identified containing some echoes from the luminal thrombus, especially if there is calcification in the vessel wall (Fig. 48.10). The waveform in the common carotid artery may show reduced or absent diastolic flow, as it now reflects the external carotid circulation with its high peripheral resistance. However, if there is significant collateral supply from the external carotid artery to the cerebral arteries through ophthalmic artery and meningeal artery anastomoses, then the external carotid artery waveform may show increased diastolic flow, sometimes called 'internalisation' of external carotid artery flow (Fig. 48.11), and care must be taken to ensure that the single branch at the bifurcation is accurately identified by observing branches or using the temporal tap technique.

Occlusion of the common carotid artery does not always result in occlusion of the internal carotid, as sufficient blood may be provided by retrograde flow down the ipsilateral external carotid artery to maintain the patency of the internal artery; this pattern of

Table 48.2 Classification of carotid plaques (from Thiele et al.[44])

Haemodynamic classification		
H1	0–20% diameter reduction	Normal to mild
H2	20–60% diameter reduction	Moderate
H3	60–80% diameter reduction	Severe
H4	80–99% diameter reduction	Critical
H5	Occluded	
Morphological components		
P1	Homogeneous	
P2	Heterogeneous	
Surface characteristics		
S1	Smooth	
S2	Irregular (defect <2 mm)	
S3	Ulcerated (defect >2 mm)	

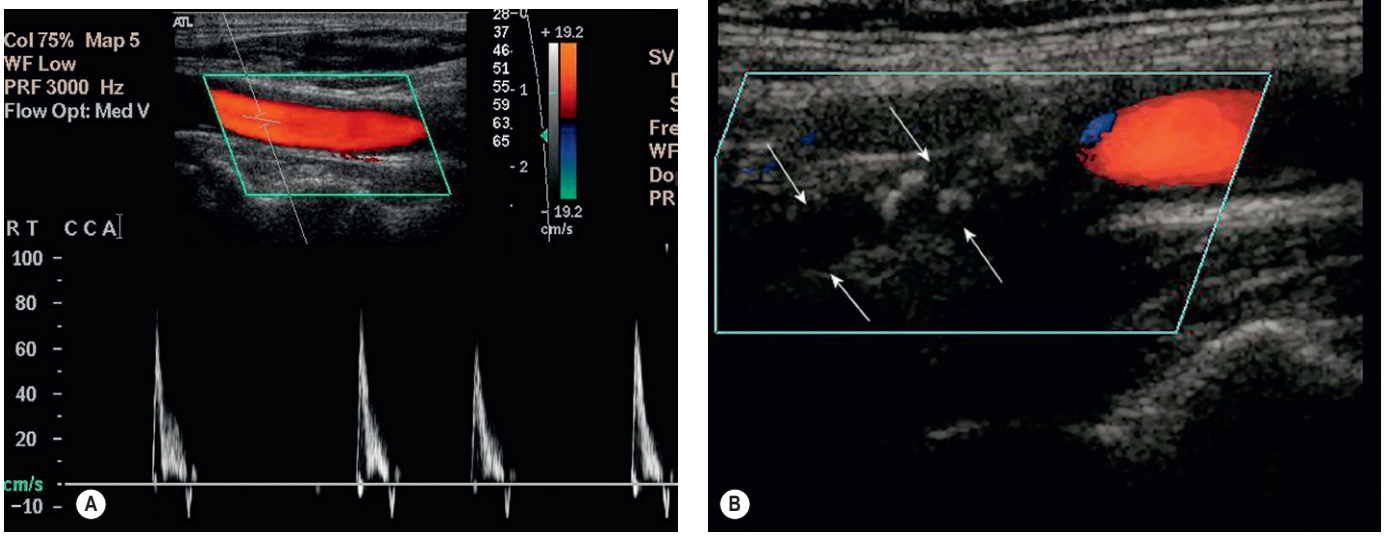

Figure 48.10 Occlusion of the internal carotid artery. A: The waveform in the CCA shows high pulsatility with absence of diastolic flow. **B:** The ICA is shown to be occluded above the bifurcation (arrows).

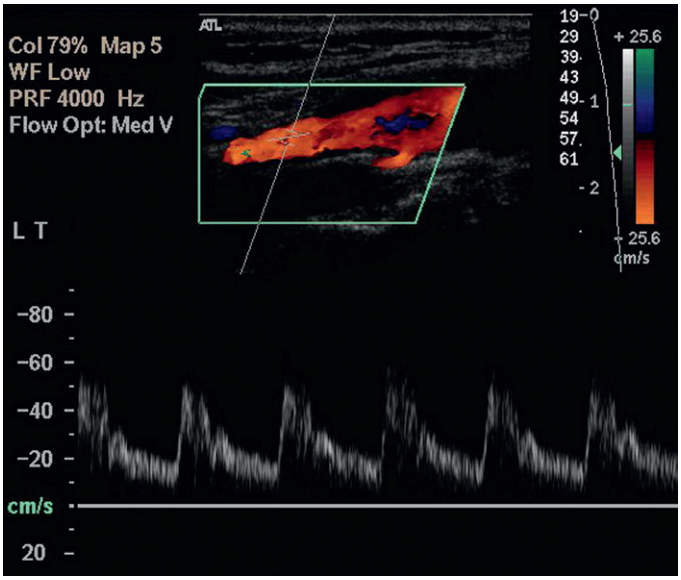

Figure 48.11 Internalisation of external carotid artery waveform. The ECA in a patient with ICA occlusion. A branch artery is present but there is increased diastolic flow.

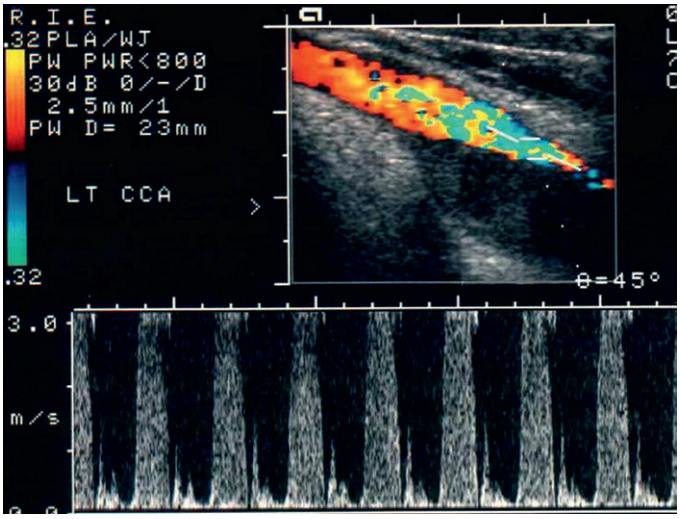

Figure 48.12 Dissection. Colour and spectral Doppler of a dissection involving a common carotid artery. The colour Doppler shows aliasing of the colour signal in the area narrowed by the thrombosed false lumen posteriorly. The spectral display shows a significantly increased velocity in excess of 3.0 m/s.

abnormal flow may be quite confusing if it is not recognised, but it is of clinical importance as these patients can still suffer ischaemic events in the relevant internal carotid artery territory.

Carotid dissection

Carotid artery dissection may result from a variety of causes. Spontaneous dissection may occur as a result of atheroma, or an aortic dissection may extend up the common carotid artery. Dissection may also occur following trauma, such as a hyperextension neck injury, or from iatrogenic damage at arteriography. The appearances and findings on Doppler ultrasound are variable. The vessel may be occluded completely; it may show a smooth tapering stenosis, with or without a recognisable haematoma/thrombosed false lumen being visible (Fig. 48.12); or a membrane with a double lumen may be seen with variable Doppler flow patterns in the two channels.[46] Recanalisation of the occluded vessel is a recognised occurrence and occurs in up to 60% of cases.[47]

Pulsatile cervical masses

The main causes of a pulsatile swelling in the neck are well shown with colour Doppler ultrasound. It allows rapid diagnosis of prominent normal or ectatic arteries in the neck and supraclavicular region. Enlarged lymph nodes, or other cervical masses adjacent to the carotid artery, are also easily defined by ultrasound: careful palpation with the transducer and observation when the patient swallows will allow fixation to the carotid sheath to be assessed (Fig. 48.13).[48]

Aneurysms

Aneurysms of the carotid artery may result from atheroma and mural degeneration; they may also occur following trauma. The diagnosis is usually apparent on ultrasound, but some difficulty may be found in assessing the patency of the internal carotid artery above the aneurysm if this is not clearly visible; flow in the ipsilateral ophthalmic artery is not necessarily evidence of patency, as this may come from collateral filling via the circle of Willis.

Causes of pulsatile cervical masses

- Normal but prominent carotid artery and bulb.
- Ectatic carotid, innominate or subclavian artery.
- Enlarged lymph node adjacent to carotid sheath.
- Aneurysm of the carotid artery.
- Carotid body tumour.

Carotid body tumours

Carotid body tumours arise at the bifurcation and characteristically spread the two branches into a 'wineglass' configuration (Fig. 48.14). Ultrasound shows a poorly reflective mass at the bifurcation and colour Doppler shows this to be a highly vascular lesion displacing the internal and external carotid arteries. The external carotid usually shows a low-resistance pattern of flow on spectral Doppler.[49]

Carotid stents

Carotid stenting has become a recognised technique for treating clinically significant stenoses of the carotid arteries. As well as being of value in identifying and categorising patients prior to the procedure, ultrasound also has a role in follow-up to identify post-procedural complications. The presence of the stent alters the characteristics and compliance of the arterial wall, so that the usual criteria for stenosis (Table 48.3) must be adapted for assessment of stenoses associated with stents. These modified criteria are still being developed but those suggested by Armstrong et al.[50] currently seem to allow reasonable assessments to be made regarding stent stenoses and the need for further intervention (Table 48.3).

Complications relating to carotid stents include inadequate stent deployment with suboptimal expansion, or lack of apposition to the arterial wall, stent deformity, residual atheromatous stenosis above or below the stent, migration of the stent, development of stenosis in the stent as the result of myointimal hyperplasia, or thrombosis and occlusion. Ultrasound can identify these and, at present, most centres use ultrasound as part of a surveillance programme to follow up carotid stent procedures.

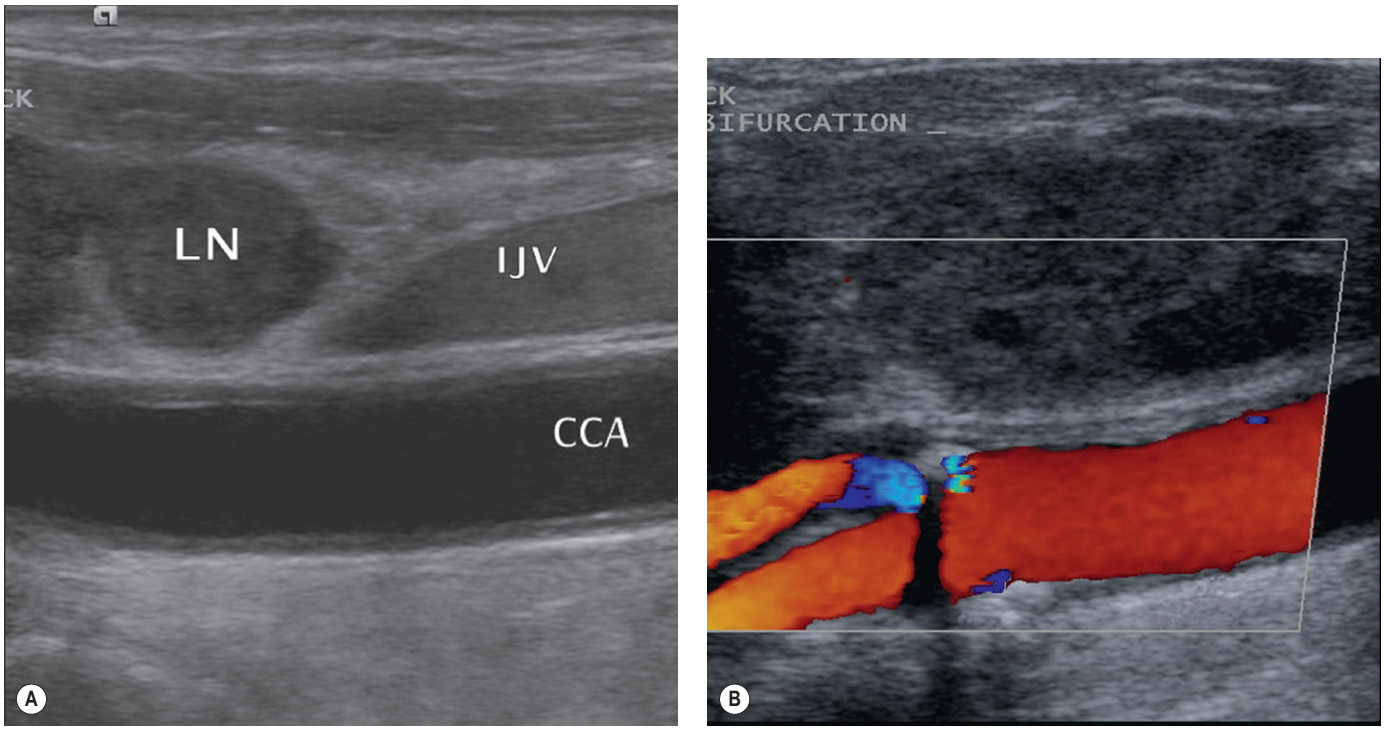

Figure 48.13 Stenosis caused by a tumour. A: Enlarged cervical lymph nodes (LN) from oropharyngeal carcinoma compressing the internal jugular vein (IJV), which contains thrombus but not affecting the adjacent carotid artery (CCA). **B:** Colour Doppler showing nodes adjacent to the bifurcation but there is no evidence of arterial compression or invasion.

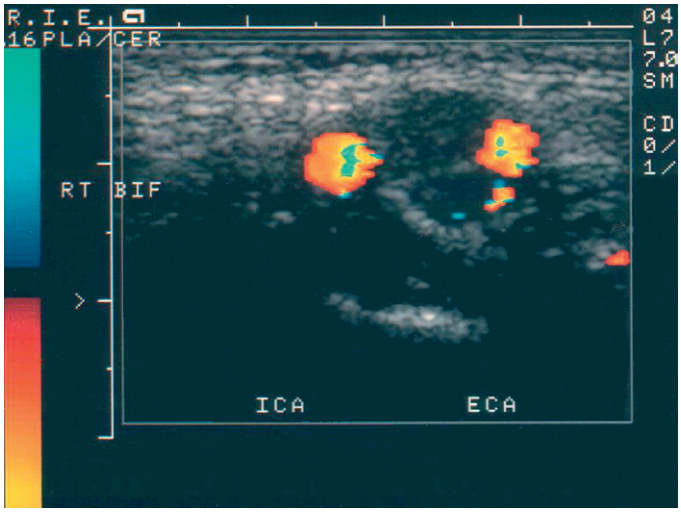

Figure 48.14 Carotid body tumour. Transverse scan of the bifurcation in a patient with a carotid body tumour showing separation of the ICA and ECA by the poorly reflective tumour.

Table 48.3 Diagnostic criteria for Doppler diagnosis of carotid stent stenosis (reproduced with permission from Armstrong et al.[50])

Diameter stenosis	Peak systolic velocity ICA (m/s)	End-diastolic velocity ICA (m/s)	PSV systolic ratio[a]
50%	>1.5	<1.25	>2
75%	>3.0	>1.25	>4

[a]*PSV ratio calculated from PSV in the stent stenosis compared with PSV in proximal stent, or CCA.*

The vertebral arteries

The vertebral arteries are normally examined briefly to ascertain their patency and the direction of flow within them. A more detailed examination will be required in patients with symptoms related to the posterior cerebral circulation. Failure to visualise an artery in the vertebral canal, in the lower neck between the subclavian artery and the cervical spine, or behind the lateral mass of the atlas, may be due to occlusion or to congenital absence/hypoplasia. In some patients specific abnormalities of the waveform may be seen which are indicative of local disease in a vertebral artery. These include colour and spectral Doppler evidence of a stenosis in the segment being examined. Alternatively, damping from significant disease affecting the proximal vertebral artery or subclavian artery may be seen (Fig. 48.15).[21] The clinical significance of vertebral artery disease is less clear than in the carotids, as the basilar artery and posterior fossa circulation is supplied by the two vertebral arteries and from the circle of Willis, allowing compensatory flow in the presence of unilateral vertebral artery obstruction or stenosis.

The phenomenon of vertebral steal occurs when a severe proximal subclavian artery stenosis or occlusion is present and blood reaches the affected arm by passing down the ipsilateral vertebral artery from the posterior fossa circulation, which is being supplied from the other vertebral artery or the circle of Willis (see Fig. 48.3B). Reversed flow is seen in the affected vertebral artery on colour and spectral Doppler. A biphasic waveform may be seen in patients with a developing steal situation; in these cases exercising the relevant arm may increase blood flow and produce full reversal of flow in the vertebral artery. Alternatively, blowing up a blood pressure cuff to occlude circulation to the arm for a couple of minutes then releasing it produces reactive hyperaemia which will also increase blood flow to the arm.

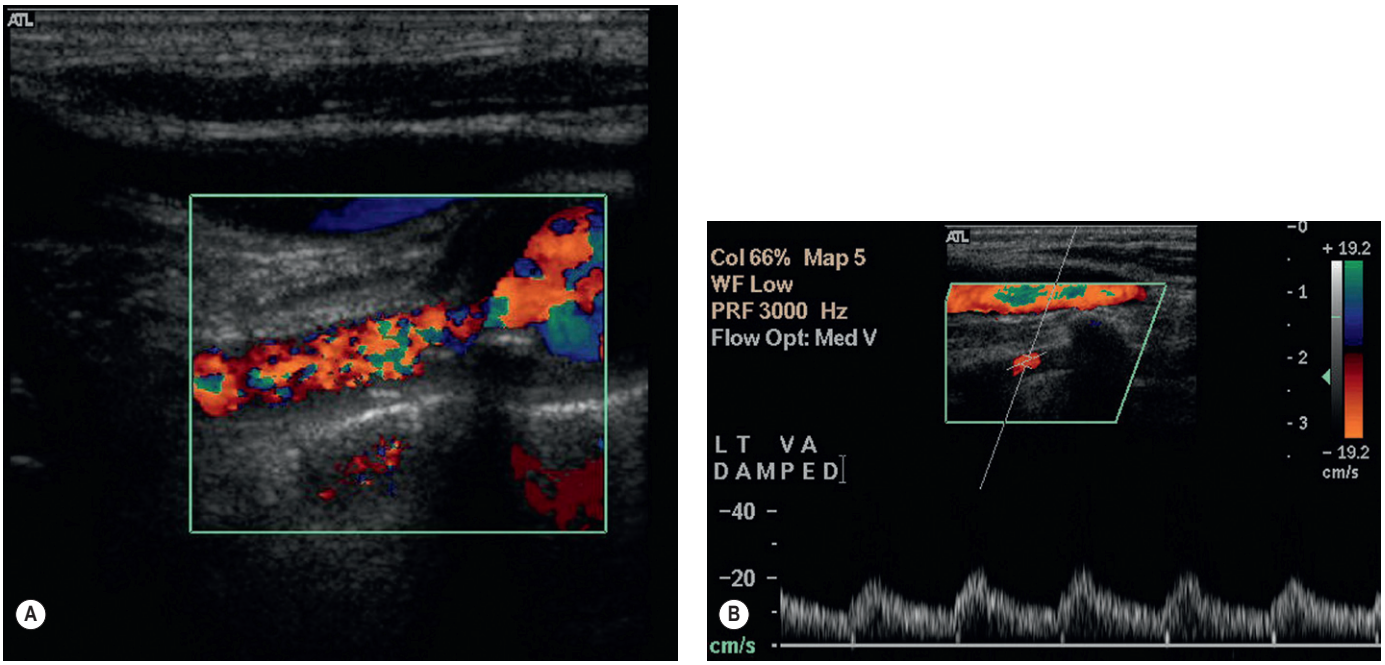

Figure 48.15 Vertebral artery disease. A: Stenosis with turbulence at the origin of a vertebral artery. **B:** Damped flow in the cervical segment of the vertebral artery above the stenosis.

TRANSCRANIAL DOPPLER ULTRASOUND

One of the first clinical applications of ultrasound in diagnosis was the assessment of midline intracranial structures using A-scan techniques. More recently high quality imaging and Doppler studies have been obtained in neonates through the patent fontanelles, or through the relatively thin bone of the neonatal skull. In 1982 Aaslid et al.[51] reported on the development of a pulsed Doppler technique which could obtain information on blood flow in the major intracranial vessels in adults, and since then the technique of pulsed transcranial Doppler (TCD) has been further developed. The technique provides useful information on the direction and velocity of blood flow and the changes that may occur with various physiological, pharmacological or pathological conditions, including intraoperative and postoperative monitoring of patients undergoing carotid stenting or endarterectomy.

More recently, developments in system performance and transducer technology have enabled real-time colour transcranial Doppler examinations to be performed, thus allowing more precise localisation of blood flow information than has been possible with 'blind' pulsed transcranial Doppler.[52]

TCD also has potential therapeutic applications in large artery ischaemic stroke. Ultrasound applied to a fluid causes formation of small bubbles which vibrate and enhance thrombus dissolution.[53] Following promising results in observational studies, the potential therapeutic effects of Doppler ultrasound for treatment of acute ischaemic stroke secondary to a large intracranial artery occlusion are now being evaluated in randomised trials (see below).[54]

The main problem in transcranial ultrasound techniques, particularly in adults, remains the marked attenuation of sound by the bone of the skull vault. Not only is the sound strongly reflected at the soft tissue/bone interfaces as it enters and leaves the skull, but the multiple interfaces in the diploë also contribute to attenuation by scattering the sound.[55] It has been shown that the degree of attenuation varies with age, sex and race, tending to be greater in older, female and black subjects and less marked in younger, male and white subjects.[56]

Echo contrast agents can be injected intravenously to help overcome beam attenuation due to poor bone windows. However, these prolong the examination and turn a completely non-invasive technique into a (slightly) more invasive one, so are best used in specific circumstances. These agents must be able to pass through the heart (without being altered by pressure changes) and lungs (<10 μm in diameter) to reach the cerebral circulation. Use of contrast agents improved vessel and tissue visualisation in about 70% of patients who had no visualisation of intracranial structures on non-contrast TCD, thus raising the success rate of colour TCD to 90% for all examinations.[52]

Anatomy

The internal carotid arteries (ICAs) enter the skull through the foramina lacera in the middle cranial fossae, passing up through the cavernous sinuses on each side of the sphenoid bone to divide on each side into the anterior and middle cerebral arteries. The anterior cerebral arteries (ACAs) pass forward and medially to the inter-hemispheric fissure, where they turn superiorly to run around the anterior aspect of the corpus callosum. The middle cerebral arteries (MCA) pass laterally into the sylvian fissure, where they turn posteriorly to pass in the fissure superiorly towards the parietal region. The vertebral arteries (VAs) enter the skull through the foramen magnum and thereafter join with each other to form the basilar artery (BA) at the level of the lower pons. This runs up the anterior aspect of the pons to divide at the upper margin into the posterior cerebral arteries (PCAs). The PCAs pass laterally and posteriorly around the cerebral peduncles of the midbrain to supply the occipital lobes. The normal circle of Willis is completed by the anterior communicating artery (ACoA) linking the two ACAs, and the two posterior communicating arteries (PCoAs) linking the terminations of the ICAs with the PCAs. The complete, classic circle of Willis is present in only 50–60% of the population.[57] In the remainder there is a wide variation in the configuration and connections of the terminal branches of the four supply vessels. The most common variants are hypoplasia or absence of the proximal ACA on one side, the distal ACA's territory being supplied from the opposite ICA via the ACoA (20%); and absence or hypoplasia of the proximal PCA, with the distal PCA being supplied from the ipsilateral ICA via the PCoA (30%).

Table 48.4 The segmental divisions of the major cerebral arteries (data from Day[58])

A1	Horizontal segment of the anterior cerebral artery (pre-communicating artery)
A2	Segment of the anterior cerebral artery after the anterior communicating artery
M1	Horizontal segment of the middle cerebral artery
M2	Interior segment
M3	Opercular segment
P1	Peduncular segment of the posterior cerebral artery (pre-communicating artery)
P2	Ambient cistern segment of the artery (post-communicating artery)

The main branches of the circle of Willis are divided into segments as listed in Table 48.4.[58] These segments can be used for descriptive purposes when reporting changes in the vessels seen on ultrasound.

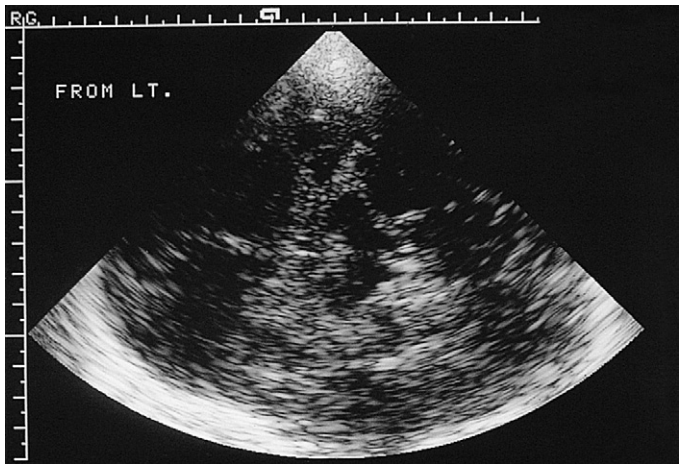

Figure 48.16 Transcranial image. Axial view of the normal brain through the temporal bone window. The face is to the left and occiput to the right. Note the brainstem (like a butterfly in the centre of the image) and third ventricle (midline bright echo to the left of the brainstem).

Examination technique

The three main ultrasonic access portals for examination of the intracranial vessels are the transtemporal window, the suboccipital window and the transorbital window. The transtemporal window is used for the circle of Willis and its major branches; the suboccipital window for the vertebral arteries and the lower basilar artery; and the transorbital window provides alternative access to the internal carotid, ophthalmic and anterior cerebral arteries.[59] A low-frequency (2 MHz) probe is used and the system is set for maximum sensitivity. Maximum power can be used through the transtemporal window in adults but it is essential to reduce the power output to the minimum necessary for the orbital approach to avoid damage to the lens. In neonates the lowest practical power output should be used at all times, regardless of the approach window used.

The transtemporal window

The examination is best started with the transtemporal approach. The size of the window can vary considerably and some searching may be required to define the useful limits of the thinner segment. A generous application of gel is necessary to ensure good sound transmission, otherwise air pockets trapped in the subject's hair will degrade the image. The transducer is placed on the side of the patient's head in front of and above the external auditory meatus and a transverse (axial) scan of the brain obtained (Fig. 48.16). A satisfactory view of the brain on the greyscale image indicates that the bone window is good, and so the arteries should be visible unless pathological. Failure to identify the cerebral peduncles, perisellar region or third ventricle usually indicates an inadequate bone window. A completely impenetrable temporal bone window occurs in about 10% of subjects, most of them elderly. Colour or power Doppler will show the location of the major cerebral arteries; usually the ipsilateral MCA is the easiest to locate: this can then be followed back to the region of the circle of Willis and the other branches tracked from there. Some cranial and caudad angling of the probe may be required to follow the artery. It is usually not possible to get the full circle of Willis on a single scan plane as the components are at different levels. The direction of flow in the vessels is noted, particularly in the A1 segments of the ACAs, as these are a major collateral pathway. Power Doppler is more sensitive for locating the arteries[60] but gives no information on the direction of flow, spectral or colour Doppler being required to make this assessment (Fig. 48.17). The use of echo-enhancing agents improves visualisation significantly compared with colour or power Doppler.[60] The three communicating arteries may not all be visible, owing to their small size or to congenital absence. The proximal and distal segments of the PCAs are also visible from the temporal approach as they pass around the lateral aspect of the cerebral peduncle to run posteriorly on the inferior aspect of the occipital lobe. The termination of the BA will also be seen in about 50% of subjects,[61] more often with power Doppler.

The ICA can be examined in the axial plane by angling the probe inferiorly to locate it in the foramen lacerum, and then angling progressively more superiorly to follow the artery through the cavernous sinus to its bifurcation. The termination of the ICA can also be visualised well by turning the transducer through 90° and scanning the medial side of the middle cranial fossa. Because of the curves of the carotid siphon several scan planes will be required to image the ICA fully.

The suboccipital window

The suboccipital window is located by scanning in the midline posteriorly at the level of the hairline and angling the probe upwards towards the foramen magnum. The third part of the VA is identified running towards the foramen magnum and is followed superiorly. Visualisation may be improved by scanning just to the side of the midline, as the central ligaments are relatively dense. The VAs can be followed superiorly through the foramen: their junction to form the BA may be identified if this lies low enough in the posterior fossa.

The transorbital window

The transorbital window is used to direct the ultrasound beam upwards and medially towards the apex of the orbit; the ophthalmic artery (OA), the carotid siphon and the contralateral ACA can be examined. The power output is reduced to the minimum, the transducer is placed on the closed eyelid, and sterile aqueous gel is used, rather than ordinary ultrasound gel, as this is less irritant for the eye. It is less convenient for colour Doppler examinations as the transducers are relatively bulky, and the need for this approach is reduced as the ACAs can usually be seen on transtemporal scanning. It is important that the flow in the OA is assessed close to the apex of the orbit, rather than immediately behind the eye, as flow in the retinal artery is always directed out towards the eye. The collaterals between the orbital branches of the external carotid circulation and the OA lie in the mid and posterior orbit, and blood

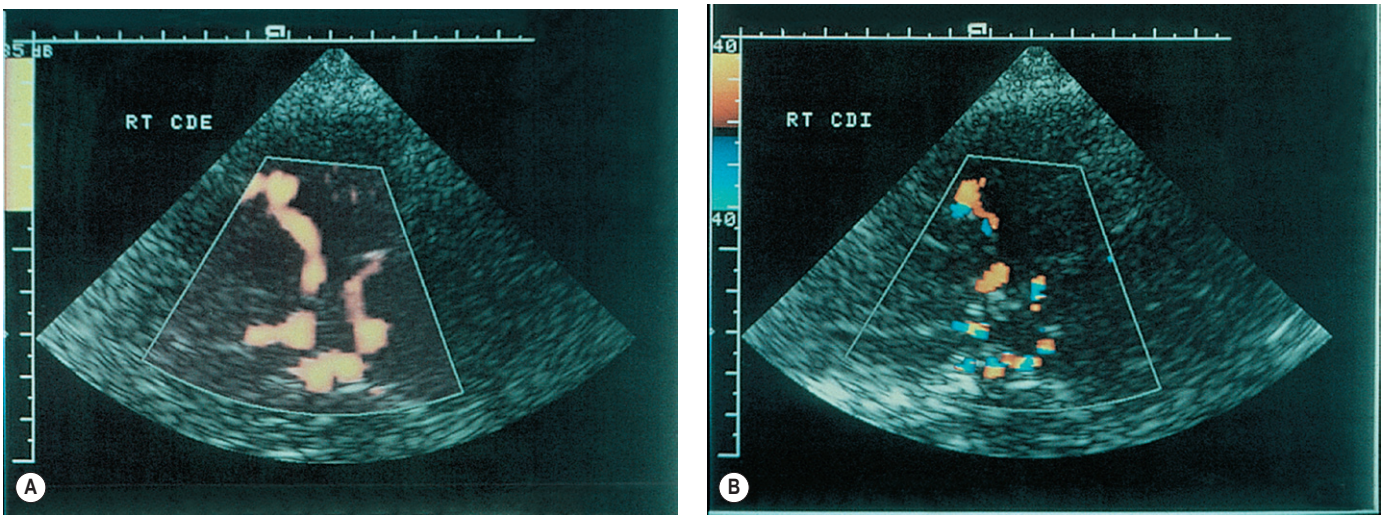

Figure 48.17 **Normal circle of Willis** viewed axially through the temporal bone window. **A:** Power Doppler and **B:** colour Doppler imaging. Note that in **A** the continuity of the arteries is much clearer and smaller branches are more visible than in **B**.

passes through these to supply the circle of Willis through the ophthalmic artery if the ipsilateral ICA is occluded.

Transcranial pulsed Doppler

The original technique of transcranial Doppler using pulsed Doppler has been developed and refined over the years. If appropriate colour Doppler equipment is not available, or is impractical to use (as may be the case in the operating theatre, where space at the patient's head is limited or prolonged monitoring is required), 'ordinary' TCD still has a role to play.

Examination technique

Using the transtemporal window, the bifurcation of the ipsilateral ICA into the MCA and ACA can usually be detected at a depth of about 65 mm and is a useful landmark – the MCA flow is directed towards the probe and that of the ACA away from it. The MCA and ACA can then be followed by adjusting to lesser and greater depths, respectively. The MCA is identified to as shallow a depth as 35 mm (if it cannot be tracked this superficially, then the insonated artery is probably not the MCA). The ipsilateral ACA is located between 65 and 75 mm deep, and by angling the probe more anteriorly than for the MCA. An arterial signal with flow directed away from the probe is demonstrated in the ACA in normal subjects. The patency of the ACA can be assessed by compressing the ipsilateral common carotid artery in the neck and the demonstration of flow reversal in the ACA. However, this is not recommended in patients suspected of having cerebrovascular disease, and is rarely necessary in any case. The PCA is identified by angling the probe posteriorly from the ICA bifurcation until a lower-velocity signal than that found in the MCA is detected directed towards the probe. This can usually only be tracked out to a depth of 55 mm, as at that point the PCA curves more deeply and posteriorly around the brainstem. The PCA can be tracked medially to the terminal basilar artery at around 75 mm, where bidirectional flow indicates the basilar bifurcation into the PCAs, which are directed one towards and the other away from the probe. As with colour Doppler, small changes of probe angle are required to follow the paths of the arteries (Fig. 48.18).

The carotid siphon is identified through the transorbital approach at a depth of 55–70 mm. The direction of flow will depend on whether the lower part of the siphon is in the beam (when flow will be towards the transducer) or the upper segment (when flow will be away from the transducer). As with colour Doppler, the power

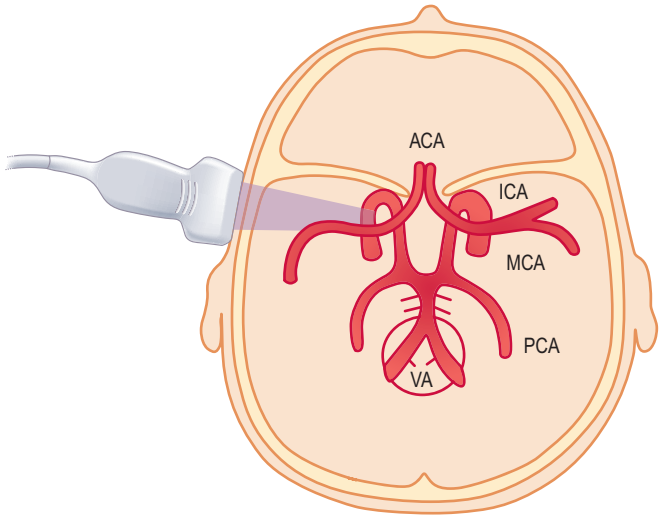

Figure 48.18 **Positioning of the probe and scan angles for pulsed TCD.**

should be reduced to the minimum necessary for an adequate examination so as to reduce the potential for damage to the lens of the eye. The vertebral arteries are located through the suboccipital approach at a depth of 40–70 mm. The origin of the basilar artery may be demonstrated a little deeper, at 70–80 mm, and traced as it passes anterior to the brainstem to a depth of 100 mm.

The normal intracranial arterial velocities depend on which artery is being insonated and the age of the patient.[62] In general the MCA velocity is higher than that of the ACA, PCA, BA and ICA, in that order, and all decline with age (Table 48.5). The MCA velocities (peak or mean) should not differ by more than 20%, as a rule of thumb. Colour Doppler allows more accurate reading of velocity by adjusting for the angle of insonation.[63]

It should be recognised that, as with any ultrasound technique, what may look easy to the unschooled observer is not: there are numerous pitfalls and tricks to obtaining good results, which only come with practice. Operators must be highly motivated, experienced and diligent in their attention to detail to obtain good results with any TCD technique.

Table 48.5 Normal average peak and time-averaged mean flow velocity values (cm/s) for the main intracranial arteries in subjects aged 40–60 years. Details of values for other ages are given in references 61,62 and 63

	Peak	Range	Time-averaged mean	Range
MCA	91	57–125	58	35–81
ACA	86	46–127	53	32–74
PCA	60	19–101	37	17–56

Applications of colour TCD imaging and pulsed TCD

- Identification of collateral pathways, occluded or stenosed arteries.
- Vasospasm complicating SAH.
- Patent foramen ovale detection.
- Brain death (not a medico legal requirement).
- Assessment of intracranial venous system.

Pulsed wave

- Monitoring during carotid surgery and in neuro-intensive care.
- Emboli detection.
- Assessment of cerebral perfusion reserve.

Colour Doppler

- Detection of intracranial aneurysms.
- Identification of feeder vessels to AVMs.

Applications

Many of the original applications of pulsed TCD are more easily and efficiently performed with colour or power Doppler. This allows easier and more consistent identification of vessel segments and correction for angle of insonation, which may be useful if longitudinal studies are being undertaken, as the same segment of vessel can be located and assessed with greater certainty on sequential examinations. Power Doppler has better signal to noise ratio than frequency-based colour Doppler, has little dependence on the angle of insonation and is not subject to aliasing so is useful where increased sensitivity for detecting small vascular structures is required (such as detection of intracranial aneurysms or delineation of focal stenoses). Frequency-based colour Doppler is useful where directional information is important, such as determining the direction of flow in potential collateral intracranial arteries of the circle of Willis. Either Doppler imaging or spectral pulsed Doppler can be used for a range of tasks and applications. There is some variation between the different countries in the use of these techniques, and individual centres will have their own preference based on local expertise and equipment.

For many of these applications the location and accessibility of the patient will determine whether colour Doppler or pulsed TCD is used. For example, it is much more convenient to take a small pulsed TCD machine to the intensive therapy unit, into theatre or to an immobile ward patient than to move a larger colour Doppler system and, for the most part, pulsed TCD will give perfectly adequate information on waveform and velocity – the probe can be mounted on the temporal bone window and held in place with a headband for continuous monitoring while the small machine footprint means that it is less likely to get in the way. The probes provided with large colour Doppler machines are generally not suitable for continuous monitoring, are heavy and uncomfortable to hold or to have placed against any of the bone windows for long. Circumstances in which pulsed TCD is used in preference to Doppler imaging TCD include the assessment of cerebral perfusion reserve and emboli counting. In the latter case, the patient can be seated reading or watching television during the recording period which may last up to an hour, with the ultrasound probe fixed in place with the headband.

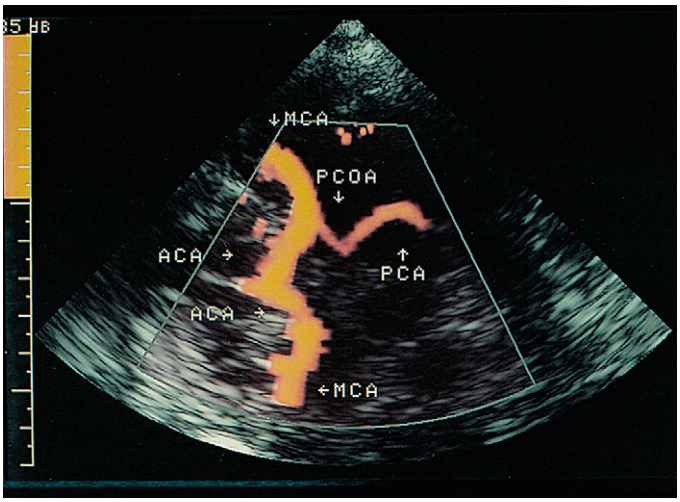

Figure 48.19 Posterior communicating artery. Large PCoA connecting the BA to the ICA in a patient with ipsilateral ICA occlusion in the neck. The flow in the PCoA was from BA to ICA.

Cerebral perfusion reserve

Cerebral perfusion reserve assessment prior to carotid endarterectomy looks at the ability of the cerebral vessels to dilate in response to a raised Pco_2, which is achieved by patient breath-holding, CO_2 rebreathing or acetazolamide injection.[64] Some vascular surgeons find this a useful technique but others find that it offers no great advantage. Some vascular surgeons find knowledge of the adequacy of collateral pathways (in the ACoA or PCoA) useful in assessing the risk of carotid surgery (Fig. 48.19).

Emboli counting

Emboli counting[65] has yet to find a place in clinical practice although it has been used as a surrogate outcome measure in secondary stroke prevention trials. It requires sensitive equipment, regular quality control, rigorous operator training and a lot of time in which both to collect and analyse the recordings and to develop the skills required to identify the characteristic embolic noises correctly (Fig. 48.20). Although automated embolus detection systems have been developed they are not yet very reliable: review by an experienced operator to exclude artefacts and to detect small emboli is still required. At least 20 minutes (preferably 60 minutes) of recording time from both MCAs is required, with corresponding analysis time. Emboli produce a characteristic 'popping' noise superimposed on the Doppler audio signal, corresponding with a high-intensity blip visible in the waveform. It has not yet proved possible to differentiate reliably between emboli of different sizes or compositions. Emboli are found in patients with a tight rather than a moderate carotid stenosis; they are more frequent before the start of aspirin treatment rather than after[66] and they decline in frequency with time following a stroke, but the clinical value of these observations is not yet clear. Embolic signals are frequently found in patients with mechanical artificial heart valves, but these are now known to be due to air drawn out of solution by the vortex effect of the value opening and closing (Fig. 48.21), not to particulate matter.[67] One clinical use of emboli detection is the diagnosis of a patent foramen ovale: microbubbles in agitated saline injected into

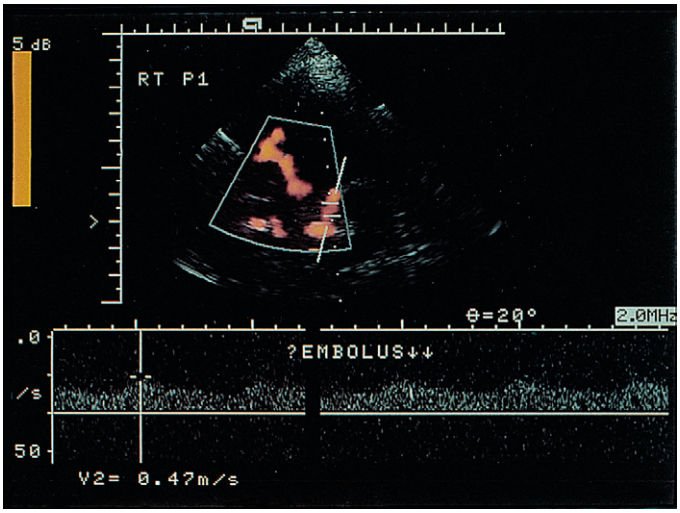

Figure 48.20 **An embolus signal detected in the PCA.**

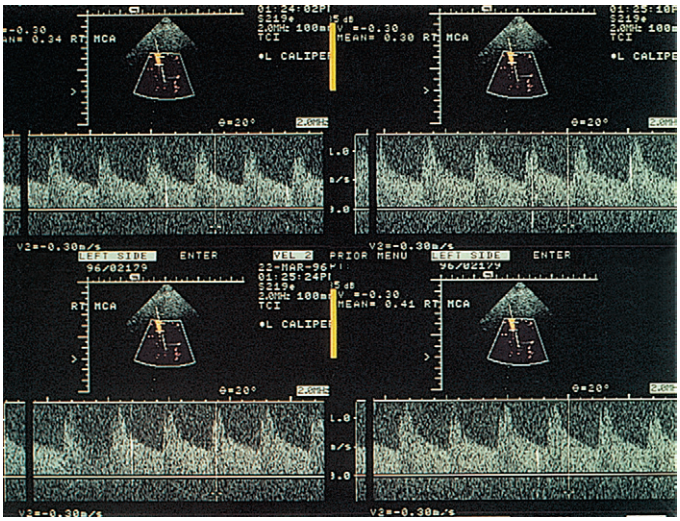

Figure 48.21 **Embolic signals in the MCA** in a patient with a mechanical artificial heart valve. Note the frequency of these signals, which were completely asymptomatic and are now known to be due to microbubbles.[44]

an arm vein should be removed by the lungs and not enter the systemic side of the circulation, unless the foramen ovale (or another right-to-left shunt) is patent, in which case the characteristic embolic noises can be detected in the MCA.[68]

Patient monitoring

Pulsed TCD is used when a prolonged period of continuous monitoring is required, such as in neuro-intensive care or during neurosurgical or carotid arterial operations. The MCA is insonated and the probe fixed to the temporal region with a headband. In neuro-intensive care pulsed TCD can be used as a surrogate measure of intracranial pressure (ICP) and cerebral blood flow. A fall in the diastolic velocity towards zero and an increase in pulsatility indicates rising ICP. However, TCD is not much used in the UK for this purpose, direct ICP monitoring being more usual.

TCD is used by some vascular surgeons in the intraoperative monitoring of patients undergoing carotid endarterectomy. The effects of clamping the carotid can be monitored so that the need for a shunt can be assessed. Tiny air emboli are a feature of this procedure, especially during shunt insertion and removal; these can be seen on the spectral trace as small, intensely reflective foci which, when multiple and occurring in rapid succession, sound rather like a Velcro fastening being undone. Particulate emboli produce a similar though generally louder noise, although it is not usually possible to distinguish between air and solid emboli. Occasional small air emboli may be accepted, but recurrent or showers of multiple emboli are a cause for concern. Postoperatively, cerebral blood flow can be monitored so that any significant reduction can be identified as soon as possible and remedial action taken.

Ischaemic stroke

Applications in major intracranial arterial occlusion in acute stroke (Fig. 48.22) can be identified using TCD, or with greater confidence using colour Doppler, and the response to therapy (e.g. recanalisation) can be monitored,[69] although currently this is a research rather than a clinical application and the findings are still not routinely used for clinical management. The evidence to support the use of TCD in identifying acute arterial occlusion,[52,70–72] assisting in determining prognosis,[73] identifying intracranial stenoses, monitoring response to reperfusion therapy (either intravenous or through more interventional means)[72,74] and therapeutically to enhance thrombus dissolution[75] is accumulating.

Intracranial larger artery occlusion, such as of the MCA, can be identified with TCD with a typical sensitivity of 83% and specificity of 94% (without the use of contrast agents) compared with magnetic resonance angiography[71] and of 100% when compared with intra-arterial digital subtraction angiography.[70] Persistent occlusion of the MCA main stem at 6 hours after stroke is associated with a poor prognosis compared with either no occlusion at presentation or with signs of early reperfusion.[73]

A classification system for documenting intracranial large artery occlusion and monitoring response to therapy on TCD has been adapted[76] from similar classifications for intra-arterial angiography for diagnosing coronary artery and intracranial large artery occlusion. The Thrombolysis in Brain Ischaemia (TIBI) classification for TCD uses flow signals (rather than angiographic appearance) to assign one of six categories of arterial status ranging from no flow, through minimal flow, blunted flow, dampened flow, stenotic to normal.[74,76] This is a useful operational standard for diagnosing the status of intracranial large arteries in acute ischaemic stroke and monitoring the response to treatment.

Intracranial arterial stenoses can be readily identified with spectral Doppler or colour TCD imaging (Fig. 48.23): these may be the cause of TIAs in patients in whom no arterial disease is present in the neck.[52,72] In our predominantly white, northern European population, intracranial stenoses are rare, but are said to be a common finding in patients with TIA and stroke in other populations, particularly Chinese Asians. Certainly it is worth looking for intracranial stenoses in patients with recurrent symptoms but no atheromatous stenosis in the carotid arteries or more proximal source of embolus.

An exciting development with TCD is its potential therapeutic usefulness to enhance spontaneous and pharmacological thrombolysis.[75] The main evidence to date comes from a trial in which 126 patients who all received intravenous recombinant tissue plasminogen activator (rt-PA) within 3 hours of acute ischaemic stroke were randomised to receive continuous TCD or placebo (probe placed on temporal bone window but not switched on) with the end point being blinded assessment of complete recanalisation or dramatic clinical recovery.[75] Forty-nine per cent of TCD-treated and 30% of non-TCD-treated patients had early recanalisation or dramatic clinical recovery (p = 0.03), although there was no difference in functional outcome at 3 months. These early and encouraging results are now being tested in further randomised trials, in some cases with addition of ultrasound contrast agents to see whether this further enhances thrombus dissolution. However, it is as yet unclear whether the enhanced thrombus lysis with TCD in

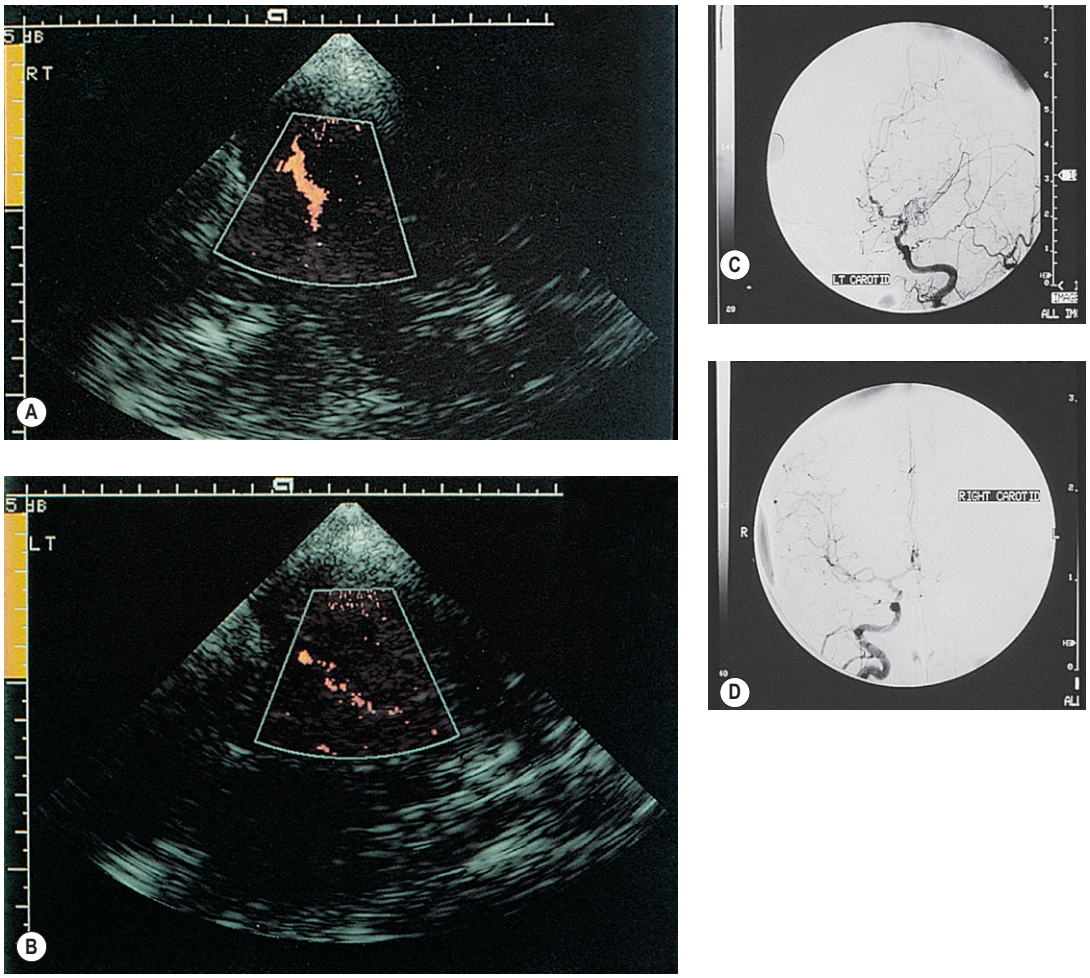

Figure 48.22 **Power Doppler examination** from right **(A)** and left **(B)** MCAs with corresponding angiography of right **(C)** and left **(D)** MCAs (performed within 30 minutes of the TCD). The left MCA is occluded near its origin and there are numerous dilated lenticulostriate arteries supplying collateral flow to the MCA territory: these are seen on TCD as pinpoints of colour in the absence of any clear MCA signal. Compare with right MCA signal in **A**.

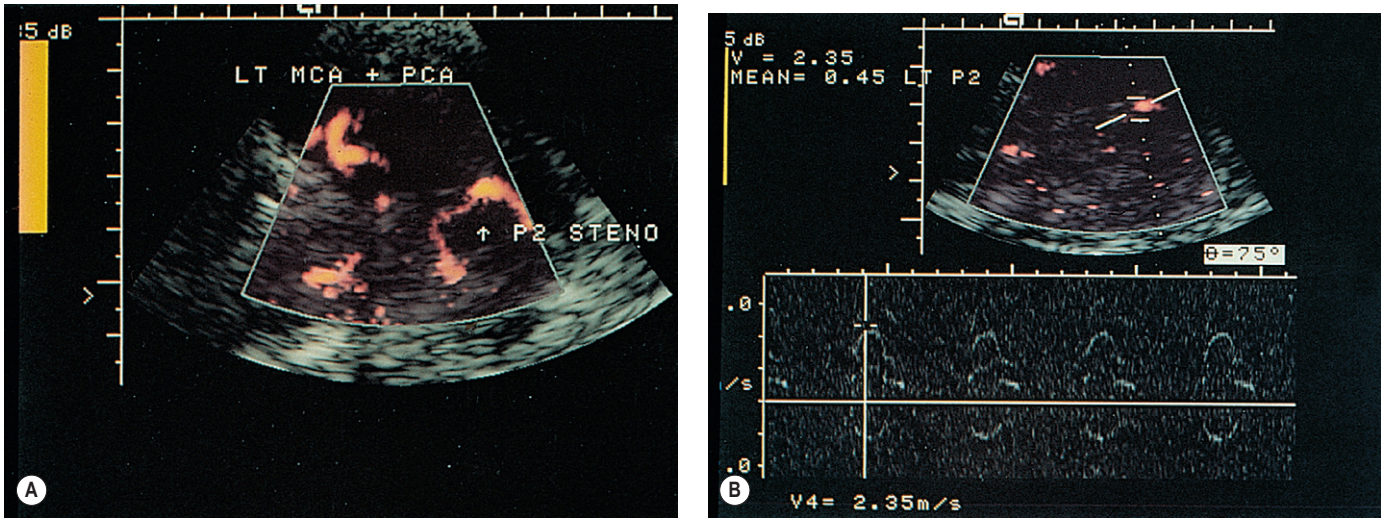

Figure 48.23 **Stenosis of the P2 segment of the PCA. A:** Power Doppler image and **B:** velocity waveform showing increased velocity and turbulence. A 'seagull' noise was heard at the point of stenosis.

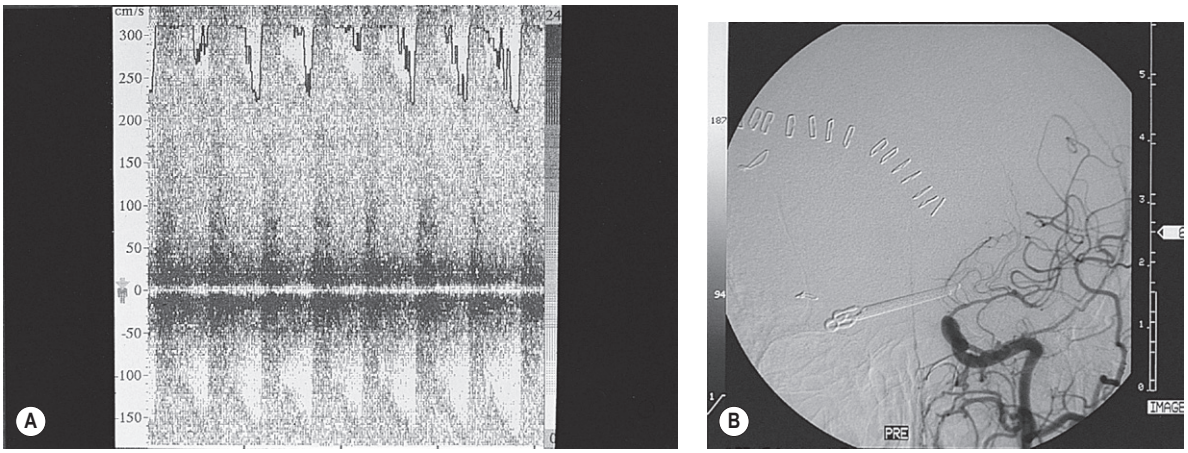

Figure 48.24 Vasospasm following subarachnoid haemorrhage. A: Velocity waveform from a patient with severe ischaemic neurological deficit. Note the gross elevation of blood velocity. **B:** Angiogram showing severe narrowing of the MCA.

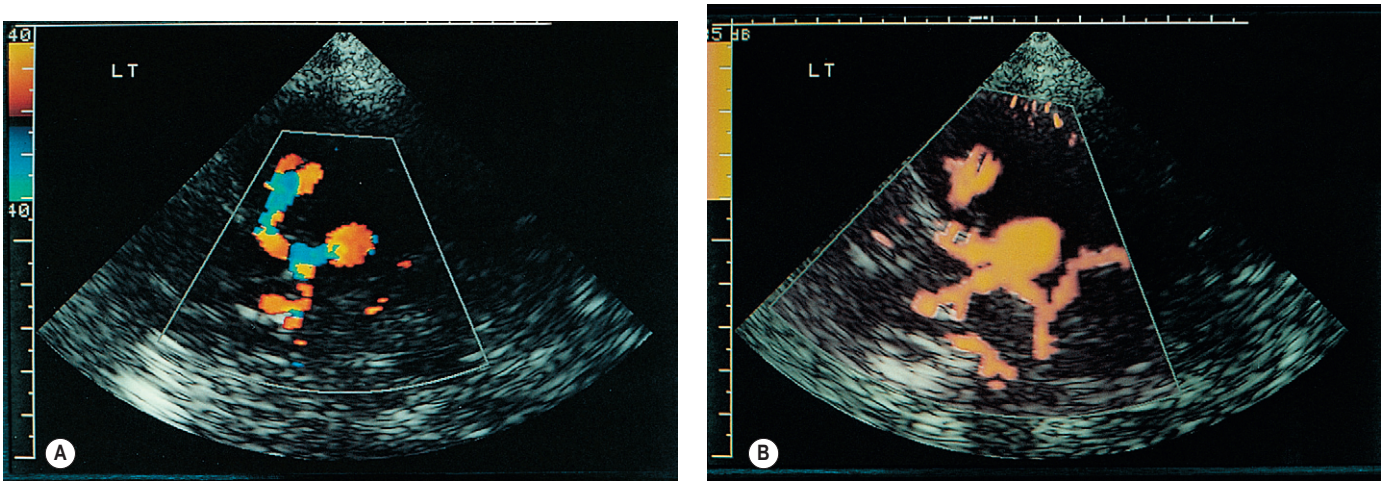

Figure 48.25 Posterior communicating artery aneurysm. A: Colour Doppler and **B:** power Doppler imaging of a large aneurysm arising at the origin of the posterior communicating artery. Again note the increased vessel visualisation with power Doppler. The swirling flow within the aneurysm is well seen with colour Doppler imaging.

the presence of rt-PA comes at the cost of increased risk of haemorrhagic transformation of the infarct with consequent clinical deterioration. Much larger trials are needed to clarify this before therapeutic TCD comes into routine use. Of course it is possible that therapeutic TCD could be used to enhance spontaneous thrombus lysis in patients who are not eligible for rt-PA or interventional neuroradiological thrombus extraction.

Subarachnoid haemorrhage

TCD is widely used to diagnose ischaemic neurological deficit after subarachnoid haemorrhage (SAH). The intracranial arterial blood velocities almost always rise following SAH, in keeping with the time course of angiographic vasospasm and, if severe, may result in focal neurological deficits or deteriorating conscious level.[77] The diagnosis is made by excluding other causes of neurological deterioration and by finding markedly elevated velocities on TCD. The increased velocity may be detected in all arteries or just one, but symptoms are usually associated with a marked increase in velocity, for example MCA mean velocities of 150 cm/s or more (Fig. 48.24). Several studies have attempted to predict which patients are likely to develop severe vasospasm, but although there are associations with blood load and the rate of rise of blood velocity over several days, none of these factors is specific.[77]

Aneurysms and arteriovenous malformations

Colour TCD imaging can identify intracranial aneurysms and feeder vessels to arteriovenous malformations. In preliminary studies colour TCD showed promise for aneurysm detection, but it is too early to say whether it could be used to identify either unruptured (in asymptomatic people) or ruptured (in SAH patients) intracranial aneurysms reliably (Fig. 48.25).

Other applications

All forms of TCD are widely used in neuroscience research. Brain parenchymal imaging in adults can be performed with TCD: ischaemic and haemorrhagic strokes and brain tumours have been identified[52] but in general for clinical practice CT and MRI are much better ways of imaging the parenchyma. TCD can be used to assess the intracranial veins and venous sinuses in suspected venous thrombosis.[78] In sagittal sinus thrombosis, venous blood flow may be increased in veins running parallel to the MCA to reach the cavernous sinus, bypassing the blocked sagittal sinus. A variety of abnormal venous drainage patterns may be identified as blood attempts to exit the cranial cavity by alternative routes. However, the reliability of this is still being evaluated. TCD can also be used to assess haemodynamic response to a range of stimuli (e.g. in the PCA to

flashing lights or the MCA to finger movement) to assess functional reserve – a sort of TCD equivalent of functional MRI.[79]

Brain death can be inferred from a change in the waveform from high diastolic flow to absent or reversed flow, indicating that the intracranial pressure and vascular resistance are greater than the mid/end-diastolic blood pressure; however, the TCD findings are not part of the criteria for the medicolegal establishment of brain death.

REFERENCES

1. European Carotid Surgery Triallists' Collaborative Group (ECST). MRC European Carotid Surgery Trial: interim results for symptomatic patients with severe (70–99%) or with mild (0–29%) carotid stenosis. Lancet 1991;337:1235–1243.
2. North American Symptomatic Carotid Endarterectomy Trial Collaborators (NASCET). Beneficial effect of carotid endarterectomy in symptomatic patients with high grade carotid stenosis. N Engl J Med 1991;325:445–453.
3. Rothwell PM, Gibson RT, Slattery J, et al. Equivalence of measurement in carotid stenosis. A comparison of three methods on 101 angiograms. Stroke 1994;25:2435–2439.
4. The ECST Collaborative Group. Endarterectomy for moderate symptomatic carotid stenosis: interim results from the MRC European Carotid Surgery Trial. Lancet 1996;347:1591–1593.
5. Cina CS, Clase CM, Haynes RB. Carotid endarterectomy for symptomatic carotid stenosis. Cochrane Database of Systematic Reviews 1999, Issue 3. Art. No.: CD001081. DOI: 10.1002/14651858.CD001081.
6. National Institute of Neurological Disorders and Stroke. Clinical advisory: carotid endarterectomy for patients with asymptomatic internal carotid artery stenosis. Stroke 1994;25:2523–2524.
7. Chambers BR, Donnan GA. Carotid endarterectomy for asymptomatic carotid stenosis. Cochrane Database of Systematic Reviews 2000, Issue 1. Art. No.: CD001923. DOI: 10.1002/14651858.CD001923.pub2.
8. Chaturvedi S, Bruno A, Feasby T, et al. Carotid endarterectomy – an evidence-based review. Neurology 2005;65:794–801.
9. Wolf PA, Kannel WB, Sorlie P, McNamara P. Asymptomatic carotid bruit and risk of stroke. The Framingham study. JAMA 1981;245:1442–1445.
10. Roederer GO, Langlois YE, Jager KA, et al. The natural history of carotid arterial disease in asymptomatic patients with cervical bruits. Stroke 1984;15:605–613.
11. Ford CS, Frye JL, Toole JF, Lefkowitz D. Asymptomatic carotid bruit and stenosis. A prospective follow-up study. Arch Neurol 1986;43:219–222.
12. Rothwell PM, Slattery J, Warlow CP, on behalf of the European Carotid Surgery Triallists Collaborative Group. Risk of stroke in the distribution of an asymptomatic carotid artery. Lancet 1995;345:209–212.
13. Ivey TD, Strandness DE, Williams DB, et al. Management of patients with carotid bruit undergoing cardiopulmonary bypass. J Thorac Cardiovasc Surg 1984;87:183–189.
14. Naylor AR, Mehta Z, Rothwell PM, Bell PRF. Carotid artery disease and stroke during coronary artery bypass: a critical review of the literature. Eur J Vasc Endovasc Surg 2002;23:283–294.
15. Naylor AR, Merrick MV, Sandercock PAG, et al. Serial imaging of the carotid bifurcation and cerebrovascular reserve after carotid endarterectomy. Br J Surg 1993;80:1278–1280.
16. Post PN, Kievit J, van Baalen JM, et al. Routine duplex surveillance does not improve the outcome after carotid endarterectomy: a decision and cost utility analysis. Stroke 2002;33:749–755.
17. de Groot E, van Leuven SI, Duivenvoorden R, et al. Measurement of carotid intima-media thickness to assess progression and regression of atherosclerosis. Nature Clin Pract Cardiovasc Med 2008;5:280–288.
18. Geroulakos G, O'Gorman DJ, Kalodiki E, et al. The carotid intima–media thickness as a marker of severe symptomatic coronary artery disease. Eur Heart J 1994;15:781–185.
19. Hollander M, Hak AE, Koudstaal PJ, et al. Comparison between measures of athereosclerosis and risk of stroke. Stroke 2003;34:2367–2372.
20. Trigaux JP, Delchambre F, Van Beers B. Anatomical variations of the carotid bifurcation: implications for digital subtraction angiography and ultrasound. Br J Radiol 1990;63:181–185.
21. Buckenham TM, Wright AR. Ultrasound of the extracranial vertebral artery. Br J Radiol 2004;77:15–20.
22. Berguer R, Kiefer E, editors. The aortic arch and its branches. In: Surgery of the arteries to the head. New York: Springer Verlag; 1992. p. 5–31.
23. Budorick NE, Rojratanakiat W, O'Boyle MK, et al. Digital tapping of the superficial temporal artery: significance in carotid duplex sonography. J Ultrasound Med 1996;15:459–464.
24. Allan PL, Mowbray PI, Lee AJ, Fowkes FG. Relationship between carotid intima–media thickness and symptomatic and asymptomatic peripheral arterial disease. The Edinburgh Artery Study. Stroke 1997;28:348–353.
25. Lim TK, Lim E, Dwivedi G, et al. Normal value of carotid intima-media thickness – a surrogate marker of atherosclerosis: quantitative assessment by B-mode carotid ultrasound. J Am Soc Echocardiogr 2008;21:112–116.
26. Hood DB, Mattos MA, Mansour A, et al. Prospective evaluation of new duplex criteria to identify 70% internal carotid artery stenosis. J Vasc Surg 1996;23:254–262.
27. Robinson ML, Sacks D, Perlmutter GS, Marinelli DL. Diagnostic criteria for carotid duplex sonography. Am J Radiol 1988;151:1045–1049.
28. Grant EG, Benson CB, Moneta GL, et al. Carotid artery stenosis: gray-scale and Doppler US diagnosis – Society of Radiologists in Ultrasound Consensus Conference. Radiology 2003;229:340–346.
29. Spencer MP, Reid JM. Quantitation of carotid stenosis with continuous wave (C-W) Doppler ultrasound. Stroke 1979;10:326–330.
30. Lee DH, Gao F-Q, Rankin RN, et al. Duplex and color flow sonography of occlusion and near occlusion of the carotid artery. Am J Neuroradiol 1996;17:1267–1274.
31. Sitzer M, First G, Siebler M, et al. Usefulness of an intravenous contrast medium in the characterization of high-grade internal carotid stenosis with color Doppler-assisted duplex imaging. Stroke 1994;25:385–389.
32. Ohm C, Bendick PJ, Monash J, et al. Diagnosis of total internal carotid occlusions with duplex ultrasound and ultrasound contrast. Vasc Endovasc Surg 2005;39:237–243.
33. Kalman CE, Gosink BB, Gardner DJ. Carotid duplex sonography: bisferious pulse contour in patients with aortic valvular disease. Am J Radiol 1991;157:403–407.
34. O'Boyle MK, Vibhakar, NI, Chung J, et al. Duplex sonography of the carotid arteries in patients with isolated aortic stenosis: imaging findings and relation to severity of stenosis. Am J Radiol 1996;166:197–202.
35. Cardullo PA, Cutler BS, Brownell Wheeler H. Detection of carotid disease by duplex ultrasound. J Diagn Med Sonogr 1986;2: 63–73.
36. Carroll BA. Carotid sonography. Radiology 1991;178:303–313.
37. Mattos MA, Hodgson KJ, Ramsey DE, et al. Identifying total carotid occlusion with colour flow duplex scanning. Eur J Vasc Surg 1992;6:204–210.
38. Lee DH, Gao F-Q, Rankin RN, et al. Duplex and color Doppler flow sonography of occlusion and near occlusion of the carotid artery. Am J Neuroradiol 1996;17:1267–1274.
39. Steffen CM, Gray-Weale AC, Byrne KE, Lusby RJ. Carotid artery atheroma: ultrasound appearances in symptomatic and asymptomatic vessels. Aust NZ J Surg 1989;59:529–534.
40. Geroulakos G, Hobson RW, Nicolaides A. Ultrasonographic carotid plaque morphology in predicting stroke risk. Br J Surg 1996;83:582–587.
41. Gronholdt M-L, Nordestgaard BG, Schroeder TV, et al. Ultrasonic echolucent carotid plaques predict future strokes. Circulation 2001;104:68–73.
42. Carotid plaque surface irregularity predicts ischemic stroke. The Northern Manhattan Study. Stroke 2006;37:2696–2701.
43. Hatsukami TS, Ferguson MS, Beach KW, et al. Carotid plaque morphology and clinical events. Stroke 1997;28:95–100.
44. Thiele BL, Jones AM, Hobson RW, et al. Standards in noninvasive cerebrovascular testing. J Vasc Surg 1992;15:495–503.
45. Kriegshauser JS, Patel MD, Nelson KD. Carotid pseudostring sign from vasa vasorum collaterals. J Ultrasound Med 2003;22:959–963.
46. de Bray JM, Lhoste P, Dubaz F, et al. Ultrasonic features of extracranial carotid dissections: 47 cases studied by angiography. J Ultrasound Med 1994;13:659–664.
47. Steinke W, Rautenberg W, Schwartz A, Hennerici M. Non-invasive monitoring of internal carotid artery dissection. Stroke 1994;25:998–1005.
48. Mann WJ, Beck A, Schreiber J, et al. Ultrasonography for evaluation of the carotid artery in head and neck cancers. Laryngoscope 1994;104:885–888.

49. Barry R, Pienaar A, Pienaar C. Duplex Doppler evaluation of suspected lesions at the carotid bifurcation. Ann Vasc Surg 1993;7:140–144.
50. Armstrong PA, Bandyk DF, Johnson BL, et al. Duplex scan surveillance after carotid angioplasty and stenting: A rational definition of stent stenosis. J Vasc Surg 2007;46:460–466.
51. Aaslid R, Markwalder TM, Nornes H. Noninvasive transcranial Doppler ultrasound recording of flow velocity in basal cerebral arteries. J Neurosurg 1982;57:769–774.
52. Baumgartner RW. Transcranial color duplex sonography in cerebrovascular disease: a systematic review. Cerebrovasc Dis 2003;16:4–13.
53. Polak JF. Ultrasound energy and the dissolution of thrombus. N Engl J Med 2004;351:21.
54. Alexandrov AV. Ultrasound-enhanced thrombolysis for stroke: clinical significance. Eur J Ultrasound 2002;16:131–140.
55. White DN, Curry GR, Stevenson RJ. The acoustic characteristics of the skull. Ultrasound Med Biol 1978;4:225–252.
56. Halsey JH. Effect of emitted power on waveform intensity in transcranial Doppler. Stroke 1990;21:1573–1578.
57. Alpers BJ, Barry RG, Paddison RM. Anatomical studies of the Circle of Willis in normal brains. Arch Neurol Psychiatry 1959;81:409–418.
58. Day AL. Arterial distributions and variants. In: Wood JH, editor. Cerebral blood flow: physiological and clinical aspects. New York: McGraw-Hill; 1987.
59. Fujioka KA, Douville CM. Anatomy and freehand examination techniques. In: Newell DW, Aaslid R, editors. Transcranial Doppler. New York: Raven Press; 1992. p. 9–31.
60. Postert T, Federlein J, Przuntek H, Buttner T. Comparison of transcranial power Doppler and contrast-enhanced color-coded sonography in the identification of intracranial arteries. J Ultrasound Med 1998;17:91–96.
61. Bogdahn U, Becker G, Winkler J, et al. Transcranial color-coded real-time sonography in adults. Stroke 1990;21:1680–1688.
62. Adams RJ, Nichols FT, Hess DC. Normal values and physiological variables. In: Newell DW, Aaslid R, editors. Transcranial Doppler. New York: Raven Press; 1992. p. 41–48.
63. Martin PJ, Evans DH, Naylor AP. Transcranial colour-coded sonography of the basal cerebral circulation. Reference data from 115 volunteers. Stroke 1994;25:390–396.
64. Otis SM, Ringelstein EB. Findings associated with extracranial occlusive disease. In: Newell DW, Aaslid R, editors. Transcranial Doppler. New York: Raven Press; 1992. p. 153–160.
65. Markus HS, Harrison MJ. Microembolic signal detection using ultrasound. Stroke 1995;26:1517–1519.
66. Ries S, Schminke U, Daffertshofer M, et al. High intensity transient signals and carotid artery disease. Cerebrovasc Dis 1995;5:124–127.
67. Kaps M, Hansen J, Weiher M, et al. Clinically silent microemboli in patients with artificial prosthetic aortic valves are predominantly gaseous and not solid. Stroke 1997;28:322–325.
68. Anzola AP, Renaldini E, Magoni M, et al. Validation of transcranial Doppler sonography in the assessment of patent foremen ovale. Cerebrovasc Dis 1995;5:194–198.
69. Babikian VL. Transcranial Doppler evaluation in patients with ischaemic cerebrovascular disease. In: Babikian VL, Wechsler LR, editors. Transcranial Doppler ultrasonography. New York: Mosby Year Book; 1993. p. 87–103.
70. Chernyshev OY, Garami Z, Calleja S, et al. Yield and accuracy of urgent combined carotid/transcranial ultrasound testing in acute cerebral ischemia. Stroke 2005;36:32–37.
71. Demchuk AM, Christou I, Wein TH, et al. Accuracy and criteria for localizing arterial occlusion with transcranial Doppler. J Neuroimaging 2000;10:1–12.
72. Egido JA, Sanchez C. Neurosonology in cerebral ischemia: future application of transcranial Doppler in acute stroke. Cerebrovasc Disc 2001;11(Suppl. 1):15–19.
73. Allendoerfer J, Coertler M, von Reutern GM, for the Neurosonology in Acute Ischemic Stroke (NAIS) Study Group. Prognostic relevance of ultra-early Doppler sonography in acute ischaemic stroke: a prospective multicentre study. Lancet Neurol 2006;5:835–840.
74. Alexandrov AV. Ultrasound-enhanced thrombolysis for stroke: clinical significance. Eur J Ultrasound 2002;16:131–140.
75. Alexandrov AV, Molina CA, Grotta JC, et al. for the CLOTBUST investigators. Ultrasound-enhanced systemic thrombolysis for acute ischemic stroke. N Engl J Med 2004;351:21.
76. Demchuk AM, Burgin WS, Christou I, et al. Thrombolysis in brain ischemia (TIBI) transcranial flow grades predict clinical severity, early recovery, and mortality in patients treated with intravenous tissue plasminogen activator. Stroke 2001;32:89–93.
77. Sloan MA. Detection of vasospasm following subarachnoid haemorrhage. In: Babikian VL, Wechsler LR, editors. Transcranial Doppler ultrasonography. New York: Mosby Year Book; 1993. p. 105–127.
78. Wardlaw JM, Vaughan GT, Steers AJW, Sellar RJ. Transcranial doppler ultrasound findings in cerebral venous sinus thrombosis. J Neurosurg 1994;80:332–335.
79. Bragoni M, Caltagirone C, Troisi E, et al. Correlation of cerebral hemodynamic changes during mental activity and recovery after stroke. Neurology 2000;55:35–40.

CHAPTER

49 Breast

Jonathan J. James and Andrew J. Evans

BREAST ULTRASOUND

Ultrasound and mammography are the two most important modalities for breast imaging. In younger women, under the age of 35 years, ultrasound is the primary tool used to investigate breast problems. Even in the older age group, ultrasound plays a vital role in breast imaging, particularly for the assessment of mass lesions.

Many years ago the role of breast ultrasound was limited to the differentiation of cystic from solid masses. The technical advances of the past 30 years have allowed radiologists to differentiate benign from malignant solid breast masses with a high level of accuracy. Ultrasound-guided core biopsy is usually performed to obtain a histological diagnosis, confirming the precise nature of benign lesions, and to provide additional information on cancers such as tumour type, grade and hormone receptor status which may influence treatment choices.

Equipment and technique

Ultrasound imaging of the breast requires the use of high-frequency linear array transducers with frequencies between 7.5 and 14 MHz. The frequency selected is dependent on the size of the breast to be examined. A balance has to be struck between the greater spatial resolution offered by higher frequencies and the penetration needed to produce satisfactory imaging of the whole thickness of the breast down to the chest wall.

The patient is positioned supine. It is helpful for the patient to extend the ipsilateral arm behind her head. If the area to be assessed lies in the lateral aspect of the breast then turning the patient slightly oblique is recommended. The aim is to flatten the breast tissue against the chest wall, reducing the thickness of breast tissue to be imaged.

It is best to scan in two planes at 90° to each other. Many operators scan the breast in a longitudinal and transverse direction. Scanning the breast in a radial direction is advocated by some operators, potentially allowing better demonstration of the duct system and ductal pathology. This involves moving the transducer in a direction similar to the pattern of the spokes of a bicycle wheel. The breast is then again imaged at 90° in an anti-radial direction.

ULTRASOUND OF BENIGN BREAST PATHOLOGY

Cystic lesions

Simple cysts

Cysts represent the commonest cause of a lump presenting to a breast clinic. They are common in premenopausal women, with the incidence decreasing rapidly after the menopause.

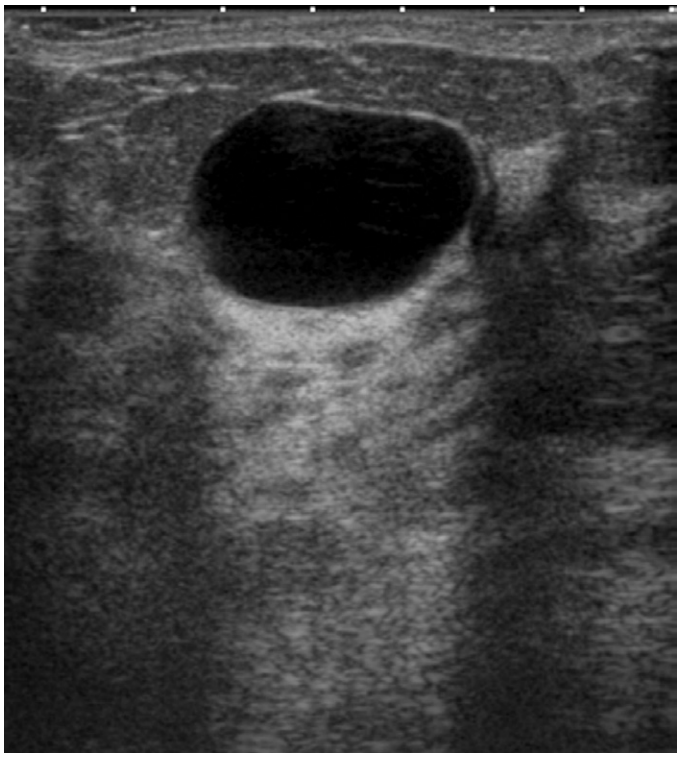

Figure 49.1 Cyst. The absence of any internal echoes and the posterior enhancement are characteristic of a simple cyst.

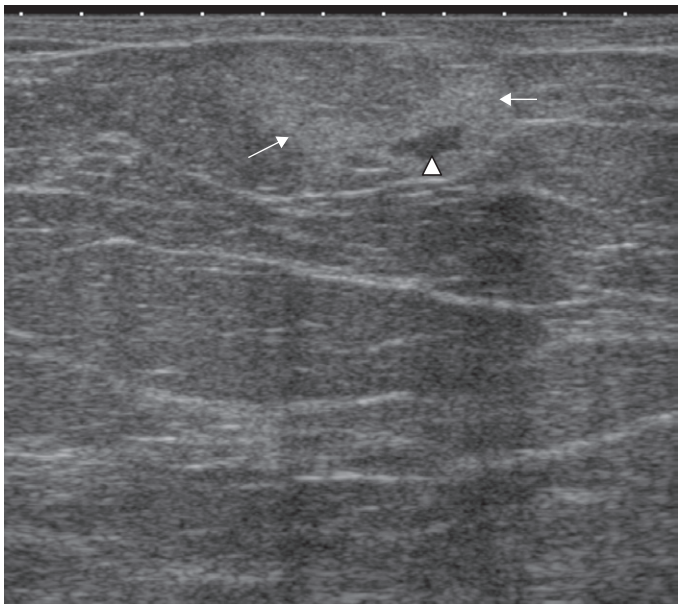

Figure 49.2 Fat necrosis. There is an area of hyperechoic change just deep to the skin (arrows). The necrotic fat can liquefy, leading to development of small fluid collections or 'oil' cysts (arrowhead). The patient gave a history of trauma.

Breast cysts have a characteristic ultrasonic appearance (Fig. 49.1). They are typically well defined, rounded or oval. They are hypoechoic, lacking any internal echoes, and exhibit characteristic posterior enhancement due to the presence of fluid. When these features exist a cyst can be diagnosed with confidence. If there is any doubt then aspiration can easily be performed under ultrasound guidance. When diagnosed, breast cysts do not require aspiration, but this can be undertaken if the patient wishes. The material aspirated is not routinely sent for cytological examination, but can be if the cyst has any atypical features or contains blood-stained fluid.

Oil cysts and fat necrosis

Injury to the breast is associated with the development of fat necrosis. Local trauma, surgery and radiotherapy are commonly associated with the development of fat necrosis. On ultrasound fat necrosis may be appreciated as rather diffuse hyperechoic change (Fig. 49.2). Often post-traumatic oil cysts may develop in areas of fat necrosis, precipitating referral for breast imaging.

Oil cysts may appear as simple cysts on ultrasound, but are more likely to have more complex features. Calcification may develop in the wall of oil cysts and with time the whole cyst may become densely calcified.

Clinically fat necrosis may mimic both benign and malignant pathology. In many cases the combination of mammography and ultrasound is diagnostic of fat necrosis. Biopsy can be performed if there is any uncertainty.

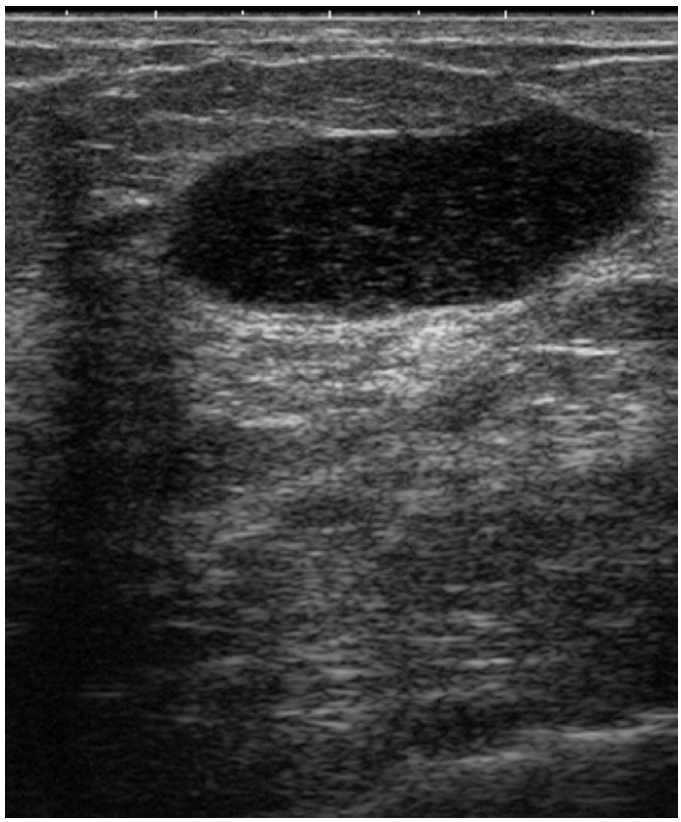

Figure 49.3 Galactocele. Echogenic material is visible within this galactocele. Ultrasound-guided aspiration of 'milky' material confirmed the diagnosis.

Galactoceles

Galactoceles are milk-filled cystic structures which develop during lactation. The contents of a galactocele are commonly echogenic, probably as the result of mixing of fat globules and water (Fig. 49.3); sometimes fat/fluid levels may be seen. The presence of internal echoes may make differentiation from a solid lesion such as a fibroadenoma difficult. Frequently the pressure of the transducer over the lesion results in movement of the particles, confirming that the mass is in fact cystic rather than solid. If there is any diagnostic doubt ultrasound-guided aspiration is easily performed, resulting in a characteristic 'milky' aspirate.

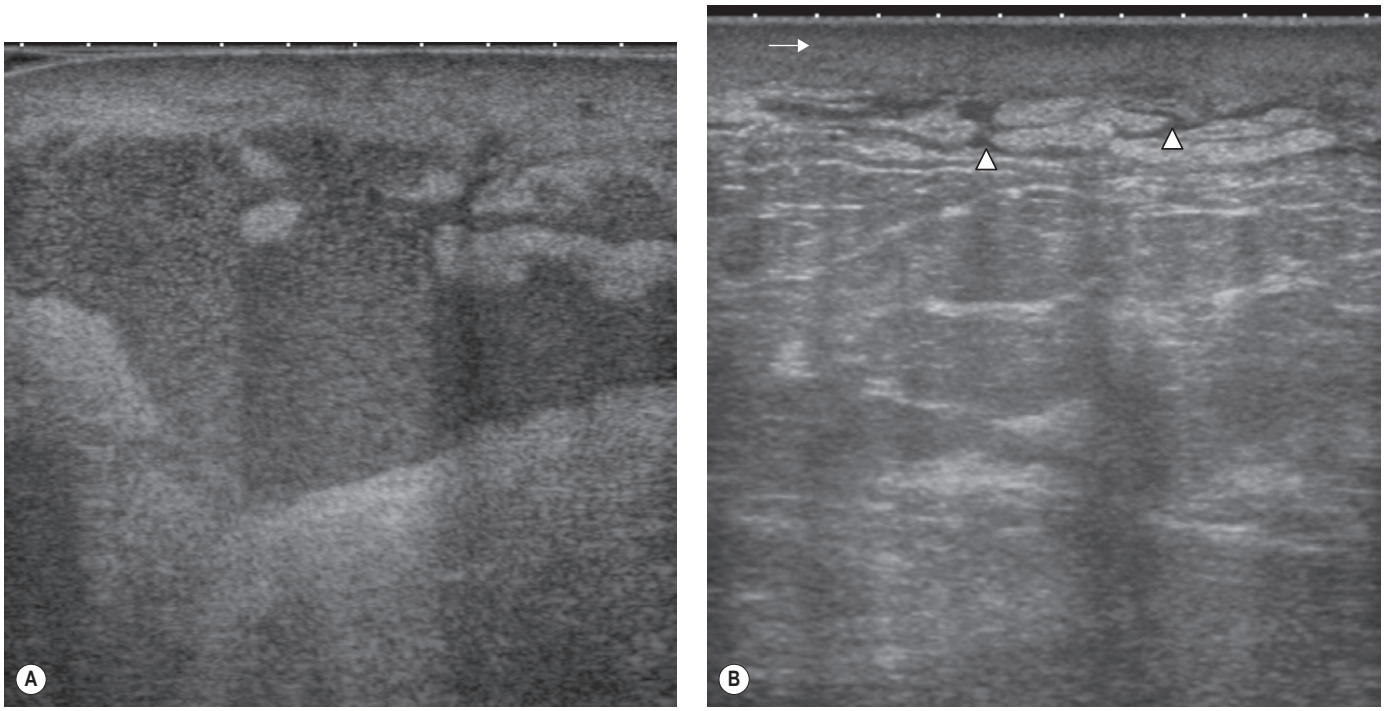

Figure 49.4 Breast abscess. A: Echogenic pus is seen within this large lactational breast abscess. **B:** There was marked subcutaneous oedema (arrowheads) and skin thickening (arrow) in the breast tissue extending some distance from the abscess cavity. This corresponded with the area of inflammation apparent clinically. The abscess was treated conservatively with repeated ultrasound-guided aspirations and antibiotics, with resolution of the ultrasound appearances.

Breast abscess

Breast abscesses are commonly associated with lactation. Women typically present with pain, swelling and tenderness. The typical organism responsible is *Staphylococcus aureus*. Ultrasound is crucial in the diagnosis of the condition, confirming the presence of a pus collection, but also plays an important role in patient management (Fig. 49.4A and B). Breast abscesses are best managed by repeated aspiration of pus under ultrasound guidance every 2 or 3 days together with oral or intravenous antibiotics. Utilising this approach, very few breast abscesses will require open surgical incision and drainage.

Aspiration is performed following the injection of local anaesthetic into the skin and subcutaneous tissues. Injection of local anaesthetic directly into the abscess cavity provides excellent pain relief. Aspiration is then undertaken using a 19G needle or larger. It is possible to place percutaneous drains into breast abscesses, but this is rarely necessary.

Breast infections and abscesses can also occur in the non-lactating breast; it can be associated with chronic conditions such as diabetes. Periareolar infection or periductal mastitis is characterised by inflammation around periareolar ducts. It is much more common in smokers. Abscess formation may occur and the acute management is identical to lactational abscesses.

Skin lesions such as sebaceous cysts can be associated with infections or abscess formation (Fig. 49.5). Surgical excision may be required to prevent recurrent infections.

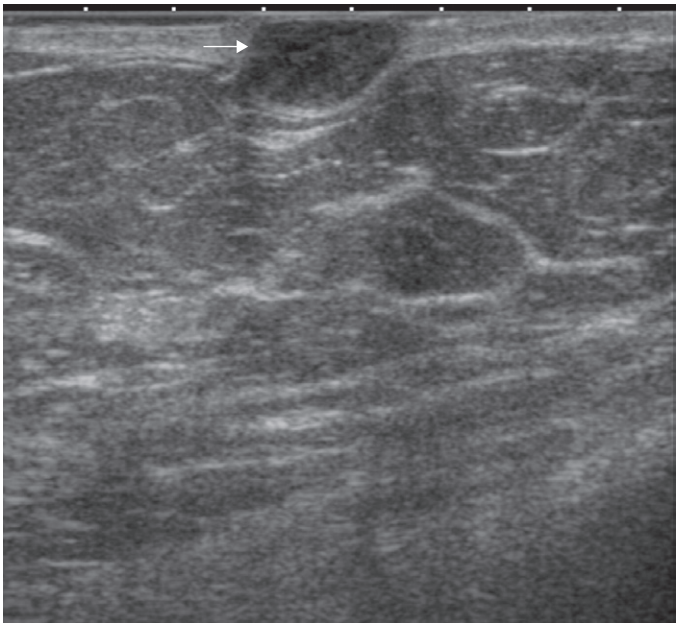

Figure 49.5 Sebaceous cyst. This superficial cyst is arising from the skin and is entirely benign (arrow).

Solid lesions

The ultrasound features of a solid lesion that are characteristic of benign pathology include hyperechogenicity compared with fat, oval shape, well-circumscribed lobulated margins and a thin echogenic pseudocapsule.[1] In contrast, features found in malignancy include spiculation, angular margins, marked hypoechogenicity, acoustic shadowing and a lesion that is 'taller than wide' (greater dimensions in the anteroposterior (AP) direction compared to the

Ultrasound features of a benign breast mass

- Well-defined edge
- Lobulated margins (macrolobulation)
- Oval shape
- Thin echogenic pseudocapsule
- Edge attenuation
- Posterior enhancement
- Homogeneous internal echo pattern
- Compressibility

transverse diameter).[1] For the vast majority of mass lesions, ultrasound-guided biopsy will be required to make the diagnosis. With careful patient selection there are situations where if several of the benign ultrasound features are present, and there are no suspicious features, biopsy can be avoided. One such group may be women under the age of 25 where the chances of any solid lesion being malignant are very small.[2]

Fibroadenomas and phyllodes tumours

Fibroadenoma is the most common benign solid mass lesion presenting to a breast clinic. They are most commonly encountered in younger women, with a peak incidence between the ages of 20 and 30.

Fibroadenomas are typically well defined, oval with smooth or gently lobulated margins (Fig. 49.6A). They are typically hypoechoic or isoechoic to the adjacent fat. Sometimes a thin echogenic pseudocapsule may be appreciated, which is characteristic of benign lesions. Coarse calcifications may develop within fibroadenomas in older women (Fig. 49.6B, C).

In the vast majority of cases, biopsy will be required to establish the diagnosis. Biopsy confirmation is important because occasionally a rapidly growing, high histological grade carcinoma can mimic a fibroadenoma.

The ultrasound appearances of a phyllodes tumour can be indistinguishable from a fibroadenoma. Occasionally slit-like cystic spaces may be seen which can suggest the diagnosis (Fig. 49.7). It is important to differentiate the two because a small number of phyllodes tumours are locally aggressive (around 25%) and occasionally even metastasise. Even the pathological features can be difficult to distinguish on core biopsy. If a phyllodes tumour is suspected then surgical excision is advised with a clear margin to minimise the risk of recurrence. It is common practice to excise larger fibroadenomas (>3 cm) to avoid missing a phyllodes tumour.

Fibroadenomas have no malignant potential and are not associated with an increased risk of breast cancer. Consequently, smaller

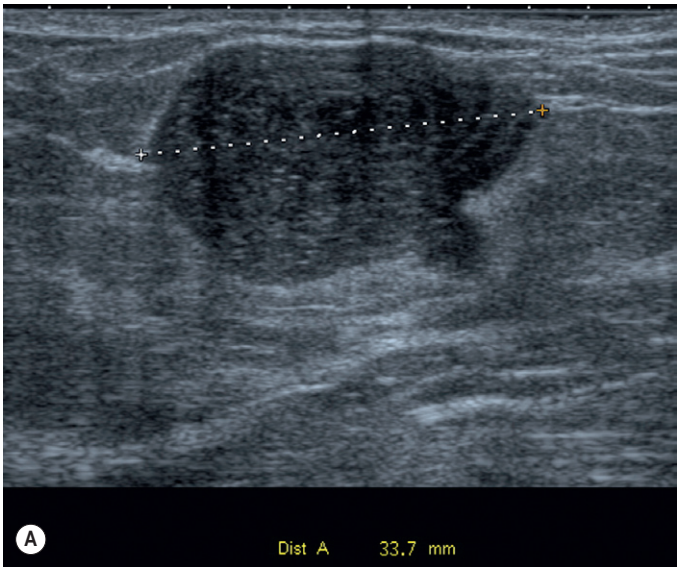

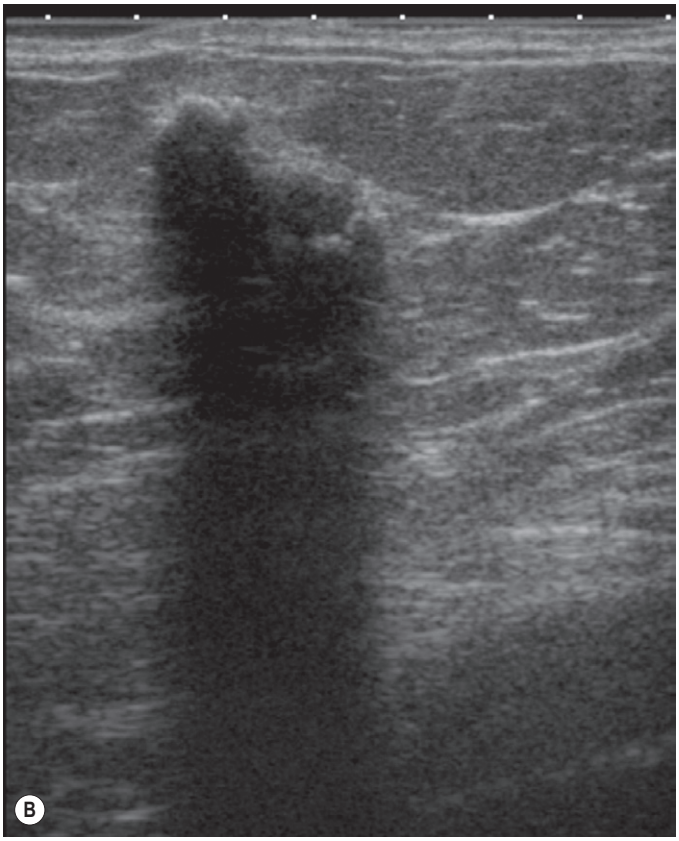

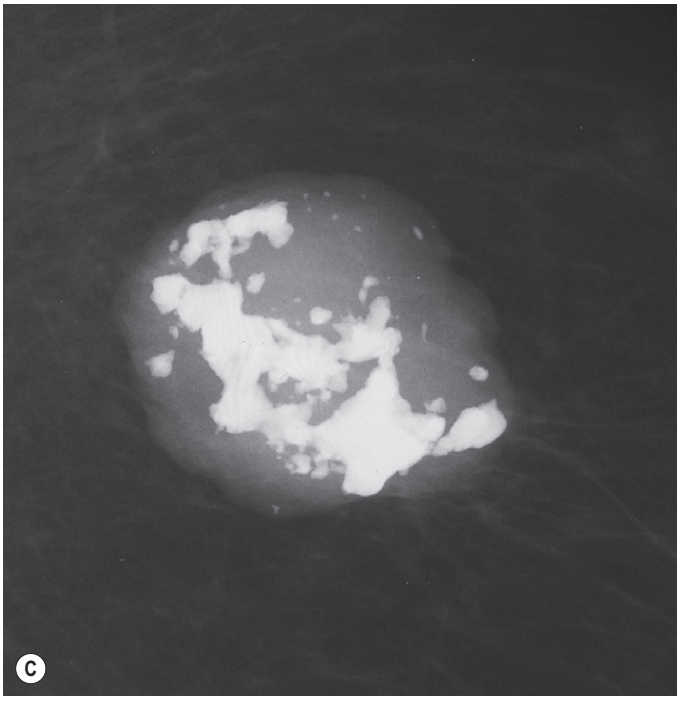

Figure 49.6 Fibroadenomas. A: A well-defined hypoechoic mass with a lobulated margin is typical of a fibroadenoma. The diagnosis was confirmed on core biopsy. Fibroadenomas >3 cm are frequently excised to avoid missing phyllodes tumours. **B:** Heavily calcified fibroadenomas may be encountered particularly in the elderly. **C:** If there is diagnostic doubt then a mammogram is helpful, showing the coarse benign 'pop-corn' calcifications typical of calcified fibroadenomas.

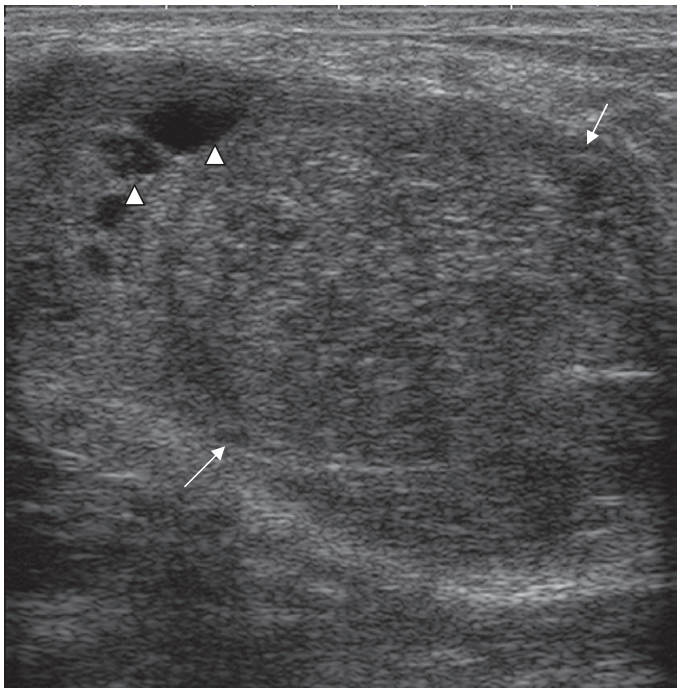

Figure 49.7 Phyllodes tumour. Phyllodes tumours can appear identical to large fibroadenomas (arrows). The presence of cystic spaces (arrowheads) raises the possibility of the diagnosis, which was confirmed on core biopsy.

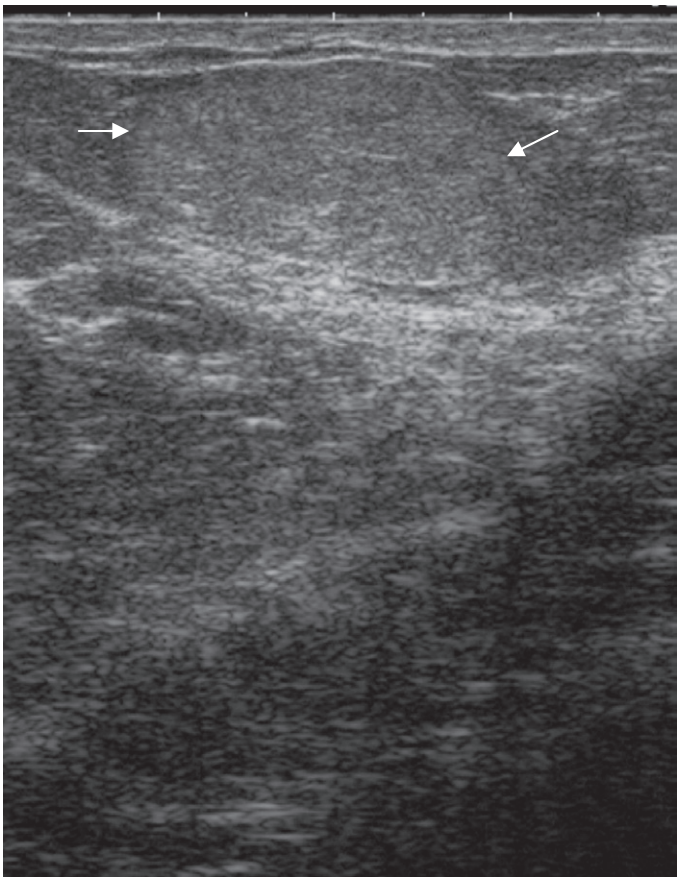

Figure 49.8 Lipoma. A well-defined mass which is uniformly hyperechoic to the surrounding breast tissue is characteristic of a lipoma (arrows).

fibroadenomas (<3 cm) are not usually excised. Surgical excision is sometimes undertaken usually at a patient's request. In recent years the development of vacuum-assisted breast biopsy devices has enabled percutaneous excision of small fibroadenomas to be performed under ultrasound guidance, as an alternative to an open surgical procedure.

Hamartomas

Hamartomas are benign breast masses composed of all the elements that make up normal breast tissue – lobular elements, stroma and fatty tissue. They usually present as either a palpable mass or are detected on screening mammography. Most hamartomas seen on screening mammography are not recalled because the well-defined edge and fat density within the mass are characteristic.

In one study the mean age of presentation of symptomatic hamartomas was 39 years and the mean size 2.9 cm. At ultrasound examination an oval, well-defined compressible mass is identified. They can have a rather heterogeneous appearance as they contain fat as well as other breast parenchymal elements. There is usually no distal effect or edge enhancement.[3] Without the presence of a well-defined capsule these lesions would be difficult to differentiate from normal breast tissue. Cystic change and calcification are occasionally seen.

The diagnosis can be made with confidence if fat is definitely identified within the mass. If there is any diagnostic doubt then percutaneous biopsy is performed. The core specimens from hamartomas are frequently reported as just showing normal tissue.

Lipomas

Breast lipomas are common and may present as a palpable mass. Ultrasound examination shows a well-defined oval compressible mass, often in a superficial location. A thin echogenic capsule is usually seen and the mass is either isoechoic or slightly hyperechoic. The echo pattern is very homogeneous. The ultrasound appearances are usually so characteristic that the diagnosis can be made with ultrasound alone with biopsy rarely required. Occasionally intramuscular lipomas can present as a breast mass and in these circumstances magnetic resonance imaging (MRI) may be helpful to confirm the diagnosis.

Papillary lesions

Papillary lesions are benign, fleshy nodules arising in a breast duct. The main concern is their association with cellular atypia and malignancy, such as atypical ductal hyperplasia (ADH), ductal carcinoma in situ (DCIS) or even invasive cancer. In addition, the papillary lesion may represent an encysted or invasive papillary carcinoma.

Papillary lesions are usually identified either at screening mammography or in the work-up of women with nipple discharge. They have a tendency to secrete watery fluid and so frequently present as a nipple discharge rather than a discrete lump.

Symptomatic lesions tend to be central and solitary whilst asymptomatic screen-detected lesions are more likely to be multiple and peripheral. The larger, solitary, centrally located lesions are less likely to be found in association with atypia or malignancy. The multiple, peripherally located lesions seem to carry a much greater malignant potential.[4] Overall, the diagnosis of a papillary lesion increases the risk of developing a subsequent breast cancer; the risk may be up to 7.5 times greater if there is associated ADH.[5]

Up until recently, all papillary lesions identified on imaging and core biopsy were surgically excised to alleviate symptoms and because of the significant risk of associated atypia and malignancy. Recently some have advocated not excising papillomas when an initial core biopsy has shown no evidence of atypia because of the

low rates of malignancy and atypia found at subsequent surgical excision. Another management alternative for this group of patients is to perform piecemeal image-guided percutaneous vacuum-assisted excision. This debate has led to interest in the possibility of using ultrasonic features to help distinguish between malignant and benign papillary lesions.

Papillary lesions have three common ultrasound correlates: a cyst with a solid or mixed cystic/solid mural nodule (Fig. 49.9A); an intraductal mass (Fig. 49.9B) or a completely solid mass where the intraductal nature of the mass cannot be appreciated.[6] Benign papillomas, presenting as a filling defect in the wall of a cyst, tend to be small and unilobulated whilst malignant papillary lesions tend to be larger, multilobulated and occur in older women. There is considerable overlap in the ultrasound features of benign and malignant solid papillary lesions. All papillary lesions tend to be vascular on Doppler examination (Fig. 49.9C). Malignant papillary lesions frequently exhibit the ultrasound features that are typical of malignancy, including being taller than wide, having an echogenic halo, exhibiting posterior enhancement and being associated with microcalcification.[7]

Radial scars or complex sclerosing lesions

Radial scars are benign lesions which were rarely identified before the advent of mammographic screening. Many more radial scars are now seen because they often present as small spiculate masses or areas of architectural distortion on screening mammograms. Radial scars greater than 2 cm in diameter are called complex sclerosing lesions. Radial scars are usually impalpable.

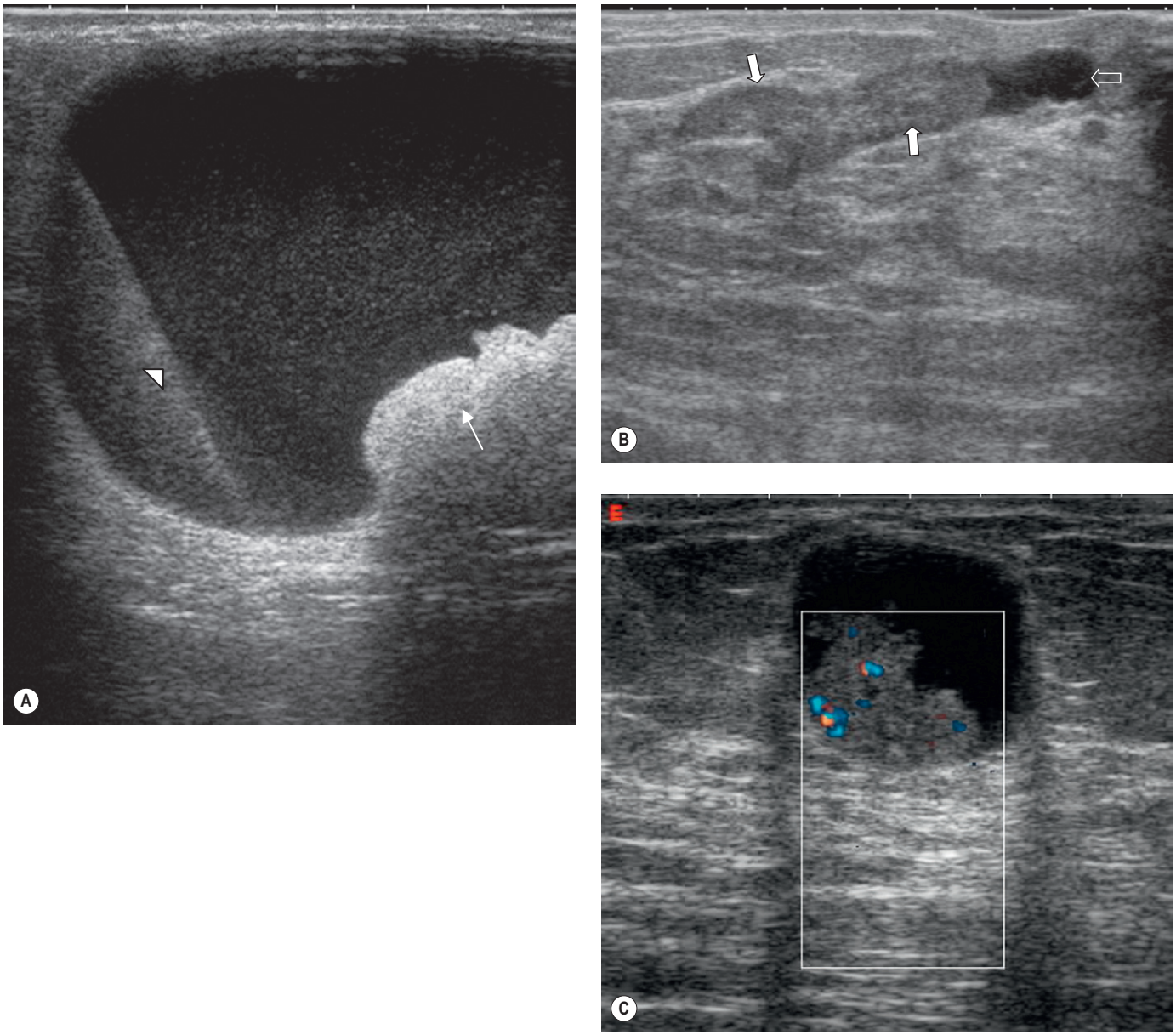

Figure 49.9 Papillary lesions. A: This papillary lesion is predominantly cystic with a mural nodule (arrow). Debris can be appreciated layering in the dependent portion of the cyst (arrowhead). Core biopsy of the solid component suggested a benign papilloma. The lesion was surgically excised. **B:** This patient with a nipple discharge had an intraductal lesion (thick arrows) partly filling a dilated duct (hollow arrow) close to the nipple. **C:** Colour Doppler is useful to confirm that this is a soft tissue nodule rather than debris within a cyst.

The mammographic and ultrasound features of low-grade carcinomas and radial scars are very similar. Sonographically, a small hypoechoic mass with distal attenuation and architectural distortion is typical. However, ultrasound examination is more frequently normal in radial scars (57%) compared with cancer (7%). A recent comparison of the sonographic features of radial scars and cancer presenting as small spiculate lesions on mammography found that an echogenic halo, distal attenuation, taller than wide shape and distortion were more commonly seen in cancers while small cysts and an echogenic component were more frequently seen in radial scars.[8] Differences were not, however, clear-cut enough to allow safe sonographic differentiation and so percutaneous biopsy is crucial in the diagnosis. When the lesion is sonographically visible, this can be performed under ultrasound guidance.

At surgical excision a proportion of radial scars have associated ADH, lobular carcinoma in situ (LCIS), DCIS or invasive cancer. Some authors also argue that a small number of radial scars may transform into invasive cancer. For this reason the standard management of radial scars has until recently been surgical excision. However, if the initial core biopsy shows no evidence of atypia or malignancy then it has been suggested that percutaneous excision using a vacuum-assisted device can be an alternative to surgery, because of the very low risk of malignancy or atypia in this subgroup. A similar approach has already been described for papillary lesions.

ULTRASOUND OF MALIGNANT BREAST PATHOLOGY

No single feature is entirely specific or sensitive for predicting malignancy and a number of benign lesions such as radial scars, inflammation and fat necrosis can mimic malignancy. The factors most useful in confirming malignancy are irregular shape, microlobulation, transverse to AP ratio of 1.4 or less (lesion taller than wide), heterogeneous echo pattern and spiculation (Fig. 49.10). Other factors such as the clinical findings, mammographic findings, patient's age and evidence of stability over time also need to be taken into consideration when assessing the likelihood of malignancy of a solid breast nodule.

Over the past 15 years a number of studies have assessed the sensitivity, specificity, and positive/negative predictive value (PPV/NPV) of individual features and combinations of features to try to optimise benign/malignant differentiation. It has been suggested that a radiologist's overall impression can be improved a little by deciding on the presence or absence of a number of features which can then be used in an algorithm to assign a level of risk. However, approximately 1–2% of lesions classified as benign on ultrasound examination are malignant at biopsy.[9,10]

Ultrasound features of a malignant breast mass

- Ill-defined margins
- Irregular shape
- Microlobulation
- Mass taller than wide
- Inhomogeneous internal echo pattern
- Spiculation
- In-pulling of Cooper's ligaments
- Ill-defined echogenic halo
- Distal attenuation
- Intraductal extension of the mass
- Calcification
- Non-compressibility

Techniques to aid the diagnosis of malignancy

Various techniques have been developed to try and aid the operator in the differentiation of malignant and benign disease. In reality, many of these techniques are of limited use as there is considerable overlap between the features found in benign and malignant breast lesions. Core biopsy is ultimately required for the diagnosis of the vast majority of breast lesions.

Ultrasound computer-aided classification

There has been recent interest in whether computers can classify breast masses as benign or malignant. The initial results are encouraging with area under the ROC curve results of around 90%. When in one study the sensitivity was set to 100% the specificity was 26% (rather better than some radiologists!).[11,12]

Doppler and contrast

All cancers, to be viable, need to have a blood supply. Neoangiogenesis occurs in invasive carcinoma and to a lesser extent DCIS. The presence of a tumour circulation can be used to help differentiate benign from malignant masses. Tumour vessels tend to be irregular and tortuous, they penetrate deeply into the tumour mass and arteriovenous shunting may occur. Benign masses mainly have vessels stretched over the surface with a few straight penetrating vessels.

In one recent study colour flow was seen in 68% of malignant lesions and 36% of benign lesions. Pulsatility index and resistive index values are higher in malignant compared to benign masses; however, there is considerable overlap between values for benign and malignant lesions.[13] A paper using three-dimensional power Doppler, scoring such features as number of vascular trees and measures of tortuosity, gave sensitivity, specificity, PPV and NPV results of 92%, 85%, 86% and 91% respectively.[14] These results appear superior to 2D Doppler studies.

The conspicuity of tumour vessels can be increased by using a contrast agent consisting of microbubbles which are injected intravenously. A number of studies suggest a moderate increase in benign/malignant differentiation when using ultrasound contrast agents. More importantly, a recent study has suggested that the use of contrast agents may improve the assessment of tumour size.[15]

Elastography

Elastography (strain imaging) is a method of assessing the stiffness of tissue. Elastography aims to use the increased stiffness of malignant lesions compared with that of benign lesions to aid diagnosis. Invasive breast cancer contains disordered fetal collagen which makes lesions poorly compressible, whilst benign lesions such as fibroadenoma are less stiff even if they contain large amounts of collagen. This is because the collagen in fibroadenomas is well-ordered, adult type collagen.

A recent study has looked at the additional value of adding strain imaging to B-mode imaging when trying to differentiate benign from malignant breast masses. They detected a small but statistically significant improvement in the area under the ROC curve from 0.88 to 0.90, $p = 0.01$. However, there was considerable inter-observer variability, with image quality also affecting observer performance.[16]

Ultrasound classification of invasive breast cancer

Some breast cancers show distinct patterns of growth and so various subtypes of cancer can be identified. Those with specific features are recognised and called special type tumours; these include

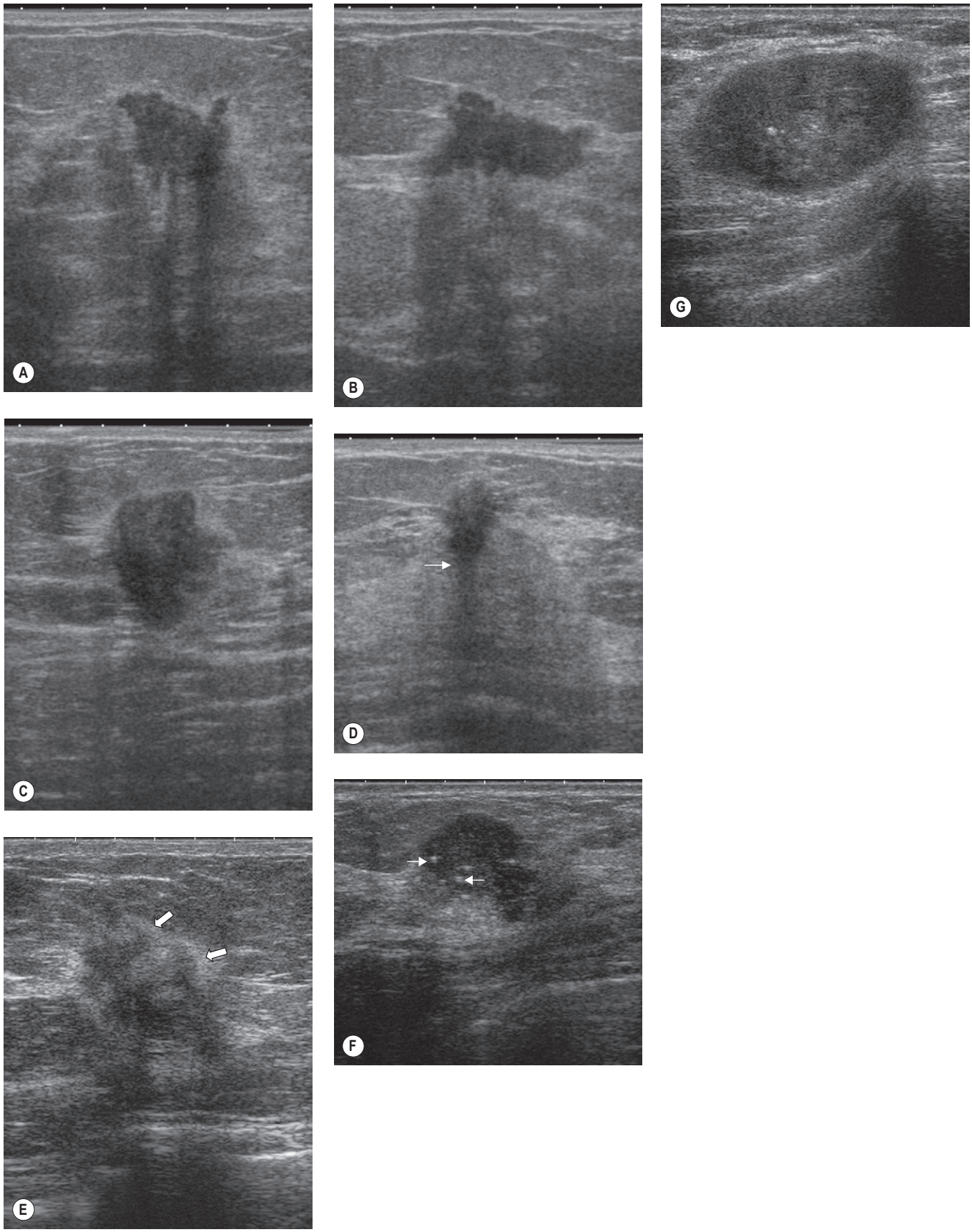

Figure 49.10 **Invasive carcinomas. A and B:** Irregular hypoechoic masses with ill-defined margins are typical of carcinomas. **C:** Malignant masses are more likely to be 'taller than wide'. **D:** Distal attenuation (arrow) obscuring the posterior margin of the tumour is frequently observed, particularly in low histological grade tumours such as this tubular carcinoma. **E:** An echogenic halo (solid arrows) may also be appreciated around malignant masses. **F:** Calcifications (arrows) may be visible in high-grade invasive cancers. **G:** Some high-grade tumours may appear well defined, mimicking a benign lesion – this shows the importance of biopsy to confirm the diagnosis.

lobular, tubular, papillary, cribriform, medullary and metaplastic carcinomas. When a tumour is assigned to a special type group it implies a recognisable pattern of growth rather than a particular cell of origin. These special type tumours exhibit different patterns of behaviour and so carry different prognoses. The vast majority of breast cancers do not fit into one of these groups and are said to be ductal carcinoma of no special type (NST or ductal NST).

The histological grade of a breast cancer has implications for tumour behaviour and prognosis. High-grade tumours are poorly differentiated, grow rapidly and are more likely to metastasise and so carry a poor prognosis compared to low-grade tumours.

Low-grade invasive ductal cancers often appear as a small hypoechoic lesion with an echogenic halo and intense distal shadowing. In contrast, high-grade cancers often show no distal shadowing and may even exhibit posterior enhancement; calcifications are also more frequently observed (Fig. 49.10F, G).[17]

Lobular cancer

Invasive lobular cancer accounts for between 10% and 15% of invasive breast cancer in both symptomatic and screening settings. The incidence of lobular cancer is rising more than other tumour types and this may be related to the use of hormone replacement therapy. Lobular cancers are almost always oestrogen receptor (ER) positive. Lobular cancers usually have low or absent e-cadherin expression. E-cadherin is a cell adhesion molecule and its absence in most cases of lobular cancer may account for the diffuse infiltrative growth pattern often seen in this tumour. The sensitivity of ultrasound for detecting lobular cancer (around 95%) is significantly higher than mammography and physical examination.[18]

Compared with other tumour types, invasive lobular cancers more frequently have an irregular shape, indistinct margins, exhibit hyper- or isoechogenicity compared to fat, and show distal shadowing and architectural distortion.[19] Lobular cancers are less frequently taller than wide compared to invasive ductal cancers.[20]

Underestimation of tumour size by ultrasound is more frequent in lobular cancer than in other tumour types. This has led to many units performing preoperative MR in women diagnosed with lobular cancer breast when breast-conserving surgery is being considered.

Tubular cancer

Tubular cancers are low-grade lesions found most frequently at mammographic screening. On a mammogram they appear as areas of distortion or small spiculated masses. They have low rates of lymph node involvement and vascular invasion and carry an excellent prognosis.

On ultrasound, tubular cancers present as small, hypoechoic masses with marked distal attenuation which may obscure the posterior border (Fig. 49.10D). They frequently have an ill-defined echogenic halo and show in-pulling of adjacent Cooper's ligaments. Tubular cancers tend not to exhibit neovascularity on Doppler examination.

Mucinous cancer

Mucinous cancers are slow-growing lesions which have a good prognosis. They are over-represented in interval cancer studies because mammographically they can appear well defined, mimicking benign lesions. At ultrasound examination mucinous cancers are hypoechoic, inhomogeneous, and commonly show distal enhancement. Partly ill-defined margins, microlobulation and an inability to aspirate an apparently cystic lesion should raise the possibility of a malignant lesion, prompting biopsy.[21,22]

Papillary carcinoma

Papillary cancers can be either encysted (papillary carcinoma in situ) or invasive. They are low-grade lesions with a good prognosis.

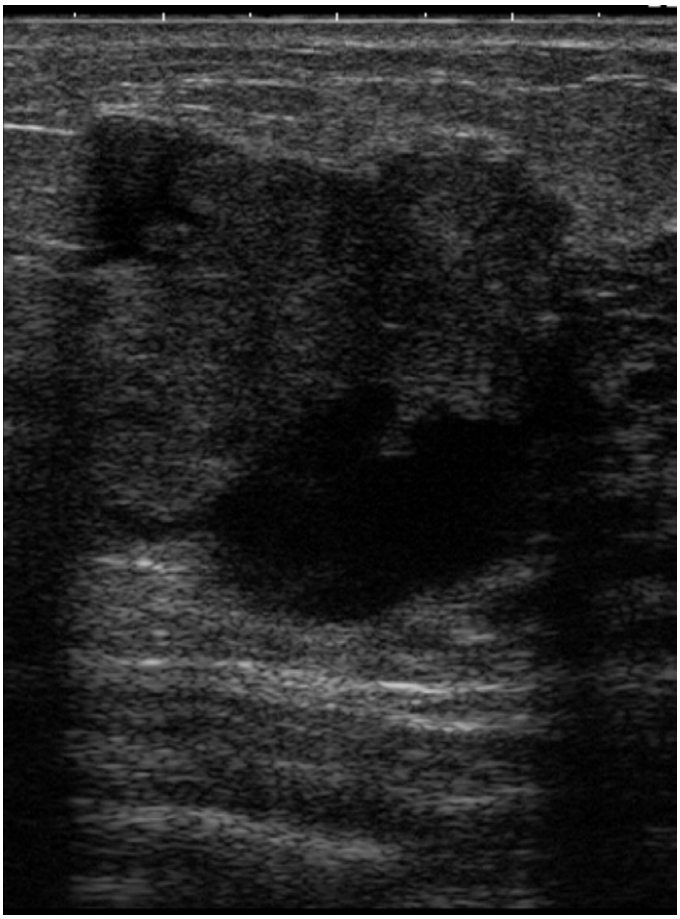

Figure 49.11 Papillary carcinoma. Large, part solid and part cystic mass lesion. The solid component has a rather lobulated appearance, which is typical of a papillary carcinoma. Ultrasound-guided core biopsy showed an invasive papillary carcinoma.

Papillary carcinomas present mammographically as ill-defined or partly well-defined masses.

At ultrasound examination, papillary carcinomas present as either hypoechoic solid or mixed cystic solid masses (Fig. 49.11). They are often well defined but may have an inhomogeneous echo pattern.[23] The intracystic papillary carcinomas tend to be multilobulated and vascular. Layering of blood/debris within the cystic component is occasionally seen. Papillary lesions tend to show either distal enhancement or no distal effect.

Cribriform carcinoma

Invasive cribriform cancers are uncommon low-grade lesions which present mammographically as spiculate masses. Unlike tubular cancers, cribriform carcinomas can be quite large. Invasive cribriform cancers appear at ultrasound examination as ill-defined inhomogeneous masses. They often have an ill-defined echogenic halo but often do not exhibit distal shadowing.[24]

Medullary carcinoma

Medullary tumours are high-grade lesions characterised histologically by a pushing margin and a lymphocytic infiltrate. On mammography, medullary tumours present as a well- or ill-defined mass. Similarly on ultrasound, medullary carcinomas may appear well or ill defined.[25] There are conflicting reports regarding the distal shadowing effect associated with these tumours.

Metaplastic carcinoma

Metaplastic cancers are high-grade tumours which may show chondroid or osseous differentiation. Mammographically they manifest as predominantly well-defined masses. Similarly, on ultrasound examination metaplastic cancers tend to have an oval shape with well-defined margins.[26] Cystic changes are common and acoustic shadowing is unusual. Lesions with osseous or cartilaginous differentiation may show coarse calcification.

BRCA1-related tumours

Some women have a high familial risk of developing breast cancer. Those who carry one of the recognised gene mutations BRCA1 or BRCA2 have a lifetime risk of developing breast cancer of around 85%. Cancers arising in BRCA1 gene carriers are high grade, ER negative and have little associated DCIS. Mammographically they manifest as well- or ill-defined masses with no associated spiculation or calcification. At ultrasound examination they tend to be well defined, have an oval shape and have little distal effect, potentially mimicking benign lesions.[27] Again, this illustrates the importance of performing ultrasound-guided biopsy on apparently benign appearing masses to avoid missing high-grade tumours.

Ultrasound of non-invasive breast cancer (ductal carcinoma in situ)

Ductal carcinoma in situ (DCIS) usually manifests as impalpable mammographic calcifications. Ultrasound of such lesions can be helpful, especially in women with dense breasts. Calcifications may be visible in dilated ducts, particularly when scanning in a radial direction (Fig. 49.12A, B). Sometimes the calcifications cannot be clearly seen but non-specific shadowing or alterations in echogenicity allow the DCIS to be localised. Visualisation of areas of DCIS with ultrasound enables biopsy to be performed under ultrasound guidance, which is both easier for the patient and the radiologist. Another important reason to ultrasound lesions that represent DCIS is to try to identify areas of occult invasion and for these areas to be preferentially biopsied.[28] Finding invasion within the surgical specimen of a lesion with a preoperative core biopsy of DCIS only is a common reason for further surgery. This is because invasive tumours require nodal staging whilst pure DCIS lesions do not.

A recent Japanese study found that 75% of DCIS lesions manifesting as mammographic calcification could be found at ultrasound examination. Ultrasound visualisation was more frequent if the calcifications were of the casting, comedo type or the area of involvement was large (Fig. 49.12B).[29]

Occasionally DCIS is visible as a mass lesion without associated calcification. This is most commonly seen in low-grade DCIS. Such lesions tend to have indeterminate ultrasound features and lack the obvious malignant features often seen in invasive breast cancer. DCIS can also present as a large multilobulated soft tissue filling defect within a cyst. Sometimes DCIS is found within benign lesions of uncertain malignant potential such a papillary lesions and radial scars. The ultrasound features in these cases are then those of the benign lesion rather than the DCIS itself. Rarely, low-grade DCIS can present mammographically and ultrasonically as a focal area of duct dilatation without calcification. A solitary or unilateral segmental group of dilated ducts requires biopsy to exclude the presence of DCIS.

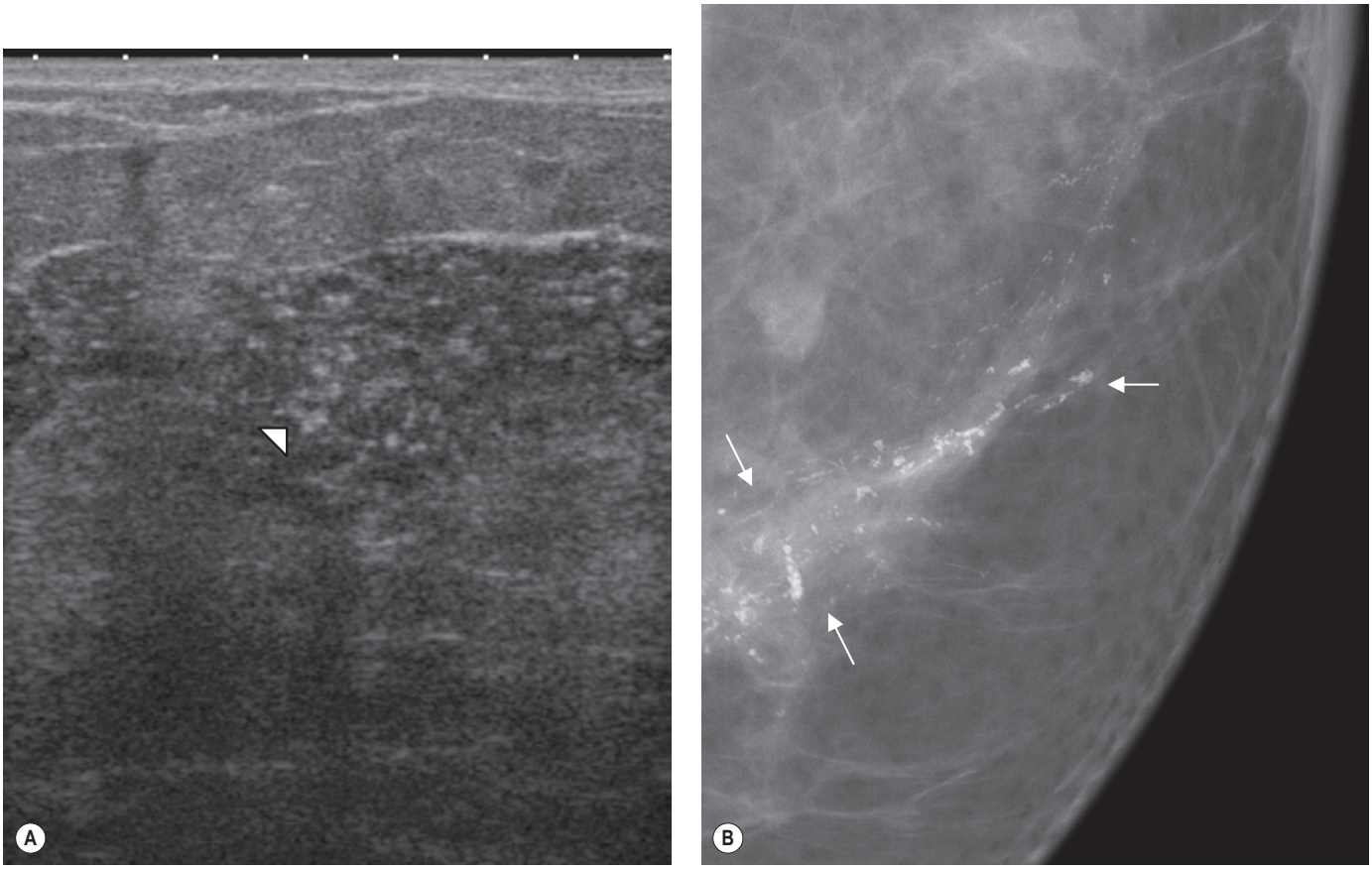

Figure 49.12 Ductal carcinoma in situ (DCIS). A: An extensive area of microcalcifications (arrowhead) is visible in this patient with high-grade DCIS. **B:** Characteristic comedo microcalcifications are visible on the mammogram (arrows).

Other malignant breast lesions

Metastases to the breast

Metastases can occur in the breast from many tumours particularly lymphoma, melanoma and lung cancer. The mammographic appearances of metastases are those of multiple well-defined masses without spiculation or calcification. At ultrasound examination metastases usually appear as well-defined masses without distal shadowing (Fig. 49.13).[30,31]

Angiosarcoma

Angiosarcomas present clinically as either a palpable mass or an area of spontaneous bruising. Angiosarcomas manifest as ill-defined masses or areas of asymmetric density on mammography. Ultrasound shows either a hyperechoic or a mixed hyper- and hypoechoic mass.[32]

Staging operable breast cancer

Once a diagnosis of malignancy is suspected the main tasks for the radiologist are to obtain a definitive histological diagnosis and to stage the cancer. Staging involves estimating invasive tumour size, diagnosing the presence and size of any intraductal component and diagnosing any further foci of tumour in the ipsilateral and contralateral breast. Staging also includes assessing the ipsilateral axillary nodes to try and diagnose axillary nodal metastases preoperatively. Ultrasound has an important role in staging primary operable breast cancer, where its role is complementary to that of mammography and MRI.

Size

Mammography and ultrasound are the standard methods of assessing invasive tumour size. The ability of mammography to accurately assess tumour size is breast density dependent. Mammography and ultrasound are equally accurate in assessing invasive tumour extent in women with a fatty mammographic pattern whilst ultrasound is superior to mammography in predicting tumour extent in women with a dense mammographic background pattern.[33] Ultrasound tends to underestimate histological tumour size by on average a few millimetres. The degree of size underestimation is tumour type dependent, with the degree of underestimation being larger in lobular cancers (7.5 mm) than in ductal tumours (2.5 mm).[34] Mammography is poor at both detecting and sizing lobular cancer, which is why MRI is often used to assess tumour extent in women with cancers with lobular features on core biopsy when breast-conserving surgery is being contemplated.

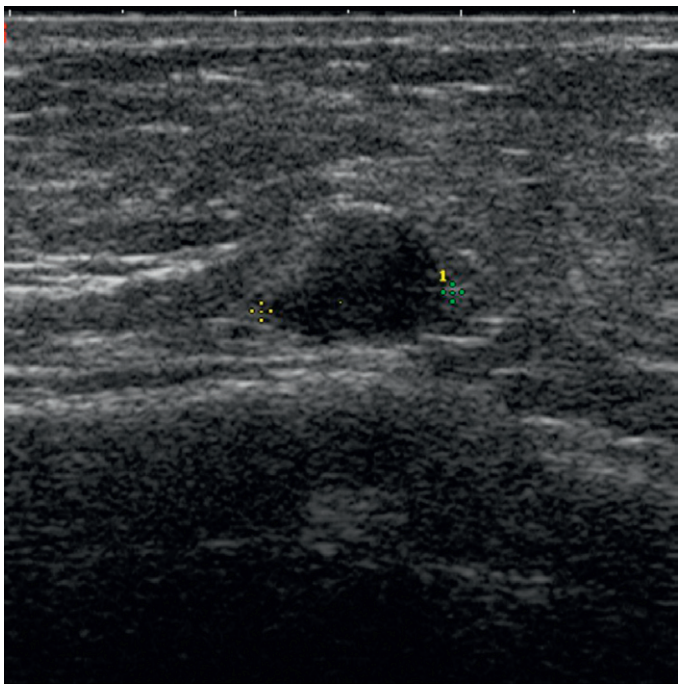

Figure 49.13 Metastasis. This relatively well-defined mass was found to be a metastasis from colonic carcinoma, which the patient had been treated for 6 years previously.

Focality

When a focus of invasive breast cancer has been detected on targeted breast ultrasound then ultrasound of the rest of the ipsilateral breast and the contralateral breast may detect further tumour foci, changing surgical management. A recent study indicated an increase in the detection of multifocal and multicentric disease by performing bilateral whole breast ultrasound, from 15% to 34%. In this study the surgical management was changed in 8% of cases.[35]

In another series, ultrasound detected further tumour foci in 18% of cases compared with 30% for MRI. In this study overestimation of lesion size and multifocality was present in 12% of ultrasound examinations and 21% of MRI examinations.[36] These findings indicate the need to obtain histological confirmation of any possible additional tumour foci with biopsy. The number of additional foci detected is much higher in the ipsilateral breast (14%) than in the contralateral breast (4%).[37]

Intraductal extension

When scanning a breast cancer, the tumour can sometimes be seen extending into adjacent ducts going either towards or away from the nipple (Fig. 49.14). Whether this phenomenon represents invasive tumour spreading down a duct or adjacent DCIS is unclear. Intraductal extension can be observed on ultrasound even when mammography shows none of the characteristic microcalcifications typical of DCIS. Identifying ductal extension by careful interrogation of the ducts adjacent to an invasive tumour is important when estimating tumour size. Some would advocate biopsy of such intraductal extension if its presence will change surgical management as dilated ducts around tumours may simply represent ducts blocked or filled by debris rather than tumour.

A number of studies have suggested that ultrasound is useful in identifying the intraductal component of tumours and that it is superior to mammography and at least equivalent to MRI in this regard.[38,39]

Axilla

Staging the axilla of women with operable breast cancer for nodal metastases is vital since lymph node staging is the strongest prognostic factor for breast cancer and adequate local treatment of lymph node metastases is important to prevent regional recurrence.

Traditionally both the prognostic information and treatment of node-positive patients was achieved by axillary lymph node dissection. This operation is associated with significant long-term morbidity and only a minority of women with nodal metastases derive benefit from the dissection.

To reduce surgical morbidity, sentinel lymph node biopsy and lymph node sampling procedures are often now performed to stage the axilla. Those women with involved nodes will then require further treatment in the form of axillary clearance or radiotherapy. Identification of node-positive patients preoperatively allows definitive axillary treatment at first operation. Ultrasound and

ultrasound-guided biopsy are currently the best way of identifying nodal positivity preoperatively in the clinically negative axilla.

Normal lymph nodes are visible in almost every axilla. Normal lymph nodes have a hypoechoic cortex with a thickness up to 2 mm, and a fatty hyperechoic central hilum (Fig. 49.15). Normal nodes can be very large but almost entirely made up of fat with a thin rim of hypoechoic cortex. Measurement of nodal length is therefore useless in predicting nodal infiltration by tumour. Normal nodes are typically oval in shape. Metastatic nodes are frequently round rather than oval (Fig. 49.16C). Reactive nodes normally have a concentrically thickened cortex while metastatic nodes show either concentric or eccentric cortical thickening of >2 mm (Fig. 49.16A, B). In a recent systematic review of 16 studies, using morphological criteria, ultrasound of non-palpable nodes showed a sensitivity of 44% and a specificity of 92% for predicting malignant nodal involvement. When size criteria were used the sensitivity was higher but the specificity was poorer. Doppler studies show an increase in peripheral flow in some patients with involved nodes. The addition of ultrasound-guided biopsy to ultrasound alone increases the specificity to almost 100% whilst reducing the sensitivity only slightly.[40] Studies of ultrasound-guided core biopsy and fine-needle aspiration of axillary nodes have yielded similar results. The sensitivity of ultrasound and ultrasound-guided biopsy is higher in women with four or more nodes involved (around 90%) and in women with high-grade disease.[41]

Axillary ultrasound and sentinel node biopsy are complementary, helping to avoid one of the common causes of a false negative sentinel node procedure. If the sentinel node is completely replaced by tumour it may not take up the isotope and so the involved sentinel node may be missed. Such cases are easily identified by ultrasound and ultrasound-guided biopsy. Axillary ultrasound and biopsy is therefore a very effective way of reducing the need for further surgery after sentinel node biopsy.

In the future it may be possible to target the sentinel node preoperatively by dual scanning with a hand-held gamma probe and an

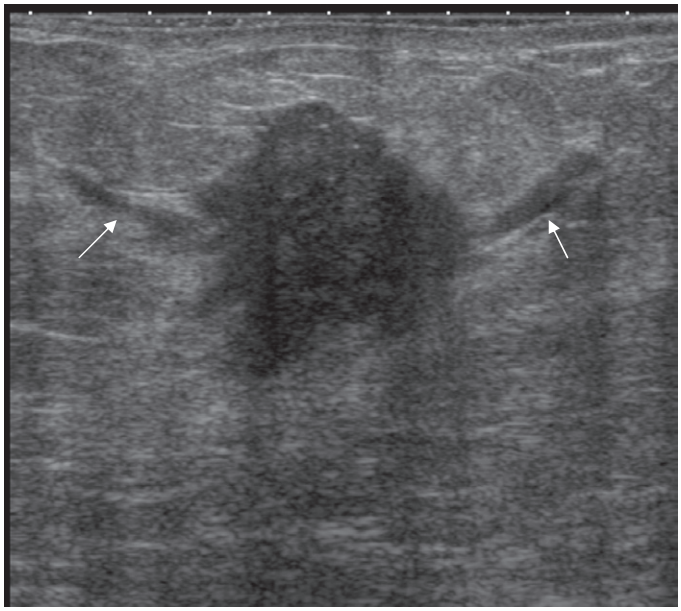

Figure 49.14 Intraductal tumour extension. Tumour can be seen extending along a duct towards and away from the nipple (arrows) in this patient with an invasive carcinoma.

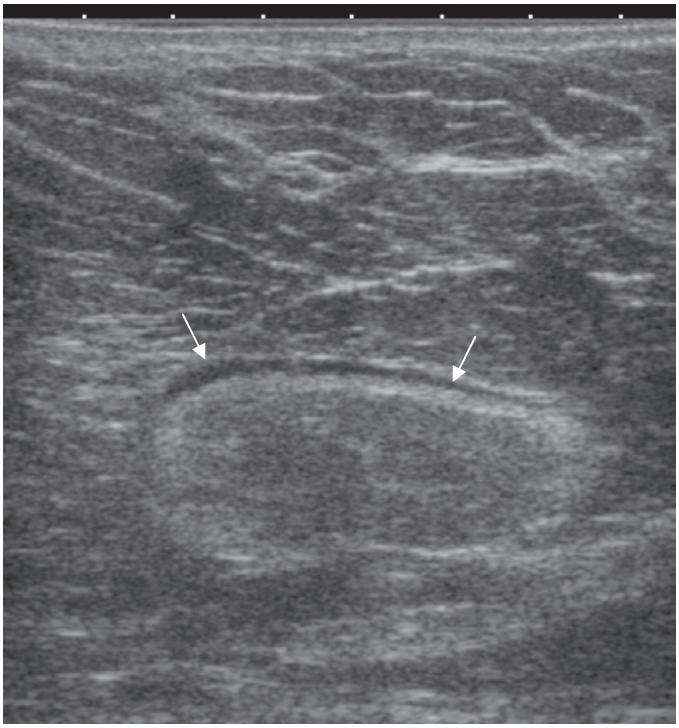

Figure 49.15 Normal axillary lymph node. Normal lymph nodes have a thin, uniform hypoechoic cortex <2 mm thick (arrows) and are oval in shape.

Ultrasound appearances suspicious of axillary lymph node metastases

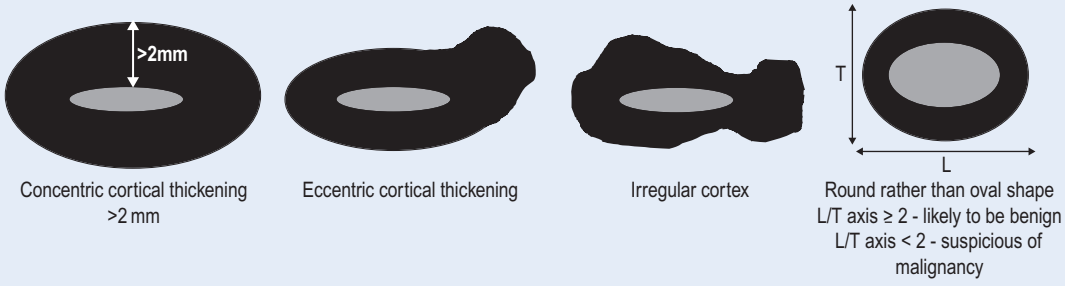

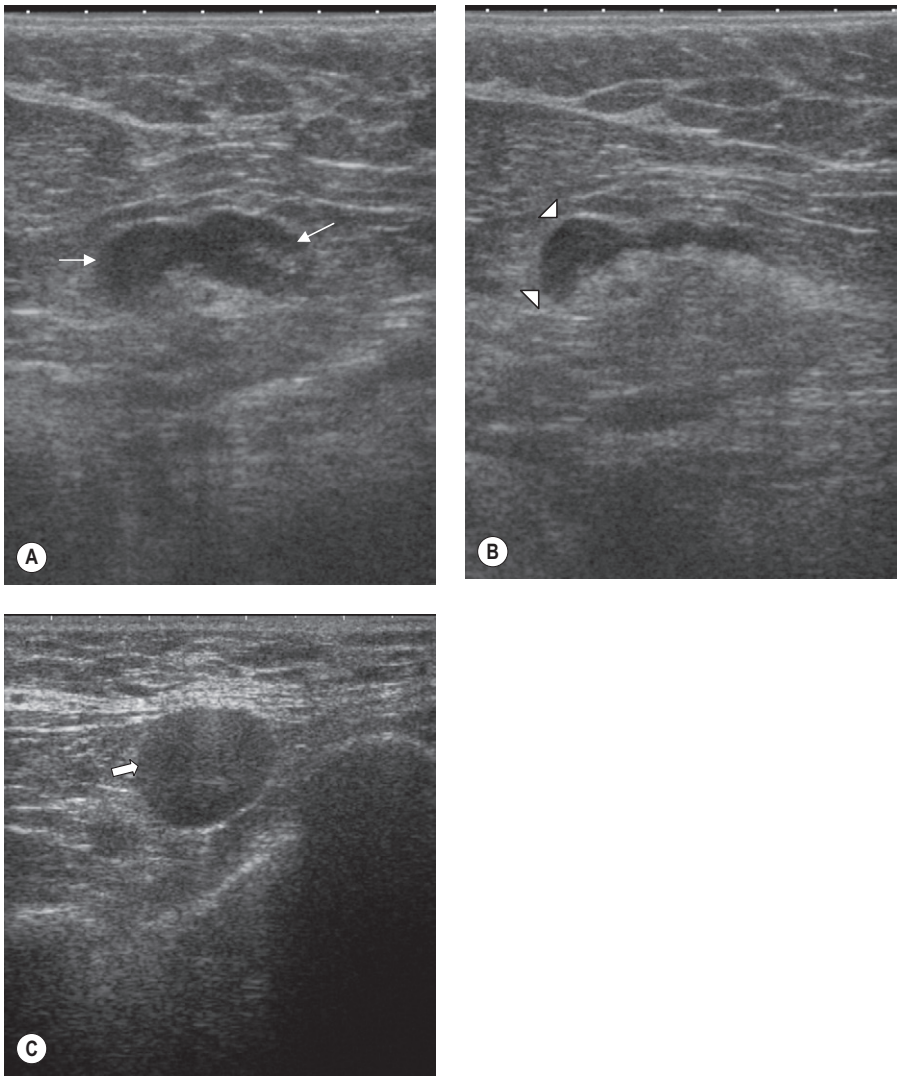

Figure 49.16 Abnormal axillary lymph nodes. Abnormal nodes may show **(A)** uniform cortical thickening (>2 mm) (arrows) or **(B)** eccentric cortical thickening (arrowheads). **C:** Metastatic nodes are frequently round rather than oval (solid arrow). These nodes from three different patients were subjected to ultrasound-guided core biopsy, allowing a preoperative diagnosis of axillary nodal metastasis.

ultrasound probe. The sentinel node could then be scrutinised selectively and heavily sampled or even removed with a vacuum-assisted biopsy device.

Assessment of response after chemotherapy

Ultrasound is useful in assessing response to chemotherapy and hormone therapy in women undergoing adjuvant systemic therapy. There is good correlation between histological tumour size and ultrasound tumour size estimation. Ultrasound is, however, insensitive to residual tumour foci that are <6 mm in diameter. In addition, foci of fibrosis in women with a pathological complete response may be misinterpreted as residual tumour on ultrasound examination.[42]

Some recent studies have suggested that Doppler examination may be helpful in predicting response to chemotherapy, with vascular tumours tending to respond more frequently than avascular tumours. It has also been suggested that changes in vascularity can be used as an early predictor of response.[43,44]

Ultrasound for breast cancer screening

Ultrasound screening in women with normal risk of breast cancer

Any radiologist working in a symptomatic clinic will soon be aware that 10–15% of palpable symptomatic cancers that are visible on ultrasound are not seen on mammography. This is particularly true in younger women with dense breasts and in women with lobular breast cancer. This has led to interest in using ultrasound as an adjunct to mammography when screening women with dense breasts. In contrast, ultrasound detects very few additional cancers in women with a fatty background pattern.

In a recent Italian study of 25572 women who attended for breast screening, 9157 (36%) had normal mammograms but a dense parenchymal pattern (BI-RADS D3–4). This group of women underwent bilateral breast ultrasound. Ultrasound detected 37 additional cancers, giving an incremental cancer detection rate of 0.4%. Ultrasound detected a higher proportion of cancers in younger women. The cancers detected by ultrasound were smaller and more

frequently node negative than the mammographically detected cancers. However, ultrasound caused additional investigations in 4.9% of women and benign surgical biopsies in 0.9%.[45]

In a study from Japan where women were screened with mammography, physical examination and ultrasound, the combination of ultrasound and mammography detected 99% of the cancers found. Ultrasound increased the cancer detection of mammography by 15%.[46]

These results suggest that ultrasound may provide an additional benefit above that seen from mammographic screening in women with dense breasts but at a substantial financial cost and marked increase in false positive results.

Ultrasound screening in women at high familial risk of breast cancer

A number of studies have compared the yield of screening women at high familial risk (>20% lifetime risk) with mammography, ultrasound and MRI. The largest study to data found that ultrasound detected only 40% of the cancers compared to 33% for mammography and 91% for MRI.[47] A number of other studies have shown similar results. It is therefore clear that ultrasound is not an ideal screening modality for women at high familial risk of breast cancer.

ULTRASOUND OF BREAST IMPLANTS

Ultrasound is frequently used to image breast implants, although MRI is the 'gold standard' for assessing the integrity of an implant, with a sensitivity and specificity of over 90%.[48,49]

Breast implants consist of a plastic shell containing a filler which is usually either silicone or saline. When an implant is placed, a fibrous capsule forms around the shell of the implant. Implant rupture can be termed either intracapsular or extracapsular depending on whether the filler leak has extended beyond the fibrous capsule. Imaging is rarely necessary for saline implants as when they leak the saline is absorbed by the body and so the volume loss is usually obvious to both the clinician and the patient!

Intracapsular rupture of silicone implants may be appreciated on ultrasound; the shell of the implant is sometimes seen floating around within the silicone filler in the form of sets of parallel lines – the 'step ladder' sign. It can be difficult to distinguish prominent folds in the shell of the implant from the 'step ladder' sign (Fig. 49.17A). The presence of internal echoes within the silicone can also indicate intracapsular rupture, probably as the result of mixing of silicone and serous fluid. Leakage of silicone into breast tissue beyond the fibrous capsule (extracapsular rupture) may result in the formation of silicone granulomas due to a foreign body giant cell reaction to the extruded material. This can present clinically as a palpable lump. Silicone granulomas have a characteristic 'snow storm' appearance on ultrasound and so usually do not require biopsy to establish the diagnosis (Fig. 49.17B). Identifying these signs makes it possible to diagnose implant rupture on ultrasound with a sensitivity of 50% and a specificity of 55%.[50]

Silicone may also migrate to more distant sites and it is not unusual to see silicone in axillary lymph nodes in cases of extracapsular rupture. The nodes are typically enlarged and also exhibit the same 'snow storm' appearance typical of the silicone granuloma.

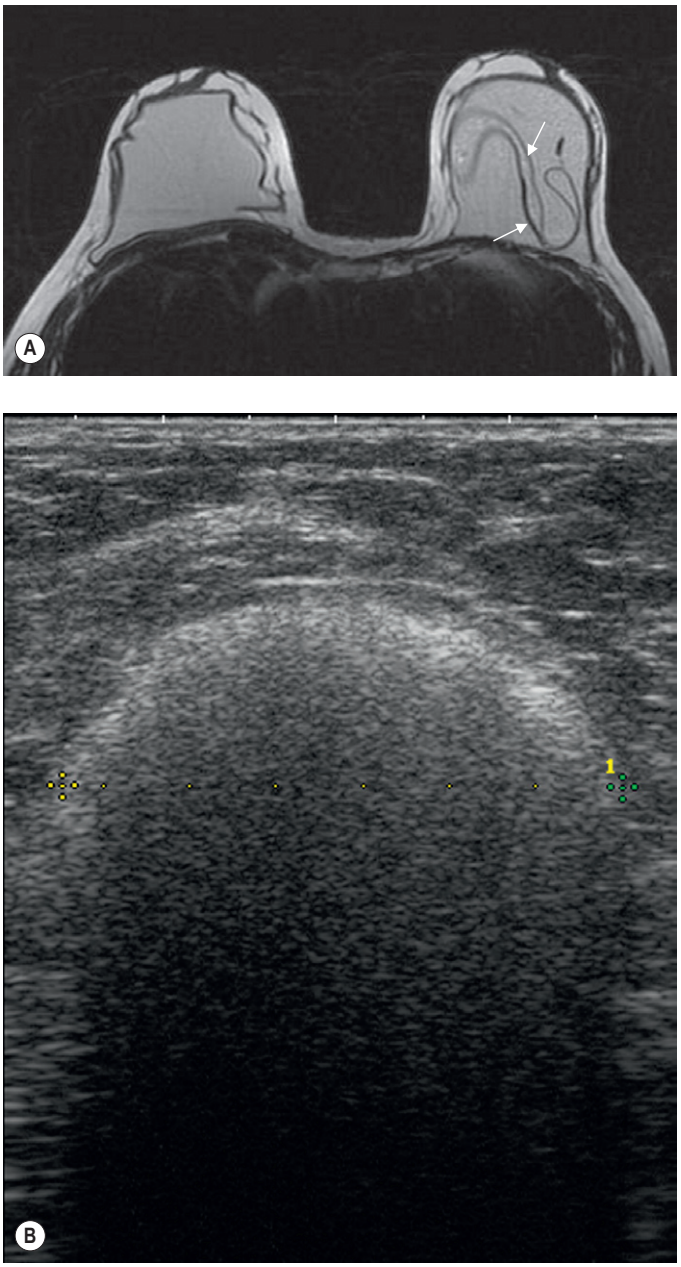

Figure 49.17 Breast implants. A: MRI is the 'gold standard' for assessing implant integrity. The left breast implant is ruptured and the shell of the implant can be seen floating in the silicone filler (arrows). On ultrasound it can be difficult to distinguish rupture from normal implant folds. **B:** A 'snow storm' appearance is characteristic of a silicone granuloma.

ULTRASOUND-GUIDED BREAST BIOPSY

The key to successful breast diagnosis is the combination of imaging, clinical examination and percutaneous needle biopsy – the so-called triple assessment. The use of percutaneous biopsy avoids the need for open surgical biopsy for breast diagnosis. Surgery should be reserved for the treatment of breast cancer or occasionally the excision of lesions of uncertain malignant potential, rather than for diagnosis.

Screening programmes account for an increasing proportion of the breast cancers diagnosed. Many of these lesions are impalpable and so image-guided percutaneous biopsy is crucial for preoperative diagnosis. Ultrasound is the preferred method of image guidance. When a lesion is not visible on ultrasound, biopsy under stereotactic X-ray guidance is required. Stereotactic biopsy is more time-consuming, involves the use of specialist equipment and ionising radiation. Abnormalities such as microcalcifications which are frequently not visible on ultrasound require biopsy under stereotactic biopsy, although with the improved spatial and contrast resolution properties of modern ultrasound machines many more microcalcifications are sonographically visible.

Table 49.1 The use of needle biopsy in breast imaging

Biopsy type	Advantages	Disadvantages
Fine-needle aspiration	(1) Shorter specimen processing times with ability to offer same day results (2) Much larger areas of the lesion can be sampled (3) Safer in more challenging areas – adjacent to vessels and breast implants	(1) Higher rates of false positives and negatives (2) Unable to differentiate between invasive and in-situ disease (3) Operator dependent with high number of inadequate samples (4) Requires highly skilled cytopathologists
Core biopsy (14G)	(1) Improved accuracy compared with FNA (2) Less operator dependent (3) Easier histopathological interpretation (4) Able to differentiate invasive from in-situ disease	(1) Minimum 24-hour lab turnaround time – longer at many hospitals (2) Higher rate of complications
Vacuum-assisted biopsy	(1) Larger volumes of tissue are removed, leading to a reduction in sampling errors (2) Reduced under-staging of DCIS (3) Complete excision of small benign/borderline lesions as an alternative to surgery	Expensive

Even when a lesion is clinically palpable, image-guided biopsy can be more accurate. When an ultrasound biopsy is performed the operator is able to verify that the needle has passed through the lesion, confirming successful biopsy. Sometimes tumours may contain necrotic material and in this situation ultrasound-guided biopsy can be targeted at viable tumour tissue. The use of ultrasound also allows the safe targeting of lesions in more anatomically challenging areas such as the axilla. In our institution, all percutaneous biopsies for ultrasound visible lesions are performed under image guidance even when clinically palpable.

There are three different types of needle biopsy that can be performed under ultrasound guidance. These are fine-needle aspiration (FNA), needle core biopsy (NCB) and large-bore vacuum-assisted biopsy or mammotomy (VAM) (Table 49.1).

Fine-needle aspiration (FNA) or core biopsy

FNA of breast lesions has been practised for many years. The technique involves the passage of a fine needle, typically 23G, through a lesion. Multiple passes are made through the area of concern, with the aim of capturing representative cells in the barrel of the needle. Suction is applied with the aim of increasing cell yield. The aspirate is then either smeared onto a microscope slide or washed into a cytology transport medium for processing in the laboratory. The procedure is easily performed under ultrasound guidance.

In the mid-1990s automated, spring loaded 'guns' were developed enabling cores of breast tissue to be obtained (Fig. 49.18A–C). After the injection of local anaesthetic, a cutting needle is positioned immediately adjacent to the area to be sampled. A 20 mm inner sampling notch is fired through the lesion and almost immediately, an outer sheath closes over the notch, trapping a core of tissue which can then be retrieved by the operator. Core biopsy devices used for breast diagnosis are typically 14G, delivering a sample weight of around 15–20 mg. Smaller bore devices are available, but tend to give less reliable results.

There are some problems with FNA. The technique is associated with higher rates of false positives and false negatives. For instance, cytological samples from conditions like fat necrosis and lactational change can be misinterpreted as potentially malignant. Also samples from low-grade tumours with lower cellularity may lead to false negative interpretations. FNA is also unable to differentiate between invasive and in-situ disease. FNA is particularly poor at diagnosing lobular cancers while core biopsy is diagnostic in over 90% of cases. FNA is more operator dependent, with a relatively high number of inadequate samples. It also requires the expertise of highly skilled cytopathologists. Ultrasound-guided core biopsy has been shown to be more accurate than FNA in breast diagnosis, with the absolute sensitivity of ultrasound-guided FNA for diagnosing malignancy being 83% compared to core biopsy at 97%.[51,52]

The improved performance of core biopsy over FNA is well illustrated in the UK National Health Service Breast Screening Programme (NHSBSP). In the early 1990s only around 10% of units were able to achieve the then minimum standard for preoperative diagnosis of breast cancer of 70%; with the move to core biopsy in the mid-1990s, dramatic improvements in performance were observed enabling the target standard of 90% preoperative diagnosis rate to be achieved.[53]

FNA does have a few advantages over core biopsy. Specimen processing time is much shorter for FNA samples and in some units this used to offer an instant reporting service in a 'one-stop' clinic. It is also possible to sample much larger areas of a lesion with FNA, as the needle can be directed to different sites during each pass. This may be helpful when undertaking preoperative sampling of axillary lymph nodes in patients with breast cancers. FNA is also potentially safer in more challenging anatomical locations, adjacent to blood vessels, breast implants, etc. For this reason some operators advocate the use of FNA for the biopsy of axillary lymph nodes, but in reality any potentially involved node is to be found lying low in the axilla, well away from the axillary vessels or other danger sites. Consequently 14G core biopsy of axillary nodes is a well-tolerated and safe technique.[41]

Large-bore vacuum-assisted biopsy

One of the reasons why a 100% preoperative diagnosis is not achieved and open surgical biopsies for breast disease still take place is due to sampling error or failure to retrieve sufficient representative tissue. Large-bore vacuum biopsy devices have been developed to try and address these problems. They can be used under ultrasound or stereotactic guidance. These devices use much larger needles, typically between 11G and 8G, to obtain larger volumes of tissue. Cores of tissue obtained with these devices typically weigh around 300 mg. Some of the systems are fully automated, allowing multiple cores to be obtained and collected from multiple sites in a relatively short period of time. Following infiltration with local anaesthetic, the needle is positioned adjacent to the area to be sampled. A vacuum is applied sucking tissue into the needle aperture, a rotating blade then spins or cuts forward capturing the specimen, which is then transported to a collection chamber or port. In the most automated systems the needle can be rotated through 360° and tissue sampled as many times as required without

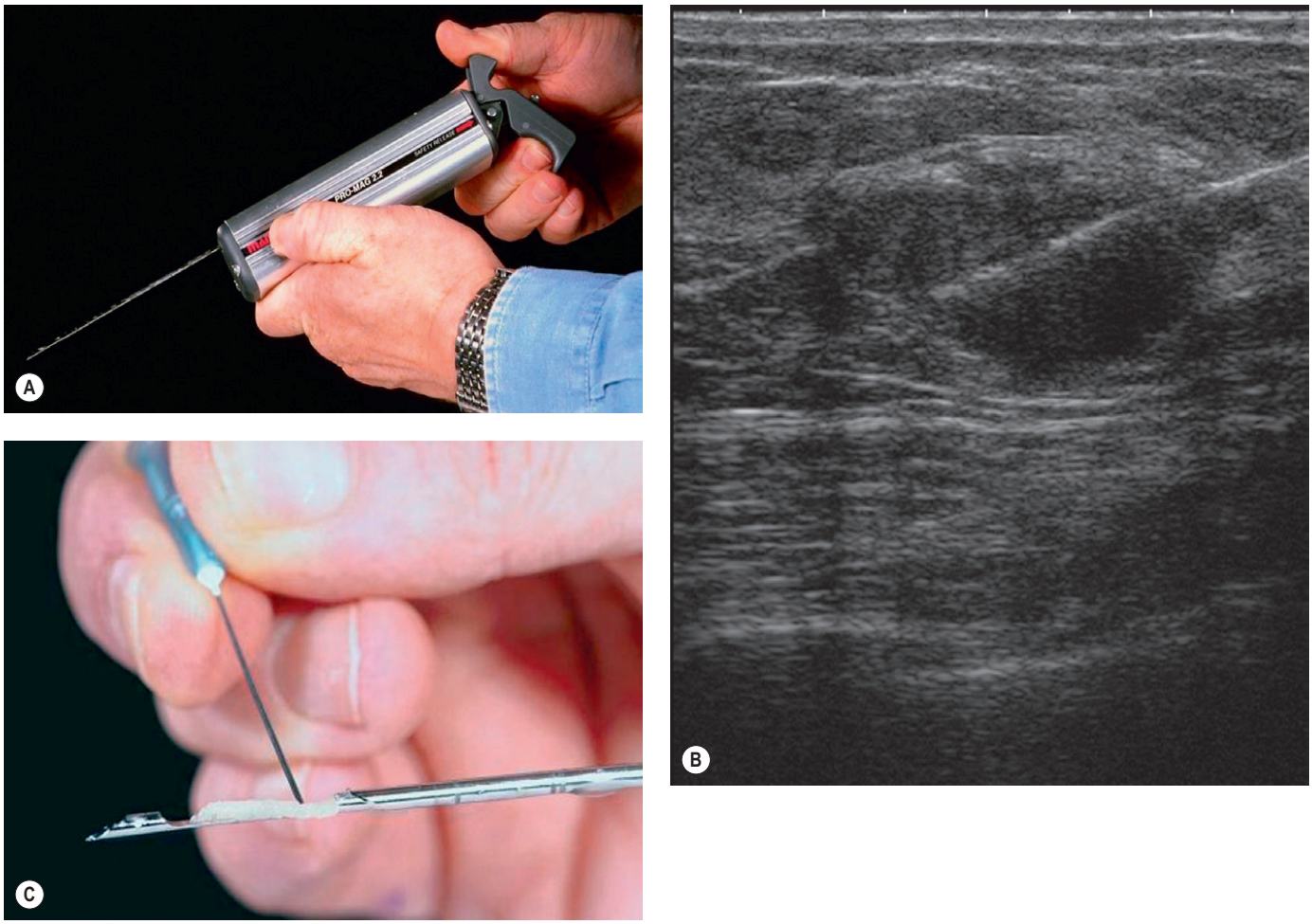

Figure 49.18 Ultrasound-guided core biopsy. A: An automated spring-loaded gun is used for ultrasound-guided core biopsies. The tip of the 14G needle is positioned adjacent to the lesion to be sampled. **B:** When the 'gun' is 'fired', the needle is visualised passing through the mass. **C:** A core of tissue is trapped within the sampling notch and can then be retrieved by the operator.

removing the needle from the breast. Consequently it is also possible to use these devices to remove small lesions from the breast.

The main benefit of performing vacuum-assisted biopsy is in the diagnosis of ductal carcinoma in situ (DCIS) and borderline lesions. The larger volume of tissue obtained reduces the risk of missing areas of invasive carcinoma within areas of DCIS, effectively understaging the disease. Core biopsy is said to under-stage the presence of invasive malignancy associated with DCIS in just over 20% of cases, whilst this is found to occur in only around 11% of cases when a vacuum-assisted biopsy is performed.[54]

For some borderline lesions, such as radial scars and papillomas, core biopsy may fail to provide a definitive diagnosis. Traditionally diagnostic surgery has been performed when these lesions have been diagnosed. A larger volume of tissue is required to avoid missing associated atypical proliferations, DCIS or invasive carcinoma. It has been suggested that vacuum-assisted excision of radial scars and papillary lesions is a safe and minimally invasive alternative to open surgical biopsy when the initial core biopsy has shown no evidence of atypia, although this approach still remains controversial.[55–57]

Ultrasound-guided vacuum-assisted biopsy can be used as an alternative to open surgery for the excision of benign lesions such as fibroadenomas. Typically fibroadenomas measuring less than 30 mm are amenable to percutaneous excision using this technique, which is safe and well tolerated by patients.

WIRE LOCALISATIONS OF IMPALPABLE BREAST LESIONS

Impalpable breast cancers require some form of localisation procedure prior to breast-conserving surgery so that the surgeon can confidently identify the tumour site. When the lesion is sonographically visible the localisation is performed under ultrasound guidance. The most commonly employed method of localisation is using a hook wire. The technique is similar to performing an ultrasound-guided biopsy, with the localisation needle inserted through the lesion under ultrasound guidance. A hook or similar structure on the end of the wire prevents movement once deployed.

When biopsies have been performed under stereotactic X-ray guidance, particularly for small clusters of microcalcifications, it is common practice to insert a marker at the biopsy site. Several proprietary brands of marker clips also contain 'gel' pellets that are ultrasound visible, enabling any subsequent localisation to be performed under ultrasound guidance even if the original abnormality was not sonographically visible.

Specimen radiography is used to ensure that the lesion has been excised with the appropriate tissue margin. For cancer surgery, the surgeon aims for a 10 mm clear margin around the tumour.

REFERENCES

1. Stavros AT, Thickman D, Rapp CL, et al. Solid breast nodules: use of sonography to distinguish between benign and malignant lesions. Radiology 1995;196:123–134.
2. Smith GEC, Burrows P. Ultrasound diagnosis of fibroadenoma – is biopsy always necessary? Clin Radiol 2008;63:511–515.
3. Chao TC, Chao HH, Chen MF. Sonographic features of breast hamartomas. J Ultrasound Med 2007;26:447–452.
4. Rizzo M, Lund MJ, Oprea G, et al. Surgical follow-up and clinical presentation of 142 breast papillary lesions diagnosed by ultrasound-guided core-needle biopsy. Annal Surg Oncol 2008;15:1040–1047.
5. Carter BA, Simpson JF. Papillomas and related lesions. In: O'Malley FP, Pinder SE, editors. Breast pathology. Edinburgh: Churchill Livingstone Elsevier; 2006.
6. Ganesan S, Karthik G, Joshi M, Damodaran V. Ultrasound spectrum in intraductal papillary neoplasms of breast. Br J Radiol 2006;79:843–849.
7. Kim TH, Kang DK, Kim SY, et al. Sonographic differentiation of benign and malignant papillary lesions of the breast. J Ultrasound Med 2008;27:75–82.
8. Cawson JN. Can sonography be used to help differentiate between radial scars and breast cancer? Breast 2005;14:352–359.
9. Paulinelli RR, Freitas-Júnior R, Moreira MA, et al. Risk of malignancy in solid breast nodules according to their sonographic features. J Ultrasound Med 2005;24:635–641.
10. Lister D, Evans AJ, Burrell HC, et al. The accuracy of breast ultrasound in the evaluation of clinically benign discrete, symptomatic breast lumps. Clin Radiol 1998;53:490–492.
11. Drukker K, Gruszauskas NP, Sennett CA, Giger ML. Breast US computer-aided diagnosis workstation: performance with a large clinical diagnostic population. Radiology 2008;248:392–397.
12. Duname VA, Shanker PM, Piccoli CW, et al. Computer aided classification of masses in ultrasonic mammography. Med Phys 2002;29:1968–1973.
13. del Cura JL, Elizagaray E, Zabala R, et al. The use of unenhanced Doppler sonography in the evaluation of solid breast lesions. AJR Am J Roentgenol 2005;184:1788–1794.
14. Huang SF, Chang RF, Moon WK, et al. Analysis of tumour vascularity using three-dimensional power Doppler ultrasound images. IEEE Trans Med Imaging 2008;27:320–330.
15. van Esser S, Veldhuis WB, van Hillegersberg R, et al. Accuracy of contrast-enhanced breast ultrasound for pre-operative tumor size assessment in patients diagnosed with invasive ductal carcinoma of the breast. Cancer Imaging 2007;7:63–68.
16. Burnside ES, Hall TJ, Sommer AM, et al. Differentiating benign from malignant solid breast masses with US strain imaging. Radiology 2007;245:401–410.
17. Rotstein AH, Neerhut PK. Ultrasound characteristics of histologically proven grade 3 invasive ductal breast carcinoma. Australas Radiol 2005;49:476–479.
18. Selinko VL, Middleton LP, Dempsey PJ. Role of sonography in diagnosing and staging invasive lobular cancer. J Clin Ultrasound 2004;32:323–332.
19. Watermann DO, Tempfer C, Hefler LA, et al. Ultrasound morphology of invasive lobular breast cancer is different compared with other types of breast cancer. Ultrasound Med Biol 2005;31:167–174.
20. Cawson JN, Law EM, Kavanagh AM. Invasive lobular carcinoma: sonographic features of cancers detected in a BreastScreen Program. Australas Radiol 2001;45:25–30.
21. Lam WW, Chu WC, Tse GM, Ma TK. Sonographic appearance of mucinous carcinoma of the breast. AJR Am J Roentgenol 2004;182:1069–1074.
22. Chopra S, Evans AJ, Pinder SE, et al. Pure mucinous breast cancer – mammographic and ultrasound findings. Clin Radiol 1996;51:421–424.
23. McCulloch GL, Evans AJ, Yeoman L, et al. Radiological features of papillary carcinoma of the breast. Clin Radiol 1997;52:865–868.
24. Stutz JA, Pinder S, Ellis IO, et al. The radiological appearances of invasive cribriform carcinoma of the breast. Clin Radiol 1994;49:693–695.
25. Yilmaz E, Lebe B, Balci P, et al. Comparison of mammographic and sonographic findings in typical and atypical medullary carcinomas of the breast. Clin Radiol 2002;57:640–645.
26. Yang WT, Hennessy B, Broglio K, et al. Imaging differences in metaplastic and invasive ductal carcinomas of the breast. AJR Am J Roentgenol 2007;189:1288–1293.
27. Hamilton LJ, Evans AJ, James JJ, et al. The imaging features of BRCA1 and BRCA2 related breast cancer. Clin Radiol 2004;59:895–902.
28. Teh WL, Wilson ARM, Evans AJ, et al. Ultrasound guided core biopsy of suspicious mammographic calcifications using high frequency ultrasound and power doppler ultrasound. Clin Radiol 2000;55:390–394.
29. Nagashima T, Hashimoto H, Oshida K, et al. Ultrasound demonstration of mammographically detected microcalcifications in patients with ductal carcinoma in situ of the breast. Breast Cancer 2005;12:216–220.
30. Ribeiro-Silva A, Mendes CF, Costa IS, et al. Metastases to the breast from extramammary malignancies: a clinicopathologic study of 12 cases. Pol J Pathol 2006;57:161–165.
31. Lyou CY, Yang SK, Choe DH, et al. Mammographic and sonographic findings of primary breast lymphoma. Clin Imaging 2007;31:234–238.
32. Yang WT, Hennessy BT, Dryden MJ, et al. Mammary angiosarcomas: imaging findings in 24 patients. Radiology 2007;242(3):725–734.
33. Fasching PA, Heusinger K, Loehberg CR, et al. Influence of mammographic density on the diagnostic accuracy of tumor size assessment and association with breast cancer tumor characteristics. Eur J Radiol 2006;60:398–404.
34. Pritt B, Ashikaga T, Oppenheimer RG, Weaver DL. Influence of breast cancer histology on the relationship between ultrasound and pathology tumour size measurements. Mod Pathol 2004;17:905–910.
35. Wilkinson LS, Given-Wilson R, Hall T, et al. Increasing the diagnosis of multifocal primary breast cancer by the use of bilateral whole-breast ultrasound. Clin Radiol 2005;60:573–578.
36. Berg WA, Gutierrez L, NessAvier MS, et al. Diagnostic accuracy of mammography, clinical examination, US and MR imaging in preoperative assessment of breast cancer. Radiology 2004;233:830–849.
37. Moon WK, Noh DY, Im JG. Multifocal, multicentric and contralateral breast cancers: bilateral whole breast US in the preoperative evaluation of patients. Radiology 2002;224:569–576.
38. Kang DK, Jeon GS, Yim H, Jung YS. Diagnosis of the intraductal component of invasive breast cancer: assessment with mammography and sonography. J Ultrasound Med 2007;26:1587–1600.
39. Sundararajan S, Tohno E, Kamma H, et al. Role of ultrasonography and MRI in the detection of wide intraductal component of invasive breast cancer – a prospective study. Clin Radiol 2007;62:252–261.
40. Alvarez S, Añorbe E, Alcorta P, et al. Role of sonography in the diagnosis of axillary lymph node metastases in breast cancer: a systematic review. AJR Am J Roentgenol 2006;186:1342–1348.
41. Damera A, Evans AJ, Cornford EJ, et al. Diagnosis of axillary nodal metastases by ultrasound-guided core biopsy in primary operable breast cancer. Br J Cancer 2003;89:1310–1313.
42. Roubidoux MA, LeCarpentier GL, Fowlkes JB, et al. Sonographic evaluation of early-stage breast cancers that undergo neoadjuvant chemotherapy. J Ultrasound Med 2005;24:885–895.
43. Kuo WH, Chen CN, Hsieh FJ, et al. Vascularity change and tumor response to neoadjuvant chemotherapy for advanced breast cancer. Ultrasound Med Biol 2008;34:857–866.
44. Kumar A, Singh S, Pradham S, et al. Doppler ultrasound scoring to predict chemotherapeutic response in advanced breast cancer. World J Surg Oncol 2007;5:99.
45. Corsetti V, Houssami N, Ferrari A, et al. Breast screening with ultrasound in women with mammography-negative dense breasts: evidence on incremental cancer detection and false positives, and associated cost. Eur J Cancer 2008;44:539–544.
46. Uchida K, Yamashita A, Kawase K, Kamiya K. Screening ultrasonography revealed 15% of mammographically occult breast cancers. Breast Cancer 2008;15:165–168.
47. Kuhl CK, Schrading S, Leutner CC, et al. Mammography, breast ultrasound, and magnetic resonance imaging for surveillance of women at high familial risk for breast cancer. J Clin Oncol 2005;23:8469–8476.
48. Berg WA, Caskey CI, Hamper U, et al. Single- and double-lumen silicone breast implant integrity: prospective evaluation of MR and US criteria. Radiology 1995;197:45–52.
49. Everson LI, Parantainen H, Detlie T, et al. Diagnosis of implant rupture: imaging findings and relative efficacies of imaging techniques. AJR Am J Roentgenol 1994;163:57–60.
50. Venta LA, Salomon CG, Flisak ME, et al. Sonographic signs of breast implant rupture. AJR Am J Roentgenol 1996;166:1412–1419.
51. Britton PD. Fine needle aspiration or core biopsy. The Breast 1999;8:1–4.
52. Britton PD, McCann J. Needle biopsy in the NHS breast screening programme 1996/7: how much and how accurate? The Breast 1999;8:5–11.
53. Litherland JC, Evans AJ, Wilson ARM, et al. The impact of core-biopsy on the preoperative diagnosis rate of screen detected breast cancers. Clin Radiol 1996;51:562–565.

54. Jackman RJ, Burbank F, Parker SH, et al. Stereotactic breast biopsy of non-palpable lesions: determinants of ductal carcinoma in situ underestimation rates. Radiology 2001;218:497–502.
55. Brenner RJ, Jackman RJ, Parker SH, et al. Percutaneous core needle biopsies of radial scars of the breast: when is excision necessary? AJR Am J Roentgenol 2002;179:1179–1184.
56. Guidelines for Breast Screening Assessment 2005 NHSBSP Publication No 49. www.cancerscreening.nhs.uk/breastscreen/publications/nhsbsp49.html.
57. Libermann L, Tornos C, Huzjan R, et al. Is surgical excision warranted after benign, concordant diagnosis of papilloma at percutaneous breast biopsy? AJR Am J Roentgenol 2006;186:1328–1334.

CHAPTER

50 Lung, pleura and chest wall

Najib M. Rahman and Fergus V. Gleeson

INTRODUCTION

Thoracic ultrasound is a valuable technique in the assessment of patients with thoracic disease. Although ultrasound is unable to penetrate normal aerated lung, and skill is required to assess the thoracic organs between the ribs, it has an important role in diagnosis and intervention within the thorax, and in fact has been used in this context for over 40 years.[1,2]

TECHNICAL REQUIREMENTS

Sonographic examination of the chest wall, axilla and supraclavicular regions (e.g. for the detection of bony metastases or lymph nodes) requires a linear array probe using frequencies of 5.0–7.5 MHz. Small footprint sector transducers allow better intercostal access for scanning the pleura and peripheral pulmonary parenchyma when abnormal. Tilting and turning the sector probe within each intercostal space will provide good views of the pleura and underlying pulmonary anatomy. Convex probes provide a wider view which can be especially helpful in assessing large pleural effusions. For the pleura and lung, frequencies from 3.5 to 5 MHz provide a good balance between depth of penetration and detail.[3] For routine clinical use in chest ultrasound, a combination of a 3.5 MHz sector or curved array probe and a 5–7.5 MHz small parts linear probe is ideal.

EXAMINATION TECHNIQUE

Patient position

Patient position should be selected to maximise ease of examination and possible views. This will in some respects depend upon whether a diagnostic scan or guided intervention is planned. As most thoracic ultrasound is performed in patients with pleural effusions, generally the patient is positioned sitting up with their arms resting on a trolley or table in front of them. This widens the intercostal spaces, and rotates the shoulder blades externally. The examination is then performed from the back and in the lateral areas of the chest. Patients may alternatively lie in the left or right lateral decubitus position (with the opposite hemithorax then available for examination) with the arm raised, exposing the axillary area. A prone, supine or lateral decubitus position is preferable if a biopsy is performed as this decreases the risk of a vasovagal episode and patients are less likely to move. When patients are in pain, immobile or bed bound (e.g. the intensive care setting) a supine position perhaps with minor elevation of the right or left side is often the only position attainable. The supine position is used to examine the anterior hemithorax.

Technique

The transducer is positioned in parallel to the ribs in the intercostal space to assess the intrathoracic anatomy (lung and pleura). Moving along the intercostal spaces and tilting the transducer within each space permits detailed information to be gathered on three-dimensional relationships within the thoracic cavity. Longitudinal and transverse sections may be helpful, especially in the diagnosis of chest wall and rib lesions. Scanning and comparison with the normal side may be of value to assist interpretation of pleural abnormalities, particularly in difficult to access areas.

CHEST WALL

Soft tissue lesions

Suspicious findings during palpation of the chest wall are most easily initially examined with ultrasound. Common lesions such as lipomas, haematomas, lymph nodes and rib metastases may be detected in this manner (Figs 50.1 and 50.2). Lymph node metastases appear as round to oval poorly reflective inhomogeneous structures (Fig. 50.3A and B). Extracapsular extension with irregular borders and diffuse infiltrating growth into vessels and the

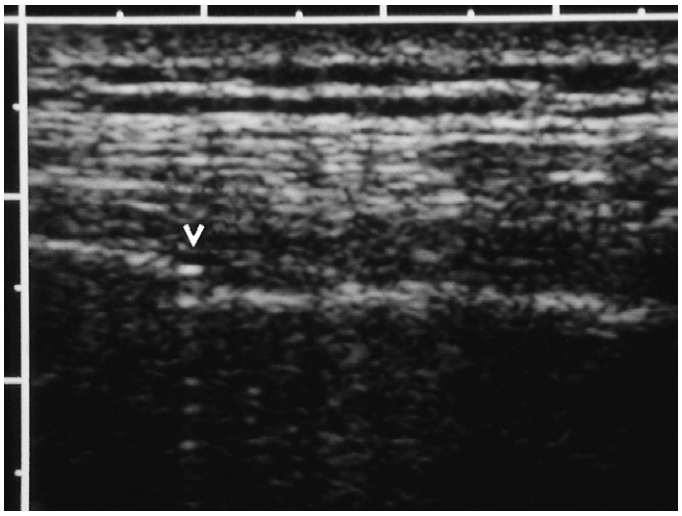

Figure 50.1 Rib fracture: 2 mm step in longitudinal section. Note reverberation echoes from the step (arrowhead).

surrounding tissue may rarely be seen. Reactive and inflammatory lymph nodes are typically oval or triangular; some are elongated with an increasingly reflective centre during healing. Malignant lymphomas also appear echo-poor. They are rounded and sharply bordered but do not infiltrate adjacent tissues. Although some ultrasound criteria help distinguish the aetiology of lymphadenopathy, similar pictures occur in different aetiologies.[3] Malignant infiltration of the chest wall by tumour is detected with a high degree of accuracy using ultrasound[4,5] (Fig. 50.4).

Bony lesions

The normal ribs are visualised sonographically as well-defined echo-poor shadows with well-defined reflective borders. Rib fractures are more easily diagnosed on ultrasound than on chest radiography, with up to a 50% increase in diagnostic sensitivity using ultrasound.[3] Typical sonographic findings are gaps, steps, dislocation, haematoma and small associated pleural effusions (Fig. 50.1). Minute dislocations and fissures may be visible by a reverberation artefact, known as the so-called 'lighthouse' or 'chimney' phenomenon.[6] This is produced by the ultrasound beam passing through the gap in the bony structure, and being reflected by the lung surface. Fracture-associated haematomas may be seen as echo-poor areas adjacent to the fracture and soft tissues. Osteolytic rib

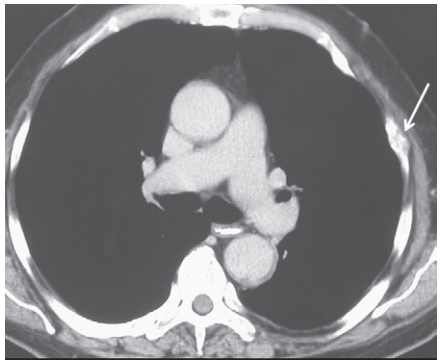

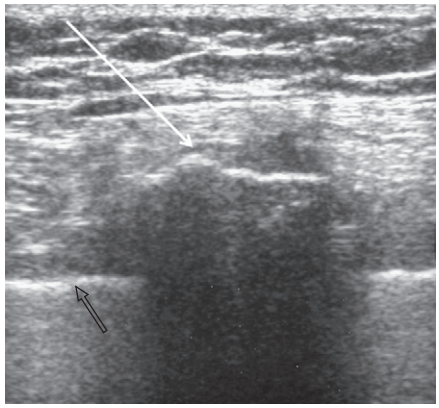

Figure 50.2 Osteolytic rib metastasis. Intracortical rib metastasis demonstrated on CT (arrow). Ultrasound demonstrates normal visceral pleural line (open arrow) and irregular periosteum (arrow). Ultrasound is transmitted beyond the periosteum to reveal echo detail distally.

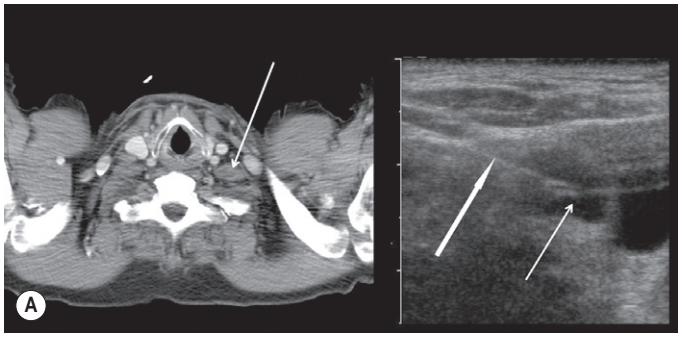

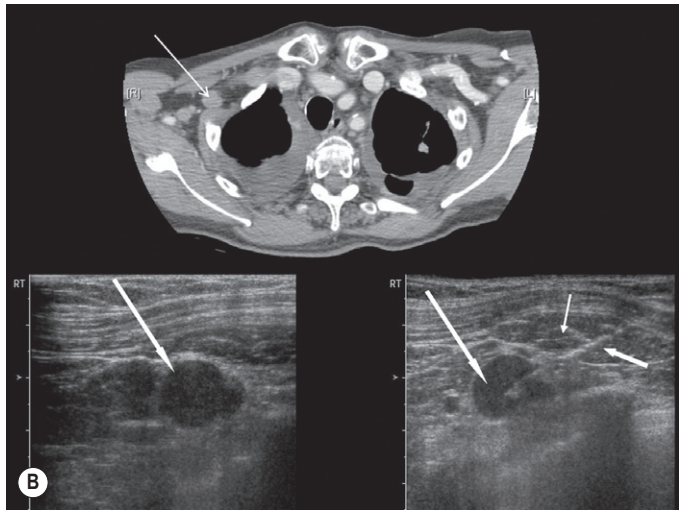

Figure 50.3 A: Left supraclavicular lymph node seen on CT (left, arrow) and ultrasound (right, thin arrow). Aspiration with direct visualisation of the needle (thick arrow) under real-time ultrasound is demonstrated. **B:** Subpectoral lymph node in a patient with recurrent breast carcinoma on CT (arrow) and ultrasound (long arrow). Biopsy under direct vision is shown on the right, with the needle clearly demonstrated (thick arrow) travelling through pectoralis (short arrow).

Sonographic appearance of ribs

- Normal ribs appear on ultrasound as echo-poor shadows with well-defined borders.
- Rib fractures may be seen as breaks in the normal cortical surface associated with gaps, steps or pleural effusion.
- Rib fractures may be associated with the 'lighthouse' effect on ultrasound.
- Rib metastases are seen as disrupted rib cortex associated with increased adjacent soft tissue.

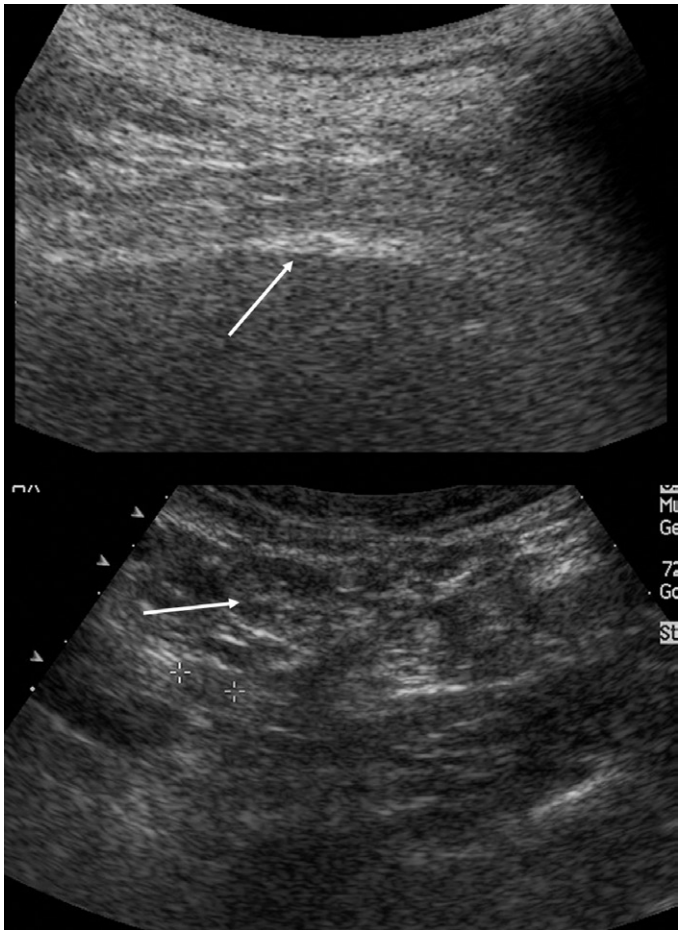

Figure 50.4 Normal chest wall (upper image) with parietal pleura marked (arrow) in comparison to malignant chest wall infiltration (lower image) Arrow demonstrates invasion of soft tissues.

metastases cause disruption of the rib cortex with abnormal ultrasound transmission and inhomogeneous lesions (Fig. 50.2) and are usually associated with an increase in adjacent soft tissue.

Peridiaphragmatic lesions

Supradiaphragmatic and infradiaphragmatic lesions can be diagnosed by ultrasound with a sensitivity similar to that of CT. However, ultrasound is superior to CT for the demonstration of abnormalities of diaphragmatic motion, e.g. paralysis, because of the real-time observation of diaphragm motility. Diaphragmatic rupture may be identified, particularly if there is an associated pleural effusion. Inflammatory thickening of the diaphragm and malignant infiltration are usually visualised with ultrasound as irregular thickening of the diaphragm (Fig. 50.5) with loss of the normal diaphragmatic layers.

Thoracic lymph nodes

Ultrasound is a valuable tool in the detection, and specifically the diagnosis by aspiration, of supraclavicular and neck lymph nodes in patients with bronchogenic carcinoma. The nodes may be identified by clinical examination or staging CT, but ultrasound has been shown to detect impalpable lymphadenopathy and nodal enlargement not detected at CT.[7] Excellent diagnostic rates have been demonstrated using ultrasound-guided aspiration.[8–10] This technique has the advantage of being very safe, and if positive for tumour cells, achieves both diagnosis and staging (i.e. metastatic disease) simultaneously.

THE PLEURA

Normal appearances

Ultrasound is unable to penetrate the normally aerated lung. In the presence of normal underlying lung, the parietal and visceral surfaces are visualised (as the 'pleural stripe') with the lung underneath. The pleural stripe is a highly reflective band which appears to be up to 2 mm in thickness (Fig. 50.6). Anatomically, the visceral and parietal pleura together measure approximately 0.3–0.4 mm. A non-echogenic layer may sometimes be seen proximal to the parietal pleural layer, representing subpleural fat.

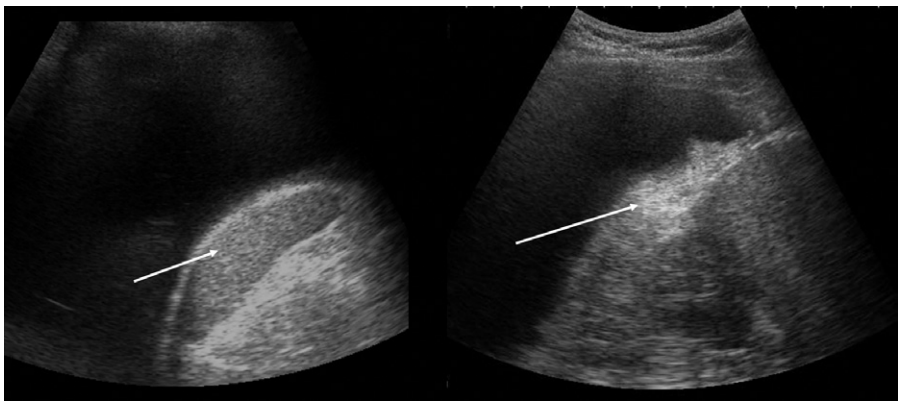

Figure 50.5 Normal hemidiaphragm (left image) with underlying spleen (arrow) in a patient with a large effusion, in comparison to thickened hemidiaphragm surface (right image) in a patient with malignant pleural disease (mesothelioma). The normal diaphragmatic layers are not differentiated and there is a central area of thickening (arrow).

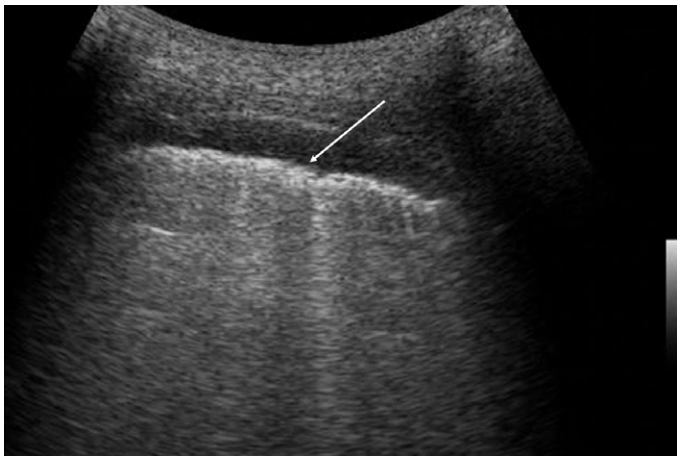

Figure 50.6 The pleural stripe in the normal lung, seen as a bright, echogenic strip (white arrow).

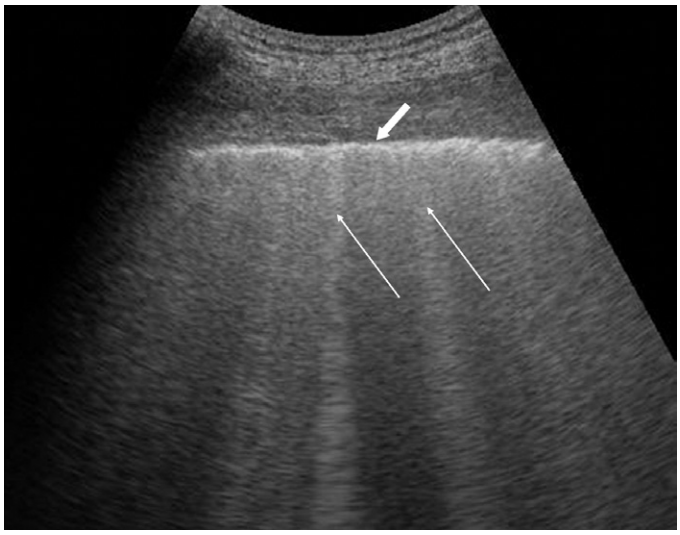

Figure 50.7 Normal lung echoes – the pleural stripe is once again seen (short arrow), and distal lung reverberation artefacts are seen in the lung (comet tails) (arrows).

Normal lung appearances

- Ultrasound is unable to penetrate normally aerated lung tissue.
- Normal lung is recognised by the presence of the 'pleural stripe', appearing as a highly reflective band with distal air artefacts ('comet tails').
- Normal movement of the visceral pleural surface against the chest wall is visualised as the 'lung gliding sign' and is absent in cases of pneumothorax or in the presence of hyper-expanded lung tissue.
- The normal hemidiaphragm surfaces are not well visualised in the absence of pleural effusion.

Normal lung tissue is easily recognisable on ultrasound, as a structure associated with multiple, echo-free areas, created by the presence of air within the lung (known as 'comet tails',[11] Fig. 50.7). Additionally, the normal lung moving up and down on respiration has a characteristic appearance on ultrasound, the so-called 'lung gliding sign'. This is the sonographic representation of normal visceral pleural movement and is often described as 'shimmering' on real-time ultrasound. The visceral pleura may not be seen to move

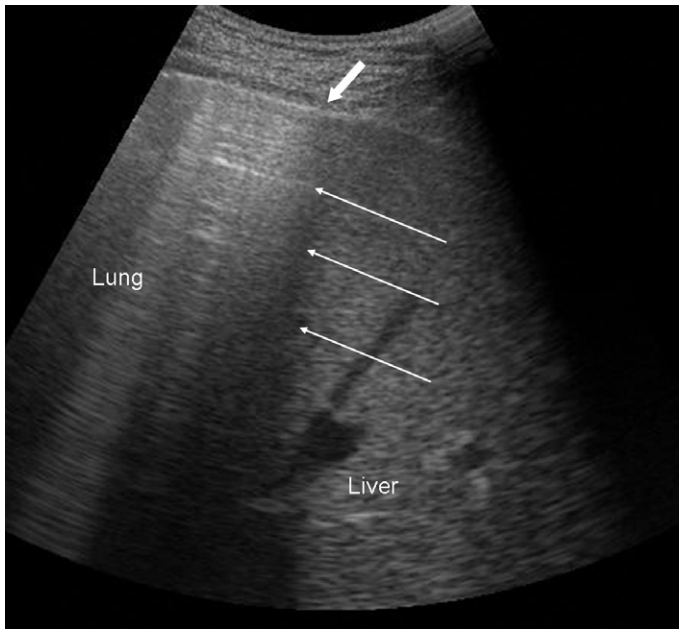

Figure 50.8 Normal right hemidiaphragm. The lung obscures the structures behind it in the costophrenic angle (short arrow). Normal liver can be seen below, and the edge of the acoustic shadow cast by the lung is visible (multiple arrows).

(especially if a previous pleural adhesion procedure had been performed), and may be particularly difficult to appreciate in the apical areas of the lung where visceral movement is minimal. This phenomenon may also be seen in patients with hyper-expanded lung due to obstructive lung disease (typically chronic obstructive lung disease).[12]

The normal left and right hemidiaphragms are not well visualised in the presence of normal aerated lung, which acts as a curtain, obscuring the medial portions of these structures (Fig. 50.8). During the respiratory cycle, the liver or spleen can be seen during expiration. Recognition of the normal appearances is an important skill when asked to differentiate between consolidation of the peripheral lung and effusion seen on a chest radiograph.

Pleural effusion

Pleural fluid detection and characteristics

Ultrasound is a far more sensitive technique for the detection of pleural fluid than chest radiography.[13] It has largely superseded the lateral decubitus chest radiographs for the detection of small pleural effusions. Pleural fluid may be particularly challenging to diagnose using chest radiography when patients are supine (e.g. trauma or the intensive care setting),[14] and thoracic ultrasound is particularly helpful in these situations. Estimation of pleural fluid volume has been shown to be more accurate using sonography than from chest radiographs.[14] Even very small volumes of pleural fluid (3–5 mL) are detectable with ultrasound.[15] Simple (i.e. free flowing, non-septated) pleural fluid is seen on ultrasound as an echo-free area. The differentiation of thickened parietal pleura and pleural fluid may be difficult, as pleural thickening may also appear as an echo-poor zone. In these cases the 'fluid colour sign' may be helpful, i.e. the movement of pleural fluid in response to cardiac pulsation and respiratory excursion results in positive colour Doppler signals with it[16] (Fig. 50.9). This is regarded as definitive evidence of free flowing fluid within the pleural cavity.[16–18]

The volume of pleural fluid present may be estimated using measurements at thoracic ultrasound.[3,19] However, these

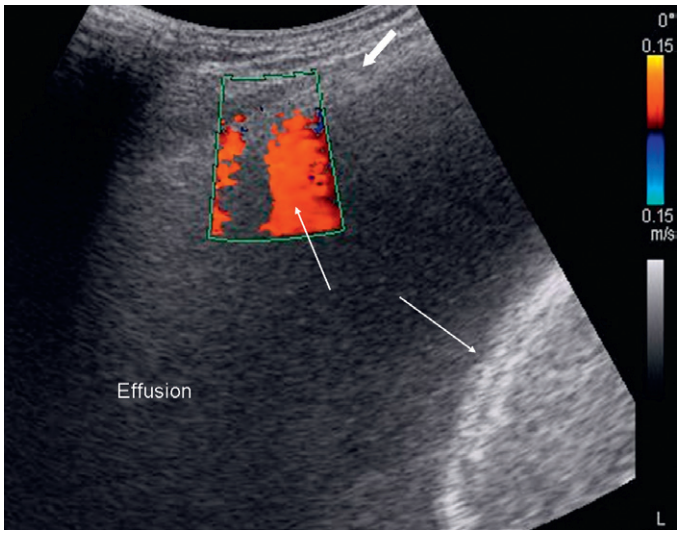

Figure 50.9 The fluid colour sign. Parietal pleural (short arrow) and diaphragmatic surface are shown (long arrow, right). The Doppler signal confirms fluid movement (arrowed).

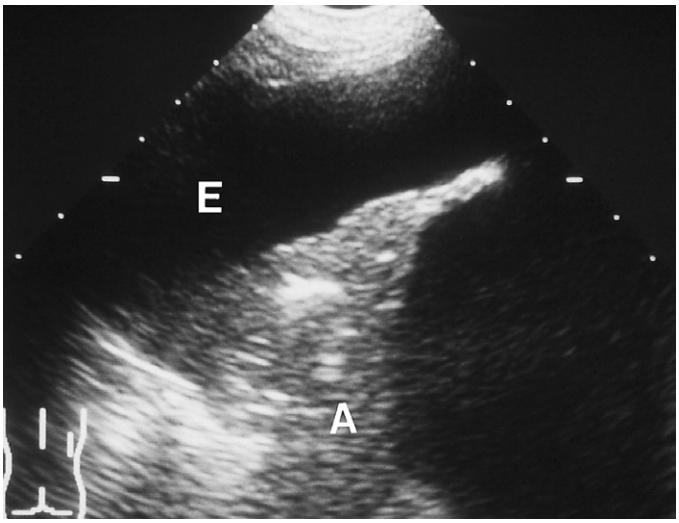

Figure 50.10 Pleural effusion (E) caused by heart failure. Note the underlying atelectasis (A).

Pleural fluid

- Ultrasound is far more sensitive in the detection of pleural fluid than chest radiography, with small (<10 mL) volumes detectable.
- Differentiation of pleural thickening from small amounts of fluid is possible using the 'fluid colour sign', where pleural fluid demonstrates Doppler signals in response to cardiac pulsation.
- The presence of an 'echogenic swirling' pattern of fluid on ultrasound is highly predictive of exudative effusion.
- Septations within pleural fluid are visualised as thin or thicker structures dividing the fluid, and may move with the cardiac cycle.
- The presence of visceral or parietal nodularity and thickening of the hemidiaphragm may suggest a malignant aetiology.

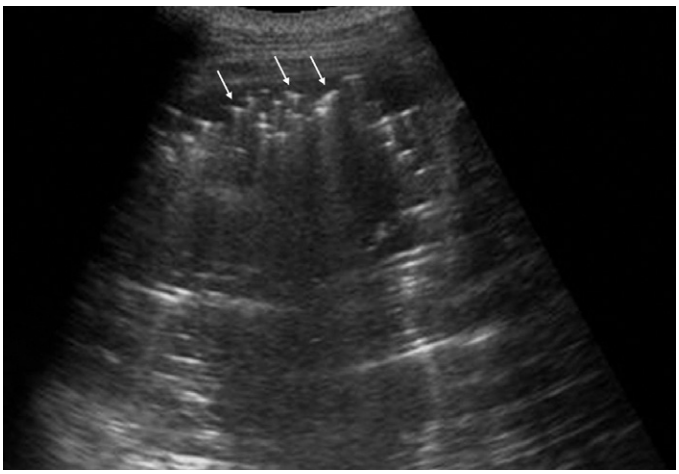

Figure 50.11 Empyema demonstrating echogenic (purulent) fluid on ultrasound, with multiple air bubbles (arrows), recognised as bright points associated with distal echogenic tails.

measurements are unlikely to be consistent and several studies have shown that the volume of a pleural effusion cannot be measured accurately, presumably because of its anatomical complexity. Furthermore, the clinical utility of measuring the exact volume of pleural fluid at sonography is not clear. In routine follow-up it is sufficient to measure the subpulmonary and lateral 'fluid level'.[3,15] A rough estimate of the size of a pleural effusion can be made, using the level of fluid posteriorly with the patient sitting upright as a guide. Fluid that is present in only the basal area is classified as a small effusion, and moderate (mid-thorax) and large (more than half the hemithorax) effusions can be similarly defined.

The characteristics of the pleural fluid should also be examined. Ultrasound is able to differentiate echogenic and non-echogenic pleural fluid, and this differentiation may be diagnostically helpful. Swirling or floating echoes indicate particles in the fluid, such as cells, protein, fibrin or blood. Pleural effusions due to a transudative cause (i.e. diseases associated with 'leak' from structurally normal pleural surfaces, e.g. heart failure) (Fig. 50.10) are always non-echogenic. Exudative effusions (i.e. diseases associated with structurally abnormal pleura, e.g. malignancy, inflammation) may be echo-free or echogenic.[20] The only exception to this is a heart failure associated effusion treated with diuretics, which may appear echogenic. The most comprehensive study in this area suggests that 'complex' effusions (i.e. septated or non-septated) and those with homogeneous echogenicity are always exudative, although the converse is not universally the case.[20]

The presence of multiple small reflective dots within pleural fluid, which move with the respiratory cycle (the 'echogenic swirling sign'), is highly predictive of exudative effusions.[21] Haemothorax may appear as brightly coloured, echo-dense fluid, and empyema may give a similar appearance,[20] often with many brightly reflective areas representing gas formed by the infecting organisms (Fig. 50.11).

The presence of septations within pleural fluid is easily demonstrated on ultrasound. These septations may be thin and easily deformed during fluid movement (secondary to respiratory and cardiac excursions) (Fig. 50.12) and are in this case largely composed of fibrin ('early septations'). They may be more solid-looking structures which move less with the surrounding fluid, composed mainly of collagen (mature septations) (Fig. 50.13). Septations may occur in any sort of effusion, but are most common in infective and metabolically active diseases (e.g. TB pleuritis). Any longstanding effusion may result in septated pleural fluid. Septations of infected fluid are a particular challenge in treatment with tube drainage. Early evidence suggested that the presence of septations in infected pleural effusions was associated with the need for surgical intervention.[22,23] However, this finding has not been prospectively tested in larger cohorts, and evidence has since emerged challenging whether

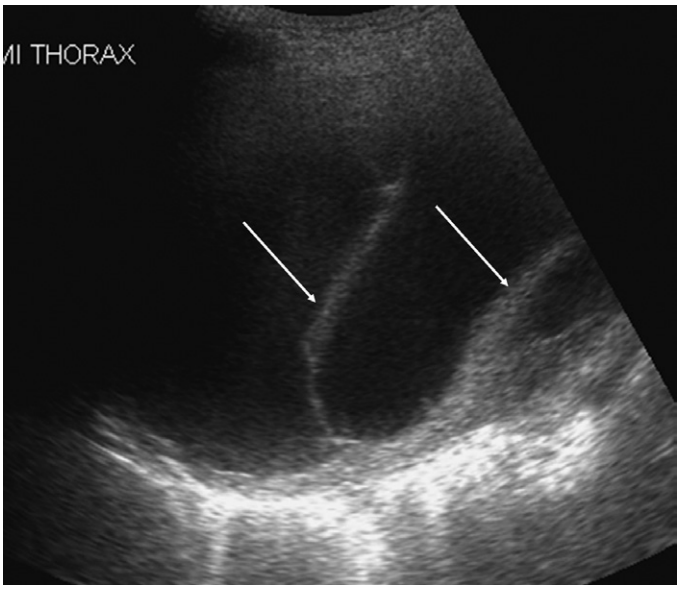

Figure 50.12 Non-echogenic fluid in association with a few thin septations (arrows), which were seen to move easily with the cardiac pulsation in real-time ultrasound.

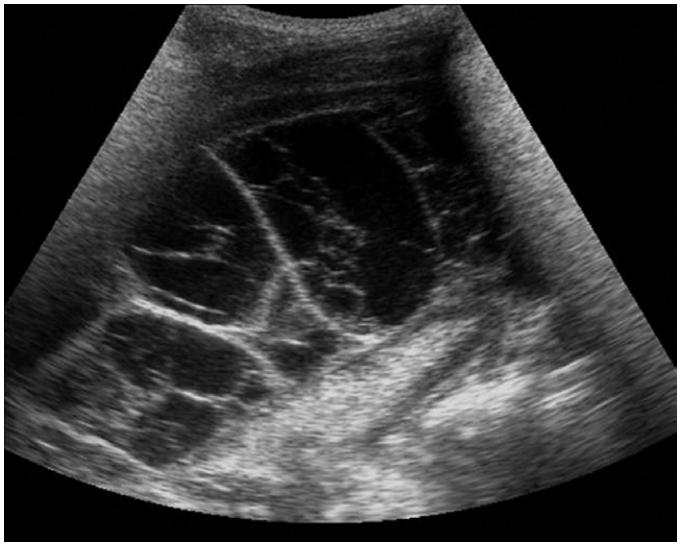

Figure 50.13 Mature, thick septations in a patient with a chronic pleural infection. Locules are seen with varying echogenicity divided by septations of varying width.

disruption of septations using intrapleural agents alters outcome.[24]

There is emerging data that ultrasound may be a useful technique in the diagnosis of malignant pleural effusions. The sonographic finding of pleural fluid, nodules or diffuse thickening in patients with known malignancy is suggestive of metastatic pleural involvement[25,26] (Fig. 50.14). The presence of similar criteria to that used in contrast-enhanced CT scanning of the pleura (i.e. parietal pleural thickening, nodularity, the presence of diaphragmatic nodules) on ultrasound has been prospectively assessed in a recent study, demonstrating reasonable sensitivity and high specificity for the diagnosis of a malignant pleural effusion.[27] It is not possible to reliably differentiate mesothelioma from secondary carcinoma-induced pleural effusions by ultrasound. The presence of an area of pleural thickening or nodules may also provide a potential biopsy target (see later section).

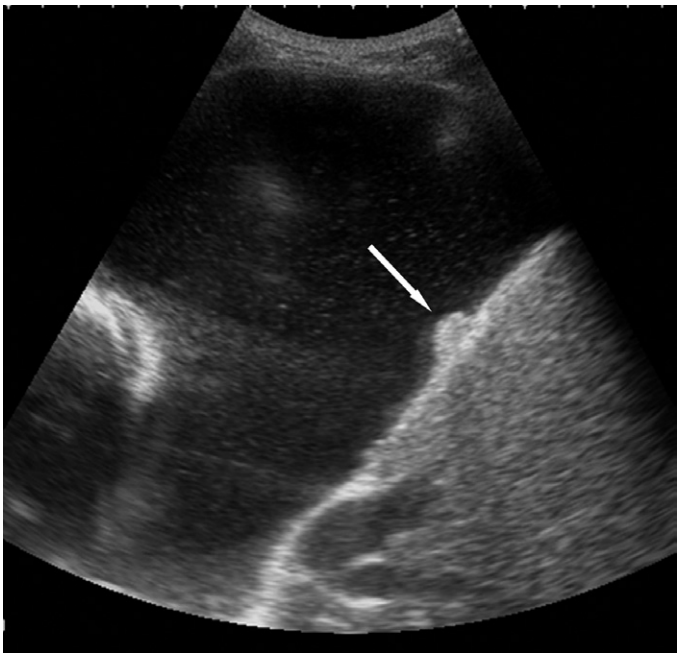

Figure 50.14 Malignant nodule (arrow) seen on the surface of the hemidiaphragm (adenocarcinoma of unknown origin).

The diaphragm

The presence of a moderate to large free-flowing pleural effusion permits excellent visualisation of the dome of the diaphragm. The normal diaphragm is a fibromuscular layer that consists of a single layer of muscle that can be divided into three regions, the sternal, costal and lumbar areas, which are named according to their sites of origin. This muscular layer is lined with the endothoracic fascial membrane superiorly and the transversalis fascial membrane inferiorly. Sonographically five distinct layers of the diaphragm are generally visible. The muscular layers appear hypoechoic and the membranous layers echogenic. The normal diaphragm generally measures <5 mm in thickness, although this is dependent on a number of factors, most importantly respiration, which results in an increase in thickness on inspiration and a decrease on expiration. The diaphragm should be gently curved (concave upward) – in the presence of large effusions, the shape of the diaphragm may change to become inverted (Fig. 50.15). This is usually associated with severe symptoms, and aspiration of even a small amount of fluid (e.g. 500 mL of a 3000 mL effusion) may reverse the inversion and result in substantial symptomatic relief.

Assessment of diaphragm movement in cases of suspected paralysis or phrenic nerve damage is easily conducted using real-time sonography, asking the patient to 'sniff' and watching for reversal of the normal downward diaphragm movement. The presence of rounded distinct nodules on the diaphragm surface (only visualised in the presence of adjacent pleural fluid) is highly suggestive of malignancy.

The lung and visceral pleura

The visceral pleura and underlying lung may also be assessed. The presence of a pleural effusion results in lung atelectasis, which appears as an echo-dense structure that moves with the cardiac pulsation and respiration (Fig. 50.16). If the underlying lung is abnormal (e.g. in effusion associated with pulmonary infarction or parenchymal infection), this may be visualised through the pleural fluid clearly, showing hyperdense lung parenchyma and specific appearances such as fluid bronchograms (see relevant sections later).

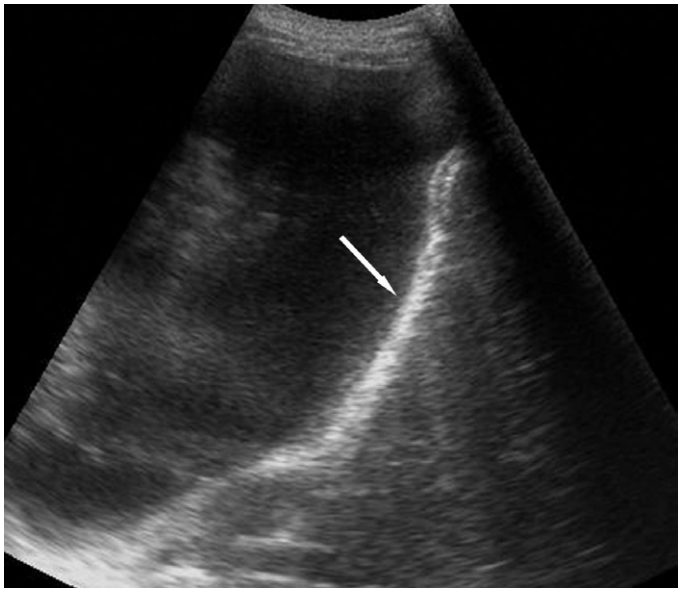

Figure 50.15 Inverted hemidiaphragm with loss of normal convex shape (arrowed) and associated with severe breathlessness.

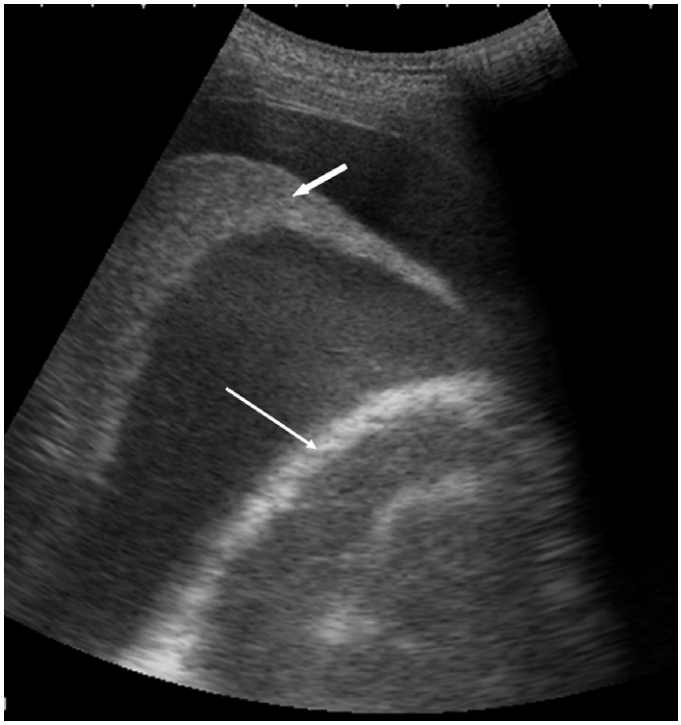

Figure 50.16 Atelectatic lung (short arrow) associated with a large simple pleural effusion and a thickened hemidiaphragm (long arrow).

Compression atelectasis of the lower lobe is frequently observed in large and moderate-sized pleural effusions at the lower edge of the lung that cannot be delineated clearly from the lung. This reflective concave structure, often shaped like a hockey stick, is seen flapping in the effusion owing to transmitted cardiac pulsation and respiratory movement. The lobe is often tightly collapsed and appears small compared to the volume of the pleural effusion, in contrast to the situation in pulmonary embolism or consolidated lung where there is little loss of volume, hyperdensity and bright echogenicity. In addition, atelectatic lung appears to be easily

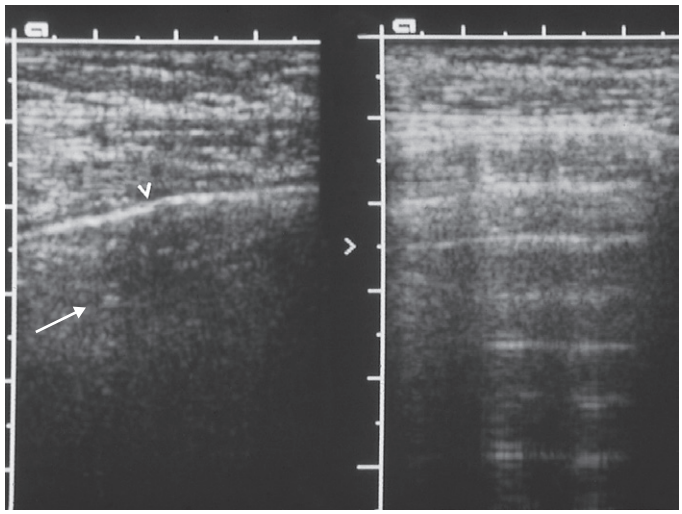

Figure 50.17 Pneumothorax. Normal side (left) with echoes from the lung surface (arrowhead) that moved in real-time. Stationary reverberations indicate the pneumothorax (right).

moved by associated cardiac pulsation and respiratory movement, whereas this is less evident with consolidation/infarction.

Pneumothorax

Pneumothorax is detectable at ultrasound, with some significant and important limitations. The presence of a pneumothorax is implied at ultrasound by:[28]

1. absence of breath-related movement of the visceral pleura ('gliding sign')
2. apparent broadening and brightening of the pleural stripe
3. increased reverberation artefacts (i.e. absence of comet tails), with a bland distal picture.

These changes are most readily recognised if compared to the non-pneumothorax side of the chest (Fig. 50.17). The presence of lung sliding in association with comet tail artefacts rules out pneumothorax with 100% negative predicative value, and the combination has a positive predictive value for the diagnosis of normal lung approaching 100%.[29–31] However, the absence of lung sliding and comet tail artefacts does not consistently diagnose pneumothorax, especially in the context of obstructive lung disease (see later).

The extent and size of pneumothorax may not be assessed using ultrasound[32] – a chest radiograph or CT is required to assess the degree of lung dehiscence from the chest wall, as ultrasound only detects the presence of a rim of air in the pleural cavity.[28] However, several studies have shown that ultrasound is more sensitive in the detection of pneumothorax post lung biopsy[32–35] and in the trauma setting[36,37] than chest radiography. Identification of the 'lung point' (which is the fleeting appearance of an ultrasound pattern of lung replacing the ultrasound pattern of pneumothorax in a particular position on the chest wall) has been associated with a 100% specificity of pneumothorax detection.[38,39] Thoracic ultrasound has also been shown to have a high sensitivity (around 92%) in the detection of 'occult' (i.e. missed on the chest radiograph) pneumothorax in trauma patients,[40,41] although false positives occur. Important limitations exist in the detection of pneumothorax at ultrasound – the differentiation of pneumothorax and lung in patients with obstructive lung disease is difficult and shown in a study to be poor and unreliable.[12]

The clinical utility of ultrasound in the detection of pneumothorax also requires some consideration, when there are excellent and sensitive tests widely available (e.g. CT which will be undertaken in the majority of major trauma victims where available). Ultrasound may be useful as a screening tool for pneumothorax in

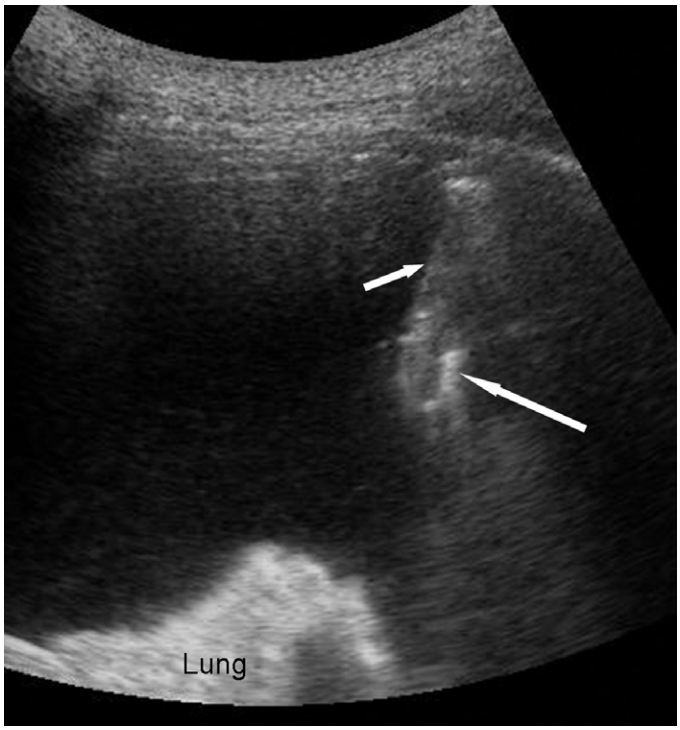

Figure 50.18 Guide-wire in pleural fluid during drain insertion (short arrow). The curved distal portion of the wire can be seen (long arrow).

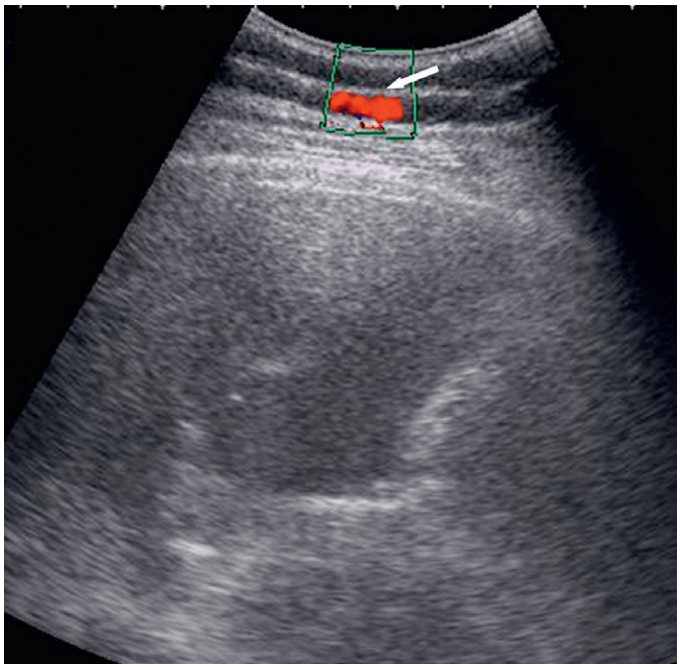

Figure 50.19 Intercostal artery on colour Doppler (arrow) – the patient was scanned posteriorly near the spinous processes, where the artery is often not shielded by the rib.

Pneumothorax

- Pneumothorax is implied at ultrasound by the absence of the lung gliding sign, absence of the pleural stripe and absence of comet tails.
- The size of pneumothorax may not be assessed using ultrasound (unable to penetrate air).
- Bullous or obstructive lung disease may appear as a pneumothorax on ultrasound and caution is required in interpretation in patients with these lung conditions.

circumstances where CT imaging is not available, but further studies are required to clarify its exact role.

Ultrasound-guided interventions for pleural effusion

The 'real-time' capability of ultrasound makes this technique ideal for guided intervention in the thoracic cavity (Fig. 50.18). Studies have demonstrated that ultrasound-guided thoracocentesis or drain insertion is safe (see below), with a complication rate that compares favourably to the quoted complication rate of 'blind' pleural aspiration (20–39%).[42]

The complication rate of pleural aspiration is reduced using ultrasound guidance.[42–44] Directly comparative studies suggest lower pneumothorax rates (0–3% versus 29–18%[42,44]) and lower need for subsequent tube thoracostomy using ultrasound guidance.[44,45] An interesting and large series suggests that the vast majority of ultrasound-guided thoracocentesis-associated pneumothoraces are due to 'trapped lung' rather than lung puncture as determined by pleural physiological characteristics.[46]

Ultrasound-guided aspiration is successful after failed 'blind' aspiration in up to 88% of cases.[47,48] In over 50% of 'dry taps' conducted without image guidance, needle puncture sites were found to be below the diaphragm on subsequent sonography.[48] In an elegant study, Diacon et al.[49] demonstrated an increase in accuracy of site selection using ultrasound scanning by 26%, and decreased organ puncture in 1 in 10 cases using ultrasound guidance, even where 'blind' aspiration was conducted by experienced clinicians.

Ultrasound is particularly useful in the intensive care unit (ICU), where positive pressure ventilation makes pneumothorax hazardous, and supine patients make diagnosis difficult on chest radiography alone. A small pneumothorax rate of 1.3% has been reported in large series of ICU patients aspirated under ultrasound control.[50]

Ultrasound permits visualisation of the underlying lung and diaphragm, thereby avoiding accidental lung puncture and pneumothorax, and visceral organ injury. The intercostal vessels may be identified using colour Doppler and thereby avoided (Fig. 50.19) – this is especially important in elderly patients (where their route is unpredictable) and for access to posterior collections (e.g. empyemas) where the intercostal arteries are likely to lie centrally in the intercostal spaces. Sonography may in addition identify areas of lung that are tethered to the pleural surface (presumably from previous parietal inflammation and adhesion), preventing accidental lung puncture (Fig. 50.20).

Although many radiologists will conduct an ultrasound examination and 'mark' a suitable area on the chest for another clinician to attempt aspiration or drain insertion, we would not recommend this except in the largest of effusions or where no other choice exists. The presence of the 'mark' on the patient's skin often leads to overconfidence by the clinician conducting the procedure, and skin marks can easily move with movement of the patient's shoulder blade or arm. Furthermore, if patients are sent to a different clinical environment in which the procedure will take place, the patient may not be placed in the same position as was used for the ultrasound scan. Interestingly, the 'X marks the spot' technique of image-guided pleural aspiration is not associated with a reduction in pneumothorax rate.[44]

It is our practice to aspirate or insert drains using direct ultrasound vision of the needle entering the pleural space, or to mark a

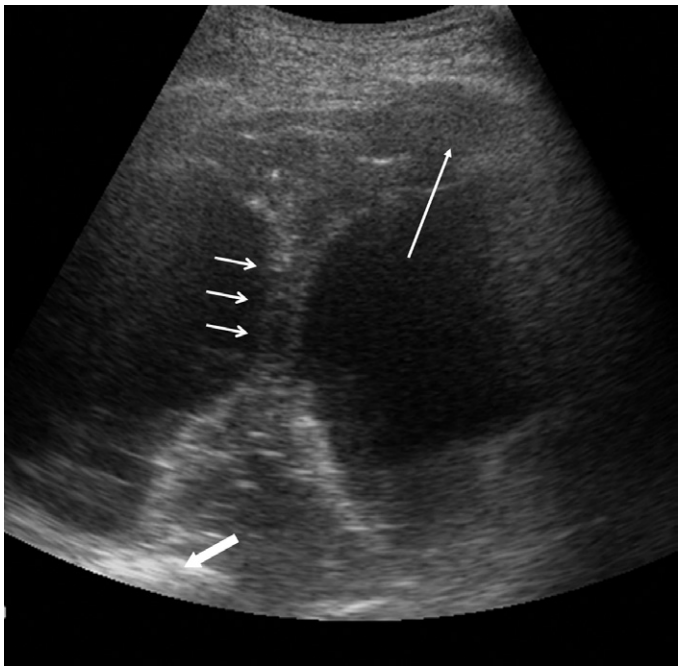

Figure 50.20 Fibrinous attachments (short arrows) between collapsed lung (thick arrow) and parietal pleura (long arrow). These were thought to have arisen as a result of previous attempts at pleural aspiration.

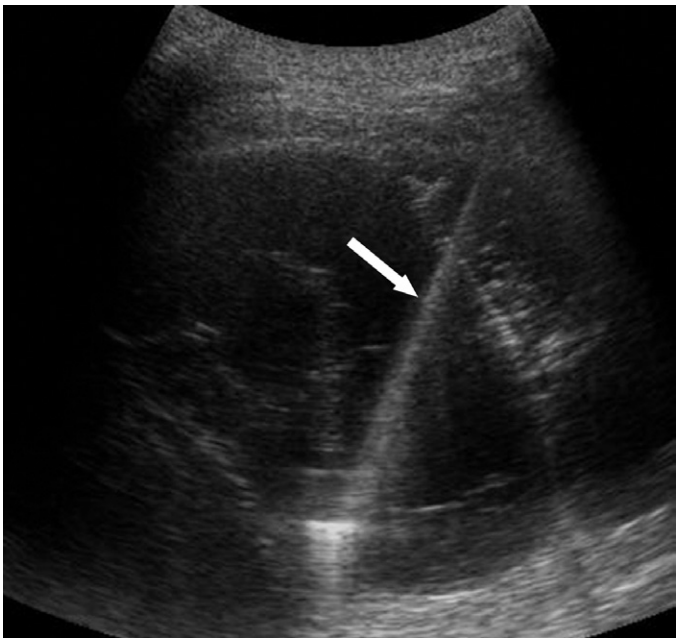

Figure 50.21 Septated effusion with guide-wire (arrow) in situ, crossing septations.

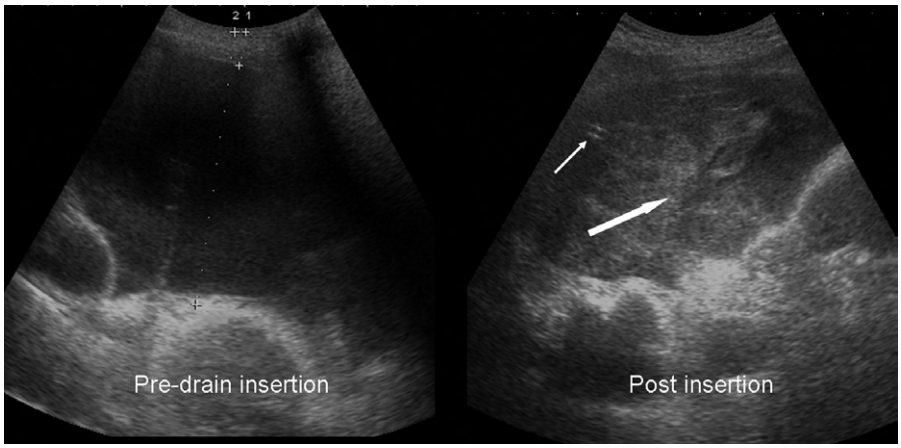

Figure 50.22 Intercostal bleed. Pre- and post-ultrasound images in a patient undergoing intercostal drain insertion. The drain can be seen on the ultrasound image (small arrow) as a bilaminar structure. Heavily echogenic material is seen in the pleural space post procedure (large arrow), representing frank blood.

site and immediately aspirate or insert a drain without moving the patient.

The real-time capability of ultrasound also permits separate puncture of loculated effusions – this has been shown to be of diagnostic value in patients with pleural infection, in which pleural fluid pH is a key diagnostic marker. The pH has been shown to be different in each locule sampled,[51] with implications for the way in which the patient was managed. For the drainage of infected pleural collections, sonographic guidance during drain insertion may permit the largest locule to be entered and septations to be disrupted during insertion of guide-wires and drains (Fig. 50.21).

Following any aspiration procedure, the amount of pleural fluid remaining may be assessed. Intercostal artery bleeding is perhaps the most serious complication of pleural intervention, due to a large space into which bleeding may occur (Fig. 50.22). Ultrasound with colour Doppler may be used to assess the pleural space post procedure to ensure blood is not accumulating and does not require urgent interventional radiology or thoracic surgical input.

Visualisation of the position of catheters within the pleural space is possible with ultrasound. They are seen as bilaminar structures within pleural fluid (Fig. 50.23), and the presence of a correctly positioned intrapleural drain may be confirmed using sterile saline flushes and assessing the 'blush' seen in the pleural space in response to the injected saline using real-time ultrasound. This is a valuable technique where drainage from a catheter has slowed or stopped, and permits decisions on further drains, intrapleural thrombolytics (in the case of septated effusions) or drain repositioning to be made. Direct demonstration of the utility of intrapleural thrombolytics in septated malignant effusions has been demonstrated.[52]

Ultrasound is increasingly used before more invasive pleural procedures such as prior to medical thoracoscopy. One small study has suggested that the use of pre-thoracoscopy ultrasound permits safe entry into the chest cavity.[53] The demonstration of a highly septated effusion associated with lung tethering suggests that the thoracoscopic procedure will be challenging, and may suggest

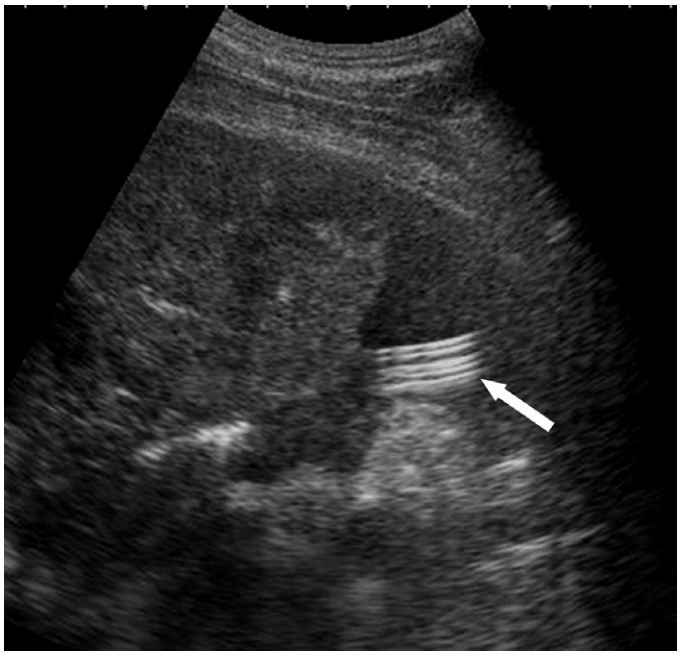

Figure 50.23 Intercostal drain in situ (arrow) in a patient with malignant pleural effusion, seen as multiple bilaminar structures.

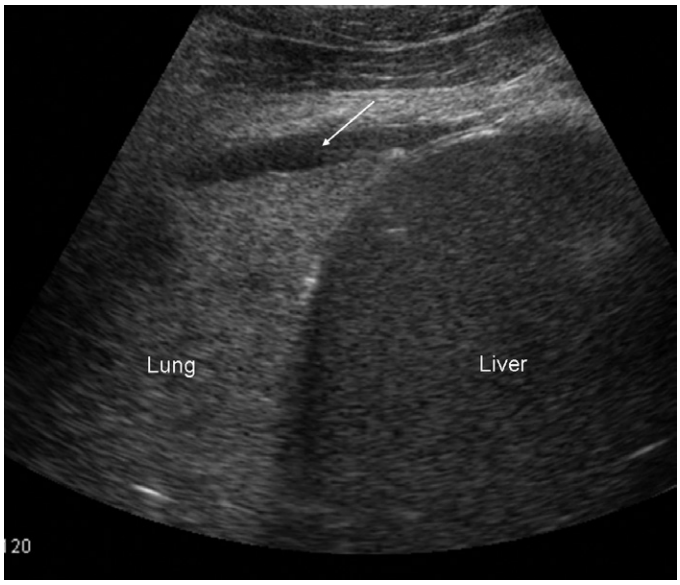

Figure 50.24 Lung consolidation seen on ultrasound as bright echogenic lung (brighter than adjacent liver) in association with a small pleural effusion (arrow).

Ultrasound-guided interventions for pleural effusion

- Ultrasound-guided aspiration and drain insertion is more accurate and safer than 'blind' procedures.
- Where possible, procedures should be conducted using real-time ultrasound or marking the skin and immediately conducting the procedure. Marking the skin with a possible procedure entry site for another clinician may lead to inaccurate aspiration/drain insertion.
- Intrapleural bleeding may be assessed post pleural procedure at ultrasound.
- The position of intercostal drains within the pleural space may be assessed using ultrasound and the injection of sterile saline.

other diagnostic tests instead (e.g. CT-guided biopsy of pleural thickening). In addition, the presence of induced pneumothorax, which is necessary for safe thoracoscopic examination of the pleural cavity, can reliably be assessed in real-time using 'on table' ultrasound during medical thoracoscopy.

Recent evidence from animal models suggests that thoracic ultrasound may be a useful technique in the assessment of a successful pleurodesis,[54] used in the case of pneumothorax or malignant pleural effusion treatment to prevent air or fluid recurrence. A single study has prospectively assessed this in patients undergoing abrasion pleurodesis for prevention of recurrent pneumothorax,[55] and found that the absence of the 'lung sliding' sign was predictive of a successful long-term outcome. Further studies assessing its use in different forms of pleurodesis and in different disease states are needed.

PERIPHERAL LUNG CONSOLIDATION

Any intraparenchymal process which extends to and involves the visceral pleural surface may be visualised using ultrasound. Recognition and identification of such lesions is important, specifically to allow differentiation of fluid requiring drainage and abnormal lung. However, the appearances are usually not specific enough to make a diagnosis based on the sonographic features alone. In conjunction with the plain chest radiograph and the patient's clinical history, sonographic analysis of the lung may provide important aetiological information.

Pneumonia

In the early congestive stage of disease, the texture of the pneumonic lung is homogeneous and similar to that of the liver. As the process progresses within the lung, and the alveolar spaces are increasingly filled with inflammatory exudate, the echotexture may become brighter than the liver (Fig. 50.24). Pneumonia shows a bizarre outline and is rarely segmented in shape like pulmonary infarction, or round like carcinomas and metastases. It is characterised by an irregular, serrated and somewhat blurred margin. A marked tree-shaped air bronchogram[56] is found in about 90% of cases. Numerous lenticular echoes measuring a few millimetres in size are frequently observed extending to the pleura.[57,58] During all stages of the disease process, the air bronchogram is more pronounced than in pulmonary embolism (Fig. 50.25).

A characteristic feature of pneumonia seen on ultrasound is that the pneumonia appears smaller on the sonogram than on plain films in more than 50% of cases, as a result of reverberation artefacts obscuring the extent of the pneumonia. Where a pneumonia appears larger on ultrasound than on the chest radiograph, this may represent parapneumonic effusion.[20,28,56,58]

Inflammatory exudate within and surrounding air spaces may be seen on ultrasound as the 'fluid bronchogram', which appears as anechoic tubular structures in the position of the bronchial tree. Bronchial walls are more reflective and wider than vessel walls, and fluid bronchogram can be differentiated from pulmonary vessels using colour Doppler imaging. The presence of persistent fluid bronchograms once the acute illness has recovered may suggest post-stenotic pneumonitis and requires further investigation (e.g. CT or bronchoscopy). Post-stenotic pneumonia can be better delineated from the tumour by ultrasound than on a plain radiograph.[20,58]

Several studies have been conducted on the aspiration of consolidated lung to achieve microbiological diagnosis.[59–61] While in these small studies the technique appears to be safe, the clinical value is not yet certain – larger studies assessing the diagnostic value and associated change in antibiotic management are required before this becomes a routine or commonplace investigation.

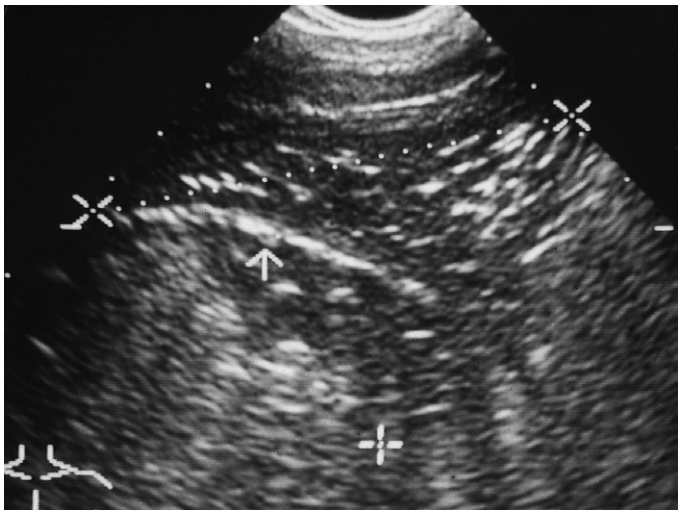

Figure 50.25 Pneumonia. Poorly demarcated consolidation with an air bronchogram (arrow).

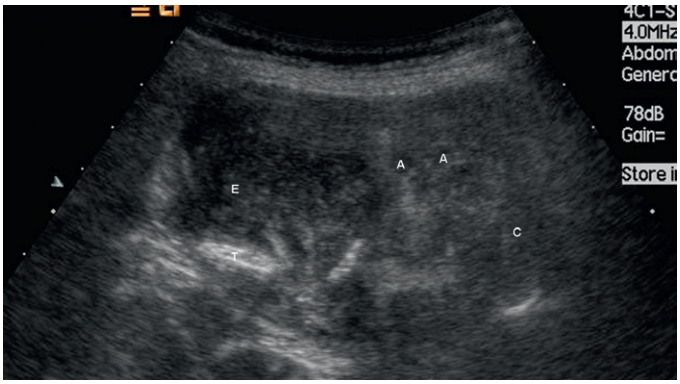

Figure 50.26 Consolidated lung (C) with several small abscess cavities (A) and associated empyema (E). A chest tube can be seen in situ (T).

Lung consolidation

- Lung consolidation appears on ultrasound as bright lung tissue of higher attenuation than adjacent soft tissue structures (e.g. liver).
- Air and fluid bronchograms may be visualised within consolidated lung and are strong evidence of the diagnosis.
- Assessment for associated pleural effusion in the context of infective lung consolidation is important as these collections may require drainage.

Lung abscesses are depicted on ultrasound as round or oval echo-free lesions (Fig. 50.26). Differentiation from small, loculated pleural collections may be challenging, and thoracic CT is the gold standard technique in this circumstance. Micro-abscesses are more easily and frequently visualised on ultrasound than on plain chest radiography. Aspiration of infected fluid under ultrasound control is feasible, to provide microbiological information and drain the infected collection. However, crossing the parietal and visceral pleural surfaces adjacent to potentially damaged lung and entering infected abscess fluid is associated with a risk of 'spilling' the abscess contents into the pleural space, resulting in empyema and potentially infected bronchopleural fistula. The majority of lung abscesses are therefore managed with directed antibiotic therapy for prolonged periods, with drainage procedures reserved for resistant or difficult cases.

Pulmonary tuberculosis is polymorphic on chest radiographs as well as on chest sonography, which reveals isolated or numerous subpleural nodular echo-poor lesions, round or irregular in shape. Concomitant pleural effusions and liquefactions in the infiltrated parenchyma are well demonstrated on sonography.

Pulmonary embolus

A moderate-sized pulmonary embolus associated with lung infarction will be associated with under-perfused peripheral lung parenchyma, and associated changes which may be visualised using thoracic ultrasound if the changes reach the visceral pleural surface. Some minutes after complete embolic occlusion of a peripheral pulmonary artery there is a breakdown of surfactant and infiltration of interstitial fluid and erythrocytes into the alveolar spaces. Congestion of the alveoli allows ultrasound imaging. In contrast to angiography and helical CT, which depict the embolus itself, chest sonography documents the outcome of pulmonary embolism at its different stages, including immediate haemorrhage or early infarct as well as long-term injury of the peripheral lung parenchyma.

Previous studies suggest that up to 40% of cases of pulmonary embolus will be associated with sonographic abnormalities.[62] Studies comparing ultrasound and pathological anatomical findings have demonstrated that early haemorrhage and infarcts are echo-poor, homogeneous, more rounded and less sharply bordered, in contrast to older infarcts which are well demarcated, wedge shaped, coarsely structured with a reflective centre corresponding to the bronchiole.[63,64] In a minority of cases, the blocked pulmonary artery may be visualised, the so-called 'vessel sign' (Fig. 50.27). On sonography the lung infarct is 1–2 cm smaller than the perfusion defect revealed by angiography or scintigraphy. As in earlier pathological studies, ultrasound studies were also able to show that the occlusive embolus lies up to 2 cm central to the infarcted area.[64] Attention should be drawn to the frequent autopsy findings of multiple pulmonary emboli and infarctions of apparently varying age (Fig. 50.28). This finding is important since it indicates that these patients suffered successive embolisations and that death might have been prevented if an early diagnosis had been made.

Prospective studies have assessed the clinical utility of thoracic ultrasound in the detection of pulmonary embolus, as compared to the 'gold standard' of CT pulmonary angiography.[65–68] These studies examined populations with variable prevalence of pulmonary embolus, and suggest in summary a thoracic ultrasound sensitivity of 76–98% and a specificity of 66–95%.

Therefore, although thoracic ultrasound is associated with very reasonable sensitivity and high specificity in the diagnosis of pulmonary embolus, the diagnostic inclusion and exclusion rates are not high enough in isolation to be able to inform clinical decisions. Ultrasound may detect small peripheral emboli not seen at perfusion scanning, but conversely may not detect large central emboli.[63] Furthermore, as radiological investigations with a higher sensitivity and specificity are available (e.g. VQ scanning, CT pulmonary angiography), the practical use of ultrasound for the diagnosis of pulmonary embolus is questionable. In areas where there is poor access to other techniques, it may have a role but remains lower than ideal in isolation for sensitivity and specificity of diagnosis.

In two-thirds of cases with pulmonary embolism, deep vein thrombosis is the source of embolism. Compression duplex ultrasound is an accurate procedure to diagnose definitively the source of pulmonary embolism in the case of deep vein thrombosis of the legs (see Chapter 64). Right atrial thrombus is a recognised predictive factor of high mortality in patients with pulmonary embolism.

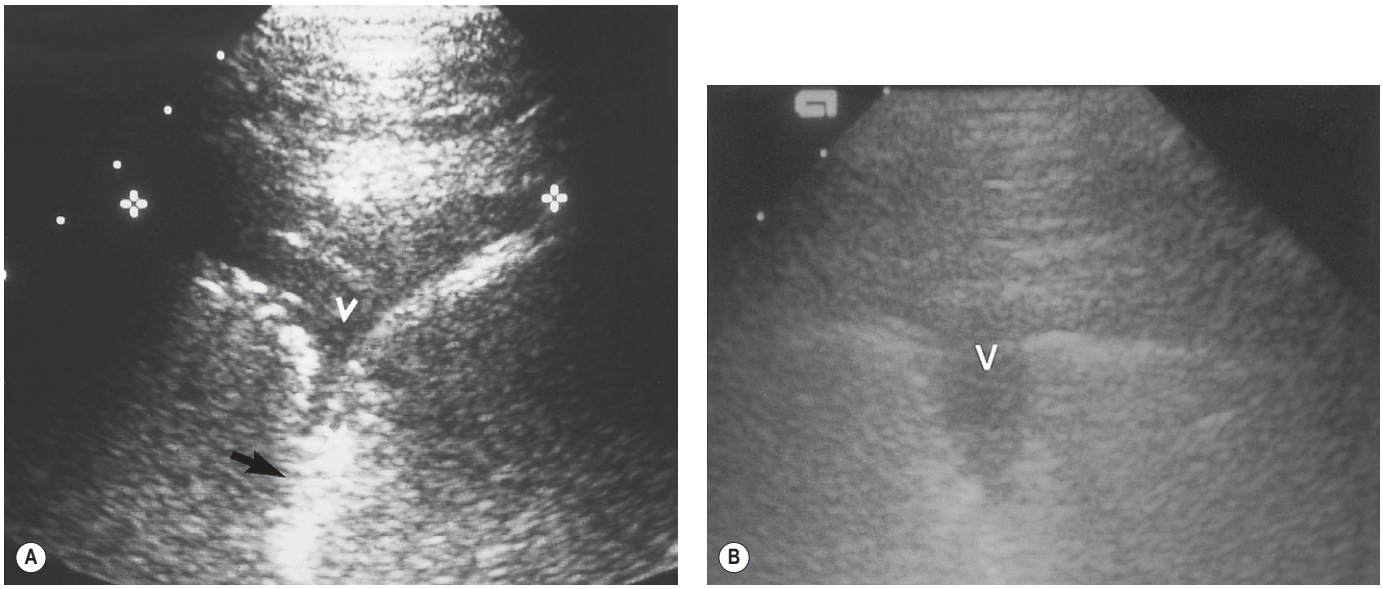

Figure 50.27 Pulmonary infarcts. A: Note the wedge-shaped, echo-poor configuration (arrowhead). **B:** The occluded supply artery is seen (arrow).

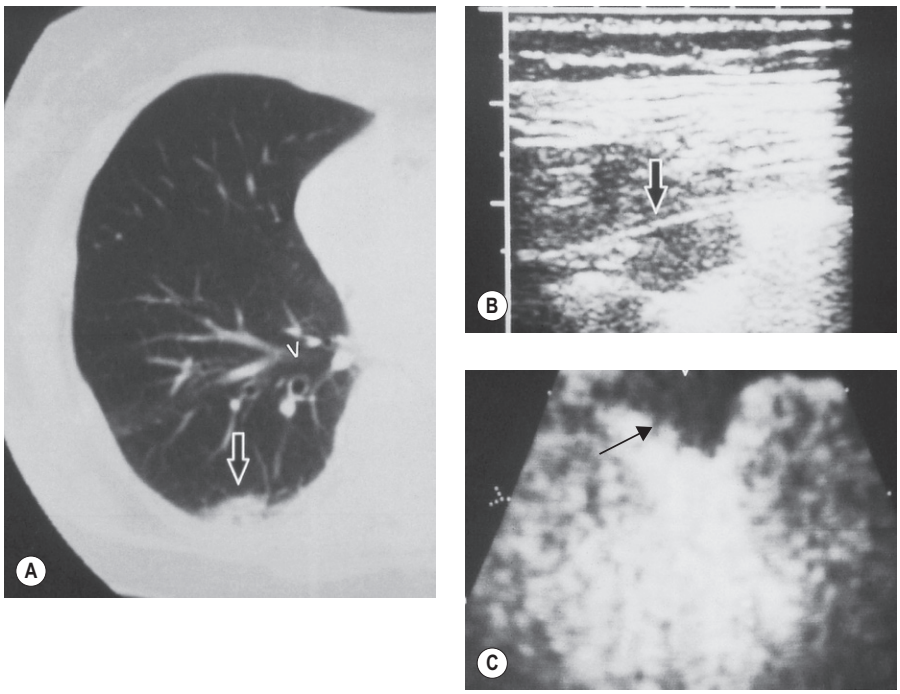

Figure 50.28 Central pulmonary embolism. A: Confirmed by spiral-CT (arrowhead) and small peripheral consolidation (arrow) similar in size to **B:** the ultrasound lesion (arrow). **C:** Further triangular infarct (13 mm), not detected on CT.

Pulmonary emboli

- Pulmonary emboli may be associated with changes visualised at thoracic ultrasound.
- Large infarcts associated with lung infarction and effusion are easily seen, whereas smaller and more central infarcts may be difficult to visualise.
- Given the excellent sensitivity and specificity of other radiological techniques, ultrasound is not recommended as a diagnostic test for pulmonary embolic disease.

Bedside leg vein scanning, echocardiography and chest ultrasound can be performed in emergency units.

Lung cancer and metastases

Peripheral lung carcinoma abutting the visceral pleural surface, and subpleural lung metastases may be visualised on ultrasound as round, oval or lobular echo-poor inhomogeneous structures. Peripheral areas of these lesions may be characterised by an echo-poor halo and spiculations, and central necrosis may be observed. Infiltration of the pleura and chest wall is well observed on thoracic

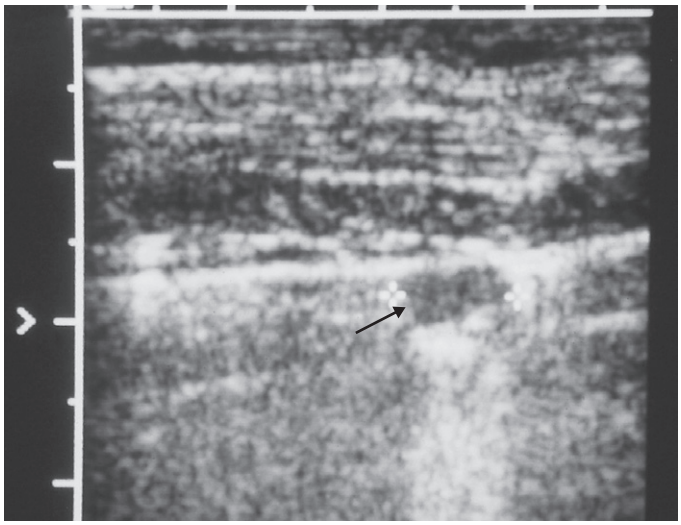

Figure 50.29 Subpleural metastasis (7 mm) from an adenocarcinoma. Similar lesions could be caused by tuberculosis, pleuritis or pulmonary embolism.

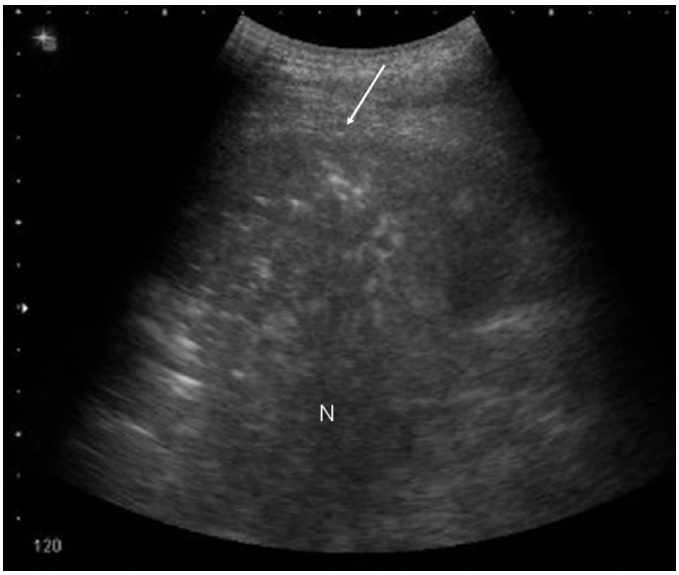

Figure 50.31 Large peripheral lung cancer. A lobulated mass with central necrosis (N).

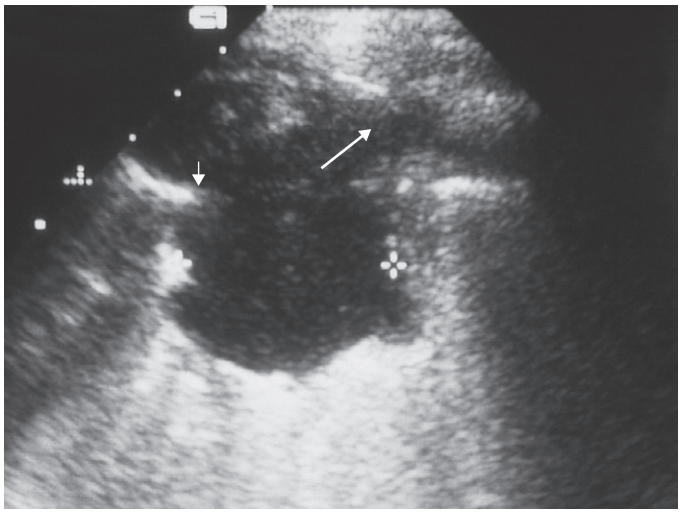

Figure 50.30 Peripheral lung cancer. The pleura is disrupted and the tumour is infiltrating the chest wall.

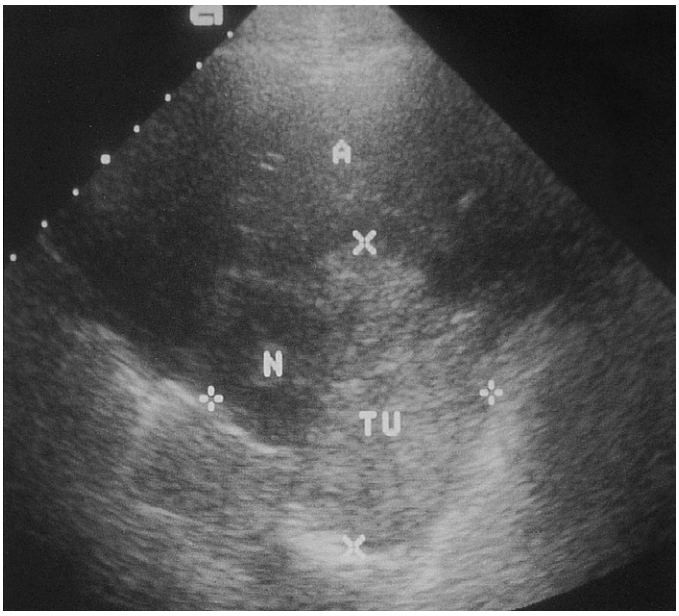

Figure 50.32 Central lung cancer (TU). The atelectasis (A) provides an acoustic window. Note the tumour necrosis (N).

ultrasound with, disruption of the pleura, infiltration of the chest wall and fixation of the tumour during breathing, and parietal pleural invasion has been shown to be more reliably reported on ultrasound than CT[27] (Figs 50.29–50.32). Although more central tumours are not normally visualised by ultrasound due to intervening aerated lung, the presence of post-obstructive atelectasis may permit their identification. Even central tumours can be depicted if there is an atelectasis extending out to the pleura.[4]

Benign and malignant lung lesions may in some cases be differentiated with the aid of colour Doppler ultrasound, due to their different vascular patterns and blood flow[69,70] (Figs 50.33 and 50.34). This ability is limited within the lung parenchyma due to poor normal visibility of pulmonary blood flow sonographically.

Ultrasound-guided biopsy

Fine-needle aspiration or larger core biopsies may be obtained using ultrasound on any intraparenchymal lung lesion abutting the pleural surface, pleural or chest wall lesions, lymph nodes in the neck or supraclavicular fossae and the mediastinum. Specifically designed needle holders and markers for biopsy purposes elsewhere in the body are not in general used in the thorax due to the presence of the ribs, which will obstruct the needle's path. Real-time ultrasound guidance is therefore usually employed with one hand holding the transducer, and the other holding the aspiration needle or a triggered biopsy gun. This approach provides interactive feedback between real-time imaging and needle manipulation.

Although there have been no comparative studies between ultrasound- and CT-guided techniques, ultrasound-guided biopsy is likely to have a similarly high diagnostic yield (over 90%) in selected patients. Several studies have reported comparative diagnostic yields for CT- and ultrasound-guided pleural biopsy in malignant disease[71,72] and in lung, mediastinal and pleural diseases.[73] For the diagnosis of pleural lesions that are visible on ultrasound, the diagnostic rate is highly likely to be far in excess of that seen using 'blind' (e.g. Abrams' needle) pleural biopsies, especially as tumour masses are often best seen in the inferior and posterior

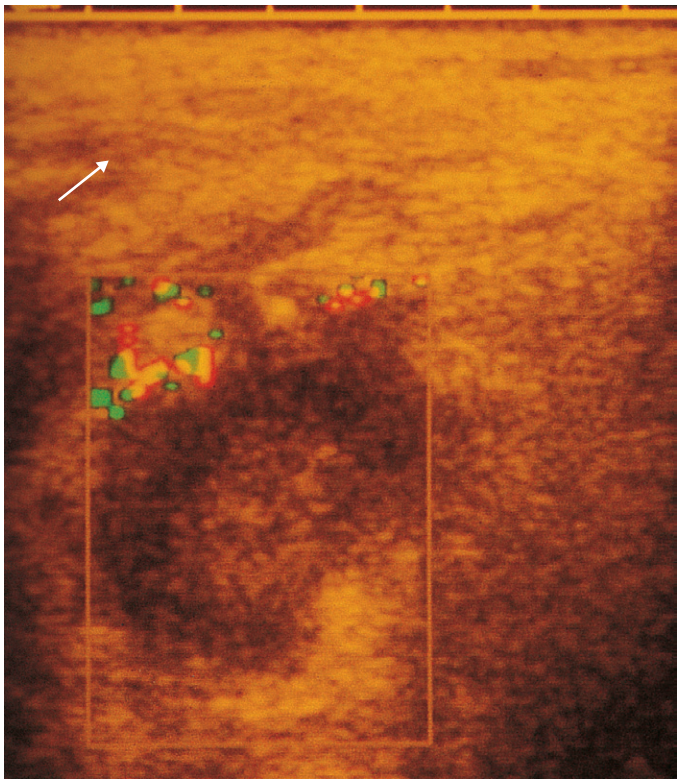

Figure 50.33 Irregular vascularisation at the margin of a lung cancer.

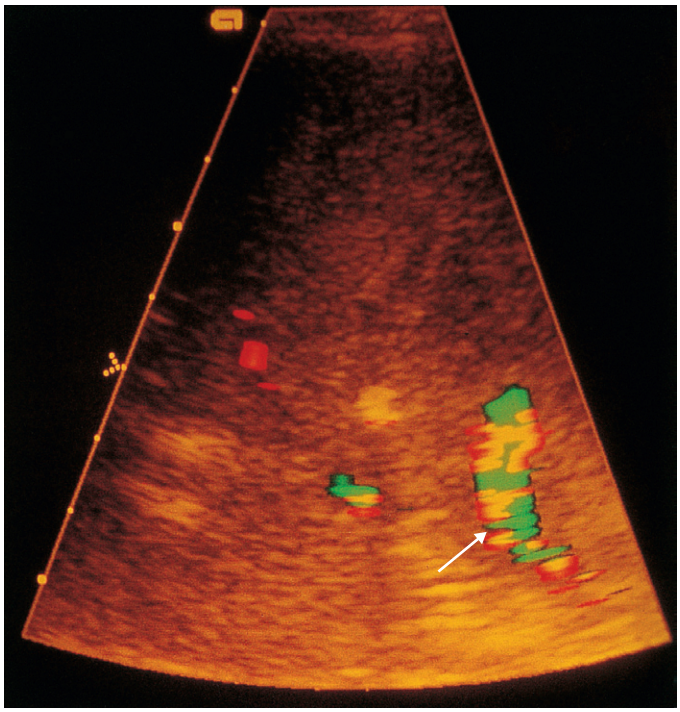

Figure 50.34 Tumour neovascularisation. The tortuous vessel produces the 'corkscrew' sign.

portions of the hemithorax, which are the areas most avoided using blind techniques.

Studies have demonstrated successful ultrasound-guided biopsies in peripheral pulmonary nodules less than 3 cm in diameter[74] and in lung consolidation associated with central necrosis.[75]

The complication rate is low: 1–2% haemoptysis; 1–3% pneumothorax; and 1% requiring chest drainage.[57,61,74–80] It should be noted that the complication of pneumothorax during an ultrasound-guided lung biopsy procedure will cause total loss of vision using the ultrasound transducer, and CT will be required for any further immediate biopsy attempts. Colour Doppler ultrasound is a helpful guide to selecting the safest route for the insertion of a needle and to avoid injury to the regional pulmonary vessels. In addition, this simple diagnostic procedure makes it possible to spare patients the discomfort of pleural endoscopies or even thoracotomies.

There is a small but important risk of 'tumour seeding' in the biopsy channel after ultrasound-guided biopsy. A review of over 95 000 cases of ultrasound-guided biopsy (not restricted to thoracic disease) found 6 metastases after fine-needle aspiration (<0.005%) and 11 after cutting needle or chest tube insertion (0.012%).[81] The significance of this in terms of patient outcomes is unknown but is unlikely to be limiting or preventative in terms of use of this technique.

Colour Doppler ultrasound

Colour Doppler permits non-invasive assessment of morphology and function of thoracic disease, as reflected in the organ blood supply and perfusion. Vascular structures in pulmonary consolidation are visualised as thin-walled, echo-poor pulsating, branched tubular structures arising from the hilar region, with blood flow detected by Doppler.[82]

Rapid respiratory movement may produce extensive artefacts in colour Doppler imaging, making analysis impossible. Non-vascular colour Doppler signals may appear within the fluid collection in the pleural space during respiratory and cardiac cycles.[16] This has been referred to as the 'colour fluid sign' and can be useful in the differentiation of echo-poor pleural thickening from pleural fluid. If there is doubt, spectral Doppler will clarify the situation.

Pulmonary sequestration is associated with specific colour Doppler ultrasound appearances:[83]

1. a large tortuous pulsating feeding artery in the consolidated lung
2. spectral Doppler reveals an arterial waveform, with a spiking systolic wave and persistent low diastolic flow; and
3. the flow is directed into the lesion from a feeding artery that arises from the aorta or from below the diaphragm.

Lung cancers and metastases are characterised by increased flow, irregular vessels, which are tortuous at the margins of the tumour, and arteriovenous malformations. A characteristic 'low resistance tumour flow' indicates the presence of abnormal neovascularisation that is frequently found in malignant tumours[69] (Fig. 50.34). Pneumonia is characterised by dilatation of normal pulmonary artery branches. The pulsatility index is higher in obstructive pneumonia than in simple pneumonia.

Colour Doppler may be helpful in the diagnosis and assessment of the perfusion status in cases of pulmonary infarction. In the early stage no pulmonary arterial blood flow is visible. However, this characteristic sonographic finding, the so-called 'consolidation with little perfusion', is only rarely detected, probably because of early reperfusion. Trans-thoracic biopsy is safer if colour Doppler imaging is available to avoid needle penetration through the main pulmonary vessels and thus reduce complications such as haemoptysis.

MEDIASTINUM

Mediastinal masses are often discovered incidentally on chest X-rays. CT plays an important role in their differential diagnosis. The mediastinum consists of solid and liquid components that allow the ultrasound beam to pass but is surrounded by 'sound-unfriendly' structures, mainly air.

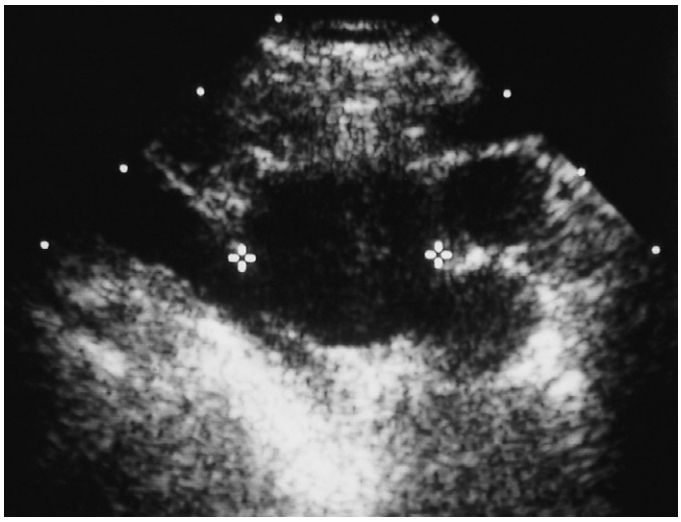

Figure 50.35 **Metastatic lymph nodes** in the upper anterior mediastinum via a suprasternal approach.

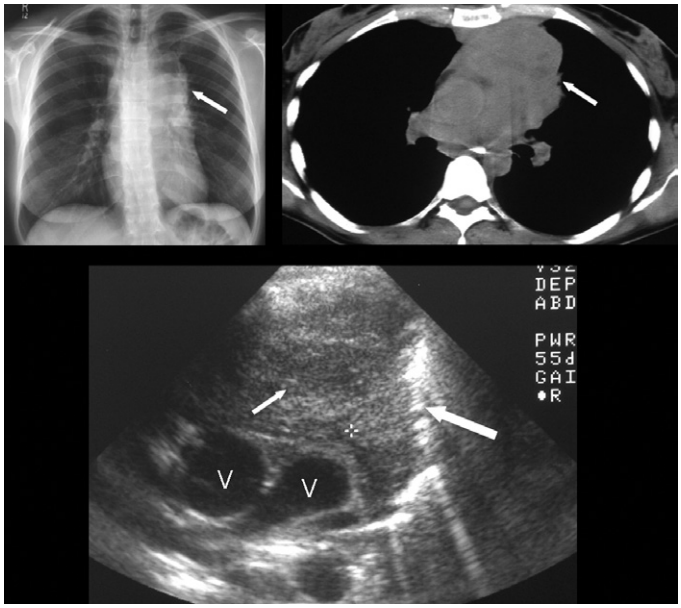

Figure 50.36 **Mediastinal mass** on chest radiograph, CT and ultrasound (arrows). The lower image shows ultrasound performed via the suprasternal notch, demonstrating normal visceral pleural (large arrow), the mass (small arrow) and distal great vessels (V).

However, access to the mediastinum can be obtained by a suprasternal or parasternal approach or occasionally via the infrasternal path. In the suprasternal approach, the patient's shoulders are supported and the head reclined to the maximum, preferably by cushioning the thoracic spine, as is done in thyroid sonography. Thus, the supra-aortic and parasternal regions as well as the aortopulmonary window can be visualised (Fig. 50.35). Parasagittal right and left, coronal and transverse sections need to be obtained. Masses such as lymphomas, retrosternal thyroids, thymomas, germ cell tumours, dermoid cysts and aortic aneurysms can be detected by this approach. Some 75% of clinically important mediastinal masses in adults lie in the anterior and medial portions of the mediastinum and are thus easily visualised by ultrasound. Although these patients will normally receive CT for full staging, ultrasound can be a quick and inexpensive means of follow-up (Fig. 50.36).

The anterior and mid-portions of the mediastinum can be evaluated using the parasternal approach with the patient in a decubitus position. The large vessels and their relationship to the heart at various levels serve as mediastinal landmarks. The examination is preferably done in expiration.

Sonographic studies of the mediastinum are limited by emphysema, scars caused by inflammation or surgery or radiotherapy, spinal deformations and movement artefacts. Moreover, sonography only shows some sections of the mediastinum. The quality of the examination depends on the experience of the examiner, the equipment and the patient's condition. A profound knowledge of mediastinal anatomy is indispensable. Colour Doppler ultrasound has made it easier to learn and perform mediastinal sonography, it shortens examination time and improves the quality and accuracy of B-mode imaging.[84]

REFERENCES

1. Joyner CR Jr, Miller LD, Dudrick SJ, et al. Reflected ultrasound in the detection of pulmonary embolism. Trans Assoc Am Physicians 1966;79:262–277.
2. Goldberg BB. Suprasternal ultrasonography. JAMA 1971;215(2): 245–250.
3. Mathis G. Thoraxsonography – Part I: Chest wall and pleura. Ultrasound Med Biol 1997;23(8):1131–1139.
4. Suzuki N, Saitoh T, Kitamura S. Tumor invasion of the chest wall in lung cancer: diagnosis with US. Radiology 1993;187(1):39–42.
5. Sugama Y, Tamaki S, Kitamura S, Kira S. Ultrasonographic evaluation of pleural and chest wall invasion of lung cancer. Chest 1988;93(2): 275–279.
6. Bitschnau R, Gehmacher O, Kopf A, Scheier M, Mathis G. [Ultrasound diagnosis of rib and sternum fractures]. Ultraschall Med 1997;18(4): 158–161.
7. van Overhagen H, Brakel K, Heijenbrok MW, et al. Metastases in supraclavicular lymph nodes in lung cancer: assessment with palpation, US, and CT. Radiology 2004;232(1):75–80.
8. Fultz PJ, Feins RH, Strang JG, et al. Detection and diagnosis of nonpalpable supraclavicular lymph nodes in lung cancer at CT and US. Radiology 2002;222(1):245–251.
9. van Overhagen H, Brakel K, Heijenbrok MW, et al. Metastases in supraclavicular lymph nodes in lung cancer: assessment with palpation, US, and CT. Radiology 2004;232(1):75–80.
10. Kumaran M, Benamore RE, Vaidhyanath R, et al. Ultrasound guided cytological aspiration of supraclavicular lymph nodes in patients with suspected lung cancer. Thorax 2005;60(3):229–233.
11. Sakai F, Sone S, Kiyono K, Imai S, et al. High resolution ultrasound of the chest wall. Rofo 1990;153(4):390–394.
12. Slater A, Goodwin M, Anderson KE, Gleeson FV. COPD can mimic the appearance of pneumothorax on thoracic ultrasound. Chest 2006;129(3):545–550.
13. Cancer Research UK Statistical Information Team. Cancer Research UK – incidence of common cancers. 2005. Email: stats.team@cancer.org.uk.
14. Eibenberger KL, Dock WI, Ammann ME, et al. Quantification of pleural effusions: sonography versus radiography. Radiology 1994;191(3):681–684.
15. Kelbel C, Borner N, Schadmand S, J et al. [Diagnosis of pleural effusions and atelectases: sonography and radiology compared]. Rofo 1991;154(2):159–163.
16. Wu RG, Yuan A, Liaw YS, et al. Image comparison of real-time gray-scale ultrasound and color Doppler ultrasound for use in diagnosis of minimal pleural effusion. Am J Respir Crit Care Med 1994;150(2):510–514.
17. Marks WM, Filly RA, Callen PW. Real-time evaluation of pleural lesions: new observations regarding the probability of obtaining free fluid. Radiology 1982;142(1):163–164.
18. Wu RG, Yang PC, Kuo SH, Luh KT. 'Fluid color' sign: a useful indicator for discrimination between pleural thickening and pleural effusion. J Ultrasound Med 1995;14(10):767–769.
19. Akhan O, Demirkazik FB, Ozmen MN, et al. Tuberculous pleural effusions: ultrasonic diagnosis. J Clin Ultrasound 1992;20(7):461–465.
20. Yang PC, Luh KT, Chang DB, et al. Value of sonography in determining the nature of pleural effusion: analysis of 320 cases. AJR Am J Roentgenol 1992;159(1):29–33.
21. Chian CF, Su WL, Soh LH, et al. Echogenic swirling pattern as a predictor of malignant pleural effusions in patients with malignancies. Chest 2004;126(1):129–134.

22. Ramnath RR, Heller RM, Ben-Ami T, et al. Implications of early sonographic evaluation of parapneumonic effusions in children with pneumonia. Pediatrics 1998;101(1 Pt 1):68–71.
23. Shankar KR, Kenny SE, Okoye BO, et al. Evolving experience in the management of empyema thoracis. Acta Paediatr 2000;89(4):417–420.
24. Maskell NA, Davies CW, Nunn AJ, et al. U.K. Controlled trial of intrapleural streptokinase for pleural infection. N Engl J Med 2005;352(9):865–874.
25. Steinberg HV, Erwin BC. Metastases to the pleura: sonographic detection. J Clin Ultrasound 1987;15(4):276–279.
26. Goerg C, Schwerk WB, Goerg K, Walters E. Pleural effusion: an 'acoustic window' for sonography of pleural metastases. J Clin Ultrasound 1991;19(2):93–97.
27. Qureshi NR, Rahman NM, Gleeson FV. Thoracic ultrasound in the diagnosis of malignant pleural effusion. Thorax 2009;64(2):139–143.
28. Targhetta R, Bourgeois JM, Chavagneux R, et al. Ultrasonic signs of pneumothorax: preliminary work. J Clin Ultrasound 1993;21(4):245–250.
29. Lichtenstein DA, Menu Y. A bedside ultrasound sign ruling out pneumothorax in the critically ill. Lung sliding. Chest 1995;108(5):1345–1348.
30. Lichtenstein D, Meziere G, Biderman P, Gepner A. The comet-tail artifact: an ultrasound sign ruling out pneumothorax. Intensive Care Med 1999;25(4):383–388.
31. Maury E, Guglielminotti J, Alzieu M, et al. Ultrasonic examination: an alternative to chest radiography after central venous catheter insertion? Am J Respir Crit Care Med 2001;164(3):403–405.
32. Sistrom CL, Reiheld CT, Gay SB, Wallace KK. Detection and estimation of the volume of pneumothorax using real-time sonography: efficacy determined by receiver operating characteristic analysis. AJR Am J Roentgenol 1996;166(2):317–321.
33. Sartori S, Tombesi P, Trevisani L, et al. Accuracy of transthoracic sonography in detection of pneumothorax after sonographically guided lung biopsy: prospective comparison with chest radiography. AJR Am J Roentgenol 2007;188(1):37–41.
34. Reissig A, Kroegel C. Accuracy of transthoracic sonography in excluding post-interventional pneumothorax and hydropneumothorax. Comparison to chest radiography. Eur J Radiol 2005;53(3):463–470.
35. Goodman TR, Traill ZC, Phillips AJ, et al. Ultrasound detection of pneumothorax. Clin Radiol 1999;54(11):736–739.
36. Blaivas M, Lyon M, Duggal S. A prospective comparison of supine chest radiography and bedside ultrasound for the diagnosis of traumatic pneumothorax. Acad Emerg Med 2005;12(9):844–849.
37. Rowan KR, Kirkpatrick AW, Liu D, et al. Traumatic pneumothorax detection with thoracic US: correlation with chest radiography and CT – initial experience. Radiology 2002;225(1):210–214.
38. Lichtenstein D, Meziere G, Biderman P, Gepner A. The 'lung point': an ultrasound sign specific to pneumothorax. Intensive Care Med 2000;26(10):1434–1440.
39. Lichtenstein DA, Meziere G, Lascols N, et al. Ultrasound diagnosis of occult pneumothorax. Crit Care Med 2005;33(6):1231–1238.
40. Soldati G, Testa A, Sher S, et al. Occult traumatic pneumothorax: diagnostic accuracy of lung ultrasonography in the emergency department. Chest 2008;133(1):204–211.
41. Soldati G, Testa A, Pignataro G, et al. The ultrasonographic deep sulcus sign in traumatic pneumothorax. Ultrasound Med Biol 2006;32(8):1157–1163.
42. Grogan DR, Irwin RS, Channick R, et al. Complications associated with thoracentesis. A prospective, randomized study comparing three different methods. Arch Intern Med 1990;150(4):873–877.
43. Jones PW, Moyers JP, Rogers JT, et al. Ultrasound-guided thoracentesis: is it a safer method? Chest 2003;123(2):418–423.
44. Raptopoulos V, Davis LM, Lee G, et al. Factors affecting the development of pneumothorax associated with thoracentesis. AJR Am J Roentgenol 1991;156(5):917–920.
45. Barnes TW, Morgenthaler TI, Olson EJ, et al. Sonographically guided thoracentesis and rate of pneumothorax. J Clin Ultrasound 2005;33(9):442–446.
46. Heidecker J, Huggins JT, Sahn SA, Doelken P. Pathophysiology of pneumothorax following ultrasound-guided thoracentesis. Chest 2006;130(4):1173–1184.
47. Hirsch JH, Rogers JV, Mack LA. Real-time sonography of pleural opacities. AJR Am J Roentgenol 1981;136(2):297–301.
48. Weingardt JP, Guico RR, Nemcek AA, Jr, et al. Ultrasound findings following failed, clinically directed thoracenteses. J Clin Ultrasound 1994;22(7):419–426.
49. Diacon AH, Brutsche MH, Soler M. Accuracy of pleural puncture sites: a prospective comparison of clinical examination with ultrasound. Chest 2003;123(2):436–441.
50. Mayo PH, Goltz HR, Tafreshi M, Doelken P. Safety of ultrasound-guided thoracentesis in patients receiving mechanical ventilation. Chest 2004;125(3):1059–1062.
51. Maskell NA, Gleeson FV, Darby M, Davies RJ. Diagnostically significant variations in pleural fluid pH in loculated parapneumonic effusions. Chest 2004;126(6):2022–2024.
52. Maskell NA, Gleeson FV. Images in clinical medicine. Effect of intrapleural streptokinase on a loculated malignant pleural effusion. N Engl J Med 2003;348(14):e4.
53. Hersh CP, Feller-Kopman D, Wahidi M, et al. Ultrasound guidance for medical thoracoscopy: a novel approach. Respiration 2003;70(3):299–301.
54. Zhu Z, Donnelly E, Dikensoy O, et al. Efficacy of ultrasound in the diagnosis of pleurodesis in rabbits. Chest 2005;128(2):934–939.
55. Leo F, Dellamonica J, Venissac N, et al. Can chest ultrasonography assess pleurodesis after VATS for spontaneous pneumothorax? Eur J Cardiothorac Surg 2005;28(1):47–49.
56. Weinberg B, Diakoumakis EE, Kass EG, et al. The air bronchogram: sonographic demonstration. AJR Am J Roentgenol 1986;147(3):593–595.
57. Mathis G. Thoraxsonography – Part II: Peripheral pulmonary consolidation. Ultrasound Med Biol 1997;23(8):1141–1153.
58. Gehmacher O, Mathis G, Kopf A, Scheier M. Ultrasound imaging of pneumonia. Ultrasound Med Biol 1995;21(9):1119–1122.
59. Hsu WH, Chiang CD, Chen CY, et al. Ultrasound-guided fine needle aspiration biopsy in the diagnosis of chronic pulmonary infection. Respiration 1997;64(5):319–325.
60. Ishida T, Hashimoto T, Arita M, et al. Efficacy of transthoracic needle aspiration in community-acquired pneumonia. Intern Med 2001;40(9):873–877.
61. Yang PC, Chang DB, Yu CJ, et al. Ultrasound guided percutaneous cutting biopsy for the diagnosis of pulmonary consolidations of unknown aetiology. Thorax 1992;47(6):457–460.
62. Arcasoy SM, Kreit JW. Thrombolytic therapy of pulmonary embolism: a comprehensive review of current evidence. Chest 1999;115(6):1695–1707.
63. Kroschel U, Seitz K, Reuss J, Rettenmaier G. [Sonographic imaging of lung emboli. Results of a prospective study]. Ultraschall Med 1991;12(6):263–268.
64. Mathis G, Dirschmid K. Pulmonary infarction: sonographic appearance with pathologic correlation. Eur J Radiol 1993;17(3):170–174.
65. Mathis G, Blank W, Reissig A, et al. Thoracic ultrasound for diagnosing pulmonary embolism: a prospective multicenter study of 352 patients. Chest 2005;128(3):1531–1538.
66. Mathis G, Metzler J, Fussenegger D, et al. Sonographic observation of pulmonary infarction and early infarctions by pulmonary embolism. Eur Heart J 1993;14(6):804–808.
67. Lechleitner P, Riedl B, Raneburger W, et al. Chest sonography in the diagnosis of pulmonary embolism: a comparison with MRI angiography and ventilation perfusion scintigraphy. Ultraschall Med 2002;23(6):373–378.
68. Mathis G, Bitschnau R, Gehmacher O, et al. Chest ultrasound in diagnosis of pulmonary embolism in comparison to helical CT. Ultraschall Med 1999;20(2):54–59.
69. Yuan A, Chang DB, Yu CJ, et al. Color Doppler sonography of benign and malignant pulmonary masses. AJR Am J Roentgenol 1994;163(3):545–549.
70. Hsu WH, Ikezoe J, Chen CY, et al. Color Doppler ultrasound signals of thoracic lesions. Correlation with resected histologic specimens. Am J Respir Crit Care Med 1996;153(6 Pt 1):1938–1951.
71. Adams RF, Gleeson FV. Percutaneous image-guided cutting-needle biopsy of the pleura in the presence of a suspected malignant effusion. Radiology 2001;219(2):510–514.
72. Adams RF, Gray W, Davies RJ, Gleeson FV. Percutaneous image-guided cutting needle biopsy of the pleura in the diagnosis of malignant mesothelioma. Chest 2001;120(6):1798–1802.
73. Diacon AH, Theron J, Schubert P, et al. Ultrasound-assisted transthoracic biopsy: fine-needle aspiration or cutting-needle biopsy? Eur Respir J 2007;29(2):357–362.
74. Yuan A, Yang PC, Chang DB, et al. Ultrasound-guided aspiration biopsy of small peripheral pulmonary nodules. Chest 1992;101(4):926–930.

75. Pan JF, Yang PC, Chang DB, et al. Needle aspiration biopsy of malignant lung masses with necrotic centers. Improved sensitivity with ultrasonic guidance. Chest 1993;103(5):1452–1456.
76. Heilo A, Stenwig AE, Solheim OP. Malignant pleural mesothelioma: US-guided histologic core-needle biopsy. Radiology 1999;211(3): 657–659.
77. Benamore RE, Scott K, Richards CJ, Entwisle JJ. Image-guided pleural biopsy: diagnostic yield and complications. Clin Radiol 2006;61(8):700–705.
78. Chang DB, Yang PC, Luh KT, et al. Ultrasound-guided pleural biopsy with Tru-Cut needle. Chest 1991;100(5):1328–1333.
79. Wernecke K, Vassallo P, Peters PE, von Bassewitz DB. Mediastinal tumors: biopsy under US guidance. Radiology 1989;172(2): 473–476.
80. Heilo A. Tumors in the mediastinum: US-guided histologic core-needle biopsy. Radiology 1993;189(1):143–146.
81. Weiss H, Duntsch U. [Complications of fine needle puncture. DEGUM survey II]. Ultraschall Med 1996;17(3):118–130.
82. Yuan A, Yang PC, Chang DB. Pulmonary infarction: use of color Doppler sonography for diagnosis and assessment of reperfusion of the lung. AJR Am J Roentgenol 1993;160(2):419–420.
83. Gudinchet F, Anderegg A. Echography of pulmonary sequestration. Eur J Radiol 1989;9(2):93–95.
84. Wernecke K, Peters PE, Galanski M. Mediastinal tumors: evaluation with suprasternal sonography. Radiology 1986;159(2):405–409.

CHAPTER

51 Muscular ultrasound – introduction

Ian Beggs

Musculoskeletal ultrasound needs appropriate equipment, careful technique, sound knowledge of anatomy and appreciation of clinical disorders.

Commercially available linear array transducers of the order of 7–12 MHz and 4 cm length are adequate for most musculoskeletal examinations. Small footprint, high-frequency transducers are often used to examine the hands, fingers and sites that are difficult to access although they have a limited field of view (FOV). Large FOV linear array transducers suffer from poor lateral resolution for superficial structures. Extended FOV imaging (Fig. 51.1) compensates for the limited range of medium-sized transducers.

Compound imaging reduces artefacts such as speckle, improves resolution and helps to overcome the effects of anisotropy in tendons and muscles. As the image is generated at different angles of insonation at least some of the sound should be perpendicular to the muscle or tendon.[1] Beam steering overcomes the effect of anisotropy although in practice experienced sonologists compensate automatically by altering the angulation of the transducer.

Colour or power Doppler is essential in the assessment of tendinopathy (Fig. 51.2) and inflammatory arthropathy. Neovascularity in tendinosis may be missed or underestimated if the tendon is under tension; therefore Doppler examination of tendons should be performed with the muscle–tendon complex relaxed (Fig. 51.3). Neovascularity has a positive correlation with pain. Contrast-enhanced techniques and pulse inversion harmonic imaging may improve sensitivity to vascular changes in inflammatory arthropathy.[2]

Good technique is important to optimise imaging and diagnostic information and to avoid repetitive stress injuries to the operator.

A stand-off is not required although copious jelly may be needed to examine superficial structures.

Generally speaking the patient should be positioned to minimise the strain on the operator's shoulder and arm by having the patient lower than the operator and the operator's hand resting on the patient. Twisting of the operator's neck and torso should be avoided.

Technique and equipment settings are subjectively determined by the operator but guidance can be offered. Detailed information about examination technique has been produced by the European Society of Musculoskeletal Radiology and is available at essr.org.[3] The transducer should be gripped around its face (i.e. at the end opposite the cable) between the thumb and forefinger with the ulnar border of the hand placed on the patient to provide maximum control of the transducer and support. The transducer cable should be held in the opposite hand to reduce the weight on the operating hand. The transducer should be moved slowly and smoothly. Fine movements may be achieved by pulling and pushing with the hand that does not hold the transducer. Slow and slight changes in angulation may be needed to overcome the effects of anisotropy and achieve a perpendicular angle of insonation to tendon or muscle. Transducer pressure should be light, although increased pressure may be needed to reach deeper structures or to displace fluid. Heavy pressure may efface muscle hernias or reduce Doppler signal.

Always ask the patient to indicate the site of symptoms although this can be misleading; pain from rotator cuff impingement, for example, is frequently felt distal to the shoulder. If there is no palpable abnormality it may help to mark the skin before starting to scan. Muscle tears and hernias may become more obvious if the patient contracts and relaxes the relevant muscles.

Comparison with the opposite side is helpful when the operator is unsure if appearances are normal or abnormal.

Neovascularity

- Neovascularity in tendons on Doppler ultrasound correlates with pain.
- Neovascularity may be missed if the tendon is under tension when examined.

Technique

- Move the transducer slowly.
- Ensure maximum support for the operator's hand.
- Pay attention to ergonomic factors.
- Compare with the opposite side if unsure if findings are normal/abnormal.

MUSCLES

Skeletal muscle is composed of elongated muscle fibres that are covered by thin connective tissue, the endomysium. Muscle fibres are grouped together in muscle bundles or fascicles and are surrounded by perimysium, or fibro-adipose septa, which contains vessels and nerves. A thicker connective tissue sheath, the epimysium, surrounds the whole muscle. Muscles lie deep to the deep fascia.

The arrangement of muscle bundles in an individual muscle depends on muscle function and shape. A parallel arrangement is seen in strap muscles such as sartorius and also in rectus abdominis which is divided into segments by transverse tendinous intersections that are echogenic. In fusiform muscles the bundles are almost parallel in mid-substance then converge as they run to the tendon. In pennate muscles the fascicles run oblique to the line of traction. This increases the insertional area of the fascicles and the force of

contraction of the muscle. Unipennate muscles (e.g. flexor pollicis longus) have a peripheral aponeurosis or tendon; bipennate muscles (e.g. rectus femoris) have a central tendon; and multipennate muscles (e.g. deltoid) have more than one tendon in the muscle substance. Muscles may have more than one muscle belly (e.g. biceps femoris) or have a spiral course (e.g. pectoralis major).[4]

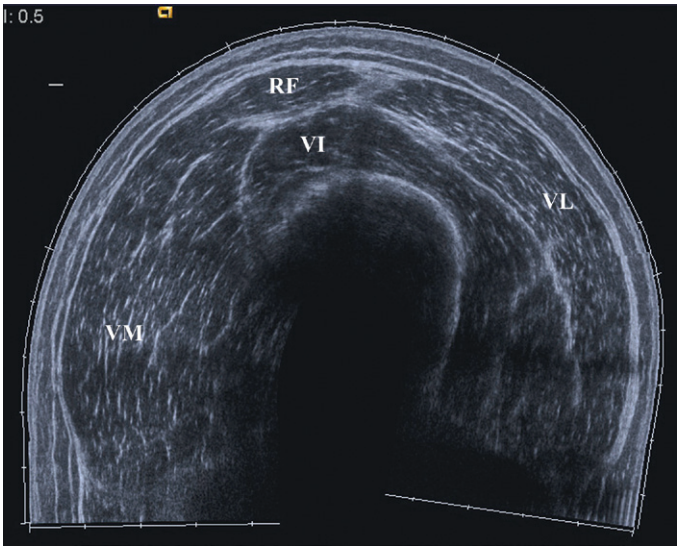

Figure 51.1 Transverse, extended FOV image of quadriceps muscle. The individual muscles are defined by the echogenic epimysium and enveloped by the echogenic deep fascia. Short echogenic streaks and 'dots' within the muscles are due to the fibro-adipose septa. RF, rectus femoris muscle; VM/VI/VL, vastus medialis/intermedius/lateralis muscles respectively.

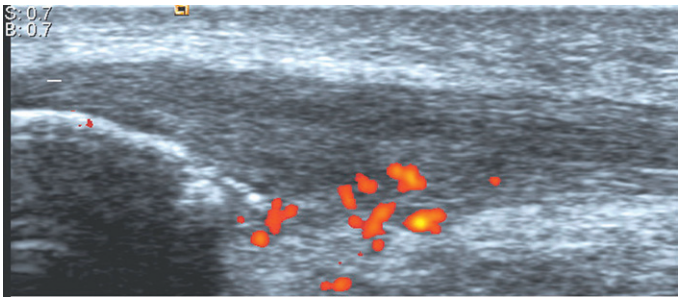

Figure 51.2 Longitudinal power Doppler scan of patellar tendon showing tendinosis adjacent to the inferior pole of the patella. The proximal tendon is swollen, hypoechic and ill-defined. There is prominent abnormal Doppler signal in the tendon and adjacent soft tissues typical of symptomatic tendinosis.

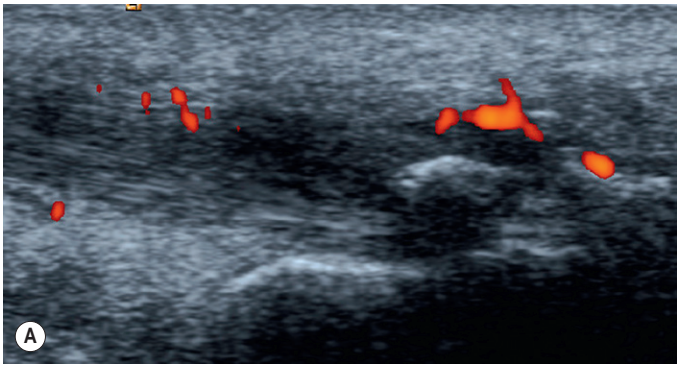

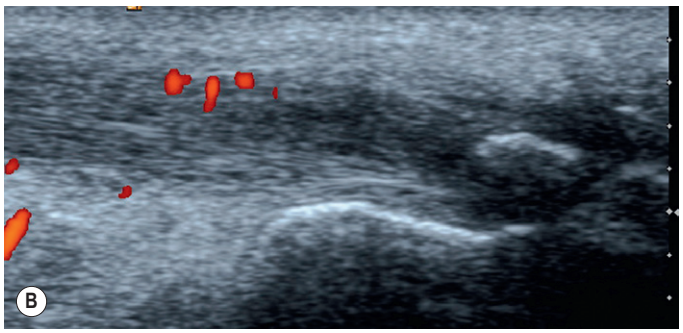

Figure 51.3 Longitudinal scans showing chronic tendinosis of the distal Achilles tendon. Neovascularity is obvious when the tendon is relaxed **(A)** but is almost completely abolished when the tendon is under tension **(B)**.

Normal muscle bundles are hypoechoic but become hyperechoic with fatty infiltration.

Fibro-adipose septa, intramuscular tendons and aponeuroses and epimysium are hyperechoic. Fibro-adipose septa appear as linear, almost parallel bands of increased echogenicity on longitudinal scans (Fig. 51.4) and as small echogenic 'dots' on transverse scans (Fig. 51.5). Echogenicity is lost if the ultrasound beam is not perpendicular to the fibro-adipose septa and the muscle then appears artefactually hypoechoic. Intramuscular tendons and aponeuroses are well defined and echogenic. They are better assessed on transverse scans.

Muscles

- Muscle bundles are hypoechoic but become echogenic with fatty infiltration.
- Fibro-adipose septa, tendons and aponeuroses are echogenic and are anisotropic.

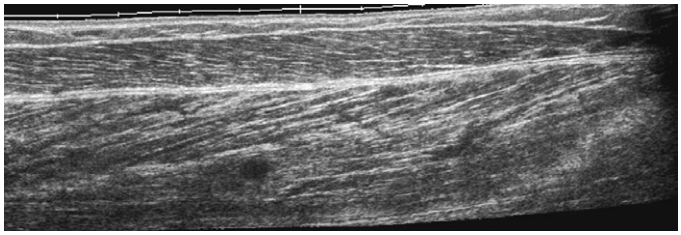

Figure 51.4 Extended FOV long-axis scan of medial head of gastrocnemius (superficial) and soleus (deep) muscles. Both are unipennate muscles. The echogenic fibro-adipose septa run obliquely to insert in the echogenic, linear aponeurosis.

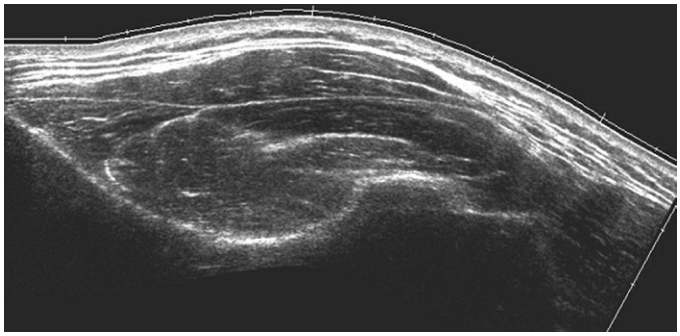

Figure 51.5 Sagittal extended FOV scan of infraspinatus muscle. The fibro-adipose septa appear as multiple 'dots' on this short-axis scan. The deeper part of the muscles is diffusely hyperechoic – individual muscles may show variable echogenicity. Comparison with the opposite side often helps to confirm that such variations are normal.

TENDONS

Tendons link muscle to bone and have great tensile strength. Tendons are largely composed of water but type 1 collagen accounts for 70% of the dry weight of a tendon. Collagen units form fibrils. Fibrils form fibres and fibres form fascicles. Tendon fibres mostly run parallel to the long axis of a tendon and to each other (Fig. 51.6) but transverse and spiral arrangements also occur.

Tendon fibrils are surrounded by an endotenon of loose connective tissue. Fibres are surrounded by peritenon and the tendon is enveloped by epitenon which may be surrounded by paratenon, the two comprising the peritendon. Tendons that curve as they run across joints (e.g. at the wrist and ankle) are surrounded by a two-layered synovial sheath that has a deep visceral layer and a superficial parietal layer. They are lined by synovial cells and connected by vincula, remnants of mesotendon, through which vessels run (Fig. 51.7). A normal tendon is avascular. Curved tendons are maintained in position by retinacula, focal thickenings of the deep fascia that are attached to bone.

Tendons that attach to bone at an acute angle and have a relatively simple action have a fibrous attachment. Tendons that insert nearly perpendicular to bone and have a more complex action such as the supraspinatus tendon have a multilayered fibrocartilaginous attachment.

Normal tendons have an echogenic appearance. On long-axis scans they have a fibrillar appearance (Fig. 51.8) with multiple thin, parallel, linear echoes due to interfaces between the collagen bundles and the endotendon.[5] Short-axis scans (Fig. 51.9A) show multiple bright dots. A more complex structure may be seen in tendons derived from more than one muscle (e.g. the quadriceps and Achilles tendons) in which the constituent tendons can be identified. Tendons and muscles are strongly anisotropic. They are composed of specular reflectors: the amplitude of the echo is greatest when the ultrasound beam is perpendicular to the reflector. Most other tissues are composed of diffuse reflectors and scatter the ultrasound beam.[1] The echogenic appearance is lost (Figs 51.8, 51.9B) if the sound beam is not perpendicular to the tendon and this may simulate tendinosis or a tear. Anisotropy may be used deliberately

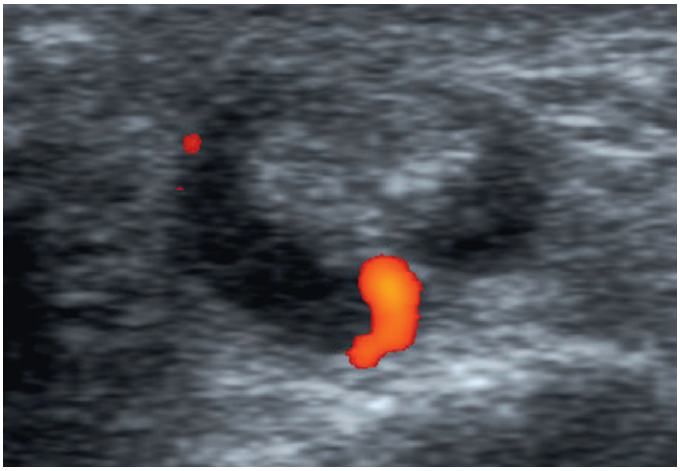

Figure 51.7 Transverse power Doppler scan of flexor tendon of finger. The tendon sheath is distended by fluid that encircles the tendon. A vessel runs across the vincula from the synovium to the tendon.

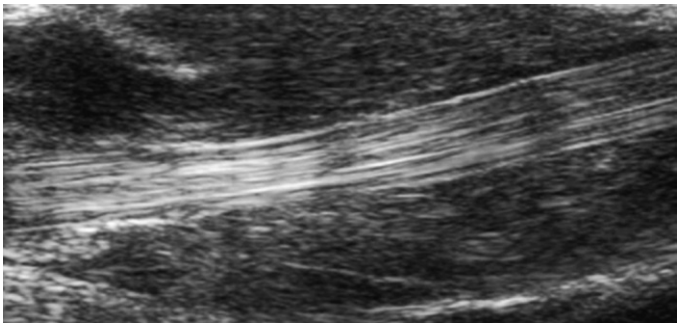

Figure 51.6 Longitudinal scan of flexor pollicis longus tendon in thenar eminence showing the parallel arrangement of the tendon fibres.

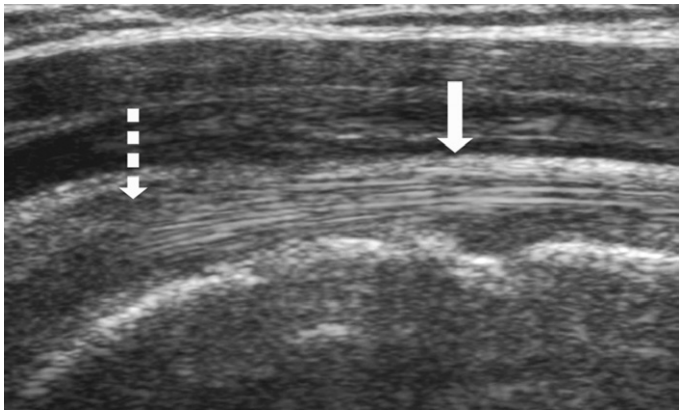

Figure 51.8 Longitudinal scan of long head of biceps tendon showing typical lamellar appearance (arrow) of tendon at 90° of insonation. The proximal tendon (broken arrow) is not seen because of the effect of anisotropy: as the tendon curves deeply the angle of the ultrasound beam to the tendon is no longer 90° and the tendon is no longer reflective.

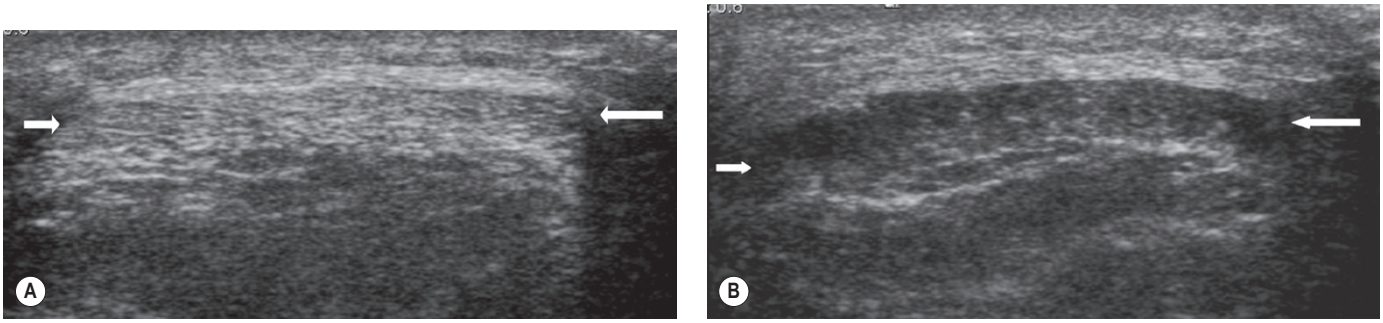

Figure 51.9 Patellar tendon. A: Short-axis scan of patellar tendon (between arrows). At 90° angle of insonation the typical echogenic speckling is seen. **B:** Short-axis scan of patellar tendon (between arrows) at same position as in **A**. The angle of insonation is now about 85° and the tendon appears hypoechoic.

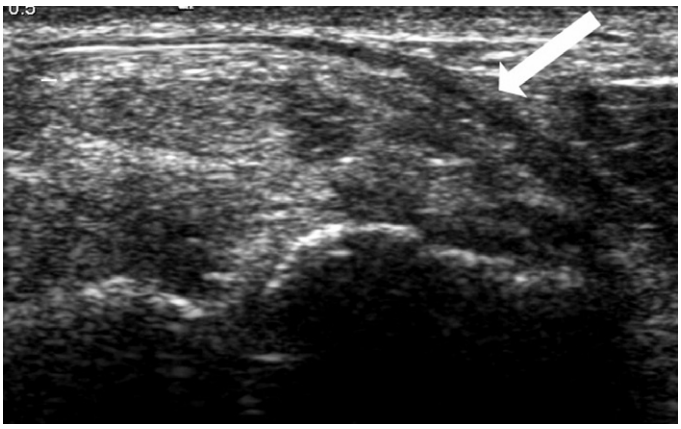

Figure 51.10 Transverse scan on medial aspect of ankle shows thin hypoechoic band of medial retinaculum (arrow).

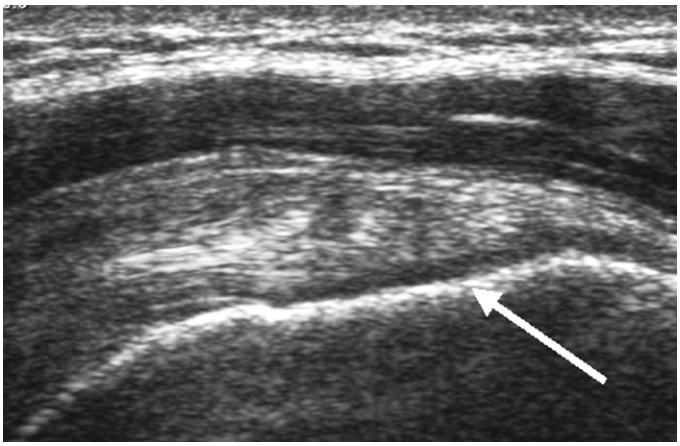

Figure 51.11 Longitudinal scan of supraspinatus tendon. The hypoechic band (arrow) at the tendon–bone interface is due to fibrocartilage.

to make a tendon more conspicuous if it is surrounded by echogenic structures, for example at the ankle. Beam edge artefact occurs at the border of large tendons, compromising tendon definition and causing distal acoustic shadowing. A thin echogenic line encircling the tendon is due to the paratenon while a synovial sheath results in a narrow hypoechoic layer in the otherwise echogenic halo around the tendon. Retinacula are thin, linear and hypoechoic (Fig. 51.10).

Muscle and tendon thickness at the musculotendinous junction have a reciprocal relationship: as one thins, the other expands proportionately. The fibrous or fibrocartilaginous attachment at the enthesis is a narrow hypoechic interface between tendon and bone (Fig. 51.11). Just proximal to this, the distal tendon may also be hypoechoic due to anisotropy as it curves to the enthesis (Fig. 51.12).

Tendons

- Tendons are echogenic. They have a fibrillar appearance on long-axis scans and a multiple-dot appearance on short-axis scans.
- Tendons are strongly anisotropic and will appear falsely hypoechoic if the angle of insonation is not 90° or very close to 90°.

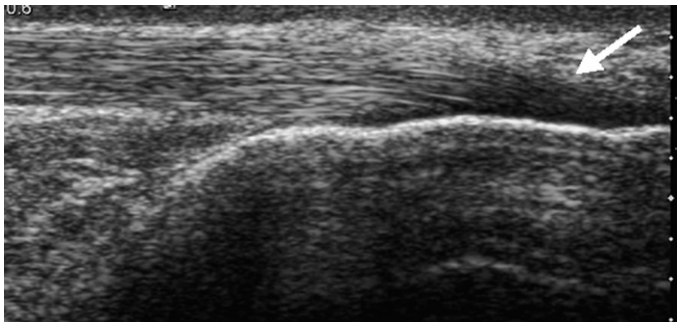

Figure 51.12 Long-axis scan of the Achilles tendon. The distal tendon becomes hypoechoic (arrow) due to anisotropy as it curves deeper to insert in the calcaneum.

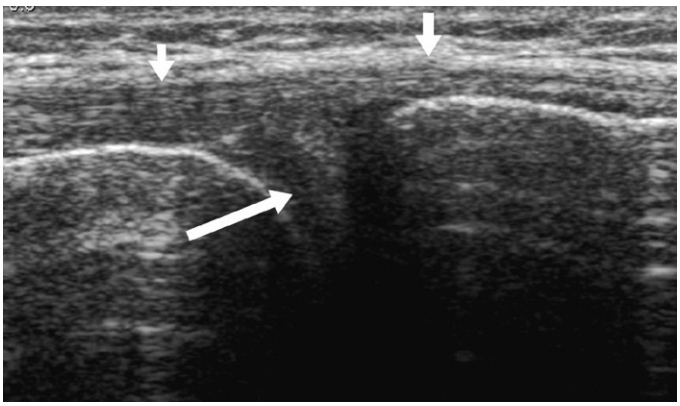

Figure 51.13 Longitudinal scan of medial collateral ligament (short arrows) of knee. The ligament has a similar lamellar appearance to tendons. The adjacent medial meniscus (long arrow) appears echogenic and triangular.

LIGAMENTS

Ligaments have broadly similar structure and ultrasound appearances to tendons. They are generally hyperechoic and lamellar (Fig. 51.13) and are affected by anisotropy. As it is not possible to scan perpendicular to the anterior and posterior cruciate ligaments because of their oblique orientation in the knee joint, they appear hypoechoic.

NERVES

Nerves appear similar in many respects to tendons. Each nerve fibre is invested by a connective tissue endoneurium. Nerve fibres are grouped together in fascicles and surrounded by perineurium while the fascicles are bundled together and sheathed by epineurium which may have two layers.

Ultrasound shows hypoechoic and hyperechoic speckling (Fig. 51.14A) on short-axis scans and a well-defined lamellar appearance on long-axis scans (Fig. 51.14B). Hypoechoic areas are separated by echogenic bands. The hypoechoic areas correspond to the nerve fascicles and the hyperechoic foci probably to perineurium.[6] Although nerves and tendons have similar ultrasound appearances they can be readily distinguished. The lamellar appearance of nerves is continuous while it is discontinuous in tendons. Contraction and relaxation of appropriate muscle groups results in to-and-fro movement of tendons but not nerves.

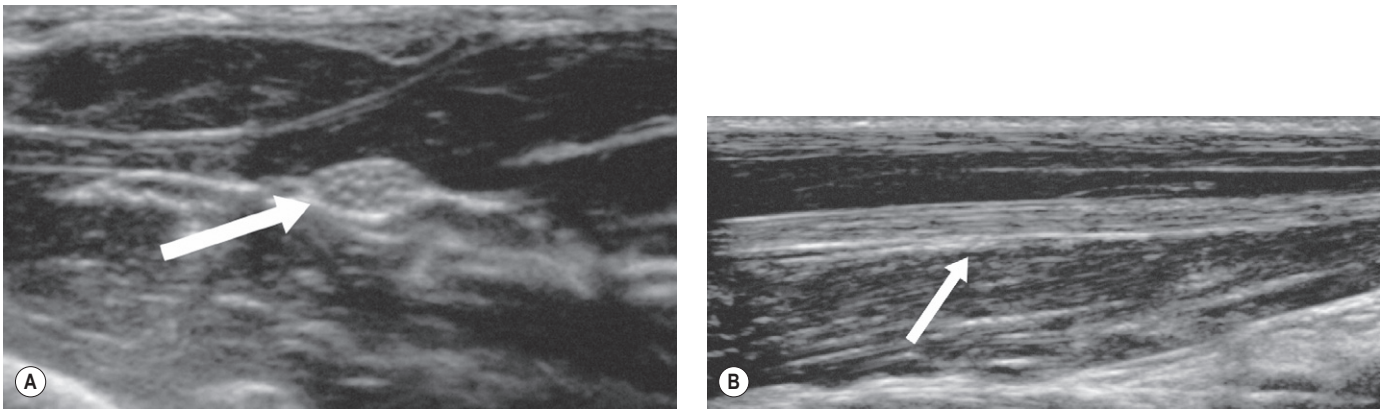

Figure 51.14 Median nerve. A: Transverse scan of median nerve (arrow) in mid forearm. It shows typical speckling. The echogenic areas are due to perineurium, the hypoechoic areas to nerve fascicles. **B:** Longitudinal scan of median nerve (arrow) in mid forearm. The alternating parallel lines of perineurium and nerve fascicles are continuous.

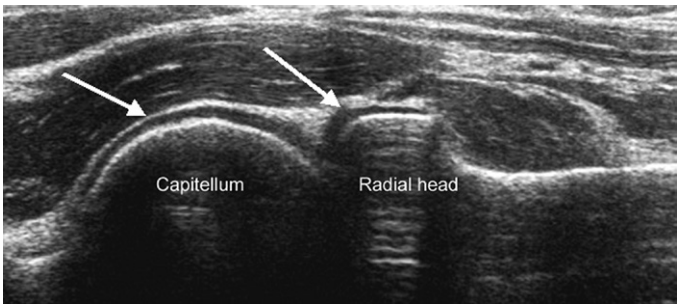

Figure 51.15 Longitudinal scan just lateral to midline on anterior aspect of elbow. The hyaline cartilage (arrows) covering the capitellum and radial head is thick and hypoechoic.

BONES

Ultrasound is of limited value in investigating bone as sound is reflected by intact cortex (Fig. 51.1). Periosteal elevation or cortical defects may be manifestations of trauma, infection or tumour. Ultrasound-guided biopsy of bone can be performed if cortex is destroyed. Erosions may be seen in inflammatory arthropathy and abnormal Doppler signal indicates that they are active. Hyperostosis at tendon insertions is a feature of enthesopathy and tendinopathy.

JOINTS

Articular cartilage is well defined and hypoechoic (Fig. 51.15). Subchondral bone is highly reflective. The layers of hyaline cartilage seen on histological examination, high-resolution MRI and in vitro using very high-frequency ultrasound transducers are not identified on conventional ultrasound. Fibrocartilage structures such as the glenoid labrum or the menisci of the knee (Fig. 51.13) are homogeneously echogenic. The joint capsule is thin and echogenic. The normal synovial membrane is too thin to be identified.

Normal joints are dry or contain only small amounts of fluid. Comparison with the opposite side may be helpful in this regard. Ultrasound cannot reliably distinguish between different types of effusion but can be used to guide aspiration.

REFERENCES

1. Lin DC, Nazarian LN, O'Kane PL, et al. Advantages of real-time spatial compound sonography of the musculoskeletal system versus conventional sonography. AJR Am J Roentgenol 2002;179:1629–1631.
2. Schueller-Weidekamm C, Krestan C, Schueller G, et al. Power Doppler sonography and pulse-inversion harmonic imaging in evaluation of rheumatoid arthritis synovitis. AJR Am J Roentgenol 2007;188:504–508.
3. European Society of Musculoskeletal Radiology (essr.org). Shoulder: http://www.essr.org/images/stories/new%20shoulder.pdf. Elbow: http://www.essr.org/images/stories/elbow.pdf. Wrist: http://www.essr.org/images/stories/wrist.pdf. Hip: http://www.essr.org/images/stories/new%20hip.pdf. Knee: http://www.essr.org/images/stories/knee.pdf. Ankle: http://www.essr.org/images/stories/ankle.pdf.
4. Erickson SJ. High-resolution imaging of the musculoskeletal system. Radiology 1997;205:593–618.
5. Martinoli C, Derchi LE, Pastorino C, et al. Analysis of echotexture of tendons with US. Radiology 1993;186:839–843.
6. Silvestri E, Martinoli C, Derchi LE, et al. Echotexture of peripheral nerves: correlation between US and histologic findings and criteria to differentiate tendons. Radiology 1995;197:291–296.

CHAPTER

52

Ultrasound of the shoulder

Simon Ostlere

INTRODUCTION

Ultrasound is an excellent method of assessing the soft tissues around the shoulder. Although magnetic resonance imaging (MRI) has similar accuracy, ultrasound is an effective first-line investigation in the majority of cases. Ultrasound is most effective when there is a precise clinical question to be answered, usually 'Is there a full thickness rotator cuff tear and how large is it?' Ultrasound can answer these questions quickly and accurately.[1] The speed of the examination is commensurate with an immediate access service.

Ultrasound, MRI and radiography are complementary techniques. Most patients will have a plain radiograph which may identify calcification and degenerative joint disease. Patients with impingement-type symptoms can be imaged with ultrasound alone. Ultrasound is not useful in the investigation of glenohumeral instability.

ANATOMY

The rotator cuff consists of the tendons of four muscles: supraspinatus, which originates from the posterior aspect of the scapula superior to the scapular spine; infraspinatus and teres minor, which originate inferior to the scapular spine; and subscapularis, which originates from the anterior blade of the scapula. All tendons with the exception of teres minor are routinely inspected during ultrasound examination of the shoulder. The tendons are echogenic structures in the young but often become more hypoechoic with age. The most important tendon is the supraspinatus, which attaches to the anterior part of the greater tuberosity (Fig. 52.1). Infraspinatus merges imperceptibly with the supraspinatus tendon about 1.5 cm posterior to the anterior edge of supraspinatus and attaches to the posterior part of the greater tuberosity. Slips of muscle extend into the infraspinatus tendon resulting in a characteristic appearance (Fig. 52.2). On axial imaging the two tendons are seen as a cuff of uniform thickness (Fig. 52.3). Teres minor attaches on the lesser tuberosity posterior to infraspinatus.

The subscapularis tendon is situated anteriorly and attaches to the lesser tuberosity (Fig. 52.4). The distal subscapularis tendon is echogenic, similar to the supraspinatus and infraspinatus tendons. More medially on transverse images, i.e. at the musculotendinous junction, the echogenic tendon slips are separated by hypoechoic muscle.

The gap in the rotator cuff between the supraspinatus and infraspinatus tendons is the rotator cuff interval. The long head of biceps tendon originates from the superior glenoid rim and traverses the rotator cuff interval where it abuts the anterior leading edge of the supraspinatus tendon. The coracohumeral and superior glenohumeral ligaments stabilise the biceps tendon and lie superficial and deep respectively to the tendon in the interval (Fig. 52.5). Distal to the rotator interval the biceps tendon enters the bicipital groove. The roof of the groove is formed by the transverse humeral ligament, which consists of fibres from the subscapularis and supraspinatus tendons (Fig. 52.6).

The subacromial/subdeltoid bursa is draped over the rotator cuff deep to the acromion and deltoid muscle and is seen as a thin hypoechoic line (Fig. 52.1), often accentuated by thin, superficial and deep layers of echogenic peri-bursal fat. The coracoacromial ligament is orientated at 90° to the supraspinatus muscle and is seen as an echogenic linear structure superficial to the subacromial bursa (Fig. 52.7). The posterior aspect of the glenohumeral joint is best appreciated in the axial plane (Fig. 52.8).

TECHNIQUE

A standard examination of the shoulder need only take a few minutes. A high-resolution probe, usually 10–15 MHz, and state of the art scanner are recommended. The shoulder is examined with the patient seated and the operator facing or standing behind the patient. The examination can be divided into two parts which can be performed in either order: (a) examination of the supraspinatus and infraspinatus tendons with the arm in the extended and internally rotated position and (b) examination of the subscapularis and biceps tendon with the arm in the neutral position. In addition, dynamic imaging for impingement and inspection of other structures such as the acromioclavicular joint may be performed in selected cases. With the hand in the 'back trouser pocket' position, the supraspinatus and infraspinatus tendons can be clearly visualised as the extended and internally rotated position exposes the important distal end of the tendons from under the acromion (Figs 52.1 and 52.2). When imaging along the long axis of the tendon the

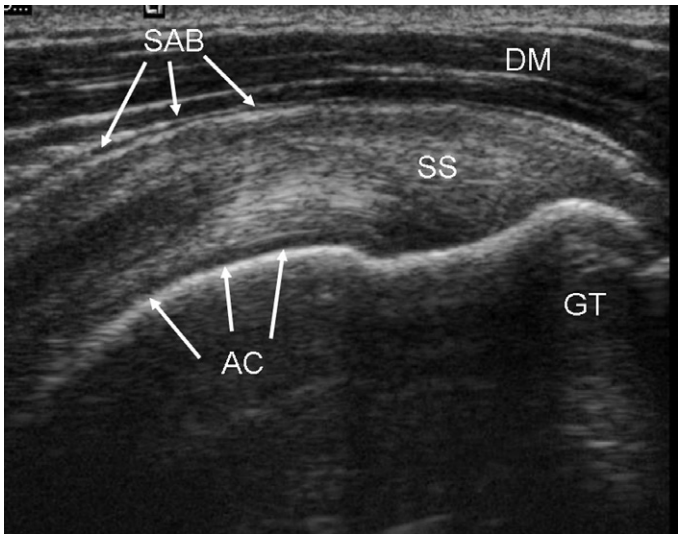

Figure 52.1 Normal longitudinal scan of supraspinatus tendon. SS, supraspinatus tendon; GT, greater tuberosity; DM, deltoid muscle; SAB, subacromial bursa; AC, articular cartilage.

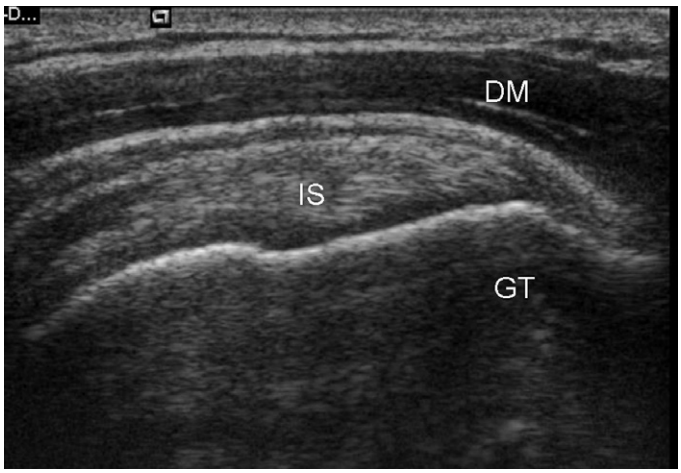

Figure 52.2 Normal infraspinatus tendon on longitudinal scan. IS, infraspinatus tendon; DM, deltoid muscle; GT, greater tuberosity.

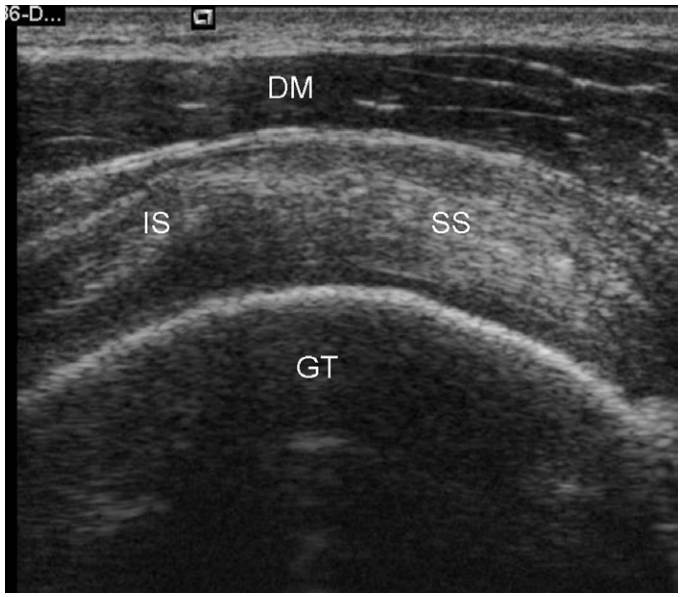

Figure 52.3 Normal rotator cuff seen in transverse section. The cuff is of uniform thickness throughout. SS, supraspinatus tendon; IS, infraspinatus tendon; DM, deltoid muscle; GT, greater tuberosity.

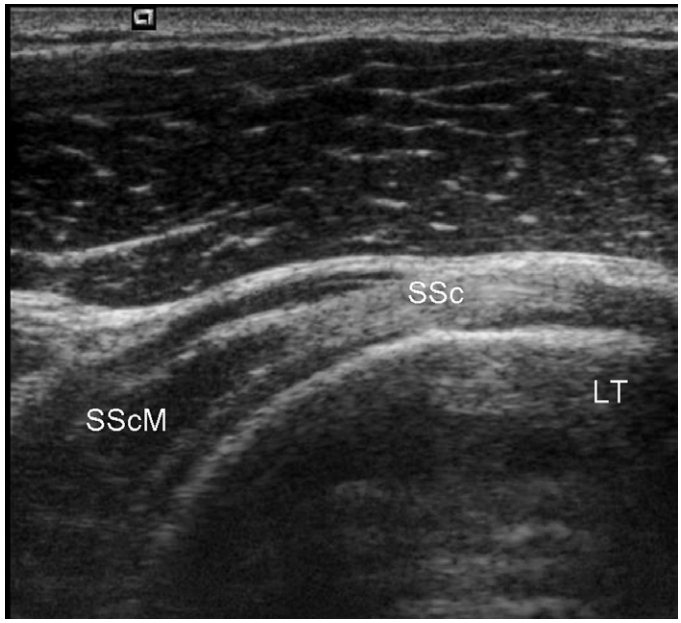

Figure 52.4 Normal subscapularis tendon. SSc, subscapularis tendon; SScM, subscapularis muscle; LT, lesser tuberosity.

probe should be inclined at around 45° to the coronal plane. The probe should initially be placed over the bicipital groove and then slowly moved posteriorly onto the anterior leading edge of the supraspinatus tendon. Careful inspection of this area is required as this is where tears are commonly found. The probe is then moved further posteriorly to cover the remainder of the supraspinatus and the infraspinatus tendon. Anisotropy can be a problem which particularly affects the distal deep fibres of the tendon, simulating focal degeneration or partial tear. Tilting the probe will eliminate this artefact (Fig. 52.9). To obtain short-axis views of the rotator cuff, the probe is rotated 90°. In this position the cuff should be scanned from its distal attachment to the musculotendinous junction. By slightly reducing the degree of internal rotation, better views of the rounded anterior leading edge of the supraspinatus can be obtained (Fig. 52.5). At some stage the lateral aspect of the greater tuberosity should be inspected as this is where fluid often collects in the subacromial/subdeltoid bursa.

In the second part of the examination the patient's hand is placed on the ipsilateral thigh with the palm facing upwards. In this position the bicipital groove, which contains the biceps tendon, points anteriorly and is best appreciated in the axial plane (Fig. 52.6). The echogenicity of the tendon is susceptible to anisotropy and dependent on the angle of the probe. The tendon can also be imaged in the sagittal plane by rotating the probe 90°. Tilting the probe slightly is needed to obtain optimal images as this keeps the tendon and probe parallel. To examine the subscapularis tendon, the patient is asked to externally rotate the arm. The tendon can then be examined along its long and short axes (Fig. 52.4).

The above description represents the minimum required for a routine examination for a patient with suspected rotator cuff

disease. Additional views may be obtained when clinically indicated. Minor movements of the shoulder and compression with the probe can help in the diagnosis of small rotator cuff tears. Some small tears are best appreciated by examining the patient in maximum internal rotation or with the arm by the patient's side. Dynamic imaging while abducting the arm may demonstrate impingement of the bursa against the coracoacromial ligament (Fig. 52.10). Impingement of the acromioclavicular joint can be demonstrated by asking the patient to slowly move the hand on the affected side onto the opposite shoulder while scanning the joint in the coronal plane.

IMPINGEMENT

Impingement syndrome is characterised by pain and restricted motion of the shoulder on abducting the arm.[2] The primary pathology is thought to be degeneration and swelling of the supraspinatus tendon resulting in impingement of the tendon and the subacromial bursa against the acromion and coracoacromial ligament.[3] This may result in bursitis, partial and full thickness tears of the rotator cuff, spur formation on the undersurface of the acromion and irregularity of the greater tuberosity. The relative importance of physical impingement versus degeneration in the pathogenesis of rotator cuff tear is unclear. Tears tend to occur at the distal hypovascular end of the tendon termed the rotator crescent which is bordered medially by a cord of thickened fibres called the rotator cable. It is thought that the cable has important biomechanical properties supporting the rotator crescent so that shoulder strength may be maintained despite tears of the distal end of the cuff. The deep portion of the cable can be identified on ultrasound in 10% of individuals.[4] Imaging with either MRI or ultrasound is used primarily to determine the degree of damage to the rotator cuff and to select patients who may be suitable for rotator cuff repair. The indications for rotator cuff repair will vary from centre to centre and from surgeon to surgeon but in general lesions considered to be suitable for repair are small and medium-sized tears

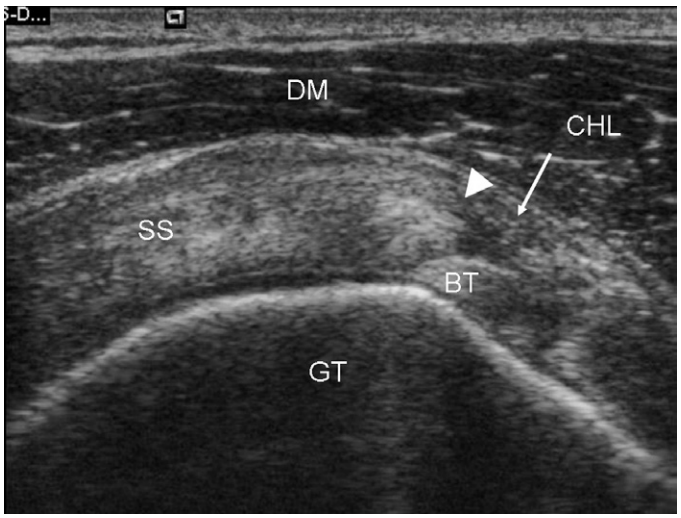

Figure 52.5 Normal appearance of the anterior leading edge of the supraspinatus tendon and rotator cuff interval in the transverse plane. The rounded edge of the supraspinatus tendon (arrowhead) overhangs the biceps tendon. The coracohumeral ligament lies superficial to the biceps tendon. SS, supraspinatus tendon; GT, greater tuberosity; DM, deltoid muscle; BT, biceps tendon; CHL, coracohumeral ligament.

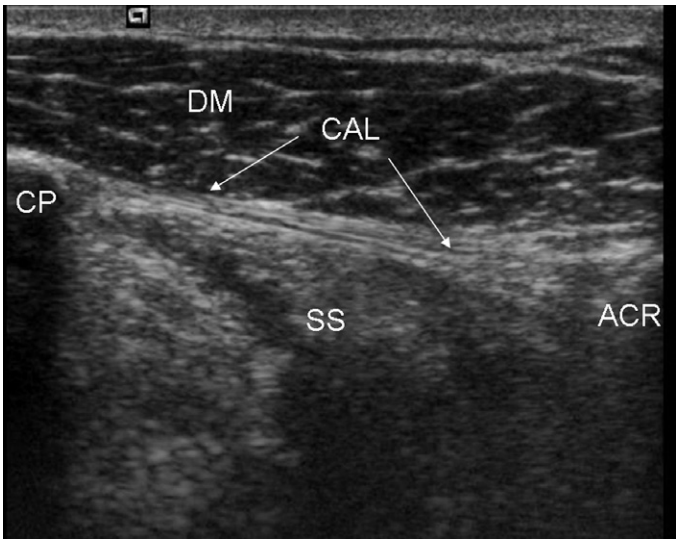

Figure 52.7 Coracoacromial ligament. The scan plane is coronal oblique along the long axis of the coracoacromial ligament. SS, supraspinatus tendon; DM, deltoid muscle; CP, coracoid process; CAL, coracoacromial ligament; ACR, acromion.

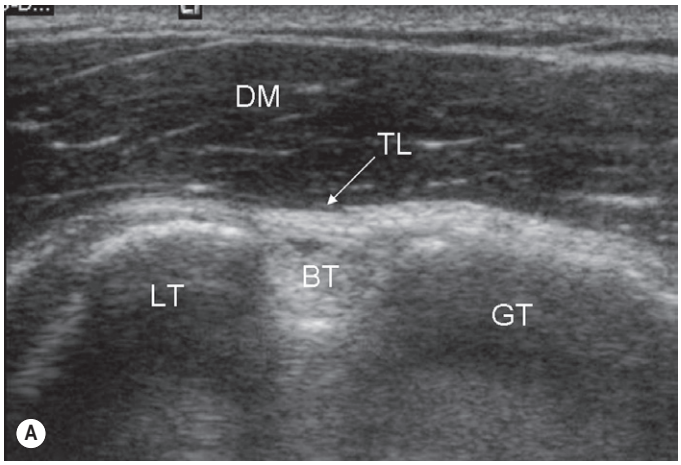

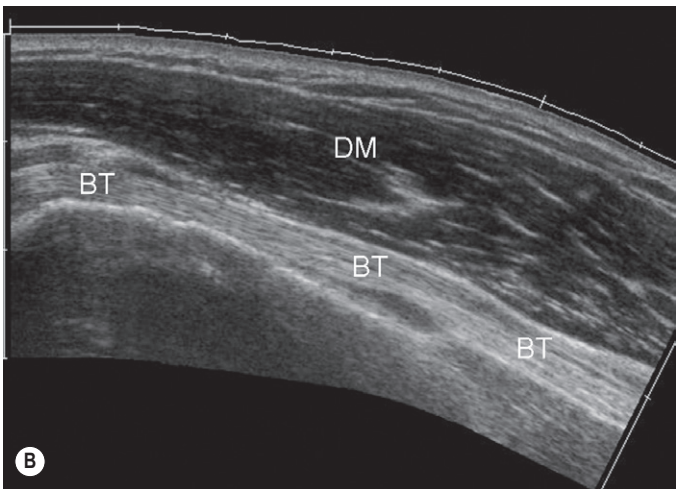

Figure 52.6 Normal biceps tendon is seen as an echogenic structure in the bicipital groove in the **(A)** transverse and **(B)** longitudinal plane. GT, greater tuberosity; LT, lesser tuberosity; DM, deltoid muscle; BT, biceps tendon; TL, transverse ligament.

in the younger population. The results of repair for large and massive tears are disappointing. Patients with no full thickness tear or a tear that is considered to be too extensive for repair may benefit from arthroscopic subacromial decompression.

DEGENERATION

The normal rotator cuff is uniformly echogenic. With age the tendon becomes degenerate and the echogenicity reduces. Degeneration may lead to swelling of the tendon, making it vulnerable to impingement in the confined space under the subacromial arch (Fig. 52.11). Often degeneration is accompanied by hypertrophy of the subacromial bursa. It may be difficult to differentiate focal degeneration from partial thickness tears.

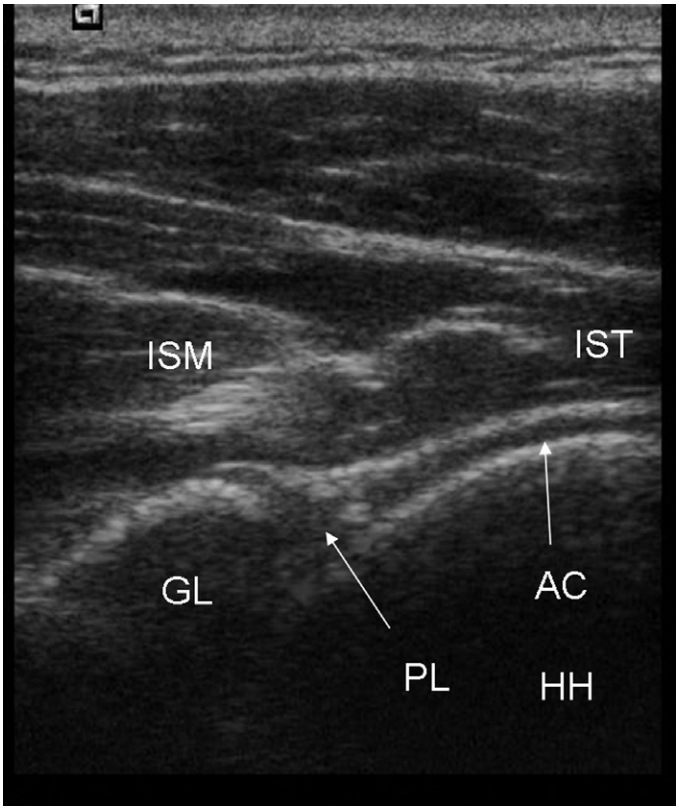

Figure 52.8 Posterior glenohumeral joint. Axial scan. IST, infraspinatus tendon; ISM, infraspinatus muscle; PL, posterior labrum; GL, glenoid; HH, humeral head; AC, articular cartilage.

FULL THICKNESS TEARS

Ultrasound is accurate in the detection of full thickness rotator cuff tears.[5] These tears, which extend from the superficial to the deep surfaces of the rotator cuff, invariably start at or near the anterior aspect of the distal end of the supraspinatus tendon before extending both anteriorly across the rotator cuff interval to involve the subscapularis and posteriorly into infraspinatus. Fluid may be seen between the tendon ends (Fig. 52.12) but more frequently there is a paucity of fluid and the tear is represented by the loss of the normal convexity of the superficial surface of the cuff with the deltoid muscle sagging into the gap (Fig. 52.13). Although most lesions can be detected while imaging along the long axis of the tendon, imaging along the short axis is useful to detect longitudinal splits-like tears and tears of the anterior leading edge of the supraspinatus tendon. The latter can be diagnosed when a gap between the anterior aspect of the supraspinatus tendon and the biceps tendon is detected (Fig. 52.14). Large and massive tears with retraction of the muscle are easy to diagnose on ultrasound. The humeral head appears bare and is covered directly by the deltoid muscle (Fig. 52.15). Sometimes smaller tears are difficult to appreciate in the presence of a thickened subacromial bursa that is of similar echogenicity to the underlying tendon. Irregularity and cystic change at the greater tuberosity are common findings in impingement syndrome and are usually accompanied by rotator cuff tear (Fig. 52.16).

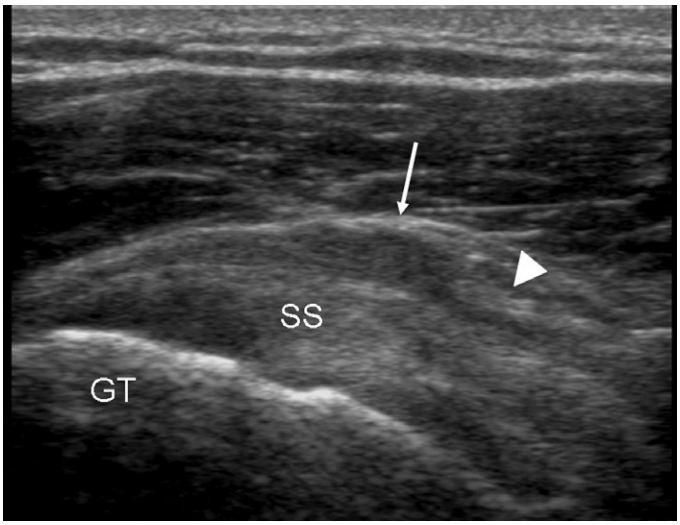

Figure 52.10 Impingement. There is bunching up of the thickened bursa (arrow) against the coracoacromial ligament (arrowhead). SS, supraspinatus tendon; GT, greater tuberosity.

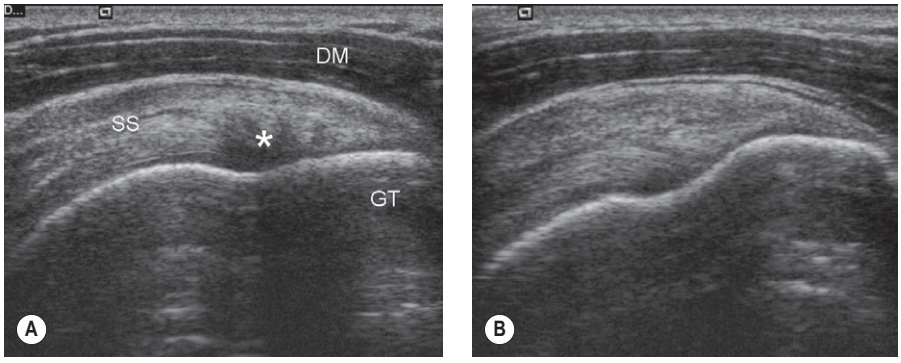

Figure 52.9 Anisotropy affecting the echogenicity of the supraspinatus tendon. **A:** The deep portion of the tendon appears hypoechoic close to its attachment to the greater tuberosity (*). **B:** The normal echogenicity is restored by angling the probe. SS, supraspinatus tendon; GT, greater tuberosity; DM, deltoid muscle.

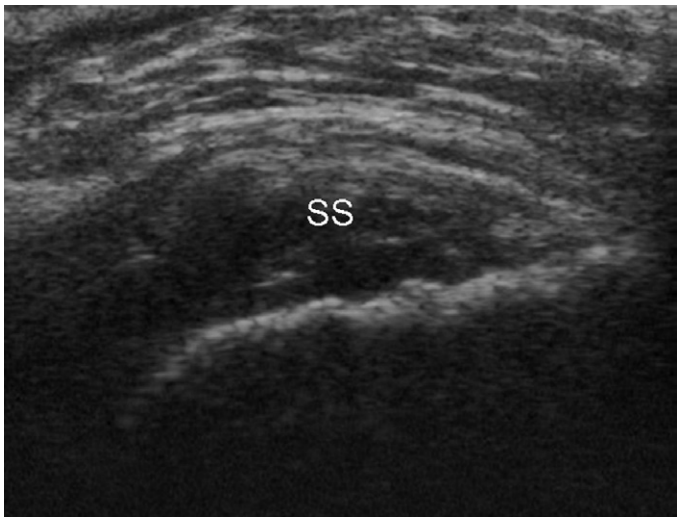

Figure 52.11 Degenerate tendon. The tendon is hypoechoic and swollen. SS, supraspinatus tendon.

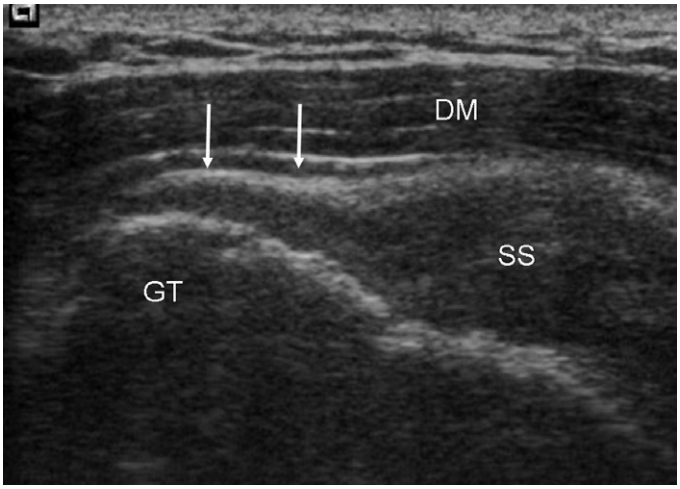

Figure 52.13 Full thickness tear of the supraspinatus tendon. There is loss of the normal convexity of the surface of the supraspinatus tendon. The deltoid is seen to sag into the tear (arrows). SS, supraspinatus tendon; GT, greater tuberosity; DM, deltoid muscle.

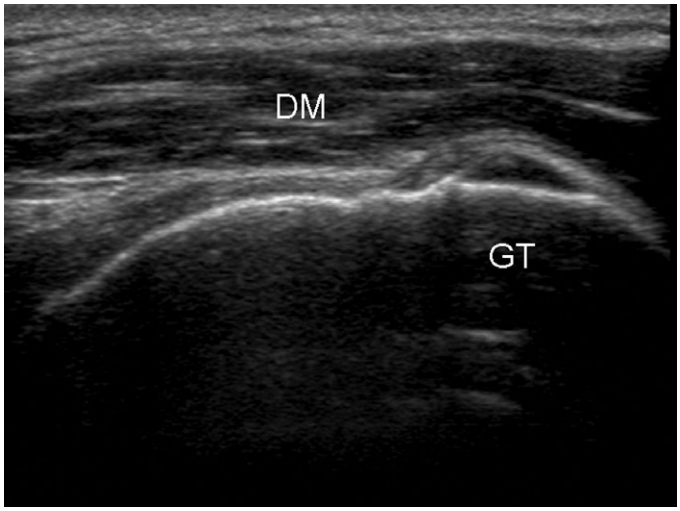

Figure 52.15 Massive rotator cuff tear. Longitudinal image. No tendon can be seen between the deltoid muscle and the humeral head. GT, greater tuberosity; DM, deltoid muscle.

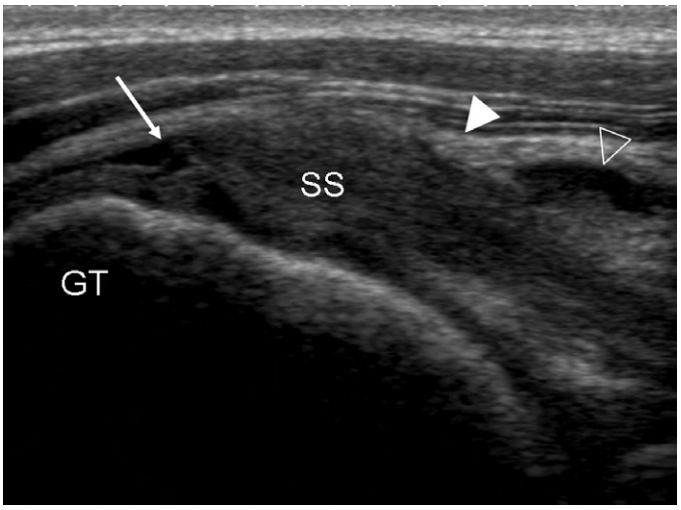

Figure 52.12 Small tear of the supraspinatus tendon. Fluid is seen in the gap in the tendon (arrow). There is fluid in the subacromial bursa (open arrowhead) seen medial to the coracoacromial ligament (arrowhead). SS, supraspinatus tendon; GT, greater tuberosity.

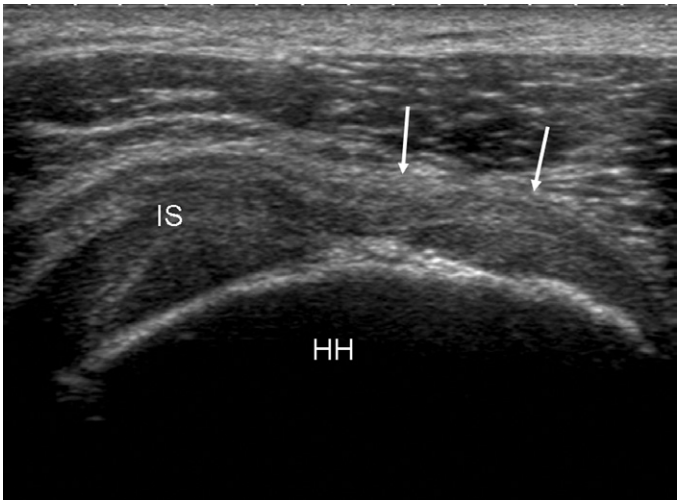

Figure 52.14 Transverse image of the rotator cuff showing a defect (arrows) representing a full thickness tear of the supraspinatus tendon. The infraspinatus tendon is intact. HH, humeral head; IS, infraspinatus.

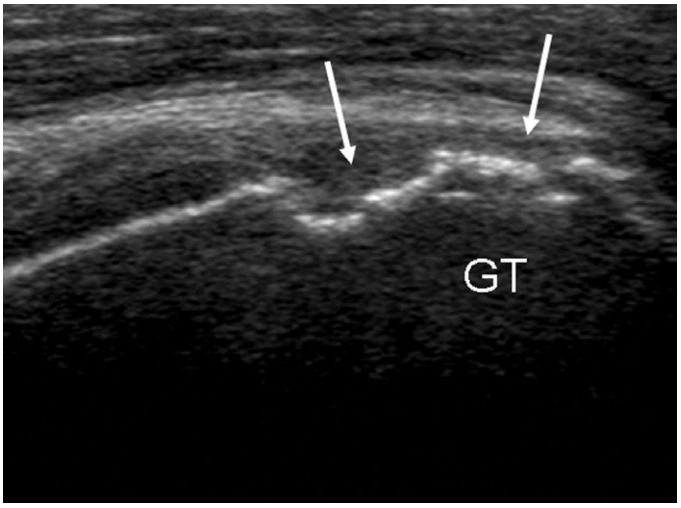

Figure 52.16 Irregularity of the greater tuberosity (arrows). This is a common finding in patients with impingement and rotator cuff tears. GT, greater tuberosity.

Most tears are of a degenerative nature but acute rupture may occur, particularly of the supraspinatus and subscapularis tendons. In acute tears the retracted tendon end can usually be identified and the large gap is filled with fluid[6] (Fig. 52.17).

The status of the rotator cuff muscles is an important predictor of success of a rotator cuff repair,[7,8] and is particularly important in centres where repair of more advanced tears is regularly undertaken. Although MRI is the more established method for identifying and grading atrophy of the muscle, ultrasound is also effective. Fatty infiltration is seen as loss of the normal pennate pattern and increase in echogenicity of the muscle[9] (Fig. 52.18). By scanning the supraspinatus muscle in the short-axis plane, a measure of atrophy can be obtained by calculating the ratio of the cross-sectional areas of the muscle to the fossa.

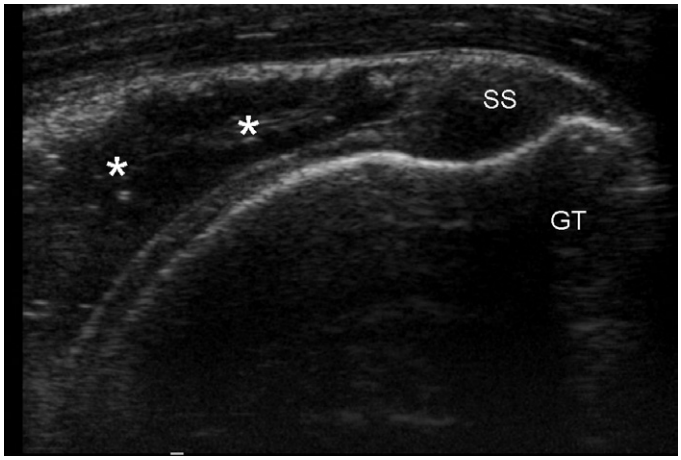

Figure 52.17 Acute rupture of the supraspinatus tendon. Longitudinal scan showing retracted tendon with fluid in the defect (*). SS, supraspinatus tendon; GT, greater tuberosity.

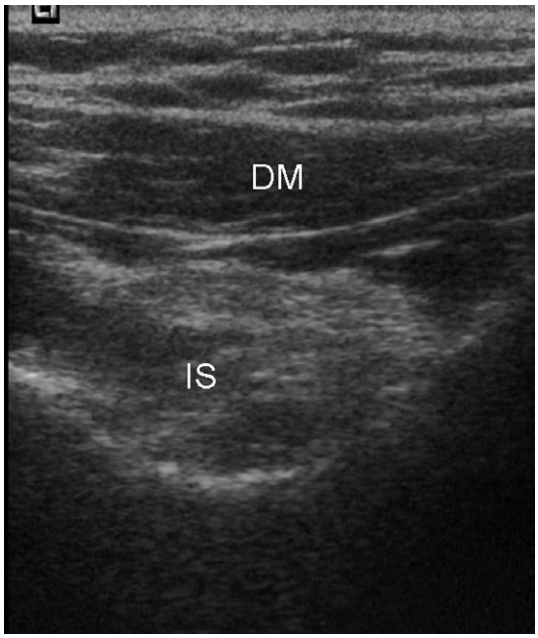

Figure 52.18 Transverse scan showing fatty infiltration of the infraspinatus muscle. The muscle is echogenic when compared to the normal deltoid. IS, infraspinatus muscle; DM, deltoid muscle.

PARTIAL THICKNESS TEARS

Partial thickness tears are hard to differentiate from focal degeneration of the tendon on ultrasound. In practice this is rarely an issue as the management of both conditions is usually the same. Partial tears usually involve the inferior surface of the tendon and are seen as focal hypoechoic lesions or mixed hyperechoic and hypoechoic lesions[10] (Fig. 52.19). A partial undersurface tear at the distal end of the supraspinatus tendon involving the medial part of the tendon attachment is termed a rim rent tear. Partial tears of the superior surface of the tendon are easier to diagnose in the presence of a bursal effusion. Delamination tears originate from full thickness or partial thickness tears and dissect medially through the cuff. They may be seen occasionally on ultrasound as a hypoechoic layer within the tendon (Fig. 52.20). Joint fluid may be forced medially along the tear to create a cyst within the distal end of the muscle.[11]

POST ROTATOR CUFF REPAIR

Ultrasound following rotator cuff repair is difficult although good results have been reported.[12] The repair may not be complete and defects in the cuff may be seen following satisfactory repair. If cuff

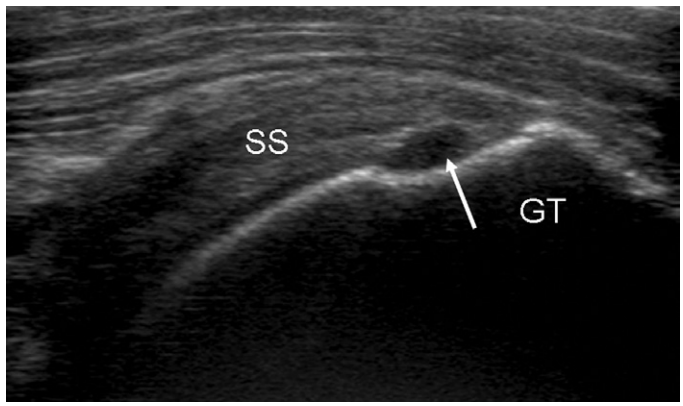

Figure 52.19 Partial articular surface tear of the supraspinatus tendon. There is a focal undersurface hypoechoic lesion at the tendon insertion (arrow). SS, supraspinatus tendon; GT, greater tuberosity.

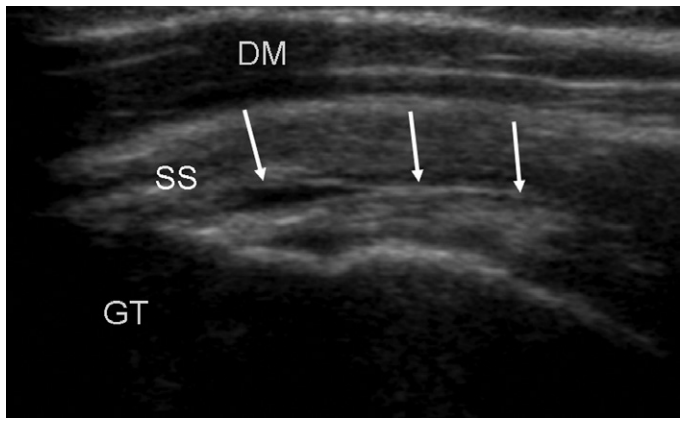

Figure 52.20 Delamination tear of the supraspinatus tendon. There is a layer of fluid within the tendon (arrows). SS, supraspinatus tendon; GT, greater tuberosity; DM, deltoid muscle.

repair involves anchoring the tendon in a bony trough in the greater tuberosity, the integrity of the repair can be assessed by identifying intact tendon in the trough. Subacromial decompression has no effect on the accuracy of ultrasound in the assessment of the rotator cuff.

BURSITIS

The subacromial/subdeltoid bursa lies superficial to the rotator cuff and deep to the acromion and deltoid muscle. Laterally the bursa extends over the greater tuberosity. The bursa is invariably involved in impingement syndrome and may be the primary source of pain. If there is a full thickness cuff tear the bursa will communicate with the glenohumeral joint. Bursitis is diagnosed when there is a bursal effusion or bursal thickening (Fig. 52.21). With the patient seated, a small effusion is best detected over the greater tuberosity, as dependent fluid initially collects here (Fig. 52.22). Bursal fluid extends into partial or full thickness tears involving the superficial surface of the cuff. More commonly bursitis is seen as a thickening of the bursa. The echogenicity may be similar to the underlying degenerate tendon, making assessment of the latter difficult. Dynamic imaging while moving the shoulder joint will help differentiate the two.

Impingement of the bursa against the acromion and coracoacromial ligament can be demonstrated by abducting the extended arm while imaging along the long axis of the supraspinatus tendon. In this position it is easy to appreciate the relationship of the bursa to the coracoacromial ligament, which is seen in cross-section as an echogenic structure on the surface of the bursa. On gentle abduction of the arm the bursa may be seen to bunch up distal to the ligament (Fig. 52.6). Further abduction is either not possible or painful. Occasionally there is a palpable click as the thickened bursa flips under the ligament. Although not required to make the diagnosis of impingement, dynamic imaging is a useful manoeuvre to demonstrate the pathology to the patient.

Injection of the bursa with steroids and local anaesthetic is an effective treatment for impingement syndrome. The procedure can be performed 'blind' by the clinician in the clinic or under ultrasound guidance. 'Blind' injections are usually performed from a posterior approach placing the needle tip on the undersurface of the acromion. Studies investigating the accuracy of the positioning of the needle show variable results.[13,14] The advantage of ultrasound guidance is that the intrabursal position of the needle tip can be demonstrated. The procedure is best performed with the patient supine to avoid syncope. The needle entry point is chosen so that the needle is near parallel to the face of the ultrasound probe. With the bevel facing downwards the needle is advanced until the tip enters the bursa at a tangent (Fig. 52.23). Free flow of local anaesthetic from the needle confirms the intrabursal position of the needle tip. The syringe is changed and the steroid is injected. The use of a small connecting tube is helpful in preventing

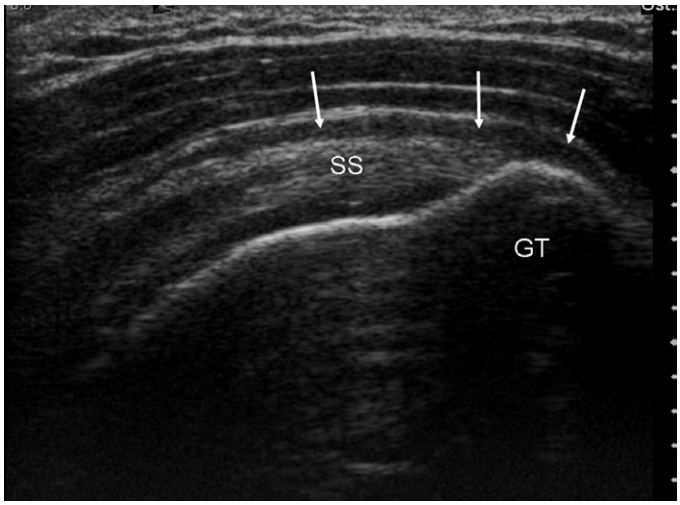

Figure 52.21 Subacromial bursitis. There is thickening of the normal hypoechoic line that represents the subacromial bursa (arrows). SS, supraspinatus tendon; GT, greater tuberosity.

Impingement

- Ultrasound is an accurate test for full thickness tears of the rotator cuff.
- Differentiating partial tears from degeneration is difficult.
- Bunching of the bursa against the coracoacromial ligament on arm abduction indicates impingement.
- Ultrasound can reliably guide injections into the bursa.

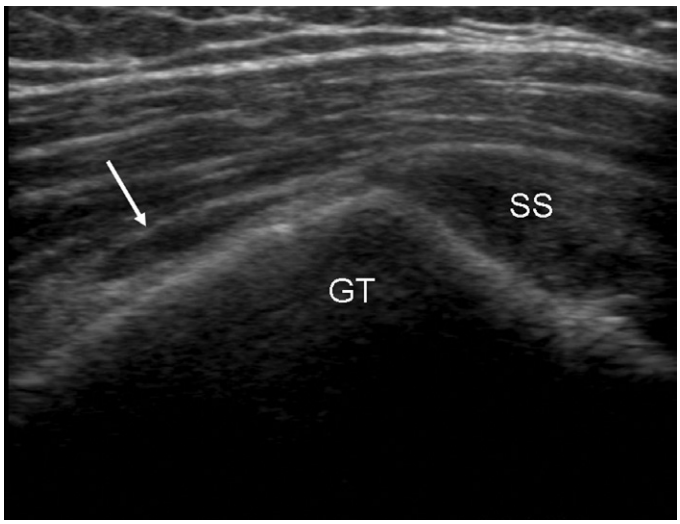

Figure 52.22 Subacromial bursal effusion. A small effusion may be missed unless the bursal extension over the greater tuberosity (arrow) is scanned. SS, supraspinatus tendon; GT, greater tuberosity.

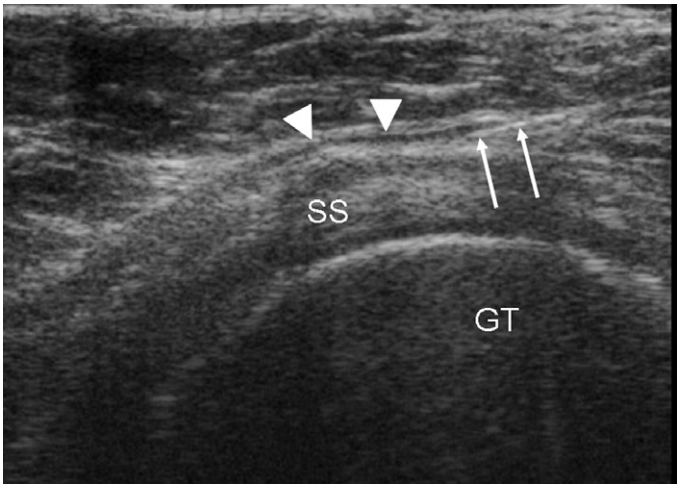

Figure 52.23 Subacromial bursal injection. The needle tip (arrows) is entering the bursa at a tangent. Fluid is seen flowing away from the needle tip (arrowheads). SS, supraspinatus tendon; GT, greater tuberosity.

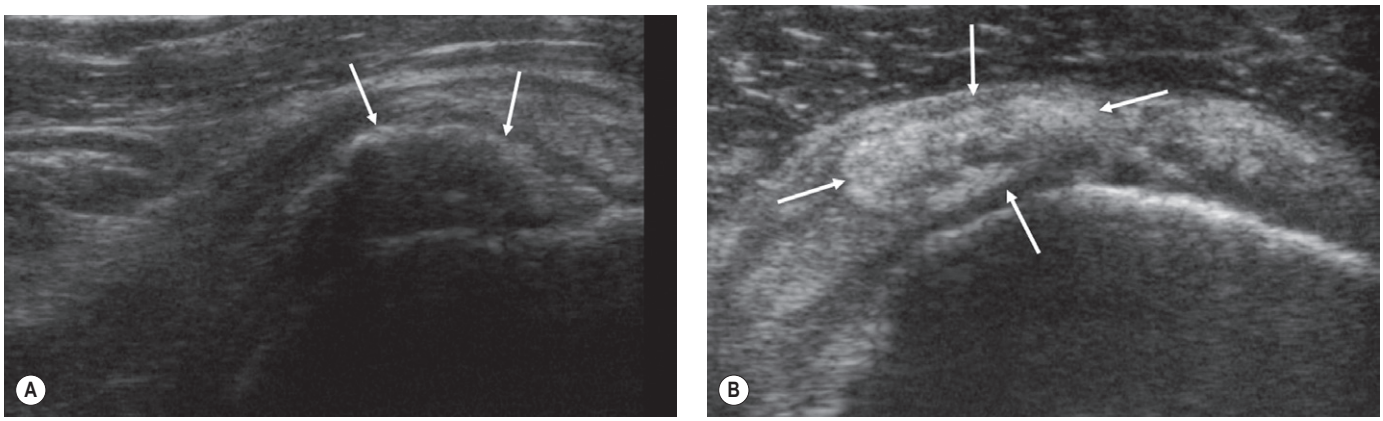

Figure 52.24 Calcific tendinitis. A: 'Hard' calcification within the tendon with a well-defined echogenic border and acoustic shadowing (arrows). **B:** 'Soft' calcification seen as ill-defined echogenic area within the cuff (arrows).

dislodgement of the needle tip while changing the syringe. The local anaesthetic usually results in a rapid improvement in symptoms. Most patients also experience longer-term benefit from the steroid. The value of injection in the presence of a full thickness tear is less reliable but may still be worth performing in some cases.

CALCIFIC TENDINITIS

Calcific tendinitis is a common condition of unknown aetiology. The calcific deposits, which may be entirely asymptomatic, can be hard or soft and paste-like. Ultrasound is very sensitive in detecting calcific deposits seen as echogenic foci usually accompanied by acoustic shadowing. With soft deposits the echogenicity may be more subtle and acoustic shadowing more variable (Fig. 52.24). All three of the main rotator cuff tendons may be involved although the supraspinatus is the most common site of symptomatic disease. Patients may present with chronic pain and impingement type symptoms or with an acute exacerbation of pain due to deposition of calcium in the tendon or extrusion of calcium into the subacromial bursa. In most cases the calcification and symptoms will resolve with time, although this may take 2 to 3 years.[15] Intervention is appropriate for patients who have disabling symptoms. Barbotage refers to the percutaneous intervention leading to the fragmentation and aspiration of calcific material. Initially a generous amount of local anaesthetic is injected into the subacromial bursa. For a well-defined calcific deposit an effective technique is to insert a needle into the deposit using a single pass and then repeatedly apply pulses of pressure to an attached syringe full of local anaesthetic. Gradually, increasing amounts of calcification are seen mixed with the local anaesthetic and the resistance to injection reduces. The calcium-containing fluid in the syringe may be exchanged for fresh saline periodically. When all the calcification has been aspirated only the outer rim is left like the skin of a balloon (Fig. 52.25). This can be broken up with multiple passes of the needle. Another described technique is to insert two needles into the deposit and irrigate the calcific material by injecting saline down one of the needles. Exclusively hard calcification can be broken up by means of multiple passes of a needle. A combination of these methods may be appropriate for any particular case. Following all of these procedures steroid may be injected into the subacromial space.[16,17]

Patients are usually very grateful as they leave the department, but they must be warned that the pain may be exacerbated the next day as inevitably there will be calcific material in the subacromial space.

SUPRASCAPULAR NERVE PALSY

Suprascapular nerve palsy results in weakness of supraspinatus and infraspinatus muscles and may be due to a number of conditions, including brachial neuritis (Parsonage–Turner syndrome), repetitive trauma in overhead sports athletes and compression of the suprascapular nerve by a posterior labral cyst that has extended posteriorly towards the spinoglenoid notch. Although MRI is usually requested when this condition is suspected, ultrasound may reveal atrophy of the infraspinatus muscle and a cyst in the spinoglenoid notch (Fig. 52.26). If the cyst extends anteriorly the branch to supraspinatus may also be affected.

FROZEN SHOULDER

Frozen shoulder is primarily a clinical diagnosis although differentiation from impingement may be difficult in some cases. Patients present with global reduction in joint movement and pain. The pathology is adhesive capsulitis involving primarily the region of the rotator cuff interval between the supraspinatus and the subscapularis. Imaging is usually negative. Arthrography may show a reduced joint space volume, and MRI thickening and contraction of the inferior recess or rotator cuff interval. Ultrasound is usually negative, but occasionally, particularly in the early stages, a hypervascular mass in the rotator cuff interval and/or thickening of the coracohumeral ligament may be seen (Fig. 52.27).[18,19]

BICEPS TENDON

Biceps tendon pathology is common and is usually associated with impingement syndrome.[20] The tendon originates from the superior glenoid rim, courses through the joint in the rotator cuff interval, enters the bicipital groove and runs along the anterior aspect of the upper part of the humerus to the musculotendinous junction. A synovial sheath surrounds the tendon, extending from the joint space to a few centimetres distal to the groove. As the sheath communicates with the joint, fluid seen in the sheath is usually a sign of glenohumeral joint effusion rather than primary pathology of the biceps tendon. A small amount of fluid is normal. All but the most proximal part of the biceps tendon can be identified on ultrasound. The normal tendon is an echogenic structure and lies in the bicipital groove. The tendon is very sensitive to anisotropy. Marked reduction of echogenicity may be encountered on slight angulation of the

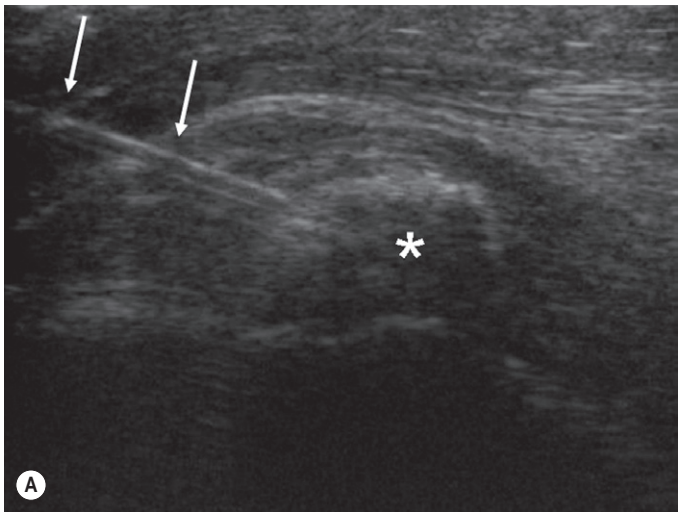

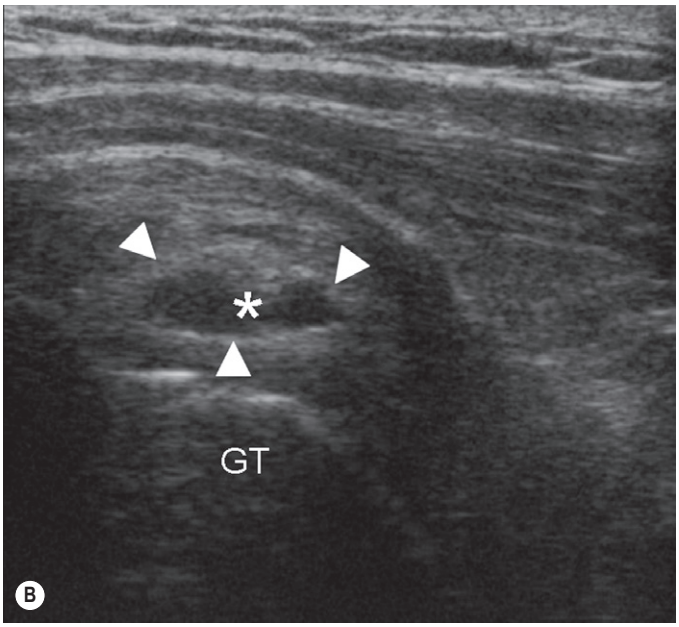

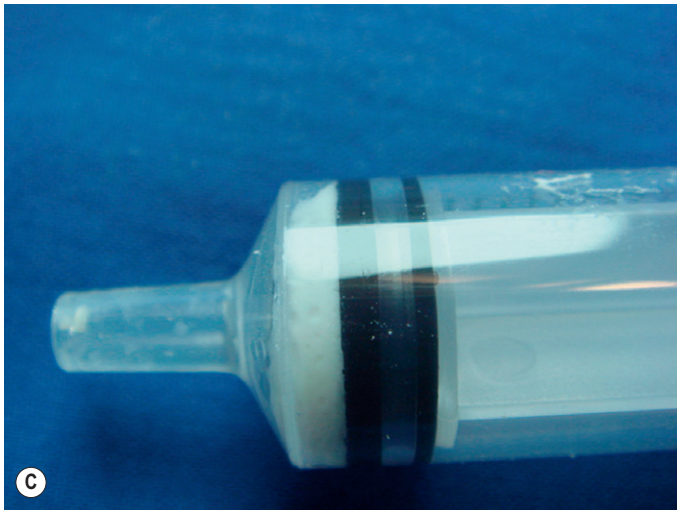

Figure 52.25 Barbotage. A: A needle (arrows) has been inserted into the calcific deposit (*). **B:** This image has been taken towards the end of the procedure with positive pressure applied to the plunger. The deposit is distended with clear fluid that has replaced the calcific material (*). The echogenic calcific rim of the deposit remains intact (arrowheads). GT, greater tuberosity. **C:** Syringe containing aspirated calcific sediment.

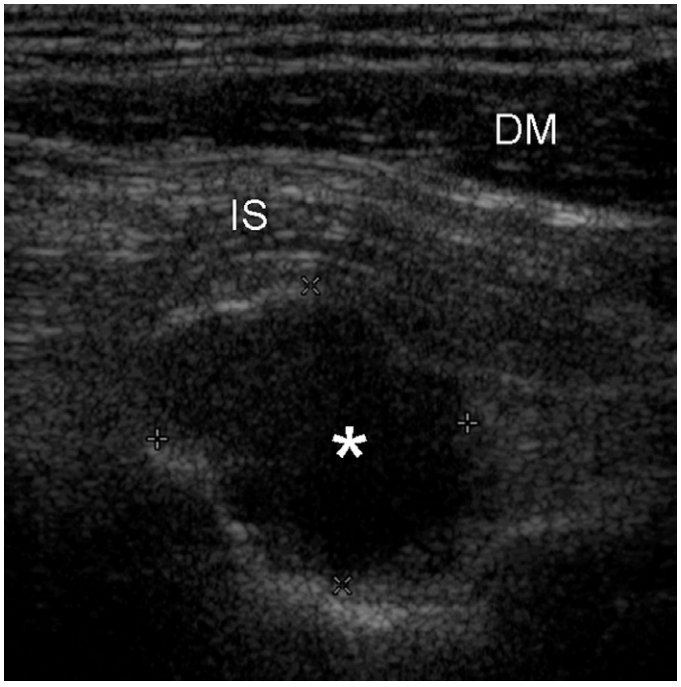

Figure 52.26 Labral cyst. The cyst (*) is seen in the spinoglenoid notch. The infraspinatus muscle is echogenic due to atrophy. IS, infraspinatus tendon; DM, deltoid muscle.

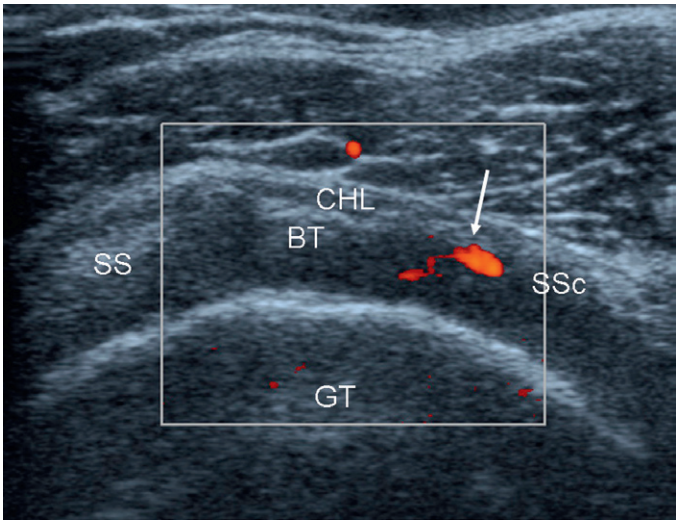

Figure 52.27 Frozen shoulder. There is hypervascularity in the rotator cuff interval (arrow). BT, biceps tendon; SS, supraspinatus tendon; SSc, subscapularis tendon; GT, greater tuberosity; CHL, coracohumeral ligament.

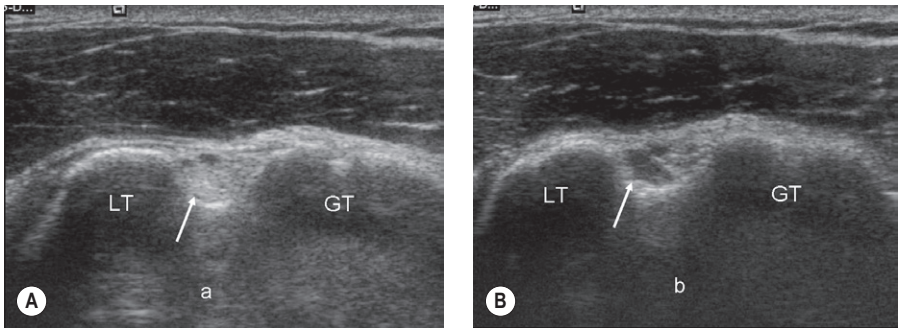

Figure 52.28 Anisotropy. A: Normal biceps tendon in transverse plane (arrow). **B:** Slight tilting of the probe results in a tendon appearing hypoechoic (arrow). GT, greater tuberosity; LT, lesser tuberosity.

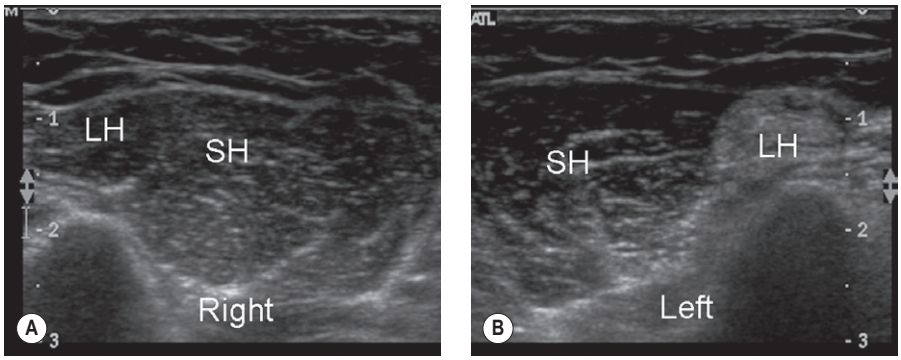

Figure 52.29 Fatty atrophy of the long head of biceps muscle on the left **(A)** due to ruptured tendon. The muscle is echogenic due to fatty atrophy. (Compare with the opposite side **(B)** which is normal.) LH, long head of biceps; SH, short head of biceps.

Rotator cuff disease other than impingement

- Ultrasound is sensitive for detecting calcific tendinitis.
- Barbotage under ultrasound control is effective.
- Imaging for frozen shoulder is generally unrewarding. Hypervascularity in the rotator cuff interval may be seen in early stages.
- Demonstration of dislocation of the biceps tendon may require dynamic imaging.

probe and care must be taken not to misdiagnose tendinosis (Fig. 52.28).

The biceps tendon is vulnerable to impingement, and chronic attrition leading to complete rupture is common in advanced rotator cuff disease. On ultrasound the tendon is attenuated or absent. Scanning in the longitudinal plane is best for determining tendon integrity. Rupture of the biceps tendon may result in the 'Popeye' sign due to retraction and bulging of the muscle belly. Chronic rupture results in atrophy of the long head of biceps muscle, which appears echogenic relative to the short head (Fig. 52.29).

Primary biceps tendinitis is quite common. The tendon is hypoechoic and hypervascular and there may be an effusion in its sheath. Absence of the biceps tendon from its groove is due to rupture or dislocation of the tendon. Dislocation is common. The main stabiliser of the tendon is the coracohumeral ligament, which acts as a sling for the tendon proximal to the bicipital groove. The transverse ligament that forms the roof of the bicipital groove is a weak stabiliser. Dislocation of the tendon from the groove is usually accompanied by subscapularis pathology. With complete rupture of the subscapularis tendon the biceps tendon is displaced medially, possibly as far as the glenoid labrum (Fig. 52.30). If subscapularis is intact the dislocated biceps often lies on the lesser tuberosity.[21] It is not uncommon for the tendon to dissect into the subscapularis tendon (Fig. 52.31).[22] Intermittent dislocation may only be unmasked on dynamic imaging by externally rotating the arm. Proximal to the bicipital groove the biceps tendon is intra-articular and lies deep to the coracohumeral ligament, which may be involved by anterior extension of a supraspinatus tendon tear. Hypervascularity in the rotator cuff interval is sometimes seen in the early phase of frozen shoulder (Fig. 52.27).

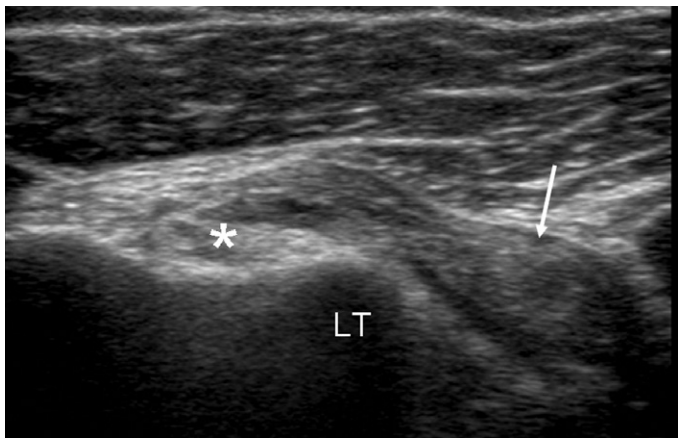

Figure 52.30 Dislocated biceps tendon. The shallow bicipital groove is empty (*). The tendon is displaced medially (arrow). There is associated tear of the subscapularis tendon. LT, lesser tuberosity.

ACROMIOCLAVICULAR JOINT

It is usually easy to differentiate acromioclavicular from glenohumeral disease as the patient will place a fingertip on the acromioclavicular joint when asked to point to the painful area. The joint is not usually included in the routine examination of the shoulder. The commonest pathology affecting the joint is osteoarthritis. Ultrasound shows osteophytes, capsular hypertrophy and an effusion. In advanced cases with loss of the intra-articular

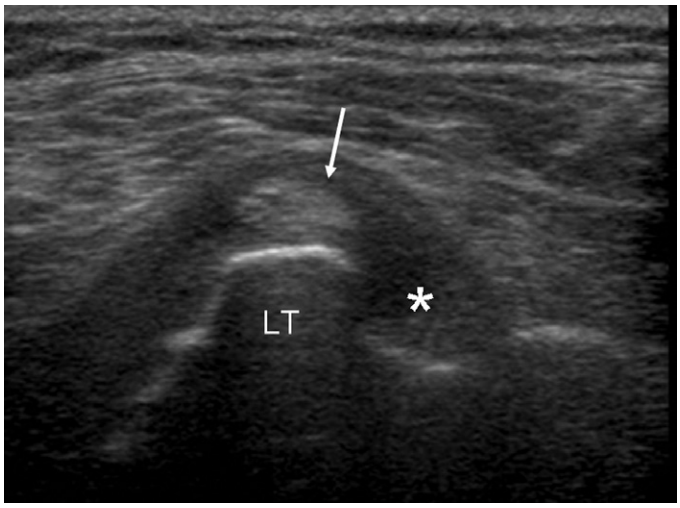

Figure 52.31 Dislocated biceps tendon. The tendon has dislocated medially and is seen to be lying within the supscapularis tendon (arrow). The shallow bicipital groove is empty (*). LT, lesser tuberosity.

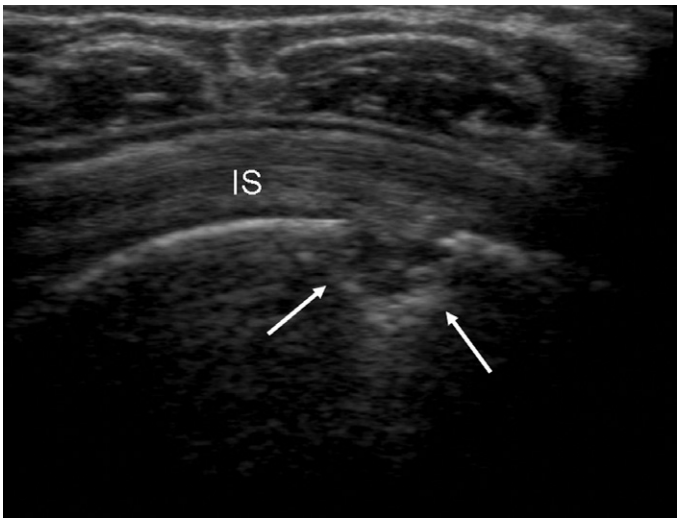

Figure 52.33 Rheumatoid arthritis. There is an erosion in the articular cortex (arrows). IS, infraspinatus tendon.

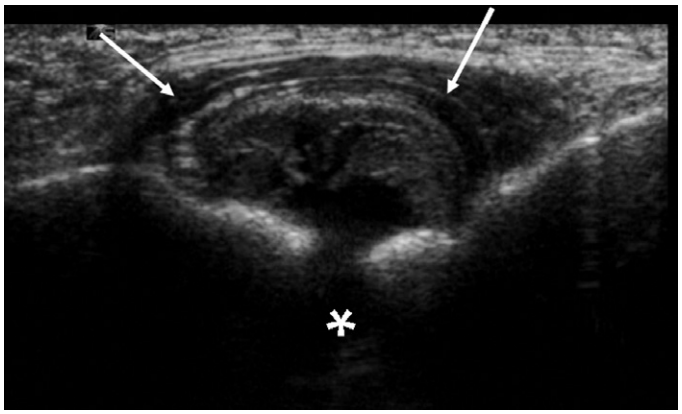

Figure 52.32 Acromioclavicular joint cyst. There is a cyst (arrows) arising from the superior aspect of the acromioclavicular joint (*).

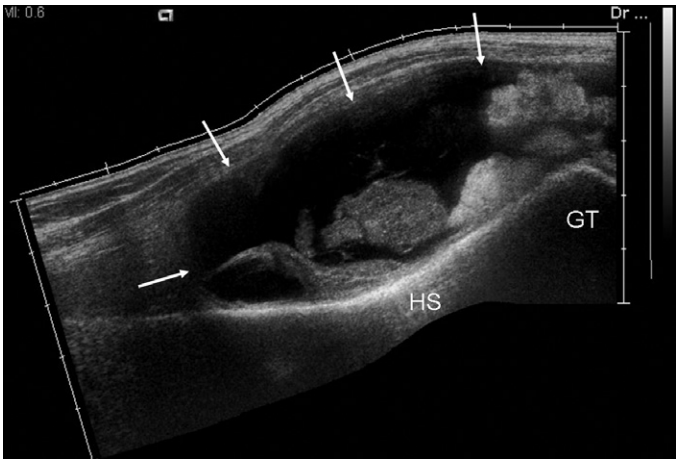

Figure 52.34 Extended field of view image showing a massive effusion of the subacromial bursa (arrows) containing debris. GT, greater tuberosity; HS, humeral shaft.

meniscus and wear of the articular cartilage, impingement of the articular surfaces may be demonstrated by asking the patient to move the hand of the affected side onto the opposite shoulder. The joint space narrows as the two articular surfaces become apposed and fluid is extruded superiorly from the joint space. An acromioclavicular joint cyst presents as a growing mass superficial to the joint. The cyst is seen to arise from the acromioclavicular joint and there is invariably an associated full thickness tear of the rotator cuff (Fig. 52.32). The cyst is due to a defect in the capsule of the joint.[23] A valve-like mechanism prevents the cyst from decompressing, resulting in a slowly growing mass which may reach the size of an orange. Although aspiration is easily performed, the fluid is likely to re-accumulate and surgery, either repair of the cuff or decompression of the cyst at the joint, may be required.[24]

Injection of the acromioclavicular joint is usually performed blind in the outpatient clinic. For ultrasound guidance the probe is positioned in the sagittal plane so that the joint space appears as a hypoechoic disc. The needle, inserted parallel to the surface of the probe, can be easily guided into the centre of the joint.

GLENOHUMERAL JOINT

A joint effusion may be seen using an anterior or posterior approach, the latter being preferred as the joint line is easier to identify. Using the axial plane the humeral head, glenoid and posterior glenoid labrum are identified. An effusion results in bulging of the posterior capsule by anechoic or hypoechoic fluid. Dynamic imaging may be helpful as small effusions are easier to see with the arm in external rotation. Aspiration is easy using a posterolateral approach. Ultrasound is also used to aid injection of the glenohumeral joint prior to MR arthrography.[25] Although in good hands this may be done blind using surface landmarks,[26] ultrasound guidance documents the correct position of the needle tip. The posterolateral approach is preferred. The needle is directed towards the articular surface of the humerus just lateral to the labrum.[27] Correct position is confirmed when fluid flows freely from the needle tip and distends the joint.

Although osteophytes, articular cartilage defects on the exposed part of the humeral head and marginal erosions can be identified

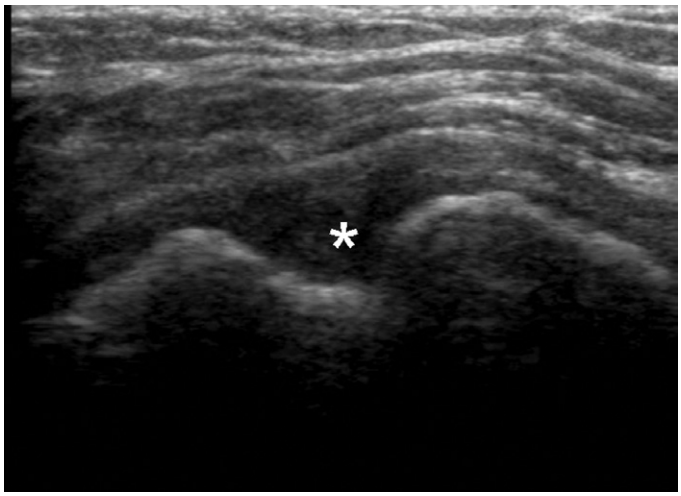

Figure 52.35 Hill–Sachs deformity. The old impaction fracture is seen as a trough in the posterolateral aspect of the humeral head (*).

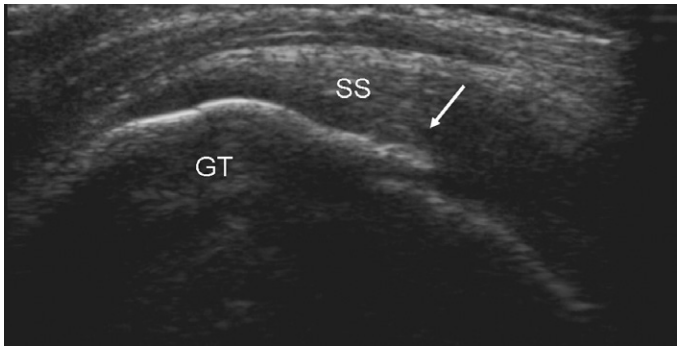

Figure 52.36 Fracture of the greater tuberosity. There is a break in the cortex indicating fracture (arrow). SS, supraspinatus tendon; GT, greater tuberosity.

The joints

- Large cysts arising from a degenerate acromioclavicular joint are associated with full thickness rotator cuff tears.
- Fluid in the biceps tendon sheath usually implies glenohumeral rather than biceps pathology.
- The posterior approach is recommended for identifying and aspirating effusion of the glenohumeral joint.
- Ultrasound has no established role in assessing instability of the glenohumeral joint.
- Spinoglenoid notch labral cyst may result in infraspinatus muscle wasting.

(Fig. 52.33), there is no established role for ultrasound in the diagnosis of osteoarthritis or inflammatory arthropathies. Rarer arthropathies such as synovial osteochrondromatosis, or amyloid arthropathy related to renal dialysis, are best assessed by MRI. Large effusions of the subacromial bursa may be seen in inflammatory arthropathies and cuff tear arthropathy resulting in a palpable mass (Fig. 52.34).

MR arthrography is the preferred technique for assessing patients with instability. The use of dynamic ultrasound for detecting subtle posterior subluxation by comparing the relationship of the humeral head to the glenoid in various arm positions has been described.[28] It has also been reported that abnormalities of the anterior glenoid labrum can be assessed with some accuracy.[29]

The Hill–Sachs deformity, indicating previous dislocation, can be readily diagnosed on ultrasound as a trough-like defect in the posterolateral aspect of the humeral head (Fig. 52.35).

FRACTURE

Ultrasound is often requested in patients with ongoing symptoms following trauma in the presence of radiographs that have been interpreted as normal. A common finding is an undisplaced fracture of the greater tuberosity. Ultrasound is sensitive for fracture as the break in the cortex is readily identified (Fig. 52.36).

REFERENCES

1. Teefey SA, Hasan SA, Middleton WD, et al. Ultrasonography of the rotator cuff. A comparison of ultrasonographic and arthroscopic findings in one hundred consecutive cases. J Bone Joint Surg Am 2000;82:498–504.
2. Neer CS, 2nd. Anterior acromioplasty for the chronic impingement syndrome in the shoulder: a preliminary report. J Bone Joint Surg Am 1972;54:41–50.
3. Hashimoto T, Nobuhara K, Hamada T. Pathologic evidence of degeneration as a primary cause of rotator cuff tear. Clin Orthop Relat Res 2003;415:111–120.
4. Morag Y, Jacobson JA, Lucas D, et al. US appearance of the rotator cable with histologic correlation: preliminary results. Radiology 2006;241:485–491.
5. Fotiadou AN, Vlychou M, Papadopoulos P, et al. Ultrasonography of symptomatic rotator cuff tears compared with MR imaging and surgery. Eur J Radiol 2008;68:174–179.
6. Teefey SA, Middleton WD, Bauer GS, et al. Sonographic differences in the appearance of acute and chronic full-thickness rotator cuff tears. J Ultrasound Med 2000;19:377–378; quiz 383.
7. Goutallier D, Postel JM, Gleyze P, et al. Influence of cuff muscle fatty degeneration on anatomic and functional outcomes after simple suture of full-thickness tears. J Shoulder Elbow Surg 2003;12:550–554.
8. Burkhart SS, Barth JR, Richards DP, et al. Arthroscopic repair of massive rotator cuff tears with stage 3 and 4 fatty degeneration. Arthroscopy 2007;23:347–354.
9. Khoury V, Cardinal E, Brassard P. Atrophy and fatty infiltration of the supraspinatus muscle: sonography versus MRI. AJR Am J Roentgenol 2008;190:1105–1111.
10. van Holsbeeck MT, Kolowich PA, Eyler WR, et al. US depiction of partial-thickness tear of the rotator cuff. Radiology 1995;197: 443–446.
11. Walz DM, Miller TT, Chen S, Hofman J. MR imaging of delamination tears of the rotator cuff tendons. Skeletal Radiol 2007;36:411–416.
12. Prickett WD, Teefey SA, Galatz LM, et al. Accuracy of ultrasound imaging of the rotator cuff in shoulders that are painful postoperatively. J Bone Joint Surg Am 2003;85-A:1084–1089.
13. Rutten MJ, Maresch BJ, Jager GJ, de Waal Malefijt MC. Injection of the subacromial-subdeltoid bursa: blind or ultrasound-guided? Acta Orthop 2007;78:254–257.
14. Naredo E, Cabero F, Beneyto P, et al. A randomized comparative study of short term response to blind injection versus sonographic-guided injection of local corticosteroids in patients with painful shoulder. J Rheumatol 2004;31:308–314.
15. Wittenberg RH, Rubenthaler F, Wolk T, et al. Surgical or conservative treatment for chronic rotator cuff calcifying tendinitis – a matched-pair analysis of 100 patients. Arch Orthop Trauma Surg 2001;121:56–59.
16. Aina R, Cardinal E, Bureau NJ, et al. Calcific shoulder tendinitis: treatment with modified US-guided fine-needle technique. Radiology 2001;221:455–461.
17. del Cura JL, Torre I, Zabala R, Legorburu A. Sonographically guided percutaneous needle lavage in calcific tendinitis of the shoulder: short- and long-term results. AJR Am J Roentgenol 2007;189:W128–134.
18. Lee JC, Sykes C, Saifuddin A, Connell D. Adhesive capsulitis: sonographic changes in the rotator cuff interval with arthroscopic correlation. Skeletal Radiol 2005;34:522–527.
19. Homsi C, Bordalo-Rodrigues M, da Silva JJ, Stump XM. Ultrasound in adhesive capsulitis of the shoulder: is assessment of the coracohumeral ligament a valuable diagnostic tool? Skeletal Radiol 2006;35:673–678.

20. Beall DP, Williamson EE, Ly JQ, et al. Association of biceps tendon tears with rotator cuff abnormalities: degree of correlation with tears of the anterior and superior portions of the rotator cuff. AJR Am J Roentgenol 2003;180:633–639.
21. Martinoli C, Bianchi S, Prato N, et al. US of the shoulder: non-rotator cuff disorders. Radiographics 2003;23:381–401; quiz 534.
22. Walch G, Nove-Josserand L, Boileau P, Levigne C. Subluxations and dislocations of the tendon of the long head of the biceps. J Shoulder Elbow Surg 1998;7:100–108.
23. Craig EV. The geyser sign and torn rotator cuff: clinical significance and pathomechanics. Clin Orthop Relat Res 1984;191:213–215.
24. Postacchini F, Perugia D, Gumina S. Acromioclavicular joint cyst associated with rotator cuff tear. A report of three cases. Clin Orthop Relat Res 1993;294:111–113.
25. Koivikko MP, Mustonen AO. Shoulder magnetic resonance arthrography: a prospective randomized study of anterior and posterior ultrasonography-guided contrast injections. Acta Radiol 2008;49:912–917.
26. Catalano OA, Manfredi R, Vanzulli A, et al. MR arthrography of the glenohumeral joint: modified posterior approach without imaging guidance. Radiology 2007;242:550–554.
27. Zwar RB, Read JW, Noakes JB. Sonographically guided glenohumeral joint injection. AJR Am J Roentgenol 2004;183:48–50.
28. Bianchi S, Zwass A, Abdelwahab I. Sonographic evaluation of posterior instability and dislocation of the shoulder: prospective study. J Ultrasound Med 1994;13:389–393.
29. Magnusson L, Kalebo P, Baranto A, et al. The value of ultrasonography in the preoperative diagnostic evaluation of patients with recurrent anterior shoulder dislocation: a prospective study of 44 patients. Knee Surg Sports Traumatol Arthrosc 2007;15:649–653.

CHAPTER

53 Ultrasound of the elbow

James Teh

INTRODUCTION

The elbow is a complicated joint which is subject to a wide range of mechanical forces making it susceptible to a variety of conditions. Ultrasound is an excellent imaging technique for evaluating the elbow joint, either as the primary imaging modality or as an adjunct to other modalities, particularly magnetic resonance imaging (MRI).[1] Ultrasound can also be used to guide interventional procedures. This chapter covers ultrasound anatomy, technique and the appearances of common disorders at the elbow.

TECHNIQUE AND ANATOMY

The elbow is a complex hinge-pivot synovial joint which combines function with stability. It has three main components: the humeroradial, humero-ulnar and radioulnar articulations. The humero-ulnar articulation allows for flexion and extension, whilst pronation and supination occur at the radioulnar articulation. For the purposes of ultrasound evaluation the elbow can be examined in four main compartments: anterior, posterior, medial and lateral.

Anterior compartment

The patient should be seated with the elbow supine and extended, resting on a couch or bed (Fig. 53.1). The most easily identified landmark is the radiocapitellar joint in the longitudinal plane. Articular cartilage is delineated as a thin low-echogenicity layer overlying the echogenic cortex. In children the cartilaginous epiphyses are low echogenicity, have smooth margins and contain randomly interspersed small echogenic foci.[2] The ossifying epiphyses develop small irregular ovoid or spherical echogenic sites of calcium deposition (Fig. 53.2).

As the probe is swept across the joint, the coronoid fossa is identified as a smooth depression in the distal humerus. Lying within the coronoid fossa is the echogenic anterior fat pad which lies superficial to the anterior joint lining.[3] The fat pad is elevated when there is a joint effusion, synovitis or haemarthrosis (Fig. 53.3).

The biceps tendon inserts onto the radial tuberosity and dips down obliquely as it courses from a superficial to deep position. With a longitudinal scan, a direct anterior approach, the elbow extended and the forearm supinated the tendon has a hyperechoic fibrillar appearance. Visualisation of the distal biceps may be difficult due to anisotropy. This may be overcome by angling the transducer slightly laterally and flexing the elbow by a few degrees. Alternatively, if the probe is placed medially and directed laterally with the elbow flexed, abducted and supinated (the FABS position[4]) the effect of anisotropy can be reduced (Figs 53.4 and 53.5). The biceps tendon should also be imaged in the axial plane. It is best to start above the musculotendinous junction and slide the probe distally.

The brachialis muscle is the most superficial muscle in the distal arm. Its tendon inserts onto the proximal ulna and should not be mistaken for the biceps.

The major artery at the elbow is the brachial artery, which runs superficial to the brachialis muscle and medial to the biceps muscle and tendon. Approximately 1–2 cm distal to the elbow joint, at the level of the radial head, it divides into the radial and ulnar arteries. The cephalic and basilic veins run in the anterior superficial soft tissues.

The median nerve follows the axillary artery and lies superficial to the brachial muscle in the upper arm. It courses over the medial aspect of the elbow joint and enters the forearm between the two heads of pronator teres. Just distal to this point it gives off the anterior interosseous branch and then continues down the forearm between the flexor digitorum superficialis and profundus.[5]

The simplest way to detect the median nerve is to scan in the axial plane at the mid forearm, where the nerve is easily identified between the flexor digitorum superficialis and profundus, and to follow the nerve proximally to the elbow.

The radial nerve travels around the humerus in the spiral groove between the medial and lateral heads of the triceps, then pierces the intermuscular septum to enter the anterior compartment of the arm. It lies between the brachialis and brachioradialis muscles at the level of the lateral epicondyle, then divides into the motor posterior interosseous nerve and the sensory superficial radial nerve at the level of the radiocapitellar joint.[6]

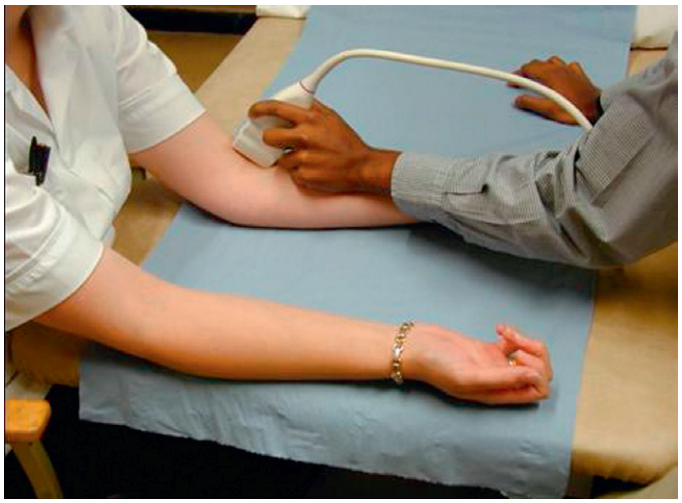

Figure 53.1 The position for performing ultrasound of the anterior compartment of the elbow.

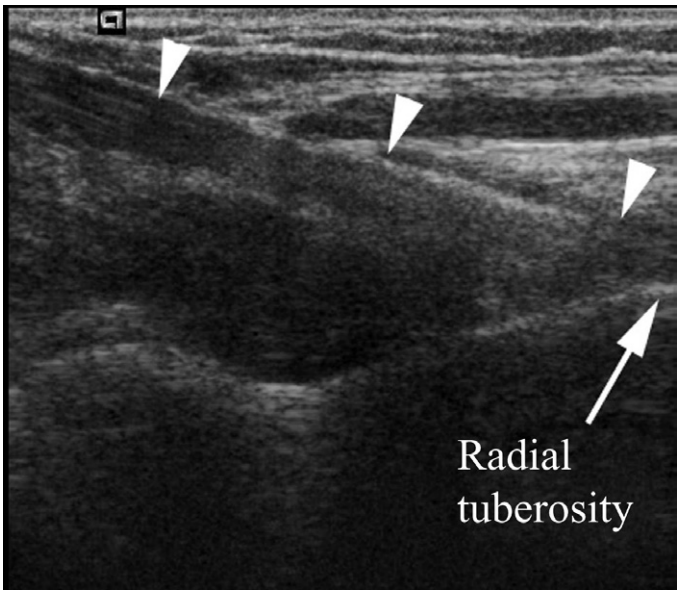

Figure 53.4 Anterior view of the biceps tendon (arrowheads). The position of the radial tuberosity is indicated.

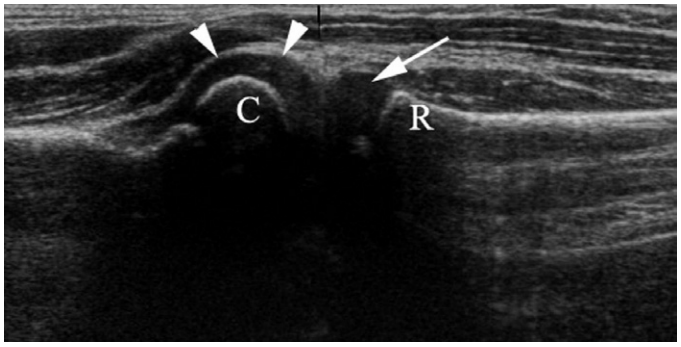

Figure 53.2 The radiocapitellar joint in a child. The arrowheads indicate the hypoechoic unossified cartilage of the capitellum (C) and the arrow indicates the unossified cartilage of the radial head (R).

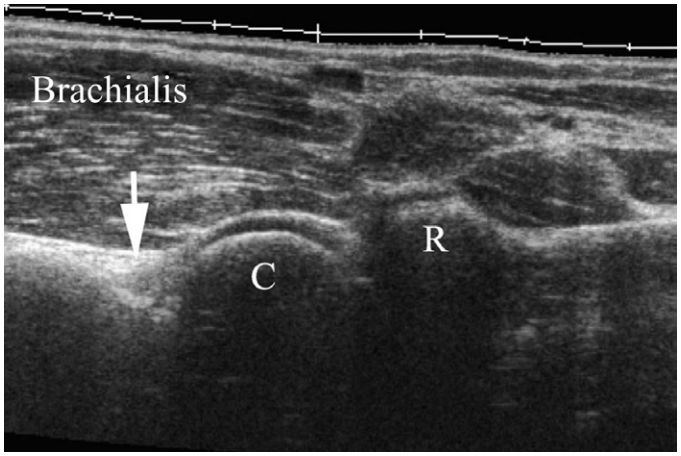

Figure 53.3 The radiocapitellar joint in an adult. The extended field-of-view (FOV) image demonstrates the capitellum (C) and radial head (R). The echogenic anterior fat pad (arrow) sits within the coronoid fossa.

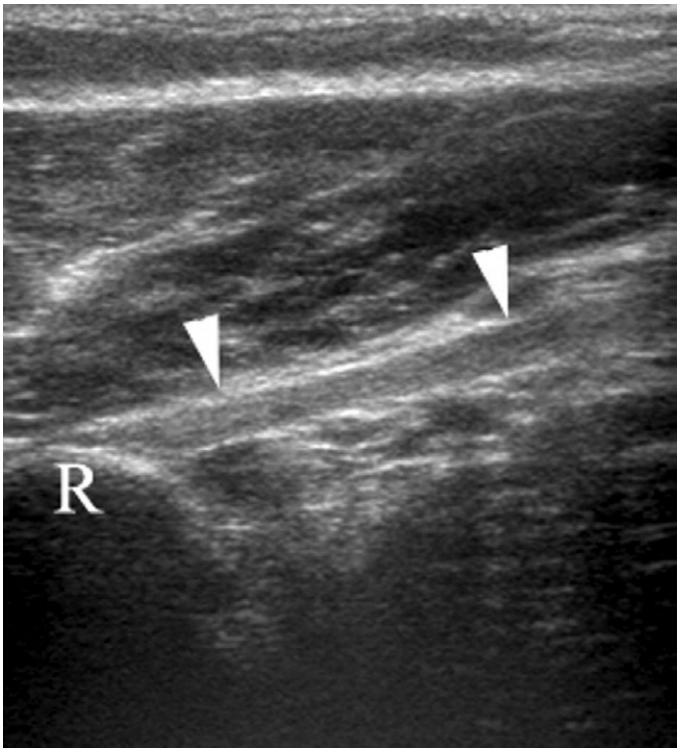

Figure 53.5 The biceps tendon (arrowheads) attaching to the radial tuberosity (R) visualised with the elbow flexed, abducted and supinated.

The posterior interosseous nerve enters the radial tunnel beneath the arcade of Frohse, a musculotendinous band formed by the upper border of supinator. A leash of arterial branches (leash of Henry) crosses over the posterior interosseous nerve just before the arcade of Frohse.

Posterior compartment

The patient should be positioned with the palm flat on the couch with the elbow flexed at 90° in the so-called crab position. A copious amount of ultrasound gel should be used to allow the tip of the olecranon to be visualised (Fig. 53.6).

The triceps tendon attaches to the tip of the olecranon. The olecranon fossa contains the echogenic posterior fat pad, which can be displaced by an effusion, synovitis or haemarthrosis (Fig. 53.7).

The ulnar nerve is demonstrated in the ulnar groove with the probe placed between the olecranon and medial epicondyle. The nerve is normally of uniform thickness, measuring approximately 2 × 3 mm. In the longitudinal plane it has a cord-like appearance with multiple linear fascicles (Figs 53.8 and 53.9). Ulnar nerve division is considered a normal variant.[7] Comparison with the contralateral side is useful for assessing suspected alterations in morphology. Flexion and extension of the elbow shows medial subluxation of the nerve over the medial epicondyle in up to 20% of subjects.[8] Subluxation is thought to be due to congenital laxity of Osborne's fascia, which forms the roof of the epicondylar groove.

Distal to the epicondylar groove the ulnar nerve crosses the elbow, giving off articular branches and branches to the flexor carpi ulnaris and the medial half of the flexor digitorum profundus. It dips between the two heads of the flexor carpi ulnaris and continues into the forearm between this muscle and the flexor digitorum profundus.

Medial compartment

The patient is positioned in front of the sonographer with the elbow extended and the forearm supinated. Alternatively the patient may be examined lying supine with the arm extended above the head. The probe is placed longitudinally over the medial epicondyle and the origin of the common flexor tendon, which is formed by the pronator teres and superficial flexor muscles. The normal tendon has a hyperechoic triangular or beak-like appearance. The tendon should be assessed for altered echogenicity, thickening, calcifications and enthesopathic change. There should be no flow on Doppler interrogation (Fig. 53.10).

The ulnar collateral ligament has three main bands: anterior, posterior and oblique. The anterior band is attached to the anterior aspect of the medial epicondyle and the medial margin of the coronoid process. It is a cord-like structure which is taut with the elbow extended, with a hyperechoic fibrillar appearance.[9] It has an important role in stabilising the elbow against valgus stress (Fig. 53.11). The posterior band attaches the postero-inferior medial epicondyle to the medial margin of the olecranon. It is a fan-like structure which is taut with the elbow flexed, but is usually difficult to visualise as a discrete structure. The oblique band passes from the medial olecranon to the medial aspect of the coronoid fossa. It plays only a minor role in stabilisation and is usually difficult to identify.

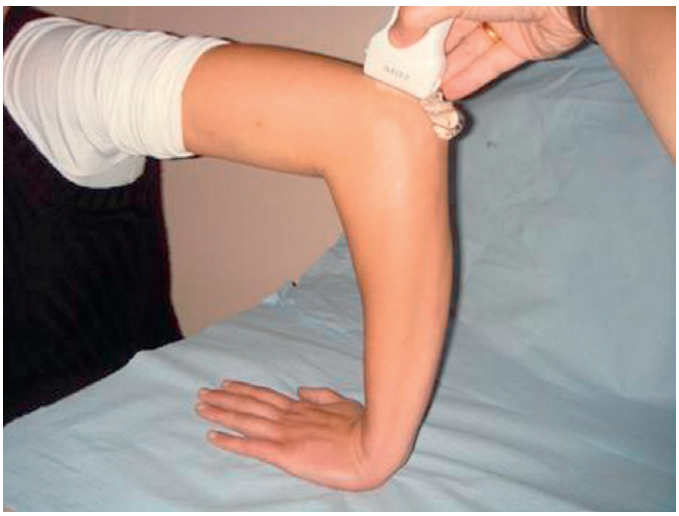

Figure 53.6 The 'crab' position for examining the posterior compartment of the elbow.

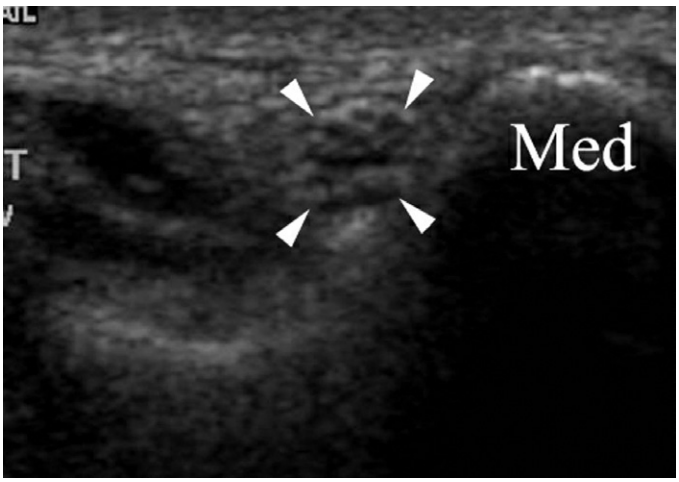

Figure 53.8 Axial view of the posteromedial aspect of the elbow demonstrating the echogenic fascicular structure of the ulnar nerve (arrowheads) sitting in the epicondylar groove.

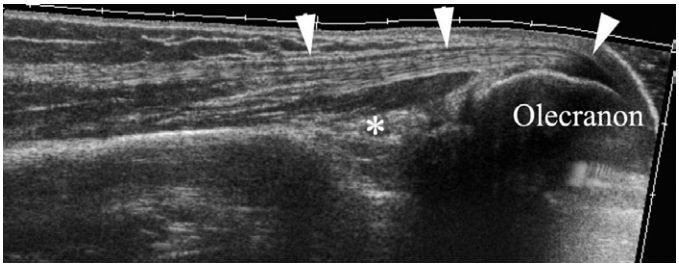

Figure 53.7 The extended FOV image of the posterior aspect of the elbow demonstrating the triceps tendon (arrowheads) inserting onto the olecranon. The echogenic posterior fat pad (asterisk) sits within the olecranon fossa.

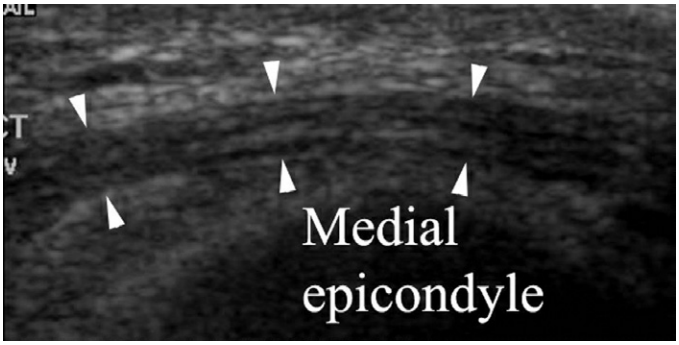

Figure 53.9 Longitudinal view of the ulnar nerve (arrowheads) at the level of the medial epicondyle demonstrating a uniform thickness.

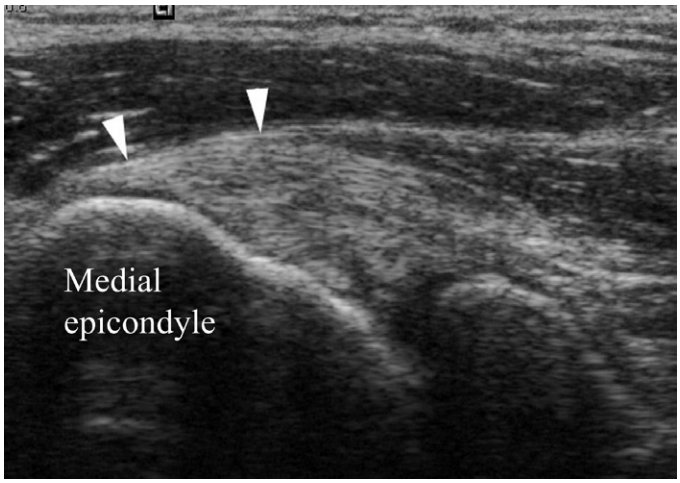

Figure 53.10 Longitudinal view of the medial aspect of the elbow demonstrating the echogenic beak-like appearance of the common flexor origin (arrowheads).

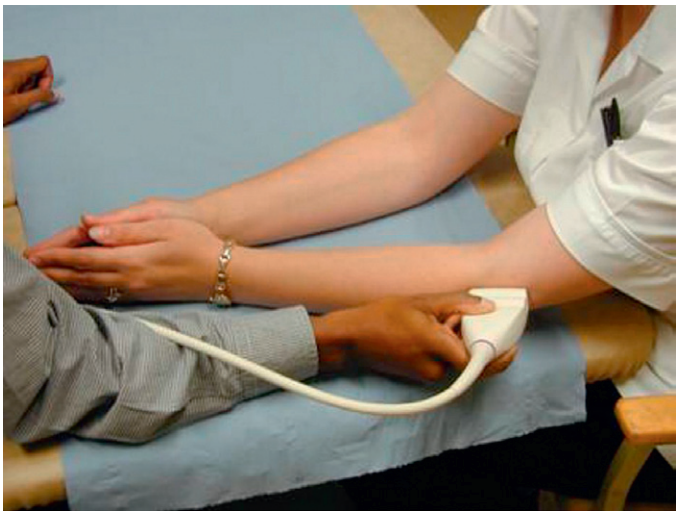

Figure 53.12 The 'praying' position for examining the lateral aspect of the elbow.

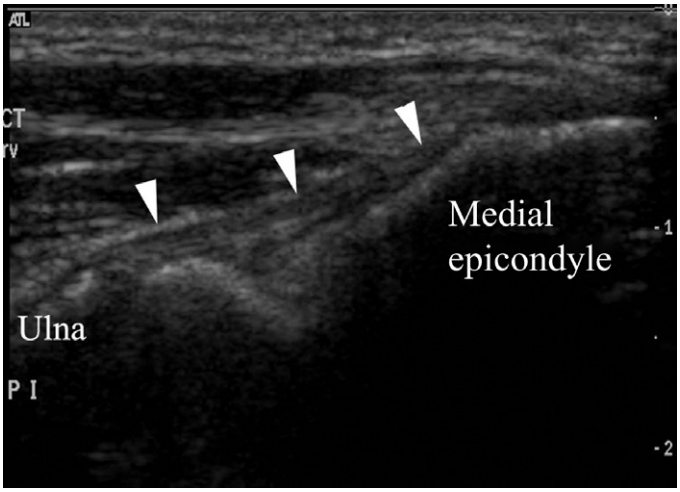

Figure 53.11 Longitudinal view of the ulnar collateral ligament (arrowheads).

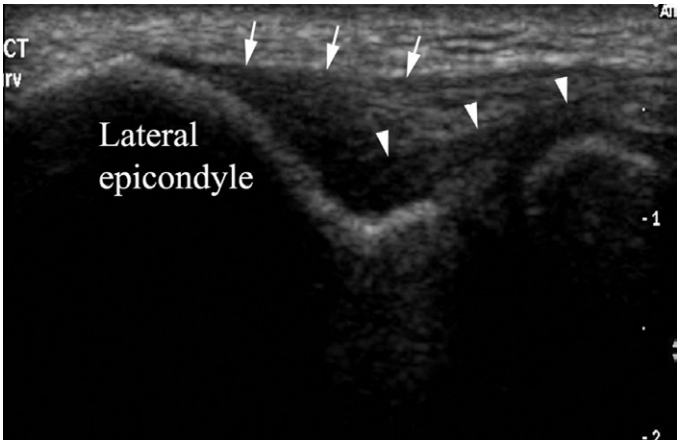

Figure 53.13 Longitudinal view of the lateral aspect of the elbow demonstrating the common extensor origin (arrows) and the radial collateral ligament (arrowheads).

Lateral compartment

The patient is positioned with the elbow in slight flexion and the forearm in the neutral position. An ideal position is easily achieved if the patient is asked to place both hands together (Fig. 53.12). In the longitudinal plane the common extensor origin has a triangular or beak-like hyperechoic fibrillar appearance, similar to the common flexor origin. The superficial fibres are composed of the extensor carpi radialis brevis, extensor digitorum, extensor digiti minimi and extensor carpi ulnaris. The deep fibres consist mainly of extensor carpi radialis brevis.[10] The common extensor origin may be affected by anisotropy. If the probe is gently tilted or rocked, the area affected by anisotropy should regain its normal echogenicity whereas true tendinopathic areas or tears remain hypoechoic (Fig. 53.13).

The radial collateral ligament is a short narrow fibrous band, less distinct than the ulnar collateral, attached above to a depression below the lateral epicondyle of the humerus and below to the annular ligament. Some of its most posterior fibres pass over the annular ligament, to be inserted into the lateral margin of the ulna.

Technique and anatomy

- Ultrasound can detect as little as 1–3 mL of fluid in the elbow joint.
- Visualisation of the distal biceps tendon may be improved by slight flexion of the elbow joint and lateral angulation of the transducer.
- The ulnar nerve subluxes from the cubital tunnel when the elbow is flexed in 20% of subjects.
- The common flexor and extensor origins appear almost identical. They are triangular, fibrillar and echogenic.

The annular ligament is attached to the margin of the trochlear notch of the ulna, and it encircles the head of the radius, functioning to keep the head in contact with the radial notch of the ulna. The proximal radioulnar joint is encapsulated by the elbow joint capsule.

INDICATIONS AND PATHOLOGICAL CONDITIONS

Effusion and synovitis

Effusions may be simple or complex, when there is associated synovial hypertrophy. An effusion may occur as a non-specific response to a wide range of insults, including trauma, infection, inflammatory arthropathy and degeneration. Ultrasound can demonstrate effusions as small as 1–3 mL.[11] The joint should be approached both anteriorly and posteriorly, preferably with the elbow slightly flexed.[11] On ultrasound there is anechoic or low-echogenicity distension of the joint with elevation of the anterior and posterior fat pads (Fig. 53.14). Synovial thickening appears more echogenic than effusion and may demonstrate Doppler flow (Fig. 53.15). Dynamic compression helps to differentiate effusion from synovium, as fluid can be displaced. Ultimately, aspiration may be required to determine the cause of effusion.

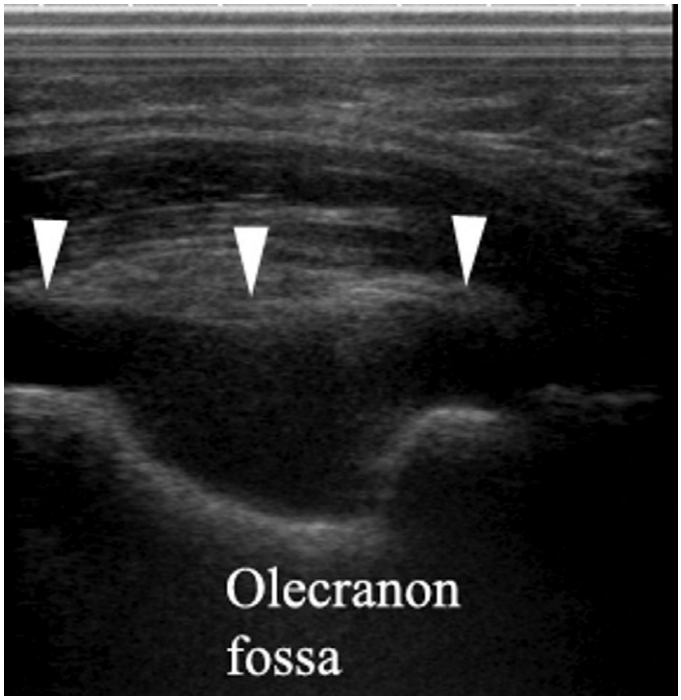

Figure 53.14 Longitudinal view of a posterior elbow joint effusion (arrowheads) with displacement of the fat pad from the olecranon fossa.

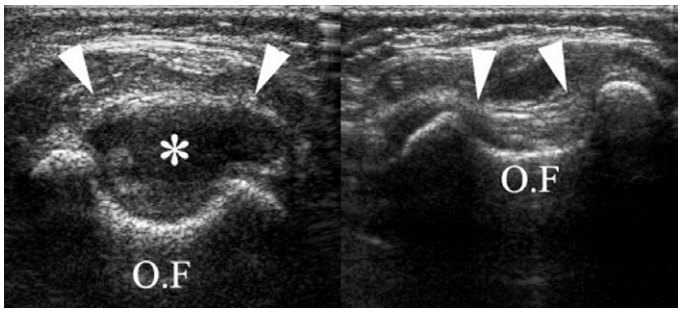

Figure 53.15 Septic joint with effusion and synovitis. Axial dual image view of the olecranon fossae (O.F.) comparing abnormal (left) with normal (right) sides. The position of the joint capsule is indicated by the arrowheads; the asterisk represents the joint effusion and synovitis.

Loose bodies

The elbow is the second most common joint for loose bodies after the knee. A loose body originates from a small detached nidus of bone, articular cartilage or synovium which can be associated with trauma, degeneration, osteochondritis dissecans or a synovial proliferative disorder. The nidus may increase in size over time, growing in a laminar fashion, receiving its nutrition from the synovial fluid.[12] Patients may present with pain, limitation of movement or locking.

If a loose body is suspected plain radiography should be performed. If a loose body is not mineralised or lies deep within the coronoid or olecranon fossae it may be missed on radiographs. Differentiation from osteophytes may be difficult in patients with osteoarthritis. Computed tomography (CT) and MRI accurately identify and localise loose bodies particularly in the presence of intra-articular contrast.[13,14]

Ultrasound is an excellent modality for demonstrating loose bodies, which usually appear echogenic with posterior acoustic shadowing. There may be an associated effusion (Fig. 53.16). If the joint is dry, injection of saline may significantly improve the conspicuity of loose bodies, particularly if they are small or of low echogenicity.[15] Injection with 10–15 mL of saline can be achieved via a posterior approach. The articular surfaces should be examined if a loose body is seen to determine if the source is an osteochondral lesion such as osteochondritis dissecans (Fig. 53.17).

Synovial osteochondromatosis

Synovial osteochondromatosis is a synovial proliferative disorder characterised by synovial metaplasia.[16] There are three recognisable phases. In the proliferative phase there is synovial hypertrophy only, with no evidence of loose bodies. In the transitional phase there is active synovial proliferation with multiple loose bodies. In the late stage of disease there are multiple ossified loose bodies with no active synovitis. In the early stage plain radiographs demonstrate fat pad elevation but no ossified loose bodies. In the

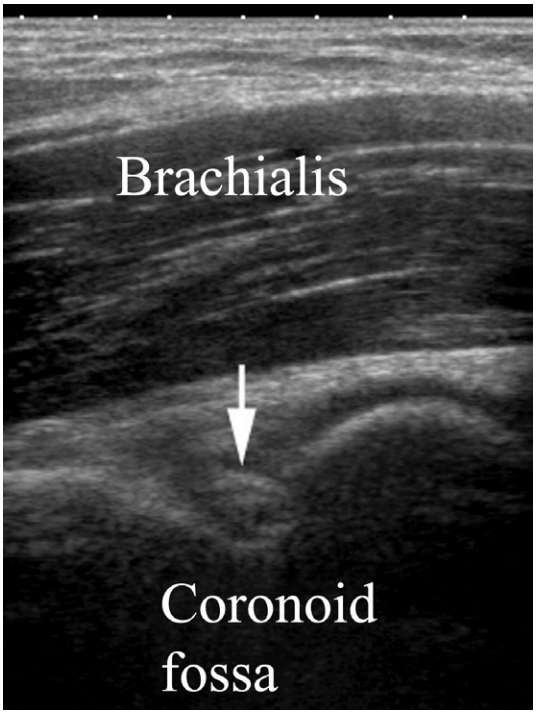

Figure 53.16 Anterior longitudinal view demonstrating an echogenic loose body (arrow) sitting within the coronoid fossa.

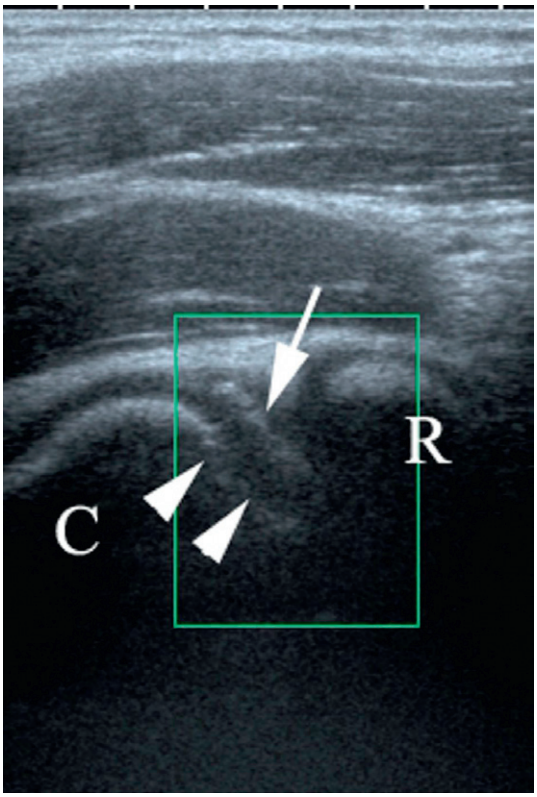

Figure 53.17 Osteochondritis dissecans in a 15-year-old gymnast demonstrating an osteochondral lesion (arrowheads) of the capitellum (C) with an in-situ fragment (arrow). The radial head is indicated (R).

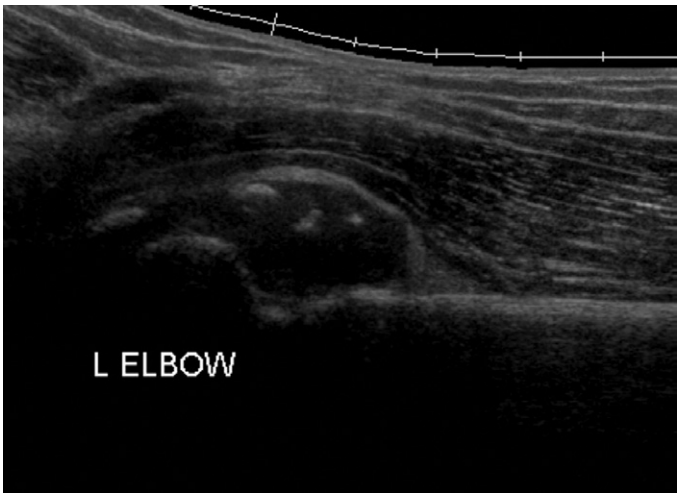

Figure 53.18 Synovial osteochondromatosis with distension of the joint capsule. Several small echogenic foci are present.

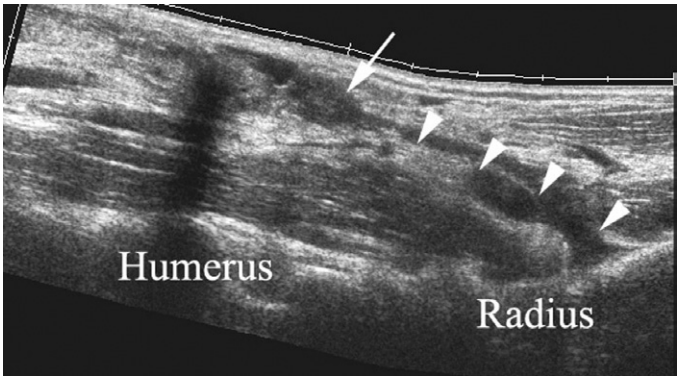

Figure 53.19 Biceps tendon rupture. Longitudinal extended FOV image demonstrating a full thickness rupture of the biceps tendon with retraction (arrow). The gap (arrowheads) lying adjacent to the brachial artery is partly filled with haematoma.

transitional and late phases ossified loose bodies can be seen. Eventually secondary osteoarthritis may occur. The presenting symptoms are usually diffuse discomfort with decreased range of motion and an accompanying gritty or locking sensation. The loose body may result in ulnar, median or radial nerve compression.[17,18] On ultrasound loose bodies can be detected prior to their appearance on radiographs. Multiple small echogenic loose bodies are typically seen with associated synovitis or effusion (Fig. 53.18).

Tendon injury

Biceps tendon injury

Distal biceps tendon injuries are uncommon, comprising around 3% of biceps injuries. The biceps tendon is typically injured by forced extension of the flexed elbow with the biceps contracted, or by lifting a heavy weight. With partial tears, the cause may be chronic attrition and there may not be a good history of acute trauma.[19] The patient is typically a middle-aged man or weight-lifter. The tendon usually ruptures at the insertion. Attempted flexion of the biceps results in the 'Popeye' sign, with bunching up of the muscle belly in the mid-arm. Bruising may be present above the elbow.

Partial tears are usually managed conservatively and complete tears dealt with surgically. Attachment to the brachialis improves flexion but not supination. Reattachment to the radial tuberosity provides the best functional outcome but usually requires two incisions and may put the radial nerve at risk. The degree of tendon retraction can be assessed, allowing the surgeon to plan the surgical approach. Significant tendon retraction indicates injury of the lacertus fibrosus, a thin fibrous band that crosses over the distal biceps tendon.[4] Conversely, an intact lacertus fibrosus prevents tendon retraction and may make assessment more difficult.

Ultrasound is a good technique for assessing biceps tendon injuries.[20,21] The biceps tendon should be approached in both the longitudinal and transverse planes. Complete rupture results in disruption of the tendon fibres and hypoechoic or mixed-echogenicity haemorrhage in the gap.[21] The position of the proximal ruptured tendon end can be marked on the skin to allow surgical planning. Occasionally, a small avulsion fragment can be demonstrated (Fig. 53.19).

With a partial tear the abnormal segment of tendon is thickened or thinned but not discontinuous.[4,20] It may have a wavy contour in the longitudinal plane indicating laxity. A partial tear may be difficult to differentiate from severe tendinosis (Fig. 53.20).

Associated features of biceps tendon tears include irregularity of the bicipital tuberosity of the radius, tenosynovitis and bicipitoradial bursitis. There may be muscle atrophy if the injury is chronic. If visualisation of the tendon is poor, MRI should be performed.

Triceps tendinosis

Triceps tendinosis is a relatively common condition usually occurring in middle-aged or elderly men. There may be associated enthesopathic change with a small traction spur seen at the olecranon. The tendon is swollen, heterogeneous and hypoechoic.

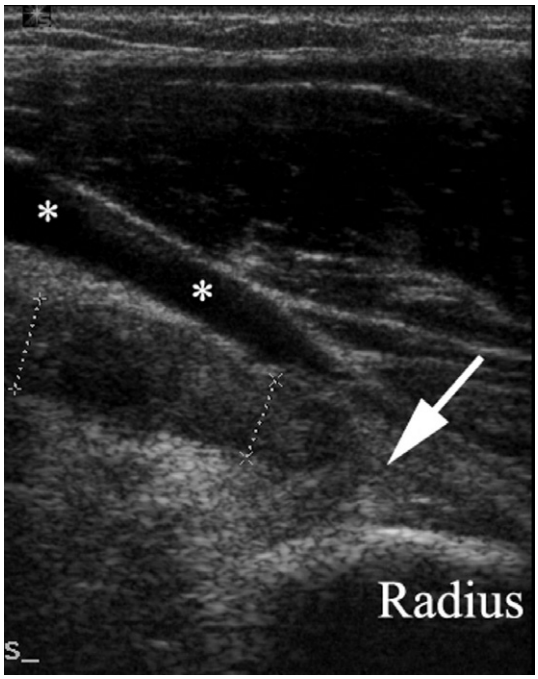

Figure 53.20 Longitudinal image demonstrating a full thickness tear of the biceps tendon with only a small gap (arrow). The tendon appears thickened and lax. The brachial artery is marked by the asterisks.

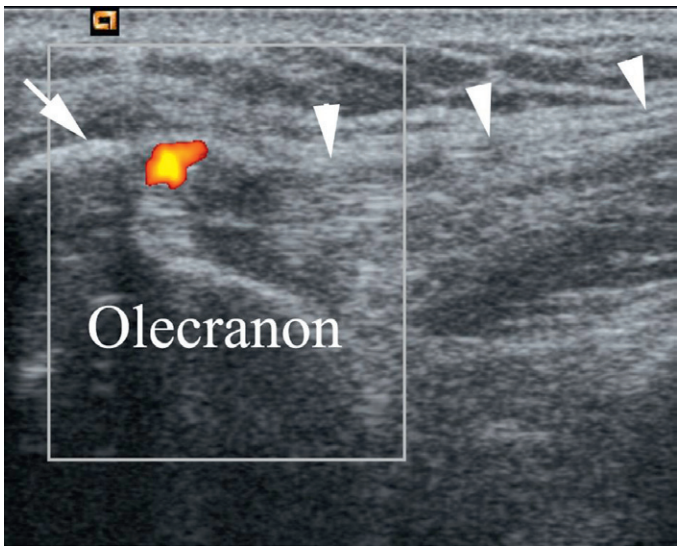

Figure 53.21 Longitudinal view demonstrating triceps tendinosis (arrowheads) with a small olecranon spur (arrow). There is minor flow on power Doppler interrogation.

There is often increased flow on Doppler interrogation. Small calcifications may be present within the tendon close to the insertion indicating enthesopathic change. Associated olecranon bursitis is common[22] (Fig. 53.21).

Triceps tendon ruptures

Triceps tendon ruptures are uncommon. They occur as a result of a direct blow to the posterior aspect of the elbow or eccentric loading on a contracting triceps.[23] Predisposing factors include inflammatory arthropathy, diabetes, gout, renal failure, local steroid injections and olecranon bursitis. Patients present with pain and swelling, and limited ability to extend. A palpable gap may be present. The tear may be partial or complete. As with biceps tendon injuries, complete tears usually require surgery whereas partial tears may heal with conservative therapy.[23] Ultrasound may identify an echogenic avulsion fragment from the olecranon with associated posterior acoustic shadowing.[24] Dynamic scanning in the longitudinal plane with the patient's elbow passively extended and flexed may allow differentiation of a partial from a complete tear. With partial tears there is disruption of the fibrillar echo pattern with remnant intact fibres seen. There may be associated thickening of the tendon due to associated tendinosis. With complete tears there is discontinuity with a hypoechoic gap in the tendon[24] (Fig. 53.22).

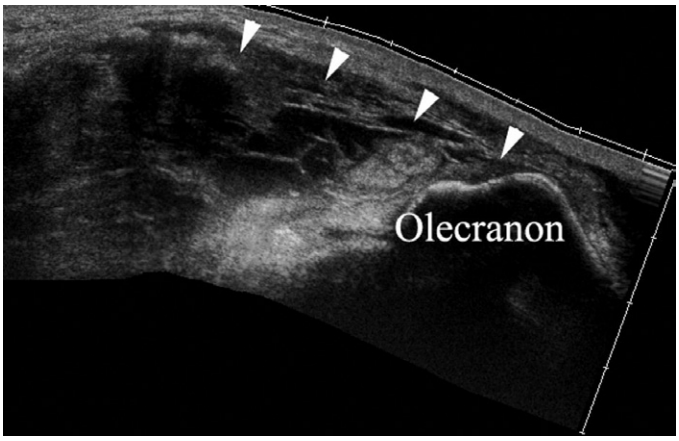

Figure 53.22 Triceps tendon rupture. Longitudinal extended FOV image demonstrating a ruptured triceps tendon with retraction (arrowheads) in a weight-lifter.

Tennis elbow

Tennis elbow or lateral epicondylitis is a common cause of elbow pain. The term 'epicondylitis' is a misnomer as there is no significant inflammatory change; rather the condition reflects tendinosis or enthesopathic change of the common extensor origin due to repetitive microtrauma during supination of the forearm and dorsiflexion of the wrist.[10,25] The microtears lead to formation of reparative tissue resulting in angiofibroblastic hyperplasia. Patients are usually aged 35–55 years and present with symptoms over the lateral epicondyle, exacerbated by use. The condition is usually diagnosed clinically and is often self-limiting. Imaging may be required if the symptoms do not respond to therapy, and if intervention or surgery is being considered.

Ultrasound shows loss of the normal echotexture of the common extensor origin with generalised or focal areas of decreased echogenicity, and loss of the fibrillar structure.[10] There may be generalised swelling of the tendon.[26] In most symptomatic cases there is increased vascularity on Doppler, indicating vascular in-growth. The deep fibres of the tendon tend to be affected more commonly than the superficial fibres. Tendon tears manifest as linear hypoechoic lines or clefts. Bony changes may be present, with traction spur formation or cortical irregularity at the lateral epicondyle[26] (Figs 53.23 and 53.24). In chronic cases there may be mineralisation within the tendon. Macroscopic partial tears of the common extensor origin are common and seen as discrete cleavage planes traversing the tendon. The adjacent radial collateral ligament may also be injured.[10] Comparison with the contralateral elbow is very useful, particularly if changes are subtle.

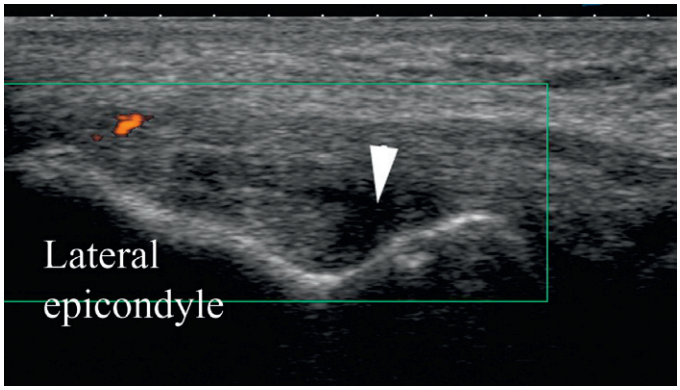

Figure 53.23 Tennis elbow. Longitudinal image of the common extensor origin demonstrating tennis elbow with a hypoechoic tear (arrowhead) of the deep fibres (extensor carpi radialis brevis). Note the presence of power Doppler signal at the tendon insertion.

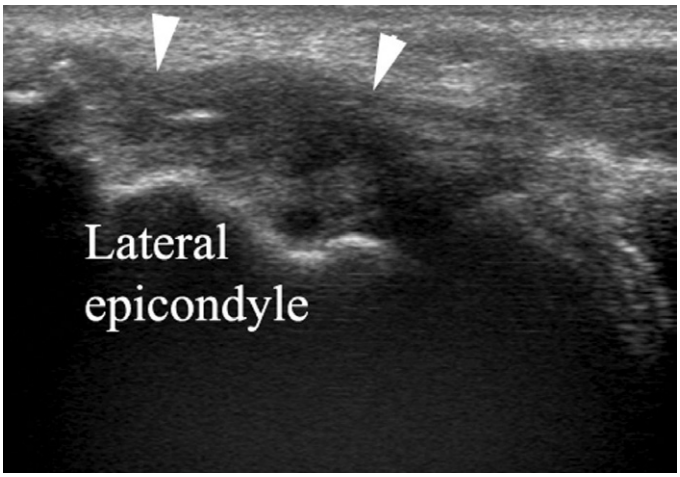

Figure 53.24 Tennis elbow. Longitudinal image of the common extensor origin demonstrating chronic tennis elbow with a heterogeneous tendon, enthesopathic change and small areas of mineralisation. The arrowheads indicate the abnormal common extensor origin.

Golfer's elbow

Golfer's elbow or medial epicondylitis, sometimes called pitcher's elbow, represents tendinosis or enthesopathic change at the common flexor origin. Patients present with focal pain and tenderness over the medial epicondyle, worse on using the arm. The ultrasound manifestations are similar to lateral epicondylitis with focal or generalised altered echotexture of the tendon and swelling. Increased Doppler signal may be present.[27]

Bursitis

Bicipitoradial bursitis

The bicipitoradial or cubital bursa is a potential space lined by synovial tissue that drapes around the distal biceps tendon but does not completely encircle it. The bursa reduces friction between the distal biceps tendon and the radial tuberosity during pronation and supination of the forearm. A normal bursa may be imperceptible or may appear as a low-echogenicity cleft surrounded by a thin hyperechoic lining.

Bursal distension may be simple or complex. With simple bursal distension there is anechoic distension of the bursa. With complex bursal distension there is a combination of fluid and synovial hypertrophy, often with increased vascularity on Doppler. Soft tissue debris, calcifications and septations[28] and occasionally rice body formation may be present.[29] Bursal distension may compress the radial or posterior interosseous nerves.[30] Bursitis is often associated with distal biceps injury[19] and may also occur with overuse, inflammatory arthropathies and infection. Occasionally, the bursa is the site for synovial proliferative disorders such as synovial osteochondromatosis. The degree of synovial hypertrophy may be so severe that it may be difficult to exclude a neoplasm on imaging grounds alone. If bicipitoradial bursitis is present the elbow joint should be carefully examined to exclude underlying joint synovitis, which may indicate inflammatory arthropathy (Figs 53.25 and 53.26).

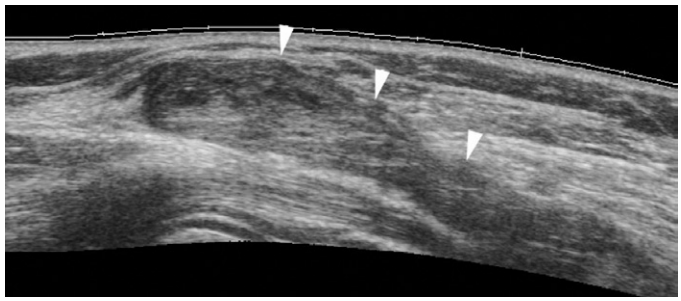

Figure 53.25 Bicipitoradial bursitis. Longitudinal extended FOV image demonstrating a sausage-shaped heterogeneous distended bicipitoradial bursa (arrowheads).

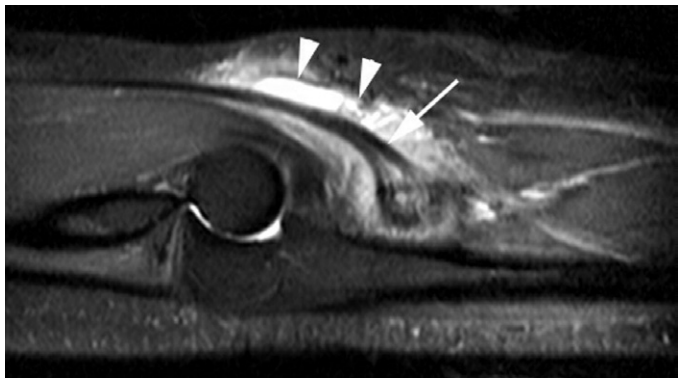

Figure 53.26 Bicipitoradial bursitis. Sagittal STIR sequence demonstrating a distended bicipitoradial bursa (arrowheads) with distal biceps tendinosis and partial tear (arrow).

Olecranon bursitis

Olecranon bursitis, also known as miner's elbow or student's elbow, is a common condition which can be caused by trauma, overuse, gout or inflammatory arthropathy. Infection is implicated in around 20% of patients with olecranon bursitis. *Staphylococus aureus* is the most common organism. Patients present with a painful swelling which may be accompanied by skin erythema. The diagnosis is usually clinical but imaging may be necessary to exclude a soft tissue neoplasm or involvement of the joint. Ultrasound shows distension of the bursa with compressible low-echogenicity fluid, usually in association with synovial thickening.[22] Sometimes the bursa has a completely solid appearance due to florid synovial hypertrophy. Doppler flow may be seen in the solid components. Calcified loose bodies are seen occasionally. If infection is suspected ultrasound allows guided aspiration (Fig. 53.27).

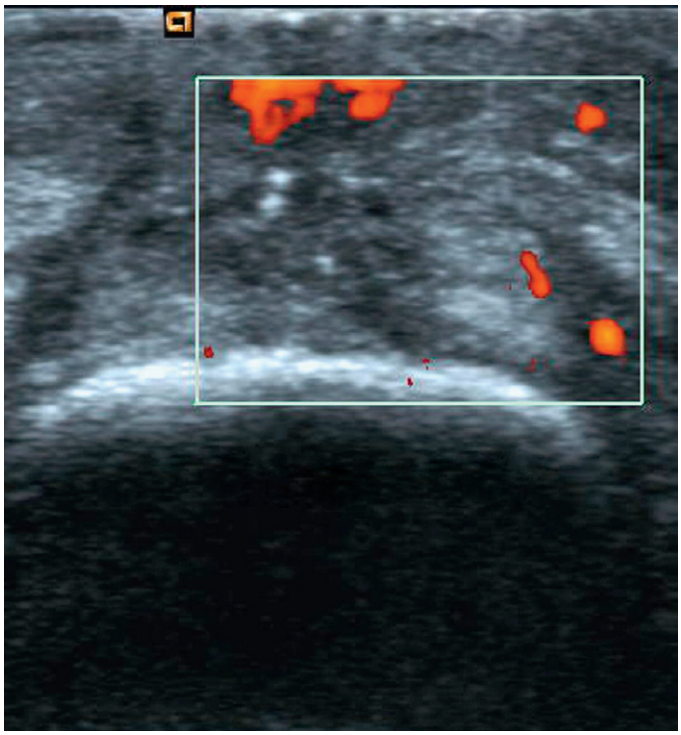

Figure 53.27 Olecranon bursitis. Axial image of a distended thickened olecranon bursa with increased vascularity on power Doppler interrogation.

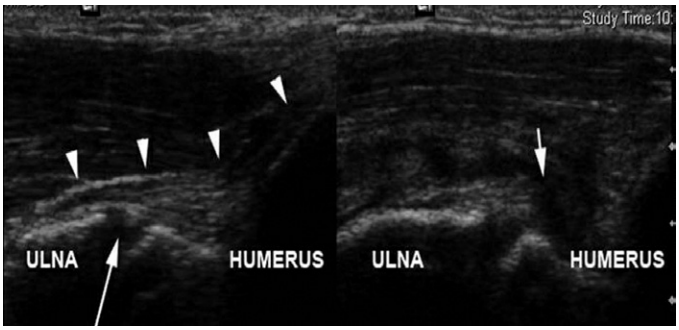

Figure 53.28 Longitudinal dual image view of the medial elbow demonstrating the normal (left, arrowheads) and torn (right, arrow) ulnar collateral ligament.

Pathological conditions

- Tears of the distal biceps tendon result in disruption of tendon fibres, haematoma in the gap and possibly tendon retraction but retraction does not occur if the lacertus fibrosus is intact.
- Bicipitoradial bursitis results in distension of the bursa with fluid or synovium.
- Intra-articular loose bodies may be better seen with an ultrasound arthrogram.
- Epicondylitis produces swelling, reduced echogenicity, loss of the normal echo pattern in the tendon ± hyperostosis and neovascularity.
- Dynamic scanning improves detection of ulnar collateral ligament tears.

Paediatric injury

- Ultrasound has a valuable role in evaluating transphyseal fractures.
- In cases of pulled elbow the radial head slips beneath the annular ligament, increasing the radiocapitellar distance.

Ligament injury

Ulnar collateral ligament injury

The ulnar collateral ligament is prone to injury when there is valgus stress on the elbow, particularly from repetitive overhead throwing sports such as basketball, javelin throwing and American football. Patients present with localised pain and instability. Chronic valgus instability (the medial tension–lateral compression phenomenon) may result in medial epicondylitis, ulnar neuropathy, posteromedial olecranon impingement and osteophytes and loose body formation.[31,32]

The ligament is usually readily identified deep to the common flexor origin and should have a well-defined fibrillar structure. Midsubstance ruptures account for nearly 90% of injuries.[33] In the acute phase following injury there is loss of the normal architecture with heterogeneous echogenicity seen in the gap due to haematoma.[34] Dynamic scanning with valgus stress improves the specificity of diagnosis, and also allows real-time assessment of instability.[35] Comparison with the contralateral side is extremely useful (Fig. 53.28).

Radial collateral ligament injury

The radial collateral ligament is often injured by dislocation of the elbow and may be associated with tendinosis or previous surgery for tennis elbow.[36,37] There is loss of the normal structure with loss of continuity of fibres on ultrasound. There may be fluid in the gap. The adjacent common extensor origin should be assessed for tendinosis or tears. On Doppler interrogation increased vascularity may be present in the common extensor origin indicating degeneration with vascular in growth.

Paediatric bony injury

Ultrasound can be used to reveal effusions, cortical breaks and transphyseal fractures through unossified epiphyseal cartilage that may be unsuspected on plain radiographs.[38–41] If a lipohaemarthrosis is demonstrated on ultrasound there is invariably an associated cortical break.[40]

Fractures of the lateral humeral condyle in children may cause difficulties in diagnosis and treatment, as the fracture line usually involves the cartilaginous trochlea, which cannot be visualised on plain radiographs. Ultrasound can differentiate stable from unstable lateral condyle fractures. The latter can be diagnosed when the fracture extends through the physis to the articular surface.[42] Unstable fractures of the lateral condyle usually require surgery whereas stable fractures can be managed conservatively.

Avulsion fractures of the medial epicondyle can also be demonstrated on ultrasound.[43] Ultrasound has also been used to assess radial neck fractures involving the physis[44] (Fig. 53.29).

Although further imaging by ultrasound, CT and MRI can reveal more injury than radiographs alone,[45,46] routine use of these modalities remains controversial as the additional information appears to have little bearing on treatment or clinical outcome.[46,47]

The pulled elbow is a common injury in young children. Most cases do not require radiographs or ultrasound. Imaging is recommended if there is a non-typical history, deformity or the child is over 6 years of age.[48] In cases of pulled elbow the radial head slips beneath the annular ligament resulting in an increase in the distance between the radial head and capitellum, and also the radiocoronoid distance[48–50] (Fig. 53.30).

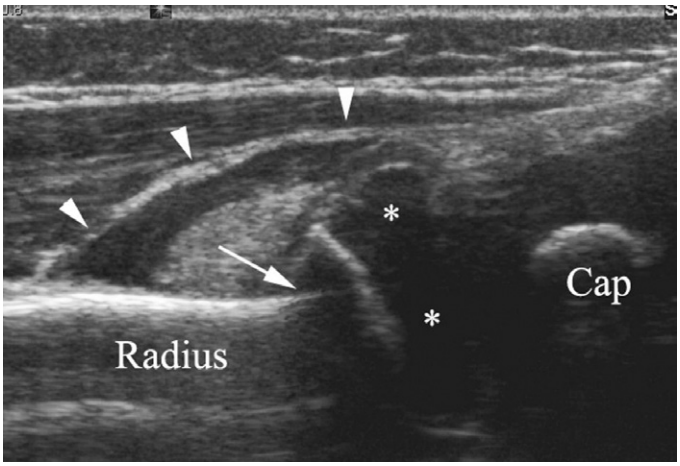

Figure 53.29 Longitudinal image of the proximal radius demonstrating a Salter–Harris type II fracture (arrow) involving the unossified physis (asterisks). There is a lipohaemarthrosis (arrowheads).

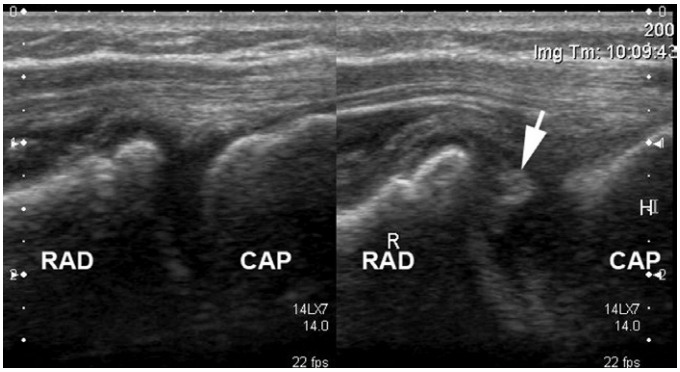

Figure 53.30 Pulled elbow. Longitudinal dual image comparing the normal (left) with a pulled elbow (right) in a 9-year-old girl. The radiocapitellar joint (marked by RAD and CAP) is widened and contains the echogenic body (arrow) shown at surgery to represent the annular ligament.

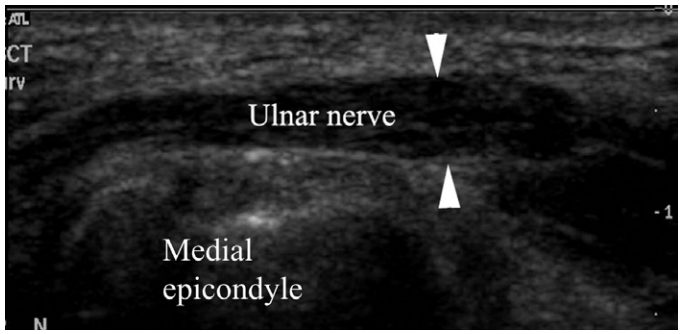

Figure 53.31 Longitudinal image demonstrating focal thickening of the ulnar nerve (arrowheads) in the epicondylar groove in a patient with a subluxing nerve.

Nerve entrapment

- An entrapped nerve may be hypoechoic and swollen, with loss of the normal fibrillar echotexture.
- Entrapment of the ulnar nerve usually occurs at the epicondylar groove.
- Entrapment of the posterior interosseous nerve may occur due to elbow synovitis.

Nerve entrapment

Ulnar nerve entrapment

The features of ulnar nerve entrapment vary from mild intermittent paraesthesia in the ring and little fingers to clawing of the digits with muscle wasting. Patients may have difficulty opening jars.

There are five potential areas of ulnar nerve compression around the elbow.[51] The most common sites of entrapment around the elbow are the olecranon groove and the cubital tunnel.

- Intermuscular septum compression may occur at the ligament of Struthers, a myofascial band seen in association with a supracondylar spur, which is a normal variant. This occurs approximately 8 cm above the medial epicondyle or at the medial head of triceps, which may snap over the medial epicondyle.
- Following a fracture of the medial epicondyle chronic stretching of the ulnar nerve may occur.
- The epicondylar groove is a fibro-osseous tunnel that is bound by the olecranon and medial epicondyle, and covered by a fibrous band. A shallow groove or disruption of the band may result in subluxation of the ulnar nerve resulting in neuritis. Spontaneous subluxation of the ulnar nerve out of the cubital tunnel occurs in 20% of the population.[8] With flexion and extension of the elbow there may be medial subluxation of the ulnar nerve, with the patient reporting a click or snap.[52,53] This important feature is usually only present with dynamic imaging and may not be appreciated on MRI. Patients with symptomatic ulnar nerve subluxation may benefit from nerve transposition surgery. Any cause of mass effect within the epicondylar groove such as a spur, synovitis or ganglion may also lead to nerve compression.
- The cubital tunnel runs between the two heads of the flexor carpi ulnaris, which are connected by a continuation of the fibrous covering of the epicondylar groove (Osborne's ligament). As the elbow flexes, the tunnel flattens.
- When the ulnar nerve exits the flexor carpi ulnaris it can be compressed at the flexor-pronator aponeurosis.

With entrapment the nerve may become hypoechoic and lose its normal speckled structure in cross-section. There may also be calibre changes. Thickening of the nerve indicates neuropathy.[54,55] A cross-sectional area greater than 0.1 cm^2 is suggestive of neuropathy. Assessment in the longitudinal plane may demonstrate focal swelling. Normally no changes are present on Doppler evaluation (Fig. 53.31).

Posterior interosseous nerve compression

Posterior interosseous neuropathy initially results in pain and weakened extension of the ring and middle fingers. Eventually there is weakness in extension of all the fingers and in thumb abduction.

To identify the posterior interosseous nerve on ultrasound, the radial nerve should first be identified at the radial groove in the axial plane. As the nerve is followed down, bifurcation of the radial nerve into superficial and deep components can be seen. The deep

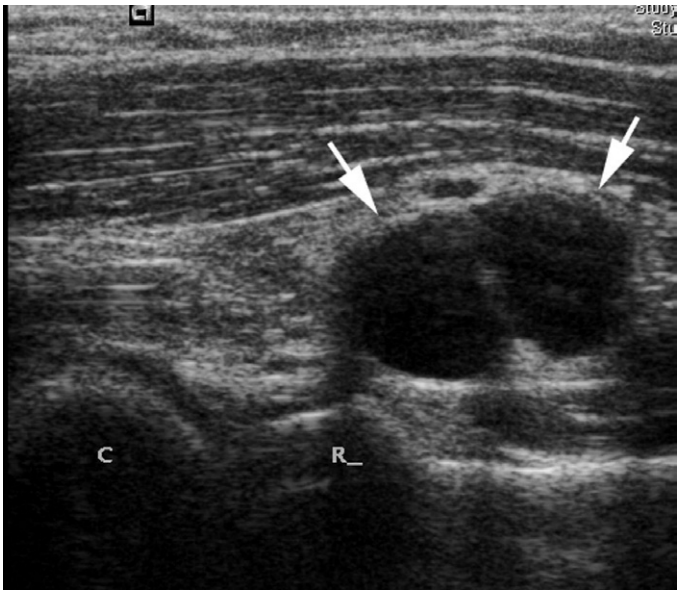

Figure 53.32 Longitudinal image of the anterior elbow joint demonstrating a radiocapitellar ganglion (arrows) in a patient with posterior interosseous nerve syndrome (supinator syndrome).

branch penetrates the supinator muscle as the posterior interosseous nerve. Entrapment of the posterior interosseous nerve may result from a variety of conditions including severe elbow joint synovitis, bicipitoradial bursitis, a radiocapitellar ganglion, trauma, misplaced surgical screws or impingement at the arcade of Frohse.[6,56,57] Nerve compression due to hypertrophy of the leash of Henry has also been documented. In supinator syndrome, the nerve may become thickened as it is impinged at the level of supinator[58] (Fig. 53.32).

ULTRASOUND-GUIDED INTERVENTIONAL PROCEDURES

Joint aspiration and injection

Elbow joint aspiration may be required in suspected infection or inflammatory arthropathy. A posterior approach is safest. The patient should be positioned with the elbow flexed and abducted. Children may be scanned sitting on a parent's lap with the elbow flexed. Ideally a probe cover should be used to ensure an aseptic technique. The probe should be positioned longitudinally over the dorsal aspect to demonstrate the effusion. A small volume of subcutaneous local anaesthetic may be used. Under continuous direct guidance the distended joint can be entered using a 20G needle. The aspirate should be routinely sent for microbiology and crystals.

Ultrasound-guided injection of the elbow may be performed for an arthrogram or therapy. The posterior approach is also recommended. The needle tip is directed into the olecranon fossa where the posterior recess is distended easily.

Injection of the common extensor and flexor origins

Physiotherapy, ultrasound and shock-wave therapy, steroid injections, dry needling, acupuncture, autologous blood injection and surgery have all been utilised for the treatment of epicondylitis, with varying success.[59–61] To date there have been no randomised controlled trials comparing the various treatments and as a result there is no consensus as to which technique is the best.[62] A recent meta-analysis has shown that physiotherapy may be more successful than steroid injections in the long term.[60]

The diagnosis of epicondylitis is often made on clinical grounds without imaging. Many clinicians perform therapeutic injections without imaging guidance. If therapy has failed, or there is doubt as to the diagnosis, the patient may be referred for ultrasound diagnosis and guided injection.

Depending on local practice, a simple steroid and local anaesthetic injection may be performed around the tendon origin using a longitudinal approach. Some practitioners advocate intratendinous injection but this carries a small risk of tendon rupture. Following introduction of local anaesthetic the tendon origin may be dry-needled, by repeated to-and-fro needle perforations of the tendon to elicit micro-haemorrhage. Autologous blood injection involves drawing a small volume of venous blood from the patient and re-injecting this in and around the tendon origin.[63] This procedure has been shown to reduce the number of interstitial tears and decrease the neovascularity.

REFERENCES

1. Teh J. Imaging of the elbow. Imaging 2007;19(3):220–233.
2. Barr LL, Babcock DS. Sonography of the normal elbow. AJR Am J Roentgenol 1991;157(4):793–798.
3. Miles KA, Lamont AC. Ultrasonic demonstration of the elbow fat pads. Clin Radiol 1989;40(6):602–604.
4. Chew ML, Giuffre BM. Disorders of the distal biceps brachii tendon. Radiographics 2005;25(5):1227–1237.
5. Andreisek G, Crook DW, Burg D, et al. Peripheral neuropathies of the median, radial, and ulnar nerves: MR imaging features. Radiographics 2006;26(5):1267–1287.
6. Chien AJ, Jamadar DA, Jacobson JA, et al. Sonography and MR imaging of posterior interosseous nerve syndrome with surgical correlation. AJR Am J Roentgenol 2003;181(1):219–221.
7. Jacob D, Creteur V, Courthaliac C, et al., Sonoanatomy of the ulnar nerve in the cubital tunnel: a multicentre study by the GEL. Eur Radiol 2004;14(10):1770–1773.
8. Okamoto M, Abe M, Shirai H, Ueda N. Morphology and dynamics of the ulnar nerve in the cubital tunnel. Observation by ultrasonography. J Hand Surg [Br] 2000;25(1):85–89.
9. Jacobson JA, Propeck T, Jamadar DA, et al. US of the anterior bundle of the ulnar collateral ligament: findings in five cadaver elbows with MR arthrographic and anatomic comparison – initial observations. Radiology 2003;227(2):561–566.
10. Connell D, Burke F, Coombes P, et al. Sonographic examination of lateral epicondylitis. AJR Am J Roentgenol 2001;176(3):777–782.
11. De Maeseneer M, Jacobson JA, Jaovisidha S, et al. Elbow effusions: distribution of joint fluid with flexion and extension and imaging implications. Invest Radiol 1998;33(2):117–125.
12. Milgram JW. The development of loose bodies in human joints. Clin Orthop 1977;(124):292–303.
13. Bianchi S, Martinoli C. Detection of loose bodies in joints. Radiol Clin North Am 1999;37(4):679–690.
14. Quinn SF, Haberman JJ, Fitzgerald SW, et al. Evaluation of loose bodies in the elbow with MR imaging. J Magn Reson Imaging 1994;4(2):169–172.
15. Miller JH, Beggs I. Detection of intraarticular bodies of the elbow with saline arthrosonography. Clin Radiol 2001;56(3):231–234.
16. Milgram JW, Synovial osteochondromatosis: a histopathological study of thirty cases. J Bone Joint Surg Am 1977;59(6):792–801.
17. Ruth RM, Groves RJ. Synovial osteochondromatosis of the elbow presenting with ulnar nerve neuropathy. Am J Orthop 1996;25(12): 843–844.
18. Nogueira A, Alcelay O, Pena C, et al. Synovial osteochondromatosis at the elbow producing ulnar and median nerve palsy. Case report and review of the literature. Chir Main 1999;18(2):108–114.
19. Williams BD, Schweitzer M, Weishaupt D, et al. Partial tears of the distal biceps tendon: MR appearance and associated clinical findings. Skeletal Radiol 2001;30(10):560–564.
20. Weiss C, Mittelmeier M, Gruber G. Do we need MR images for diagnosing tendon ruptures of the distal biceps brachii? The value of ultrasonographic imaging. Ultraschall Med 2000;21(6): 284–286.

21. Miller TT, Adler RS. Sonography of tears of the distal biceps tendon. AJR Am J Roentgenol 2000;175(4):1081–1086.
22. Blankstein A, Ganel A, Givon U, et al. Ultrasonographic findings in patients with olecranon bursitis. Ultraschall Med 2006;27(6):568–571.
23. Mair SD, Isbell WM, Gill TJ, et al. Triceps tendon ruptures in professional football players. Am J Sports Med 2004;32(2):431–434.
24. Kaempffe FA, Lerner RM. Ultrasound diagnosis of triceps tendon rupture. A report of 2 cases. Clin Orthop Relat Res 1996;332:138–142.
25. Nirschl RP, Pettrone FA. Tennis elbow. The surgical treatment of lateral epicondylitis. J Bone Joint Surg Am 1979;61(6A):832–839.
26. Maffulli N, Regine R, Carrillo F, et al. Tennis elbow: an ultrasonographic study in tennis players. Br J Sports Med 1990;24(3):151–155.
27. Suresh SP, Ali KE, Jones H, Connell DA. Medial epicondylitis: is ultrasound guided autologous blood injection an effective treatment? Br J Sports Med, 2006;40(11):935–939; discussion 939.
28. Liessi G, Cesari S, Spaliviero B, et al. The US, CT and MR findings of cubital bursitis: a report of five cases. Skeletal Radiol 1996;25(5): 471–475.
29. Spence LD, Adams J, Gibbons D, et al. Rice body formation in bicipito-radial bursitis: ultrasound, CT, and MRI findings. Skeletal Radiol, 1998;27(1):30–32.
30. Skaf AY, Boutin RD, Dantas RW, et al., Bicipitoradial bursitis: MR imaging findings in eight patients and anatomic data from contrast material opacification of bursae followed by routine radiography and MR imaging in cadavers. Radiology 1999;212(1):111–116.
31. Mirowitz SA, London SL. Ulnar collateral ligament injury in baseball pitchers: MR imaging evaluation. Radiology 1992;185(2):573–576.
32. Thornton R, Riley GM, Steinbach LS. Magnetic resonance imaging of sports injuries of the elbow. Top Magn Reson Imaging 2003;14(1): 69–86.
33. Conway JE, Jobe FW, Glousman RE, Pink M. Medial instability of the elbow in throwing athletes. Treatment by repair or reconstruction of the ulnar collateral ligament. J Bone Joint Surg Am 1992;74(1):67–83.
34. Miller TT, Adler RS, Friedman L. Sonography of injury of the ulnar collateral ligament of the elbow – initial experience. Skeletal Radiol 2004;33(7):386–391.
35. De Smet AA, Winter TC, Best TM, Bernhardt DT. Dynamic sonography with valgus stress to assess elbow ulnar collateral ligament injury in baseball pitchers. Skeletal Radiol 2002;31(11): 671–676.
36. Potter HG, Weiland AJ, Schatz JA, et al. Posterolateral rotatory instability of the elbow: usefulness of MR imaging in diagnosis. Radiology 1997;204(1):185–189.
37. Ring D, Koris M, Jupiter JB. Instability after total elbow arthroplasty. Orthop Clin North Am 2001;32(4):671–677, ix.
38. Markowitz RI, Davidson RS, Harty MP. Sonography of the elbow in infants and children. AJR Am J Roentgenol 1992;159(4):829–833.
39. Davidson RS, Markowitz RI, Dormans J, Drummond DS. Ultrasonographic evaluation of the elbow in infants and young children after suspected trauma. J Bone Joint Surg Am 1994;76(12): 1804–1813.
40. Zuazo I, Bonnefoy O, Tauzin C, et al. Acute elbow trauma in children: role of ultrasonography. Pediatr Radiol 2008;38(9):982–988.
41. Brown J, Eustace S. Neonatal transphyseal supracondylar fracture detected by ultrasound. Pediatr Emerg Care 1997;13(6):410–412.
42. Vocke-Hell AK, Schmid A. Sonographic differentiation of stable and unstable lateral condyle fractures of the humerus in children. J Pediatr Orthop B 2001;10(2):138–141.
43. May DA, Disler DG, Jones EA, Pearce DA. Using sonography to diagnose an unossified medial epicondyle avulsion in a child. AJR Am J Roentgenol 2000;174(4):1115–1117.
44. Lazar RD, Waters PM, Jaramillo D. The use of ultrasonography in the diagnosis of occult fracture of the radial neck. A case report. J Bone Joint Surg Am 1998;80(9):1361–1364.
45. Carey J, Spence L, Blickman H, Eustace S. MRI of pediatric growth plate injury: correlation with plain film radiographs and clinical outcome. Skeletal Radiol 1998;27(5):250–255.
46. Blickman JG, Dunlop RW, Sanzone CF, et al. Is CT useful in the traumatized pediatric elbow? Pediatr Radiol 1990;20(3):184–185.
47. Griffith JF, Roebuck DJ, Cheng JC, et al. Acute elbow trauma in children: spectrum of injury revealed by MR imaging not apparent on radiographs. AJR Am J Roentgenol, 2001;176(1):53–60.
48. Scapinelli R, Borgo A. Pulled elbow in infancy: diagnostic role of imaging. Radiol Med (Torino) 2005;110(5–6):655–664.
49. Kim MC, Eckhardt BP, Craig C, Kuhns LR. Ultrasonography of the annular ligament partial tear and recurrent 'pulled elbow'. Pediatr Radiol, 2004;34(12):999–1004.
50. Kosuwon W, Mahaisavariya B, Saengnipanthkul S, et al. Ultrasonography of pulled elbow. J Bone Joint Surg Br, 1993;75(3): 421–422.
51. Posner MA. Compressive ulnar neuropathies at the elbow: I. Etiology and diagnosis. J Am Acad Orthop Surg 1998;6(5):282–288.
52. Jacobson JA, Jebson PJ, Jeffers AW, et al. Ulnar nerve dislocation and snapping triceps syndrome: diagnosis with dynamic sonography – report of three cases. Radiology 2001;220(3):601–605.
53. Grechenig W, Mayr J, Peicha G, Boldin C. Subluxation of the ulnar nerve in the elbow region – ultrasonographic evaluation. Acta Radiol 2003;44(6):662–664.
54. Beekman R, Schoemaker MC, van der Plas JPL, et al. Diagnostic value of high-resolution sonography in ulnar neuropathy at the elbow. Neurology 2004;62(5):767–773.
55. Kutlay M, Colak A, Simşek H, et al., Use of ultrasonography in ulnar nerve entrapment surgery – a prospective study. Neurosurg Rev 2009;32(2):225–232.
56. Ly JQ, Barrett TJ, Beall DP, et al. MRI diagnosis of occult ganglion compression of the posterior interosseous nerve and associated supinator muscle pathology. Clin Imaging 2005;29(5):362–363.
57. Ogawa H, Akaike A, Ishimaru D, et al. Posterior interosseous nerve palsy related to rheumatoid synovitis of the elbow. Mod Rheumatol 2007;17(4):327–329.
58. Bodner G, Harpf C, Meirer R, et al. Ultrasonographic appearance of supinator syndrome. J Ultrasound Med 2002;21(11):1289–1293.
59. Binder AI, Hazleman BL. Lateral humeral epicondylitis – a study of natural history and the effect of conservative therapy. Br J Rheumatol 1983;22(2):73–76.
60. Boisaubert B, Brousse C, Zaoui A, Montigny JP. [Nonsurgical treatment of tennis elbow]. Ann Readapt Med Phys 2004;47(6): 346–355.
61. Ernst E. Conservative therapy for tennis elbow. Br J Clin Pract 1992;46(1):55–57.
62. Johnson GW, Cadwallader K, Scheffel SB, Epperly TD. Treatment of lateral epicondylitis. Am Fam Physician 2007;76(6):843–848.
63. Connell DA, Ali KE, Ahmad M, et al. Ultrasound-guided autologous blood injection for tennis elbow. Skeletal Radiol 2006;35(6):371–377.

CHAPTER

54 Ultrasound of the wrist and hand

Carlo Martinoli, Alberto Tagliafico and Gerd Bodner

INTRODUCTION

Ultrasound (US) provides exquisite detail of superficial structures, dynamic assessment and rapid examination and is the first-line imaging modality in the assessment of the soft tissues of the wrist and hand.[1,2] Applications of US include the diagnosis of extensor and flexor tendon abnormalities, retinacula-related disorders, some ligament injuries and compressive or traumatic neuropathies. Accurate diagnosis and adequate treatment is essential given the importance of normal hand function in sporting, professional and everyday activity. The aim of this chapter is to review the clinically relevant anatomy and US appearances of tendons, ligaments and nerves of the wrist and hand and to emphasise the role of US in assessing them. Rheumatological disorders are described in Chapter 59.

NORMAL ANATOMY AND SCANNING TECHNIQUE

The wrist is crossed by flexor and extensor tendons along its ventral and dorsal aspects respectively. The **extensor tendons** pass through a series of osteofibrous tunnels composed of depressions in the surface of the radius and ulna that are covered by the extensor retinaculum. From the deep surface of the retinaculum, vertical fibrous bands insert into the bone, dividing the extensor tunnel into six compartments numbered from radial (I) to ulnar (VI). As shown in Figure 54.1, the first compartment contains the abductor pollicis longus (APL) and extensor pollicis brevis (EPB) tendons. Medial to this, the second compartment houses the extensor carpi radialis longus (ECRL) and brevis (ECRB), which insert on the base of the second and third metacarpals. The third compartment is separated from the second by the bony prominence of Lister's tubercle, and contains extensor pollicis longus (EPL) which, with EPB, forms the dorsal and volar boundaries of the anatomical snuff-box. The fourth compartment is wide and encloses the four tendons of extensor digitorum communis (EDC) for the II–V fingers, and the tendon of the extensor indicis proprius (EIP), which is absent or rudimentary in approximately 40% of normal subjects. The fifth compartment encloses the extensor digiti minimi (EDM). The sixth compartment includes extensor carpi ulnaris (ECU), which inserts into the base of the fifth metacarpal. These tunnels give lateral stability to the extensor tendons during wrist and fingers movements.

US depicts each tendon as a rounded or oval echogenic fibrillar structure from the musculotendinous junction to its insertion.[3,4] Dynamic scanning during passive finger flexion and extension may help to assess their integrity and gliding quality.

Transverse US images are first obtained at the distal radius to identify the Lister tubercle, the landmark that separates the second and third compartments. Then the probe is swept proximally and distally along the axis of the tendon or directed radially or ulnarly to change the compartment to be examined. Depending on probe positioning, the normal extensor retinaculum surrounding the tendons may assume a hypoechoic appearance from anisotropy. This should not be misinterpreted as tenosynovitis.[5]

In the fingers, the extensor tendons become broad and flat, like an aponeurotic expansion, that covers the dorsal aspect of the metacarpophalangeal joint (MCPJ) and proximal phalanx and narrows distally (extensor hood). Each tendon has three slips: one central, which runs in the midline to insert onto the middle phalanx, and two lateral, which pass on each side of the central to insert on the distal phalanx. Over the metacarpal head, the extensor tendon complex is stabilised by a retinaculum, which is known as the sagittal band.[6]

When examining the dorsal wrist, transverse planes are the best to depict and correctly identify the extensor tendons. Longitudinal images may be helpful to assess tendon gliding and check the distal tendon insertions dynamically.

At the volar aspect of the wrist, nine **flexor tendons** cross the carpal tunnel: they include four slips from the flexor digitorum superficialis (FDS) and four from the flexor digitorum profundus (FDP) for the II–V fingers and the flexor pollicis longus (FPL) (Fig. 54.2). At the wrist, the FDS and FDP tendons have a common synovial sheath, whereas the FPL crosses the tunnel enveloped by a separate sheath. After exiting the carpal tunnel, the flexor tendons diverge to reach the respective fingers. At the base of the proximal phalanx, the FDS tendon divides into two slips which pass on each side of the FDP tendon. More distally, the FDS slips cross dorsal to the FDP and insert into the shaft of the middle phalanx, whereas the FDP continues its straight course to reach the base of the distal phalanx. The FPL tendon traverses the thenar eminence between the superficial and deep bellies of the flexor pollicis brevis muscle. It then enters the thumb, passing in between the sesamoids to insert at the base of the distal phalanx.

US shows the finger flexor system in excellent detail.[3,4] In each finger, the flexor tendon are invested by a single synovial sheath and stabilised by a fibrous envelope consisting of a complex system of **annular pulleys** and cruciform bands.[7] The annular pulleys are located at five specific locations along the tendon sheath and are numbered from proximal (A1) to distal (A5) (Fig. 54.3). Of the five pulleys, the A2 is the strongest and the A4 has the greatest stiffness. Both attach to the bone while the A1, A3 and A5 pulleys arise from the palmar plates. In the thumb, the flexor digital sheath includes two pulleys lying over the MCPJ (A1) and the head of the proximal

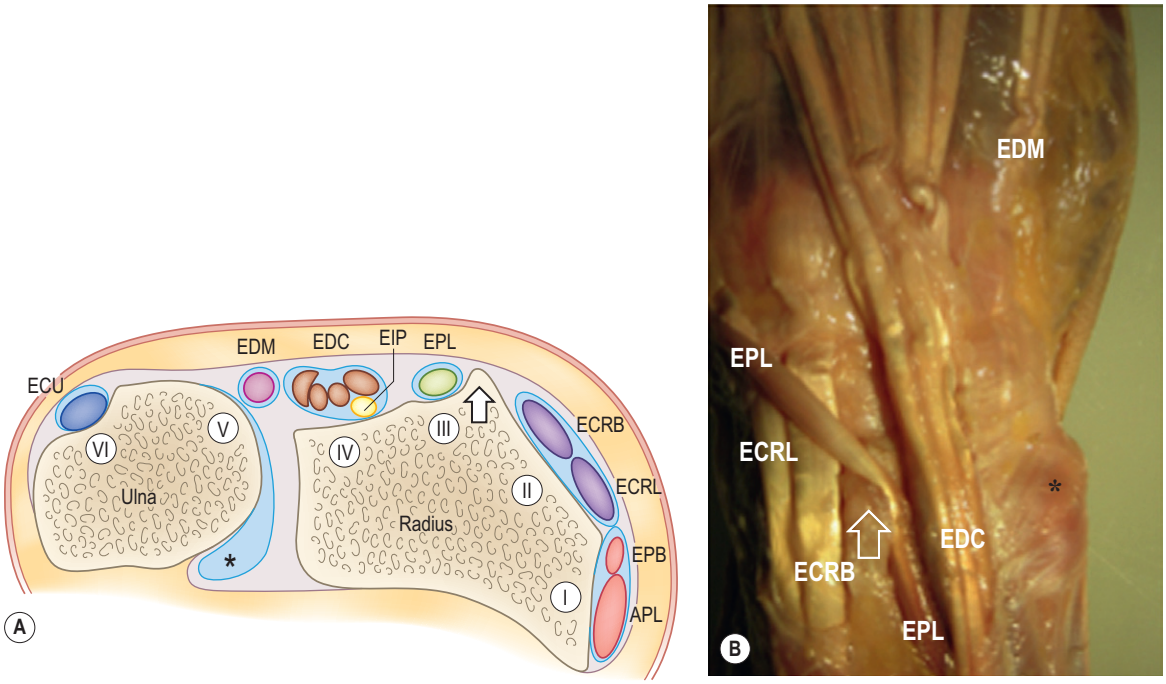

Figure 54.1 **Extensor tendons. A:** Schematic drawing of the six compartments of the extensor tendons numbered I–VI from radial to ulnar: abductor pollicis longus (APL), extensor pollicis brevis (EPB), extensor carpi radialis longus (ECRL), extensor carpi radialis brevis (ECRB), extensor pollicis longus (EPL), extensor digitorum communis (EDC), extensor indicis proprius (EIP), extensor digiti minimi (EDM) and extensor carpi ulnaris (ECU). Arrow, Lister tubercle; asterisk, distal radioulnar joint. **B:** Cadaveric view shows the EPL tendon running alongside the Lister tubercle (arrow). Distally EPL deflects toward the thumb crossing over the ECRB and ECRL. Asterisk, ulnar head.

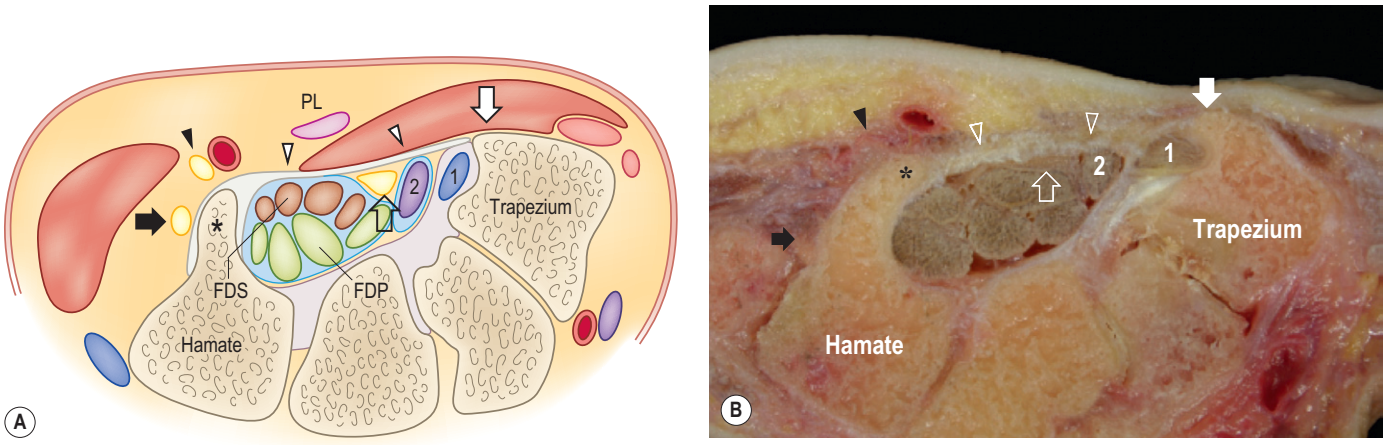

Figure 54.2 **Flexor tendons. A:** Schematic drawing illustrates the carpal tunnel at its distal level. The transverse carpal ligament (hollow arrowheads) inserts on the tubercle (white arrow) of the trapezium and the hook (asterisk) of the hamate. Nine tendons cross the carpal tunnel: four from flexor digitorum superficialis (FDS), four from flexor digitorum profundus (FDP) and flexor pollicis longus (2). The flexor carpi radialis (1) travels outside the tunnel, close to the trapezium. The median nerve (hollow arrow) lies radially in the carpal tunnel, immediately deep to the transverse carpal ligament. At the hamate level, the ulnar nerve has already divided into superficial sensory (black arrowhead) and deep motor (black arrow) branches. PL, palmaris longus tendon. **B:** Corresponding cadaveric slice of the distal carpal tunnel. The tunnel is delimited by carpal bones and a fibrous roof formed by the transverse carpal ligament (arrowheads) that inserts on the tubercle (white arrow) of trapezium and the hook (asterisk) of the hamate. The flexor digitorum tendons from the FDS and FDP are bundled up in the tunnel. Relative to them, the FCR (1) and the FPL (2) assume a more radial position.

phalanx (A2) and an oblique pulley over the volar shaft of the proximal phalanx. The primary flexors of the wrist, the flexor carpi radialis (FCR) and the flexor carpi ulnaris (FCU), travel outside the carpal tunnel. The FCR is a long tendon invested by its own synovial sheath and inserts on the second metacarpal after coursing close to the scapho-trapezio-trapezoid (triscaphe) joint. The FCU is not invested by a synovial sheath and courses on the ulnar side of the wrist to insert into the pisiform (which is considered a sesamoid bone in the tendon), the hook of the hamate and the fifth metacarpal. The palmaris longus (PL) tendon is a thin tendon which passes midline and superficial to the transverse carpal ligament.

The two most important intrinsic ligaments of the wrist are the **scapholunate** (SLL) and **lunotriquetral** (LTL) ligaments. On dorsal transverse planes, the SLL is a compact echogenic fibrillar band between the lunate and the scaphoid, just distal to the Lister tubercle. The SLL is fundamental to carpal stability. Identification of a normal ligament is useful. Non-visualisation of the ligament on dorsal scans does not necessarily indicate a complete tear as its

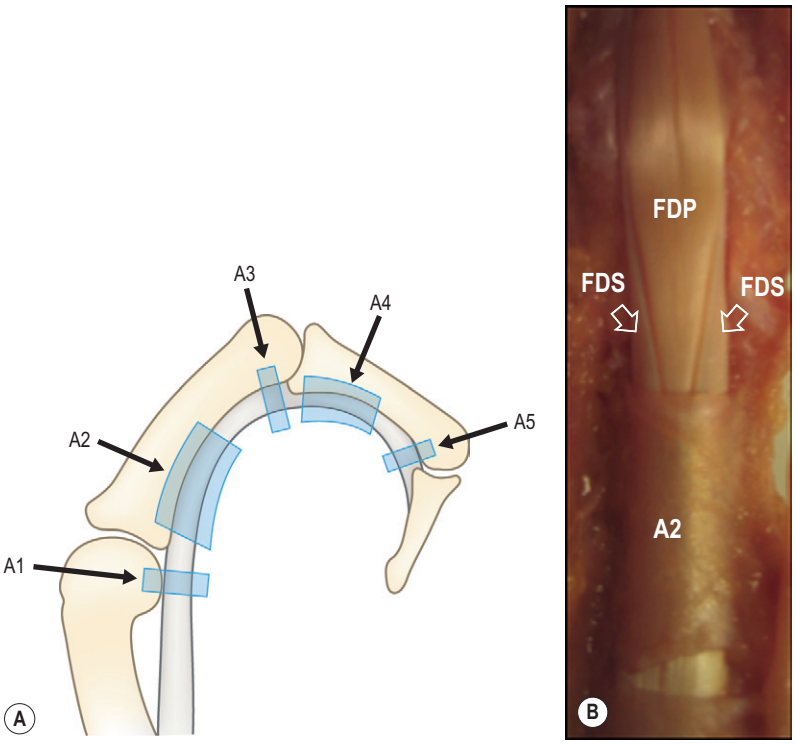

Figure 54.3 Annular pulley system. A: Schematic drawing shows the positions of the five annular pulleys. The A1, A3 and A5 pulleys lie over the heads of the metacarpal, proximal phalanx and distal phalanx, whereas the A2 and A4 pulleys attach to the shaft of the proximal and middle phalanx respectively. **B:** Cadaveric dissection of the flexor tendons at the level of the proximal phalanx illustrates the two slips of the FDS tendon passing on each side of the FDP. They are firmly restrained by the A2 pulley.

ventral part might be intact.[8] The LTL can be located by shifting the probe slightly to the ulnar side. Its US appearance is similar to that of the SLL.[3]

The **triangular fibrocartilage** complex (TFC) or radioulnar disc is attached by its apex to a depression between the styloid process and the head of the ulna; and by its thin base to the prominent edge of the radius, which separates the ulnar notch from the carpal articular surface. It is interposed between the distal radioulnar and radiocarpal joints. At US, it appears as a homogeneously echogenic inverted triangular structure deep to the ECU tendon.[3]

Three **nerves** cross the wrist: median (MN), ulnar (UN) and the superficial cutaneous branch of the radial (RN).[9,10] In the wrist, the UN is accompanied by the ulnar artery (UA) and the MN gives off a secondary sensory nerve, the palmar cutaneous branch (PCB_{MN}).

In the distal forearm, the MN courses in the hyperechoic fascial plane between the FDS and FDP. As the MN approaches the wrist, it shifts radially and then moves superficial passing alongside the lateral margin of the FDS to align itself in the midline before entering the carpal tunnel. On short-axis planes, the MN has an oval cross-section at the proximal tunnel and becomes more flattened as it progresses distally to the level of the hamate hook. Throughout the carpal tunnel, it is covered by a localised thickening of fascia known as the flexor retinaculum or transverse carpal ligament. In carpal tunnel syndrome the cross-sectional area (CSA_{MN}) of the MN[11] should be sampled at the site where the MN is maximally enlarged and histopathological changes are maximal. In general, this occurs just cranial to the proximal boundary of the retinaculum, a position located slightly cranial to the pisiform. Two methods are used to measure the CSA_{MN}: the indirect method, based on calculation of the nerve diameters by callipers and application of the ellipse formula (transverse diameter × anteroposterior diameter × $\pi/4$) and the direct method, based on manual tracing and automated calculation of the area.[11,12] There is a high degree of correlation between the methods,[12,13] which are easily learned.[13] Probe positioning can potentially affect the variability of CSA measurements. The US beam should be always directed perpendicular to the MN, even when the nerve runs obliquely from superficial to deep. Optimal probe orientation can be defined dynamically by tilting the probe over the nerve or inducing slight changes in the carpal position.

Normal anatomy

- The wrist is traversed by a series of twelve extensor and twelve flexor tendons, most of which are invested by synovial sheaths, and by three nerves, the median, ulnar and the sensory branch of the radial nerve.
- The MN and nine tendons from the FDS, FDP and FPL pass through the carpal tunnel.
- The Guyon tunnel houses the UN and the UA.
- In the fingers, both flexor and extensor tendons insert into the middle and the distal phalanges.

The UN crosses the wrist through the Guyon tunnel, which is superficial and medial to the carpal tunnel. It is bounded by the pisiform (medially), the transverse carpal ligament (floor) and the palmar carpal ligament (roof). The UN bifurcates within the tunnel into the superficial (sensory) branch and the deep (motor) branch, the latter supplying most of the intrinsic muscles of the hand. Distal to the Guyon tunnel, the sensory branch has a straight course while the motor branch reflects across the palm to end at the first interosseous space.

On the radial aspect of the distal forearm, the superficial cutaneous branch of the RN pierces the fascia between the tendons of the ECRL and the brachioradialis to move into the subcutaneous tissue that overlies the anatomical snuff-box, traversing the extensor tendons of the first compartment in close relationship with the cephalic vein.

TENDON TEARS

Most **extensor tendon tears** occur in the fingers, causing typical deformities that are easily diagnosed at physical examination. On the other hand, identification of extensor tendon ruptures in the wrist may not be straightforward clinically and US can be invaluable. In closed injuries, US can recognise the cause of the tear, often due to bony spurs or attrition from surgical hardware.

The most frequently torn extensor tendon in the hand is EPL, which is also the second most commonly injured tendon in the upper limb. EPL tears produce loss of extension at the interphalangeal joint of the thumb and inability to grip with the other fingers. US shows a gap between tendon ends that is occupied by a continuous or discontinuous hypoechoic interval due to debris or frayed residual fibres. The tendon ends may appear stump-like or, following elongation trauma, tapered.[14,15] Apart from spontaneous ruptures in patients with rheumatoid arthritis, on local or systemic steroids or due to sports/work-related repetitive stress, EPL rupture may be due to injury and wrist fractures, impingement by orthopaedic devices (e.g. Kirschner wire fixation, volar plating) or stab wounds. There is an increased risk of EPL rupture in non-displaced radial fractures (Fig. 54.4). The intact extensor retinaculum causes decreased compliance and raised compartmental pressure in the osteofibrous tunnel delimited by the Lister tubercle.[16] A vascular watershed in the tendon at the Lister tubercle level may increase tendon vulnerability. In EPL tears that occur following volar plate fixation, US may show the tips of the screws perforating the dorsal radial cortex of the radius and causing the tendon rupture (Fig. 54.5).[17] This may be difficult to assess with magnetic resonance (MR) imaging due to metallic artefact. In patients with EPL rupture, the status of the EIP should be evaluated as it may be used as a graft. US can also confirm tears of tendons that cannot be easily assessed clinically, such as the EIP, ECRB and ECRL.

Flexor tendon injuries are less frequent than extensor tears. Rupture usually follows a penetrating injury or in association with systemic disorders or therapy with steroids or quinolones. Preoperatively, US is particularly helpful in locating the two ends of the ruptured tendon as they may be retracted considerable distances from the tear. Accurate localisation helps to plan the surgical approach (Fig. 54.6). If there is significant retraction, use of extended field-of-view images can improve the presentation of the US information for the surgeon. Alternatively, the position of the tendon ends can be related to landmarks that are palpable (e.g. bones) or can be readily identified by the surgeon. Dynamic scanning may help to distinguish partial from complete tears when the injury has occurred with an elongation mechanism. In **jersey finger**, US confirms the traumatic FDP tendon avulsion from the distal phalanx and shows if the tendon is attached to an avulsed bone fragment.[18]

Many factors influence recovery following flexor tendon tears, the most important of which is the location of the injury. Flexor tendon injuries are divided into five zones, as follows: *zone 1*, distal to the FDS insertion; *zone 2*, from the A1 pulley to zone 1; *zone 3*: from the distal edge of the flexor retinaculum to the A1 pulley; *zone 4*, within the carpal tunnel; *zone 5*, proximal to the carpal tunnel. The functional outcome of zone 2 injury is poorer and the complication rate, including adhesions, contracture, triggering and pulley failure, is greater than that associated with injury in other zones.[19] Postoperatively, a repaired tendon usually appears more

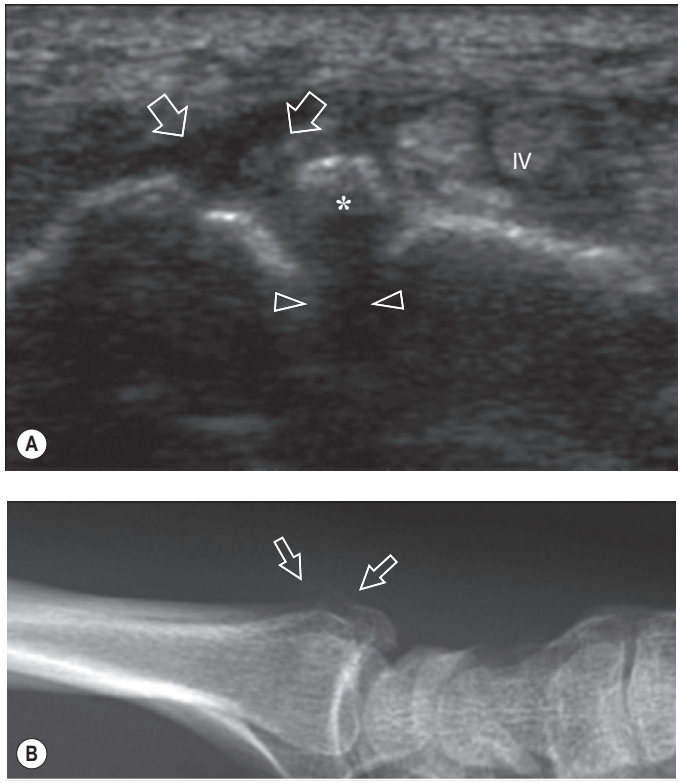

Figure 54.4 Extensor pollicis longus tendon tear presenting as weak thumb extension after distal radial fracture. **A:** Transverse US shows fragmentation (asterisk) and discontinuity (arrowheads) of the floor of the third compartment at the level of the Lister tubercle and an empty EPL tendon sheath (arrows) due to a torn and retracted EPL tendon. **B:** Correlative lateral radiograph demonstrates a non-displaced fracture (arrows) of the distal radius.

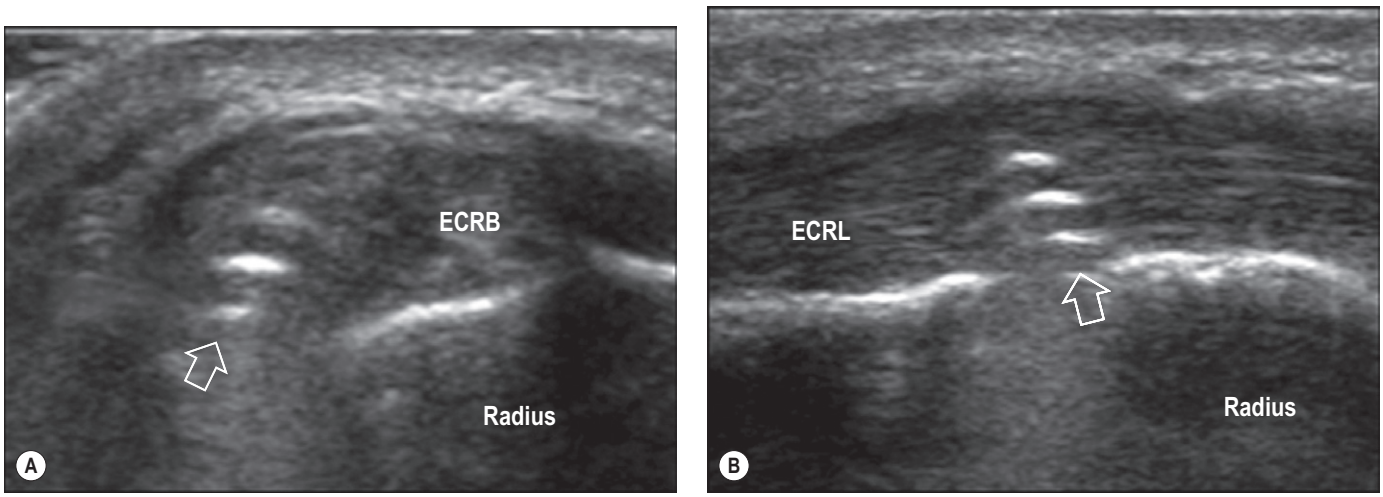

Figure 54.5 Screw tip impingement of the ECRL tendon following volar plating for distal radial fracture. Transverse **(A)** and longitudinal **(B)** US images obtained over the second compartment at the level of the Lister tubercle show the tip of a screw (arrow) protruding inside the ECRL tendon. The adjacent ECRB is spared.

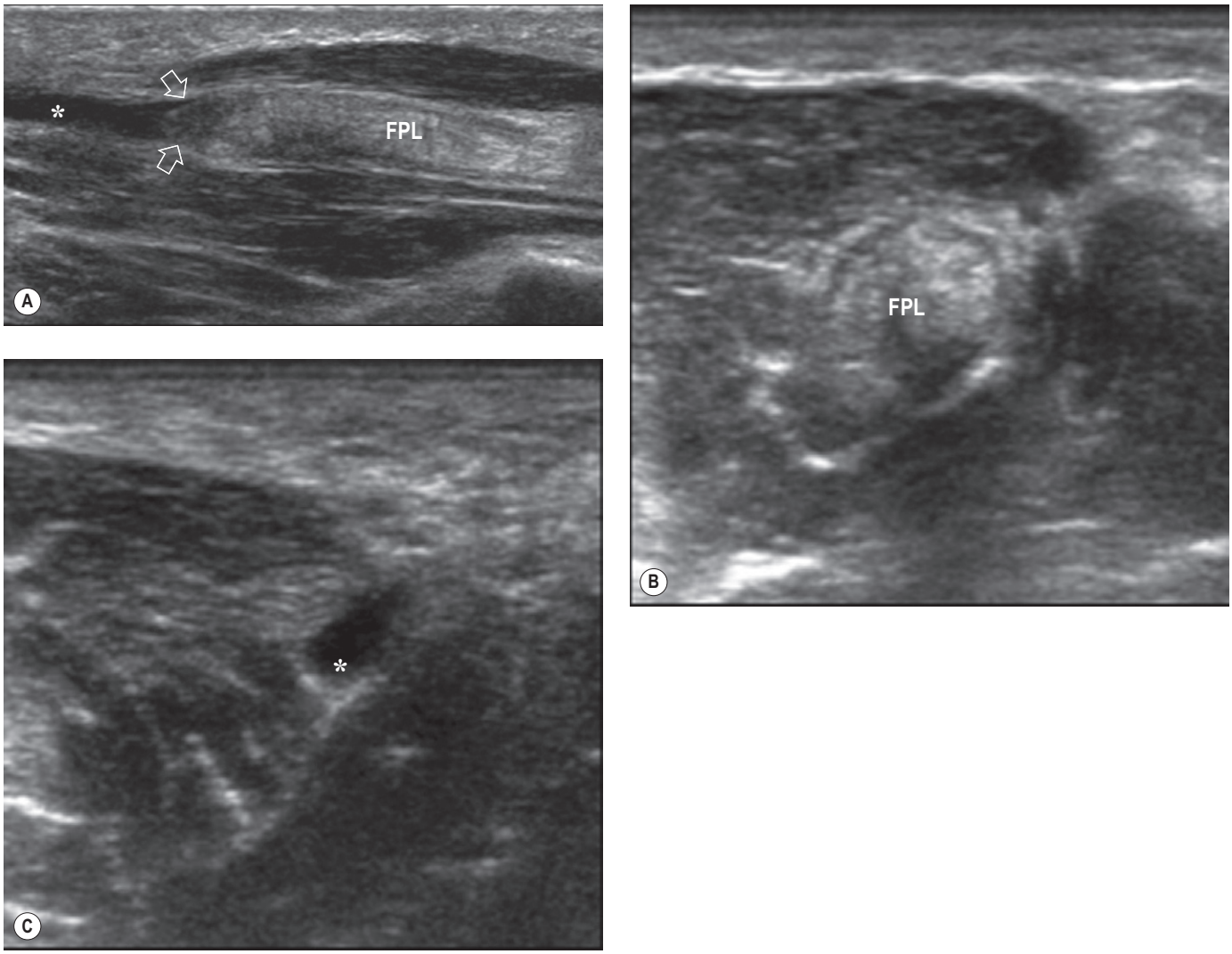

Figure 54.6 Flexor tendon tear. A: Longitudinal US image over the thenar compartment demonstrates complete rupture of the FPL tendon. The torn tendon appears slightly hypoechoic with loss of the fibrillar echoes. Fluid (asterisk) in the empty sheath is visible distal to the tendon end (arrows). **B, C:** Corresponding transverse US images obtained **(B)** over the ruptured tendon and **(C)** distal to the rupture.

heterogeneous than normal. The tendon boundaries are often undefined as a result of fibrotic changes. Intratendinous sutures may be seen as bright linear echoes with faint reverberation artefact. Dynamic scanning during finger flexion and extension is a critical means to assesses how the tendon glides and to rule out adhesions. Passive traction of peritendinous tissues during tendon movement is the main sign indicating adhesions between the parietal and visceral layers of the tendon sheath and confirms the need for further rehabilitation or tenolysis. Discontinuity in the tendon and detection of sutures floating freely in an empty sheath indicate a re-tear.

OVERUSE TENDINOPATHIES AND RETINACULA-RELATED DISORDERS

Some wrist tendons may be involved by specific overuse or degenerative changes. The **proximal intersection syndrome**, also known as 'oarsman's forearm' or 'crossover syndrome', arises on the dorsoradial aspect of the distal forearm, several centimetres proximal to the Lister tubercle. It results from friction between the myotendinous junctions of the APL and EPB with the tendon sheath containing the ECRB and ECRL[20,21] and is typically encountered in activities that involve repetitive flexion and extension of the wrist, such as in rowing, weight-lifting, canoeing and rice-harvesting. It may mimic de Quervain disease. The limited gliding space between the radius and the extensor fascia of the forearm seems to play a predisposing role.[20] US may identify fluid surrounding the radial wrist extensors at the crossing point and loss of definition between the two compartments.

The **distal intersection syndrome** involves the crossover of the ECRB and ECRL (second compartment) and the EPL tendon (third compartment) just distal to the Lister tubercle. It is not related to overuse. In most cases, the deep surfaces of the second compartment tendons are impinged by bony spurs due to osteoarthritis, SLAC wrist (scapho-lunate advanced collapse) or Colles fracture[16] that cause distension of the ECRB–ECRL sheath. The retinaculum of the third compartment is likely to exert a constricting role, making the EPL vulnerable. US demonstrates a variable combination of tendinosis and tenosynovitis affecting the second and third compartments (which may communicate) and underlying bony spurs impinging on the tendons.

On the volar aspect of the wrist, degenerative osteoarthritis affecting the triscaphe (scapho-trapezio-trapezoid) joint may lead to **FCR tendinopathy** due to impingement by a ridge of osteophytes on the ventral aspect of the scaphoid.[22] FCR tendinopathy may occur in isolation but is most often associated with a SLAC wrist.

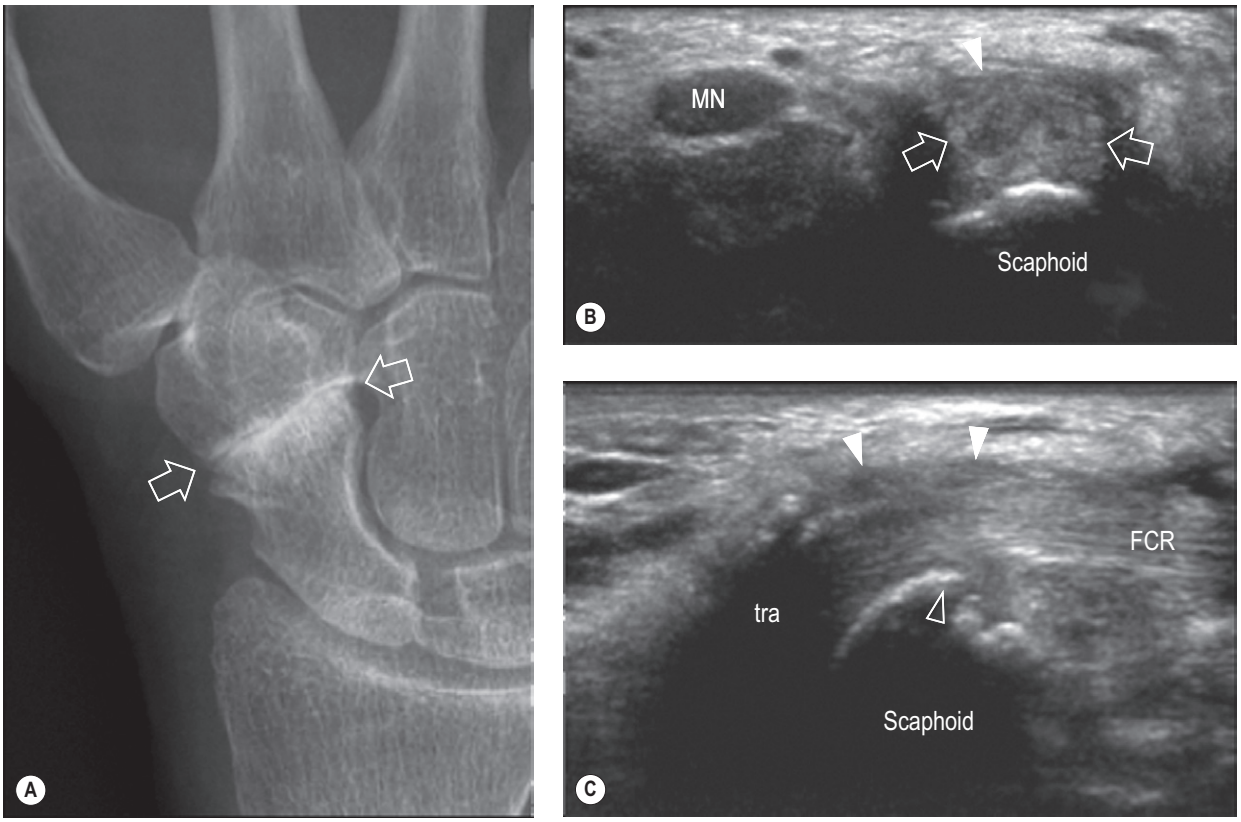

Figure 54.7 Flexor carpi radialis tendinopathy in a 65-year-old woman complaining of a painful palpable lump over the ventral radial aspect of the right wrist. The patient was referred for US examination for a suspected ventral ganglion cyst. **A:** Anteroposterior radiograph reveals scapholunate diastasis and advanced triscaphe arthritis (arrows). **B:** Transverse US image over the lump demonstrates a swollen and heterogeneous FCR tendon (arrows) stabilised over the scaphoid tubercle by a thickened retinaculum (white arrowhead). **C:** Longitudinal US image shows bony spurs (hollow arrowhead) from the ventral aspect of the scaphoid and the trapezium (tra) impinging on the undersurface of the abnormal tendon. The retinaculum is thickened (solid arrowheads).

US demonstrates a swollen and heterogeneous FCR with tenosynovial fluid, longitudinal splits, thickening of the retinaculum and peritendinous tissues and scaphoid osteophytes encroaching on the FCR (Fig. 54.7). Patients complain of a painful lump and tenderness over the ventral radial aspect of the wrist. The role of US is to exclude a ganglion and redirect the diagnosis. **FCU tendinopathy** is rare, mainly occurs in the context of calcific tendinitis[23] and is related to repetitive activities such as typing. US shows calcific material in a swollen and heterogeneous tendon, proximal to the pisiform (Fig. 54.8). In acute phases, deposits may be semiliquid.

As a result of fibrosing degeneration, retinacula and annular pulleys may become thickened, producing painful gliding, blockage or triggering (a partial blockage that abruptly unblocks) of the underlying tendons, usually at the level of the A1 pulleys (trigger finger) for the flexor tendons or at the first compartment of the extensor tendons (de Quervain disease).[24,25] Patients with **trigger finger** complain of either blockage or triggering of one or more fingers (the middle finger most commonly) from flexion to extension caused by stenosing tenosynovitis at the level of the A1 pulley, possibly extending distally between the A1 and A2 pulleys. US shows a thickened A1 pulley, local swelling of the flexor tendons distal to the pulley, distal tenosynovitis and small cysts at the pulley boundaries due to fluid trapping.[26] In severe cases, dynamic scanning during passive flexion and extension shows difficult tendon gliding underneath the abnormal pulley. Doppler imaging may depict a hypervascular pattern in the A1 pulley and surrounding soft tissues.[25] It is unclear if thickening of the A1 pulley initiates the blockage and tendon inflammation or if the thickening is secondary to tendinopathy.[26] Surgical release of the A1 pulley is the treatment of choice. Steroid injection into the flexor sheath at the level of the A1 pulley is an alternative but is ineffective in patients with type 1 diabetes, and surgical release remains the treatment of choice in this subset of patients.[27] US may have value guiding intrasheath steroid injections and assisting percutaneous release of the pulley.[28,29]

De Quervain disease causes pain around the radial styloid associated with movement of the thumb. It is most common in the 30–50-year-old age group with high prevalence in new mothers (baby wrist).[30] The main US signs of de Quervain disease include a thickened retinaculum, local fusiform swelling of APL and EPB tendons, tenosynovial fluid distal to the retinaculum and intra- and peritendinous hyperaemia at Doppler imaging (Fig. 54.9A).[24] Dynamic imaging shows difficult gliding of the tendons as they pass under the retinaculum during thumb extension. In severe disease, the tendons may form a rounded complex on the short-axis view under a thickened and hypo-anechoic retinaculum and cannot be distinguished from each other. Care should be taken not to confuse the retinaculum (non-compressible and located at the level of the radial styloid) for intrasheath fluid (compressible and usually found distal to the radius). Surgical release may be required when the retinaculum is markedly thickened. Mild abnormalities may be treated conservatively. Occasionally a vertical septum splits the compartment into two subtunnels for each of the tendons.[31] As de Quervain disease may selectively involve only the dorsal tunnel containing EPB (Fig. 54.9B) and the septum may form a barrier to drug diffusion, the clinician should be informed if this variant is present in order that steroids are injected into the appropriate half of the compartment or that both tunnels are decompressed at surgery.[32]

The main function of retinacula and annular pulleys is to stabilise tendons.[7] Tears lead to tendon subluxation or dislocation, most

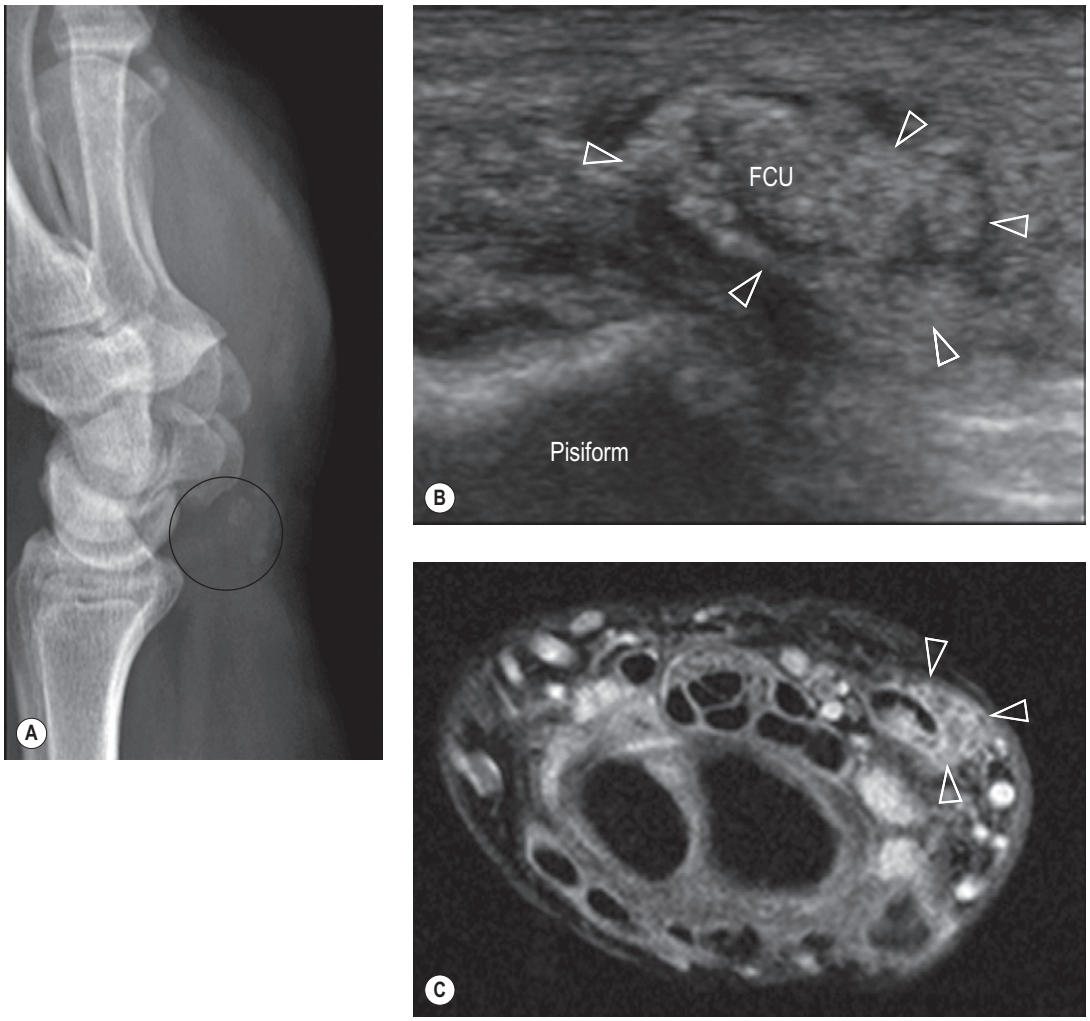

Figure 54.8 **Flexor carpi ulnaris tendinopathy** in a 50-year-old patient with sudden onset of pain in the right pisiform region. **A:** A radiograph reveals amorphous calcific deposits (ring) proximal and volar to the pisiform. **B:** US identifies a conglomerate of slurry echogenic calcifications (arrowheads) within and around a heterogeneous FCU tendon. **C:** Correlative fat-suppressed gradient-echo T2*-weighted MR image confirms a hyperintense peritendinous mass (arrowheads) related to reactive inflammatory changes.

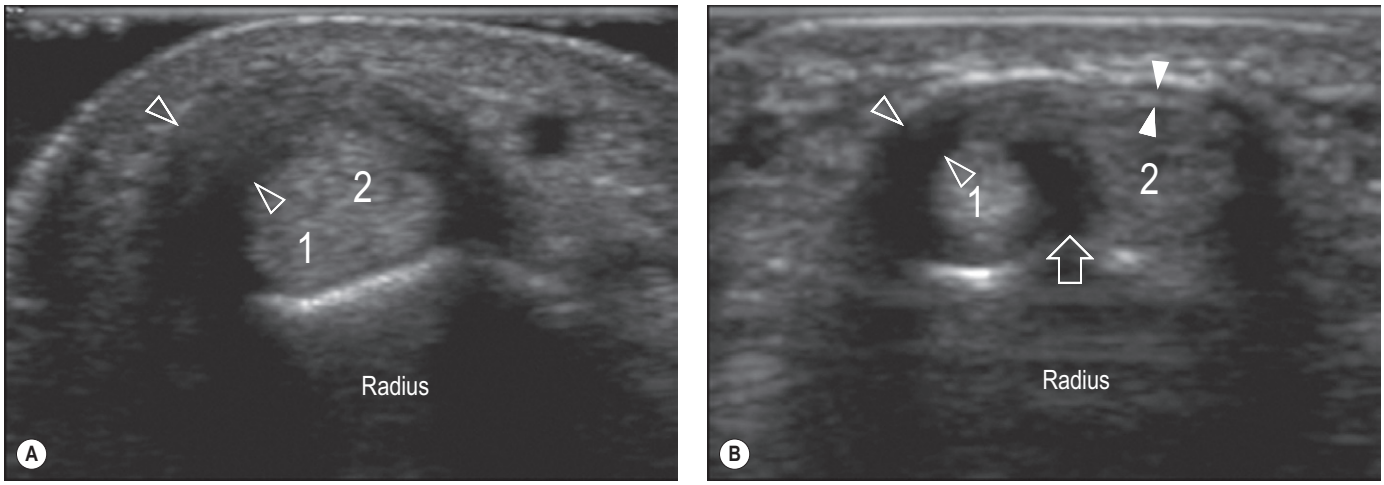

Figure 54.9 **de Quervain disease:** spectrum of findings. **A:** Transverse US image obtained over the radial styloid reveals a thickened and hypoechoic retinaculum (arrowheads) and the swollen EPB (1) and APL (2). The two tendons form a rounded complex and cannot be separated from each other as they are constricted by the abnormal retinaculum. **B:** Transverse US image obtained over the radial styloid shows selective thickening of the dorsal portion of the retinaculum (hollow arrowheads) and the vertical septum (arrow) enveloping the EPB tendon (1), whereas the more ventral portion of the retinaculum (white arrowheads) and the APL tendon (2) retain a normal appearance. In this case, steroids were selectively injected into the sheath of the EPB.

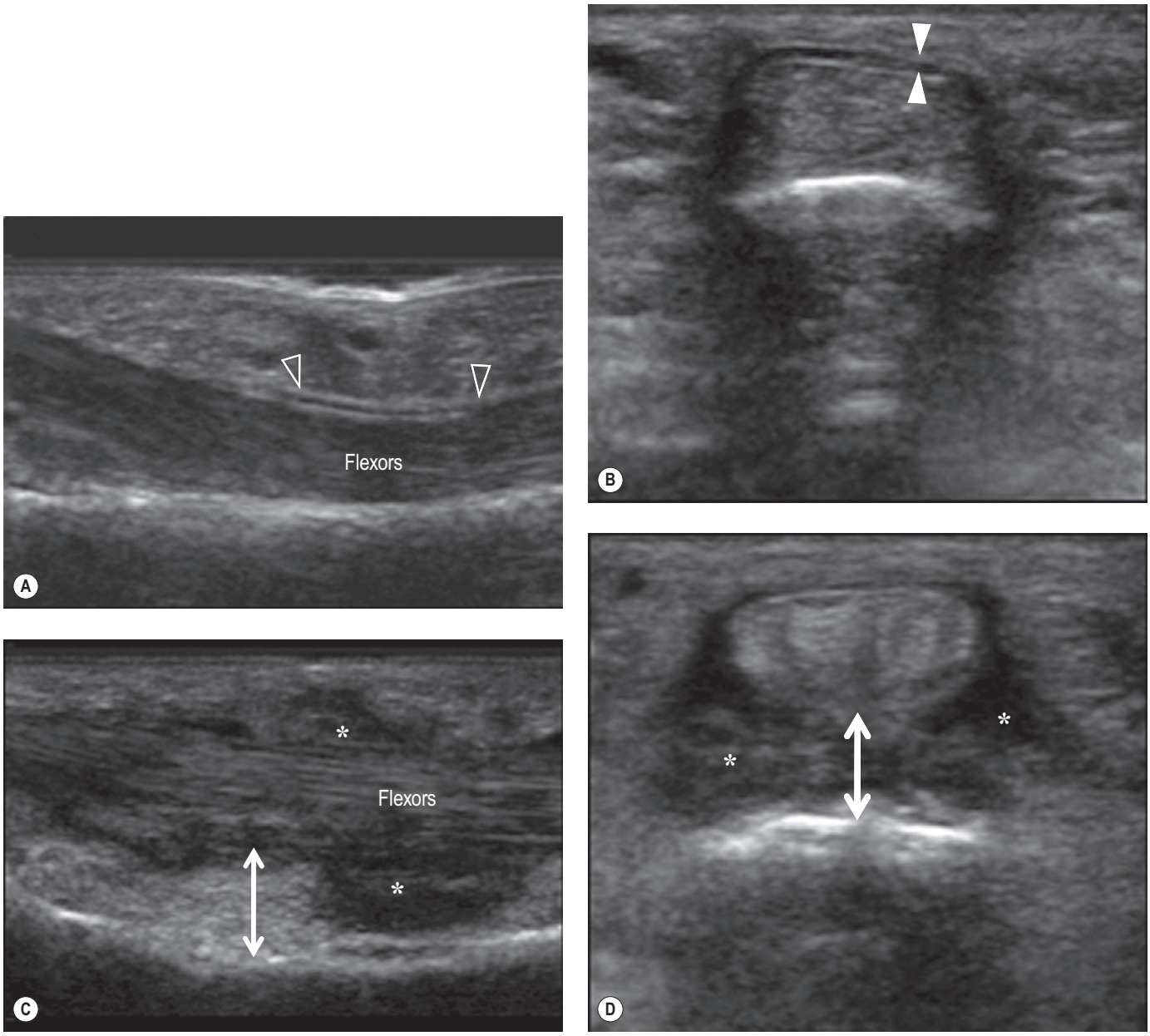

Figure 54.10 Annular pulleys and climber's finger. Longitudinal **(A)** and transverse **(B)** US images over the left long finger of an elite rock-climber show the normal A2 pulley as a thin hypoechoic band (arrowheads) restraining the flexor tendons against the shaft of the proximal phalanx. Longitudinal **(C)** and transverse **(D)** US images over the injured right long finger of the same patient demonstrate bowstringing and volar displacement of the flexor tendons secondary to A2 pulley rupture with an increased tendon-to-bone distance (double arrow) over the proximal phalanx and an effusion (asterisks) between tendons and bone.

commonly at the sixth extensor compartment for the ECU, over the dorsal aspect of the metacarpal heads for the extensors (boxer's knuckle) and on the ventral aspect of the fingers for the flexors (climber's finger). Depending on the site and applied biomechanical forces, tendon instability may occur during specific joint movements and muscle contraction (transient) or even at rest (permanent). In intermittent instability, dynamic US demonstrates the tendon dislocating and relocating relative to its groove.

ECU instability typically occurs in professional tennis players. Repeated sudden pronation movements from a supinated position strip the ventral attachment of the retinaculum from the ulnar head causing volar tendon subluxation or dislocation.[33] The patient usually complains of a painful 'snap' over the ulnodorsal aspect of the wrist, particularly on forearm rotation.[34] ECU instability is often observed in patients with longstanding rheumatoid arthritis, causing hypertrophic ECU tenosynovitis and distal radioulnar joint (DRUJ) changes.[35] Pannus disrupts the retinaculum. The ECU tends to migrate to the volar surface of the ulna and behaves as a flexor of the wrist rather than an extensor, permitting dislocation of the distal ulna relative to the radius. US shows the status of the ECU and its position relative to the ulnar groove at rest and during stressing.[36,37]

Sagittal band rupture over the dorsal aspect of MCPJs is typically encountered in boxers as a result of repetitive direct trauma, but may occur from trivial injury. It most often involves the long finger and leads to ventral dislocation of the extensor tendon over the ulnar or, less commonly, radial slope of the metacarpal head during fist clenching.[38] Physical examination usually establishes the diagnosis. Dynamic US may help to differentiate sagittal band injuries from partial tendon tears if the tendon position cannot be palpated because of soft tissue swelling or clinical findings are atypical.[38] Dislocation of the extensor tendon is easily visualised during finger

flexion by placing the probe in the transverse plane over the metacarpal head. Treatment is by splinting in full extension or direct repair of the torn sagittal band and relocation of the central tendon.

Annular pulley tears are typically encountered in extreme rock-climbers who use fingers-holds, often consisting of one or two fingers only, to hang their body weight.[39] This creates tremendous overload on the pulley system during proximal interphalangeal joint (PIPJ) flexion, leading to various combinations of A2, A3 and A4 pulley tears. US may be particularly helpful to confirm isolated A2 or A4 pulley tears that may not be easily recognised at physical examination. Dynamic US examination along the long axis of the finger during resisted flexion shows that instead of coursing along the concavity of the phalanx in contact with the bone, the tendon lies at a variable distance from the bone (Fig. 54.10).[7,39–41] The site of maximal volar bowstringing usually corresponds to the position of the torn pulley.

LIGAMENT AND FIBROCARTILAGE DISORDERS

Injuries to the extrinsic (i.e. radiocarpal and ulnocarpal) and intrinsic (i.e. intercarpal) wrist ligaments can lead to chronic wrist pain and carpal instability.[42,43] US identifies the dorsal bands of the scapholunate (SLL) and lunotriquetral (LTL) ligaments in 97% and 61% of cases. Their palmar bands are visible in 93% and 40% of cases respectively when the transducer is placed over the ventral wrist.[42] On the palmar side of the wrist, the radioscaphocapitate, radiolunotriquetral, ulnotriquetral and scaphotriquetral ligaments can also be visualised.[42,44]

The dorsal band of the SLL can be considered torn if its fibres are not visualised and instability of the scapholunate articulation is observed while scanning during ulnar and radial deviation of the wrist. Irregularity of the ligamentous fibres indicates a partial tear or fraying.[45,46] An increase in joint width and abnormal mobility of the scaphoid and lunate during ulnar deviation of the wrist suggest a complete tear and indicate that further imaging is required to confirm the diagnosis (Fig. 54.11).[8,44,47,48] Using tricompartmental wrist arthrography as the reference standard, US results seem more promising for the SLL (100% sensitivity; 92% specificity) than for the LTL (25–50% sensitivity; 100% specificity).[46]

The **triangular fibrocartilage** complex can be evaluated by coronal scans using the ECU tendon as an acoustic window. Detection of an intrasubstance hypoechoic cleft or defect is the most reliable signs of TFC disc tear on US (86% sensitivity and 100% specificity).[46] A thinned fibrocartilage may also be associated with a tear. However, part of the TFC cannot be evaluated as it is obscured by the ulnar styloid. In the authors' opinion, US seems inadequate to distinguish traumatic from degenerative lesions.

Tears of the ulnar collateral ligament (UCL) of the MCPJ of the thumb (**gamekeeper's thumb** or '**skier's thumb**') are reliably assessed by US.[49] The UCL is an important stabiliser of the first MCPJ and limits valgus opening during forceful grasp. It lies deep to the aponeurosis of the adductor pollicis (AddPA). Tear patterns include avulsion of the distal ligament insertion with avulsion of a bone fragment from the base of the proximal phalanx; an intrasubstance tear when the ligament ends remain deep to the AddPA; and a displaced tear with proximal migration of the ligament superficial to the cranial edge of the aponeurosis, the **Stener lesion**. Distinguishing a displaced from a non-displaced tear is important as displacement of the proximal end of the ruptured UCL over the AddPA aponeurosis prevents healing. Surgical repair is needed to avoid permanent instability and early osteoarthritis.[50–52] In undisplaced tears, the UCL appears swollen (partial tear) or discontinuous (complete tears) and the AddPA can be appreciated as a thin gliding band overlying the abnormal ligament during flexion and extension of the interphalangeal joint (Fig. 54.12A). In the Stener lesion the ruptured ligament appears as a rounded hypoechoic nodule retracted over the metacarpal neck. During flexion and

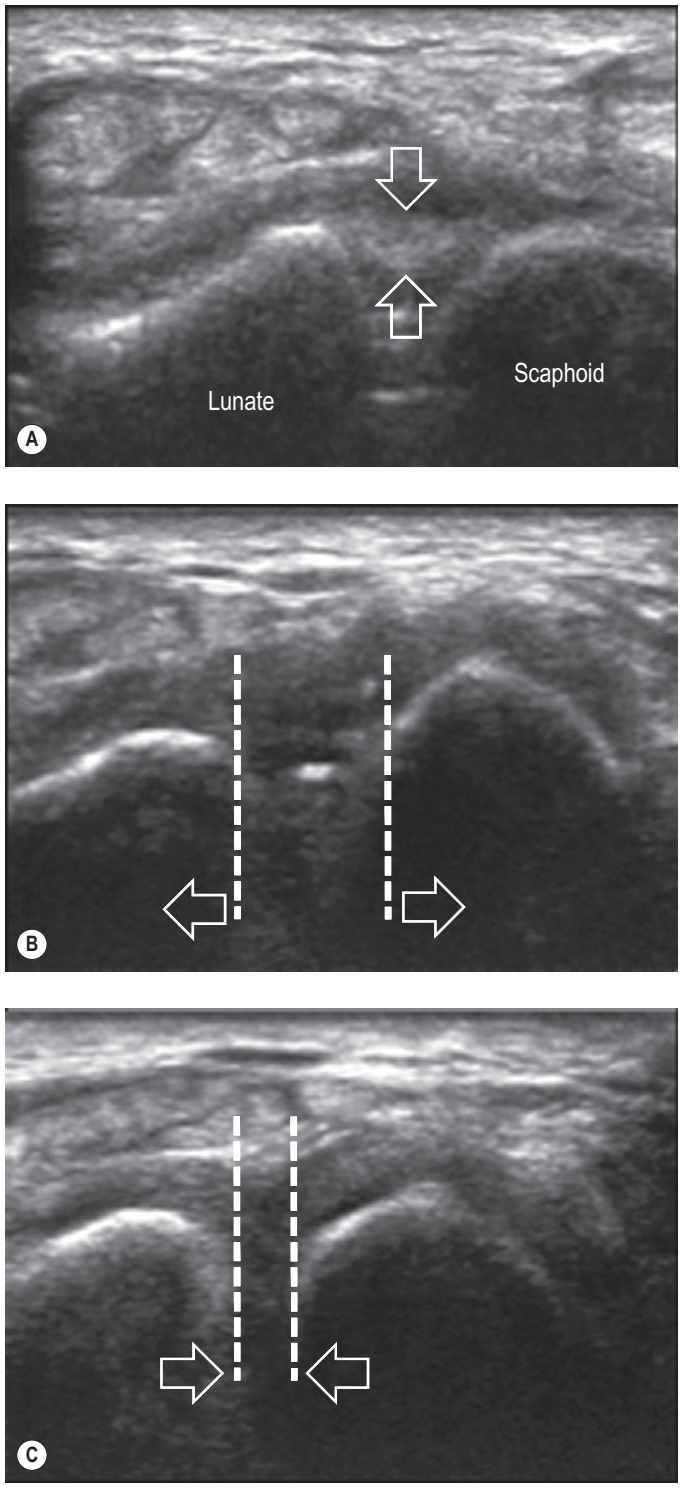

Figure 54.11 Scapholunate ligament. A: Transverse US image over the dorsal aspect of the wrist shows the normal dorsal component of the scapholunate ligament (arrows) which appears as an echogenic fibrillar band. **B, C:** Scapholunate dissociation. Transverse US images over the dorsal aspect of the scapholunate joint obtained **B** with ulnar (diverging arrows) and **C** radial deviation (converging arrows) of the wrist demonstrate non-visualisation of the ligament and widening of the scapholunate distance (distance between the vertical bars) in ulnar deviation. This can be considered an indirect sign of ligament tear.

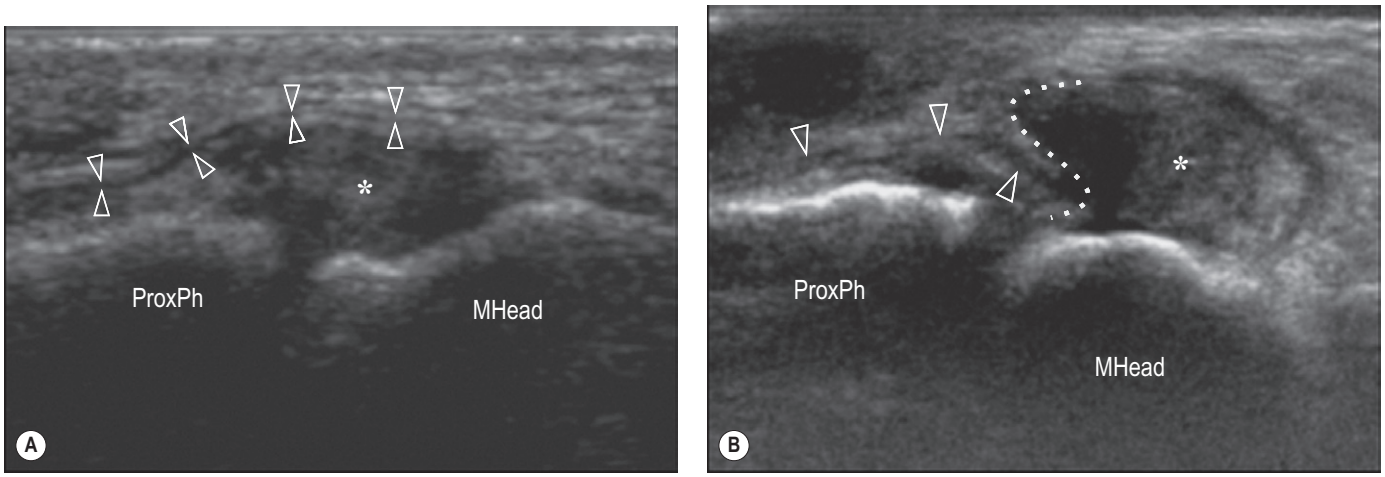

Figure 54.12 Gamekeeper's thumb and Stener lesion. A: Non-displaced ligament tear. Coronal US image obtained over the ulnar aspect of the MCPJ of the thumb shows an abnormally thickened ligament (asterisk) lying deeply to the adductor aponeurosis (arrowheads). **B:** Stener lesion. Coronal US image over the ulnar aspect of the first MCPJ reveals a swollen and retracted ulnar collateral ligament presenting as a hypoechoic pseudomass (asterisk) located proximally and in a more superficial position relative to the AddPA (arrowheads). ProxPh, proximal phalanx; MHead, metacarpal head.

Tendon tears, retinacula-related and ligament disorders

- In tendon tears, dynamic scanning may help to distinguish partial from complete tears. US accurately measures the gap length and assesses the position of the retracted proximal tendon end in complete tears.
- In de Quervain and trigger finger diseases, thickened retinacula and annular pulleys may lead to painful gliding, blockage or triggering of the underlying tendons.
- Traumatic rupture of retinacula and annular pulleys cause tendon subluxation or dislocation.
- Dynamic US helps to evaluate scapholunate ligament tears.
- In the gamekeeper's/skier's thumb, US distinguishes between undisplaced ulnar collateral ligament tears and Stener lesions.

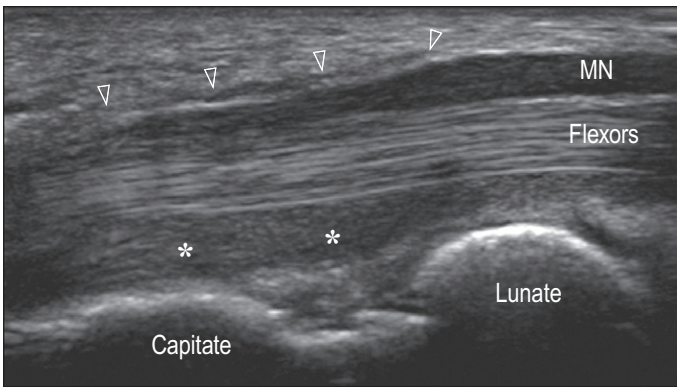

Figure 54.13 Carpal tunnel syndrome. Longitudinal US image over the carpal tunnel shows the MN as it passes underneath the proximal edge of the retinaculum (arrowheads). The MN appears flattened in the carpal tunnel and swollen proximal to it. Note synovial sheath distension of the underlying flexor tendons (asterisks).

extension of the distal phalanx, the AddPA is seen as a straight echogenic line clashing against this nodule (Fig. 54.12B). This figure recalls the 'yo-yo sign' visible at MR imaging and increases diagnostic confidence in distinguishing displaced from undisplaced tears.

Collateral ligament injuries of the finger joints are common in sportsmen, especially in ball-handing sports, such as volleyball and basketball. Most occur at the PIPJ level and can be readily assessed with US. Joint synovitis secondary to phalanx dislocation, avulsion of small flecks of bone at the ligament insertion sites and palmar plate injuries are often associated with these lesions.[6]

In the fingers, hyperextension trauma or longitudinal compression may cause PIPJ instability in the sagittal plane leading to **palmar plate tear** without or with collateral ligament injury. These tears occur when the base of the middle phalanx is driven against the head of the proximal phalanx. The impact of the force is absorbed by the volar capsule, resulting in simple avulsion of the palmar plate, avulsion of the palmar plate plus a chip of bone from the base of the middle phalanx that can be diagnosed on radiographs or a tear at the attachment of the accessory collateral ligament to the palmar plate. In the absence of a fracture, US shows avulsion and proximal migration of the palmar plate over the neck of the proximal phalanx leading to a decreased distance between the flexor tendons and the head of the phalanx.

WRIST NEUROPATHIES

US is a well-recognised diagnostic modality to evaluate the MN, the UN, the RN and their divisional branches as they cross the wrist and hand.[2,9,10]

Carpal tunnel syndrome (CTS) is the most common entrapment neuropathy of the upper limb. The main US signs include: an increased CSA_{MN} at the proximal tunnel or, more commonly, at the proximal edge of the flexor retinaculum and flattening of the nerve within the distal tunnel (Figs 54.13 and 54.14).[53,54] Occasionally the US changes are inverted and the swollen segment of MN is located distally, just beyond the distal edge of the retinaculum. In severe cases and longstanding disease, Doppler imaging depicts intraneural hyperaemia[55] and increased palmar bowing of the retinaculum.[53] Dynamic scanning may reveal restricted motion of the compressed nerve beneath the retinaculum during flexion and extension of the fingers. Measurement of the maximum CSA_{MN} is the most reliable parameter to diagnose nerve compression but there is no consensus

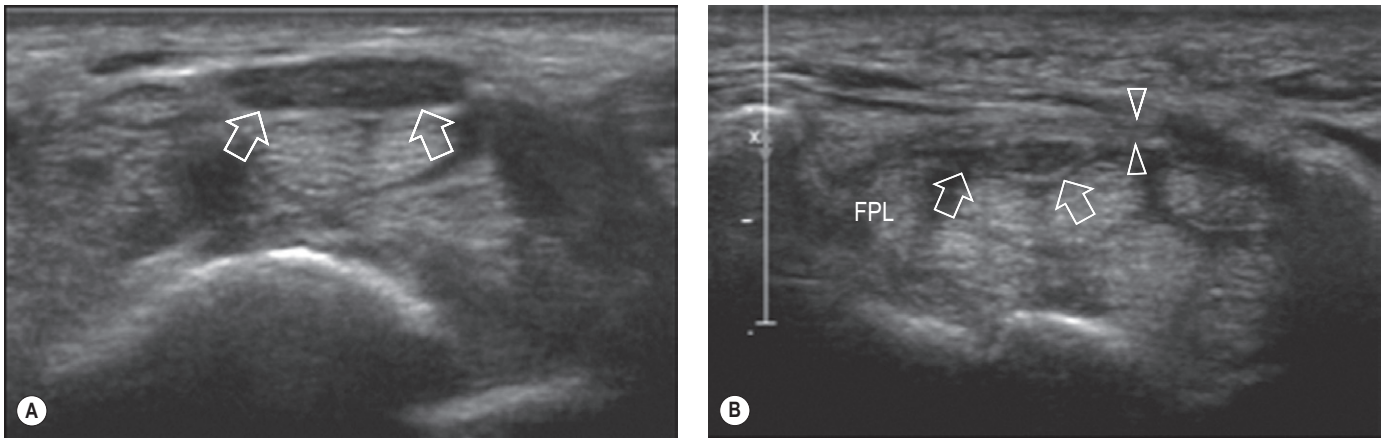

Figure 54.14 Carpal tunnel syndrome. Transverse US images obtained **(A)** at the distal radius and **(B)** at the distal tunnel level. In **A**, the MN (arrows) is markedly enlarged and its individual fascicles are less clearly defined. In **B**, marked narrowing of the MN (arrows) is observed deep to the thickened flexor retinaculum (arrowheads).

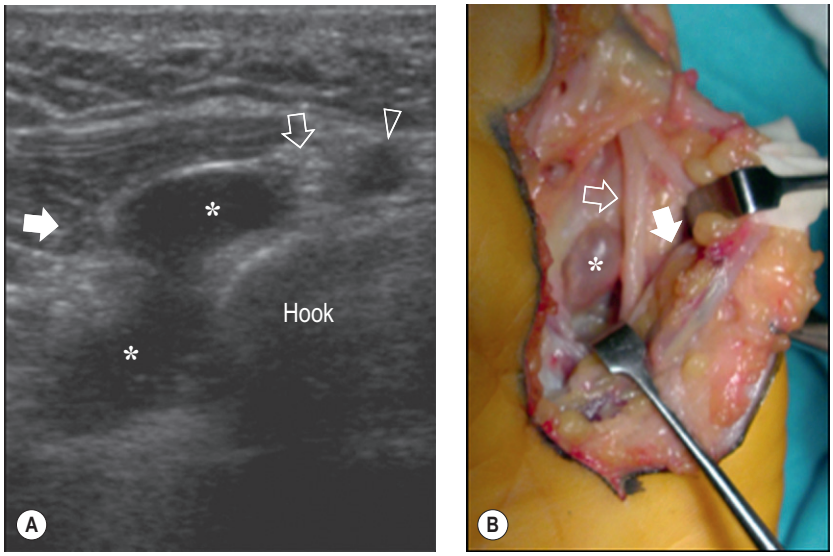

Figure 54.15 Guyon tunnel syndrome. **A:** Transverse US image over the hook of the hamate reveals an hourglass-shaped ganglion (asterisks) compressing the motor branch (white arrow) of the UN. The superficial sensory branch (hollow arrow) and the ulnar artery (arrowhead) are spared. **B:** Operative view obtained before resection shows the close relationship of the cyst (asterisk) with the branches (arrows) of the UN.

on the most appropriate threshold for establishing the diagnosis, and cut-off values ranging from 9 mm^2 to 12 mm^2 have been proposed.[56] Factors including gender, weight, body mass index and race are responsible for the lack of consensus.[57] Comparison between CSA_{MN} measurements obtained at the carpal tunnel and the pronator quadratus[58] or mid-forearm[59] have been proposed to eliminate intersubject and internerve variability.

Although US measures a different parameter (nerve swelling) from the nerve conduction velocities measured at electrodiagnostic study, a positive correlation has been found between the CSA_{MN} and the severity of electromyographic findings.[56] In the diagnostic work-up of suspected CTS, US has been suggested as the initial diagnostic test. If US yields positive results, CTS is confirmed. If the results are negative, the patient could be referred for an electrodiagnostic study.[60] Besides assessing the area of the MN, US can demonstrate extrinsic causes of nerve entrapment, including tenosynovitis of flexor tendons, ganglion cysts, soft tissue tumours, anomalous muscles and displaced bone.[9] If symptoms persist or recur after carpal tunnel release, US may show residual nerve entrapment due to fibrous scarring or incomplete sectioning of the retinaculum or demonstrate palmar cutaneous branch injury.[61,62] After decompression, MN swelling may be reversed. The higher the CSA_{MN} reduction on postoperative US, the better the clinical outcome.[63]

At the ventral ulnar aspect of the wrist, the UN can be trapped in the Guyon tunnel (zone I). Distally, its divisional branches can be selectively damaged as they pass alongside (motor branch – zone II) or over the tip (sensory branches – zone III) of the hamate hook. Ganglion cysts arising from the hamate-triquetrum or the pisotriquetrum joints are the most frequent cause of **Guyon tunnel syndrome**[10] and compress the main nerve trunk against the pisiform or its motor branch against the hamate hook (Fig. 54.15). Pseudoaneurysms of the ulnar artery and anomalous muscles (e.g. accessory abductor digiti minimi) are rare causes of nerve entrapment in this area.

Over the radial aspect of the wrist, the sensory branch of the RN can be damaged **(Wartenberg syndrome)** as a result of penetrating trauma, a tight watch-strap or iatrogenically (e.g. due to cephalic vein cannulation or retinaculum release in de Quervain disease). The patient presents with pain and sensory loss over the dorsoradial aspect of the hand and dorsal thumb (cheiralgia paraesthetica). US can detect scar encasement of the nerve secondary to previous surgery or a stump neuroma involving the main nerve trunk or one of its distal branches as a result of penetrating trauma.

US is accurate and reliable in assessing **penetrating and closed injuries of nerves** in the wrist and hand. In complete nerve tears, assessing the exact location of the nerve ends and measuring the length of the gap on longitudinal scans is crucial preoperatively. US

Wrist neuropathies

- In carpal tunnel syndrome the cross-sectional area of the median nerve is increased at the proximal edge of the retinaculum and the nerve is flattened within the distal tunnel.
- Accessory signs of median neuropathy include palmar bowing of the retinaculum, decreased mobility of the median nerve during passive flexion and extension of the index and long fingers and hyperaemia of the nerve.
- In carpal tunnel syndrome, there is no consensus on what is an abnormal cross-sectional area measurement of the median nerve: proposed values range from 9 mm^2 to 12 mm^2.
- Comparison between the cross-sectional area of the median nerve obtained at the carpal tunnel and more proximally may be an alternative.
- US accurately identifies compressive and traumatic neuropathies of the ulnar and radial nerves in the wrist and hand.

is more accurate than MR in the acute setting because oedema and haemorrhage lead to high signal intensity on T2-weighted images that may be similar to the hyperintense signal of the nerve ends. As any traumatic neuroma should be excised when the nerve is repaired, the measurement should be taken by adding the neuroma length to the actual gap length (starting measurement at the base of neuroma, where the normal CSA and fascicular echotexture of the nerve bundle are preserved). In partial nerve tears, meticulous US assessment establishes the percentage of CSA with injured fascicles and shows that usually superficial fascicles are interrupted whereas deep ones appear normal. In other cases, a fusiform hypoechoic swelling develops in the absence of nerve discontinuity. Penetrating injuries of the MN often involve contiguous structures, such as the FCR and the palmaris longus. UN tears often coexist with FCU and UA injuries. In the hammer syndrome, repeated microtrauma over the ventral ulnar aspect of the wrist may cause damage to the divisional branches of the UN around the hamate hook.

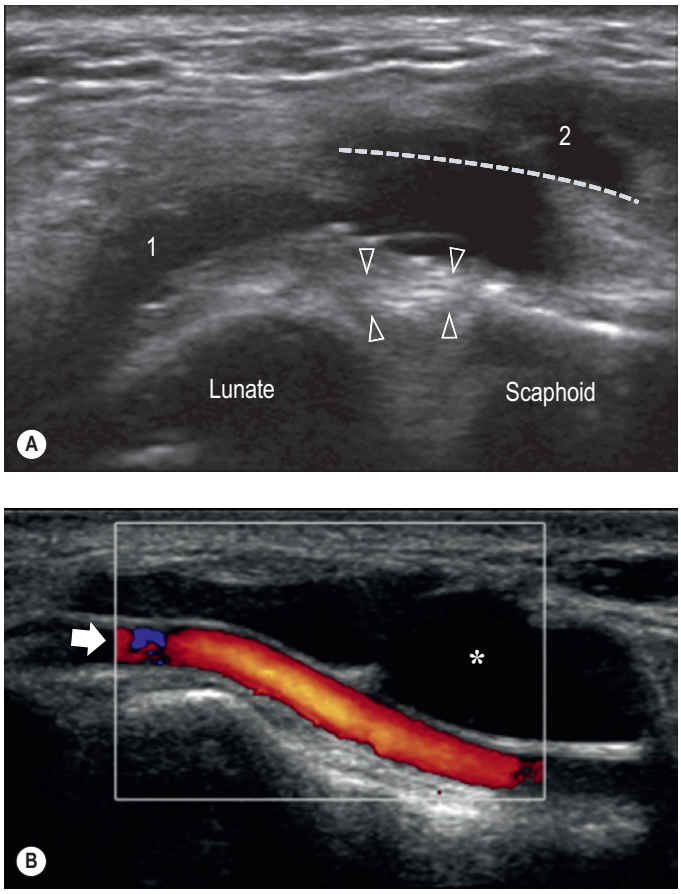

Figure 54.16 Wrist ganglia. A: Dorsal wrist ganglion. Transverse US image over the scapholunate ligament (arrowheads) demonstrates an irregularly shaped fluid-filled anechoic mass developing inside the dorsal capsular layers (1) and partially extruding into the superficial soft tissues (2). The dashed line indicates the assumed level of the outer capsular boundaries crossed by the cyst. **B:** Ventral wrist ganglion. Longitudinal colour Doppler US image obtained over a palpable lump reveals an elongated anechoic cyst (asterisk) alongside the radial artery (arrow).

SPACE-OCCUPYING LESIONS

The most common masses of the wrist and hand are **ganglion cysts**. They are well-defined cystic masses and contain jelly-like viscous fluid and an epithelial lining.[64] US demonstrates ganglia as anechoic cystic masses of variable size and shape, usually located near a joint. They have posterior acoustic enhancement and may exhibit fine septa, a lobulated appearance and a thin and tortuous stalk connecting the cyst with the joint capsule. At the wrist, 70% of ganglia are dorsal and 30% volar.[2] Most dorsal wrist ganglia originate from the level of the joint capsule, just superficial to the SLL (Fig. 54.16A). The capsule here is not reinforced by the dorsal radiocarpal ligament and seems to be vulnerable to shear stresses during forced dorsal and palmar flexion of the wrist.[65] Small ganglia may be occult at physical examination. Dorsal ganglia tend to expand between the II and IV compartments of the extensor tendons.[65] Ventral ganglia are usually located on the radial aspect of the wrist (Fig. 54.16B), arise from the triscaphe joint and typically expand between the FCR and the radial artery. If large, they may displace the artery. In the fingers, ganglia usually present as small stiff cysts located palmar to the proximal phalanx, in close relationship with the A1 pulley. Rarely, ganglia originate from a tendon sheath or expand within the tendon substance. Dynamic US shows that an intratendinous ganglion moves with excursion of the tendon. US can guide cyst aspiration and injection of steroids.[66]

Giant cell tumour of tendon sheath (GCTTS), also referred to as 'localised pigmented villonodular synovitis', is a solid slow-growing mass which arises from the synovium of tendon sheaths and can cause bone erosions.[67] US demonstrates a solid well-delineated hypoechoic mass adjacent to a flexor tendon, often encircling the tendon and adjacent phalanx[67,68] (Fig. 54.17). The mass does not move with the tendon as it arises from the parietal sheath and not from the tendon. Although highly suggestive, the US appearances do not allow a conclusive diagnosis. MR imaging confirms the diagnosis by showing susceptibility artefact on T2*-weighted images.[67]

Other soft tissue masses in the wrist and hand include neurogenic tumours, lipomas, pseudoaneurysms, accessory muscles and glomus tumour.[69] **Schwannomas** and **neurofibromas** are solid hypoechoic masses in continuity with the nerve of origin at their proximal and distal poles.

Hand **lipomas** are indolent lobulated masses with ill-defined margins. They typically develop over the palmar aspect of the hand and the thenar eminence, extending with elongated processes between muscles and tendons. US can characterise these lesions based on their echotexture and compressibility but it may be difficult to assess the full extent of large, deep-seated lesions.

In **aneurysms** and **pseudoaneurysms**, Doppler imaging shows the afferent artery and whirling blood flow within a pulsatile mass. **Accessory muscles** may present as painless lumps mimicking soft tissue tumours (e.g. extensor digitorum brevis manus) or disturb

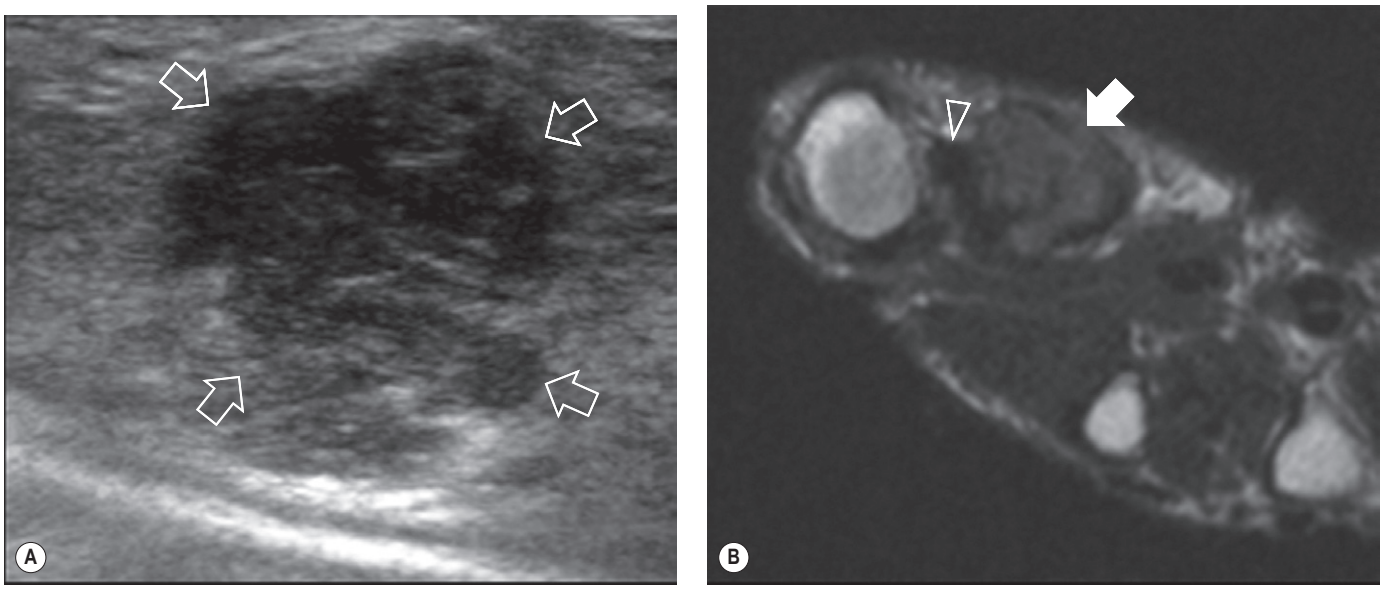

Figure 54.17 **Giant cell tumour of the tendon sheath. A:** Longitudinal US image in a patient with a painless mass in the thenar region demonstrates a lobulated, solid hypoechoic mass (arrows). **B:** Corresponding T2-weighted turbo spin-echo MR image shows a low signal intensity mass (arrow). Note the close relationship of the tumour with the FPL tendon (arrowhead).

Space-occupying lesions

- Ganglion cysts are well-defined cystic masses. They may exhibit fine septa and a thin and tortuous stalk connecting the cyst with the joint.
- Giant cell tumour of tendon sheath presents as a homogeneous, hypoechoic, well-delineated solid mass in close contact with a tendon.

nerve function if located in proximity to or within osteofibrous tunnels (e.g. accessory abductor digiti minimi, reversed palmaris, anomalous FDS of the index finger). The US diagnosis relies on recognition of their typical location, echotexture and contraction pattern.[70,71] The **glomus tumour** takes its origin from the neuromyoarterial glomus beneath the nail or over the palmar aspect of the fingertip. US reveals a small solid hypoechoic mass beneath the nail, pressure erosion of the distal phalanx and a hypervascular pattern at Doppler imaging.[72]

Note: Figures 54.13–54.15 were obtained with a 12.5 MHz transducer. All other images were obtained with a 17.5 MHz transducer.

REFERENCES

1. Middleton WD, Teefey SA, Boyer MI. Hand and wrist sonography. Ultrasound Q 2001;17:21–36.
2. Tagliafico A, Rubino M, Autuori A, et al. Wrist and hand ultrasound. Semin Musculoskelet Radiol 2007;11:95–104.
3. Lee JC, Healy JC. Normal sonographic anatomy of the wrist and hand. RadioGraphics 2005;25:1577–1590.
4. De Maeseneer M, Marcelis S, Jager T, et al. Sonography of the finger flexor and extensor system at the hand and wrist level: findings in volunteers and anatomical correlation in cadavers. Eur Radiol 2008;18:600–607.
5. Robertson BL, Jamadar DA, Jacobson JA, et al. Extensor retinaculum of the wrist: sonographic characterization and pseudotenosynovitis appearance. AJR Am J Roentgenol 2007;188:198–202.
6. Boutry N, Lardé A, Demondion X, et al. Metacarpophalangeal joints at US in asymptomatic volunteers and cadaveric specimens. Radiology 2004;232:716–724.
7. Boutry N, Titecat M, Demondion X, et al. High-frequency ultrasonographic examination of the finger pulley system. J Ultrasound Med 2005;24:1333–1339.
8. Jacobson JA, Oh E, Propeck T, et al. Sonography of the scapholunate ligament in four cadaveric wrists: correlation with MR arthrography and anatomy. AJR Am J Roentgenol 2002;179:523–527.
9. Martinoli C, Bianchi S, Gandolfo N, et al. US of nerve entrapments in osteofibrous tunnels of the upper and lower limbs. RadioGraphics 2000;20:199–217.
10. Bianchi S, Montet X, Martinoli C, et al. High-resolution sonography of compressive neuropathies of the wrist. J Clin Ultrasound 2004;32:451–461.
11. Duncan I, Sullivan P, Lomas F. Sonography in the diagnosis of carpal tunnel syndrome. AJR Am J Roentgenol 1999;173:681–684.
12. Yesildag A, Kutluhan S, Sengul N, et al. The role of ultrasonographic measurements of the median nerve in the diagnosis of carpal tunnel syndrome. Clin Radiol 2004;59:910–915.
13. Alemán L, Berná JD, Reus M, et al. Reproducibility of sonographic measurements of the median nerve. J Ultrasound Med 2008;27:193–197.
14. De Maeseneer M, Marcelis S, Osteaux M, et al. Sonography of a rupture of the tendon of the extensor pollicis longus muscle: initial clinical experience and correlation with findings at cadaveric dissection. AJR Am J Roentgenol 2005;184:175–179.
15. Santiago FR, Plazas PG, Fernández JM. Sonography findings in tears of the extensor pollicis longus tendon and correlation with CT, MRI and surgical findings. Eur J Radiol 2008;66:112–116.
16. Parellada AJ, Gopez AG, Morrison WB, et al. Distal intersection tenosynovitis of the wrist: a lesser-known extensor tendinopathy with characteristic MR imaging features. Skeletal Radiol 2007;36:203–208.
17. Bianchi S, van Aaken J, Glauser T, et al. Screw impingement on the extensor tendons in distal radius fractures treated by volar plating: sonographic appearance. AJR Am J Roentgenol 2008;191:199–203.
18. de Gautard G, de Gautard R, Celi J. Sonography of jersey finger. J Ultrasound Med 2009;28:389–392.
19. Tang JB. Clinical outcomes associated with flexor tendon repair. Hand Clin 2005;21:199–210.
20. De Lima JE, Kim HJ, Albertotti F, et al. Intersection syndrome: MR imaging with anatomic comparison of the distal forearm. Skeletal Radiol 2004;33:627–631.
21. Roger PL, Hatem SF, Recht MP. Extended MRI findings of intersection syndrome. Skeletal Radiol 2009;38:157–163.
22. Parellada AJ, Morrison WB, Reiter SB. Flexor carpi radialis tendinopathy: spectrum of imaging findings and association with triscaphe arthritis. Skeletal Radiol 2006;35:572–578.
23. Holt PD, Keats TE. Calcific tendinitis: a review of the usual and unusual. Skeletal Radiol 1993;22:1–9.

24. Giovagnorio F, Andreoli C, De Cicco ML. Ultrasonographic evaluation of de Quervain disease. J Ultrasound Med 1997;16:685–689.
25. Guerini H, Pessis E, Theumann N, et al. Sonographic appearance of trigger fingers. J Ultrasound Med 2008;27:1407–1413.
26. Serafini G, Derchi LE, Quadri P, et al. High resolution sonography of the flexor tendons in trigger fingers. J Ultrasound Med 1996;15: 213–219.
27. Nimigan AS, Ross DC, Gan BS. Steroid injections in the management of trigger fingers. Am J Phys Med Rehabil 2006;85:36–43.
28. Godey SK, Bhatti WA, Watson JS, et al. A technique for accurate and safe injection of steroid in trigger digits using ultrasound guidance. Acta Orthop Belg 2006;72:633–634.
29. Jou IM, Chern TC. Sonographically-assisted percutaneous release of the A1 pulley: a new surgical technique for treating trigger digit. J Hand Surgery 2006;31:191–199.
30. Anderson SE, Steinbach LS, De Monaco D, et al. "Baby wrist": MRI of an overuse syndrome in mothers. AJR Am J Roentgenol 2004;182: 719–724.
31. Diop AN, Ba-Diop S, Sane JC, et al. Role of US in the management of de Quervain's tenosynovitis: review of 22 cases. J Radiol 2008;89: 1081–1084.
32. Mahakkanukrauh P, Mahakkanukrauh C. Incidence of a septum in the first dorsal compartment and its effects on therapy of de Quervain's disease. Clin Anat 2000;13:195–198.
33. Montalvan B, Parier J, Brasseur JL, et al. Extensor carpi ulnaris injuries in tennis players: a study of 28 cases. Br J Sports Med 2006;40:424–429.
34. Tagliafico AS, Ameri P, Michaud J, et al. Wrist injuries in non professional tennis players: relationships with different grips. Am J Sports Med 2009;37:760–767.
35. Egi T, Inui K, Koike T, et al. Volar dislocation of the extensor carpi ulnaris tendon on magnetic resonance imaging is associated with extensor digitorum communis tendon rupture in rheumatoid wrists. J Hand Surg [Am] 2006;31:1454–1460.
36. Pratt RK, Hoy GA, Bass Franzcr C. Extensor carpi ulnaris subluxation or dislocation? Ultrasound measurement of tendon excursion and normal values. Hand Surg 2004;9:137–143.
37. MacLennan AJ, Nemechek NM, Waitayawinyu, et al. Diagnosis and anatomic reconstruction of extensor carpi ulnaris subluxation. J Hand Surg [Am] 2008;33:59–64.
38. Lopez-Ben R, Lee DH, Nicolodi DJ. Boxer knuckle (injury of the extensor hood with extensor tendon subluxation): diagnosis with dynamic US – report of three cases. Radiology 2003;228:642–646.
39. Martinoli C, Bianchi S, Cotten A. Imaging of rock climbing injuries. Semin Musculoskelet Radiol 2005;9:334–345.
40. Martinoli C, Bianchi S, Nebiolo M, et al. Sonographic evaluation of digital annular pulley tears. Skeletal Radiol 2000;29:387–391.
41. Klauser AS, Frauscher F, Bodner G, et al. Finger pulley injuries in extreme rock climbers: depiction with dynamic US. Radiology 2002;222:755–761.
42. Boutry N, Lapegue F, Masi L, et al. Ultrasonographic evaluation of normal extrinsic and intrinsic carpal ligaments: preliminary experience. Skeletal Radiol 2005;34:513–521.
43. Renoux J, Zeitoun-Eiss D, Brasseur JL. Ultrasonographic study of wrist ligaments: review and new perspectives. Semin Musculoskelet Radiol 2009;13:55–65.
44. Finlay K, Lee R, Friedman L. Ultrasound of intrinsic wrist ligament and triangular fibrocartilage injuries. Skeletal Radiol 2004;33:85–90.
45. Dao KD, Solomon DJ, Shin AY, et al. The efficacy of ultrasound in the evaluation of dynamic scapholunate ligamentous instability. J Bone Joint Surg [Am] 2004;86:1473–1478.
46. Taljanovic MS, Sheppard JE, Jones MD, et al. Sonography and sonoarthrography of the scapholunate and lunotriquetral ligaments and triangular fibrocartilage disk. J Ultrasound Med 2008;27:179–191.
47. Griffith JF, Chan DP, Ho PC, et al. Sonography of the normal scapholunate ligament and scapholunate joint space. J Clin Ultrasound 2001;29:223–229.
48. Mohr A, Guermazi A, Genant HK. Value of sonography of the scapholunate ligament. AJR Am J Roentgenol 2003;181:275–277.
49. Bronstein AJ, Koniuch MP, von Holsbeeck M. Ultrasonographic detection of thumb ulnar collateral ligament injuries: a cadaveric study. J Hand Surg [Am] 1994;19:304–312.
50. O'Callaghan BI, Kohut G, Hoogewoud HM. Gamekeeper's thumb: identification of the Stener lesion with US. Radiology 1994;192:477–480.
51. Hergan K, Mittler C, Oser W. Ulnar collateral ligament: differentiation of displaced and nondisplaced tears with US and MRI imaging. Radiology 1995;194:65–71.
52. Ebrahim FS, De Maeseneer M, Jager T, et al. US diagnosis of UCL tears of the thumb and Stener lesions: technique, pattern-based approach, and differential diagnosis. RadioGraphics 2006;26: 1007–1020.
53. Buchberger W, Judmaier W, Birbamer G, et al. Carpal tunnel syndrome: diagnosis with high-resolution sonography. AJR Am J Roentgenol 1992;159:793–798.
54. Wiesler ER, Chloros GD, Cartwright MS, et al. The use of diagnostic ultrasound in carpal tunnel syndrome. J Hand Surg [Am] 2006;31:726–732.
55. Mallouhi A, Pülzl P, Trieb T, et al. Predictors of carpal tunnel syndrome: accuracy of gray-scale and color Doppler sonography. AJR Am J Roentgenol 2006;186:1240–1245.
56. Beekman R, Visser LH. Sonography in the diagnosis of carpal tunnel syndrome: a critical review of the literature. Muscle Nerve 2003:27: 26–33.
57. Thoirs K, Williams MA, Cert G, et al. Ultrasonographic measurements of the ulnar nerve at the elbow. J Ultrasound Med 2008;27:737–743.
58. Hobson-Webb LD, Massey JM, Juel VC, et al. The ultrasonographic wrist-to-forearm nerve area ratio in carpal tunnel syndrome. Clin Neurophysiol 2008;119:1353–1357.
59. Klauser AS, Halpern EJ, DeZordo T, et al. Carpal tunnel syndrome assessment with US: value of additional cross-sectional area measurements of the median nerve in patients versus healthy volunteers. Radiology 2009;250:171–177.
60. Wong SM, Griffith JF, Hui AC, et al. Carpal tunnel syndrome: diagnostic usefulness of sonography. Radiology 2004;232:93–99.
61. Mondelli M, Filippou G, Aretini A, et al. Ultrasonography before and after surgery in carpal tunnel syndrome and relationship with clinical and electrophysiological findings: a new outcome predictor? Scand J Rheumatol 2008;37:219–224.
62. Tagliafico A, Pugliese F, Bianchi S, et al. High-resolution sonography of the palmar cutaneous branch of the median nerve. AJR Am J Roentgenol 2008;191:107–114.
63. Smidt MH, Visser LH. Carpal tunnel syndrome: clinical and sonographic follow-up after surgery. Muscle Nerve 2008;38: 987–991.
64. Nguyen V, Choi J, Davis KW. Imaging of wrist masses. Curr Probl Diagn Radiol 2004;33:147–160.
65. Cardinal E, Buckwalter KA, Braunstein EM, Mih AD. Occult dorsal carpal ganglion: comparison of US and MR imaging. Radiology 1994;193:259–262.
66. Ho PC, Griffiths J, Lo WN, et al. Current treatment of ganglion of the wrist. Hand Surg 2001;6:49–58.
67. De Schepper AM, Hogendoorn PC, Bloem JL. Giant cell tumors of the tendon sheath may present radiologically as intrinsic osseous lesions. Eur Radiol 2007;17:499–502.
68. Middleton WD, Patel V, Teefey SA, Boyer MI. Giant cell tumors of the tendon sheath: analysis of sonographic findings. AJR Am J Roentgenol 2004;183:337–339.
69. Bianchi S, Della Santa D, Glauser T, et al. Sonography of masses of the wrist and hand. AJR Am J Roentgenol 2008;191:1767–1775.
70. Timins ME Muscular anatomic variants of the wrist and hand: findings on MR imaging. AJR Am J Roentgenol 1999;172:1397–1401.
71. Harvie P, Patel N, Ostlere SJ. Ulnar nerve compression at Guyon's canal by an anomalous abductor digiti minimi muscle: the role of ultrasound in clinical diagnosis. Hand Surg 2003;8:271–275.
72. Fornage BD Glomus tumors in the fingers: diagnosis with US. Radiology 1988;167:183–185.

CHAPTER

55 Musculoskeletal ultrasound of the adult hip and groin

Philip Robinson

INTRODUCTION AND TRANSDUCER CHOICE

When assessing the pelvic region for musculoskeletal abnormality the examination should commence with the highest frequency transducer available (>12 MHz) followed by lower frequencies if image quality dictates.

Ultrasound evaluation of musculoskeletal disease in the adult pelvis has limitations, but the technique plays an important role in diagnosis, intervention and dynamic evaluation of the region. This chapter reviews the role of ultrasound in musculoskeletal hip and pelvis disease for diagnosis and intervention.

HIP JOINT EFFUSION

The presence of an effusion can be difficult to define. Causes are varied and the ultrasound appearances frequently non-specific (Table 55.1).[1–3]

Ultrasound evaluation for hip joint effusion is made using an anterior approach parallel to the longitudinal axis of the femoral neck (Fig. 55.1). At the junction of the femoral neck and head the normal capsular margin should follow this bony contour. Effusion or other intra-articular pathology produces outward capsular displacement.

Capsular measurements and comparison with the opposite hip have previously been proposed for detection of capsular abnormality and effusion.[2,3] Measurements include capsular thickening or displacement in excess of 5–10 mm or asymmetry of >2 mm between the two hips. In practice normal variation is quite marked and a thickened capsule can normally be present as part of ageing, degenerative disease, post surgery or in previously treated synovitis (Figs 55.2 and 55.3). Direct visualisation of anterior fluid is the most specific feature for effusion but its absence does not exclude effusion as fluid can settle in the posterior recess of the joint, escaping detection.[1]

Purely hypoechoic fluid suggests simple fluid. Complex fluid with internal echoes suggests active inflammation or infection (Fig. 55.2B). These features should be used to support any underlying clinical diagnosis as ultimately normal or markedly abnormal ultrasound features are not disease specific (Table 55.1).

Ultrasound-guided aspiration and injection of the hip

Ultrasound provides an excellent guide for needle placement for aspiration or injection of the hip joint. Techniques include 'blind' or direct visualisation (see below). Common to all techniques is marking of an appropriate skin entry point, chosen while scanning, followed by aseptic skin preparation. Local anaesthetic is injected at the skin site followed by introduction of the aspiration needle. For aspiration this ideally should be at least 18-gauge in size and over 5 cm long; however, choice will vary with patient body habitus. If an effusion is present but is too thick to aspirate, sterile normal saline should be injected through the needle and then re-aspirated. An aseptic technique is essential to avoid sample contamination and reduce the risk of iatrogenic infection. The risk of infection should be explained when consent is sought, although in reality the incidence of iatrogenic infection is extremely low (<1/1000).[2]

'Blind' aspiration or injection

In this method ultrasound is used to visualise the long axis of the femoral neck and the margins of the probe footprint are be marked. The probe is removed and the centre of the footprint marked. After skin preparation the aspiration needle is introduced vertically

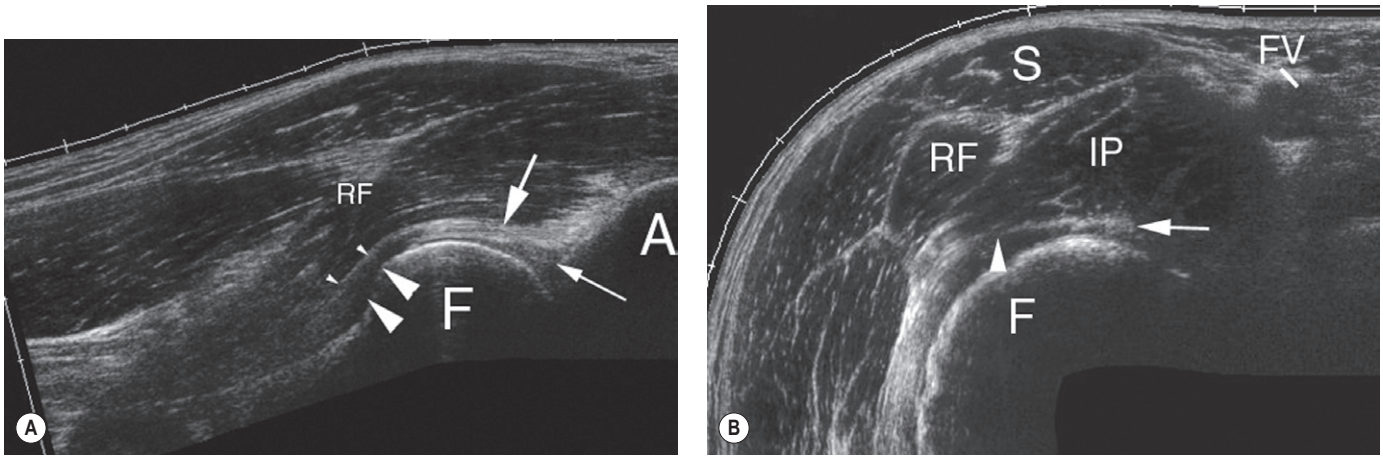

Figure 55.1 **A:** Longitudinal extended field-of-view (eFOV) sonogram shows femoral head (F), acetabulum (A), rectus femoris (RF) and triangular labrum (small arrow). At the anterior joint margin is the capsule (arrowheads) merging with overlying iliopsoas tendon (large arrow). **B:** Transverse eFOV sonogram shows right femoral head (F), sartorius (S), femoral vessels (FV), rectus femoris (RF) and iliopsoas muscle (IP). Iliopsoas tendon (arrow) adjacent to labrum and anterior capsule (arrowhead).

Table 55.1 Causes of adult hip joint effusion and capsular thickening

Cause	Primary	Secondary
Infection	Post surgery/arthroplasty, e.g. *Staphylococcus*, TB	Intravenous drug abuse (from psoas and abdomen)
Inflammatory arthritides	Seropositive Seronegative	Treatment complications (avascular necrosis, infection)
Intra-articular trauma	Femoral neck fracture Osteochondral fracture	Avascular necrosis
Degenerative disease	Primary disease	Secondary to articular debris, inflammatory arthritis and osteonecrosis
Post surgery/arthroplasty	Infection (acute/chronic) Aseptic loosening	Wear debris (granulomatous disease, metal wear)
Intra-articular neoplasm	Bone – osteoid osteoma, giant cell tumour Soft tissue – pigmented villonodular synovitis, synovial osteochondromatosis	

Summary of main uses

- Hip effusion and aspiration.
- Hernia detection and classification.
- Muscle and tendon abnormality.
- Guided therapeutic injection.

through the footprint centre, advanced until bone is reached and aspiration performed. This technique is particularly useful in patients who are agitated or have a large body habitus because once the area is marked needle advancement is rapid with no need to coordinate probe movement.

Direct needle visualisation

Direct needle visualisation requires a needle skin entry site at the margin of the probe and is performed in either the transverse or longitudinal plane of the femoral neck, although the transverse position is easier to perform (Fig. 55.4). After skin preparation the aspiration needle can be advanced under direct guidance into the joint and effusion aspirated.

This technique is also preferred for hip injection as it allows confirmation of needle and injectate position. Diagnostic procedures include intra-articular local anaesthetic to confirm joint-based symptoms and contrast for magnetic resonance (MR arthrography). Therapeutic procedures include corticosteroid injection for arthritides. When the needle is in the joint there should be little resistance to injection. The injectate flows away from and does not collect around the needle tip (Fig. 55.4). Local pooling indicates an extra-articular position.

TRAUMA – FEMORAL NECK FRACTURE

MR imaging is the technique of choice for definition of radiographically occult fracture. Ultrasound may show an intra-articular haematoma but is insensitive and non-specific.

LABRAL ABNORMALITIES AND FEMOROACETABULAR IMPINGEMENT

The labrum is a rim of fibrocartilage around the acetabulum that plays an important role in stabilising the hip joint by increasing the functional articular surface area of the acetabulum (Fig. 55.1). Labrum degeneration and deformity can result in pain and limitation of movement, particularly on flexion and internal rotation. The

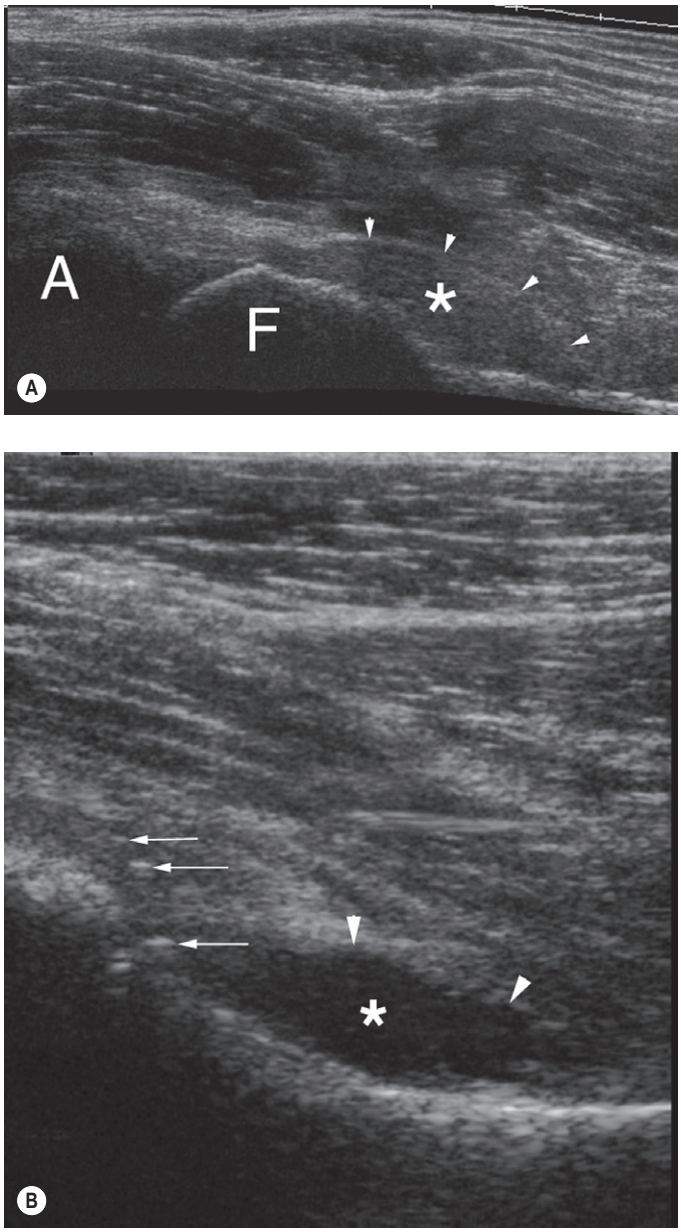

Figure 55.2 Longitudinal eFOV sonograms show **(A)** irregular degenerate femoral head (F), acetabulum (A), capsular bulging (arrowheads) with asymptomatic solid capsular thickening (*) and **(B)** capsular bulging (arrowheads), fluid (*) with complex echoes (arrows) adjacent to the femoral head consistent with gas shown to be septic arthritis.

anterior and superior labrum may develop a linear tear from acute injury or more commonly from femoro-acetabular impingement (FAI)[4] due to a primary acetabular deformity ('pincer') (Fig. 55.5) or more commonly prominence of the femoral head and proximal neck ('cam').[4] Associated femoral head and acetabular cartilage damage are frequent and a paralabral cyst can also form (Fig. 55.5B). Treatment is surgical with osteotomy of the femoral prominence, labral repair/trimming and chondroplasty.

MR arthrography is the examination of choice for FAI, although there are recognised limitations in the assessment of cartilage.[4] Ultrasound can only assess the anterior and superior labrum (where most pathology occurs) but is insensitive for undisplaced tears or articular cartilage damage. Ultrasound can show labral thickening, an associated cyst or alternative diagnoses such as iliopsoas tendon abnormalities or hernias.[5,6]

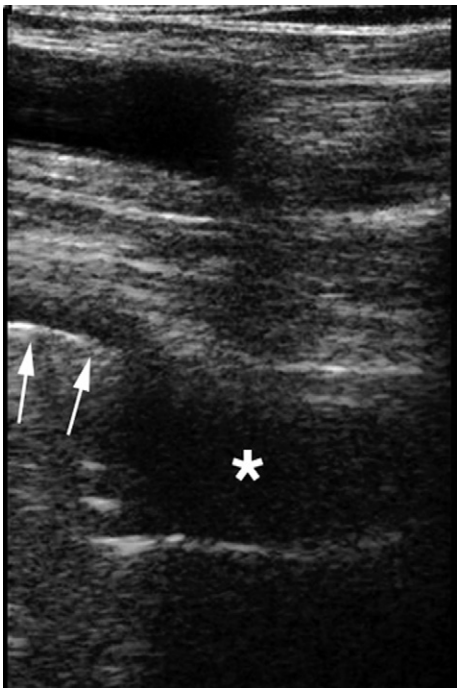

Figure 55.3 Longitudinal sonogram shows resurfacing femoral hip prosthesis (arrows) with effusion (asterisk) shown to be sterile and presumed reactive.

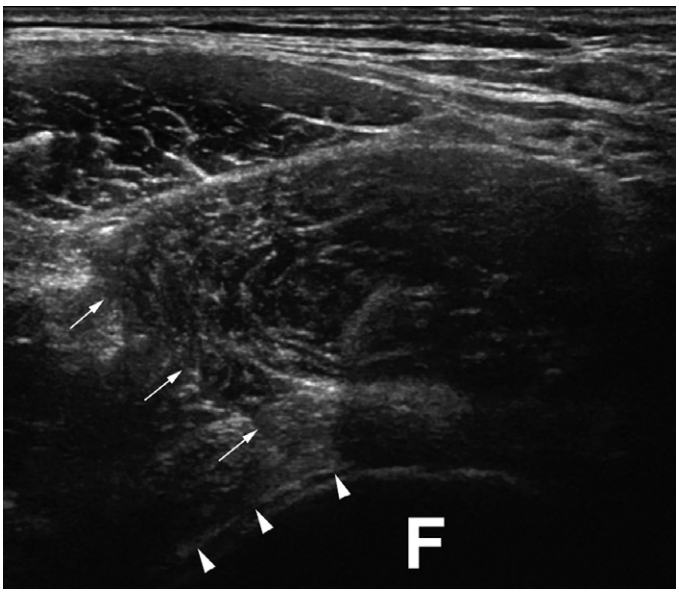

Figure 55.4 Direct guidance needle placement for hip injection or aspiration (see text). Transverse sonogram shows 22-gauge needle (arrows) and air (arrowheads) in injectate flowing away from the needle tip over femoral head (F).

HIP ARTHROPLASTY AND INSTRUMENTATION

Complications of hip arthroplasty are well recognised and are not uncommon because of the large volume of procedures performed.

Normally after any articular procedure the hip capsule appears thickened on ultrasound due to scar tissue and haemorrhage at operation. The metal prosthesis has a very echogenic margin and causes varying degrees of reverberation artefact.[3] Complications

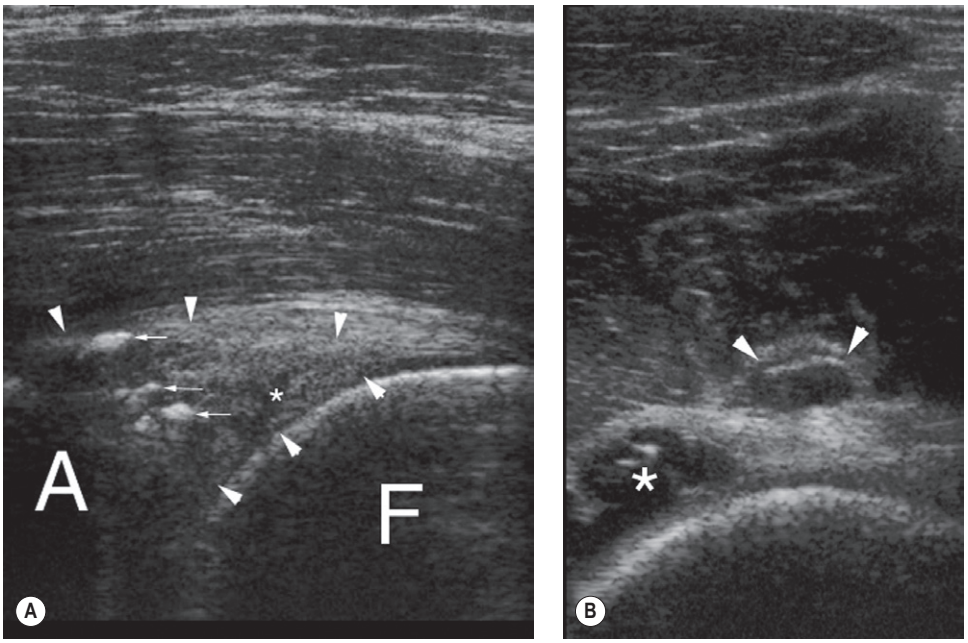

Figure 55.5 Labral tears. A: Dysplastic labral tear. Longitudinal sonogram shows markedly enlarged labrum (arrowheads), dystrophic calcification (arrows) and fissuring (*). A, acetabulum; F, femur. **B:** Transverse sonogram shows torn deformed labrum (*) and paralabral cyst (arrowheads).

include infection (acute or chronic), aseptic implant loosening and granulomatous disease (wear disease secondary to debris) (Fig. 55.3).[7] All can produce effusion and other non-specific imaging features. Large periarticular effusions and masses with resurfacing femoral head arthroplasties may be secondary to a localised, non infectious, immune response.[7]

Ultrasound plays an important role in detecting and aspirating joint effusions, hypoechoic periarticular collections and oedema associated with metalwork infection which are not seen on radiography or obscured by artefact on MR imaging (Fig. 55.6).[3] Ultrasound detects associated diagnoses such as gluteal muscle tears or snapping tendons (see below).

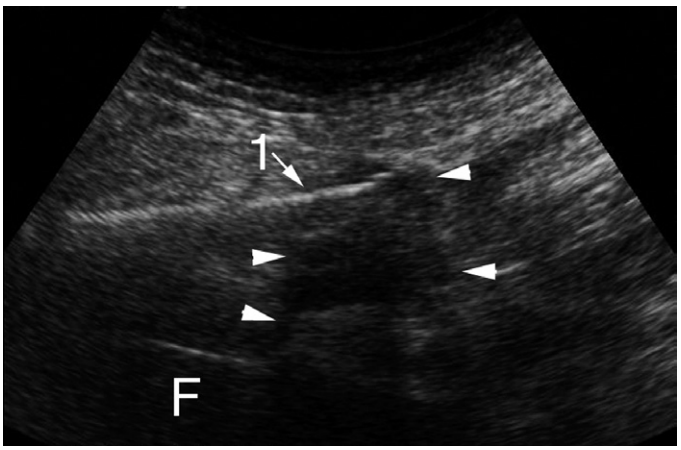

Figure 55.6 Right hip pain thought to be due to aseptic metal loosening. Longitudinal sonogram shows loosened screw (1), femur (F) and surrounding complex oedematous tissues (arrowheads) confirmed as infected at surgery.

PELVIC MUSCLE AND TENDON INJURY

Acute pelvic muscle injuries and overuse injuries (athletic or degenerative) resulting in tendinopathy are common[8,9] but catastrophic tears of normal tendons are rare.

During activity tendons and not muscles go through the greatest range of movement shortening and lengthening to transmit and absorb associated forces. The muscle–tendon–bone unit is weakest at the myotendinous junction in normal skeletally mature patients while the bone (apophysis) is weakest in skeletally immature patients. In older patients a chronically degenerate tendon can rupture with relatively minor trauma. Injuries occurring in unusual sites for a patient's age should be treated with suspicion; for example, a tendon tear in a young patient may indicate steroid abuse or bone avulsion in an elderly patient may indicate a pathological fracture.

Muscle and tendon

- Grading of acute muscle and tendon injury.
- Evaluation of healing and complications of muscle injury.
- Diagnosis of tendon snapping.
- Guided injection of symptomatic tendons, especially iliopsoas, hamstrings, gluteals and adductors.

Overuse (training errors), injury elsewhere in the kinetic chain, adjacent pathology (e.g. joint degeneration) or increasing age can alter a tendon's matrix, collagen composition and consequently its susceptibility to injury.

Ultrasound evaluation and findings for muscle and tendon disease are discussed in Chapter 60, and the same principles apply when investigating the pelvic region. Full muscle and tendon visualisation can be difficult due to tendon obliquity and increased soft tissue bulk in the pelvis when compared to the shoulder, knee and ankle regions. Careful technique is essential to eliminate anisotropy as a cause of hypoechoic change both from obliquity (e.g. iliopsoas) or crossing of multiple fibrils (e.g. adductor, hamstring and gluteal tendons).

In the pelvis the main tendons that present symptomatically are those of the proximal hamstring, adductor longus, gluteal, tensor fascia lata and iliopsoas muscles. Areas of mechanical friction are

important for the development of chronic damage and tendon snapping occurring at the iliopectineal eminence (iliopsoas tendon), greater trochanter (gluteal tendons and TFL) or from overlap of adjacent tendons (gluteal and proximal hamstring tendons).[5,10–13] Adductor longus tendinopathy is common but can be asymptomatic while tenoperiosteal disease seems to be a more important source of chronic groin pain (see later).

Although MR imaging may give a larger and more consistent field of view of the pelvic musculoskeletal soft tissues, ultrasound is still excellent for focused and dynamic examination of muscle, tendon and adjacent bone abnormality, and for targeted intervention.[3]

Anterior thigh

Iliopsoas

This compound muscle has a primary function of hip flexion and lateral rotation. It originates from the spine and pelvis. Its distal tendon attaches to the lesser trochanter of the femur.[5,11] The tendon can be difficult to visualise in the last few centimetres but anterior to the iliopectineal eminence and hip joint it is well seen (Fig. 55.1) and can be assessed for tendinopathy, bursitis, snapping and any adjacent hip or iliopectineal abnormality (Figs 55.7–55.9).[5,13,14] Primary tendon or paratenon abnormality arises from overuse injuries, especially in runners. Secondary involvement can be due to adjacent hip disease or bony irregularity (osteophytes, prosthesis/cement or fracture) (Fig. 55.8).[15] Iliopsoas tendinopathy or bursitis can be difficult to diagnose clinically and should always be considered as part of the ultrasound investigation of hip or groin pain.

Ultrasound evaluation is made in the transverse plane at the level of the iliopectineal eminence and hip joint.[5,13] Tendinopathy appears hypoechoic with thickening and loss of the normal fibrillar pattern. Adjacent bony abnormality (spur, osteophyte or prominent acetabular prosthesis) may be present. Tendon sheath fluid is seen often with a normal tendon. The iliopsoas tendon and hip joint frequently communicate and joint pathology may be the cause of fluid in the tendon sheath fluid rather than a primary tenosynovitis (Fig. 55.7).

Clinically iliopsoas snapping is felt as a sudden flick that can be reproduced on hip flexion and extension. This may be due to intrinsic tendinopathy but is more commonly secondary to paratenon oedema from overuse at the level of the iliopectineal eminence. Ultrasound visualisation is best in the transverse plane at the iliopectineal imminence where the tendon lies just medial to the anterior inferior iliac spine (Fig. 55.9). The tendon may appear normal but there is usually some hypoechoic oedema which can be quite subtle. Snapping is confirmed on dynamic hip flexion. The normal smooth translation of the tendon from lateral to medial is replaced by juddering and sudden displacement correlating with symptoms.[13] Ultrasound-guided injection of steroid and anaesthetic is an effective treatment to reduce inflammation and allow rehabilitation.[5,14] The injection is performed under direct guidance using a transverse approach. The needle is introduced from the lateral aspect to avoid the femoral vessels (Fig. 55.9B).

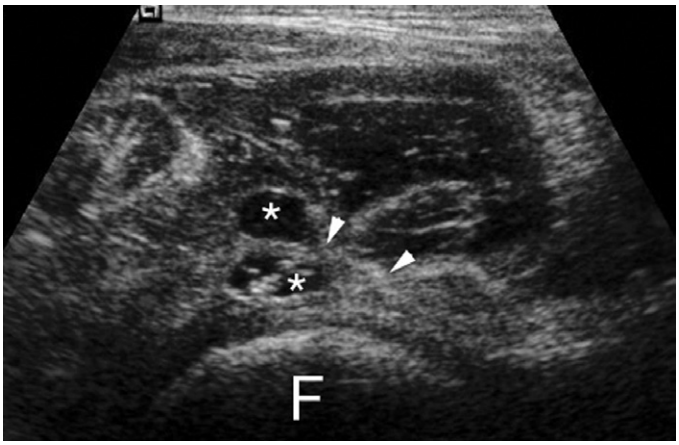

Figure 55.7 Transverse sonogram shows femoral head (F) with no effusion, iliopsoas tendinopathy (arrowheads) and complex bursitis (*).

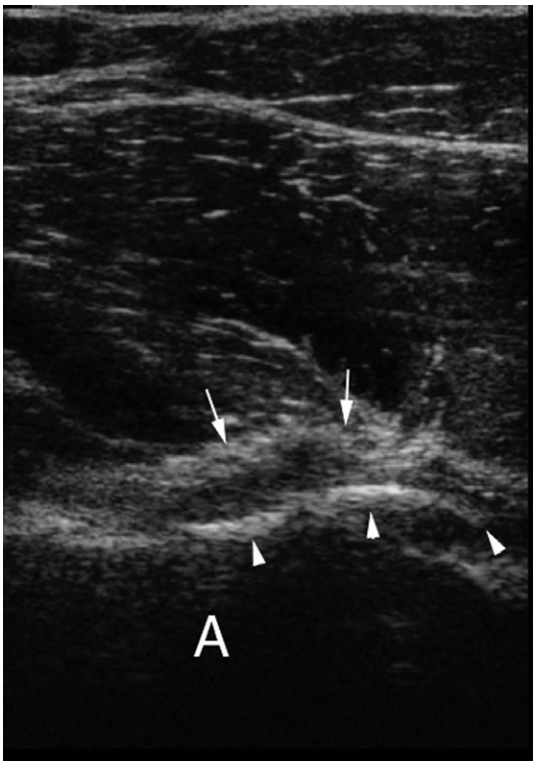

Figure 55.8 Longitudinal sonogram shows iliopsoas tendinopathy (arrows) impinging on osteophyte (arrowheads) arising from acetabulum (A).

Quadriceps and sartorius

Rectus femoris is the most frequently injured quadriceps muscle as it has a dual head proximally and spans two joints, increasing its susceptibility to eccentric injury. Proximally its two tendons originate from the anterior inferior iliac spine (long head) and acetabulum (short or reflected head) adjacent to the hip capsular margin. Proximal tendon disease is rare but acute apophyseal avulsions occur at the anterior inferior iliac spine in skeletally immature patients usually during kicking or tackling. This mechanism also commonly affects the sartorius origin from the superior iliac spine. A large bone fragment can be confirmed on plain film but avulsions frequently involve the superficial fibrocartilage with only a small flake of bone. Ultrasound shows the intact tendon, and associated bone and cartilage fragment and the extent of displacement which determines if surgical reattachment is necessary (Fig. 55.10).

In skeletally mature athletes proximal myotendinous injuries occur at the merger of the two heads of rectus femoris just distal to the level of the hip joint. This injury is not as common as distal myotendinous injuries but occurs particularly in kicking athletes when the leg is drawn back, with hip extension and knee flexion producing significant eccentric loading at this point. The quadriceps muscles are also common sites for scarring and myositis ossificans because of frequent athletic injury and contusion.

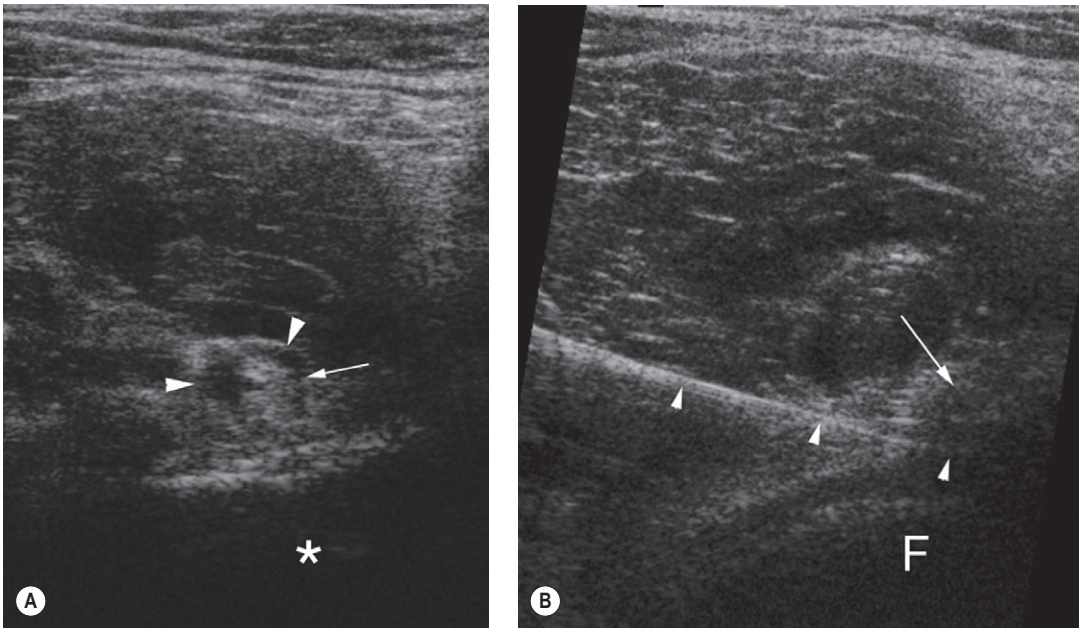

Figure 55.9 Snapping iliopsoas tendon and injection. Transverse sonograms show **(A)** iliopectineal eminence (*), iliopsoas tendon (arrow) and oedema (arrowheads), **(B)** injection needle (arrowheads) placed in oedematous sheath deep to tendon (arrow). F, femoral head.

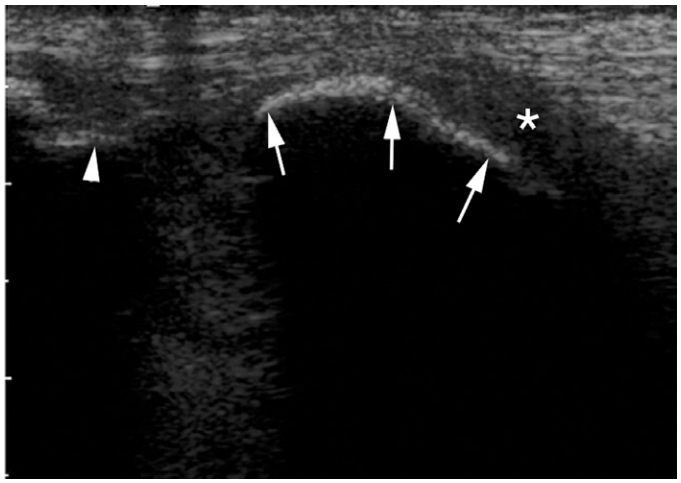

Figure 55.10 Longitudinal sonogram shows acute sartorius avulsion with intact cartilage (*), avulsed bone (arrows) from origin (arrowhead).

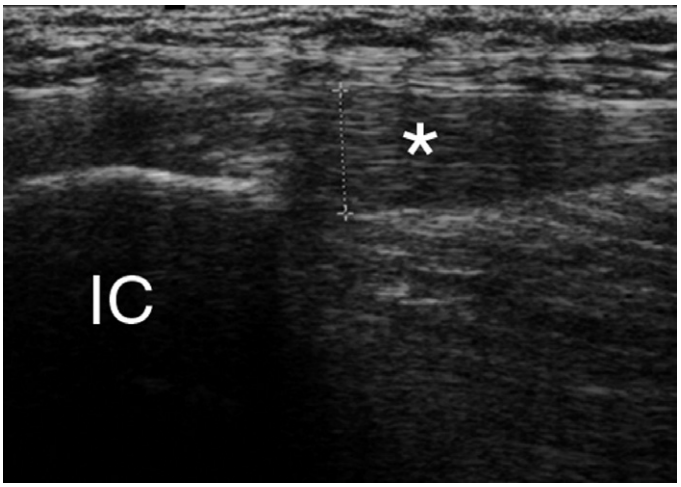

Figure 55.11 Longitudinal sonogram shows proximal TFL tendinopathy (*) arising from the iliac crest (IC).

Posterior and lateral thigh

Tensor fascia lata (TFL)

The TFL originates from the iliac crest with a broad short tendon extending to the muscle, which then forms the iliotibial band that extends distally to the tibia. The main function of the fascia and muscle is to stabilise the knee in flexion and extension. The tendon occasionally undergoes a proximal partial tear or tendinopathy at the iliac crest and may cause groin pain. At ultrasound the proximal tendon appears swollen, hypoechoic and loses its normal fibrillar pattern (Fig. 55.11).[10]

Slightly more distally impingement of the iliotibial band over the greater trochanter and adjacent gluteal tendons can result in tendinopathy and snapping. At ultrasound the tendon appears hypoechoic with adjacent bony irregularity and abnormal movement on hip flexion.[13]

Direct shearing injury of the tensor fascia lata at its junction with the overlying subcutaneous fat and fascia results in haematoma between the fascia and the fat with resulting fat necrosis. This can occur in contact sport athletes and in elderly patients after a simple fall. The underlying TFL appears normal. This is easier to appreciate on ultrasound as the complex hypoechoic fluid and oedema overlying the fascia can obscure this detail on MR imaging. Particularly in elderly patients the haematoma may persist and become walled off and present as a persisting soft tissue mass known as Morel–Lavallée lesion (see Chapter 58).

Hamstrings

Overuse tendinopathy and paratenon inflammation of the proximal hamstring tendons is seen in athletes, particularly footballers and distance runners, and can result in debilitating symptoms. Anatomically the area is complex as the tendons overlap as they originate from the ischial tuberosity. Although commonly described as

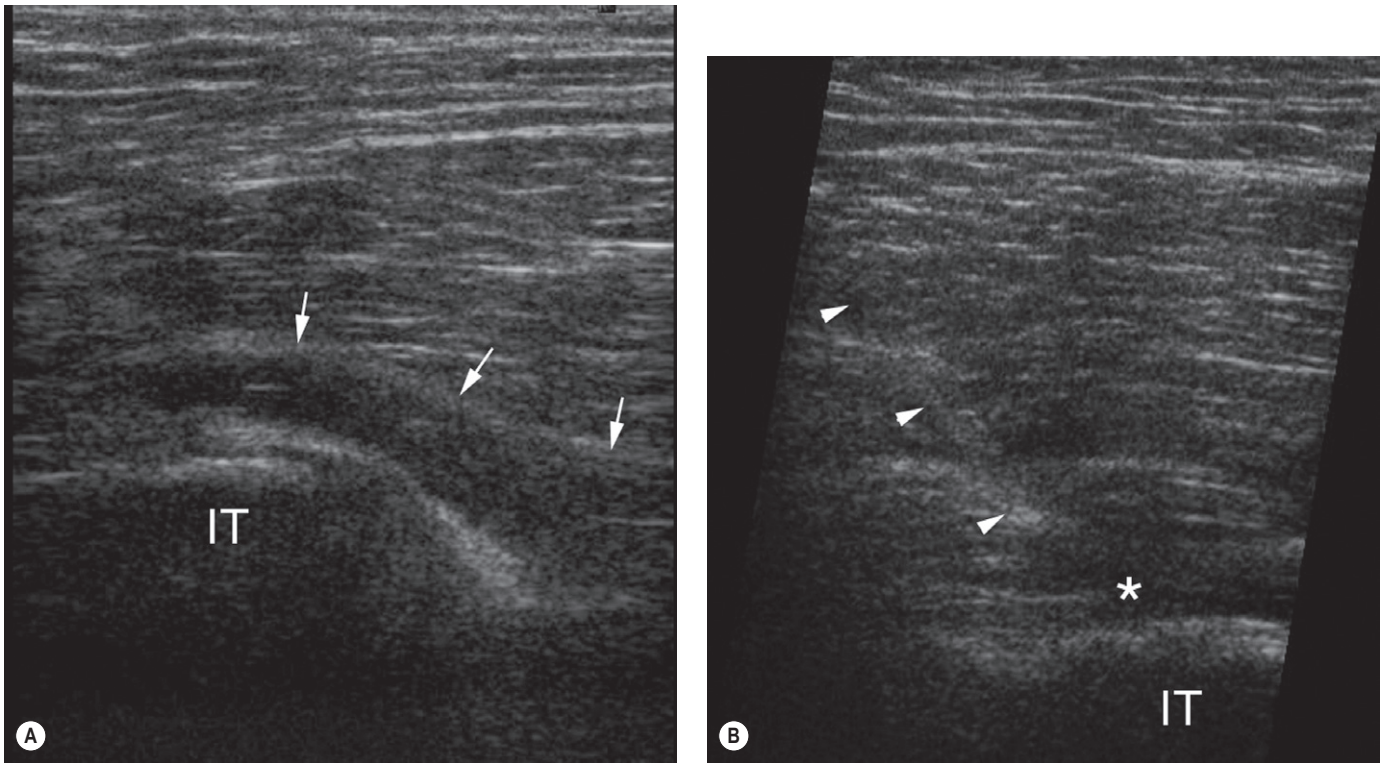

Figure 55.12 Hamstring paratendinopathy and injection. Paratenon change seen on MRI. Transverse sonograms show **(A)** subtle hypoechoic oedematous and ill-defined tissues (arrows) at ischial tuberosity (IT) and **(B)** needle placement (arrowheads) into oedematous tissues (*) at injection.

bursitis, discrete fluid collections are rarely seen. Subtle paratenon oedematous changes are more easily seen at MR imaging than ultrasound (Fig. 55.12A). The tendons often appear normal but can be thickened if the process is longstanding, the athlete is elderly or there has been previous hamstring muscle injury. Ultrasound-guided injection of steroid and anaesthetic for treatment of symptomatic paratenon oedema resistant to conservative management is best performed with a transverse approach to allow direct visualisation of the needle and avoid the sciatic nerve (Fig. 55.12B).

The hamstring muscles are the most commonly injured of all muscles due to athletic activities. Biceps femoris is most frequently affected. Proximal hamstring muscle injuries can present with diffuse symptoms because of haematoma causing direct sciatic nerve irritation or muscle spasm. Ultrasound can evaluate the site and grade of acute injury as well as haematoma or subsequent chronic scar tissue impingement on the sciatic nerve. In skeletally immature patients ischial tuberosity avulsions are also common.

Gluteal

The gluteal muscles are important postural muscles that act on the hip and femur to produce abduction and external rotation during normal gait. Gluteal tendinopathy particularly of medius and minimus is commonly symptomatic where they attach to the greater trochanter and are crossed by gluteus maximus and TFL. Bursae occur between the individual tendons and between the tendons and the greater trochanter (Fig. 55.13).[16,17] Although symptoms in this area are commonly attributed to bursitis, in practice a fluid collection is rarely seen and tendinopathy and oedema are more commonly found on imaging (Fig. 55.14). Clinical correlation is necessary as asymptomatic tendinopathy, tendon thickening and entheseal changes (ossification and irregularity of greater trochanter) are common in elderly patients.[12,17] Ultrasound can be used to guide injection of steroid and anaesthetic for treatment.

Acute gluteal tendon tears are rare and occur mainly in elderly patients, especially if they have undergone previous hip replacement surgery (Fig. 55.15). Muscle atrophy is a common asymptomatic finding in hip replacement patients. Tendon avulsions are rare in asymptomatic patients and should be considered clinically significant.[17]

Medial thigh

The thigh adductor muscle group consists of adductors longus, brevis and magnus and the gracilis muscle. They originate from the pubic body and inferior pubic ramus and pass distally to the femur and tibia. Their main action is thigh adduction with some hip flexion and they are functionally important in sports where frequent changes of direction are required.[18] The adductor muscles are best visualised as they originate from the pubis and inferior pubic ramus with the thigh in abduction and external rotation and the knee flexed. In this position adductor longus is the most prominent muscle and is easily palpable. The transducer is placed on the longitudinal axis of the muscle and is moved obliquely along this plane towards the symphysis pubis, following the muscle through the myotendinous junction to its tendon and origin at the pubis (Fig. 55.16).[19]

Acute muscle injuries usually occur when the leg undergoes forced abduction. Adductor longus is the most commonly injured muscle with tears occurring at the proximal or distal myotendinous junction. Proximal tendon avulsion is more common in mature athletes due to chronic background tendinopathy (Fig. 55.17).[18]

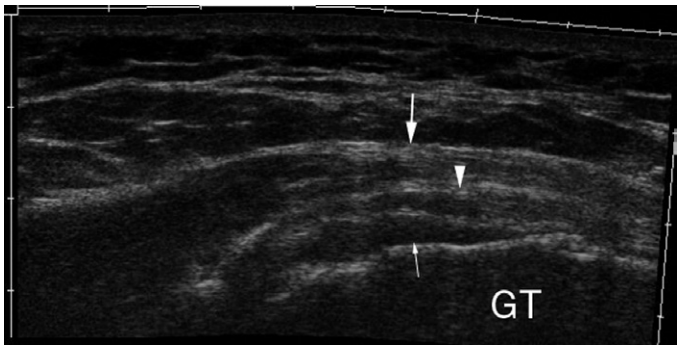

Figure 55.13 Longitudinal eFOV sonogram shows normal irregularity of greater trochanter (GT) and the overlapping gluteal tendons (arrowhead and arrows).

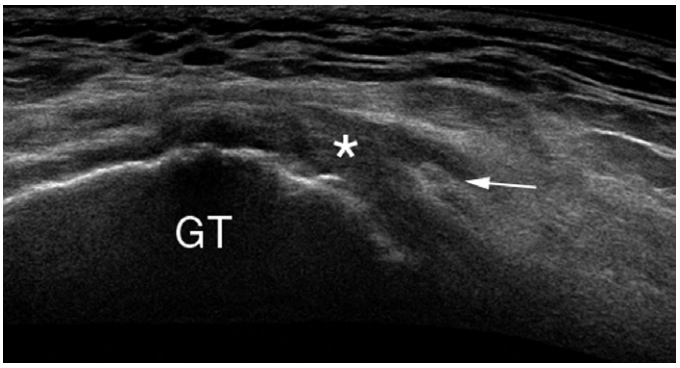

Figure 55.15 Longitudinal eFOV sonogram shows gluteus medius tendon tear with haematoma (*), adjacent greater trochanter (GT), retracted muscle and tendon (arrow).

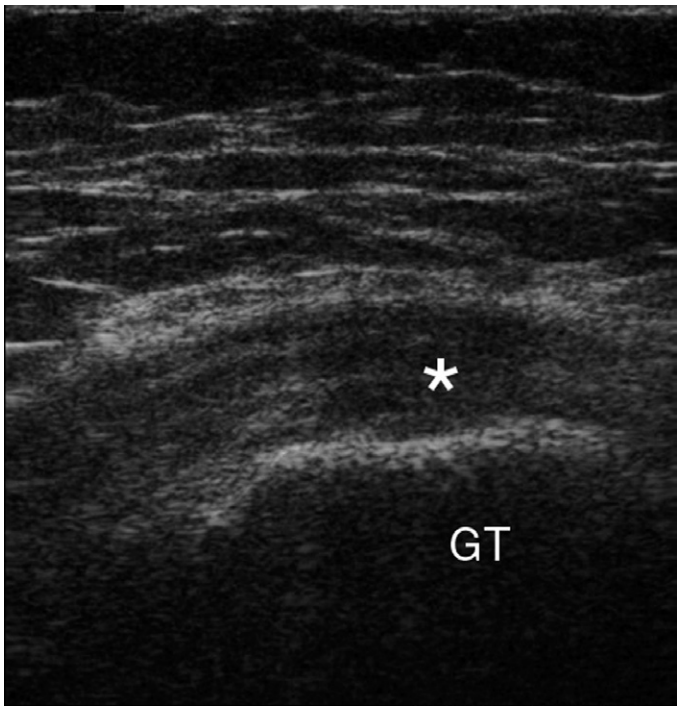

Figure 55.14 Longitudinal sonogram shows gluteal tendinopathy (*) and greater trochanter (GT). The tendon is hypoechoic and swollen.

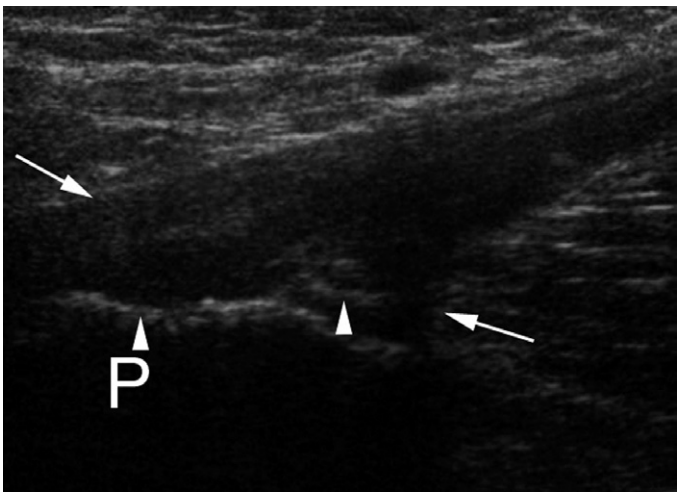

Figure 55.16 Asymptomatic adductor tendinopathy. Longitudinal sonogram shows fanning out (arrows) of normal adductor tendon over the pubis (P) with anisotropy and cortical irregularity (arrowheads).

ABDOMINAL MUSCLES

The musculature of the lower abdominal wall includes the external oblique, internal oblique, transversus abdominis and rectus abdominis muscles. They have an important postural function and a linear configuration. The rectus abdominis lies either side of the midline raphe running inferiorly to blend with the superior aspect of the symphysis pubis and the adductor musculature.[20] The other muscles form three layers at the lateral margin of the rectus abdominis. The external oblique is outermost, transversus abdominis innermost and internal oblique lies between.[21] Acute injuries are relatively rare except in athletes. Rectus abdominis is the most commonly affected (especially in weight-lifters, tennis players and gymnasts). Haematomas form after trauma, surgery or spontaneously in patients taking anticoagulants. This group of muscles is best evaluated transversely in the midline, locating rectus abdominis and then moving laterally to the oblique abdominal muscles. The rectus sheath is visualised as thick echogenic fascia, which blends with the investing fascia of the oblique muscles. Once the anatomy of these muscles has been defined, the position of any pathology or hernia can be identified.

HERNIAS

Inguinofemoral hernias

Overview and differing imaging modalities

The majority of clinically significant hernias can be diagnosed on clinical examination and managed without the use of diagnostic imaging. However, a significant proportion of patients with symptoms suggestive of a hernia are found to have inconsistent clinical examination findings.[22,23] Surgical exploration can be performed if symptoms are severe, but as this is invasive and has potential morbidity there is a role for imaging in patients with equivocal clinical features.

Herniography is sensitive but non-specific and demonstrates asymptomatic hernias in 6–18% of patients.[24,25] Herniography has a low complication rate but is relatively invasive and requires ionising radiation.[24,26,27] False negative herniography findings occur due

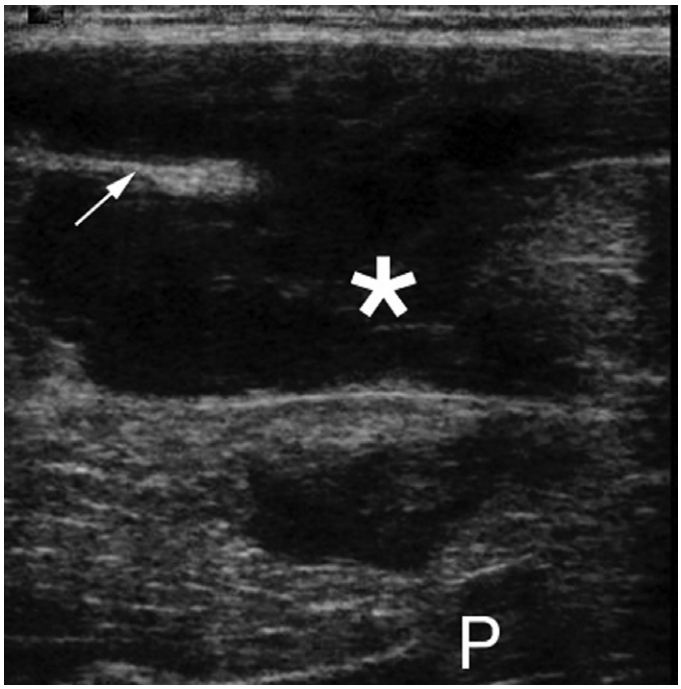

Figure 55.17 Acute adductor longus tendon tear secondary to tendinopathy. Transverse sonogram shows haematoma (*), pubis (P) and irregular retracted tendon (arrow).

to small hernias, loculation of contrast preventing flow into the hernial sac or hernias that predominantly consist of fat.[6,25]

Studies of computed tomography (CT) and MR imaging have not been performed in patients with equivocal clinical findings but reviews of abdominal CT series have shown this to be an effective technique for defining abdominal hernias in patients with symptoms and palpable abnormality.[28–30] Although some studies of dynamic MR technique have been performed in patients with clinically evident hernias prior to surgery, MR studies have not been widely accepted or evaluated in clinical practice.[31]

Ultrasound in infants can confirm clinically evident inguinal hernias but a varied accuracy is reported for assessment of the contralateral inguinal canal.[32,33] In adults ultrasound is accurate both for confirming hernias evident on clinical examination (sensitivity 86–100% and specificity 82–97%)[31,34–36] and for clinically equivocal patients.[6] More varied accuracy is reported for hernia classification (45–85%),[31,34–36] although use of lower-frequency transducers may be responsible for poor results.[31,35] Ultrasound detects fat-filled hernias not seen at herniography, probably because real-time visualisation of the hernia contents does not depend on the secondary sign of peritoneal contrast movement.[6] False negative findings for ultrasound have been attributed to small hernias or technical errors due to operator inexperience.[31,35] False positive findings have been attributed to over-reporting of bulging and inguinal lipomas as direct and indirect hernias respectively.[31,35]

Inguinal canal evaluation

Normal anatomy

The inguinal canal transmits vessels, nerves, lymphatics and the spermatic cord (round ligament in females) from the abdomen to the external genitalia.[21] The posterior wall of the canal is formed by the muscle, aponeurosis and fascia of transversus abdominis and also part of the internal oblique. The anterior wall is formed from the fascia of the external oblique muscle. The deep (internal) inguinal ring is a defect in the transversus abdominis fascia that allows the contents to enter the canal and leave the abdomen (Figs 55.18 and 55.19) before extending obliquely, medially and inferiorly through the canal to exit at the superficial (external) inguinal ring, a defect in the external oblique fascia. Superficial to the canal are subcutaneous fat and skin. Deep to the canal lie the iliopsoas muscle medially and the external iliac vessels laterally (Figs 55.18 and 55.19). Peritoneum and small bowel lie posterosuperiorly.

The inferior epigastric vessels are an important landmark. They arise from the external iliac vessels and course superiorly to lie deep to rectus abdominis. Just after their origin from the external iliac vessels they lie immediately medial to the deep inguinal ring. If a hernia arises lateral to these vessels, it is indirect (passing through the internal ring) but if it arises medial to the vessels it is a direct hernia (passing through the posterior wall).

Examination technique and normal ultrasound appearances

Initially it is important to identify the inferior epigastric vessels and deep inguinal ring.[6] One method is to scan rectus abdominis transversely, identify the inferior epigastric vessels within the deep aspect of the rectus sheath, then scanning continuously in the transverse plane to follow the vessels inferiorly where they join the external iliac vessels. In obese patients it is difficult to continuously scan inferiorly because of abdominal protrusion and another technique is to identify the femoral vessels in the transverse plane and move cranially until the epigastric vessels are seen at their origin. A longitudinal image of the inguinal canal is then obtained. The inguinal ligament is a linear fibrillar echogenic structure deep to the subcutaneous fat and blends with the deep fascia (Fig. 55.18A). Deep to the ligament are multiple hyperechoic and hypoechoic linear structures (representing vessels, nerves and cord) within the canal. Deep to the canal are the psoas muscle, echogenic peritoneum and hypoechoic bowel (and a varying amount of preperitoneal fat).[6]

The canal should also be assessed in its short axis, which is the anatomical sagittal plane (Fig. 55.19A). To obtain this view the external iliac/femoral vessels should be scanned longitudinally and the transducer moved medially to view the short axis of the inguinal canal, its hypoechoic tubular contents with peritoneum and bowel posterosuperiorly.

Assessment of the canal with the patient at rest and straining (performing a slow Valsalva manoeuvre) is performed. It is important to instruct the patient to perform the Valsalva manoeuvre slowly (i.e. not cough) and to ensure that transducer pressure is not applied too firmly, otherwise any potential hernia will be maintained in reduction. Normally there may be mild bulging of the posterior wall and peritoneum but it should not occlude the canal (see later) (Fig. 55.20). On straining in a normal subject, there may be slight vessel dilatation and sliding of contents within the canal but bowel should only move towards the canal and not completely efface or enter it.[6]

Ultrasound appearance of inguinal hernias

In the transverse plane an indirect hernia arises lateral to the epigastric vessels and extends through the long axis of the canal (Fig. 55.18B). When scanning sagittally (short axis of the canal) the indirect hernia distends the canal and effaces its contents (Fig. 55.19B).

Examination technique

- Can normally use a linear transducer in most patients.
- Identify inferior epigastric vessels in the transverse plane.
- The canal is assessed in the long and short axis during slow Valsalva manoeuvre.
- Same principles are applied for patients with postoperative pain.

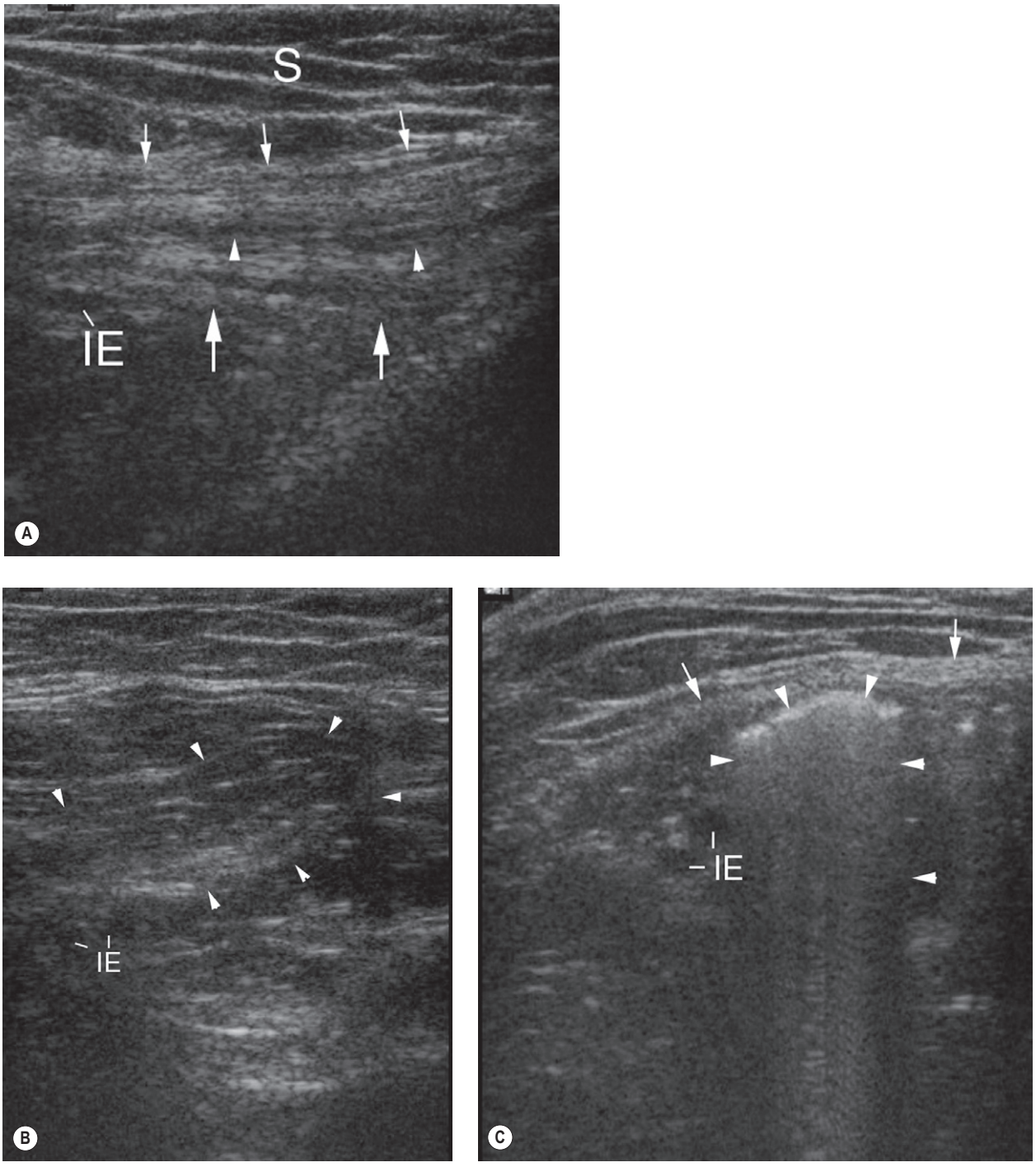

Figure 55.18 Normal right inguinal canal anatomy and hernias (longitudinal axis). **A:** Longitudinal sonogram of inguinal canal shows subcutaneous fat (S), inferior epigastric vessels (IE) laterally, inguinal ligament (small arrows), deep transversalis fascia (large arrows) and linear contents (arrowheads). **B:** Indirect hernia (arrowheads) of fat and bowel entering the canal lateral to the epigastric vessels (IE). **C:** Direct hernia (arrowheads) of bowel (note echogenic gas) entering the canal medial to the epigastric vessels (IE), displacing the inguinal ligament (arrows).

The hernia usually consists of hyperechoic peritoneum, fat and hypoechoic bowel. Occasionally the hernia is congenital due to a persistent processus vaginalis, but this can be an incidental finding seen in 29% of adults. A persistent processus vaginalis appears similar to peritoneum with two thin opposing echogenic layers seen sliding over each other on straining.

Direct inguinal hernias occur due to a defect in the posterior inguinal wall and rarely continue distally along the inguinal canal, being much more localised in comparison to indirect hernias. In the transverse plane a direct hernia protrudes through the posterior defect medial to the epigastric vessels (Fig. 55.18C). In the sagittal plane the direct hernia pushes into the canal from the posterior aspect and effaces its contents (Fig. 55.19C).

Occasionally preperitoneal fat also herniates into the canal and appears more homogeneous and hyperechoic compared to bowel and sometimes moving with the bowel and peritoneum. Careful note should be made of less common inguinal abnormalities, e.g. lipoma, haematoma, lymph node, cyst of Nuck or undescended testicle.

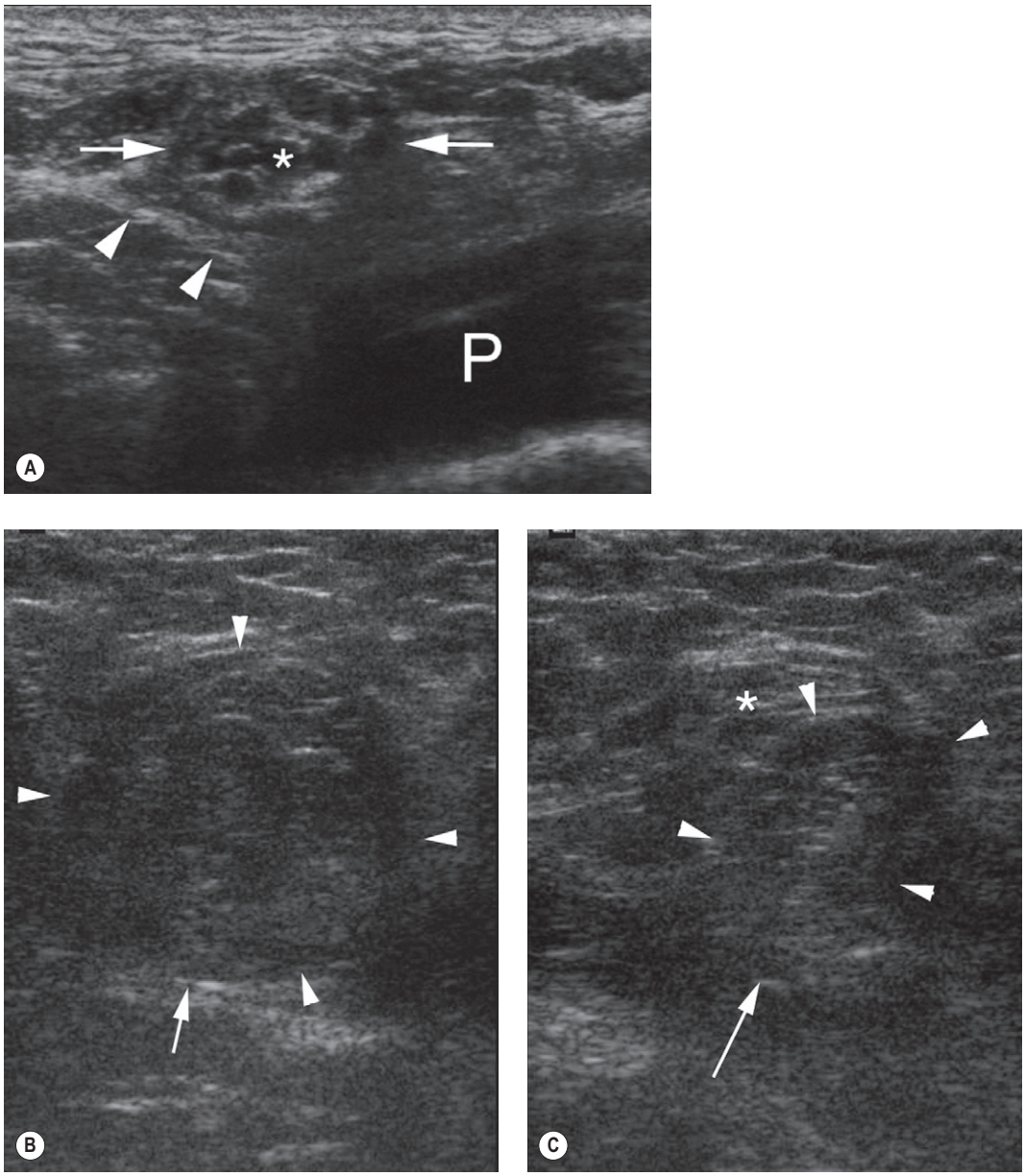

Figure 55.19 Normal inguinal canal anatomy and hernias (short axis). **A:** Sonogram of inguinal canal shows inguinal canal (arrows), vessels (*), peritoneum (arrowheads) and psoas (P). **B:** Indirect hernia (arrowheads) of fat and bowel expanding the canal with intact echogenic deep fascia (arrow). **C:** Direct hernia (arrowheads) entering the canal through a fascial defect (arrow) and compressing the canal contents (*).

'Bulging' and 'pre-hernia complex'

Bulging of the transversalis fascia, where the posterior inguinal wall almost occludes the canal on straining without actual herniation, has been proposed as a source of pain or 'pre-hernia' condition (Fig. 55.20). Ultrasound[6,37,38] and herniography[27,39] do not confirm that this correlates with pain or is part of the spectrum of direct hernia. As it does not represent a definite hernia it should be cautiously interpreted. Comment can be made when wall bulging occurs on the symptomatic side and is markedly asymmetrical with the asymptomatic side.

Postoperative evaluation

Several surgical procedures are described for hernia repair. In principle all involve reduction of the hernia and correction of the defect by oversewing or mesh insertion. When a mass recurs after surgical repair, ultrasound can help differentiate between recurrent hernia and a static haematoma, infection or seroma. Mesh is seen as a hyperechoic linear structure just adjacent to the epigastric vessels (Fig. 55.21A). Occasionally after repair of indirect hernias, peritoneum is seen entering the canal although the repair is sufficient to prevent bowel herniation. This is because the peritoneal sac is often left intact to reduce any trauma to the spermatic vessels during surgery. Patients can also develop a preperitoneal lipoma which shows only minor movement on straining. Neuralgia is another relatively common postoperative complication (2%) and ultrasound is usually normal. Focal pain may be due to post-surgical neuromas and stitch granulomas (Fig. 55.21B).

Femoral hernia – technique and appearance

The femoral canal is a potential space that contains fat and lymph nodes and lies medial to the femoral vein just distal to the inguinal

ligament. Femoral hernias are relatively infrequent in male patients and are commoner in middle-aged female patients. Pathologically the hernia sac passes from the abdomen deep to the inguinal canal and into the femoral canal. Quite commonly bowel does not completely enter the canal but pushes preperitoneal fat into it.

The femoral canal is located just inferior to the inguinal canal and immediately medial to the femoral vein.[6,40] Normally on performing a Valsalva manoeuvre the femoral vein should distend and the adjacent tissues are not distorted. This expansion of the vein into the potential space of the adjacent femoral canal implies there is no mass effect from within the canal itself.

A femoral hernia expands the canal, compressing or preventing the normal expansion of the femoral vein (Fig. 55.22). The hernia should be confirmed by scanning over the canal in the longitudinal plane. Bowel and peritoneum extend inferiorly, deep to the inguinal canal and into the femoral canal.

Hernias

- Accurate technique for patients with clinically equivocal findings.
- Currently superior to other techniques for inguinal, femoral and abdominal hernias.
- Inguinal 'bulging' not fully evaluated and currently not a reliable finding.
- Postoperative patients can be evaluated using the same techniques.

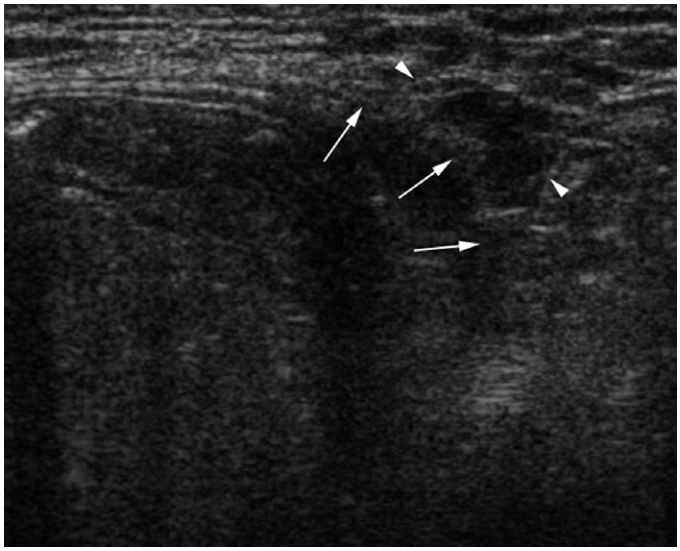

Figure 55.20 Inguinal wall bulging. Sonogram shows short-axis inguinal canal (arrowheads) on straining with movement (arrows) and compression of the canal into a crescent shape.

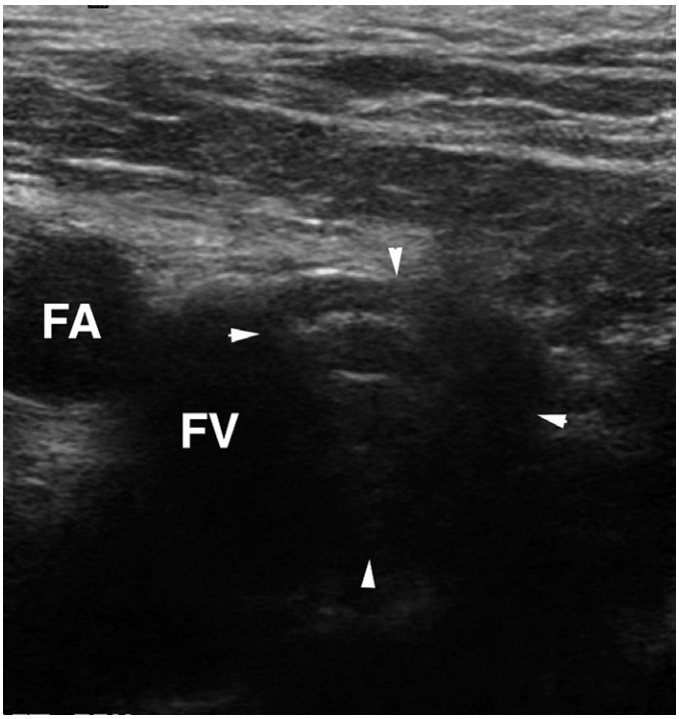

Figure 55.22 Femoral hernia. Transverse sonogram taken during straining shows femoral artery (FA), femoral hernia (arrowheads) expanding the canal and compressing adjacent vein (FV).

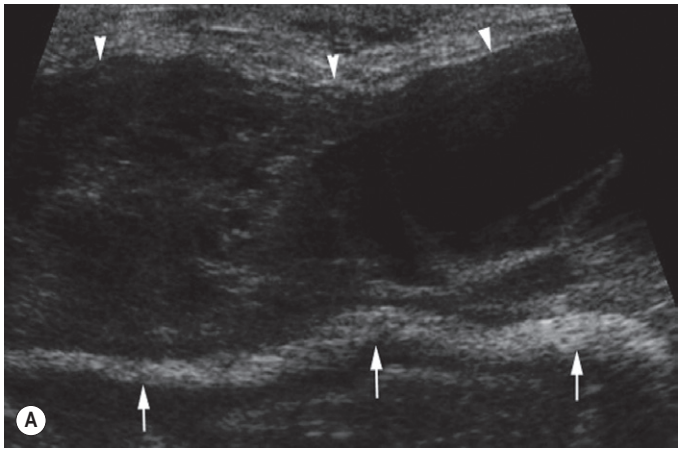

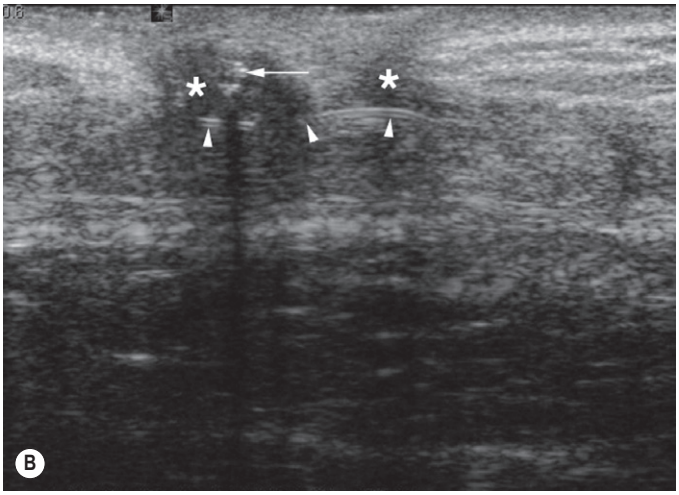

Figure 55.21 Patients with postoperative pain. A: Large hypoechoic haematoma (arrowheads) expanding the long axis of the canal and outlining the thickened echogenic mesh (arrows) inserted at surgery. **B:** Stitch granuloma and infection with oedematous hypoechoic tissue (*) surrounding echogenic suture (arrowheads) and granuloma (arrow).

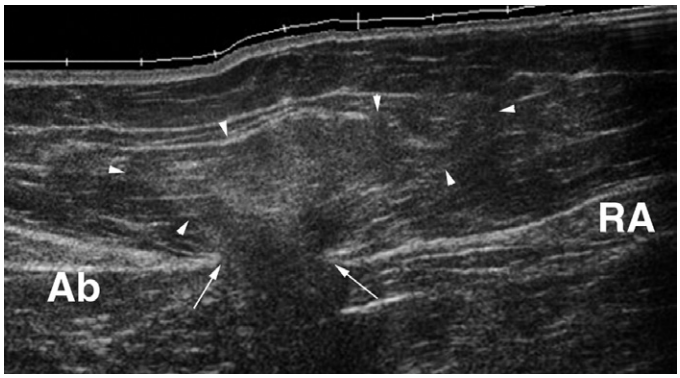

Figure 55.23 Transverse eFOV sonogram shows Spigelian hernia (arrowheads) of fat herniating through defect (arrows) between rectus abdominis (RA) and lateral abdominal muscles (Ab).

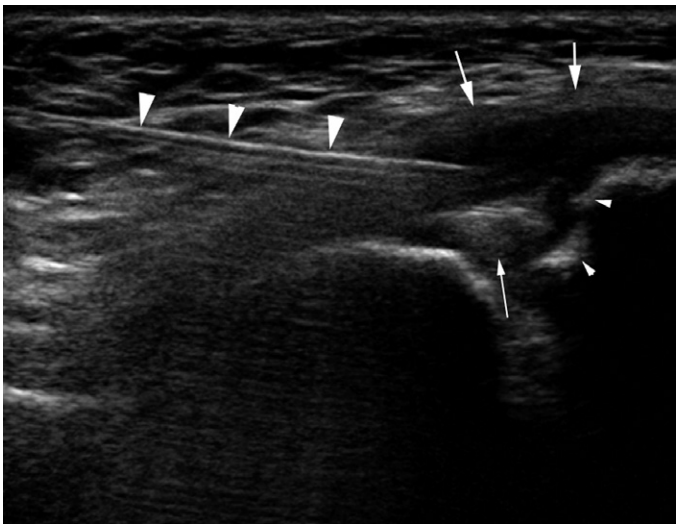

Figure 55.24 Symphysis pubis. Transverse oblique sonogram shows anterior capsule (large arrows), normal irregular pubic body cortical margin (small arrowheads) and ill-defined echogenic disc (small arrow) and needle placement (large arrowheads) during joint injection.

Abdominal wall and incisional hernias

These hernias involve protrusion of at least peritoneum and preperitoneal fat through a defect in the abdominal wall musculature and fascia. They can be classified as Spigelian, incisional and umbilical.[6,28]

Spigelian hernias occur through a weakness of the lateral rectus abdominis sheath at its margin with the oblique muscles (linea semilunaris), particularly at the point where the inferior epigastric vessels penetrate the rectus sheath (Fig. 55.23).

Incisional hernias arise from muscular weakness and fascial defects due to previous surgery and scar tissue. This is a common clinical problem with an estimated 10% of all hernia operations being for repair of this type of hernia. Umbilical or paraumbilical hernias present in the midline and can be congenital, postpartum or in patients with abdominal distension (obesity or ascites).

For all these conditions the area to be evaluated can be confirmed on taking a history. The role of ultrasound is to confirm the presence and contents of the hernia (fat and/or bowel) as well as measuring the size of the defect in the echogenic deep fascia (Fig. 55.23).

ATHLETIC GROIN PAIN (PUBALGIA)

Although a large number of pathologies can cause groin pain, including infection, neuralgia and tumour, the following discussion will concentrate on chronic athletic groin pain (pubalgia).

Anatomy and normal ultrasound appearances

Symphysis pubis and adductor muscles

The anatomy and ultrasound appearances of the adductor muscles and inguinal soft tissues have already been described. Chronic tendinopathy, especially of the proximal adductor longus, is common in many athletes and is often relatively asymptomatic (Fig. 55.16).[41]

The symphysis pubis is a fibrocartilaginous joint and is the confluence for the thigh adductors, rectus abdominis and the medial aspect of the inguinal ligament.[20,21] The superior and anterior echogenic pubic cortex is visualised on ultrasound by scanning rectus abdominis transversely and moving inferiorly to the symphysis. The hypoechoic capsular margin and superior pubic ligament merge anteriorly with a fibrocartilaginous disc occasionally seen within the joint as an echogenic stripe (Fig. 55.24).

Chronic degeneration and irregularity of the symphysis pubis is a non-specific finding commonly seen in elderly people, postpartum women and professional athletes (Fig. 55.24).[9,42] Joint margin irregularity also occurs secondary to chronic enthesopathy at the adductor origins or with more acute inflammatory joint conditions (e.g. fracture or osteomyelitis).

Clinical overview

Chronic insidious-onset groin pain is a significant clinical problem that has potentially poor prognostic implications for athletes. Considerable biomechanical stresses are produced across the anterior pelvis, particularly in single stance (changing direction or kicking). Players who develop chronic pain describe slight discomfort at the end of a game gradually progressing to stiffness on waking in the mornings. Initially features ease with warming up but soon symptoms appear during playing and are exacerbated by cutting-in and kicking.

Pathologies that have been proposed as the primary cause of symptoms include osteitis pubis, adductor tenoperiosteal (enthesis) injury, pubic subchondral bone stress fractures, rectus abdominis insertion tears and inguinal canal abnormalities (pre-hernia complex, subclinical inguinal hernias or external oblique and conjoint tendon dehiscence).[41] Neuralgia of the ilioinguinal nerve has also been described, resulting either from posterior inguinal canal weakness with ballooning on straining (see section on 'bulging' and 'pre-hernia complex', earlier), or from small tears in the abdominal muscles (mainly external oblique).[43] Referred pain from the spine or hip (FAI) should also be considered.[4]

Clinical definition of these various pathologies is difficult as symptoms and examination findings are similar or overlap markedly.[18] Most players respond to active rehabilitation and core stabilisation but may take many months to return to full activity.[8] Several surgical procedures have developed to treat non-responders but no controlled trials have been described.

Radiological evaluation of athletes with pubalgia includes MR imaging, ultrasound and herniography.[9,27,37,44] Conventional radiographs and scintigraphy are often unhelpful. Pubic sclerosis, irregularity and increased isotope uptake are commonly seen in asymptomatic athletes, presumably due to chronic shearing forces and remodelling.

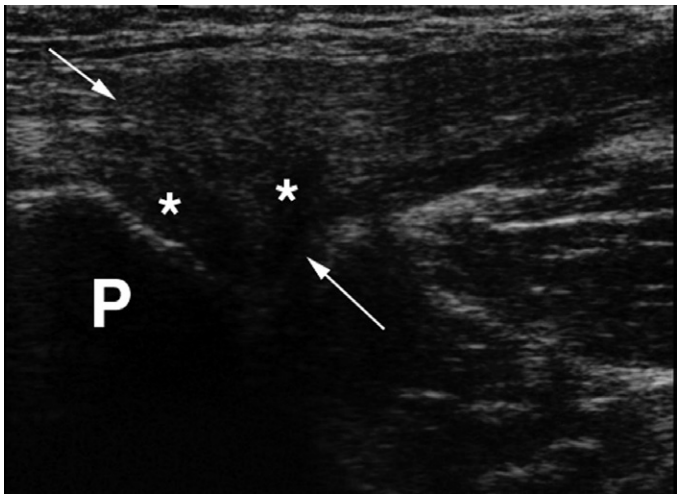

Figure 55.25 Symptomatic adductor longus tendinopathy. Longitudinal sonogram shows tendinopathy with convex swelling (arrows) and focal hypoechoic areas (*) shown not to be anisotropy.

The role of ultrasound

Ultrasound is initially performed in parasymphyseal pain to rule out inguinal hernia or acute on chronic tendon or muscle strain (particularly of adductor longus). Features that suggest that an area of chronic tendinopathy may be symptomatic are marked focal tenderness on transducer pressure and evidence of superimposed acute changes within the tendon including haematoma or oedema causing convex swelling (Fig. 55.25).

If ultrasound is normal and the clinician confident of an inguinal soft tissue abnormality (e.g. external oblique or conjoint tendon tear), no other imaging is performed as ultrasound cannot detect the small tears described in surgical series or subtle adductor enthesis change.[41,43] If the clinical opinion is that the pain is symphyseal in origin, MR imaging can assess the degree of symphyseal and adductor entheseal oedema, which significantly correlates with symptoms.[9,44,45]

Ultrasound-guided intervention

Ultrasound-guided symphysis pubis injection may help refine the clinical diagnosis or provide long-term symptom relief.[46–48] Its overall benefit is not proven. Some studies that lacked control groups have reported an early return to pain-free activity.[46–48] When unilateral symptoms predominate infiltration around the adductor tendon origin (enthesis) may be sufficient.

For both types of injection a freehand technique can be used. For injection of the symphysis pubis a 22-gauge spinal needle is introduced using a transverse oblique approach (Fig. 55.24), as a pure transverse position may lead to piercing of the medial inguinal contents. When infiltrating around the adductor tendon origins, a 20-gauge needle usually suffices, as the adductor muscle is relatively superficial when the thigh is abducted and externally rotated.

Pubalgia

- Pubalgia = chronic athletic groin pain (>3 months).
- Multiple aetiologies implicated involving the symphyseal and inguinal soft tissues.
- Athletes commonly have some background asymptomatic adductor tendinopathy.
- MR imaging can define symptomatic adductor entheseal change.
- Ultrasound is used to exclude hernia or acute tendon injury but is frequently negative in athletes with chronic symptoms.
- Ultrasound allows image-guided injection of the symphysis pubis or adductor region.

PELVIC MUSCULOSKELETAL SOFT TISSUE MASSES

The ultrasound appearances of soft tissue masses and neoplasms are described in Chapter 58. Pseudomasses, particularly haematomas, subcutaneous fat necrosis and Morel–Lavellée lesions, are particularly frequent in the pelvis and proximal thigh region secondary to trauma.

REFERENCES

1. Weybright PN, Jacobson JA, Murry KH, et al. Limited effectiveness of sonography in revealing hip joint effusion: preliminary results in 21 adult patients with native and postoperative hips. AJR Am J Roentgenol 2003;181:215–218.
2. McNally E. Ultrasound of the hip. In McNally E, ed. Practical musculoskeletal ultrasound. London: Churchill Livingstone; 2004.
3. Van Holsbeeck M, Introcasco J. Musculoskeletal ultrasound. St Louis, MO: Mosby; 2001.
4. Pfirrmann CW, Mengiardi B, Dora C, et al. Cam and pincer femoroacetabular impingement: characteristic MR arthrographic findings in 50 patients. Radiology 2006;240:778–785.
5. Adler RS, Buly R, Ambrose R, Sculco T. Diagnostic and therapeutic use of sonography-guided iliopsoas peritendinous injections. AJR Am J Roentgenol 2005;185:940–943.
6. Robinson P, Hensor E, Lansdown MJ, et al. Inguinofemoral hernia: accuracy of sonography in patients with indeterminate clinical features. AJR Am J Roentgenol 2006;187:1168–1178.
7. Pandit H, Glyn-Jones S, McLardy-Smith P, et al. Pseudotumours associated with metal-on-metal hip resurfacings. J Bone Joint Surg Br 2008;90:847–851.
8. Holmich P, Uhrskou P, Ulnits L, et al. Effectiveness of active physical training as treatment for long-standing adductor-related groin pain in athletes: randomised trial. Lancet 1999;353:439–443.
9. Robinson P, Barron DA, Parsons W, et al. Adductor-related groin pain in athletes: correlation of MR imaging with clinical findings. Skeletal Radiol 2004;33:451–457.
10. Bass CJ, Connell DA. Sonographic findings of tensor fascia lata tendinopathy: another cause of anterior groin pain. Skeletal Radiol 2002;31:143–148.
11. Blankenbaker DG, Tuite MJ. Iliopsoas musculotendinous unit. Semin Musculoskelet Radiol 2008;12:13–27.
12. Connell DA, Bass C, Sykes CA, et al. Sonographic evaluation of gluteus medius and minimus tendinopathy. Eur Radiol 2003;13: 1339–1347.
13. Pelsser V, Cardinal E, Hobden R, et al. Extraarticular snapping hip: sonographic findings. AJR Am J Roentgenol 2001;176:67–73.
14. Wank R, Miller TT, Shapiro JF. Sonographically guided injection of anesthetic for iliopsoas tendinopathy after total hip arthroplasty. J Clin Ultrasound 2004;32:354–357.
15. Trousdale RT, Cabanela ME, Berry DJ. Anterior iliopsoas impingement after total hip arthroplasty. J Arthroplasty 1995;10:546–549.
16. Pfirrmann CW, Chung CB, Theumann NH, et al. Greater trochanter of the hip: attachment of the abductor mechanism and a complex of three bursae – MR imaging and MR bursography in cadavers and MR imaging in asymptomatic volunteers. Radiology 2001;221:469–477.
17. Pfirrmann CW, Notzli HP, Dora C, et al. Abductor tendons and muscles assessed at MR imaging after total hip arthroplasty in asymptomatic and symptomatic patients. Radiology 2005;235:969–976.
18. Anderson K, Strickland SM, Warren R. Hip and groin injuries in athletes. Am J Sports Med 2001;29:521–533.
19. Robinson P. Ultrasound of groin injury. In: McNally E, ed. Practical musculoskeletal ultrasound. London: Churchill Livingstone; 2004.
20. Robinson P, Salehi F, Grainger A, et al. Cadaveric and MRI study of the musculotendinous contributions to the capsule of the symphysis pubis. AJR Am J Roentgenol 2007;188:W440–445.
21. Agur A. Grant's atlas of anatomy. Baltimore, MD: Williams and Wilkins; 1991.

22. Rutkow IM. Demographic and socioeconomic aspects of hernia repair in the United States in 2003. Surg Clin North Am 2003;83:1045–1051, v–vi.
23. Kark A, Kurzer M, Waters KJ. Accuracy of clinical diagnosis of direct and indirect inguinal hernia. Br J Surg 1994;81:1081–1082.
24. Ekberg O, Blomquist P, Olsson S. Positive contrast herniography in adult patients with obscure groin pain. Surgery 1981;89:532–535.
25. van den Berg JC, Strijk SP. Groin hernia: role of herniography. Radiology 1992;184:191–194.
26. Ekberg O. Complications after herniography in adults. AJR Am J Roentgenol 1983;140:491–495.
27. Smedberg SG, Broome AE, Gullmo A, Roos H. Herniography in athletes with groin pain. Am J Surg 1985;149:378–382.
28. Aguirre DA, Casola G, Sirlin C. Abdominal wall hernias: MDCT findings. AJR Am J Roentgenol 2004;183:681–690.
29. Jaffe TA, O'Connell MJ, Harris JP, et al. MDCT of abdominal wall hernias: is there a role for valsalva's maneuver? AJR Am J Roentgenol 2005;184:847–851.
30. Hara AK, Johnson CD, MacCarty RL, Welch TJ. Incidental extracolonic findings at CT colonography. Radiology 2000;215:353–357.
31. van den Berg JC, de Valois JC, Go PM, Rosenbusch G. Detection of groin hernia with physical examination, ultrasound, and MRI compared with laparoscopic findings. Invest Radiol 1999;34:739–743.
32. Chou TY, Chu CC, Diau GY, et al. Inguinal hernia in children: US versus exploratory surgery and intraoperative contralateral laparoscopy. Radiology 1996;201:385–388.
33. Toki A, Watanabe Y, Sasaki K, et al. Ultrasonographic diagnosis for potential contralateral inguinal hernia in children. J Pediatr Surg 2003;38:224–226.
34. Bradley M, Morgan D, Pentlow B, Roe A. The groin hernia – an ultrasound diagnosis? Ann R Coll Surg Engl 2003;85:178–180.
35. Kraft BM, Kolb H, Kuckuk B, et al. Diagnosis and classification of inguinal hernias. Surg Endosc 2003.
36. Zhang GQ, Sugiyama M, Hagi H, Urata T, et al. Groin hernias in adults: value of color Doppler sonography in their classification. J Clin Ultrasound 2001;29:429–434.
37. Orchard JW, Read JW, Neophyton J, Garlick D. Groin pain associated with ultrasound finding of inguinal canal posterior wall deficiency in Australian Rules footballers. Br J Sports Med 1998;32:134–139.
38. Steele P, Annear P, Grove JR. Surgery for posterior inguinal wall deficiency in athletes. J Sci Med Sport 2004;7:415–421; discussion 422–423.
39. Kesek P, Ekberg O, Westlin N. Herniographic findings in athletes with unclear groin pain. Acta Radiol 2002;43:603–608.
40. Deitch EA, Soncrant MC. The value of ultrasound in the diagnosis of nonpalpable femoral hernias. Arch Surg 1981;116:185–187.
41. Fricker PA. Management of groin pain in athletes. Br J Sports Med 1997;31:97–101.
42. Slavotinek JP, Verrall GM, Fon GT, Sage MR. Groin pain in footballers: the association between preseason clinical and pubic bone magnetic resonance imaging findings and athlete outcome. Am J Sports Med 2005;33:894–899.
43. Ziprin P, Williams P, Foster ME. External oblique aponeurosis nerve entrapment as a cause of groin pain in the athlete. Br J Surg 1999;86:566–568.
44. Verrall GM, Slavotinek JP, Fon GT. Incidence of pubic bone marrow oedema in Australian rules football players: relation to groin pain. Br J Sports Med 2001;35:28–33.
45. Cunningham PM, Brennan D, O'Connell M, et al. Patterns of bone and soft-tissue injury at the symphysis pubis in soccer players: observations at MRI. AJR Am J Roentgenol 2007;188:W291–296.
46. Holt MA, Keene JS, Graf BK, Helwig DC. Treatment of osteitis pubis in athletes. Results of corticosteroid injections. Am J Sports Med 1995;23:601–606.
47. O'Connell MJ, Powell T, McCaffrey NM, et al. Symphyseal cleft injection in the diagnosis and treatment of osteitis pubis in athletes. AJR Am J Roentgenol 2002;179:955–959.
48. Schilders E, Bismil Q, Robinson P, et al. Adductor-related groin pain in competitive athletes. Role of adductor enthesis, magnetic resonance imaging, and entheseal pubic cleft injections. J Bone Joint Surg Am 2007;89:2173–2178.

CHAPTER

56

Ultrasound of the knee

Ian Beggs

INTRODUCTION

Ultrasound is a valuable tool in the investigation of the knee. Although unable to compete with magnetic resonance imaging (MRI) in the investigation of the menisci, cruciate ligaments or bony abnormalities, ultrasound provides superb detail of anatomy and pathology in the extensor mechanism, popliteal fossa, and medial and lateral knee and distinguishes cystic from solid masses.

ANATOMY AND ULTRASOUND EXAMINATION

The examination should be performed using a high-frequency linear array transducer. The European Society of Skeletal Radiology provides detailed guidance on examination technique at http://essr.org/html/img/pool/knee.pdf. The knee is best considered as having four separate quadrants: anterior, posterior, medial and lateral.

The anterior knee includes the quadriceps muscles and tendon, patella, patellar tendon, suprapatellar recess and infrapatellar (Hoffa's) fat. The anterior knee is examined with the hip extended and the knee in slight flexion with the patient supine and a small pad under the knee.

The quadriceps muscles (Fig. 56.1) consist of the rectus femoris muscle which lies superficially and in the midline, vastus intermedius which lies deep to rectus femoris, and vastus medialis and lateralis on either side of rectus femoris and superficial to vastus intermedius. The quadriceps muscles narrow inferiorly to form the quadriceps tendon. The rectus femoris component of the tendon is the first to form proximally, then vastus intermedius. The vastus medialis and vastus lateralis muscles extend quite far distally, particularly lateralis, and join the tendon obliquely.

The suprapatellar recess (Fig. 56.2) lies deep to the quadriceps tendon. It is seen as a thin echogenic line if there is no fluid in the recess.

The quadriceps tendon inserts into the upper pole of the patella although fibres cross the front of the patella in continuity with the patellar tendon, which runs from the inferior pole of the patella to the tibial tuberosity. The patellar tendon (Fig. 56.3) is uniform in calibre and texture although both ends are slightly expanded and the edges tapered (Fig. 56.4A,B). The tendon measures 10–15 mm in width and 3–6 mm in depth.[1] The medial and lateral retinacula are thin hypoechoic structures that extend from the patella on transverse images.

With the leg slightly externally rotated, the medial structures are examined. The medial collateral ligament (Fig. 56.5) extends from the medial femoral epicondyle to the medial cortex of the proximal tibia. The ligament is usually of uniform texture and is slightly wider inferiorly. Occasionally a small bursa lies between its deep and superficial layers. The medial meniscus (Fig. 56.5) is deep to and in continuity with the collateral ligament. The pes anserinus tendons, from anterior to posterior, sartorius, gracilis and semitendinosus, lie posteromedial to the medial collateral ligament and insert on the proximal tibia alongside semimembranosus.

The lateral structures are examined with the leg slightly internally rotated. The iliotibial band (Fig. 56.6) is the most anterior structure. It inserts on Gerdy's tubercle on the anterolateral aspect of the proximal tibia. Behind this is the lateral collateral ligament, which runs obliquely from the lateral femoral epicondyle to insert on the fibular head, usually in a conjoined tendon with biceps femoris, which is the most posterior of the lateral structures.

The posterior structures are examined with the patient prone and the knee extended or minimally flexed. The medial and lateral heads of gastrocnemius arise from the respective femoral condyles. The popliteal vessels lie between the gastrocnemius heads. The pes anserinus tendons lie medial to the medial head of gastrocnemius. The semimembranosus tendon lies just deep to semitendinosus; the two tendons may be hypoechoic and simulate cysts if the transducer is not perpendicular (Fig. 56.7). The common peroneal nerve lies on the lateral border of the lateral head of gastrocnemius, and runs distally around the neck of the fibula.

ANTERIOR KNEE

Patellar tendinosis

Tendinosis usually affects the proximal end of the patellar tendon ('jumper's knee') and is thought to be the result of overuse, although

Patellar tendon

- The patellar tendon may appear hypoechoic due to anisotropy.

Focused examination

- Ultrasound examination of the knee is usually targeted on a specific problem and does not examine the whole knee.

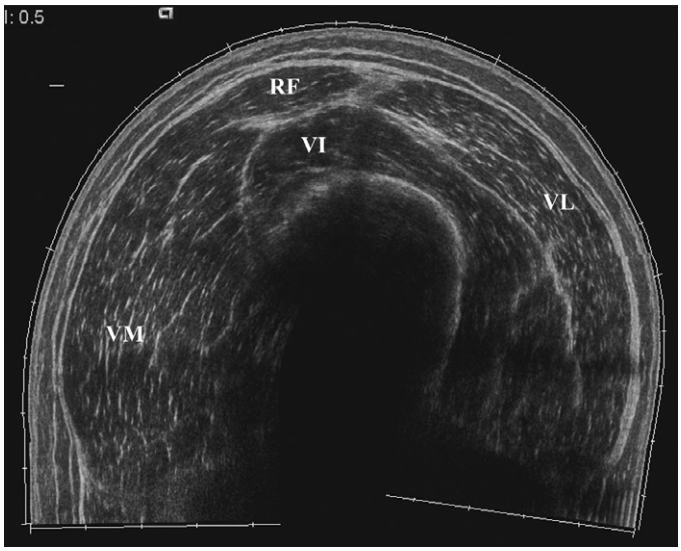

Figure 56.1 Quadriceps muscles: transverse, extended field-of-view image (RF, rectus femoris muscle; VM/VI/VL, vastus medialis/intermedius/lateralis muscles respectively).

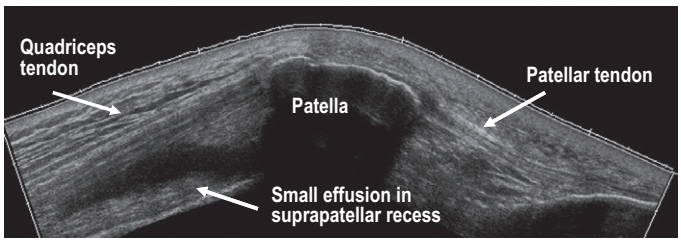

Figure 56.2 Quadriceps tendon, patella and patellar tendon: longitudinal extended field-of-view image. There is a small effusion in the suprapatellar recess.

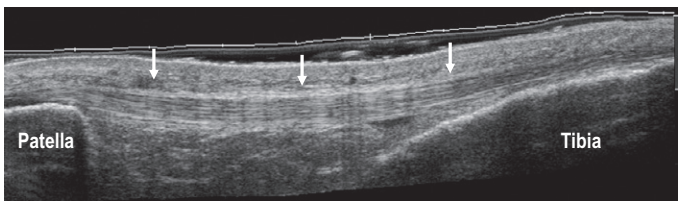

Figure 56.3 Longitudinal scan of patellar tendon (arrows) running from inferior pole of patella to tibial tuberosity. The tendon is well defined and uniform in calibre and texture.

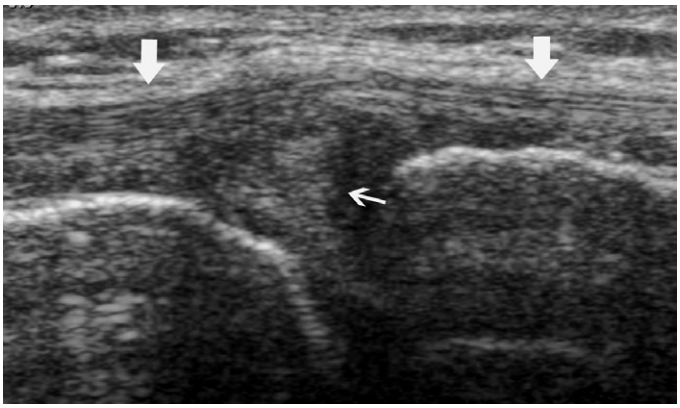

Figure 56.5 Longitudinal scan of medial collateral ligament (thick arrows) showing similar appearance to tendons. The medial meniscus (small arrow) is deep to the ligament and is triangular and echogenic.

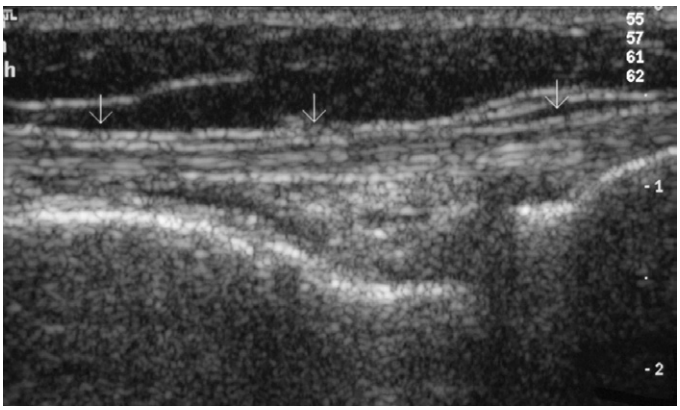

Figure 56.6 The iliotibial band (arrows) appears identical to other ligamentous structures.

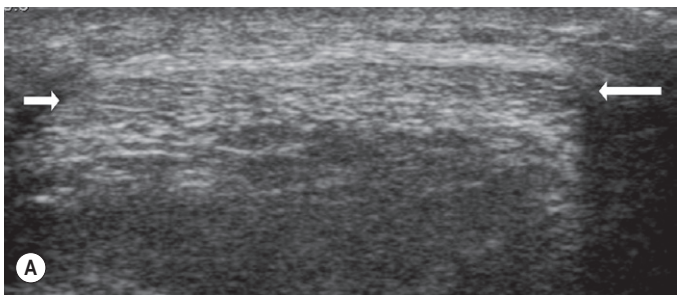

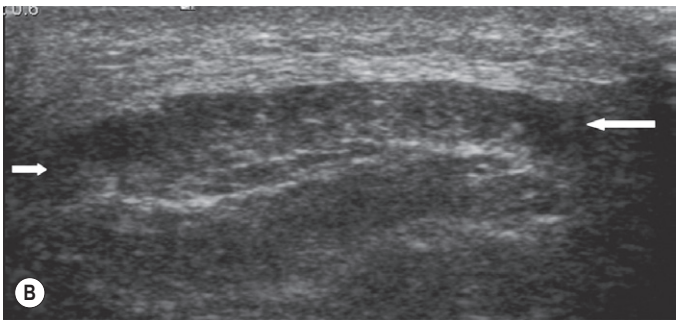

Figure 56.4 Patellar tendon. A: Transverse scan of patellar tendon (arrows). It is well defined, echogenic and uniform in calibre and texture although its edges are tapered. **B:** Same position as **A**. Altering the angle of insonation from 90° makes the tendon hypoechoic and more conspicuous.

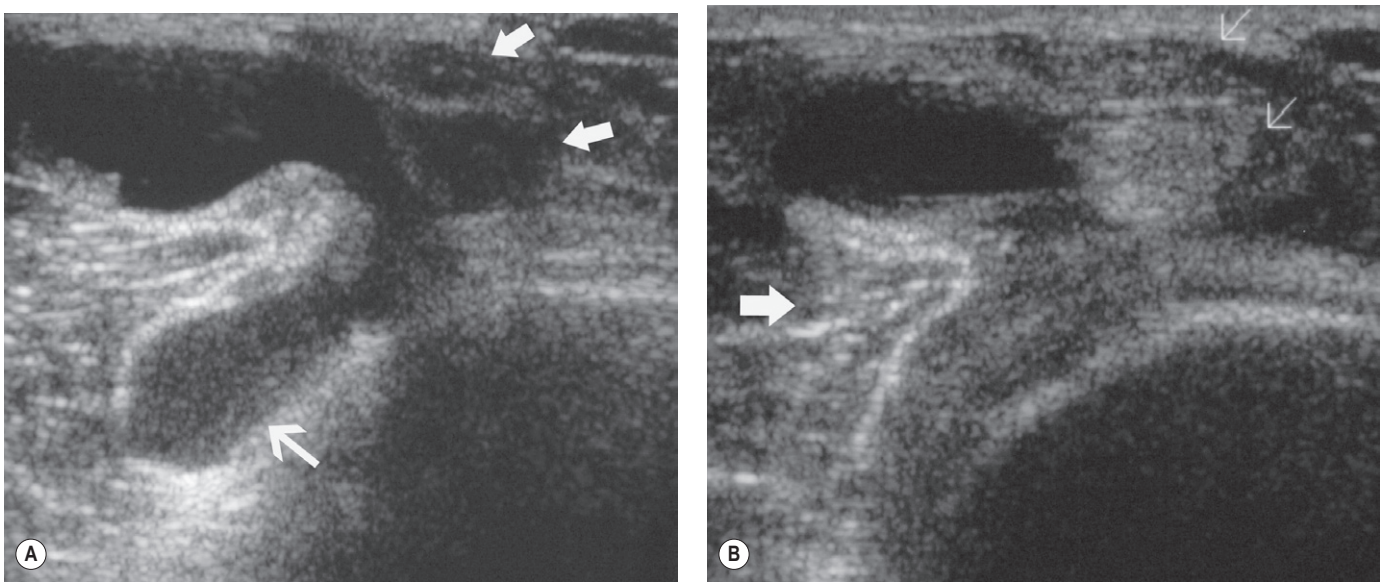

Figure 56.7 Semimembranosus and semitendinosus tendons. A: Transverse scan of popliteal fossa showing neck (narrow arrow) of small Baker's cyst emerging between medial head of gastrocnemius (between neck and cyst) and semimembranosus and semitendinosus tendons (short arrows). The tendons are virtually anechoic due to anisotropy. This effect can be used to make tendons more conspicuous. **B:** Altering transducer angulation makes the tendons (small arrows) appear echogenic. The broader arrow points to the medial head of gastrocnemius.

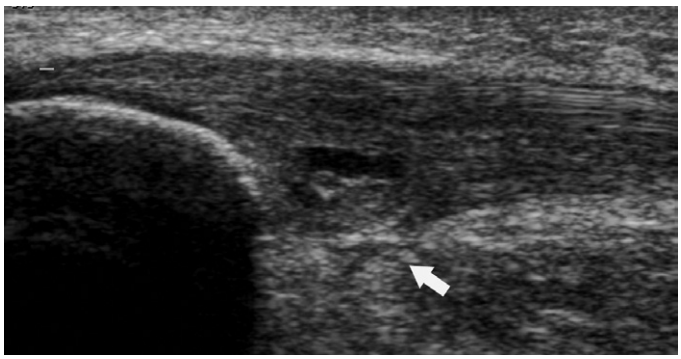

Figure 56.8 Longitudinal scan of jumper's knee: the proximal patellar tendon (arrow) adjacent to the lower pole of the patella is swollen, hypoechoic and ill defined. Cystic change is present.

various aetiological theories have been proposed.[1–4] Histologically the normal, highly organised pattern of collagen bundles is disrupted. Increased amounts of mucoid ground substance and cellular infiltrates, particularly tenocytes, are present. Capillary proliferation and deposits of cartilage and bone are also features. Inflammatory changes are absent.[2,5]

Ultrasound shows hypoechoic swelling (Fig. 56.8) of the proximal patellar tendon adjacent to the inferior pole of the patella. The swelling is focal, usually posterior, and involves only part of the width of the tendon. The deep surface is ill defined. The paratenon may be thickened. Echogenic foci of ossification or calcification (Fig. 56.9) in the tendon and hyperostosis at the inferior pole of the patella may be present in longstanding cases. There is generally good agreement between ultrasound and MRI in assessing the extent of morphological changes but asymptomatic morphological changes are common.[1,5] Neovascularity (Figs 56.10–56.12) on colour or power Doppler correlates strongly with pain.[6,7] Abnormal Doppler signal is less conspicuous when the tendon is under tension

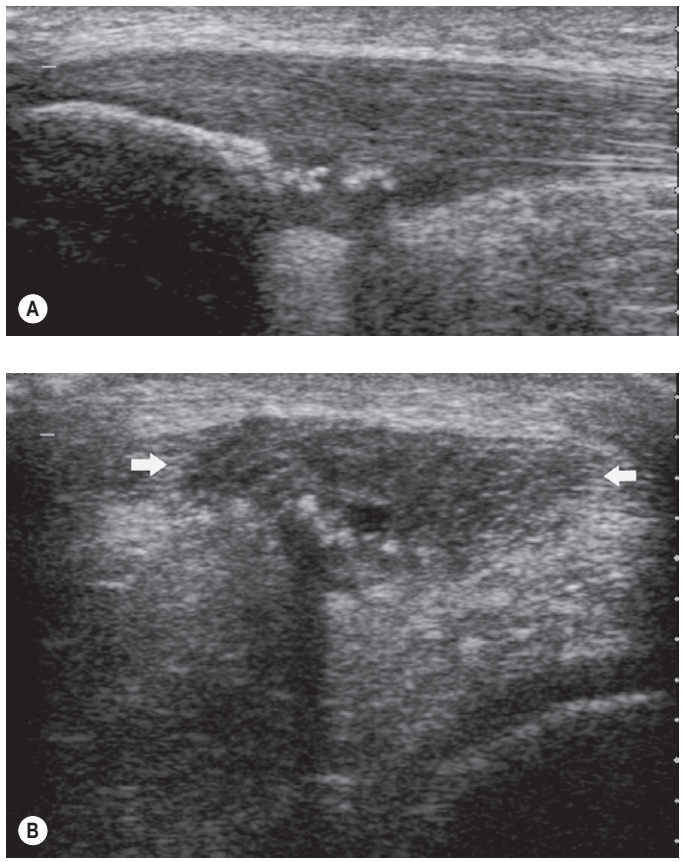

Figure 56.9 Tendinosis. A: Longitudinal scan: microcalcification is present in the segment of tendinosis. **B:** The transverse scan shows that the tendinosis involves only part of the width of the tendon (arrows at tendon margins). The swelling is posterior. Calcification and cystic change are also present.

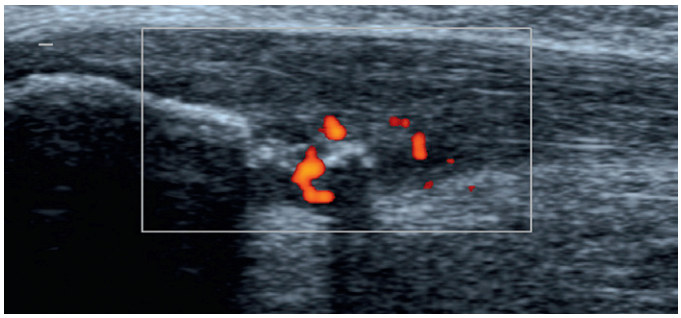

Figure 56.10 Neovascularity on power Doppler correlates with symptomatic tendinosis. The tendon is swollen, hypoechoic, ill defined and contains echogenic foci of calcification or ossification.

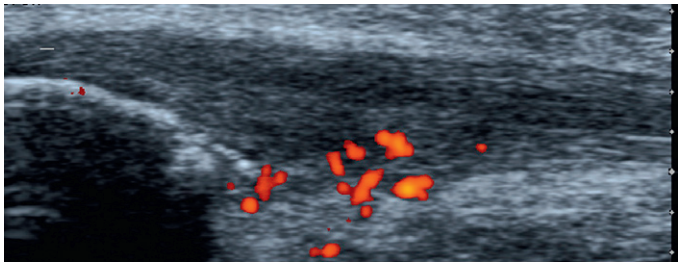

Figure 56.11 Neovascularity typically extends into adjacent soft tissues.

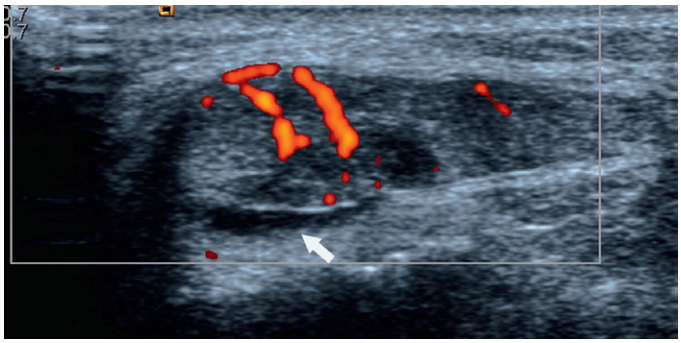

Figure 56.12 Transverse power Doppler scan of tendinosis at distal end of patellar tendon. The tendon is eccentrically swollen, heterogeneously hypoechoic and contains new vessels. The adjacent paratenon (arrow) is thickened and hypoechoic.

Tendon changes

- Morphological changes in the patellar tendon may be asymptomatic. Neovascularity correlates with pain.

and more obvious after exercise.[8] Neovascularity suggests a better prognosis and inhomogeneity a poorer outcome.[9] Progression from tendinosis to a full thickness tear is rare.

Treatment of jumper's knee is usually conservative and involves physiotherapy. However, dry needling and injections of autologous blood or sclerosants under ultrasound guidance have been advocated as treatments that are directed at the neovascularity.[1]

Tears of quadriceps and patellar tendons

Tears of the quadriceps and patellar tendons occur less often than tears of the rotator cuff or Achilles tendon.

Quadriceps tears are due to sudden contraction of the extensor mechanism. Patients are usually middle-aged or older and may have a systemic disease such as rheumatoid arthritis, gout, systemic lupus erythematosus, diabetes mellitus, chronic renal failure or hyperparathyroidism. Patients present with swelling and inability to extend the knee although a post-traumatic joint effusion without tendon damage may have an identical clinical presentation, while extension may still be possible with partial tears.

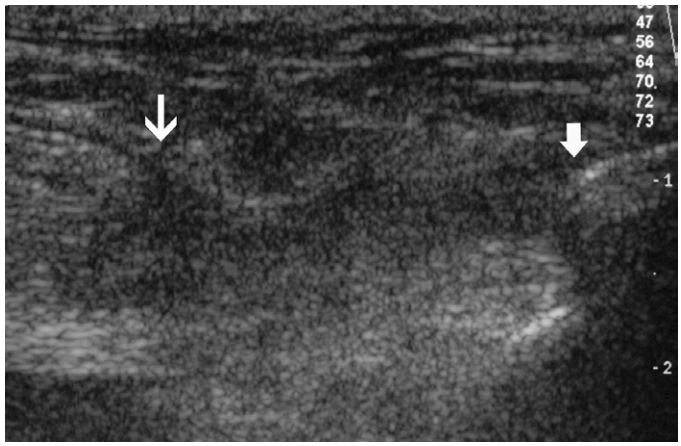

Figure 56.13 Longitudinal scan of tear of quadriceps tendon (arrows at tear margins). Hypoechoic haematoma occupies the gap.

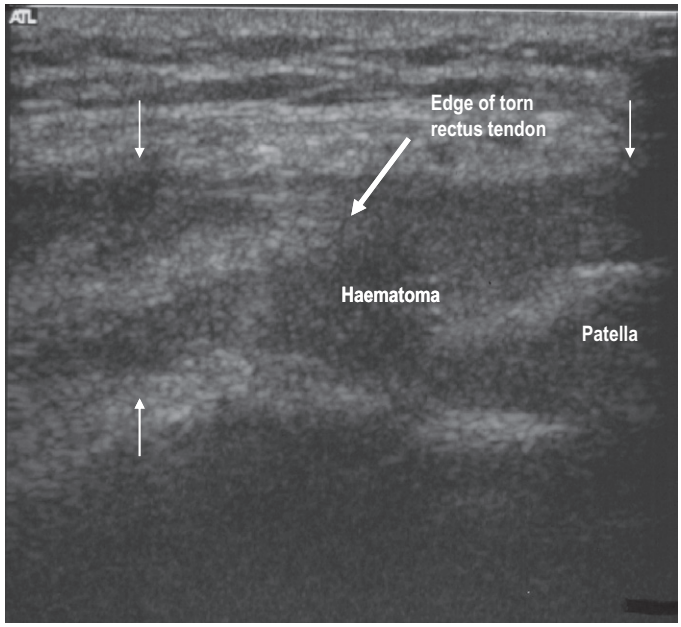

Figure 56.14 Longitudinal scan of tear of rectus femoris tendon. Haematoma between the patella and retracted tendon extends superficial to the patella and superficial and deep to the rectus tendon (arrows).

Most quadriceps tears are incomplete and involve the superficial rectus femoris component of the quadriceps tendon. The tear occurs in the distal 1–2 cm of the tendon or at its insertion into the patella.[10] Ultrasound shows a gap (Fig. 56.13) in the tendon fibres that is easier to identify if occupied by hypoechoic haematoma, which may track subcutaneously and between muscle and tendon layers (Fig. 56.14). The proximal tendon edge is retracted and may be made more conspicuous by gentle flexion of the knee.

Complete tears of the quadriceps tendon also involve the distal tendon although occasionally the proximal pole of the patella (Fig. 56.15) is avulsed. All layers of tendon are involved and the swollen tendon edges are separated by a liquid haematoma which may

track into adjacent tissues. Traction on the patella makes the defect more obvious and helps to distinguish between complete and incomplete ruptures.

Ultrasound has 100% sensitivity for partial and complete quadriceps tendon tears and 100% specificity for complete tears.[10,11]

Patellar tendon ruptures involve the proximal tendon. They are less frequent than quadriceps tears and are due to sporting injuries in younger patients. There may be pre-existing tendinosis. Patients present with pain, swelling and inability to extend the knee. Radiographs show proximal retraction of the patella. Ultrasound demonstrates a fluid-filled defect in the tendon[12] and an irregular, redundant appearance of the distal tendon.

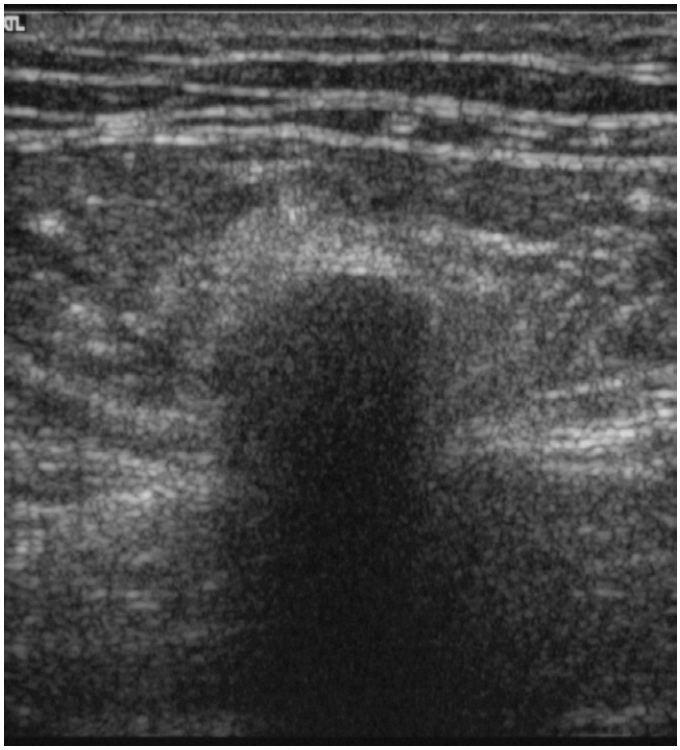

Figure 56.15 Quadriceps tendon tear. Transverse scan: the echogenic focus is a small fragment of the proximal pole of the patella that has been avulsed with the quadriceps tendon still attached.

Quads and patellar tendon tears

- Tears of the quadriceps and patellar tendons may be more conspicuous if the examination is performed with the knee flexed.

Osgood–Schlatter disease

Osgood–Schlatter disease occurs in adolescents and is the result of chronic avulsive stress where the patellar tendon inserts into the tibial apophysis. Hirano et al.[13] have shown that the primary injury is in the apophysis and that the tendon changes are secondary. Patients present with pain, tenderness and swelling. The diagnosis is usually clinical.

Ultrasound shows swelling of the distal patellar tendon, apophyseal cartilage and pretibial soft tissues, fragmentation of the ossification centre and distension of the infrapatellar bursa. Neovascularity may be present in the tendon and bursa. Similar changes at the inferior pole of the patella are seen in Sinding-Larsen–Johansson disease.[14,15]

Joint effusion

Ultrasound detects small amounts of fluid (Fig. 56.16) in the suprapatellar recess, first seen in the recesses on either side of the patella. Larger effusions extend proximally and clinically may simulate a solid mass. Early synovial hypertrophy results in hypoechoic thickening of the wall of the suprapatellar recess. In advanced cases the recess is distended by solid pannus. Colour and power Doppler distinguish between active pannus, which is vascular, and fibrous pannus, which is hypovascular.[16] Contrast-enhanced power Doppler shows reduced perfusion in response to treatment.[17]

A post-traumatic haemarthrosis contains hypoechic fluid although echogenic thrombi may also be present. A lipohaemarthrosis is due to escape of medullary fat through an intra-articular fracture. Ultrasound performed soon after the injury shows two layers and an intervening fluid–fluid level (Fig. 56.17) as the echogenic fat floats on the hypoechoic blood. After about 3 hours the serum and red blood cells (RBCs) separate and a three-layer, two fluid–fluid levels appearance may develop. The superior echogenic band of fat, middle almost anechoic layer of serum and synovial fluid, and dependent layer of hypoechoic RBCs are separated by thin fluid–fluid levels.[18,19] Ultrasound is more accurate than radiographs in the identification of lipohaemarthrosis.[20]

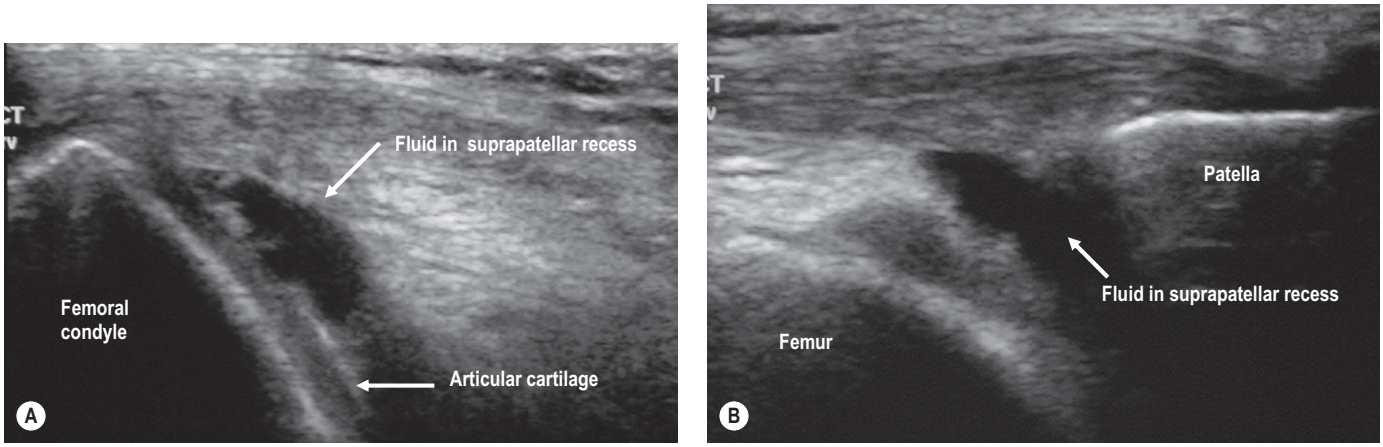

Figure 56.16 Joint effusion. A: Transverse scan showing tiny joint effusion in suprapatellar recess beside femoral condyle. Hypoechoic articular cartilage lies between the fluid and the condyle. **B:** Longitudinal scan showing small effusion in suprapatellar recess between patella and femur.

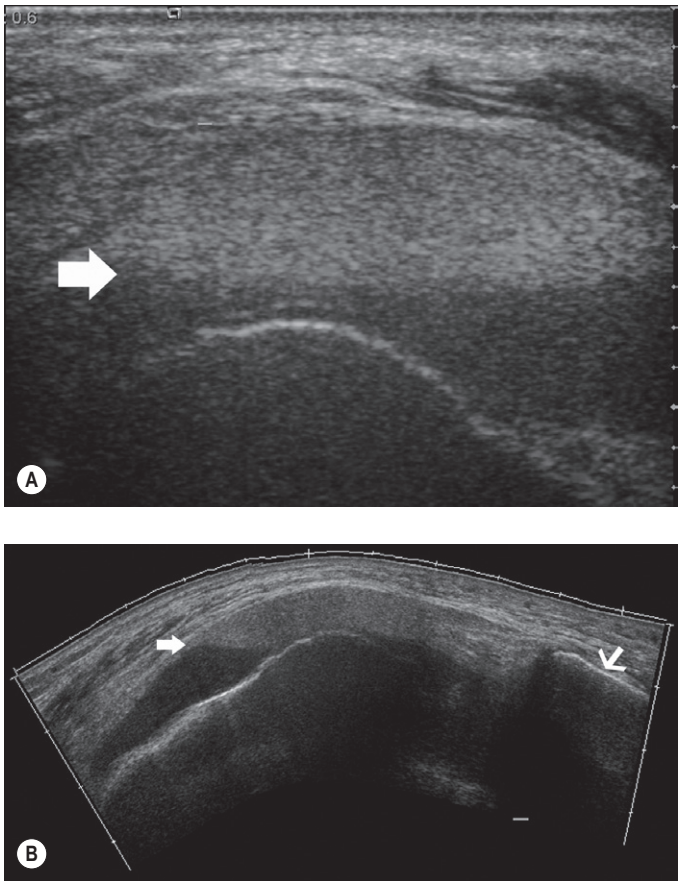

Figure 56.17 Lipohaemarthosis. A: Transverse scan of lipohaemarthosis. The echogenic fat lies superficial to the blood and synovial fluid forming a fluid–fluid level (arrow). **B:** Longitudinal scan of fluid–fluid level (broad arrow) due to lipohaemarthosis in suprapatellar recess. The narrow arrow points to the patella.

Joint effusions

- Small joint effusions can be identified by ultrasound.
- A fluid–fluid level is typical of a lipohaemarthrosis and indicates that a fracture is present.

Other anterior bursae

A small amount of fluid in the deep infrapatellar bursa which lies posterior to the distal patellar tendon is normal. Deep infrapatellar bursitis may occur in association with distal patellar tendinopathy but the difference between normal and pathological bursae has not been defined.

Fluid in the prepatellar bursa may be symptomatic and caused by prolonged kneeling, 'housemaid's knee' superficial to the patella and 'clergyman's knee' superficial to the patellar tendon. The bursal wall may be thickened, abnormal flow present on colour or power Doppler, and pain produced by palpation in bursitis,[12] but small amounts of fluid in the prepatellar bursa may be without clinical significance. Synovial hypertrophy may be present (Fig. 56.18).

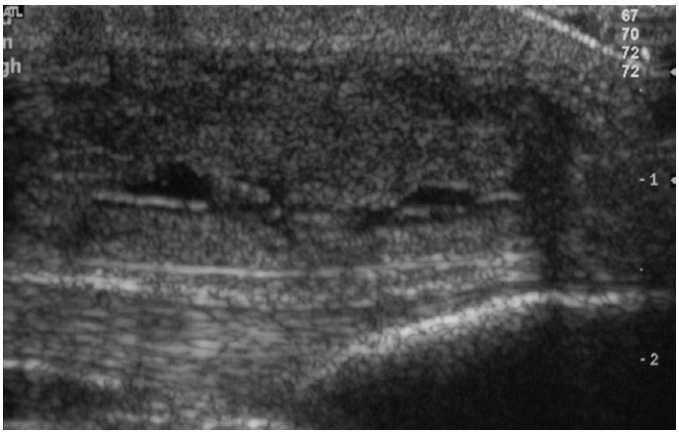

Figure 56.18 Longitudinal scan of distended prepatellar bursa overlying distal patellar tendon. Echogenic synovium and a small amount of fluid fill the bursa.

POSTERIOR KNEE

Baker's cyst

The most frequent indication for ultrasound examination of the posterior knee is to confirm the presence and define the nature of a space-occupying lesion in the popliteal fossa, usually due to a semimembranosus–gastrocnemius bursa or Baker's cyst or other synovial cyst. They are generally anechoic and well defined, although hypoechic fluid contents may be present. Prominence of a normal medial or lateral head of gastrocnemius muscle also accounts for a number of referrals.

Baker's cysts are common and frequently asymptomatic, although they may present with swelling and/or mild discomfort. An MRI study of asymptomatic knees found Baker's cysts in 20% of knees, almost all <3 cm in diameter.[21] The essential criterion for the diagnosis of a Baker's cyst is identification of the fluid-filled neck (Fig. 56.7) of the cyst running from the posterior aspect of the knee joint between the medial head of gastrocnemius laterally and the semimembranosus and semitendinosus tendons medially.[22] This is best achieved on transverse scans with the knee very slightly flexed. The neck of the cyst is narrow, may be effaced by pressure between gastrocnemius and semimembranosus when the knee is fully extended and can function as a one- or two-way valve resulting in a swelling that waxes and wanes. In uncomplicated cysts either or both the gastrocnemius and semimembranosus components of the cyst contain anechoic fluid and may extend distally or proximally respectively. The fluid may be partly or wholly replaced by hypoechoic pannus or contain echogenic foci (Fig. 56.19) of synovial osteochondromatosis.

Rupture of a Baker's cyst presents with a painful, swollen calf that clinically resembles a deep vein thrombosis (DVT). Both a ruptured cyst and a DVT should be sought on ultrasound as they may coexist. Cyst rupture (Fig. 56.20) usually occurs distally and the shape of the distal border of the cyst changes from convex to pointed. Rupture results in cyst deflation although the cyst re-expands when the leak seals. The fluid tracks along tissue planes, subcutaneously and between muscles. Anticoagulated patients may present with a swollen, painful calf due to haemorrhage into a Baker's cyst resulting in hypoechoic fluid or echogenic clots in the cyst. Cyst haemorrhage and rupture may coexist.

If no abnormality is found, the transducer should be moved distally to look for a 'tennis leg' by identifying a tear of the medial head of gastrocnemius or a fluid collection between the aponeuroses of the soleus and medial head of gastrocnemius muscles.[23]

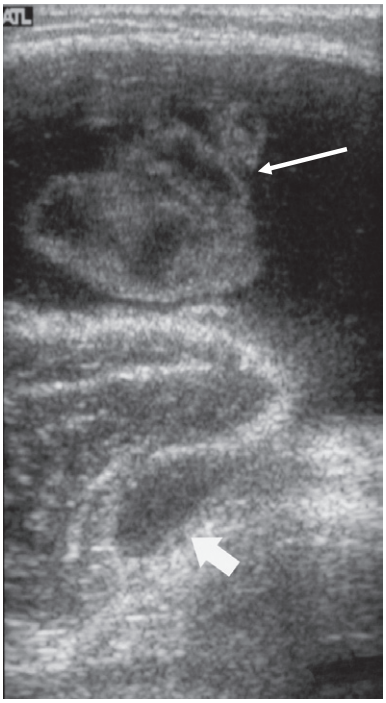

Figure 56.19 Transverse scan of small Baker's cyst (wide arrow points to neck of cyst) that contains an irregular, echogenic focus of synovial osteochondromatosis (narrow arrow).

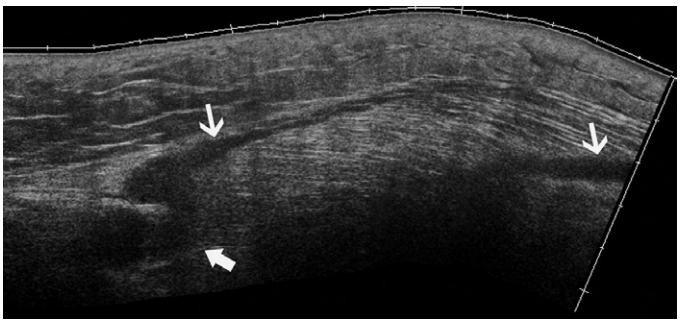

Figure 56.20 Ruptured Baker's cyst (broad arrow). Fluid (narrow arrows) tracks deep and superficial to the medial gastrocnemius muscle.

Baker's cysts

- The stalk of a Baker's cyst lies between medial head of gastrocnemius and the semimembranosus and semitendinosus tendons. The tendons may appear hypoechoic and cystic due to anisotropy.
- Rupture of a Baker's cyst may present like a DVT.

Cruciate ligaments

Normal cruciate ligaments are not well demonstrated on ultrasound because of their oblique orientation and the effect of anisotropy. Tears of the cruciate ligaments are frequently associated with other bone and soft tissue injuries and are best investigated with MRI. However, the ultrasound appearances of cruciate injuries have been reported.

The normal posterior cruciate ligament (PCL) is seen on longitudinal scans as a hypoechoic band running obliquely to its insertion on the posterior margin of the tibia inferior to the tibial plateaux. Tears of the PCL result in focal discontinuity or diffuse swelling compared with the opposite PCL.[24]

The normal anterior cruciate ligament is not seen on ultrasound but a hypoechoic haematoma on the lateral wall of the intercondylar notch on a posterior transverse scan is said to indicate the presence of an anterior cruciate ligament tear.[25]

Anechoic, well-defined ganglion cysts are occasionally seen in or adjacent to the cruciate ligaments.[26]

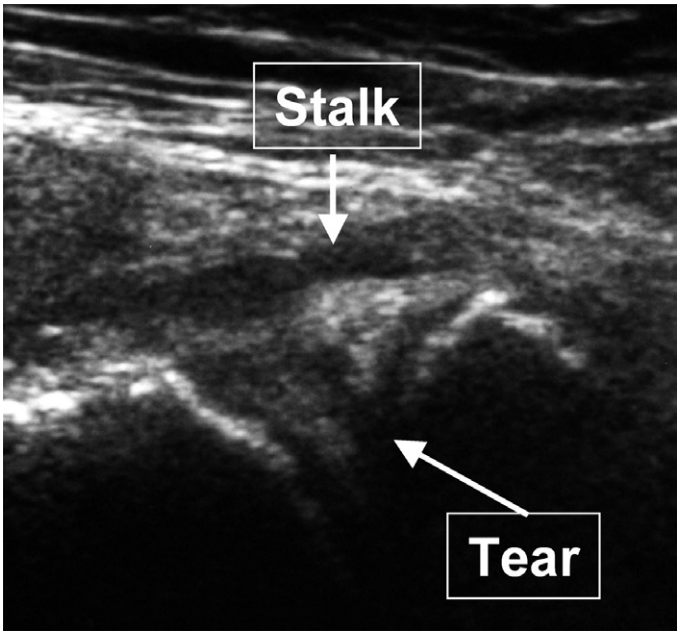

Figure 56.21 Torn medial meniscus and stalk of associated meniscal cyst.

MEDIAL KNEE

Medial collateral ligament

Isolated injuries of the medial collateral ligament (MCL) result from valgus stress. Most are treated conservatively and require no imaging. MRI is indicated if more complex injuries are suspected.

Most MCL injuries are proximal and involve the deep layer more frequently than the superficial layer. A grade I sprain is really a peri-ligamentous injury without instability and produces hypoechoic fluid and swelling adjacent to the MCL. A grade II sprain is a partial tear and additionally results in instability and swelling of the MCL. A grade III injury is a complete tear and causes gross instability. Hypoechoic fluid or haematoma occupies the defect in the disrupted deep and superficial layers. Thickening or calcification, the Pellegrini–Stieda lesion seen on radiographs, adjacent to the medial epicondyle represents an old injury.[27]

Medial meniscus

MRI rather than ultrasound is the imaging examination of choice for the meniscus. The normal medial meniscus is triangular and echogenic (Fig. 56.5). Tears (Fig. 56.21) appear as anechoic or hypoechoic, occasionally hyperechoic, clefts or as an absent or truncated meniscus. Swelling, reduced echogenicity and extrusion occur in meniscal degeneration. Focal echogenic areas suggest meniscal calcification. A gap between the meniscus and the MCL suggests meniscocapsular separation.

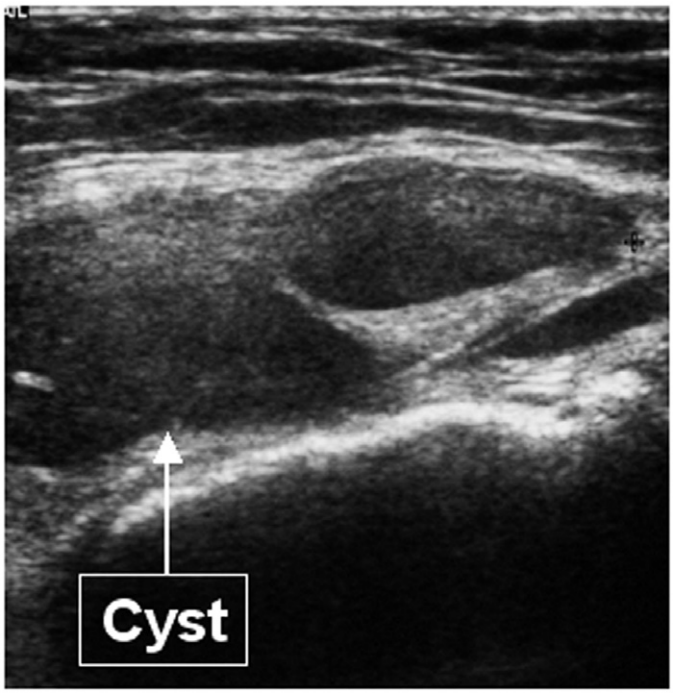

Figure 56.22 **Multiloculated meniscal cyst.**

Meniscal cysts

- Meniscal cysts are usually associated with meniscal tears.

Meniscal cysts (Figs 56.21 and 56.22) present with pain and swelling at the joint margin, although not all cysts are symptomatic. They develop as a consequence of an underlying meniscal tear that allows joint contents to leak into the para-meniscal tissues. Cyst appearances reflect their contents and range from hypoechoic masses to uni- or multilocular cystic masses that contain anechoic or hypoechoic fluid. The characteristic feature is that the mass lies alongside the meniscus.[28]

Pes anserinus bursa

The pes anserinus bursa lies deep to the tendons of sartorius, gracilis and semitendinosus as they run to insert on the medial aspect of the tibia. Bursitis presents with localised pain and swelling. Ultrasound shows the fluid-filled bursa between the tendons and the proximal tibia.[29]

LATERAL KNEE

Lateral collateral ligament

Sprains of the lateral collateral ligament are usually investigated by MRI as part of a suspected more complex injury. Isolated sprains are uncommon and produce focal swelling or discontinuity on ultrasound.

Iliotibial band

Chronic friction due to sporting activities results in iliotibial band friction syndrome where the iliotibial band runs over the lateral femoral condyle. Ultrasound shows thickening and reduced echogenicity of the affected segment of the iliotibial band and may also show a deeper hypoechoic area due to bursitis or soft tissue inflammation.[30]

Iliotibial band tendinopathy occurs in older patients who have osteoarthritis or a knee prosthesis and results from altered stresses due to an angular deformity or rubbing against the edge of the tibial component respectively. It causes lateral or anterior knee pain. Ultrasound shows swelling, reduced echogenicity and loss of the normal fibrillar pattern of the distal iliotibial band. Changes may be subtle and comparison with the opposite side may help.[31]

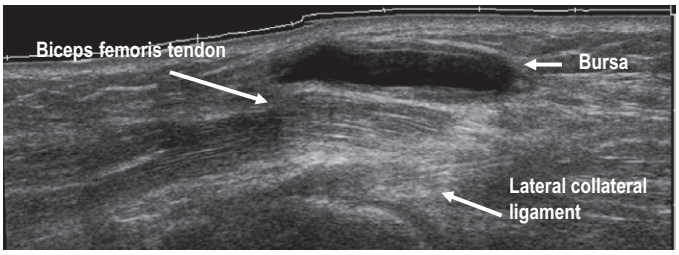

Figure 56.23 **Thick-walled bursa** overlying distal biceps femoris muscle and lateral collateral ligament.

Lateral meniscus

Tears and cysts of the lateral meniscus appear identical to those in the medial meniscus. Fluid around the popliteus tendon as it runs through the posterior horn of the meniscus should not be mistaken for a cyst.

Biceps femoris and popliteus tendons

Tendinopathy results in swelling and reduced echogenicity but is not common. A superficial bursa may be present (Fig. 56.23).

Proximal tibiofibular joint

Synovial cysts or ganglia may emerge from the anterior or posterior aspects of the proximal tibiofibular joint. They are frequently asymptomatic but may become palpable. Anterior cysts that run across the anterior and lateral aspects of the fibular neck may compromise or invade the common peroneal nerve as it runs from the popliteal fossa, between the peroneus longus muscle and the fibular neck to lie anterior to the proximal fibula.

The cyst or ganglion is identified on ultrasound as a well-defined anechoic mass. It is usually oval or pear-shaped, with its narrower end close to the tibiofibular joint, and has a thick wall. A narrow stalk may connect the joint and the cyst.[32]

REFERENCES

1. Peace KAL, Lee JC, Healy J. Imaging the infrapatellar tendon in the elite athlete. Clin Radiol 2006;61:570–578.
2. Khan KM, Cook JL, Bonar F, et al. Histopathology of common tendinopathies. Update and implications for clinical management. Sports Med 1999;27(6):393–408.
3. Maganaris CN, Narici MV, Almekinders LC, Maffulli N. Biomechanics and pathophysiology of overuse tendon injuries: ideas on insertional tendinopathy. Sports Med 2004;34(14):1005–1017.
4. Wilson JJ, Best TM. Common overuse tendon problems: a review and recommendations for treatment. Am Fam Physician 2005;72(5):811–818.
5. Khan KM, Bonar F, Desmond PM, et al. Patellar tendinosis (jumper's knee): findings at histopathologic examination, US, and MR imaging. Victorian Institute of Sport Tendon Study Group. Radiology 1996;200:821–827.

6. Cook JL, Malliaras P, De Luca J, et al. Neovascularization and pain in abnormal patellar tendons of active jumping athletes. Clin J Sport Med 2004;14:296–299.
7. Warden SJ, Kiss ZS, Malara FA, et al. Comparative accuracy of magnetic resonance imaging and ultrasonography in confirming clinically diagnosed patellar tendinopathy. Am J Sports Med 2007;35:427–436.
8. Cook JL, Kiss ZS, Ptasznik R, Malliaras P. Is vascularity more evident after exercise? Implications for tendon imaging. AJR Am J Roentgenol 2005;185:1138–1140.
9. Zanetti M, Metzdorf A, Kundert H-P, et al. Achilles tendons: clinical relevance of neovascularization diagnosed with power Doppler ultrasound. Radiology 2003;227:556–560.
10. Bianchi S, Zwass A, Abdelwahab IF, Banderali A. Diagnosis of tears of the quadriceps tendon of the knee: value of sonography. AJR Am J Roentgenol 1994;162:1137–1140.
11. La S, Fessell DP, Femino JE, et al. Sonography of partial-thickness quadriceps tendon tears with surgical correlation. J Ultrasound Med 2003;22:1323–1329.
12. Carr JC, Hanly S, Griffin J, Gibney R. Sonography of the patellar tendon and adjacent structures in pediatric and adult patients. AJR Am J Roentgenol 2001;176:1535–1539.
13. Hirano A, Fukubayashi T, Ishii T, Ochiai N. Magnetic resonance imaging of Osgood-Schlatter disease: the course of the disease. Skeletal Radiol 2002;31:334–342.
14. De Flaviis L, Nessi R, Scaglione P, et al. Ultrasonic diagnosis of Osgood-Schlatter and Sinding-Larsen-Johansson diseases of the knee. Skeletal Radiol 1989;18:193–197.
15. Blankstein A, Cohen I, Heim M, et al. Ultrasonography as a diagnostic modality in Osgood-Schlatter disease. A clinical study and review of the literature. Arch Orthop Trauma Surg 2001;121:536–569.
16. Carotti M, Salaffi F, Manganelli P, et al. Power Doppler sonography in the assessment of synovial tissue of the knee joint in rheumatoid arthritis: a preliminary experience. Ann Rheum Dis 2002;61: 877–882.
17. Salaffi F, Carotti M, Manganelli P, et al. Contrast-enhanced power Doppler sonography of knee synovitis in rheumatoid arthritis: assessment of therapeutic response. Clin Rheumatol 2004;23:285–290.
18. Bianchi S, Zwass A, Abdelwahab IF, et al. Sonographic evaluation of lipohemarthrosis: clinical and in vitro study. J Ultrasound Med 1995;14:279–282.
19. Costa DN, Cavalcanti CF, Sernik RA. Sonographic and CT findings in lipohemarthrosis. AJR Am J Roentgenol 2007;188(4):W389.
20. Bonnefoy O, Diris B, Moinard M, et al. Acute knee trauma: role of ultrasound. Eur Radiol 2006;16:2542–2548.
21. Tschirch FT, Schmid MR, Pfirrmann CW, et al. Prevalence and size of meniscal cysts, ganglionic cysts, synovial cysts of the popliteal space, fluid-filled bursae, and other fluid collections in asymptomatic knees on MR imaging. AJR Am J Roentgenol 2003;180:1431–1436.
22. Helbich TH, Breitenseher M, Trattnig S, et al. Sonomorphologic variants of popliteal cysts. J Clin Ultrasound 1998;26:171–176.
23. Delgado GJ, Chung CB, Lektrakul N, et al. Tennis leg: clinical US study of 141 patients and anatomic investigation of four cadavers with MR imaging and US. Radiology 2002;224:112–119.
24. Miller TT. Sonography of injury of the posterior cruciate ligament of the knee. Skeletal Radiol 2002;31:149–154.
25. Ptasznik R, Feller J, Bartlett J, et al. The value of sonography in the diagnosis of traumatic rupture of the anterior cruciate ligament of the knee. AJR Am J Roentgenol 1995;164:1461–1463.
26. DeFriend DE, Schranz PJ, Silver DA. Ultrasound-guided aspiration of posterior cruciate ligament ganglion cysts. Skeletal Radiol 2001;30: 411–414.
27. Friedman L, Finlay K, Jurrians E. Ultrasound of the knee. Skeletal Radiol 2001;30:361–377.
28. Seymour R, Lloyd DC. Sonographic appearances of meniscal cysts. J Clin Ultrasound 1998;26:15–20.
29. Ptasznik R. Ultrasound in acute and chronic knee injury. Radiol Clin North Am 1999;37:797–830.
30. Bonaldi VM, Chhem RK, Drolet R, et al. Iliotibial band friction syndrome: sonographic findings. J Ultrasound Med 1998;17:257–260.
31. Martinoli C, Bianchi S. Ultrasound of the musculoskeletal system. Berlin: Springer, 2007;693–694.
32. Bianchi S, Zwass A, Abdelwahab IF, et al. Sonographic evaluation of intramuscular ganglia. Clin Radiol 1995;50:235–236.

CHAPTER

57 Ultrasound of the ankle and foot

David Wilson and Gina Allen

INTRODUCTION

Ultrasound examination of the foot and ankle is a clinically valuable technique which has gained popularity due to improved knowledge of anatomy, recognition of the value of dynamic stress imaging and improvement in ultrasound resolution for superficial soft tissue structures.

Most of the important structures in the foot are close to the surface and easily examined by ultrasound with the exception of the internal structure of bones. Increasing use of ultrasound has led to increased understanding of the technique and appreciation of its strengths and weaknesses, particularly when compared with conventional radiographs and magnetic resonance imaging (MRI). Knowledge of the pathophysiology of each syndrome and disease is essential in order to recognise both advanced and early changes. The same disease will give different findings depending on its duration and severity.[1–3]

The European Society of Skeletal Radiology Ultrasound Sub Committee presents a standard set of imaging planes as a basis for each examination (http://www.essr.org/cms/website.php?id=/en/index/educational_material.htm).

ANATOMY AND TECHNIQUE (Figs 57.1 to 57.3)

Examination technique will often include comparison with the normal side. Particular note should be made of tender or symptomatic areas, using ultrasound examination to identify the structure involved.

Posterior ankle

Achilles region

The Achilles tendon is the largest weight-bearing tendon of the body, carrying up to 50 newtons when the individual is standing. It is formed from the medial and lateral heads of the gastrocnemius muscle and the soleus muscle and has a posterior portion from the gastrocnemius muscles and an anterior portion from the soleus muscle. These components may be likened to a rope with two twisted elements that run in a spiral pattern in different planes. The bundles are easily distinguished using good quality ultrasound machines. Dynamic examination in the transverse plane shows a moving image of the rotation and clearly separates the two major parts of the tendon.

The Achilles tendon varies in length from 0 to 9 cm,[4] and measures approximately 5 mm in maximum sagittal diameter. It is either ovoid or kidney bean shaped in cross-section with a little increase in bulk medially. There is normally an anterior indentation or smooth convexity in its mid-portion although it is rounder near to the insertion.

The accessory soleus has been described as an additional muscle attaching to the tendon (Fig. 57.4), but a better description may be that it is a normal variation of the muscle insertion into the tendon with a low musculotendinous junction leading to a shortened free component of the Achilles tendon.

Normal variants due to incomplete fusion of the gastrocnemius and soleus tendons can lead to split or accessory tendons.

Rather than having a tendon sheath the Achilles has a loose connective tissue surrounding called the paratenon. This is less adherent posteriorly than anteriorly and is bound to the back of the calcaneus by fascia that acts as a 'retinaculum'. Bursae are present anterior and posterior to the tendon at the level of the calcaneus. and act as cushion pads. In utero the bursae contain synovium which can persist. The whole unit acts like a synovial joint in the fetus with extension into the plantar fascia. It is part of the 'enthesis organ' where the tendon is attached to the calcaneus by fibrocartilage which extends into the bone in plugs that penetrate the cortical bone and show a 'sieve'-like appearance on ultrasound

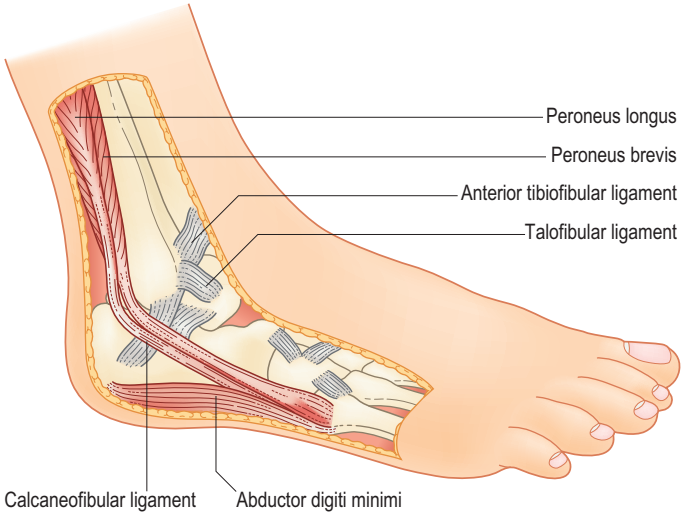

Figure 57.1 Anatomy of the lateral ankle.

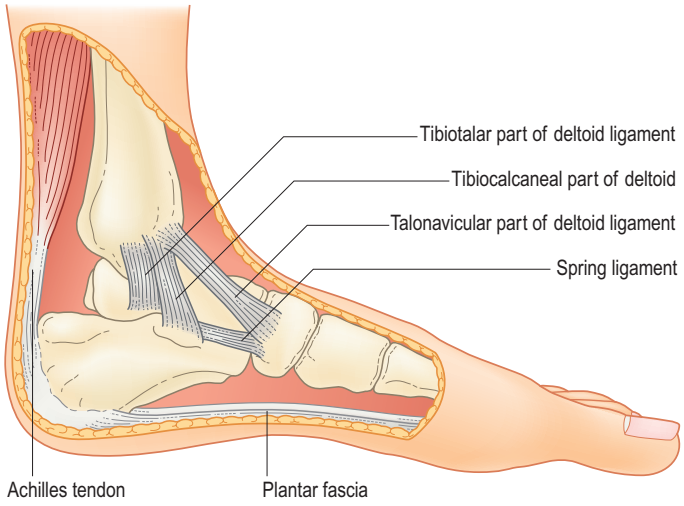

Figure 57.2 Anatomy of the medial ankle ligaments.

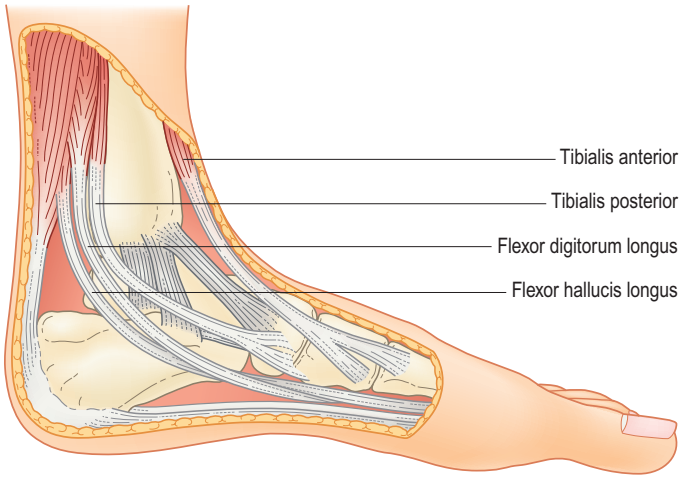

Figure 57.3 Anatomy of the medial ankle tendons.

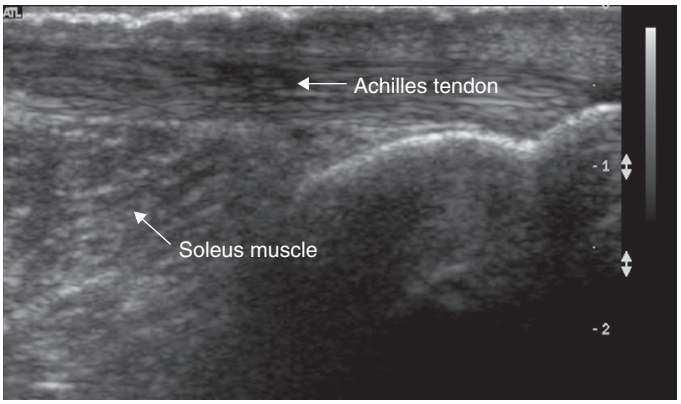

Figure 57.4 Longitudinal ultrasound image of the distal Achilles tendon with a low-lying 'accessory' soleus.

Important anatomy to know in the ankle

Posterior ankle
- Achilles tendon
- Plantaris tendon
- Pre Achilles bursa
- Post Achilles bursa
- Kager's fat pad
- Sural nerve
- Saphenous vein

Medial ankle
- Tibialis posterior tendon
- Flexor digitorum
- Flexor hallucis longus
- Posterior tibial nerve
- Posterior tibial artery
- Posterior tibial vein
- Deltoid ligament
- Spring ligament

Lateral ankle
- Peroneus longus tendon
- Peroneus brevis tendon
- Peroneus tertius tendon
- Peroneus quartus tendon
- Common peroneal nerve
- Peroneal artery and vein
- Anterior talofibular ligament
- Anterior inferior tibiofibular ligament
- Calcaneofibular ligament

Anterior ankle
- Tibialis anterior tendon
- Extensor hallucis longus tendon
- Extensor digitorum

examination. Kager's fat pad lies deep to the tendon. In motion it slides against the bursa and tendons, dissipating the load of the body evenly through the tendon[5] (Fig. 57.5).

Ultrasound examination of the Achilles tendon is best performed with the patient prone and the feet hanging off the end of the couch (Fig. 57.6), allowing the sonographer to plantar- or dorsiflex the foot in order to assess the integrity of the Achilles tendon or the size of a tear in the tendon. With dorsiflexion some stretch can be placed on the Achilles tendon and the echogenicity and size of the tendon can be assessed (Figs 57.7 and 57.8). The foot should be placed in plantarflexion to assess neovascularisation, which can be obliterated by extreme dorsiflexion. Care should be taken in looking at the

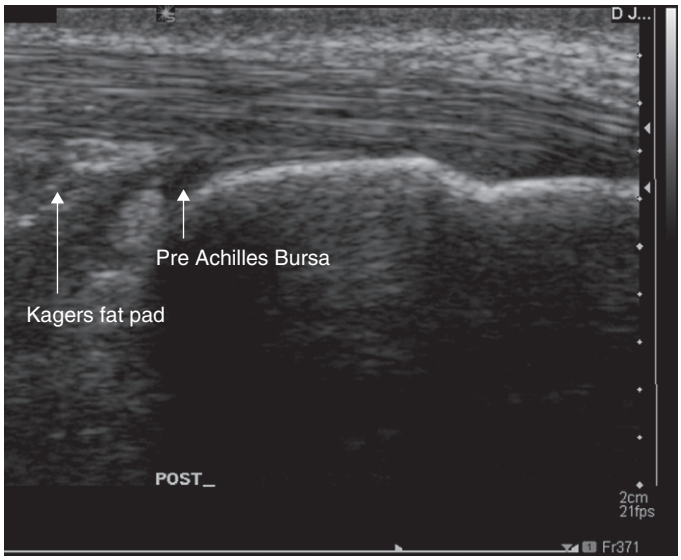

Figure 57.5 Longitudinal ultrasound image of the distal Achilles tendon with the Kager's fat pad seen indenting the pre Achilles bursa.

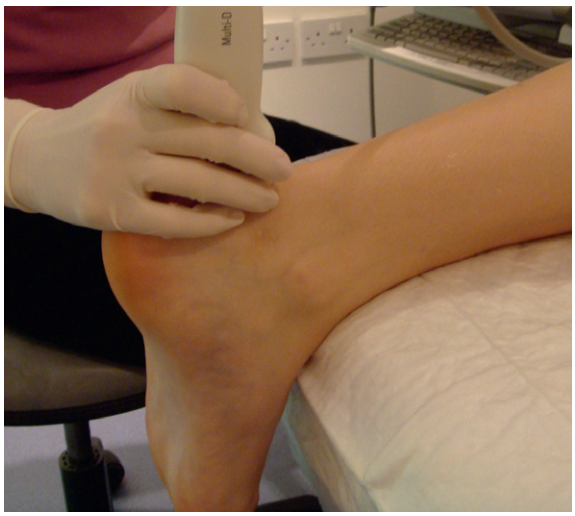

Figure 57.6 A patient lying prone with the foot off the end of the bed with the foot held in dorsiflexion while examining the Achilles tendon with ultrasound.

medial and lateral margins of the Achilles tendon on transverse and longitudinal scans as these areas can be obscured by edge artefact and may be a site for tearing or paratenon inflammation. Sclerosing tendinopathy can occur and the importance of dynamic assessment cannot be overstated. Scanning the tendon during the motion that brings on the patient's symptoms can be useful, for example when examining a ballerina who is standing en pointe.

Plantaris

Approximately 90% of individuals have an additional muscle/tendon called the plantaris, which arises from the lower part of the supracondylar line of the femur and the oblique popliteal ligament. It forms a tendon that runs obliquely between the gastrocnemius and soleus muscles to lie on the medial side of the Achilles tendon[6] as a separate tendon that runs to the calcaneus or merges with the Achilles at varying levels (Fig. 57.9). It may take over some of the function of a ruptured Achilles tendon and mask the clinical signs of rupture. Plantaris may be used for tendon reconstruction.

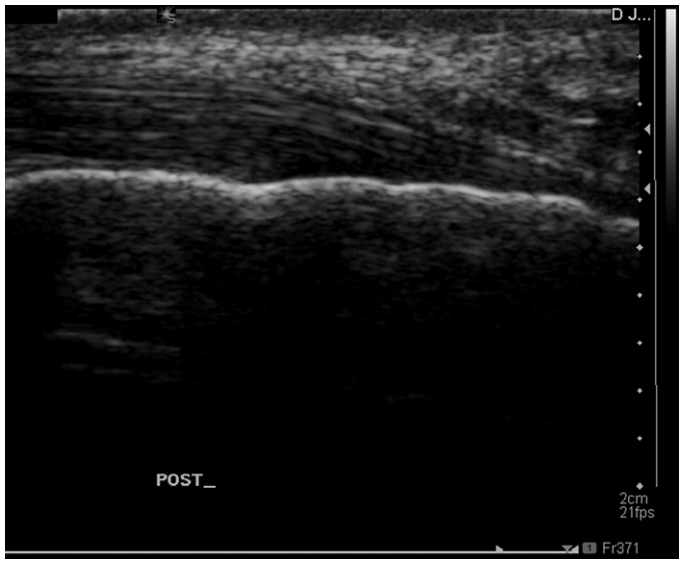

Figure 57.7 Longitudinal ultrasound image taken of the distal Achilles tendon with the foot in dorsiflexion.

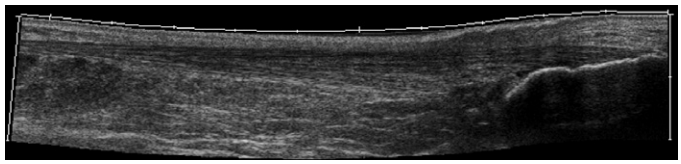

Figure 57.8 Extended field-of-view longitudinal image of the Achilles tendon.

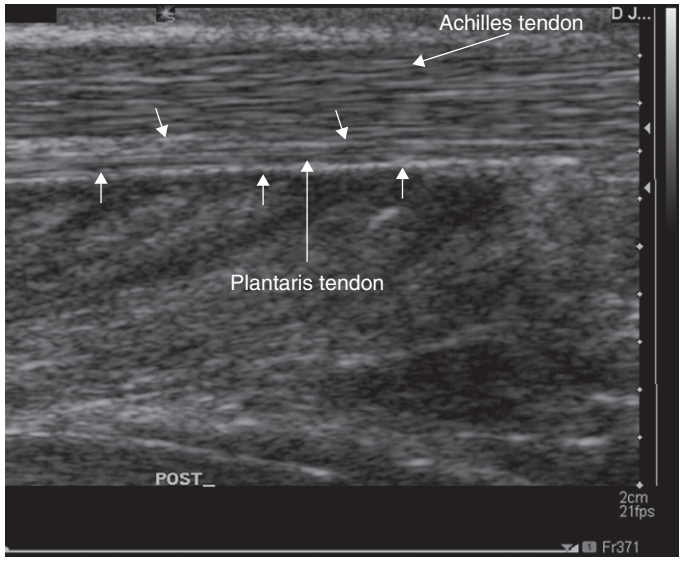

Figure 57.9 Longitudinal ultrasound image of the plantaris tendon.

The plantaris tendon can be found on the medial and anterior aspect of the Achilles tendon when it is present. Both axial and longitudinal images are useful in first identifying the tendon and then tracing it to its insertion.

The sural nerve descends lateral to the Achilles tendon with the short saphenous vein and passes distal to the lateral malleolus, supplying the lateral side of the foot and little toe.

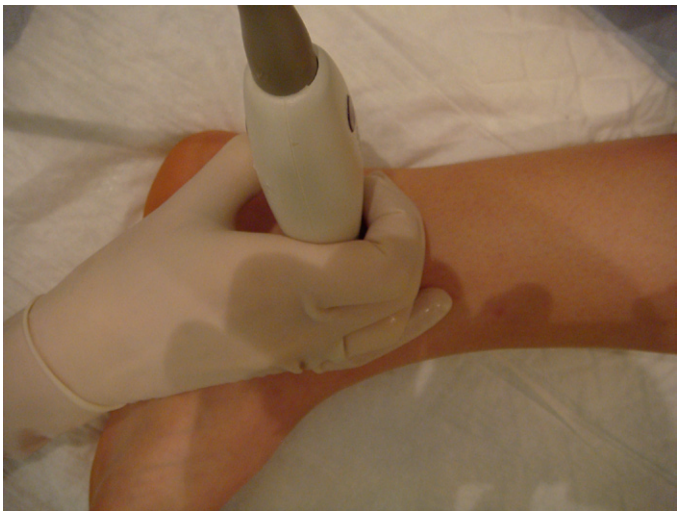

Figure 57.10 A patient lying with their medial ankle uppermost, lying slightly on the hip while examining the medial ankle tendons.

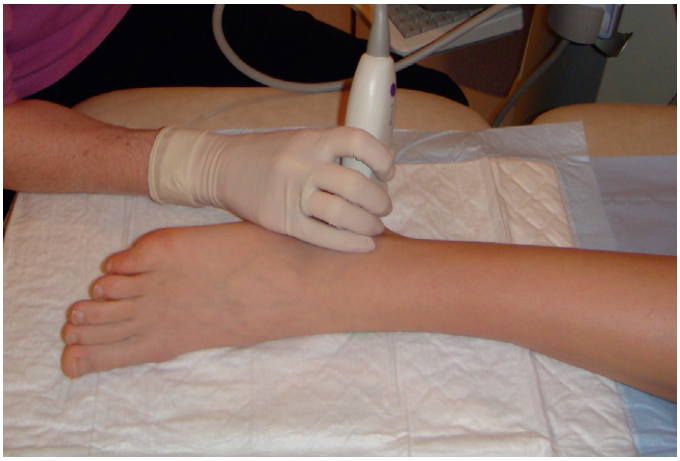

Figure 57.11 A patient lying with their lateral ankle uppermost, lying slightly on the hip while examining the lateral ankle tendons.

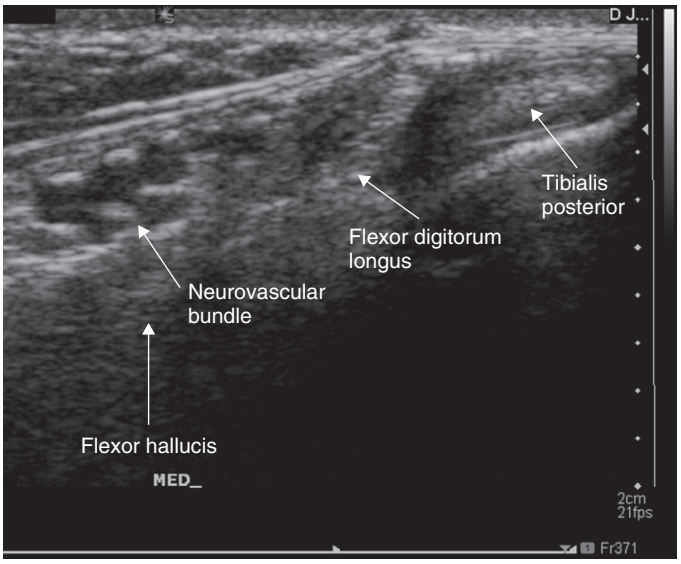

Figure 57.12 Transverse ultrasound image of the tibialis posterior, flexor digitorum, flexor hallucis tendons and the neurovascular bundle.

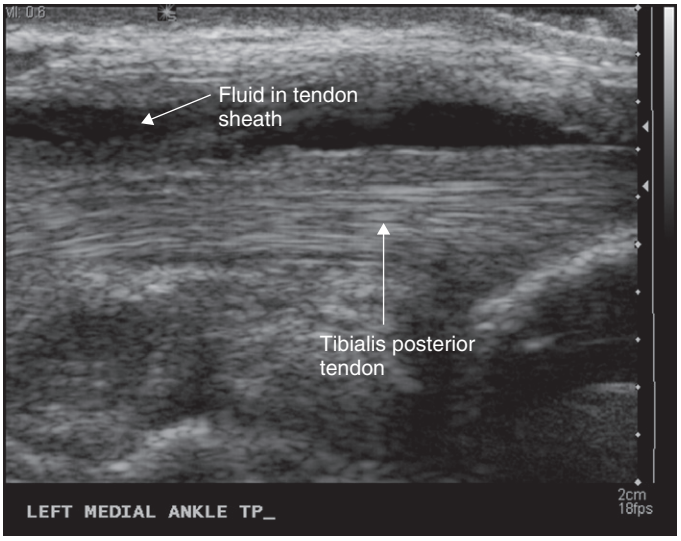

Figure 57.13 Longitudinal ultrasound image of the distal insertion of the tibialis posterior tendon in a patient with tendinopathy.

Medial ankle

The medial aspects of the ankle are best assessed with the patient sitting, the knee flexed and the leg pushed slightly outwards (Figs 57.10 and 57.11).

On the medial side of the ankle are from anterior to posterior the tibialis posterior, flexor digitorum and flexor hallucis longus tendons. A neurovascular bundle lies between the flexor digitorum longus tendon and the deeper flexor hallucis longus (FHL) tendon. A mnemonic that helps is '**T**om, **D**ick **a**nd **v**ery **n**ervous **H**arry' (**T**ibialis posterior, flexor **D**igitorum longus, **A**rtery, **V**ein, **N**erve, flexor **H**allucis longus) (Fig. 57.12).

The **posterior tibial nerve** is the largest nerve second only to the sciatic nerve in the lower limb. It arises from the sciatic nerve above the popliteal fossa with the common peroneal nerve and gives rise to the medial and lateral plantar calcaneal nerves at the level of the calcaneus.

The **tibialis posterior** tendon extends from the tibialis muscle, which originates on the posteromedial aspect of the tibia and runs to the navicular, with a second slip of the distal tendon extending on the undersurface of the foot forming the medial arch of the foot and inserting it into the cuneiforms and bases of the metatarsals (Fig. 57.13). An accessory ossicle, os naviculare may be incorporated in the distal navicular attachment.

The **flexor digitorum longus** tendon develops from the flexor digitorum muscle, which arises from the anterior medial tibia and extends to the terminal phalanges of the toes excepting the great toe. The flexor hallucis longus muscle arises from the posterior medial tibia and its tendon inserts into the terminal phalanx of the great toe. The **flexor hallucis brevis** (FHB) tendon also inserts by two slips into the terminal phalanx but this muscle is formed in the plantar aspect of the foot. Within the two tendon slips of the FHB are the sesamoid bones at the level of the metatarsophalangeal (MTP) joint (Fig. 57.14).

The medial ligamentous complex, the **deltoid ligament,** is made up of a fan of ligaments that pass from the medial malleolus (Fig. 57.2). The superficial portion comprises from anterior to posterior the tibionavicular ligament, tibiospring ligament and tibiocalcaneal ligament (Fig. 57.15).

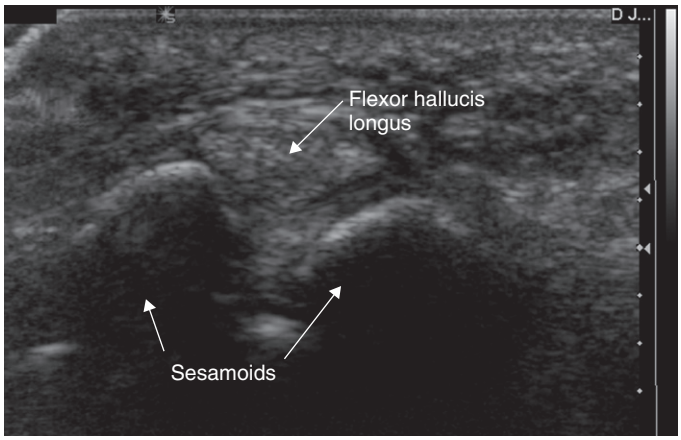

Figure 57.14 Transverse ultrasound image of the sesamoid bones of the great toe with the flexor hallucis longus tendon centrally.

The tibionavicular ligament may be difficult to identify on imaging. The deep portion consists of the anterior and posterior tibiotalar ligaments. The anterior tibiotalar ligament is absent in 50% of people.[7] The ligament is crossed by the tibialis posterior and flexor digitorum longus tendons.

The **spring ligament** or plantar calcaneonavicular ligament spans from the sustentaculum tali to the navicular and fuses with the distal fibres of the anterior portion of the deltoid ligament[8] (Fig. 57.16).

Anterior ankle

The anterior aspect of the ankle is best examined with the patient sitting and the foot relaxed. The anterior tendons are well demonstrated in this position (Fig. 57.17A and B).

The anterior joint can also be visualised at this point (Fig. 57.18).

The anterior tendons and muscles across the ankle are from medial to lateral **T**ibialis anterior, extensor **H**allucis and extensor **D**igitorum ('**T**om **H**ates **D**ick'). The tibialis anterior arises from the

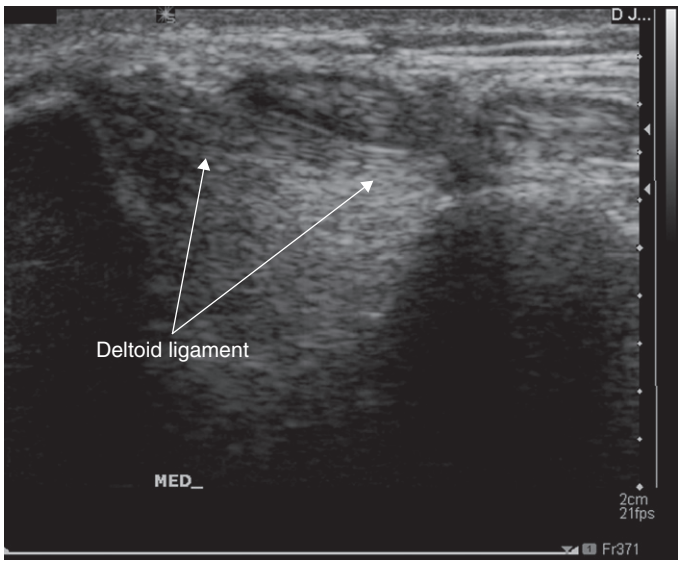

Figure 57.15 Longitudinal ultrasound image of deltoid ligament, superior medial component; the tibiocalcaneal segment.

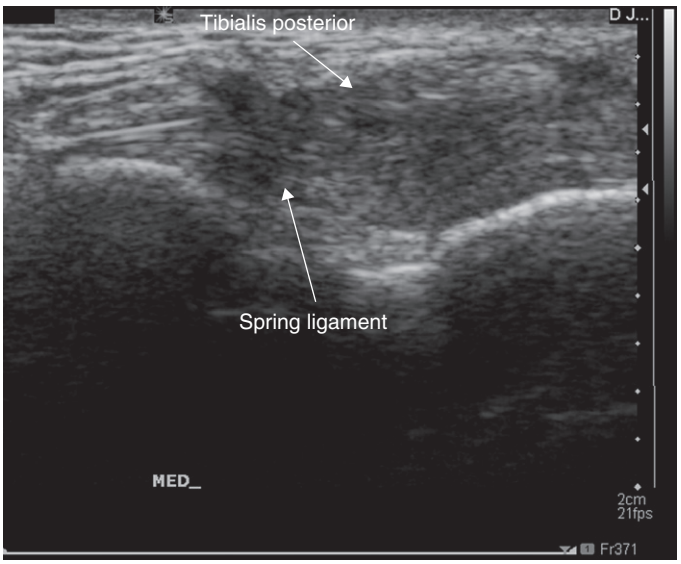

Figure 57.16 Longitudinal ultrasound image of spring ligament under the tibialis posterior tendon.

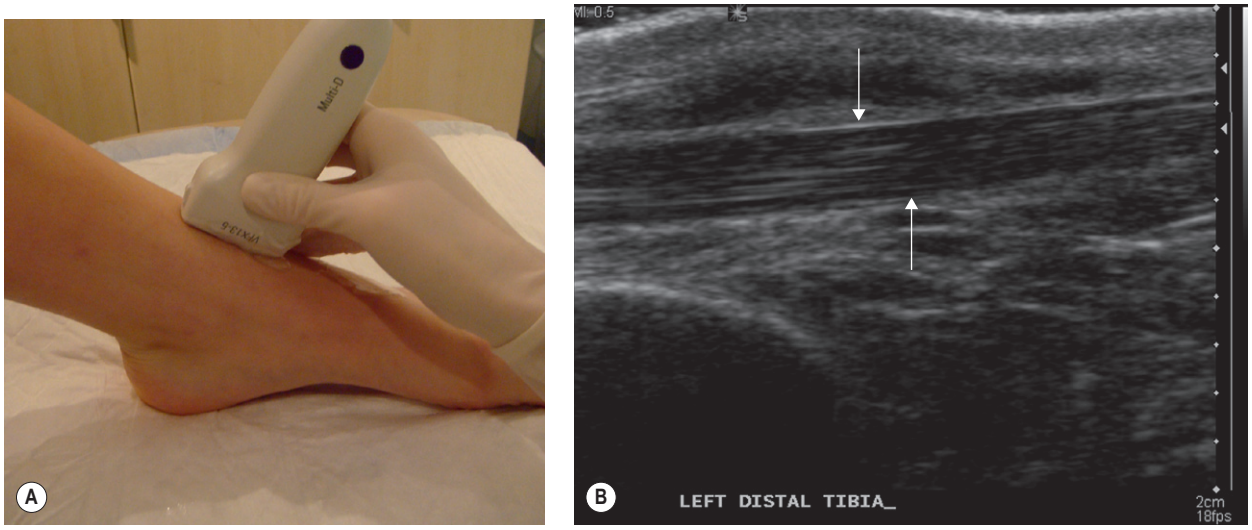

Figure 57.17 A: A patient sitting with the probe on the anterior aspect of the ankle. **B:** Tibialis anterior tendon.

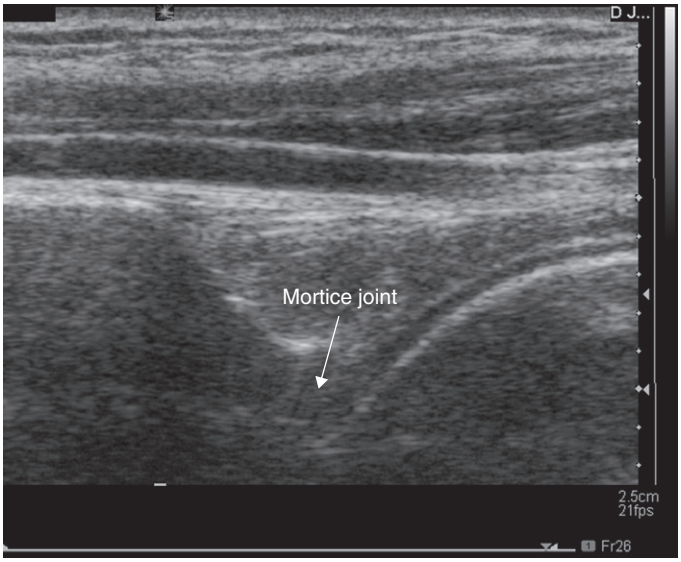

Figure 57.18 Ultrasound image of the anterior ankle mortise joint with the probe in a similar position as shown in Figure 57.17.

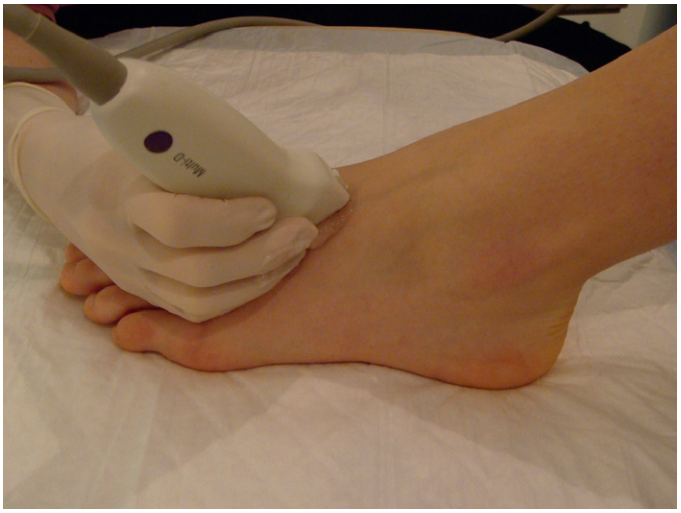

Figure 57.19 A patient sitting with the probe on dorsum of the foot to see the midfoot bones and ligaments.

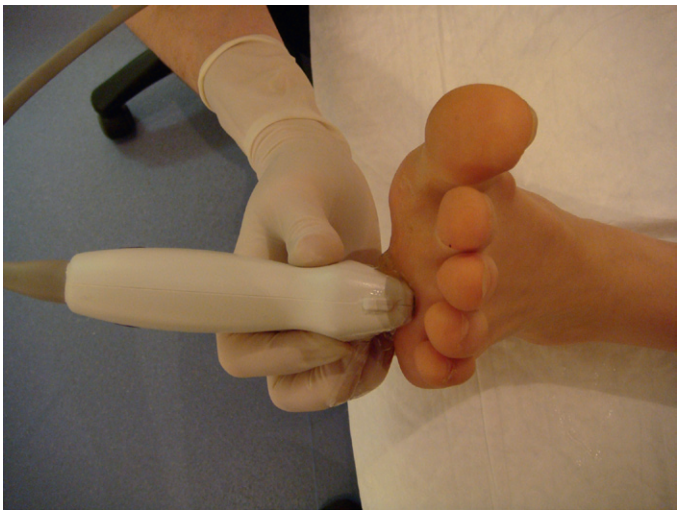

Figure 57.20 A patient sitting with the probe on the plantar aspect of the foot looking for a Morton's neuroma.

proximal lateral tibia and passes under the superior and inferior extensor retinacula to attach to the inferior and medial aspect of the medial cuneiform and the adjacent base of the first metatarsal. The **tibialis anterior** tendon is the most commonly affected tendon in the anterior aspect of the foot from inflammatory arthropathy or overuse injury. A split of its distal portion is a normal variant seen in around 18% of individuals, with attachments to the talus, first metatarsal head, base of the proximal phalanx of the great toe and the extensor retinaculum having been recorded.

Extensor hallucis longus arises from the medial and middle fibula and anterior intraosseous membrane. Its tendon passes under the extensor retinacula laterally and inserts into the base of the proximal phalanx of the great toe. Sometimes it unites with the extensor digitorum tendon to send a second slip to the second toe.

The **extensor digitorum longus** arises from the lateral condyle of the tibia, proximal and medial surface of the fibula, anterior intraosseous membrane and muscular septa. The tendon passes under the superior extensor retinaculum and forms four slips as it passes under the inferior retinaculum with the peroneus tertius. The tendons of the second, third and fourth toes are joined by the tendons of extensor digitorum brevis at the level of the MTP joints, laterally. The dorsal expansions are formed at the level of the proximal phalanges with contributions from the interosseous muscles and the lumbricals. The tendon splits into three, forming a central slip that attaches to the base of the dorsum of the middle phalanx and two collateral slips that insert into the base of the distal phalanx dorsally.

The foot

The dorsum of the foot is best assessed with the patient sitting and the sole of the foot resting on the couch (Fig. 57.19). To study the plantar aspect the patient should be supine with the hips and knees extended, the heel on the couch and the toes pointing up (Fig. 57.20).

Lateral ankle (Fig. 57.1)

The lateral aspects of the ankle are best assessed with the patient sitting, the knee flexed and the leg pushed slightly inwards (Figs 57.10, 57.11).

The lateral tendons of the ankle are the peroneus longus and the peroneus brevis. The **peroneus longus** muscle arises from the lateral aspect of the proximal fibula and adjacent deep fascia and intermuscular septa and occasionally from the lateral condyle of the tibia. The peroneus longus tendon passes around the outer edge of the ankle behind the lateral malleolus and 'goes a long way round'. It enters a tunnel formed by a groove in the fibula which has the superior peroneal retinaculum as its roof. It travels with the **peroneus brevis** tendon and then runs in a canal formed by a groove on the plantar aspect of the cuboid and the long plantar ligament. At this point it may contain a sesamoid bone, the os peroneum. The distal tendon splits and inserts into the base of the lateral side of the first metatarsal and the medial cuneiform. The peroneus brevis has a more distal musculotendinous junction than peroneus longus. A transverse image at the level of the ankle may show the peroneus longus tendon and the peroneus brevis tendon with part of its muscle (Fig. 57.21). Peroneus brevis inserts into the lateral tubercle on the base of the fifth metatarsal.

The peroneal tubercle on the anterolateral aspect of the calcaneus splits the peroneus longus from the brevis in 60% of people, with the peroneus longus lying inferiorly[7] (Fig. 57.22).

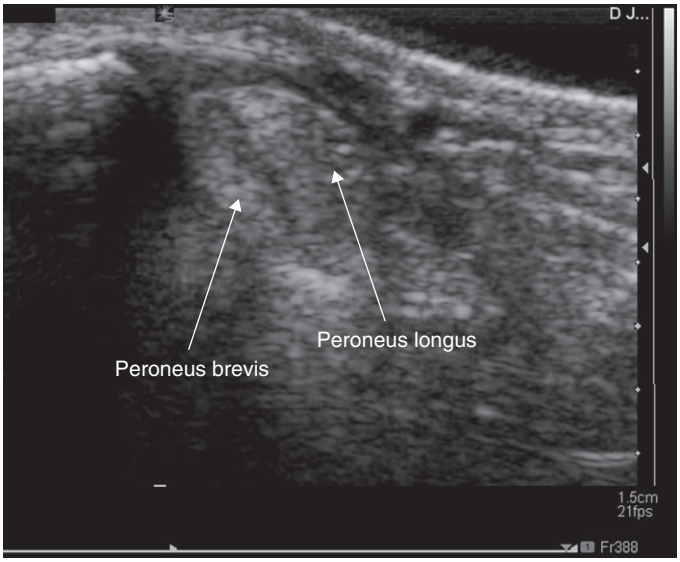

Figure 57.21 Transverse ultrasound image of the peroneal tendons at the level of the lateral malleolus.

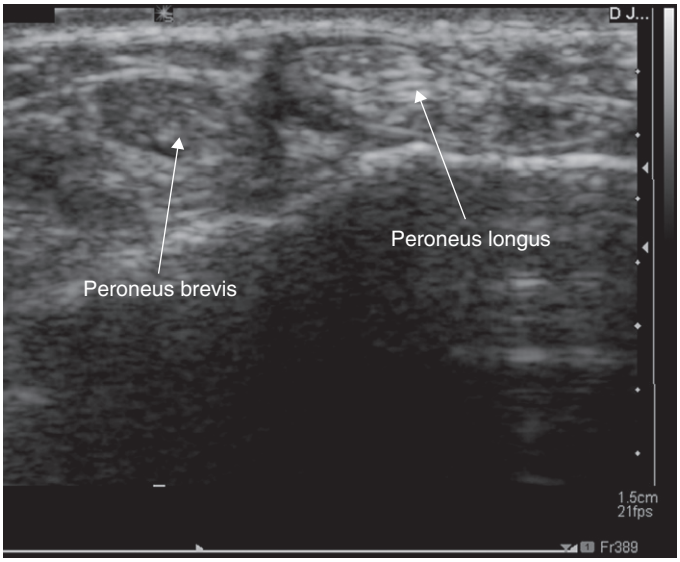

Figure 57.22 Transverse ultrasound image of the peroneal tendons at the level of the peroneal tubercle.

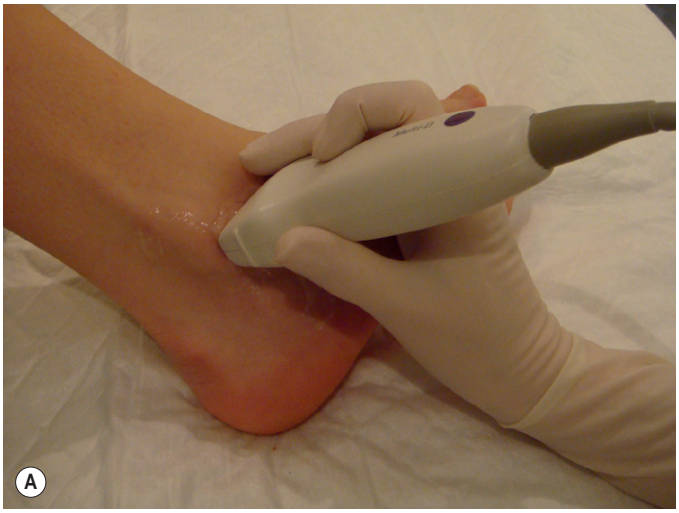

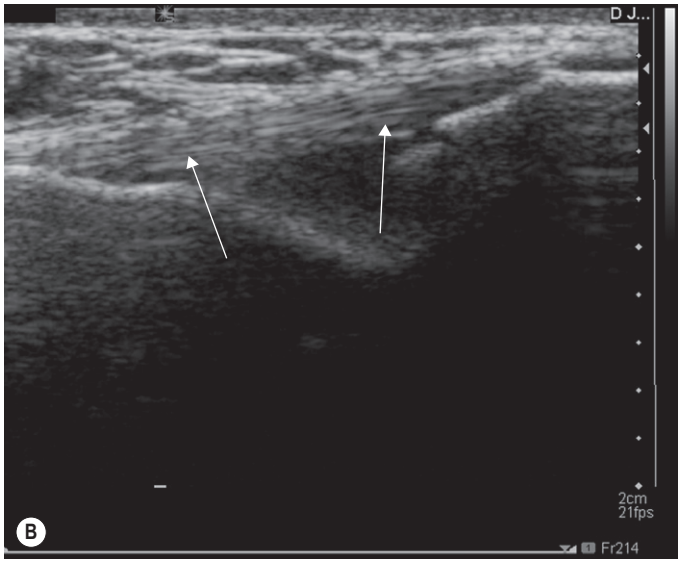

Figure 57.23 Anterior talofibular ligament. A: A patient lying with their lateral ankle uppermost, lying slightly on the hip, with the foot in slight inversion and the probe parallel to the base of foot to examine the ATFL. **B:** Ultrasound image of the ATFL with the probe in the position shown in **A**.

The ligaments are identified as echogenic bands when the probe is perpendicular to their axis. If even a small tilt in the incident beam is allowed then the ligament will appear hypoechoic due to anisotropy and may aid the examiner in identifying the course of the ligament, which is sometimes easier to identify when seen as a darker structure.

The **lateral ligamentous complex** is composed of the anterior and posterior talofibular ligaments and the calcaneofibular ligament and is more commonly injured than the medial ligamentous complex. The anterior talofibular ligament (ATFL) is easily identified by scanning from the fibula to the calcaneus with the probe position parallel to the base of the foot whilst the foot is inverted (Fig. 57.23A and B). If the ultrasound probe is then moved in a proximal direction from the ATFL, the anterior tibiofibular ligament can be identified. The calcaneofibular ligament is the largest ligament in the ankle and is seen as a broad band parallel to the posteromedial calcaneus extending under the peroneal tendons to the distal fibula. It is identified by placing the probe parallel to the back of the calcaneus in an upright oblique position (Fig. 57.24A and B). By putting some stress on the lateral aspect of the ankle with the foot in inversion these ligaments can be better assessed, resolving doubts about their mechanical integrity.

Normal variants include the peroneus tertius and peroneus quartus muscles. The **peroneus tertius** (fibularis tertius) is seen as an additional tendon[9] and appears to be part of the extensor digitorum longus (EDL) arising from the distal third of the fibula, adjacent interosseous membrane and intermuscular septum. It shares space with the EDL within the inferior extensor retinaculum loop and inserts into the medial and dorsal base of the fifth metatarsal. It can also insert into the fourth metatarsal and is present in approximately 17% of people.[10] The **peroneus quartus** lies posterior to peroneus brevis and longus and inserts into the calcaneus.[11]

The anterior and posterior inferior tibiofibular ligaments add support to the tibiofibular syndesmosis with the transverse tibiofibular ligament and the interosseous ligament.

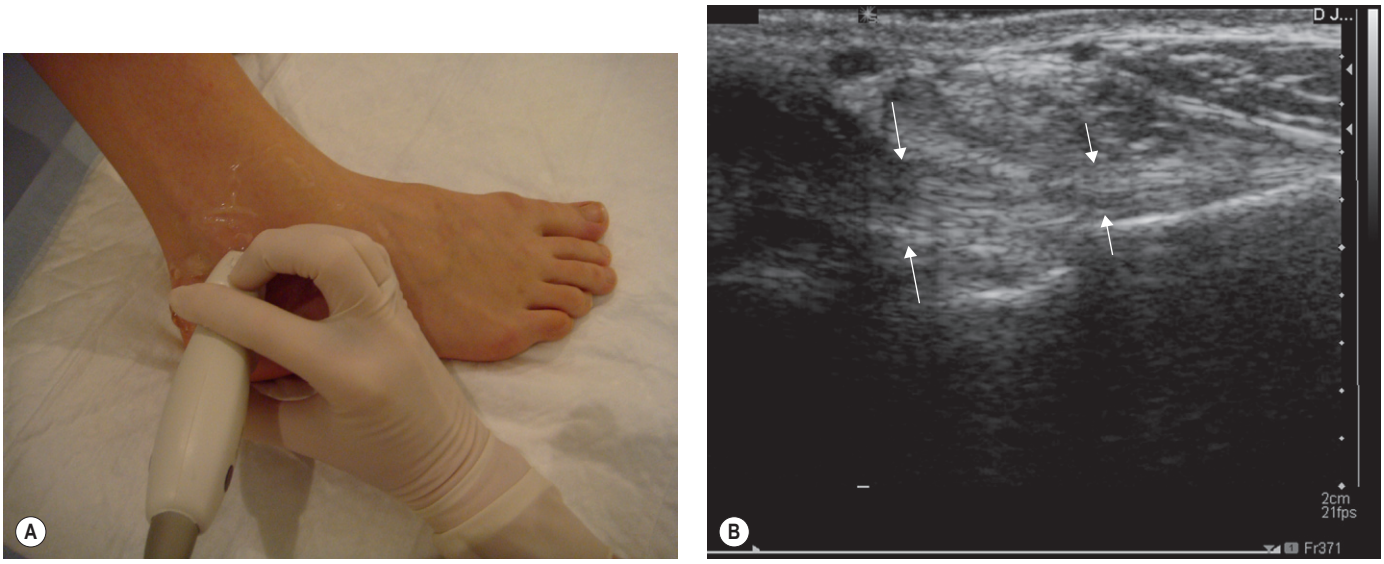

Figure 57.24 Calcaneofibular ligament. A: A patient lying with their lateral ankle uppermost, lying slightly on the hip, with the foot in slight inversion and the probe parallel to the back of the foot to examine the CFL. **B:** Ultrasound image of the CFL with the probe in the position shown in **A**.

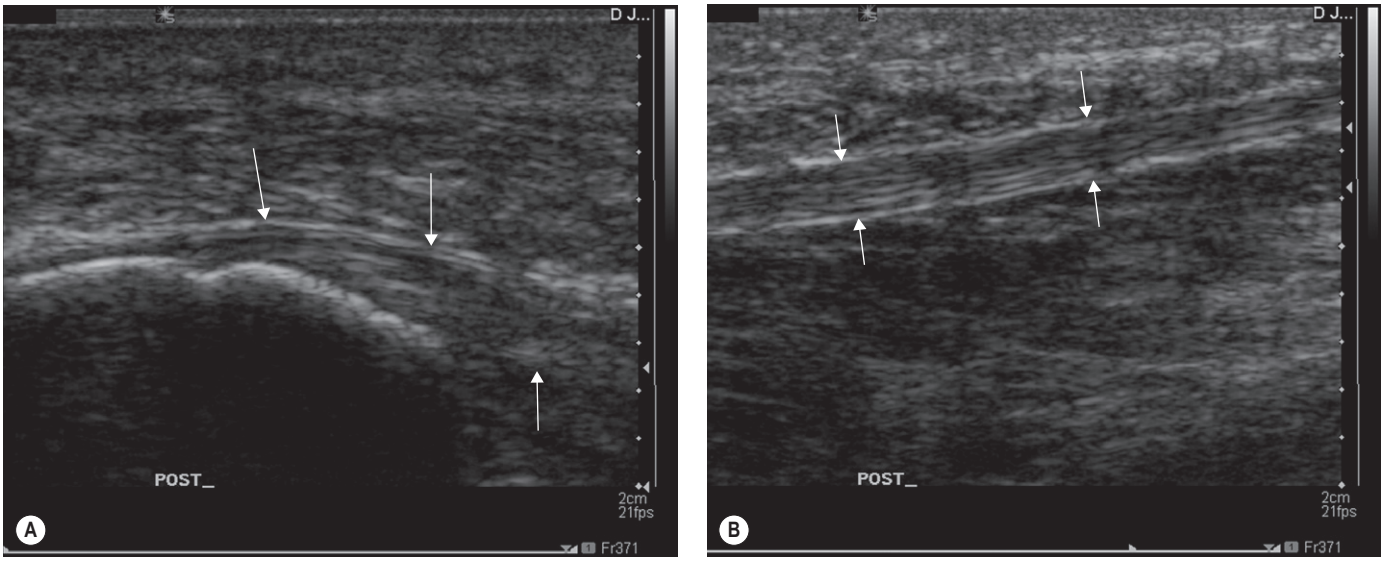

Figure 57.25 A and B: Longitudinal ultrasound image taken of plantar fascia at the heel **(A)** and in the midfoot **(B)**.

The **common peroneal nerve** divides into superficial and deep branches at the level of the proximal part of the peroneus longus and gives branches to the toes. These structures can be identified using ultrasound examination.

Plantar aspect of foot

The **plantar fascia** is the fibrous tissue that helps support the arch of the foot and extends from the undersurface of the calcaneus to the rays of the foot. It arises from an enthesis on the calcaneus within a small bony indentation. At this point it is normally less than 4 mm in depth. As the fascia passes distally to insert on the bases of the proximal phalanges, it fans out and its depth diminishes to about 2 mm. It is a predominantly low-echogenicity structure although high-resolution images will show linear areas of higher echogenicity as it is formed of several layers producing a striped dark–light–dark–light–dark pattern making approximately five layers[12,13] (Fig. 57.25A and B).

Important anatomy to know in the foot

- Plantar fascia
- Tarsal bones
- Flexor hallucis longus
- Flexor hallucis brevis
- Chopart ligaments
- Lisfranc ligaments
- Extensor hallucis brevis
- Dorsalis pedis artery
- Intermetatarsal bursa

The plantar fascia can be examined with the patient prone with the feet dangling off the edge of the bed or the toes resting on the couch, or supine with the heel on the couch and the toes pointing up (Fig. 57.26). Copious amounts of gel are needed as the thick dry skin on the base of the foot can sometimes cause dragging of the ultrasound probe.

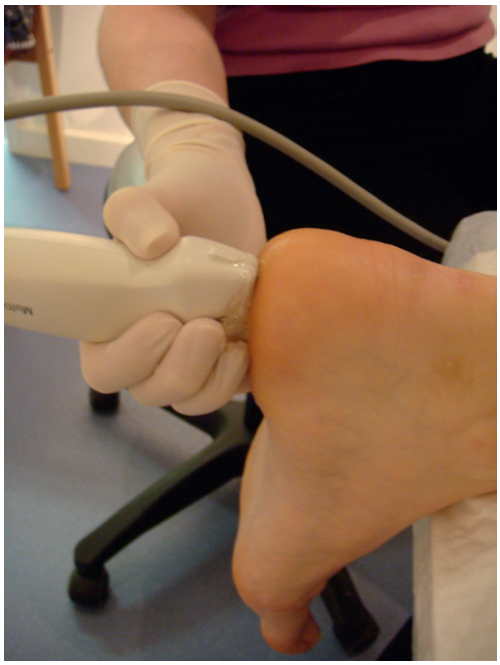

Figure 57.26 **A patient lying prone with the probe on the calcaneus insertion of the plantar fascia.**

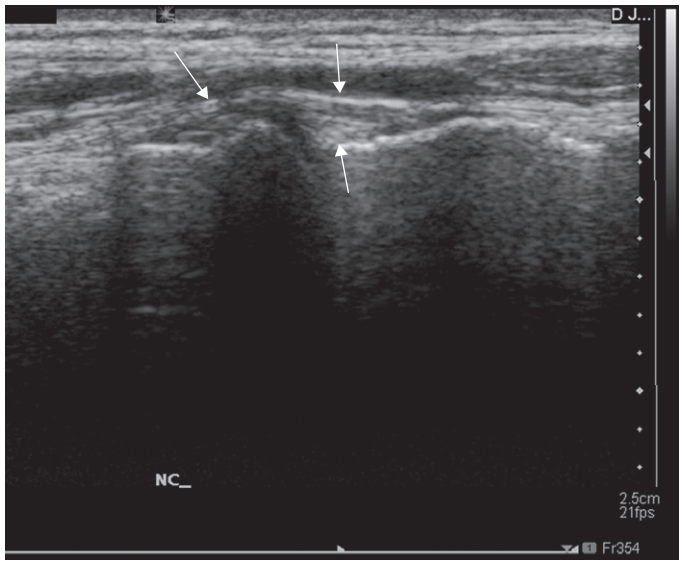

Figure 57.27 **A longitudinal image of the Chopart ligament.**

Examination technique for the ankle and foot

- High frequency probe 12 MHz and above, preferably a small 'hockey stick' probe for small structures.
- Lots of thick gel especially on the plantar aspect of the foot.
- Comfortable position for patient.
- Prone position for plantar fascia, Achilles tendon and other posterior structures.
- Supine and sitting for the anterior ankle and forefoot.
- Supine and on one side for medial and lateral ankle structures.

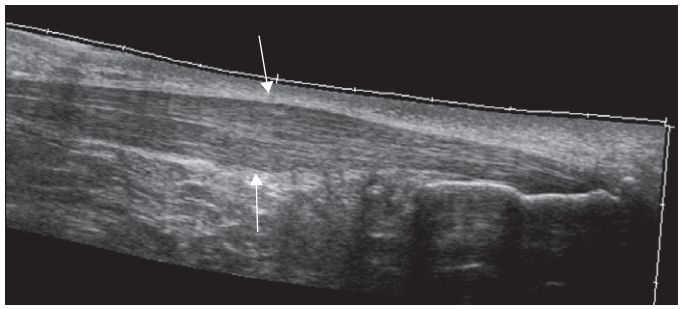

Figure 57.28 **Extended field-of-view longitudinal ultrasound image of the Achilles tendon** with the foot in dorsiflexion showing fusiform swelling and some reduction in echogenicity in a tendinosis.

The **short muscles** of the foot and the long tendons that pass around each malleolus and over the anterior (superior) aspect of the foot are each bound by retinacula. All these structures can be identified using ultrasound. The amount of fluid in each tendon sheath should normally be less in cross-section than the tendon itself with the exception of the flexor hallucis longus tendon sheath, which commonly communicates with the ankle joint. A joint effusion can increase the fluid volume in the FHL tendon sheath. Although this is the result of an anatomical variant it is not normal and is a reflection of disease in the ankle.

Detailed knowledge of bony architecture is needed. More than 140 accessory ossicles have been described in the foot. The most frequently found are the os trigonum behind the ankle joint and an accessory navicular at the tibialis posterior tendon insertion.

Interosseous ligaments span the midfoot joints and are seen as echogenic bands joining the bone surfaces. Dynamically stressing the foot tightens these ligaments and increases their conspicuity. This test confirms structural integrity in cases of suspected chronic instability but may be difficult to achieve in painful acute injuries (Fig. 57.27).

DISEASE PROCESSES

Posterior ankle

Achilles tendinopathy

Early in tendinopathy there may be thickening of or a small amount of fluid in the paratenon. The tendon itself is swollen and focally hypoechoic due to oedema. More pronounced focal hypoechoic areas are due to central delaminating tears or mucoid degeneration (Fig. 57.28) Neovascularisation represents a repair process and correlates with pain. It can be florid in acute tendinopathy (Fig. 57.29). Chronic tendinopathy results in diffuse swelling of the tendon, and some reduction in echogenicity. Neovascularisation may be absent and there may be focal calcification.

There is debate over the safety and efficacy of injections in and around tendons. There is general consensus that ultrasound guidance is an advantage as it allows accurate placement whilst avoiding damaging tendons and the neurovascular structures. However, there is evidence that anaesthetic agents placed near tendons with intrinsic disease render the tendon at risk of rupture due to

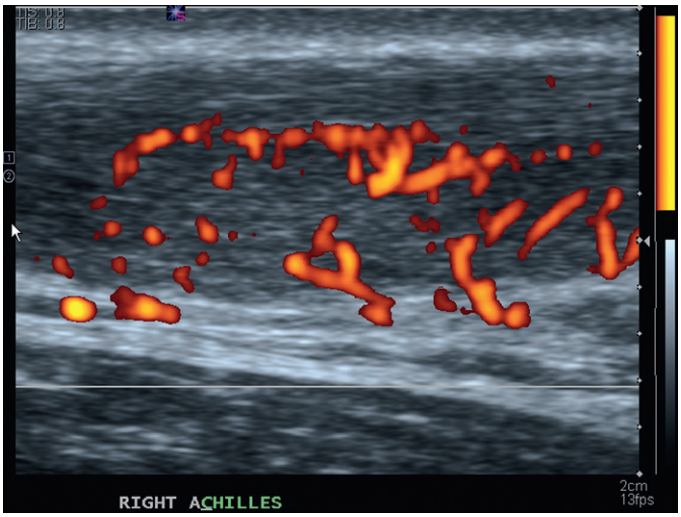

Figure 57.29 Longitudinal power Doppler ultrasound image of the mid Achilles tendon with the foot relaxed showing neovascularisation in an acute tendinosis.

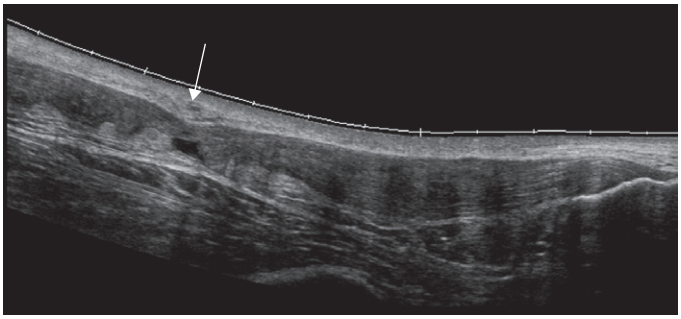

Figure 57.30 Extended field-of-view longitudinal ultrasound image of the Achilles tendon with the foot in dorsiflexion showing a complete rupture of the tendon.

inadvertent loading. Corticosteroid injection may worsen this risk by extending the period of analgesia and reducing the healing response. If injections around abnormal tendons are being offered it should be with an agreed period of mechanical splint protection.

Currently there are no randomised controlled trials to support treatments such as local anaesthetic and steroid injection, dry needling of the tendon, injection of autologous blood, saline stripping and injection of sclerosing substances which are discussed further in the interventional chapter (Chapter 62).

Tendon tears

Most Achilles ruptures are due to an abnormal load being placed through an ageing and therefore less elastic tendon.

Complete tears of the Achilles tendon frequently result in a palpable defect in the tendon, inability to stand on tiptoes and are clinically obvious. However, soft tissue swelling may obscure the defect and the patient may still be able to stand on tiptoes if the plantaris tendon is intact. Ultrasound examination is useful to confirm the nature, location and extent of a tear.

The ends of the torn tendon are often thickened and irregular as the tendon buckles (Fig. 57.30). Edge artefact from the tendon remnant may be present. The defect in the tendon fills with a localised haematoma which may be echo-free (liquid) or contain particulate debris (clot and fibrin). There is often extensive soft tissue oedema and, within a short period, adjacent neovascularisation.

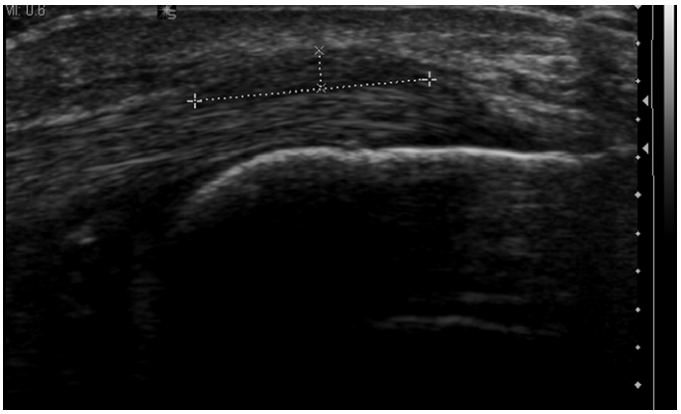

Figure 57.31 Longitudinal ultrasound image of the distal Achilles tendon with the foot in dorsiflexion showing post Achilles bursitis.

Dynamic examination by plantar/dorsiflexion of the foot may make a tear more conspicuous and shows if the tear margins become apposed on plantarflexion. The latter observation will help to decide whether conservative treatment in an 'equinus' (plantarflexed) plaster will be effective. If surgery is being considered, marking the tendon ends on the skin with the foot in an agreed (normally neutral) position will aid the surgeon and permit smaller incisions. Accurate placement of the markers permits effective surgical repair under local anaesthesia.

Partial ruptures tend to affect one component of the Achilles (gastrocnemius or soleal) and are identified as a focal defect bridged by the intact portion. Dynamic testing is the most effective means of determining the integrity of all or part of the tendon. Even in the most acute injury the degree of motion required to show tendon separation is rarely painful and is normally less than 1 cm of movement of the toes. Review of the cine loop acquired by capturing a dynamic examination gives the clearest picture of the nature of the tear. The stress may be applied by passively moving the foot or manually compressing the calf muscles. Voluntary movement may be difficult in acute injury.

The plantaris tendon should be visualised if present. It may have a tendinopathy or tear as well. If intact it can be used to surgically reinforce the ruptured Achilles.

Bursitis

Bursitis leads to thickening of the bursal wall, fluid in the bursa and adjacent neovascularisation (Fig. 57.29). Bursitis may be the result of inflammatory joint disease, infection or chronic impingement. The ultrasound appearances are similar and non-specific. Fluid in the bursa with or without particulate matter, wall thickening and adjacent neovascularisation may be observed. The clinical circumstances and history are important discriminating features. In cases suspected of infection ultrasound-guided aspiration for microbiological examination is effective and easy to perform. Exudates should also be examined for crystals in case of gout or pseudo-gout (Fig. 57.31).

Enthesopathy

Enthesopathy results in focal tenderness and pain at the Achilles tendon insertion. It is seen as roughening of bone at the attachment of the tendon, oedema in the tendon and neovascularity in the tendon and surrounding soft tissues (Fig. 57.32). Focal tenderness and pain are the principal clinical features and ultrasound localisation is helpful in determining which tendon insertion hurts. Ultrasound examination is less sensitive than T2-weighted fat-suppressed

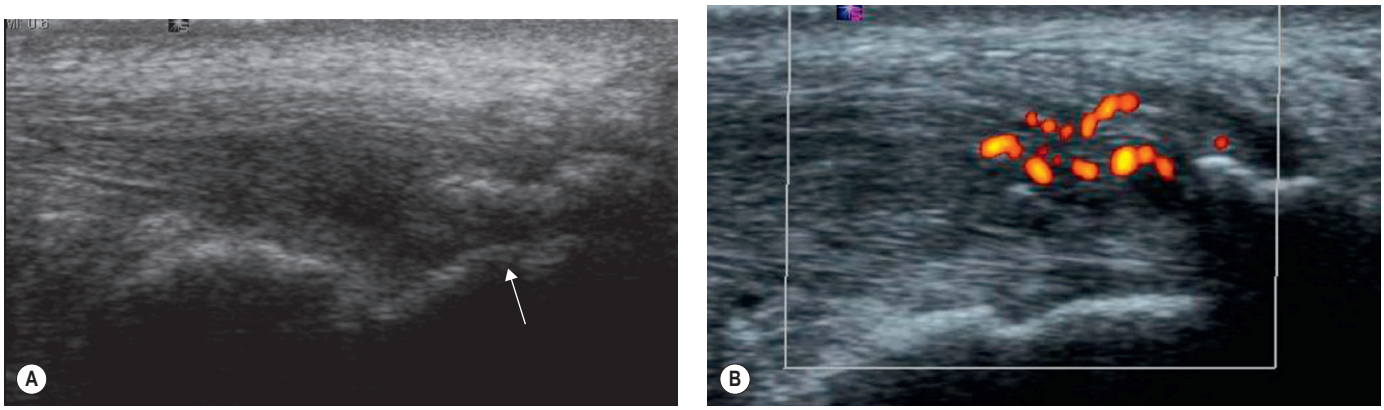

Figure 57.32 Enthesopathy. A: Longitudinal ultrasound image of the distal Achilles tendon showing enthesopathy with marked roughening of the cortex of the calcaneus. **B:** Same case as **A** with colour Doppler.

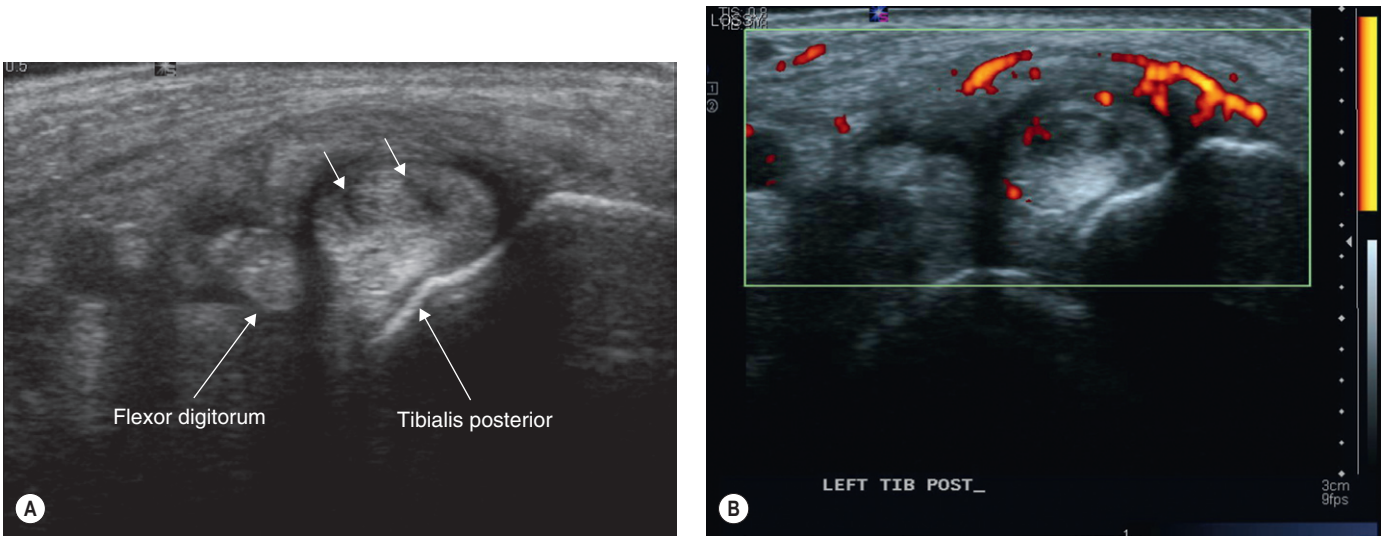

Figure 57.33 Tibialis posterior tendinopathy. A: Transverse ultrasound image of a tibialis posterior tendinopathy with internal splits (arrows). **B:** Power Doppler image of the same tendon as in **A**.

or STIR MRI sequences in demonstrating oedema in the enthesis. Only MRI can demonstrate the oedema sometimes seen in the bone. However, ultrasound is a reasonable first examination as it is fast, excludes tears and detachments and localises the symptoms to a specific structure. MRI is rarely of additional diagnostic value despite its superior sensitivity to oedema.

Haglund's deformity is thought to be due to footwear with a high-backed shoe causing an extra portion of bone to arise from the posterior calcaneus. This leads to focal pressure on the Achilles and a focal tendinopathy. The deformity and any associated neovascularisation in soft tissue are well defined by ultrasound examination.[14]

Xanthomata and calcific mass lesions

Xanthomatous or gouty deposits produce echogenic foci in the Achilles tendon. Calcium deposits are especially reflective and cast acoustic shadows. They are much more readily seen using ultrasound examination than with conventional radiographs or MRI.

Medial ankle

Tendons

Tibialis posterior

The second most likely tendon to cause symptoms in the ankle, the tibialis posterior tendon, may be affected by the same range of diseases as the Achilles including tears, tendinopathy and inflammatory conditions. Internal splits or delamination are common and typically seen around the medial malleolus where the tendon turns the corner.

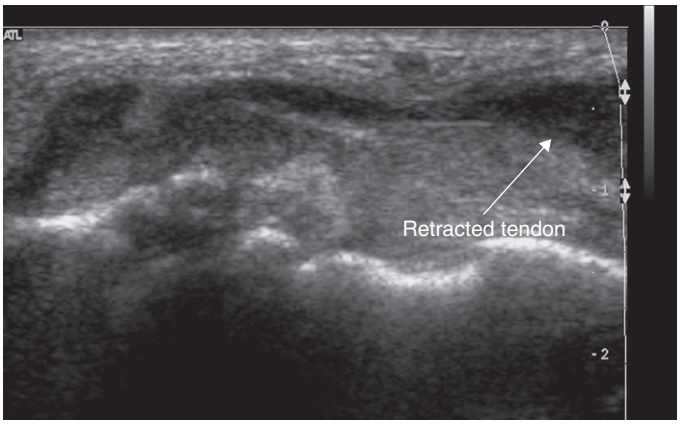

Figure 57.34 Longitudinal ultrasound image of a complete rupture of the tibialis posterior tendon.

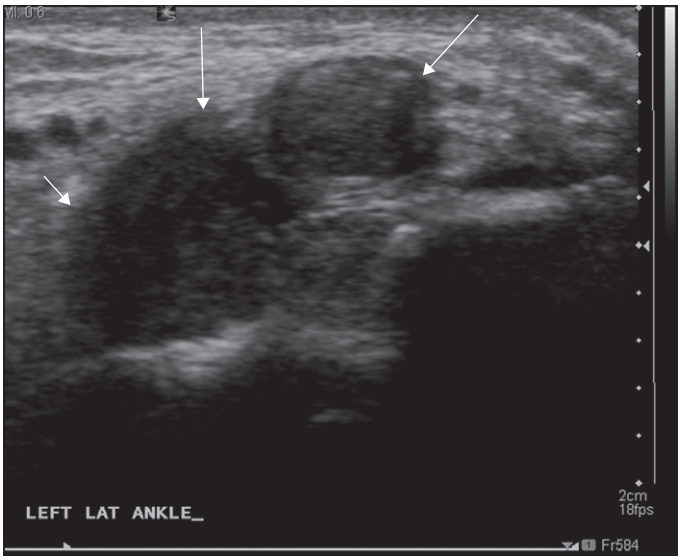

Figure 57.35 Ultrasound image of the synovitis seen 'mushrooming' from the ankle joint in the lateral gutter syndrome.

Ultrasound examination is probably the most sensitive method of delineating these conditions. Axial images of the tendon are best to show delamination and neovascularity whilst longitudinal views demonstrate tears (Fig. 57.33A and B). The tendon may be swollen or thinned, irregularly marginated and contain heterogeneous hypoechic areas or frank defects. Its tendon sheath may be distended with fluid and neovascularity may be present.

The insertion of the tendon onto the navicular is seen as a fan-shaped widening with a less clearly visualised extension of the remainder of the tendon under the forefoot.

Rupture and retraction tends to occur around the malleolus (Fig. 57.34). The acute dropped arch with an everted hind foot typically seen in older women is often attributed to tibialis posterior rupture but ultrasound has shown that there is often an acute tendinopathy with an intact tendon and loss of function.[15]

Flexor tendons

The flexor digitorum and flexor hallucis longus tendons are best located by moving the appropriate digit whilst imaging in axial section. The tendon moves with the toes.

These tendons are affected by the same conditions including tendinopathy acute and chronic, atrophic tendinopathy and the rarely hypertrophic tendinopathy. These probably reflect the same mechanisms but different expressions depending on the local trauma and repair response. The flexor hallucis longus tendon sheath very often communicates with the ankle joint so that fluid in the ankle joint may track into an otherwise normal tendon sheath, indicating joint disease rather than tendon disease.

Ligaments

The **medial ligament complex** is uncommonly injured; the deltoid more commonly than the spring ligament especially in bimalleolar fractures.[16] There is a high association with tibialis posterior tendon injuries and osteochondral damage to the talar dome. When injured it is most commonly the superior-medial portion of the ligament that is damaged first.

Imaging medial ligament damage is difficult whether using ultrasound or MRI, They are thin and short structures with sometimes curved courses, especially when not under load. The advantage of ultrasound examination is that the ligament may be tensed by loading the foot and ankle, thereby increasing its conspicuity and confirming or refuting the suspicions of rupture. If the bones move apart excessively then the ligament is deficient. The normal limit for a patient can be judged by examining the opposite side. This is especially useful in younger patients where ligament laxity may be normal.

Using ultrasound imaging, ligaments appear as laminated echogenic lines between the bone margins. If the beam is slightly away from a true 90° to the ligament then anisotropy causes the ligament to appear black. The position where it appears echogenic is a very limited angle. To recognise a tear when there is no oedema or haematoma (chronic) is difficult unless the examiner is very confident of the normal appearances. It is always harder to determine if a structure is missing. Despite this, those used to examining ligaments with MRI and ultrasound usually prefer the latter as more specific, faster and easier to interpret.

The spring ligament lies deep to the distal part of the tibialis posterior tendon. It is readily found using ultrasound and larger tears may be identified. More subtle tears and deficiencies may be harder to detect than with other ankle ligaments as its course is hard to examine in profile and stress is difficult to achieve.[8,17]

Joints

Joint effusion is best detected using ultrasound examination; the capsule is distended and displaced by the fluid, which is most often echo-free. Occasionally echogenic effusions are seen in fresh haemarthroses and in inflammatory joint disease. Dynamic assessment of fluid motion differentiates echogenic effusions from synovial proliferation.

The joint can be affected by an inflammatory arthropathy, when synovitis and neovascularisation can be seen. In severe ligamentous injury, synovitis may be seen secondary to instability of the ankle.

In athletes (especially soccer and hockey players) anterolateral gutter syndrome can occur when there is focal synovitis associated with impingement. This is initially a thickening of the synovium with neovascularisation but may become a chronic synovitis. Fibrosis results in reduced echogenicity of the synovium with no vascularity, although occasionally synovial calcification occurs. The synovitis acts as a mass lesion and may produce a mechanical block to the ankle.[18] Ultrasound examination has been shown to be a sensitive method of making this diagnosis largely because of the dynamic component of the examination. Moderate pressure on the malleoli will compress the synovitic mass, causing it to emerge anteriorly. This looks like a 'mushroom' pushing out of the gutter (Fig. 57.35).

Osteoarthritis may be diagnosed when bone spurs are seen at the joint margins. A ganglion can arise from the joint in association with degenerative arthropathy and is seen as an anechoic mass. A neck

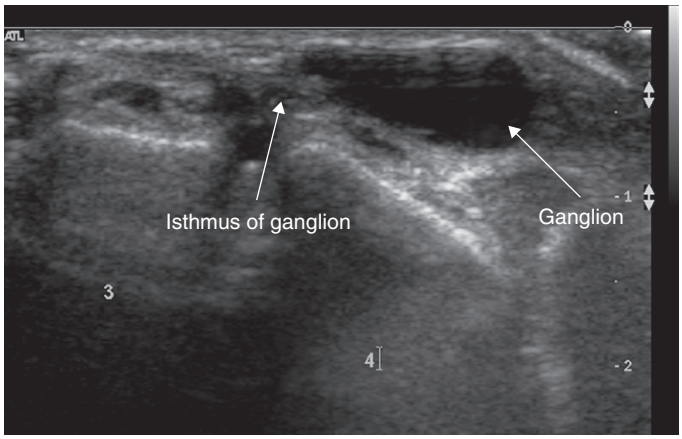

Figure 57.36 Ultrasound image of ganglion arising from a midfoot joint.

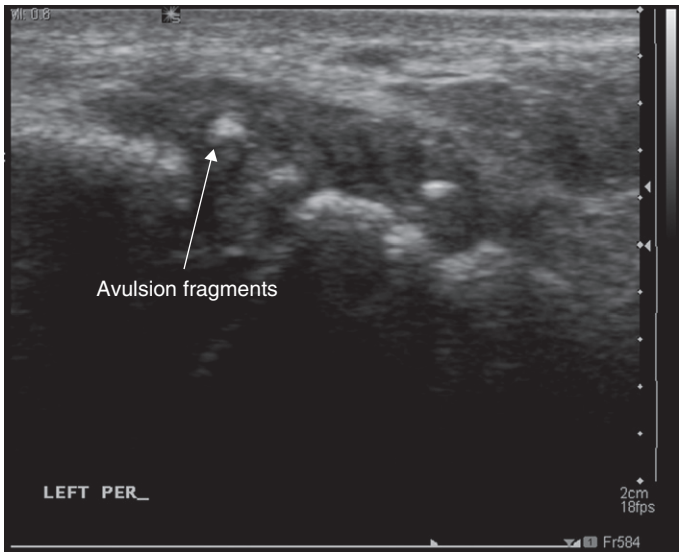

Figure 57.37 Longitudinal ultrasound image of a complete rupture of the ATFL with small avulsion fractures from the talus.

or isthmus extending from the joint to the mass indicates the origin of the ganglion and is specific for the diagnosis (Fig. 57.36).

Transient subluxation of joints secondary to ligament injury or laxity may be observed dynamically using ultrasound or equally by fluoroscopic examination.

The subtalar joint cannot be adequately examined with ultrasound and is better examined using MRI and computed tomography.

Neurovascular bundle

Neuromas and schwannomas of the tibial nerve are relatively hypoechoic masses. They are considered in more detail in Chapter 61.

Aneurysms and varicosities of the posterior tibial vessels appear tubular or ovoid. There may be areas of internal blood clot which are echogenic. The nature and waveform of flow will determine the type of vessel when the parent structure is not obvious.

Tarsal tunnel syndrome may be identified by enlargement of the tibial nerve as it enters the region under the malleolus[19] or by the presence of an accessory flexor digitorum longus muscle,[20] ganglion or other mass lesion.

Lateral ankle

Tendons

The **peroneal** tendons are affected by the same range of conditions as are the tendons on the medial side of the ankle. In disease processes often the peroneus brevis tendon becomes flattened and the peroneus longus erodes the centre of the tendon, eventually leading to splits in the tendon.

The imaging criteria and examination methods are the same with one exception: these tendons are held beneath the lateral malleolus by a retinaculum that may tear, leading to transient or sometime permanent subluxation. The clicking painful sensation that occurs is associated with a flicking of the tendons over the malleolus. Axial imaging with ultrasound, whilst dynamically loading to the point of the symptoms by inverting the foot, is the only way of confirming transient subluxation.

Ligament injury

All of the ligaments around the ankle can be torn either completely or partially.

The most common site of injury is the lateral ligament complex and the ATFL is the most common of these ligaments (Fig. 57.37). Injury to the calcaneofibular ligament (CFL) is often associated with peroneal tendon injury. This is a more serious injury and occurs in approximately 30% of cases of sprain. The anterior tibiofibular ligament is a component of the syndesmosis and if this is injured a diastasis may result. Injury can lead to an avulsion of a small fragment of bone at the attachment of the ligament. This may not be visible on plain radiographs but is usually easily detected on ultrasound examination.

The most important ligament structurally is the calcaneofibular ligament. It is difficult to examine with MRI as its course is so variable. The tilt or axis of the ligament varies from almost horizontal to close to vertical. The optimum MR plane is hard to find and the ligament may be seen partly and obliquely on several slices. As a result its integrity is hard to judge. Using ultrasound a simple rotation of the probe allows the correct alignment in a moment and then inversion load shows the integrity of the ligament immediately after.

Sinus tarsi syndrome is best examined using MRI where focal oedema assists its detection. Ultrasound examination may suggest that the pain arises in the anatomical location but will give little more information.

Anterior ankle

In the anterior tendons it is unusual to see tendinopathy with the exception of the rheumatoid patient, when the tibialis anterior tendon may be involved (Fig. 57.38).

Joint disease

Osteophytes may be seen around the ankle, especially in athletes where they often arise from the talar neck or the anterior distal tibia. Commonly seen entities are the osteophytes seen arising from the anteromedial talar neck in 'footballer's ankle' due to the impaction of the ball on the anteromedial talus.

Bone

Stress fractures of the fibula are the only common stress fractures encountered in the ankle and may be seen as a laminated focal periosteal reaction. The double line on the bone surface that results

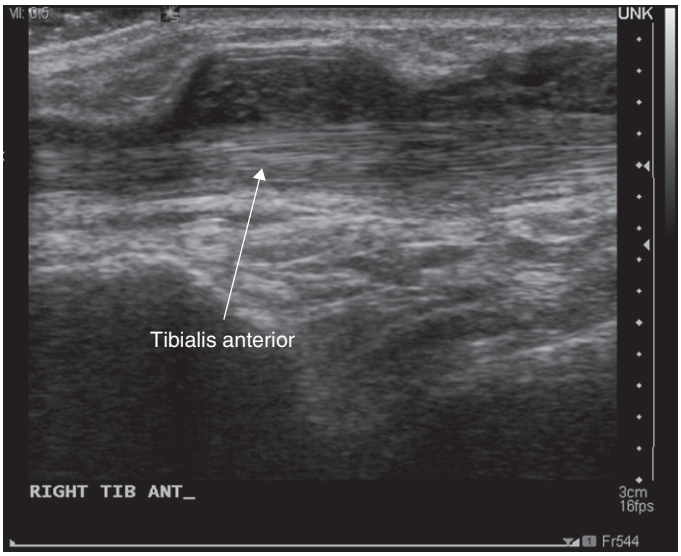

Figure 57.38 Longitudinal ultrasound image of a tibialis anterior tendinopathy seen in rheumatoid arthritis.

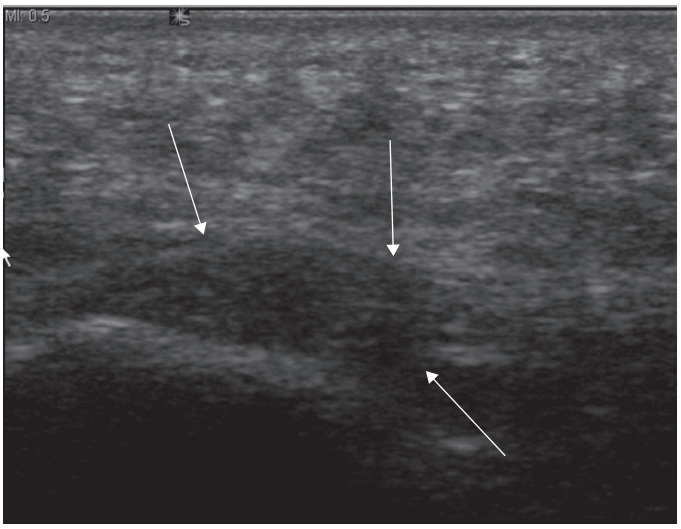

Figure 57.39 Longitudinal ultrasound image of plantar fasciitis.

is easily detected using ultrasound. Callus and cortical defects are also sensitively detected. However, in early stress lesions, before the cortex or periosteum are affected, MRI shows bone oedema and is the more sensitive test to exclude stress lesions.

An ankle effusion following acute trauma may herald the presence of an osteochondral fracture or intra-articular lesion and MRI is then recommended to assess for cartilage or occult fractures.

Plantar fasciitis, fibromatosis and fibroma

Plantar fasciitis is common and causes pain predominantly on the heel but also extending typically into the medial aspect of the plantar fascial arch. Ultrasound examination often shows reduced echogenicity of the plantar fascia with loss of the normal linear echo change and an increase in thickness (4 mm or more) (Fig. 57.39). In the acute phase there may be some neovascularisation but commonly this is not is observed. An associated enthesopathy with roughening of the cortex of the calcaneus at the insertion of the plantar fascia suggests the possibility of an inflammatory arthropathy.

Fibromatosis is an irregular thickening of the plantar fascia with reduction of echogenicity and loss of the normal linear echo pattern. It can be focal (a fibroma) or diffuse when it is irregular in outline. There is often a family history as the condition is inherited as an autosomal dominant and it is associated with Dupuytren's contracture in the hand. Fibromas may be part of a generalised disorder or may occur in isolation. There are rare cases of malignant fibrous lesions and sarcomas in the same structures.

Morton's neuroma is seen between the metatarsal heads predominantly at the third/fourth or second/third web spaces (Fig. 57.40), especially in middle-aged women. 'Neuroma' is a misnomer as this is a thickening of fibrous tissue around and involving the interdigital nerve rather than a true neuroma. A Morton's neuroma may be asymptomatic and may not be the cause of a patient's pain. The neuroma is often associated with a bursitis when the patient is symptomatic.

Morton's neuromas are round or oval, well defined and usually hypoechoic although increased echogenicity or cystic areas may be seen. Morton's neuroma and an intermetatarsal bursa/bursitis may coexist. If the transducer is held on the plantar aspect of the foot and the operator presses the skin on the dorsum of the foot, compression of the mass or alteration of its echogenicity indicates that a bursa is present. Any non-compressible area is usually due to a Morton's neuroma.[21]

Ultrasound is the best way of making this distinction. Bursitis is high signal on T2-weighted and STIR MRI images. The neuroma may be low to intermediate signal but if oedematous it may look identical to bursitis. If the neuroma is large (over 1 cm) then the possibility of other nerve-related tumours should be considered including schwannomas and neurofibromas. Large swellings on the interdigital nerve that cause deviation of the digits should be excised. Ultrasound-guided injections of long-acting local anaesthetic and corticosteroids or alcohol are used in many centres but their efficacy is debated.[22] Studies on injections of alcohol suggest that repeated injections are needed to obtain benefit.[23]

Other causes for forefoot pain include **metatarsalgia**, which is not seen on ultrasound examination and for which MRI is needed.[24] However, when assessing the forefoot the position of the metatarsal heads should be assessed. Often in forefoot pain and even in the presence of a Morton's neuroma one of the metatarsal heads lies in a more plantar position than the other metatarsal heads. There may be crowding of the metatarsal heads with impingement that can be observed when manually compressing the foot from side to side. The patient's response to compression is a useful pointer to this diagnosis. MRI shows oedema in the metatarsal head and confirms metatarsal impingement as the cause of pain.

Stress fractures are a cause of forefoot pain sometimes identified using ultrasound. It helps to palpate the area of pain and then place the probe on the area of bone that is tender. A stress fracture with cortical reaction will be seen as a focal irregularity of the cortex of the bone with periosteal oedema and neovascularisation. If ultrasound is normal and a stress fracture is suspected MRI is required. MRI is superior to ultrasound, shows bone oedema on T2-weighted or STIR images and the fracture line on T1-weighted images. Conventional radiography may overlook stress fractures and the presence of a normal radiograph does not exclude the diagnosis.

Other causes of forefoot pain

Pain in the great toe can be due to flexor hallucis longus tendinopathy but is more commonly due to sesamoiditis, inflammation around the sesamoid bones within the flexor hallucis brevis tendon. This most often affects the medial sesamoid and may show ultrasound signs of local oedema (swelling and reduced echo pattern)

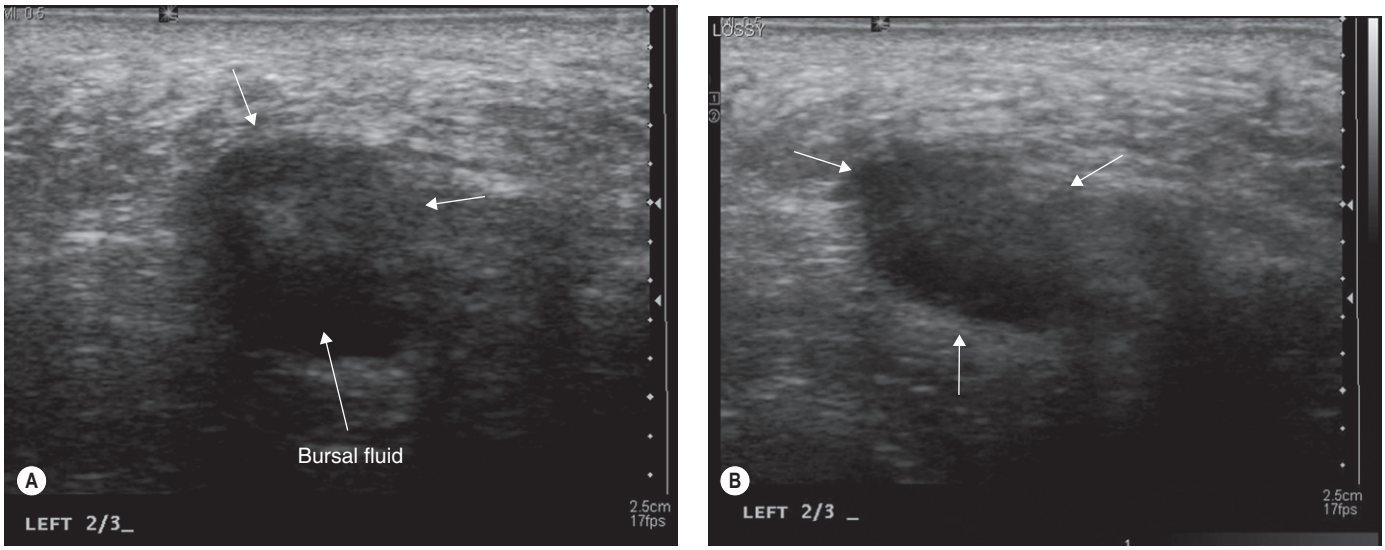

Figure 57.40 Longitudinal ultrasound image of a Morton's neuroma (A) pre compression and **(B)** post compression showing the presence of an associated bursitis also.

and bone surface bone irregularity. Sesamoid fractures and bifid medial sesamoids may appear morphologically similar on ultrasound but fractures have surrounding oedema and often some neovascularisation. In case of doubt MRI shows if oedema is present in the bony fragments. Hammer toe is best assessed by MRI for similar reasons. The bone oedema will be easily identified.

Freiberg's disease

Fragmentation of the second metatarsal head due to Freiberg's osteochondrosis can sometimes be seen with ultrasound. Contour changes are apparent later in the disease but early on there may simply be a focal synovitis.

Mass lesions

Mass lesions around the foot are often due to ganglion formation and ultrasound can be used to detect the presence of a fluid-filled ganglion and the joint from which it arises. Rarely soft tissue tumours are observed; they range from benign lesions like lipoma (echogenic), fibroma (see above) and haemangioma (vessels with low flow on Doppler ultrasound examination) to malignant lesions including secondary deposits and sarcomas. Ultrasound examination can exclude a soft tissue mass without need for further investigation. However, the ultrasound appearances of soft tissue masses that contain any solid tissue are not sufficiently characteristic to exclude the need for histological diagnosis. Therefore when a mass lesion is not a Morton's neuroma (position, size <1 cm, echo pattern and symptoms) then referral to a specialist tumour service is indicated for local staging by MRI and biopsy.

Synovitis

In inflammatory arthropathy synovitis results in effusions and synovial thickening in joints and tendon sheaths and marginal erosions in joints. Joint disease can be staged based on the size of effusion, extent of synovitis, presence of erosions and neovascularity. Erosions are best seen on transverse ultrasound images at the level of the metatarsal head. Examination of the feet is often combined with examination of the hands. Simple ultrasound examination is faster than and arguably as accurate as MRI, which requires repeat examination after injection of contrast agent (GdDTPA).

Disease processes

- *Tendinosis* – fluid and synovial thickening in the tendon sheath, intrinsic change within the tendon with a reduction in echogenicity. May show focal low echoes in keeping with mucoid degeneration (misnomer cysts).
- *Partial tendon tear* – disruption of some of the tendon fibres.
- *Complete tendon tear* – disruption of the tendon fibres and dynamic assessment shows the tendon ends moving apart.
- *Partial ligament tear* – disruption of some of the ligament fibres.
- *Complete ligament tear* – disruption of the ligament fibres and dynamic assessment shows the ligament ends moving apart. Sometimes the ligament avulses a small bone fragment that may not be seen on radiographs.
- *Stress fractures* – cortical irregularity and increased colour Doppler signal beside the bone cortex.
- *Morton's neuroma* – low-echo lesion in web space at level of metatarsal head that does not compress.
- *Intermetatarsal bursitis* – low-echo lesion in web space at level of metatarsal head that compresses.
- *Ganglion versus solid lesions* – a ganglion should appear 'cystic' ie anechoic with distal acoustic enhancement.

Traumatic lesions

Traumatic lesions around the foot can include ligamentous disruption and ultrasound can be used for this. In the authors' practice, however, MRI using a 3T scanner is the preferred imaging method as fractures can also be excluded. Ultrasound has a secondary role in judging the dynamic stability of ligament injuries; the joint may be examined with and without stress and compared to the unaffected side.

REFERENCES

1. Fessell DP, Vanderschueren GM, Jacobson JA, et al. US of the ankle: technique, anatomy, and diagnosis of pathologic conditions. Radiographics 1998;18(2):325–340.
2. Bianchi S, Martinoli C, Gaignot C, et al. Ultrasound of the ankle: anatomy of the tendons, bursae, and ligaments. Semin Musculoskelet Radiol 2005;9(3):243–259.

3. Khoury V, Guillin R, Dhanju J, Cardinal E. Ultrasound of ankle and foot: overuse and sports injuries. Semin Musculoskelet Radiol 2007;11(2):149–161.
4. Pang BS, Ying M. Sonographic measurement of achilles tendons in asymptomatic subjects: variation with age, body height, and dominance of ankle. J Ultrasound Med 2006;25(10):1291–1296.
5. Shaw HM, Vázquez OT, McGonagle D, et al. Development of the human achilles tendon enthesis organ. J Anat 2008;213(6):718–724.
6. Incavo SJ, Alvarez RG, Trevino SG. Occurrence of the plantaris tendon in patients sustaining subcutaneous rupture of the achilles tendon. Foot Ankle 1987;8(2):110–111.
7. Zanetti M. Founder's lecture of the ISS 2006: borderlands of normal and early pathological findings in MRI of the foot and ankle. Skeletal Radiol 2008;37(10):875–884.
8. Mansour R, Teh J, Sharp RJ, Ostlere S. Ultrasound assessment of the spring ligament complex. Eur Radiol 2008;18(11):2670–2675.
9. Ellis H. Morphology of peroneus tertius muscle. Clin Anat 2007; 20(2):230.
10. Chepuri NB, Jacobson JA, Fessell DP, et al. Sonographic appearance of the peroneus quartus muscle: correlation with MR imaging appearance in seven patients. Radiology 2001;218(2):415–419.
11. Zammit J, Singh D. The peroneus quartus muscle. Anatomy and clinical relevance. J Bone Joint Surg Br 2003;85(8):1134–1137.
12. Cardinal E, Chhem RK, Beauregard CG, et al. Plantar fasciitis: sonographic evaluation. Radiology 1996;201(1):257–259.
13. Gibbon WW, Long G. Ultrasound of the plantar aponeurosis (fascia). Skeletal Radiol 1999;28(1):21–26.
14. Sofka CM, Adler RS, Positano R, et al. Haglund's syndrome: diagnosis and treatment using sonography. HSS J, 2006;2(1):27–29.
15. Kong A, Van Der Vliet A. Imaging of tibialis posterior dysfunction. Br J Radiol 2008;81(970):826–836.
16. Chen PY, Wang TG, Wang CL. Ultrasonographic examination of the deltoid ligament in bimalleolar equivalent fractures. Foot Ankle Int 2008;29(9):883–886.
17. Harish S, Jan E, Finlay K, et al. Sonography of the superomedial part of the spring ligament complex of the foot: a study of cadavers and asymptomatic volunteers. Skeletal Radiol 2007;36(3):221–228.
18. McCarthy CL, Wilson DJ, Coltman TP. Anterolateral ankle impingement: findings and diagnostic accuracy with ultrasound imaging. Skeletal Radiol 2008;37(3):209–216.
19. Kinoshita M, Okuda R, Yasuda T, Abe M. Tarsal tunnel syndrome in athletes. Am J Sports Med 2006;34(8):1307–1312.
20. Gumusalan Y, Kalaycioglu A. Bilateral accessory flexor digitorium longus muscle in man. Ann Anat 2000;182(6):573–576.
21. Quinn TJ, Jacobson JA, Craig JG, van Holsbeeck MT. Sonography of Morton's neuromas. AJR Am J Roentgenol 2000;174(6):1723–1728.
22. Markovic M, Crichton K, Read JW, et al. Effectiveness of ultrasound-guided corticosteroid injection in the treatment of Morton's neuroma. Foot Ankle Int 2008;29(5):483–487.
23. Hughes RJ, Ali K, Jones H, et al. Treatment of Morton's neuroma with alcohol injection under sonographic guidance: follow-up of 101 cases. AJR Am J Roentgenol 2007;188(6):1535–1539.
24. Iagnocco A, Coari G, Palombi G, Valesini G. Sonography in the study of metatarsalgia. J Rheumatol 2001;28(6):1338–1340.

CHAPTER

58 Ultrasound of soft tissue masses

Rob Campbell

INTRODUCTION

Evaluation of a soft tissue mass is a common indication for ultrasound (US) examination of the musculoskeletal system. The cause of the mass may be apparent on clinical examination, but frequently the diagnosis is uncertain. US may provide an image-specific diagnosis. More critically it aids the clinician in determining a management plan.

The causes of soft tissue masses vary from pseudo-masses to primary soft tissue sarcomas (STS). Most masses are benign. STS accounts for about 1% of all malignancies[1] and has an incidence of approximately 20 per million per year. Soft tissue metastases from other primary malignancies are rarer, with the exception of regional lymph node metastases. Even in regional sarcoma centres, primary STS comprises less than 10% of case load.[2]

Clinical findings that raise suspicion of a sarcoma include:

- mass >5 cm
- mass increasing in size
- mass deep to the fascia
- pain.

However, many lesions that include one or more of these characteristics are benign. Conversely some sarcomas may not fulfil any of the above criteria, or may be mistaken clinically for other processes. Imaging complements the clinical examination and may help to reduce the incidence of 'whoops' lesions, where an unsuspected STS is incompletely excised without a preliminary diagnosis.

Magnetic resonance imaging (MRI) and US are complementary methods for imaging soft tissue mass lesions. Both have advantages and disadvantages. A good rule of thumb is to reserve MRI for deeper and larger soft issue masses. US is particularly useful for small superficial masses. When an image-specific diagnosis cannot be made, referral to the regional sarcoma service is recommended. Biopsy should not be performed outside a sarcoma centre except for regional lymph nose metastases. It may be appropriate to perform excision biopsy on small non-specific soft tissue masses. However, masses of indeterminate nature that fulfil any of the suspicious criteria should not be surgically excised without prior consultation with the sarcoma multidisciplinary team.

Lesions that may present as a soft tissue mass

- Pseudo-tumours
- Bursae and cysts
- Proliferative synovial disorders
- Surface lesions of bone
- Inflammatory masses
- Benign soft tissue tumours
- Regional lymph node metastases
- Primary soft tissue sarcomas
- Soft tissue metastases
- Soft tissue lymphoma
- Soft tissue extension of bone tumours

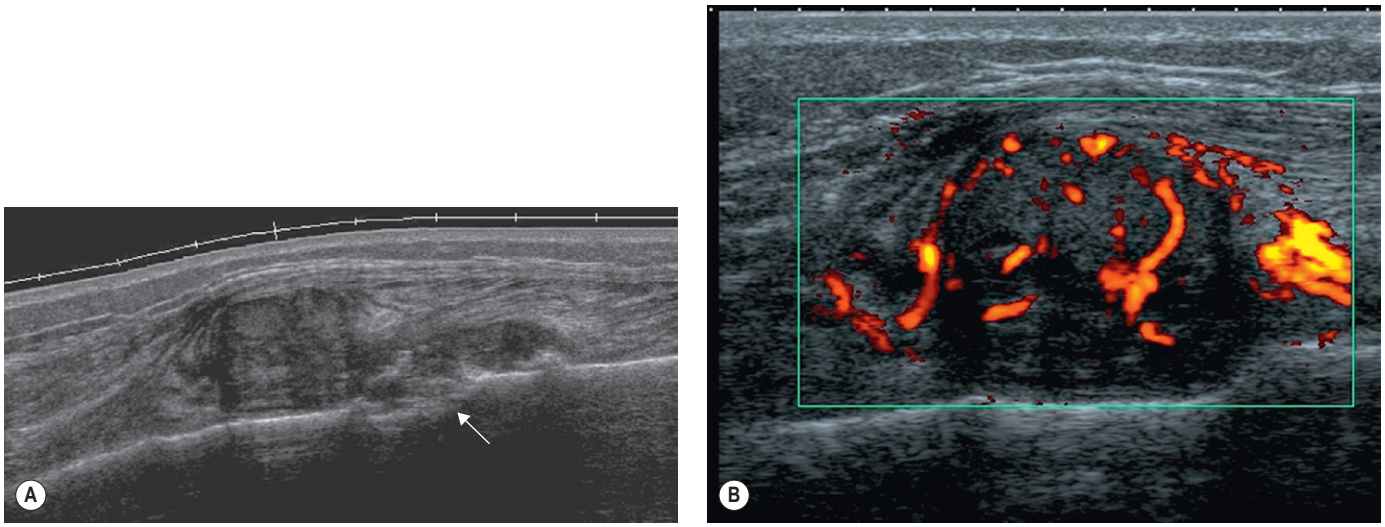

Figure 58.1 Soft tissue mass/Ewing's sarcoma. Panoramic greyscale **(A)** and Doppler **(B)** sonograms of a 16-year-old female patient presenting with a soft tissue mass of the lower limb. There is a vascular soft tissue mass which lies in contact with the underlying cortex of the fibula with irregular areas of cortical destruction (white arrow). Radiographs revealed a typical Ewing's sarcoma of bone.

Soft tissue masses that may be painful

- Abscesses
- Inflammatory bursae
- Ganglion cysts
- Neural sheath tumours
- Thrombosed varicose veins
- Nodular fasciitis
- Rapidly growing sarcomas
- Soft tissue metastases

ULTRASOUND TECHNIQUE

A thorough US technique is required at the site of a soft tissue swelling to avoid overlooking a lesion. All layers of the soft tissues should be examined from the subcutaneous tissues to the periosteal surface of the underlying bone. Good knowledge of musculoskeletal anatomy is needed to recognise individual muscle groups and major neurovascular bundles. Radiographs should be obtained. Surface lesions of bone or bony malignancies with soft tissue extension may present as soft tissue masses (Fig. 58.1). Radiographs are also recommended if there is soft tissue calcification, or when there is suspected joint involvement.

The sonologist should take a history from the patient and perform a clinical examination, as pertinent information may be elicited, e.g. a history of previous local trauma. The age and sex of the patient and relevant clinical findings such as skin changes or the presence of pain should be recorded in the radiological report as this helps define the differential diagnosis.

Although high-frequency linear array probes (10–15 MHz) are most appropriate for evaluation of musculoskeletal structures, lower-frequency probes and even curvilinear array probes may be required for larger and deeper masses. Extended field-of-view imaging is particularly useful for demonstrating the entire lesion and its relationship to other structures.[3] Accuracy of measurements from panoramic images is within 5%.[4]

Compound imaging and frequency harmonic imaging improve image contrast and lesion conspicuity (Fig. 58.2). Compound imaging and beam steering reduce anisotropic effects and facilitate lesion detection in anisotropic tissues such as muscle. Doppler imaging should be employed to assess the vascularity of masses and surrounding soft issue structures.[3]

Refractile shadowing is often seen at the edge of lesions and may help to identify masses which share a similar echodensity to surrounding soft issues. Compound imaging reduces refractile shadowing.[5] If no mass is immediately apparent it is worthwhile employing frequency harmonic imaging. Acoustic enhancement is usually encountered with cysts and other fluid-filled lesions, but may also occur in association with echo-poor solid masses.

When a lesion has been identified its US characteristics should be evaluated in order to define the differential diagnosis.

Size and shape

Size alone is not a discriminating factor, but only 5% of benign soft issue tumours exceed 5 cm in diameter.[6] Larger lesions increase the index of suspicion for malignancy.

Sarcomas tend to grow in a centripetal fashion[7] and are usually round or ovoid. Some lipomas that grow within the intrafascial layer may have a lenticular morphology and can attain quite large transverse dimensions, whilst remaining no more than a few millimetres in depth (Fig. 58.3). The size and shape of the mass should be documented as clinical evaluation may be difficult for deep lesions or if there is prominent subcutaneous fat.

Location

Compartmental involvement is important as it directly influences differential diagnosis, tumour staging and surgical management.[8] The mass may be subcutaneous, intramuscular, intermuscular, or may arise from nerves, blood vessels, joints, bursae or tendons. Masses that cross more than one compartment are usually malignant or inflammatory, although many STS are confined to one compartment until late in the disease.[7] Bone or neurovascular involvement is a predictor of malignancy.[6]

Some tumours have a tendency to occur at specific sites, e.g. a small, round mass in the second or third intermetatarsal space of the foot is likely to be a Morton's neuroma.

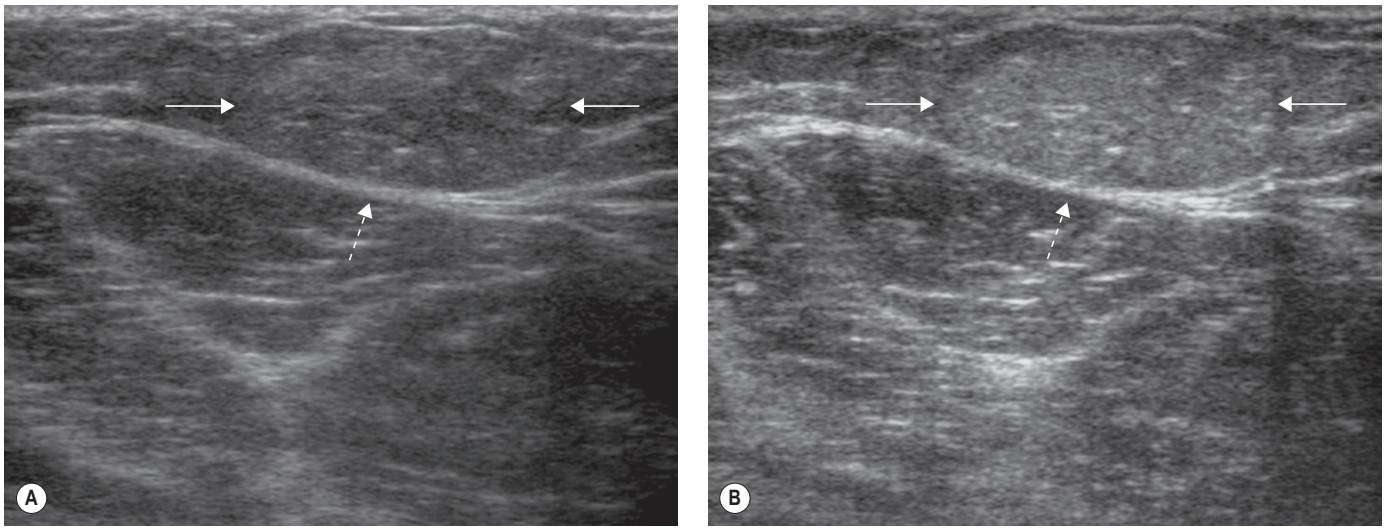

Figure 58.2 Lipoma. Fundamental **(A)** and tissue harmonic **(B)** US images of a simple subcutaneous lipoma. The mass is similar in echodensity with the surrounding subcutaneous fat (white arrows), but there is improved definition and contrast of the lipoma on the tissue harmonic images. The underlying fascia is indented by the lipoma (broken arrow), which also helps identify the presence of a focal mass lesion.

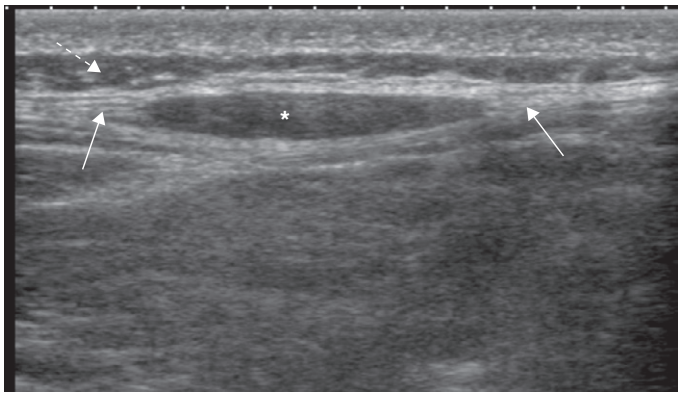

Figure 58.3 Sonogram of a simple lipoma (asterisk) arising within the echo-bright fascia (white arrows), and similar in echodensity to the deep subcutaneous fat layer (broken arrow). The lipoma is constrained by the fascia and grows along the plane of the intrafascial tissues, resulting in a lenticular morphology that is no more than a few millimetres in depth.

Masses arising from tendons or the tendon sheath

- Ganglia
- Rheumatoid nodules
- Xanthomas
- Giant cell tumour of the tendon sheath (GCTTS)
- Synovial chondromatosis
- Tendon sheath lipoma

Margin

Both benign and malignant soft tissue tumours typically have smooth well-defined borders, with a clear transition from normal to abnormal tissue. As an STS grows it compresses rather infiltrates adjacent soft tissue structures, creating a fibrous pseudocapsule,[7] although a rim of low-echo peri-lesional oedema may be identified (Fig. 58.4).

Lesions with irregular or poorly defined margins

- Early haematoma
- Soft tissue abscess
- Pyomyositis
- Aggressive fibromatosis
- Haemangiomas
- Infiltrating intramuscular lipomas
- Soft tissue endometriosis
- Soft tissue lymphoma or metastases

Exceptions include aggressive or deep fibromatoses, which often have irregular or spiculated borders (Fig. 58.5) and satellite lesions. Irregular borders are also typical of inflammation, lymphoma and soft tissue metastases and may occur in benign tumours such as haemangiomas and some intramuscular lipomas.

Echo pattern

Soft tissue masses vary from anechoic to brightly echoic. An anechoic mass with posterior acoustic enhancement is the hallmark of a cystic or fluid-filled lesion. Lipomas are often brightly echoic and similar in echo pattern to adjacent subcutaneous fat. Many soft tissue masses are hyporeflective compared to adjacent structures. Benign and malignant tumours may be composed of more than one mesenchymal tissue type and appear heterogeneous on US. Heterogeneity due to haemorrhage or central necrosis is most frequently seen in STS,[6] and lymphoma. Distinguishing necrotic tumours from simple haematomas and abscesses may be difficult.

Calcification

Mineralisation may be present and vary from complete ossification to foci of calcification of variable size, appearance and location within the mass. Mature myositis ossificans may produce a curvilinear echo-bright line with no appreciable mass due to extensive acoustic shadowing. Microcalcification demonstrates no acoustic shadowing if the areas of calcification are smaller than the width of the US (Fig. 58.6). Both benign and malignant soft tissue masses

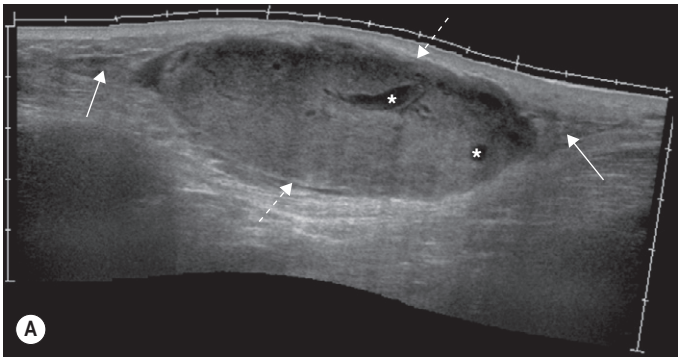

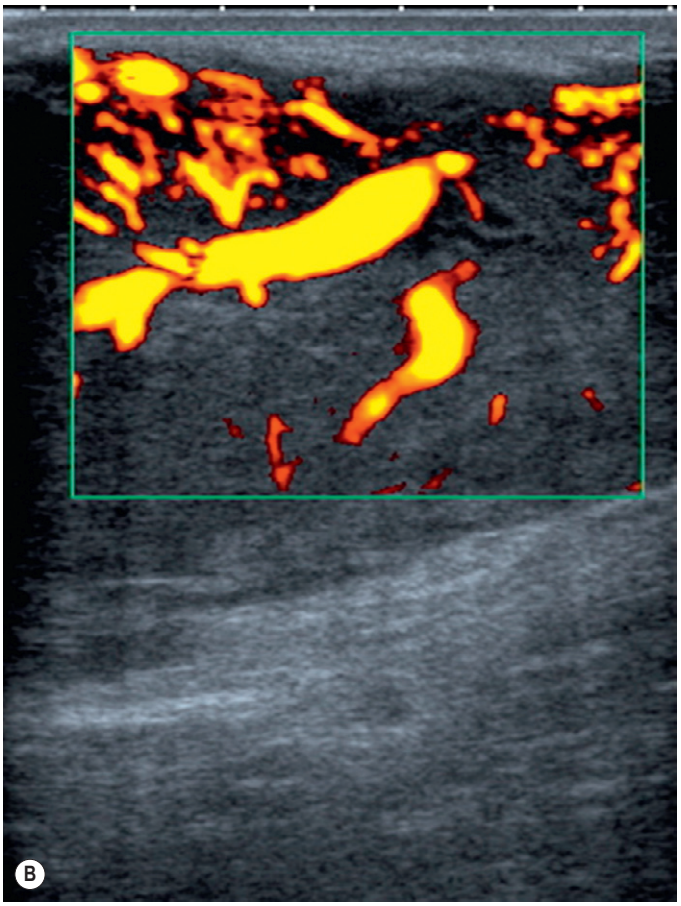

Figure 58.4 **Sonogram of a high-grade subcutaneous leiomyosarcoma** with well-defined margins **(A)**. A thin echo-bright pseudocapsule (broken arrows) is present associated with areas of peri-lesional soft tissue oedema (white arrows). There are prominent anechoic vascular channels (white asterisks), and the lesion is highly vascular on power Doppler imaging **(B)**.

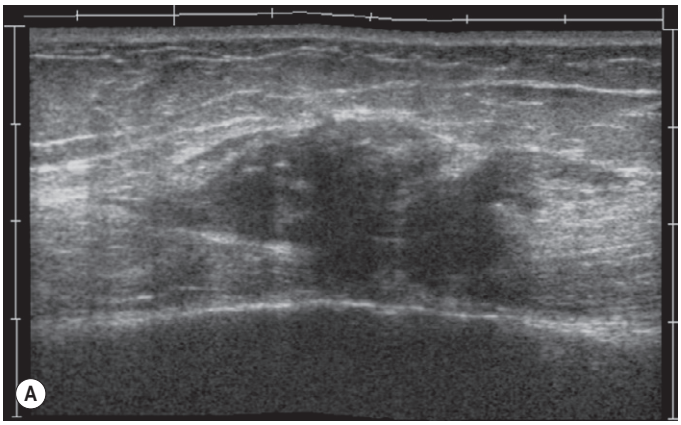

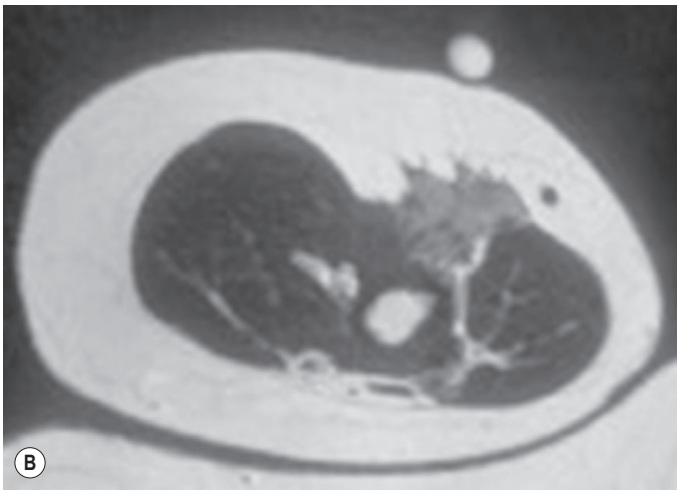

Figure 58.5 **Aggressive fibromatosis.** Sonogram **(A)** and T2-weighted **(B)** MR images of a patient with an immobile soft tissue mass in the upper arm. The mass is echo-poor on US, and has irregular and spiculated borders on both US and MRI. The mass is intermediate signal intensity on the MR image. The diagnosis of aggressive fibromatosis was confirmed on biopsy.

may calcify or ossify. Many other causes of soft issue calcification are not associated with masses.

Tissue density/compressibility

Sonopalpation (using the US probe to compress a mass) may distinguish a solid from a cystic mass. A bursa filled with thickened synovium or debris may mimic a solid mass, but will often compress easily. Movement of echogenic debris within a bursa or abscess during sonopalpation also helps to confirm the nature of the lesion. Not all cystic structures are compressible. Many ganglia are firm and do not deform on sonopalpation.

Elastography, an emerging technology, identifies tissue with abnormal elastic shear properties,[9] and highlights differences in the stiffness of soft tissues (Fig. 58.7). No validated role has been established for the use of elastography in evaluation of soft tissue masses. It is unlikely that it will reliably distinguish benign from malignant neoplasms but it may increase conspicuity of tumours by enhancing the contrast between normal and abnormal tissue.

Soft tissue masses that frequently calcify

Benign
- Myositis ossificans
- Haemangiomas
- Fat necrosis
- Soft tissue chondromas
- Leiomyomas

Malignant
- Leiomysarcoma
- Synovial sarcoma
- Extraskeletal osteosarcoma
- Extraskeletal chondrosarcoma

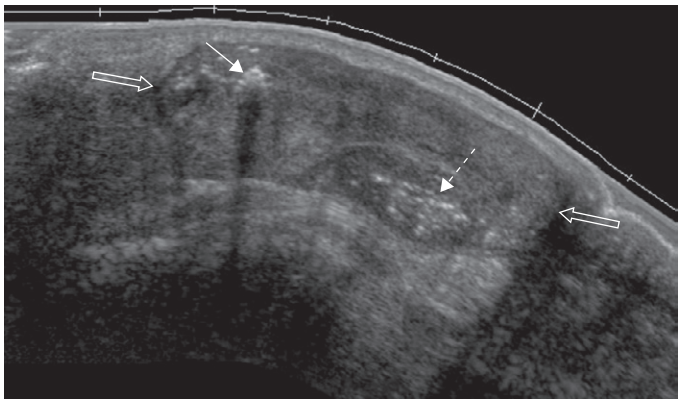

Figure 58.6 Sonogram of a superficial leiomyoma. The mass (open arrows) is echogenic and contains areas of calcification with acoustic shadowing (white arrow), and smaller areas of microcalcification without acoustic shadowing (broken arrow). Prominent vascularity was present on Doppler imaging.

Vascularity

All soft tissue masses should be assessed by colour or power Doppler imaging. The presence of vascularity confirms the solid nature of a mass. Occasionally characteristic patterns are seen (Fig. 58.8). Doppler US may be crucial in diagnosing vascular lesions such as aneurysms and arteriovenous malformations, or in distinguishing subtypes of haemangiomas.[10] Power Doppler US may identify hyperaemia surrounding inflammatory lesions.[11] Conversely the vascularity of benign and malignant tumours often overlap and Doppler examination may add little practical diagnostic value,[6] e.g. benign schwannomas are often highly vascular, while some STSs, such as low-grade liposarcoma, may be relatively avascular.

No validated role for the use of sonographic contrast agents has been established.

At the conclusion of the examination, the sonologist should summarise the findings with the specific diagnosis or a differential diagnosis. The radiological report should include recommendations for subsequent management. It is useful to develop local imaging algorithms that can be applied whenever a soft tissue mass is referred for imaging.

TUMOUR-LIKE MASSES

Pseudo-masses

Many pseudo-masses originate from muscle. Anomalous muscles such as the accessory soleus are relatively common and may present as a soft issue mass if there is asymmetry with the contralateral limb.[12] Anatomical knowledge of muscle groups is crucial, and comparison with the opposite side is helpful.

Muscle hernias are protrusions through defects in the overlying fascia. They are often the result of injury, and are most common in the lower extremity. Most are clinically apparent, but dynamic US during muscle contraction and relaxation can confirm the diagnosis in cases of doubt (Fig. 58.9), and document the size of the fascial defect.[13,14]

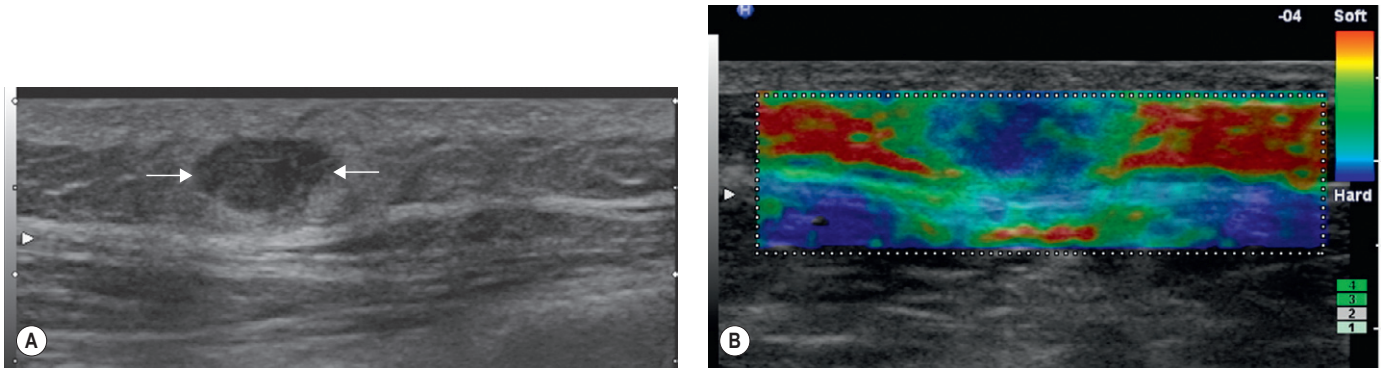

Figure 58.7 Sonogram of a small hyporeflective subcutaneous mass (white arrows) **(A)**. The sono-elastographic image **(B)** demonstrates increased stiffness of the mass (blue) compared to the adjacent subcutaneous fat (orange), but the US features are non-specific.

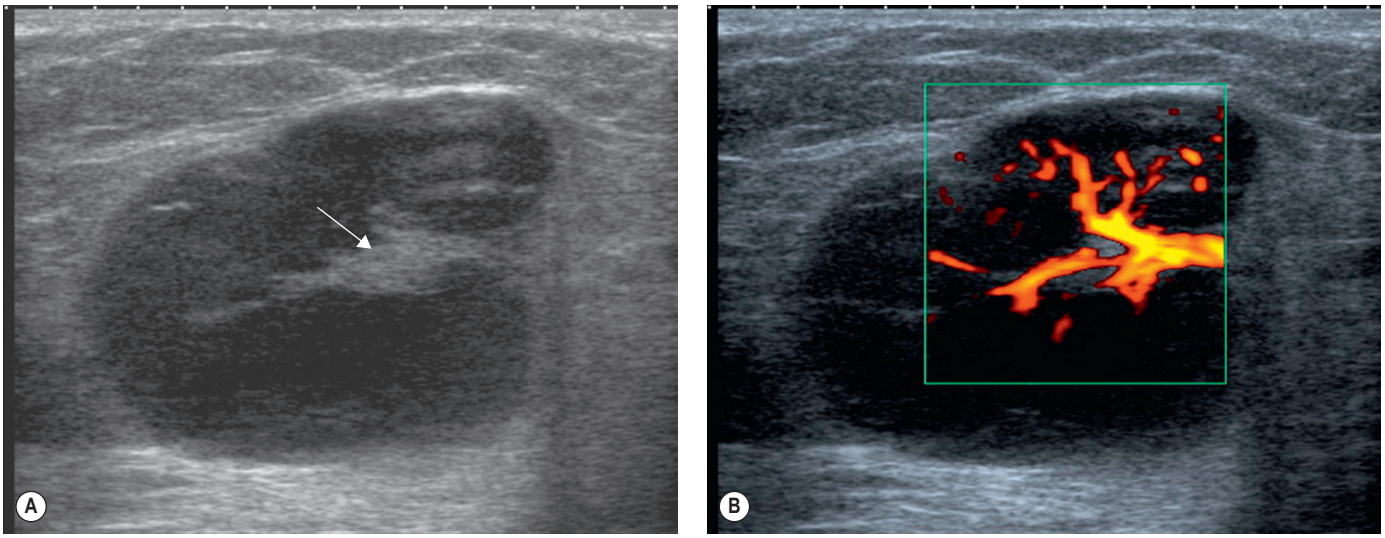

Figure 58.8 Sonogram of a patient presenting with a mass in the groin. US shows the typical appearance of an enlarged lymph node with a fatty hilum **(A)** (white arrow), and the characteristic blood supply arising from the hilum on power Doppler imaging **(B)**. The subsequent CT staging demonstrated widespread retroperitoneal lymphadenopathy and lymphoma was confirmed on lymph node biopsy.

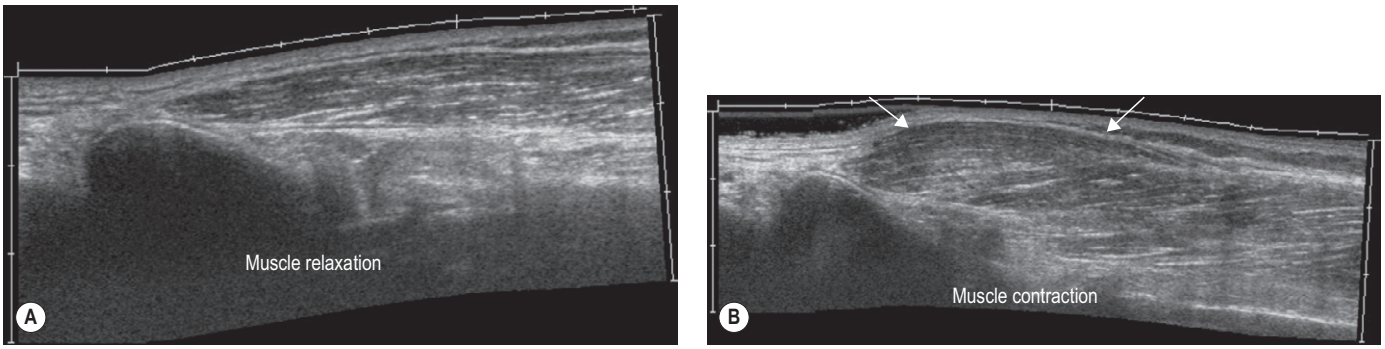

Figure 58.9 Panoramic sonograms of the proximal peroneal muscle belly. The normal outline of the superficial muscle fascia is demonstrated during muscle relaxation **(A)**. A prominent hernia bulging through a fascial defect becomes apparent on muscle contraction **(B)** (white arrows).

Chronic muscle tears occasionally present as a soft tissue masses, particularly when the history of injury is not recalled by the patient. A 'mass' is palpable due the bunching of the proximal muscle belly. This is frequently encountered in chronic quadriceps ruptures, usually rectus femoris.[15] Identification of the torn end of the muscle tissue may be aided by the presence of refractile shadowing. Associated atrophy results in loss of bulk and increased echogenicity in the affected muscle, and is most obvious by comparison with the contralateral limb.

Other pseudo-masses include normal but prominent subcutaneous fat, often asymmetrical, and sometimes encountered after periods of significant weight loss or gain. Careful evaluation is required to avoid missing a lipoma.

Pseudo-masses may be caused by deformity of underlying bone, e.g. mal-union of fractures rib anomalies or asymmetry of costal cartilage (Fig. 58.10).

Once the diagnosis of a pseudo-mass has been established, it is important to reassure the patient that no actual mass or tumour is present.

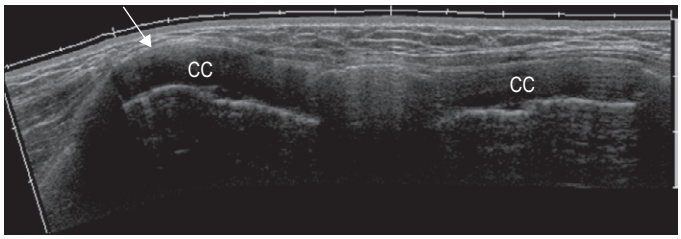

Figure 58.10 Transverse sonogram of the anterior chest wall in a patient with a painless swelling. The costal cartilages (CC) are clearly identified as echo-poor structures either side of the sternum. On the right side there is deformity with anterior bowing of the costal cartilage (white arrow), but without associated mass.

Masses of traumatic origin

Traumatic lesions include haematoma, myositis ossificans and traumatic fat necrosis. A history of injury may not be recalled by the patient.

Muscle haematomas usually occur by overstretching muscle or by direct contusion. A spontaneous haematoma in the absence of anticoagulation or injury raises the suspicion of an underlying sarcoma, and interval US scanning to assess resolution or follow-up MRI may be indicated.

Initially a haematoma has poorly defined margins, and is generally hyperechoic. Within 1–2 days the haematoma becomes more hypoechoic. Cellular material may be seen within the fluid

component, and visualisation is enhanced by sonopalpation. As the haematoma matures over several weeks it organises, shrinks and becomes more solid with a heterogeneous echo pattern. This appearance may mimic a soft tissue tumour, although an organising haematoma is usually avascular on Doppler imaging. The combination of history, intramuscular location and US appearances are usually sufficient to make a confident diagnosis. Occasionally a haematoma remains serous and persists indefinitely as an intramuscular 'cyst'.

Myositis ossificans usually results from muscle contusion and occurs in large muscles of the extremities.[16] Zonal maturation occurs with central areas of necrotic muscle and proliferating fibroblasts, a middle zone of immature osteoid tissue and cartilage, and a peripheral zone of calcification which eventually ossifies. In the early stages, an intramuscular hyporeflective mass is seen, which may show some central zonal hyper-reflectivity. Calcification develops 6–8 weeks after the original injury. US shows calcification up to 2 weeks earlier than radiographs.[17] The calcification is at the periphery of the mass, and may not demonstrate acoustic shadowing initially (Fig. 58.11). When there is doubt about the diagnosis, interval scanning shows maturing ossification over 2–3 weeks. Early biopsy is to be avoided as the histological differentiation from soft tissue osteosarcoma can be difficult.

Ossification with dense acoustic shadowing is seen with mature myositis ossificans. Radiographs or computed tomography (CT) confirm the diagnosis. Calcific myonecrosis is a rare complication of muscle injury and results in a central area of cystic change with a calcified peripheral rim.[18]

Superficial injuries may result in subcutaneous haematoma or fat necrosis. Subcutaneous haematomas appear similar to intramuscular haematomas. Fat necrosis has variable appearances that include a mass with both hyper- and hypoechoic fat lobules and internal septa. A pseudocapsule is sometimes present, although the margin may be poorly defined (Fig. 58.12). Internal fluid is not usually present.[19]

Post-traumatic seromas, 'Morel–Lavallée lesions', occasionally occur in the proximal thigh between the deep subcutaneous fat and the fascia and are due to shearing forces. US demonstrates a well-defined anechoic or hypoechoic lenticular mass with a pseudocapsule overlying the surface of the fascia.[20]

Cysts and bursae

Synovial cysts originate from joints and have a lining of synovial tissue. The commonest is the popliteal or Baker's cyst, which arises from the knee between the medial head of gastrocnemius and the semimembranosus tendon. In adults they are related to underlying joint disorders.[21] The synovial layer is not appreciable on US unless there is synovial thickening, which may be hypervascular in patients with inflammatory arthritis. The fluid within the cyst may be anechoic or contain debris and loose bodies, which may be calcified and mobile or attached to the synovium.[22]

Meniscal cysts at the knee are associated with meniscal tears, and may be clinically palpable as a hard mass. The cystic nature is evident on US, and the underlying meniscal tear may be

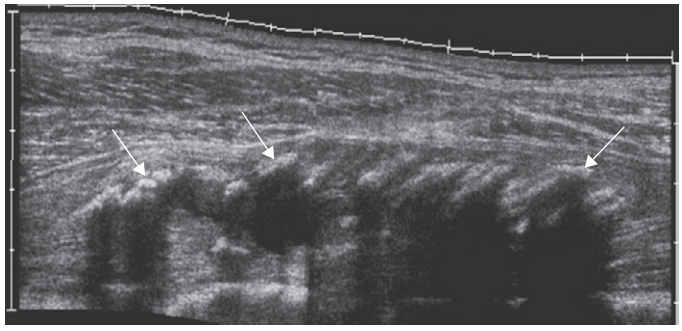

Figure 58.11 Longitudinal sonogram of an area of early myositis ossificans in the thigh of a soccer player. There are areas of peripheral calcification, some of which (white arrows) are starting to display acoustic shadowing. The central portion of the mass is largely obscured by the developing calcification. (Image courtesy of Dr Philip O'Connor, Leeds, UK.)

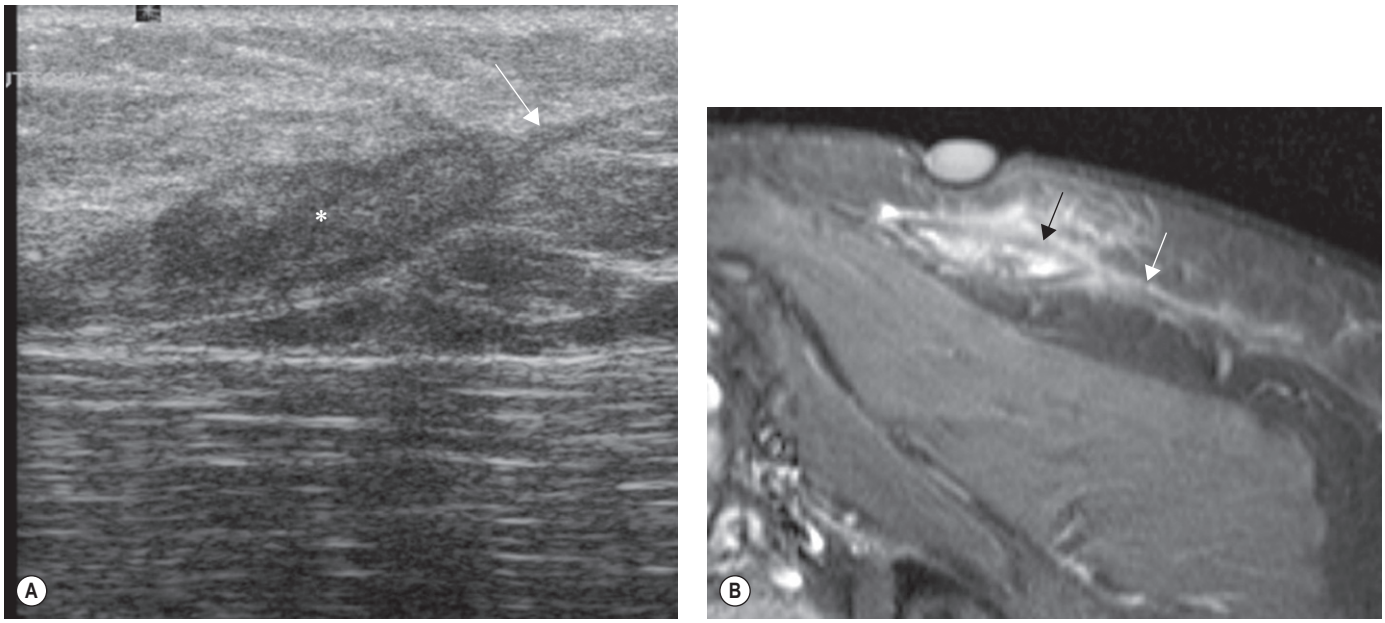

Figure 58.12 Fat necrosis. Sonogram **(A)** and axial fat-saturated T2-weighted MR image **(B)** of an area of subcutaneous fat necrosis. There is a poorly reflective fat lobule (asterisk) with a subtle hyporeflective pseudocapsule and extrinsic low-echo stranding in the adjacent subcutaneous fat (broken arrow). The same features are present on MRI with a high signal intensity fat lobule (black arrow) with low signal pseudocapsule, and extrinsic high signal stranding (white arrow). No calcification is present. (Image courtesy of Dr Philip Robinson, Leeds, UK.)

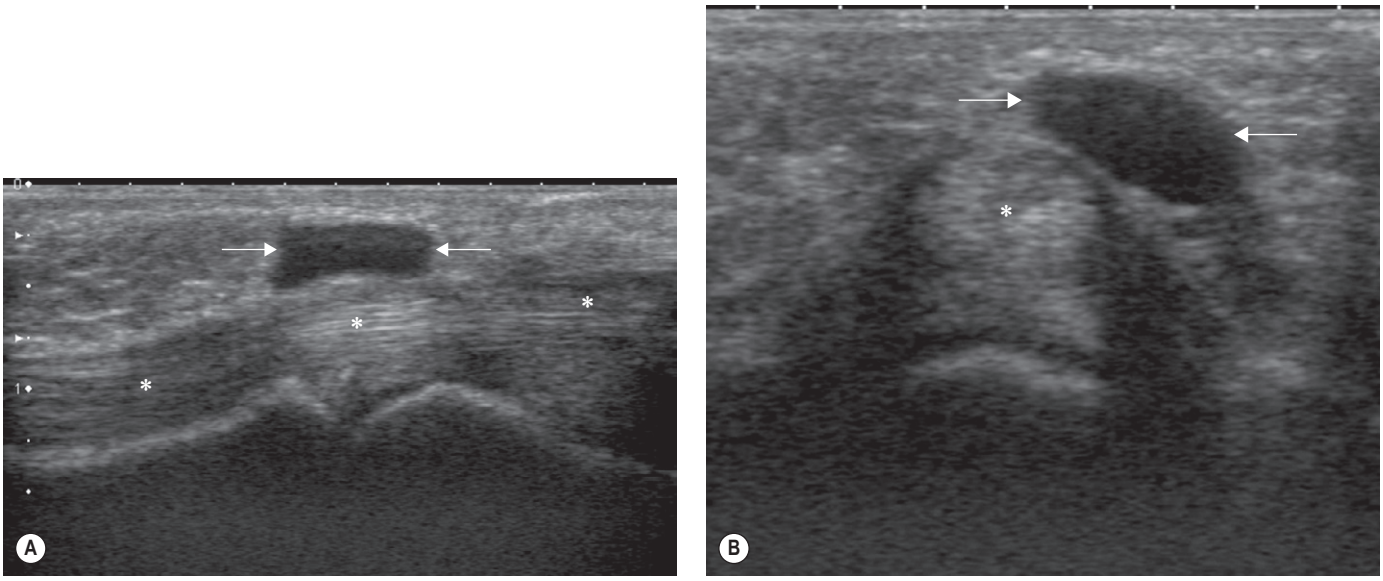

Figure 58.13 Ganglion. Longitudinal **(A)** and transverse sonograms **(B)** of a tendon sheath ganglion of the finger at the level of the metacarpophalangeal joint. The anechoic ganglion (white arrows) lies superficial to the flexor tendon (asterisks), and demonstrates posterior acoustic enhancement.

identified.[23] Paralabral cysts at the hip and shoulder rarely present as soft tissue masses.

Ganglion cysts are of uncertain histogenesis, but are probably caused by myxomatous degeneration of periarticular connective tissues.[24] Although communication with the underlying joint may occur, it is reported to be uncommon.[25] Ganglia contain viscous material and have no synovial layer. Periarticular ganglia often present as masses, most commonly in the hands and feet. They may be painful. A classic location is the dorsal aspect of the wrist, arising from a degenerate scapholunate joint. Tendon sheath ganglia occur most frequently in the fingers.

Ganglia may vary in size over time. The diagnosis is often clinically obvious. Imaging may be indicated as cysts can present some distance from the joint of origin. US identifies the origin, which must be excised to avoid recurrence. Cysts vary from small and round to elongated and loculated. They are classically anechoic with posterior acoustic enhancement,[26] and vary from tense to easily compressible (Fig. 58.13). Chronic ganglia may become echogenic due to internal septation and wall thickening.

Synovial bursae may become enlarged due to inflamed synovium in inflammatory arthritis or crystal deposition disease. The nature of the swelling may be uncertain clinically if the bursa is deep such as the bicipito-radial bursa.[27] Bursae are anechoic if filled with simple fluid, or echogenic due to thickened synovium or fibrinous exudate. In crystal deposition disorders, bursal contents may be highly echogenic.[28]

Subcutaneous cystic masses are usually epidermal inclusion cysts (sebaceous cysts, keratin cysts). Most are less than 5 cm in size, anechoic and have discrete margins and posterior enhancement.[29] They can become echogenic when distended by keratinous material (Fig. 58.14) and may be mistaken for solid masses. Sonopalpation may not reveal their cystic nature.

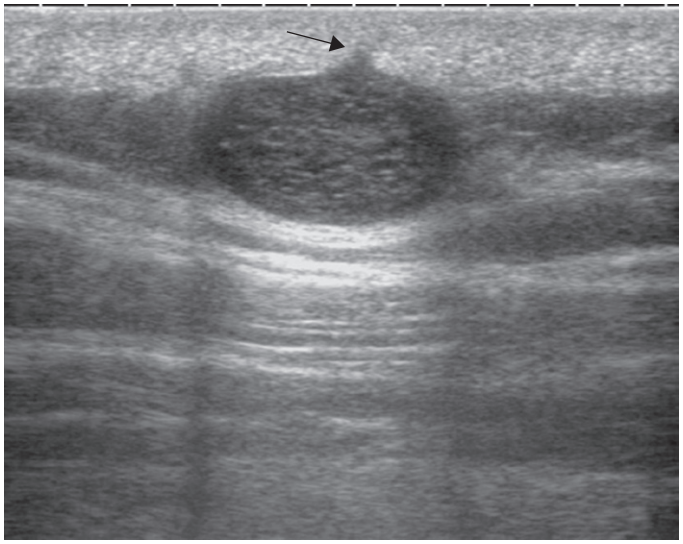

Figure 58.14 Sonogram of a small subcutaneous sebaceous cyst. The mass demonstrates posterior acoustic enhancement, and refractile shadowing, but there are internal echoes due to the presence of keratinous material. The small tail (black arrow) on the superficial surface indicates the origin from a sebaceous gland. No vascularity was present on Doppler imaging.

Inflammatory masses

Acute soft tissue infection is recognised clinically by soft tissue swelling, cellulitis and raised inflammatory markers. US confirms and localises abscesses prior to drainage,[30] and distinguishes reactive adenopathy from abscess.

Abscesses vary in echo pattern from poorly to highly reflective depending on the amount of cellular debris. Debris moves on sonopalpation,[31] although this may be limited by pain and tenderness. The margins of the abscess may be poorly defined. Adjacent soft tissues are highly vascular on Doppler imaging.[32] US can facilitate image-guided drainage, but if the abscess is large or loculated, MRI is required to document the full extent of the abscess and assess if surgical drainage is required. When an abscess lies close to a joint, the joint should be evaluated for an effusion to exclude septic arthritis, which may require aspiration or surgical wash-out.

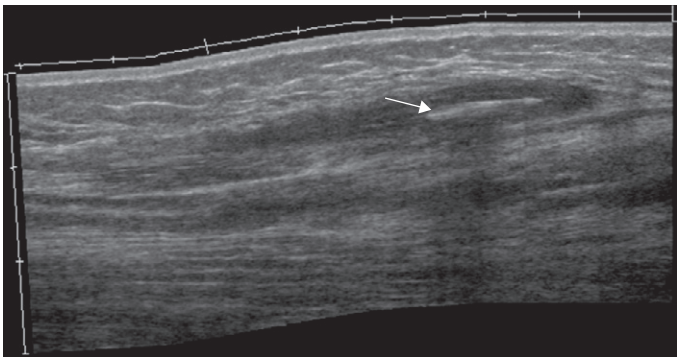

Figure 58.15 Longitudinal sonogram of a chronic foreign body (wooden splinter) granuloma in the forearm. The patient fell from a tree some years previously, and had a residual soft tissue swelling, but did not recall any history of penetrating injury. The splinter is identified as a linear echogenic area (white arrow) with posterior acoustic shadowing within a hyporeflective chronic granuloma. No vascularity was seen on Doppler imaging.

Pyomyositis is usually bacterial and is frequently associated with diabetes mellitus and immunocompromised patients.[33] The affected muscle is swollen, diffusely hyperechoic and hyperaemic on US.[30] Small hypoechoic areas due to tissue necrosis and eventually frank abscesses may develop. Tuberculous abscesses lack clinical features of inflammation. Aspiration is required in 'at risk' patients who present with a soft tissue fluid collection. Chronic TB abscesses may become heavily calcified.

Hydatid disease (*Echinococcus granulosus*) most commonly affects the liver and lungs. Soft tissue disease is rare and usually involves muscles. Hydatid cysts are anechoic but may contain septa. Cyst walls may calcify, and there may be daughter cysts.[34]

Foreign body granulomas may present as soft tissue masses and can create clinical difficulties if the history of a trauma is not recalled by the patient. US demonstrates the echogenic foreign body surrounded by a hyporeflective granuloma which may display varying degrees of vascularity on Doppler imaging depending on chronicity (Fig. 58.15).

Vascular masses

Aneurysms of the extremities are present clinically as pulsatile soft tissue masses but may mimic soft issue tumours, particularly if there is no palpable pulse. The popliteal artery is most commonly affected.[35] Doppler US distinguishes an aneurysm from other masses. Adventitial cystic disease also affects the popliteal artery most commonly and presents as a multiloculated cyst that may compromise the arterial lumen.[36] Pseudo-aneurysms are usually the result of injury, frequently iatrogenic resulting from arterial puncture. They may remain static for years. Thrombosed pseudo-aneurysms may present diagnostic difficulty unless there is a history of trauma.

Varicose veins are easily diagnosed clinically, but thrombosed varicose veins are occasionally mistaken for soft tissue masses, especially if there are no widespread varicosities. Doppler US demonstrates the associated perforating and draining veins which help establish the diagnosis (Fig. 58.16).

Miscellaneous tumour-like masses

Rheumatoid nodules are rounded hypoechoic masses, often located at pressure points.[37] They occur in 20–30% of rheumatoid patients with elevated rheumatoid factor. Gouty tophi are common in the hands, feet and elbows, and are heterogeneous with areas of hyper-reflective crystal deposits. Occasionally internal calcification is seen. Increased attenuation (about 160 Hounsfield units) on CT is the most specific imaging sign of gout,[38] although the diagnosis of rheumatoid nodules or gouty tophi is usually apparent from the clinical history.

Extraperitoneal endometriomas may occur within abdominal scars following pelvic surgery. Rarely they are located in the line of the round ligament in the groin. The masses are typically hypoechoic with irregular margins.

Xanthomas are focal deposits of histiocytes containing large amounts of lipids, and occur in patients with primary or secondary hyperlipidaemia. Skin and subcutaneous nodules in the hands and feet are the commonest manifestation, but tendon involvement, usually the Achilles tendon (Fig. 58.17), also occurs. US reveals either diffuse low-echo tendon enlargement or focal hypoechoic tendon masses.[39]

SOFT TISSUE TUMOURS

Soft tissue tumours are classified according to their tissue of origin and biological behaviour. Diagnosis may require a combination of histology and immunochemistry. Imaging frequently helps to make a specific diagnosis and may avoid the need for biopsy. A comprehensive description of all tumour types is beyond the scope of this chapter, which is limited to a description of the more common benign and malignant tumours and to conditions where an image-specific diagnosis may be possible. Readers are referred to specialist texts for a comprehensive discussion of soft tissue tumours.

Lipomatous tumours

Lipomatous lesions are the commonest of all mesenchymal tumours. The benign group comprises lipomas, lipoma variants, a variety of infiltrating lipomatoses and hibernomas. Liposarcoma is the second commonest soft tissue sarcoma.

Lipomas

Most lipomas are subcutaneous, soft or rubbery on palpation and relatively compressible. They occur anywhere on the trunk or extremities. They are usually solitary, but may be multiple in 5–15% of cases.[40]

Ultrasound shows an, ovoid or elliptical, encapsulated subcutaneous mass that is avascular on Doppler imaging and may contain short echo-bright internal striations that run parallel to the skin. Most lipomas are <10 cm in size, 80% are <5 cm.[41] They vary from echo-bright to echo-poor depending on the relative composition of fat, connective tissue and water (Figs 58.2 and 58.3).[42] The lobulated appearance of normal fat can be difficult to distinguish from a focal lipoma and sonopalpation and tissue harmonic imaging may help to delineate the margin of a lipoma.

Deeper subcutaneous lipomas that are adherent to or lie within the deep fascia typically have a lenticular morphology with concavity of the underlying fascial plane (Fig. 58.3).

Deep intra- or intermuscular lipomas, are less common than superficial lipomas and are frequently larger. Clinical differentiation from sarcoma can be difficult. The presence of a well-defined hyperechoic intramuscular mass is usually diagnostic (Fig. 58.18). However, lipomas may be nearly isoechoic to surrounding muscle and the margins of the mass may be poorly defined even if well defined on MRI. Infrequently lipomas diffusely infiltrate an entire muscle belly[43] and appear similar to fatty atrophy with generalised increase in reflectivity and loss of the normal pennate structure, but with normal or increased muscle bulk.

Intermuscular lipomas extend along fascial planes between muscles. MRI better documents their relationship to neurovascular structures than US.

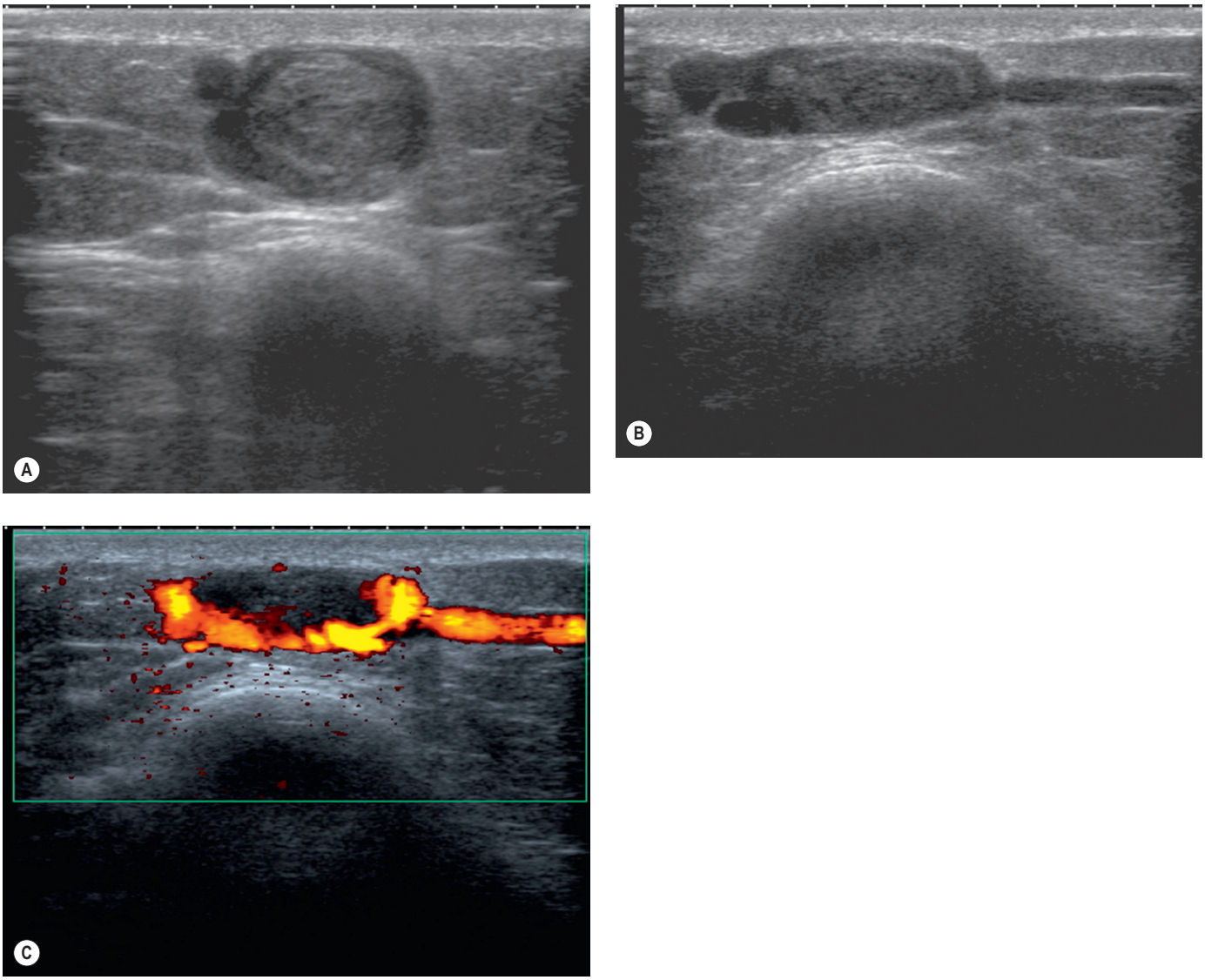

Figure 58.16 Sonographic images (A, B) of a thrombosed varicose vein presenting as a painless superficial mass. There is echogenic intraluminal clot within a small varix. The relationship to the proximal vein is easily identified. Blood flow within the superficial vein and around the intraluminal clot on the Doppler image **(C)** helps confirm the diagnosis.

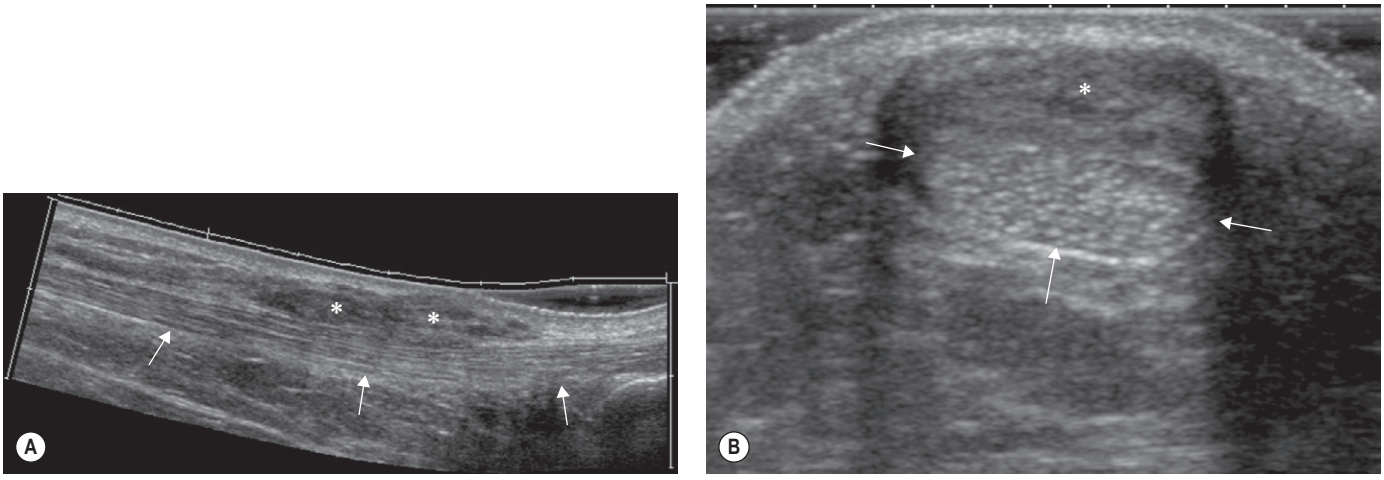

Figure 58.17 Longitudinal (A) and transverse (B) sonograms of the Achilles tendon (white arrows) in a patient with hyperlipidaemia. There is a superficial hyporeflective xanthoma (asterisks) arising from the adventitial layer of the tendon sheath. No internal vascularity was demonstrated on Doppler imaging.

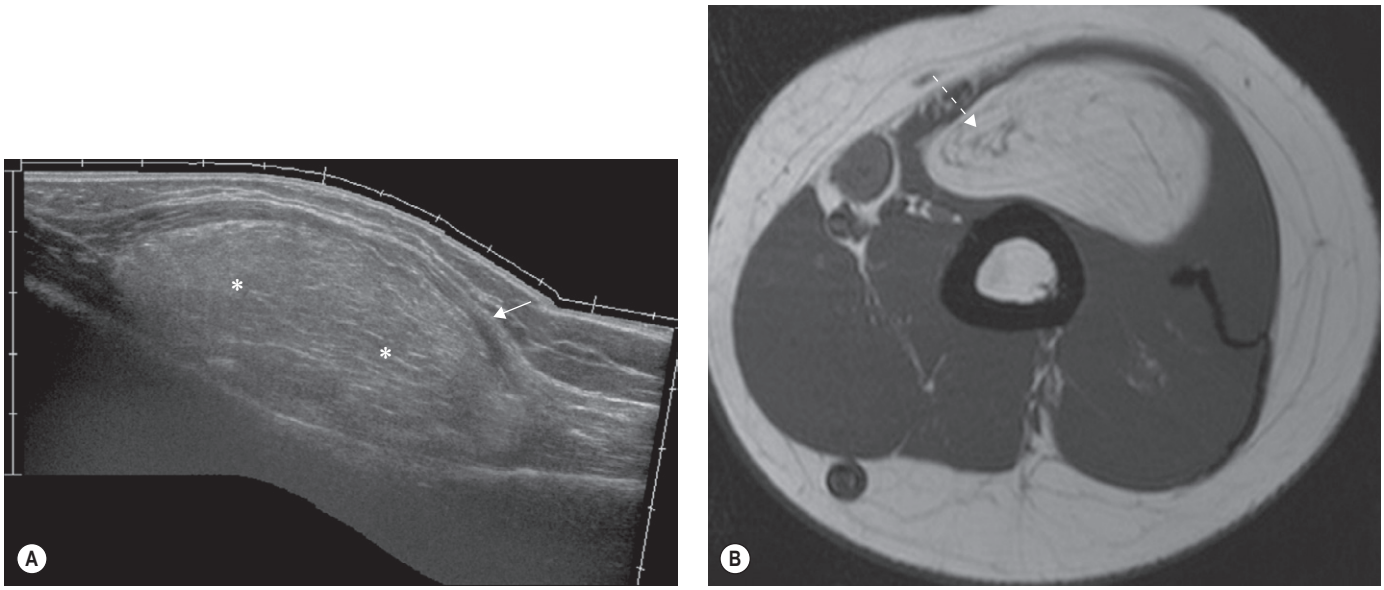

Figure 58.18 Lipoma. Longitudinal sonogram **(A)** and axial T1-weighted MR image **(B)** of a large intramuscular lipoma in a 22-year-old woman. The US image shows a characteristic echo-bright lipoma (asterisks) with well-defined margins within the triceps muscle (white arrow). The features of large tumour size, deep location and areas of non-lipomatous tissue stranding within the lesion on MRI (broken arrow) indicate that low-grade liposarcoma cannot be excluded.

Lipoma variants

Lipoma variants including fibrolipoma and angiolipoma contain varying amounts of other mesenchymal tissues which affect their US appearances. Heterogeneity within a lipomatous lesion merits further evaluation with MRI. Hibernomas arise from brown fat. They are usually well-marginated hyperechoic masses with internal vascularity on Doppler imaging.

Liposarcoma

Liposarcomas account for 16–18% of all soft tissue sarcomas.[44] Low-grade well-differentiated liposarcoma, the commonest subtype (approximately 50%), has the best prognosis and is composed predominantly of fat (usually >75%).[45] Heterogeneity on imaging may be due to connective tissue striations and areas of non-lipomatous tissue. Calcification is present in up to 10% of cases but is seen occasionally in benign lipomas. Distinction from benign lipomas can be difficult even with MRI. Large fatty tumours (>10 cm) with striations but otherwise homogeneous appearances are sometimes referred to as atypical lipomas (Fig. 58.18). Biopsy is prone to sampling errors and these tumours are best presumed to be low-grade liposarcomas until proven otherwise either by surgical excision or by interval MRI scanning depending on clinical circumstances and the index of clinical suspicion.

Higher-grade myxoid or pleomorphic liposarcoma subtypes usually display little or no appreciable fat on US or MRI and often have non-specific imaging features. Diagnosis relies on tissue biopsy.

Nerve tumours and tumour-like lesions

Nerve tumours derived from Schwann cells include benign neurofibromas and schwannomas (neurolemmoma) and malignant peripheral nerve sheath tumours. Clinical diagnosis is straightforward if the patient has a positive Tinel sign (pain or paraesthesia in the distribution of the nerve on palpation). Sonopalpation may also reproduce a Tinel sign. The key US feature is recognition that the mass arises from a nerve.

Less common tumours with neurogenic histiogenesis include fibrolipomatous hamartoma, paraganglioma, ganglioblastoma, clear cell sarcoma, extraskeletal Ewing's sarcoma and primitive neuroectodermal tumours (PNET).

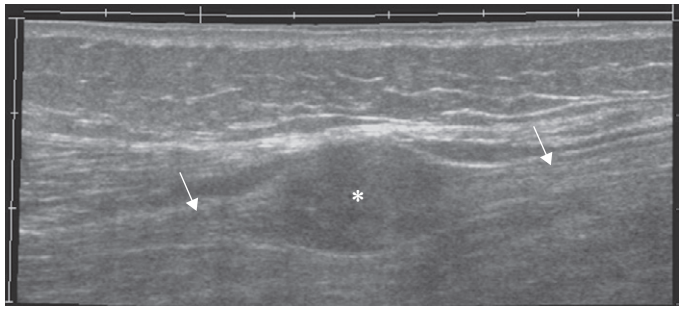

Figure 58.19 Longitudinal sonogram of schwannoma arising from the posterior tibial nerve. The tumour (asterisk) has a homogeneous echo-poor appearance. The proximal and distal nerve fibres (white arrows) can be seen tapering into the neuroma, which confirms the diagnosis of a neural sheath tumour. However, the mass is not eccentric to the nerve in this case, and cannot be reliably distinguished from a neurofibroma.

Non-tumorous nerve masses include stump neuromas in amputees and Morton's neuromas in the intermetatarsal spaces of the forefoot. Intraneural ganglia are cystic masses which most frequently involve the proximal common peroneal nerve.

Schwannoma

Schwannomas usually arise in the extremities and are composed of neoplastic cells that have the phenotype of Schwann cells but without the presence of axons.[46] They are usually solitary, eccentric to the nerve axis and are round or oval. US shows a uniformly hypoechoic mass with posterior acoustic shadowing and moderate vascularity on Doppler imaging. The proximal nerve may be thickened, hypoechoic and taper into the mass (Fig. 58.19) due to infiltration of tumour cells along the nerve fascicles.[47]

Cystic degeneration and calcification may occur in longstanding schwannomas or 'ancient schwannomas'.[48]

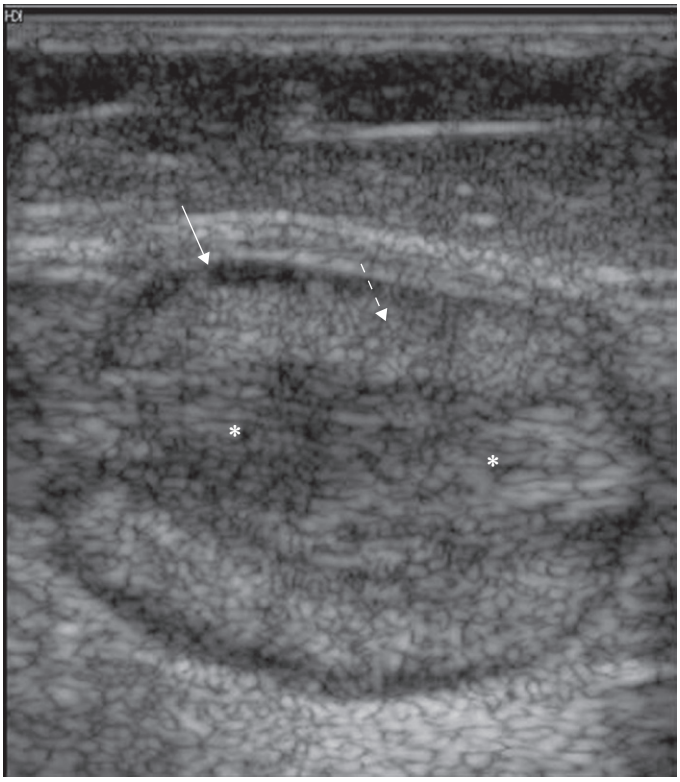

Figure 58.20 Sonogram of a neurofibroma. The nerve can be seen running through the mass (asterisks). There is an outer hyporeflective myxoid layer (white arrow) and a central hyperreflective zone (broken arrow) producing a 'target' sign.

Neurofibroma

Neurofibromas are composed of a mixture of cell types including perineural cells which spread through the epineurium.

There are three distinct types of neurofibroma: focal, diffuse and plexiform.

Focal neurofibromas are the most common, usually solitary, and account for up to 90% of cases.[49] They arise anywhere along a nerve, from the spinal canal to the most terminal superficial branch. The characteristic appearance is of a fusiform mass arising from a nerve, cf. the eccentric morphology of schwannomas. A central fibrotic relatively hyperechoic area surrounded by a hypoechoic rim of myxomatous tissue may produce a 'target sign' (Fig. 58.20).[50] Neurofibromas are generally less vascular then schwannomas on Doppler imaging. However, appearances overlap and distinction between neurofibroma and schwannoma may not be possible.[47]

Multiple focal neurofibromas and diffuse and plexiform neurofibromas are associated with neurofibromatosis type 1. Multiple focal neurofibromas are often located in the skin and subcutaneous tissues. The nerve of origin is usually too small to identify. Diffuse neurofibromas are usually seen as an ill-defined area of subcutaneous thickening, particularly at the ankle or neck.[49]

Plexiform neurofibromas have pathognomonic appearances with multiple neurofibromas arising from the fascicles of a large nerve trunk over a long distance and extending into the terminal branches. On US they are convoluted and multinodular and may have a 'bag of worms' appearance.[49]

Malignant peripheral nerve sheath tumours (MPNST)

MPNST is suggested by a recently or rapidly enlarging soft tissue mass which arises from a peripheral nerve. MPNSTs may arise de novo, as a result of malignant transformation of a pre-existing neurofibroma in a patient with neurofibromatosis or secondary to previous radiotherapy. A change in size of a previously stable lump in a patient with neurofibromatosis requires immediate imaging and biopsy. US may show a mass with irregular borders, but appearances are otherwise indistinguishable from benign nerve sheath tumours.[47]

Biopsy of nerve sheath tumours should be undertaken with care, as the procedure may cause excruciating pain. Anaesthetic infiltration around the nerve proximal to the mass as well as at the biopsy site may provide an effective nerve root block. Surgical excision of a schwannoma can usually be achieved without neurological deficit. Resection of a neurofibroma may result in nerve damage although some neurofibromas can be dissected out without permanent deficit.

Vascular tumours

Vascular tumours are a common cause of soft issue masses, particularly in young adults, and may be confused clinically with other soft tissue tumours, especially if there is no overlying skin discoloration. Imaging often demonstrates characteristic features.

Haemangiomas

Benign haemangiomas (vascular malformations) comprise 7% of all soft tissue tumours. The presence of non-vascular elements, such as fat, smooth muscle and fibrous tissues, can make subclassification difficult but haemangiomas are usually classified by their predominant vascular channel (capillary, cavernous, arteriovenous or venous),[51] although there may be significant degrees of overlap.

Capillary haemangiomas are commonest in infants and children, are usually associated with characteristic naevi and frequently involute spontaneously.

Cavernous haemangiomas have dilated vessels filled with blood and lined by epithelium. They typically present in adolescents and young adults with a deep intramuscular mass that may fluctuate in size and be painful, especially after exercise. Superficial lesions may demonstrate bluish discoloration of the skin.

Arteriovenous haemangiomas or arteriovenous malformations (AVMs), are either superficial or deep. Deep AVMs are high-flow lesions with arteriovenous shunting, and occasionally present with cardiovascular symptoms and focal limb enlargement.

The US appearances of haemangiomas partly depend on the various histological constituents. Lesions with a large fat component are hyperechoic (Fig. 58.21).[52] Compressible vascular spaces may contain slow moving echogenic blood. Doppler US appearances vary from high flow to no detectable Doppler signal depending on the predominant vessel type. Low-resistance forward vascular flow during both systole and diastole may be seen,[53] but there are no Doppler patterns that reliably distinguish haemangiomas from other vascular tumours.

Phleboliths cause acoustic shadowing in 20–67% of cavernous haemangiomas (Fig. 58.22). Other patterns include curvilinear or amorphous calcification. Haemangiomas close to bone may induce periosteal reaction which is usually mature and non-aggressive. Cortical thickening or erosion is less common.[54] Radiographs may show areas of soft tissue calcification.

The margins of haemangiomas are variable. Lesions may be discrete or diffuse, extending across more than one anatomical compartment. MR imaging often reveals characteristic features,[55] and is useful for local staging prior to surgery or sclerotherapy. MR angiography or conventional angiography may 'map out' the feeding vessels and draining veins.

Angiomatosis

Angiomatosis is a diffuse infiltration of soft tissues by haemangiomatous or lymphangiomatous lesions and may also involve bone

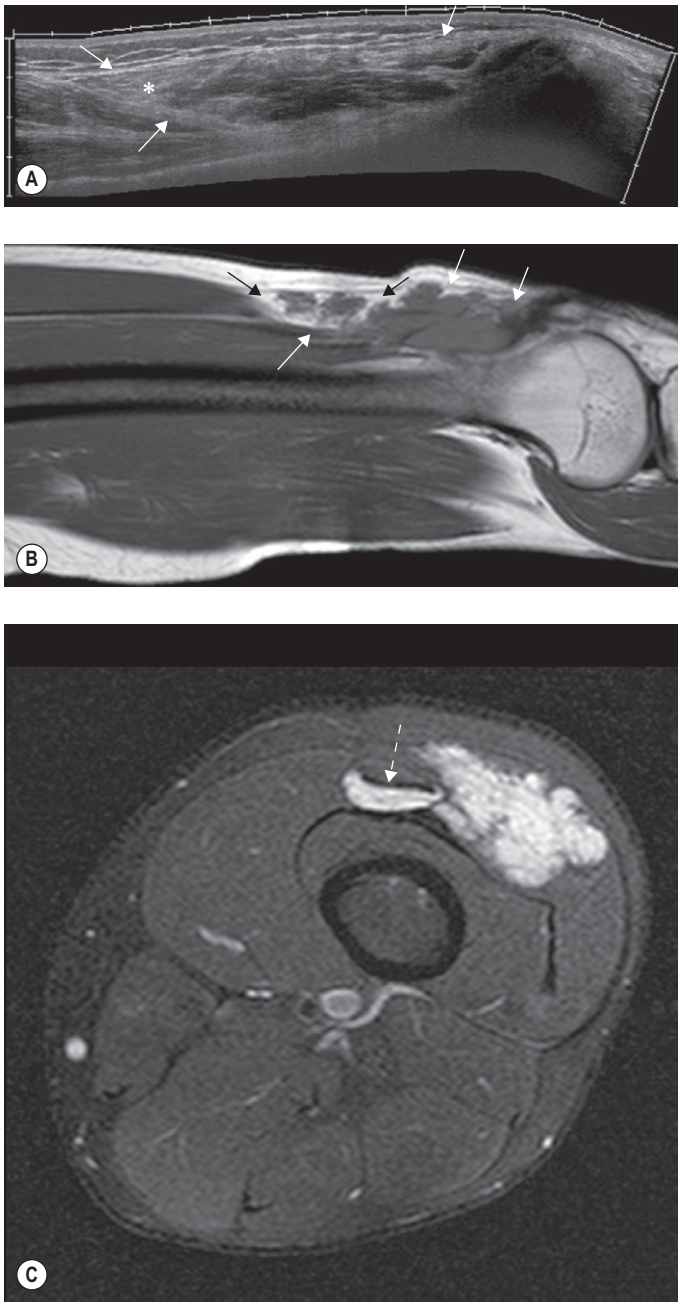

Figure 58.21 Haemangioma. Longitudinal sonogram **(A)**, sagittal T1-weighted MR image **(B)** and axial fat saturated T2-weighted MR image **(C)** of a haemangioma of the distal thigh. The haemangioma has rather poorly defined margins on both US (white arrows) and MRI. There is an echo-bright fatty component on ultrasound (asterisk), which is also seen on the sagittal MR image (black arrows). A prominent draining vein is identified on the axial MR image (broken arrow). Non-specific vascularity was present on Doppler imaging (not shown).

and viscera.[56] US features are similar to those of focal haemangiomas, but lesions are more widespread.

Angiomatosis may be associated with Mafucci's, Osler–Weber–Rendu and Klippel–Trénaunay–Weber syndromes. Imaging may be required where complications arise, e.g. malignant transformation of enchondromas or haemangiomas in Mafucci's syndrome. MRI is usually the investigation of choice.

Intermediate vascular tumours

Haemangioendothelioma and haemangiopericytoma are vascular tumours of intermediate aggressiveness and have several histological subtypes. Adults are usually affected. Recurrence rates are variable. Mortality rates are low but metastases may be encountered.[57] US and MRI features are often non-specific, usually comprising a solid mass with a high-flow vascular component. The prognosis is good following wide local excision, but there is a risk of local recurrence.

Malignant vascular tumours

Angiosarcoma involves the skin and deeper soft tissues, usually in older patients. Visceral involvement also occurs. Lymphoedema, typically post-mastectomy, is a recognised predisposing factor and occurs in 10% of cases.[58] The clinical diagnosis may be obvious. Imaging features are non-specific although a skin lesion with underlying solid vascular mass on US and diffuse subcutaneous oedema is suggestive.

Kaposi's sarcoma is a malignant vascular tumour of the skin and occurs in association with HIV infection. The diagnosis is clinical and confirmed by biopsy.

Muscle tumours

Many tumours arising within muscle are not of muscle tissue origin, e.g. intramuscular haemangiomas and lipomas. Conversely tumours of muscle origin, either smooth muscle (rhabdomyoma) or skeletal muscle (leiomyoma), may arise outside muscle.

Leiomyoma

Superficial leiomyomas and angiomyoleiomas occur in the skin and subcutaneous soft tissue.[59] They are uncommon, usually ovoid, have a heterogeneous echo pattern and may demonstrate areas of calcification and vascularisation (Fig. 58.6). Deep soft tissue leiomyomas may be intra- or intermuscular, and are often large and prone to calcification.[60] Rhabdomyomas rarely occur in the extremities.

Myxoma

Intramuscular myxomas are hypocellular tumours composed of gelatinous myxoid stroma. They are commonest in the fifth to seventh decades and in the thigh (>50%). On US they are well defined and markedly hypoechoic, often with small anechoic cysts and acoustic enhancement. There is little or no vascularity on Doppler imaging. Differentiation from soft tissue sarcoma can be difficult and MRI and biopsy are required. Myxomas are associated with fibrous dysplasia in Mazabraud's syndrome.

Other varieties of myxoma include juxta-articular, subcutaneous and deep aggressive angiomyxoma.

Malignant muscle tumours

Malignant leiomyosarcomas account for nearly 10% of all soft tissue sarcomas in adults. They are located in or outside muscle,[44] and may be large and have central necrosis. Vascularity is variable. Mineralisation occurs in 12% of cases (Fig. 58.4).[61] Rhabdomyosarcoma is the commonest soft tissue sarcoma of childhood;[62] 15% occur in the extremities. Imaging shows a non-specific intramuscular mass. Rhabdomyosarcoma is very rare and has a particularly poor prognosis in adults. Local bone invasion and distant metastases are frequently found at presentation.

Fibrous and fibrohistiocytic tumours

The benign group includes fibroblastic proliferations such as nodular fasciitis and the fibromatoses. The malignant group

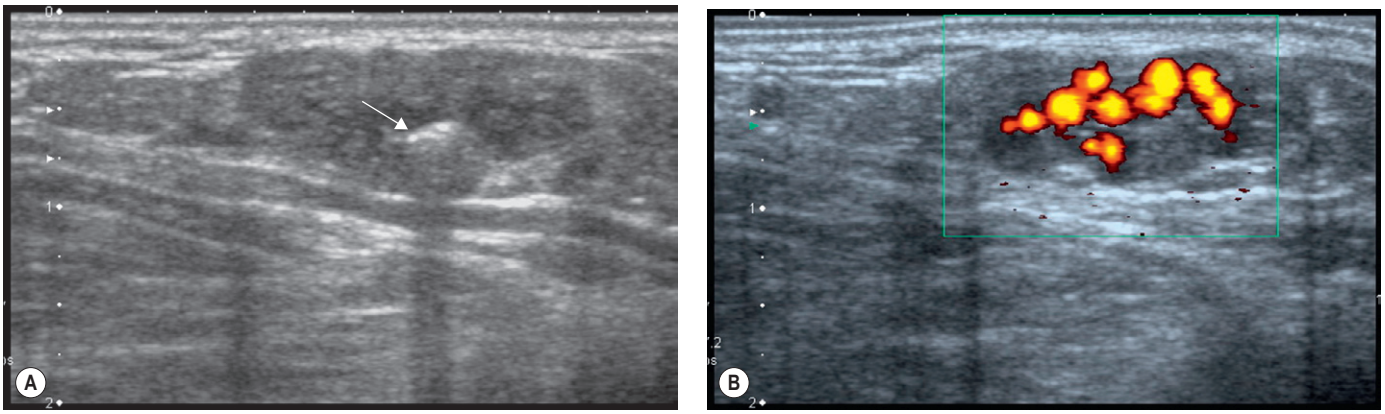

Figure 58.22 Superficial haemangioma of the dorsal aspect of the foot. The haemangioma contains a small phlebolith with posterior acoustic shadowing **(A)** (white arrow), which was also visible on radiographs. There is prominent vascularity on the power Doppler image **(B)**.

comprises dermatofibrosarcoma protuberans (DFSP) and fibrosarcoma/malignant fibrohistiocytoma.

Nodular fasciitis

Nodular fasciitis is a reactive condition that occurs in young adults, most commonly in the upper limb. It is often initiated by local trauma or an inflammatory process, and is characterised by an initial phase of rapid growth. The commonest form is a subcutaneous soft tissue nodule of up to 3–4 cm in size. Intrafascial or intramuscular lesions may be larger.[63] Local pain and tenderness are common. Calcification is rare. The US appearances are of a non-specific soft tissue mass of intermediate echogenicity with well-defined borders.[64] Larger lesions cannot be distinguished from sarcoma. Local excision is usually curative.

Elastofibroma

Elastofibroma is a fibroblastic pseudo-tumour that presents as a mass at the inferior angle of the scapula deep to the latissimus dorsi muscle and is probably due to chronic friction between the scapula and chest wall. Up to two-thirds of cases are bilateral. Elastofibromas grow slowly and usually do not present until reaching 5–10 cm in size in the fifth to seventh decades of life.[65] Small asymptomatic lesions are not infrequently seen incidentally on chest CT.[66]

Elastofibromas are composed of fibroblasts interposed with mature adipose tissue. The US appearance of an ellipsoid mass of moderate reflectivity due to the fat content combined with the classic location is usually diagnostic.[67] Resection, if required, is curative.

Fibromatosis

The fibromatoses are a group of soft tissue lesions characterised by proliferation of fibrous tissue with spindle-shaped cells surrounded by variable amounts of collagen. They can be indolent or locally aggressive with a tendency to local recurrence. They are generally divided into superficial and deep fibromatosis.

Superficial fibromatosis

This group comprise palmar and plantar fibromatosis. Palmar fibromatosis consists of small fibrous nodules that progress to contractures of the hand (Dupuytren's contracture). It is a clinical diagnosis.

Plantar fibromatosis typically presents as small soft issue nodules on the sole of the foot, frequently multiple and bilateral in 20–50%.[68] US reveals a characteristic hypoechoic ovoid mass arising from the plantar fascia usually on the medial aspect (Fig. 58.23). Small lesions are often avascular. Larger lesions above 2–3 cm may demonstrate a mixed hyper- and hyporeflective appearance reflecting areas of fibrous and cellular tissue, and may demonstrate internal vascularity on Doppler US.[69] There is an overlap with deep fibromatosis.

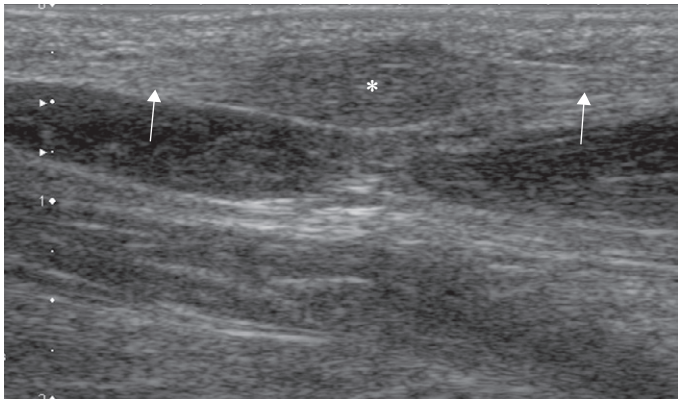

Figure 58.23 Longitudinal sonogram of a patient with three small nodules on the sole of the foot. The US image of one of the lesions demonstrates a small ovoid echo-poor mass (asterisk) arising from the plantar fascia (white arrows). The other lesions appeared identical. The location, US appearance and presence of more than one lesion confirms the diagnosis of multiple plantar fibromas.

Deep fibromatosis

These lesions affect the fascia and aponeuroses between muscles, although subcutaneous masses may be seen. Lesions in the extremities are usually distinguished from abdominal wall desmoids. Extremity lesions are referred to as aggressive fibromatosis because of the propensity to recur locally following surgical resection, although a wide spectrum of behaviour is encountered. Lesions are usually solitary, although synchronous and metachronous tumours may occur.[70] US reveals a hyporeflective mass that may be well defined or have irregular margins (Fig. 58.5), with posterior acoustic shadowing and varying degrees of internal vascularity. Areas of both low and high signal intensity on T2-weighted MR images are typical.[71,72] MRI is indicated to document the extent of the lesion prior to biopsy and surgery. Wide excision reduces the risk of local recurrence but may be precluded because of the cosmetic or functional consequences. Adjuvant chemotherapy and radiotherapy may be required.

Dermatofibrosarcoma protuberans (DFSP)

DFSP accounts for about 6% of soft tissue sarcomas and occurs in the third to fifth decades of life.[44] About equal numbers occur in the trunk and extremities. DFSP presents as a protuberant mass involving the skin and subcutaneous tissues, typically causing reddish-brown to blue skin discoloration and occasionally skin ulceration. DFSP may grow slowly over a long period of time, although phases of accelerated growth may happen. Lesions are occasionally multiple or there may be satellite nodules.

Imaging shows a non-specific well-defined protuberant non-mineralised hypervascular mass.[73,74] Larger lesions may invade deeper structures. Treatment is by wide local excision. Local recurrence rates can be as high as 20%.

Fibrosarcoma and malignant fibrous histiocytoma (MFH)

The classification of other malignant fibrous sarcomas is complex and based upon factors including cellular patterns. Tumours vary from low to high grade and occasionally present with a spontaneous haematoma.

MFH is the commonest STS of late adult life.[75] Some cases are associated with previous radiotherapy. MFH is usually deep and intramuscular. Fibrosarcoma is a less frequent diagnosis following recent subclassifications of the fibrous sarcomas. The internal structure is variable and depends on the relative amounts of collagen, myxoid tissue, necrosis and haemorrhage. In both tumours US typically demonstrates a large, deep, well-defined mass with a heterogeneous echo pattern and increased vascularity on Doppler imaging. Rarely MFH presents with a spontaneous haematoma. Ultrasound shows the haematoma but the tumour may be small or not detected, in which case interval scanning with US or MRI or excision should be considered.

Synovial tumours

Tumours of synovial origin arise from joints, bursae, tendon sheaths or de novo in other soft tissues. Eccentric joint lesions may present as soft tissue masses. If joint involvement is suspected, correlation with radiographs is mandatory. Cross-sectional imaging frequently provides a specific diagnosis.

Pigmented villonodular synovitis (PVNS)

PVNS usually occurs in the third and fourth decades of life in large joints, particularly the knee, hip, shoulder and elbow, and rarely involves more than one joint. PVNS has large frond-like synovial proliferations which are typically red due to haemosiderin deposition.[76] US reveals a prominent joint effusion with synovial thickening and fronding.[76,77] Vascularity is variable. Calcification is usually absent. Radiographs may show pressure erosion of bone. Demonstration of haemosiderin on gradient-echo MRI is characteristic but not invariable.[78]

The joint is usually diffusely involved, but lesions may present as a mass if there is involvement of a communicating bursa or cyst, e.g. within a Baker's cyst. There is also a localised form termed focal nodular synovitis. Treatment is usually by synovectomy.

Giant cell tumour of the tendon sheath (GCTTS)

GCTTS is histologically similar to PVNS, but arises most commonly in the hands and feet and clinically mimics ganglion cysts. US reveals rounded or ovoid masses that encircle the tendon, are usually heterogeneous and have moderate internal vascularity.[79,80] Large lesions can scallop underlying bone. Haemosiderin deposition is best identified on MRI. A diffuse form also occurs (proliferative synovitis or extra-articular PVNS).

Synovial osteochondromatosis

Synovial chondromatosis is a metaplastic condition that results in the formation of multiple intra-articular cartilaginous nodules. Over time nodules may enlarge and calcify or ossify. Large joints are usually involved, especially the knee, hip and shoulder. Occasionally more than one joint is affected. Pressure erosion of bone is common. Involvement of a bursa or tendon sheath is more likely to present as a soft tissue mass (Fig. 58.24). US reveals multiple echogenic intrasynovial masses which may be mobile, and, if small, are sometimes referred to as rice bodies.[81] The differential diagnosis of rice bodies includes rheumatoid arthritis and TB. Acoustic shadowing is present when the nodules begin to calcify (two-thirds of cases), and is characteristic.

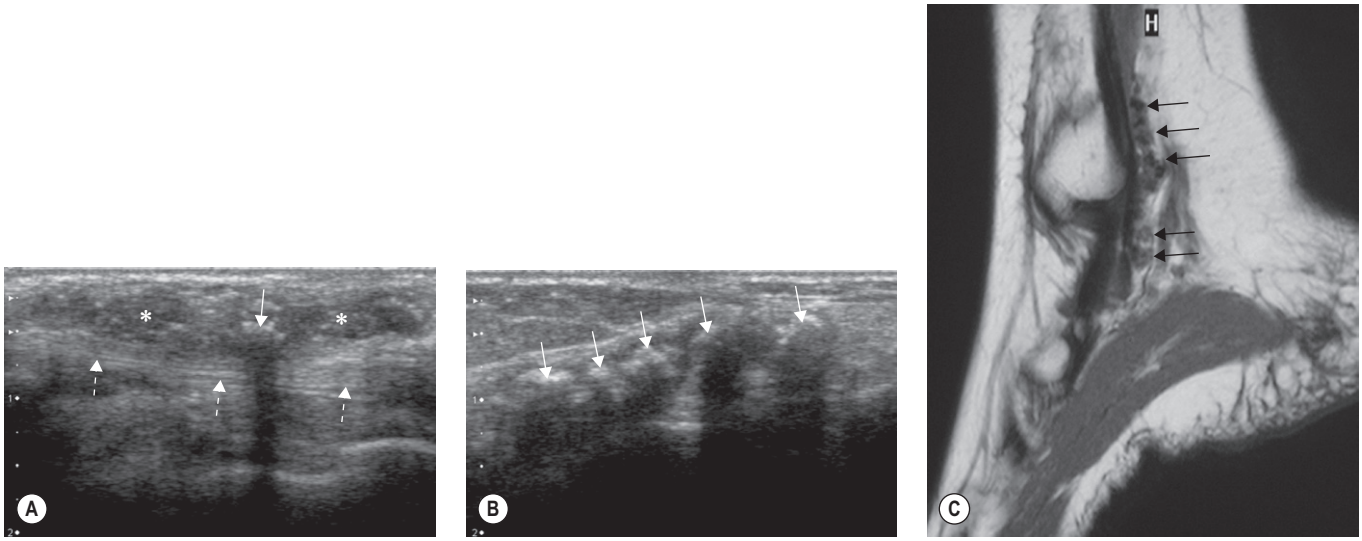

Figure 58.24 Synovial chondromatosis. Longitudinal sonograms **(A, B)** and sagittal T1-weighted MR image **(C)** of a patient presenting with a painless, poorly defined swelling of the medial aspect of the ankle. The tendon sheath (asterisks) of the tibialis posterior tendon (broken arrows) is thickened and hypoechoic and contains multiple echogenic foci (white arrows) with posterior acoustic shadowing due to multiple calcified cartilaginous nodules secondary to synovial chondromatosis of the tendon sheath. The calcified bodies are clearly seen as low signal masses (black arrows) behind the tendon on the corresponding MR image.

Synovial sarcoma

A common misconception is that synovial sarcomas arise from joints. They are nearly always extra-articular and probably arise from undifferentiated mesenchymal tissue. Joint involvement usually results from local spread. Biological activity is variable, but local recurrence and metastases are common, particularly in larger lesions, with 5-year survival rates of 27–61%.

Synovial sarcoma is most frequent at 15–35 years although older age groups may be affected. Most cases occur in the extremities and present with a palpable mass which is often painful and slow growing.[44]

US reveals a non-specific mass, round or lobulated and usually well defined. Calcification present in up to one-third of cases may occur at the periphery of the tumour. Lesions are frequently hypervascular and heterogeneous due to haemorrhage, cystic areas and fluid–fluid levels.[82] Synovial sarcomas may induce periosteal reaction or invade bone.[83]

Extraskeletal osseous tumours

This group of tumours includes the rare extraskeletal osteosarcoma and mesenchymal chondrosarcoma. The patterns of tumour matrix calcification may be characteristic. Correlation with radiographs is essential.

Benign soft tissue chondromas present as well-defined nodules of adult hyaline cartilage. They frequently calcify, and larger deeper masses may be difficult to distinguish from malignant chondrosarcomas.

REFERENCES

1. Rydholm A. Improving the management of soft tissue sarcoma. Diagnosis and treatment should be given in specialist centres. BMJ 1998;317(7151):93–94.
2. Improving outcomes for people with sarcoma. London: National Institute for Health and Clinical Excellence; 2006.
3. Derchi LE, Rizzatto G. Technical requirements. In: Martinoli C, Bianchi S, editors. Ultrasound of the musculoskeletal system. Berlin: Springer; 2007. p. 3–16.
4. Fornage BD, Atkinson EN, Nock LF, Jones PH. US with extended field of view: phantom-tested accuracy of distance measurements. Radiology 2000;214(2):579–584.
5. Claudon M, Tranquart F, Evans DH, et al. Advances in ultrasound. Eur Radiol 2002;12(1):7–18.
6. Kransdorf JM, Murphey M. Imaging of soft tissue tumours. In: Imaging of soft tissue tumours. Philadelphia: Lippincott Williams & Wilkins; 2006. p. 38–79.
7. Peabody TD, Simon MA. Principles of staging of soft-tissue sarcomas. Clin Orthop Relat Res 1993;(289):19–31.
8. Kransdorf JM, Murphey M. Compartmental anatomy. In: Imaging of soft tissue tumors. Philadelphia: Lippincott Williams & Wilkins: 2006. p. 573–576.
9. Bamber JC. Ultrasound elasticity imaging: definition and technology. Eur Radiol 1999;9(Suppl. 3):S327–S330.
10. Paltiel HJ, Burrows PE, Kozakewich HP, et al. Soft-tissue vascular anomalies: utility of US for diagnosis. Radiology 2000;214(3):747–754.
11. Newman JS, Adler RS, Bude RO, Rubin JM. Detection of soft-tissue hyperemia: value of power Doppler sonography. AJR Am J Roentgenol 1994;163(2):385–389.
12. Bianchi S, Abdelwahab IF, Oliveri M, et al. Sonographic diagnosis of accessory soleus muscle mimicking a soft tissue tumor. J Ultrasound Med 1995;14(9):707–709.
13. Beggs I. Sonography of muscle hernias. AJR Am J Roentgenol 2003;180(2):395–399.
14. Bianchi S, Abdelwahab IF, Mazzola CG, et al. Sonographic examination of muscle herniation. J Ultrasound Med 1995;14(5):357–360.
15. Temple HT, Kuklo TR, Sweet DE, et al. Rectus femoris muscle tear appearing as a pseudotumor. Am J Sports Med 1998;26(4):544–548.
16. Thomas EA, Cassar-Pullicino VN, McCall IW. The role of ultrasound in the early diagnosis and management of heterotopic bone formation. Clin Radiol 1991;43(3):190–196.
17. Peetrons P. Ultrasound of muscles. Eur Radiol 2002;12(1):35–43.
18. Batz R, Sofka CM, Adler RS, et al. Dermatomyositis and calcific myonecrosis in the leg: ultrasound as an aid in management. Skeletal Radiol 2006;35(2):113–116.
19. Robinson P, Farrant JM, Bourke G, et al. Ultrasound and MRI findings in appendicular and truncal fat necrosis. Skeletal Radiol 2008;37(3): 217–224.
20. Parra JA, Fernandez MA, Encinas B, Rico M. Morel-Lavallee effusions in the thigh. Skeletal Radiol 1997;26(4):239–241.
21. Miller TT, Staron RB, Koenigsberg T, et al. MR imaging of Baker cysts: association with internal derangement, effusion, and degenerative arthropathy. Radiology 1996;201(1):247–250.
22. Torreggiani WC, Al-Ismail K, Munk PL, et al. The imaging spectrum of Baker's (popliteal) cysts. Clin Radiol 2002;57(8):681–691.
23. Rutten MJ, Collins JM, van Kampen A, Jager GJ. Meniscal cysts: detection with high-resolution sonography. AJR Am J Roentgenol 1998;171(2):491–496.
24. Steiner E, Steinbach LS, Schnarkowski P, et al. Ganglia and cysts around joints. Radiol Clin North Am 1996;34(2):395–425, xi–xii.
25. McCarthy CL, McNally EG. The MRI appearance of cystic lesions around the knee. Skeletal Radiol 2004;33(4):187–209.
26. Paivansalo M, Jalovaara P. Ultrasound findings of ganglions of the wrist. Eur J Radiol 1991;13(3):178–180.
27. Spence LD, Adams J, Gibbons D, et al. Rice body formation in bicipito-radial bursitis: ultrasound, CT, and MRI findings. Skeletal Radiol 1998;27(1):30–32.
28. Campbell RS, Montgomery RJ. A cholesterol-containing foreign body granuloma presenting as an inter-metatarsal bursa. Skeletal Radiol 2005;34(4):239–243.
29. Lee HS, Joo KB, Song HT, et al. Relationship between sonographic and pathologic findings in epidermal inclusion cysts. J Clin Ultrasound 2001;29(7):374–383.
30. Chau CL, Griffith JF. Musculoskeletal infections: ultrasound appearances. Clin Radiol 2005;60(2):149–159.
31. Loyer EM, DuBrow RA, David CL, et al. Imaging of superficial soft-tissue infections: sonographic findings in cases of cellulitis and abscess. AJR Am J Roentgenol, 1996;166(1):149–152.
32. Arslan H, Sakarya ME, Bozkurt M, et al. The role of power Doppler sonography in the evaluation of superficial soft tissue abscesses. Eur J Ultrasound 1998;8(2):101–106.
33. Gordon BA, Martinez S, Collins AJ. Pyomyositis: characteristics at CT and MR imaging. Radiology 1995;197(1):279–286.
34. Polat P, Kantarci M, Alper F, et al. Hydatid disease from head to toe. Radiographics 2003;23(2):475–494; quiz 536–537.
35. Ross GJ, Ross LV, Hartz WH, Fairman RM. Case report 723. Popliteal artery aneurysm. Skeletal Radiol 1992;21(3):190–193.
36. Peterson JJ, Kransdorf MJ, Bancroft LW, Murphey MD. Imaging characteristics of cystic adventitial disease of the peripheral arteries: presentation as soft-tissue masses. AJR Am J Roentgenol 2003;180(3):621–625.
37. Nalbant S, Corominas H, Hsu B, et al. Ultrasonography for assessment of subcutaneous nodules. J Rheumatol 2003;30(6):1191–1195.
38. Gerster JC, Landry M, Dufresne L, Meuwly JY. Imaging of tophaceous gout: computed tomography provides specific images compared with magnetic resonance imaging and ultrasonography. Ann Rheum Dis 2002;61(1):52–54.
39. Bureau NJ, Roederer G. Sonography of Achilles tendon xanthomas in patients with heterozygous familial hypercholesterolemia. AJR Am J Roentgenol 1998;171(3):745–749.
40. Murphey MD, Carroll JF, Flemming DJ, et al. From the archives of the AFIP: benign musculoskeletal lipomatous lesions. Radiographics 2004;24(5):1433–1466.
41. Rydholm A, Berg NO. Size, site and clinical incidence of lipoma. Factors in the differential diagnosis of lipoma and sarcoma. Acta Orthop Scand 1983;54(6):929–934.
42. Fornage BD, Tassin GB. Sonographic appearances of superficial soft tissue lipomas. J Clin Ultrasound 1991;19(4):215–220.
43. Matsumoto K, Hukuda S, Ishizawa M, et al. MRI findings in intramuscular lipomas. Skeletal Radiol 1999;28(3):145–152.
44. Kransdorf MJ. Malignant soft-tissue tumors in a large referral population: distribution of diagnoses by age, sex, and location. AJR Am J Roentgenol 1995;164(1):129–134.
45. Kransdorf MJ, Bancroft LW, Peterson JJ, et al. Imaging of fatty tumors: distinction of lipoma and well-differentiated liposarcoma. Radiology 2002;224(1):99–104.
46. Woodruff JM. The pathology and treatment of peripheral nerve tumors and tumor-like conditions. CA Cancer J Clin 1993;43(5):290–308.

47. Reynolds Jr DL, Jacobson JA, Inampudi P, et al. Sonographic characteristics of peripheral nerve sheath tumors. AJR Am J Roentgenol 2004;182(3):741–744.
48. Isobe K, Shimizu T, Akahane T, Kato H. Imaging of ancient schwannoma. AJR Am J Roentgenol 2004;183(2):331–336.
49. Murphey MD, Smith WS, Smith SE, et al. From the archives of the AFIP. Imaging of musculoskeletal neurogenic tumors: radiologic-pathologic correlation. Radiographics 1999;19(5):1253–1280.
50. Lin J, Jacobson JA, Hayes CW. Sonographic target sign in neurofibromas. J Ultrasound Med 1999;18(7):513–517.
51. Olsen KI, Stacy GS, Montag A. Soft-tissue cavernous hemangioma. Radiographics 2004;24(3):849–854.
52. Derchi LE, Balconi G, De Flaviis L, et al. Sonographic appearances of hemangiomas of skeletal muscle. J Ultrasound Med 1989;8(5):263–267.
53. Dubois J, Soulez G, Oliva VL, et al. Soft-tissue venous malformations in adult patients: imaging and therapeutic issues. Radiographics 2001;21(6):1519–1531.
54. Ly JQ, Sanders TG, Mulloy JP, et al. Osseous change adjacent to soft-tissue hemangiomas of the extremities: correlation with lesion size and proximity to bone. AJR Am J Roentgenol 2003;180(6):1695–1700.
55. Teo EL, Strouse PJ, Hernandez RJ. MR imaging differentiation of soft-tissue hemangiomas from malignant soft-tissue masses. AJR Am J Roentgenol 2000;174(6):1623–1628.
56. Paley D, Evans DC. Angiomatous involvement of an extremity. A spectrum of syndromes. Clin Orthop Relat Res 1986;(206):215–218.
57. Weiss SW, Goldblum J. Haemangioendothelioma: vascular tumours of intermediate malignancy. In: Weiss EA, editor. Soft tissue tumours. St Louis, MO: Mosby; 2001. p. 891–915.
58. Nakazono T, Kudo S, Matsuo Y, et al. Angiosarcoma associated with chronic lymphedema (Stewart-Treves syndrome) of the leg: MR imaging. Skeletal Radiol 2000;29(7):413–416.
59. Weiss SW. Smooth muscle tumors of soft tissue. Adv Anat Pathol 2002;9(6):351–359.
60. Ledesma-Medina J, Oh KS, Girdany BR. Calcification in childhood leiomyoma. Radiology 1980;135(2):339–341.
61. Bush CH, Reith JD, Spanier SS. Mineralization in musculoskeletal leiomyosarcoma: radiologic-pathologic correlation. AJR Am J Roentgenol 2003;180(1):109–113.
62. McCarville MB, Spunt SL, Pappo AS. Rhabdomyosarcoma in pediatric patients: the good, the bad, and the unusual. AJR Am J Roentgenol 2001;176(6):1563–1569.
63. Montgomery EA, Meis JM. Nodular fasciitis. Its morphologic spectrum and immunohistochemical profile. Am J Surg Pathol 1991;15(10):942–948.
64. Wilson DJ. Ultrasonic imaging of soft tissues. Clin Radiol 1989;40(4):341–342.
65. Nagamine N, Nohara Y, Ito E. Elastofibroma in Okinawa. A clinicopathologic study of 170 cases. Cancer 1982;50(9):1794–1805.
66. Kransdorf MJ, Meis JM, Montgomery E. Elastofibroma: MR and CT appearance with radiologic-pathologic correlation. AJR Am J Roentgenol 1992;159(3):575–579.
67. Bianchi S, Martinoli C, Abdelwahab IF, et al. Elastofibroma dorsi: sonographic findings. AJR Am J Roentgenol 1997;169(4):1113–1115.
68. Lee TH, Wapner KL, Hecht PJ. Plantar fibromatosis. J Bone Joint Surg Am 1993;75(7):1080–1084.
69. Griffith JF, Wong TY, Wong SM, et al. Sonography of plantar fibromatosis. AJR Am J Roentgenol 2002;179(5):1167–1172.
70. Rock MG, Pritchard DJ, Reiman HM, et al. Extra-abdominal desmoid tumors. J Bone Joint Surg Am 1984;66(9):1369–1374.
71. Sundaram M, McGuire MH, Schajowicz F. Soft-tissue masses: histologic basis for decreased signal (short T2) on T2-weighted MR images. AJR Am J Roentgenol 1987;148(6):1247–1250.
72. Vandevenne JE, De Schepper AM, De Beuckeleer L, et al. New concepts in understanding evolution of desmoid tumors: MR imaging of 30 lesions. Eur Radiol 1997;7(7):1013–1019.
73. Ehara S, Oda Y. Deep dermatofibrosarcoma protuberans. AJR Am J Roentgenol 2002;179(6):1643; author reply 1643.
74. Torreggiani WC, Al-Ismail K, Munk PL, et al. Dermatofibrosarcoma protuberans: MR imaging features. AJR Am J Roentgenol 2002;178(4):989–993.
75. Kransdorf JM, Murphey M. Malignant fibrous and fibrohistiocytic tumours. In: Imaging of soft tissue tumours. Philadelphia: Lippincott Williams & Wilkins; 2006. p. 257–297.
76. Dorwart RH, Genant HK, Johnston WH, Morris JM. Pigmented villonodular synovitis of synovial joints: clinical, pathologic, and radiologic features. AJR Am J Roentgenol 1984;143(4):877–885.
77. Martinoli C, Bianchi S. Knee. In Martinoli C, Bianchi S, editors. Ultrasound of the musculoskeletal system. Berlin: Springer; 2007. p. 637–744.
78. Al-Nakshabandi NA, Ryan AG, Choudur H, et al. Pigmented villonodular synovitis. Clin Radiol 2004;59(5):414–420.
79. Horcajadas AB, Lafuente JL, de la Cruz Burgos R, et al. Ultrasound and MR findings in tumor and tumor-like lesions of the fingers. Eur Radiol 2003;13(4):672–685.
80. Middleton WD, Patel V, Teefey SA, Boyer MI. Giant cell tumors of the tendon sheath: analysis of sonographic findings. AJR Am J Roentgenol 2004;183(2):337–339.
81. Cho KH, Park BH, Yeon KM. Ultrasound of the adult hip. Semin Ultrasound CT MR 2000;21(3):214–230.
82. Jones BC, Sundaram M, Kransdorf MJ. Synovial sarcoma: MR imaging findings in 34 patients. AJR Am J Roentgenol 1993;161(4):827–830.
83. Elias DA, White LM, Simpson DJ, et al. Osseous invasion by soft-tissue sarcoma: assessment with MR imaging. Radiology 2003;229(1):145–152.

CHAPTER

59

Ultrasound imaging in rheumatological disease

Andrew J. Grainger and Philip O'Connor

INTRODUCTION

Ultrasound has an important part to play in the assessment and management of rheumatological conditions. Broadly it has roles in three main areas. These are:

- diagnosis
- assessment of disease severity and monitoring change in disease status as a result of disease progression or response to therapy
- guiding therapeutic and diagnostic procedures.

This has come about partly as improvements in ultrasound technology have occurred, but perhaps more significantly the role of ultrasound has developed as a result of changes in the way the inflammatory arthritides are managed clinically. The introduction of expensive biological therapies for a broad range of inflammatory arthritides has rendered the use of more costly diagnostics relatively cost effective.

This chapter will review the appearances of arthritis on ultrasound and the areas where ultrasound has an application both in current clinical practice and potentially in the future. The role of ultrasound in guiding therapeutic and diagnostic procedures will also be briefly discussed.

TECHNICAL ASPECTS OF RHEUMATOLOGICAL ULTRASOUND

Musculoskeletal ultrasound requires high-frequency probes in order to achieve the necessary resolution for accurate diagnosis. The majority of joints are superficial and can be imaged effectively using probe frequencies of 7.5 MHz or higher. These probes should be linear array, with curvilinear transducers available where necessary. The advent of beam steering technology and compound imaging on modern machines has allowed many manufacturers to provide widened field of views on linear probes with a trapezoid configuration. This can be a useful facility for improved demonstration of the anatomy of larger structures, such as the hip joint, on a single image.

Near-field resolution has greatly improved over the past decade with the need for a gel stand-off pad no longer necessary for most musculoskeletal applications. There are, however, still a few occasions when a stand-off can be of value. When examining superficial structures with Doppler techniques, probe pressure can significantly affect flow within lesions. Minimal probe pressure can be achieved by applying and maintaining a layer of jelly interposed between the skin and probe. Extended field-of-view and three-dimensional techniques are of debatable value in diagnostic terms but are useful when demonstrating an abnormality to clinicians or colleagues.

To achieve high diagnostic yield the examiner should use the highest possible probe frequency to give sufficient penetration to visualise the tissue of interest. The focal zones should be centred at the level of the tissue of interest, utilising the lowest frame rate possible to allow dynamic assessment of the tissue.

Artefacts that may interfere with ultrasound assessment of tendons include anisotropy and beam edge artefact. If the incident sound beam is not perpendicular to the long axis of an anisotropic structure such as a tendon, there may be dramatic reduction in the echogenicity of the tendon. Beam edge artefact is most evident around the margins of large tendons. It results in a characteristic appearance at the edge of the tendon with loss of signal and distal acoustic shadowing that may obscure fluid or inflammation in the paratenon (Fig. 59.1).

Doppler imaging plays an important role in the assessment of synovium and can be used to assess disease activity. An important artefact is flash artefact, which results from movement of the transducer or patient while scanning using power or colour Doppler.[1] Power Doppler is more susceptible to this artefact, which can be minimised by increasing the pulse repetition frequency and reducing gain. Altering the persistence may also help. Doppler artefact may also be produced from bone cortex deep to its interface with the overlying soft tissues (Fig. 59.2).[2]

Joint ultrasound should be methodical and cover all areas of the joint in longitudinal and transverse planes. Joint motion can be important in the demonstration of small joint effusions.

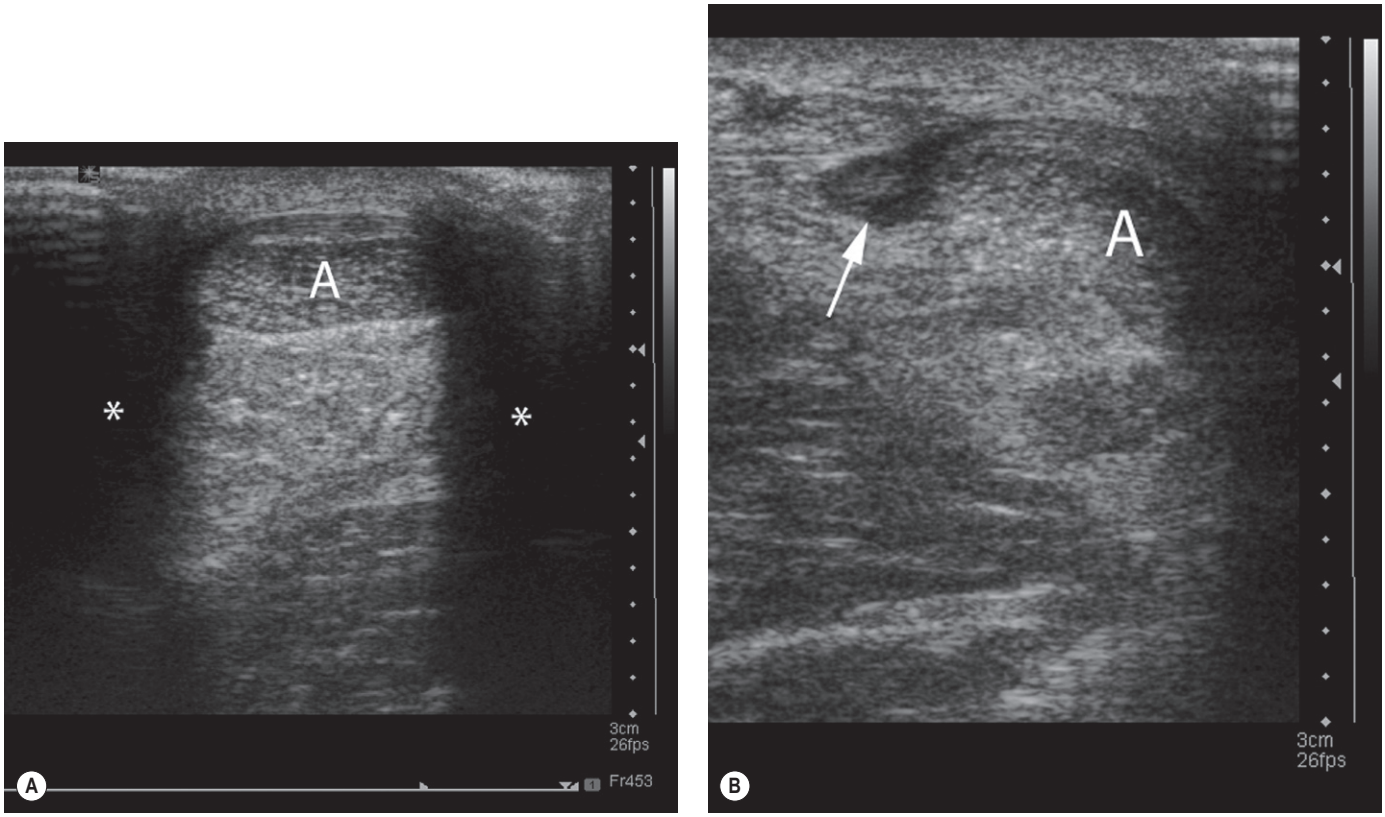

Figure 59.1 Beam edge artefact. A: Transverse ultrasound of the Achilles tendon (A). There is severe beam edge artefact on either side of the tendon shown as low reflective areas (*). **B:** When the probe is moved to interrogate the tissues at the side of the tendon (A) low reflective inflammatory change in the paratenon is demonstrated (arrow), which was not visualised previously due to the beam edge artefact.

Introduction and technical aspects

- Ultrasound has an important role in the assessment and management of rheumatological conditions.
- The introduction of expensive biological therapies for inflammatory arthritis has rendered diagnostics relatively cost effective.
- Improved near-field resolution means that a gel stand-off pad is no longer necessary for most musculoskeletal applications.
- To achieve high diagnostic yield use the highest possible probe frequency to give sufficient penetration to visualise the tissue of interest.
- The focal zones should be centred at the level of the tissue of interest, utilising the lowest frame rate possible to allow dynamic assessment of the tissue.
- Increase the pulse repetition frequency and reduce gain to avoid power Doppler flash artefact.

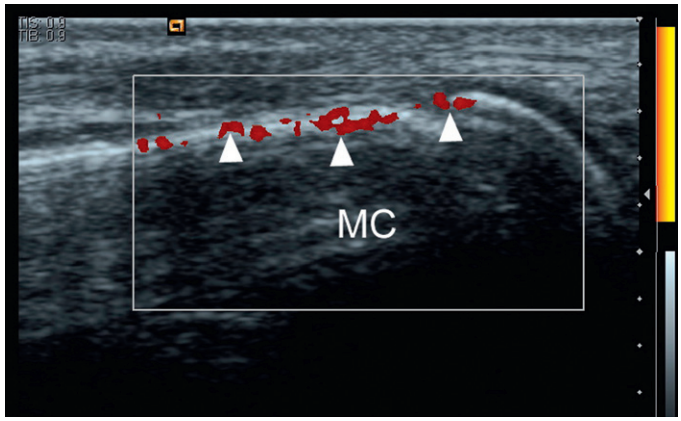

Figure 59.2 Flash artefact. Longtitudinal power Doppler image through second metacarpophalangeal joint. The flash artefact is clearly demonstrated (arrowheads) at the bone cortex of the distal metacarpal (MC).

ULTRASOUND FEATURES OF ARTHRITIS

Synovitis

Synovial joints, bursae and tendon sheaths are lined by a thin synovial membrane. In joints the synovial membrane lines the joint capsule and intra-articular ligaments. It covers exposed bone, but stops short of the margins of articular cartilage. Histologically the synovial membrane has distinct layers with a surface comprising one to three layers of synovial cells applied to a thin connective tissue layer containing capillaries. Despite this complex structure the normal synovial membrane is not usually visualised on ultrasound as a discrete structure. Thickening and inflammation of the synovium are hallmarks of the inflammatory arthritides but are also seen following trauma, as part of the osteoarthritis spectrum and as features of other joint diseases including septic arthritis. Synovitis is readily demonstrated on ultrasound.

The OMERACT group have defined the appearance of articular synovitis on ultrasound as:

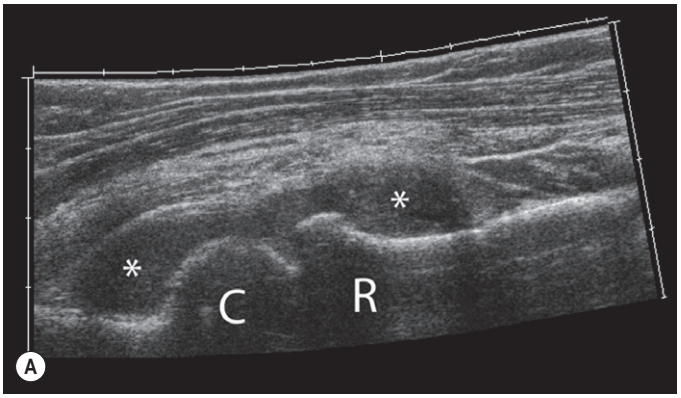

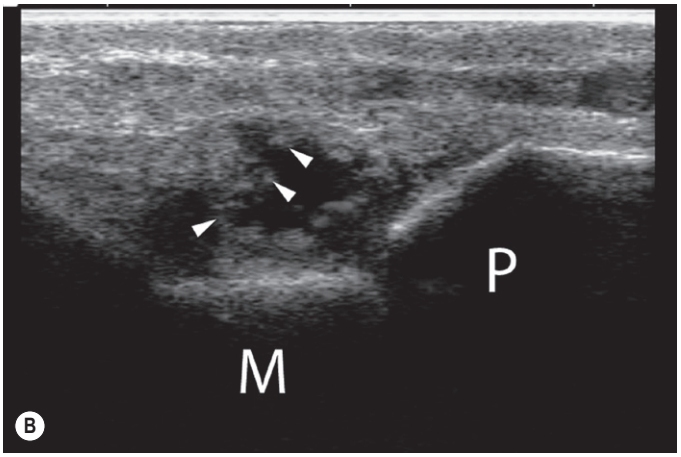

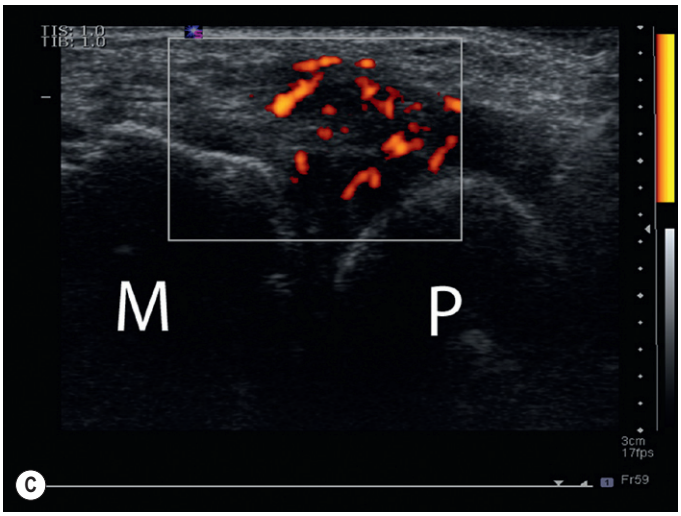

Figure 59.3 Synovitis. A: Extended field-of-view longitudinal ultrasound of the radiocapitellar joint in a patient with rheumatoid arthritis. There is severe synovitis present seen as low reflective intra-articular tissue bulging the anterior joint capsule (*). C, capitellum; R, radial head. **B:** Longitudinal ultrasound of the first metatarsophalangeal joint. There is again synovitis present but in this case it is seen in combination with a joint effusion as frond-like material with intermediate echogenicity (arrowheads). The effusion is seen as anechoic areas within the joint. P, proximal phalanx; M, metatarsal head. **C:** Longitudinal ultrasound of the first metatarsophalangeal joint in a patient with rheumatoid arthritis showing intense power Doppler signal from the low reflective synovium. P, proximal phalanx; M, metatarsal head.

Abnormal hypoechoic (relative to subdermal fat, but sometimes may be isoechoic or hyperechoic) intra-articular tissue that is nondisplaceable and poorly compressible and which may exhibit Doppler signal.[3]

The three points, that synovitis

1. is non-displaceable
2. is poorly compressible
3. may exhibit Doppler signal

are particularly important in assisting the ultrasonographer to distinguish synovitis from effusion, as will be discussed in the next section.

The echogenicity of thickened synovial tissue is highly variable, as suggested by the definition, and is related to the amount of extracellular fluid; the more fluid present, the less echogenic the tissue. As a result it is possible for synovitis to have an almost anechoic appearance. The morphology of the inflamed synovium is also variable, sometimes appearing as a solid mass lesion and sometimes having a more frond-like appearance (Fig. 59.3A and B). In the inflammatory arthritides, synovitis is often seen in characteristic sites in individual joints, such as the suprapatellar pouch of the knee, ulnar aspect of the wrist or along the radial and ulnar aspects of the metacarpophalangeal (MCP) joints.[4]

Synovitis shows varying degrees of vascularity as assessed with Doppler imaging. Both colour and power Doppler signal are detected in synovitis. As the direction of flow is generally not of interest and the technique is not angle dependent, assessment of vascularity with power Doppler imaging is generally preferred (Fig. 59.3C). Pressure may occlude vessels in synovium and prevent flow and visualisation of vessels. Consequently light transducer pressure is necessary. A stand-off or water bath can be used, but generally the use of a liberal amount of acoustic jelly allows virtually no pressure to be exerted on the joint.

There has been considerable focus on the quantification of synovitis vascularity using Doppler techniques. Disease activity correlates with synovial vascularity and will be discussed later in this chapter. Ultrasound contrast media can be detected following injection as it reaches the synovium and makes any vascularity extremely obvious. This may have a role to play in the quantification of vascularity.

Ultrasound is a reliable method of demonstrating synovitis compared with magnetic resonance imaging (MRI) as a gold standard[5–7] and, as it is more sensitive than clinical examination, is of increasing importance as the trend towards the early diagnosis of inflammatory arthropathies continues.[5,8,9]

Synovitis

- The normal synovial membrane is not usually visualised on ultrasound.
- Thickening and inflammation of the synovium are hallmarks of the inflammatory arthritides.
- Relative to effusion, synovitis is non-displaceable, poorly compressible and may exhibit Doppler signal.
- Probe pressure may occlude vessels in synovium and prevent flow and visualisation of vessels.
- Ultrasound is a reliable method of demonstrating synovitis compared with MRI.

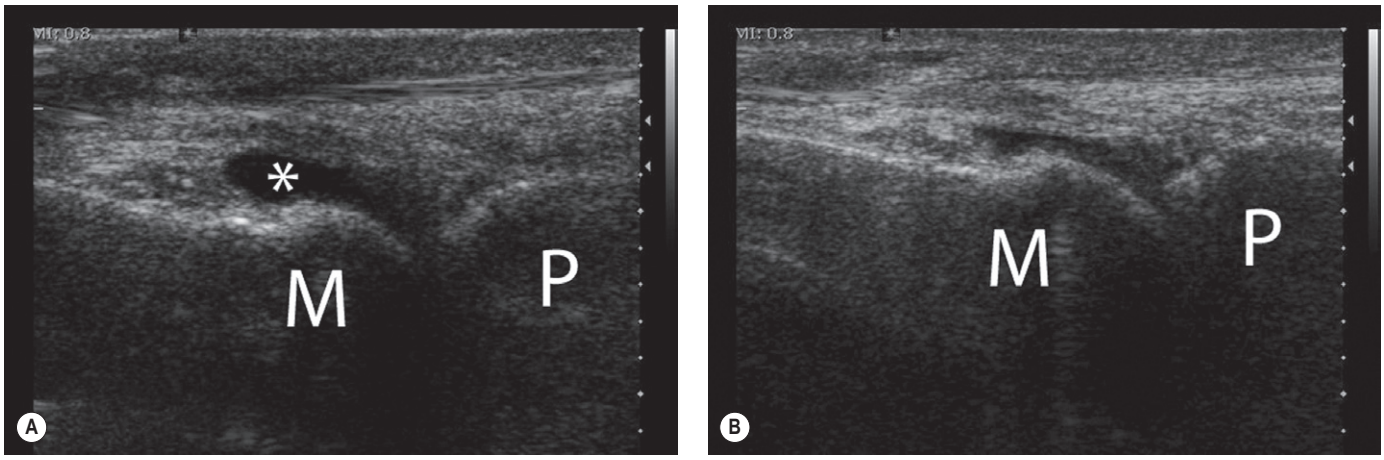

Figure 59.4 Effusion. A: Joint effusion in metatarsophalangeal joint on longitudinal ultrasound (*). **B:** Following compression with the probe, fluid is squeezed into other parts of the joint so the effusion is compressible, distinguishing it from synovitis, which would appear non-compressible. P, proximal phalanx, M, metatarsal head.

Effusion

Joint fluid most frequently appears anechoic but occasionally has a more complex echo appearance. Knowledge of the normal joint anatomy, in particular the capsular attachments and recesses, is important when examining a joint for fluid. Generally fluid is best identified in capsular recesses such as the suprapatellar pouch of the knee and the biceps sheath of the shoulder. Hyaline cartilage is anechoic and can occasionally be difficult to distinguish from adjacent fluid. Usually a thin hyperechoic interface between the two is visible.

Fluid appears compressible. Probe pressure will squeeze fluid into other parts of the joint and, along with an absence of Doppler signal, distinguishes fluid from hypo- or anechoic synovitis (Fig. 59.4). This distinction can be difficult, particularly with more complex echogenic fluid with an apparent internal structure. Such effusions may result from more proteinaceous fluid, crystal deposition, fibrin or cellular debris. Compression of more complex fluid with the probe (sonopalpation) may bring about movement of internal echoes, distinguishing fluid from solid tissue.

It is rarely possible to visualise all parts of a joint with ultrasound and so an attempt must be made to displace any fluid into sonographically accessible areas by moving the joint while scanning.

Like synovitis the presence of an effusion is a non-specific finding. The echo characteristics of an effusion do not provide information as to its aetiology. This is particularly important in the context of septic arthritis. An effusion due to infection can appear anechoic, hypoechoic or complex in nature. A common misconception is that anechoic effusions are unlikely to be due to sepsis. The only way to reliably exclude joint sepsis is by aspirating the joint. While the presence of an effusion is a non-specific finding, the absence of an effusion does effectively rule out infection.

Erosions

Breaks in the bone cortex, erosions, are important indicators of inflammatory arthritis and provide prognostic information (Fig. 59.5). As with synovitis the OMERACT group has produced a definition for the ultrasound diagnosis of erosion:

An intra-articular discontinuity of the bone surface visible in 2 perpendicular planes.[3]

An important part of this definition is the need to demonstrate the discontinuity in two perpendicular planes. This helps to distinguish erosions from normal variations in bony contour that might otherwise be confused for erosions. Comparison with the contralateral joint can be useful.

With ultrasound imaging erosions are often seen to be associated with synovitis (Fig. 59.5A). Unlike MRI, ultrasound gives no information regarding the bone adjacent to the erosion, such as the presence of marrow oedema.

The high-resolution and multiplanar capabilities of ultrasound make it more sensitive than radiographs to erosion detection.[10,11] Ultrasound detects 6.5 times as many erosions in 7.5 times as many patients in early rheumatoid arthritis and 3.4 times as many erosions in 2.7 times as many patients in late rheumatoid arthritis as radiographs.[10] Ultrasound and MRI are of comparable sensitivity (Fig. 59.5B and C)[12,13] and are more sensitive than CT for smaller erosions.[14]

Ultrasound will miss erosions at sites not amenable to ultrasound such as the radial and ulnar sides of the middle and ring MCP joints that cannot be visualised with ultrasound.

Ultrasound also depends on the experience and skill of the operator. Using experienced sonographers, Wakefield et al. reported intraclass correlation coefficients (ICC) of 0.75 for intra-observer agreement and 0.76 for inter-observer agreement.[10]

Effusion

- Fluid is compressible on sonopalpation.
- Sonopalpation of more complex fluid may produce movement of internal echoes, distinguishing fluid from solid tissue.
- The only way to reliably exclude joint sepsis is by aspirating the joint.

Erosions

- Erosions cause intra-articular discontinuity of the bone surface visible in two perpendicular planes.
- Synovitis is often seen with erosions in inflammatory arthritis.
- Ultrasound is more sensitive than radiographs in erosion detection.

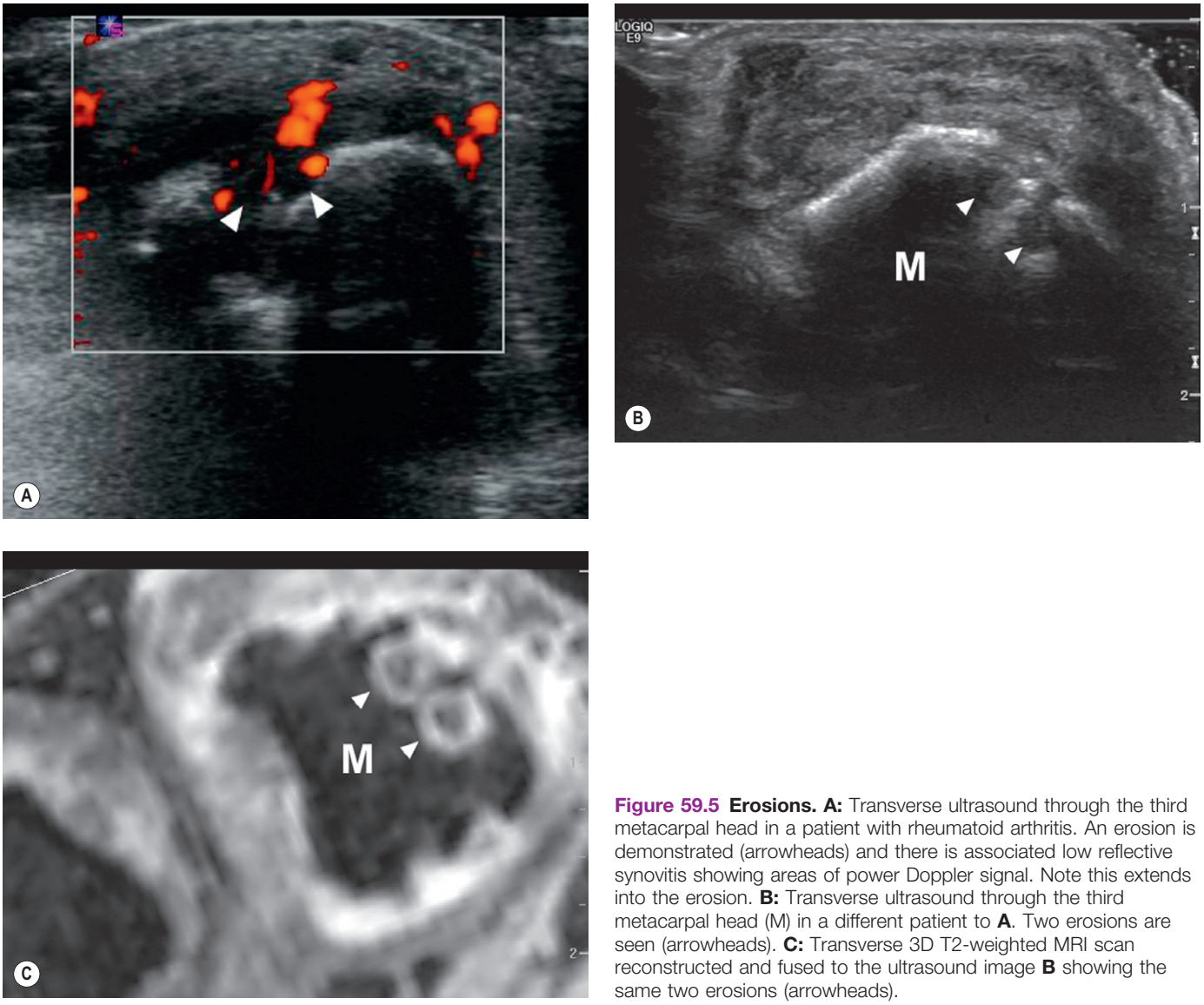

Figure 59.5 **Erosions. A:** Transverse ultrasound through the third metacarpal head in a patient with rheumatoid arthritis. An erosion is demonstrated (arrowheads) and there is associated low reflective synovitis showing areas of power Doppler signal. Note this extends into the erosion. **B:** Transverse ultrasound through the third metacarpal head (M) in a different patient to **A**. Two erosions are seen (arrowheads). **C:** Transverse 3D T2-weighted MRI scan reconstructed and fused to the ultrasound image **B** showing the same two erosions (arrowheads).

Other bone changes and cartilage

Ultrasound demonstrates joint space loss and cartilage thinning in both inflammatory and mechanical (osteo) arthritis,[15–17] osteophytes in osteoarthritis, and at the knee joint may show meniscal degeneration and Baker's cyst formation.[16,18,19] Although osteoarthritis is not considered in the same group as the inflammatory arthritides, it has an inflammatory component. Synovitis, if demonstrated, indicates that intra-articular corticosteroid treatment may be helpful.

Crystal deposition on articular cartilage is seen in 92% of joints affected by gout and demonstrates a characteristic double contour sign. Crystals may also be detected within the joint fluid or synovium itself (Fig. 59.6).[20]

Tendon disease

Inflammatory change associated with tendons in the form of tenosynovitis is an important finding seen in the inflammatory arthritides and is a feature of early rheumatoid arthritis. Tenosynovitis represents an inflammation of the synovial sheath which surrounds some tendons (the tenosynovium). Not all tendons have a tenosynovium. It tends to be present in tendons that pass through narrow, confined spaces, or change direction of travel by passing around other anatomical structures such as the flexor and extensor tendons of hands and feet.

Features of tenosynovitis are thickening of the tenosynovium surrounding the tendons (synovitis) and fluid within the tendon sheath. While both fluid and thickening of the synovium may be seen, often one component predominates. As in joints, the thickened synovium may appear of low or increased reflectivity and show Doppler signal due to hypervascularisation. Synovial hypertrophy may produce a uniformly thickened mass or may have a frond-like pattern (Fig. 59.7).

Tendinopathic change may occur within tendons in association with tenosynovitis or as a result of impingement of the tendon on bony prominences and irregularities that result from the arthropathic process. This change may progress to partial thickness tearing and ultimately to tendon rupture.

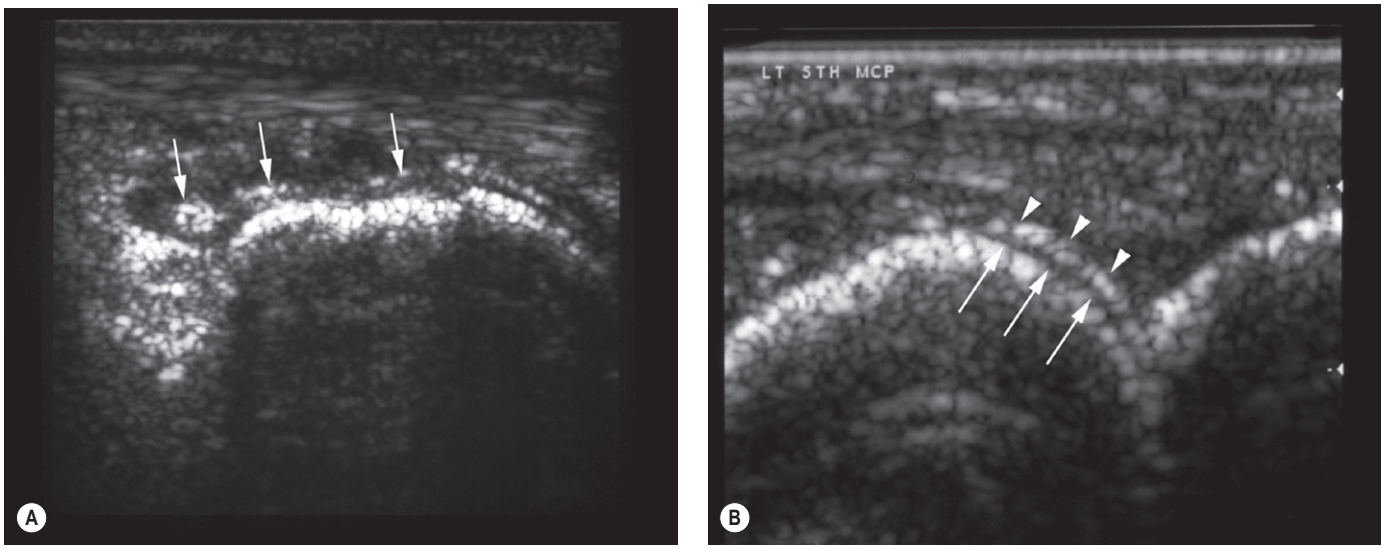

Figure 59.6 **Gout. A:** Crystal deposition in a first metatarsophalangeal joint in a patient with gout. Multiple brightly echogenic foci are seen within the joint (arrows). **B:** Longitudinal ultrasound of the fifth metacarpophalangeal joint in a patient with gout. Crystal deposition in the articular cartilage over the metacarpal head results in a double contour sign (arrowheads) paralleling the bone interface of the metacarpal head itself (arrows).

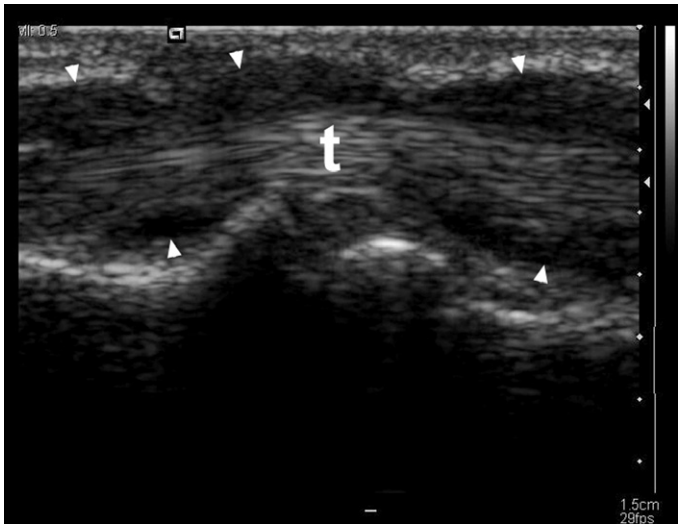

Figure 59.7 **Flexor tenosynovitis** seen on longitudinal ultrasound at the level of the second proximal interphalangeal joint in a patient with rheumatoid arthritis. The tenosynovium is markedly thickened, appearing as a lobulated low reflective mass (arrowheads) surrounding the normal tendon (t).

Rheumatoid nodules may also be seen in tendons; see later discussion.

Entheseal disease

Inflammation of the enthesis (enthesitis) is a characteristic feature of the seronegative arthritides such as ankylosing spondylitis and psoriatic arthritis. The enthesis refers to the point of insertion of ligaments, tendons and capsular tissues into bone. We are increasingly understanding the complex nature of these insertions which involve multiple histological components including fibrocartilage.[21]

Tendons and entheseal disease

- Tenosynovitis is inflammation of the synovial sheath.
- Not all tendons have a tenosynovium. Tendons passing through fibro-osseous tunnels typically have tendon sheaths.
- Tendinopathic change may occur in tendons in association with tenosynovitis or as isolated findings.
- The enthesis is the point of insertion of ligaments, tendons and capsule into bone.
- Inflammation of the enthesis is characteristic of the seronegative arthritides.
- Ultrasound shows surface changes in bone erosion and enthesophyte formation, and Doppler ultrasound demonstrates neovascularisation and tendinopathic change.

Changes occur in both the inserting structure and the adjacent bone. The inserting tendon or ligament shows features typical of tendinopathy with thickening and low reflective change centred on the insertion point (Fig. 59.8). Doppler ultrasound may demonstrate neovascularisation of the tendon. Ultrasound shows surface changes in bone: erosion and enthesophyte formation (Fig. 59.8A). In contrast, MRI also shows changes in adjacent marrow signal.

Erosions are similar in appearance to marginal erosions seen in joints in rheumatoid arthritis with a cortical break shown in two planes. Enthesophytes are seen as brightly reflective proliferative new bone on the bone surface at the enthesis site. The new bone may lie both in and adjacent to the inserting soft tissue structure. The earliest bone change in enthesitis is subtle surface irregularity, equivalent to the periostitis seen on plain films.

Bursitis is frequently associated with enthesitis, particularly retrocalcaneal bursitis in association with Achilles enthesitis and infrapatellar bursitis associated with patellar tendon enthesitis.

In digits the demonstration of enthesitis is difficult although periosteal new bone may be visualised. Frequently there is more generalised inflammatory change in the form of dactylitis with flexor tenosynovitis and generalised, non-specific soft tissue oedema.[22–24]

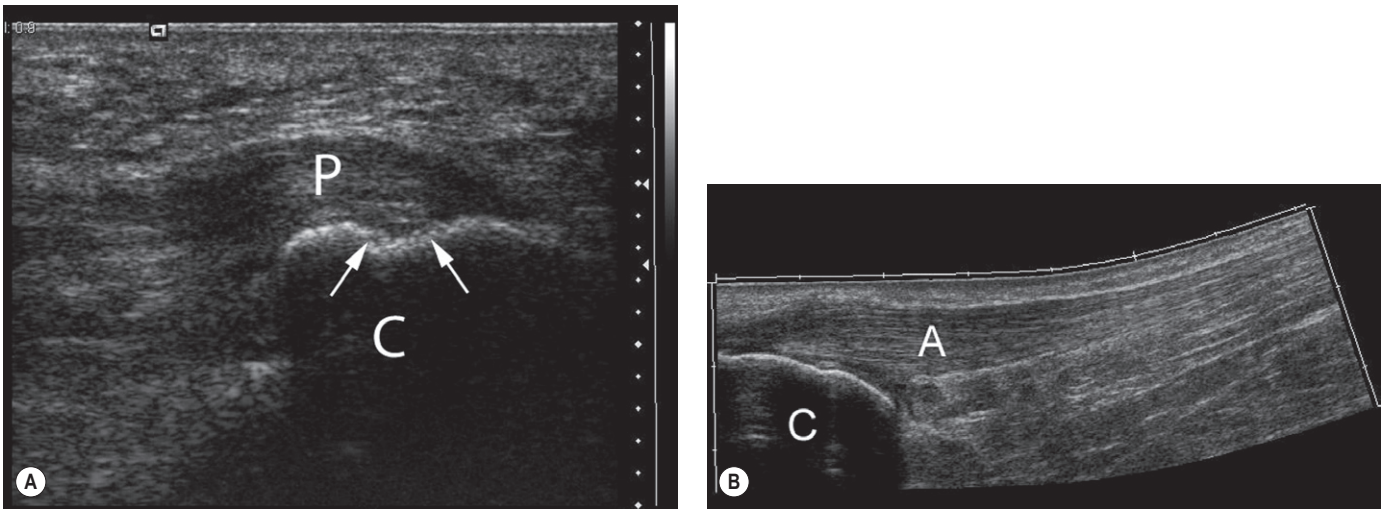

Figure 59.8 **Enthesitis. A:** Longitudinal ultrasound of the plantar fascia insertion in a patient with psoriatic arthritis. Enthesitis is evident with low reflective thickening of the plantar fascia itself (P) along with erosion of the calcaneum at the entheses site (arrows). C, calcaneum. **B:** Extended field-of-view longitudinal ultrasound of the Achilles tendon insertion in the same patient. Again entheseal disease is evident, with thickening and low reflective change seen within the tendon at its enthesis (A). C, calcaneum.

USING ULTRASOUND TO MONITOR DISEASE PROGRESSION

The use of modern disease-modifying anti-rheumatic drugs (DMARDs), which are capable of stopping joint destruction and preventing functional debility, requires accurate assessment of disease activity and progression or response to treatment. Increasingly imaging is used to assess disease activity. If the disease process fails to respond to a particular drug or drug combination, then a different drug treatment regimen can be instituted.

MRI techniques have evolved for assessing disease activity. These include quantification of synovitis through volume measurement or rate of gadolinium uptake and scoring of erosions. However, MRI can be poorly tolerated by patients, particularly those with severe arthropathy. Assessment of synovitis usually requires intravenous injection of gadolinium, the imaging process is time-consuming and expensive and it is difficult to assess multiple joints. Ultrasound in contrast is well tolerated and multiple joints can be assessed in a short time. Ultrasound markers of disease activity that can be assessed include effusion, synovial volume and vascularity and erosions.

Although volume of effusion can be assessed with ultrasound, this is easier to do in the larger superficial joints such as the knee than in deeper joints such as the hip or smaller joints such as those of the hands and feet. Ultrasound assessment of effusion in finger and toe joints does not achieve the levels of inter-observer agreement that are obtained for assessments of synovitis and erosion.[25] Poor reproducibility of effusion volume measurements may be because the effusion pools in areas of the joint that cannot be assessed easily with ultrasound, or because pressure on the probe displaces fluid elsewhere in the joint. Nevertheless ultrasound monitoring of joint effusions in longitudinal studies has shown change with treatment in both rheumatoid arthritis and the seronegative arthritides.[6]

Unlike MRI it is relatively difficult to obtain an accurate quantification of synovial volume, although semi-quantitative methods have been described.[7] Instead many ultrasound studies have concentrated on the use of Doppler techniques to assess the vascularity of the inflamed synovium. This is largely based on MRI and histological studies that have shown an association between synovial vascularisation and disease activity.[26–29] Although colour and power Doppler can be used, power Doppler is more sensitive and is a reliable measure of synovial blood flow,[30,31] although not without problems. Transducer pressure must be as light as possible to avoid occluding flow. Variations in ambient temperature and variation between different machines, in particular differences in spatial and temporal resolution and post processing algorithms, can make high levels of reproducibility difficult to obtain. This is a particular problem when power Doppler is used in longitudinal studies with follow-up at multiple time points.

Power Doppler has been used in combination with ultrasound contrast agents to demonstrate synovial vascularity and one study has shown high levels of agreement with contrast-enhanced MRI.[32] Another study used arthroscopy as a reference to show that contrast-enhanced power Doppler sonography is more accurate than power Doppler sonography in demonstrating synovial hypervascularity in the knee joint.[33] Despite this, contrast-enhanced power Doppler in the investigation of synovitis has not entered the mainstream partly as a result of the additional cost, time and invasiveness.

The use of power Doppler to monitor disease activity has so far largely involved small-scale studies producing preliminary data in a research environment. Both quantitative and semi-quantitative measures of vascularity have been applied. Quantification of power Doppler signal can be undertaken by counting the number of pixels showing power Doppler signal and this is a technique that has been applied in cross-sectional and longitudinal studies.[34–38]

An alternative method of quantification makes use of the resistive index (RI) calculated from spectral Doppler measurements of

Monitoring disease progression

- Ultrasound is well tolerated and multiple joints can be assessed at a single visit.
- Ultrasound markers of disease activity that can be assessed include effusion, synovial volume and vascularity and erosions.
- Ultrasound monitoring of joint effusions in longitudinal studies has shown changes in response to treatment but has poor reproducibility.
- The use of power Doppler to monitor disease activity has so far largely involved small-scale studies producing preliminary data in a research environment.

flow.[37–39] An increasing resistive index, suggesting reduced hypervascularity of synovium, has been shown following treatment.[37,39]

PERIARTICULAR MASSES AND ARTHRITIS MIMICS

Periarticular mass lesions may arise from or be related to underlying arthritis. Other pathological entities can present as periarticular swelling or with clinical features of arthritis.

Two synovial based masses warrant special consideration. Pigmented villonodular synovitis (PVNS) and synovial chondromatosis arise from joint synovium. PVNS is seen on ultrasound as a focal or diffuse mass or thickening of joint, tendon or bursal synovium. Usually only one joint is affected. There may be associated bone erosion. There are no specific features relating to the echo characteristics of the mass. When suspected, MRI is valuable because PVNS can be diagnosed if areas of low-signal intensity due to haemosiderin deposition are seen on gradient-echo images. Synovial chondromatosis is a benign proliferative condition of synovium associated with metaplastic cartilaginous nodules within the joint, tendon sheath or bursa. Although ultrasound appearances are relatively non-specific, cartilage nodules may undergo ossification (synovial osteochondromatosis), in which case the synovial mass will be seen to be associated with multiple calcific bodies. These have typical ultrasound appearances of bright surface reflectivity and posterior acoustic shadowing. Single joint involvement, no associated arthropathy or a disparity between the severity of arthropathy and the number of bodies should raise the possibility of primary synovial osteochondromatosis.

Other mass lesions that can occur in clinical practice are masses related to crystal deposition and rheumatoid nodules.

Tophi in chronic gout occur in the periarticular soft tissues and have fairly characteristic ultrasound appearances (Fig. 59.9). They usually have heterogeneous echotexture with the crystal material varying in echogenicity from hyperechoic to hypoechoic. Lesions are clearly demarcated and normally have a well-defined surrounding anechoic margin. Tophi are associated with neovascularity and can demonstrate marked hyperaemia on Doppler examination. Erosion of adjacent bone is common and seen more often in the feet than the hands. About two-thirds of tophi in the feet are associated with erosion compared with only a quarter in the hands. Where there is diagnostic doubt ultrasound is an excellent tool for diagnostic aspiration.

Rheumatoid nodules are a common extra-articular feature of rheumatoid arthritis, occurring in approximately one-quarter of rheumatoid arthritis patients. They are most common in the periarticular subcutaneous tissues and have a predilection for developing in pressure areas such as the elbow or heel but can occur in a wide variety of tissues including tendons, kidney, lung and heart.[40] In the soft tissues they have well-defined margins with generally more homogeneous hyperechoic echotexture than tophi.[41] Central necrosis can occur and results in central heterogeneity or hypoechogenicity. Rheumatoid nodules adjacent to bone can be associated with cortical remodelling, although cortical erosion occurs less frequently than with tophi. Tendon-related rheumatoid nodules characteristically occur immediately adjacent to the tendon rather than in the tendon (Fig. 59.10). They may result in triggering as they 'catch' on adjacent structures such as annular pulleys and retinacula. Dynamic examination may demonstrate the triggering.

Masses and arthritis mimics

- Periarticular mass lesions may arise from or be related to underlying arthritis.
- Pigmented villonodular synovitis (PVNS) produces a diffuse mass or thickening of joint, tendon or bursal synovium affecting usually only one site. There are no specific echo characteristics.
- Synovial chondromatosis has typical ultrasound appearances of bright surface reflectivity and posterior acoustic shadowing with single joint involvement.
- There is no associated arthropathy or a disparity between the severity of arthropathy and the number of bodies.
- Gouty tophi usually have heterogeneous echotexture, with the crystal material varying in echogenicity from hyperechoic to hypoechoic.
- Two-thirds of tophi occur in the feet.
- Rheumatoid nodules are seen commonly in seropositive rheumatoid arthritis.
- Rheumatoid nodules have a predilection for developing in pressure areas such as the elbow or heel and have well-defined margins with generally more homogeneous hyperechoic echotexture than tophi.
- Amyloid infiltration of tendons is well recognised and can be detected at ultrasound as thickening of the tendon.
- Amyloid infiltration needs to be considered in the differential diagnosis of conditions producing tendon infiltration including gout.

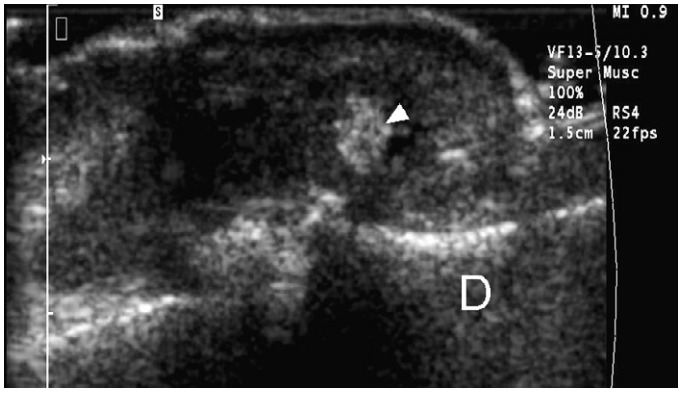

Figure 59.9 Gout tophus in a first toe. Note the brightly echogenic crystal deposits in the lesion centre (arrowhead). D, distal phalanx.

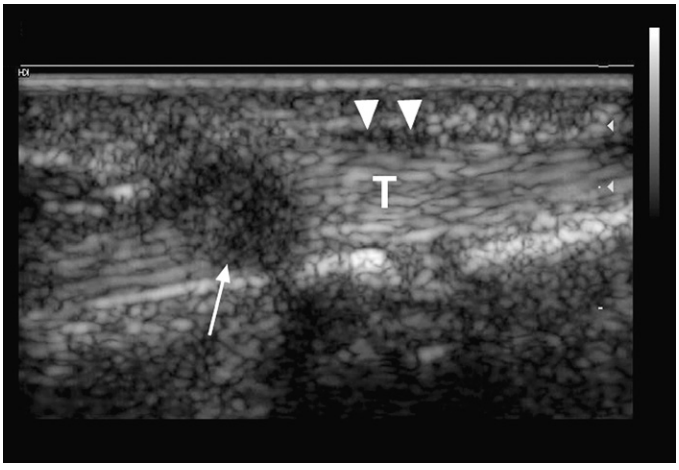

Figure 59.10 Longitudinal ultrasound along a digital flexor tendon (T). The tendon contains a rheumatoid nodule seen as a low reflective lesion (arrow). A thickened annular pulley is seen close by as a low reflective band overlying the tendon (arrowheads) and the patient was experiencing triggering as the nodule passed under the pulley.

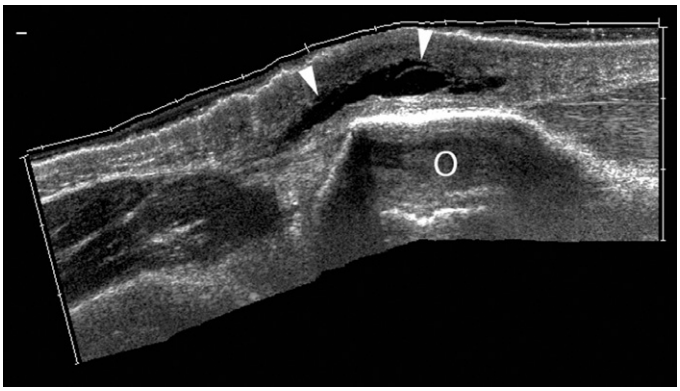

Figure 59.11 Olecranon bursitis. Extended field-of-view longitudinal ultrasound showing olecranon bursitis, which is seen as a pocket of anechoic fluid (arrowheads) overlying the olecranon (O).

Bursae

Bursae are pouches of fluid that facilitate movement between structures by reducing friction.

Two types of bursae are recognised:

- Synovial lined bursae tend to occur in well-recognised positions and may communicate with the adjacent joint.
- Adventitial bursae have no synovial lining and are acquired as a result of friction between two structures leading to the collection of fluid within the tissues separating them. They are much more variable in location and may develop at specific sites relating to a patient's occupation or a sporting activity.

Bursae normally contain only a trace of fluid. However, if a bursa becomes inflamed as a result of trauma, infection or autoimmune condition then it will become distended with fluid. Associated thickening of the bursal synovial lining may be demonstrated with ultrasound. Thickened bursal synovium shows a similar range of ultrasound appearances to those seen in joint synovitis.

Although the fluid will often appear anechoic, the presence of haemorrhage or infection will lead to fluid with a more complex and echogenic appearance. Bursae around individual joints can be very variable, especially the hip and knee. However, the distribution of bursae around some joints is more predictable, including the subacromial bursa of the shoulder, the olecranon bursa at the elbow (Fig. 59.11), the retrocalcaneal bursa of the ankle and some bursae about the anterior knee. Bursae which communicate with joints may become distended in the presence of synovitis and effusion; for instance, popliteal cysts in adults are often secondary to a primary knee abnormality such as osteoarthritis.[42–44] A distended Baker's cyst has a characteristic 'speech bubble' appearance that should be identified to make the diagnosis (Fig. 59.12). In other cases joint communication is variable, as with the iliopsoas bursa, which may or may not communicate with the hip.

Periarticular cysts

Periarticular cysts are readily identified on ultrasound and may be indicators of underlying joint disease. As part of the spectrum of rheumatological disease, fibrocartilaginous degeneration and tearing may be seen, typically in the menisci of the knee and labrum of the shoulder and hip. When this occurs it may be associated with cyst formation. The first presentation of a patient with knee osteoarthritis may be with a lump resulting from a meniscal cyst associated with a degenerate and extruded meniscus. Around the hip and shoulder, cysts associated with degeneration or tearing of the acetabular or glenoid labrum may also be identified.[45–47]

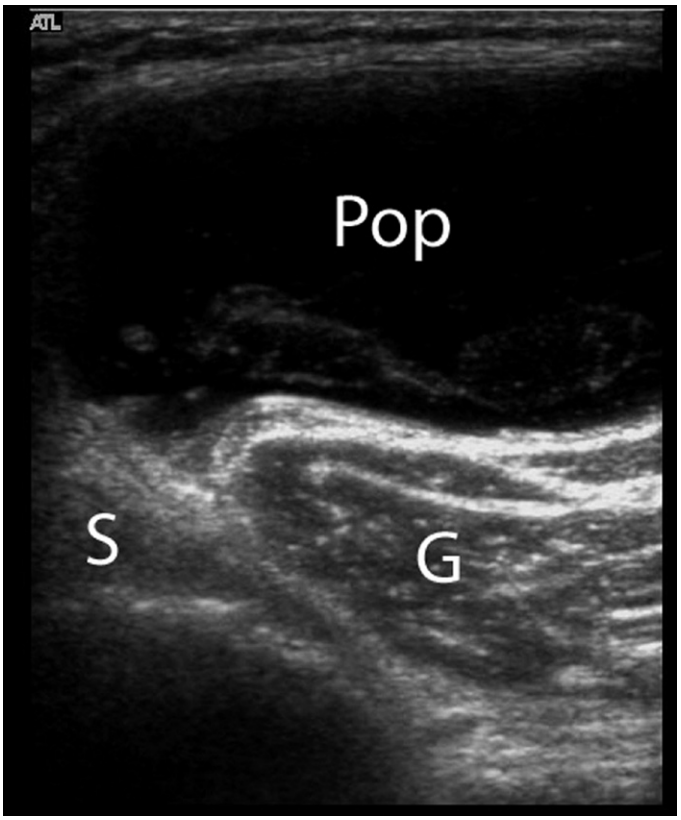

Figure 59.12 A large popliteal cyst is demonstrated in transverse section (Pop). Characteristically the neck of the cyst is demonstrated extending deeper towards the knee joint between the medial head of gastrocnemius (G) and semimembranosus tendon (S), giving the cyst a 'speech bubble' configuration.

Amyloidosis

Ultrasound has been utilised in the diagnosis and monitoring of periarticular amyloidosis although the findings are not specific. Amyloid infiltration of tendons is well recognised and can be detected at ultrasound as thickening of the tendon. This has been most frequently described in the rotator cuff tendons, but it also occurs in other tendons.[48–51] Amyloid should be considered in the differential diagnosis of conditions giving tendon infiltration including gout. Additional findings in amyloidosis include thickening of the joint capsule and synovitis.[51] There is evidence from a longitudinal study in patients with dialysis-related amyloidosis that the thickness of the supraspinatus tendon can be related to the duration of dialysis, suggesting there may be a role for ultrasound in monitoring the disease progress.[51]

JOINT INFECTION AND ULTRASOUND

The presence or absence of joint infection is one of the key diagnoses made in clinical practice. Ultrasound can help in making this diagnosis. The clinical presentation of infection is variable. Patients usually present with pain and swelling in the affected joint. Pain is particularly prominent and in patients complaining of severe pain infection must be excluded. Occasionally patients present with relatively low-grade symptoms. These tend to be patients who are immunocompromised or cases where the infective agent is less aggressive.

Diagnostic radiographic features of infection are delayed and the classic appearances of periarticular osteopenia with panarticular

Intervention and infection

- Ultrasound is ideally suited for guiding diagnostic and therapeutic injections into joints, tendon sheaths and bursae.
- Pain is particularly prominent in infection. In patients complaining of severe pain infection must be excluded.
- Ultrasound assessment of possible infection should look for effusion, synovitis and subperiosteal collections.
- Assessment of the periosteum adjacent to joints is particularly important in skeletally immature patients where subperiosteal abscesses are more common.
- The accuracy of ultrasound in demonstrating effusions in large joints like the hip is more limited than one might think.
- As a result, when effusion is demonstrated and infection is clinically suspected, diagnostic aspiration is needed.

joint space loss take time to develop. MR and ultrasound appearances are relatively non-specific with inflammatory change and effusion present in the affected joint. In the skeletally immature patient infection can begin in the growth plate of the bone with secondary extension of infection into either the subperiosteal or joint space. Ultrasound assessment involves the diagnosis of effusion, synovitis and subperiosteal collections. Assessment of the periosteum adjacent to joints is particularly important in skeletally immature patients where subperiosteal abscesses are more common. The accuracy of ultrasound in demonstrating effusions in large joints like the hip can be somewhat limited[52] and where there is strong clinical suspicion recourse to MR assessment may be required. Where abnormality is seen within the joint, power Doppler assessment should be performed and can help differentiate synovitis from effusions. Some studies suggest that using ultrasound contrast agents can help more reliably to identify synovitis in the large joints though there is some persisting doubt.[53] In infection substantial power Doppler signal is seen in the periarticular soft tissues. Synovial thickening within the joint is one of the key features. Even in paediatric patients where there is good sonographic access to the joint, the sensitivity, specificity and positive predictive value for infection versus transient synovitis is between 85% and 90%.[54] As a result, when effusion is demonstrated and infection is clinically suspected, diagnostic aspiration needs to be performed under ultrasound guidance to confirm or refute the presence of infection. This should be performed under strict sterile conditions to avoid introducing infection. Samples should be sent for microscopy, culture and sensitivity and TB culture. One study looked at percutaneous treatment of paediatric septic arthritis with repeated aspiration and washout without arthrotomy.[55] This proved effective in 24 of 34 patients, with earlier return to normal activity and no complications.

Ultrasound is less promising in the assessment of periprosthetic infection in hip replacements and is not advised as a standalone assessment.[56]

USE OF ULTRASOUND IN GUIDING DIAGNOSTIC AND THERAPEUTIC INTERVENTION

Ultrasound is ideally suited for guiding diagnostic and therapeutic injections into joints, tendon sheaths and bursae. The purpose of a diagnostic injection is to determine if symptoms arise from a specific site by showing if they are abolished by injection of local anaesthetic. The need for accurate needle placement is clear. Local anaesthetic and corticosteroid can be combined for a therapeutic injection.

REFERENCES

1. Bude RO, Rubin JM. Power Doppler sonography. Radiology 1996;200(1):21–23.
2. Cardinal E, Lafortune M, Burns P. Power Doppler US in synovitis: reality or artifact? Radiology 1996;200(3):868–869.
3. Wakefield RJ, Balint PV, Szkudlarek M, et al. Musculoskeletal ultrasound including definitions for ultrasonographic pathology. J Rheumatol 2005;32(12):2485–2487.
4. Hau M, Schultz H, Tony HP, et al. Evaluation of pannus and vascularization of the metacarpophalangeal and proximal interphalangeal joints in rheumatoid arthritis by high-resolution ultrasound (multidimensional linear array). Arthritis Rheum 1999;42(11):2303–2308.
5. Backhaus M, Kamradt T, Sandrock D, et al. Arthritis of the finger joints: a comprehensive approach comparing conventional radiography, scintigraphy, ultrasound, and contrast-enhanced magnetic resonance imaging. Arthritis Rheum 1999;42(6):1232–1245.
6. Fiocco U, Cozzi L, Rubaltelli L, et al. Long-term sonographic follow-up of rheumatoid and psoriatic proliferative knee joint synovitis. Br J Rheumatol 1996;35(2):155–163.
7. Szkudlarek M, Narvestad E, Klarlund M, et al. Ultrasonography of the metatarsophalangeal joints in rheumatoid arthritis: comparison with magnetic resonance imaging, conventional radiography, and clinical examination. Arthritis Rheum 2004;50(7):2103–2112.
8. Conaghan PG, Wakefield R, O'Connor P, et al. The metacarpophalangeal joints in early arthritis: a comparison of clinical, radiographic, MRI and ultrasonographic findings. Ann Rheum Dis 1999;58(Eular Congress Suppl.):28.
9. Koski JM, Anttila P, Hamalainen M, Isomaki H. Hip joint ultrasonography: correlation with intra-articular effusion and synovitis. Br J Rheumatol 1990;29(3):189–192.
10. Wakefield RJ, Gibbon WW, Conaghan PG, et al. The value of sonography in the detection of bone erosions in patients with rheumatoid arthritis: a comparison with conventional radiography. Arthritis Rheum 2000;43(12):2762–2770.
11. Weidekamm C, Koller M, Weber M, Kainberger F. Diagnostic value of high-resolution B-mode and Doppler sonography for imaging of hand and finger joints in rheumatoid arthritis. Arthritis Rheum 2003;48(2):325–333.
12. Magnani M, Salizzoni E, Mule R, et al. Ultrasonography detection of early bone erosions in the metacarpophalangeal joints of patients with rheumatoid arthritis. Clin Exp Rheumatol 2004;22(6):743–748.
13. Wakefield RJ, Gibbon WW, Emery P. The current status of ultrasonography in rheumatology. Rheumatology (Oxford) 1999;38(3):195–198.
14. Alasaarela E, Suramo I, Tervonen O, et al. Evaluation of humeral head erosions in rheumatoid arthritis: a comparison of ultrasonography, magnetic resonance imaging, computed tomography and plain radiography. Br J Rheumatol 1998;37(11):1152–1156.
15. Iagnocco A, Coari G, Zoppini A. Sonographic evaluation of femoral condylar cartilage in osteoarthritis and rheumatoid arthritis. Scand J Rheumatol 1992;21(4):201–203.
16. Keen HI, Wakefield RJ, Grainger AJ, et al. Can ultrasonography improve on radiographic assessment in osteoarthritis of the hands? A comparison between radiographic and ultrasonographic detected pathology. Ann Rheum Dis 2008;67(8):1116–1120.
17. Grassi W, Lamanna G, Farina A, Cervini C. Sonographic imaging of normal and osteoarthritic cartilage. Semin Arthritis Rheum 1999;28(6):398–403.
18. Helbich TH, Breitenseher M, Trattnig S, et al. Sonomorphologic variants of popliteal cysts. J Clin Ultrasound 1998;26(3):171–176.
19. Rutten MJ, Collins JM, van Kampen A, Jager GJ. Meniscal cysts: detection with high-resolution sonography. AJR Am J Roentgenol 1998;171(2):491–496.
20. Thiele RG, Schlesinger N. Diagnosis of gout by ultrasound. Rheumatology (Oxford) 2007;46(7):1116–1121.
21. Benjamin M, McGonagle D. The anatomical basis for disease localisation in seronegative spondyloarthropathy at entheses and related sites. J Anat 2001;199(Pt. 5):503–526.
22. Kane D, Greaney T, Bresnihan B, et al. Ultrasonography in the diagnosis and management of psoriatic dactylitis. J Rheumatol 1999;26(8):1746–1751.
23. Olivieri I, Barozzi L, Favaro L, et al. Dactylitis in patients with seronegative spondylarthropathy. Assessment by ultrasonography and magnetic resonance imaging. Arthritis Rheum 1996;39(9):1524–1528.
24. Wakefield RJ, Emery P, Veale D. Ultrasonography and psoriatic arthritis. J Rheumatol 2000;27(6):1564–1565.

25. Szkudlarek M, Court-Payen M, Jacobsen S, et al. Interobserver agreement in ultrasonography of the finger and toe joints in rheumatoid arthritis. Arthritis Rheum 2003;48(4):955–962.
26. Lindblad S, Hedfors E. Intraarticular variation in synovitis. Local macroscopic and microscopic signs of inflammatory activity are significantly correlated. Arthritis Rheum 1985;28(9):977–986.
27. Tamai K, Yamato M, Yamaguchi T, Ohno W. Dynamic magnetic resonance imaging for the evaluation of synovitis in patients with rheumatoid arthritis. Arthritis Rheum 1994;37(8):1151–1157.
28. Huang J, Stewart N, Crabbe J, et al. A 1-year follow-up study of dynamic magnetic resonance imaging in early rheumatoid arthritis reveals synovitis to be increased in shared epitope-positive patients and predictive of erosions at 1 year. Rheumatology (Oxford) 2000;39(4):407–416.
29. Ostergaard M, Stoltenberg M, Lovgreen-Nielsen P, et al. Quantification of synovistis by MRI: correlation between dynamic and static gadolinium-enhanced magnetic resonance imaging and microscopic and macroscopic signs of synovial inflammation. Magn Reson Imaging 1998;16(7):743–754.
30. Newman JS, Laing TJ, McCarthy CJ, Adler RS. Power Doppler sonography of synovitis: assessment of therapeutic response – preliminary observations. Radiology 1996;198(2):582–584.
31. Walther M, Harms H, Krenn V, et al. Correlation of power Doppler sonography with vascularity of the synovial tissue of the knee joint in patients with osteoarthritis and rheumatoid arthritis. Arthritis Rheum 2001;44(2):331–338.
32. Magarelli N, Guglielmi G, Di Matteo L, et al. Diagnostic utility of an echo-contrast agent in patients with synovitis using power Doppler ultrasound: a preliminary study with comparison to contrast-enhanced MRI. Eur Radiol 2001;11(6):1039–1046.
33. Fiocco U, Ferro F, Cozzi L, et al. Contrast medium in power Doppler ultrasound for assessment of synovial vascularity: comparison with arthroscopy. J Rheumatol 2003;30(10):2170–2176.
34. Teh J, Stevens K, Williamson L, et al. Power Doppler ultrasound of rheumatoid synovitis: quantification of therapeutic response. Br J Radiol 2003;76(912):875–879.
35. Taylor PC, Steuer A, Gruber J, et al. Comparison of ultrasonographic assessment of synovitis and joint vascularity with radiographic evaluation in a randomized, placebo-controlled study of infliximab therapy in early rheumatoid arthritis. Arthritis Rheum 2004;50(4):1107–1116.
36. Taylor PC, Steuer A, Gruber J, et al. Ultrasonographic and radiographic results from a two-year controlled trial of immediate or one-year-delayed addition of infliximab to ongoing methotrexate therapy in patients with erosive early rheumatoid arthritis. Arthritis Rheum 2006;54(1):47–53.
37. Kasukawa R, Shio K, Kanno Y, et al. Doppler ultrasound measurements of knee joint synovitis in rheumatoid arthritis patients treated with infliximab. Mod Rheumatol 2007;17(5):376–379.
38. Kasukawa R, Shio K, Kanno Y, et al. Power Doppler and spectral Doppler measurements of knee-joint synovitis in rheumatoid arthritis patients with superficial pattern signals and in those with deep pattern signals. Mod Rheumatol 2007;17(4):267–272.
39. Terslev L, Torp-Pedersen S, Qvistgaard E, et al. Estimation of inflammation by Doppler ultrasound: quantitative changes after intra-articular treatment in rheumatoid arthritis. Ann Rheum Dis 2003;62(11):1049–1053.
40. Batalov AZ, Kuzmanova SI, Sapoundjiev LI. Intraarticular rheumatoid nodule detection in the knee joint using ultrasonography. Folia Med (Plovdiv) 2000;42(4):27–29.
41. Nalbant S, Corominas H, Hsu B, et al. Ultrasonography for assessment of subcutaneous nodules. J Rheumatol 2003;30(6):1191–1195.
42. Fielding JR, Franklin PD, Kustan J. Popliteal cysts: a reassessment using magnetic resonance imaging. Skeletal Radiol 1991;20(6):433–435.
43. Janzen DL, Peterfy CG, Forbes JR, et al. Cystic lesions around the knee joint: MR imaging findings. AJR Am J Roentgenol 1994;163(1):155–161.
44. Murphey MD, Gross TM, Rosenthal HG, Neff JR. Magnetic resonance imaging of soft tissue and cystic masses about the knee. Top Magn Reson Imaging 1993;5(4):263–282.
45. Schnarkowski P, Steinbach LS, Tirman PF, et al. Magnetic resonance imaging of labral cysts of the hip. Skeletal Radiol 1996;25(8):733–737.
46. Tirman PF, Feller JF, Janzen DL, et al. Association of glenoid labral cysts with labral tears and glenohumeral instability: radiologic findings and clinical significance. Radiology 1994;190(3):653–658.
47. Tung GA, Entzian D, Stern JB, Green A. MR imaging and MR arthrography of paraglenoid labral cysts. AJR Am J Roentgenol 2000;174(6):1707–1715.
48. Kay J, Benson CB, Lester S, et al. Utility of high-resolution ultrasound for the diagnosis of dialysis-related amyloidosis. Arthritis Rheum 1992;35:926–932.
49. McMahon LP, Radford J, Dawborn JK. Shoulder ultrasound in dialysis related amyloidosis. Clin Nephrol 1991;35:227–232.
50. Ferrara MA, Marcelis S. Ultrasound examination of the wrist. J Belge Radiol 1997;80:78–80.
51. Jadoul M, Malghem J, Vande Berg B, van Ypersele de Strihou C. Ultrasonographic detection of thickened joint capsules and tendons as marker of dialysis-related amyloidosis: a cross-sectional and longitudinal study. Nephrol Dial Transplant 1993;8:1104–1109.
52. Weybright PN, Jacobson JA, Murry KH, et al. Limited effectiveness of sonography in revealing hip joint effusion: preliminary results in 21 adult patients with native and postoperative hips. AJR Am J Roentgenol 2003;181(1):215–218.
53. Wamser G, Bohndorf K, Vollert K, et al. Power Doppler sonography with and without echo-enhancing contrast agent and contrast-enhanced MRI for the evaluation of rheumatoid arthritis of the shoulder joint: differentiation between synovitis and joint effusion. Skeletal Radiol 2003;32(6):351–359.
54. Zamzam MM. The role of ultrasound in differentiating septic arthritis from transient synovitis of the hip in children. J Pediatr Orthop B 2006;15(6):418–422.
55. Givon U, Liberman B, Schindler A, et al. Treatment of septic arthritis of the hip joint by repeated ultrasound-guided aspirations. J Pediatr Orthop 2004;24(3):266–270.
56. Eisler T, Svensson O, Engstrom CF, et al. Ultrasound for diagnosis of infection in revision total hip arthroplasty. J Arthroplasty 2001;16(8):1010–1017.

CHAPTER

60 Sonography of muscle injury

Justin C. Lee and Jeremiah C. Healy

INTRODUCTION

The physical and psychosocial benefits of regular exercise are widely documented. Regular sporting activity can prolong life and reduce the risk of ischaemic heart disease and stroke.[1–3] However, the increase in exercise levels in the general population and the ever greater demands on professional athletes have increased the risk of sports-related injuries especially to muscle.

The radiologist is central to the diagnosis and management of skeletal muscle injury. Whilst magnetic resonance imaging (MRI) provides excellent lesion detection and anatomical localisation, it is expensive, time consuming and acquires a static image. Although sonography is limited by its reduced contrast resolution, operator dependence and limited image field, it is cheap, readily accessible, provides dynamic examination and has superior spatial resolution to MRI. Most machines are now capable of extended field-of-view imaging which facilitates image interpretation to the non-ultrasound specialist.[4] High quality ultrasound can be achieved using portable machines, useful in the early diagnosis and follow-up of muscle injury.

In this chapter, we describe sonographic normal anatomy, optimal technique, and features of acute and chronic skeletal muscle injury.

SONOGRAPHIC TECHNIQUE

Recent developments in ultrasound technology have led to significant advances in ultrasound imaging of skeletal muscle injury. Several commercially available machines are now capable of imaging at 17 MHz, allowing extremely fine spatial resolution in the near field although they are limited by their reduced tissue penetration. This can be a problem in athletes in whom muscle hypertrophy may limit assessment of deep muscle injury, particularly in the thigh. In deep muscle injury, it may be necessary to either use a reduced frequency linear transducer (7–13 MHz) or, for larger patients, a curvilinear array transducer (3.5–7.5 MHz). Extended field-of-view imaging further enhances the value of sonography.[5]

The ultrasound examination is aided by obtaining a brief history and physical examination of the patient. In the sonographic assessment of muscle injury, it is advisable to consider the muscle compartment as a whole and then to focus on the injured individual muscle. Comprehensive sonographic examination of the injured muscle compartment is recommended as muscle injuries are not always accurately localised clinically.[6] Liberal use of gel couplant is advisable. The operator should not press too firmly as excess pressure can reduce detection of blood flow on Doppler imaging, obscure small tears by distorting fibre orientation and displacing myofascial fluid collections/haemorrhage or reduce myofascial hernias (see later section).[7] The patient may need to be scanned in different patient positions to increase the conspicuity of a lesion. For example, during the assessment of anterior compartment or peroneal compartment myofascial hernia, it may be useful to scan the patient in the squat position as this increases intra-compartmental pressure, forcing any occult hernias into view.[8]

The transducer must remain perpendicular to the bulk of the muscle fibres to prevent anisotropy artefact.[9] The normal juxtaposition of areas of hyper- and hypoechogenicity within a single muscle may lead to misinterpretation of muscle oedema. Therefore, it is important to alter the angle of obliquity repeatedly when scanning for muscle oedema to ensure that the increased reflectivity is a constant finding.

Dynamic scanning during active and passive muscle movement is a major advantage of sonography over MRI and is essential as significant disruption of muscle fibres may only become apparent during contraction.[9]

Extended field-of-view (EFOV) imaging, now commonly available, allows the sonographer and clinician to assess the muscle in relation to its surrounding anatomy.[10] EFOV imaging improves the reliability of sonographic diagnosis of muscle atrophy.[11]

Standard muscle injury sonographic assessment protocol

1. Liberal gel couplant
2. Patient positioned with affected muscle compartment easily accessible
3. Whole compartment scanned
   a. Series of axial images from proximal to distal
4. Individual affected muscle scanned from origin to insertion
   a. Axial
   b. Sagittal
   c. Obliquely along line of fibres
   d. Extended field-of-view images in above three planes
   e. Exclude paratendinitis as this may mimic muscle tear
5. Dynamic assessment of injured muscle
   a. Active against resistance (may require assistant)
   b. Passive without resistance
6. Scan in different patient position
   a. Squat for peroneal/anterior leg compartment myofascial hernia assessment

NORMAL ANATOMY

Skeletal muscle is innervated by somatic nerves and forms the bulk of the muscle tissue in the human body. Although skeletal muscle mass varies between individuals, it typically contributes up to 35% of total body weight in women and up to 50% in men.[12] Before considering the gross morphological appearances of muscle, knowledge of skeletal muscle microstructure is useful in understanding how a muscle injury develops and how chronic complications can occur following injury.

Microstructure

Several cell types in the human body are capable of changing shape by altering elements of their cytoskeleton, for example macrophages during phagocytosis. However, in muscle tissue, the parallel arrangement of the abundant molecular *myofilament* proteins of actin and myosin (and their related proteins) ensures that changes at the molecular level result in contraction of the whole cell in a single direction. When grouped together in this parallel fashion, these contractile proteins are referred to as *myofibrils* (Fig. 60.1).

The cellular unit of skeletal muscle has a variety of different terms: *muscle cells*, *muscle fibres*, and *myocytes*. For the purposes of this chapter, we will refer to the cellular unit as a muscle fibre. These long cylindrical structures tend to be consistent in size within a given muscle but vary greatly between muscles. The connective tissue of skeletal muscle provides the framework for maintaining the shape of the muscle in both the contracted and relaxed state. The *endomysium* is a delicate network of connective tissue, which surrounds individual muscle fibres and contains the vessels and nerves that supply the muscle fibres as well as the proteoglycan matrix for ion flux and metabolic exchange.[12] The *perimysium* is continuous with the endomysium and surrounds groups of parallel muscle fibres, known as *fasciculi.* The perimysium is significantly thicker than the endomysium and contains larger vessels and nerves and accommodates the neuromuscular spindles.

The perimysium is formed by inward extensions of the connective tissue layer that surrounds the whole muscle, which is known as the *epimysium* (Fig. 60.1). The endomysium, perimysium and epimysium come together as the muscle fuses together into tendons, aponeuroses or fasciae.

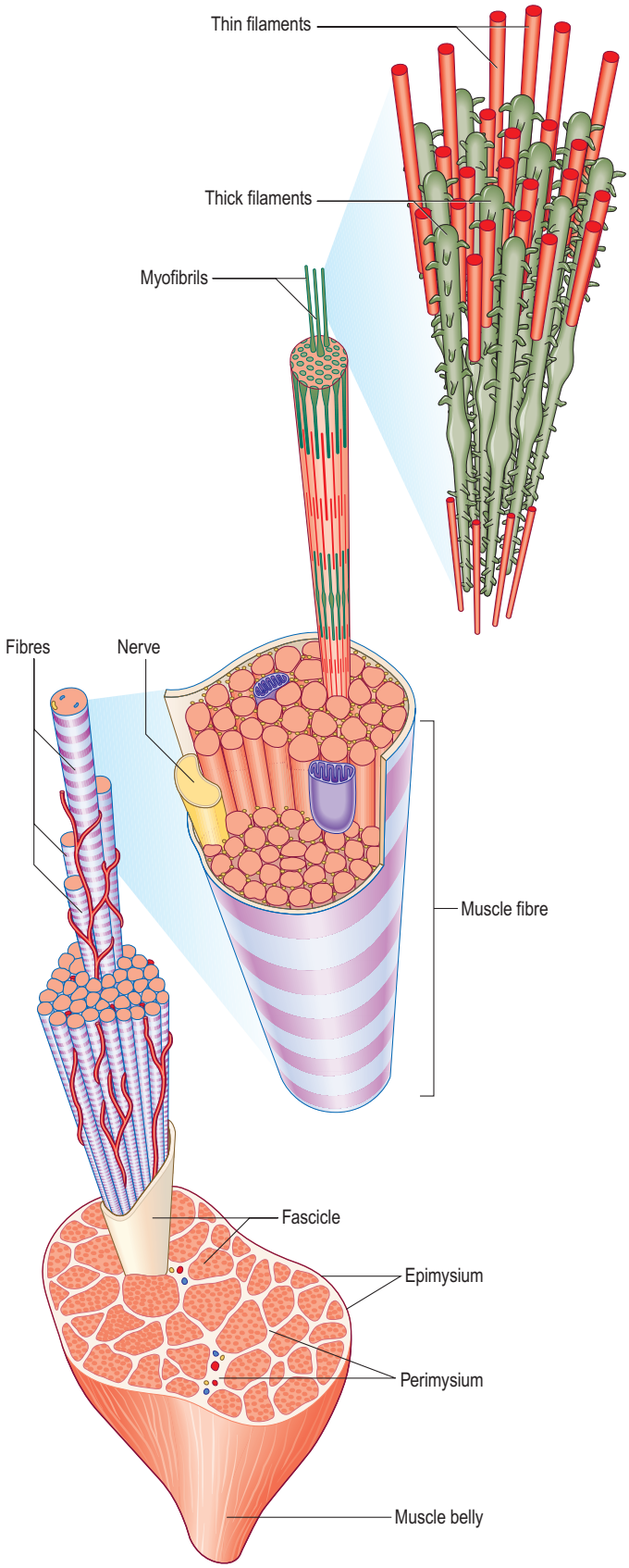

Figure 60.1 The microstructure of skeletal muscle from muscle belly to myofilaments. (Reproduced with permission from Standring S, et al. (eds), Gray's Anatomy, 40th edn, Edinburgh, Churchill Livingstone, 2008.)

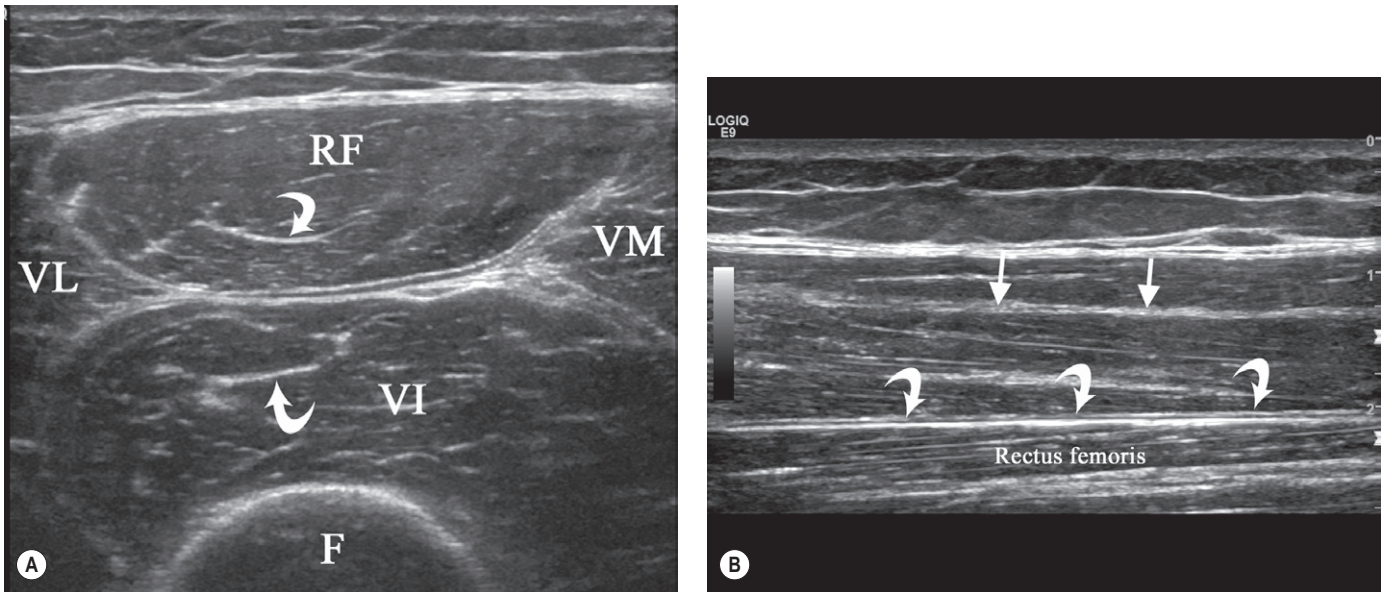

Figure 60.2 Normal sonographic muscle appearance. A: Transverse section through the anterior compartment of the thigh. Note the dot-like perimysium within the hypoechoic background muscle fibres and the normal comma-shaped echogenic central tendons within the centre of the muscle (curved arrow). RF, rectus femoris; VM, vastus medialis; VI, vastus intermedius; VL, vastus lateralis. **B:** Longitudinal section through the rectus femoris muscle. The perimysium is seen as multiple linear echogenic interfaces (straight arrows) on a background of hypoechoic muscle fibres. Note the brightly echogenic central tendon (curved arrows).

NORMAL SONOGRAPHIC MUSCLE APPEARANCE

During ultrasound scanning in the transverse plane, the epimysium is identified as an echogenic envelope surrounding the muscle belly, whilst the perimysium is seen as dot echoes, or short lines scattered throughout the hypoechoic background, representing the bulk of the muscle fibres (Fig. 60.2). The intermuscular septa and aponeuroses are brightly echogenic linear structures in all imaging planes. Similarly, intramuscular extensions of tendons are identified as thick, fibrillar, echogenic structures. In the longitudinal plane, the perimysium is seen as oblique, parallel echogenic striae against a hypoechoic background of muscle fibres (Fig. 60.2). During contraction muscle alters shape and becomes hypoechoic with increased angulation of the echogenic septa in relation to the central tendon.

MORPHOLOGICAL TYPES, COMPARTMENTAL ANATOMY, ACCESSORY MUSCLES

Morphological types

Skeletal muscles may be classified according to their morphology and fibre orientation relative to the line of contraction, i.e., parallel or oblique (Fig. 60.3). Parallel orientation of muscle fibres ensures a maximum range of mobility of the muscle whereas oblique orientation of fibres reduces range but increases force of contraction.

Parallel muscles

Short flat muscles (e.g. pronator quadratus in the forearm), and long strap-like muscles (e.g. gracilis or sartorius in the thigh) have their fibres orientated parallel to their line of contraction. Some of the individual fibres may run the entire length of the muscle unless the muscle is crossed by tendinous intersections, as in rectus abdominis (Fig. 60.3).

Oblique orientation fibres

Fusiform-shaped muscles (e.g. biceps brachii) have their fibres arranged in near parallel orientation in the belly and converge to a tendon at one or both ends. Muscles that have their fibres oblique to the line of contraction may be triangular (pectoralis, adductor longus) or pennate (feather-like) (Fig. 60.3). Pennate muscles can be further subdivided into unipennate (e.g. flexor pollicis longus), bipennate (e.g. rectus femoris, dorsal interossei), multipennate (e.g. deltoid), and circumpennate or cylindrical (e.g. tibialis anterior).

Some muscles have their fibres arranged in a spiral fashion so that the fibres originating medially turn 180° as they reach their lateral insertion (e.g. the sternocostal fibres of the pectoralis major and latissimus dorsi muscles). Others spiral around a bone (e.g. supinator in the forearm) or have fibres orientated in different directions in a cruciate fashion (e.g. adductor magnus muscle). Many muscles have more than one of the above arrangements to allow for different functional roles.

Compartmental anatomy

The sonographic localisation of a muscle injury requires the operator to have a clear understanding of the organisation of muscles within each compartment of the upper and lower limb.

Upper limb

The muscles of each compartment are listed in Table 60.1.

- **Arm:** The arm extends from the shoulder to the elbow joint and is divided into anterior and posterior compartments by the humerus and the medial and lateral intermuscular septa (Fig. 60.4).

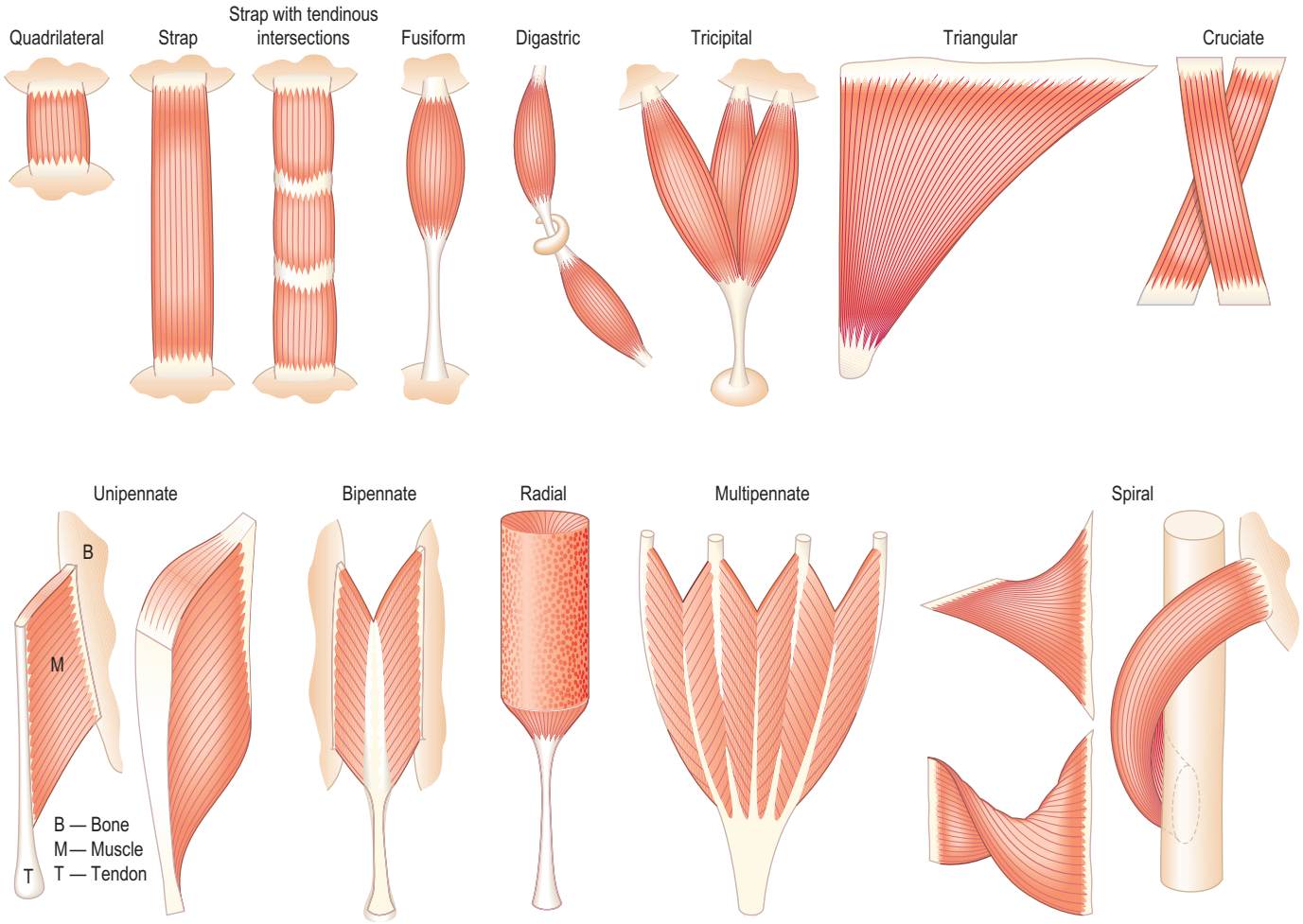

Figure 60.3 The different morphological types of skeletal muscle. (Reproduced with permission from Standring S, et al. (eds), Gray's Anatomy, 40th edn, Edinburgh, Churchill Livingstone, 2008.)

Table 60.1 Upper limb

Section	Compartment		Muscles
Arm	Anterior		Biceps brachii Coracobrachialis Brachialis
	Posterior		Triceps
Forearm	Anterior	Superficial	Pronator teres Flexor carpi radialis Palmaris longus Flexor digitorum superficialis
		Deep	Flexor digitorum profundus Flexor pollicis longus Pronator quadratus
	Posterior	Superficial	Anconeus Supinator Brachioradialis Extensor carpi radialis longus and brevis Extensor digitorum (communis) Extensor digiti minimi Extensor carpi ulnaris
		Deep	Extensor pollicis brevis and longus Abductor pollicis longus Extensor indicis

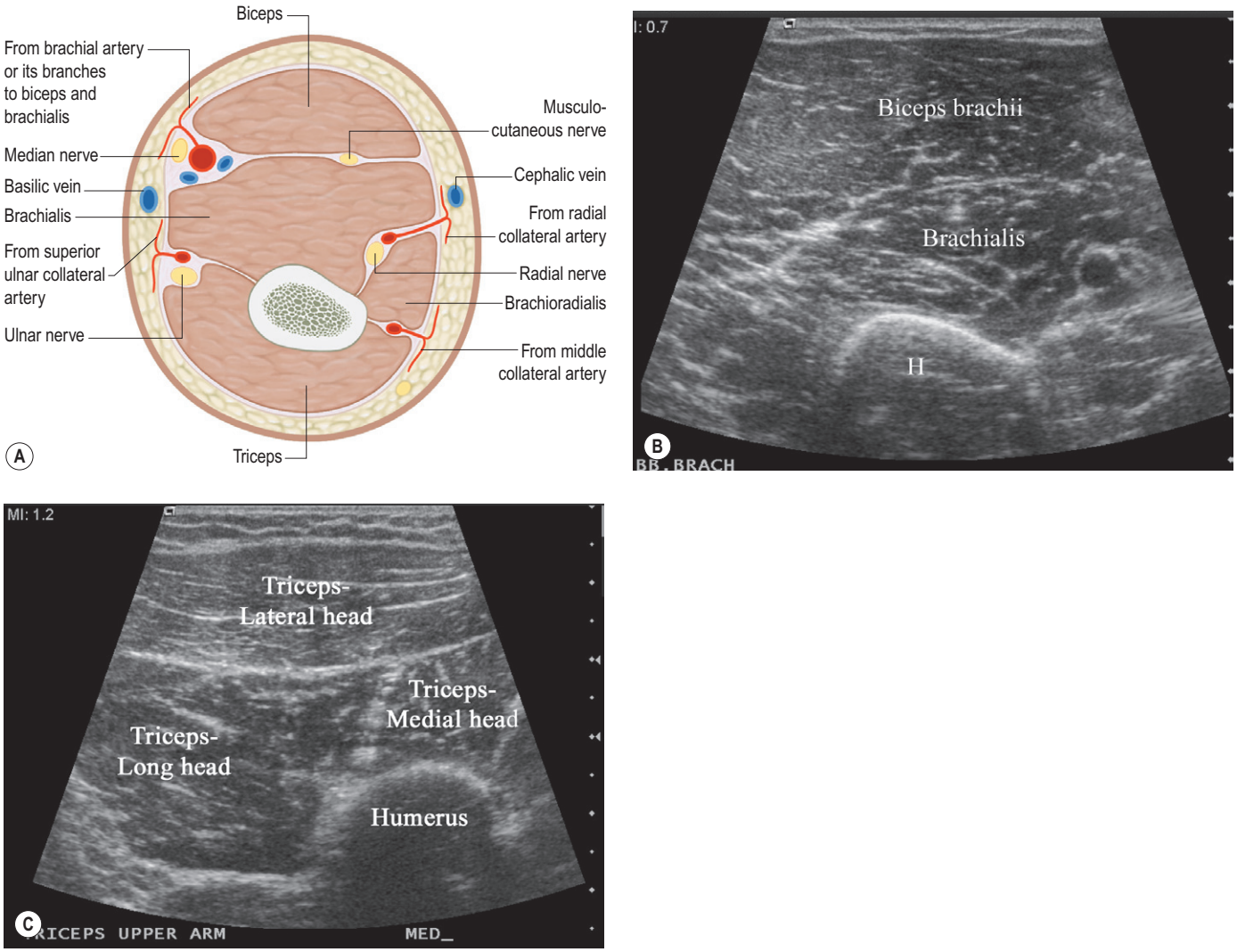

Figure 60.4 **Arm. A:** Line drawing of the compartmental anatomy of the arm. (Reproduced with permission from Standring S, et al. (eds), Gray's Anatomy, 40th edn, Edinburgh, Churchill Livingstone, 2008.) **B:** Transverse sonogram of the anterior compartment of the arm. H, humerus. **C:** Transverse sonogram of the posterior compartment of the arm.

- **Forearm:** The forearm extends from the elbow to the wrist joint and is similarly divided into anterior and posterior compartments by the radius, ulna and interosseous membrane (Fig. 60.5). The anterior compartment is subdivided into superficial and deep groups.

Lower limb

The muscles of each compartment are listed in Table 60.2.

- **Thigh:** The thigh extends from the hip to the knee joint. It is divided into three compartments; posterior (hamstring), anterior (extensor) and medial (adductor) (Fig. 60.6). The first two compartments are separated by a well-defined lateral intermuscular septum. The posterior and medial compartments are not separated by a defined septum as the adductor magnus has both hamstring (flexor) and adductor function.
- **Leg:** The leg refers to that part of the lower limb between the knee and the ankle joint. There are three muscular compartments: anterior (extensor), lateral (peroneal) and posterior (flexor), which are separated by the tibia, fibula, interosseous membrane, and the anterior and posterior intermuscular septa (Fig. 60.7). The posterior compartment is subdivided further into deep and superficial groups.

Accessory muscles

Anatomical variations include muscle agenesis, supernumerary muscles and muscles with anomalous origins or insertions. An accessory muscle is a distinct muscle unit in addition to the normal group of muscles in that region.[13] Most normal variants pass unnoticed but some are clinically detectable in the form of localised swellings or by compression of adjacent neurovascular structures.

Accessory muscles of the upper limb include the accessory brachialis, anconeus epitrochlearis, accessory head of flexor pollicis longus, accessory flexor digitorum superficialis indicis, flexor carpi radialis brevis vel profundus, accessory hypothenar muscles, extensor digitorum brevis manus and the accessory extensor carpi radialis (Table 60.3).[14,15] The most commonly encountered clinically relevant accessory upper limb muscles are anconeus epitrochlearis and accessory abductor digiti.[16,17] The anconeus epitrochlearis muscle arises from the medial border of the olecranon and inserts

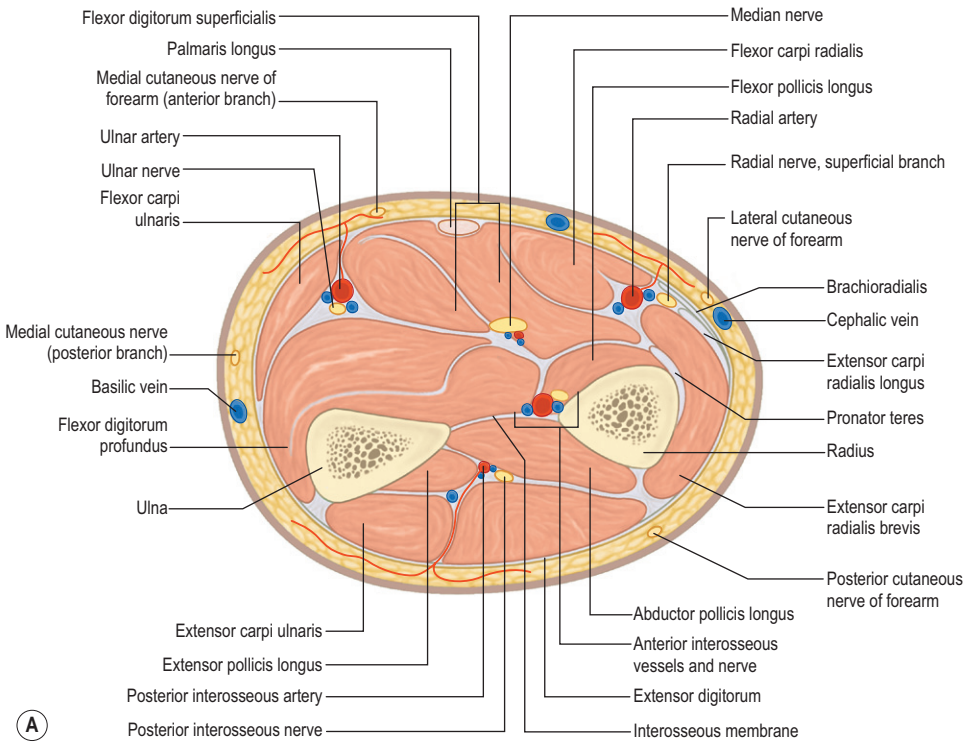

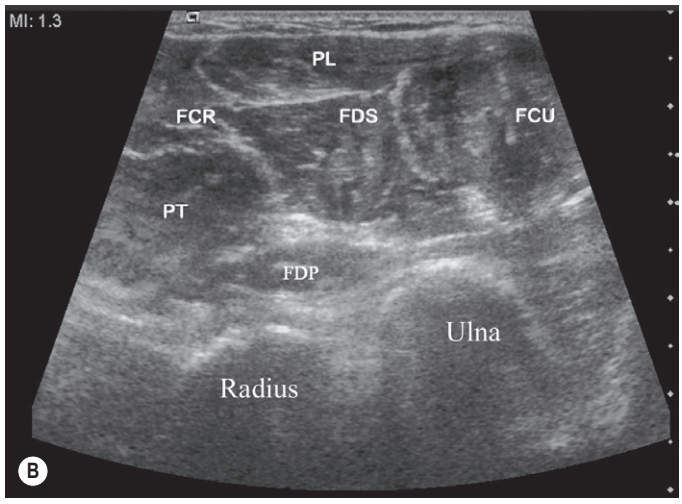

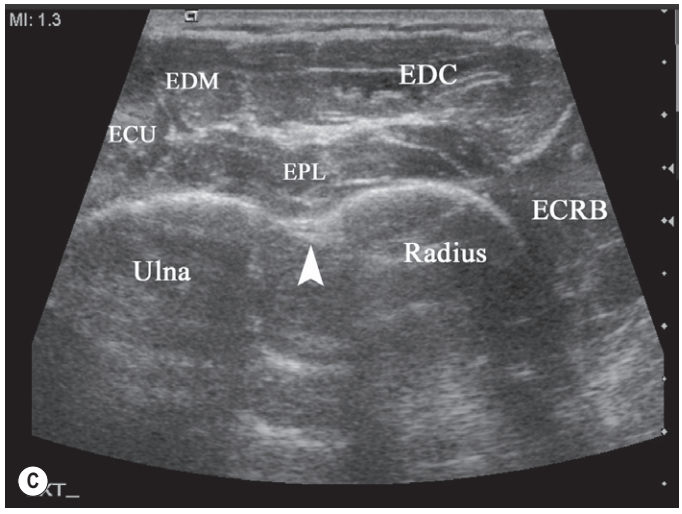

Figure 60.5 **Forearm. A:** Line drawing of the compartmental anatomy of the forearm. (Reproduced with permission from Standring S, et al. (eds), Gray's Anatomy, 40th edn, Edinburgh, Churchill Livingstone, 2008.) **B:** Transverse sonogram of the upper forearm anterior compartment muscles. PT, pronator teres; FCR, flexor carpi radialis; PL, palmaris longus, FCU; flexor carpi ulnaris; FDP, flexor digitorum profundus; FDS, flexor digitorum superficialis. **C:** Transverse sonogram of the posterior compartment of the forearm. ECU, extensor carpi ulnaris; EDM, extensor digiti minimi; EPL, extensor pollicis longus; EDC, extensor digitorum communis; ECRB, extensor carpi radialis brevis. Arrowhead, interosseous membrane.

Table 60.2 Lower limb

Section	Compartment		Muscles
Thigh	Medial/Adductor		Pectineus Gracilis Adductor brevis, longus and magnus (adductor portion)
	Anterior/Extensor		Quadriceps femoris Sartorius Tensor fascia lata
	Posterior/Flexor/Hamstring		Biceps femoris Semimembranosus Semitendinosus Adductor magnus (hamstring portion)
Leg	Anterior/Extensor		Tibialis anterior Extensor hallucis longus Extensor digitorum longus Peroneus tertius
	Lateral/Peroneal		Peroneus longus and brevis
	Posterior/Flexor	Superficial	Medial and lateral gastrocnemei Soleus Plantaris
		Deep	Popliteus Tibialis posterior Flexor digitorum longus Flexor hallucis longus

onto the inferior margin of the medial epicondyle superficial to the ulnar nerve (Fig. 60.8). The location within the tight confines of the osseofibrous cubital tunnel may lead to compression of the ulnar nerve at the elbow following exercise or at rest when combined with other space-occupying lesions such a ganglion cyst.[18,19] The ulnar nerve may be compressed more distally along its course by the accessory abductor digiti minimi (AADM) muscle in Guyon's canal (Fig. 60.9).[20] This short muscle arises from the palmaris longus tendon and antebrachial fascia and passes into Guyon's canal alongside the ulnar artery and nerve before inserting onto the base of the proximal phalanx of the little finger via the ulnar side of the metacarpophalangeal joint capsule.[21]

Accessory muscles of the lower limb include the tensor fasciae suralis muscle, accessory popliteus, accessory peroneal muscles, flexor digitorum accessorius longus, peroneocalcaneus internus, accessory soleus and the tibiocalcaneus internus muscles (Table 60.4).[13] The most commonly encountered clinically relevant accessory lower limb muscles are accessory soleus and peroneus quartus muscles. The accessory soleus originates from the deep surface of the soleus proper and/or from the fibula and soleal line of the tibia, descends deep to soleus and inserts onto the superior or medial surface of the calcaneus either via muscle directly onto bone or via a tendon (Fig. 60.10). The muscle usually presents clinically as a posteromedial mass behind the ankle but has been described as a cause of posteromedial ankle pain.

The peroneus quartus muscle arises from the distal fibula or peroneal muscles and descends posteromedial to the peroneal tendons to insert in a variable fashion on the posterolateral side of the ankle.[22] The most common site of insertion is the retrocalcaneal eminence of the calcaneus but it may insert on the peroneal tubercle, the cuboid bone or the peroneal tendons.[23] It is important to recognise a peroneus quartus muscle on ultrasound as it may be confused with a longitudinal tear of the peroneus brevis tendon. Longitudinal tears of the peroneus brevis tendon usually result in two components of roughly equal size, whereas a peroneus quartus tendon is significantly smaller than peroneus brevis (Fig. 60.11).[24]

ACUTE SKELETAL MUSCLE INJURY

Traumatic skeletal muscle injury may be divided into direct (extrinsic) and indirect (intrinsic) types.

Direct muscle injury

When an external force is applied to muscle a direct injury occurs. Penetrating trauma with a sharp or high-velocity object leads to laceration of the muscle, whereas blunt trauma classically results in muscle contusion, haematomas and later myositis ossificans.

Muscle laceration

Penetrating muscle trauma usually results in a linear laceration that heals by scar formation and may lead to muscle weakness or loss of function.[25] The laceration is initially identified as a hypoechoic linear abnormality crossing the perimysial echogenic striae of the muscle and may involve more than one muscle (Fig. 60.12). In the healing or healed phase scar tissue around the laceration is an echogenic linear abnormality which may cross the fascial planes, differentiating it from normal tendons or aponeuroses.

Muscle contusion

Sports-related blunt trauma classically occurs in those muscles closely applied to bone, e.g. vastus intermedius. During a direct blow to the front of the thigh, the superficial quadriceps muscles are able to dissipate the energy laterally during the compression but the majority of the force is dissipated away from the bone via the vastus intermedius muscle, resulting in local haemorrhage which may extend through the perimysial layers forming an intramuscular contusion (Fig. 60.13). Imaging shows that all layers are affected but the maximum injury occurs in the muscle closest to bone.

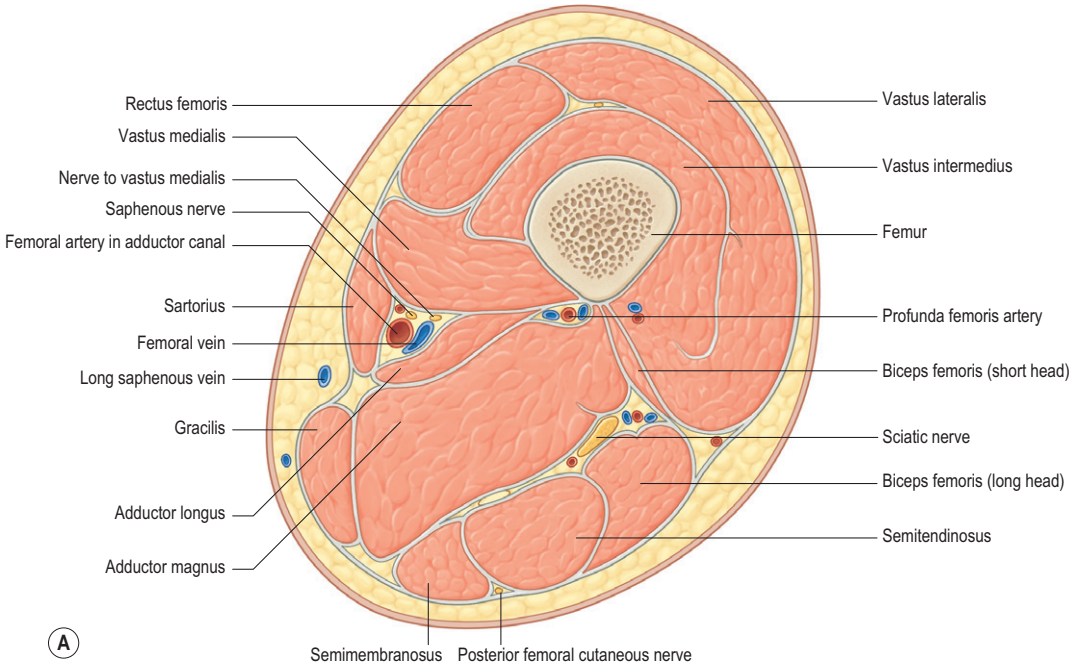

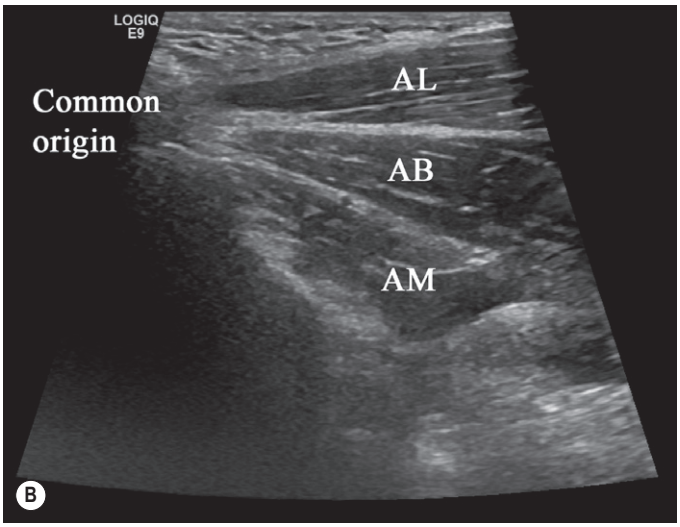

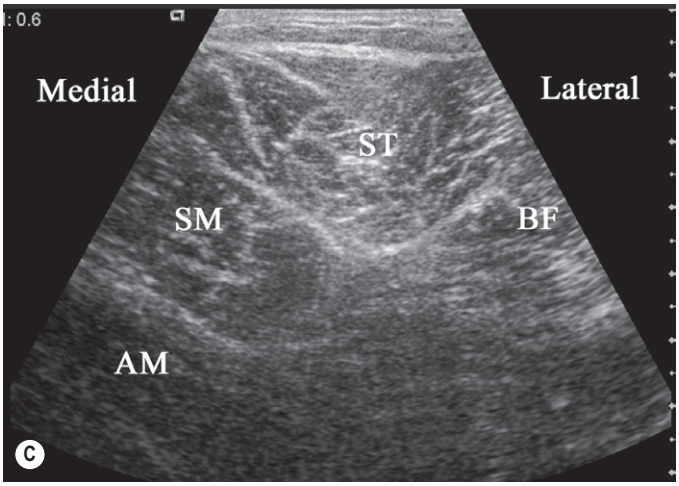

Figure 60.6 **Thigh. A:** Line drawing of the compartmental anatomy of the thigh. The three compartments comprise the medial (adductor), posterior (hamstring flexor) and anterior (extensor). (Reproduced with permission from Standring S, et al. (eds), Gray's Anatomy, 40th edn, Edinburgh, Churchill Livingstone, 2008.) **B:** Transverse sonogram of the medial compartment of the thigh at the level of the pubis. AL, adductor longus; AB, adductor brevis; AM, adductor magnus. **C:** Transverse sonogram of the posterior compartment of the thigh. SM, semimembranosus; ST, semitendinosus; BF, biceps femoris; AM, adductor magnus.

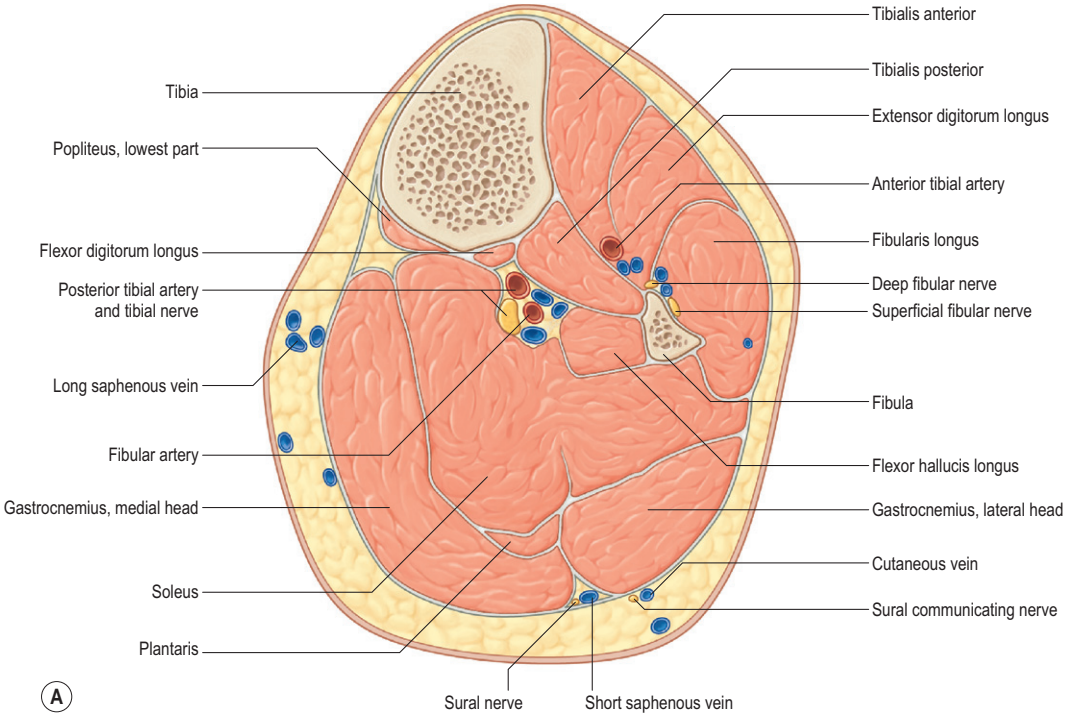

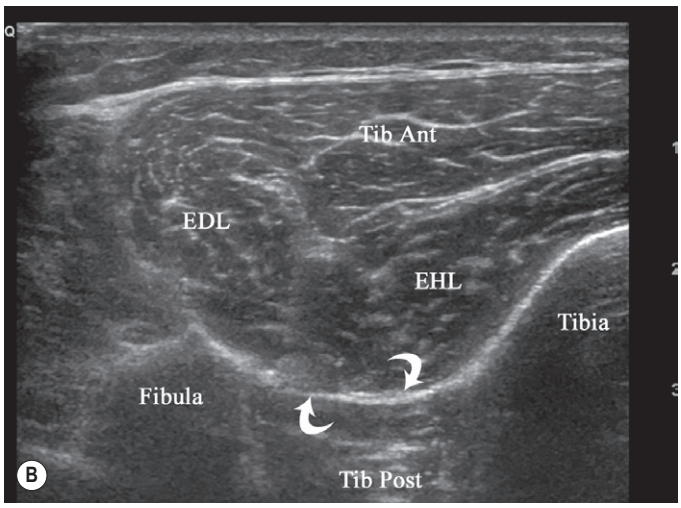

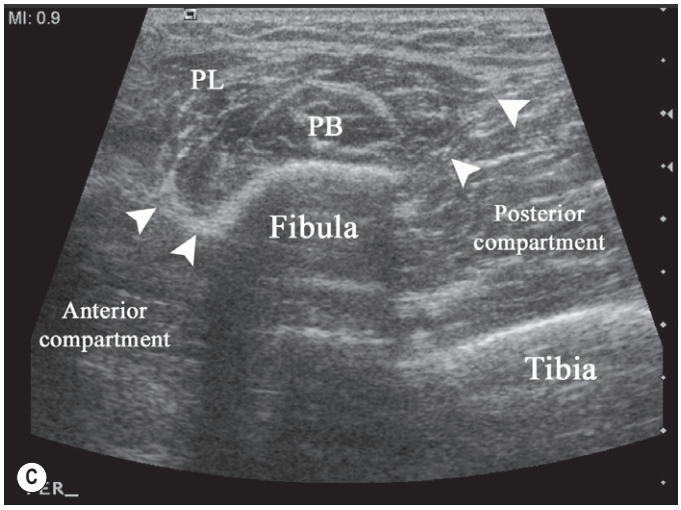

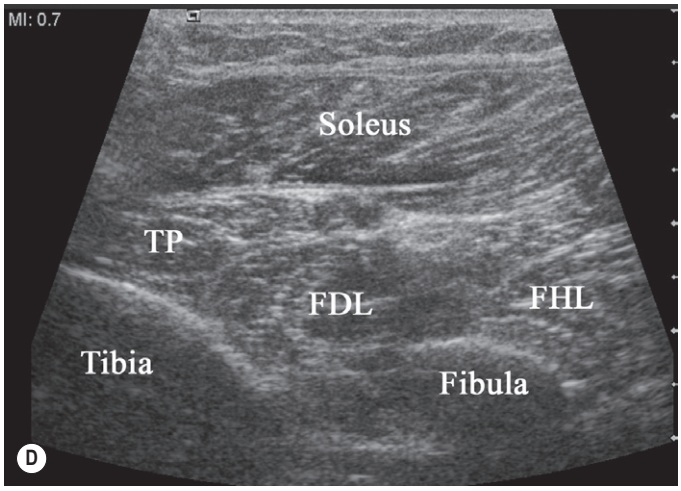

Figure 60.7 **Leg. A:** Line drawing of the compartmental anatomy of the leg. (Reproduced with permission from Standring S, et al. (eds), Gray's Anatomy, 40th edn, Edinburgh, Churchill Livingstone, 2008.) **B:** Transverse sonogram of the anterior compartment of the leg. Tib Ant, tibialis anterior; EHL, extensor hallucis longus; EDL, extensor digitorum longus. Note echogenic interosseous membrane (curved arrows). **C:** Transverse sonogram of the peroneal compartment of the leg. PL, peroneus longus; PB, peroneus brevis. Note anterior and posterior intermuscular septa (arrowheads). **D:** Transverse sonogram of the superficial posterior compartment of the leg. TP, tibialis posterior; FDL, flexor digitorum longus; FHL, flexor hallucis longus.

Table 60.3 Accessory muscles of the upper limb (adapted from Sookur et al.[13])

Name	Origin	Insertion	Prevalence	Clinical relevance
Additional heads of biceps brachii	1. Humeral shaft between coracobrachialis and brachialis muscles 2. Coracobrachialis insertion 3. Intertubercular sulcus 4. Slip passes to pronator teres posterior fascia	Biceps muscle belly	Rare	Slip to pronator teres may compress median nerve and brachial artery
Accessory brachialis	Medial mid-shaft of humerus	Common forearm flexor origin lateral epicondyle	Rare	Distal tendon may split to enclose and compress the median nerve
Anconeus epitrochlearis	Medial olecranon	Inferior surface medial humeral epicondyle superficial to ulnar nerve	11%	Ulnar nerve compression in cubital tunnel
Accessory head of flexor pollicis longus	1. Humeral medial epicondyle 2. Coronoid process 3. Dual origin from 1 and 2 4. FDS muscle belly	Base of thumb	45–66%	Compression of anterior interosseous nerve or median nerve
Accessory flexor digitorum superficialis indicis (aFDSI)	FDS tendon adjacent to transverse carpal ligament May have muscle belly in forearm	Index finger A1 pulley	Rare	Palmar mass Median nerve compression in carpal tunnel
Accessory abductor digiti minimi (aADM)	1. Antebrachial fascia and runs into Guyon's canal 2. Palmaris longus muscle	Ulnar base of 5th metacarpal	24%	Ulnar nerve compression Guyon's canal
Flexor carpi radialis brevis vel profundus	Volar aspect distal radius	1. Capitate 2. Bases of 3rd and 4th metacarpals	Rare	Carpal tunnel syndrome
Extensor digitorum brevis manus (EDBM)	1. Dorsal wrist capsule 2. Distal radius 3. Deep carpal fascia	Extensor hood index and/or middle finger	1.6%	Soft tissue swelling dorsum wrist
Accessory extensor carpi radialis brevis (ECRB)	Medial aspect of normal ECRB	1. Base of 2nd/3rd metacarpal 2. Extensor hood index/middle finger	Rare	Soft-tissue mass Mimics a split ECRB tendon on US/MRI
ECR intermedius	Between ECRB and extensor carpi radialis longus (ECRL) origins	1. Base of 2nd/3rd metacarpal 2. Abductor pollicis longus muscle	12–24%	Mass effect
ECR accessorius	ECRL and passes deep to extensor retinaculum in its own compartment	Abductor pollicis longus/brevis muscle	Extremely rare	Mass effect

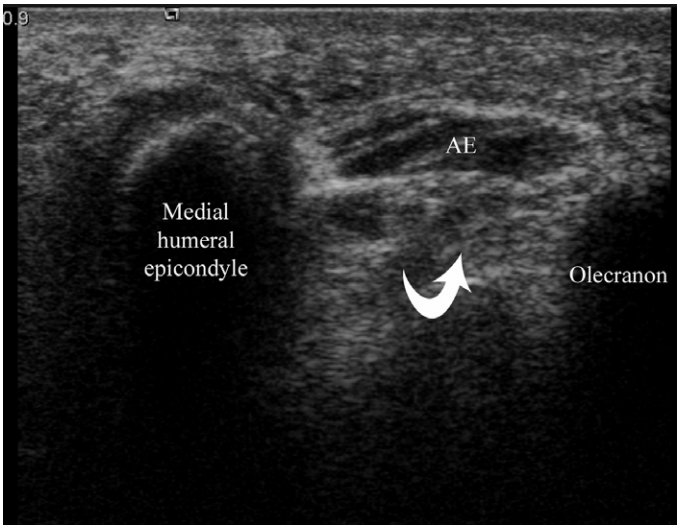

Figure 60.8 Transverse sonogram of the posteromedial elbow demonstrating the presence of an anconeus epitrochlearis (AE) overlying the ulnar nerve (arrow). This accessory muscle may compress the ulnar nerve within the cubital tunnel.

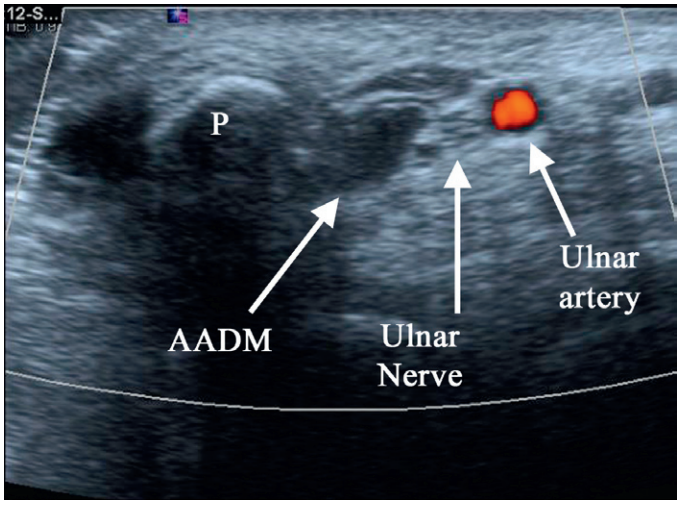

Figure 60.9 Transverse sonogram of the ulnar wrist demonstrating the presence of an accessory abductor digiti minimi (AADM) muscle within Guyon's canal. This accessory muscle may be associated with ulnar nerve compression. P, pisiform.

Table 60.4 Accessory muscles of the lower limb (adapted from Sookur et al.[13])

Name	Origin	Insertion	Prevalence	Clinical relevance
Accessory slips of medial and lateral gastrocnemei	Medial head: intercondylar notch Lateral head: posterior femoral condyle and remains lateral to popliteal vessels	Slips may enclose the popliteal vessels	Medial head slip seen in 21% patients with PAES Lateral head slip seen in 30% patients with PAES	Popliteal artery entrapment syndrome (PAES)
Tensor fascia suralis muscle	Distal semitendinosus muscle. Passes into the popliteal fossa between the semimembranosus and biceps femoris muscles	1. Posterior fascia of leg 2. Medial head gastrocnemius 3. Superficial part of Achilles tendon	Not defined	Popliteal soft tissue mass
Accessory popliteus	Lateral gastrocnemius origin	Posteromedial joint capsule	Rare	?compressive effect
Peroneus tertius	Anterior compartment of leg. Anterior fibula and anterior EDL muscle	Base dorsum 5th metatarsal	83–95%	Snapping over lateral talar dome
Peroneus quartus	Variable Peroneus brevis muscle is most common	Medial and posterior to other peroneal tendons with variable insertion: retrocalcaneal eminence, peroneal tubercle, peroneus longus tendon, cuboid, inferior peroneal retinaculum	13–26%	Mimics a peroneal tendon split on axial imaging
Flexor digitorum accessorius longus (FDAL)	1. Medial margin tibia 2. Deep posterior fascia 3. Any structure of the posterior compartment	Course beneath flexor retinaculum into tarsal tunnel Inserts into quadratus plantae muscle or flexor digitorum longus tendon	6–8%	Tarsal tunnel syndrome (FDAL found in 12% of cases)
Peroneocalcaneus internus (PCI)	Lower fibula	Runs posterolateral to and displaces flexor hallucis longus in the tarsal tunnel Inserts onto medial aspect calcaneus below sustentaculum tali	1%	Tarsal tunnel syndrome Posterior ankle impingement syndrome
Accessory soleus	1. Anterior surface soleus 2. Fibula 3. Soleal line tibia	Descends anterior or anteromedial to Achilles tendon. Variable insertion which may be fleshy or tendinous onto: Achilles tendon Upper surface os calcis Medial aspect os calcis	0.7–5.5%	Soft tissue mass Pain: 1. Local compartment syndrome 2. Posterior tibial nerve compression
Tibiocalcaneal internus (TCI)	Medial crest tibia	Through tarsal tunnel onto medial surface of os calcis	Rare	Mimics FDAL and accessory soleus

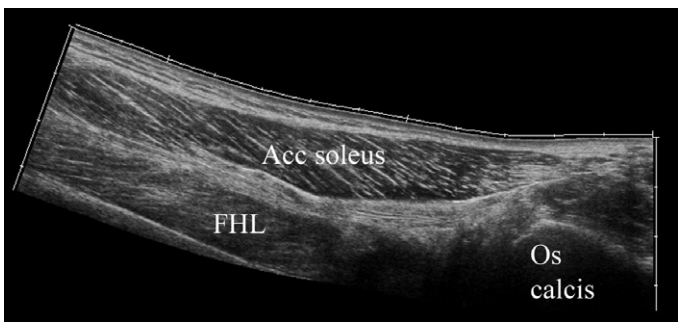

Figure 60.10 Extended longitudinal field-of-view sonogram of the accessory soleus. Note large muscle bulk extending down to the level of the os calcis. FHL, flexor hallucis longus.

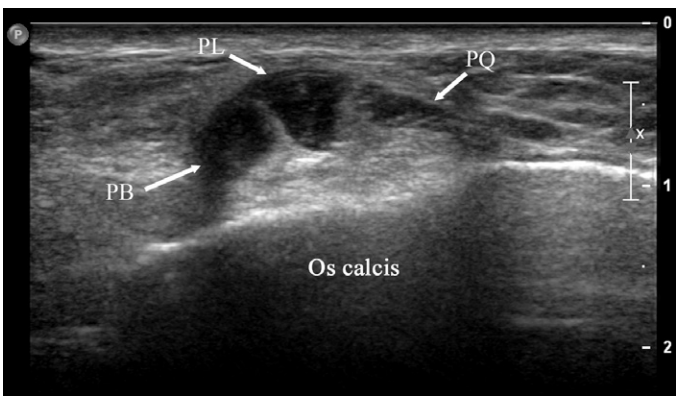

Figure 60.11 Transverse sonogram of the peroneal tendons just proximal to the retrocalcaneal eminence on the lateral margin of the os calcis. Note the presence of three tendons: PB, peroneus brevis; PL, peroneus longus; PQ, peroneus quartus. The tendons are conspicuous because they are hypoechoic due to the effect of anisotropy.

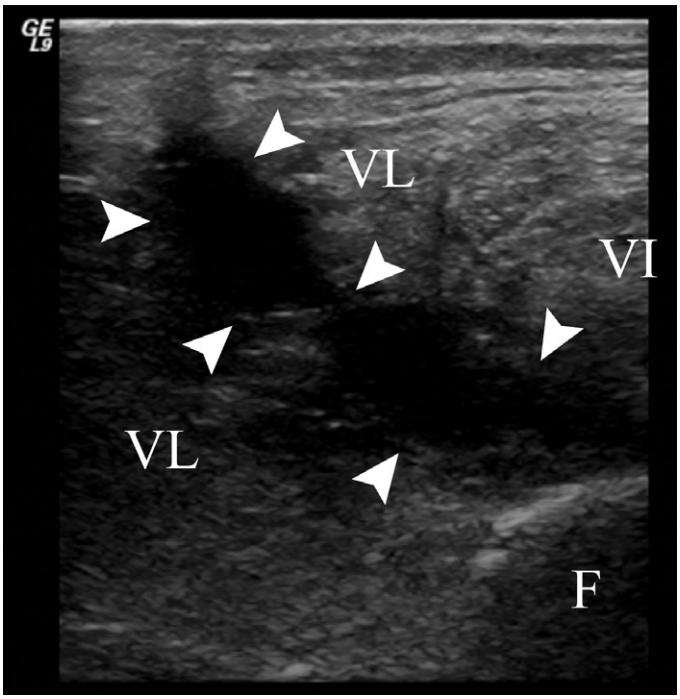

Figure 60.12 Muscle laceration. Transverse sonogram of laceration (arrows) of the vastus lateralis (VL) and vastus intermedius (VI) muscle tissue down to the level of the femur (F).

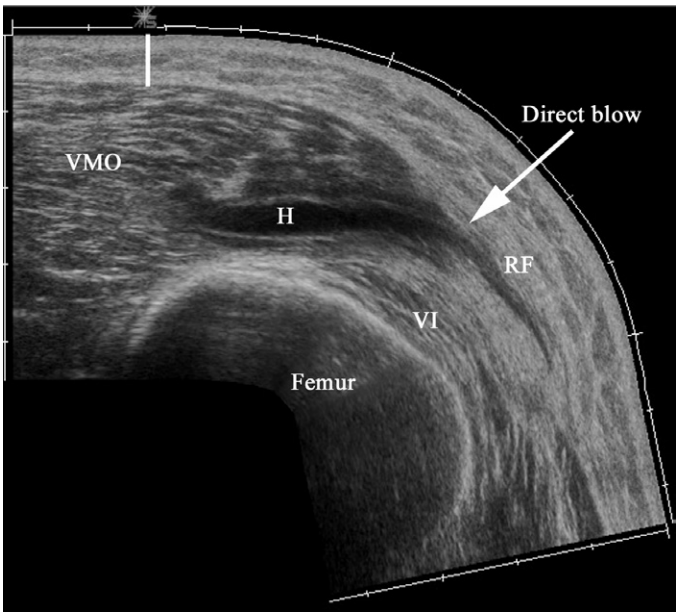

Figure 60.13 Muscle contusion. Transverse extended-field-of-view sonogram of the anterior thigh following a direct blow to the thigh. Note that all layers in the line of the externally applied force are injured although the greatest injury is at the vastus intermedius (VI). The skin and subcutaneous tissues are thickened (cf. more medial skin/subcutaneous thickness (straight line)). The rectus femoris (RF) and vastus intermedius (VI) demonstrate global increased reflectivity consistent with muscle contusion. The blow was of sufficient force to cause a local haematoma (H) formation. VMO, vastus medialis obliquus.

A three-stage *clinical* grading system has been described which may be used to direct treatment and provide a prognosis of muscle contusion.[26]

- *Mild contusion.* Range of motion loss less than one-third normal. Average loss of activity is 6 days.
- *Moderate contusion.* Range of motion loss one-third to two-thirds of normal. Average loss of activity is 56 days.
- *Severe contusion.* Greater than two-thirds loss of range of motion. Average loss of activity is more than 60 days.

On ultrasound, a contusion is seen as an ill-defined area of hyperechogenicity within the muscle, which crosses fascial boundaries (Fig. 60.13). In the hyperacute situation, the injured muscle initially appears swollen and may be isoechoic with adjacent unaffected muscle.[27]

If there is significant separation of muscle fibres the injury may result in an intramuscular or intermuscular haematoma. In the first 1–2 days, intramuscular haematoma may appear as an irregularly outlined muscle laceration separated by hypoechoic fluid with marked increased reflectivity in the surrounding muscle (Fig. 60.13). During this period, the haematoma may solidify and become hyperechoic to the surrounding muscle. After 3 days, the intramuscular haematoma starts to develop into a clearly defined hypoechoic fluid collection with an echogenic margin (Fig. 60.14). This echogenic margin gradually enlarges and 'fills in' the haematoma in a centripetal fashion, a process that may take several months to complete (Fig. 60.15).[28] After 4 weeks, the margin of the haematoma may start to calcify (see section on myositis ossificans below). If the haematoma is causing intense pain and/or exerts local mass effect on adjacent neurovascular structures, or is placing the limb at risk of compartment syndrome, then evacuation of the clot may be necessary. This can be performed under ultrasound guidance, in most cases usually 10–14 days following initial injury.[29]

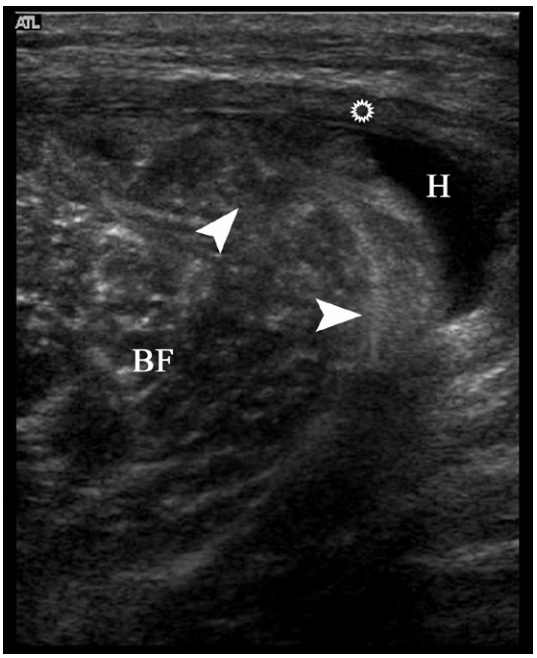

Figure 60.14 Transverse sonogram of posterior thigh demonstrating a myofascial tear (arrowheads) of the biceps femoris (BF) muscle with haematoma formation (H) deep to the fascia lata (asterisk).

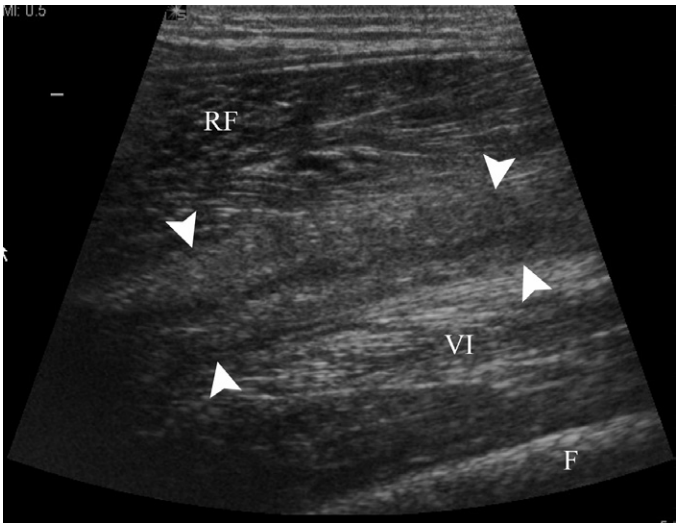

Figure 60.15 Longitudinal sonogram of the anterior compartment of the thigh demonstrating a healing haematoma between rectus femoris (RF) and vastus intermedius (VI). F, femur. The margins of the haematoma are echogenic (arrowheads).

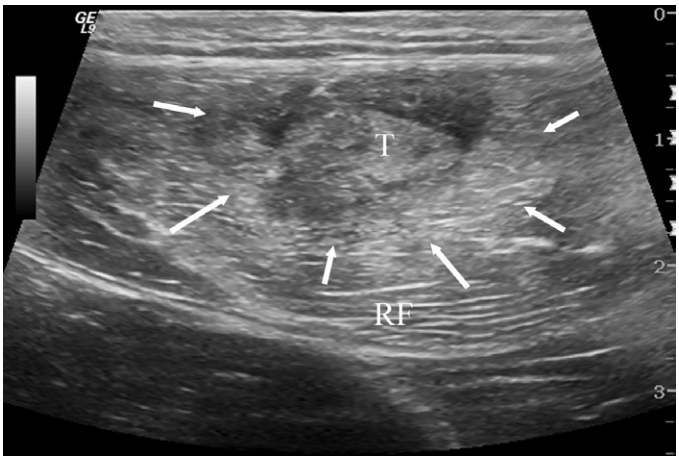

Figure 60.16 Muscle tear. Transverse sonogram of the anterior thigh in a professional soccer player. There is a tear of the rectus femoris muscle (RF) centred on the central tendon (T). The overall size of the tear measured 25% of the overall width of the muscle consistent with a grade II injury.

Sports-specific muscle strains

- Rectus abdominis – tennis serve
- External/internal oblique – cricket bowling
- Hamstring – sprinters
- Rectus femoris – soccer kicking
- Hip rotators – soccer/rugby twist/turn

Indirect muscle injury – muscle strain

Indirect injury usually occurs during periods of excessive eccentric muscle contraction and results in disruption of the myotendinous or myofascial unit, i.e. muscle strain, or delayed onset muscle soreness (DOMS).

Biomechanical aspects

Muscle contractions are classified as concentric, isometric or eccentric and during activity most active muscles exhibit all three types of contraction. The difference between these contraction types is illustrated by the movements involved in a 'biceps curl'. When the weight is lifted, the biceps brachii contracts and simultaneously shortens, i.e. it *concentrically* contracts. If the weight-lifter holds the weight at halfway, the muscle contracts but does not shorten, i.e., it *isometrically* contracts. However, when the weight is lowered, the biceps brachii still contracts but is passively lengthened, i.e., it *eccentrically* contracts. During such eccentric contractions, the muscle is at risk of disruption as the force of active contraction is added to the passive stretching force being applied to the muscle.

Clinical features

Muscle strain produces a characteristic clinical presentation of acute limb pain usually localised to a single muscle occurring during a period of eccentric muscle contraction. On clinical examination, depending on the size of the injury and the presence of a haematoma, a palpable defect may be present. The muscle will be weak and the patient will complain of pain during concentric contraction. Some muscle strains are 'sports-specific'.

In elite athletes, skeletal muscle injury is a major cause of prolonged loss of competitive activity and accounts for up to a third of all sports-related injuries.[30–32] The hamstring muscle complex of the posterior thigh is particularly susceptible to indirect trauma and is the most common site of muscle injury in UEFA Champions League footballers,[33] and elite rugby union players, resulting in an average loss of playing time of 17 days post injury.[34]

Risk factors include the older athlete and previous injury in the same muscle.[35] Specific predisposing risk factors may be athlete-related or muscle-specific. Athlete-related risk factors include male sex, improper warm-up and fatigue. Muscle-specific risk factors include muscles that have a high proportion of fast-twitch (type II) fibres, cross multiple joints, have complex anatomy or are subject to eccentric loading.[35]

Hence, the biceps femoris, rectus femoris and medial gastrocnemius are the most commonly strained muscles.[33,36]

Clinical grading system

The severity spectrum of muscle strain ranges from muscle soreness to complete myotendinous dissociation. Several grading systems have been described based on clinical examination and histology.[37,38] The most commonly used system has a three-step clinical grading score as follows:

- grade I strain: a small tear resulting in less than 5% loss of function
- grade II strain: a larger tear with 5–50% loss of function
- grade III: complete muscle–tendon or muscle–fascia separation
- grade IIIB: an occasionally used term to describe an avulsion fracture at a tendon attachment.

Strain location within the muscle

A muscle strain occurs when the stretching force applied to a muscle elongates it beyond its normal range of elasticity. The myotendinous junction is the weakest part of the muscle–tendon–bone unit (MTBU) and is the point at which most muscle tears occur (Fig. 60.16).[35] Muscle strains may occur elsewhere: at the myofascial surface (Fig. 60.14); intramuscular (not involving the tendon or fascia) (Fig. 60.17); or direct avulsion from bone. Myofascial injury is not uncommon in the thigh, accounting for up to 36% of hamstring strains. The biceps femoris muscle is particularly at risk.

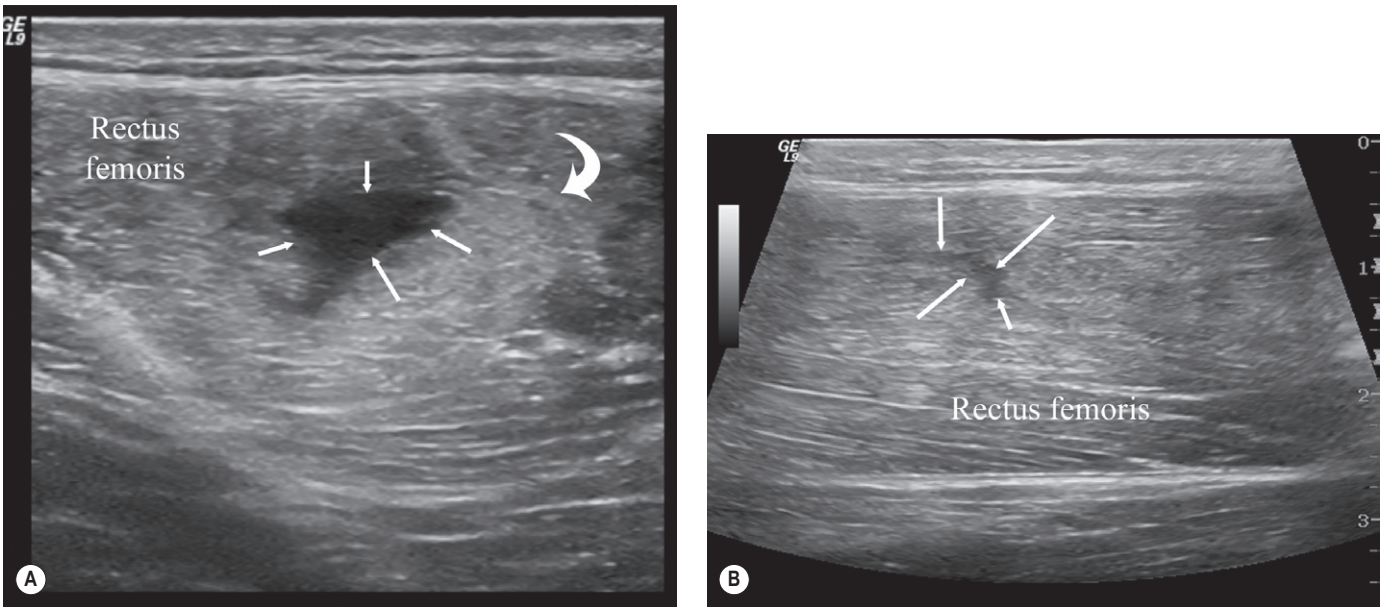

Figure 60.17 Intramuscular tear. A: Transverse sonogram of an intramuscular tear of the rectus femoris muscle. The tear is located medial to the central tendon (curved arrow), which is displaced laterally by the intramuscular haematoma (arrows). **B:** Longitudinal sonogram at 4 weeks following initial injury. Note that the haematoma has almost resolved (arrows).

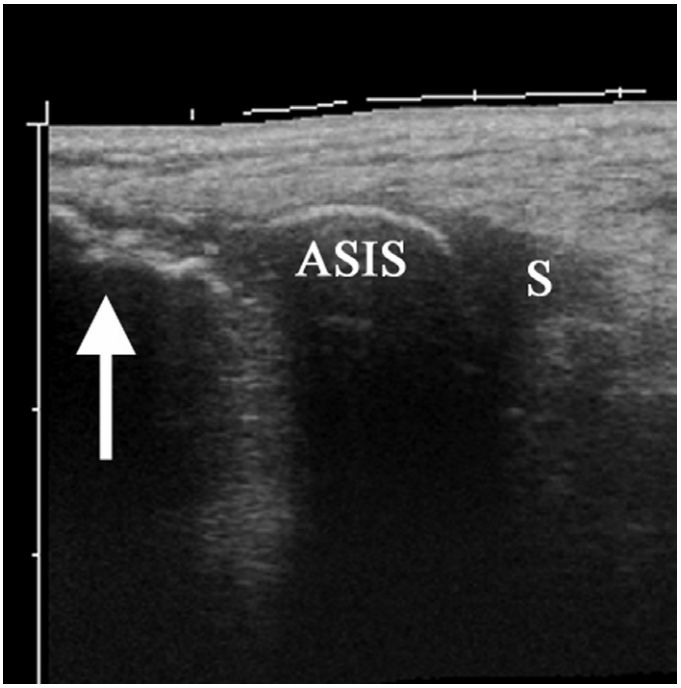

Figure 60.18 Avulsion injury. Longitudinal extended-field-of-view sonogram of the upper anterior thigh in an adolescent soccer player. The anterior superior iliac spine (ASIS) has been avulsed from the ilium (arrow) by the action of sartorius (S).

The tear usually occurs at the union of short and long heads, possibly due to differential contraction of the different components resulting in a distracting force at the myofascial surface.[39] Muscle strains away from the MTBU and the myofascial surface are rare and their pathophysiology is poorly understood (Fig. 60.17). Strains also occur at the muscle–bone interface when no tendon is present such as in pectineus and short head biceps femoris.[40]

In the paediatric immature skeleton, the weakest point of the MTBU is at the tendon–bone junction and therefore avulsion injuries of the apophysis are more common in this group (Fig. 60.18).[41]

Sonographic assessment of muscle strain

Information required on ultrasound muscle injury report:
- Muscle involved
- Tear characteristics
  - Grade
  - Size
  - Location within muscle
    Musculotendinous junction
    Myofascial junction
    Intramuscular (away from tendon and fascia)
    Proximal, middle or distal third
- Presence or absence of haematoma
- Underlying intramuscular scar present or absent

Clinical-sonographic correlation

In the assessment of muscle strain, sonography can be used to identify which muscles are involved, the grade and size of the tear, and the site of the tear in relation to the central tendon and myofascial surface. Sonography is as accurate as MRI in detecting the presence of a muscle injury at presentation.[39] MRI and sonographic correlation of the three-stage clinical grading system has been described.[42,43]

Grade I strain involves less than 5% of the muscle volume. Grade I strains may have a normal sonographic appearance or show focal or general areas of increased echogenicity (Fig. 60.19). Up to 50% may demonstrate generalised hyperechogenicity. Although there is no significant (<5%) separation of muscle fibres at the musculotendinous junction, perifascial fluid may be seen and may be hyperechoic due to the presence of blood in the extravascular space.

Grade II strain involves more than 5% and up to 50% of the muscle cross-sectional area. Disruption of the musculotendinous or myofascial junction results in local haematoma formation at the tear site. Intramuscular fluid collection and fibre disruption is the characteristic combination used to describe a grade II tear. On ultrasound, there is discontinuity of the echogenic perimysial striae

Muscle strain severity grading system

Grade	Clinical findings	MRI findings	US findings
I	<5% loss of function	'Feather-type' pattern of oedema within the muscle Centred on myotendinous or myofascial junction and radiating along muscle fibres Little or no perifascial fluid	May be normal Focal or generalised areas of increased reflectivity within the muscle Centred on myotendinous or myofascial junction Little or no perifascial fluid
II	5–50% loss of function	Focal disruption of normal fibrillar pattern involving between 5% and 50% of the muscle volume Centred on myotendinous or myofascial junction Moderate volume of perifascial fluid Muscle oedema as in grade I	Marked focal increased reflectivity within muscle Centred around focal area of fibrillar disruption at musculotendinous or myofascial junction Moderate perifascial fluid
III	>50% loss of function	Extensive muscle oedema Complete myotendinous separation Fluid in tear gap Large perifascial fluid	Complete myotendinous separation Fluid in tear gap 'Bell-clapper' sign Large perifascial fluid

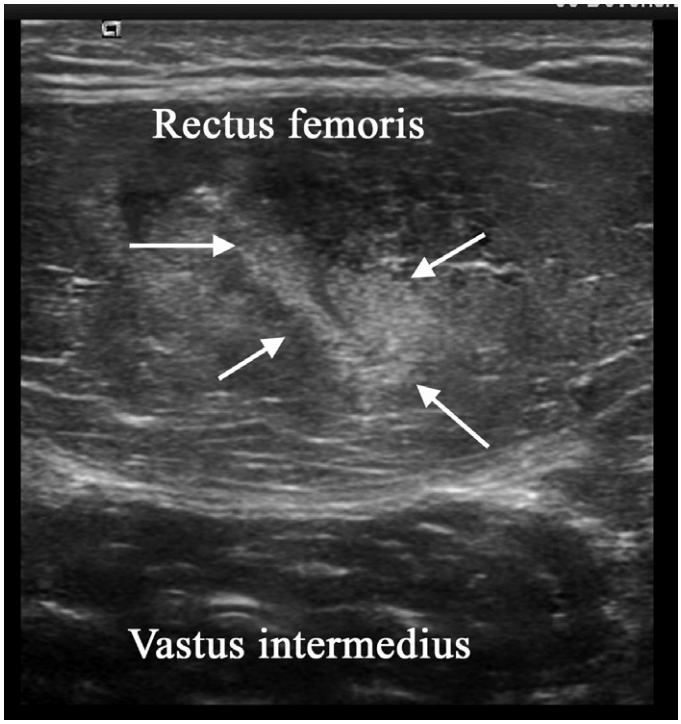

Figure 60.19 Transverse sonogram of the rectus femoris muscle demonstrating a grade I musculotendinous junction tear (arrows).

either at the myotendinous or myofascial junction (Fig. 60.16).[44] An intramuscular fluid collection may be seen with a surrounding hyperechoic halo. Hypervascularity around the disrupted muscle fibres may increase conspicuity if colour Doppler sonography is used. Partial retraction of muscle fibres may produce a mass-like effect clinically and dynamic scanning during contraction may increase the conspicuity of the tear by promoting fluid movement into the perifascial space or by increasing the mass-like effect of the tear.[22] Intermuscular and perifascial fluid collections are common in grade II injuries.

'Tennis leg', a subtype of grade II strain, includes partial detachment of muscle from the adjacent fascia or aponeurosis that it shares with another muscle. This occurs most commonly at the

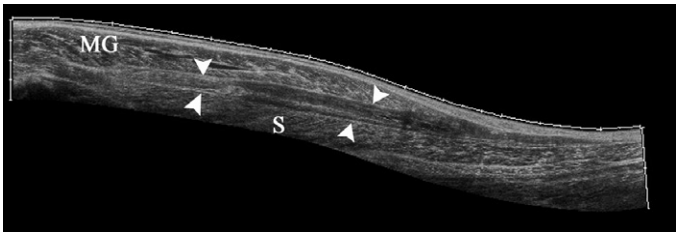

Figure 60.20 Longitudinal extended-field-of-view sonogram of a case of 'tennis leg' (arrowheads). MG, medial head of gastrocnemius; S, soleus.

aponeurosis between the medial gastrocnemius and soleus muscles[45] (Fig. 60.20). It typically occurs in the more mature athlete or the 'weekend warrior' and is only infrequently seen in elite athletes. Tennis leg presents with sudden-onset calf pain during a period of eccentric muscle contraction, typically during the push-off phase of a sudden movement. The condition clinically mimics a high Achilles tendon rupture as a palpable and audible 'snap' are common presenting features. Deep venous thrombosis is both a differential diagnosis and a complication of this condition and assessment of the calf veins at the time of the scan is mandatory.[46]

Grade III strain involves complete myotendinous dissociation or tendo-osseous avulsion. Surgery is rarely required but has been advocated in avulsion injuries with more than 2–3 cm of retraction (Fig. 60.21).[38] Ultrasound demonstrates complete discontinuity of the muscle fibres at the myotendinous junction and haematoma in the gap. Occasionally, haematoma obscures an avulsed tendon end on MRI whilst sonography can readily separate the two. The surrounding muscle is hyperechoic and intermuscular, perifascial and subcutaneous fluid collections are common (Fig. 60.22). On dynamic scanning, there is bunching of the torn muscle ends. Retracted echogenic muscle fragments surrounded by hypoechoic haematoma result in the 'bell-clapper' sign, a specific finding for muscle strain (Fig. 60.23). Although more common in grade III injuries, it may also be seen in grade II tears.[47]

Repeat sonography may be used to assess haematoma resolution and muscle tear healing and may guide the patient's rehabilitation programme to try to prevent re-injury (Fig. 60.24).[48]

Delayed-onset muscle soreness

Delayed-onset muscle soreness (DOMS) is usually observed 12–24 hours following unaccustomed strenuous exercise but may also be

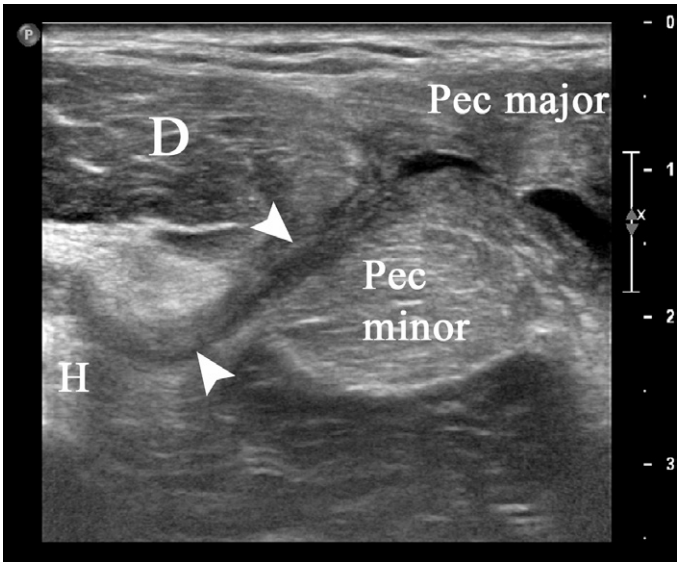

Figure 60.21 Transverse sonogram of surgically proven grade III tear of the pectoralis major muscle–tendon junction (arrowheads). D, deltoid; H, humerus.

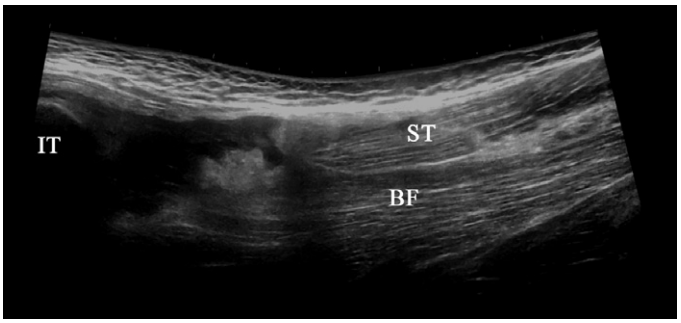

Figure 60.22 Longitudinal extended-field-of-view sonogram of the hamstring compartment demonstrating a grade III tear of the common hamstring origin from the ischial tuberosity (IT). ST, semitendinosus; BF, biceps femoris.

seen in elite athletes, typically during pre-season when training intensity is increased rapidly or in the early post-rehabilitation phase following injury. It typically affects multiple limbs and is associated with excessive eccentric muscle contractions. The severity of symptoms correlates with the intensity and duration of the activity.[49] The soreness increases to a peak between 24 and 72 hours then subsides by 7 days.[50] Histologically, there is damage to the connective tissue elements of the muscle, disruption of myofibrils and accumulation of interstitial fluid.[51] Myofibrillar repair begins at 3 days and is complete by 7 days.[52] MRI may demonstrate increased intramuscular signal on fat-suppressed fluid-sensitive sequences, similar in appearance to grade I muscle strain, but typically affects more than one muscle and possibly more than one compartment.[53] Ultrasound may be normal, or demonstrate geographical hyperechogenicity affecting several muscles across different compartments. Imaging alone may not be able to distinguish DOMS from grade I muscle strain and clinical correlation is required. DOMS classically presents at 24–48 hours and completely resolves after 4–5 days with conservative treatment, whereas a grade I strain will present acutely and takes 1–2 weeks to resolve.

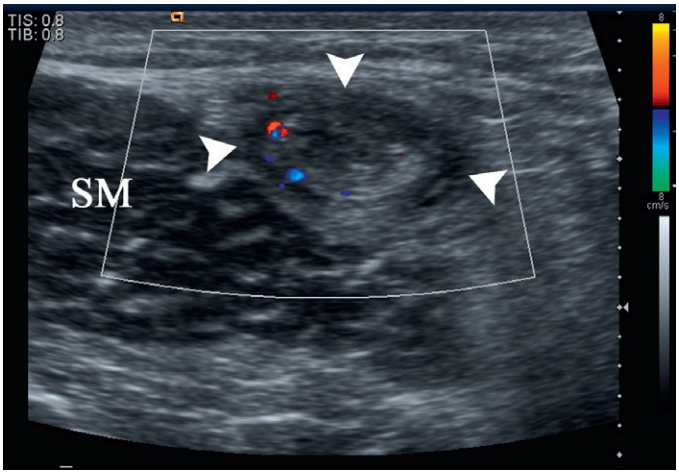

Figure 60.23 'Bell-clapper' sign. Transverse sonogram demonstrating a biceps femoris tear with tendon retraction surrounded by hypoechoic haematoma (arrows). SM, semimembranosus.

Prognostic value of sonography in acute muscle tear

MRI features of hamstring muscle strain associated with a prolonged recovery time include complete myotendinous transection, muscle tear involving more than 50% of the cross-sectional area or volume of muscle, deep muscle tears, distal tears, ganglion cyst-type fluid collections and intramuscular haemorrhage.[39,54] The location of the tear within the muscle, and the presence of a fluid collection or intramuscular haemorrhage do not correlate with delayed return to competitive activity.[39] Sonography can be used to predict recovery time following muscle injury as measurement of affected cross-sectional area is equivalent on sonography and MRI.[36] The location of the tear within the length of the muscle may have prognostic value, although the data regarding this is conflicting.[36,39,54]

Following a muscle strain, the risk of re-injury is high, particularly in the first 8 weeks after injury.[55,56] Recurrent strains tend to be larger than the original injury.[57] Unfortunately, the same imaging criteria used to assess recovery time do not appear to correlate with risk of recurrent injury and clinical factors appear to be more significant.[58]

CHRONIC MUSCLE INJURY

Most acute muscle injuries heal without any long-term sequelae but chronic complications may occur and include intramuscular scar formation, myositis ossificans (post-blunt trauma), fatty atrophy of muscle, myofascial hernia (post-penetrating trauma) and acute compartment syndrome. Chronic non-exertional compartment syndrome does not usually follow muscle trauma but is a recognised cause of recurrent muscle pain and will be considered in this section.

Chronic intramuscular scar/fibrosis

Muscle tears heal by a combination of muscle regeneration and scar formation. In larger tears, muscle regeneration may be insufficient and intramuscular fibrosis may dominate the repair process. The presence of an intramuscular scar alters the normal muscle contraction vector, reducing strength and increasing fatigue.[48,59] The combination of altered muscle biomechanics and increased muscle fatigue results in an increased risk of re-injury.[60,61]

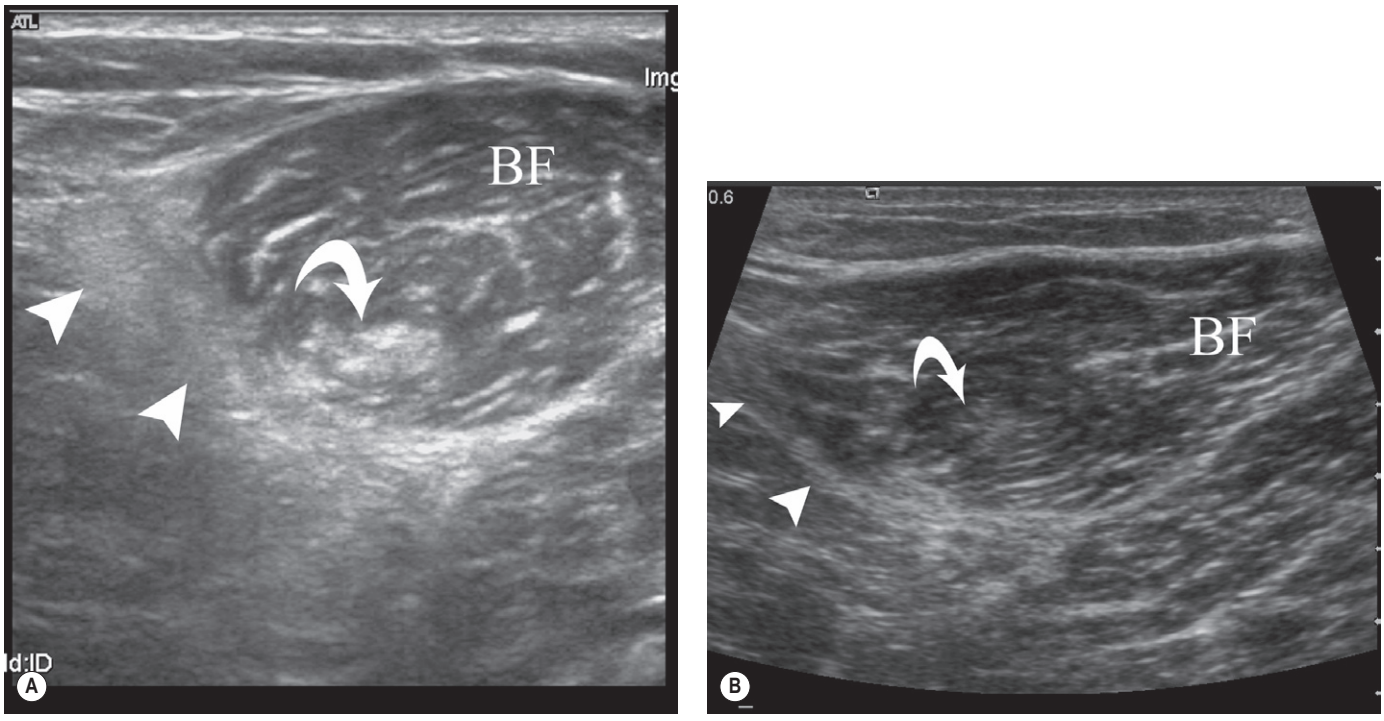

Figure 60.24 **Tear follow-up. A:** Transverse sonogram demonstrating a tear of the biceps femoris (BF) musculotendinous junction (curved arrow) with adjacent myofascial haematoma (arrowheads). **B:** Six weeks post injury in same position. Note how the tendon is now of normal reflectivity (curved arrow) and that the haematoma has resolved (arrowheads).

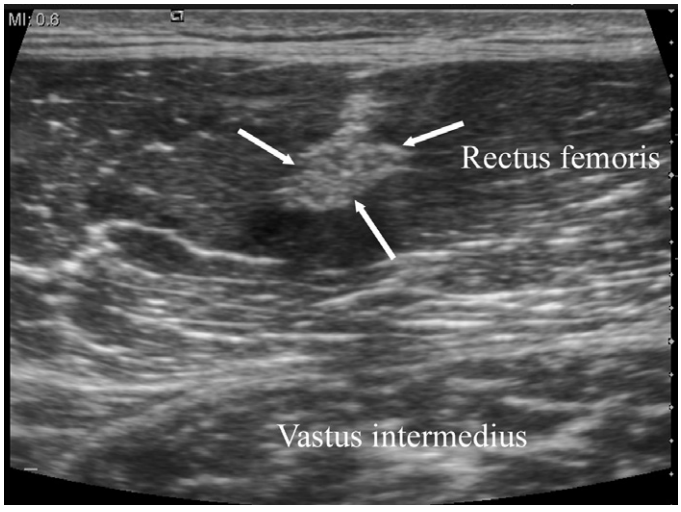

Figure 60.25 **Intramuscular scar.** Transverse sector-mode sonogram demonstrating stellate hyperechoic scar at the musculotendinous junction (arrows).

On ultrasound, an intramuscular scar appears hyperechoic, or heterogeneous hypoechoic, linear or stellate adherent to the musculotendinous junction (Fig. 60.25). The stellate form usually follows muscle contusion from a direct blow, whereas the linear form typically follows a muscle strain and commonly surrounds the musculotendinous junction. In 'tennis leg', the scar may extend the length of the medial gastrocnemius–soleus aponeurosis (Fig. 60.26). On dynamic scanning, there may be distortion of normal muscle fibre movement at the scar with overall reduced elasticity of the muscle.[62]

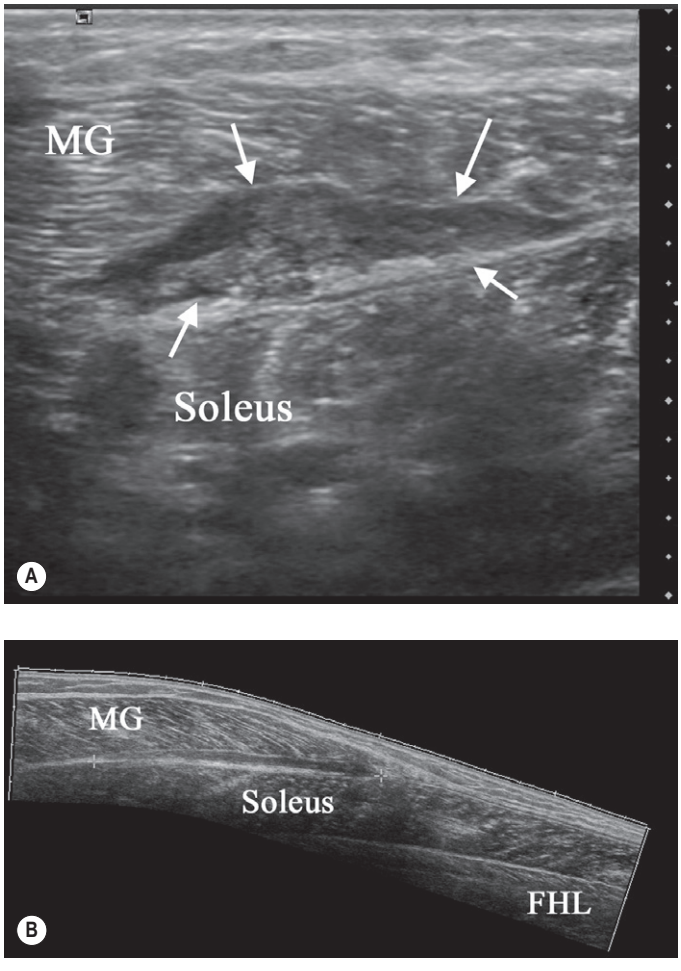

Figure 60.26 **Tennis leg scar** in **(A)** transverse and **(B)** longitudinal extended-field-of-view images. The length of the scar is marked with callipers on the image. MG, medial gastrocnemius; FHL, flexor hallucis longus.

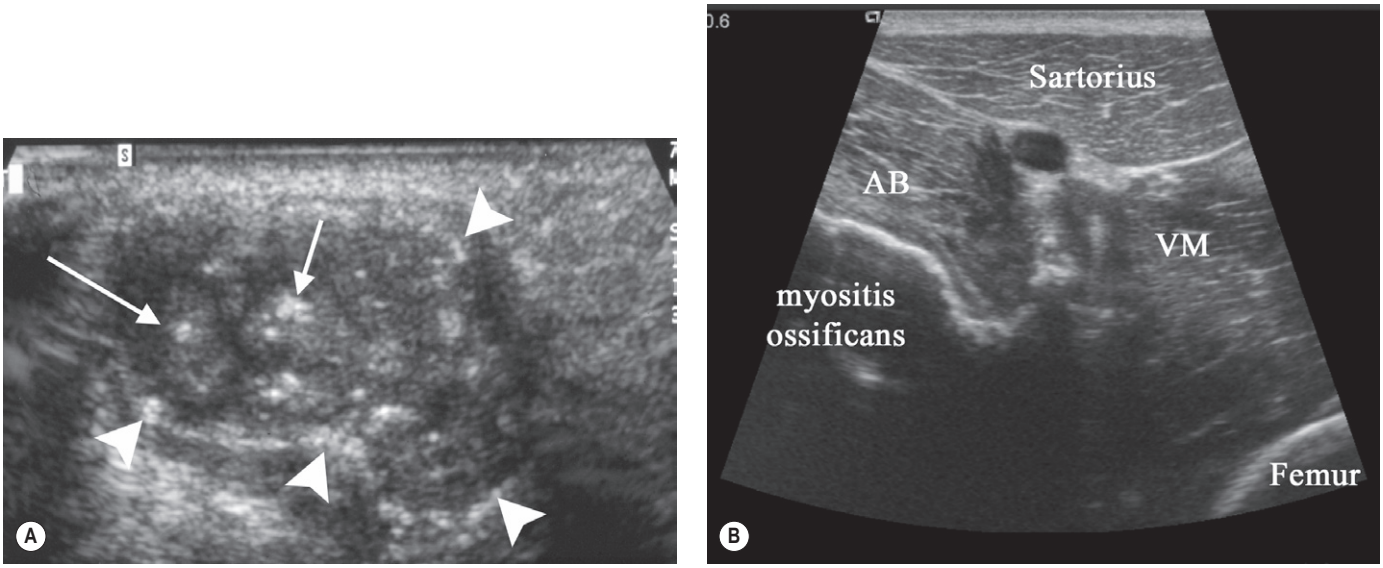

Figure 60.27 **Myositis ossificans. A:** Early stage. Note the peripheral laminar calcification (arrowheads) and the central punctuate calcification (arrows). **B:** Late stage. Transverse sonogram of the upper medial thigh demonstrating mature calcification within the adductor longus muscle. AB, adductor brevis; VM, vastus medialis.

Myositis ossificans

Heterotopic bone formation within muscle (myositis ossificans) may follow trauma, surgery, burns, neurological insults, and immobilisation.[63] Large muscle contusions and haematomas are particularly associated.[64,65] Myositis ossificans initially presents with swelling and loss of function disproportionate to the severity of the initial trauma. Three distinct phases are recognised clinically: (1) the acute or pseudo-inflammatory phase; (2) the subacute or pseudo-tumoral phase; and (3) the chronic healing phase.[66]

Stages 1 and 2 myositis ossificans typically demonstrate non-specific areas of muscle inflammation on both MRI and ultrasound. During the chronic healing phase, osteoid material is laid down at the margin of the haematoma in a lamellar fashion. Peripheral calcification is visible on computed tomography (CT) and plain radiographs at approximately 6 weeks and ossification occurs by 6 months.[67] Sonography detects the early stages of myositis ossificans 2 weeks before radiographic evidence of calcium is evident.[68] Ultrasound initially demonstrates a hypoechoic mass with sheets of peripheral echogenic material (Fig. 60.27).[69,70] Later, areas of coarse calcification casting acoustic shadows, often parallel to the adjacent diaphysis, may be seen.[71] CT is recommended to confirm the diagnosis in equivocal cases and is considered the gold-standard diagnostic imaging tool for myositis ossificans.

Fatty atrophy

Fatty replacement of muscle may follow a denervation injury but is also seen following intrinsic muscle injury. The detection of fatty atrophy in muscle can be challenging as initial findings of generalised increased muscle reflectivity are non-specific. However, assessment of muscle fatty atrophy may have important implications in post-surgical prognosis, particularly following rotator cuff repair.[72] Although MR imaging can clearly demonstrate changes in muscle fat content, a confident diagnosis of fatty atrophy can be made on ultrasound if there is complete loss of clarity of the muscle contour, the normal muscle pennate pattern or the central tendon, and if there is significantly higher generalised reflectivity within the muscle compared to the adjacent non-injured muscle (Fig. 60.28).[73]

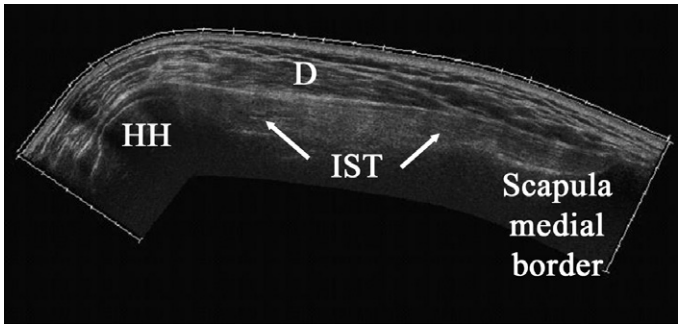

Figure 60.28 **Fat atrophy.** Extended-field-of-view transverse sonogram of the posterior shoulder demonstrating fatty atrophy of the infraspinatus (IST) muscle. Note the loss of normal fibrillar echo pattern and generalised increased reflectivity compared to the overlying deltoid (D). HH, humeral head. (Image courtesy of Dr Andrew Dunn, Consultant Musculoskeletal Radiologist, Royal Liverpool University Hospital.)

Myofascial hernia

Herniation of muscle tissue through the superficial epimysial surface produces a visible and palpable lump in the subcutaneous tissues mimicking a tumour. A myofascial hernia characteristically enlarges in the erect position or during active muscle contraction and reduces in the supine rested position. Hernias usually occur in the lower limb and classically affect the tibialis anterior muscle in young adults.[74] The defect in the fascia may be secondary to trauma but fascial weakness may also be seen in chronic compartment syndrome and at sites of enlarged perforating vessels.[75]

Careful scanning technique is essential. Liberal use of gel to produce a 'gel stand-off', gentle pressure by the transducer and scanning the patient in the standing or squatting position may be necessary to reveal the abnormality. The initial scan may reveal a focal defect or thinning of the superficial fascia at rest (Fig. 60.29). Active muscle contraction or raising the compartmental pressure

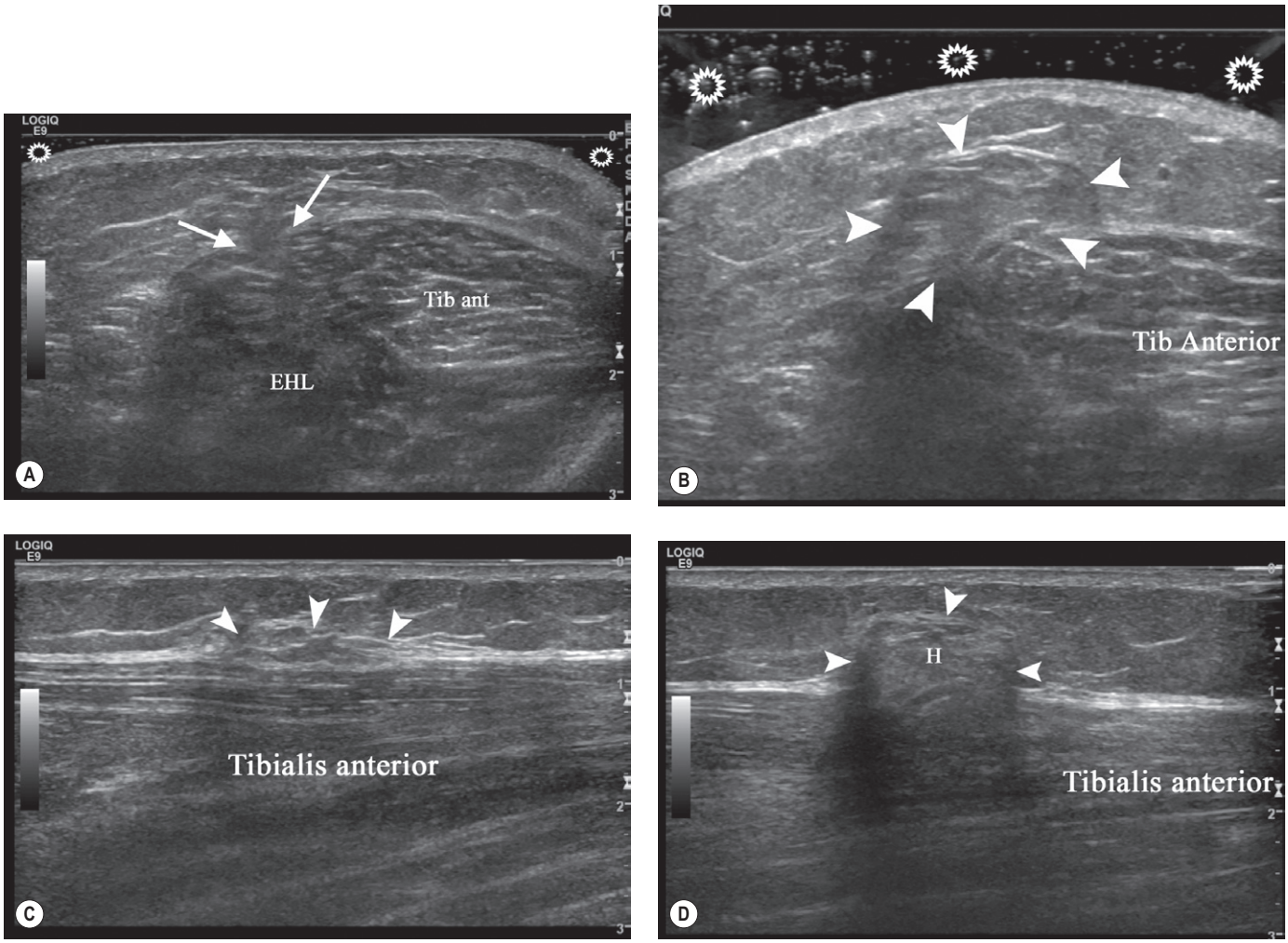

Figure 60.29 Myofascial hernia. Transverse sonogram **(A)** before and **(B)** after removing excess transducer pressure. When too much pressure is applied, the hernia is reduced. Using a good gel stand-off (asterisks) and reducing pressure allowed the hernia (arrowheads) to protrude. EHL, extensor hallucis longus. Longitudinal view in the relaxed **(C)** and contracted **(D)** state demonstrating how the muscle hernia (H) changes dynamically.

(e.g. by squatting), may make the margins of the defect more obvious as the herniated muscle tissue protrudes through the defect (Fig. 60.29). Herniated muscle fibres are usually hypoechoic and prominent arterial pulsations may be seen in the herniated muscle on Doppler imaging. If the fascia is focally weakened but not perforated, a generalised bulge of the muscle surface is seen during contraction.[76]

Treatment is usually limited to reassurance and compression stockings at most. Surgical closure of the fascial defect has been associated with development of acute compartment syndrome,[77] although this can be avoided by patching the defect.

Compartment syndromes

Acute compartment syndrome

When a patient complains of pain within a limb out of proportion to the degree of injury, it is important to consider compartment syndrome as a cause. Unfortunately, the diagnosis may not be made until there is irreversible muscle and nerve damage.[78]

Following muscle injury, the presence of interstitial oedema and local haematoma can lead to an increase in intra-compartmental pressure. The normal intra-compartmental pressure is between 0 and 4 mmHg. Once it rises above 15 mmHg, capillary blood flow is compromised and irreversible muscle ischaemia results, i.e. acute compartment syndrome. This complication is more common in those muscle compartments with tight fascial coverings, e.g. the superficial posterior and peroneal compartments of the leg, and the flexor compartment of the forearm.[79,80] In the first sonographic description of acute compartment syndrome, the authors described cystic replacement of the muscle by necrotic material with normal Doppler arterial and venous flow waveforms.[81] However, this feature is only seen in advanced cases of muscle necrosis. In the early stages of acute compartment syndrome, sonography only demonstrates the primary muscle injury and therefore plays a limited role in the diagnosis. Ultrasound may demonstrate generalised muscle oedema and dampened arterial waveforms on Doppler imaging but the gold standard diagnostic test for compartment syndrome is an intra-compartmental pressure measurement of greater than 15–20 mmHg at rest or 5 minutes after exercise.[82] Initial management may be conservative but if the compartmental pressure remains over 30 mmHg or continues to rise despite conservative management, or the patient complains of paraesthesia or weakness, surgical decompression will be necessary.[83]

Chronic exertional compartment syndrome

A separate but related condition is chronic exertional compartment syndrome (CECS). It presents with gradual-onset unicompartmental

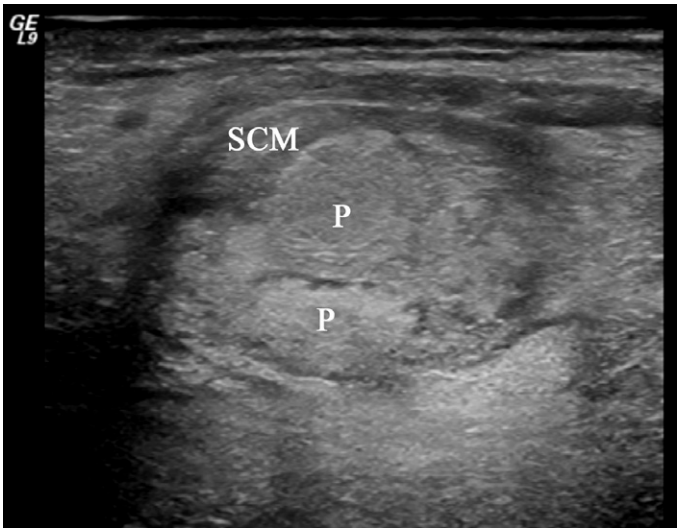

Figure 60.30 Pyomyositis. Transverse sonogram demonstrating echogenic pus (P) in the centre of the sternocleidomastoid muscle (SCM).

limb pain during exercise which gradually increases in severity until the activity is stopped. During strenuous exercise, muscle volume may increase by up to 20%, which in turn raises intra-compartmental pressure leading to muscle ischaemia.[84] Symptoms are frequently bilateral, recurrent and tend to occur at a consistent time after the onset of exercise.[85]

Sonography of the affected area is usually normal but occasionally the muscle will demonstrate generalised increased reflectivity with some sparing of the periphery.[22] Although changes in cross-sectional area of the muscle compartment have been described following exercise, there does not appear to be a significant difference in these changes in patients with CECS compared to control groups.[86,87]

Muscle infection

Most infections in muscle are secondary to an underlying medical condition such as osteomyelitis, trauma, diabetes mellitus, rheumatoid arthritis, leukaemia, lymphoma, sepsis, bleeding dyscrasia and autoimmune disease.[88] Infective myositis (pyomyositis) initially demonstrates non-specific heterogeneous increased reflectivity (Fig. 60.30).[89] If untreated, intramuscular abscesses may develop. Abscesses are well-defined hypoechoic fluid-collections with thick echogenic walls. Abscess contents may be highly echogenic due to inspissated fluid or haemorrhage, in which instance it may be necessary to perform biopsy of the lesion. The fluid may be septated or contain internal debris, and needle aspiration may be necessary for diagnostic and therapeutic purposes.[90]

REFERENCES

1. Sherman SE, D'Agostino B, Sibershatz H, et al. Comparison of past versus recent physical activity in prevention of premature death and ischaemic heart disease. Am Heart J 1999;138:900–907.
2. Ellekjaer H, Holmen J, Ellekjaer E, et al. Physical activity and stroke mortality in women: ten-year follow-up of the Nord-Trondelag Health Survey, 1984–1986. Stroke 2000;31:14–18.
3. Hu FB, Stampfer MJ, Colditz GA, et al. Physical activity and stroke risk in women. JAMA 2000;283:2961–2967.
4. Vlychou M, Teh J. Muscle injury. Curr Prob Diagn Radiol 2008;37:219–230.
5. Lin EC, Middleton WD, Teefey SA. Extended field of view sonography in musculoskeletal imaging. J Ultrasound Med 1999;18(2):147–152.
6. Jamadar DA, Jacobson JA, Caoili EM, et al. Musculoskeletal sonography technique: focused versus comprehensive evaluation. AJR Am J Roentgenol 2008;190(1):5–9.
7. Bianchi S, Abdelwahab IF, Mazzola CG, et al. Sonographic examination of muscle herniation. J Ultrasound Med 1995;14(5):357–360.
8. Martinoli C, Bianchi S, Derchi LE. Tendon and nerve sonography. Radiol Clin North Am 1999;37:691–711.
9. van Holsbeeck M, Introcasco J. Musculoskeletal ultrasound. 2nd edn. St Louis, MO: Mosby; 2001.
10. Barberie JE, Wong AD, Cooperberg PL, Carson BW. Extended field-of-view sonography in musculoskeletal disorders. AJR Am J Roentgenol 1998;171:751–757.
11. Kavanagh EC, Koulouris G, Parker L, et al. Does extended-field-of-view sonography improve interrater reliability for the detection of rotator cuff muscle atrophy? AJR Am J Roentgenol 2008;190(1):27–31.
12. Functional anatomy of the musculoskeletal system. In: Gray's anatomy. 39th edn. London: Elsevier; 2005.
13. Sookur PA, Naraghi AM, Bleakney RR, et al. Accessory muscles: anatomy, symptoms, and radiologic evaluation. RadioGraphics 2008;28:481–499.
14. Zeiss J, Guilliam-Haidet L. MR demonstration of anomalous muscles about the volar aspect of the wrist and forearm. Clin Imaging 1996;20:219–221.
15. Timins ME. Muscular anatomic variants of the wrist and hand: findings on MR imaging. AJR Am J Roentgenol 1999;172:1397–1401.
16. Okamoto M, Abe M, Shirai H, Ueda N. Diagnostic ultrasonography of the ulnar nerve in cubital tunnel syndrome. J Hand Surg (Br) 2000;25:499–502.
17. Zeiss J, Guilliam-Haidet L. MR demonstration of anomalous muscles about the volar aspect of the wrist and forearm. Clin Imaging 1996;20:219–221.
18. Hodgkinson PD, McLean NR. Ulnar nerve entrapment due to epitrochleo-anconeus muscle. J Hand Surg (Br) 1994;19(6):706–708.
19. Hsu RW, Chen CY, Shen WJ. Ulnar nerve palsy due to concomitant compression by the anconeus epitrochlearis muscle and a ganglion cyst. Orthopedics 2004;27(2):227–228.
20. Harvie P, Patel N, Ostlere SJ. Ulnar nerve compression at Guyon's canal by an anomalous abductor digiti minimi muscle: the role of ultrasound in clinical diagnosis. Hand Surg 2003;8:271–275.
21. Soldado-Carrera F, Vilar-Coromina N, Rodríguez-Baeza A. An accessory belly of the abductor digiti minimi muscle: a case report and embryologic aspects. Surg Radiol Anat 2000;22:51–54.
22. Saupe N, Mengiardi B, Pfirrman CW, et al. Anatomic variants associated with peroneal tendon disorders: MR imaging in volunteers with asymptomatic ankles. Radiology 2007;242:509–517.
23. Cheung YY, Rosenberg ZS, Ramsinghani R, et al. Peroneus quartus muscle: MR imaging features. Radiology 1997;202:745–750.
24. Schweitzer ME, Eid ME, Deely D, et al. Using MR imaging to differentiate peroneal splits from other peroneal disorders. AJR Am J Roentgenol 1997;168(1): 129–133.
25. Garrett Jr WE. Injuries to the muscle-tendon unit. AAOS Instr Course Lect 1988;37:275–282.
26. Jackson DW, Feagin JA. Quadriceps contusions in young athletes. Relation of severity of injury with treatment and prognosis. J Bone Joint Surg (Am) 1973;55(1):95–105.
27. Aspelin P, Ekberg O, Thorsson O, et al. Ultrasound examination of soft tissue injury of the lower limb in athletes. Am J Sports Med 1992;20:601–603.
28. Lehto M, Alanen A. Healing of a muscle trauma – correlation of sonographic and histological findings in an experimental study in rats. J Ultrasound Med 1987;6(8):425–429.
29. Fornage BD. Soft tissue masses: the underutilization of sonography. Semin Musculoskelet Radiol 1999;3(2):115–134.
30. Orchard J, Seward H. Epidemiology of injuries in the Australian Football League, seasons 1997–2000. Br J Sports Med 2002;36:39–44.
31. Yard EE, Schroeder MJ, Fields SK, et al. The epidemiology of United States high school soccer injuries, 2005–2007. Am J Sports Med 2008;36(10):1930–1937.
32. Arnason A, Sigurdsson SB, Gudmundsson A, et al. Risk factors for injuries in football. Am J Sports Med 2004;32:5S–16S.
33. Walden M, Hagglund M, Ekstrand J. Br J Sports Med 2005;39(8): 542–546.
34. Brooks JHM, Fuller CW, Kemp SPT, Reddin DB. Incidence, risk, and prevention of hamstring muscle injuries in professional rugby union. Am J Sports Med 2006;34:1297–1306.
35. Garrett WE. Muscle strain injuries: clinical and basic aspects. Med Sci Sports Exerc 1990;8:73.
36. De Smet AA, Best TM. MR imaging of the distribution and location of acute hamstring injuries in athletes. AJR Am J Roentgenol 2000;174: 393–399.

37. Ryan AJ. Quadriceps strain. Rupture and charley horse. Med Sci Sports Exerc 1969;1:106.
38. O'Donoghue D. Principles in the management of specific injuries. In: Treatment of injuries to athletes. 4th edn. Philadelphia: Saunders; 1984. p. 39–91.
39. Connell DA, Schneider-Kolsky ME, Hoving JL, et al. Longitudinal study comparing sonographic and MRI assessments if healing hamstring injuries. AJR Am J Roentgenol 2004;183:975–984.
40. Slavotinek JP, Verrall GM, Fon GT. Hamstring injury in athletes: using MR imaging measurements to compare extent of muscle injury with amount of time lost from competition. AJR Am J Roentgenol 2002;179:1621–1628.
41. Stevens MA, El-Khoury GY, Kathol MH, et al. Imaging features of avulsion injuries. Radiographics 1999;19:655–672.
42. De Smet AA, Fisher DR, Heiner JP, et al. Magnetic resonance imaging of muscle tears. Skeletal Radiol 1990;19(4):283–286.
43. Takebayashi S, Takasawa H, Banzai Y, et al. Sonographic findings in muscle strain injury: clinical and MR imaging correlation. J Ultrasound Med 1995;14:899–905.
44. Fornage BD. The case for ultrasound of muscles and tendons. Semin Musculoskelet Radiol 2000;4:375–390.
45. Bianchi S, Martolini C, Abdelwahab IF, et al. Sonographic evaluation of tears of the gastrocnemius medial head ('tennis leg'). J Ultrasound Med 1998;17:157–162.
46. Delgado GJ, Chung CB, Lektrakul N, et al. Tennis leg: clinical US study of 141 patients and anatomic investigation of four cadavers with MR imaging and US. Radiology 2002;224(1):112–119.
47. Fornage BD, Touche H, Segal P, Rifkin MD. Ultrasonography in the evaluation of muscular trauma. J Ultrasound Med 1983;2:549–554.
48. Taylor DC, Dalton JD, Seaber AV, Garrett WE. Experimental muscle strain injury. Early functional and structural deficits and the increased risk of reinjury. Am J Sports Med 1993;21(2):190–194.
49. Abraham WM. Factors in delayed muscle soreness. Med Sci Sports 1977;9(1):11–20.
50. Armstrong RB. Mechanisms of exercise-induced delayed onset muscular soreness: a brief review. Med Sci Sports Exerc 1984;16(6):529–538.
51. Newnham DJ, McPhail G, Mills KR, et al. Ultrastructural changes after concentric and eccentric contractions of human muscle. J Neurol Sci 1983;61(1):109–122.
52. Clarkson PM, Tremblay I. Exercise-induced muscle damage, repair and adaption in humans. J Appl Physiol 1988;65(1):1–6.
53. Nurenberg P, Giddings CJ, Stray-Gundersen J, et al. MR imaging-guided muscle biopsy for correlation of increased signal intensity with ultrastructural change and delayed-onset muscle soreness after exercise. Radiology 1992;184(3):865–869.
54. Pomeranz SJ, Heidt RS. MR imaging of the prognostication of hamstring injury. Radiology 1993;189:897–900.
55. Orchard JW. Intrinsic and extrinsic risk factors for muscle strain injuries in Australian football. Am J Sports Med 2001;29:300–303.
56. Orchard JW, Best TM. The management of muscle strain injuries: an early return versus the risk of recurrence. Clin J Sports Med 2002;12:3–5.
57. Koulouris G, Connell DA, Brukner P, Schneider-Kolsky M. Magnetic resonance imaging parameters for assessing risk of recurrent hamstring injuries in elite athletes. Am J Sports Med 2007;35:1500–1506.
58. Verrall GM, Slavotinek JP, Barnes PG, et al. Clinical risk factors for hamstring muscle strain injury: a prospective study with correlation of injury by magnetic resonance imaging. Br J Sports Med 2001;35:435–440.
59. Speer KP, Lohnes J, Garrett WE. Radiographic imaging of muscle strain injury. Am J Sports Med 1993;21(1):89–95.
60. Crosier JL. Factors associated with recurrent hamstring injuries. Sports Med 2004;34(10):681–695.
61. Verrall GM, Slavotinek JP, Barnes PG, et al. Clinical risk factors for hamstring muscle strain: a prospective study with correlation of injury by magnetic resonance imaging. Br J Sports Med 2001;35(6):435–439.
62. Lee JC, Healy JC. Sonography of lower limb muscle injury. AJR Am J Roentgenol 2004;182:341–351.
63. Kransdorf MJ, Meis JM, Jelinek JS. Myositis ossificans: MR appearance with radiologic-pathological correlation. AJR Am J Roentgenol 1991;157:1243–1248.
64. Huss CD, Puhl JJ. Myositis ossificans of the upper arm. Am J Sports Med 1980;8:419–424.
65. Kransdorf MJ, Murphey MD. Extraskeletal osseous and cartilaginous tumors. In: Imaging of soft-tissue tumors. Philadelphia: WB Saunders; 1997. p. 317–349.
66. Bouchardy L, Garcia J. Magnetic resonance imaging in the diagnosis of myositis ossificans circumscripta. J Radiol 1994;75:101–110.
67. Shirkhoda A, Armin AR, Bis KG, et al. MR imaging of myositis ossificans: variable patterns at different stages. J Magn Reson Imaging 1995;5(3):287–292.
68. Peetrons P. Ultrasound of muscle. Eur Radiol 2002;12:35–43.
69. Fornage BD, Eftekhari F. Sonographic diagnosis of myositis ossificans. J Ultrasound Med 1989;8(8):463–466.
70. Bodley R, Jamous A, Short D. Ultrasound in the early diagnosis of heterotopic ossification in patients with spinal injuries. Paraplegia 1993;31(8):500–506.
71. Peck RJ, Metreweli C. Early myositis ossificans: a new echographic sign. Clin Radiol 1988;39:586–588.
72. Goutallier D, Postel JM, Gleyze P, et al. Influence of cuff muscle fatty degeneration on anatomic and functional outcomes after simple suture of full-thickness tears. J Shoulder Elbow Surg 2003;12:550–554.
73. Strobel K, Hodler J, Meyer DC, et al. Fatty atrophy of supraspinatus and infraspinatus muscles: accuracy of US. Radiology 2005;237(2):584–589.
74. Bianchi S, Abdelwahab IF, Mazzola CG, et al. Sonographic examination of muscle herniation. J Ultrasound Med 1995;14:357–360.
75. Braunstein JT, Crues JV. Magnetic resonance imaging of hereditary hernias of the peroneus longus muscle. Skeletal Radiol 1995;24: 601–604.
76. Beggs I. Sonography of muscle hernias. AJR Am J Roentgenol 2003;180:395–399.
77. Miniaci A, Rorabeck CH. Tibialis anterior muscle hernia: a rationale for treatment. Can J Surg 1987;30:79–80.
78. Seddon HJ. Volkmann's ischaemia in the lower limb. J Bone Joint Surg (Br) 1966;48:627–636.
79. Gwynne Jones DP, Theis JC. Acute compartment syndrome due to closed muscle rupture. Aust NZ J Surg 1997;67:227–228.
80. Thennnavan AS, Funk L, Volans AP. Acute compartment syndrome after muscle rupture in a non-athlete. J Accid Emerg Med 1999;7:182–190.
81. Auerbach DN, Bowen 3rd AD. Sonography of leg in posterior compartment syndrome. AJR Am J Roentgenol 1981;136(2):407–408.
82. Pedowitz RA, Hargens AR, Mubarak SJ, et al. Modified criteria for the objective diagnosis of chronic compartment syndrome of the leg. Am J Sports Med 1990;18:35–40.
83. Robinson D, On E, Halperin N. Anterior compartment syndrome of the thigh in athletes: indications for conservative treatment. J Trauma 1992;32:183–186.
84. Fronek J, Mubarak SJ, Hargens AR, et al. Management of chronic exertional anterior compartment syndrome of the lower extremity. Clin Orthop 1987;220:217–227.
85. Fraipont MJ, Adamson GJ. Chronic exertional compartment syndrome. J Am Acad Orthop Surg 2003;11(4):268–276.
86. Gershuni DH, Gosink BB, Hargens AR, et al. Ultrasound evaluation of the anterior musculofascial compartment of the leg following exercise. Clin Orthop Relat Res 1982;(167):185–190.
87. Birtles DB, Minden D, Wickes SJ, et al. Chronic exertional compartment syndrome: muscle changes with isometric exercise. Med Sci Sports Exerc 2002;34(12):1900–1906.
88. vanSonnenberg E, Wittich GR, Casola G, et al. Sonography of thigh abscess: detection, diagnosis, and drainage. AJR Am J Roentgenol 1987;149(4): 769–772.
89. Chau CL, Griffith JF. Musculoskeletal infections: ultrasound appearances. Clin Radiol 2005;60(2):149–159.
90. Craig JG. Infection: ultrasound-guided procedures. Radiol Clin North Am 1999;37(4):669–678.

CHAPTER

61

Ultrasound of the peripheral nerves

Stefano Bianchi, Ferdinando Draghi and Ian Beggs

INTRODUCTION

Disorders affecting the peripheral nerves (PNs) are common in clinical practice and can mimic a variety of musculoskeletal diseases. Accurate clinical evaluation including history taking, physical examination and electrodiagnostic tests are the mainstays of diagnosis,[1,2] but imaging examinations are frequently obtained to confirm the clinical data and plan treatment.[3,4]

Standard radiographs and computed tomography (CT) do not visualise the PNs. However, they can help in assessing entrapment neuropathies by evaluating adjacent anatomical structures such as bones and joints, add information on extrinsic nerve compression and assist in surgical planning. A typical example is entrapment of the ulnar nerve in the cubital tunnel by osteoarthritis of the elbow. In this setting radiographs and CT are invaluable in showing marginal osteophytes responsible for narrowing of the tunnel and nerve compression.

Magnetic resonance imaging (MRI) directly shows PNs and their size and internal structure. In addition it provides a detailed muscle assessment and evaluation of denervation on a precise anatomical basis.[5,6] When properly implemented, MR neurography is capable of providing high-quality information about PN disorders.[7,8] MRI is, however, not widely available in every country, is expensive, not well accepted by every patient and has relative and absolute contraindications.

Recent advances in ultrasound (US) technology, including high-resolution, electronic broadband transducers and enhanced software capabilities, have led to improved assessment of the musculoskeletal system.[9–11] US is considered an optimal imaging technique to evaluate the normal anatomy and disorders of PNs.[12–20] Advantages include the ability to assess long segments of nerve quickly and perform dynamic examinations; US is also cheap, well tolerated by patients, has no contraindications and is considered by several authors to be the primary technique for imaging PN pathology.[12–17,19]

In this chapter we present a brief description of the normal and US anatomy of the peripheral nerves followed by a description of the US technique of PN examination. Then we present the basic US appearance of the most frequent PN disorders. More detailed description of nerve disorders will be found in the chapters dealing with specific anatomical regions.

NORMAL ANATOMY AND US ANATOMY

Peripheral nerves are composed of hundreds/thousands of axons (nerve fibres). Some axons are surrounded by myelin sheath, a fat-rich membrane, while others are non-myelinated.[13,21–23] Both types are surrounded by Schwann cells and by the endoneurium, a thin layer of connective tissue that maintains the homeostasis of the endoneurial fluid that surrounds the individual myelinated nerve fibres and groups of unmyelinated nerve fibres.[23] Nerve fibres are grouped together in bundles, called nerve fascicles. The size and number of fascicles in PNs is highly variable and depends on the size of the nerve, its location and its type.[13] Fascicles are surrounded by the perineurium and separated by the epineurium, which has a supportive action and houses elastic fibres and vessels (vasa nervorum). The epineurium also surrounds the nerve trunk to form the peripheral nerve sheath. The sheath has variable thickness in different nerves as well as in different segments of the same nerve, a peculiar arrangement that seems correlated to the degree of external pressure on the nerve. A thicker epineurium is usually found in locations such as inextensible fibro-osseous tunnels where PNs are subject to physiological compression or stretching.

The US appearance of PNs closely correlates to the histological findings in both transverse and longitudinal images.[22] Normal PNs appear as echogenic tubular structures containing hypo/anechoic discontinuous segments (Fig. 61.1). On transverse scans PNs appear as hyperechoic structures containing oval-to-round hypoechoic areas. The echogenic background corresponds to the supportive connective tissue while the hypo/anechoic component corresponds to the fascicles or groups of fascicles. A focal homogeneous hypoechoic appearance of the nerve with loss of the normal fascicular pattern can be found in normal subjects in sites where the nerve is subject to physiological compression, for example in the ulnar nerve as it runs through the cubital tunnel. PNs are flexible structures that, when submitted to stretching or external compression, can change in shape. The size of a single nerve decreases when examined from proximal to distal due to branches leaving the main nerve trunk. Usually no internal blood flow can be detected with colour Doppler. As a general rule, detectable internal flow must be considered pathological. The cross-sectional area (CSA) of the PN correlates with the body mass index, and most closely with the patient weight. There seems not to be any statistical difference in nerve CSA between dominant and non-dominant arms.[24]

US TECHNIQUE OF EXAMINATION

US examination of PNs requires knowledge of normal anatomy and anatomical variations as well as rigorous examination technique.

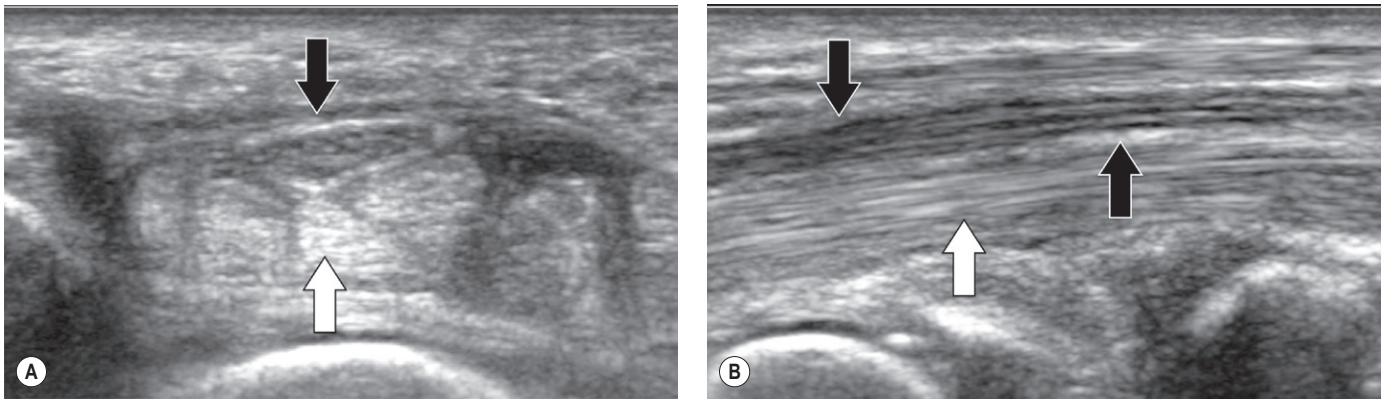

Figure 61.1 Normal US of a peripheral nerve. Axial **(A)** and longitudinal **(B)** sonograms obtained over the median nerve (black arrows) at the carpal tunnel. The transverse scan shows the nerve has a background of hyperechoic connective tissue containing oval-to-round hypoechoic areas that correspond to the nerve fascicles. In the longitudinal image the nerve appears tubular and has hypo-anechoic discontinuous segments, the so-called fascicular pattern. Note that the adjacent tendons (white arrows) show a different pattern (fibrillar pattern) made by hyperechoic fibrils packed together.

When starting the examination, transverse images of the area to be evaluated are useful since they are more panoramic and allow simultaneous detection of muscle, vessel, bone and joint outlines. These structures are more easily identified than PNs and serve as excellent anatomical landmarks. PNs can then be detected on the basis of their internal echostructure and/or relationship with adjacent anatomical structures. In particular vessels that run alongside nerves act as useful landmarks. Once identified the nerve must be followed on axial images obtained during alternating cranial and caudal displacement of the transducer, the so-called 'elevator technique'.[12,16,17,20] During transducer movement the sonologist must be aware of changes in size, morphology and echogenicity of the nerve as well as of appearance of the surrounding structures. Multiple 'up-and-down' scanning may be necessary to recognise all the different anatomical structures and accurately assess them. For optimal evaluation of PNs the transducer must always be positioned perpendicular to the nerve to avoid artefactual changes in its echogenicity and this requires continuous modification of transducer tilt. With experience this can be accomplished also in complex anatomical areas where nerves are difficult to examine. After assessment in the transverse plane, the nerve is evaluated by longitudinal images These are usually more difficult to obtain due to the curvilinear course of most nerves. Longitudinal sonograms are most valuable in cases of focal nerve compression as they display in the same image the compressed pathological portion of the nerve together with its swollen proximal and distal components.

The dynamic nature of US allows exquisite assessment of nerve stretching and/or movement in normal[25,26] as well as in pathological conditions.[27] Dynamic US examination shows how PNs change their shape and position with stretching and application of external pressure related to joint movements or muscle contraction.[28,29] Nerves can be seen displacing because of adaptation to the position of adjacent structures (e.g. translation of the median nerve in the axial plane due to movements of the flexor tendons inside the carpal tunnel)[30] or they can show adaptive changes in their size and morphology due to increased tension. These changes are related to changes in the relationship between internal fascicles made possible by the presence of loose connective tissue and elastic fibres inside the epineurium.

ANATOMICAL VARIATIONS OF PERIPHERAL NERVES AND ADJACENT STRUCTURES

Several anatomical variations of PNs and surrounding structures can be easily detected by US and are frequently encountered during routine US examination. Most variations are not clinically significant but can be interpreted as pathological by the inexperienced sonologist, while others can predispose to nerve compression. The most relevant anatomical variations can affect the nerve itself (size, shape, position) or affect the adjacent structures.

Common anatomical variations that could affect the peripheral nerves

- Nerve shape
  - Bifid median nerve
- Nerve position
  - Anterior instability of the ulnar nerve
- Anatomical structures adjacent to the nerves
  - Median artery
  - Supracondylar process of the humerus (less frequent)
  - Accessory muscles

The most frequent variation affecting PNs is the presence of a high division of the median nerve (2.4% of normal individuals), the so-called 'bifid' median nerve.[31–33] Bifid median nerves usually have a larger cross-sectional area than non-bifid nerves and this can predispose to carpal tunnel syndrome.[33] Ultrasound shows two nerves running close to each other at the distal forearm and inside the carpal tunnel (Fig. 61.2). The US appearance correlates well to MRI[31,32] and to anatomical findings.[31] The size of the two nerves is highly variable. Most frequently they are approximately the same size. An asymmetric presentation with one larger and one smaller nerve is less frequent. Presence of a bifid median nerve must be always reported by the sonologist since one of the nerves may be injured during arthroscopic decompression of the carpal tunnel (Fig. 61.3).

Anomalies of nerve position are less frequent. Rarely the median nerve may show a vertical tilt at the level of the proximal carpal tunnel but this is not associated with pathological alterations. Instability of a PN is usually intermittent with temporary dislocation/reduction in response to changes of position of an adjacent joint. Intermittent instability affects typically the ulnar nerve at the elbow. Absence of the superficial retinaculum at the proximal cubital tunnel predisposes to anterior instability of the nerve during elbow flexion.[27] Such instability can be found as a normal anatomical variation and usually does not lead to any pathological nerve changes but in a minority of patients chronic friction during displacement

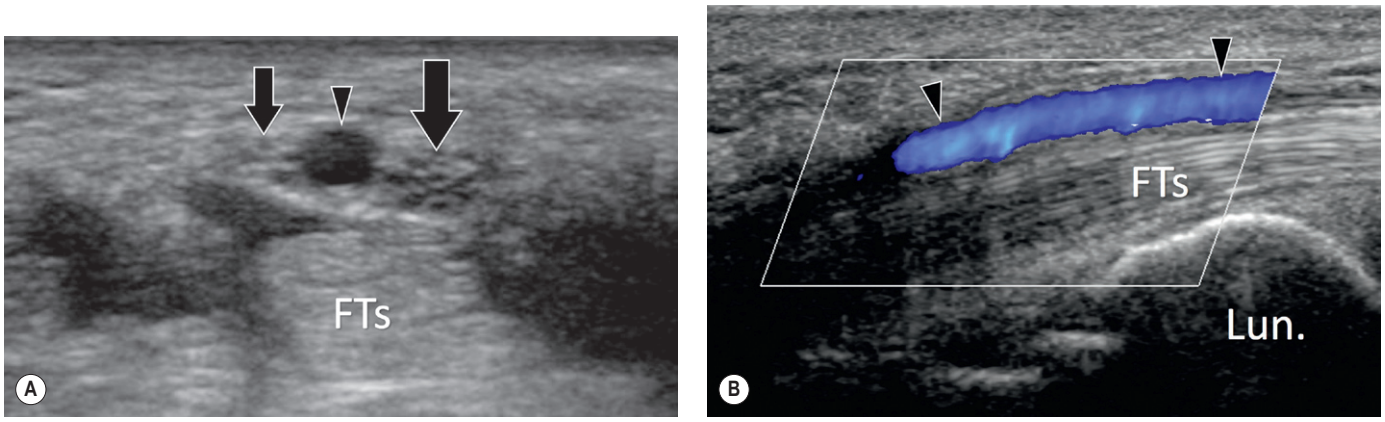

Figure 61.2 Bifid median nerve and persistent median artery. Axial **(A)** and longitudinal colour Doppler **(B)** sonograms obtained over the proximal carpal tunnel. In **A** the median nerve appears bifid and has a large medial component (large arrow) and a smaller lateral portion (small arrow). Both components show a normal internal fascicular structure. Between the two components runs a persistent median artery (arrowhead). In **B** note the internal flow signal of the median artery (arrowheads). FTs, flexor tendons; Lun, lunate.

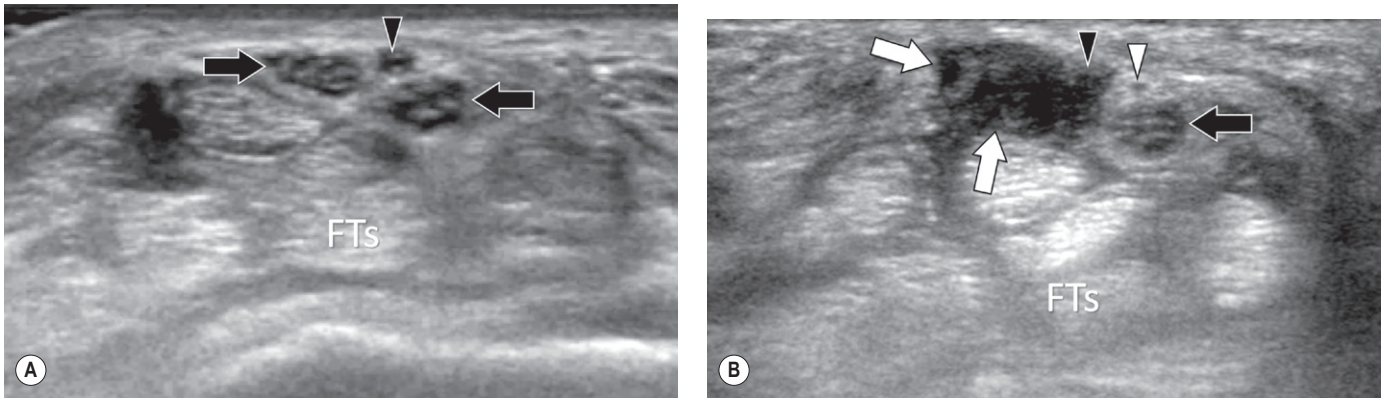

Figure 61.3 Surgical damage to bifid median nerve. Axial sonograms obtained at the distal forearm **(A)** and proximal carpal tunnel **(B)** in a patient with persistent symptoms after carpal tunnel release. In **A** the median nerve (arrows) appears bifid. A persistent median artery (arrowhead) is seen running between the two nerves. In a more distal sonogram **(B)** the lateral nerve is normal (black arrow) while the medial nerve is hypoechoic and enlarged because of a post-traumatic neuroma (white arrows) related to arthroscopic trauma. The persistent median artery (black arrowhead) is located very close to the neuroma. Note the normal sensory palmar branch of the median nerve (white arrowhead). FTs, flexor tendons.

can lead to nerve swelling and impaired function. Axial sonograms of the cubital tunnel during elbow flexion show that the nerve is suddenly displaced anterior to the medial epicondyle. It returns to the cubital tunnel on extension.

Anatomical variations of structures adjacent to the PN can produce pathological nerve changes. The persistent median artery is a frequent anatomical variation (Fig. 61.2). It is a supernumerary artery, usually originating from the ulnar artery, that joins the median nerve in the middle third of the forearm, then runs alongside the nerve to the distal forearm and the carpal tunnel.[34,35] This artery normally involutes after birth but occasionally persists and can be associated with a normal or bifid median nerve. A persistent median artery that is larger than 3 mm or is thrombosed can compress the median nerve in the carpal tunnel[35] (Fig. 61.4). The presence of a persistent median artery must always be noted in the radiology report. During open release of the carpal tunnel, the anomalous vessel is easily detected by the surgeon but it may go unrecognised and be injured when an arthroscopic approach is used.

The supracondylar process of the humerus is a bony exostosis on the medial aspect of the distal metaphysis of the humerus. It points medially. A strong fibrous ligament, the ligament of Struthers, joins the tip of the process to the distal humeral epiphysis. The bony process or the ligament can compress the median or ulnar nerves.[36] Although the supracondylar process can be detected at US as a thin hyperechoic structure with posterior acoustic shadowing, its detection is easier on radiographs.

Accessory muscles can cause a mass effect and produce compressive neuropathies, particularly when the anomalous muscle is hypertrophied or runs with the nerve inside an inextensible osteofibrous tunnel. US shows the distinctive internal architecture of muscle and excludes tumour. The accessory abductor digiti minimi, the most common accessory muscle of the wrist found in approximately 24% of normal individuals, runs inside Guyon's canal at the wrist in close contact with the ulnar artery and nerve. Although mostly asymptomatic, when hypertrophied it may cause compression of the ulnar nerve. US not only diagnoses the accessory muscle but also evaluates ulnar nerve changes secondary to compression[37–39] and colour Doppler allows evaluation of the ulnar artery. Ultrasound can also detect compression of other nerves by anomalous muscles.[40,41]

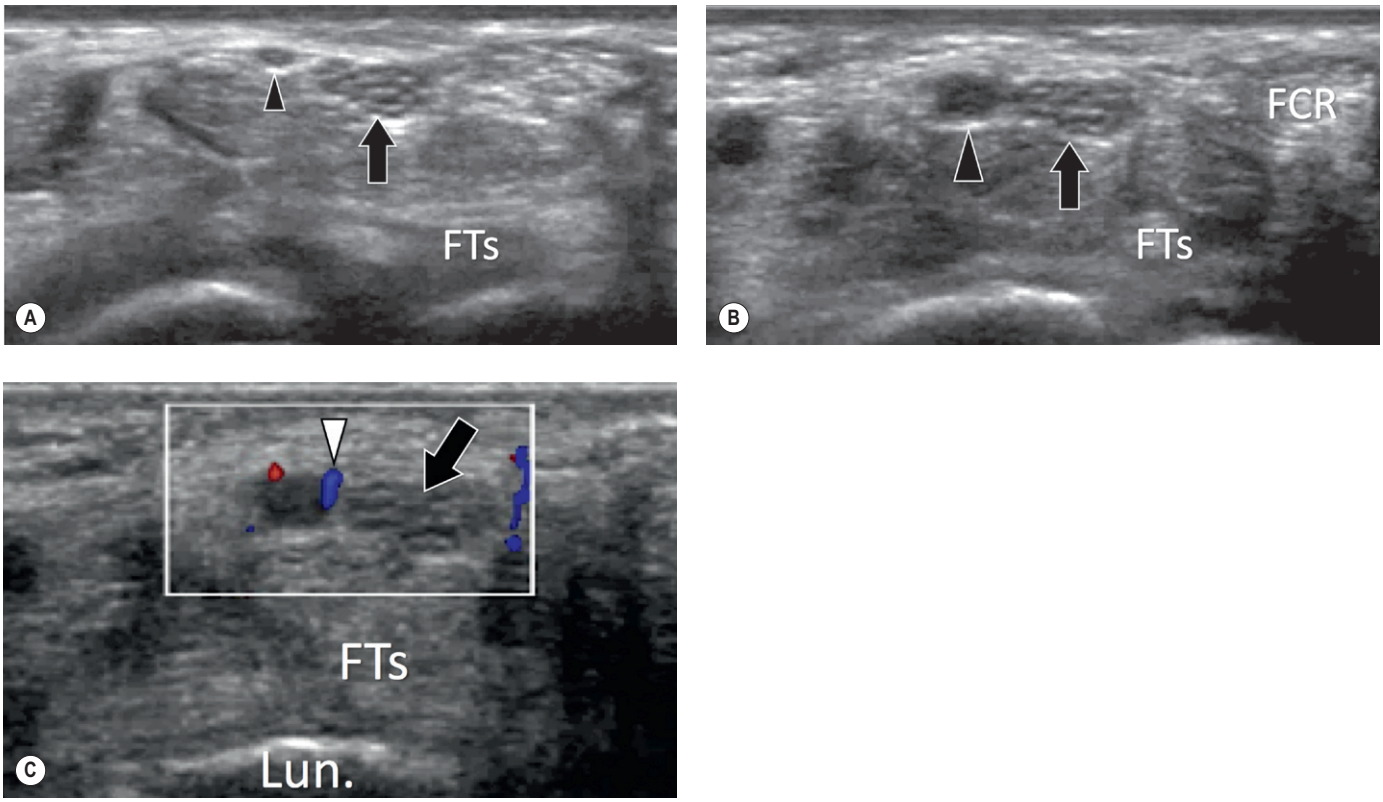

Figure 61.4 Thrombosis of a persistent median artery. Axial sonograms obtained over the distal forearm **(A)** and proximal carpal tunnel **(B)**, and axial colour Doppler sonogram **(C)** in a patient with a thrombosed persistent median artery causing carpal tunnel syndrome. In **A** the median nerve (arrow) and the normal appearing median artery (arrowhead) run close to each other. Note the small size of the artery compared to the nerve. In **B** the anomalous vessel shows significant increase in size due to internal thrombosis (large arrowhead). In **C** the persistent median artery shows absent internal flow signals due to internal thrombosis. Note hypervascular changes of the arterial wall (white arrowhead) corresponding to thrombophlebitis. FTs, flexor tendons; FCR, flexor carpi radialis tendon; Lun, lunate.

BASIC PATHOLOGICAL CHANGES OF PERIPHERAL NERVES

We will describe here only the basic pathological changes of peripheral nerves in trauma (acute and chronic), tumour and some miscellaneous disorders. For details of specific pathological entities the reader is referred to other chapters dealing with joints and limb segments.

Trauma

Trauma of peripheral nerves can be acute or chronic. Acute trauma can cause temporary alterations to nerve function not associated with morphological change, or partial or complete tears. US can only detect morphological alterations such as tears. PN tears can be secondary to exogenous trauma such as penetrating knife injuries or endogenous trauma such as humeral shaft fractures that result in tearing of the radial nerve. Tears due to exogenous trauma may be difficult to assess in the presence of an open wound.

A partial nerve tear appears as focal discontinuity of several nerve fascicles (Fig. 61.5) and mainly follows exogenous trauma. The size of the tear depends on the strength of the trauma and the location of the nerve trunk (superficial or deep). As for most PN disorders, transverse images are first obtained since they allow a rapid and efficient scanning of long nerve segments. Sagittal images are then obtained over pathological nerve segments. Partial tears cause interruption of one or more nerve fascicles and hypoechoic areas interposed among the torn fascicles. Often transducer pressure at the level of the tears helps localise the site of tear by triggering local pain and paraesthesia. The percentage of the cross-sectional area affected by the tear can be judged in transverse images. Typically no nerve gap can be detected in partial tears. In complete tears US shows total nerve transection and two nerve stumps separated by an irregular hypoechoic area. The gap between the nerve stumps can measure several centimetres in severe trauma. US accurately detects complete nerve transection soon after injury and can alter the evaluation and management of peripheral nerve injuries.[42] Both partial and complete tears may result in traumatic neuromas, proliferative masses due to disorganised attempts at nerve regeneration.[43] In-continuity neuromas are observed when the nerve stumps are both connected with the poles of neuroma (Fig. 61.6). Terminal (amputation) neuromas are mostly found at the proximal stump and are frequent in lower limb amputations. Traumatic neuromas appear as focal irregular hypoechoic masses found along the course of a nerve. They are usually painful when pressure is applied through the transducer. US can assess surgical repair of complete nerve section (Fig. 61.7).

Entrapment neuropathies (EN) are a heterogeneous group of conditions in which PNs are chronically compressed or stretched.[3] They result from congenital or acquired disorders or a combination of both. Nerve changes and clinical symptoms depend on the degree and duration of compression. High pressures applied for long periods can severely alter the morphology and function of nerves and eventually result in irreversible damage. Some congenital conditions predispose to EN. Hereditary neuropathy with liability to pressure palsies (HNPP) is an autosomal dominant-inherited demyelinating disorder that affects PNs and presents clinically as recurrent sensory and motor mononeuropathies.[44] US demonstrates

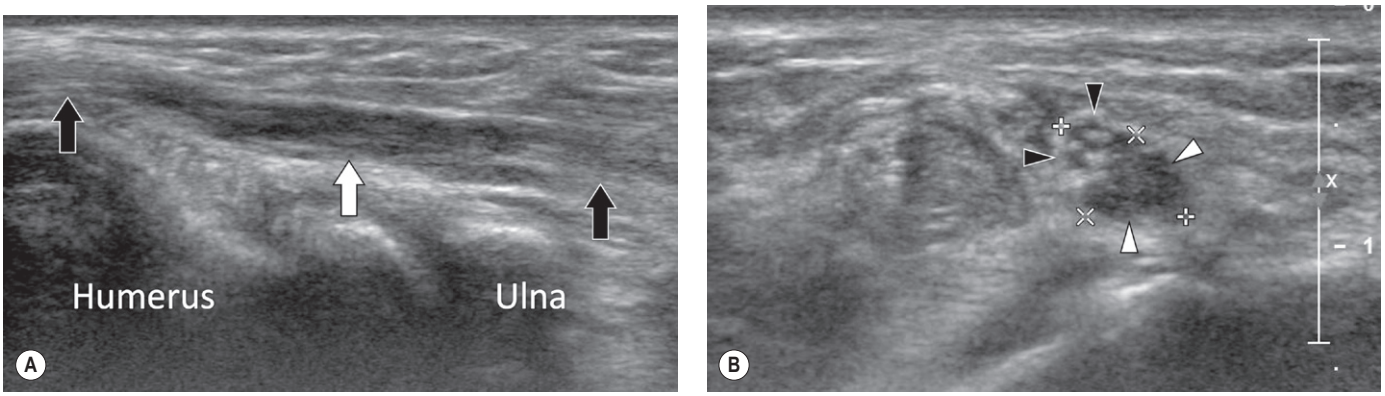

Figure 61.5 Trauma. Traumatic partial tear of the ulnar nerve at the elbow. Sagittal **(A)** and axial **(B)** sonograms obtained over the cubital tunnel in a patient with a history of local trauma. **A:** The sagittal image shows a hypoechoic focal swelling of the ulnar nerve (white arrow). The nerve presents a normal fascicular pattern proximally and distally (black arrows). **B:** The axial sonogram, obtained over the injured portion of the nerve (callipers), shows a normal appearance of the anterior fascicles (black arrowheads) and a hypoechoic post-traumatic neuroma (white arrowheads) affecting the posterior part of the nerve.

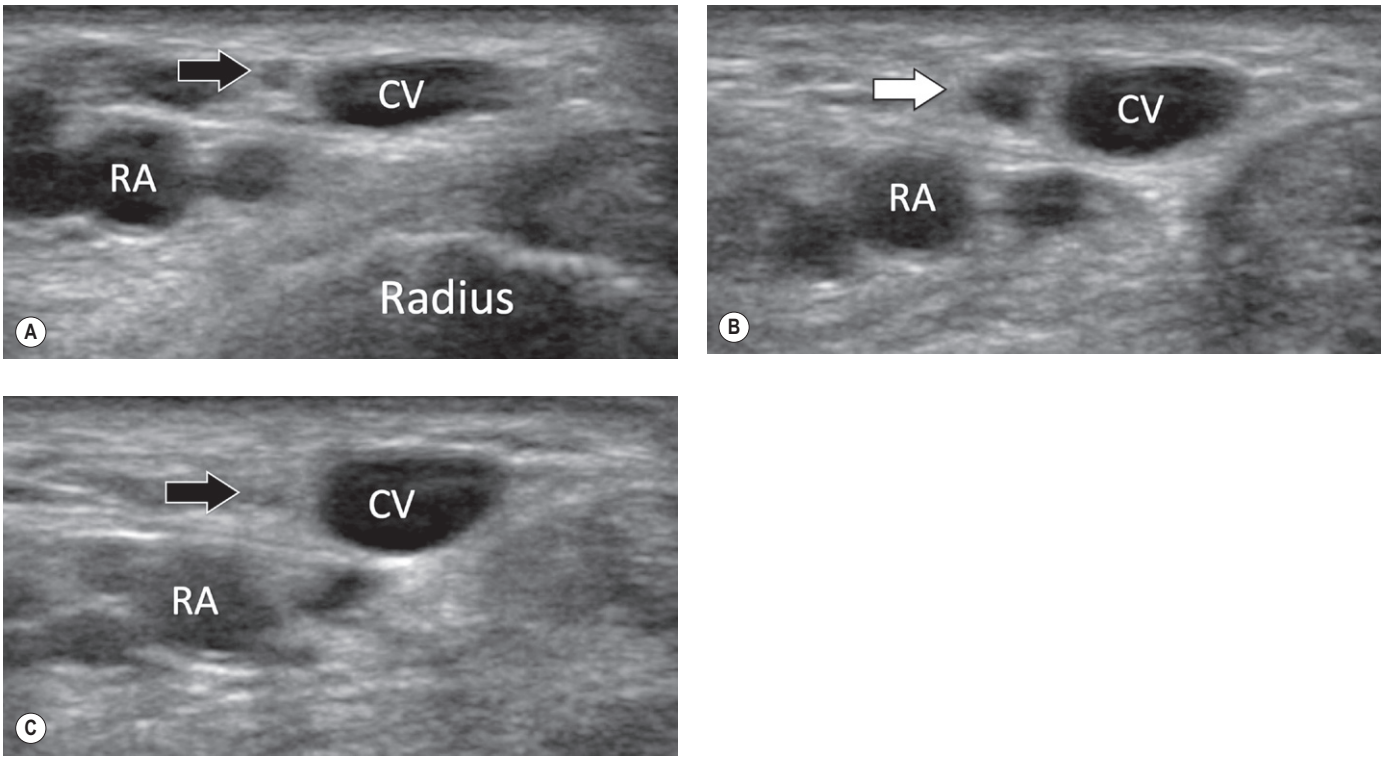

Figure 61.6 Trauma. Neuroma of the sensory branch of the radial nerve. Axial sonograms obtained from proximal to distal **(A–C)** over the distal aspect of the forearm in a patient suffering distal paraesthesia after cannulation of the cephalic vein. Sonograms show a normal appearance of the sensory branch of the radial nerve (black arrows) in **A** and **C**. In **B** the nerve appears irregular, swollen and hypoechoic due to formation of an in-continuity neuroma (arrow) related to needle trauma during cannulation of the adjacent cephalic vein (CV). Local pressure through the transducer was painful and induced distal paraesthesia and tingling (Tinel sign). RA, radial artery.

diffuse enlargement and hypoechogenicity of several PNs running extending outside osteofibrous tunnels. PNs that are clinically unaffected may also show this abnormal appearance.[45] As discussed previously, accessory congenital muscles are common anatomical variants that can compress a PN when they run alongside each other in inextensible osteofibrous tunnels.[7,46] Other congenital variations of the nerves or adjacent structure (bifid median nerve, persistent median artery) can produce entrapment.

Chronic nerve compression leads to internal changes in the PN that are initially reversible then become irreversible leading to impairment of nerve function. First, impaired venous flow leads to increased intraneural interstitial pressure causing reversible intraneural oedema of the connective tissue. When compression is prolonged, ischaemia due to damage to the vasa nervorum, the small vessels that supply the nerve trunk, appears and is followed by irreversible internal fibrosis. This results finally in myelin sheath and axonal degeneration. Such morphological changes alter the function of nerve conduction, with subsequent sensory or motor impairment depending on the type of nerve affected. Chronic compression has the same US appearance regardless of the cause (Fig. 61.8). The nerve is typically focally thinned at the site of compression associated with proximal fusiform swelling.

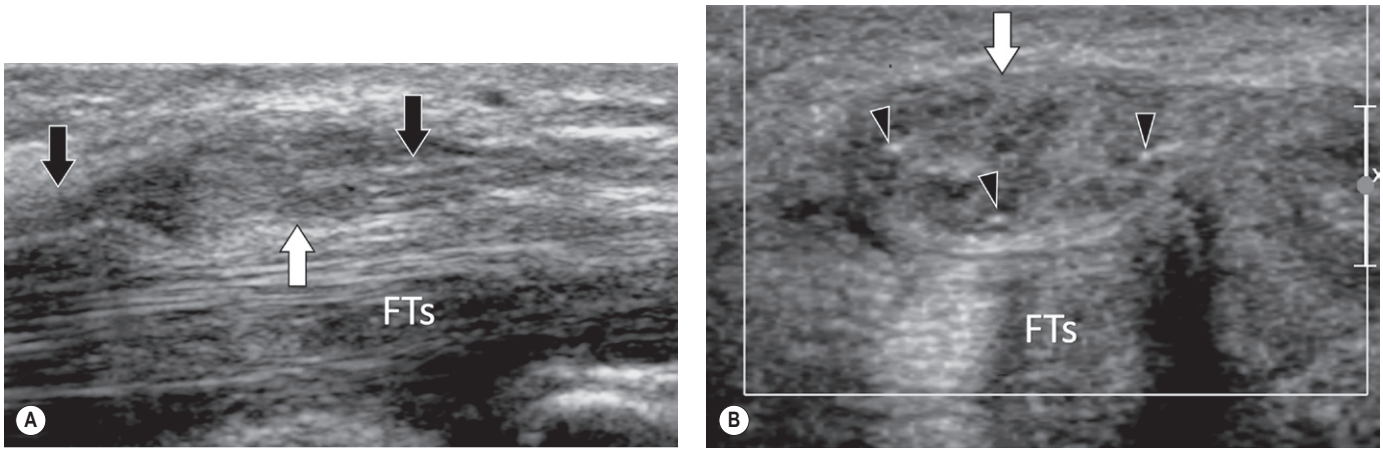

Figure 61.7 Trauma. Postsurgical appearance. A: Sagittal image obtained over the palmar aspect of the distal forearm shows a postsurgical neuroma (white arrow) as a focal fusiform swelling of the median nerve (black arrows). The axial sonogram **(B)**, obtained over the neuroma, shows multiple internal hyperechoic foci corresponding to surgical stitches (arrowheads) in the swollen nerve. FTs, flexor tendons.

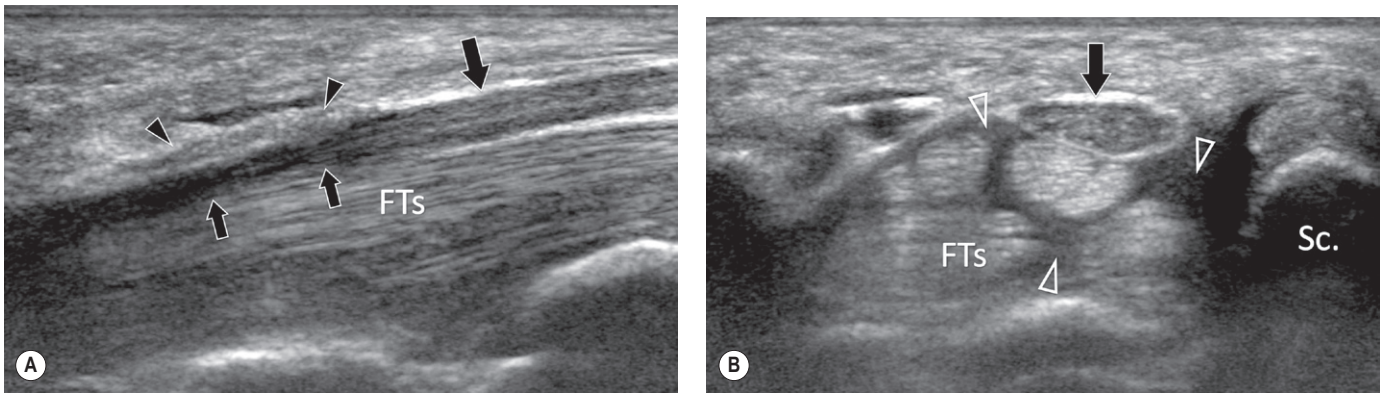

Figure 61.8 Entrapment neuropathy. Carpal tunnel syndrome. Sagittal **(A)** and axial **(B)** sonograms obtained over the median nerve at the carpal tunnel. **A:** The sagittal image shows the transverse ligament (arrowheads) as a hyperechoic band. The median nerve is thinned at the level of the ligament (small arrows) and swollen proximal to it (large arrow). **B:** In the axial image, obtained at the proximal tunnel, the nerve appears swollen (arrow) and displaced in a palmar direction by the hypertrophied tendon synovium (hollow arrowheads). Note partial loss of internal fascicular pattern of the nerve. FTs, flexor tendons; Sc, scaphoid.

US changes of peripheral nerves in entrapment neuropathies

- Nerve shape
  - Swelling proximal to the site of compression
  - Thinning at the site of compression
  - Swelling distal to the site of compression (less frequent)
- Nerve internal structure
  - Overall hypoechoic appearance
  - Loss of fascicular pattern
  - Internal hyperaemia on colour Doppler (less frequent)
- Nerve position
  - Displacement of the nerve

Measurements of the nerve area in the transverse plane at proximal level as well as the ratio between proximal and distal areas have been used to establish diagnostic cut-off values, particularly in carpal tunnel syndrome.[12,13] The site of nerve compression can be detected by showing an abrupt transition between the swollen proximal portion and the thinned compressed part. This 'notch sign' is useful in pointing to the site of nerve compression when focal masses are not evident. Rarely enlargement of the nerve is observed distal to the compression site. Intranerve changes are non-specific and US is not able to differentiate between intraneural oedema and fibrosis. The nerve appears more or less homogeneously hypoechoic because of diminished echogenicity of endoneurium and interfascicular perineurium. Changes in the echogenicity of the endo- and perineurium are responsible for the disappearance of the fascicular pattern. Increased vascular signals can be seen inside the affected nerve with colour Doppler.

In addition to assessing PN changes, US helps in detecting and assessing a variety of causes of nerve compression.[12,13,27–29] Masses are easily detected and US can evaluate their size, borders, internal structure and vascularity (Fig. 61.9). Frequently US allows a specific diagnosis on the basis of mass appearance (accessory muscle, mucoid cyst, lipoma, ganglion, etc.), obviating the need for other imaging examinations (Fig. 61.10). As for all musculoskeletal examinations, integration of clinical data and US appearance helps accurate diagnosis. If a local injection is needed, US guidance can avoid inadvertent nerve damage during the procedure (Fig. 61.11). Entrapment neuropathies can affect a wide variety of nerves. The most commonly involved are the median,[16,17,27,28] ulnar[10,11,16,28] and radial nerves.[47–49]

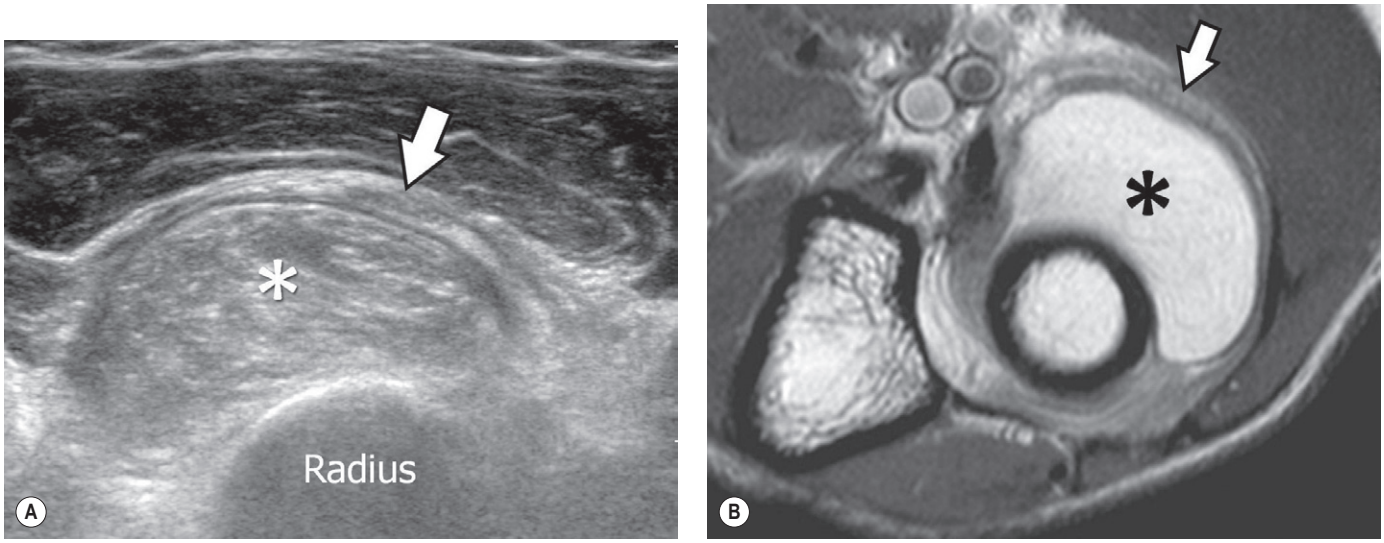

Figure 61.9 Entrapment neuropathy. Compression of the posterior interosseous nerve by an intramuscular lipoma. Axial sonogram **(A)** and corresponding axial T1-weighted MR image **(B)**. In **A** the supinator muscle appears swollen and irregular because of an intramuscular hyperechoic mass (asterisk) suggesting a lipoma. Colour Doppler (not shown) did not show any intralesional flow signals. The posterior interosseous nerve (arrow) appears compressed by the lipoma against the arcade of Frohse. MR image **(B)** confirms the diagnosis of an intramuscular lipoma (*). Note the flattened appearance of the compressed nerve (arrow).

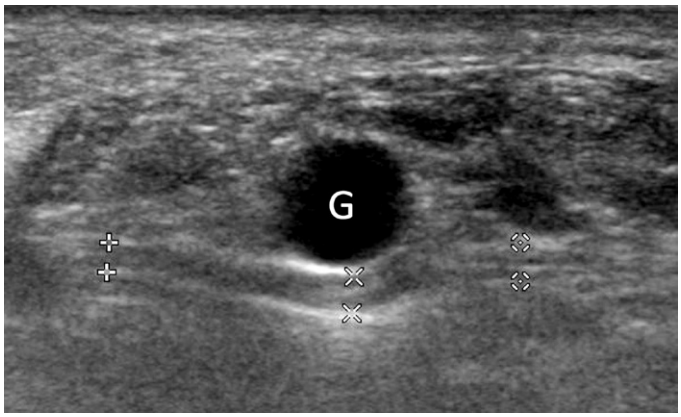

Figure 61.10 Entrapment neuropathy: Guyon tunnel syndrome. Sagittal oblique sonogram in a patient suffering from weakness of the intrinsic hand muscles. Sonogram, obtained medial to the hamate hook, shows a well-defined anechoic ganglion (G) compressing the motor branch of the ulnar nerve (callipers). Note how the ganglion displaces the adjacent nerve, which is locally swollen and hypoechoic.

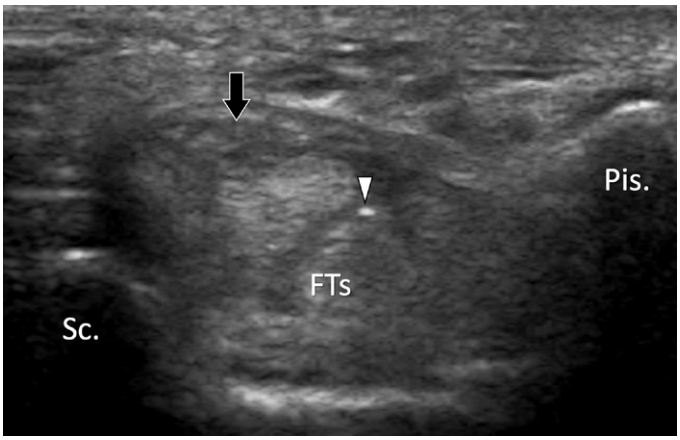

Figure 61.11 Carpal tunnel syndrome: US-guided procedures. Axial image obtained over the carpal tunnel during US-guided steroid injection shows correct location of the needle's tip (arrowhead) inside the inflamed synovial tendon sheath. Arrow, median nerve; Sc, scaphoid; Pis, pisiform.

TUMOURS AND OTHER MASSES

Peripheral nerve tumours are mostly benign and include two major benign histotypes – schwannomas (also called neurilemmomas) and neurofibromas.[50–53] Malignant peripheral nerve sheath tumours are rare and usually derive from the sarcomatous transformation of a neurofibroma.

The differentiation between schwannomas and neurofibromas is important. Neurofibromas infiltrate nerve trunks and spread among the nerve fascicles (Fig. 61.12). Many neurofibromas cannot be removed without sacrificing the nerve, requiring nerve resection and grafting. Schwannomas usually displace the nerve fascicles and can be shelled out while preserving nerve continuity[39,40] (Fig. 61.13). Benign nerve tumours are round, oval or fusiform hypoechoic masses with well-defined margins. Internal cystic changes as well as posterior enhancement may be observed. The most important criterion for the US diagnosis of a nerve tumour is the relation of the mass to a nerve.[51,52] This can be easily accomplished if the nerve is 2 mm or more in size and if the nerve lies in the superficial tissues. Assessment of the relation with the nerve can be very difficult in deep masses or when the nerve is small as in the subcutaneous tissues. In a recent study of 76 peripheral nerve tumours, the relationship with the nerve was undetermined at US in 40% of schwannomas and 53.8% of neurofibromas.[51] Axial images are usually more effective in assessing nerve/tumour relation. The nerve is first detected proximally and then followed distally to the level of the mass. Longitudinal images can also be useful but visualisation of the nerve entering and leaving the mass in the same image can be difficult to achieve. Distinction between

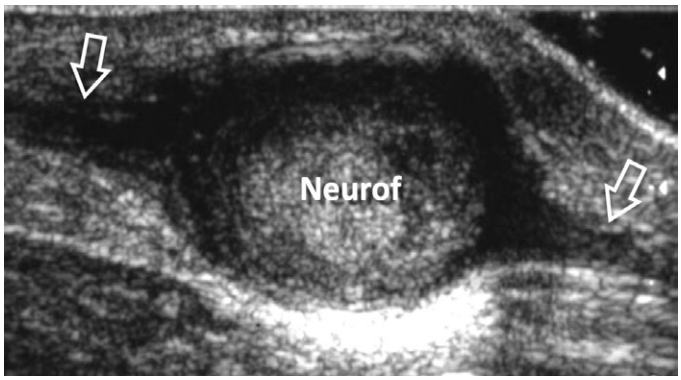

Figure 61.12 Neurofibroma of sural nerve. The nerve (arrows) enters and leaves the mass in a central position.

schwannomas and neurofibromas is difficult with US. No ultrasonographic finding currently allows a definite differentiation between them[51] but a nerve eccentrically entering the mass strongly suggests a schwannoma while a central position suggests a neurofibroma. Intratumour cystic changes and a hypervascular pattern on colour Doppler are also more common in schwannomas.

The majority of cysts (mucoid cysts, ganglia) responsible for compression of PNs arise from the anterior aspect of the superior tibiofibular joint (STFJ) (Fig. 61.14).[54,55] There are two types of such cysts: intramuscular and intraneural. Both are mucoid cysts, with a fibrous external capsule and no synovial lining, that contain viscous fluid. With intramuscular cysts the compression on the nerve is external while with intraneural cysts the fascicles are compressed by the mucoid ganglion that develops inside the nerve perineurium. Intramuscular ganglia arising from the STFJ usually develop inside the muscles of the anterolateral compartment of the leg and

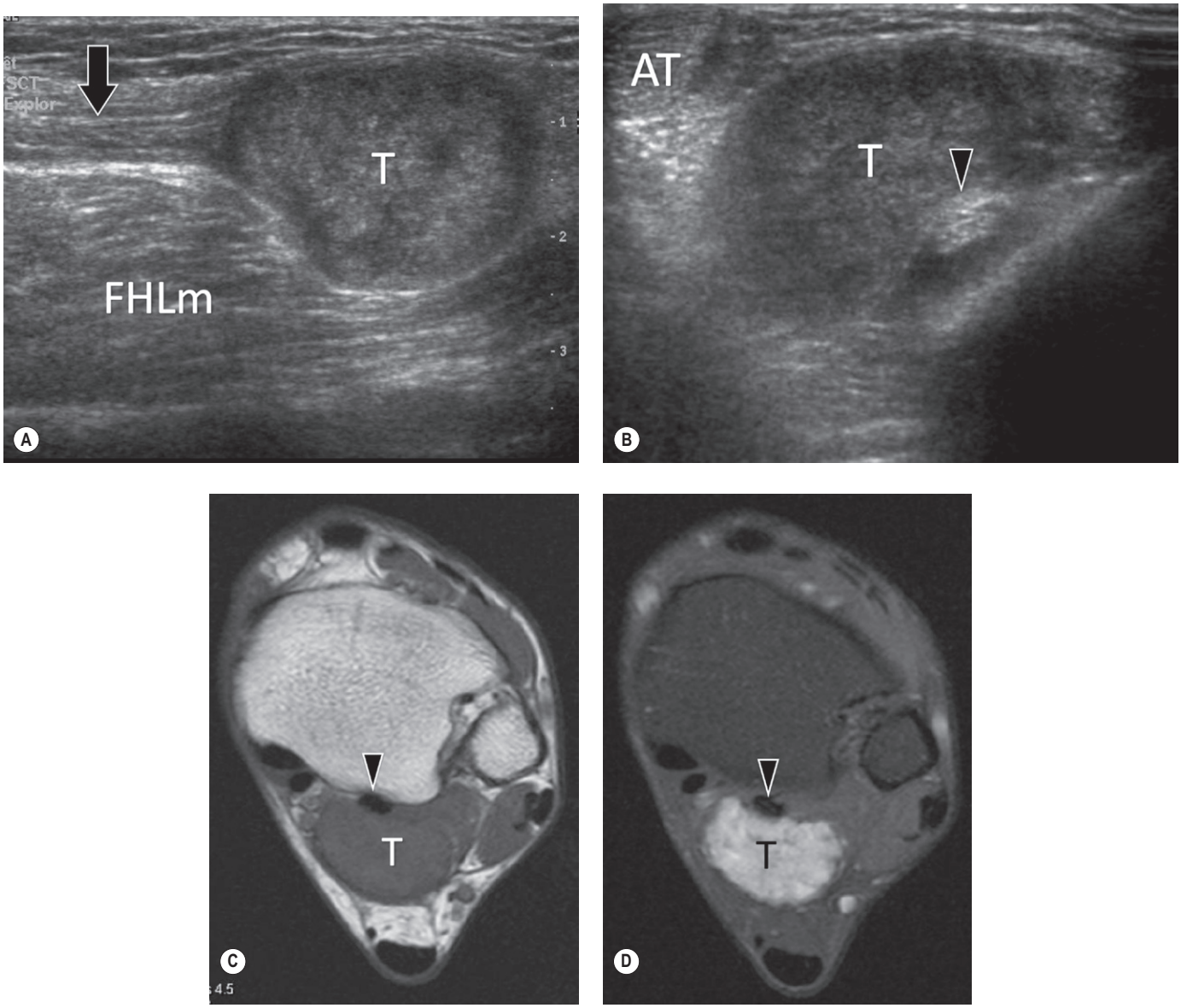

Figure 61.13 Schwannoma of the tibial nerve. Sagittal **(A)** and axial **(B)** sonograms, axial T1-weighted **(C)** and gadolinium-enhanced T1-weighted **(D)** MRI images obtained over the distal tibial nerve. In **A** and **B** note the presence of an irregular hypoechoic solid tumour (T) located inside the tibial nerve (arrow). The tumour is located close to the flexor hallucis longus muscle (FHLm) and tendon (arrowhead). AT, Achilles tendon. **C:** MRI axial image corresponding to **B**. **D:** After gadolinium gadopentate injection note enhancement of the tumour. The FHL tendon (arrowhead in **C** and **D**) is compressed by the mass. Histological examination showed a schwannoma.

Nerves most frequently affected in entrapment neuropathies

Suprascapular nerve
- Shoulder
  - Coracoglenoid notch
  - Spinoglenoid notch

Median nerve
- Elbow
  - Supracondylar process syndrome
  - Pronatore teres syndrome
  - Lacertus fibrosus syndrome
  - Flexor digitorum superficialis syndrome
- Wrist
  - Carpal tunnel syndrome

Ulnar nerve
- Elbow
  - Cubital tunnel syndrome
  - Supracondylar process syndrome
- Wrist
  - Guyon tunnel syndrome

Radial nerve
- Elbow
  - Supinator syndrome
- Wrist
  - Wartenberg syndrome

Lateral femoral cutaneous nerve
- Hip
  - Meralgia paraesthetica

Peroneal nerve
- Knee
  - Intramuscular ganglia
  - Intraneural ganglia
  - Peroneal tunnel

Tibial nerve
- Ankle
  - Tarsal tunnel syndrome
- Foot
  - Morton neuroma

can compress the peroneal nerves, causing motor deficit and ill-defined pain in the anterolateral aspect of the leg. Intraneural ganglia enter the articular nervous branch and then dissect cranially inside the peroneal nerve towards the sciatic nerve. US demonstrates intramuscular ganglia as pear-shaped, anechoic expansible lesions with the proximal pointed portion closely related to the STFJ and a distal rounded portion extending inside the muscle.[54] Septations arising from the internal side of the fibrous wall are usually evident in larger ganglia. The relations of the cyst with the peroneal nerves and anterior tibial artery can be assessed by US. Needle aspiration guided by real-time US is not curative but can ameliorate the patient's symptoms by reducing intracystic pressure and pressure on the adjacent nerve. Intraneural cysts are smaller than intramuscular ganglia and appear as tubular anechoic structures inside the nerve. US shows hypoechoic enlargement of the articular branch of the common peroneal nerve and cranial extension of the cyst. A high-resolution transducer can show the compressed nerve fascicles displaced by the cyst, which appears surrounded by the epineurium.

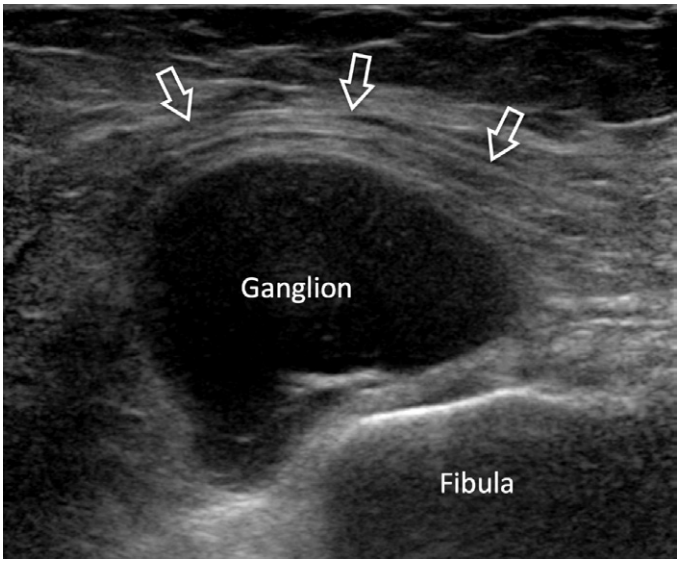

Figure 61.14 Ganglion of the superior tibiofibular joint compressing the peroneal nerve. Axial oblique sonogram obtained over the fibular head shows a well-marginated anechoic soft tissue mass arising from the superior tibiofibular joint. The appearance is typical of a ganglion. The cyst displaces the adjacent peroneal nerve (arrows).

MISCELLANEOUS DISORDERS

Due to its high resolution US can also assess other disorders of the PNs. US can assess pathological nerve changes in Charcot–Marie–Tooth disease[56] and helps in defining the Charcot–Marie–Tooth type 1A from other types of the disease. In leprosy detection of endoneural colour flow signals indicate active reversal reactions[57] and suggest prompt anti-reactional treatment. Fibrolipomatous hamartoma mainly affects the median nerve. It presents at US as a marked enlargement of the nerve, which appears hyperechoic because of the increased internal echogenic fat surrounding the normal appearing nerve fascicles.[58] There is increasing use of ultrasound in guiding needle placement for local anaesthesia.[59,60]

REFERENCES

1. Bard H. Les syndromes canalaires vus en rhumatologie. Numéro pedagogique. Rev Rhum 2007;74:315–433.
2. Bard H. Avant-propos: Les syndrome canalaires. In: Les syndromes canalaires vus en rhumatologie. Rev Rhum 2007;74:315–318.
3. Spratt JD, Stanley AJ, Grainger AJ, et al. The role of diagnostic radiology in compressive and entrapment neuropathies. Eur Radiol 2002;12:2352–2364.
4. Kim S, Choi JY, Huh YM, et al. Role of magnetic resonance imaging in entrapment and compressive neuropathy – what, where, and how to see the peripheral nerves on the musculoskeletal magnetic resonance image: part 1. Overview and lower extremity. Eur Radiol 2007;17:139–149.
5. Bashir WA, Connell DA. Imaging of entrapment and compressive neuropathies. Semin Musculoskelet Radiol 2008;12(2):170–181.
6. Allen JM, Greer BJ, Sorge DG, Campbell SE. MR imaging of neuropathies of the leg, ankle, and foot. Magn Reson Imaging Clin N Am 2008;16(1):117–131, vii.
7. Filler AG, Maravilla KR, Tsuruda JS. MR neurography and muscle MR imaging for image diagnosis of disorders affecting the peripheral nerves and musculature. Neurol Clin 2004;22(3):643–682, vi–vii.
8. Bendszus M, Stoll G. Technology insight: visualizing peripheral nerve injury using MRI. Nat Clin Pract Neurol 2005;1(1):45–53.
9. van Holsbeeck M, Introcaso JH, eds. Musculoskeletal ultrasound. St Louis, MO: Mosby; 2001.

10. McNally E, ed. Practical musculoskeletal ultrasound. Philadelphia: Elsevier; 2004.
11. Bianchi S, Martinoli C, eds. Ultrasound of the musculoskeletal system. Berlin: Springer-Verlag; 2007.
12. Valle M, Zamorani MP. Nerve and vessels. In: Bianchi S, Martinoli C, eds. Ultrasound of the musculoskeletal system. Berlin: Springer-Verlag; 2007. p. 97–136.
13. Peer S, Bodner G. eds. High-resolution sonography of the peripheral nervous system. 2nd ed. Berlin: SpringerVerlag; 2008.
14. Martinoli C, Bianchi S, Cohen M, et al. Echographie des nerfs peripheriques. J Radiol 2005;86:1869–1878.
15. Créteur V, Bacq C, Fumière E, et al. [Sonography of peripheral nerves. Part II: lower limbs] J Radiol 2007;88:349–360.
16. Créteur V, Bacq C, Widelec J. [Sonography of peripheral nerves – first part: upper limb] J Radiol 2004;85:1887–1899.
17. Bianchi S, Demondion X, Bard H, et al. Echographie du nerf médian [Ultrasound of the median nerve]. Rev Rhum 2007;74:376–383.
18. Beekman R, Visser LH. High-resolution sonography of the peripheral nervous system – a review of the literature. Eur J Neurol 2004;11:305–314.
19. Stuart RM, Koh ESC, Breidahl WH. Sonography of peripheral nerve pathology. AJR Am J Roentgenol 2004;182:123–129.
20. Bianchi S. Ultrasound of the peripheral nerves. Joint Bone Spine. 2008 Sep 25. [Epub ahead of print]
21. Lundborg G, Dahlin LB. Anatomy, function, and pathophysiology of peripheral nerves and nerve compression. Hand Clinics 1996;12(2): 185–193.
22. Silvestri E, Martinoli C, Derchi LE, et al. Echotexture of peripheral nerves: correlation between US and histologic findings and criteria to differentiate tendons. Radiology 1995;197:291–296.
23. Stewart JD. Peripheral nerve fascicles: anatomy and clinical relevance. Muscle Nerve 2003;28:525–541.
24. Cartwright MS, Shin HW, Passmore LV, Walker FO. Ultrasonographic findings of the normal ulnar nerve in adults. Arch Phys Med Rehabil 2007;88(3):394–396.
25. Dilley A, Summerhayes C, Lynn B. An in vivo investigation of ulnar nerve sliding during upper limb movements. Clin Biomech (Bristol, Avon) 2007;22:774–779.
26. Julius A, Lees R, Dilley A, et al. Shoulder posture and median nerve sliding. BMC Musculoskelet Disord 2004;5:23.
27. Martinoli C, Bianchi S, Gandolfo N, et al. Ultrasound of nerve entrapments in osteofibrous tunnels. Radiographics 2000;20:S199–S213.
28. Bianchi S, Montet X, Martinoli C, et al. High-resolution sonography of compressive neuropathies of the wrist. J Clin Ultrasound 2004;32:451–461.
29. Bianchi S, Montet X, Martinoli C, et al. Echographie des nerfs des membres inférieures [Ultrasound of nerves of the lower extremity]. Rev Rhum 2007;74:415–423.
30. Wright TW, Gloweczewskie F, Wheeler D, et al. Excursion and strain of the median nerve. J Bone Joint Surg Am 1996;78A:1897–1903.
31. Propeck T, Quinn TJ, Jacobson JA, et al. Sonography and MR imaging of bifid median nerve with anatomic and histologic correlation. AJR Am J Roentgenol 2000;175:1721–1725.
32. Iannicelli E, Chianta GA, Salvini V, et al. Evaluation of bifid median nerve with sonography and MR imaging. J Ultrasound Med 2000;19:481–485.
33. Bayrak IK, Bayrak AO, Kale M, et al. Bifid median nerve in patients with carpal tunnel syndrome. J Ultrasound Med 2008;27(8):1129–1136.
34. Gassner EM, Schocke M, Peer S, et al. Persistent median artery in the carpal tunnel: color Doppler ultrasonographic findings. J Ultrasound Med 2002;21:455–461.
35. Kele H, Verheggen R, Reimers CD. Carpal tunnel syndrome caused by thrombosis of the median artery: the importance of high-resolution ultrasonography for diagnosis. Case report. J Neurosurg 2002;97:471–473.
36. Sener E, Takka S, Cila E. Supracondylar process syndrome. Arch Orthop Trauma Surg 1998;117:418–419.
37. Bianchi S, Santa DD, Glauser T, et al. Sonography of masses of the wrist and hand. AJR Am J Roentgenol 2008;191(6):1767–1775.
38. Spiess AM, Gursel E. Entrapment of the ulnar nerve at Guyon's canal by an accessory abductor digiti minimi muscle. Plast Reconstr Surg 2006;117(3):1060–1061.
39. Harvie P, Patel N, Ostlere SJ. Ulnar nerve compression at Guyon's canal by an anomalous abductor digiti minimi muscle: the role of ultrasound in clinical diagnosis. Hand Surg 2003;8(2):271–275.
40. Malloy MA, Finger DR. Clinical image: carpal tunnel syndrome from accessory lumbrical muscles. Arthritis Rheum 2000;43(3):707.
41. Kinoshita M, Okuda R, Morikawa J, Abe M. Tarsal tunnel syndrome associated with an accessory muscle. Foot Ankle Int 2003;24(2):132–136.
42. Cartwright MS, Chloros GD, Walker FO, et al. Diagnostic ultrasound for nerve transection. Muscle Nerve 2007;35(6):796–799.
43. Spencer PS. The traumatic neuroma and proximal stump. Bull Hosp Joint Dis 1974;35:85–102.
44. Li J, Krajewski K, Shy ME, et al. Hereditary neuropathy with liability to pressure palsy: the electrophysiology fits the name. Neurology 2002;58:1769–1773.
45. Beekman R, Visser LH. Sonographic detection of diffuse peripheral nerve enlargement in hereditary neuropathy with liability to pressure palsies. J Clin Ultrasound 2002;30:433–436.
46. Sammarco GJ, Stephens MM. Tarsal tunnel syndrome caused by flexor digitorum accessorius longus. J Bone Joint Surg 1990;72A:453–454.
47. Bodner G, Huber B, Schwabegger A, et al. Sonographic detection of radial nerve entrapment within a humerus fracture. J Ultrasound Med 1999;18:703–706.
48. Bodner G, Harpf C, Meirer R, et al. Ultrasonographic appearance of supinator syndrome. J Ultrasound Med 2002;21:1289–1293.
49. Bodner G, Buchberger W, Schocke M, et al. Radial nerve palsy associated with humeral shaft fracture: evaluation with US – initial experience. Radiology 2001:219:811–816.
50. Beaman FD, Kransdorf MJ, Menke DM. Schwannoma: radiologic-pathologic correlation. Radiographics 2004;24:1477–1481.
51. Tsai WC, Chiou HJ, Chou YH, et al. Differentiation between schwannomas and neurofibromas in the extremities and superficial body: the role of high-resolution and color Doppler ultrasonography. J Ultrasound Med 2008;27:161–166.
52. Reynolds DL Jr, Jacobson JA, Inampudi P, et al. Sonographic characteristics of peripheral nerve sheath tumors. AJR Am J Roentgenol 2004;182:741–744.
53. Gruber H, Glodny B, Bendix N, et al. High-resolution ultrasound of peripheral neurogenic tumors. Eur Radiol 2007;17:2880–2888.
54. Bianchi S, Abdelwahab IF, Kenan S, et al. Intramuscular ganglia arising from the superior tibio-fibular joint: CT and MR evaluation. Skeletal Radiol 1995;24:253–256.
55. Bianchi S, Zwass A, Abdelwahab IF, et al. Sonographic evaluation of intramuscular ganglia. Clin Radiol 1995;50:235–236.
56. Martinoli C, Schenone A, Bianchi S, et al. Sonography of the median nerve in Charcot-Marie-Tooth disease. AJR Am J Roentgenol 2002;178(6):1553–1556.
57. Martinoli C, Derchi LE, Bertolotto M, et al. US and MR imaging of peripheral nerves in leprosy. Skeletal Radiol 2000;29(3):142–150.
58. Toms AP, Anastakis D, Bleakney RR, Marshall TJ. Lipofibromatous hamartoma of the upper extremity: a review of the radiologic findings for 15 patients. AJR Am J Roentgenol. 2006;186(3):805–811.
59. Marhofer P, Chan VW. Ultrasound-guided regional anesthesia: current concepts and future trends. Anesth Analg 2007;104(5):1265–1269.
60. Gray AT. Ultrasound-guided regional anesthesia: current state of the art. Anesthesiology 2006;104(2):368–373.

CHAPTER

62

Interventional musculoskeletal ultrasound

Catherine L. McCarthy and Eugene G. McNally

INTRODUCTION

Ultrasound is ideal for guiding interventional musculoskeletal procedures. It provides real-time visualisation of needle advancement, confirmation of accurate needle placement and observation of interventional procedures such as aspiration, injection and biopsy. Aspiration of cystic lesions may be both diagnostic and therapeutic. Aspiration of joints helps differentiate between seropositive, seronegative, crystal and septic arthropathy. Injection may be diagnostic or therapeutic. A diagnostic injection is targeted at a specific site to determine if it is the source of the patient's symptoms by assessing the response to local anaesthetic injection. A therapeutic injection usually contains corticosteroids to give an anti-inflammatory effect. Biopsy of solid soft tissue masses and bone lesions that involve the cortex can be performed under ultrasound guidance. The aim of this chapter is to provide a practical description of the most commonly performed procedures.

Several points are common to most ultrasound-guided interventional procedures.

An appropriate patient history including allergies and medication, specifically anticoagulation drugs, should be obtained. Informed patient consent should be obtained following discussion of the risks of infection, bleeding, initial increase in pain and allergic reaction. Fat necrosis and skin discoloration are potential complications following superficial steroid injections. With sterile precautions, extra-articular soft tissue injections have a remarkably low complication rate.

Potential risks of musculoskeletal interventional procedures

- Infection
- Bleeding
- Initial increase in pain
- Allergic reaction
- Fat necrosis
- Skin discoloration
- Steroid flare
- Tendon rupture
- Local trauma (nerves, vessels, articular cartilage)

High-frequency linear array transducers with a centre frequency of 9.5–12.5 MHz are usually used. Occasionally a lower-frequency 5 MHz curved array transducer is required for imaging deeper joints such as the hip in obese patients. The focal zone should be centred at the depth of the target and the gain settings should be adjusted to allow differentiation between cystic and solid lesions. Stand-off pads are not recommended because of the difficulty of keeping the puncture point sterile.

A full ultrasound examination should be completed before localisation of the intended target structure. Time should be spent determining the best transducer position, puncture point and approach route while avoiding other soft tissue structures and nearby neurovascular bundles. The puncture site is marked in a number of ways. Skin marking pens are commonly used but may be smudged or wiped clear during skin sterilisation if they are water soluble or stain the probe if not water soluble. Pressure with the blunt end of a needle or needle cover avoids this. Pressure for 10 seconds produces an impression that lasts for about 5 minutes, which is enough time for scrubbing and skin preparation. Skin pressure can be combined with a marker pen to indicate the puncture site. Marking a line rather than a single point gives the initial needle direction as well as the puncture point. The relationship of the puncture point to the intended target can be shown by placing a metal marker such as an extended paperclip on the marked puncture site. The transducer over the paperclip creates an artefact characterised by ring down, an echo pattern caused by reverberation, which is projected through the tissues towards the target. With practice, the needle can be inserted blind then advanced the final distance under ultrasound guidance to its intended target.

The degree of sterility varies with the procedure, personal practice and local guidelines. Thorough skin antisepsis and sterile contact jelly should be minimal requirements. For intra-articular injections, particularly with implanted joints, a higher level of sterility is warranted with gloved hands, meticulous skin preparation, skin drapes and sterile probe covers.

Lidocaine 1% is generally used for local anaesthesia and is injected along the course that will be traversed by the needle. Care must be taken not to inject air bubbles as they may obscure the region of interest. The initial sting from some anaesthetic

preparations can be reduced by the addition of a 1% bicarbonate solution. Adequate time should be given for local anaesthesia to work. With more complex preparations, such as the application of a sterile probe cover, skin preparation and local anaesthesic injection are carried out first. Ultrasound guidance can be used to infiltrate local anaesthetic around a mass prior to biopsy, particularly if the lesion is expected to contain neural elements. Certain bone biopsies may be performed under ultrasound guidance and it is important to generously infiltrate local anaesthetic around the periosteum at the biopsy site because of the hypersensitivity of the periosteal envelope. In children, the use of topical local anaesthetic cream or ethyl chloride spray helps to reduce the discomfort of the initial injection. These preparations can also be used in adults in areas that are more uncomfortable such as the sole of the foot but whether they have any more than a placebo effect in adults is debatable.

The distance of the target from the skin puncture point can be measured to choose the appropriate needle length. A 21G green (4 cm) needle is usually sufficient to puncture relatively superficial structures in the majority of cases. A 21G spinal (9 cm) needle is used for deeper structures. Rarely, it may be necessary to use longer needles such as a Chiba needle for very large patients. A wider-bore 17–19G needle may be used for aspiration of viscous fluid from an abscess or ganglion. A variety of biopsy needles are available for soft tissue and synovial biopsy. A 14–16G biopsy needle is usually used. It is important to be familiar with the throw length of the needle to ensure adequate sampling and to avoid nearby vital structures.

Needle placement technique is similar regardless of the type of needle and whether the intention is to aspirate, inject or biopsy. Ideally the patient should not see the needle until it is about to be inserted into the skin. A minor distraction at the time of needle insertion such as asking the patient to take a deep breath or directing a question may help. The needle entry is usually aligned with the ultrasound transducer in the longitudinal plane so that the shaft of the needle is seen as a bright echogenic linear structure. Reverberation artefacts may be seen posterior to the needle as its axis approaches 90° to the ultrasound beam. Once the needle is in the target structure, the location of the needle tip can be confirmed in the transverse plane where it is seen as a single echogenic dot in the centre of the target. With practice, the dexterity required to manipulate the needle improves and the needle may be held in either the right or left hand with an approach from above or below the transducer.

Needle visualisation in interventional musculoskeletal ultrasound is generally excellent because of the high-resolution transducers and relatively superficial musculoskeletal structures. There are several techniques for optimising needle visualisation. The needle should be advanced as parallel to the face of the transducer as possible to maximise needle conspicuity by providing a single strong sound interface that should render the needle visible regardless of the acoustic properties of surrounding tissues. Repeated small backwards and forwards movements of the needle are useful in showing the needle tip, particularly when injecting deep structures. If there is still doubt, a small injection of local anaesthetic or sterile saline which is almost invariably accompanied by a little gas is ultrasonically visible and will localise the injection even if the needle tip cannot be seen. With the needle in place, colour flow can be used during an injection. The location of the colour jet will confirm that needle placement is correct (Fig. 62.1D).

The injection tray should be prepared in advance and kept out of the patient's sight until needed. Drugs should not be drawn up in full view of the patient, particularly children. The most frequently used therapeutic cocktail is a combination of corticosteroid mixed with a long- or short-acting local anaesthetic such as 40 mg triamcinolone and a long-acting local anaesthetic. For more superficial injections, where there is a risk of a subcutaneous leak, methylprednisolone replaces triamcinolone as the corticosteroid of choice as there is some evidence to suggest methylprednisolone is less likely to cause subcutaneous fat necrosis or skin depigmentation.

Corticosteroid should not be injected directly into tendons as a focal area of necrosis may lead to tendon rupture. If there is uncertainty about needle placement into a tendon sheath, a preliminary injection of a small quantity of local anaesthetic will distend the tendon sheath, confirming correct needle placement with free flow of anaesthetic within the sheath and away from the needle. The needle should be repositioned if undue resistance is encountered. Injections around large weight-bearing tendons, such as the Achilles and patellar tendons, should only be performed after discussion of the risks and benefits with both the patient and clinical team.

Tips to optimise needle visualisation

- Advance needle as parallel to transducer as possible.
- Use small back and forward movements to localise needle.
- Inject small amount of local anaesthetic or sterile saline to localise needle tip.
- Use colour flow during needle placement or injection.

SHOULDER

Subacromial subdeltoid bursal injection

Introduction

Ultrasound-guided injections can be quickly and easily performed following the diagnostic shoulder examination, which ends with the patient and transducer in the correct position for injection. A quick clean with a sterile swab followed by the bursal injection allows the diagnostic examination to be combined with a guided injection with little prolongation of the overall examination time.

Equipment

A 21G needle is adequate for all but the deepest bursae. The subacromial subdeltoid bursa is a large structure and can accommodate a considerable volume of fluid but a combination of 40 mg triamcinolone and a long-acting local anaesthetic totalling 5–10 mL is usually used.

Patient position

The shoulder is usually examined with the operator standing behind the seated patient. The patient is asked to leave their arm in the final position of the diagnostic examination with the shoulder adducted and internally rotated. Some sonologists prefer the patient to be supine to reduce the risk of a vasovagal reaction.

Transducer position

The transducer is placed in the same position as used to create a coronal image of the supraspinatus tendon.

Puncture point

The needle can approach from either above or below the transducer. A common approach for a right-handed operator, for a right shoulder injection, is to hold the transducer in the right hand and the needle in the left hand while standing behind the seated patient. The reverse is true for a left shoulder injection. With this technique, the skin is punctured above the transducer, lateral to the tip of the

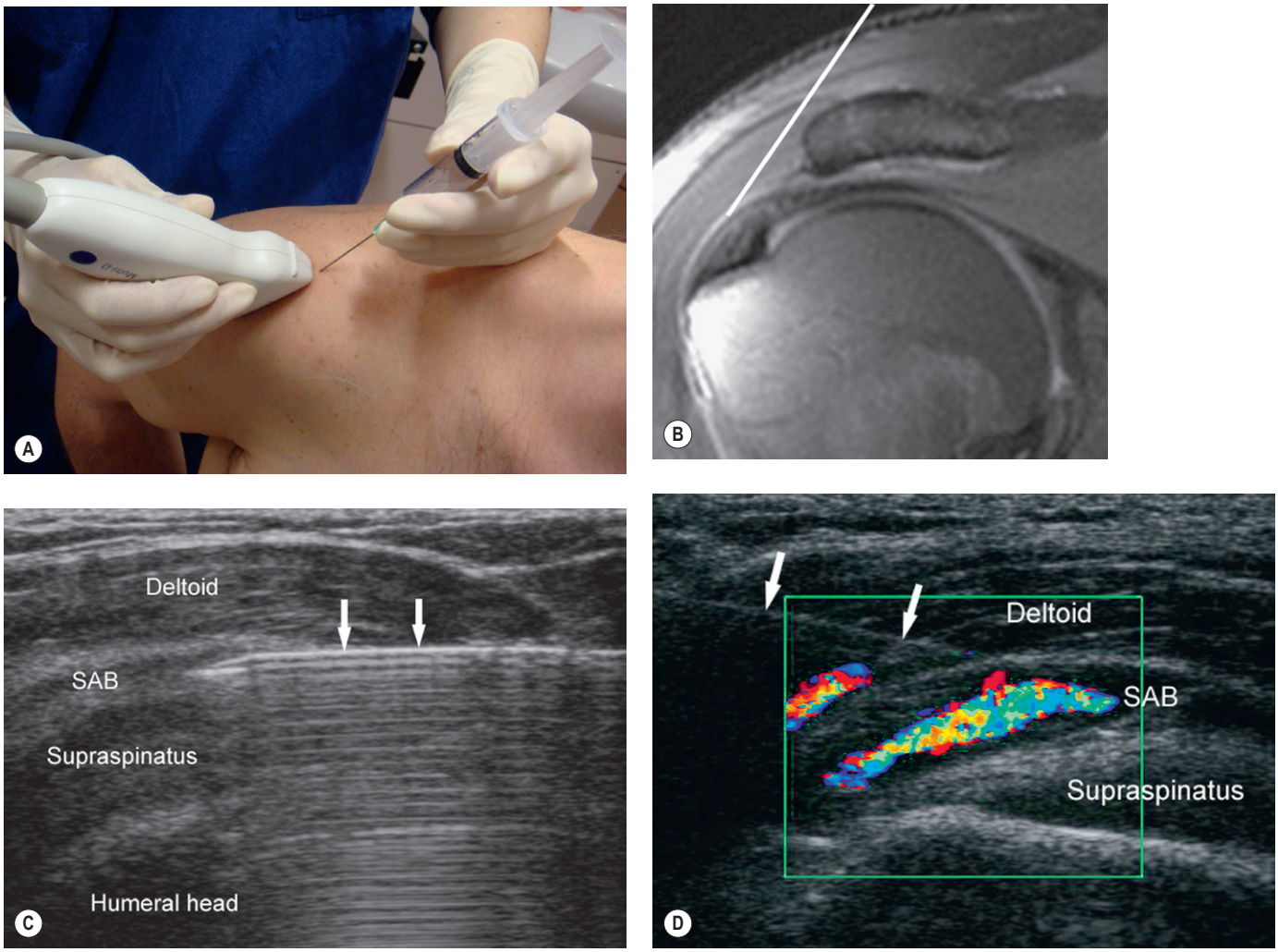

Figure 62.1 Subacromial subdeltoid bursal injection. A: The patient leaves the arm in the final position of the diagnostic examination with the shoulder adducted and internally rotated. The preferred approach to the bursa is with the needle above the transducer. **B:** Coronal proton density MR image shows the approach of the needle, lateral to the tip of the acromion and parallel to the bursa, close to the superolateral margin of supraspinatus. **C:** Comparative ultrasound image shows the needle (arrows) entering the bursa (SAB) between the deltoid muscle and supraspinatus tendon. Reverberation artefact is seen posterior to the needle. **D:** Ultrasound image with colour Doppler flow shows the needle (arrows) with a colour jet in the bursa (SAB) confirming correct needle placement during the bursal injection.

acromion and the needle directed anterolaterally into the bursa. An approach from above the transducer has the advantage of the transducer cable not getting in the way of the needle (Fig. 62.1). If the patient is supine, the needle can be inserted along the same axis in the opposite direction by puncturing the skin distal to the transducer. An alternative is to place the transducer transversely in an anterior position until the anterior free edge of the supraspinatus tendon and the subacromial subdeltoid bursa are visualised. The skin is punctured just medial to the transducer and the needle directed into the bursa (Fig. 62.2).

Target point

Provided that the needle is kept in the same plane as the transducer, it can be visualised until it reaches the superior surface of the supraspinatus tendon. An initial injection in this position may confirm correct needle placement in the bursa as the injected material flows away from the needle tip. It helps if the bevel of the needle is inferior. Focal accumulation of injected fluid indicates incorrect positioning with the needle tip most commonly on the deltoid side of the bursa. Gentle advancement of the needle with a slight

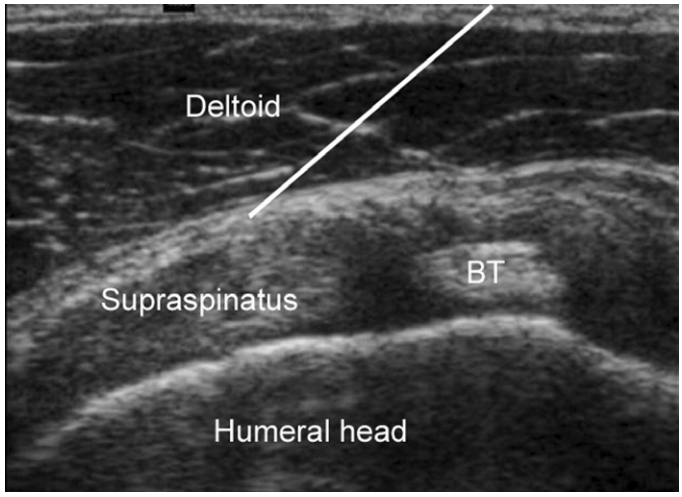

Figure 62.2 Subacromial subdeltoid bursal injection via anterior approach. Anterior transverse ultrasound image shows the anterior free edge of supraspinatus and biceps tendon (BT) with the needle directed into the bursa from a medial puncture point.

hooking action to direct the needle under the reflective bursal surface is usually adequate to ensure placement within the bursa and the injection can be completed.

Post procedure

Following the injection it is often useful to gently manipulate the shoulder and determine whether the patient's range of movement within the painful arc has improved. A reduction of symptoms with an increased range of motion is termed a positive impingement test.

Barbotage of calcific supraspinatus tendinopathy

Introduction

Calcific tendinopathy is caused by the deposition of calcium hydroxyapatite crystals. It is not always symptomatic and barbotage is usually reserved for patients who suffer acute pain. Symptoms may be so acute that a diagnosis of septic arthritis is frequently considered. It is difficult to determine which lesions are likely to respond to treatment. Inflammatory change in the adjacent tendon and poorly demarcated calcification with faint or absent acoustic shadowing are clues.[1] Plain films may be more useful in making this assessment. Ill-defined faint cloudy appearances on the plain radiograph suggest milk of calcium, which is more easily aspirated and likely to respond to the procedure. Well-defined dense calcification is usually longstanding and unlikely to respond to barbotage.

Equipment

A single or double needle technique may be used with 18–21G needles. The calcium may be easier to flush out by using one needle to inject saline and a second needle for aspiration.[1] Multiple needle punctures of the rotator cuff with larger 18G needles are not known to compromise tendon integrity or increase the risk of a tendon tear.

Patient position

The technique is similar to a subacromial subdeltoid bursa injection previously described and can be carried out with the patient seated or supine. The patient should be warned that barbotage may be painful and in many cases the examination is best carried out with the patient in an oblique decubitus position.

Transducer position

Although the coronal approach frequently provides the best view of the calcification, this is not always true. The transducer should be positioned for optimal visualisation of the calcification and the most direct approach to it.

Puncture point

Once the best transducer position has been decided, the skin is usually punctured at the midpoint of the lateral short axis of the transducer.

Target point

The needle is initially directed into the subacromial subdeltoid bursa, which is injected with local anaesthetic before the barbotage procedure as barbotage may release calcium crystals into the bursa, which can be very painful. The same needle is then advanced into the calcium (Fig. 62.3). The distal part of the needle is usually not visible within the dense calcium because of posterior acoustic shadowing generated by calcium. Correct needle location can be verified when gentle movement of the needle is transmitted to the calcific deposit and observed by ultrasound. Aspiration of calcium is initially attempted. If aspiration is unsuccessful, then needling the lesion can help encourage calcium fragmentation and dispersion. Saline may be injected to help flush out the calcium. Subsequent aspiration may then be performed via the same needle or a second needle may be inserted so that the saline is injected via one needle and aspirated with the other. Extracted calcium is identified in the syringe as solid white gritty material or milk-like fluid. Lavage is usually continued until the aspirate is free of calcific particles but it is not essential to remove the calcium deposit completely. Excellent results have been reported following partial removal of calcium.[1,2] In these cases, needling may decompress the calcium-containing cavity and allow sufficient disruption and localised bleeding to facilitate spontaneous resorption of the remaining calcium or its dispersion into the subacromial space.[1,2] Reduction in the size of the calcification or a decrease in its echogenicity are associated independently with improved symptomatic relief.[1,2] Following barbotage, a small quantity of local anaesthetic and hydrocortisone may be injected into the residual calcium.

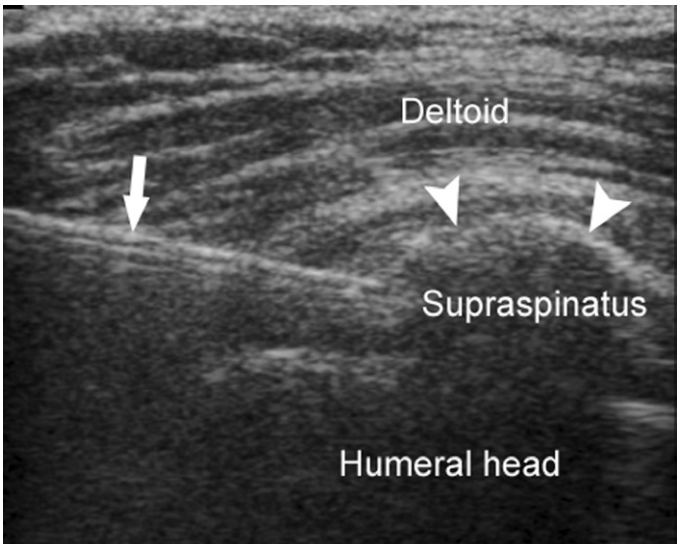

Figure 62.3 Supraspinatus calcification barbotage. Coronal ultrasound image showing the needle (arrow) directed into an echogenic calcium deposit (arrowheads) within the distal supraspinatus tendon.

Tips to barbotage supraspinatus tendon

- Better response if ill-defined calcification, faint acoustic shadowing, peritendinous inflammation, reduction in calcium size and echogenicity post procedure.
- Position transducer for most direct approach to calcification.
- Start with local anaesthetic injection into subacromial bursa.
- Needle calcium to encourage fragmentation and dispersion.
- Needle movement transmitted to calcification aids in localisation.
- Use saline to flush out calcium.
- Use single or double needle technique to aspirate calcium.
- Follow barbotage with local anaesthetic and hydrocortisone injection into residual calcium or subacromial bursa.

Shoulder joint injection

Introduction

Guided shoulder injections may be used for therapeutic purposes or direct magnetic resonance (MR) arthrography. MR arthrography

is useful to depict the intra-articular abnormalities that contribute to an unstable shoulder following shoulder dislocation. As the majority of dislocations and structures of interest are anterior, a posterior approach is best to reduce any artefacts that may hinder interpretation of the study. Injection may be performed under ultrasound or fluoroscopic guidance to reduce the risk of failure associated with a blind injection. Ultrasound equipment is portable and thus more readily available in remote MR units.

Equipment

A 21G spinal needle is recommended. The injectate depends on the indication for the procedure; either a mixture of 40 mg triamcinolone and a long-acting local anaesthetic for a therapeutic injection or approximately 12–20 mL of 0.1 mL gadolinium diluted in 20 mL saline for an MR arthrogram.

Patient position

The patient may be seated with the operator standing behind the patient. Alternatively the patient may be placed in a semi-prone position with the affected shoulder uppermost and the ipsilateral arm resting over a bolster or pillow to maintain the semi-prone position and optimise patient comfort.

Transducer position

The transducer is best aligned beneath the scapular spine in the axial plane directly over the posterior glenohumeral joint and manipulated until the posterior glenoid margin with its attached labrum is visualised.

Puncture point

The needle is introduced just lateral to the ultrasound transducer and directed obliquely along a path where the humeral head slopes towards the posterior labrum.

Target point

The needle is directed in the axial plane aiming for a point approximately halfway between the most posterior aspect of the humeral head and the glenoid margin. The path of the needle is adjusted so that the needle tip passes into the joint space directly beneath the free margin of the glenoid labrum (Fig. 62.4). Care should be taken not to aim for the glenoid margin itself as a large labrum may displace the needle posteriorly and prevent accurate placement into the joint. This lateral approach avoids the suprascapular nerve and circumflex scapular vessels that course medial to the glenoid rim. As the needle passes through the infraspinatus tendon or its musculotendinous junction, the needle tip may be deflected off course as it dissects into and along the path of the tendon fibres. This tendency can be reduced by advancing the needle with the bevel of the needle tip facing away from the humeral head.[3] Rotation of the needle tip through 180° so that the bevel faces towards the humeral head may be required to find a resistance-free intracapsular location.[3] The intra-articular position of the needle can be confirmed by injecting a small amount of local anaesthetic. The arthrographic material or an anti-inflammatory cocktail may then be injected. In the early stages of the injection, distension of the posterior glenohumeral joint recess is typically not evident on real-time scanning as the injected substance passes into the non-visualised dependent anterior joint recess. Towards the end of the injection, if a sufficiently large volume of fluid has been instilled, the posterior recess of the glenohumeral joint begins to distend and the posterior capsule is seen displacing away from the humeral head.

Other indications for ultrasound-guided procedures around the shoulder joint include injection of the biceps tendon sheath, anterior interval and aspiration-injection of paralabral or supraglenoid cysts, which are best performed with a transversely orientated transducer.

Acromioclavicular joint injection

Equipment

A 21G green needle and 20 mg methylprednisolone mixed with a long-acting local anaesthetic is suggested. The acromioclavicular joint is a small joint and is unlikely to accept more than 1–1.5 mL.

Patient position

The procedure is performed with the patient seated or supine and the operator beside the patient.

Transducer position

The acromioclavicular joint is most easily visualised in the coronal plane but best injected in the sagittal plane. To identify the joint in the sagittal plane, the transducer is initially placed over the outer end of the clavicle and then moved laterally until the bony reflection disappears, indicating that it is now positioned directly over the joint. Further lateral movement shows the echogenic surface of the acromion.

Puncture point

The needle is inserted from superoposterior parallel to the transducer with the transducer in the sagittal plane along the anterior aspect of the joint (Fig. 62.5). Reversing needle and transducer is equally effective.

Target point

The needle is easily seen entering the rounded poorly reflective joint.

ELBOW

Common extensor origin injection

Introduction

The main indication for injecting the common extensor origin is persistent tennis elbow that has failed to respond to physiotherapy and blind injection. The same procedure can be used to inject the common flexor origin on the medial side of the elbow for persistent golfer's elbow.

Equipment

A 21G green needle is used. For a corticosteroid injection, a combination of 40 mg methylprednisolone mixed with a long-acting local anaesthetic totalling 2–3 mL is suggested. An alternative procedure that does not involve corticosteroids is to make multiple punctures of the tendon with the needle, which is termed dry needling. It is postulated that dry needling fenestrates the tendon, causing fibrillar disruption and internal bleeding to initiate a healing response.[4] Dry needling can be combined with an injection of 2 mL autologous blood. It is hypothesised that growth factor-β and fibroblast growth factor carried in the blood will act as humoral mediators to induce the healing cascade.[4]

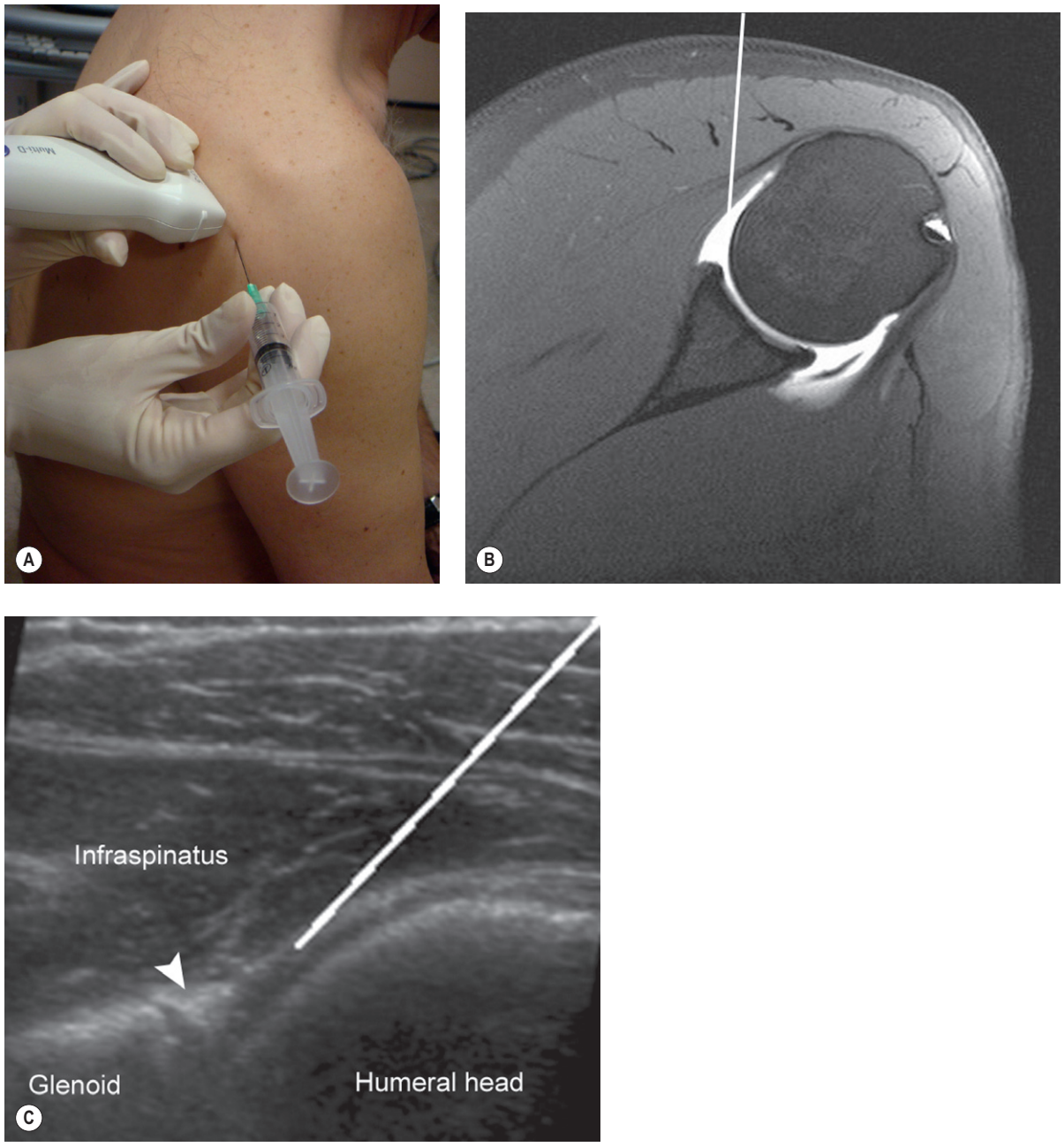

Figure 62.4 Shoulder joint injection. A: The transducer is placed in the axial plane over the posterior shoulder with the patient in a seated or semi-prone position. The puncture point is lateral to the transducer. **B:** Axial fat-saturated T1-weighted MR arthrogram indicating the path of the needle along the humeral head as it slopes towards the posterior labrum into the posterior glenohumeral joint. **C:** Ultrasound image at the same position shows the direction of the needle into the joint space directly beneath the free margin of the posterior glenoid labrum (arrowhead).

Patient position

Injection of the common extensor origin is usually performed with the patient seated opposite the operator with both arms extended on the examination table and palms together in the so called 'prayer position'.

Transducer position

The transducer is positioned in the coronal plane along the lateral aspect of the elbow.

Puncture point

The skin is punctured distal to the transducer and the needle advanced proximally and medially to the extensor origin.

Target point

The line of approach should allow the needle to be advanced to the deep portion of the common extensor origin, which is usually the site of maximal tendon injury. The radiocapitellar joint is a useful landmark for this purpose (Fig. 62.6).

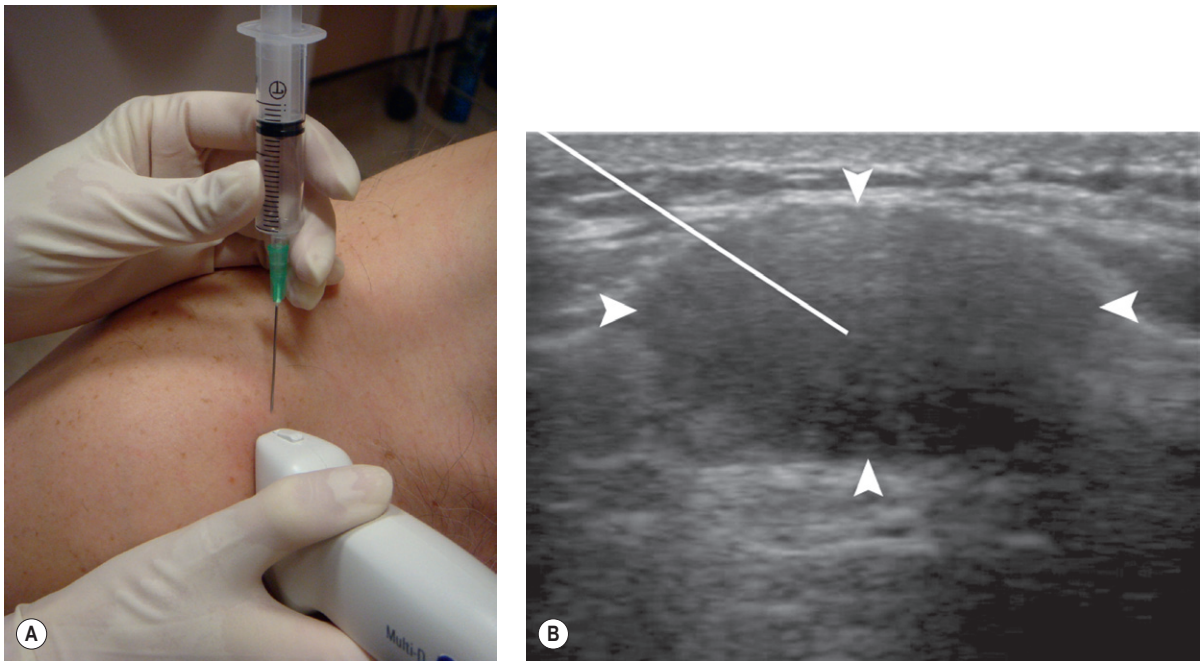

Figure 62.5 Acromioclavicular joint injection. A: The acromioclavicular joint is best injected in the sagittal plane. The transducer is usually along the anterior aspect of the joint with the needle inserted from superoposterior. Reversing needle and transducer is equally effective. **B:** Ultrasound image showing the acromioclavicular joint as a rounded, poorly reflective structure (arrowheads) in the sagittal plane and the approach of the needle.

Elbow joint injection

Equipment

A 21G green needle is usually adequate to access the elbow joint; 40 mg triamcinolone mixed with a long-acting local anaesthetic is a common combination for a therapeutic injection. The joint generally accepts 8–10 mL. Ultrasound may be used as guidance for joint distension and gadolinium injection prior to MR arthrography. Saline arthrosonography can be used to detect radiographically occult osseous and cartilaginous loose bodies within the joint.[5]

Patient position

The patient may be seated with the elbow flexed at 90° and forearm perpendicular to the examination table in the so-called 'crab position' or lying down with their arm positioned across their chest. In children with suspected septic arthritis, the child sits facing the mother on her lap with the arms wrapped around the mother's side. A nurse or assistant can stand behind the mother and hold the child's hands to prevent excessive movement. This position allows access to the posterior aspect of the elbow joint for examination and aspiration.

Transducer position

A posterior approach is simplest, particularly in the presence of an elbow joint effusion. The transducer is best positioned in a sagittal plane along the posterior aspect of the joint.

Puncture point

With a posterior approach, the puncture point is proximal to the transducer and a path adjacent to the triceps tendon rather than through it is recommended (Fig. 62.7). An alternative approach in adults is through the radiocapitellar joint, which is palpated as a soft spot on the lateral aspect of the flexed elbow. A third approach in adults is just lateral to the olecranon process where a small groove can be palpated between the olecranon and the humerus.

Target point

The elbow joint is readily identified by any of the approaches described. Once the needle is inserted, it is helpful to move the probe to visualise the olecranon fossa prior to injecting. This allows confirmation of joint filling and visualisation of loose bodies as mobile echogenic foci with or without posterior acoustic shadowing.[5]

WRIST AND HAND

Tendon sheath injection

Introduction

Injection of a tendon sheath is a relatively easy procedure due to the superficial location and elongated structure which provides a large target area.

Equipment

A 21G green needle and 40 mg triamcinolone mixed with a long-acting local anaesthetic is used. A large tendon sheath will usually accept 5 mL.

Patient position

The patient is seated opposite the operator with the forearm extended on the examination table and rotated to allow access to the relevant tendon sheath.

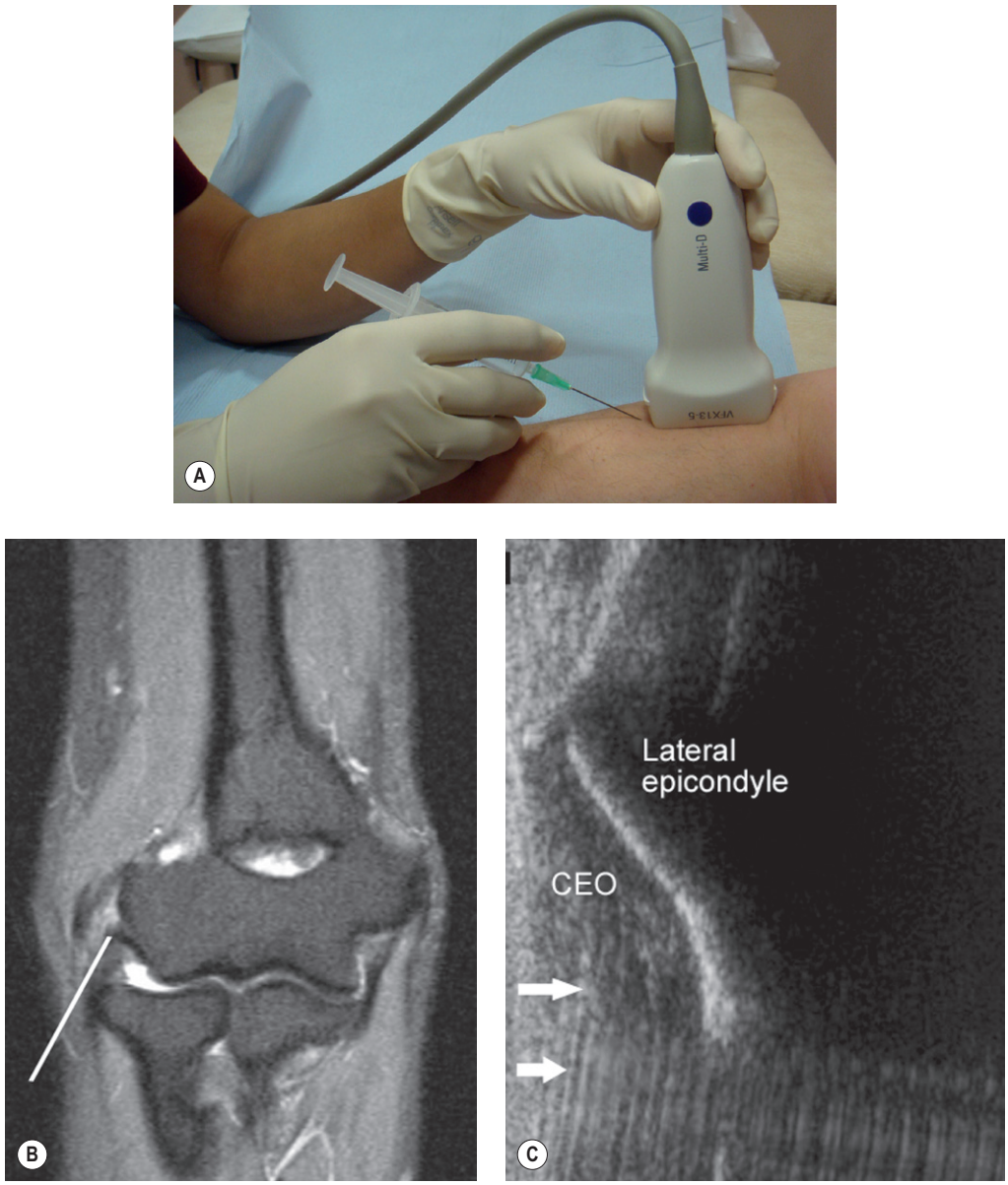

Figure 62.6 Common extensor origin injection. A: The patient is seated with arm extended and the transducer positioned in the coronal plane along the lateral elbow. The puncture point is usually distal to the transducer. **B:** Coronal STIR MR image shows the line of the needle towards the extensor origin and radiocapitellar joint. **C:** Corresponding ultrasound image shows the needle (arrows) being advanced towards the deep portion of the common extensor origin (CEO) with reverberation artefacts.

Transducer position

The transducer is orientated along the long axis of the tendon sheath to be injected.

Puncture point

The puncture point may be proximal or distal to the transducer with the needle directed at a relatively shallow angle towards the tendon sheath. A line rather than a point mark helps to indicate both the puncture site and direction of needle advancement. If local anaesthetic is used, the skin can be anaesthetised along the direction indicated by the line. When the transducer is placed in position, the needle tip will be found to lie close to its target area.

Target point

Under ultrasound guidance, the needle is advanced with further infiltration of local anaesthetic to provide pain relief and to distend the tendon sheath. Rotating the needle so that the bevel points towards the tendon helps reduce the possibility of tendon puncture. Once correct needle placement has been confirmed by the free flow of local anaesthetic within the sheath away from the needle, the full injection can be administered (Fig. 62.8). The injection should result in distension of the tendon sheath with filling on both sides of the tendon. If filling is limited to only one side of the tendon it is likely that the needle lies outside the tendon sheath. In de Quervain's tenosynovitis, the sclerosing nature of the disease limits the amount that can be injected and needle placement can be more difficult and painful.

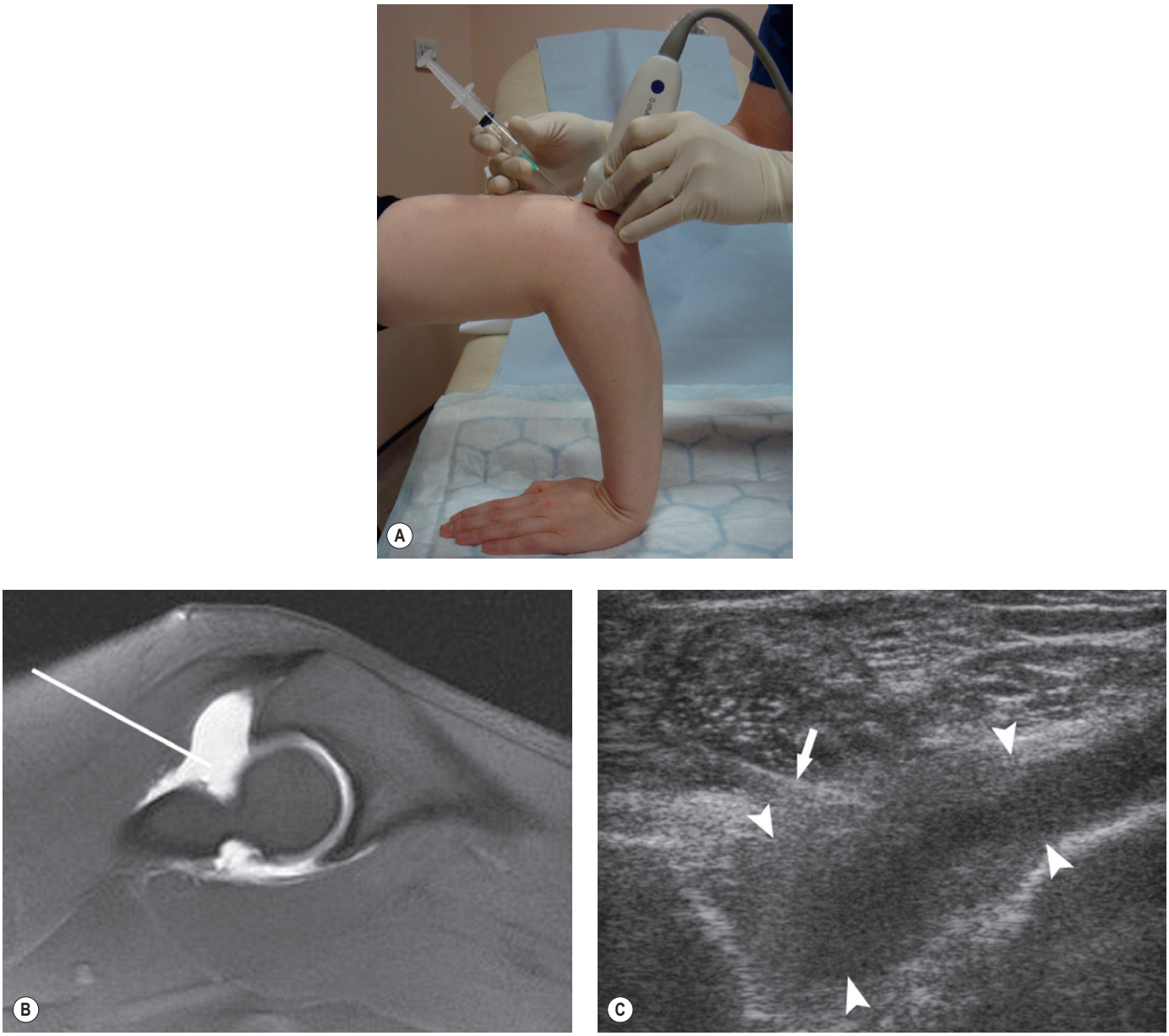

Figure 62.7 Elbow joint injection. A: The elbow joint is usually accessed from a dorsal approach with the transducer in a sagittal plane. The puncture point is proximal to the transducer, adjacent to the triceps tendon. **B:** Sagittal T1-weighted arthrogram with fat saturation showing the direction of the needle into the posterior joint space. **C:** Corresponding ultrasound image shows the needle (arrow) passing into an effusion within the olecranon fossa (between arrowheads).

Tips to inject tendon sheath

- Distinguish inflammation from infection, which should not be injected.
- Beware injecting weight-bearing tendons.
- Insert needle at relatively shallow angle.
- Insert needle with bevel down.
- Lead with local anaesthetic.
- Ensure fluid distends sheath and surrounds tendon after injection.
- De Quervain's tenosynovitis may be sclerosing with little or no fluid.

Carpal tunnel injection

Equipment

A 21G green needle and 40 mg triamcinolone mixed with a long-acting local anaesthetic is used.

Patient position

The patient is seated opposite the operator with the forearm extended and supinated on the examination table.

Transducer position

The standard injection point for a carpal tunnel injection is between the flexor carpi radialis tendon and the median nerve. The puncture

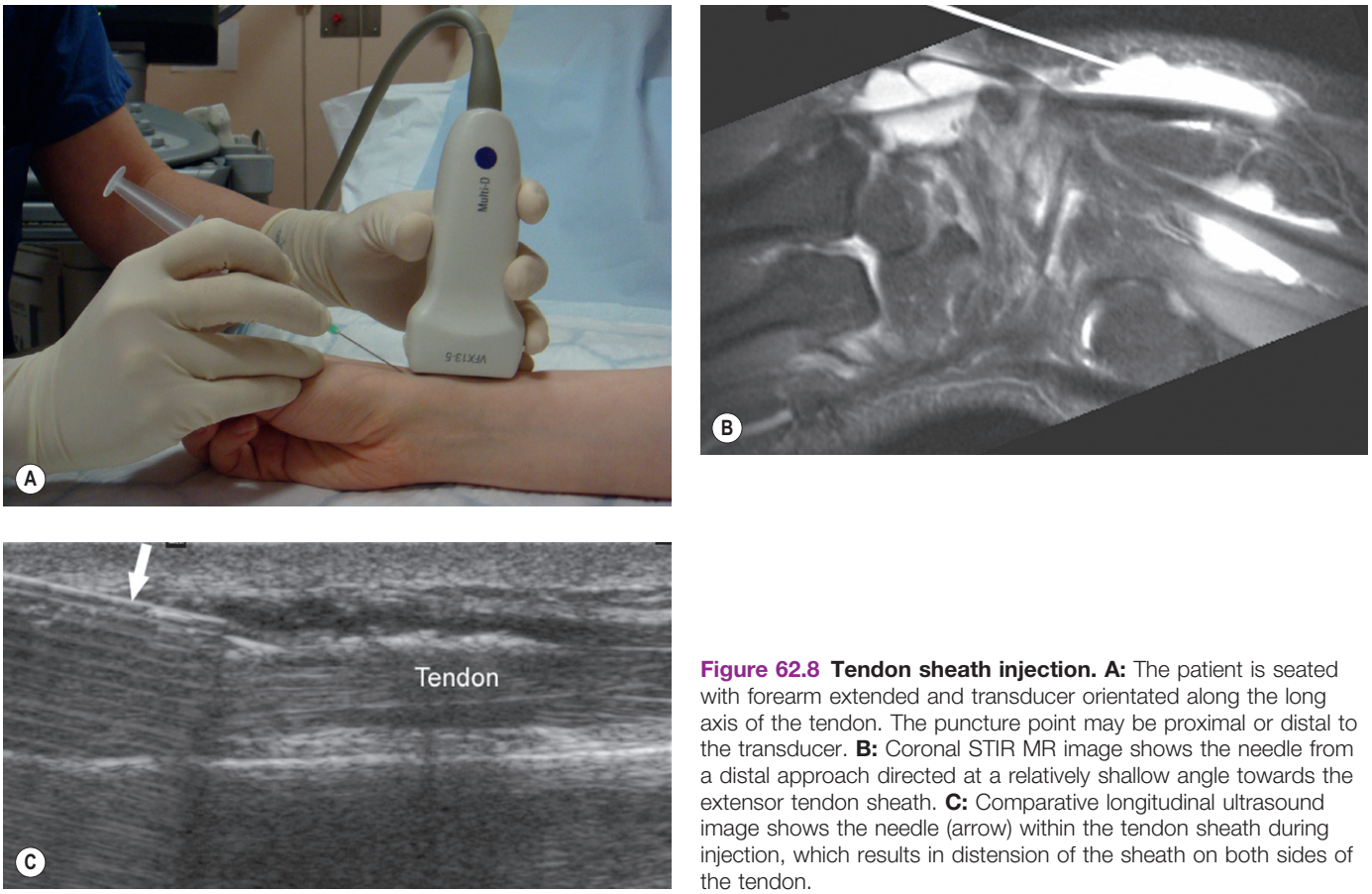

Figure 62.8 Tendon sheath injection. A: The patient is seated with forearm extended and transducer orientated along the long axis of the tendon. The puncture point may be proximal or distal to the transducer. **B:** Coronal STIR MR image shows the needle from a distal approach directed at a relatively shallow angle towards the extensor tendon sheath. **C:** Comparative longitudinal ultrasound image shows the needle (arrow) within the tendon sheath during injection, which results in distension of the sheath on both sides of the tendon.

point is determined by placing the transducer in the transverse plane to identify these two structures. The transducer is then rotated through 90° until its midpoint is centred over the space between the flexor carpi radialis tendon and median nerve in the sagittal plane.

Puncture point

The puncture point is proximal to the transducer and the flexor retinaculum.

Target point

The needle is directed under ultrasound guidance into the target space between the flexor carpi radialis tendon and median nerve. The small size of the target space means that a combination of sagittal and axial views with the transducer is helpful in confirming accurate needle placement.

Carpal joint injection

Equipment

A 21G green needle and 40 mg methylprednisolone mixed with a long-acting local anaesthetic is recommended for therapeutic injections. The carpal joint generally accepts 5 mL.

Patient position

The seated patient is positioned opposite the operator with the pronated forearm resting on the examination table. A rolled up towel or pad beneath the wrist allows slight wrist flexion.

Transducer position

The transducer is positioned in a sagittal plane along the dorsal aspect of the radiocarpal joint.

Puncture point

The preferred puncture point is distal to the transducer about 1 cm distal to Lister's tubercle at the level of the proximal scaphoid pole.

Target point

The needle is directed proximally to enter the radiocarpal joint beneath the dorsal rim of the distal radius (Fig. 62.9). With therapeutic injections, the injectate is directly visualised entering the carpal joint. Ultrasound differentiates between a joint effusion and synovitis in patients presenting with wrist pain and swelling, thus appropriately guiding joint aspiration and synovial biopsy to assist in the diagnosis of an arthropathy.

Ultrasound is useful to guide aspiration and injection of ganglia arising from the carpal joint (Fig. 62.10). Ganglia are the commonest soft tissue mass around the wrist and up to 70% arise from the dorsal scapholunate joint. Aspiration may be difficult as the ganglion usually contains viscous fluid and a wider bore 17–19G needle is usually required. Aspiration is followed by an injection of 20 mg methylprednisolone.

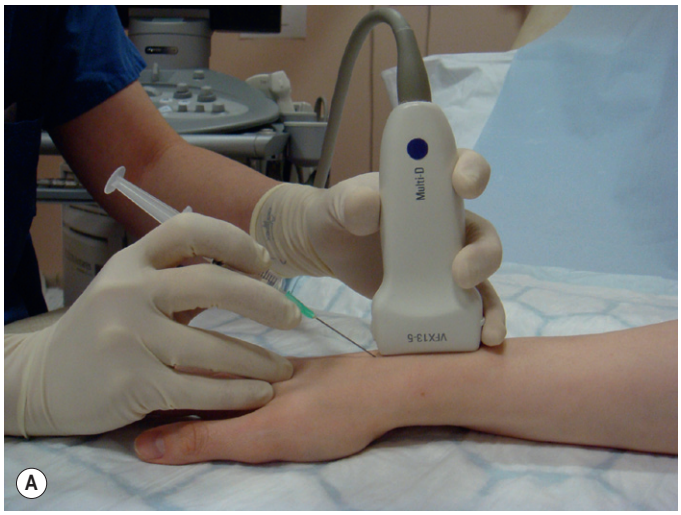

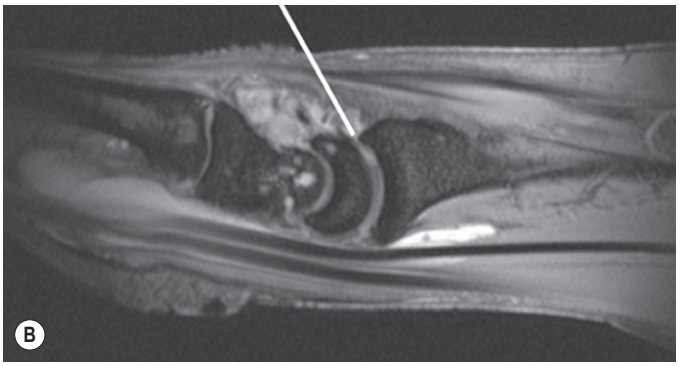

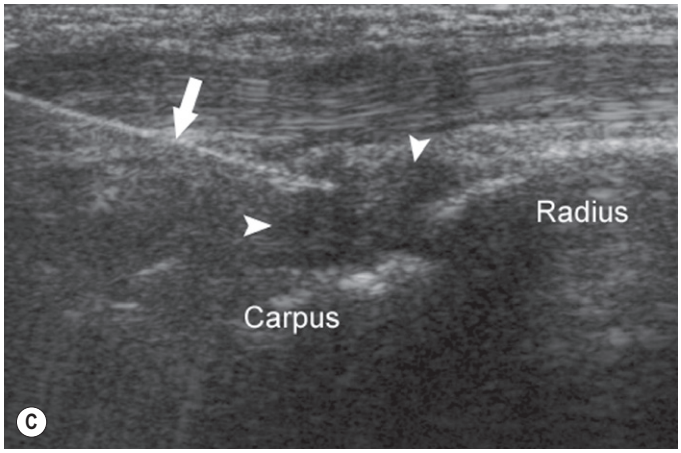

Figure 62.9 Carpal joint injection. A: The patient is seated with forearm pronated and transducer in a sagittal plane along the dorsal radiocarpal joint. The preferred puncture point is distal to the transducer at the level of the proximal scaphoid pole. **B:** Sagittal T2-weighted MR image with fat saturation in a rheumatoid patient showing carpal joint synovitis and the direction of the needle into the dorsal radiocarpal joint. **C:** Corresponding ultrasound image shows the needle (arrow) advancing into an area of low echogenicity synovitis (arrowheads) in the dorsal radiocarpal joint.

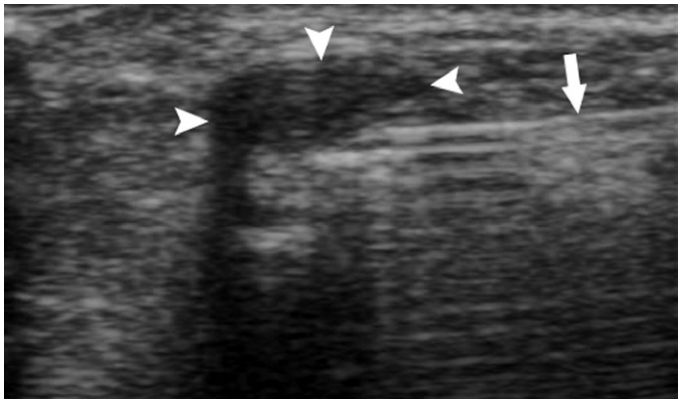

Figure 62.10 Aspiration of dorsal wrist ganglion. Longitudinal ultrasound image shows the needle (arrow) in a dorsal wrist ganglion (demarcated by arrowheads) prior to aspiration and injection.

Injection of the small joints of the hand

Introduction

Ultrasound-guided needle placement in small joints is more accurate than a palpation-guided approach.[6]

Equipment

A 21G green needle is used. For therapeutic injections, 30 mg methylprednisolone mixed with a long-acting local anaesthetic is recommended. The small joints of the hand generally accept 1–2 mL.

Patient position

Seating the patient opposite the seated operator with the patient's hand resting on the examination table provides good access to the small joints of the hand.

Transducer position

A small footprint ultrasound transducer is best as it allows the puncture point to be closer to the centre of the image. The transducer is best positioned in the sagittal plane along either the volar or dorsal aspect of the joint.

Puncture point

A proximal puncture point is preferred although a distal puncture site can be used. The puncture point is just to the side of the flexor or extensor tendon. The position of the joint space relative to the puncture point can be confirmed by interposing a sterile needle between the transducer and the skin and moving the needle to overlie the joint space.

Target point

A proximal puncture point allows the needle to parallel the curved head of the more proximal metacarpal or phalanx and be directed under the rim of the more distal bone (Fig. 62.11). The inclination of the needle is almost parallel to the skin surface to access the very superficial small joints. Once the needle tip is visualised within the joint space, anti-inflammatory therapeutic agents are injected. The intra-articular location of the needle is confirmed by visualising diffuse distension of the joint capsule during the injection. Joint aspiration and sampling of periarticular erosions is diagnostically useful to differentiate between seropositive, seronegative, crystal and other causes of an arthropathy. Synovial fluid may be aspirated in the presence of a joint effusion. If joint aspiration is unsuccessful, joint lavage with up to 1 mL of sterile saline followed by aspiration has been successful in obtaining synovial cells in up to 63% of cases.[6] Ultrasound guidance can also be used to sample periarticular erosions. A 19–21G needle is manipulated into the base of the erosion under direct visualisation and manipulated from side to side before being withdrawn using gentle suction with a syringe to remove a small amount of histological material for cytological analysis.[7]

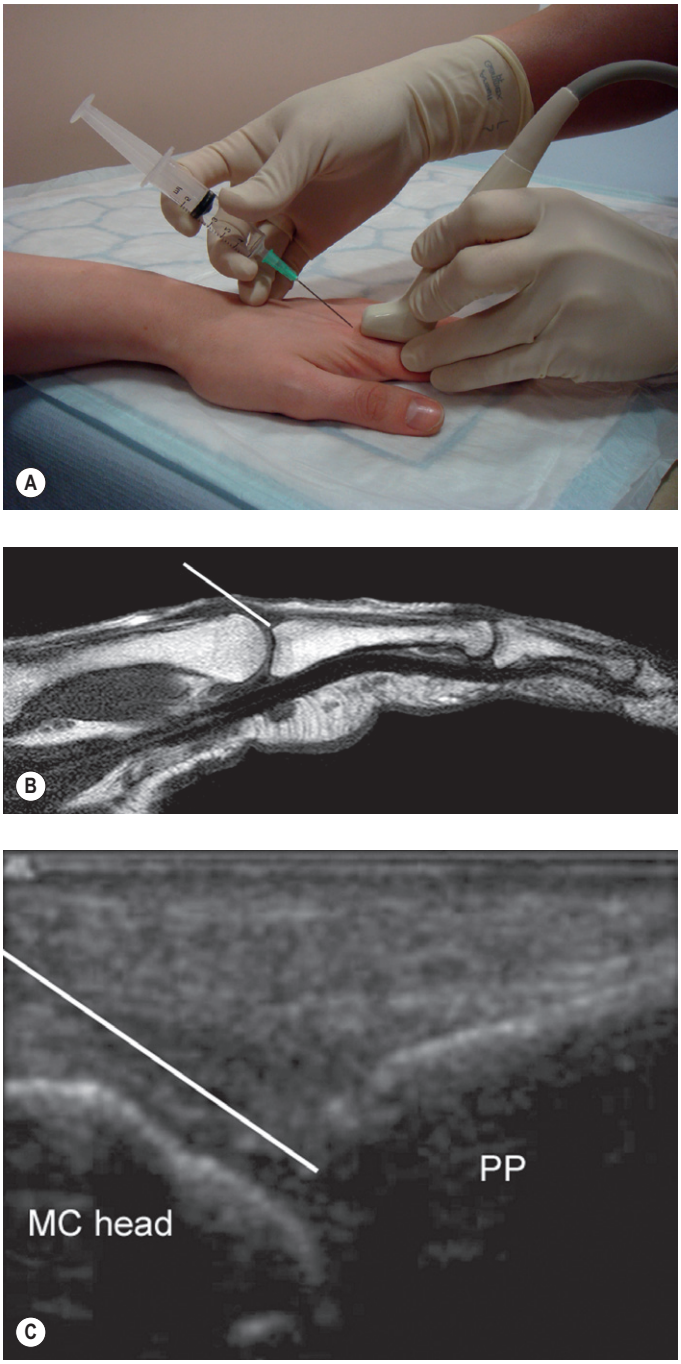

Figure 62.11 Injection of metacarpophalangeal joint of the hand. A: A small footprint transducer allows the puncture point to be closer to the centre of the image. The transducer is best positioned in the sagittal plane and a proximal puncture point is preferred. **B:** Sagittal T1-weighted MR image and **(C)** corresponding ultrasound image show the line of the needle from a proximal puncture point parallel to the curved metacarpal (MC) head and directed under the rim of the proximal phalanx (PP).

PELVIS

Adductor origin injection

Introduction

Adductor origin sprain or enthesopathy can be injected under ultrasound guidance. Ultrasound findings may not be prominent and correlation with areas of inflammation on corresponding MR images is often helpful.

Equipment

A 21G spinal needle with 40 mg triamcinolone mixed with a long-acting local anaesthetic totalling about 4–5 mL is used.

Patient position

The adductor origin is best exposed with the patient lying in the supine position with the thigh abducted and externally rotated and the knee flexed.

Transducer position

The transducer is orientated along the long axis of the adductor tendons. The bony landmark of the inferior pubic ramus, from which the adductor tendons originate, is easily seen at the proximal aspect of the transducer.

Puncture point

The puncture point is usually from below the transducer so the needle can be inserted close to the adductor origin.

Target point

The needle should be directed close to and paralleling the adductor origin so that the greatest area of infiltration is achieved (Fig. 62.12).

Symphysis pubis injection

Introduction

As with adductor origin injections, correlation with corresponding MR images may be helpful. Abnormal symphyseal MR signal may be detected in the asymptomatic athlete and radiological findings must always be correlated with clinical examination and history.

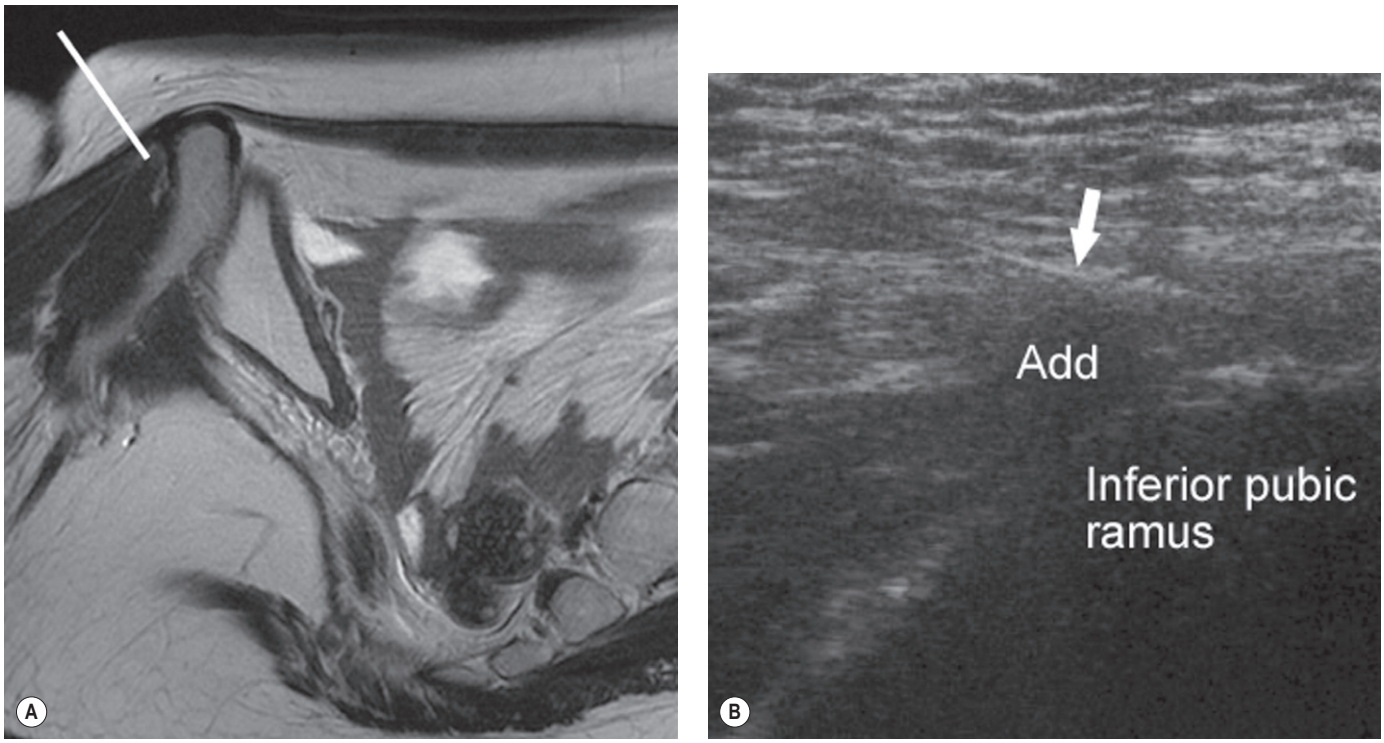

Figure 62.12 Adductor origin injection. A: Sagittal T2-weighted MR image demonstrates a distal approach of the needle to the adductor origin beneath the inferior pubic ramus. **B:** Ultrasound image with the transducer aligned along the long axis of the adductor tendons shows the needle (arrow) directed close to the adductor origin (Add) prior to injection.

Equipment

A 21G green needle with 40 mg triamcinolone mixed with a long-acting local anaesthetic totalling about 2–3 mL is used.

Patient position

Injection into the symphysis is best achieved with the patient lying supine.

Transducer position

The symphysis can be injected axially but a sagittal approach is often easier. Moving the transducer from side to side identifies the echogenic landmarks of the pubic bones and it becomes clear when the transducer is positioned directly over the hypoechoic symphyseal cleft. This technique is similar to isolating the acromioclavicular joint.

Puncture point

The puncture point is either proximal or distal to the transducer.

Target point

The needle is advanced under ultrasound visualisation into the top of the symphysis. The patient should be warned that a symphyseal injection can be painful.

HIP

Aspiration and injection of the adult hip

Introduction

Hip aspiration and injection may be performed for suspected infection, for MR arthrography or for therapeutic purposes. The depth of the adult hip joint results in the anatomy not being as well visualised as in the child. In obese patients a lower-frequency probe may be required. These probes inherently have a lower spatial resolution, which combined with the oblique needle approach makes visualisation of the needle more difficult. Capsular distension that follows a hip injection can also be more difficult to identify with certainty. In these patients, a fluoroscopic guided hip injection using iodinated contrast media may be more prudent to ensure that an intra-articular injection has been achieved. Ultrasound, however, has the advantage of distinguishing joint effusions from synovial inflammation and guiding synovial biopsy, which is a useful adjunct for investigation of the complicated hip replacement.

Equipment

A 21G spinal needle and 40–80 mg triamcinolone mixed with a long-acting local anaesthetic are used for a therapeutic injection. The hip joint will usually accept 5–8 mL. Viscosupplementation of the hip joint with hyaluronic acid or its derivatives has been effective for the symptomatic relief of osteoarthritis in individual cases.[8]

Patient position

The patient lies in the supine position with the hips extended.

Transducer position

Two approaches can be used depending on personal preference, patient body habitus and the presence of a joint effusion. With the standard sagittal approach, the transducer is orientated along the femoral neck to give a view of the anterior joint space. In thin patients and non-distended joints, a good view of the anterior joint can be obtained with the transducer turned into an axial position over the femoral head.

Puncture point

With the sagittal approach, the puncture point is usually distal to the transducer with the needle directed proximally towards the joint (Fig. 62.13). With the axial anterior approach, the puncture point is lateral to the transducer and femoral vessels, remembering that the femoral nerve lies most lateral and is not as conspicuous (Fig. 62.14). This is the same approach as an iliopsoas bursal injection.

Target point

With the sagittal approach, the needle is directed towards the anterior femoral head–neck junction until the needle tip is visible in the capsule adjacent to the femoral neck. With the axial approach, the rounded contour of the anterior femoral head contrasts with the triangular shaped acetabulum. The needle is advanced medially anterior to the femoral head and directed to a point just lateral to the anterior acetabular labrum. If the needle tip is intra-articular, no fluid should pool around the needle on injection.

Synovial biopsies may be more valuable than aspiration of fluid in infected hip replacements. Ideally, three separate specimens should be obtained, using a different needle each time to reduce the possibility of contamination. Restrained use of lidocaine is recommended as it is bacteriostatic. Ultrasound is also useful to guide aspiration of the potentially infected native hip joint. If no effusion fluid is initially aspirated, 3–4 mL of sterile non-bactericidal saline can be injected into the joint with re-aspiration of the fluid for microbiological assessment.

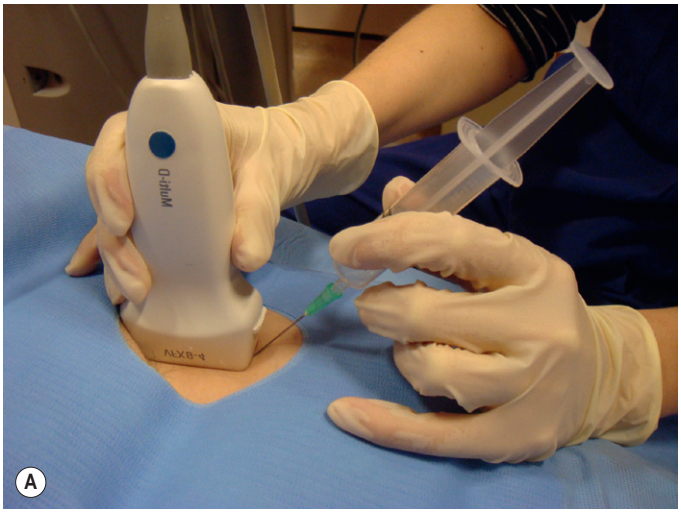

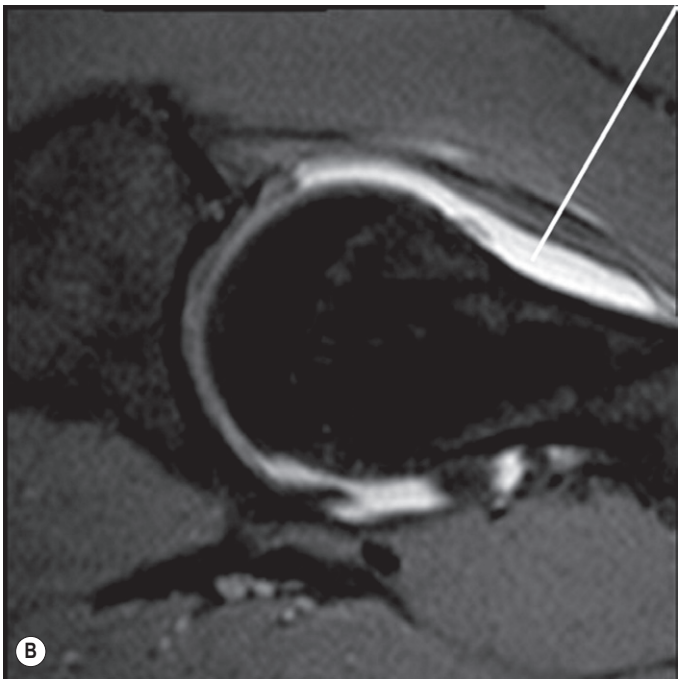

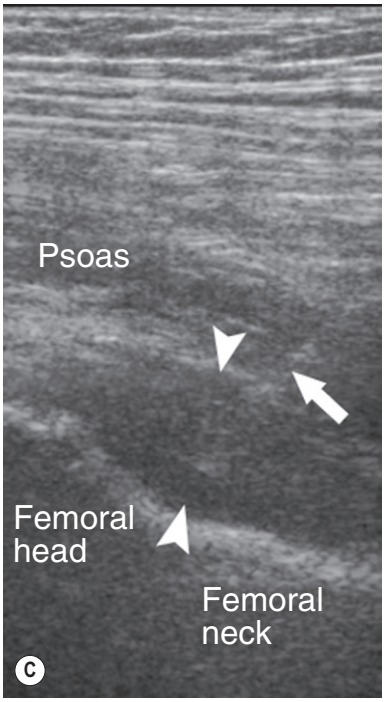

Figure 62.13 Standard sagittal approach to adult hip. A: The patient is supine with hips extended and transducer positioned to give a sagittal view of the anterior joint space. The puncture point is usually distal to the transducer. **B:** Sagittal T1-weighted MR arthrogram with fat saturation shows the needle directed proximally towards the anterior femoral head–neck junction. **C:** Comparative ultrasound image shows the needle (arrow) directed towards the anterior femoral head–neck junction prior to aspiration of an effusion (between arrowheads).

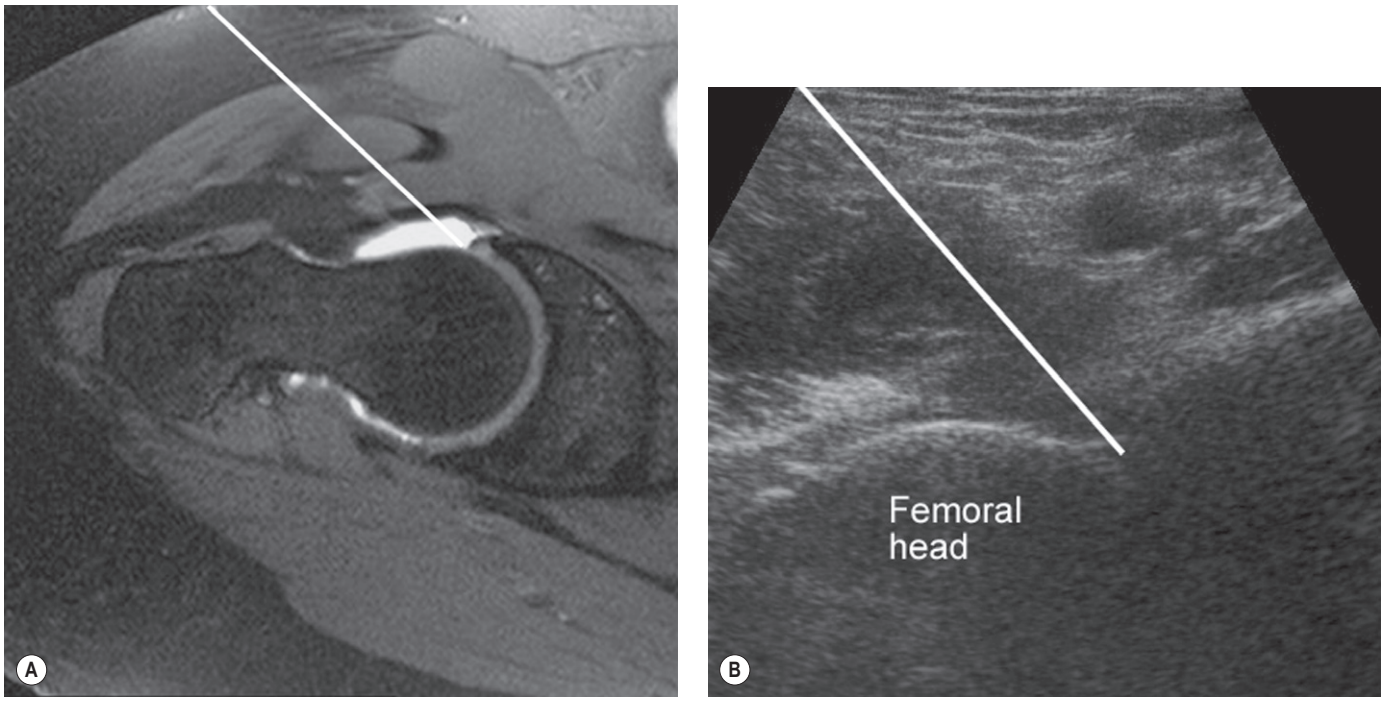

Figure 62.14 Alternative axial approach to adult hip. A: Axial T1-weighted MR arthrogram with fat saturation shows the direction of the needle with a puncture point lateral to the transducer. **B:** Ultrasound image with the transducer in an axial position over the femoral head shows the needle directed medially anterior to the femoral head to a point just lateral to the anterior labrum.

Aspiration of the paediatric hip

Introduction

A painful irritable hip is one of the commonest non-traumatic acute paediatric presentations in orthopaedic practice. Ultrasound is an important early diagnostic technique to detect a hip joint effusion and to guide aspiration to exclude sepsis. The commonest cause of the irritable hip is transient synovitis. Those who support a conservative approach to paediatric hip aspiration point to the vast majority of effusions being sterile and the potential risk of introducing infection at the time of aspiration. Ultrasound appearances cannot determine the cause of an effusion and clinical and laboratory parameters such as fever, peripheral white cell count and erythrocyte sedimentation rate (ESR) do not always reliably predict hip sepsis.[9,10] This has led those in favour of routine aspiration to emphasise that a delayed diagnosis of septic arthritis can result in serious damage to the hip joint with rapid destruction of the femoral head, degenerative arthritis and permanent deformity. This group argue that aspiration is quick and has a very low complication rate with no reported cases of septic arthritis arising from diagnostic aspiration. It is suggested that the trauma of hip aspiration is little more than drawing blood and that direct evidence of septic arthritis from synovial fluid is better than indirect evidence from a white cell count or ESR. Aspiration reduces intra-articular pressure, which may produce immediate pain relief avoiding hospital admission and possibly reduces the risk of avascular necrosis.[11,12]

Equipment

Topical anaesthetic cream such as Emla cream (Astra Pharmaceuticals, Kings Langley, UK) is applied to the skin in the region of the anterior skin crease of the affected hip as soon as the patient presents to hospital. The optimal time between the application of the cream and the examination depends on the anaesthetic preparation used but is between 20 and 90 minutes. A 21G green needle and 5 mL syringe are used and the aspirate is placed in both sterile microbiology and blood culture bottles.

Patient position

The child lies supine with the legs comfortably extended. Slight internal rotation of the hip is advantageous as it results in a more horizontal ultrasound appearance of the femoral neck, moves the femoral neurovascular bundle medially out of the path of the needle and prevents tightening of the joint capsule with subsequent posterior displacement of synovial fluid. The presence of a family member near the head of the bed often helps to calm the child.

Transducer position

Aspiration of the paediatric hip is one of the few ultrasound procedures that is not carried out under real-time visualisation. The transducer is placed in a sagittal plane along the anterior aspect of the affected hip and positioned over the point of maximal anterior capsular distension. The transducer must be held vertically over the hip at an angle of 90° to the skin to ensure accurate localisation. The introduction of angles in determining the puncture point requires that the needle is at the same angle for aspiration, and replication of angles other than 90° is difficult.

Puncture point

With the transducer in the correct position, the point of maximal anterior capsular distension is marked for aspiration. Several techniques can be used to indicate the puncture point and these are often best used in combination. The first method involves marking the midpoint of all four sides of the transducer. When the transducer is removed, the intersection of these opposite points identifies the central puncture point. Another method is to place an extended paperclip beneath the transducer and move it until its acoustic shadow falls over the point of maximal capsular

distension. This can be used on its own or in conjunction with marking the midpoints on the narrow ends of the transducer. The intersection between the marker points and the position indicated by the paperclip gives the puncture point. Another useful method which provides confirmation of the marking technique is to apply a small amount of pressure with the transducer once the site of maximal capsular distension has been identified. If the transducer is then quickly removed, the blanched footplate of the transducer can be identified on the skin and a mark placed at its centre. Combining these methods provides firmer reassurance of the correct puncture point. The accuracy of the puncture point is checked by replacing the transducer over the mark in both longitudinal and transverse orientations. The transducer should not be removed until the operator is fully confident that the marked puncture point lies directly over the deepest aspect of the joint effusion, which should result in a quick, successful aspiration with minimal trauma to the child.

Target point

Once the puncture point is determined, the transducer is removed and with a sterile technique, the joint is punctured with a vertical needle positioned at 90° to the skin (Fig. 62.15). At this point it is often helpful for a parent to hug the child, obscuring the view of the needle. The needle is advanced until the femoral neck is encountered and then withdrawn 1–2 mm before aspiration is attempted. Accurate needle placement is confirmed by successful aspiration of joint fluid. There is correlation between the size of the effusion, pain, restriction of movement and intra-articular pressure.[11] Aspiration should thus be as complete as possible as this may result in more rapid resolution of symptoms and a shorter hospital stay.

Tips to aspirate paediatric hip

- Allow time for topical anaesthetic cream to take effect.
- Position with slight internal rotation of hip.
- Family member present to reassure and obscure needle.
- Mark point of maximal anterior capsular distension.
- Use combination of techniques to mark puncture point.
- Keep transducer 90° to skin.
- Only remove transducer when confident mark is vertically over deepest aspect of effusion
- 'Blind' approach.
- Aspirate dry.

Gluteal insertion injection

Introduction

Perigluteal bursitis is a common condition causing pain along the lateral aspect of the hip. Symptoms may be due to either subgluteal or trochanteric bursitis. The trochanteric bursa is the largest of the lateral hip bursae and lies posterior to the greater trochanter. Ultrasound features of bursitis are variable but often the bursa is not particularly distended with fluid and is more commonly seen as a thickened rind of tissue in comparison with the contralateral side. The subgluteus minimus and medius bursae lie more anterior and deep to the tendons of gluteus minimis and medius respectively.

Equipment

A 21G spinal needle and 40 mg triamcinolone mixed with a long-acting local anaesthetic are used. The bursa usually accepts at least 5 mL.

Patient position

The bursae are best approached with the patient lying in the lateral decubitus position with the affected side upwards.

Transducer position

The transducer is placed in a coronal or axial position so that the greater trochanter is visualised. The transducer remains in this position if the subgluteal bursae are to be injected. The transducer is moved slightly posteriorly if the trochanteric bursa is to be injected.

Puncture point

The skin may be punctured either proximal or distal to the transducer.

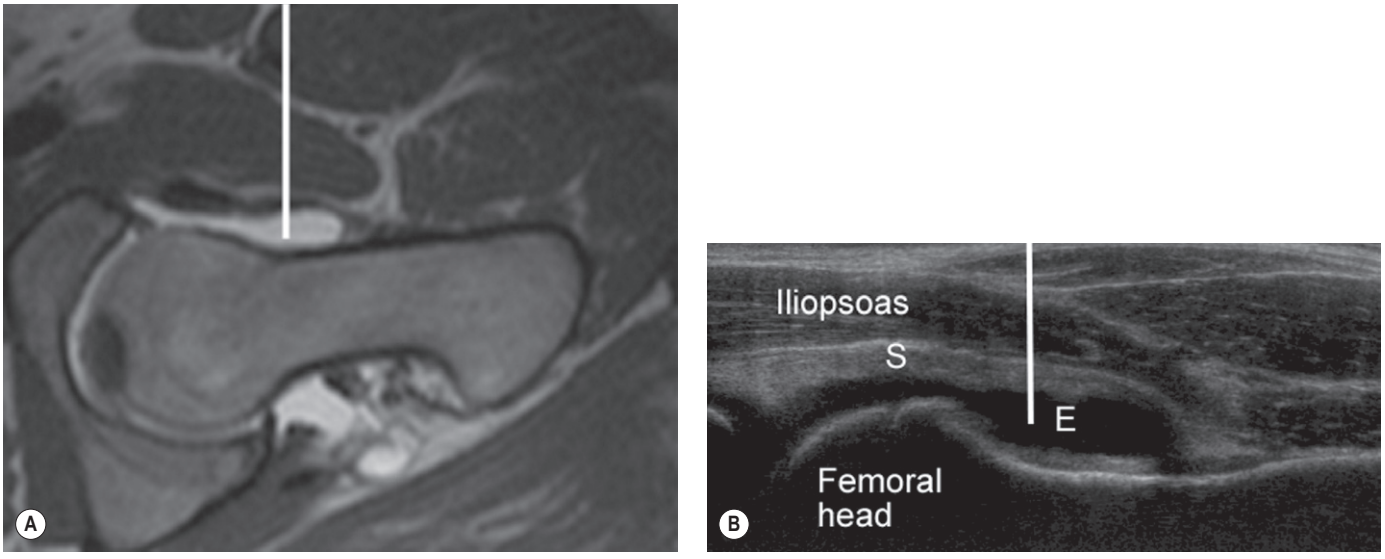

Figure 62.15 Paediatric hip aspiration. Sagittal T2-weighted MR image **(A)** and comparative ultrasound image **(B)** show the vertical approach of the needle into the deepest portion of the effusion (E), which is surrounded by thickened synovium (S).

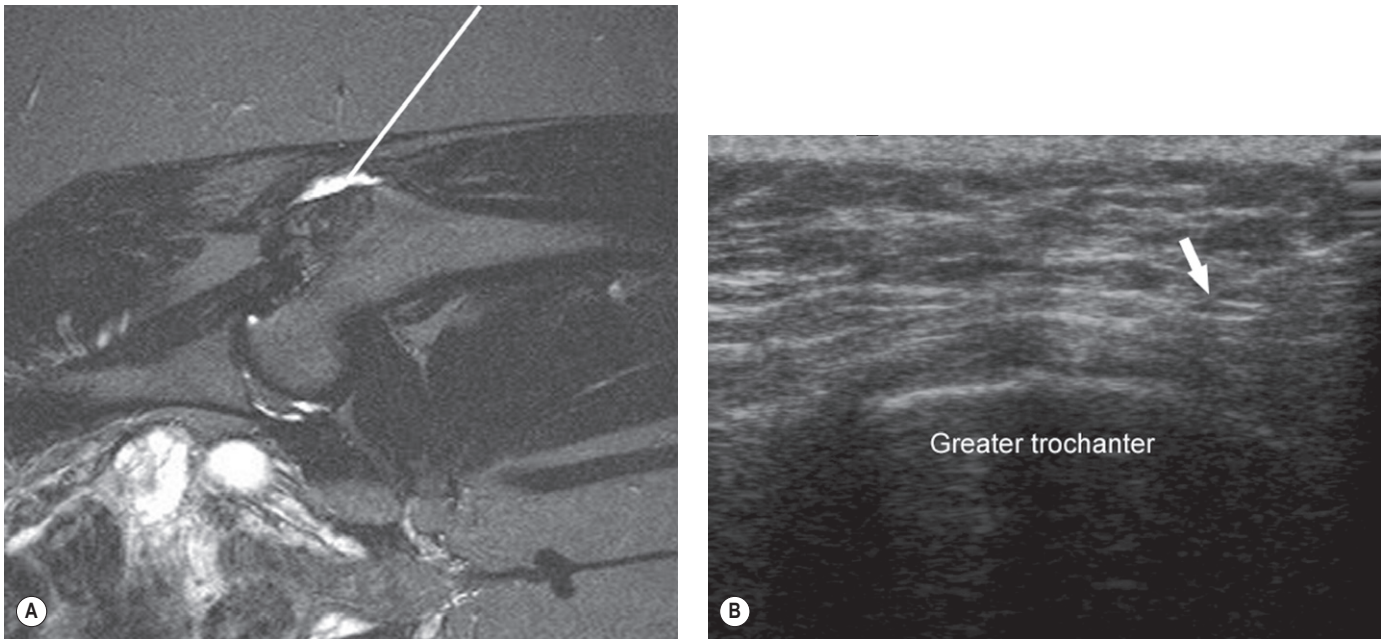

Figure 62.16 Trochanteric bursal injection. Coronal STIR MR image **(A)** and comparative coronally orientated ultrasound image **(B)** show the needle (arrow) directed towards an inflamed bursa along the posterolateral aspect of the greater trochanter.

Target point

With a trochanteric bursal injection, the needle is directed into the bursa deep to the gluteus maximus insertion along the posterolateral aspect of the greater trochanter (Fig. 62.16). The subgluteal bursae are reached by advancing the needle deep to the tendons of gluteus minimus and medius along the anterolateral aspect of the greater trochanter. When the needle tip is correctly positioned, the injectate should be seen to flow freely within the bursa and no resistance should be encountered.

Iliopsoas bursal injection

Introduction

Injection into the iliopsoas bursa has been used to treat iliopsoas tendinopathy and bursitis. Iliopsoas bursal injection has benefited patients with impingement of the iliopsoas tendon on a prominent acetabular cup following a hip replacement[13] and patients with a clinically suspected snapping iliopsoas tendon, even if the snapping tendon is not visualised at ultrasound.[14] Pain relief after an iliopsoas bursal steroid and anaesthetic injection has correlated with a good outcome following surgical release of the iliopsoas tendon.[14]

Equipment

A 21G spinal needle and 40 mg triamcinolone mixed with a long-acting local anaesthetic are used. The bursa usually accepts 5–8 mL.

Patient position

The patient is in the supine position with the hips extended.

Transducer position

The iliopsoas bursa is best identified lying lateral to the femoral vessels at the level of the acetabular brim and is distinguished from the vessels by using colour flow. The transducer is best placed in an axial position overlying the femoral artery.

Puncture point

The puncture point is lateral to the transducer and femoral vessels.

Target point

The needle is advanced medially into the iliopsoas bursa, deep to the tendon and posterior to the femoral artery (Fig. 62.17). In patients with iliopsoas tendon impingement following hip replacement, the tendon may be situated in a more anterior and medial position. A small test injection of lidocaine may be helpful to confirm correct needle placement with echogenic microbubbles seen entering the bursa and subsequent bursal distension.

KNEE

Knee joint aspiration and synovial biopsy

Equipment

A 21G green or spinal needle depending on the depth of the joint and 40 mg triamcinolone mixed with a long-acting local anaesthetic are used for a therapeutic injection. The knee joint can hold a large amount of fluid but up to 8–10 mL is adequate for a therapeutic injection.

Patient position

Aspiration and injection of the knee joint is best achieved with the patient supine and the knee slightly flexed in a position of comfort.

Transducer position

The suprapatellar recess is the easiest point to access the distended knee joint and is best viewed with the transducer in a sagittal plane just lateral to the distal quadriceps tendon.

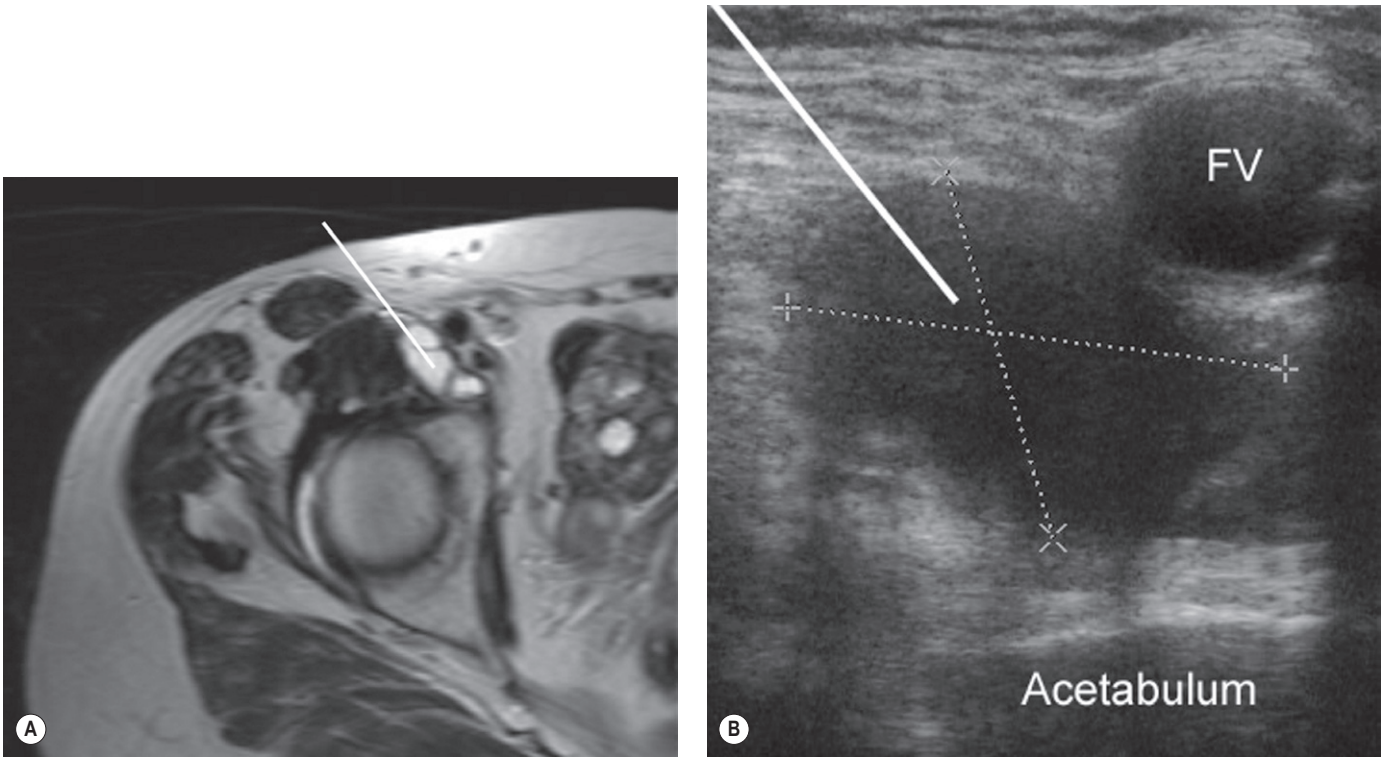

Figure 62.17 Iliopsoas bursal injection. A: Axial T2-weighted MR image shows a distended iliopsoas bursa lateral to the femoral vessels and the direction of the needle into the bursa. **B:** Corresponding axial ultrasound image indicating the medial approach of the needle into the bursa (indicated by callipers), which may be distinguished from the femoral vessels (FV) by using colour flow.

Puncture point

A puncture point proximal to the transducer allows cannulation of the superolateral aspect of the suprapatellar bursa.

Target point

The needle is directed distally into the bursa. Aspiration of large effusions is straightforward. The area between the patella and the distal femur is an excellent target point for small effusions. As in the hip, synovial biopsy is better than simple joint fluid aspiration in diagnosing the microbiological content of the septic joint replacement (Fig. 62.18). In view of the relative thinness of the synovium, biopsy is best achieved by inserting the needle parallel to the area of synovium to be biopsied. A slight vibration of the needle allows the specimen to embed in the biopsy port prior to closure.

Other intra-articular lesions of the knee amenable to aspiration and injection include cysts and ganglia. Hoffa's ganglia are more easily aspirated from an anterior approach with the transducer orientated in the axial plane overlying the patellar tendon. The needle is inserted adjacent to the patellar tendon from either a medial or lateral approach depending on the position of the ganglion (Fig. 62.19). Cruciate ganglia are more difficult to aspirate. A posterior approach is required either medial or lateral to the popliteal vessels and posterior tibial nerve. Visualisation is often limited by their depth and it is difficult to be certain that the ganglion has been aspirated completely. As with ganglia in other locations, aspiration may be difficult in view of their thick gelatinous content, and recurrence following aspiration is not unusual. The outcome following cruciate ganglion aspiration-injection is variable but relief of pain and mechanical symptoms is well described.[15]

Impingement of the lateral infrapatellar fat pad is well identified using MRI as focal high T2-weighted signal between the patellar tendon and lateral femoral condyle. Corresponding ultrasound abnormalities include hypoechogenicity and increased vascularity with Doppler imaging. The authors have performed ultrasound-guided steroid injection of the fat pad in a limited number of patients with impingement with initial promising results. Inhibiting the inflammatory process may reduce the volume of tissue and thus relieve the impingement.

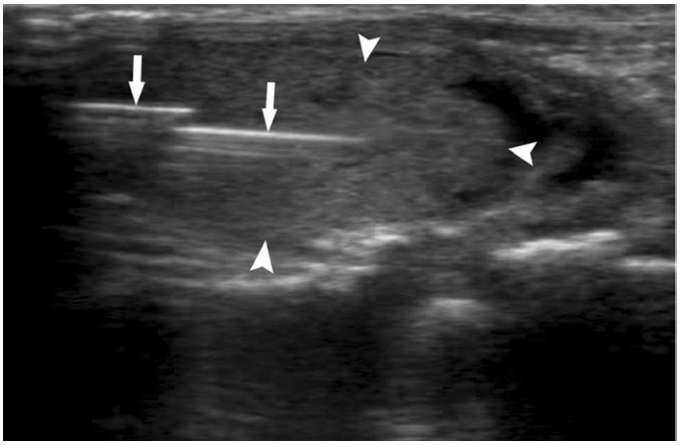

Figure 62.18 Knee joint biopsy. Longitudinal ultrasound image with transducer over the suprapatellar recess shows an open biopsy needle (arrows) within an area of synovitis (arrowheads).

Extra-articular interventional procedures around the knee joint include peripatellar tendon injection for patellar tendinopathy. A combination of steroid and long-acting local anaesthetic can be injected around the inflamed patellar tendon under ultrasound guidance and is best visualised with the transducer in an axial position.

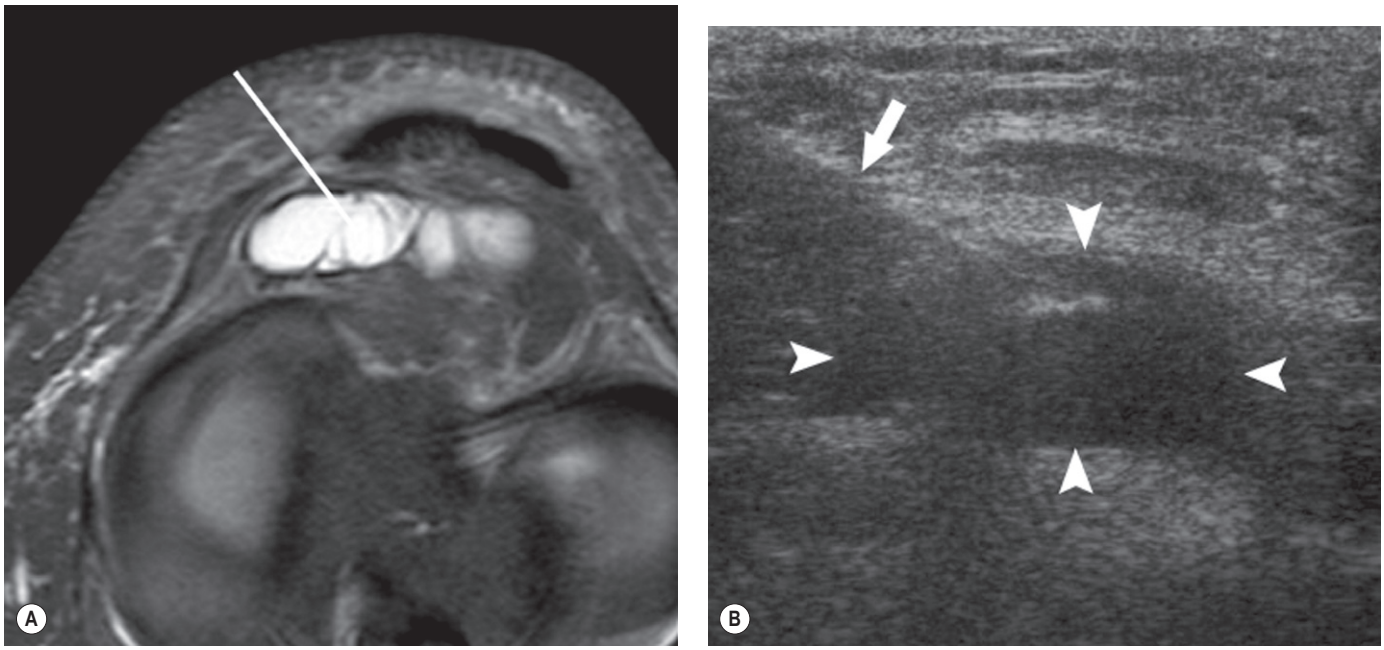

Figure 62.19 Hoffa's ganglion aspiration. Axial T2-weighted MR image with fat saturation **(A)** and corresponding axial ultrasound image **(B)** show the needle (arrow) inserted adjacent to the patellar tendon into a Hoffa's ganglion (arrowheads) prior to aspiration and injection.

Proximal tibiofibular joint aspiration and injection

Equipment

A 21G green needle and 40 mg triamcinolone mixed with a long-acting local anaesthetic are used for a therapeutic injection. The joint accepts about 2–3 mL.

Patient position

Access to the proximal tibiofibular joint is best achieved with the patient in a lateral decubitus position with the affected knee upwards.

Transducer position

The transducer is best positioned in an axial orientation along the posterolateral aspect of the proximal calf. The axial image depicts the superolateral aspect of the proximal tibiofibular joint as a triangular space between the echogenic bony surfaces of the tibia and adjacent fibula.

Puncture point

The puncture point is proximal to the transducer.

Target point

The needle is directed distally into the triangular space representing the superior aspect of the joint between the proximal tibia and fibula.

FOOT AND ANKLE

Tibiotalar joint injection

Equipment

A 21G needle and 40 mg triamcinolone mixed with a long-acting local anaesthetic totalling about 5 mL are used for a therapeutic injection.

Patient position

The patient lies prone with the foot slightly plantar flexed to access the anterior aspect of the joint.

Transducer position

An anterior sagittal approach provides a good view of the anterior tibiotalar joint. The transducer is positioned either medial or lateral to the dorsalis pedis artery and adjacent deep peroneal nerve.

Puncture point

A puncture point distal to the transducer allows the needle to be directed into the anterior tibiotalar joint beneath the anterior rim of the distal tibia.

Target point

The needle tip is usually clearly visualised within the joint space and the injected material seen to flow away from the needle. This anterior approach can also be used to aspirate fluid from the joint in the presence of an effusion.

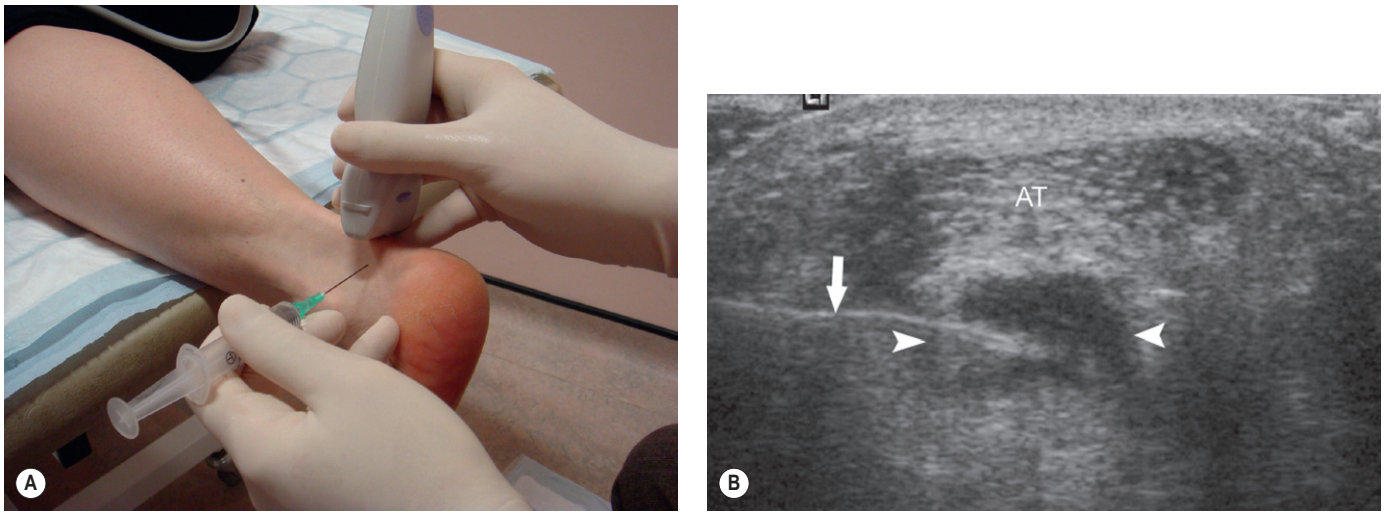

Figure 62.20 Pre-Achilles bursal injection. A: The patient is prone with feet extended over the end of the examination couch. The transducer is axially orientated with a lateral puncture point. **B:** Transverse ultrasound image shows the needle (arrow) entering the pre-Achilles bursa (between arrowheads) anterior to the Achilles tendon (AT).

Hindfoot injections: Achilles bursa injection

Equipment

A 21G green needle and 30 mg methylprednisolone mixed with a long-acting local anaesthetic are used. The bursa easily accepts 5 mL but 2–3 mL is usually sufficient.

Patient position

The patient is positioned prone with the feet extended over the end of the examination couch as per the Achilles tendon examination.

Transducer position

The ultrasound transducer is positioned in the axial plane directly over the distal Achilles tendon.

Puncture point

The Achilles bursa is best approached with a puncture point lateral to the transducer. For a pre-Achilles bursal injection, the puncture point must be sufficiently anterior to the Achilles tendon to prevent penetrating it with the needle.

Target point

Advancing the needle parallel to the axially orientated transducer provides an excellent view of the needle approaching from the lateral side. The needle should remain anterior to the Achilles tendon and relatively close to the superior margin of the calcaneum to reach the pre-Achilles bursa, particularly if the degree of bursal distension is mild (Fig. 62.20). Preliminary injection of a small quantity of local anaesthetic may be helpful to distend a small bursa and confirm intrabursal positioning.

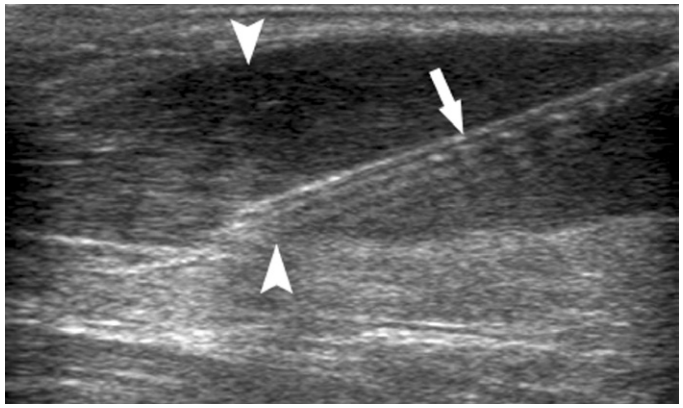

Figure 62.21 Achilles dry needling. Longitudinal ultrasound image shows the needle (arrow) within the Achilles tendon (between arrowheads) during dry needling.

Peri-Achilles tendon injection

Introduction

Injection around the Achilles tendon for tendinopathy and paratendinitis is controversial. Some authors advocate the use of large volumes of either normal saline or local anaesthetic into the paratenon to disrupt adhesions that may have formed between the paratenon and the tendon and to reduce blood flow in neovessels.[16] A small volume paratenon injection may be combined with dry needling of the Achilles tendon to cause fibrillar disruption and internal bleeding to initiate a healing response (Fig. 62.21). Ultrasound and colour Doppler have been used to guide sclerosing polidocanol injections of neovessels just outside the ventral aspect of the Achilles tendon in patients with chronic painful mid-portion Achilles tendinosis. Initial results appear promising, with significantly reduced tendon pain during activity and resolution of neovascularisation on follow-up imaging.[17,18] Correlation of neovascularity with painful Achilles tendinosis in these studies suggests that neovascularisation may be a potential source of pain in chronic mid-portion Achilles tendinosis.[19]

Equipment

A 21G green needle is suggested. For large volume injection into the Achilles paratenon, 10 mL of a long-acting local anaesthetic and up to 40 mL of injectable normal saline have been used.[16] The inclusion of a corticosteroid is thought to increase the risk of tendon rupture.

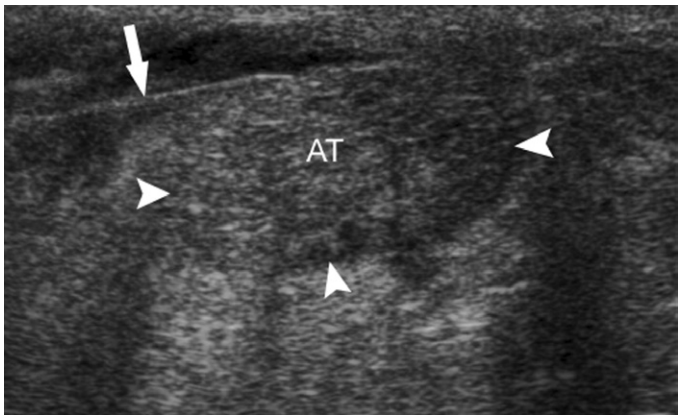

Figure 62.22 Achilles paratenon injection. Transverse ultrasound image confirms correct needle placement (arrow) along the dorsal aspect of the tendon sheath and ensures the Achilles tendon (AT, demarcated by arrowheads) has not been penetrated.

Patient position

The patient is positioned prone with the feet extended over the end of the examination couch as per the Achilles tendon examination.

Transducer position

A sagittally orientated transducer is best.

Puncture point

The puncture point is usually proximal to the transducer.

Target point

For injection into the Achilles paratenon, the needle is advanced onto the dorsal aspect of the tendon sheath. Axial imaging is useful to confirm correct needle placement and ensure that the tendon itself has not been penetrated (Fig. 62.22). Large volumes are injected into the paratenon until Doppler imaging confirms a significant reduction in blood flow in the neovessels along the ventral portion of the tendon.

Plantar fascia injection

Equipment

A 21G green needle and 40 mg methylprednisolone mixed with approximately 5 mL of a long-acting local anaesthetic are used.

Patient position

Injection of the plantar fascia is usually carried out with the patient lying prone and feet extended over the end of the examination couch.

Transducer position

The transducer is initially placed in a sagittal position over the abnormal fascia. Depending on technique, the injection is then carried out either with the transducer remaining in the sagittal plane or after rotating it through 90° to show the plantar fascia in axial section.

Tips to inject plantar fascia

- Patient prone with feet extended over couch or supine with feet on couch.
- Three injection techniques.
- Medial and midfoot puncture points less painful.
- Select approach angle so needle can reach deep and superficial to fascia.
- Inject superficial and deep to the fascia.
- Dry needling may be performed.

Puncture point

Three injection techniques are possible. The standard sagittal approach is with a puncture point proximal to the transducer (Fig. 62.23). The puncture point should be chosen so the needle can traverse the plantar fascia at its origin from the os calcis to inject along its deep surface. A second sagittal approach is to puncture distal to the transducer. This technique has the advantage of being easier to angle the needle between the fascia and the os calcis to inject the deep aspect of the fascia. The injection point is the midfoot rather than the heel and the procedure is potentially less painful as the skin in this region is thinner. The main disadvantage of this method is that manipulation of the needle and syringe is a little more awkward and the patient may need to be turned from the prone examining position into a supine position for the injection. A third technique, the authors' preference, is to rotate the transducer into an axial plane prior to injection. A medial puncture point, ideally at the same level as the maximal site of plantar fasciitis, is used (Fig. 62.24). Although anatomical localisation is initially less familiar, this approach allows easy access to both superficial and deep surfaces of the fascia and is said to be less painful.

Target point

The authors prefer to inject both superficial and deep to the plantar fascia so the puncture point and angle of approach should be chosen to allow for this. The superficial surface is infiltrated first before manipulating the needle to the deep surface where the injection is augmented. Dry needling of the fascia may be performed.

Forefoot injections: Morton's neuroma injection

Introduction

The rationale of injecting corticosteroid in the treatment of Morton's neuroma is based on the theory that there is compression and subsequent irritation of the common interdigital nerve against the overlying transverse intermetatarsal ligament which is caused by chronic repetitive low-grade trauma during walking. This is believed to trigger degenerative changes and an increase in the volume and size of the tissue in the intermetatarsal space, forming a visible neural nodule on imaging. Corticosteroid injection is thought to induce atrophy of the neuroma and perineural web space tissue and thus decrease compression and inflammation of the neuroma.[20] Alcohol ablation using ethyl alcohol diluted in local anaesthetic is another treatment option in Morton's neuromas. Ethanol injected around a nerve produces chemical neurolysis through dehydration and necrosis.[21] Alcohol injections are given on three or four occasions 2 weeks apart.

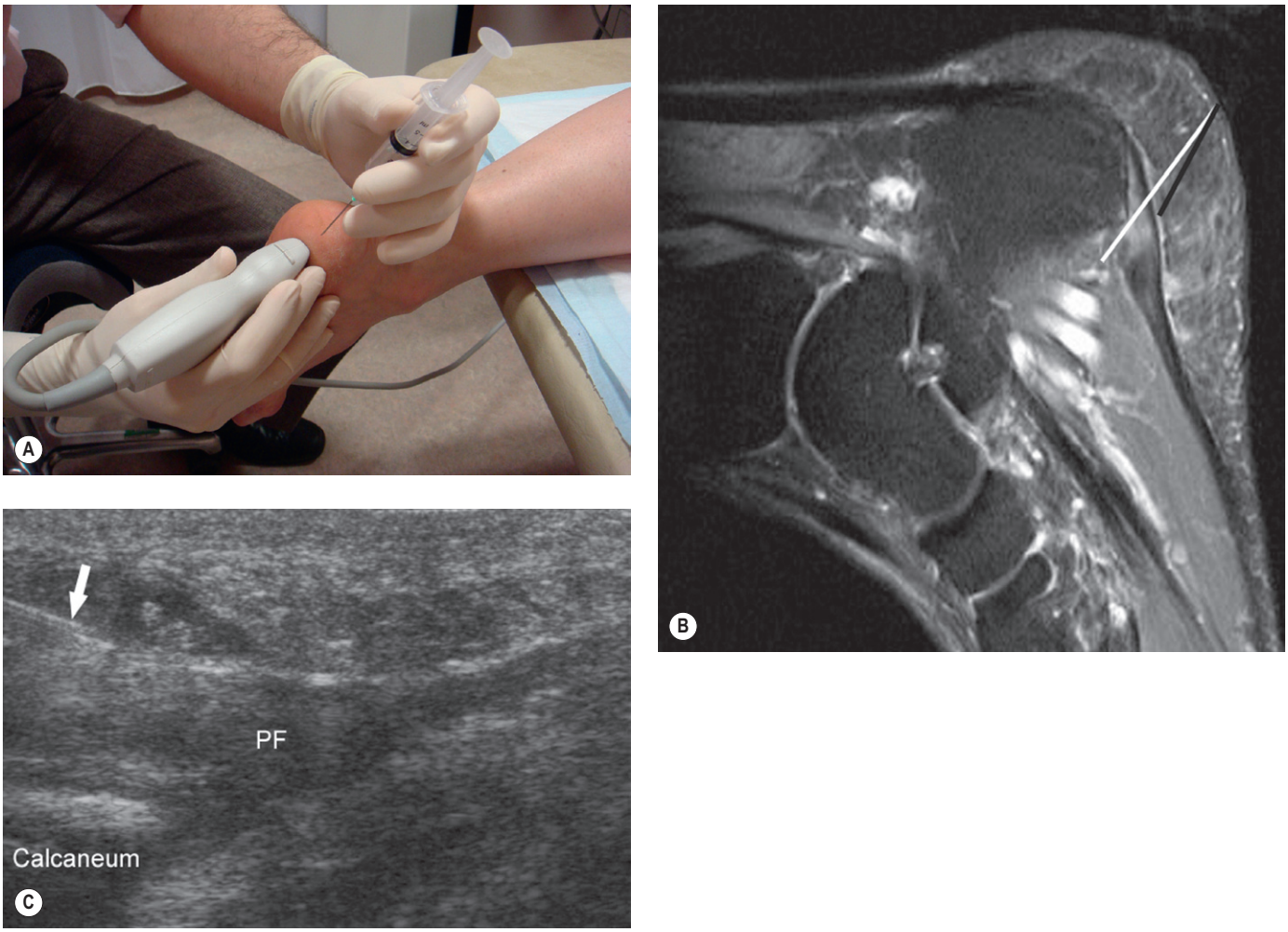

Figure 62.23 Standard sagittal approach to plantar fascia. A: The patient is prone, with the transducer in a sagittal position and proximal puncture point. **B:** Sagittal STIR MR image shows the direction of the needle to inject the superficial surface of the fascia (black line) before manipulating the needle to the deep surface (white line) where the injection is augmented. **C:** Corresponding longitudinal ultrasound image shows the needle (arrow) superficial to the plantar fascia (PF) during injection.

Equipment

A 21G green needle and 40 mg methylprednisolone mixed with 1 mL of a long-acting local anaesthetic are used.

Patient position

The patient is positioned supine on the examination couch.

Transducer position

The transducer is placed in the sagittal plane along the plantar surface of the foot with the neuroma visible within the metatarsal interspace. There is often direct correlation between the visualised sonographic lesion and the patient's site of pain.

Puncture point

The puncture point may be on the plantar or dorsal surface of the forefoot. To approach from the plantar surface, the puncture site is at the centre of the distal end of the transducer between the toes of the involved interspace. To approach from the dorsal surface of the forefoot, it is useful to apply pressure between the toes with the blunt end of a needle to confirm the optimal puncture point over the neuroma and mark the skin (Fig. 62.25). The dorsal route is through thinner skin and may be less painful but visualisation of the needle may not be as good as the needle tip is more perpendicular rather than parallel to the ultrasound probe. The second and third toes may also lie close together and even overlap in some patients, making the dorsal approach more difficult.

Target point

Once the needle has been inserted at the puncture point, it is usually seen to lie close to the neuroma when the transducer is placed in the sagittal position. It is then straightforward to advance the needle into the neuroma and inject the anti-inflammatory cocktail. Rotating the transducer into the axial plane to show the needle in the interspace prior to injection is a helpful confirmatory procedure. Fluid can be visualised swirling within the lesion, probably in the intermetatarsal bursa, during the injection.

FOREIGN BODY LOCALISATION

Foreign bodies are readily seen with high-resolution ultrasound even if they are quite small. Most superficial foreign bodies are easily located close to the skin puncture point. Unless there is a fibrous reaction around the foreign lesion, ultrasound localisation can be followed by removal either by aspiration through a

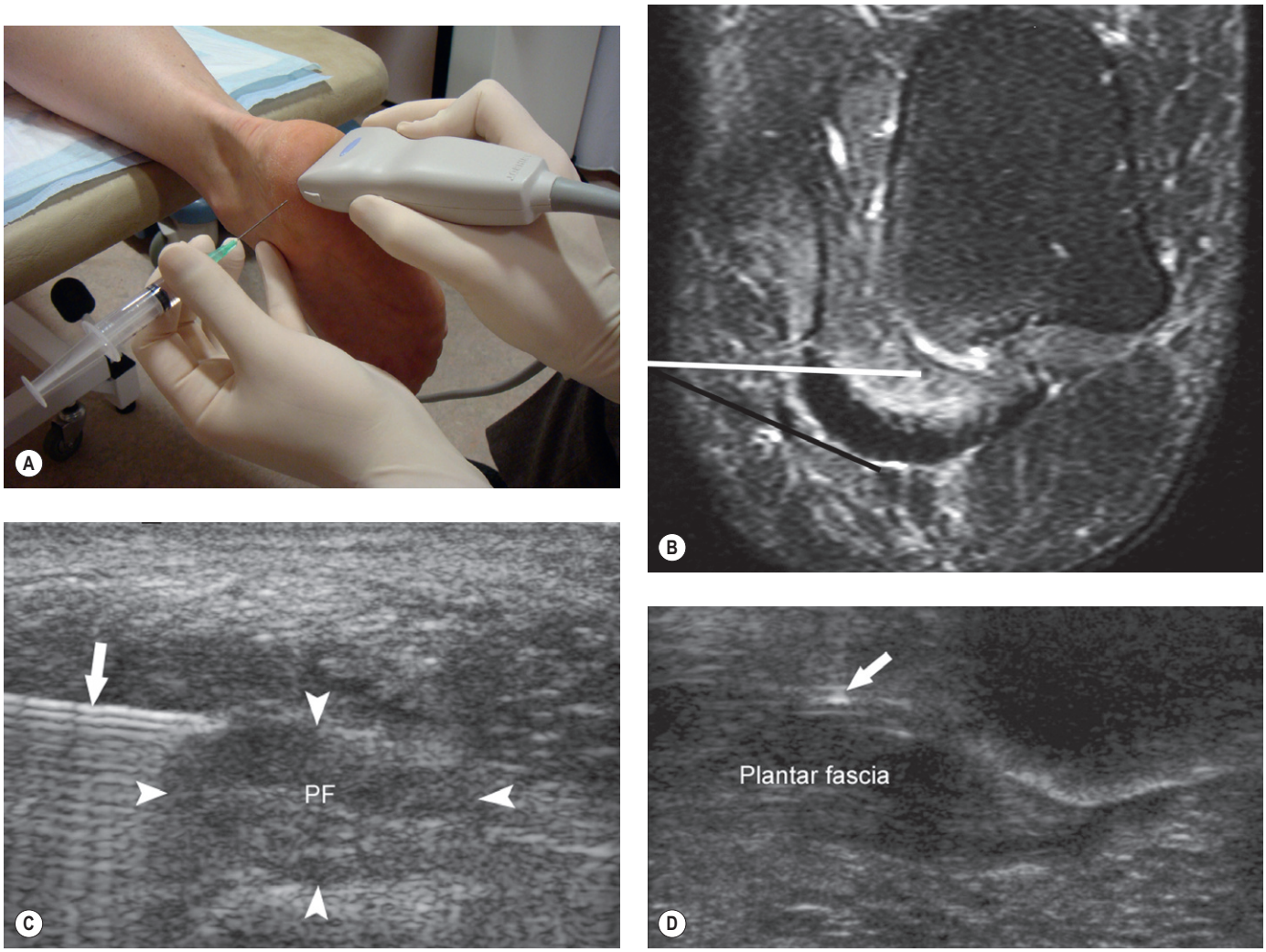

Figure 62.24 Axial approach to plantar fascia. A: The patient is prone, with the transducer in a transverse position and medial puncture point. **B:** Axial STIR MR image shows the needle approach to the superficial (black line) and deep (white line) surfaces of the fascia. **C:** Transverse ultrasound image shows the needle (arrow) superficial to the plantar fascia (PF, between arrowheads) during injection. **D:** Corresponding sagittal ultrasound image confirms the needle (arrow) in cross-section superficial to the plantar fascia.

wide-bore needle or by a limited skin incision. With deeply located or fibrosed foreign bodies, the skin overlying the foreign material can be marked to guide surgical removal.

MASSES

Biopsy of solid soft tissue masses and bone lesions

Prior to biopsy of potentially malignant soft tissue tumours, adequate local staging with MRI must be performed and the biopsy, including the proposed biopsy approach, should be discussed with the relevant tumour surgeon. The biopsy tract must be in a position that can be excised during subsequent surgical resection of the lesion to prevent needle track recurrence and should not cross an uninvolved compartment as this would adversely alter the staging and potentially the prognosis of a malignant tumour. Ultrasound-guided biopsy ensures that tissue is taken from solid components of the lesion and not from liquid or necrotic areas, which have a lower diagnostic yield (Fig. 62.26). The vascular nature of lesions becomes readily apparent using Doppler imaging and highly vascular portions may be avoided to prevent excessive haemorrhage.

Biopsy of bone tumours is traditionally performed under CT or fluoroscopic guidance. Ultrasound may be used to guide biopsy of lesions that are subperiosteal or cortical in location or destroy the bone cortex. Ultrasound accurately demonstrates the cortical

Tips to biopsy soft tissue masses

- Stage with MRI and discuss approach with operating surgeon first.
- Distinguish cystic from solid lesions.
- Ensure biopsy tract will be excised during surgical resection.
- Identify tissue planes to avoid compartment cross-contamination.
- Avoid necrotic, vascular, fibrosed or other atypical areas within tumour.
- Avoid biopsy in aneurysms, plantar fibroma, foreign body granuloma.
- Review if needle biopsy is appropriate in neural tumours, fatty tumours, fibromatosis, haemangioma.
- Identify cortical breach to allow transcortical biopsy.
- Adequate local anaesthesia for neural lesions and periosteal bone biopsies.

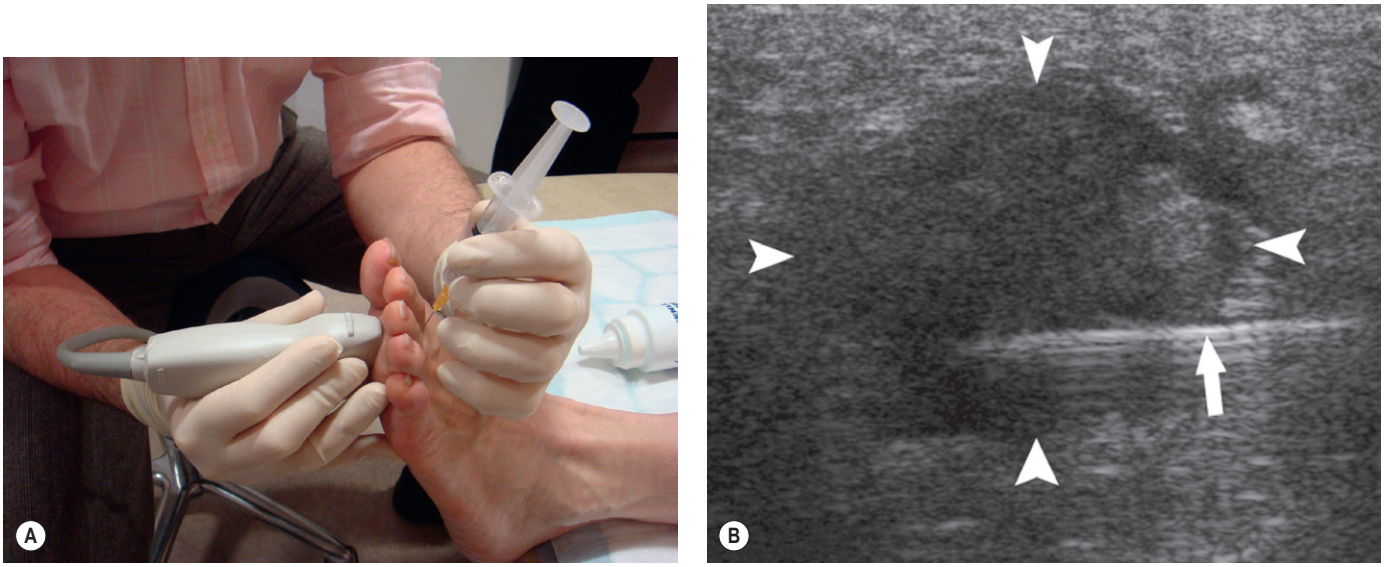

Figure 62.25 Morton's neuroma injection. A: The patient is supine, with the transducer in a sagittal plane along the plantar surface of the foot. This image illustrates a puncture point on the dorsal surface of the forefoot. **B:** Longitudinal ultrasound image shows the needle (arrow) advanced into a neuroma (between arrowheads) prior to injection.

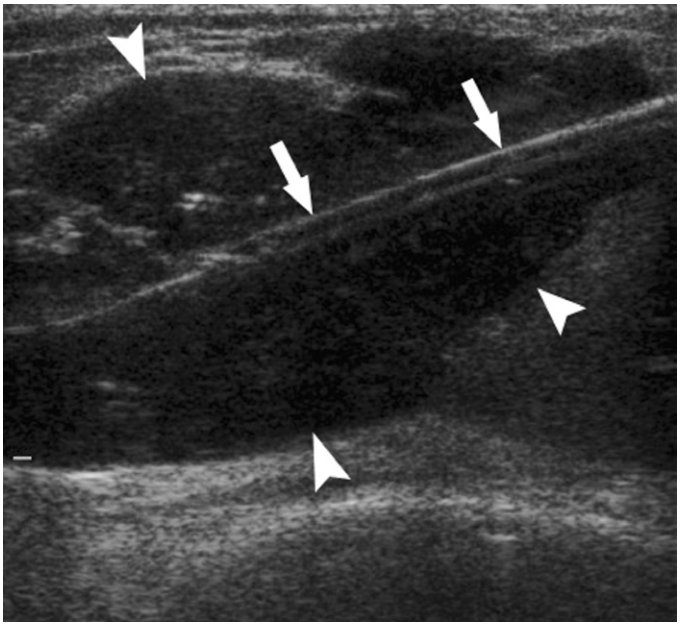

Figure 62.26 Soft tissue tumour biopsy. Ultrasound is valuable in guiding the biopsy needle (arrows) into more solid tumour components (demarcated by arrowheads) for a better diagnostic yield and to ensure the biopsy tract does not cross limb compartments.

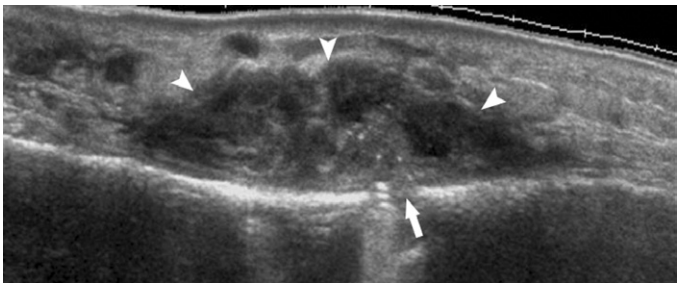

Figure 62.27 Cortical bone tumour biopsy. Ultrasound identifies a cortical defect as a breach in the echogenic bone surface (arrow) to allow transcortical biopsy. Biopsy of an associated soft tissue component (arrowheads) can be performed at the same time.

breach, which can sometimes be difficult to clearly visualise at fluoroscopy (Fig. 62.27). Generous infiltration of local anaesthetic around the periosteum is required because of the hypersensitivity of the periosteal envelope. Biopsy of an associated soft tissue component can be performed at the same time.

Aspiration of cystic lesions

Ganglia and simple cystic lesions may be aspirated to relieve swelling and pain. Colour Doppler should always be performed prior to aspiration to ensure the lesion is not a vascular structure such as a pseudo-aneurysm. A large-calibre needle, e.g. 17–19G, is used for aspiration of ganglia as the contents tend to be viscous. Injection of up to 40 mg of corticosteroid into a ganglion following decompression has been associated with symptomatic relief and complete resolution or reduction in size of the ganglion.[22] Injection into the residual ganglion is confirmed by visualising echogenic material exiting from the needle tip into the ganglion. The injection is usually continued until the previously anechoic ganglion is uniformly echogenic in an attempt to maximise the symptomatic response while minimising extravasation and thus local cutaneous side effects.[22]

Aspiration of abscesses is indicated to obtain fluid for microbiological analysis and possibly for cytological examination (Fig. 62.28). Tissue around the abscess is hypersensitive and ample local anaesthesia should precede the aspiration.

Liquefied haematomas are aspirated for pain relief, compartment syndrome and probable infection. Uncomplicated haematomas should not be aspirated due to the risk of infection, and drainage catheters placed for prolonged use are contraindicated as the risk of infection is too high.

Large collections may be aspirated using a freehand technique without the transducer. The distance from the skin to the centre of the lesion can initially be measured. The puncture point is then marked by placing the transducer in the longitudinal axis over the greatest length of the lesion and marking the centre of the narrow

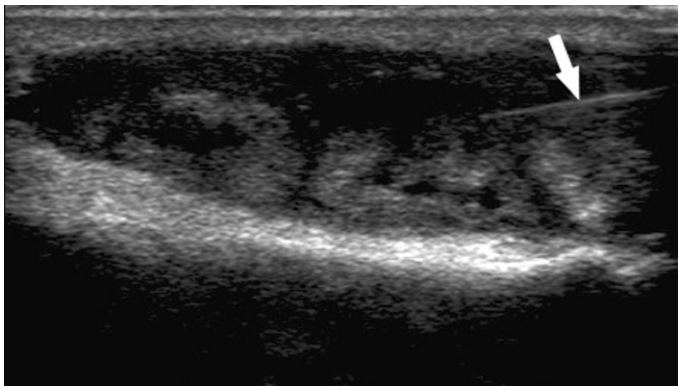

Figure 62.28 Abscess aspiration. Longitudinal ultrasound image shows the needle (arrow) within a superficial abscess to obtain fluid for microbiological analysis.

ends of the transducer. The transducer is then rotated 90° to find the maximum width of the lesion and again marking the centre of the narrow ends of the transducer. The transducer is removed and lines connected to mark the central puncture point. The needle is placed at the intersection of the coordinates at right angles to the skin and directed as deep as the centre of the mass prior to aspiration.

REFERENCES

1. Farin PU, Rasanen H, Jaroma H, Harju A. Rotator cuff calcifications: treatment with ultrasound guided percutaneous needle aspiration and lavage. Skeletal Radiol 1996;25:551–554.
2. Aina R, Cardinal E, Bureau NJ, et al. Calcific shoulder tendonitis: treatment with modified US-guided fine needle technique. Radiology 2001;221:455–461.
3. Zwar RB, Read JW, Noakes JB. Sonographically guided glenohumeral joint injection. AJR Am J Roentgenol 2004;183:48–50.
4. Connel DA, Ali KE, Ahmad M, et al. Ultrasound guided autologous blood injection for tennis elbow. Skeletal Radiol 2006;35:371–377.
5. Miller JH, Beggs I. Detection of intraarticular bodies of the elbow with saline arthrosonography. Clin Radiol 2000;56:231–234.
6. Raza K, Lee CY, Pilling D, et al. Ultrasound guidance allows accurate needle placement and aspiration from small joints in patients with early inflammatory arthritis. Rheumatology 2003;42:976–979.
7. McGonagle D, Gibbon W, O'Connor P, et al. A preliminary study of ultrasound aspiration of bone erosions in early rheumatoid arthritis. Rheumatology 1999;38:329–331.
8. Van den Bekerom MP, Lamme B, Sermon A, Mulier M. What is the evidence for viscosupplementation in the treatment of patients with hip osteoarthritis? Systematic review of the literature. Arch Orthop Trauma Surg 2008;128:815–823.
9. Bennett OM, Namnyak SS. Acute septic arthritis of the hip joint in infancy and childhood. Clin Orthop 1992;281:123–132.
10. Del Beccaro MA, Champoux AN, Bockers T, Mendelman PM. Septic arthritis versus transient synovitis of the hip: the value of screening laboratory tests. Ann Emerg Med 1992;21:1418–1422.
11. Rydholm U, Wingstrand H, Egund N, et al. Sonography, arthroscopy and intracapsular pressure in juvenile chronic arthritis of the hip. Acta Orthop Scand 1986;57:295–298.
12. Fink AM, Berman L, Edwards D, Jacobson SK. The irritable hip: immediate ultrasound guided aspiration and prevention of hospital admission. Arch Dis Child 1995;72:110–114.
13. Adler RS, Buly R, Ambrose R, Sculco T. Diagnostic and therapeutic use of sonography guided iliopsoas peritendinous injections. AJR Am J Roentgenol 2005;185:940–943.
14. Blankenbaker DG, De Smet AA, Keene JS. Sonography of the iliopsoas tendon and injection of the iliopsoas bursa for diagnosis and management of the painful snapping hip. Skeletal Radiol 2006;35:565–571.
15. DeFriend DE, Schranz PJ, Silver DAT. Ultrasound guided aspiration of posterior cruciate ligament ganglion cysts. Skeletal Radiol 2001;30:411–414.
16. Chan O, O'Dowd D, Padhiar N, et al. High volume image guided injections in chronic Achilles tendinopathy. Disabil Rehabil 2008;19:1–12.
17. Lind B, Ohberg L, Alfredson H. Sclerosing polidocanol injections in mid-portion Achilles tendinosis: remaining good clinical results and decreased tendon thickness at 2-year follow-up. Knee Surg Sports Traumatol Arthrosc 2006;14:1327–1332.
18. Alfredson H, Ohberg L. Sclerosing injections to areas of neo-vascularisation reduce pain in chronic Achilles tendinopathy: a double-blind randomised controlled trial. Knee Surg Sports Traumatol Arthrosc 2005;13:338–344.
19. Alfredson H, Ohberg L, Forsgren S. Is vasculo-neural ingrowth the cause of pain in chronic Achilles tendinosis? An investigation using ultrasonography and colour Doppler, immunohistochemistry, and diagnostic injections. Knee Surg Sports Traumatol Arthrosc 2003;11:334–338.
20. Markovic M, Crichton K, Read JW, et al. Effectiveness of ultrasound guided corticosteroid injection in the treatment of Morton's neuroma. Foot Ankle 2008;29:483–487.
21. Hughes RJ, Ali K, Jones H, et al. Treatment of Morton's neuroma with alcohol injection under sonographic guidance: follow up of 101 cases. AJR Am J Roentgenol 2007;188:1535–1539.
22. Breidahl WH, Adler RS. Ultrasound guided injection of ganglia with corticosteroids. Skeletal Radiol 1996;25:635–638.

FURTHER READING

McNally EG. Musculoskeletal interventional ultrasound. In: McNally EG, ed. Practical musculoskeletal ultrasound. Edinburgh: Churchill Livingstone; 2005. p. 283–307.

CHAPTER

63 Peripheral arteries

Colin R. Deane and David E. Goss

INTRODUCTION

Ultrasound is used extensively in the investigation of arterial disease and circulation in the limbs. For over forty years the measurement of arterial pressure at the ankle using continuous wave Doppler ultrasound and pressure cuffs has been shown to be effective in establishing the presence and severity of occlusive peripheral arterial disease in the legs. More recently, duplex ultrasound scanning has been used to identify specific sites of stenosis and occlusion prior to angioplasty or surgery. Ultrasound imaging is competitive and complementary to angiography, computed tomography angiography (CTA) and magnetic resonance angiography (MRA) for many arterial investigations, even when the circulation is seriously compromised.

For superficial arteries, duplex ultrasound provides a combination of detailed imaging of anatomy and morphology with an understanding of the haemodynamic implications of stenoses, thrombosis, fistulae, aneurysms and pseudo-aneurysms. The ability to measure haemodynamic parameters is particularly important for the investigation of the circulation in the limbs. For these applications ultrasound has developed from being primarily an instrument of physiological measurement in the early days of continuous wave Doppler, to the present where imaging, colour flow imaging and measurement are combined to present a more complete picture of anatomy and function to the physician or surgeon.

PERIPHERAL ARTERIAL DISEASE – THE CLINICAL PROBLEM

The onset of symptomatic peripheral arterial disease (PAD) affecting the leg arteries may be either a gradual or a sudden deterioration depending on whether it is the result of a slow build-up of plaque or an acute thrombotic event. This may be followed by a period of stability or even improvement due to a combination of collateral artery development, changing muscle metabolism and the training effects of exercise. However, the disease is progressive and deterioration may progress, leading ultimately to limb-threatening ischaemia. Whilst peripheral arterial disease is a significant cause of morbidity, it is concurrent disease of the circulations to the brain and heart that carries the highest mortality: 40–60% of patients will die of cardiac disease, 10–20% of cerebrovascular disease and 10% of other vascular causes, chiefly ruptured aortic aneurysm. Only 30% of patients with asymptomatic disease will progress to intermittent claudication, of whom 75% will stabilise. Of these claudicants, only 5% proceed to reconstructive surgery or percutaneous transluminal angioplasty. About 5% will suffer critical ischaemia and 1% will require an amputation.[1] Therefore the majority of patients with leg artery disease require no local treatment but are a high-risk group. Ultrasound techniques can readily identify subclinical atherosclerosis and the measurement of ankle brachial pressure index using continuous wave Doppler has been suggested as a screen to identify those at risk from cardiovascular disease.[2]

In intermittent claudication the arterial supply to the limb is adequate at rest but the increased metabolic demands of exercising muscle cannot be met due to the high resistance of the diseased arteries. In severe disease, ischaemia of the tissues occurs at rest and this may eventually lead to ulceration, gangrene and loss of the extremity.

By far the most common mechanism of arterial narrowing and occlusion is atherosclerosis and the associated complications and pathologies of thrombosis, embolisation and aneurysm formation. Atherosclerosis produces raised lesions in the wall of the artery, plaques, which reduce or obliterate the lumen. Disruption of the intima and ulceration results in platelet adhesion and the formation of thrombus which may occlude the vessel locally or embolise downstream to lodge at bifurcations of the artery or where the tapering of the artery prevents further passage. This thromboembolic occlusion can lead to acute ischaemia and gangrene. Complex atherosclerotic plaque can also give rise to cholesterol emboli which typically lodge in small arteries producing patches of cutaneous ischaemia in the foot or toes.

Changes of peripheral arterial disease are found at all levels of the arterial tree but atheroma has an apparent predilection for certain sites, particularly at bifurcations and bends in the artery where haemodynamic shear stresses are low or flow separation occurs. In the lower limb the most common site is the superficial femoral artery at adductor canal level and the second most common is the aorto-iliac segment. Diabetic patients suffer with more distal disease in the tibial and peroneal arteries. Symptomatically, more proximal disease produces more proximal intermittent claudication. A more proximal occlusion often has greater clinical effect than a distal. There are limited collateral vessels available to bypass an iliac artery occlusion, whereas the profunda femoris and geniculate branches provide good collateral routes around a superficial femoral artery occlusion and cross branches between the three arteries in the lower half of the calf and foot are extensive. In multisegmental disease symptoms are worse due to the effect of stenoses and occlusions in series, although each successive stenosis has a lesser effect than the preceding one. Management of lower limb ischaemia is complicated; it must be decided in which segments disease is clinically (or haemodynamically) significant and whether stenoses proximal to, or disease distal to the reconstruction will reduce flow to such an extent that angioplasty or bypass grafts will fail. Consequently, much effort has been directed towards the assessment of the aorto-iliac segment in multisegmental disease and the evaluation of arterial outflow and peripheral resistance in distal reconstructions.

Other pathological conditions, some related to atherosclerosis, may affect arterial flow and distal perfusion. These include local thrombosis, embolisation and downstream occlusion. Aneurysmal dilatation is a serious clinical threat because of leak or rupture, or associated mural thrombus which may cause local occlusion or distal embolisation. Abdominal aortic aneurysms are often clinically silent yet are readily diagnosed with B-mode ultrasound. Popliteal artery aneurysms are a common site of thrombus formation and sudden occlusion of the arterial supply at this level causes acute limb-threatening ischaemia.

The arteries supplying the limbs are low-resistance conduits between the heart and the tissues; in the absence of narrowing or occlusion, the pressure difference between heart and arterioles is small. When a certain degree of narrowing is reached pressure loss and flow reduction occur, which has clinical consequences. Invasive treatment therefore aims to improve or bypass the diseased segment of the artery. Reconstructive surgery is reserved for critical ischaemia and limb salvage, although it is also performed for disabling and worsening intermittent claudication. The use of less invasive percutaneous angioplasty and stenting techniques has reduced the threshold for intervention.

The diabetic patient, with a more distal distribution of disease and complicating factors of neuropathy and infection, poses special problems in diagnosis and management. Medial arterial wall calcification, also known as Mönckeberg's sclerosis or 'pipe stem' calcification because of its radiological appearance, affects ultrasound diagnosis but has probably little clinical impact.

EQUIPMENT

Continuous wave ultrasound

Continuous wave Doppler ultrasound offers a relatively low-cost means of insonating the peripheral arteries for measuring pressure and to provide a quick assessment of vessel patency. Hand-held models are available with an audio output of Doppler frequencies. More sophisticated machines incorporate a spectral analyser and display, enabling the flow spectral waveform to be seen and analysed with measurements of major parameters (e.g. peak frequency, pulsatility index, resistance index) (Fig. 63.1).

Transducers are usually available in a range of frequencies and these are used as follows: 8–10 MHz for the distal limb arteries below the knee and elbow; 4–6 MHz for the proximal limb arteries; and 2–3 MHz for the aorta and iliac arteries, or the femoral arteries in obese patients.

Ultrasound scanners

Ultrasound scanners should have good sensitivity to blood flow in both spectral and colour Doppler modes. Linear arrays are usually used for the limbs from the subclavian to ulnar and radial arteries and the femoral to pedal arteries. Although the field of view is limited, the parallel alignment of the scan lines and the ability to steer the colour Doppler box make it easier to interpret colour velocity changes through stenoses. For the thigh, 3–8 MHz

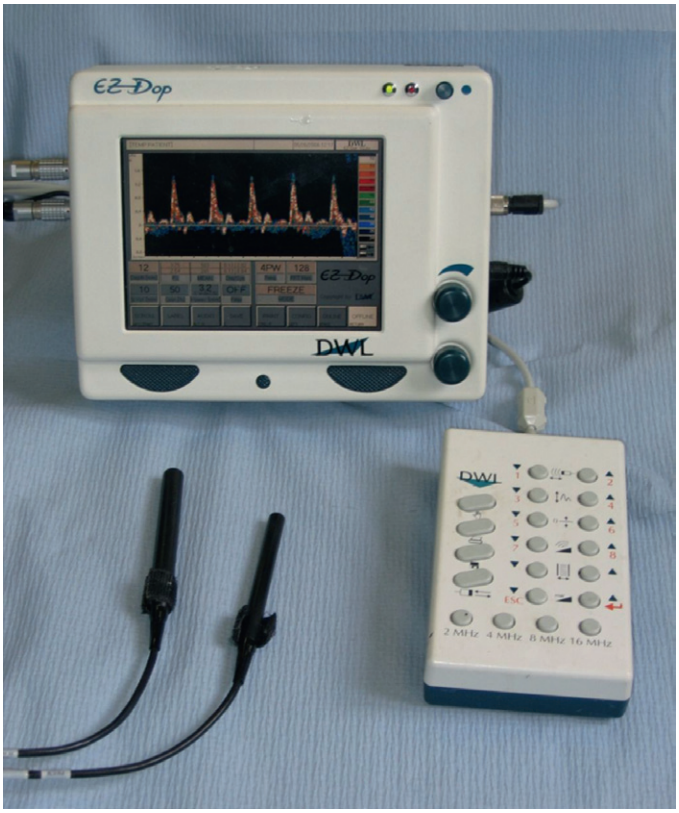

Figure 63.1 CW Doppler system. Continuous wave Doppler ultrasound device with a spectral display. Probes with frequencies of 2, 4, 8 and 16 MHz can be used.

linear arrays are usually optimum. However, these may not have sufficient penetration in obese patients, in which case lower-frequency curvilinear arrays are helpful. In distal vessels, flow velocities decrease, especially in the presence of disease, and 7–10 MHz linear arrays are advisable. In patients with diabetes or chronic renal failure, calcification and low flows may severely reduce the clarity of both B-mode and Doppler images, especially at depth.

For pelvic vessels, the orientation of the arteries in relation to the ultrasound beam leads to poor definition of the lumen in B-mode. Doppler sensitivity is of the utmost importance in displaying iliac artery flow. Curvilinear array transducers in the 1–4 MHz range usually provide adequate penetration while giving the sensitivity necessary for the range of velocities encountered. Curvilinear and phased array transducers are also useful when examining the proximal subclavian and innominate arteries where the clavicle restricts ultrasound access, although frequencies of 4–7 MHz are probably better suited to this application.

CONTINUOUS WAVE DOPPLER ULTRASOUND OF PERIPHERAL ARTERIAL OCCLUSIVE DISEASE

Blood flow measurement using continuous wave (CW) Doppler ultrasound was pioneered in vascular laboratories in the 1970s.[3–5] Simple CW Doppler ultrasound machines are now found throughout hospitals in vascular laboratories, clinics and surgical wards. They are also used in the community, notably as a screen for peripheral vascular disease in the assessment of venous leg ulcers.[6]

Although less sophisticated than colour duplex scanners, CW Doppler ultrasound can provide valuable first-line diagnostic evidence as to the presence, site and severity of disease. In the hierarchy of investigations for peripheral vascular disease, a CW Doppler ultrasound examination should be performed before more expensive and time-consuming duplex scanning and more invasive arteriography. When used in conjunction with systolic pressure measurement and stress testing, these instruments provide physiological information on the functional severity of the disease and, additionally, arterial velocity waveform analysis provides an indication as to the level of significant disease.

Ankle brachial pressure index (ABPI)

The use of continuous wave Doppler ultrasound to measure the ankle systolic pressure and compare it with the systolic pressure in the brachial artery was first described by Yao.[7] The ankle brachial systolic pressure index is defined as ankle systolic pressure divided by the brachial systolic pressure. The use of a pressure index rather than the absolute pressure allows serial comparison of results from the same patient in the presence of changing systemic arterial pressure, as well as comparisons between individuals. The technique is simple and robust but must be performed with correct technique.[8]

The brachial cuff is placed in the standard position[9] and the distal edge of the ankle cuff is placed just above the ankle. Any suitable site distal to the occlusion cuff may be used as a site of insonation to detect reappearance of flow on cuff deflation. A cuff that is too wide will underestimate the blood pressure, whereas too narrow a cuff will overestimate the pressure.[10] The patient should be lying supine with upper arm and ankles at the same level (approximately that of the heart). Blood pressure should be measured in both arms as significant differences between the arms has been shown in patients with arterial disease[11,12] and with leg ulcers.[13]

An ABPI value of less than 1.0 is used to diagnose the presence of peripheral vascular disease. The more severe the disease and the more arterial segments involved, the lower the pressure index.[7] There is an overlap in pressure index between those with and without disease[14] and lower decision thresholds have been applied.[15] Typically a pressure index of <0.8 is found in patients with mild intermittent claudication and this level of index would contraindicate venous compression bandaging in patients with leg ulceration.[16] An index of 0.5 is associated with severe claudication and indices of 0.3 or less with ischaemic rest pain, ulceration and gangrene.[17] A significant change in ABPI over time has been taken as 0.1[18] and 0.15.[19]

Calcification in the media of the artery wall is a source of error which results in the overestimation of ankle pressure.[20] The artery wall is stiffened and so resists compression by the ankle occlusion cuff and, on cuff deflation, reopens at intraluminal pressures that are less than the cuff pressure. This complication may be obvious but the greater danger of misinterpretation of ABPI lies with patients in whom a partial increase in stiffness of the artery wall results in a seemingly realistic but in fact falsely raised reading. Methods have been suggested to overcome this deficiency[21,22] but routine careful comparison of ABPI with pedal artery velocity waveform shape is prudent.

Stress testing is used in conjunction with ABPI measurements. It utilises the relationship between increased flow due to hyperaemia and corresponding increase in pressure loss across a stenosis to provide further information on the functional and haemodynamic consequences of peripheral vascular disease. Cuff-induced reactive hyperaemia,[23] static ergometer exercise[24] and, most commonly, treadmill testing[5] are used. Standardised treadmill exercise protocols have been suggested[25] but methods vary. Patients may typically be exercised on the level or on a slope of up to 12% at speeds of 2–4 km/h for a duration of 1–5 minutes[26] or until limited by symptoms. Disease not detected at rest can be unmasked and claudication distance assessed but the latter is poorly reproducible. The real value in stress testing is demonstration of a post-exercise pressure drop which confirms the presence of a physiologically significant lesion.

Velocity waveform analysis

The shape of the arterial velocity waveform is characteristic to individual arteries and their circulations and to specific sites along the arteries (Fig. 63.2). As with ABPI, the velocity flow waveform shape is representative of physiological function and disease. It is often used to assess the severity of vascular disease proximal to the site of insonation but factors distal, local and proximal to the site of insonation affect its shape. Damping of the arterial waveform results from proximal disease (Fig. 63.3). An increase in velocity can be detected at the site of a stenosis and disturbed flow demonstrated immediately distal to this.[5] Proximal factors affecting the waveform include cardiac output and collateral vessels; distal factors include the impedance from downstream arteries and arterioles. Distal stenosis or increased peripheral microvascular resistance as a result of cold temperatures, drugs or spasm causes an increase in waveform pulsatility. Vasodilation occurs in the presence of increased ambient temperature, wound healing and infection, critical ischaemia and with reactive hyperaemia after exercise or temporary occlusion. A combination of these factors will usually affect the waveform at any particular site.

Changes in the arterial waveform can be assessed successfully by eye.[27] Many of the features of the waveform such as systolic acceleration and reverse flow components are readily distinguished by the trained eye or ear. However, more objective and quantifiable methods are desirable. A variety of mathematical descriptions of the waveform have been employed, of which the most widely used in peripheral vascular disease is the pulsatility index (PI), which is non-dimensional and independent of the angle of insonation in relation to the direction of blood flow. Table 63.1 defines some of the measurements used in descriptions of the arterial waveform, which are illustrated in Figure 63.4.

Although the pulsatility index has been shown to reflect changes in the presence of a proximal stenosis,[28] it also reflects changes in peripheral resistance.[29,30] Pourcelot's resistive index is another simple, commonly used, measure of pulsatility. It was designed for

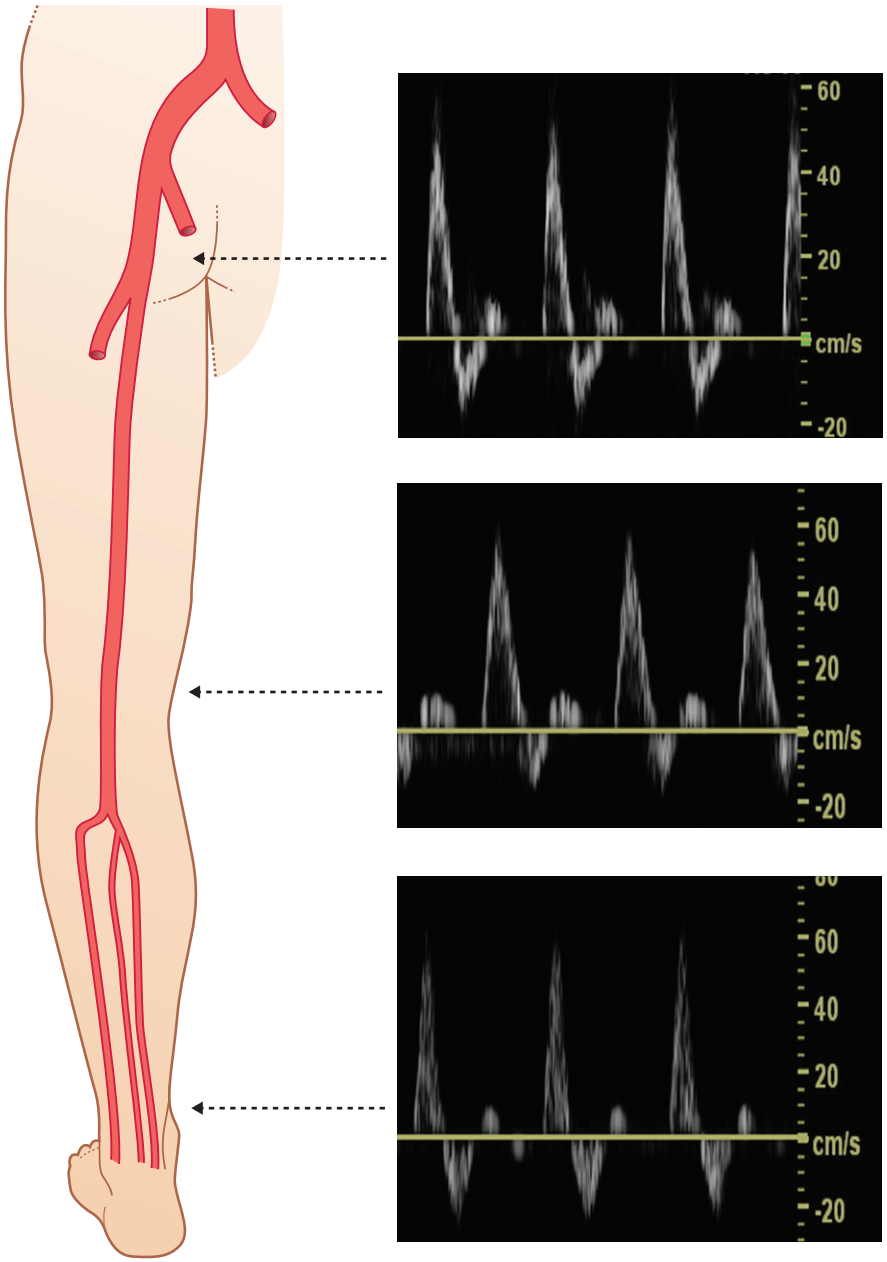

Figure 63.2 Normal arterial waveforms. Normal arterial waveforms of common femoral, popliteal and posterior tibial arteries.

the cerebral circulation and to reflect distal resistance rather than proximal stenosis.[31]

The increased utility and popularity of duplex scanning with the use of velocity ratios to identify significant lesions has meant that simple visual examination of the waveform is used to screen for the presence of proximal disease. Visual waveform inspection at the common femoral artery is also useful when aorto-iliac scanning is precluded by poor quality images.[27]

Summary

In the investigation of leg artery disease, continuous wave ultrasound waveform analysis and ankle pressure measurement are relatively inexpensive, quick and simple to perform. They are non-invasive and, unlike most imaging methodologies, are a measurement of haemodynamic and physiological function that is proportional to the severity of the disease. Their role therefore is as a preliminary diagnostic tool prior to angiography and duplex scanning. They are repeatable, so are well suited to follow up studies of treatment and in trials; they are also used for monitoring disease in screening and epidemiological study.

DUPLEX ULTRASOUND OF PERIPHERAL ARTERIAL DISEASE

Duplex ultrasound is increasingly used to specify the level and severity of occlusive disease in legs, to monitor bypass grafts and to identify run-off arteries suitable for use in distal reconstructions. With its ability to determine and measure occlusions, it can be instrumental in planning angioplasty or surgery.[32–35]

In current clinical practice, duplex ultrasound complements and competes against contrast- and non-contrast-enhanced magnetic resonance angiography (MRA) and computed tomography angiography (CTA). Intra-arterial contrast angiography was previously regarded as the gold reference standard against which other modalities were compared but is performed much less frequently now as

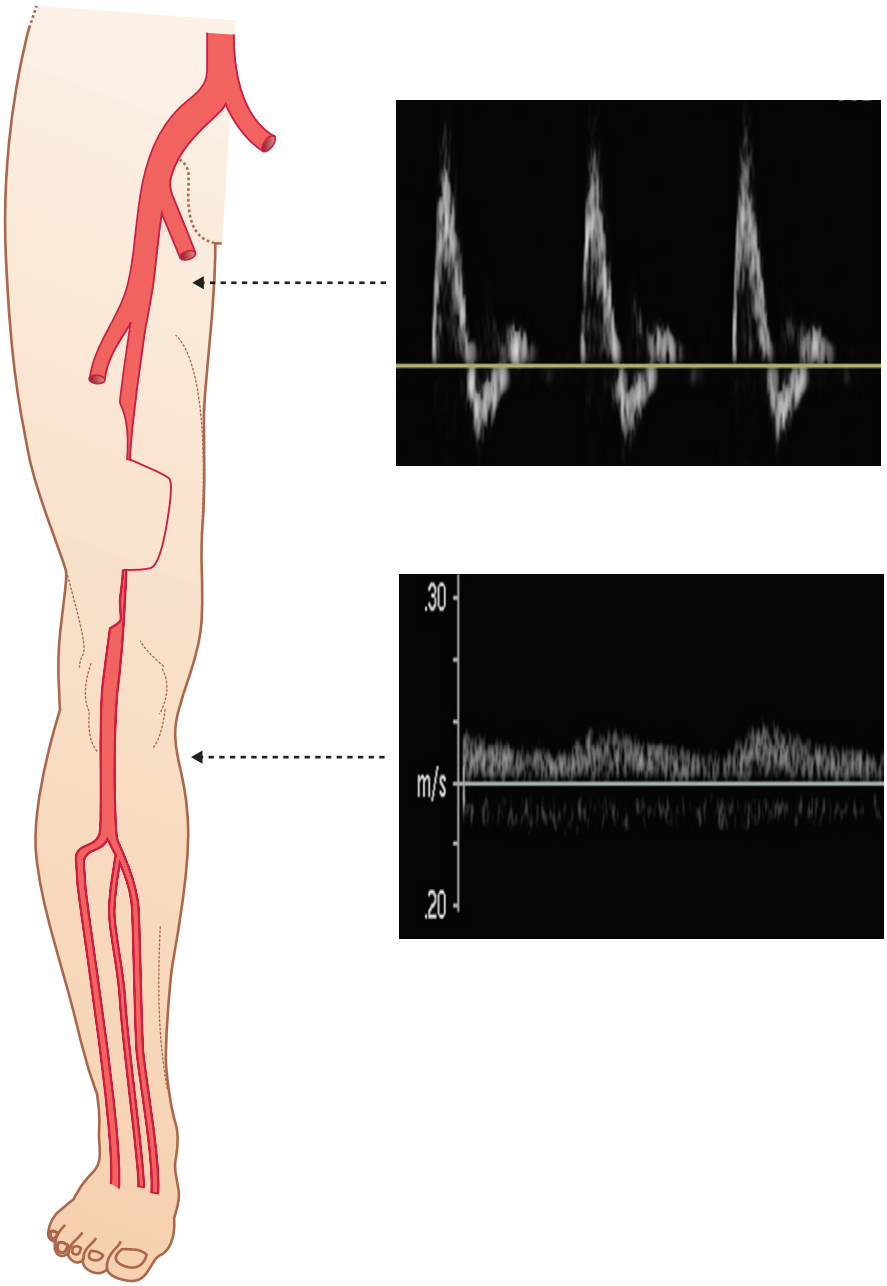

Figure 63.3 The arterial waveform with an occlusion. Common femoral and popliteal artery waveform with a long occlusion of the superficial femoral artery as shown diagrammatically. The popliteal artery waveform shows severely damped flow resulting from a low pressure pulse inflow and distal vasodilatation.

non-catheter techniques have improved. In a review of comparative studies,[36] contrast-enhanced MRA was shown to have slightly better agreement with arterial contrast angiography than duplex ultrasound and CT angiography, although it was also concluded that duplex ultrasound is sensitive to the presence of disease and is unlikely to misclassify a limb as normal if disease is present. Arterial angiography also carries a low, but consistently reported, complication rate with a risk of injury to the artery (false aneurysm, dissection, embolisation) and contrast agent reactions. Local practice is dependent on the resources and expertise available and the implementation of local diagnostic pathways. Other factors, including patient tolerance, radiation safety and the safety of contrast agents in patients with impaired renal function may also play a part in choosing which imaging to use.[37]

Duplex ultrasound has the advantage of combining anatomical and morphological information with a haemodynamic assessment of the lesions. Against this, the examination of the leg arteries is time-consuming, requiring 30–60 minutes for investigation of the major arteries from aorta to the lower tibial arteries. The examination requires considerable skill and training if accurate results are to be produced. In addition, the small field of view of linear arrays makes it comparatively difficult to demonstrate anatomy convincingly to third parties.

Stenosis criteria

Because of the depth, orientation and presence of atherosclerotic disease in the arteries under investigation, B-mode images of the lumen are often insufficiently clear to obtain a measure of the degree of narrowing, especially in high-grade stenoses. This is particularly true in the iliac vessels, where the course of the arteries may not be at all apparent in the B-mode image. In these cases, vessel/beam angles provide conditions more suitable for a colour image of the artery (Fig. 63.5). The presence of a stenosis results in a compensatory increase in velocity though the stenosis lumen (Fig. 63.6). Diagnosis of disease is made by measurements of the ratio of velocity in the stenosis to that in the more proximal lumen above the stenosis. The velocity change is depicted in the colour image by a change of hue, often with aliasing depending on the settings used (Figs 63.6, 63.7).

Table 63.1 Measurements used in descriptions of the arterial waveform (from Allan, Dubbins, Pozniak and McDicken: Clinical Doppler Ultrasound, Churchill Livingstone, 2006)

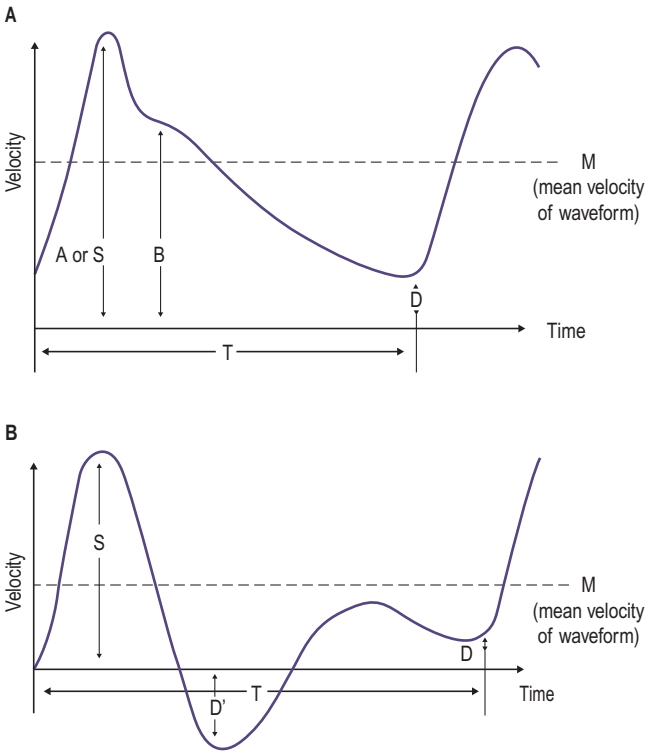

$$RI = \frac{S-D}{S}$$

$S/_D$ ratio (umbilical and uterine arteries)

$A/_B$ ratio (carotid arteries)

$$PI = \frac{\text{Maximum velocity excursion}}{\text{Mean velocity}}$$

$$= \frac{S-D}{M} \text{ in } \mathbf{A}$$

$$= \frac{S+D'}{M} \text{ in } \mathbf{B}$$

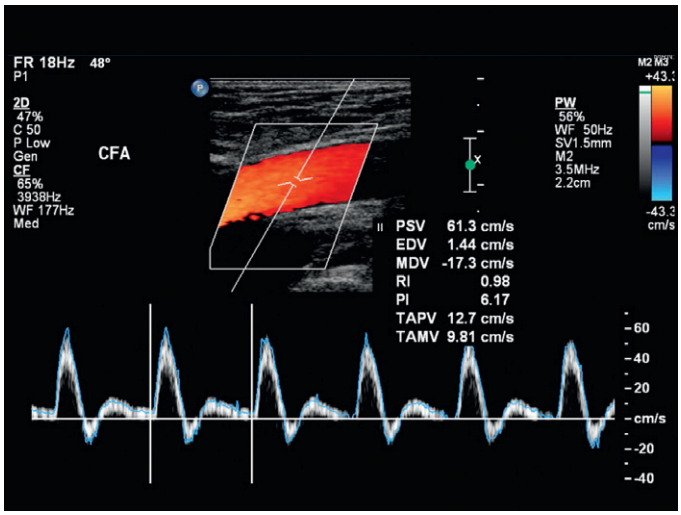

Figure 63.4 Waveform parameters. Flow waveform of a common femoral artery. Several parameters are measured from the automatic trace of the flow outline. PSV, peak systolic velocity; EDV, end-diastolic velocity; MDV, minimum diastolic velocity; RI, resistance index; PI, pulsatility index; TAPV, time-averaged peak velocity, also referred to as time-averaged maximum velocity and also time-averaged mean maximum velocity; TAMV, time-averaged mean velocity (weighted mean of the sonogram).

In a stenosis, the change in mean velocity rises in proportion to the decrease in cross-sectional area. Unfortunately, mean velocity is difficult to measure accurately, particularly in the stenosis jet. The change in peak systolic velocity (PSV) (Fig. 63.7) through a narrowing is more complex and depends on the flow profile proximal to and within the stenosis. The PSV is more easily measured, however, and is less susceptible to other variables (such as distal impedance) than other measurements of velocity. In a comparison of PSV and angiographic measurements of peripheral artery stenosis severity,[38] the PSV ratios showed a better correlation with percentage stenosis than absolute velocities, which were affected by other physiological variables. Most studies have used a velocity ratio for stenosis quantification.

The most common threshold used to describe a haemodynamically significant stenosis is a 50% reduction in diameter. PSV ratios for this degree of stenosis have been reported from 1.8 to 2.5 in a range of studies for aorto-iliac and femoropopliteal disease, although a ratio of 2.0 is most commonly reported and used.[32,33,39,40] The range reflects differences of interpretation in ultrasound and arteriography measurements and illustrates the problem inherent in defining a stenosis by its diameter. A study to examine progression of femoral artery disease[41] observed that stenoses with velocity ratios >3.0 had a high incidence of early occlusion and that at this level early intervention is advised. A 50% reduction in diameter produces a 75% reduction in area if the stenosis is concentric and 50% reduction in area if the stenosis is semicircular. Mean and peak flow through the two profiles will be markedly different. In practice, stenoses are rarely concentric or semicircular and their irregular shape further compounds technical limitations and errors in converting the velocity increase to stenosis diameter.

For accurate quantification of the stenosis, the peak systolic velocity is measured in the artery above the stenosis, where there is no or minimal disease and at the point of maximum velocity increase (Fig. 63.7). Angle correction should be made in line with the direction of the artery. In practice this may under- or overestimate the PSV in the stenosis jet in cases of asymmetric plaque but it may be difficult to identify the direction of the true velocity vector and a systematic method within a department will lead to less operator-dependent variation. Attempts have been made to quantify pressure loss from measured velocities using a modified Bernoulli equation with limited success.[42,43]

The use of velocity ratios in multiple stenoses is somewhat controversial. While some reports have suggested that velocity ratios produce lower accuracy in the presence of severe adjacent disease,[44,45] others suggest that criteria are unaffected.[35] In practice, assessment of a lower limb with serial stenosis in the arteries will depend on the clinical situation as well as the Doppler findings.

Ultrasound in the diagnosis of peripheral arterial disease

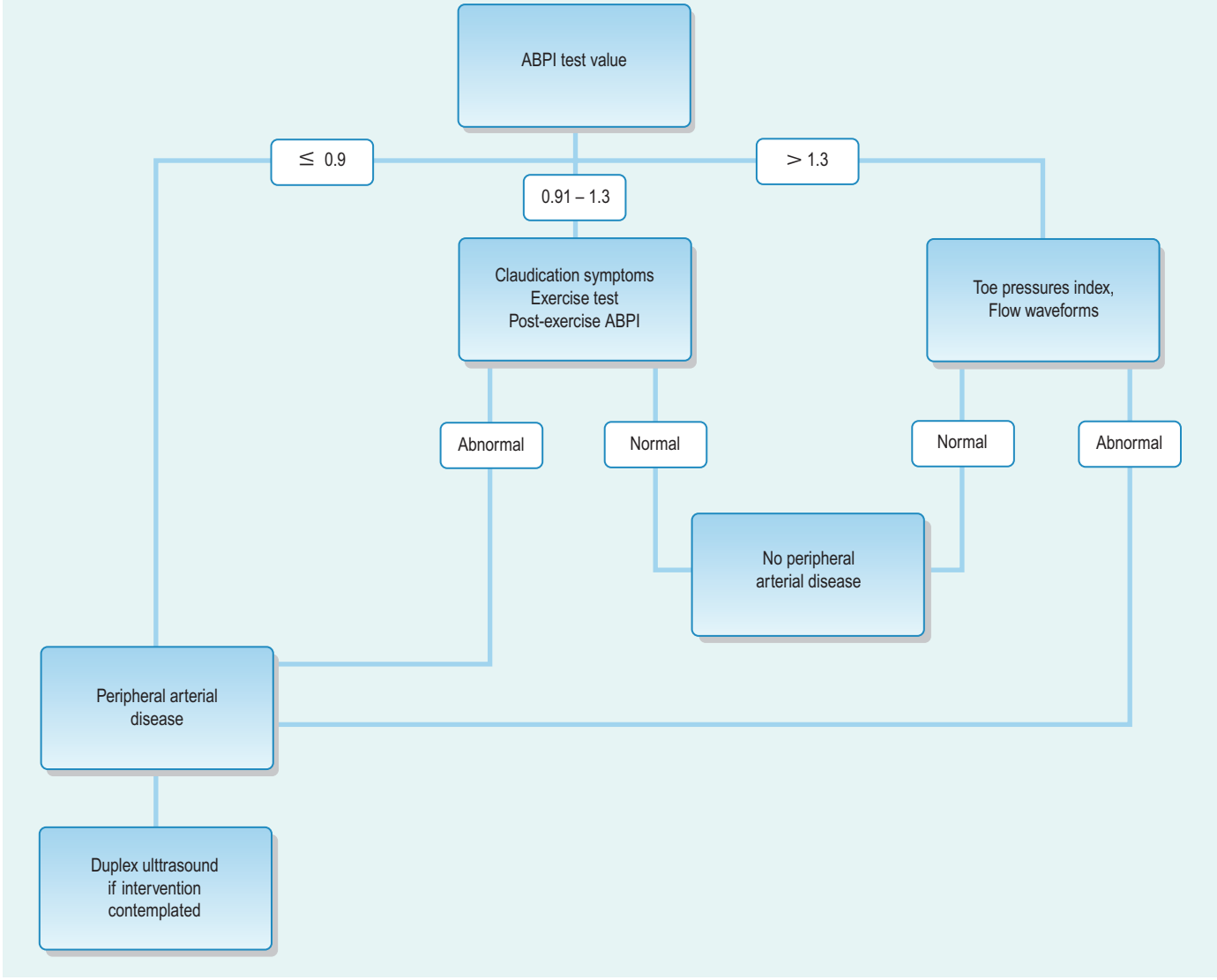

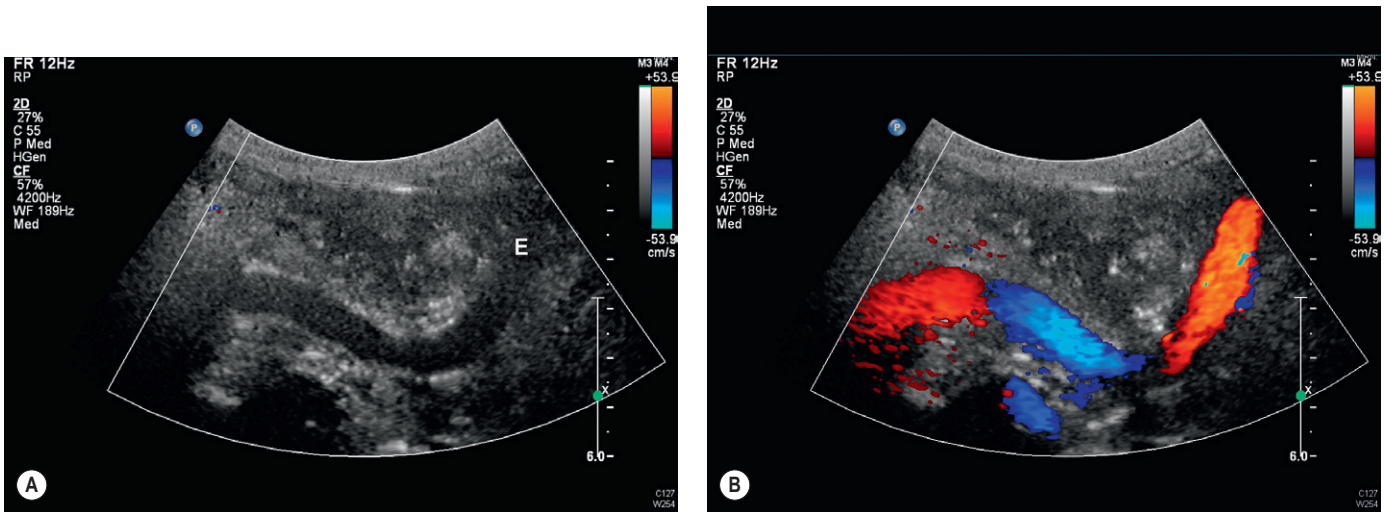

Figure 63.5 B-mode (A) and colour Doppler (B) images of an external iliac artery. Curvature in the artery causes a wide range of beam/vessel angles when insonated with a curvilinear transducer. The distal artery is not seen clearly on the B-mode image (E); the orientation of the vessel at this point leads to a clear colour flow image.

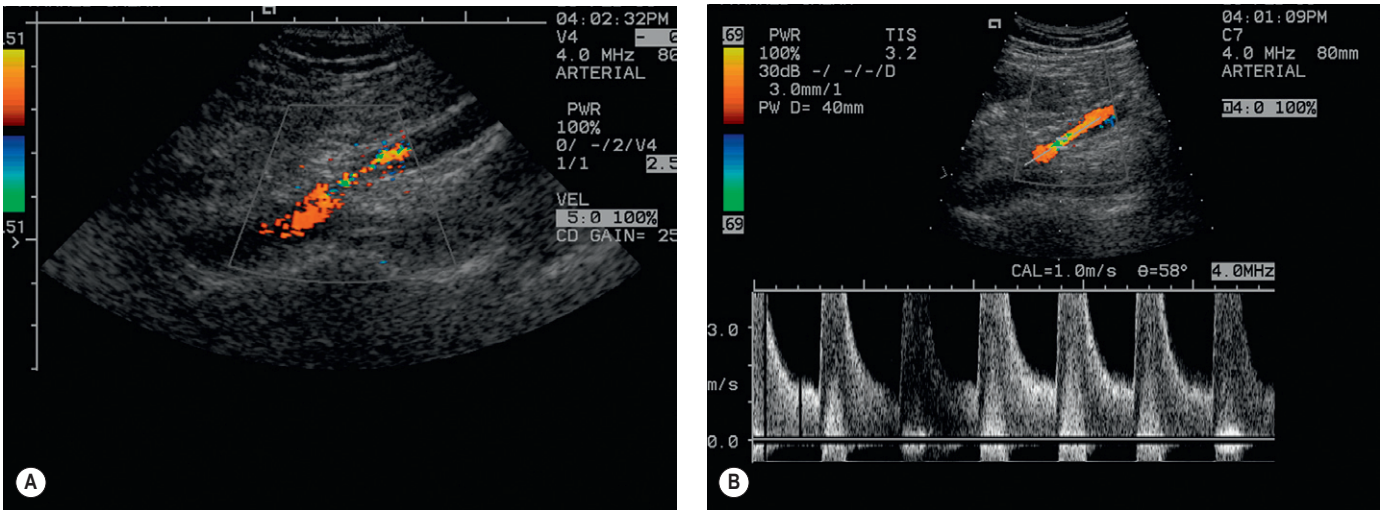

Figure 63.6 External iliac stenosis. The colour Doppler image **(A)** shows aliasing and a loss of colour flow filling. Spectral Doppler **(B)** shows very high velocities with aliasing and peak velocities of approximately 5 m/s. The depth and high velocities prevent unambiguous display of the spectral image without aliasing.

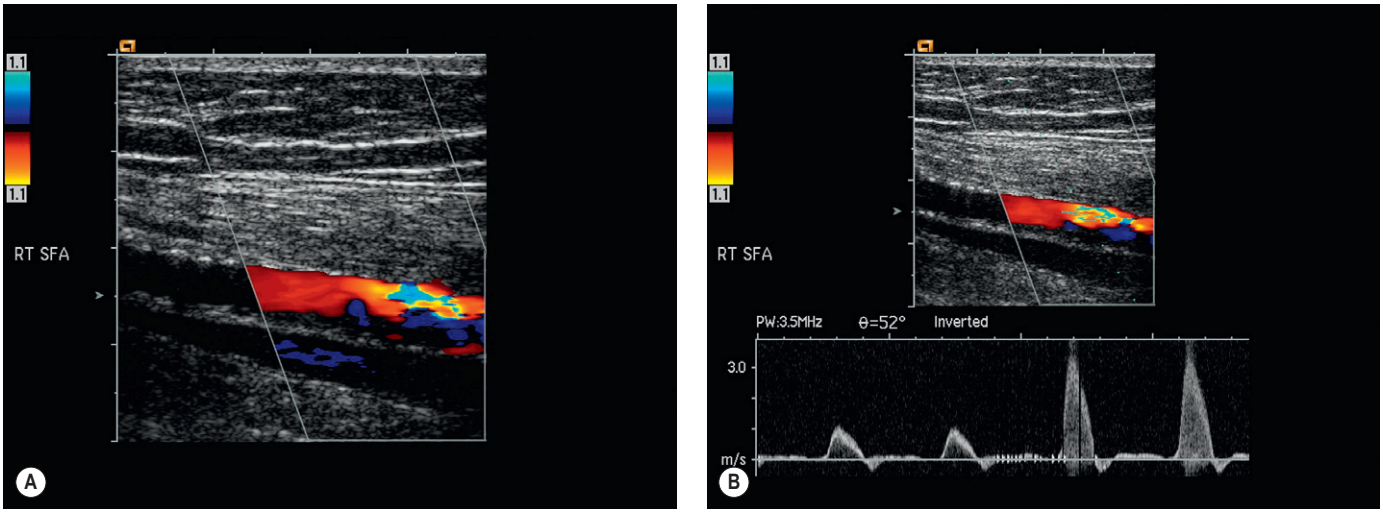

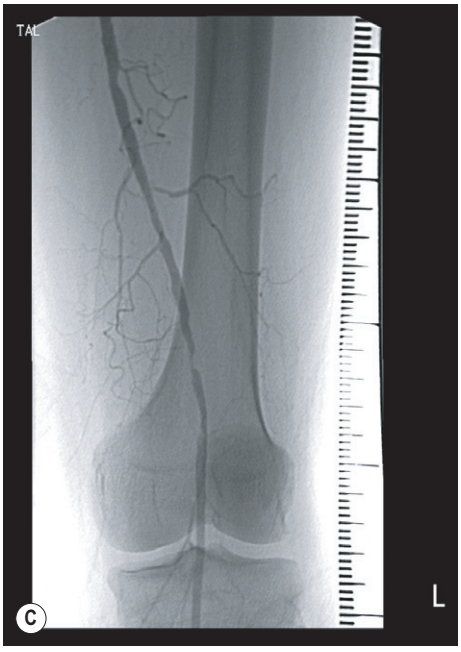

Figure 63.7 Images of a superficial femoral artery stenosis. The colour flow image **(A)** shows an area of aliasing in the artery associated with high Doppler shifts. Note the high colour flow scale of 1.1 m/s mean velocity. The sonogram **(B)** shows the flow waveform in the pre-stenosis artery and at the stenosis. There is a greater than threefold velocity increase with peak velocity >3 m/s. Angiography shows a tight stenosis **(C)**.

Scanning technique

Since quantification of stenoses is based on velocities and velocity increases, scanning of the arteries is undertaken longitudinally. In the aorto-iliac segment, fasting is recommended to reduce the difficulties caused by gas. The aorta and proximal iliac vessels are usually scanned with a curvilinear or phased array transducer. From the external iliac to mid-calf vessels, linear arrays are most commonly used, although high-frequency curvilinear arrays produce a greater field of view.

Atherosclerotic changes produce inconsistent effects in the B-mode image. Because of this, the colour image is used extensively to identify the location of the artery, voids in the flow signal indicating occlusion (Figs 63.8, 63.9, 63.10) and regions of increased velocity (Figs 63.6. 63.7, 63.11) suggesting narrowing of the lumen. Areas of concern can then be tested using spectral Doppler. For linear arrays, beam steering can enhance the Doppler image in both colour

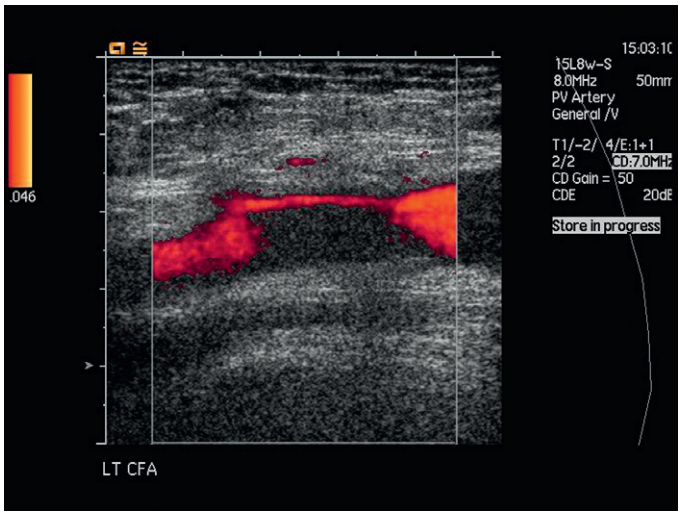

Figure 63.9 Common femoral artery stenosis. A tight stenosis in a common femoral artery. The power Doppler image shows a small patent lumen with a severe (>90%) stenosis.

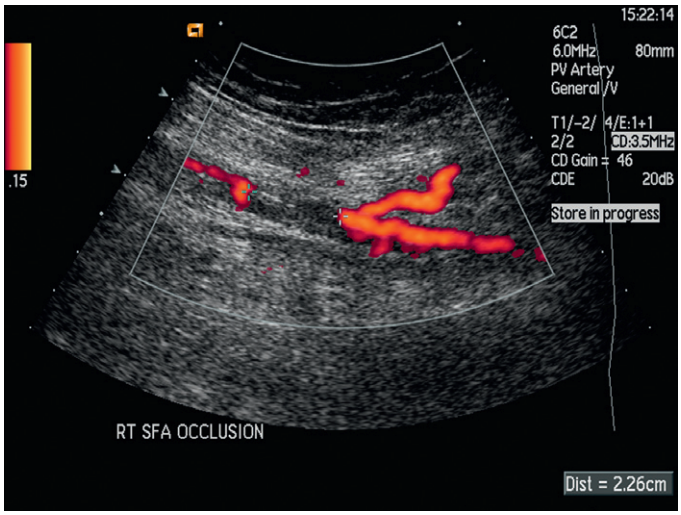

Figure 63.8 Superficial femoral artery occlusion. Power Doppler image showing a short occlusion of a superficial femoral artery. A collateral artery supplying the distal femoral artery is evident.

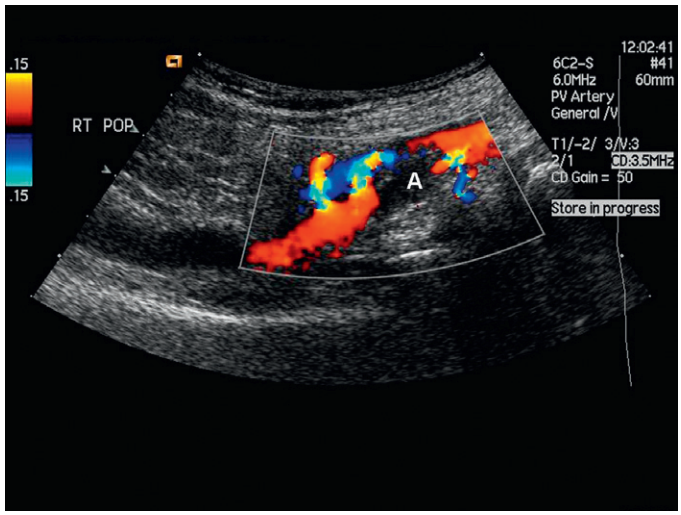

Figure 63.10 Popliteal artery occlusion. Colour flow image showing a popliteal artery occlusion with two large collateral arteries arising proximal to the occlusion (A).

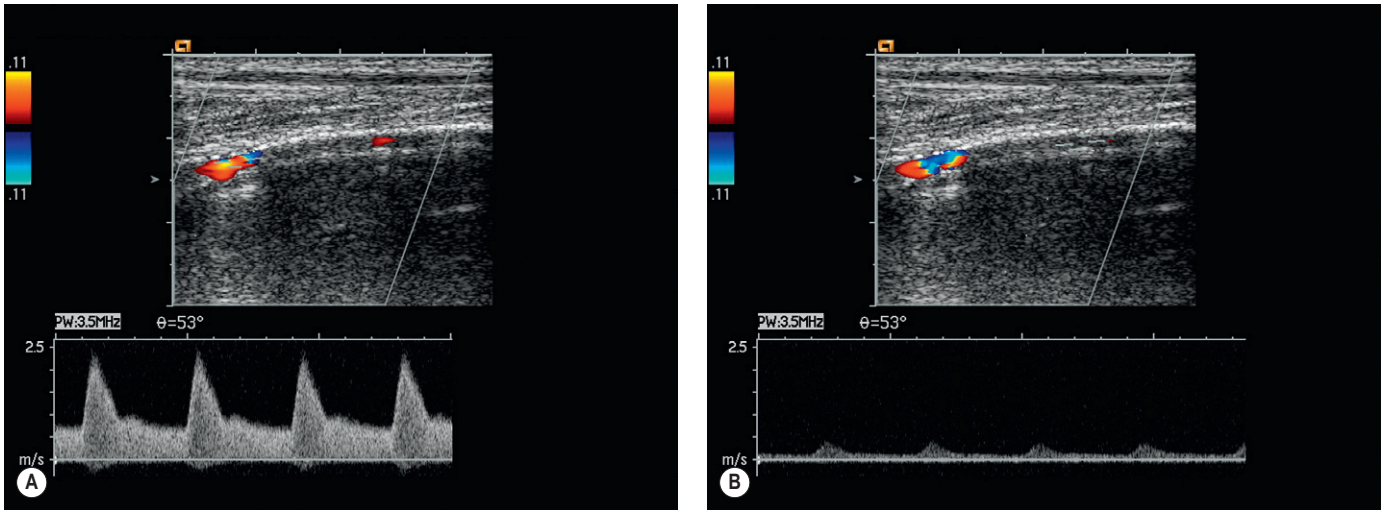

Figure 63.11 Tibial artery stenosis. Colour flow aliasing indicates high peak velocities, measured as 2.4 m/s on spectral Doppler **(A)**. Downstream **(B)** the course of the artery is visible on B-mode although there is no colour filling. Spectral Doppler shown on the same scale as **(A)** indicates the reduction in velocity post-stenosis.

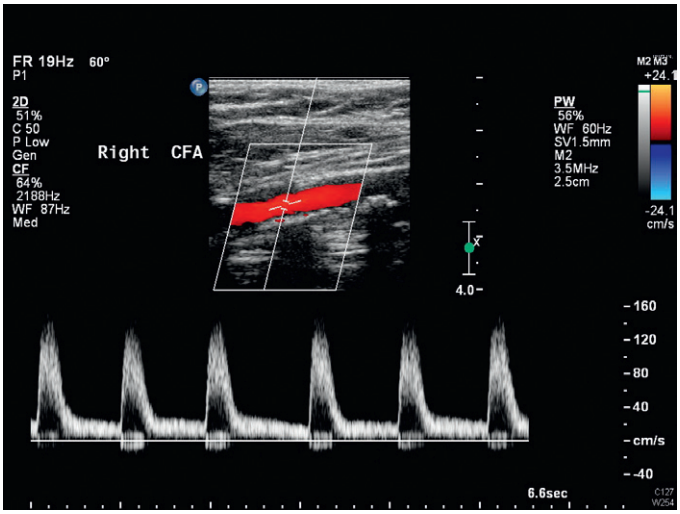

Figure 63.12 Monophasic flow waveform in a common femoral artery. The loss of the reverse flow component and forward flow throughout diastole are indicative of proximal disease.

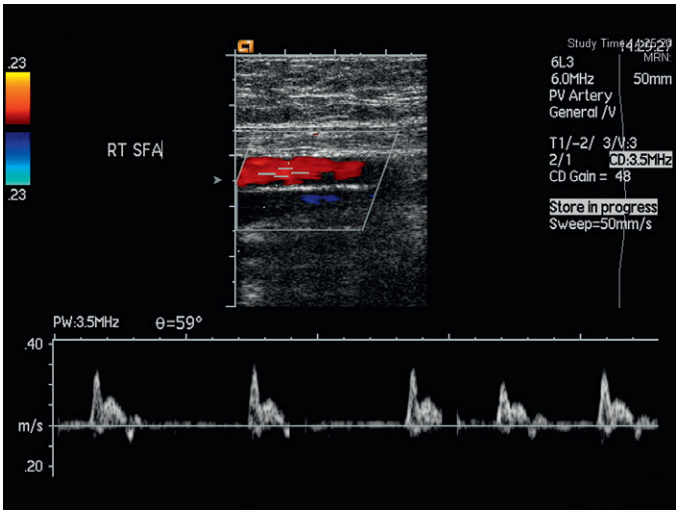

Figure 63.13 Abnormal superficial femoral artery flow waveform. The low velocities, absent diastolic flow and short initial peak are indicative of severe distal disease, in this case an occlusion of the femoral artery at mid-thigh level.

and spectral modes, although attenuation is least when the Doppler beam is unsteered.

The degree of stenosis is obtained by measuring peak systolic velocity from the spectral Doppler sonogram. As usual when using spectral Doppler ultrasound to calculate velocities, care should be taken when using beam/flow angles greater than 60°, although the use of velocity ratios means that errors are usually acceptable at angles up to 70°. When determining occlusion, low pulse repetition frequencies and power Doppler should be used to check for low volume, low velocity flow in any residual lumen in the vessel.

Flow waveforms in healthy arteries exhibit pulsatile flow with reverse flow in late systole – triphasic or biphasic flow (Fig. 63.2). Changes in flow waveform shape can be an indication of proximal disease (Fig. 63.12) or distal occlusion (Fig. 63.13). Although attempts have been made to use measurement of subtle changes to indicate proximal disease, these have not become established in clinical practice. However, experienced sonographers use visual changes in the waveforms and abnormally low or high velocities as indications of abnormal circulation warranting further investigation.

Aorto-iliac and femoropopliteal segments

The examination normally begins with the identification and assessment of the common femoral artery at the groin. Even if colour Doppler appears unremarkable, a spectral Doppler trace should be made, as changes may be demonstrated indicating proximal disease, necessitating careful direct assessment of the iliac arteries. This is best carried out by following the external iliac artery superiorly, identifying the origin of the internal iliac artery, then following the common iliac artery up to its origin from the aorta. If the vessels cannot be followed in continuity up from the groin, then starting at the bifurcation and moving inferiorly is of value.

The common femoral artery is then followed distally to its bifurcation where the origin of the profunda femoris artery is assessed, together with the upper 5–6 cm of the vessel. The superficial femoral artery is examined using colour Doppler from its origin down to the adductor canal, with spectral Doppler assessments being obtained from any areas of concern demonstrated on colour Doppler. In patients with severe disease, collateral vessels may be seen connecting with the main artery, or within the tissues of the thigh.

The patient is then asked to move into a decubitus position so that the medial aspect of the thigh and knee being examined are uppermost and the adductor canal and popliteal regions can be examined. The artery may be difficult to follow through the adductor canal but it is important to ensure that it is visualised in its entirety in this region as there is a risk that short segment stenoses or occlusions may be missed. In difficult cases the superficial femoral artery can be tracked down the thigh as far as possible and the skin marked to identify this point. The popliteal artery is then followed superiorly to the point marked on the skin. If concern persists about disease in this segment, spectral Doppler waveforms from the lower superficial femoral artery and upper popliteal artery segments should be obtained to ensure that there are no changes that might suggest significant intervening disease.

In a meta-analysis of duplex ultrasound studies[46] that used velocity ratios to investigate occlusions and stenoses >50% diameter, there was technical success of over 90% for the aorto-iliac segment. The pooled sensitivity and specificity for occlusion were 94% and 99% and for stenoses greater than 50% diameter, 80% and 95%, respectively.

In the same meta-analysis, results for the femoropopliteal segments were similar. The pooled sensitivity and specificity for occlusion were 90% and 97% and for stenoses greater than 50% diameter, 82% and 96%, respectively. When compared with angiography, ultrasound has been shown sometimes slightly to underestimate the length of occlusions, a finding attributed to poor contrast filling adjacent to the occlusion limits on the arteriogram.[47]

Below-knee segments

The popliteal artery is followed to its bifurcation and the origin of the anterior tibial artery and then on to the bifurcation of the tibioperoneal trunk. This segment is another site of predilection of disease and careful assessment is required. The posterior tibial and peroneal arteries are best examined from a medial approach; the peroneal artery lies deep to the posterior tibial artery with this approach. The anterior tibial artery is examined from an anterolateral approach as it lies on the interosseous membrane between the tibia and fibula. The peroneal artery may also be seen from this approach. In cases where the calf arteries are difficult to visualise, using power Doppler, or scanning transversely and using the companion veins to identify their location may be of help. This latter

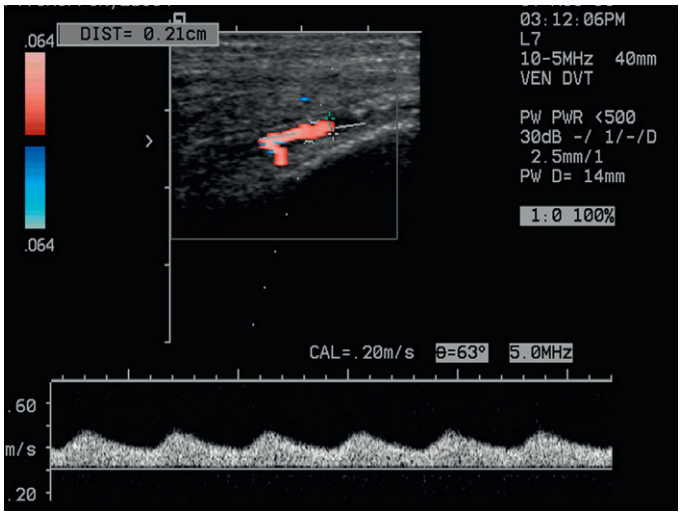

Figure 63.14 Collateral artery supplying a dorsalis pedis artery. Ultrasound identifies the level of vessel patency and the artery diameter.

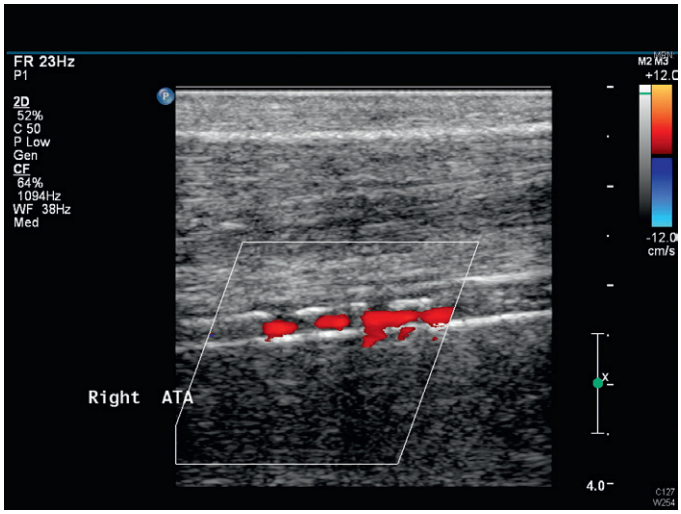

Figure 63.15 Calcification in the tibial arteries. Calcification in the tibial arteries causes loss of colour flow deep to high levels of calcification. In severe cases flow may not be detected by colour or spectral Doppler.

approach is facilitated if the patient can sit on the edge of the couch with their leg dependent.

The calf arteries are followed down to the ankle. The pedal arteries are examined if clinically indicated, usually if the dorsalis pedis artery is being considered for a distal graft insertion, or there are particular questions about the arterial circulation in the foot (Fig. 63.14).

For infrapopliteal examinations, patency of the distal anterior tibial, posterior tibial and peroneal arteries is identified. Arteries are described in terms of diameter, patent length with evidence of stenoses, waveform shape and evidence of communication with the pedal arch.

There have been fewer studies reporting on ultrasound scanning of infrapopliteal arteries. In comparison with scanning the proximal arteries, investigation of vessels in the lower leg is time-consuming with a lower reported success rate, especially for peroneal artery stenosis.[48,49] The presence of extensive, severe calcification can preclude full investigation of calf arteries; this is a practical constraint on the many patients presenting with diabetes or chronic renal failure (Fig. 63.15). Nevertheless, a study comparing angiography and duplex scanning assessment of vessel patency[48] concluded that

Table 63.2 Causes of graft failure (from Allan, Dubbins, Pozniak and McDicken: Clinical Doppler Ultrasound, Churchill Livingstone, 2006)

Intrinsic	Extrinsic
Stenosis	Inflow disease progression
Proximal or distal anastomosis	Outflow disease progression
Mid-graft	Entrapment or kinking
	Clamp injury
Diffuse myointimal hyperplasia	Thromboembolism
	Hypercoagulation states
Aneurysm	Sepsis
Anastomotic	
Mid-graft	

Haemodynamic failure occurs when the graft is patent but the limb remains ischaemic.

agreement between the two modalities was similar to agreement between radiologists reporting on angiograms. For these arteries, colour flow is particularly useful for identifying the course of vessels and the presence of collateral flow.

Ultrasound has been shown to be effective in evaluating run-off vessels suitable for femorodistal reconstructions.[50] For these preoperative examinations, flow and velocities are often very low indeed. High-frequency transducers are required using low colour and spectral pulse repetition settings.

Reporting

Ultrasound images are constrained by the transducer width and field of view. This presents difficulties in presenting findings to referring clinicians. It is common to present ultrasound findings on a diagram of the leg, highlighting the presence and size of occlusions and aneurysms, the site and severity of stenoses and major collateral pathways identified at the scan. An example is shown in Figure 63.16.

PERIPHERAL ARTERY BYPASS GRAFTS

Ultrasound is used extensively to monitor bypass grafts, permitting early intervention to prolong graft life and to enhance limb salvage rates. Grafts (both autologous vein and synthetic) can fail for a variety of reasons (Table 63.2).

In general, bypass grafts terminating at or above femoral artery level have a higher patency rate than those terminating at the infrainguinal level. These proximal grafts tend to make more use of artificial materials and tend to fail as a result of thrombosis. Ultrasound is used to assess grafts to determine patency, identify any stenosis (particularly in the proximity of the anastomoses), thrombosis, technical errors, mismatches in lumen size and abnormal haemodynamics (disturbed flow, regions of low velocity).

The most effective application of ultrasound in bypass grafts has been for infrainguinal vein grafts. Here the comparatively high failure rate, clinical implications of graft failure and the gradual onset of failure from hyperplasia-induced stenoses may justify the investment required for an intensive programme of surveillance.

Preoperative vein scanning for arterial reconstruction

In addition to the examination of proximal and run-off arteries in relation to an occluded segment, ultrasound is also used to identify veins suitable for use in surgery. The most commonly used vein is

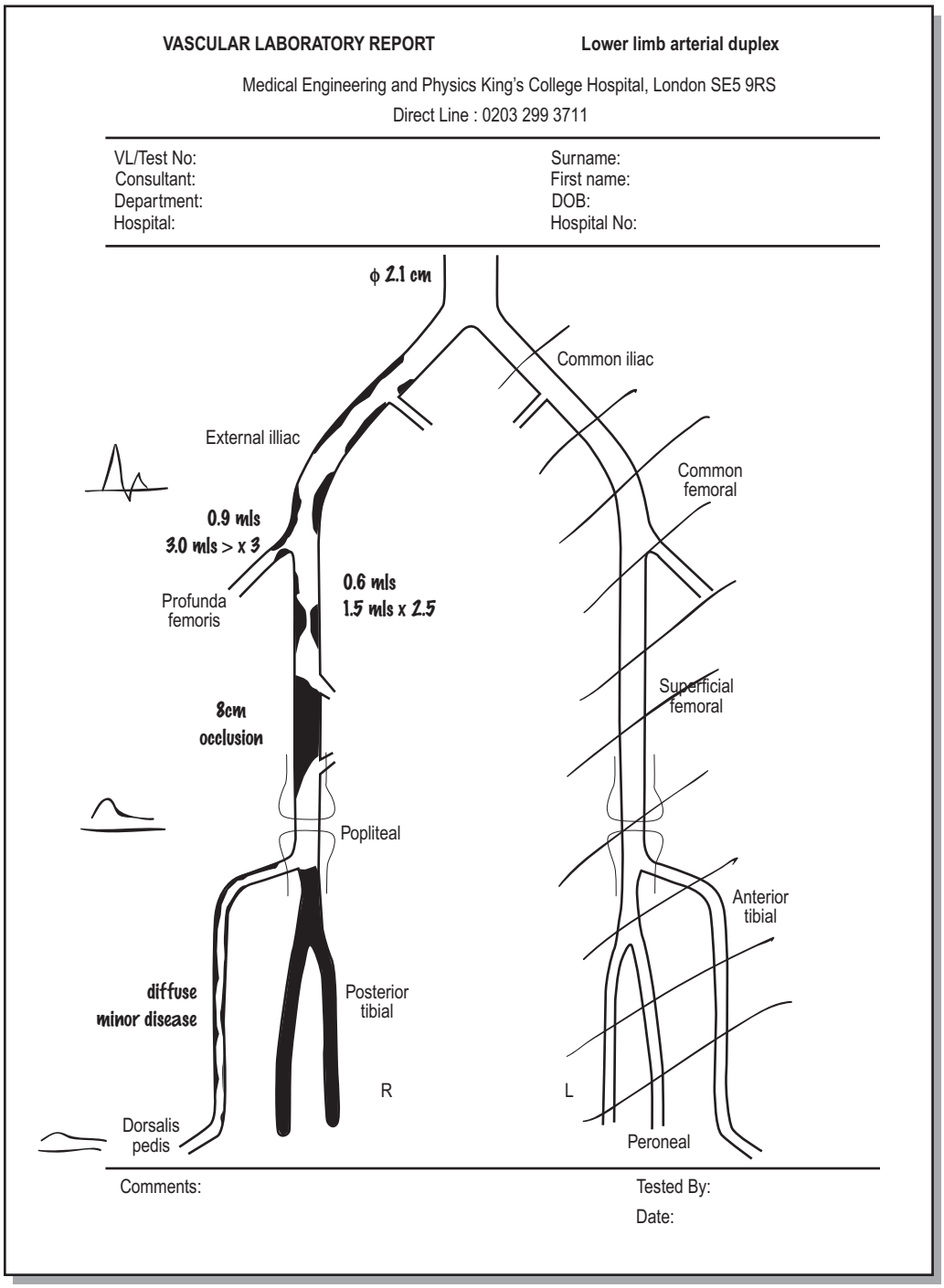

Figure 63.16 Report of leg artery duplex examination. Diagrammatic representation of ultrasound findings in right leg arteries including PSV changes, occlusions and waveforms.

the long saphenous vein, although the short saphenous vein, or the cephalic or basilic veins in the arm may be used where necessary. Veins are examined for size (Fig. 63.17), patency, evidence of varicosities and their course mapped on the skin. The patient should be tested with their upper body elevated above the level of the veins, or sitting on the couch with the legs dependent in order to distend the veins; alternatively the patient can be asked to stand for the examination. Proximal venous occlusion has been advocated as providing a more realistic assessment of a vein's diameter postoperatively when used as a graft.[51] Ideally the chosen vein should have a diameter of 3–4 mm for most of its length and be at least 2 mm at the ankle if a long length of graft is being considered.

Normally the long saphenous vein is used. This is followed down the medial aspect of the leg to the medial malleolus and its course marked with an indelible marking pain (Fig. 63.18). Care needs to be taken in the calf as the long saphenous vein has two calf tributaries, the longer and more useful one being the anterior division which passes down the medial calf to the medial malleolus at the ankle. Once the line of the vein has been marked in, transverse scanning can be used to identify perforator veins and superficial collateral venous channels, which are also marked on the skin prior to surgery. This is particularly important for in-situ vein grafts as arteriovenous fistulae may develop if the collateral channels are not all tied off.

Postoperative scanning of femorodistal bypass grafts

Duplex ultrasound is seen as particularly important in evaluating vein grafts as it can identify problems in the graft before they are evident from clinical indications or from ankle/brachial pressure measurements. The superficial location of grafts allows use of high frequencies with corresponding good detail resolution (Fig. 63.19).

Failure is most common in the early postoperative period. Graft surveillance programmes using duplex ultrasound reflect the need for close monitoring over the first postoperative year and routine scanning at 1, 3, 6, 9 and 12 months postoperatively is typical. Continued follow-up has been advocated beyond the first year,[52] although the low rate of late failure and low incidence of de novo stenoses after the first 6 months has led others to suggest that programmes should be restricted to the first 6[53] or 12[54] months for grafts showing no evidence of deterioration.

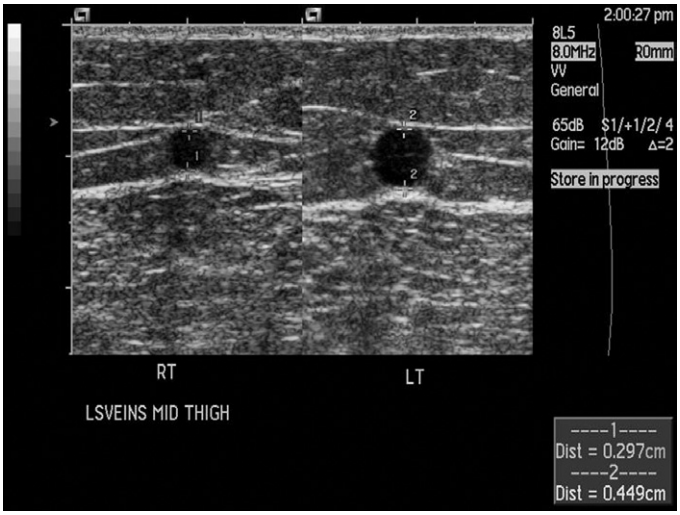

Figure 63.17 Vein calibre suitable for use as a graft. Transverse images of the right and left long saphenous veins at mid thigh. Diameter measurements of 3 mm and 4.5 mm are useful in determining suitability for bypass conduit.

Causes of graft failure are given in Table 63.2. The timing of graft failure is associated with the cause of the failure. Failure within 6–8 weeks of the operation is usually due to technical problems arising from the surgery. Approximately 3–5% of grafts will fail at this stage. Failures in the period from 3 months to about 2 years after surgery are usually due to neo-intimal hyperplasia; the majority of these failures occur in the first 12 months. Approximately 12–37% of grafts fail during this period, accounting for some 70–80% of all graft failures. After 2 years from surgery the usual cause of failure is progression of atherosclerosis in the native vessels, or the graft itself.[55]

Practical constraints may limit access in the first few days postoperatively. In artificial grafts, small air bubbles can cause strong reflection of ultrasound at the graft surface in the initial postoperative period. Nevertheless, graft patency can be established quickly, even with restricted access. Once scanning of the full length of the graft is possible, the graft is examined for stenoses (Fig. 63.19), thrombosis, collections (Fig. 63.20) and any other anomalies evident on B-mode or Doppler ultrasound. Inflow and outflow is assessed in terms of flow waveform shape and peak systolic velocity and can be compared with previous results. Because the graft offers a low

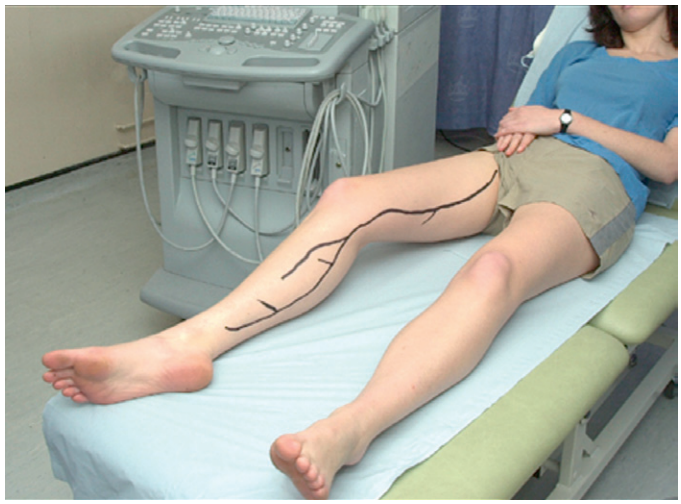

Figure 63.18 Vein mapping. The long saphenous vein and major tributaries are marked on the skin using an indelible marking pen.

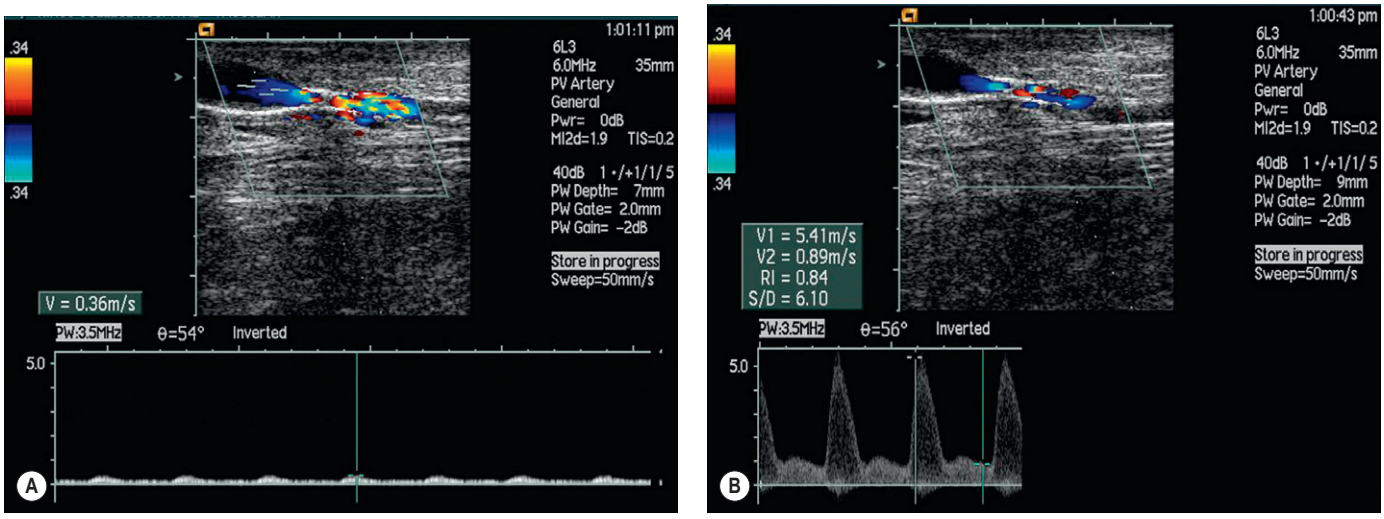

Figure 63.19 Tight stenosis in a vein graft. Velocities rise over 10-fold from 0.36 m/s above the stenosis **(A)** to 5.4 m/s in the stenosis **(B)**. The severity of the stenosis is evident on the B-mode image.

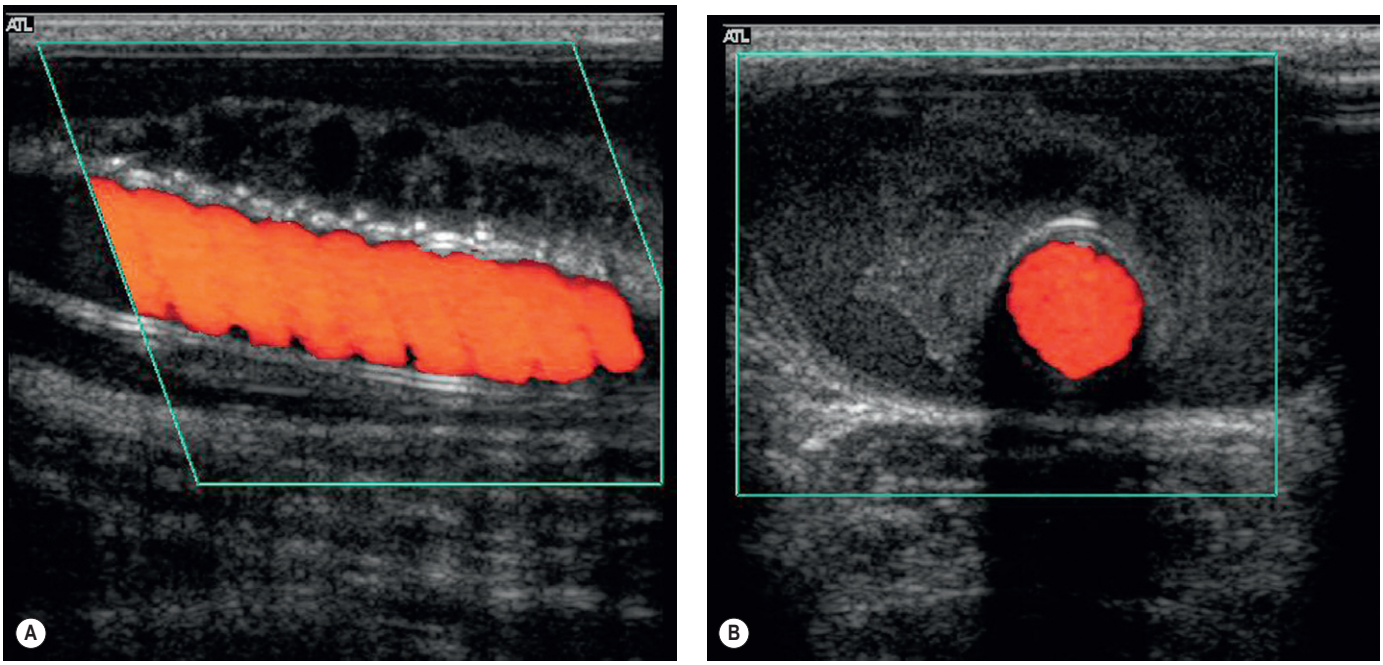

Figure 63.20 Infected peri-graft collection. Longitudinal **(A)** and transverse **(B)** colour Doppler images of a PTFE graft with echogenic proteinaceous material and fluid around it.

Recommendations for duplex ultrasound surveillance of grafts

- Routine follow-up should be undertaken in femoral-popliteal and femoral-tibial vein grafts.
- Graft surveillance intervals are approximately 3, 6, 12 months postoperatively and yearly.
- PSV ratios of 2.0 are indicative of stenosis, 3.0 of severe stenosis.
- Minimum in-graft PSV is 45 cm/s.

resistance path for the circulation with little pressure loss, run-off flow at the distal anastomosis is commonly both antegrade to distal vessels and retrograde to proximal vessels (Fig. 63.21).

Stenosis criteria are generally divided between moderate stenoses for which continued surveillance is indicated and severe, haemodynamically significant lesions which indicate the need for urgent revision. Although absolute velocities have been used to define stenosis level, the variation in graft diameters between patients leads to similar variance in normal velocities. By using the velocity ratio of peak systolic velocity in the stenosis to that in an adjacent undiseased segment, variation in diameter (and in flow) is taken into account. For moderate stenoses, velocity ratios of 1.5[53] and 2.0[54] have been proposed. For severe stenoses, velocity ratios of 3.0[53] and 3.5[56] are indicative of impending failure. At this level of stenosis, a decrease in ABPI of >0.15 is evident, although in comparison to duplex ultrasound, the ABPI is insensitive to graft stenoses. Care must be taken in suggesting stenosis at the lower anastomosis as the disparity in calibre between the graft and a smaller native artery may result in a physiological rather than pathological stenosis.

Low velocities in a graft are indicative of inadequate inflow or outflow and are associated with early occlusion and graft failure. A PSV of 45 cm/s below which velocities should not fall has been suggested for both vein[56] and PTFE[57] grafts.

Recently, the cost-effectiveness of ultrasound surveillance programmes has been questioned, particularly its effectiveness in improving limb salvage rates.[58,59] This multicentre study with some 600 patients showed no significant difference in graft patency and limb salvage rates between patients on a surveillance programme and those undergoing standard clinical management. However, duplex ultrasound continues to have a major role in the assessment of graft problems, particularly if there is clinical concern.

ANGIOPLASTY AND STENTS

Duplex ultrasound is used to assess lesions suitable for angioplasty, reducing the need for diagnostic arteriography prior to intervention. Ultrasound has also been used to guide angioplasty in femoral and iliac lesions.[60,61] This permits an immediate assessment of the outcome of balloon inflation by haemodynamic parameters.

For follow-up of angioplasty procedures, velocity ratio criteria can be used to measure relief of the constriction, showing good agreement with angiographic appearance.[62] The diagnostic potential of these measurements is uncertain. In a study[63] using a velocity ratio >2 to indicate stenosis of >50% 5 days post-procedure, arteries with a residual stenosis exceeding 50% had a significantly worse patency rate (11%) at one year compared with lower levels of residual narrowing, which had patency rates of 80%. Another study,[64] using the same criteria, measured velocities within 16 hours of the procedure and found that there was no significant difference in long-term patency between arteries with high-grade and low-grade stenoses. Technical errors arising from angioplasty, including raised intimal flaps and subintimal tunnelling, may also be evident on ultrasound, allowing any appropriate action to be undertaken in a timely manner.

Duplex ultrasound has been advocated for the assessment of stenosis severity in relation to arterial stents placed in lower limb arteries. In a retrospective study comparing ultrasound with angiography[65] using peak systolic velocity and the velocity ratio (Vr) of in-stenosis to pre-stenosis peak systolic velocities. A PSV ≥190 cm/s and a velocity ratio ≥1.5 were most accurate for prediction of ≥50% stenosis and a peak systolic velocity ≥275 cm/s and a ratio ≥3.5 were optimum values for prediction of a ≥80% stenosis. Duplex criteria for ≥50% stenosis preceded changes in the ABPI and may aid in determining the need for more intensive surveillance.

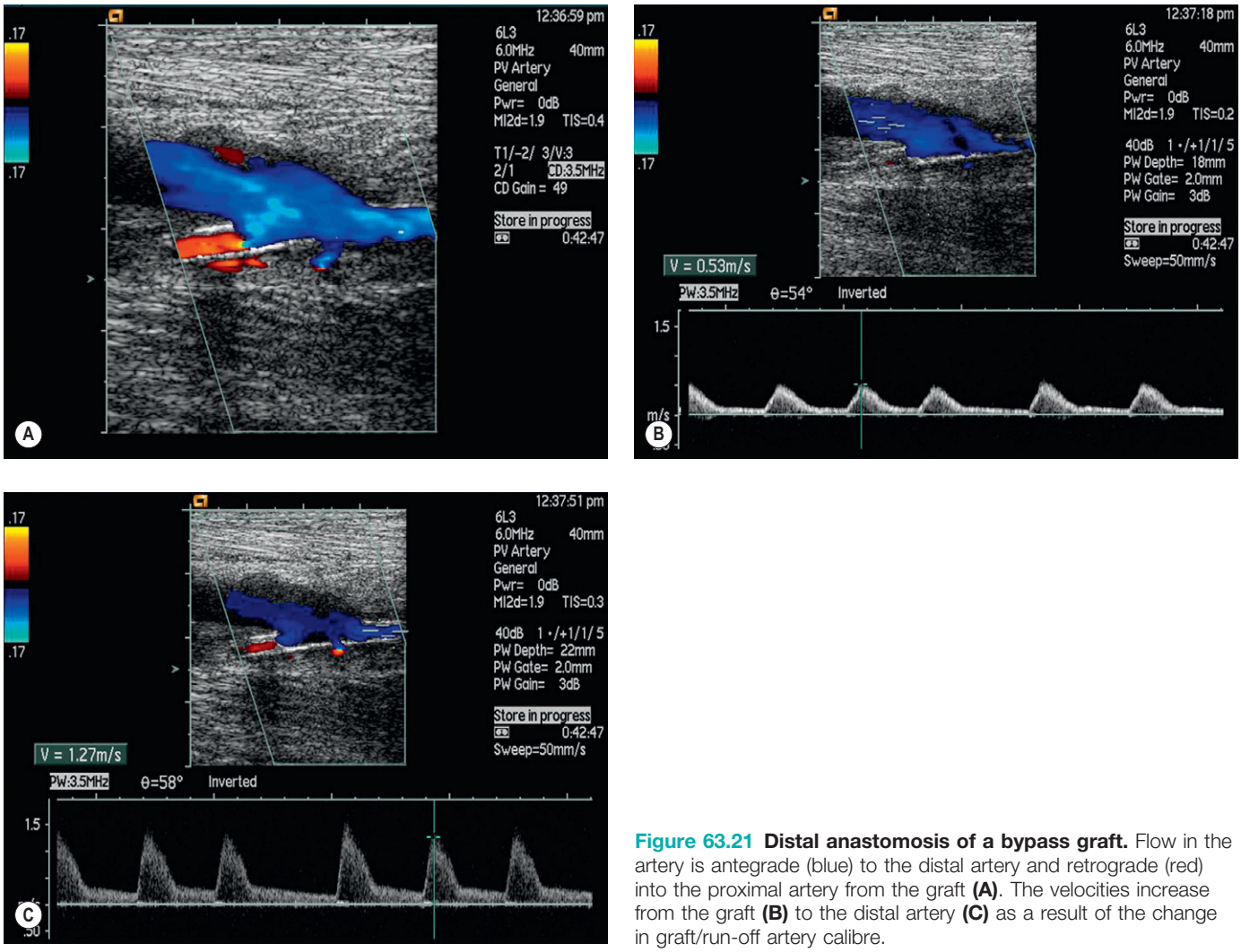

Figure 63.21 Distal anastomosis of a bypass graft. Flow in the artery is antegrade (blue) to the distal artery and retrograde (red) into the proximal artery from the graft **(A)**. The velocities increase from the graft **(B)** to the distal artery **(C)** as a result of the change in graft/run-off artery calibre.

ACUTE ISCHAEMIA

Acute ischaemia in limbs usually arises from two main causes: acute thrombosis on existing plaque – often described as acute on chronic; and embolism from a proximal source, usually the heart or an aneurysm. These emboli commonly lodge at a bifurcation. In both cases there is a rapid onset of ischaemia with pain and coldness in the limb and risk of tissue loss. Left untreated, systemic adverse effects can occur leading to organ failure and death. The use of ultrasound in the assessment of these cases depends on its availability and the speed with which it can be used compared with angiography. Ultrasound can be useful in identifying the location of the occlusion, its proximal and distal extent and the arterial access for intervention.

POPLITEAL ENTRAPMENT

Occlusion of the distal popliteal artery can be produced by plantar flexion of the foot in patients suffering from popliteal entrapment.[66] It can be assessed by a reduction in ankle blood pressure, reduction in continuous wave flow signals at ankle level or by colour Doppler ultrasound, which shows the site of occlusion and the presence of collateral circulation. However, the phenomenon of popliteal occlusion in response to plantar flexion can be elicited in over 50% of young, healthy normal volunteers,[67] making it sufficiently prevalent to render this test of limited diagnostic use, and decisions on treatment must be based on a clinical assessment of the level of impairment of normal function.

ANEURYSMS

The role of ultrasound in diagnosis and follow-up of abdominal aortic aneurysms and aortic stents is covered in Chapter 40. Aneurysms also occur in the limbs, most commonly in the popliteal artery (Fig. 63.22), less often in the femoral artery. Iliac aneurysms are usually associated with aortic aneurysms and isolated iliac aneurysms are rare. Complications are acute thrombosis, rupture, and compression of the adjacent vein possibly causing deep vein thrombosis.

High rates of coexistent aneurysms have been found in patients with popliteal aneurysms (78%) and common femoral aneurysms (95%).[68] In patients undergoing routine follow-up of popliteal aneurysm, 32% developed new aneurysms over a 5-year period.[69] In cases of suspected distal embolism, the major arteries from the popliteal artery proximally to the aorta should be investigated to

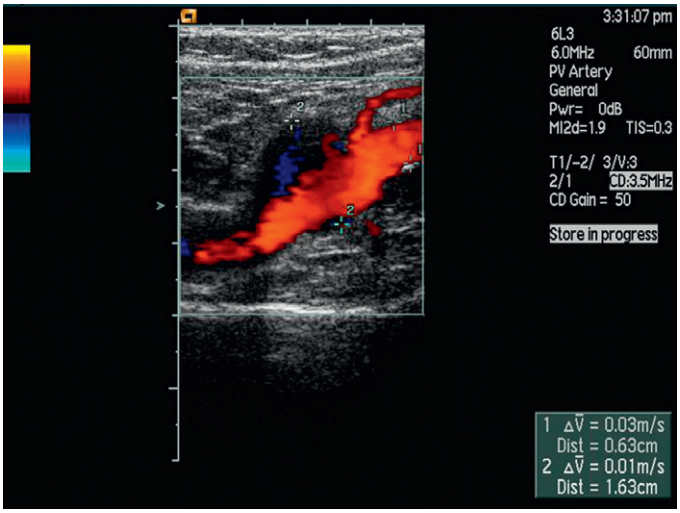

Figure 63.22 Popliteal artery aneurysm. Colour Doppler image of a popliteal artery aneurysm showing reverse flow (dark blue) within the aneurysm.

identify any aneurysm that might have acted as a source of emboli. If an aneurysm at iliac or distal level is identified during an investigation of leg arteries, the patient should be screened for aortic aneurysm.

ARTERIAL INJURIES

Duplex ultrasound is a rapid and accurate means for the diagnosis of arterial injuries following puncture or compression trauma. These occur most commonly as iatrogenic injuries following invasive diagnostic or therapeutic procedures; more rarely they may result from a fracture, blunt trauma, crush injuries, gunshot or stab wounds, and accidental or self-inflicted wounds. The most common complication is a pseudo-aneurysm; others include arteriovenous fistula, thrombosis, dissection, intimal flap and haematoma.[70,71] The most common site is at the common or proximal superficial femoral artery (resulting from catheterisation) but these complications can occur in any of the major arteries in the upper or lower limb.

Pseudo-aneurysms

Pseudo-aneurysms appear as a hypoechoic region adjacent to the artery where blood leaks from the artery into adjacent tissue. Flow in the pseudo-aneurysm sac is characterised by a swirling motion which produces bi-directional colour flow signals (Fig. 63.23A). Flow in the communicating track from the damaged artery exhibits a characteristic to-and-fro motion as blood flows in during systole and flows out in diastole (Fig. 63.23B). There may be evidence of partial thrombus within the cavity (Fig. 63.23C). The appearances of a pseudo-aneurysm can be mimicked both by structures overlying an artery (e.g. an enlarged lymph nodes) and by underlying structures displacing an artery superficially. In both cases, the patient may present with a pulsatile lump. Ultrasound can quickly exclude or confirm a pseudo-aneurysm.

Ultrasound can be effective in treating pseudo-aneurysms by inducing thrombosis with guided compression using the transducer.[72] After locating the neck of the aneurysm, pressure can be applied and colour flow used to observe cessation of flow into the pseudo-aneurysm. The length of time required for adequate compression is reported to vary from 15 to 60 minutes. Thrombosis of the sac can be confirmed by B-mode and colour flow. The initial echogenic appearance of the thrombosis becomes progressively less echogenic over time (Fig. 63.24). Patency of the artery should be confirmed post-compression. Complications can include distal embolus and hypotension.[73] Failure of compression is more common in long-standing pseudo-aneurysms and in patients undergoing treatment with anticoagulation.

Compression of pseudo-aneurysms is, however, tiring and may be painful for both the patient and operator. Many centres now use ultrasound-guided thrombin injection as a quicker and effective alternative to compression therapy.[74] A thin needle (21–25G) is located in the patent component of the false aneurysm and a small amount of human thrombin solution is injected using an insulin syringe to titrate the small amount of thrombin solution that is normally required to produce complete thrombosis and exclusion of the aneurysm from the circulation (Fig. 63.25). Normally 400–1000 IU of thrombin is sufficient to produce thrombosis in 20–30 seconds. Following the procedure the patient should rest in bed for 2–3 hours with regular review of the distal circulation. Most centres perform a follow-up scan at about 24 hours to confirm continued complete thrombosis; in some cases a small residual area of patency may require a second injection.[74]

Arteriovenous fistulae

Traumatic arteriovenous fistulae result from a puncture of adjacent artery and vein with a corresponding low-resistance, high-pressure gradient and consequent high flows.[75] Flow in the supplying artery exhibits a high-velocity, low-resistance flow waveform and the draining vein may show arterial-type pulsations (Fig. 63.26). At the site of the fistula, the high-velocity flow jet can produce ambiguous and confusing colour and spectral Doppler signals, together with possible artefact from adjacent tissue vibration.[76] Distal to the fistula, haemodynamics may be altered with a vascular steal syndrome possible. In patients undergoing interventional therapy for fistulae, ultrasound is used to monitor the outcome of the occlusion procedure.

Dissection

Dissection of the lower limb arteries may extend down from an aortic dissection, or be the result of local trauma, typically from vascular access procedures. As is the case with an aortic dissection, the dissection flap may be seen on ultrasound, although different angles of insonation may be required to get an image of the flap, depending on its orientation to the ultrasound beam (Fig. 63.27). Colour Doppler will show flow in the patent channels, which often shows different characteristics depending on the haemodynamics of the dissection. Sometimes one of the channels may thrombose, producing an apparent long stenosis of the vessel which can be difficult to recognise if the diagnosis of dissection has not been considered.

ARTERIAL DISEASE IN THE ARM

Patients presenting with ischaemia of the arms and hands do so for a more diverse range of aetiologies than for legs and feet, where atherosclerosis is the predominant cause. Ultrasound, in conjunction with pressure measurements, plays an important role in eliciting the cause, or excluding possible causes, of arterial insufficiency in the upper limb. Broadly, causes can be divided into diseases of large arteries, suitable for investigation by duplex scanning, and of small arteries, where higher-frequency continuous wave Doppler may be helpful.

Ultrasound investigation of arm arteries

Duplex ultrasound can be used to investigate the arteries from the innominate/brachiocephalic and subclavian arteries to axillary,

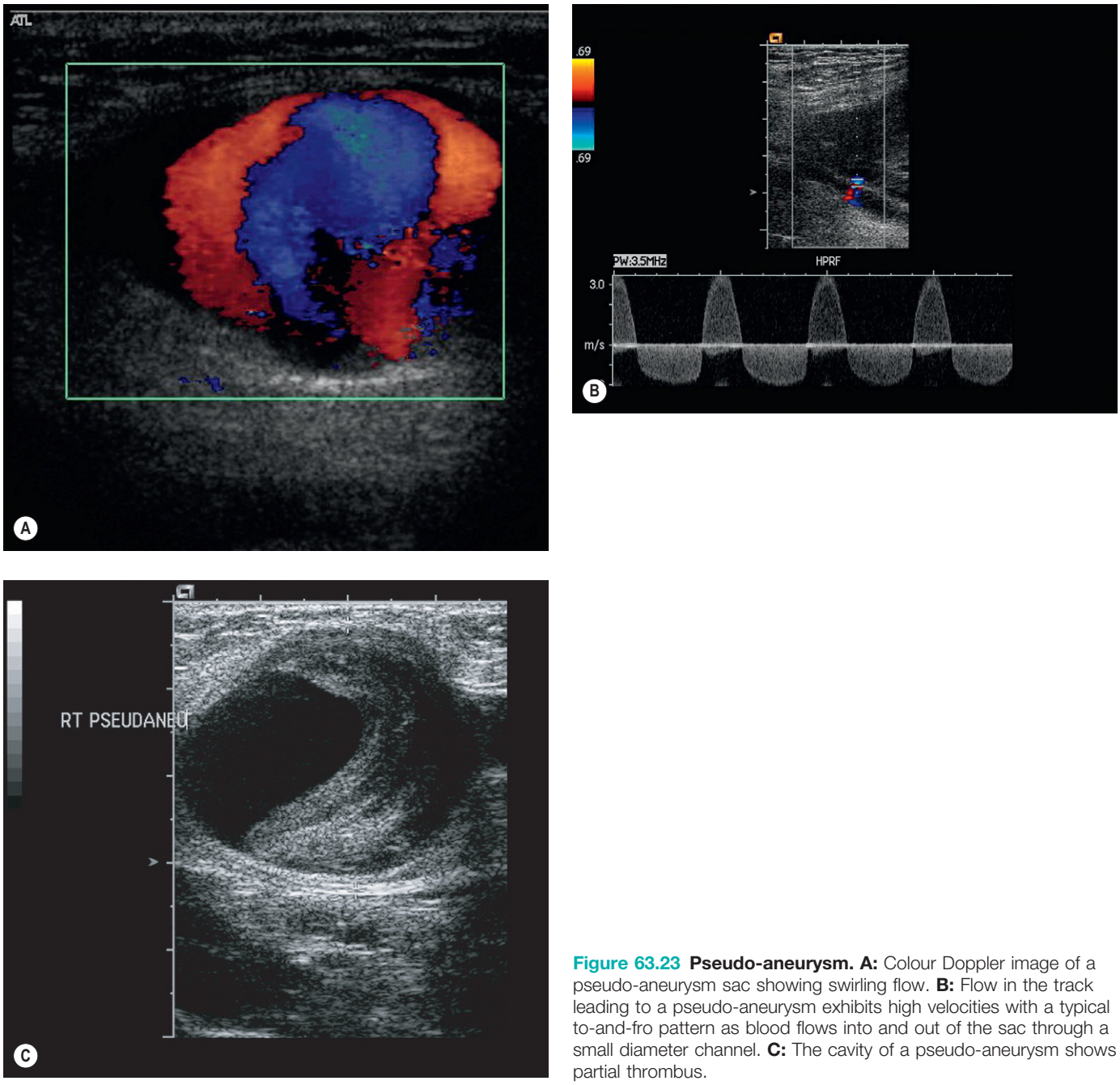

Figure 63.23 **Pseudo-aneurysm. A:** Colour Doppler image of a pseudo-aneurysm sac showing swirling flow. **B:** Flow in the track leading to a pseudo-aneurysm exhibits high velocities with a typical to-and-fro pattern as blood flows into and out of the sac through a small diameter channel. **C:** The cavity of a pseudo-aneurysm shows partial thrombus.

brachial, radial and ulnar arteries. Because the arteries are relatively superficial, high quality images can usually be obtained. The main areas of difficulty likely to be encountered are in the subclavian artery, where both supra- and infraclavicular approaches are often required to obtain adequate views, and the proximal innominate and left subclavian arteries, where the location behind the sternum and orientation of the vessel to the beam result in poor visualisation and contrast resolution.

The axillary artery is best examined with the arm abducted so that the vessel can be followed across the axilla and along the medial aspect of the upper arm. The brachial artery usually divides into the radial and ulnar arteries just below the cubital fossa and these are followed down the anterior (palmar) aspect of the forearm. If the radial or ulnar artery is difficult to follow down from the elbow, the vessel can be found at the wrist and then traced proximally. Colour Doppler imaging can be helpful in identifying the radial and ulnar arteries, which can be small. The palmar and digital arteries may be examined if there are specific concerns about these vessels.

If thoracic outlet syndrome is suspected with compression of the subclavian artery by a fibrous band as it passes over the first rib, then the subclavian artery should be assessed with the arm elevated in varying degrees of abduction to identify any changes in flow that may result. Should a subclavian steal syndrome be suspected, exercise of the ipsilateral hand increases blood flow in the arteries supplying the forearm muscles and exacerbates the haemodynamic effects of the stenosis including increased mean reversed velocities in the vertebral artery, accentuating the abnormal flow.

Resting flow waveforms in the arm are usually pulsatile (Fig. 63.28), exhibiting characteristics typical of high distal resistance. In

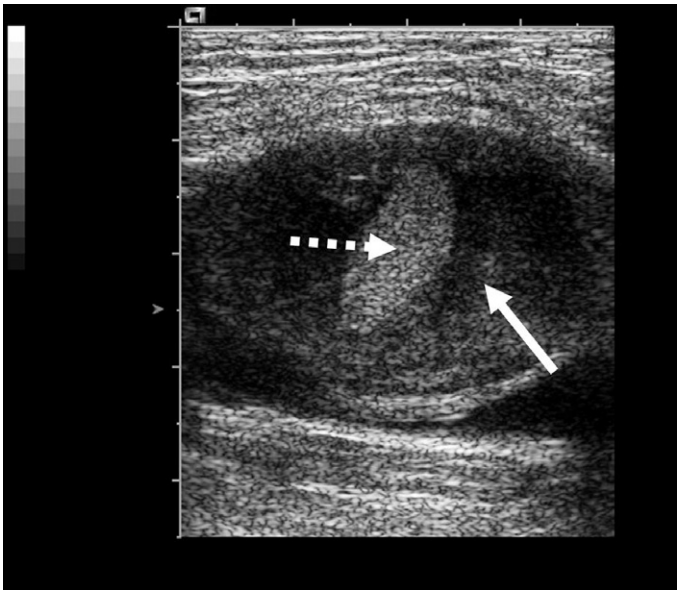

Figure 63.24 Pseudo-aneurysm following occlusion of the tract. The centre of the sac shows bright echoes (dotted arrow) from blood which has just started to form thrombus. Older thrombus appears as darker echoes (solid arrow).

comparison with the leg arteries, flow waveforms in the arm are altered more by changes in temperature, reflecting the thermoregulatory nature of skin blood flow in the hand and the comparatively low muscle mass. In response to heating or exercise, the tri- (or more) phasic flow waveform shape becomes monophasic, though often with pulsations superimposed on a raised mean velocity.

Clinical applications

Occlusive arterial disease

Atherosclerosis occurs most frequently in the proximal arteries, particularly at the origins of the innominate and subclavian arteries from the aorta. Depending on its location, plaque may be imaged on real-time imaging (Fig. 63.29). The general criteria for assessment of upper limb atheroma are similar to those used for the lower limb arteries.

If the stenosis at the subclavian artery origin is severe enough to cause a pressure loss, a subclavian steal syndrome may result which can reliably be diagnosed using ultrasound.[77] Characteristics of a steal syndrome include high velocity and disturbed flow at the subclavian artery stenosis, with either reduced systolic flow or partial or completely reversed flow in the ipsilateral vertebral artery (Figs 63.29 and 63.30). Distal arteries in the affected arm demonstrate damped flow (Fig. 63.31). The effect of the stenosis can be quantified by non-invasive pressure measurements bilaterally.

In patients undergoing coronary artery surgery using the internal mammary artery, the artery can be imaged preoperatively using an intercostal approach; patency can be established and the diameter and peak velocities measured.[78] The subclavian artery should also be scanned for evidence of stenosis. Postoperative internal mammary artery flow shows low systolic and increased diastolic flow typical of coronary arteries.

The major source of emboli in the arm is either the heart, or a proximal aneurysm, which occur most commonly in the subclavian artery. The arteries can be imaged using real-time ultrasound to examine for aneurysms and mural thrombi. Colour Doppler can identify sites of occlusion in the arm arteries down to radial and ulnar level.

Takayasu's arteritis

Takayasu's arteritis is a rare autoimmune disorder with granulomatous infiltration of the vessel wall and subsequent fibrosis and scarring; occasionally ectasia or aneurysm formation may be seen. The clinical presentation can vary from very little to severe ischaemic symptoms and asymmetrical or absent pulses; in the acute phase 50% of patients will have systemic symptoms. Medical treatment is with steroids and cytotoxic agents, with stenting or surgery reserved for critical ischaemic circumstances. The condition is characterised by long segment stenoses or occlusions[79] (Fig. 63.32). Duplex ultrasound has been shown to be of use in monitoring regression in response to therapy.[80]

Thoracic outlet syndrome

Thoracic outlet syndrome describes a range of disorders affecting the subclavian artery and vein as they cross the first rib at the thoracic outlet. The most likely causes for this compression are congenital fibrous bands at the insertions of the anterior and middle scalene muscles, with or without an associated cervical rib. Although some degree of compression may be seen in 20% of normal subjects,[81] this does not result in symptoms. The symptoms may only occur with certain positions of the arm, or posture. The patient should asked to replicate the trigger position. Normally the diagnosis can be made simply by identifying the loss of the pulse in the arm in the appropriate position. In cases of uncertainty duplex scanning can detect stenotic (Fig. 63.33) or aneurysmal causes for vascular thoracic outlet syndrome. The point of compression or occlusion may not be directly accessible to the transducer due to the position of the arm and shoulder. In these cases Doppler can show the change or reduction in the systolic waveform as the arm is moved into the relevant position and the artery is compressed.[82]

Raynaud's disease

Raynaud's disease causes spasm of the digital arteries, usually in response to cold, leading to digital ischaemia. Duplex ultrasound does not contribute directly to diagnosis of Raynaud's disease but is used to exclude other vascular abnormalities, such as stenosis, thrombosis or aneurysms, down to wrist level.[83] High-frequency (10 MHz and above) continuous wave Doppler ultrasound has sufficient sensitivity to assess digital artery patency and can be used to compare patency at room temperature and following a cold challenge. However, modern ultrasound equipment has sufficient sensitivity to be able to demonstrate the digital arteries directly on colour Doppler (Fig. 63.34).

ULTRASOUND OF HAEMODIALYSIS ACCESS

Permanent haemodialysis access, through a fistula or graft, requires high flows through a superficial vein or graft which can be repeatedly needled, is easy to keep clean and is comfortable for the patient during their periods of dialysis – typically three times a week, each of around 4 hours' duration. American and European reviews and guidelines[84,85] have been produced and are regularly updated to foster good haemodialysis practice. In both guidelines, ultrasound is identified as important in identifying appropriate vessels for dialysis access surgery, for follow-up of problems in the access circuit and as a means of measuring volume flow. The role of ultrasound in routine surveillance is still controversial.

The high flows, unusual haemodynamics and anatomy of fistulae and grafts can make this a challenging investigation but it is potentially a rewarding one. Ultrasound is a quick, safe and effective means to identify existing and impending problems, enabling early radiological or surgical intervention to prolong the use of the existing access and to plan effective alternatives.

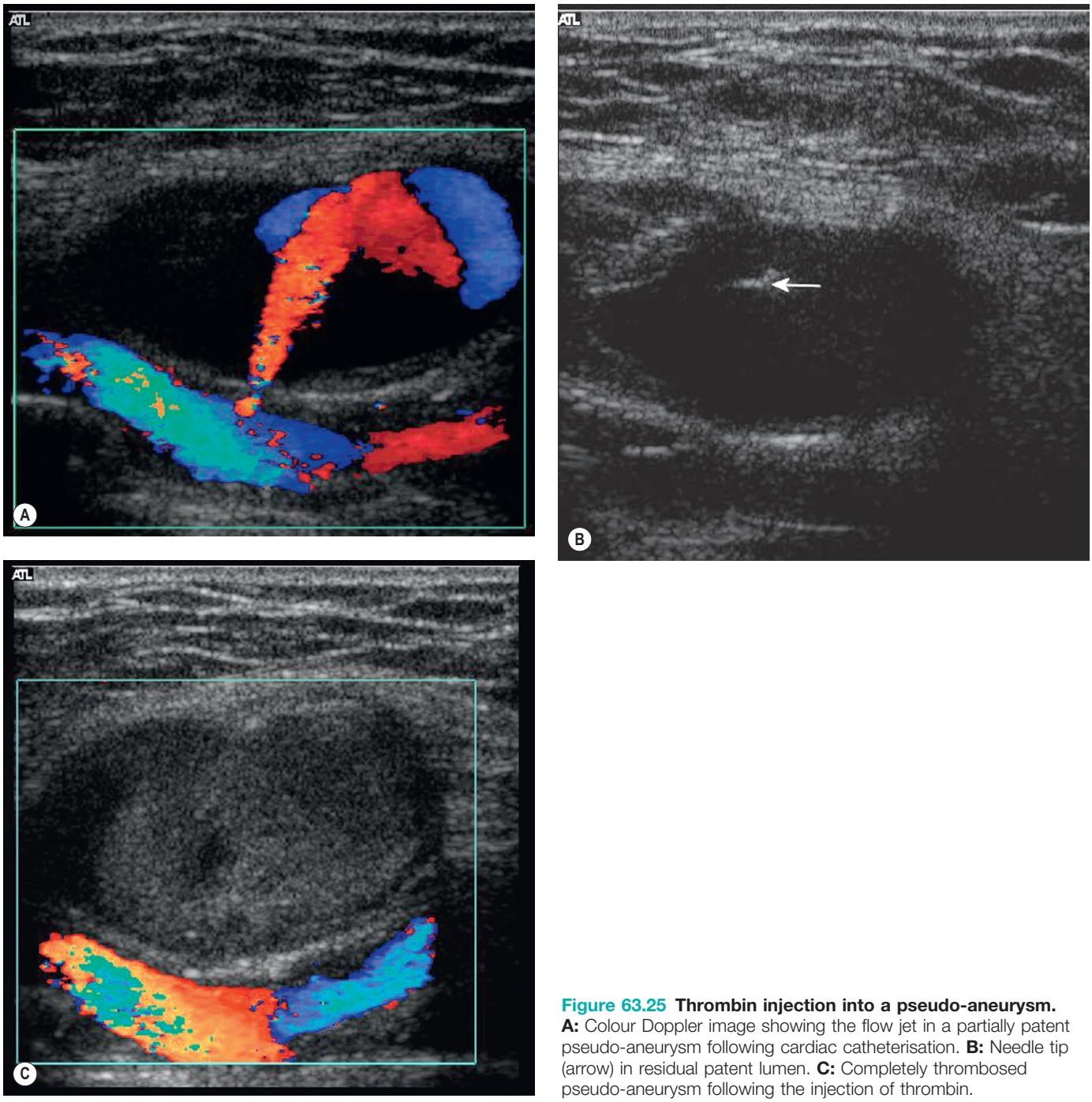

Figure 63.25 Thrombin injection into a pseudo-aneurysm. **A:** Colour Doppler image showing the flow jet in a partially patent pseudo-aneurysm following cardiac catheterisation. **B:** Needle tip (arrow) in residual patent lumen. **C:** Completely thrombosed pseudo-aneurysm following the injection of thrombin.

Access sites

There are two main types of permanent haemodialysis access site. A fistula between an adjacent artery and vein can be created surgically where the vein is used for needle access, or a synthetic graft can be placed between an artery and vein. Fistulae generally have a lower incidence of complications than grafts and superior long-term patency. However, they take time to develop and mature following surgery, with first use typically 6 weeks postoperatively, whereas grafts can be used earlier following surgery.

The arms are the preferred site for arteriovenous connections for dialysis access. There are several possible sites for fistulae and grafts in the arms. Once arm access sites are exhausted, leg vessels may be used. Several unusual variations of grafts and veins are possible where access is difficult, depending on the preference of the surgeon and the availability and access of suitable arteries and veins. The main sites in approximate order of preference are given in Table 63.3. A major advantage of a distal fistula is that it may leave more proximal vessels available for future accesses.

Temporary access – role of ultrasound

Ultrasound can be used to assess central veins to ensure patency for emergency central dialysis catheter placement in patients with acute renal failure or failed permanent access. The patient should be lying flat so that the central veins are not collapsed. The internal

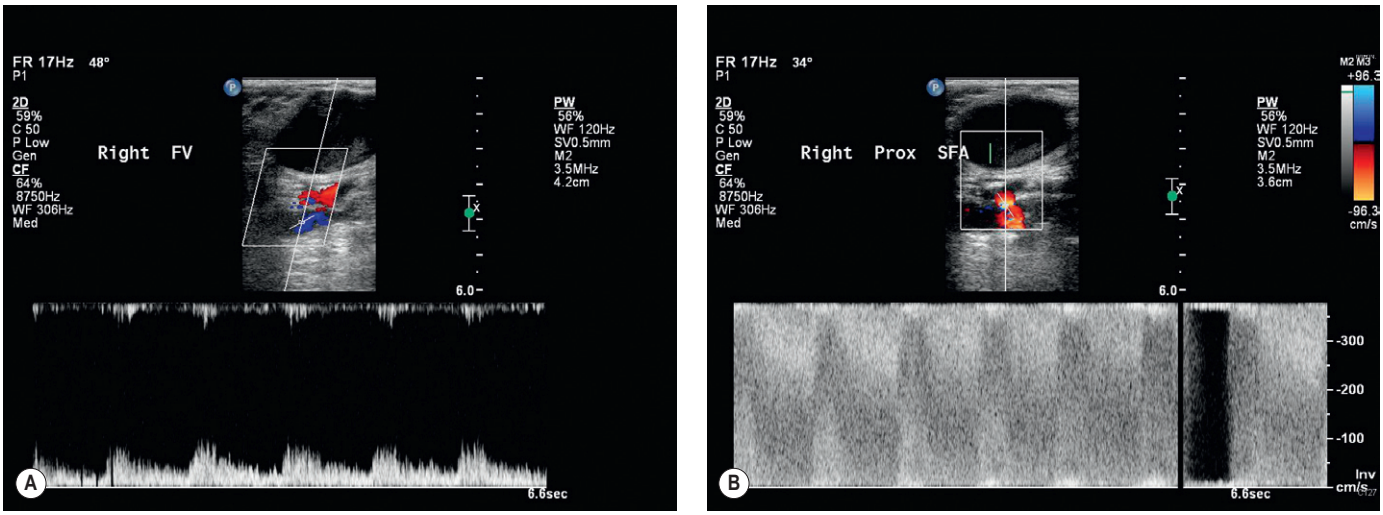

Figure 63.26 Flow through an iatrogenic arteriovenous fistula. A: Spectral Doppler from the femoral vein shows evidence of arterial pulsations. **B:** The large pressure gradient across the fistula produces very high velocities which, in this case, were difficult to image unambiguously.

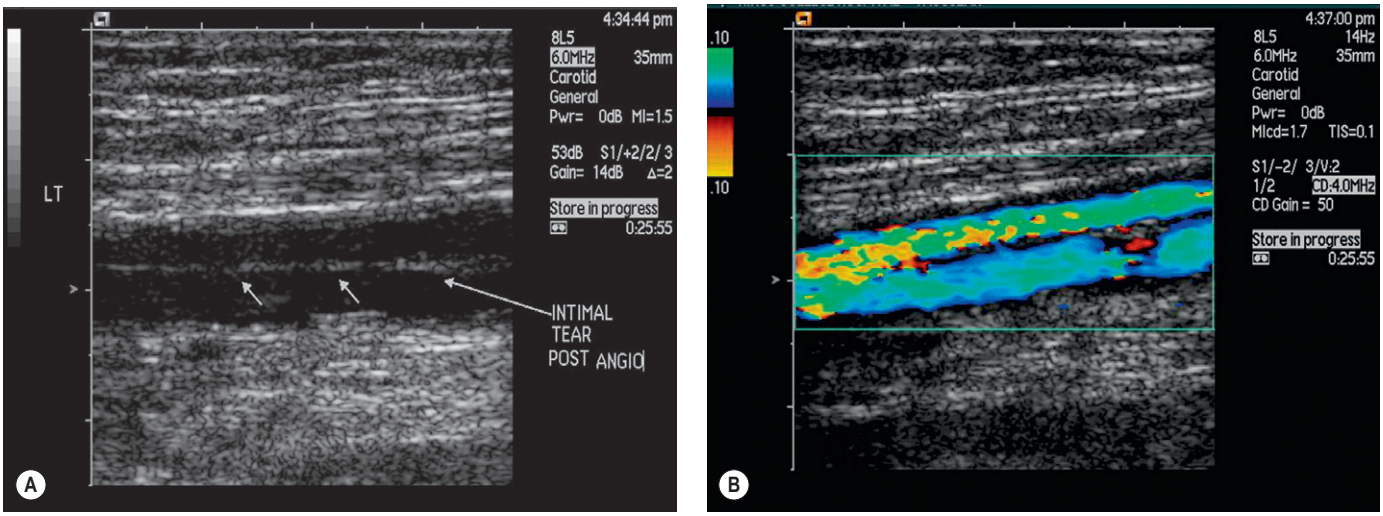

Figure 63.27 Dissection in a femoral artery. The B-mode image **(A)** shows the flap in the vessel lumen (arrows) and the colour Doppler image **(B)** shows flow in both of the channels.

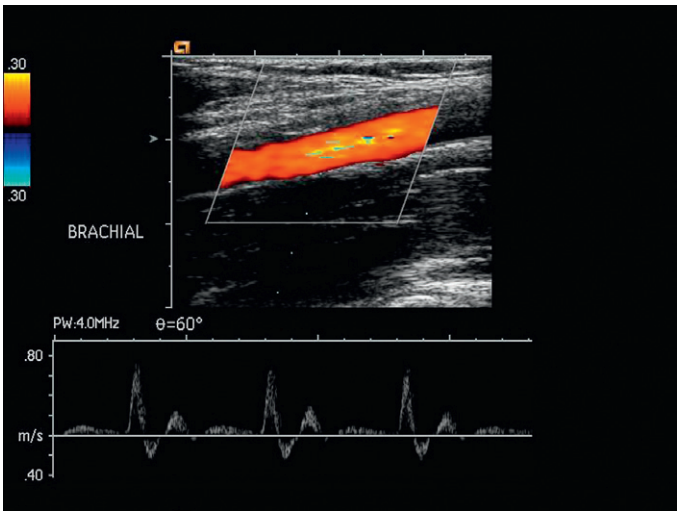

Figure 63.28 Normal resting flow waveforms in a brachial artery. The flow waveform is pulsatile with reverse flow evident.

Table 63.3 Types of arteriovenous connection for dialysis access

Radiocephalic fistula
Brachiocephalic fistula
Brachial artery–transposed basilic vein fistula
Forearm graft from radial artery to cubital fossa vein
Looped graft from brachial artery to cubital fossa vein
Upper arm graft from brachial artery to axillary vein
Femoral–femoral loop graft
Axillary artery to contralateral axillary vein graft

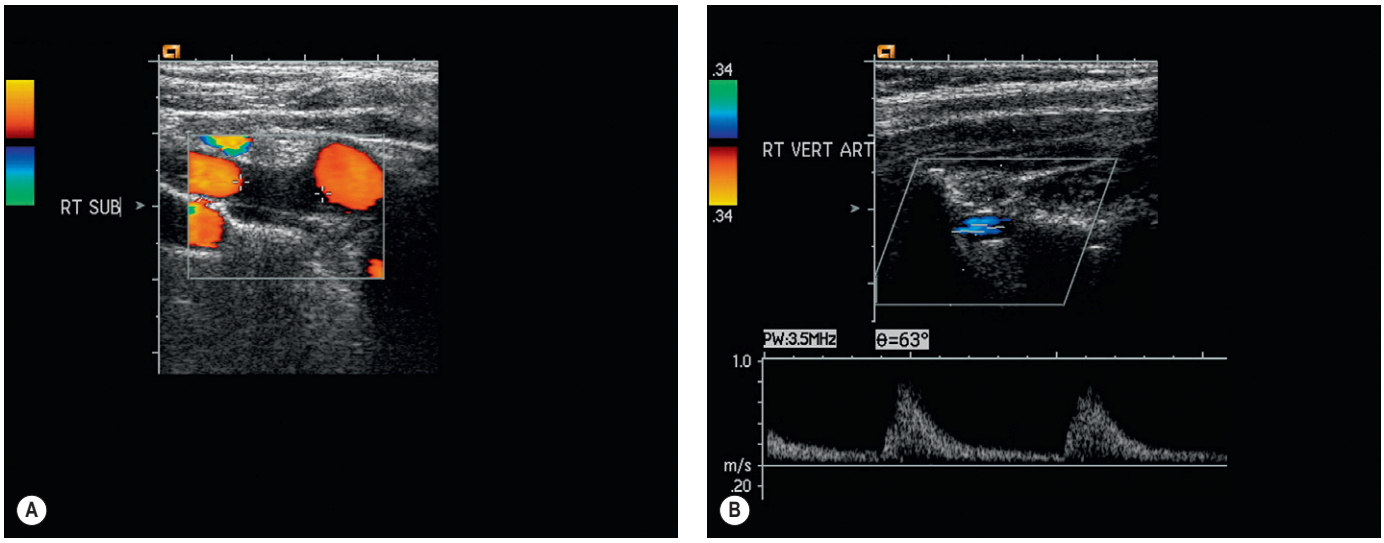

Figure 63.29 **Subclavian artery occlusion. A:** Right subclavian artery occlusion (callipers) between the origins of common carotid and vertebral artery origins. **B:** The vertebral artery shows reverse flow (blue) supplying the right arm arteries.

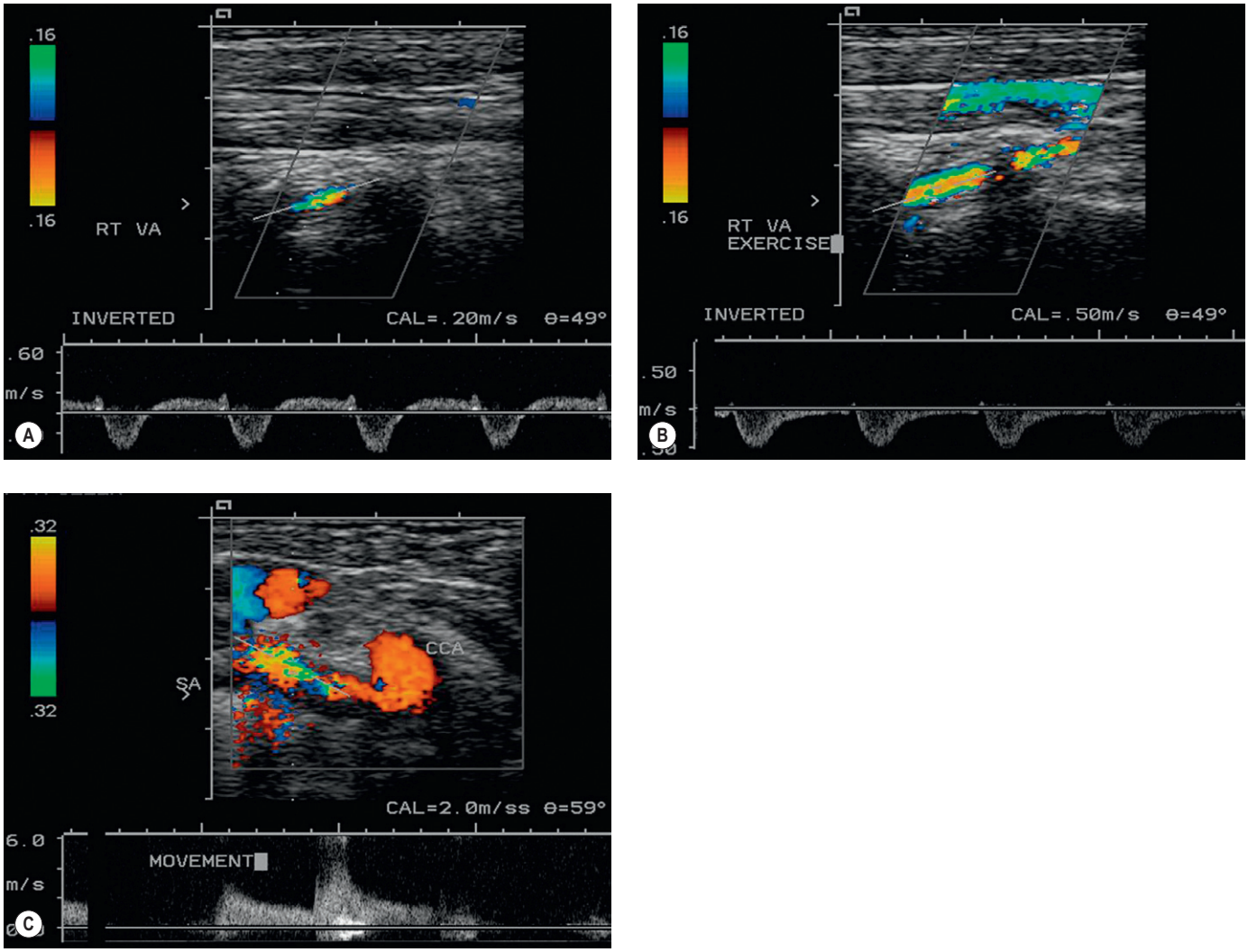

Figure 63.30 **Subclavian steal syndrome. A:** The vertebral artery shows reverse flow in systole indicating a partial steal syndrome. **B:** Following exercise, there is reverse flow throughout the cardiac cycle caused by an increased pressure gradient through the subclavian artery origin stenosis. **C:** Colour Doppler image of the subclavian artery origin shows high velocities associated with a tight stenosis and an associated tissue bruit. Patient movement results in a sonogram that is not displayed continuously.

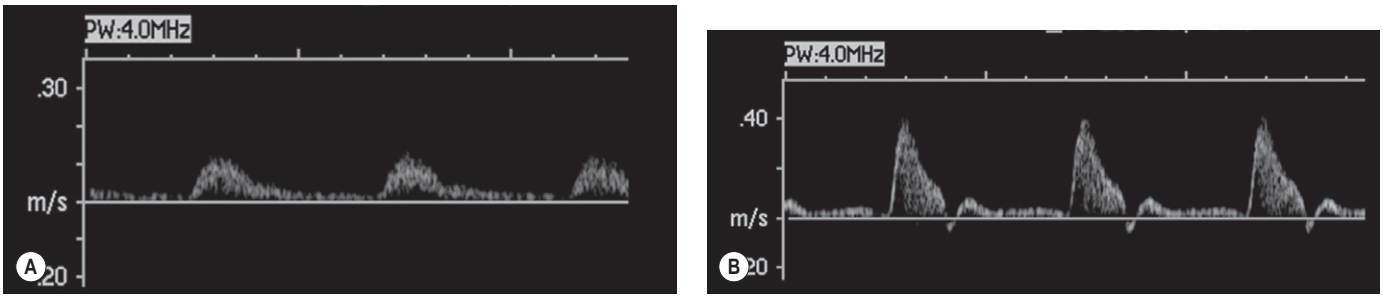

Figure 63.31 Spectral Doppler waveform with proximal occlusion. Axillary artery spectral waveforms in the right **(A)** and left **(B)** arms; the damped waveform on the right indicating proximal occlusion/stenosis of the right arm arteries.

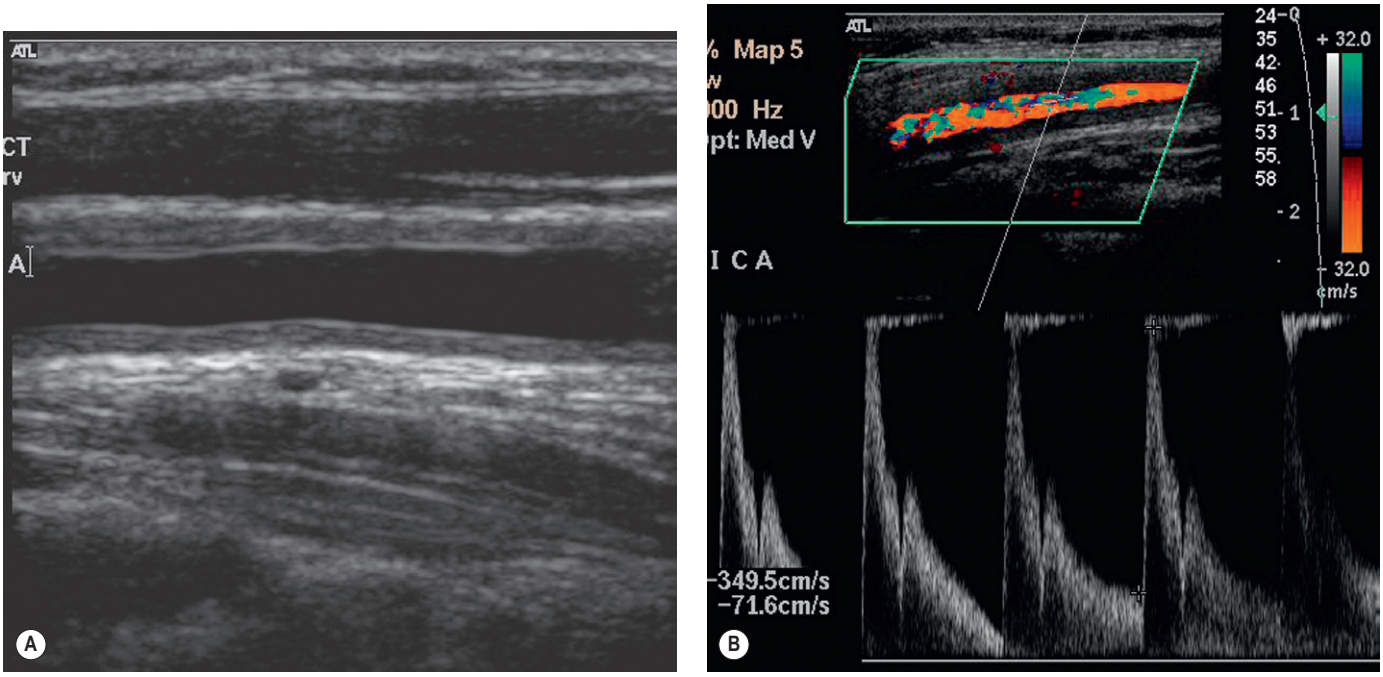

Figure 63.32 Takayasu's arteritis. A: Real-time image of a common carotid artery showing marked and extensive thickening of the artery wall. **B:** Colour and spectral Doppler of the internal carotid artery in the same patient showing a long stenosis with a PSV of 3.5 m/s.

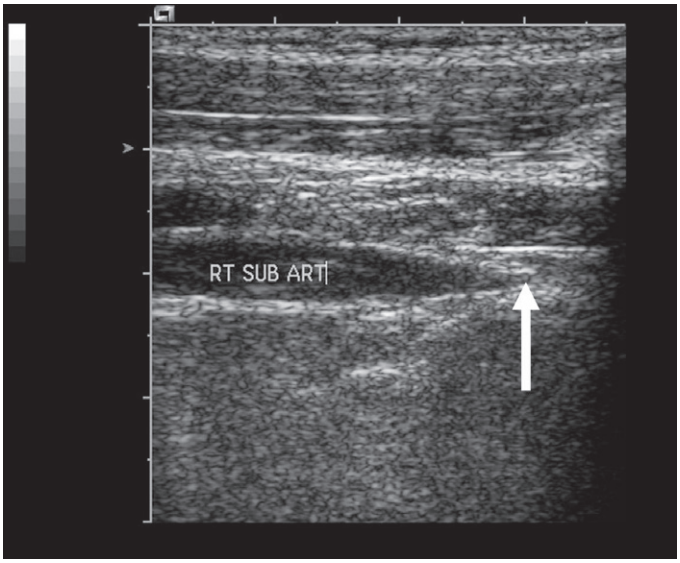

Figure 63.33 Compression of the subclavian artery on arm abduction. The subclavian artery is compressed as it passes over the first rib (arrow).

and external jugular veins are examined using a low-frequency (4–8 MHz) linear array using colour and spectral Doppler to ensure patency and normal venous flow patterns. The subclavian veins may be imaged using either a supra- or infraclavicular approach. The proximal internal jugular veins and subclavian veins may be difficult to image with a linear array due to clavicle, sternum and ribs which restrict ultrasound access. However, patency of the central veins can be inferred if there is normal cardiac pulsatility and respiratory phasicity on spectral Doppler.

Permanent access: pre-assessment

Poor selection of vessels for permanent access is associated with high failure rates. As dialysis is increasingly offered to older patients and those with diabetes and arterial disease, ultrasound has an important role to complement physical examination in identifying the most suitable site for access surgery. For radiocepahlic fistulae European recommendations are that the minimum diameter of radial artery and cephalic vein at the wrist level should be 2 mm.

Scanning is undertaken with a high-frequency linear array. A tourniquet may be applied proximal to the measurement sites to occlude venous return and to allow the veins to expand. It is important to use very light pressure; even with a tourniquet, as veins are

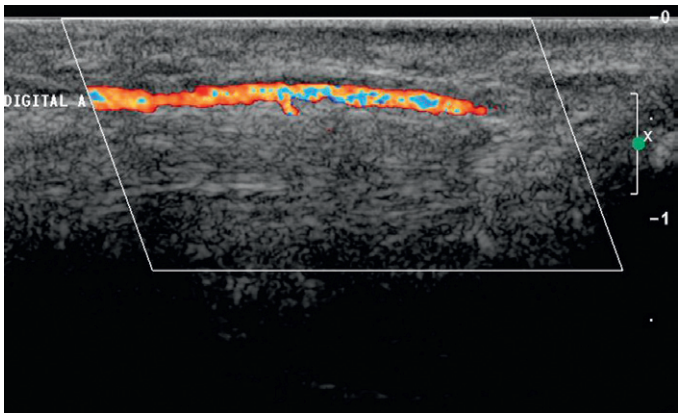

Figure 63.34 Digital artery. Colour Doppler image of a digital artery showing a smaller branch vessel origin.

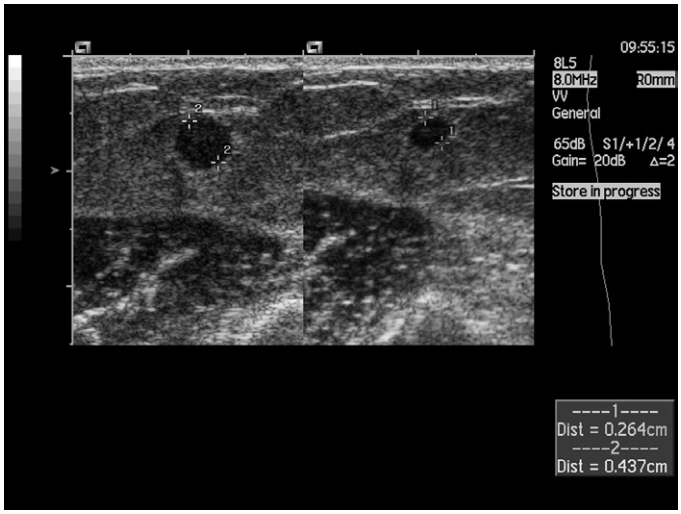

Figure 63.35 Measuring vein diameter. Transverse views of cephalic vein diameter measurement with a proximal tourniquet (left image) and without a tourniquet (right image).

readily compressed and the diameter may be underestimated. The vein diameters are measured in transverse section (Fig. 63.35) and are scanned through their length to check for patency, narrowing, particularly near confluences, anatomical variations (for example large veins communicating with the deep veins) and continuity of flow. The proximal cephalic vein may be compressed extrinsically by the clavipectoral fascia just before its insertion to the subclavian vein. This is sometimes relieved by relaxation of the arm.

The deep veins are imaged to ensure patency for the outflow of the fistula. Spectral waveforms in the proximal veins should show phasicity with respiration and cardiac pulsatility (Fig. 63.36). Absent or reduced phasicity is an indication of possible proximal vein occlusion or stenosis; if there is doubt the waveforms can be compared with those on the contralateral side.

The arteries should be examined for normal pulsatile flow to wrist level. The internal diameter of the radial artery should be measured and note is taken of arterial disease, including general calcification in the arm arteries. Even moderate stenoses should be noted as they can become more haemodynamically significant with the larger flow volumes that occur after fistula creation. It is important to identify the brachial bifurcation level if surgery in the cubital fossa is contemplated.

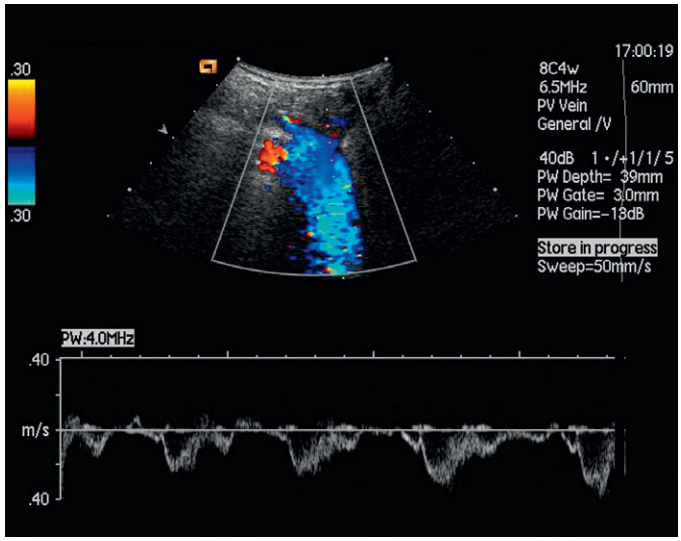

Figure 63.36 Normal venous pulsatility. The right brachiocephalic vein shows continuity of flow on colour flow imaging. The sonogram shows phasicity of flow corresponding to right atrial pressure changes.

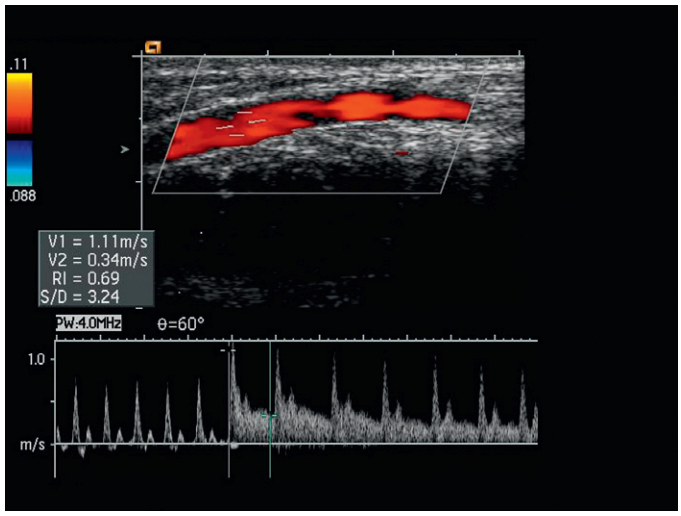

Figure 63.37 Hyperaemic response. following a 2-minute distal occlusion causes an instantaneous increase in flow accompanied by changes in the flow waveform in the radial artery. The resistance index (RI) is a measure of the decreased distal resistance.

For radiocephalic fistulae, it has been suggested that measurement of flow waveform changes in an induced hyperaemic response in the radial artery (Fig. 63.37) prior to surgery is a good measure of the likelihood of success of the fistula. A low resistance index (RI <0.7) in the initial period of hyperaemia was associated with a markedly improved outcome when compared with fistulae formed from arteries with an index ≥0.7,[86] although others have been unable to show the same discrimination between fistula success and failure.[87] A checklist of observations and measurements made is listed in.

Table 63.4 Complications of dialysis fistulae

Early complications
Inadequate/inappropriate vessels
Thrombosis
Inappropriate venous return to deep veins
Stenosis of artery, anastomosis, or vein
Late complications
Stenosis
Thrombosis
Aneurysm, or pseudo-aneurysm
Infection
Steal syndrome
Venous hypertension
Congestive heart failure

Measurements and checklist for arm pre-assessment scan for haemodialysis access

- Cephalic vein diameter upper arm/lower arm*
- Basilic vein diameter upper arm/lower arm*
- Anomalies (thrombus/stenosis/unusual anatomy) of superficial veins
- Patency of deep veins including brachial, axillary, subclavian and braciocephalic veins
- Radial artery internal diameter at wrist
- Normal flow waveforms in major arm arteries (including radial/ulnar/brachial)
- Normal flow augmentation in radial artery in response to hyperaemia
- Level of brachial artery bifurcation
- Anomalies (calcification/occlusion/unusual anatomy) of arm arteries.

Note: It should be stated whether the * measurements of superficial vein diameter are made with or without a proximal tourniquet.

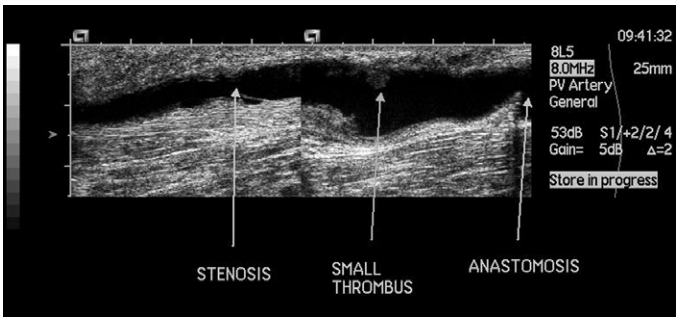

Figure 63.38 Longitudinal image of the cephalic vein in an arteriovenous fistula. The vein shows changes in diameter, a common feature in veins following repeated needling.

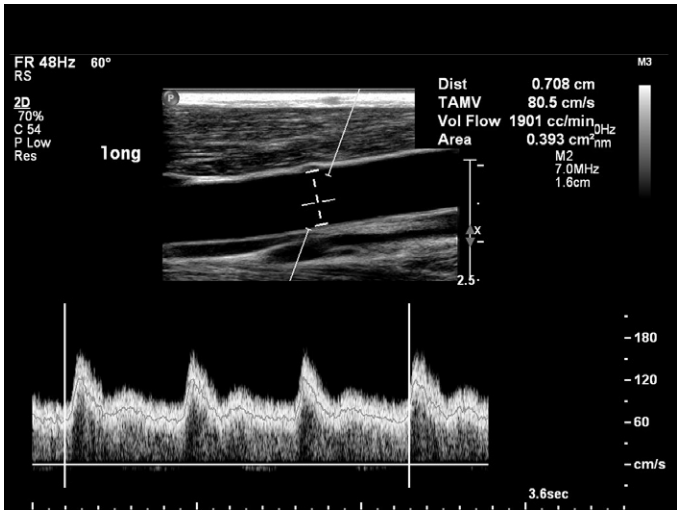

Figure 63.39 Ultrasound measurement of volume flow. The scanner combines a measurement of artery diameter with the time-averaged mean velocity (TAMV) over several cardiac cycles to calculate volume flow.

Permanent access: postoperative assessment

Postoperatively, flow through the fistula causes the vein to enlarge (Fig. 63.38). There is an initial large increase of flow into the vein followed by a gradual further increase for several weeks. Grafts have a higher initial flow and can be used earlier. It is our practice to measure flow by duplex ultrasound at 1 and 6 weeks postoperatively and to record the size and depth of the fistula vein as a baseline record. This early scan also shows potential difficulties including multiple venous returns, venous occlusions and abnormal flows, particularly low flows. In radiocephalic fistulae, early postoperative flows <400 mL/min have a high incidence of non-maturation and failure.[88]

If the fistula fails to mature or the dialysis staff have concerns about function, then a full ultrasound investigation is performed. Complications that may occur in the early stages include use of inappropriate vessels, thrombosis, venous return through communicating veins to deep veins, or stenosis affecting the anastomosis, supplying arteries or draining veins, which may be the result of undiagnosed pre-existing stenosis or perioperative clamp injuries.

Once in use, later complications of fistulae and grafts may occur; these are listed in Table 63.4. These may result in inadequate dialysis access function and require revision of the fistula or graft.

The most common complication affecting grafts is thrombosis; for fistulae the most common complication is reduced flow from stenosis. Stenosis in the access circuit is commonplace even in fistulae and grafts with good function. The presence of a stenosis without other clinical or haemodynamic anomalies is not sufficient to classify the access as a dysfunctional access. These stenoses can usually be left untreated but can be monitored by ultrasound.

Volume flow

Volume flow is an important indication of the health of the access. The ultrasound examination should always include a measurement of volume flow through the fistula or graft (Fig. 63.39). Volume flows may range from 200 to 3000 mL/min in fistulae and grafts, although most fall in the range 600–1500 mL/min. Fistulae tolerate lower flows better than do grafts but there is a high risk of thrombosis if flow falls below 300 mL/min in a fistula or 600 mL/min in a graft. In addition, volume flows of <300 mL/min are inadequate for efficient dialysis. Both the European and American guidelines for fistula management have produced guidelines for further instituting investigations into the possible cause of low or reduced flow or if flows show a reduction in volume in consecutive scans. Recommended criteria are given in Table 63.5.

Most ultrasound systems now provide a calculation package to assess volume flow in a blood vessel. Ultrasound measurement of volume flow is calculated using the equation:

$$\text{Volume flow (mL/min)} = \text{cross-sectional area (cm}^2\text{)} \times \text{time-averaged mean velocity (cm/s)} \times 60.$$

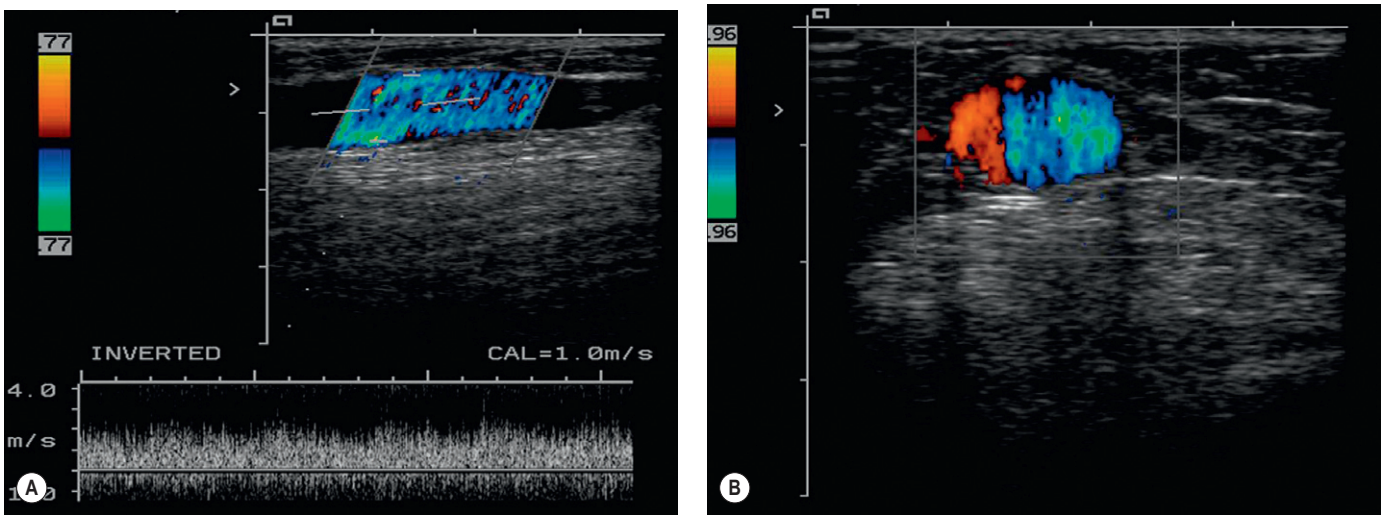

Figure 63.40 Complex flow patterns in the cephalic vein. Colour Doppler images showing complex disturbed flow in a cephalic vein draining an arteriovenous fistula; **A:** longitudinal and **B:** transverse views. The sonogram **(A)** shows turbulent flow associated with high velocity, non-axial flow. In these conditions, angle correction accuracy is limited and volume flow measurements cannot be made reliably.

Table 63.5 Criteria for further investigation/intervention of access of dialysis fistulae/grafts

European Best Practice Guidelines (EBPG)	
Grafts	<600 mL/min
	>20% reduction in flow volume/month
Forearm fistulae	<300 mL/min
National Kidney Foundation guidelines	
Grafts	<600 mL/min
	Flow 1000 mL/min with decrease >25% over 4 months
Fistulae	No absolute measure recommended. Flows should be considered for individuals. It is noted that levels of <400 mL/min and 650 mL/min have been proposed

The weighted time-averaged velocity is obtained by measuring the velocity of blood flow across the lumen of the vessel over several cardiac cycles. The cross-sectional area of the vessel can be measured directly on a transverse scan at the point where the velocity has been measured; however, most ultrasound systems measure the time-averaged velocity and the diameter of the vessel on a single longitudinal view and extrapolate the diameter to obtain a figure for cross-sectional area (Fig. 63.39).

The fistula volume flow is best calculated from the supplying brachial artery proximal to the fistula as arteries have a circular cross-section, enabling a more accurate calculation of the area to be obtained from diameter. In addition, flow velocities in the artery are predominantly axial in the direction of the vessel, allowing good approximation of mean velocity to be measured, and the arteries are relatively straight, permitting accurate Doppler angle correction. The assumption is made that with the arm at rest the vast majority of brachial artery flow will supply the fistula with only a small proportion of flow supplying the arm or hand distal to the fistula. If necessary, distal blood flow below the fistula can be excluded temporarily with an inflated blood pressure cuff.

In radiocephalic fistulae, flow to the fistula is usually from both the radial artery and ulnar artery via the palmar arch. Measuring flow in the subclavian or brachial artery will therefore account for all of the flow to the fistula/graft.

Measurements of volume flow form the venous side of a fistula are prone to error from turbulent non-axial flow velocities and non-circular cross-sectional area (Fig. 63.40). In addition, the venous side of the fistula may divide into two or more channels with resulting dissipation of flow and subsequent underestimation of the overall volume of blood crossing the fistula or graft.

It is well recognised that measurements of volume flow are fraught with possible errors resulting from errors in diameter measurement, where a 10% error in measurement of the diameter leads to an error of over 20% in calculating the cross-sectional area. Similarly, errors in the measurement of the time-averaged velocity may result from errors in Doppler beam/flow angle measurement, or incomplete insonation of all the velocities across the artery or inclusion of negative venous velocities in the sonogram. Despite these possible errors, the high flows in dialysis accesses and large changes in a failing access make volume flow calculation a practical and useful measurement in clinical practice.

As well as estimating flow at the time of each examination, the finding that flow volumes have decreased significantly since the last scan makes it imperative to seek possible causes that may be rectified before fistula failure occurs.

Scanning the access circuit

The entire circuit should be examined, as problems can occur anywhere from the proximal arteries, across the fistula to the subclavian vein. High-frequency linear arrays should be used although the high superficial velocities at some stenoses can exceed the upper limits of measurable velocities. An initial rapid transverse scan of the vessels with colour flow can identify major anomalies including aneurysms, partial thrombus and collections and can ascertain the presence of multiple unsuspected venous returns or venous occlusions. A more detailed examination is then carried out to assess any area of potential abnormality.

The access circuit is scanned from subclavian artery through the fistula/graft to the draining veins and back to the central veins, A measurement of volume flow is made in the brachial artery; three measurements may be made and the mean value recorded. Any abnormalities, such as thrombus, intimal flaps, aneurysms, pseudoaneurysms, or collections should be examined and assessed. Similarly, any areas of abnormal flow or stenosis should be assessed and the relevant velocity measurements (PSV and systolic ratio) obtained

to quantify the degree of any stenosis. If diameters at a stenosis are measurable on the real-time image, then these can also be used to quantify the degree of stenosis. If there are problems gaining access with the cannulas, the diameter and depth of the vein can be measured. If multiple draining veins are found, then their location and the route of blood returning to the central veins should be described.

Normal characteristics

For fistulae with good function, flow in the supplying artery is characterised by high velocity and low pulsatility flow (Fig. 63.39). At the site of the fistula, velocities are usually very high and may be difficult to measure accurately. Close to the anastomosis venous flow may be turbulent (Fig. 63.40) and exhibits non-axial flow vectors which reorganise more proximally downstream from the anastomosis. The vein normally exhibits arterial-like pulsations up to axillary/subclavian vein level. More proximally, venous pulsations become more evident. The vein calibre should be adequate for repeated needling and a diameter of at least 5 mm is recommended; care should be taken to avoid artefactual compression of the superficial vein by excessive pressure from the transducer.

There may be a degree of physiological increase in velocity as the cephalic vein penetrates the clavipectoral fascia just below the clavicle and it is important to distinguish this from a clinical stenosis which may occur at this point. In radiocephalic fistulae, flow to the vein is commonly from antegrade flow in the radial artery and retrograde flow from the lower radial artery distal to the anastomosis through the palmar arches from the ulnar artery.

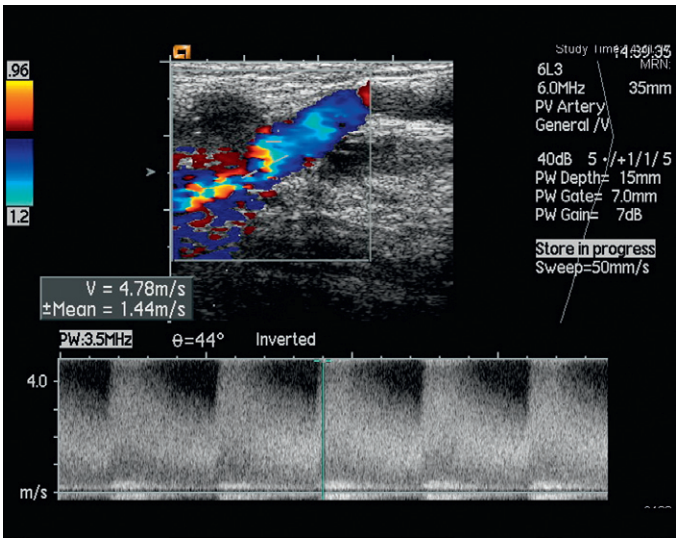

Figure 63.41 Cephalic vein stenosis. High velocities in a cephalic vein stenosis in an arteriovenous fistula. The stenosis causes vibration leading to colour flow signal in adjacent tissue.

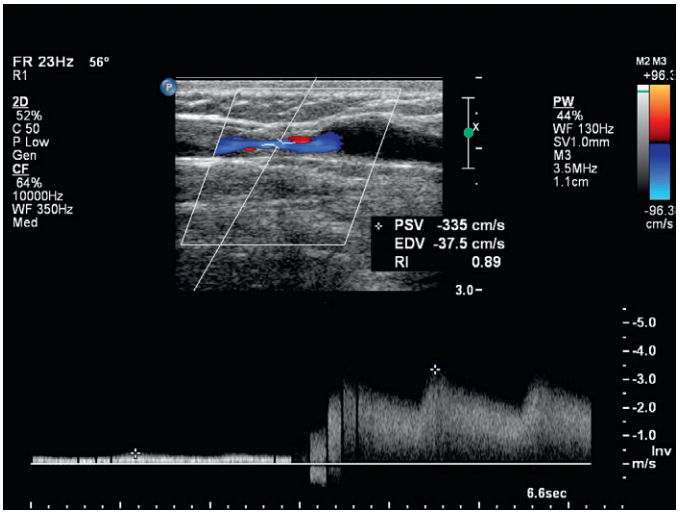

Figure 63.42 Tight stenosis in a fistula vein. The difference in diameter is evident in the colour Doppler image and the significant change in the peak velocity.

Abnormalities and complications

Thrombosis

In cases of vein and graft thrombosis, flow in the supplying artery shows a high distal resistance, usually with a triphasic flow waveform, similar to a normal brachial artery. Thrombus is evident in the vein or graft and may be partial, with a small channel of flow around it, or complete. Thrombosis may occur in the artery leading to the fistula, particularly in the radial artery in radiocephalic fistulae. It is important to determine the site and length of thrombus to aid planning of surgical or radiological intervention.

Stenoses, aneurysms, pseudo-aneurysms

Access sites frequently contain stenoses (Figs 63.41, 63.42) aneurysms, pseudo-aneurysms (Fig. 63.43) or hybrid aneurysms/pseudo-aneurysms, as a result of the continuing trauma from repeated needle puncture. By themselves they do not necessarily preclude successful dialysis. Older fistulae can develop multiple aneurysms at the needling sites yet still be viable for dialysis, or partial thrombus may be evident, particularly at the needling site. Aneurysms, stenoses and the presence of partial thrombus give rise to complex flows with turbulence and areas of recirculation which may promote thrombus formation around the dialysis needle. Aneurysms and pseudo-aneurysms are visible on real-time and colour Doppler imaging, which allow measurement of the lumen of the aneurysm/pseudo-aneurysm and the presence of any associated thrombus to be assessed.

Stenoses may be evident on colour Doppler but must be quantified by their PSV (Fig. 63.41) and the peak systolic velocity ratio (Fig. 63.42) of pre-stenotic flow to in-stenosis flow. Typical criteria used to suggest a significant stenosis are a PSV >400 cm/s and/or a PSV ratio >3:1.[89]

Steal syndromes

A steal may occur with dialysis fistulae and grafts if there is excessive shunting of blood through the access circuit with inadequate flow to distal tissues. This can result in pain in the hand and fingers and, if severe, tissue changes associated with ischaemia. It has been shown that steal syndromes may be aggravated by coexistent disease and stenosis in the arteries of the affected arm.[90,91] Ultrasound can be used to determine vascular anatomy, vessel patency and qualitative evaluation of the circulation in the arm and hand. Occlusion of the venous side of the fistula by manual pressure, or a cuff inflated above the venous pressure but below arterial pressure may result in improved flow to the arm and hand below the fistula (Fig. 63.44). This finding is useful if flow reduction surgery at the fistula is being considered.

Other findings

Collections and haematomas should be noted; these can lead to difficulties when needling fistulae and can cause extrinsic compression of the access circuit.

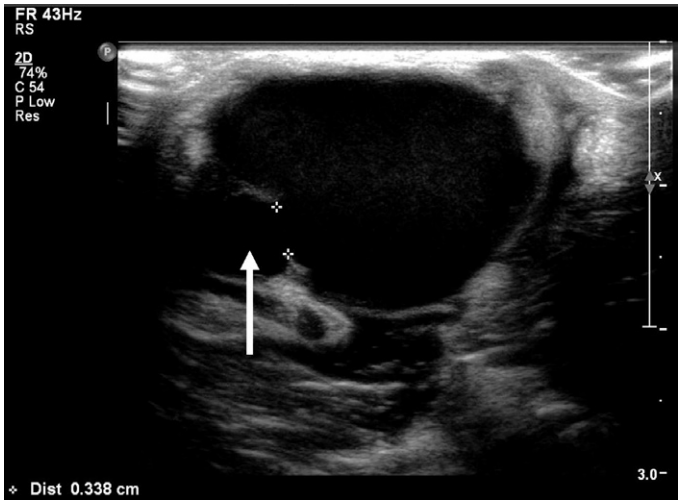

Figure 63.43 **Pseudo-aneurysm** A large pseudo-aneurysm in a fistula vein (arrow). The size of the tear in the vein wall is evident (callipers).

Protocol for evaluating haemodialysis arm access postoperatively

- Measure flow in the brachial or subclavian artery supplying the access.
- Scan the circuit from subclavian artery through the fistula/graft to the draining veins to central veins.
- Note any abnormality (thrombus, aneurysms, pseudo-aneurysms, collections).
- Note any abnormal flows (unusual flow velocities or pulsatility, flow direction in veins).
- If there are multiple venous paths, draw them and state approximately the flow through each. Note where flow returns to the deep veins.
- Measure vein diameter and depth, especially if there are needling problems. Note any sudden change in vein direction and the presence of thrombus/intimal flaps, etc. in the needling area.
- Note any stenoses and measure them on B-mode and with peak systolic velocity and ratios of stenosis to pre/post-stenosis velocities.

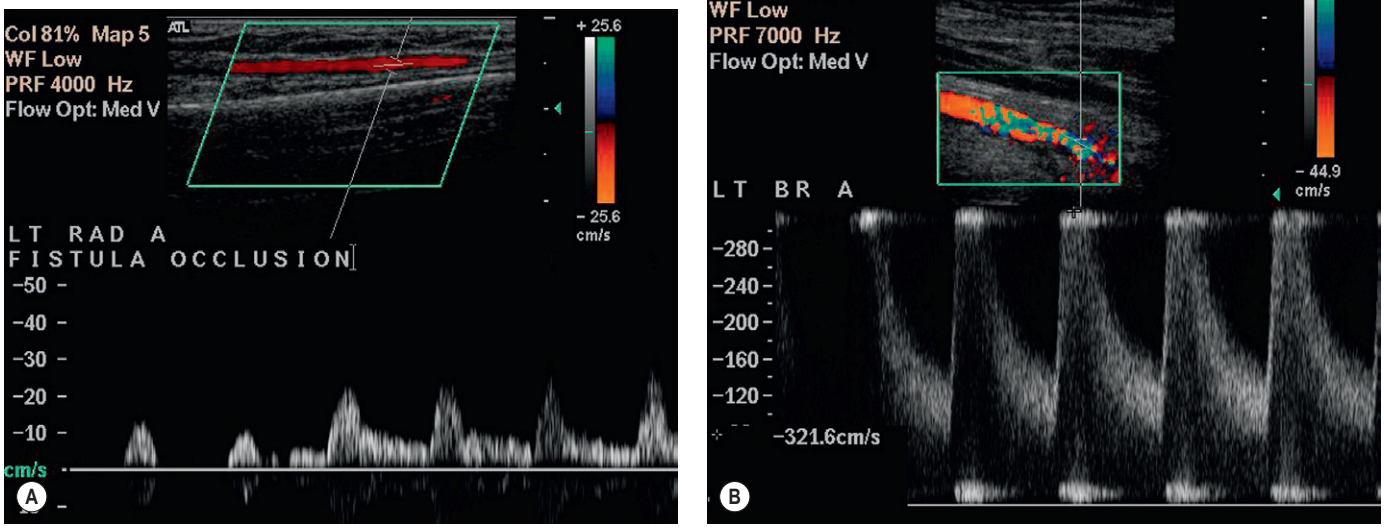

Figure 63.44 **Steal syndrome. A:** Colour and spectral Doppler images of the radial artery showing the initial poor flow, which improves significantly when the venous side of the fistula is occluded by manual pressure. **B:** Examination of the brachial artery shows a tight stenosis with a tissue bruit and peak systolic velocity of 3.2 m/s.

Very high volume flows may be found and these can lead to high output cardiac problems if flow rates are greater than 1400–2000 mL/min. Ultrasound can be used to quantify the flow and monitor therapy.

Reporting dialysis fistula examinations

The report should describe the main features of the examination. Volume flow in the brachial artery is recorded, together with any significant changes to flow when compared with previous investigations. Peak systolic velocities at stenoses should be given and ratios calculated. The presence of thrombus, aneurysms, pseudo-aneurysms and collections should be noted and dimensions recorded. In cases where needling is difficult, the diameter of the vein should be determined, together with its depth. If the fistula flow returns through more than one pathway then these should be described. It is important to report unusual flow pathways and flow in unsuspected directions. We use diagrams of the access to aid dialysis staff where needling is difficult, if there are multiple or unusual flow channels, or as a guide for planning radiological intervention or surgery (Fig. 63.45).

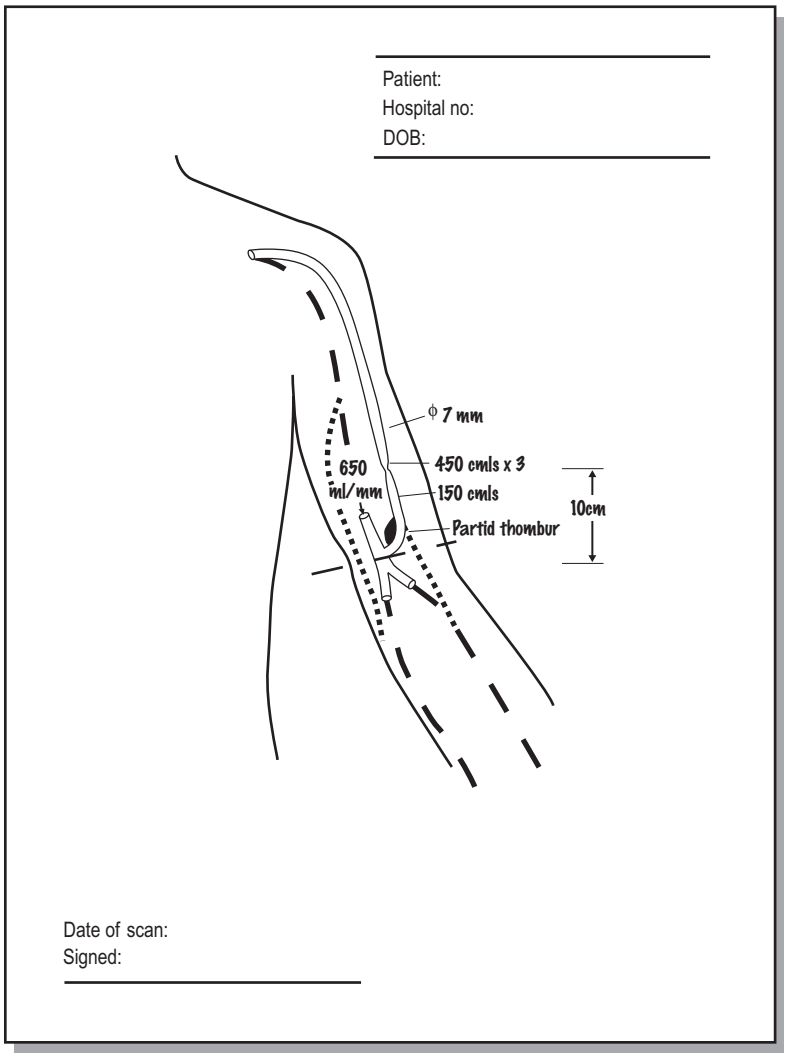

Figure 63.45 Report diagram. Diagrammatic representation of an arteriovenous fistula with the site and severity of a stenosis indicated to guide intervention.

REFERENCES

1. Dormandy JA, Ray S. The natural history of peripheral arterial disease. In: Tooke JE, Lowe GDO, editors. A textbook of vascular medicine. London: Arnold; 1996. p. 162–175.
2. Fowkes FGR, Price JF, Leng GC. Targeting subclinical atherosclerosis. BMJ 1998;316:1764–1770.
3. Raines JK, Darling CD, Buth J, et al. Vascular laboratory criteria for the management of peripheral vascular disease of the lower extremities. Surgery 1976;79:21–29.
4. Froneck A, Coel M, Bernstein EF. The importance of combined multi segmental pressure and Doppler flow velocity studies in the diagnosis of peripheral arterial occlusive disease. Surgery 1978;84:840–847.
5. Yao ST. Haemodynamic studies in peripheral arterial disease. Br J Surg 1970;57:761–766.
6. Anderson I. Doppler ultrasound recording of ankle brachial pressure index in the community. J Wound Care 1995;4:325–327.
7. Yao ST, Hobbs JT, Irvine WT. Ankle systolic pressure measurements in arterial disease affecting the lower extremities. Br J Surg 1969;59:676–679.
8. Ray SA, Scrodon PD, Taylor RS, Dormandy JA. Reliability of ankle brachial pressure index measurement by junior doctors. Br J Surg 1994;8:188–190.
9. Shapiro D, Jamner LD, Lane JD, et al. Blood pressure publication guidelines. Society for Psychophysical Research. Psychophysiology 1996;3:1–12.
10. Rastam L, Prineas RJ, Gomez-Marin O. Ratio of cuff width arm circumference as a determinant of arterial blood pressure measurements in adults. J Intern Med 1990;227:225–232.
11. O'Flynn I. Three methods of taking brachial systolic pressure: which one is best? J Vasc Nurs 1993;11:71–75.
12. Moll F, Six J, Janssens A, Mutsaerts D. Misleading upper extremity blood pressure measurements in vascular occlusive disease. Bruit 1983;8:18–19.
13. Stubbing NJ, Bailey P, Poole M. Protocol for the accurate assessment of ABPI in patients with leg ulcers. J Wound Care 1997;6:417–418.
14. Goss DE, de Trafford J, Roberts VC, et al. Raised ankle/brachial pressure index in insulin treated diabetic patients. Diabet Med 1989;6:576–578.
15. Laing SL, Greenhalgh RM. The detection and progression of asymptomatic arterial disease. Br J Surg 1983;70:628–630.
16. Lambourne LA, Moffatt CJ, Jones AC, et al. Clinical audit and effective change in leg ulcer services. J Wound Care 1996;5: 348–351.
17. Yao ST. Lower limb systolic pressure measurements: technique and clinical applications. Int Angiol 1985;4:31–39.
18. Sumner DS, Strandness DE. Aortoiliac reconstruction in patients with combined iliac and superficial femoral artery occlusion. Surgery 1978;84:348–355.
19. Baker JD, Dix D. Variability of Doppler ankle pressures with arterial occlusive disease: an evaluation of ankle index and brachial ankle pressure gradient. Surgery 1981;89:134–137.

20. Hobbs JT, Yao St, Lewis JD, Needham TN. A limitation of the Doppler ultrasound method of measuring ankle systolic pressure. VASA 1974;3:160–162.
21. Goss DE, Stevens M, Watkins PJ, Baskerville PA. Falsely raised ankle/brachial pressure index: a method to determine tibial artery compressibility. Eur J Vasc Surg 1991;5:23–26.
22. Smith FCT, Shearman CP, Simms MH, Gwynn BR. Falsely elevated ankle pressures in severe leg ischaemia: The pole test – an alternative approach. Eur J Vasc Surg 1994;8:408–412.
23. Ouriel K, McDonnell AE, Metz CE, Zarins CK. A critical evaluation of stress testing in the diagnosis of peripheral vascular disease. Surgery 1982;91:686–693.
24. Cameron AEP, Porter A, Rosser S, et al. The stresst'er ergometer as an alternative to treadmill testing in patients with claudication. Eur J Vasc Endovasc Surg 1997;14:433–438.
25. Laing SL, Greenhalgh RM. Standard exercise test to assess peripheral arterial disease. BMJ 1980;280:13–16.
26. Strandness DE. Abnormal exercise responses after successful reconstructive surgery. Surgery 1966;59:325–333.
27. Sensier Y, Bell PRF, London NJ. The ability of quantitative assessment of the common femoral Doppler waveform to screen for significant aortoiliac disease. Eur J Vasc Endovasc Surg 1998;15:357–364.
28. Johnston KW, Kassam M, Cobbold RSC. Relationship between Doppler pulsatility index and direct femoral pressure measurements in the diagnosis of aortoiliac disease. Ultrasound Med Biol 1983;9:271–281.
29. Evans DH, Barrie, WW, Asher MJ, et al. The relationship between ultrasonic pulsatility index and proximal arterial stenosis in a canine model. Circ Res 1980;46:470–475.
30. Clifford PC, Skidmore R, Bird DR, et al. The role of pulsatility index in the assessment of lower limb ischaemia. J Med Technol 1981;5:237–241.
31. Planiol T, Pourcelot L. Doppler effect study of the carotid circulation. In: 2nd World Congress on Ultrasonics in Medicine. Amsterdam: Excerpta Medica; 1973. p. 104–111.
32. Jager KA, Phillips DJ, Martin RL, et al. Noninvasive mapping of lower limb arterial lesions. Ultrasound Med Biol 1985;11:515–521.
33. Legemate DA, Teeuwen C, Hoeneveld H, Eikelboom BC. Value of duplex scanning compared with angiography and pressure measurements in the assessment of aortoiliac arterial lesions. Br J Surg 1991;78:1003–1008.
34. Whyman MR, Gillespie I, Ruckley CV, et al. Screening patients with claudication from femoropopliteal disease before angioplasty using Doppler colour flow imaging. Br J Surg 1992;79:907–909.
35. Sensier Y, Hartsthorne T, Thrush A, et al. A prospective comparison of lower limb colour-coded duplex scanning with arteriography. Eur J Vasc Endovasc Surg 1996;11:170–175.
36. Collins R, Burch J, Cranny G, et al. Duplex ultrasonography, magnetic resonance angiography, and computed tomography angiography for diagnosis and assessment of symptomatic, lower limb peripheral arterial disease: systematic review. BMJ 2007;334:1257–1265.
37. Norgren L, Hiatt WR, Dormandy JA, et al. TASC II working group. Inter-Society Consensus for the management of peripheral arterial disease (TASCII) J Vasc Surg 2007;45:S5A–S67A.
38. Ranke C, Creutzig A, Alexander K. Duplex scanning of the peripheral arteries: correlation of the peak velocity ratio with angiographic diameter reduction. Ultrasound Med Biol 1992;18:433–440.
39. Polak JF, Karmel MI, Mannick JA, et al. Determination of the extent of lower-extremity peripheral arterial disease with color-assisted duplex sonography: a comparison with angiography. AJR Am J Roentgenol 1990;155:1085–1089.
40. Langsfeld M, Nepute J, Hershey FB, et al. The use of deep duplex scanning to predict hemodynamically aortoiliac stenoses. J Vasc Surg 1988;7:395–399.
41. Whyman MR, Ruckley CV, Fowkes FG. A prospective study of the natural history of femoropopliteal artery stenosis using duplex ultrasound. Eur J Vasc Surg 1993;7:444–447.
42. Strauss AL, Roth FJ, Rieger H. Non-invasive assessment of pressure gradients across iliac artery stenoses; duplex and catheter correlative study. J Ultrasound Med 1993;12:17–22.
43. Legemate DA, Teeuwen C, Hoeneveld H, Eikelboom BC. How can the assessment of the hemodynamic significance of aortoiliac arterial stenosis by duplex scanning be improved? A comparative study with intraarterial pressure measurement. J Vasc Surg 1993;17:676–684.
44. Allard L, Cloutier G, Durand L-G, et al. Limitations of ultrasonic duplex scanning for diagnosing lower limb arterial disease in the presence of adjacent segment disease. J Vasc Surg 1994;19:650–657.
45. Bergamini TM, Tatum CM, Marshall C, et al. Effect of multilevel sequential stenosis on lower extremity arterial duplex scanning. Am J Surg 1995;169:564–566.
46. Koelemay MJW, Hratog DD, Prins MH, et al. Diagnosis of arterial disease of the lower extremities with duplex ultrasonography. Br J Surg 1996;83:404–409.
47. Collier P, Wilcox G, Brooks D, et al. Improved selection of patients for angioplasty utilizing colour Doppler imaging. Am J Surg 1990;160:171–174.
48. Sensier Y, Fishwick G, Owen R, et al. A comparison between colour duplex ultrasonography and arteriography for imaging for infrapopliteal arterial lesions. Eur J Vasc Endovasc Surg 1998;15:44–50.
49. Hatsukami TS, Primozich JF, Zierler RE, et al. Color Doppler imaging of infrainguinal arterial occlusive disease. J Vasc Surg 1992;16:527–531.
50. Wilson YG, George JK, Wilkins DC, Ashley S. Duplex assessment of run-off before femorocrural reconstruction. Br J Surg 1997;84:1360–1363.
51. Davies AH, Magee TR, Jones DR, et al. The value of duplex scanning with venous occlusion in preoperative prediction of femoro-distal vein bypass graft diameter. Eur J Vasc Surg 1991;5:633–636.
52. Bergamini TM, George SM, Massey HT, et al. Intensive surveillance of femoropopliteal-tibial autogenous vein bypasses improves long-term graft patency and limb salvage. Ann Surg 1995;221:507–515.
53. Idu MM, Buth J, Cuypers P, et al. Economising vein-graft surveillance programs. Eur J Vasc Endovasc Surg 1998;15:432–438.
54. Giannoukas AD, Androulakis AE, Labropoulos N, Wolfe JHN. The role of surveillance after infrainguinal bypass grafting. Eur J Vasc Endovasc Surg 1996;11:279–289.
55. Mills JL. Mechanisms of graft failure: the location, distribution and characteristics of lesions that predispose to graft failure. Semin Vasc Surg 1983;6:78–91.
56. Westerband A, Mills JL, Kistler S, et al. Prospective validation of threshold criteria for intervention in infrainguinal vein grafts undergoing duplex surveillance. Ann Vasc Surg 1997;11:44–48.
57. Davies AH, Magee TR, Tennant SWG, et al. Criteria for identification of the 'at risk' infrainguinal bypass graft. Eur J Vasc Surg 1994;8:315–319.
58. Davies AH, Hawdon AJ, Sydes MR, Thompson SG. Is duplex surveillance of value after leg vein bypass grafting? Principal results of the Vein Graft Surveillance Randomised Trial (VGST). Circulation 2005;112:1985–1991.
59. Landry GJ, Liem TK, Mitchell EL, et al. Factors affecting symptomatic vs asymptomatic vein graft stenoses in lower extremity bypass grafts. Arch Surg 2007;142:848–854.
60. Cluley SR, Brener BJ, Hollier L, et al. Transcutaneous ultrasonography can be used to guide and monitor balloon angioplasty. J Vasc Surg 1993;17:23–30.
61. Katzenschlager R, Ahmadi A, Minar E, et al. Femoropopliteal artery: initial and 6-month results of color duplex US-guided percutaneous transluminal angioplasty. Radiology 1996;199:331–334.
62. Nyamekye I, Sommerville K, Raphael M, et al. Non-invasive assessment or arterial stenoses in angioplasty surveillance: a comparison with angiography. Eur J Vasc Endovasc Surg 1996;12:471–481.
63. Kinney EV, Bandyk DF, Mewissen MW, et al. Monitoring functional patency of percutaneous transluminal angioplasty. Arch Surg 1991;12:743–747.
64. Sacks D, Robinson ML, Summers TA, Marinelli DL. The value of duplex sonography after peripheral artery angioplasty in predicting subacute restenosis. AJR Am J Roentgenol 1994;162:179–183.
65. Baril DT, Rhee RY, Kim J, et al. Duplex criteria for determination of in-stent stenosis after angioplasty and stenting of the superficial femoral artery. J Vasc Surg 2009;49:133–139.
66. Miles S, Roediger W, Cooke P, Mieny CJ. Doppler ultrasound in the diagnosis of the popliteal artery entrapment syndrome. Br J Surg 1977;64:883–884.
67. Erdoes LS, Devine JJ, Bernhard VM, et al. Popliteal compression in a normal population. J Vasc Surg 1994;20:978–986.
68. Dent TL, Lindenauer SM, Ernst CB, Fry WJ. Multiple arteriosclerotic arterial aneurysms. Arch Surg 1972;105:338–344.
69. Dawson I, van Bockel JH, Brand R, Terpstra JL. Popliteal artery aneurysms. Long-term follow-up of aneurysmal disease and results of surgical treatment. J Vasc Surg 1991;13:398–407.
70. Bynoe RP, Miles WS, Bell RM, et al. Noninvasive diagnosis of vascular trauma by duplex ultrasonography. J Vasc Surg 1991;14:346–352.

71. Knudson MM, Lewis FR, Atkinson K, Neuhaus A. The role of duplex ultrasound imaging in patients with penetrating extremity trauma. Arch Surg 1993;128:1033–1037.
72. Fellmeth BD, Roberts AC, Bookstein JJ, et al. Postangiographic femoral artery injuries: nonsurgical repair with US guided compression. Radiology 1991;178:671–675.
73. Coley BD, Roberts AC, Fellmeth BD, et al. Postangiographic femoral artery pseudoaneurysms: further experience with US guided compression repair. Radiology 1995;194:307–311.
74. Maleux G, Hendrickx S, Vaninbrouckx J, et al. Percutaneous injection of human thrombin to treat iatrogenic femoral pseudoaneurysms: short and mid-term ultrasound follow up. Eur Radiol 2003;13:209–212.
75. Igidbachian VN, Mitchell DG, Middleton WD, et al. Iatrogenic femoral arteriovenous fistula: diagnosis with color Doppler imaging. Radiology 1989;170:749–752.
76. Middleton WD, Erickson S, Melson GL. Perivascular color artifact: pathological significance and appearance on color Doppler US images. Radiology 1989;17:647–652.
77. Ackerstaff RG, Hoeneveld H, Slowikowski JM, et al. Ultrasonic duplex scanning in atherosclerotic disease of the innominate, subclavian and vertebral arteries. A comparative study with angiography. Ultrasound Med Biol 1984;10:409–418.
78. Strauss AL, Soeparwate R. Is preoperative evaluation of the internal mammary artery for suitability in coronary bypass surgery possible? Vasa Suppl 1991;33:212–213.
79. Sun Y, Yip PK, Jeng JS, et al. Ultrasonic study and long-term follow-up of Takayasu's arteritis. Stroke 1996;27:2178–2182.
80. Reed AJ, Fincher RM, Nichols FT. Takayasu arteritis in a middle-aged Caucasian woman: clinical course correlated with duplex ultrasound and angiography. Am J Med Sci 1989;298:324–327.
81. Longley DG, Schwabacher S, Yedicka JW, et al. Thoracic outlet syndrome: evaluation of the subclavian vessels by colour duplex sonography. Am J Radiol 1992;158:623–630.
82. Rush MP, McNally DM, Rossman ME, Otis S. Non-invasive vascular diagnosis of thoracic outlet syndrome. Bruit 1983;7:56–59.
83. Baxter BT, Blackburn D, Payne K, et al. Noninvasive evaluation of the upper extremity. Surg Clin North Am 1990;70:87–97.
84. National Kidney Foundation. NKF-K/DOQI clinical practice guidelines for vascular access: update 2006. Am J Kidney Dis 2006;48(Suppl. 1):S177–S277.
85. Tordoir J, Canaud B, Haage P, et al. European Best Practice Guidelines on Vascular Access. Nephrol Dial Transplant 2007;22(Suppl. 2): ii88–ii117.
86. Malovrh M. Native arteriovenous fistula: preoperative evaluation. Am J Kidney Dis 2002;39:1218–1225.
87. Lockhart ME, Robbin ML, Allon M. Preoperative sonographic radial artery evaluation and correlation with subsequent radiocephalic fistula outcome. J Ultrasound Med 2004;23:161–168.
88. Tordoir JHM, Rooyens P, Dammers R, et al. Prospective evaluation of failure modes in autogenous radiocephalic wrist access for hemodialysis. Nephrol Dial Transplant 2003;18:378–383.
89. Older RA, Gizieski TA, Wilcowski MJ, et al. Hemodialysis access stenosis: early detection with color Doppler US. Radiology 1998;207:161–164.
90. Leon C, Asir A. Arteriovenous access and hand pain: the distal hypoperfusion ischemic syndrome. Clin J Am Soc Nephrol 2007;2:175–183.
91. Malik J, Slavikova M, Maskova J. Dialysis access-associated steal syndrome: the role of ultrasonography. J Nephrol 2003;16:903–907.

CHAPTER

64 Peripheral veins

Grant M. Baxter and David E. Goss

LOWER LIMB VENOUS IMAGING FOR DEEP VEIN THROMBOSIS

Introduction

Deep venous thrombosis is a common clinical condition which is known to have a number of well-recognised potentially life-threatening complications and, more chronically, complications related to the lower limb itself secondary to valve damage and venous incompetence. Most general imaging departments will be familiar with patients who present acutely on a daily basis and require careful evaluation. Accurate diagnosis is therefore essential but despite its frequent clinical presentation and the well-evaluated methods of investigation and assessment, it nevertheless can remain a difficult diagnostic and therapeutic dilemma. With regard to its prevalence in the USA it is estimated that approximately 20 million cases of deep venous thrombosis (DVT) occur per year, with an incidence of 100 persons per 100 000 per year of which approximately 600 000 will develop pulmonary thromboembolism (PTE),[1,2] a potentially life-threatening condition. The consequences of a missed diagnosis, or delay in diagnosis are well recognised, the 28-day mortality rate for a first time DVT being 11% in a large venous thromboembolism epidemiological study.[3] With regard to figures in the United Kingdom there may be anything upward of 20 000 deaths per year from pulmonary embolus.[4] Unfortunately the classical appearances of an acute venous thrombosis, i.e. a red, hot, swollen leg, are far from universal and indeed, even the presence of this triad of clinical signs may not in itself indicate an underlying deep venous occlusion. As a consequence, the clinical diagnosis is at best 50% accurate and this in itself necessitates the need for both a reliable and reproducible diagnostic technique.

The historical, conventional imaging modality is venography and for many, this has long been accepted as the 'gold standard' technique in the investigation of this condition, being both accurate and reproducible. However, it has many well-recognised drawbacks including being invasive as it requires cannulation of a foot vein, which can be painful, and in the presence of oedema this may be difficult or even unsuccessful in a small percentage of patients. It also involves exposure to radiation, albeit small and there is the potential risk of contrast reaction. Paradoxically, venography may even induce thrombosis secondary to the local venotoxic effects of the contrast agent itself; although, since the advent of the osmolar non-ionic contrast agents, this is of less concern.[5,6] The interpretation of venograms may vary between radiologists by as much as 10–15% of studies.[7] For these reasons, the search for a suitable non-invasive alternative to venography has always been a priority.

A number of different techniques have been evaluated in the investigation of DVT and these include radio-isotope scans, impedance plethysmography, thermography and light reography. All have had their advocates; however, due to their limitations, none of these techniques has ever been accepted clinically as suitable for routine use. Radio-isotope scanning,[8–10] whilst accurate within the calf, has reduced sensitivity and specificity in the proximal venous system,[11] probably the most important area clinically in relation to the risk of a thromboembolic event. Thermography,[12–14] on the other hand, has difficulty differentiating superficial thrombophlebitis from DVT, leading to false positive scans. Impedance plethysmography gives an overall assessment of venous return from the limb but does not accurately identify the position of the thrombosis and may miss more distal situated lesions.[15,16]

The introduction of real-time ultrasound in the mid-1980s had a huge impact on the imaging of DVT as it was cheap, universally available and a relatively rapid method for assessment of possible

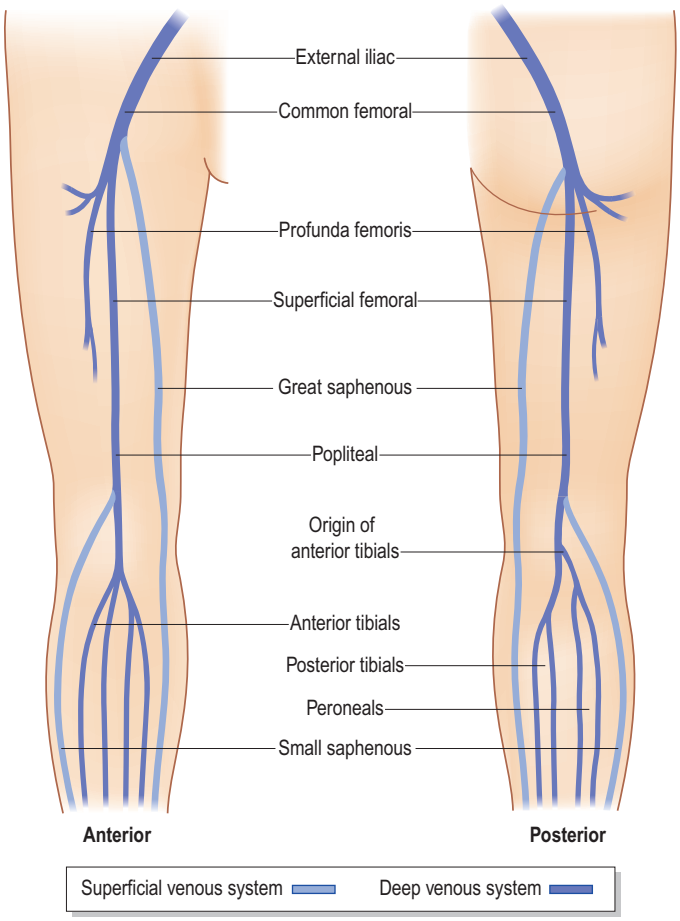

Figure 64.1 **Anatomy of the lower limb venous system.**

Basic facts

- There are approximately 20 million cases of DVT per year in the USA.
- There are approximately 20 000 deaths per year from PTE in the UK.
- Ultrasound, real-time or colour Doppler, is the primary method of diagnosis of DVT worldwide.
- Duplication of the femoral and popliteal veins occurs in 20–35% of people.

DVT. Many studies from centres all over the world have shown ultrasound to be reliable in the assessment of both the femoral and popliteal veins.[17–19] The addition of colour flow imaging in the late 1980s and early 1990s led to a more graphic, instantaneous, visual appreciation of flow, or its absence, within the venous system and the technique was rapidly adopted by most centres as the first-line imaging modality. Numerous rigorous trials have shown ultrasound to have an extremely high sensitivity and specificity of over 95% in the diagnosis of femoral and popliteal vein thromboses.[20,21] This high level of performance has been maintained over many years.[22] Some centres have also suggested that similar results can be achieved below the knee, assuming good imaging conditions and careful technique.[23–25] However, routine imaging of the calf veins has not been generally adopted clinically due to many inherent difficulties of scanning in this area.

With regard to venography, this is now utilised largely as a second-line alternative to ultrasound in the assessment of DVT for patients in whom there may be a technical difficulty or equivocal results. Even in such patients often a repeat ultrasound study is all that is required to enable a clinical decision to be made. Indeed, currently the number of venograms being performed, not just in the UK but worldwide, has probably never been as low, and in many centres is now non-existent.

Venous anatomy

The venous system of the lower limb (Fig. 64.1) can be divided into the deep and superficial systems with small communicating veins between. With regard to the deep veins there are three paired calf veins below the knee, each being accompanied by a single artery. These calf veins join behind the knee to form the popliteal vein, which becomes the femoral vein at the level of the adductor canal; at the groin the femoral vein joins with the profunda femoris vein to become the common femoral vein, which then drains into the iliac veins. The two sets of iliac veins join to form the inferior vena cava (IVC). It is well recognised that segments of the lower limb veins may be duplicated and this occurs in up to 20% of femoral veins and 35% of popliteal veins.[26,27]

The superficial system consists of the great saphenous vein, which courses along the medial aspect of the calf and thigh to join the common femoral vein at the level of the inguinal ligament. The small saphenous system runs along the posterolateral aspect of the calf to join the popliteal vein behind the knee. These two venous systems are connected by a series of small communicating veins, which are more numerous below the knee than above; they are prominent in the medial aspect of the lower leg connecting the posterior arch branch of the great saphenous vein with the deep veins of the calf. Normal venous drainage is from the superficial to the deep system. However, when this malfunctions and flow direction reverses, it may be associated with the clinical scenario of venous incompetence.

TECHNIQUE

Real-time compression ultrasound

This is by design a simple technique. Imaging is performed with the probe perpendicular to the direction of vascular flow. Scanning generally begins at the groin with identification of the common femoral vein and artery, with the vein lying medial to the artery. Scanning is performed with a linear probe which may vary in frequency from 5–12 MHz depending on the type of ultrasound system. Clearly, the most appropriate frequency will depend on the patient build and the degree of swelling and soft tissue change within the limb. The probe straddles both the artery and vein and very light pressure is initially applied so as not to collapse the walls of the vein. Following this, further pressure is applied with the probe and if the vein is patent, the anterior and posterior walls of the vein will meet completely. On release of pressure, the lumen of the vein will return to normal. However, if the vein contains thrombus, it does not collapse when probe pressure is applied and the vein remains distended (Fig. 64.2). Reflective thrombus may also be visualised within the vein lumen (Fig. 64.3).

This technique is applied from the groin to the adductor canal, moving the transducer at approximately 1 cm intervals. The femoral vein lies at its deepest point in the adductor canal and it can be difficult both to visualise and to perform a compression scan at this point. Visualisation may be aided by pushing the hamstring tendon upwards from behind the lower thigh: this has the effect of bringing the vessels closer to the probe and allowing a modified compression test to be performed.

To examine the popliteal vein the patient is turned into a decubitus position with the knee partially flexed. Approaching from the posterior popliteal fossa, the vein is now seen lying superficial to the artery and it is once again imaged in the transverse plane. The vein can be followed both superiorly to the adductor canal and inferiorly to the tibio-peroneal trunk with the same compression test being applied. At this point the examination is complete.

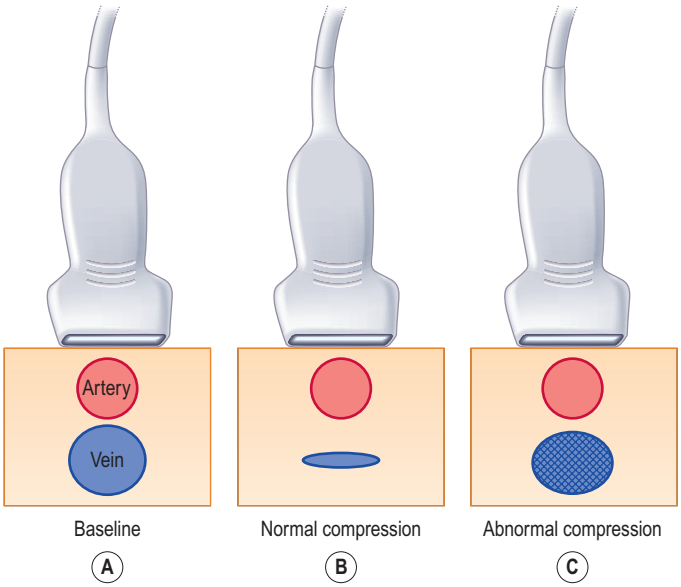

Figure 64.2 The real-time compression ultrasound technique. The ultrasound probe straddles the vessels transversely and pressure is applied. If the vein is patent the anterior and posterior walls oppose completely, as in **B**; if thrombus is present then the vein remains dilated, as in **C**.

Colour Doppler imaging

Technique

Imaging is performed using the same 5–12 MHz range of linear probes. The patient lies supine and a liberal amount of ultrasonic jelly is applied continuously from the groin to the level of the adductor canal. The leg itself should be slightly abducted by 10–15°. As with the real-time compression technique, initial imaging is performed in a transverse plane to identify both the common femoral artery and vein. These can easily be differentiated by their anatomical positions (the vein invariably lies medial to the artery) and by spectral Doppler analysis of the vessels. The triphasic waveform of the femoral artery is significantly different from the monophasic waveform of the vein. Transverse scanning will also identify any dual segments of the femoral vein.

The common femoral vein can be traced proximally to the external iliac vein, which is routinely imaged until it passes deep into the pelvis. This is often a good vein to obtain a spectral Doppler waveform from. This will normally be monophasic, increasing on expiration and reducing on inspiration (Fig. 64.4). Indeed, if doubt persists, with regard to the presence of respiratory variation the simple task of asking the patient to breath in and out will often confirm such phasic variation. The absence of such variation may indicate a more proximal obstructing or compressing lesion and in this situation further investigation is often merited.[28] A Valsalva manoeuvre is also routinely performed and this is a further indirect assessment of more proximal venous patency (see 'Assessment of the iliac system and inferior vena cava'). Following satisfactory imaging of the external iliac vein the examination proceeds caudally and, from this point onwards, imaging is routinely performed in the longitudinal plane.

The common femoral, upper profunda femoris and femoral veins are routinely imaged longitudinally. The profunda femoris is normally only imaged for the first 3–5 cm and if this is patent then most effort is concentrated on examining the femoral vein which, in the

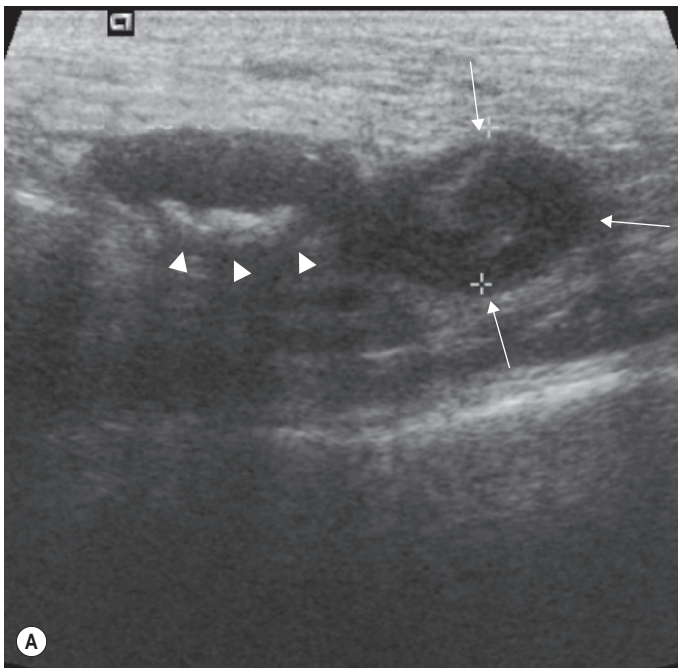

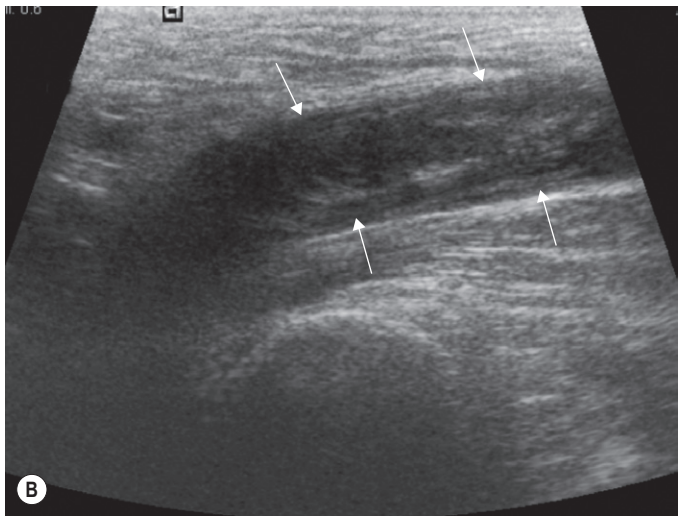

Figure 64.3 Acute thrombus. A: Transverse B-mode image of the femoral vein (arrows) containing solid echogenic material consistent with acute thrombus. This vein was non-compressible on ultrasound, a feature highly supportive of the diagnosis. The femoral artery is noted adjacent to the vein containing calcification (arrowheads) in its posterior wall. **B:** Sagittal scan of the femoral vein confirms the presence of echogenic thrombus (arrows).

vast majority of individuals, lies deep to the femoral artery. The vein can be tracked continuously from the groin to the level of the adductor canal. As for all venous imaging techniques, light probe pressure is mandatory and an awareness of anatomical variants is essential (see 'Problems and pitfalls'). Colour Doppler flow may on occasion be difficult to visualise in the femoral vein at the adductor canal due to the depth of the vessel. This can be overcome by utilising a number of techniques, one of which is calf compression, which increases flow within the distal femoral venous segment (see 'Problems and pitfalls'). In addition, removing the steering angle on the colour Doppler box may also be helpful, as this aids sensitivity. The final option is to use power Doppler, if available.

When the examination of the femoral segment is complete, the patient is turned into the decubitus position and imaging of the popliteal vein can be performed. The knee is normally flexed 20–25°. The popliteal vein from the posterior approach is visualised superficial to the popliteal artery and it can be followed both superiorly to the adductor canal and inferiorly to the tibio-peroneal trunk. Flow within this vessel is normally spontaneous and completely fills the vein lumen; little distal compression, if any, is required to visualise it.

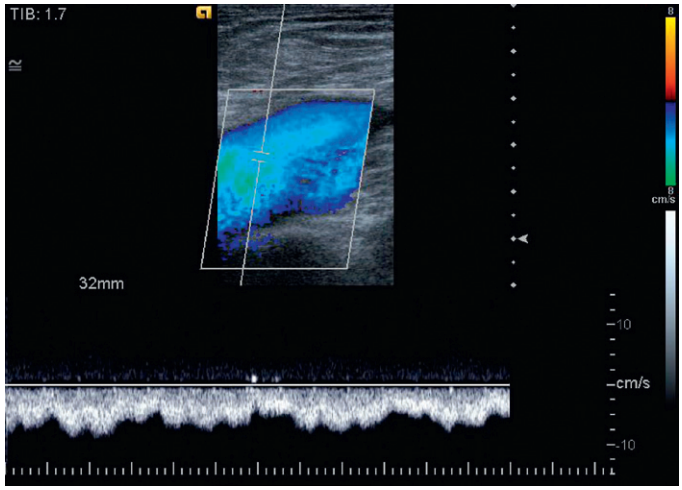

Figure 64.4 Spectral Doppler waveform of the distal external iliac vein. Flow decreases on inspiration and increases with expiration. Loss of phasic swing may occur with more proximal thromboses or be secondary to vein compression from a pelvic lesion.

Diagnostic criteria

A number of diagnostic criteria are routinely utilised to assess venous patency with the colour Doppler technique. These include the following:

Spontaneous flow

Flow within the iliac, femoral and popliteal veins is normally spontaneous and normally completely fills the vein lumen (Fig. 64.5). On occasion, colour Doppler across the vein lumen may be incomplete; however, this should never be persistent. Incomplete intraluminal colour flow filling is more likely to occur

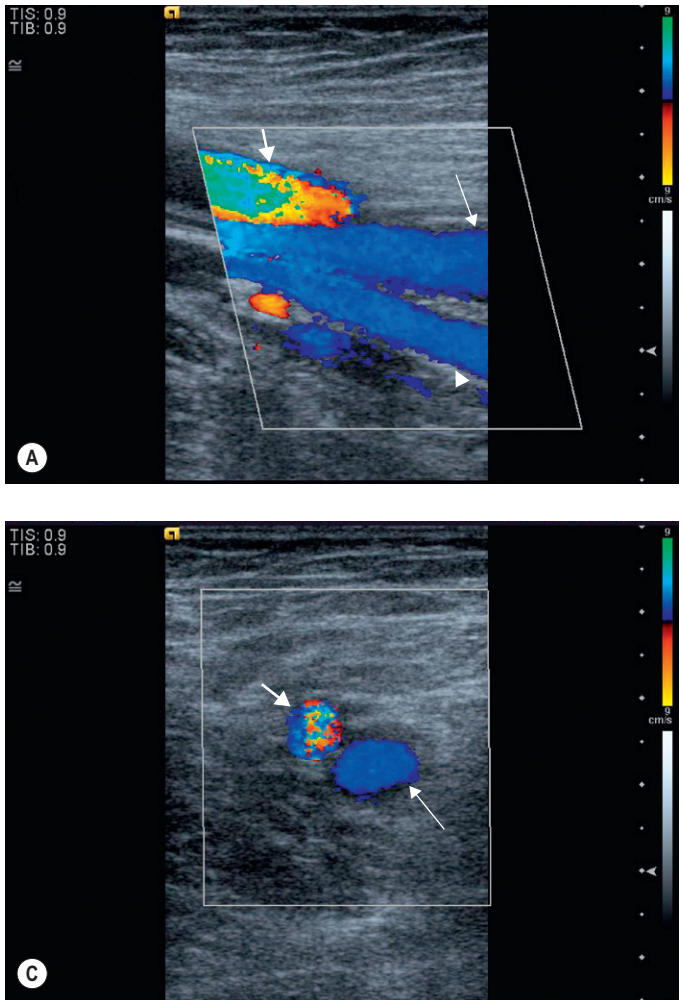

Figure 64.5 Spontaneous flow. A: Longitudinal colour Doppler scan of the femoral vein (thin arrow) lying posterior to the artery (thick arrow) at the groin. There is complete filling of the vein lumen with spontaneous colour flow indicative of patency. The deeper vein is the profunda femoris (arrowhead). **B:** Similar longitudinal scan at mid-thigh showing the femoral vein (thin arrow) lying in its normal anatomical position posterior to the artery (thick arrow). **C:** The same vessels as in **B** but seen in the transverse plane, the vein (thin arrow) lying medial to the artery (thick arrow).

in pregnancy when the increase in intra-abdominal pressure can reduce venous return from the lower limbs. The judicious use of distal compression should largely resolve any problem areas. Persistent underfilling of a venous segment strongly indicates the presence of a small focal area of thrombus.

Reflective material

The normal vein lumen, when using colour Doppler, is filled with colour-coded venous flow. It should be devoid of any echogenic reflective material; this finding is indicative of venous thrombosis.

Distal augmentation

The application of distal augmentation by squeezing the calf will result in increased venous return and thus an increase in the Doppler signal from the vein (Fig. 64.6). This increased signal indicates that the venous segment between the point of compression and the position of the probe is patent. Although this is the case in the majority, there are some very well-recognised pitfalls that can result in reassuringly false negative scans and this particular manoeuvre, despite being helpful on a number of occasions, should not be relied upon in isolation to confirm or refute a diagnosis of DVT. In addition, augmentation should be performed in a controlled manner, given the potential risk of dislodging thrombus and a resultant pulmonary embolus[29,30] (see 'Problems and pitfalls').

Response to probe compression

Although this particular manoeuvre is more historically related to the real-time compression technique it can nevertheless also be utilised with colour Doppler. When the probe is transverse to the artery and vein and light pressure applied, the walls of the vein should meet each other completely. Should the vein lumen remain visible then thrombus is present.

Variation of the spectral waveform with respiration

Examination of the common femoral and external iliac veins using spectral Doppler normally shows a phasic venous waveform which varies with respiration. The presence of such a waveform is predictive of proximal venous patency. Respiratory variation is not normally as marked in the more distal veins of the leg as it is more proximally.

The absence of phasicity in the common femoral vein is suspicious of either a more proximal obstructing venous thrombus or a large pelvic or abdominal lesion with accompanying venous compression.[28] Flat venous waveforms may also be seen in collateral vessels; these should not be confused with the primary deep venous system.

Venous dilatation

This often occurs in the presence of acute DVT. It can be a helpful confirmatory sign, especially when thrombus is fresh and anechoic as this tends to expand the vein. It should be noted, however, that dilatation is not universal and is not seen in all cases of acute thrombosis (Fig. 64.7).

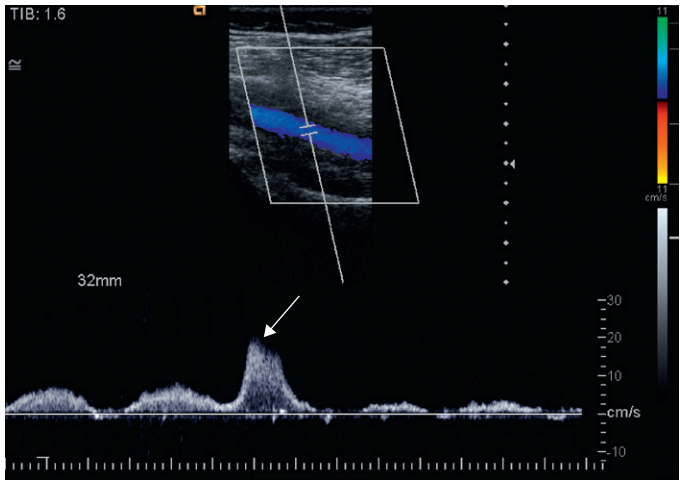

Figure 64.6 Spectral Doppler waveform of the popliteal vein following distal manual compression of the calf. The amplitude of the spectral trace has significantly increased following this augmentation manoeuvre (arrow), suggesting patency of the calf veins. Complete reliance on this manoeuvre in isolation may lead to incorrect conclusions – see 'Problems and pitfalls'.

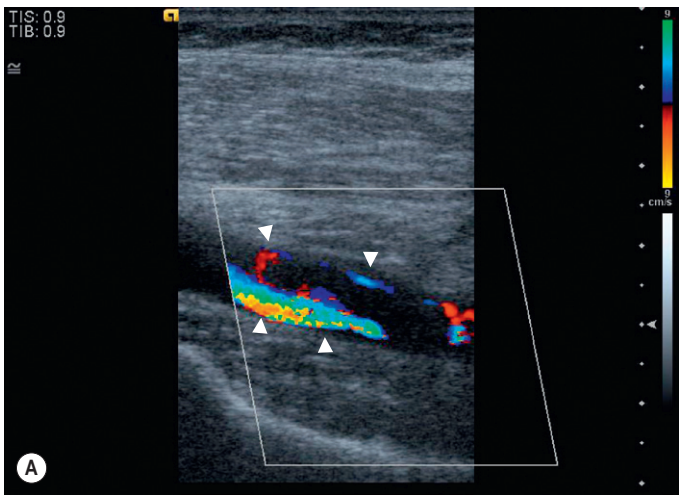

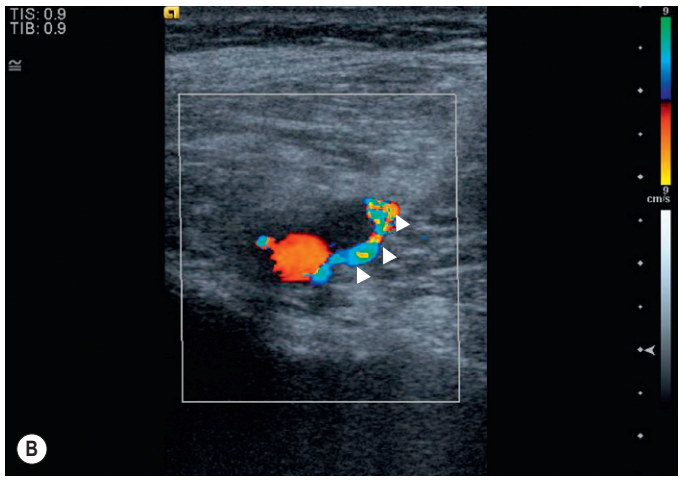

Figure 64.7 Thrombus in popliteal vein. A: Longitudinal colour flow scan through the popliteal vein. The popliteal vein contains thrombus with some surrounding flow (arrowheads). **B:** The same vein seen transversely showing central vein thrombus with surrounding peripheral wall flow (arrowheads) in keeping with non-occlusive thrombus. The popliteal vein, however, is not particularly dilated. Venous dilatation often accompanies DVT but is not an absolute requirement for diagnosis.

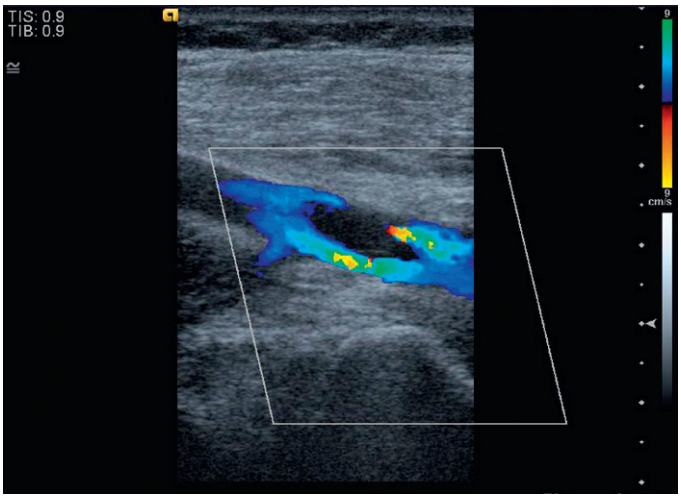

Figure 64.8 Longitudinal colour flow image through the distal femoral vein. The femoral vein contains an area of non-occlusive thrombus with flow surrounding the periphery of the clot encircling both its proximal and distal aspects.

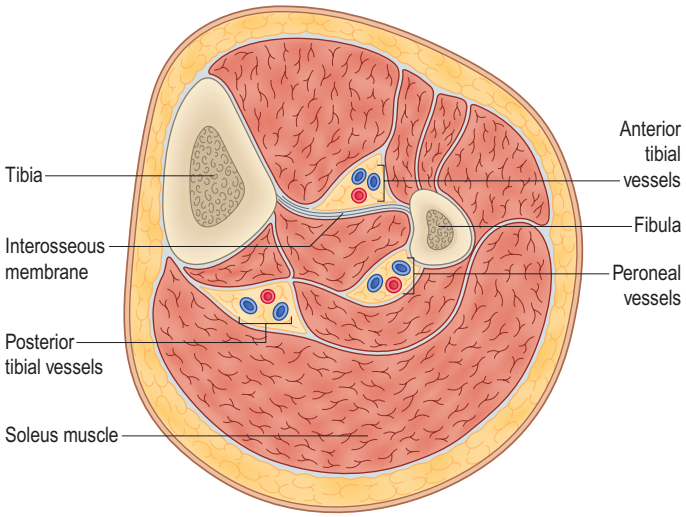

Figure 64.9 Cross-sectional anatomy of the calf showing the position of the calf veins, accompanying arteries and their anatomical landmarks.

Ultrasonic findings in normal and thrombosed veins

- The femoral vein normally lies medial to the artery.
- Complete apposition of the vein walls is an indicator of vein patency (probe pressure applied in the transverse plane).
- Colour Doppler flow in the femoral and popliteal veins is normally spontaneous.
- Spectral Doppler flow in the common femoral vein is normally phasic; a flat waveform is indicative of more proximal disease.
- With colour Doppler a combination of absent spontaneous intraluminal flow and the presence of intraluminal thrombus is indicative of venous thrombosis.

Table 64.1 Colour Doppler imaging in suspected deep venous thrombosis: diagnostic criteria

Diagnostic criteria	Patent	Thrombosis
Spontaneous flow	Present	Absent
Augmentation of flow[a]	Present	Absent
Response to probe compression	Present	Absent or diminished
Doppler waveform	Present + phasic	Absent
Intraluminal echoes[b]	Absent	Present
Colour Doppler imaging[b]	Fills lumen completely	Absent or incomplete filling of lumen

[a]*Beware of false negative results; see 'Problems and pitfalls'.*
[b]*Most important diagnostic criteria.*

Diagnosis of deep venous thrombosis

A positive diagnosis of DVT using colour Doppler depends upon a number of factors including a lack of spontaneous flow within the vein, the presence of reflective material within the lumen, dilatation of the vein itself, poor response to augmentation manoeuvres and non compressibility of the vein. Although all of these criteria can be sought individually, with experience using colour Doppler, the diagnosis is often visual (Fig. 64.8) and indeed on many occasions, instantaneous. Spectral analysis is generally unnecessary except for the indirect assessment of the proximal veins of the iliac system. With regard to everyday working criteria, the two main diagnostic ones are those of absent spontaneous flow and the presence of reflective material within the vein lumen (Table 64.1).

Calf vein imaging

Imaging of the calf veins is not routinely performed in many centres. However, a number of studies have suggested that applying the technique to the calf veins may have a useful role.[24] Each of the three major calf arteries is normally accompanied by paired veins (Fig. 64.9); indeed, the method of identification of these vessels is normally first to identify the artery (although these may be occluded in patients with severe vascular disease) and then subsequently apply distal calf compression to visualise the paired veins. Spontaneous colour flow is generally absent below the knee although on occasion it is seen in the young, fit individual. Flow augmentation within the calf veins is normally performed manually (the most common method) or can be performed with the aid of a compressive cuff, which is a more reproducible method.

The posterior tibial veins are normally visualised by placing the probe to the medial side of the tibia. These veins are more superficially placed than the deeper situated common peroneal veins which can also be visualised in the same imaging plane, albeit with slight alteration of probe angulation. The anterior tibial veins are normally visualised by imaging from the lateral aspect of the tibia, where they lie in a more superficial position on the interosseous membrane between the tibia and fibula. The common peroneal veins can also be visualised from this approach, as they lie deep to the interosseous membrane. Should the common peroneal veins be difficult to visualise from both the medial and lateral approaches, then they can be visualised from a more posterior position.

When scanning the calf veins the patient is initially assessed supine as for the femoral and popliteal veins. Should visualisation be poor or suboptimal, the patient can be positioned sitting with their legs suspended over the edge of the examination table and the foot supported on a rest. This simple manoeuvre has the affect of distending the calf veins and thus improving visualisation[24] (Fig. 64.10). The anterior tibial veins are regarded as the least important set as they are almost invariably associated with simultaneous thrombosis of the posterior tibial or common peroneal veins.[31] For this reason many centres that employ this technique do not routinely include them in their imaging protocols.

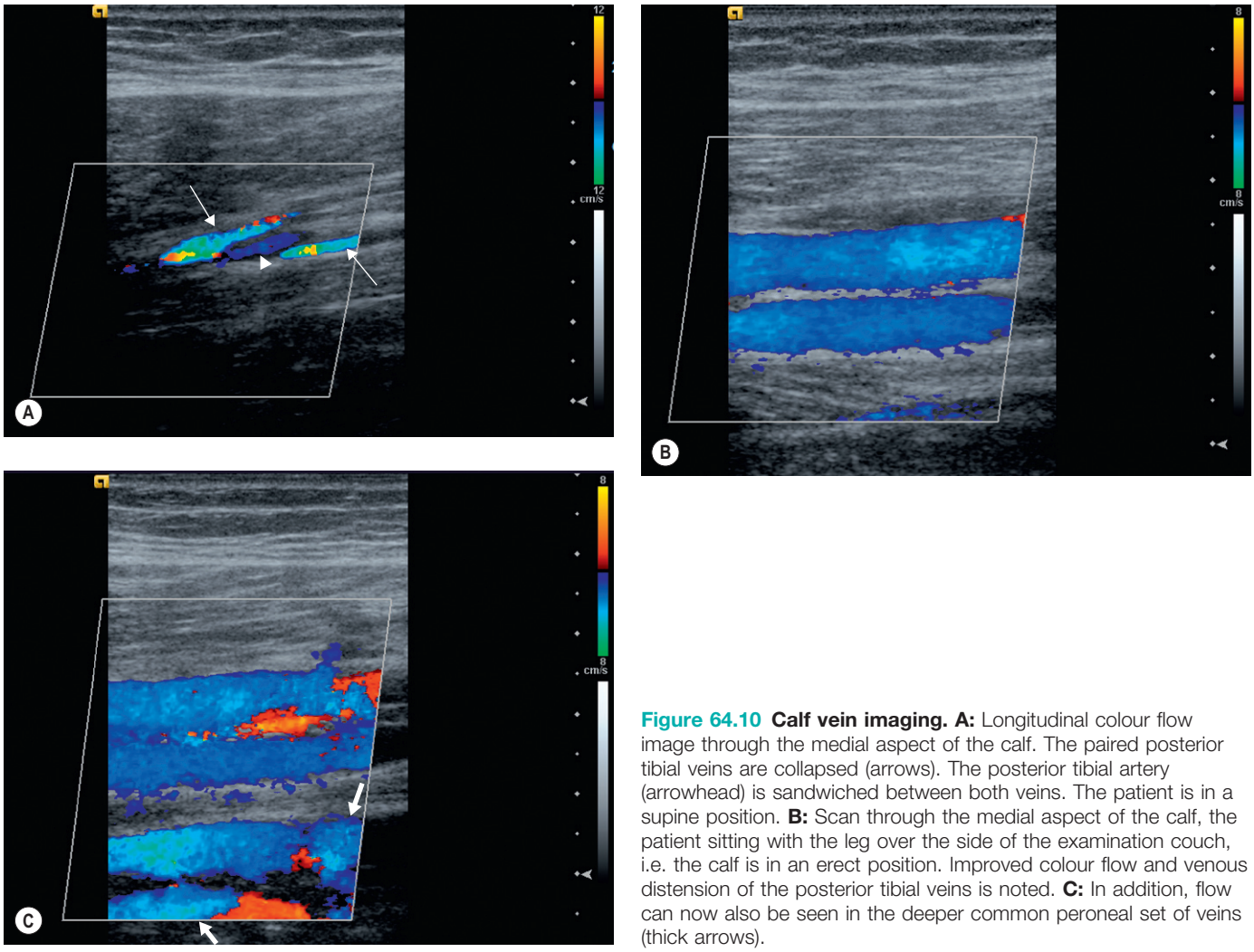

Figure 64.10 **Calf vein imaging. A:** Longitudinal colour flow image through the medial aspect of the calf. The paired posterior tibial veins are collapsed (arrows). The posterior tibial artery (arrowhead) is sandwiched between both veins. The patient is in a supine position. **B:** Scan through the medial aspect of the calf, the patient sitting with the leg over the side of the examination couch, i.e. the calf is in an erect position. Improved colour flow and venous distension of the posterior tibial veins is noted. **C:** In addition, flow can now also be seen in the deeper common peroneal set of veins (thick arrows).

The diagnostic criteria of calf vein thrombosis are essentially those used for above-knee thrombosis. Spectral Doppler is not normally required. The main criteria once again, are absence of flow, venous distension and the presence of reflective material within the vein lumen (Fig. 64.11). The limitations of this technique are simply that it will show significant thrombosis, confined to one or multiple sets of calf veins,[32] but it will not reliably and routinely detect a small focal segment of thrombosis; equivocal scans and persistent symptoms can be approached with a number of alternative strategies. A limited venogram of the area of concern may be considered but venography is now so rarely performed in many centres, that there are very few radiologists familiar with the technique. An alternative approach is to rescan the patient at a time interval of 3–7 days to exclude any significant potential clot propagation into the popliteal vein.

Assessment of the iliac system and inferior vena cava

Unfortunately, despite improvements in probe technology and adequate patient preparation including fasting and a full bladder, the iliac veins can still be difficult to visualise in up to 50% of cases.[33] This is often due to a combination of factors including patient build, the relatively deep position of these veins within the pelvis and the presence of bowel gas, particularly on the left side where the

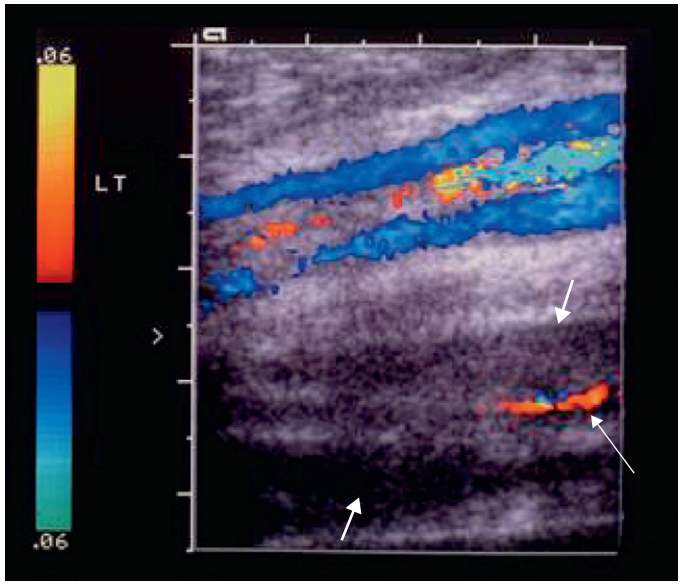

Figure 64.11 **Longitudinal scan of the medial aspect of the calf showing thrombus** within the common peroneal veins. The artery is delineated in red (thin arrow) and the dilated thrombus filled common peroneal veins are seen on either side (thick arrow).

sigmoid colon lies superficial to the iliac vessels. Assessment of these large veins in many patients is therefore dependent on indirect criteria.

Respiratory variation of the spectral waveform

As noted previously, the external iliac and common femoral veins should have a phasic spectral Doppler waveform. If this is absent and the waveform is clearly flat, then this is suspicious of either external compression secondary to a pelvis mass or a more proximal obstructing thrombosis.[28] Further investigation, usually with computed tomography (CT) scanning, may be required to determine the aetiology of the obstruction.

Valsalva manoeuvre

The patient can be asked to perform a Valsalva manoeuvre whilst the common femoral vein is imaged transversely. A normal response results in complete retardation of femoral vein flow and venous dilatation, with the diameter of the vein increasing by at least 50%[34] (Fig. 64.12). Although these would appear definite criteria, the presence of conditions such as congestive cardiac failure can dampen this normal response and potentially result in misinterpretation. As a consequence, more reliance and emphasis is placed on the presence or absence of respiratory swing of the Doppler waveform, with rebound increase in flow following a short breath hold: this is routinely used in combination with the Valsalva manoeuvre.

Calf vein imaging, pitfalls and complications of venous ultrasound

- Relatively few centres routinely perform calf vein imaging.
- Spontaneous flow is not seen in the calf veins; distal calf compression is applied to assess the calf veins.
- The posterior tibial and common peroneal sets of veins are the most important with regard to calf vein imaging.
- Reliance on the distal augmentation manoeuvre, in isolation, for above-knee venous assessment is inadvisable due to many potential interpretative pitfalls.
- Recorded cases of PTE following calf compression are extremely rare.

Problems and pitfalls

There are many potential problems and pitfalls with colour Doppler imaging. However, with good examination technique these can usually be avoided.

Technical

The ultrasound system should be optimised for a venous examination. This means correct setting of the focal zone, low velocity settings – normally around 6 cm/s, and the use of a low level filter. If machine optimisation is ignored then it is possible to get a false positive result for venous occlusion.

Associated medical conditions

An accurate medical history is of paramount importance, as many general conditions can influence venous flow. If the sonographer is aware of these, they may explain some of the ultrasonic findings and avoid any potential misinterpretation; for example, the common femoral vein waveform response to the Valsalva manoeuvre may be masked in the presence of congestive cardiac failure. A known pelvic malignancy may explain a flat non-phasic femoral spectral waveform. The presence of an arteriovenous fistula may explain increased or turbulent flow within the vein. A history of previous DVT may also be of importance in interpretation of the venous findings.

Anatomical variants

Duplication of the femoral and popliteal veins is common, with a prevalence of 20% in the femoral vein segments and 35% in the popliteal vein[27] (Fig. 64.13). An appreciation of normal anatomy and variation in size of the veins, particularly with a duplicated venous system where the veins are generally smaller, aids recognition.[26] Awareness of this variant may be clinically relevant because thrombus can be confined to one limb of the duplicated system.[35] However, despite the relative prevalence of duplicated systems, this clearly has not affected the overall accuracy of ultrasound in DVT diagnosis and it therefore must be assumed that such confined thrombus is likely to be uncommon.

Distal augmentation

This manoeuvre was designed to help in the evaluation of venous segments that either could not be visualised or were difficult to

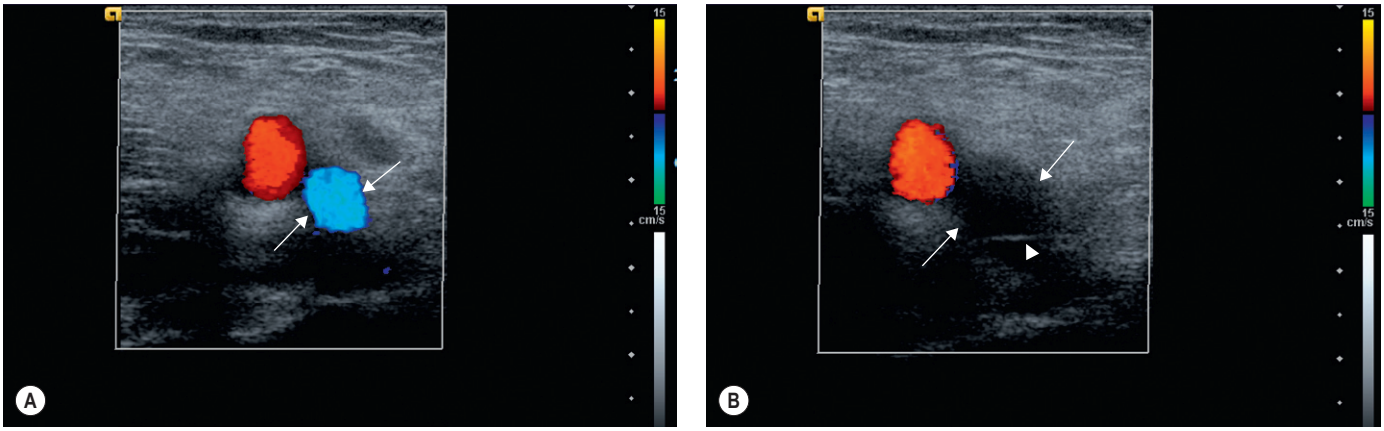

Figure 64.12 Transverse image of the common femoral vein at **(A)** rest and **(B)** following the Valsalva manoeuvre (arrows). There is marked venous dilatation following this manoeuvre, which is also accompanied by complete retardation of flow. This positive response is an indirect sign of more proximal patency although in patients with conditions such as congestive cardiac failure this response may be masked. A thin valve cusp can be seen (arrowhead).

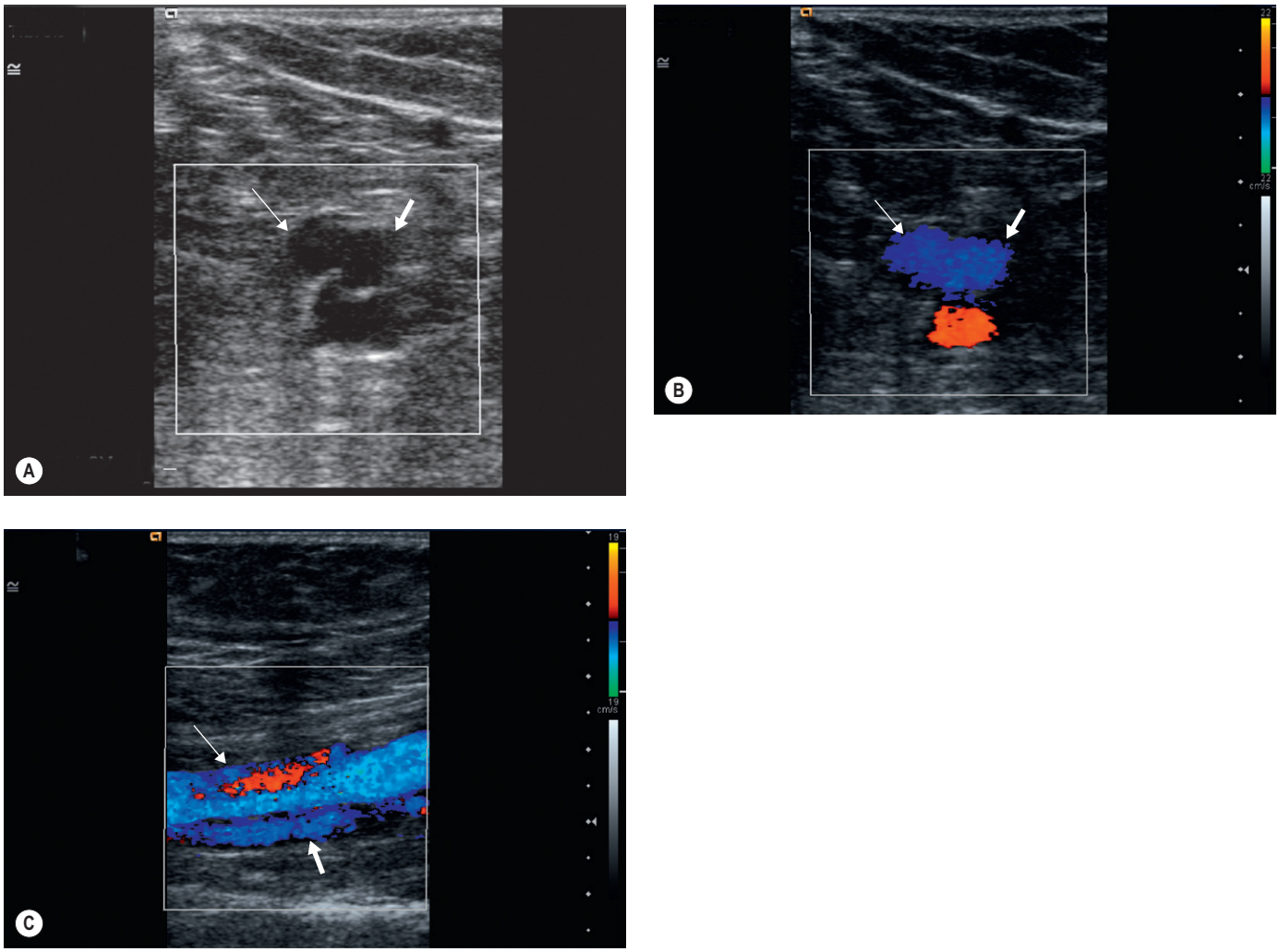

Figure 64.13 **Duplicate vein. A:** B-mode and **B:** colour flow scan showing a duplicated popliteal vein (thin and thick arrow). This is much more difficult to appreciate on the longitudinal view **(C)** where the veins lie side by side (thin and thick arrow). Very often this appearance is best appreciated on the transverse image.

visualise directly. It depends upon the premise that if a venous segment is patent and the distal limb is compressed, the amplitude of the spectral waveform increases significantly as a result, inferring that the non-visualised segment between the point of augmentation and the probe is patent. Although this is indeed the case in most circumstances, the presence of collateral vessels and segments of non-occlusive thrombus makes reliance on this technique in isolation potentially misleading (Fig. 64.14).

Collateral veins

Collateral vessels develop as alternative pathways of venous drainage in cases of chronic thrombosis. They can reach sizes comparable with the native veins, although in most cases they are generally smaller. They can usually be differentiated from the normal venous system because they often occupy unusual anatomical positions. On spectral analysis they may have flat waveforms. When such collateral veins lie close to the normal position of the major veins, differentiation can be difficult.

Induction of pulmonary thromboembolism

Recorded cases of PTE following calf compression have been described,[29] but these are rare. However, it is prudent to avoid such calf compression manoeuvres unless these are likely to aid diagnosis.

CLINICAL APPLICATIONS

Acute DVT

Symptomatic DVT

Using the techniques described earlier, colour Doppler ultrasound has the advantage of being able not only to diagnose DVT with a high sensitivity and specificity but also to differentiate it from other conditions that may result in similar symptoms, such as a ruptured Baker's cyst, post-traumatic subfascial haematoma, tumours and pseudo-aneurysms,[1] and may occur in up to 26% of positive studies of the lower limb[36] (Fig. 64.15). It can also diagnose superficial thrombophlebitis, which is important, as this is treated with non-steroidal anti-inflammatory drugs and does not require anticoagulation.

When there is a clinical suspicion of DVT, examination of the symptomatic limb only is required. Previous studies have supported this approach; in one study of 206 patients not only was it

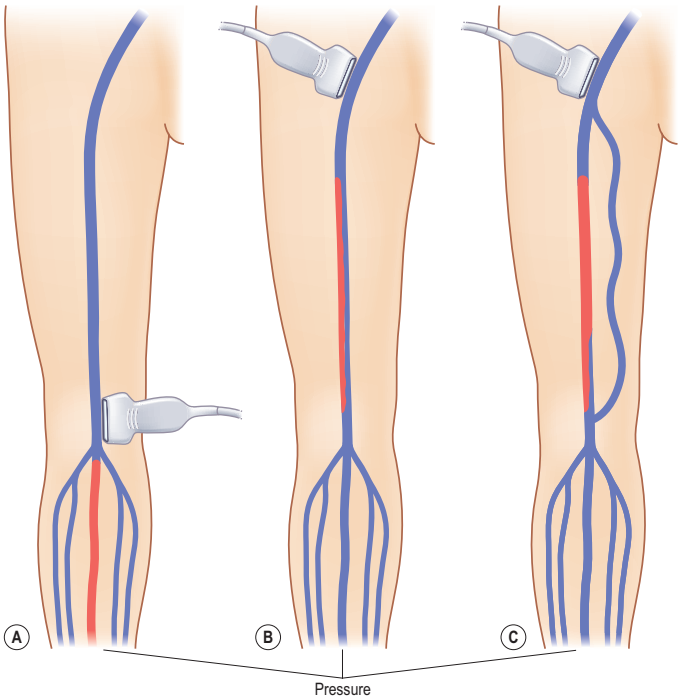

Figure 64.14 Distal augmentation may be used to help determine whether a venous segment is patent. The results of this manoeuvre must never be interpreted in isolation from other diagnostic criteria as it can on occasion lead to a false negative result in the type of situations illustrated above, i.e. where there are alternative routes of venous return or the thrombus is non-occlusive.

Table 64.2 Wells clinical score

	Score
Active cancer (treatment ongoing or within previous 6 months or palliative)	1
Paralysis, paresis or recent plaster immobilisation of lower limb	1
Bedridden ≥3 days or major surgery <12 weeks	1
Localised tenderness along distribution of deep venous system	1
Entire leg swollen	1
Calf swollen ≥3 cm compared to asymptomatic leg	1
Pitting oedema (greater in symptomatic leg)	1
Collateral superficial veins (non varicose)	1
Previously documented DVT	1
Alternative diagnosis as likely or greater than that of DVT	–2
DVT unlikely if score <2	
DVT possible if score ≥2	

shown that all the ultrasonically demonstrated thromboses were confined to the symptomatic limb but that the asymptomatic limb was normal within the entire study group.[37] This has been confirmed in other studies which support this approach for outpatients with unilateral symptoms.[38] In an inpatient, however, there is a higher risk of clinically silent contralateral thrombosis (34%), which is also seen in patients with an active malignancy (38%), and it is felt that these patients should have bilateral studies.[38] Colour Doppler allows a clinical decision to be made in the vast majority of patients with symptoms suggestive of DVT. The sensitivity and specificity of the technique have been shown to be greater than 95% sensitivity and almost 100% for specificity; with a more recent systematic review showing a sensitivity of 96.4% and a specificity of 94.3%.[39] In addition, a negative scan has reassuringly been shown in long-term follow-up studies to be a very reliable indicator of normality with a serious risk of a major adverse event of less than 0.5%.[40,41]

Scanning of calf veins remains a more controversial topic as does treatment of calf vein thrombosis.[42] Before distal imaging techniques can be employed there is undoubtedly a learning curve and comparison with venography at the introduction of these techniques would have been prudent. Unfortunately this is no longer possible, which makes learning of the technique difficult. There is no doubt, however, that when visualisation of the calf veins is satisfactory, the sensitivity and specificity of the technique is similar to that for above-knee thrombus. Unfortunately, as the calf veins are only adequately visualised in 60–80% of patients at best, the accuracy of the technique is reduced for distal (calf vein) thrombosis.[43,44]

Given the difficulties and added time needed for calf vein study, many institutions employ an alternative imaging strategy to that of direct calf vein visualisation. In patients with a negative scan of the femoral and popliteal veins at the time of clinical presentation, a repeat colour Doppler scan can be performed at any time up to 7 days. This second examination excludes or confirms the presence of proximal venous propagation of clot from a previously undiagnosed calf vein thrombosis;[41] this may occur in up to 20% of thrombi confined to the calf vein in whom treatment is withheld.[45] It also allows re-evaluation of any equivocal findings on the initial scan, although this is required infrequently. Increased resources are clearly necessary to adopt such a two-scan policy; in one study[41] 1300 additional scans were required to detect a further 12 DVTs on the repeat study. Nevertheless, this has been shown to be a very safe approach, with a 3-month thromboembolic event rate of 0.6% in untreated patients.[42]

D-dimer testing has gained wide acceptance throughout the world as a screening test to exclude DVT. It is of particular use in the outpatient population referred to emergency departments with suspected DVT or pulmonary embolism. It has been shown repeatedly to have a very high sensitivity and therefore a very high negative predictive value of 99%.[46,47] The negative predictive value alone is 98.4–99.3% for a normal rapid enzyme-linked immunosorbent assay (ELISA) VIDAS D-dimer test <500 ng/mL irrespective of clinical score. This increases to greater than 99% for a negative ultrasound when combined with either a negative SimpiRED test or ELISA VIDAS result of <1000 ng/mL.[48] D-dimer is used in combination with a clinical scoring system (the Wells score,[49] Table 64.2) and based upon this assessment, further evaluation with ultrasound can be confirmed or discounted. In our institution a number of patients with a negative ultrasound will require a repeat ultrasound scan at about 7 days. Many departments will have very similar imaging schemes – it is often easier to appreciate how these tests interact by viewing a standard imaging pathway (Fig. 64.16).

High quality scanning is required if the impact of the colour Doppler technique is to be maintained. This will depend upon local practice. Some centres have promoted 'limited three point scanning'.[41] This involves scanning the common femoral vein and popliteal segments only, on the premise that some studies have shown that clot confined to the femoral vein, without simultaneous involvement of the popliteal or common femoral vein, is extremely rare at less than 3%.[50] Another recent, prospective randomised study of two-point ultrasonography versus whole leg sonography on 2098 patients showed no difference in detection rates of DVT.[51] There were also no adverse events with up to 3 months of follow-up in those patients with negative studies. Although both techniques can be used safely, many people believe that any potential time gain with the limited techniques is minimal and that doing a complete

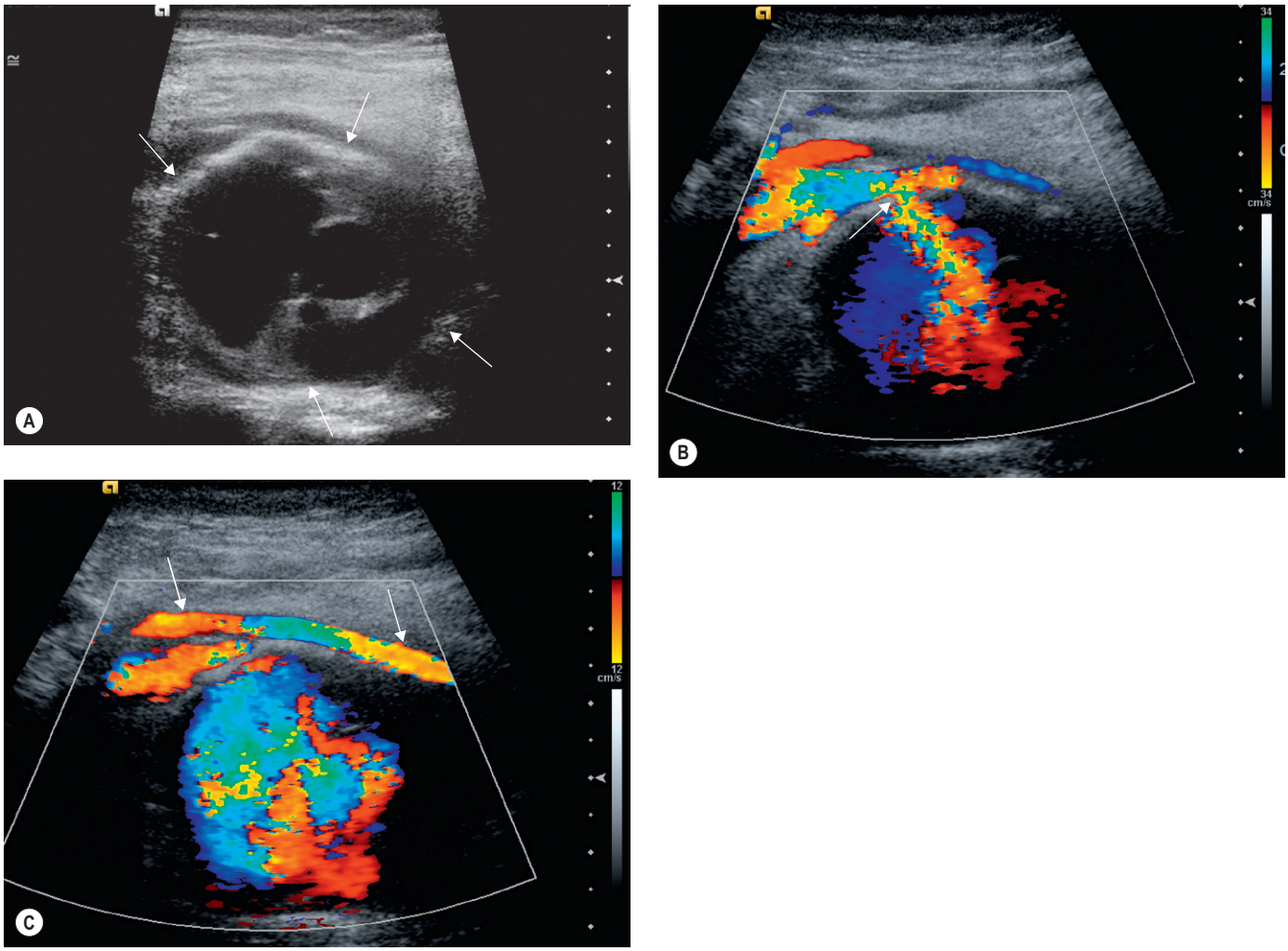

Figure 64.15 **Pseudo-aneurysm. A:** B-mode image of the popliteal fossa in a patient with lower limb swelling, worse below knee. This shows a large, thick, septated cystic collection (arrows). **B:** Colour flow image of the same area showing that the 'cyst' contains swirling flow and is actually a pseudo-aneurysm. Its source is the popliteal artery, the jet being easily visualised (arrow). **C:** On this image the pseudo-aneurysm is again easily visualised. The popliteal vein anteriorly is compressed (arrows) and presumably this accounts for the patient's presenting symptoms of calf swelling.

examination of the deep venous system is not significantly more time-consuming.

Asymptomatic DVT

Results are generally less impressive for detection of asymptomatic thrombus using colour Doppler than in the symptomatic patient group. Even in the best centres, sensitivity is significantly lower at 38–80%, although specificity can still be maintained.

There are a number of well-recognised reasons for this. A large part of the difference in the sensitivity reflects the different patient populations being studied; the vast majority of the asymptomatic group are postoperative patients with, for example, hip or knee joint replacements. They are often immobile, have excessive soft tissue oedema and are likely to be on some form of anticoagulation regimen, which may influence the type of thrombus formed and hence its ease of detection. Previous venographic studies have shown that in many of these cases, thrombus may be confined to the calf, which is often reflected in the reduced sensitivity, whereas in other patients there may be small focal areas of non-occlusive thrombosis, which requires very careful and accurate technical assessment to identify (Fig. 64.17). This is reflected in some studies which show a sensitivity of only 10%, reflecting the large number of thromboses confined to the calf.[52]

Although the clinical application of ultrasound in asymptomatic patients is less certain, there have undoubtedly been significant improvements in both ultrasound technology and technique, so that re-evaluation of this patient group has shown improved results, with sensitivity values ranging from 60% to 93% being quoted.[53,54]

Chronic venous thrombosis

It is well recognised that following an acute DVT of the femoral and popliteal veins only approximately 50% of patients will completely recanalise their deep venous system by one year.[55,56] In the remaining 50% abnormalities will persist, often for many years following the initial episode. This, therefore, creates a difficulty in patients who present with signs and symptoms similar to the primary thrombotic event, representing a diagnostic imaging dilemma. Although there are specific ultrasonic patterns and criteria that may help differentiate acute from chronic venous thrombosis, the full set of classic features in combination is relatively rare (Table 64.3). The classic description of chronic thrombosis is that of a narrowed major vein, with thickened walls of increased reflectivity and multiple surrounding collateral vessels. Spontaneous colour flow is often reduced and may be absent, only being detectable following more distal compression. Reduced vein wall compressibility may also be present. Should this pattern be visualised, then chronic DVT is

strongly suggested (Fig. 64.18). Unfortunately, for most patients there remains an overlap of both acute and chronic thrombotic ultrasonic features.[55] In essence, therefore, the presence of reflective material within the lumen, a reduction in spontaneous flow and incomplete vein compressibility is as likely to be due to chronic as acute DVT, all of which adds to the difficulty of imaging the post-phlebitic limb (Fig. 64.19).

Attempts have been made to age the thrombus based on its reflectivity. However, the experiences of others would suggest that these attempts are largely futile.[57] It has also been suggested that a

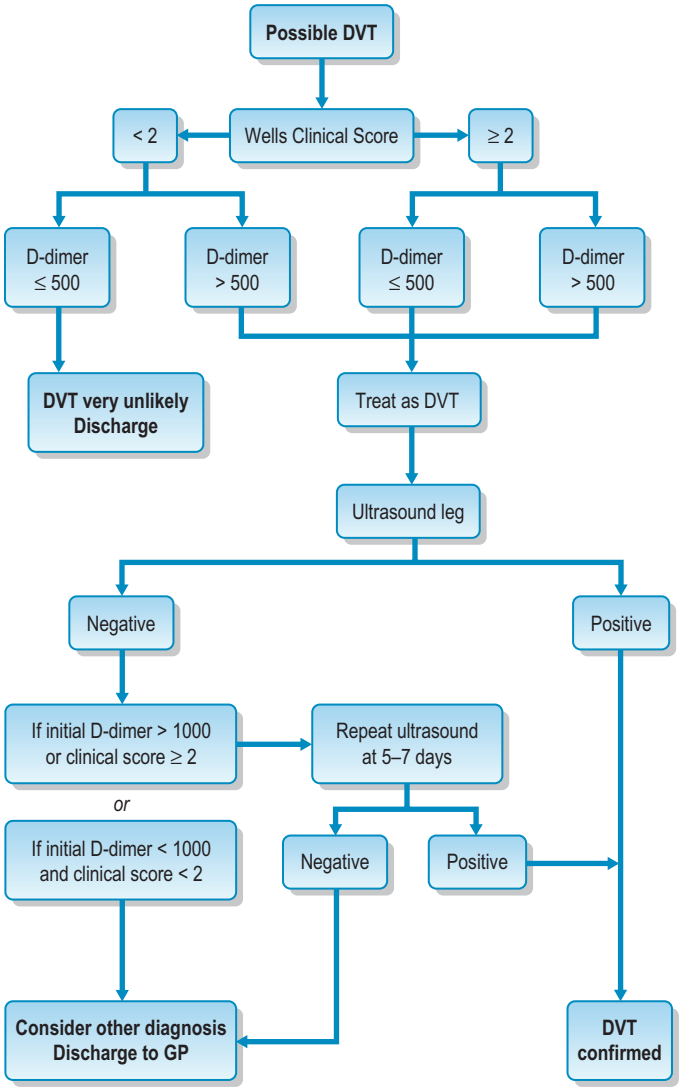

Figure 64.16 Decision algorithm for symptomatic patients with suspected lower limb DVT.

Clinical applications and role of venous ultrasound

- Alternative diagnoses may occur in up to 26% of positive studies for suspected DVT in symptomatic patients.
- Sensitivity and specificity of colour Doppler ultrasound for DVT diagnosis is >95% in the symptomatic patient.
- Most centres have an agreed algorithm combining clinical risk factors, D-dimer levels and ultrasound for the imaging of suspected DVT.
- Repeat ultrasound will be performed on a selected group of patients with an initial negative ultrasound study within 5–7 days of initial presentation depending on local protocol.
- There is a significant reduction in ultrasound sensitivity in the evaluation of asymptomatic DVT.

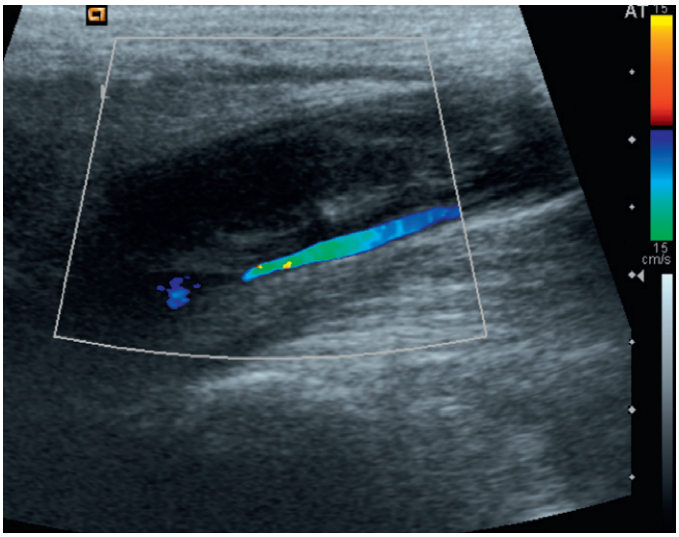

Figure 64.17 Non-occlusive thrombus. Longitudinal scan of the common femoral vein showing an area of focal non-occlusive thrombus. This is typical of localised focal thrombi and can be seen in postoperative hip replacement patients.

Table 64.3 Differentiation of acute from chronic venous thrombosis

CRITERIA	ACUTE DVT	CHRONIC DVT	
		Complete recanalisation	Partial recanalisation
Intraluminal echoes	Present	Absent	Present
Thrombus characteristics	Low echoes	–	Variable
Venous distension	Present	Absent	Variable
Collateral vessels	None, few	Variable	Variable
Spontaneous flow	Absent	Reduced	Reduced
Augmented flow	Absent	Normal	Reduced
Vein wall thickening	Absent	Present	Absent
Response to probe compression	Absent	Normal or slightly reduced	Markedly reduced

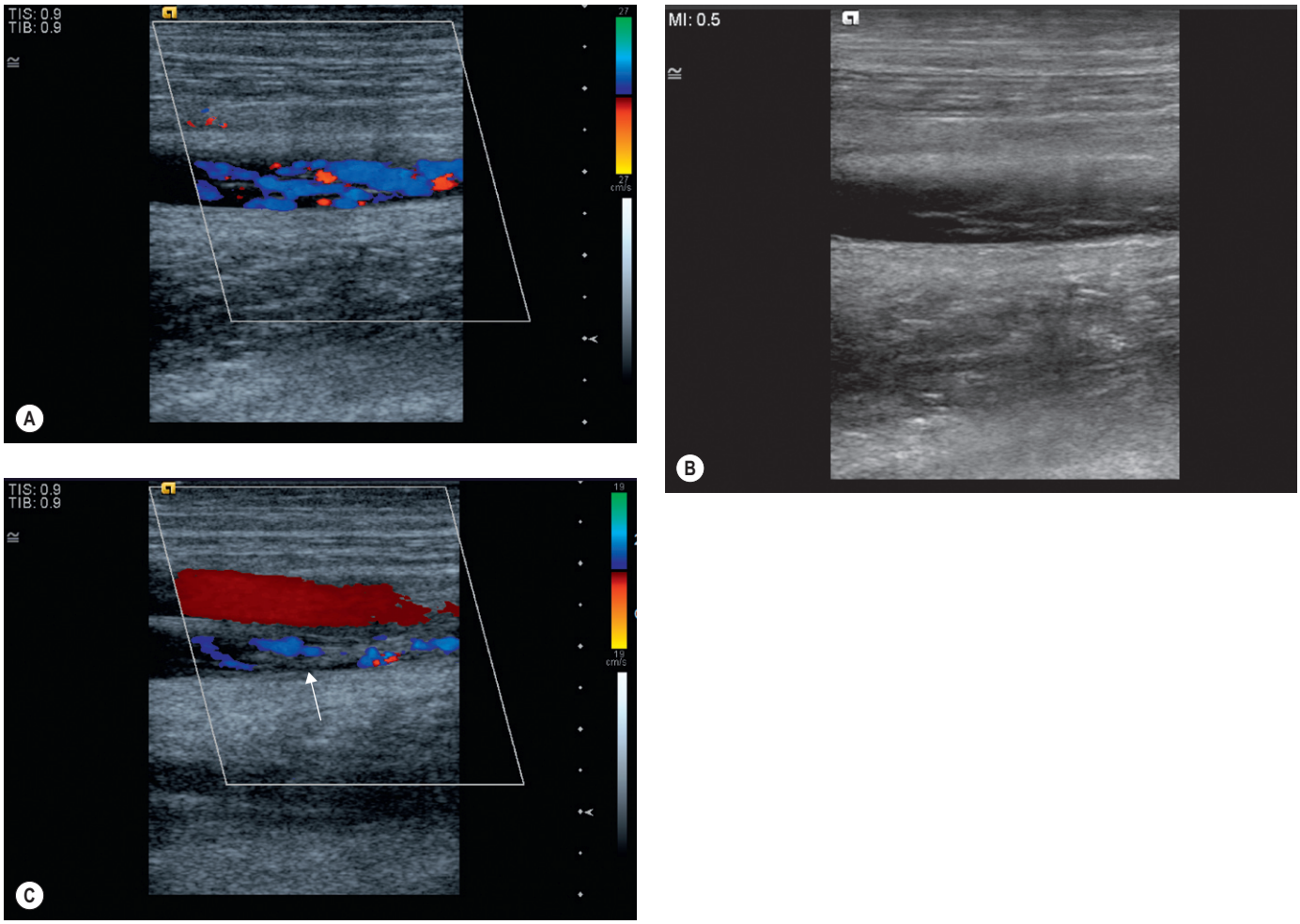

Figure 64.18 **Chronic venous thrombosis. A:** Longitudinal colour flow scan of the mid femoral vein showing incomplete vein filling with small areas of flow reversal and the suggestion of intraluminal echogenic material. **B:** B-mode image of the same area clearly demonstrating echogenic material within the vein lumen. **C:** Colour flow image of the same vein more distally (arrow) showing a very similar appearance to that in **A** and **B**. This appearance of mixed flow and echogenic material is seen typically in patients with chronic venous thrombosis undergoing recanalisation.

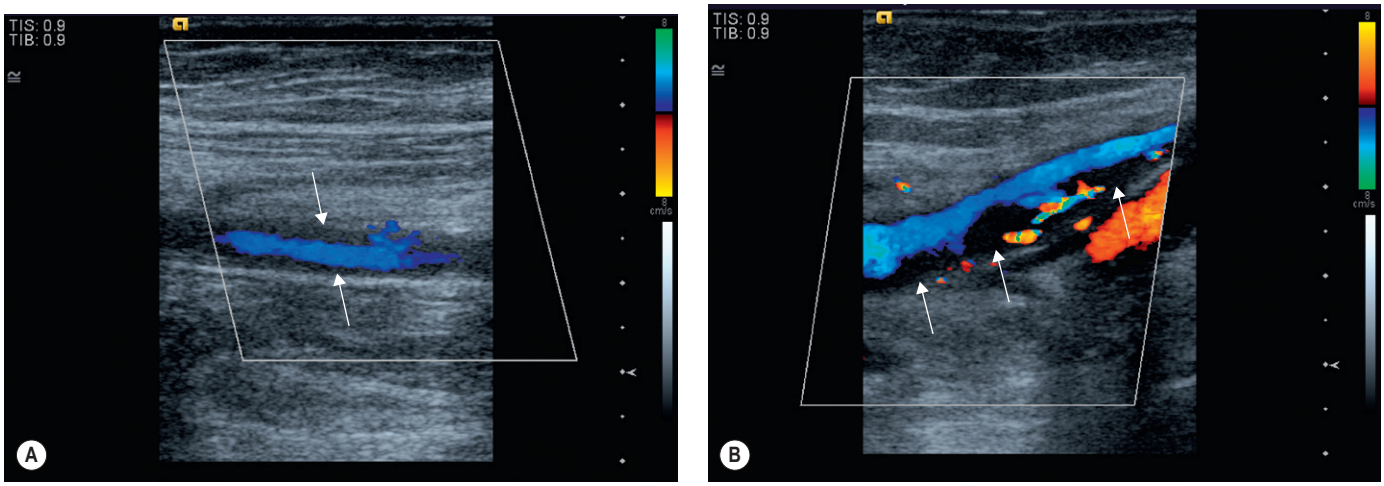

Figure 64.19 **A:** Longitudinal scan through the distal femoral vein in a patient with lower limb symptoms. The vein, if anything, is of slightly reduced calibre with clear evidence of wall thickening (arrows) suggestive of chronic change. **B:** Longitudinal scan in the same patient of the popliteal vein. The vein is slightly distended and contains three areas (arrows) of non-occlusive thrombus with flow along the near wall of the vein. The appearances are highly suggestive of acute DVT superimposed on chronic change (above knee).

baseline scan at 6 months after the initial thrombosis would allow comparison with any later scans and potentially be of use; however, this has generally not been adopted clinically, not least because the additional workload implications would be significant.

In conclusion, patients with previous venous thrombosis represent significant diagnostic dilemmas. A normal scan is clearly helpful; one with venous or multiple venous abnormalities must be interpreted with care and ultimately not in isolation from the clinical information. Alternative techniques including venography and isotope scanning are also of similarly limited use in this group of patients. D-dimer estimation may have a role in this difficult patient group. One recent study of 105 outpatients with clinically suspected acute recurrent lower limb deep vein thrombosis demonstrated that in patients with an unlikely clinical probability and negative D-dimer the negative predictive value for DVT was 94.4%.[47]

Monitoring of clot lysis

Non-invasive ultrasound could be of use in monitoring the therapeutic response in venous occlusive disease. Reports of faster and more complete clot lysis in patients with non-occlusive thrombosis than in those with occlusive disease have been published.[58] Although standard therapy involves the use of heparin (or its analogues) and oral anticoagulants, such as warfarin, alternative treatment regimens do exist and it is not unusual for patients to receive subcutaneous heparin as their entire treatment regime. Alternative treatment options depending on the site of thrombosis include streptokinase, urokinase or tissue plasminogen activator (TPA); this is often reserved for patients with conditions such as superior vena cava obstruction, which is often secondary to malignant compression.

Ultrasound microbubbles

Microbubble contrast agents are now playing an increased role in many areas of ultrasound, in particular in the evaluation of focal liver lesions and also to a lesser extent in other areas, such as the kidney and vascular tree. Recent European guidelines[59] have suggested a number of areas in which these agents may play a clinically useful role but the diagnosis of venous thromboembolism has not been included and this may reflect the high quality of the conventional colour Doppler scan. One small reported trial using such a microbubble agent identified some free-floating thrombus in seven of nine patients which had not been visualised on conventional scanning.[60] However, current practice suggests that the use of microbubbles in the assessment of deep vein thrombosis is not particularly valuable.

One of the potential exciting developments for the future is the possibility of tagging a microbubble contrast agent with labelled fibrinogen which would accumulate at the site of thrombosis. Microbubbles could also be labelled with tissue plasminogen activator, so that when the microbubbles are destroyed with the ultrasound beam, TPA is released and the process of lysis begins.[61] A decade ago such possibilities were largely theoretical but a lot of development work is underway and undoubtedly a number of these therapeutic options will be introduced within the next ten years.

UPPER LIMB VENOUS IMAGING

Upper limb DVT is relatively uncommon, accounting for only 1–2% of venous thrombosis.[62] Many predisposing factors are recognised (Table 64.4) but the most common is related to recurrent central venous catheterisation. As in the lower limb, conventional upper limb venous anatomy is well recognised (Fig. 64.20), although variations may occur.

Table 64.4 Upper limb thrombosis: predisposing factors

Traumatic	
Venous catheterisation	
Fracture dislocation of clavicle or first rib	
Irritants:	Contrast agents
	Chemotherapy
	Stress (effort) thrombosis
Spontaneous	
Idiopathic	
Secondary to:	Congestive cardiac failure
	Malignancy
	Coagulopathies

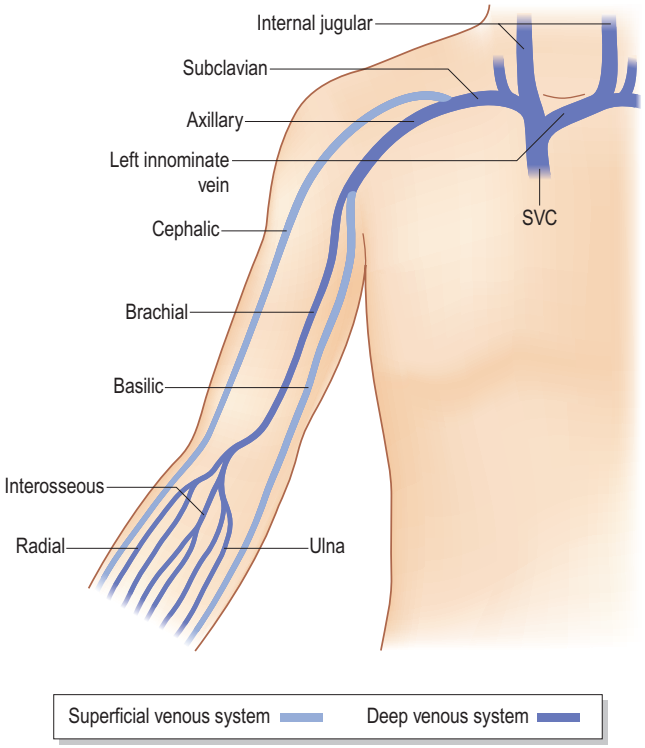

Figure 64.20 Anatomy of the upper limb venous system.

Diagnostic criteria

Excellent anatomical detail can still be observed on real-time imaging alone (Fig. 64.21) and the colour Doppler technique is similar to that used for the lower limb. With experience, the appearance of thrombosis is normally apparent and this is the only practical criterion used.[63] Prior to colour Doppler ultrasound, patients were asked to perform various manoeuvres such as sniffing or Valsalva and the response of the Doppler waveform and vein were observed. These manoeuvres are now essentially historical.[64,65]

The main difference between imaging the upper and lower limb veins is that the Doppler waveform in the upper limb veins is much more pulsatile because of its relative proximity to the heart and the influence of the right heart contractions on the Doppler spectral tracing (Fig. 64.22). It is therefore possible for those unfamiliar with these fluctuations to confuse this venous waveform with that of the artery, although for experienced operators this is unlikely.

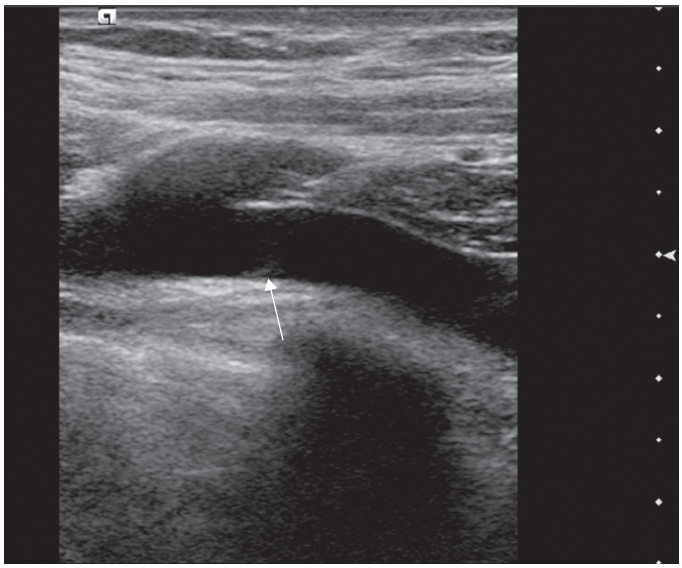

Figure 64.21 Longitudinal greyscale image of the subclavian vein. A small valve leaflet (arrow) can just be visualised.

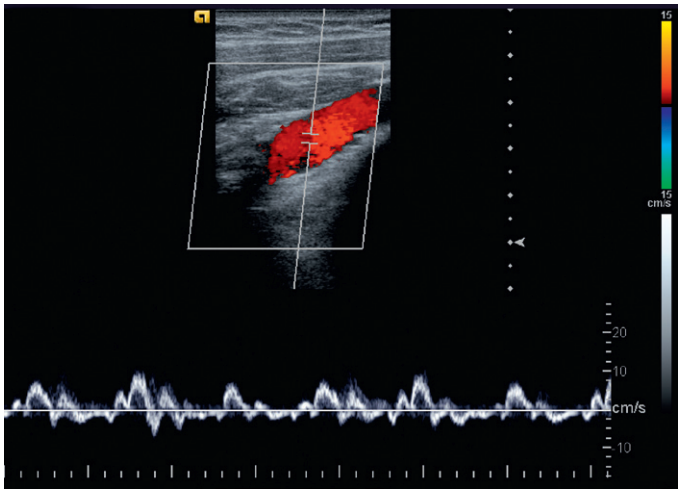

Figure 64.22 Spectral Doppler trace of the subclavian vein showing a more pulsatile venous waveform. Both forward and reverse flow are normally appreciated. This is normal and should not be confused with that of the accompanying artery. These variations are related to right heart contractions and tricuspid valve closure.

Only the axillary and subclavian veins need be assessed in patients with symptoms that may be attributable to DVT. The internal jugular vein can also be visualised with ultrasound, which is a major advantage over upper limb venography, particularly if venous access sites are being sought.[66] The limitations of ultrasound are that it can, at best, only visualise the proximal innominate vein, the distal innominate vein and superior vena cava being ultrasonic blind spots. Loss of cardiac pulsatility on spectral Doppler may suggest proximal occlusion but if a central site of thrombosis is suspected clinically, then CT, magnetic resonance or contrast venography would be preferred for assessment.

Colour Doppler ultrasound is a good first-line assessment in patients with suspected thrombus in the axillary or subclavian veins with both a high sensitivity and specificity of 78–100% and 82–100% respectively[67] (Fig. 64.23); it can also provide clinically useful information on the patency of the internal jugular veins. Although this technique is suitable for the diagnosis of thrombosis,

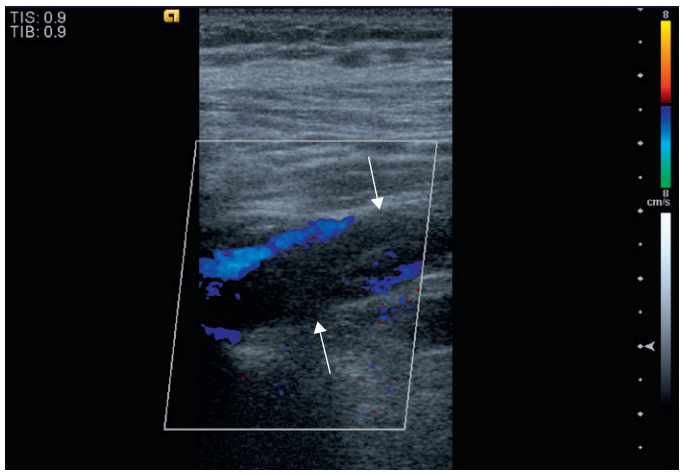

Figure 64.23 Colour flow image showing a dilated subclavian vein (arrows) with thrombus and surrounding peripheral flow consistent with a subclavian vein thrombosis.

it can be difficult to detect stenosis of a vein which may occur following multiple venous catheterisations. These lesions lie beneath the clavicle in up to 40% of patients and can therefore be difficult to visualise with ultrasound.[63] Therefore if a stenosis is to be conclusively excluded prior to a procedure, such as fashioning a haemodialysis fistula, then one of the alternative imaging techniques is preferred.

Limitations with regard to the upper limb are those of any ultrasonic technique; oedema and obesity may be a challenge in some studies. In spite of these limitations, colour Doppler ultrasound remains an extremely useful technique, not only in the detection of upper limb thrombosis, but also in the mapping of venous access sites prior to central line insertion procedures. Where findings are equivocal and clinical suspicion remains high, then an alternative imaging technique will be required.[68]

The presence of an arteriovenous fistula, either traumatic or surgical, will alter the haemodynamics in the upper limb. The arterial waveform becomes monophasic rather than triphasic and venous flow has a very pulsatile and arterialised character. A colour Doppler tissue bruit may be observed within the soft tissues secondary to transmitted wall vibrations.[69] Observation of these ultrasonic findings suggests the diagnosis. Further details on haemodialysis fistulae are discussed in Chapter 63.

In addition to its diagnostic role, ultrasound can be used for guiding the insertion of central lines such as Hickman and dialysis lines. The preferred route, where possible, is via the internal jugular vein due to the reduced incidence of pneumothorax when compared with the subclavian approach. Given the superficial position of this vein, it is easily visualised with a high-frequency probe and the needle tip easily identified, enabling the puncture needle to be inserted into the vein lumen with minimal trauma and avoiding inadvertent puncture of the adjacent carotid artery.

IMAGING OF SUSPECTED PULMONARY THROMBOEMBOLIC DISEASE

Many differing algorithms have been suggested for using colour Doppler ultrasound in the diagnosis of pulmonary thromboembolic disease, but the introduction of CT pulmonary angiography, with or without delayed scanning through the proximal femoral veins, has made this less of an issue. As a result, venous ultrasound does not play a primary role in the diagnosis of pulmonary embolus and, if it is used, then this is further down the main investigative pathway and only applies to a relatively small proportion of patients.

There is no evidence to support the universal use of venous ultrasound in patients with suspected pulmonary embolus, as negative results do not exclude embolism. Indeed, previous studies have shown that 50% of patients with high probability ventilation/perfusion (V/Q) isotope lung scans have no detectable evidence of lower limb deep vein thrombosis.[70] There is some evidence that a non-invasive approach to pulmonary thromboembolic disease may still be worthwhile. One study[71] suggested that a combination of clinical probability, D-dimer and complete bilateral lower limb ultrasound resulted in a significant reduction in the number of CT scans. However, since that study was performed, the widespread introduction of multislice CT with a negative predictive value of >99%[48] makes many of these more complicated algorithms less relevant.

The current investigation pathway for pulmonary thromboembolic disease therefore includes a combination of D-dimer blood test with CT pulmonary angiography (Fig. 64.24) and venous ultrasound is reserved only for relatively few patients in whom a diagnosis remains an issue. In those patients who have a V/Q scan as a primary investigation and have an indeterminate result, any potential role of venous ultrasound has been usurped, the clinical question being resolved by CT pulmonary angiography.

Other applications of venous ultrasound

- Venous abnormalities persist on ultrasound in up to 50% of patients with DVT for a year or greater.
- Acute DVT can be difficult to differentiate from chronic disease with ultrasound in some cases.
- To date microbubble contrast agents play no role in venous imaging.
- Colour Doppler ultrasound is the first-line test for suspected axillary and/or subclavian vein thrombosis.
- In patients presenting with suspected PTE, ultrasound has a limited role.

VENOUS INCOMPETENCE

Venous anatomy

Anatomical venous nomenclature has varied widely; recent publications have attempted to reach a consensus[72] and describe the anatomy as demonstrated by ultrasound.[73]

The superficial system consists of the great and small saphenous veins and their tributaries, which are connected to the deep veins by a network of perforator veins. The great saphenous vein (GSV) starts anterior to the medial malleolus, courses upwards along the medial aspect of the calf; a posterior division joins the main vein below the knee joint. The main trunk then continues up the medial aspect of the thigh and joins the common femoral vein at the saphenofemoral junction (SFJ) at the level of the groin skin crease. Several other veins join the great saphenous vein close to the junction including the anterior and posterior accessory saphenous veins (Fig. 64.25). Distally, the small saphenous vein (SSV) originates posterior to the external malleolus and then runs along the posterior aspect of the calf, usually joining the popliteal vein at the saphenopopliteal junction (SPJ) about 4 cm above the knee crease. However, the presence and level of the SPJ can vary and the SSV may continue superiorly and terminate in the thigh as a superficial or perforating vein, or join with the GSV in the medial thigh (Giacomini vein) (Fig. 64.26). The two saphenous veins are connected by communicating branches in the upper calf. There is a third, usually much smaller, lateral superficial venous system which is usually only investigated when obviously varicose.

Perforating veins connect the superficial and deep veins. They are more numerous below the knee than above and are more commonly found medially in the calf and thigh. Normal venous drainage, promoted by competent valves, is from the superficial to the deep system via the saphenous junctions and perforating veins.

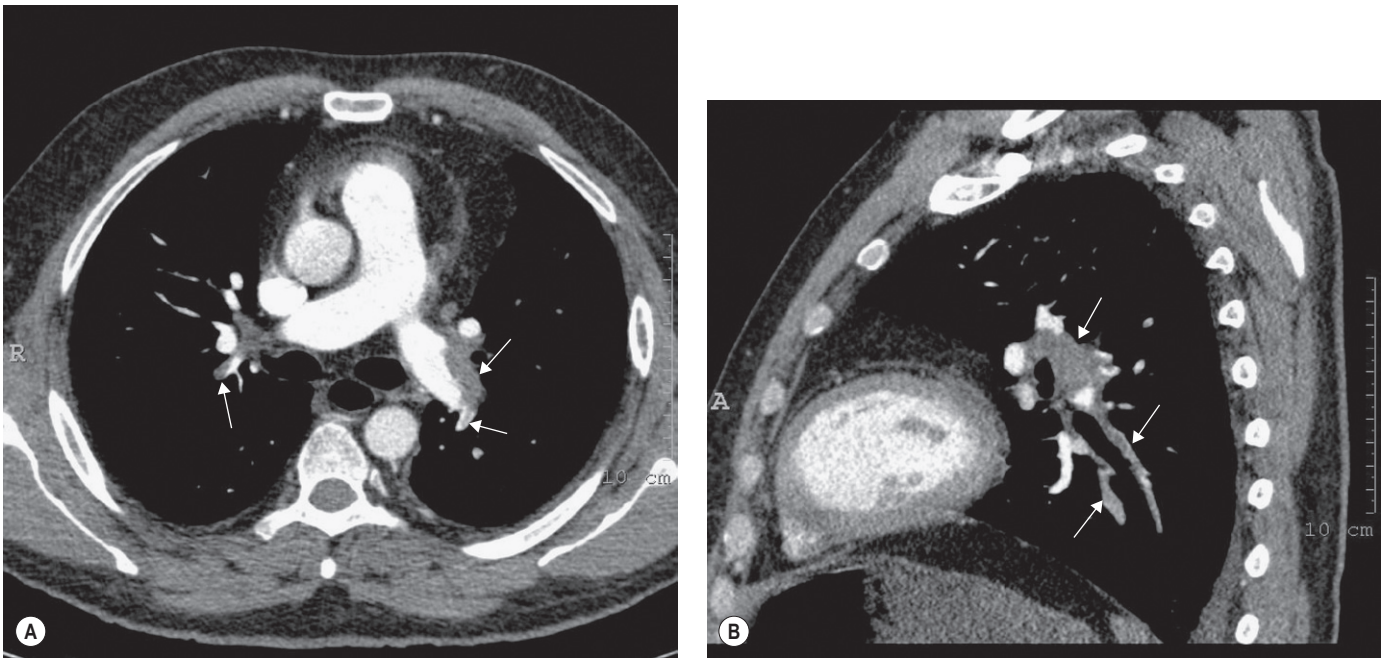

Figure 64.24 Pulmonary thromboembolism. A: Axial CT pulmonary angiogram showing filling defects in the left main pulmonary artery and lower lobe vessel and the right hilar segmental vessels (arrows) consistent with PTE. **B:** A sagittal section through the left hilum and lung showing extensive PTE involving the left pulmonary artery and multiple lower lobe vessels (arrows).

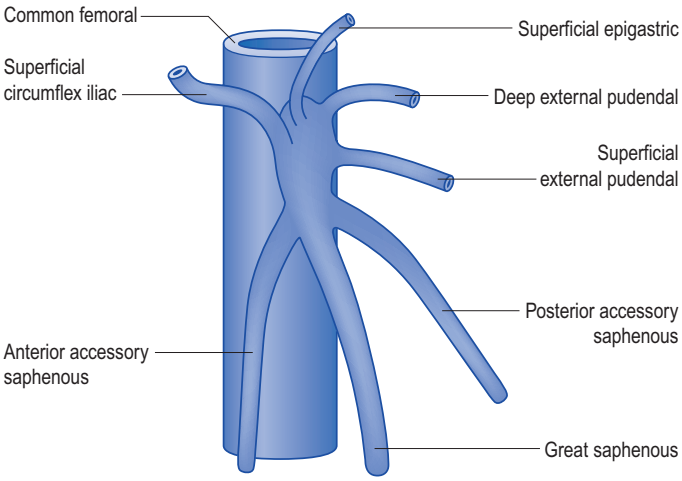

Figure 64.25 The saphenofemoral junction and the proximal great saphenous vein with its main tributaries.

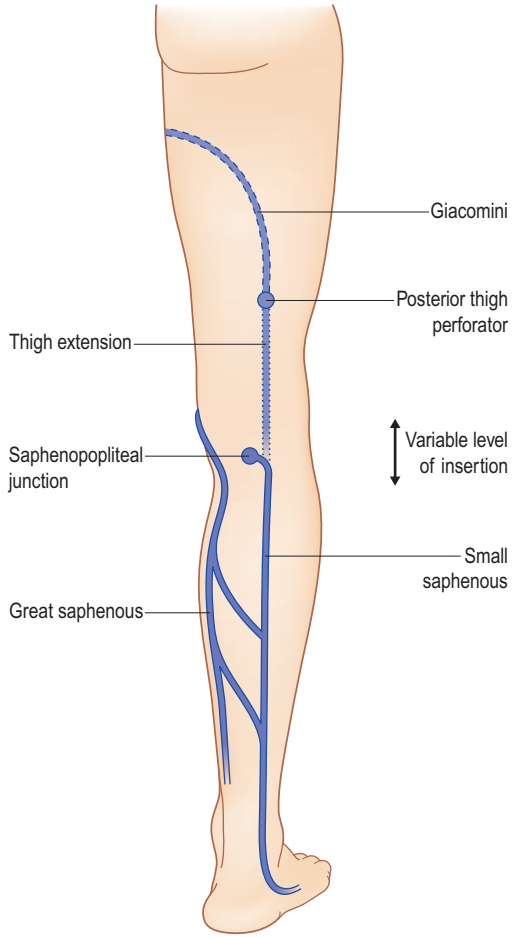

Figure 64.26 The variable anatomy associated with the small saphenous vein shown in a posterior view of the right leg. The SSV may terminate at the saphenopopliteal junction (SPJ) or continue (with or without an insertion at the SPJ) to the thigh extension vein terminating in the thigh. If it continues further to the GSV it is known as the Giacomini vein.

Chronic venous insufficiency

Background

The signs and symptoms of venous incompetence are due to venous valve failure permitting retrograde venous flow and causing raised distal venous pressure. This may be due to primary valve failure and can occur in the superficial or deep systems or a combination of both. Secondary incompetence is usually found after a deep vein thrombosis and subsequent recanalisation. A further relevant long-term sequela of thrombosis is chronic outflow obstruction which increases resistance to venous flow from the limb. Long-term incompetence, outflow obstruction or a combination of the two can result in swelling and ulceration characteristic of the post-phlebitic limb.

The signs and symptoms that result from venous incompetence range from none whatsoever through telangiectasia to active ulceration. There is a hierarchy of symptoms which is incorporated into a classification system known as the Clinical-Etiology-Anatomy-Pathophysiology (CEAP) classification.[74] The lowest score, C_0, describes no visible or palpable signs of disease followed by telangiectasia and reticular veins, varicose veins, oedema, skin pigmentation and eczema, lipodermatosclerosis, healed ulcer and finally C_6 active ulceration (Table 64.5).

The prevalence of venous disease varies according to studies and populations. The Edinburgh vein study[75] examined a random sample from the general population. It found venous reflux can be present in the absence of varicose veins. Varicose veins were found in 14% of women aged around 30 years and in 51% aged around 60 years. Unusually, the prevalence was found to be slightly greater in men. It may be that the prevalence in males is changing, or previous

Table 64.5 The Clinical-Etiology-Anatomy-Pathophysiology classification (CEAP) (from Eklöf B, et al.[74])

Clinical	Etiology
C_0: no visible or palpable signs of venous disease	E_c: congenital
C_1: telangiectases or reticular veins	E_p: primary
C_2: varicose veins	E_s: secondary (post-thrombotic)
C_3: oedema	E_n: no venous cause identified
C_{4a}: pigmentation or eczema	
C_{4b}: lipodermatosclerosis or atrophic blanche	
C_5: healed venous ulcer	
C_6: active venous ulcer	
Each category can be classified further as symptomatic (S), or asymptomatic (A):	

Anatomical	Pathophysiological
A_s: superficial veins	P_r: reflux
A_p: perforator veins	P_o: obstruction
A_d: deep veins	$P_{r,o}$: reflux and obstruction
A_n: no venous location identified	P_n: no venous pathophysiology identified

Advanced CEAP classification

This is the same as the basic CEAP but with the addition that any of 18 named venous segments can be used as locators for venous pathology

studies may have overestimated the prevalence in women due to poor or biased sampling.

Investigation of venous reflux

Duplex ultrasound scanning has become the standard test for venous incompetence and has added to our knowledge of the variations in venous anatomy and pathology.[72] Continuous wave Doppler ultrasound can be used to assess reflux but has the drawback that little anatomical information is provided, as the exact vein insonated is not reliably known. Previously, venography with tourniquets was used to assess incompetence and direct injection of contrast (varicography) was used to illustrate local venous anatomy, especially at the saphenopopliteal junction.

Photoplethysmography measures changes in local skin blood volume at ankle level. With superficial venous flow controlled by tourniquets, this technique provides an estimation of the level of incompetence and involvement of the deep or superficial systems, giving comparable results to direct pressure measurements.[76]

The physiological gold standard remains ambulatory venous pressure measurement; also used with tourniquets, it measures distal venous pressure via a cannulated dorsal foot vein.[77]

Colour duplex ultrasound examination

Real-time ultrasound provides precise identification of the variable venous anatomy and colour Doppler imaging, together with spectral Doppler, provides evidence of venous reflux in the deep and superficial veins. The aim of the examination is to provide information as to the exact site of venous reflux, which may be related to the deep or superficial veins, a specific venous confluence, perforator veins, or a combination of these. Ultrasound is used as a primary diagnostic technique, prior to surgery and more recently during less invasive varicose vein treatments.

Technique

Patient position

Ideally the patient is investigated standing, in order to fill the leg veins and promote venous reflux in the presence of incompetent valves. A degree of weight-bearing will improve the repeatability of the examination. The patient should be asked to put their weight on the contralateral limb whilst slightly bending the examined limb at the knee and keeping the foot and heel flat on the floor. If this is not possible then a degree of head-up tilt can be applied for the bed-bound patient. The infirm but mobile patient can sit on the edge of a raised couch with their feet on the floor.

Equipment

The examination is best performed using a linear transducer with a frequency of 5–9 MHz. Examination of the superficial veins requires less penetration than for the deep veins and high sensitivity to low flow velocities is desirable. The final choice of transducer depends on the size of the patient and whether deep or superficial veins are being examined.

Identification of anatomy

The key to a successful venous examination is the correct identification of anatomy with ultrasound. The main trunks of the great and small saphenous veins lie within a fascial envelope which has a typical appearance on ultrasound sometimes referred to as an 'Egyptian eye' (Fig. 64.27A). Tributaries, branches and perforators to the two main saphenous trunks lie outside this fascial sheath and superficial to the deep fascia (Fig. 64.27B). The recognition of the deep fascia on the real-time image is therefore crucial in correctly identifying the superficial veins.

Ultrasound and venous incompetence

- The signs and symptoms of venous incompetence are due to valve failure, which permits retrograde flow known as venous reflux.
- The symptoms of venous incompetence are described and graded using the Clinical-Etiology-Anatomy-Pathophysiology classification (CEAP).
- Duplex ultrasound is the standard test for venous incompetence and is used to locate the exact site of reflux.
- The patient should preferably be investigated standing in order to promote venous filling and demonstrate any reflux flow.
- The examination is best performed in the transverse scan with colour flow used to identify venous reflux.
- Reflux is best produced by manual muscle compression followed by its rapid release.
- A duration of greater than 0.5 seconds is used to define significant reflux.

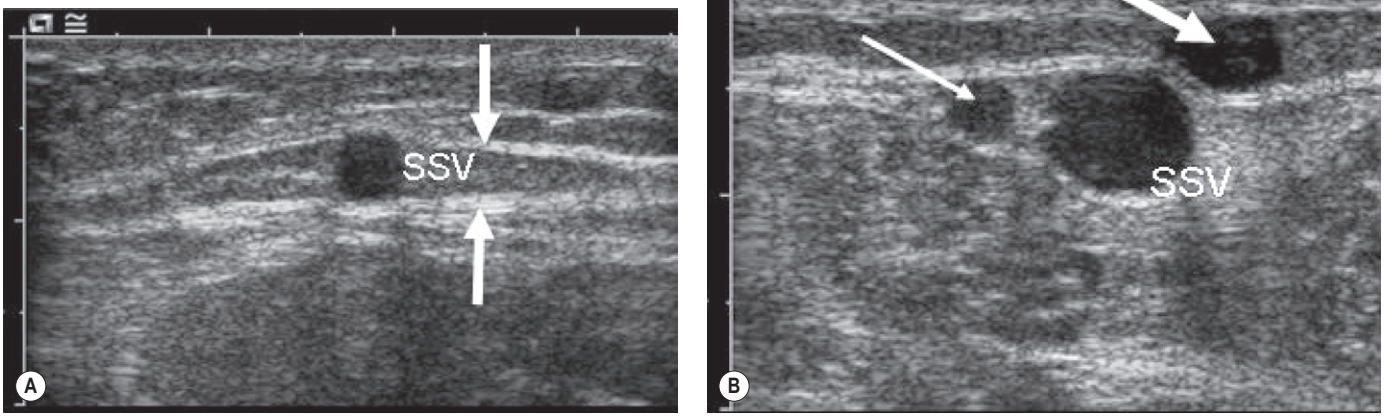

Figure 64.27 Transverse section of a small saphenous vein. A: The vein between the superficial and deep fascia (arrows). **B:** SSV with a subcutaneous tributary which lies outside the fascial sheath (large arrow) and a smaller tributary which runs for a short distance inside the sheath (small arrow) before inserting into the SSV.

The perforating veins run from the superficial to the deep veins, passing through the deep fascia (Fig. 64.28) and connecting the two systems. They tend to lie along the course of the main saphenous trunks (Fig. 64.29) and are most easily identified by scanning transversely along the deep or superficial vein. A fairly rapid transducer movement, whilst concentrating on the vein scanned, will show the perforating veins passing from deep to superficial on the image or vice versa. This apparent movement of the vein image with transducer movement is an invaluable aid to perforator identification and in tracing the course of veins.

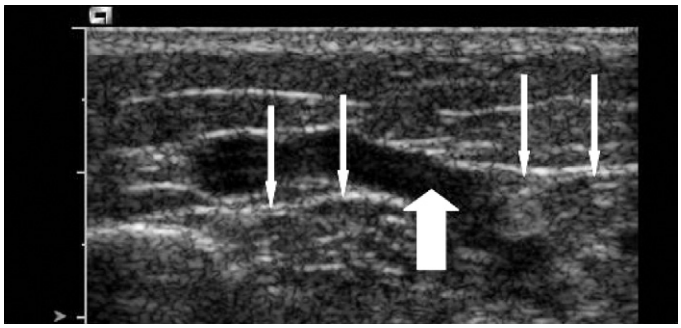

Figure 64.28 A perforating vein penetrating the fascia (large arrow) and lying on the deep fascia (small arrows). Perforators may be simple as in this case, or more complex with an intramuscular branch deep and close to the site where it penetrates the fascia.

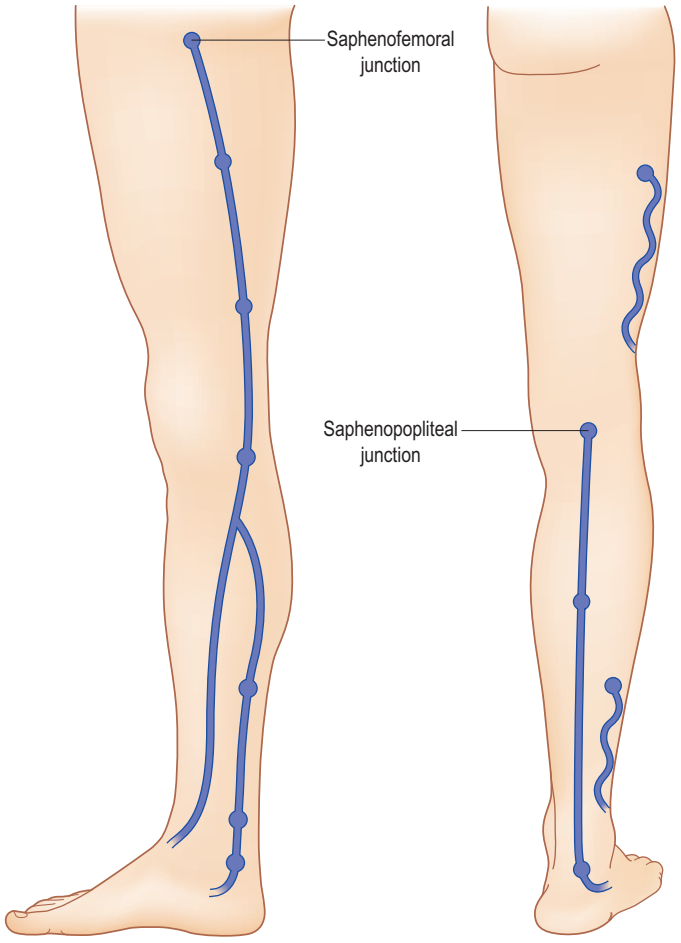

Figure 64.29 Common sites of perforating veins which are usually but not invariably close to the GSV and SSV. Note the lateral thigh perforator, which may be the source of lateral thigh varicose veins.

The great saphenous vein may be duplicated with two veins within the saphenous sheath, or there may be additional communications with accessory veins distally in the thigh or upper calf. If a Giacomini vein is present, this provides another communicating pathway between the great and small saphenous systems. The multiple venous connections found in the leg have implications when identifying the true source and exact path of reflux flow prior to treatment.

The examination is best performed in the transverse plane, as this helps ensure all veins are located and identified. When scanning transversely, optimal images of the vein wall will be achieved with the ultrasound beam orthogonal to the vein wall; however, optimal colour flow images require physical angulation of the transducer to ensure that there is an angle between flow direction and the ultrasound beam (Fig. 64.30).

Quantifying venous reflux

Venous reflux is best produced by squeezing the calf muscle, slowly and firmly, and then rapidly releasing the grip. This has the effect of emptying the compressed calf veins and creating a potential venous volume that can be filled on release of compression either normally from the more distal veins, or rapidly by retrograde flow if there are incompetent proximal valves. Care should be taken to compress the bulk of the muscle and not merely pinch the skin, which is both painful and ineffective (Fig. 64.31). The thigh and foot can be similarly compressed. Usually compression is applied distal to the site of insonation and the resultant flow observed on release of compression. It is possible and sometimes useful, e.g. with calf perforators, to compress and release proximal to the insonation site and observe the effect on flow. If the competence of pelvic veins must be established or if the calf is incompressible due to oedema or gross lipodermatosclerosis, then other methods must be used to induce flow/reflux. A Valsalva manoeuvre may be the only alternative although ill, bed-bound patients may have difficulty producing sufficient force. The converse is the over-enthusiastic patient, in whom a vigorous Valsalva can produce reflux in veins which are probably competent under normal physiological conditions. Cuff inflation systems are available to provide reproducible pressures for research studies but these tend to be time-consuming and cumbersome in routine clinical use.

A colour Doppler scan in the transverse plane can be used to distinguish between normal flow direction with no reflux and obvious reflux (Figs 64.32 and 64.33). If a permanent record of reflux is required or if quantification of reflux is required in the case of borderline findings, then a spectral Doppler trace of the flow recorded should be taken (Fig. 64.34).

A commonly used discriminant value for abnormal reflux is >0.5 s.[78] However, reliable quantification of reflux is problematic as it is dependent upon a number of factors including venous pressure and tone. For example, at the end of the day venous tone is reduced and previously competent veins may appear incompetent. Also it is not unusual to observe quite normal veins quickly becoming incompetent if the patient begins to feel faint with associated vasodilatation and loss of venous tone. It should be remembered that colour and spectral Doppler are velocimetric and not volume flow measurements; the volume of any observed reflux will depend on the diameter of the vessel investigated and the duration of the reflux.

Sources of superficial reflux

Successful treatment depends upon identifying the ultimate source of reflux. This is straightforward in cases of saphenofemoral junction incompetence to the great saphenous vein and saphenopopliteal incompetence to the small saphenous vein. In the latter case,

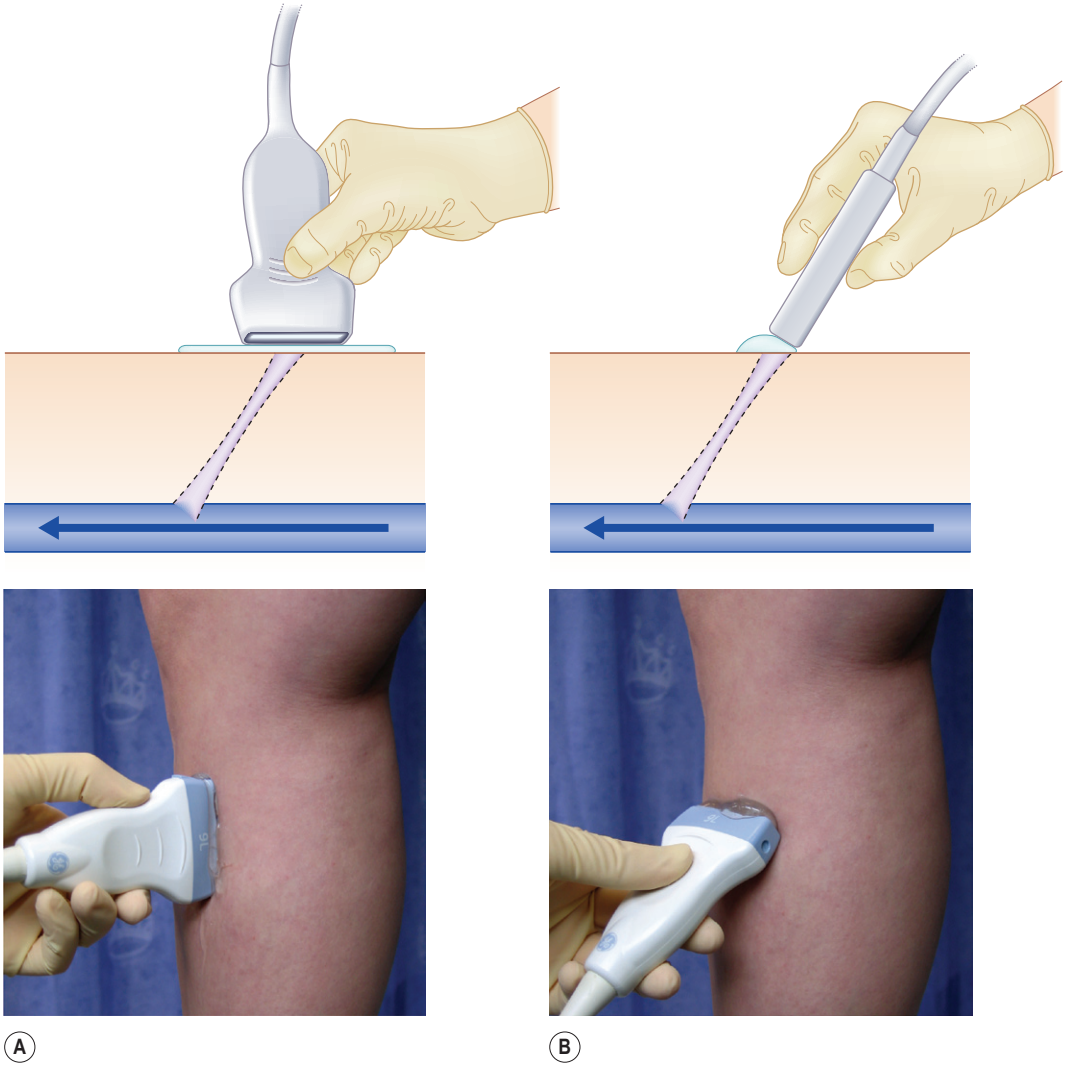

Figure 64.30 **An angle between the ultrasound beam and blood flow direction** is necessary in order to detect flow (which may be low velocity). In a longitudinal scan **(A)** the beam is steered electronically whilst in a transverse scan **(B)** the transducer must be physically angled.

the level above the knee crease and orientation (deep, superficial, lateral or medial insertion) of the small saphenous vein confluence with the popliteal vein should be reported. However, there may be multiple sources of reflux, from the saphenous vein junctions and/or from perforating veins. Varicose veins may show reflux from an unlikely source such as subcutaneous collaterals between the great and small saphenous systems, or a Giacomini vein. The source and pattern of reflux should be identified by tracing the anatomical pathway from the varicose veins back to their superficial and deep vein source(s).

Recurrent venous incompetence after varicose vein surgery may result from neovascularisation, whereby small collateral veins form a connection from a source of reflux to a vein remnant or varicose veins (Fig. 64.35). At the saphenofemoral junction, the source may be from the site of the junction, or from superficial or deep tributaries to the junction, or the great saphenous vein close to the junction (Fig. 64.36A–D). A further common source of recurrent reflux is a thigh perforating vein that communicates with a remnant of the main saphenous trunk (Fig. 64.36E). In the calf, incompetent medial perforating veins are sometimes found in association with recurrent varicose veins, or a non-healing ulcer. Other scenarios include new reflux from a previously competent vein and local superficial reflux with no identifiable deep source.

Treatments for venous incompetence

The usual treatment for deep venous incompetence is compression stockings or, in the case of ulceration, multilayer compression bandaging. Superficial reflux can be treated with conventional surgery. Commonly, this involves flush ligation of the saphenofemoral junction and stripping of the great saphenous vein.

There are now newer less invasive treatments available with the potential advantages of a rapid recovery for the patient and the absence of surgical incisions. They also avoid the surgical exposure and ligation of the saphenous junctions, which itself may contribute to neovascularisation and recurrence. These procedures include ablation of the main saphenous trunk using sclerosant foam, endovenous laser treatment (EVLT) and radio-frequency ablation.

Ultrasound is used during foam sclerotherapy to guide the injection of foam and compress the vein. In endovenous ablation, cannulation of the vein and the passing of a guidewire and a catheter-mounted ablation device is performed under ultrasound guidance. These catheter-based ablation techniques require an injection of local anaesthetic to provide anaesthesia, thermally insulate the treated vein from surrounding tissues and move the vein deeper

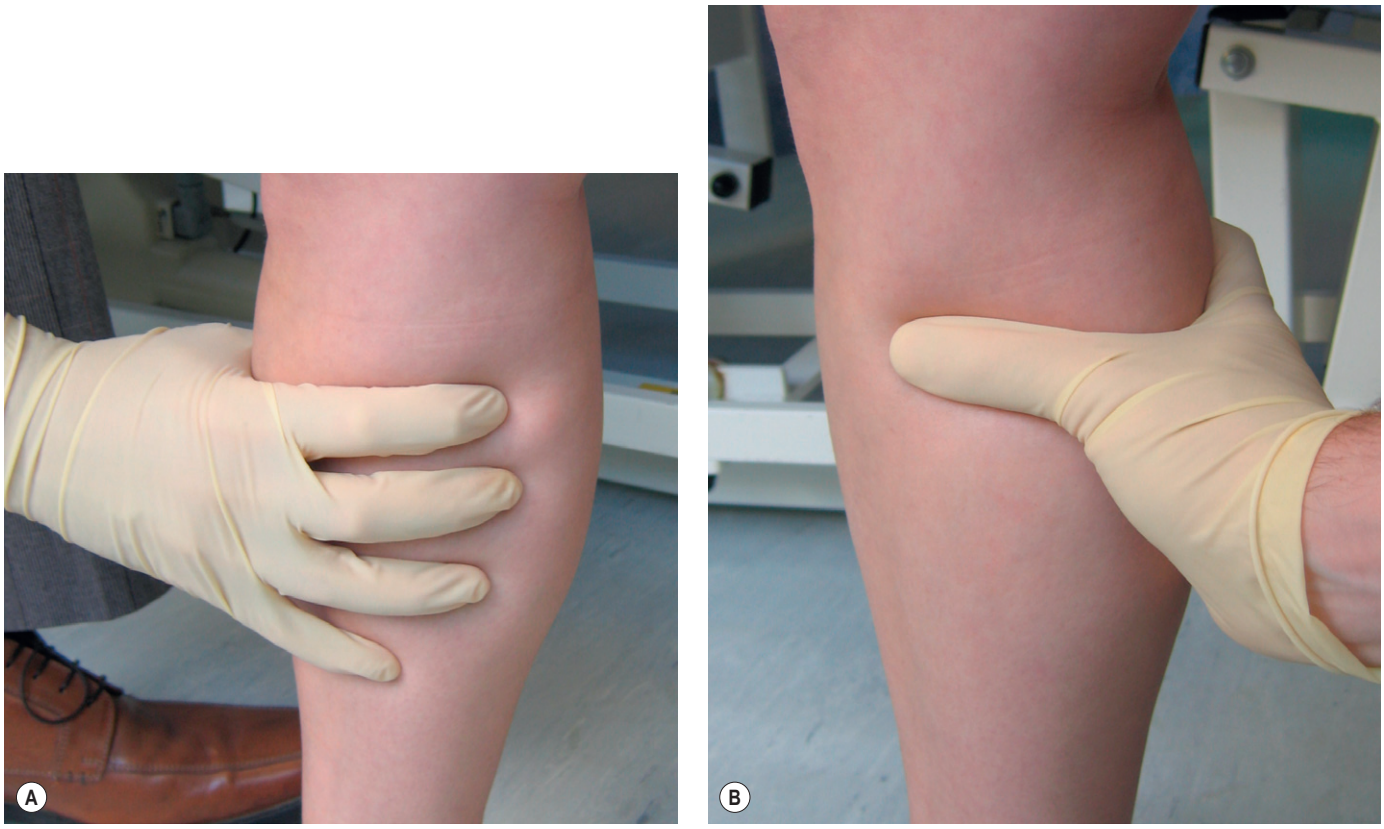

Figure 64.31 **A:** An ineffective approach to generating reflux. **B:** Compressing the bulk of the muscle empties the veins efficiently.

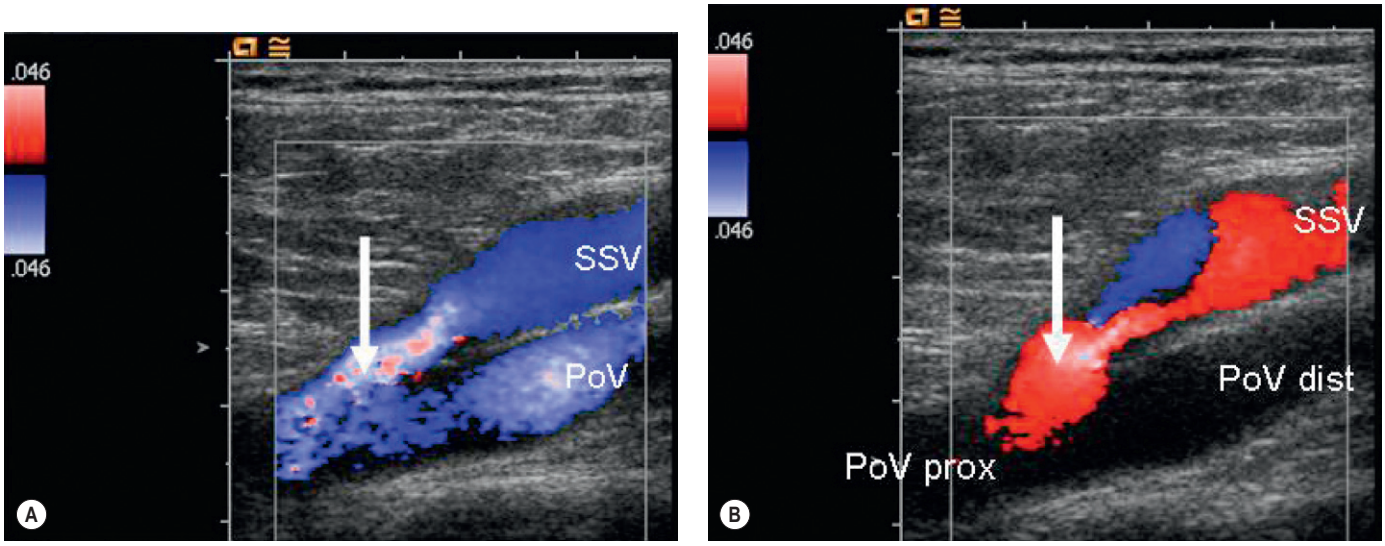

Figure 64.32 **Longitudinal colour flow scan of the saphenopopliteal junction** (arrow). **A:** Normal flow (blue) on calf compression in the popliteal vein (PoV) and SSV. **B:** Reflux flow (red) on release of compression in the SSV with an area of blue disturbed or helical flow. There is no colour flow in the distal popliteal vein (PoV dist), indicating no reflux. In the proximal popliteal vein (PoV prox) there is poor colour filling (red) due to the larger diameter and lower velocities in the popliteal vein compared with the SSV.

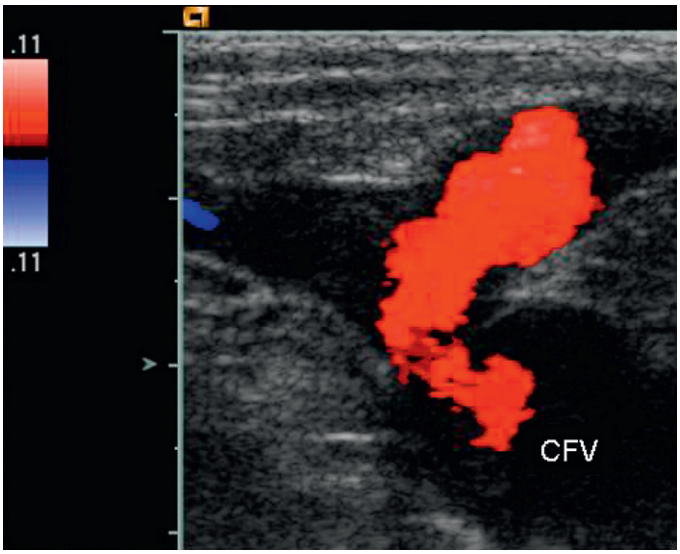

Figure 64.33 Reflux in a transverse scan at the saphenofemoral junction. The red is reflux flow, across the junction, towards the transducer from deep to superficial vein. CFV, common femoral vein.

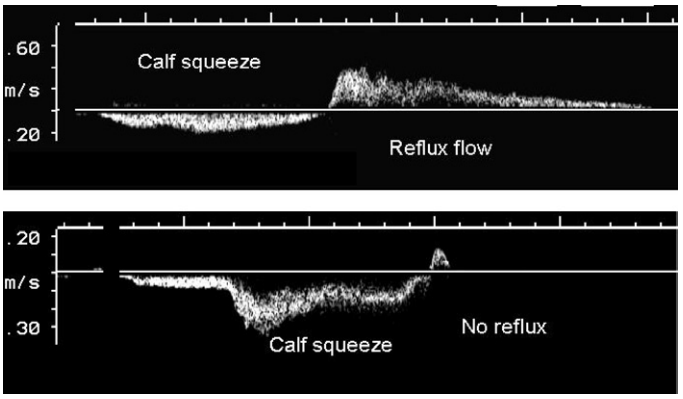

Figure 64.34 Normal cephalad flow produced with calf compression distal to point of insonation. On release of compression, the top trace shows reflux flow, towards the transducer, above the baseline; the lower trace shows no reflux flow but a short period of reverse flow less than 0.5 s in duration.

from the skin. The injection of fluid also reduces the vein diameter, squeezing out blood and ensuring a close fit between the vein wall and the device. The injection is performed under ultrasound guidance when the cannulated vein is visualised and the injected anaesthetic agent is imaged in the surrounding tissue. The surgeon, when trained, is usually best placed to simultaneously perform the ultrasound and procedure.

Studies have shown that the new procedures have a good outcome with comparable results to surgery but their relative merits should be assessed for the individual patient and type of varicose vein.[79,80] One drawback of the newer procedures is that there is, as yet, no information on their relative long-term performance compared with traditional methods. The success and outcomes for all of these procedures can be assessed using ultrasound.

PRE-ARTERIAL BYPASS VEIN MAPPING

A further use of superficial vein ultrasound scanning is to assess and mark veins prior to coronary artery or leg artery bypass procedures. Vein diameter and usable length can be assessed and the presence of tributaries and perforators identified. The ipsilateral great saphenous vein is the first choice for most leg artery bypass procedures. However, the contralateral vein can be used, if required, as can the small saphenous vein or superficial arm veins.

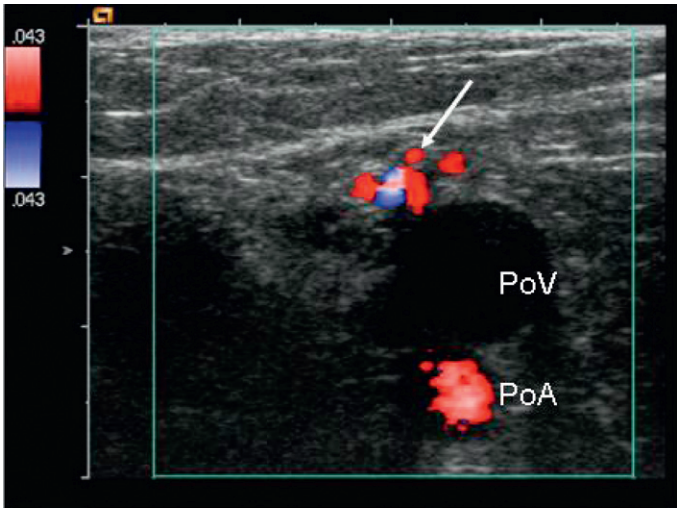

Figure 64.35 Recurrent saphenopopliteal reflux. Neovascularisation has formed small veins (arrow) that supply reflux from the popliteal vein to the SSV, which is not in the image. PoA, popliteal artery; PoV, popliteal vein.

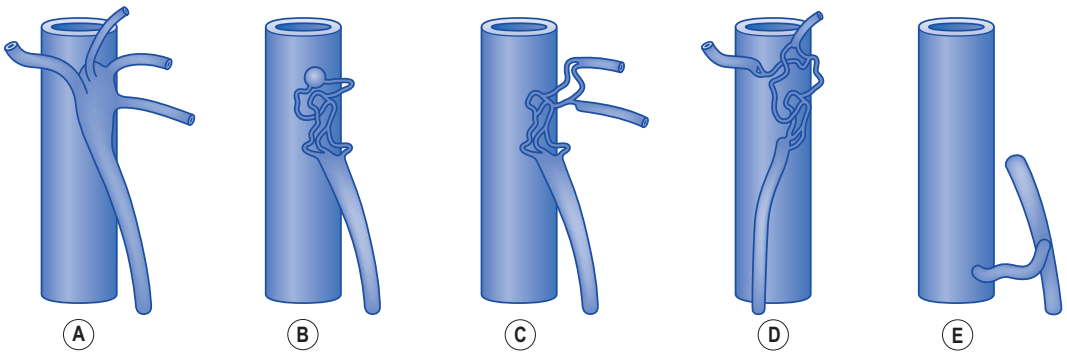

Figure 64.36 Common sources of recurrent saphenofemoral incompetence. Compare this figure with the presurgical appearance of the junction in Figure 64.25. **A:** Intact junction after failed surgery. **B:** Neovascularisation from the site of the junction to GSV remnant or accessory vein. **C:** Pudendal or medial tributary. **D:** Superficial abdominal veins. **E:** Medial thigh perforating vein.

REFERENCES

1. Useche JN, de Castro AM, Galvis GE, et al. Use of US in the evaluation of patients with symptoms of deep venous thrombosis of the lower extremities. Radiographics 2008;28:1785–1797.
2. White RH. The epidemiology of venous thromboembolism. Circulation 2003;107:1–4.
3. Cushman M, Tsai A, Heckbert SR, et al. Incidence rates, case fatality and recurrence rates of deep vein thrombosis and pulmonary embolus: the Longitudinal Investigation of Thromboembolism Etiology (LITE). Am J Med 2004;117:19–25.
4. Kakkar W. Deep vein thrombosis: detection and prevention. Circulation 1975;51:8–19.
5. Lea Thomas M, Keeling FP, Piaggio RB, Treweeke PS. Contrast agent induced thrombophlebitis following leg phlebography: iopamidol versus meglumine iothalamate. Br J Radiol 1984;57:205–207.
6. Albrechtson U, Olsson CG. Thrombotic side effects of lower limb venography. Lancet 1976;i:723–724.
7. McLachlan MSF, Thomson JG, Taylor DW, et al. Observer variation in the interpretation of lower limb venograms. AJR Am J Roentgenol 1979;132:227–229.
8. Christensen SW, Wille-Jorgensen P, Kjaer L, et al. Contact thermography, 99mTc-plasmin scintimetry and 99mTc-plasmin scintigraphy as screening methods for deep venous thrombosis following major hip surgery. Thromb Haemost 1987;58(3): 831–833.
9. Gomes AS, Webber MM, Buffkin D. Contrast venography vs radionuclide venography: a study of their discrepancies and their possible significance. Radiology 1982;142:719–728.
10. Zorba J, Schier D, Posmituck G. Clinical value of blood pool radionuclide venography. AJR Am J Radiol 1986;146:1051–1055.
11. Prescott SM, Tikoff G, Coleman RE, et al. 13lI labelled fibrinogen in the diagnosis of deep venous thrombosis of the lower extremities. AJR Am J Roentgenol 1978;131:451–453.
12. Pochaczevsky R, Pillari G, Feldman F. Liquid crystal contact thermography of deep venous thrombosis. AJR Am J Radiol 1982;138:717–723.
13. Ritchie WGM, Soulen RL, Lapayowker MS. Thermographic diagnosis of deep venous thrombosis. Radiology 1979;131:341–344.
14. Sandler DA, Martin JF. Liquid crystal thermography as a screening test for deep vein thrombosis. Lancet 1985;i:665–668.
15. Ramchandani P, Soulen RL, Fedullo LM, Gaines VD. Deep vein thrombosis: significant limitations of non invasive tests. Radiology 1985;156:47–49.
16. Goodacre S, Sampson F, Stevenson M, et al. Measurement of the clinical and cost effectiveness of non invasive diagnostic testing strategies for deep vein thrombosis. Health Technol Assess 2006;10(15):1–168, iii–iv.
17. Aitken AGF, Godden DJ. Real time ultrasound diagnosis of deep vein thrombosis: a comparison with venography. Clin Radiol 1987;38:309–313.
18. Cronan JJ, Dorfman GS, Scola FH, et al. Deep venous thrombosis: US assessment using vein compression. Radiology 1987;162:191–194.
19. Lensing AWA, Prandoni P, Brandges D, et al. Detection of deep venous thrombosis by real time B-mode ultrasonography. N Engl J Med 1989;320:342–345.
20. Baxter GM, MacKechnie S, Duffy P. Colour Doppler ultrasound in deep venous thrombosis: a comparison with venography. Clin Radiol 1990;42:32–36.
21. Foley WD, Middleton WD, Lawson TL, et al. Colour Doppler ultrasound imaging of lower extremity venous disease. AJR Am J Radiol 1989;152:371–376.
22. Gaitini D. Current approaches and controversial issues in the diagnosis of deep vein thrombosis via duplex Doppler ultrasound. J Clin Ultrasound 2006;34(6):289–297.
23. van Bemmelin PS, Bedford G, Strandness DE. Visualisation of calf veins by colour flow imaging. Ultrasound Med Biol 1990;16(1):15.
24. Baxter GM, Duffy P. Calf vein anatomy and flow: Implications for colour Doppler imaging. Clin Radiol 1992;46:84–87.
25. Polak JF, Culter SS, O'Leary DH. Deep veins of the calf: Assessment with colour Doppler flow imaging. Radiology 1989;171:481–485.
26. Thomas ML. Phlebography of the lower limb. Edinburgh: Churchill Livingstone; 1982. p. 162–163.
27. Polak JF. Peripheral vascular sonography. Baltimore, MD: Williams & Wilkins; 1992. p. 158.
28. Bach AM, Hann LE. When the common femoral vein is revealed as flattened on spectral Doppler sonography: is it a reliable sign for diagnosis of proximal venous obstruction? AJR Am J Roentgenol 1997;168(3):733–736.
29. Perlin SJ. Pulmonary embolism during compression ultrasound of the lower extremity. Radiology 1992;184:165–166.
30. Bahvican M, Elmali M, Karamustafa H, et al. A rare cause of pulmonary emboli in a patient with deep vein thrombosis: Doppler ultrasonographic compressibility. Cardiovasc Intervent Radiol 2007;30(4):803–805.
31. Nicolaides AN, Kakkar W, Field ES, Renney JTG. The origin of deep vein thrombosis: a venographic study. Br J Radiol 1971;44: 653–663.
32. Baxter GM, Duffy P, Partridge E. Colour flow imaging of calf vein thrombosis. Clin Radiol 1992;46:198–201.
33. Richardson GD, Beckwith TC, Sheldon M. Ultrasound windows to abdominal and pelvic veins. Phlebology 1991;6:125.
34. Effeney DJ, Friedman MB, Gooding GAW. Iliofemoral venous thrombosis: real time ultrasound diagnosis, normal criteria, and clinical application. Radiology 1984;150:787–792.
35. Quinn KL, Vandeman FN. Thrombosis of a duplicated superficial femoral vein. Potential error in compression ultrasound diagnosis of lower extremity deep venous thrombosis. J Ultrasound Med 1990;9(4):235–238.
36. Sutter ME, Turnipseed SD, Diercks DB, et al. Venous ultrasound testing for suspected thrombosis: incidence of significant non thrombotic findings. J Emerg Med 2008; epub.
37. Sheiman RG, McArdle CR. Bilateral lower extremity US in the patient with unilateral symptoms of deep venous thrombosis: assessment of need. Radiology 1995;194:171–173.
38. Pennell RC, Mantese VA, Westfall SG. Duplex scan for deep vein thrombosis – defining who needs an examination of the contralateral asymptomatic leg. J Vasc Surg 2008;48(2):413–416.
39. Goodacre S, Sampson F, Thomas S, et al. Systematic review and meta analysis of the diagnostic accuracy of ultrasonography for deep vein thrombosis. BMC Med Imaging 2005;5:6.
40. Vaccaro JP, Cronan JJ, Dorfman GS. Outcome analysis of patients with normal compression US examinations. Radiology 1990;175:645–649.
41. Cogo A, Lensing AWA, Koopman MMW, et al. Compression ultrasonography for diagnostic management of patients with clinically suspected deep vein thrombosis: prospective cohort study. BMJ 1998; 316:17–20.
42. Righini M, Bounameaux H. Clinical relevance of distal deep vein thrombosis. Curr Opin Pulmon Med 2008;14(5):408–413.
43. Orbell JH, Smith A, Burnand KG, Waltham M. Imaging of deep vein thrombosis. Br J Surg 2008;95(2):137–146.
44. Kearon C, Julian JA, Newman TE, Ginsberg JS. Noninvasive diagnosis of deep venous thrombosis. McMaster Diagnostic Imaging Practice Guidelines Initiative. Ann Intern Med 1998;128(8):663–677.
45. Lagerstedt CI, Olsson CG, Fagher BO, et al. Need for long term anticoagulant treatment in symptomatic calf vein thrombosis. Lancet 1985;2:515–518.
46. Righini M, Perrier A, DeMoerloose P, Bounameaux H. D-Dimer for venous thromboembolism diagnosis: 20 years later. J Thromb Haemost 2008;6(7):1059–1071.
47. Aguilar C, del Villar V. Combined D-dimer and clinical probability are useful for exclusion of recurrent deep venous thrombosis. Am J Hematol 2007;82(1):41–44.
48. Michiels JJ, Gadisseur A, van der Planken M, et al. Screening for deep venous thrombosis and pulmonary embolism in outpatients with suspected DVT or PE by the sequential use of clinical score: a sensitive quantitative D-dimer test and non-invasive diagnostic tools. Semin Vasc Med 2005;5(4):351–364.
49. Wells PS, Anderson DR, Rodger M, et al. Evaluation of D dimer in the diagnosis of suspected deep vein thrombosis. N Engl J Med 2003;349:1227–1235.
50. Cogo A, Lensing AWA, Prandoni P, Hirsh J. Distribution of thrombosis in patients with symptomatic deep vein thrombosis. Arch Intern Med 1993;153:2777–2780.
51. Bernardi E, Camporese G, Buller HR, et al. Serial 2 point ultrasonography plus D-dimer vs whole leg color coded Doppler ultrasonography for diagnosing suspected symptomatic deep vein thrombosis: a randomised controlled trial. JAMA 2008;300(14):1653–1659.
52. Ciccone 2nd WJ, Fox PS, Neumyer M, et al. Ultrasound surveillance for asymptomatic deep venous thrombosis after total hip replacement. J Bone Joint Surg Am 1998;80(8):1167–1174.
53. Lensing AWA, Doris I, McGrath FP, et al. A comparison of compression ultrasound with color Doppler ultrasound for the

diagnosis of symptomless postoperative deep vein thrombosis. Arch Intern Med 1997;157:765–768.
54. Kalodiki E, Nicolaides AN, al-Katoubi A, et al. Duplex scanning in the postoperative surveillance of patients undergoing total hip arthroplasty. J Arthroplasty 1997;12(3):310–316.
55. Baxter GM, Duffy P, MacKechnie S. Colour Doppler ultrasound of the post-phlebitic limb: sounding a cautionary note. Clin Radiol 1991;43:301–304.
56. Cronan JJ, Leen V. Recurrent deep venous thrombosis: limitations of US. Radiology 1989;170:739–742.
57. Murphy TP, Cronan JJ. Evolution of deep venous thrombosis: a prospective evaluation with US. Radiology 1990;177:543–548.
58. Meyerovitz MF, Polak JF, Goldhaber SZ. Short-term response to thrombolytic therapy in deep venous thrombosis: predictive value of venographic appearance. Radiology 1992;184:345–348.
59. Claudon M, Cosgrove D, Albrecht T, et al. Guidelines and good clinical practice recommendations for contrast enhanced ultrasound (CEUS) – Update 2008. Ultraschall (European Journal of Ultrasound) 2008;29:28–44.
60. Schott U, Laniado M, Duda SH, et al. Echo contrast agents for the colour Doppler sonographic diagnosis of deep femoral venous thrombosis. Rofo Fortschr Geb Rontgenstr Neuen Bildgeb Verfahr 1995;162(3):194–198.
61. Harvey CJ, Pilcher JM, Eckersley RJ, et al. Advances in ultrasound. Clin Radiol 2002;57(3):157–177.
62. Coon WW, Willis PW. Thrombosis of axillary and subclavian veins. Arch Surg 1966;94:657.
63. Baxter GM, Kincaid W, Jeffrey RF, et al. Comparison of colour Doppler ultrasound with venography in the diagnosis of axillary and subclavian vein thrombosis. Br J Radiol 1991;64:777–781.
64. Falk RL, Smith DL. Thrombosis of upper extremity thoracic inlet veins: diagnosis with duplex Doppler sonography. AJR Am J Roentgenol 1987;149:677–682.
65. Hightower DR, Gooding GAW. Sonographic evaluation of the normal response of subclavian veins to respiratory manoeuvres. Radiology 1985;20:517–520.
66. Wing V, Schieble W. Sonography of jugular vein thrombosis. AJR Am J Roentgenol 1983;140:333–336.
67. Sajid MS, Ahmed N, Desai M, et al. Upper limb deep vein thrombosis: a literature review to streamline the protocol for management. Acta Haematol 2007;118(1):10–18.
68. Chin EE, Zimmerman PT, Grant EG. Sonographic evaluation of upper extremity deep venous thrombosis. J Ultrasound Med 2005;24(6):829–838.
69. Igidbashian VN, Mitchell DG, Middleton WD, et al. Iatrogenic femoral arteriovenous fistula: diagnosis with color Doppler imaging. Radiology 1989;170:749–752.
70. Smith LL, Iber C, Sirr S. Pulmonary embolism: confirmation with venous duplex US as adjunct to lung scanning. Radiology 1994;191:143–147.
71. Elias A, Cazanave A, Elias M, et al. Diagnostic management of pulmonary embolism using clinical assessment plasma D-dimer assay, complete lower limb venous ultrasound and helical computed tomography of pulmonary arteries. A multi centre clinical outcome study. Thrombos Haemostas 2005;93(5):982–988.
72. Caggiati A, Bergan JJ, Gloviczki P, et al. Nomenclature of the veins of the lower limbs: an international interdisciplinary consensus statement. J Vasc Surg 2002;36(2):416–422.
73. Cavezzi A, Labropoulos N, Partsch S, et al. Duplex ultrasound investigation of the veins in chronic venous disease of the lower limbs – UIP Consensus Document. Part II. Anatomy. Eur J Vasc Endovasc Surg 2006;31(3):288–299.
74. Eklöf B, Rutherford R, Bergan J, et al. Revision of the CEAP classification for chronic venous disorders: Consensus statement. J Vasc Surg 2004;40(6):1248–1252.
75. Evans CJ, Fowkes FG, Ruckley CV, et al. Prevalence of varicose veins and chronic venous insufficiency in men and women in the general population: Edinburgh Vein Study. J Epidemiol Commun Health 1999;53(3):149–153.
76. Abramowitz HB, Queral LA, Flinn WT, et al. The use of photoplethysmography in the assessment of venous insufficiency. A comparison to venous pressure measurements. Surgery 1979;86:434–441.
77. Nicolaides AN, Zukowski AJ. The value of dynamic venous pressure measurements. World J Surg 1986;10:919–924.
78. Labropoulos N, Tiongson J, Pryor L, et al. Definition of venous reflux in lower extremity veins. J Vasc Surg 2003;38:793–798.
79. Hoggan BL, Cameron AL, Maddern GJ. Systematic review of endovenous laser therapy versus surgery for the treatment of saphenous varicose veins. Ann Vasc Surg 2009;23(2):277–287.
80. Leopardi D, Hoggan BL, Fitridge RA, et al. Systematic review of treatments for varicose veins. Ann Vasc Surg 2009;23(2):264–276.

CHAPTER

65 The neonatal brain

Rob Dineen and Tim Jaspan

INTRODUCTION

It is now over fifty years since ultrasound was first used to demonstrate intracranial pathology, when an A-mode device was used to demonstrate shift of the cerebral midline.[1] Thirty years have elapsed since real-time B-mode scanning of the infant brain via the anterior fontanelle became a possibility, allowing detailed ultrasound evaluation of structural brain abnormalities.[2–4] The development of portable units followed shortly after and facilitated the explosion of literature regarding the use of ultrasound in the characterisation of the cerebral and ventricular complications of prematurity which occurred during the 1980s. In the late 1980s and early 1990s, the value of Doppler ultrasound for assessing intracranial vasculature and cerebral haemodynamic changes was demonstrated.[5]

From the mid-1990s the literature regarding neuroimaging in neonates has been dominated by studies of magnetic resonance imaging (MRI), and it is clear that appropriately performed MRI has exquisite sensitivity for many of the pathological states of the neonatal period, such as ischaemia and haemorrhage. While advances in cranial ultrasound over the past fifteen years may not have been as spectacular as in the field of MRI, there have been steady improvements in scanner technology, leading to significant improvements in image quality.

Cranial ultrasound (CUS) remains an extremely important neuroimaging technique in infants, and the technique is well established as providing clinically important information in a convenient and safe bedside environment. Although the safety issues associated with transferring neonates to an MRI scanner have been partially ameliorated by the development of MRI compatible monitoring and incubator systems, ultrasound remains the first line in the assessment of the unwell or haemodynamically unstable neonate. Additionally, cranial ultrasound is established for a wide range of indications beyond the neonatal period. Concern about the health risks associated with ionising radiation in the very young has focused attention on alternatives to computed tomography (CT). The potential applications, advantages and limitations of ultrasound are discussed in this chapter. Recognition of the weaknesses of the technique, as well as its strengths, is important in order to maintain the rightful place of ultrasound in the investigation of neurological problems in this age group.

TECHNIQUE AND ANATOMY

Technique

Scanning in the neonate requires a 5–8 MHz sector probe for visualisation of the whole of the brain. High-frequency (8–17 MHz) sector, curved or linear array probes are excellent for demonstrating the superficial extracerebral spaces and to delineate the sulcal pattern and corticomedullary regions in the near field.[6,7] Focal zones should be adjusted to optimise visualisation in the near, mid and far fields.

Premature babies can be examined within the incubator with minimal disturbance, and reduction in image quality due to movement is unusual due to the relative immobility of premature infants. In term neonates and in infancy, excessive movements may hamper the examination, in which case feeding before or during the investigation may help to reduce movement. A cine-loop facility is of particular value in older infants, enabling an optimal image to be 'grabbed' from a short segment of real-time scanning.

Routine cranial ultrasound examination via the anterior fontanelle allows evaluation of the majority of the infant brain, and

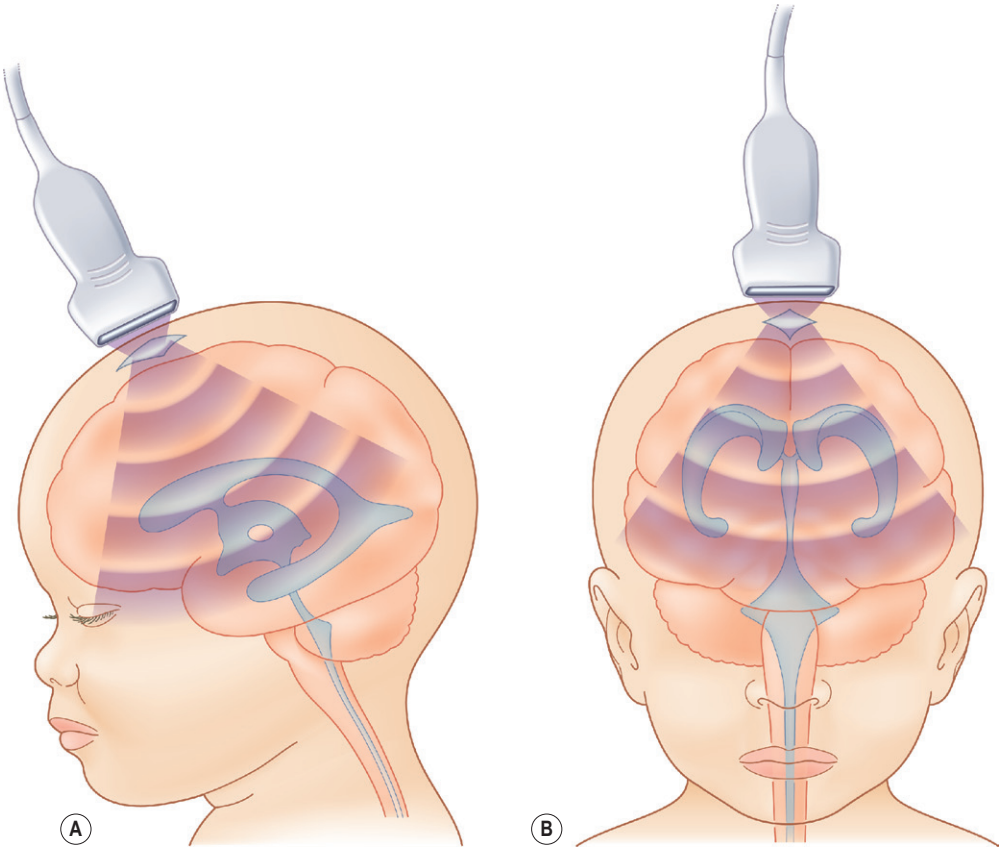

Figure 65.1 Technique of trans-fontanellar scanning. A: Coronal, **B:** Sagittal.

includes an assessment of the anatomical structures and locations where the frequently seen pathologies commonly occur. The brain is scanned in the sagittal and coronal planes via the anterior fontanelle and representative images are recorded.

Exact protocols for the standard views required vary from institution to institution, but the use of the same protocol for serial scanning allows direct comparison of images and the evaluation of evolving pathology between studies. Although a series of standard images is recorded, the scan is performed as a continuous real-time study and the structures between the standard views should be carefully scrutinised for the presence of pathology, and if identified the findings should be stored as images for future reference.

The routine views form a 'fan' pivoting around the window provided by the fontanelle (Fig. 65.1). Although referred to as sagittal and coronal images, only the midline sagittal image is truly sagittal, and the posteriorly angled coronal views more closely resemble the axial plane used in computed tomography. The brain and extra-axial spaces lying in the high convexities of the frontal and parietal regions are difficult to evaluate via the anterior fontanelle. Views of these areas can be improved by off-centring the angulation of the probe on the anterior fontanelle. When specific detail is required of the near-field structures, changing to a high-frequency linear array transducer will provide much more detailed information about the extra-axial spaces, surface vessels and brain surface. However, an appreciation of the relative blind spots is important to the understanding of the limitations of cranial ultrasound.

Routinely obtained views should be supplemented by additional views to evaluate other brain areas or structures as required.[8] The choice of additional views is dictated by the clinical scenario and to a certain extent by the skill and experience of the operator, but may include scanning via the posterior[9,10] or mastoid (posterolateral) fontanelles,[11,12] the foramen magnum,[13] or through the sutures. When required, specific information regarding the evaluation of blood or cerebrospinal (CSF) flow requires the use of Doppler ultrasound.

Technical problems that may be encountered include over-riding of sutures due to birth moulding, which can significantly narrow the anterior fontanelle, a small or prematurely closed fontanelle, and a large amount of thick hair over the fontanelle. These problems may be overcome by insonating with a lower frequency or if necessary using one of the alternative acoustic windows as indicated above.

Meticulous attention to detail is required when scanning to ensure correct identification of landmarks and alignment of the probe during scanning. Radiological convention for image display is employed, such that the coronal images are viewed with the right side of the brain on the left side of the display. Sagittal images are displayed with the anterior structures to the left side of the display. Side markers should always be included on the recorded images, and care should be taken to make sure these are correct. Standardised positioning of the patient will help to minimise labelling errors and reduce artefactual variability in images on serial scanning. At our institution the infant is scanned with the head in the lateral position with right cheek to the cot (Fig. 65.2), unless the infant's clinical condition prohibits positioning in this way.

Scanning conditions can make a significant impact on the quality of the images obtained. If the CUS is undertaken in a well-lit or bright environment, the gain settings will be inappropriately set, resulting in excessively bright stored images. As a matter of routine, room lighting should be decreased to a tolerable minimum, especially within the neonatal unit when the quality of imaging can often be paramount when evaluating subtle parenchymal abnormalities.

Anatomy (Fig. 65.3)

A clear understanding of the normal sonographic anatomy of the infant brain is critical to ensure identification of anatomical landmarks, for understanding pathological variation from the normal anatomy and for the correct description of the location of pathology.

The ventricular system consists of the lateral ventricles (anterior horns, body, occipital and temporal horns); the third ventricle, which communicates with the lateral ventricles via the foramina of Monro, and the fourth ventricle, which communicates with the third ventricle via the aqueduct of Sylvius (or cerebral aqueduct). The fourth ventricle outflow channels are in the midline into the cisterna magna (foramen of Magendie) and laterally into the perimedullary cisterns (the paired foramina of Luschka). All these compartments can be identified by ultrasound to a greater or lesser degree, depending on the age of the infant. In the premature infant the ventricular system is well defined, with separation of the walls, whereas in the full-term and older infant the ventricles are less distended and consequently the ventricular walls are more often apposed, such that the reflective borders of the ventricles become the identifiable landmarks.

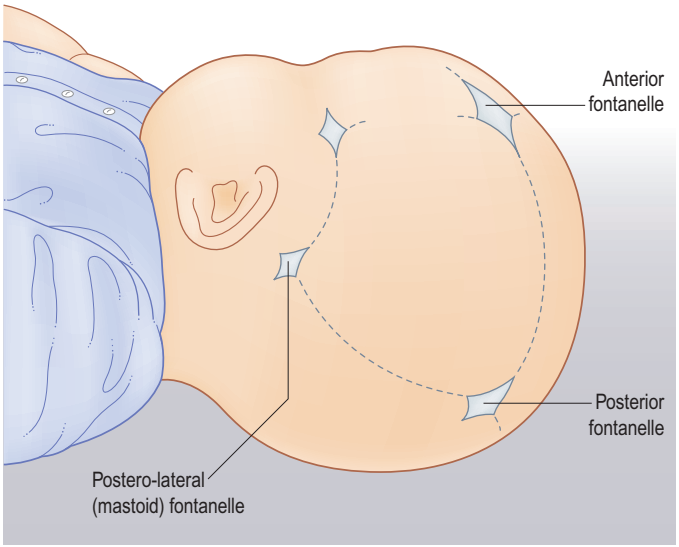

Figure 65.2 Location of the major ultrasound windows.

Around the ventricles are situated solid structures which are important both anatomically and pathologically. The caudate nucleus, specifically the head, lies directly beneath the anterior horn of the lateral ventricle, forming its inferior border. Between the caudate nucleus and the anterior horn lies the germinal matrix, although this structure is not directly visualised by ultrasound. The caudothalamic groove or notch forms a variably echogenic linear marking between the head of the caudate nucleus and the thalamus below.

The normal ventricular size has been extensively investigated using axial, coronal and sagittal measurements, and compared with equivalent measurements made by CT and MRI (Table 65.1).[14–16] The ventricular index (VI), a transverse measurement taken from the midline to the lateral margin of the lateral ventricle on coronal images at the level of the foramen of Monro (e.g. Fig. 65.13), is an easily applied and long-established ultrasound surrogate of ventricular size.[17] Centile charts based on this measurement can be used for early detection of ventricular dilatation. However, this measure may be insensitive to the 'ballooning' of the ventricles which occurs as an early feature in developing hydrocephalus and hence may not be as reliable as other linear ultrasound indices, or compared with subjective expert review.[18] In addition, ventricular dilatation in the premature infant tends to result in disproportionate expansion of the posterior parts of the lateral ventricles; strict adherence to VI may thus not fully reflect the degree of ventricular enlargement. Measurement of ventricular volume can be made, but this is more time-consuming. Mild degrees of asymmetry are common:[19] the normal bias is for the left to be slightly larger than the right.

Another important landmark is the choroid plexus: it helps define the levels of scans in the coronal and sagittal planes.[20] In the temporal horn the choroid plexus adheres to the roof medially and is thin, but around the thalamus it increases in thickness to form the glomus as it passes posteriorly into the trigone of the lateral ventricle (Fig. 65.3H). The position and thickness of the choroid plexus within the body are variable: it is essential to recognise this when assessing the possible presence of blood clot. The echotexture and surface outline of the choroid plexus tend to be uniform and smooth. Focal irregularity and/or extension posteriorly into the occipital horn coupled with a heterogeneous echotexture should raise the suspicion of choroidal and/or intraventricular haemorrhage.

Choroid plexus cysts are a common finding in CUS and are of no neurological significance when occurring in a karyotypically normal infant. Choroid plexus cysts are commonly located in the bodies of the choroid plexus within the lateral ventricles. They are typically small (measuring up to several millimetres in diameter), spherical, and are often multiple.[21]

Table 65.1 Some measurements of ventricular size on cranial ultrasound

Measure	Reference no.	Description	Comment
Ventricular index (VI)	17	Horizontal measurement from the midline to the lateral margin of the lateral ventricle on coronal images at the level of the foramen of Monro	Widely used Long established Centile charts available May be insensitive to early 'ballooning' of the ventricles
Diagonal width	15, 18	Ventrolateral to dorsomedial width of the lateral ventricle at the level of the foramen of Monro	Excellent correlation with expert clinical judgement
Ventricular height	18	Ventricular height in the parasagittal plane adjacent to the foramen of Monro	Excellent correlation with expert clinical judgement
Frontal and occipital horn ratio	16	The average of the greatest diameter of the frontal horns and the greatest diameter of the occipital horns, divided by the greatest biparietal diameter	Excellent correlation with ventricular volume measurements

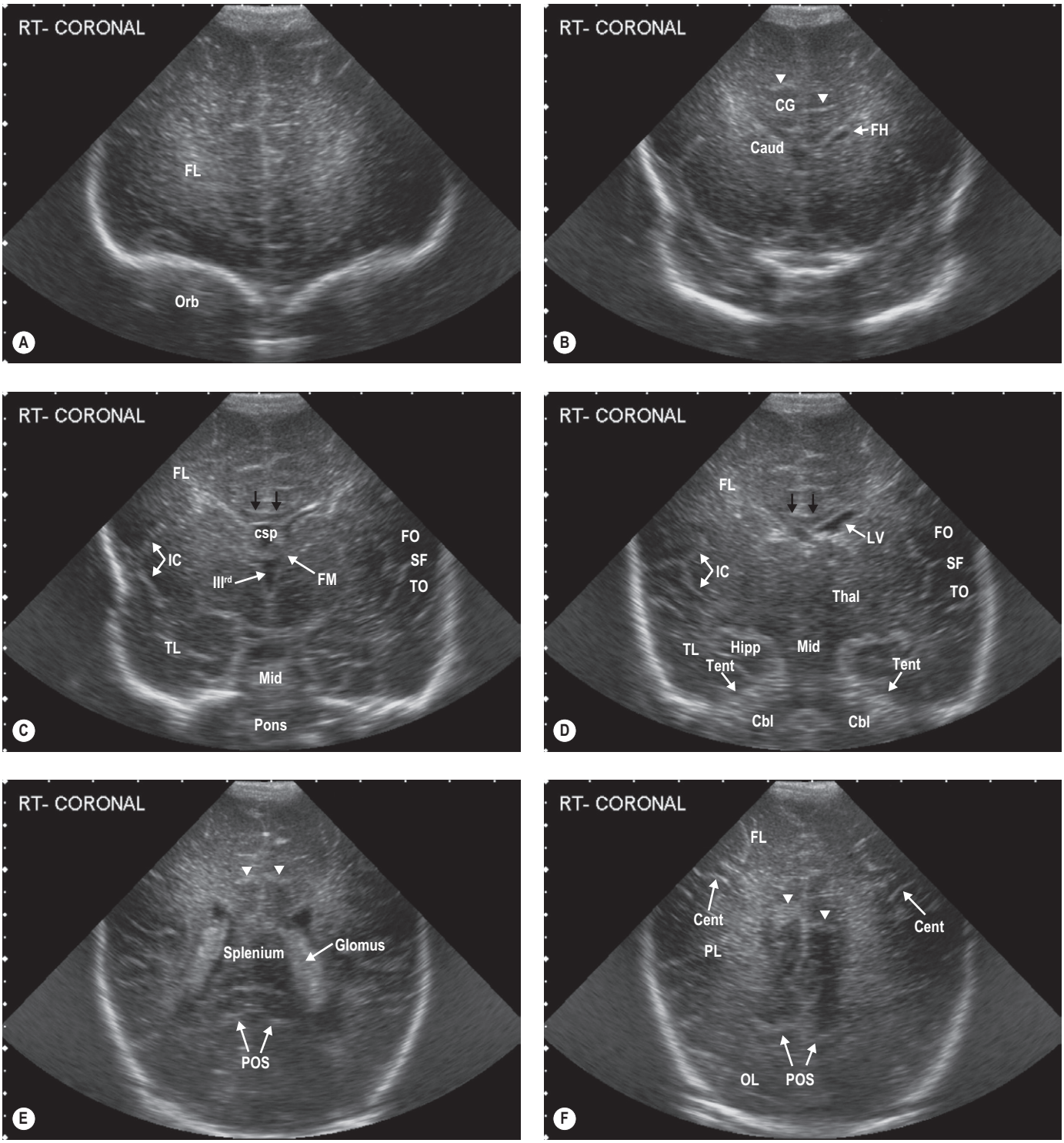

Figure 65.3 Normal anatomy. Coronal images from anterior to posterior and sagittal images from lateral to medial. **A–F:** Routine coronal images are recorded through **(A)** the frontal lobes anterior to the frontal horns, **(B)** the frontal horns, **(C)** the foramina of Monro, **(D)** the thalami, **(E)** the trigones of the lateral ventricles and **(F)** the parietal and occipital lobes dorsal to the ventricular system. **G–J:** Routine sagittal images, from lateral to medial, recorded through **(G)** the white matter lateral to the ventricular system, **(H)** the lateral ventricle, **(I)** the caudothalamic notch and **(J)** the midline. Small black arrows indicate corpus callosum, small white arrowheads the cingulate sulcus. IIIrd, third ventricle; IVth, fourth ventricle; Amyg, amygdala; Caud, caudate nucleus; Cbl, cerebellum; Cent, central sulcus; CF, choroidal fissure; CG, cingulate gyrus; CM, cisterna magna; Csp, cavum septum pellucidum; CTG, caudothalamic groove; CTN, caudothalamic notch; FH, frontal horn of the lateral ventricle; FL, frontal lobe; FM, foramen of Monro; FO, frontal operculum; Hipp, hippocampus; IC, insular cistern; LV, lateral ventricle; Med, medulla; Mid, midbrain; MTG, middle temporal gyrus; OH, occipital horn of the lateral ventricle; OL, occipital lobe; Orb, orbit; PL, parietal lobe; POS, parieto-occipital sulcus; SF, sylvian fissure; STG, superior temporal gyrus; Tent, tentorium cerebelli; Thal, thalamus; TL, temporal lobe; TO, temporal operculum.

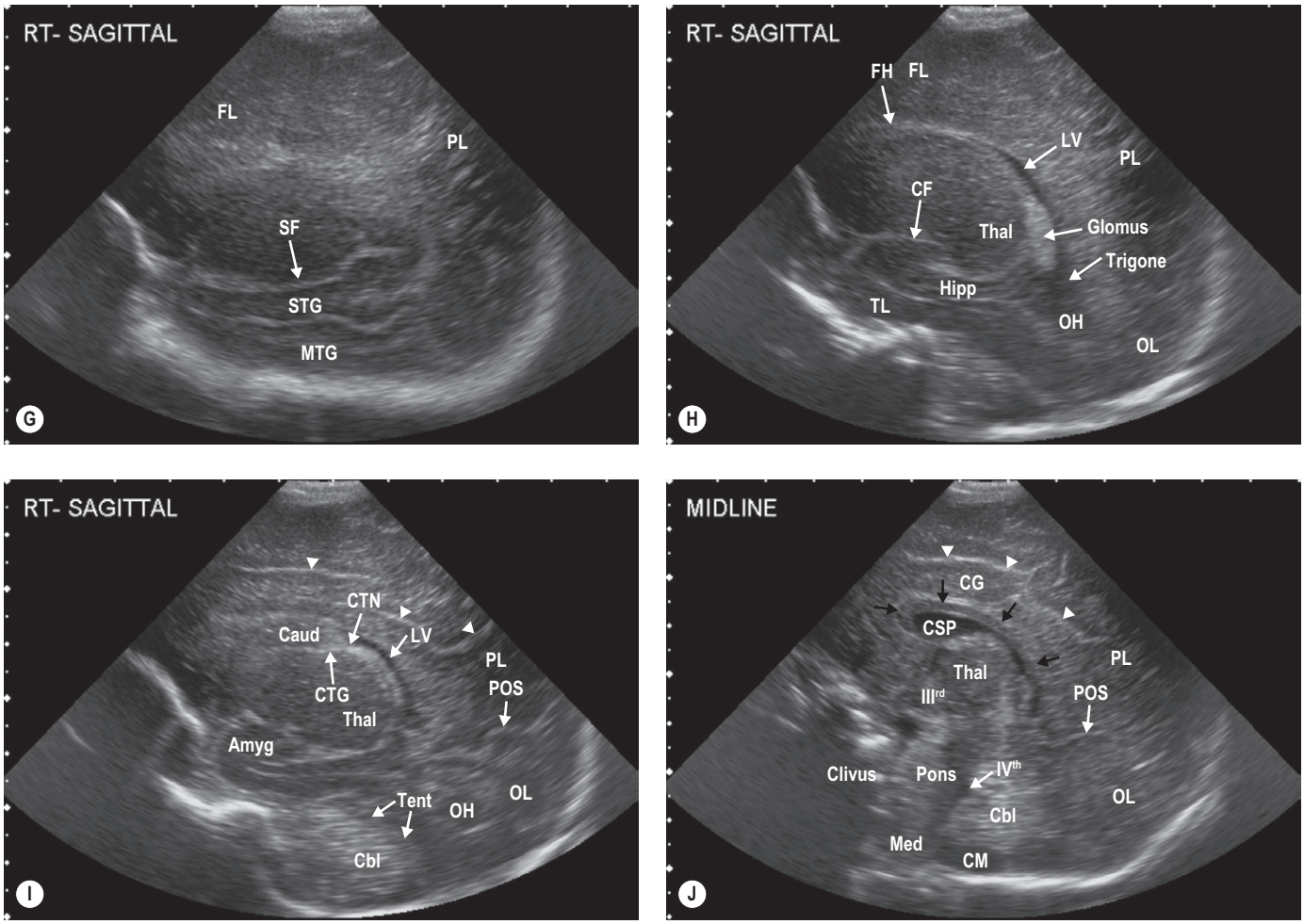

Figure 65.3 *Continued*

The thalamus comprises paired ovoid structures lying on either side of the third ventricle; their reflectivity is slightly greater than that of the adjacent brain. They lie posterior to the foramina of Monro and below the inferior concavity of the lateral ventricle (Fig. 65.3D and I). A midline rounded or oval structure, the massa intermedia, connects the thalami. The massa intermedia is not identifiable in the normal infant but becomes identifiable with enlargement of the third ventricle, or if it is enlarged owing to a small or absent corpus callosum.

Normally the third ventricle is poorly seen as a slit in the coronal plane or as a vague rectangular or trapezoid structure in the midline sagittal plane. When dilated its full outline can be visualised more easily, with the massa intermedia lying centrally.

The cavum septum pellucidum and cavum vergae are CSF-filled spaces lying between the lateral ventricles and beneath the corpus callosum. The septum pellucidum is a thin laminated structure that forms the medial walls of the lateral ventricles. In utero the leaves of the septum pellucidum are separated creating the cavum septum pellucidum and cavum vergae, which are usually in continuity, but during the late in-utero and early postnatal period the cavity progressively obliterates in the caudal to cranial direction. The finding of cavum septum pellucidum and cavum vergae is thus common in neonates (Fig. 65.3C and J), being seen in up to 90% of preterm and 50% of term infants. By 2 months of age 85% of infants have no remaining visible cavum. A midline cystic space in the absence of dilatation of the ventricles represents a persistent cavum, and as it has no clinical sequela in this age group, it can be considered a normal variant.[21] In the context of intraventricular haemorrhage and evolving ventriculomegaly, the cavum may enlarge in synchrony with the ventricular dilatation and correspondingly contracts as the ventricles decrease in size, suggesting communication between the compartments.

The echo-poor corpus callosum lies above the roof of the lateral ventricles (Fig. 65.3C and J) bordered by the pericallosal sulcus, which communicates with the reflective inter-hemispheric fissure. In the normal state, the overlying cingulate gyrus parallels the corpus callosum; loss of this parallelism accompanies abnormalities of the corpus callosum. Other noteworthy anatomical landmarks are the sylvian fissures, choroidal fissures and the tentorium cerebelli (Fig. 65.3D and G–I). Variable amounts of fluid may be present in the cisternal spaces around the tentorium cerebelli and in the cisterna magna.

The normal periventricular vessels produce fine reflective striae in the frontal lobes and also posterior to the bodies of the lateral ventricles. These should not be misinterpreted as pathological 'flares' or parenchymal ischaemic lesions, which generally appear as coarser, linear more reflective areas interspersed by cystic foci (see below).

Juxtaventricular cysts, also referred to as connatal cysts, characteristically occur immediately lateral to the frontal horns of the lateral ventricles, anterior to the foramina of Monro.[21] Juxtaventricular cysts are said to arise as a result of apposition of the lateral

walls of the frontal horns, effectively 'pinching off' a portion of the ventricle to form the cyst. These are an incidental finding on CUS, and usually resolve spontaneously. As they carry no pathological or prognostic significance, juxtaventricular cysts can essentially be considered as a normal variant.[22,23]

The cerebellum is moderately reflective and can be visualised through the anterior fontanelle. However, clearer views may be obtained by using the temporoparietal approach.[8,11] In the midline sagittal plane, the vermis appears as a strikingly echogenic structure (Fig. 65.3J), the numerous folia between the segments of the vermis resulting in multiple echogenic interfaces. More laterally, the cerebellar hemispheres have a more uniform lower echogenicity. The convoluted superior surface of the cerebellum is highly echogenic on both sagittal and coronal imaging. The brainstem can be visualised on sagittal sections via the anterior fontanelle. The ventral pons has a brightly echogenic appearance compared with the dorsal pons; this echogenicity has been attributed to crossing bundles of the transverse pontocerebellar fibre pathways and the intermixed pontine nuclei.[24]

The sulci and cerebral fissures are prominent linear markings which help to define the surface anatomy and major lobar divisions of the brain. In the normal brain the sulci appear echogenic owing to the pulsating pial vessels and interface between the brain and CSF in the subarachnoid spaces. If the subarachnoid spaces are enlarged or prominent, the CSF within the sulci and the fissures appears as echo-free spaces between the brain surface. The cerebral cisterns, although CSF-filled, may appear paradoxically reflective owing to the presence of pulsatile blood vessels, particularly the inter-peduncular cistern. The cisterna magna can usually be seen as a wedge-shaped sonolucency below the vermis and behind the medulla, and has a normal depth of up to 8 mm when measured from the undersurface of the inferior vermis to the plane of the echogenic posterior lip of the foramen magnum.[25]

Variation in appearance with gestational age

There is considerable variation in the normal appearances of the brain as a result of gestational age alone. In extremely premature infants of 23+ weeks gestational age the primary fissures (interhemispheric fissure, horizontal or sylvian fissure) are present, but the sulci and gyri of the brain are not yet formed, leading to a smooth appearance to the surface of the brain (Fig. 65.4). The opercula are not well formed and as a result the sylvian fissures often appear open and box-like in shape. Below the age of 28 weeks the subarachnoid spaces around the cerebrum often appear prominent, which is a normal finding. This is particularly pronounced posterior to the cerebral hemispheres. As the brain matures, there is progressive formation of the sulci and gyri, starting with the central, parieto-occipital, calcarine and cingulate sulci. The opercula enlarge, closing the sylvian fissure and covering the insular cortex. Beyond around 33 weeks of gestational age, the middle of the third trimester, the process of sulcation and opercularisation is largely complete.

The appearance of the images may change beyond this time and into the post-term equivalent period, but this is largely due to technical factors such as increasing head size or the presence of hair on the scalp, as opposed to brain maturation per se. CUS via the anterior fontanelle is possible up to the age of 6 months and occasionally longer, particularly if the fontanelle is kept enlarged by the presence of intracranial mass effect. Image quality becomes progressively more limited, although depth penetration can be maintained by use of low-frequency transducers in the 3–5 MHz range. Eventually assessment of the brain parenchyma becomes too poor for diagnostic purposes, but CUS can still be useful as a quick screening tool for the presence of lateral ventricular dilatation. However, confirmation of findings by more definitive imaging should be sought. Clinicians should be made fully aware of the limitations of CUS beyond this period and requests for a scan to look for suspected pathology, other than hydrocephalus, should be resisted. Evaluation of cerebral vasculature by Doppler imaging may, however, be performed throughout childhood (and indeed through adulthood) via the transtemporal widow, but this will not be dealt with here.

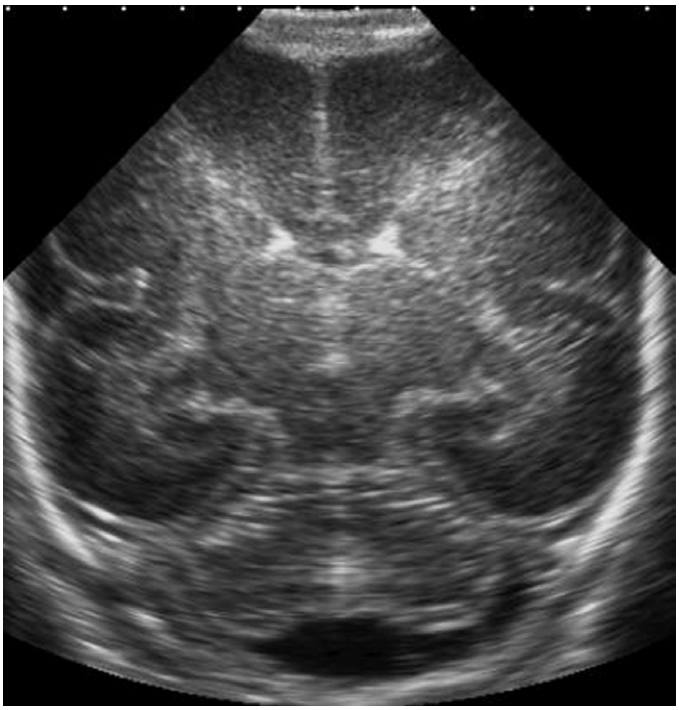

Figure 65.4 Appearance of the brain in a 24-week gestational age infant. Compare with the image from a 32-week gestational age infant shown in Figure 65.3D.

Vascular anatomy

Visualisation of the major intracranial arteries and much of the dural venous system can be achieved using colour Doppler ultrasound. To achieve maximal visualisation of the vascular system the operator will need to insonate via several of the natural ultrasound windows (Fig. 65.5, Table 65.2). The anterior fontanelle provides clear visualisation of the terminal portions of the internal carotid arteries and the anterior cerebral arteries (Fig. 65.6A). The horizontal portions of the middle cerebral arteries can often be seen via this window, but demonstration of flow by colour Doppler can be unreliable in view of the direction of flow angle being perpendicular to the angle of insonation. Angulation of the probe on the fontanelle can improve visualisation and is essential if measurements of flow are being made, when angle correction may also be required to achieve accurate measurements. The transtemporal route provides the best view of the ipsilateral horizontal (M1) segment of the middle cerebral arteries (Fig. 65.6B), as well as a view of the circle of Willis. The sonographer should be aware of the natural variability in arrangements of the circle of Willis. In particular, one or both posterior communicating arteries may be dominant with hypoplastic or absent proximal (P1) portions of the contralateral posterior cerebral artery.

A number of direct and derived measurements can be made from the Doppler waveform, and these measurements can be used to characterise the pattern of cerebral blood flow. Direct measurements include the peak systolic (PSV) and end-diastolic (EDV) velocities. Derived parameters include the mean cerebral blood velocity (mCBV), Pourcelot resistive index (RI) and pulsatility index (PI). The mCBV is the time-averaged mean of the maximum velocity curve of the waveform over at least one cardiac cycle. RI is defined as (PSV – EDV)/PSV, and PI as (PSV – EDV)/mCBV.

There are significant changes in cerebral haemodynamics in the early postnatal period. In term infants, there is an increase in the

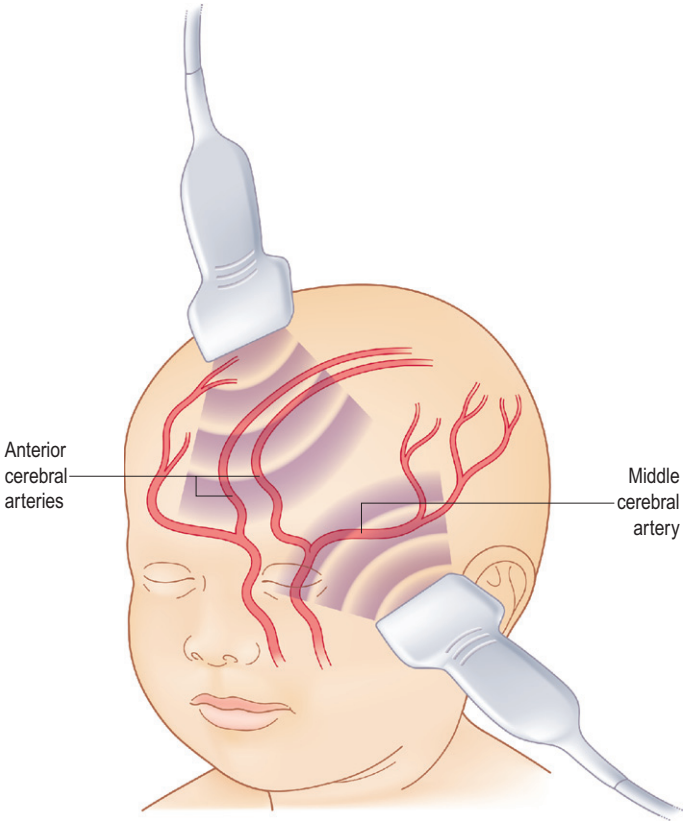

Figure 65.5 **Arterial Doppler ultrasound windows.**

mCBV, PSV and EDV in pulsatility over the first 5–7 days.[26,27] Velocity measurements in different vessels correlate well, but absolute velocities vary depending on site, with velocities from the middle cerebral artery (MCA) being higher than those from the anterior cerebral artery (ACA). A minor initial reduction in PSV and EDV over the first few hours has also been reported.[28] A similar pattern of increasing PSV and EDV, with reducing RI, has been demonstrated in premature infants over the first 3 days of life.[29]

RI values for the intracranial internal carotid artery (ICA), MCAs and ACAs from healthy term infants obtained during the first 24 hours of life have a mean of 0.72 and lie between 0.55 and 0.9 (Fig. 65.6A and B) (a minimum RI value of 0.47 was found for a measurement of the right MCA via the transtemporal window, but the potential causes and significance of this outlier are not considered by the researchers).[30] Of note, no significant difference was found for the RI measurements of the MCA vessels via the anterior fontanelle and via the transtemporal window despite the very different angles of insonation.

The dural venous system can be imaged by cranial ultrasound. The majority of the dural sinuses lie immediately adjacent to the inner table of the skull, in many cases directly under fontanelles or sutures and hence near-field scanning using a high-frequency linear probe can provide high-resolution imaging of the sinuses. Colour Doppler can be used to demonstrate flow within sinuses provided enough angulation between the beam direction and direction of flow can be achieved.

The superior sagittal sinus can be imaged from the anterior fontanelle to the posterior fontanelle through the sagittal suture (Fig. 65.7A). On real-time imaging, the sinus is hypoechoic, appearing triangular in shape in the coronal plane and as a tubular structure on midline sagittal images. Venous blood flow within the sinuses can be readily confirmed with colour Doppler ultrasound, which will also demonstrate the cortical draining veins entering into the

Table 65.2 **Doppler assessment of intracranial arteries**

Vessel	Window and view	Comments	Usual direction of flow
Internal carotid artery	Anterior fontanelle	Seen on parasagittal slices immediately lateral to sphenoid bone	Toward probe
	Transtemporal window	Ipsilateral ICA, Supraclinoid portion	Toward probe
Anterior cerebral artery	Anterior fontanelle	Excellent visualisation of most of the ACA passing anterior to callosal genu. Right and left vessels often cannot be discriminated	Toward probe
	Transtemporal window	Ipsilateral A1 segment, extends medially from the carotid tip	Away from probe
Middle cerebral artery	Anterior fontanelle, coronal plane	M1 segment may be difficult to visualise and measure velocities due to angle of insonation. M2 segment usually visualised	M1 segment: Toward probe proximally, often away from probe distally. M2 segment: toward probe
	Transtemporal window	Excellent visualisation of ipsilateral M1 segment	Toward probe
Posterior cerebral artery	Transtemporal window	P1 segments seen arising from basilar tip ventral to the midbrain	Toward probe
Posterior communicating artery	Transtemporal window	May be visible running between distal ICA and PCA	Variable, ipsilateral vessel often flows away from probe
Basilar artery	Anterior fontanelle	Anterior to brainstem	Toward probe
	Transtemporal window	Anterior to brainstem	Toward probe
	Foramen magnum	Anterior to brainstem	Away from probe
Vertebral arteries	Foramen magnum	Anterolateral to medulla and lower pons	Away from probe

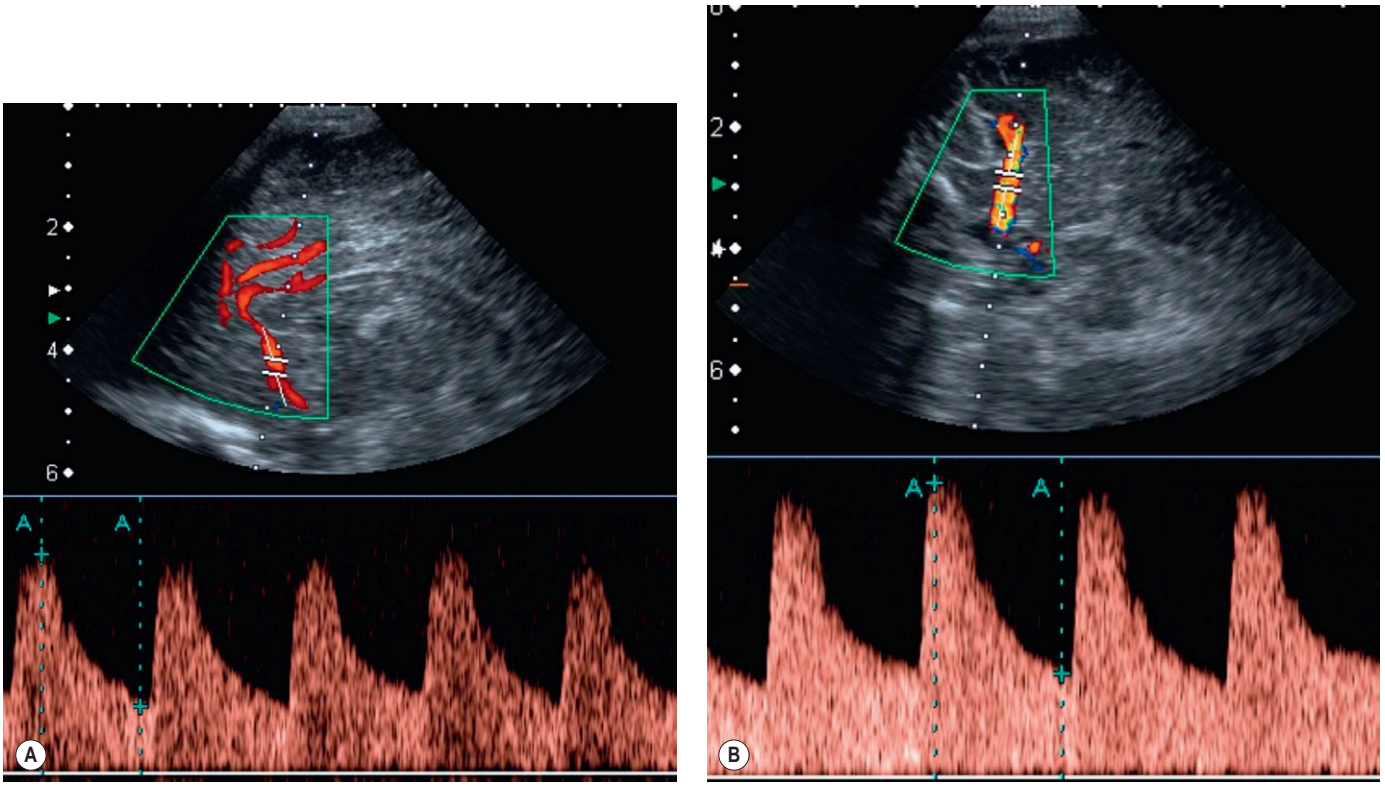

Figure 65.6 Colour Doppler ultrasound of intracranial arteries. A: Evaluation of the anterior cerebral artery on midline sagittal image via the anterior fontanelle. Normal waveform with RI of 0.70. **B:** Evaluation of the ipsilateral middle cerebral artery via the transtemporal window. Normal waveform with RI of 0.65.

sinus. The posterior portion of the superior sagittal sinus, straight sinus, torcula and medial transverse sinuses are harder to visualise but can often be identified at depth via the anterior fontanelle. The lateral aspects of the transverse sinuses and sigmoid sinuses can be seen via the mastoid fontanelles (Fig. 65.7C).[11]

CEREBROVASCULAR COMPLICATIONS

The bedside identification and evaluation of cerebrovascular complications in neonates is one of the most important uses of cranial ultrasound. The pattern of cerebrovascular injury in neonates depends on several key factors. Gestational age is a major determinant of susceptibility of different brain structures to hypoxia or hypotension and the pattern of injury in preterm infants differs markedly from infants who are near or at term. For this reason, this section is divided into two main subdivisions based on gestational age. The other main factor thought to determine pattern of injury, particularly in term infants, is severity and duration of hypoxia or hypotension.

Premature infants

Prematurity is defined as a gestational age of less than 37 weeks. However, the patterns of brain injury seen in response to cerebrovascular stress in prematurity occur with much greater frequency in those born below 33 weeks. The main patterns seen in this age group are germinal matrix/intraventricular haemorrhage, periventricular haemorrhagic infarction and periventricular leukomalacia.

Germinal matrix – intraventricular haemorrhage

The germinal matrix is the area in the developing fetal brain that gives rise to the neuronal cells which will later constitute the grey matter of the brain. The germinal matrix first appears at 7 weeks of gestational age and increases in size to the 23rd week, when it lies adjacent to the ventrolateral wall of the lateral ventricles.[31] After the 26th to 28th week the germinal matrix rapidly regresses to a small zone adjacent to the ventricular margin, between the head of the caudate nucleus and the thalamus. The location of the germinal matrix at this time can be found by identifying the caudothalamic groove (Fig. 65.3I). The germinal matrix almost completely involutes by 33 weeks, which accounts for the reduction in new germinal matrix haemorrhage seen after this time.

The germinal matrix is a highly vascularised and metabolically active structure and is thus susceptible to undergoing haemorrhage during hypoxic or ischaemic stress. Although the exact mechanism resulting in germinal matrix haemorrhage (GMH, also referred to as subependymal haemorrhage, SEH) is not fully elucidated, it appears to be predominantly of venous origin.[32,33] The rich microvasculature of the germinal matrix is prone to haemorrhage during periods of venous congestion. The vascular fragility of the germinal matrix capillary bed is multifactorial and includes factors such as rapid angiogenesis, paucity of pericytes and a lack of mesenchymal support.[34] In addition, the cerebral circulation in extremely preterm infants is virtually pressure-passive, and hence fluctuations in systemic blood pressure are not compensated for by cerebral autoregulatory mechanisms.

GMH frequently coincides with intraventricular haemorrhage (IVH), and there is no doubt that the two conditions are usually aetiologically related. The strength of the association is such that the two conditions are often referred to under the bracket term of germinal matrix – intraventricular haemorrhage (GMH-IVH) or alternatively periventricular haemorrhage (PVH). It is proposed that the haemorrhage within the germinal matrix ruptures through the ependymal surface to enter the ventricular system. However, it should be borne in mind that there are other potential causes of IVH in preterm infants, particularly haemorrhage from the choroid plexus.

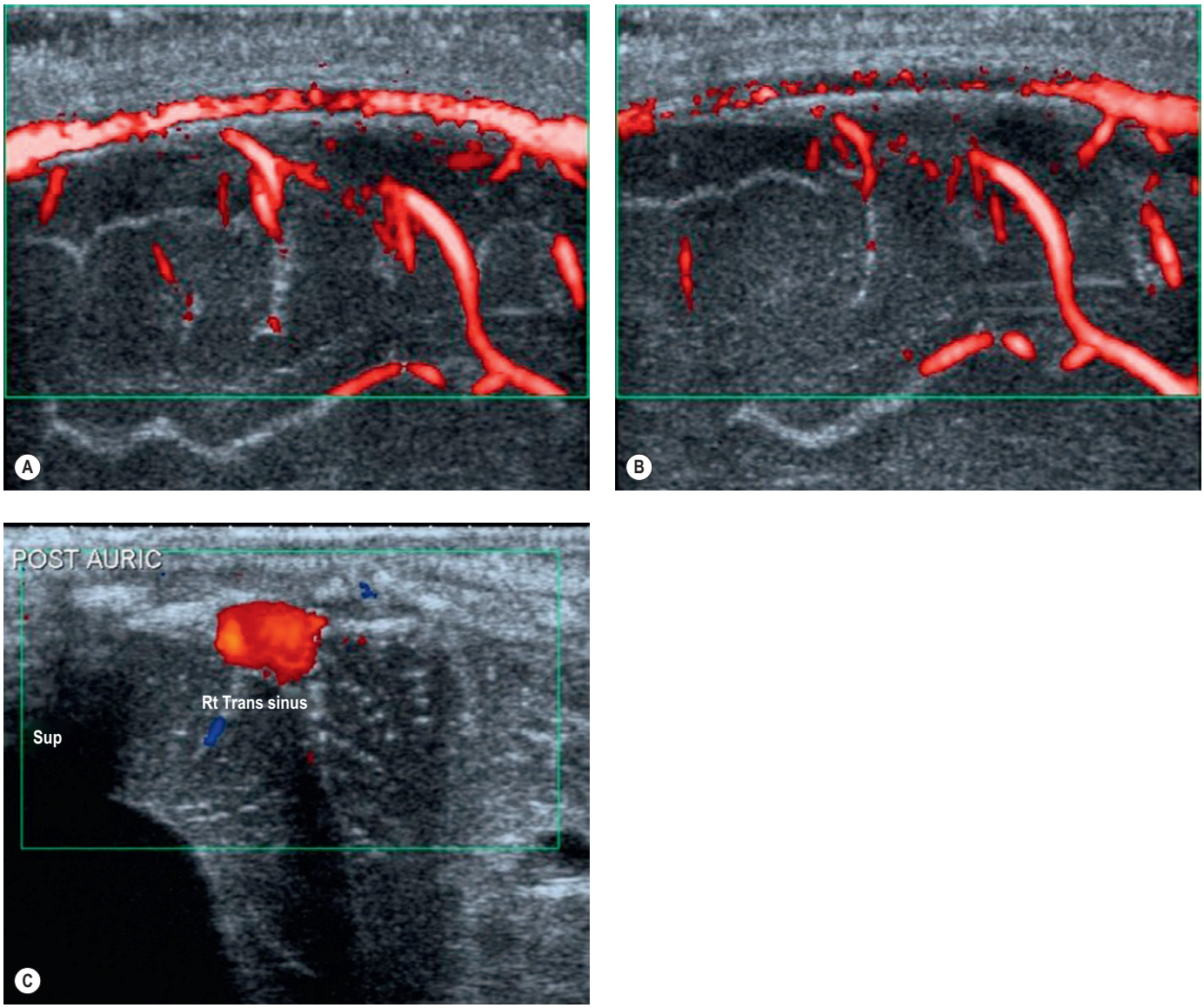

Figure 65.7 Colour Doppler of the venous system. A: Power Doppler evaluation of the superior sagittal sinus in the midline sagittal plane via the anterior fontanelle. Care must be taken not to inadvertently compress the fontanelle during scanning **(B)**, as this can lead to diminished detection of flow. **C:** Coronal view of the right transverse sinus via the lambdoid suture. The tentorium is seen deep to the sinus, with the occipital lobe above (to the left of the image) and the cerebellum below (to the right of the image).

Ventricular dilatation occurring in the context of IVH can be multifactorial. Large acute IVH can directly distend the ventricles. However, in the majority of cases the dilatation is a combination of obstruction to CSF flow through the ventricular system by clot and adhesions, and blockage of CSF resorption at the level of the arachnoid granulations by haemorrhagic debris.

In advanced cases GMH-IVH is associated with areas of periventricular haemorrhagic infarction (PHI), which is unilateral in two-thirds of cases, and strikingly asymmetrical in the majority of the remaining cases.[35] Studies have shown the infarction is likely to be predominantly venous in origin.[36,37] The deep hemispheric parenchyma drains towards the terminal vein, which passes through the region of the germinal matrix before draining into the deep venous system. GMH has been shown to distort the terminal vein and reduce venous flow as detected by Doppler ultrasound (Fig. 65.8).[38] It has thus been proposed that venous congestion in the parenchyma resulting from GMH leads to the haemorrhagic parenchymal infarction. Other factors, such as systemic haemodynamic parameters and ventricular dilatation (which could lead to increased pressure and shearing forces in periventricular tissue) could contribute to the tissue injury.

GMH-IVH and PHI are early postnatal events, with 75% of intraventricular haemorrhages being detectable in the first 3–5 days.[39] It is also clear from clinical practice that GMH-IVH can occur as an in-utero event, as evidenced by detection of haemorrhage on fetal MRI, and the finding of maturing GMH-IVH on CUS performed on the first day of life.

Several grading systems have been proposed for GMH-IVH. The most commonly used is the system described by Papile in 1978 which was originally based on CT findings, but has since been widely applied to ultrasound (Table 65.3).[40] This system has the advantage that it is relatively simple to use, is widely enough applied to be part of the 'common lexicon' of neonatal care, and the grades relate well to outcome. However, recently there has been criticism of the system based on the fact that the four-point grade system implies that GMH-IVH and periventricular haemorrhagic infarction are a pathophysiological continuum of increasing severity. This implication is misleading as IVH can occur without GMH

Table 65.3 Grading of germinal matrix – intraventricular haemorrhage

Traditional (Papile) grading		PROGNOSIS: Death	PROGNOSIS: Cerebral palsy in surviving infants	Descriptive grading
Grade I	Isolated GMH			GMH (yes or no) IVH (yes or no) Ventricular dilatation (yes or no) Parenchymal abnormality (yes or no)
Grade II	GMH with IVH, but no ventricular dilatation			
Grade III	IVH with ventricular dilatation	27.6%	7.4%[a]	
Grade IV	Parenchymal involvement (with or without IVH or ventriculomegaly)	37%	48.7%[a]	

[a]*Brouwer A, et al., Neurodevelopmental outcome of preterm infants with severe intraventricular hemorrhage and therapy for post-hemorrhagic ventricular dilatation. The Journal of Pediatrics 2008;152:648-654.*

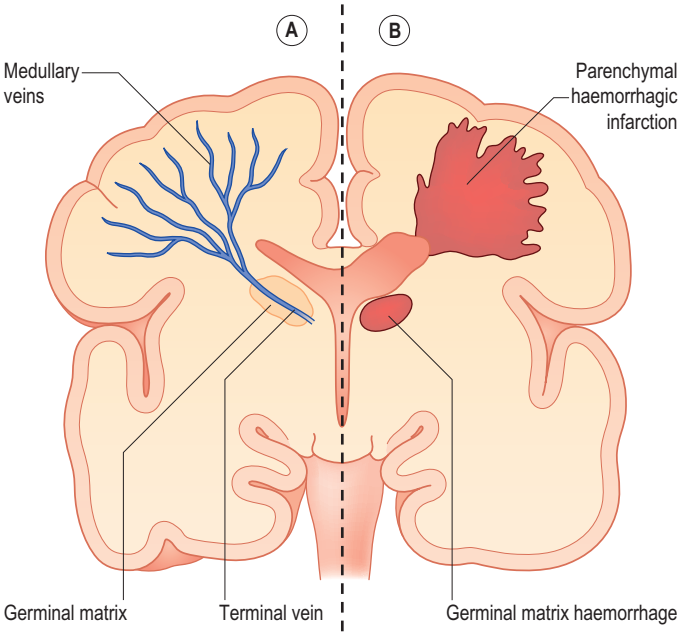

Figure 65.8 Venous anatomy and parenchymal haemorrhagic infarction. A: Medullary veins converge to form the terminal vein in the region of the germinal matrix. **B:** In the context of GMH and ventricular distension, venous congestion has been proposed as a mechanism precipitating parenchymal haemorrhagic infarction (modified from Volpe JJ. Brain injury in the premature infant – from pathogenesis to prevention. Brain and Development 1997; 19: 519–534, figure 2).

(in the case of choroid plexus haemorrhage), ventricular dilatation can occur for reasons other than the presence of IVH, and parenchymal haemorrhage is not a direct extension of the IVH into parenchyma (as evinced by some cases occurring in the absence of any or significant IVH). For this reason a more descriptive approach to GMH-IVH has been proposed where the independent components constituting the grades are listed if present (final column in Table 65.3).[41]

Ultrasound findings

Acute GMH is identified as echogenicity in the subependymal location immediately anterior to the caudothalamic notch (Fig. 65.9). Size varies considerably, and the haemorrhage may be unilateral or bilateral. As the GMH matures it becomes less echogenic and will often develop a hypoechoic core as the haematoma liquefies (Fig. 65.9C). A cyst can sometimes be identified at the site of GMH in the late stages of evolution, but small GMH often resolves completely on ultrasound.

IVH is identified as material of increased echogenicity within the ventricular system. Acute haemorrhage is hyperechoic to brain parenchyma. Small amounts of IVH will often be adherent to the ventricular margin (Fig. 65.10). It can be difficult to differentiate small IVH from the choroid plexus. Haemorrhage adherent to the choroid plexus is often slightly hyperechoic to the choroid plexus, and can be expected to evolve or resolve on subsequent scans. A useful rule of thumb is that the choroid plexus does not extend more anteriorly in the lateral ventricles than the foramina of Monro, and does not extend into the occipital horn, and hence echogenic material at these sites indicates IVH as opposed to normal choroid plexus. IVH within the third ventricle can be identified as echogenic material which often adheres to the massa intermedia or settles within the anterior recesses. Haemorrhage can also be seen within the cavum septum pellucidum and cavum vergae as part of the IVH spectrum, and this should be actively looked for.

When large, IVH fills and expands the ventricles and can track between the ventricles via the third ventricle. As IVH matures it becomes progressively more hypoechoic (Fig. 65.11). Small IVHs disappear over several days to several weeks. Larger IVHs tend to undergo a process of central liquefaction before clot breakdown and resorption, often leaving debris and stranding within the ventricles for several months.

IVH is usually accompanied by the development of ependymal echogenicity (see Fig. 65.32A). This is presumed to be a reaction of the ependyma to the presence of irritant blood products in the ventricular system. Occult IVH can be identified by the finding of transient ependymal echogenicity, often accompanied by a transient, minor increase in ventricular size, but without the identification of overt IVH.

Ultrasound is of critical importance for detecting and monitoring progressive ventricular dilatation with the aim of identifying infants who require CSF aspiration or shunt insertion. Measurement of ventricular size, for example with the ventricular index (VI), can be of use in serial ultrasound to demonstrate developing hydrocephalus. Clinical factors, including measurement of head circumference, will also inform the decision to intervene. The assessment of post-haemorrhagic ventricular dilatation is dealt with in detail in the section on hydrocephalus.

PHI appears as areas of parenchymal echogenicity (sometimes described as a 'flare') with associated mass effect (Fig. 65.12). Periventricular white matter in the frontal, parietal and temporal regions is most commonly affected. With maturation, the haemorrhagic infarction becomes more hypoechoic and may undergo liquefaction. Breakdown of the adjacent ventricular wall can allow communication of the haemorrhagic cavity with the ventricle. During this phase, there is frequently an echogenic mass, probably a composite of tissue debris and organised haemorrhage, within the cavity with the ventricle extending through the defect in the ventricular margin into the underlying portion of the ventricle.

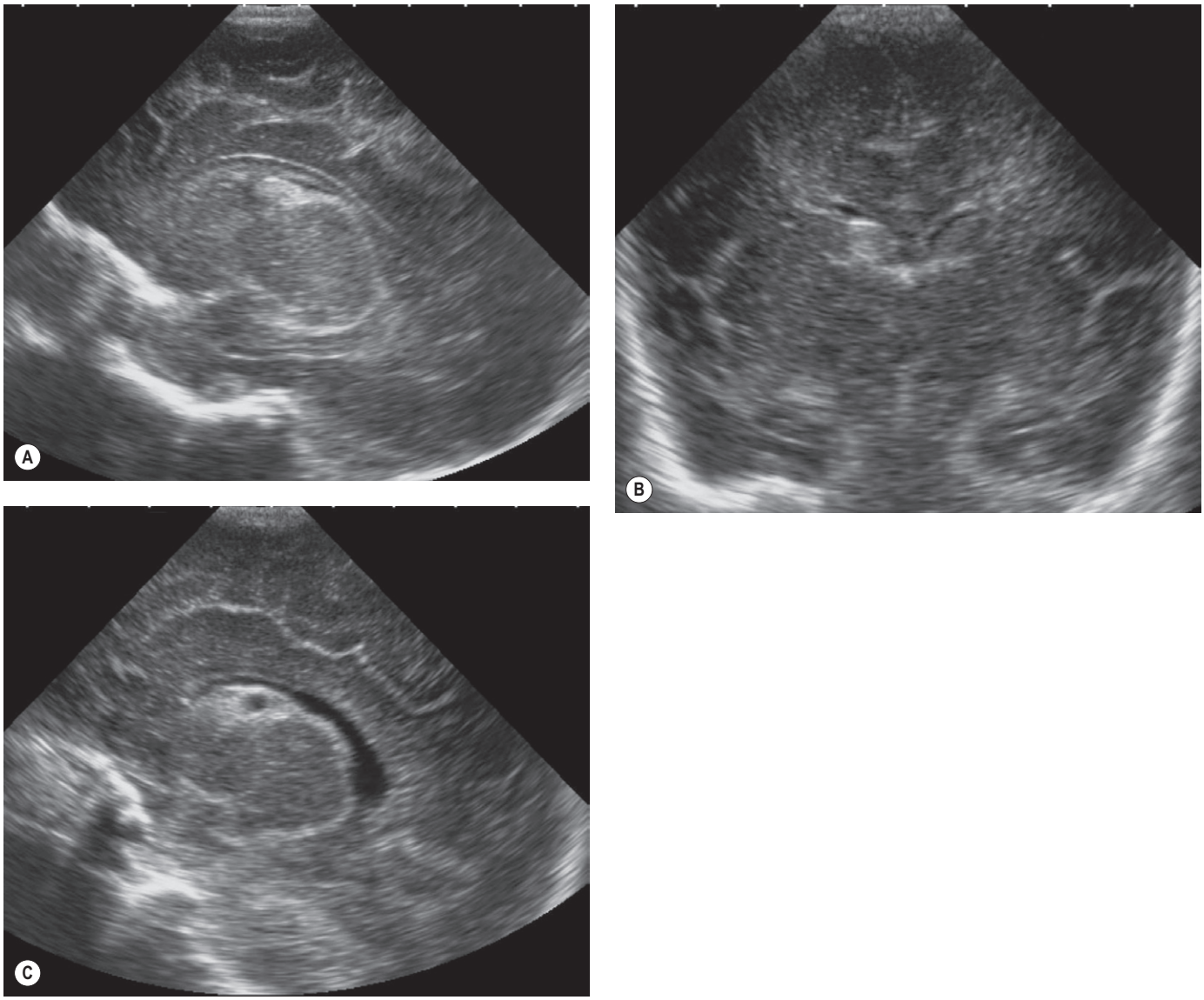

Figure 65.9 **Germinal matrix haemorrhage**. **A, B:** Right GMH, day 7 scan. **C:** Day 21 scan showing evolution of the right GMH with development of central hypoechogenicity.

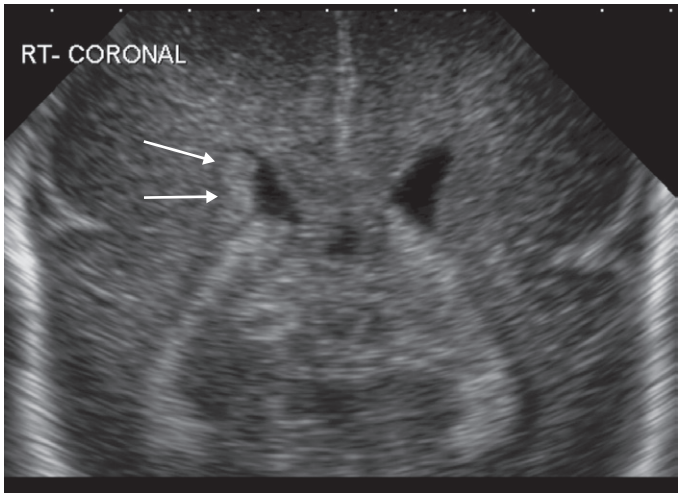

Figure 65.10 **Small right IVH** adherent to the lateral wall of the left lateral ventricle (arrows).

It is clear that that GMH-IVH and PHI can occur in utero, with unexpected GMH and IVH elegantly demonstrated by fetal MRI. When CUS of neonates in the first few days shows haemorrhagic changes which are more mature than would be expected, an in-utero event is likely. In-utero GMH leading to a mature, encysted appearance on early postnatal CUS is one of the more common causes of germinolytic cysts.

Periventricular leukomalacia

Periventricular leukomalacia (PVL) is the result of ischaemic injury in the border zones and arterial end zones of the preterm brain.[42] This particular pattern of ischaemic injury is specific to preterm infants because of the distribution of the arterial border zones and end zones in the immature brain (Fig. 65.13).[43,44] The deep periventricular zones fall at the watershed between the long penetrating distal branches of the middle cerebral artery (and to a lesser extent the anterior and posterior cerebral arteries) and lenticulostriate perforating vessels. These periventricular watershed zones are thus susceptible to ischaemia during falls in cerebral perfusion pressure, as can occur during episodes of cardiorespiratory distress. This effect may be exacerbated in very preterm infants who have

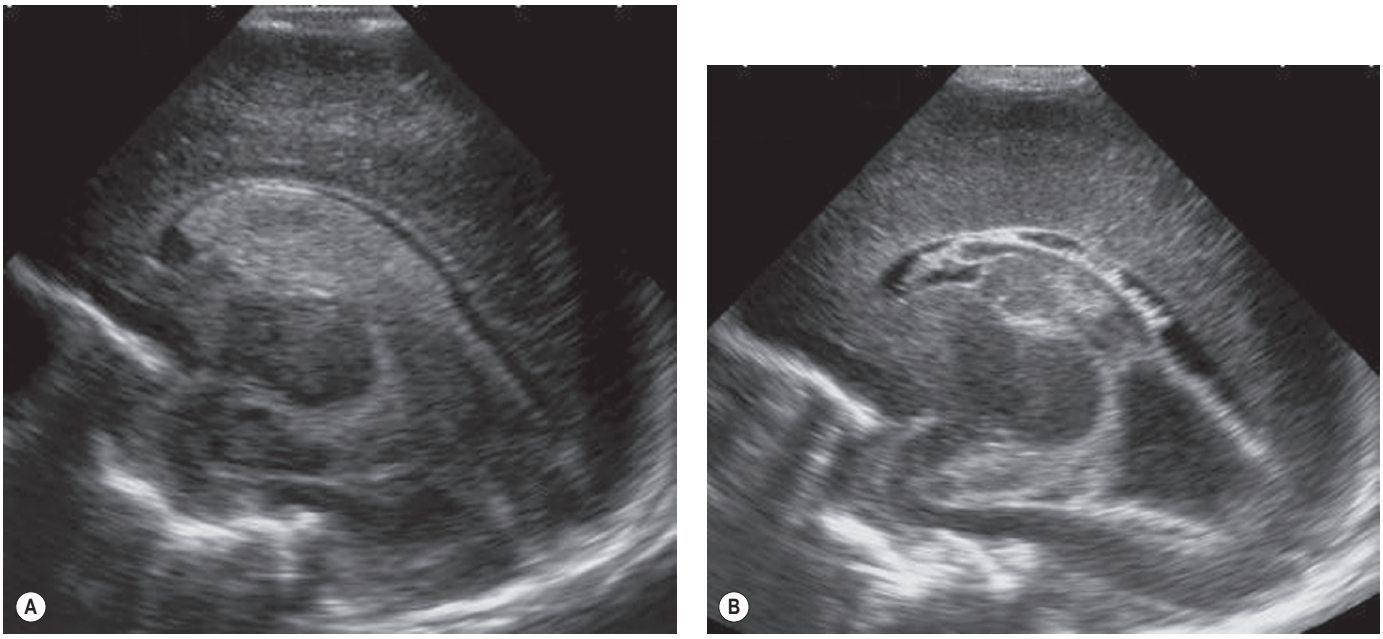

Figure 65.11 Evolution of intraventricular haemorrhage. A: Day 8 scan showing GMH and IVH filling and expanding the lateral ventricle. **B:** Day 36 scan showing hypoechogenicity within the intraventricular haematoma and retraction of clot in the frontal horn.

pressure-passive cerebral circulation. Additionally, there is a maturation-dependent susceptibility of oligodendrocytes in the immature brain, and hence white matter in very preterm infants is at increased risk of cellular injury in the watershed territories during reduced cerebral perfusion.[42]

Incidence of PVL varies depending on the population studied and method of identification used. PVL is found on ultrasound in 3–15% of infants with birth weights below 1500 g, but figures are much higher when based on histopathology. Incidence of PVL appears to peak around 28 weeks, but it is unclear whether worse survival outcomes below this age skew the peak upwards.[42]

As PVL matures, two main patterns of PVL emerge, namely non-cystic and cystic. The non-cystic pattern is more common and is characterised histologically by astrogliosis, oligodendrocyte injury and subsequent impairment of myelination.[42] Cystic PVL is characterised by focal necrosis within periventricular white matter with subsequent cyst formation.

Ultrasound findings

PVL usually becomes apparent on CUS during the first few days after the episode of cardiovascular compromise, although this itself is not always documented.[45] The ultrasound findings of PVL in the acute stages are of increased echogenicity in the white matter superolateral to the margins of the lateral ventricles (Fig. 65.14). At its most subtle, PVL may be detected as a coarsening of the white matter echotexture. Unlike PHI, PVL is rarely strikingly asymmetrical and does not have significant associated mass effect.

The echogenicity of PVL can increase over the first week following initial detection. After this time, non-cystic PVL starts to become less obvious, to the point where it is no longer detectable. Cystic change in PVL tends to become obvious within the first week following initial detection. The appearance tends to be of numerous small cysts distributed throughout the PVL (Fig. 65.14B and C), as opposed to the development of a solitary large cavity as seen with PHI. Juxtaventricular cysts can be differentiated from frontal cystic PVL by the fact that the former do not evolve or have surrounding parenchymal echogenicity, and lie immediately lateral to the frontal horns (as opposed to superolateral location of cystic PVL).[21]

With maturation the cysts may coalesce, and breakdown of the adjacent ventricular wall may lead to communication of the ventricle with the PVL. This is manifest on CUS as irregularity and outpouching of the ventricular wall at the sites of previous PVL. Over the following 1–3 months the cysts disappear, leaving gliosis and periventricular white matter volume loss.[42]

Although CUS is sensitive for the detection of cystic PVL, it is well recognised that CUS can be insensitive for non-cystic PVL. Comparison of CUS with histology has shown that 30–70% of white matter abnormalities are not visualised on CUS.[46–48] It could be suggested that improvements in ultrasound technology since these studies were performed might improve detection of non-cystic PVL. However, a more recent study of CUS in very low birth weight, preterm infants during the first 6 weeks of life has shown a sensitivity of only 26% and positive predictive value of 36% for the detection of non-cystic PVL, compared to a gold standard of MRI performed at term-equivalent age.[49] For this reason, many centres now perform MRI in surviving ex-preterm infants at term-equivalent age as a documentation of the extent of white matter injury.

Severe diffuse white matter injury leads to generalised atrophy which can be detected on CUS as parenchymal volume loss with gradual enlargement and contour irregularity of the ventricles and widening of the cerebral sulci (Fig. 65.14B). Differentiation from hydrocephalus can be made by correlation with serial head circumference measurements which will increase disproportionately if hydrocephalus is present, and may fail to increase appropriately in the presence of cerebral atrophy. In reality, ventriculomegaly detected on ultrasound is often a combination of atrophy and hydrocephalus secondary to previous IVH or intracranial infection.

Term infants

Hypoxic ischaemic encephalopathy

Hypoxic ischaemic encephalopathy (HIE) describes the syndrome of neurological dysfunction resulting from perinatal asphyxia. Perinatal asphyxia occurs in 3-5 infants per 1000 live births, and HIE develops in 0.5-1 per 1000 live births.[50] There has been a continued trend towards decreasing incidence of HIE in the United Kingdom, the decline being attributed to improved perinatal care, although HIE remains a significant clinical problem.[51]

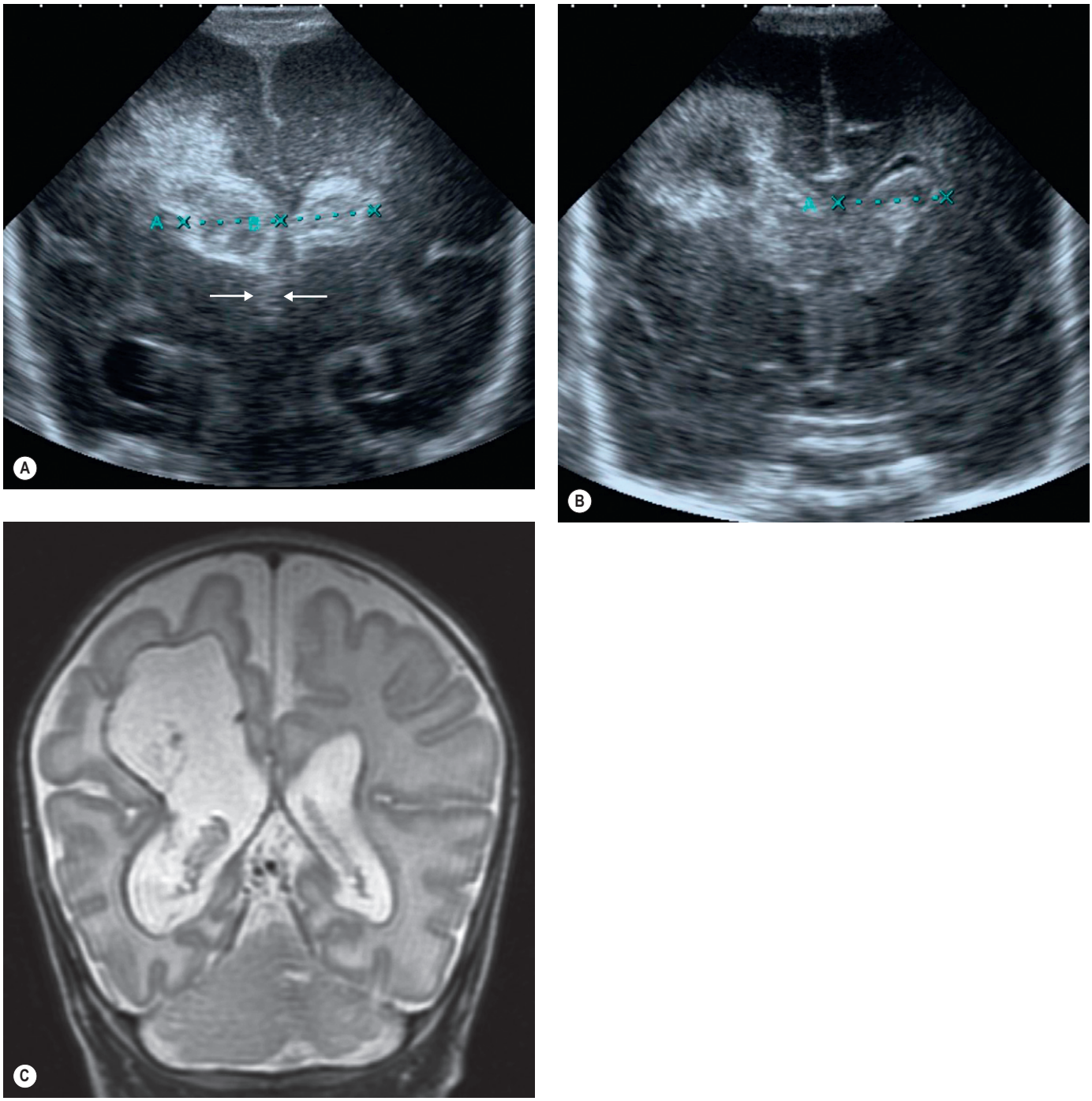

Figure 65.12 **Periventricular haemorrhagic infarction** in a 26-week gestational age infant. **A:** Day 2 scan showing right periventricular 'flare'. Note also IVH in the lateral ventricles and third ventricle (arrows). **B:** Day 9 scans demonstrating development of central hypoechogenicity within the area of PHI. **C:** Coronal T2-weighted MRI scan at the equivalent of term age. The area of PHI has undergone cavitation with free communication with the lateral ventricle. A small amount of debris/stranding persists in the cavity.

Perinatal asphyxia is manifest clinically as progressive hypoxia and hypercapnia, and the development of metabolic acidosis.[50] Unless the asphyxial state is reversed, a pathophysiological cascade ensues which results in cell death in the fetal/infant brain. Structures within the brain show different susceptibility to cellular injury, with acute severe asphyxia resulting in preferential injury to the thalami, basal ganglia and brainstem. Cortical injury is also frequently seen, with the peri-Rolandic cortex being particularly susceptible in term infants.

Diagnosis of HIE is primarily clinical, and is supported by laboratory, neurophysiological and neuroimaging criteria. Clinical features and grading of HIE are shown in Table 65.4. In recent years MRI has gained prominence in the imaging evaluation of HIE. It is clear that MRI is sensitive for detecting HIE and is the current clinical imaging gold standard. However, many of the published head-to-head comparisons of ultrasound and MRI are limited by wide interval between US and MRI being performed, were performed using ultrasound systems which would now be considered out of

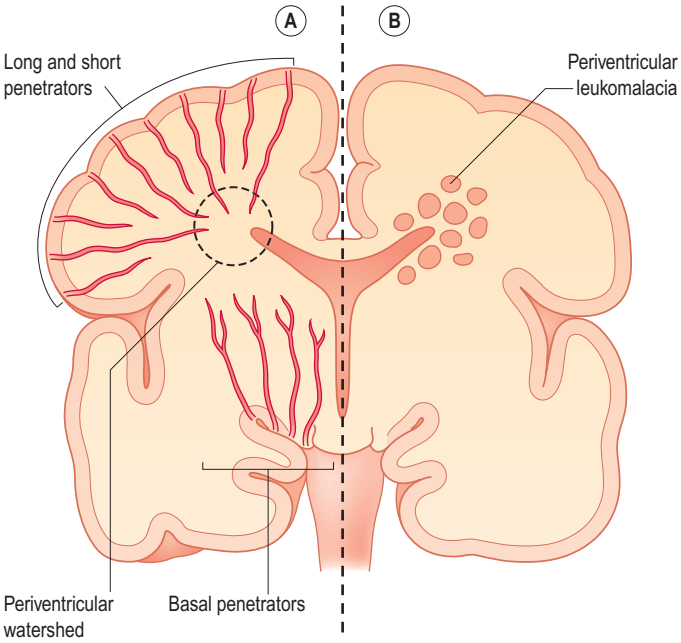

Figure 65.13 Arterial anatomy and periventricular leukomalacia. A: In the preterm infant the watershed areas between the basal and surface penetrating arteries fall in the periventricular area (modified from Volpe JJ. Brain injury in the premature infant – from pathogenesis to prevention. Brain and Development 1997; 19: 519–534, Figure 65.9). **B:** Typical location of PVL (modified from Weindling M. Clinical aspects of brain injury in the preterm infant. In: Lagercrantz H, Hanson M, Evrard P, Rodeck C. (Eds) The Newborn Brain: Neuroscience and Clinical Applications. Cambridge, UK: Cambridge University Press (2001). pages 443–478. Fig 20.1).

Cranial ultrasound findings in HIE

- Brain swelling (ventricular effacement).
- Diffuse increased white matter echogenicity.
- Exaggerated grey–white matter differentiation.
- Basal ganglia echogenicity (particularly thalamic).
- Cortical echogenicity.
- Haemodynamic alterations demonstrated by Doppler.

date, or with non-optimised ultrasound techniques.[6] State-of-the-art ultrasound still has an important role in the evaluation of post-asphyxiated infants, providing detailed structural and haemodynamic information at the bedside without the logistical and safety issues involved with MRI.

Ultrasound findings

One of the earliest detectable changes on B-mode ultrasound is of transient brain swelling. This is often visible on early scans as effacement of the third and lateral ventricles (Fig. 65.15), with a return to normal ventricular visualisation after several days. Brain swelling may be accompanied by alterations in parenchymal echogenicity, but in the authors' experience the transient loss of ventricular visualisation can be the only B-mode finding in cases of low grade HIE.

The typical description of sonographic findings of brain parenchyma in HIE is of diffusely increased echogenicity of the brain parenchyma (Fig. 65.15). In the early phase, high-resolution imaging reveals an increase in echogenicity of the subcortical white matter, resulting in increased grey–white matter differentiation (GWMD) with relative hypoechogenicity of the cortical stripe. The white matter echogenicity can range from subtle to gross. Although the increase in white matter echogenicity is often diffuse, with high-resolution imaging it is possible to identify focal lesions which show good correlation with ischaemic lesions identified using DWI.[6] For the inexperienced sonographer inappropriate gain settings may lead to over-reporting of diffuse white matter echogenicity. As well as optimising machine settings, identification of increased GWMD using cortical echogenicity as a reference can help to minimise interpretation error. It should be noted that increased white matter echogenicity is not specific for HIE and may be seen in other white matter processes such as disorders of myelination.

Selective neuronal necrosis in response to prolonged ischaemia preferentially affects the cerebellar cortex, brainstem, thalami and hippocampi[52]. Sonographically deep grey matter injury is represented by echogenicity which appears between 1 and 5 days following the hypoxic episode (Fig. 65.16). In mild cases the echogenicity may be transient. In severe cases neuronal death is accompanied by gliosis and hypermyelination of astrocytic processes resulting in marked basal ganglial echogenicity, termed status marmoratus. Extensive infarction in the thalami, particularly if accompanied by haemorrhage, should always prompt a search for thrombosis of the straight sinus and internal cerebral veins, as described below.

Additionally, in the term neonatal brain layers 3, 5 and 6 of the neocortex show a particular susceptibility to ischaemia. Cortex within the depths of the sulci, particularly in the frontal and parietal regions, is preferentially involved. Focal cortical injury is identified on ultrasound as cortical echogenicity and swelling, and can be extensive (Fig. 65.17). When the cortical infarction is widespread, it may not be possible to clearly identify alterations in GWMD due to simultaneous involvement of both grey and white matter.

Watershed infarction is an uncommon but well-recognised pattern of ischaemic injury in term infants.[53] Ischaemic lesions are seen in the parasagittal cortical watershed areas between the MCA and ACA and MCA and posterior cerebral artery (PCA) territories, in a similar distribution to cortical watershed infarction seen in older children and adults. This is therefore in contrast to the pattern of watershed abnormality seen in premature infants where the watershed zone is located in the periventricular white matter. In the term age group watershed infarction results from partial asphyxia or hypotension resulting in reduced perfusion to the border zones between the major arterial territories.[52,54]

CUS shows bilateral parasagittal echogenicity and swelling involving the cortex (Fig. 65.18A). In contrast to infarction occurring in the territory of the major cerebral arteries, the changes associated with watershed infarction occur along the boundary zones between the major arterial territories. Serial scanning may reveal progressive atrophy and cystic encephalomalacia in the affected tissue over the weeks following the insult (Fig. 65.18B). Preferential atrophy at the depth of sulci leads to ulegyria, with the gyri taking on a mushroom-shaped appearance. When suspected, findings can be confirmed by MRI.[55] Superior sagittal sinus thrombosis, which can also result in parasagittal swelling and infarction, should be actively excluded by colour Doppler examination.

Evolution of appearances on cranial ultrasound in surviving infants post-HIE tends to be characterised by atrophy which is often more widespread than the extent of injury visualised on the acute imaging. The onset of atrophy can be rapid in severe cases, appearing after 3–4 weeks. In practice, once the acute phase of HIE has passed and provided the infant remains clinically stable, there is little role for repeated cranial ultrasound. MRI scanning at the age of one year is often performed to evaluate the end-stage appearances of the post-HIE brain.

Doppler ultrasound is able to detect the cerebral haemodynamic changes that occur in the hours to days following birth asphyxia, and Doppler-derived biomarkers have been shown to have a predictive value for neurological outcome.

A number of different patterns of haemodynamic response have been described in early HIE, all of which reflect to some extent the

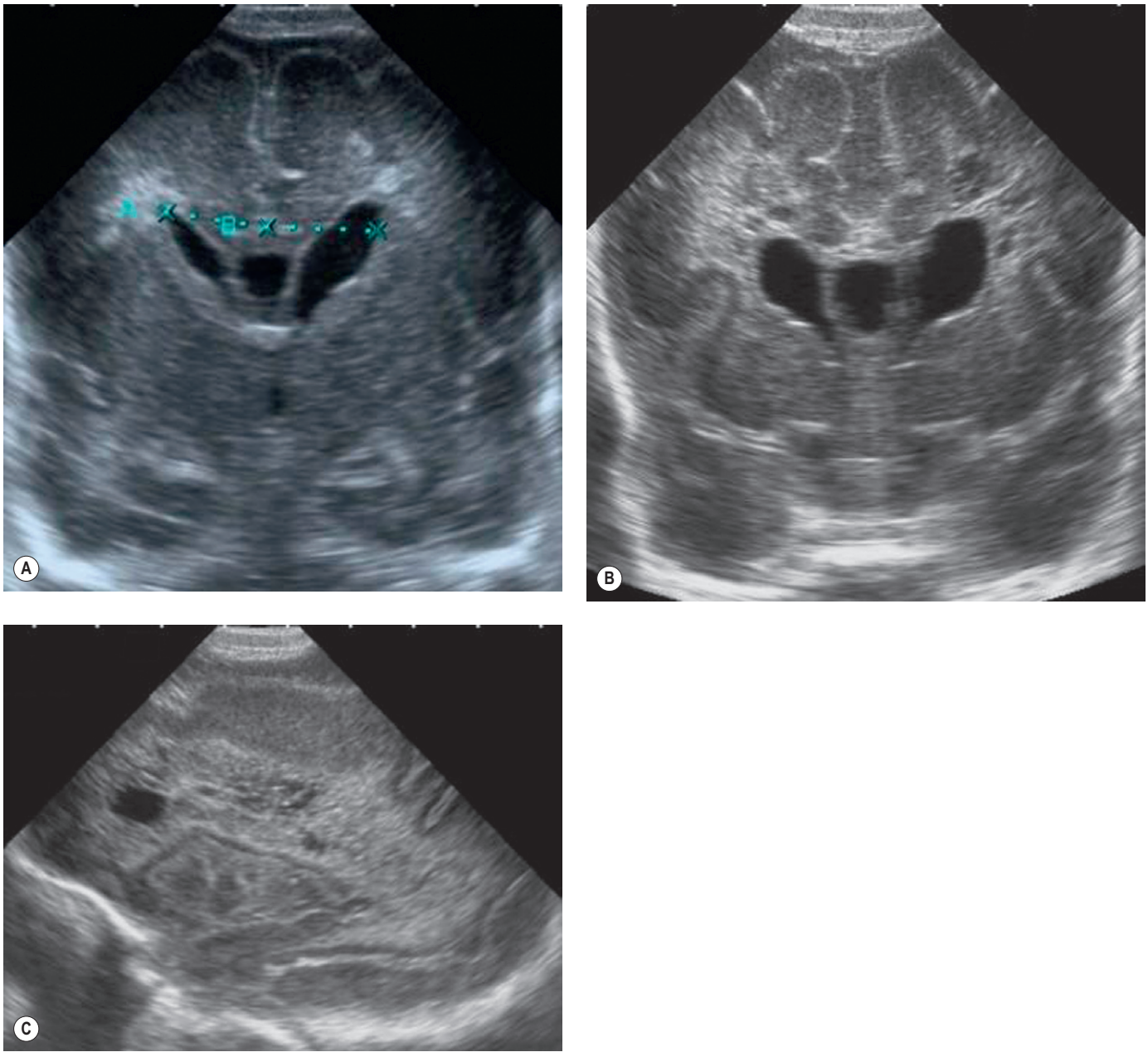

Figure 65.14 **Periventricular leukomalacia** in a 26-week gestational age infant. **A:** Day 28 scan showing areas of increased echogenicity in the periventricular regions bilaterally. **B, C:** Day 42 scan showing evolution to cystic PVL. Note also widening of subarachnoid spaces and ventricular enlargement as a result of progressive atrophy.

Table 65.4 **Clinical features and grading of HIE (adapted from Sarnat and Sarnat, 1976[a])**

Grade	Mild	Moderate	Severe
Level of consciousness	Alert	Lethargy	Coma
Tendon reflexes	Normal or hypertonia	Hypotonia	Flaccidity
Primitive reflexes	Uninhibited	Depressed	Absent
Autonomic function	Sympathetic overactivity	Generalised parasympathetic	Both systems depressed
Seizures	Absent	Common; focal or multifocal	±Frequent and often refractory
Others	Irritability, jitteriness	Brainstem dysfunction	±Elevated intracranial pressure
Outcome	Normal	20–40% abnormal	100% abnormal

[a]*Sarnat HB and Sarnat MS. Neonatal encephalopathy following fetal distress. A clinical and electroencephalographic study. Archives of Neurology, 1976:33:696-705.*

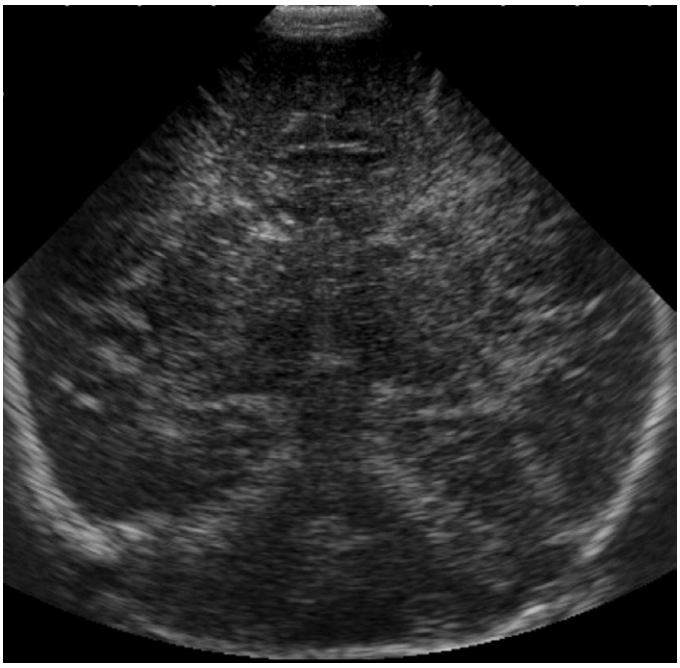

Figure 65.15 Hypoxic ischaemic encephalopathy. Day 2 cranial ultrasound of a term infant showing effacement of the ventricular system with diffuse increase in echogenicity of the brain parenchyma.

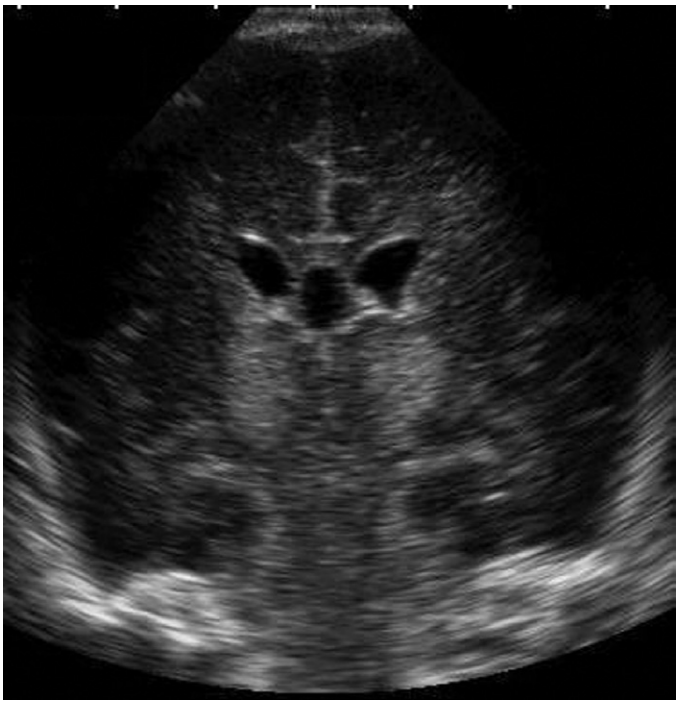

Figure 65.16 Bilateral thalamic echogenicity following perinatal asphyxia.

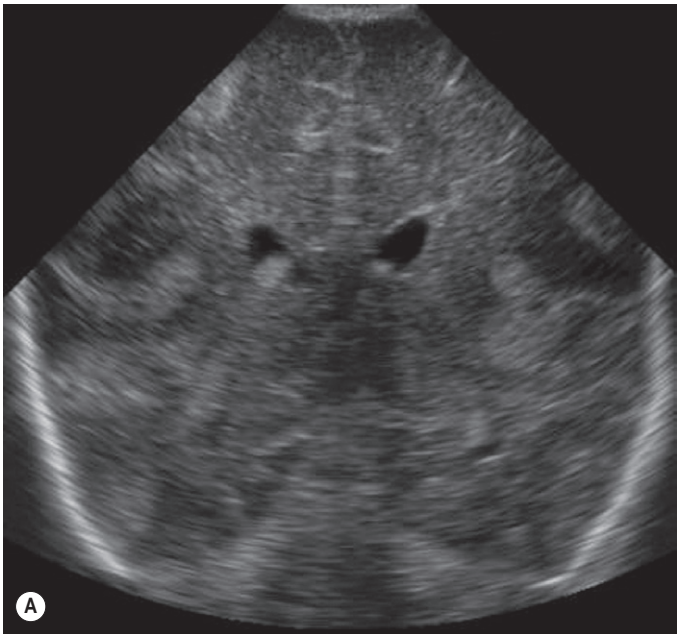

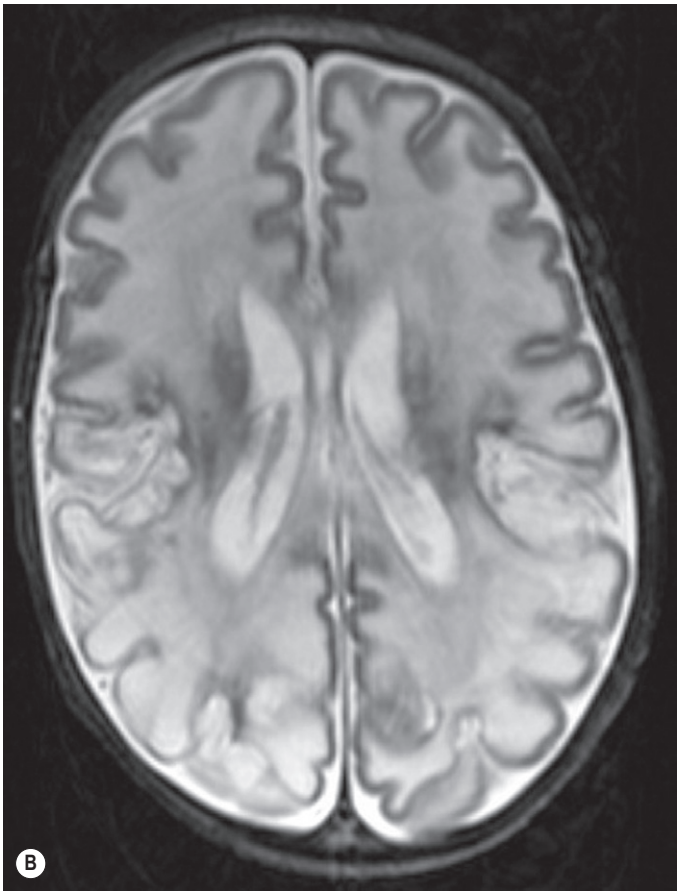

Figure 65.17 Diffuse cortical ischaemic injury. A: Day 3 cranial ultrasound of a term infant showing diffuse swelling and hyperechogenicity of the cerebral cortex. **B:** Follow-up MRI at 2 months reveals cortical thinning and underlying gliosis in the perisylvian and parieto-occipital regions, particularly on the right. The frontal lobes are relatively spared.

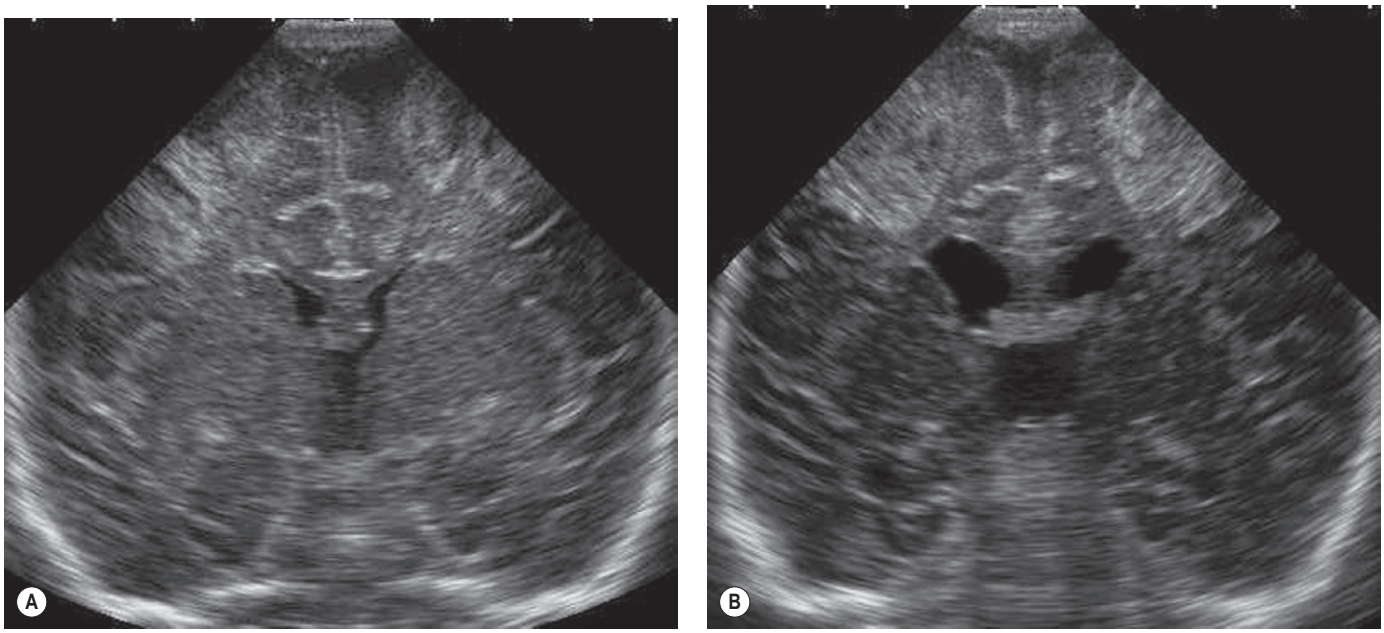

Figure 65.18 Watershed infarction. Term infant undergoing abdominal surgery in the first week of life. Watershed infarction thought to have resulted from haemodynamic instability during the perioperative period. **A:** Cranial ultrasound 1 day after surgery showing cortical swelling and hyperechogenicity in the parasagittal areas bilaterally. **B:** Ultrasound at 1 month showing more clearly defined bilateral parasagittal changes. Note the sparing of the paramedian anterior cerebral artery territories, and the onset of atrophy as evidenced by expansion of the ventricles and subarachnoid spaces.

loss of cerebrovascular regulation following the ischaemic insult. Abnormal mCBV appears to be a robust marker of poor prognosis, with values greater than 3 standard deviations above or more than 2 standard deviations below the normative mean having a 94% positive predictive value for death or severe disability.[56] There is some evidence that those infants with low mCBV at 12 hours of age may have a slightly better prognosis than those with elevated mCBV.[57,58] Derangements in vascular resistance are common in HIE. RI values below 0.55 (Fig. 65.19) are associated with a poor outcome,[5,59] with an 84% positive predictive value of death or severe disability.[56] Elevated RI values are seen when EDV is diminished, absent or reversed and are also considered a poor prognostic marker.[60,61] It should, however, be noted that many of the studies of the utility of Doppler for predicting prognosis were performed in the late 1980s and early 1990s, and hence will not take account of potential improvements in prognosis due to recent improvements in neonatal care.

Timing is of critical importance in view of both the normal physiological changes following birth and the time course of cerebral haemodynamic changes in evolving HIE. Doppler measurements made within the first 6 hours are of little value as they are frequently normal.[57,62] By between 6 and 12 hours measurable differences in cerebral Doppler measurements of normal infants and those with HIE emerge,[60] with robust data showing significant intergroup differences by 12 hours.[57,58] Abnormal Doppler indices are present by 62 hours and are unlikely to emerge beyond this time.[5] Abnormal Doppler measurements can return to normal as early as day 2, and are usually all normalised by day 7.[63] Thus it can be seen that there is a relatively short window for optimal detection of Doppler abnormalities which lies between 12 and 36 hours post-delivery.

Cerebral haemodynamic parameters can potentially be affected by a number of other physiological factors present in (or imposed upon) encephalopathic neonates. Cardiovascular parameters such as myocardial dysfunction[64] and patent ductus arteriosus[65] can impact on cerebral circulation. Therapeutic measures such as inotropic support[66] or indomethacin administration[67] can potentially affect Doppler measurements. Mechanical ventilation does not appear to alter cerebral haemodynamics per se, but arterial carbon dioxide levels, which may be altered by mechanical ventilation, can affect cerebral blood flow.[68] Hypocapnia ($PaCO_2$ <30 mmHg) can result in loss of end-diastolic flow. Conversely, hypercapnia can result in elevated end-diastolic flow due to vasodilatation in cerebral arterioles.[69] Induced hypothermia is used as a therapeutic measure for HIE in some centres, and is associated with modest reduction in heart rate and stroke volume, and reduction in cardiac output by up to 67% of the level following rewarming.[70] At present, the effect of induced hypothermia on Doppler measurements of cerebral haemodynamics in HIE is unclear, and the relationship between Doppler measurements and outcome is undefined in this group of patients.

Arterial infarction

Perinatal arterial territory infarction can occur in term infants as an apparently sporadic and idiopathic event. Such infants typically have an absence of clinical evidence of significant hypoxia or haemodynamic compromise, and have good Apgar scores at birth. Infants often present with seizures in the first 72 hours, but presentation can be delayed or cases may be identified incidentally during neuroimaging of the neonate for other reasons.[71] A prevalence of between 1 in 2300 and 4000 live births has been estimated based on symptomatic cases undergoing imaging, but the true incidence is unknown.[72,73] There is a male predominance, with 60% of neonatal strokes occurring in males infants.[74] The cause of neonatal arterial stroke remains unclear, but a high incidence of thrombophilia has been noted in these infants.[75]

The vast majority of arterial strokes occur in the MCA territories, although anterior and posterior cerebral artery territory infarcts also occur.[71] MCA territory infarction may involve the entire territory or cortical branches of the MCA territory. Arterial infarction is usually unilateral, although smaller areas of infarction can be present in the contralateral hemisphere, and occasionally the infarction can be truly bilateral. For unknown reasons, the left cerebral hemisphere is more frequently affected than the right hemisphere.

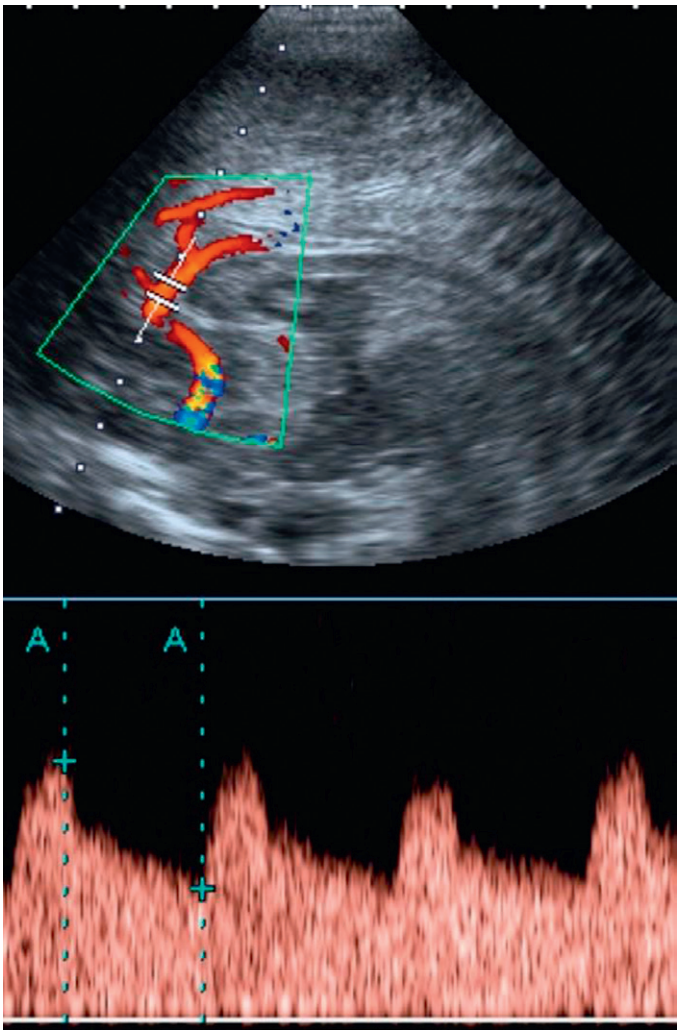

Figure 65.19 Doppler ultrasound in hypoxic ischaemic encephalopathy. Infant aged 18 hours following perinatal asphyxia. Resistive index of the anterior cerebral artery was measured as 0.50.

On ultrasound, acute arterial infarction appears as an area of echogenicity and swelling. In this regard, the appearances are non-specific, but the shape and distribution of the changes are characteristic for arterial territory infarction. The area of echogenicity and swelling is often wedge-shaped and conforms to the vascular territory. The cortex in particular may appear thickened and echogenic. Infarction of cortical branches will appear as smaller, more peripherally located areas of wedge-shaped echogenicity, again with cortical involvement.

Less commonly, territorial infarction of the basal perforating arteries may occur, particularly the lenticulostriate and thalamic perforator groups, which can also be detected on CUS. These tend to be seen as well-defined echogenic areas in the basal ganglia (Fig. 65.20), which may be single lesions representing a solitary perforator event, or may be multiple or associated with cortical infarction in the MCA territory suggesting a common thrombotic or embolic aetiology.

While it is clear that CUS can demonstrate arterial infarction, there has been debate regarding the value of the technique, with sensitivities for acute stroke of as low as 30% being reported.[76] When performed in the first 3 days CUS is abnormal in 68% of arterial strokes, and this figure can increase to 86% if CUS is performed between 4 and 14 days. However, even with this higher rate of detection of abnormality CUS only predicted correct

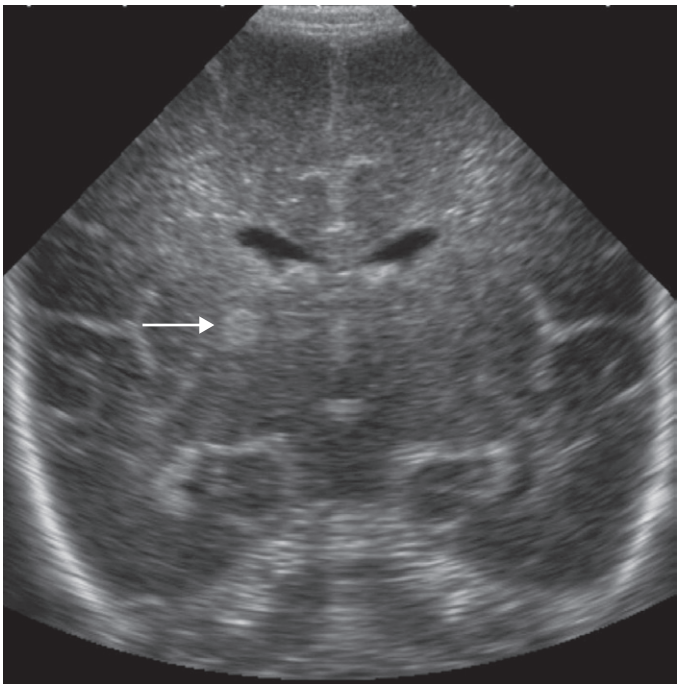

Figure 65.20 Solitary perforator infarct (arrow) in the right lateral thalamus/internal capsule.

lateralisation and site of the stroke in just over half of cases.[71] As with all ultrasound there is heavy dependence on the skill and knowledge of the user and the technical qualities of the system being used, but the general recommendation is that when arterial infarction is suspected clinically, whether CUS demonstrates a lesion or not, MRI scanning should be performed to confirm.

Parenchymal haemorrhage in term infants

Parenchymal haemorrhage in term infants can occur due to abnormalities of clotting including fetal alloimmune thrombocytopenia, following infarction or in the presence of underlying structural abnormalities such as an arterior venous malformation (AVM). Often, however, no underlying cause is found. Presentation is most commonly with seizures.[77] CUS demonstrates the haemorrhage as large solitary areas of echogenicity with associated mass effect (Fig. 65.21). The centre of the haematoma often shows heterogeneous hypoechogenicity consistent with liquefaction of haematoma. These areas proportionately increase and become more sonolucent as the haematoma matures and the blood products clear, until a residual cystic cavity remains.

There is growing awareness of the incidence of cerebellar haemorrhage in preterm infants.[78,79] The cause is not clear, but GMH-IVH or PHI are present in three-quarters of affected infants. This pattern of haemorrhage should be specifically looked for in preterm infants (Fig. 65.22).

Venous thrombosis and infarction

Venous thrombosis occurs in childhood at an estimated rate of 0.67 per 100 000 children per year, and within this group is most frequently seen in the neonatal group.[80] Risk factors for the development of venous thrombosis in neonates includes dehydration, sepsis, perinatal complications and prothrombotic states. Presentation is most commonly with seizures, decreased conscious level, jittery movements and occasionally focal neurology such as hemiparesis or cranial nerve signs.

Venous thrombosis leads to venous congestion and subsequent infarction and haemorrhage. The distribution of the parenchymal changes depends on the vessel involved. Thrombosis of the straight

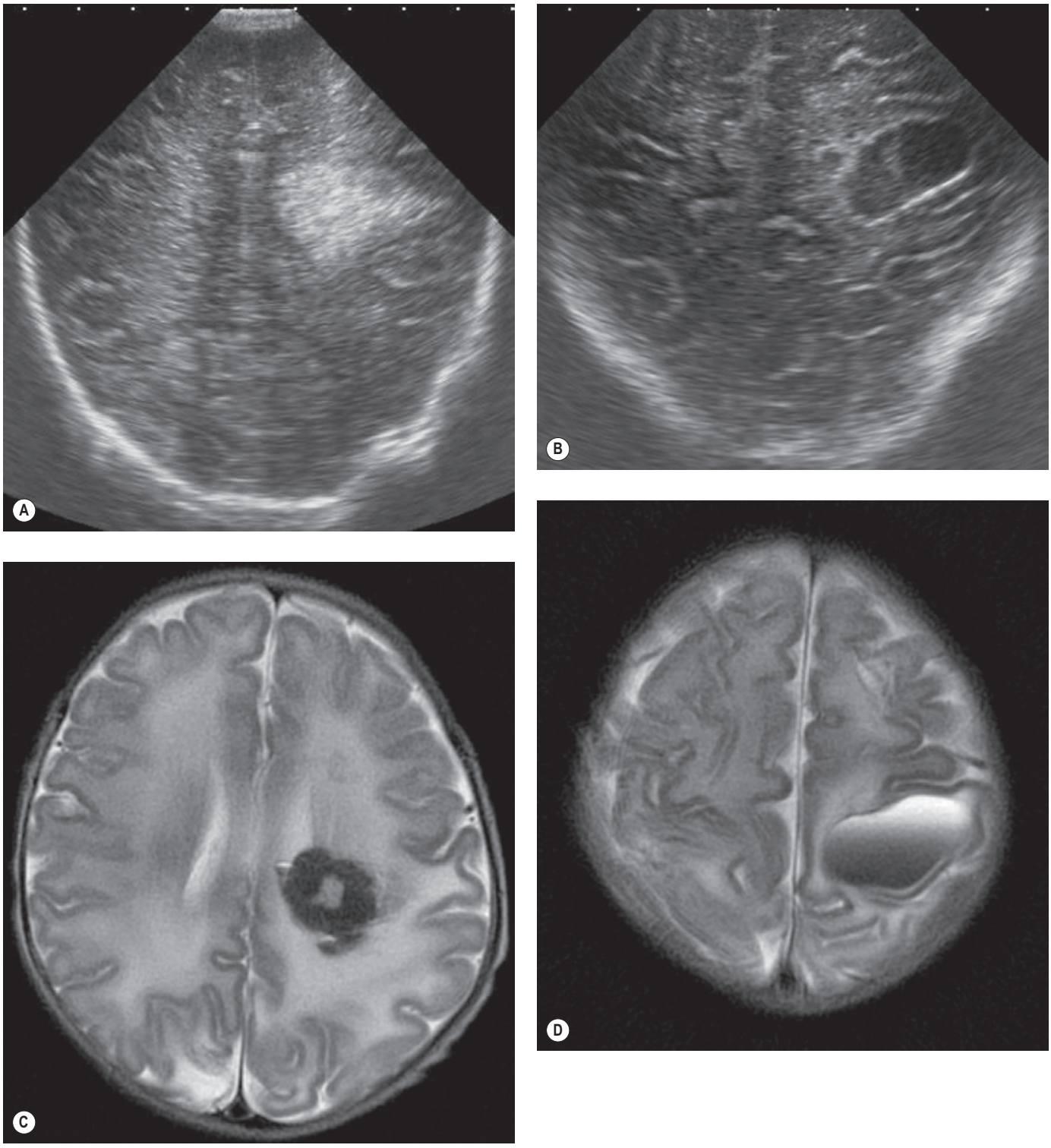

Figure 65.21 Left parietal parenchymal haematoma. Cranial ultrasound showing **(A)** echogenic haematoma in the centrum semiovale, with **(B)** a hypoechoic cystic area immediately dorsally. **C, D:** Respective axial T2-weighted MRI demonstrating close correlation with the cranial ultrasound findings.

sinus, vein of Galen and internal cerebral veins results in injuries to the deep cerebral structures, particularly the thalami. The thalamic changes are often bilateral but not always symmetrical. Thrombosis of superior sagittal sinus leads to changes in the frontal and parietal parasagittal territories drained by cortical venous tributaries to the sinus. Transverse or sigmoid thrombosis may result in temporal lobe involvement if the drainage of the vein of Labbé is compromised, and cerebellar haemorrhage may occur if cerebellar draining veins are occluded.

The parenchymal findings on cranial ultrasound are of swelling and increased echogenicity, which may become more heterogeneous in the presence of overt haemorrhagic transformation of the venous infarct (Fig. 65.23). Recognition of the patterns of parenchymal changes is key to raising the possibility of venous thrombosis.

If suspected clinically, or on B-mode ultrasound findings, detailed examination of the venous sinuses should be made using colour Doppler or power Doppler ultrasound. With meticulous technique, the majority of the dural venous system can be visualised by cranial ultrasound.

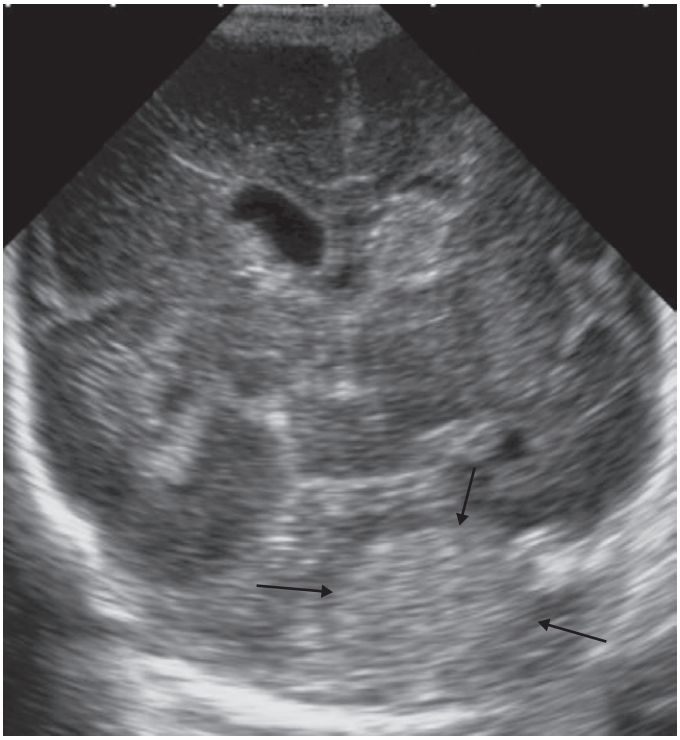

Figure 65.22 Preterm infant with left sided cerebellar haemorrhage (arrows). Note also bilateral IVH with ventricular dilatation.

Thrombosed dural sinuses appear echogenic and expanded, and demonstrate an absence of flow on Doppler ultrasound (Fig. 65.23B).[81] Care must be taken not to mistake the absence of colour flow due to angle of insonation as thrombosis, and angulation of the probe or examination of the same segment of the vessel from different angles can help to overcome this error. Furthermore, inadvertent compression of the superior sagittal sinus during scanning via the anterior fontanelle can lead to marked reduction in venous flow (Figs 65.7A and B) and hence false positive diagnosis of venous thrombosis. Doppler ultrasound is a useful tool for diagnosing or excluding the majority of venous sinus thromboses at the bedside, which may be helpful in critically ill infants, but confirmation of the finding by MRI should be sought.[80]

Lenticulostriate vasculopathy

Lenticulostriate vasculopathy (LSV) is the term given to the appearance of prominent echogenicity of the lenticulostriate vessels and associated perivascular spaces. The typical sonographic appearance is of linear branching echogenicities in the region of the basal ganglia and thalamus, often referred to as a 'candelabra' appearance (Fig. 65.24). The vascular nature of these linear echogenicities can be easily confirmed by colour Doppler ultrasound.[82]

Histopathologically LSV is characterised by thickened hypercellular walls without hyalinisation or fibrosis, and deposition of amorphous basophilic material, calcium and iron in the vessel wall and perivascular space.[83] LSV has been found in association with a number of abnormal states including in-utero TORCH infection, particularly cytomegalovirus, congenital malformations, hypoxic/ischaemic events and fetal exposure to maternal substances of abuse.[83,84] However, it is clear from clinical practice that LSV frequently occurs in infants who do not have any of the described causes and who have an unremarkable clinical course. In a large prospective study of infants receiving neonatal care, 2.5% were found to have LSV, and this was bilateral in nearly half of cases.[83] Compared to control infants without LSV, the LSV group included more multiple births, but did not have any other adverse features or outcomes, suggesting that the presence of LSV per se carries no direct prognostic significance.

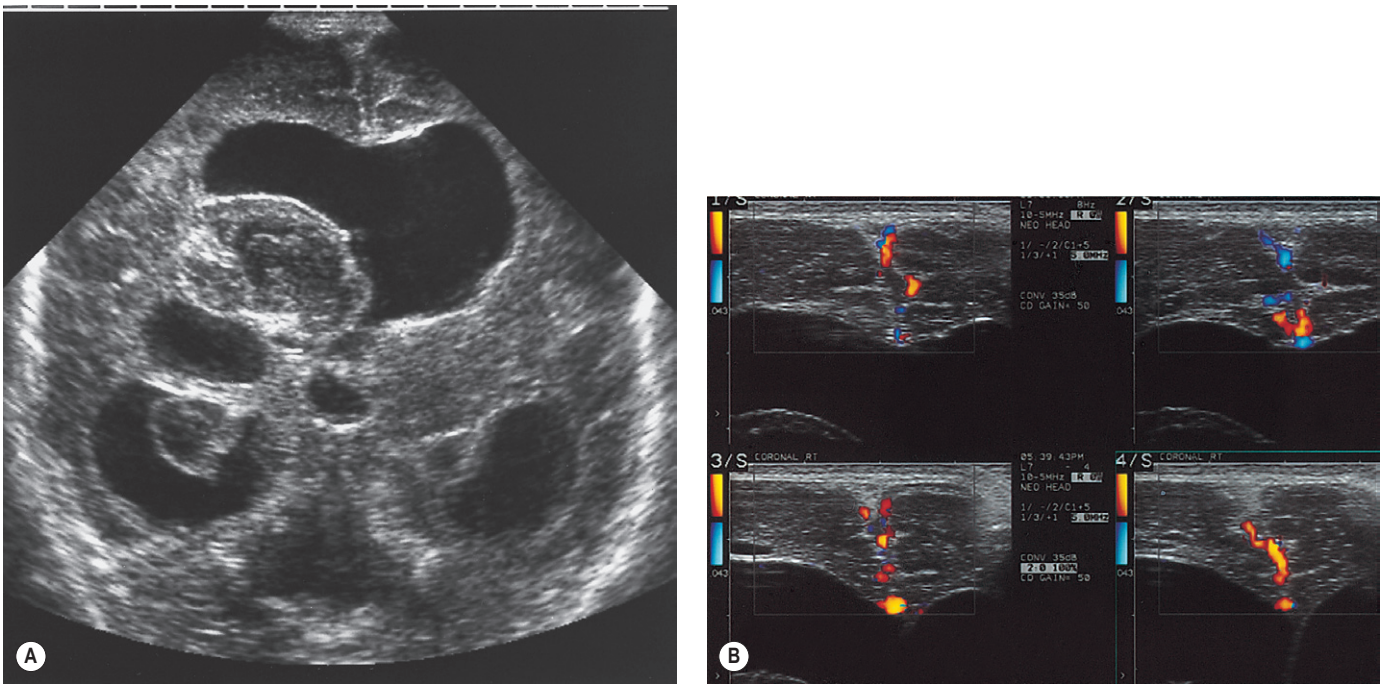

Figure 65.23 Venous haemorrhagic infarction. A: Coronal section demonstrating a thalamic-based haematoma undergoing liquefaction. Haemorrhage has extended into the adjacent lateral ventricles with hydrocephalus. **B:** High-resolution coronal colour Doppler imaging shows no flow in the superior sagittal sinus.

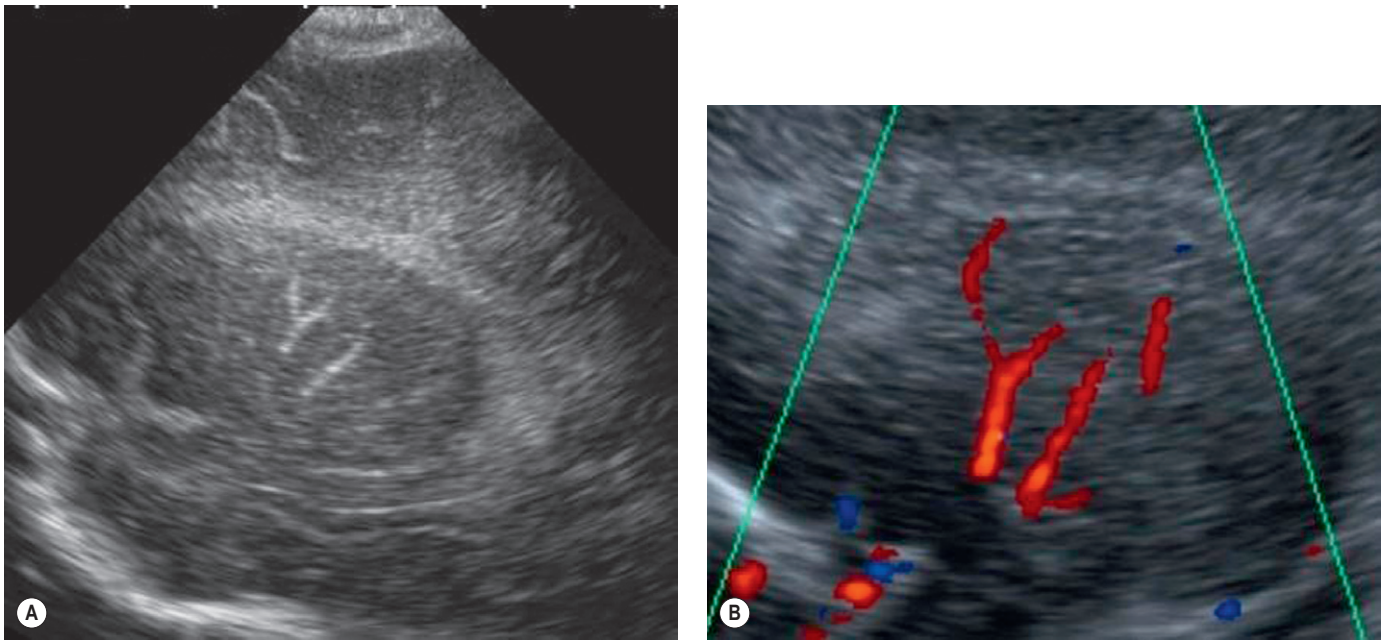

Figure 65.24 Lenticulostriate vasculopathy. A: Branching linear echogenicities with **(B)** prominent flow detected on colour Doppler ultrasound.

INFECTION

Prenatal causes

Congenital infections with cytomegalovirus, rubella, herpes simplex and *Toxoplasma gondii* all cause variable degrees of cerebral abnormality, the extent and severity depending on the stage of maturational development the brain had reached at the time of infection. Rubella and herpes simplex both infect the brain, and ultrasonic changes of ventriculitis have been described in rubella,[85] with calcification seen on CT in both herpes and rubella.[86] Toxoplasmosis may cause ventriculomegaly with associated cerebral calcification, and has been recognised in utero. Calcification is seen in the thalamus, the basal ganglia and in a periventricular distribution, as well as in the cerebral cortex (Fig. 65.25). There are also recognised systemic manifestations. Cytomegalovirus classically produces periventricular calcifications which can be detected with ultrasound,[87] although they are more easily recognised on CT. They have also been detected in utero.[88] Lenticulostriate vasculopathy is also a recognised finding, but is not specific.

HSV type 2 is the most common congenital infection to present with overt neurology at birth. Parenchymal involvement is often patchy and widespread, and does not necessarily conform to the temporal lobe distribution which is more common in childhood and adult infection (which is more often due to HSV type 1). Cranial ultrasound shows increased echogenicity and swelling of involved parenchyma (Fig. 65.26), and haemorrhage may occur. As the acute phase subsides there may be rapid onset of encephalomalacia and atrophy with enlargement of the ventricular system.[89,90] Cystic change and dystrophic cortical calcification frequently develop in the injured brain parenchyma.

Postnatal causes

Meningitis is the most commonly encountered form of intracranial infection in the neonate and older infant. Preceding focal sepsis or bacteraemia is usual, with group B streptococci, *Haemophilus influenzae*, *Streptococcus pneumoniae* and *Neisseria meningitidis* being the most common pathogens. The more common sequelae of intracranial sepsis and meningitis are cerebritis and abscess, subdural effusions and empyema, infarction, ventriculitis, hydrocephalus and end-stage encephalomalacia and atrophy.

Meningitis is primarily a clinical diagnosis, which is confirmed by a lumbar puncture and culture of the infective organisms. CT and ultrasound are used in severe cases to assess the sequelae of the infection. Both bacterial and viral agents may cause meningitis, but it is predominantly the bacterial infections that produce anatomical cerebral damage. Ultrasound may detect increased reflectivity of the sulci secondary to leptomeningeal inflammation and pus,[91,92] but it is usually unhelpful in the early acute phase. Cerebral vasculitis and thrombophlebitis may prevail and, coupled with oedema, result in focal or diffuse highly echogenic lesions. Within these areas of abnormality infarction or abscesses may develop, often multiple. Cerebral infarction may be segmental or gyral in distribution.[87] Gyral infarction is seen on ultrasound as characteristic swelling of the cortex.

Cerebral abscesses in neonates are usually secondary to bacterial meningitis, particularly involving *Citrobacter* (Fig. 65.27) and *Proteus spp*. They may develop into large hemispheric lesions. Venous sinus thrombosis may also occur, producing more complex patterns of brain injury, including venous ischaemia and haemorrhage. The resultant damage, in surviving infants, is widespread areas of encephalomalacia, gliosis and atrophy, with the architecture of the brain grossly destroyed and a diffuse increase in reflectivity and/or multicystic change.

Subdural effusions are seen in older infants, most commonly in association with *H. influenzae*. Ultrasound can readily detect the extra-axial nature of the fluid and differentiate it from prominent subarachnoid effusions, which are also frequently present (Fig. 65.28).[91] The subdural collections may be echo-free but more often contain low levels of reflectivity indicative of mobile particulate matter, or may contain septations (Fig. 65.29). The more reflective the collection, the more likely it is to represent an empyema. CT or preferably MRI scanning with contrast should be performed if this diagnosis is suspected, and the fluid explored either by percutaneous aspiration or at craniotomy with evacuation of these life-threatening collections.

Involvement of the choroid plexuses and spread to the ventricular system results in ventriculitis and hydrocephalus.[93] The

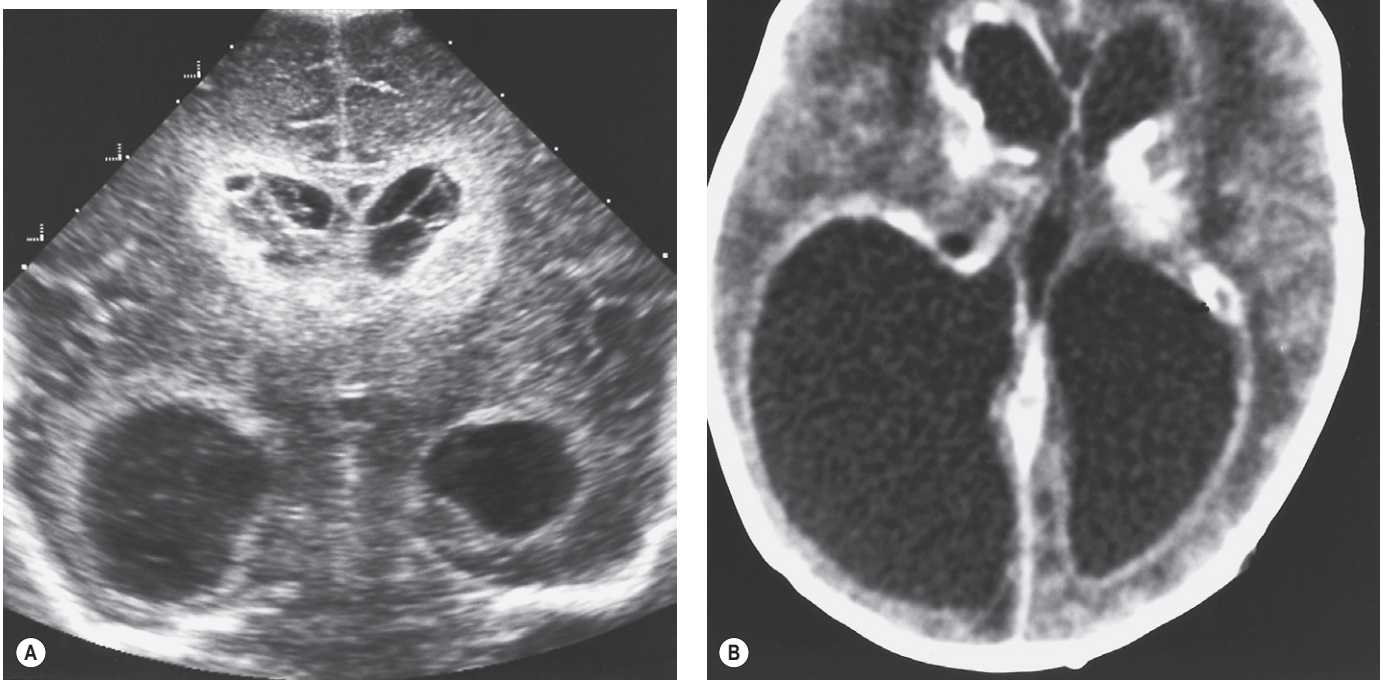

Figure 65.25 In-utero toxoplasmosis. A: Coronal section showing strong periventricular and thalamic reflectivity with intraventricular debris and septations. **B:** Axial CT scan more clearly demonstrates the extensive calcifications, but the intraventricular abnormalities are not as clearly identified.

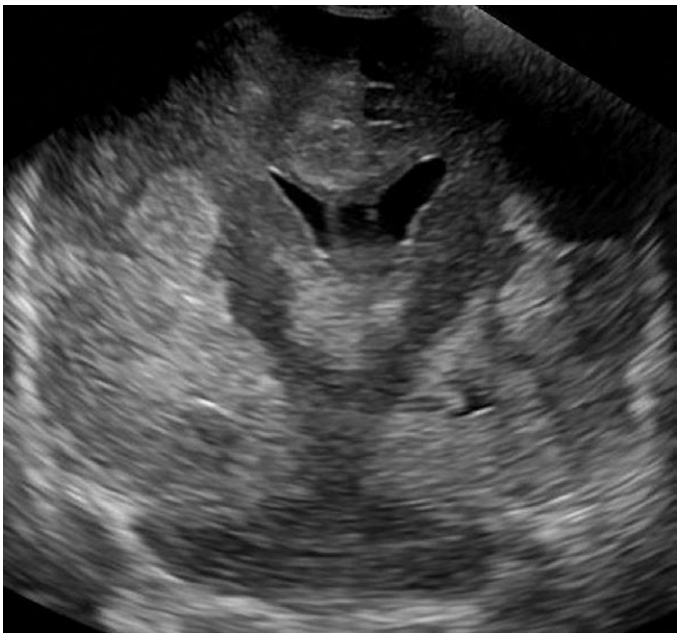

Figure 65.26 Neonatal HSV encephalitis. Extensive bilateral parenchymal echogenicity and swelling, particularly involving the temporal lobes, peri-insular areas, the thalami and the right cingulate gyrus. (Image courtesy of Dr Fiona Dickinson.)

ventricular margins become more echogenic, indicating a generalised ependymitis. Particulate debris may be seen floating in the ventricles,[91] becoming particularly evident as the child moves or cries, thereby stirring up the debris. As the disease progresses multiple septations and band adhesions appear, with the evolution of often complex and multicompartmentalised hydrocephalus which is frequently resistant to effective shunting. The hydrocephalus is compounded by fibrinous basal arachnoiditis, which may result in a grossly enlarged and loculated fourth ventricle.

In the special care baby unit fungal infection with *Candida albicans* is becoming more frequent; it particularly affects the brain, heart and kidneys, brain involvement occurring in two-thirds of cases of systemic candidiasis. Cerebral infection with *Candida* manifests as multifocal ill-defined echogenic areas throughout the brain parenchyma (Fig. 65.30). As the lesions evolve they may develop hypoechogenicity centrally, presumably representing central liquefaction. Transient, minor ventricular dilatation is a common feature. In the healing phase the lesions often disappear completely on ultrasound, or may develop into discrete echogenic foci representing calcification. These lesions can be seen on MRI, but in the authors' experience CUS is often more sensitive than MRI for detecting the parenchymal lesions in the acute phase, and screening CUS should be considered in infants on the neonatal unit with *Candida* isolated from blood or other sites.[94,95]

HYDROCEPHALUS

Hydrocephalus is an excessive accumulation of cerebrospinal fluid (CSF) leading to expansion of the ventricular system, the subarachnoid spaces overlying the brain, or a combination of both. The aetiology is an imbalance between the production and absorption

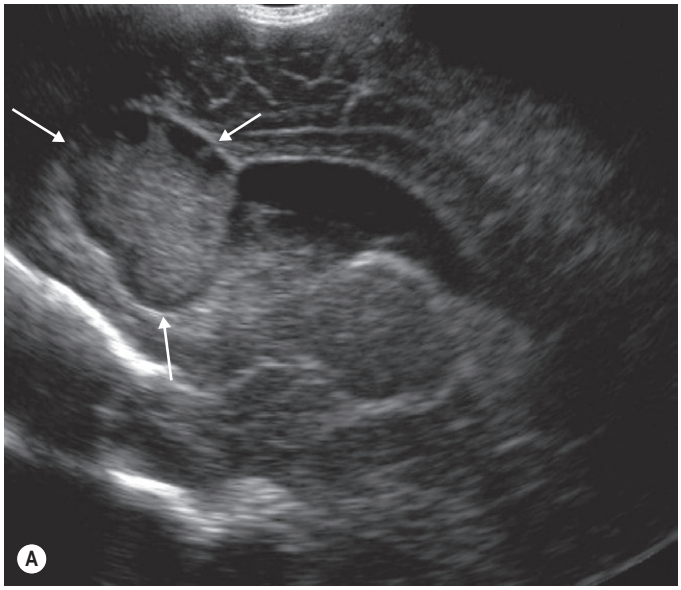

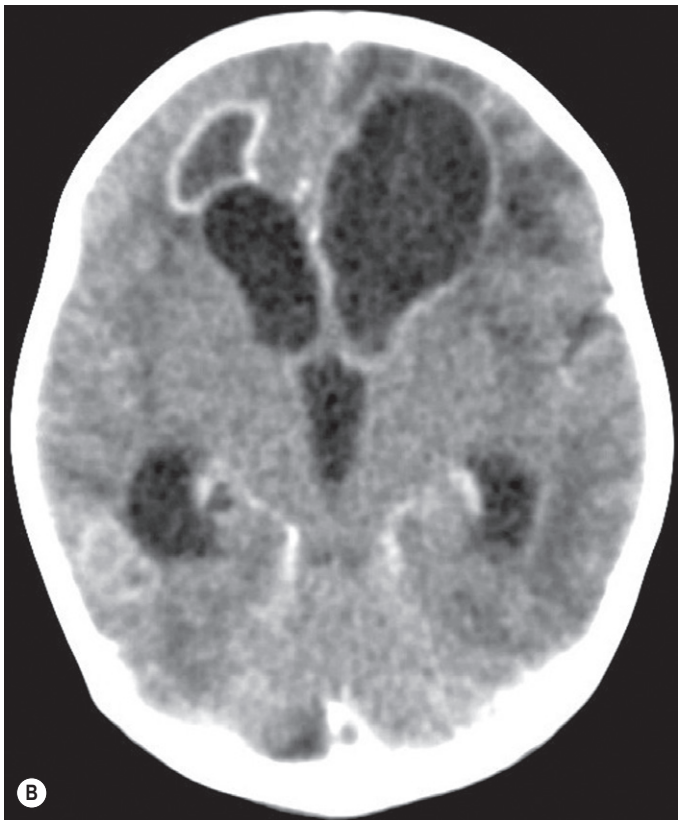

Figure 65.27 ***Citrobacter*** **meningitis with abscess. A:** Left parasagittal cranial ultrasound showing round echogenic area (arrows) adjacent to the frontal horn, with debris in the lateral ventricle. **B:** Subsequent post-contrast cranial CT showing free communication between the abscess cavity and the left frontal horn, with further areas of abscess formation adjacent to the right frontal and temporal horns.

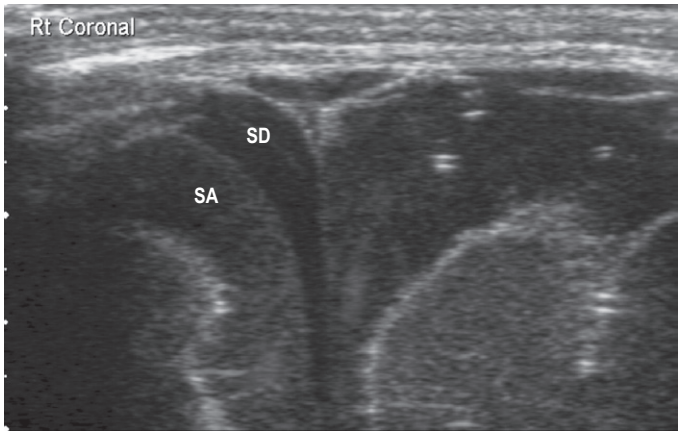

Figure 65.28 **Right paramedian subdural effusion** (SD) can be seen as clearly separate from the underlying subarachnoid (SA) space.

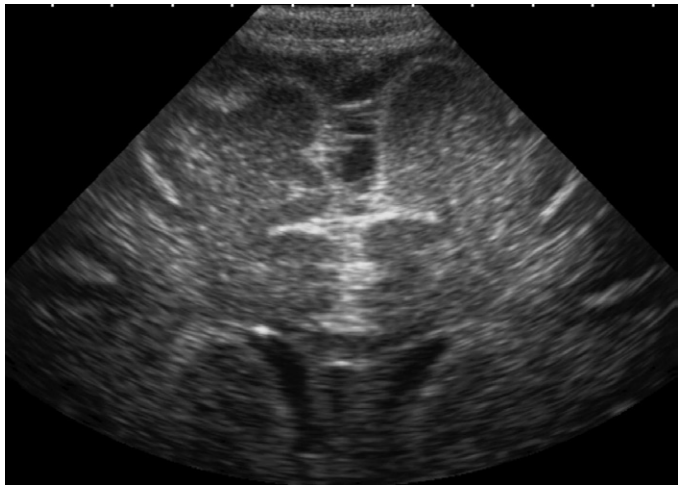

Figure 65.29 **Septated left paramedian subdural collection.**

of CSF, or an obstruction to the free flow of CSF. CSF is primarily produced by the intraventricular choroid plexus, after which there is flow through the ventricular system and into the basal cisterns via the foramina of Luschka and Magendie. The CSF then circulates around the spinal cord and basal cisterns before being resorbed by the arachnoid granulations adjacent to the major dural venous sinuses, with additional sources of resorption in the cranial nerves and probably the brain itself. In addition to this bulk flow, CSF undergoes to-and-fro motion with the cardiac cycle. Expansion of the brain tissue (and to a lesser extent the choroid plexuses and basal arteries) during systole leads to transmission of the cardiac pulsations to the CSF.

Hydrocephalus is described as communicating (extraventricular obstruction to CSF flow) or non-communicating (intraventricular obstruction to CSF flow, the level of obstruction being up to the level of the outlet foramina of the fourth ventricle). Rarely excessive CSF production may result in hydrocephalus, as is said to occur with choroid plexus papillomas, although intraventricular haemorrhage and excessive protein production by these tumours may contribute by impairing CSF resorption.

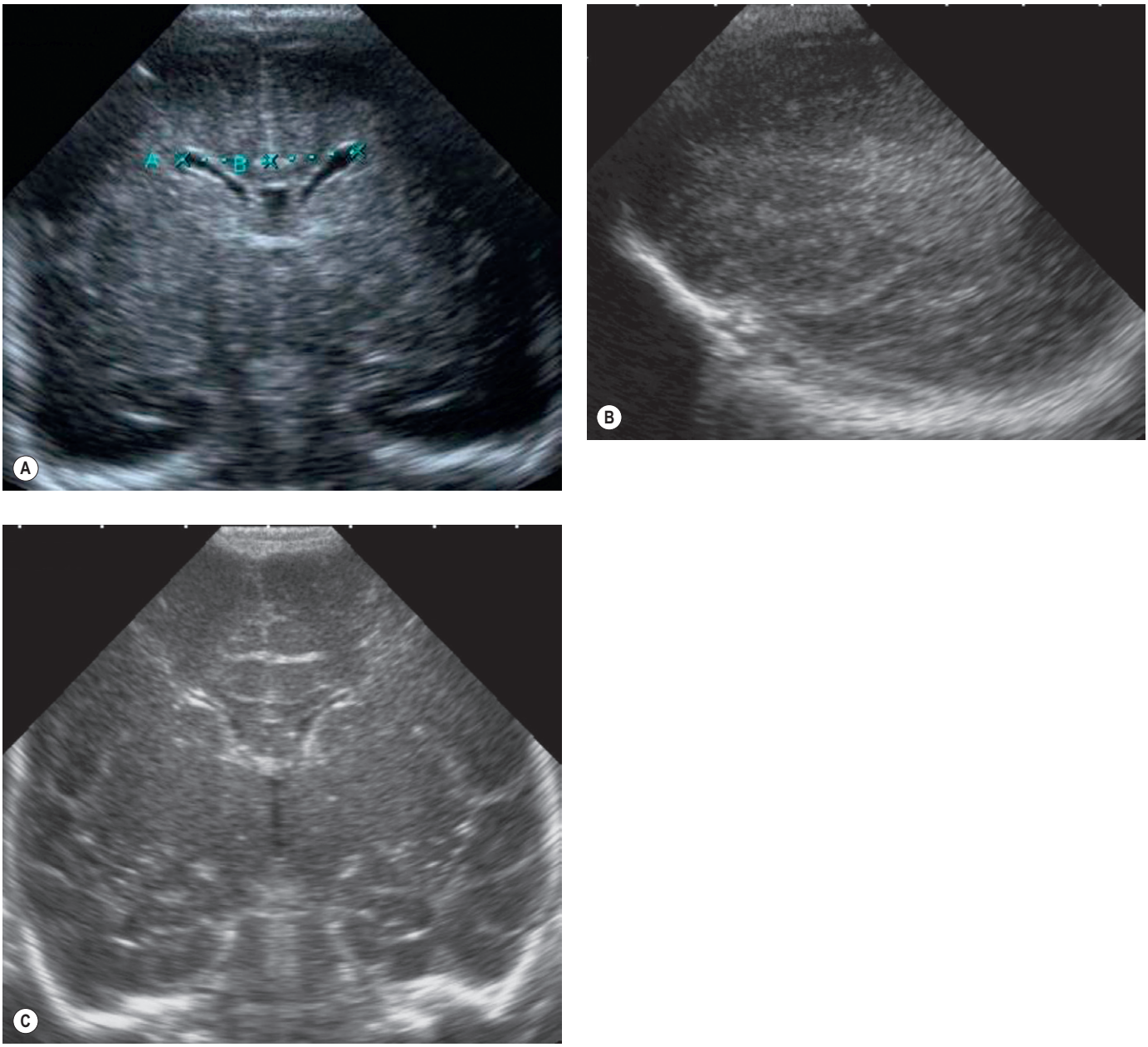

Figure 65.30 **Cerebral candidiasis** in a 2-week-old preterm infant with candidaemia. **A:** Coronal and **B:** parasagittal ultrasound images showing diffuse, ill-defined parenchymal echogenicities. **C:** Scan at 6 weeks of age following treatment shows multiple discrete highly echogenic foci consistent with healing lesions.

For the cranial ultrasound practitioner, hydrocephalus is likely to occur in one of two main contexts. The first is in infants encountered on the neonatal unit who are being examined for complications of prematurity or for suspected or known intracranial sepsis. The second is in infants who have been found by the health visitor or clinician to have a large head or rapidly increasing head circumference with a full or bulging anterior fontanelle.

In the neonatal unit hydrocephalus is most commonly the sequel of post-haemorrhagic hydrocephalus or infection (either as a pre- or a postnatal event). A combination of factors most probably applies. Intraventricular obstruction secondary to blood clots and an ependymal reaction, particularly at the aqueductal level (Fig. 65.31 and Fig. 65.35A), occurs in association with a basal adhesive arachnoiditis and impaired function of the arachnoid granulations (Fig. 65.32). Intraventricular septations are frequently identified. Complex cases, particularly following surgical intervention, can be associated with loculated compartments of the ventricular system and focal herniation of the ventricles, particularly the medial part of the trigone of the lateral ventricle into the superior cerebellar cisterns, mimicking an arachnoid cyst. Less common causes of acquired hydrocephalus are tumours and cysts obstructing the ventricles at varying sites, the sequelae of meningitis and post-traumatic communicating hydrocephalus.

Congenital causes include X-linked aqueduct stenosis, hydrocephalus associated with the Chiari II malformation (particularly following repair of an associated myelomeningocele), and the Dandy–Walker malformation. Aqueduct stenosis is seen as dilatation of the lateral and third ventricles with a normal fourth ventricle. If the diagnosis is delayed the massive dilatation may mimic other congenital anomalies, such as hydranencephaly and holoprosencephaly (Fig. 65.33). In such cases near-field ultrasound can be useful for differentiation by the demonstration of the presence of the inter-hemispheric fissure, which should be present in cases of hydrocephalus. The diagnosis of congenital hydrocephalus is

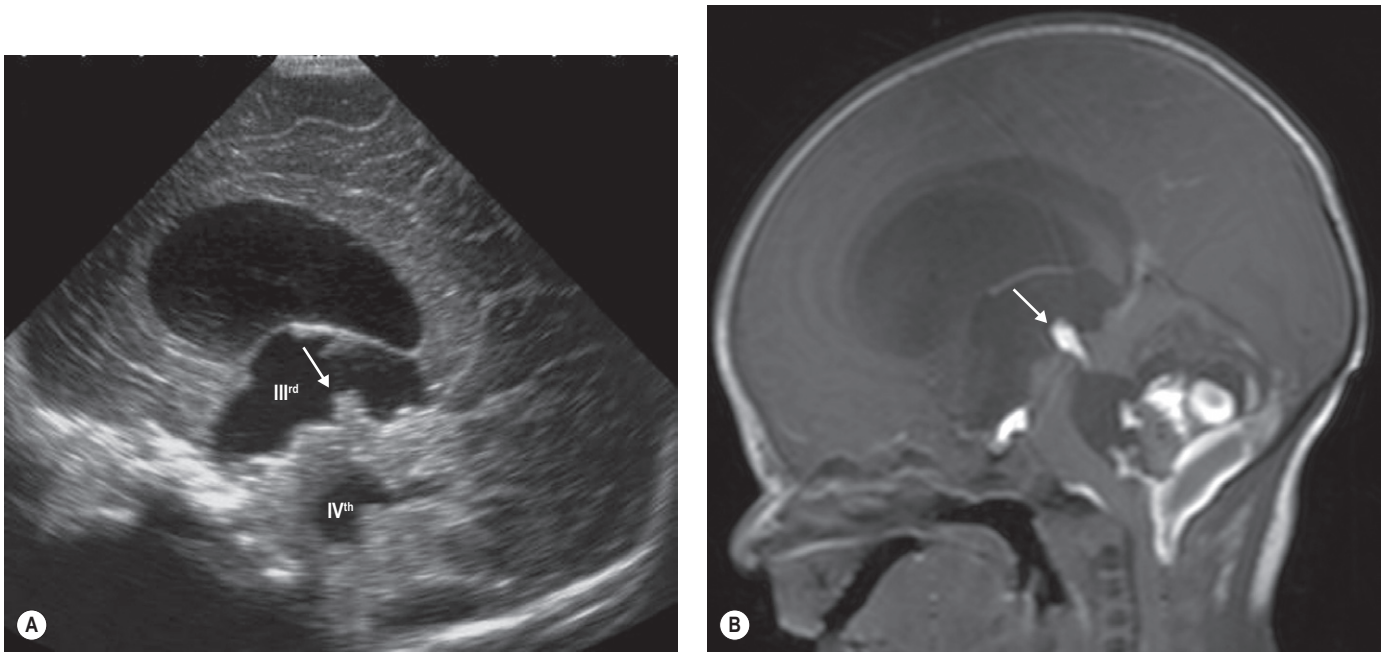

Figure 65.31 **Obstructive hydrocephalus. A:** Clot (arrow) occluding the midbrain aqueduct. Note also irregular echogenicity posterior to, and distorting, the fourth ventricle, consistent with cerebellar haematoma. **B:** Corresponding sagittal T1-weighted MRI demonstrates high signal clot plugging the aqueduct (arrow), as well as haematoma in the anterior third ventricle and the cerebellum, and subdural haemorrhage in the posterior fossa.

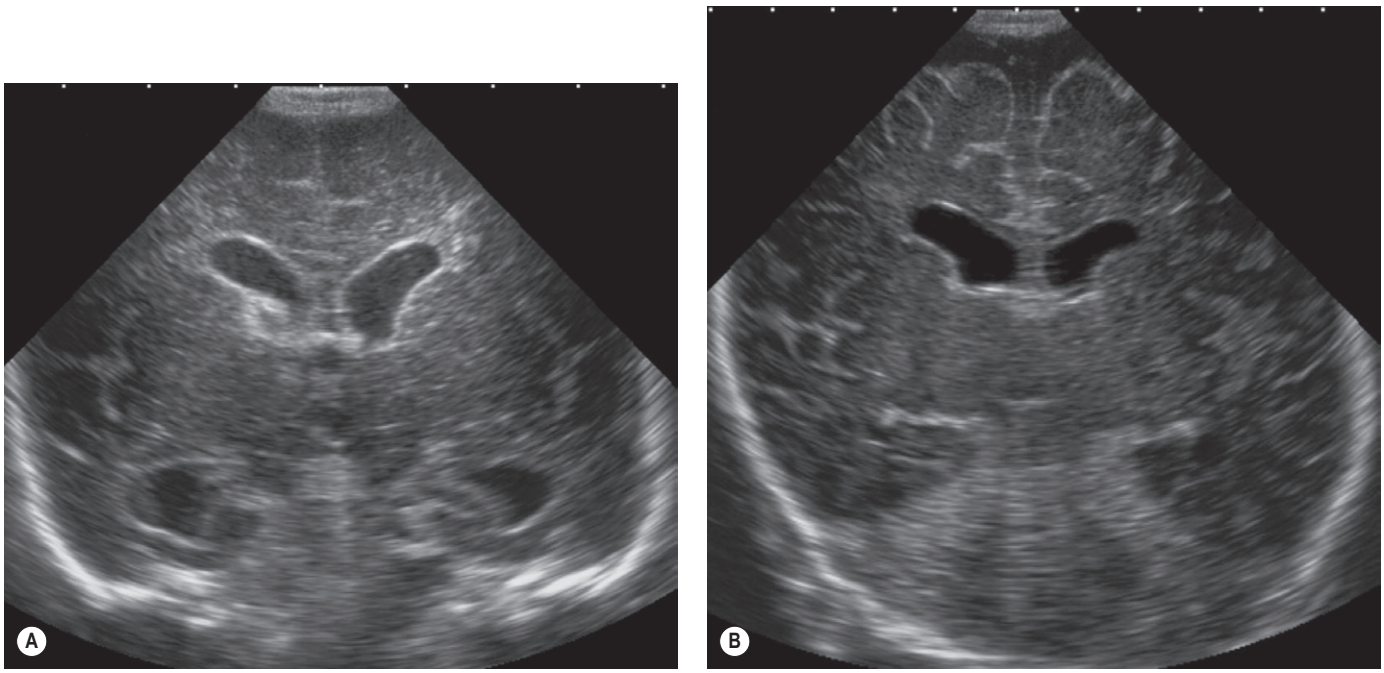

Figure 65.32 **CSF resorption block. A:** Day 8 ultrasound showing right GMH, with minor ventriculomegaly and bilateral ependymal echogenicity, indicative of IVH. **B:** Ultrasound at 2 months demonstrated persistent mild ventriculomegaly and marked widening of the subarachnoid spaces over the high cerebral convexities.

now often made in utero by ultrasound and evaluated further by fetal MRI, enabling management plans to be made early on, including termination of the pregnancy.

Another important type of hydrocephalus in infancy is external hydrocephalus (EH). This is a form of communicating hydrocephalus, thought to result from transient immaturity of the arachnoid granulations or villi, and is characterised by an enlargement (in excess of 5 mm) of the subarachnoid spaces overlying the cerebral hemispheres, particularly overlying the frontal convexities, and in the inter-hemispheric fissure.[96] There is associated mild or moderate ventricular dilatation. The syndrome occurs in the first year of life, the infant presenting with a large head crossing the centile charts and/or exceeding the 95th centile, and is usually a self-limiting process that resolves without treatment, in most cases by 2 years of age.[97] It should be remembered that the extracerebral subarachnoid spaces in infants are larger than in older children and adults.

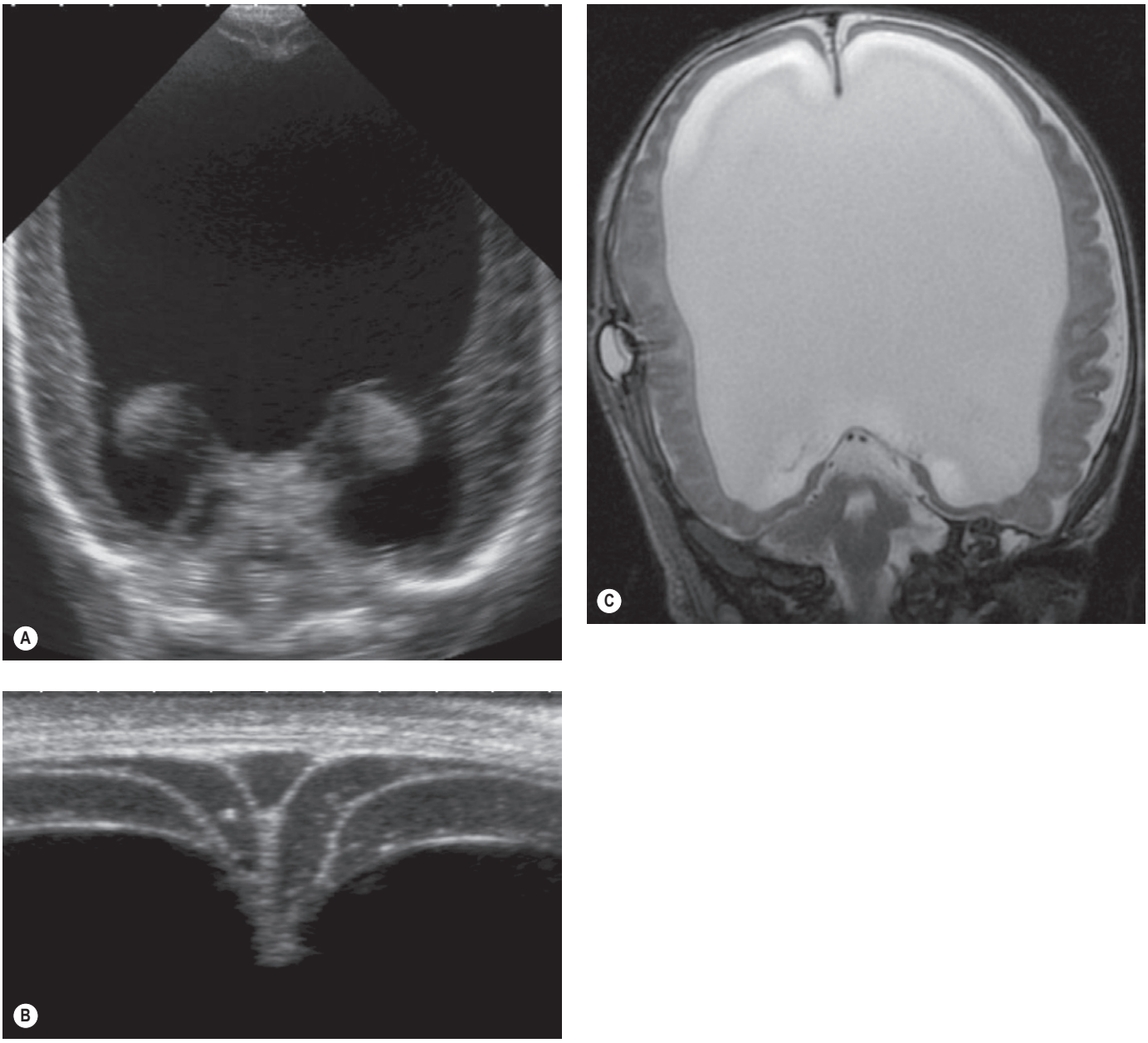

Figure 65.33 Gross congenital hydrocephalus secondary to aqueduct stenosis. A: Coronal ultrasound could be misinterpreted as holoprosencephaly (compare with Fig. 65.38), but near-field ultrasound **(B)** demonstrates the presence of the inter-hemispheric fissure. **C:** Correlating coronal T2-weighted MRI scan.

Libicher and Tröger suggest an upper limit of 3 mm, measured as the distance from the superior sagittal sinus to the adjacent cortex on coronal ultrasound scans in normal infants.[98] Others have suggested that the figure should be higher.[99] In the authors' experience 4–5 mm is generally the upper limit; however, the figure must not be taken in isolation but should be correlated with serial head circumference measurements and the clinical context.

Ultrasound evaluation

The characteristic finding of hydrocephalus is of enlargement of the ventricles. Numerous authors have outlined the normal ventricular measurements (see Table 65.1) and these indices can be used to confirm the diagnosis and monitor the cause of hydrocephalus. Cranial ultrasound will often demonstrate the cause of hydrocephalus, such as blood clots, adhesions or mass lesions. However, when the cause of hydrocephalus is not seen, the level of obstruction to CSF flow can often be postulated from the imaging findings; obstruction at the level of the foramina of Monro leads to lateral ventricular dilatation, at the level of the aqueduct leads to third and lateral ventricular dilatation, and at the level of the fourth ventricular outflow or in the extraventricular compartment leads to dilatation of all ventricles.

Serial ultrasound images and measurements demonstrating progressive hydrocephalus should prompt discussion between clinicians and the neurosurgical team to allow timely intervention, if required. Ultrasound can also be utilised to assess the efficacy of ventricular shunting procedures, avoiding the need for CT scanning with its accompanying radiation burden. Additionally, ultrasound may reveal focal areas of brain parenchymal injury following therapeutic ventricular aspiration for the treatment of hydrocephalus (Fig. 65.34).

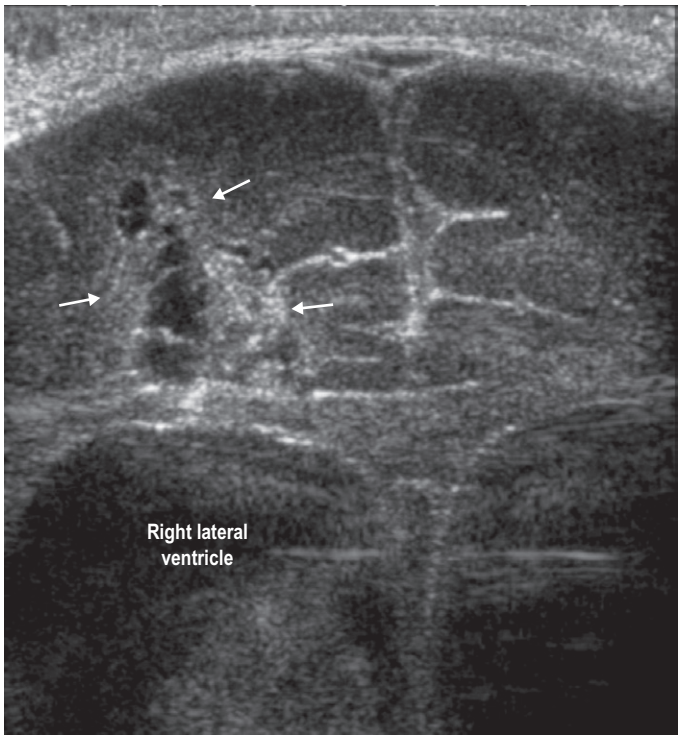

Figure 65.34 Parenchymal injury following therapeutic ventricular aspiration. Coronal ultrasound showing irregular heterogeneous echogenicity along the line of needle tract (arrows). Intraventricular CSF under high pressure is presumed to leak into the parenchyma at the time of aspiration leading to the appearance of multiple small cysts.

In the case of EH, ultrasound can be of crucial importance in differentiating the excess of fluid overlying the cerebral hemispheres from subdural hygromas. In EH ultrasound clearly demonstrates the excess fluid residing in the subarachnoid compartment and dipping into the sulci whereas subdural collections flatten the surface of the brain. The ultrasound findings of EH in isolation may be difficult to differentiate from atrophy, from whatever cause. However, these entities can be separated clinically as the latter is marked by a small head or declining head circumference on serial measurements.

Colour flow Doppler plays a useful role in determining the patency of the ventricular system in infants with hydrocephalus.[100] Particulate matter and microbubble formation in CSF passing through the aqueduct results in flow-related colour-encoded jets (Fig. 65.35). CSF flow produces a highly characteristic sinusoidal spectral Doppler waveform indicative of the cyclical to-and-fro motion of CSF within the ventricular system (Fig. 65.35C). Sagittal imaging examining the mid- and hindbrain allows assessment of patency of the aqueduct and fourth ventricular outflow foramina. In the presence of dilatation of the supratentorial ventricles, complete absence of flow through the aqueduct is strongly suspicious for obstruction at this level, whereas free passage of CSF through the ventricles and out into the basal cisterns confirms a diagnosis of communicating hydrocephalus.

CONGENITAL MALFORMATIONS

Congenital malformations occur as a result of primary errors of development or from destructive injuries in utero. Classification of congenital abnormalities of the central nervous system is complex, and readers are referred to specialist texts considering this area in more detail.[101,102] MRI has become the gold standard for imaging congenital central nervous system malformations, but ultrasound can provide useful information on structural brain abnormalities. Ultrasound is often the first imaging used when congenital abnormality is suspected based on fetal ultrasound, fetal MRI or clinical features, and hence operators need to be familiar with the patterns and spectrum of congenital malformations. In this section, the sonographic appearances of some of the more common and more important malformations are discussed, but it should be noted that the discussion is by no means exhaustive.

Dysgenesis of the corpus callosum

The corpus callosum is the major commissural tissue connecting the two cerebral hemispheres. It forms during the first 8–12 weeks of gestation and is derived from the lamina terminalis. Growth probably proceeds superiorly and posteriorly. An insult before the 12th gestational week results in callosal agenesis. The midline fibres do not cross but become orientated postero-anteriorly as the bundles of Probst, lying along the superomedial aspect of the lateral ventricles. There is characteristic elongation and superior displacement of the third ventricle, wide separation of the lateral ventricles, with narrow peaked anterior horns and dilatation of the occipital horns (Fig. 65.36). The sulci, which normally parallel the corpus callosum, may be seen to diverge radially from the abnormal third ventricle in the midline sagittal view.

Destructive insults, such as infection or ischaemic injury, occurring after formation of the corpus callosum lead to secondary callosal dysgenesis and varying degrees of partial absence. The posterior half of the corpus callosum tends to be predominantly affected. The varying degree of dysgenesis is reflected by the ultrasound appearances with variable displacement of the third ventricle.[103–105] The clinical sequelae of the isolated anomaly are surprisingly mild, the diagnosis sometimes being made incidentally in apparently normal adults. This condition may be associated with other cerebral abnormalities, including the Chiari II malformation, encephaloceles, the Dandy–Walker malformation, inter-hemispheric arachnoid cysts and intracranial lipomas. In these cases the neurological deficit tends to be more severe.

Dandy–Walker complex

Included in this group is the true Dandy–Walker (DW) malformation, which is associated with a large posterior fossa and ballooned fourth ventricle, and inferior vermian and cerebellar hypoplasia. The DW variant represents a lesser degree of vermian hypoplasia and fourth ventricular dilatation. A mega-cisterna magna and Blake's pouch cyst come into the syndrome complex.[106,107]

The DW malformation is commonly diagnosed in utero[108,109] by the demonstration of a large posterior fossa cyst associated with dilatation of the lateral ventricles (Fig. 65.37). The cyst is the result of atresia of the foramina of Magendie and Luschka, producing enlargement of the fourth ventricle and a small cerebellum with an absent inferior vermis. The dilatation of the lateral ventricles is disproportionate to the size of the cyst. There are reported associations with other anomalies, including encephaloceles, agenesis of the corpus callosum and malformations of cortical development.[101]

Retrocerebellar fluid collections appear as an anechoic space located behind the inferior vermis extending to the posterior lip of the foramen magnum. There is often lateral extension behind the cerebellar hemispheres, which can be asymmetrical. Linear bands, thought to be dural reflections, are sometimes seen running inferiorly through the fluid.[21] This appearance may be due to mega cisterna magna or Blake's pouch cyst, both of which are putatively part of the Dandy–Walker complex, or an unrelated arachnoid cyst. In the latter there is no communication between the fluid collection and the fourth ventricle. In practice, differentiation of these entities

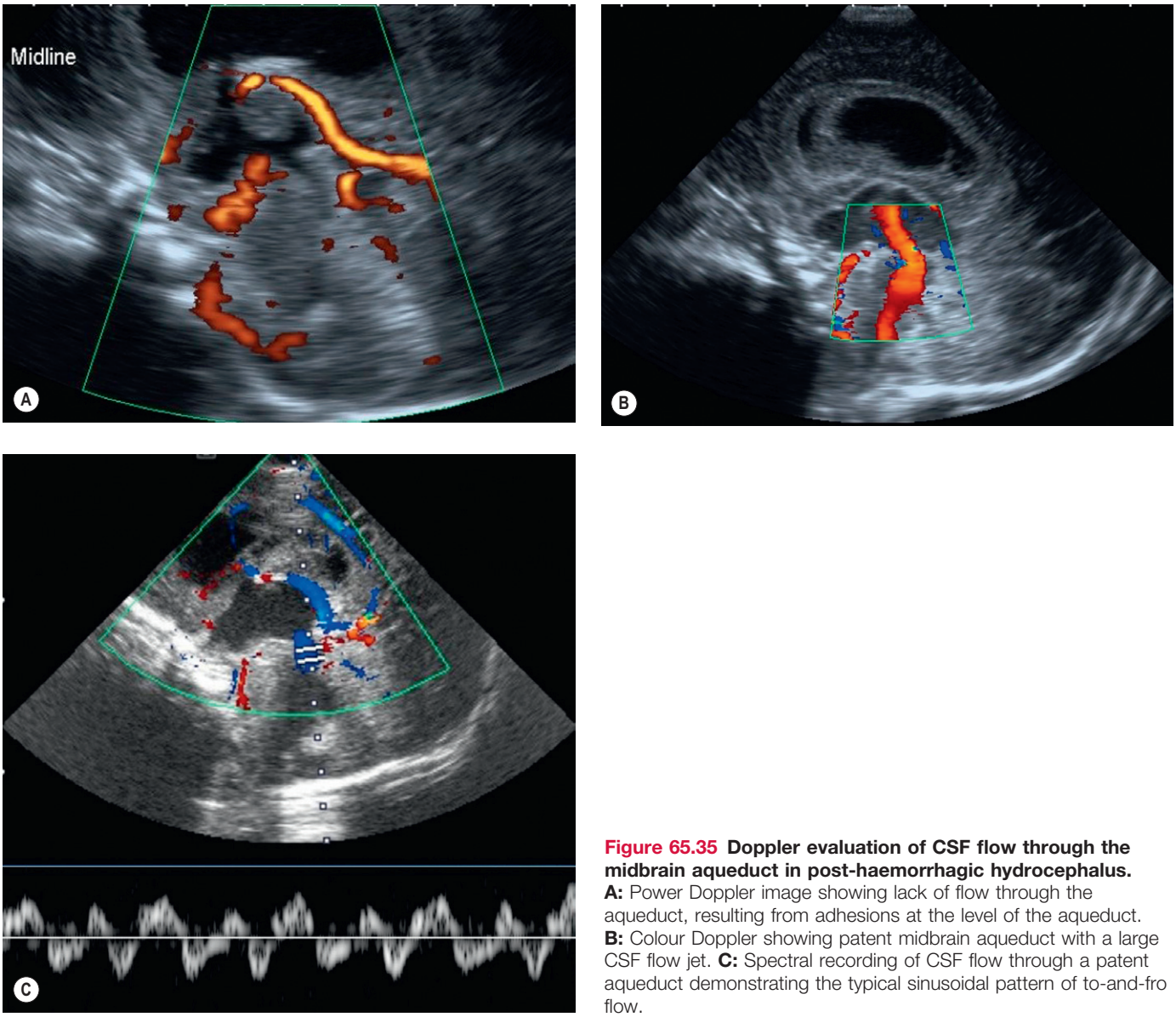

Figure 65.35 Doppler evaluation of CSF flow through the midbrain aqueduct in post-haemorrhagic hydrocephalus. **A:** Power Doppler image showing lack of flow through the aqueduct, resulting from adhesions at the level of the aqueduct. **B:** Colour Doppler showing patent midbrain aqueduct with a large CSF flow jet. **C:** Spectral recording of CSF flow through a patent aqueduct demonstrating the typical sinusoidal pattern of to-and-fro flow.

is rarely possible on CUS, and is of little value if asymptomatic and without other associated abnormalities. However, the finding of enlarged cisterna magna should prompt detailed examination of the brain for other features of the Dandy–Walker complex.

Holoprosencephaly

Failure of the prosencephalon of the 5–10-week-old fetus to divide into two telencephalic vesicles (to form the cerebral hemispheres) and the diencephalon (to form the thalamus and hypothalamus) results in varying degrees of fusion of the cerebral hemispheres, thalami and olfactory tracts. The result is a spectrum of abnormalities, ranging from a large single midline ventricle with a dorsal cyst (alobar), partial division of the cerebral hemispheres but fused thalami (semilobar), to minimal failure of separation of the frontal lobes accompanied by absence of the septum pellucidum (lobar). These children also have varying degrees of hypotelorism, with cyclops being the most severe. Other midline defects may be associated, such as cleft palate and nasal abnormalities, including rudimentary nose and median proboscis.

The ultrasonic appearances in the alobar and semilobar types are a single, dilated ventricle with fused thalami and a variable thickness of cerebral tissue (Fig. 65.38). The third ventricle is absent or small in alobar holoprosencephaly and is incorporated into the single ventricle in the semilobar form. In the alobar type the fourth ventricle is present but the aqueduct may be small.

Lobar holoprosencephaly is the least severe type, with absence of the septum pellucidum producing squaring of the frontal horns. The cerebellum and midbrain are normal in all types.

Isolated absence of the septum pellucidum is rare[110,111] but can be an incidental finding on cranial ultrasound (Fig. 65.39). Careful evaluation of the rest of the brain is required to exclude associated abnormalities. An absent septum can be associated with abnormalities of the optic apparatus and hypothalamic-pituitary axis in septo-optic dysplasia (De Morsier's syndrome), which has overlaps with lobar holoprosencephaly. When an absent septum is incidentally found by cranial ultrasound, clinical review is advisable and MRI examination should be considered.

Disorders of sulcation and migration

Occurring between the second and sixth months of gestation, abnormalities of the process of neuroblast formation, radial and

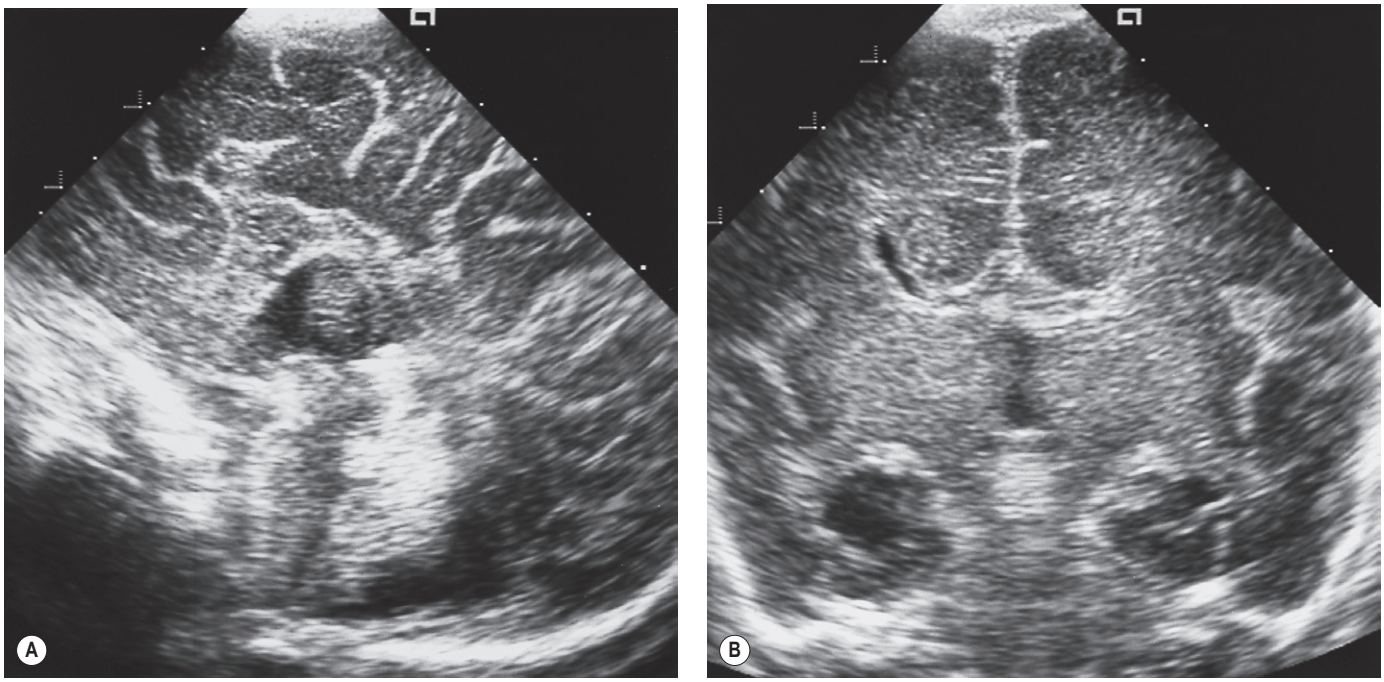

Figure 65.36 Agenesis of the corpus callosum. A: Sagittal image demonstrates radially orientated sulci and a high-riding third ventricle. **B:** Coronal scan shows the widely separated lateral ventricles and absent corpus callosum.

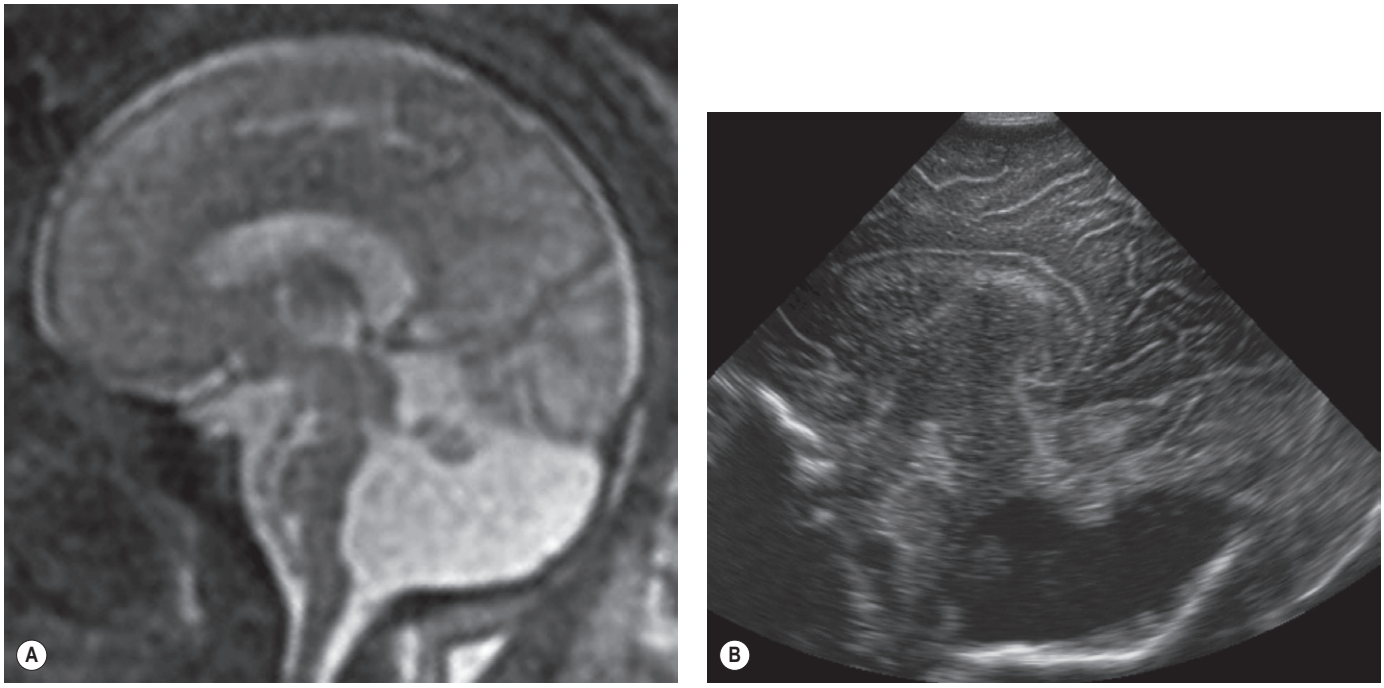

Figure 65.37 Dandy–Walker malformation. A: Midline sagittal fetal MRI at 32 weeks gestation showing large posterior fossa cyst and dysplastic small vermis. **B:** Sagittal cranial ultrasound on the first day of life. Note the corpus callosum is present in this case.

tangential migration to the cerebral cortex result in a spectrum of disorders which includes lissencephaly, focal or diffuse cortical dysplasias, schizencephaly and grey matter heterotopias. Injuries (infective or ischaemic) at an early stage can disrupt normal cortical development, but some of these lesions are due to chromosomal deletional abnormalities.

In lissencephaly the cerebral sulci and gyri fail to develop fully, with a thick smooth four-cell layered cortex resembling an hourglass in the coronal plane. Two types are encountered. In type I lissencephaly (Miller–Dieker, Norman–Roberts syndromes) microcephaly, facial dysmorphism and severe mental disability are the rule. On ultrasound, and particularly on MRI, the cerebral cortex resembles a 24-week fetus with no cerebral sulci and wide sylvian fissures.[112] Type II lissencephaly (characterised by the Walker–Warburg syndrome) typically presents with macrocephaly secondary to obstructive hydrocephalus. Ultrasound can help to identify

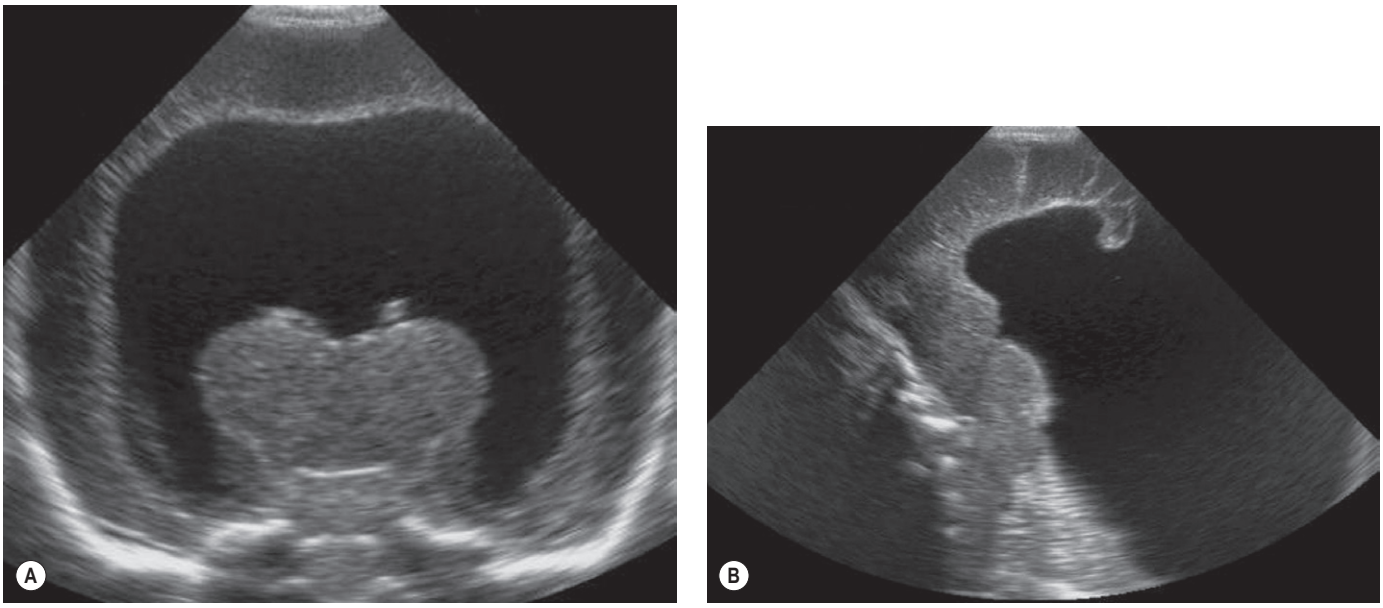

Figure 65.38 Alobar holoprosencephaly. A: Coronal and (B) sagittal images. Large single midline ventricle with dorsal cyst. Note the absence of the inter-hemispheric fissure, fusion of the thalami and absence of the third ventricle.

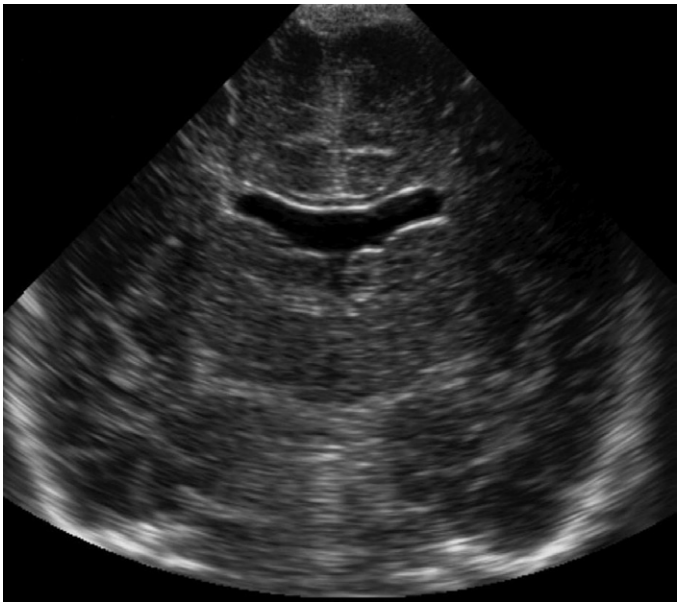

Figure 65.39 Absence of the septum pellucidum.

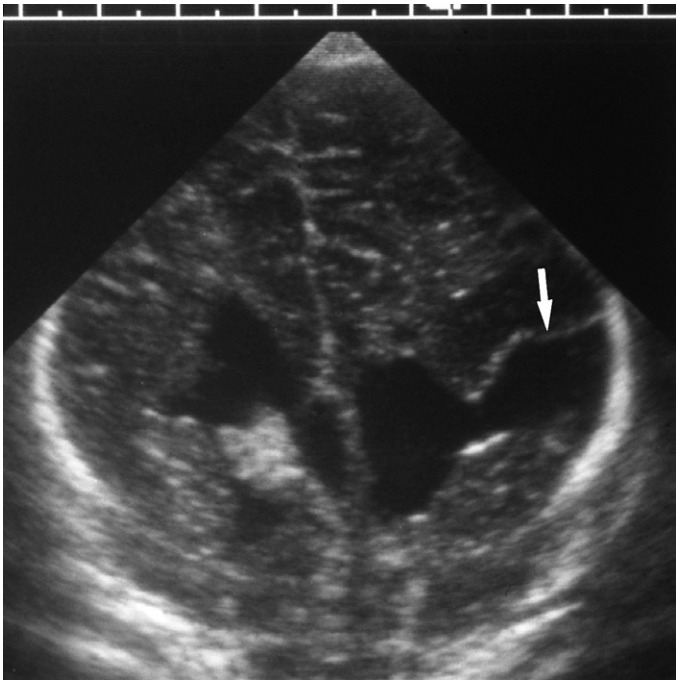

Figure 65.40 Open-lipped schizencephaly. Coronal section demonstrating a wide trans-cerebral cleft (arrow) in the left cerebral hemisphere.

the agyric cortex, despite severe ventricular dilatation, which can be difficult to identify on CT scanning.

Schizencephaly represents a focal abnormality or area of damage to the radially migrating neuroblasts, resulting in closed (fused) or open-lipped trans-cerebral clefts lined by dysplastic, most often polymicrogyric, cortex. The open-lipped type may be easily diagnosed by ultrasound, where a transonic cavity extends from the surface of the brain to fuse with the lateral wall of the lateral ventricle (Fig. 65.40). Focal eversion or outpouching of the ventricular margin in addition to the polymicrogyric lining of the cyst characterises this type of lesion, helping to differentiate it from other destructive juxtaventricular cystic abnormalities. Although ultrasound can make the diagnosis, a more complete evaluation requires MRI, particularly for the closed-lipped type and to define the associated cortical dysplasia that is invariably present.

Tuberous sclerosis

Tuberous sclerosis is characterised clinically by the triad of adenoma sebaceum, mental disability and seizures. Hamartomatous lesions are the hallmark and may be present in all parts of the brain. A subependymal location is most common and may be detected as a small focal highly reflective nodule in the wall of the lateral ventricle (Fig. 65.41).

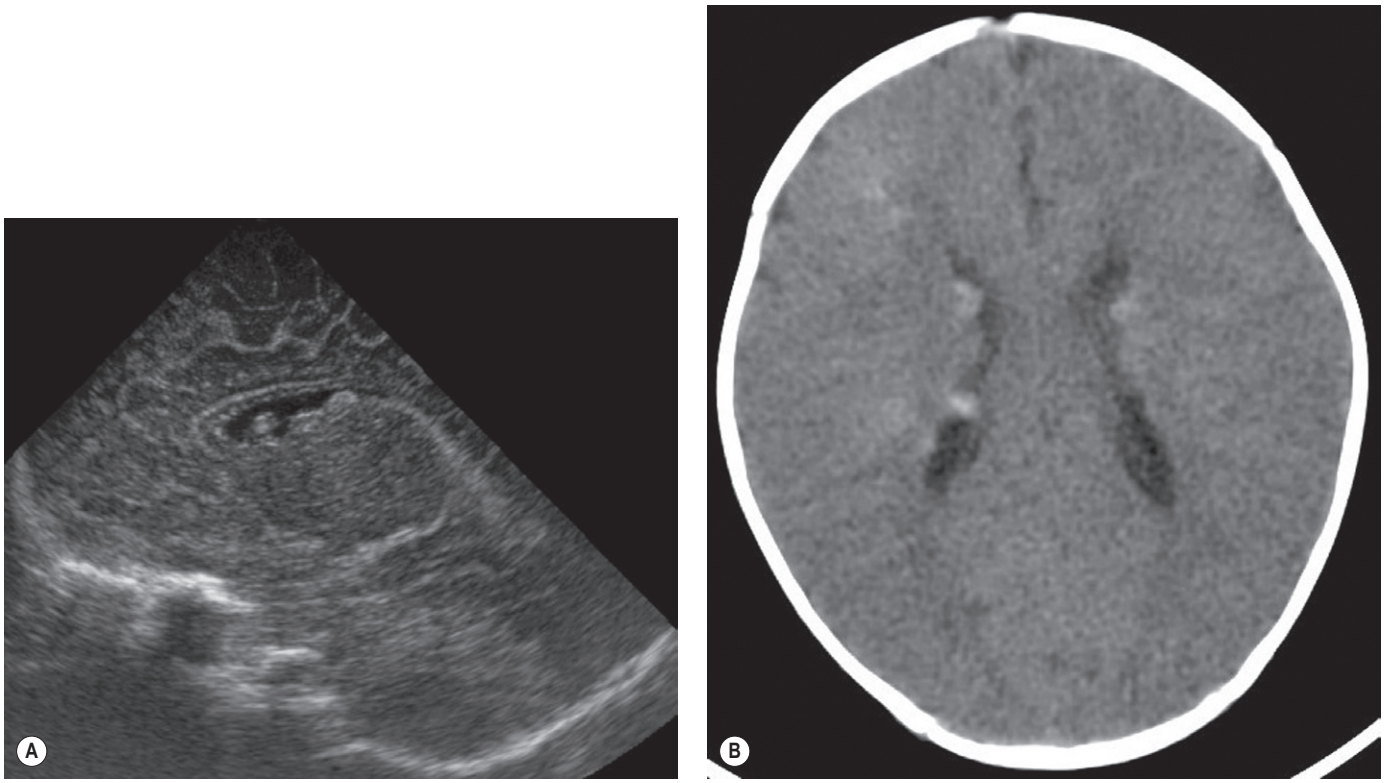

Figure 65.41 Tuberous sclerosis. A: Right parasagittal image showing subependymal nodules, with **(B)** corresponding CT.

Destructive brain lesions

Hydranencephaly results from in-utero occlusion of the supraclinoid internal carotid arteries between the 12th and 26th weeks of gestation. This may result from a variety of causes, including infection and trauma, and leads to destruction of the formed cerebral hemispheres. A fluid-filled membranous sac fills the calvarium (Fig. 65.42) but the falx is still present, differentiating this condition from holoprosencephaly. There is preservation of a varying amount of frontal and occipital lobe, and the thalami, basal ganglia, midbrain and posterior fossa contents are essentially normal. Macrocephaly is usual, though the head may be normal or even small in size.

Destruction of brain tissue in the first or early second trimester results in areas of cystic damage without a gliotic reaction. The resultant lesion, referred to as porencephaly, may or may not communicate with the ventricles and is not lined by grey matter, unlike schizencephaly. The term porencephaly should be restricted to true in-utero causes of cystic brain damage.

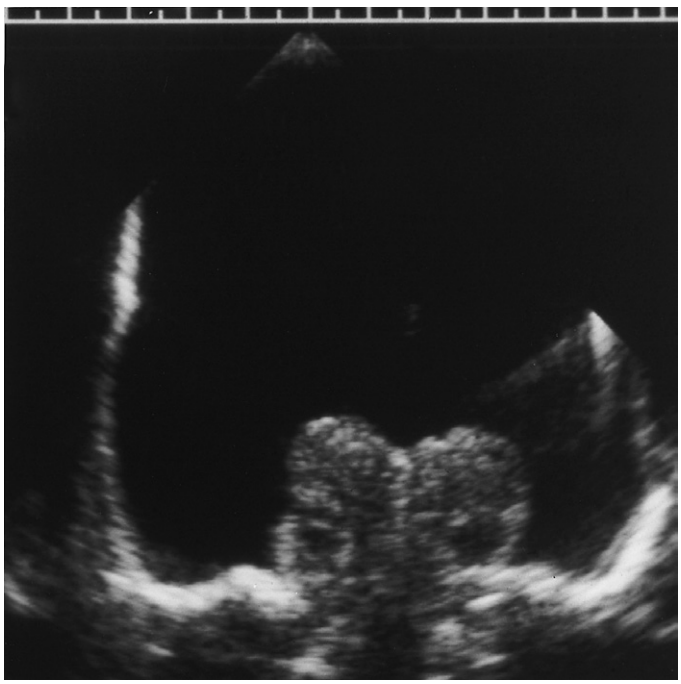

Figure 65.42 Hydranencephaly. Coronal section showing the fluid-filled sac almost completely replacing the cerebral hemispheres. The thalami and a small portion of the medial temporal lobes are preserved.

METABOLIC DISORDERS

Hypoglycaemia

Hypoglycaemia during the neonatal period can lead to neurological dysfunction and brain injury. The infant brain is relatively resistant to mild transient hypoglycaemia, which is often asymptomatic, due to its ability to metabolise non-glucose organic substrates such as ketones, fatty acids, lactate and pyruvate to provide energy.[113] Severe hypoglycaemia, however, is often symptomatic and presents with stupor, tremulousness, seizures and respiratory depression. Patients at high risk for developing severe hypoglycaemia during the immediate postnatal period include infants born to diabetic

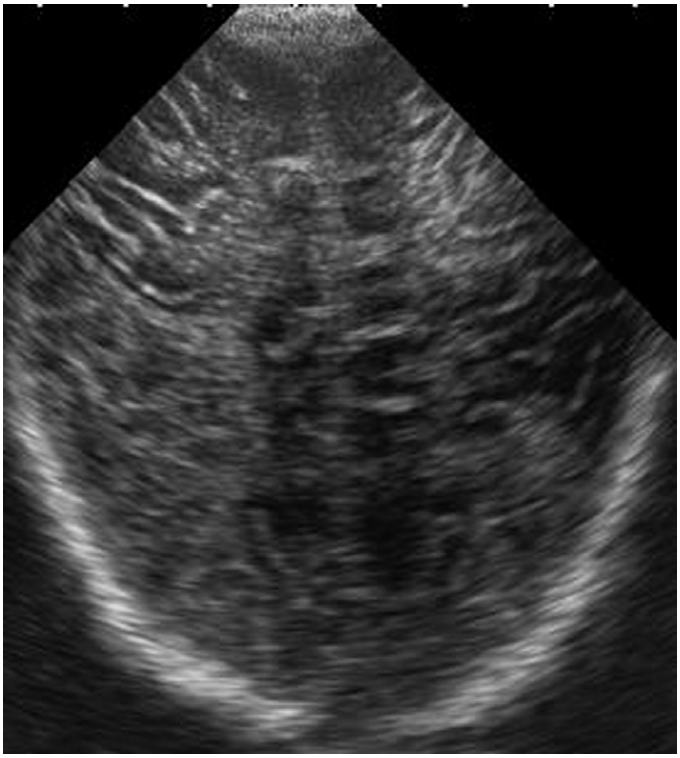

Figure 65.43 Neonatal hypoglycaemia. Day 3 scan showing echogenicity and loss of sulcal visualisation in the parieto-occipital regions bilaterally.

mothers, infants who are small for gestational age, and those who sustained perinatal asphyxia.[113]

A classical distribution of parietal and occipital abnormality, with occasional basal ganglia involvement, has been reported in MRI studies of neonatal hypoglycaemia,[114] and a similar pattern can be detected by ultrasound.[115] Affected areas appear hyperechoic on ultrasound (Fig. 65.43).[116] MRI has shown a greater sensitivity for the parenchymal changes in hypoglycaemia than ultrasound, but abnormalities are frequently absent on both modalities.[115] In infants who sustained perinatal asphyxia, parenchymal changes may be a combination of hypoglycaemic injury and HIE.

Inborn errors of metabolism

A variety of ultrasound findings have been reported in infants with inborn errors of metabolism, including germinolytic cysts, calcifications, grey and white matter echogenicity and structural abnormalities.[117] Ultrasound findings appear to correlate with findings demonstrated by MRI, and in selected cases may be a useful bedside test to support a diagnosis of metabolic disorder. Although appearances in metabolic disorders can overlap with HIE, non-progression of appearances on serial CUS goes against the latter. However, the role of CUS in the assessment of metabolic disorders is not well established and MRI remains the definitive neuroimaging in these cases.

SPACE-OCCUPYING LESIONS IN THE INFANT BRAIN

These are divided into cystic and solid lesions and include neoplasms, cysts and arteriovenous malformations.

Neoplasms

Neoplasms in the infant brain are very rare, with an incidence of 2 per 100 000.[118] The majority of brain tumours in children under 1 year of age are supratentorial[119] and are therefore readily accessible to diagnosis by ultrasound. Primitive neuroectodermal tumours, atypical teratoid rhabdoid tumours, astrocytomas, ependymomas and choroid plexus tumours are the most common histological types.[120] MRI now forms the mainstay of diagnostic imaging in infantile intracranial tumours, but ultrasound remains a useful tool for identifying and characterising intracranial masses.[121–123] Ultrasound can also be used intraoperatively to identify the site of the tumour and monitor the progress of the procedure.[124]

Almost all are large at presentation and of heterogeneously increased echogenicity (Fig. 65.44). Cystic foci and highly reflective punctate or craggy calcifications may also be encountered. Depending on their location the tumours may produce hydrocephalus and usually present with a rapidly expanding head (Fig. 65.45). Astrocytomas, primitive or developmental tumours, choroid plexus papillomas (Fig. 65.46) and desmoplastic infantile gangliogliomas are the most frequently encountered, in that order. Although ultrasound is usually able to detect – and in some cases characterise – these lesions, definitive investigation of the entire neuraxis, to define the tumour accurately, plan surgery and demonstrate distant spread, is now almost entirely the province of MRI.

Cysts

Cysts can occur in all parts of the brain. Those occurring at birth and located adjacent to or communicating with the ventricles are known as porencephalic cysts. They are usually the result of previous infection, infarction or haemorrhage, representing areas of encysted necrotic brain damage.[125] Arachnoid cysts are developmental lesions probably caused by disordered leptomeningeal formation coupled with hypogenesis of the adjacent brain, and as such seldom cause mass effect unless very large. They are found in various supratentorial sites, particularly in the middle cranial fossa, and in the posterior fossa. Lesions abutting the ventricular system may cause obstructive hydrocephalus. Suprasellar arachnoid cysts may lead to some diagnostic confusion, simulating a greatly enlarged third ventricle. Ultrasound is, however, able to define the wall of the lesion extending over and obstructing the foramina of Monro. Arachnoid cysts are usually an incidental finding.

Vascular malformations

True vein of Galen malformations most commonly present in neonates and in early infancy with high-output cardiac failure, hydrocephalus and failure to thrive. They are developmental lesions probably related to a defect in the evolution of the embryonic galenic venous system.[126] There is a variable composition of arteriovenous shunts within the syndrome complex, the classification of which is outside the scope of this chapter. The ultrasound hallmark of the lesion is a midline echo-free pulsatile mass, probably representing a grossly dilated median prosencephalic vein. Ultrasound has proved particularly useful in both the diagnosis and the treatment of these lesions, especially with the adjunctive use of colour Doppler imaging (Fig. 65.47).[127,128] The diagnosis may be confirmed by MRI, but definitive assessment and treatment is now effected by angiography and endovascular therapy. The arterial feeding pedicles can be clearly identified and monitored by ultrasound during endovascular treatment; ultrasound can also be used intraoperatively to assess the progress of surgery.[128]

Congenital arteriovenous malformations, particularly pial arteriovenous fistulae, may be more difficult to identify by ultrasound. A high index of suspicion should be maintained in an infant presenting with high-output cardiac failure.

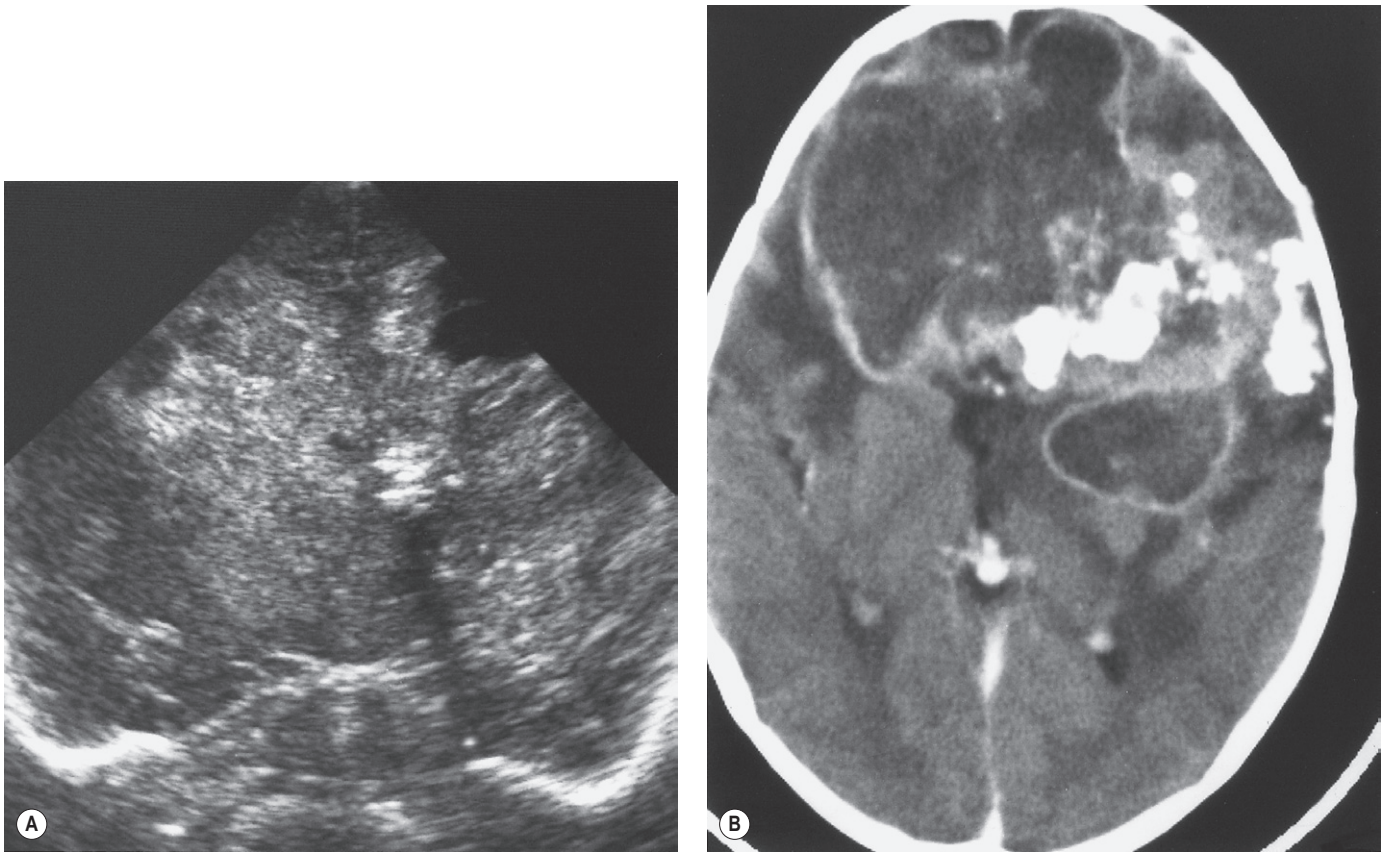

Figure 65.44 Primitive rhabdoidal tumour of the frontal lobe. A: Coronal scans demonstrate a huge heterogeneous frontal mass distorting and obscuring the local anatomy. Cysts and calcifications are present. **B:** Axial CT scan more clearly defines the full extent of the tumour.

TRAUMA

Trauma during the first year of life may be divided into birth-related causes, and accidental and non-accidental injury.

Birth-related injury

Injuries related to the birth process may be due to abnormal presentation, specifically breech, or to surgical instrumentation. Forceps-assisted deliveries or ventouse extraction can produce injury to the scalp (cephalhaematoma), extra-axial bleeding (subdural or extradural haematoma) or intraparenchymal haemorrhage (usually a delayed cerebellar bleed). The newborn baby typically appears bruised, with a misshapen head and overriding calvarial bones. Most infants with significant intracranial haemorrhage have normal Apgar scores at birth and may initially appear relatively normal; however, signs and symptoms generally evolve over the ensuing 36 hours.[129] Near-field scanning can readily demonstrate the scalp lesions, which can sometimes be very large and slow to resolve. Trans-cranial scanning is useful to delineate fully the extent of subdural haemorrhages (SDH) that typically occur around the tentorium, being related to tentorial laceration and tearing of the contained venous sinuses. Infratentorial haematomas, however, are difficult to diagnose and easy to miss. A CT scan should be performed if there is any suspicion of abnormality in this region. High-convexity subdural haematomas may be missed unless trans-cranial scanning is performed owing to the 'blind spot' adjacent to the anterior fontanelle. CT scanning is necessary, however, to confirm the diagnosis and provide more definitive imaging, particularly in the context of potential litigation.

There is now a growing awareness of the presence of birth-related subdural haematomas in asymptomatic infants with atraumatic birth histories[130] which can be detected by cranial ultrasound.[131] These are typically shallow, occurring around the occipital poles or in the posterior fossa (Fig. 65.48), and resolve by 4 weeks of age.

Accidental injury

As neonates and young infants are relatively immobile they are unlikely to fall of their own accord. Falls from beds, settees and the arms of carers are, however, not uncommon. Significant intracranial injury from such falls is very uncommon, with skull fractures usually being the only major damage sustained.[132] Fractures occurring as a result of an accidental fall are typically parietal, simple and linear. If subdural haemorrhage occurs it usually underlies the fracture. Parenchymal injury is rare. Ultrasound scanning, particularly trans-cranial, can detect the collections adequately, but CT scanning should also be performed, particularly if there is clinical concern.

Non-accidental head injury

Infants are particularly susceptible to intracranial trauma because of their large head-to-body ratio, poor neck muscles and the poorly myelinated brain with its high water content. In addition, the infant brain has more space in which to move about in the intracranial compartment owing to the relatively large CSF volume overlying the brain and the greater plasticity of the skull, with its open fontanelles and unfused sutures. The mechanism of injury in child abuse probably involves a combination of vigorous to-and-fro shaking and some element of blunt impact, against either a hard or a padded surface.[133] Neuro-imaging must be obtained at the earliest

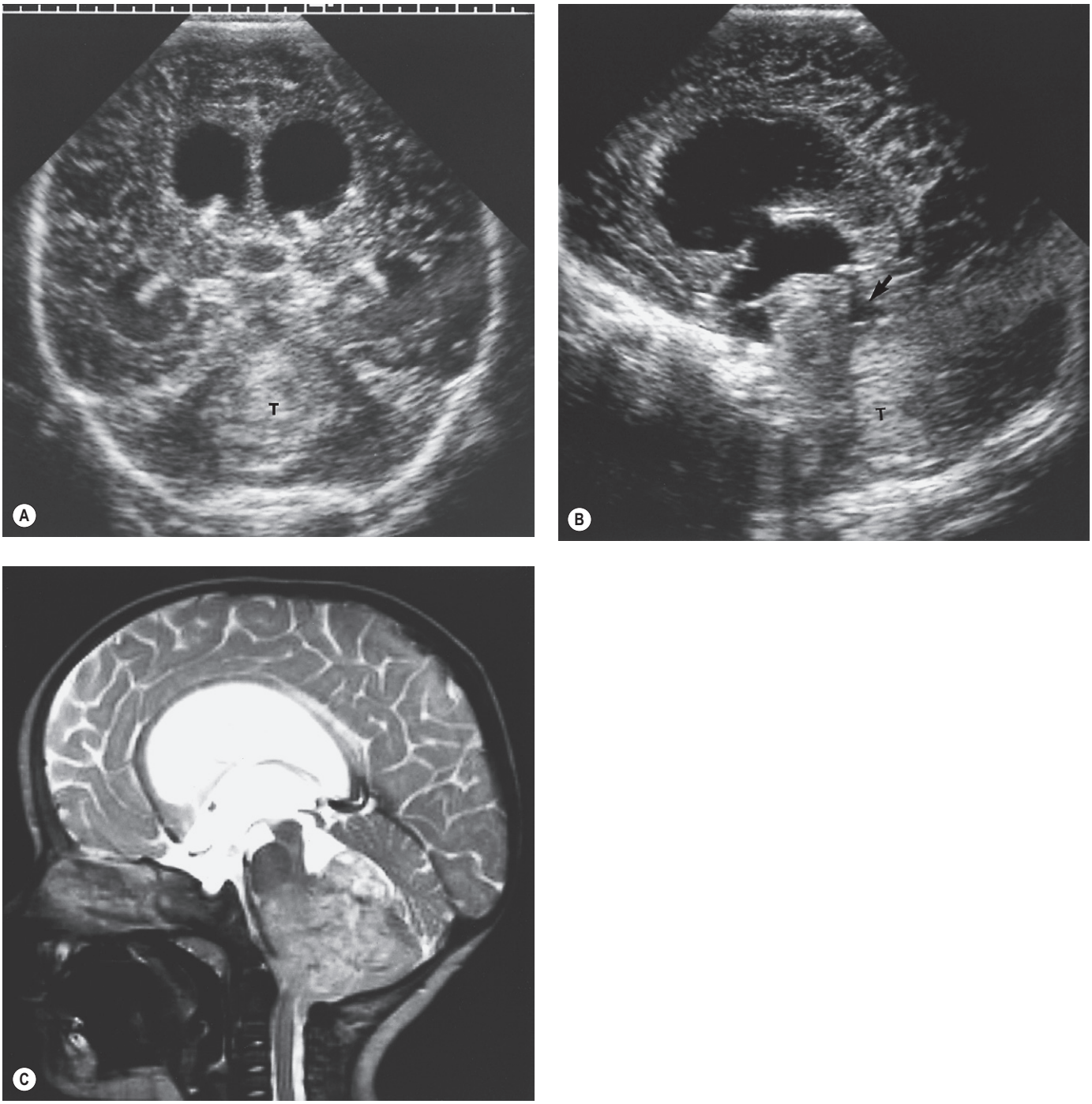

Figure 65.45 Posterior fossa primitive neuro-ectodermal tumour (PNET). A: Coronal and **B:** sagittal scans show a large midline posterior fossa tumour (T) producing supratentorial hydrocephalus. Note the fourth ventricle displaced superiorly (arrow). **C:** Sagittal T2-weighted MR image defines the extent of the tumour more fully.

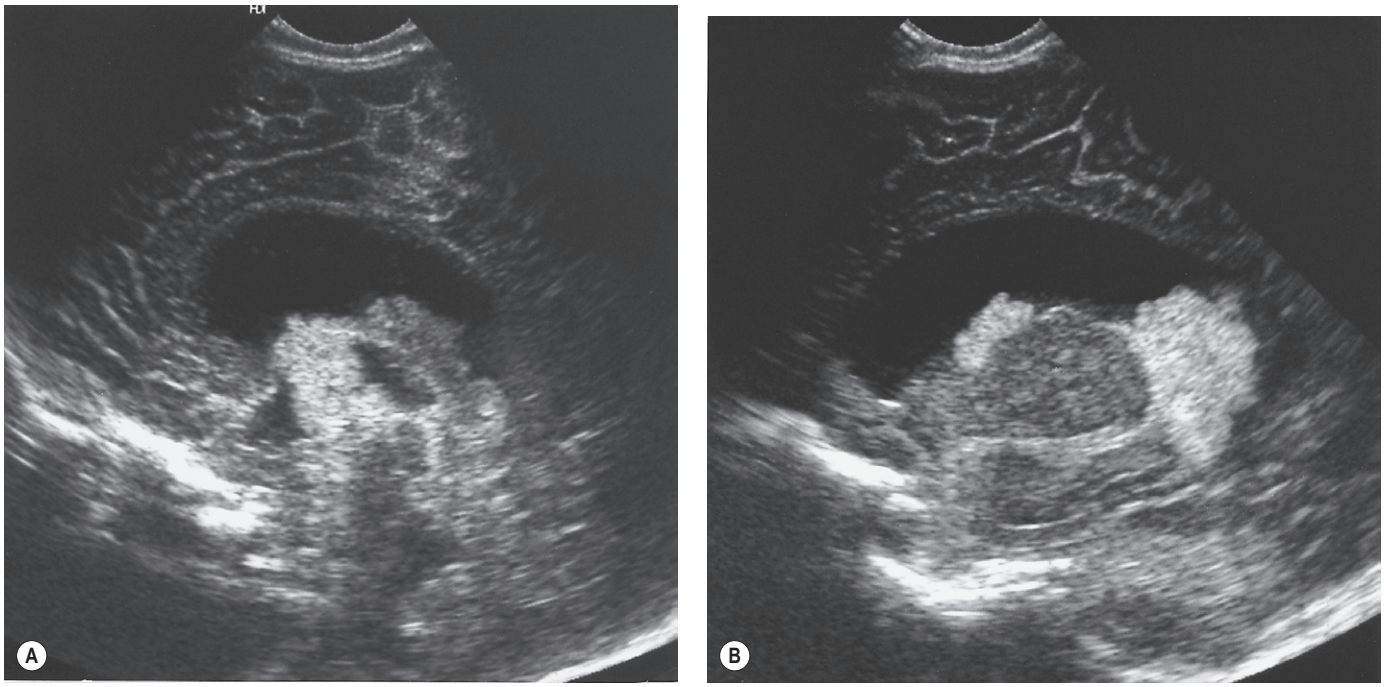

Figure 65.46 Multifocal choroid plexus papillomas. A: Midline sagittal and **B:** parasagittal sections showing at least three strongly reflective tumours in the third and lateral ventricles.

possible time following the child's admission and stabilisation of his/her medical condition if severely injured. A cranial CT scan is mandatory to document the presence of haemorrhage, particularly when fresh, and determine the need for urgent therapeutic intervention, such as evacuation of a large subdural haematoma.[134] Cranial ultrasound is helpful to confirm the location of extra-axial fluid collections and can be particularly sensitive in the detection of subtle parenchymal injuries, such as corticomedullary contusional tears, which CT can miss.[135] An ultrasound examination can also be the most practical first step in the most severely injured infants, who are highly unstable. Reliance on paper copies of images, poor ultrasound technique and the use of poor-quality ultrasound units discredits ultrasound as a diagnostic tool in this area of radiology. A strict protocol for the investigation of suspected non-accidental head injury (NAHI) should be adopted and adhered to in all cases,[134] ultrasound forming an important adjunct to the work-up of such cases. It should, however, be borne in mind that the limitations of ultrasound are real, and that it should never be over-relied upon, particularly in the older infant, when scan quality declines progressively. In cases of suspected NAHI, every step should be taken to obtain an early CT scan.

A wide range of injuries may be sustained in NAHI. The injuries may be considered to be primary (a direct result of the inflicted trauma), secondary (a delayed consequence of the primary injury) and chronic.

Primary injuries include scalp bruising, skull fractures, subdural and subarachnoid haemorrhage and parenchymal brain injury. The latter includes shearing injuries, cortical contusions, major transcerebral lacerations and lobar disruption. The ultrasound appearances of subdural haemorrhage have already been discussed. Acute subdural haemorrhage should be looked for particularly carefully in the inter-hemispheric region, where it may be subtle, appearing as excessive reflectivity of the falcine complex (Fig. 65.49), and over the cerebral convexity using a near-field linear array transducer (Fig. 65.50). The demonstration of membranes within a subdural collection can be helpful in indicating that the subdural haematoma is of mixed age. Parenchymal injuries detected by ultrasound include delicate echo-free linear or branching contusional injuries indicative of injuries involving shearing forces. These lesions are seen particularly at the grey–white matter interface of the frontoparietal parts of the brain using high-resolution ultrasound (Fig. 65.51).[135] Gliding contusions, larger areas of mixed reflectivity representing haemorrhagic contusions, and lobar disruption, which typically occur in the basal parts of the brain as a result of the brain striking the hard skull base in an impact injury, can also be readily detected. Transcerebral lacerations are identified as reflective blood-filled lesions or echo-free clefts in the brain, usually extending from the surface of the brain towards a ventricular margin.

Secondary damage to the brain evolves as a result of the primary injury and includes cerebral oedema and swelling, hypoxic or ischaemic injury and hydrocephalus. Cerebral swelling occurs within hours of a major inflicted injury and probably reflects increased cerebral blood volume (hyperaemia). The intracranial pressure can rise precipitately, with subsequent death if left untreated. Cerebral oedema is a complex phenomenon, with primary brain damage, vascular injury or secondary infarction leading to increased brain water (oedema). On ultrasound imaging this is shown by focal or diffuse areas of increased reflectivity of the brain, which takes on a rather featureless appearance as normal anatomical landmarks are obscured.

Evolving regional or diffuse increased reflectivity may be seen over the ensuing few days to weeks following injury. The cortex in particular can become thickened and strongly reflective, accompanying the haemorrhagic laminar cortical necrosis or infarction which is not infrequently seen in severely affected infants. Hydrocephalus is usually the consequence of impaired CSF resorption secondary to traumatic subarachnoid and/or subdural haemorrhage. Prominent subarachnoid spaces underlying a subdural haematoma are readily detected and may indicate chronicity of the SDH, communicating hydrocephalus being a recognised sequela of cranial injury. The diagnosis needs to be made with caution as cerebral atrophy can also lead to marked widening of the subarachnoid spaces. Correlation with serial head circumference measurements helps to differentiate between these two, cerebral atrophy resulting in cessation of head growth.

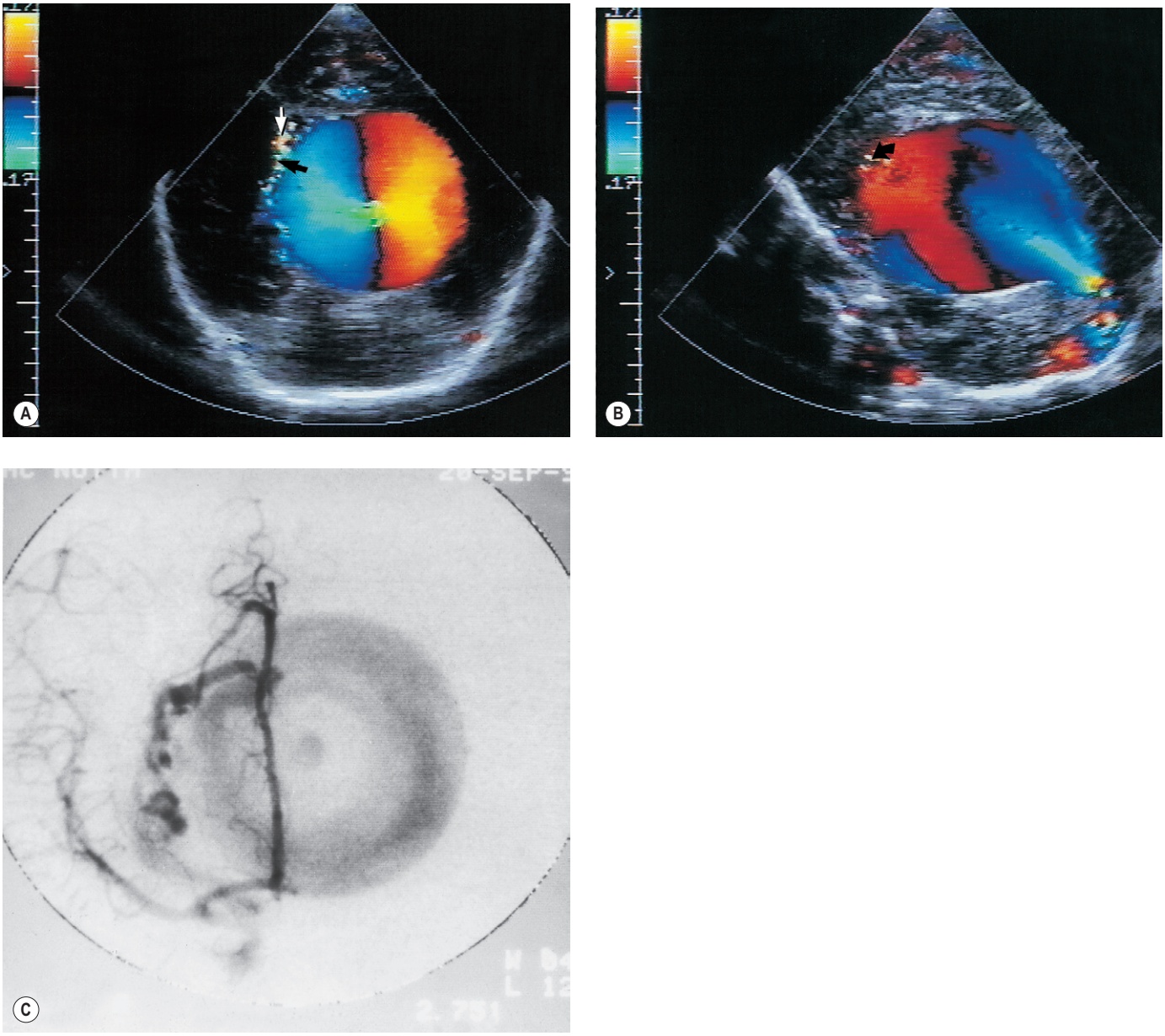

Figure 65.47 **Vein of Galen malformation. A:** Coronal and **B:** sagittal colour Doppler images demonstrating aneurysmal dilatation of the vein of Galen. The arterial inflow can be identified on the superolateral wall of the aneurysm (arrows). **C:** A digital subtraction angiogram demonstrates the arterial supply and the doughnut appearance of the venous sac.

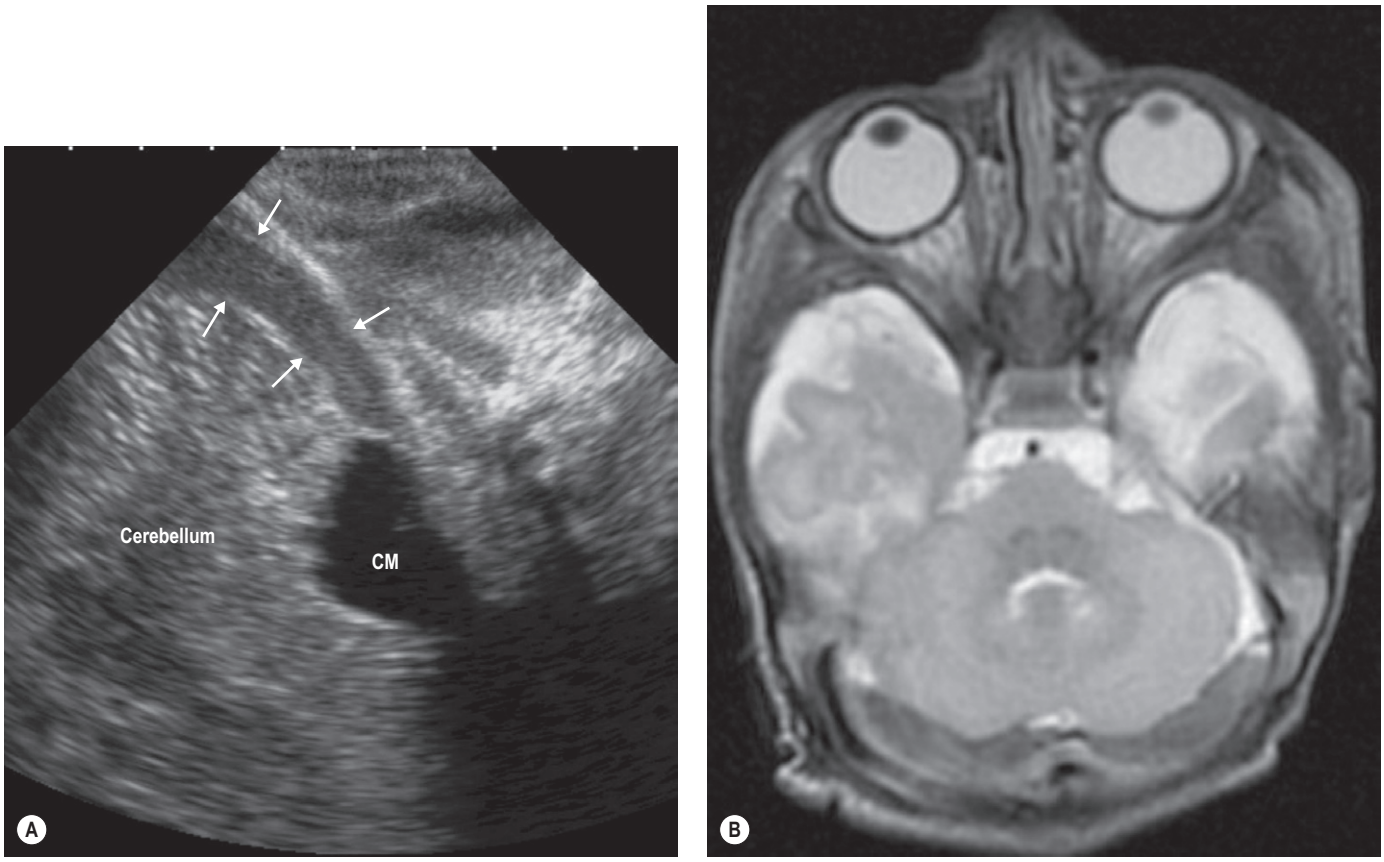

Figure 65.48 Birth-related subdural haematoma. A: Transverse cranial ultrasound via the mastoid fontanelle showing echogenic fluid (arrows) dorsal to the cerebellum. CM, cisterna magna. **B:** Axial T2-weighted image confirms the presence of bilateral posterior fossa

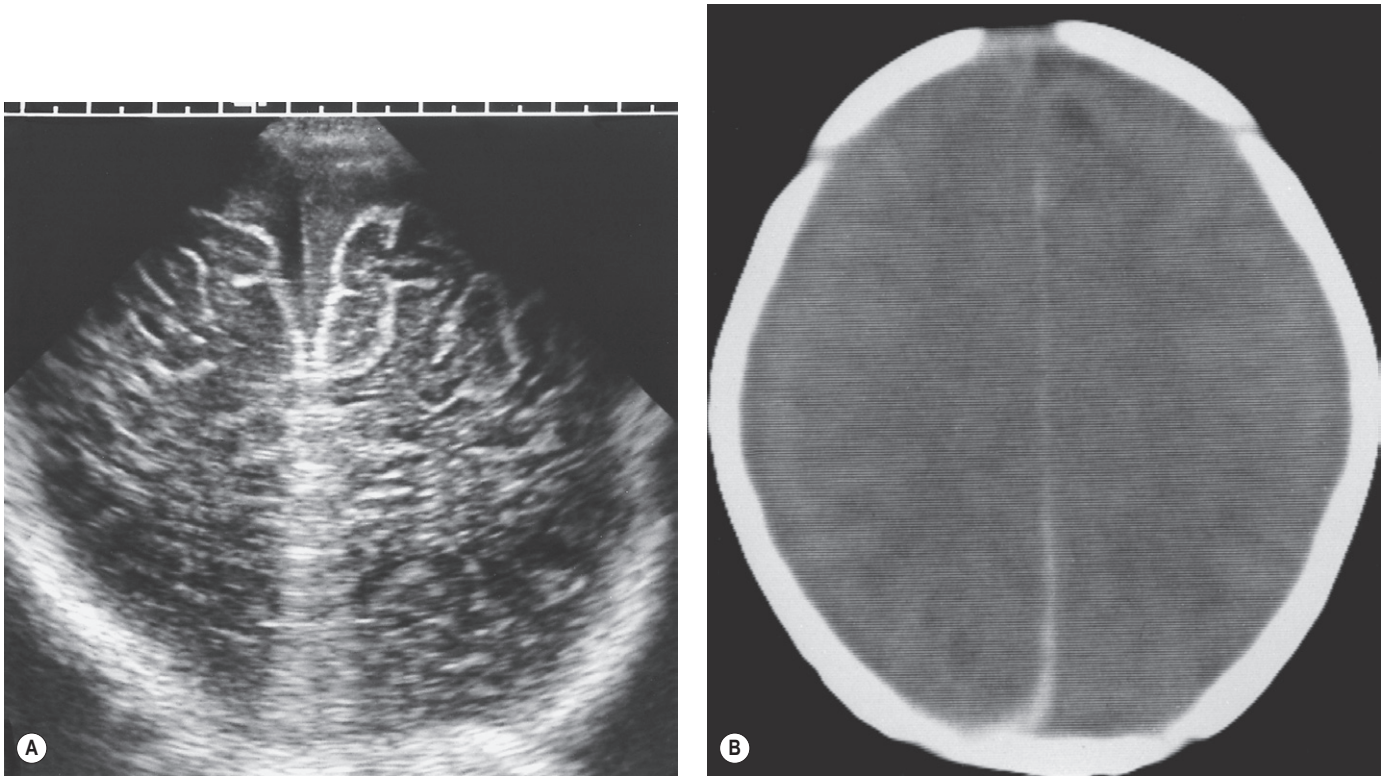

Figure 65.49 Posterior inter-hemispheric acute subdural haematoma. A: Coronal scan shows a prominent appearance of the posterior falx complex. **B:** Axial CT scan shows the delicate hyperdense collection lying along the right side of the falx posteriorly.

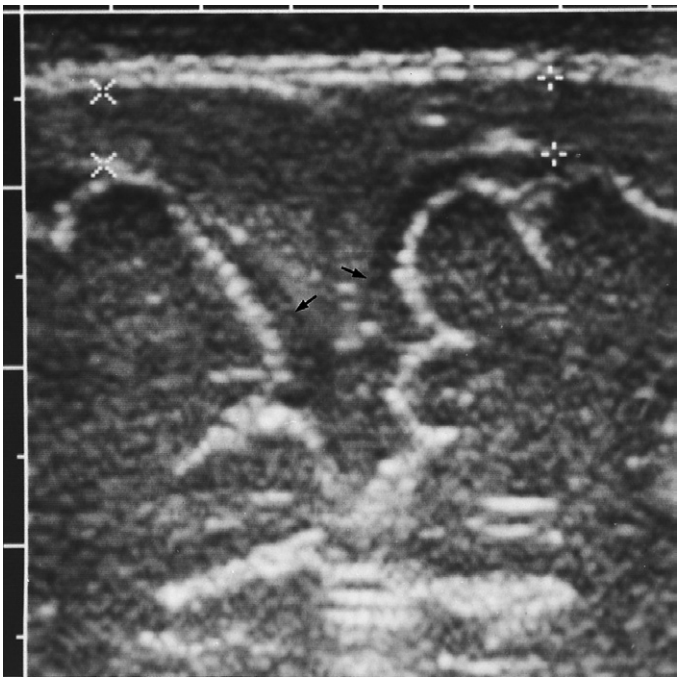

Figure 65.50 Acute subdural haematomas overlying the high cerebral convexities. Cursors identify the collections. Note the echo-free subarachnoid fluid (arrows) underlying the subdural haematomas.

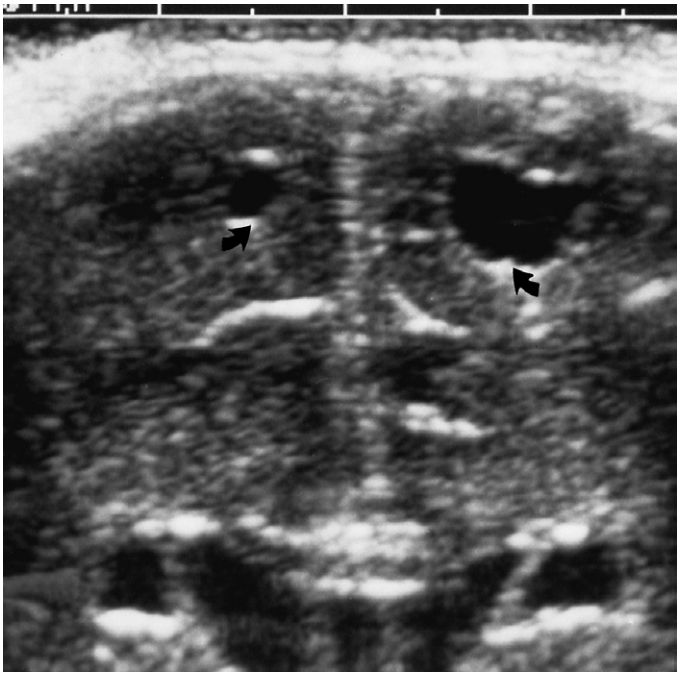

Figure 65.51 Corticomedullary junction contusional tears. High-resolution coronal scanning clearly identifies two characteristic lesions (curved arrows) in the parasagittal frontoparietal regions.

EVALUATION OF BRAIN DEATH

Doppler ultrasound provides a specific and sensitive test for the confirmation of brain death in adults and children over the age of 2 years.[136,137] During the evolution of cerebral circulatory arrest there is a progressive reduction of diastolic flow which becomes absent,

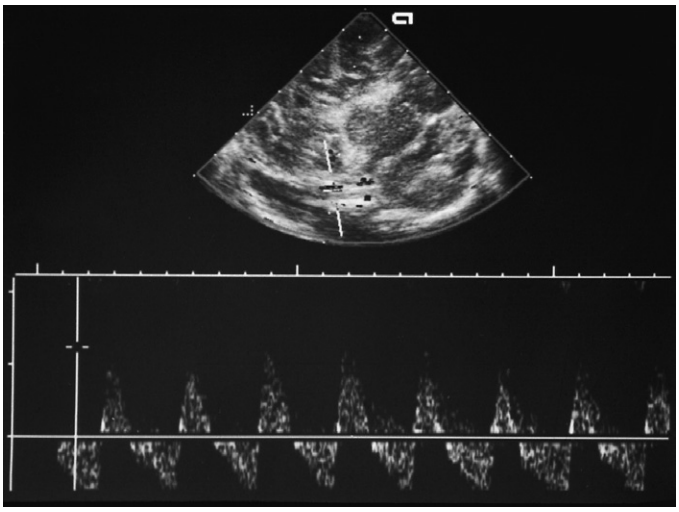

Figure 65.52 Reversed diastolic blood flow on spectral Doppler imaging.

followed by an agonal reversal of diastolic flow and the development of short systolic spikes.[137] Reversal of diastolic flow detected by cranial Doppler has been shown to occur in infants with brain death (Fig. 65.52).[138] However, reversal of diastolic flow can occur in infants without brain death when there is raised intracranial pressure due to other causes such as tumour or status epilepticus.[139] While complete absence of detectable blood flow is a lethal sign, an isolated finding of reversed diastolic flow is not a reliable sign of brain death in infants.[140]

REFERENCES

1. de Vliega M, de Sterke A, Molin CE, van der Ven C. Ultrasound for two-dimensional echoencephalography. Ultrasonics 1963;1:148–151.
2. Pape KE, Blackwell RJ, Cusick G, et al. Ultrasound detection of brain damage in preterm infants. Lancet 1979;1:1261–1264.
3. Dewbury KC, Aluwihare AP. The anterior fontanelle as an ultrasound window for study of the brain: a preliminary report. Br J Radiol 1980;53:81–84.
4. Ben-Ora A, Eddy L, Hatch G, Solida B. The anterior fontanelle as an acoustic window to the neonatal ventricular system. J Clin Ultrasound 1980;8:65–67.
5. Archer LN, Levene MI, Evans DH. Cerebral artery Doppler ultrasonography for prediction of outcome after perinatal asphyxia. Lancet 1986;2:1116–1118.
6. Daneman A, Epelman M, Blaser S, Jarrin JR. Imaging of the brain in full-term neonates: does sonography still play a role? Pediatr Radiol 2006;36:636–646.
7. Winkler P. Advances in paediatric CNS ultrasound. Eur J Radiol 1998;26:109.
8. Di Salvo DN. A new view of the neonatal brain: clinical utility of supplemental neurologic US imaging windows. Radiographics 2001;21:943–955.
9. Correa F, Enriquez G, Rossello J, et al. Posterior fontanelle sonography: an acoustic window into the neonatal brain. AJNR Am J Neuroradiol 2004;25:1274–1282.
10. De Vries LS, Eken P, Beek E, et al. The posterior fontanelle: a neglected acoustic window. Neuropediatrics 1996;27:101–104.
11. Enriquez G, Correa F, Aso C, et al. Mastoid fontanelle approach for sonographic imaging of the neonatal brain. Pediatr Radiol 2006;36:532–540.
12. Luna JA, Goldstein RB. Sonographic visualization of neonatal posterior fossa abnormalities through the posterolateral fontanelle. AJR Am J Roentgenol 2000;174:561–567.
13. Sudakoff GS, Montazemi M, Rifkin MD. The foramen magnum: the underutilized acoustic window to the posterior fossa. J Ultrasound Med 1993;12:205–210.
14. Leijser LM, Srinivasan L, Rutherford MA, et al. Structural linear measurements in the newborn brain: accuracy of cranial ultrasound compared to MRI. Pediatr Radiol 2007;37:640–648.

15. London DA, Carroll BA, Enzmann DR. Sonography of ventricular size and germinal matrix hemorrhage in premature infants. AJR Am J Roentgenol 1980;135:559–564.
16. O'Hayon BB, Drake JM, Ossip MG, et al. Frontal and occipital horn ratio: a linear estimate of ventricular size for multiple imaging modalities in pediatric hydrocephalus. Pediatr Neurosurg 1998;29:245–249.
17. Levene MI. Measurement of the growth of the lateral ventricles in preterm infants with real-time ultrasound. Arch Dis Child 1981;56:900–904.
18. Grasby DC, Esterman A, Marshall P. Ultrasound grading of cerebral ventricular dilatation in preterm neonates. J Paediatr Child Health 2003;39:186–190.
19. Shackelford GD. Neurosonography of hydrocephalus in infants. Neuroradiology 1986;28:452–462.
20. Fiske CE, Filly RA, Callen PW. The normal choroid plexus: ultrasonographic appearance of the neonatal head. Radiology 1981;141:467–471.
21. Epelman M, Daneman A, Blaser SI, et al. Differential diagnosis of intracranial cystic lesions at head US: correlation with CT and MR imaging. Radiographics 2006;26:173–196.
22. Rosenfeld DL, Schonfeld SM, Underberg-Davis S. Coarctation of the lateral ventricles: an alternative explanation for subependymal pseudocysts. Pediatr Radiol 1997;27:895–897.
23. Thun-Hohenstein L, Forster I, Kunzle C, et al. Transient bifrontal solitary periventricular cysts in term neonates. Neuroradiology 1994;36:241–244.
24. Yousefzadeh DK, Naidich TP. US anatomy of the posterior fossa in children: correlation with brain sections. Radiology 1985;156:353–361.
25. Goodwin L, Quisling RG. The neonatal cisterna magna: ultrasonic evaluation. Radiology 1983;149:691–695.
26. Archer LN, Evans DH, Levene MI. Doppler ultrasound examination of the anterior cerebral arteries of normal newborn infants: the effect of postnatal age. Early Hum Dev 1985;10:255–260.
27. Fenton AC, Shortland DB, Papathoma E, Evans DH, Levene MI. Normal range for blood flow velocity in cerebral arteries of newly born term infants. Early Hum Dev 1990;22:73–79.
28. Hayashi T, Ichiyama T, Uchida M, et al. Evaluation by colour Doppler and pulsed Doppler sonography of blood flow velocities in intracranial arteries during the early neonatal period. Eur J Pediatr 1992;151:461–465.
29. Evans DH, Levene MI, Shortland DB, Archer LN. Resistance index, blood flow velocity, and resistance-area product in the cerebral arteries of very low birth weight infants during the first week of life. Ultrasound Med Biol 1988;14:103–110.
30. Allison JW, Faddis LA, Kinder DL, et al. Intracranial resistive index (RI) values in normal term infants during the first day of life. Pediatr Radiol 2000;30:618–620.
31. Kinoshita Y, Okudera T, Tsuru E, Yokota A. Volumetric analysis of the germinal matrix and lateral ventricles performed using MR images of postmortem fetuses. AJNR Am J Neuroradiol 2001;22:382–388.
32. Ghazi-Birry HS, Brown WR, Moody DM, et al. Human germinal matrix: venous origin of hemorrhage and vascular characteristics. AJNR Am J Neuroradiol 1997;18:219–229.
33. Nakamura Y, Okudera T, Fukuda S, Hashimoto T. Germinal matrix hemorrhage of venous origin in preterm neonates. Hum Pathol 1990;21:1059–1062.
34. Braun A, Xu H, Hu F, et al. Paucity of pericytes in germinal matrix vasculature of premature infants. J Neurosci 2007;27:12012–12024.
35. Guzzetta F, Shackelford GD, Volpe S, et al. Periventricular intraparenchymal echodensities in the premature newborn: critical determinant of neurologic outcome. Pediatrics 1986;78: 995–1006.
36. Gould SJ, Howard S, Hope PL, Reynolds EO. Periventricular intraparenchymal cerebral haemorrhage in preterm infants: the role of venous infarction. J Pathol 1987;151:197–202.
37. Takashima S, Mito T, Ando Y. Pathogenesis of periventricular white matter hemorrhages in preterm infants. Brain Dev 1986;8:25–30.
38. Taylor GA. Effect of germinal matrix hemorrhage on terminal vein position and patency. Pediatr Radiol 1995;25(Suppl 1):S37–S40.
39. Perlman JM, Rollins N. Surveillance protocol for the detection of intracranial abnormalities in premature neonates. Arch Pediatr Adolesc Med 2000;154:822–826.
40. Papile LA, Burstein J, Burstein R, Koffler H. Incidence and evolution of subependymal and intraventricular hemorrhage: a study of infants with birth weights less than 1,500 gm. J Pediatr 1978;92:529–534.
41. Leviton A, Kuban K, Paneth N. Intraventricular haemorrhage grading scheme: time to abandon? Acta Paediatr 2007;96:1254–1256.
42. Volpe JJ. Brain injury in the premature infant. Neuropathology, clinical aspects, pathogenesis, and prevention. Clin Perinatol 1997;24:567–587.
43. De Reuck JL. Cerebral angioarchitecture and perinatal brain lesions in premature and full-term infants. Acta Neurol Scand 1984;70:391–395.
44. Takashima S, Tanaka K. Development of cerebrovascular architecture and its relationship to periventricular leukomalacia. Arch Neurol 1978;35:11–16.
45. Blankenberg FG, Barnes PD. Structural and functional imaging of hypoxic-ischemic injury (HII) in the fetal and neonatal brain. In: Stevenson DK, Benitz WE, Sunshine P, editors. Fetal and neonatal brain injury. 3rd ed. Cambridge, UK: Cambridge University Press; 2003. p. 455.
46. Hope PL, Gould SJ, Howard S, et al. Precision of ultrasound diagnosis of pathologically verified lesions in the brains of very preterm infants. Dev Med Child Neurol 1988;30:457–471.
47. Paneth N, Rudelli R, Monte W, et al. White matter necrosis in very low birth weight infants: neuropathologic and ultrasonographic findings in infants surviving six days or longer. J Pediatr 1990;116:975–984.
48. Carson SC, Hertzberg BS, Bowie JD, Burger PC. Value of sonography in the diagnosis of intracranial hemorrhage and periventricular leukomalacia: a postmortem study of 35 cases. AJNR Am J Neuroradiol 1990;11:677–683.
49. Inder TE, Anderson NJ, Spencer C, et al. White matter injury in the premature infant: a comparison between serial cranial sonographic and MR findings at term. AJNR Am J Neuroradiol 2003;24:805–809.
50. Sunshine P. Perinatal asphyxia: an overview. In: Stevenson DK, Benitz WE, Sunshine P, editors. Fetal and neonatal brain injury. 3rd ed. Cambridge, UK: Cambridge University Press; 2003. p. 3–29.
51. Smith J, Wells L, Dodd K. The continuing fall in incidence of hypoxic-ischaemic encephalopathy in term infants. BJOG Int J Obste Gynaecol 2000;107:461–466.
52. Hill A. Current concepts of hypoxic-ischemic cerebral injury in the term newborn infant. Pediatr Neurol 1991;7:317–325.
53. Volpe JJ, Pasternak JF. Parasagittal cerebral injury in neonatal hypoxic-ischemic encephalopathy: clinical and neuroradiologic features. J Pediatr 1977;91:472–476.
54. Volpe JJ, Herscovitch P, Perlman JM, et al. Positron emission tomography in the asphyxiated term newborn: parasagittal impairment of cerebral blood flow. Ann Neurol 1985;17:287–296.
55. Groenendaal F, de Vries LS. Watershed infarcts in the full term neonatal brain. Arch Dis Child Fetal Neonatal Ed 2005;90:F488.
56. Levene MI, Fenton AC, Evans DH, et al. Severe birth asphyxia and abnormal cerebral blood-flow velocity. Dev Med Child Neurol 1989;31:427–434.
57. Ilves P, Lintrop M, Metsvaht T, et al. Cerebral blood-flow velocities in predicting outcome of asphyxiated newborn infants. Acta Paediatr 2004;93:523–528.
58. Ilves P, Talvik R, Talvik T. Changes in Doppler ultrasonography in asphyxiated term infants with hypoxic-ischaemic encephalopathy. Acta Paediatr 1998;87:680–684.
59. Stark JE, Seibert JJ. Cerebral artery Doppler ultrasonography for prediction of outcome after perinatal asphyxia. J Ultrasound Med 1994;13:595–600.
60. Kirimi E, Tuncer O, Atas B, et al. Clinical value of color Doppler ultrasonography measurements of full-term newborns with perin atal asphyxia and hypoxic ischemic encephalopathy in the first 12 hours of life and long-term prognosis. Tohoku J Exp Med 2002;197:27–33.
61. Bennhagen RG, Weintraub RG, Lundström NR, Svenningsen NW. Hypoxic-ischaemic encephalopathy is associated with regional changes in cerebral blood flow velocity and alterations in cardiovascular function. Biol Neonate 1998;71:275–286.
62. Eken P, Toet MC, Groenendaal F, de Vries LS. Predictive value of early neuroimaging, pulsed Doppler and neurophysiology in full term infants with hypoxic-ischaemic encephalopathy. Arch Dis Child Fetal Neonatal Ed 1995;73:F75–F80.
63. Chang L, Wang Y, Liu W. Measurements of cerebral blood flow in post-asphyxiated newborns by color Doppler imaging (CDI). J Tongji Med Univ 1996;16:249–252.
64. Van Bel F, Walther FJ. Myocardial dysfunction and cerebral blood flow velocity following birth asphyxia. Acta Paediatr Scand 1990;79:759–762.
65. Shortland DB, Gibson NA, Levene MI, et al. Patent ductus arteriosus

and cerebral circulation in preterm infants. Dev Med Child Neurol 1990;32:386–393.
66. Robel-Tillig E, Knüpfer M, Pulzer F, Vogtmann C. Cardiovascular impact of dobutamine in neonates with myocardial dysfunction. Early Hum Dev 2007;83:307–312.
67. Evans DH, Levene MI, Archer LN. The effect of indomethacin on cerebral blood-flow velocity in premature infants. Dev Med Child Neurol 1987;29:776–782.
68. Shortland DB, Field D, Archer LN, et al. Cerebral haemodynamic effects of changes in positive end expiratory pressure in preterm infants. Arch Dis Child 1989;64:465–469.
69. Van Bel F, Van de Bor M, Baan J, Ruys JH. The influence of abnormal blood gases on cerebral blood flow velocity in the preterm newborn. Neuropediatrics 1988;19:27–32.
70. Gebauer CM, Knuepfer M, Robel-Tillig E, et al. Hemodynamics among neonates with hypoxic-ischemic encephalopathy during whole-body hypothermia and passive rewarming. Pediatrics 2006;117:843–850.
71. Cowan F, Mercuri E, Groenendaal F, et al. Does cranial ultrasound imaging identify arterial cerebral infarction in term neonates? Arch Dis Child Fetal Neonatal Ed 2005;90:F252–F256.
72. Estan J, Hope P. Unilateral neonatal cerebral infarction in full term infants. Arch Dis Child Fetal Neonatal Ed 1997;76:F88–F93.
73. Schulzke S, Weber P, Luetschg J, Fahnenstich H. Incidence and diagnosis of unilateral arterial cerebral infarction in newborn infants. J Perinatal Med 2005;33:170.
74. Golomb MR, Fullerton HJ, Nowak-Gottl U, deVeber G, for the International Pediatric Stroke Study Group. Male predominance in childhood ischemic stroke. findings from the International Pediatric Stroke Study. Stroke 2009;40(1):52–57.
75. Suppiej A, Franzoi M, Gentilomo C, et al. High prevalence of inherited thrombophilia in 'presumed peri-neonatal' ischemic stroke. Eur J Haematol 2008;80:71–75.
76. Golomb MR, Dick PT, MacGregor DL, et al. Cranial ultrasonography has a low sensitivity for detecting arterial ischemic stroke in term neonates. J Child Neurol 2003;18:98–103.
77. Sandberg DI, Lamberti-Pasculli M, Drake JM, et al. Spontaneous intraparenchymal hemorrhage in full-term neonates. Neurosurgery 2001;48:1042–1048.
78. Limperopoulos C, Benson CB, Bassan H, et al. Cerebellar hemorrhage in the preterm infant: ultrasonographic findings and risk factors. Pediatrics 2005;116:717–724.
79. Muller H, Beedgen B, Schenk J-P, et al. Intracerebellar hemorrhage in premature infants: sonographic detection and outcome. J Perinatal Med 2007;35:67–70.
80. DeVeber GA, Andrew M, Adams C, et al. Cerebral sinovenous thrombosis in children. N Engl J Med 2001;345:417–423.
81. Lam AH. Doppler imaging of superior sagittal sinus thrombosis. J Ultrasound Med 1995;14:41–46.
82. Ben-Ami T, Yousefzadeh D, Backus M, et al. Lenticulostriate vasculopathy in infants with infections of the CNS. Sonographic and Doppler findings. Pediatr Radiol 1990;20:575–579.
83. Makhoul IR, Eisenstein I, Sujov P, et al. Neonatal lenticulostriate vasculopathy: further characterisation. Arch Dis Child Fetal Neonatal Ed 2003;88:F410–F414.
84. Coley BD, Rusin JA, Boue DR. Importance of hypoxic/ischemic conditions in the development of cerebral lenticulostriate vasculopathy. Pediatr Radiol 2000;30:846–855.
85. Carey BM, Arthur RJ, Houlsby WT. Ventriculitis in congenital rubella ultrasound demonstration. Pediatr Radiol 1987;17:415–416.
86. Grant EG, Williams AL, Schellinger D, Slovis TL. Intracranial calcifications in the infant and neonate: evaluation by sonography and CT. Radiology 1985;157:63–68.
87. Babcock DS, Han BK. Sonographic recognition of gyral infarction in meningitis. AJR Am J Roentgenol 1985;144:833–836.
88. Fisher RM, Lipinski JK, Cremin BJ. Ultrasonic assessment of infectious meningitis. Clin Radiol 1984;35:267–273.
89. Cleveland RH, Herman TE, Oot RF, Kushner DC. The evolution of neonatal herpes encephalitis as demonstrated by cranial ultrasound with CT correlation. Am J Perinatol 1987;4:215–219.
90. Ramsden WH, Sapherson DA. Case report: the sonographic appearance of neonatal herpes simplex encephalitis. Clin Radiol 1995;50:574–576.
91. Yikilmaz A, Taylor GA. Sonographic findings in bacterial meningitis in neonates and young infants. Pediatr Radiol 2008;38:129–137.
92. Han BK, Babcock DS, McAdams L. Bacterial meningitis in infants: sonographic findings. Radiology 1985;154:645–650.
93. Frank JL. Sonography of intracranial infection in infants and children. Neuroradiology 1986;28:440–451.
94. Kirpekar M, Abiri MM, Hilfer C, Enerson R. Ultrasound in the diagnosis of systemic candidiasis (renal and cranial) in very low birth weight premature infants. Pediatr Radiol 1986;16:17–20.
95. Tung KT, MacDonald LM, Smith JC. Neonatal systemic candidiasis diagnosed by ultrasound. Acta Radiol 1990;31:293–295.
96. Maytal J, Alvarez LA, Elkin CM, Shinnar S. External hydrocephalus: radiologic spectrum and differentiation from cerebral atrophy. AJR Am J Roentgenol 1987;148:1223–1230.
97. Alvarez LA, Maytal J, Shinnar S. Idiopathic external hydrocephalus: natural history and relationship to benign familial macrocephaly. Pediatrics 1986;77:901–907.
98. Libicher M, Tröger J. US measurement of the subarachnoid space in infants: normal values. Radiology 1992;184:749–751.
99. Frankel D, Fessel DP, Wolfson WP. High resolution sonographic determination of the normal dimensions of the intracranial extraaxial compartment in the newborn infant. J Ultrasound Med 1998;17:411–415.
100. Perkins AC, Lawes SC, Mitchell LA, Jaspan T. A simple simulation for the visualisation of CSF flow in infants with hydrocephalus. Ultrasound Med Biol 1994;20:21–26.
101. Barkovich AJ. Pediatric neuroimaging. 4th ed. Philadelphia: Lippincott Williams & Wilkins; 2005.
102. Norman MG, McGillivray B, Kalousek DK, et al. Congenital malformations of the brain: pathologic, embryologic, clinical, radiological and genetic aspects. New York: Oxford University Press; 1995.
103. Babcock DS. The normal, absent and abnormal corpus callosum: sonographic findings. Radiology 1984;151:449–453.
104. Atlas SW, Shkolnik A, Naidich TP. Sonographic recognition of agenesis of the corpus callosum. AJR Am J Roentgenol 1985;145:167–173.
105. Gebarski SS, Gebarski KS, Bowerman RA, Silver TM. Agenesis of the corpus callosum: sonographic features. Radiology 1984;151:443–448.
106. Barkovich AJ, Kjos BO, Norman D, Edwards MS. Revised classification of posterior fossa cysts and cystlike malformations based on multiplanar MR imaging. AJR Am J Roentgenol 1989;153:1289–1300.
107. Calabro F, Arcuri T, Jinkins JR. Blake's pouch cyst: an entity within the Dandy-Walker continuum. Neuroradiology 2000;42:290–295.
108. Has R, Ermis H, Yuksel A, Ibrahimoglu L, et al. Dandy-Walker malformation: a review of 78 cases diagnosed by prenatal sonography. Fetal Diagn Ther 2004;19:342–347.
109. Adamsbaum C, Moutard ML, Andre C, et al. MRI of the fetal posterior fossa. Pediatr Radiol 2005;35:124–140.
110. Scoffings DJ, Kurian KM. Congenital and acquired lesions of the septum pellucidum. Clin Radiol 2008;63:210–219.
111. Supprian T, Sian J, Heils A, et al. Isolated absence of the septum pellucidum. Neuroradiology 1999;41:563–566.
112. Babcock DS. Sonographic demonstration of lissencephaly (agyria). J Ultrasound Med 1983;2:465–466.
113. Vannucci RC, Vannucci SJ. Hypoglycemic brain injury. Semin Neonatol 2001;6:147–155.
114. Barkovich AJ, Ali FA, Rowley HA, Bass N. Imaging patterns of neonatal hypoglycemia. AJNR Am J Neuroradiol 1998;19:523–528.
115. Kinnala A, Rikalainen H, Lapinleimu H, et al. Cerebral magnetic resonance imaging and ultrasonography findings after neonatal hypoglycemia. Pediatrics 1999;103:724–729.
116. Cakmakci H, Usal C, Karabay N, Kovanlikaya A. Transient neonatal hypoglycemia: cranial US and MRI findings. Eur Radiol 2001;11:2585–2588.
117. Leijser LM, de Vries LS, Rutherford MA, et al. Cranial ultrasound in metabolic disorders presenting in the neonatal period: characteristic features and comparison with MR Imaging. AJNR Am J Neuroradiol 2007;28:1223–1231.
118. Schoenberg BS, Schoenberg DG, Christine BW, Gomez MR. The epidemiology of primary intracranial neoplasms of childhood. Mayo Clin Proc 1976;51:51–56.
119. Rickert CH. Epidemiological features of brain tumors in the first 3 years of life. Childs Nerv Syst 1998;14:547–550.
120. Brown K, Mapstone TB, Oakes WJ. A modern analysis of intracranial tumors of infancy. Pediatr Neurosurg 1997;26:25–32.
121. Han BK, Babcock DS, Oestreich AF. Sonography of brain tumours in infants. AJR Am J Roentgenol 1984;143:31–36.
122. Strassburg HM, Sauer Weber S, Gilsbach J. Ultrasonographic

diagnosis of brain tumours in infancy. Pediatr Radiol 1984;14:284–287.
123. Winkler P, Helmke K. Ultrasonographic diagnosis and follow up of malignant brain tumours in childhood. Pediatr Radiol 1985;15:215–219.
124. Babcock DS, Barr LL, Crone KR. Intraoperative uses of ultrasound in the pediatric neurosurgical patient. Pediatr Neurosurg 1992;18:84–91.
125. Grant EG, Kerner M, Schellinger D, et al. Evolution of porencephalic cysts from intraparenchymal hemorrhage in neonates. Sonographic evidence. AJR Am J Roentgenol 1982;138:467–470.
126. Raybaud CA, Strother CM, Hald JK. Aneurysms of the vein of Galen: embryonic considerations and anatomical features relating to the pathogenesis of the malformation. Neuroradiology 1989;31:109–128.
127. Cohen HL, Haller JO. Advances in perinatal neurosonography. AJR Am J Roentgenol 1994;163:801–810.
128. Rubin JM, Hatfield MK, Chandler WF, et al. Intracerebral arteriovenous malformations: intraoperative color Doppler flow imaging. Radiology 1989;170:219–222.
129. Hanigan WC, Morgan AM, Stahlberg LK, Hiller JL. Tentorial hemorrhage associated with vacuum extraction. Pediatrics 1990;85:534–539.
130. Whitby EH, Griffiths PD, Rutter S, et al. Frequency and natural history of subdural haemorrhages in babies and relation to obstetric factors. Lancet 2004;363:846–851.
131. Rooks VJ, Eaton JP, Ruess L, et al. Prevalence and evolution of intracranial hemorrhage in asymptomatic term infants. AJNR Am J Neuroradiol 2008;29:1082–1089.
132. Lyons TJ, Oates RK. Falling out of bed: a relatively benign occurrence. Pediatrics 1993;92:125–127.
133. Kleinman PK. Diagnostic imaging in infant abuse. AJR Am J Roentgenol 1993;155:703–712.
134. Jaspan T, Griffiths PD, McConachie NS, Punt JAG. Neuroimaging for non-accidental injury in childhood: a proposed protocol. Clin Radiol 2003;58:44–53.
135. Jaspan T, Narborough G, Punt JA, Lowe J. Cerebral contusional tears as a marker of child abuse – detection by cranial sonography. Pediatr Radiol 1992;22:237–245.
136. Ducrocq X, Braun M, Debouverie M, et al. Brain death and transcranial Doppler: experience in 130 cases of brain dead patients. J Neurol Sci 1998;160:41–46.
137. Hadani M, Bruk B, Ram Z, et al. Application of transcranial doppler ultrasonography for the diagnosis of brain death. Intensive Care Med 1999;25:822–828.
138. Glasier CM, Seibert JJ, Chadduck WM, et al. Brain death in infants: evaluation with Doppler US. Radiology 1989;172:377–380.
139. Chiu NC, Shen EY, Lee BS. Reversal of diastolic cerebral blood flow in infants without brain death. Pediatr Neurol 1994;11:337–340.
140. Chiu NC, Shen EY, Ho CS. Outcome in children with significantly abnormal cerebral blood flow detected by Doppler ultrasonography: focus on the survivors. J Neuroimaging 2003;13:53–56.

CHAPTER

66

Head and neck masses in children

Laurence Abernethy

INTRODUCTION

Ultrasound is ideally suited to the examination of lesions of the head and neck in children. It is helpful to have a range of transducers with different footprints for children of different ages. High-resolution linear transducers, using frequencies up to 17 MHz, are generally most useful. Ultrasound examination is painless and non-invasive, and with patience, diagnostic images can be obtained even with a restless child. The plane of imaging is infinitely variable and can be adapted to the anatomical location of the lesion. Gentle pressure applied with the transducer can be used to determine whether lesions are compressible. Colour Doppler is uniquely valuable in allowing assessment of blood flow in real-time, making it immediately apparent whether a fluid-filled structure is cystic or vascular and if vascular whether it is fast or slow flowing in nature.

Ultrasound is limited in the assessment of deep lesions and some anatomical locations are not easy to visualise. The field of view may not be sufficient to demonstrate the full extent of large lesions, although extended field-of-view sonography may be helpful. High-frequency ultrasound cannot penetrate bone and air, and so may fail to demonstrate deep extension of lesions around the skull base, cervical spine, pharynx and trachea. Magnetic resonance imaging (MRI) is often complementary to ultrasound in these situations, as the field of view is not limited by the presence of bone, dense calcification, and air. However, MRI does not offer the same capability for real-time imaging that ultrasound can provide; imaging times are relatively long, and as the images are easily degraded by movement artefact, younger children may require sedation or general anaesthesia.

Investigation of head and neck masses in children requires a very different diagnostic approach from that which would be appropriate for adults. Most head and neck lesions in children are benign, and the child's age is an important factor in the differential diagnosis. Congenital and inflammatory lesions are common, especially in young children. The most common inflammatory masses are reactive or suppurative lymphadenitis, which typically present following an upper respiratory tract, middle ear or pharyngeal infection; infection also occurs in congenital cystic lesions. Malignant tumours are uncommon, but should be suspected when there is a solid, progressively enlarging mass. When malignant disease is suspected, fine-needle aspiration under ultrasound guidance is not usually recommended, except for focal thyroid and salivary gland lesions in older children and adolescents. In young children, tumours that can be readily diagnosed by cytology, such as carcinomas, are rare; small round cell tumours and lymphomas are much more common, and usually require an open biopsy to obtain sufficient tissue for diagnosis. When lymphoma is suspected, excision biopsy of an entire lymph node is desirable.

CONGENITAL CYSTIC LESIONS

Thyroglossal duct cysts

The thyroid gland develops in the floor of the primitive pharynx, descending from the tongue through the floor of the mouth, anterior to the developing hyoid bone, to reach its final location in the neck by the seventh week of gestation. The thyroglossal duct connects the gland to the tongue during migration and normally involutes by the end of the tenth week of gestation. The foramen caecum on the tongue is the site of the original opening of the duct. Persistence of any part of the thyroglossal duct may result in a cyst.

Clinically a thyroglossal duct cyst usually presents as an enlarging, painless anterior neck mass in or near the midline, although it may become painful due to infection. On ultrasound the cyst may appear anechoic (Fig. 66.1), hyperechoic or heterogeneous (Fig. 66.2) due to the presence of proteinaceous material. The cyst may be complex, containing septations, and can be very mobile, sometimes changing from one side of the neck to the other. Movement in association with the tongue can be observed with ultrasound.[1]

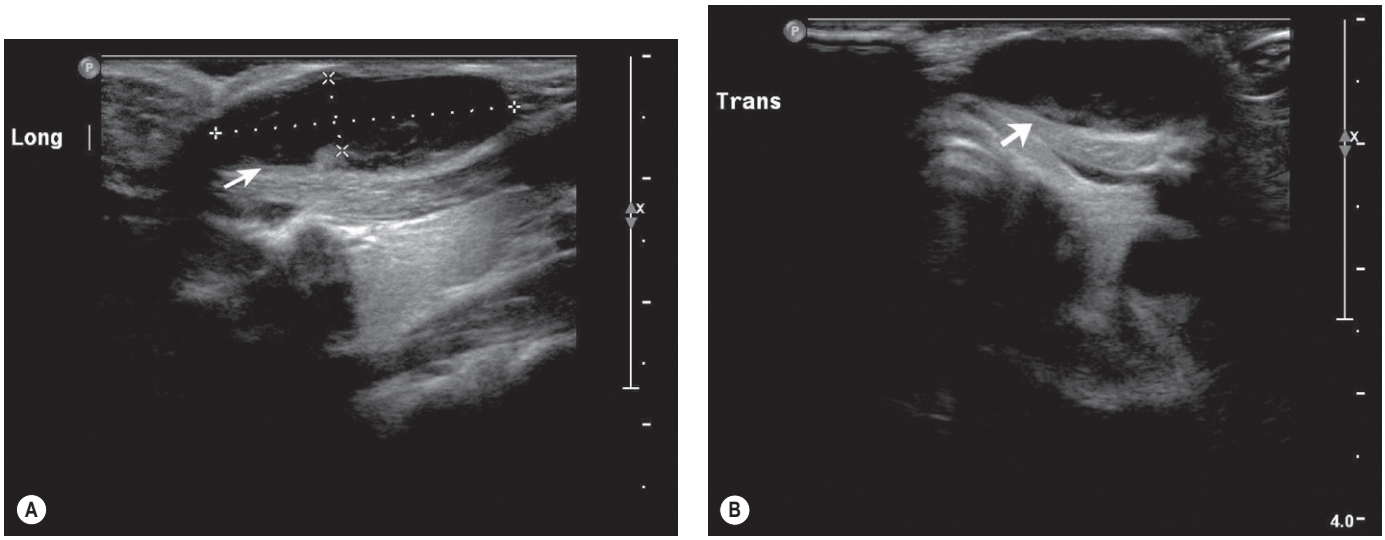

Figure 66.1 **Thyroglossal duct cyst** (arrows). Longitudinal **(A)** and transverse **(B)** ultrasound images.

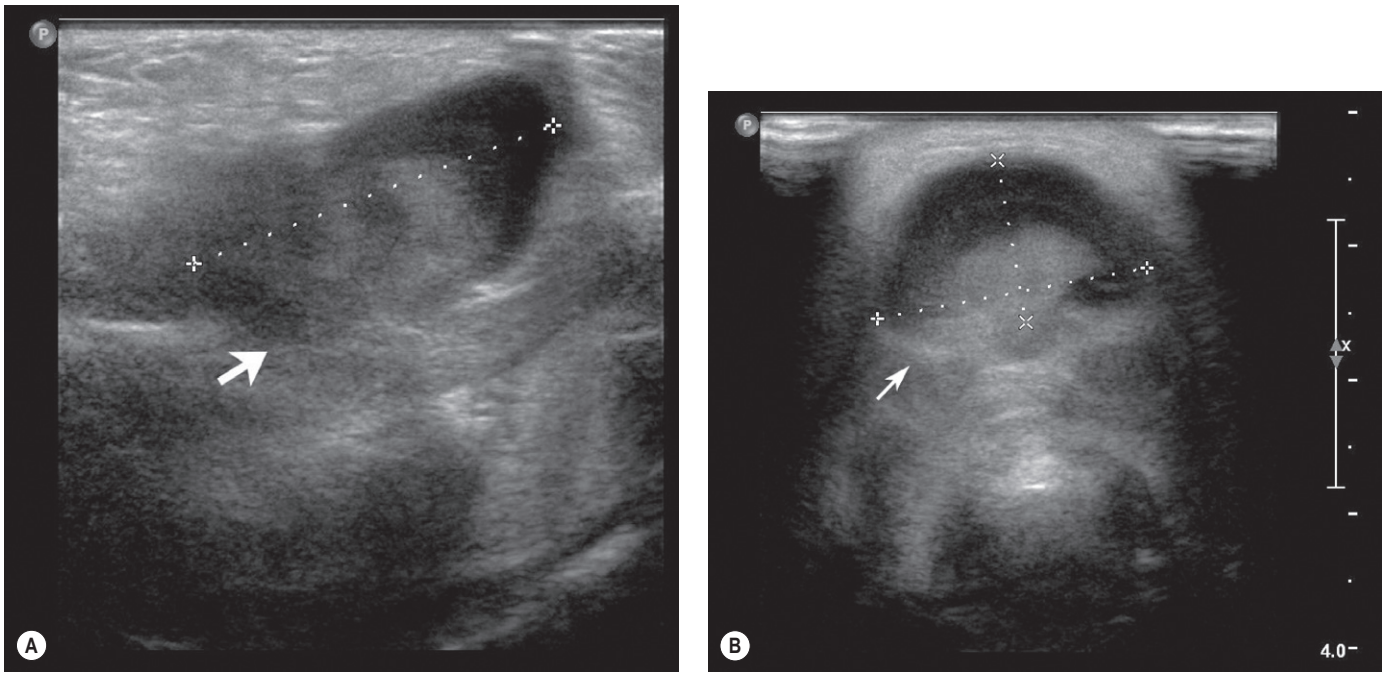

Figure 66.2 **Thyroglossal duct cyst** with echogenic content (arrows). Longitudinal **(A)** and transverse **(B)** ultrasound images.

Papillary thyroid carcinoma is reported to develop in 1% of thyroglossal duct cysts, but this is usually a histological diagnosis following surgery.

Lymphatic malformations

Lymphatic malformations consist of fluid-filled cystic structures, formed from lymphatic vessels which fail to connect with normal drainage pathways. The lesions may be unilocular or multilocular, and there is a wide variation in the size of the individual cysts. Lymphatic malformations may be macrocystic or microcystic. Microcystic lymphatic malformations (previously known as lymphangiomas) consist of multiple tiny cysts within a solid matrix; macrocystic lymphatic malformations (cystic hygromas) may be very large and exert significant mass effect on adjacent structures. Individual cysts typically contain straw-coloured, protein-rich fluid. Both types may undergo rapid enlargement as a result of haemorrhage or infection.

Lymphatic malformations may occur at any anatomical location except in the central nervous system, but the neck, axilla and mediastinum are the commonest sites. Cervical lymphatic malformations are associated with trisomy syndromes, Turner syndrome, Noonan syndrome, and fetal alcohol syndrome, but most are sporadic. Soft tissue lymphatic malformations may be associated with overgrowth of adjacent skeletal structures, particularly in the craniofacial region.

Ultrasound in macrocystic lymphatic malformations characteristically reveals large, thin-walled, fluid-filled cystic spaces (Fig. 66.3), which may contain internal septations. If there has been previous haemorrhage or infection, mobile echogenic debris may be visible. The cysts may be mobile but are usually not compressible. Colour Doppler typically shows only sparse blood vessels around the walls of the cysts. Microcystic lymphatic malformations are shown to consist of multiple tiny cysts, sometimes at the limit of ultrasound resolution, within a densely echogenic solid matrix (Fig. 66.4A). Greyscale ultrasound appearances may be similar to those of a

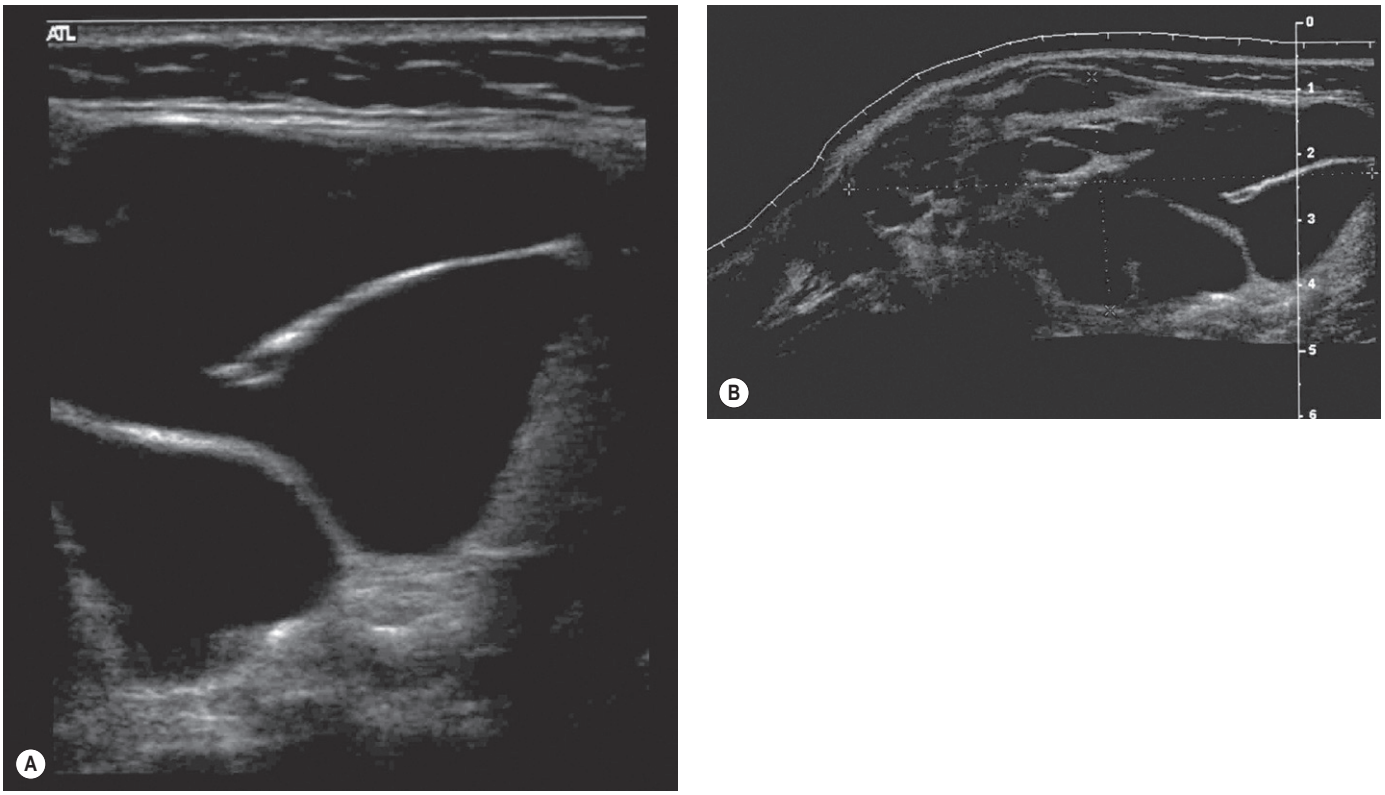

Figure 66.3 **Macrocystic lymphatic malformation. A:** Ultrasound shows multiple thin-walled, fluid-filled cystic structures. **B:** Extended field-of-view sonography demonstrates the full extent of the lesion.

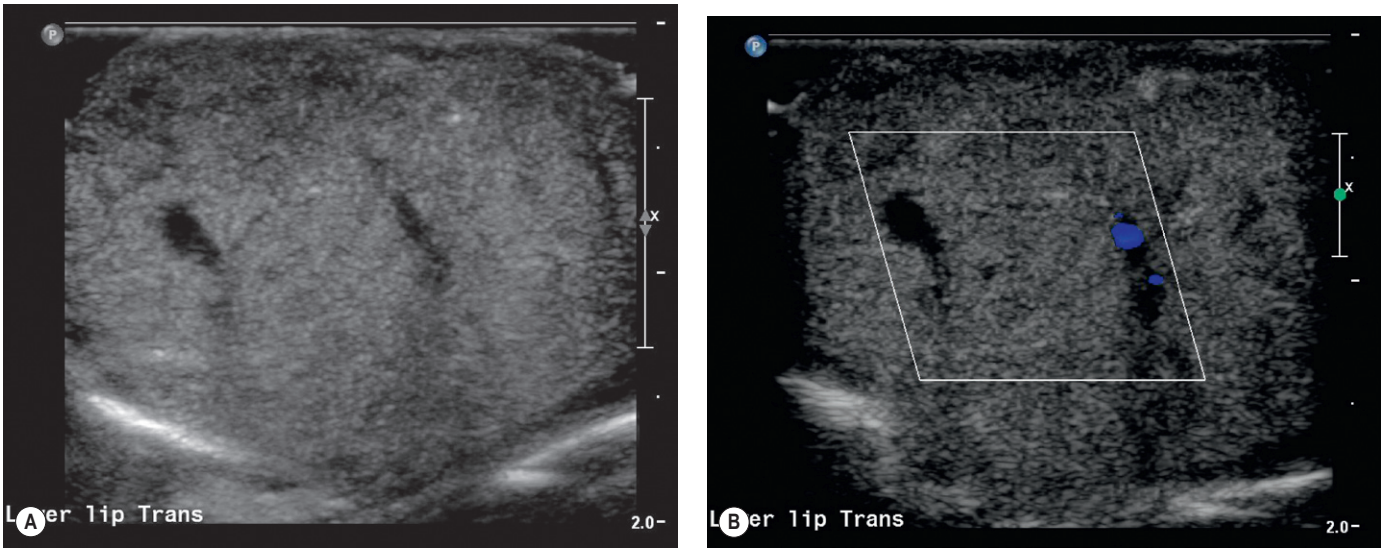

Figure 66.4 **Microcystic lymphatic malformation. A:** High-resolution greyscale image shows a mass containing tiny, fluid-filled cysts within a solid, echogenic matrix. **B:** Colour Doppler image shows sparse vessels within the lesion.

proliferative haemangioma, but colour Doppler shows that a microcystic lymphatic malformation is much less vascular and lacks the high density of small vessels typically seen in a proliferative haemangioma (Fig. 66.4B).

MRI is the optimal modality for assessing the deep extension of lymphatic malformations in areas that are not accessible to ultrasound; for example, deep to the carotid and jugular vessels, into the retropharyngeal region and upper mediastinum.[2]

Branchial cysts

Branchial cleft anomalies may take the form of cysts, sinuses or fistulae. Sinuses have an external opening to the skin surface, whereas fistulae have both external and internal (e.g. pharyngeal) openings. Cysts tend to present in older children or young adults, whereas sinuses and fistulae are often noticed in early childhood. The abnormalities are bilateral in 2–3% of cases and can be familial.

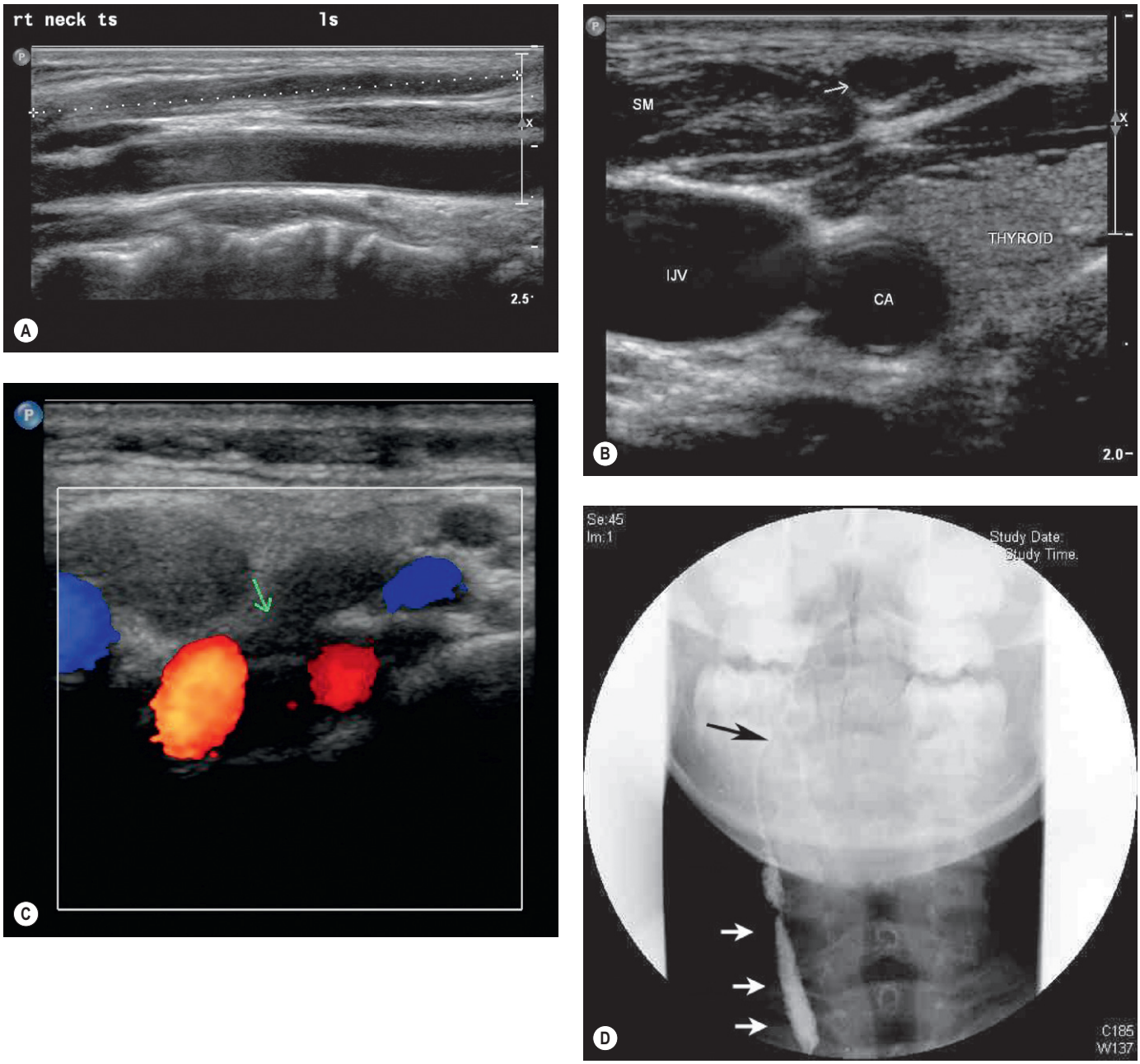

Figure 66.5 **Branchial fistula. A:** Longitudinal image. The fistula is visible as a long tubular structure (marked by callipers) anterior to the carotid artery. **B:** Transverse image. The fistula (arrow) is visible at the medial margin of the sternomastoid muscle (SM), anterior to the right lobe of the thyroid, common carotid artery (CA) and internal jugular vein (IJV). **C:** Transverse colour Doppler image at a higher level shows the fistula (arrow) passing between the internal and external carotid arteries, just above the carotid bifurcation. **D:** Fistulogram: water-soluble contrast introduced into the cutaneous opening demonstrates the full extent of the fistula (white arrows); its upper end (black arrow) penetrates deeply to open into the tonsillar fossa.

First branchial cleft abnormalities occur in the region between the external auditory meatus, the parotid gland and the submandibular triangle. They may present clinically with recurrent inflammation in the region of the ear or angle of the mandible. The cyst may be superficial or deep to the parotid gland.

Second branchial cleft anomalies are the commonest, accounting for 90% of all branchial abnormalities. Seventy-five per cent of these are cysts, which are usually located in the anterior triangle of the neck, along the line of the anterior border of the sternomastoid muscle, anterolateral to the internal jugular vein and carotid artery, and lateral to the thyroid. A second branchial cleft fistula passes from the tonsillar fossa to the supraclavicular region of the neck, with the ostium lying just above the clavicle (Fig. 66.5). On ultrasound, a second branchial cleft cyst typically displaces the sternomastoid posteriorly, and its contents may be anechoic, or contain debris (Fig. 66.6).[3,4]

Third and fourth branchial cleft abnormalities are rare. They may present in childhood or adult life and mainly occur on the left side. Third branchial cleft cysts lie posterior to the carotid artery and sternomastoid muscle. In fourth branchial cleft anomalies, only sinuses have been reported; they run a very long course into the mediastinum and are associated with ectopic parathyroid glands and parathyroid adenomas.

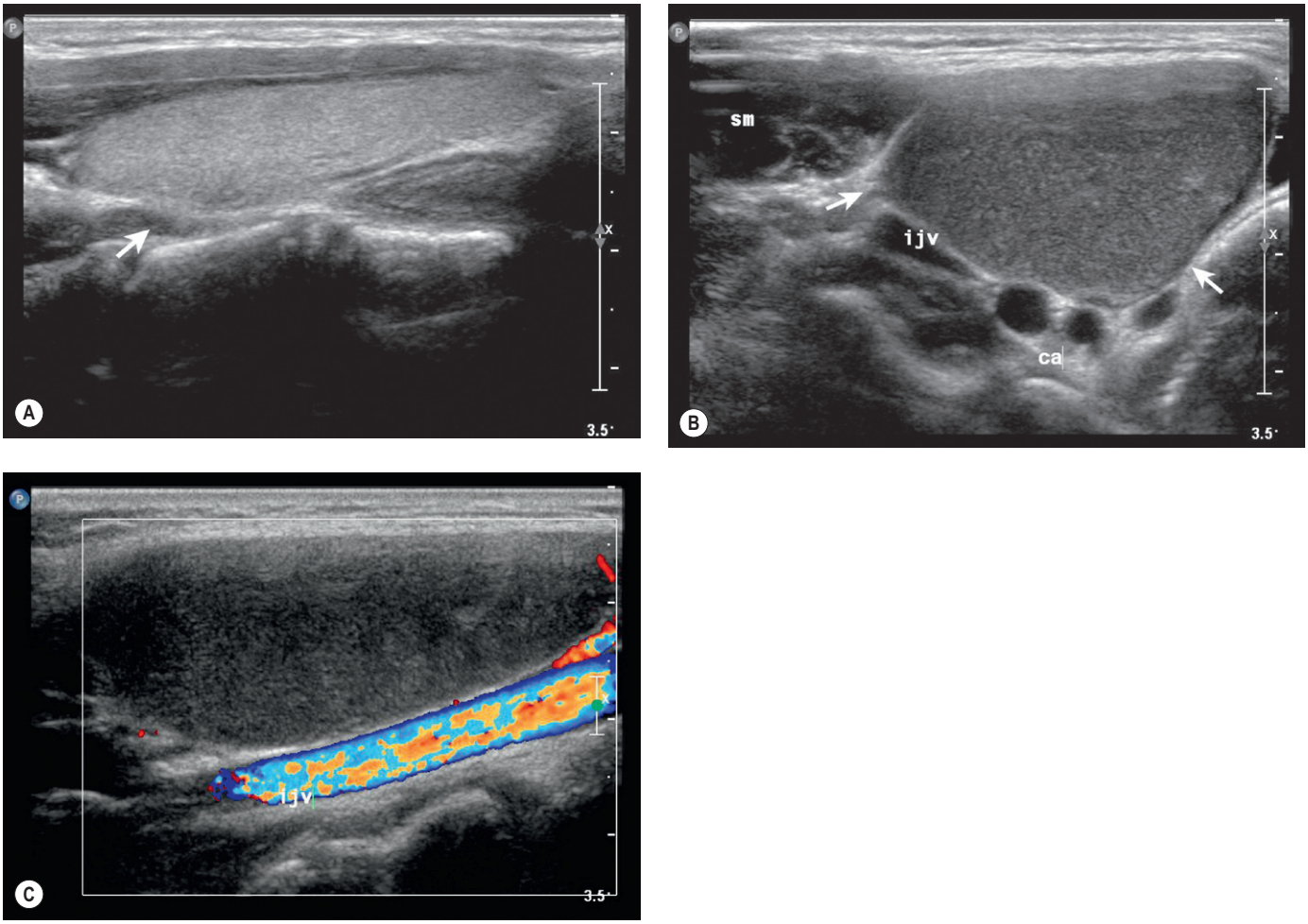

Figure 66.6 Branchial cyst (arrows). Longitudinal **(A)** and transverse **(B)** ultrasound images, demonstrating relationships to sternomastoid muscle (sm), internal jugular vein (ijv) and carotid artery (ca). **C:** Longitudinal colour Doppler image shows that the cyst itself is avascular, and lies just anterior to the common carotid artery.

Dermoid cysts

Dermoid cysts frequently occur in the head and neck. Ultrasound of dermoid cysts typically shows a mainly hypoechoic structure with well-defined walls, containing echogenic elements due to the presence of fat or calcification (Fig. 66.7). Cranial lesions may be fixed to the outer table of the skull and are often closely related to cranial sutures. The lateral and medial margins of the orbit are common sites. Midline cranial lesions in particular require careful investigation to exclude intracranial extension. Ultrasound is valuable in initial assessment but further imaging with computed tomography (CT) or MRI is often necessary.

Dermoid cysts also occur in the neck, typically in the midline above the hyoid, but sometimes between the hyoid and the isthmus of the thyroid (Fig. 66.8). Lesions in this location may be difficult to differentiate from thyroglossal cysts, but dermoid cysts tend not to show movement with the tongue. Dermoid cysts can also occur adjacent to or within the thyroid.[3,4]

Thymic and parathyroid cysts

The embryonic thymus descends from the third pharyngeal pouches, following which the thymo-pharyngeal duct normally

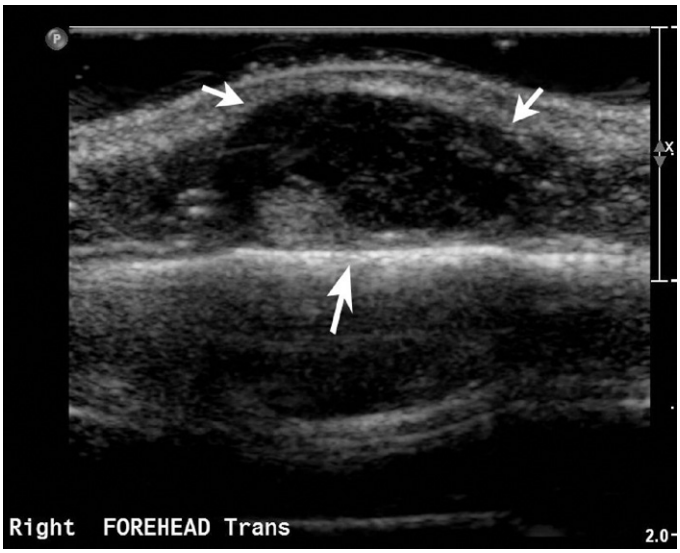

Figure 66.7 Dermoid cyst on the forehead (short arrows). Solid, echogenic areas are visible within a mainly cystic structure. Note the close relationship to the outer table of the skull (long arrow).

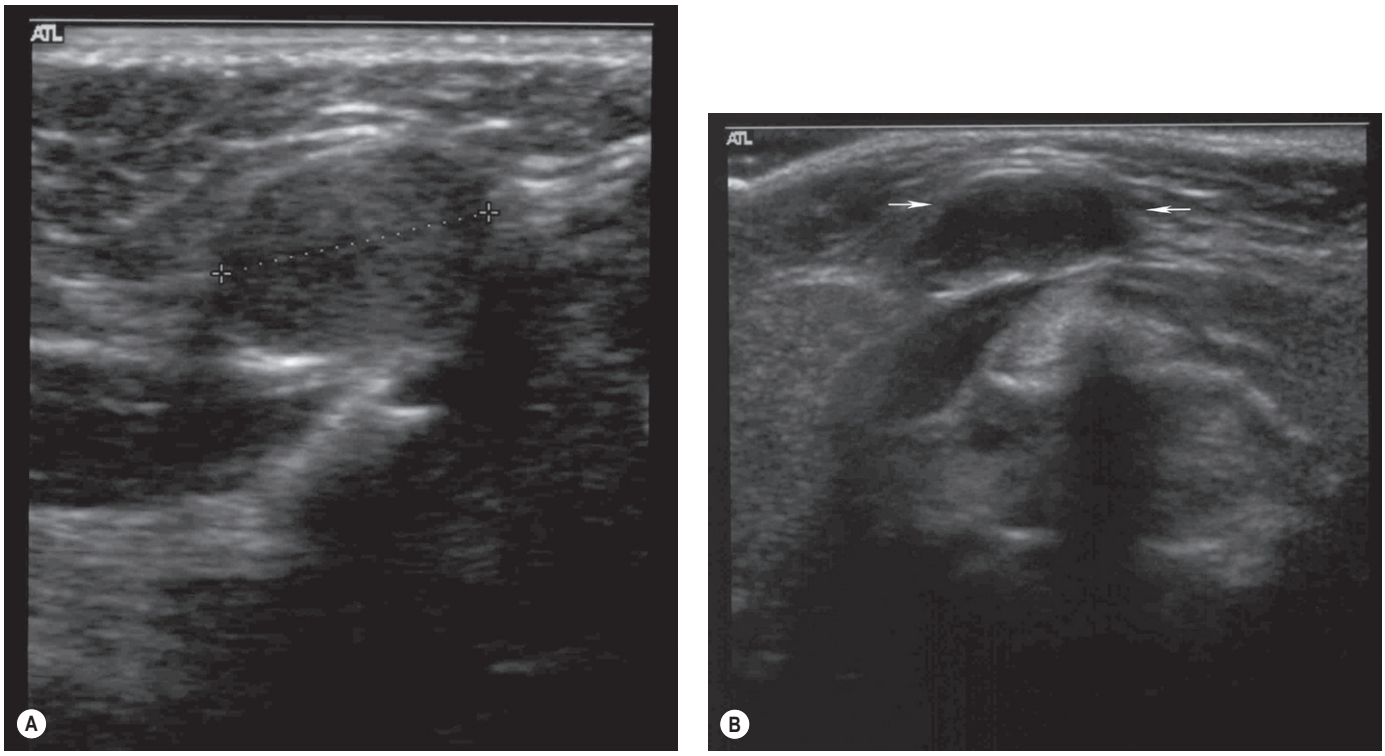

Figure 66.8 Dermoid cyst in the neck, lying in the midline above the isthmus of the thyroid. Lesions in this location may be difficult to distinguish from thyroglossal duct cysts. **A:** Longitudinal image (cyst marked by callipers). **B:** Transverse image (cyst indicated by arrows).

Congenital cystic lesions

- Thyroglossal duct cysts are the commonest congenital cysts in the neck, usually lie in or near the midline, and move with the tongue.
- Cystic lymphatic malformations may be macrocystic or microcystic.
- Second branchial cleft cysts and fistulae occur along a line passing from the tonsillar fossa, along the anterior border of the sternomastoid muscle to the supraclavicular region.
- Dermoid lesions on the head, especially those in the midline, may have intracranial extension.

involutes. Remnants of the duct or possibly cystic degeneration may result in the presence of a thymic cyst, usually presenting as a swelling on the lateral aspect of the lower third of the neck. Although the cysts are usually simple, they may be mulitilocular and contain echogenic fluid if there has been previous haemorrhage or infection. In 50% of cases there is mediastinal extension and it may be possible to demonstrate continuity with the thymus on ultrasound.[3,4]

Parathyroid cysts are usually located at the lateral margins of the thyroid and differentiating them from thyroid cysts may be difficult. Most occur in the inferior parathyroid glands. Parathyroid cysts arise from the remnants of the third and fourth pharyngeal pouches, but may also occur as a result of cystic degeneration of adenomas, rarely causing hyperparathyroidism if a component of functional parathyroid adenoma is present.

Congenital foregut malformations

Although bronchogenic cysts are usually found in the mediastinum, and duplication cysts similarly are found in the mediastinum or abdomen, they can occasionally extend into the neck and so should be considered in the differential diagnosis of a cystic mass at the root of the neck or in the thoracic inlet.[3]

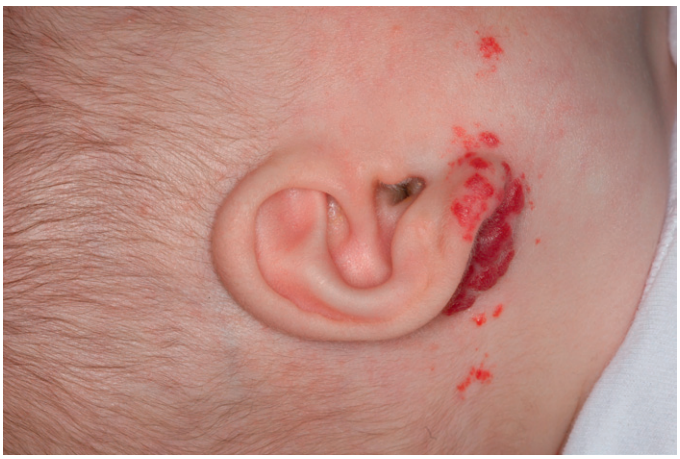

Figure 66.9 Common infantile (proliferative) haemangioma: typical appearance of a superficial cutaneous lesion ('strawberry naevus').

VASCULAR LESIONS

Haemangiomas

Proliferative haemangiomas (common infantile haemangiomas) are benign vascular tumours which may occur at any site but seem to have a particular predilection for the parotid region. Superficial cutaneous lesions are easily recognised as typical 'strawberry naevi' (Fig. 66.9), but deeper lesions may cause diagnostic difficulty.

Proliferative haemangiomas usually appear shortly after birth, although some cutaneous manifestation may be visible at birth in up to 40% of affected children. These lesions undergo a proliferative

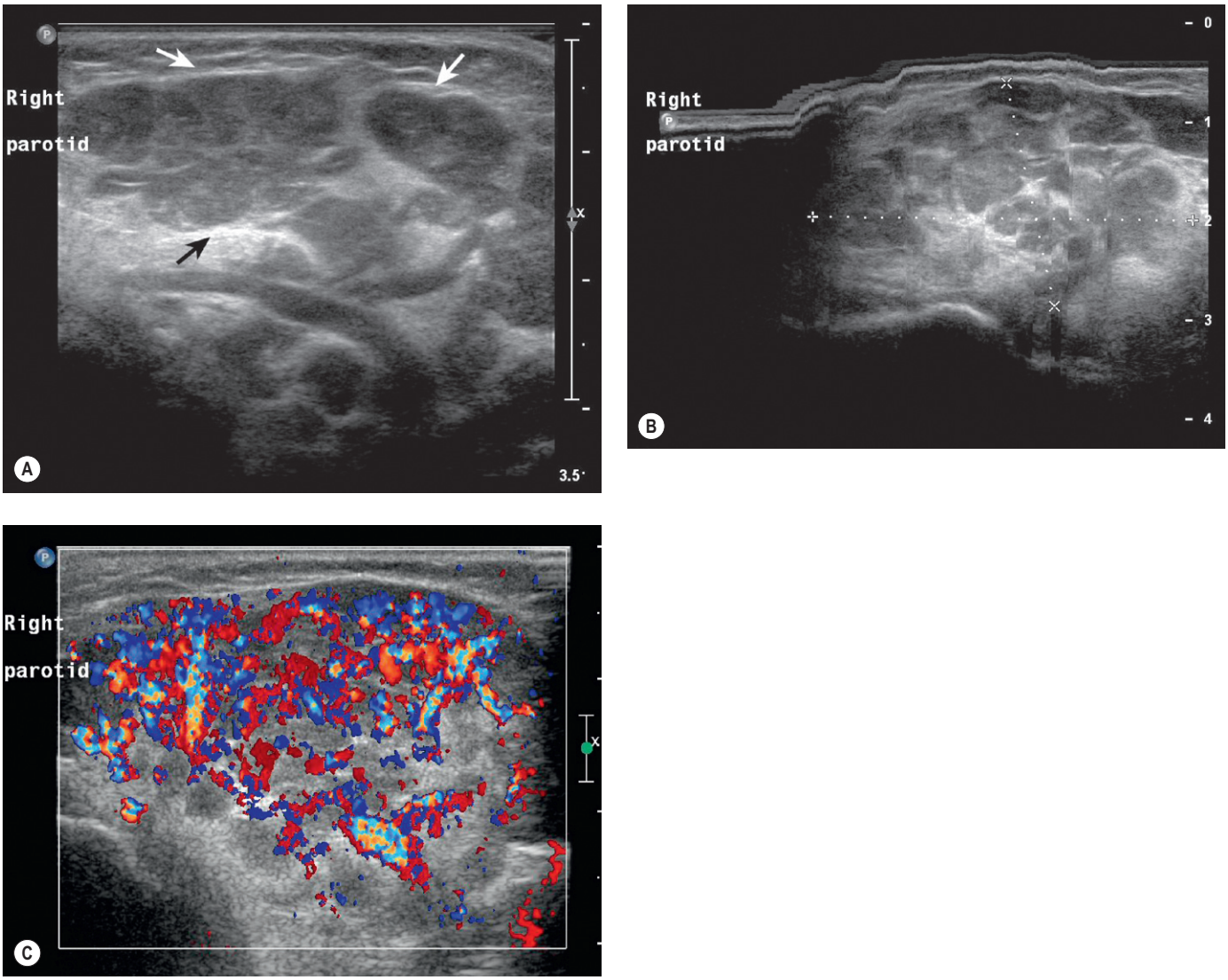

Figure 66.10 Common infantile (proliferative) haemangioma. A: Greyscale image (arrows indicate haemangioma). **B:** Extended field-of-view sonography. **C:** Colour Doppler ultrasound appearances.

phase of rapid growth, becoming raised, bulky, compressible lesions with a characteristic strawberry-red colour. Following a few weeks of proliferation and growth, they typically enter a phase of stabilisation lasting for several months, followed by a phase of involution. The rate of regression is variable; 50% enter the phase of involution by 5 years of age, and 90% by the age of 9 years. The prognosis for cosmetic outcome is not universally favourable; even after involution, some residual abnormality is present in 20–40% of cases, including telangiectasia, increased or decreased pigmentation, and persisting fibrofatty masses.

Proliferative haemangiomas occur more frequently in girls than in boys; there is a significant association with prematurity. Systemic haemangiomatosis is a condition in which multiple cutaneous and visceral haemangiomas occur; although this condition is rare, it is usually recommended that infants with multiple cutaneous lesions should have an abdominal ultrasound scan to exclude hepatic or splenic lesions.

These lesions usually only require treatment if they cause secondary problems such as airway obstruction or difficulty with feeding. Although eventual stabilisation and regression can be expected, proliferative haemangiomas may cause significant symptoms. Ulceration, bleeding and secondary infection may occur, particularly in perioral lesions. Large lesions close to the eye and airway may have disastrous consequences. In the young infant, permanent visual impairment may occur if the eye is occluded for more than one week; a large proliferative haemangioma on the eyelid therefore requires urgent investigation and treatment. Similarly, lesions involving the oropharynx, larynx or trachea may rapidly progress to cause airway obstruction, and require prompt intervention.

Imaging is not usually necessary for typical cutaneous proliferative haemangiomas, but it can be valuable in determining the extent of particularly large lesions and those at dangerous sites. If the nature of the lesion is not certain on the basis of its clinical features, ultrasound and colour Doppler may be helpful in showing a typical appearance of a well-defined, solid, echogenic mass which is intensely vascular, containing a high density of small vessels with high blood flow velocity (Fig. 66.10). Vessel density in excess of 5/cm^2 and high peak arterial blood flow velocities are highly specific when taken together and give a positive predictive value of 97% for the diagnosis of a proliferative haemangioma.[5] However, appearances change as the lesion undergoes stabilisation and regression. The lesions become relatively less vascular, and the residual vascular spaces enlarge as the solid components regress. In the past, lesions with these appearances were sometimes described as 'cavernous haemangiomas', but it is now recognised that this is a phase in the development of a common infantile haemangioma, rather than a separate entity.[2]

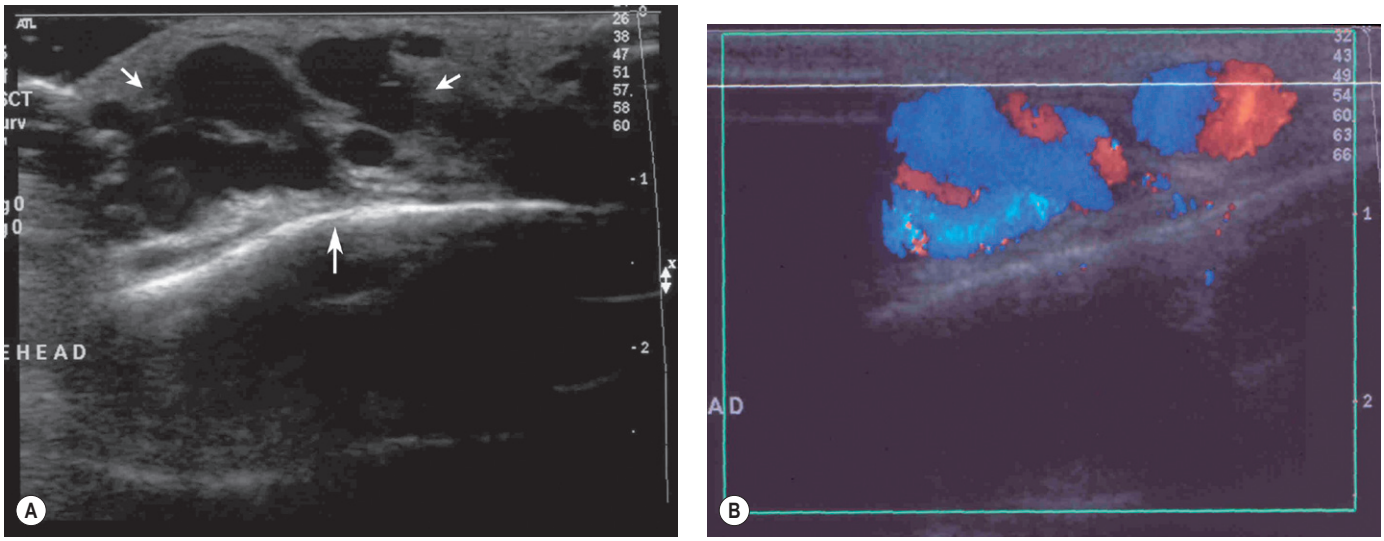

Figure 66.11 Venous malformation on forehead. A: Greyscale image. The short arrows indicate the malformation; the longer arrow shows the outer table of the skull. **B:** Colour Doppler.

Some haemangiomas are present at birth and show differing patterns of biological behaviour; the rapidly involuting congenital haemangioma (RICH) regresses spontaneously, whereas the non-involuting congenital haemangioma (NICH) does not.[6] Rarer vascular tumours, such as kaposiform haemangioendotheliomas and tufted haemangiomas, are much more serious and may cause a severe coagulation disorder due to platelet consumption (Kasabach–Merritt syndrome). The characteristic features of Kasabach–Merritt syndrome are an enlarging, highly vascular soft tissue mass associated with a severe systemic bleeding disorder and marked reduction in platelet count, which may be impossible to correct by platelet transfusion.

Vascular lesions

- Haemangiomas are vascular tumours which grow by cellular proliferation.
- Common infantile (proliferative) haemangiomas typically regress spontaneously after a period of rapid growth. However, at sensitive sites they may cause serious complications.
- Rarer types of haemangioma, such as kaposiform haemangioendothelioma and tufted angioma, are aggressive, rapidly growing lesions, sometimes presenting with consumptive coagulopathy (Kasabach–Merritt syndrome).
- Vascular malformations are present at birth and do not proliferate or regress spontaneously.
- Jugular varix is the commonest venous malformation in the neck, but is usually of no clinical significance.
- Carotico-jugular fistula may be caused by central venous catheter insertion.

Vascular malformations

Arteriovenous malformations and venous malformations are congenital lesions that do not grow by cellular proliferation in the same way as haemangiomas, and do not spontaneously regress. However, arteriovenous malformations may progressively enlarge as a result of increasing blood flow and arteriovenous shunting. Colour Doppler US shows that these lesions consist mainly of dilated vascular spaces; arteriovenous malformations typically show high blood flow velocities, whereas venous malformations are low flow, low pressure lesions.

Arteriovenous malformations consist of a network of abnormal vascular channels comprising both feeding arteries and draining veins. Clinically, high flow vascular malformations present as a soft tissue mass with cutaneous discoloration, locally increased temperature and palpable arterial pulsation. Arteriovenous malformations tend to be present at birth, and to grow in parallel with the growth of the child, although some lesions manifest unpredictable, aggressive growth, sometimes precipitated by trauma, infection, surgery, puberty or pregnancy. Tissue ischaemia and venous hypertension may cause severe local pain, particularly on exercise. Skin ulceration and uncontrollable haemorrhage may occur, and large lesions may result in high-output cardiac failure.

Ultrasound is helpful in confirming the vascular nature of the lesion and demonstrating high-velocity blood flow within it. A careful search for arteriovenous fistulae is necessary; high-velocity, pulsatile blood flow can be demonstrated in most arteriovenous malformations.[2]

Venous malformations are varied and complex; some patients have diffuse malformations involving both deep and superficial systems, whereas others have localised or segmental abnormalities. Localised, superficial lesions have characteristic clinical features; they are bluish in colour, and there is no local increase in skin temperature. They are easily compressible and typically increase in size on Valsalva manoeuvre. However, deeper lesions are impossible to assess fully on clinical criteria alone, and are often much more extensive than initially expected. Greyscale ultrasound reveals the vascular spaces as hypoechoic structures. Varicosities, stenoses, complex interconnecting channels and venous lakes are typical.[2,7] Colour Doppler shows slow, turbulent flow within dilated, compressible vascular spaces (Fig. 66.11).

Jugular varix (jugular vein ectasia or phlebectasia) is a common venous malformation, which presents as a bluish neck swelling in infants due to dilatation of the external or internal jugular vein. It may enlarge alarmingly when the child cries or strains, but is usually of no clinical significance, and becomes less prominent with age. Ultrasound examination is often reassuring,[8] revealing simple dilatation of the jugular vein with no evidence of venous obstruction, thrombosis or an arteriovenous fistula (Fig. 66.12).

Carotid artery disease is rare in childhood, but aneurysms may occur following trauma, septicaemia (mycotic aneurysms) and in Kawasaki disease and Takayasu's arteritis. An arteriovenous fistula in the neck may occur as a complication of insertion of a central

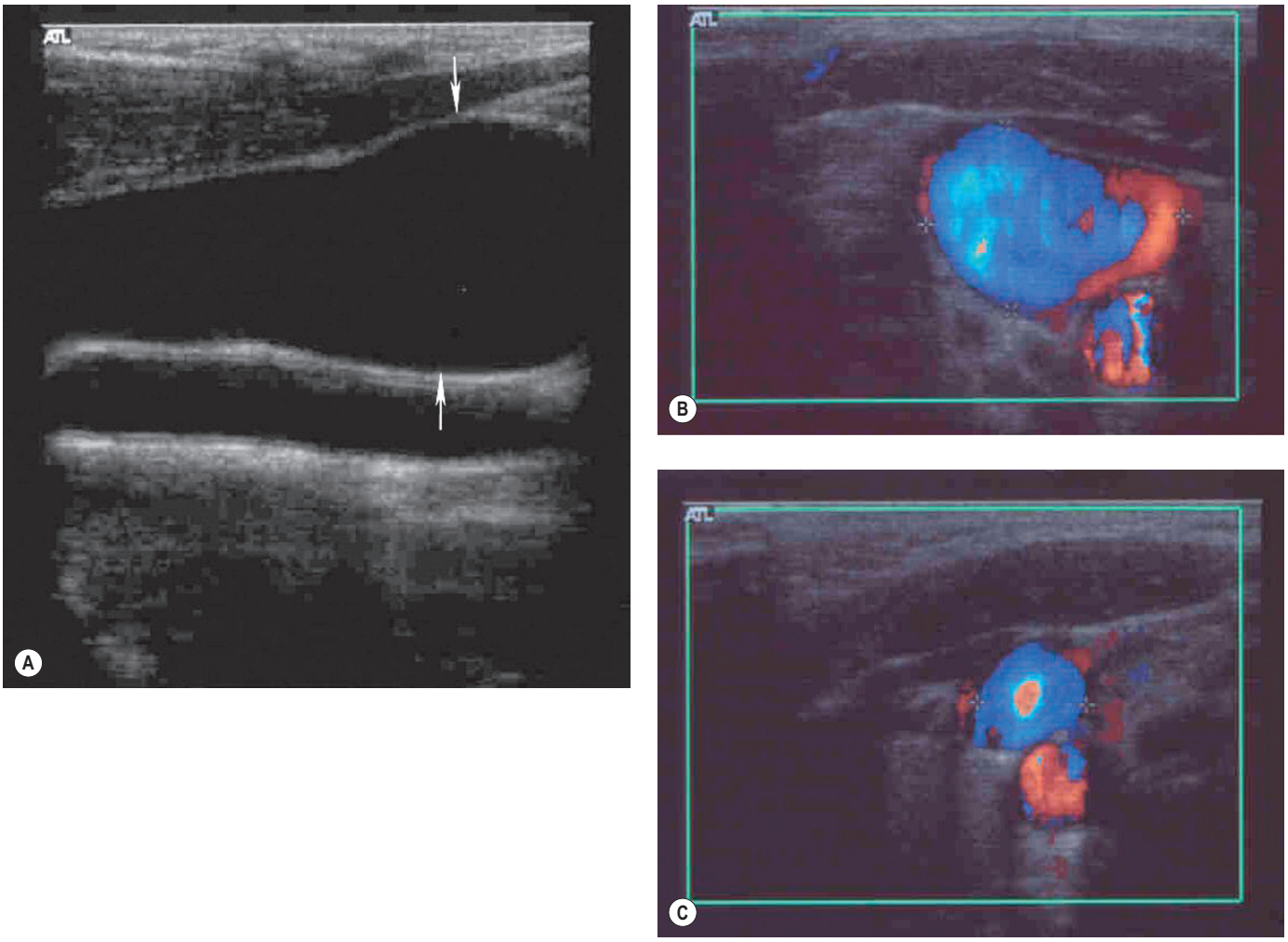

Figure 66.12 **Jugular varix. A:** Longitudinal greyscale image (arrows indicate the varix). **B:** Colour Doppler shows enlargement of the jugular vein (marked by callipers) when the child cries. **C:** In quiet breathing the jugular vein appears relatively normal.

venous catheter, caused by inadvertent puncture of the common carotid artery through the internal jugular vein. Colour Doppler ultrasound shows a dilated internal jugular vein with turbulent, arterialised blood flow, and the fistula may be recognised as the site of a high-velocity jet of blood from the common carotid artery into the internal jugular vein.[9]

FIBROMATOSIS

Fibroma and fibromatosis are terms used for tumours that are mainly composed of fibroblasts. Although they appear histologically benign, some behave aggressively, and may be locally invasive, with a tendency to recur following local excision. Some may present with multifocal tumours, but true metastases do not occur. In some types, spontaneous regression is typical.

Benign sternomastoid tumour of infancy (fibromatosis colli)

Benign sternomastoid tumour of infancy is characterised by diffuse or focal enlargement of the sternomastoid muscle, typically first recognised at 2–8 weeks after birth. It is often associated with a history of birth trauma, suggesting that it may be caused by haematoma formation and healing with fibrosis. However, associations with hip dysplasia and tibial torsion suggest that some cases may be caused by abnormal fetal position in utero. Shortening of the muscle may cause torticollis. Spontaneous resolution usually occurs over a period of 4–8 months, and may be helped by physiotherapy, but a minority of cases require surgery for persisting torticollis. Severe, untreated cases may result in strabismus, facial asymmetry and plagiocephaly.

Ultrasound shows a well-defined mass within the belly of the muscle, which is usually isoechoic or slightly hypoechoic in comparison with normal muscle, but may be hyperechoic (Fig. 66.13).[10,11] Calcification may be present. Sometimes there is diffuse enlargement of the whole of the muscle.

Most cases are so obvious clinically that imaging is used infrequently.

Other forms of fibromatosis

Congenital generalised fibromatosis, also known as infantile myofibromatosis, is a deep form of fibromatosis. Solitary and multicentric forms occur with equal frequency. Most cases present in early infancy. Microscopically the lesions consist of spindle cells with features of both fibroblasts and smooth muscle cells. Prognosis is better in the solitary form without visceral or bone involvement and some lesions may undergo spontaneous regression. Cutaneous

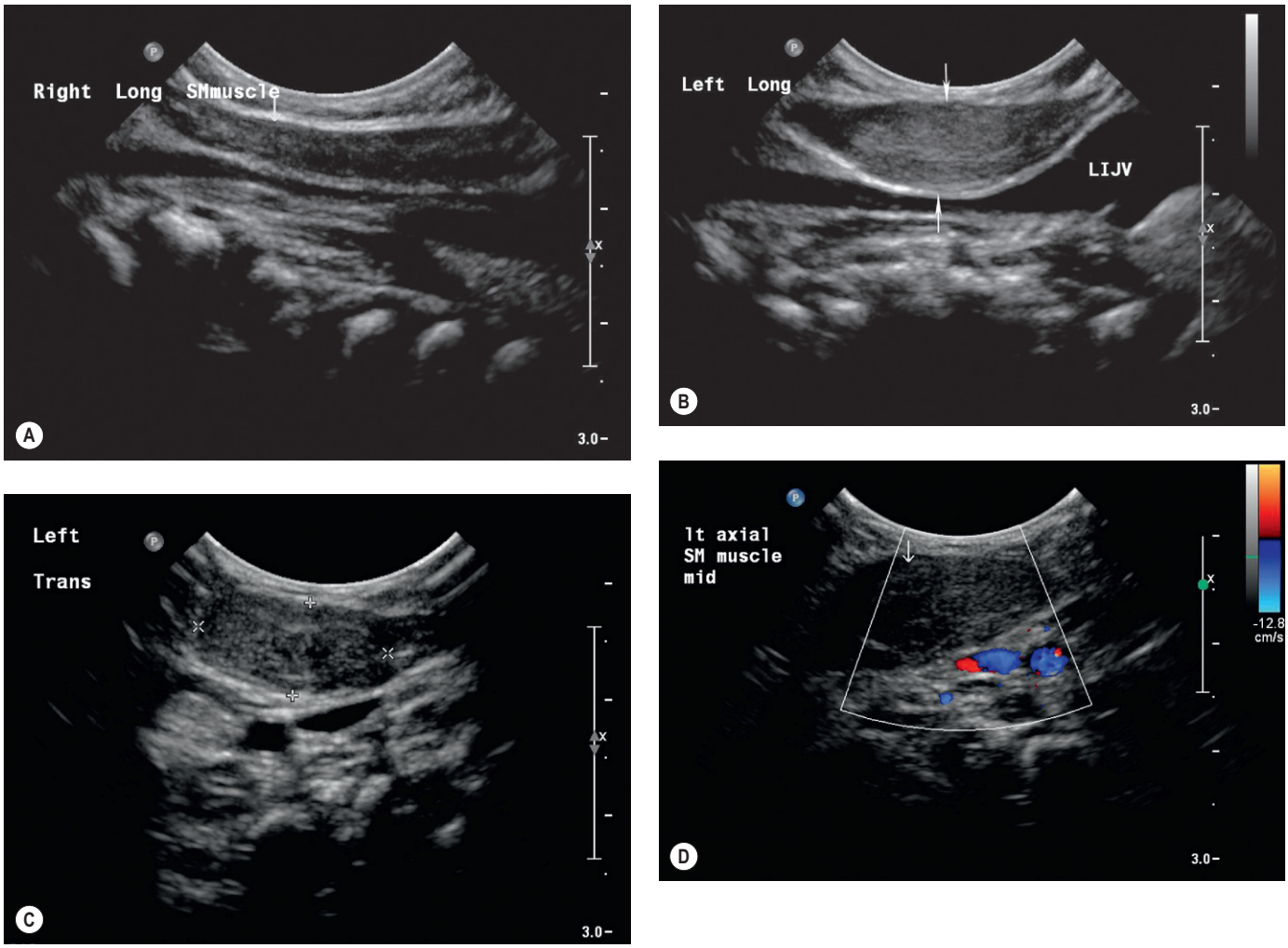

Figure 66.13 Sternomastoid tumour of infancy (fibromatosis colli). **A:** Normal sternomastoid muscle (longitudinal image). **B:** Sternomastoid tumour (arrows). LIJV, left internal jugular vein. **C:** Transverse image of sternomastoid tumour (marked by callipers). **D:** Colour Doppler shows that the sternomastoid tumour is not vascular.

nodules often occur on the head and neck, and may clinically resemble haemangiomas.

Infantile (desmoid-type) fibromatosis is a benign but sometimes locally aggressive tumour, which typically occurs between birth and 5 years of age, arising as a solitary mass in skeletal muscle or the adjacent soft tissues. The lesion often grows along nerve sheaths or vascular bundles. Sites of predilection include the head and neck.

Nodular fasciitis consists of reactive myofibroblastic proliferative lesions found in the subcutaneous tissues, fascia and skeletal muscle, the former site being the most common. These lesions have a large histological variability, but can be classified into myxoid, cellular and fibrous. In infants and children these benign lesions are most commonly found in the head and neck region. The usual history is that of a rapidly growing, painless mass. Uncommon variants include intravascular, cranial, ossifying and proliferative fasciitis. Cranial fasciitis involves both the scalp and the underlying skull.

Ultrasound appearances of all of these forms of fibrosis are non-specific. Ultrasound usually shows a homogeneous, echogenic, solid mass with poorly defined margins.[4,12] Colour Doppler is helpful as the absence of a high density of small vessels within these lesions helps to differentiate them from common infantile haemangiomas. Treatment is by complete surgical excision, and there is a risk of local recurrence, and so imaging is important in preoperative staging and postoperative follow-up.

INFLAMMATORY MASSES AND LYMPHADENOPATHY

Cervical lymphadenopathy

Cervical lymphadenopathy is very common in childhood, although less common in infants under 1 year of age. Many normal children have palpable cervical lymph nodes that are not associated with infection or a systemic illness. In children over 1 year of age, normal cervical lymph nodes can measure up to 10 mm, whereas the upper limit of normal in infancy is 3 mm (short-axis diameter).[4]

In most cases, enlarged cervical lymph nodes in children are reactive, caused by a response to infection, or immunisation. Biopsy of these nodes shows non-specific reactive hyperplasia. Virtually all paediatric viral infections can cause lymphadenopathy and different organisms are prevalent in different age groups. Infective causes of lymphadenopathy include childhood illnesses (measles, mumps, rubella, chicken-pox) as well as adenovirus, rhinovirus and enteroviruses. Cervical lymphadenopathy caused by these illnesses generally resolves spontaneously within 2 weeks.

In normal nodes an ovoid shape is maintained and sonographically glands are hypoechoic, sometimes appearing pseudocystic, with an echogenic vascular hilum from which the vessels radiate

(Fig. 66.14). Reactive nodes are larger, may be ovoid or rounded in shape, and are often hypervascular, but hilar vascular architecture is preserved (Fig. 66.15). The most important group of cervical lymph nodes is in the anterior triangle: these are the submandibular and internal jugular chain nodes, which are all medial to the sternomastoid muscle. These drain the mouth and pharynx. Any viral or bacterial infection of the upper respiratory tract or pharynx can cause enlargement, including mouth infections such as herpetic stomatitis, or dental infection. Posterior cervical or occipital lymphadenopathy may be caused by scalp infection or dermatitis, roseola or rubella infection. Postauricular lymphadenopathy is characteristic of rubella although not specific, and preauricular lymph nodes may enlarge as a result of eye infections or cat scratch disease (*Bartonella henselae*).[4,12]

Acute suppurative lymphadenitis

Acute suppurative lymphadenitis is common in young children and is usually diagnosed clinically. It classically occurs following an upper respiratory tract infection, pharyngitis, tonsillitis or otitis media. Affected children present with rapid unilateral enlargement of cervical lymph nodes with warmth, erythema and tenderness to palpation, and are frequently irritable and pyrexial. Leukocytosis is common. *Staphylococcus aureus* or group A beta-haemolytic streptococci are the usual causative organisms.

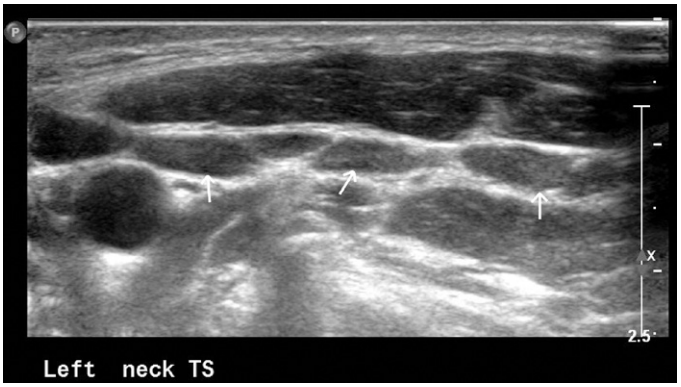

Figure 66.14 Normal cervical lymph nodes (arrows).

Ultrasound is useful to differentiate simple lymph node enlargement from confluent or suppurating nodes. Inflammatory nodes are round to oval masses, usually discrete but may enlarge and become confluent (Fig. 66.16). Colour Doppler shows increased blood flow. With suppuration the central part of the node becomes hypoechoic, and necrotic nodes may have areas of decreased vascularity. Infected cystic lesions can mimic acute suppurative lymphadenitis. Abscesses are hypoechoic or anechoic masses with a variably thick rim of solid tissue and may be septated or have a serpiginous configuration (Fig. 66.17). Abscesses can be missed if the contents are echogenic but in some cases it may be possible to demonstrate mobility of the contents with gentle pressure.[12] Acute suppurative lymphadenitis is treated with antibiotics, but abscesses may require surgical drainage.

Retropharyngeal and mastoid infection

Nasopharyngeal and tonsil infection may involve the retropharyngeal lymph nodes, which can suppurate and perforate into the retropharyngeal space. Retropharyngeal lymphadenopathy is a common location for bacterial lymphadenitis in children aged 1–5 years and there may be no visible or palpable cervical mass to suggest the diagnosis. Symptoms such as pharyngeal pain, drooling, dysphagia and torticollis are highly suspicious. In most cases lymphadenopathy extends from the neck into the retropharyngeal space. The involved nodes may then suppurate and develop into an abscess. In severe cases, infection may extend from the neck into the mediastinum. Diagnosis by ultrasound is difficult and CT or MRI may be required to assess extent of infection, abscess formation and involvement of the carotid sheath.

Suppurative mastoid infection (coalescent mastoiditis) may break through the cortex of the mastoid process and present as an abscess in the overlying soft tissues (Fig. 66.18A). In some cases, abscesses secondary to mastoid infection may occur in unusual sites; for example, pneumatisation of the zygomatic process may allow mastoid infection to spread into the temporal region and face (Luc's abscess).

Internal jugular vein thrombosis may occur as a result of severe infections originating in the mastoid or oropharynx (Lemierre's syndrome). Unusual anaerobic organisms such as fusobacteria are often implicated. There is a high risk of septic pulmonary embolism. Colour Doppler ultrasound of the internal jugular veins is indicated in severe, spreading infections of the neck to enable early diagnosis of this dangerous complication (Fig. 66.18B).

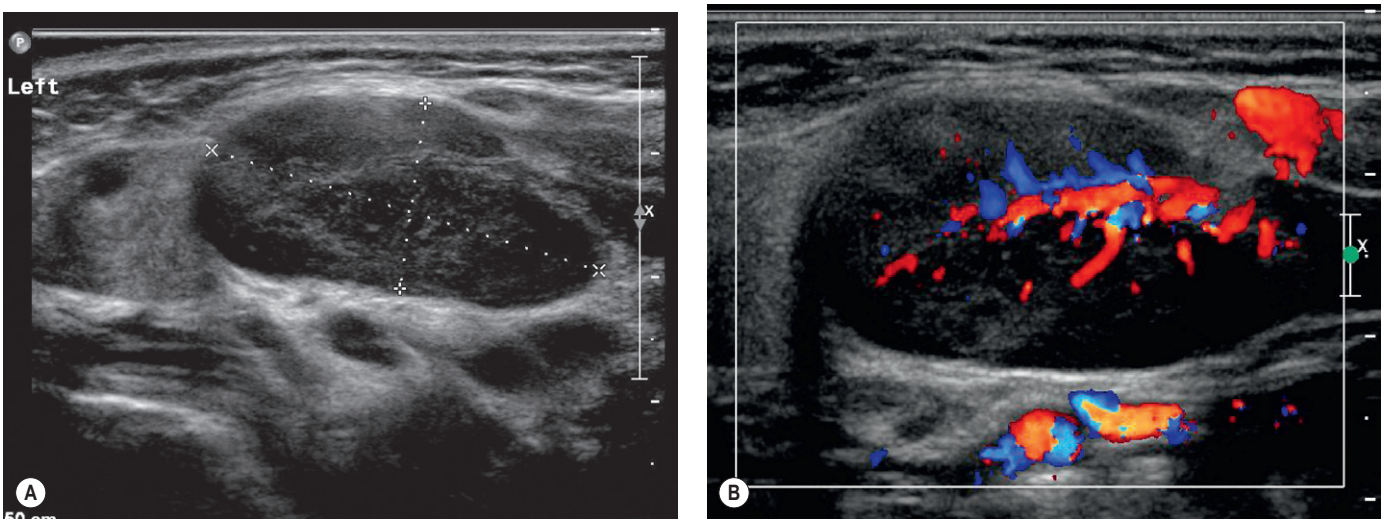

Figure 66.15 Enlarged cervical lymph node in a child with infectious mononucleosis. **A:** Greyscale ultrasound. **B:** Colour Doppler shows preservation of normal hilar vascular architecture.

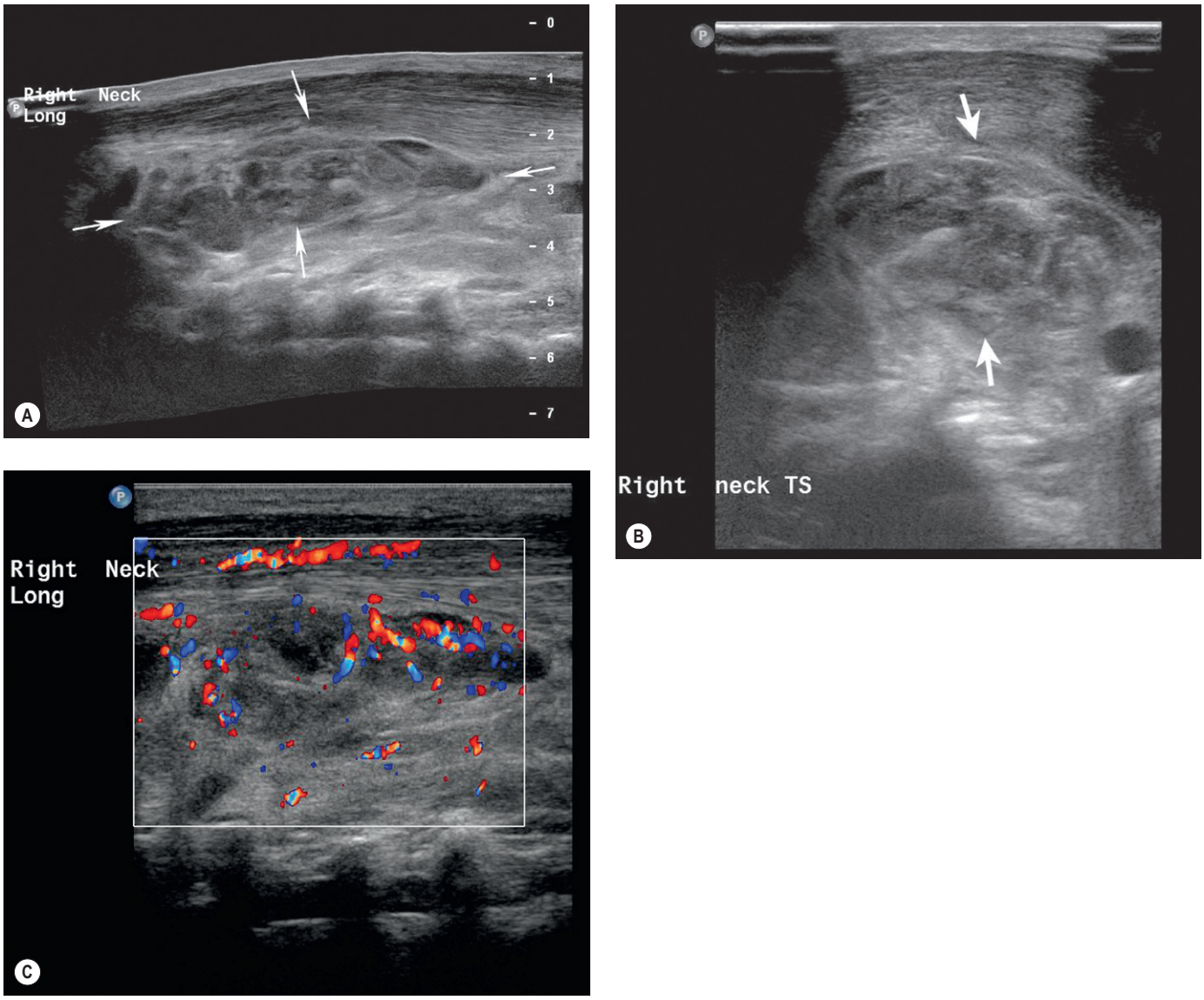

Figure 66.16 **Confluent lymph node mass** (arrows) deep to the sternomastoid muscle. **A:** Longitudinal extended field-of-view sonography. **B:** Transverse image. **C:** Colour Doppler.

Subacute or chronic cervical lymphadenitis

Children may present with enlarged, minimally tender, mildly inflamed nodes without a prodromal illness or systemic symptoms. The causes are numerous, but the most common is a viral infection such as infectious mononucleosis (Epstein–Barr virus) or cytomegalovirus (CMV) infection. Less common causes include tuberculosis (TB) or atypical mycobacterial infection, cat scratch disease (*Bartonella henselae*), human immunodeficiency virus (HIV), sarcoid and fungal infection (histoplasmosis, actinomycosis).

Abdominal ultrasound is helpful to detect enlargement of the spleen or liver. Other tests such as chest radiography, full blood count, monospot and a Mantoux test are also indicated. Usually nodal enlargement persisting longer than 6–8 weeks that has not responded to antibiotics requires biopsy.

Mycobacterial lymphadenitis

Mycobacterial infection is an important cause of subacute or chronic lymphadenitis in children. In most developed countries, infection with atypical mycobacteria (*Mycobacterium avium intracellulare*, *M. kansaii* and *M. haemophilum*) has a higher incidence than infection with *Mycobacterium tuberculosis* (TB). Overall, mycobacterial lymphadenitis represents about 8% of all chronic lymphadenitis in children, often involving the head and neck region. Most affected children are aged between 1 and 5 years and infection is much less common over the age of 12 years. Atypical mycobacterial infection is usually indolent in the immunocompetent child. If infection is disseminated or extensive the child should be investigated for impaired immunity, for example HIV infection. The portal of entry for atypical mycobacteria is usually the mucous membrane of the mouth, pharynx and tonsils (e.g. during the teething). The submandibular and jugulodigastric nodes are most commonly affected and the overlying skin, soft tissues and salivary glands may also be involved. Inflammatory changes in the surrounding soft tissues are characteristically less severe than with bacterial lymphadenitis. The nodes are typically minimally tender and rubbery, usually asymmetric, with a dominant 2–4 cm node that may be solid or partially necrotic. There may be a draining sinus or fistula present. Systemic symptoms are rare unless the patient is immunocompromised.

TB lymphadenitis usually occurs in older children and is usually accompanied by systemic symptoms. With TB, lymphadenopathy

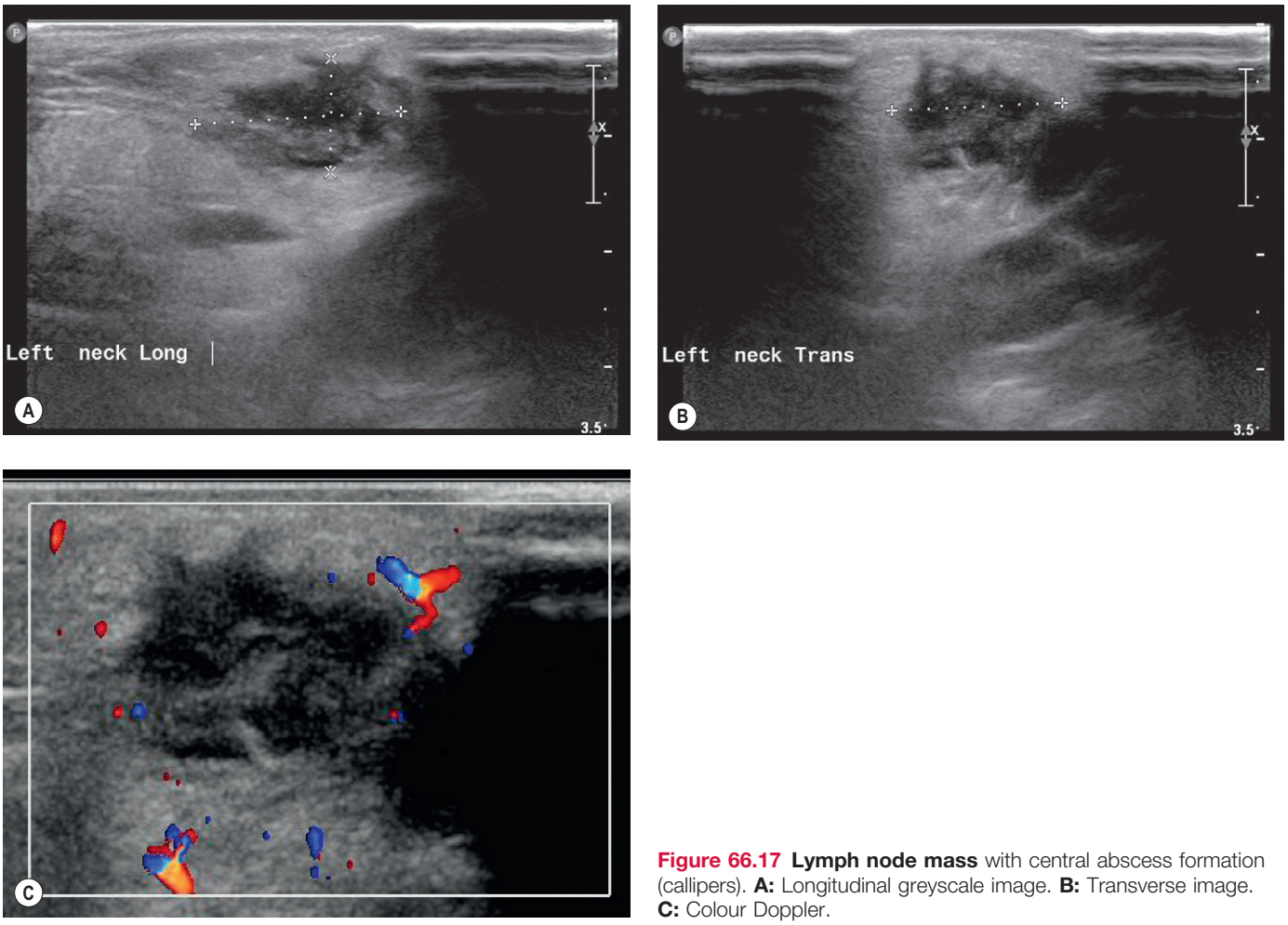

Figure 66.17 **Lymph node mass** with central abscess formation (callipers). **A:** Longitudinal greyscale image. **B:** Transverse image. **C:** Colour Doppler.

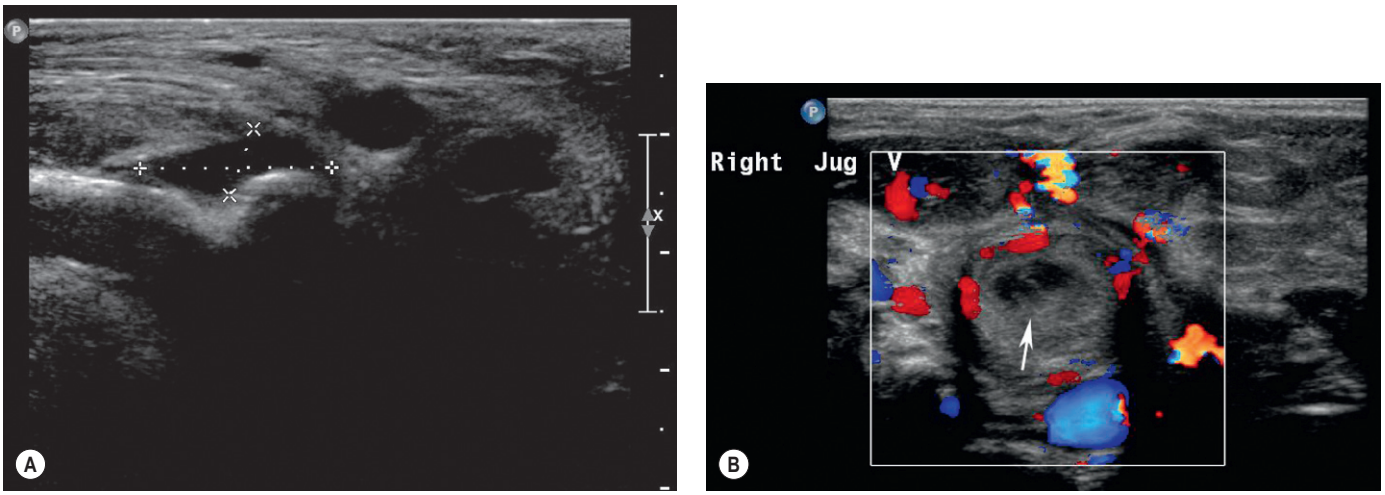

Figure 66.18 **Mastoid infection. A:** Facial abscess secondary to mastoid infection (Luc's abscess) (marked by callipers). **B:** Internal jugular vein thrombosis secondary to mastoid infection (arrow).

is generally bilateral and more diffuse. Supraclavicular nodes are often involved from extension of primary pulmonary infection. The nodes may be solid or necrotic and in advanced disease the nodal capsule may rupture, resulting in adherence of multiple nodes and formation of a cold abscess that may discharge through a sinus tract to the skin.

The Mantoux test is usually strongly positive in TB infection, but negative in up to 50% of patients with atypical mycobacterial infection. Differentiation between the two types of mycobacterial infection is important because therapy is completely different. Atypical mycobacterial infection is treated by complete surgical excision, whereas TB lymphadenitis requires a prolonged course of chemotherapy.

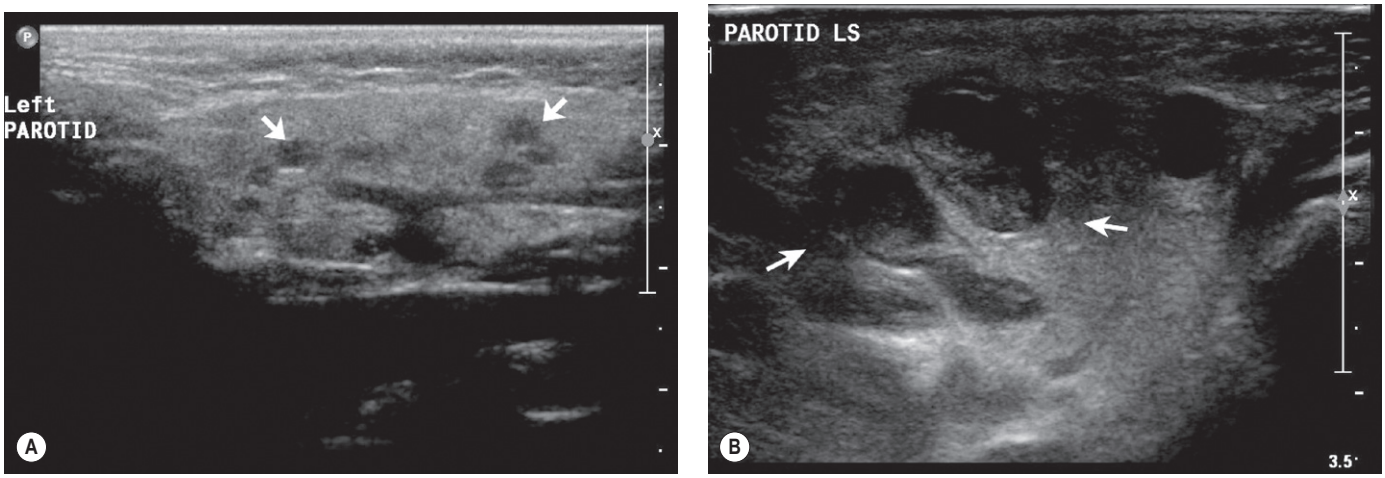

Figure 66.19 Parotid gland. A: Normal parotid with small intraparotid lymph nodes (arrows). **B:** Acute parotitis with intraparotid lymph node enlargement and abscess formation (arrows).

Inflammatory masses and lymphadenopathy

- Cervical lymphadenopathy in children is usually due to simple infection, but ultrasound and other imaging modalities cannot reliably distinguish between benign and malignant lymphadenopathy.
- Lymphoma should be suspected if cervical lymphadenopathy is painless, enlarges progressively, involves supraclavicular nodes, or persists for more than 6 weeks.
- Atypical mycobacterial infection is an important cause of subacute or chronic cervical lymphadenitis.

Neoplastic cervical lymphadenopathy

Lymphoma and leukaemia are the commonest causes of malignant cervical lymphadenopathy in children. Metastatic cervical lymphadenopathy is uncommon, but can occur in neuroblastoma and rhabdomyosarcoma.

Lymphoma should be suspected if cervical lymphadenopathy is painless, shows progressive enlargement, involves supraclavicular nodes, or persists for more than 6 weeks despite antibiotic treatment, especially in older children and adolescents. The majority of children with simple lymphadenopathy due to infection will respond to a 2-week course of antibiotics. Generally, any non-resolving neck mass that has been present for 6 weeks despite antibiotic treatment requires further investigation. In the absence of definite evidence of a benign cause (such as infectious mononucleosis) excision biopsy of an entire lymph node is necessary to exclude lymphoma, as fine-needle aspirate for cytology or percutaneous core biopsy may give misleading results.

Lymphoma accounts for half of all head and neck malignancy in children. Non-Hodgkin's lymphoma is commoner than Hodgkin's lymphoma in young children, but Hodgkin's lymphoma is commoner in older children and adolescents. Extranodal disease is more common in non-Hodgkin's lymphoma, whereas Hodgkin's lymphoma is almost exclusively nodal in origin. Ultrasound readily demonstrates lymph node masses. They may be ovoid or round, can have increased flow on colour Doppler and may also coalesce into masses. The affected lymph nodes are typically enlarged, ovoid or round, and less echogenic than normal lymph nodes with loss of normal internal architecture. They may appear hypervascular on colour Doppler, and it may also be possible to recognise loss of the normal radial distribution of hilar vessels. These appearances may be sufficient to raise the possibility of lymphoma, but they are not specific and infection may produce identical ultrasound appearances. Central necrosis may occur, mimicking abscess formation. Calcification is uncommon in untreated lymphoma but may be identified after chemotherapy or radiotherapy.[4,12]

SALIVARY GLANDS

The parotid and submandibular glands are readily accessible for ultrasound examination, although the much smaller sublingual glands are difficult to identify. On ultrasound, the normal parotid is triangular to ovoid in shape and homogeneous with increased echogenicity compared with adjacent muscle. Small intraparotid lymph nodes are frequently seen in normal children, measuring up to 5–6 mm in their short-axis diameter, and should not be mistaken for focal lesions (Fig. 66.19A).

Acute parotitis

The most common cause of a parotid swelling is infection, usually viral, with the most common causes being mumps, infectious mononucleosis (caused by Epstein–Barr virus) and CMV. In 75% of cases the swelling is bilateral.

Bacterial parotitis is rare in children, most often occurring in premature neonates and children with an underlying systemic illness. *Staphylococcus aureus* is the usual infective organism and retrograde spread from the mouth may be the underlying mechanism of infection. It is usually unilateral and commonly associated with fever, dehydration and immunosuppression.

In parotitis, ultrasound shows diffuse enlargement of the parotid; the internal architecture of the gland may be normal, or it may appear heterogeneous and hypoechoic. Intraparotid lymph nodes are often enlarged and there may be associated cervical lymphadenopathy. Parotid abscess can develop secondary to bacterial parotitis or upper respiratory tract infection, with spread of infection to intraparotid lymph nodes and subsequent suppuration (Fig. 66.19B). Enlargement of intraparotid lymph nodes can be seen with any cause of lymphadenopathy, including tuberculosis and atypical mycobacterial infection.

Recurrent acute parotitis

This disorder, otherwise known as juvenile recurrent parotitis, is characterised clinically by intermittent attacks of pain and unilateral or bilateral parotid swelling often associated with fever and malaise. Typical age of onset is between 2 and 6 years of age in an

otherwise well child and the symptoms tend to diminish or cease to occur around puberty or late adolescence but may persist into adulthood. The aetiology is unknown, but possible causes include congenital duct abnormality with recurrent episodes of ascending infection, acquired duct damage caused by ascending infection which predisposes to further bouts of infection, and reduced flow of saliva. Some patients respond to antibiotics and prophylaxis may be helpful.

Ultrasound typically demonstrates a heterogeneous gland, with multiple round hypoechoic areas 2–4 mm in diameter within the parenchyma which represent peripheral sialectasis and lymphatic infiltration (Fig. 66.20). The appearances are similar to chronic parotitis, although the gland may be enlarged during an acute episode.[13]

Chronic parotitis

Chronic parotitis is uncommon in children and is associated with autoimmune disorders such as Sjögren's syndrome, systemic lupus erythematosus or Raynaud's disease. Patients usually have a low-grade, persistent or intermittent parotid swelling and pain without signs of acute infection. Sometimes underlying ductal obstruction with stones is identified. Ultrasound demonstrates a heterogeneous gland with small punctate echogenic areas or small multiple hypoechoic areas.

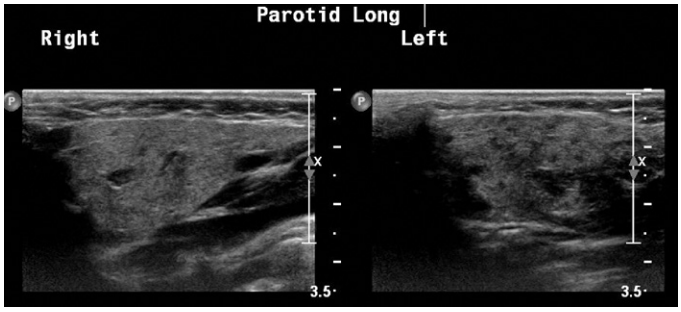

Figure 66.20 Juvenile sialectasis. The right parotid gland shows normal, uniform echogenicity. The left parotid contains multiple focal areas of low echogenicity.

Other causes of parotid enlargement

Granulomatous disorders such as cat scratch disease, sarcoidosis and TB may involve the parotid and cause enlargement of the gland.

In children with HIV infection, all of the salivary glands may be affected, but chronic parotid enlargement is most common. Ultrasound typically shows multiple lymphoepithelial cysts of varying size, sometimes replacing most of the parotid glands or causing marked enlargement (Fig. 66.21).

Sialolithiasis

Salivary calculi are uncommon in childhood but should be suspected with a history of recurrent painful salivary gland swelling related to eating. The majority of cases (90%) affect the submandibular glands, and the remainder the parotid.

Stones may be intraglandular or intraductal. Eighty per cent of submandibular stones are radio-opaque, whereas only 20% of parotid stones are visible on radiographs. Ultrasound is more sensitive than radiography at detection of intraglandular sialolithiasis, but sialography may be required if ultrasound and plain radiography are inconclusive.

Salivary gland tumours

Salivary gland tumours are uncommon in children, representing only 1% of all childhood neoplasms and 10% of all paediatric head and neck tumours. The parotid is involved in up to 90% of cases, and approximately half are malignant, the majority of these occurring in children over 10 years of age.

Pleomorphic adenoma is the most common benign salivary gland tumour after haemangioma and lymphatic malformations. They present as hard, mobile, painless, slow growing masses and usually occur in older children or adolescents. They occur more commonly in the parotid but may also occur in the submandibular glands. On ultrasound, a pleomorphic adenoma is usually well-defined and hypoechoic compared with the rest of the gland and may contain small calcifications. Distal acoustic enhancement is characteristic (Fig. 66.22).

Mucoepidermoid carcinoma is the most common malignant tumour of the salivary glands in children, and is also the most

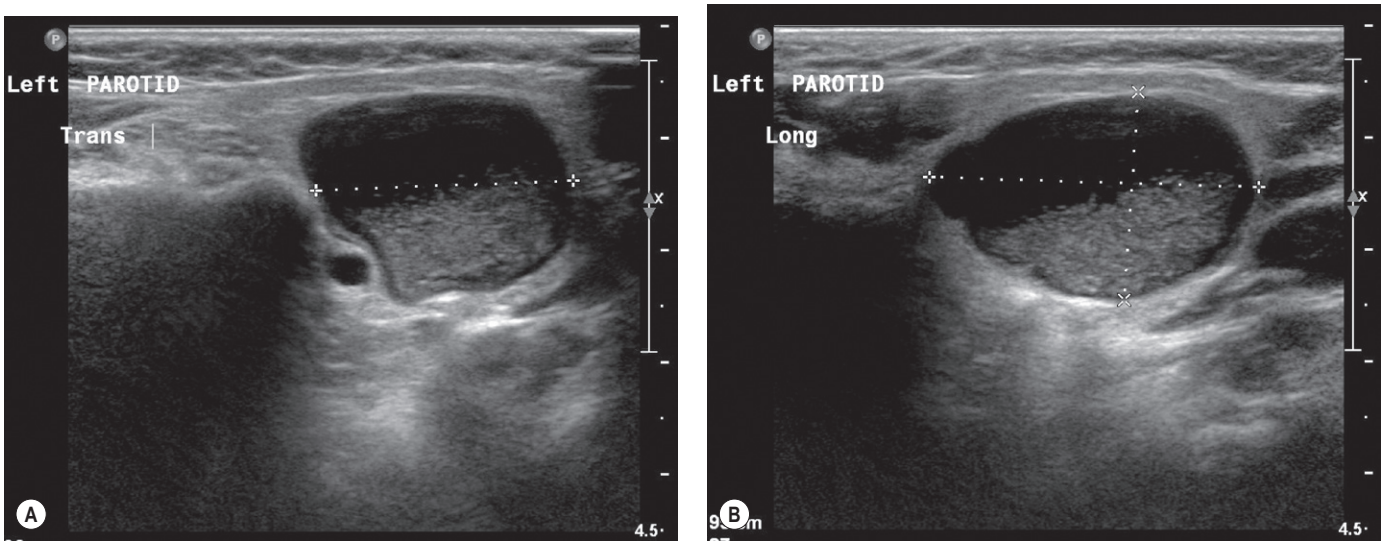

Figure 66.21 Multiple parotid cysts containing layered echogenic debris in a child with HIV infection. **A:** Transverse image. **B:** Longitudinal image.

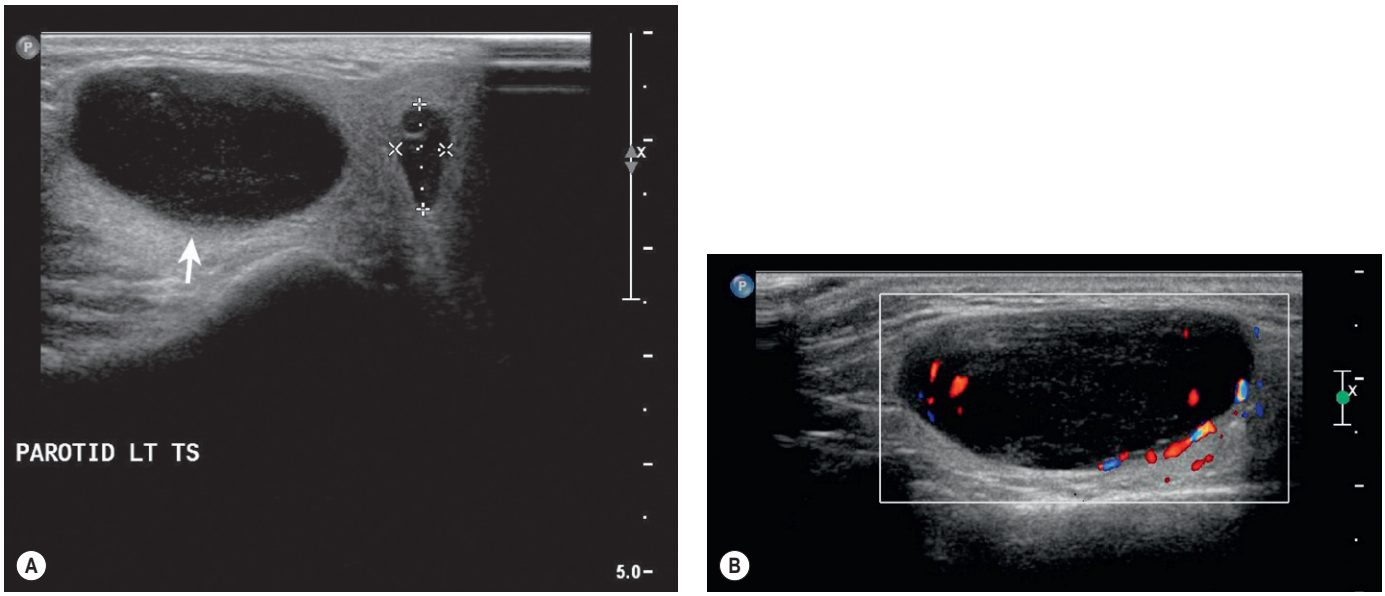

Figure 66.22 Pleomorphic adenoma of the parotid. A: Ultrasound shows a well-defined ovoid mass within the parotid gland, with relatively low echogenicity, and distal acoustic enhancement (arrow). An adjacent intraparotid lymph node is marked by callipers. **B:** Colour Doppler shows that the lesion has a vascular capsule and a few vessels are visible in its centre.

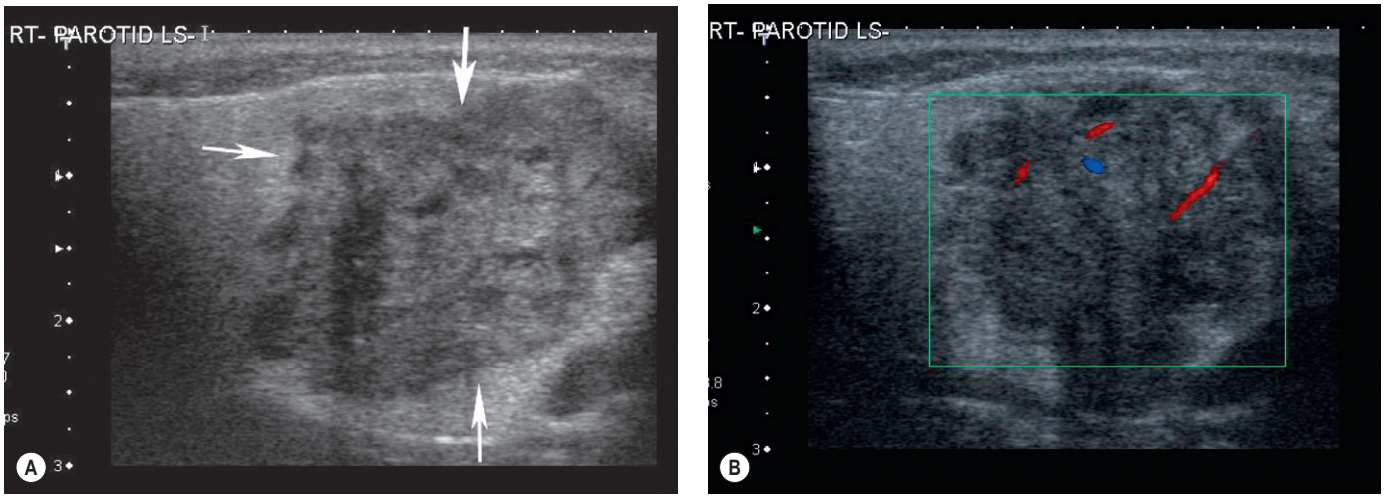

Figure 66.23 Mucoepidermoid carcinoma of the parotid. A: Ultrasound shows a solid, poorly defined mass within the parotid gland, with mixed echogenicity and some small cystic areas (arrows). **B:** Colour Doppler shows sparse vessels within the tumour.

common radiation-induced salivary gland tumour. Rapid increase in size of the mass, facial nerve paralysis or lymphadenopathy associated with a salivary gland mass are suspicious of malignancy. On ultrasound, malignant tumours usually appear heterogeneous, relatively hypoechoic in comparison with the normal gland, with indistinct borders, and may contain cystic or necrotic areas (Fig. 66.23).[12,14]

THYROID

The thyroid gland consists of two lobes at the level of the thyroid cartilage joined by an isthmus. Occasionally an extra lobe known as the pyramidal lobe extends superiorly. Normally the thyroid gland has a homogeneous appearance, but it is not unusual to find small cystic areas, known as colloid cysts, within it, measuring up to 3 mm in diameter (Fig. 66.24). Occasionally one lobe of the thyroid may be absent, which may give a clinical impression of a swelling on the contralateral side.

The thyroid gland may also be ectopic, which usually results in a deficiency of thyroid hormone. The ectopic thyroid may be situated anywhere along the course of descent, but most often it is lingual or sublingual in location. On ultrasound, the ectopic thyroid appears as a rounded structure with uniform echogenicity, similar to normal thyroid, just above the hyoid, and the thyroid is absent from its normal position. When hypothyroidism is detected on neonatal screening, these ultrasound appearances are sufficient to make a confident diagnosis of lingual ectopic thyroid. In a minority of cases, the ectopic lingual thyroid maintains sufficient function to prevent overt hypothyroidism, and may present later in childhood as an enlarging mass at the base of the tongue, sometimes sufficiently large to cause airway obstruction.[4]

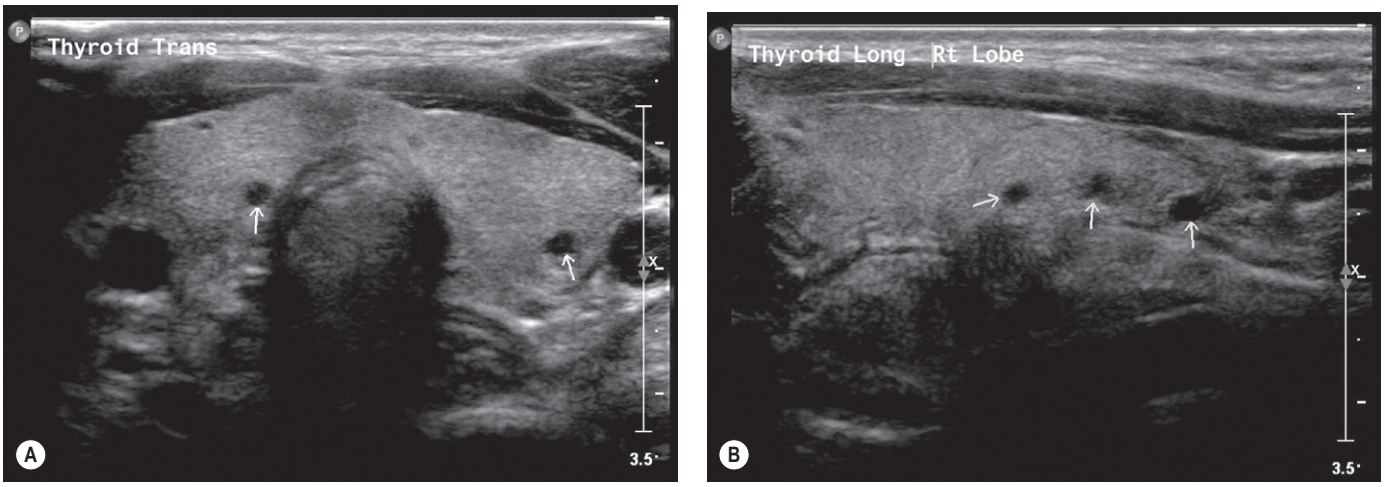

Figure 66.24 **Normal thyroid with colloid cysts** (arrows). **A:** Transverse image. **B:** Longitudinal image.

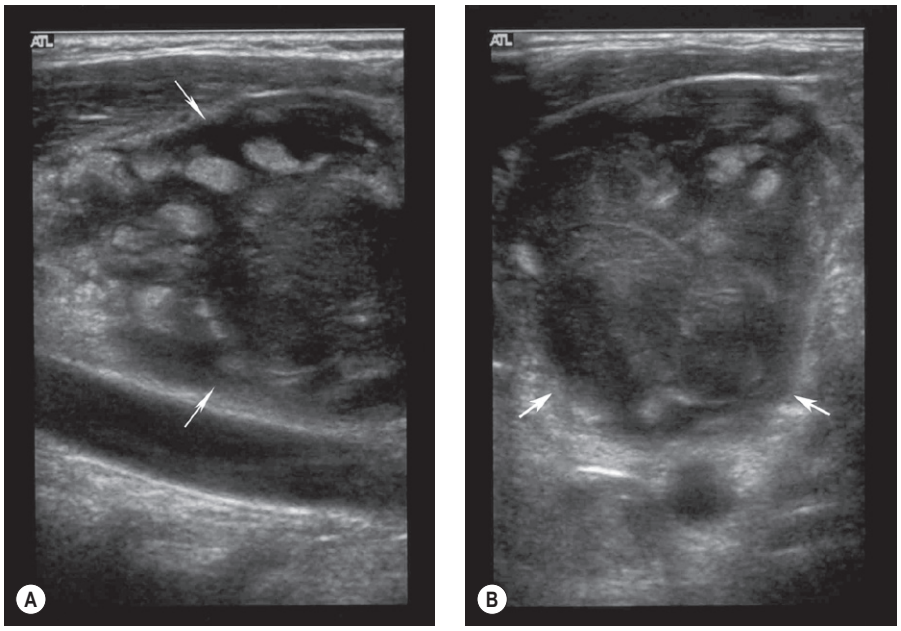

Figure 66.25 **Thyroid abscess** caused by *Aspergillus* infection in an immunocompromised child with leukaemia (arrows). **A:** Longitudinal image. **B:** Transverse image.

Acute suppurative thyroiditis

Acute suppurative thyroiditis is usually caused by blood-borne bacterial infection, but a rare cause is a congenital fistula, between the pyriform sinus and a lobe of thyroid, usually the left. Ultrasound shows a complex mass within the thyroid which commonly develops into an abscess. In immunocompromised children, a thyroid abscess may occur as a result of opportunistic infection by unusual organisms such as *Aspergillus* (Fig. 66.25).

Diffuse thyroid disease

Graves' disease, Hashimoto's thyroiditis and multinodular goitre are much less common in children than in adults but may occasionally present with a neck swelling in childhood. In some parts of the world simple goitre due to dietary iodine deficiency is common.

Graves' disease is an autoimmune disease which causes thyrotoxicosis. On ultrasound the gland is diffusely enlarged, with a lobulated margin. The echogenicity may be normal or hyperechoic, but the most striking feature is that it is markedly hypervascular (Fig. 66.26).

Hashimoto's thyroiditis is also an autoimmune disease, which may occur in adolescent girls. As the disease progresses most patients become hypothyroid. It is the commonest cause of acquired hypothyroidism. On ultrasound the thyroid gland is enlarged and hypoechoic, with a coarse heterogeneous echotexture. If the gland becomes fibrotic there may be areas of increased echogenicity. Calcification and lymphadenopathy may be present.[3]

Multinodular goitre is uncommon in childhood. It is usually idiopathic but may occur in association with congenital defects of thyroid hormone synthesis (dyshormonogenesis), McCune–Albright syndrome and Hashimoto's thyroiditis. On ultrasound the gland is enlarged and contains multiple nodules, which are usually hypoechoic but are sometimes hyperechoic and may contain calcification (Fig. 66.27).

Focal thyroid lesions

Thyroid adenomas are the most common thyroid nodules in children and are usually solitary. Typically on ultrasound the rest of the gland is normal and the adenoma is seen as a hypoechoic lesion, with a sonolucent rim, but haemorrhage, necrosis or calcification

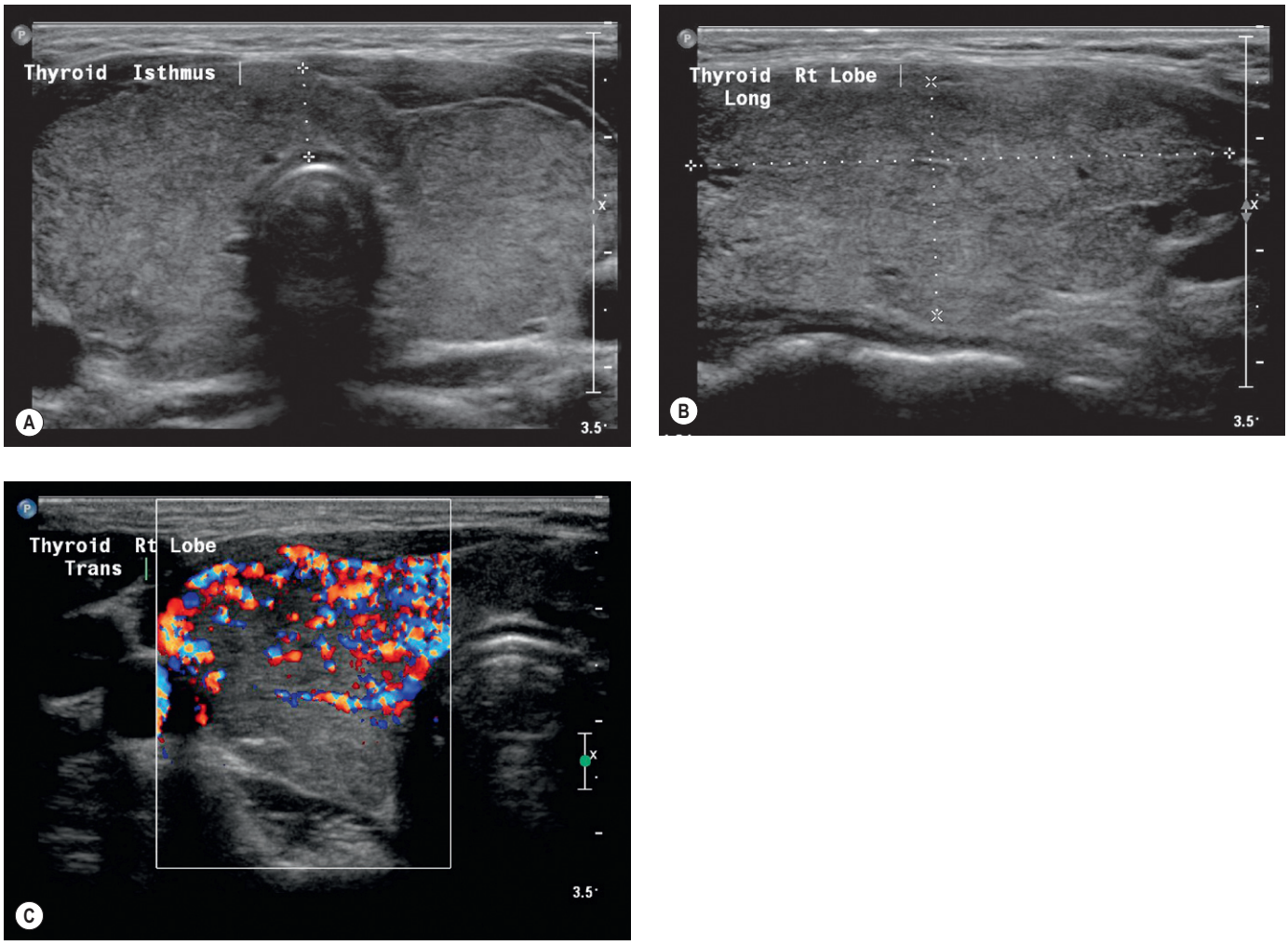

Figure 66.26 Graves' disease. Transverse **(A)** and longitudinal **(B)** images show diffuse enlargement of the thyroid. **C:** Colour Doppler shows marked hypervascularity of the whole of the thyroid.

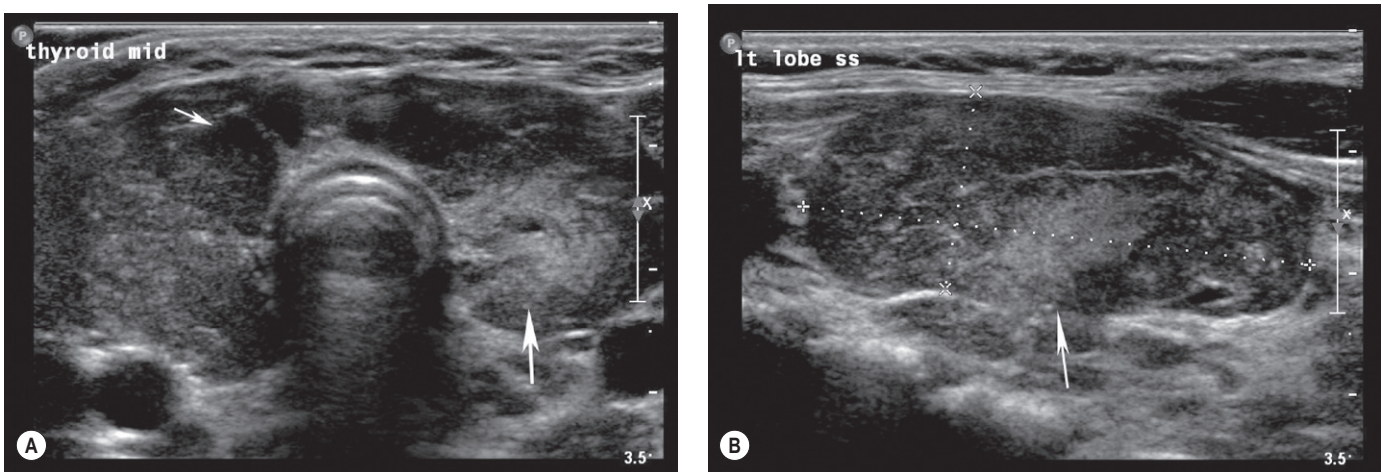

Figure 66.27 Multinodular goitre. Transverse **(A)** and longitudinal **(B)** images show diffusely abnormal thyroid architecture with discrete nodules with both increased (long arrow) and decreased (short arrow) echogenicity.

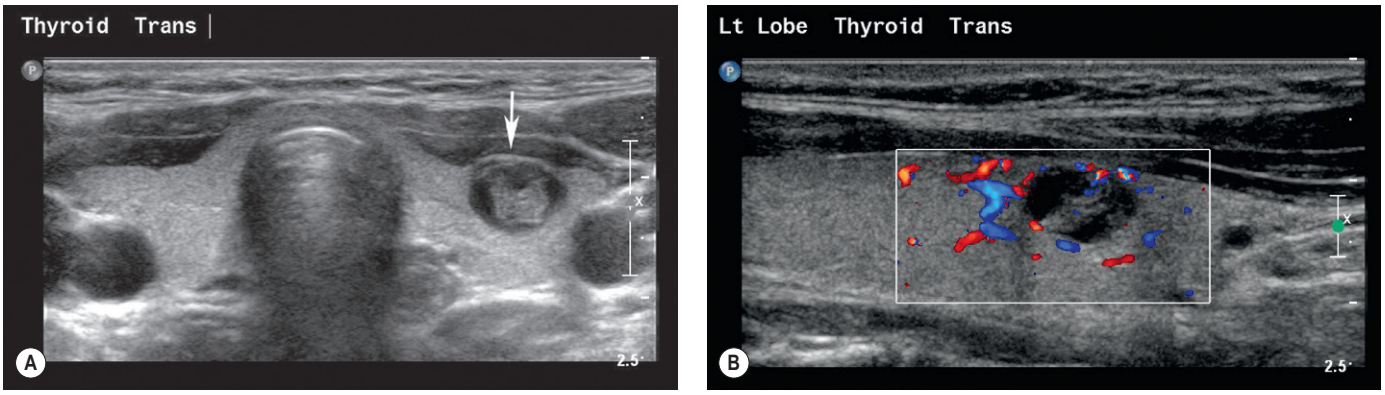

Figure 66.28 Thyroid adenoma. A: Ultrasound shows a well-defined, solitary focal lesion within the left lobe of the thyroid, with a hypoechoic rim (arrow). **B:** Colour Doppler shows that the margin of the lesion is vascular.

Salivary gland and thyroid lesions

- Haemangiomas and lymphatic malformations are the commonest causes of parotid masses in young children. Pleomorphic adenomas are commoner in older children and adolescents, but mucoepidermoid carcinomas also occur in this age group.
- Ectopic lingual thyroid may present as an enlarging mass at the base of the tongue.
- Thyroid adenomas are the most common cause of solitary thyroid nodules in children. Thyroid carcinoma can occur in childhood but is uncommon. The majority of cases are papillary carcinoma. Ultrasound alone cannot reliably distinguish between benign and malignant thyroid nodules.

may alter this appearance. On colour Doppler ultrasound it typically has a vascular rim (Fig. 66.28).

Thyroid carcinoma accounts for about 1% of malignancies in children under 15 years of age; 70–90% of cases are papillary carcinoma, with follicular carcinoma accounting for 10–20%. Medullary carcinoma of the thyroid is associated with multiple endocrine neoplasia syndromes and occurs in 1–10% of cases. Thyroid carcinoma may be multicentric and bilateral. On ultrasound most are hypoechoic, but they can be hyperechoic or isoechoic. They may also have a regular or irregular border and may have a sonolucent rim, as is the case with an adenoma. Calcification may occur in medullary cell carcinoma. At the time of diagnosis nodal metastases are present in 55–90% of cases.[3,4]

Ultrasound alone cannot reliably distinguish between benign and malignant thyroid nodules and further investigation with fine-needle aspiration or biopsy is required.

OTHER NEOPLASTIC MASSES

Head and neck neoplasms account for only 5% of all malignancy in children, of which over 50% are soft tissue sarcomas and lymphoma. On ultrasound, malignant tumours usually appear solid and uniformly echogenic, but may contain areas of necrosis or calcification. Malignant tumours typically have irregular, ill-defined margins with evidence of vascular encasement and invasion of normal structures, but the presence of an apparently well-defined capsule should not give false reassurance; soft tissue sarcomas and other malignant tumours may have pseudocapsules. Imaging appearances are non-specific and, in the absence of a histological diagnosis, a suspicious clinical history is the single most important factor in determining whether a child's neck mass could be malignant. Typically malignant cervical lesions are painless, firm, fixed masses that may be accompanied by systemic symptoms. A firm hard mass, rapid or progressive growth, and fixation to skin or deep structures are important indicators of possible malignancy. Because ultrasound appearances are non-specific, any lesion that does not fulfil criteria for a benign lesion warrants biopsy.[12] Unlike the situation with adult head and neck tumours, fine-needle aspiration of solid soft tissue masses in children is usually inappropriate, except for focal thyroid or salivary gland lesions (see above). Most of the soft tissue tumours of childhood are small, round cell tumours which cannot easily be differentiated by cytology.

Rhabdomyosarcoma is the commonest soft tissue sarcoma of childhood, with about 40% occurring in the head and neck. Age distribution is biphasic, with peaks in early childhood and in the teenage years. Rhabdomyosarcomas are usually bulky, sometimes partly necrotic, aggressive tumours that rapidly invade surrounding structures and metastasise to regional lymph nodes. However, some cases present in an indolent manner and may be mistaken for inflammatory cervical lymphadenopathy. Rhabdomyosarcomas are sometimes highly vascular, but do not usually contain the high density of small vessels typical of a haemangioma, and are usually firm, whereas a haemangioma is soft and easily compressible.[4,15]

Neuroblastoma is a malignant tumour of childhood originating from neural crest cells. Most cases occur in the first 5 years of life. The most common location is in the abdomen; less than 5% of primary tumours occur in the neck and these have a relatively favourable prognosis. Cervical tumours may extend into the spinal canal through the neural foramina, and may present with symptoms of cord or nerve root compression or an ipsilateral Horner's syndrome. CT or MRI is necessary to assess spinal extension, which cannot be reliably demonstrated with ultrasound. Metastatic involvement of cervical nodes occurs from primary sites in the abdomen or thorax, often involving the left supraclavicular nodes.[12,15]

Other neurogenic tumours such as nerve sheath tumours, neurofibromas, ganglioneuroma and ganglioneuroblastoma may have identical appearances to neuroblastoma (Fig. 66.29). Plexiform neurofibroma is a peripheral nerve sheath tumour that is typically associated with neurofibromatosis type 1. The tumour produces diffuse enlargement and distortion of nerves; it is histologically benign but may be locally aggressive (Fig. 66.30).

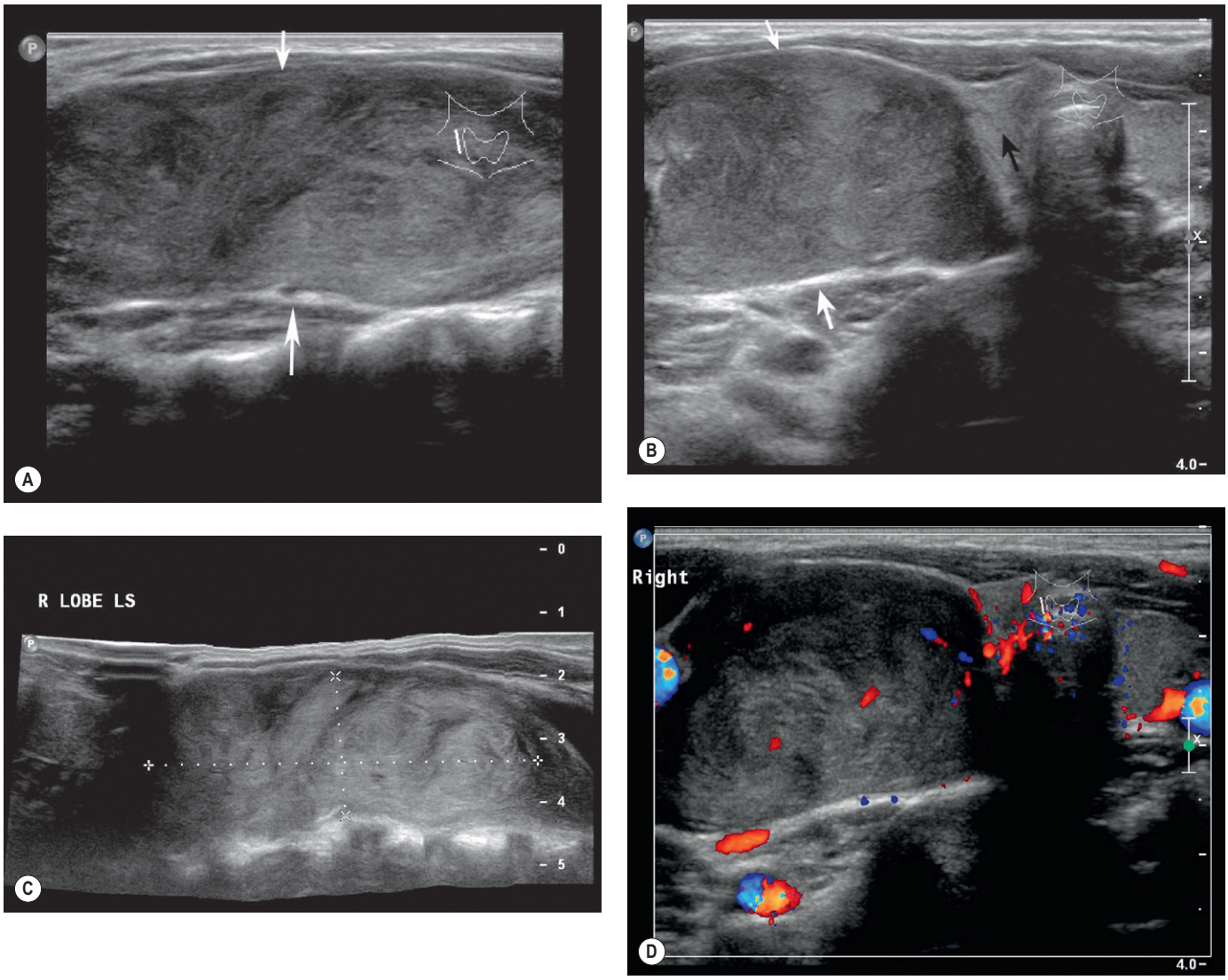

Figure 66.29 **Ganglioneuroma.** Ultrasound shows a solid, echogenic mass (white arrows) adjacent to the thyroid (black arrow). **A:** Longitudinal image. **B:** Transverse image. **C:** Extended field-of-view sonography shows the full extent of the lesion and its relationship to the adjacent cervical vertebrae. **D:** Colour Doppler shows scattered vessels throughout the solid tumour.

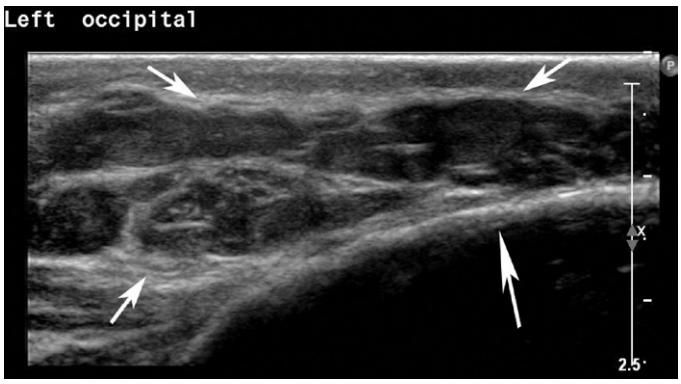

Figure 66.30 **Plexiform neurofibroma** involving the scalp in a child with neurofibromatosis type 1. Short arrows indicate the lobulated and cord-like solid structures, which are enlarged, thickened nerves. The long arrow marks the outer table of the occipital bone.

Neoplastic masses

- Malignant soft tissue tumours of childhood, such as rhabdomyosarcoma and neuroblastoma, have non-specific and variable ultrasound appearances.
- Urgent biopsy is indicated for any mass which is solid and shows rapid or progressive enlargement, fixation to deep structures, or is associated with signs of spinal cord or nerve root compression or a Horner's syndrome.
- The presence of a well-defined capsule or pseudocapsule does not exclude malignancy.
- Fine-needle aspiration is usually not appropriate for the diagnosis of neoplastic masses in children, except for thyroid and salivary gland nodules.
- Neuroblastoma and other neurogenic tumours may extend into the spinal canal but this cannot be reliably demonstrated with ultrasound.

REFERENCES

1. Ahuja AT, King AD, Metreweli C. Sonographic evaluation of thyroglossal duct cysts in children. Clin Radiol 2000;55:770–774.
2. Abernethy LJ. Paediatric neck lumps III – vascular and lymphatic malformations. Ultrasound 2007;15(3):142–147.
3. Alton H. Paediatric neck lumps II – Congenital cystic lesions in the neck and thyroid abnormalities. Ultrasound 2007;15(3):136–141.
4. Siegel MJ. Face and neck. In: Siegel MJ, editor. Pediatric sonography. 3rd edn. Philadelphia, PA: Lippincott Williams and Wilkins; 2002.
5. Dubois J, Patriquin HB, Garel L, et al. Soft tissue haemangiomas in infants and children: diagnosis using Doppler sonography. AJR Am J Roentgenol 1998;171:247–252.
6. Rogers M, Lam A, Fischer G. Sonographic findings in a series of rapidly involuting congenital haemangiomas (RICH). Pediatr Dermatol 2002;19:5–11.
7. Trop I, Dubois J, Gruibard L, et al. Soft tissue venous malformations in pediatric and young adult patients: diagnosis with Doppler US. Radiology 1999;212:841–845.
8. Chao HC, Wong KS, Lin SJ, et al. Ultrasonographic diagnosis and colour flow Doppler sonography of internal jugular venous ectasia in children. J Ultrasound Med 1999;18:411–416.
9. Lopez-Quinones M, Bargallo X, Biasco J, et al. Iatrogenic carotid-jugular arteriovenous fistula; color Doppler sonographic findings and treatment with covered stent. J Ultrasound Med 2006;34:301–305.
10. Ablin DS, Jain K, Howell L, West DC. Ultrasound and MR imaging of fibromatosis colli (sternomastoid tumour of infancy). Pediatr Radiol 1998;28:230–233.
11. Bedi DG, John SD, Swischuk LE. Fibromatosis colli of infancy: variability of sonographic appearance. J Clin Ultrasound 1998;26:345–348.
12. Williams H. Paediatric neck lumps I – Inflammatory and neoplastic lesions including salivary gland abnormalities. Ultrasound 2007;15(3):124–135.
13. Nozaki H, Harasawa A, Hara H, et al. Ultrasonographic features of recurrent parotitis in childhood. Pediatr Radiol 1994;24:98–100.
14. Garcia CJ, Flores PA, Arce JD, et al. Ultrasonography in the study of salivary gland lesions in children. Pediatr Radiol 1998;28:418–425.
15. Turkington JRA, Patterson A, Sweeney LE, Thornbury GD. Neck masses in children. Br J Radiol 2005;78:75–85.

CHAPTER

67 The infant spine

Tim Jaspan and Rob Dineen

INTRODUCTION

Development of real-time ultrasound and high-frequency linear array technology has taken imaging of the spine in early life well beyond early reports of using articulated arm static scanners. Clearer and more detailed information about spinal anatomy and pathology has made the modality increasingly useful.[1–4] Its use in the older child and adult is severely limited by the presence of the surrounding posterior bony vertebral arches, whereas in the neonate these structures are incompletely ossified. At birth the posterior portions of the neural arches and spinous processes are still cartilaginous, providing an acoustic window into the spinal canal, which can be imaged in the sagittal (longitudinal) and axial (transverse) plane.

By the end of the first year of life, fusion of the lamina into a bony arch is complete in the lumbar region; ossification progresses cranially and is complete in the cervical region by 2 years of age. Visualisation of the spinal canal in the older child is only possible when a congenital or surgical bony defect is present, but ultrasound scanning rarely provides useful or diagnostic information in such cases and there should be no hesitation in proceeding to magnetic resonance imaging (MRI).

Spinal ultrasound is most useful in the first few weeks of life, when the posterior elements are unossified. The quality of information can be unrivalled if performed with care and attention to detail.[5]

Although MRI is now the modality of choice for spinal imaging, the neonatal spine presents a difficult challenge for MRI because of the small size of the baby, lack of suitable dedicated neonatal spinal surface coils and the high water content and immature myelination of the spinal cord, leading to relatively poor tissue contrast and signal-to-noise ratio compared to older infants and children. Pulsatile hyperdynamic cerebrospinal fluid (CSF) flow in the spine is particularly pronounced in infancy and early childhood, presenting additional interpretive problems, generating complex CSF flow pulsation artefacts on spinal MRI.[6] Conversely, ultrasound can reveal exquisite anatomical detail, guiding subsequent imaging triage.

TECHNIQUE

The infant's back should be inspected for cutaneous stigmata of occult spinal dysraphism. Although such findings may be the trigger for the study, clinicians sometimes miss subtle physical features (such as skin pits). Care should be made to look for a tiny ostium that may mark a dermal sinus track, which can be difficult to identify by ultrasound scanning.

A high-quality real-time ultrasound machine is needed. A curved linear or sector transducer is preferable for scanning the craniocervical junction. Linear array transducers are best for imaging the rest of the spine. In the neonate frequencies of 7.5–12 MHz are routinely used.

The infant should be examined in the prone position, the spine slightly flexed to flatten out the natural lower spinal lordotic curvature, lying prone over a pillow or bolster placed on the lap of the person holding the infant. Flexion maximises the acoustic window in axial scanning.

Performing the examination following a feed may ensure the baby is settled and more likely to lie still. Slightly warmed ultrasound gel will reduce the disturbance to the baby. Plenty of coupling gel on the skin should be maintained throughout the examination.

The entire spine, from craniocervical junction to coccyx, is scanned in the sagittal and axial planes, capturing representative images from each zone. A split-screen facility enables contiguous sagittal sections of the spine to be displayed together, providing a composite image of a longer length of spine.[3] This is useful for determining anatomical landmarks, counting spinal vertebral levels and delineating the full extent of more complex pathological structures. The extended field-of-view facility on some scanners achieves the same result.

The examination starts at the sacrococcygeal level; identifying the five sacral vertebral bodies provides a landmark for anatomical localisation. The presence and direction of spinal cord and nerve root movement should be looked for. A clip store helps in the

appreciation of cord and root dynamics. With changes of position and with crying the spinal cord normally shows dorsoventral movement and the echogenic roots of the cauda equina move freely within the transonic CSF in the thecal sac. Pulsations of the anterior spinal artery and 'dancing' motion of individual nerve roots may also be seen.[1] The spinal cord does not normally pulsate with the cardiac cycle.[2]

In up to 10% of cases, a second (or more) dysraphic abnormality is present elsewhere in the neuraxis. Cord cavitation distant from the site of the lesion should be looked for, emphasising the need to examine the entire length of the cord.

INDICATIONS FOR SPINAL ULTRASOUND

Requests for spinal ultrasound often depend upon local experience and availability of appropriate sonographic expertise. Another factor is a lack of awareness amongst many referring clinicians as to the uses and limitations of ultrasound in early life.

Ultrasound is recommended as the initial examination in suspected spinal disease in the neonate. Where ultrasound is inconclusive or reveals pathology it should be followed by MRI. Over-reliance on ultrasound carries the risk of diagnostic errors and failure to detect potentially significant pathology. There should be a low threshold for proceeding to MRI.

CONTRAINDICATIONS FOR SPINAL ULTRASOUND

The only absolute contraindication is an open neural tube defect because of the risk of contamination and infection. Increasing age is a relative contraindication; visualisation of the spinal canal is limited beyond early infancy. Over-reliance on ultrasound as the primary imaging modality outside of the first few weeks of life should be strongly resisted. Severe spinal deformity and bony vertebral anomalies can make ultrasound difficult. Scanning in the axial plane is most useful in these cases.

ULTRASOUND VERSUS MRI

In a study of spinal disorders in infants undertaken in the 1990s, ultrasound was equally sensitive to MRI in the diagnostic yield.[7] Thirty children with a mean age of 5.5 months underwent 38 spinal ultrasound scans; in 32 cases ultrasound matched the information seen on MRI. In 5 cases ultrasound showed the main abnormality but MRI gave additional information. In all 24 MRI studies that demonstrated a spinal abnormality, ultrasound identified the index lesion. MRI confirmed normal appearances in all spinal ultrasound scans reported as normal, suggesting excellent sensitivity for ultrasound.

However, caution must be exercised in evaluating studies that include older children and where older generation MRI systems were used. Current state-of-the-art MRI, with superior surface coil technology, gradient systems, CSF and cardiac gating techniques, has improved the quality of MRI in the first few months of life.

Indications for ultrasound scanning in early infancy

High risk	Medium risk	Low risk
Multiple congenital anomalies	Complicated sacral dimple (>5 mm diameter, >2.5 cm above anus)	Uncomplicated sacral pit or dimple (<5 mm diameter, <2.5 cm above anus)
Suspected birth-related cord damage	Subcutaneous soft tissue mass	Strawberry naevus or Mongolian blue spot
Atypical or discharging skin pit	High-risk skin markers (hairy tufts, associated haemangioma, tail buds)	Isolated diffuse hairiness

NORMAL ANATOMY

Extraspinal and spinal anatomy

Extraspinal

The skin surface appears as a narrow echogenic bilaminar stripe in the near field. Below this subcutaneous fat forms an intermediate to low echogenicity plane, immediately deep to which lies the lumbosacral fascia. This commences in the coccygeal region (Fig. 67.1), forming a strongly echogenic unbroken stripe, which in turn blends with the hypoechoic interspinous ligaments and posterior paraspinal musculature in the lumbosacral region (Fig. 67.2). Gas within the rectum appears as an echogenic structure immediately deep to the coccyx (Fig. 67.1).

Spinal

The spinal column is composed of 33 individual segments, which are unfused in the cervical (7 segments), thoracic (12 segments) and lumbar (5 segments) regions. The 5 sacral and 4 coccygeal segments are partially fused. At term, echogenic ossification centres are present in all the vertebral bodies except the coccyx, and in paired centres that form the posterior neural arches. The latter do not fuse in the midline until the end of the first year of life.

On sagittal plane imaging, the vertebral bodies form strongly echogenic complexes lying deep to the anechoic CSF-filled thecal sac. The appearance of the posterior neural arches lying superficial to the thecal sac varies with the level of the spine and age of the patient, and they cast variable echogenic shadowing within the

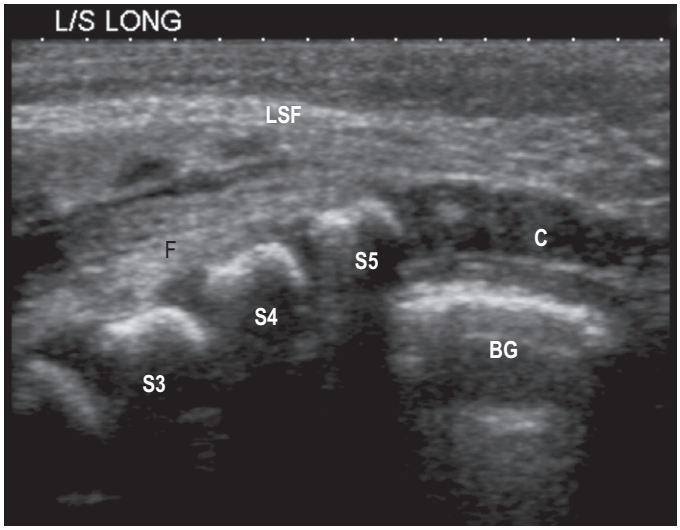

Figure 67.1 Sagittal image of sacrum and coccyx. The subcutaneous fat is hypoechoic, immediately below which lies the echogenic lumbosacral fascia (LSF). The echogenic sacral vertebral bodies (S) contrast with the hypoechoic coccyx (C). Note echogenic fat (F) in the sacral spinal canal and echogenic bowel gas (BG).

canal. With increasing age, they become more echogenic and an increasing barrier to insonation of the underlying structures. In the first few weeks of life, the unossified coccyx appears as a tubular hypoechoic structure extending caudally from the fifth sacral body (Fig. 67.1). Identification of the five echogenic, rectangular ossified sacral vertebral bodies, forming a curved sweep in the sagittal plane, is the basis for localisation of the spinal level (Fig. 67.2).

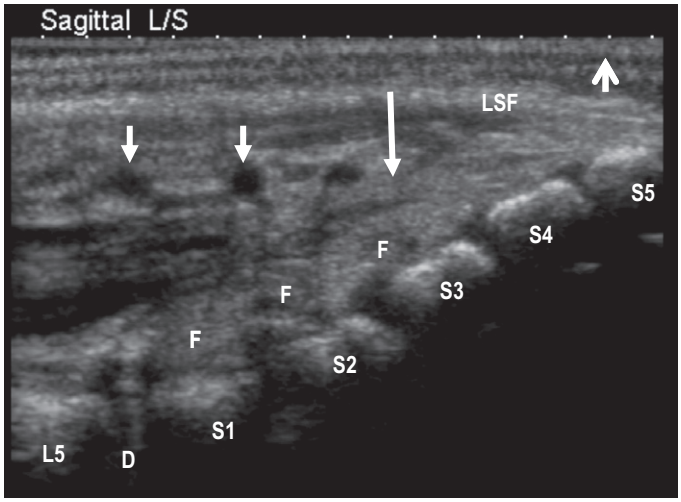

Figure 67.2 Sagittal image of sacrum. The bilaminar skin surface complex is readily seen (arrowhead), with the underlying hypoechoic subcutaneous fat and echogenic lumbosacral fascia (LSF). The hypoechoic spinous processes (short arrows) are bridged by more echogenic interspinous ligaments. The sacral vertebral bodies (S) lie deep to the epidural fat (F) filling the sacral canal. The sacral cul-de-sac (long arrow) can be difficult to differentiate from the echogenic fat. The hypoechoic L5/S1 disc (D) lies between the bodies of S1 and L5.

The lumbar vertebrae have a cleft in the midbody region, containing the basivertebral veins (Fig. 67.3). Intervening intervertebral discs are hypoechoic, reflecting the gel-like nucleus pulposus. The nucleus pulposus is particularly large in the first year of life, thereafter gradually decreasing in size.

The vertebral bodies of the upper cervical spine and ossification centres of the clivus form constant strongly echogenic landmarks. The intervening anterior arch of C1 is poorly visualised. The spinous processes are cartilaginous in the first few months of life; however, in the cervical spine they ossify earlier than the remainder of the spinal column and may appear echogenic (Fig. 67.4).

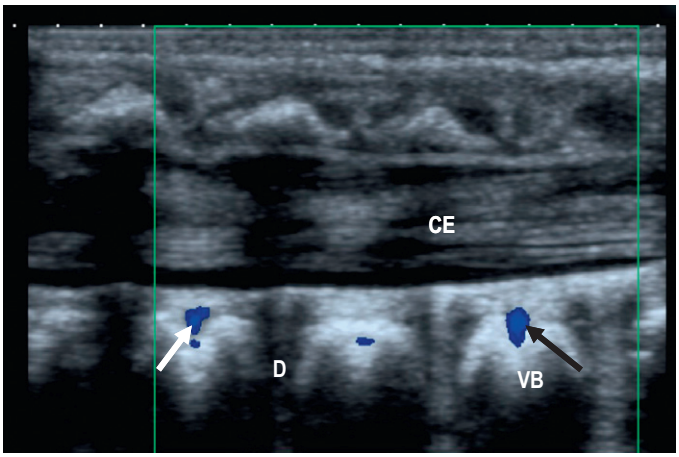

Figure 67.3 Sagittal image of the lumbar spine with colour Doppler imaging. The vertebral bodies (VB) form strongly echogenic structures immediately deep to the anterior wall of the thecal sac. The intervertebral disc (D) is hypoechoic but contains a central echogenic stripe. CE, cauda equina. The basivertebral veins are readily identified on colour Doppler imaging (arrows).

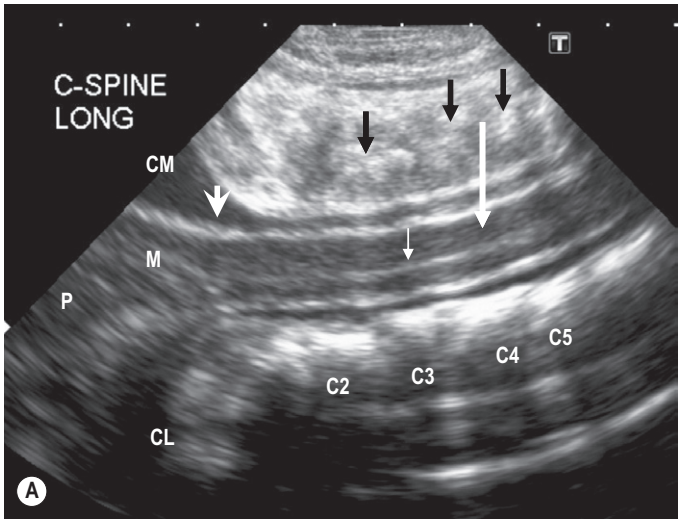

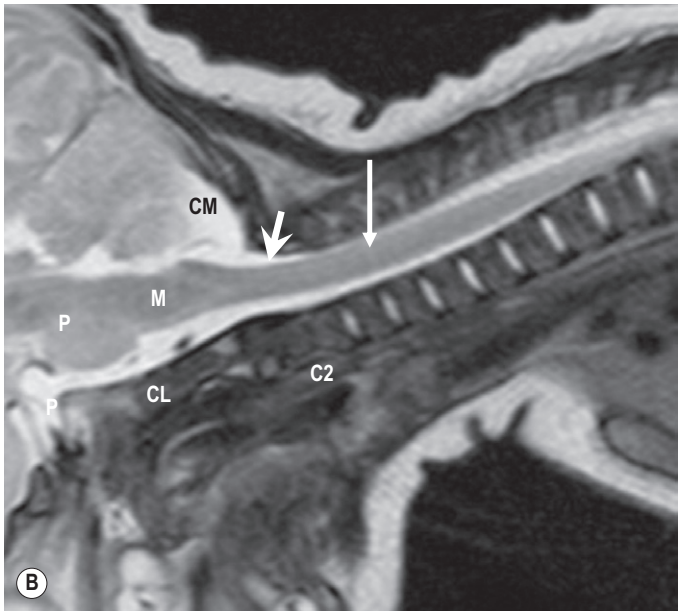

Figure 67.4 Craniocervical region. A: Sagittal image of upper cervical spine with a sector transducer. Note the lower brainstem (P, pons; M, medulla), craniocervical junction (arrowhead) and cervical cord (long arrow). The spinous processes are more echogenic (black arrows). Short arrow indicates the central echo complex. CL, clivus; C, cervical vertebral body. **B:** Sagittal T2 MR image (displayed horizontally). The internal architecture of the cord is not as well visualised as on the corresponding ultrasound image. Note good correlation of the anatomy of the brainstem. P, pons; M, medulla; CM, cisterna magna; CL, clivus; craniocervical junction indicated by arrowhead and upper cervical cord by arrow.

In the axial plane the posterior neural arches are delta- or gull-shaped echogenic structures casting variable acoustic shadowing (Figs 67.5 and 67.6). In the thoracic region, the paired ribs appear as posteriorly convex echogenic structures sweeping away from the vertebral bodies, overlying the echogenic lungs (Fig. 67.6).

Intraspinal anatomy

Sacrum and coccygeal region

Echogenic epidural fat fills the sacral spinal canal, blending with the theca and its contained anechoic cerebrospinal fluid (CSF) at the sacral cul-de-sac (Fig. 67.1).

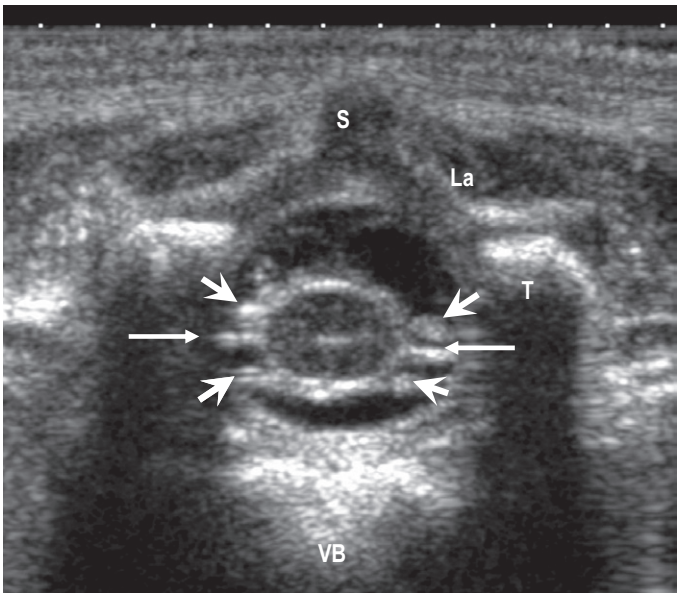

Figure 67.5 Axial image through mid thoracic cord. The spinal cord lies towards the anterior half of the spinal canal, suspended by the echogenic dentate ligaments (arrows) in the anechoic CSF. T, transverse process; La, lamina; S, spinous process; VB, vertebral body; arrowheads indicate ventral and dorsal nerve rootlets.

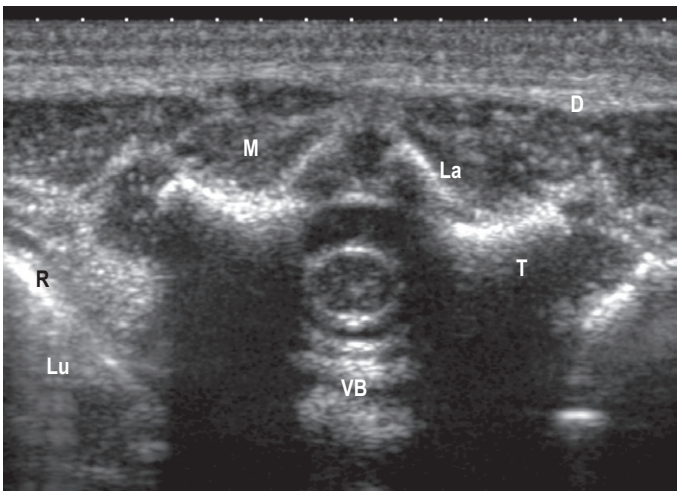

Figure 67.6 Axial image through the upper thoracic spine. The spinal cord is round and hypoechoic with a clearly defined central echo complex. D, deep fascial layer; La, lamina; T, transverse process; M, paraspinal muscle; R, rib; Lu, lung; VB, vertebral body.

Lumbar region

The echogenic vertebral bodies form the deep extent of the spinal canal on sagittal scanning, separated from the echogenic anterior thecal sac wall by a thin band of intermediate echogenicity fat in the anterior epidural space. The echogenic posterior thecal sac wall lies immediately deep to the posterior neural arches. The CSF within the thecal sac contains the linear echogenic nerve roots of the cauda equina (Fig. 67.7).

In the axial plane the roots of the cauda equina form an amorphous mass of echogenic structures filling much of the thecal sac in the lower lumbar spinal canal (Fig. 67.8). In the upper lumbar spine they become progressively more symmetrical, clustered either side of the midline (Fig. 67.9).

The filum terminale, a single strand of neuroglial tissue, may be identified on sagittal images as a fine linear midline echogenic structure within or posterior to the cauda equina. The filum extends caudally from the tip of the conus medullaris to pierce the thecal sac and attach to the posterior aspect of the coccyx.[8] No nerve roots arise from the filum terminale.

Anatomical landmarks

Anatomical site	Ultrasound appearance	Comment
Coccyx	Hypoechoic, tubular	Use to locate fifth sacral segment
Sacrum	5 echogenic segments	Count up from coccyx to locate S1
Lumbar spine	5 echogenic segments	Contains linear echogenic cauda equina; conus lies from T12 to lower L2
Thoracic spine	12 echogenic segments	Tubular hypoechoic cord, lies towards ventral part of canal. Central echo complex
Cervical spine	7 echogenic segments	Triangular hypoechoic cisterna magna behind craniocervical junction, echogenic elements of clivus anterior

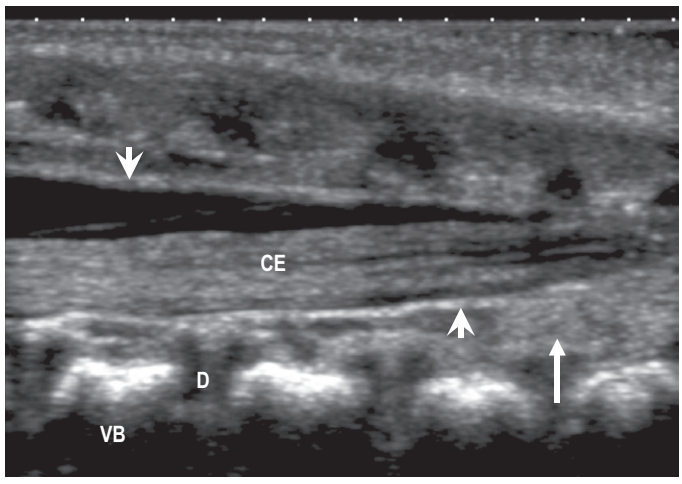

Figure 67.7 Sagittal image of the lumbar spine. The cauda equina (CE) fills the thecal sac. The thecal sac wall (arrowheads) is separated from the echogenic cauda equina by anechoic CSF. VB, vertebral body; D, intervertebral disc; arrow indicates anterior (ventral) echogenic epidural fat.

Thoracic region and conus

The conus medullaris, the termination of the spinal cord, is located anywhere between T12 and lower L2.[9] The conus is the last segment of the cord from which nerve roots arise; none arise from the filum. This distinction can be crucial; if cord tethering (see later) is considered to be the cause of a child's neurological deficit, the filum may be safely surgically divided. A tethered cord often becomes thinned and attenuated, blending imperceptibly with a thickened filum terminale. The surgeon must be aware of the transition point so as not to divide a low-lying spinal cord, which could result in devastating neurological sequelae. Elective division of a thickened tethering filum to prevent late neurological problems was prevalent in many centres in the past; the evidential efficacy of this practice is lacking, and is now largely abandoned.

In the lower thoracic/upper lumbar region the hypoechoic cord is focally enlarged (lumbar expansion) before funnelling down to the conus. The conus is identified in the sagittal plane as a conical structure, surrounded by echogenic cauda equina (Fig. 67.10A). Although MRI, particularly T2-weighted imaging, is the gold standard, the high-resolution detail afforded by ultrasound in early infancy provides exquisite detail that may not be achievable by MRI (Fig. 67.10B). In the axial plane the lumbar expansion is flanked by echogenic lumbosacral nerve roots (Fig. 67.11). The conus is surrounded by a symmetrical arrangement of the echogenic cauda equina (Fig. 67.12).

The split-screen facility enables a more complete evaluation of the position of the lower spinal cord (Fig. 67.13). The spinal cord normally lies a third to halfway between the anterior and posterior margins of the upper thoracic spinal canal[6] (Fig. 67.14).

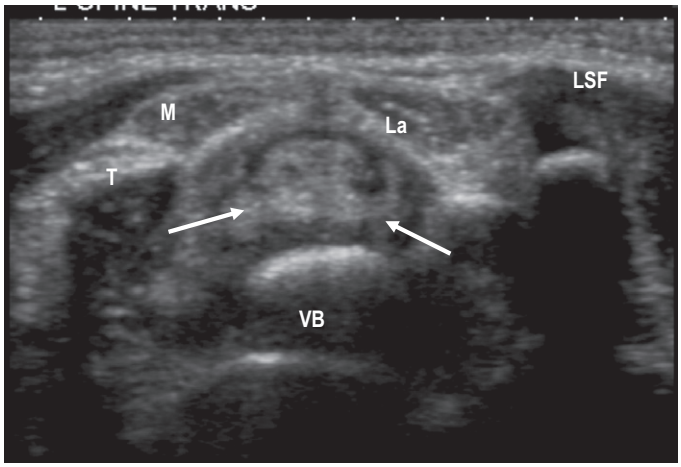

Figure 67.8 Axial image at the lumbosacral junction. The thecal sac is largely filled by the echogenic cauda equina (arrows) with little visible CSF. La, lamina; M, paraspinal muscle; T, transverse process; VB, vertebral body; LSF, lumbosacral fascia.

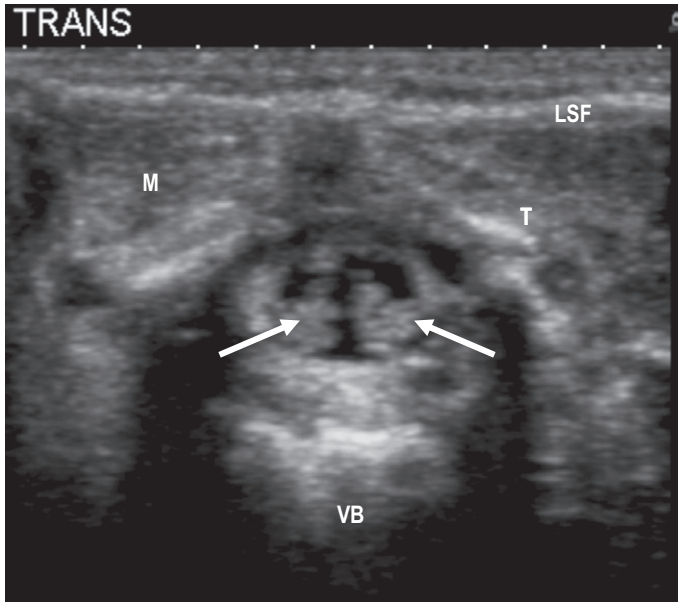

Figure 67.9 Axial image in the mid lumbar region. The echogenic nerve roots of the cauda equina are clumped together into two symmetrical groups (arrows) within the thecal sac. T, transverse process; M, paraspinal muscle; LSF, lumbosacral fascia; VB, vertebral body.

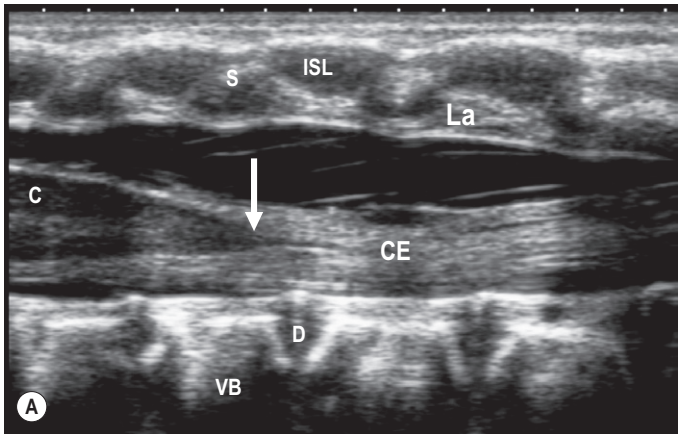

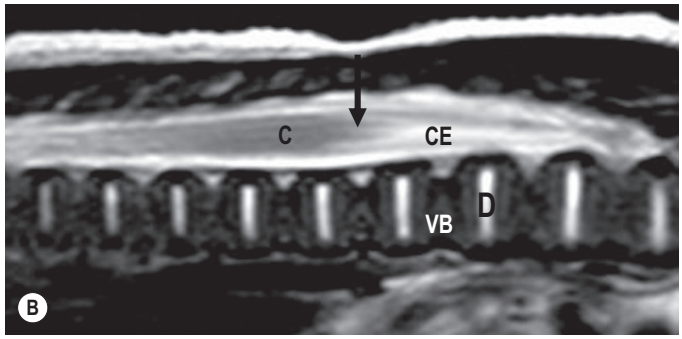

Figure 67.10 Distal cord. A: Sagittal image of the distal cord (C) and conus (arrow). The echogenic nerve roots of the cauda equina encase the conus and extend caudally in the transonic CSF. Echogenic vertebral bodies (VB) lie immediately deep to the anterior thecal sac wall with the hypoechoic intervening intervertebral discs (D). S, spinous process; ISL, interspinous ligament; La, lamina. **B:** Sagittal T2 MR image at the same level in a 9-day-old infant. Note that the cord (C), cauda equina (CE), conus medullaris (arrow), posterior neural arches and ligamentous anatomy are not as clearly visualised as on ultrasound at this age.

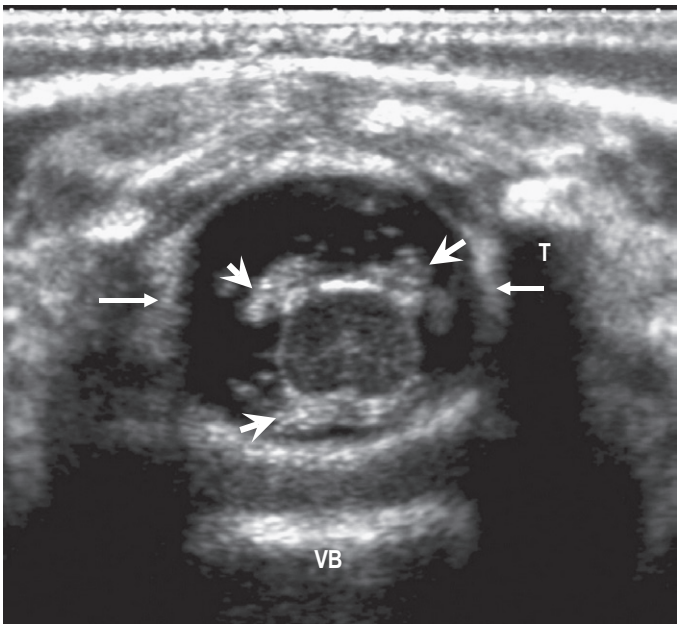

Figure 67.11 Axial image through the lower thoracic spine. Note the relatively large size of the anechoic CSF-filled thecal sac compared to the spinal cord. T, transverse process; VB, vertebral body; arrowheads indicate dorsal and ventral nerve rootlets; short arrows indicates thecal sac wall.

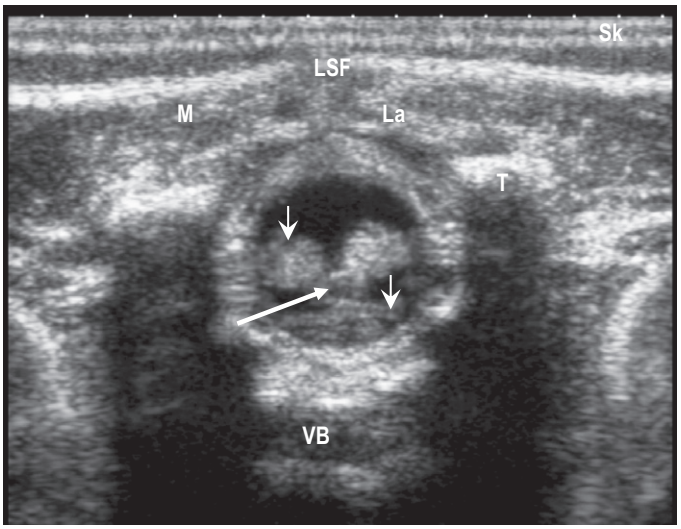

Figure 67.12 Axial image at the conus. The nerve roots forming the cauda equina (arrowheads) are grouped together like a four-bladed fan around the conus (arrow). Sk, skin; LSF, lumbosacral fascia; M, paraspinal muscles; La, lamina; T, transverse process; VB, vertebral body.

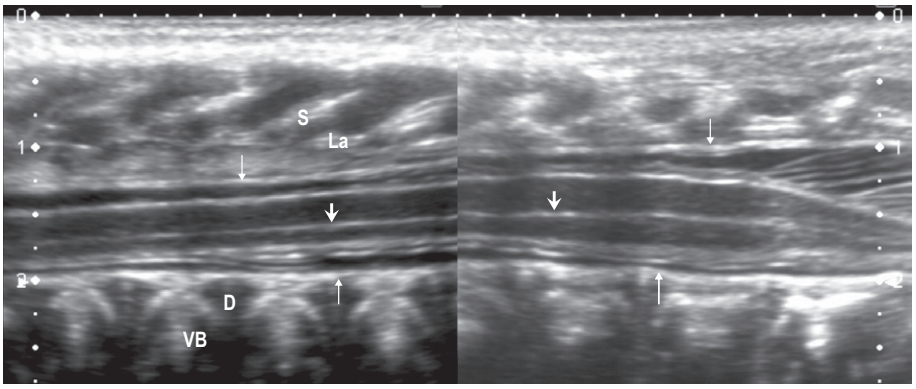

Figure 67.13 Normal thoracic spine. Sagittal image of the mid and lower thoracic cord using the split-screen facility. Note the focal expansion of the lower thoracic cord due to the lumbar enlargement. Arrowheads indicate central echo complex; arrows indicate thecal sac wall; VB, vertebral body; D, intervertebral disc; S, spinous process (echogenic due to early ossification); La, lamina.

The central echo complex forms a single strongly echogenic line or pair of lines within the spinal cord on sagittal images (Fig. 67.15) and a central echogenic 'dot' (or ring) on axial images (Fig. 67.16).[10,11] The central echo complex probably represents the central canal of the spinal cord. Physiological enlargement of the central canal or a dilated ventriculus terminalis is continuous with and splays the central echo complex, which funnels down to a single central echo complex both caudal and cephalad to the widened central echo complex.

Axial images in the mid and upper thoracic region reveal an oval/round hypoechoic cord lying freely within the CSF. Paired dorsal and ventral roots may be identified in addition to the dentate ligaments, which suspend the spinal cord within the spinal canal, arising from the cord at its equator and extending laterally to the thecal sac wall (Fig. 67.5).

Cervical region

Sagittal scanning employing a sector transducer is required to image the upper cervical spine and craniocervical junction, permitting visualisation of the cisterna magna, pons and medulla oblongata (Fig. 67.4). The pons and medulla appear relatively hypoechoic. CSF in the cisterna magna appears as a triangular transonic space dorsal to the craniocervical junction and medulla.

The grey and white matter of the spinal cord is homogeneously hypoechoic. The anatomy correlates well with MRI, which provides high quality anatomical portrayal of this region. However, MRI lacks the ability to show delicate cord detail in the first few months of life (Fig. 67.4)

Vascular structures

The anterior spinal artery may be seen as a tiny tubular midline structure on the ventral surface of the cord, its vascular nature confirmed by colour Doppler imaging (CDI) (Fig. 67.17).

Veins forming the vertebral venous complex, located in the epidural fat surrounding the thecal sac, appear as transonic structures on both sagittal and axial ultrasound. CDI reveals the vascular nature of these transonic structures (Fig. 67.18). The veins may appear disproportionately large in the neonate. The basivertebral veins, which drain the vertebral bodies into the venous plexus

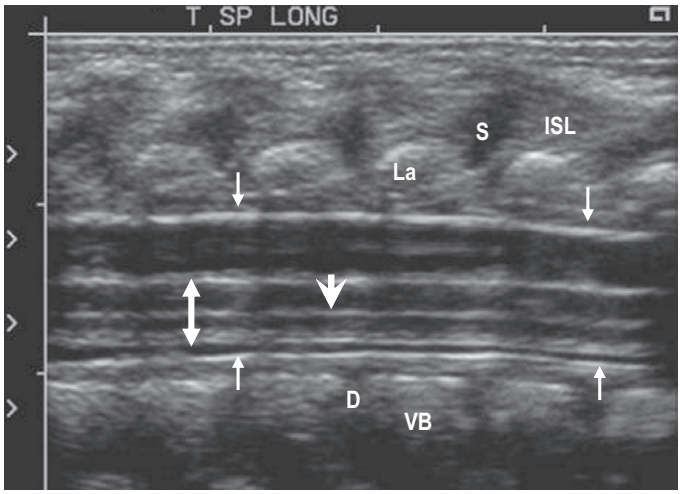

Figure 67.14 Normal cervicothoracic spine. Sagittal image at the cervicothoracic junction. The cord lies anteriorly within the spinal canal. ISL, interspinous ligament; La, lamina; S, spinous process; VB, vertebral body; D, intervertebral disc; double-headed arrow indicates spinal cord; small white arrows indicate thecal sac wall; arrowhead indicates central echo complex.

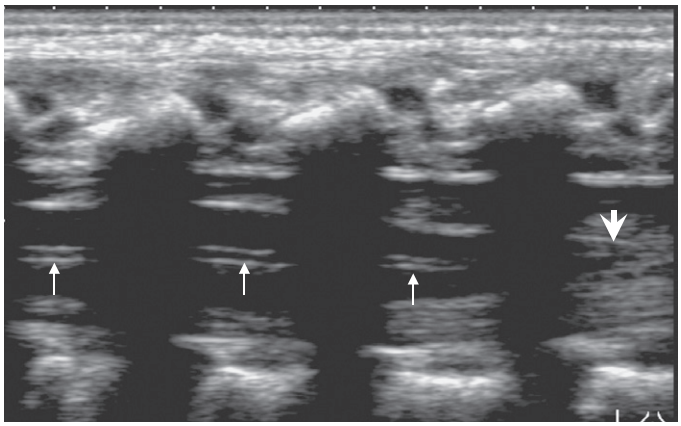

Figure 67.15 Central echo complex. Sagittal image of the lower thoracic spine demonstrating a prominent central echo complex within the hypoechoic cord (arrows), funnelling down to a single delicate echogenicity at the level of the conus (arrowhead).

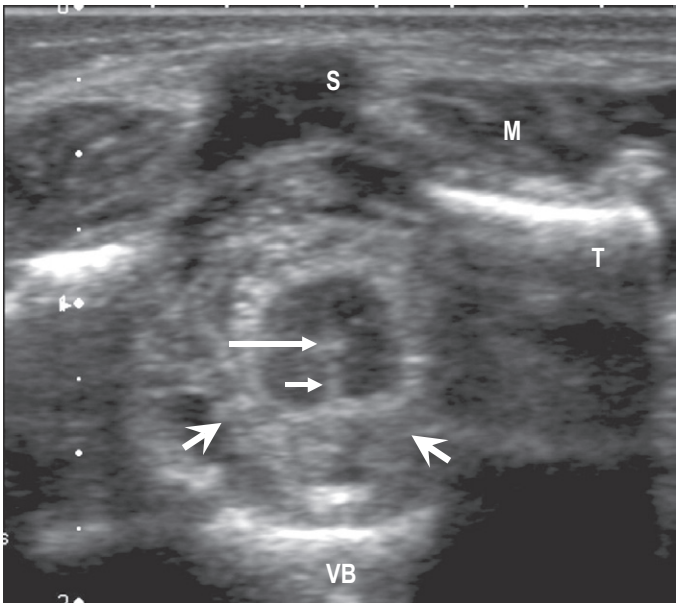

Figure 67.16 Central echo complex. Axial image of the lower thoracic spine at the level of the lumbar expansion. Note the anterior fissure of the cord (small arrow) extending down to the central echo complex (long arrow). T, transverse process; VB, vertebral body; S, spinous process; M, paraspinal muscle; arrowheads indicate echogenic nerve roots.

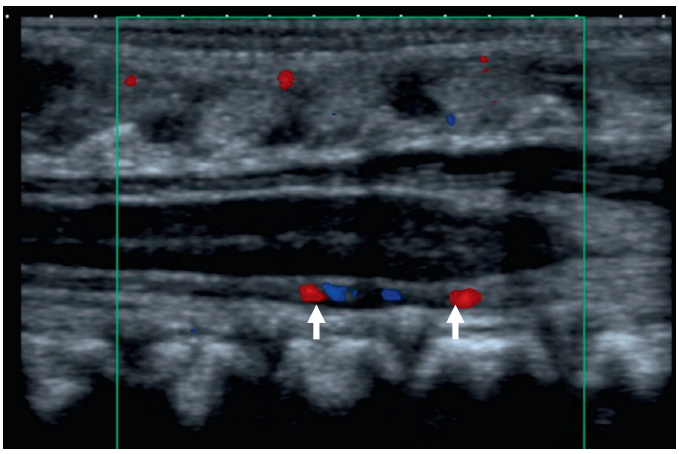

Figure 67.17 Sagittal colour Doppler image in the lower thoracic region. The anterior spinal artery is readily identified on the ventral surface of the cord (arrows).

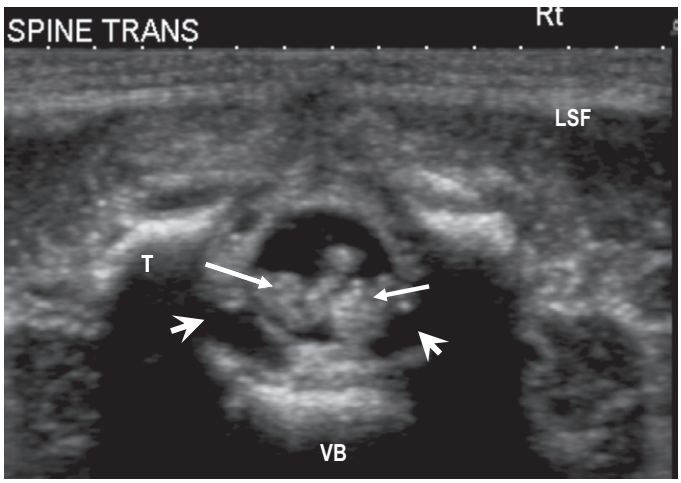

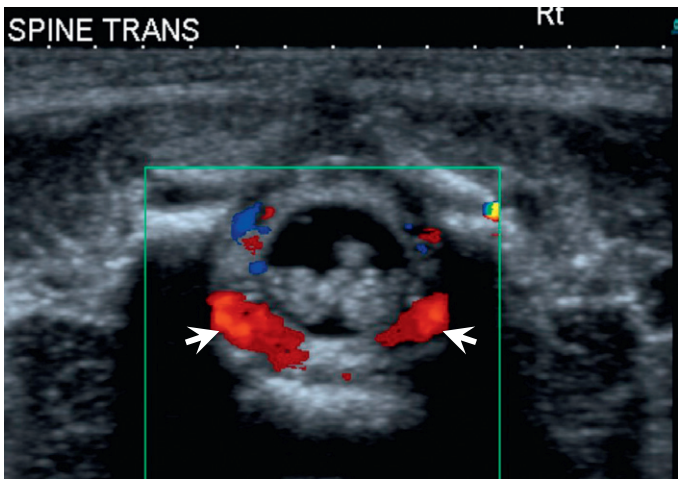

Figure 67.18 Axial imaging in the mid lumbar region. The echogenic cauda equina (arrows) are arranged symmetrically in the transonic CSF. Epidural veins, appearing as transonic structures lying outside the thecal sac (arrowheads) on real-time scanning, can only be fully appreciated with colour Doppler imaging. LSF, lumbosacral fascia; VB, vertebral body; T, transverse process.

within the spinal canal, lie within the cleft in the vertebral bodies posteriorly (Fig. 67.3).

EMBRYOLOGY

The embryological aspects of spinal development are addressed elsewhere, to which the reader is referred as well as further literature addressing the complex issues associated with spinal formation and development.[12–19] The development of the embryonic spine and neural elements involves a complex series of events; errors in these processes may result in a diverse group of abnormalities, collectively known as spinal dysraphism.

CLINICAL APPLICATIONS

Spinal dysraphism

The commonest application of spinal ultrasound is suspected spinal dysraphism. This term refers to all forms of incomplete fusion or malformation of the midline embryonic structures involving cutaneous, osseous and neural elements, either alone or in combination. Spinal dysraphism therefore includes:

1. all forms of anomalies in which there is incomplete fusion of the neural tube, meninges, vertebral column or skin
2. failure of separation of the germinal layers, e.g. a deep dermal sinus
3. abnormal growth of ectopic cell rests, e.g. dermoid or epidermoid cyst
4. disturbance of growth of an otherwise normal tissue, e.g. an intraspinal or intramedullary lipoma.

Spinal dysraphism manifests itself clinically as open defects (lacking in skin covering) or closed defects (skin covered) and are thus classified as open spinal dysraphism (OSD) and closed spinal dysraphism (CSD).[20]

Open spinal dysraphism (OSD)

In OSD there is incomplete closure of the bony elements of the spinal canal, with posterior protrusion of part or all of its contents. Open dysraphism is subdivided into spina bifida aperta (completely deficient skin covering), and spina bifida cystica (poorly epithelialised skin covering) and includes:

1. meningocele: extension of a CSF-filled arachnoid sac through a posterior spina bifida
2. myelocele: an externalised midline plaque of neural tissue, exposed, and flush with, the skin surface
3. myelomeningocele: a myelocele that has been elevated above the skin surface by expansion of the underlying subarachnoid space.

In spina bifida aperta the externalised neural tissue is clearly visible and vulnerable, making ultrasound inadvisable. A second abnormality occurs cephalad or caudad to the myelomeningocele in up to 75% of patients[8,21] (see below).

In spina bifida cystica the primarily epithelialised sac may be imaged; however, MRI has supplanted ultrasound for the investigation of such lesions. Ultrasound of the craniocervical junction may demonstrate a Chiari II malformation, invariably associated with myelomeningoceles;[22] transfontanellar ultrasound may detect ventricular dilatation that develops in most cases, usually requiring shunting.[8]

Closed spinal dysraphism (CSD)

As skin and neural tissues share a common ectodermal origin, anomalies of both frequently coexist. Clinical detection of a midline skin lesion in an otherwise well baby often triggers a request for imaging to exclude an underlying lesion. Dysraphic abnormalities characterised by a covering of normal skin are classified as closed spinal dysraphism (CSD). The majority are associated with a subcutaneous (usually fatty) mass, or a cutaneous abnormality, such as a hairy tuft, a naevus or a sinus, indicating an underlying developmental anomaly.

Closed dysraphic abnormalities associated with a subcutaneous mass include lipomyelomeningoceles and myelocystoceles (terminal expansion of the central canal of the spinal cord associated with expansion of the dural tube). Those not usually accompanied by a subcutaneous mass include anterior sacral meningocele, split notochord syndrome (including diastematomyelia), dorsal dermal sinus, tight filum terminale syndrome and intraspinal lipomas.

Anterior meningocele

This is a rare entity characterised by a CSF-filled sac that protrudes through a bony defect, usually in the sacrococcygeal region where sacral dysgenesis is usually present. Meningoceles may be asymptomatic or present with bowel/bladder dysfunction and/or a pelvic mass. The sac, by definition, contains no cord tissue (although neuroglial tissue may course through it) and represents a focal expansion of the meninges through an anterior sacral defect.

Ultrasound shows an anechoic fluid-filled sac directly continuous with the spinal canal. Although generally echo-free, the meningocele may be multilocular or traversed by fine adhesions that do not enter the spinal canal. The sac may change size and shape with position or Valsalva manoeuvre.

Spinal lipoma

Spinal lipomas constitute 20–50% of CSDs. These masses of fat and connective tissue are variably encapsulated and have a connection with the leptomeninges or spinal cord. In general lipomas are highly echogenic and relatively easily discernible on ultrasound examination,[2] with accompanying defects of the posterior neural arches and a low position of the commonly tethered spinal cord. Three types occur:

Open spinal dysraphism

Type	Cord position	Investigation
Myelomeningocele	Raised above skin surface	Craniospinal MRI
Myelocele	Level with adjacent skin	Craniospinal MRI
Posterior meningocele	Inside spinal canal	Spinal MRI

Closed spinal dysraphism

With subcutaneous mass	Without subcutaneous mass
Lipomyelomeningocele	Diastematomyelia
Lipomyeloschisis	Dermal sinus
Terminal myelocystocele	Thickened filum terminale
	Intraspinal lipoma
	Anterior sacral meningocele

1. Lipomyelomeningocele and lipomyeloschisis

These constitute up to 50% of skin-covered lumbosacral masses. They present before 6 months of age with a subcutaneous mass, or later in life with neurological symptoms. The subcutaneous component is typically asymmetric, presenting as a fleshy expansion towards one side of the low back or in one buttock.

Large masses of complex echogenic fatty tissue extend deep from the subcutaneous plane into the spinal canal through a posterior spina bifida. The normal relatively hypoechoic subcutaneous fat is deficient at the site of the lipoma. The bony lamina, paraspinal muscles and lumbodorsal fascia are separated in the midline.

The interface between spinal cord and lipoma may lie within (lipomyeloschisis syn: lipomyelocele) or outside of the spinal canal (lipomymelomeningocele). In reality, the majority of lesions straddle the spinal canal with varying degrees of expansion of the underlying subarachnoid space. The meningeal sac may be identified as a discrete transonic pouch within the soft tissue mass or as finger-like transonic projections into the mass, echogenic neuroglial strands forming pseudosepta within the sac. The spinal cord lies in a low position, firmly applied to the posterior aspect of the canal with variable posterior extension into the meningeal sac in the subcutaneous mass (Fig. 67.19).

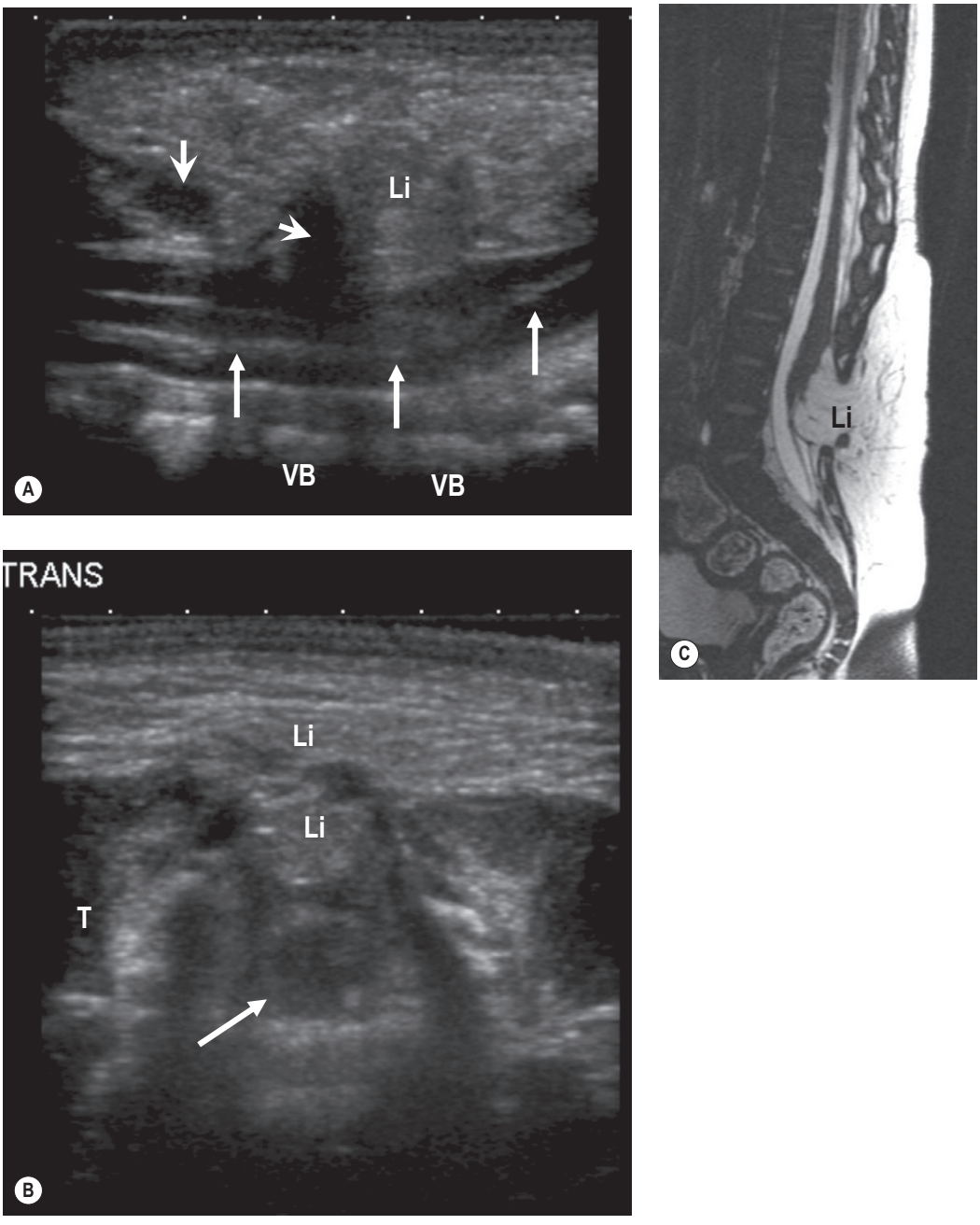

Figure 67.19 **Mixed lipomyeloschisis. A:** Sagittal image in the lumbar region showing a large echogenic lipoma (Li) extending from the subcutaneous region deep to enter the spinal canal through a wide defect in the posterior neural arches of the lower lumbar spine (note absence of echogenic posterior elements), blending with and tethering the low-lying cord (arrows). Focal finger-like projections of CSF-filled pouches are present around the extraspinal part of the lesion (arrowheads). VB, vertebral bodies. **B:** Axial image in the lower lumbar spine. The echogenic lipoma (Li) is difficult to differentiate from adjacent fat but note loss of definition of the normal thin echogenic line of the dermis. The lipoma extends through a wide posterior neural arch defect into the spinal canal to blend with the low-lying cord (arrow). T, transverse process. **C:** Sagittal high-resolution T2 image showing the low-lying cord tethered to the lipoma (Li) entering into the spinal canal.

2. Intradural lipomas

These present with neurological symptoms at any age, but predominantly in the second and third decades. The overlying skin is usually normal; the bony canal can also be normal, but commonly there is focal enlargement and a localised posterior neural arch defect. The lipomas are well encapsulated, often lobulated and occur most commonly in the lumbar region. The lesions are usually subpial, less commonly partially intramedullary or rarely completely intramedullary. On ultrasound imaging the appearances are typically those of a hyperechogenic intradural juxtamedullary mass.[2]

3. Fibrolipoma of the filum terminale (filar lipoma)

The increasing use of MRI has led to the realisation that lipomatous infiltration of the filum terminale is common, found in 1.5–5% of spinal MRIs undertaken for unrelated symptoms, though they may present with symptoms of a tethered cord as late as the seventh decade.[23,24] In many cases the lipoma appears as a small, gracile thickening of the filum terminale located posteriorly in the spinal canal, not infrequently lying away from the midline. These lesions can be easily missed if the possibility is not considered in an infant presenting with cutaneous risk factors. Larger lesions may be identified as an echogenic mass in the filum (Fig. 67.20), particularly when associated with a low-lying cord.

Tight filum terminale syndrome

This is a complex of neurological and orthopaedic deformities associated with a short thick filum and a low position of the conus. A thickened filum terminale is one of several dysraphic abnormalities

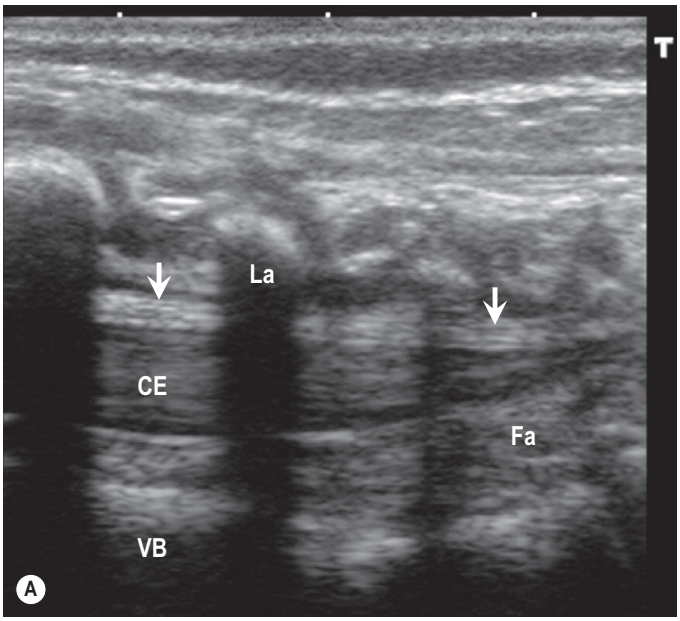

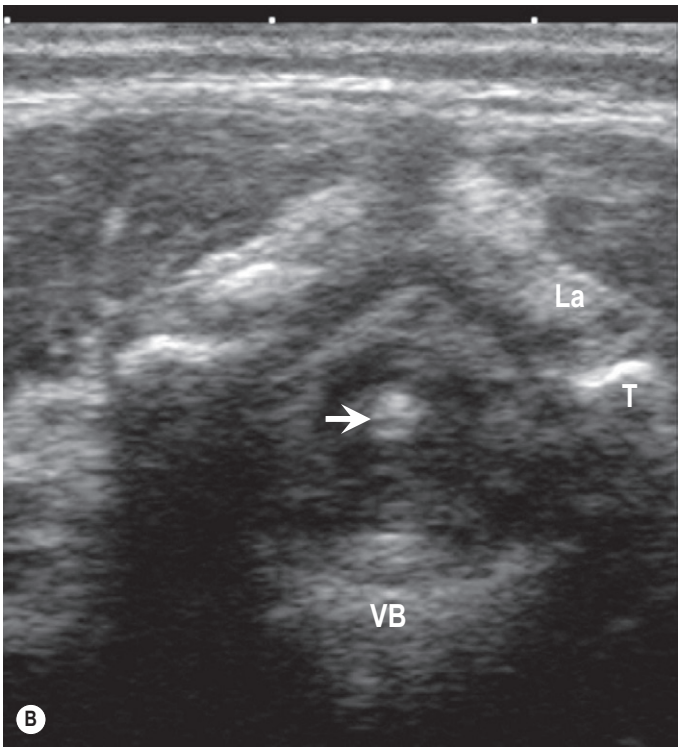

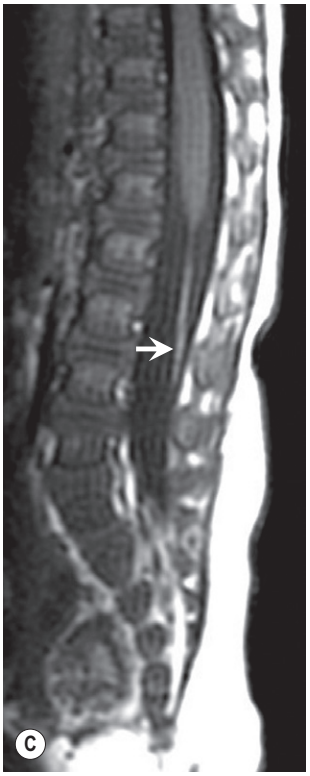

Figure 67.20 Lipoma of the filum terminale. A: Sagittal image in the lumbar region demonstrating a thickened, echogenic filum terminale (arrowheads), which lies posterior to the cauda equina (CE). La, lamina; VB, vertebral body; Fa, epidural fat in the ventral sacral spinal canal. **B:** Axial image in the mid lumbar region. The filum terminale is markedly thickened and echogenic (arrowhead). La, lamina; T, transverse process; VB, vertebral body. **C:** Sagittal T1-weighted image, demonstrating focal thickening and hyperintensity of the filum terminale (arrowhead).

associated with tethering of the spinal cord, resulting in the so-called tethered cord syndrome. With growth, neurological symptoms may develop due to distortion of neural structures, particularly the cord, which may come under increasing tension.

Cord traction and tension may impair cord microcirculation, leading to progressive cord ischaemia.[25] Whilst debate continues as to whether early or even any intervention is indicated to prevent irreversible neurological damage,[26,27] early detection of cord tethering is justifiable in terms of identifying patients at future risk of developing neurological damage.[28] Neurological sequelae include difficulty in locomotion, bladder dysfunction, orthopaedic problems and exertional low back pain. Scoliosis is present in 20%[19] and 50% of patients have an associated cutaneous stigma.

Three criteria are used in the ultrasound diagnosis of a tethering filum terminale:

1. the conus medullaris cannot be identified and separated from an enlarged filum terminale
2. the spinal cord adopts an abnormal position, lying in the dorsal thecal sac (Fig. 67.21)
3. normal cord movement is damped or absent.[3]

The filum is thickened (more than 2 mm at the L5/S1 level) and in 30% of cases contains an echogenic fibrolipoma.

Sonographical features of cord tethering

- Low-lying conus (below L2/3)
- Cord lies posteriorly in spinal canal
- Cord movements damped or absent
- Cord adherent to mass (lipoma, dermoid, subcutaneous mass)
- Cauda equina movements damped or absent
- Filum thickened, echogenic

Diastematomyelia

Diastematomyelia is partial or complete sagittal clefting of the spinal cord into two hemicords (not necessarily symmetrical), each containing a central canal. Each hemicord is associated with its own dorsal and ventral nerve roots. Cutaneous stigmata of the underlying abnormality are present in 50–75% of cases and cord tethering in 75%.[29] The patient may present with signs and symptoms at any age. Females are much more commonly affected than males (9:1). Orthopaedic problems are present in over 50% of cases. The neurological symptoms are non-specific.

Type I diastematomyelia (40–50%): a fibro-osseous bony spur is interposed between the two hemicords.[30] The fibro-osseous spur determines that each hemicord lies in its own dural tube. Vertebral anomalies, including a range of malsegmentation anomalies, and scoliosis are common.[31]

Type II diastematomyelia (50–60%): both hemicords lie within a single dural tube, continuous with the normal thecal sac, with no interposed fibro-osseous spur. The most common location is the thoracolumbar region (50–75%); however, they may also be seen elsewhere including the cervical spine.

Hydromyelia occurs in 50% of cases, more commonly in type I diastematomyelia. The spine is nearly always abnormal.

The bony anomalies make ultrasound examination difficult. The spinal cord typically terminates at an abnormally low level. At the level of the diastematomyelia two hemicords are seen lying side by side or less commonly dorsoventral to each other. In type I cases, an echogenic bony spur and/or hydromyelia may be identified. The hemicords usually combine to reform a single cord.[5] Less commonly the two hemicords do not rejoin below the cord cleft, continuing as separate, thickened fila terminale. The spinal canal is enlarged and the vertebral bodies are often widened and abnormal in appearance.

In type II the spinal cord may be partially or completely split into two hemicords of variable size (Fig. 67.22). A fibrous septum may be present in the latter, although this may be very subtle, evading detection.

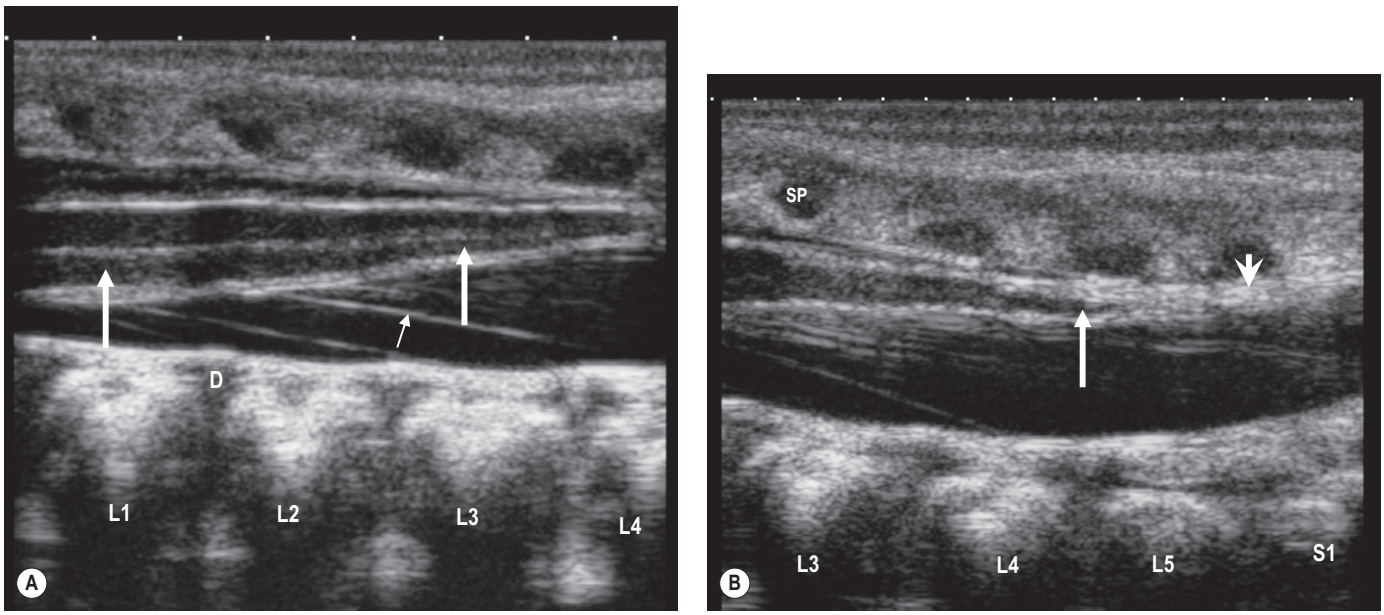

Figure 67.21 Tethered cord. A: Sagittal image in the lumbar spine of a low tethered cord. The cord (arrows) is displaced and held posteriorly within the thecal sac (real-time imaging showed no cord movement). Note nerve roots (small arrow) extending anteriorly through the CSF within the thecal sac. D, intervertebral disc; L, lumbar vertebra. **B:** Sagittal image of lower lumbar canal. The cord is held tightly posteriorly in the thecal sac, tapering down to the conus medullaris, which is located at the L4/5 level (white arrow). The filum terminale is thickened and echogenic (arrowhead). SP, spinous process; L, lumbar vertebral body; S, sacral vertebral body.

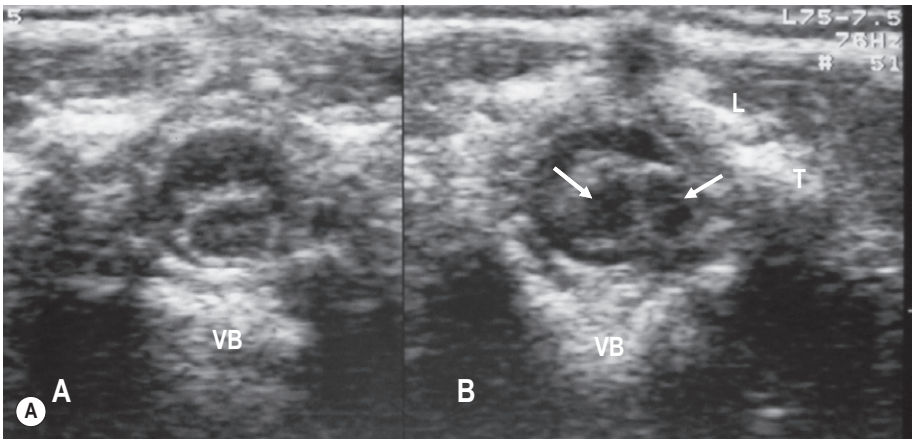

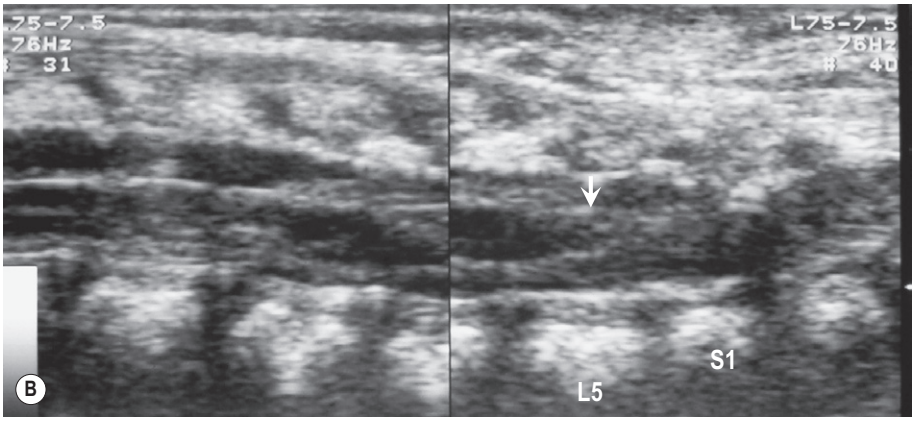

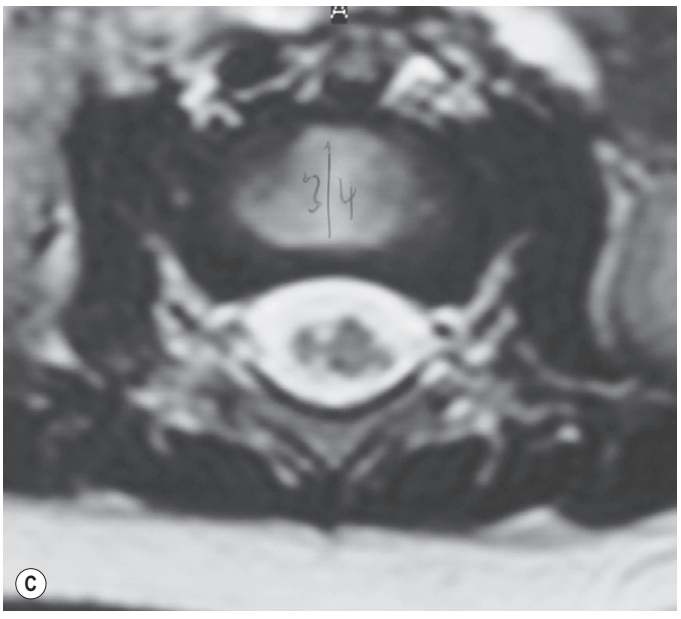

Figure 67.22 Type II diastematomyelia. **A:** Axial images immediately rostral to (left image) and at the level of (right image) the cord split, which lies within a single dural tube. Note the two separate hemicords (arrows). L, lamina; VB, vertebral body; T, transverse process. **B:** Sagittal combined image with partial overlap. The cord is low-lying with the conus at mid L5 (arrowhead). There is subtle distortion of the cord anatomy with loss of clear visualisation of the central echo complex, which should raise suspicion of a cord clefting defect. **C:** Axial T2 MR image at the L3/4 level. There is asymmetric clefting of the cord, with a larger left hemicord. Note absence of an intervening fibro-osseous septum.

Dorsal dermal sinuses

Dorsal dermal sinuses are epithelial lined tubes extending inwards from the skin surface for varying distances. Approximately 50% extend into the spinal canal up to the thecal sac or pierce the dura to enter the thecal sac. Dermal sinuses extending into the thecal sac may terminate within the spinal canal as an echogenic dermoid cyst or may adhere to the spinal cord.

Dermal sinuses occur anywhere from the skull to the coccyx, though the majority arise in the lumbosacral region. A history of intermittent discharge of fluid from a pit or sinus should be sought; recurrent episodes of meningitis in early life should act as a red flag sign for a dermal sinus located somewhere along the neuraxis and calls for careful examination of the skin over the entire spine and head.

The cutaneous lesion may be tiny, with a midline or occasionally a paramedian ostium that may contain hairs. There are frequently other associated cutaneous stigmata but the ostium may be difficult to identify and not infrequently evades detection.

On ultrasound scanning the sinus track may appear as an echogenic tube if the lumen is narrow, or with a hypoechoic centre if the lumen is wide enough to resolve (Fig. 67.23). The track extends obliquely, initially caudally, to the spinal column, piercing the lumbodorsal fascia, and then in a cephalad direction into the spinal canal. Intraspinal extension can be difficult to assess, but may be inferred by a low-lying spinal cord or an associated echogenic mass within the thecal sac or cord, suggesting a dermoid or matted nerve roots from arachnoiditis. Full evaluation with MRI is the definitive examination.[5,19]

Caudal regression syndrome (CRS)

This group of disorders involves varying degrees of dysgenesis of the sacrococcygeal spine and may occur in association with abnormalities of genitourinary, gastrointestinal and pulmonary structures; there is a recognised association with maternal diabetes mellitus. CRS may be associated with syndrome complexes such as VACTERL (vertebral abnormality, anal imperforation, tracheo-oesophageal fistula, renal abnormalities, limb deformities) and Currarino's triad (see below).[19,20]

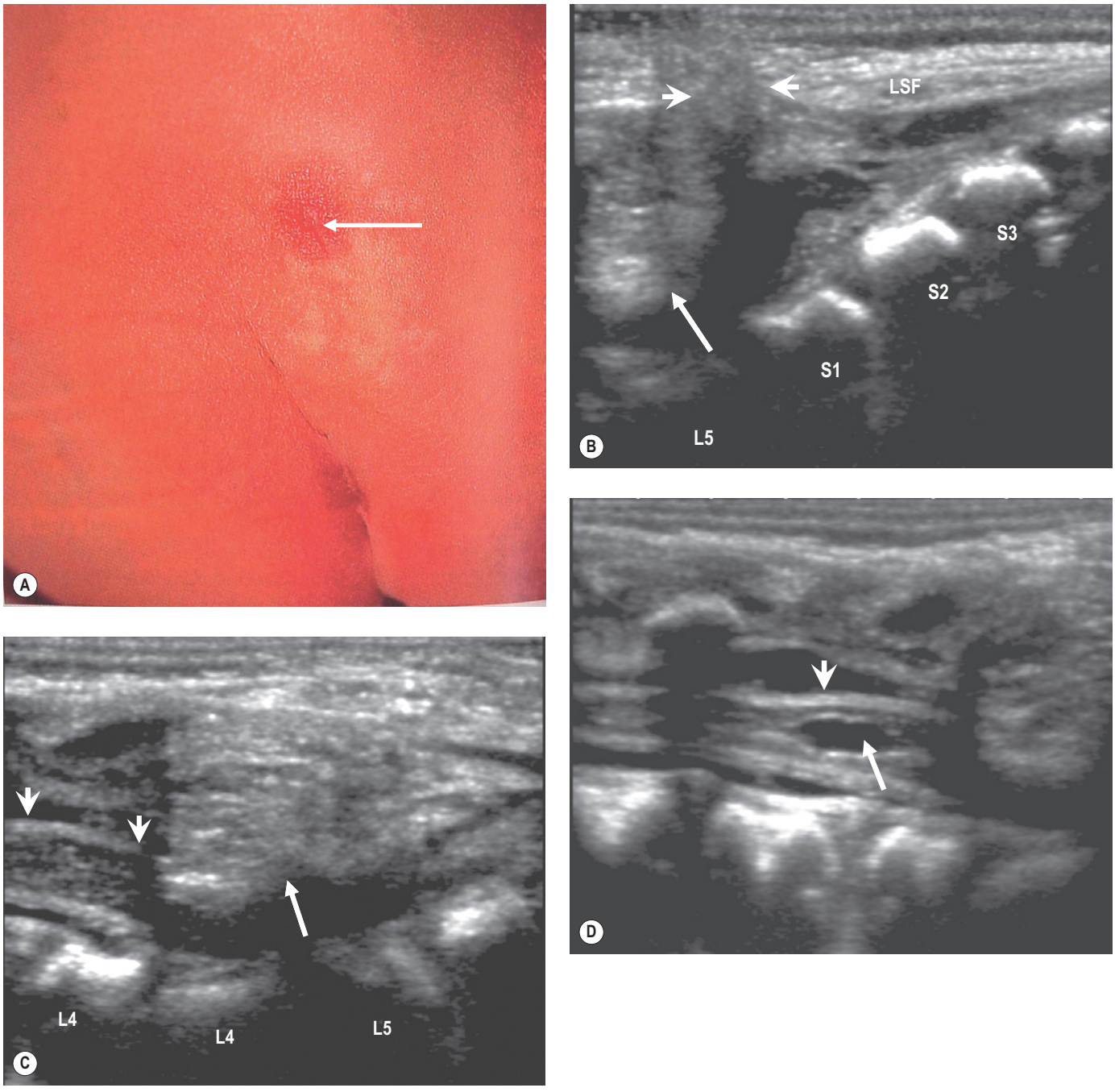

Figure 67.23 Dermal sinus and dermoid cyst. A: Photograph of the back of a 2-week-old baby presenting with a discharging sinus in the lower lumbar region. A small cutaneous pit is present just off the midline (arrow). **B:** Sagittal image in the lumbosacral region. There is a poorly defined hypoechoic channel (arrowheads) breaching the lumbosacral fascia (LSF), extending deep from the skin surface to the spinal canal to blend with a hyperechogenic mass within the spinal canal (arrow). **C:** Sagittal image in the lower lumbar region. The intraspinal mass (arrow) is well defined and echogenic. The spinal cord (arrowheads) is displaced anteriorly and is tethered by the mass. L, lumbar vertebral body. **D:** Sagittal image in the mid-lumbar region. The cord is mildly swollen (arrowhead) and contains a discrete small hydrosyringomyelic cavity (arrow).

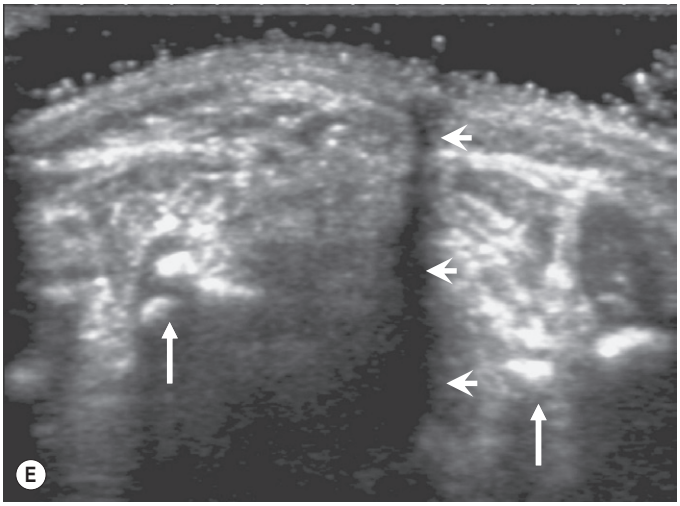

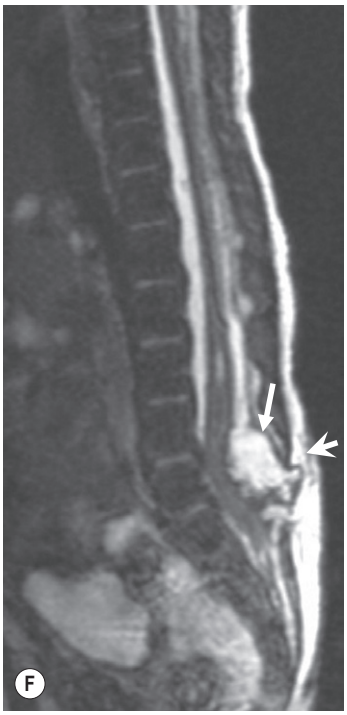

Figure 67.23 *Continued* **E:** Axial image at level of the discharging cutaneous pit. The dermal sinus track is hypoechoic (arrowheads), extending deep into the spinal canal through a wide posterior neural arch defect. The everted posterior neural arch is seen to be widely splayed (arrow). **F:** Sagittal high-resolution T2 image. A dermal sinus (arrowhead) extends caudally into the spinal canal, where it blends with a discrete mass (arrow) adherent to the dorsal surface of the tethered cord. The syrinx seen on ultrasound (Fig. 67.23D) can be identified as a poorly defined linear hyperintense streak in the spinal cord.

The CRS is divided into:

- Type I – severe or total sacral agenesis with an abnormally high location of the cord, which may have an abruptly truncated or 'sawn-off' configuration. In most cases, the last spinal segment is L5–S2. Tethering of the cord is generally not present.
- Type II – the commonest manifestation of CRS, with a variable degree of sacral hypogenesis which is accompanied by an elongated and stretched spinal cord, often tethered by a thickened filum terminale.[19] Less frequently the low-lying cord may be tethered by an intradural lipoma, lipomymelomeningocele or anterior sacral meningocele.

On ultrasound scanning, the dysgenetic sacrum and absent coccyx are readily identified by loss of visualisation of the normal five echogenic sacral vertebral segments and hypoechoic coccyx (Fig. 67.24A). In a minority of cases, where there is only minimal sacral hypogenesis, the conus will be normally located; however, in most cases detailed scanning will detect a low-lying conus (Fig. 67.24B) and thickened filum, particularly when associated with a filar lipoma, which is more easily identified by MRI (Fig. 67.24C).

Syringomyelia and hydromyelia

Syringomyelia and hydromyelia are cystic abnormalities of the spinal cord. Syringomyelia refers to an abnormal CSF-filled cavity within the cord, lying external to the central canal of the cord and lined by glial cells. Hydromyelia is characterised by an accumulation of CSF within an enlarged central canal of the spinal cord, lined by ependymal cells. Syringomyelia (or syrinx) is the generally used term that encompasses both. In reality, clinical findings and imaging cannot differentiate between the two.

Syringomyelia may be focal or may extend to involve the full length of the cord, and is associated with a range of spinal dysraphic abnormalities. On ultrasound the cord may be enlarged and the normal single central echo split (see Fig. 67.25), the anterior and posterior walls of the central canal being separated by anechoic fluid.

Syringomyelia should be clearly differentiated from a dilated ventriculus terminalis, which represents incomplete embryonal regression of the terminal vesicle. The latter occurs immediately cephalad to a normally located conus medullaris, is not associated with other dysraphic anomalies and is non-progressive on follow-up MRI.

Cutaneous pits, dimples, skin tags, clefts and sinuses

The commonest request for spinal ultrasound imaging in the neonatal period is for exclusion of dysraphism in a baby found to have a cutaneous abnormality of the lower back during a routine postnatal check. Clinicians are frequently unclear as to which lesions warrant imaging and if so what type of imaging is required. Over 90% of patients with CSD will have some form of cutaneous stigmata heralding the underlying abnormality. Cutaneous markers of CSD include localised hairy patches or tufts, atypical dimples (deep, more than 5 mm above the gluteal cleft), cutaneous pits away from the midline, vascular lesions such as haemangioma/telangiectasia (but not a Mongolian blue spot), a skin tag or subcutaneous (fatty) mass. If only one of these cutaneous markers is present, the risk of an underlying CSD is less than 1%.[32] Co-occurrence of two or more significantly increases the likelihood of an associated CSD.[33]

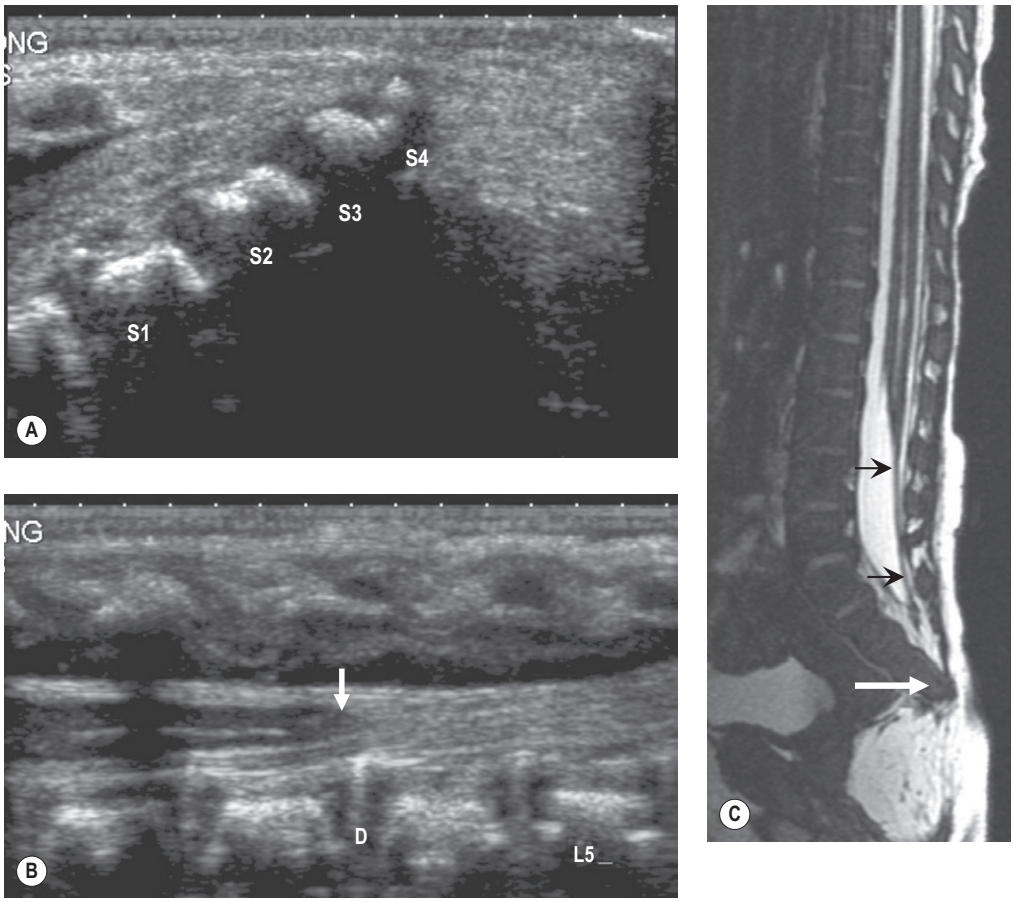

Figure 67.24 Caudal regression syndrome. A 3-day-old baby with sacral hypogenesis and a low tethered cord. **A:** Sagittal image in the sacral region showing a dysgenetic sacrum, a small fourth sacral segment and absent fifth segment and coccyx. **B:** Sagittal image in the lower lumbar region. The spinal cord is low-lying, the conus (arrow) being at the L3/4 level. D, intervertebral disc. **C:** Sagittal high-resolution T2 image. The dysgenetic sacrum is more clearly defined (arrow), as is the low-lying cord and thickened tethering filum terminale (arrowheads).

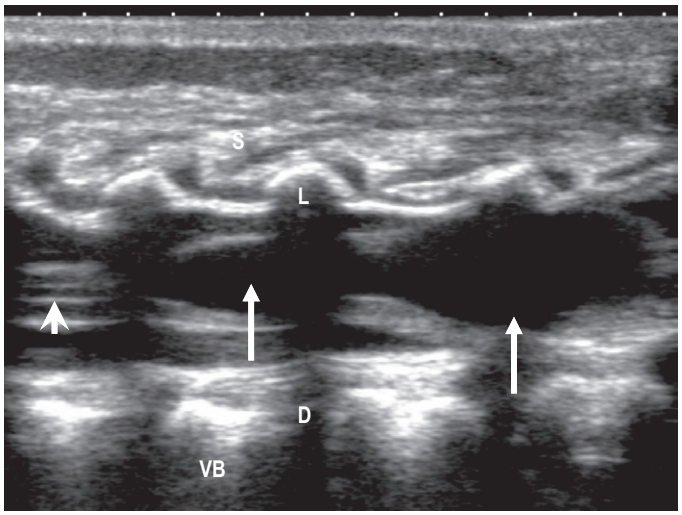

Figure 67.25 Syringomyelia in a low tethered spinal cord. Sagittal image in the upper lumbar region. There is a large hydrosyringomyelic cavity (arrows) in the enlarged spinal cord, tapering down to the central echo complex (arrowhead). VB, vertebral body; D, intervertebral disc; L, lamina; S, spinous process.

In a retrospective study of 223 infants who had undergone spinal ultrasound examinations over a 10-year period, 29 had CSD lesions.[34] In all 86 patients with simple sacral dimples, pits or sinuses none had evidence of an underlying dysraphic lesion. In a separate study of 207 term babies, 216 cutaneous stigmata were detected on clinical examination, of which 180 were dimples; the remaining 36 had haemangiomas, hairy patches, subcutaneous masses or tails.[35] None of the patients with a simple midline dimple had a spinal dysraphic abnormality. Of the 36 with other cutaneous stigmata, 14 (39%) had a dysraphic lesion. In 20 cases, there was an atypical dimple and of these, 8 had an underlying dysraphic lesion. In all 8 cases, the clefts occurred more than 2.5 cm from the anus; the clefts were large (>5 mm) in 3, and 5 had other cutaneous stigmata. The authors concluded that only atypical dimples, those more than 2.5 cm from the anus or associated with other cutaneous stigmata carry a significant risk of dysraphism.

Diffuse lower lumbar hairiness, a skin pit or dimple located within the natal cleft (less than 2.5 cm above the anus) or simple deviation of the gluteal fold is almost always innocent. Although routine scanning for simple natal cleft pits is unnecessary and should be discouraged, demonstration of normality can be reassuring for both parents and clinicians. When there are two or more cutaneous markers, detailed ultrasound serves as an excellent screening tool. The presence of a skin tag in a low lumbosacral location, particularly if accompanied by an anorectal malformation, has a significant risk of an associated CSD (Fig. 67.26).

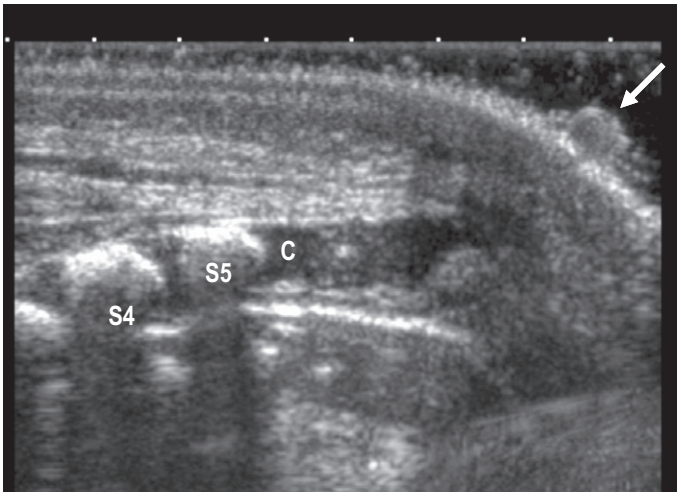

Figure 67.26 Skin tag in a newborn baby. Sagittal image through the sacrum and coccyx (same case as Fig. 67.21). A small skin tag (arrow) overlies the caudal most part of the coccyx (C). There is focal distortion of the tip of the coccyx and disruption of the normal subcutaneous and deep fascial layers.

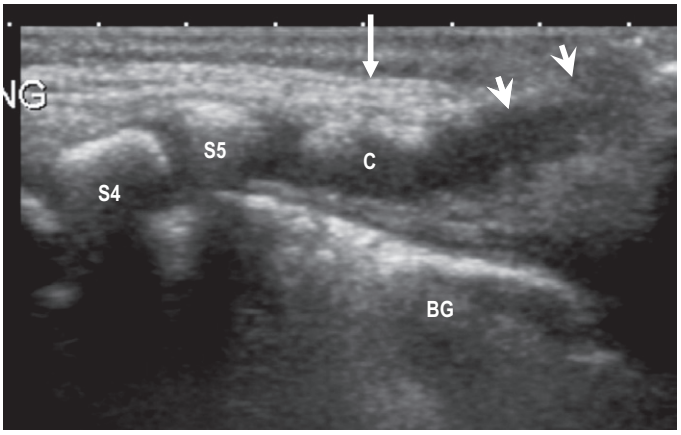

Figure 67.27 Coccygeal tract. Three-day-old baby presenting with a low gluteal cleft cutaneous pit. Sagittal image showing a hypoechoic tract (arrowheads) extending from the tip of the coccyx to the skin surface, breaching the deep fascia (arrow). S, sacrum; C, coccyx; BG, bowel gas.

If undertaken in neonates with isolated simple cutaneous pits or low risk dimples (<5 mm diameter and <2.5 cm from the anus), particularly coccygeal lesions, ultrasound is almost always normal. Coccygeal pits are common, occurring in up to 4% of the population.[32,35] In some cases a hypoechoic track may be identified extending from a coccygeal pit down to the coccyx (Fig. 67.27). The track may breach the deep fascial layer but does not extend into the spinal canal. An integral part of the examination must, however, be an assessment of the spinal canal to exclude an intraspinal anomaly.

Trauma

Injury to the spinal cord in early infancy usually occurs during birth. A less common aetiology is inflicted injury (the so-called shaken impact syndrome), where the brainstem and upper spinal cord may suffer shear-stress injuries. These infants suffer injuries that rarely result in macroscopic, imageable cord, brainstem or soft tissue damage, in contrast to birth-related cord damage.

Sonographical features of cervical cord injury

- Focal or diffuse cord expansion
- Focal or diffuse hyperechogenicity
- Loss of visualisation of central echo complex
- Echogenic extra-axial collections (subdural haematoma)

Although recognised for over a century, spinal cord injury is often overlooked in stillbirth, perinatal death or severe neurological morbidity in the newborn, when the lesion may be ascribed to an intracranial catastrophe. Towbin ascribed severe spinal cord or brainstem injury as a causal factor in 10% of neonatal deaths in the USA.[36] Difficult breech extraction is the commonest cause,[36–39] although there are several reports associated with difficult cephalic deliveries[40,41] and hyperextension of the fetal neck in utero.[39]

There are well-recognised predisposing factors, particularly prematurity, asphyxia, dystocia and intrauterine malposition.[39,42,43] A unifying mechanism is longitudinal stretching of the cord associated with hyperextension of the head and/or rotational forces related to forceps manipulation.[37–40] Liberalisation of the criteria for caesarean section has led to a reduction in the incidence of these injuries, which are now rare.

Most lesions associated with breech deliveries occur in the lower cervical and upper thoracic segments.[37–39] Those related to cephalic deliveries tend to affect the upper cervical cord (above C4).[40,41,44] Cord laceration or even transection may result from either impaction of neural tissue on adjacent bony structures or vertebral dislocation, although clinically evident skeletal injury is rare. Vascular mechanisms have also been implicated, with disruption of the arterial supply to the cord at watershed areas such as the cervicothoracic junction.[36,45]

Ultrasound evaluation of the cervical spine and craniocervical junction has been shown to provide good morphological delineation of this region.[46–48] The infant may present with a complete neurological deficit at or below the brachial plexus level in the commoner lower cervical segment injuries. Those suffering an upper cervical or brainstem lesion are more profoundly affected and may be ventilator dependent from birth, early death being an almost invariable outcome. Ultrasound examination offers the least disruptive form of investigation, enabling a high-definition cotside assessment of the whole neuraxis.

In the acute phase cord injury may be identified as either complete discontinuity, indicative of transection, or focal swelling. At birth, cord myelination is immature and the water content is relatively high. As a result, normal cord appears relatively hypoechoic and the central echo complex is readily discernible. Loss of visualisation of the normal cord anatomy coupled with abnormal cord echogenicity and cord swelling enables ready detection of acute cord injury (Fig. 67.28A–C). The abnormal echogenicity most probably reflects a combination of oedema and haemorrhagic contusion.[49]

The high water content of the normal spinal cord in the infant results in a hyperintense appearance on T2-weighted MR images. As acute injury is manifested primarily by oedema, which is identified by T2 hyperintensity, cord damage may be difficult to detect or define fully on MRI in the first few days of life (Fig. 67.28C). If the child survives, the cord swelling recedes. Extra-axial haemorrhage within the spinal canal and cisterna magna or in the extraspinal soft tissues may also be seen with acute injuries. CT may fail to detect the acute cord injury but may identify the extra-axial haemorrhage, particularly subdural haematoma that frequently accompanies such injuries. T1-weighted MRI generally provides optimal demonstration of subacute extra-axial haemorrhage, particularly subdural haematoma, in this region (Fig. 67.28D); however, it is difficult to perform on a vulnerable infant and specialised MRI compatible equipment is required.

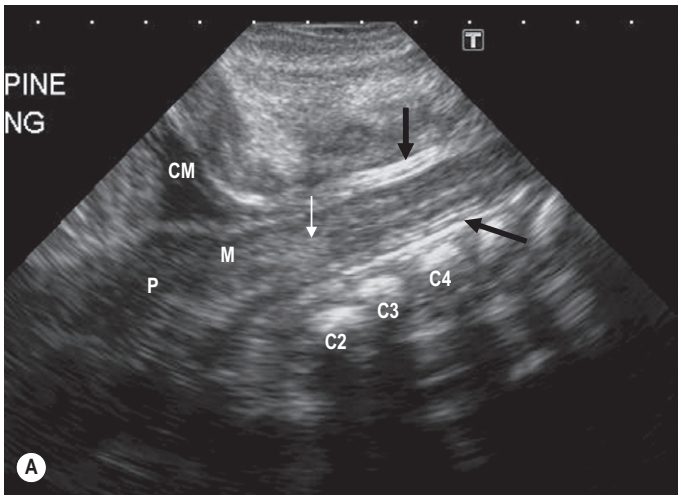

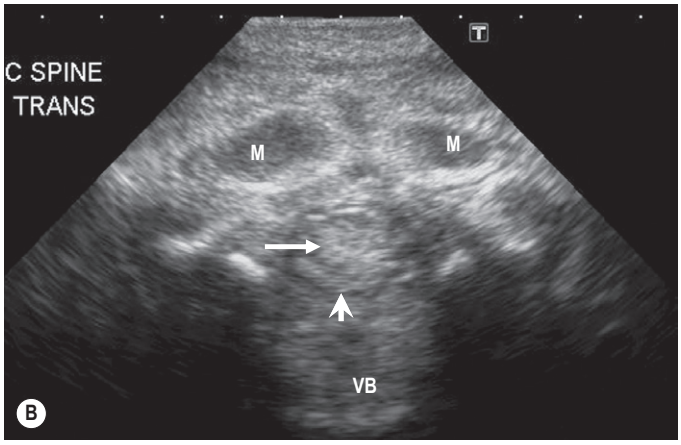

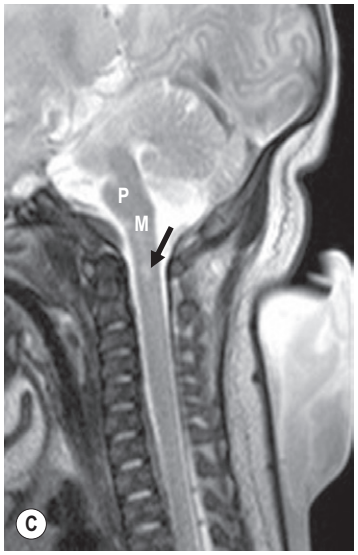

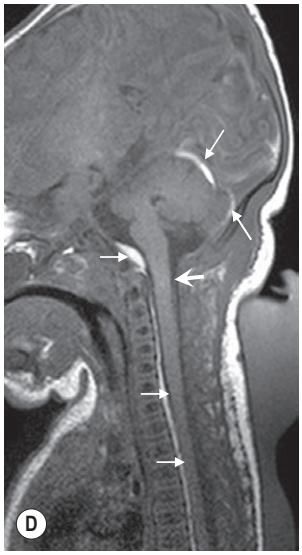

Figure 67.28 **Cervical cord trauma. A:** Sagittal image in a 2-day-old baby with absent limb movements and respiratory distress following a difficult forceps delivery. There is focal cord echogenic abnormality at the C1/2 level (arrow), extending up towards the medulla (M). Extra-axial echogenic haemorrhage is present dorsal and ventral to the cord (black arrows), probably in the subdural space. The normal cord hypoechogenicity and central echo complex is lost in the affected segment of the cord but is revisualised at C4. P, pons; CM, cisterna magna. **B:** Axial image at the C1/2 level. The mildly swollen cord is diffusely echogenic (arrow) with loss of visualisation of the central echo complex. M, paraspinal muscles; VB, vertebral body; arrowhead, extra-axial, probable subdural, haematoma. **C:** Sagittal T2 MR image at 4 days of life. There is a poorly defined hyperintense (bright) area of abnormality at the C2 level (arrow), extending rostrally into the medulla (M). P, pons. **D:** Sagittal T1 image. There is subtle hyperintensity at the C2 level (arrowhead), indicative of blood products (extracellular methaemoglobin). There is hyperintense (bright) subdural haematoma in the posterior fossa over the cerebellar hemispheres, dorsal to the clivus and in the spinal canal (arrows).

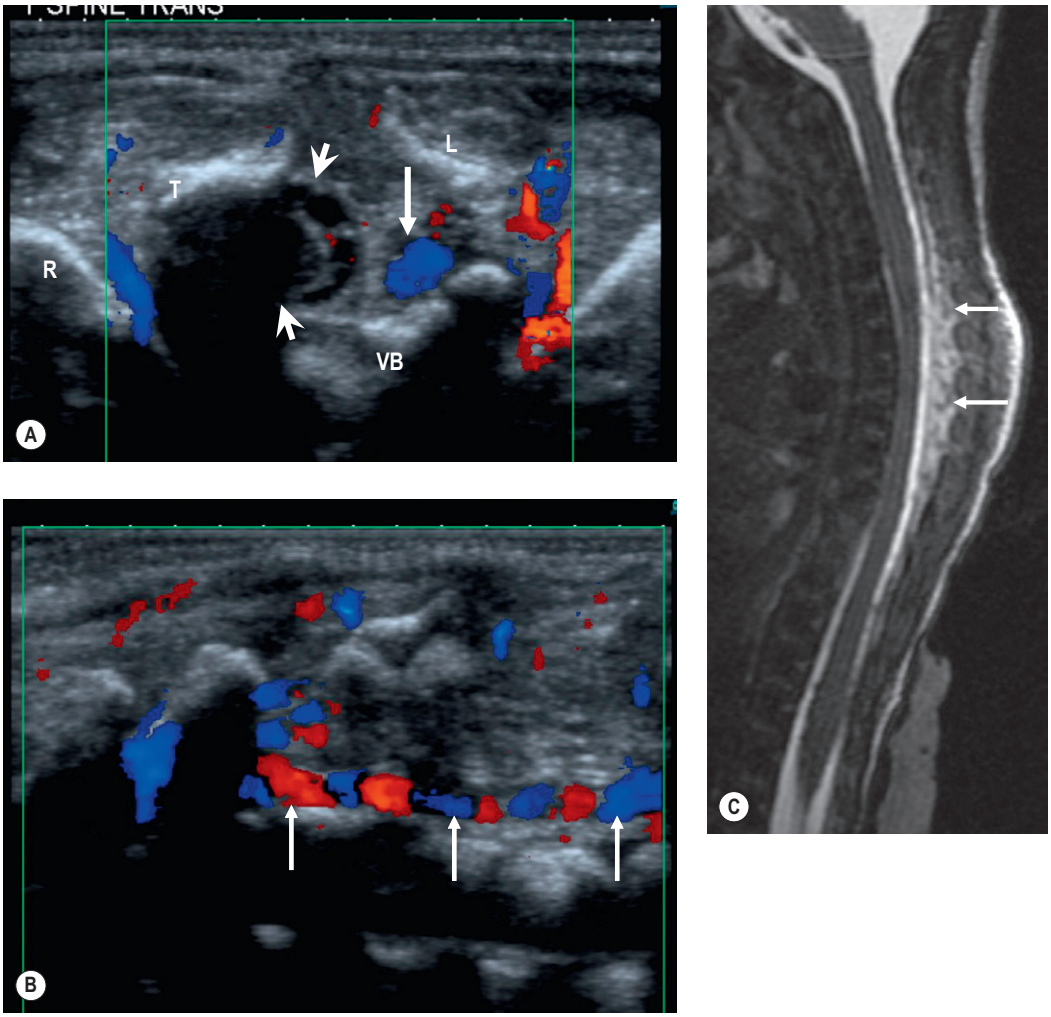

Figure 67.29 Spinal column deformity. A: Axial colour Doppler image at the apex of a complex mid-thoracic scoliotic deformity in a 2-day-old infant. Prenatal imaging showed an expanded spinal canal associated with vertebral body and neural arch defects but a normal spinal cord. The thecal sac and spinal cord (arrowheads) are displaced to the right side of the spinal canal with epidural fat and prominent veins (arrow) filling the left side of the canal. L, lamina; T, transverse process; R, rib; VB, dysplastic wide vertebral body. **B:** Parasagittal colour Doppler image demonstrating the enlarged vertebral venous plexus (arrows). **C:** Sagittal 3D T2 volume image, reconstructed to compensate for the scoliosis, demonstrating a normal spinal cord. Note irregular signal voids in the enlarged epidural fat (arrows).

High quality ultrasound seems to be at least as accurate as MRI in the investigation of suspected acute spinal cord damage in the neonate.[46] A combined approach is, however, recommended. In cases where the spinal cord appears entirely normal, cranial ultrasound should be performed to exclude an intracerebral cause for any neurological deficit. Where spinal ultrasound is abnormal or equivocal, MRI should be obtained to confirm the ultrasound findings. Confirmation of the presence of a spinal injury is important, both to guide the infant's future management and, increasingly, for medicolegal documentation.

Vascular anomalies

Vascular anomalies do not tend to present during infancy. Colour Doppler imaging permits localisation of normal vascular structures and offers the opportunity for haemodynamic assessment of the intraspinal contents in the normal and diseased states. Experience in this area is as yet limited. Prominence of the normal vertebral venous plexus is a normal finding in infancy. Expansion of the vertebral venous plexus may also be seen in association with an enlarged spinal canal that may occur with complex vertebral column anomalies, which does not necessarily reflect a vascular malformation (Fig. 67.29). CDI may be helpful in demonstrating or confirming a vascular nature of a discoloured subcutaneous mass, and also for excluding any deep extension into the spinal canal (Fig. 67.30).

Tumours

Compared to adults, childhood tumours involving the spinal canal and its contents are relatively infrequent, accounting for only a small percentage of spinal tumours in the first decade of life.[50–52] The presentation is often misleading, the signs and symptoms being frequently non-neurological. Motor weakness and, to a lesser extent, spinal deformity may be the only objective indicators. Spinal tumours have traditionally been compartmentalised into extradural and intradural lesions. Sacrococcygeal tumours are considered separately.

Determination of which spinal compartment a lesion lies in depends upon identification of the dural sac wall. An extradural location of a lesion can be ascertained by demonstrating displacement of the dura from the margins of the spinal canal on either side

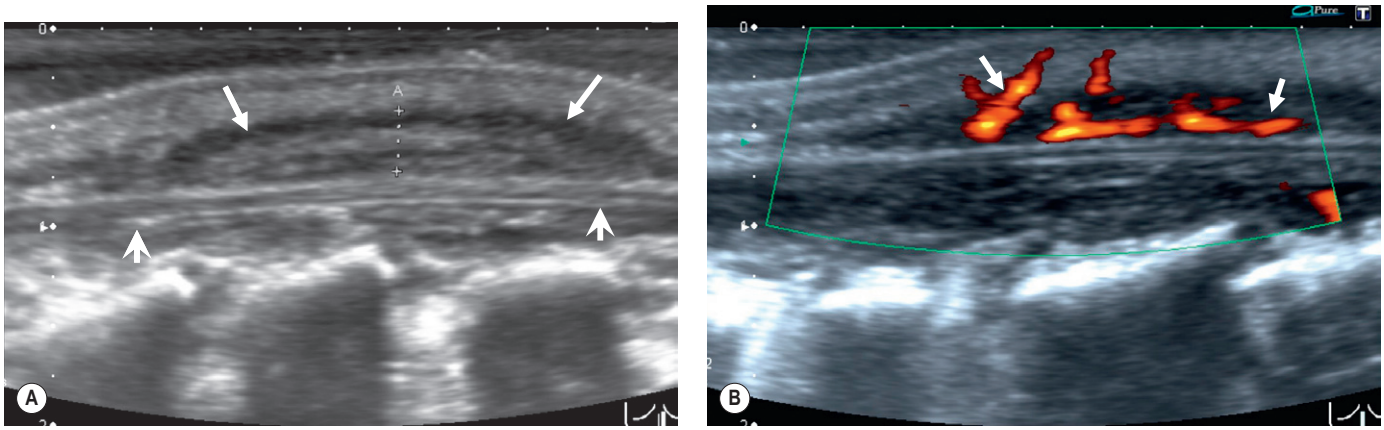

Figure 67.30 Subcutaneous vascular malformation. A: Sagittal image over a low lumbar subcutaneous mass (arrows), which is hypoechoic, containing central linear echoes, overlying the lumbodorsal fascia (arrowheads) and underlying echogenic posterior neural arches. **B:** Axial image at same level employing colour Doppler imaging. Prominent vessels are readily detected within the lesion (arrows), indicating its vascular nature (pulsed Doppler image, not shown, showed venous waveform). Conservative management has been elected for, the lesion being assumed to represent a venous phase low-flow vascular malformation.

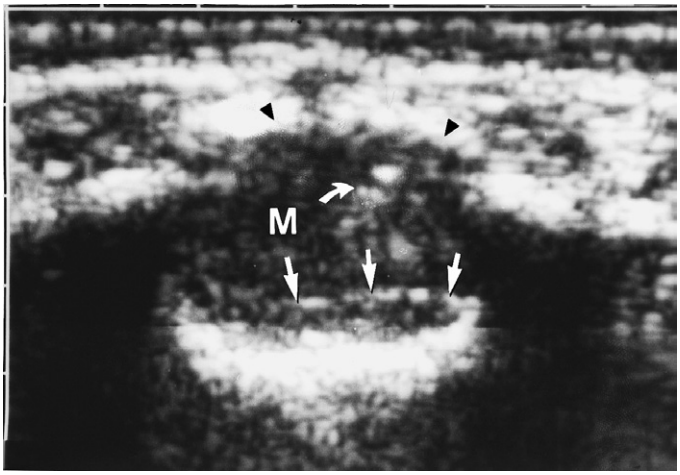

Figure 67.31 Localisation of intraspinal compartments. Axial ultrasound image in a 3-month-old infant. A large extradural mass (M) lies dorsal to the thecal sac, which is compressed anteriorly but clearly identified by its highly reflective margins (arrows). Note the calcifications within the tumour (curved arrow). Arrowheads indicate lamina.

of the mass (Fig. 67.31). With intradural lesions the dura remains in a normal position, closely apposed to the bony spinal canal margins. Intramedullary masses appear as discrete or more diffuse heterogeneous hyperechogenicity intrinsic to an expanded spinal cord, readily distinguishable from the uniformly hypoechoic normal cord. A severely enlarged cord is associated with widening of the spinal canal. Intratumoral cysts appear as transonic cavities within echogenic tumour matrix. In contrast, extramedullary tumours compress the cord and displace it away from the mass; the normal ring-like integrity of the thecal sac wall is, however, maintained.

Extradural tumours

The most important extradural tumour encountered in infancy is the neuroblastoma, with a higher incidence in females (2:1).[53] Derived from neural crest cells, these tumours are endocrinologically active, producing catecholamines that can be measured in the urine. They arise most frequently in the adrenal medulla but may occur at the site of any sympathetic nervous tissue, particularly in the paravertebral abdominal region.

Intradural tumours

Compared to brain tumours, spinal cord tumours are much less common in children. Astrocytomas (60%) and ependymomas (30%) form the large majority of intramedullary lesions,[54,55] with an upper spinal predominance. The presentation in infants may be primarily with weakness, especially of the upper limbs, rigidity or severe pain. Expansion of the spinal canal is often present on ultrasound, astrocytomas showing mixed or reduced echogenicity. Peritumoral cysts are present in 20–40% of cases.[55] MRI is the imaging modality of choice for the investigation of intraspinal lesions in childhood,[56] and is the examination of choice in the infant, particularly after the first few weeks of life.

Extramedullary tumours such as meningiomas, schwannomas and neurofibromas are rare in early childhood. However, CSF seeding of intracranial tumours is more common than in adults and so is particularly important in childhood. Posterior fossa medulloblastomas are the most common source, particularly the well-differentiated histological types; however, ependymomas, germ cell tumours, low-grade (pilocytic) astrocytomas and glioblastoma multiforme all share an increased propensity for spinal CSF-borne spread.[57] Detection of metastatic spread is the preserve of T1-weighted contrast-enhanced MRI,[58] leaving little role for ultrasound.

Sacrococcygeal tumours

These rare congenital tumours are derived from pluripotential cells from the trilaminar germinal disc. Presentation is with a large skin-covered sacral soft tissue mass. There is an increased incidence of other malformations associated with caudal cell mass aberrations, such as anomalies of the anorectum, genitourinary tract and sacral vertebrae.[59]

Sacrococcygeal teratomas occur most frequently in females (3:1) and are benign in 80% of cases. In descending order of frequency they occur as purely dorsal sacral lesions; combined external and presacral masses; entirely presacral; primarily intra-abdominal; or pelvic and intraspinal.[60] Ultrasound reveals a heterogeneous mass which may contain intratumoral calcifications (Fig. 67.32). Spinal canal expansion or sacral erosion may be seen. The tumour may displace or surround the caudal spinal roots.

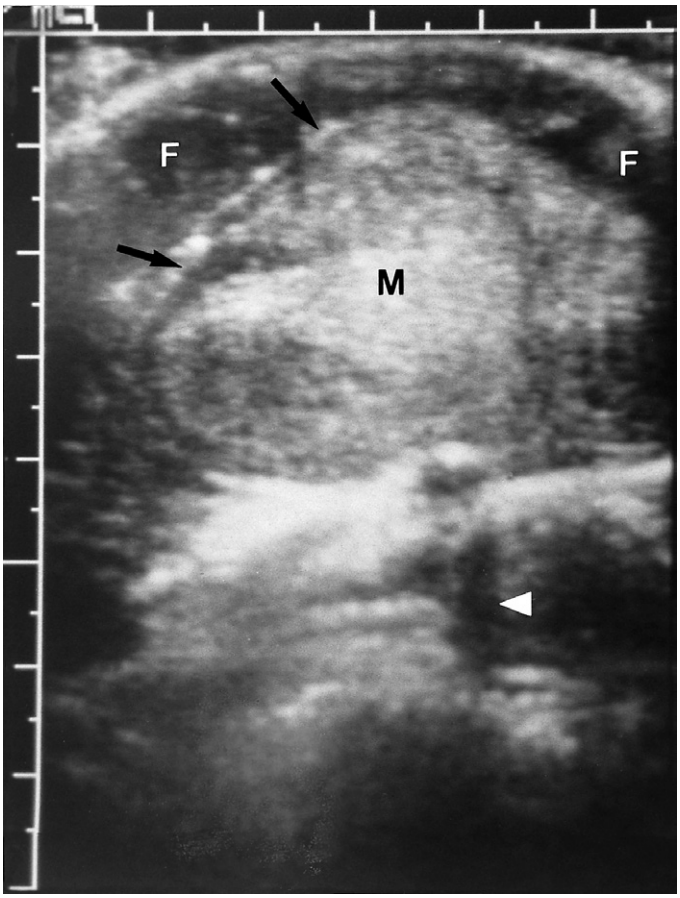

Figure 67.32 Sacrococcygeal teratoma. Axial ultrasound image in a 27-month-old female presenting with a large, tense mass below the natal cleft. A myelogram performed at 3 months of age for a deep natal cleft pit was normal. The tumour (M) is of heterogeneously increased reflectivity. The lesion appears well encapsulated (arrows), as found at surgery. Subcutaneous fat (F) surrounds the mass. A deep extension (arrowhead) consisted mainly of tumour cyst.

Currarino's triad

Currarino's triad is a rare hereditary condition characterised by complex caudal anomalies consisting of (1) an anorectal malformation, (2) sacral bony defect and (3) a presacral mass.[61,62] The underlying defect probably reflects abnormal endo-ectodermal adhesions and/or notochordal defects in early gestational life, resulting in development of a fistula between the gut and spinal canal. Enteric elements will be associated with the ventral end of the defect and neural elements at the dorsal end. The more commonly associated presacral masses include ventral meningocele, benign teratoma, dermoid cyst and lipoma. Duplication cysts of the vagina, uterus and urinary tract may be occasional findings. Ultrasound in the first few days of life may identify the presacral anechoic meningocele or a more complex echogenic mass associated with an anterior defect of the body of the sacrum (Fig. 67.33). Once identified, MRI is required for more complete evaluation and as a baseline for future imaging, which is frequently required for the surgical management of these difficult cases.

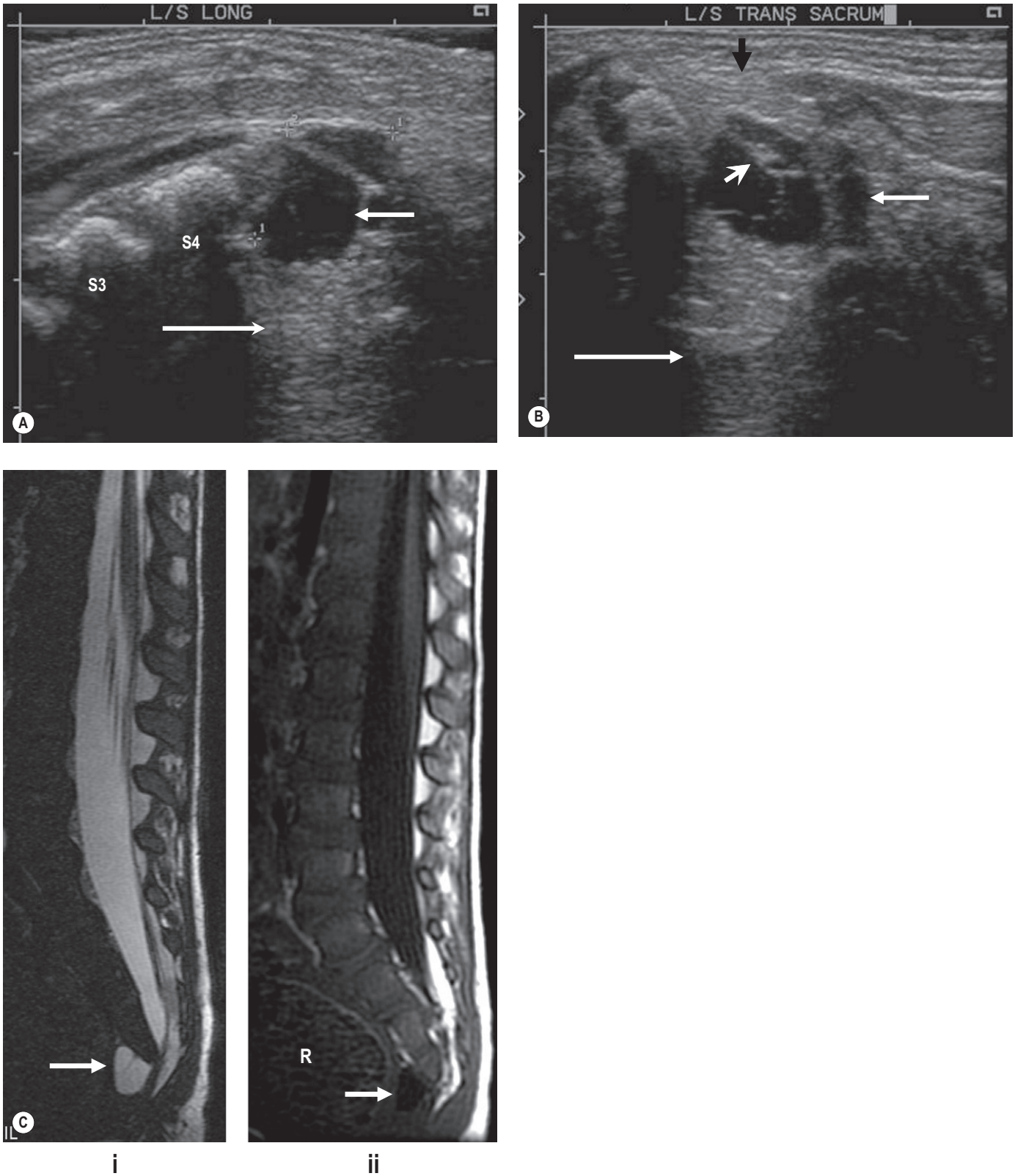

Figure 67.33 **Currarino's triad. A:** Sagittal image in a 2-week-old baby, showing a septated anterior meningocele (short white arrow) immediately posterior to the distended echogenic rectum (long white arrow). **B.** Axial image at the caudal sacrum. The posterior neural arch is absent (black arrow). Underlying the defect the meningocele is seen (short white arrow), containing the thickened filum terminale (arrowhead) and internal septa. Deep to the meningocele lies the echogenic rectum (long white arrow). **C:** Sagittal high-resolution T2 (i) and sagittal T1 (ii) MR images showing the anterior sacral meningocele (arrow). There is a thickened tethering filum terminale. The sacrum is dysgenetic with only four segments. The rectum (R) is grossly distended.

REFERENCES

1. Naidich TP, McLone DG, Shkolnik A, Fernbach S. Sonographic evaluation of caudal spine anomalies in children. Am J Neuroradiol 1983;4:661–664.
2. Naidich TP, Fernbach SK, McLone DG, Shkolnik A. Sonography of the caudal spine and back: congenital anomalies in children. AJR Am J Roentgenol 1984;142:1229–1242.
3. Raghavendra BN, Epstein FJ, Pinto RS, et al. The tethered spinal cord: diagnosis by high resolution real time ultrasound. Radiology 1983;149:123–128.
4. Jequier S, Cramer B, O'Gorman AM. Ultrasound of the spinal cord in neonates and infants. Ann Radiol 1985;28:225–231.
5. Naidich T, Radkowski MA, Britton J. Real time sonographic display of caudal spinal anomalies. Neuroradiology 1986;28:512–527.
6. Dick EA, Patel K, Owens CM, De Bruyn R. Spinal ultrasound in infants. Br J Radiol 2002;75:384–392.
7. Rohrschneider WK, Forsting M, Darge K, Troger J. Diagnostic value of spinal US: comparative study with MR imaging in pediatric patients. Radiology 1996;200:383–388.
8. Naidich TP, McLone DG. Congenital pathology of the spine and spinal cord. In: Taveras JM, Ferrucci JT, editors. Radiology. Philadelphia: JB Lippincott; 1986.
9. Hill CA, Gibson PJ. Ultrasound determination of the normal location of the conus medullaris in neonates. Am J Neuroradiol 1995;16:469–472.
10. St Amour TE, Rubin JM, Dohrmann GJ. The central canal of the spinal cord: ultrasonic identification. Radiology 1984;152:767–769.
11. Nelson MD, Sedler JA, Gilles FH. Spinal cord central echo complex: histoanatomic correlation. Radiology 1989;170:479–481.
12. Langman J. Medical embryology. Baltimore: Williams & Wilkins; 1963.
13. French BN. The embryology of spinal dysraphism. In: Proceedings of the Congress of Neurological Surgeons, Toronto, Ontario, Canada, 1982. Clinical neurosurgery. Baltimore: Williams & Wilkins; 1983. p. 295–340.
14. Van Allen MI, Kalousek DK, Chernoff GF, et al. Evidence for multisite closure of the neural tube in humans. Am J Med Genet 1993;47: 723–743.
15. Kunitomo K. The development and reduction of the tail and of the caudal end of the spinal cord. Contrib Embryol 1918;8:161–198.
16. Lemire RJ, Loeser JD, Leech RW, Alvord EC. Normal and abnormal development of the human nervous system. Hagerstown, MD: Harper & Row; 1975.
17. Tarlov IM. Structure of the filum terminale. Arch Neurol Psychiatry 1938;40:117.
18. Kallen B, Weinberg J. Caudal mesoderm pattern of anomalies: from renal agenesis to sirenomyelia. Teratology 1974;9:99–111.
19. Barkovich AJ. Congenital anomalies of the spine. In: Pediatric neuroimaging. 4th ed. New York: Raven Press; 2005. p. 704–772.
20. Tortori-Donati P, Rossi A, Cama A. Spinal dysraphism: a review of neuroradiological features with embryological correlations and proposal for a new classification. Neuroradiology 2000;42:471–491.
21. Naidich TP, Harwood-Nash DC, McLone DG. Radiology of spinal dysraphism. Clin Neurosurg 1983;30:341–365.
22. Naidich TP, McLone DG, Fulling KH. The Chiari II malformation: part IV. The hind brain deformity. Neuroradiology 1983;25:179–197.
23. Unchino A, Mori T, Ohino M. Thickened fatty filum terminale: MR imaging. Neuroradiology 1991;33:331–333.
24. Brown E, Matthes JC, Bazan C, Jinkins JR. Prevalence of incidental intraspinal lipoma of the lumbosacral spine as determined by MRI. Spine 1994;19:833–836.
25. Warder DE. Tethered cord syndrome and occult spinal dysraphism. Neurosurg Focus 2001;10:1–9.
26. Koyanagi I, Iwasaki Y, Hida K, et al. Surgical treatment supposed natural history of the tethered cord with occult spinal dysraphism. Child Nerv Syst 1997;13:268–274.
27. van der Meulen WD, Hoving EW, Staal-Schreinemacher A, Begeer JH. Analysis of different treatment modalities of tethered cord syndrome. Child Nerv Syst 2002;18:513–517.
28. Williams H. Spinal sinuses, dimples, pits and patches: what lies beneath? Arch Dis Child Pract Ed 2006;91:75–80.
29. Egelhoff JC. MR imaging of congenital anomalies of the pediatric spine. Magn Reson Imaging Clin N Am 1996;4:797–833.
30. Byrd SE, Darling CF, McClone DG, Tomita T. MR imaging of the pediatric spine. Magn Reson Imag Clin N Am 1996;4:797–833.
31. Rossi A, Cama A, Piatelli G, et al. Spinal dysraphism: MR imaging rationale. J Neuroradiol 2004;31:3–24.
32. Guggisberg D, Hadj-Rabia S, Viney C, et al. Skin markers of occult spinal dysraphism in children. Arch Dermatol 2004;140:1109–1115.
33. Ackerman LL, Menezes AH. Spinal congenital dermal sinuses: a 30-year experience. Pediatrics 2003;58:1227–1233.
34. Robinson AJ, Russell S, Rimmer S. The value of ultrasonic examination of the lumbar spine in infants with specific reference to cutaneous markers of occult spinal dysraphism. Clin Radiol 2005;60:72–77.
35. Kriss VM, Desai NS. Occult spinal dysraphism in neonates: assessment of high-risk cutaneous stigmata on sonography. AJR Am J Roentgenol 1998;171:1687–1692.
36. Towbin A. Latent spinal cord and brain stem injury in newborn infants. Develop Med Child Neurol 1969;11:54–68.
37. Yates PO. Birth trauma to the vertebral arteries. Arch Dis Child 1959;34:436–441.
38. Hellstrom B, Sallmander U. Prevention of spinal cord injury in hyperextension of the fetal head. JAMA 1968;204:1041–1044.
39. Abroms IF, Bresnan MJ, Zuckerman JE, et al. Cervical cord injuries secondary to hyperextension of the head in breech presentations. Obstet Gynecol 1973;41:369–378.
40. Shulman ST, Madden JD, Esterly JR, Shanklin DR. Transection of spinal cord. A rare obstetrical complication of cephalic delivery. Arch Dis Child 1971;46:291–294.
41. Gould SJ, Smith JF. Spinal cord transection, cerebral ischaemic and brainstem injury in a baby following a Kielland's forceps rotation. Neuropathol Appl Neurobiol 1984;10:151–158.
42. Koch BM, Eng GM. Neonatal spinal cord injury. Arch Phys Med Rehab 1979;60:378–381.
43. De Souza SW, Davis JA. Spinal cord damage in a newborn infant. Arch Dis Child 1974;49:70–71.
44. Norman MC, Wedderburn LC. Fetal spinal cord injury with cephalic delivery. Obstet Gynecol 1973;42:355–358.
45. Castillo M, Quencer RM, Green BA. Cervical spinal cord injury after traumatic breech delivery. Am J Neuroradiol 1989;10:S99.
46. Fotter R, Sorantin E, Schneider U, Ranner G, et al. Ultrasound diagnosis of birth-related spinal cord trauma: Neonatal diagnosis and follow up and correlation with MRI. Pediatr Radiol 1994;24:241–244.
47. Jequier S, Cramer BC, O'Gorman AM. Ultrasound of the spinal cord in neonates and infants. Ann Radiol 1985;28:225–231.
48. Cramer BC, Jequier S, O'Gorman AM. Sonography of the neonatal craniocervical junction. AJR Am J Roentgenol 1986;147:133–139.
49. Babyn PS, Chuang SH, Daneman A, Davidson GS. Sonographic evaluation of spinal cord birth trauma with pathologic correlation. AJR Am J Roentgenol 1988;151:763–766.
50. Grant FC, Austin GM. The diagnosis, treatment and prognosis of tumours affecting the spinal cord in children. J Neurosurg 1956;13:665–668.
51. Iraci G, Ruberti R. Intraspinal tumours of the cervical tract. A study of 68 cases. Int Surg 1966;46:154–167.
52. Steinke CR. Spinal tumours: statistics on a series of 330 collected cases. J Nerv Ment Dis 1918;47:418–426.
53. de Lorimer AA, Bragg KU, Linden G. Neuroblastoma in childhood. Am J Dis Child 1969;118:441–450.
54. Arseni C, Samitca DC. Primary intraspinal tumours in children and adolescents: a report on 12 cases. J Neurosurg 1961;18:135–138.
55. Epstein F, Epstein N. Intramedullary tumors of the spinal cord. In: Shillito Jr J, Matson DD, editors. Pediatric neurosurgery: surgery of the developing nervous system. New York: Grune & Stratton; 1982. p. 529–540.
56. Sze G, Krol G, Zimmerman RD, Deck MDF. Intramedullary disease of the spine: diagnosis using Gd-DTPA-enhanced MR imaging. Am J Neuroradiol 1988;9:847–858.
57. Packer RJ, Siegel KR, Sutton LN, et al. Leptomeningeal dissemination of primary CNS tumors of childhood. Ann Neurol 1985;18:217–221.
58. Sze G, Abramson A, Krol G, et al. Gadolinium–DTPA in the evaluation of intradural, extramedullary spinal disease. AJR Am J Roentgenol 1988;150:911–921.
59. Stark GD. Spina bifida: problems and management. Oxford: Blackwell Scientific Publications; 1977.
60. Altman RP, Randolph JG, Lily JR. Sacrococcygeal teratoma: American Academy of Pediatrics Surgical Section Survey – 1973. J Pediatr Surg 1974;9:389–398.
61. Riebel T, Maurer J, Teichgraber UK, Bassir C. The spectrum of imaging in Currarino triad. Eur Radiol 1999;9:348–353.
62. Martucciello G, Torre M, Belloni E. Currarino syndrome: proposal of a diagnostic and therapeutic protocol. J Pediatr Surg 2004;39:1305–1311.

CHAPTER

68 Paediatric chest

Edward Y. Lee and Marilyn J. Siegel

INTRODUCTION

Ultrasonography (US) is a widely used and valuable imaging modality, particularly in paediatric patients, due to its widespread availability, relative ease of performance, and absence of sedation or harmful ionising radiation exposure. In addition, the real-time nature of the examination, which allows evaluation of moving structures (e.g. the diaphragm) in different planes, and the ability to perform the examination using portable equipment are unique in comparison to other commonly used imaging modalities, including plain radiography, computed tomography (CT) and magnetic resonance imaging (MRI). Although conventional chest radiography remains the initial imaging study for evaluating chest diseases in children, US as a secondary test may provide clinically relevant information in selected situations.

This chapter addresses the sonographic technique for evaluating non-vascular chest disease processes, discusses normal anatomy, and reviews clinical and sonographic features of selected common pulmonary, pleural, mediastinal, diaphragmatic and chest wall lesions in infants and children.

TECHNIQUE

Prior to the US, the conventional chest radiograph should be reviewed in order to localise the area of interest so that the clinical question can be optimally answered. If there are available cross-sectional imaging studies, such as CT or MRI, they should be carefully reviewed since they often provide useful information to further define the area of interest to be interrogated.

Ultrasound transducers

The choice of ultrasound transducer depends on the age and size of the patient and the location of the abnormality with a goal of obtaining an optimal acoustic 'window' to transmit sound and generate diagnostic quality sonographic images.[1–6] While curved or linear array transducers are commonly used for evaluation of pulmonary, pleural, mediastinal, diaphragmatic and chest wall abnormalities, sector or vector transducers, which are smaller in size than the curved or linear array transducers, are often preferred when there is a need for imaging via a small acoustic window (e.g. between the ribs). Higher-frequency, 7.5–15.0 MHz, transducers, which provide higher-resolution images but have a lower ability for soft tissue penetration, are suitable for evaluating the chest in infants and young children with smaller amounts of subcutaneous fat.[1–6] In contrast, lower-frequency transducers (<5 MHz), which provide better soft tissue penetration but with lower image resolution, are required for older children or adolescents with relatively large amounts of subcutaneous fat.[1–6] Colour Doppler sonography is useful for evaluating vascular structures and blood flow patterns, especially in cases of pulmonary sequestration (i.e. for detecting anomalous vessels) and masses (for evaluating underlying vascularity). Linear high-frequency transducer and tissue-equivalent stand-off materials can improve the evaluation of superficial chest wall lesions.

Patient positioning and imaging approach

Proper patient positioning can increase patient comfort and optimise the acoustic window.[1–6] Most ultrasound evaluation of the chest is performed with the patient in the supine or upright position. Placing a pillow or blanket on the dependent side of the patient for the lateral decubitus view or behind the shoulder to help extend the neck for the supraclavicular or suprasternal notch view can increase patient comfort and facilitate the examination.

There are several different sonographic imaging approaches, depending on the location of the abnormality, including: (1)

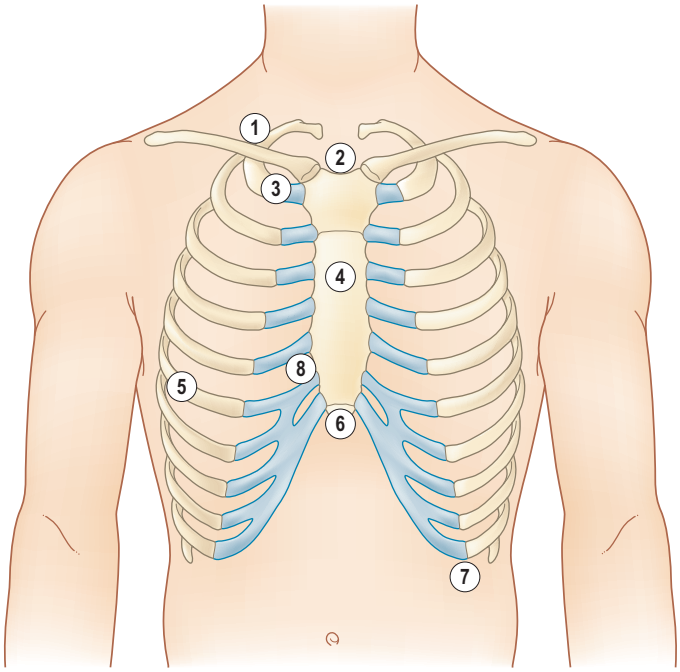

Figure 68.1 Locations of acoustic windows for chest ultrasound examinations. (1) supraclavicular; (2) suprasternal; (3) parasternal; (4) trans-sternal; (5) intercostal; (6) subxiphoid; (7) subdiaphragmatic; and (8) posterior paraspinal approaches.

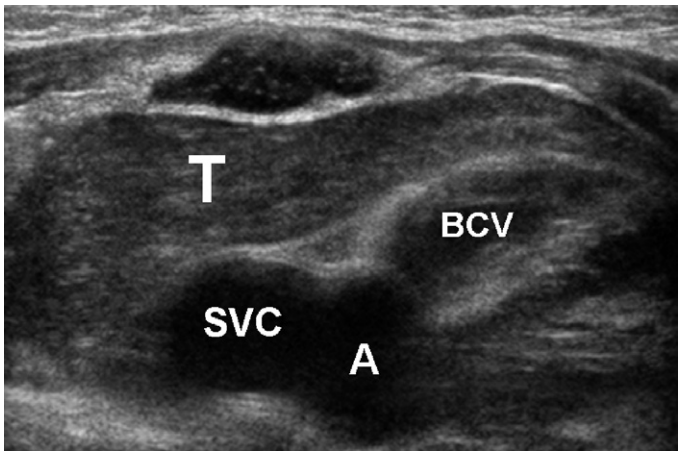

Figure 68.2 Normal thymus. Transverse view of the normal thymus at the horizontal portion of the left brachiocephalic vein in a 9-week-old boy. The thymus (T) is relatively homogeneous in echogenicity with smooth and well-marginated outer borders. It is located anterior to the superior vena cava (SVC), aorta (A) and the horizontal portion of the left brachiocephalic vein (BCV).

supraclavicular; (2) suprasternal; (3) parasternal; (4) trans-sternal; (5) intercostal; (6) subxiphoid; (7) subdiaphragmatic; and (8) posterior paraspinal approaches (Fig. 68.1).[1–6] Supraclavicular and suprasternal approaches, obtained with the transducer placed above the clavicle or sternum, respectively, are helpful for evaluating the superior and anterior mediastinum, lung apices and great vessels. The parasternal approach, acquired by placing the transducer parallel to the sternum, and the trans-sternal approach, acquired by positioning the transducer directly over the sternum, can be useful for evaluating anterior mediastinal structures such as the thymus in infants who have unossified sternums that allow transmission of the ultrasound beam. The intercostal approach, obtained by placing the transducer between the ribs, provides the best acoustic window for evaluating the pleural space and peripheral lung parenchyma. The subxiphoid and subdiaphragmatic approaches, acquired by placing the transducer beneath the xiphoid and diaphragm, respectively, are helpful in imaging juxtaphrenic lesions. The posterior paraspinal approach, obtained by locating the transducer parallel to the spine with the patient in an upright or lateral decubitus position, is used for evaluating paravertebral lesions. For the evaluation of moving structures such as the diaphragm, sagittal scanning using the liver on the right and the spleen on the left as acoustic windows is helpful.[5] Comparison of the diaphragmatic motion of the hemidiaphragms can be best achieved via a subxiphoid approach in the transverse plane with the transducer angled cephalad toward the posterior leaflets of the hemidiaphragms and the patient breathing quietly. In neonates the two sides can often be very well compared using a direct coronal subcostal approach.

NORMAL ANATOMY

Thymus

The thymus produces hormones which stimulate maturation of T cells, playing an important role in the immune system in humans.[7–9] The thymus is located anterior to the great vessels, extending cranially to the horizontal portion of the left brachiocephalic vein and caudally to the origin of great vessels, and is usually confined to the anterior mediastinum.[5] Inferior extension almost to the level of the diaphragm can be occasionally seen. Due to its relatively large size in comparison to the rest of the thorax and its location within the anterior mediastinum, ultrasound with suprasternal, trans-sternal or parasternal approaches can be easily used for thymic evaluation in neonates and infants with non-ossified sternums. In a prospective evaluation of the thymus in 140 infants and children (newborn to 8 years old), Liang and Huang reported that normal thymus was easily and clearly visualised with ultrasound in the majority (95%) of cases.[10]

To avoid errors in diagnosis, understanding the characteristic sonographic appearance of the thymus is paramount. In neonates and infants, the thymus is quadrilateral shaped; in contrast in older children it typically has a triangular shape. Characteristic sonographic findings include: (1) homogeneous echotexture; (2) mild hypoechogenicity relative to adjacent thyroid gland or liver; (3) smooth and well-marginated borders due to a fibrous outer capsule; (4) change in shape with respiration and cardiac pulsation; (5) no associated mass effect on adjacent mediastinal structures (e.g. trachea and great vessels) (Fig. 68.2).[1–6,11]

Lung and pleura

The normal pleural surface is characterised by a hyperechoic line beneath the chest wall and ribs (Fig. 68.3).[5] The aerated lung, which is a barrier to sound, lies underneath the echogenic pleural surface. The acoustic interface between the chest wall and normal aerated lung produces characteristic echogenic reverberations behind the visceral pleura and mirror image artefacts.[1–6,12] The mirror image artefacts are created by sound wave reflection, which occurs when the ultrasound beam encounters the lung surface. This results in a dual or mirror image with the liver or spleen projecting above the diaphragm mimicking parenchymal consolidation.[1–6,12] During respiration, a characteristic to-and-fro movement of the aerated normal lung along the adjacent parietal pleural surface is typical, a finding referred to as the 'gliding sign'.[2]

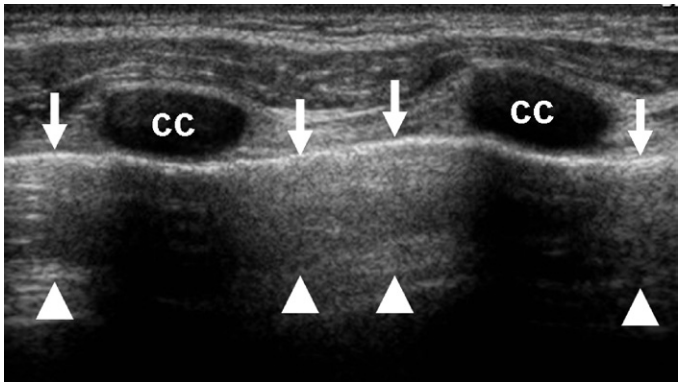

Figure 68.3 Normal pleura and lung. Transverse view of the normal pleural surface (arrows) and the aerated lung imaged with a high-frequency ultrasound probe (15 MHz) in a 4-week-old girl. Echogenic reverberations (arrowheads) are seen within the aerated lung. CC, costochondral cartilages of the ribs.

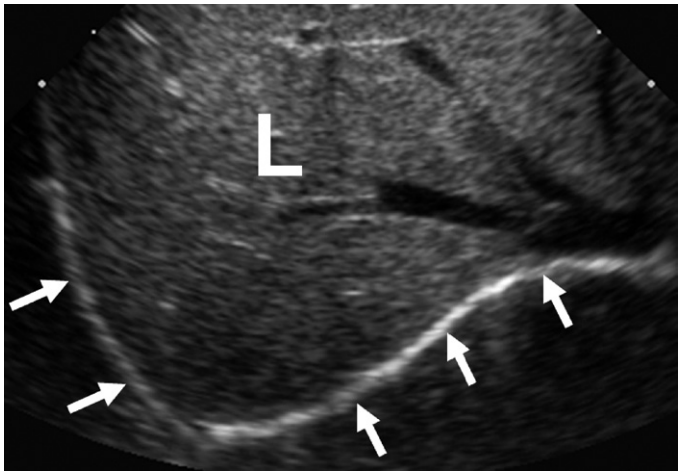

Figure 68.4 Normal diaphragm. Transverse view of the right hemidiaphragm (arrows) in a 10-year-old boy imaged with a subxiphoid approach using the liver (L) as an acoustic window. The normal diaphragm (arrows) appears as a smooth but echogenic band.

Diaphragm

The diaphragm is a dome-shaped musculofibrous structure composed of a central tendon and peripheral muscle leaflets which separate the thoracic from the abdominal cavity.[5,13] It is primarily innervated by the phrenic nerve and performs a crucial function in respiration. The diaphragm can be best imaged with a subxiphoid approach using the liver on the right and spleen or left lobe of the liver on the left as an acoustic window.[1,5] Evaluation of the right hemidiaphragm is usually easier than the left hemidiaphragm, because of impedance of the ultrasound beam on the left by gas within the stomach or splenic flexure of the colon. Distending the stomach by administering fluid orally or via a nasogastric tube can improve visualisation of the left hemidiaphragm.[5]

The normal diaphragm appears as a relatively smooth but slightly undulating echogenic band (Fig. 68.4).[5] The crural parts of the diaphragm are tendinous portions, which extend to the anterolateral surfaces of the upper lumbar vertebral bodies and also to the medial and lateral arcuate ligaments, which cover the anterior surfaces of the psoas and quadratus lumborum muscles.[5] The crural parts of the diaphragm appear as relatively hypoechoic, linear structures near the midline.[5]

Common clinical indications for chest sonography in infants and children

- Confirming normal or ectopic thymus.
- Characterising peripheral opacity (i.e. parenchymal versus pleural disease) detected on plain chest radiography.
- Characterising a mediastinal lesion.
- Assessing diaphragmatic motion and anatomical abnormalities.
- Diagnosing palpable chest wall lesion.
- Localising pleural fluid for thoracentesis or a mass for biopsy.

With real-time imaging capability, diaphragmatic motion during a respiratory cycle can be reliably assessed.[14–19] The transverse plane provides simultaneous identification of both hemidiaphragms and is useful for identification of diaphragmatic motion abnormality (i.e. paralysis or paresis).[5,14–20] The longitudinal plane allows visualisation of the relationship between the diaphragm and intrathoracic structures (e.g. lungs and heart), and intra-abdominal structures (e.g. liver and spleen) and is helpful for assessing structural integrity and diaphragmatic hernias.[5,14–20] The excursion of the middle and posterior thirds of the diaphragm is greater than that of the anterior third. In the longitudinal plane, the mean excursion (and standard deviation) for anterior, middle and posterior thirds of the diaphragm are 2.6±0.1, 3.6±0.2 and 4.5±0.2 mm, respectively.[20]

CLINICAL INDICATIONS

The common clinical indications for ultrasonography of the chest in infants and children include: (1) confirming normal or ectopic thymus; (2) characterising peripheral opacity (i.e. parenchymal versus pleural disease) detected on plain chest radiography; (3) characterising a mediastinal lesion; (4) assessing diaphragmatic motion and anatomical abnormalities; (5) diagnosing palpable chest wall lesions; and (6) localising pleural fluid for thoracentesis or a mass for biopsy.

THYMUS

During its caudal migration in utero, descent of the thymus can be arrested resulting in an ectopic location, most commonly within the lower neck, suprasternal region or posterior mediastinum.[21–26] In this situation, ultrasound can confirm a direct connection between the ectopically positioned and normally positioned thymic tissue within the anterior mediastinum, thereby excluding a pathological mass and obviating further imaging studies such as CT or MRI. In older children or adolescents who do not have adequate acoustic windows for evaluation of thymus due to an ossified sternum, CT or MRI demonstrates thymic pathology better than ultrasound.[27–29] The ultrasound diagnosis of ectopic thymic tissue is based on a direct continuity with the anterior mediastinal thymic tissue along with an echogenicity similar to that of normal thymic tissue and the absence of mass effect on the adjacent mediastinal vessels and the tracheobronchial tree (Fig. 68.5). Ultrasound also can be used to confirm the presence of a normal thymus in infants with a suspected mass or consolidation on plain chest radiographs (Fig. 68.6).

PULMONARY PARENCHYMA

Atelectasis and consolidation

The evaluation of normally aerated lungs with ultrasound is limited. However, atelectatic and consolidated lungs can transmit

sound and be visible by ultrasound, although differentiation between the two conditions is usually not possible. In practice, definite differentiation between atelectasis and consolidation is better achieved with chest radiography or CT.

On ultrasound, consolidated or atelectatic lung is usually poorly-defined and hypoechoic compared with highly reflective normal lung and adjacent liver and spleen.[5,30–32] Air-filled bronchi within consolidated lung produce multiple bright punctate and branching linear structures extending from the centre of the consolidated or collapsed lung to the periphery (Fig. 68.7). This appearance is termed the 'sonographic air bronchogram', which is equivalent to the air bronchogram seen on chest radiographs.[1–6] When aerated bronchi are replaced with fluid or mucoid material, branching anechoic or hypoechoic tubular structures are seen on ultrasound, termed the 'sonographic fluid bronchogram' (Fig. 68.8).[5,6] Branching pulmonary vessels in a radiating pattern can be seen on colour Doppler ultrasound (Fig. 68.9).[6] Normal pulmonary vessels cannot be seen in aerated lung by ultrasound. Occasionally, consolidated or atelectatic lung has a predominantly homogeneous echogenic appearance with few bronchi visible mimicking liver, referred to as 'hepatisation' of the lung (Fig. 68.10).[1,6]

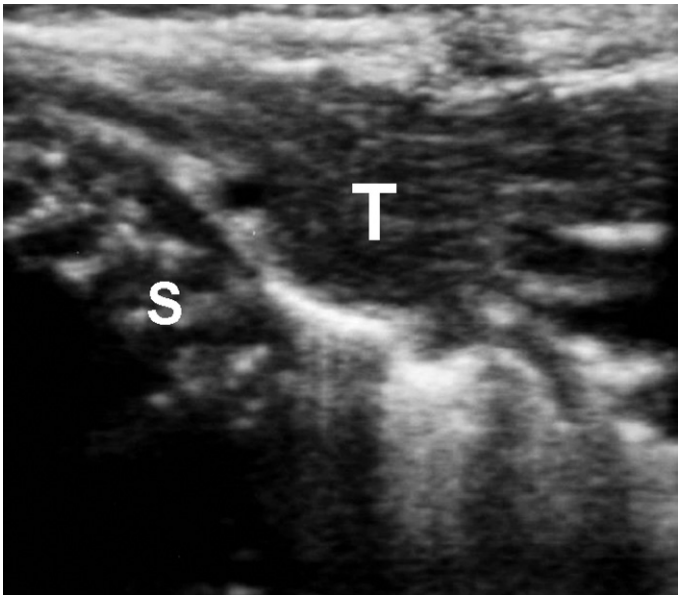

Figure 68.5 Ectopic thymus, superior neck extension. Longitudinal scan to the left of midline shows normally echogenic thymus (T) extending into the lower neck anterior to the cervical spine (S).

Lung necrosis and abscess

Lung necrosis (i.e. necrotising pneumonia) and lung abscess are complications of severe parenchymal infection.[33–38] Necrotising pneumonia occurs when infected lung compresses and occludes alveolar capillaries, resulting in decreased vascular supply to the lung parenchyma.[36,37] On ultrasound the affected lung is heterogeneous, containing poorly marginated cystic areas representing necrosis and solid areas related to consolidation (Fig. 68.11). Decreased or absent blood flow can also be seen on colour Doppler ultrasound.

Lung abscess refers to suppuration of lung tissue and formation of cavities containing necrotic debris or gas surrounded by a well-formed inflammatory capsule.[5,33–35] Although lung abscess typically develops from primary lung infection, recurrent infection in the same area should raise a high suspicion for underlying abnormalities such as a foreign body, pulmonary sequestration, lung cyst and pneumatocele. Lung abscess typically presents as a round or ovoid hypoechoic mass with thick and irregular hyperechoic walls (Fig. 68.12). Hyperechoic areas with posterior acoustic shadowing may be observed if the abscess cavity contains gas (Fig. 68.13). In patients with lung abscess, ultrasound can also be used to guide percutaneous needle aspiration and drainage tube placement.[1,5,6]

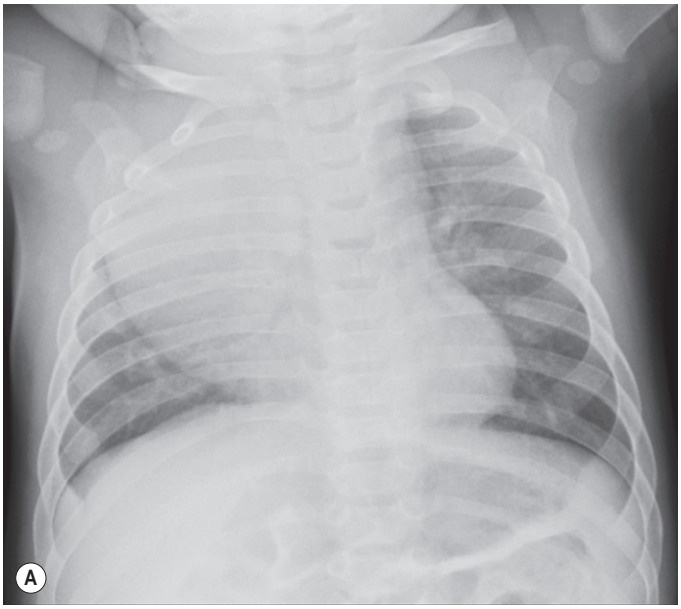

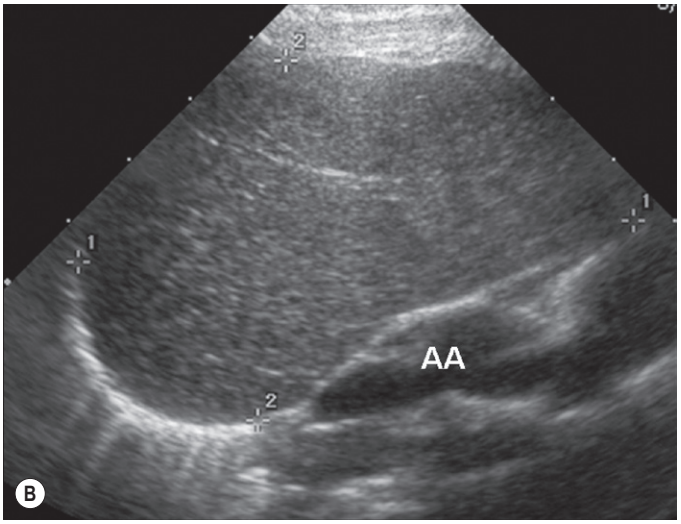

Figure 68.6 Normal thymus. A: A frontal view of a 5-month-old boy with coughing and fever shows a large opacity in the right upper lung zone, possibly representing consolidation. **B:** Transverse view of superior mediastinum at the level of aortic arch (AA) demonstrates a large but normal thymus (callipers) characterised by homogeneous echotexture with smooth and well-marginated borders.

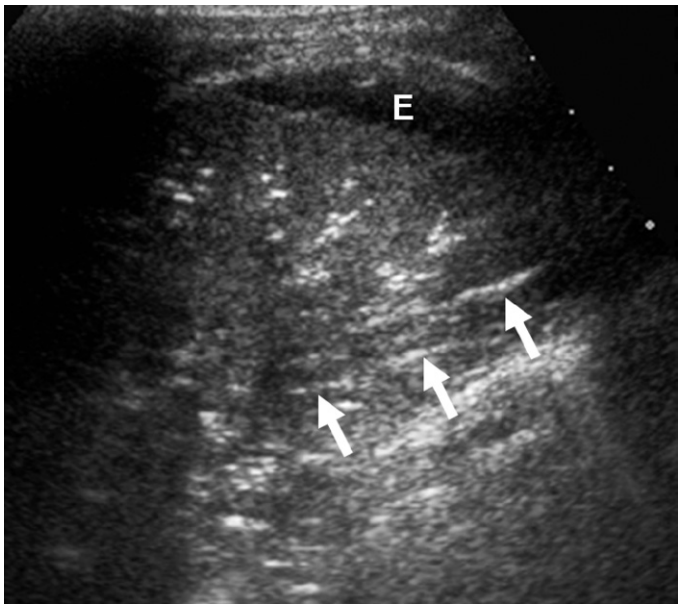

Figure 68.7 Parenchymal consolidation. US was performed to evaluate for pleural effusion. Transverse view of a consolidated right lower lobe in a 9-year-old boy with *Streptococcus* pneumonia demonstrates multiple bright punctuate and branching linear structures (arrows) representing air within the bronchi ('sonographic air bronchogram' sign). A small amount of pleural effusion (E) is also noted.

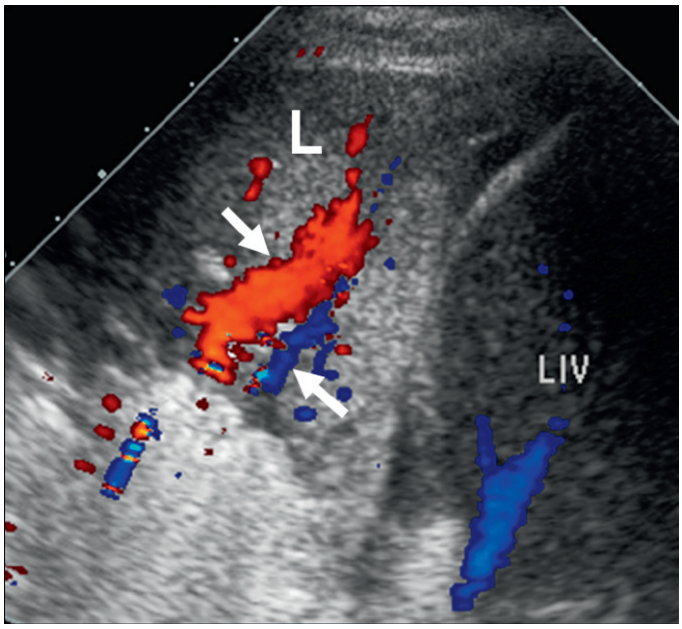

Figure 68.9 Parenchymal consolidation. US was performed to evaluate for pleural effusion. Longitudinal colour Doppler scan of the right lower hemithorax in an 8-year-old girl with *Staphylococcus* pneumonia demonstrates branching pulmonary vessels (arrows) within the consolidated lung (L). LIV, liver.

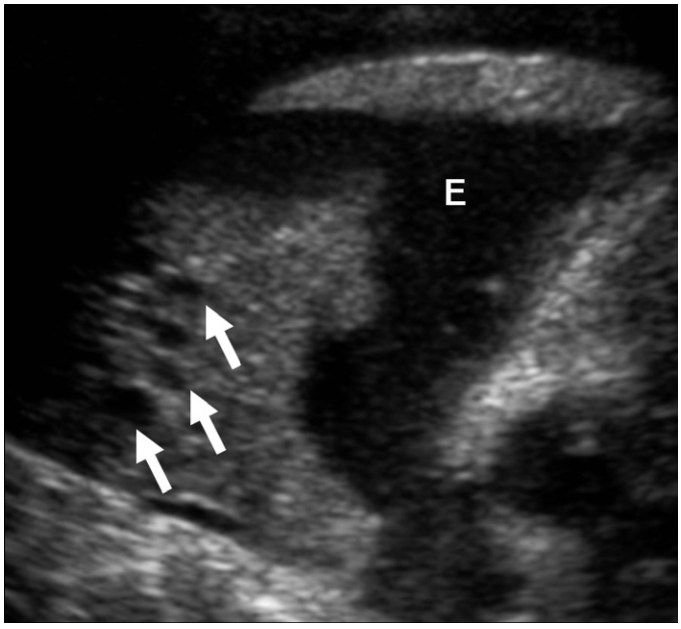

Figure 68.8 Parenchymal consolidation. Longitudinal view of the right lower hemithorax in a 4-year-old boy with *Streptococcus* pneumonia shows hypoechoic tubular structures (arrows), representing dilated bronchi with purulent material ('sonographic fluid bronchogram' sign). E, pleural effusion.

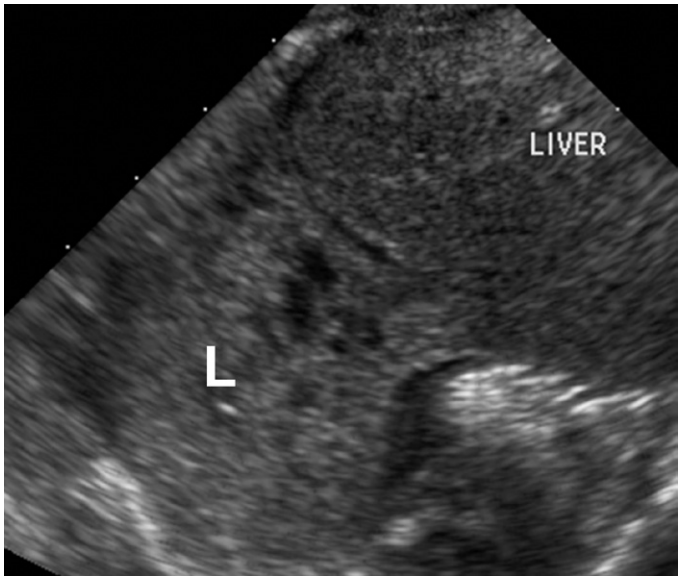

Figure 68.10 Hepatisation of the lung. Transverse view of the right lower hemithorax in a 10-year-old boy with *Streptococcus* pneumonia. The echogenicity of the consolidated right lower lobe (L) is similar to that of liver (LIVER) (i.e. 'hepatisation').

Congenital parenchymal masses

CT and MRI are the most commonly used imaging modalities for confirming or further evaluating a known or suspected lesion seen on prenatal imaging studies or postnatal chest radiography.[39–41] With the exception of pulmonary sequestration, ultrasound usually has a limited role in evaluating congenital lung masses. However, occasionally, congenital lesions, particularly congenital cystic adenomatoid malformation (CCAM) and congenital lobar emphysema, can show increased pulmonary opacity on chest radiographs obtained soon after birth, secondary to impaired drainage of fetal lung fluid. Ultrasound can show the fluid-filled nature of these lesions and aid in diagnosis.

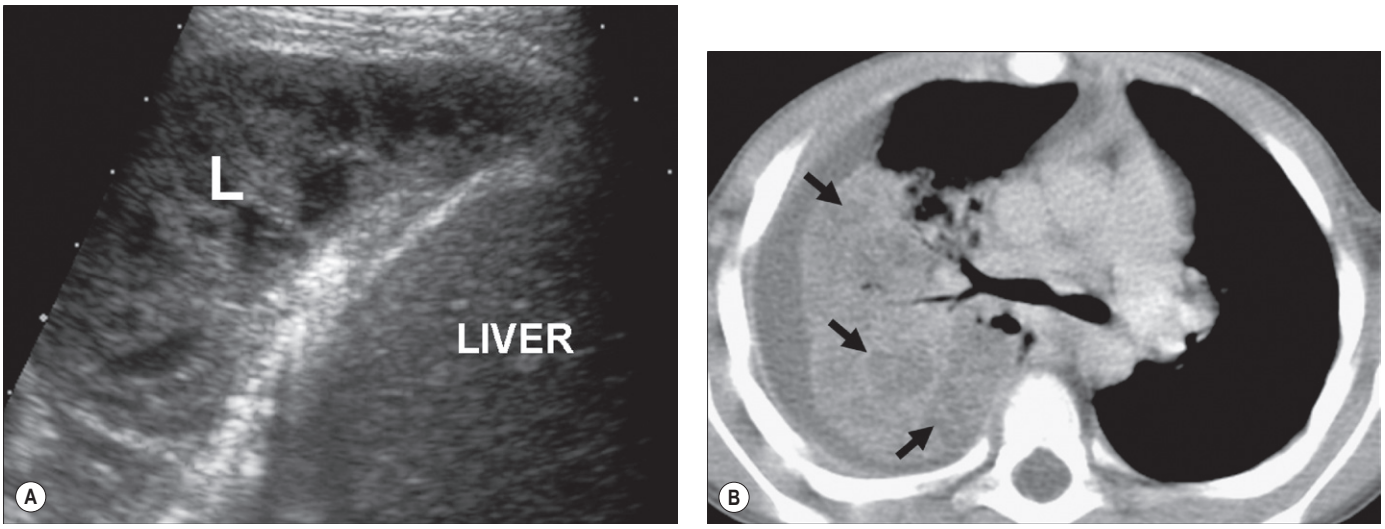

Figure 68.11 Necrotising pneumonia A: Longitudinal view of the right lower hemithorax in a 4-year-old boy demonstrates heterogeneous lung parenchyma with cystic areas surrounded by areas of consolidated lung (L). **B:** Axial CT scan shows low attenuation foci (arrows) representing areas of necrosis and decreased contrast enhancement in the consolidated right lung.

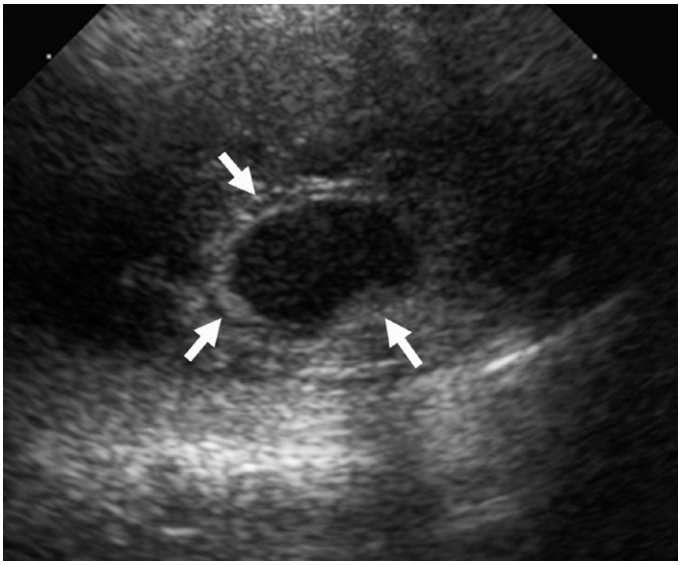

Figure 68.12 Lung abscess. Transverse view of the left lower lobe in a 7-year-old girl shows an oval-shaped hypoechoic mass with surrounding thick and irregular walls (arrows).

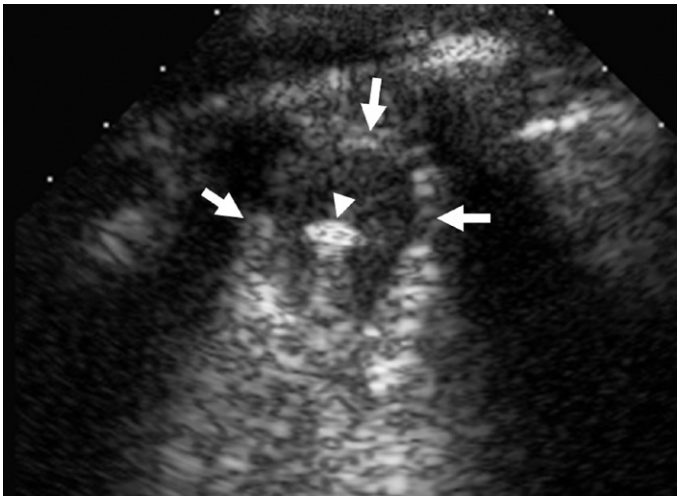

Figure 68.13 Lung abscess. Transverse view of the right lower lung in a 16-year-old boy shows a hypoechoic mass containing a hyperechoic focus, representing gas (arrowhead). The abscess is surrounded by thick and irregular walls (arrows).

Bronchopulmonary sequestration is a non-functioning malformed mass of lung tissue which is associated with anomalous systemic arterial blood supply and has no communication with the tracheobronchial tree.[5,39,40] Traditionally, bronchopulmonary sequestration has been classified into two types: intralobar and extralobar.[39,40] Intralobar sequestration is contained within the lung parenchyma and is enclosed by normal visceral pleura. It is associated with anomalous arterial supply from the descending thoracic aorta and usually has anomalous venous drainage into the inferior pulmonary vein. Extralobar sequestration lies outside the normal lung parenchyma and is enclosed in its own pleural investment. The arterial supply is from the thoracic or abdominal aorta and venous drainage is typically into the systemic circulations, such as the azygos vein, right atrium or portal vein.[39,40] Most patients with intralobar sequestrations present in childhood or later in life with signs of chronic or recurrent segmental or subsegmental pneumonitis, especially at a lung base. Extralobar sequestration is usually asymptomatic and can either present as an abdominal mass in a neonate when it is infradiaphragmatic in location or as a lung mass on chest radiographs.[39,40,42,43]

When plain chest radiography demonstrates a persistent infiltrate or mass, ultrasound with pulsed or colour flow Doppler imaging is a valuable study for identifying the aberrant blood supply associated with sequestration, especially in the neonate when the lesion is adjacent to the diaphragm or liver. On ultrasound, bronchopulmonary sequestration appears as an echogenic mass at a lung base. Cystic changes may be seen in intralobar sequestration due to superimposed infection (Fig. 68.14) or if there is an associated cystic adenomatoid malformation.[44] Extralobar sequestrations rarely are infected and usually present as a homogeneous echogenic mass in the posteromedial thorax next to the diaphragm (Fig. 68.15). Cystic areas also may be noted if there is an associated cystic adenomatoid malformation. Colour Doppler imaging can confirm the number and origin of the anomalous arteries associated with the sequestration (Fig. 68.16).[1–6,45] In older patients, CT or MR imaging is superior to sonography for

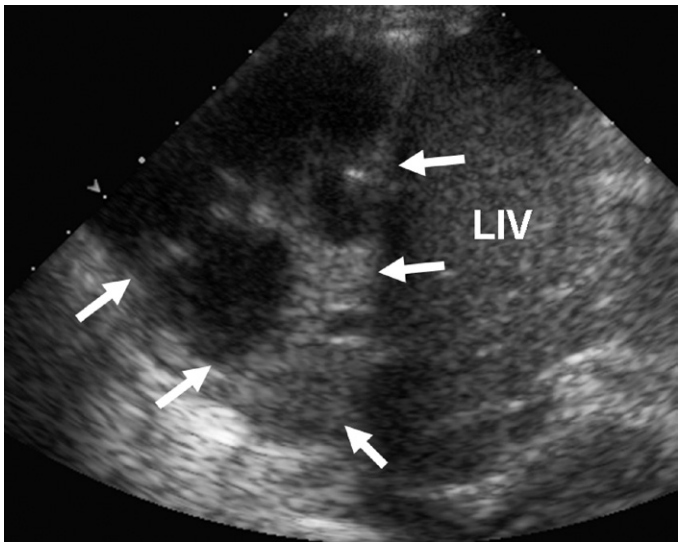

Figure 68.14 Intralobar sequestration. Longitudinal view of the right lower hemithorax in a 3-year-old boy with recurrent right lower lobe pneumonia shows a complex echogenic mass (arrows) with multiple varying sized cysts. CT (not shown) revealed anomalous arterial supply from the descending aorta and anomalous venous drainage into the right inferior pulmonary vein. LIV, liver.

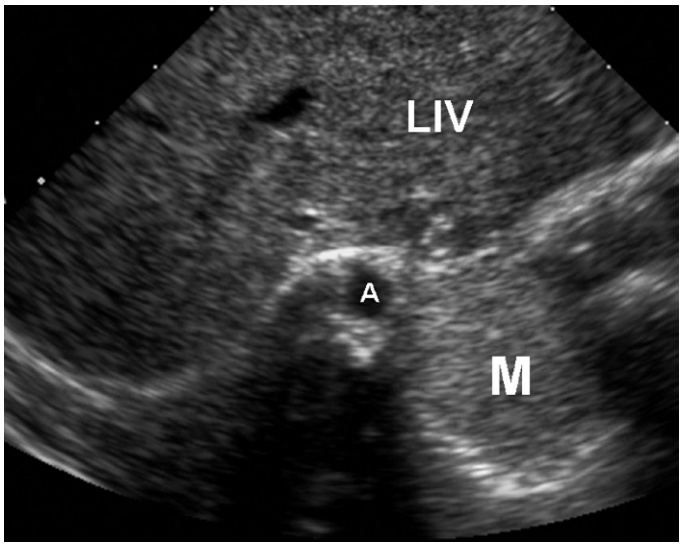

Figure 68.15 Extralobar sequestration. Transverse view of the left lower hemithorax in a 2-week-old girl with a prenatal ultrasound diagnosis of left thoracic mass shows a relatively homogeneous echogenic mass (M). LIV, liver; A, aorta.

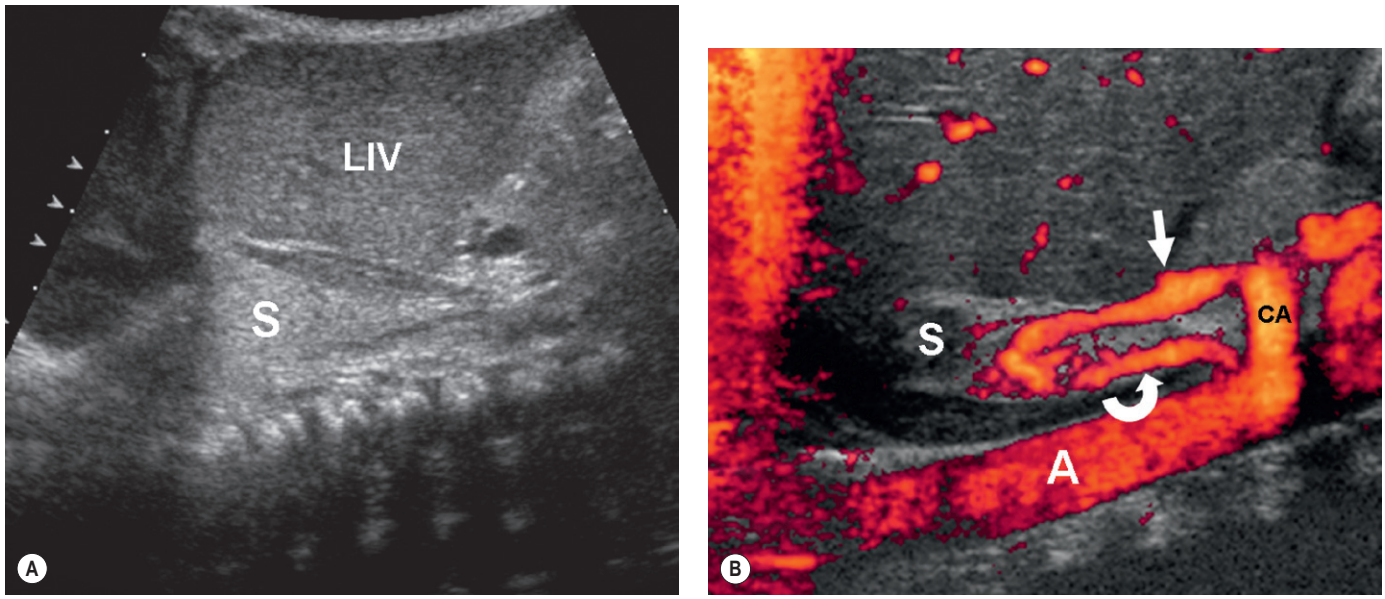

Figure 68.16 Extralobar sequestration. A: Longitudinal view through the right lung base and upper abdomen in a newborn infant boy with a history of prenatal diagnosis of lower thoracic and upper abdominal mass shows a homogeneously echogenic sequestration (S) below the diaphragm and posterior to the liver (LIV). **B:** Colour Doppler longitudinal view of demonstrates two anomalous feeding arteries – one from the descending aorta (curved arrow) and the other from the coeliac axis (straight arrow) feeding the sequestration (S). A, descending aorta; CA, coeliac axis.

demonstrating the sequestered lung and the arterial and venous connections, because of the absence of a good acoustic window.

CCAM is a congenital lung mass composed of disorganised adenomatoid and hamartomatous bronchioles that has a normal communication with the underlying bronchial tree and normal vascular supply and drainage.[5,39,40,46] Pathologically, three major types are recognised: type I (accounting for 50% of cases) contains at least one dominant cyst >2 cm in diameter; type II (40% of cases) contains multiple small cysts <2 cm in diameter; and type III (10% of cases) appears solid on visual inspection, but contains microscopic cysts.[5,39,40] Ultrasound is useful in neonates when the lesion appears opaque on X-ray (secondary to retained fluid), thus, mimicking an intrathoracic mass or pleural effusion. On ultrasound, CCAM demonstrates variable sized cysts and echogenic septations (Figs 68.17 and 68.18).[5,46,47] Acoustic shadowing occurs when the cysts contain air. The lesion is relatively avascular on pulsed or colour flow Doppler ultrasound.

Congenital lobar emphysema is a condition characterised by hyperinflation of a lobe without destruction of alveolar septa.[5,40] Plain radiographs are diagnostic if the obstructed lobe is air-filled,

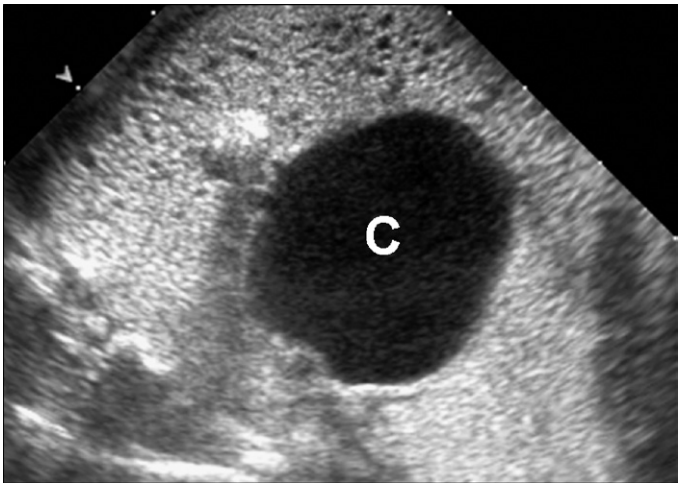

Figure 68.17 Cystic adenomatoid malformation. Transverse view of the right lower lung in a 1-week-old girl with an abnormal chest radiograph obtained for respiratory distress demonstrates a large cystic lesion (C) with thin walls, consistent with a type 1 CCAM.

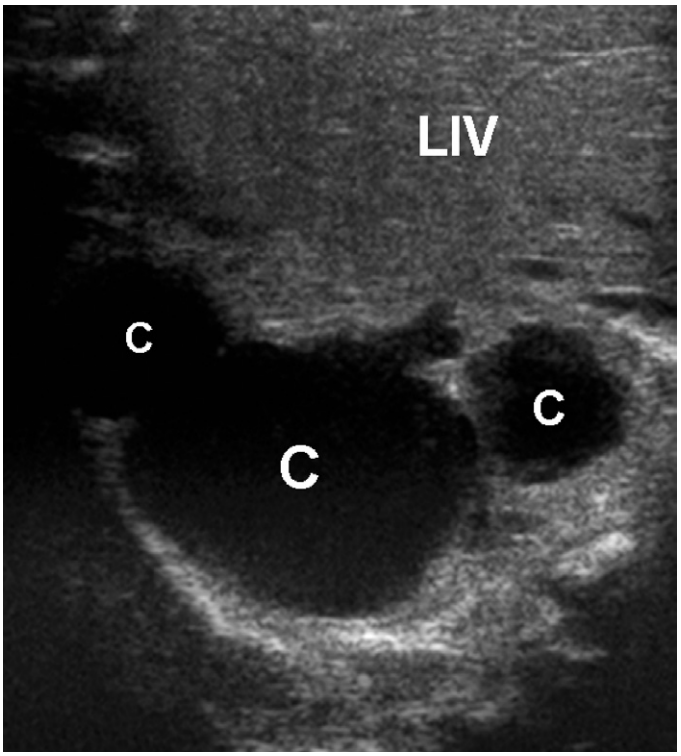

Figure 68.18 Cystic adenomatoid malformation. Transverse view of the right lower lung in an 8-week-old girl with a known prenatal diagnosis of a right lower lobe mass shows multiple cystic lesions (C) with thin walls, consistent with a type 2 CCAM. LIV, liver.

but immediately after birth fetal lung fluid may be trapped in the affected lobe, resulting in an opaque hemithorax on X-ray.[40] In this circumstance, sonography can help suggest the diagnosis of an emphysematous lobe. Congenital lobar emphysema appears as a homogeneous, hypoechoic lobe with enhanced sound transmission and atelectasis of the adjacent lung. The affected lobe is avascular.

Sonographic signs of pulmonary disease

- Sonographic air bronchogram, which is equivalent to air bronchogram on chest radiographs, typically presents as multiple bright punctate and branching linear structures extending from the centre of the consolidated or collapsed lung to the periphery.
- Lung abscess usually presents as a round or ovoid hypoechoic mass with thick and irregular hyperechoic walls. Hyperechoic areas with posterior acoustic shadowing may be observed if the abscess cavity contains gas.
- Anomalous arteries associated with an echogenic lung mass seen on colour Doppler imaging can confirm the diagnosis of pulmonary sequestration.
- Variable sized cysts and echogenic septations without associated anomalous arteries are typically seen in Congenital Cystic Adenomatoid Malformation.

Pulmonary neoplasm

Most lung neoplasms in children are metastases rather than primary neoplasms.[39,48] These are routinely identified on chest radiography or CT. However, they may be detected incidentally by US in patients who have examinations for pleural effusion. Primary and metastatic lung tumours appear as homogeneous or heterogeneous echogenic masses. Colour Doppler ultrasound demonstrates internal blood flow (Fig. 68.19).

PLEURA

Pleural effusions

Conventional radiographs usually suffice to distinguish between atelectasis and consolidation versus pleural fluid, but ultrasound can be useful when the diagnosis is equivocal. In evaluation of a small amount of pleural effusion, ultrasound is more sensitive than supine or decubitus radiographs.[49] Pleural effusions can be serous (transudate), purulent (exudate), haemorrhagic or chylous.[50] Serous effusion is low in protein and results from congestive heart failure, renal failure, cirrhosis, hypoalbuminaemia and overhydration. Purulent (exudate) effusion is high in protein and lactate dehydrogenase and is almost always a complication of bacterial infection. Haemorrhagic effusion ('haemothorax') contains a high haematocrit level and usually follows blunt or penetrating chest trauma, but it may be secondary to a bleeding diathesis. Chylous effusion (chylothorax) contains intestinal lymph (i.e. chyle) composed of high protein and fatty acid and typically is a complication of thoracic duct rupture or obstruction by primary or metastatic neoplasm, but it can be idiopathic.[50] Left-sided chylous effusion occurs when there is an injury of the upper thoracic duct while right sided chylous effusion is typically associated with injury of the distal duct.

A simple pleural effusion appears as anechoic fluid collection (Fig. 68.20). A complex pleural effusion contains multiple internal echoes, septations, loculations, and is surrounded by thickened echogenic pleura (Figs 68.21, 68.22 and 68.23). Serous or chylous effusions tend to be simple effusions and anechoic, while purulent and haemorrhagic effusions are more likely to be complex (Figs 68.24 and 68.25). However, sonographic imaging findings are not specific and anechoic effusions can represent exudative processes. A definite diagnosis requires pleural fluid analysis. With moderate or large pleural effusions, compressive atelectasis occurs in the adjacent lung. The collapsed lobe is displaced anteriorly and toward the hilum.

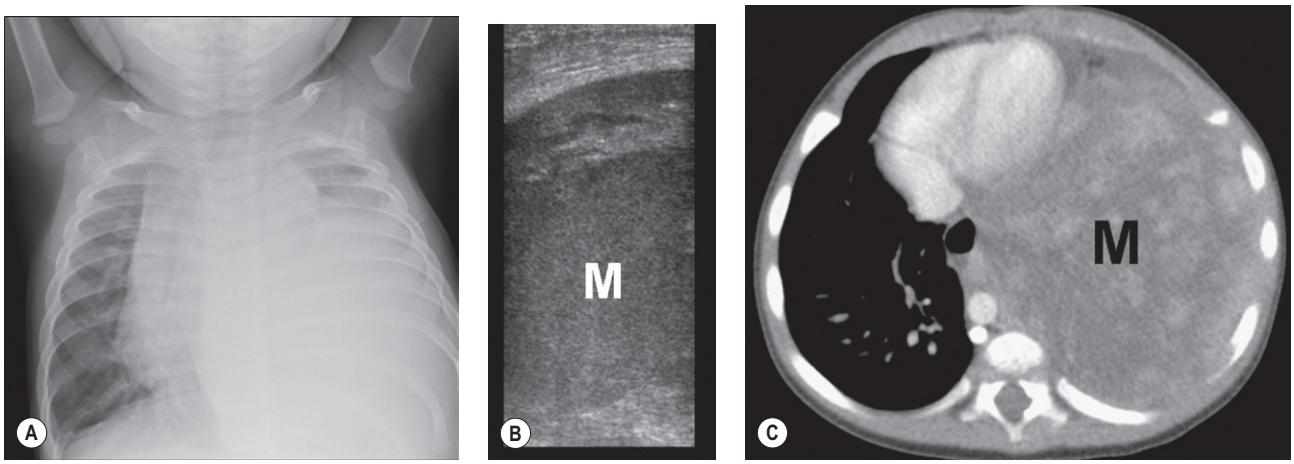

Figure 68.19 Primary lung sarcoma. A: Frontal view of the chest radiograph in a 10-month-old boy demonstrates a large opacity in the left mid to lower hemithorax associated with the mediastinal shift to the right. **B:** Longitudinal sonographic view of the left mid hemithorax shows a relatively homogeneous mass (M). **C:** CT confirms the mass (M). Surgical pathology showed undifferentiated sarcoma arising from the lung.

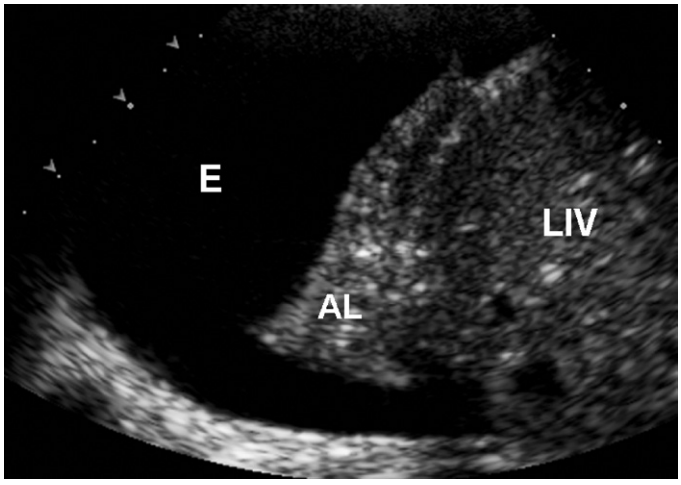

Figure 68.20 Simple pleural effusion. A longitudinal view of the right hemithorax in a 12-year-old girl with congestive heart failure demonstrates a large anechoic pleural effusion (E). Also noted is adjacent atelectatic lung (AL). LIV, liver.

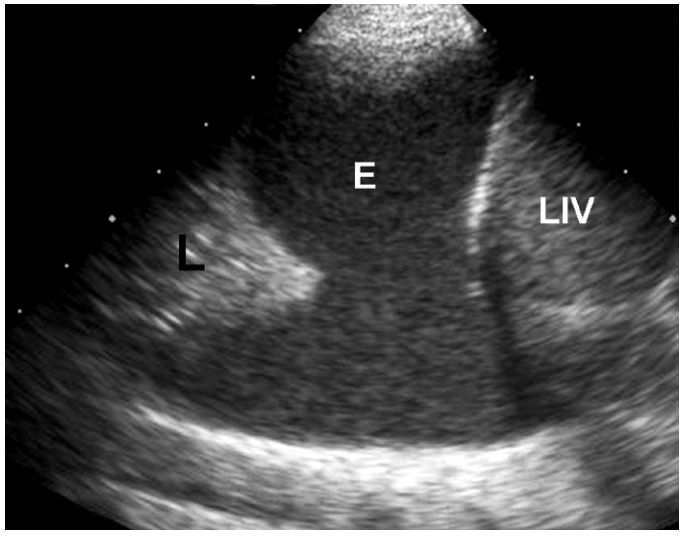

Figure 68.21 Complex effusion. A longitudinal view of the right hemithorax in a 14-year-old boy shows a large pleural effusion (E) containing multiple internal echoes. L, Lung; LIV, liver.

Scanning the patient in both erect and lateral decubitus positions can help to differentiate between freely flowing and loculated pleural fluid. Ultrasound findings of free-flowing fluid include: (1) changes in configuration and shape of the fluid related to changes in patient respiration or positioning; (2) demonstration of mobile particles on greyscale or colour Doppler ultrasound (termed a 'fluid colour sign'); and (3) absence of septations.[1–6,51,52] Visualisation of multiple thickened septa and/or no changes in configuration of the shape of the fluid related to changes in respiration or position generally imply a purulent fluid collection (i.e. empyema).[5,38] The normal gliding motion between the visceral pleural surfaces also persists when there is free effusion, whereas the gliding motion disappears in patients with loculated effusions. Sonography can be used to predict the success of the thoracentesis and also guide the drainage procedure. Free-flowing effusions generally have a relatively low viscosity and are amenable to needle aspiration, whereas a complex effusion implies a high viscosity collection or pleural thickening and is less likely to respond to thoracentesis. In general, ultrasound is superior to CT in detection of septations.

Sonographic signs of pleural disease

- A simple pleural effusion appears as anechoic fluid collection.
- A complex pleural effusion contains multiple internal echoes, septations, loculations, and is surrounded by thickened echogenic pleura.
- Sonographic findings of free-flowing pleural fluid include: (1) changes in configuration and shape of the fluid related to changes in patient respiration or positioning; (2) demonstration of mobile particles on greyscale or colour Doppler ultrasound (termed a 'fluid colour sign') and (3) absence of septations.
- Primary pleural masses, commonly from metastatic disease rather than primary neoplasm, typically present as pleural based echogenic nodules or masses often associated with pleural effusion.
- Sonographic findings associated with a pneumothorax include: (1) absence of the normal gliding motion of the lung due to loss of normal tension between the visceral and parietal pleural layers when air is introduced into the pleural space; and (2) absence of the normal reverberations (i.e. comet-tail artefacts) at the pleura–lung interface with subsequent development of a homogeneous posterior acoustic shadow.

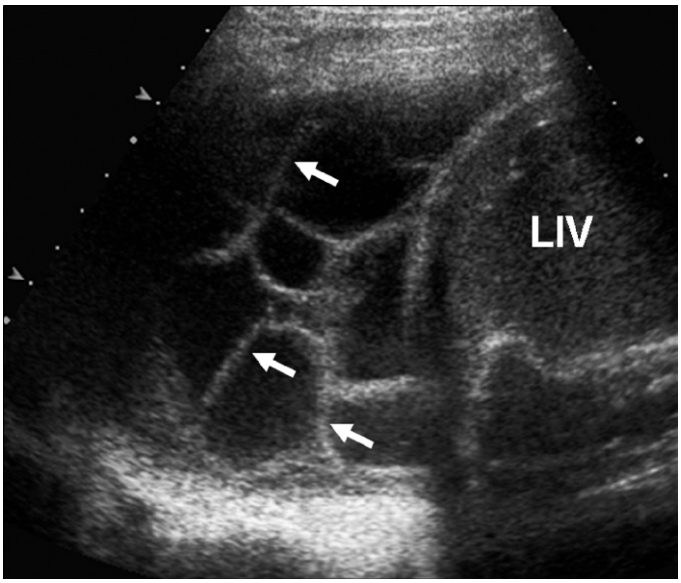

Figure 68.22 Complex effusion. A longitudinal view of the right hemithorax in a 10-year-old girl with pneumonia demonstrates a large complex pleural effusion with multiple internal septations (arrows). LIV, liver.

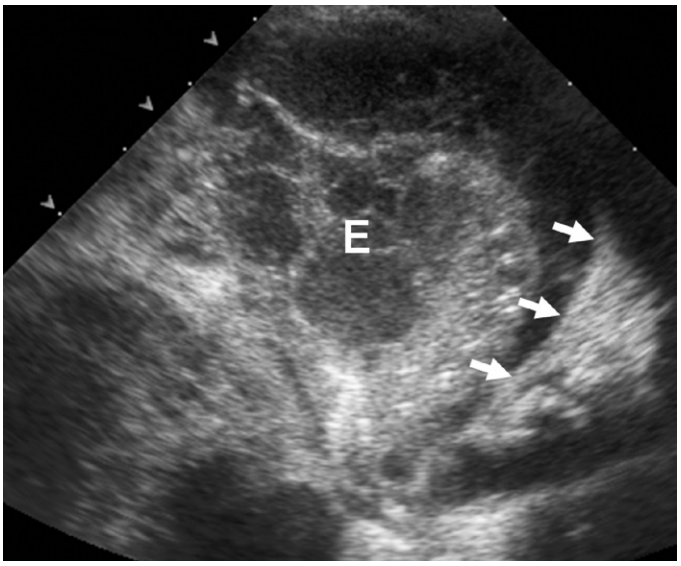

Figure 68.24 Empyema. A transverse view of the left lower hemithorax in a 1-month-old shows a large pleural effusion (E) containing echogenic particles, septations and heterogeneous adjacent lung parenchyma (arrows).

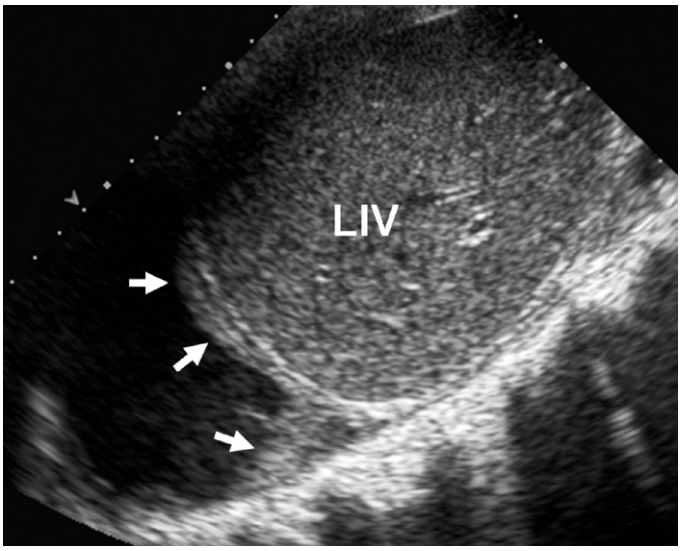

Figure 68.23 Complex effusion. A longitudinal view of the right hemithorax in an 8-year-old girl shows a large effusion and thickened and echogenic adjacent pleura (arrows). LIV, liver.

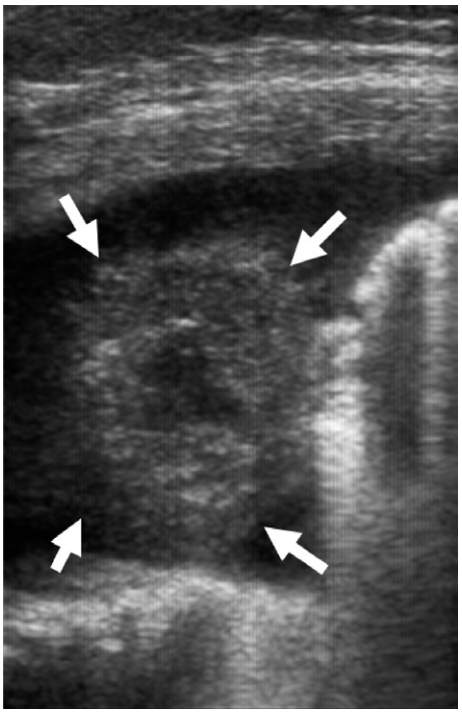

Figure 68.25 Haemothorax. A longitudinal view of the left hemithorax in a 7-week-old girl with an effusion on chest radiography following repair of aortic coarctation. Organised blood clot (arrows) appears as a heterogeneously echogenic mass surrounded by pleural effusion.

Pleural masses

Primary pleural masses are commonly from metastatic disease rather than primary neoplasm. They typically present as pleural based echogenic nodules or masses often associated with pleural effusion which may contain echogenic or haemorrhagic debris (Figs 68.26 and 68.27).

Pneumothorax

Chest radiography is the imaging modality of choice for detecting pneumothorax in paediatric patients. However, understanding the characteristic sonographic appearance of pneumothorax is paramount since a pneumothorax can be present incidentally during ultrasound examinations performed for another clinical indication. Sonographic findings associated with a pneumothorax include: (1) absence of the normal gliding motion of the lung due to loss of normal tension between the visceral and parietal pleural layers when air is introduced into the pleural space; and (2) absence of the normal reverberations (i.e. comet-tail artefacts) at the

Sonographic findings of mediastinal masses

- Teratoma is a complex mass containing an admixture of tissues, including sebum or serous fluid, which appears hypoechoic, and hair, calcifications, bone or fat which appear hyperechoic.
- Enlarged lymph nodes and thymic infiltration appear as well marginated, heterogeneous or homogeneous masses in lymphoma.
- Foregut duplication cysts, regardless of type or location, are typically thin-walled hypoechoic cystic lesions with increased through-transmission.
- Neuroblastoma typically appears as a sharply marginated, fusiform paraspinal mass which may contain hypoechoic areas representing cystic necrosis or degeneration and echogenic areas due to associated calcification.

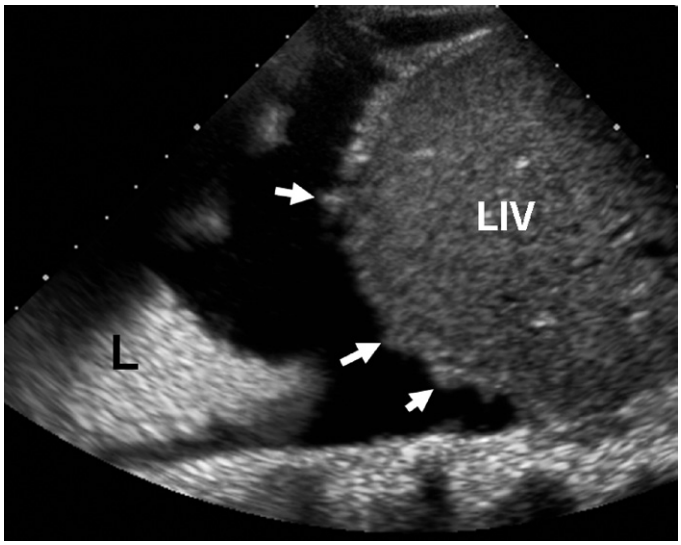

Figure 68.26 Pleural metastases. A longitudinal view of the right lower hemithorax in a 16-year-old girl with a known metastatic papillary thyroid carcinoma shows multiple echogenic pleural based metastatic nodules (arrows). L, lung. LIV, liver.

pleura–lung interface with subsequent development of a homogeneous posterior acoustic shadow.[5,6,53,54] Loss of the normal gliding motion is known as the 'curtain sign'.[2] Mobile air–fluid levels are a finding of hydropneumothorax.[55]

MEDIASTINUM

Chest masses are most commonly located within the mediastinum in infants and children.[56] In general, CT or MRI are studies of choice for confirmation and further characterisation of mediastinal masses detected on chest radiography. Ultrasound is not routinely used for evaluation of the mediastinum although in the neonate or young infant with a mediastinal mass, ultrasound can characterise the cystic, solid or vascular nature of the lesion if it is located close to the diaphragm or thymus, which can serve as acoustic windows. Masses also can be detected incidentally on ultrasound examinations performed for evaluation of pleural effusions and the associated mass may be imaged. The ultrasound features of common mediastinal masses are discussed below.

Anterior mediastinal masses

Teratomas and lymphomas are the common anterior mediastinal masses. Teratoma is a complex mass containing an admixture of tissues, including sebum or serous fluid, which appear hypoechoic, and hair, calcifications, bone or fat, which appear hyperechoic.[5,57] Teratoma is typically avascular or hypovascular. Because they are non-pliable, they compress and displace adjacent structures.

Lymphoma, especially Hodgkin's disease, is the most common malignant tumour involving the mediastinum in older children and adolescents.[5] In younger children non-Hodgkin's lymphoma will give similar appearances. Mediastinal involvement may involve lymph nodes, the thymus, or both. Enlarged lymph nodes and thymic infiltration appear as well-marginated, heterogeneous or homogeneous masses (Fig. 68.28). They may be hypoechoic or isoechoic relative to adjacent soft tissues.[5] The abnormal thymus loses its pliability, and it may deform and compress adjacent structures. Lymphomatous nodes and thymic infiltration are relatively avascular on Doppler imaging. By comparison, inflammatory and malignant adenopathy secondary to metastases are often hypervascular.

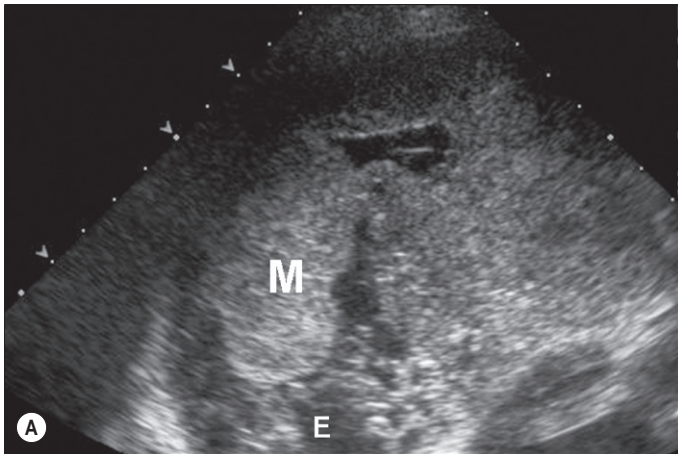

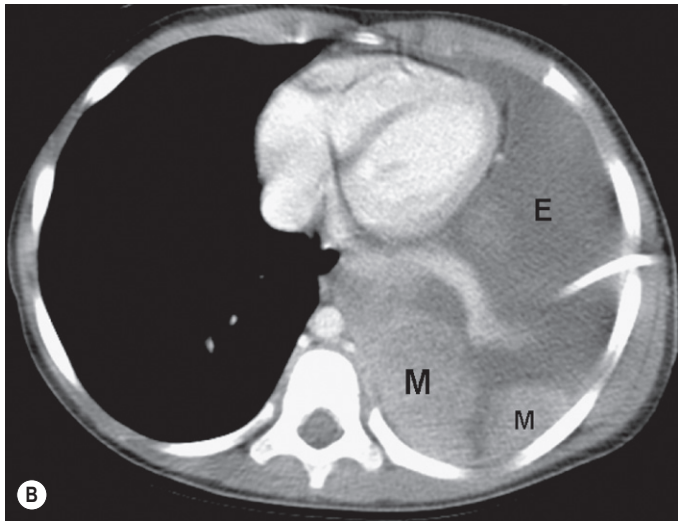

Figure 68.27 Pleural metastases. A: A transverse view of the left lower hemithorax in a 7-year-old girl with an immature teratoma demonstrates an echogenic mass (M) surrounded by a complex pleural effusion (E). **B:** CT scan confirms pleural based metastatic masses (M) surrounded by a large pleural effusion (E). The highly dense linear structure is a left chest tube.

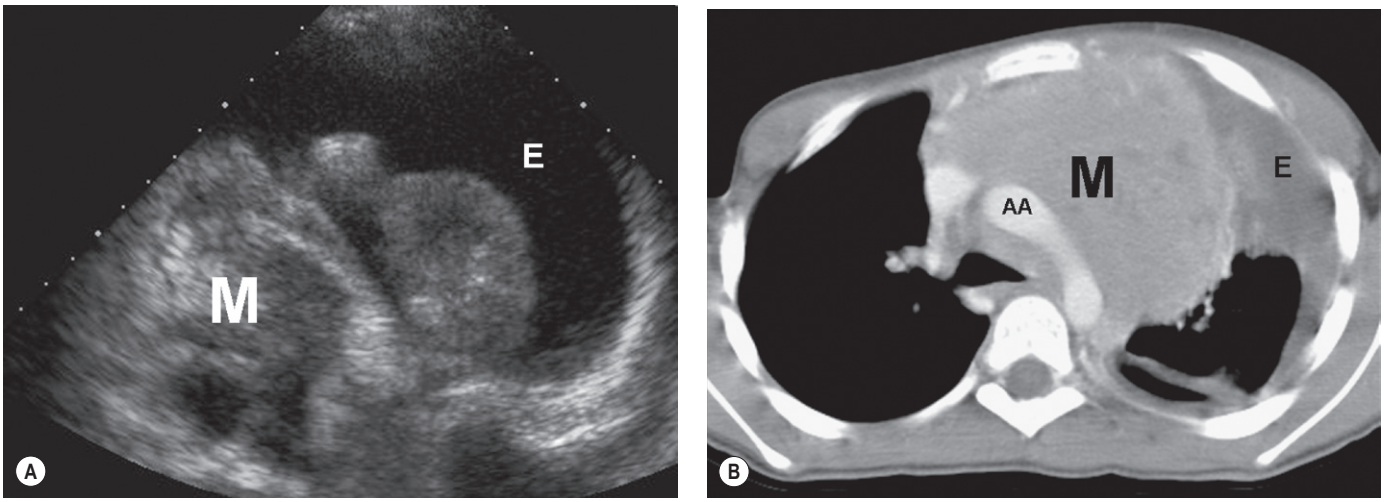

Figure 68.28 Hodgkin's lymphoma. A: A transverse view of the upper left hemithorax demonstrates a heterogeneous mass (M) surrounded by pleural effusion (E). **B:** CT image at the level of aortic arch (AA) confirmed a heterogeneous mass (M), representing infiltrated thymus, with adjacent pleural effusion (E).

Middle mediastinal masses

Middle mediastinal masses are mostly adenopathy secondary to infection, lymphoma or metastatic disease and foregut malformations.[5,56] Enlarged lymph nodes appear as multiple discrete or confluent hypoechoic or isoechoic masses relative to adjacent muscle. Increased blood flow can be seen on colour Doppler ultrasound.

Foregut cysts are classified as bronchogenic, enteric or neurenteric.[5,40,56] Bronchogenic cysts are lined by respiratory epithelium and most are located in the subcarinal or right paratracheal regions. Enteric duplications are lined by gastrointestinal mucosa and usually are located close to or within the oesophageal wall. Neurenteric cysts are lined by gastrointestinal epithelium and are connected to the meninges through a midline defect in one or more vertebral bodies.

Foregut duplication cysts, regardless of type or location, are typically thin-walled hypoechoic cystic lesions with increased through-transmission (Fig. 68.29).[5,6] Increased echogenicity can be seen if the contents of the cyst contain mucoid or proteinaceous material, debris or air. Uncomplicated cysts are avascular. Increased blood flow within the wall or surrounding soft tissues can be seen if the cyst is infected.

Posterior mediastinal masses

Posterior mediastinal masses are usually neurogenic tumours, most commonly neuroblastoma.[5,56] Neuroblastoma appears as a sharply marginated, fusiform paraspinal mass. It is iso- or hyperechoic relative to thymus or chest wall muscle and it may contain hypoechoic areas representing cystic necrosis or degeneration and echogenic areas due to associated calcification (Fig. 68.30). Intraspinal extension can be recognised by ultrasound if the tumour causes cord displacement. Although ultrasound can show intraspinal extension, CT or MRI is the preferred imaging modality for evaluating extent of tumour involvement.

Cardiophrenic angle masses

Pericardial cysts are rare and commonly located within the right cardiophrenic angle; however, they can be also located anywhere along the pericardium.[58] They typically are unilocular, well marginated and anechoic or hypoechoic (Fig. 68.31). The echogenicity increases if the fluid is haemorrhagic or viscous. Pericardial cysts usually do not displace or compress adjacent mediastinal structures.

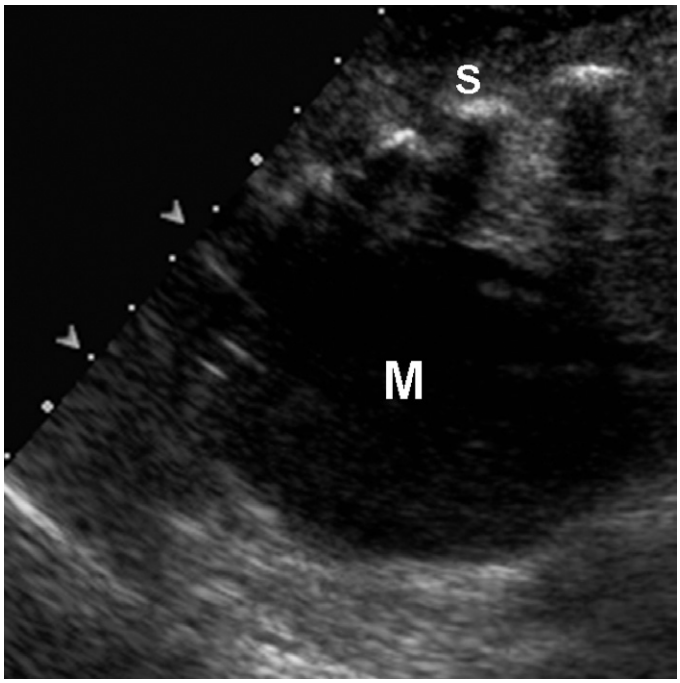

Figure 68.29 Bronchogenic cyst. A paraspinal view of the mid thorax in a 2-week-old girl demonstrates a large cystic mass (M) with imperceptible walls located within the middle/posterior mediastinum. S, spine.

DIAPHRAGMATIC ABNORMALITIES

Diaphragmatic hernias

Diaphragmatic hernia represents protrusion of abdominal contents into the thoracic cavity via a defect in the diaphragm.[5,13] Congenital

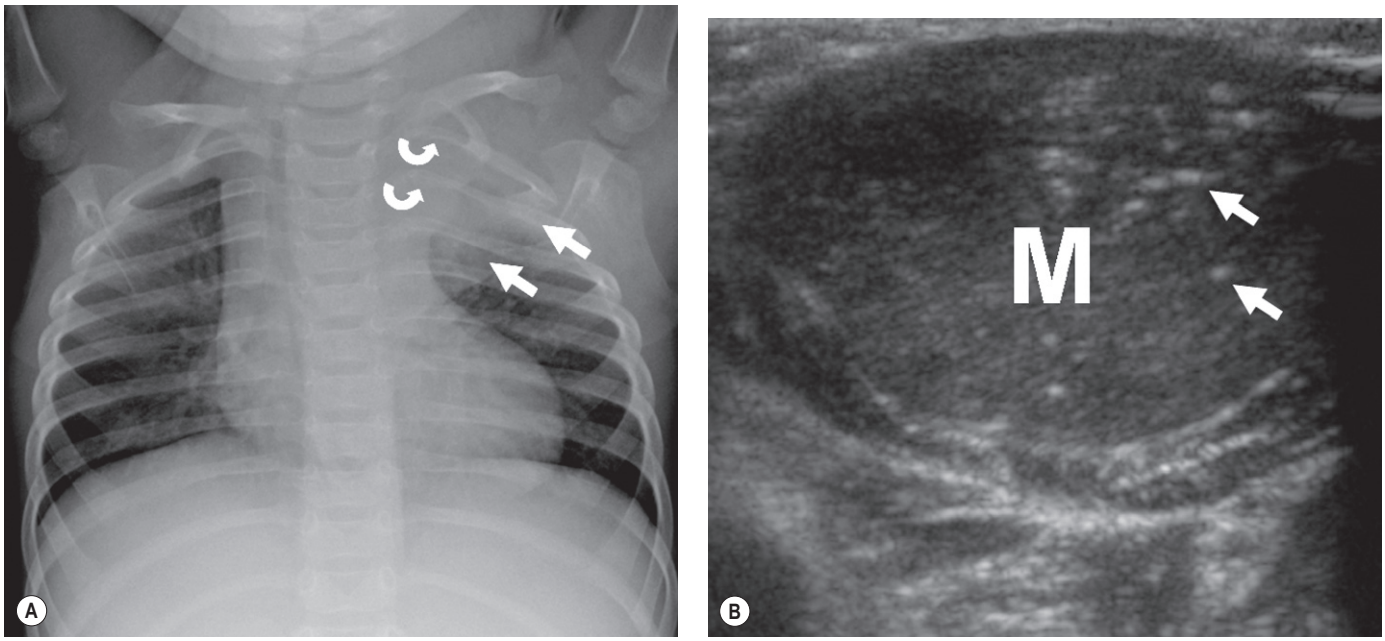

Figure 68.30 **Neuroblastoma. A:** A frontal view of the chest demonstrating left upper hemithorax opacity (arrows) resulting in mediastinal shift to the right. Associated cortical irregularity (curved arrows) of the second and third left ribs is also noted. **B:** A transverse ultrasound through the superior mediastinum demonstrates a relatively hypoechoic solid mass (M) with small echogenic areas (arrows) due to associated calcification.

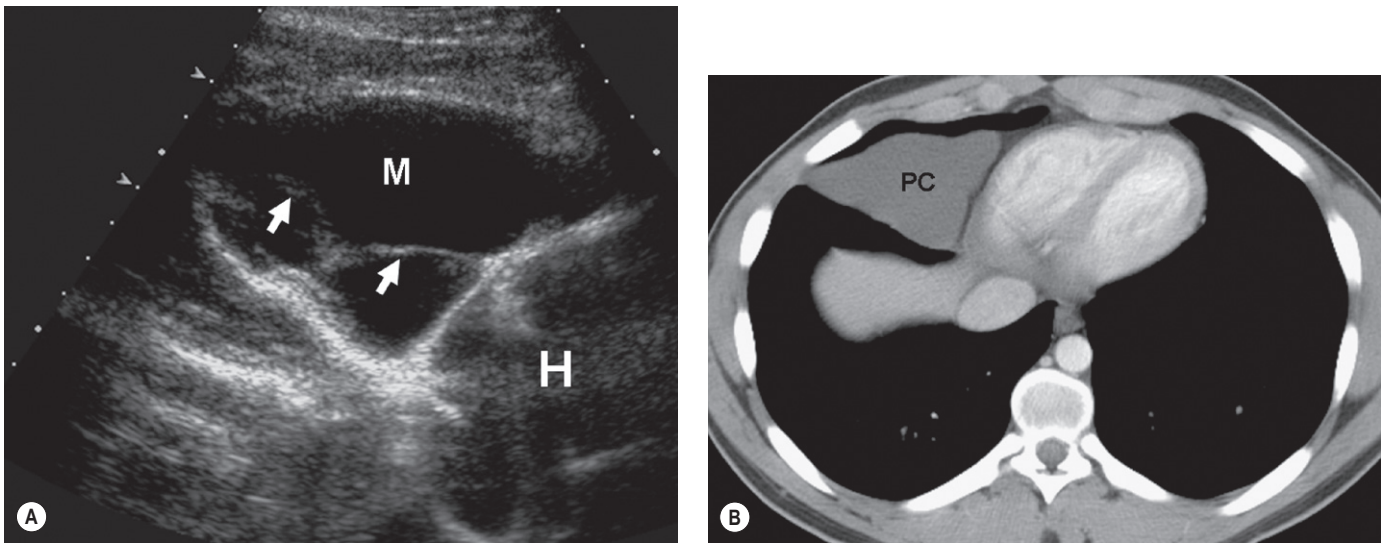

Figure 68.31 **Pericardial cyst. A:** A transverse view of the lower hemithorax in an 18-year-old male with a cardiophrenic mass on chest radiography demonstrates a cystic mass (M) with a few septations (arrows) abutting the heart (H). **B:** An enhanced axial CT image confirmed the pericardial cyst (PC).

Sonographic findings in diaphragmatic abnormalities

- Sonographic findings of both congenital and acquired diaphragmatic hernias include discontinuity of the normal linear diaphragmatic echoes and the presence of intra-abdominal contents within the thoracic cavity.
- Eventration of the diaphragm presents as a focally thinned, but intact diaphragm that protrudes superiorly and is adjacent to the liver or spleen.
- In diaphragmatic paralysis or paresis the sonographic findings are absent or paradoxical diaphragmatic motion during deep inspiration and expiration.

diaphragmatic hernia is more common than acquired herniation in infants and children. Acquired diaphragmatic hernia is typically associated with penetrating or blunt trauma. There are two types of congenital diaphragmatic hernia: Morgagni hernia and Bochdalek hernia. Bochdalek hernia, which is more common than Morgagni hernia, is located posteriorly while Morgagni hernia is positioned anteriorly. Diaphragmatic hernias are more common on the left side than right side, which is presumed to be due to the protective effect of the liver. Left-sided defects can contain the left lobe of the liver, the spleen, the stomach, the large or small bowel, or the kidney. Right-sided defects contain the right lobe of the liver and occasionally other abdominal viscera.

The diagnosis of a diaphragmatic hernia can be confidently established when air-filled bowel loops are visualised in the chest on

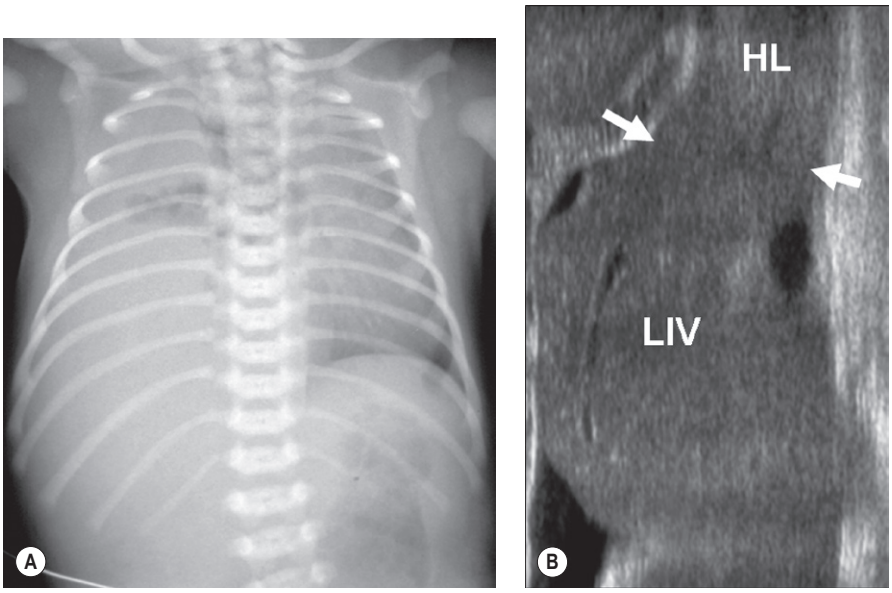

Figure 68.32 Bochdalek diaphragmatic defect. A: A frontal chest radiograph of a newborn boy who presented with respiratory distress shows opacity in the right hemithorax associated with non-visualisation of the ipsilateral hemidiaphragm. **B:** A sagittal view of the right mid hemithorax demonstrates superiorly herniated liver (HL) in the lower right thorax through a large diaphragmatic defect (arrows). LIV, intra-abdominal liver.

plain radiographs. However, the diagnosis may not be obvious when the hernia contains fluid-filled bowel loops, which can mimic an elevated hemidiaphragm, pleural effusion or intrathoracic mass. In these instances, ultrasound can provide helpful diagnostic information.

Ultrasound findings of congenital and acquired diaphragmatic hernias are similar and include discontinuity of the normal linear diaphragmatic echoes and the presence of intra-abdominal contents (i.e. bowel, liver, spleen, kidney and omentum) within the thoracic cavity (Fig. 68.32).[1,5,6,59] A hernia containing predominantly solid organs, such as the liver, spleen or kidney, appears echogenic. A hernia containing fluid-filled bowel loops appears hypoechoic. A definite diagnosis of herniated bowel loops can be made when the characteristic echogenic inner lining of mucosa and a hypoechoic rim of smooth muscle is present. Herniated omentum can appear hypoechoic, isoechoic or hyperechoic relative to the liver. Colour Doppler ultrasound can demonstrate omental vessels in the herniated omentum.

Eventration

Eventration of the diaphragm refers to a congenital weakness or thinness of the central tendon or muscle of the diaphragm resulting in poor diaphragmatic function.[5,60] The cause is thought to be hypoplasia of the diaphragmatic muscle. Eventration is more often left-sided than right-sided and usually focal, affecting the anteromedial portion of the right diaphragm.[5] Less commonly it involves an entire hemidiaphragm. Ultrasound findings are a focally thinned, but intact diaphragm that protrudes superiorly and is adjacent to the liver or spleen (Fig. 68.33).[5] Diaphragmatic motion is decreased or absent. It is important to note that ultrasound differentiation of diaphragmatic eventration from hernia may be difficult when the affected portion of diaphragm is markedly thinned.[5]

Paralysis and paresis

Diaphragmatic paralysis or paresis is usually a result of phrenic nerve injury due to mediastinal or cardiac surgery, birth injury, trauma, chest tube placement or inflammatory conditions such as pneumonia or subphrenic abscess. The sonographic diagnosis of paralysis is made when diaphragmatic motion is absent or paradoxical during deep inspiration and expiration.[1,5,14–20] When motion is paradoxical, the affected hemidiaphragm moves cranially during inspiration and caudally during expiration (Fig. 68.34).[5] In patients with a paretic or weak diaphragm the degree of excursion of the anterior, middle and posterior portions of the diaphragm is similar. Of note, normally excursion of the middle and posterior thirds of diaphragm is greater than that of the anterior third.[5]

CHEST WALL LESIONS

High-resolution ultrasound with colour Doppler can provide valuable information about the cystic, solid or vascular nature of a chest wall lesion and also the extent of the lesion. In general, non-tender, cystic and vascular chest wall lesions tend to be benign, while painful, growing and solid masses are more likely to be malignant. For definite diagnosis, surgical biopsy/resection with histological analysis is required for most chest wall lesions with the exception of benign lesions with pathognomonic findings, such as haemangioma and lipoma.

Soft tissue lesions

Benign masses

The common benign masses of the chest wall include congenital lesions (haemangiomas and vascular malformation, lipomas), infections (cellulitis, abscess) and haematoma.[61,62] Haemangiomas are the most common tumours in infancy typically appearing in the first week of life.[63,64] They are characterised by spontaneous course of an initial rapid postnatal growth, a variable period of stability, and then followed by subsequent slow involution. Although the correct diagnosis of most haemangiomas can be relatively easily made based on clinical examination, which typically demonstrates a soft tissue mass with associated reddish overlying skin discoloration, imaging study is helpful for evaluating extent of the haemangioma, particularly for deep haemangiomas with normal overlying skin. It has been reported that ultrasound is the best imaging modality to define and characterise haemangiomas. On ultrasound with colour Doppler, chest wall haemangioma typically presents as a well-circumscribed soft tissue mass with variable echogenicity with increased internal blood flow during the proliferative phase (Fig. 68.35).[5,63–66] Haemangioma is typically characterised by: (1) a high vessel density (>5 vessels/cm^2); (2) a high Doppler shift (>2 kHz); (3) low resistance; and (4) little or no evidence of arteriovenous shunting.[64,65] On the other hand, during the involution phase, the

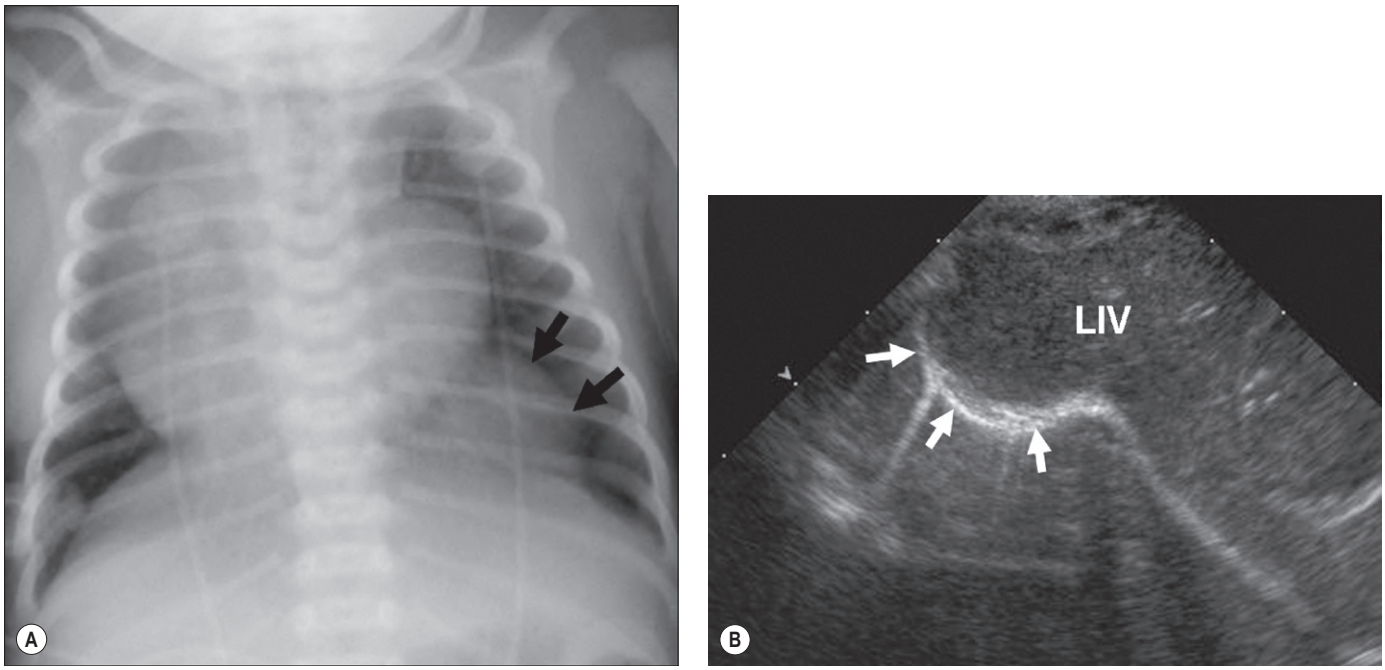

Figure 68.33 Diaphragmatic eventration. A: A frontal chest radiograph of a 2-day-old boy with tetralogy of Fallot shows a well-marginated opacity abutting the medial left hemidiaphragm (arrows). **B:** Transverse sonogram demonstrates a focal diaphragmatic bulge (arrows) containing liver (LIV). Note that the diaphragm is intact.

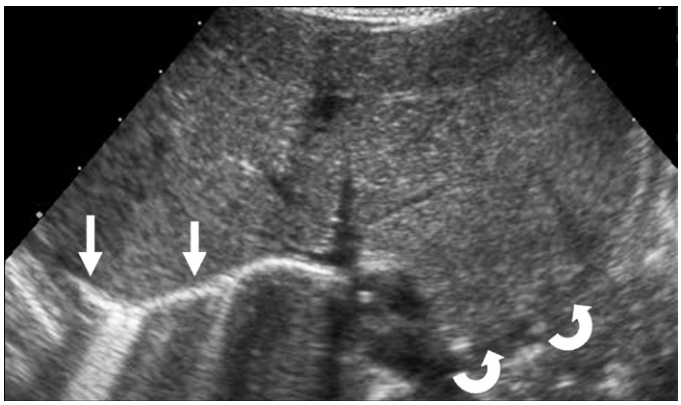

Figure 68.34 Diaphragmatic paralysis. A transverse view of the diaphragm in a 6-month-old boy during expiration demonstrates normal anterior movement of the right hemidiaphragm (arrows) and no excursion of the left hemidiaphragm (curved arrows).

Sonographic findings in chest wall masses

- Sonographic findings of haemangioma are typically a well-circumscribed echogenic mass in the subcutaneous tissues with increased central flow and dilated feeding vessels on colour Doppler ultrasound.
- Lymphatic malformation usually appears as a multiloculated cystic mass with internal septa of varying thickness.
- Chest wall abscesses are typically hypoechoic or anechoic fluid collections with internal echoes, septations or fluid–fluid levels, and posterior acoustic enhancement.
- Malignant chest wall masses are heterogeneous echogenic, vascular soft tissue masses with ill-defined or irregular borders often associated with underlying rib destruction and pleural effusion.
- Unossified costochondral and cartilaginous abnormalities appear hypoechoic compared with adjacent echogenic cortex.

decrease in number of vessels while maintaining high systolic flow within the remaining vessels is typically seen on ultrasound with colour Doppler (Fig. 68.35).[5,63–65] Scattered, more focal hyperechoic areas may be seen if the lesion contains dystrophic calcification or fat.

Vascular malformations are developmental anomalies of the embryonic vascular system which occur between the fourth and tenth weeks of gestation.[64] Based on the currently accepted classification of vascular lesions by Mulliken and Glowacki,[63,67] vascular malformations are currently subdivided into high-flow arteriovenous malformations and low-flow capillary, venous, lymphatic or combined malformations. Although vascular malformations are typically present at birth similar to haemangioma, vascular malformations do not spontaneously regress unlike haemangioma.

Arteriovenous malformations (AVMs) are characterised by abnormal communications between arteries and veins without intervening normal capillary bed.[64] On ultrasound with colour Doppler, AVMs are characterised as a heterogeneous mass with feeding vessels, high vessel density and high systolic flow, and multiple areas of arteriovenous shunting.[64] Arterialisation of veins is present in AVMs in contrast to haemangiomas.[64]

Venous malformations are soft and compressible masses associated with overlying bluish skin discoloration. On ultrasound, venous malformations are characterised by a soft tissue mass with a mixed echogenicity with occasional (16%) association with phleboliths.[64] Either low flow, monophasic flow, or no flow at all can be detected on ultrasound with Doppler. It is important to note that underlying thrombosis may be the reason for no flow within venous malformations.

Lymphatic malformations typically present as smooth soft tissue masses before the second year of life. Lymphatic malformation can be further subcategorised into macrocystic, microcystic and mixed types.[64] Ultrasound imaging findings reflect the different subtypes of lymphatic malformation. While ultrasound typically shows a multiloculated cystic mass without internal flow except the internal septa of varying thickness in cases of macrocystic type lymphatic

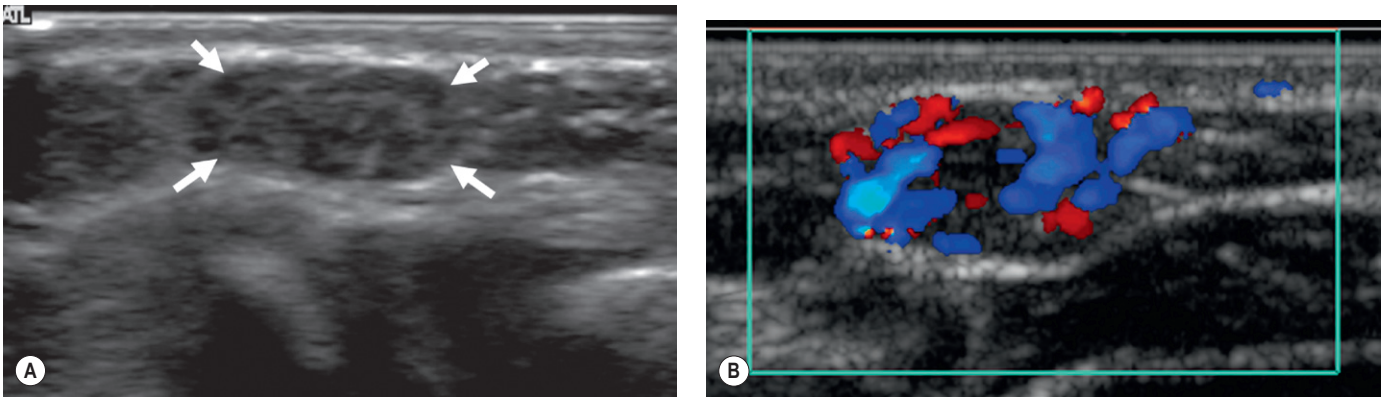

Figure 68.35 Haemangioma. A: A transverse view of a palpable mass in the right anterior chest wall in a 2-year-old girl demonstrates a well-marginated echogenic mass (arrows) with scattered hyperechoic areas representing fatty stroma. **B:** A transverse colour Doppler image demonstrates multiple vascular channels within the mass.

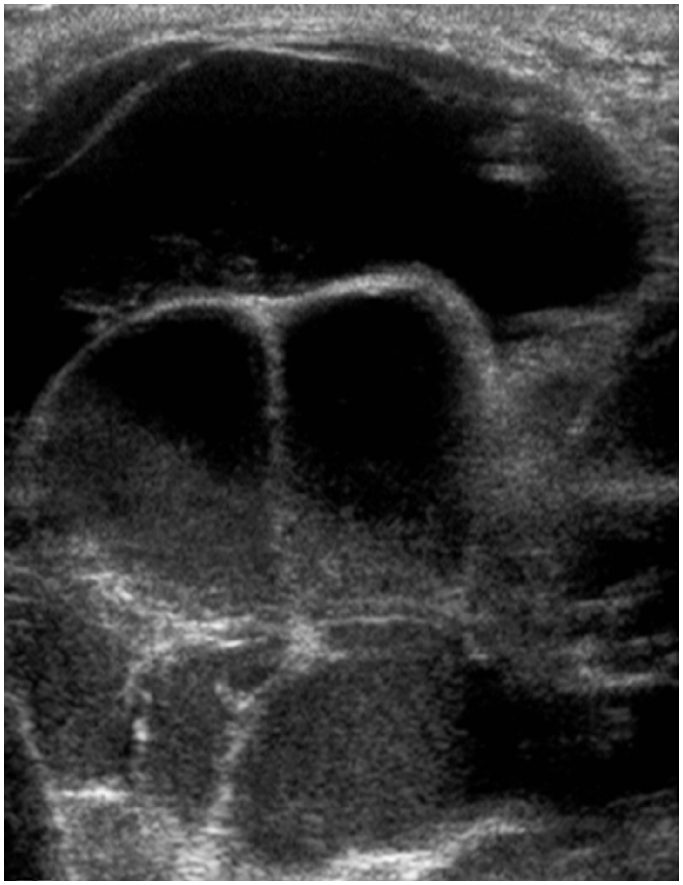

Figure 68.36 Lymphangioma. A transverse view of the right mid chest wall in a 9-month-old girl demonstrates a multiloculated hypoechoic mass with internal septa.

malformation (Fig. 68.36),[1,5,64] microcystic type lymphatic malformation are typically hyperechoic due to underlying numerous sonographic interfaces without underlying blood flow on ultrasound with Doppler. Low-level echoes in the fluid portion of the lymphatic malformation suggest haemorrhage or infection.

Lipoma is a benign tumour consisting of fatty tissue. On ultrasound, lipomas are typically avascular echogenic masses with either well-circumscribed or imperceptible borders.[5]

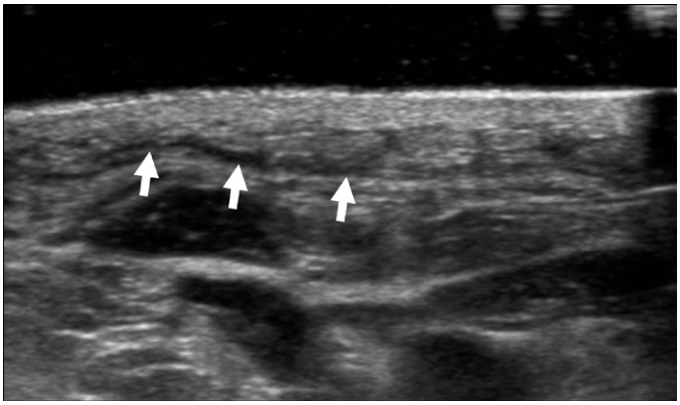

Figure 68.37 Cellulitis. A longitudinal view of the left lateral chest wall in a 10-year-old girl with a insect bite shows thickened and hyperechoic subcutaneous tissues with reticular hypoechoic striations (arrows) secondary to oedema.

Cellulitis results from an acute infection of the deep subcutaneous tissues of the dermis. *Staphylococcus aureus* and group A *Streptococcus* are the two common inciting bacterial organisms.[5] Ultrasound findings include increased echogenicity of the subcutaneous tissues, a reticular pattern of anechoic or hypoechoic striations secondary to oedema dissecting along the subcutaneous tissue septa, and increased blood flow on colour Doppler images (Fig. 68.37).[5]

Aggressive subcutaneous infection of the chest wall can result in abscess formation. Ultrasound can be useful in both diagnosis and guidance of percutaneous drainage procedures. Abscesses are typically hypoechoic or anechoic fluid collections with internal echoes, septations or fluid–fluid levels, and posterior acoustic enhancement (Fig. 68.38). Highly reflective foci suggest gas within the abscess cavity. Other findings include a thick wall around the cyst and associated cellulitis. Doppler imaging shows flow around the periphery of the abscess and in the adjacent soft tissue. The centre of the abscess is avascular. Associated osteomyelitis should be considered when there is disruption or irregular thickening of the cortex of adjacent ribs (Fig. 68.39).

Haematoma is a relatively common soft tissue mass in children. It is almost always associated with prior trauma and less commonly with underlying bleeding diatheses. Acute haematomas are hyperechoic due to the presence of fibrin and have relatively ill-defined margins. Subacute haematomas have hypoechoic central areas and well-marginated echogenic borders. Chronic haematomas are anechoic, well-circumscribed masses.[5]

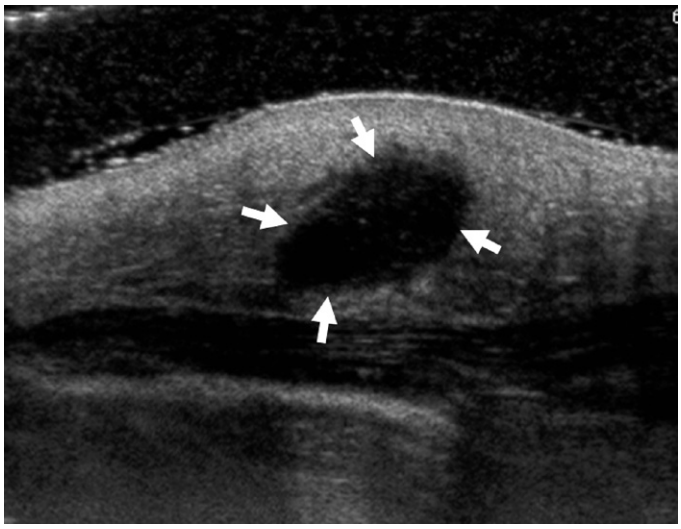

Figure 68.38 Soft tissue abscess. A transverse view of the right lower chest wall in a 4-year-old boy with skin erythema and fever demonstrates a hypoechoic fluid collection (arrows) with scattered internal echoes. Also note thickened and echogenic subcutaneous tissues due to cellulitis.

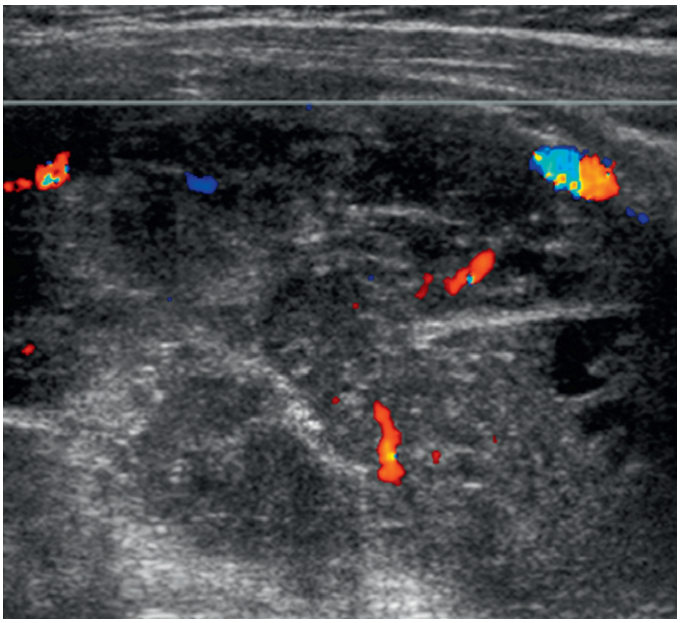

Figure 68.40 Rhabdomyosarcoma. A transverse colour Doppler scan of the left lateral chest wall just below the axilla in a 6-year-old girl who presents with an enlarging chest wall mass shows a heterogeneous, vascular solid mass with ill-defined margins.

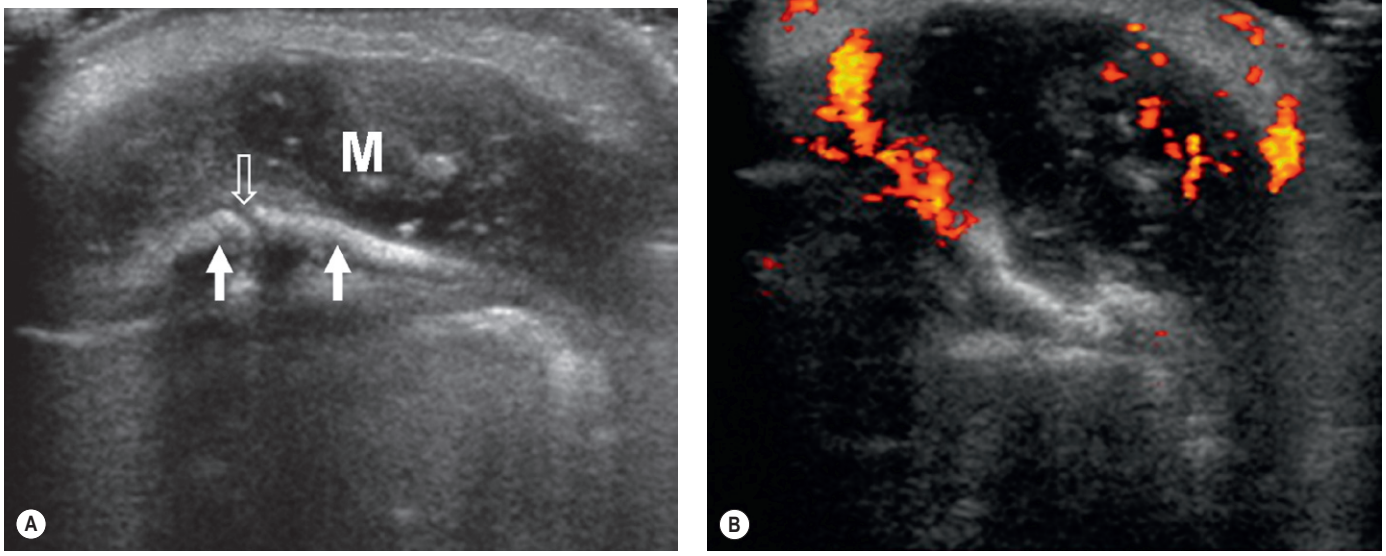

Figure 68.39 Soft tissue abscess with osteomyelitis. A: Transverse scan of the lower left chest wall over an area of soft tissue swelling shows a heterogeneous, hypoechoic mass (M) immediately anterior to the left ninth rib (arrows). The cortex of the rib is irregular and thickened, consistent osteomyelitis. There also is focal cortical disruption (fracture) (open arrow). **B:** Colour Doppler scan shows peripheral flow around the abscess.

Malignant masses

The common malignant chest wall masses in children include rhabdomyosarcoma, fibrosarcoma, primitive neuroectodermal tumour and the Ewing family of tumours.[68,69] Sonographic findings vary widely but, in general, the diagnosis of a malignant chest wall mass should be considered when a heterogeneously echogenic, vascular soft tissue mass with ill-defined or irregular borders is observed on ultrasound (Fig. 68.40).[5] Associated rib destruction and pleural effusion support the diagnosis.[70] However, ultrasound features are not specific for malignancy and the findings can mimic those of benign conditions such as haematomas, abscess and some benign soft tissue tumours. Biopsy is needed for definitive diagnosis.

Cartilaginous and osseous lesions

Cartilaginous rib abnormalities can present as firm chest wall masses in children and ultrasound may be the initial diagnostic imaging study. The common skeletal lesions include asymmetric cartilaginous costochondral junctions, enlarged rib ends,

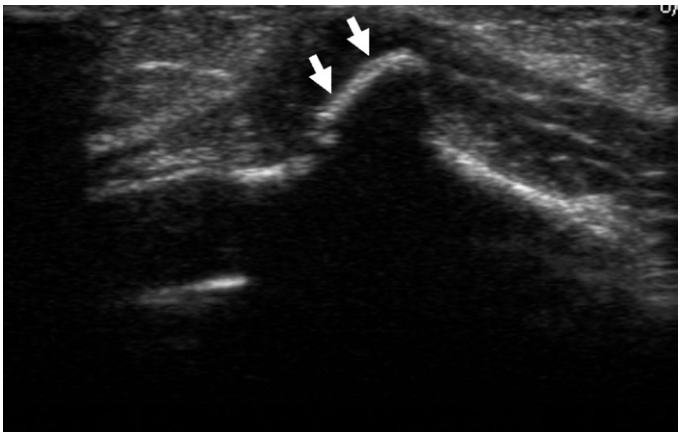

Figure 68.41 Osteochondroma. A 7-year-old boy who presents with a longstanding, non-tender and palpable left chest wall mass. A transverse ultrasound demonstrates enlargement of the end of the left seventh rib (arrows). The cartilaginous part of the rib is hypoechoic, whereas the cortex is echogenic.

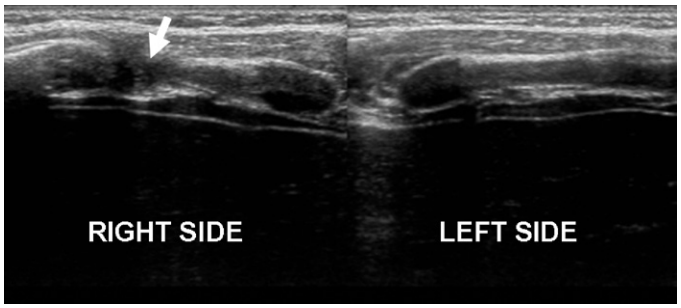

Figure 68.42 Fracture. Longitudinal split screen scan of the upper anterior ribs bilaterally in an 11-year-old boy who was involved in a dirt bike accident demonstrates cortical disruption of the right rib (arrow) near the costochondral junction. The cortex of the left-sided rib is intact.

osteochondromas, and acute or healing rib fractures (Figs 68.41 and 68.42).[1,5,71] Unossified costochondral and cartilaginous abnormalities will appear hypoechoic compared with adjacent echogenic cortex.[5] Acute rib fractures are associated with cortical disruption and surrounding soft tissue swelling.[70,72,73] A healing rib fracture can show callous formation manifested as thickened cortex on ultrasound. Comparison views of the contralateral side can be useful when ultrasound findings on the affected side are equivocal.

REFERENCES

1. Coley BD. Pediatric chest ultrasound. Radiol Clin North Am 2005; 43(2):405–418.
2. Ben-Ami TE, O'Donovan JC, Yousefzadeh DK. Sonography of the chest in children. Radiol Clin North Am 1993; 31:517–531.
3. Koh D, Burke S, Davies N, Padley SP. Transthoracic US of the chest: clinical uses and applications. Radiographics 2002; 22:1e.
4. Kim OH, Kim WS, Kim MJ, et al. US in the diagnosis of pediatric chest diseases. Radiographics 2000; 20(3):653–671.
5. Siegel MJ. Chest. In: Siegel MJ, ed. Pediatric sonography. Philadelphia: Lippincott Williams & Wilkins; 2002: 167–211, 2010;164–199.
6. Enriquez G, Aso C, Serres X. Chest ultrasound. In: Lucaya J, Strife JL, eds. Pediatric chest imaging. Berlin: Springer Science + Business Media; 2008: 1–35.
7. Boehm T. Thymus development and function. Curr Opin Immunol 2008; 20(2):178–184.
8. Nishino M, Ashiku SK, Kocher ON, et al. The thymus: a comprehensive review. Radiographics 2006; 26(2):335–348.
9. Jacobs MT, Frush DP, Donnelly LF. The right place at the wrong time: historical perspective of the relation of the thymus gland and pediatric radiology. Radiology 1999; 210(1):11–16.
10. Liang CD, Huang SC. Sonographic study of the thymus in infants and children. J Formos Med Assoc 1997; 96(9):700–703.
11. Adam EJ, Ignotus PI. Sonography of the thymus in healthy children: frequency of visualization, size, and appearance. AJR Am J Roentgenol 1993; 161:153–155.
12. Pozniak MA, Zagzebski JA, Scanlan KA. Spectral and color Doppler artifacts. Radiographics 1992; 12(1):35–44.
13. Skandalakis JE, Gray SW, Ricketts RR. The diaphragm. In: Skandalakis JE, Gray SW, eds. Embryology for surgeons. 2nd edn. Baltimore: Williams & Wilkins; 1994: 491–539.
14. Houston JG, Fleet M, Cowan MD, McMillan NC. Comparison of ultrasound with fluoroscopy in the assessment of suspected hemidiaphragmatic movement abnormality. Clin Radiol 1995; 50(2):95–98.
15. Houston JG, Angus RM, Cowan MD, et al. Ultrasound assessment of normal hemidiaphragmatic movement: relation to inspiratory volume. Thorax 1994; 49(5):500–503.
16. Gottesman E, McCool FD. Ultrasound evaluation of the paralyzed diaphragm. Am J Respir Crit Care Med 1997; 155(5):1570–1574.
17. Gerscovich E, Cronan M, McGahan J, et al. Ultrasonographic evaluation of diaphragmatic motion. J Ultrasound Med 2001; 20: 597–604.
18. Patel AS, O'Donnell C, Parker MJ, Roberts DH. Diaphragm paralysis definitively diagnosed by ultrasonography and postural dependence of dynamic lung volumes after seven decades of dysfunction. Lung 2007; 185:15–20.
19. Summerhill EM, El-Sameed YA, Glidden TJ, McCool FD. Monitoring recovery from diaphragm paralysis with ultrasound. Chest 2008; 133(3):737–743.
20. Laing IA, Teele RL, Stark AR. Diaphragmatic movement in newborn infants. J Pediatr. 1988; 112:638–643.
21. Park JJ, Kim JW, Kim JP, et al. Two cases of ectopic cervical thymus: case reports and a review of the literature. Auris Nasus Larynx 2006; 33(1):101–105.
22. Scott KJ, Schroeder AA, Greinwald JH Jr. Ectopic cervical thymus: an uncommon diagnosis in the evaluation of pediatric neck masses. Arch Otolaryngol Head Neck Surg 2002; 128(6):714–717.
23. De Foer B, Vercruysse JP, Marien P, et al. Cervical ectopic thymus presenting as a painless neck mass in a child. JBR-BTR 2007; 90(4):281–283.
24. Koumanidou C, Vakaki M, Theophanopoulou M, et al. Aberrant thymus in infants: sonographic evaluation. Pediatr Radiol 1998; 28:987–989.
25. Krysta MM, Gorecki WJ, Miezynski WH. Thymic tissue manifesting as a posterior mediastinal mass in two children. J Pediatr Surg 1998; 33(4):632–634.
26. Han BK, Yoon HK, Suh YL. Thymic ultrasound: Diagnosis of aberrant cervical thymus. Pediatr Radiol. 2001; 31:480–487.
27. Cohen MD, Weber TR, Sequeira FW, et al. The diagnostic dilemma of the posterior mediastinal thymus: CT manifestations. Radiology 1983; 146(3):691–692.
28. Cory DA, Cohen MD, Smith JA. Thymus in the superior mediastinum simulating adenopathy: appearance on CT. Radiology 1987; 162 (2):457–459.
29. Slovis TL, Meza M, Kuhn JP. Aberrant thymus – MR assessment. Pediatr Radiol 1992; 22(7):490–492.
30. Targhetta R, Chavagneux R, Bourgeois JM, et al. Sonographic approach to diagnosing pulmonary consolidation. J Ultrasound Med 1992; 11:667–672.
31. Lichtenstein DA, Lascols N, Meziere G, Gepner A. Ultrasound diagnosis of alveolar consolidation in the critically ill. Intensive Care Med 2004; 30(2):276–281.
32. Mathis G. Thoraxsonography – Part II: Peripheral pulmonary consolidation. Ultrasound Med Biol 1997; 23(8):1141–1153.
33. Puligandla PS, Laberge JM. Respiratory infections: pneumonia, lung abscess, and empyema. Semin Pediatr Surg 2008; 17(1):42–52.
34. Patradoon-Ho P, Fitzgerald DA. Lung abscess in children. Paediatr Respir Rev 2007; 8(1):77–84.
35. Hogan MJ, Coley BD. Interventional radiology treatment of empyema and lung abscesses. Paediatr Respir Rev 2008; 9(2):77–84.
36. Hsieh YC, Hsiao CH, Tsao PN, et al. Necrotizing pneumococcal pneumonia in children: the role of pulmonary gangrene. Pediatr Pulmonol 2006; 41(7):623–629.

37. Lin CJ, Chen PY, Huang FL, et al. Radiographic, clinical, and prognostic features of complicated and uncomplicated community-acquired lobar pneumonia in children. J Microbiol Immunol Infect 2006; 39(6):489–495.
38. Chen K, Liaw Y, Wang H, et al. Sonographic septations: a useful prognostic indicator of acute thoracic empyema. J Ultrasound Med 2000; 19:837–843.
39. Yikilmaz A, Lee EY. CT imaging of mass-like nonvascular pulmonary lesions in children. Pediatr Radiol 2007; 37(12):1253–1263.
40. Lee EY, Boiselle PM, Cleveland RH. Multidetector CT evaluation of congenital lung anomalies. Radiology 2008; 247(3):632–648.
41. Siegel MJ. Lungs, pleura and chest wall. In: Siegel MJ, ed. Pediatric Body CT. 2nd edn. Philadelphia: Lippincott Williams & Wilkins; 2008:69–120.
42. Rosado-de-Christenson ML, Frazier AA, Stocker JT, Templeton PA. Extralobar sequestration: radiologic-pathologic correlation. Radiographics 1993; 13:425–441.
43. Ceola AF, Angtuaco TL. US case of the day: extralobar pulmonary sequestration. Radiographics 1999; 19:817–819.
44. Benya EC, Bulas DI, Selby DM, Rosenbaum KN. Cystic sonographic appearance of extralobar pulmonary sequestration. Pediatr Radiol 1993; 23:605–607.
45. Schlesinger AE, DiPietro MA, Statter MB, Lally KP. Utility of sonography in the diagnosis of bronchopulmonary sequestration. J Pediatr Surg 1994; 29:52–55.
46. Rosado-de-Christenson ML, Stocker JT. Congenital cystic adenomatoid malformation. Radiographics 1991; 11:865–886.
47. Berrocal T, Madrid C, Novo S, et al. Congenital anomalies of the tracheobronchial tree, lung, and mediastinum: embryology, radiology, and pathology. Radiographics 2004; 24:e17.
48. Weldon CB, Shamberger RC. Pediatric pulmonary tumors: primary and metastatic. Semin Pediatr Surg 2008; 17(1):17–29.
49. Kocijancic I, Vidmar K, Ivanovi-Herceg Z. Chest sonography versus lateral decubitus radiography in the diagnosis of small pleural effusion. J Clin Ultrasound 2003; 31:69–74.
50. Fraser R, Colman N, Muller NL, Pare PD. Pleural disease. In: Fraser R, Colman N, Muller NL, Pare PD. Synopsis of diseases of the chest. 3rd edn. Philadelphia: Elsevier Saunders; 2005: 188–221.
51. Wu RG, Yang PC, Kuo SH, Luh KT. "Fluid color" sign: a useful indicator for discrimination between pleural thickening and pleural effusion. J Ultrasound Med 1995; 14:767–769.
52. Yang P. Applications of colour Doppler ultrasound in the diagnosis of chest diseases. Respirology 1997; 2: 231–238.
53. Dulchavsky SA, Schwarz KL, Kirkpatrick AW, et al. Prospective evaluation of thoracic ultrasound in the detection of pneumothorax. J Trauma 2001; 50:201–205.
54. Rowan KR, Kirkpatrick AW, Liu D, et al. Traumatic pneumothorax detection with thoracic US: correlation with chest radiography and CT – initial experience. Radiology 2002; 225:210–214.
55. Targhetta R, Bourgeois JM, Chavagneux R, et al. Sonographic approach to diagnosing hydropneumothorax. Chest 1992; 101:931–934.
56. Franco A, Mody NS, Meza MP. Imaging evaluation of pediatric mediastinal masses. Radiol Clin North Am. 2005; 43(2):325–353.
57. Wu TT, Wang HC, Chang YC, et al. Mature mediastinal teratoma: sonographic and imaging patterns and pathologic correlation. J Ultrasound Med 2002; 21:759–765.
58. Patel J, Park C, Michaels J, et al. Pericardial cyst: case reports and a literature review. Echocardiography 2004; 21(3):269–272.
59. Taylor GA, Atalabi OM, Estroff JA. Imaging of congenital diaphragmatic hernias. Pediatr Radiol 2008; Jul 8. [Epub ahead of print].
60. Deslauriers J. Eventration of the diaphragm. Chest Surg Clin N Am 1998; 8(2):315–330.
61. Tateishi U, Gladish GW, Kusumoto M, et al. Chest wall tumors: radiologic findings and pathologic correlation: part 1. Benign tumors. Radiographics 2003; 23(6):1477–1490.
62. Watt AJ. Chest wall lesions. Paediatr Respir Rev 2002; 3(4):328–338.
63. Mulliken JB, Fishman SJ, Burrows PE. Hemangiomas and other vascular tumors. In: Mulliken JB, Fishman SJ, Burrows PE, eds. Current problems in surgery: vascular anomalies. St Louis, MO: Mosby; 2000: 529–551.
64. Dubois J, Garel L. Imaging and therapeutic approach of hemangiomas and vascular malformations in the pediatric age group. Pediatr Radiol 1999; 29(12):879–893.
65. Dubois J, Patriquin HB, Garel L, et al. Soft-tissue hemangiomas in infants and children: diagnosis using Doppler sonography. AJR Am J Roentgenol 1998; 171:247–252.
66. Dubois J, Garel L, David M, Powell J. Vascular soft-tissue tumors in infancy: distinguishing features on Doppler sonography. AJR Am J Roentgenol 2002; 178:1541–1545.
67. Mulliken JB, Glowacki J. Hemangiomas and vascular malformations in infants and children: a classification based on endothelial characteristics. Plast Reconstr Surg 1982;69: 412–422.
68. van den Berg H, van Rijn RR, Merks JH. Management of tumors of the chest wall in childhood: a review. J Pediatr Hematol Oncol 2008; 30(3):214–221.
69. Tateishi U, Gladish GW, Kusumoto M, et al. Chest wall tumors: radiologic findings and pathologic correlation: part 2. Malignant tumors. Radiographics 2003; 23(6):1491–1508.
70. Sistrom C, Wallace CK, Gay SB. Thoracic sonography for diagnosis and intervention. Curr Probl Diagn Radiol 1997; 26:2–49.
71. Donnelly LF, Frush DP. Abnormalities of the chest wall in pediatric patients. AJR Am J Roentgenol 1999; 173:1595–1601.
72. Mathis G. Thoraxsonography – Part I: chest wall and pleura. Ultrasound Med Biol 1997; 23:1131–1139.
73. Bitschnau R, Gehmacher O, Kopf A, et al. Ultrasound in the diagnosis of rib and sternal fracture. Ultraschall Med 1997; 18:158–161.

CHAPTER

69

Paediatric liver and bile ducts, gallbladder, spleen and pancreas

Helen Williams

THE LIVER AND BILE DUCTS

Technique and anatomy

In many instances the indications for liver imaging in children do not differ significantly from indications in adults. Common indications for ultrasound scanning include hepatomegaly, a suspected liver mass, jaundice or liver dysfunction, pre and post liver transplantation, monitoring of chronic liver disease and trauma. With the exception of acute trauma, ultrasound is the primary imaging modality and is a standard part of the evaluation of liver disease. The imaging appearances of many hepatic diseases in children such as diffuse parenchymal disease are similar to those in adults but specific clinical indications and pathological disorders in children are unique or more common in the paediatric age group; for example, the investigation of neonatal jaundice, segmental or split liver transplantation and evaluation of a hepatic mass.

A 4–6-hour or overnight fast is recommended if the gallbladder is to be examined but no other preparation or sedation is required when the liver is to be examined using ultrasound. Using a curvilinear probe with frequency appropriate to the child's size, the majority if not all of the paediatric liver can be examined from an anterior subcostal approach. However, the subdiaphragmatic part of the right liver lobe may require an intercostal approach, especially in larger children or adolescents. The ultrasound appearances of the normal liver and its anatomy do not differ significantly from appearances in adults. Normal liver parenchyma in childhood has a fine homogeneous echotexture. In the neonate and young infant the hepatic echotexture is either slightly lower than that of the renal cortex, or is comparable (Fig. 69.1). Usually by 6 months of age, the liver is slightly more echogenic than the renal cortex (Fig. 69.2). Some if not all of this difference relates to the change in renal echogenicity. Small rounded hyperechoic areas in the liver parenchyma represent periportal fibrofatty tissue and ligaments.

The internal measurements of the common bile duct (CBD) should not exceed 1.6 mm in neonates and infants up to 1 year of age; and 3 mm in childhood and early adolescence, with the CBD having a similar diameter to the adjacent hepatic artery. However, the CBD is a distensible structure and does vary slightly in calibre with fluctuations in bile flow especially postprandially.[1] Compared with the spleen, the normal liver is slightly hypoechoic. The upper limit of spleen size in infants and children according to age is given in Table 69.1.

Anatomical variants associated with abnormal position of the liver and spleen

Cardiac malposition and abnormalities of cardiac situs are associated with abnormal position of the liver and spleen. Mirror-image dextrocardia is the most common, and is associated with abdominal situs inversus in which the otherwise normal liver is left-sided and the spleen is right-sided. The liver is usually right-sided in cases of dextroversion with situs solitus. Asplenia and polysplenia syndromes occur with cardiac malpositions and are usually associated with complex congenital heart disease and pulmonary malformations.[3] In both asplenia and polysplenia the liver often lies in the midline and microgastria may be present.[4] It is not possible to confirm complete absence of splenic tissue with ultrasound, but radionuclide studies are definitive (although rarely clinically indicated). Polysplenia is more easily diagnosed with ultrasound and associated abnormalities of the abdominal vasculature should be sought, as there is an increased incidence of interrupted inferior vena cava with azygos continuation. If no spleen is detected in the left upper quadrant, splenic tissue should be looked for in unusual locations in the abdomen.

A 'wandering spleen' refers to a spleen that does not have normal fixed ligamentous attachments (gastrosplenic and splenorenal ligaments). The ligamentous attachments are elongated, allowing the spleen to be highly mobile. Many patients are asymptomatic but the condition can be associated with intermittent abdominal pain if the spleen is undergoing intermittent torsion and de-torsion.

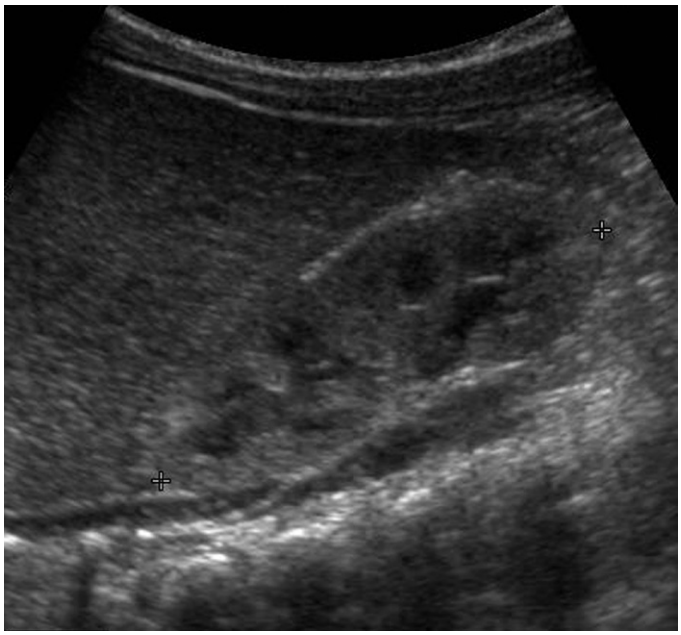

Figure 69.1 Normal liver in a 3-month-old. The echogenicity of the liver and right renal cortex are comparable.

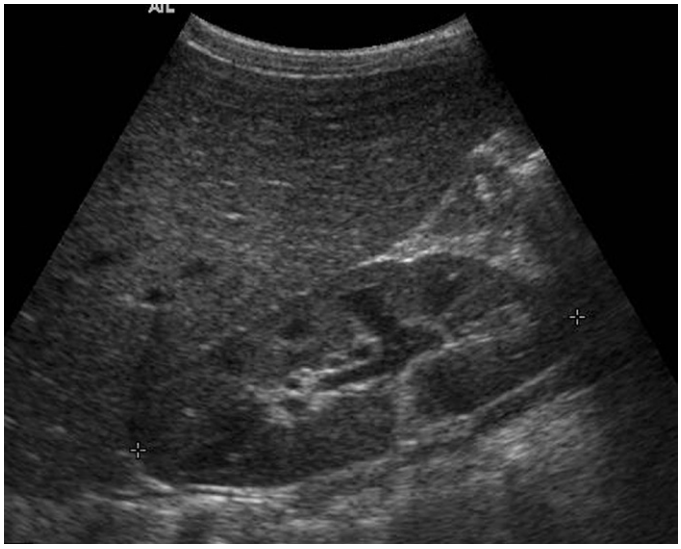

Figure 69.2 Normal liver in a 10-month-old. The liver is slightly more echogenic than the right renal cortex.

Occasionally patients may present with an acute abdomen if the spleen undergoes torsion and infarction.[5]

An accessory spleen or splenunculus is seen on ultrasound as a rounded 'mass' near the inferior border of the spleen or in the splenic hilum (Fig. 69.3). Splenosis results from splenic rupture secondary to trauma or surgery, leading to dissemination or autotransplantation of small amounts of splenic tissue within the peritoneal cavity or, less commonly, elsewhere in the body. Splenic nodules in splenosis are round hypoechoic masses, indistinguishable from accessory spleens.[6] Postnatal persistence of splenic connections with hepatic, gonadal and renal tissue results in splenohepatic, splenogonadal or splenorenal fusions.

Diffuse parenchymal disease

Acute hepatitis is characterised by inflammation and necrosis of the liver. The underlying cause may be infection (viral or non-viral),

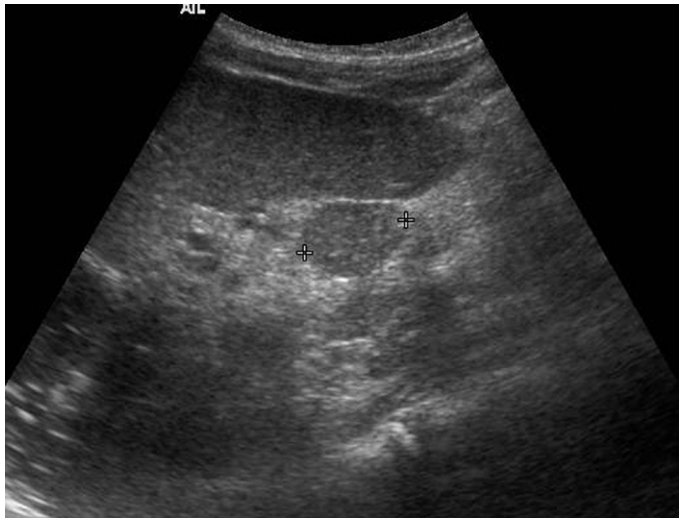

Figure 69.3 Small splenunculus measuring 2 cm at the inferior border of the spleen. The echogenicity of the spleen and splenunculus are comparable.

Table 69.1 Normal spleen size in infants and children[2]

Age	Upper limit of normal spleen length (cm)
0–3 months	6
3–6 months	6.5
6–12 months	7
1–2 years	8
2–4 years	9
4–6 years	9.5
6–8 years	10
8–10 years	11
10–12 years	11.5
12–15 years	12
15–20 years	
Female:	12
Male:	13

autoimmune disease, a metabolic disorder or toxic agent, including certain drugs. A list of infective causes of acute hepatitis is given in Table 69.2.[7] Chronic hepatitis may be caused by a wide range of diseases, with distinct aetiologies that typically lead to slowly progressive inflammatory damage and liver fibrosis. Hepatitis due to viral infection may evolve from an acute inflammatory process to chronicity; autoimmune and drug-induced liver disease are other important causes of chronic hepatitis. In up to 10% of patients with chronic hepatitis the cause remains unknown, or cryptogenic. The ultrasound appearance of acute hepatitis depends more on the severity of disease than its underlying cause. The liver may be normal in size or enlarged with diffuse increase in the parenchymal echogenicity and increased echogenicity of the walls of the portal veins due to hepatocyte oedema. In acute hepatitis the gallbladder wall may also be thickened.[8] In chronic active hepatitis a generalised decrease in hepatic echogenicity is usually seen, with coarsening of the parenchymal echotexture and decreased visualisation of the peripheral portal venous system.[8]

Liver disease is a frequent presentation of many inborn errors of metabolism. Most patients present in the neonatal period with cholestasis or acute liver failure but many of these disorders will

Table 69.2 Infective causes of acute hepatitis[7]

Hepatotrophic viruses	Non-hepatotrophic viruses	Non-viral causes of hepatic infection
Hepatitis A	RNA viruses:	Bacteria:
Hepatitis B, C and D	Paramyxovirus (measles)	*Bartonella henselae/quintana*
Hepatitis E	Togavirus (rubella)	*Brucella melitensis*
Hepatitis F	Enteroviruses	*Legionella pneumophilia*
Hepatitis G	Echovirus	*Leptospira ictohaemorrhagica*
	Coxsackie virus	*Listeria monocytogenes*
	Flaviviruses	*Mycobacterium tuberculosis*
	Yellow fever	*Salmonella typhi*
	Dengue fever	
	Filoviruses	Protozoa:
	Marburg virus	*Toxoplasma gondii*
	Ebola virus	
	Arenavirus (Lassa fever)	Helminths (worms):
		Cestodes (tapeworms)
	DNA viruses:	*Echinococcus multilocularis*
	Parvovirus B19	*Echinococcus granulosus*
	Adenovirus	
	Herpes viruses	Nematodes (roundworms):
	Herpes simplex types 1 and 2	*Ascaris lumbricoides*
	Varicella-zoster virus	*Toxocara canis/T. catis*
	Cytomegalovirus	
	Epstein–Barr virus	Trematodes (flukes):
	Human herpes virus 6	*Schistosoma mansoni*
		Schistosoma japonicum
		Fasciola hepatica

Table 69.3 Metabolic causes of liver disease in childhood and their common presenting features[9]

Presenting feature	Metabolic conditions
Liver failure	Galactosaemia Tyrosinaemia type I Hereditary fructose intolerance Mitochondrial respiratory chain defects Long chain fatty acid oxidation defects Neonatal haemochromatosis α_1-antitrypsin deficiency
Encephalopathy	Fatty acid oxidation defects Organic acidaemias Urea cycle defects
Cholestasis (in the neonatal period or later)	All disorders that cause liver failure *plus* Peroxisomal disorders Congenital disorders of glycosylation Lysosomal storage disorders Niemann–Pick type C disease Bile acid synthesis defects
Isolated hepatomegaly or hepatosplenomegaly	Glycogen storage diseases Lysosomal storage diseases Congenital disorders of glycosylation

not become clinically evident until later in infancy or childhood. Presentation with metabolic liver disease is variable and includes acute or fulminant liver failure, hepatic encephalopathy associated with liver dysfunction, cholestasis and hepatomegaly or hepatosplenomegaly. Some examples of metabolic disorders that present with liver disease are given in Table 69.3.[9] Wilson's disease is an autosomal recessive disorder of copper metabolism. The affected gene encodes a copper-transporting protein that excretes copper into bile. The condition presents at an average age of 10–13 years (rarely before 3 years of age) usually with either neurological symptoms or liver disease. Hepatic involvement ranges from asymptomatic transaminitis to acute liver failure with jaundice, cirrhosis, hepatic necrosis and encephalopathy. The ultrasound appearances of all metabolic disorders affecting the liver are non-specific, with the liver often appearing hyperechoic with decreased visualisation of the peripheral portal venous vasculature[8] (Fig. 69.4). The diagnosis is made from clinical information and laboratory tests, with some cases requiring liver biopsy.

Cirrhosis is a chronic disease process characterised by parenchymal destruction, scarring, fibrosis and nodular regeneration which distorts the hepatic lobular and vascular architecture. It represents the end stage of many chronic processes affecting the liver, including infective hepatitis, biliary atresia, metabolic disease and vascular disorders affecting the liver (e.g. Budd–Chiari syndrome). The sonographic findings of cirrhosis include a small right hepatic lobe and medial segment of the left lobe with compensatory hypertrophy of the lateral segment of the left lobe and caudate lobe; nodular liver edge; coarse or heterogeneous parenchymal echotexture; increased parenchymal echogenicity with attenuation of the ultrasound beam; hyper- or hypoechoic regenerative nodules; and a small or non-visualised gallbladder[10] (Fig. 69.5A and B). There may also be signs of coexistent portal hypertension (see 'Vascular disorders and portal hypertension' section below).

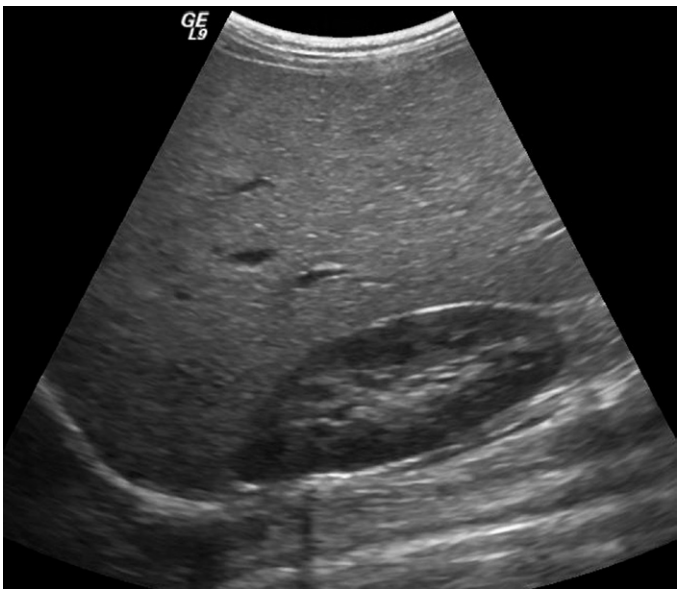

Figure 69.4 Enlarged, hyperechoic liver in a child with a glycogen storage disorder.

Cystic fibrosis (CF) is the most common lethal genetic defect in white populations. It is caused by defects in the CF transmembrane regulation (CFTR) gene on chromosome 7. The disorder produces abnormally thick secretions in multiple organ systems with the lungs, pancreas, liver, intestine and reproductive tract being primarily affected. Hepatic involvement in cystic fibrosis is common and ranges from fatty infiltration of the liver to focal biliary fibrosis and eventually multilobular biliary cirrhosis. There is an increasing incidence of liver involvement with age, although only 1–5% of cases

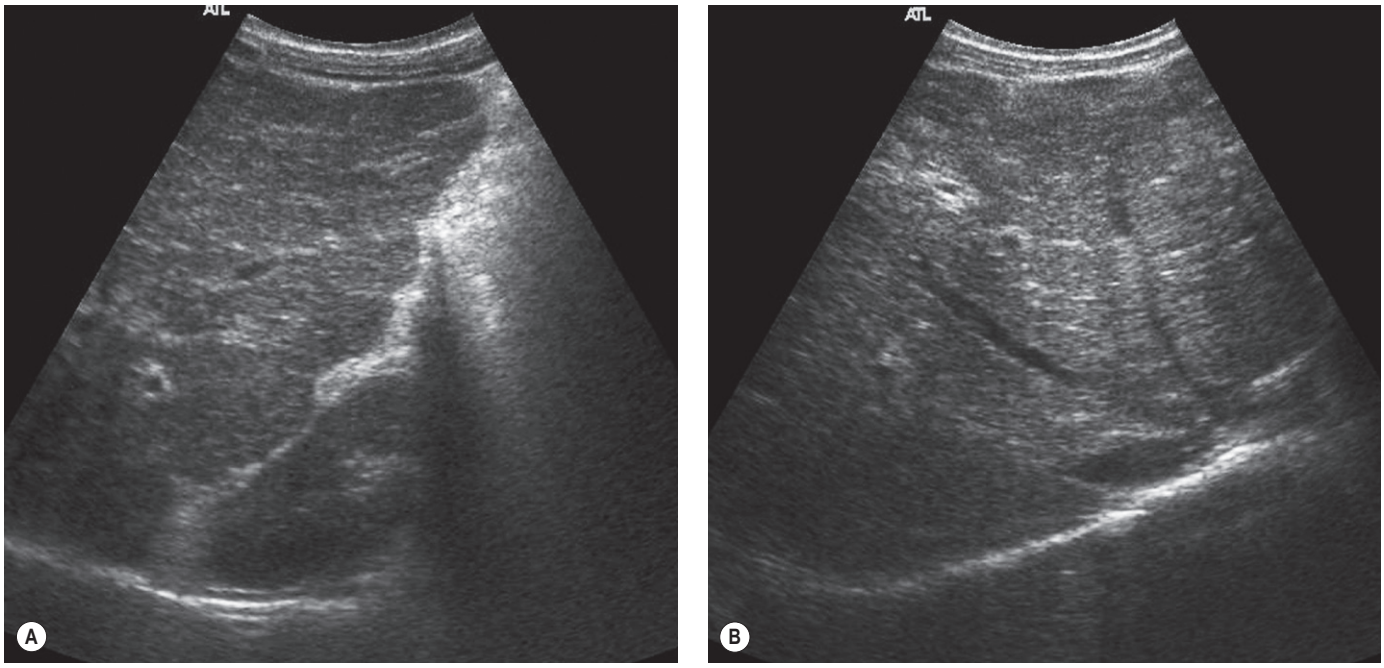

Figure 69.5 Coarse, nodular cirrhotic liver in a child with Niemann–Pick disease. **A:** Right longitudinal ultrasound image showing an irregular liver edge. **B:** Right transverse subcostal view showing minor distortion of the hepatic veins.

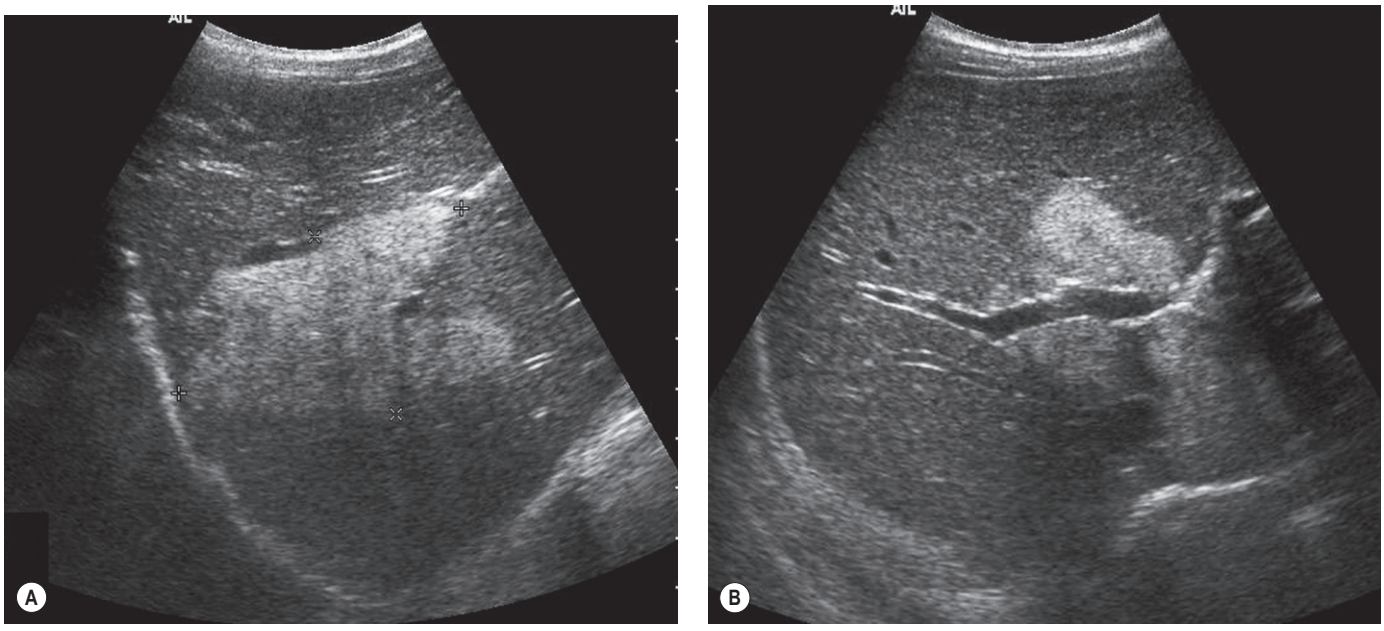

Figure 69.6 Focal fatty infiltration in the right liver lobe on a longitudinal image **(A)** and around the intrahepatic portal vein **(B)** – right transverse view. The margins of the infiltrated hyperechoic fatty areas are well defined and there is no associated mass effect.

progress to clinically apparent liver disease.[11] Hepatic enlargement and increased parenchymal echogenicity representing fatty infiltration are typically seen sonographically. In focal biliary fibrosis, which affects >20% of children and adolescents with CF-related liver disease, there is hyperechoic periportal thickening due to fibrosis or focal fatty deposition in addition to increased parenchymal echogenicity.[12] In the small proportion of cases of focal biliary fibrosis (approximately 5%) that progress to multilobular biliary cirrhosis the liver is small and nodular sonographically, with an irregular echotexture. With the development of portal hypertension, splenic enlargement, portosystemic collateral vessels and occasionally ascites are seen on abdominal ultrasound. Patients with CF also have an increased incidence of gallstones.

Fatty infiltration (steatosis) due to excess accumulation of triglycerides within the hepatocytes occurs in two morphological types: microvacuolar and macrovacuolar. Microvacuolar steatosis occurs in fulminant liver diseases or following the administration of drugs and is usually irreversible. Macrovacuolar steatosis is usually asymptomatic and may be secondary to nutritional abnormalities such as obesity, starvation or parenteral nutrition; metabolic abnormalities such as diabetes mellitus, hyperlipidaemia and galactosaemia; drugs (e.g. corticosteroids); viral infections; and CF. Macrovacuolar steatosis is reversible if the underlying abnormality is removed or corrected. Fatty infiltration of the liver manifests as parenchymal echogenicity, and can be diffuse or focal producing a 'geographic' appearance (Fig. 69.6A and B). The most commonly

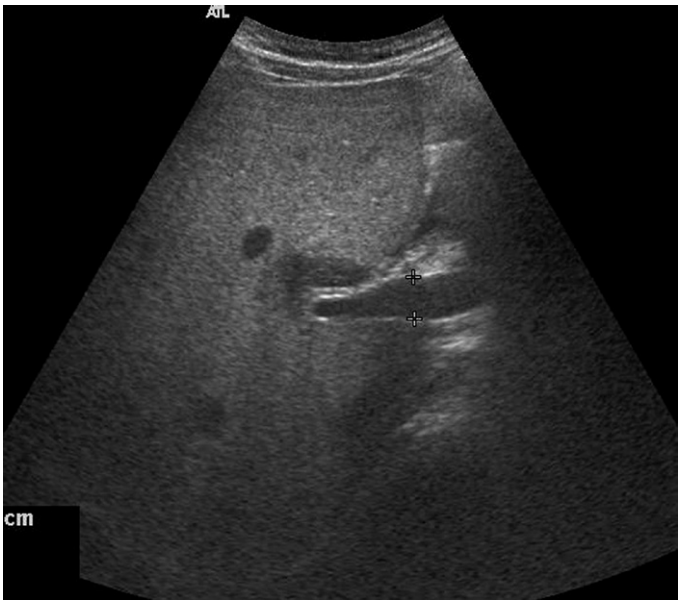

Figure 69.7 Diffuse fatty infiltration of the liver in an obese child, with some focal fatty sparing around the proximal intrahepatic portal vein. This area is hypoechoic in contrast to the remainder of the liver.

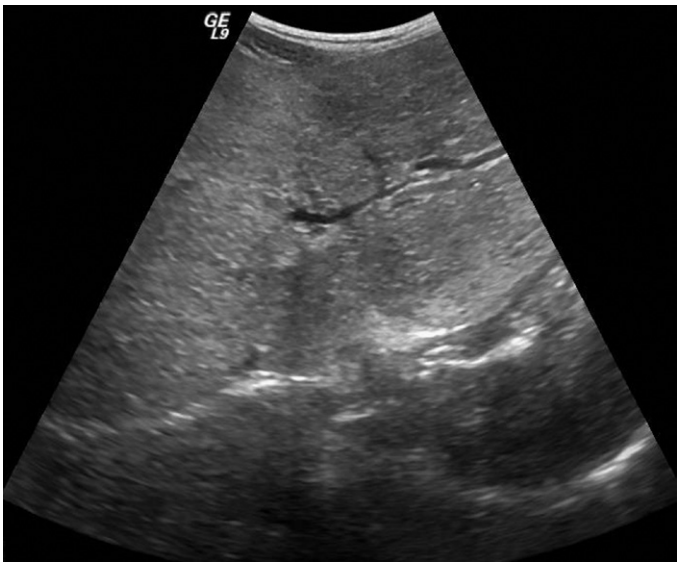

Figure 69.8 Congenital hepatic fibrosis in a 7-year-old with autosomal recessive polycystic kidney disease (ARPKD). The liver is heterogeneous and there is intrahepatic bile duct dilatation.

affected sites of focal fatty infiltration are just anterior to the portal vein bifurcation and gallbladder neck, and medial segment of the left hepatic lobe adjacent to the interlobar fissure. In diffuse fatty infiltration the liver may be enlarged and the attenuation of the ultrasound beam can result in poor visualisation of the intrahepatic vessels, posterior part of the liver and the diaphragm. Occasionally focal fatty infiltration can mimic a hepatic mass, although the affected liver does not have mass effect and never distorts the hepatic contour. Similarly, areas of liver that are spared from fatty infiltration appear hypoechoic in contrast to the remaining steatotic liver (Fig. 69.7). Occasionally these may be mistaken for a mass lesion.

Congenital hepatic fibrosis is a rare condition that has been associated with autosomal recessive polycystic kidney disease (ARPKD) and other disorders such as Meckel–Gruber syndrome, vaginal atresia, tuberous sclerosis, nephronophthisis and rarely autosomal dominant polycystic kidney disease, but may also be sporadic.[13] Patients present with hepatomegaly and signs of portal hypertension usually in late childhood or adolescence. Liver function is usually normal unless there is established cirrhosis. Histologically the bile ducts and portal tracts are affected with no damage to hepatocytes. Sonographic findings include patchy or diffuse parenchymal echogenicity and dilated bile ducts[14] (Fig. 69.8). In ARPKD the kidneys are also affected (see section on ARPKD in Chapter 71).

Diffuse parenchymal disease in children

- Acute hepatitis may be caused by infection, autoimmune disease, a metabolic disorder or toxic agent, including drugs.
- Ultrasound appearances in acute hepatitis depend more on the severity of disease rather than the underlying cause.
- In acute hepatitis the liver may be normal in size or enlarged and liver echogenicity may be altered, although it can appear normal.
- Cirrhosis represents the end stage of many chronic processes including infective hepatitis, CF, extra hepatic biliary atresia, metabolic disease and vascular disorders affecting the liver.
- The liver is commonly involved in children with CF, ranging from fatty infiltration to multilobular biliary cirrhosis.
- Fatty infiltration of the liver in children may be caused by nutritional or metabolic disturbance, metabolic disorders, drugs, viral infections and CF.

Focal hepatic lesions

The liver is an uncommon site for an abdominal mass in a child, with focal hepatic masses accounting for only 5–6% of all abdominal masses in children. Primary hepatic neoplasms are rare, representing only 0.5–2% of all paediatric malignancies,[15] but are the third most common abdominal tumour in children after Wilms' tumour and neuroblastoma. Metastatic disease affecting the liver is much less common in children than in adults. Most children with a liver mass present with abdominal distension or a mass on examination. Other symptoms such as pain, jaundice, weight loss, vomiting, a paraneoplastic syndrome, or acute abdomen due to tumour rupture are less common. When evaluating a child with a liver mass, in addition to the clinical presentation an important differentiating factor is the child's age. The differential diagnosis will also vary depending on whether there is a single lesion or multifocal disease, and whether the serum alpha-fetoprotein (AFP) level is elevated. See Table 69.4: Differential diagnosis of hepatic masses in children.

The main role of imaging is to define the extent of a hepatic mass, its relationship to vascular and biliary structures and segmental anatomy. This is particularly important with neoplastic lesions in order to determine resectability. Most children with a liver mass will initially be evaluated using ultrasound, which helps to determine the cystic or solid nature of the lesion (or lesions) and whether it contains vascular flow. Once this has been established most children will undergo computed tomography (CT) or magnetic resonance imaging (MRI) in order to stage disease and/or plan treatment.

Malignant hepatic neoplasms

There are no particular pathognomonic imaging features to indicate that a liver mass is malignant and biopsy is required in order to confirm the diagnosis.

Hepatoblastoma is the most common primary malignant liver tumour in childhood, accounting for approximately 45% of all childhood liver masses.[15,16] It primarily affects children under 3

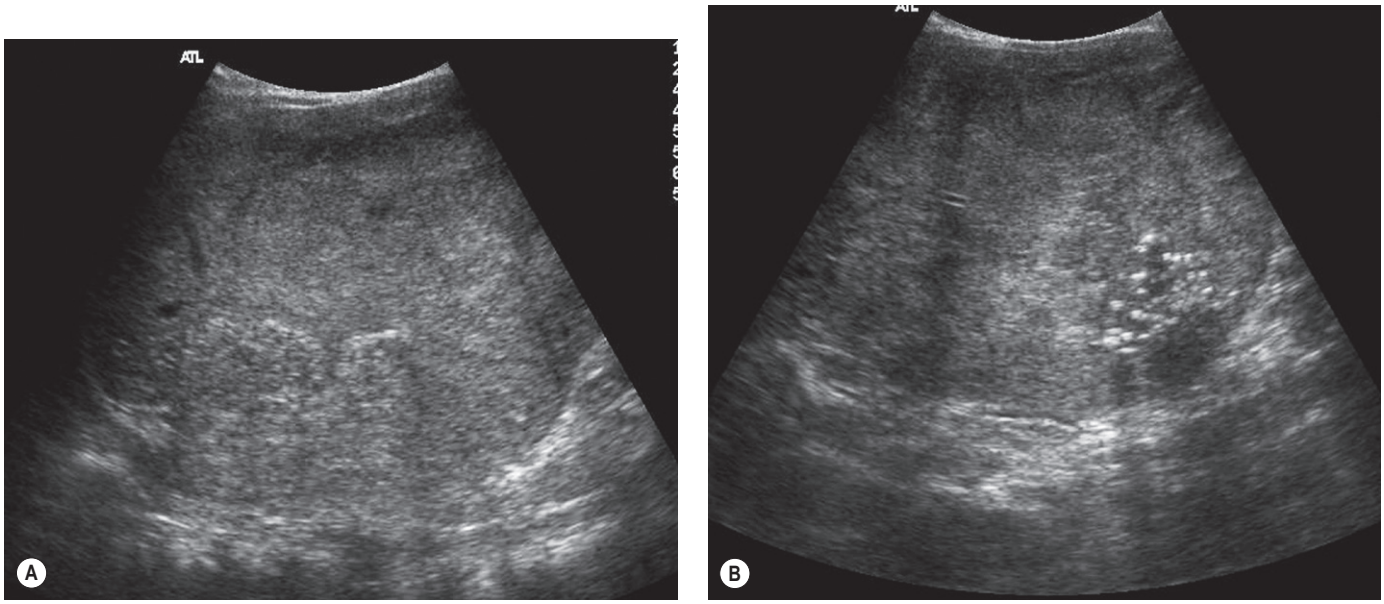

Figure 69.9 Hepatoblastoma in a 10-month-old who presented with an abdominal mass. Left transverse image **(A)** shows a large, heterogeneous, mildly hyperechoic mass replacing most of the left liver. Coarse punctate calcification with acoustic shadowing is seen in the inferior part of the tumour on left longitudinal view **(B)**.

Table 69.4 Differential diagnosis of hepatic masses in children (adapted from Donnelly and Bisset[15])

Newborn to 5 years:
Hepatoblastoma
Haemangioendothelioma
Mesenchymal hamartoma
Metastatic disease (neuroblastoma, Wilms' tumour)
Age >5 years:
Hepatocellular carcinoma
Undifferentiated/embryonal sarcoma
Hepatic adenoma
Lymphoma
Metastatic disease
Immunocompromised patients:
Post-transplant lymphoproliferative disorder
Bacterial or fungal abscesses
Metastatic disease
Multiple lesions:
Metastatic disease (neuroblastoma or Wilms' tumour)
Bacterial or fungal abscesses
Lymphoma or post-transplant lymphoproliferative disease
Adenomas
Cat scratch disease

years of age and most cases are sporadic. There is an increased incidence of hepatoblastoma in children with Beckwith–Wiedemann syndrome, hemihypertrophy, familial adenomatous polyposis (FAP), renal/adrenal agenesis, neurofibromatosis, Prader–Willi syndrome and trisomy 18. Environmental factors associated with an increased incidence of this tumour include maternal oral contraceptive use, fetal alcohol syndrome and very low birth weight (<1500 g).[17] Hepatoblastoma originates from early hepatic progenitor cells and is an embryonal neoplasm composed of malignant epithelial tissue with variable differentiation. Some tumours may contain mesenchymal elements. Between the ages of 6 months and 3 years, serum AFP is elevated in over 90% of cases, which is a useful marker both at diagnosis and for monitoring treatment. Most children with hepatoblastoma present with a combination of abdominal distension, pain, a mass, vomiting and failure to thrive but the tumour may produce other hormones in addition to AFP (such as human chorionic gonadotrophin (hCG), thrombopoietin, erythropoietin or renin) and cause paraneoplastic effects. Sonographically, the tumour is usually heterogeneous and mildly hyperechoic (Fig. 69.9A). Less commonly, it may be hypoechoic or anechoic due to central necrosis or haemorrhage. The hepatic vessels may be distorted and calcification within the lesion may be seen[18] (Fig. 69.9B). Involvement of portal lymph nodes and intravascular extension may also be identified.

Hepatocellular carcinoma (HCC) is the second most common hepatic tumour in childhood after hepatoblastoma, although it is the most common over 4 years of age. There are two age peaks in childhood: between 4 and 5 years of age and more commonly at 12–14 years. Pre-existing liver disease (e.g. hepatitis B infection, tyrosinaemia, type I glycogen storage disease, haemochromatosis, α_1-antitrypsin deficiency, familial cholestatic cirrhosis) is present in more than half of patients with HCC.[16] Pathologically, the tumour consists of large pleomorphic, multinucleated cells with variable degrees of differentiation. The tumour spreads by vascular and lymphatic invasion and is often bilobar, multifocal or extensively invasive at presentation, with metastatic disease in at least half of patients.[17] Abdominal distension and a right upper quadrant mass are the most common presenting features. Serum AFP is elevated in over two-thirds of patients, with the exception of the fibrolamellar variant of HCC which occurs in adolescents and young adults without pre-existing liver disease. In the fibrolamellar variant AFP is elevated in only 11%.[18] The imaging features of HCC are similar to hepatoblastoma, except that calcification is much less common, seen in only 10% of cases. The typical sonographic appearance is a large, heterogeneous, predominantly hyperechoic mass, but the tumour can appear isoechoic or hypoechoic compared with the surrounding normal liver tissue. Fibrolamellar HCC has variable echogenicity and is commonly solitary and well marginated. A central scar and calcification is seen in a high proportion of cases (approximately 70%[16]), but this feature is best appreciated with CT or MRI scanning.

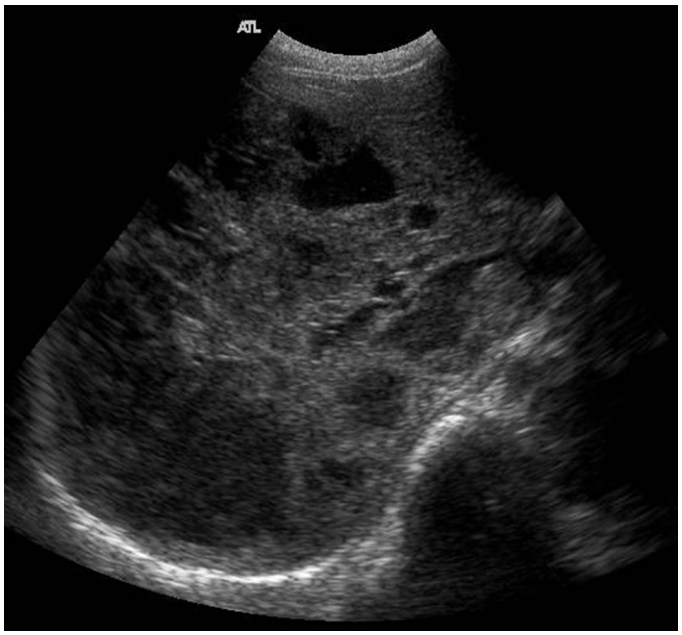

Figure 69.10 Embryonal sarcoma of the liver in a 14-year-old boy who presented with pain and a mass following a minor episode of trauma. There is a large, predominantly cystic/necrotic mass replacing most of the right liver lobe on ultrasound.

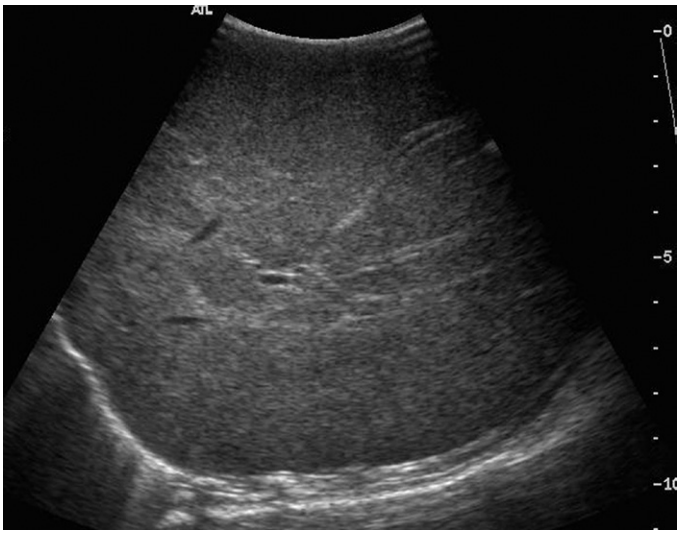

Figure 69.11 Stage IV neuroblastoma in a neonate with diffuse liver involvement and hepatomegaly. Right longitudinal ultrasound image showing heterogeneous liver echogenicity with an irregular liver edge.

Other primary hepatic malignancies are uncommon in children. The third most common tumour is undifferentiated embryonal sarcoma, which is usually a large, well-defined mass on imaging and may have large cystic elements with septations and an appearance similar to a mesenchymal hamartoma (Fig. 69.10). Serum AFP is normal and undifferentiated embryonal sarcoma tends to occur in a completely different age group, most commonly between 6 and 10 years of age[15] and also in adolescents. Other primary paediatric hepatic malignancies include angiosarcoma, rhabdoid tumour, endodermal sinus tumour and lymphosarcoma. The most common malignancy to arise from the biliary tree in children is the rare embryonal rhabdomyosarcoma. (See 'Biliary dilatation and obstruction' section below.)

Treatment of primary liver tumours depends on the tumour type. Hepatoblastoma usually shows good response to chemotherapy, which helps to decrease tumour size and achieve better resectability, although cure is largely dependent on a complete resection of the primary tumour. HCC does not usually respond to chemotherapy or radiotherapy and complete resection is necessary in order to achieve cure. Unfortunately the majority of HCCs in children are not primarily resectable, with vascular invasion and lymph node or distant metastases at presentation, and a poor prognosis. For localised but unresectable malignant tumours orthotopic liver transplantation (OLT) may be appropriate and curative.[19]

Hepatic metastases may appear hypoechoic or hyperechoic on ultrasound, or a diffuse infiltrative pattern may be seen (Fig. 69.11). There may be evidence of mass effect with displacement of vessels, vessel invasion or amputation. Childhood tumours that most frequently metastasise to the liver are Wilms' tumour, neuroblastoma (stage IV and IV-S disease), rhabdomyosarcoma and lymphoma. Clinically patients with liver metastases present with hepatomegaly, jaundice, abdominal pain, a palpable mass or abnormal liver function tests.

Involvement of the liver is present in up to 50% of children with post-transplant lymphoproliferative disease (PTLD). The imaging appearances of PTLD are similar to metastatic disease but three distinct patterns have been described. There may be discrete hypoechoic nodules measuring 1–4 cm; poorly defined infiltrative lesions with hepatomegaly; or direct involvement of the portal hepatis with periportal infiltration or involvement of the biliary tree which can cause biliary obstruction.[16]

Benign hepatic neoplasms

Benign tumours of the liver can be classified according to their tissue of origin as mesenchymal (e.g. haemangioma, haemangioendothelioma and mesenchymal hamartoma) or epithelial (e.g. focal nodular hyperplasia, adenoma and cysts). In children, mesenchymal tumours are more common than epithelial types.

Haemangioendothelioma is the most common benign hepatic tumour seen in childhood and belongs to the group of vasoproliferative lesions that also includes infantile haemangioma, epithelioid haemangioendothelioma and angiosarcoma. These types of vascular tumour may be single or multiple and occur in young patients – typically under 6 months of age, many in the neonatal period. Presentation is with an abdominal mass associated with high output cardiac failure related to vascular shunting within the tumour and up to 50% of affected neonates will have similar vascular lesions on the skin.[20] Some lesions are even detected antenatally. These vascular tumours may be complicated by consumptive coagulopathy or haemorrhage. The sonographic appearance of haemangioendothelioma is variable and the lesions may be hypoechoic or hyperechoic, well defined or diffuse but are typically heterogeneous[15] (Fig. 69.12A and B). Punctate calcification may be seen. Doppler studies demonstrate prominent arterial and venous flow. Sometimes multiple lesions are present and the appearance may be confused with metastatic disease (Fig. 69.13A and B). Many haemangioendotheliomas and haemangiomas regress spontaneously but treatment is indicated if there is cardiac failure or a complication that endangers life such as consumptive coagulopathy or respiratory compromise. Corticosteroids and α-interferon are used but may take several weeks to take effect. Hepatic artery ligation or embolisation may be required in the acute situation to control life-threatening symptoms or when medical treatment fails. Resection of localised lesions or liver transplantation are occasionally necessary.[17]

Mesenchymal hamartoma of the liver is a rare, benign, predominantly cystic liver mass which almost always presents before 2 years of age, although prenatal diagnosis has been reported.[21] The lesion consists of a mixture of mesenchymal tissue and bile ducts and is often considered to be a developmental abnormality rather

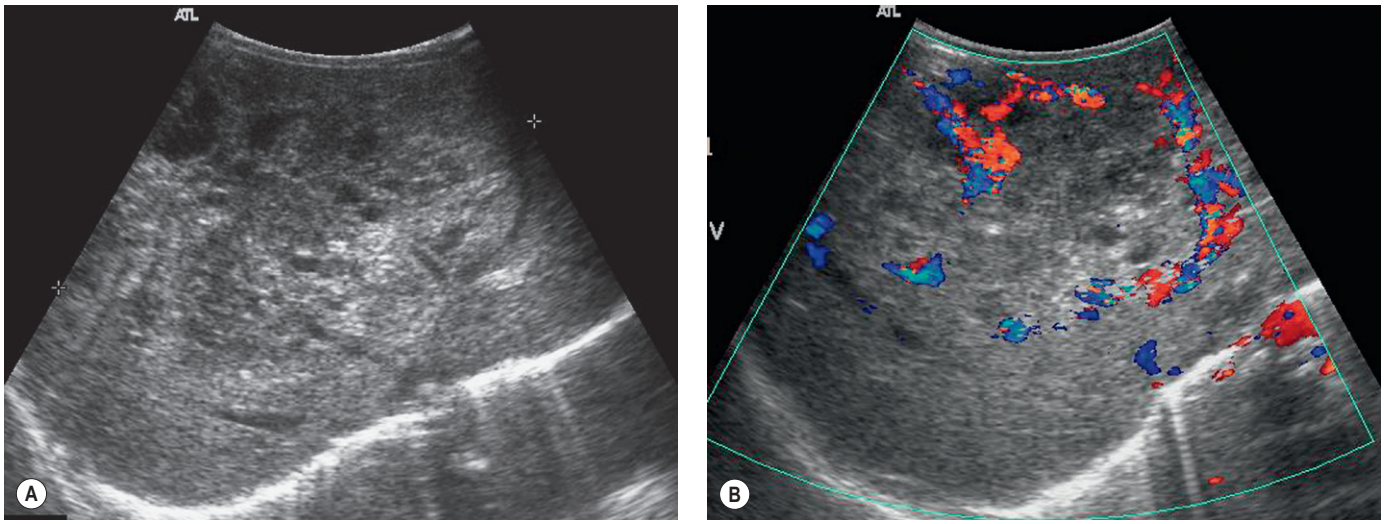

Figure 69.12 Large haemangioendothelioma of the liver in a neonate who presented with cardiac failure. Greyscale **(A)** and colour Doppler **(B)** transverse images of the liver show a heterogeneous mass with peripheral vascularity.

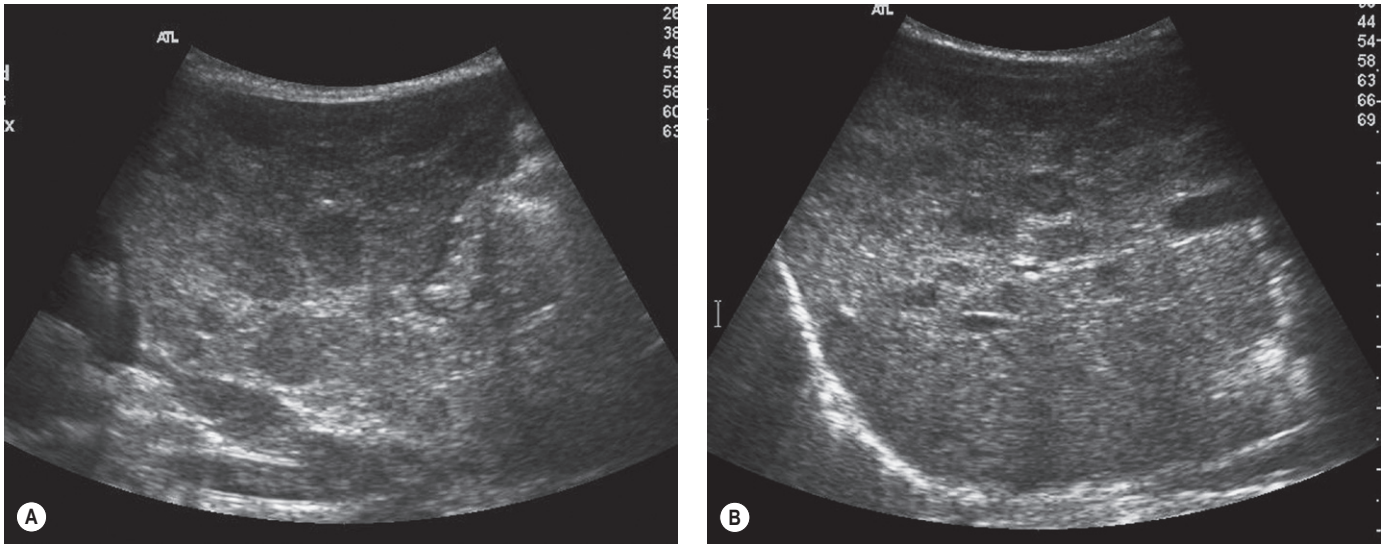

Figure 69.13 Multiple hepatic haemangiomas in a 3-month-old who presented with hepatomegaly and mild cardiac failure. Left **(A)** and right **(B)** longitudinal ultrasound images showing multiple rounded hypoechoic lesions of varying size and definition throughout most of the liver.

than a true neoplasm. The lesion is usually confined to a single lobe (more often the right lobe), is often pedunculated and has solid and cystic components. It enlarges slowly as serous or mucoid fluid accumulates within the cysts and most patients present with an abdominal mass or abdominal distension, but are otherwise asymptomatic. Sonographically, large hypoechoic or anechoic multicystic masses are seen with thin internal septations. Occasionally they appear more solid with multiple smaller cysts and the internal septations may be vascular. Treatment is complete surgical resection. There are rare reports of malignant transformation of mesenchymal hamartomas and local recurrence is occasionally seen.[17]

Focal nodular hyperplasia (FNH) is a benign tumour that may be small or large, single or multiple. It is more common in females, presenting at any age in childhood but is most frequent in young women taking the oral contraceptive pill (OCP). Most patients have an asymptomatic liver mass. The lesions are variably echogenic on ultrasound (Fig. 69.14), with a central scar typically seen on CT or MRI. FNH are not pre-malignant and most are managed conservatively following histological confirmation.

Hepatic adenomas are rare in children but may be associated with a pre-existing disorder such as glycogen storage disease types I and IV, Fanconi's anaemia, transfusion associated haemosiderosis, Hurler's disease, severe combined immunodeficiency, galactosaemia or FAP. In adults there is a well-established link with the OCP and anabolic steroids. They are usually asymptomatic solitary lesions discovered incidentally, but may be multiple and consist of benign hepatocytes lacking portal or biliary structures and Kuppfer cells. They have variable echogenicity on ultrasound and are best imaged using MRI, which may demonstrate fibrofatty change, haemosiderin deposition or haemorrhage. Due to their small risk of malignant transformation or rupture, surgical excision is the treatment of choice.[19]

Hepatic cysts are rare in children. They may be congenital, arising from intrahepatic bile ducts that fail to involute, or acquired, resulting from inflammation, trauma or parasitic disease. Multiple cysts may be seen in association with autosomal dominant polycystic kidney disease. Most cysts are detected incidentally but some patients present with a mass. Sonographically, cysts are

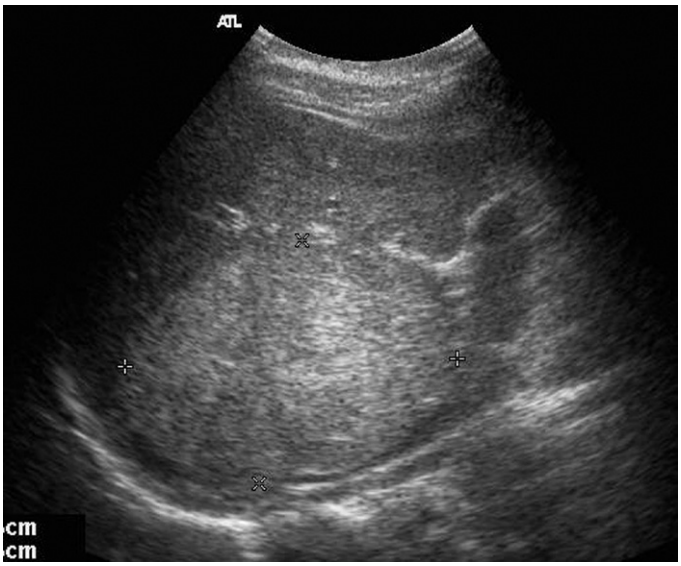

Figure 69.14 Focal nodular hyperplasia in a 14-year-old girl. Longitudinal ultrasound image showing a well-defined, predominantly hyperechoic mass in the right liver.

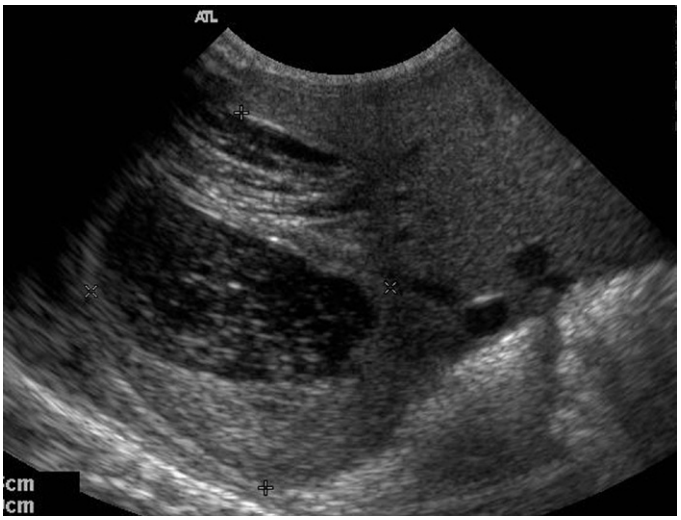

Figure 69.16 Liver abscess secondary to necrotising enterocolitis (NEC) in a neonate. Transverse image showing a large, mixed echogenicity, multiloculated/septated mass in the right lobe.

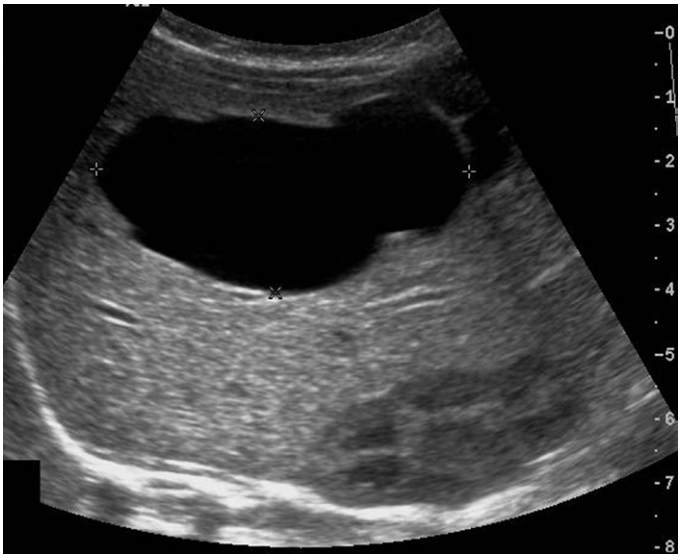

Figure 69.15 Antenatally detected large, simple liver cyst in an asymptomatic 5-week-old.

Focal hepatic lesions in children

- Primary hepatic neoplasms are rare, representing only 0.5–2% of all paediatric malignancy, but primary liver tumours are the third most common type of abdominal tumour in children.
- Most children with liver masses present with abdominal distension and a palpable mass.
- There are no pathognomonic imaging features to indicate that a mass is malignant.
- Hepatoblastoma is the most common primary malignant tumour in childhood, predominantly affecting children <3 years of age.
- Hepatocellular carcinoma almost always occurs in children with pre-existing liver disease.
- Haemangioendothelioma is the most common benign liver tumour in childhood, usually affecting children <6 months of age.
- Wilms' tumour, neuroblastoma, lymphoma and rhabdomyosarcoma may metastasise to the liver in children.

typically thin-walled and anechoic (Fig. 69.15). Parasitic cysts are generally due to *Echinococcus* or hydatid disease and are uncommon in newborns. Hydatid is endemic in Greece, eastern Europe, South America, Australia and South Africa. The cysts may be calcified and contain daughter cysts (cyst within a cyst).[22]

Echogenic liver lesions are often seen in the fetus and neonatal follow-up is advised. They are always less than 5 mm in diameter. The histology of these has never been confirmed. If they cast a shadow they are likely to be calcified and congenital infection is a possibility. If not they have been presumed to be haemangiomas. They have not been shown to have any postnatal significance.

Inflammatory masses and abscesses

Inflammatory liver masses and abscesses in children are rare in developed countries. They may be related to bacterial, fungal or granulomatous infections and may reach the liver by direct inoculation (e.g. penetrating trauma), contiguous spread from adjacent organs such as the lung, or from remote sites via the arterial or portal venous route. Immunocompromised children are particularly susceptible to abscesses caused by enteric organisms and fungal infection, e.g. *Candida albicans* and *Aspergillus* species. Patients present with fever, upper abdominal pain and occasionally a mass, although infection may be occult in the immunocompromised host. Abscesses are typically hypoechoic sonographically (Fig. 69.16), although thick, viscid contents may be isoechoic and difficult to detect in the initial stages of infection. Cat scratch disease is a granulomatous or suppurative reaction to the organism *Bartonella henselae*, a Gram-negative bacillus. The usual presentation is with fever and regional lymphadenopathy after being scratched by a domestic cat. Infection involves the liver in approximately 10% of patients, producing multiple small nodular lesions (granulomas) ranging from 3 mm to 2 cm in diameter,[15,16] although this appearance is non-specific and can be seen in other infectious diseases including tuberculosis (TB), and in metastatic disease.

Amoebic liver abscesses are rare, seen in areas where *Entamoeba histolytica* is endemic such as Mexico, western South America, south Asia and west and southeastern Africa. In approximately half of patients the hepatic abscesses remain small and can be medically treated; the other half require percutaneous aspiration or

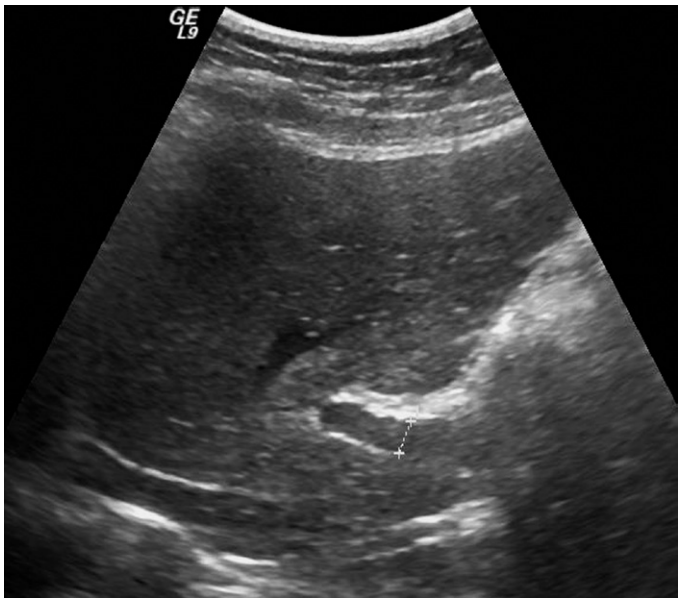

Figure 69.17 **Normal portal vein** with well-defined echogenic wall.

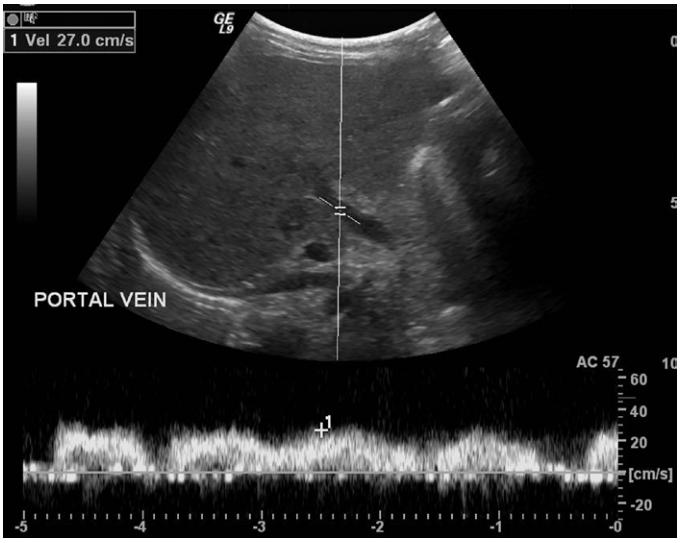

Figure 69.18 **Normal portal vein Doppler trace** showing mild variation in flow with respiration.

surgical drainage because of persistent abdominal pain, sepsis, an abscess cavity over 6 cm or one that has ruptured or is at risk of rupture.[22]

Misplaced umbilical venous catheters within the liver can result in a hepatic mass related to laceration and haematoma, or to the infusion of fluid such as parenteral nutrition into the line. The appearances of haematoma within the liver vary depending on the age of the haematoma, and some may resemble abscesses.

Vascular disorders and portal hypertension

The portal vein, formed from the superior mesenteric vein (SMV) and splenic vein, is valveless and contributes approximately 75% of blood flow to the liver. Its wall is thick, like an artery, and contains a high proportion of collagen and fat which produces an echogenic rim on ultrasound[23] (Fig. 69.17). On Doppler studies, normal portal blood flow is towards the liver (hepatopetal) and the flow varies slightly with respiration (Fig. 69.18). Normal portal flow increases postprandially. A portosystemic shunt is the diversion of portal blood into a systemic vein without the blood passing through the liver and may be extrahepatic (e.g. congenital atresia of the portal vein) or intrahepatic, resulting from a connection between the portal venous system within the liver and either the hepatic veins or inferior vena cava.

Congenital absence of the portal vein was first described by Abernathy in 1793. In this situation, blood from the SMV and splenic vein bypasses the liver and drains into a systemic vein. A type I shunt occurs when all portal venous blood is shunted into a systemic vein so that there is complete bypass of the liver. In this situation the shunt is the only drainage pathway for portal blood. A type II shunt occurs when only part of the portal venous flow bypasses the liver. Classification of the shunt is important for prognosis and treatment, as type II shunts can be successfully treated by banding or occlusion of the shunt whereas type I shunts cannot.[24,25] Congenital absence of the portal vein is associated with other congenital abnormalities including cardiac and skeletal anomalies and abnormalities of situs. Other liver abnormalities are also associated with congenital portal vein absence, e.g. biliary atresia, portal hypertension and an increased incidence of primary liver tumours such as hepatoblastoma and HCC.[26]

A **hypoplastic portal vein** is commonly found in patients with biliary atresia and has been linked to an increased incidence of complications post liver transplant, such as portal vein thrombosis and decreased graft survival.[27] Hypoplasia of the portal vein, portal vein atresia and stenosis cause obstruction and portal hypertension leading to splenomegaly and the development of extrahepatic portosystemic shunts which cause gastrointestinal haemorrhage. Portal vein atresia can involve the entire vein or may be localised to the portion just proximal to its division at the porta hepatis[23] and is distinct from congenital absence of the portal vein where the portal blood is diverted directly into a systemic vein. Absence of a main portal vein branch may be congenital, or caused by atrophy of the vein secondary to a pathological process.

Preduodenal portal vein is when the portal vein lies anterior to the first part of the duodenum, rather than in its usual posterior location. When the portal vein is anterior, it can cause duodenal obstruction by compression, or may be associated with intestinal malformations such as duodenal web, stenosis or malrotation. Two-thirds of children with a preduodenal portal vein present in the first week of life with symptoms. Other associations include biliary atresia, annular pancreas, situs inversus, preduodenal common bile duct and cardiovascular malformations.[28] Duplication of the portal vein is extremely rare, with isolated case reports in the literature.

Portal vein thrombosis may cause partial or total occlusion of portal flow. Risk factors associated with portal vein thrombosis include exchange transfusions, hypercoagulability states, congenital portal vein malformations, umbilical vein catheterisation, omphalitis, sepsis, trauma, manipulation of the portal vein, malignancy and abdominal operations including splenectomy.[29] In some cases, an underlying cause cannot be identified. Acute thrombus can sometimes be identified on ultrasound, either floating in the portal vein lumen or completely occluding it (Fig. 69.19). The vessel proximal to the thrombus may be dilated. Collateral vessels start to form with ongoing obstruction by thrombus in addition to the development of portal hypertension with splenomegaly, hypersplenism, ascites and portosystemic shunts that cause gastrointestinal bleeding. Chronic portal vein thrombosis can lead to the development of multiple collateral channels within and around a stenosed or occluded portal vein, known as *cavernous transformation of the portal vein*. The appearance of the collateral vessels is sometimes referred to as a *portal cavernoma*. Cavernous transformation of the portal vein has been demonstrated on ultrasound as early as 6–20 days after the thrombotic event,[30] and is identified by the appearance of an increased number of hypoechoic vascular structures at and around the porta hepatis which show venous flow on

Doppler studies. The collateral vessels can vary in size from multiple tiny vessels with little detectable flow to large channels with turbulent flow (Figs 69.20 and 69.21).

An aneurysm of the portal vein, otherwise (and more correctly) known as **portal vein varix,** is a localised dilatation of the vessel which may be intra- or extrahepatic in location. This abnormality is rare in children and the aetiology is unknown with both congenital and acquired theories proposed in order to explain its occurrence. These include a congenital weakness of the vessel wall and failure of the right vitelline vein to obliterate fully during embryogenesis, leaving a diverticulum that leads to a varix of the SMV. Complications associated with portal vein varix include duodenal or bile duct compression, portal hypertension or rupture.[23]

Portal hypertension results from an increase in resistance to venous flow through the liver. An increase in portal pressure leads to splenomegaly and the development of portosystemic collaterals (varices) at various sites including the distal oesophagus, anal canal, falciform ligament, abdominal wall and retroperitoneum. Varices around the porta hepatis can compress the bile ducts and cause obstructive jaundice. Portal hypertension can cause mucosal oedema in the small intestine leading to malabsorption, protein-losing enteropathy and failure to thrive. Portal hypertension is defined as an increased hepatic venous pressure gradient (>5 mmHg), which is the difference between wedged hepatic venous pressure (an indicator of portal venous pressure) and free hepatic venous pressure. A gradient of >12 mmHg is necessary for the development of oesophageal varices. Although the consequences of increased pressure in the portal venous system, i.e. splenic enlargement and hypersplenism, ascites, and bleeding oesophageal varices, are the same at all ages, the aetiology, appropriate management and outcome are quite different in children compared with adults. Even when portal hypertension is the result of cirrhosis in children, active management with optimisation of nutritional state and quality of life, rather than palliation, is the goal of treatment.

Aetiologically, portal hypertension is traditionally divided into prehepatic, intrahepatic and posthepatic causes depending on the anatomical site of obstruction. Prehepatic obstruction results from abnormalities of the portal vein such as portal vein thrombosis and stenosis. These conditions are relatively unique to the paediatric age group and patients generally retain good synthetic function of the liver although the manifestations of portal hypertension such as variceal haemorrhage and hypersplenism are pronounced. Intrahepatic causes of portal hypertension are diverse and include intrinsic liver disease (e.g. cirrhosis with its multiple causes and hepatic fibrosis) and diseases that primarily affect the venous circulation through the liver such as hepatoportal sclerosis, veno-occlusive disease and schistosomiasis.[31]

Veno-occlusive disease (VOD) is the result of toxic insult to the sinusoidal endothelium in the liver leading to occlusion of centrilobular veins and hepatic venules, sinusoidal congestion and hepatocyte necrosis. In Western countries this is seen after irradiation and/or cytotoxic drug injury to the liver[32] and there is an increased incidence of this disorder in bone marrow transplant recipients. In the West Indies, South Africa, India and the Middle East toxins found in some foods and herbal teas are associated with the condition. The clinical features of VOD are rapid onset of painful hepatomegaly and ascites, with jaundice. When the disorder is associated with bone marrow transplant it usually occurs within one

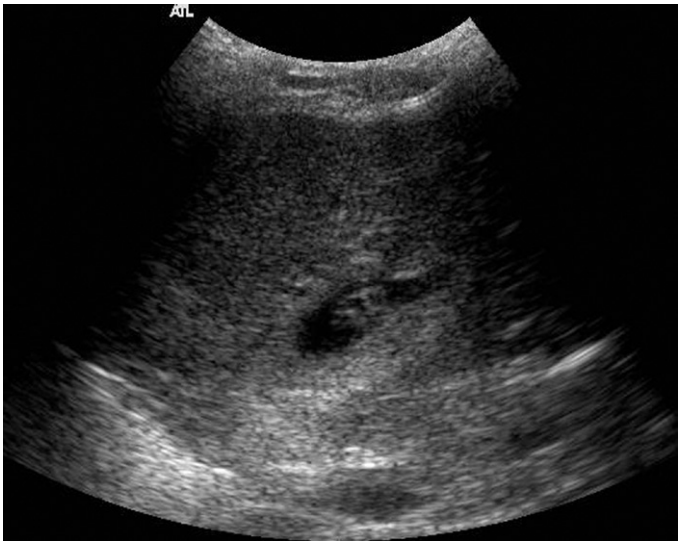

Figure 69.19 Non-occlusive portal vein thrombus in a segment II and III reduced liver graft.

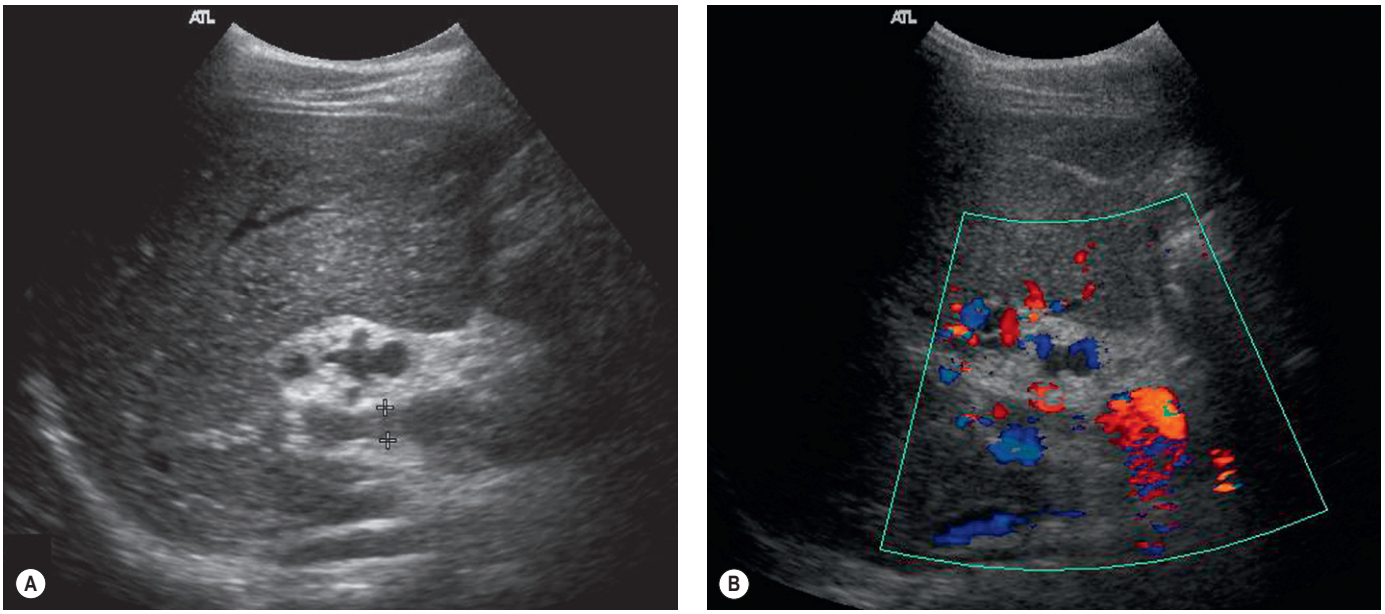

Figure 69.20 Portal cavernoma. Greyscale **(A)** and colour Doppler **(B)** images showing multiple small collateral vessels at the porta hepatis and no normal portal vein in a 13-year-old girl who presented with signs of portal hypertension.

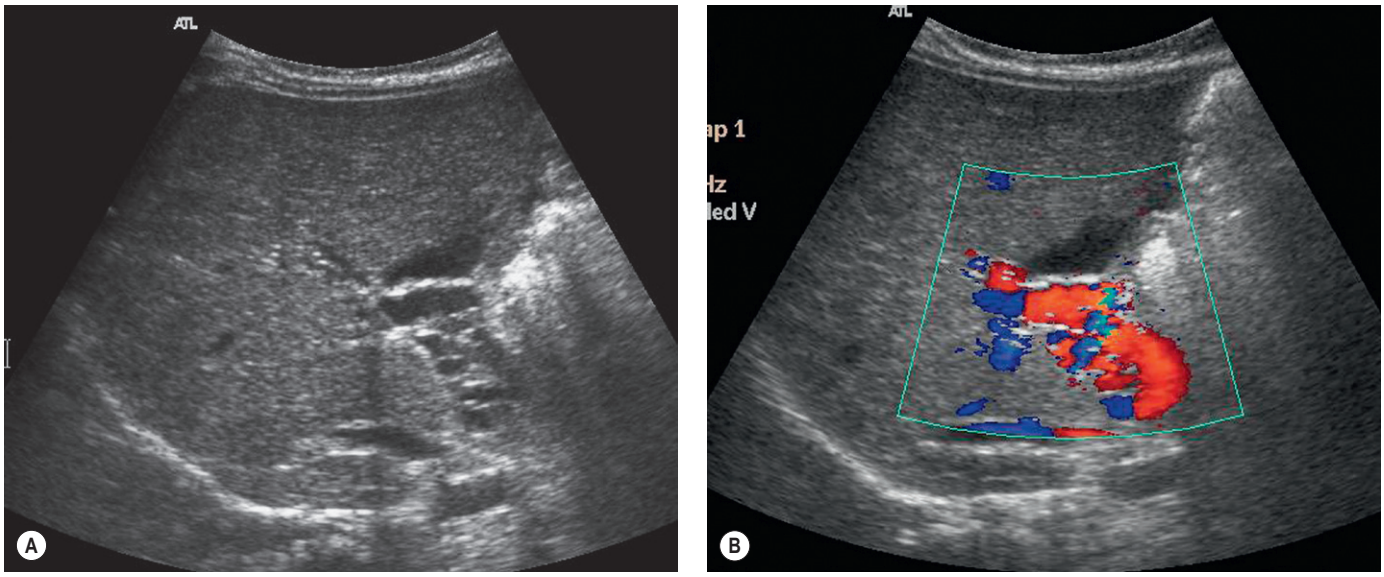

Figure 69.21 Portal cavernoma. Greyscale **(A)** and colour Doppler images showing multiple collateral vessels at the porta hepatis in a 5-month-old who presented with signs of portal hypertension. The left and right intrahepatic portal vein branches were not identified at ultrasound.

Vascular disorders and portal hypertension in children

- Portal vein atresia, hypoplasia and stenosis are rare congenital abnormalities that may cause portal hypertension in childhood.
- Portal vein thrombosis is an important cause of portal hypertension in childhood.
- A portal cavernoma refers to the collateral vessels that develop following portal vein thrombosis.
- The aetiology, management and outcome of portal hypertension in childhood is different to that in adults, with most complications in children actively managed, even if the underlying cause is cirrhosis.
- A diagnosis of veno-occlusive disease may be supported by ultrasound findings of slow or reversed portal flow, dampened hepatic venous flow, increased hepatic artery RI and gallbladder thickening.
- The Budd–Chiari syndrome is rare in children, with identical imaging features to adults.

month of grafting. The diagnosis is made clinically, supported by ultrasound findings which may include slow or reversed (hepatofugal) portal venous flow, decreased or reversed diastolic flow in the hepatic artery and an increase in hepatic artery resistive index (RI ≥0.75), monophasic flow in the hepatic veins, thickening of the gallbladder wall (≥6 mm), as well as hepatomegaly and ascites.[33] Treatment is mostly supportive, although defibrotide, a drug with antithrombotic and thrombolytic properties, has been shown to improve outcome if treatment is started early in the course of the disease.[34]

Posthepatic causes of portal hypertension include hepatic venous obstruction and cardiac or chronic constrictive pericardial disease. Congenital webs in the hepatic veins or inferior vena cava may obstruct blood flow.[35] The **Budd–Chiari syndrome** refers to the clinical manifestations of hepatic venous obstruction at any level from the small hepatic veins to the junction of the IVC and right atrium, regardless of cause. Thrombosis of the hepatic veins is usually due to an underlying hypercoagulable state or myeloproliferative disorder and is rare in children, occurring most commonly in young adults. Clinical features in children are similar to those in adults with the development of hepatomegaly, ascites, symptoms and signs of portal hypertension, progressive cachexia, and variable jaundice. Sonographically, there is segmental or lobar atrophy and enlargement of the caudate lobe, which is spared because of its independent drainage into the IVC. Ascites and splenomegaly are seen, together with narrowing, lack of visualisation or thrombus in the hepatic veins. Absent, monophasic or reversed flow in the hepatic veins and/or IVC may be appreciated on Doppler studies and intrahepatic collateral pathways may also be identified.[36] (See Chapter 12.)

Neonatal jaundice

Unconjugated bilirubin, which is lipid soluble, is formed from haem following breakdown of red blood cells. Because bilirubin is highly insoluble in water, it must be converted into a soluble conjugate prior to elimination from the body. In the liver, the enzyme uridine diphosphate (UDP)-glucuronyl transferase converts bilirubin to a mixture of monoglucuronides and diglucuronides, referred to as conjugated bilirubin, which is then secreted into the bile by an ATP-dependent transporter. Unconjugated hyperbilirubinaemia is a normal physiological event that occurs in up to 50% of normal full-term infants and a higher percentage of premature infants, causing transient jaundice 3–5 days after birth. This is physiological and due to mildly elevated bilirubin levels from breakdown of haemoglobin (newborn infants are relatively polycythaemic) and immaturity of hepatic enzyme glucuronosyl transferase. In general, physiological jaundice peaks on day 3 of life, but may persist for as long as 2 weeks and can last longer in breastfed infants.

A small proportion of patients with physiological jaundice have more than mildly elevated unconjugated hyperbilirubinaemia and require treatment to reduce the bilirubin level because unconjugated bilirubin is neurotoxic. Elevated serum levels can cause brain damage or kernicterus as a result of bilirubin binding to specific parts of the brain, e.g. the basal ganglia. This can cause a severe movement disorder (choreoathetosis), learning disability, deafness or even death. Therefore, if the bilirubin reaches a critical level these infants are treated with phototherapy or even exchange transfusion to prevent complications. Other causes of pathologically elevated blood levels of unconjugated bilirubinaemia are haemolysis, sepsis, systemic disease, inherited enzyme defects, hypothyroidism, pyloric stenosis and dehydration.[37] There is no role for imaging in determining the cause of unconjugated hyperbilirubinaemia.

Prolonged neonatal jaundice and conjugated hyperbilirubinaemia

Not all babies with jaundice in the neonatal period have benign physiological jaundice and even amongst health professionals, neonatal jaundice is often assumed to be completely harmless. Diseases that reduce the rate of secretion of conjugated bilirubin into the bile or the flow of bile into the intestine produce a mixed or predominantly conjugated hyperbilirubinaemia due to reflux of conjugates back into the plasma. Conjugated bilirubinaemia nearly always reflects hepatic dysfunction. This can be due to many different disorders, both surgical or medical, and long-term outcome depends on the underlying cause.

The true incidence of infantile jaundice in the UK is unknown, but it has been suggested from previous studies that between 2% and 15% of neonates will remain jaundiced after 14 days of age.[38] The current recommendation is that jaundice in any infant persisting beyond 2 weeks of age should be investigated (>3 weeks in preterm babies). Initially, it must be determined whether this is due to conjugated or unconjugated hyperbilirubinaemia. If the level of conjugated bilirubin constitutes >20% of the total, and/or total bilirubin is >200 μmol/L, the child should be referred promptly to a paediatrician for further investigation.[39] However, the number that require investigation is relatively small and only 0.2–0.4% of jaundiced infants >14 days of age will have cholestatic jaundice due to a medical or surgical condition.[38] Investigations may include blood tests, ultrasound, hepatic scintigraphy, liver biopsy and more invasive imaging investigations to determine patency of the biliary system. The numerous medical causes of neonatal conjugated hyperbilirubinaemia are collectively referred to as the **neonatal hepatitis syndrome** (NHS). NHS is a non-specific inflammatory disorder of the neonatal liver that develops secondary to a variety of causes including intrauterine infection, endocrine disorders, metabolic defects and familial cholestasis syndromes.

Causes of neonatal conjugated hyperbilirubinaemia[40]

1. **Congenital infection** – e.g. TORCH infections (toxoplasmosis, rubella, cytomegalovirus, herpes viruses), syphilis, hepatitis A, B or C, human immunodeficiency virus (HIV), parvovirus B19, enteric viral sepsis (echoviruses, Coxsackie A and B, adenoviruses)
2. **Genetic syndromes** – trisomies 18 and 21, cat eye syndrome
3. **Endocrine disorders** – hypopituitarism, hypothyroidism
4. **Metabolic disorders** – α_1-antitrypsin deficiency, cystic fibrosis (CF), galactosaemia, hereditary fructosaemia, tyrosinaemia, glycogen storage disease type IV, Niemann–Pick types A and C, Wolman's disease, disorders of bile acid synthesis, Byler's disease, Zellweger's syndrome
5. **Immune disorders** – neonatal lupus erythematosus, neonatal hepatitis with autoimmune haemolytic anaemia, neonatal haemochromatosis
6. **Duct paucity syndromes** – Alagille's syndrome, non-syndromic duct paucity
7. **Structural disorders of the biliary system** – extrahepatic biliary atresia, choledochal cyst and Caroli's syndrome, neonatal sclerosing cholangitis, spontaneous perforation of the common bile duct, inspissated bile syndrome, hair-like bile duct syndrome.

Ultrasound in the neonatal hepatitis syndrome (NHS)

Ultrasound has a limited role early on in the investigation of neonates with conjugated hyperbilirubinaemia caused by NHS. The main reason for performing ultrasound is to exclude some surgical causes and biliary dilatation, but often the examination is normal. Non-specific signs of parenchymal disease may be identified such as an enlarged liver, increased parenchymal echogenicity and signs of reduced hepatic compliance on Doppler studies, including raised hepatic arterial RI and dampened hepatic venous waveform. The final diagnosis is made by other means – usually blood tests and liver biopsy.

The most common causes of conjugated hyperbilirubinaemia in neonates are: NHS, extrahepatic biliary atresia (EHBA) and choledochal cyst (CDC). Distinguishing between these is very important because NHS is managed medically whilst EHBA and CDC require surgery. It is particularly important to diagnose EHBA early, in order that surgical intervention is successful in establishing bile flow. Delayed diagnosis leads to progressive biliary cirrhosis requiring transplantation.

Surgical causes of neonatal jaundice

Extrahepatic biliary atresia

Extrahepatic biliary atresia (EHBA) is the most important condition to distinguish from other causes of prolonged conjugated hyperbilirubinaemia in the neonatal period because it requires early surgical intervention to prevent biliary cirrhosis. EHBA is the cause of liver disease in approximately 20% of infants presenting with prolonged conjugated hyperbilirubinaemia.[41] Infants with EHBA have an obstructive jaundice due to an obliterative inflammatory process that results in progressive destruction of the extrahepatic bile ducts, with scarring, obliteration and damage to small and medium-sized intrahepatic ducts. Untreated, it leads to progressive biliary cirrhosis, failure to thrive and death within 2 years. EHBA is found in all racial groups, worldwide, and is the leading indication for liver transplant in childhood. The overall incidence of this disorder is approximately 1 in 10000–15000 neonates[42] with an incidence of 1 in 16700 live births in the UK and Ireland.[43] The aetiology is unknown although proposed mechanisms include perinatal viral infections, ischaemic or immune-mediated insult to the biliary tree.[44] The time of onset is variable, but most affected infants are jaundiced from birth.

There are three main subtypes of EHBA as classified by Kasai.[45] Type 3 is the most common type (90%) and all the extrahepatic ducts are affected. In type 2 (2%) the common hepatic duct (CHD) is affected and the right and left hepatic ducts remain patent; type 2a has obliteration of the CHD only and type 2b obliteration of the CHD, cystic duct and CBD. In type 1 EHBA only the CBD is affected; this is the most easily correctable, but applies to only 8% of all patients with EHBA (Fig. 69.22).

Although ultrasound is a mandatory investigation in infants with prolonged conjugated hyperbilirubinaemia, it does have limitations. The role of ultrasound is not to distinguish between NHS and EHBA, but to rule out other causes of cholestasis, especially other surgical causes such as choledochal cyst. However, ultrasound may give clues to the diagnosis of EHBA. The liver size may be normal or increased in both NHS and EHBA, and the parenchyma may have normal or increased echogenicity. The intrahepatic bile ducts are not usually dilated in either condition. The main differences are that in EHBA the gallbladder is usually small or absent (90%), measuring <15 mm in length[46] (Fig. 69.23), whereas in NHS it may be small, normal or enlarged. It is important to ensure that the patient is adequately fasted in order to examine the gallbladder and it can also be helpful to use a high-frequency linear ultrasound probe to look for a small gallbladder. Furthermore gallbladder contractility usually occurs in NHS, but not in EHBA. Sonographic evidence of a bile duct remnant at the porta hepatis, the 'triangular cord sign', has been evaluated as being a sensitive and specific indicator of EHBA in patients with prolonged conjugated hyperbilirubinaemia.[47–49] The triangular cord sign consists of a focal echogenic triangular, tube-shaped or ovoid area measuring more than 4 mm, just cranial to the portal vein bifurcation, and has been shown to represent a cone-shaped mass of fibrous tissue replacing

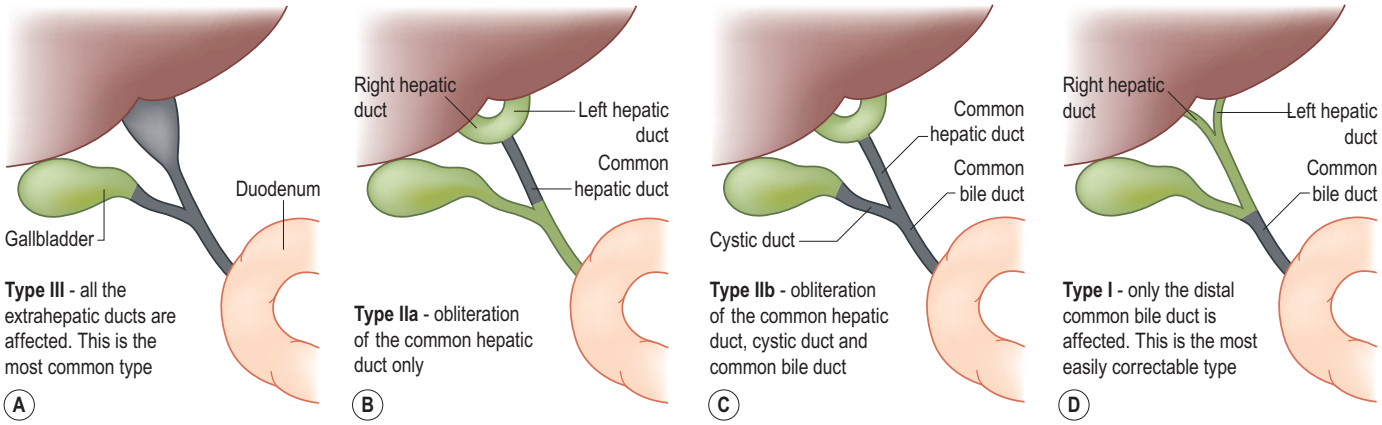

Figure 69.22 The different types of extrahepatic biliary atresia (EHBA). (Modified from http://emedicine.medscape.com/article/366004-overview; accessed 18/09/2009.)

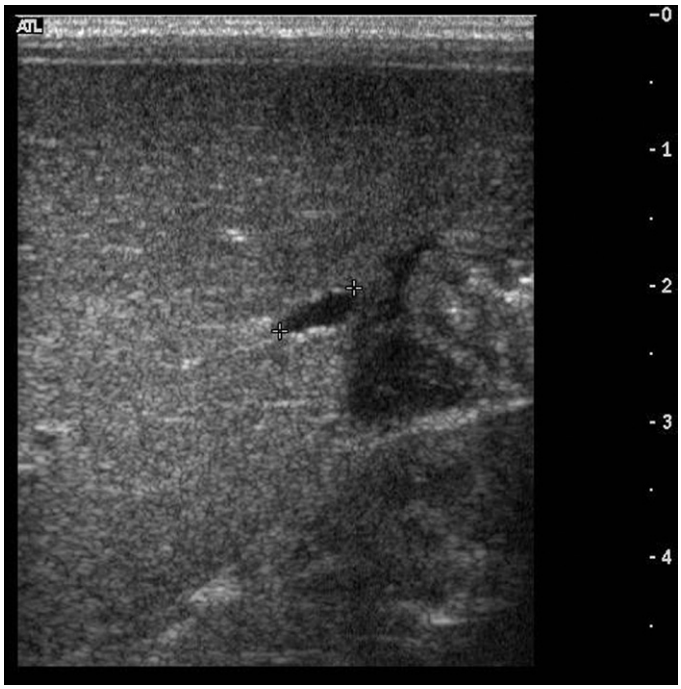

Figure 69.23 Ultrasound of the gallbladder in a patient with EHBA. The gallbladder is abnormally small (length 6 mm) and undistended despite an adequate fast. It was not identified using a lower-frequency curvilinear probe.

the bile ducts.[50] Other abnormalities are seen in 10–20% of patients with EHBA; these include polysplenia, azygos continuation of the IVC, anomalous hepatic arteries, preduodenal portal vein, abnormalities of situs and diaphragmatic, renal or cardiac abnormalities, and are often referred to as the 'biliary atresia–splenic malformation syndrome'[51] (Fig. 69.24A and B). Liver biopsy is the most useful investigation in making the diagnosis of EHBA, although ultrasound remains a mandatory part of the investigative pathway. Hepatic scintigraphy helps to separate medical causes of conjugated hyperbilirubinaemia from EHBA, but ultimately the final diagnosis rests on liver biopsy and intraoperative cholangiography.

The treatment of EHBA is the Kasai portoenterostomy, which serves to restore bile drainage. The operation consists of dissection of the diseased bile ducts and fibrous tissue with excision at the porta hepatis behind the portal vein bifurcation. The exposed patent bile ducts are then anastomosed to a Roux-en-Y bowel loop to re-establish bile drainage. The operation needs to be performed early, ideally less than 6 weeks of age. After 100 days the outcome is much poorer.[43,52] For infants that present late, the Kasai portoenterostomy is usually tried unless there are signs of established portal hypertension, in which case transplantation is the only suitable treatment option. The success of the operation is variable and long-term complications of the Kasai portoenterostomy include ascending bacterial cholangitis, the metabolic and nutritional consequences of cholestasis, intrahepatic cyst formation, hepatopulmonary syndrome and pulmonary hypertension, cirrhosis with portal hypertension and occasionally malignant change in the liver.[31] All patients require regular follow-up including serial ultrasound scanning for monitoring, and most patients with EHBA eventually require transplantation.

Choledochal cysts

Choledochal cysts (CDC) are congenital, localised dilatations of the bile ducts. Overall, they are rare, with an incidence of approximately 1 in 100 000 live births in Western countries but are more common in people from East Asia and in girls (F:M, 3:1). More than two-thirds are diagnosed before 10 years of age and antenatal detection, from 15 weeks gestation, is increasing. Infants typically present with obstructive jaundice (approximately one-third of all cases), and older children with abdominal pain and sometimes intermittent jaundice. The classic triad of jaundice, pain and abdominal mass is uncommon.[16] CDC may be complicated by stones, infection, rupture, biliary cirrhosis, pancreatic disease, portal hypertension or malignant change.

CDC can be classified into five types.[53] Type I is a cystic or fusiform dilatation of the common bile duct (CBD). This is the most common type, accounting for over 70% of all cases. Type II is a diverticulum of the CBD (approximately 2%) and type III is a choledochocele involving the intraduodenal part of the distal CBD (1–5%). The type IV cyst is subdivided into type IVA, which is the second most common type consisting of multiple intra- and extrahepatic cystic dilatations, and type IVB where there are multiple extrahepatic cystic dilatations only. The type V cyst or Caroli's disease consists of single or multiple cystic dilatations of the intrahepatic bile ducts. Classification of types IV and V is controversial and they are considered by some authors to be separate disorders entirely (Fig. 69.25).

The cause of CDC is unknown but two main aetiological theories exist. The first is that they may represent an acquired weakness of duct wall, as CDCs are frequently associated with an abnormal junction between distal CBD and pancreatic duct, where the ducts

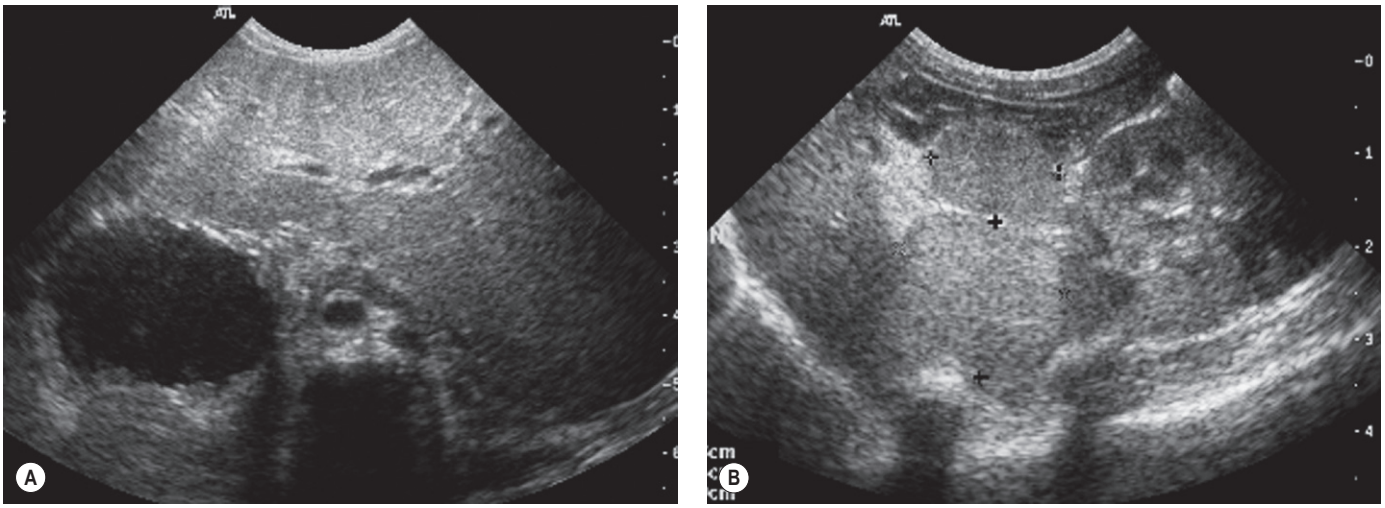

Figure 69.24 Biliary atresia–splenic malformation syndrome. Midline transverse **(A)** and right longitudinal **(B)** ultrasound images in a patient with EHBA, situs inversus, right-sided polysplenia and azygos continuation of the IVC. Note the right-sided stomach.

unite outside the duodenal wall and have a long common channel. This causes some degree of obstruction and encourages reflux of pancreatic juice into the bile duct, which may weaken the duct wall, and could also predispose to the development of malignancy in adulthood.[54] An abnormal CBD–pancreatic duct union is seen most commonly in CDC types I and IVA. The second theory is that duct dilatation occurs secondary to CBD obstruction, e.g. stricture.[55] Genetic factors may play a part. However, familial CDCs are rare and twin studies have not identified any clear genetic predisposition.[56] CDC and biliary atresia occasionally coexist in neonates.[57]

Sonographically, a spectrum of abnormalities is seen in patients with CDC. The main role of ultrasound is to define the biliary anatomy and look for associated parenchymal or vascular abnormalities. CBD dilatation is defined as >2 mm in infants and >3.5 mm in older children. A well-defined, fluid-filled cyst may be seen at the porta hepatis separate from the gallbladder (Fig. 69.26), and this may contain stones or debris (Fig. 69.27). Intrahepatic duct dilatation is usually limited to the central portions of the left and right main hepatic ducts (Fig. 69.28). Further imaging with magnetic resonance cholangiopancreatography (MRCP), endoscopic retrograde cholangiopancreatography (ERCP) or percutaneous transhepatic cholangiogram (PTC) to confirm the biliary origin and anatomy preoperatively may be required; or operative cholangiogram if these are not available or are inconclusive. Hepatic scintigraphy may be used to confirm communication of the cyst with the biliary tract but anatomical detail is limited. The treatment of CDC is radical excision and hepaticoenterostomy to reduce the incidence of complications, but patients require long-term follow-up postoperatively as they remain at increased risk for development of anastomotic stricture, cholangitis, progressive biliary cirrhosis and adhesive bowel obstruction.

Inspissated bile syndrome

Bile duct obstruction in the neonatal period or early infancy caused by sludge, gallstones or plugs of thickened bile typically occurs in patients with a history of perinatal complications often related to prematurity or sepsis, or those that have undergone intestinal resection or stoma formation. Other predisposing factors include parenteral nutrition, haemolysis, phototherapy, dehydration or diuretic treatment.[38,58] Rarely, an underlying congenital structural biliary abnormality is found at cholangiography, e.g. abnormal entry of the CBD into the duodenum, that may predispose to inspissated bile syndrome (IBS).

Ultrasound shows dilatation of the intrahepatic or extrahepatic bile ducts that contain moderately echogenic material without acoustic shadowing or highly echogenic foci with acoustic shadowing. Similar contents may be seen in the gallbladder which itself may be contracted and thick-walled (Fig. 69.29A and B). IBS can be distinguished from EHBA on ultrasound because EHBA lacks biliary dilatation. The definitive investigation is PTC, which can be therapeutic. Irrigation may sometimes be achieved with ERCP. Laparotomy with opening and wash-out of the CBD may be necessary. Medical treatment with ursodeoxycholic acid or cholecystokinin (CCK) may obviate the need for surgery.[31]

Spontaneous perforation of the common bile duct

Spontaneous perforation of the CBD in infancy is a rare but important surgical cause of conjugated hyperbilirubinaemia. Affected infants present at 2–4 weeks of age with acute onset of abdominal distension, jaundice and acholic stools, sometimes accompanied by irritability and vomiting. Bilious ascites may stain the scrotum, hernias, hydroceles and umbilicus. There is typically no preceding history of jaundice in contrast to other causes, although occasionally the onset of obstructive jaundice may be insidious, mimicking CDC or EHBA.

The cause of this condition is unknown but perforation always occurs at the junction of the cystic duct and CBD, and is usually described as 'punched out', suggesting a congenital weakness.[59,60] Biliary sludge or stricture are often associated but these findings may be secondary to perforation rather than the primary cause of obstruction leading to a sudden elevation of biliary pressure.[61] Ultrasound may show a complex mass or 'pseudocyst' at the porta hepatis which can mimic an infected or perforated CDC (Fig. 69.30A). Inflammatory reaction may cause distal CBD stricture with dilatation of intrahepatic ducts. Generalised ascites sometimes containing echogenic debris or fine septations may be present, and gallbladder or distal CBD sludge or stones may be seen.[62] Nuclear scintigraphy may be non-excreting but can show localised or generalised leak into peritoneal cavity (Fig. 69.30B). Operative cholangiogram is confirmatory and the treatment is surgical repair of the defect; however, accurate preoperative and operative diagnosis is extremely important, both to confirm the leak and to exclude distal obstruction or a pancreaticobiliary malformation.

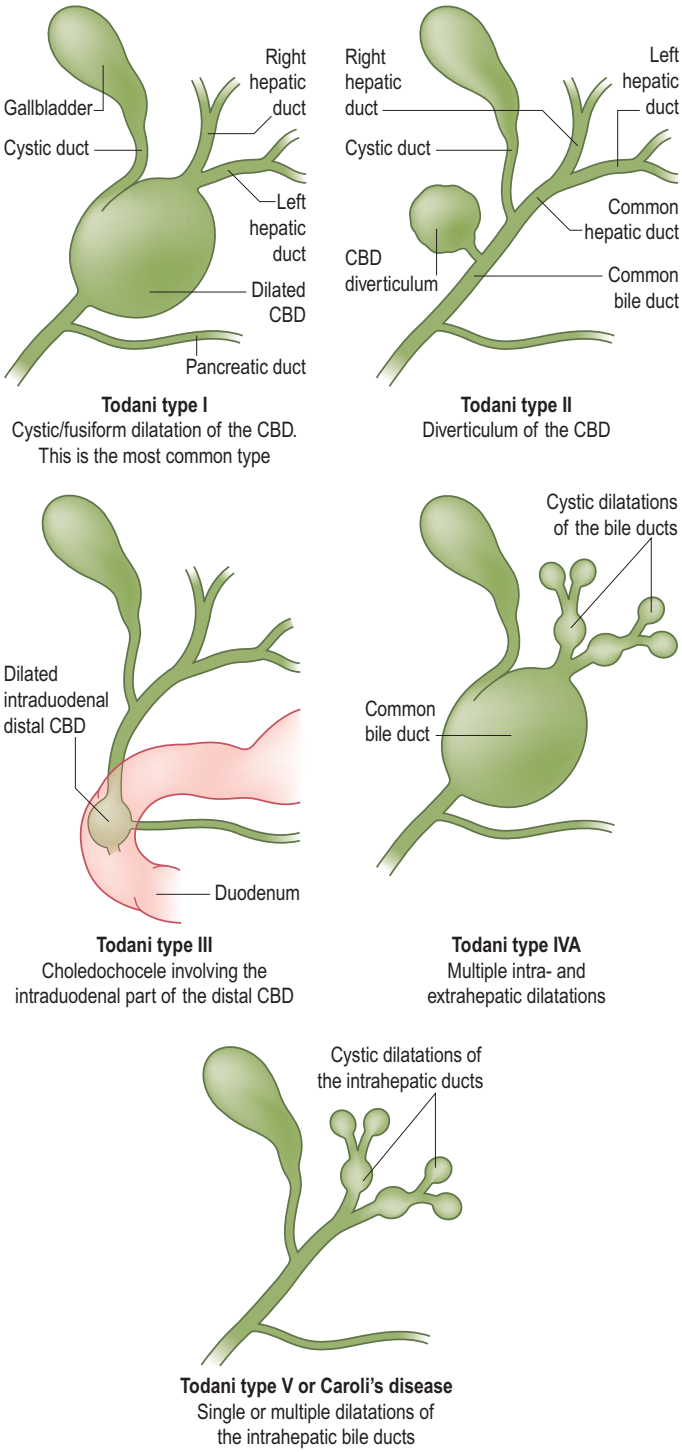

Todani type I
Cystic/fusiform dilatation of the CBD. This is the most common type

Todani type II
Diverticulum of the CBD

Todani type III
Choledochocele involving the intraduodenal part of the distal CBD

Todani type IVA
Multiple intra- and extrahepatic dilatations

Todani type V or Caroli's disease
Single or multiple dilatations of the intrahepatic bile ducts

Figure 69.25 Types of choledochal cyst (CDC). (Modified from http://emedicine.medscape.com/article/366004-overview; accessed 18/09/2009.)

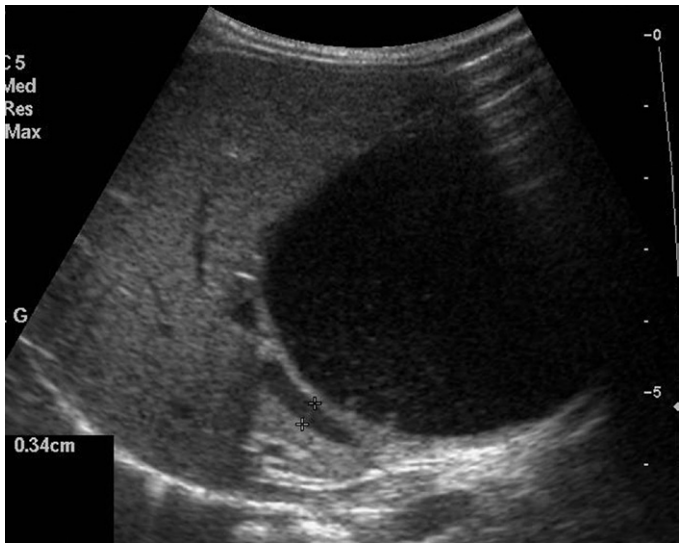

Figure 69.26 Todani type I choledochal cyst in a neonate with conjugated hyperbilirubinaemia. Right transverse ultrasound image showing a 4 cm, well-defined cyst at the porta hepatis, anterior to the portal vein.

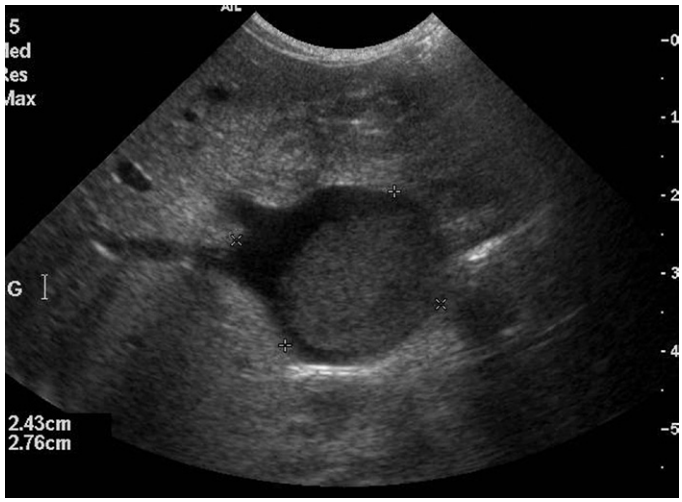

Figure 69.27 Todani type IVA choledochal cyst in a neonate with conjugated hyperbilirubinaemia. Right longitudinal ultrasound image showing a 24×28 mm cyst at the porta hepatis, containing debris.

Biliary hypoplasia and Alagille's syndrome

Biliary hypoplasia is characterised by a very small, but visible and patent extrahepatic biliary ductal system and is a manifestation of a variety of hepatobiliary disorders causing neonatal hepatitis, e.g. α_1-antitrypsin deficiency, Alagille's syndrome and non-syndromic paucity of the intrahepatic bile ducts. The diagnosis is made at surgical exploration for neonatal conjugated hyperbilirubinaemia. The prognosis is variable, depending on the primary disease, and

Neonatal jaundice

- Unconjugated hyperbilirubinaemia is a normal physiological event that occurs in up to 50% of term infants.
- Prolonged neonatal jaundice (>2 weeks of age) should be investigated.
- Conjugated hyperbilirubinaemia almost always reflects hepatic dysfunction.
- The neonatal hepatitis syndrome (NHS) refers to the numerous medical causes of conjugated hyperbilirubinaemia.
- The most common causes of conjugated hyperbilirubinaemia are NHS, EHBA and CDC.
- The role of ultrasound in neonatal conjugated hyperbilirubinaemia is limited, but it helps to rule out some surgical causes such as CDC and cholelithiasis or sludge causing biliary obstruction.
- In EHBA a good prognosis depends on early operative treatment to re-establish bile flow and prevent progressive biliary cirrhosis.

cannot be improved by surgical procedures. Alagille's syndrome, also known as *syndromic bile duct paucity* or *arteriohepatic dysplasia*, is an autosomal dominant disorder with low penetrance. In this condition, bile duct hypoplasia/paucity is found on liver biopsy in association with cardiac, facial, ocular and skeletal abnormalities (Fig. 69.31). Patients usually present in the first 3 months of life but may be diagnosed in older children with persistent cholestatic jaundice and even in adults after diagnosis in a related child.[63]

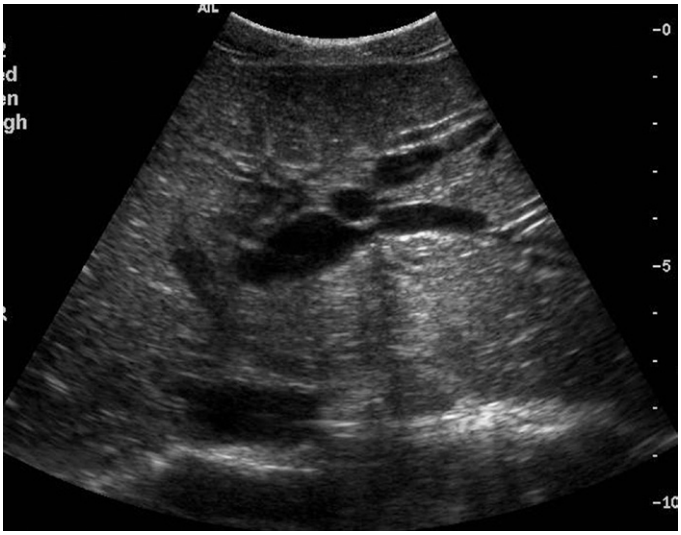

Figure 69.28 Todani type IVA choledochal cyst. Transverse ultrasound in a 14-year-old with recurrent abdominal pain and jaundice showing dilatation of the left and right intrahepatic ducts.

Jaundice in older children

The multiple causes of jaundice in infants beyond the neonatal period and in older children can be broadly divided into two categories: primary diseases of the hepatocytes, and obstructive causes. (See sections on diffuse parenchymal disease above, and biliary dilatation and obstruction, below.)

Biliary dilatation and obstruction

Biliary dilatation with obstruction in children may be seen in association with cholelithiasis, in IBS in neonates (see 'Inspissated bile syndrome' section above), with benign strictures of the biliary system, and in malignant disease of the biliary system. Presenting symptoms in children with CDC are variable but the typical presentation is with obstructive jaundice, occasionally with sludge or stone formation in the biliary system. Isolated, benign bile duct strictures in children may occur following trauma, surgery, radiotherapy or spontaneous perforation of the CBD[64] or may be idiopathic.[65] Multiple biliary strictures are seen in patients with sclerosing cholangitis, and following ischaemic injury to the bile ducts, e.g. post transplantation.

Bile duct tumours

Although uncommon, a tumour arising from the bile ducts should always be considered in the differential diagnosis of a child presenting with painless obstructive jaundice. Malignant bile duct tumours are more common than benign lesions in childhood, with rhabdomyosarcoma being the most common primary biliary tumour in children. Most tumours are found in the extrahepatic biliary tree and pre-school age children are predominantly affected. Presentation is usually with obstructive jaundice, often accompanied by

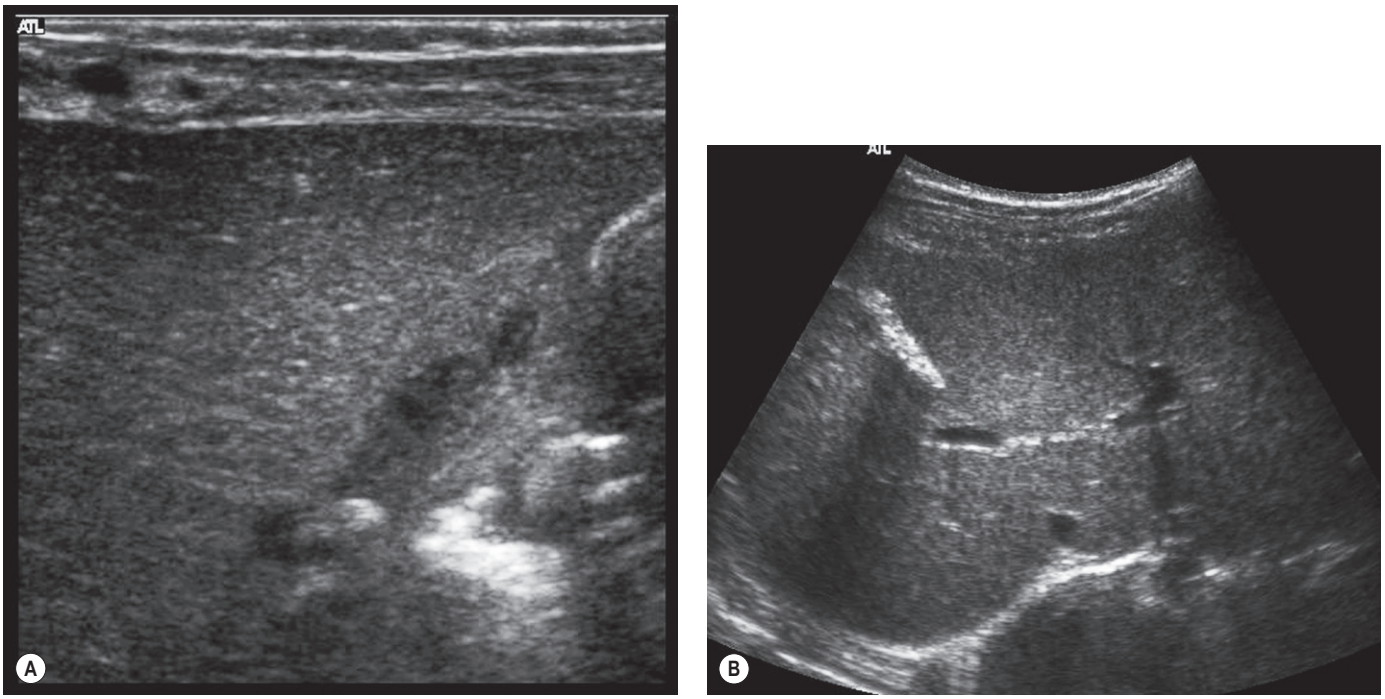

Figure 69.29 Inspissated bile syndrome in a neonate on parenteral nutrition. Images of the gallbladder from two different ultrasound examinations. The gallbladder is thick-walled and contains echogenic material **(A)**. One week later, the gallbladder is filled with echogenic sludge and casts an acoustic shadow **(B)**.

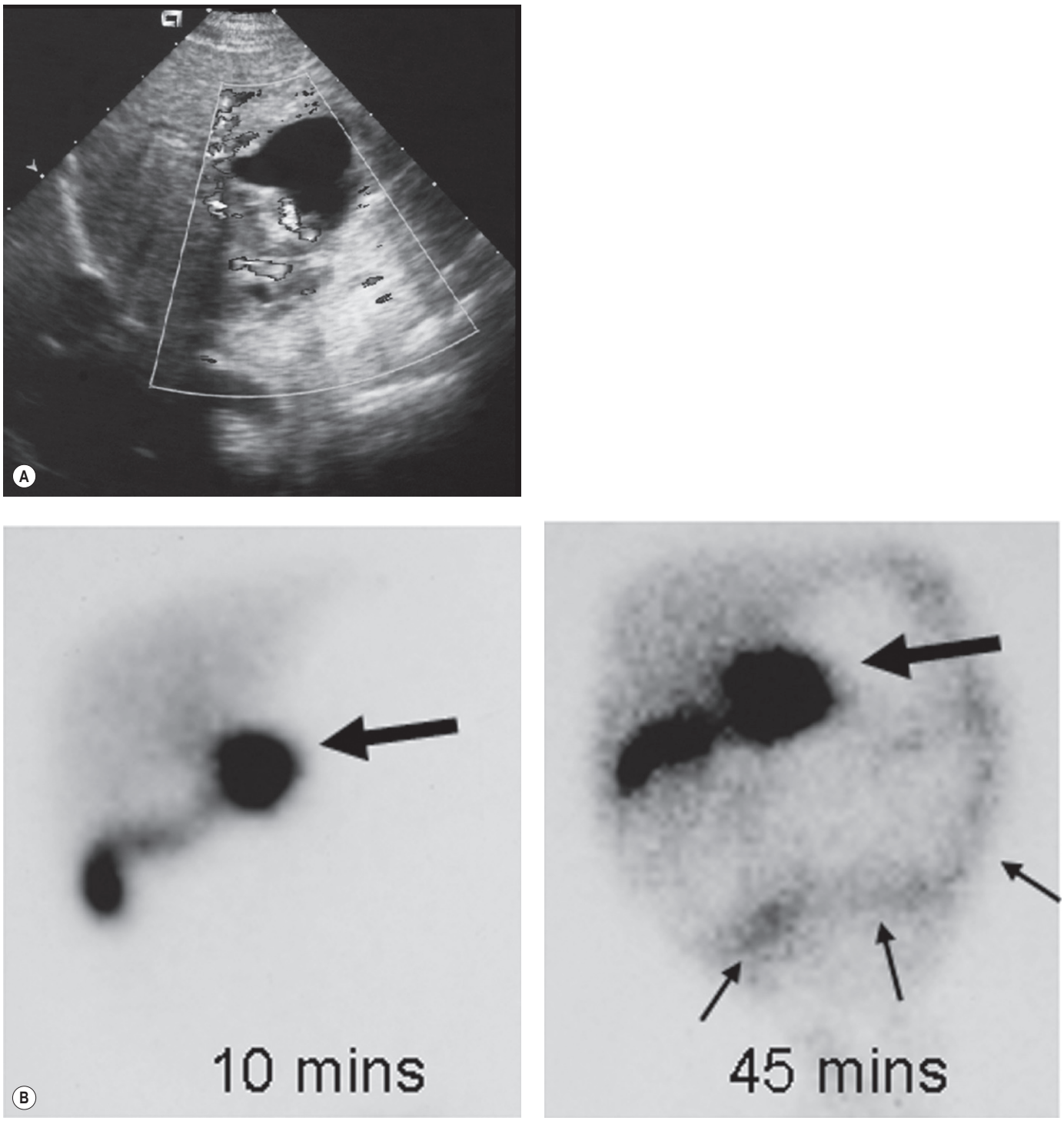

Figure 69.30 Spontaneous perforation of the common bile duct (CBD) in a neonate who presented with poor feeding, jaundice and abdominal distension. Ultrasound **(A)** shows a cyst at the porta hepatis; free intraperitoneal fluid was also demonstrated. Hepatobiliary iminodiacetic acid (HIDA) scan **(B)** showed a bile leak with accumulation of tracer at the porta hepatis (large arrows) and within the peritoneal cavity (small arrows). Perforation of the CBD at its junction with the cystic duct was confirmed at laparotomy. (Images courtesy of Dr A. Paterson, Royal Belfast Children's Hospital.)

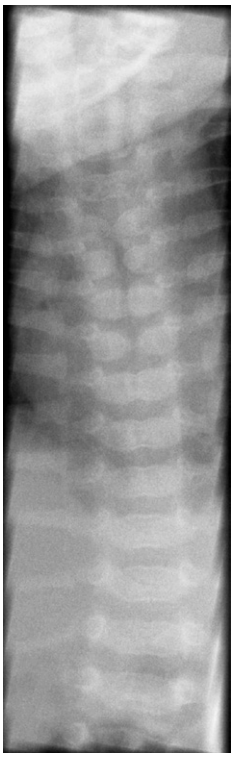

Figure 69.31 Alagille's syndrome. Thoracic spine radiograph showing several 'butterfly' vertebrae, a characteristic skeletal manifestation of the syndrome.

weight loss, abdominal pain and fever. Biliary rhabdomyosarcomas arise most frequently at the porta hepatis, and involve the cystic duct. Ultrasound typically shows intra- and extrahepatic biliary dilatation and solid material within the bile ducts which does not cast an acoustic shadow. Biliary rhabdomyosarcoma can be misdiagnosed as choledochal cysts or cholelithiasis, unless it is recognised that the biliary system contains solid material (Fig. 69.32A and B). Histologically they are embryonal or botryoid tumours which are locally invasive, and approximately 20% of children have metastases at presentation.[66] Carcinoma may arise in the biliary tract of patients with untreated or residual (incompletely resected) choledochal cysts although the youngest reported case is a patient of 17 years of age.[67]

Jaundice in older children

- Jaundice outside the neonatal period may be caused by hepatocellular disease or biliary obstruction.
- Overall, bile duct tumours are rare in children but malignant bile duct tumours occur more commonly than benign tumours.
- Gallbladder disease in children including cholelithiasis is increasing in incidence; this is probably due to dietary changes, increased use of parenteral nutrition and better detection using ultrasound.
- Risk factors for the development of gallstones in children include biliary stasis, excess bilirubin load (e.g. haemolysis), and lithogenic bile.
- Children who have undergone ileal resection, or who have ileal Crohn's disease or CF are at an increased risk of developing gallstones.

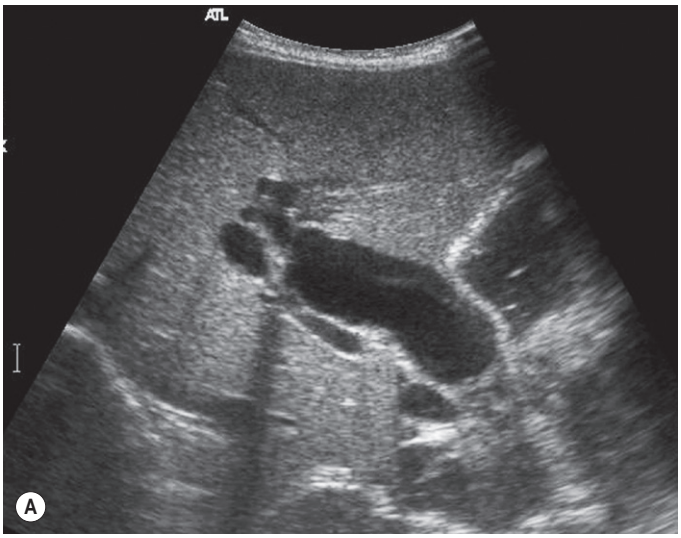

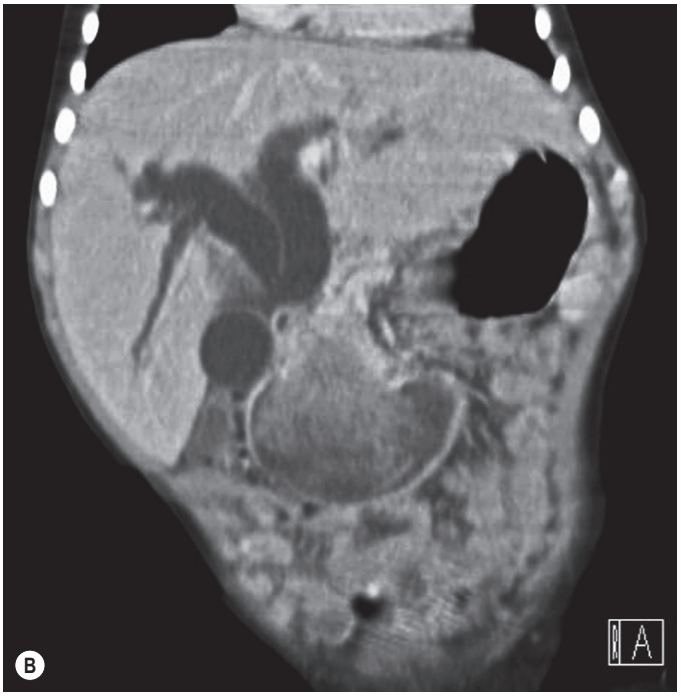

Figure 69.32 Biliary rhabdomyosarcoma in a 20-month-old referred with a diagnosis of probable choledochal cyst. Ultrasound **(A)** shows marked dilatation of the common bile duct. The intrahepatic ducts were also dilated and there was a 4 cm diameter soft tissue mass in the duodenum. CT scan (coronal reconstruction) performed for staging purposes demonstrates all of these abnormalities together with marked duodenal dilatation **(B)**. At surgery the tumour was found to arise from the distal CBD/sphincter of Oddi and was projecting into the duodenum.

Benign tumours of the biliary tracts include inflammatory 'pseudo-tumours', papillomas and granular cell tumours. All are rare in children and require surgical excision following histological confirmation.

GALLBLADDER

Normal appearances in children and congenital variants

The normal gallbladder can always be identified using ultrasound, provided the patient has been adequately fasted. There is a wide range of gallbladder size in childhood, and measurements of gallbladder width and length are of limited use in the evaluation of gallbladder pathology. In neonates and infants the gallbladder measures 1.3–3.4 cm in length (mean 2.5 cm), and 0.5–1.2 cm in width (mean 0.9 cm). In children aged 2–16 years gallbladder length ranges from 2.9 to 8 cm (mean 5 cm), and width 1 to 3.2 cm (mean 1.8 cm).[68] The normal gallbladder wall is thin, well defined and hyperechoic with a maximum wall thickness of 3 mm.[68] Folds in the gallbladder, particularly at the junction of the gallbladder neck and body, can produce an acoustic shadow giving the impression of stones, a septum or dilated CBD. The 'phrygian cap' appearance is produced by folding of the gallbladder fundus. Folds should be easily differentiated from pathology by scanning in multiple planes.

Agenesis of the gallbladder is very rare and may be associated with biliary atresia. Ectopic gallbladder may be found in the left or right retrohepatic space, suprahepatic space, within the liver itself or rarely, elsewhere in the abdomen.[69] In gallbladder duplication, the gallbladder lumen is divided by a partition, with each compartment having a separate cystic duct. Less commonly the gallbladder may be bilobed, with a single cystic duct. Triple and quadruple gallbladders are also described.[70] Septated gallbladders contain a variable number of thin septations, which may be partial or complete and are associated with stasis and stone formation.[69]

Cholelithiasis and gallbladder disease

Gallbladder disease in children is being diagnosed with increasing frequency. This is most likely due in part to dietary changes in developed countries, an increased incidence of gallbladder disease associated with parenteral nutrition in infancy, and the widespread use of ultrasound. The incidence of gallstones in children varies according to geographic location and age, and is variably quoted in the literature from 0.5% of neonates in Germany and 0.13–0.2% of infants and children in Italy to less than 0.13% of children in Japan.[31] Most studies show a bimodal distribution with a small peak in infancy and a steady rise in incidence from early adolescence onwards. In childhood, boys and girls are equally affected but in adolescence girls are more often affected, with other risk factors such as obesity in common with adult cholelithiasis. In children, the main risk factors associated with the development of biliary sludge or gallstones are biliary stasis (e.g. parenteral nutrition, fasting, impaired gallbladder emptying, immobilisation and cholestatic liver disease per se), excess bilirubin load (e.g. haemolytic disorders), and an increased tendency to develop stones due to the nature of the bile or *lithogenic bile*, which occurs in conditions such as cystic fibrosis and when bile composition is altered iatrogenically or secondary to a pre-existing disorder.[71] Patients who have undergone ileal resection or have ileal Crohn's disease have a tendency to develop gallstones, most likely due to a reduction in the normal recirculation of bile salts, which are usually absorbed in the ileum. This leads to a relative bile salt deficiency, incomplete solubilisation of unconjugated bilirubin and calcium bilirubinate stones.

Clinical suspicion of gallstones is easily confirmed on ultrasound following an appropriate fast. Gallstones are mobile and cast an acoustic shadow, whatever their composition. Biliary sludge is

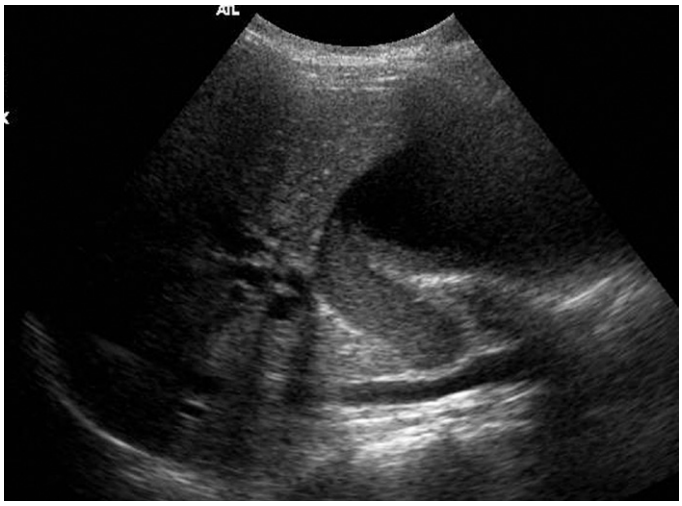

Figure 69.33 **Echogenic sludge in the gallbladder.**

echogenic and may or may not cast an acoustic shadow (Fig. 69.33). Although spontaneous resolution of gallstones is reported in some infants, the likelihood of this occurring in older children is low and they remain at risk of developing complications such as biliary obstruction and gallstone pancreatitis. Cholecystectomy is indicated in symptomatic patients with gallstones, but the perceived benefit of elective cholecystectomy needs to be considered together with the risks of surgery in asymptomatic patients.

Gallbladder hydrops and acalculous cholecystitis

Gallbladder hydrops and acalculous cholecystitis are probably manifestations of the same disease entity but represent different points on a spectrum of symptoms and clinical signs. Acute distension of the gallbladder with wall oedema (hydrops) in the absence of any other biliary tract disease or an inflammatory component is rare but has been reported in association with sepsis and hypovolaemic states including Kawasaki disease, severe diarrhoea with dehydration, hepatitis, scarlet fever and mesenteric adenitis. In this condition it is thought that bile stasis leads to functional obstruction of the cystic duct. The diagnosis is suspected in patients with a palpable, non-tender or mildly tender right upper quadrant mass that is subsequently confirmed to be the gallbladder with ultrasound. Secondary infection of a distended, hydropic gallbladder resulting from invasion of the gallbladder wall by organisms in the bile produces the clinical symptoms and signs of acalculous cholecystitis. In Western countries, acalculous cholecystitis may develop after shock, systemic sepsis, trauma, cardiac surgery, burns, *Salmonella* infection or in patients on parenteral nutrition. Many of these are patients receiving intensive care and initially the diagnosis may be occult. Clinical features include abdominal pain, vomiting, fever and localised right upper quadrant tenderness over the gallbladder which may be palpable. Patients typically have a raised white cell count and inflammatory markers. Ultrasound shows a markedly distended, thick-walled gallbladder, often containing echogenic debris. Patients are managed with intravenous fluid and antibiotics and bowel rest. Cholecystectomy or cholecystotomy are indicated in patients who fail to respond to conservative management and continue to deteriorate clinically.[31,70]

Gallbladder wall lesions

Polypoid lesions of the gallbladder, projecting from the wall into the lumen, are rare in children compared with adults, in whom neoplastic lesions account for up to 15% of all lesions.[72] At any age, the differential diagnosis includes an adherent gallstone, sludge

ball or blood clot, so the fixed nature of the mass should be confirmed on serial ultrasound scans. Most children reported to have gallbladder polyps are asymptomatic and pathology is variable, including adenomas, epithelial hyperplasia, gastric heterotopia and cholesterol polyps which may be associated with cholesterolosis of the gallbladder and have no malignant potential.[73] In adults, adenomas can be complicated by the development of carcinoma in situ or adenocarcinoma.[74] Three conditions are known to be associated with the development of gallbladder polyps in children: metachromatic leukodystrophy, Peutz–Jeghers syndrome and pancreaticobiliary mal-union with choledochal cyst formation.[73] Metachromatic leukodystrophy is an inherited neurodegenerative metabolic disorder caused by a deficiency of the lysosomal enzyme arylsulphatase A. In this disorder metachromatic sulphatides accumulate in various tissues including the gallbladder wall. In the Peutz–Jeghers syndrome, polyps are more common in adults and are hamartomatous lesions that vary in size and number. Recommended management of gallbladder polyps varies from observation with serial ultrasound to radical cholecystectomy and will obviously depend on the underlying cause. In general, cholecystectomy is advised if there are biliary symptoms, concerns about malignancy or if the polyp is ≥1 cm in size.[73]

LIVER TRANSPLANTATION IN CHILDREN

Orthotopic liver transplant (OLT) is the treatment for acute or chronic liver failure for which there is no other treatment option. There once was a shortage of suitably sized donors for children requiring transplantation, and many patients died because of this. However, it is now standard practice to transplant reduced or segmental (also referred to as cut-down) liver grafts from donors in whom the whole organ would have been too large for the intended recipient, although whole liver grafts from a similar sized donor will be transplanted if available. As with adults, reduced grafts may be from cadavers (harvested from donors on life support prior to this being withdrawn), or less commonly live donors. The preoperative assessment is similar to adult patients requiring transplant, but due to the nature of the reduced donor organ, the postoperative imaging features and some of the complications that may be encountered in children are different.

The success of reduced liver transplantation is based on two unique properties of the organ: its segmental anatomy, and the ability of the liver to regenerate. The most common reduced liver grafts in younger children are part of the left lobe (segments II and III) or the entire left lobe – segments II–IV. Right lobes (segments V–VIII) or extended right lobes (segments IV–VIII) are usually reserved for larger children or adults. Regeneration of the liver occurs rapidly and transplanted grafts in adults can double in size in as little as 3 weeks.[75] In some instances the whole graft is split with the smaller part (e.g. segments II and III) being transplanted into a child and the remaining extended right lobe transplanted into another patient, usually an adult.

In reduced liver grafts there are three main anatomical differences in relation to the postoperative imaging; there is a cut edge representing the line of separation from the remaining organ; bile drainage is often into a Roux-en-Y loop rather than an end-to-end biliary anastomosis; and there is an alteration in the position and number of the hepatic vessels depending on the number of liver segments that have been transplanted. For example; a segment II and III graft would have a main hepatic artery (HA) and portal vein (PV) with two segmental vessels respectively, and a single hepatic vein. An extended right lobe graft (segments IV–VIII) has main HA and PV with five segmental branches of each, and two hepatic veins. The position of the neo-porta hepatis and the arterial structures is altered in left lobe grafts with the PV coursing laterally towards the graft and entering its inferior right lateral aspect (Fig. 69.34). With right lobe or extended right lobe grafts the neo-porta hepatis is more medially placed, similar to the native liver.

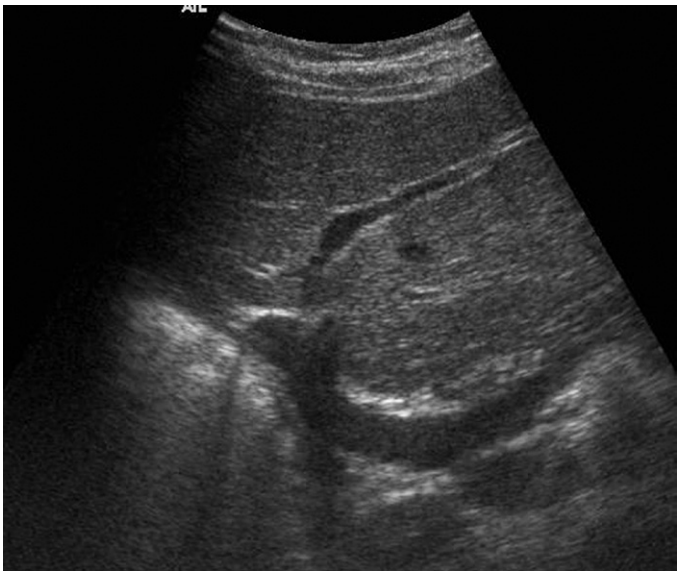

Figure 69.34 Reduced left lobe liver graft (segments II and III) showing position of the portal vein.

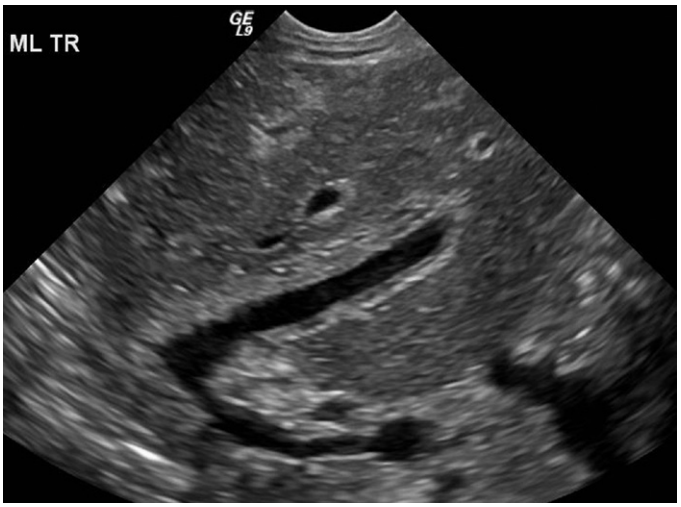

Figure 69.35 Periportal oedema in a reduced left lobe graft, day 1 post transplantation.

Complications after liver transplantation may involve the liver parenchyma, vasculature, bile ducts and perihepatic space. Alteration in the route of the graft vessels, problems associated with small vessel anastomoses (e.g. anastomotic breakdown, thrombosis or stenosis) and increased abdominal pressure due to intestinal and mesenteric oedema, or sheer size of the graft can result in vascular compromise and threaten graft viability. The normal liver transplant has a homogeneous or slightly heterogeneous appearance, whilst marked heterogeneity, especially reduced echogenicity of one or more segments raises the possibility of ischaemic injury. Some degree of periportal echogenicity or oedema is typical in the first week post-transplantation but usually resolves over time (Fig. 69.35). There is also normally a small amount of free fluid in the subhepatic space and remainder of the upper abdomen postoperatively. Fluid collections along the cut edge of the graft may represent serous fluid, haematoma or bile collections and should be monitored for size on follow-up studies, as they can become infected or increase in size and require percutaneous drainage.

Patency of the main graft vessels (and the segmental branches if required by the transplant surgeon) should be confirmed with

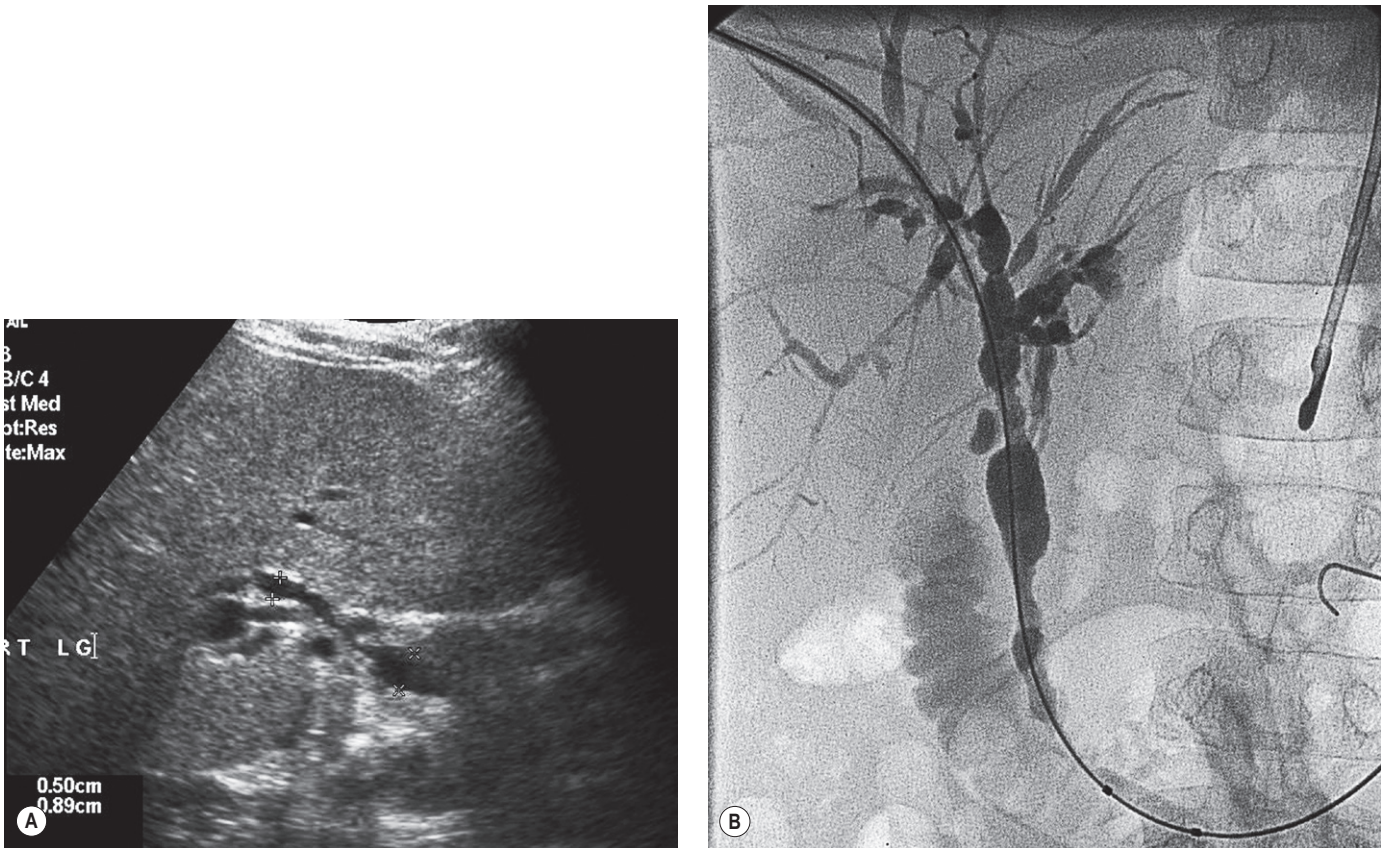

Figure 69.36 Multiple bile duct strictures in a liver graft secondary to arterial ischaemia. Ultrasound **(A)** shows dilatation and irregularity of the common bile duct. Image from a percutaneous transhepatic cholangiogram in the same patient **(B)** demonstrates multiple intra- and extrahepatic biliary strictures with areas of duct dilatation.

Liver transplantation in children

- Orthotopic liver transplantation (OLT) is the treatment for acute or chronic liver disease where there is no other treatment option.
- Reduced or segmental liver grafts have enabled small children to be successfully transplanted when there is no similar sized donor available.
- Reduced liver grafts have a cut-edge, bile may drain into a Roux-en-Y loop and the vascular anatomy differs from whole liver grafts.
- Complications following reduced liver graft transplantation may involve the parenchyma, vessels, bile ducts or perihepatic space.
- Many postoperative complications of reduced liver graft transplantation are related to problems associated with small vessel anastomoses.

Doppler studies in the immediate postoperative period and on long-term follow-up studies. The normal hepatic arterial trace shows a rapid systolic upstroke with continuous forward flow in diastole, and the normal RI should lie between 0.5 and 0.7. The normal PV waveform is a continuous flow towards the liver and varies slightly in velocity with the respiratory cycle as with a native liver. It is not uncommon to see dampening of the hepatic venous Doppler traces on early postoperative scans, rather than the usual triphasic pattern.

The Roux-en-Y anastomosis may be identified near the neo-porta-hepatis, especially if there is a stent across it. Bile leaks and anastomotic breakdown at the Roux-en-Y site can occur and a fluid collection in this region may indicate a bile leak. Conversely, anastomotic strictures may occur at the Roux-en-Y, although these are not easily identified using ultrasound, often requiring PTC. If there is graft bile duct dilatation, this complication should be suspected. However, bile duct dilatation in a liver transplant can occur for a variety of other reasons including ascending cholangitis and rejection so it is a relatively non-specific finding. Non-anastomotic bile duct strictures may result from arterial ischaemia and can be extensive, involving much of the graft (Fig. 69.36A and B).[76] Cholecystectomy is performed routinely on all donor liver grafts so the gallbladder is never visualised on transplant recipients. Long-term complications of liver transplantation include rejection, recurrence of the original liver disease (e.g. tumour) and PTLD.

PANCREAS AND SPLEEN

The normal pancreas and congenital variations

Sonographic examination of the pancreas is more reliable in children compared with adults due to their smaller body mass and relatively large left hepatic lobe which acts as an acoustic window. However, visualisation can be hampered by the presence of excess air in the stomach and duodenum, particularly if the child has been crying. Imaging of the distal body and tail in the prone position using the left kidney as an acoustic window may be helpful in some cases.[77] In childhood the gland is normally isoechoic or of slightly increased echogenicity compared with the liver. However, in the

neonatal period the pancreas is more often hyperechoic. In 10% of patients the gland is hypoechoic compared with the liver, probably due to the relatively large amounts of glandular tissue and lack of fibrosis or fat found in older individuals.

Part or all of the normal pancreatic duct can be seen in at least 50% of healthy children. The duct appears either as a single echogenic linear structure, or a tubular structure with smooth parallel walls and an anechoic lumen (Fig. 69.37). The upper limit of normal duct diameter is 2 mm in childhood. Side branches of the main pancreatic duct are not usually seen sonographically unless the duct is dilated. It is usual to see the common bile duct as a round anechoic structure in the head of the pancreas. The most growth and consequent variation in size of the pancreas occurs in the first year of life, after which there is a gradual increase in size throughout childhood.[78]

Agenesis of the dorsal pancreatic bud leads to a congenitally short pancreas with absence of the pancreatic neck, body and tail. Only a short rounded pancreatic head is found adjacent to the duodenum. It may be an isolated finding but has been reported in association with polysplenia syndromes. As most of the islet cells are located in the distal pancreas, affected patients have an increased incidence of diabetes mellitus.[77]

Pancreas divisum is the most common congenital pancreatic anatomical variant and is the result of failure of fusion of the dorsal and ventral pancreatic ducts, so that there is persistence of two separate ductal systems. The abnormality is said to exist in up to 11% of the population.[79] In this anatomical variation, the longer dorsal pancreatic duct drains the anterior part of the head, the body and tail via the minor papilla; and the ventral pancreatic duct drains the inferior part of the head and uncinate process via the major papilla. This anomaly may be associated with recurrent abdominal pain and pancreatitis although the aetiological theories are controversial; including a relative or functional stenosis of the minor papilla, which is too small to transmit the volume of secretions from the majority of the gland, with consequent pooling of secretions leading to pancreatitis. Ultrasound has no role in defining the ductal anatomy of the pancreas, which is best imaged non-invasively using MRI.

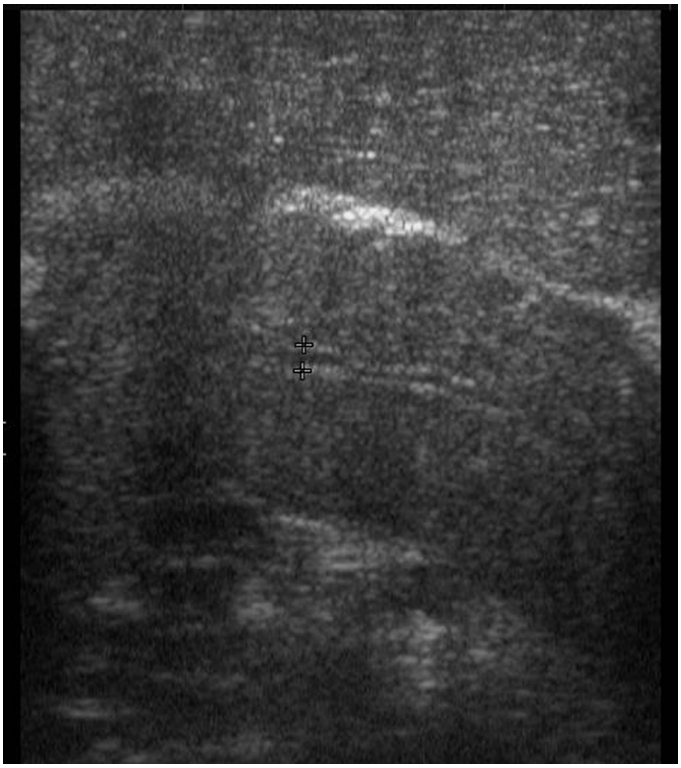

Figure 69.37 Normal pancreatic duct in a child (shown by callipers).

Annular pancreas is a congenital pancreatic abnormality in which pancreatic tissue encircles the duodenum. Several aetiological theories for the developmental of this anomaly have been proposed.[77,79] The abnormality often causes duodenal obstruction in the neonatal period, and is associated with other congenital abnormalities including duodenal stenosis or atresia, trisomy 21, oesophageal atresia and congenital heart disease.[77] The abnormality may be identified using ultrasound whereby the pancreas appears as a circumferential band of pancreatic tissue encircling the proximal duodenum, which may be fluid-filled and dilated. Occasionally, presentation is later in life with recurrent vomiting, or the abnormality may be asymptomatic.

Congenital pancreatic cysts

True single congenital cysts of the pancreas are extremely rare. They are more common in females and typically located in the pancreatic tail or body. Solitary pancreatic cysts may be discovered incidentally or present as a mass lesion, with epigastric pain, jaundice or vomiting related to compression of nearby structures. They have been described in association with other congenital abnormalities including renal tubular ectasia, polydactyly, anorectal malformations, polycystic kidneys and Jeune's syndrome. The cysts typically measure up to 5 cm in diameter and sonographically are thin-walled, anechoic structures.[80] The pancreas is an uncommon site for an enteric duplication cyst but in this location may be confused with a pancreatic pseudocyst or neoplasm. Over 50% of pancreatic duplication cysts reported in the literature are located in the pancreatic head, and the most common presentation is with abdominal pain, nausea and vomiting being the second most common presentation.[81] Sonographically, duplication cysts in any location typically have a two-layered wall consisting of an inner echogenic mucosal lining and outer hypoechoic smooth muscle layer. The cyst contents may be anechoic or it may contain debris.

Multiple congenital pancreatic cysts are usually part of a systemic disorder with pancreatic involvement, such as von Hippel–Lindau disease (VHL) or autosomal dominant polycystic kidney disease (ADPKD). VHL is an autosomal dominant disorder with variable penetrance, characterised by retinal angiomas, central nervous system haemangioblastomas, cysts and tumours in other organs such as the pancreas, kidneys and adrenal glands. Most pancreatic cysts in this disorder are asymptomatic, discovered on screening examinations. Approximately 10% of patients with ADPKD have pancreatic cysts, and cysts may also be found in the adrenal glands, liver and spleen in addition to the kidneys.[82]

Acute and chronic pancreatitis in children

Acute pancreatitis is characterised by an acute inflammatory process involving the gland with variable involvement of adjacent tissues. The process is triggered by ductal obstruction, physical or chemical injury to the gland and leads to protease activation within the acinar cells. Proteolytic enzymes are released into the pancreatic interstitium causing a cascade of leukocyte activation and cytokine release which in turn causes a systemic inflammatory response. The most severe cases are associated with pancreatic haemorrhage and necrosis with major organ failure, and local complications such as abscess and pseudocyst formation are common. The causes of acute pancreatitis in children are more diverse and numerous than in adults. The most common cause of acute pancreatitis in children is trauma, followed by drugs and biliary causes such as gallstones, biliary sludge, microlithiasis and pancreaticobiliary malunion.[83] Other recognised causes in children include viral infections (e.g. mumps, Epstein–Barr virus, Coxsackie B, influenza), metabolic disorders or metabolic disturbance (e.g. diabetes, CF, hyperlipidaemia,

hyperparathyroidism, organic acidaemias) and hereditary pancreatitis. A small number of cases remain idiopathic. The clinical signs of acute pancreatitis include abdominal pain and tenderness, vomiting and fever, and the diagnosis is based on clinical findings and biochemical tests.

Ultrasound views can be limited by overlying bowel gas in acute pancreatitis but may reveal pancreatic swelling, oedematous/echogenic peripancreatic tissues, peripancreatic fluid collections, ascites, biliary stones or sludge and biliary or pancreatic duct dilatation (Fig. 69.38). Enhanced CT is the modality of choice in acute pancreatic trauma and for demonstrating acute complications of pancreatitis such as pancreatic haemorrhage or necrosis, and abscess formation. Pseudocyst formation is the most common complication associated with acute pancreatitis. Pseudocysts are collections of amylase-rich pancreatic juice surrounded by a wall of granulation tissue that arise following acute pancreatic inflammation or trauma, and normally form over several weeks (Fig. 69.39). Ultrasound has a particular role in follow-up of pseudocysts. Ultrasound or CT may be used to guide percutaneous drainage of pancreatic or extrapancreatic fluid collections.

Chronic pancreatitis is characterised by progressive destruction of the pancreatic parenchyma leading to permanent morphological change in the gland. There is usually calcification within the gland and focal or diffuse ductal dilatation and strictures. Causes in children include hereditary pancreatitis, CF, metabolic disorders and pancreas divisum. The disease often causes recurrent abdominal pain but the diagnosis may be delayed because the symptoms and episodes of hyperamylasaemia are transient, or the gland initially looks normal on ultrasound. The sonographic hallmark of chronic pancreatitis is pancreatic or ductal calcification which is identified as focal areas of hyperechogenicity, with or without acoustic shadowing. The main pancreatic duct is often dilated (>2 mm in diameter) and may appear tortuous (Fig. 69.40A and B). Other findings include parenchymal atrophy, an irregular pancreatic contour, and heterogeneous or increased parenchymal echogenicity secondary to fibrosis or fatty replacement.[78] Pseudocyst formation, peripancreatic

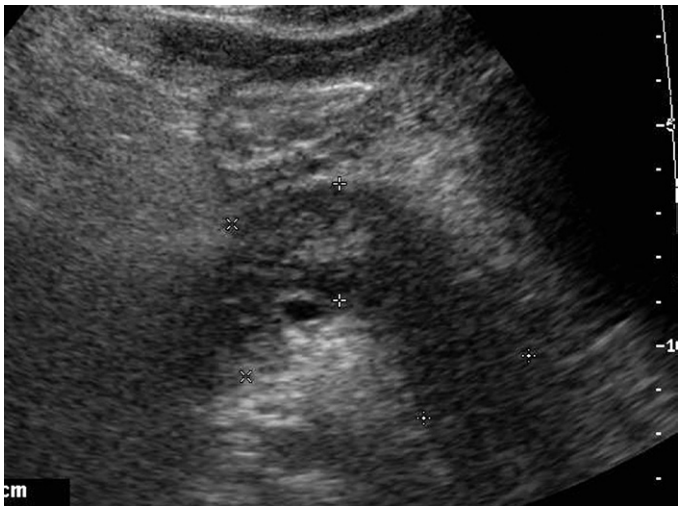

Figure 69.38 Acute pancreatitis in a 9-year-old. Transverse ultrasound showing pancreatic swelling and heterogeneous echotexture, especially in the head and neck of the gland.

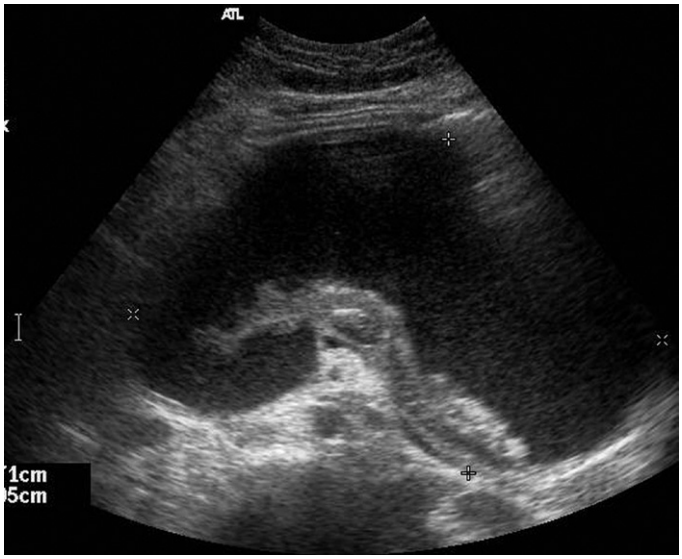

Figure 69.39 Pancreatic pseudocyst in the same patient as Figure 69.38. Transverse ultrasound showing a massive fluid-filled cyst anterior to the pancreas and surrounding much of the pancreatic head.

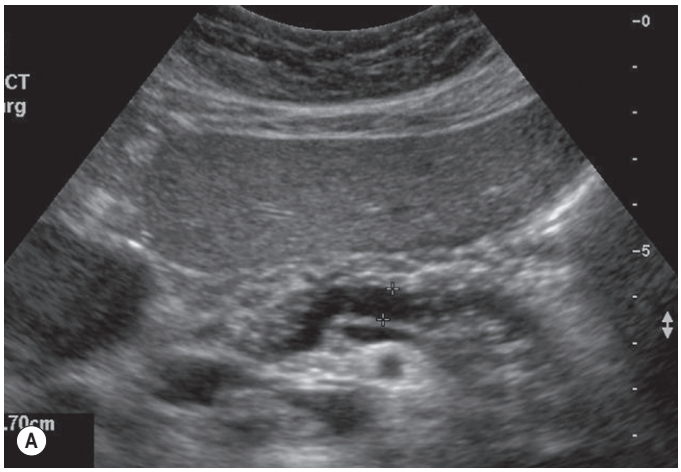

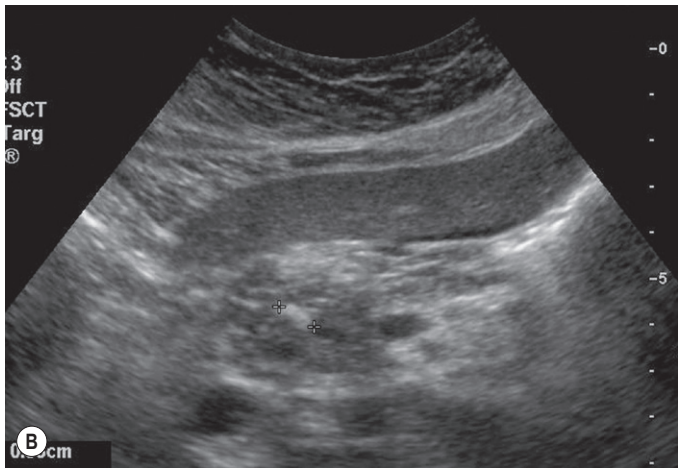

Figure 69.40 Chronic pancreatitis in a 15-year-old. The gland is atrophic and heterogeneous with duct dilatation (7 mm) **(A)** and there are stones in the pancreatic head **(B)**.

inflammatory changes and biliary dilatation may also be seen in association with chronic pancreatitis.

The pancreas in cystic fibrosis

Patients with CF develop pancreatic exocrine dysfunction secondary to obstruction of the small pancreatic ductules by abnormally thick mucoid secretions. This leads to ductal dilatation, tissue destruction and atrophy. Eventually the gland is replaced by fibrosis and fatty tissue, appearing heterogeneous or echogenic sonographically. The gland may calcify and a variable number of small cysts may develop within it, typically measuring <3 mm in diameter. Occasionally the pancreas is almost completely replaced by macroscopic cysts (>1 cm in diameter), a condition referred to as *cystosis*.

Spleen size in children and splenomegaly

The spleen is the largest lymphoid organ in the body. Together with the lymph nodes it forms the major components of the mononuclear-phagocyte system (reticuloendothelial system). This serves as a system of filters that remove damaged cells, microorganisms, and particulate matter, and deliver antigens to the immune system. The splenic tissue consists of red and white pulp lying in a capsule. Blood enters the spleen through the splenic artery, and travels into the smaller arterioles to reach the white pulp. The white pulp receives plasma for antigen processing and the remaining haemoconcentrated blood continues into the red pulp that forms the bulk of the splenic tissue and consists of splenic cords. Circulation through the splenic cords is slow and congested. This delay provides prolonged exposure of blood cells, bacteria, and particulate matter to the dense mononuclear-phagocyte elements in the red pulp. Blood from the red pulp drains into the splenic vein, uniting with the superior mesenteric vein to form the portal vein. Because no valves are present in the splenic venous system, the pressure in the splenic vein reflects the pressure in the portal vein.

Spleen size varies throughout childhood, according to patient age. The upper limit of normal spleen size in infants and children according to age is indicated in Table 69.1. There are numerous causes of splenomegaly in childhood and these are summarised in Table 69.5. The most common causes are infection, non-malignant haematological disorders and malignancies such as leukaemia and lymphoma. Despite the wide differential diagnosis for an enlarged spleen, it is rarely the primary site of disease. Therefore, investigations are not directed at the spleen itself; rather to identifying an underlying systemic cause for splenomegaly. Hypersplenism is the occurrence of thrombocytopenia, and occasionally leukopenia and anaemia, in the context of significant splenomegaly. Associated cytopenias are usually mild but may contribute to overall morbidity. Ultrasound can confirm the presence of an enlarged spleen, or space-occupying lesions (e.g. splenic cyst or abscess), and helps to distinguish between splenic enlargement and other causes of a left subchondral mass (e.g. a renal mass). It is also useful in confirming or excluding splenomegaly in obese patients in whom clinical examination may be difficult.

Splenic calcification

See Chapter 17.

Pancreas and spleen

- Pancreas divisum is the most common congenital pancreatic anatomical variant and is associated with recurrent abdominal pain and pancreatitis.
- Solitary congenital pancreatic cysts in children are rare, and multiple congenital cysts are usually associated with a systemic disorder such as von Hippel–Lindau disease, polycystic kidney disease or CF.
- The most common cause of acute pancreatitis in children is pancreatic trauma.
- The causes of acute pancreatitis in children are more diverse and numerous than in adults.
- The imaging appearances of acute pancreatitis and associated complications are the same as in adults.
- Spleen size varies in childhood according to age.
- The most common causes of splenomegaly in childhood are infection, non-malignant haematological disorders and malignancy such as lymphoma or leukaemia.
- The spleen is rarely the primary site of disease and investigations in splenomegaly are usually directed at identifying an underlying systemic cause.

Table 69.5 Causes of splenomegaly in children

Infection:
Viral infection – most childhood viral illnesses; including Epstein–Barr virus (EBV), cytomegalovirus (CMV), human immunodeficiency virus (HIV)
Bacterial, e.g. pneumococcal infection, *Salmonella*, bacterial endocarditis
Fungal, e.g. candidiasis in immunocompromised patients
Parasitic, e.g. malaria and schistosomiasis in endemic areas
Inflammatory causes:
Collagen vascular disorders
Juvenile idiopathic arthritis
Haematological causes – non-malignant:
Thalassaemia major
Severe iron deficiency anaemia
Acute splenic sequestration crisis in sickle cell anaemia
Haemolytic anaemias, e.g. hereditary spherocytosis
Bone marrow failure, e.g. aplastic anaemia, osteopetrosis
Malignancy:
Leukaemia
Lymphoma
Metastatic disease, e.g. neuroblastoma
Obstructed venous blood flow:
Extrahepatic portal venous obstruction, e.g. portal vein thrombosis
Intrahepatic causes of portal hypertension, e.g. any cause of cirrhosis
Congestive or right heart failure
Storage disorders:
Glycogen storage diseases
Lysosomal storage diseases (including lipid storage disorders such as Niemann–Pick, Gaucher's; and the mucopolysaccharidoses)
Miscellaneous:
Splenic trauma with subcapsular haematoma or cyst formation
Langerhans cell histiocytosis
Splenic abscess (bacterial, fungal or parasitic causes)

Splenic trauma and infarction

See Chapter 17.

Splenic masses/cysts

See Chapter 17.

REFERENCES

1. Hernanz-Schulman M, Ambrosino MM, Freeman PC, Quinn CB. Common bile duct in children: sonographic dimensions. Radiology 1995; 195(1):193–195.
2. Rosenberg HK, Markowitz RI, Kolberg H, et al. Normal splenic size in infants and children: sonographic measurements. AJR Am J Roentgenol 1991; 157(1):119–121.
3. Hernanz-Schulman M, Ambrosino MM, Genieser NB, et al. Pictorial essay. Current evaluation of the patient with abnormal visceroatrial situs. AJR Am J Roentgenol 1990; 154(4):797–802.
4. Mandell GA, Heyman S, Alavi A, Ziegler MM. A case of microgastria in association with splenic-gonadal fusion. Pediatr Radiol 1983; 13(2):95–98.
5. Brown CV, Virgilio GR, Vazquez WD. Wandering spleen and its complications in children: a case series and review of the literature. J Pediatr Surg 2003; 38(11):1676–1679.
6. Maillard JC, Menu Y, Scherrer A, et al. Intraperitoneal splenosis: diagnosis by ultrasound and computed tomography. Gastrointest Radiol 1989; 14(2):179–180.
7. Davison S. Acute hepatitis. In: Kelly DA, ed. Diseases of the liver and biliary system in children. 2nd edn. Wiley-Blackwell; 2004: 92–106.
8. Gubernick JA, Rosenberg HK, Ilaslan H, Kessler A. US approach to jaundice in infants and children. Radiographics 2000; 20(1):173–195.
9. Chakrapani A, Green, A. Metabolic liver disease in the infant and older child. In: Kelly DA, ed. Diseases of the liver and biliary system in children. 2nd edn. Wiley-Blackwell, 2004: 211–242.
10. Siegel MJ. Liver. In: Siegel MJ, ed. Pediatric sonography. 3rd edn. Philadelphia: Lippincott Williams and Wilkins; 2002: 213–274.
11. Robertson MB, Choe KA, Joseph PM. Review of the abdominal manifestations of cystic fibrosis in the adult patient. Radiographics 2006; 26(3):679–690.
12. Haber HP. Cystic fibrosis in children and young adults: findings on routine abdominal sonography. AJR Am J Roentgenol 2007; 189(1):89–99.
13. Lonergan GJ, Rice RR, Suarez ES. Autosomal recessive polycystic kidney disease: radiologic-pathologic correlation. Radiographics 2000; 20(3):837–855.
14. Davies CH, Stringer DA, Whyte H, et al. Congenital hepatic fibrosis with saccular dilatation of intrahepatic bile ducts and infantile polycystic kidneys. Pediatr Radiol 1986; 16(4):302–305.
15. Donnelly LF, Bisset GS, 3rd. Unique imaging issues in pediatric liver disease. Clin Liver Dis 2002; 6(1):227–246, viii.
16. Siegel MJ. Pediatric liver imaging. Semin Liver Dis 2001; 21(2): 251–269.
17. Stringer MD. Liver tumors. Semin Pediatr Surg 2000; 9(4):196–208.
18. Lowe LH. Imaging hepatobiliary disease in children. Semin Roentgenol 2008; 43(1):39–49.
19. von Schweinitz D. Management of liver tumors in childhood. Semin Pediatr Surg 2006; 15(1):17–24.
20. von Schweinitz D. Neonatal liver tumours. Semin Neonatol 2003; 8(5):403–410.
21. Isaacs H, Jr. Fetal and neonatal hepatic tumors. J Pediatr Surg 2007; 42(11):1797–1803.
22. Meyers RL, Scaife ER. Benign liver and biliary tract masses in infants and toddlers. Semin Pediatr Surg 2000; 9(3):146–155.
23. Corness JA, McHugh K, Roebuck DJ, Taylor AM. The portal vein in children: radiological review of congenital anomalies and acquired abnormalities. Pediatr Radiol 2006; 36(2):87–96, quiz 170–1.
24. Morgan G, Superina R. Congenital absence of the portal vein: two cases and a proposed classification system for portasystemic vascular anomalies. J Pediatr Surg 1994; 29(9):1239–1241.
25. Howard ER, Davenport M. Congenital extrahepatic portocaval shunts – the Abernethy malformation. J Pediatr Surg 1997; 32(3):494–497.
26. De Gaetano AM, Gui B, Macis G, et al. Congenital absence of the portal vein associated with focal nodular hyperplasia in the liver in an adult woman: imaging and review of the literature. Abdom Imaging 2004; 29(4):455–459.
27. Mitchell A, John PR, Mayer DA, et al. Improved technique of portal vein reconstruction in pediatric liver transplant recipients with portal vein hypoplasia. Transplantation 2002; 73(8):1244–1247.
28. Fernandes ET, Burton EM, Hixson SD, Hollabaugh RS. Preduodenal portal vein: surgery and radiographic appearance. J Pediatr Surg 1990; 25(12):1270–1272.
29. Gurakan F, Eren M, Kocak N, et al. Extrahepatic portal vein thrombosis in children: etiology and long-term follow-up. J Clin Gastroenterol 2004; 38(4):368–372.
30. De Gaetano AM, Lafortune M, Patriquin H, et al. Cavernous transformation of the portal vein: patterns of intrahepatic and splanchnic collateral circulation detected with Doppler sonography. AJR Am J Roentgenol 1995; 165(5):1151–1155.
31. Stringer MD, Howard ER. Surgical disorders of the liver and bile ducts and portal hypertension. In: Kelly DA, ed. Diseases of the liver and biliary system in children. 2nd edn. Wiley-Blackwell; 2003: 324–362.
32. DeLeve LD, Shulman HM, McDonald GB. Toxic injury to hepatic sinusoids: sinusoidal obstruction syndrome (veno-occlusive disease). Semin Liver Dis 2002; 22(1):27–42.
33. Lassau N, Leclere J, Auperin A, et al. Hepatic veno-occlusive disease after myeloablative treatment and bone marrow transplantation: value of gray-scale and Doppler US in 100 patients. Radiology 1997; 204(2):545–552.
34. Corbacioglu S, Greil J, Peters C, et al. Defibrotide in the treatment of children with veno-occlusive disease (VOD): a retrospective multicentre study demonstrates therapeutic efficacy upon early intervention. Bone Marrow Transplant 2004; 33(2):189–195.
35. Hoffman HD, Stockland B, von der Heyden U. Membranous obstruction of the inferior vena cava with Budd-Chiari syndrome in children: a report of nine cases. J Pediatr Gastroenterol Nutr 1987; 6(6):878–884.
36. Brancatelli G, Vilgrain V, Federle MP, et al. Budd-Chiari syndrome: spectrum of imaging findings. AJR Am J Roentgenol 2007; 188(2):W168–176.
37. Maisels MJ. Neonatal jaundice. Pediatr Rev 2006; 27(12):443–454.
38. Davenport M, Betalli P, D'Antiga L, et al. The spectrum of surgical jaundice in infancy. J Pediatr Surg 2003; 38(10):1471–1479.
39. Children's Liver Disease Foundation: Jaundice Protocol. Early Identification and referral of liver disease in infants. Birmingham, UK: www.childliverdisease.org, 2007.
40. Roberts EA. The jaundiced baby. In: Kelly DA, ed. Diseases of the liver and biliary system in children. 2nd edn. Wiley-Blackwell; 2003: 35–73.
41. Mowat AP, Davidson LL, Dick MC. Earlier identification of biliary atresia and hepatobiliary disease: selective screening in the third week of life. Arch Dis Child 1995; 72(1):90–92.
42. Tan Kendrick AP, Phua KB, Ooi BC, Tan CE. Biliary atresia: making the diagnosis by the gallbladder ghost triad. Pediatr Radiol 2003; 33(5):311–315.
43. McKiernan PJ, Baker AJ, Kelly DA. The frequency and outcome of biliary atresia in the UK and Ireland. Lancet 2000; 355(9197):25–29.
44. Sokol RJ, Mack C. Etiopathogenesis of biliary atresia. Semin Liver Dis 2001; 21(4):517–524.
45. Kasai M. Treatment of biliary atresia with special reference to hepatic porto-enterostomy and its modifications. Prog Pediatr Surg 1974; 6:5–52.
46. Tan Kendrick AP, Phua KB, Ooi BC, et al. Making the diagnosis of biliary atresia using the triangular cord sign and gallbladder length. Pediatr Radiol 2000; 30(2):69–73.
47. Kotb MA, Kotb A, Sheba MF, et al. Evaluation of the triangular cord sign in the diagnosis of biliary atresia. Pediatrics 2001; 108(2):416–420.
48. Kanegawa K, Akasaka Y, Kitamura E, et al. Sonographic diagnosis of biliary atresia in pediatric patients using the "triangular cord" sign versus gallbladder length and contraction. AJR Am J Roentgenol 2003; 181(5):1387–1390.
49. Park WH, Choi SO, Lee HJ, et al. A new diagnostic approach to biliary atresia with emphasis on the ultrasonographic triangular cord sign: comparison of ultrasonography, hepatobiliary scintigraphy, and liver needle biopsy in the evaluation of infantile cholestasis. J Pediatr Surg 1997; 32(11):1555–1559.
50. Choi SO, Park WH, Lee HJ, Woo SK. 'Triangular cord': a sonographic finding applicable in the diagnosis of biliary atresia. J Pediatr Surg 1996; 31(3):363–366.
51. Davenport M, Savage M, Mowat AP, Howard ER. Biliary atresia splenic malformation syndrome: an etiologic and prognostic subgroup. Surgery 1993; 113(6):662–668.
52. Davenport M, De Ville de Goyet J, Stringer MD, et al. Seamless

management of biliary atresia in England and Wales (1999–2002). Lancet 2004; 363(9418):1354–1357.
53. Todani T, Watanabe Y, Narusue M, et al. Congenital bile duct cysts: classification, operative procedures, and review of thirty-seven cases including cancer arising from choledochal cyst. Am J Surg 1977; 134(2):263–269.
54. Babbitt DP. [Congenital choledochal cysts: new etiological concept based on anomalous relationships of the common bile duct and pancreatic bulb]. Ann Radiol (Paris) 1969; 12(3):231–240.
55. Spitz L. Experimental production of cystic dilatation of the common bile duct in neonatal lambs. J Pediatr Surg 1977; 12(1):39–42.
56. Lane GJ, Yamataka A, Kobayashi H, et al. Different types of congenital biliary dilatation in dizygotic twins. Pediatr Surg Int 1999; 15(5–6):403–404.
57. Torrisi JM, Haller JO, Velcek FT. Choledochal cyst and biliary atresia in the neonate: imaging findings in five cases. AJR Am J Roentgenol 1990; 155(6):1273–1276.
58. St-Vil D, Yazbeck S, Luks FI, et al. Cholelithiasis in newborns and infants. J Pediatr Surg 1992; 27(10):1305–1307.
59. Davenport M, Heaton ND, Howard ER. Spontaneous perforation of the bile duct in infants. Br J Surg 1991; 78(9):1068–1070.
60. Bingol-Kologlu M, Karnak I, Ocal T, Tanyel FC. Idiopathic perforation of the bile duct in an infant. J Pediatr Gastroenterol Nutr 2000; 31(1):83–85.
61. Davenport M, Howard ER. Macroscopic appearance at portoenterostomy – a prognostic variable in biliary atresia. J Pediatr Surg 1996; 31(10):1387–1390.
62. Haller JO, Condon VR, Berdon WE, et al. Spontaneous perforation of the common bile duct in children. Radiology 1989; 172(3):621–624.
63. Harb R, Thomas DW. Conjugated hyperbilirubinemia: screening and treatment in older infants and children. Pediatr Rev 2007; 28(3):83–91.
64. Howard ER. Benign extrahepatic bile duct obstruction and cholestatic syndromes. In: Howard ER, Stringer MD, Colombani PM, eds. Surgery of the liver, bile ducts and pancreas in children. 2nd edn. London: Arnold; 2002: 175–187.
65. Bowles MJ, Salisbury JR, Howard ER. Localized, benign, nontraumatic strictures of the extrahepatic biliary tree in children. Surgery 2001; 130(1):55–59.
66. Spunt SL, Lobe TE, Pappo AS, et al. Aggressive surgery is unwarranted for biliary tract rhabdomyosarcoma. J Pediatr Surg 2000; 35(2):309–316.
67. Czaja MJ, Goldfarb JP, Cho KC, et al. Bile duct carcinoma in an adolescent. Am J Gastroenterol 1985; 80(6):486–489.
68. McGahan JP, Phillips HE, Cox KL. Sonography of the normal pediatric gallbladder and biliary tract. Radiology 1982; 144(4):873–875.
69. Meilstrup JW, Hopper KD, Thieme GA. Imaging of gallbladder variants. AJR Am J Roentgenol 1991; 157(6):1205–1208.
70. Siegel MJ. Gallbladder and biliary tract. In: Siegel MJ, ed. Pediatric sonography. 3rd edn. Philadelphia: Lippincott Williams & Wilkins; 2002: 275–304.
71. Afdhal NH. Epidemiology, risk factors and pathogenesis of gallstones. In: Afdhal NH, ed. Gallbladder and biliary tract diseases. New York: Marcel Dekker; 2000: 127–146.
72. Yang HL, Sun YG, Wang Z. Polypoid lesions of the gallbladder: diagnosis and indications for surgery. Br J Surg 1992; 79(3):227–229.
73. Stringer MD, Ceylan H, Ward K, Wyatt JI. Gallbladder polyps in children – classification and management. J Pediatr Surg 2003; 38(11):1680–1684.
74. Boulton RA, Adams DH. Gallbladder polyps: when to wait and when to act. Lancet 1997; 349(9055):817.
75. Crossin JD, Muradali D, Wilson SR. US of liver transplants: normal and abnormal. Radiographics 2003; 23(5):1093–1114.
76. Berrocal T, Parron M, Alvarez-Luque A, et al. Pediatric liver transplantation: a pictorial essay of early and late complications. Radiographics 2006; 26(4):1187–1209.
77. Nijs E, Callahan MJ, Taylor GA. Disorders of the pediatric pancreas: imaging features. Pediatr Radiol 2005; 35(4):358–373; quiz 457.
78. Siegel MJ. Adrenal glands, pancreas, and other retroperitoneal structures. In: Siegel MJ, ed. Pediatric sonography. 2nd edn. Philadelphia: Lippincott Williams and Wilkins; 2002: 475–528.
79. Benya EC. Pancreas and biliary system: imaging of developmental anomalies and diseases unique to children. Radiol Clin North Am 2002; 40(6):1355–1362.
80. Auringer ST, Ulmer JL, Sumner TE, Turner CS. Congenital cyst of the pancreas. J Pediatr Surg 1993; 28(12):1570–1571.
81. Hunter CJ, Connelly ME, Ghaffari N, et al. Enteric duplication cysts of the pancreas: a report of two cases and review of the literature. Pediatr Surg Int 2008; 24(2):227–233.
82. Johnson PR, Spitz L. Cysts and tumors of the pancreas. Semin Pediatr Surg 2000; 9(4):209–215.
83. Stringer MD. Pancreatitis and pancreatic trauma. Semin Pediatr Surg 2005; 14(4):239–246.

CHAPTER

70 Paediatric bowel and mesentery

Marilyn J. Siegel and Edward Y. Lee

INTRODUCTION

With the technical advances in real-time scanners, ultrasound has emerged as an important diagnostic tool in the evaluation of a variety of gastrointestinal tract disorders.[1,2] Barium examinations are still the method of choice for assessing the mucosal surface and contour of the bowel lumen, but they provide limited information about the bowel wall or extrinsic abnormalities. Ultrasound allows direct visualisation of the bowel wall and surrounding tissues, and thus it can offer information affecting patient diagnosis and management. In some disorders, such as pyloric stenosis and appendicitis, it has become the primary imaging technique for establishing a diagnosis. This chapter addresses the ultrasound findings of the common disorders of the gastrointestinal tract in children. Techniques for examining each segment of the gastrointestinal tract are also discussed.

GASTRO-OESOPHAGEAL JUNCTION

Technique and normal anatomy

The distal oesophageal segment and the gastro-oesophageal junction are imaged via a subcostal or subxiphoid approach, using the liver as an acoustic window. The examination is performed with the patient supine or in the right lateral decubitus position and the transducer positioned in the midline or slightly to the left at the level of the diaphragm.[3] Scans are obtained in transverse and sagittal planes. This technique is used to detect gastro-oesophageal reflux.

The normal distal oesophagus is best seen on long-axis views appearing as a tubular structure anterior to the aorta, posterior to the left lobe of the liver and adjacent to the diaphragm (Fig. 70.1). On short-axis views it has a bull's-eye or target appearance, owing to the central reflective mucosa and submucosa surrounded by an outer echo-poor muscular wall. Small amounts of fluid and gas may be seen within the oesophageal lumen.

Gastro-oesophageal reflux

Gastro-oesophageal reflux is the retrograde flow of gastric contents into the oesophagus. Affected children typically present with vomiting and occasionally with dysphagia, haematemesis, failure to thrive, recurrent pneumonias, wheezing or apnoea. Barium oesophagography has been the conventional imaging method for the diagnosis of gastro-oesophageal reflux, but several authors have shown that real-time ultrasound can also be used to diagnose gastrointestinal reflux in infants.[3–5]

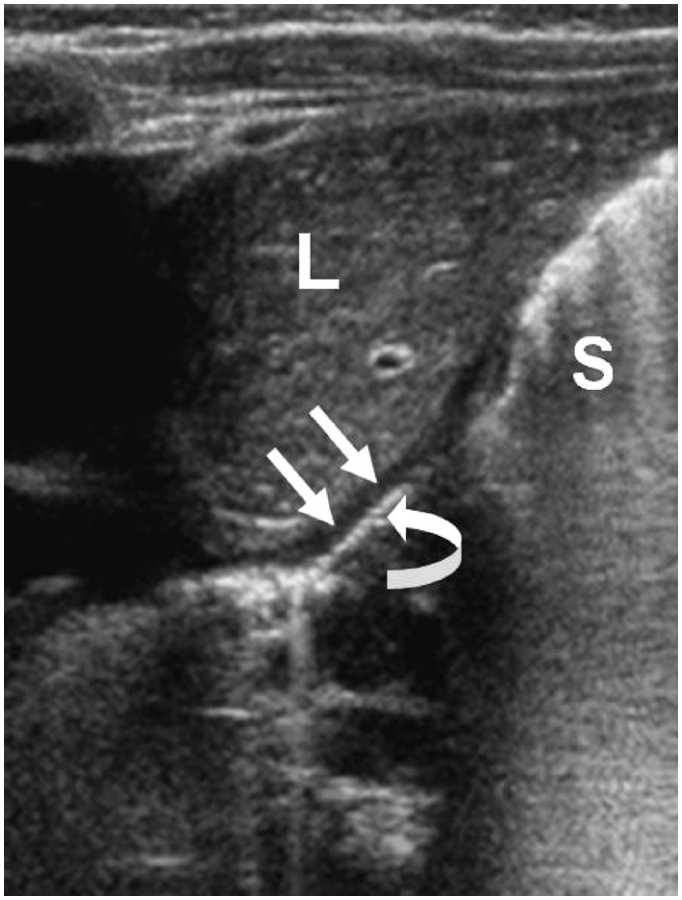

Figure 70.1 Normal gastro-oesophageal junction. Longitudinal scan at the level of the gastro-oesophageal junction shows a virtually collapsed oesophagus with only a small amount of hypoechoic fluid (straight arrows) and echogenic air (curved arrow) in the lumen. L, liver; S, stomach. Reproduced with permission from Siegel MJ, ed. Pediatric Sonography, 4th edition. Philadelphia: Lippincott Williams & Wilkins; 2010.

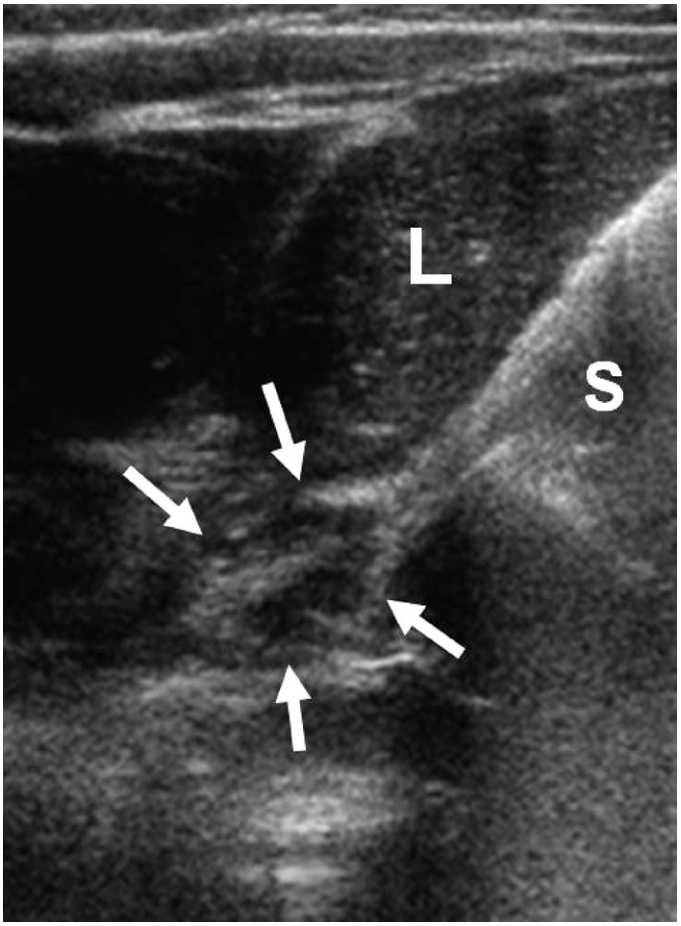

Figure 70.2 Gastro-oesophageal reflux. Refluxed gastric contents, containing echogenic air and hypoechoic fluid, are seen in a dilated distal oesophagus (white arrows) at the level of the gastro-oesophageal junction. L, liver; S, stomach. Reproduced with permission from Siegel MJ, ed. Pediatric Sonography, 4th edition. Philadelphia: Lippincott Williams & Wilkins; 2010.

The ultrasound appearance of gastro-oesophageal reflux varies with the relative amounts of fluid and gas in the refluxed material. Refluxed fluid alone is anechoic or echo-poor. When there is an admixture of fluid and air the refluxed gastric contents appear highly reflective (Fig. 70.2). Another finding of reflux is oesophageal dilatation. Complementary use of colour Doppler ultrasound may facilitate the detection of gastro-oesophageal reflux.[6,7] Based on pH monitoring, which is considered the reference standard for the diagnosis of reflux, the sensitivity of both greyscale and colour Doppler ultrasound for the diagnosis of gastro-oesophageal reflux is approximately 95%.[3,6,7] Additional studies have shown that ultrasound measurements of abdominal oesophageal length (i.e. the point where the oesophagus penetrates the diaphragm to the anterior surface of the fundus of the stomach) can further increase confidence in the diagnosis of reflux.[8] Children with gastro-oesophageal reflux have significantly shorter abdominal oesophageal lengths compared with neonates and infants without reflux. In neonates ultrasound also can predict the severity of reflux.

Because ultrasound is time-consuming and difficult to perform, particularly in the crying child, in whom there may not be a good acoustic window, it has not gained widespread use for diagnosing reflux and a barium study remains the recommended examination. However, reflux may be detected on studies performed for other indications, such as pyloric stenosis, and thus, its sonographic features need to be recognised.

Oesophagus

- On long-axis views the normal oesophagus appears as a tubular structure.
- On short-axis views the oesophagus has a bull's-eye or target appearance.
- Appearance of gastro-oesophageal reflux varies with the relative amounts of fluid and air.
- Colour Doppler ultrasound may facilitate the detection of gastro-oesophageal reflux.
- Length of abdominal oesophagus is decreased in reflux.

STOMACH

Technique and normal anatomy

Most gastric pathology in children involves the gastric antrum and antropyloric region. Scans of the antrum and antropyloric region are obtained with the patient in a right lateral decubitus position using the liver as an acoustic window. A curved or linear array transducer is positioned to the right of midline and transverse and longitudinal images are obtained. The examination should be performed after the stomach is distended with clear fluids, such as water or glucose solution.

On cross-sectional scans the gastric antrum has a target appearance, showing the echo-free fluid-filled lumen, the adjacent reflective mucosa and submucosa, and the outer echo-poor muscularis propria. On longitudinal scans the antrum is a tubular structure in which the appearance of the lumen varies, depending on the relative amounts of fluid and air within it (Fig. 70.3). With the gastric lumen fully distended, the wall thickness is 3 mm or less, measured from the inner border of the submucosa to the outer border of the muscularis propria.[9,10]

Obstruction

Hypertrophic pyloric stenosis

Hypertrophic pyloric stenosis (HPS) is a disorder characterised by hypertrophy of the circular muscle of the pylorus. The incidence of HPS is approximately 3 in 1000 and boys are affected four to five times more commonly than girls. There is also a familial predisposition. Affected patients usually present between 2 and 6 weeks of age, with projectile non-bilious vomiting. An olive-shaped mass may be palpated in the epigastrium.

Ultrasound has virtually replaced the barium examination in the diagnosis of hypertrophic pyloric stenosis because it is non-invasive and does not utilise ionising radiation. Other advantages of ultrasound are the ability to directly visualise the pyloric muscle and to obtain measurements of muscle thickness.[10–12] The examination is performed with a 5.0 or 7.5 MHz curved or linear array transducer. Longitudinal and transverse images are obtained with the infant in the right posterior oblique position. In this position any fluid in the fundus of the stomach moves into the antrum and pyloric region, distending these regions. The stomach should not be emptied prior to the examination as this makes identification of the antropyloric area difficult. If there is inadequate distension of the antrum the infant can be given a glucose solution or water, orally or via a nasogastric tube. If fluid is administered by tube it can be removed at the end of the examination to prevent further vomiting and the risk of aspiration.

The ultrasound evaluation of HPS includes assessment of both morphological and quantitative features. The classic findings of HPS are of a thickened pyloric muscle and an elongated pyloric canal (Fig. 70.4).[10–12] On transverse images, the hypertrophic pylorus

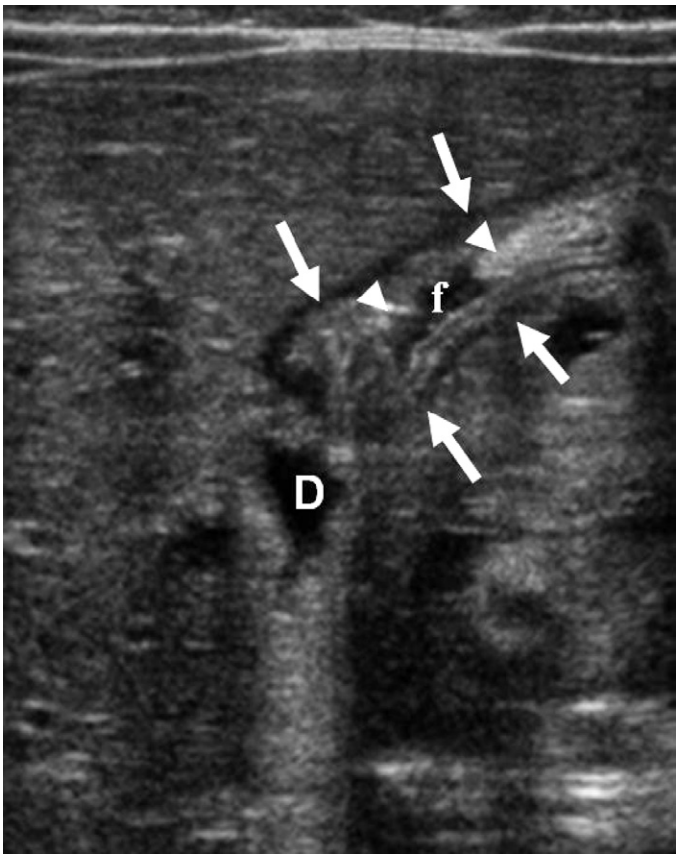

Figure 70.3 Normal antrum. Transverse scan through the distal stomach shows echo-poor muscle (arrows) surrounding the inner mucosa/submucosal layer (arrowheads). Wall thickness is 3 mm. A small amount of fluid (f) is present in the gastric lumen. Also noted normal fluid-filled duodenal bulb (D).

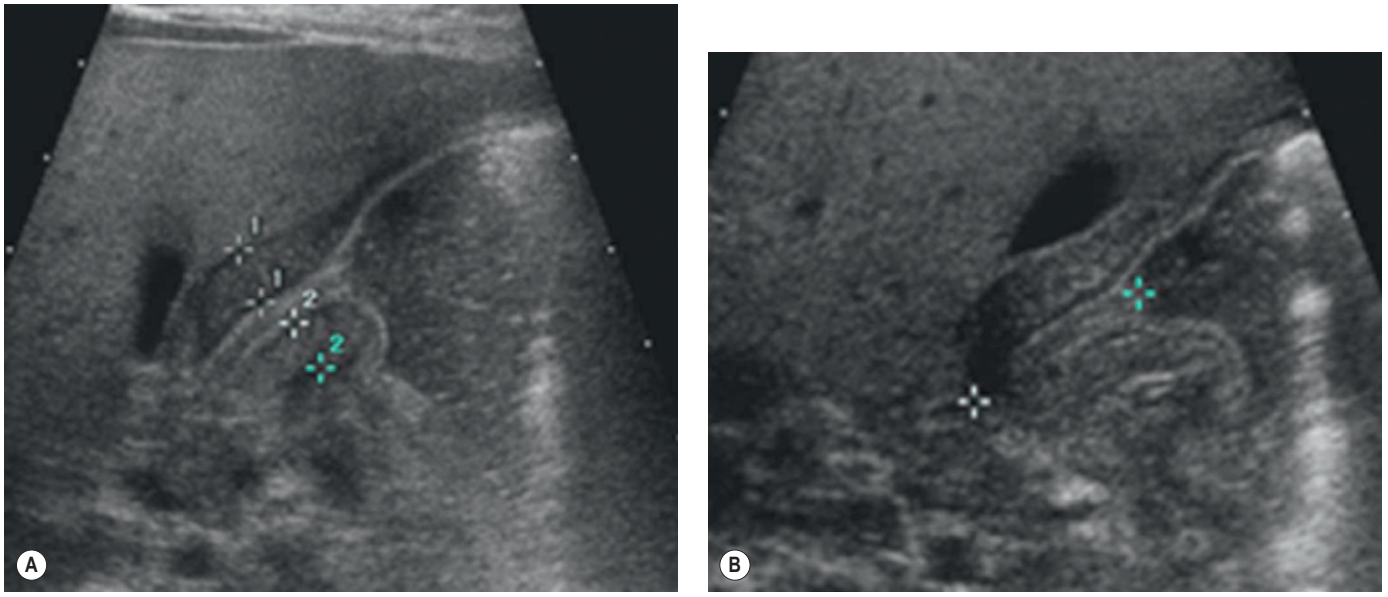

Figure 70.4 Pyloric stenosis. A: Long-axis scan. Electronic callipers (labelled 1 and 2) delineate the pyloric muscle thickness on each side of the echogenic central mucosa. The pyloric thickness in this patient is increased, measuring 4 mm. **B:** Long-axis scan. Electronic callipers show the length of the pyloric canal. Channel length is elongated, measuring 19 mm.

has a doughnut appearance, representing the reflective central mucosa and submucosa surrounded by echo-free muscle. Another finding on longitudinal scans is a 'double-track' sign produced by the presence of small amounts of fluid in the crevices of the echogenic mucosal folds.[13] Other signs on longitudinal scans include exaggerated peristaltic waves that terminate abruptly at the level of the pylorus and oesophageal reflux, absence of opening of the pyloric channel, and little if any passage of fluid from the stomach into the descending duodenum.[14]

As a general guide a pyloric channel length greater than 15 mm, muscle thickness greater than 3.0 mm, and transverse serosal-to-serosal diameter greater than 15 mm is consistent with HPS[9,11,15] (Fig. 70.4). At least two values should be abnormal. Based on these measurements, the sensitivity, specificity and accuracy of ultrasound in the diagnosis of HPS is virtually 100%.[15] A muscle thickness less than 2.0 mm is unequivocally normal. A muscle thickness between 2 and 2.9 mm is abnormal but non-specific, and can be seen in gastritis and pylorospasm as well as in HPS. Borderline muscle thickness measurements are more likely to occur in premature than in term infants.[16] In premature infants, the ultrasound diagnosis of HPS is based on the thickness of the pyloric muscle relative to the rest of the stomach and the length of the pyloric canal.

False negative diagnoses may be made if the stomach is overdistended. Overdistension of the stomach can displace the pylorus posteriorly, making it difficult to visualise the pyloric canal.[10] If the scan is not in the midline, or is tangential to the antrum, the antral wall can simulate a thickened pyloric muscle, leading to a false positive diagnosis.[10]

Hypertrophic pyloric stenosis is usually an isolated finding, but it has been associated with prostaglandin-induced foveolar hyperplasia.[17] An increased incidence of renal anomalies has been reported in patients with HPS. These include pelvi-ureteric junction obstruction, primary mega-ureter, duplex kidneys, renal agenesis or ectopia, nephroblastomatosis and horseshoe kidney. Because of this association, the kidneys should be examined when there is ultrasound evidence of HPS.[18,19]

The treatment for HPS is pyloromyotomy, in which the hypertrophic muscle is split longitudinally. The pyloric muscle thickness usually returns to normal within 2–12 weeks after surgery, but in some cases it may not return to normal for up to 5 months.[20,21]

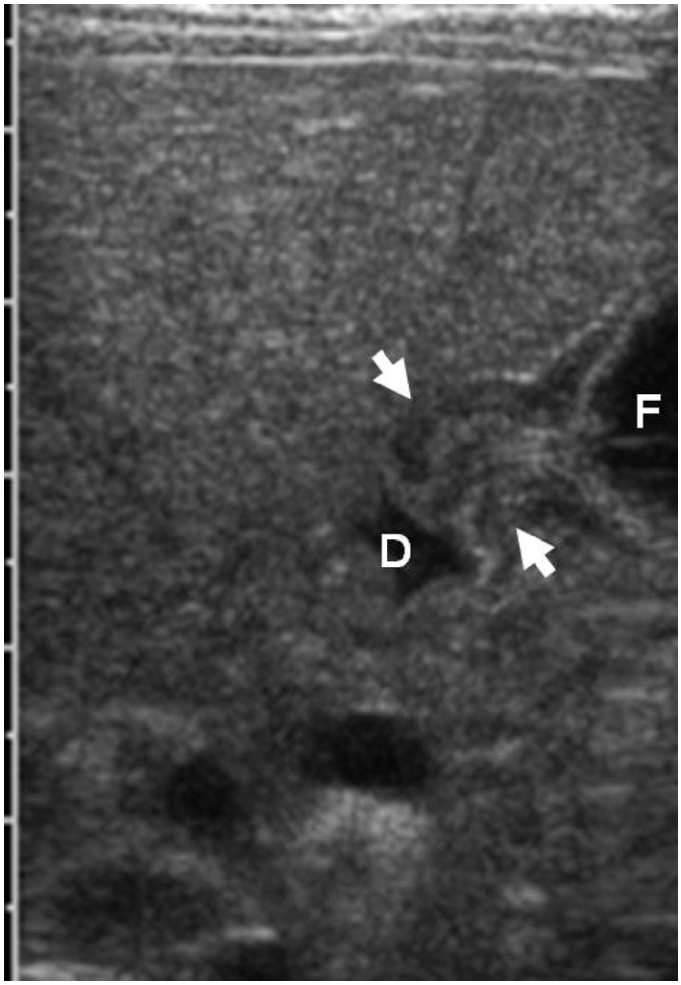

Figure 70.5 Pylorospasm in a 6-week-old boy with persistent vomiting. The distal stomach is contracted and elongated. The thickness of the echo-poor muscular wall (arrows) of the collapsed antrum is normal, measuring 2 mm. A small amount of fluid (F) is present in the lumen of the stomach proximal to the collapsed antrum. D, fluid-filled duodenum.

Pylorospasm

The major differential diagnostic considerations of non-bilious vomiting are gastro-oesophageal reflux (see above) and pylorospasm (also known as antral dyskinesia). The ultrasound findings of pylorospasm are elongation and narrowing of the antral/pyloric region, decreased peristalsis and delayed gastric emptying. With persistent scanning, it is possible to observe that eventually the pyloric canal opens and fluid passes into the descending duodenum. The thickness of the antral wall is normal and less than 3.0 mm (Fig. 70.5).[10] The problem is essentially one of spasm, rather than anatomical obstruction.

Gastric wall thickening

Gastric wall thickening is not a common problem in children. The differential diagnosis includes gastritis due to peptic ulcer disease, chronic granulomatous disease, and Ménétrier's disease. Chronic granulomatous disease of childhood is an X-linked recessive disorder that results in a defect in the bactericidal activity of the polymorphonuclear leukocytes. Most patients are diagnosed before 3 years of age and present with lymphadenopathy, hepatosplenomegaly, pneumonia or intermittent abdominal pain. The antrum is the most frequently involved part of the gastrointestinal tract. Ménétrier's disease is a protein-losing gastropathy characterised by giant hypertrophy of the gastric mucosa. Most childhood cases affect patients in the second decade of life. The clinical findings include oedema of the extremities or eyelids, ascites, pleural effusions and abdominal pain.

The ultrasound findings of gastric wall inflammation are non-specific and include thickened gastric mucosa and submucosa, with poorly defined mural layers indicating loss of stratification (Fig. 70.6). In Ménétrier's disease, an additional finding is large tortuous echo-poor rugae in the fundus and body of the stomach.[22]

Gastric masses

Gastric duplications

Gastric duplications account for less than 10% of all gastrointestinal tract duplications.[23] Most are diagnosed in infants under 1 year of age. Typical clinical features include an abdominal mass or distension on physical examination. Infrequent presentations include acute pain due to intestinal obstruction or intussusception and gastrointestinal haemorrhage. Gastric duplications are usually located along the greater curvature, measure less than 12 mm in diameter

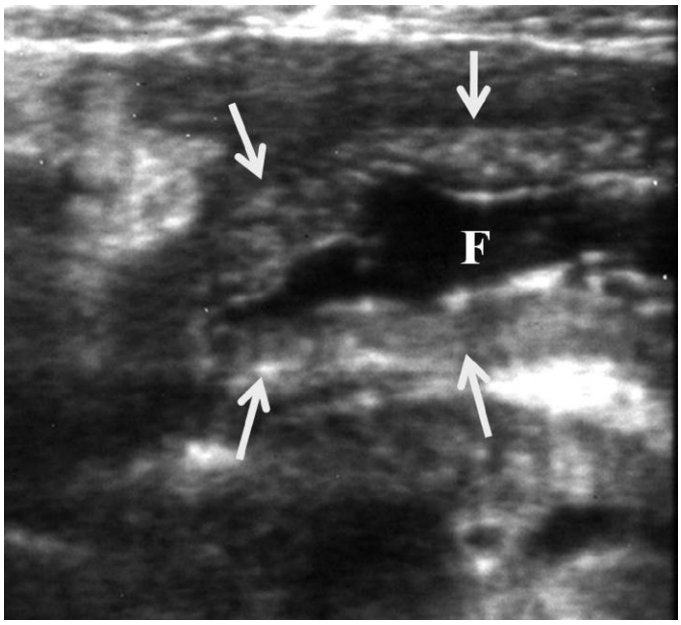

Figure 70.6 Chronic granulomatous disease of childhood. Long-axis scan of the distal stomach showing a fluid-filled antrum (F) surrounded by a thick wall (arrows).

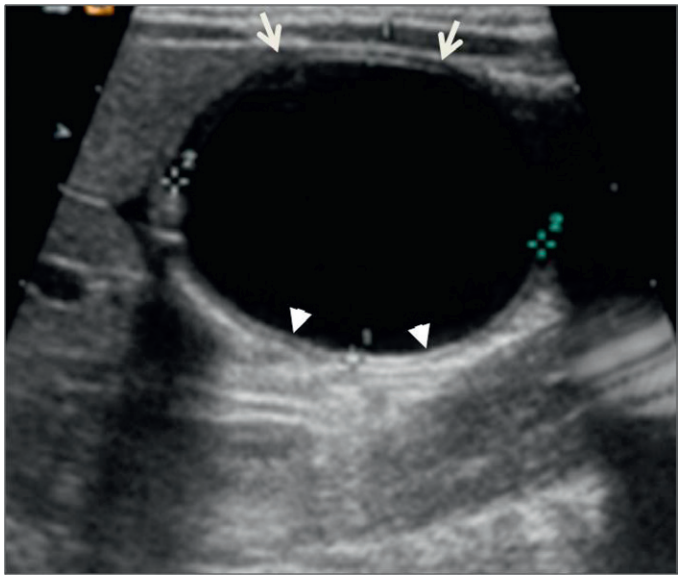

Figure 70.7 Gastric duplication. Transverse scan of the left upper quadrant shows a fluid-filled duplication cyst (callipers). The cyst wall is barely perceptible. Note the inner reflective layer (arrowheads) representing the mucosal lining and an outer echo-poor rim representing the muscular wall (arrows).

and do not communicate with the gastric lumen. The characteristic ultrasound findings are an echo-poor mass with good through-transmission reflecting the fluid contents of the cyst, an inner reflective layer representing the mucosal lining and an outer echo-poor rim representing the muscular wall (Fig. 70.7). If the cyst becomes infected or undergoes haemorrhage the internal contents may become more reflective or contain septations. The mucosal layer may be destroyed as a result of extensive ulceration by gastric enzymes.[24]

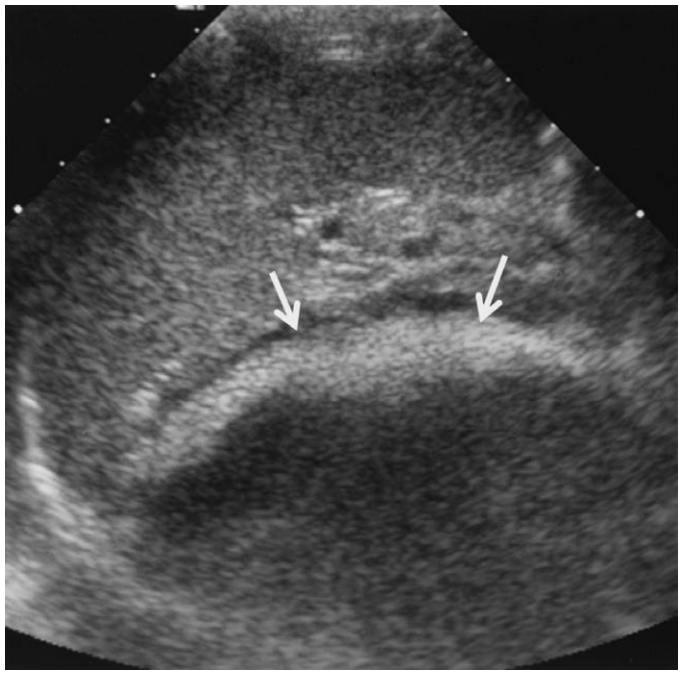

Figure 70.8 Gastric bezoar. Transverse sonogram demonstrates a hyperechoic curvilinear band (arrows) that has marked distal acoustic shadowing. The band represents the anterior aspect of the bezoar which was composed almost entirely of hair, accounting for the echogenicity.

Gastric teratomas

Gastric teratomas are benign extraluminal masses that contain an admixture of fluid, fat and calcification. On ultrasound they appear either as a predominantly cystic mass or as a complex mass with cystic and solid components. Highly reflective foci with acoustic shadowing, owing to the presence of calcification, may also be seen. The lesions are often both intra- and extraluminal.[25]

Bezoars

Trichobezoars (hair) and lactobezoars (inspissated powdered milk) are the two common types of bezoars in children. Phytobezoars (vegetable matter) are seen more often in adults. Children with gastric bezoars usually present with an epigastric mass or tenderness, vomiting, early satiety and weight loss. The typical sonographic finding is of a mobile intraluminal highly reflective mass (Fig. 70.8).[26] In trichobezoars, air is often trapped in and around the hair fibres, so acoustic shadowing is common. This shadowing may obscure the posterior margins of the trichobezoar. Acoustic shadowing is a less common feature of phyto- or lactobezoars. Water administration can be useful in outlining the mass and confirming the intraluminal location.

Neoplasms

Although they are extremely rare, benign gastric tumours such as leiomyoma and polyps, and malignant tumours, including gastrointestinal stromal tumour, carcinoma and lymphoma, can occur in children.[27] On ultrasound they appear as polypoid intraluminal masses, areas of gastric wall thickening or a large exophytic mass (Fig. 70.9).

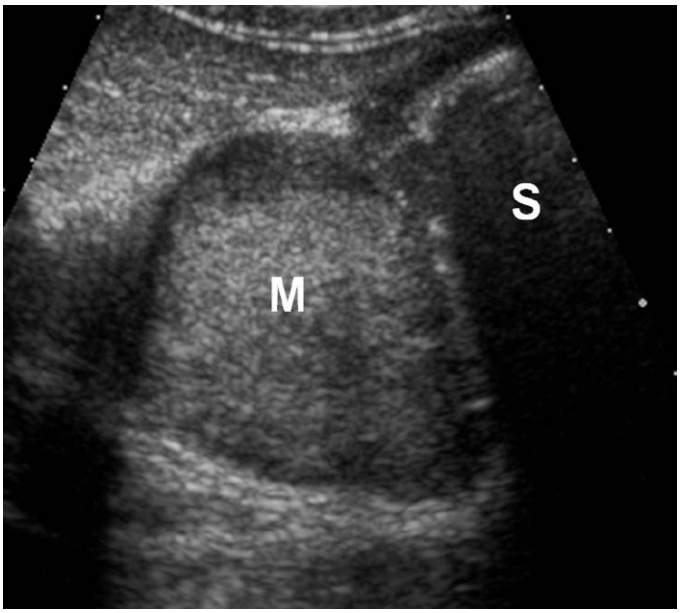

Figure 70.9 Gastrointestinal stromal tumour (GIST) of stomach in an 8-year-old girl with epigastric pain. Transverse scan of the upper abdomen shows a heterogeneous mass (M) arising exophytically from the stomach (S). (Case courtesy of Edward Lee MD.)

Stomach

- On long-axis scans the antrum is a tubular structure.
- On short-axis scans the gastric antrum has a target appearance.
- Ultrasound has replaced the barium examination in diagnosis of pyloric stenosis (HPS).
- Findings of HPS are of a thickened pyloric muscle, an elongated pyloric canal and absent gastric emptying.
- Findings of pylorospasm are normal pyloric muscle thickening, an elongated and narrowed antral/pyloric region, decreased peristalsis and delayed gastric emptying.
- Findings of gastric wall inflammation are non-specific and include thickened gastric mucosa and submucosa, with loss of stratification.
- Most common gastric masses are duplication cysts and bezoars.

SMALL BOWEL

Normal anatomy

The duodenum and small bowel are not usually identifiable as discrete structures on ultrasound, either because they are collapsed or because they are filled with air. However, when fluid filled, the duodenal bulb and other parts of the small bowel may be recognisable (Fig. 70.10). The mucosa, submucosa and muscular layers can be delineated in loops that contain fluid. Internal echoes, representing gas bubbles or food particles, may be seen in the fluid-filled lumen. The small bowel valvulae conniventes may also be seen, as intraluminal linear structures 3–5 mm apart. When the duodenum and small bowel are distended, the wall thickness should not exceed 3 mm.

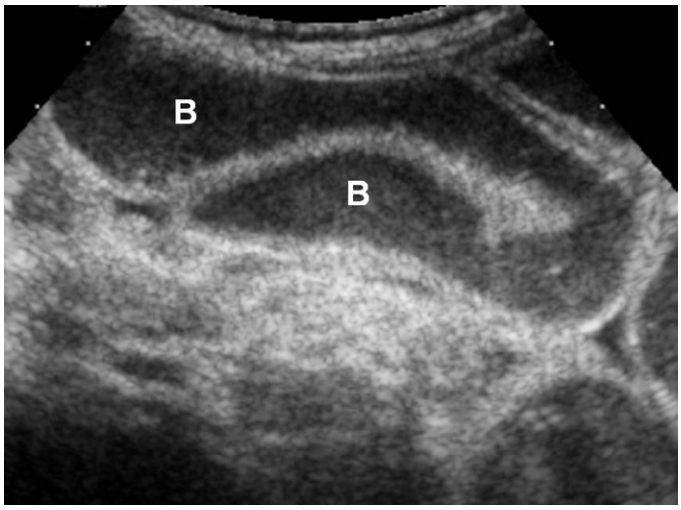

Figure 70.10 Small bowel obstruction. Longitudinal scan of the right lower quadrant showing dilated, fluid-filled bowel loops (B) in a 10-month-old boy with a distal small bowel obstruction secondary to intussusception.

Obstruction

When plain radiographs show a complete bowel obstruction, additional imaging is not usually needed. However, ultrasound can be helpful when the abdomen is gasless by showing the presence of an unsuspected mass, ascites or bowel obstruction. The characteristic features of small bowel obstruction are hyperperistaltic, dilated fluid-filled loops proximal to the site of obstruction (Fig. 70.10). These findings are, however, non-specific, and may also be seen with gastroenteritis.

Duodenal atresia

Duodenal atresia is the most common cause of proximal bowel obstruction in the neonate. It is thought to be the result of an error in bowel canalisation. The atresia obstructs near the ampulla of Vater and leads to vomiting of bilious material within the first 24 hours after birth. Other anomalies are present in about one-half of patients, including Down's syndrome, malrotation, congenital heart disease, oesophageal atresia, renal anomalies, imperforate anus and biliary atresia.

Abdominal radiography is usually diagnostic of duodenal atresia, showing the classic 'double-bubble' sign, produced by a markedly dilated stomach and duodenum. With this appearance further imaging studies are unnecessary. Ultrasound can, however, provide valuable information in infants who have duodenal atresia and oesophageal atresia without an associated tracheo-oesophageal fistula. In these cases the conventional radiographic diagnosis of duodenal atresia is difficult, as the abdomen is gasless. Because the distal oesophagus, stomach and duodenum are filled with fluid they provide an excellent acoustic window. The ultrasound findings of duodenal atresia are a markedly dilated, fluid-filled stomach, proximal duodenum and distal oesophagus (Fig. 70.11).

Obstruction by a duodenal membrane, duodenal stenosis or an annular pancreas have clinical and ultrasound findings similar to those of duodenal atresia. An additional finding that has been described in an infant with a duodenal membrane is a reflective band in the dilated proximal duodenum.[28]

Jejuno-ileal atresia and meconium ileus

Jejuno-ileal atresia is the result of an in-utero vascular accident. Meconium ileus results from inspissation of abnormally thick,

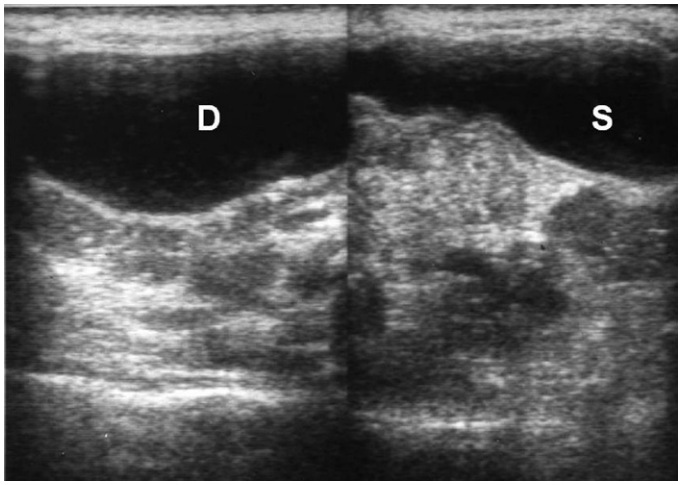

Figure 70.11 Duodenal atresia in a neonate with oesophageal atresia. Transverse dual-screen image of the upper abdomen shows a dilated duodenal bulb (D) and stomach (S).

tenacious meconium in the distal small bowel. The end result of both disorders is bowel obstruction.

A contrast enema examination is still the primary imaging study to diagnose distal bowel obstruction. However, ultrasound may provide diagnostic information if the clinical or plain radiographic findings are atypical. The ultrasound findings of ileal atresia are multiple loops of dilated small bowel filled with fluid and air; peristalsis may be normal or increased. In meconium ileus there are multiple loops of bowel filled with highly reflective material (Fig. 70.12), indicating the presence of thick, tenacious meconium; peristalsis is often decreased.[29] Additional findings of both disorders include meconium peritonitis and meconium pseudocyst.

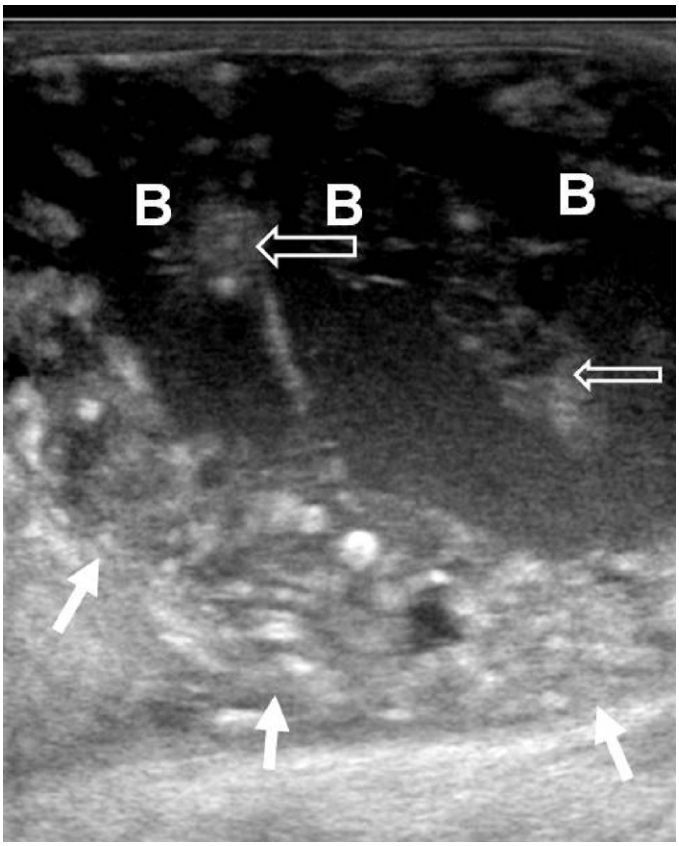

Figure 70.12 Meconium ileus. Longitudinal scan of the right lower quadrant, showing a dilated loop of small bowel (arrows) filled with highly reflective meconium. More proximal dilated small bowel (B) contains some meconium (open arrows) along with fluid and air.

Meconium peritonitis

Meconium peritonitis is the result of antenatal bowel perforation resulting in leakage of sterile meconium into the peritoneal cavity and a non-bacterial chemical peritonitis. In many fetuses, the perforation seals in utero and the only postnatal findings are scattered calcifications in the peritoneal cavity. In some neonates, there may be associated bowel obstruction. On ultrasound, meconium peritonitis produces multiple discrete, very highly reflective foci, with acoustic shadowing or occasionally diffuse peritoneal reflectivity (referred to as a 'snowstorm' appearance) (Fig. 70.13).[30] Ascites containing reflective material, related to calcification or air, may also be seen.[31]

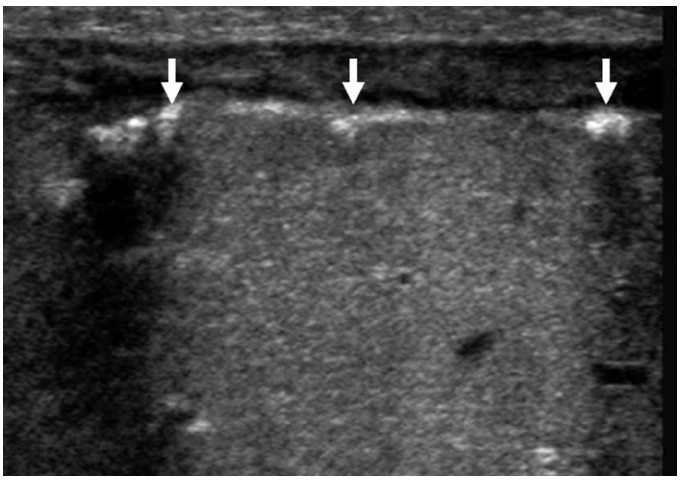

Figure 70.13 Meconium peritonitis. Transverse scan shows highly reflective foci (arrows) with acoustic shadowing beneath the right lobe of the liver. This patient had a bowel perforation proximal to an area of ileal atresia. Reproduced with permission from Siegel MJ, ed. Pediatric Sonography, 4th edition. Philadelphia: Lippincott Williams & Wilkins; 2010.

Meconium pseudocyst

The meconium pseudocyst is a cystic mass that results when the extruded meconium becomes walled-off by fibrous adhesions. Calcifications within the cyst wall are frequent. At sonography, the meconium pseudocyst appears as a well-defined fluid-filled mass with reflective contents representing a combination of air and meconium (Fig. 70.14). Highly echogenic calcifications can be seen in the cyst lumen or in the wall.

Malrotation

Midgut malrotation is an anomaly of intestinal rotation and fixation. It encompasses a spectrum of rotational abnormalities including non-rotation (colon in the left abdomen, small bowel in the right abdomen), reverse non-rotation (small bowel on the left, colon on the right), reverse rotation (duodenum anterior and colon posterior to the superior mesenteric artery, small bowel in the right abdomen), and incomplete rotation (a range of rotational abnormalities between non-rotation and normal rotation). In malrotation, the attachment of the bowel is abnormally short, resulting in a narrowed mesenteric pedicle and an abnormally positioned ligament of Treitz.[32] The normal duodenojejunal junction lies posterior and to the left of the spine, whereas the abnormal junction is anterior and to the right of the spine.

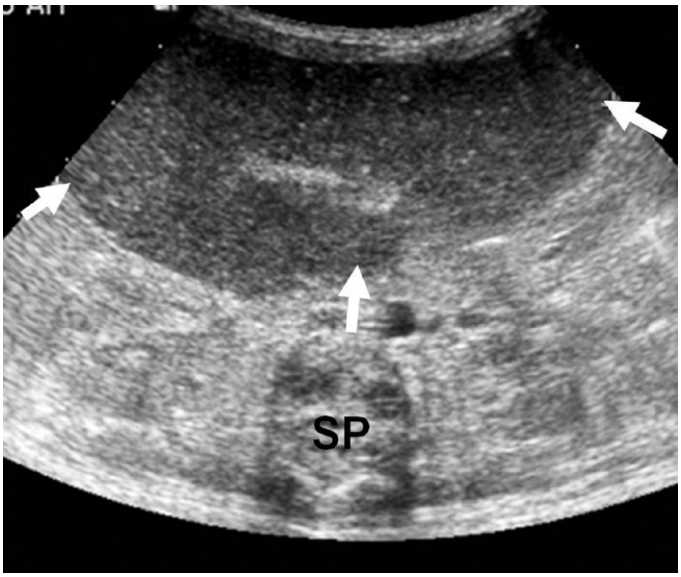

Figure 70.14 Meconium pseudocyst. Transverse scan showing a large cystic mass (arrows) filled with echogenic contents representing air and meconium. SP, spine. The patient had ileal atresia.

Infants with malrotation present with symptoms caused by obstruction from peritoneal bands (i.e. Ladd's bands), midgut volvulus or a combination of the two. Bilious vomiting is the hallmark of the obstruction. Approximately 90% of patients with malrotation present in the first month of life with vomiting. Peritoneal bands typically obstruct the second and third parts of the duodenum as they pass from the malpositioned caecum to the liver or posterior peritoneum. Midgut volvulus is the more serious complication of malrotation. The bowel twists in a clockwise manner on the narrowed mesenteric pedicle. Because the pedicle contains the superior mesenteric artery and vein, the twisting occludes the blood supply to the midgut and may lead to ischaemia or infarction.

Because of the potentially catastrophic consequences of failing to recognise the diagnosis of malrotation, any infant with bilious vomiting should be considered to have malrotation and imaging should be performed immediately. The upper gastrointestinal (UGI) series is considered the examination of choice to confidently identify malrotation. The UGI series can accurately show the abnormally positioned ligament of Treitz (duodenojejunal junction) and the proximal jejunum to the right of the midline.

If the significance of the bile-stained vomitus is not appreciated, a sonogram may be the first examination requested, and thus, the radiologist should be familiar with these findings of malrotation. The ultrasound finding of malrotation is inversion of the usual relationship between the superior mesenteric artery and vein. Normally, the origin of the superior mesenteric artery lies to the left of the superior mesenteric vein. Reversal of this relationship suggests midgut malrotation (Fig. 70.15).[32–34] However, vessel inversion can be found in patients with normal midgut rotation and, conversely, mesenteric inversion can be absent in patients with malrotation.[34] Because the ultrasound finding of malrotation is not specific, the upper gastrointestinal barium examination is still the preferred study for diagnosis of malrotation.

The classic ultrasound findings of associated midgut volvulus are clockwise swirling of the superior mesenteric vein, proximal small bowel and mesentery around the superior mesenteric artery (whirlpool sign) and stretching of the mesenteric vessels.[35,36] Additional findings of volvulus include a fluid-filled proximal duodenum, a hyperpulsatile superior mesenteric artery, peritoneal fluid, and thickened highly reflective bowel wall as a result of haemorrhage or oedema.[37]

Intussusception

Intussusception occurs when a segment of bowel (the intussusceptum) prolapses into a more caudal segment of intestine (the intussuscipiens). It is the most common acute abdominal disorder of early childhood, typically affecting children between 3 months and 2 years of age. The classic clinical features of intussusception are paroxysmal abdominal pain, vomiting, 'redcurrant jelly' stools (containing blood and mucus), and a palpable abdominal mass. Approximately 90% of intussusceptions are ileocolic; the remainder are ileo-ileocolic, colocolic or ileo-ileal. More than 90% have no pathological lead point and are believed to result from hypertrophy of lymphoid tissues following a viral infection, which leads to altered intestinal peristalsis and intussusception. Lead points in the other 10% of cases are Meckel's diverticula, intestinal polyps, enteric duplication cysts, intramural haematoma, and lymphoma. Lead points should be strongly suspected in children under 3 months or over 3 years of age. Other conditions associated with intussusception include lymphoma, haematoma and cystic fibrosis.

Ultrasound is becoming the study of choice to screen children suspected of having intussusception.[38–40] In other cases intussusception may be encountered as an unsuspected finding on a scan performed for the evaluation of other clinical conditions, such as suspected appendicitis.

The graded-compression sonographic technique is utilised for investigation of intussusception. On transverse images, the intussusception appears as a complex mass with multiple high- and low-reflectivity rings surrounding a reflective centre (termed 'doughnut' or 'target' sign).[38–41] The hypoechoic layers represent the oedematous wall of the intussusceptum and the more echogenic reflective layers represent compressed mesentery, mucosa and intestinal contents. On longitudinal images, the intussusception appears as an oval or reniform mass with bright central echoes (termed the 'pseudo-kidney' sign) (Fig. 70.16). A mass within the central dilated loop of bowel may be seen when there is a lead mass.[42] An echo-poor mass usually represents a duplication cyst or haematoma, although fluid trapped within the intussuscepted mesentery can mimic a cyst.[43] Other ultrasound findings in intussusception include free peritoneal fluid[44] and left–right inversion of the superior mesenteric vessels.[45]

The conventional treatment for intussusception has been reduction using an air or contrast enema examination. Ultrasound-guided hydrostatic reduction has been proposed as an alternative method of treatment to avoid the ionising radiation associated with fluoroscopic-guided reduction.[46,47] A saline or tap water enema is administered under sonographic guidance until there is complete disappearance of the intussusception.

Colour flow imaging has been used to identify changes of ischaemia in the intussuscepted bowel. The presence of blood flow suggests viable bowel, whereas its absence suggests that gangrenous changes may have occurred.[48,49] Several investigators have suggested that the success rate of hydrostatic or air reduction appears to be higher when blood flow is present in the intussuscepted loops (Fig. 70.17) than when it is absent.[48] However, the true reliability of these findings has not been established. Other findings such as a wall thickness greater than 1 cm, large amounts of trapped fluid, and lymph nodes larger than 1 cm within the intussusception have also been correlated with a decreased enema reduction rate, although again the reproducibility of these findings has not yet been determined.[50–52]

The sensitivity of greyscale and colour Doppler ultrasound for the diagnosis of intussusception ranges between 95% and 100%, with a negative predictive value of 100%.[50,51] The specificity ranges between 88% and 100%. False positive diagnoses are caused by faecal contents, inflammatory bowel disease, intramural haematoma and volvulus (Fig. 70.18).

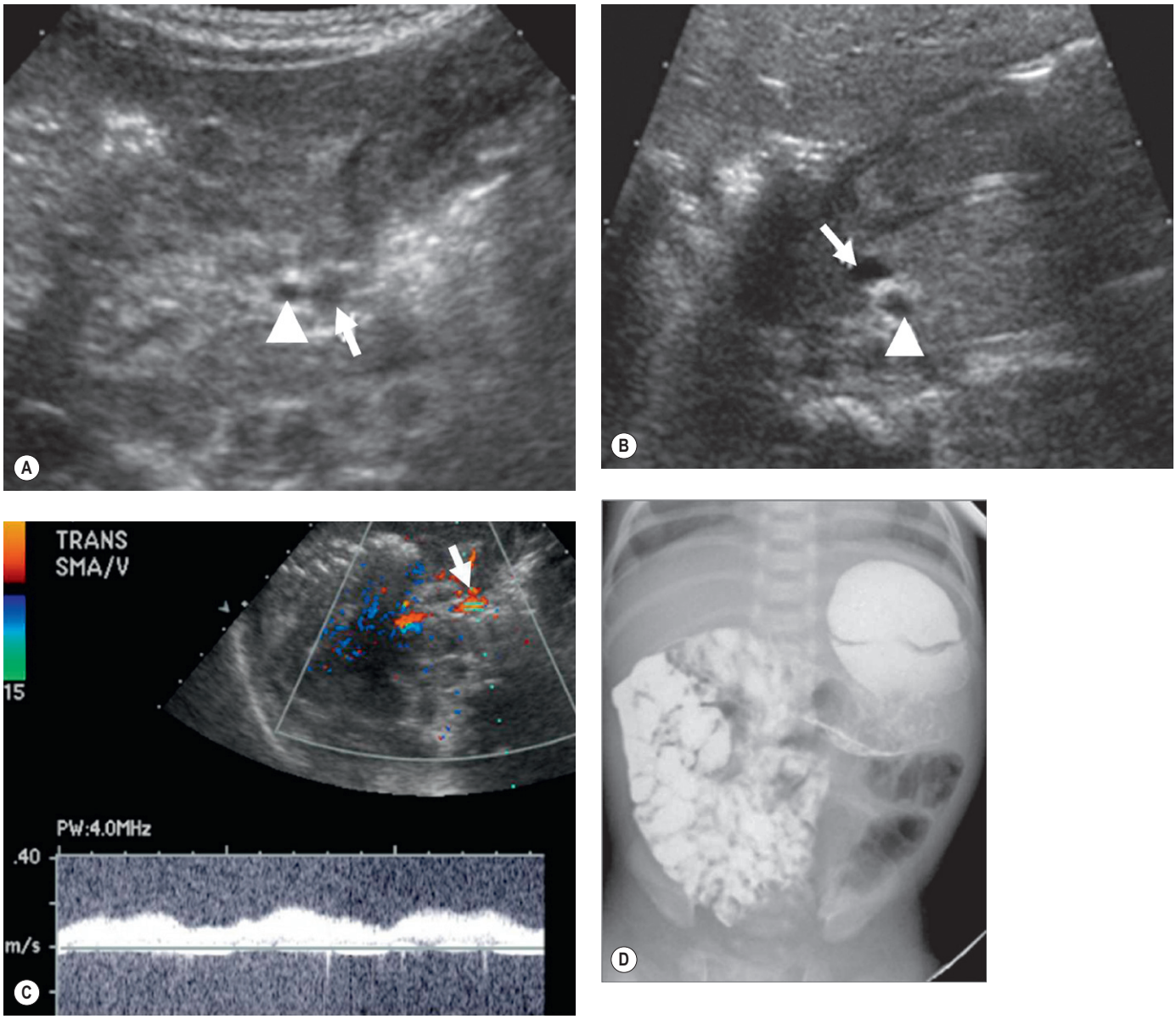

Figure 70.15 Malrotation. Six-week-old boy with non-bilious vomiting. Ultrasound was performed to rule out pyloric stenosis. **A:** Transverse scan through the upper abdomen shows the superior mesenteric vein (arrow) anterior and to the left of the superior mesenteric artery (arrowhead). The inverted position of the vessels suggests malrotation. **B:** Normal relationship between the superior mesenteric artery and vein. Transverse scan shows the vein (arrow) anterior and to the right of the artery (arrowhead). The artery can be differentiated from the vein by its thicker and more echogenic wall. **C:** Doppler interrogation of the superior mesenteric vein (arrow) demonstrates a venous waveform. **D:** Subsequent upper gastrointestinal study with barium shows small bowel loops in the right side of abdomen consistent with malrotation.

Transient small bowel intussusception

Transient small bowel intussusception is a common event, particularly in children with hyperperistaltic bowel. These intussusceptions tend to occur in older children (mean age 4 years) and are more frequently found in the proximal small bowel in the left upper quadrant.[53] Common clinical findings are abdominal pain, vomiting, and diarrhoea. A palpable mass and redcurrant jelly stools characteristic of ileocolic intussusception are absent. Ultrasound findings of transient small bowel intussusception are small size without a thickened bowel wall, short segment involvement, preserved wall motion, and absence of a lead point.[53] Spontaneous resolution of the intussusception usually can be observed with continuous scanning.

Small bowel obstruction

- Ultrasound is the initial study of choice to diagnose intussusception.
- Ultrasound can be helpful in diagnosis of other bowel obstruction when the abdomen is gasless by showing an unsuspected mass, ascites or bowel obstruction.
- Finding of malrotation is inversion of the superior mesenteric artery and vein relationship.
- Findings of midgut volvulus are clockwise swirling of the superior mesenteric vein, small bowel and mesentery around the superior mesenteric artery (whirlpool sign) and stretching of mesenteric vessels.
- Intussusception appears as a complex mass with high- and low-reflectivity rings surrounding a reflective centre ('doughnut' or 'target' sign).

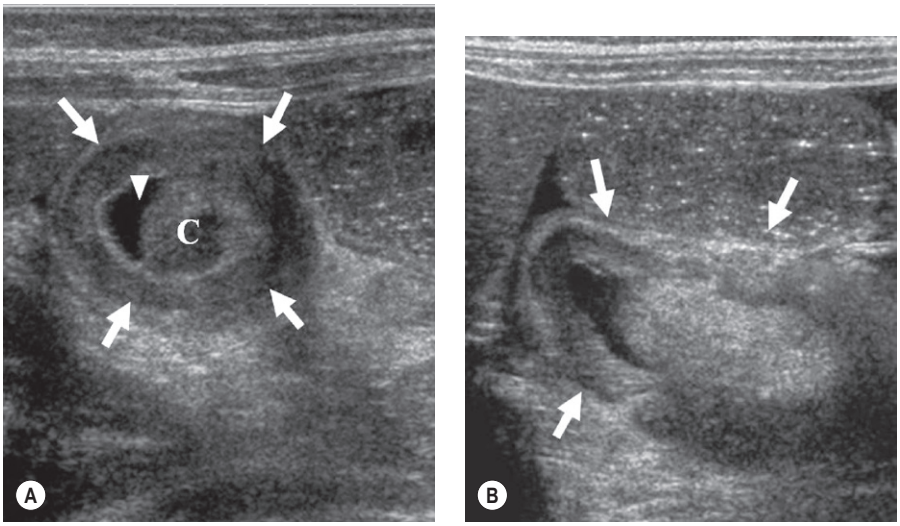

Figure 70.16 Intussusception. **A:** Transverse scan shows a mass with a reflective centre (C), a surrounding echo-poor ring (arrowhead), and a more reflective outer ring (arrows) in the right mid-abdomen. **B:** On a longitudinal image the intussusception has a reniform shape (arrows).

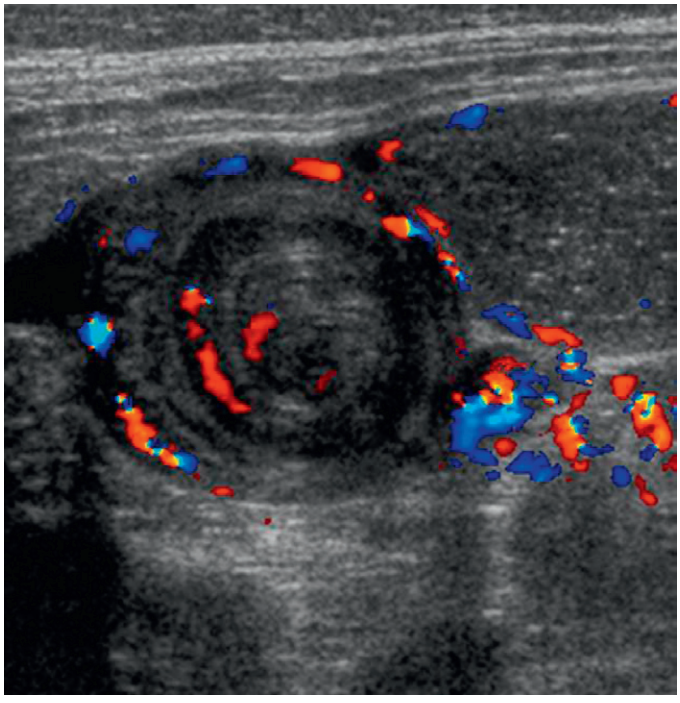

Figure 70.17 Intussusception. Transverse colour flow image shows flow within the intussuscepted loop of bowel. The intussusception was reducible by air-contrast enema.

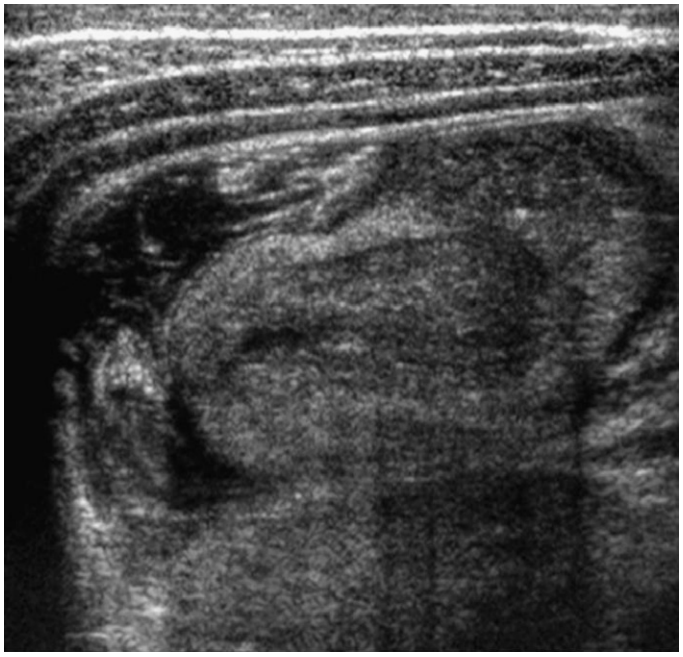

Figure 70.18 False positive diagnosis of intussusception. Transverse scan of the right lower quadrant shows an ovoid mass, considered to be an intussusception. Thickened bowel wall and no intussusception was shown on contrast enema. Cultures grew *Escherichia coli*.

Bowel wall thickening

Crohn's disease

Crohn's disease or regional enteritis is the most frequent inflammatory disease of the small bowel in children. The peak incidence is between 20 and 40 years of age, but approximately 25% of cases present in childhood. Most children present after 10 years of age, with abdominal pain and diarrhoea occurring in 70–75%. Other common clinical findings are fever, anorexia, weight loss, growth failure, peri-anal fistulae and arthritis. Rarely patients present with findings mimicking acute appendicitis.

Barium examination remains the imaging study of choice for determining the mucosal extent of Crohn's disease. Ultrasound can be used for the diagnosis of extramural complications and hydronephrosis.[54–57] On longitudinal images the findings of Crohn's disease are a partially compressible, tubular structure that communicates with adjacent bowel (i.e. no blind ending) (Fig. 70.19). The bowel wall is thickened, measuring between 4 and 10 mm in diameter, and is echo-poor.[57] Peristalsis may be present but diminished. On axial images, the abnormal bowel has a bull's-eye appearance, representing the outer echo-poor wall and the central reflective mucosa. Colour flow Doppler imaging shows increased blood flow in the thickened segment of bowel wall (Fig. 70.20).[54,55,57]

Mesenteric adenopathy, abscess, fistulae or sinus tracts and stenosis are common extraintestinal complications of Crohn's disease. Ultrasound can be used to identify these complications. Enlarged mesenteric nodes appear as oval or round echo-poor structures with echogenic central hila in the region of the inflamed bowel,

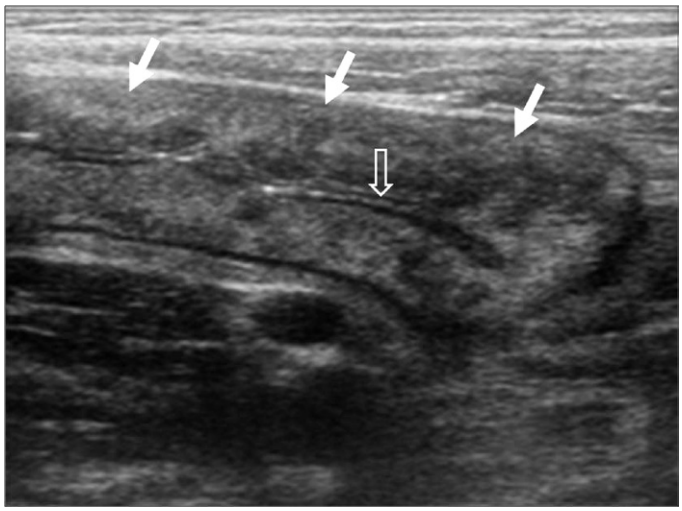

Figure 70.19 Crohn's disease. Longitudinal scan of the right lower quadrant showing abnormal ileum with thickened echo-poor walls (arrows); the wall thickness ranged between 8 and 10 mm. The central stripe represents mucosa (open arrow). The bowel lumen is narrowed by the apposed thick bowel walls.

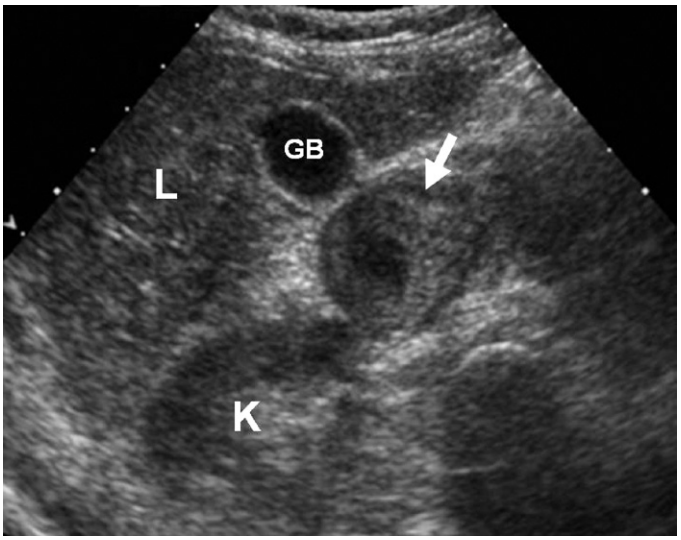

Figure 70.21 Henoch–Schönlein purpura. Transverse scan of the upper abdomen showing circumferential thickening of the descending duodenum (arrow). GB, gallbladder; K, right kidney; L, liver.

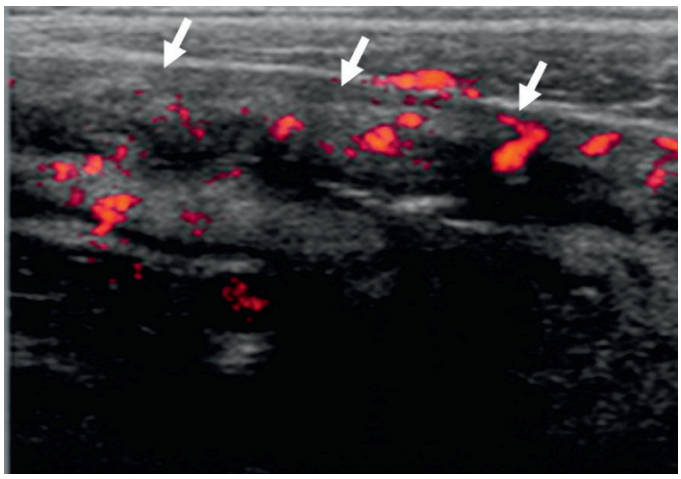

Figure 70.20 Crohn's disease. Same patient as in Figure 70.19. Colour flow Doppler image showing a thickened terminal ileum (arrows) with increased flow in the mucosal and submucosal layers.

usually measuring 1 cm or less in diameter. An abscess appears as an echo-poor mass with more reflective irregular borders. Highly reflective internal echoes can be present, representing gas or debris. The moderately reflective wall of an abscess helps to differentiate it from a thickened bowel loop, which typically has an echo-poor wall. Fistulae appear on ultrasound as echo-poor tracts between intestinal loops and other structures. They may contain highly reflective foci corresponding to air.[56] Stenosis appears as a thickened bowel wall with a narrowed lumen and increased peristalsis and dilatation of bowel proximal to the stenotic loop.

Acute terminal ileitis

Acute terminal ileitis may be caused by *Yersinia enterocolitica*, *Campylobacter jejuni*, *Salmonella* typhus and Behçet's syndrome, though they more usually produce a mild gastroenteritis. In acute terminal ileitis the abdominal pain may mimic appendicitis.[58] The distal ileum and colon are the common sites of involvement.

Small bowel wall thickening

- Crohn's disease is the most frequent inflammatory bowel disease in children.
- Findings of Crohn disease are a partially compressible, non-blinding tubular structure on long-axis views and bull's-eye appearance on short-axis views.
- Findings of acute terminal ileitis are a thickened echo-poor wall, diminished peristalsis and enlarged mesenteric lymph nodes.
- Findings of bowel wall haemorrhage are wall thickening with varying echotexture depending on the age of the haematoma.
- Acute haematomas are more reflective than chronic haematomas.
- Bowel wall thickness in inflammatory and haemorrhagic diseases is <1 cm.

In patients who present with symptoms mimicking appendicitis ultrasound can suggest the diagnosis of unsuspected acute terminal ileitis.[58,59] The ultrasound findings are similar to those of Crohn's disease, including a thickened echo-poor wall, diminished peristalsis and enlarged mesenteric lymph nodes. The nodes usually range between 7 and 21 mm in diameter and are echo-poor with a highly reflective centre.[59] Colour Doppler shows increased flow within the inflamed mucosa.[54,55] A specific diagnosis of infectious or inflammatory bowel disease requires stool culture or tissue sampling.

Haemorrhage

Bowel wall haemorrhage in children is usually the result of Henoch–Schönlein purpura or trauma. Rare causes of haemorrhage are bleeding diathesis and leukaemia.

Henoch–Schönlein purpura

This is an idiopathic systemic vasculitis of small vessels characterised by purpura, abdominal pain and arthralgia, and sometimes nephritis. Abdominal pain can precede the onset of the skin lesions and mimic an acute abdomen. In such patients, ultrasound can detect findings of bowel disease, which are a circumferentially thickened bowel wall (Fig. 70.21) that is hypervascular on colour flow imaging (Fig. 70.22).[60–62] Initially, the acute haematoma appears

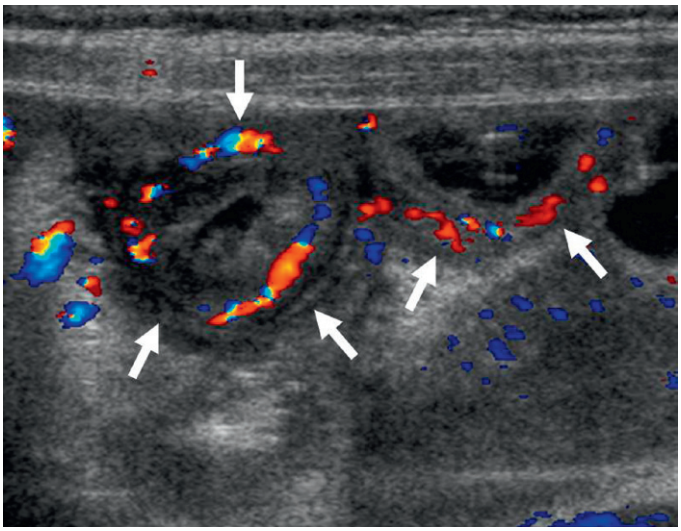

Figure 70.22 Henoch–Schönlein purpura. Transverse colour Doppler scan showing thick-walled hypervascular loops of proximal jejunum (arrows). Reproduced with permission from Siegel MJ, ed. Pediatric Sonography, 4th edition. Philadelphia: Lippincott Williams & Wilkins; 2010.

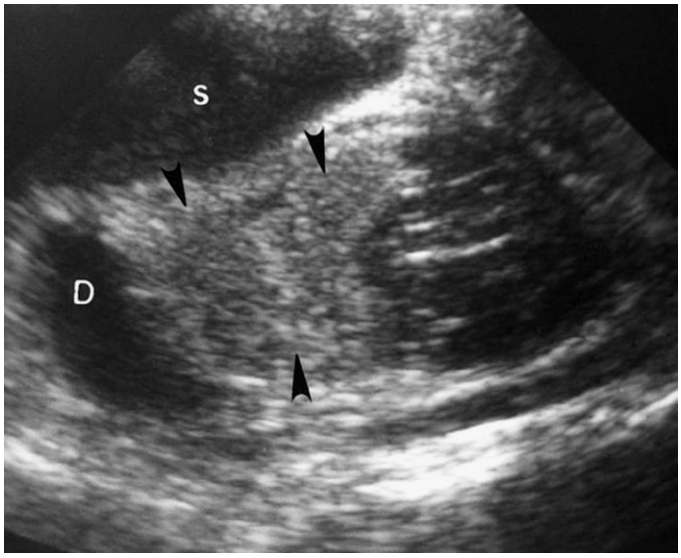

Figure 70.23 Duodenal haematoma. Longitudinal scan of the upper abdomen showing marked wall thickening of the transverse duodenum (arrowheads). S, stomach; D, dilated descending duodenum.

more reflective than the surrounding tissues. With subsequent liquefaction the haematoma becomes less reflective. The duodenum and jejunum are the common sites of bowel involvement. Ultrasound can also be used to detect intussusception which is a complication of Henoch–Schönlein purpura. The sensitivity and specificity of ultrasound for diagnosis of Henoch–Schönlein purpura are approximately 83% and 100%, respectively.[62]

Duodenal haematoma

Duodenal haematoma is a relatively common complication of blunt abdominal trauma, including non-accidental child abuse. The sonographic findings of duodenal haematoma are similar to those in Henoch–Schönlein purpura and include bowel wall thickening with a varying echotexture depending on the age of the haematoma.[63,64] With large haematomas, there may be apposition of the mucosal surfaces of the thickened walls, obliterating the bowel lumen (Fig. 70.23). The duodenum usually is dilated proximal to the site of the haematoma. Associated injuries to the liver, spleen or kidneys should be excluded in patients with blunt or non-accidental abdominal trauma.

Masses

Duplication

Duplication cysts can arise anywhere in the gastrointestinal tract but most (35%) are found in the distal ileum, distal oesophagus (20%) and stomach (9%). The remainder are scattered throughout the bowel. Frequent signs and symptoms are a palpable mass, abdominal pain, vomiting secondary to bowel obstruction and haemorrhage. Abdominal pain is usually the result of compression of the adjacent bowel; rarely it is due to intussusception. Gastrointestinal haemorrhage may result from peptic ulceration occurring in duplications that contain gastric mucosa.

On ultrasonography a duplication cyst appears as a well-defined, unilocular echo-poor mass with good through-transmission. Rarely the contents are reflective or contain septations secondary to haemorrhage or inspissated material within the lumen. Characteristically, duplication cysts have an inner highly reflective mucosa and an outer echo-poor muscular wall (Fig. 70.24).[23,65] The presence of a reflective lining is relatively specific for the diagnosis of duplication cyst and is useful to exclude other cystic masses, such as mesenteric or omental cyst, choledochal cyst, ovarian cyst, pancreatic pseudocyst or abscess. However, the reflective lining may be absent as a result of extensive mucosal ulceration by gastric enzymes. In these cases the appearance of the duplication cyst is similar to that of other cystic lesions.

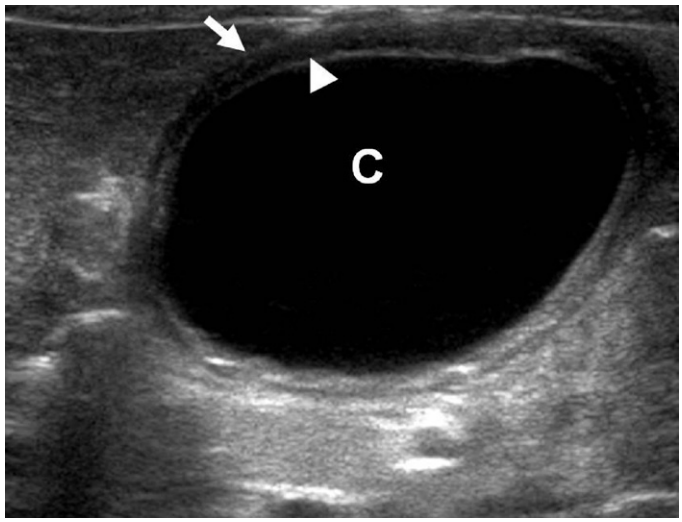

Figure 70.24 Duodenal duplication. Transverse scan of the upper abdomen showing an echo-poor mass (C) with an inner layer of echogenic mucosa (arrowhead) and an outer wall of hypoechoic muscle (arrow).

Lymphoma

Lymphoma, usually non-Hodgkin's lymphoma, is the most common primary malignancy of the small bowel in childhood and the terminal ileum is the most common site of lymphomatous involvement because it contains the greatest amount of lymphoid tissue. Children with small bowel lymphoma often present with a palpable abdominal mass, or with abdominal pain and vomiting

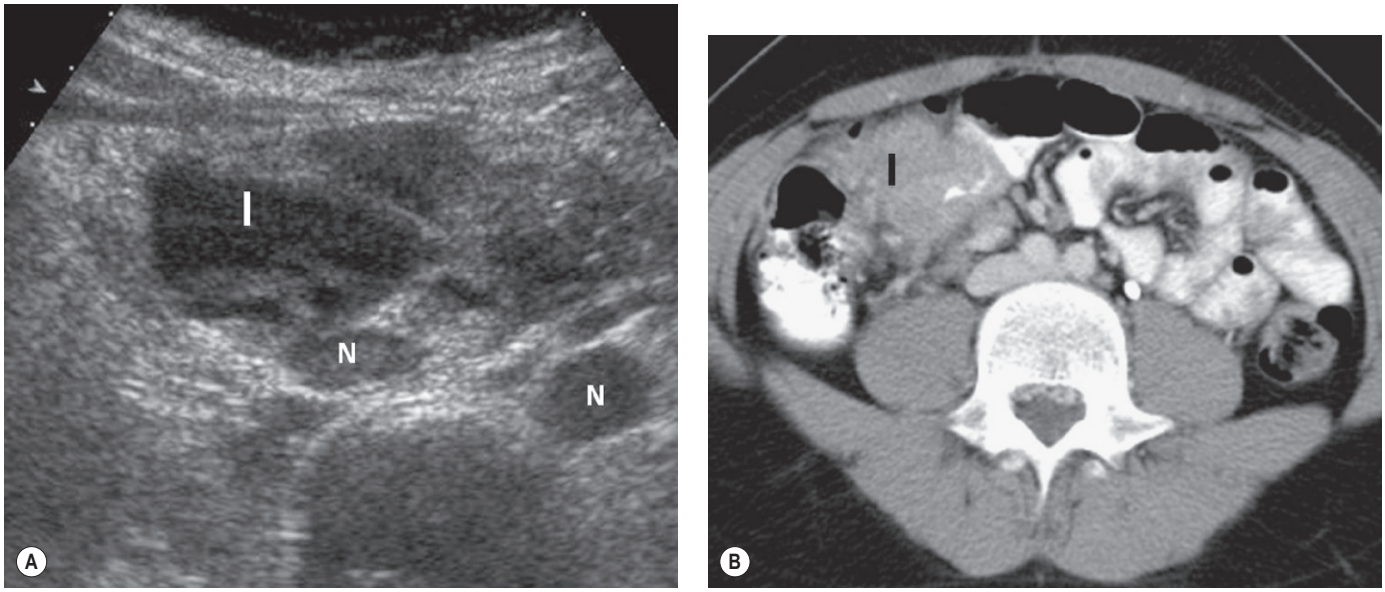

Figure 70.25 Non-Hodgkin's lymphoma. A: Transverse scan of the lower abdomen showing a thick-walled loop of ileum (I). N, lymph nodes. **B:** CT scan confirms thick-walled terminal ileum (I).

Small bowel masses

- Duplication cyst appears as a well-defined, unilocular echo-poor mass with good through-transmission, inner highly reflective mucosa and outer echo-poor wall.
- Lymphoma is the most common small bowel malignancy in childhood.
- Finding of lymphoma is echo-poor wall thickening, usually >1 cm.

due to intestinal obstruction. Systemic manifestations, such as malaise, anorexia, weight loss and fever, are also common.

On ultrasound the bowel wall is echo-poor and the wall thickness usually exceeds 1 cm (Fig. 70.25). Aneurysmal dilatation of the bowel lumen may be seen, secondary to mucosal invasion and excavation.[66] Intussusception is an occasional complication. Other findings include splenomegaly and mesenteric and retroperitoneal adenopathy. The enlarged nodes are usually echo-poor, lack a highly reflective centre, and may contain areas of necrosis. Leiomyosarcoma and adenocarcinoma have been reported in childhood but they are extremely rare. On ultrasound these tumours appear as large solid masses with necrotic centres.

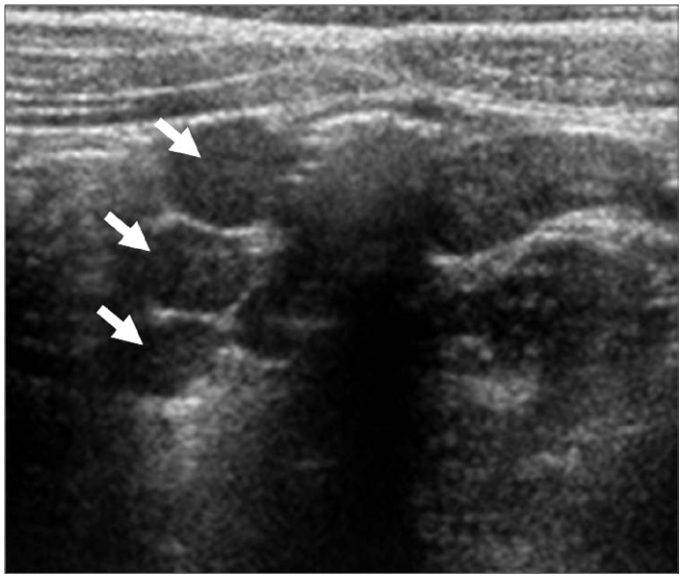

Figure 70.26 Mesenteric adenitis. Multiple echo-poor lymph nodes (arrows) are noted on this longitudinal scan of the right lower quadrant.

MESENTERIC ADENITIS

Mesenteric lymphadenitis is a clinical entity characterised by benign inflammation of the lymph nodes.[67–69] It is commonly viral in origin, but *Yersinia enterocolitica* has been implicated in some cases. Affected patients present with acute abdominal pain, mimicking appendicitis. The condition is usually self-limited and treated symptomatically.

Multiple enlarged, echo-poor mesenteric lymph nodes greater than 3 in number and 5 mm in anteroposterior diameter, with or without mild bowel wall thickening, establishes the diagnosis on ultrasound (Fig. 70.26).[69] The nodes usually are isoechoic or echo-poor relative to surrounding tissues and muscles and may retain their echogenic central hila. Colour Doppler ultrasound usually shows central flow in the hilar areas (Fig. 70.27).

APPENDIX

Acute appendicitis is the commonest cause of emergency abdominal surgery in children.[70–73] Typical signs and symptoms are present in most patients and include abdominal pain, nausea, vomiting, anorexia and fever. About one-third of patients have atypical findings: in these cases high-resolution graded-compression ultrasound may be of value to establish the diagnosis of appendicitis and to aid in the diagnosis of other abdominal or pelvic conditions that may mimic the disorder.[70–76]

The graded-compression technique, described by Puylaert, is used to compress the right lower quadrant.[77] Gentle gradual pressure is applied to the anterior abdominal wall with a linear array

or curved array transducer (5 or 7.5 MHz). At the start of the examination the patient is asked to point with one finger to the site of maximal tenderness and pain. This self-localisation expedites the search for an inflamed appendix, especially an aberrantly located one, and reduces the time of the examination.[78,79] Adequate examinations are achieved in over 95% of patients. Technical failures are due to the presence of severe pain, marked ascites or obesity, which preclude satisfactory compression.

Normal air-filled bowel loops are easily compressed and displaced from the right lower quadrant, but the inflamed obstructed appendix is not compressible. On the long-axis image the inflamed appendix appears as a fluid-filled non-compressible tubular structure with one blind end and a diameter, from outside wall to outside wall of at least 6 mm[70,73,80] (Fig. 70.28). In early non-perforated appendicitis an inner reflective lining, representing submucosa, can be noted. In the short-axis plane the appendix has a target appearance, representing the fluid-filled centre, the subjacent submucosa and the outer echo-poor muscular wall. Intraluminal reflective foci are occasionally identified and may indicate the presence of an appendicolith (Fig. 70.29) or intraluminal gas. Colour flow Doppler interrogation demonstrates flow in the wall of the appendix (Fig. 70.30).[81–83] Enlarged mesenteric nodes may be identified and a small amount of fluid may be seen adjacent to the appendix, even in the absence of perforation.

The normal appendix is visible with the graded-compression technique in about 5–10% of patients.[70,71] It is compressible, blind-ending and measures 6 mm or less in maximum diameter. The thin echogenic inner layer of mucosa/submucosa and the hypoechoic outer zone representing the muscularis propria are usually identifiable (Fig. 70.31). A small amount of fluid or gas may be noted within the lumen.[84] There usually is no demonstrable flow on colour flow Doppler imaging.[81–83]

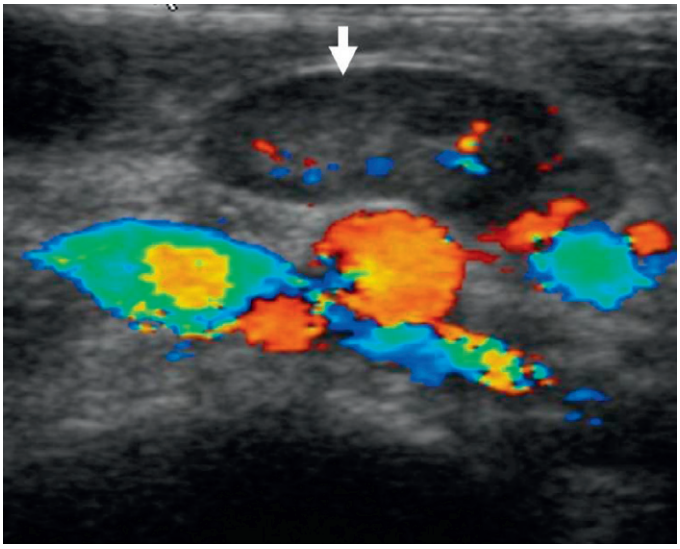

Figure 70.27 Mesenteric adenitis. Transverse colour flow imaging of the right lower quadrant shows central flow within an enlarged lymph node (arrow).

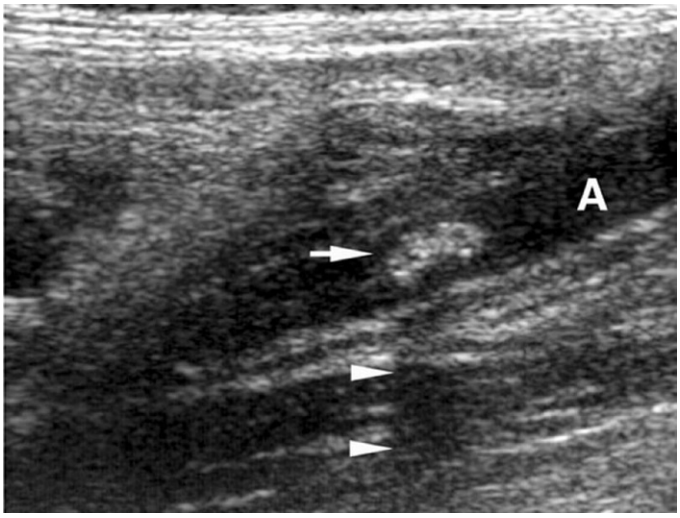

Figure 70.29 Acute appendicitis. The appendix (A) is fluid-filled and contains an appendicolith (arrow) with acoustic shadowing (arrowheads).

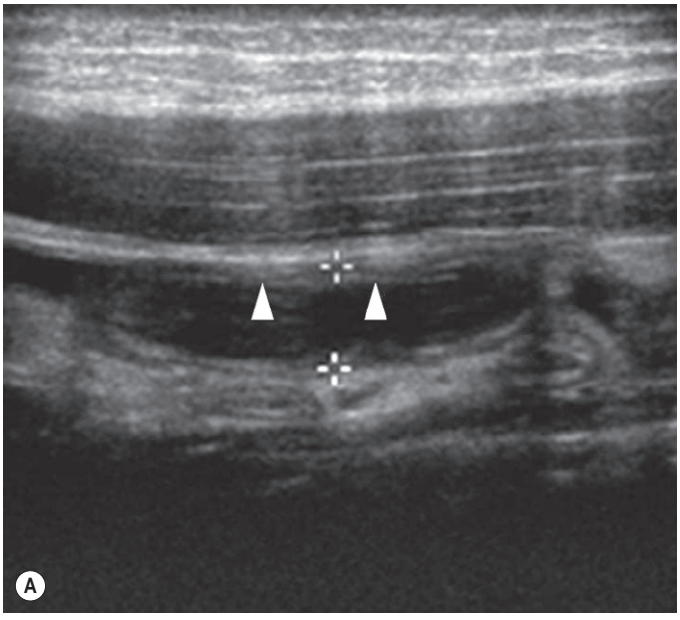

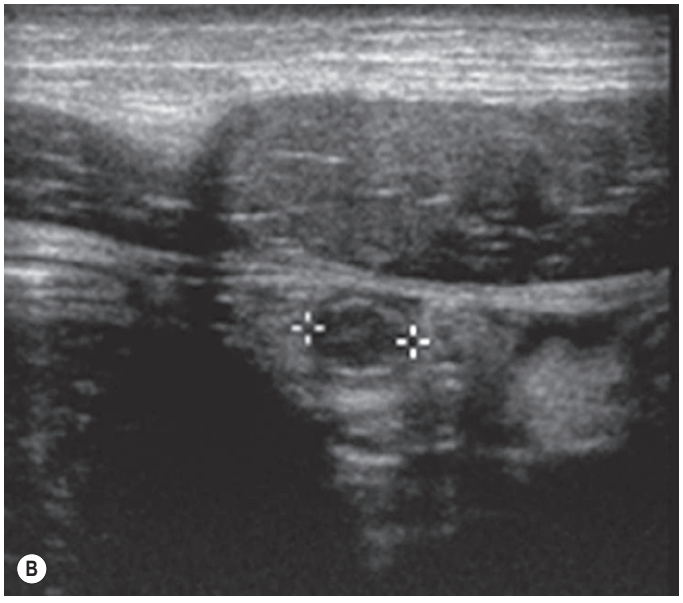

Figure 70.28 Acute appendicitis. A: Scan of the right lower quadrant shows a tubular fluid-filled appendix (callipers) with a reflective submucosal lining (arrowheads). **B:** On a transverse scan the appendix (callipers) has a target appearance.

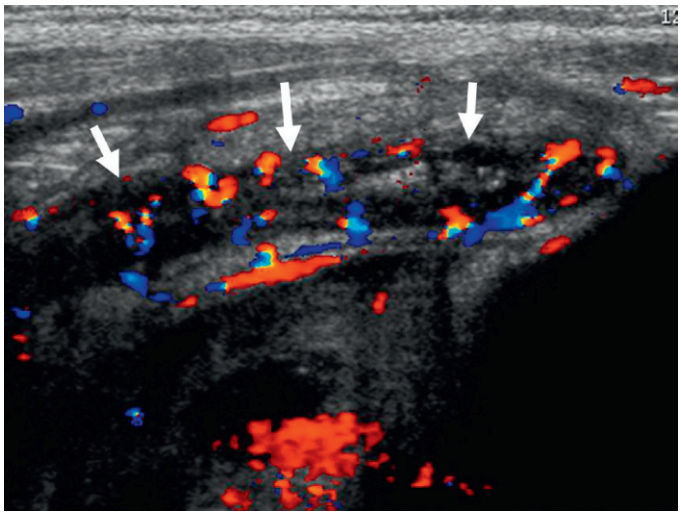

Figure 70.30 Acute appendicitis. Colour flow Doppler image shows a dilated appendix (arrows) with peripheral hypervascularity.

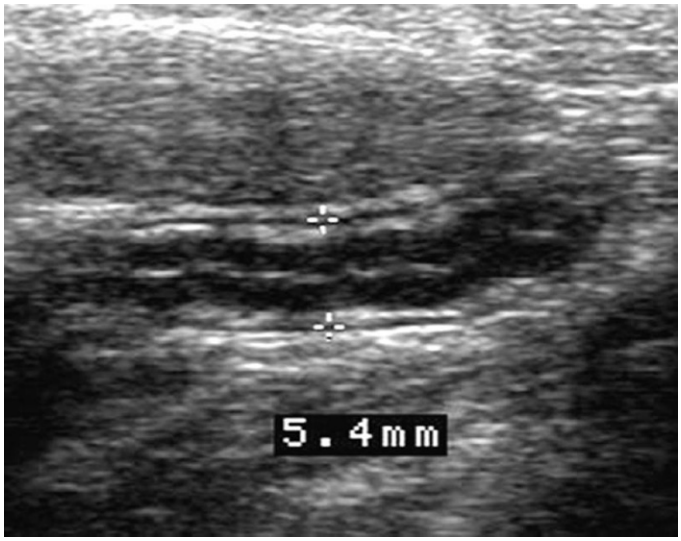

Figure 70.31 Normal appendix. Scan of the right lower quadrant showing a tubular structure (callipers) measuring 5.4 mm in diameter with a reflective mucosal centre.

Complications

Perforation occurs in 20–30% of children with appendicitis. The best predictors of perforation are loss of the reflective submucosa, increased peri-appendiceal reflectivity and abscess formation (Fig. 70.32).[85] The appendix itself is visible in only 40–60% of children with perforation.[83,85]

Abscesses can be limited to the right lower quadrant or they can extend into the pelvis or the peritoneal spaces of the upper abdomen. Appendiceal abscess appears as an echo-poor or complex mass (Fig. 70.33). Colour Doppler ultrasound shows flow in the wall of the abscess.[86] Peritonitis, another complication of appendicitis, is suggested by dilated fluid-filled bowel loops with thick, echogenic walls usually associated with ascites (Fig. 70.34). Colour flow imaging demonstrates increased flow in the bowel wall and adjacent soft tissues.

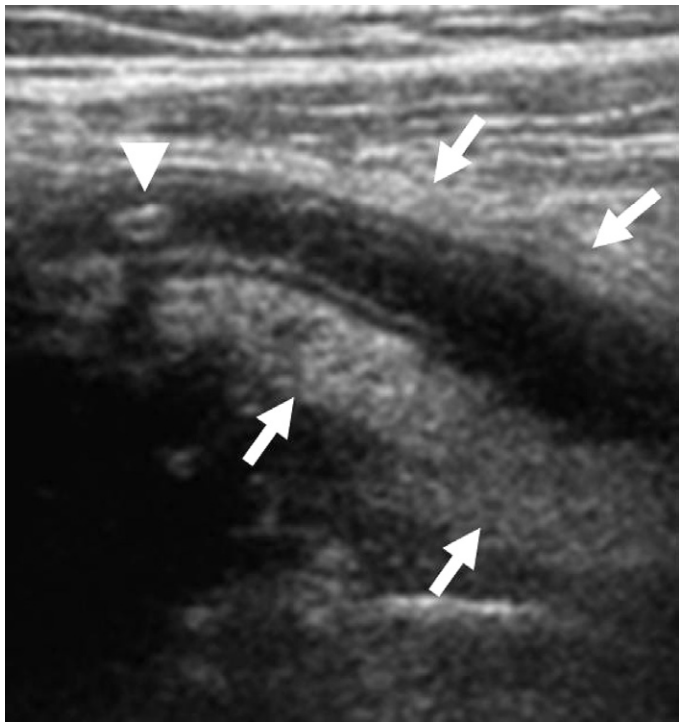

Figure 70.32 Perforated appendicitis. Longitudinal scan showing a dilated appendix and marked peri-appendiceal reflectivity (arrows). An appendicolith (arrowhead) within the lumen of the appendix is also seen. Peri-appendiceal phlegmon was documented at surgery.

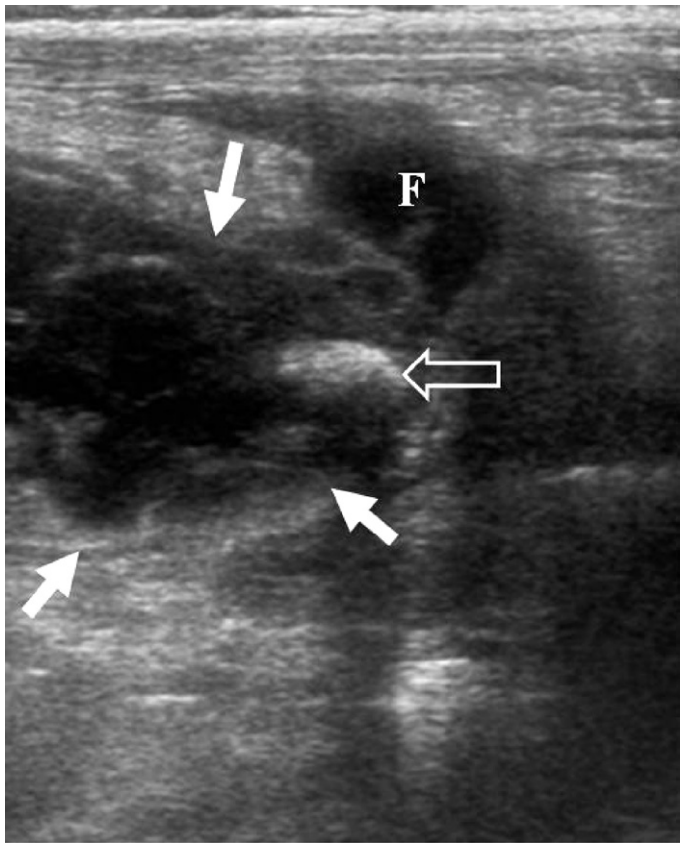

Figure 70.33 Appendiceal abscess. Longitudinal scan of the pelvis showing a complex fluid collection (arrows) in the right lower quadrant. A separate appendix could not be identified. The abscess cavity contains an appendicolith (open arrow) with a posterior acoustic shadowing. F, free pelvic fluid.

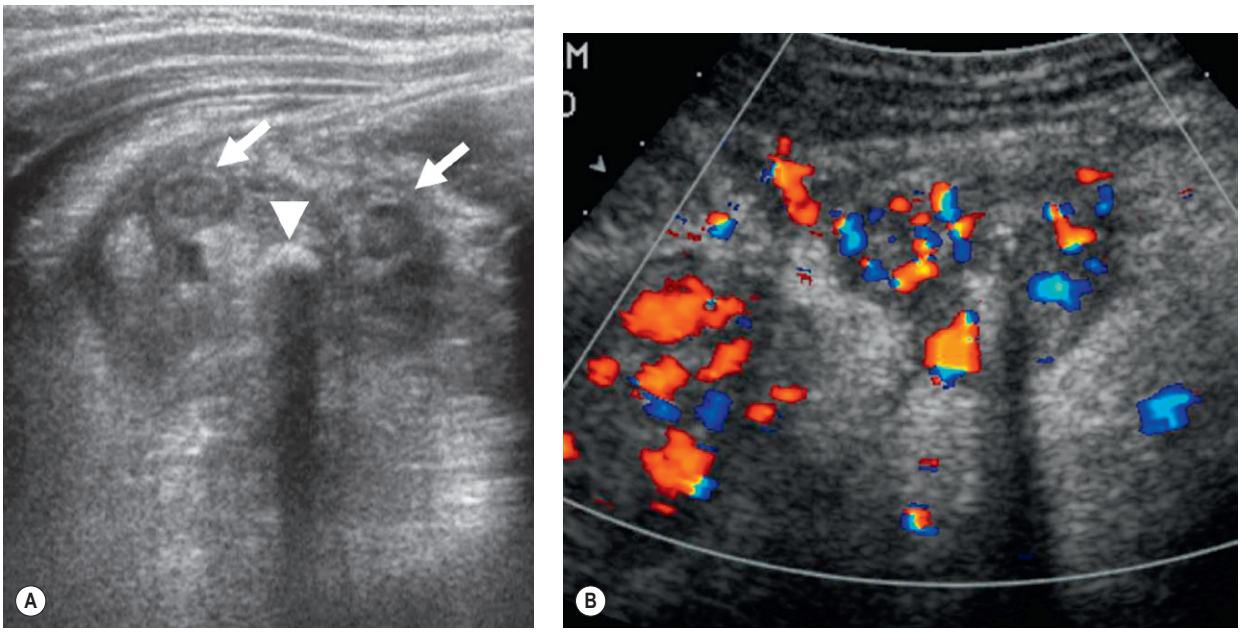

Figure 70.34 Peritonitis. A: Transverse scan of the right lower quadrant demonstrates fluid-filled bowel loops (arrows) with thick, echogenic walls. An extraluminal appendicolith (arrowhead) is also seen. **B:** Colour Doppler interrogation of the right lower quadrant shows increased blood flow within the bowel wall and adjacent soft tissues. Reproduced with permission from Siegel MJ, ed. Pediatric Sonography, 4th edition. Philadelphia: Lippincott Williams & Wilkins; 2010.

Diagnostic efficacy

The sensitivity of ultrasound for diagnosing appendicitis ranges between 80% and 95%, the specificity from 89% to 100% and the accuracy from 90% to 96%.[70–76,87] The sensitivity and specificity of colour Doppler are approximately 90% and 95%, respectively.[83] Colour Doppler does not increase the sensitivity of the examination but it makes interpretation of the greyscale ultrasound findings easier and can increase observer confidence in the diagnosis of appendicitis.

False negative diagnoses

False negative diagnoses may result from inability to compress the right lower quadrant because of severe pain or tense ascites; an aberrant location of the appendix, such as a retrocaecal position (Fig. 70.35); perforation; or early appendicitis. The problem of a retrocaecal appendix can be minimised by having the patient identify the site of maximal tenderness before the start of the examination. Although the appendix is not recognisable in many patients with perforation the identification of secondary findings, such as thickening of adjacent aperistaltic bowel loops, interloop fluid, phlegmon or abscess, can help to suggest the diagnosis. Another pitfall is early inflammation limited to the appendiceal tip, which can be missed if only the proximal appendix is imaged.[88]

False positive diagnoses

Causes of false positive diagnoses include the normal appendix and other inflammatory diseases which may secondarily affect the appendix, such as Crohn's disease or pelvic inflammatory disease. An inflamed Meckel's diverticulum may also mimic appendicitis.

When ultrasound fails to identify findings of acute appendicitis it is important to examine the pelvis and upper abdomen.[70–73] Approximately one-quarter to one-third of children referred for sonographic evaluation of suspected appendicitis will have that condition and another one-quarter to one-third of children will have specific alternative diagnoses, usually gynaecological diseases, gastrointestinal tract abnormalities or renal diseases. Between one-third and one-half of children will have resolution of abdominal pain without a specific diagnosis being established.[70–73]

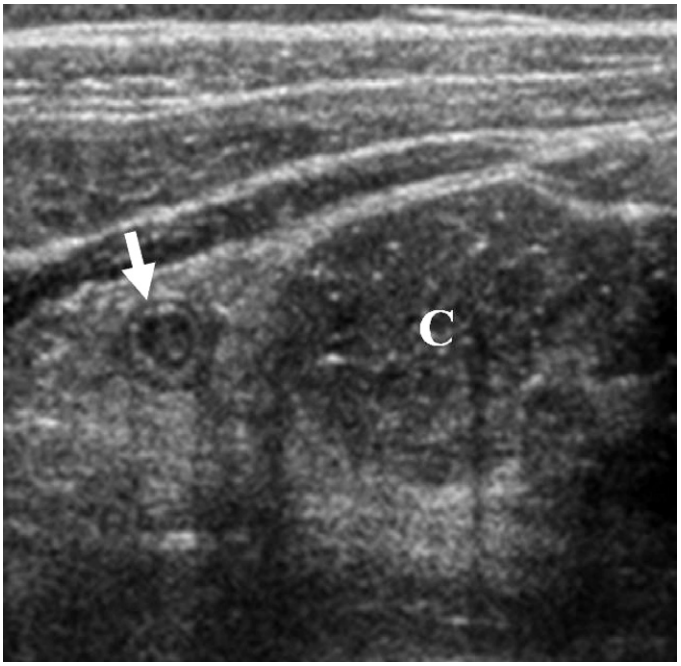

Figure 70.35 Retrocaecal appendix. Transverse scan of the right lower quadrant shows a dilated appendix (arrow) located lateral to the caecum (C).

Appendicitis

- Acute appendicitis is the most common abdominal emergency in children.
- Appendicitis appears as a fluid-filled non-compressible tubular structure with one blind end and a diameter of at least 6 mm.
- Colour flow Doppler demonstrates flow in the inflamed, appendiceal wall.
- A normal appendix is a compressible, blind-ending structure, 6 mm or less in diameter.
- Perforation occurs in 20–30% of children with appendicitis.
- Appendiceal abscess appears as an echo-poor or complex mass with hyperaemic walls.

COLON

Normal anatomy

With the exception of the right colon and rectum most of the large bowel is not amenable to ultrasound scanning because the faecal contents and gas produce intense reflection, with acoustic shadowing. When the lumen is fluid filled, the submucosa and the echo-poor muscularis can be identified. For practical purposes, the role of ultrasound in the colon is limited to evaluation of inflammatory bowel disease. A rarer indication is the evaluation of imperforate or ectopic anus.

Imperforate or ectopic anus

Imperforate or ectopic anus is characterised by an abnormal termination of the hindgut. The important consideration for surgical management is the relationship of the most caudal portion of the hindgut to the puborectalis or levator sling. Ultrasound has been used to measure the distance from the distal rectal pouch to the perineum. Longitudinal midline images are obtained through the perineum. The examiner's finger is placed on the perineum at the site of the anal dimple and the distance from the distal rectal pouch to the perineum is measured (Fig. 70.36). A pouch–perineum distance of less than 1.0 cm suggests a low lesion, a distance of 1.0–1.5 cm indicates an intermediate lesion, and more than 1.5 cm implies a high lesion.[89] The disadvantages of ultrasound are that it is time-consuming and there is overlap in the measurements between high and low lesions. A high lesion can be mistaken for a low one if the ultrasound scan is performed when the infant is crying, as this displaces the pouch caudally. Because of the lack of reproducibility, this technique is not widely used to evaluate the end of the hindgut.

Colon

- In imperforate anus ultrasound has been used to measure the distance between the distal rectal pouch and perineum to determine if a lesion is low or high.
- Ultrasound is used in colitis to establish the diagnosis and complications.
- Colitis produces non-specific wall thickening, hyperaemia on colour Doppler imaging, enlarged mesenteric lymph nodes and ascites.
- Necrotising enterocolitis produces thick-walled, fluid-filled loops of bowel, pneumatosis intestinalis, absent peristalsis, and portal venous air.

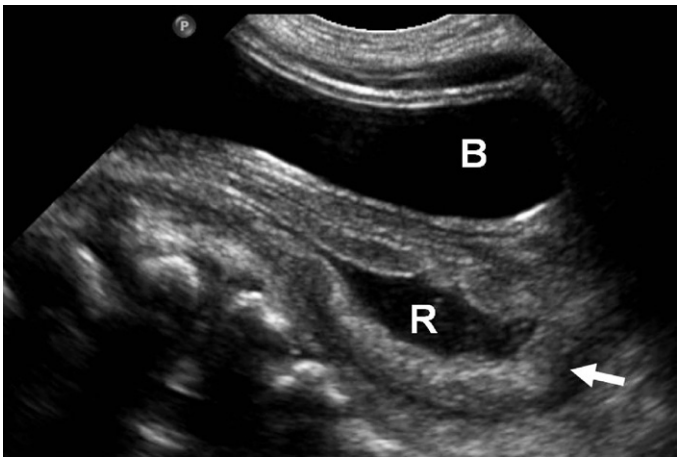

Figure 70.36 Low imperforate anus. Longitudinal scan through the perineum showing a fluid-filled distal rectal pouch (R). The pouch–perineum distance was less than 1.0 cm. Arrow, distal end of the rectal pouch; B, bladder.

Colitis

Ultrasound is used in colitis to establish the diagnosis of colitis and to detect complications, such as ascites or abscess. Colitis produces colonic wall thickening.[56–59,90–93] Such thickening is non-specific and can be seen in granulomatous colitis, ulcerative colitis, pseudomembranous colitis, neutropenic colitis (typhlitis), haemolytic uraemic syndrome, and infectious diseases such as *Yersinia*, *Salmonella* or *Shigella* colitis (Fig. 70.37). Additional findings of colitis include enlarged mesenteric lymph nodes, peritoneal or retroperitoneal fluid and abscess.

Although wall thickening is non-specific, the severity (mucosal or transmural inflammation) and distribution can sometimes help in diagnosis. **Granulomatous colitis** is a transmural inflammatory process usually involving the right colon, terminal ileum and rectum, with areas of normal bowel (i.e. skip areas) in between.[56–59] **Ulcerative colitis** is a mucosal process that typically begins in the rectum and extends proximally in a contiguous pattern.[56–59] **Pseudomembranous colitis** involves primarily the mucosa and occurs almost exclusively in patients who have been on antibiotic therapy. It is a pancolonic disease caused by toxin-producing *Clostridium difficile* bacteria.[90,92] In addition to colonic wall thickening, it can produce exaggerated haustral markings. **Neutropenic colitis** is a necrotising mucosal and/or transmural inflammatory process that affects immunocompromised patients, including neutropenic children undergoing chemotherapy and patients with acquired immunodeficiency syndrome (AIDS). It is usually localised to the caecum and right colon. The **haemolytic uraemic syndrome** is thought to be an antigen–antibody reaction to bacterial toxins, *Escherichia coli* 0157:H7 being one of the most frequent pathogens. This serotype produces a verotoxin, resulting in a vasculitis that damages endothelium which in turn causes deposition of fibrin microthrombi in the kidneys. It can involve the whole colon. **Infectious diseases** are typically mucosal infections and may involve part or all of the colon.

If the inflammatory process primarily involves the mucosa, the inner echogenic mucosal layer becomes thickened; the outer muscular layer of the colonic wall remains thin. When there is transmural inflammation, there is thickening of the entire colonic wall (mucosa, submucosa and muscularis).

Colour Doppler ultrasound demonstrates hyperaemia of the thickened colonic segments in most inflammatory and infectious processes. In the early stages of the haemolytic uraemic syndrome, colour Doppler scanning demonstrates a hypovascular colon, probably related to fibrin microthrombi. In the recovery stage the colonic wall becomes hypervascular, indicating reperfusion.[94]

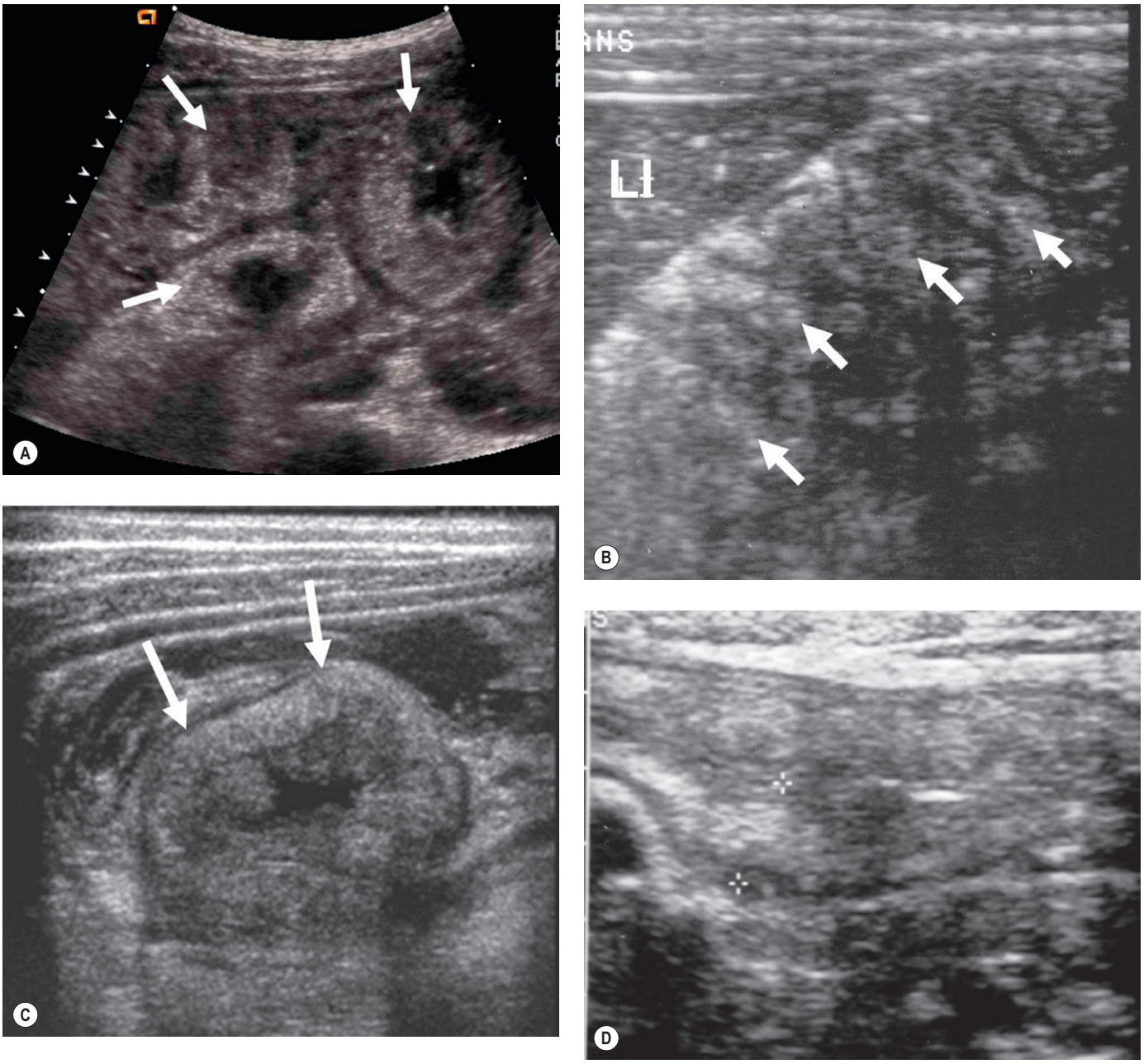

Figure 70.37 Colitis. A: Neutropenic colitis. Longitudinal scan showing a thickened right colon (arrows). **B: Pseudomembranous colitis.** Transverse scan shows markedly thickened right hepatic flexure and prominent haustral pattern (arrows). Because of the extensive inflammation individual bowel layers cannot be identified. LI, liver. **C: *Shigella* colitis.** Transverse ultrasound of the caecum shows concentric thickening of the caecal wall (arrows). **D: Haemolytic uraemic syndrome.** Longitudinal scan of the right colon shows diffuse wall thickening (callipers). In panels **A**, **C** and **D**, there is thickening of the mucosal and submucosal layers; the thin hypoechoic wall is relatively preserved.

Necrotising enterocolitis

Necrotising enterocolitis is an ischaemic disease of bowel, usually affecting premature newborn infants. Plain abdominal radiography has been the traditional method to establish the diagnosis, but ultrasound can be useful when plain radiographs are equivocal. The ultrasound findings of necrotising enterocolitis are thick-walled, fluid-filled loops of bowel, pneumatosis intestinalis, absent peristalsis, and portal venous air.[95–97] Pneumatosis intestinalis may be visible on sonography before it is seen on radiographs, appearing as small echogenic foci in the non-dependent wall or as a continuous echogenic ring (Fig. 70.38). Portal venous gas appears as small echogenic foci within the liver (Fig. 70.39). Ultrasound findings of ascites with fluid/debris levels is suggestive of perforation. Increased flow velocity in the coeliac and superior mesenteric arteries, most likely due to vasoconstriction, has been noted on Doppler ultrasound.[98]

Neoplasms

Polyps and duplications are the most common benign colonic masses in children and lymphoma is the common malignant tumour. These masses present clinically as a palpable mass, bowel obstruction or rectal bleeding. On ultrasound the appearance is

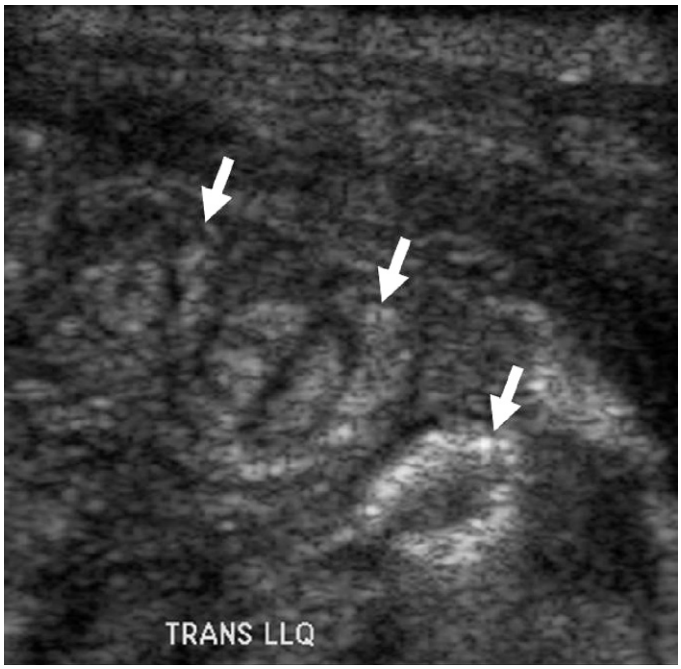

Figure 70.38 Necrotising enterocolitis. Transverse scan showing multiple highly reflective areas representing gas (arrows) within the bowel wall.

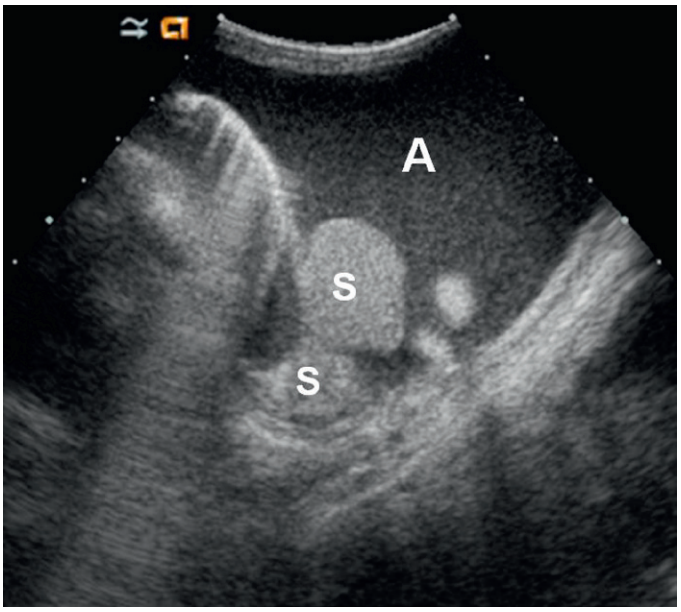

Figure 70.40 Ascites. Longitudinal scan of the right lower quadrant showing echogenic ascites (A) surrounding several small bowel loops (S). Chylous ascites was proven by aspiration.

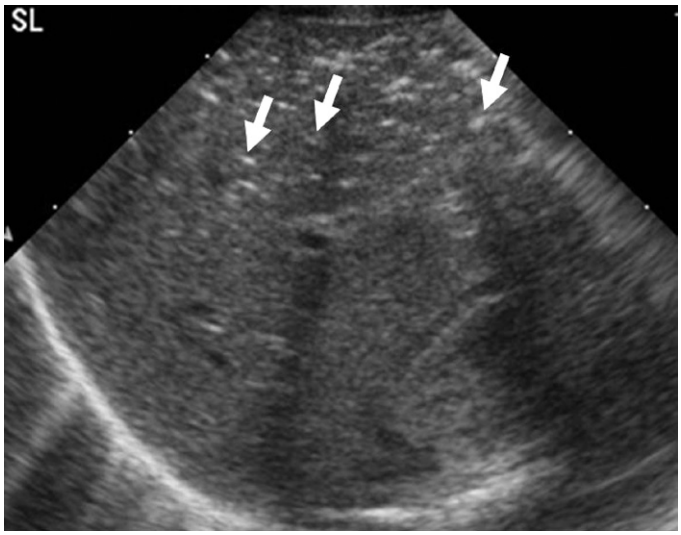

Figure 70.39 Necrotising enterocolitis. Scan through the liver shows multiple, punctate echogenic foci (arrows) representing portal venous air.

similar to that of gastrointestinal polyps, duplications and lymphomas elsewhere in the bowel (see above).

PERITONEAL CAVITY

Ascites

Ultrasound is a sensitive method for detecting peritoneal fluid. The common causes of ascites are hypoalbuminaemia, 'third-spacing' (shift of fluid into the peritoneal cavity secondary to shock), infectious or inflammatory processes, bleeding, lymphatic obstruction and urine leakage. Ascites can appear echo-free or complex. Transudative, chylous or uriniferous ascites are usually echo-free, whereas haemorrhagic, infectious, neoplastic or pancreatic ascites tend to be more complex with internal echoes or septations. Chylous ascites also may sometimes be echogenic if the chyle has a high lipid content (Fig. 70.40). Intraperitoneal fluid accumulates chiefly in the right perihepatic space, Morison's pouch and the cul-de-sac. With a large amount of ascites the small bowel loops are displaced centrally within the abdomen and fluid accumulates adjacent to and between loops.

Loculated ascites, caused by postoperative or inflammatory adhesions, produces a septated fluid collection that may displace adjacent structures. On ultrasound scanning loculated ascites may simulate other pathology, such as a duplication cyst, meconium pseudocyst, dilated bowel, urachal cyst, lymphocele, haematoma or abscess. Differentiation requires clinical correlation and, in some instances, percutaneous needle aspiration.

Inflammatory disease

Abdominal abscesses in children are usually the result of intestinal perforation secondary to appendicitis or Crohn's disease, but they may also follow pelvic surgery or trauma or be a sequel of pelvic inflammatory disease. Patients typically present with fever, leukocytosis and abdominal pain. The characteristic ultrasound appearance of intraperitoneal abscess is an echo-poor mass (see Fig. 70.33) with a reflective rim. Occasionally fluid/debris levels, septations or gas can be encountered. Gas can be recognised as intensely reflective foci, usually with acoustic shadowing. Careful observation while holding the transducer still may show the mobile gas bubbles in anaerobic abscesses.

Omental infarction

Segmental infarction of the greater omentum is another cause of acute abdominal pain that can mimic acute appendicitis. Ultrasound shows a heterogeneous, highly reflective mass within the

omental fat (Fig. 70.41). It characteristically is located at the anterior abdominal wall near the transverse or ascending colon.[99,100] The margins of the lesion may be well circumscribed or ill defined.

Tumours of the mesentery and peritoneum

Benign lesions

Mesenteric cysts, also known as lymphangiomas, result from a developmental malformation of the lymphatic system. Affected patients typically present with a palpable abdominal mass or chronic pain, but they may present with acute abdominal pain if the cyst undergoes torsion. Characteristically mesenteric cysts are large, thin-walled, multilocular masses (Fig. 70.42);[101–104] they are rarely unilocular. Debris and internal septations may be present secondary to prior haemorrhage or infection Most are located in the small bowel mesentery, with the mesocolon and omentum being less common sites of origin.

Pseudocysts are encountered in children with ventriculoperitoneal shunts. Adhesions develop around a shunt catheter following localised peritonitis, limiting the distribution of fluid in the peritoneal cavity and resulting in a cerebrospinal fluid pseudocyst. A pseudocyst appears as a well-circumscribed anechoic mass (Fig. 70.43). The shunt catheter may be visualised within the fluid, appearing as a linear echogenic structure with distal acoustic shadowing.

Teratomas occasionally arise in the mesentery. They usually contain an admixture of tissue, including large cystic components and echogenic fat, calcification and soft tissues. Benign lesions tend

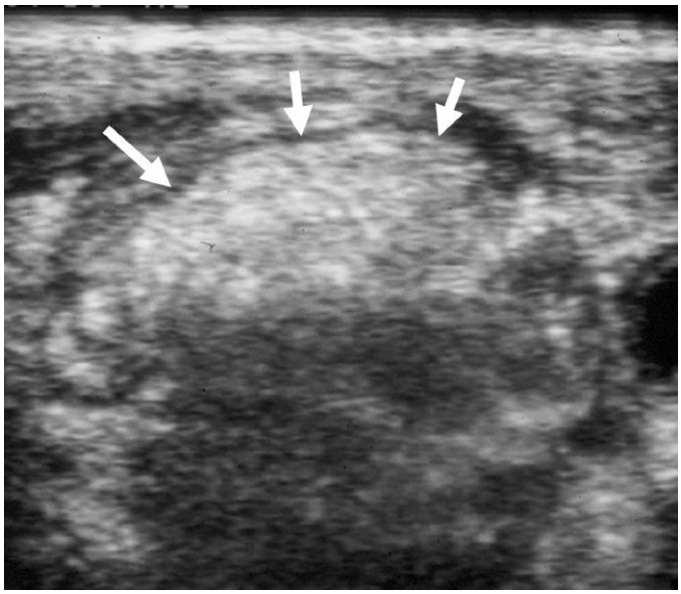

Figure 70.41 Omental infarct. Transverse view through the upper abdomen demonstrates a highly reflective mass (arrows) beneath the rectus muscles.

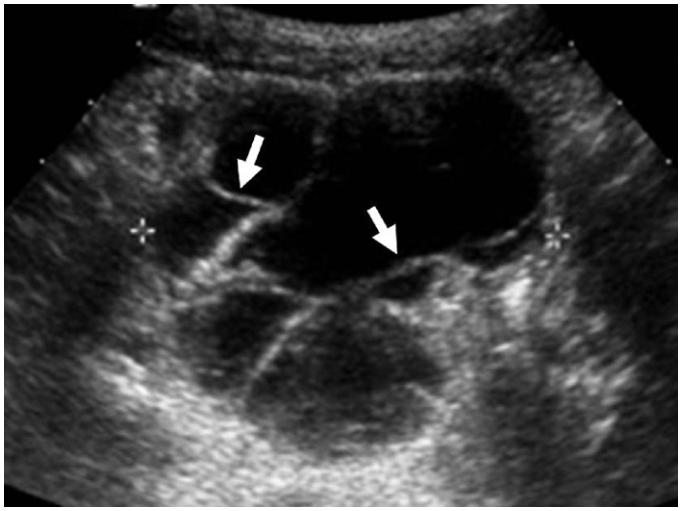

Figure 70.42 Mesenteric cyst. Longitudinal scan of the mid-abdomen showing a large complex mass (callipers) with multiple fluid-filled spaces separated by septa (arrows).

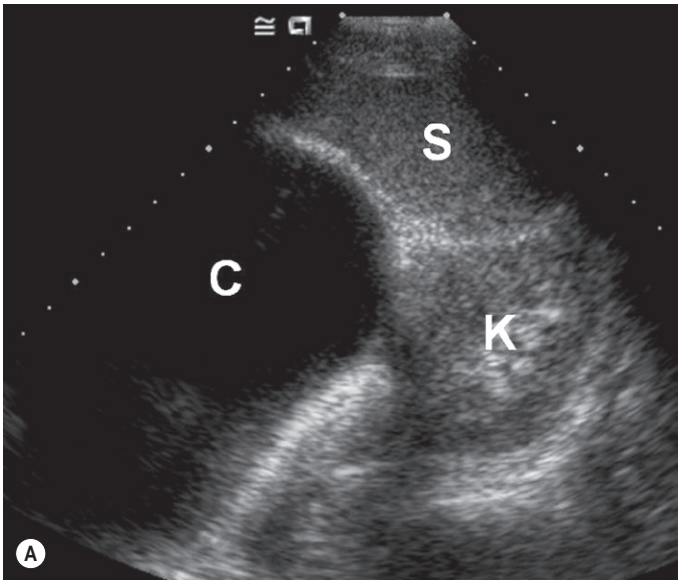

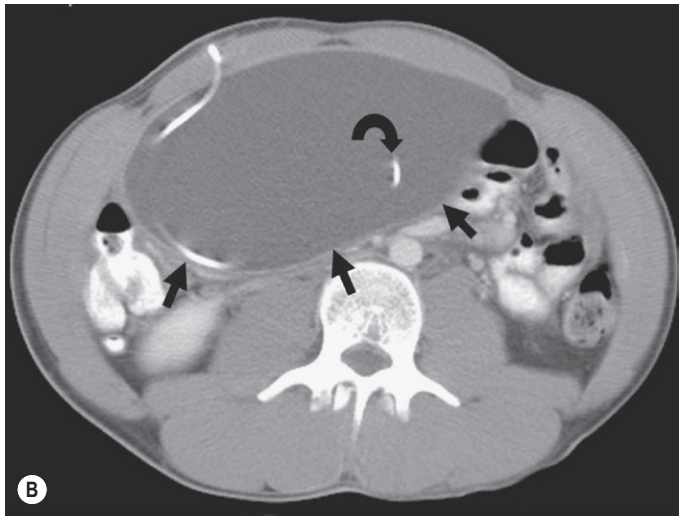

Figure 70.43 Cerebrospinal pseudocyst in a 17-year-old boy. A: Transverse scan of the left upper quadrant shows a large anechoic cystic mass (C) adjacent to the spleen (S) and left kidney (K). **B:** Axial CT image confirmed cerebrospinal pseudocyst (arrows), which contains ventriculoperitoneal shunt catheter (curved arrow).

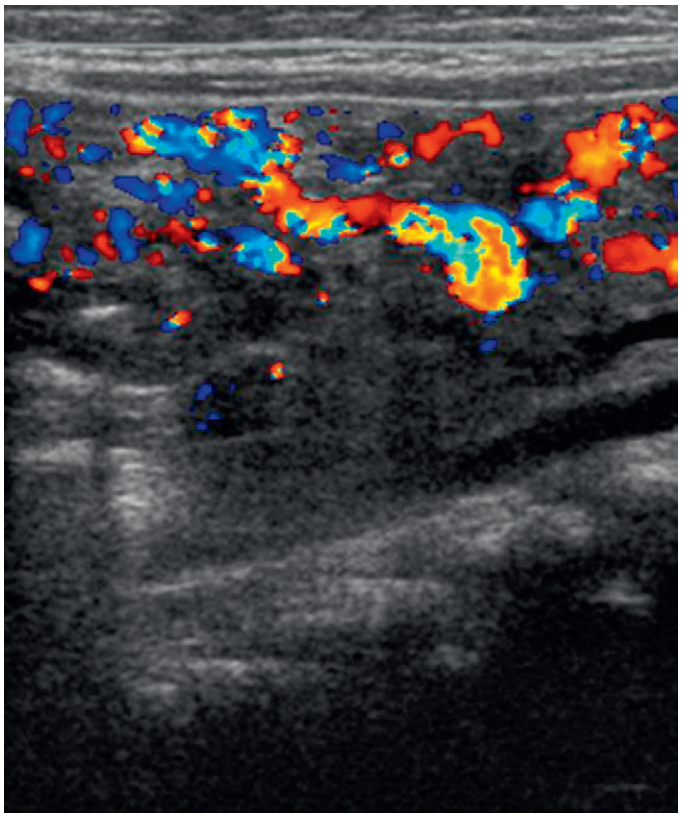

Figure 70.44 Mesenteric haemangioma in a 4-month-old girl with massive gastrointestinal bleeding. Colour Doppler longitudinal view of the mid-abdomen shows multiple tubular vascular structures within the mesentery, representing dilated arterial channels. (Case courtesy of Edward Lee MD.)

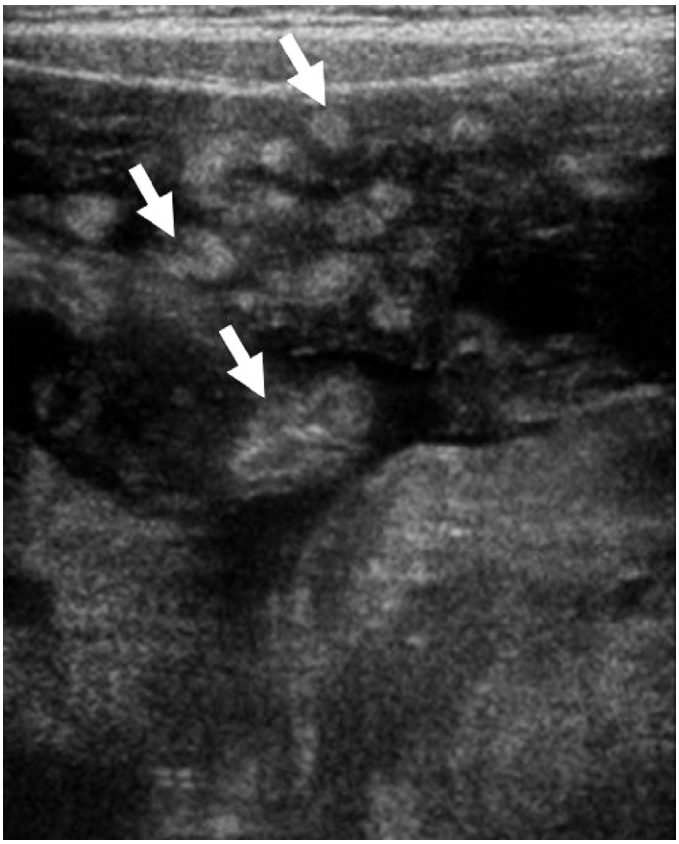

Figure 70.45 Non-Hodgkin's lymphoma. Transverse scan of the lower abdomen showing multiple enlarged lymph nodes (arrows) in the small bowel mesentery. (Case courtesy of Edward Lee MD.)

Peritoneal cavity

- Ascites can appear echo-free or complex.
- Abdominal abscesses are usually the result of intestinal perforation secondary to appendicitis or Crohn's disease.
- Finding of intraperitoneal abscess is an echo-poor mass.
- Lymphangioma is the most common mesenteric mass, appearing as a thin-walled, multilocular mass.
- Lymphoma is the most common malignant mesenteric neoplasm, appearing as enlarged mesenteric lymph nodes or large confluent masses.

to have a predominance of fluid elements, whereas malignant teratomas have a predominance of soft tissue.

Haemangiomas also may involve the mesentery. They are echogenic and usually associated with increased blood flow and large feeding vessels (Fig. 70.44).[105]

Malignant tumours

Lymphoma is the most common malignant neoplasm of the mesentery in childhood.[106] The characteristic ultrasound finding is enlarged mesenteric lymph nodes, ranging from multiple, small well-circumscribed round lymph nodes to large confluent masses infiltrating the mesentery (Fig. 70.45). Characteristically lymphomatous nodes are echo-poor or echo-free, but they can be isoechoic to adjacent soft tissue. The central echogenic hila are absent. The finding of small mesenteric lymph nodes is non-specific and can be seen in acute appendicitis and inflammatory diseases of bowel, such as Crohn's disease.

Less frequent malignant intraperitoneal tumours in children include rhabdomyosarcoma, neuroblastoma, primitive neuroectodermal tumour, extragonadal germ cell tumours, and mesothelioma.[106] These have a variety of appearances, ranging from small peritoneal or mesenteric nodules to a large peritoneal mass. Additional findings may include ascites, bowel wall thickening and omental caking.

REFERENCES

1. John SD, Hollingsworth C. The pediatric gastrointestinal tract. In: Rumack CM, Wilson SR, Charboneau JA, eds. Diagnostic ultrasound. 3rd edn. St Louis, MO: Elsevier Mosby; 2005;1941–1975.
2. Siegel MJ. Gastrointestinal tract. In: Siegel MJ, ed. Pediatric sonography. 4th edn. Philadelphia: Lippincott Williams & Wilkins; 2010;339–383.
3. Gomes H, Lallemand A, Lallemand P. Ultrasound of the gastroesophageal junction. Pediatr Radiol 1993;23:94–99.
4. Westra SJ, Wolf BHM, Staalman CR. Ultrasound diagnosis of gastroesophageal reflux and hiatal hernia in infants and young children. J Clin Ultrasound 1990;18:477–485.
5. Wright LL, Baker KR, Meny RG. Ultrasound demonstration of gastroesophageal reflux. J Ultrasound Med 1988;7:471–475.
6. Hirsch W, Kedar R, Preiss U. Color doppler in the diagnosis of the gastroesophageal reflux in children: comparison with pH measurements and B-mode ultrasound. Pediatr Radiol 1996;26:232–235.
7. Jang HS, Lee JS, Lim GY, et al. Correlation of color Doppler sonographic findings with pH measurements in gastroesophageal reflux in children. J Clin Ultrasound 2001;29:212–217.
8. Koumanidou C, Vakaki M, Pitsoulakis G, et al. Sonographic measurements of the abdominal esophagus length in infancy: a diagnostic tool for gastroesophageal reflux. AJR Am J Roentgenol 2004;183:801–807.

9. O'Keeffe FN, Stansberry SD, Swischuk LE, Hayden CK, Jr. Antropyloric muscle thickness at US in infants: what is normal? Radiology 1991;178:827–830.
10. Swischuk LE, Hayden CK Jr, Stansberry SD. Sonographic pitfalls in imaging of the antropyloric region in infants. Radiographics 1989;9:437–447.
11. Hernanz-Schulman M, Sells LL, Ambrosino MM, et al. Hypertrophic pyloric stenosis in the infant without a palpable olive: accuracy of sonographic diagnosis. Radiology 1994;193:771–776.
12. Rohrschneider WK, Mittnacht H, Darge K, Troger J. Pyloric muscle in asymptomatic infants: sonographic evaluation and discrimination from idiopathic hypertrophic pyloric stenosis. Pediatr Radiol 1998;28:429–434.
13. Cohen HL, Schecter S, Mestel AL, et al. Ultrasonic 'double track' sign in hypertrophic pyloric stenosis. J Ultrasound Med 1987;6: 139–143.
14. Finkelstein MS, Mandell GA, Tarbell KV. Hypertrophic pyloric stenosis: volumetric measurement of nasogastric aspirate to determine the imaging modality. Radiology 1990;177:759–761.
15. Hernanz-Schulman M. Vomiting in the infant. In: Bluth EI, Benson CB, Ralls PW, Siegel MJ, eds. Ultrasound: A practical approach to clinical problems. 2nd edn. New York: Thieme; 2007;489–400.
16. Bisset RAL, Gupta SC. Hypertrophic pyloric stenosis, ultrasonic appearances in a small baby. Pediatr Radiol 1988;18:405.
17. Calahan MJ, McCauley RG, Patel H, Hijazi ZM. The development of hypertrophic pyloric stenosis in a patient with prostaglandin-induced foveolar hyperplasia. Pediatr Radiol 1999;29:748–751.
18. Atwell JD, Levick P. Congenital hypertrophic pyloric stenosis and associated anomalies in the genitourinary tract. J Pediatr Surg 1981;16:1029–1035.
19. Kaminsky CK, Cleveland RH. Midgut malrotation. In: Siegel BA, Proto AV, eds. Pediatric disease (fourth series). Test and syllabus. Reston, VA: American College of Radiology; 1993;376–404.
20. Okorie NM, Dickson JAS, Carver RA, Steiner GM. What happens to the pylorus after pyloromyotomy? Arch Dis Child 1988;63: 1339–1340.
21. Yoshizawa J, Eto T, Higashimoto Y, et al. Ultrasonographic features of normalization of the pylorus after pyloromyotomy for hypertrophic pyloric stenosis. J Pediatr Surg 2001;36:582–586.
22. Goldwag SS, Bellah RD, Ward KJ, Kogutt MS. Sonographic detection of Menetrier's disease in children. J Clin Ultrasound 1994;22:5567–5570.
23. Macpherson RI. Gastrointestinal tract duplications: clinical, pathologic, etiologic, and radiologic considerations. Radiographics 1993;13:1063–1080.
24. Segal SR, Sherman NH, Rosenberg HK, et al. Ultrasonographic features of gastrointestinal duplications. J Ultrasound Med 1994;13:863–870.
25. Bowen B, Ros PR, McCarthy MJ, et al. Gastrointestinal teratomas: CT and US appearance with pathologic correlation. Radiology 1987;162:431–433.
26. Malpani A, Ramani SK, Wolverson MK. Role of sonography in trichobezoars. J Ultrasound Med 1988;7:661–663.
27. Park J, Rubinas TC, Fordahn LA, Phillips JD. Multifocal gastrointestinal tumor (GIST) of the stomach in an 11-year-old girl. Pediatr Radiol 2006;36:1212–1214.
28. Cremin BJ, Solomon DJ. Ultrasonic diagnosis of duodenal diaphragm. Pediatr Radiol 1987;17:489–490.
29. Neal MR, Seibert JJ, Vanderzalm MD, Wagner CW. Neonatal ultrasonography to distinguish between meconium ileus and ileal atresia. J Ultrasound Med 1997;16:263–266.
30. Lawrence PW, Chrispin A. Sonographic appearances in two neonates with generalized meconium peritonitis: the snowstorm sign. Br J Radiol 1984;57:340–342.
31. Wu CC. Sonographic findings of generalized meconium peritonitis presenting as neonatal ascites. J Clin Ultrasound 1988;16:48–51.
32. Strouse PJ. Disorders of intestinal rotation and fixation ('malrotation'). Pediatr Radiol 2004;34:837–851.
33. Weinberger E, Winters WD, Liddell RM, et al. Sonographic diagnosis of intestinal malrotation in infants: importance of the relative positions of the superior mesenteric artery and vein. AJR Am J Roentgenol 1992;159:825–828.
34. Zerin JM, DiPietro MA. Superior mesenteric vascular anatomy at US in patients with surgically proved malrotation of the midgut. Radiology 1992;183:693–694.
35. Pracros JP, Sann L, Genin G, et al. Ultrasound diagnosis of midgut volvulus: the 'whirlpool' sign. Pediatr Radiol 1992;22:18–20.
36. Shimanuki Y, Aihara T, Takano H, et al. Clockwise whirlpool sign at color Doppler US: an objective and definite sign of midgut volvulus. Radiology 1996;199:261–264.
37. Smet MH, Marchal G, Ceulemans R, Eggermont E. The solitary hyperdynamic pulsating superior mesenteric artery: an additional dynamic sonographic feature of midgut volvulus. Pediatr Radiol 1991;21:156–157.
38. Beasley S. Intussusception. Pediatr Radiol 2004;34:302–304.
39. Daneman A, Navarro O. Intussusception. Part I: A review of diagnostic approaches. Pediatr Radiol 2003;33:79–85.
40. del-Pozo G, Albillos J C, Tejedor D. Intussusception: US findings with pathologic correlation – the crescent-in-doughnut sign. Radiology 1996;199: 688–692.
41. Itagaki A, Uchida M, Ueki K, Kajii T. Double target sign in ultrasonic diagnosis of intussuscepted Meckel diverticulum. Pediatr Radiol 1991;21:148–149.
42. Patenaude Y, Jéquier S, Russo P. Pediatric case of the day. Duplication cyst of distal ileum. Radiographics 1993;13: 218–220.
43. Kenney IJ. Ultrasound in intussusception: a false cystic lead point. Pediatr Radiol 1990;20:348.
44. Swischuk LE, Stansberry SD. Ultrasonographic detection of free peritoneal fluid in uncomplicated intussusception. Pediatr Radiol 1991;21:350–351.
45. Papadopoulou F, Efremidis S C, Raptopoulou A, et al. Distal ileocolic intussusception: another cause of inversion of superior mesenteric vessels in infants. AJR Am J Roentgenol 1996;167:1243–1246.
46. Peh WCG, Khong KL, Lam C, et al. Reduction of intussusception in children using sonographic guidance. AJR Am J Roentgenol 1999;173:985–988.
47. Yoon CH, Kim HJ, Goo HW. Intussusception in children: US-guided pneumatic reduction-initial experience. Radiology 2001;218: 85–88.
48. Kong MS, Wong HF, Lin SL, et al. Factors related to detection of blood flow by color Doppler ultrasonography in intussusception. J Ultrasound Med 1997;16:141–144.
49. Lim HK, Bae SH, Lee KH, et al. Assessment of reducibility of ileocolic intussusception in children: usefulness of color Doppler sonography. Radiology 1994;191:781–785.
50. del-Pozo G, González-Spinola J, Gómez-Ansón B, et al. Intussusception: trapped peritoneal fluid detected with US – relationship to reducibility and ischemia. Radiology 1996;201: 379–383.
51. John. The value of ultrasound in children with suspected intussusception. Emerg Radiol 1998;5:297–305.
52. Koumanidou C, Vakaki M, Pitsoulakis G, et al. Sonographic detection of lymph nodes in the inutssusception of infants and young children. Clinical evaluation and hydrostatic reduction. AJR Am J Roentgenol 2002;178:445–450.
53. Kim JH. US features of transient small bowel intussusception in pediatric patients. Korean J Radiol 2004;5:178–184.
54. Quillin SP, Siegel MJ. Color Doppler US of children with acute lower abdominal pain. Radiographics 1993;13:1281–1293.
55. Quillin SP, Siegel MJ. Gastrointestinal inflammation in children: color Doppler ultrasonography. J Ultrasound Med 1994;13:751–756.
56. Alison M, Kheniche A, Axoulay R, et al. Ultrasonography of Crohn disease in children. Pediatr Radiol 2007;27:1071–1082.
57. Siegel MJ, Friedland JA, Hildebolt CF. Bowel wall thickening in children: differentiation with US. Radiology 1997;203:631–635
58. Puylaert JBCM, Lalisang RI, van der Werf SDJ, Doornbos L. Campylobacter ileocolitis mimicking acute appendicitis: differentiation with graded-compression US. Radiology 1988;166:737–740.
59. Matsumoto T, Iida M, Sakai T, et al. Yersinia terminal ileitis: sonographic findings in eight patients. AJR Am J Roentgenol 1991;156:965–967.
60. Couture A, Veyrac C, Baud C, et al. Evaluation of abdominal pain in Henoch-Schonlein syndrome by high frequency ultrasound. Pediatr Radiol 1992;22:12–17.
61. John SD SL, Hayden DK, Jr. Gastrointestinal sonographic findings in Henoch-Schonlein purpura. Emerg Radiol 1996;3:4–8.
62. Nichimi A, Khamis J, Paquoit I, et al. Significance of bowel wall abnormalities at ultrasound in Henoch-Schonlein purpura. Pediatr Gastroenterol Nutr 2008;46:48–53.
63. Hernanz-Schulman M, Genieser NB, Aubrosino U. Sonographic diagnosis of intramural duodenal hematoma. J Ultrasound Med 1989;8:273–276.

64. Orel SG, Nussbaum AR, Sheth S, et al. Duodenal hematoma in child abuse: sonographic detection. AJR Am J Roentgenol 1988;151: 147–149.
65. Barr LL, Hayden CK Jr, Stansberry SD, Swischuk LE. Enteric duplication cysts in children: are their ultrasonographic wall characteristics diagnostic? Pediatr Radiol 1990;20:326–328.
66. Georg C, Schwerk WB, Goerg K. Gastrointestinal lymphoma: sonographic findings in 54 patients. AJR Am J Roentgenol 1990;155:795–798.
67. Puylaert JB, van der Zant FM. Mesenteric lymphadenitis or appendicitis? AJR Am J Roentgenol 1995;165:490.
68. Sivit CJ, Newman KD, Chandra RS. Visualization of enlarged mesenteric lymph nodes at US examination: Clinical significance. Pediatr Radiol 1993;23:471–475.
69. Swischuk LE, John SD. Mesenteric adenitis – acute ileitis: a constellation of findings definable with ultrasound. Emerg Radiol 1998;5:210–218.
70. Siegel MJ. Acute appendicitis in childhood: the role of US. Radiology 1992;185:341–342.
71. Siegel MJ, Carel C, Surratt S. Ultrasonography of acute abdominal pain in children. JAMA 1991;266:1987–1989.
72. Sivit CJ, Siegel MJ, Applegate KE, et al. When appendicitis is suspected in children. Radiographics 2001;21:247–262.
73. Sivit CJ. Imaging the child with right lower quadrant pain and suspected appendicitis: current concepts. Pediatr Radiol 2004;34:447–453.
74. Axelrod DA, Sonnad SS, Hirschl RB. An economic evaluation of the sonographic examination of children with suspected appendicitis. J Pediatr Surg 2000;35:1236–1241.
75. Kaneko K, Tsudo M. Ultrasound-based decision making in the treatment of acute appendicitis in children. J Pediatr Surg 2004;39:1316–1320.
76. Sivit CJ, Applegate KE, Stallion A, et al. Imaging evaluation of suspected appendicitis in a pediatric population: effectiveness of sonography versus CT. AJR Am J Roentgenol 2000;175:977–980.
77. Puylaert JBCM. Acute appendicitis: US evaluation using graded compression. Radiology 1986;158:355–360.
78. Chesbrough RM, Burkhard TK, Balsara ZN, et al. Self-localization in US of appendicitis: an addition to graded compression. Radiology 1993;187:349–351.
79. Soda K, Nemoto K, Yoshizawa S, et al. Detection of pinpoint tenderness on the appendix under ultrasonography is useful to confirm acute appendicitis. Arch Surg 2002;136:1136–1140.
80. Sivit CJ. Diagnosis of acute appendicitis in children: spectrum of sonographic findings. AJR Am J Roentgenol 1993;161:147–152.
81. Lim HK, Lee WJ, Kim TH, et al. Appendicitis: usefulness of color Doppler US. Radiology 1996;200:221–225.
82. Quillin SP, Siegel MJ. Appendicitis in children: color doppler sonography. Radiology 1992;184:745–747.
83. Quillin SP, Siegel MJ. Appendicitis: efficacy of color Doppler sonography. Radiology 1994;191:557–560.
84. Rettenbacher T, Hollerweger A, Macheiner P, et al. Presence of absence of gas in the appendix: additional criteria to rule out or confirm acute appendicitis – evaluation with US. Radiology 2000;214:183–187.
85. Quillin SP, Siegel MJ, Coffin CM. Acute appendicitis in children: value of sonography in detecting perforation. AJR Am J Roentgenol 1992;159:1265–1268.
86. Quillin SP, Siegel MJ. Diagnosis of appendiceal abscess in children with acute appendicitis: value of color Doppler sonography. AJR Am J Roentgenol 1995;164:1251–1254
87. Applegate KE, Sivit CJ, Salvator AE, et al. Effect of cross-sectional imaging on negative appendectomy and perforation rates in children. Radiology 2001;220:103–107.
88. Lim HK, Lee WJ, Lee SJ, et al. Focal appendicitis confined to the tip: diagnosis at US. Radiology 1996;200:799–801.
89. Donaldson JS, Black CT, Reynolds M, et al. Ultrasound of the distal pouch in infants with imperforate anus. J Pediatr Surg 1989;24:465–468.
90. Downey DB, Wilson SR. Pseudomembranous colitis: sonographic features. Radiology 1991;180:61–64.
91. McMorrow Tuohy AM, O'Gorman M, Byington C, et al. Yersinia enterocolitis mimicking Crohn's disease in a toddler. Pediatrics 1999;104:e36.
92. Ros PR, Buetow PC, Pantograg-Brown L, et al. Pseudomembranous colitis. Radiology 1996;198:1–9.
93. Ueda D, Sato T, Yoshida M. Ultrasonographic assessment of Salmonella enterocolitis in children. Pediatr Radiol 1999;29:469–471.
94. Friedland JA, Herman TE, Siegel MJ. *Escherichia coli* 0157:H7-associated hemolytic–uremic syndrome: value of colonic color Doppler sonography. Pediatr Radiol 1995;25: 865–867.
95. Goske MJ, Goldblum JR, Applegate KE, et al. The "circle sign": a new sonographic sign of pneumatosis intestinalis – clinical, pathologic and experimental findings. Pediatr Radiol 1999;29:530–535.
96. Miller SF, Seibert JJ, Kinder DL, Wilson AR. Use of ultrasound in the detection of occult bowel perforation in neonates. J Ultrasound Med 1993;12:531–535.
97. Patel U, Leonidas JC, Furie D. Sonographic detection of necrotizing enterocolitis in infancy. J Ultrasound Med 1990;9:673–675.
98. Deeg KH, Rupprecht T, Schmid E. Doppler sonographic detection of increased flow velocities in the celiac trunk and superior mesenteric artery in infants with necrotizing enterocolitis. Pediatr Radiol 1993;23:578–582.
99. Grattan-Smith JD, Blews DE, Brand T. Omental infarction in pediatric patients: sonographic and CT findings. AJR Am J Roentgenol 2002;178:1537–1539.
100. Schlesinger AE, Dorfman SR, Braverman RM. Sonographic appearance of omental infarction in children. Pediatr Radiol 1999;29:598–601.
101. Konen O, Tahaus V, Dlugh E, et al. Childhood abdominal cystic lymphangioma. Pediatr Radiol 2002;32:88–94.
102. Levy AD, Cantisani V, Miettinen M. Abdominal lymphangiomas: imaging features with pathologic correlation. AJR Am J Roentgenol 2004;182:1485–1491.
103. Stoupis C, Ros PR, Abbitt PL, et al. Bubbles in the belly: imaging of cystic mesenteric or omental masses. Radiographics 1994;14:729–737.
104. Wootton-Gorges SL, Thomas KB, Harned RK, et al. Giant cystic abdominal masses in children. Pediatr Radiol 2005;35:1277–1288.
105. Chateil J-F, Saragne-Feuga C, Perel Y, et al. Capillary haemangioma of the greater omentum in a 5-month-old female infant: a case report. Pediatr Radiol 2000;30:837–839.
106. Chung CJ, Bui V, Fordham LA, et al. Malignant intraperitoneal neoplasms of childhood. Pediatr Radiol 1998;28:317–321

CHAPTER

71

The paediatric renal tract and adrenal gland

Gurdeep S. Mann

PAEDIATRIC RENAL TRACT

Ultrasound is the imaging modality of choice in the initial evaluation and follow-up of the neonatal and paediatric urinary tract and is often critical in informing the subsequent clinical management of children presenting with suspected urinary tract pathology. Ultrasound provides invaluable real-time anatomical information. A contemporary renal tract ultrasound is an extremely useful adjunct in interpreting functional urinary tract imaging studies such as scintigraphy or voiding cystourography (VCUG).

This chapter focuses on the paediatric aspects of renal disease as applied to ultrasound imaging practice. The aim of this chapter is not only to concentrate upon pathology exclusive to children but also to describe the unique paediatric features of conditions common to both adults and children.

Renal tract embryology

Kidneys and ureters

The kidneys progress through three distinct phases of development in utero: the pronephros, mesonephros and metanephros (Fig. 71.1A). Each is mesodermal in origin and arises from the nephrogenic cord.

The pronephros (fetal forekidney) is non-functioning, and develops from paired cervical intermediate mesoderm around the third week of gestation. The pronephros rapidly involutes and is replaced by the mesonephros, which forms immediately caudal to the pronephros.

The mesonephros (mid kidney) develops around the fourth week in the thoracic region. These are transient excretory organs in fetal life and function as interim kidneys until the permanent kidneys develop.[1] Each consists of glomerular tubules which drain into the mesonephric ducts. These regress at around 8 fetal weeks.

The metanephros (permanent kidney) develops around the fifth week from two sources: the metanephric diverticulum (ureteric bud) and the metanephric blastema. The ureteric bud arises from the mesonephric duct close to its insertion into the cloaca and grows toward the nephrogenic cord giving rise to the ipsilateral ureter, pelvicalyceal system and collecting tubules. The latter undergo successive branching and induce clusters of mesenchymal cells in the metanephric blastema to form nephrons (Fig. 71.1B–E). By the third month of gestation the nephrons are analogous to those of an adult. The permanent kidneys are formed by the fusion of multiple renal lobes (renunculi), each composed of a medullary pyramid and overlying cortex. The fully formed definitive fetal kidney shows a normal lobulated appearance.

The permanent kidneys initially lie within the pelvis. With abdominal growth the kidneys begin to move apart and ascend until they eventually assume their normal retroperitoneal locations within each renal fossa (Fig. 71.2). When the kidney reaches the adrenal gland its cranial ascent ceases.

Urinary bladder and urethra

The lower urinary tract arises from the cloaca, which drains the mesonephric ducts and distal embryonic ureters. The urorectal septum divides the cloaca into dorsal anorectal canal and ventral urogenital sinus at around 4–6 weeks gestation (Fig. 71.3). The bladder arises from the upper urogenital sinus. The cranial portion is continuous with the allantois and forms most of the bladder. The allantois regresses to form the urachus, a thick fibrous cord that extends from the umbilicus to the roof of the bladder. The caudal portion descends toward the genital tubercle and contributes to the

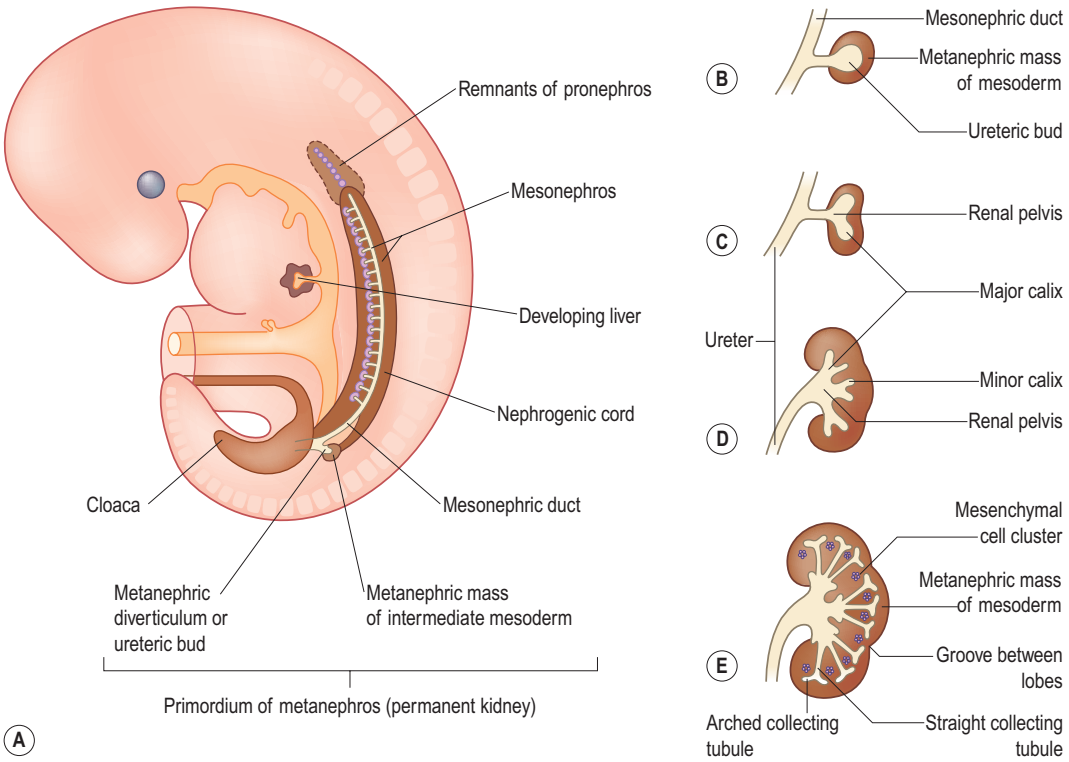

Figure 71.1 Normal development of the permanent kidney (metanephros) (reproduced with permission from Moore KL, Persaud TVN. The Developing Human. Clinically Oriented Embryology, 6th Edition. Philadelphia. WB Saunders. 1998). **A:** Lateral view of a 5-week embryo showing the development of the metanephric primordium. **B–E:** Longitudinal section through the metanephros of an embryo between 5 and 8 weeks showing the development of the metanephric diverticulum (ureteric bud), collecting tubules, calyces, renal pelvis and ureter.

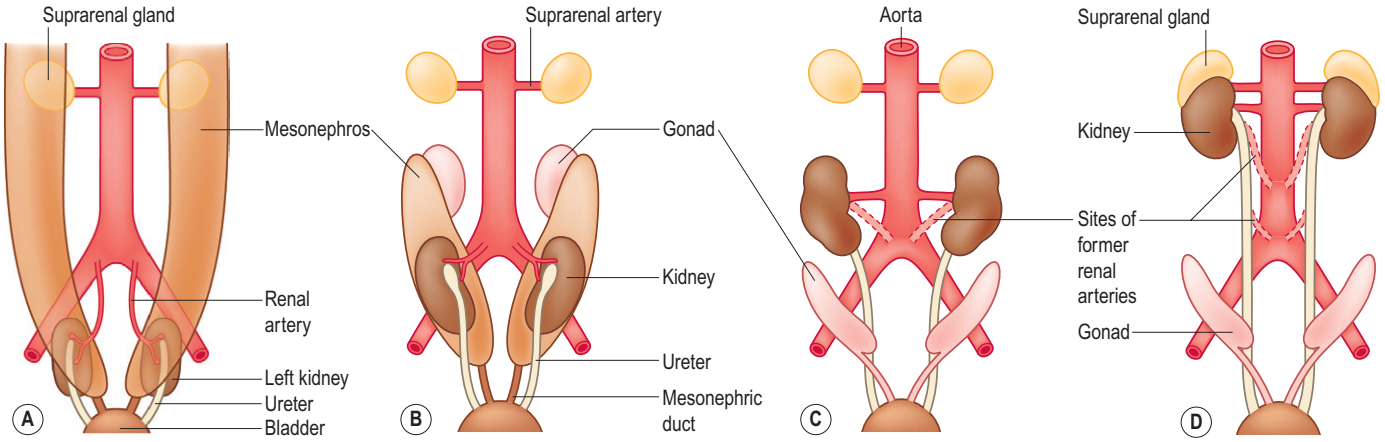

Figure 71.2 Normal development, rotation and migration of the kidneys from the pelvis to the abdomen (reproduced with permission from Moore KL, Persaud TVN. The Developing Human. Clinically Oriented Embryology, 6th Edition. Philadelphia. WB Saunders. 1998). Line diagrams showing ventral views of the fetal abdomen and pelvis between 6 and 9 weeks. **A, B:** There is regression of the mesonephros. **C, D:** Each kidney ascends and undergoes rotation such that its hilum is normally directed anteromedially. Note that the renal blood supply arises from progressively higher levels as the kidney ascends.

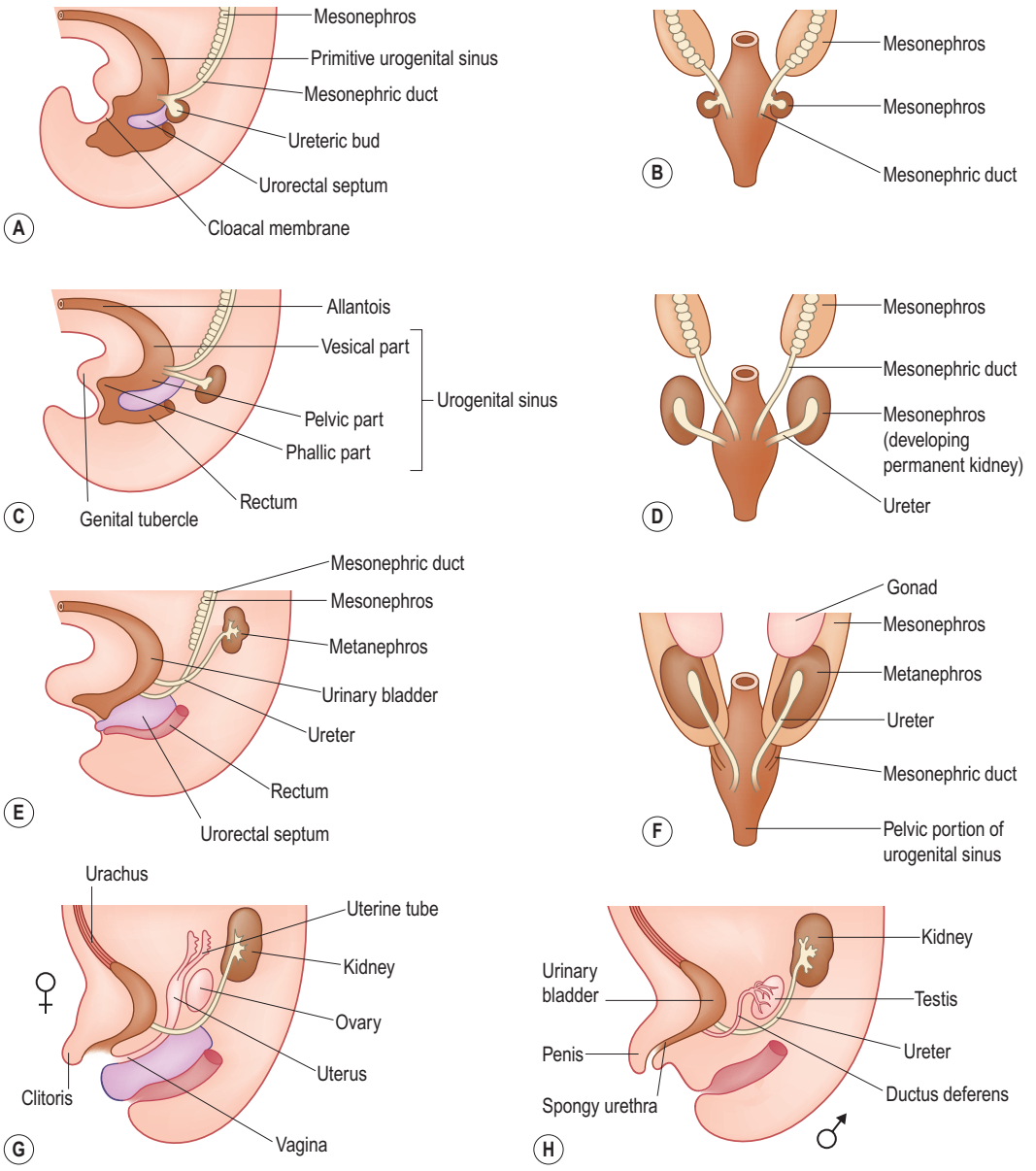

Figure 71.3 Cloacal subdivision into the urogenital sinus and rectum; development of the urinary bladder, urethra and urachus (reproduced with permission from Moore KL, Persaud TVN. The Developing Human. Clinically Oriented Embryology, 6th Edition. Philadelphia. WB Saunders. 1998). **A:** Lateral views of fetal lower abdomen and pelvis at 5 weeks. **B, D, F:** Dorsal views. **C, E:** Lateral views. **G, H:** Lateral views at 12 weeks.

bladder neck, entire female urethra and in males the prostatic urethra and ejaculatory ducts. The distal ureters and mesonephric duct separate at this time. The bladder trigone is formed from the mesonephric ducts. The distal ureters move superolaterally and obliquely insert through the bladder base.

The epithelium of the urethra develops from the endoderm of the urogenital sinus. In the male the distal urethra is also formed by superficial ectoderm.

Renal tract ultrasound technique

Examinations should be performed with the child well hydrated and with a full urinary bladder. The bladder should be assessed first and if sufficiently distended then the pelvic component of the examination should be undertaken. Oral clear fluids or intravenous fluids in patients nil by mouth can be given if the bladder is poorly distended. In the newborn the urinary bladder will often empty quickly and a further feed can be given if required.

Assessment of the upper renal tracts with a full urinary bladder may overestimate trivial upper renal tract dilatation. Post-micturition views may very occasionally underestimate significant upper tract dilatation. In practical terms a quick assessment of the upper tracts should be made with a full bladder and a more detailed assessment post voiding. An over-distended bladder also increases the likelihood of non-compliance during the study.

Neonates should ideally be assessed with a small footprint curvilinear broadband probe (7–9 MHz). Small children should be scanned using a larger footprint curvilinear probe (4–7 MHz) and larger children with a 3–5 MHz curvilinear probe. If an abnormality is detected then imaging with a linear high-resolution probe should always be considered. Optimised colour flow and pulsed Doppler wave imaging can demonstrate vascular structures, enable differentiation between cyst and solid and delineate regional blood flow.

Kidneys

Greyscale imaging

Each kidney should be assessed carefully across its entire long and short axis. Evaluation of the kidney should include an assessment of:

- renal position and outline
- cortical echogenicity relative to adjacent liver or spleen
- corticomedullary differentiation and medullary echogenicity
- cortical depth – looking for scarring
- focal lesion – stone, mass or cyst (noting dimensions, position and echotexture)
- renal pelvic diameter anteroposterior (AP)
- presence of calyceal distension and/or proximal hydroureter
- measurement of size – bipolar lengths and depending on local practice volumes
- renal bed.

A combination of the supine, lateral decubitus, posterior oblique and prone positions may be required to scan each kidney. Each examination should be tailored to the individual patient. Children with significant scoliosis often present a considerable challenge to obtain satisfactory views. The prone position is recommended in order to obtain a non-magnified maximal bipolar renal length.

Longitudinal views should be used to assess:

- renal cortical echogenicity compared to adjacent liver or spleen (Fig. 71.4A)
- relative size of the kidney versus the liver or spleen (Fig. 71.4B, C).
- renal length (Fig. 71.4D), prone length (Fig. 71.4E)
- cortical depth (Fig. 71.4E).

Transverse views should also be used to:

- assess the entire short axis of the kidney from upper pole through the renal pelvis and to the lower pole (Fig. 71.5)
- document renal AP pelvic diameter.

Renal AP pelvic diameter is assessed in transverse plane and the maximal measurement is obtained (Fig. 71.5C). Colour Doppler is helpful in differentiating between normal hilar vessels and the hypoechoic renal pelvis

Doppler imaging

Doppler evaluation should form part of the routine examination of the kidneys. The success of scanning does depend greatly upon patient cooperation and may not be practicable in all children. Colour Doppler is particularly useful in delineating regional perfusion (Fig. 71.6A), vessel patency (Fig. 71.6B) and in assessing renal vascular resistance using estimates of the resistive index (RI) (Fig. 71.6C). A renal vessel of sufficient length should be interrogated in order to obtain a good quality trace. The intrarenal arteries are more readily sampled and are a useful surrogate in those children where good quality traces of the main renal artery are not possible. Each kidney should be assessed using the same optimised parameters.

Ureters

Distal ureteric dilatation can be assessed in the transverse plane (Fig. 71.7A) and along the ureteral long axis in the oblique parasagittal plane (Fig. 71.7B) by using the urinary bladder as an acoustic window. Ureteric dilatation during voiding or which persists following complete emptying of the bladder is likely to be pathological. The dilated ureter may be traced proximally to the renal pelvis and in severe cases be massively distended (Fig. 71.7B) and easily confused with bowel loops. The ureters should not usually exceed 5 mm in calibre in normal individuals.[2] Urothelial thickening should be assessed from the ureterovesical junction to the ureteropelvic junction.

Urinary bladder, prostate gland and seminal vesicles

The urinary bladder is assessed by carefully sweeping the probe in transverse and longitudinal planes perpendicular to the anterior abdominal wall. By avoiding the temptation to simply sweep through the bladder by angulating the probe at a fixed point, it is unlikely that a focal lesion in the bladder wall will be missed. The suprapubic region is also better assessed by this method looking for urachal abnormalities.

Pre-micturition and post-micturition residual volumes should be measured (Fig. 71.8). Bladder wall thickness in the distended state is measured and should be less than 3 mm (Fig. 71.9).[3] Measurement should be made away from the trigone, which is the thickest portion of the bladder.

In the older male child the prostate gland and seminal vesicles are usually identifiable on ultrasound and are best appreciated in the transverse plane deep to an adequately distended urinary bladder (Fig. 71.10). The male urethra may be evaluated using a transperineal window or by scanning along the shaft of the penis.

Normal imaging anatomy and appearances

Both kidneys are bean-shaped retroperitoneal organs lying at around the T12 to L3 regions. The left kidney is usually a little more cranial in position relative to the right. Both lower poles are normally more laterally placed.

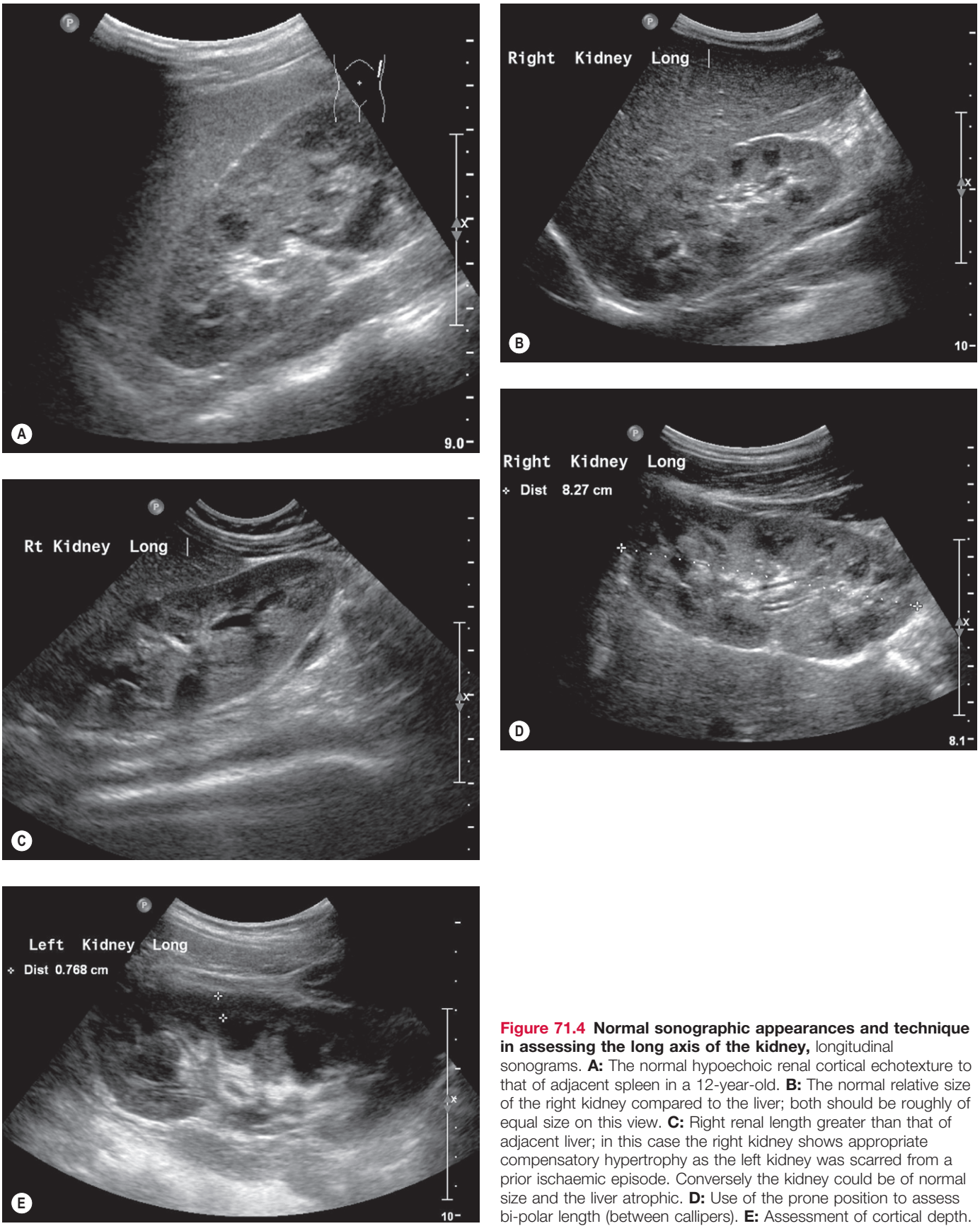

Figure 71.4 Normal sonographic appearances and technique in assessing the long axis of the kidney, longitudinal sonograms. **A:** The normal hypoechoic renal cortical echotexture to that of adjacent spleen in a 12-year-old. **B:** The normal relative size of the right kidney compared to the liver; both should be roughly of equal size on this view. **C:** Right renal length greater than that of adjacent liver; in this case the right kidney shows appropriate compensatory hypertrophy as the left kidney was scarred from a prior ischaemic episode. Conversely the kidney could be of normal size and the liver atrophic. **D:** Use of the prone position to assess bi-polar length (between callipers). **E:** Assessment of cortical depth.

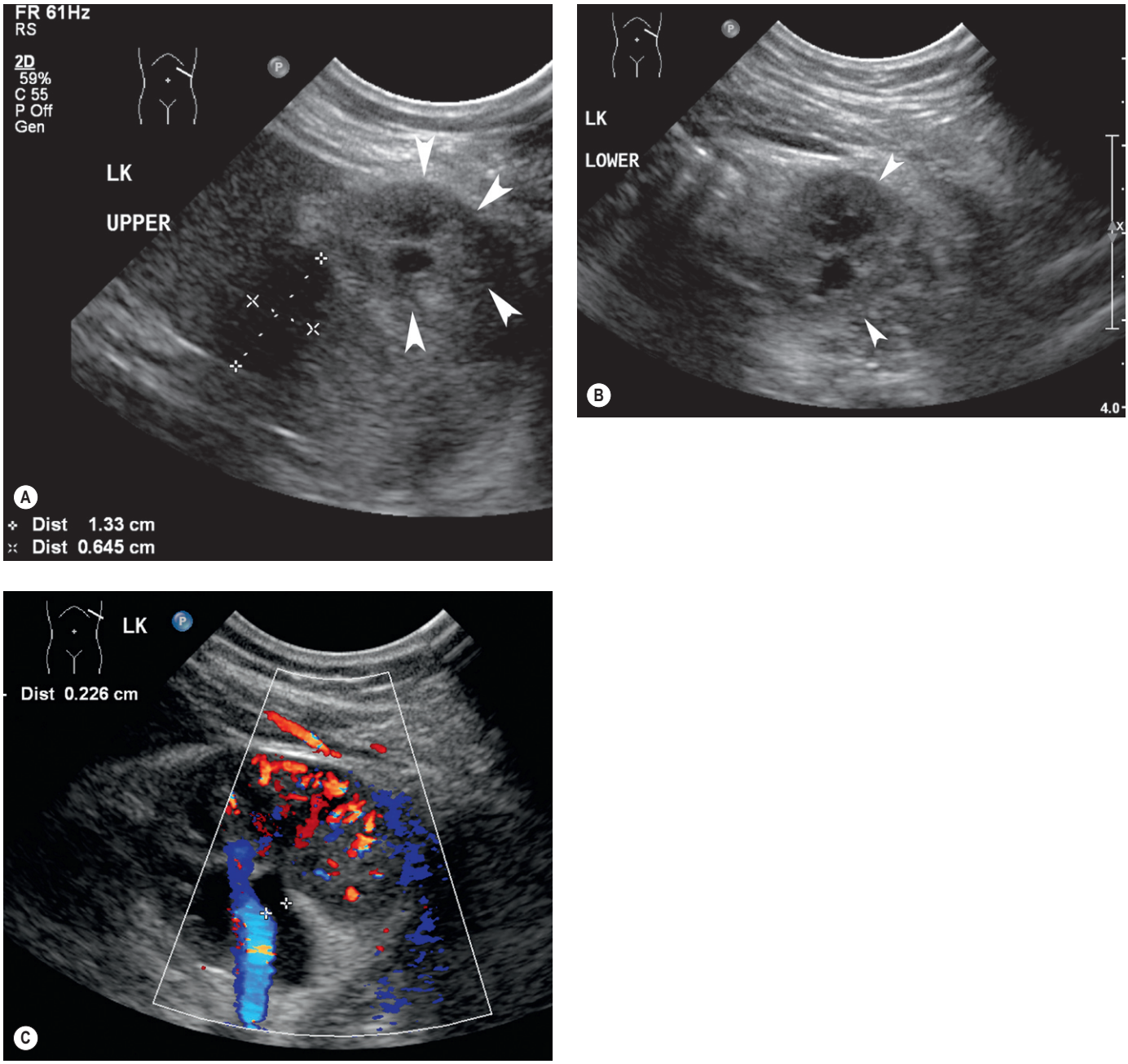

Figure 71.5 Normal sonographic appearances and technique in assessing the short axis of the kidney. A: Transverse sonogram showing a normal upper renal pole (arrowheads) adjacent to a complex cyst in the adrenal gland following adrenal haemorrhage. The cyst resolved on follow-up ultrasound. **B:** Normal lower renal pole. **C:** Colour Doppler image showing the utility of Doppler in demonstrating a normal hypoechoic renal pelvis.

Normal sonographic appearances of the kidneys

The kidneys of the newborn differ in several ways from those of the older child and adult.

At birth the renal cortex normally appears relatively bright, and is either isoechoic or slightly hyperechoic to the normal liver and spleen (Fig. 71.11). This is accounted for by increased cortical cellularity and the relatively high proportion of cortical glomeruli at this age. Renal cortical echogenicity is similar to that of an adult in most children by around 4–6 months of age and in almost all children by 12 months.

Unique sonographic features of the neonatal kidney compared to the older child

- Cortical echogenicity is increased and isoechoic or slightly hyperechoic to liver and spleen.
- Medullary pyramids are prominent and hypoechoic.
- Absent echogenic renal sinus.

The renal medullae in newborns are relatively prominent, well-defined hypoechoic structures (Fig. 71.11). Care should be taken not to misinterpret these as cysts. Medullary echogenicity and size relative to the cortex normalises by 12 months of age.

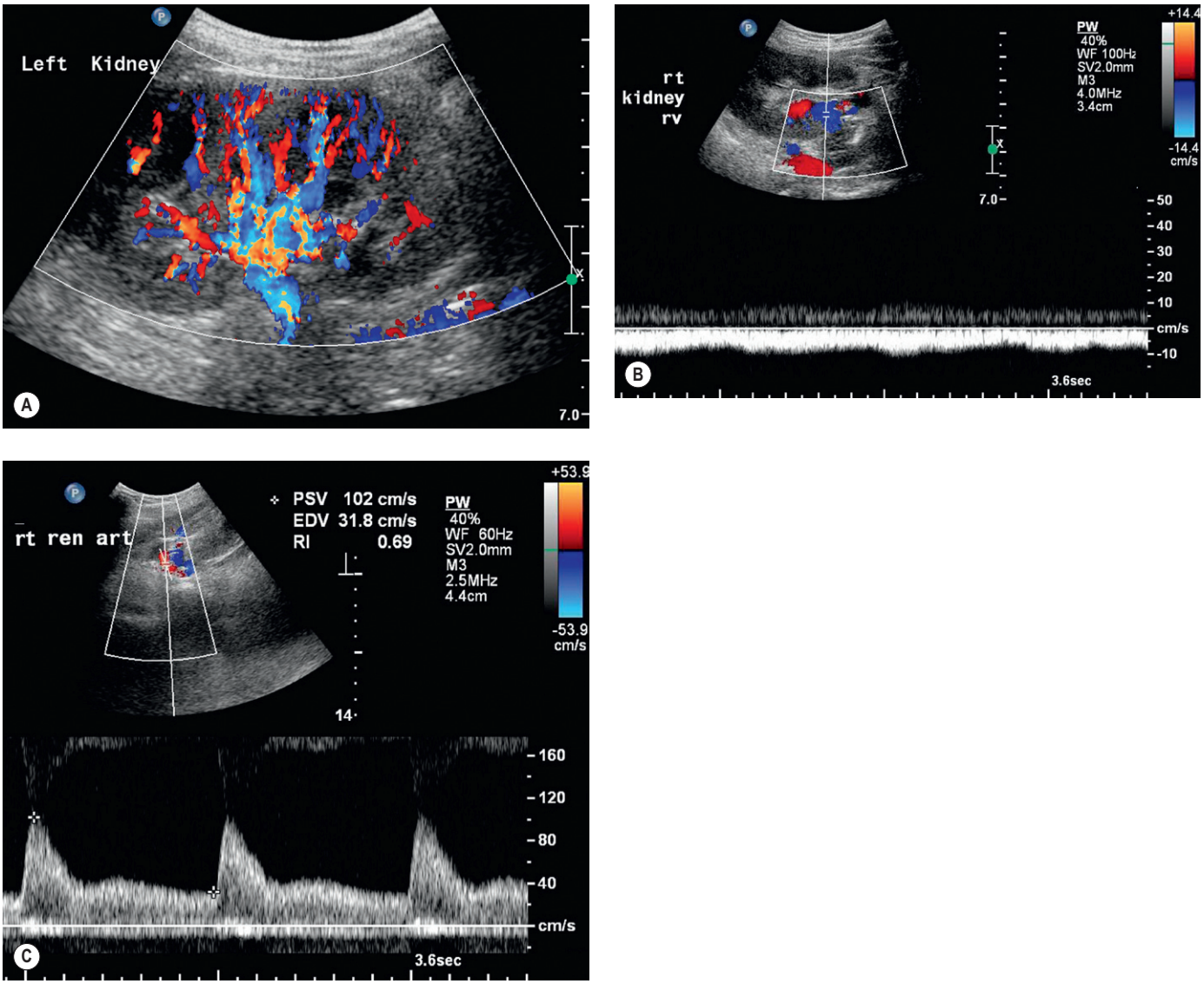

Figure 71.6 Doppler sonography. A: Normal renal colour flow pattern and relationship of the renal vessels to the collecting system, pyramids and cortex. **B:** Normal Doppler waveform in a patent native renal vein showing phasicity with gentle respiration. **C:** Assessment of resistive index (RI) in a normal native main renal artery.

Neonates also typically lack hyperechoic renal sinus fat. Most children will show a normal hyperechoic renal sinus by the time they reach teenage years.

Fetal lobulation may affect either of the kidneys although it is more pronounced on the left and results from incomplete fusion of the fetal renal lobes. This is normal at birth and is characterised by sharp cortical indentations along the outer border of the kidney that occur between the underlying calyces (Fig. 71.12). Fetal lobulation disappears in most children by 5 years of age but can persist in a very small number and should be considered a normal variant.

A number of other variations in normal ultrasound appearance are common in childhood and are summarised in Table 71.1. The spleen often causes an impression upon the upper pole of left kidney and this is frequently seen on ultrasound and nuclear medicine studies. Normally a single renal pyramid has a single medulla which opens into a single 'simple calyx'. A compound calyx results from a developmental anomaly in which two or more medullae are fused and open into a single compound calyx. This is normally located at the polar regions of the kidney, which can be prone to intrarenal reflux of urine and in the case of urinary tract infection may explain the vulnerability of the polar regions to scarring.

An extrarenal pelvis is a normal anatomical configuration which should not be confused with hydronephrosis. In extrarenal pelvis there is no calyceal dilatation and the transverse AP renal pelvic diameter does not exceed 10 mm (Fig. 71.13). In hydronephrosis the AP renal pelvic diameter (APRPD) exceeds 10 mm and there is accompanying calyceal dilatation. The degree of hydronephrosis is moderate when the APRPD is between 10.1 and 14.9 mm, and severe if the APRPD exceeds 15 mm.

Normal sonographic values

Renal length and volume varies with body mass and age.

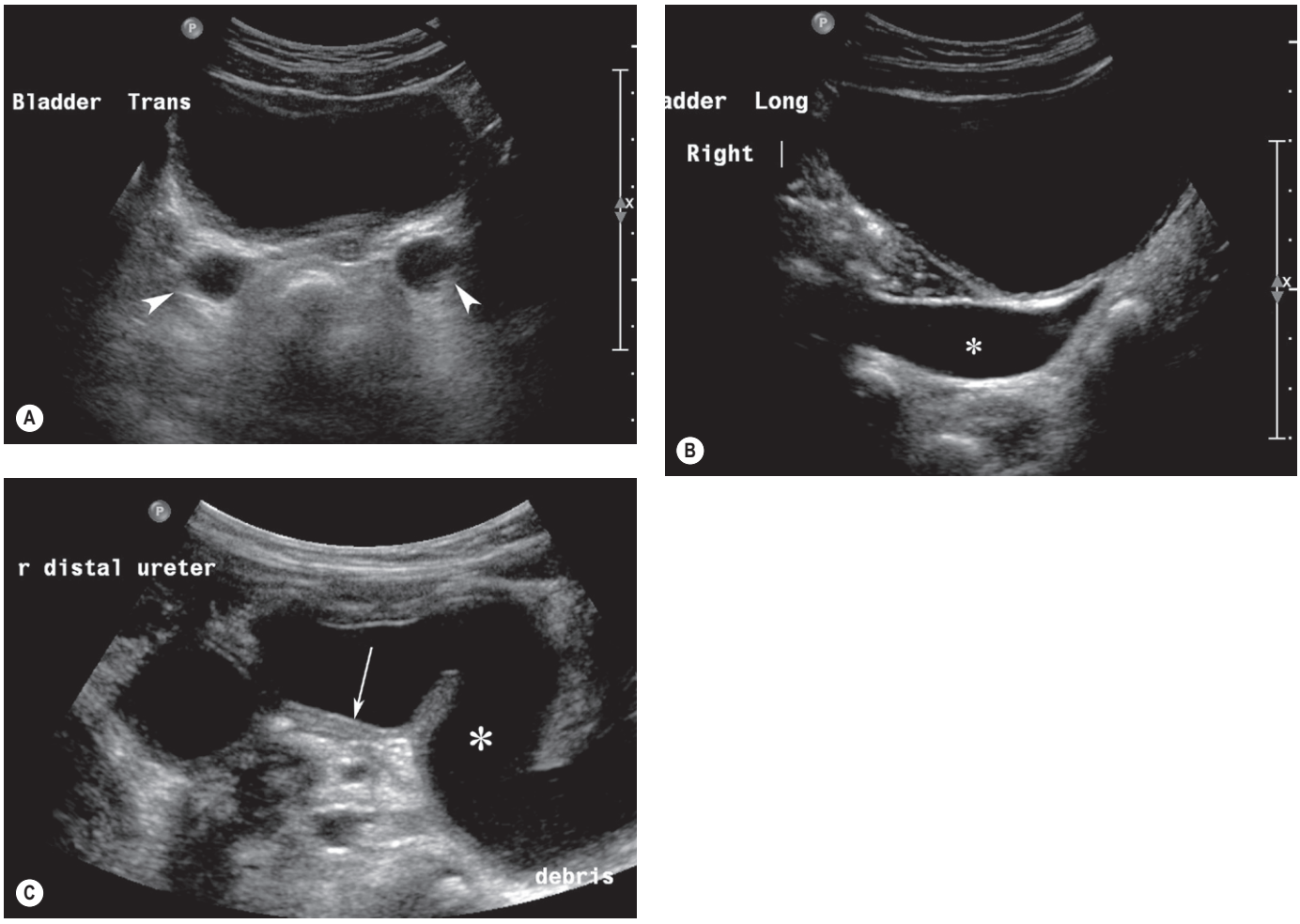

Figure 71.7 **Ureteric assessment. A:** Transverse sonogram in a newborn female with bilateral distended distal ureters (arrowheads) behind the urinary bladder. **B:** Oblique sonogram in the same patient showing distal ureteric dilatation (*) to the vesico-ureteric junction. **C:** Longitudinal sonogram in a newborn male with vesico-ureteric reflus showing a dilated ureter (*) with urothelial thickening (arrow) and some dependent debris. The ureter could be traced from the pelvis to the kidney.

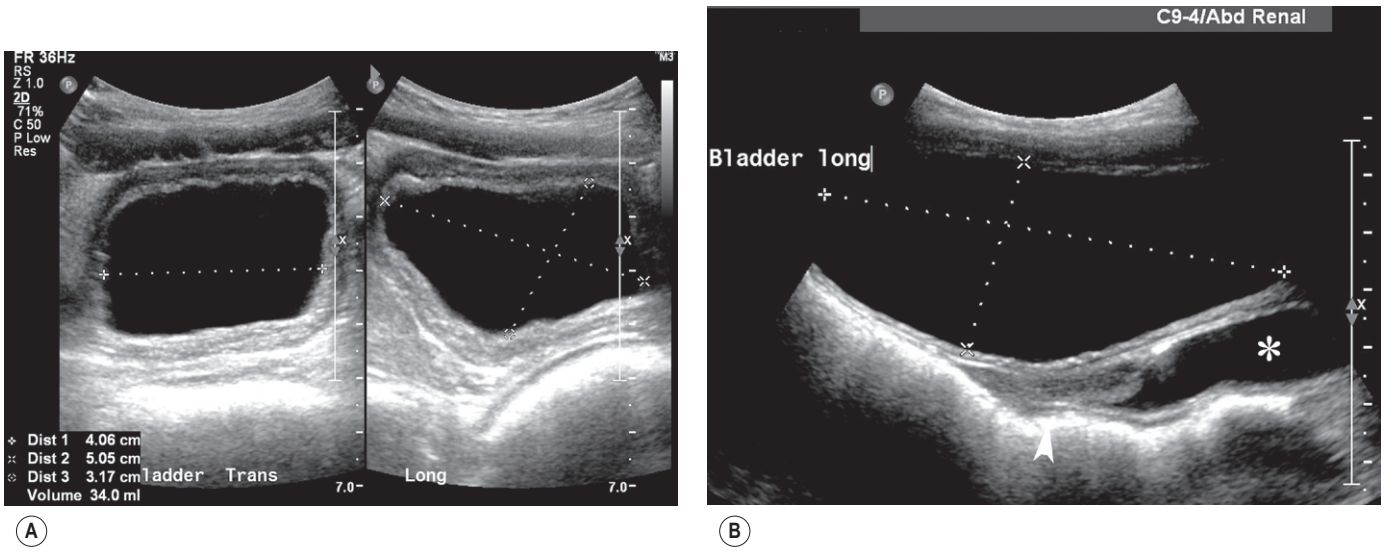

Figure 71.8 **Bladder volume assessment. A:** Dual screen sonogram showing post-micturition volume calculation. **B:** Longitudinal sonogram in a neonate showing an incidental finding of reflux of urine into the vagina during micturition. Arrowhead indicates uterus. *, Anechoic urine refluxed into the vagina.

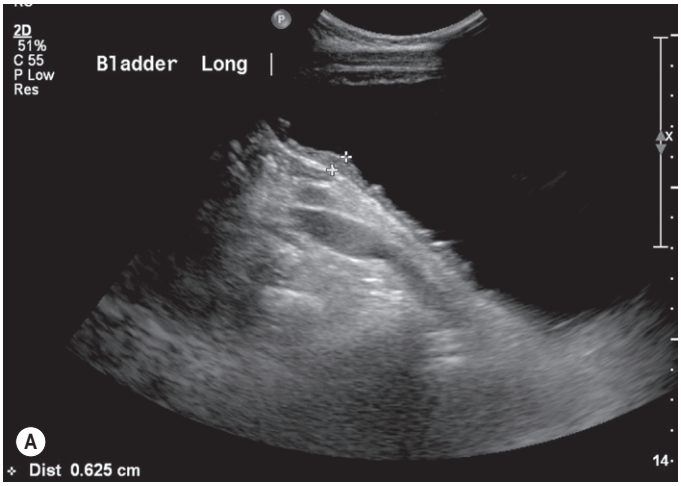

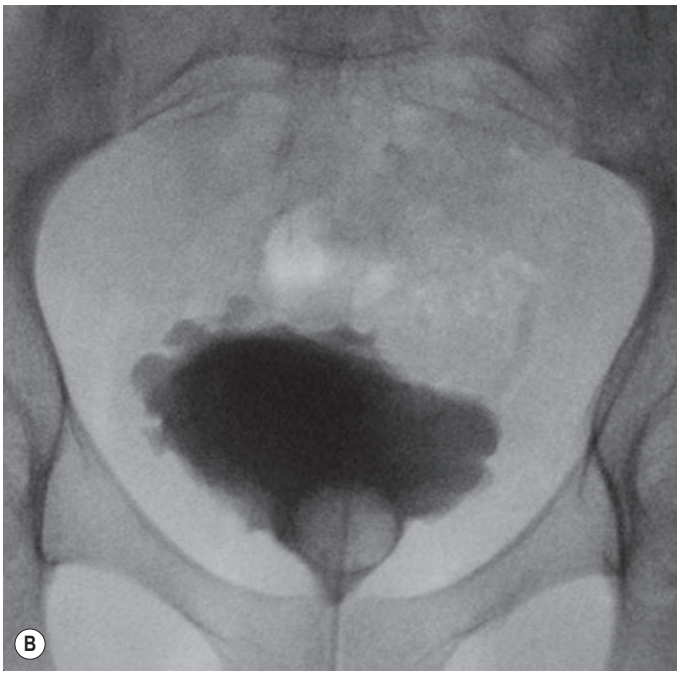

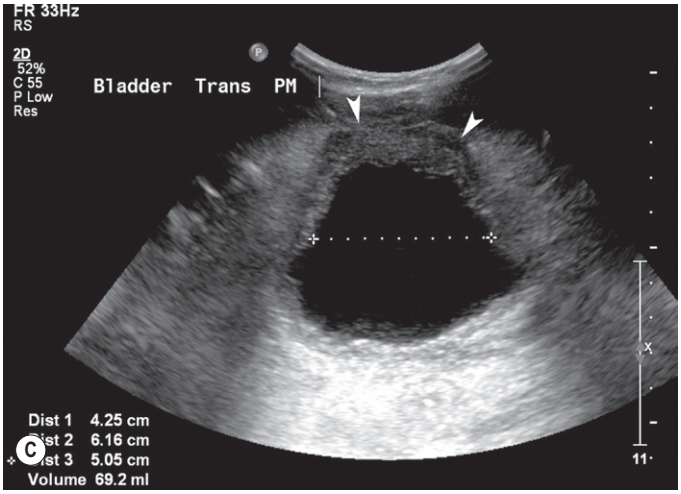

Figure 71.9 Bladder wall thickness. A: Longitudinal sonogram showing a thick-walled urinary bladder (between callipers) in a boy with **(B)** a markedly trabeculated urinary bladder on VCUG. **C:** Transverse post-micturition sonogram in the same child showing impressive focal wall bladder wall thickening (arrowheads). Measurements should be taken from the mucosa to the serosa.

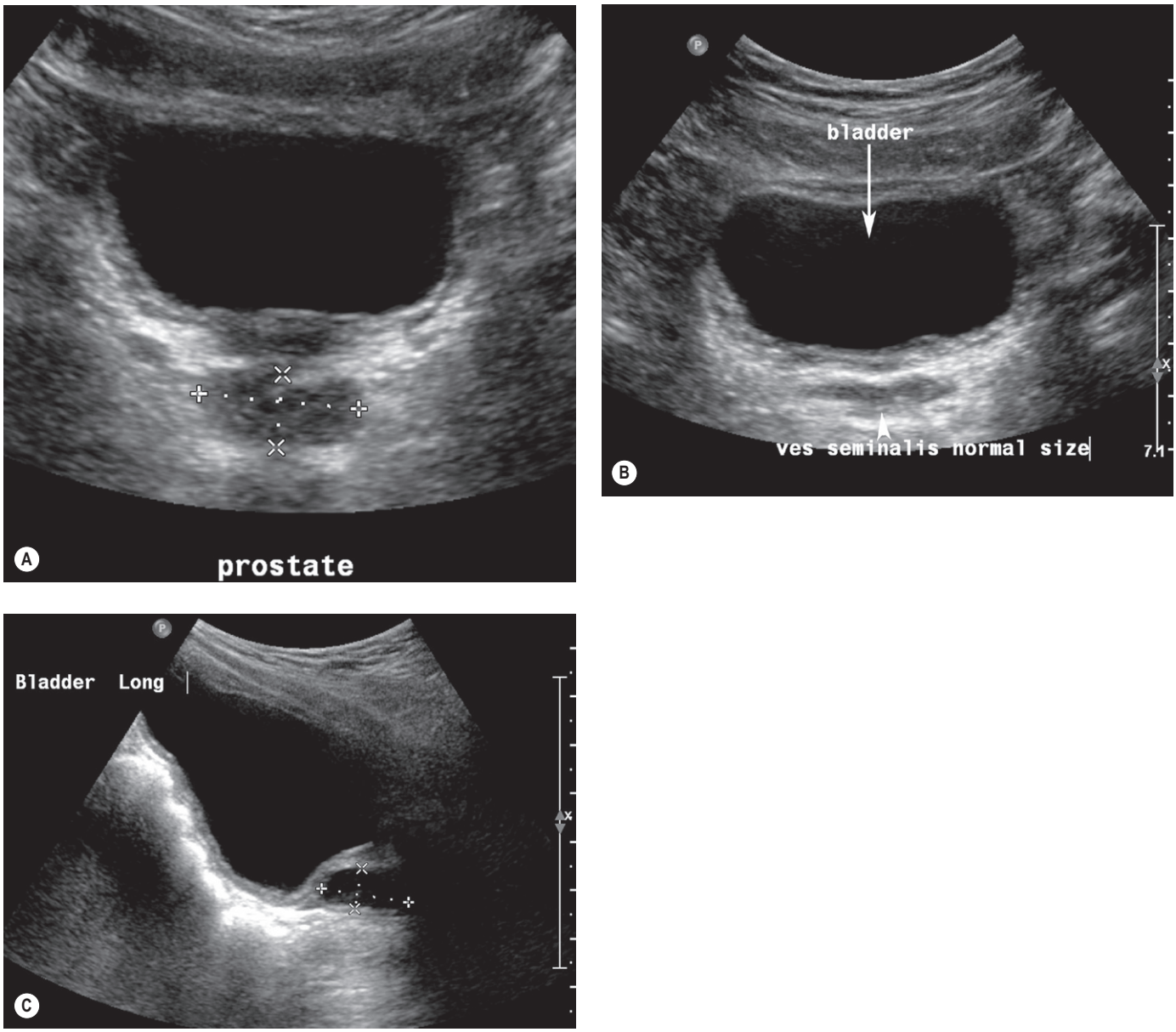

Figure 71.10 The prostate gland and seminal vesicles. Transverse sonograms showing **(A)** the normal prostate gland and **(B)** typical 'bow tie' arrangement of the seminal vesicles. **C:** Longitudinal sonogram showing a contained cyst (between callipers) deep to the base of the urinary bladder in the expected position of the prostate gland in keeping with a prostatic utricle.

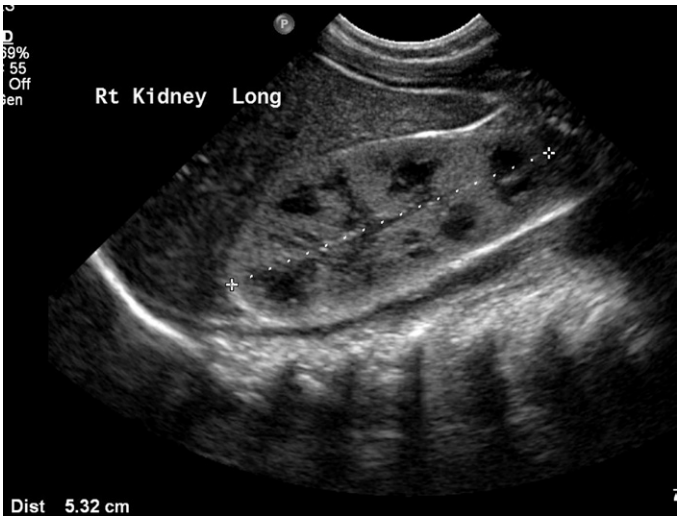

Figure 71.11 The normal neonatal kidney. Longitudinal sonogram of the right kidney in a healthy neonate. The renal medullae are relatively prominent hypoechoic structures. The normal neonatal renal cortex is isoechoic or very slightly hyperechoic to adjacent liver. The cortex is relatively thinner and there is a distinct lack of hyperechoic renal sinus fat seen normally in older children.

Table 71.1 Normal sonographic variants (data from Paspulati and Bhatt[4])

Normal variant/ Pseudolesion	Sonographic finding
Persisting fetal lobulation	Refers to persistence of normal fetal development with pronounced notching of the external surface of the cortex midway between adjacent calyces cf. renal scarring, which occurs directly over a calyx (Fig. 71.12)
Hypertrophied column of Bertin	Represents unresorbed polar junctional parenchyma from one or more of fetal subkidneys (renunculi) that fuse to form the normal kidney (Fig. 71.14)
Junctional parenchymal defect	Thin echogenic triangular notch resulting from lack of fusion of the fetal subkidneys; more common on the right kidney. Anterosuperior or posteroinferior in location
Interrenicular septum	Echogenic line connecting a junctional parenchymal defect to the renal hilum (Fig. 71.15)
Dromedary hump	Represents an additional mass of normal tissue found at the lateral portion of the left kidney
Compound calyx	Fused renal papillae which drain into fused calyces Commonly found at the poles (usually the upper pole) Thought to increase the risk of internal reflux and scarring

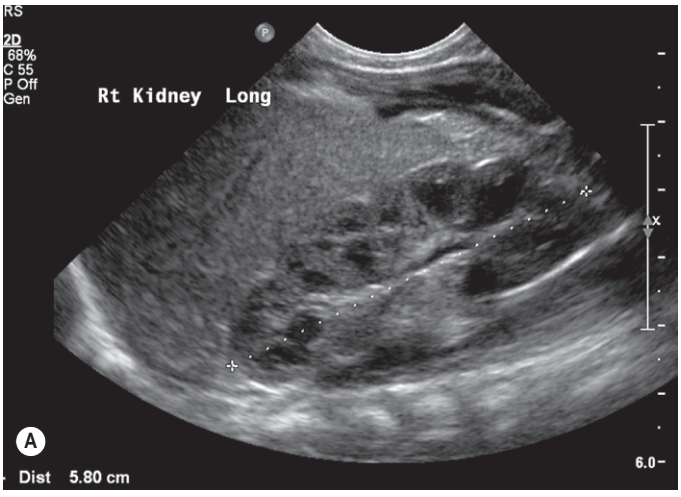

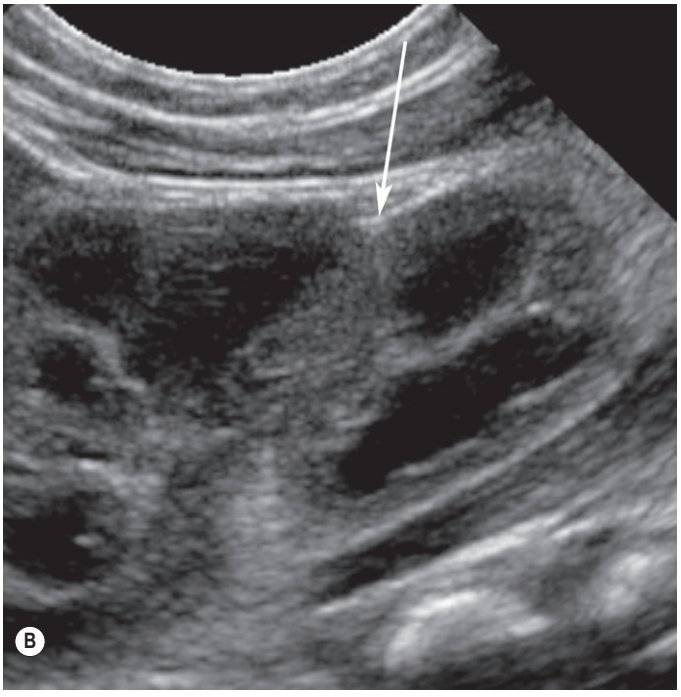

Figure 71.12 Fetal lobulation. A: Longitudinal sonogram of the right kidney in a 1-month-old infant showing the typical pattern of fetal lobulation. **B:** Magnified image showing a sharp indentation in the outer cortical border (arrow) between the renal pyramids; this may be differentiated from renal scarring where the affected area is seen as a broad-based cortical defect or zone of parenchymal thinning overlying a renal pyramid.

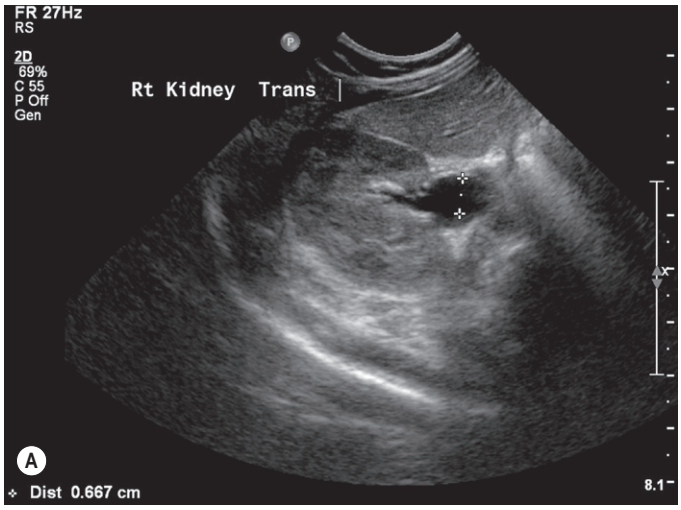

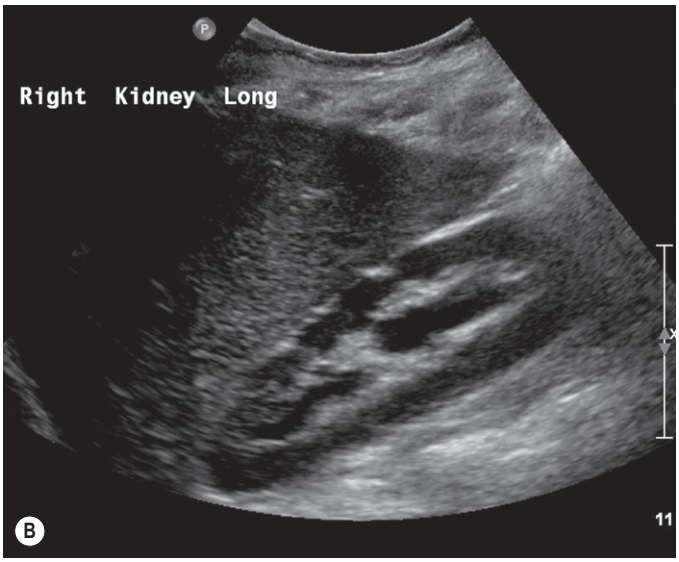

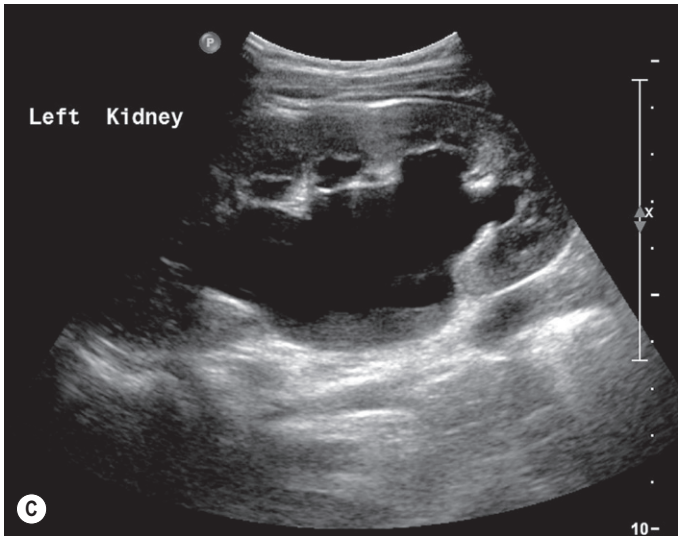

Figure 71.13 Extrarenal pelvis and terminology in upper renal tract dilatation. A: Transverse sonogram showing a prominent extrarenal pelvis or 'isolated pelviectasis'. **B:** Longitudinal sonogram showing a mild calyceal distension only or 'isolated caliectasis'. **C:** Longitudinal sonogram showing pelvicaliectasis.

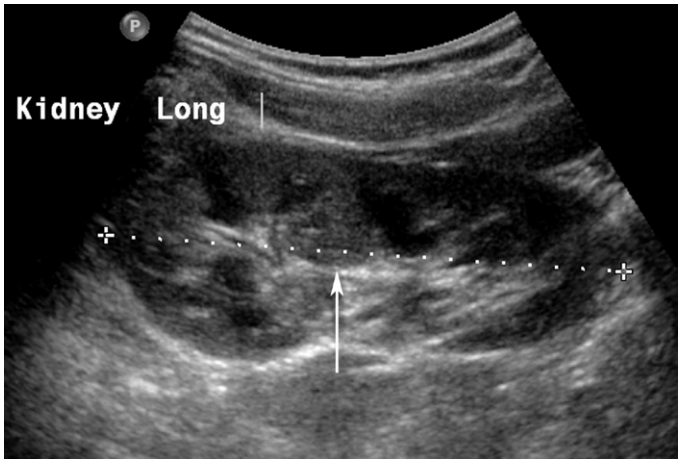

Figure 71.14 Hypertrophied column of Bertin. Longitudinal sonogram showing a column of normal cortical tissue (arrow) extending from the renal cortex towards the hyperechoic renal sinus.

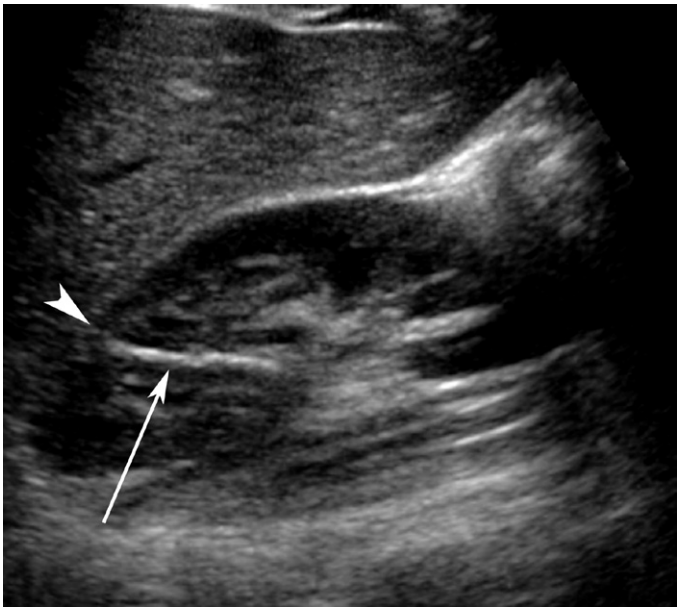

Figure 71.15 Interrenicular septum. Longitudinal ultrasound showing an oblique echogenic line (arrow) connecting the junctional parenchymal defect (arrowhead) to the renal sinus.

Normal sonographic measurements of the paediatric urinary tract

Renal size

- Renal length discrepancy of no more than 10 % is acceptable.
- Renal size (length or volume) should be compared against age or ideally body-weight-related normative data.
- Renal volumes tend to correlate better than renal length with weight-related data.
- Anteroposterior (AP) renal pelvic diameter should not exceed 10 mm.

Ureteral calibre

Normal ureteral diameter rarely exceeds 5 mm.[2]

Bladder wall thickness

Upper limit of normal:
fully distended = 3 mm
non-distended = 5 mm.[3]

Bladder volume

Formulae for normal expected capacity in cm^3:
(age in years + 2) × 30
(age in years × 30) + 60
(age in years × 60) + 70.[5]

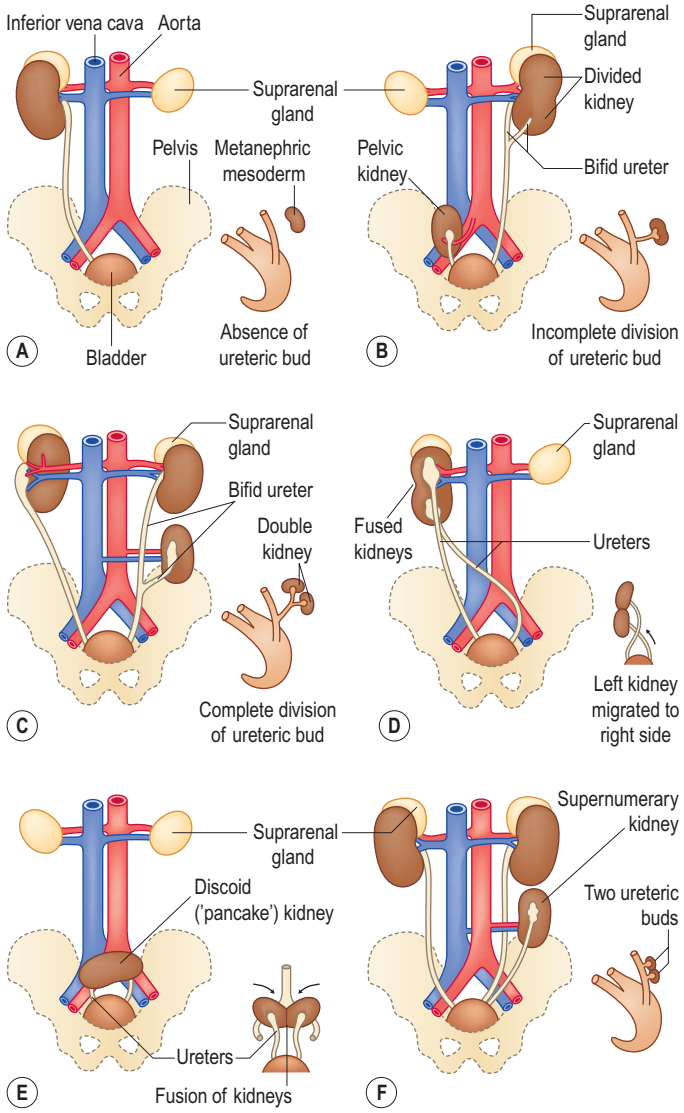

Figure 71.16 Congenital anomalies of the renal tract (reproduced with permission from Moore KL, Persaud TVN. The Developing Human. Clinically Oriented Embryology, 6th Edition. Philadelphia. WB Saunders. 1998). **A:** Unilateral renal agenesis. **B:** Right pelvic kidney with left divided kidney and accompanying bifid ureter. **C:** Right renal malrotation and left supernumerary kidney with bifid ureter. **D:** Crossed fused renal ectopia with the left kidney across the midline to fuse with normally sited right kidney. **E:** Discoid pelvic kidney. **F:** Supernumerary left kidney.

Kidneys

Measurement of renal size and determining interval growth are an important part of assessing the renal tract in childhood. Renal length is measured along the long axis of the kidney from upper to lower pole – bipolar length. A difference of up to 10% in renal lengths is acceptable. The obtained renal lengths should be compared to normative data[6] and documented. Plotting renal lengths obtained on serial examinations on a chart is helpful in demonstrating the serial trend in growth.

Observer variation in the sonographic measurement of renal length is equivalent to about 2 years of normal growth.[7] Similar variation has been described in assessing renal volumes.[8]

Renal volume is calculated from the outer diameters of the kidney using the formula for a prolate ellipsoid: volume (mL) = length × width × AP (depth) × 0.523. The correlation between relative volume measured by ultrasound and relative renal function as measured on DMSA (dimercaptosuccinic acid) scintigraphy for normal and abnormal kidneys in children has been evaluated. The difference in relative volume and function was 5.9% in normal kidneys and 10.9% in abnormal kidneys.[9] Renal volumes tend to correlate better than renal length with weight-related normative data.

Abnormalities of the upper renal tract

Abnormalities of renal number

Unilateral renal agenesis

This abnormality occurs in around 1 in 500–1500 newborn infants and results from failure of the ureteric bud to meet the metanephric blastema and stimulate the development of a normal kidney (Fig. 71.16A). This usually has no clinical significance. The contralateral kidney will show appropriate compensatory hypertrophy (Fig. 71.4C); if this is not case then the remaining kidney should be evaluated for underlying dysplasia or hypoplasia. Apparent unilateral renal agenesis may also result from failure to account for an ectopic kidney or an involuting multicystic dysplastic kidney. A DMSA scan is useful in localising functioning renal tissue and confirming a solitary kidney.

The ipsilateral adrenal gland may show hypoplasia in around 10% of cases. Another feature of renal agenesis or renal ectopia is that the ipsilateral adrenal gland is slender and elongated showing the so-called 'lying down' adrenal gland sign[10] (Fig. 71.17). Other associations include ipsilateral hypoplasia of the ureter, Wolffian anomalies in the male (seminal vesicle cyst, vas deferens/testicular hypoplasia or aplasia) or Müllerian anomalies in females.[11]

Bilateral renal agenesis (Potter's syndrome) is not compatible with life.

Supernumerary kidney

Supernumerary kidneys are exceedingly rare (Fig. 71.16F). They tend to be small, dysplastic and ectopic in location, and are best confirmed by a combination of ultrasound and DMSA scan.

Abnormalities of position

Rotational anomalies

The permanent fetal kidneys normally undergo 90° rotation about their long axes during cranial ascent from the pelvis. Malrotation of the pelvi-ureteric connection is relatively common and may be diagnosed on ultrasound or cross-sectional imaging (Fig. 71.16C). The most common type of rotational anomaly is incomplete rotation (less than 90°). Other types include:

- absent rotation (ventral malrotation)
- rotation of more than 90° (dorsal malrotation)
- negative rotation (lateral malrotation).

Rotational anomalies usually result in a degree of pelvi-ureteric obstruction and hydronephrosis.

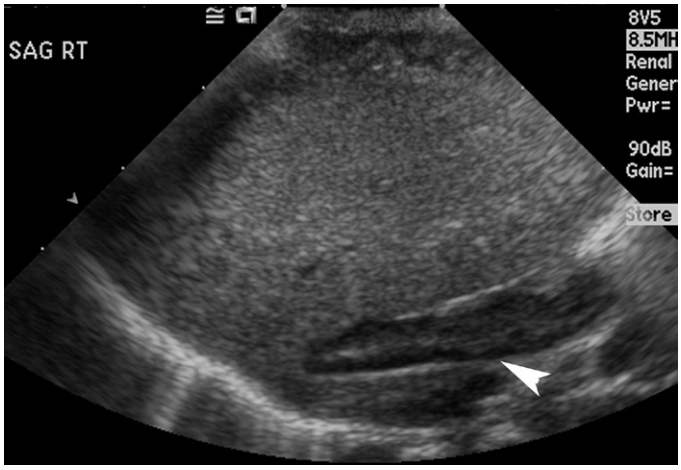

Figure 71.17 The adrenal gland in renal agenesis. Longitudinal sonogram showing the characteristic appearances of an elongated 'straight' or 'lying down' adrenal gland (arrowhead) in ipsilateral renal agenesis or ectopia.

Ectopic kidney and nephroptosis

Congenital renal ectopia occurs when the kidney has not ascended to its normal position in the renal fossa. Renal ptosis refers to abnormal caudal movement of the kidney from the renal fossa when changing from the supine to upright position. In congenital renal ectopia the ureter is short, whereas in renal ptosis the ureter is of normal length but kinks when the patient is erect. The ectopic kidney may be located in a low sacral position behind the urinary bladder or anywhere along the normal cranial migration path towards the renal fossa. The ectopic kidney is most commonly located in the pelvis (Figs 71.16D and 71.18A). Blood supply is via adjacent vessels usually directly from the iliac arteries or aorta.

A discoid kidney refers to a fused solitary pelvic kidney, which drains via a common ureter (Figs 71.16E and 71.18B).

Thoracic kidney

Thoracic kidney results from excessive cephalad migration. The kidney comes to lie below a deficient or thinned membranous portion of the diaphragm. There is a male and left-sided preponderance. The diagnosis is usually suspected on a chest X-ray (Fig. 71.19) but confirmed by ultrasound. The origin of the renal vasculature can be normal or high and may enter through the foramen of Bochdalek.

Horseshoe kidney

Horseshoe kidney is the most common renal fusion anomaly and occurs in 1 in 400–800 live births. A bridging isthmus results in fusion of the poles of both kidneys – usually the lower poles. The isthmus often consists of functioning parenchyma and will be demonstrable on both ultrasound and a ^{99m}Tc DMSA scan (Fig. 71.20). Occasionally the bridging tissue is fibrous. The isthmus almost always lies anterior to the aorta and is usually located just below the origin of the inferior mesenteric artery with blood supply arising from the aorta or iliac arteries. Both kidneys show a degree of malrotation. There is a higher incidence of hydronephrosis, urinary tract infection and calculi. The overall risk of malignancy in horseshoe kidney is not believed to be increased; however, the

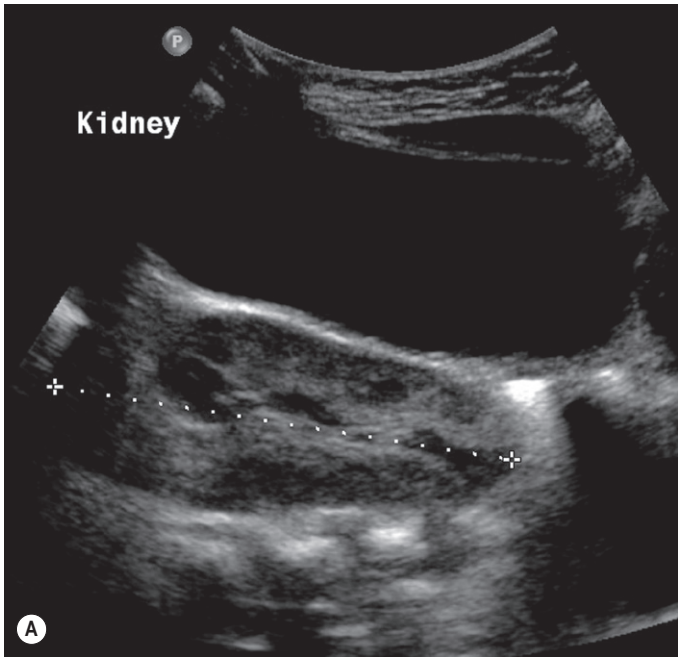

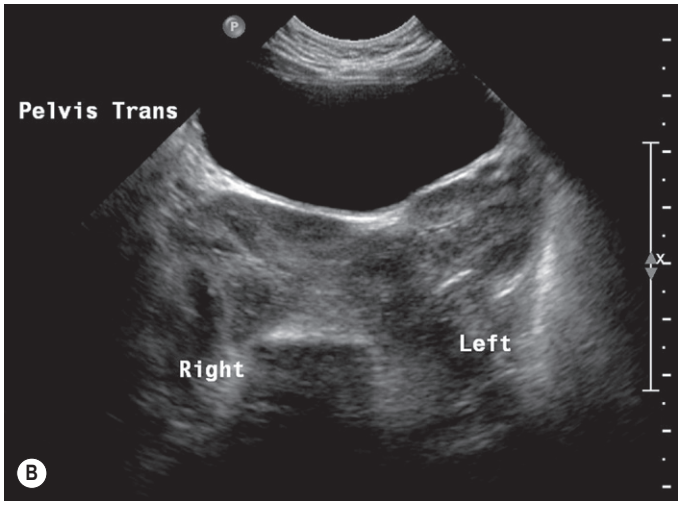

Figure 71.18 Pelvic and discoid kidneys. A: Longitudinal sonogram of an ectopic right pelvic kidney deep to the urinary bladder. **B:** Transverse sonogram showing a discoid pelvic kidney deep to the urinary bladder initially thought to be a pelvic horseshoe kidney.

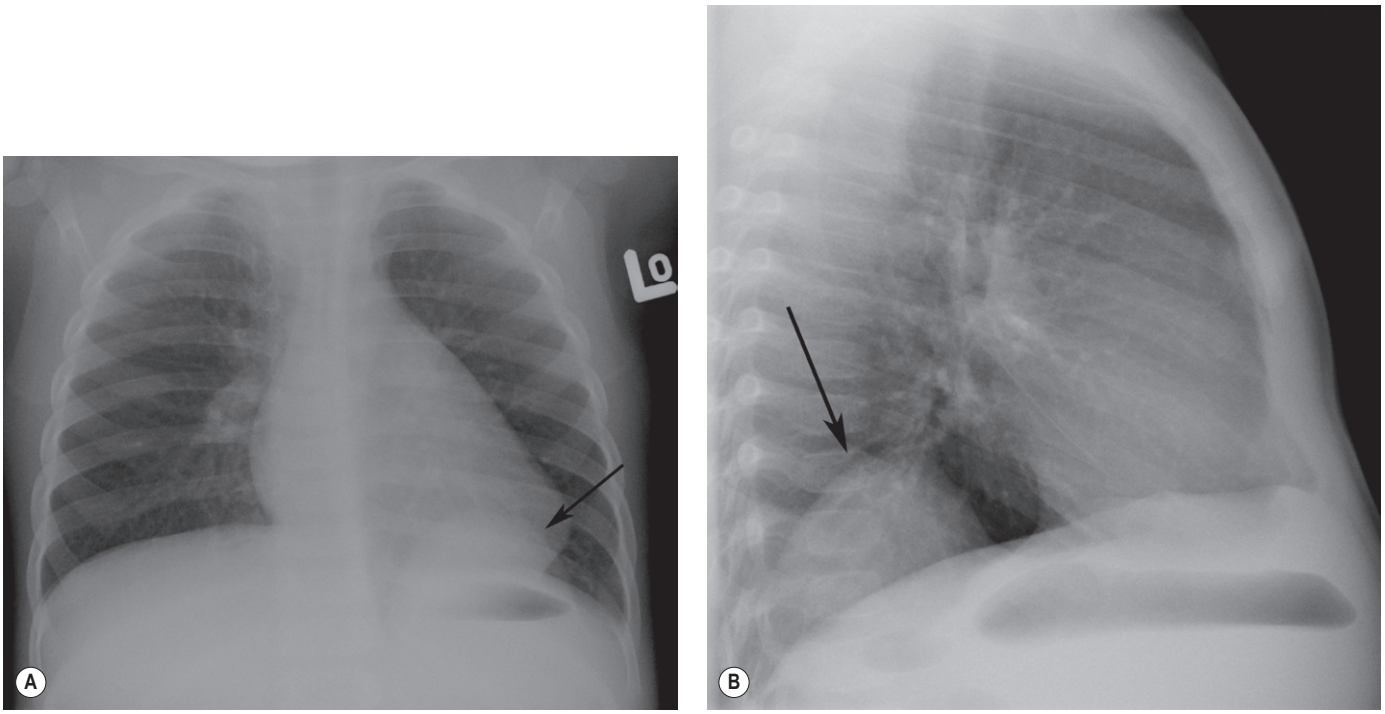

Figure 71.19 Intrathoracic kidney. Chest X-ray – AP and lateral views showing an egg-shaped hump in the contour of the left hemidiaphragm (arrow) found to represent focal thinning of the hemidiaphragm. Dynamic ultrasound confirmed this to contain a high-riding kidney within the abdomen. There was no evidence of diaphragmatic hernia. An intrathoracic kidney is a rare association of a Bochdalek malformation.

relative incidence of Wilms' tumour in the paediatric population[12] and transitional cell carcinoma in adults is increased[13] (Fig. 71.20C).

Crossed fused ectopia

Crossed ectopia occurs when a kidney is located on the opposite side of the midline from its ureteral orifice. This is more common in males. The crossing kidney usually arises from the left side and is located caudal to the normal right kidney (Figs 71.16D and 71.21).

Duplex anomalies of the kidney

Renal duplication anomalies represent a spectrum of disorders ranging from a bifid renal pelvis to complete duplication of the kidney and ureter to the level of the urinary bladder. This represents the most common type of congenital renal anomaly. Duplex anomalies of the ureter are around two to five times more common in girls.

Duplication may be complete but is more often partial. Duplication of the renal collecting system results from premature branching of the metanephric duct. The urogenital sinus (UGS) gives off two ureteral buds instead of one. The ureteral bud closest to the UGS drains the lower renal pole, inserting at the bladder trigone, and is referred to as the 'orthotopic' ureter. The upper renal pole is drained by the 'ectopic' ureter, which inserts into the bladder in a more medial and caudal location. The ectopic ureter may drain below the urinary bladder. In boys this may occur at the level of the prostatic urethra, seminal vesicles, vas deferens or epididymis. In girls ectopic drainage may occur into the vagina, uterus or even below the voluntary urinary sphincter directly into the urethra, resulting in urinary incontinence. The latter cannot be diagnosed on ultrasound but may be demonstrated on intravenous urography (IVU) or magnetic resonance urography (MRU). The ureters may fuse at any level, from the kidney to the bladder and drain into a single ureteric orifice.

Duplication anomalies of the kidney are best demonstrated by sonography along the long axis of the kidney.

Bifid renal pelvis and partial duplication anomalies

These are not usually clinically significant. The duplicated non-obstructed kidney is often enlarged, and has two separate pelvicalyceal systems, which may fuse at the renal pelvis (bifid renal pelvis) (Fig. 71.22) or anywhere along the length of the ureter (partial duplication).

Duplex kidney

A 'duplex kidney' comprises two renal masses (moieties) (Fig. 71.23), each with its own separate pelvicalyceal system, ureter, ureteral orifice and site of insertion. As described above, the typical configuration is:

- upper pole moiety drains via an ectopic ureter usually inserting below and inferomedially to the lower moiety ureter
- lower pole moiety drains via an orthotopic ureter and inserts into the lateral angle of the trigone.

Duplex kidneys may be unilateral or bilateral. The duplicated ureters are typically separate but may fuse to an abnormal common ureteral orifice.

With complete duplication, the Weigert–Meyer rule may be seen, whereby the:

- upper moiety ureter is more prone to obstruction due to ureteric stenosis at the ectopic ureteral orifice and is frequently associated with an 'ectopic ureterocele' (see below)
- lower pole moiety often demonstrates a perpendicular course rather than the normal oblique course through the ureteral orifice, resulting in an incompetent valve mechanism increasing the likelihood of vesico-ureteric reflux.

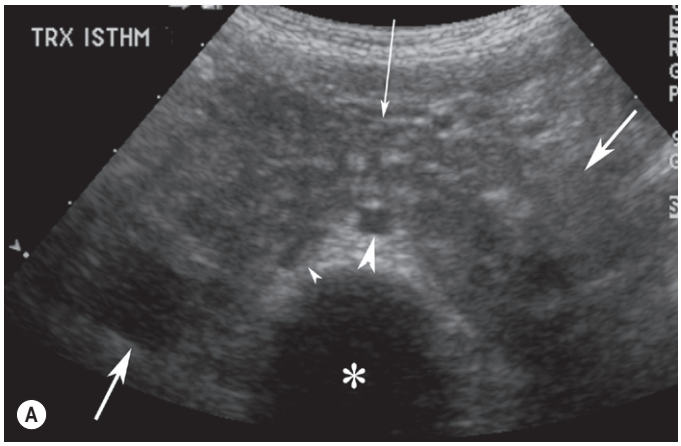

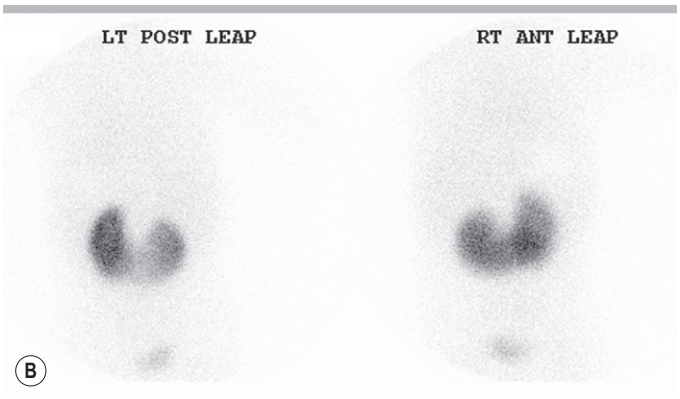

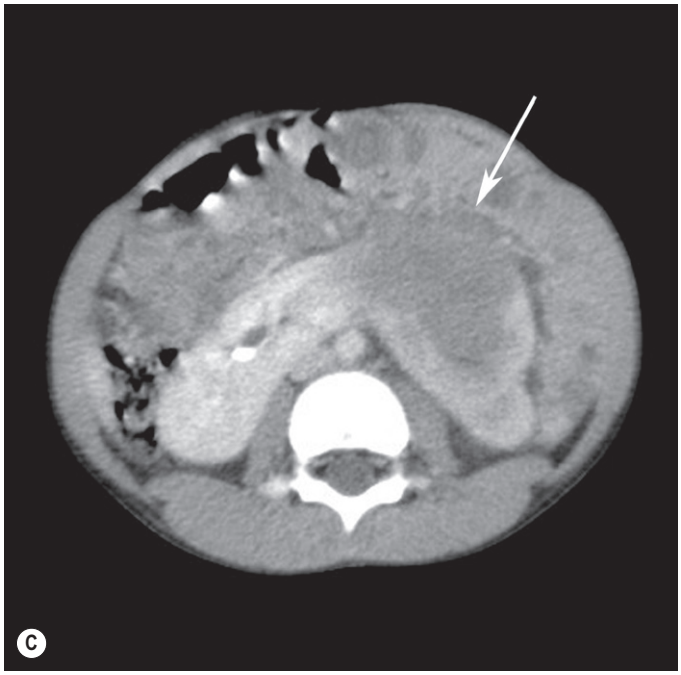

Figure 71.20 **Horseshoe kidney. A:** Transverse sonogram in a 13-year-old male showing a parenchymal isthmus (thin arrow) fusing the lower poles of both kidneys (thick arrows) in a typical horseshoe configuration with fusion of the lower poles and malrotation of the renal hilum. The spine (*), IVC (short arrowhead) and aorta (large arrowhead) are labelled. **B:** DMSA scan in the same patient confirming uptake in the functioning tissue within the isthmus. **C:** Axial contrast-enhanced CT scan showing a Wilms' tumour (arrow) arising from the left side of the isthmus of a horseshoe kidney in a 5-year-old boy.

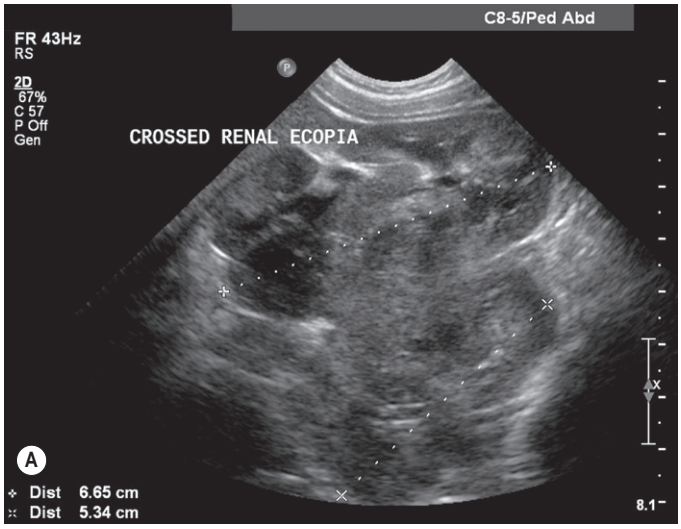

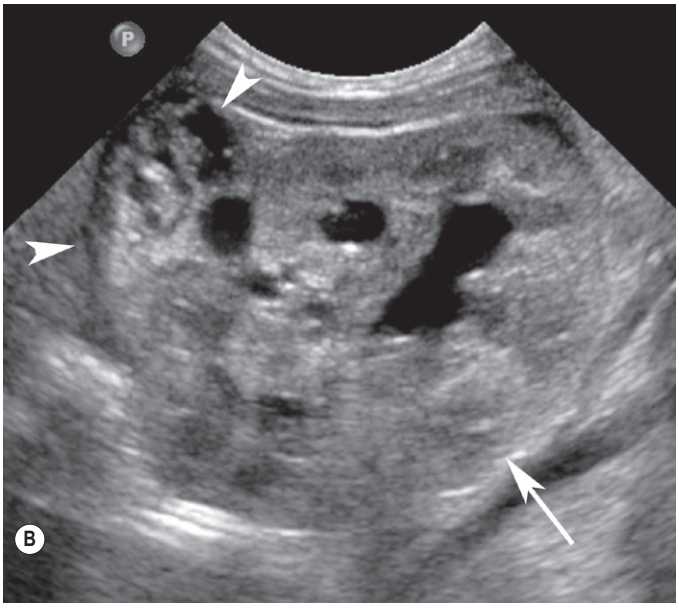

Figure 71.21 **Renal crossed fused ectopia. A:** Transverse sonogram showing a crossed left kidney fused to the caudal aspect of the normally sited right kidney. **B:** Oblique sonogram revealing an unusual crossed fused ectopia arrangement in which the relatively normal crossing left kidney (arrow) is fused to a multicystic dysplastic right kidney (arrowheads).

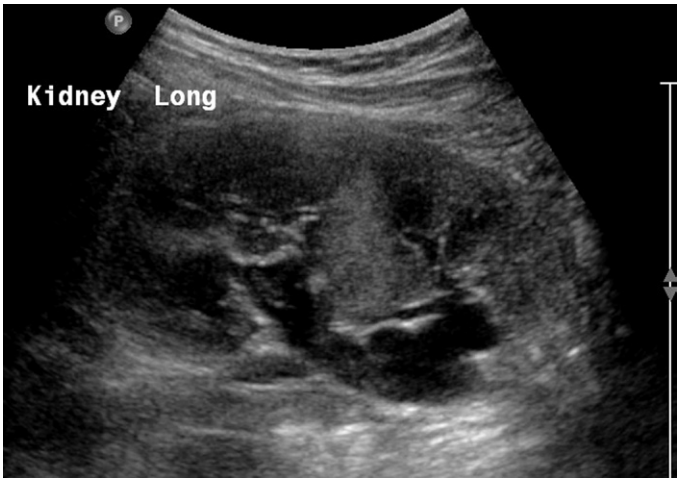

Figure 71.22 Bifid renal pelvis. Longitudinal sonogram showing a bridge of renal sinus fat separating the upper and lower collecting systems which fuse at the renal hilum.

Ureterocele

A ureterocele is a congenital abnormality resulting from 'saccular', submucosal dilatation of the intravesical portion of the ureter. Ureteroceles are more common in females and are usually seen in relation to a duplex kidney. A simple ureterocele can be seen in a single renal system and accounts for around 20% of all ureteroceles.

Ectopic ureterocele refers to a ureterocele with an orifice located in an abnormal position, such as the urethra or bladder neck, and typically arise from the upper pole moiety of a duplicated collecting system. These are more commonly identified in the paediatric population.

Orthotopic ureterocele refers to a ureterocele with an orifice that is located in the normal anatomical position within the bladder and usually arises from a single renal unit with one collecting system. This is usually detected in adulthood.

The sonographic features of ureteroceles include the following:

- A rounded, thin-walled, fluid-filled structure at the base of the urinary bladder (Fig. 71.24).[14]
- Hydroureter and hydronephrosis usually involves the upper moiety in the duplicated ectopic system (non-stenotic ectopic/infantile form) or the whole kidney in the simple single system stenotic type. When ectopia exists in a single system the associated kidney is likely to be severely dysplastic rather than hydronephrotic.
- Infected ureteroceles may contain multiple internal echoes.

Complications of ureteroceles include obstructive uropathy, which may manifest as failure to thrive, renal compromise and recurrent pain; secondary renal calculi; and urinary tract sepsis. In these cases surgical treatment may be required with urgent endoscopic incision, followed by a definitive bladder reconstruction to maintain continence and prevent troublesome vesico-ureteric reflux. Rarely a ureterocele may prolapse in a female and present as a bulging mass at introitus (Fig. 71.25). The differential diagnosis includes imperforate hymen with hydrocolpos, urethral prolapse, perineal abscess, paraurethral cyst, Skene duct cyst or vaginal rhabdomyosarcoma.[15]

Abnormalities of the lower urinary tract

Megaureter

Primary megaureter results from dilatation of the ureter proximal to an aperistaltic segment at the ureterovesical junction (UVJ) (Fig. 71.26). Primary megaureter is non-refluxing. Many cases are diagnosed antenatally. Initial investigation should include ultrasound, VCUG and MAG-3 renogram. Most will resolve spontaneously. Conservative management is all that is required with prophylactic antibiotic therapy and ultrasound follow-up. If renal function is deteriorating then surgical management is required with resection of the adynamic segment, reduction in the calibre of the dilated segments and ureteric reimplantation into the bladder.[16] Secondary megaureter may result from either reflux, obstruction or both.

Vesico-ureteric reflux

Vesico-ureteric reflux (VUR) is one of the commonest pathologies in children, affecting 1–2% of the paediatric population. VUR occurs when urine refluxes across the UVJ into the ureter and depending on the grade of severity to the renal pelvis (Fig. 71.27). This can be detected on an indirect MAG-3 cystogram or by meticulous ultrasound.[18] VUR is, however, best demonstrated by the more invasive and less physiological VCUG, which remains the reference standard. Harmonic echo-enhanced cystosonography has been advocated as an accurate, non-ionising alternative but is currently not in widespread clinical use.[19] The role of imaging is to define the grade of reflux and to assess for any associated renal damage. The most common form is primary congenital reflux. VUR is also associated with:

- duplex kidney
- bladder outflow obstruction (posterior urethral valve, hypospadias, bladder exstrophy)
- multicystic dysplastic kidney
- urinary tract infection (UTI)
- post surgical (following de-roofing of a ureterocele or post nephrectomy).

There is no doubt that children with recurrent UTI and proven reflux are at higher risk of upper renal tract damage such as scarring. More recently antenatal obstruction and reflux rather than postnatal reflux are thought to be the most significant contributors to long-term renal damage[20] and account for the gradual trend away from intensive investigation of VUR in the older child.

Higher grades of severity of VUR may require surgical intervention in order to preserve renal function. Treatment options for VUR include using the subureteric transurethral injection procedure (STING) (Fig. 71.28), hydrodistension–implantation technique (HIT) or distal ureteric reimplantation.

VACTERL association

VACTERL syndrome (vertebral, anorectal, cardiac, tracheo-esophageal, renal and limb anomalies) is associated with renal dysplasia usually from significant vesico-ureteric reflux. Other renal anomalies include renal hypoplasia, aplasia, horseshoe kidney, duplex kidney, multicystic dysplastic kidney (MCDK) and crossed fused renal ectopia. Ultrasound of the renal tract and spine are routinely performed in children with this condition.

Posterior urethral valve

Posterior urethral valve (PUV) results from a membrane formed by anterior fusion of two abnormal mucosal folds that descend from either side of the verumontanum forming a 'windsock' which balloons and obstructs the posterior urethra during micturition. Antegrade flow of urine is severely compromised but urethral catheterisation is readily achievable and provides relief. Most cases are detected antenatally and vary in severity. Complications include oligohydramnios, fetal bladder distension, hydronephrosis, cystic renal dysplasia, urinoma and urinary ascites. Hydronephrosis is usually bilateral but preferential decompression into one ureter will spare the contralateral kidney the ill effects of severe pressure overload and better preserve overall renal function. Prenatal ultrasound

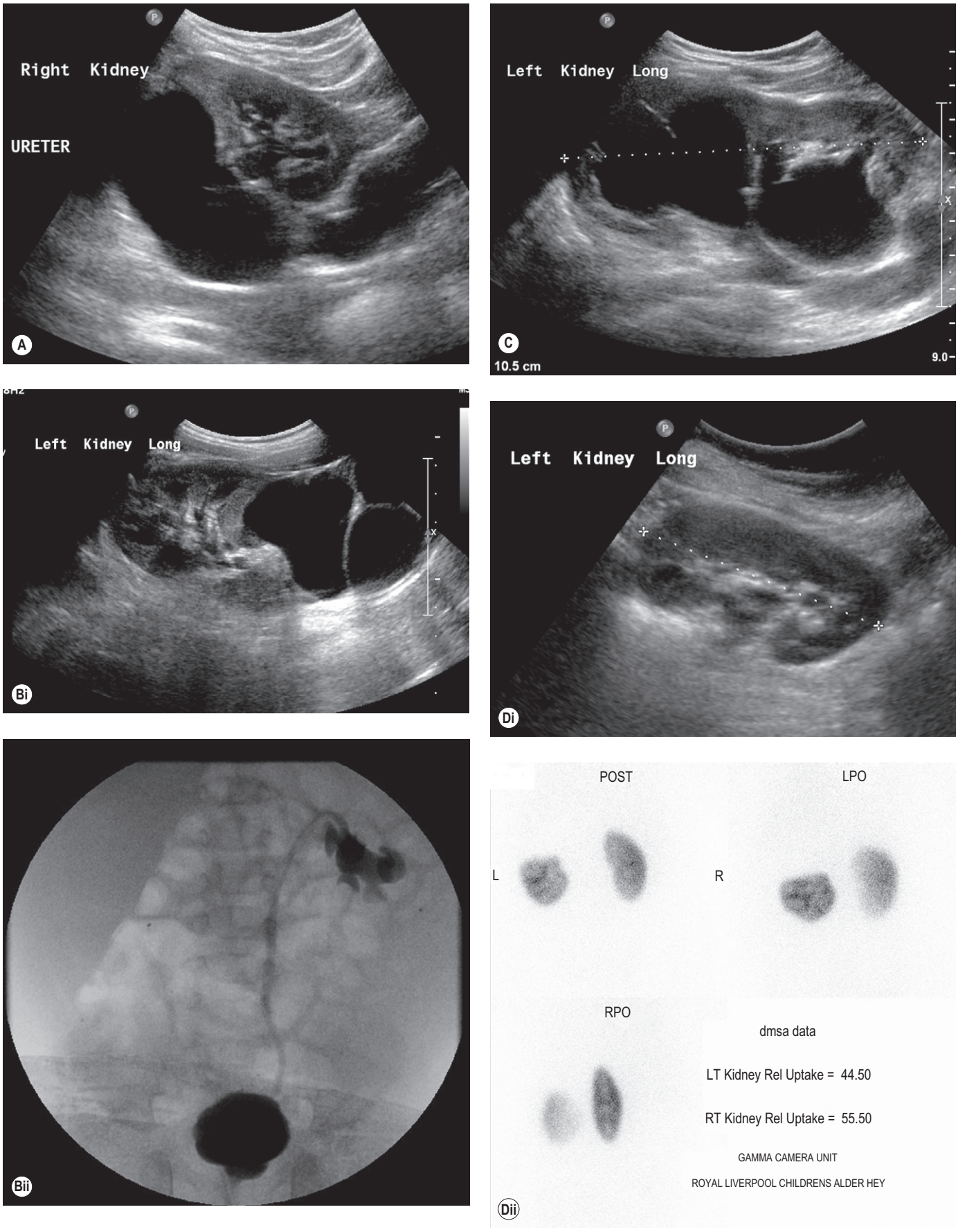

Figure 71.23 **Renal duplication anomalies. A:** Longitudinal sonogram showing a dilated upper pole moiety with a proximal hydroureter due to a ureterocele. **B:** Longitudinal sonogram showing a dilated lower pole moiety due to vesico-ureteric reflux with marked parenchymal thinning; The VCUG in the same patient shows characteristic reflux into a 'dropping lily' lower moiety. **C:** Longitudinal sonogram showing dilated upper pole and lower moieties. **D:** Longitudinal sonogram and DMSA scan in a child with left duplex kidney which required upper pole hemi-nephrectomy for problematic vesico-ureteric reflux.

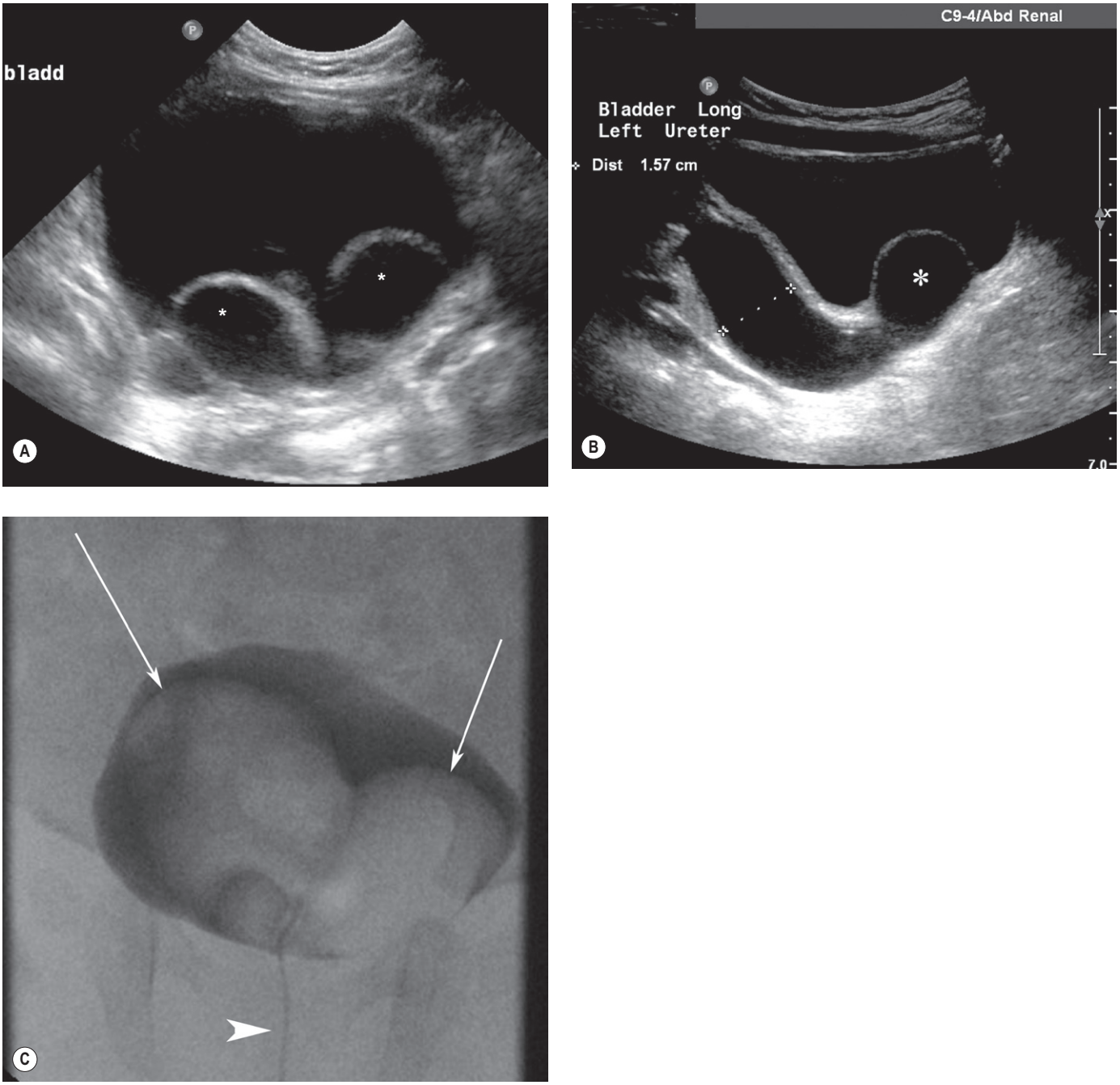

Figure 71.24 **Ureteroceles. A:** Transverse sonogram in a young girl with bilateral duplex kidneys revealing well-defined intravesical rounded cystic structures (*) with thin echogenic walls in keeping with bilateral ureteroceles. **B:** Longitudinal sonogram showing a simple ureterocele (*) at the level of the trigone with accompanying ureteric dilatation. **C:** VCUG in the same patient showing corresponding filling defects on early filling (arrows) of the bladder with a urinary catheter in situ (arrowhead).

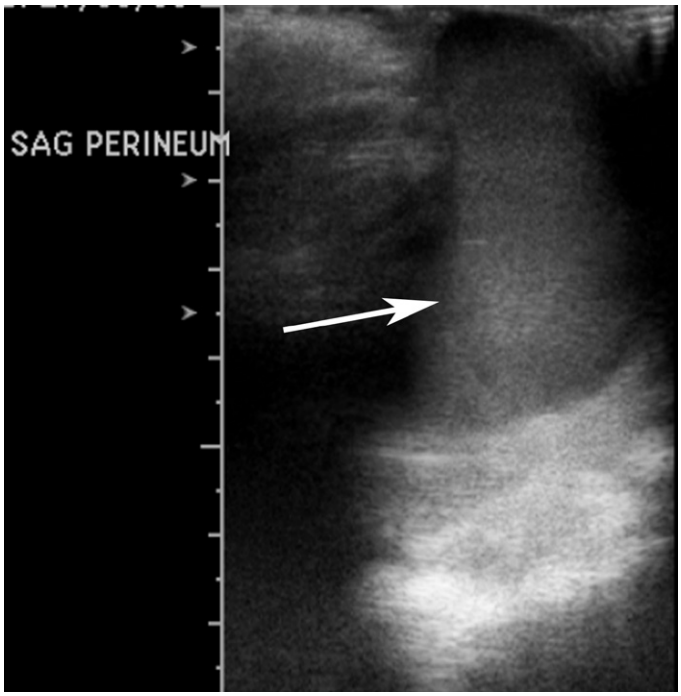

Figure 71.25 Prolapsed ureterocele. Sagittal transperineal sonogram in a young girl with a perineal mass showing a cyst (arrow) containing multiple internal echoes. An infected prolapsed ureterocele was confirmed at operation.

will show a typical keyhole appearance as the distended bladder fills the dilated posterior urethra (Fig. 71.29).

The postnatal diagnostic hallmarks of PUV relate to the bladder's attempt to overcome the urethral obstruction and include a dilated posterior urethra, trabeculated thick-walled bladder, tortuous dilated hydroureters and hydronephrosis. Urinoma formation results from calyceal rupture decompressing the upper renal tract. These features are readily demonstrable on a VCUG (Fig. 71.30) but can also be seen on ultrasound. Sonographic demonstration of a 'keyhole' dilated posterior urethra (measuring greater than 7 mm) is possible if a urinary catheter has not been passed. Meticulous technique is required to demonstrate a distended posterior urethra. The transabdominal approach requires marked caudal tilt of the transducer. Perineal scanning can also be performed by placing the transducer in the sagittal plane behind the elevated scrotum.[14] In this position the posterior urethra is directed anteriorly.

In practical terms it is critical to relieve the obstruction promptly and bypass the valve with aseptic urinary catheterisation. These children are at high risk of urinary tract infection. Placement of a catheter should not be delayed whilst awaiting urgent imaging including ultrasound and VCUG. The treatment of choice is cystoscopic urethral valve ablation. Approximately one-third of infants with PUV progress to end-stage renal failure; around half of these children undergo renal transplantation. Renal transplantation does not improve bladder function. At the time of writing a randomised prospective study is in progress to determine if intrauterine vesicoamniotic shunting for fetal bladder outflow obstruction, compared to non-interventional conservative care, improves prenatal and postnatal renal function and mortality.[21]

Delayed presentations of PUV are not unheard of. Late onset in utero increases the likelihod that the kidneys will only be mildly hydronephrotic at birth. PUV should be considered in a boy presenting with either diurnal enuresis, dysuria with a history of poor voiding stream, unexplained hydronephrosis or renal failure.

Bladder ear(s)

Bladder ear(s) result from inferolateral protrusion of the urinary bladder through the internal inguinal ring and inguinal canal and are more commonly seen in infants on a VCUG. The infant bladder assumes a more abdominal position, which places it in close proximity to the internal inguinal ring. As the pelvis grows, the bladder position descends into the pelvis, making a bladder ear much less likely (Fig. 71.31).

Bladder diverticula

Bladder diverticula result from herniation of the bladder mucosa through bladder wall detrusor muscle (Fig. 71.31). They may result from obstruction, infection or iatrogenic causes. Multiple diverticula occur in trabeculated bladders. Diverticula may protect the proximal urinary tract from high pressure by acting as 'blow off' space in an obstructive uropathy such as PUV and may resolve when the valve is ablated. Conversely diverticula may contribute to dysfunctional bladder emptying. Small-necked diverticula may empty poorly, promoting urine stasis leading to calculus formation or mucosal dysplasia. Diverticula situated close to the ureteric orifices may promote VUR. Surgical resection is usually indicated when associated with VUR or recurrent symptoms.

Neurogenic bladder

In this condition the dysfunctional urinary bladder may be unable to retain urine, empty normally or both. There are two broad groups of patients who may be referred for imaging: the newborn with spinal dysraphism or anorectal malformation and older children undergoing long-term urology follow-up. The imaging modality of choice is urodynamic investigation (video cystometrogram), which provides functional information concerning urine pressure, flow rate and volume. The main role of ultrasound is in assessing pre- and post-micturition bladder volumes and bladder wall thickening. Neurogenic bladder is a common cause of bladder wall trabeculation and thickening (Fig. 71.32). Complications include VUR and UTI.

Megacystis

Physiological enlargement of the fetal urinary bladder is observed in the first trimester of pregnancy and also normally seen in female fetuses towards the end of pregnancy. Pathological megacystis can be observed in conditions such as posterior urethral valve, urethral stricture and diverticulum, megacystis microcolon hypoperistalsis syndrome, sacral meningomyelocele, sacrococcygeal teratoma, Ehlers–Danlos syndrome and pelvic neuroblastoma. Overfilling of fetal bladder results in marked bladder distension associated with severe high-grade vesico-ureteric reflux. In an infant presenting with an enlarged thin-walled urinary bladder and massive VUR, the possibility of the megacystis–megaureter syndrome should be considered. A vicious cycle is established whereby a large proportion of the bladder volume is preferentially recycled by refluxing back into the upper tracts.

Urachal abnormalities

The connection between the allantois and fetal bladder apex normally involutes to form the medial umbilical ligament. Failure to do so results in a urachal remnant (Fig. 71.33). Urachal remnants are a rare finding. The most common type of anomaly is a cyst or sinus followed by a patent urachus, with urachal diverticulum the least common finding. High-resolution scanning of the dome of an adequately distended urinary bladder should suffice to confirm the diagnosis in most cases. Occasionally a sinogram is required to delineate a discharging remnant, or computed tomography (CT) scan.[22] Intercurrent infection within the sinus tract may present in

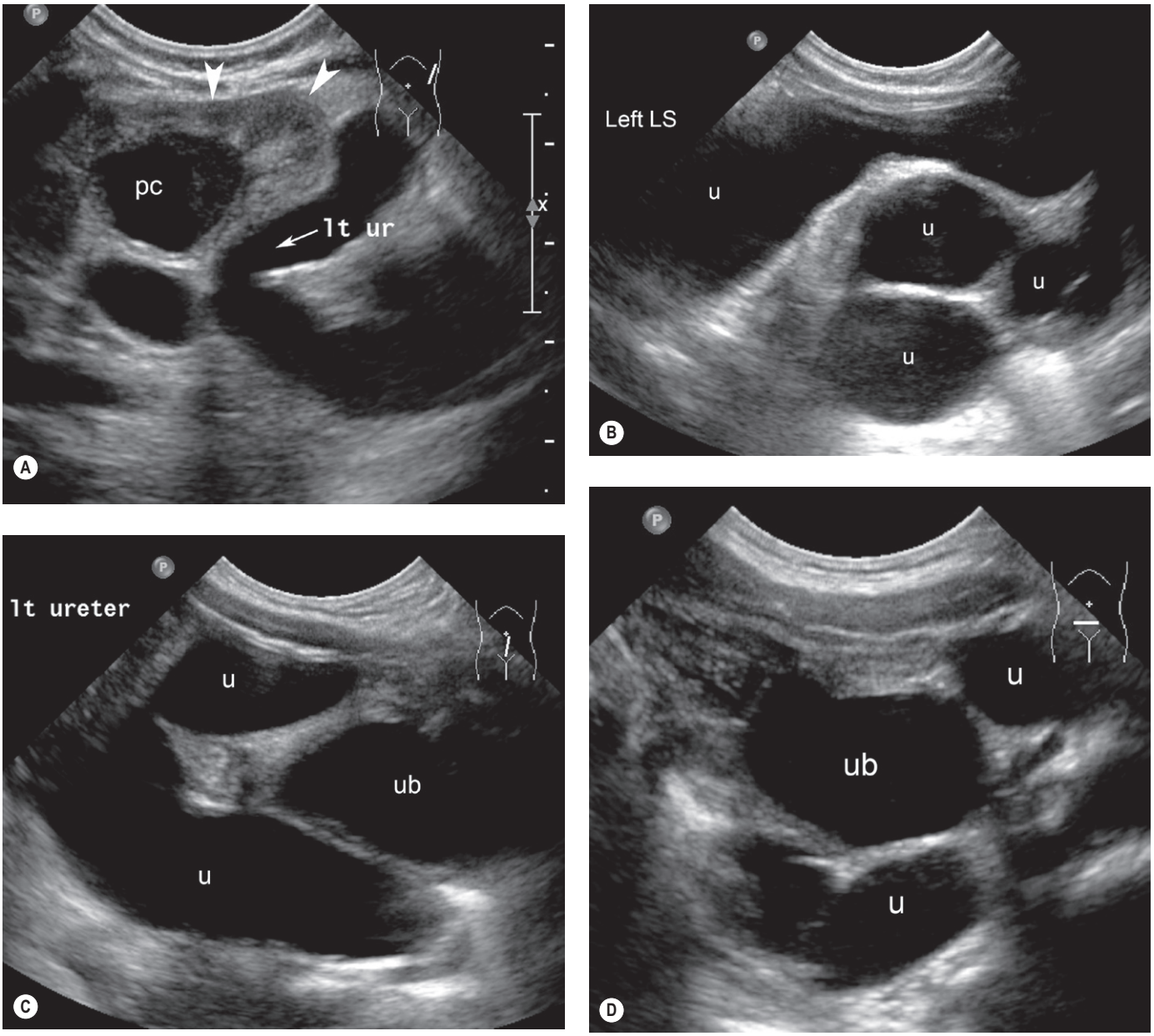

Figure 71.26 **Non-refluxing primary megaureter.** Newborn male with antenatally detected left hydroureter confirmed to be non-refluxing on an early postnatal VCUG. **A:** Longitudinal sonogram showing a markedly distended left ureter up to the pelvicalyceal system (PC), which shows debris. The left kidney (arrowheads) is dysplastic. **B:** Longitudinal image showing a dilated and ectatic left ureter (u). **C, D:** Longitudinal **(C)** and transverse **(D)** sonograms showing ureteric dilatation to the left vesico-ureteric junction posterior to the bladder (ub).

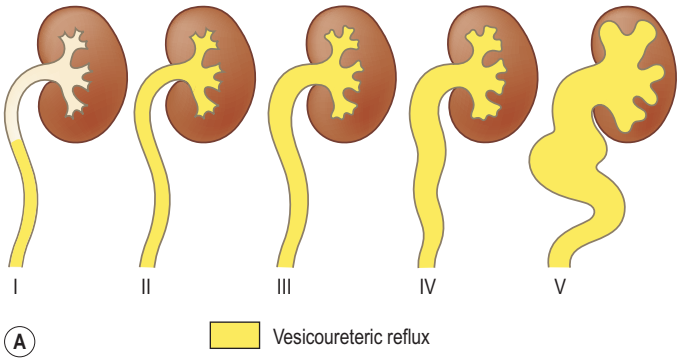

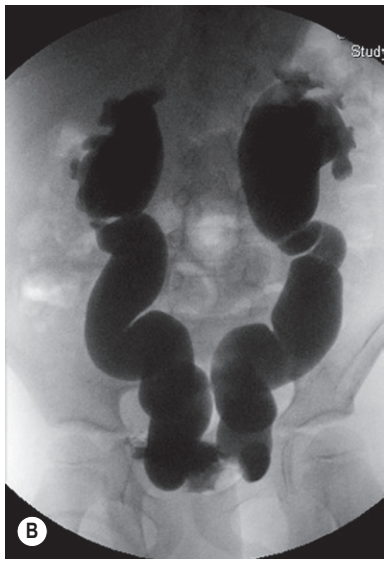

Figure 71.27 Vesico-ureteric reflux. A: Line diagram showing a grading scale commonly used in clinical practice to document the severity of vesico-ureteric reflux based on guidelines of the International Reflux Study Committee.[17] **B:** VCUG in a 2-year-old girl with bilateral grade 5 vesico-ureteric reflux; some of the calyces show preserved morphology. Reflux was only demonstrated during the latter stages of bladder emptying.

a child with periumbilical tenderness, a discharging umbilicus or umbilical granulation tissue. Rare cases of malignancy have been reported. Surgical resection is indicated when the acute infection has resolved.

Prune belly syndrome

Prune belly syndrome (Eagle–Barrett syndrome) is characterised by the association of a lax and markedly thin anterior abdominal wall – 'prune belly', prostatic hypoplasia with a dilated and elongated prostatic urethra, grossly distended smooth and thick-walled urinary bladder, bilateral cryptorchidism, dilated refluxing ureters and renal dysplasia. The degree of upper renal tract involvement is variable. At the most severe end of the spectrum there is effectively

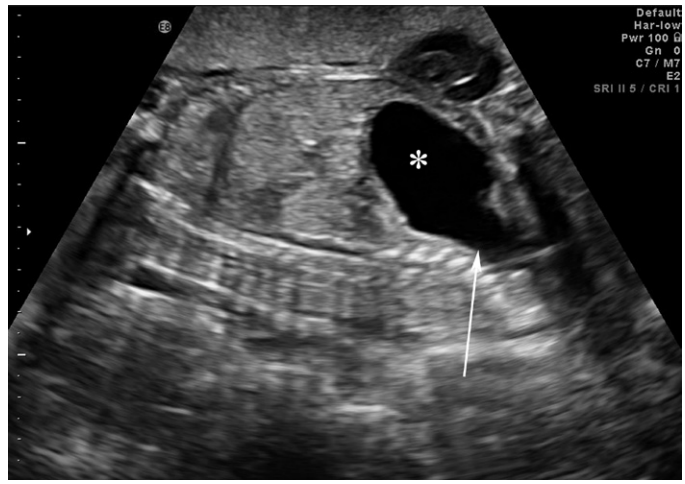

Figure 71.29 Antenatal imaging of posterior urethral valve. Longitudinal second trimester scan of a singleton male fetus with a markedly dilated urinary bladder (*) and the characteristic keyhole appearance (arrow) of a dilated posterior urethra seen in posterior urethral valve, antenatal urethral strictures or atresias.

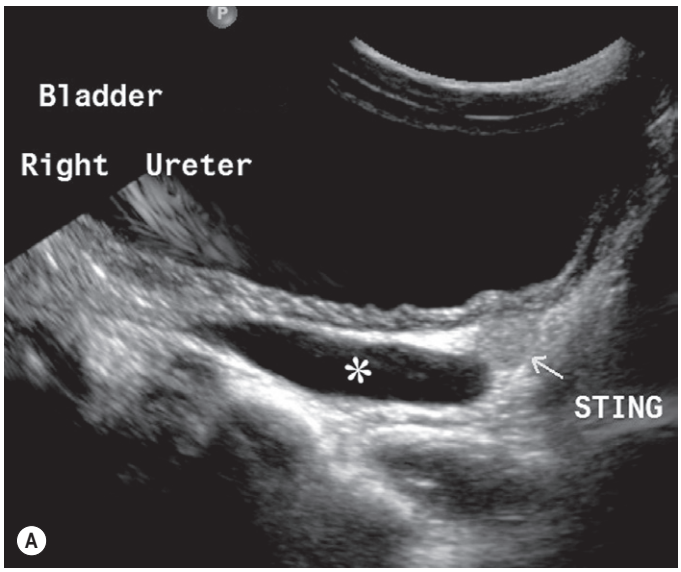

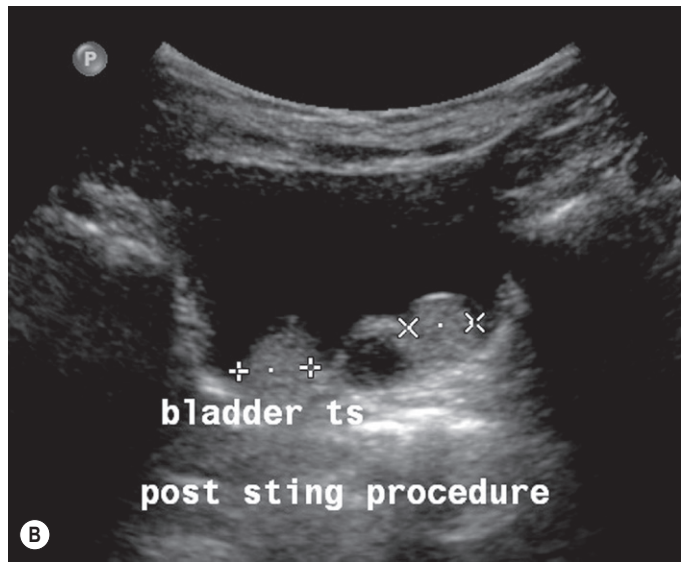

Figure 71.28 Subureteric transurethral injection or 'STING' procedure. This involves submucosal injection of a bolus of Teflon, which increases the length of the ureter and can also act as a fixation point used in the treatment of vesico-ureteric reflux. **A:** Longitudinal sonogram showing mild ureteric dilatation (*) proximal to the rounded echogenic focus of Teflon. **B:** Transverse sonograms showing bilateral treatment (between callipers).

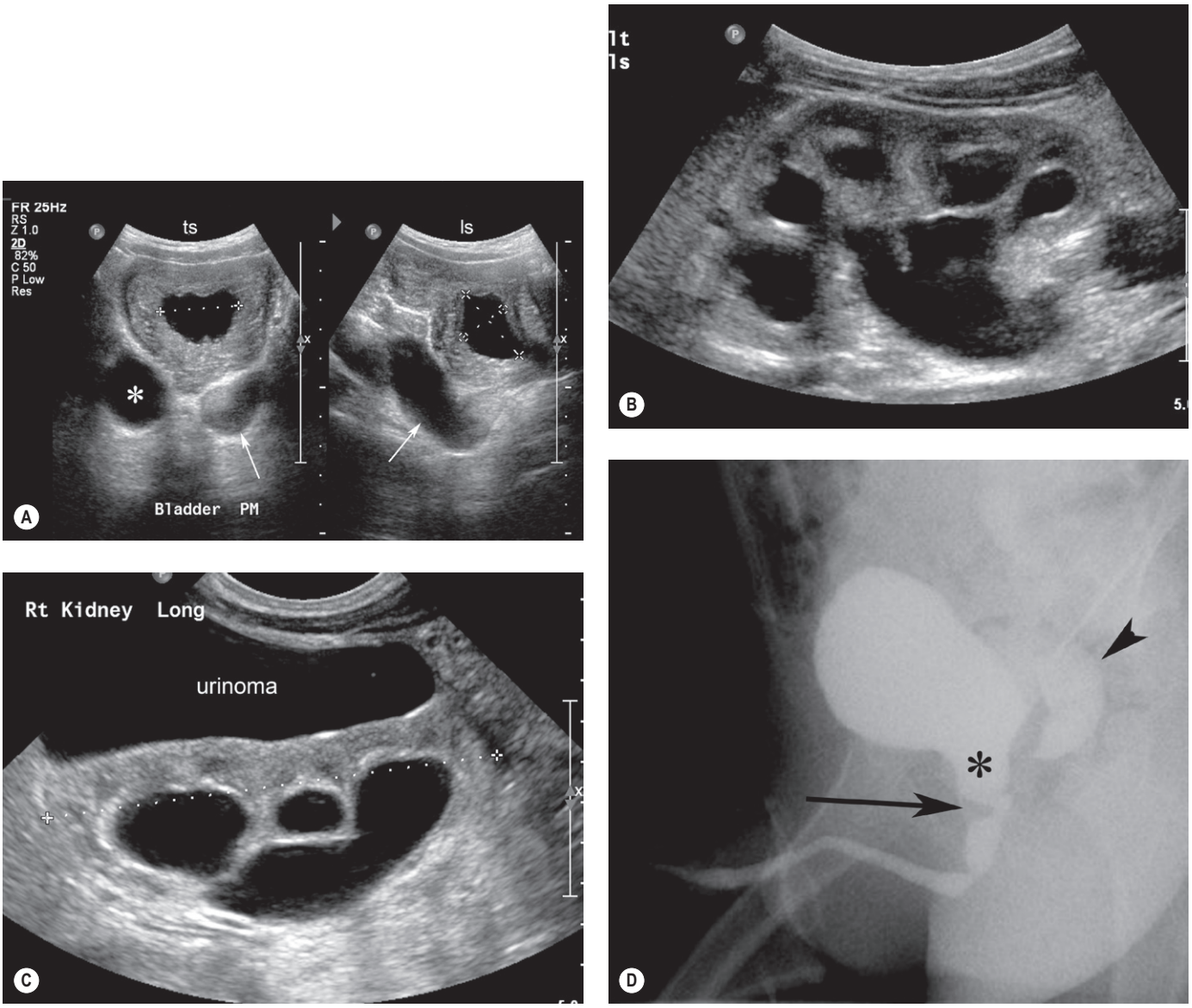

Figure 71.30 Postnatal imaging of posterior urethral valve (PUV). Newborn male with PUV. **A:** Post-micturition views of the urinary bladder showing a thick-walled trabeculated bladder (between callipers) and reflux into the right (*) and left (arrow) ureters. Longitudinal sonograms which show **(B)** a moderately hydronephrotic left kidney; **(C)** moderately hydronephrotic right kidney which has decompressed into an extrarenal subcapsular urinoma; **(D)** voiding cystourethrogram showing a dilated posterior urethra (*), posterior urethral valve (black arrow) and ureteric reflux (black arrowhead).

urethral atresia resulting in megacystis, bilateral severe ectatic hydroureters and bilateral hydronephrosis with accompanying cystic renal dysplasia.

Gastrointestinal, respiratory, cardiovascular and musculoskeletal anomalies are also associated with prune belly syndrome. The exact aetiology is unclear but is probably due to a combination of a primary defect in the anterior abdominal wall and severe bladder outflow obstruction. Females may also present but only with bladder abnormalities and abdominal wall deficiencies.

Cloacal exstrophy

Cloacal exstrophy results from the urinary bladder opening onto and through a defect in the anterior abdominal wall and is seen in both males and females.

Cloacal malformation and urogenital sinus

These are discussed in detail in Chapter 72 (see Fig. 72.11).

Obstructive uropathy

Ureteropelvic junction obstruction

Ureteropelvic junction obstruction (UPJO), also referred to as PUJ obstruction, represents the most common cause of hydronephrosis in the neonate and is also a common cause of renal pelvic dilatation in children. The aetiology is thought to relate to an intrinsic developmental abnormality resulting in a short segment of aperistaltic smooth muscle at the UPJ. Secondary causes include extrinsic compression from a fibrous band, adhesion, crossing vessel or ureteric kink.

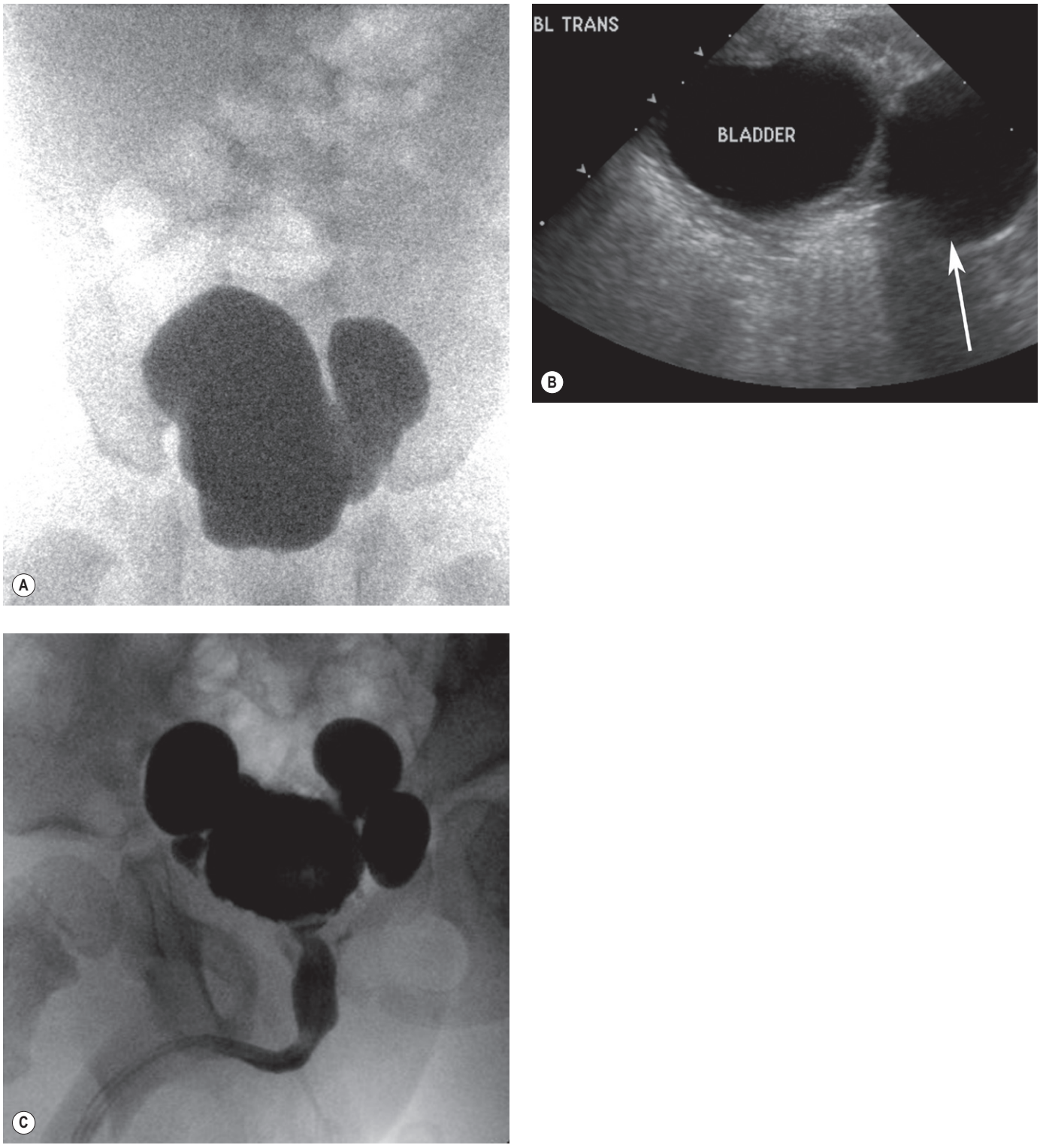

Figure 71.31 **Bladder ears and diverticula. A:** VCUG showing a left bladder ear. **B:** Transverse sonogram of the urinary bladder in the same patient showing the bladder ear (arrow). **C:** VCUG in a young male child with multiple diverticula showing the typical 'Mickey mouse ears' appearance.

The sonographic hallmarks of UPJO are the presence of 'pyelectasis' with renal pelvic dilatation greater than 10 mm in the AP plane and 'caliectasis' – calyceal distension. The degree of pyelocaliectasis is typically proportionate to the degree of renal parenchymal thinning (Fig. 71.34).

Renal complications of UPJO range from minimal cortical thinning to more severe dysplasia with echogenic parenchyma, dysplastic cortical cysts and urinoma formation.

The presence of pyelectasis alone with no calyceal distension or parenchymal thinning should alert the sonographer to the

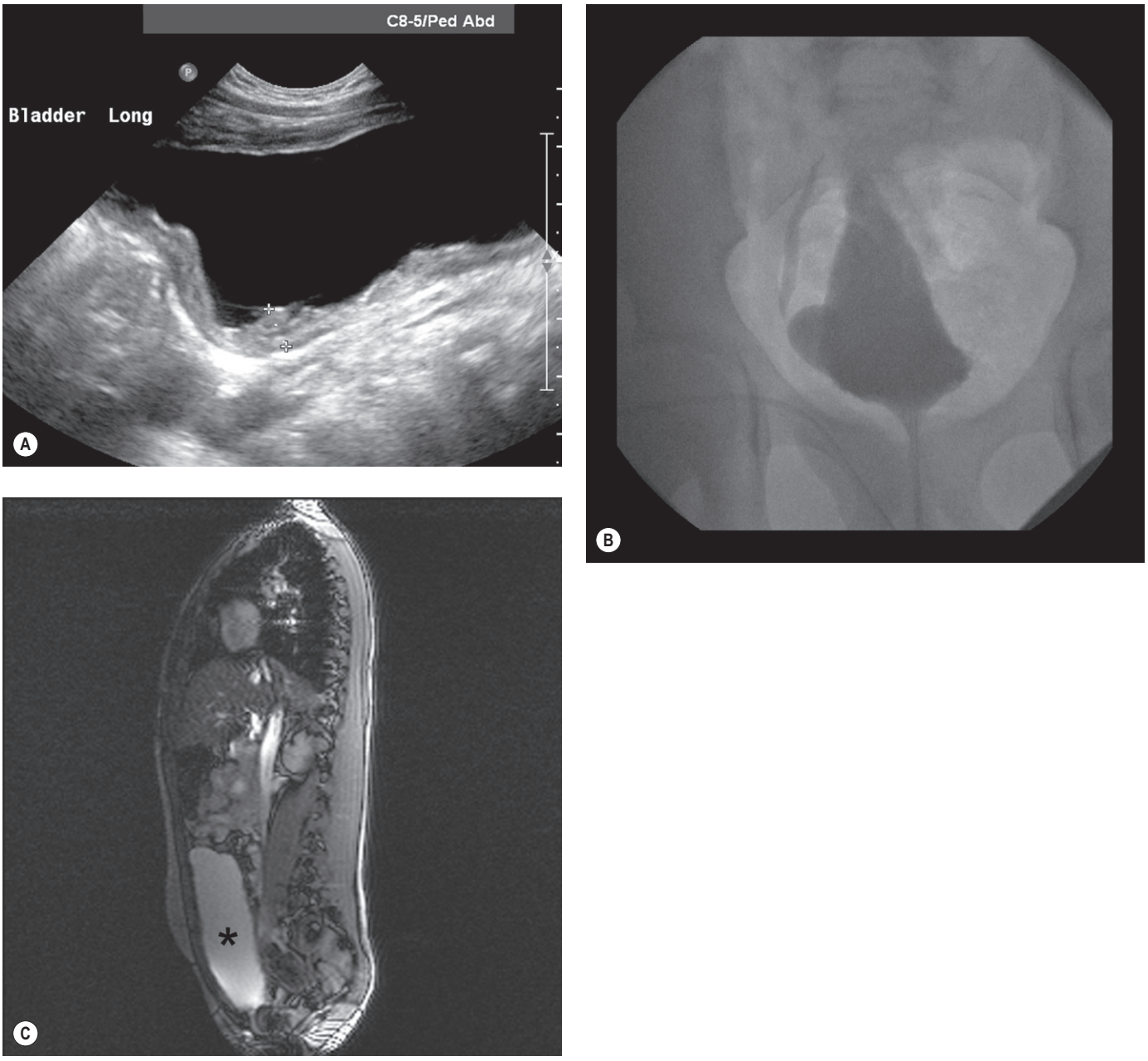

Figure 71.32 Neurogenic urinary bladder: imaging of a 7-year-old boy. **A:** Longitudinal ultrasound showing bladder wall thickening in a large capacity bladder. **B:** VCUG showing typical 'Christmas tree' appearance of the neurogenic bladder. **C:** Sagittal T2 MRI of the spine showing a massive urinary bladder (*) in this child.

diagnosis of a prominent extrarenal pelvis which in itself is not clinically significant (Fig. 71.13A).

Most cases of UPJO are diagnosed on routine antenatal sonography and require serial follow-up including postnatal ultrasound assessment. Around 10% of cases are bilateral. Occasionally UPJO may be massive, resulting in a large cystic mass lesion occupying most of the ipsilateral abdomen and pelvis with an imperceptible shell of renal parenchyma (Fig. 71.34) and making the organ of origin difficult to assign. Cyst decompression with a percutaneous nephrostomy and urinalysis may be indicated. Rarely the ipsilateral ureter may reflux and here the diagnostic dilemma is to determine whether there is both ureteric reflux and obstruction. As in other cases of ureteric dilation a VCUG and MAG-3 renogram are helpful in determining the level of obstruction and presence of VUR.

Acquired renal obstruction

Fungal balls in the neonate, calculus, blood clot (related to tumour, infection or post biopsy), pus or rarely polyp and tumour all may cause intrinsic ureteric obstruction.

Extrinsic ureteric obstruction can be seen in cases of trauma, iatrogenic injury (surgery), inflammatory mass (Crohn's disease, appendix mass) or tumour (typically lymphoma).

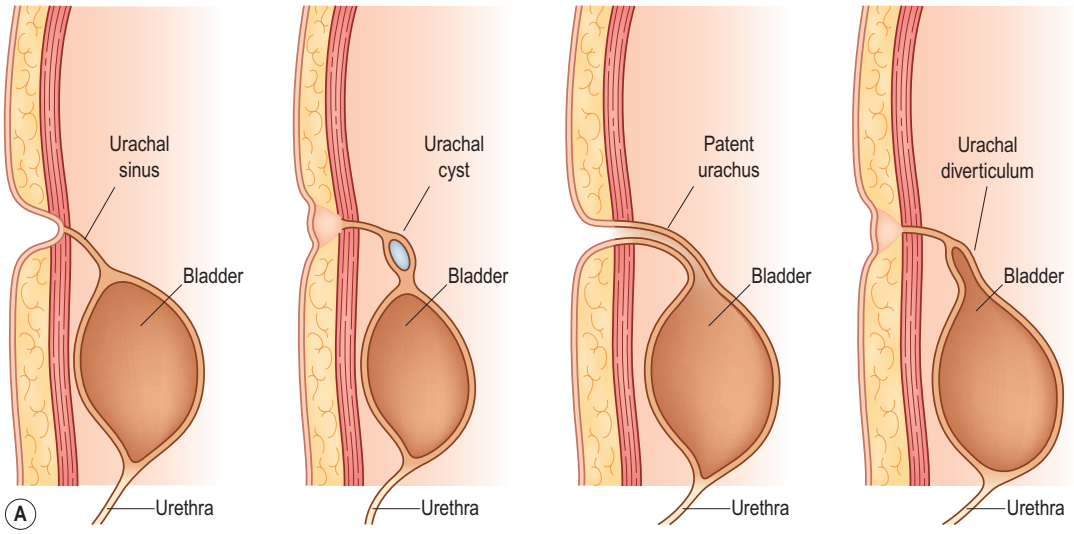

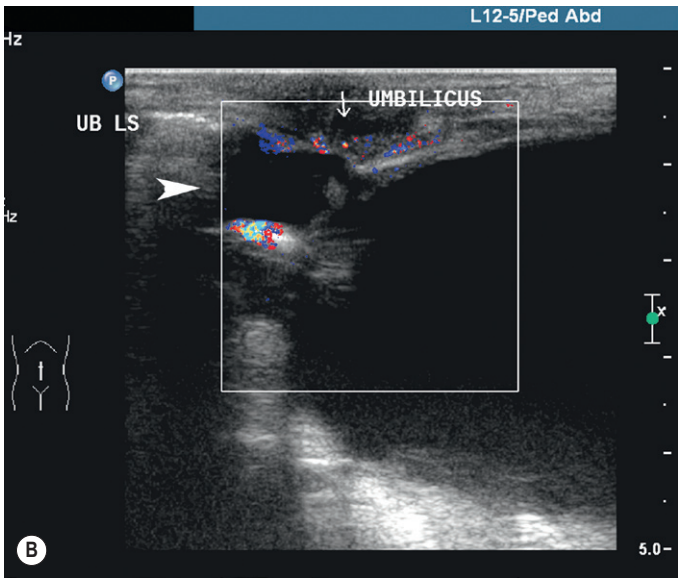

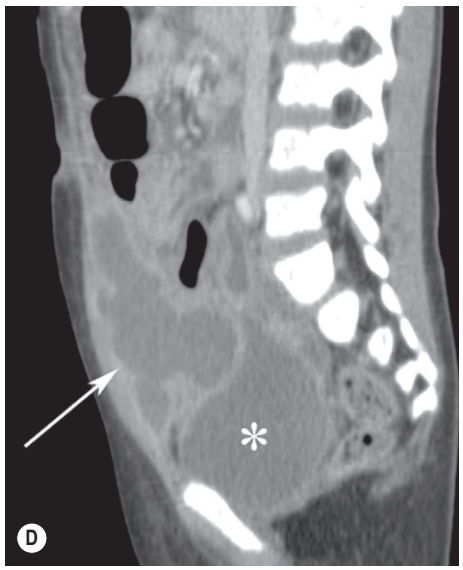

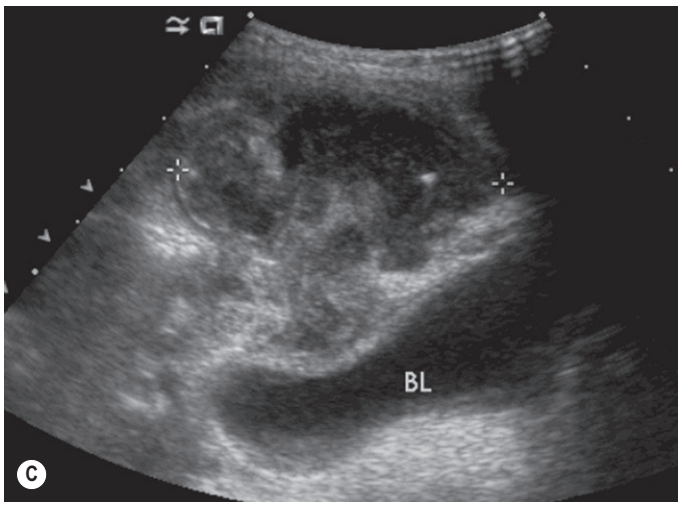

Figure 71.33 Urachal remnants. A: Line diagram summarising the various types of urachal remnant (reproduced with permission from H. Carty, F. Brunelle, D.A. Stringer, S. Kao (eds): Imaging Children, 2nd edn, Elsevier Churchill Livingstone, 2005). **B:** Longitudinal colour Doppler image of the bladder dome showing an extravesical cyst (arrowhead) in the midline just below the umbilicus of a 1-year-old boy with a weeping indurated umbilicus. This was confirmed to be a urachal cyst. **C:** Longitudinal high-resolution ultrasound showing debris within an infected urachal cyst (between callipers). BL, urinary bladder. **D:** Seen as an enhancing collection on a sagittal reconstructed contrast-enhanced abdominopelvic CT (arrow) draped over the bladder dome (*). This was resected when the initial infection had subsided.

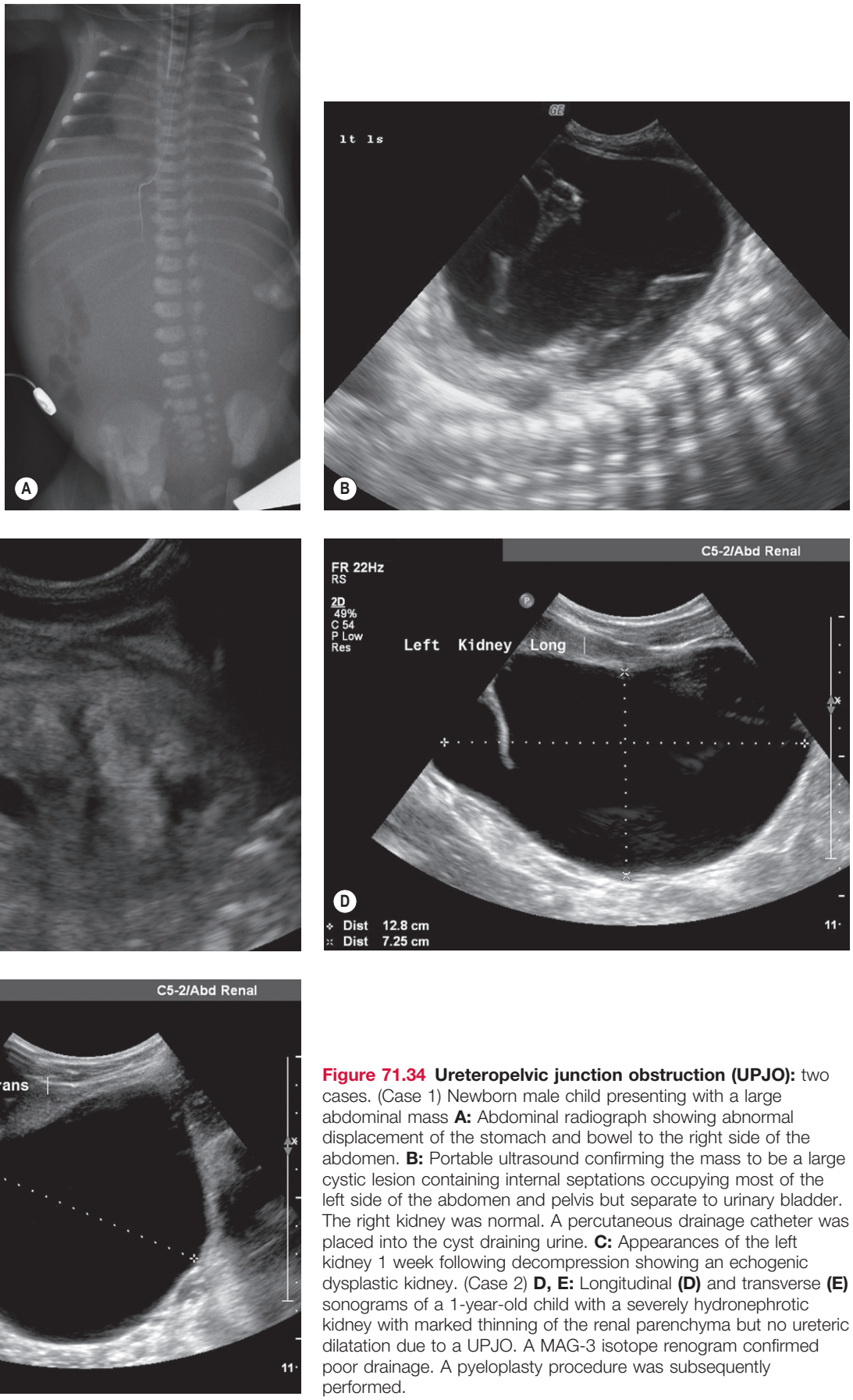

Figure 71.34 Ureteropelvic junction obstruction (UPJO): two cases. (Case 1) Newborn male child presenting with a large abdominal mass **A:** Abdominal radiograph showing abnormal displacement of the stomach and bowel to the right side of the abdomen. **B:** Portable ultrasound confirming the mass to be a large cystic lesion containing internal septations occupying most of the left side of the abdomen and pelvis but separate to urinary bladder. The right kidney was normal. A percutaneous drainage catheter was placed into the cyst draining urine. **C:** Appearances of the left kidney 1 week following decompression showing an echogenic dysplastic kidney. (Case 2) **D, E:** Longitudinal **(D)** and transverse **(E)** sonograms of a 1-year-old child with a severely hydronephrotic kidney with marked thinning of the renal parenchyma but no ureteric dilatation due to a UPJO. A MAG-3 isotope renogram confirmed poor drainage. A pyeloplasty procedure was subsequently performed.

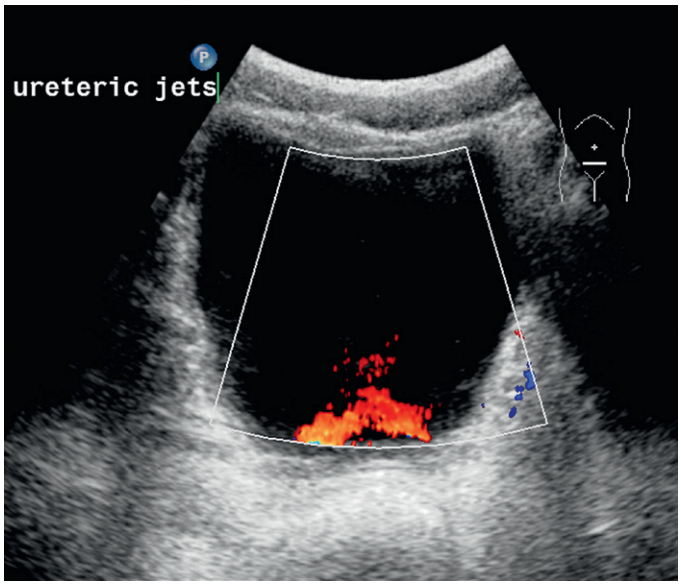

Figure 71.35 Ureterovesical flow jet. Axial colour Doppler interrogation of the ureterovesical orifices showing bilateral normal colour flow jets. This technique is useful in assessing antegrade flow of urine across the UVJ. Absent or reduced flow jets are seen in obstruction; comparison between the two sides is particularly useful in unilateral obstruction.

High-grade mechanical obstruction of the ureter results in an absent or diminished colour jet or flow velocity on Doppler imaging of the vesico-ureteric junction (Fig. 71.35).

Postnatal evaluation of antenatally detected renal tract dilatation

Hydronephrosis in the newborn

Urinary tract dilatation is the most commonly detected antenatal abnormality, with an incidence of around 0.5–1%. In most cases only mild renal pelvic dilatation is identified. Only a small proportion of this largely asymptomatic cohort of babies is at risk of developing clinically significant renal compromise. This poses a dilemma for the obstetrician, urologist and sonologist. Further postnatal investigation is required; but there is a lack of consensus as to when and how much imaging is necessary or desirable, particularly in excluding vesico-ureteric reflux.

Postnatal urinary tract dilatation may result from vesico-ureteric reflux seen in around a third of cases, and obstruction or combination of the two processes in the remainder. The severity of obstructive uropathy depends upon the level, degree and duration of obstruction. The differential diagnosis of antenatally detected hydronephrosis includes ureteropelvic junction (UPJ) obstruction, megaureter, ureterovesical junction (UVJ) obstruction, posterior urethral valves (PUV), urethral atresia or stricture, prune belly syndrome, vesico-ureteral reflux (VUR), duplicated collecting system with ureterocele and multicystic dysplastic kidney (MCDK).

Severe fetal urinary tract obstruction can lead to oligohydramnios resulting in lung hypoplasia and respiratory failure. Recognised orthopaedic complications include limb contractures and talipes equinovarus. Not all cases are detected antenatally and screened postnatally. Urinary obstruction may present in the neonate with sepsis or respiratory distress and in the older child with urinary tract infection, poor urinary stream, failure to thrive or nephrolithiasis.

General principles of postnatal imaging for antenatally detected urological abnormality

All antenatally detected uropathy should be assessed postnatally including:

- dilated renal pelvis
  - RPD >5 mm at 18–22 weeks[23]
  - RPD >10 mm at any gestation
  - increasing dilatation (even if RPD <10 mm)
- caliectasis
- ureteric dilatation
- ureterocele or bladder abnormality
- altered renal echotexture or renal cyst
- single kidney or ectopic kidney.

Scanning should be performed on day 2–3 of life when well hydrated and earlier only if there is severe hydronephrosis of both kidneys or a single functioning kidney.

Postnatal AP renal pelvic diameter less than or equal to 10 mm is normal in virtually all cases. Repeat imaging at 4 to 6 weeks is recommended to confirm initial normal findings.

Suggested imaging algorithms for postnatal evaluation of antenatally renal pelvic dilatation are summarised (Fig. 71.36).

Antenatal ultrasound findings

Anteroposterior renal pelvic diameter (RPD) assessed at the 18–22-week scan is the most useful predictor of renal disease. As a general rule 1 mm RPD is allowed per gestational month.

Transient physiological hydronephrosis is the most common cause of mild antenatal hydronephrosis and results from a prominent 'baggy' unobstructed extrarenal pelvis. VUR is the most likely pathological diagnosis in cases of mild antenatal hydronephrosis (RPD 5–9 mm). More severe antenatal hydronephrosis (RPD >10 mm) tends to be more commonly associated with UPJ obstruction.[24]

Postnatal evaluation of antenatally detected hydronephrosis

Physical examination of the neonate with proven antenatally detected hydronephrosis should precede ultrasound. UPJ obstruction or MCDK may present as a ballotable mass. Deficient abdominal wall musculature with bilateral undescended testes is seen in prune belly syndrome. A palpable urinary bladder is commonly noted in patients with PUV.

Infants with a prenatal ultrasound demonstrating a RPD greater than 5 mm should have renal ultrasounds repeated after birth at the first and sixth weeks of life.

The initial ultrasound scan should be performed after 2–3 days of life when the baby is well hydrated. Ultrasounds performed in the first 24 hours of life have a high false negative rate due to postnatal dehydration and oligoanuria which may mask obstructive uropathy. Immediate postnatal evaluation is warranted with a renal ultrasound and VCUG if the antenatal ultrasound demonstrates unilateral severe hydronephrosis in a single functioning kidney or bilateral severe hydronephrosis.[25]

A cut-off of 10 mm is used by most units for a normal postnatal renal AP pelvic diameter. More recently a meta-analysis of mainly observational studies has suggested that a cut-off of 12 mm was not associated with significant long-term morbidity or requirement for intervention.[26]

Suggested imaging algorithms for specific types of antenatal uropathy are summarised below:

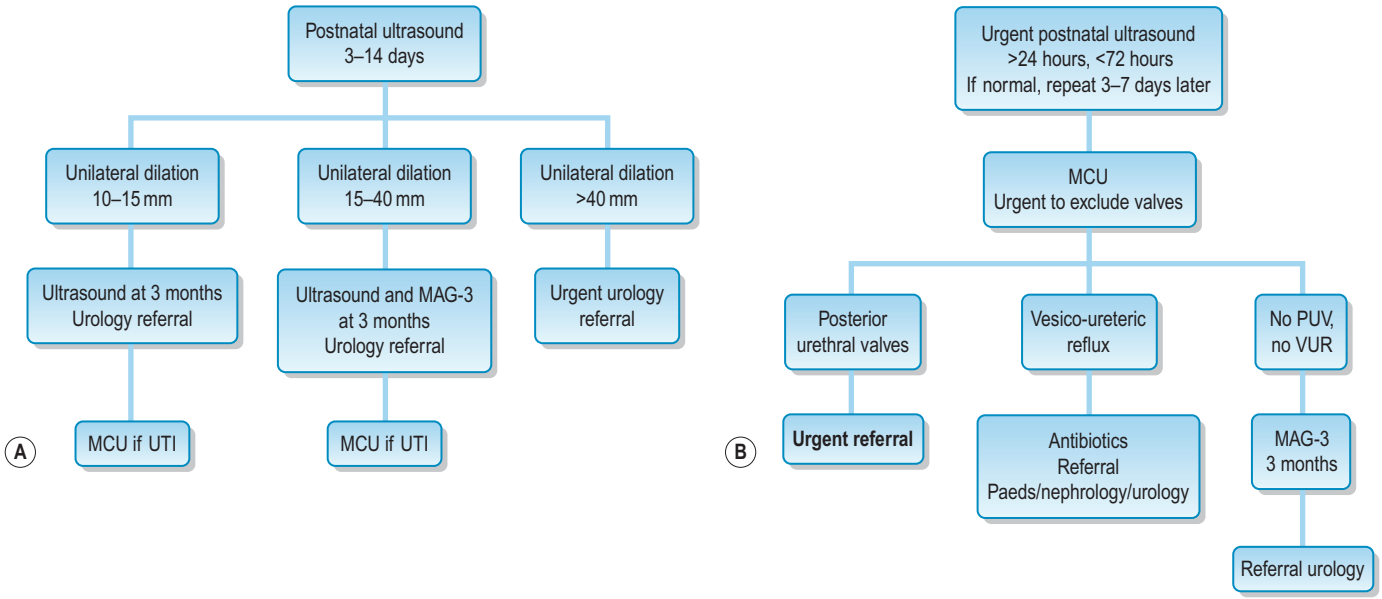

Figure 71.36 Imaging protocols for antenatally detected renal tract abnormalities. A: Protocol for isolated unilateral renal pelvic dilatation – without bladder or ureteric abnormality. **B:** Protocol for bilateral renal dilatation or unilateral dilatation with ureteric or bladder abnormality. MCU, micturating cystourethrogram. (Courtesy of the Regional Department of Paediatric Urology. Alder Hey Children's Hospital NHS Foundation Trust.)

- isolated unilateral renal pelvic dilatation (Fig. 71.36A)
- bilateral renal pelvic dilatation, single kidney with severe dilatation and ureteric dilatation or bladder abnormality (Fig. 71.36B).

The role of prophylactic antibiotics to prevent breakthrough infections is controversial but should be considered for any ureteric or bladder abnormality and significant upper tract dilatation.

Multicystic dysplastic kidney

Multicystic dysplastic kidney (MCDK) is a relatively common congenital form of renal dysplasia which occurs sporadically and is frequently detected on prenatal imaging. The condition probably relates to significant disruption of the developing ureteral bud in early fetal life resulting in discontinuity between the glomeruli and calyces.

The characteristic features of MCDK include:

- multiple non-communicating renal cysts of varying size on ultrasound (Fig. 71.37)
- absent kidney on functional imaging (DMSA or MAG-3 renogram)
- atretic ipsilateral ureter and pelvicalyceal system.

MCDK is usually a unilateral disorder. The prognosis of children with unilateral MCDK is dependent on the condition of the contralateral kidney. Contralateral abnormalities include UPJ obstruction and reflux. In the vast majority the overall prognosis is very good. A proportion will involute in utero and account for many cases of single kidney. Most postnatally detected MCDKs will undergo partial or complete involution. Associations include hypertension, urinary tract infection, vesico-ureteric reflux and rarely malignancy. The imaging strategies for the postnatal evaluation of MCDK are summarised in Figure 71.38.

The role and timing of nephrectomy is controversial. In many centres it is no longer regarded as routine clinical practice and most patients will undergo long-term imaging follow-up instead. Bilateral MCDK is rare and usually fatal.

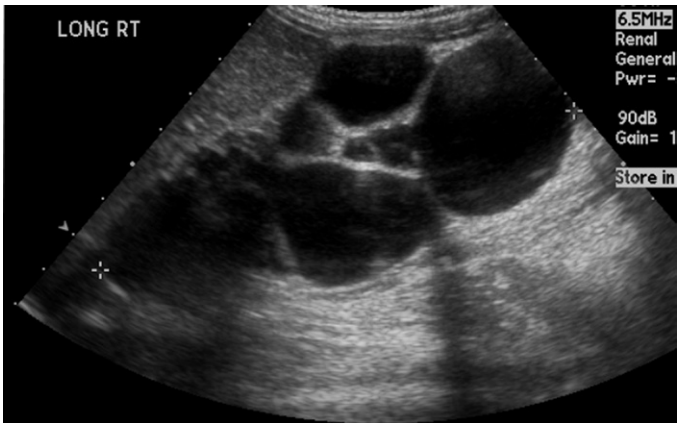

Figure 71.37 Multicystic dysplastic kidney (MCDK). Longitudinal sonogram showing multiple renal cysts of varying size and location centred on the right kidney in keeping with an MCDK (between callipers). No renal cortex or collecting system is identifiable. A DMSA scintigram confirmed no uptake in the non-functioning right kidney.

Renal cystic disease

Cystic renal disease refers to a broad range of conditions in which one or more microscopic or macroscopic renal cysts are present. These cysts can be solitary or multiple and unilateral or bilateral (Table 71.2). Renal cysts may be congenital in origin or acquired, detected antenatally or postnatally, syndromal, inherited or non-inherited (Table 71.3).

Ultrasound is the imaging modality of choice in the initial investigation of suspected renal cystic disease. Ultrasound should be

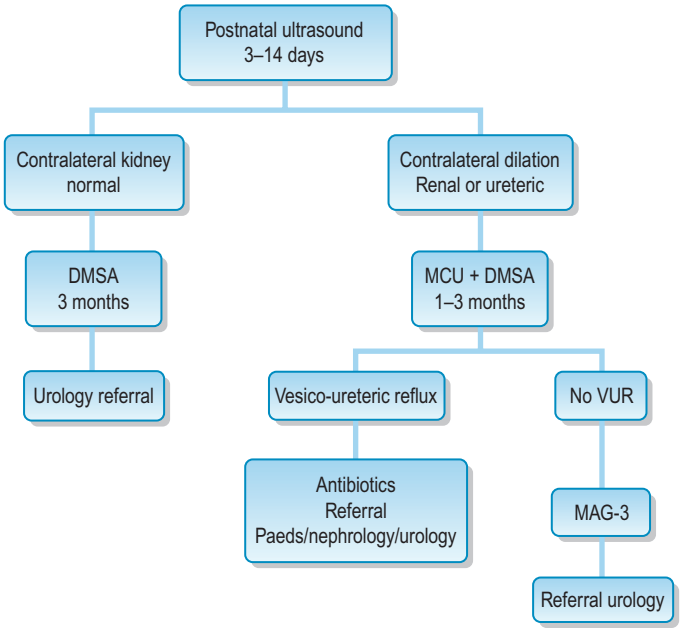

Figure 71.38 Imaging protocols for the postnatal evaluation of suspected multicystic dysplastic kidney. (Courtesy of the Regional Department of Paediatric Urology. Alder Hey Children's Hospital NHS Foundation Trust.)

Table 71.2 Cystic renal disease in children

Unilateral	Bilateral
Multicystic dysplastic kidney[a]	Autosomal recessive polycystic kidney disease (ARPKD)
Simple cyst	Autosomal dominant polycystic kidney disease (ADPKD)
Multilocular cystic nephroma	Juvenile nephronophthisis
Cystic renal dysplasia[b]	Glomerulocystic disease
	Medullary cystic disease
	Syndromic renal cystic disease
	Medullary sponge kidney

[a]*Bilateral disease is not compatible with life.*
[b]*Often bilateral.*

sufficient to document the extent of cystic renal disease in most cases and formulate the most likely differential diagnosis when appropriate clinical information is available at referral. In specific cases further imaging may be warranted as outlined below.

Useful clinical information in assessing a child with suspected cystic renal disease

- Maternal obstetric history.
- Antenatal history and imaging (liquor volumes and appearances of renal tract).
- Clinical findings of child being assessed (laboratory data, clinical genetics).
- Family history (imaging findings, clinical genetics, histology).

Documenting the extent of renal cystic disease

Ultrasound evaluation should ideally include assessment of:

Renal
Nature of cyst(s): simple versus complex (septation, associated solid mass, calcification, debris)
Colour Doppler flow findings
Number of cysts
Size of cysts: document range of sizes and size of largest cyst in each affected kidney
Location: cortical versus medullary or both
Distribution: unilateral versus bilateral
Renal lengths (comparison with age- or weight-related normative data)
Cortical and medullary echotexture: corticomedullary differentiation

Liver and spleen
Size
Presence of cysts
Parenchymal echogenicity
Bile duct dilatation
Features of portal hypertension

Cysts in solid viscera elsewhere

Table 71.3 Genetic classification of cystic renal disease (data from de Bruyn and Gordon[27])

GENETIC			NON-GENETIC
Autosomal recessive	**Autosomal dominant**	**Syndromal renal cystic disease**	
ARPKD	ADPKD	Joubert syndrome	Cystic renal dysplasia
Juvenile nephronophthisis	Medullary cystic disease	Ivemark syndrome	Simple cyst
Syndromal recessive	Glomerulocystic disease[b]	Laurence–Biedl–Moon	Parapelvic cyst
Zellweger syndrome[a]	*Syndromal dominant*	Von Hippel–Lindau	Medullary sponge kidney
Meckel–Gruber syndrome	Tuberous sclerosis	Trisomies 13, 18 and 21	Multilocular cystic nephroma
Oral-facial digital syndrome	Von Hippel–Lindau syndrome	Conradi syndrome	Acquired cystic renal disease
Jeune's syndrome			Wilms' tumour
			Glomerulocystic disease

[a]*Associated with glomerulocystic disease.*
[b]*With small kidneys.*

Autosomal recessive polycystic kidney

Autosomal recessive polycystic kidney (ARPKD) is a relatively uncommon condition characterised by cystic dilatation of the renal collecting tubules and hepatic involvement with bile duct ectasia (Caroli's disease) and liver parenchymal fibrosis. The severity of renal involvement tends to be inversely proportional to the degree of liver disease.

The antenatal sonographic diagnosis of ARPKD is frequently made on the basis of bilateral enlarged echogenic kidneys in the setting of oligohydramnios. The differential diagnosis of these antenatal findings includes autosomal dominant polycystic kidney disease, cystic renal dysplasia, syndromal cystic renal disease and glomerulocystic disease.

Neonates and infants usually present severe renal impairment or hypertension with little or no hepatic involvement. Typical ultrasound findings include bilateral enlarged kidneys with echogenic cortex and medullae with loss of corticomedullary differentiation (Fig. 71.39). The cysts are typically small (1–2 mm) and are best seen on high-resolution ultrasound and affect both the cortex and medullae. The multiple fluid interfaces resulting from the small cysts account for the bright renal parenchyma. Many neonates succumb to respiratory failure from the resulting pulmonary hypoplasia. Survivors often require renal replacement therapy as a bridge to renal transplantation.

In older children the kidneys are less markedly enlarged. The renal manifestations are more in keeping with autosomal dominant polycystic kidney and the predominant problems are hepatic fibrosis, portal hypertension with hepatosplenomegaly and abdominal varices.

Autosomal dominant polycystic kidney disease in the paediatric population

The renal manifestations of autosomal dominant polycystic kidney (ADPKD) are usually detected in adulthood. Rarely cases may be seen prenatally. Most paediatric cases are identified throughout childhood and adolescence in known at-risk families undergoing screening or in de novo presentations. Renal cysts develop as a result of pathological dilatation of the collecting tubule.

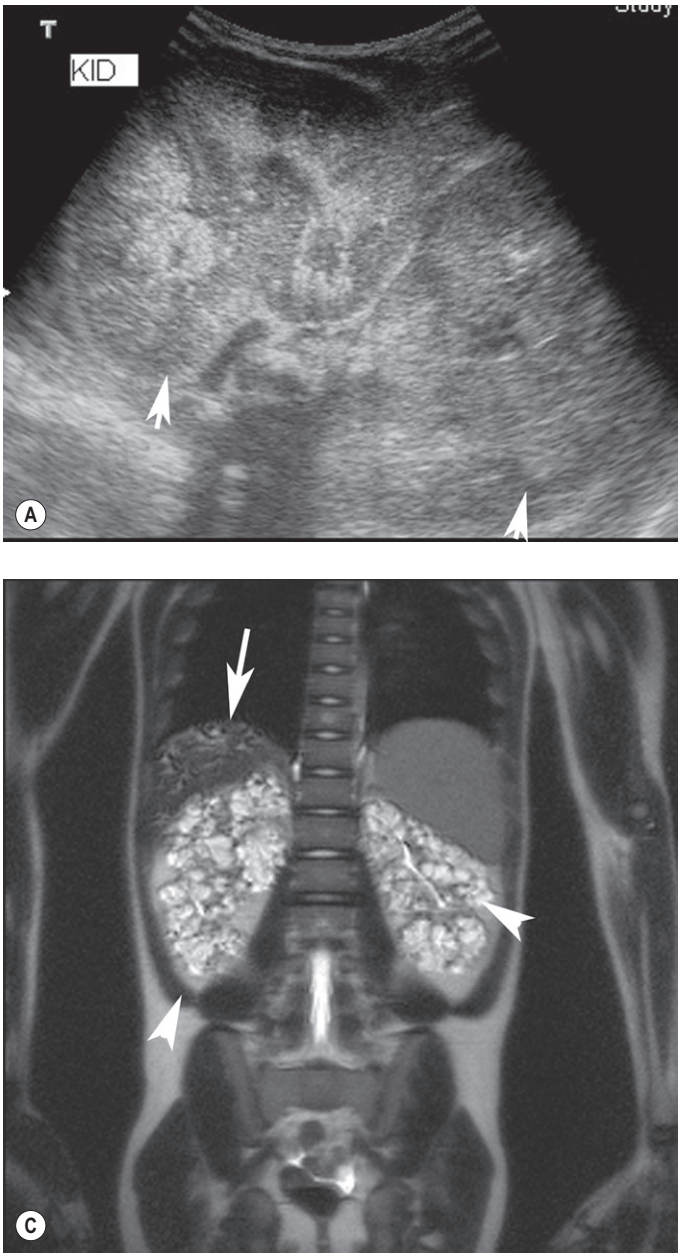

Figure 71.39 Autosomal recessive polycystic kidney disease (ARPKD). A: Transverse sonogram showing two very large echogenic kidneys (arrowheads) occupying most of the abdomen in a newborn premature female with antenatal history of oligohydramnios. **B:** Longitudinal high-resolution sonogram in a 1-year-old with ARPKD showing echogenic renal parenchyma with loss of corticomedullary differentiation and small cysts (arrow); these are often only seen at higher resolution. **C:** Coronal T2 gradient-echo MR image showing typical features of ARPKD – with intrahepatic bile duct dilatation and liver fibrosis (arrow), and bilateral enlarged kidneys containing multiple small cysts (arrowheads).

Antenatal and neonatal sonographic findings include bilateral enlarged kidneys which show loss of corticomedullary differentiation. Small cysts may be seen. The ultrasound features are very similar to ARPKD. Whilst oligohydramnios, hepatic fibrosis and significant neonatal renal impairment or hypertension are extremely unusual; such clinical features are not necessarily helpful in differentiating between neonatal ADPKD and ARPKD and can be seen in both conditions but more usually in ARPKD.

The sonographic findings in older children are similar to those in adults and include bilateral renal enlargement, echogenic parenchyma with loss of corticomedullary differentiation, variable cortical thickness, and multiple large cysts which are of varying size and parenchymal distribution within the renal cortex and medulla (Fig. 71.40). Large cysts are at greater risk of haemorrhage. Urinary tract infection is another presenting feature and like haemorrhage a cause of sedimentation within the renal cyst. Occasionally a haemorrhagic cyst is difficult to differentiate from a renal tumour. Follow-up ultrasound in patients with known ADPKD is an option, but CT or magnetic resonance imaging (MRI) is often required as part of the work-up (Fig. 71.41). Hypertension and end-stage renal failure are late complications. Cysts may also be seen in the liver, spleen, pancreas, adrenal gland, thyroid gland, testis or uterus. The first degree relatives of affected children are usually offered genetic counselling and sonographic screening.

Cystic renal dysplasia

Cystic renal dysplasia is a disorder of metanephric differentiation resulting in persisting fetal renal tissue. The condition may be segmental or diffuse and affect one or both kidneys depending on the underlying disorder. Antenatal obstructive or refluxing uropathy usually developing later in fetal life than MCDK is a common cause. In infants this is most commonly seen in the posterior urethral valve but can also be seen in urethral stricture/atresia, ureteropelvic and ureterovesical junction stenosis and occlusion.

Dysplastic kidneys show poor renal function on DMSA scintigraphy and can be difficult to differentiate from true renal scarring. DMSA and VCUG should be performed in infants with dysplastic

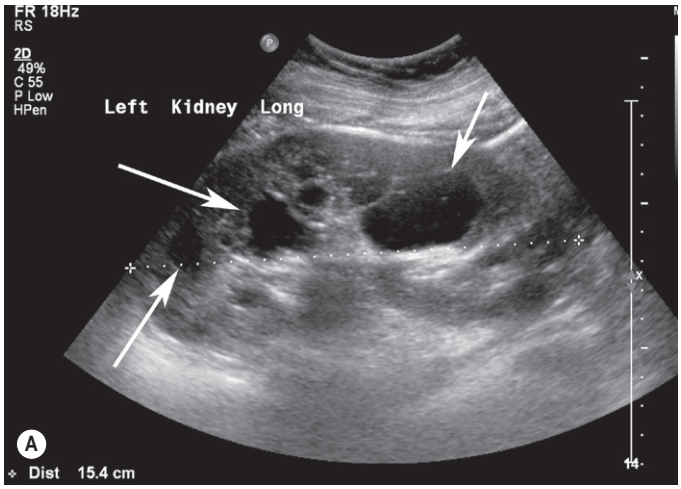

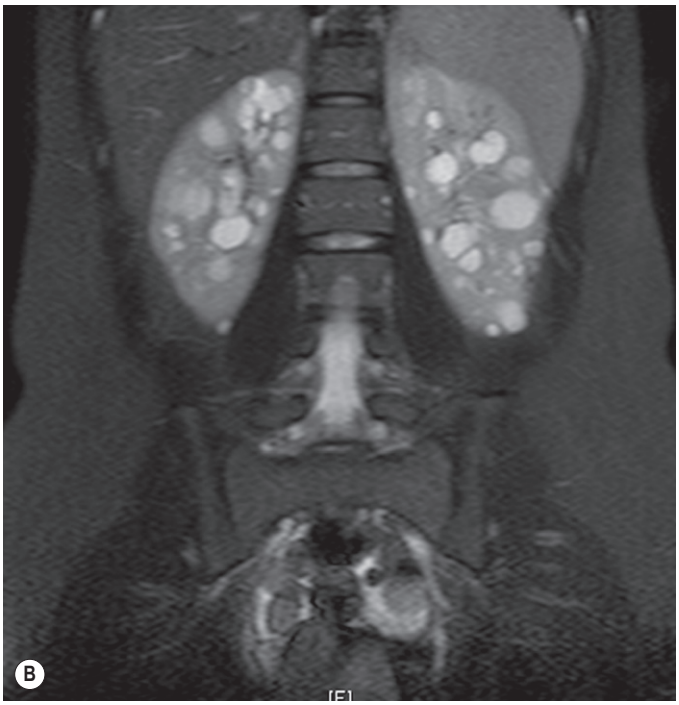

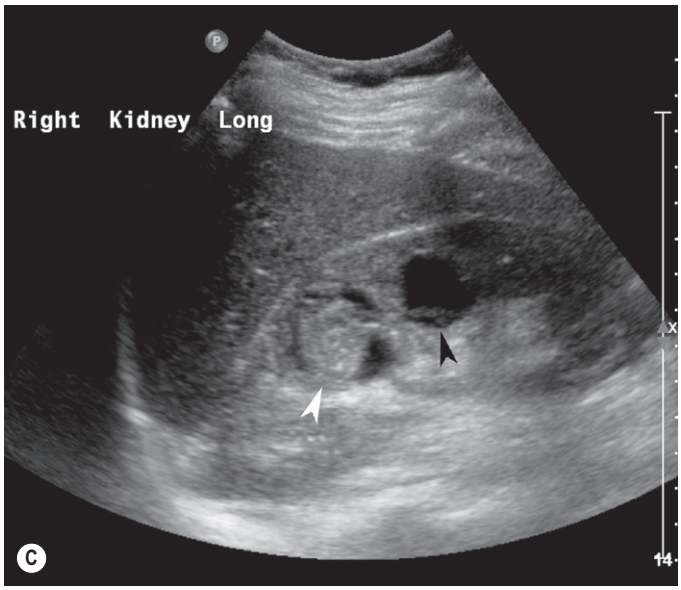

Figure 71.40 **Autosomal dominant polycystic kidney disease (ADPKD). A:** Longitudinal sonogram of an enlarged left kidney showing multiple simple cysts (arrows) of varying size. **B:** Coronal T2 gradient-echo image in the same patient showing multiple renal cysts throughout both kidneys. This child had a family history of PKD1-type ADPKD. **C:** Longitudinal sonogram of the right kidney in another patient with ADPKD presenting with loin pain showing two renal parenchymal cysts with varying amount of echogenic material from recent haemorrhage (arrowheads).

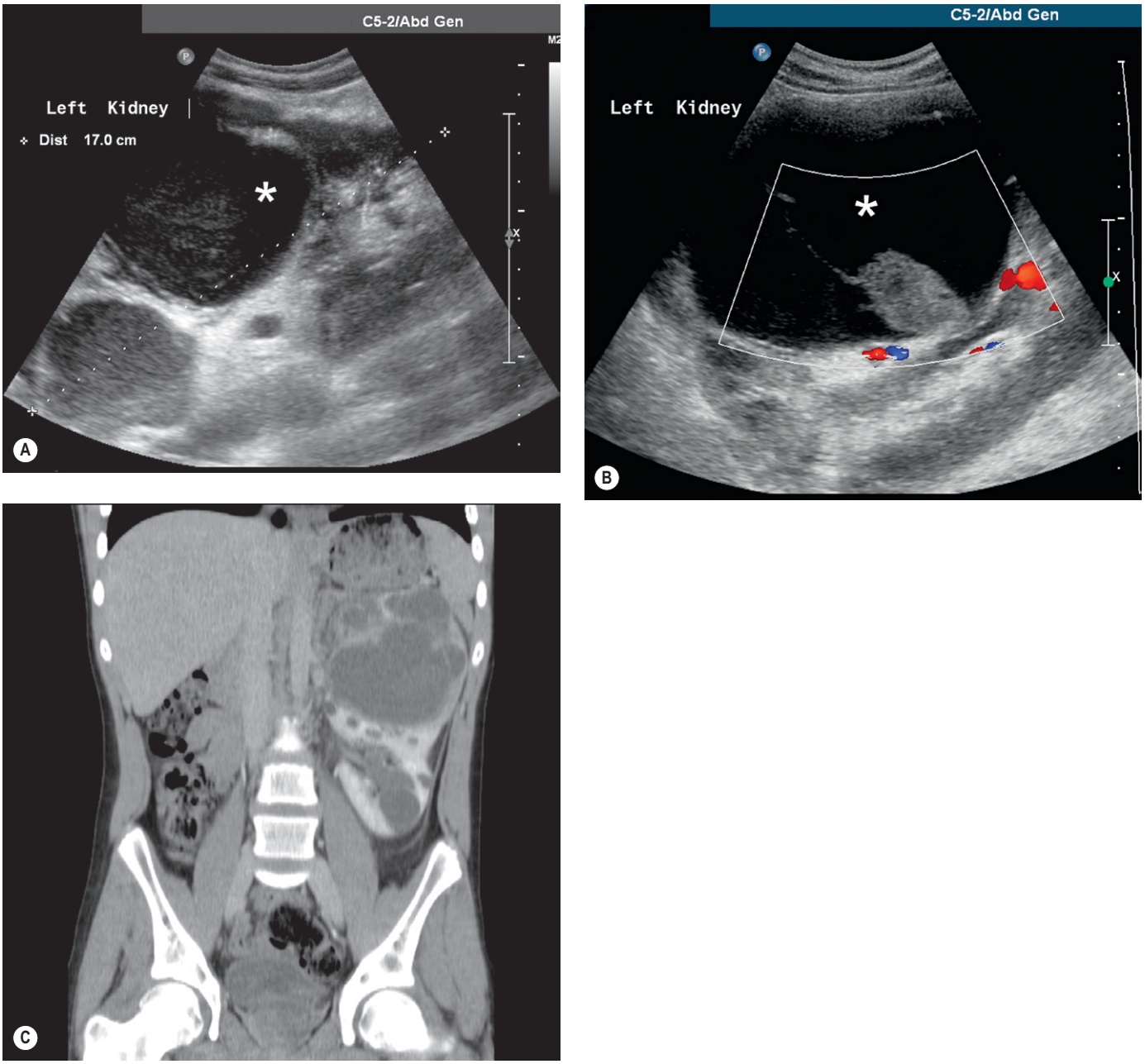

Figure 71.41 Autosomal dominant polycystic kidney disease (ADPKD) post-traumatic complex cyst. Teenage skateboarder with known ADPKD presenting with haematuria and left loin pain. Longitudinal **(A)** and transverse **(B)** sonogram of an enlarged polycystic left kidney showing a large complex cyst (*). **C:** Coronal reformatted image from a contrast-enhanced CT scan delineating the upper pole haemorrhagic cyst.

kidneys. Typical sonographic findings include small kidneys with loss of corticomedullary differentiation, and multiple small cortical cysts within echogenic renal parenchyma in the presence of an obstructive uropathy (Fig. 71.42).

Medullary cystic disease

Medullary cystic disease (MCD) is an autosomal dominant condition which manifests as late-onset chronic renal failure. The familial juvenile form, juvenile nephronophthisis (JN), is an autosomal recessive disorder characterised by a chronic sclerosing tubulo-interstitial salt-losing nephropathy leading to progressive renal failure in childhood. The resulting decreased urine-concentrating ability manifests as polydipsia, polyuria, enuresis, anaemia, failure to thrive and short stature.

The sonographic hallmark of JN at presentation is the presence of normal sized hyperechoic kidneys in a child with progressive renal failure. The diagnosis of JN is made at renal biopsy. Medullary or corticomedullary cysts (<2 cm) typically present during the later stages of the disease when there is established end-stage renal failure.[28] Small hyperechoic kidneys eventually result from cortical loss.

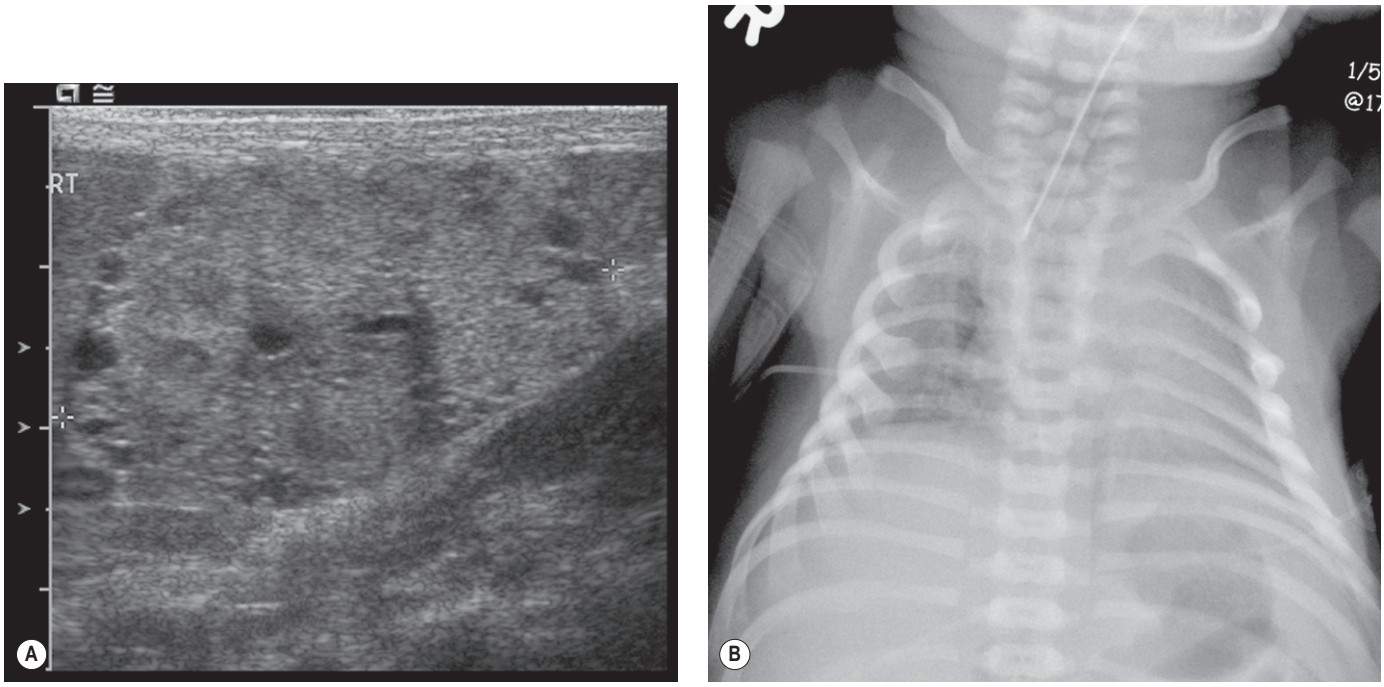

Figure 71.42 Cystic renal dysplasia. A: High-resolution longitudinal sonogram in a newborn male, showing a small uniformly echogenic kidney with loss of corticomedullary differentiation, containing multiple small renal subcortical cysts. **B:** Chest X-ray of the same child intubated at birth for respiratory distress showing pulmonary hypoplasia.

Medullary sponge kidney

Medullary sponge kidney (MSK) is rarely encountered in the paediatric population. The condition relates to cystic dilatation (tubular ectasia) affecting the renal medullae.

IVU is diagnostic, showing a characteristic contrast blush centred on the renal medullae (Fig. 71.43A). The ultrasound findings depend on the stage of the disease. The kidneys are sonographically normal in early disease and later on show increased medullary echogenicity in normal sized kidneys progressing to medullary nephrocalcinosis (Fig. 71.43B). Complications of MSK include infection, renal calculi and haematuria.

Glomerulocystic kidney disease

Glomerulocystic kidney disease (GCKD) is an uncommon heterogeneous group of conditions characterised by dilatation of the first portion of the proximal convoluted tubule. Clinical subtypes include (i) heritable or sporadic non-syndromic forms, (ii) heritable syndromal forms and (iii) part of dysplastic kidney disease which may be syndromal.

Affected infants usually present with palpable enlarged kidneys and renal impairment. Ultrasound features include enlarged kidneys, increased cortical and medullary echogenicity, loss of corticomedullary differentiation, and subcapsular cysts (typically <1 cm) which may eventually involve all the renal cortical parenchyma. Periportal liver fibrosis and bile duct dilatation may also be seen. In practice it may be difficult clinically and on imaging to differentiate GCKD from ARPKD.

Hereditary and syndromal renal cystic disease

Many syndromes are associated with renal cysts; these are summarised in Table 71.3.

Tuberous sclerosis is an autosomal dominant condition characterised by mental retardation, seizures and hamartomas affecting multiple organ systems. Renal manifestations include simple cortical and medullary cysts (Fig. 71.44). Renal angiomyolipomata are another feature. Hamartomas also involve the brain, skin (adenoma sebaceum), retinas (phakomata), heart (rhabdomyoma) and bones.

Von Hippel–Lindau (VHL) disease is an autosomal dominant condition comprising multiple visceral cysts and solid masses affecting several organ systems with the potential to undergo malignant transformation in adulthood. The abdominal and pelvic manifestations of children with VHL include simple cysts which may affect the kidneys (multiple and bilateral cortical cysts), pancreas or epididymes. There is a recognised association of VHL with phaeochromocytoma in children. Regular screening with ultrasound is sensible under the direction of a clinical geneticist.

Simple cyst

Simple renal cysts in children are rare and should be considered a diagnosis of exclusion. A compound calyx may be mistaken for a renal cyst. Care should be taken to ensure that a true parapelvic cyst is differentiated from a calyceal diverticulum (Fig. 71.45). The latter is a risk for nephrolithiasis. An upper pole renal cyst may in fact represent a rudimentary duplex system.

Follow-up ultrasound is recommended to ensure further cysts do not develop. Should a cyst show disproportionate interval growth or become more complex with interval septation or calcification or develop a solid component, then an underlying malignancy should be excluded. Biopsy with a view to nephron-sparing surgery should be considered.

Multilocular cystic nephroma

This benign 'tumour' typically occurs in boys under the age of 2 years or adult females. The ultrasound findings in multilocular cystic nephroma are of a fairly well-circumscribed multicystic mass containing internal septations of variable thickness (Fig. 71.46). The presence of solid components or parenchymal flow should alert the

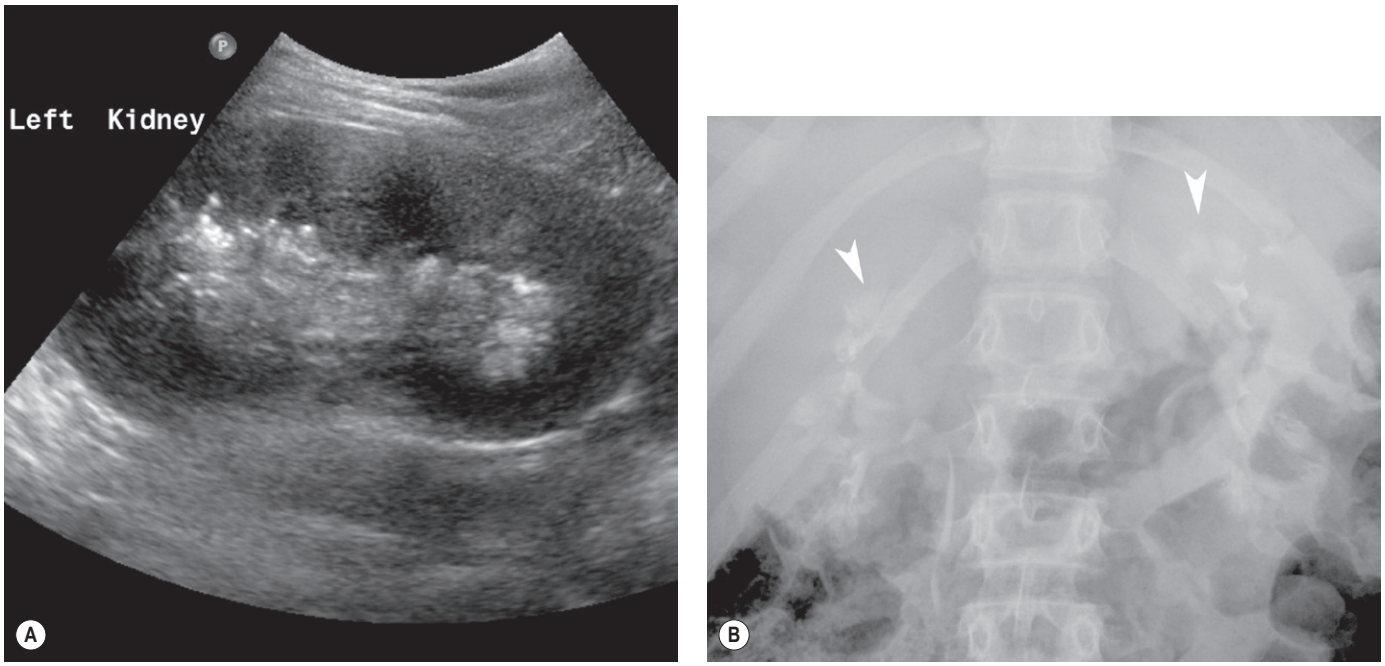

Figure 71.43 Medullary sponge kidney (MSK). Imaging of child with Rabson–Mendenhall syndrome, which is a rare condition characterised by severe insulin resistance and is associated with MSK. MSK is rare in the paediatric population. **A:** Longitudinal sonogram showing medullary nephrocalcinosis. **B:** 5-minute cross kidney film from an IVU series showing characteristic discrete linear densities within the renal papillae (arrowheads). The IVU findings are specific.

Unilateral renal cysts in children

- Ultrasound is usually sufficient to diagnose renal cystic disease.
- A simple renal cyst is uncommon in paediatric practice and merits further investigation and nephrology or urology input. Long term follow-up ultrasound should be undertaken to monitor the development of new cysts.
- Intravenous pyelography is helpful in demonstrating a calyceal cyst or duplex system.
- A complex cyst (particularly with solid portions or colour flow) should be treated as being suspicious for malignancy and should undergo biopsy with a view to nephron-sparing resection.

clinician to the presence of associated renal malignancy. The cysts can contain internal echoes from mucoid debris or internal haemorrhage and may be difficult to differentiate from normal parenchyma. In practice multilocular cystic nephroma cannot be differentiated from Wilms' tumour by imaging. Cross-sectional imaging should be undertaken and the lesion treated as malignant until proven otherwise.

The diffusely echogenic kidney

Increased renal reflectivity, also referred to as the 'bright' or echogenic kidney, is recognised when the renal parenchymal echogenicity is greater than that of normal liver or spleen parenchyma (Fig. 71.47). This abnormal finding is very non-specific and there are numerous causes of echogenic kidneys in children.

Useful information in the clinical referral of such patients include: relevant prenatal history, the age of onset, clinical presentation and family history.

Commonly encountered patterns include:

- enlarged echogenic kidneys with abnormal echotexture (Table 71.4)
- hyperechoic renal medulla with normal architecture (Table 71.5)
- small echogenic kidneys with abnormal echotexture.[29]

Table 71.4 Enlarged echogenic kidneys with abnormal echotexture

Acute tubular necrosis (can be normal sized)
Renal vein thrombosis
Recessive polycystic kidney disease
Dominant polycystic kidney disease
Dominant polycystic kidney disease with glomerulocystic disease
Sporadic glomerulocystic disease
Diffuse cystic renal dysplasia
Dysplastic renal disease associated with a syndrome
Congenital nephrotic syndrome
Haemolytic uraemic syndrome
Contrast nephropathy
Transient nephromegaly
Renal candidiasis
Renal involvement in biliary atresia
Renal glycogen storage disease
Renal leukaemic infiltrate

Bilateral small echogenic kidneys

The vast majority of small kidneys with hyperechoic parenchyma and abnormal architecture in young children are the result of cystic dysplasia associated with urinary tract obstruction (Fig. 71.42). Other causes include hypoplastic dysplastic kidneys and cortical and medullary necrosis in the newborn.

In older children established medical renal disease and renal scarring (see Fig. 71.60) are common causes of bilateral small echogenic kidneys.

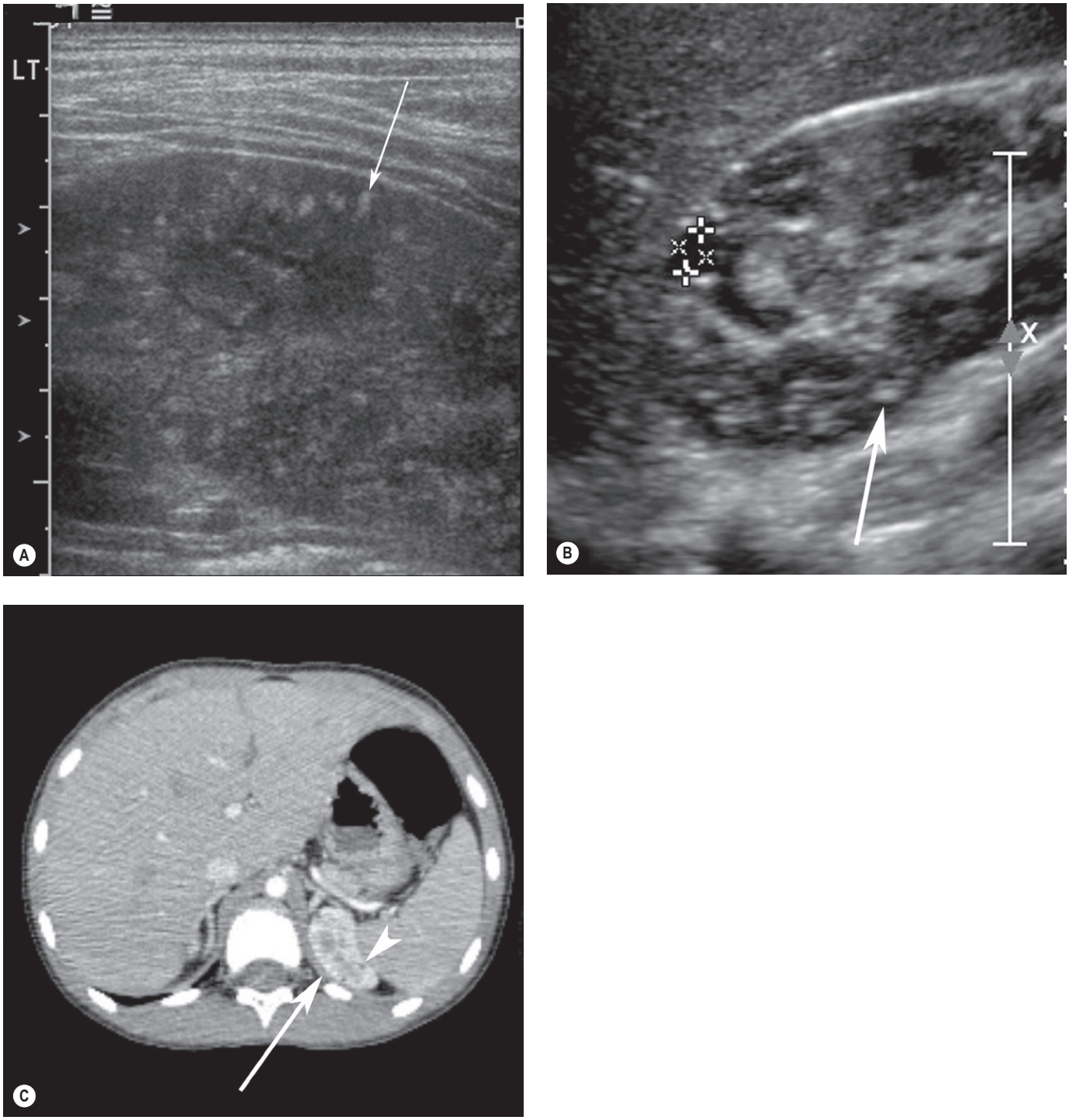

Figure 71.44 **Renal manifestations of tuberous sclerosis (TS). A:** High-resolution longitudinal sonogram showing multiple small hyperechoic foci throughout the renal parenchyma (arrow) typical of angiomyolipomata (AML). **B:** Ultrasound showing a renal cyst in a TS patient (between callipers) and AML (arrow). **C:** Axial contrast-enhanced CT of the same patient showing multiple small peripheral enhancing AML (arrow) and small renal cysts (arrowhead).

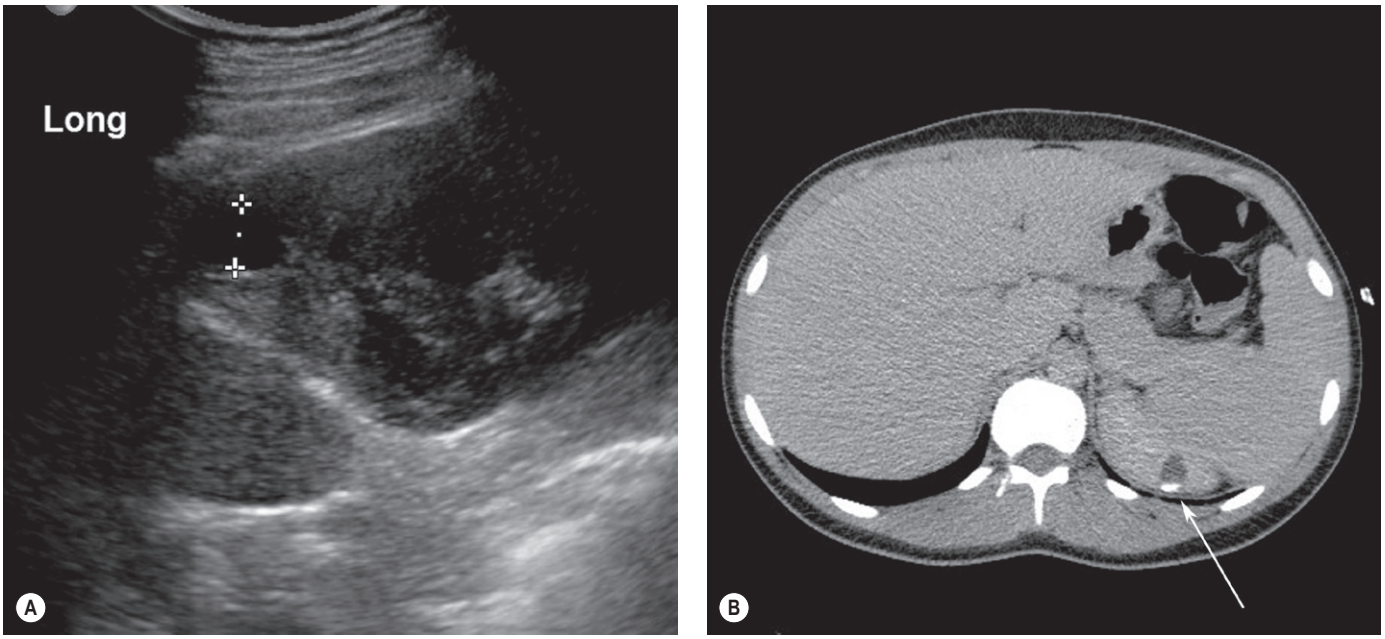

Figure 71.45 Calyceal diverticulum. A: Longitudinal sonogram in an oncology follow-up patient demonstrating what was thought to be an incidental renal cyst (between callipers). **B:** Previous contrast-enhanced CT scan in retrospect showed this cyst to fill with excreted intravenous contrast (arrow) consistent with a calyceal diverticulum. Renal cysts in children are rare and merit specialist follow-up.

Table 71.5 Increased medullary echogenicity with preserved architecture

Hypercalcaemia
Idiopathic nephrocalcinosis (Williams syndrome, absorptive hypercalciuria)
Oxalosis
Renal tubular acidosis
Iatrogenic (furosemide, treatment for hypophosphotaemic rickets)
Tamm–Horsfall proteinuria
Infection (CMV, *Candida*)
Sickle cell nephropathy
Rare causes: Bartter syndrome, Cushing syndrome, lipoid necrosis, Lesch–Nyhan syndrome, thyroid dysfunction

Table 71.6 Common causes of echogenic kidney in the older child

Glomerulonephritides
Vasculitides
Tubular interstitial nephritides (prerenal causes such as ATN, sepsis, drugs and toxins)
Renal cystic disease
Renal dysplasia
End-stage renal failure
Hypertensive nephrosclerosis
Tumour infiltration (lymphoma, leukaemia, nephroblastomatosis)
Deposition disorders (glycogen storage disease)

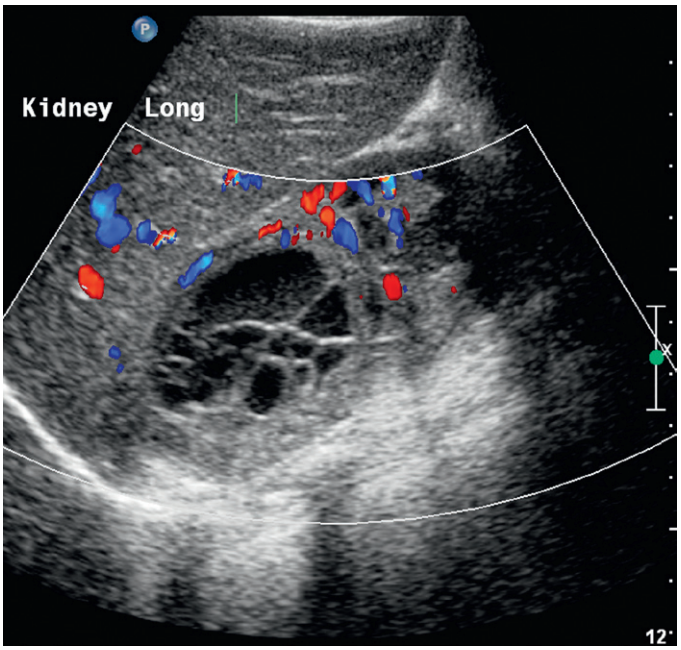

Figure 71.46 Multilocular cystic nephroma. Longitudinal colour Doppler sonogram in a 1-year-old boy with a well-circumscribed multicystic mass lesion in the upper pole of the right kidney. The majority of cysts are anechoic with echogenic septa. The largest imaged cyst contains debris.

The echogenic kidney in the older child

There are numerous causes of hyperechoic kidneys in older children. Common or important causes are listed in Table 71.6.

Medical renal disease

Persisting haematuria or proteinuria, nephritic syndrome, nephrotic syndrome, tubular dysfunction, systemic hypertension, acute and chronic renal failure are all manifestations of medical renal disease for which medical imaging may be required.

Renal failure

Renal failure may be acute (ARF) or chronic (CRF) and further subdivided based on the site of disease as any combination of:

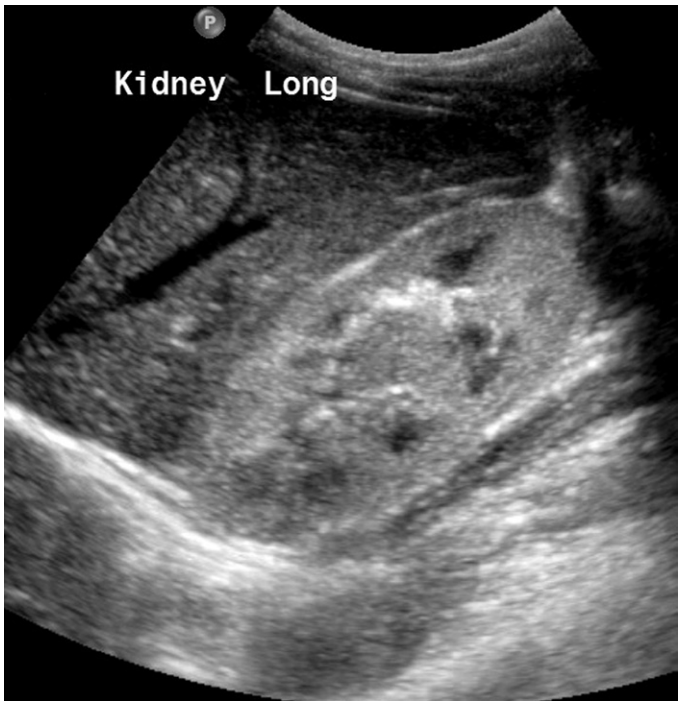

Figure 71.47 Echogenic kidney. Longitudinal sonogram in a 13-year-old girl presenting with an acute glomerulonephritis with renal impairment and haematuria; showing a normal sized kidney with bright cortex and loss of corticomedullary differentiation. Glomerulonephritis was confirmed by an ultrasound-guided renal biopsy.

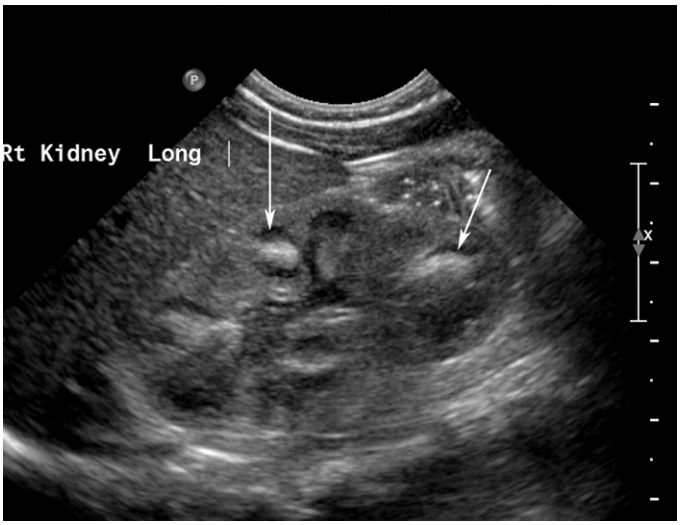

Figure 71.48 Tamm–Horsfall proteinuria. Longitudinal sonogram of the right kidney in a newborn male showing focal hyperechogenicity of the tips of several medullary pyramids (arrows).

- prerenal
- renal
- postrenal.

Renal tract ultrasound and a chest X-ray usually suffice in the initial management. Renal biopsy should be reserved for those cases where the clinical and imaging features alone are insufficient to make a definitive diagnosis. Biopsy is useful when there is poor response to treatment or persisting haematuria.

Abdominal ultrasound should address the following questions:

- What is the renal size, position and outline? (ARF – normal or enlarged kidneys: CRF – normal in medullary cystic disease but small in most other causes.)
- What is the renal parenchymal echogenicity and corticomedullary differentiation?
- Are there any focal lesion(s) (such as cysts, wedge-shaped infarcts)?
- Is there renal tract dilatation?
- Are the renal veins and inferior vena cava (IVC) patent?
- Is aortic calibre and aortic and renal perfusion normal?
- Is there nephrocalcinosis or nephrolithiasis?
- Is there ascites? (A pleural or pericardial effusion may be visible.)
- Are there any visceral cysts or liver parenchymal abnormality to suggest cystic disease?

A chest X-ray is helpful in documenting heart size, pleural effusions or pulmonary congestion.

Acute tubular necrosis

Acute tubular necrosis (ATN) refers to renal tubular injury as seen in shock (prerenal), exposure to nephrotoxins (renal) or obstructive uropathy (postrenal). Ultrasound reveals diffuse enlargement of the kidneys with loss of corticomedullary differentiation and echogenic parenchyma. ATN is frequently seen in neonates.

Tamm–Horsfall proteinuria (transient medullary hyperechogenicity)

This entity results from mucoprotein deposition, predominately Tamm–Horsfall protein, produced by nephrons which may transiently obstruct the renal tubules resulting in oligoanuria and stasis nephropathy in the newborn period. Ultrasound shows hyperechoic medullary pyramids (Fig. 71.48). This is a benign self-limiting process. The sonographic findings normalise within the first week of life with no long-term sequelae.

Vasculitides

Henoch–Schönlein purpura (HSP), also referred to as IgA nephropathy, is the most common vasculitis in childhood; it usually follows an intercurrent chest infection. Clinical manifestations include a characteristic purpuric rash, abdominal pain, arthralgia and renal disease. The diagnosis is often made clinically. The renal imaging findings are non-specific but demonstration of a small bowel intussusception or submucosal haemorrhage and typical clinical history are highly suggestive of the diagnosis (Fig. 71.49).

Other vasculitides involving the kidneys in childhood include Kawasaki disease, polyarteritis nodosa (PAN), Wegener's granulomatosis, Churg–Strauss syndrome and systemic lupus erythematosus. Renal biopsy may be required in these cases. Angiography is indicated in PAN.

Haemolytic uraemic syndrome

Haemolytic uraemic syndrome (HUS) is the most common cause of acute renal failure in children and typically follows a prodromal illness such as an *Escherichia coli* (O157:H7) gastroenteritis or occasionally an upper respiratory tract infection. HUS is characterised by a microangiopathic haemolytic anaemia, thrombocytopenia, oligo-anuric renal failure with microscopic haematuria, proteinuria and hypertension.

Abdominal symptoms predominate with bowel wall thickening (Fig. 71.50A). Initial renal sonographic findings may be normal. With more severe involvement the kidneys are enlarged and show diffuse increase in cortical echotexture (Fig. 71.50B). Most patients recover completely. Mortality is around 10% and renal impairment may persist in a third of cases.

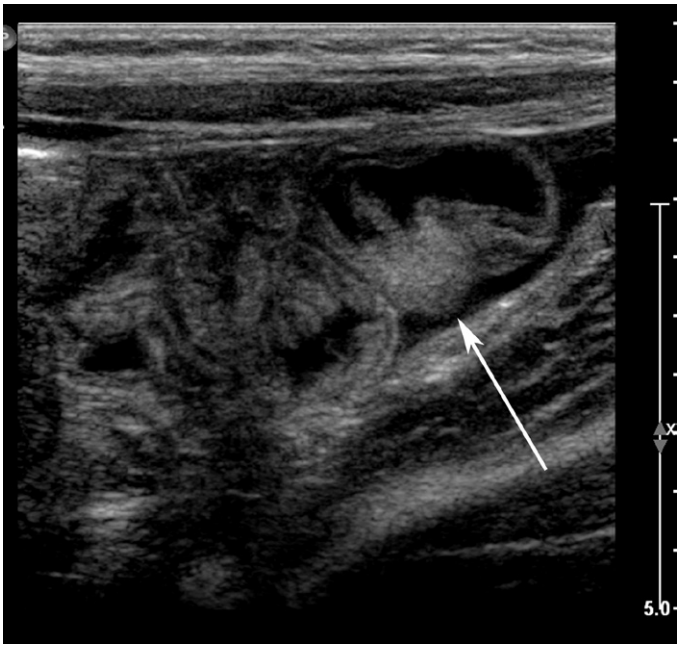

Figure 71.49 Henoch–Schönlein purpura. Transverse high-resolution sonogram of the left iliac fossa in a 7-year-old boy with purpuric rash, abdominal pain, haematuria and renal impairment. There is an abnormal hyperechoic focus within the wall of a loop of small bowel (arrow). Multiple such lesions were seen in keeping with submucosal haemorrhage. The kidneys appeared normal.

Cortical and medullary necrosis

Renal cortical and medullary necrosis are severe complications of perinatal asphyxia and shock. The mortality rate is high. The ensuing cortical infarction spares the medulla, juxtamedullary cortex and a thin rim of subcapsular cortex in all but the most severe cases. The kidneys initially are echogenic, normal sized to slightly enlarged and show poor perfusion but subsequently become smaller and remain echogenic. Affected areas may be become calcified and usually are non-functioning.

End-stage renal failure and renal transplantation

End-stage renal failure

Children with end-stage renal failure are at risk of poor growth and development due to the metabolic disturbances resulting from reduced creatinine clearance. Nutritional status is improved by parenteral or permanent enteral feeding, in order to achieve an optimum weight for renal transplantation. Colour Doppler ultrasound is frequently requested to assess for potential sites of central venous access. Ultrasound is an alternative to a contrast linogram in looking for catheter-related thrombus. Pericatheter fluid collections are also well seen on ultrasound.

Effective renal replacement therapy can be achieved with continuous ambulatory peritoneal dialysis (CAPD) until a suitable transplant becomes available. Ultrasound may be required in cases of suspected bacterial peritonitis to exclude a contained collection. Radiographs are useful to show the position of the tip of the CAPD catheter and demonstrate intrathoracic leakage of peritoneal dialysate. CAPD patients are at risk of intra-abdominal hernias, which are readily seen on ultrasound.

The major benefits of renal transplantation in children are in the avoidance of dialysis-related complications and providing the best opportunity for normal growth and development. The increasing availability of a live related donor for a child (often a parent) has

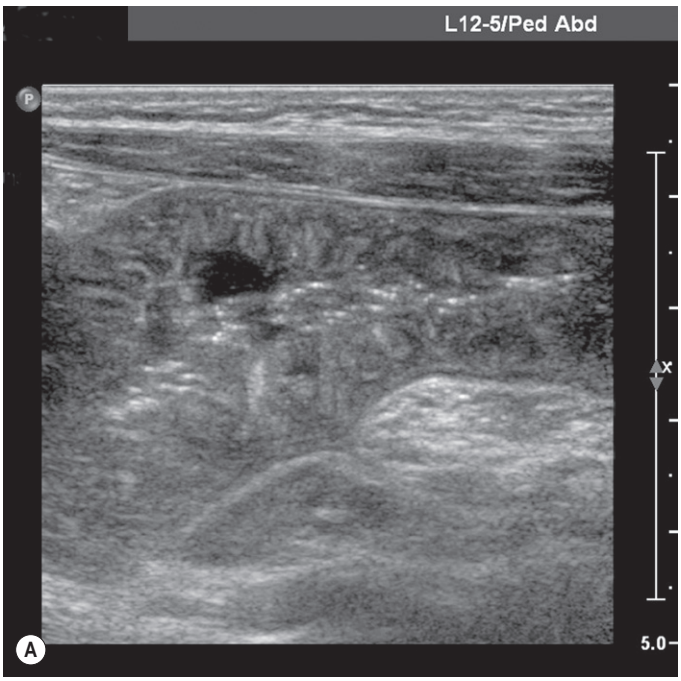

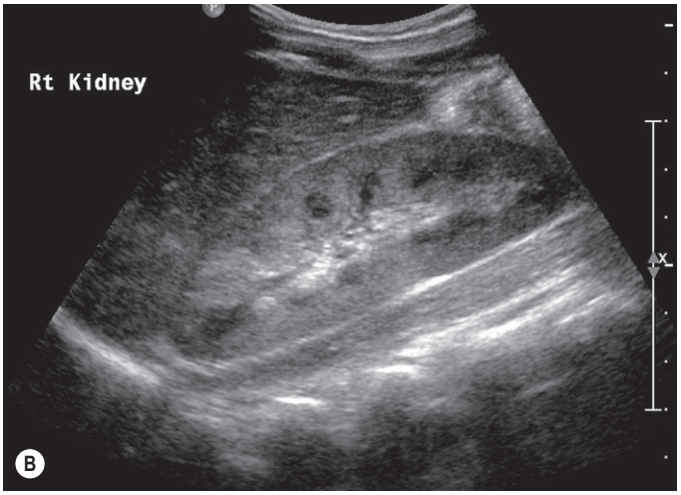

Figure 71.50 Haemolytic uraemic syndrome (HUS). A: High-resolution sonogram of the transverse colon in a child with a clinical picture of HUS showing marked bowel wall thickening; this finding is by no means specific for the diagnosis. **B:** Longitudinal sonogram of the same child showing an enlarged right kidney with diffuse increase in cortical texture. Bowel involvement in HUS is more common than renal disease.

greatly improved the chance of graft survival compared to unrelated cadaveric donor kidney. Long-term outcomes in younger children are now becoming equivalent to those in older children.[30]

Preoperative evaluation

Ultrasound of the native kidneys will have usually been performed serially prior to consideration for transplantation. Nephrectomy of the native kidneys is rarely required for successful renal transplantation. Exceptions include: renal cancer, cystic renal disease, infection, or if the native kidney is the source of severe refractory hypertension.

Detailed non-invasive screening of the aorta, IVC and iliac vessels should be undertaken for children with end-stage renal failure prior to transplantation. Ultrasound will usually suffice but phase contrast MR angiography may be required.[31] Accurate knowledge of vascular anomalies will influence the technical procedures required during renal transplantation and may affect patient survival.

Transplantation anatomy in children

In smaller children the renal allograft is usually sited intra-abdominally, with the donor renal vein and artery anastomosed to the distal inferior vena cava and aorta (Fig. 71.51A). In the older child the pelvic retroperitoneal position is favoured, with the transplant renal vein anastomosed end-to-side to the internal iliac vein and the transplant renal artery end-to-end to the internal iliac artery (Fig. 71.51B). The donor ureter is usually anastomosed to the patient's urinary bladder via a ureteroneocystostomy but if there is bladder dysfunction then an ileal conduit is formed for urinary diversion. The sonographer should ideally have the transplant operation note or an anatomical summary prior to undertaking ultrasound.

Sonographic appearances and complications of renal transplantation in the child

The imaging techniques, normal ultrasound appearances and complications demonstrable by ultrasound in children following renal transplantation are analogous to those routinely encountered in adult practice. These are described in detail in Chapter 28.

It is important to note that most children will receive an adult transplant kidney. Both paediatric and adult renal pathology should be anticipated in such cases.

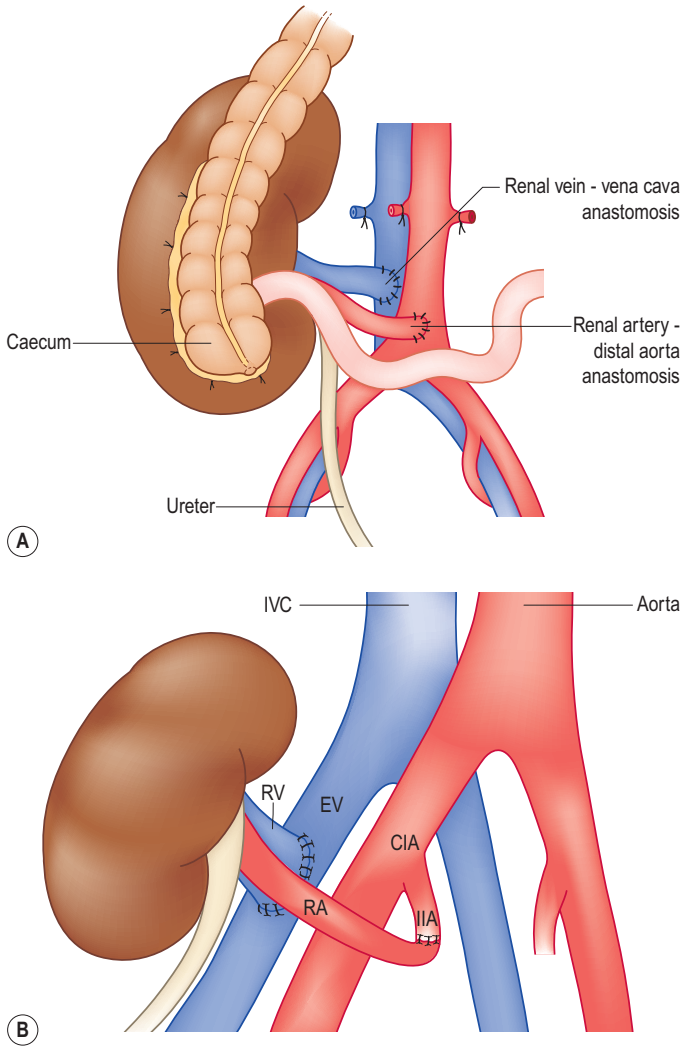

Figure 71.51 Renal transplantation anatomy in children (modified from Seigel MJ, Paediatric Sonography, 3rd edition, LWW, 2002). Line diagrams showing the vascular anastomoses in renal transplantation. **A:** In smaller children the renal allograft is typically sited intra-abdominally, with the donor renal vein and artery anastomosed to the distal inferior vena cava and aorta. **B:** In the older child the kidney is placed in a pelvic retroperitoneal position with the transplant renal vein anastomosed end-to-side to the internal iliac vein and the transplant renal artery end-to-end to the internal iliac artery.

Urolithiasis

Urolithiasis refers to the formation of a calculus within the renal collecting system, ureter, urinary bladder or urethra. Urolithiasis is uncommon in children. In European children infection-related stones predominate.[32] The epidemiology of paediatric nephrolithiasis in the United Kingdom has been reported more recently.[33] A slightly higher incidence of renal calculi was seen in males; the majority of stones formed in the upper renal tract; but higher proportions were metabolic (44%). The remainder included infective (33%) or idiopathic (26%). Coexisting urinary tract infection (49%) was common in the metabolic group, with infection in many cases masking the underlying metabolic condition.

Calcium-containing stones (opaque on X-ray) tend to occur in older children, particularly if there is coexisting nephrocalcinosis or an underlying metabolic abnormality including:

- *Idiopathic hypercalciuria* – results from increased intestinal absorption of calcium or reduced renal tubular resorption of calcium.
- *Hyperoxaluria* (densely opaque) – primary disease is a rare autosomal recessive condition associated with highly echogenic kidneys. Secondary disease is due to enteric malabsorption seen in cystic fibrosis and inflammatory bowel disease.
- *Hyperparathyroidism* – rare in children.

Other specific stones include:

- *Struvite stones* (opaque): infective stones are frequently diagnosed in boys aged less than 5 years of age. The vast majority have infected urine at the time of diagnosis. There is an association with congenital structural abnormalities such as megaureter, neurogenic bladder and bladder exstrophy.
- *Uric acid stones* (radiolucent) are uncommon in children and seen in myeloproliferative disorders, other haematological conditions and Lesch–Nyhan syndrome.
- *Cysteine stones* (faintly radio-opaque) occur at all ages and result from inborn errors of metabolism. These may form as single small stones anywhere in the urinary tract or coalesce into a staghorn arrangement.

All children with renal stones should be evaluated in a systematic fashion. The main role of ultrasound is in determining the size and number of calculi, monitoring disease progress and evaluating any related complications. Careful high-resolution ultrasound of the renal tract will reliably identify most renal tract calculi. Stones are more difficult to identify in the middle and proximal thirds of the ureter. It is still sensible to obtain an abdominal radiograph at initial presentation. Small stones on ultrasound appear as echogenic foci. Acoustic shadowing (Fig. 71.52) can be detected in calculi of at least 5 mm in size. In general stones that are more radio-opaque on radiographs tend to be stronger reflectors but US cannot reliably differentiate between different stone types. Colour Doppler 'twinkle artefact' sign should be actively sought (Fig. 71.53). This appears as a rapid fluctuating mixture of Doppler signals imitating turbulent flow with an associated characteristic flat Doppler spectrum behind a strongly reflecting interface as seen in calculi or parenchymal calcifications.[34]

The most important consideration is to exclude renal tract obstruction. In most cases the stone will eventually pass. The presence of an obstructive uropathy with secondary pyonephrosis mandates urgent treatment in the form of a percutaneous nephrostomy.

The treatment of paediatric renal stone disease includes medical therapy for cysteine and uric acid stones. Extracorporeal shock wave lithotripsy (ESWL) is now the preferred treatment for persisting, symptomatic or complicated stone disease. Nephrolithotomy is an alternative where ESWL is not an option.

Nephrocalcinosis

Nephrocalcinosis refers to abnormally increased calcium deposition within the renal parenchyma and may coexist with renal tract calculus formation. Nephrocalcinosis is classified as cortical, medullary or diffuse. The various causes of nephrocalcinosis in children are summarised in Tables 71.7 and 71.9. As most of the underlying conditions are systemic, nephrocalcinosis is almost always bilateral and typically symmetric. Exceptions include prior renal vein thrombosis, unilateral obstructive hydronephrosis[35] or perfusion anomaly such as renal artery occlusion.

Nephrocalcinosis is an uncommon condition in childhood. It is often asymptomatic, particularly in infancy. High-resolution ultrasound has been found to be a sensitive and reliable method for the detection of nephrocalcinosis.[36] Ultrasound is more sensitive in detecting nephrocalcinosis than plain abdominal radiographs. The normal renal pyramid is hypoechoic relative to the renal cortex. An increase in medullary echotexture should raise the suspicion of medullary nephrocalcinosis (Fig. 71.54). A widely used ultrasound-based nephrocalcinosis grading scale outlining the progressive sonographic changes seen in medullary nephrocalcinosis is summarised in see Table 71.8.

Selective cortical nephrocalcinosis is rare. The main causes are summarised in Table 71.9.

Investigation of paediatric nephrolithiasis

1. Urinalysis
2. Radiological investigation (options include ultrasound and radiograph, low-dose non-contrast-enhanced renal tract CT or intravenous pyelography; the latter is now rarely used)
3. Metabolic screen
4. Stone biochemical analysis

Role of ultrasound in investigating urinary tract infection

- Detect findings consistent with active infection.
- Identify predisposing conditions (VUR, neurogenic bladder, calculus or structural anomaly such as cloacal anomaly or UPJO).
- Identify immediate complications such as focal abscess.
- Identify long-term complications such as renal scarring.
- Document bipolar renal length.
- Serial follow-up to assess interval renal growth.

Table 71.7 Causes of medullary nephrocalcinosis

Idiopathic nephrocalcinosis (Williams syndrome, absorptive hypercalciuria)
Renal tubular acidosis
Iatrogenic (furosemide, treatment for hypophosphotaemic rickets)
Oxalosis
ARPKD
Sickle cell disease
Rare causes: Bartter syndrome, Cushing syndrome, lipoid necrosis, Lesch–Nyhan syndrome, thyroid dysfunction

Table 71.8 Nephrocalcinosis grading scale (adapted from Dick et al.[36])

Grade	
0	Normal echogenicity of the medullary pyramids
I	Mild increased echogenicity around the border of the medullary pyramid
II	Mild diffuse increased echogenicity of the entire medullary pyramid
III	Greater, more homogeneous increase in the echogenicity of the entire medullary pyramid

Table 71.9 Causes of cortical nephrocalcinosis

Acute cortical necrosis
Primary hyperoxaluria
Sickle cell disease
Chronic hypercalcaemia

Figure 71.52 Urolithiasis. A: Longitudinal sonogram of the kidney with an echogenic focal calculus in the upper pole casting an acoustic shadow. **B:** Longitudinal sonogram of the kidney showing a large non-obstructing calculus in the renal pelvis. **C:** Transverse sonogram of the pelvis showing a stone (between callipers) at the left vesico-ureteric junction. **D:** Transverse sonogram of the pelvis in another patient showing a very large stone within the urinary bladder. A foreign body could act as a nidus for renal stone formation but this was not the case in this child. **E:** Post-micturition transverse sonogram of the urinary bladder (*) in a teenage boy with a calculus (between callipers) in the prostate gland (arrowhead). **F:** Longitudinal high-resolution scan along the shaft of the penis demonstrating a urethral calculus (arrow).

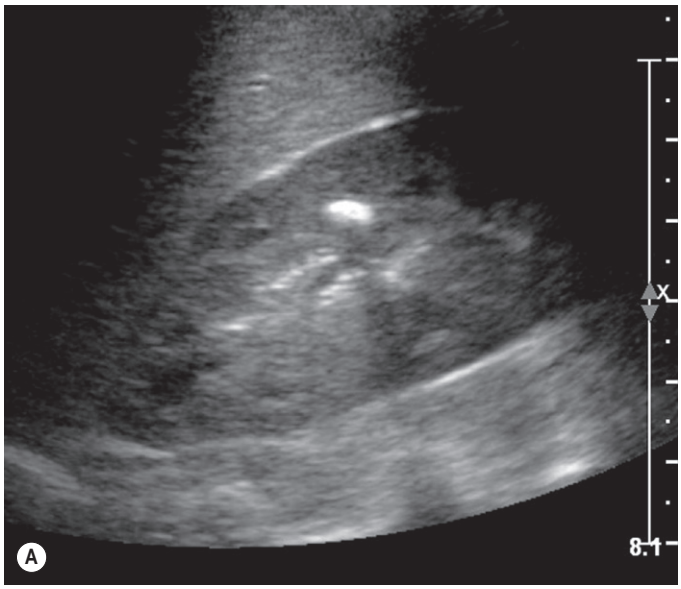
A

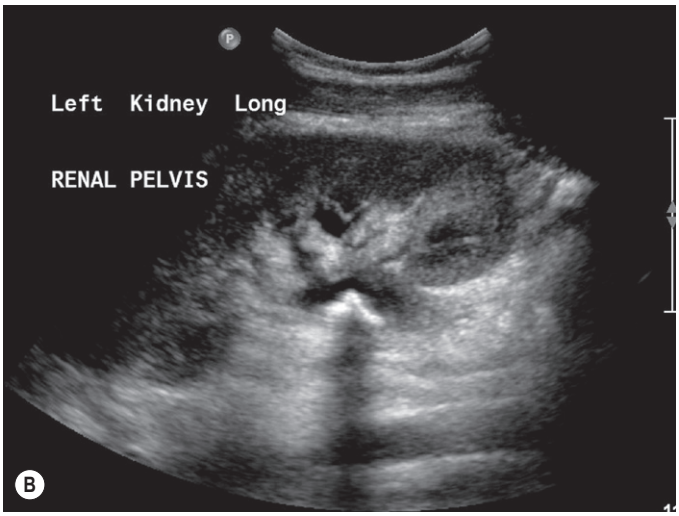
Left Kidney Long
RENAL PELVIS
B

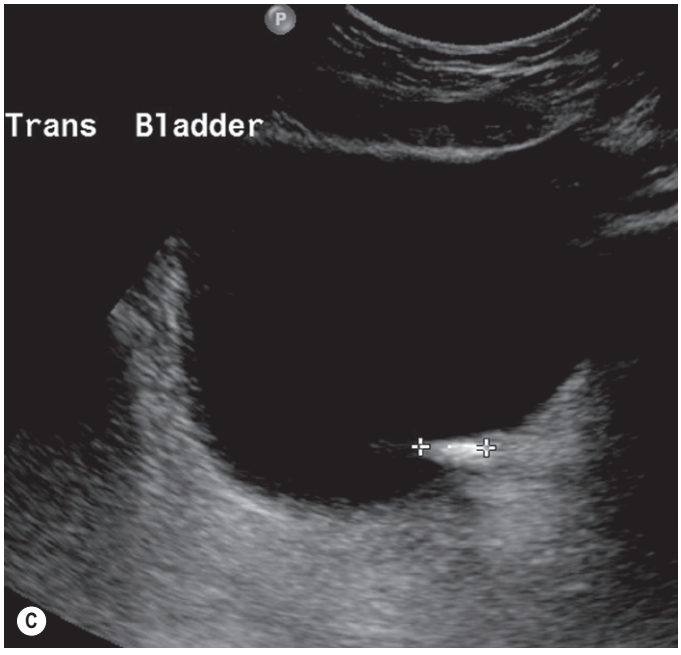
Trans Bladder
C

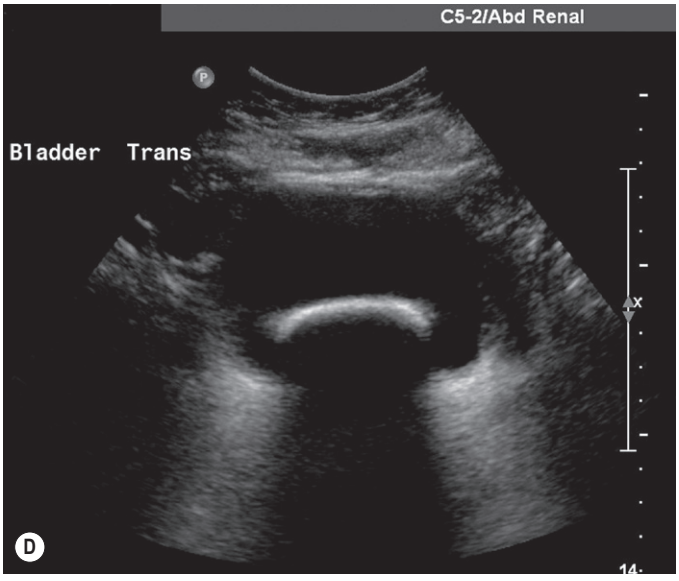
C5-2/Abd Renal
Bladder Trans
D

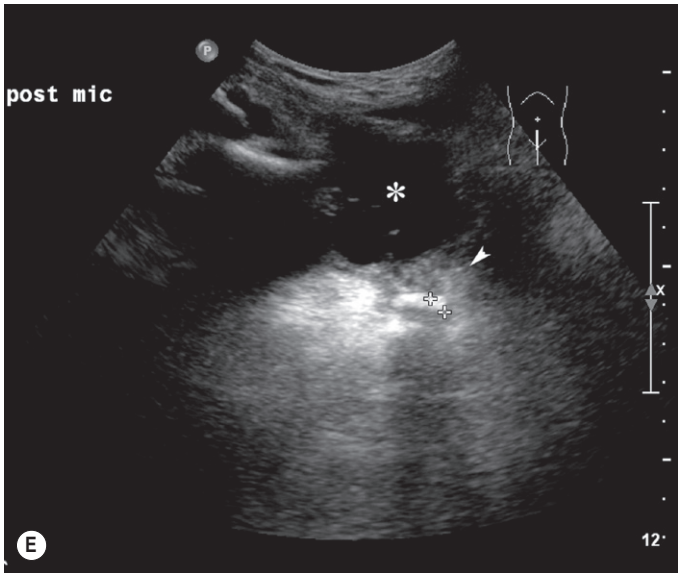
post mic
E

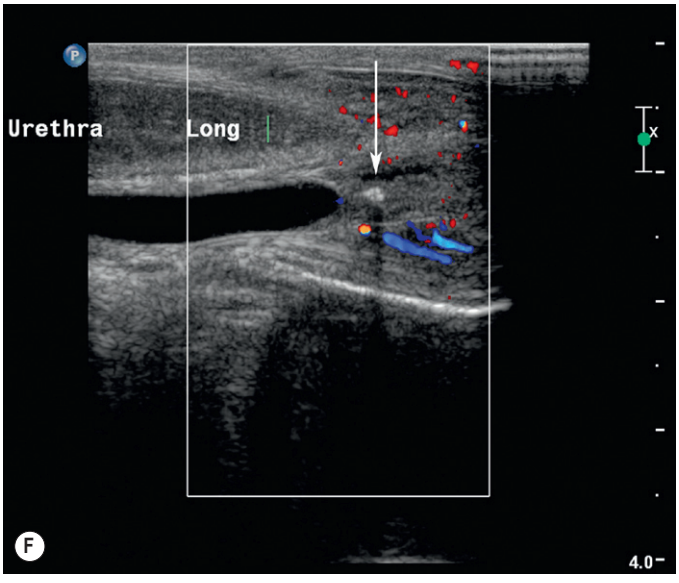
Urethra Long
F

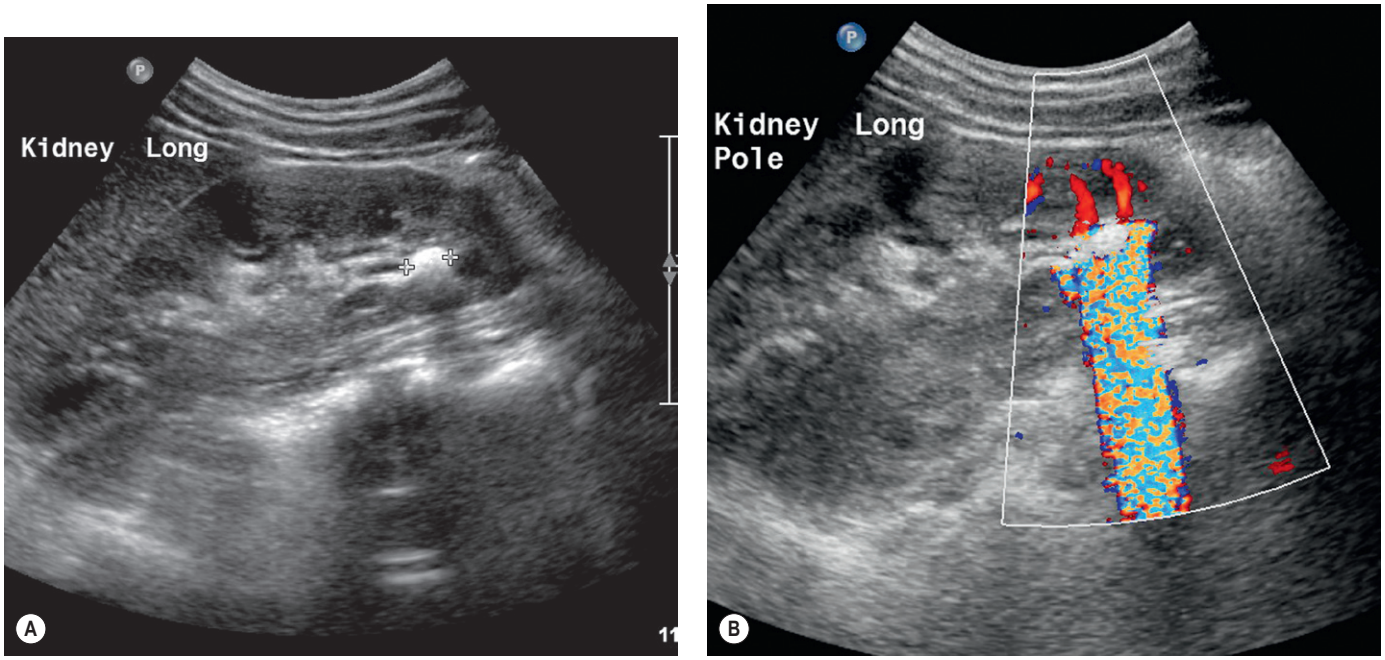

Figure 71.53 Urolithiasis. Longitudinal sonograms of the right kidney. **A:** Greyscale image. **B:** Corresponding colour Doppler image. The latter shows the characteristic 'twinkle artefact' seen in strong reflectors of sufficient size, such as renal calculi, when interrogated with optimised colour Doppler.

Urinary tract infection in children

Urinary tract infection (UTI) is one the commonest pathologies in children and is defined by the presence of a positive urine culture specimen yielding a growth of pathogens greater than or equal to 10 000 colony-forming units per cubic millimetre of urine. A slightly higher incidence is seen in uncircumcised boys under the age of 1 year; otherwise in all other age groups girls are around three times more likely to be affected than boys.

The clinical and laboratory diagnosis of UTI in children is challenging. Imaging is often required as an aid to the diagnosis and future management. Ultrasound is the first-line diagnostic imaging test in UTI. Symptoms of UTI in the younger child include fever, loss of appetite, vomiting, lethargy and failure to thrive. Abdominal pain, loin pain, frequency and dysuria are common symptoms in the older child. The urine may be smelly but regardless a sterile sample must still be sent for microbiological assessment. *Escherichia coli* accounts for 75–90% of infections.

Asymptomatic bacteriuria refers to a significant number of bacteria present in the urine that occurs without causing any of the ill effects associated with UTI. Routine treatment is not necessary as a high proportion of patients will tend to recolonise with bacteria despite antibiotic therapy.

The ultrasound findings in acute renal infection are highly variable. Infection may involve the upper renal tract (acute pyelonephritis) or the lower renal tract (cystitis or ureteritis). There may also be established changes from pre-existing renal damage caused by previous episodes of UTI (chronic pyelonephritis).

Upper urinary tract infection

Acute pyelonephritis

Sonographic findings in acute pyelonephritis (APN) (Fig. 71.55) include:

- increased volume – volume increase may be focal or generalised
- loss of corticomedullary differentiation
- areas of abnormal echotexture (heterogeneous, decreased or increased)
- renal sinus hyperechogenicity
- pyonephrosis
- urothelial thickening at the renal pelvis and ureter
- abscess formation
- subcapsular collection (Fig. 71.56)
- perirenal fat hyperechogenicity
- juxtarenal process.

Juxtarenal process refers to disease processes affecting retroperitoneal perirenal space. Pathologies include infection, urine extravasation and haemorrhage (Fig. 71.57). The echogenicity of the kidney and perirenal fascia is dependent upon the disease process. Urine is usually hypoechoic. Pus is more complex and may contain gas; the presence of gas may also indicate a urinoma. The appearance of haemorrhage varies with time and is described in more detail in relation to renal tract trauma.

Pyonephrosis on ultrasound is seen as multiple echoes within a distended pelvicalyceal system and results from pus, debris or haemorrhage (Fig. 71.58). Urothelial thickening (Fig. 71.58) is a fairly non-specific finding seen in infection, VUR, stone disease and obstruction. Placement of a percutaneous nephrostomy is urgently indicated in cases of an infected obstructed system and is usually secondary to a renal stone or structural abnormality such as UPG obstruction. Abscess formation that does not respond to an appropriate course of conservative therapy may also require surgical intervention (Fig. 71.59).

As infection may be focal or diffuse a meticulous approach to ultrasound technique is required. Careful examination should actively look for renal calculi, caliectasis, pelviectasis, hydroureter and evidence of vesico-ureteric reflux (VUR) or an underlying structural abnormality. *Proteus* infection is usually more common in boys and has a strong association with congenital obstructive uropathy and struvite renal stone formation. Infection may be

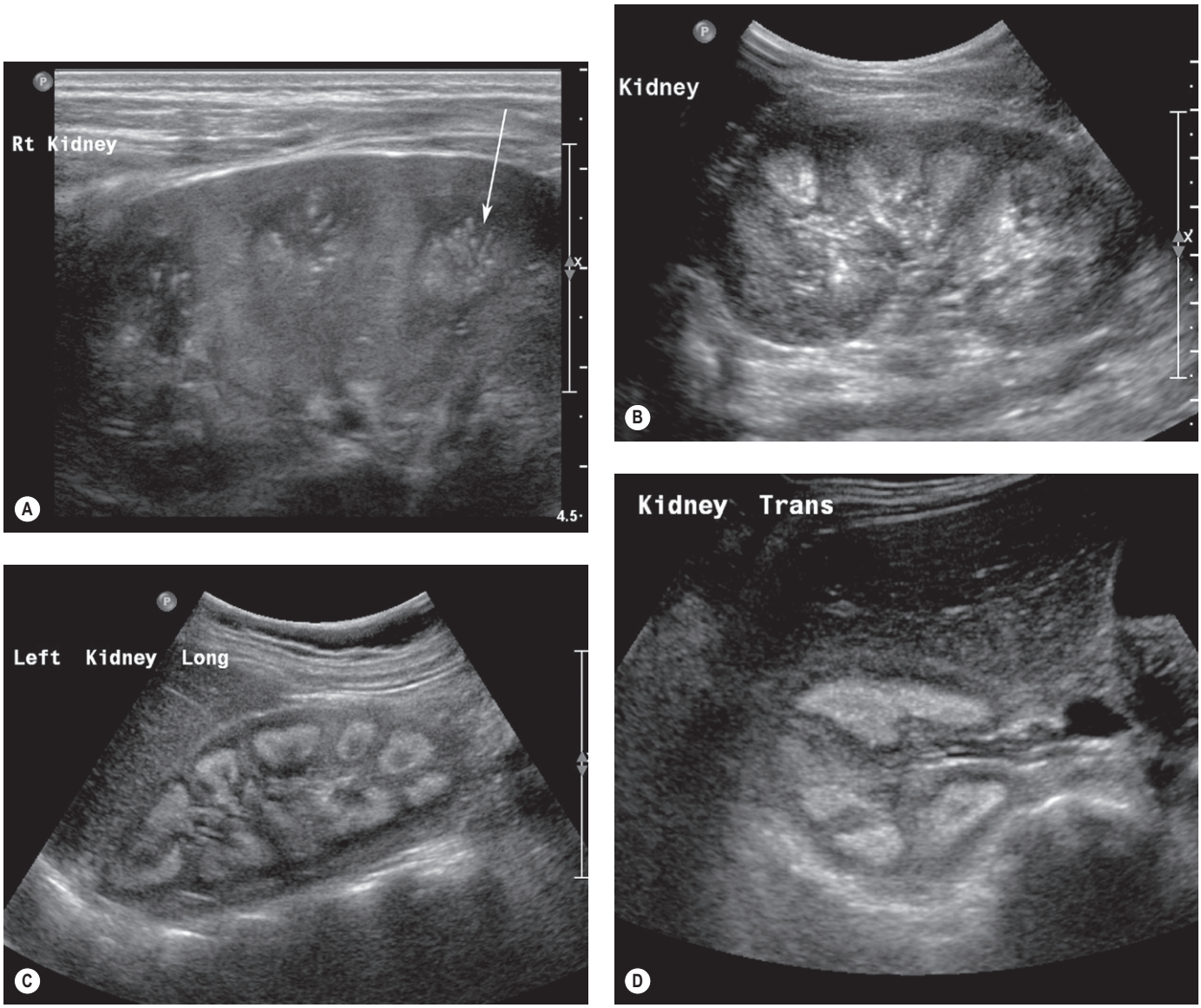

Figure 71.54 Medullary nephrocalcinosis. A: Longitudinal sonogram of the kidney showing discrete stippled foci of calcification centred on the medullary pyramids (arrow); these were not visible on plain film imaging. Ultrasound and CT are more sensitive than plain radiographs in detecting medullary nephrocalcinosis. **B:** Longitudinal sonogram of the kidney showing nephrocalcinosis predominantly affecting the periphery of the medullary pyramids. **C, D:** Longitudinal **(C)** and transverse **(D)** sonograms in a child with infantile hypercalcaemia showing striking homogeneous increased texture centred on the renal pyramids in keeping with grade 3 medullary nephrocalcinosis.[36]

repetitive resulting from reflux nephropathy, also referred to as chronic pyelonephritis. Features of chronic pyelonephritis should be actively sought (see below).

Colour Doppler may increase the sensitivity of ultrasound in the detection of APN; however, Doppler findings in APN are also highly variable. Hyperaemia with a reduction in Doppler indices is seen secondary to the acute infection. Focal oedema and capsular distension results in diminished blood flow to the affected renal parenchyma. The more typical pattern is reduced flow and an increase in Doppler indices (Fig. 71.55).[37]

Chronic pyelonephritis

Repetitive episodes of APN can result in parenchymal loss referred to as renal scarring. Ultrasound has a very high specificity but relatively lower sensitivity for the detection of renal scarring (Fig. 71.60). A high level of vigilance is required in the detection of scarring. Only with careful assessment of parenchymal depth across the entire length and breadth of each kidney can ultrasound maintain a high level of sensitivity. DMSA scintigraphy is considered the gold standard in the evaluation of renal scarring[38] (Fig. 71.60). The differential diagnosis for renal scarring includes antenatal dysplasia and cortical necrosis. Recurrent pyelonephritis may cause hypertension, renal insufficiency and end-stage renal failure.

Lower urinary tract infection

Cystitis and ureteritis will present with lower urinary tract symptoms such as dysuria and frequency. A urine culture sample should

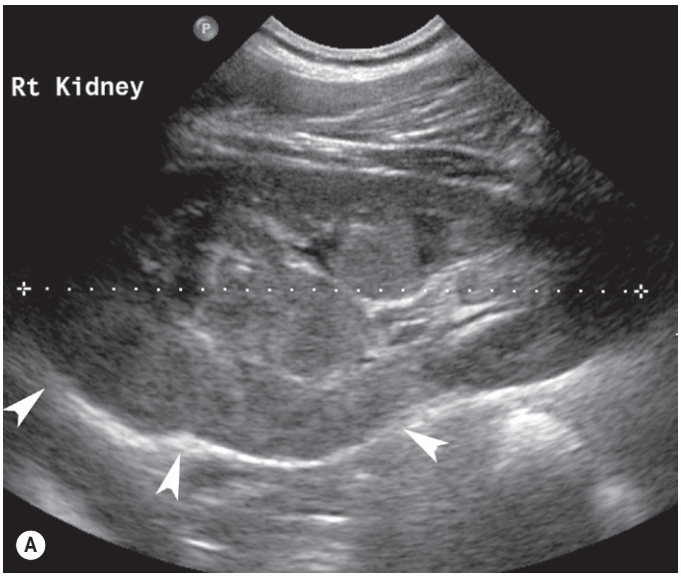

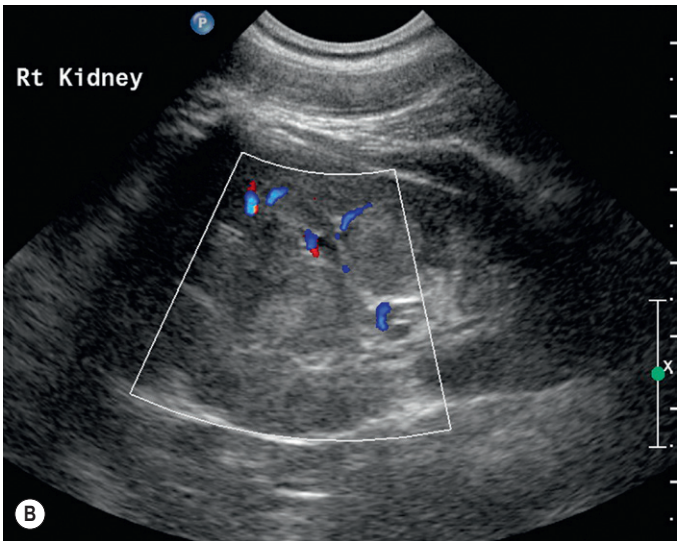

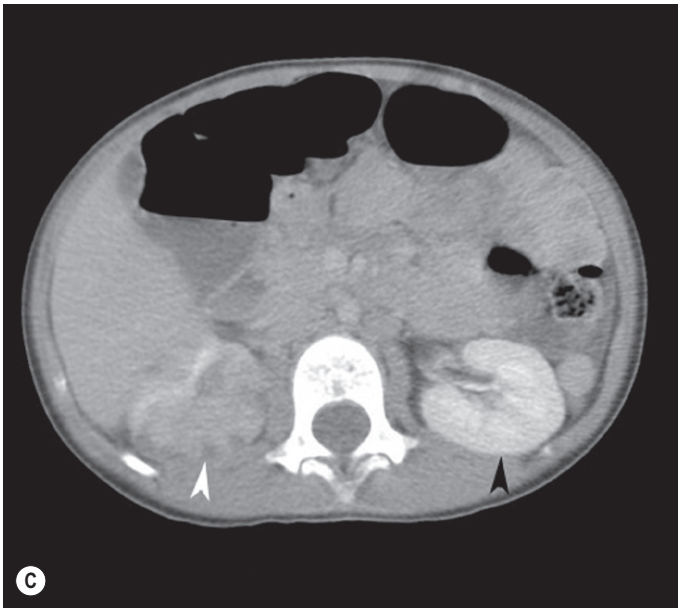

Figure 71.55 Acute pyelonephritis (APN): 13-year-old girl with flank pain and high fever. **A:** Longitudinal sonogram of the right kidney demonstrating a focal area of swollen parenchyma showing homogeneous slightly increased echogenicity (arrowheads) deforming the renal contour. **B:** Corresponding colour Doppler image showing reduced perfusion to affected area. **C:** Axial contrast-enhanced CT in the same patient showing a characteristic patchy striated nephrogram (white arrowhead) compared to normal left kidney (black arrowhead). Both kidneys were seen to excrete. The CT scan was performed at an external institution for suspected acute appendicitis. Cystic change is indicative of liquefaction and abscess formation.

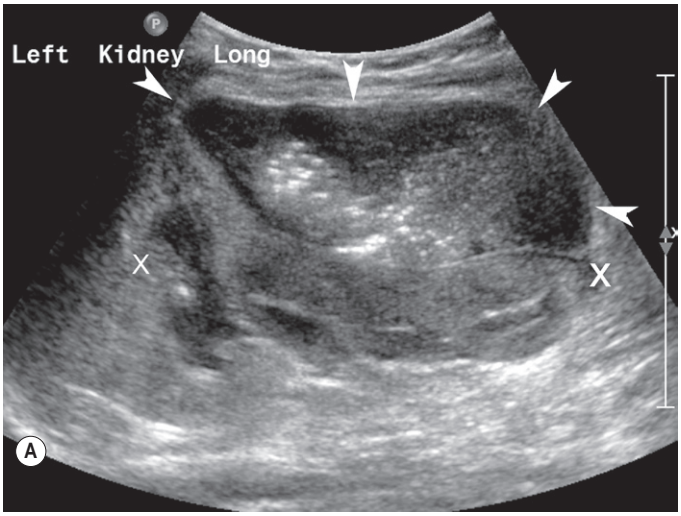

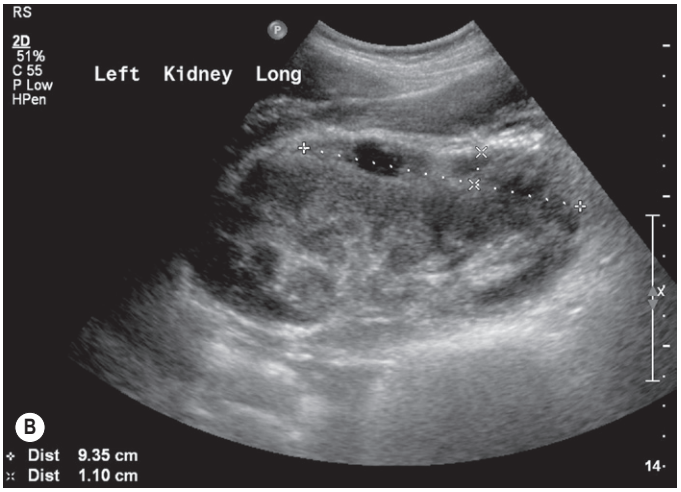

Figure 71.56 Subcapsular and perirenal space collections. Longitudinal sonograms of the left kidney. **A:** 1-week-old male with posterior urethral valve and secondary infection of a urinoma (arrowheads) compressing the left kidney. This contains mixed echoes; the bright echoes are due to gas. Urine cultures were positive for mixed coliform organisms. **B:** Lenticular subcapsular collection in a teenager following percutaneous renal biopsy (between callipers); infection could have given rise to similar appearances. Ultrasound cannot differentiate between blood and pus. The clinical history is important in determining the most likely aetiology.

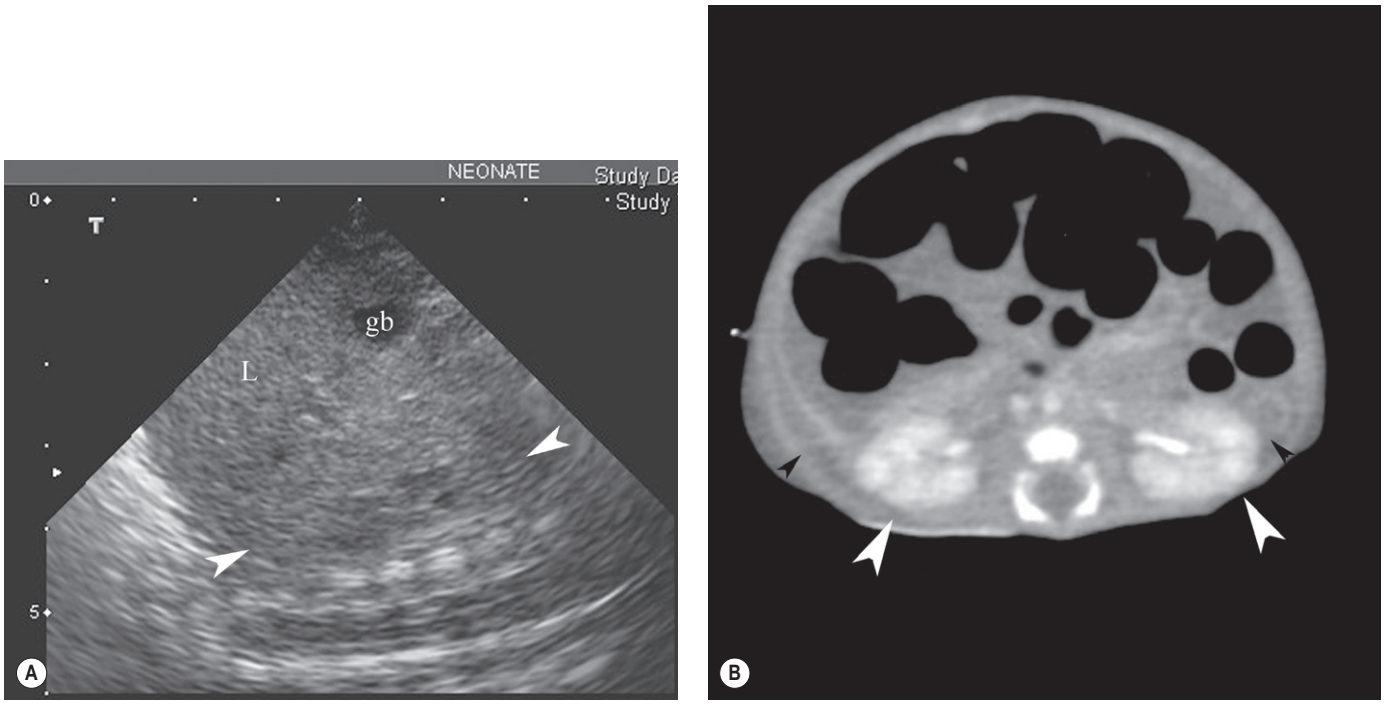

Figure 71.57 **Juxtarenal processes. A:** Longitudinal sonogram of the right kidney in a hypotensive neonate. The kidneys were extremely difficult to define as discrete structures (white arrowheads). **B:** Axial contrast-enhanced CT performed shortly after the ultrasound showing retroperitoneal haemorrhage (black arrowheads) surrounding the normally enhancing kidneys (white arrowheads). Conditions that affect the perirenal and pararenal spaces such as infection, acute haemorrhage or response to chronic urine leakage may give rise to such sonographic appearances.

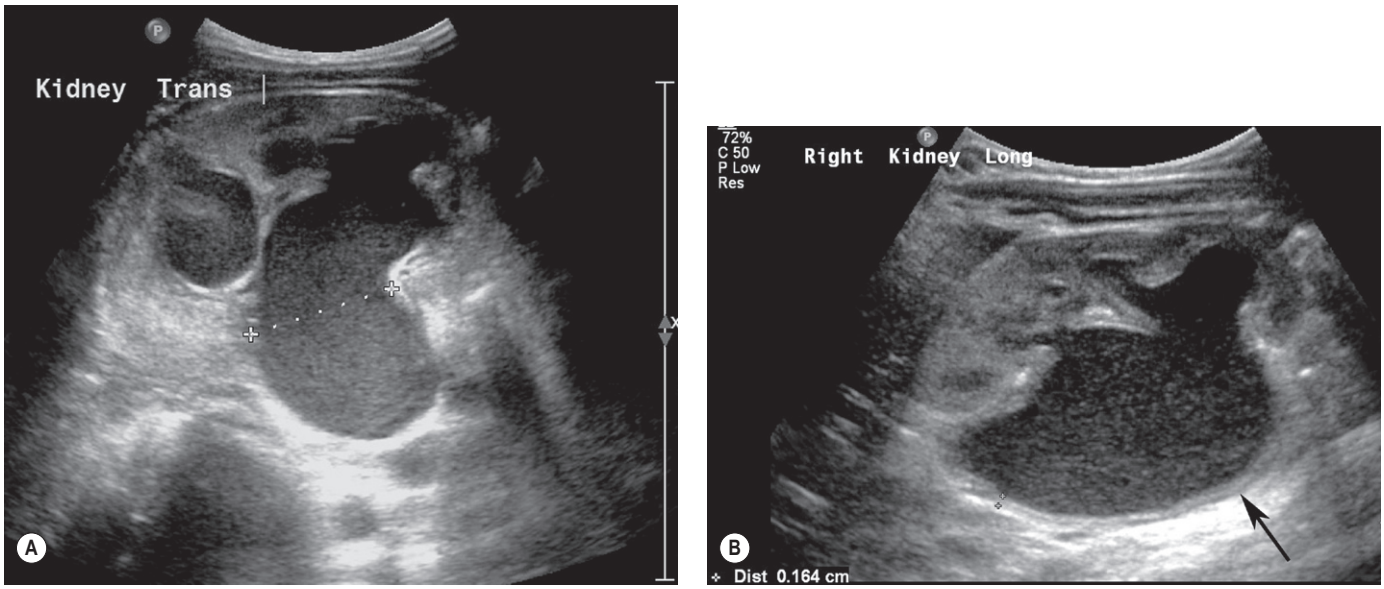

Figure 71.58 **Pyonephrosis.** Transverse **(A)** and longitudinal **(B)** sonograms of the right kidney in a child with secondary infection of a ureteropelvic junction obstruction; manifesting as a fluid debris level and urothelial thickening (arrow). Urgent decompression with a percutaneous nephrostomy was performed.

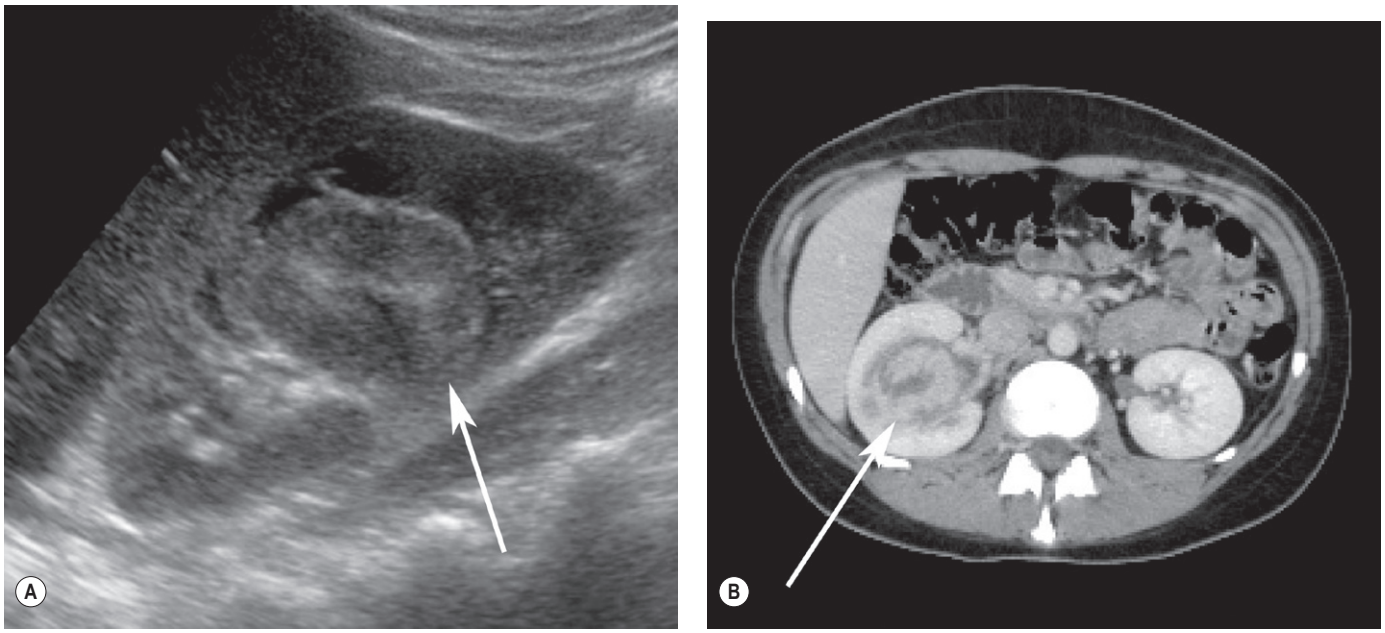

Figure 71.59 Renal abscess. A: Axial sonogram showing a well-defined mass lesion within the interpolar region of the right kidney (arrow), containing a small central hypoechoic area. This was suspected to be a necrotic tumor. **B:** Axial contrast-enhanced CT of the same child showing a thick-walled enhancing mass lesion (arrow). Percutaneous biopsy was performed yielding pus. This resolved following aspiration and treatment with parenteral antibiotics.

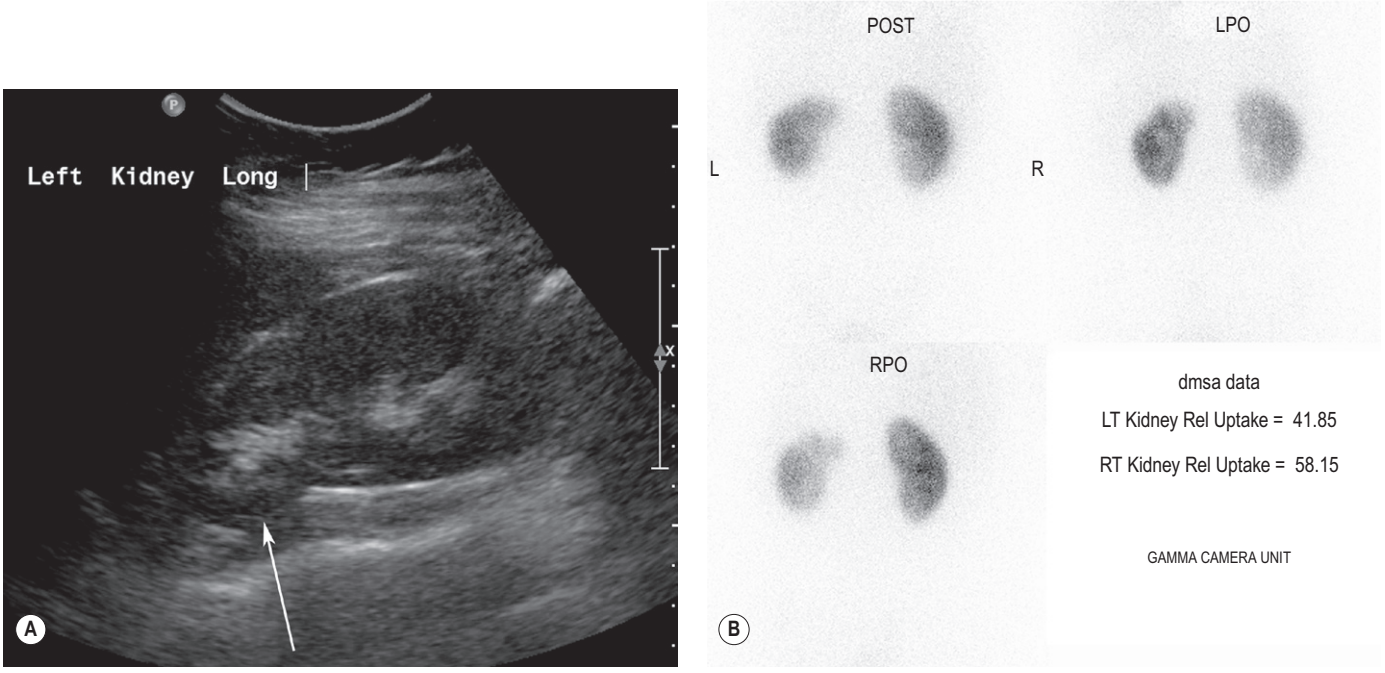

Figure 71.60 Renal scarring. A: Longitudinal sonogram of the right kidney. There is focal thinning of the upper pole (arrow) due to renal parenchymal scarring. **B:** DMSA scan showing a focal defect in the upper pole of the left kidney with accompanying volume loss. Scarring results from reflux and non-reflux pyelonephritis. DMSA scintigraphy is highly sensitive for detecting renal scarring but cannot differentiate this from antenatal renal dysplasia.

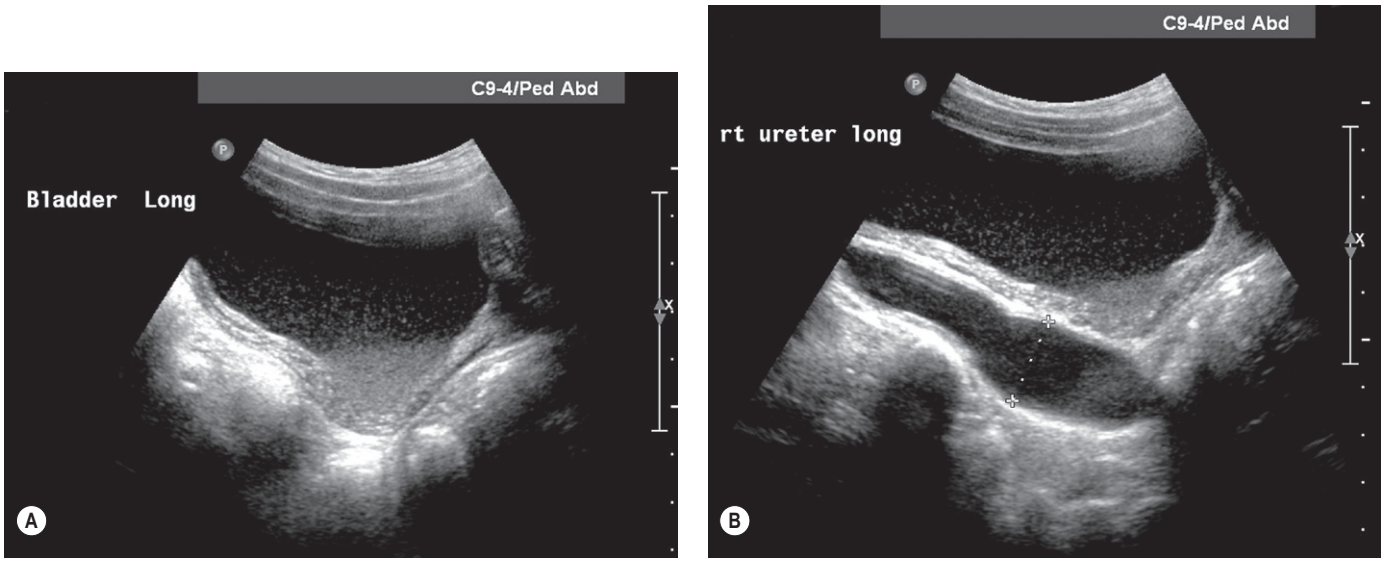

Figure 71.61 Lower urinary tract infection: a child with typical symptoms including frequency and dysuria with positive urine cultures. Longitudinal sonograms of the bladder **(A)** and right ureter **(B)** showing fluid–debris levels and urothelial thickening. The ureteric dilatation (between callipers) was later confirmed to be grade 3 vesico-ureteric reflux.

suffice for the diagnosis. Ultrasound is indicated in recurrent episodes of suspected lower urinary tract infection where there is concern for an underlying structural abnormality. Ultrasound can exclude bladder outlet obstruction and bladder calculi (Fig. 71.61).

Imaging protocols for UTI in children

The appropriate imaging strategy of UTI is dependent upon a number of factors including age at presentation, number of symptomatic or culture-proven episodes, site of infection and geographic location of the patient. A variety of imaging algorithms exist.[39,40] These geographical variations in consensus opinion are testament to the fact that the pathophysiology of paediatric UTI is not completely understood and that there are fundamental differences in opinion on what constitutes acceptable investigation and management. It is important that there are locally agreed guidelines in place for the diagnostic work-up of children with suspected and proven UTI. The infant and neonate with UTI should have ultrasound, DMSA scan and VCUG. A MAG-3 renogram is useful in assessing drainage of dilated ureter or collecting system. In the older child ultrasound of the renal tract should be the starting point of radiological assessment and is usually all that is required. The acutely unwell child with febrile UTI or suspected APN which does not respond to appropriate medical therapy should undergo prompt renal tract ultrasound.

Atypical renal infection

Xanthogranulomatous pyelonephritis

Xanthogranulomatous pyelonephritis (XGP) is a severe, atypical variant of chronic pyelonephritis and is rare in children. XGP is characterised by the destruction of renal parenchyma and replacement by granulomatous tissue containing lipid-laden macrophages.

XGP is classified as being either focal or diffuse, the latter being more common in children.[41] The variable extent of the inflammatory process into the perirenal tissues and adjacent organs results in a great deal of clinical variation at presentation. Presenting features include a chronic febrile illness, loin pain, palpable mass, malaise, weight loss, anaemia, elevated inflammatory markers and high white cell count.[42]

The aetiology is poorly understood but major contributing factors include urinary tract sepsis and chronic obstruction typically in the presence of a renal calculus. Urine cultures may be positive; organisms include *Proteus mirabilis* and *Escherichia coli*.[42]

Typically a solid mass is present showing areas of cystic necrosis. Abnormal tissue may breach the renal capsule and is frequently mistaken for a Wilms' tumour. The presence of dense calcification should serve as a clue to the diagnosis (Fig. 71.62). Cross-sectional imaging is often performed preoperatively. Nephrectomy of the non-functioning kidney is the treatment of choice, with the diagnosis frequently coming to light only after surgery.

Renal candidiasis

This is infrequent in the paediatric population. The highest prevalence is in preterm neonates, usually associated with acute systemic candidiasis. Other associations include a congenital malformation of the urinary tract (such as posterior urethral valve), diabetes and immunosuppressed states.

In systemic infection the kidney(s) may show diffuse increase in texture with loss of corticomedullary differentiation. Renal fungus balls appear as round hyperechoic foci located within the pelvicalyceal systems (Fig. 71.63). These show no acoustic shadowing or Doppler twinkle artefact. The main differential in the newborn is Tamm–Horsfall proteinuria (Fig. 71.48) although this always occurs in the first week of life and *Candida* urinary tract involvement is usually much later in onset. Renal fungal balls may precipitate urinary tract obstruction ranging from focal calyceal dilatation to hydronephrosis with rapid destruction of renal parenchyma. A combination of urine culture and ultrasound is the most reliable method for diagnosis of renal fungus balls. Intermittent follow-up renal ultrasound is usually performed until microbiological cultures are clear and the fungus balls resolve with recovery of normal renal parenchymal echogenicity.

Other infections

Tuberculosis, hydatid disease and schistosomiasis affecting the paediatric renal tract are uncommon in the West, but should always be considered in a child with the appropriate demographic or travel

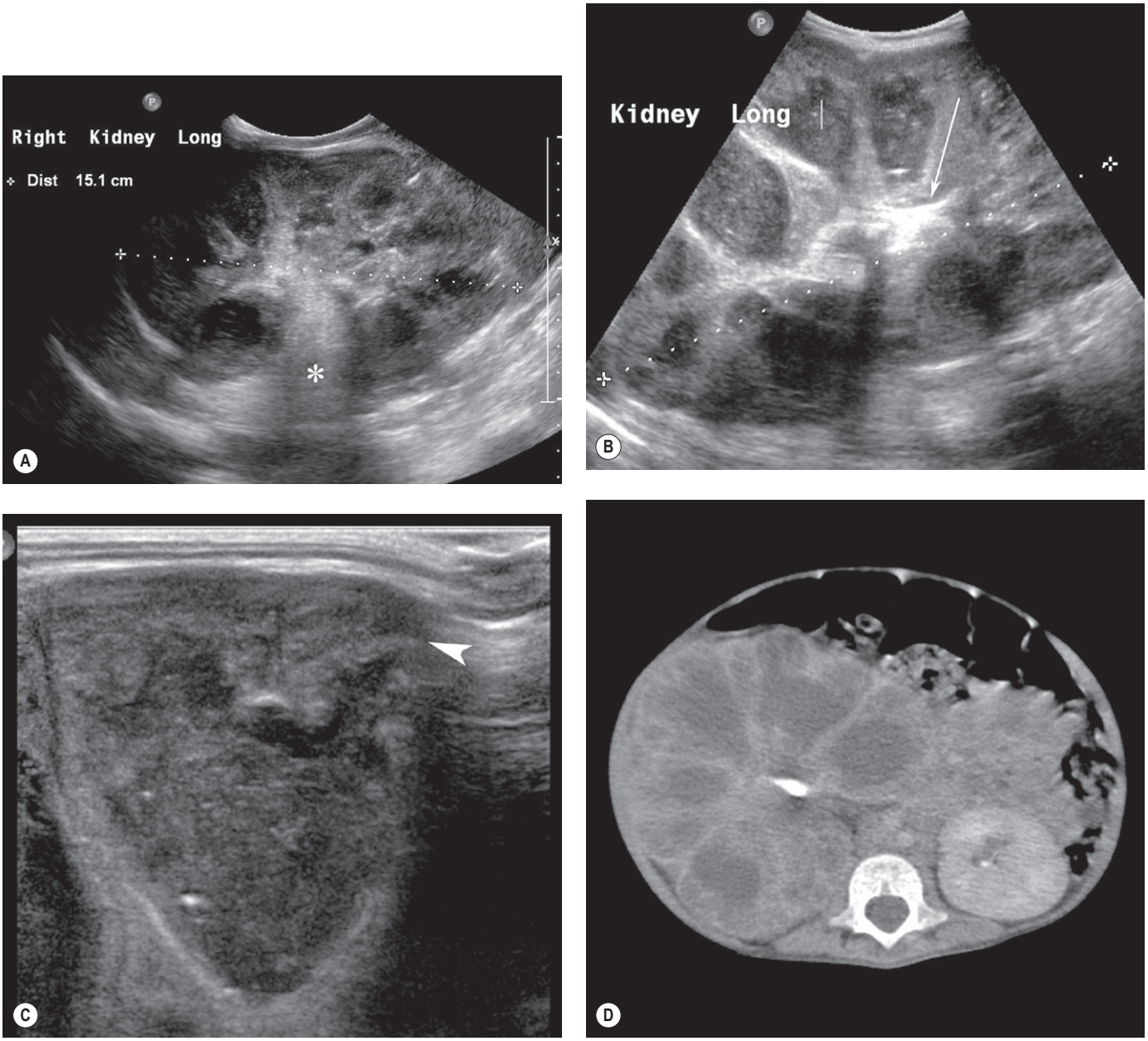

Figure 71.62 Xanthogranulomatous pyelonephritis (XGP). A: Longitudinal sonogram of the right kidney in a 2-year-old girl with a febrile illness showing an enlarged kidney with diffusely abnormal echotexture, prominent hyperechoic renal sinus and acoustic shadowing (*). **B:** Small renal calculi were present (arrow). **C:** High-resolution sonogram from the same study showing loss of corticomedullary differentiation and cortical thinning (arrowhead). **D:** Axial contrast-enhanced CT showing a central calculus in the enlarged non-functioning right kidney. A right nephrectomy was performed.

history from endemic areas. The imaging features are similar to those in adults and described in Chapter 24.

Renovascular disease

Renal vein thrombosis

Renal vein thrombosis (RVT) occurs most commonly in the neonatal period following periods of stress such as hypovolaemia, hypoxia, sepsis and coagulopathy. Infants of diabetic mothers and children with nephrotic syndrome are at particularly high risk. Thrombus initially propagates in the arcuate and interlobular veins and can extend into the renal vein and IVC. RVT is usually unilateral but when bilateral the child is oliguric or anuric. Adrenal haemorrhage and enlargement may be seen following concomitant adrenal vein occlusion and is usually left-sided.

Greyscale sonographic features of RVT include

- generalised renal enlargement from congestion
- increased parenchymal echogenicity
- loss of corticomedullary differentiation
- echogenic interlobular streaking – related to calcification of the interlobular veins[43]
- cortical loss may be seen if the thrombotic episode is of sufficient severity and duration.

Colour Doppler imaging is useful. Absent parenchymal flow can be seen in either arterial or venous thrombosis; flash arterial flow

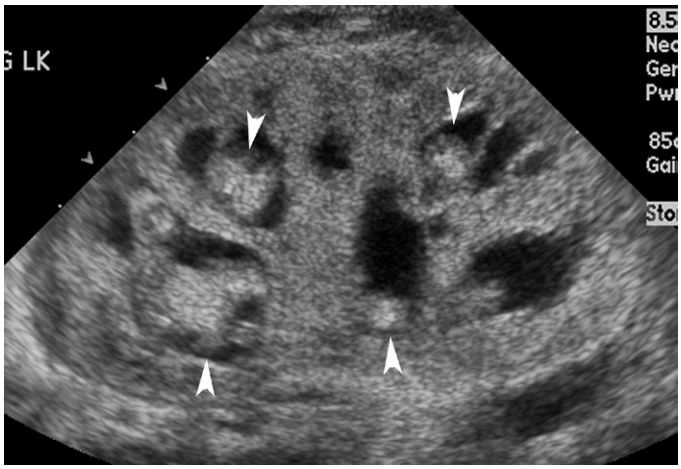

Figure 71.63 Renal *Candida*. Longitudinal sonogram of the left kidney in a 3-day-old neonate with systemic sepsis demonstrating multiple echogenic fungal balls (arrowheads) within a non-obstructing collecting system These were seen to be mobile. Urine culture and follow-up scan were normal 10 days after commencing antifungal therapy.

corresponding to peak systole is more suggestive of venous thrombosis; other patterns include 'to and fro' flow. These correspond to absent spectral flow, absent diastolic flow or reversed diastolic flow respectively (Fig. 71.64). The latter appearances are non-specific and can be seen in neonatal RVT or acute tubular necrosis. An occluded proximal IVC may give similar Doppler waveforms in both kidneys and does not necessarily indicate bilateral renal vein thrombosis.

Renal artery thrombosis

Renal arterial thrombosis in native kidneys is rare and usually seen in neonates as a complication of an aortic arterial line or umbilical arterial catheterisation (Fig. 71.65). Thrombus may propagate in the aorta, main renal artery or a smaller branch and like renal vein thrombus present as an echogenic luminal filling defect. Acutely affected areas show wedge-shaped hypoechoic parenchyma and corresponding absent Doppler flow with normal renal size. Complications depend upon the degree and duration of thrombosis and range from renal scarring to a non-functioning kidney.

Renal artery stenosis

Most cases of renal artery stenosis (RAS) in children are due to fibromuscular dysplasia; other causes are summarised in Table 71.10 (Hypertension in children, Aortic and renovascular disease section). A size discrepancy may be noted in unilateral RAS, with the affected kidney being smaller (difference of >1.5 cm).

Doppler Ultrasound in RAS may reveal slowing and dampening of the systolic waveform distal to the stenosis; the so-called parvus-tardus appearance. Many pitfalls hinder the utility of Doppler ultrasound. Non-compliant downstream vessels may not display the parvus-tardus response. The finding of bilateral renal artery parvus-tardus waveform may indicate a proximal aortic obstruction such as coarctation rather than bilateral renal artery disease. Doppler findings even if suggestive of proximal flow obstruction are often insufficient to rule out the need for angiography. The sensitivity of Doppler ultrasound in detecting treatable renovascular disease is poor. In a prospective study of children with suspected renovascular hypertension undergoing Doppler ultrasound and angiography, those with an initial negative Doppler US study but subsequent positive renal angiogram had a much higher likelihood of a cure achieved with endovascular therapy or surgery than those with an initial positive ultrasound.[44]

Table 71.10 Hypertension in children

Aortic and renovascular disease	Coarctation of the aorta (commonest cause under 1 year of age) Renal artery stenosis Fibromuscular hyperplasia/dysplasia Neurofibromatosis Ostial stenosis Williams syndrome Vasculitides (Takayasu disease, Kawasaki disease, polyarteritis nodosa) Homocysteinuria Mid-aortic syndrome Vascular trauma
Non-vascular renal disease (most common cause of secondary hypertension over 1 year of age)	Renal parenchymal disease Renal pelvic dilatation Renal cystic disease Renal tumour Renal transplantation (renal artery thrombosis, anastomotic stenosis, anti-rejection therapy – ciclosporin and corticosteroids)
Adrenal disease	Phaeochromocytoma Adrenal cortical adenoma Neuroblastoma Adrenal carcinoma Congenital adrenal hyperplasia

Hypertension in children

Hypertension forms an important part of the clinical workload of the paediatric nephrologist. The main causes of secondary hypertension in children are summarised in Table 71.10. Secondary hypertension is more common in preadolescent children and tends to be more severe in the younger patient. Under the age of 1 year, aortic coarctation is the most common cause of sustained hypertension. After 1 year of age, renal disease is the most common cause of secondary hypertension. Complications of untreated severe hypertension include poor growth, cardiac failure in younger children and acute hypertensive crises – headache, vomiting, hypertensive retinopathy and convulsions.

The clinical diagnosis of hypertension can be difficult to establish, particularly in younger children and in the primary care setting. How much imaging investigation is required once the diagnosis of hypertension is made is dependent on several factors including:

- clinical presentation (signs, symptoms and complications of hypertension)
- severity of hypertension and responsiveness to medical therapy
- treatment compliance
- clinical index of suspicion of a remediable underlying cause.

Radiological imaging of secondary hypertension

A number of imaging tests are often performed prior to undertaking renal arteriography in the child with suspected renovascular hypertension. Arteriography is the criterion standard in demonstrating renovascular disease but owing to its highly invasive

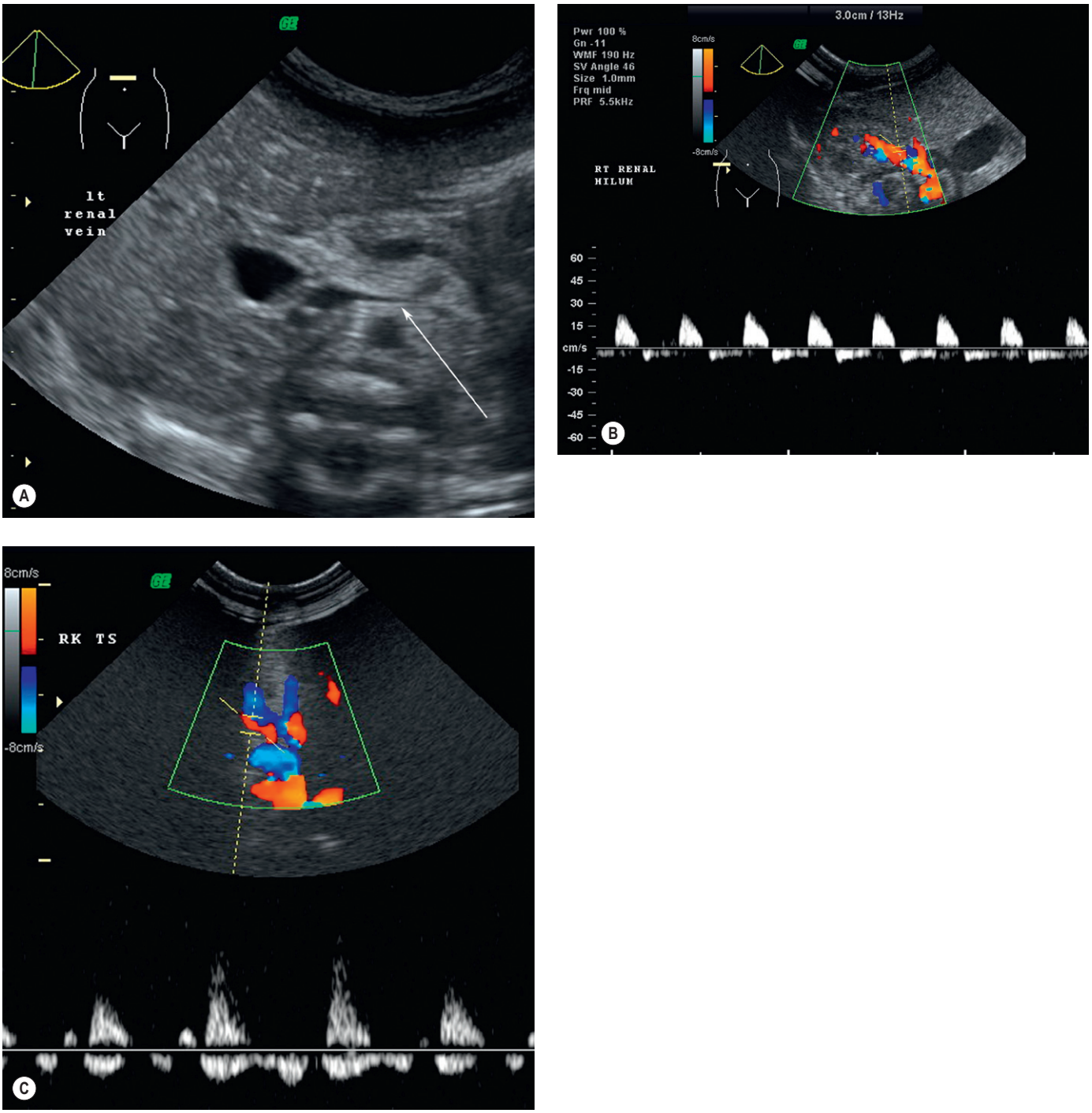

Figure 71.64 **Renal vein thrombosis (RVT). A:** Transverse image of a neonate at the level of the renal veins. Only the left renal vein was visualised (arrow). The right kidney was enlarged. **B:** Colour Doppler trace showing reversed diastolic flow. Whilst this finding may be described as sensitive for acute RVT it is by no means specific and can be seen in various conditions including acute tubular necrosis and a patent ductus arteriosus. **C:** Follow-up colour Doppler trace shows the more characteristic finding of a 'w' or 'inverted m' pattern of biphasic reversed diastolic flow in RVT.

nature other less specific tests are performed and only a small number of children will undergo angiography.

Renal tract ultrasound

Doppler ultrasound of the renal tract and abdomen is often requested as the first-line investigation. Younger children are much less likely to be compliant with the demands of a detailed Doppler examination owing to restlessness. A meticulous examination of the urinary tract should initially be performed. The scan should concentrate on:

- documenting renal lengths and the presence of scarring
- evaluating the renal parenchyma
- looking for urinary tract anomalies (hydroureteronephrosis)

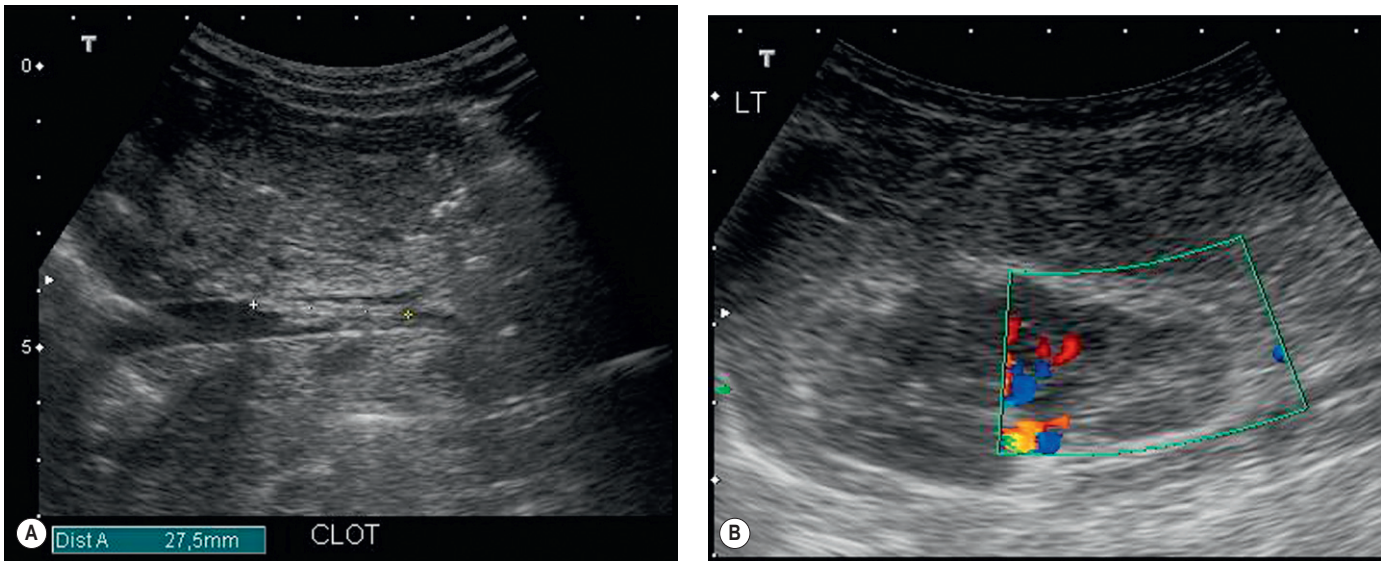

Figure 71.65 Renal artery thrombosis. A: Longitudinal sonogram in a hypertensive premature neonate with renal impairment. Aortic thrombus is demonstrated at the level of the origin of the renal arteries (between callipers) following umbilical arterial catheterisation. **B:** Doppler sonogram of the left kidney shows focal hypoperfusion to the lower pole.

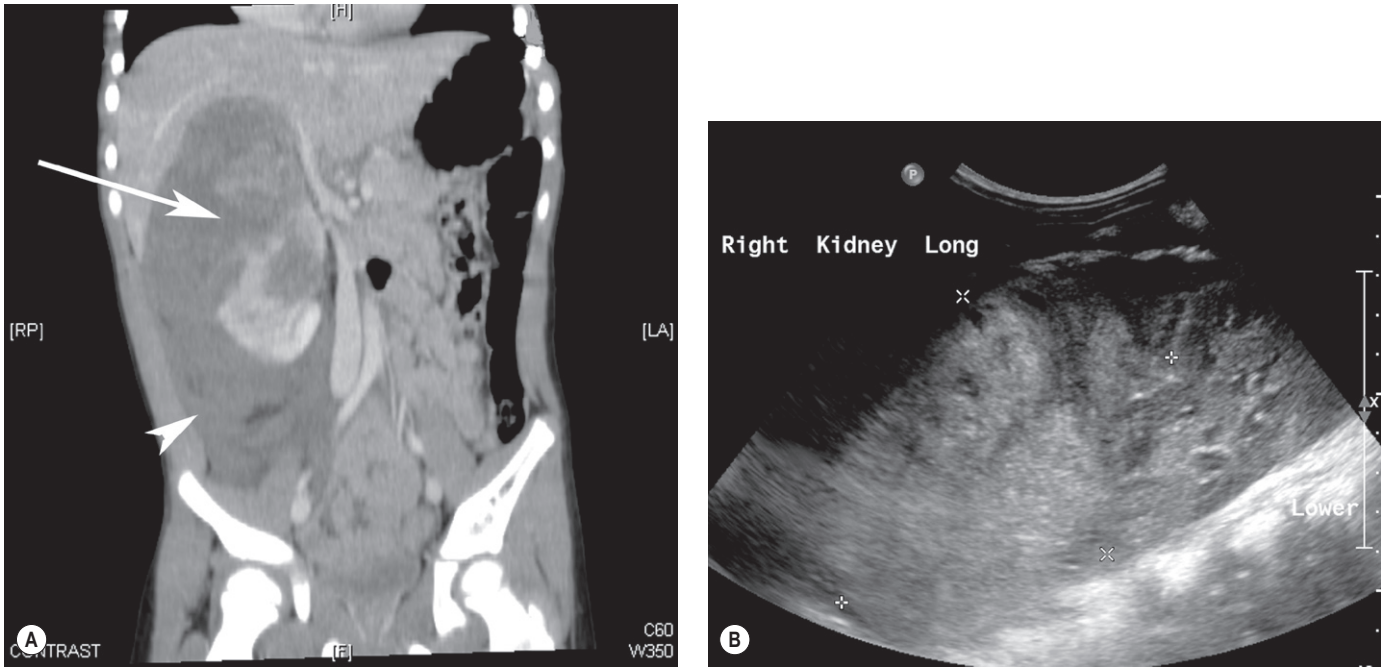

Figure 71.66 Renal trauma: 5-year-old boy 1 day following a fairly innocuous fall complaining of marked flank tenderness and presenting with fever. **A:** Contrast-enhanced CT scan showing complete disruption of the mid and upper poles of the right kidney (arrow) and large retroperitoneal haematoma and laceration (arrowhead). **B:** Longitudinal sonogram showing complete loss of normal architecture of the upper and mid pole of the right kidney (between callipers). Active bleeding necessitated embolisation. Renal biopsy performed at the same time confirmed Wilms' tumour.

- looking for abdomino-pelvic masses (Wilms' tumour or adrenal tumours)
- assessing the calibre of the aorta (aortic coarctation or mid-aortic syndrome).

Older children are usually able to cooperate with a thorough Doppler examination. If possible this should also be performed in younger children at the end of the study although it is often as unrewarding as it is time-consuming. Time is better spent performing a thorough baseline examination of the abdomen and pelvis.

The Doppler examination should concentrate on evaluating:

- the main and intrarenal vasculature for aneurysm formation or post-stenotic dilatation
- the abdominal aorta.

Renal trauma

Most renal trauma in children results from blunt injury. An appropriate clinical history and the presence of macroscopic haematuria should alert the clinician to the diagnosis. The paediatric kidney

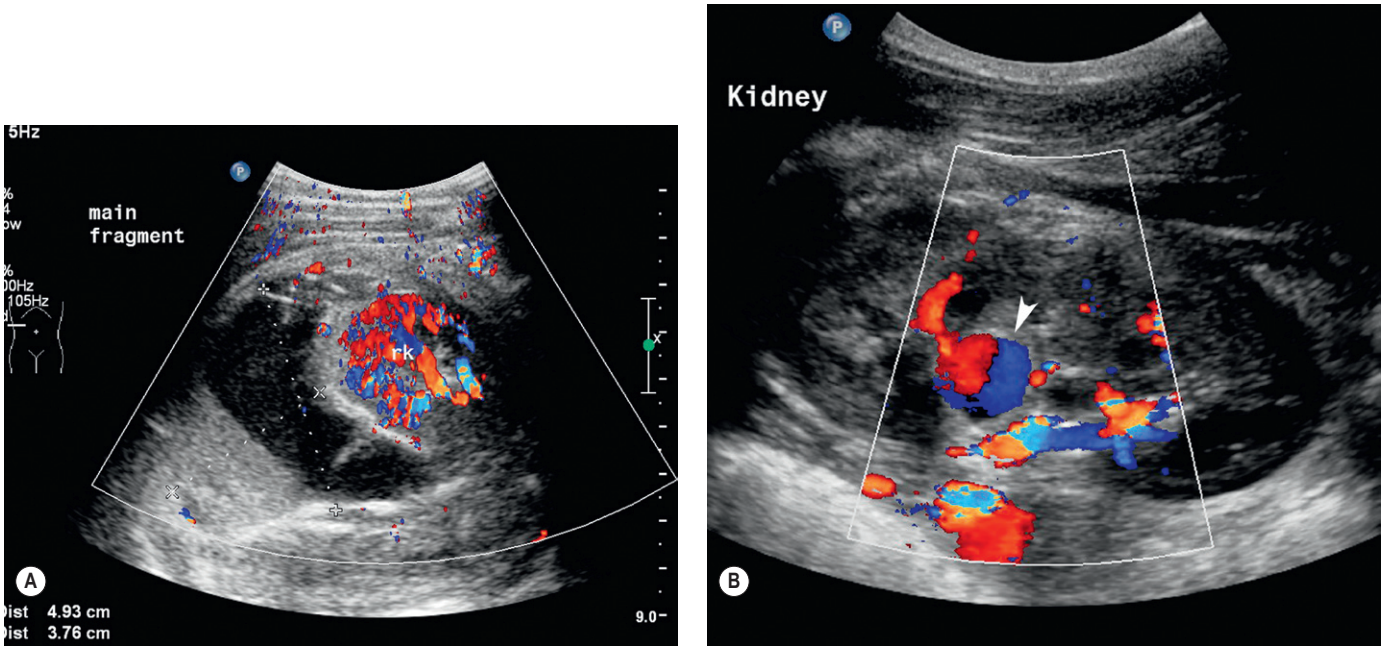

Figure 71.67 Renal trauma follow-up. A: Transverse colour Doppler sonogram of the right kidney showing a fluid debris level within a urinoma (between callipers). A retrograde JJ ureteric stent was required to effect drainage. **B:** Colour Doppler longitudinal sonogram showing post-traumatic pseudo-aneurysm (arrowhead); this was hypoechoic on greyscale imaging. This was treated with selective angiographic coiling.

is vulnerable to injury due to its relatively large size, poorly developed surrounding thoraco-abdominal wall and lack of perirenal fascia. Minor trauma may provoke significant renal injury in an already diseased kidney; examples include massive hydronephrosis, renal tumour (Fig. 71.66) or enlarged polycystic kidney (Fig. 71.41).

Contrast-enhanced multi-detector CT without oral contrast is the imaging technique of choice for staging post-traumatic abdominal injuries. CT is an effective, non-invasive method of accurately assessing the extent of renal injury in children who have sustained trauma[45] and also provides useful functional information concerning renal excretion and urine extravasation. Frequent limitations of ultrasound in the acute setting include the presence of dressings, local tenderness, suboptimal breath-holding and ileus. Imaging should only be undertaken in the haemodynamically stable patient and should not delay urgent treatment.

The main role of ultrasound is in the serial follow-up of stable renal injuries including laceration and subcapsular and retroperitoneal haematomas. Ultrasound is also suitable for detecting specific complications such as urinoma (Fig. 71.67A) or pseudo-aneurysm formation (Fig. 71.67B) and arteriovenous malformation (AVM).

Renal tract malignancy

A palpable abdominal mass in the first year of life is usually renal in origin. Common causes include congenital abnormalities such as hydronephrotic kidney or multicystic dysplastic kidney. Only a small proportion of renal masses are due to tumour. Whenever an abdominal or flank mass is clinically suspected in a child, of any age, ultrasound including colour Doppler should be the initial imaging modality of choice to evaluate the underlying cause.

Wilms' tumour

Wilms' tumour is one of the most common malignancies in children, and the most common solid renal neoplasm in childhood, accounting for over 90% of renal tumours in this age group. Presenting features include a mass, fever, haematuria and hypertension. Most will present between the ages of 3 and 5 years. Wilms' tumour is unilateral in over 90% of affected children. Bilateral synchronous nephroblastomas are observed in around 5% of affected children and are usually associated with the presence of nephrogenic rests and congenital anomalies such as horseshoe kidney (Fig. 71.20C). A number of associated conditions include predisposing overgrowth syndromes (Beckwith–Wiedemann, Simpson–Golabi–Behmel, Perlman) and non-overgrowth syndromes (familial Wilms', WAGR syndrome, aniridia, Denys–Drash syndrome, Fraser syndrome).[46]

In the vast majority of patients, ultrasound will confirm the renal origin of an intra-abdominal tumour and forms an essential part of the local staging of tumour. The staging of Wilms' tumour is summarised in Table 71.11. Intrarenal tumours tend to distort renal architecture and may show a claw of compressed surrounding renal parenchyma (Fig. 71.68). Extrarenal lesions such adrenal neuroblastomas (see Fig. 71.78) tend to infiltrate, displace and efface the kidney. Wilms' tumour usually distorts and displaces the pelvicalyceal system. Wilms' tumours are typically large at

Table 71.11 Staging of Wilms' tumour (reproduced with permission from Cohen[49])

Stage	
I	Tumour is confined by the renal capsule with no vascular invasion and is completely excised
II	Tumour has spread beyond the capsule or with vascular infiltration, but is completely excised
III	Positive abdominopelvic lymph nodes, tumour spill at operation, peritoneal invasion, unresectable tumour or incomplete tumour resection
IV	Distant metastases beyond the abdomen and pelvis (lung, liver, bone, brain, nodal)
V	Bilateral renal involvement at presentation

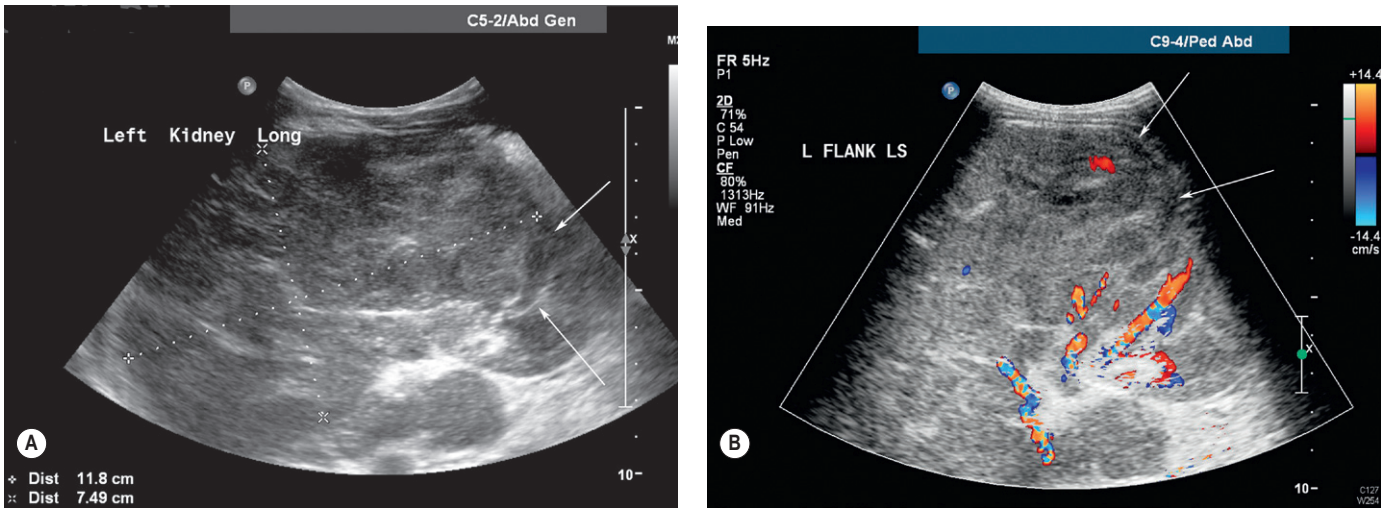

Figure 71.68 Wilms' tumour. Longitudinal greyscale **(A)** and Doppler sonogram **(B)** showing a pseudocapsule (arrows) formed by a large heterogeneous tumour (between callipers). Anechoic areas are caused by a combination of haemorrhage, cysts or necrosis.

Table 71.12 Comparative features of Wilms' tumour and adrenal neuroblastoma

Feature	Wilms' tumour	Neuroblastoma
Age of presentation	2–5 years	<2 years
Organ of origin	Kidney(s)	Neural crest tissue (usually retroperitoneal)
Laterality	5–10%	85–95%
Calcifications	5–10%	85–95%
Mass effect	Intrarenal (claw sign)	Extrinsic compression
Local invasion	Displaces renal vessels Direct extension into renal vein, IVC and potentially the right atrium	Encases and displaces vessels Neural foramen extension
Common sites of metastases	Lung	Bone

presentation. Right-sided tumours can compress the inferior vena cava and left-sided tumours displace the abdominal aorta. The comparative sonographic findings in Wilms' tumour and abdominal neuroblastoma are summarised in Table 71.12.

The echotexture of Wilms' tumour is heterogeneous with solid areas interspersed with hypoechoic and anechoic areas caused by haemorrhage, cysts or necrosis (Fig. 71.68). Internal calcifications are uncommon. Tumour margins are usually smooth and well defined as a result of pseudocapsule formation.

Tumour can spread locally by breaching the renal capsule. Microscopic breach cannot be detected on imaging. The outline of the tumour capsule should be carefully assessed to look for possible rupture. Ancillary features of direct local spread include free abdominal fluid and remote abdominal masses. Suspected invasion of adjacent local organs can be excluded by independent movement of the tumour with breathing.

Contiguous growth of tumour into the renal vein and IVC is seen in 4–10% of patients, but rarely into the heart[47] (Fig. 71.69). Colour Doppler ultrasound sonography is the best modality to determine the patency of the renal veins and IVC.[48] Tumour may rarely grow directly into the liver.

Enlarged retroperitoneal lymph nodes (Fig. 71.70) might be found although these are more usual in neuroblastoma. Retrocrural adenopathy is specific for neuroblastoma. Ultrasound is unable to differentiate between tumour and reactive lymphadenopathy.

Wilms' tumour metastasises predominantly to the lung (in about 10% of patients at diagnosis), the liver (around 2%), and very rarely to other sites. Screening of the liver should be performed to exclude liver metastasis. When examining the abdomen, a thorough examination of the contralateral kidney is necessary. If bilateral tumours are found each kidney should be locally staged separately but overall staging is stage V.[49] Histology is divided into favourable (90%) or unfavourable if anaplastic elements are present.

In all cases, additional cross-sectional imaging will be required for staging purposes. CT or MRI is performed for local staging with a chest X-ray or CT of the thorax to assess lungs.

In Europe, the International Society of Paediatric Oncology (SIOP) treatment protocol is based on chemotherapy followed by surgery to prevent the risk of perioperative tumour rupture. Imaging (ultrasound, CT and MRI), clinical history and examination will help predict whether the findings are consistent with Wilms' tumour. Preoperative chemotherapy can then be started without the need for biopsy or histological confirmation.

In the United Kingdom preoperative image-guided biopsy is advised to help identify the small group of patients who, despite typical imaging features of Wilms' tumour, have other forms of renal neoplasia (discussed below) that require alternative management.[50]

In North America the National Wilms' Tumor Study group treatment protocol mandates early tumour resection unless there is evidence of tumour thrombus, massive tumour or evidence of extracapsular spread. In these higher risk cases preoperative neoadjuvant chemotherapy is given.

Regular ultrasound surveillance for 3 years after therapy is considered to reveal most abdominal recurrences.[51] The SIOP protocol recommends only abdominal US surveillance, although other examinations such as CT or MRI are clinically indicated and undertaken in the initial post-surgical follow-up.

Wilms' tumour screening

Sonographic surveillance should be offered to children identified as being at greater than 5% risk of Wilms' tumour following review by a clinical geneticist. Ultrasound should be performed every

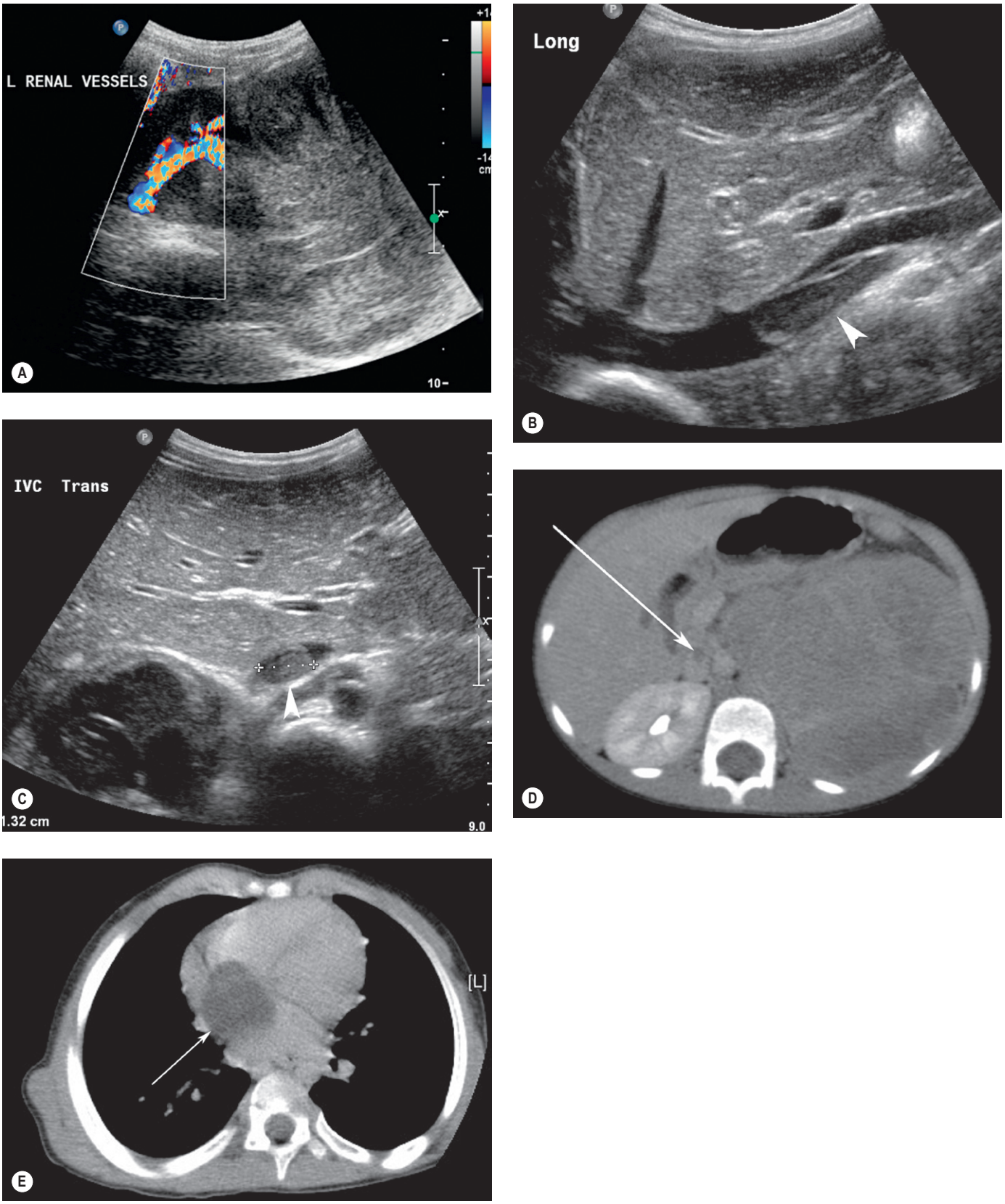

Figure 71.69 **Wilms' tumour thrombus. A–D:** 2-year-old boy with a large, unilateral, left renal intracapsular Wilms' tumour. **A:** Colour Doppler sonography showing absent flow in the right renal vein. **B, C:** Longitudinal and transverse ultrasound of the IVC showing non-occlusive tumour thrombus (arrowheads). **D:** Axial contrast-enhanced CT showing filling defect consistent with tumour thrombus within the IVC (arrow). Note that the heterogeneous left renal tumour is displacing but not encasing the adjacent aorta and IVC. **E:** Axial contrast-enhanced CT in another patient showing tumour thrombus occupying the right atrium (arrow). One of the most critical roles of ultrasound in imaging Wilms' tumour is in the detection of tumour extension into the renal vein, IVC and right atrium.

3 months until 5 years of age. In certain conditions (Beckwith–Wiedemann syndrome, aniridia, Simpson–Golabi–Behmel syndrome and specific familial Wilms' pedigrees) surveillance should continue until 7 years.[52]

Nephroblastomatosis

Nephroblastomatosis is characterised by persisting metanephric blastemal rests and represents a premalignant precursor reported in around 30–40% cases of unilateral and almost all cases of bilateral Wilms' tumour. Nephroblastomatosis manifests as either diffuse or multifocal disease.[53] Disease involvement may be perilobar (PL), intralobar (IL), combined (PL and IL) or universal. The affected portions of the kidneys are typically enlarged. The ultrasound appearances are highly variable and include well-defined hypoechoic, isoechoic or hyperechoic nephrogenic foci which may be multiple. Contrast-enhanced CT or MRI is often more helpful in characterising a macroscopic lesion identified on initial ultrasound (Fig. 71.71).

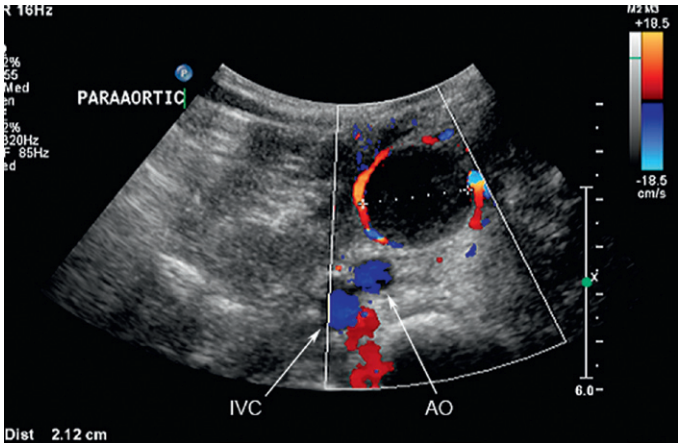

Figure 71.70 Wilms' tumour. Transverse Doppler sonogram demonstrating para-aortic adenopathy (between callipers). IVC, inferior vena cava; AO, aorta.

Congenital mesoblastic nephroma

This is the most common solid renal tumour in newborns. Tumour typically presents as a large, solid, abdominal mass. On ultrasound tumour mass is hypoechoic relative to normal renal parenchyma. Most tumours are locally invasive for which treatment involves nephrectomy.[54] Metastases are rare. Follow-up imaging is required to look for local recurrence.

Lymphoma and leukaemia

Ultrasound of the abdomen should be performed in all children presenting with lymphoma or leukaemia prior to the commencement of therapy.

The kidneys contain no lymphoid tissue. Primary lymphoma of the kidneys is rare. Lymphomatous infiltration of both kidneys is not uncommon and is usually associated with disease elsewhere. Most cases are non-Hodgkin's lymphoma – Burkitt's type. Abdominal ultrasound is useful in evaluating the size and involvement of the solid abdominal viscera and for lymphadenopathy. Cross-sectional imaging such as CT or PET-CT is required for definitive staging and follow-up. Ultrasound in renal lymphoma typically demonstrates markedly enlarged kidneys with hypoechoic areas corresponding to foci of cellular infiltrates (Fig. 71.72).

Leukaemic infiltration of the kidneys may also cause bilateral diffuse renal enlargement. This is more commonly seen in acute lymphoblastic leukaemia. On ultrasound the kidneys are hyperechoic, with loss of corticomedullary differentiation with affected areas showing mottled texture which can distort normal calyceal architecture.

Angiomyolipoma

Up to 80% of children with tuberous sclerosis are predisposed to develop angiomyolipomata during their lifetime. Angiomyolipomata are also rarely associated with neurofibromatosis and von Hippel–Lindau syndrome. Angiomyolipomata are considered to be benign tumours or hamartomas which increase in size and number with advancing age. They consist of varying quantities of adipose tissue, blood vessels and smooth muscle. The lesions are cortically based and on ultrasound are recognisable as hyperechoic foci by virtue of their fatty content (Fig. 71.44). Masses near the normally fatty renal sinus may therefore be missed. Symptoms are dependent

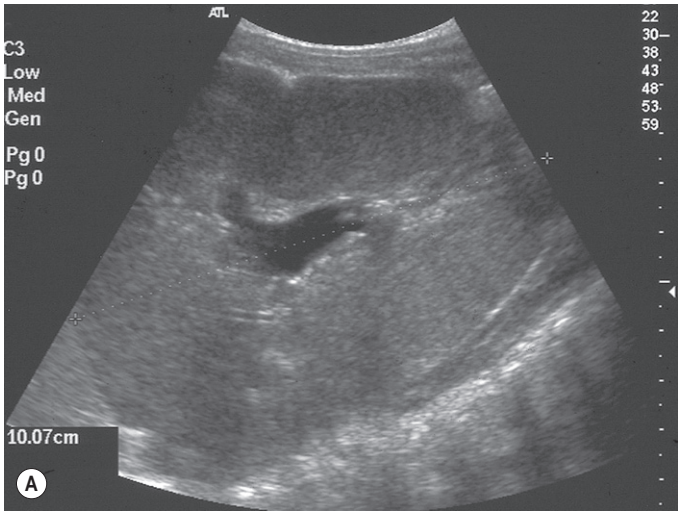

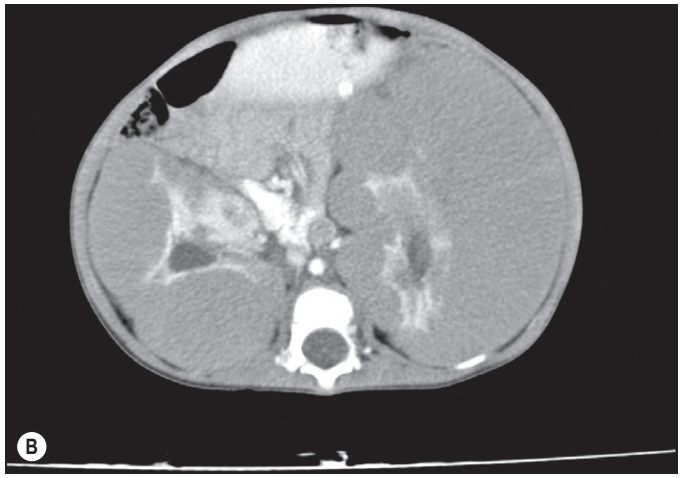

Figure 71.71 Nephroblastomatosis. A: Longitudinal sonogram demonstrating marked enlargement of the right kidney resulting from diffuse, homogeneous subcapsular nephroblastomatosis. **B:** Axial contrast-enhanced CT of the abdomen at the level of the kidneys showing a very large burden of nephroblastomatosis in both kidneys compressing the normal enhancing renal parenchyma. (Images courtesy of Andrew B. Rickett FRCR, University Hospitals of Leicester, Leicester, UK.)

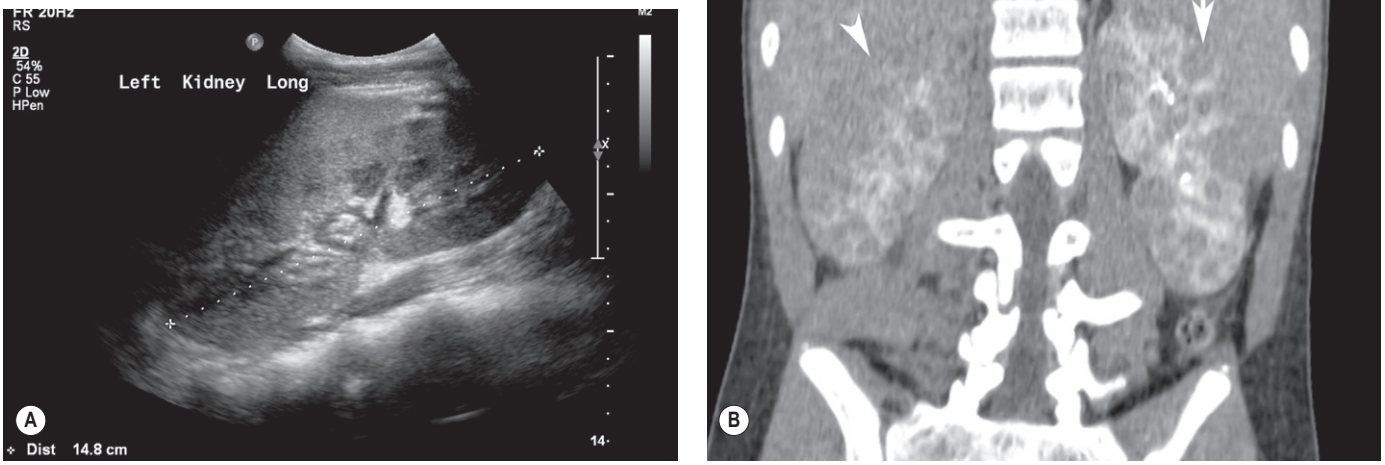

Figure 71.72 Lymphoproliferative disease. A: Longitudinal sonogram in a teenage boy with widespread lymphadenopathy and B-cell symptoms showing renal enlargement. **B:** Coronal reformatted image from a contrast-enhanced CT scan of the abdomen performed shortly afterwards, showing multiple hypo-attenuating foci of disease (arrow). The disease burden is greater in the right kidney (arrowhead). The spleen is also enlarged.

on lesion size; those smaller than 4 cm are usually asymptomatic. Larger lesions are at risk of acute and occasionally severe haemorrhage. Patients present with acute loin pain, shock and anaemia. Management of symptomatic lesions ideally should be conservative and nephron sparing. Catheter embolisation is a favourable alternative to partial nephrectomy.[55]

Clear cell sarcoma

This accounts for approximately 4% of paediatric renal neoplasms. Many of the clinical features are similar to those of Wilms' tumour. The ultrasound and cross-sectional imaging features are also indistinguishable (Fig. 71.73). Bilateral disease has not been reported.[56] Metastatic disease is common although unlike Wilms' tumour bony metastases are frequent.

Renal cell carcinoma

This tumour is rare and usually only seen in the older child with von Hippel–Lindau syndrome. The imaging features are similar to those seen in adults ranging from a complex cyst to a solid mass with areas of fat, haemorrhage, necrosis and calcification.

Rhabdoid tumour

Rhabdoid tumour is a rare aggressive malignant neoplasm of childhood accounting for 2–3% of solid renal tumours. The prognosis is poor as tumour typically metastasises before presentation. Recognised associations include hypercalcaemia and primary or metastatic central nervous neoplasms.[57] Tumour typically arises centrally from the renal hilum. In most cases the imaging features are indistinguishable from Wilms' tumour.

Urinary tract rhabdomyosarcoma

The genitourinary tract is a common site for paediatric rhabdomyosarcoma. Tumour may arise from the urinary bladder wall, prostate gland (Fig. 71.74) or genital tract (see Fig. 72.27). Urinary outflow obstruction is a common presenting symptom in prostatic or bladder rhabdomyosarcoma. The appearances range from a solid echogenic tumour to one with marked internal necrosis. MRI is particularly useful in local staging and in assessing for nodal and distant hepatic or bony metastases.

Enuresis

Enuresis is defined as recurrent episodes of uncontrolled spontaneous voiding of urine in a child 5 years or older. Nocturnal enuresis is common and the diagnostic yield of radiological investigations is often disappointing, but ultrasound of the renal tract should still be considered useful. Diurnal enuresis is less common and more likely to have an underlying cause.

Ultrasound is helpful in:

- demonstrating a major structural urinary tract abnormality
- providing reassurance in normal studies
- predicting patients with bladder dysfunction who are unlikely to respond to medical or cognitive therapy and who will benefit from further urodynamic investigation.

Bladder wall thickness, pre- and post-micturition bladder volumes should be assessed. Ultrasound has been shown to have a high predictive value when using urinary bladder measurements (volume and wall thickness indices) to identify abnormal bladder function in children with enuresis or urinary tract infection.[58]

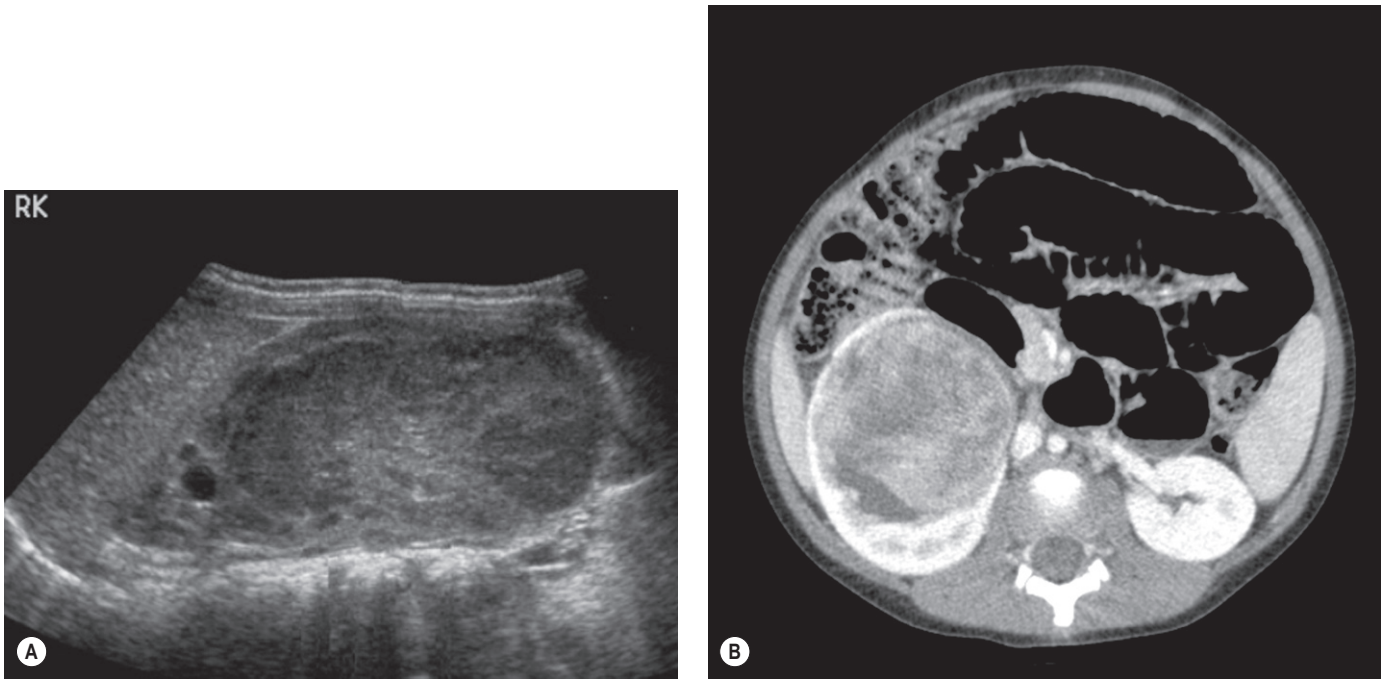

Figure 71.73 Clear cell sarcoma. Longitudinal ultrasound **(A)** and axial contrast-enhanced CT scan **(B)** showing a large heterogeneous necrotic tumour mass arising from within the right kidney. This is indistinguishable from many other tumours including Wilms' tumour.

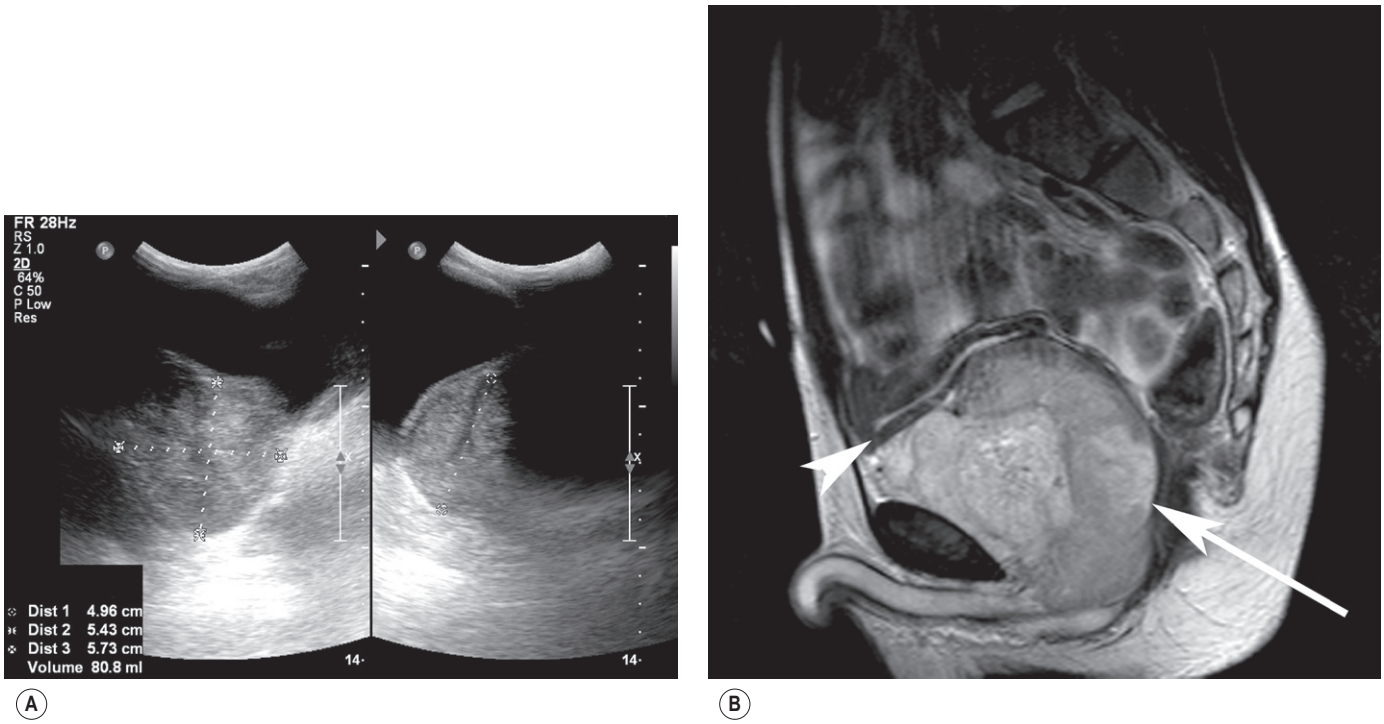

Figure 71.74 Prostatic rhabdomyosarcoma: teenage boy presenting with obstructive uropathy following blunt perineal trauma. **A:** Dual screen image of the pelvis showing diffuse enlargement of the prostate gland (between callipers). **B:** Follow-up sagittal T2-weighted MR scan showing a very large prostatic mass lesion (arrow) displacing the collapsed urinary bladder superiorly (arrowhead). The tumour arising from the prostate gland had breached its capsule anteriorly.

ADRENAL GLAND

Embryology

The adrenal glands are paired retroperitoneal organs located at the anteromedial aspect of the upper pole of each kidney. The fetal adrenal cortex is derived from mesoderm whilst the medulla originates from neuroectoderm. The fetal adrenal gland forms when the cortex envelops the medulla.

Imaging anatomy

The adrenal glands are relatively large in utero and are approximately 20 times their relative adult size at birth. The adrenals are well seen by ultrasound from birth until around one month of age when the fetal adrenal cortex rapidly involutes to leave the permanent cortex, at which time the gland attains adult-like proportions and morphology. The adrenals are typically V- or Y-shaped and show a characteristic hypoechoic cortex and hyperechoic medulla (Fig. 71.75). The adrenal gland may appear elongated in ipsilateral renal agenesis or ectopia (Fig. 71.17).

Adrenal haemorrhage

Adrenal haemorrhage more commonly occurs during periods of physiological stress such as hypoxia resulting in adrenal ischaemia and haemorrhagic infarction but can occasionally be seen in bleeding disorders (Figs 71.5A and 71.76). Most cases occur during delivery or shortly after birth but may rarely occur in utero. Approximately 10% of cases are bilateral. Clinical presentations include:

- Palpable abdominal mass – isolated adrenal haemorrhage results in a suprarenal mass. Renal vein thrombosis and adrenal haemorrhage may coexist resulting in adrenal and renal enlargement.
- Anaemia from bleeding.
- Hypotension and adrenal insufficiency are an unusual complication of bilateral adrenal haemorrhage.
- Jaundice.

In the acute setting the adrenal gland is enlarged by heterogeneously hyperechoic and isoechoic blood. Over time there is clot lysis resulting in a complex cystic mass which eventually involutes. Residual dystrophic calcifications may be seen. Follow-up ultrasound is recommended. If these temporal changes in appearance are not demonstrated then alternative diagnoses such neuroblastoma, duplex upper renal moiety and adrenal cyst should be considered together with intra-abdominal pulmonary sequestration and gastric duplication cyst if the lesion is on the left.

Congenital adrenal hyperplasia

This is also referred to as adrenogenital syndrome and is discussed in Chapter 72 (Fig. 72.11).

Adrenal abscess

Adrenal abscess is part of the differential diagnosis of a complex suprarenal mass but is extremely rare in children. This can complicate an adrenal haemorrhage or result from systemic infection.

Adrenal cysts

A suprarenal cyst in a neonate often relates to a resolving adrenal bleed. In children of all ages an obstructed upper moiety of a duplex kidney should be considered. True adrenal cysts are extremely rare in children but can be seen in Beckwith–Wiedemann syndrome (Fig. 71.77) or metastases. Cystic neuroblastoma is an unusual variant of neuroblastoma and is also rare.

Neuroblastoma

Neuroblastoma is the third most common paediatric tumour after central nervous system and haematological malignancies. Neuroblastoma is an embryonal tumour derived from neural crest tissue and may develop anywhere along the sympathetic chain or within the adrenal medulla. Common sites of origin include the adrenal gland, retroperitoneum and posterior mediastinum.

Prognosis and treatment are dependent upon age, clinical stage (Table 71.13), site of primary and tumour biology. Most children

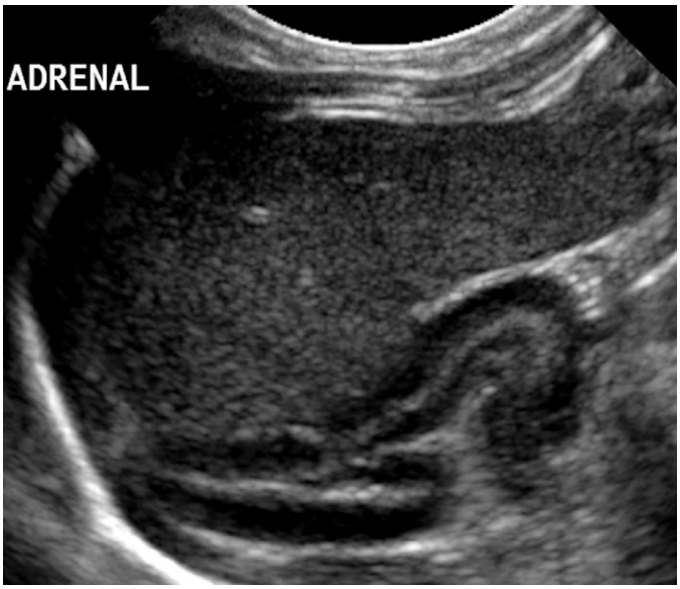

Figure 71.75 The normal adrenal gland. Longitudinal sonogram in a newborn term infant showing a normal prominent neonatal adrenal gland with echo-bright medulla and hypoechoic cortex.

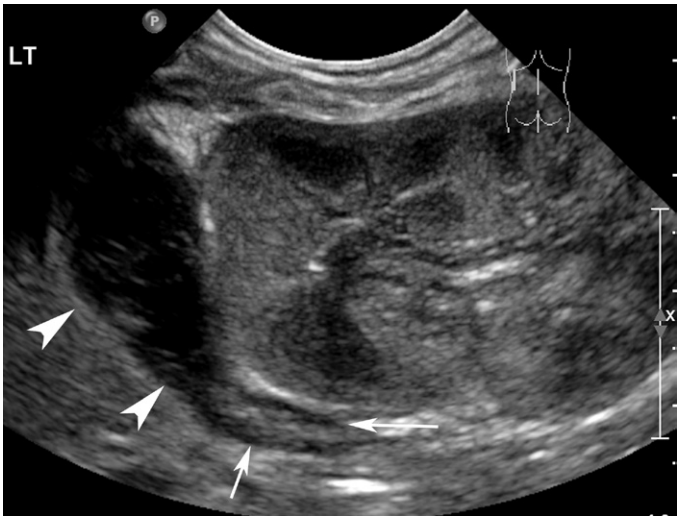

Figure 71.76 Adrenal haemorrhage. Longitudinal sonogram in a neonate with recent adrenal haemorrhage seen as a suprarenal cystic lesion (arrowheads). The two limbs of the adrenal gland were preserved in this example (arrows). This resolved on follow-up scans.

present by 4 years of age (median 2 years); many of these have high-risk disease with an unfavourable outcome. Patients with low- to intermediate-risk disease usually have an excellent prognosis. Younger children with extra-abdominal disease have a better prognosis; this includes antenatally detected and neonatal neuroblastoma. Neonates with metastases limited to the liver, skin or bone marrow referred to as stage 4S also tend to have a favourable course.

The main differential is Wilms' tumour. The comparative features between neuroblastoma and Wilms' tumour are summarised in Table 71.12. Ultrasound is an effective screening tool to assess gross local disease. The echotexture of tumour is variable, reflecting the histological findings of necrosis, haemorrhage, solid tumour and calcifications (Fig. 71.78). In neuroblastoma tumour tends to displace rather than invade the kidney, whilst the vessels are typically encased and displaced. Local nodal involvement and intraspinal extension are difficult to quantify on ultrasound, and cross-sectional imaging (either MRI or CT) is necessary for complete locoregional staging. ^{99m}Tc MDP bone scan and ^{123}I MIBG scintigraphy, bone

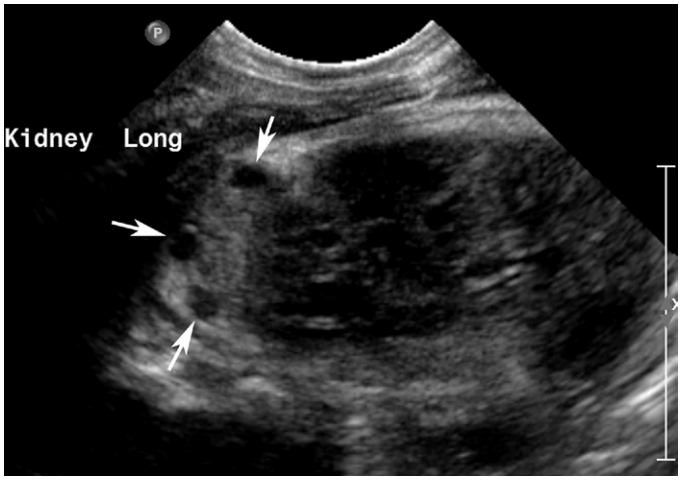

Figure 71.77 Adrenal cysts in Beckwith–Wiedemann syndrome. Longitudinal sonogram of the left kidney and adrenal gland. Bilateral small adrenal cysts (arrows) were demonstrated in this child undergoing routine surveillance sonography.

Table 71.13 Staging of neuroblastoma. International Neuroblastoma Staging System (INSS) (reproduced with permission from[59])

Stage 1	Localized tumour confined to the organ of origin; complete gross resection with or without microscopic residual tumour; ipsilateral and contralateral lymph nodes are microscopically negative
Stage 2A	Localized tumour with incomplete gross resection; ipsilateral and contralateral lymph nodes are microscopically negative
Stage 2B	Unilateral tumour with or without complete gross resection; ipsilateral lymph nodes are positive; contralateral lymph nodes are microscopically negative
Stage 3	Tumour crosses the midline with or without regional lymph node involvement, unilateral tumour associated with positive contralateral lymph nodes, or a midline tumour with positive bilateral locoregional lymph nodes
Stage 4	Distant metastases (liver, bone marrow, distant lymph nodes and other organs)
Stage 4S (occurs in infants)	Localized tumour that does not cross midline but with metastatic disease – confined to the liver, skin, and bone marrow (<10% tumour cells in bone marrow)

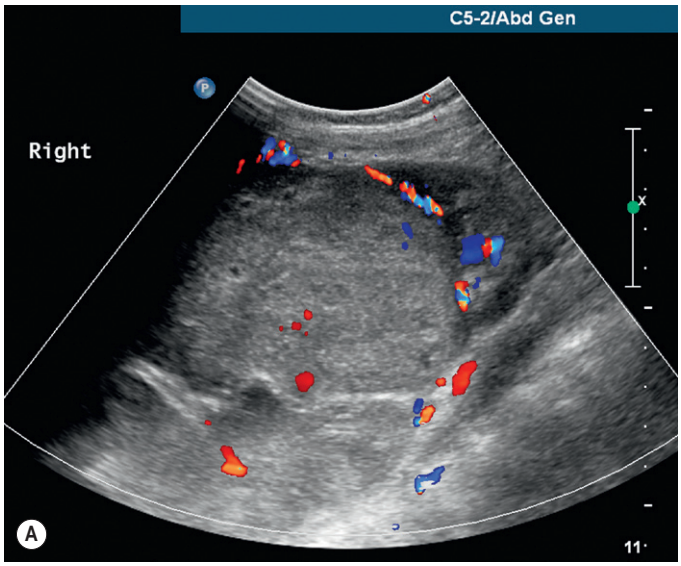

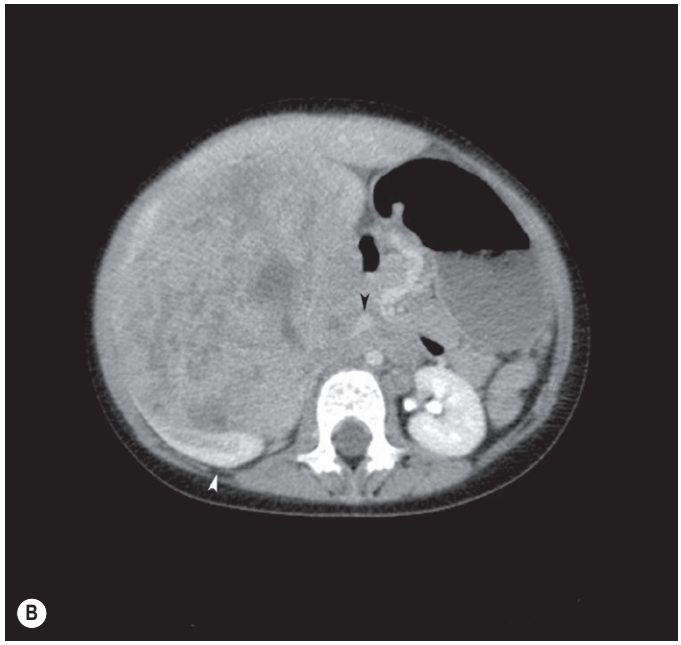

Figure 71.78 Intra-abdominal neuroblastoma. A: Longitudinal Doppler sonogram showing a large heterogeneous suprarenal mass lesion with poor vascularity intimately related to the upper pole of the right kidney. **B:** Axial contrast-enhanced CT image showing tumour effacing a small rim of enhancing lower renal pole parenchyma (white arrowhead). Typical features of neuroblastoma include calcifications; and encasement and displacement of adjacent vessels. In this case the inferior vena cava is encased (black arrowhead). Direct invasion of the kidney is an unusual finding.

Role of ultrasound in imaging nephrogenic and retroperitoneal masses

Ultrasound is the initial diagnostic imaging modality of choice in evaluating a suspected renal mass. Ultrasound should concentrate on:

- the organ of origin, local disease extent and the contralateral kidney
- adenopathy
- calcifications
- renal vessels – to look for tumour thrombus and vascular encasement
- liver metastases.

Staging normally requires CT or MRI.

marrow aspirates and local biopsy are also required for staging and risk stratification.

Ganglioneuroblastoma and ganglioneuroma

Ganglioneuroma is a well-differentiated form of neural crest tumour and is often detected incidentally on an ultrasound or chest X-ray. Ganglioneuroblastoma is an intermediate form with imaging features of both neuroblastoma and ganglioneuroma. Ultrasound usually reveals a well-defined solid mass. Calcifications are not uncommon. Management includes complete excision with radiological follow-up.

Other tumours

Adrenocortical carcinoma, phaeochromocytoma and Conn's adenoma are rare pathologies in children. Their clinical and radiological features are similar to those of adults and are discussed in the adult adrenal chapter (Chapter 33).

REFERENCES

1. Moore KL, Persaud TVN. Development of the urinary system. In: The developing human: clinically oriented embryology. 6th edn. Philadelphia: WB Saunders; 1998;305–319.
2. Hellström M, Hjälmås K, Jacobsson B, et al. Normal ureteral diameter in infancy and childhood. Acta Radiol Diagn 1985;26(4):433–439.
3. Jequier S, Rousseau O. Sonographic measurements of the normal bladder wall in children. AJR Am J Roentgenol 1987;149:563–566.
4. Paspulati RM, Bhatt S. Sonography in benign and malignant renal masses. Radiol Clin North Am 2006;44(6):787–803.
5. Zerin JM, Chen E, Ritchey ML, Bloom DA. Bladder capacity as measured at voiding cystourethrography in children: relationship to toilet training and frequency of micturition. Radiology 1993;187:803–806.
6. Han BK, Babcock DS. Sonographic measurements and appearance of normal kidneys in children. AJR Am J Roentgenol 1985;145:611–616.
7. Schlesinger AE, Hernandez RJ, Zerin JM, et al. Interobserver and intraobserver variations in sonographic renal length measurements in children. AJR Am J Roentgenol 1991;156:1029–1032.
8. Sargent MA, Long G, Karmali M, Cheng SM. Interobserver variation in the sonographic estimation of renal volume in children. Pediatr Radiol 1997;27:663–666.
9. Sargent MA, Gupta SC. Sonographic measurement of relative renal volume in children: comparison with scintigraphic determination of relative renal function. AJR Am J Roentgenol 1993;161:157–160.
10. Hoffman CK, Filly RA, Callen PW. The 'lying down' adrenal sign: a sonographic indicator of renal agenesis or ectopia in fetuses and neonates. J Ultrasound Med 1992;11:533–536.
11. Silva JM, Jafri ZHS, Cacciarelli AA, Barry KA. Abnormalities of the kidney: embryogenesis and radiologic appearance. In: Haller J, ed. Textbook of neonatal ultrasound. New York: Parthenon Publishing Group;1998;101–116.
12. Neville H, Ritchey ML, Shamberger RC, et al. The occurrence of Wilms tumor in horseshoe kidneys: a report from the National Wilms Tumor Study Group (NWTSG). J Pediatr Surg 2002;37:1134–1137.
13. Decter RM. Renal duplication and fusion anomalies. Pediatr Clin North Am 1997;44:1323–1341.
14. Cremin BJ. A review of the ultrasonic appearances of posterior urethral valve and ureteroceles. Pediatr Radiol 1986;16:357–364.
15. Nussbaum AR, Lebowitz RL. Interlabial masses in little girls: review of imaging and recommendations. AJR Am J Roentgenol 1983;141:65–71.
16. Merlini E, Spina P. Primary non-refluxing megaureters. J Pediatr Urol 2005;1(6):409–417.
17. Lebowitz RL, Olbing H, Parkkulainen KV, et al. International system of radiographic grading of vesicoureteric reflux. Pediatr Radiol 1985;15:105–109.
18. Avni EF, Ayadi K, Rypens F, et al. Can careful ultrasound examination of the urinary tract exclude vesicoureteric reflux in the neonate? Br J Radiol 1997;70:977–982.
19. Darge K, Zieger B, Rohrschneider W, et al. Contrast-enhanced harmonic imaging for the diagnosis of vesicoureteral reflux. AJR Am J Roentgenol 2001;177:1411–1415.
20. Moorthy I, Easty M, McHugh K, et al. The presence of vesico-ureteric reflux does not identify a population at risk for renal scarring following a first urinary tract infection. Arch Dis Child 2005;90:733–736.
21. The Pluto Collaborative Study Group. PLUTO trial protocol: percutaneous shunting for lower urinary tract obstruction randomized controlled trial. Br J Obst Gynaecol 2007;114:904–e4.
22. Yiee JH, Garcia N, Baker LA, et al. A diagnostic algorithm for urachal anomalies. J Pediatr Urol 2007;3(6):500–504.
23. Jaswon MS, Dibble L, Puri S, et al. Prospective study of outcome in antenatally diagnosed renal pelvis dilatation. Arch Dis Child Fetal Neonatal Ed 1999;80:F135–F138.
24. Podevin G, Mandelbrot L, Vuillard E, et al. Outcome of urological abnormalities prenatally diagnosed by ultrasound. Fetal Diagn Ther 1996;11:181– 190.
25. Shokeir AA, Nijman RJ. Antenatal hydronephrosis: changing concepts in diagnosis and subsequent management. BJU Int 2000;85:987–994.
26. Sidhu G, Beyene J, Rosenblum ND. Outcome of isolated antenatal hydronephrosis: a systematic review and meta-analysis. Pediatr Nephrol 2006;21:218–224.
27. de Bruyn R, Gordon I. Imaging in cystic renal disease. Arch Dis Child 2000;83:401–407.
28. Blowley Dl, Querfeld U, Geary D, et al. Ultrasound findings in juvenile nephronophthisis. Pediatr Nephrol 1996;10:22–24.
29. Slovis T, Bernstein J, Gruskin A. Hyperechoic kidneys in the newborn and young infant. Pediatr Nephrol 1993;7:294–302.
30. Humar A, Arrazola L, Mauer M, et al. Kidney transplantation in young children: should there be a minimum age? Pediatr Nephrol 2001;16:941–945.
31. Yata N, Nakanishi K, Uemura S, et al. Evaluation of the inferior vena cava in potential pediatric renal transplant recipients. Pediatr Nephrol 2004;19:1062–1064.
32. Hulton S-A. Evaluation of urinary tract calculi in children. Arch Dis Child 2001;84:320–323.
33. Coward RJM, Peters CJ, Duffy PG, et al. Epidemiology of paediatric renal stone disease in the UK. Arch Dis Child 2003;88:962–965.
34. Rahmouni A, Bargoin R, Herment A, et al. Color Doppler twinkling artifact in hyperechoic regions. Radiology 1996;199(1):269–271.
35. Navarro O, Daneman D, Kooh SW Asymmetric medullary nephrocalcinosis in two children. Pediatr Radiol 1998;28:687–690.
36. Dick PT, Shuckett BM, Tang B, et al. Observer reliability in grading nephrocalcinosis on ultrasound examinations in children. Pediatr Radiol 1999;29:68–72.
37. Dubbins PA. The kidney. In: Clinical Doppler ultrasound. London: Churchill Livingstone; 2000;169–190.
38. Moorthy I, Wheat D, Gordon I. Ultrasonography in the evaluation of renal scarring using DMSA scan as the gold standard. Paediatr Nephrol 2004;19:153–156.
39. National Institute for Health and Clinical Excellence (NICE). Urinary tract infection in children. Urinary tract infection: Diagnosis, treatment and long-term management of urinary tract infection in children. Available from: http://www.nice.org.uk/CG54 (accessed 10 March 2009).
40. Dacher JN, Hitzel A, Avni FE, Vera P. Imaging strategies in pediatric urinary tract infection. Eur Radiol 2005;15:1283–1288.

41. Quinn FMJ, Dick AC, Corbally MT, et al. Xanthogranulomatous pyelonephritis in childhood. Arch Dis Child 1999;81:483–486.
42. Cousins C, Somers J, Broderick N, et al. Xanthogranulomatous pyelonephritis in childhood: ultrasound and CT diagnosis. Pediatr Radiol 1994;24(3):210–212.
43. Wright NB, Blanch G, Walkinshaw S, Pilling DW. Antenatal and neonatal renal vein thrombosis: new ultrasonic features with high frequency transducers. Pediatr Radiol 1996;26:686–689.
44. Garel L, Dubois J, Robitaille P, et al. Renovascular hypertension in children: curability predicted with negative intrarenal Doppler US results. Radiology 1995;195:401–405.
45. Turnock RR, Sprigg A, Lloyd DA. Computed tomography in the management of blunt abdominal trauma in children. Br J Surg 1993;80:982–984.
46. Owens CM, Brisse HJ, Olsen ØE, et al. Bilateral disease and new trends in Wilms' tumour. Pediatr Radiol 2008;38(1):30–39.
47. Lall A, Pritchard-Jones K, Walker J, et al. Wilms' tumor with intracaval thrombus in the UK Children's Cancer Study Group UKW3 trial. J Pediatr Surg 2006;41:382–387.
48. Ritchey ML, Kelalis PP, Breslow N, et al. Intracaval and atrial involvement with nephroblastoma: review of National Wilms' Tumor Study-3. J Urol 1998;140:1113–1118.
49. Cohen MD. Commentary: Imaging and staging of Wilms' tumors: problems and controversies. Pediatr Radiol 1996;26:307–311.
50. Brisse HJ, Smets AM, Kaste SC, Owens CM. Imaging in unilateral Wilms' tumour. Pediatr Radiol 2008;38:18–29.
51. Daw NC, Kauffman WM, Bodner SM, et al. Patterns of abdominal relapse and role of sonography in Wilms' tumor. Pediatr Hematol Oncol 2002;19:107–115.
52. Scott RH, Walker L, Olsen ØE, et al. Surveillance for Wilms tumour in at-risk children: pragmatic recommendations for best practice. Arch Dis Child 2006;91:995–999.
53. Lonergan GJ, Martinez-Leon MI, Agrons GA, et al. Nephrogenic rests, nephroblastomatosis, and associated lesions of the kidney. Radiographics 1998;18:947–968.
54. Hartman DS, Lesar MS, Madewell JE, et al. Mesoblastic nephroma: radiologic-pathologic correlation of 20 cases. AJR Am J Roentgenol 1981;136(1):69–74.
55. Geller E, Smergel EM, Lowry PA. Renal neoplasms of childhood. Radiol Clin North Am 1997;35:1391–1413.
56. Lowe LH, Isuani BH, Heller RM, et al. Pediatric renal masses: Wilms tumor and beyond. Radiographics 2000;20(6):1585–1603.
57. Agrons GA, Kingsman KD, Wagner BJ, Sotelo-Avila C. Rhabdoid tumor of the kidney in children: a comparative study of 21 cases. AJR Am J Roentgenol 1997;168(2):447–451.
58. Sreedhar B, Yeung CK, Leung VYF, Chu CW. Ultrasound bladder measurements in children with severe primary nocturnal enuresis: pretreatment and posttreatment evaluation and its correlation with treatment outcome. J Urol 2008;179(4):1568–1572.
59. Brodeur GM, Pritchard J, Berthold F, et al. Revisions of the international criteria for neuroblastoma diagnosis, staging, and response to treatment. J Clin Oncol 1993;11(8):1466–1477.

CHAPTER

72

The paediatric uterus, ovaries and testes

Gurdeep S. Mann, Maria E.K. Sellars and Paul S. Sidhu

UTERUS AND OVARIES

Ultrasound is the imaging technique of choice in the initial assessment and follow-up of a variety of symptoms and pathologies relating to the female paediatric pelvis. These include: disorders of sexual differentiation (formerly known as intersex), disorders of sexual maturation (precocious puberty and pubertal delay), menstrual dysfunction, pelvic mass lesion, pelvic pain and vaginal discharge.

Evaluation of the developmental status of the uterus and ovaries from the neonatal period through to puberty, menarche and establishment of regular ovulatory menstrual cycles forms the bulk of the paediatric gynaecological ultrasound workload for an imaging department. Effective pelvic ultrasound in girls requires a good understanding of the normal sonographic anatomy, applied physiology, endocrinology and embryology of the developing genitalia. As the embryologies of the renal and gynaecological tracts are intertwined and the adrenal gland mediates sexual differentiation, the renal tract and adrenal glands should always be routinely assessed in the appropriate clinical setting.

Embryology

Normal development of the ovaries

Genetic sex is determined at fertilisation. The principal sex organ (gonad) in the female is the ovary. Prior to 7 weeks gestation the gonads are identical in both sexes and termed 'indifferent gonads'. Female gonadal development is dependent upon the presence of germ cells, a paternal X chromosome and crucially the absence of a male SRY protein. The ovaries play no significant role in female sexual differentiation or in the development of the uterus, vagina and external female genitalia.

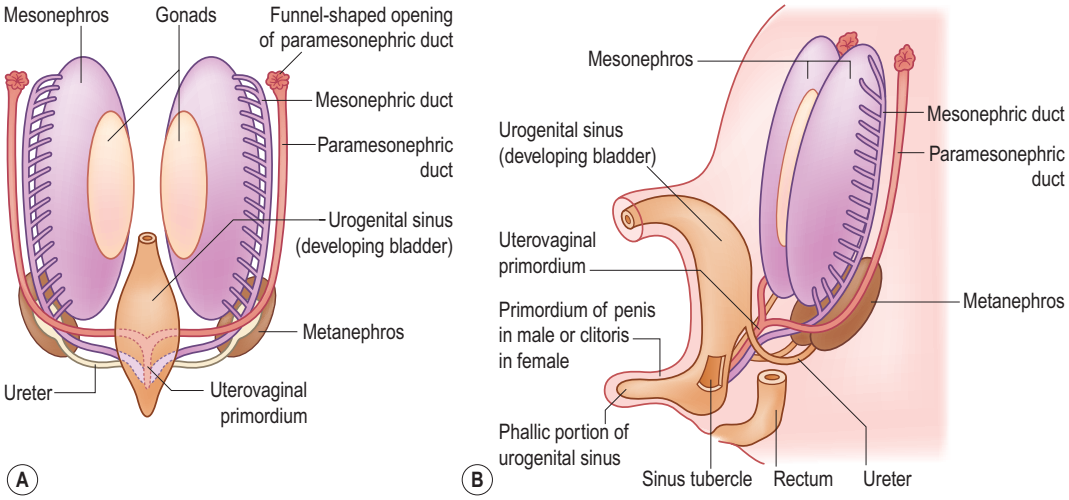

Figure 72.1 Normal development of the female genital tract. Ventral view **(A)** and lateral view **(B)** showing the development of the fallopian tubes, uterus and upper vagina from the paired paramesonephric (Müllerian) ducts. The lower vagina develops from the urogenital sinus. The hymen develops from the posterior wall of the urogenital sinus at the sinus tubercle. (Reproduced with permission from Moore KL, Persaud TVN. The Developing Human. Clinically Oriented Embryology, 6th Edition. Philadelphia: WB Saunders; 1998.)

Ovarian tissue arises from germinal epithelium covering the urogenital ridge, mesenchymal cells of the urogenital ridge and germ cells derived from the yolk sac. Gonadal differentiation occurs in the second month of fetal life when germ cells from the yolk sac proliferate and differentiate under the influence of placental gonadotrophins. Germ cells migrating to the urogenital ridge undergo a series of mitotic divisions differentiating into several million oogonia. Each oogonium is derived from a primordial germ cell surrounded by flattened squamous granulosa cells arising from germinal epithelium. A proportion of the oogonia at the genital ridges enter the first phase of meiosis and become dormant (meiotic arrest). First meiosis does not commence until the onset of ovulation.

By 16 to 20 weeks, primordial follicles begin to organise within the fetal ovarian cortex, consisting of an immature or primary oocyte surrounded by a single layer of flattened support cells. The follicle is subsequently enveloped by the mesenchyme arising from the urogenital ridge.

By birth only around a million primordial follicles remain and by menarche less than half that number. Follicles undergo varying rates of maturation and involution during life. The vast majority remain quiescent and eventually involute. The remainder can be dormant for several decades.

Normal development of the uterus, vagina and fallopian tubes

In a normal female two paired Müllerian ducts ultimately develop into the structures of the female reproductive tract including the upper two-thirds of the vagina, the cervix, uterus and both fallopian tubes (Fig. 72.1). The lower one third of the vagina and the ovaries have separate embryological origin. The principal developmental processes occurring in female sexual differentiation are:

Müllerian organogenesis

The paired Müllerian ducts (paramesonephric) originate in embryonal mesoderm lateral to each Wolffian duct (mesonephric duct) (Fig. 72.2). Both ducts grow in caudal and medial directions. The most cephalad portions of the ducts remain separate and form the fallopian tubes.

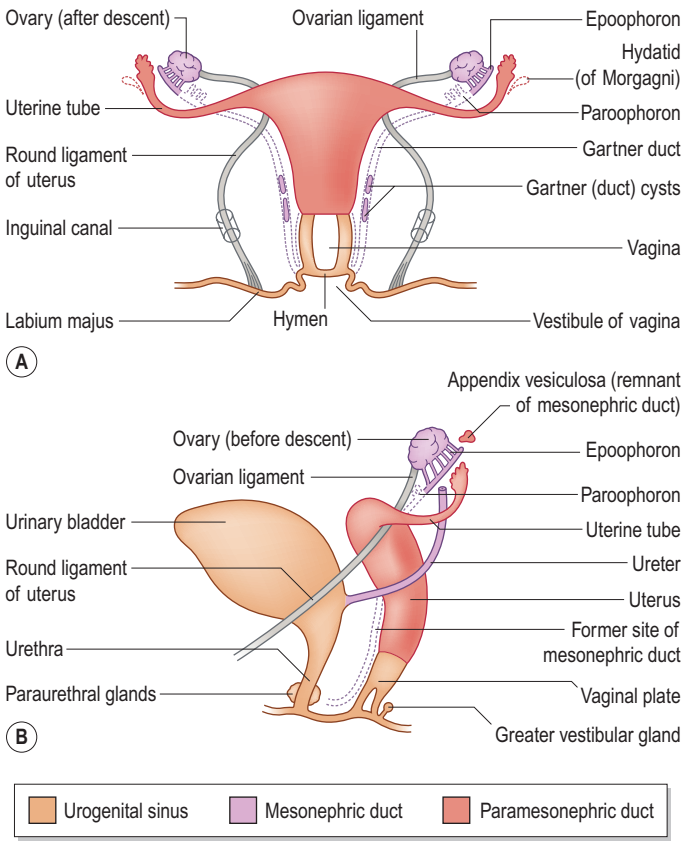

Figure 72.2 A: Schematic diagram showing the fully developed female reproductive tract including vestigial structures. **B:** Lateral view showing the position of the ovary prior to its descent towards the pelvis. (Reproduced with permission from Moore KL, Persaud TVN. The Developing Human. Clinically Oriented Embryology, 6th Edition. Philadelphia: WB Saunders, 1998.)

Lateral and vertical fusion

Lateral fusion (7–9 weeks gestation) occurs when the lower segments of the Müllerian ducts fuse. Vertical fusion (around 8 weeks gestation) occurs when the lower Müllerian system fuses with the ascending endodermal sinovaginal bulb and the lower third of the vagina is formed and canalises. The sinovaginal bulb inserts into the urogenital sinus at Müller's tubercle. The hymen develops and is normally perforate by birth.

Septal resorption

The uterus and upper third of the vagina develop into a single canal as the midline septum regresses at around 20 weeks gestation (Fig. 72.3).

In a normal male, Wolffian structures (seminal vesicles, vas deferens and epididymis) develop under the influence of testosterone from Leydig cells in the fetal testis with Müllerian duct regression. Involution of Müllerian structures in the male is dependent upon the secretion of anti-Müllerian hormone (AMH), around the 6th to 8th week of fetal life. AMH is produced by normally functioning Sertoli cells in the fetal testis and acts on target tissues principally by local diffusion and primarily inhibits the Müllerian structures on the same side as the gonad. A normal testis will therefore prevent Müllerian structures developing on the ipsilateral side. The presence of an ovary, non-functioning or poorly functioning/dysgenetic testis will permit a degree of ipsilateral Müllerian development whilst the absence of androgenic (testosterone) stimulation prevents the development of Wolffian structures.

The development of the Müllerian and the Wolffian ducts is intertwined and requires adequate development of the mesonephric system. This accounts for the frequent association of anomalies of the female genital system and urinary tract. Renal anomalies associated with uterovaginal anomalies include ipsilateral renal agenesis, ectopic kidney, duplex collecting system and cystic dysplasia.

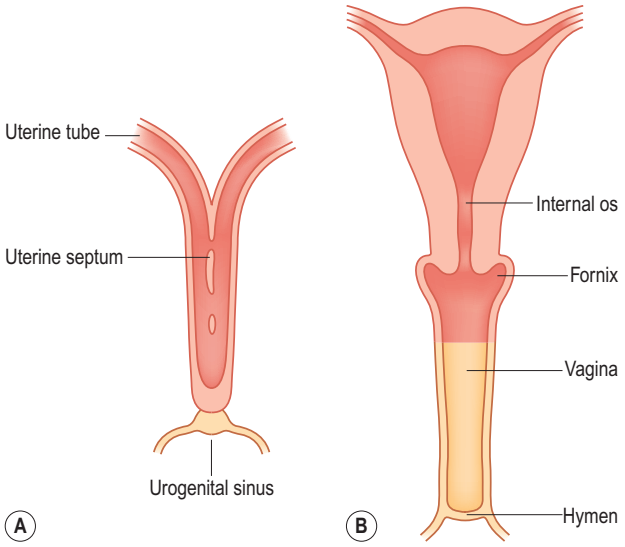

Figure 72.3 Formation of the uterus and vagina (modified from Brenner C and De Bruyn R. Imaging of benign paediatric gynecological disorders. *Imaging*, Volume 15(2003) Number, 53–62. © The British Institute of Radiology). **A:** The formation of the uterus from the lateral fusion of the paramesonephric ducts and septal resorption. **B:** The vagina developing from vertical fusion of tissue at the junction of urogenital sinus and uterus.

Normal female endocrine development (birth to puberty)

Puberty is the normal developmental process associated with the appearance of both primary and secondary sexual characteristics and occurs between the ages of 8 and 15 years in girls.

The hypothalamic-pituitary-gonadal axis is functional in the normal fetus. Following birth, the levels of gonadotrophins (leuteinising hormone, LH, and follicle-stimulating hormone, FSH) and sex hormones are similar to those seen in adults. These levels reduce in the first few months after birth. Pulsed gonadotrophin-releasing hormone (GnRH) secretion reduces in amplitude thereafter during childhood. A variety of mechanisms suppress the onset of puberty including central neural suppression of GnRH secretion and hormonal feedback.

The onset of puberty is triggered by the release of pulses of GnRH from the hypothalamus. Pulsatile GnRH secretion from the hypothalamus increases in amplitude and frequency just prior to puberty. GnRH secretion progresses to nocturnal secretion and eventually circadian 24-hour secretion is established. The initial hormonal induction of puberty is predominantly LH dependent. There is a nocturnal rise in LH pulsatility and the amplitude of LH secretion gradually increases corresponding in oestrogen production sufficient to induce breast development. The trigger for puberty comes from higher centres and is partially under neural control. This process is complex, multifactorial and incompletely understood.

Thelarche is usually the first clinically recognisable stage of puberty and typically occurs between 10 and 12 years of age and is characterised by the appearance of a 'breast bud' (Tanner stage 2). During this period the uterus grows and develops into its adult pear-shaped configuration. This is usually followed by adrenarche and the appearance of pubic hair as a result of adrenal and gonadal androgen secretion. Approximately 2 years prior to the onset of clinically apparent puberty, hormonal activity increases in the adrenal gland. This corresponds with maturation of the adrenal cortex and is independent of the hypothalamic-pituitary-ovarian axis. It is during adrenarche that the ovaries mature and enlarge. In response to nocturnal gonadotrophin pulsatility, the ovaries develop multicystic morphology (also interchangeably referred to as multifollicular).[1] The ovary contains more than six follicles 4 mm in diameter, or greater. This morphology is distinct from polycystic ovarian (PCO) appearance.[2] The multicystic ovarian appearance is a marker for the presence of pulsatile nocturnal gonadotrophin secretion. Adrenarche may arise independently of puberty.

The latter stages of puberty include a growth spurt, gonadarche (pubertal hypothalamic-pituitary-gonadal axis reactivation) and menarche. Menarche is the onset of menstrual bleeding and does not occur until Tanner breast stage 4 or 5.

Normal pubertal development is a dynamic sequential process. If onset of puberty is either too early (precocious puberty), too late (delayed puberty), out of sequence or does not occur at all then pubertal dysfunction is present.

Imaging technique

A full urinary bladder is required to serve as an acoustic window for transabdominal imaging of the pelvis. Optimal distension allows for sufficient displacement of gaseous pelvic bowel loops and visualisation of the uterus and ovaries.

The neonatal pelvis is particularly suited to transabdominal examination given the paucity of fat. Dedicated high-frequency (6–9 MHz), small footprint curvilinear probes are widely available commercially and capable of producing high-resolution images. The uterus and ovaries are more readily visualised in the early neonatal period whilst under the influence of maternal and placental hormones. Neonates should be examined in a warm room, preferably shortly after a feed. The urinary bladder should be assessed

early as it is liable to fill and empty quickly. If sufficiently distended then a full evaluation of the pelvis should be made. The first time a patient attends for a pelvic ultrasound, the examination should also ideally include both kidneys and adrenal glands, as structural anomalies of the uterus are associated with renal and gastrointestinal tract malformations. The adrenal glands should be assessed in suspected cases of disorders of sexual differentiation and pubertal dysfunction.

For older children, the timing of the patient's scan whilst in the department is important. An under-filled bladder should prompt the patient to drink more clear fluids and be reassessed every 20–30 minutes thereafter. Care should also be taken not to over-distend the bladder as this can distort normal pelvic anatomy and make for an uncomfortable examination, increasing the likelihood of non-cooperation. A post-micturition view is often very helpful.

Small children ideally should be scanned using a broadband (4–7 MHz) curvilinear probe. In the older patient, particularly those with more generous soft tissue coverage, an adult approach can be helpful using a 3–5 MHz curvilinear probe. If an abnormality is detected then imaging with a linear high-resolution probe should always be considered. Optimised colour flow and pulsed Doppler wave imaging can demonstrate vascular structures, enable differentiation between cyst and solid, and delineate regional blood flow.

The role of transvaginal (TV) scanning in children is very limited. Few dedicated paediatric imaging centres offer TV scanning. TV scanning should only be considered in sexually active adolescents. In all cases the benefits of not requiring a transvesical acoustic window and improved near-field resolution should be weighed up against the limited field of view, the invasiveness of the procedure, the need for an appropriate chaperone and issues regarding obtaining informed consent. In children where TA scanning is considered insufficient then alternatives such as transperineal ultrasound scanning or pelvic magnetic resonance imaging (MRI) should be considered.

Recent advances in ultrasound technique such as 3D scanning, saline infusion sonohysterography and contrast bubble agent dynamic scanning currently have limited clinical application in paediatric practice and are not discussed further.

Scanning planes

The ovaries are identified by scanning transversely through the full urinary bladder usually at the level of the uterine fundus and by using oblique parasagittal planes in the angle between the iliac vessels and bladder. It should, however, be remembered that particularly in the neonate the ovaries can lie in the abdomen rather than the pelvis and ovaries containing cysts can be located anywhere in the abdomen. The ovaries are measured in three axes and the ovarian volume calculated. The number, size and distribution of the follicles should also be recorded.

The uterus is identified by scanning transversely and longitudinally through the urinary bladder. The uterine length is measured along the longitudinal axis and the anteroposterior measurements taken at the cervix and fundus transversely. Uterine volume calculation can also be made. If the endometrium is detected, its contour, echogenicity and thickness are documented. Endometrial stripe thickness is measured at the maximum depth of the body away from the cervix.

Normal sonographic appearances of the developing ovaries

Ovarian position

Ovaries and testes show analogous embryological development. The fetal ovaries are initially located juxtarenally, on the medial surface of the urogenital ridge on each side of the spine. Ovarian descent towards the pelvis begins at 3 months of fetal life and is guided by the gubernaculum, connecting the lower pole of the ovary to the uterus, to form the round ligaments of the uterus and utero-ovarian ligaments. The suspensory ligament is attached to the upper pole of the ovary; its elongation forms the infundibulopelvic ligament. At birth the ovaries normally lie in the superior margin of the broad ligament referred to as the mesovarium. By puberty the ovaries lie deeper within the pelvis either posterolateral or lateral to the uterus.

Non-visualisation of an ovary

In the neonatal period one or both ovaries are normally readily visible whilst under the influence of maternal hormones. Non-visualisation of one or more ovaries in older children is not uncommon. In approximately 10–20% of transabdominal examinations one or both ovaries are not visualised.[3] The most likely causes of non-visualisation of the ovary are technical, including suboptimal bladder filling, bowel obscuring an ovary, body habitus and operator inexperience. Ovarian dysplasia (e.g. Turner's streak ovary), ovarian atresia and maldescent are uncommon causes of non-visualisation.

Unlike testicular migration, ovarian migration disorders are rare. Ovarian descent may be arrested anywhere from the lower pole of the kidney to the uterine broad ligament (Fig. 72.2B). Ovarian maldescent results in the upper pole being located above the pelvic brim, and is associated with a short infundibulopelvic ligament, mesovarium and an elongated utero-ovarian ligament. Maldescent is rarely associated with Müllerian duct and renal anomalies.[4] Descent below the broad ligaments is also rare and seen with inguinal ovarian hernias.

Ovarian outline and volume

Most premenarchal ovaries are ovoid in shape. Ovarian volume measurement is estimated using the formula for a prolate ellipsoid structure (volume = 0.523 × length × width × thickness). The volume of the ovary is affected by the presence of large follicles (primordial or ovulatory) and corpus luteal cysts and may not be reliably calculated when these structures are present.

Mean ovarian volumes in patients less than 2 years old are around 1.1 cm^3 for the first year of life and 0.67 cm^3 for the second year of life.[5] There appear to be two particular periods of increased growth rate of the ovary. The first occurs at approximately 8 years of age, coinciding with adrenarche. The second growth spurt occurs immediately before and during puberty. Ovarian growth is most rapid between Tanner breast developmental stages 2 and 4.[6] Mean ovarian volumes for a particular age are summarised in Table 72.1.

Ovarian echotexture and follicles

The normal ovary contains moderately echogenic stroma and multiple small follicles (Fig. 72.4). In infancy, follicular activity and development is a dynamic continuous process related to the influence of maternal hormones. The size and the number of visible follicles is variable. Numerous follicles may be demonstrated by ultrasound. Occasionally a follicle may act as a sufficiently large fulcrum to precipitate tubo-ovarian torsion. As maternal hormonal influence subsides the size of the ovaries decreases. The ovary is poorly vascularised in infants and young children.

Between the ages of 2 and 8 years the ultrasound appearances of ovaries are most stable; this is also the period where the ovaries tend to be most difficult to visualise. Despite this, ovarian follicles increase in size and number throughout childhood. Prepubertally, the ovaries may appear quite active, with follicles of up to 9 mm in size. However, the lower levels of gonadotrophin in prepubertal girls can result in slightly larger follicles of up to 12 mm, limiting the value of follicular diameter in assessing pubertal status.[7] Ovarian vascularisation slowly increases during childhood. By 6–8 years of age both the ovarian cortex and medulla are usually identifiable.

Table 72.1 Normal ovarian volumes in neonates, infants and throughout childhood

Chronological age	Mean volume (cm^3)	Standard deviation ($\pm cm^3$)
Birth to 3 months	1.06	0.96
4–12 months	1.05	0.67
13–24 months	0.67	0.35
2 years	0.75	0.4
4 years	0.8	0.35
6 years	1.2	0.35
8 years	1.1	0.5
10 years	2.2	0.7
12 years	3.8	1.4
13 years	4.2	2.3

Data (birth to 24 months) from Cohen et al.[5]
Data (2–13 years) from Orsini et al.[3]

At around 8–9 years of age the ovaries become multifollicular,[2] defined on ultrasound as more than six follicular cysts of at least 4 mm in diameter. This coincides with nocturnal, pulsatile luteinising hormone secretion and the onset of puberty. Follicles continue to increase in size throughout puberty. Around 11–12 years of age, primordial follicles are evenly distributed throughout the layers of the cortex. Constant maturation and involution of the follicles results in the wide range of diameters seen at different pubertal stages. Follicles may become atretic at any stage of their development. By around 12–13 years ovulation begins. Thereafter, non-primordial ova containing follicles are present. A gradual reduction of the primordial follicles is seen until none remain in the mature ovary at around 14 years of age.

Menarche

The establishment of regular ovulatory cycles heralds the end of puberty. The principal regulators of ovarian function are luteinising hormone (LH) and follicle-stimulating hormone (FSH). In response to rising levels of FSH, between 5 and 12 primordial follicles start to enlarge and are now called primary follicles. They gradually enlarge until a follicle of at least 16 mm is attained. Follicular secretion of oestrogen results in the development of the endometrium.

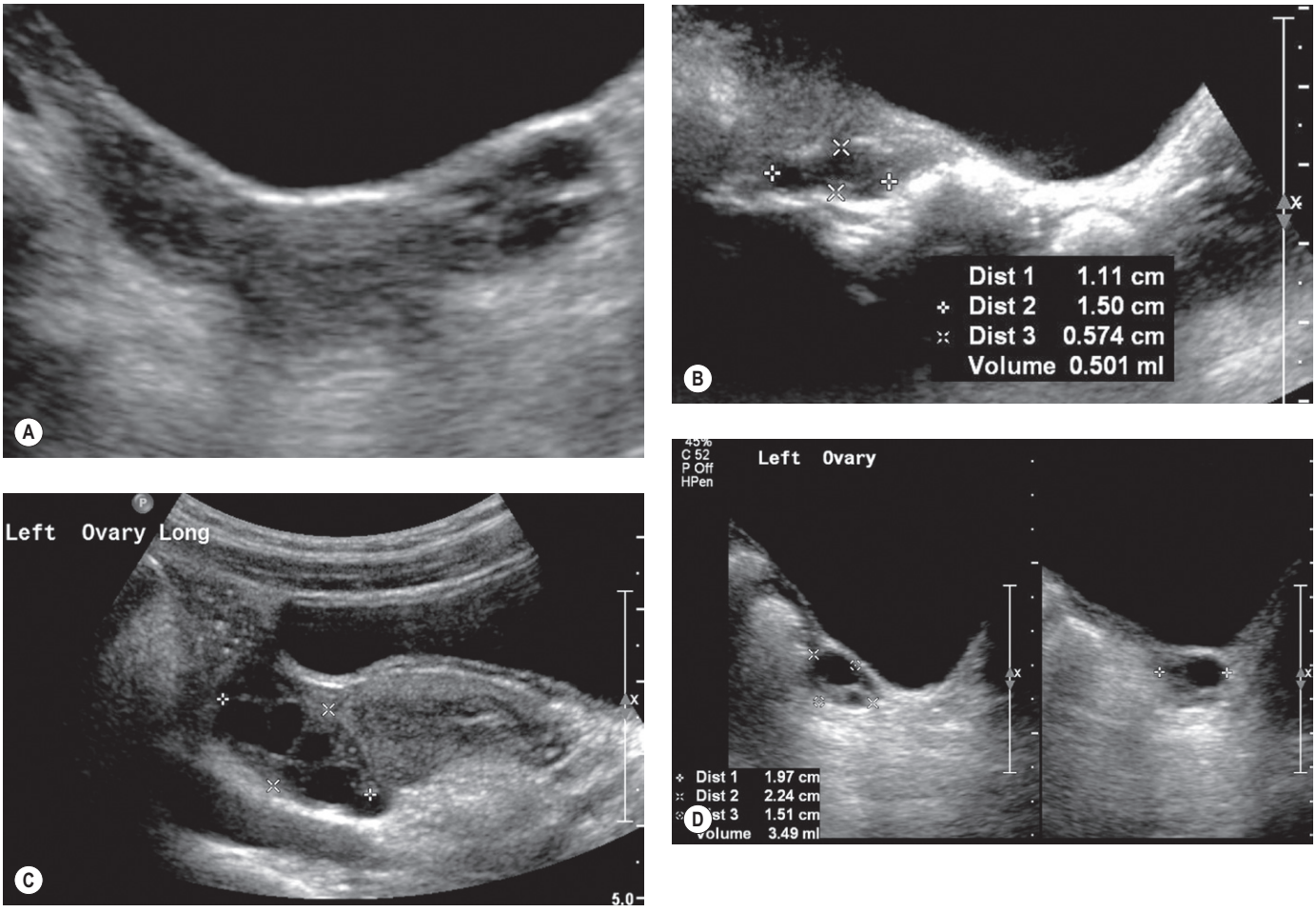

Figure 72.4 Normal ovarian appearance at various developmental stages. A: Transverse sonogram showing the uterus and both ovaries. The uterine endometrial stripe is visible and both ovaries show multiple small follicles related to maternal hormonal influence. **B:** Oblique sonogram in a 13-month-old girl showing a typical small volume ovary (between callipers). The ovaries are most difficult to visualise between the ages of 13 months and 6 years as they poorly vascularised and relatively quiescent. **C:** Oblique sonogram of the left ovary (between callipers) showing 'multicystic'/ multifollicular morphology in early puberty. This appearance signifies the onset of pubertal maturation. **D:** Oblique sonograms of the left ovary (between callipers) in a 13-year-old girl showing a dominant follicle. This is the final stage of follicular development and its presence suppresses all other follicular activity.

In an anovulatory cycle, the follicle regresses and the subsequent fall in oestrogen level results in a withdrawal menstrual bleed. Eventually, when a follicle diameter of over 20 mm is achieved, that follicle gains primacy, while the other follicles recruited during the cycle degenerate. The remaining follicle is now known as a mature or dominant graafian follicle. After ovulation the granulosa cells of the ruptured follicle wall begin to proliferate and give rise to the corpus luteum, which is an endocrine structure that secretes steroid hormones that maintain the uterine endometrium in readiness to receive an embryo. If no embryo implants, the corpus luteum degenerates after about 14 days.

Ovarian growth and follicular development

The complete, unruptured graafian follicle may regress without expelling the ovum, first by the oocyte dying and then by undergoing coagulation necrosis with eventual formation of the corpus restiforme, which vanishes without trace. In fetal and postnatal life this generally occurs before the follicle has reached an appreciable size. If the follicle expels the ovum (ovulation) then either a fully developed corpus luteum results, or the remaining follicle becomes luteinised and regresses. The distinguishing feature of the post-pubertal follicle is the ability of the follicle to liberate its ovum (ovulation) and be converted into a corpus luteum.

Normal sonographic appearances of the developing uterus

At birth the uterus remains under the influence of maternal hormones. The endometrial stripe is normally visible as a thin echogenic line and is often marginated by a hypoechoic halo. A small amount of free fluid can normally be seen in the endometrial cavity. The anteroposterior (AP) width of the cervix is slightly greater than, or more often equal to that of the fundus (Fig. 72.5). The uterus may therefore resemble an inverted pear-shape but the majority show tubular configuration.[8]

Beyond the neonatal period the AP width of the uterine fundus becomes proportionately smaller. The uterus assumes a prepubertal tubular configuration. The endometrial stripe becomes difficult to visualise even on high-resolution imaging. From infancy to around 7 years no significant uterine growth is seen.[3] The uterus is considered prepubertal if the length is less than 4.5 cm and width no greater than 1.0 cm.[9]

Uterine growth is proportional to chronological age, bone age and pubertal stage.[10] Between 8 years and puberty the uterus enlarges and thickens under the influence of local ovarian oestrogens. The mean rate of growth of the uterus is slowest until 8 years old, intermediate aged 9–11 years and higher still during the progression of gonadotrophin-dependent puberty. At puberty the uterus is located deep within the pelvis. The fundus enlarges relative to the cervix and the endometrial stripe is more readily visualised as a midline echogenic stripe. Ultimately the uterus assumes adult proportions and demonstrates the typical post-pubertal 'pear-shaped' configuration. The ultrasound appearances of the developing uterus are summarised in Table 72.2.

Detailed reference tables are available with normative data for uterine length, width and volumes.[3] Many centres do not routinely document volume calculations as the uterus changes shape with time and it is arguable whether a reliable estimate can be made using the formula for a prolate ellipsoid.

Developmental anomalies of the uterus and vagina

Congenital uterovaginal malformations

In the general population, the prevalence of congenital uterine and vaginal anomalies is unknown but estimated to be around 0.5% for uterine and 0.025% for vaginal anomalies.[11] Anomalies are caused by alterations in the development or fusion of the Müllerian ducts. Detailed classifications of congenital anomalies have been published.[12] A pictorial overview of the main congenital Müllerian malformations is given in Figure 72.6. A more simplified classification is presented in Table 72.3.

A small proportion of cases will present in the neonatal period as an obstructive pelvic mass lesion with hydrocolpos or in relation to a complex urogenital problem at birth such as urogenital sinus or cloacal malformation.[13,14] The palpable pelvic or abdominal mass is due to an obstructed fluid-filled vagina lying between the rectum and urinary bladder. A fluid–debris level is not uncommon (Fig. 72.7). Occasionally the mass may be sufficiently large to cause urinary tract obstruction.

Congenital uterovaginal anomalies most often present later in childhood and adolescence. A high incidence of decreased fertility and obstetric complications is common. Presenting symptoms include delayed onset of menarche, primary amenorrhoea or cyclical pelvic pain at the onset of menarche. A pelvic mass may occur as a result of haematocolpos or haematometrocolpos. Obstructive Müllerian anomalies (imperforate hymen, vaginal septa, genital tract atresias and stenosis) preclude the outflow of menstruation allowing the collection of blood in the uterus and the vagina, increasing the likelihood of retrograde menstruation. Imperforate hymen (Fig. 72.8) is usually not associated with any other Müllerian abnormality and occurs as a result of incomplete canalisation of the urogenital sinus with the Müllerian system.[15] Imperforate hymen cannot be differentiated from a low transverse vaginal septum by ultrasound. Transverse vaginal septum is not associated with other urological or Müllerian anomalies. Longitudinal vaginal septum is variable and ranges from no symptoms to cyclic pain and abnormal bleeding. This condition is usually associated with uterus didelphys (Fig. 72.9), absent or hypoplastic ipsilateral kidney[16] and rarely multicystic dysplastic kidney.[17]

Müllerian agenesis

The most common form of Müllerian duct dysgenesis is Mayer–Rokitansky–Kuster–Hauser (MRKH) syndrome, with combined agenesis of the uterus, cervix and upper vagina. Atypical configurations may be encountered which are not readily classified by ultrasound. MRI is particularly useful in defining complex anatomy.

Cloacal anomalies

The cloaca is a terminal portion of the fetal hindgut and is a common channel for genital secretions, faecal residue and urine. Failure of the urorectal septum to partition the cloaca into rectum, vagina and urethra results in a persisting cloacal malformation (Fig. 72.10). An imperforate anus and single perineal opening in a newborn female should immediately alert the clinician to the presence of a cloacal malformation. An ultrasound of the pelvis and urinary tract is required prior to urgent surgical treatment. A defunctioning colostomy is formed to alleviate bowel obstruction and prevent faecal contamination of the renal and gynaecological tracts. Spinal ultrasound and echocardiography should be performed to look for associated defects following surgery.

Disorders of sexual differentiation

Ultrasound is the method of choice for screening the neonate with ambiguous genitalia. Ultrasound provides a rapid, accurate and non-invasive means of identifying the presence or absence of a uterus, which is normally well visualised in the neonatal period.

Great sensitivity is required towards the parents and carers during this often distressing period. It is crucial not to make preliminary pronouncements as to the likely gender of the child being assessed based solely upon the imaging findings. Best practice is to defer to the multidisciplinary team involved in the child's overall

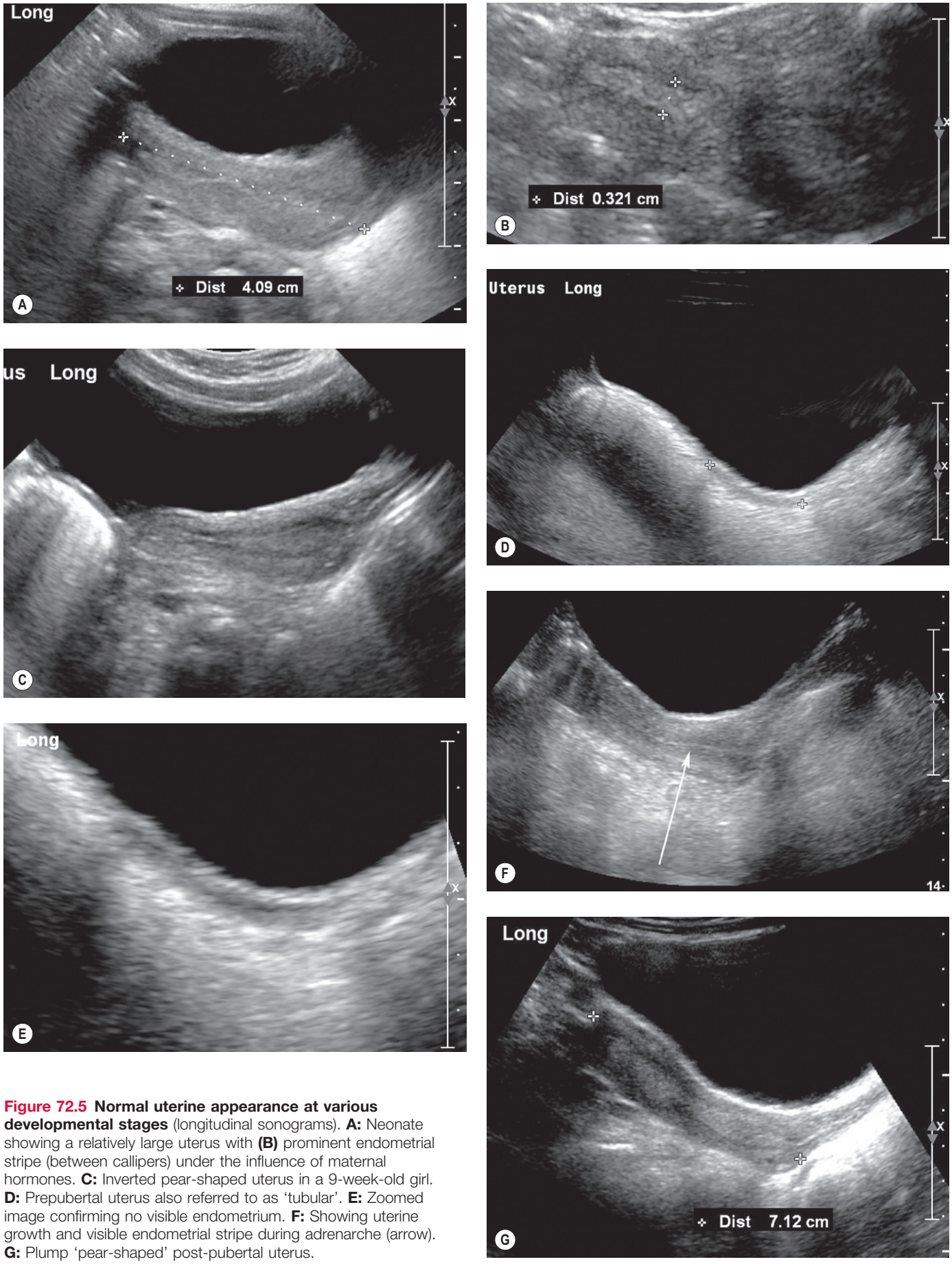

Figure 72.5 Normal uterine appearance at various developmental stages (longitudinal sonograms). **A:** Neonate showing a relatively large uterus with **(B)** prominent endometrial stripe (between callipers) under the influence of maternal hormones. **C:** Inverted pear-shaped uterus in a 9-week-old girl. **D:** Prepubertal uterus also referred to as 'tubular'. **E:** Zoomed image confirming no visible endometrium. **F:** Showing uterine growth and visible endometrial stripe during adrenarche (arrow). **G:** Plump 'pear-shaped' post-pubertal uterus.

Table 72.2 Uterine dimensions, volumes and morphology in neonates and throughout childhood

	Uterine length (cm)	Uterine fundal width (cm)	Endometrial stripe	AP fundus/cervix ratio	Uterine shape
Neonate (visible 94%)	2.3–4.6	1.2 (range 0.8–2.1)	Echogenic stripe seen in 98%	1:2	Tubular (58%) Inverted pear shape (32%) Fundal narrowing relative to cervix as oestrogen levels fall
Prepubertal	2.5–4.0	Less than 1.0	Rarely visible	1:1	Tubular
Post-pubertal	5.0–8.0	1.6–3.0	Visible echogenic stripe Cyclical endometrium as seen in adult menstrual cycle	2–3:1	Pear-shaped

Data summarised from Garel et al.[9]

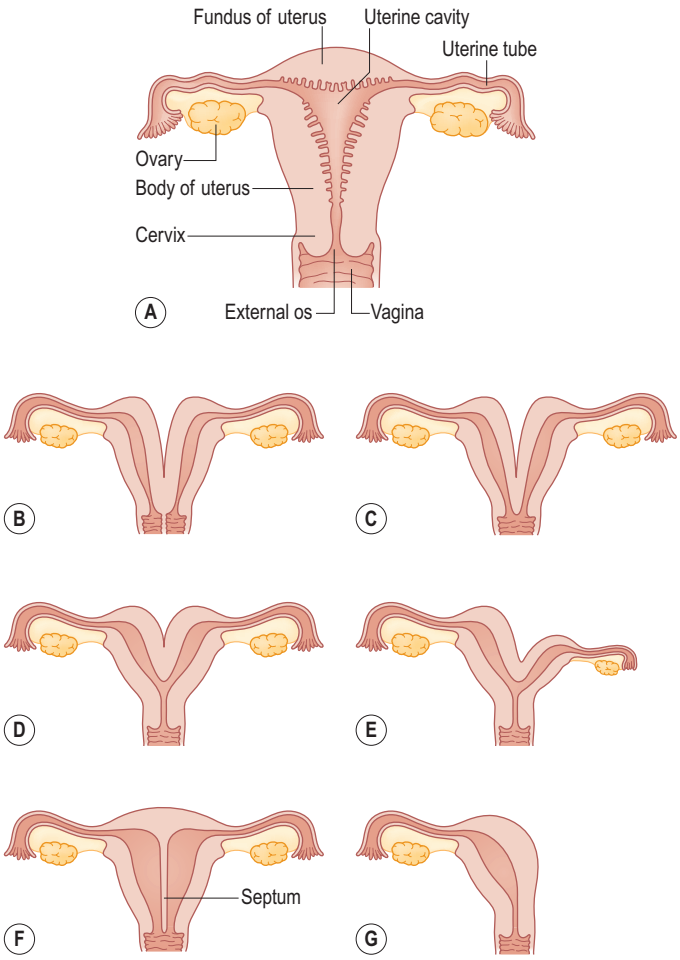

Figure 72.6 The various types of congenital abnormalities of uterovaginal formation. A: Normal vagina and uterus. **B:** Double vagina and uterus (uterus didelphys). **C:** Single vagina and double uterus. **D:** Bicornuate uterus. **E:** Bicornuate uterus with rudimentary left horn. **F:** septate uterus. **G:** unicornuate uterus. (Reproduced with permission from Moore KL, Persaud TVN. The Developing Human. Clinically Oriented Embryology, 6th Edition. Philadelphia: WB Saunders; 1998.)

Table 72.3 Simplified classification of congenital abnormalities of uterovaginal formation

Organogenesis	Inadequate development of one or more Müllerian ducts (Müllerian agenesis/dysgenesis)	Uterine agenesis (MRKH) Uterine hypoplasia
Fusion	Lateral fusion defect Vertical fusion defect	Bicornuate Uterus didelphys (Fig. 72.9) Unicornuate uterus with a rudimentary horn Cervical atresia Vaginal septa Imperforate hymen
Septal resorption	Failure of resorption	Septate uterus

care. Assigning a correct gender for the baby is complex and will require evaluation of a combination of investigations including hormonal profiles, chromosomal analysis, sonographic findings, additional radiology where indicated (genitography and MRI) and occasionally gonadal biopsy. The aim is to provide an accurate gender as soon as is practicable. The role and timing of surgical intervention for ambiguous genitalia remains controversial.[18]

Children with ambiguous genitalia requiring imaging assessment include:

- female phenotypes with clitoromegaly and/or fused labia
- female phenotypes found to have a gonad present in a hernial sac
- male phenotypes with bilateral impalpable testes and perineal hypospadias
- male phenotypes with unilateral undescended testis with hypospadias.

Children with an appropriate family history should also be assessed.[19] Various types of intersex states have been described (Table 72.4).

Female pseudohermaphrodites are genetic females (46,XX) who possess ovaries but with masculinised external genitalia. This is the most frequent cause of ambiguous external genitalia. The most common underlying cause is congenital adrenal hyperplasia, a

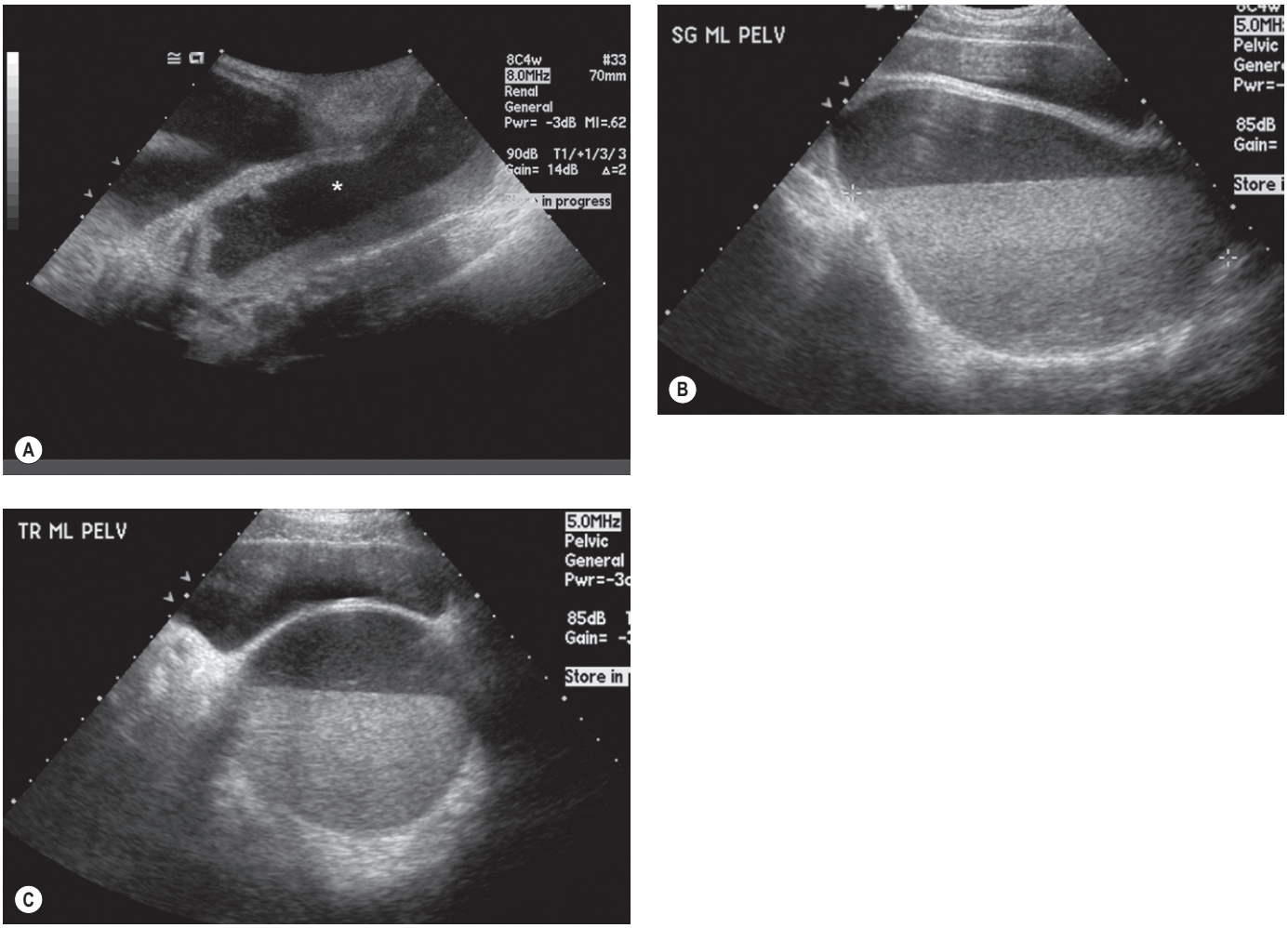

Figure 72.7 Hydrocolpos and hydrometrocolpos. A: Longitudinal sonogram in a newborn female with a large fluid-filled mass (*) behind the urinary bladder showing typical sonographic appearances of a distended vagina. **B, C:** Longitudinal **(B)** and transverse **(C)** sonograms in a 12-year-old girl showing a fluid–debris level in the distended vagina at the onset of menstruation.

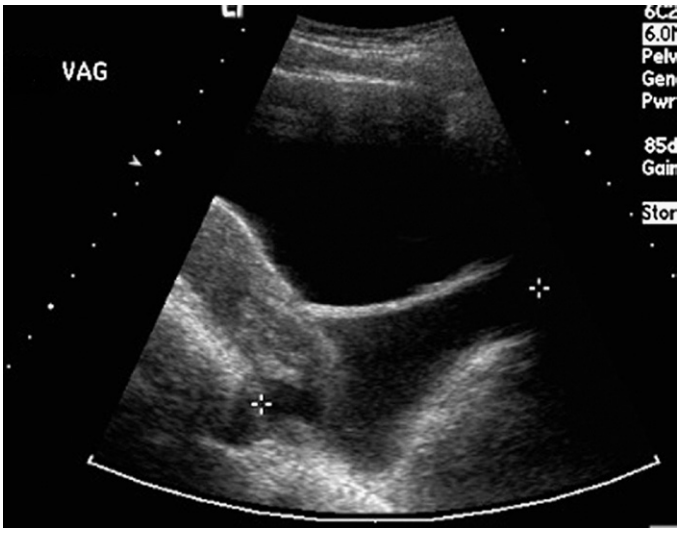

Figure 72.8 Imperforate hymen. Longitudinal sonogram showing a fluid-distended vagina in a 13-year-old girl confirmed at surgery to be an imperforate hymen.

spectrum of inborn errors of adrenogenital metabolism resulting in faulty enzyme(s) which normally mediate the production of cortisol; and results in an abnormal increase in circulating fetal androgens. The external genitalia are abnormal with fusion of the labioscrotal folds, urethral folds and clitoromegaly. A urogenital sinus is usually present in such cases and there may be accompanying characteristic enlargement of the adrenal glands (Fig. 72.11).[20]

The role of ultrasound in all cases of intersex is to confirm the presence and location of Müllerian and gonadal structures. The presence of the uterus and ovaries indicates a female pseudohermaphrodite whilst absence indicates a male pseudohermaphrodite. Müllerian abnormalities may be associated with renal anomalies such as ipsilateral renal agenesis. Ultrasound of the kidneys and adrenal glands should therefore also be performed in all cases. Identifying the location of the gonads is also important. In general an ovary is not located within or below the lower inguinal canal unless in a hernia (Fig. 72.12). Gonads found within the lower inguinal region or scrotum should be considered to be testes.

Although exceedingly rare, the next most likely intersex state for a genetic female (46,XX) is a true hermaphrodite. *True hermaphrodites* are manifested by the presence of an atypical gonad referred to as an ovotestis which contains both ovarian follicles and testicular tubular tissue. Sonographically an ovotestis lacks the uniform

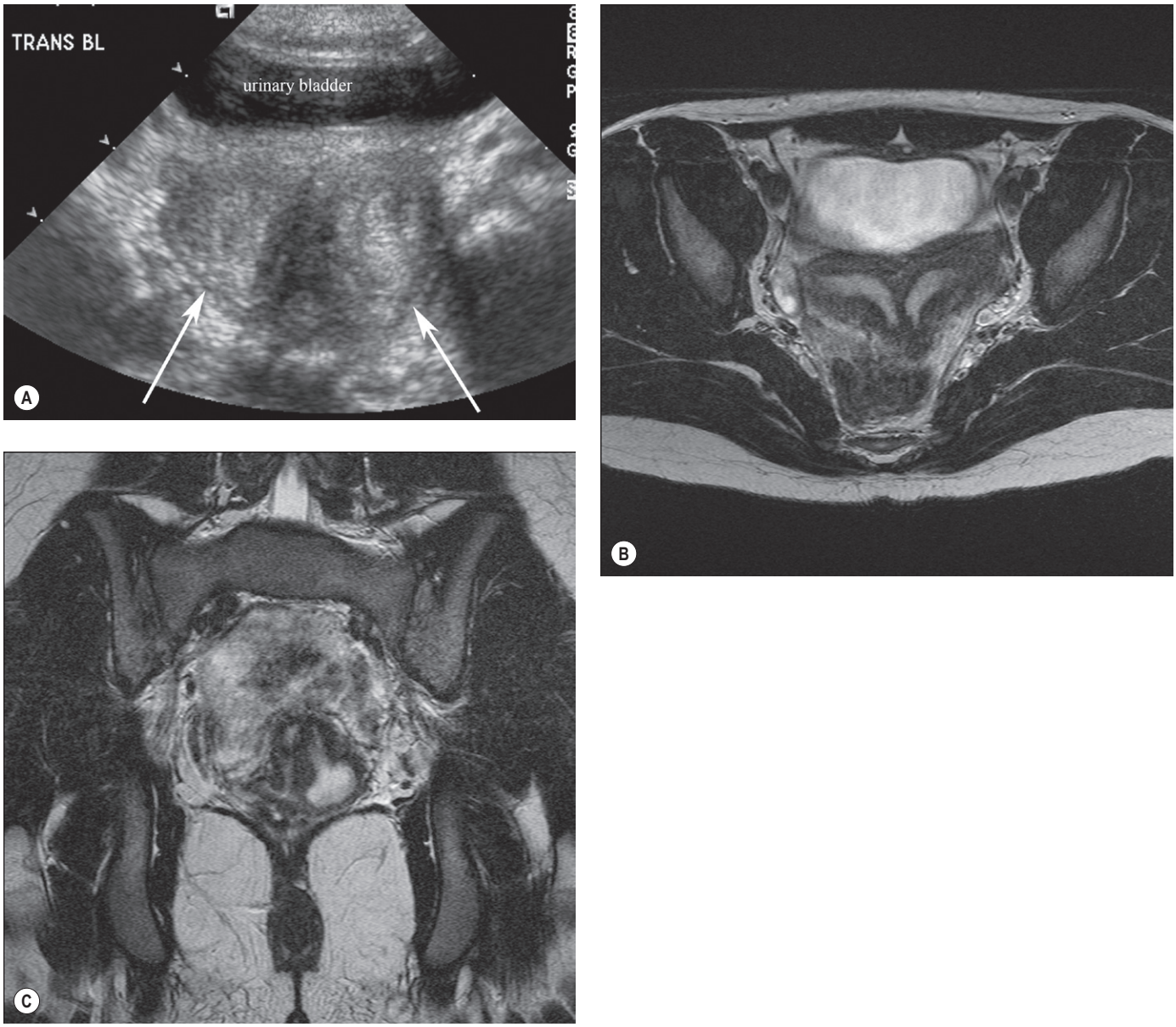

Figure 72.9 Uterus didelphys. A: Transverse sonogram showing double uterine cavities (arrows) which are best seen on transverse imaging. **B, C:** Axial **(B)** and coronal **(C)** T2-weighted MRI in the same patient showing uterus didelphys.

echotexture of the normal testicle and will contain follicles. The usual combination is paired ovotestes or ovotestis-ovary.[21]

Male pseudohermaphrodites are genetic males (46,XY) with female external genitalia and apparent female gender identity. The main causes are testosterone deficiency due to:

- inborn errors in the adrenogenital enzymatic production of testosterone
- absent or ineffective end-organ androgen receptors referred to as androgen insensitivity syndrome (AIS; also known as testicular feminisation syndrome) with normal to high circulating testosterone levels.

As testicles are present anti-Müllerian hormone is produced and Müllerian structures involute. The mesonephric ducts do not differentiate. The testes fail to descend and external genitalia range from complete female phenotype to ambiguous genitalia with hypospadias.

Gonadal dysgenesis is characterised by variable involution of Müllerian structures due to the absence or diminished production of anti-Müllerian hormone. In pure gonadal dysgenesis both gonads are dysfunctional. In mixed gonadal dysgenesis a testis is present along with an abnormal streak gonad. Patients with mixed gonadal dysgenesis may show considerable anatomical variation, depending on the duration and level of anti-Müllerian hormone production by the dysgenetic gonad(s). Most will at least retain a rudimentary uterus. A fallopian tube is often present on the side of the streak gonad. The fallopian tube normally regresses on the side of the testis due to the effects of local anti-Müllerian hormone.

Gonadal dysgenesis can be found in patients with Turner's syndrome. Sonographic studies in patients with chromosomal mosaicism, such as 45XO/46,XX, show a spectrum of findings which range from infantile uterus with absent ovaries to normal-sized uterus and gonads. Patients with the 45XO karyotype typically have elongated 'streak gonads' consisting of connective tissue with few germ cells that are not seen on ultrasound.[22] In these patients, the size and configuration of the uterus remains prepubertal (Fig. 72.13).

In Turner's syndrome infantile gonads are present at birth. During childhood the gonads often regress and may be absent at puberty. A small increased risk of germ cell tumour,

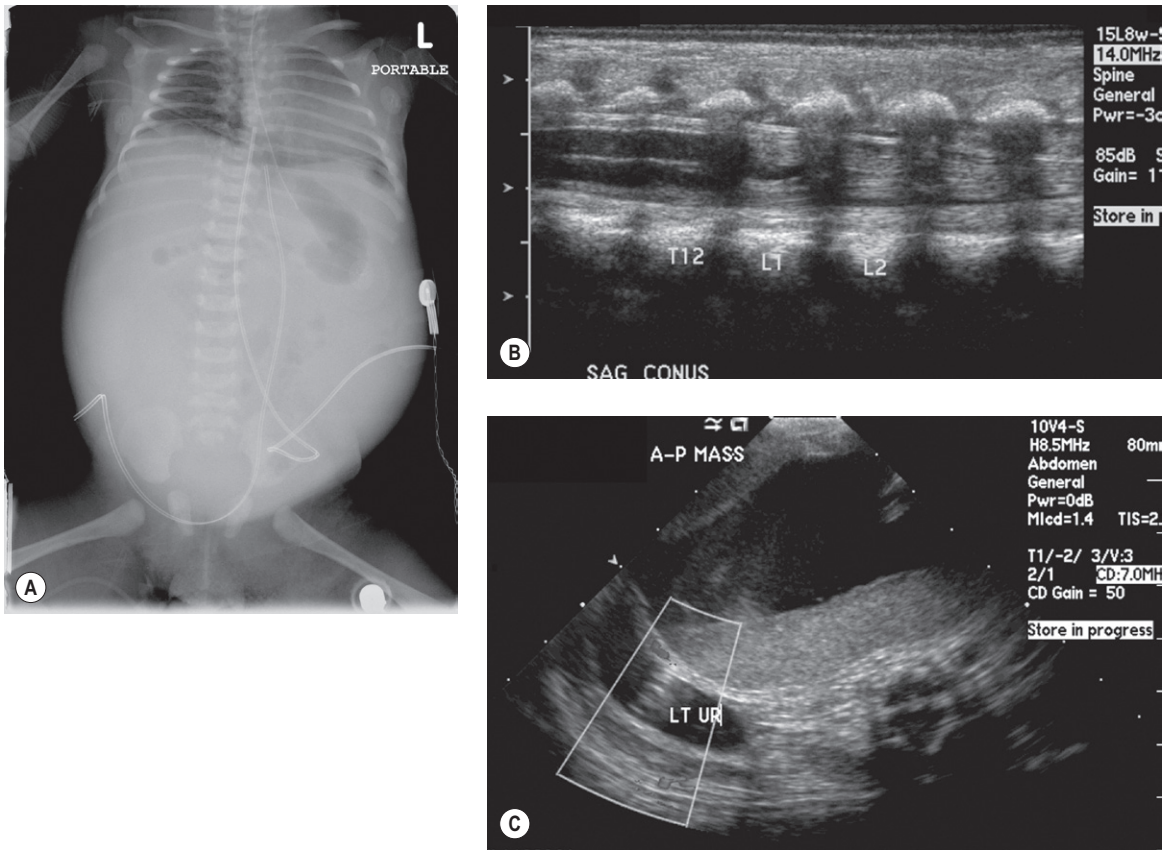

Figure 72.10 Cloacal malformation. Newborn female with imperforate anus. **A:** AP radiograph showing absent sacrum and T5 hemivertebra. **B:** High-resolution sonogram showing abnormal morphology of the conus typical of caudal regression ('cut off' appearance). **C:** Longitudinal sonogram showing a fluid–debris level within a distended viscus (cloaca) and distal left ureteric dilatation. A defunctioning colostomy was performed immediately following the scan.

Table 72.4 Image findings in disorders of sexual differentiation

	Genotype	Gonadal phenotype	Müllerian phenotype	External genitalia
Female pseudohermaphrodite Congenital adrenal hyperplasia Elevated maternal hormones	46,XX	Normal ovaries	Normal uterus and vagina	Virilised
Mixed gonadal dysgenesis Turner's syndrome	45,XO 45,XO/46,XX* Turner's with Y: increased risk of gonadoblastoma	Testis and streak Absent or streak ovaries * (may appear normal)	Persisting infantile uterus * (may appear normal)	Female
True hermaphrodite	46,XX + mosaics 46,XY with Y line	Testicle and ovaries Ovotestis	Uterus normal in 10%	Male
Male pseudohermaphrodite Androgen insensitivity Impaired testosterone production Congenital adrenal hyperplasia (rarely)	46,XY	Normal male gonads or crypto-orchid testes	Absent uterus and cervix	Female or ambiguous

gonadoblastoma, has been reported in the presence of Y chromosome material in patients with Turner's syndrome.[23] Other associations include horseshoe kidney.

Disorders of sexual maturation

Precocious puberty

Precocious puberty in a girl is defined as the development of secondary sexual characteristics or gonadal maturation before the age of 8 years. The pelvic sonographic findings of disorders of premature sexual maturation are described below and summarised in Table 72.5.

Central precocious puberty (isosexual)

Precocious puberty may be referred to as 'central' or gonadotrophin-dependent when it is identical to normal puberty but occurs prematurely due to the early activation of the hypothalamic-pituitary-gonadal axis resulting in elevated levels of FSH and

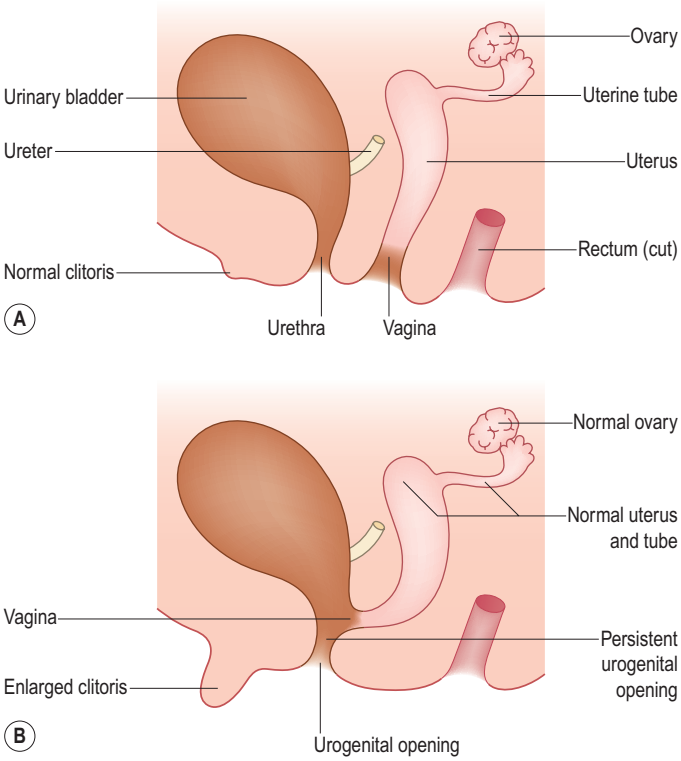

Figure 72.11 Congenital adrenal hyperplasia and urogenital sinus. A, B: Schematic diagrams showing **(A)** normal and **(B)** persisting urogenital sinus. **C:** Contrast genitogram depicting a urogenital sinus. **D:** Axial sonogram showing characteristic 'cerebriform' enlargement of the adrenal gland in congenital adrenal hyperplasia. (A, B reproduced with permission from Moore KL, Persaud TVN. The Developing Human. Clinically Oriented Embryology, 6th Edition. Philadelphia: WB Saunders; 1998.)

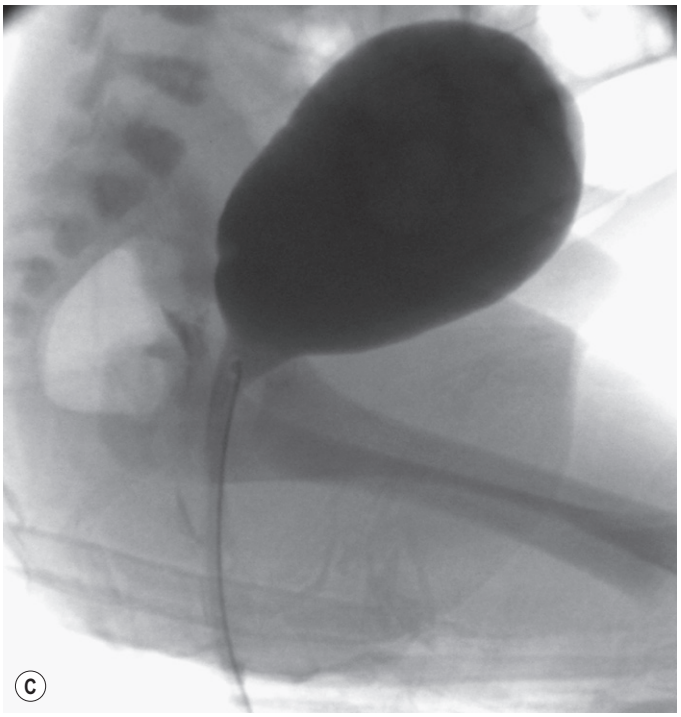

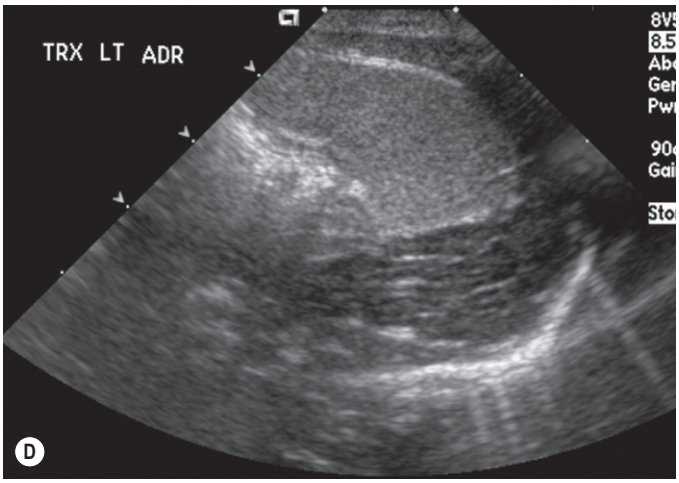

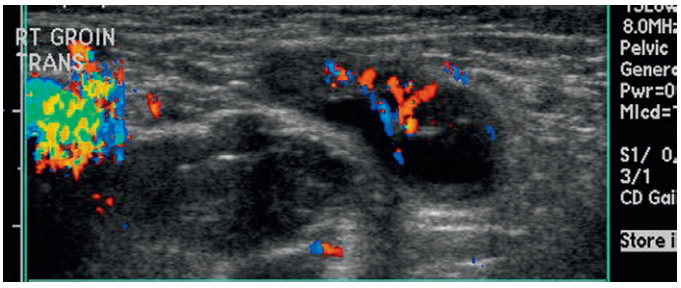

Figure 72.12 Inguinal ovary. High-resolution colour Doppler image showing an inguinal hernia containing an ovary.

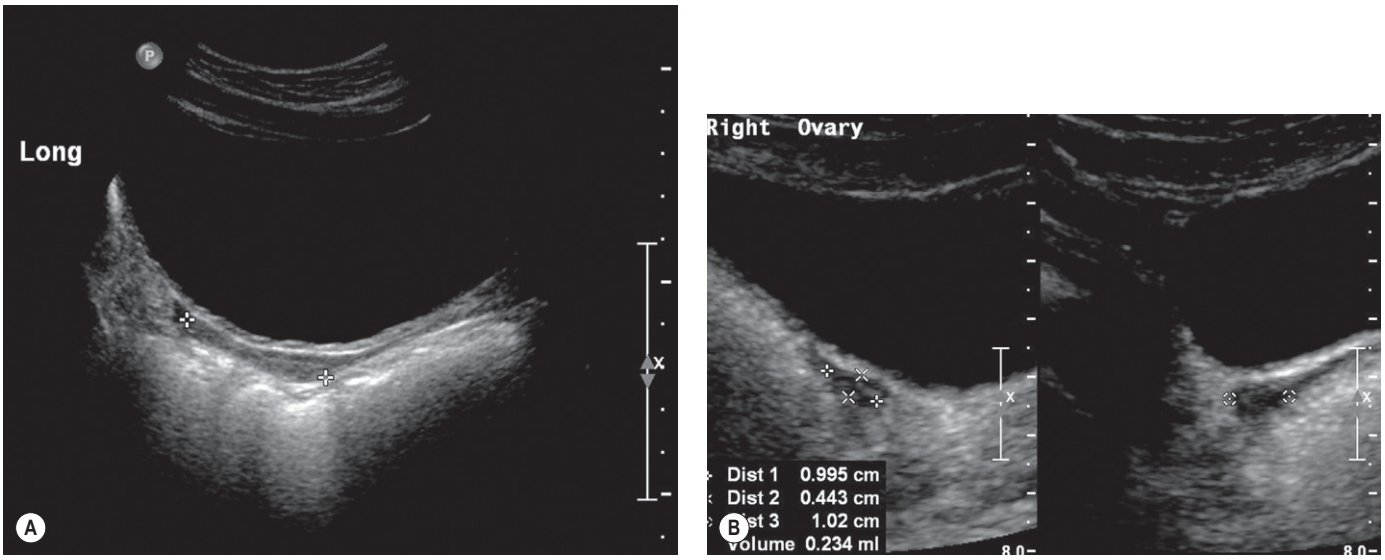

Figure 72.13 Turner's syndrome. A: Longitudinal sonogram showing prepubertal appearance to the uterus. **B:** Oblique sonograms showing a 'streak' ovary.

Table 72.5 Sonographic findings in precocious puberty

	Ovaries	Uterus
Precocious puberty	Stimulated	Large Adult pear shape Endometrial stripe present
Pseudoprecocious puberty	Unstimulated	Small Prepubertal tubular shape No endometrial stripe
Isolated premature thelarche	Unstimulated	Small Prepubertal tubular shape No endometrial stripe
Isolated premature adrenarche	Unstimulated	Small Prepubertal tubular shape No endometrial stripe

The role of ultrasound in evaluation of sexual maturation

- Pelvic ultrasound is the mainstay of imaging for the evaluation of pubertal dysfunction.
- A thorough ultrasound examination should include the uterus, both ovaries, kidneys and adrenal glands.
- Ovarian morphology can be used as an index of gonadotrophin secretion.
- Uterine volume and endometrial thickness provide a measure of oestrogen secretion.
- Uterine artery Doppler has also been advocated in assessing pelvic maturation.[26]

LH. Most cases are idiopathic. Gonadotrophin-dependent causes include hypothalamic tumours and cysts, low-dose cranial irradiation and primary hypothyroidism with elevated FSH secretion.

Ultrasound in central precocious puberty shows large multifollicular ovaries.[24] Multicystic or multifollicular morphology is usually present in girls with central precocious puberty, and in girls with normal puberty. Uterine enlargement and endometrial proliferation occurs due to gonadal oestrogen secretion. Ultrasound measurement of uterine volume had a reported sensitivity and specificity of 100% (cut-off value, 1.8 mL), while ultrasound determination of ovarian volume had a sensitivity of 82% and a specificity of 95% (cut-off value, 1.2 mL) in the detection of early central precocious puberty in a comparative study of patients with precocious puberty, premature thelarche and control group.[25]

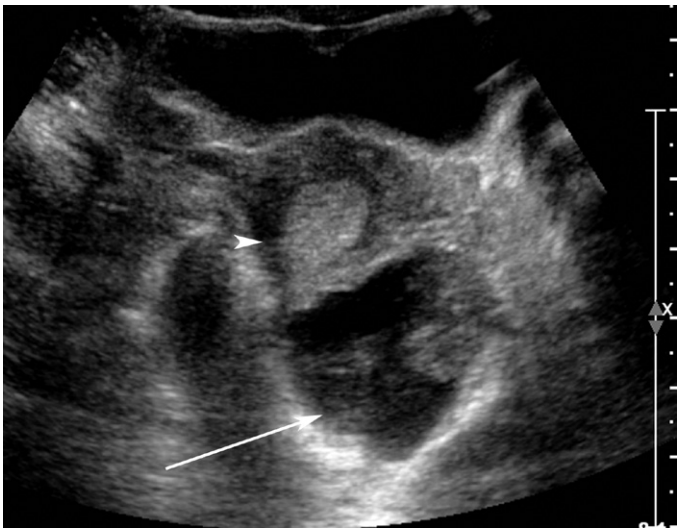

Figure 72.14 Pseudoprecocious puberty. Oblique sonogram in a 3-year-old girl presenting with precocious puberty showing a complex ovarian tumour mass (arrow) and marked endometrial hypertrophy (arrowhead).

Pseudoprecocious puberty (pseudosexual)

Pseudoprecocious puberty or gonadotrophin-independent precocious puberty is characterised by low levels of FSH and LH. Gonadotrophin-independent causes of precocious puberty include premature thelarche, premature thelarche variant, isolated menarche, McCune–Albright syndrome and hypomelanosis of Ito. The condition is also caused by autonomous oestrogen production from an ovarian or adrenal tumour (Fig. 72.14). The most common

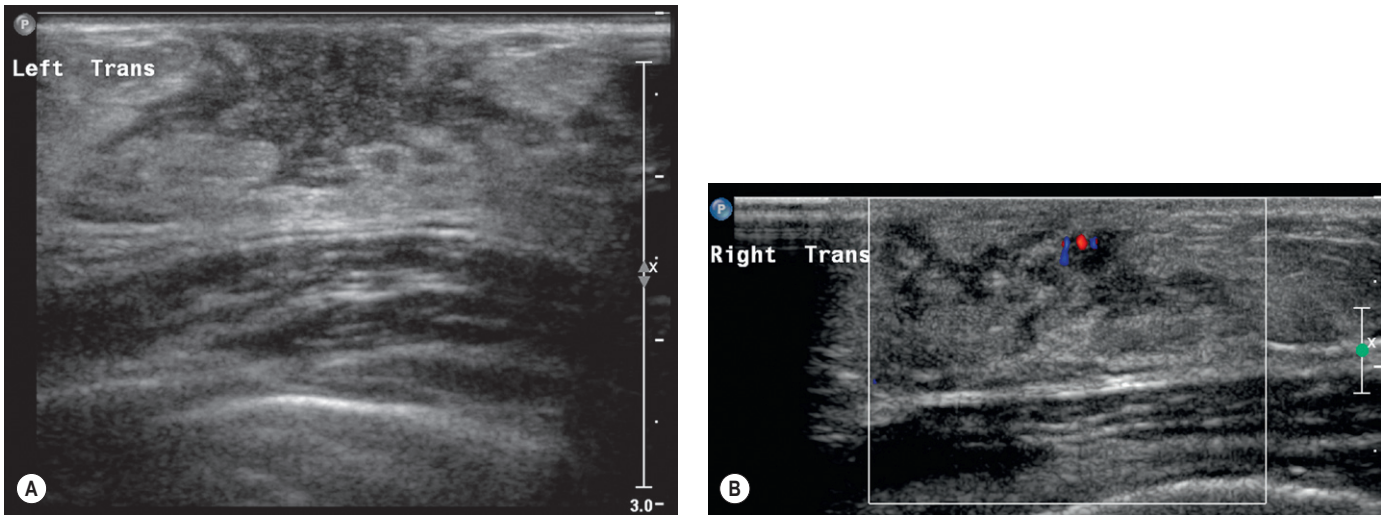

Figure 72.15 Premature thelarche. A: High-resolution ultrasound of a 2-year-old presenting with cyclical breast enlargement showing premature breast bud development. **B:** Colour Doppler flow image showing normal relatively avascular breast bud.

ovarian lesions to present with pseudosexual precocious puberty are granulosa theca cell tumours. The uterus is large and there is endometrial proliferation. Ultrasound may also detect large follicular ovarian cysts that are functional[27] and are easily distinguished from tumours and those of mixed echogenicity.

Isolated premature thelarche

Premature thelarche is isolated breast development without progression through puberty. Breast development often has an atypical appearance with relatively immature nipple development, is usually asymmetric, and not beyond Tanner stage 3 (Fig. 72.15).[28] The uterus is usually normal. Girls with premature thelarche have been shown to show no significant difference in pelvic ultrasound measurements when compared with age-matched controls.[25]

Isolated premature adrenarche

Premature adrenarche is the premature development of pubic or axillary hair with no other signs of puberty. The uterus and ovaries are generally normal. Polycystic ovarian morphology has been demonstrated in 8 of 12 girls examined with premature adrenarche.[2]

Pubertal delay

It is generally accepted that puberty is delayed when there is no sign of pubertal development by 15 years of age in girls. The initial imaging of a female with delayed puberty should include assessment of bone age and pelvic ultrasound.

Constitutional delay in growth and puberty occurs in patients with delayed bone age but who have always grown at a normal rate for their bone age and so would be expected to have a delay in the onset of puberty. This normal variation is often familial. Puberty usually begins by the time the bone age reaches 11 years in girls. Ultrasound demonstrates normal uterus and ovaries (usually multifollicular).

Low gonadotrophin levels (hypogonadotrophic hypogonadism) are often seen in chronic serious illness such as cystic fibrosis, anorexia nervosa and Crohn's disease. Central causes of gonadotrophin deficiency include central nervous system cysts and tumours, idiopathic hypopituitarism, growth hormone deficiency and acquired hypothyroidism. Elevated gonadotrophins (hypergonadotropic hypogonadism) result from primary gonadal failure. Ovarian failure is seen in patients with variants of Turner's syndrome, gonadal dysgenesis, galactosaemia or following pelvic irradiation.

Table 72.6 Causes of primary and secondary amenorrhoea

Primary amenorrhoea

- Chromosomal abnormalities: Turner's syndrome
- Congenital obstruction of the genital tract (e.g. imperforate hymen), uterovaginal atresia
- Disorders of sexual differentiation such as testicular feminisation syndrome
- Hypothalamic lesion
- Neoplasm: virilising tumours, pituitary tumour
- Drugs: androgens

Secondary amenorrhoea

- Pregnancy/Breastfeeding
- Contraceptives
- Stress
- Medication: chemotherapy drugs, oral corticosteroids, antidepressants and antipsychotics
- Radiotherapy
- Chronic illness
- Endocrine: polycystic ovarian syndrome, adrenal hyperplasia and tumours, hypopituitarism, hypothyroidism
- Low body weight: anorexia or bulimia
- Excessive exercise

Disorders of menstruation

Amenorrhoea

Primary amenorrhoea affects less than 1% of adolescent girls. Secondary amenorrhoea is much more common than primary amenorrhoea. The causes of amenorrhoea are listed in Table 72.6.

Patients with primary amenorrhoea show the prepubertal appearance of the uterus and ovaries. Those with secondary amenorrhoea can show a marked regression in the size of the uterus and ovaries such as in anorexia nervosa where the ovaries become quiescent and show no follicular activity. Pelvic ultrasound is a suitable method for determining the 'target' or 'ideal' weight required for

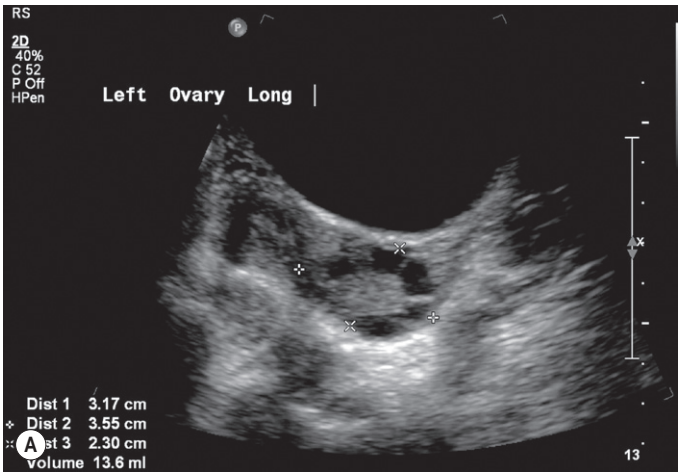

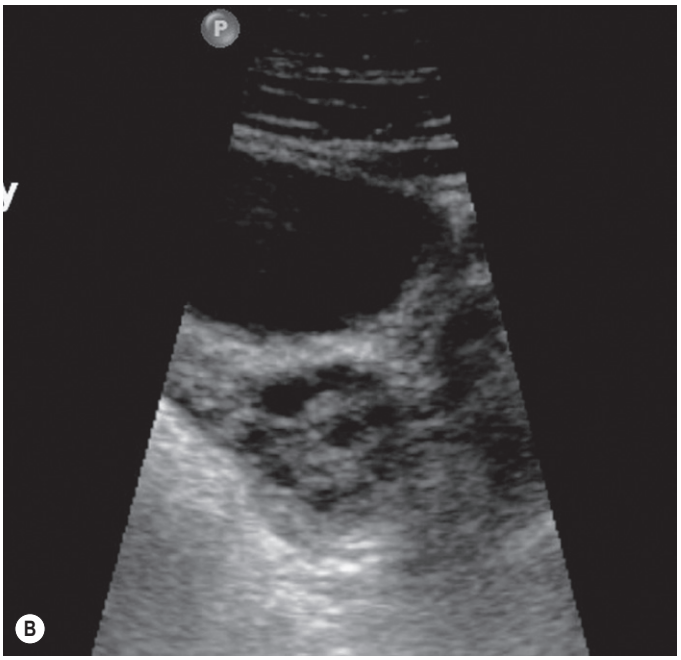

Figure 72.16 Polycystic ovarian syndrome. High-resolution oblique sonograms showing the characteristics features of PCOS. **A:** Enlarged ovary with abundant central echogenic stroma. **B:** Necklace of multiple peripheral small follicles (2–8 mm in diameter).

Imaging of amenorrhoea

- Abnormalities of the pituitary gland or hypothalamus are best evaluated with MRI.
- Adrenal hyperplasia and masses are initially best assessed with ultrasound, if abnormal MRI should be considered in favour of CT scan.
- The main role of pelvic ultrasound is to identify the presence, shape, size and maturation of the uterus, vagina and ovaries looking for genital causes of amenorrhoea

recovery of ovarian function and resumption of menstruation. Underweight patients tend to have smaller volume, immature ovaries. Normalised ovaries indicate favourable outcome and physical recovery.[29] More recently an algorithmic approach in sonographic assessment of pelvic maturity has been advocated in determining an individual's healthy weight in the management of anorexia nervosa.[30]

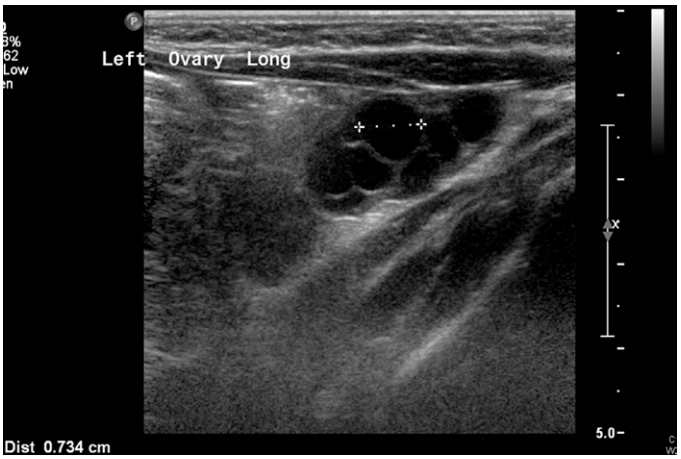

Figure 72.17 Multifollicular ovary. High-resolution oblique sonogram showing characteristic appearances of a multifollicular ovary in early pubertal development.

Polycystic ovarian syndrome

Polycystic ovarian syndrome (PCOS) should not be confused with polycystic ovaries (PCO), which are a distinct morphological entity (see next section). The main clinical features of PCOS are disturbances of menstruation, hyperandrogenism (elevated luteinising hormone levels with reduced follicle-stimulating hormone levels) and obesity. Androgen excess and ovarian dysfunction are central to the condition. High androgen levels result in ovarian stromal hyperstimulation with an increase in the number of atretic antral ovarian follicles. Other associations include hyperinsulinaemia, insulin resistance and metabolic syndrome in adolescence.

Consensus criteria have been developed and refined in establishing the clinical diagnosis of PCOS. Not all clinical, biochemical and sonographic features are required to make the diagnosis. The 1990 National Institutes of Health criteria[31] define androgen excess and ovarian dysfunction in the absence of other causes as consistent with PCOS. Latterly the typical appearances of the ovary on ultrasound have been considered important criteria for the diagnosis of PCOS in adolescents with suggestive clinical features. The 2003 Rotterdam criteria[32] require two of the following three criteria for a diagnosis: chronic oligo-anovulation, biochemical or clinical evidence of hyperandrogenism and a polycystic appearance on ovarian ultrasound (Fig. 72.16). The aetiology of PCOS is unknown. The condition manifests at puberty. It has been speculated that abnormalities of ovarian androgen production which mediate PCOS may occur in the fetus or during childhood.[34]

Polycystic ovaries

The incidence of PCO in the normal adult population is 22–25%.[33]PCO morphology as defined on ultrasound includes one or more of the following features[35] (Fig. 72.17):

- ovaries with an increased ovarian volume (>10 cm^3)
- a necklace of follicles with at least 12 follicles around the periphery of the ovary measuring between 2 and 9 mm
- increased quantity of hyperechoic stroma.

Transabdominal ultrasound has revealed bilateral enlarged ovaries (8–14 mL) in up to 70% of symptomatic patients and has demonstrated that the follicles are usually peripherally located but may also be scattered throughout the ovarian stroma.[36] Typically affected ovaries lose their normal ovoid shape and appear more spherical. Normal ovarian volume does not exclude the diagnosis; up to one third of adult patients assessed transvaginally with polycystic ovarian morphology had normal ovarian volumes (range 4–10 cm^3).[33] PCO has been described in the young as early as 6 years of age.[37] A single PCO is sufficient for the diagnosis.

If follicular diameter is greater than 10 mm, repeat ultrasound at a time of ovarian quiescence should be considered in order to calculate more meaningful ovarian volumes. Transvaginal ultrasound-based antral follicle counts, which are used to identify polycystic ovaries, have been found to have adequate inter-observer and intra-observer reproducibility.[38]

Ovarian stromal echogenicity is assessed relative to the uterus and may show considerable variation. Increased stromal echogenicity and/or stromal volume are specific to PCO, but it has been shown that the measurement of ovarian volume is a reasonable surrogate marker for quantification of the stromal volume.[35]

Other conditions with hyperandrogenism such as premature adrenarche and late-onset congenital adrenal hyperplasia may also show PCO morphology.

Pelvic masses in the neonate

These can be detected antenatally or present in infancy. The main role of ultrasound is in differentiating between a cystic mass or solid lesion and to ascribe an organ of origin. The most common finding in the neonate is a palpable urinary bladder. If the lesion is sufficiently large then determining the origin of the mass becomes more difficult and further imaging may be required. The most important point to stress is that in most cases ultrasound will be sufficient to characterise the nature and extent of a cystic mass but if tumour is suspected then cross-sectional imaging is required. Attempts to aspirate a pelvic cyst should not be undertaken until it is clear that rare causes of conditions such as meningocele or neuroenteric cyst have been excluded (Table 72.7).

Neonatal ovarian cysts

Neonatal ovarian cysts are thought to be functional and arise from disordered follicular development under the influence of maternal and placental hormones. The vast majority of these will eventually involute without complication. These cysts are frequently detected antenatally. Occasionally fetal ovarian cysts may result in polyhydramnios, vaginal dystocia or cyst rupture at delivery.[39] Most cysts detected at birth are asymptomatic. Postnatal ultrasound follow-up should be undertaken for all suspected ovarian cysts.

The ultrasound appearances of uncomplicated neonatal ovarian cysts are fairly typical (Fig. 72.18). Simple cysts are unilocular, elliptical or spherical anechoic lesions, with a barely perceptible wall. The differential diagnosis for simple ovarian cysts includes enteric duplication cyst and mesenteric cyst. Duplication cysts have typical features; the so-called 'double wall sign' (Fig. 72.19) due to enteric mucosa and the hypoechoic muscularis in 50% of cases. If present, a small 'daughter cyst' (Fig. 72.20) in the wall of the primary cyst is a specific sign suggestive of an ovarian cyst.[40] Omental cysts may bleed and can be indistinguishable from complex ovarian cysts. An omental cyst should be considered in a female neonate with a complex cystic mass in whom both ovaries are visualised.[41]

Neonatal ovarian cysts may present as complex lesions secondary to haemorrhage or rarely salpingotorsion, the risk of torsion being higher in larger cysts. These cysts may rupture or even amputate and migrate from the usual pelvic location. Complex cysts show specific characteristics such as a debris–fluid level, septa of variable thickness, a retracting clot, fibrotic mural nodule, calcification and echogenicity mimicking a solid appearance (Fig 72.21). Ovarian tumours are so rare in infants that a haemorrhagic ovarian cyst should be considered even when the mass appears solid.

Ovarian cysts may present as an abdominal mass in the neonatal period and if sufficiently large result in life-threatening pulmonary compression, bowel or urinary tract obstruction.[42] The management of most neonatal ovarian cysts is expectant and conservative. Serial ultrasound follow-up is all that is required until the cyst regresses and involutes spontaneously. If large (over 5 cm) and simple (unilocular, echo-free and without significant mass effect), they may be aspirated under ultrasound guidance. The cyst fluid is high in oestrogens. Management of larger cysts may rarely require surgical intervention.

Adnexal cysts in the older child

Prepubertal ovarian cysts

Microcysts, defined as cysts up to 9 mm in diameter, are frequent in the prepubertal girl, and increase in number with advancing age.[43] A simple, anechoic, thin-walled follicular cyst up to 10 mm diameter should be considered a normal finding. Larger ovarian cysts are uncommon in prepubertal girls but may result from

Table 72.7 Pelvic mass lesions arising from the female neonate

Cystic mass	Solid mass
Urinary bladder	Sacrococcygeal teratoma
Ovarian cyst (Fig. 72.18)	Neuroblastoma
Adnexal torsion (Fig. 72.29)	Pelvic kidney
Enteric duplication cyst (Fig. 72.19)	
Meconium pseudocyst (Fig. 72.19)	
Hydrocolpos (Fig.72.7)	
Cloacal malformation (Fig.72.10)	
Veno-lymphatic malformation (omental and mesenteric cyst)	
Neuroenteric cyst	
Anterior meningomyelocele	

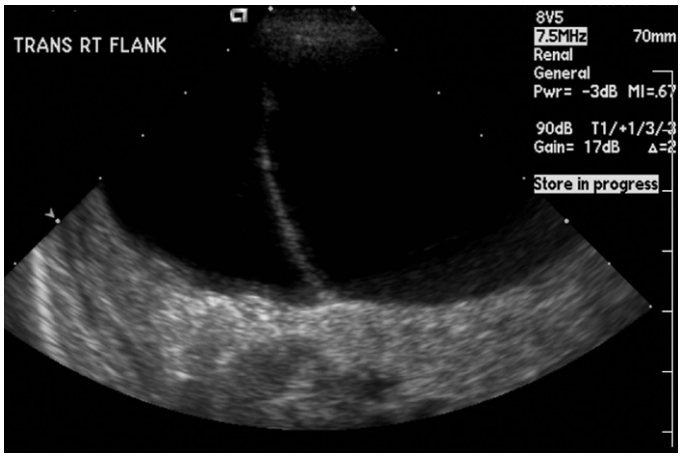

Figure 72.18 Neonatal ovarian cyst showing a single septation and no other internal echoes.

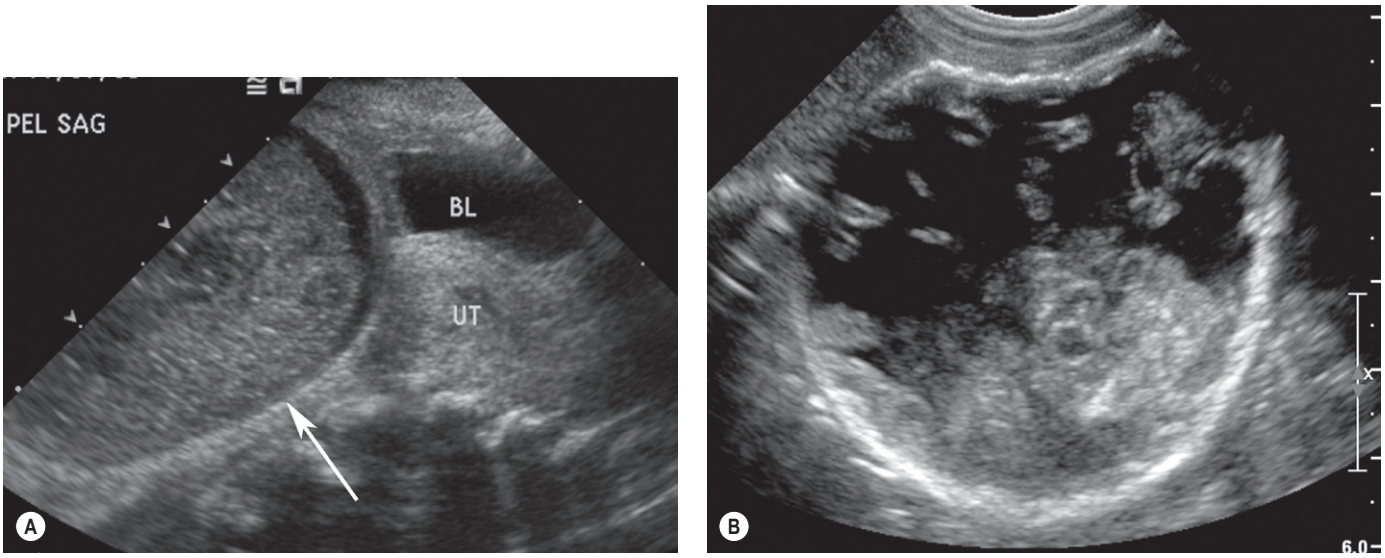

Figure 72.19 Non-ovarian neonatal pelvic cystic masses. A: Longitudinal sonogram of an enteric duplication cyst containing multiple internal echoes. The characteristic 'gut signature' or 'double wall' sign is present (arrow). BL, urinary bladder; UT, uterus. **B:** Transverse sonogram showing a thick-walled meconium pseudocyst with multiple complex internal echoes and debris.

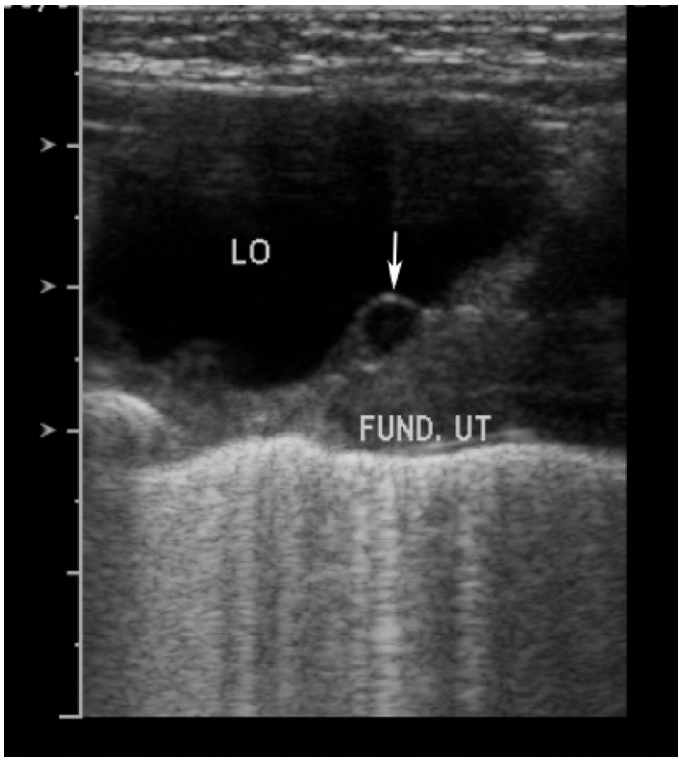

Figure 72.20 Ovarian cyst. High-resolution longitudinal sonogram showing a simple ovarian cyst (LO) containing a small internal daughter cyst (arrow).

failure of involution of follicles stimulated by intermittent release of gonadotrophins from the developing pituitary gland.[44] Prepubertal cysts like neonatal cysts are follicular in origin; the vast majority will resolve spontaneously. Larger cysts in this age group may be associated with sexual precocity and may require more extensive evaluation.[45] Cysts in this age group should be observed only if: (1) the cyst is clearly of ovarian origin, (2) the cyst is not complex, (3) alpha-fetoprotein (AFP) and beta human chorionic gonadotrophin (β-hCG) levels are normal, (4) the patient is asymptomatic, and (5) the cyst decreases in size.[46]

Prepubertal cysts should decrease in size over a period of a couple of weeks. Once a decrease in size is documented at 2- to 3-weekly follow-up, monthly ultrasound should be considered until resolution. Whilst the risk of malignancy is very low, any prepubertal ovarian cyst that does not decrease in size, persists or is complex merits a surgical opinion.

Ovarian cysts in adolescence

Cystic lesions of the adolescent ovary most commonly occur as a result of 'dysfunctional' ovulation and persistence of the remaining follicle. Most girls present with menorrhagia, irregular menstrual cycles and occasionally a palpable mass. Follicular cysts develop in the first half of the menstrual cycle. These are typically anechoic, thin-walled, around 2 to 3 cm in diameter and usually resolve during the second half of the menstrual cycle (Fig. 72.22). If ovulation does not occur, follicular cysts can continue to grow under hormonal stimulation, occasionally to very large sizes. Functional ovarian cysts in adolescence may also arise from persistence of the corpus luteum formed from a ruptured follicle. Corpus luteum cysts can grow up to sizes in excess of 6 cm and may rupture, leading to significant intraperitoneal haemorrhage. Most follicular and corpus luteum cysts resolve spontaneously. The vast majority of patients will require ultrasound follow-up alone. A minimum of 2 to 3 months or menstrual cycles of ultrasound follow-up has been suggested by some; other authors recommend observation for longer periods of time in the asymptomatic patient.[47] Large cysts that do not resolve are at higher risk of torsion and haemorrhage. Complex cysts in the adolescent are most often due to haemorrhage into a functional cyst (see below) but excluding neoplasia (most usually a benign mature ovarian teratoma) is difficult by imaging alone. If AFP and β-hCG levels are normal then the risk of malignancy is low.[46] Surgery is reserved for patients with refractory symptoms and non-resolving cysts (large simple cysts and complex cyst of any size). Surgery may be laparoscopic or open, ovary conserving (cyst aspiration, cystectomy and cyst fenestration) or radical.[46]

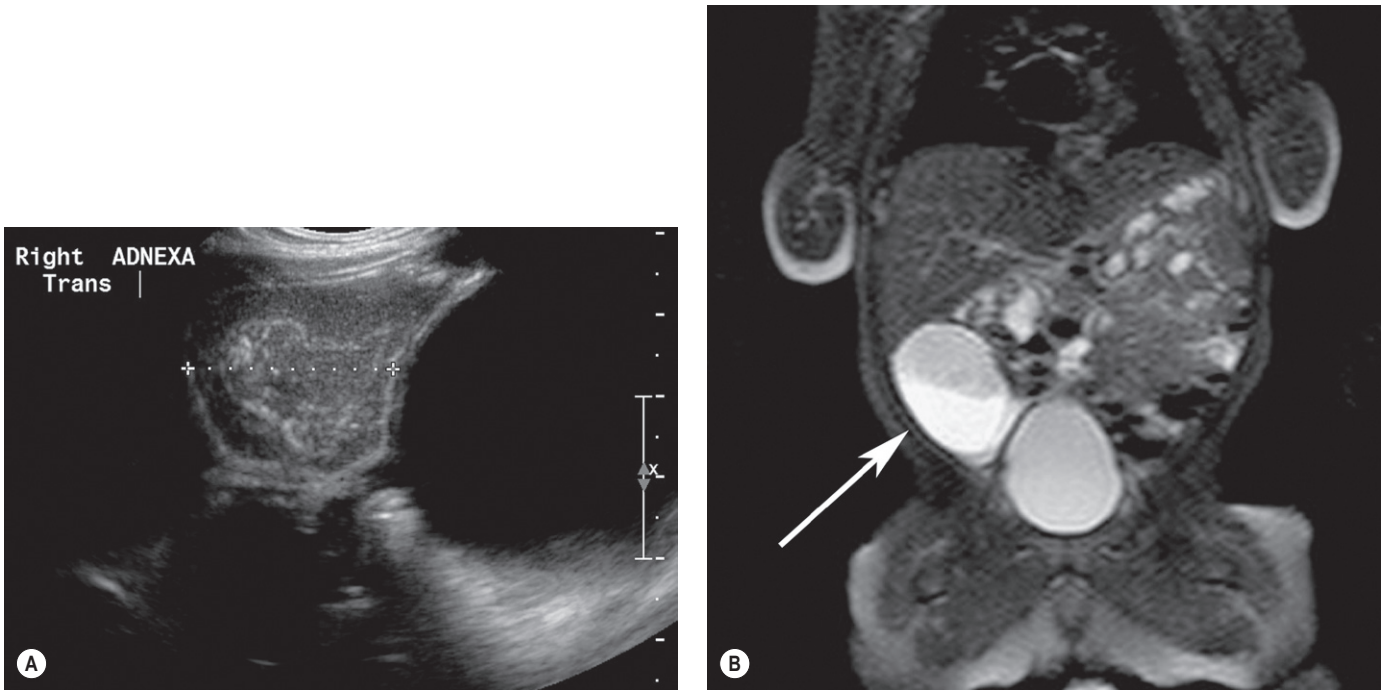

Figure 72.21 Neonatal ovarian cyst. A: Longitudinal postnatal sonogram of an antenatally detected pelvic cyst showing a complex thin-walled right adnexal cyst containing a large amount of debris and relatively poor through-transmission. **B:** Coronal T2-weighted MRI in the same patient confirming a right ovarian cyst (arrow) with a large fluid–debris level (study performed without anaesthetic or sedation).

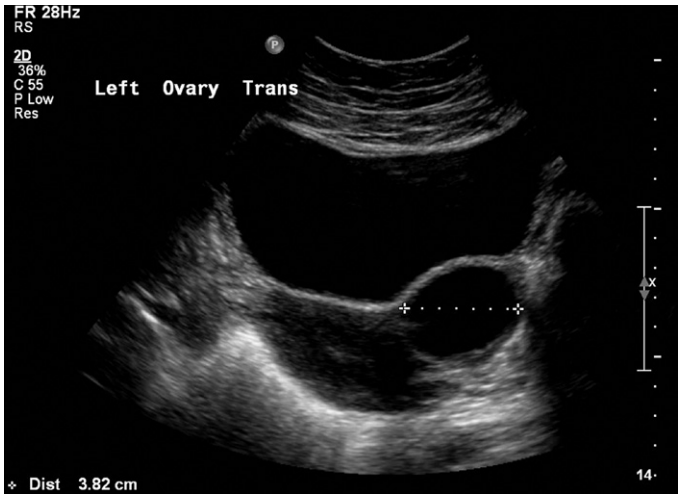

Figure 72.22 Dominant follicular ovarian cyst. Transverse sonogram showing a prominent left ovarian follicular cyst which resolved on follow-up scan after 4 weeks.

Haemorrhagic ovarian cyst

Complex cysts in the adolescent are most often due to haemorrhage into a functional cyst. Bleeding into a follicle can occur during the first 2 to 3 weeks of the menstrual cycle or into a luteal cyst at the end of the menstrual cycle. Acute, severe lower abdominal or pelvic pain coinciding with the mid-cycle is the typical clinical presentation. Enlarged haemorrhagic cysts are less likely to spontaneously resolve, increasing the risk of intraperitoneal rupture or adnexal torsion. Cyst rupture may result in significant intraperitoneal haemorrhage and hypovolaemic shock.

Ultrasound findings depend on the age of haemorrhage within the cyst (Fig. 72.23). Acute intracystic haemorrhage may appear isoechoic to ovarian stroma resulting in apparent uniform ovarian enlargement. Recent cyst haemorrhage may contain numerous thin echoes and shows increased through-transmission (comparable to transmission seen through the urinary bladder) reflecting the underlying cystic structure. Other described sonographic findings that suggest haemorrhage into a cyst include a complex heterogeneous mass, changes associated with clot retraction/lysis, fluid–debris level, septa, calcification in the cyst wall and pelvic free fluid.[48] Complex cysts in the adolescent girl should always raise concern for dermoid cysts or other neoplasms. Differentiating a haemorrhagic cyst from a tumour or endometrioma is often difficult.

Paraovarian cysts

Paraovarian cysts are not true ovarian masses. They arise from mesothelial, mesonephric (Wolffian) or paramesonephric (Müllerian) structures adjacent to a normal ipsilateral ovary (Fig. 72.2). They usually occur in the mesosalpinx between the ovary and fallopian tube. The cysts are thin-walled and anechoic. Paraovarian cysts are difficult to correctly identify prospectively by transabdominal ultrasound.[49] More recently transvaginal scanning has been advocated in differentiating paraovarian cysts, hydrosalpinges and peritoneal inclusion cysts,[50] although this is not appropriate in most children. MRI can obviate the need for TV scanning in sonographically indeterminate adnexal masses.[51]

Ovarian neoplasms

Ovarian neoplasms are extremely rare, accounting for less than 1% of all paediatric tumours. Approximately half of all lesions of the ovary in childhood are neoplastic. Only a small proportion (10–30%) of neoplastic lesions contain malignant elements.

Primary paediatric ovarian tumours can be categorised into three broad groups based on the cell type of origin:[52]

- Germ cell tumours predominate and may be further subdivided based on the differentiation of the malignant cells (teratoma is the most common subtype) (Fig. 72.24).

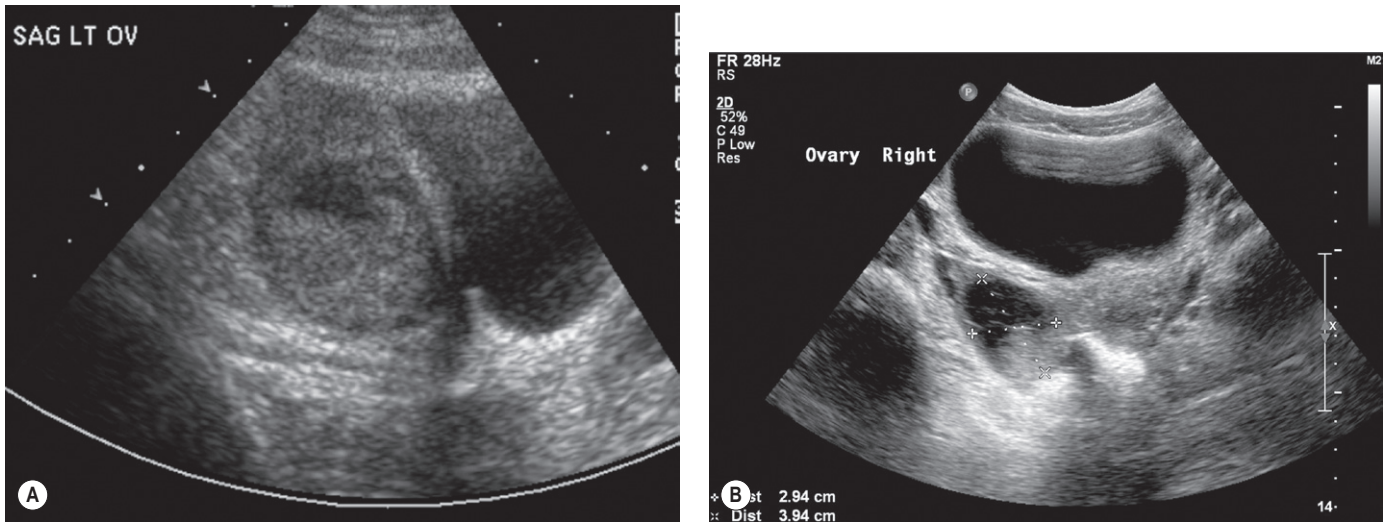

Figure 72.23 **Haemorrhagic ovarian cyst. A:** Longitudinal sonogram in a 16-year-old girl showing fluid–debris level in the left adnexa. **B:** Oblique sonogram in another 16-year-old girl presenting with suspected acute appendicitis showing a right ovarian fluid–debris level. Both scans show that lesions show reasonable through-transmission and posterior acoustic enhancement suggestive of an underlying cyst.

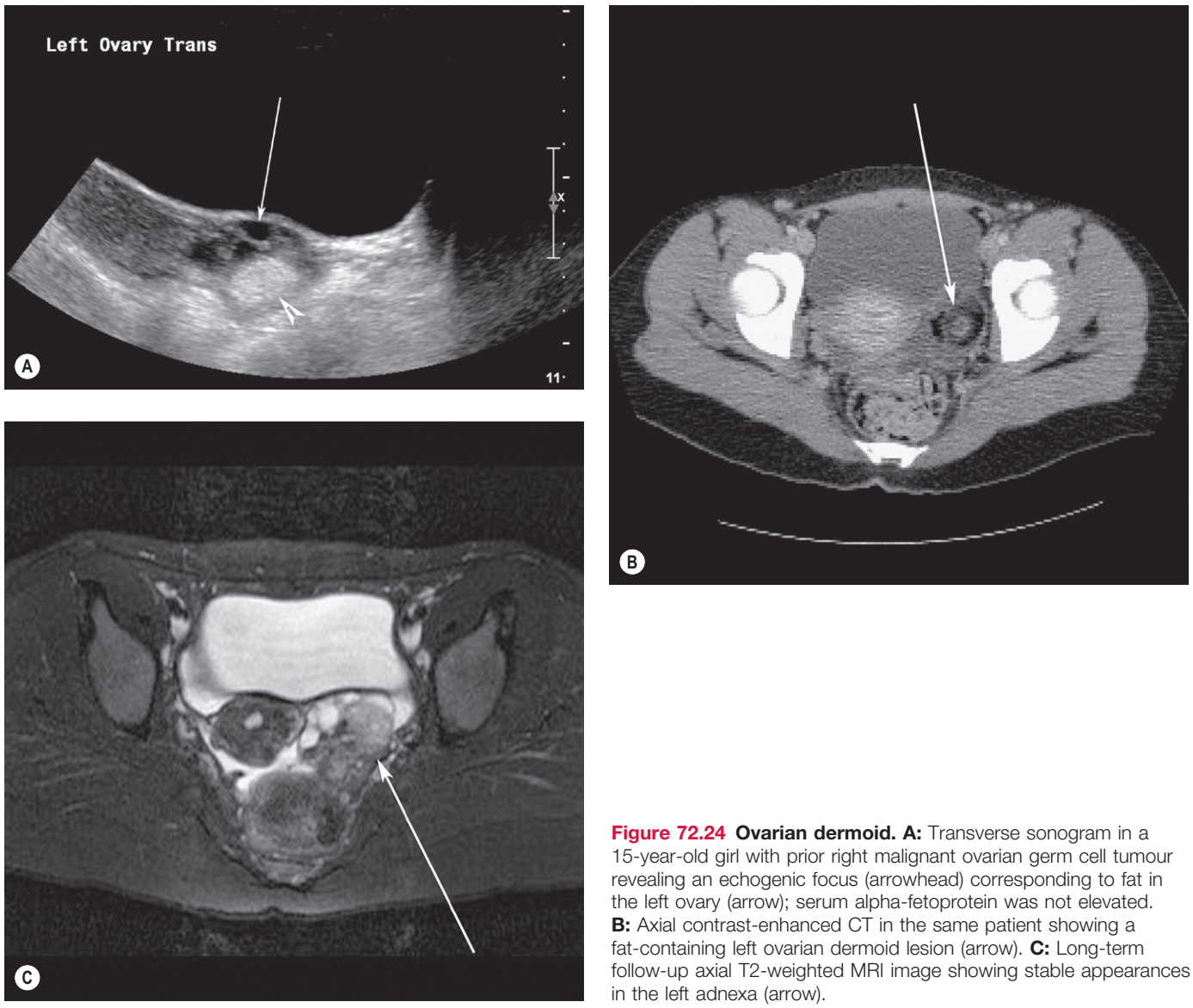

Figure 72.24 **Ovarian dermoid. A:** Transverse sonogram in a 15-year-old girl with prior right malignant ovarian germ cell tumour revealing an echogenic focus (arrowhead) corresponding to fat in the left ovary (arrow); serum alpha-fetoprotein was not elevated. **B:** Axial contrast-enhanced CT in the same patient showing a fat-containing left ovarian dermoid lesion (arrow). **C:** Long-term follow-up axial T2-weighted MRI image showing stable appearances in the left adnexa (arrow).

- Epithelial cell tumours (thecomas, fibromas, gonadoblastomas, serous and mucinous cystadenoma and malignant serous or mucinous cystadenocarcinoma), which are most common in adults but only account for approximately 15% of ovarian tumours in children and are extremely rare prior to menarche.
- Sex-cord stromal tumours (granulosa theca cell tumours and Sertoli–Leydig cell tumours) are tumours of low malignant potential which account for approximately 15% of ovarian tumours (Fig. 72.25).

Rarely, ovarian tumours may be functional hormone-secreting tumours such as granulosa theca tumours associated with pseudoprecocious puberty and andrenoblastoma associated with virilisation. Leukaemia, lymphoma, mesothelioma, metastatic neuroblastoma and gonadoblastoma account for the small remaining group of tumours.

Whatever the tumour type, most patients will present with localised disease. Common presenting symptoms are fairly non-specific and include abdominal pain and fullness. A palpable mass may be present. A degree of urinary tract and gastrointestinal obstruction is seen if the tumour is sufficiently bulky. Acute pain should alert the clinician to the possibility of associated ovarian torsion or recent tumoral haemorrhage.

Germ cell tumours – teratomas

Benign cystic teratomas are the most common ovarian tumours. Teratomas may be mature, immature or malignant. In general, the greater the proportion of immature elements the more aggressively the tumour is likely to behave locally. The risk of a malignant teratoma is greater the younger the child. Around 30% of teratomas are malignant and these are associated with elevated serum AFP levels. Ultrasonically they can have a characteristic appearance, with highly reflective areas of calcification from teeth and bone, hyperechoic fat and hypoechoic cystic areas. Fat–fluid levels may be seen. Occasionally teratomas are predominantly solid (Fig. 72.26).

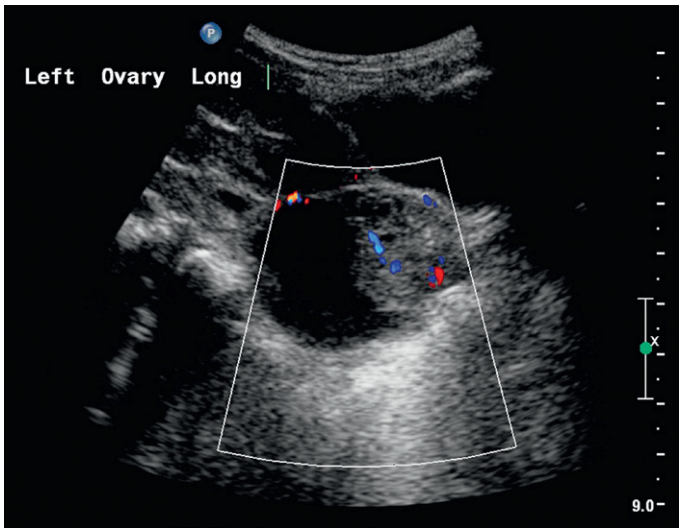

Figure 72.25 Ovarian sex cord stromal tumour. Longitudinal colour Doppler sonogram showing a part solid, part cystic left ovarian tumour.

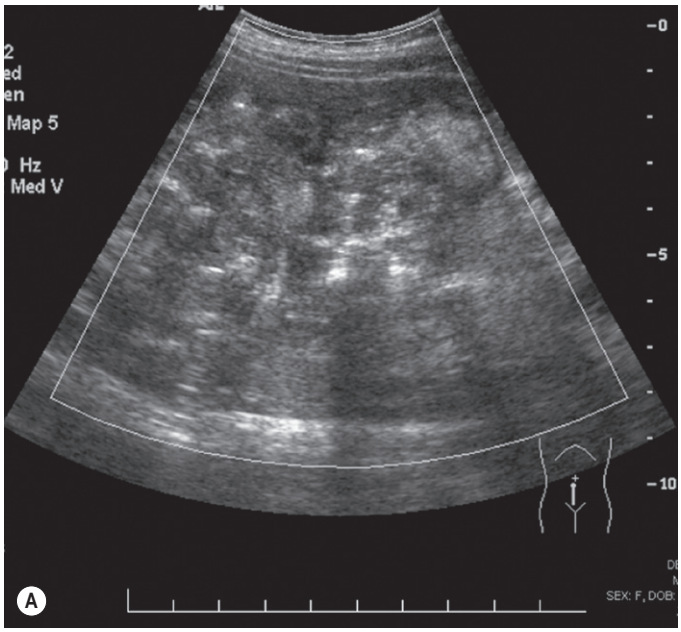

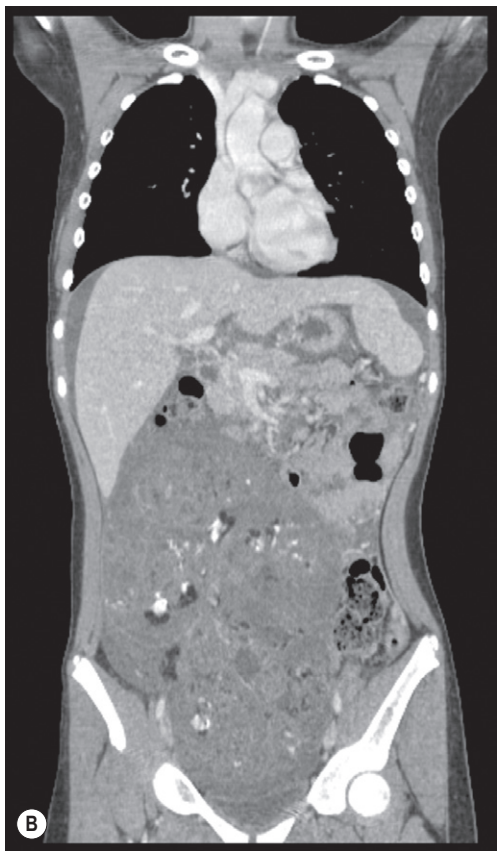

Figure 72.26 Malignant germ cell tumour. A: Longitudinal sonogram showing a mixed echotexture mass lesion found to occupy most of the abdomen and pelvis. The bright echogenic areas represent calcification, intermediate echogenic areas correspond to fat and smaller echo-poor areas represent cyst or necrosis reflecting that the tumour arises from all three germ cell layers. **B:** Coronal reformatted image from a contrast-enhanced CT showing the large abdominopelvic mass lesion and ascites.

The role of ultrasound in evaluation of pelvic masses

- Principal role is as a screening tool and long-term imaging surveillance in treated patients.
- Define echotexture; origin, extent and relationship of mass to normal pelvic structures.
- Delineate complications such as urinary tract obstruction and hydrocolpos.
- Detect local lymph node involvement.
- Evaluate distant spread: hepatic metastases.

In general tumour markers and imaging are sufficient to make the diagnosis. Surgical treatment is dependent on the risk of malignancy. Resection of a benign mass with ovarian conservation is the treatment of choice, preserving chances for future fertility.[53]

Other malignant tumours

The sonographic appearances of ovarian tumours are heterogeneous. Most benign tumours are complex masses that are hypoechoic with avascular peripheral mural nodules, which may mimic acoustic shadowing. Malignant tumours are complex, often vascular soft tissue masses with central necrosis (Fig. 72.25). Other features of malignancy include ill-defined and irregular borders with thick septa or papillary projections. Other than ovarian teratoma none of the ovarian tumours can be reliably differentiated from a haemorrhagic or torted ovarian cyst.

The overall role of ultrasound in the assessment of pelvic masses is principally to delineate the size, extent and organ of origin of the pelvic mass. Ultrasound enables evaluation of the contralateral ovary, the omentum, and is useful in evaluating for local nodal spread and for hepatic metastases. Pelvic free fluid in the pouch of Douglas and ascites are well seen on ultrasound. Complications such as hydroureteronephrosis can also be accurately depicted. In addition to ultrasound, preoperative cross-sectional imaging is required for staging purposes and may include contrast-enhanced computed tomography (CT) or MRI. MRI is particularly useful in assessing local disease extent and cystic lesions but CT remains a valid technique to evaluate solid lesions and to assess for nodal disease, omental involvement and distant metastases. If imaging suggests locally invasive disease then preoperative chemotherapy is recommended prior to surgery. Intraoperative staging remains the current gold standard.[53]

Vaginal and uterine tumours

Rhabdomyosarcoma

Rhabdomyosarcoma is the most common malignant neoplasm of the lower female genital tract during childhood and adolescence, accounting for approximately 4–6% of all malignancies in this age group. The peak incidence is bimodal, with an initial peak between 2 and 6 years of age and a further peak in the second decade of life.

Presenting symptoms may include vaginal discharge or irregular vaginal bleeding. Tumour can also present as a prolapsing fleshy mass at the introitus. Vaginal lesions have a better prognosis than cervical lesions. Outcome is dependent upon tumour size, local extent at the time of presentation and histological subtype; embryonal is the most common subtype with the most favourable outlook. The botryoid variant of embryonal rhabdomyosarcoma often presents in infancy as a submucosal polypoidal mass, arising from the vagina or urinary bladder and rarely from the uterine cervix. The usual location is the anterior vaginal wall just below the cervix. The typical appearances are of a polypoidal mass resembling a cluster of grapes within a hollow structure.[54]

The role of ultrasound is to delineate the size, extent and vascularity of tumour mass. Ultrasound is also useful for evaluating the regional lymph nodes for nodal spread and the solid viscera of the abdomen to look for hepatic metastases. Pelvic rhabdomyosarcoma will usually present as a heterogeneous soft tissue mass within the vagina or uterus (Fig. 72.27). The solid portions will show colour flow. The hypoechoic regions correspond to areas of ulceration, haemorrhage and necrosis. Obstructing lesions can lead to a build-up of fluid in the uterine cavity. Ultrasound is a very useful screening tool but is insufficient for accurate local staging, which will require MRI with its multiplanar capabilities and superior soft tissue contrast resolution. Following a tissue diagnosis other staging investigations are required, including CT scan of the thorax and bone scan to look for distant metastases. Treatment relates to tumour stage and ranges from local excision of the tumour to radical hysterectomy with pelvic exenteration following neo-adjuvant chemotherapy with or without radiotherapy or brachytherapy.[55]

Other malignant tumours

Clear cell carcinoma of the cervix and vagina is a very rare tumour in the paediatric population. Many of these tumours were associated with prior maternal intrauterine diethylstilbestrol exposure. These tumours present in similar fashion to rhabdomyosarcoma and are sonographically indistinguishable.

Endodermal sinus tumour (yolk sac tumour) of the vagina is an extremely rare and highly malignant form of germ cell tumour that is found exclusively in children less than 3 years of age.[56]

Pelvic pain

Gynaecological causes of pelvic pain

Lower abdominal and pelvic pain is a common indication for ultrasound examination in the paediatric population. Pelvic pain in children is often a fairly non-specific clinical symptom. Adnexal pathology seen commonly in adults is becoming much more prevalent in adolescents. The sonographer should keep in mind the possibility of pregnancy (ectopic or otherwise), tubo-ovarian abscess as a complication of pelvic inflammatory disease and endometrioma in the differential of pelvic pain or adnexal mass lesion in the adolescent. These topics are covered in detail in the relevant adult chapters (see Chapters 35 and 39).

Adnexal torsion

Adnexal torsion (ovarian, tubo-ovarian or tubal) is defined as partial or complete rotation of the ovarian vascular pedicle resulting in obstruction to venous outflow, lymphatic circulation and arterial inflow. If this persists, arterial perfusion eventually becomes sufficiently compromised resulting in adnexal infarction. Tubo-ovarian torsion is an uncommon surgical emergency that may occur in both pre- and postmenarchal girls. The presenting signs and symptoms are frequently non-specific. The condition mimics other causes of acute abdomen and delays in diagnosis and treatment are not uncommon.

Ovarian torsion can be associated with a lead point such as a physiological cyst or tumour. Ovarian cysts usually occur during menarche or in the first year of life. Tumour associated with torsion is typically seen in adolescents, most commonly a benign mature cystic teratoma. In-utero torsion is not usually associated with an identifiable lead point.

Ultrasound is the mainstay of imaging in the evaluation of ovarian torsion. Ultrasound enables identification of a lead point and provides real-time functional information concerning perfusion. The role of imaging is in establishing a prompt diagnosis ultimately leading to timely surgical treatment. Surgical management may be conservative with ovarian detorsion for a viable ovary or radical with adnexectomy for established adnexal infarction.[57]

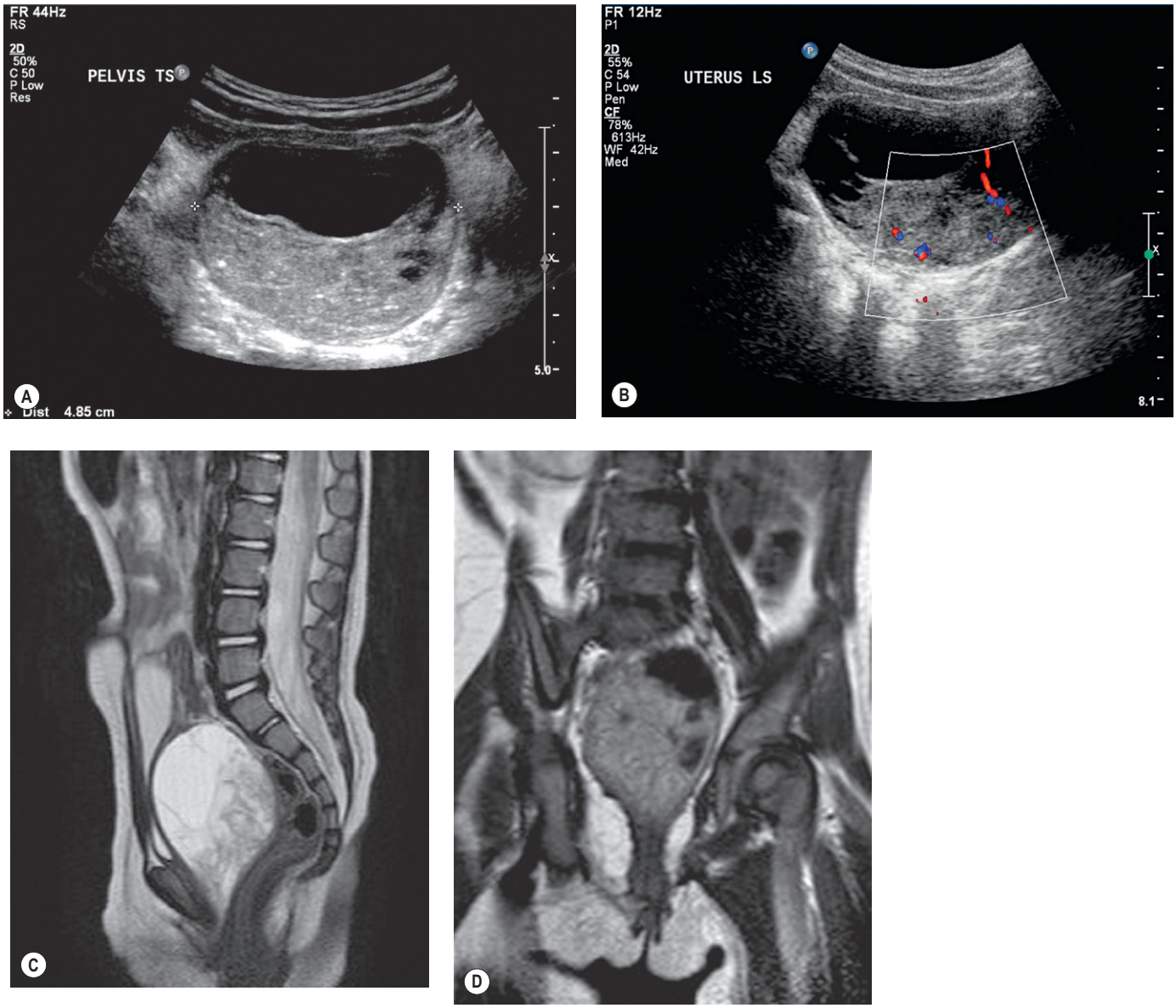

Figure 72.27 Vaginal rhabdomyosarcoma. Two-year-old girl presenting with vaginal bleeding and fleshy material bulging the introitus. **A:** Transverse sonogram and **(B)** transverse colour Doppler image showing a pelvic heterogeneous mass lesion with colour Doppler flow thought to be within distended uterus or vagina. **C, D:** Sagittal T2 **(C)** and coronal T1 **(D)** post intravenous gadolinium MR confirming an enhancing vaginal mass.

The sonographic findings in tubo-ovarian torsion are dependent upon:

- the degree of vascular compromise
- presence of a lead point.

The most consistent finding in ovarian torsion is the presence of a unilateral enlarged ovary with or without a solid hypoechoic or hyperechoic adnexal mass (Figs 72.28 and 72.29). Ovarian enlargement occurs due to congestion. The volume ratio of the torted adnexa compared to that of the normal side can predict if there is an underlying ovarian mass which may potentially be the lead point of the torted ovary.[58] Multiple peripheral cortical follicles (8–12 mm in size) in an enlarged ovary are an uncommon but highly specific sign of ovarian torsion and are thought to relate to vascular compromise causing transudation of fluid into the follicles.[59] A torted ovary may be normal, particularly in younger children. Torsion of the ipsilateral fallopian tube usually appears as an echogenic tubular structure leading from the ovary to the uterus; in turn adjacent adnexal structures may also become compromised. The uterus will often deviate towards the affected ovary.

Colour Doppler imaging can be useful in assessing ovarian viability. Preservation of central venous flow in tubo-ovarian torsion has been reported to be an indicator of ovarian viability.[60] The presence of intraovarian flow may indicate the affected ovary is still viable, particularly if central; however, intraovarian arterial flow cannot exclude torsion. The ovary may also receive collateral supply from the uterine artery. The presence of intraovarian artery flow may simply reflect acute, intermittent or partial torsion resulting from initial occlusion of the ovarian vein without compromise of arterial inflow. Absence of arterial flow in the twisted vascular pedicle may indicate that the ovary is not viable but is not a reliable finding.[58]

Pelvic free intraperitoneal fluid results from lymphatic and venous congestion or haemorrhagic infarction with intraperitoneal haemorrhage.

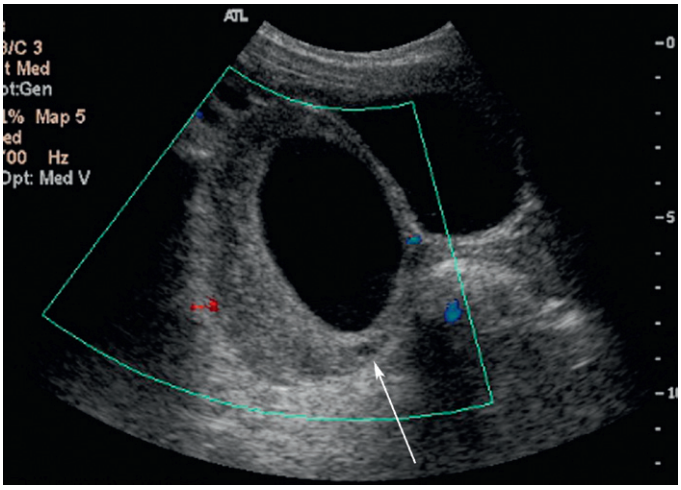

Figure 72.28 Ovarian torsion. Oblique sonogram in 14-year-old girl presenting with acute right iliac fossa pain showing an enlarged, echogenic, adnexal mass with a small peripheral follicle (arrow). Intralesional colour flow was not seen. This was later confirmed at laparoscopy to be a torted ovary.

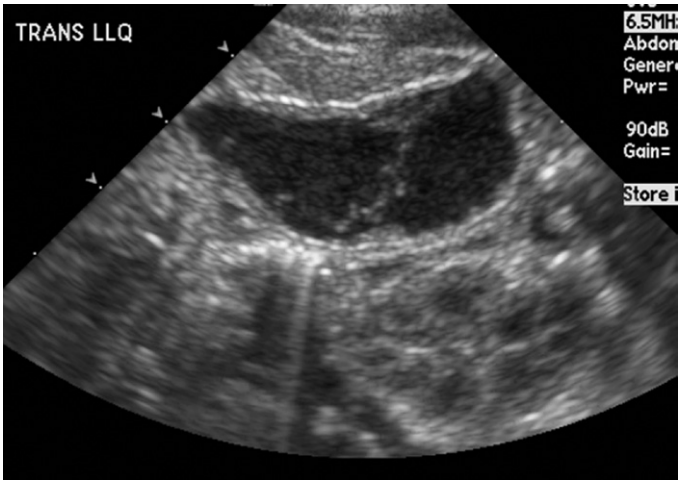

Figure 72.29 Neonatal ovarian torsion. Transverse sonogram showing a complex ovarian cyst. An antenatal torsion may show a calcific focus in the wall of the cyst.

Non-gynaecological causes of pelvic pain

Appendicitis, appendix abscess, inflammatory bowel disease from Crohn's disease, renal colic and Meckel's diverticulum are important and relatively common non-gynaecological causes of right iliac fossa pain. These topics are covered in much greater depth in the paediatric gastrointestinal and renal imaging sections of this book (see Chapters 70 and 71).

Vaginal discharge

Vaginal bleeding in the neonate is unusual. Maternal hormones can stimulate endometrial hypertrophy, seen on ultrasound as a prominent midline endometrial stripe which is then shed once maternal hormonal influence subsides. The diagnostic yield of pathology from ultrasound in these patients is very low. A normal ultrasound examination confirming a lack of ovarian and adrenal pathology with a normal sized uterus should be reassuring to all concerned. Follow-up is not required unless symptoms persist.

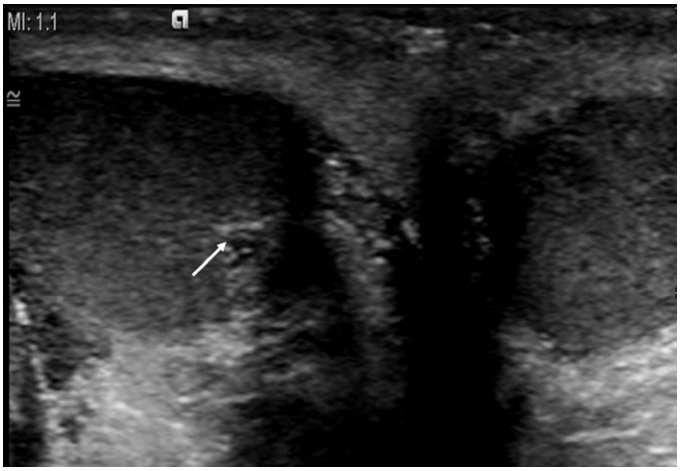

Figure 72.30 Normal testis. The 'spectacle' view of the testes in a pubertal boy demonstrating the mid-level reflectivity. The mediastinum testis (arrow) is seen, with some prominence of the rete testis; a normal appearance.

Vaginal bleeding or discharge in the absence of pubertal development may be due to the presence of vaginal trauma or foreign body. Ultrasound will often demonstrate a retained vaginal foreign body either directly as acoustic shadowing or indirectly with slight indentation on the posterior wall of the urinary bladder.[61] Under most circumstances direct visualisation will normally be required if a foreign body is suspected. The main role of ultrasound is to exclude a significant lesion such as gynaecological tract malignancy.

PAEDIATRIC TESTIS

Ultrasound is well established in the assessment of scrotal abnormalities in the adult and paediatric population. The most common clinical manifestations in the male child are pain, swelling, palpable mass or 'redness'. Ultrasound provides an objective assessment and allows selection of patients that need urgent treatment.

Ultrasound imaging technique

No preparation is required for imaging the genitourinary tract in the paediatric population. The patient is supine with a towel supporting the scrotal sac in the older child. The testes are readily examined using a linear high-frequency transducer with a suitable footprint, with copious amounts of warm ultrasound gel. The scrotal contents are examined with both B-mode and colour Doppler ultrasound.

Normal anatomy of the testis

The testis should always be present in the scrotal sac. On occasion a retractile testis may be seen at the external inguinal ring area; it is important to distinguish it from a distal inguinal canal undescended testis. The normal testis is of medium level reflectivity, with the epididymis seen as a separate entity and of slightly higher reflectivity. Testicular echogenicity increases with the development of germ cell tissue, usually after 8 years of age. The tunica albuginea appears as a thin high reflective line surrounding the testis and the mediastinum testis is a thin high reflective line coursing across the testis (Fig. 72.30). The appendix testis and appendix epididymis may be identified in the presence of a hydrocele. Colour Doppler flow depicting the intra-testicular vessels is not always present in

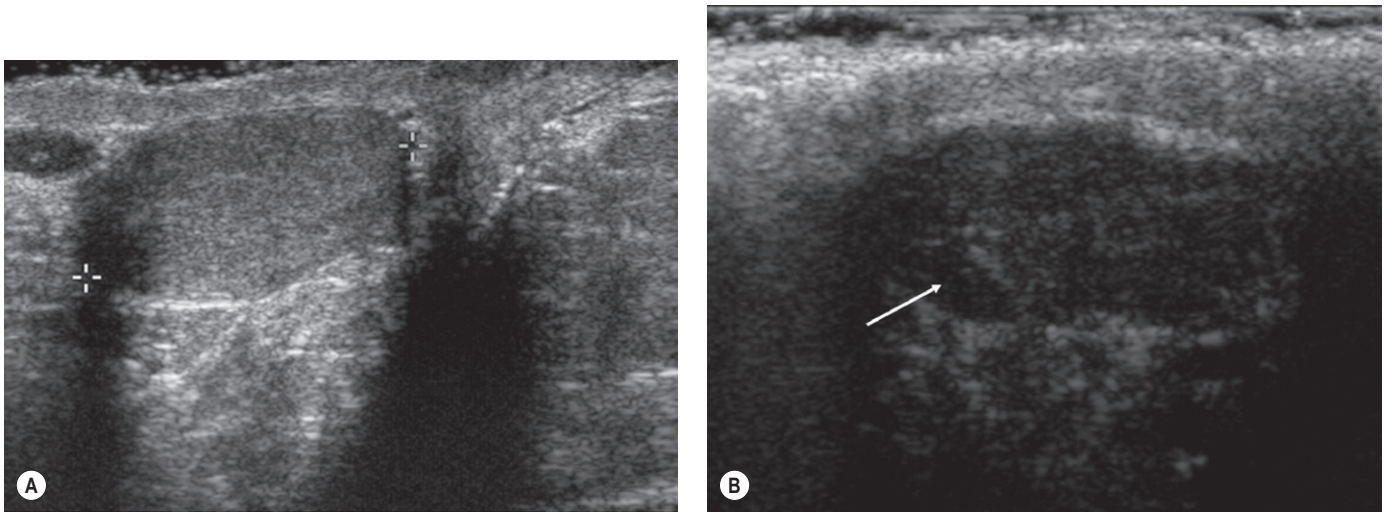

Figure 72.31 Inguinal testis. A: An oval-shaped mid-level reflectivity undescended testis (between cursors) lying in the left inguinal canal. **B:** A low reflective oval-shaped inguinal testis (arrow); the testis has infarcted and is no longer viable with total absence of colour Doppler flow signal.

the normal infant testis, and is more reliably detected as the testicular volume increases at puberty.[62,63]

Congenital anomalies

Cryptorchidism

Failure of the normal descent of the testes through the inguinal canal during the seventh month of intrauterine life is a common problem in male infants, which manifests as a unilateral or bilateral empty scrotum.[64] The undescended testis may lie anywhere along the line of descent. The incidence is estimated at 3–4% of full-term male births rising to 30% in premature male births, falling to 0.8% at one year; 80–90% will be in the inguinal canal and in 10% of cases both testes are affected (Fig. 72.31). Complications that arise with the undescended testis include testicular atrophy, infertility and an increased incidence of malignant change. Ultrasound may be used to search for the undescended testis lying at or near the inguinal canal but is less successful in locating an intra-abdominal testis; MRI should be used for localising an intra-abdominal testis.[65,66] The kidneys should also routinely be imaged to assess for urological anomalies as there is an association with duplex collecting systems, renal agenesis, hypoplasia and malrotation.

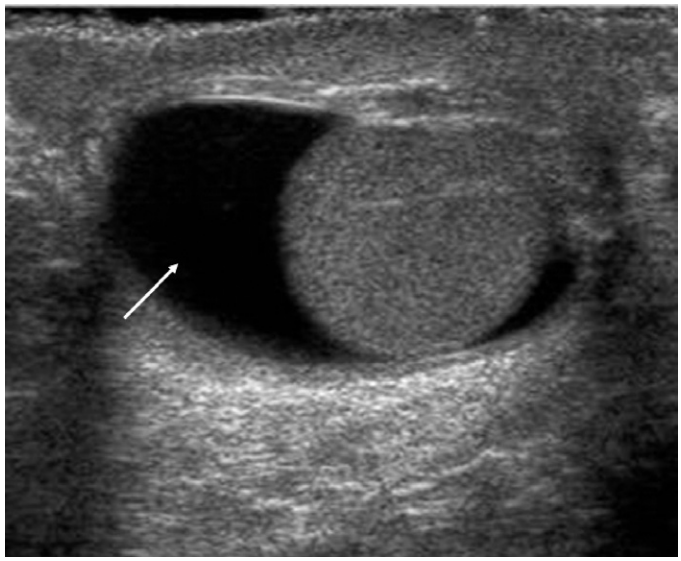

Figure 72.32 Hydrocele. The right testis is outlined by anechoic fluid (arrow), representing a hydrocele.

Hydrocele

This is the most common cause of a scrotal mass in an infant; it may be either congenital or acquired and unilateral or bilateral (Fig. 72.32). Acquired hydroceles may be secondary to inflammation, trauma, torsion or tumour and usually occur in the older child. In the younger child, at closure of the processus vaginalis, a variable amount of fluid may be trapped between the visceral and parietal layers of the tunica vaginalis, forming a stable hydrocele. The fluid should be anechoic and unilocular; debris and septations suggest an inflammatory or traumatic aetiology. With a persistent patent processus vaginalis the hydrocele may vary in size, requiring surgery to close the patent processus vaginalis. A stable hydrocele usually reabsorbs before the age of 2 years. In rare cases, a painful hydrocele may be the presenting symptom of appendicitis if a persistent patent processus vaginalis allows pus to track down into the scrotal sac.[67]

Inguinal-scrotal hernia

The passage of intestinal loops or omentum or both into the scrotal sac constitutes an inguinal-scrotal hernia, more common on the right. Clinical findings are normally conclusive; ultrasound may be reserved for difficult cases. The ultrasound features of omentum are those of a highly reflective structure whereas loops of bowel may demonstrate peristalsis.[68]

Congenital torsion

Prenatal torsion of the testis is rare, with a necrotic testis present at birth. On ultrasound, the affected testis may be small and highly reflective or enlarged and of low reflectivity, containing multiple cystic spaces.[69] There may be an associated simple anechoic or

complex mixed reflective hydrocele. An inguinal hernia is invariably present. Increased blood flow is seen within the periphery of the scrotum, with no flow demonstrated in the testis on colour Doppler ultrasound.

Cystic dysplasia

Cystic dysplasia is a rare congenital anomaly. Multiple irregular anechoic cystic spaces can be seen along the mediastinum testis on ultrasound.[70,71] As with most congenital testicular disorders, the renal tracts must be examined. Cystic dysplasia is associated with ipsilateral renal agenesis, renal duplication and multicystic dysplastic kidney.[69]

Testicular microlithiasis

Testicular microlithiasis is asymptomatic and is an incidental finding on ultrasound (Fig. 72.33). The areas of microcalcification appear as bright non-shadowing foci. There is an association of testicular microlithiasis with cryptorchidism, alveolar microlithiasis, Klinefelter syndrome and primary malignancy of the testis. Ultrasound surveillance has been suggested.[72]

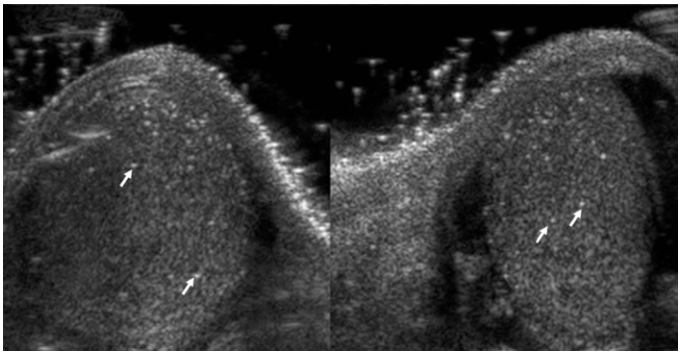

Figure 72.33 Testicular microlithiasis. Bilateral testicular microlithiasis seen as foci of high reflectivity without the presence of acoustic shadowing (arrows).

Varicocele

A varicocele is an abnormal dilatation of veins in the pampiniform plexus, mostly found on the left in older children over the age of 9 years.[73] A cause must be sought in the younger child (Fig. 72.34). On ultrasound the veins appear as anechoic tubular structures along the spermatic cord, with reflux demonstrated on colour Doppler during the Valsalva manoeuvre. A varicocele may cause testicular growth arrest[74] and treatment may be indicated.

Acute scrotum

Ultrasound of the scrotal sac and its contents can be extremely difficult in the child presenting with pain. The asymptomatic side should be examined first to obtain the child's confidence and a baseline image for comparison with the affected side.

Epididymo-orchitis

Inflammation of the epididymis is normally the consequence of infection, but may arise following trauma, reactive to spermatic cord torsion or testicular appendage torsion.[75] The epididymis is enlarged and of high reflectivity on ultrasound with an increase in colour Doppler flow[76] (Fig. 72.35). Isolated orchitis is rare, often causing irregular areas of low reflectivity within the testis. Isolated orchitis is normally associated with the mumps virus, whereas infection of the epididymis often spreads to the testis resulting in epididymo-orchitis and is bacterial in origin.[77] Epididymo-orchitis following bacterial infection in sexually active boys, if florid and untreated, may be complicated by abscess formation and testicular infarction. Renal anomalies such as a duplex collecting system with insertion of the ectopic ureter into the vas deferens or seminal vesicles must be excluded.[78]

Spermatic cord torsion

Spermatic cord torsion occurs most commonly in infants and adolescents, 12–18 years of age. The testis rotates like a 'bell-clapper' due to a narrow mesenteric attachment extending from the spermatic cord to the testis and epididymis.[79] Only 30% of boys who present with acute scrotal pain will have spermatic cord torsion, as

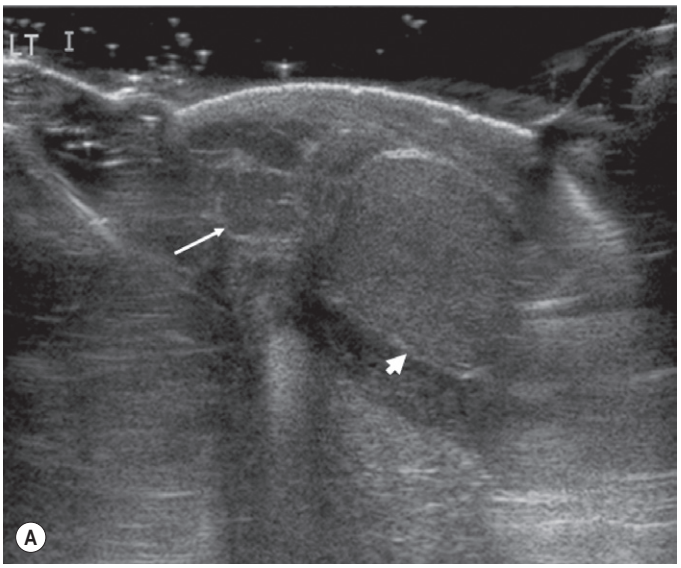

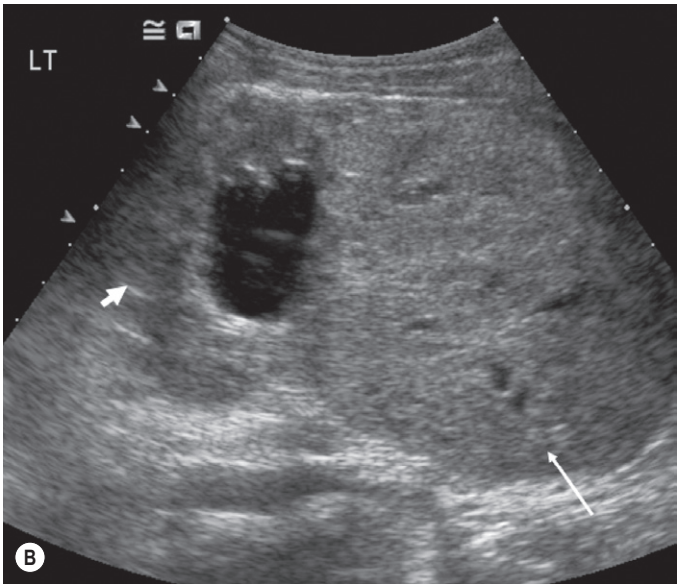

Figure 72.34 Varicocele and tumour. A: The left testis (arrowhead) is normal with evidence of dilatation of the veins at the level of the left pampiniform plexus (arrow) in a child 4 years of age complaining of scrotal pain. **B:** Ultrasound of the left flank demonstrates a large heterogeneous mass (arrow) arising from the left kidney (arrowhead), causing obstruction of the pelvicalyceal system; a nephroblastoma.

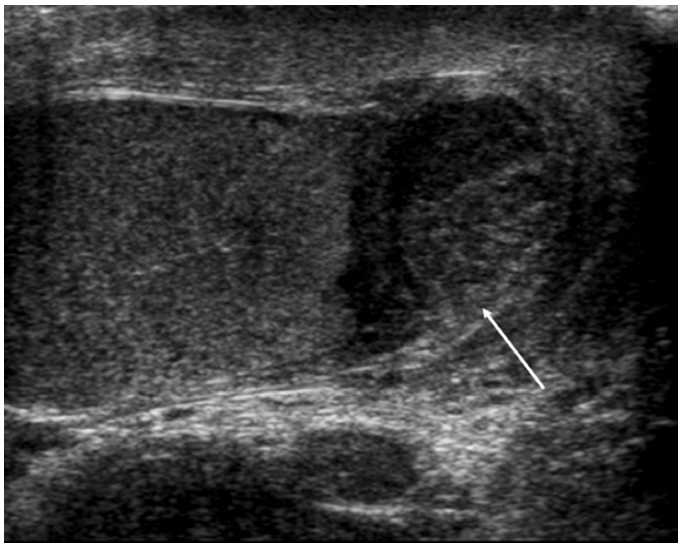

Figure 72.35 Acute epididymitis. An ultrasound image of the tail of the epididymis (arrow) in a child with a painful scrotum demonstrating a thickened epididymal tail.

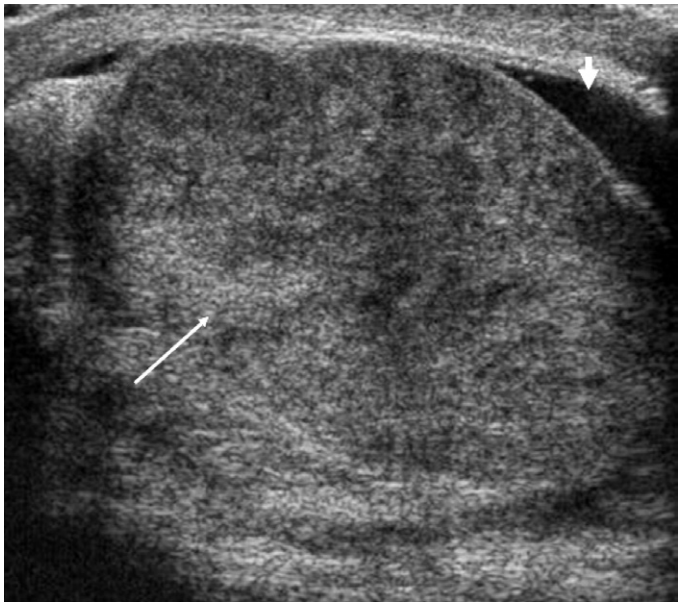

Figure 72.36 Testicular torsion. A heterogeneous enlarged testis (arrow) with a small hydrocele (arrowhead) in a patient with scrotal pain of 24 hours' duration. There is no colour Doppler signal present in the testis.

a cause, requiring surgery. Early surgery is the preference rather than relying on imaging to differentiate between spermatic cord torsion and other causes of acute scrotal pain; testicular salvage is more likely if the patient is treated within 6 hours.[80] Ultrasound appearances are variable depending on the duration of symptoms and the degree of twisting of the spermatic cord. In the early phase (<24 hours' duration) the epididymis and testis are enlarged and blood flow within the affected testicle may be absent or reduced. After 24 hours, no blood flow is seen on colour Doppler ultrasound, and the testis becomes of high reflectivity and heterogeneous due to haemorrhage and infarction[81] (Fig. 72.36).

In the paediatric population the ultrasound diagnosis of testicular torsion is even more problematic than in the adult patient.[82] There is often asymmetry in the blood flow in the normal underdeveloped testes and comparison with the unaffected side may not help.[62,63] Intermittent torsion and incomplete torsion may produce normal, increased or decreased blood flow on Doppler ultrasound. Ultrasound is not therefore always reliable in diagnosing testicular torsion and care must be taken in dismissing the diagnosis in the child who presents with an acutely painful scrotum and has a normal ultrasound.[79]

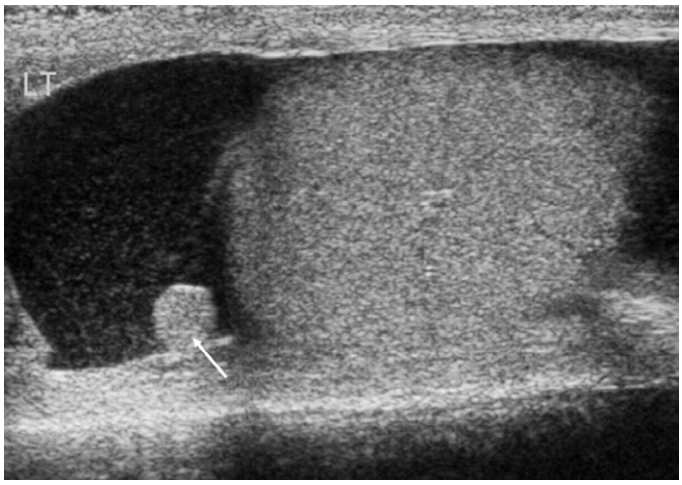

Figure 72.37 Torsion of an appendix testis. A high reflective appendix testis (arrow) surrounded by fluid-containing echogenic debris in a child with intermittent scrotal pain.

Torsion of the testicular appendix

The appendix testis lies at the upper pole of the testis in the groove between the testis and head of the epididymis and is best seen in the presence of a hydrocele (Fig. 72.37). The appendix measures between 1 and 7 mm in length and is of similar reflectivity to the epididymal head.[83] Torsion of the testicular appendix is more common than testicular torsion, occurring in boys between the ages of 3 and 13 years.[84] Patients present with pain at the upper aspect of the testis, with a small bluish nodule; the 'blue-dot' sign. In torsion of the appendix, ultrasound of the testis is normal with low resistance arterial blood flow on Doppler ultrasound. Often there is an inflammatory reaction in the epididymis, which is enlarged, and hyperaemic.[85] The appendix itself tends to be of higher reflectivity although 30% are of reduced reflectivity with a surrounding reactive hydrocele.[86] No surgical intervention is required and the condition settles.

Testicular trauma

Testicular trauma results from a direct blow to the testis, from sporting activity, straddle accident or a motor vehicle accident (Fig. 72.38). Ultrasound appearances are variable depending on the extent of injury. Extra-testicular haematomas may be large and of high reflectivity in the acute stage, becoming smaller and anechoic with time. An intra-testicular haematoma may be high or low reflective, depending on the age, often associated with a complex heterogeneous haematocele.[87] If the margins of the testis are poorly defined, a testicular rupture may be present which requires surgery to repair the disordered tunica albuginea.[88]

Scrotal tumours

The prevalence is estimated at 2.0 cases per 100 000 boys manifesting as a painless swelling. Ultrasound is able to distinguish the location of the tumour as intra-testicular or extra-testicular. The most common extra-testicular tumour is a rhabdomyosarcoma and the most common intra-testicular tumour is a yolk sac tumour. Intra-testicular tumours account for 1% of all solid paediatric tumours and peak before the age of 3 years.[89]

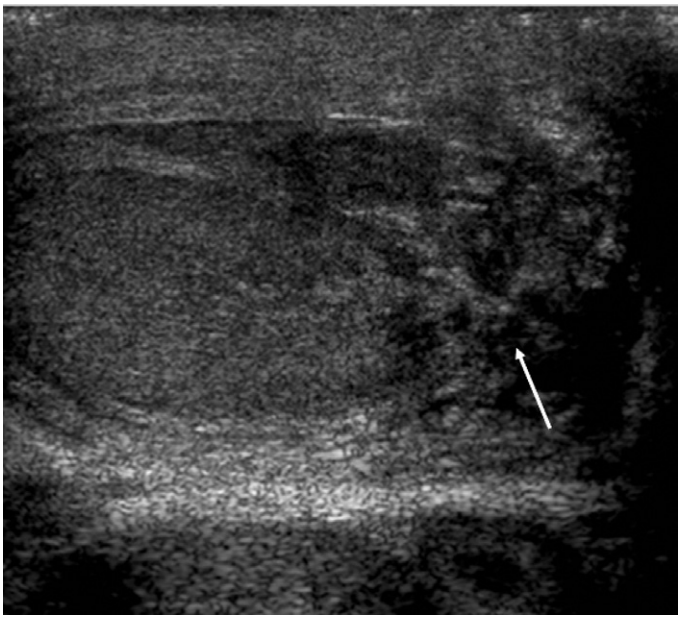

Figure 72.38 Testicular trauma. There is disruption to the normal contour of the lower aspect of the right testis (arrow) in a child with a straddle injury. Surgical exploration demonstrated disruption to the tunica albuginea.

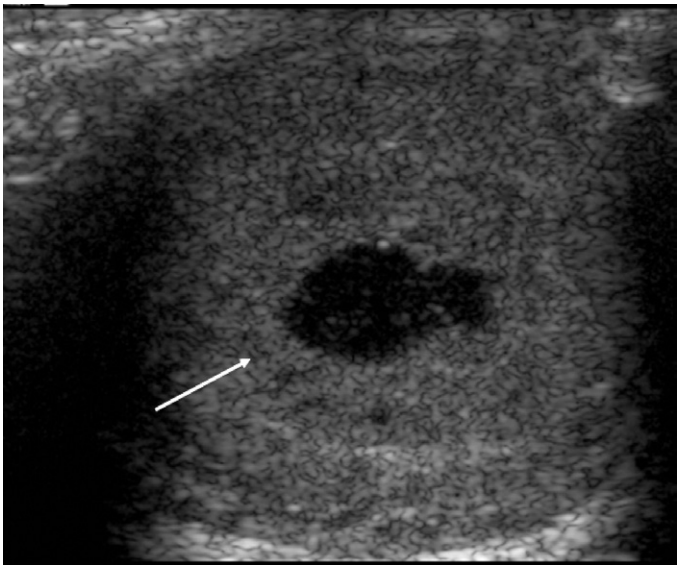

Figure 72.39 Testicular tumour. A focal testicular lesion (arrow) in the lower aspect of the testis representing a yolk sac tumour.

Testis

- Ultrasound is not successful in locating the intra-abdominal testis.
- Hydrocele is the commonest cause of a scrotal mass in the infant.
- Ultrasound diagnosis of testicular torsion is difficult in the paediatric population.
- Torsion of the testicular appendix is more common than testicular torsion.
- Germ cell tumours may present at ultrasound with a focal mass or a diffusely enlarged testis.

Intra-testicular tumours

Germ cell tumours

Germ cell tumours, which are divided into seminomatous and non-seminomatous, are the commonest primary testicular tumours. Seminomatous tumours are rare in children, whereas 80% of non-seminomatous tumours present in children under the age of 2 years.[90,91] A yolk sac tumour (infantile embryonal carcinoma) produces alpha-fetoprotein (AFP) exclusively and is the most common cell type in children. On ultrasound, the testis may be enlarged or the tumour may appear as a focal low or high reflective mass (Fig. 72.39). Focal or diffu se areas of increased vascularity may also be seen along with cystic change as a consequence of areas of necrosis. Teratoma is the next most common tumour in children, benign in the prepubertal child and allowing tissue-sparing surgery, but malignant in the adolescent and requiring orchidectomy.

Non-germ cell tumours

Leydig cell tumours are the most common stromal tumour. The peak age for presentation is 4 years and these children tend to present with precocious puberty. Sertoli cell tumours usually present around 18 months and tend to be benign.

Lymphoma and leukaemia

Less than 10% of testicular tumours are metastatic deposits, most commonly from lymphoma or leukaemia. Primary testicular lymphoma is very rare. The testes are enlarged with infiltration diffusely or focal hypoechoic in nature; often imaging is non-specific.

Extra-testicular tumours

Rhabdomyosarcoma

A rhabdomyosarcoma is a malignant tumour which may involve the spermatic cord, epididymis or testis. The majority occur in the first two decades of life, and appear as a low reflective solid mass that invades the epididymis and testis with increase in colour Doppler flow. Long-term survival is best in patients under the age of 10 years with disease confined to the scrotum[92] and depends on histological type.

Other extra-testicular tumours

Epididymal benign tumours in children include epididymal cysts, spermatocele and adenomatoid tumours. The latter is rare in children, often seen as a smooth mass in the poles of the epididymis, with colour Doppler flow identified.

Systemic disease with scrotal involvement

In children, Henoch–Schönlein purpura may cause acute pain secondary to haemorrhagic orchitis seen on ultrasound as non-specific bilateral focal hyporeflective areas, scrotal wall thickening, epididymal enlargement and a reactive hydrocele.[93] Clinical history and presence of purpura suggests the diagnosis, with up to 37% testicular involvement reported. Acute haemorrhagic oedema of infancy presents with similar findings seen in Henoch–Schönlein purpura but affects children less than 2 years of age. Acute idiopathic scrotal oedema occurs as a sudden onset of a painful swollen scrotum in children between 4 and 7 years which resolves spontaneously. Ultrasound demonstrates thickening of the scrotal wall, with increased colour Doppler flow but with normal underlying testis and epididymis.[94]

REFERENCES

1. Stanhope R, Adams J, Jacobs HS, Brook CG. Ovarian ultrasound assessment in normal children, idiopathic precocious puberty, and during low-dose pulsatile gonadotrophin-releasing hormone treatment of hypogonadotrophic hypogonadism. Arch Dis Child 1985;60:116–119.
2. Adams J, Franks S, Polson DW, et al. Multifollicular ovaries: clinical and endocrine features and response to pulsatile gonadotrophin-releasing hormone. Lancet 1985;ii:1375–1379.
3. Orsini LF, Salardi S, Pilu G, et al. Pelvic organs in premenarcheal girls: real-time ultrasonography. Radiology 1984;153(1):113–116.
4. Trinidad C, Tardáguila F, Fernández GC, et al. Ovarian maldescent. Eur Radiol 2004;14(5):805–808.
5. Cohen HL, Shapiro MA, Mandel FS, Shapiro ML. Normal ovaries in neonates and infants: a sonographic study of 77 patients 1 day to 24 months old. AJR Am J Roentgenol 1993;160(3):583–586.
6. Holm K, Laursen EM, Brocks V, Müller J. Pubertal maturation of the internal genitalia: an ultrasound evaluation of 166 healthy girls. Ultrasound Obstet Gynecol 1995;9(3):175–181.
7. De Bruyn R. The female reproductive system. In: Pediatric ultrasound. London: Churchill Livingstone; 2005. p. 227–229.
8. Nussbaum AR, Sanders RC, Jones MD. Neonatal uterine morphology as seen on real-time US. Radiology 1986;160(3):641–643.
9. Garel L, Dubois J, Grignon A, et al. US of the pediatric female pelvis: a clinical perspective. Radiographics 2001;21(6):1393–1407.
10. Herter LD, Golendziner E, Flores JAM, et al. Ovarian and uterine sonography in healthy girls between 1 and 13 years old: correlation of findings with age and pubertal status. AJR Am J Roentgenol 2002;178:1531–1536.
11. Saleem SN. MR imaging diagnosis of uterovaginal anomalies: current state of the art. Radiographics 2003;23(5):e13.
12. The American Fertility Society classifications of adnexal adhesions, distal tubal occlusion, tubal occlusion secondary to tubal ligation, tubal pregnancies, Müllerian anomalies and intrauterine adhesions. Fertil Steril 1988;49:944–955.
13. Blask AR, Sanders RC, Gearhart JP. Obstructed uterovaginal anomalies: demonstration with sonography. Part I. Neonates and infants. Radiology 1991;179(1):79–83.
14. Banerjee AK, Clarke O, MacDonald LM. Sonographic detection of neonatal hydrometrocolpos. Br J Radiol 1992;65(771): 268–271.
15. Burgis J. Obstructive Müllerian anomalies: case report, diagnosis, and management. Am J Obstet Gynecol 2001;185:338–344.
16. Orazi C, Lucchetti MC, Schingo PM, et al. Herlyn-Werner-Wunderlich syndrome: uterus didelphys, blind hemivagina and ipsilateral renal agenesis. Sonographic and MR findings in 11 cases. Pediatr Radiol 2007;37(7):657–665.
17. Prada Arias M, Muguerza Vellibre R, Montero Sanchez M, et al. Uterus didelphys with obstructed hemivagina and multicystic dysplastic kidney. Eur J Pediatr Surg 2005;15:441–445.
18. Rangecroft L. Surgical management of ambiguous genitalia. Arch Dis Child 2003;88:799–801
19. Wright NB, Smith C, Rickwood AM, Carty HM. Imaging children with ambiguous genitalia and intersex states. Clin Radiol 1995;50:823–829.
20. Avni EF, Rypens F, Smet MH, Galetty E. Sonographic demonstration of congenital adrenal hyperplasia in the neonate: the cerebriform pattern. Pediatr Radiol 1993;23(2):88–90.
21. Eberenz W, Rosenberg HK, Moshang T, et al. True hermaphroditism: sonographic demonstration of ovotestes. Radiology 1991;179(2):429–431.
22. Massarano AA, Adams JA, Preece MA, et al. Ovarian ultrasound appearances in Turner syndrome. J Pediatr 1989;114:568–573.
23. Gravholt CH, Fedder J, Naeraa RW, Müller J. Occurrence of gonadoblastoma in females with Turner syndrome and Y chromosome material: a population study. J Clin Endocrinol Metab 2000;85(9):3199–3202.
24. Salardi S, Orsini LF, Cacciari E, et al. Pelvic ultrasonography in girls with precocious puberty, congenital adrenal hyperplasia, obesity or hirsutism. J Pediatr 1988;112:880–887.
25. Haber HP, Wollmann HA, Ranke MB. Pelvic ultrasonography: early differentiation between isolated premature thelarche and central precocious puberty. Eur J Pediatr 1995;154:182–186.
26. Battaglia C, Mancini F, Regnani G, et al. Pelvic ultrasound and color Doppler findings in different isosexual precocities. Ultrasound Obstet Gynecol 2003;22(3):277–283.
27. Lyon AJ, De Bruyn R, Grant DB. Transient sexual precocity and ovarian cysts. Arch Dis Child 1985;60:819–822.
28. Stanhope R, Traggiai C. Precocious puberty (complete, partial). Endocr Dev 2004;7:57–65.
29. Sobanski E, Hiltmann W, Blanz B. Pelvic ultrasound scanning of the ovaries in adolescent anorectic patients at low weight and after weight recovery. Eur Child Adolesc Psychiatry 1997;6(4):207–211.
30. Mason HD, Key A, Allan R, Lask B. Pelvic ultrasonography in anorexia nervosa: what the clinician should ask the radiologist and how to use the information provided. Eur Eat Disorders Rev 2007;15:35–41.
31. Zawadzki JK, Dunaif A. Diagnostic criteria for polycystic ovary syndrome: towards a rational approach. In: Dunaif A, Givens JR, Haseltine F, Merriam GR, eds. Polycystic ovary syndrome. Cambridge, MA: Blackwell Scientific Publications; 1992. p. 377–384.
32. Rotterdam ESHRE/ASRM-Sponsored PCOS Consensus Workshop Group. Revised 2003 consensus on diagnostic criteria and long-term health risks related to polycystic ovary syndrome. Fertil Steril 2004;81:19–25.
33. Polson DW, Adams J, Wadsworth J, Franks S. Polycystic ovaries – a common finding in normal women. Lancet 1988;i:870–872.
34. Franks S. Adult polycystic ovary syndrome begins in childhood. Best Pract Res Clin Endocrinol Metab 2002;16:263–272.
35. Balen AH, Laven JSE, Tan S, Dewailly D. Ultrasound assessment of the polycystic ovary: international consensus definitions. Hum Reprod Update 2003;9(6):505–514.
36. Hann LE, Hall DA, McArdle CR, Seibel M. Polycystic ovarian disease: sonographic spectrum. Radiology 1984;150:531–534.
37. Bridges NA, Cook A, Healy MJR, et al. Standards for ovarian volume in childhood and puberty. Fertil Steril 1993;60:456–460.
38. Scheffer GJ, Broekmans FJ, Bancsi LF, et al. Quantitative transvaginal two- and three-dimensional sonography of the ovaries: reproducibility of antral follicle counts. Ultrasound Obstet Gynecol 2002;20: 270–275.
39. Nussbaum AR, Sanders RC, Hartman DS, et al. Neonatal ovarian cysts: sonographic-pathologic correlation. Radiology 1988;168(3):817–821.
40. Lee HJ, Woo SK, Kim JS, Suh SJ. 'Daughter cyst' sign: a sonographic finding of ovarian cyst in neonates, infants, and young children. AJR Am J Roentgenol 2000;174:1013–1015.
41. Enriquez G, Durán C, Torán N, et al. Conservative versus surgical treatment for complex neonatal ovarian cysts: outcomes study. AJR Am J Roentgenol 2005;185:501–508.
42. Muller-Leisse C, Bick U, Paulussen K, et al. Ovarian cysts in the fetus and neonate: changes in sonographic pattern in their follow-up and management. Pediatr Radiol 1992;22:395–400.
43. Cohen HL, Eisenberg P, Mandel F, Haller JO. Ovarian cysts are common in premenarchal girls: a sonographic study of 101 children 2–12 years old. AJR Am J Roentgenol 1992;159(1):89–91.
44. Miller D, Blake JM, Stringer DA, et al. Prepubertal ovarian cysts: 5 year experience. Obstet Gynecol 1993;81:434–438.
45. Peinkowski C, Baunin C, Gayrard M, et al. Ovarian cysts in prepubertal girls. Endocr Dev 2004;7:66–76.
46. Brandt ML, Helmrath MA. Ovarian cysts in infants and children. Semin Pediatr Surg 2005;14(2):78–85.
47. Strickland JL. Ovarian cysts in neonates, children and adolescents. Curr Opin Obstet Gynecol 2002;14:459–465.
48. Baltarowich OH, Kurtz AB, Pasto ME, et al. The spectrum of sonographic findings in hemorrhagic ovarian cysts. AJR Am J Roentgenol 1987;148(5):901–905.
49. Barloon TJ, Brown BP, Abu-Yousef MM, Warnock NG. Paraovarian and paratubal cysts: preoperative diagnosis using transabdominal and transvaginal sonography. J Clin Ultrasound 1996;24(3):117–122.
50. Savelli L, Ghi T, De Iaco P, et al. Paraovarian/paratubal cysts: comparison of transvaginal sonographic and pathological findings to establish diagnostic criteria. Ultrasound Obstet Gynecol 2006;28(3):330–334.
51. Adusumilli S, Hussain HK, Caoili EM, et al. MRI of sonographically indeterminate adnexal masses. AJR Am J Roentgenol 2006;187(3):732–740.
52. von Allmen D. Malignant lesions of the ovary in childhood. Semin Pediatr Surg 2005;14:100–105.
53. Templeman C, Fallat ME. Benign ovarian masses. Semin Pediatr Surg 2005;14:93–99.
54. Agrons GA, Wagner BJ, Lonergan GJ, et al. From the archives of the AFIP. Genitourinary rhabdomyosarcoma in children: radiologic-pathologic correlation. Radiographics 1997;17(4):919–937.
55. McDowell HP. Update on childhood rhabdomyosarcoma. Arch Dis

Child 2003;88:354–357.
56. Hwang EH, Han SJ, Lee MK. Clinical experience with conservative surgery for vaginal endodermal sinus tumor. J Pediatr Surg 1996;31:219–222.
57. Aziz D, Davis V, Allen L, Langer JC. Ovarian torsion in children: is oophorectomy necessary? J Pediatr Surg 2004;39:750–753.
58. Servaes S, Zurakowski D, Laufer MR, et al. Sonographic findings of ovarian torsion in children. Pediatr Radiol 2007;37:446–451.
59. Graif M, Itzchak Y. Sonographic evaluation of ovarian torsion in childhood and adolescence. AJR Am J Roentgenol 1988;150:647–649.
60. Fleischer AC, Stein SM, Cullinan JA, et al. Color Doppler sonography of adnexal torsion. J Ultrasound Med 1995;14:523–528.
61. Caspi B, Zalel Y, Katz Z, et al. The role of sonography in the detection of vaginal foreign bodies in young girls: the bladder indentation sign. Pediatr Radiol 1995;25(suppl 1):S60–S61.
62. Ingram S, Hollman AS. Colour Doppler sonography of the normal paediatric testis. Clin Radiol 1994;49:266–267.
63. Albrecht T, Lotzof K, Hussain HK, et al. Power Doppler US of the normal prepubertal testis: does it live up to its promises? Radiology 1997;203:227–231.
64. Friedland GW, Chang P. The role of imaging in the management of the impalpable undescended testis. AJR Am J Roentgenol 1988;151:1107–1111.
65. Gersovich EO. High-resolution ultrasound in the diagnosis of scrotal pathology. Normal scrotum and benign disease. J Clin Ultrasound 1993;21:355–373.
66. Siemer S, Humke U, Uder M, et al. Diagnosis of nonpalpable testes in childhood: comparison of magnetic resonance imaging and laparoscopy in a prospective study. Eur J Pediatr Surg 2000;10:114–118.
67. Satchithananda K, Beese RC, Sidhu PS. Acute appendicitis presenting with a testicular mass: ultrasound appearances. Br J Radiol 2000;73:780–782.
68. Chou TY, Chu CC, Diau GY, et al. Inguinal hernia in children: US versus exploratory surgery and intraoperative contralateral laparoscopy. Radiology 1996;201:385–388.
69. Blews DE. Sonography of the neonatal genitourinary tract. Radiol Clin North Am 1999;37:1199–1208.
70. Jimenez-López M, Ramírez-Garrido F, López-González Garrido JD, et al. Dilatation of the rete testis: ultrasound study. Eur Radiol 1999;9:1327–1329.
71. Sellars MEK, Sidhu PS. Pictorial review: ultrasound appearances of the rete testis. Eur J Ultrasound 2001;14:115–120.
72. Miller FNAC, Sidhu PS. Does testicular microlithiasis matter? A review. Clin Radiol 2002;57:883–890.
73. El-Saeity NS, Sidhu PS. 'Scrotal varicocele, exclude a renal tumour'. Is this evidence based? Clin Radiol 2006;61:593–599.
74. Thomas JC, Elder JS. Testicular growth arrest and adolescent varicocele: does varicocele size make a difference? J Urol 2002;168:1689–1691.
75. Hollman AS, Ingram S, Carachu R, Davis C. Colour Doppler imaging of the acute paediatric scrotum. Pediatr Radiol 1993;23:83–87.
76. Horstman WG, Middleton WD, Melson GL. Scrotal inflammatory disease: Color Doppler US findings. Radiology 1991;179:55–59.
77. Cook JL, Dewbury K. The changes seen on high-resolution ultrasound in orchitis. Clin Radiol 2000;55:13–18.
78. Shalaby-Rana E, Lowe LH, Blask AN, Majid M. Imaging in paediatric urology. Pediatr Clin North Am 1997;44:1065–1089.
79. Sidhu PS. Clinical and imaging features of testicular torsion: role of ultrasound. Clin Radiol 1999;54:343–352.
80. Lindsey D. Boys with acute testicular pain should be presumed to have a torsion until proved otherwise. J Emerg Med 1994;12:531.
81. Patriquin HB, Yazbeck S, Trinh B, et al. Testicular torsion in infants and children: Diagnosis with Doppler sonography. Radiology 1993;188:781–785.
82. Wallace AD, Hollman AS. Colour Doppler ultrasound of the paediatric scrotum. Imaging 1996;8:324–334.
83. Sahni D, Jit I, Joshi K, Sanjeev S. Incidence and structure of the appendices of the testis and epididymis. Anatomy 1996;189:341–348.
84. Sellars MEK, Sidhu PS. Ultrasound appearances of the testicular appendages: pictorial review. Eur Radiol 2003;13:127–135.
85. Strauss S, Faingold R, Manor H. Torsion of the testicular appendages: sonographic appearance. J Ultrasound Med 1997;16:189–192.
86. Hesser U, Rosenborg M, Gierup J, et al. Gray-scale sonography in torsion of the testicular appendages. Pediatr Radiol 1993;23:529–532.
87. Purushothaman H, Sellars ME, Clarke JL, Sidhu PS. Intra-testicular haematoma: differentiation from tumour on clinical history and ultrasound appearances in two cases. Br J Radiol 2007;80:e184–e187.
88. Dogra VS, Gottlieb RH, Oka M, Rubens DJ. Sonography of the scrotum. Radiology 2003;227:18–36.
89. Woodward PJ, Sohaey R, O'Donoghue MJ, Green DE. Tumors and tumorlike lesions of the testis: radiologic-pathologic correlation. Radiographics 2002;22:189–216.
90. Barth RA, Teele RL, Colodny A, et al. Asymptomatic scrotal masses in children. Radiology 1984;152:65–68.
91. Luker GD, Siegel MJ. Asymptomatic scrotal masses in children. Radiology 1994;191:561–564.
92. Woodward PJ, Schwab CM, Sesterhenn IA. Extratesticular scrotal masses: radiologic-pathologic correlation. Radiographics 2003;23:215–240.
93. Ben-Sira L, Laor T. Severe scrotal pain in boys with Henoch-Schonlein's purpura: incidence and sonography. Pediatr Radiol 2000;30:125–128.
94. Klin B, Lotan G, Efrati Y, et al. Acute idiopathic scrotal edema in children: revisited. J Pediatr Surg 2002;37:1200–1202.

CHAPTER

73 Paediatric musculoskeletal imaging

Caren J. Landes

Musculoskeletal imaging with ultrasound is now a well-recognised technique used by both radiologists and sonographers.

In the paediatric setting the absence of ionising radiation and the ability to visualise soft tissues and joints make this a useful tool in the assessment of a number of musculoskeletal pathologies.

TECHNIQUE

When scanning children it is often necessary to be opportunistic in order to acquire the best images. Children can be unpredictable and uncooperative and, although it is important to have a routine for scanning an area, it is also important to recognise areas of interest beyond the area in focus. This allows the assessment of pathology as early as possible during the scan before the infant or child becomes restless.

For superficial musculoskeletal imaging it is appropriate to use the highest frequency transducer available; usually this is in the form of a 17 MHz probe. A small footprint transducer, often known as a 'hockey stick' probe and usually with a frequency of 15 MHz, can be invaluable in paediatric imaging.

For older children and for the visualisation of deeper structures a lower-frequency transducer may be useful.

Other considerations during scanning should be the application of colour Doppler and in some instances pulsed wave. The use of extended field-of-view settings that allow the operator to visualise an area larger than the footprint of the transducer has uses in the limbs in particular.

There should also be the capacity to perform measurements, such as lengths, volumes and angles, including hip angles in the assessment of developmental dysplasia of the hip (DDH).

HIPS

Developmental dysplasia of the hip (previously congenital dysplasia of the hip) is a term applied to abnormal development of the hip joint.

In the normal hip the femoral head lies within the acetabulum as a ball in socket joint. In developmental dysplasia the acetabulum is poorly developed, resulting in a less secure joint. The femoral head becomes mobile within the joint and may be subluxed or completely dislocated.

Infants with clicky hips at the neonatal assessment according to a Barlow or Ortolani test (Fig. 73.1) should be screened for DDH, as should other infants with risk factors for DDH (Table 73.1).

Girls are three times more likely to be affected than boys and the left hip is four times more likely to be affected than the right (probably related to the left occiput anterior fetal lie in utero).[1]

Early detection and intervention has been shown to dramatically improve outcome and in 1969 a national UK screening programme was introduced to clinically assess at-risk infants.[2–4]

The femoral head is unossified in infants and starts to ossify between 6 and 12 months of age.

Plain radiography will demonstrate the ossified portion of the acetabulum, but will not show the unossified femoral head, and it is widely recognised that ultrasound is the best method for assessment of DDH.

Ultrasound will show the non-ossified cartilage of the femoral head and its relationship to both the ossified and unossified components of the acetabulum. It also allows multiplanar and dynamic assessment of stability (Fig. 73.2).

Unfortunately once the femoral head begins to ossify and causes acoustic shadowing, ultrasound becomes less useful.

There is, however, no universally agreed method for hip ultrasound. At least two methods are available as described by Graf[5] and Harcke.[6]

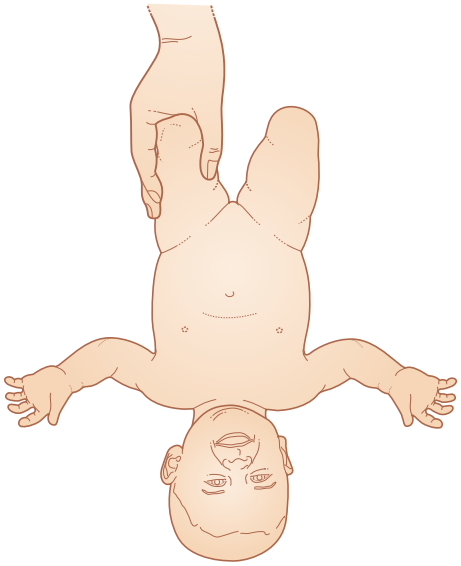

Figure 73.1 The position of the infant and examiner for the Barlow/Ortolani test.

Table 73.1 Risk factors for developmental dysplasia of the hip (DDH)

Breech presentation
A family history of DDH
Oligohydramnios
Talipes
Spinal dysraphism
Arthrogryposis
Generalised ligamentous laxity

It is acknowledged that ultrasound is operator dependent and it is important that the operator involved in the screening programme, whether it be a radiologist or a sonographer, is performing hip scans on a frequent, regular basis.

Sonographic anatomy

In infants the hyaline cartilage of the femoral head is echo-poor with fine vascular echoes throughout. The ossification centre of the femoral head is visible on ultrasound several weeks before it can be demonstrated radiographically,[6] although the age of ossification can vary widely.

In the normal hip, the femoral head should be seated within the bony acetabulum formed by the ossification centres of the ilium, ischium and pubis, which are separated by the triradiate cartilage (Fig. 73.2).

This cartilaginous roof is predominantly echo-poor hyaline cartilage except for a small reflective fibrocartilaginous tip.[7] The iliofemoral ligament and hip joint capsule cannot generally be separated on ultrasound and appear as a common reflective band lateral to the femoral head.

Sometimes curvilinear echoes can be seen outlining the capital femoral epiphysis during movement of the hip. This is thought to represent small bubbles of nitrogen within the joint space (the vacuum phenomenon).[8]

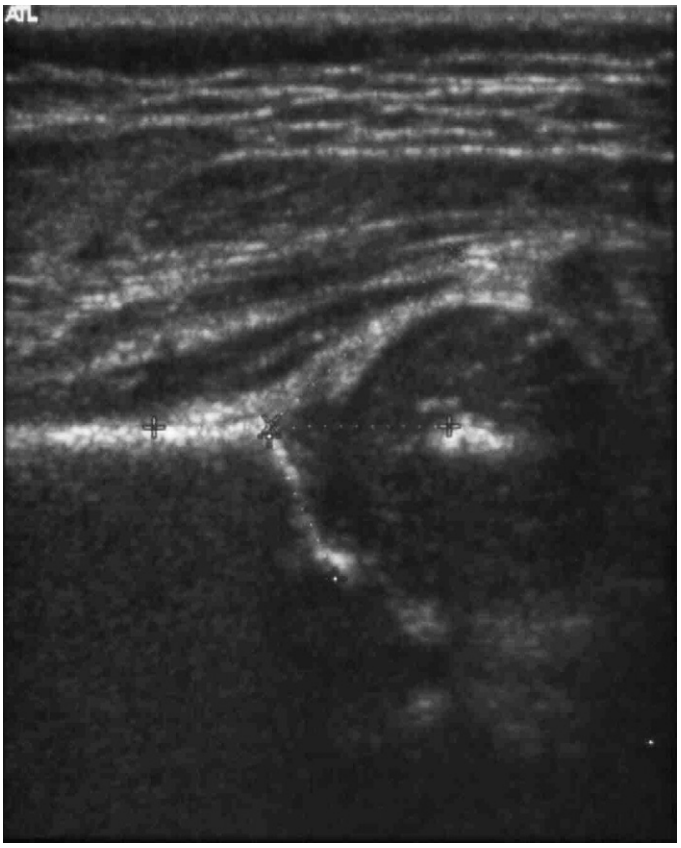

Figure 73.2 Ultrasound of the normal hip showing the femoral head within the joint and the landmarks for the measurement of the alpha angle.

Clinical examination of the infant hip (Fig. 73.1)

Barlow test

The hip is held in flexion with the leg abducted. In this position, posterior pressure (push) is applied to determine whether the hip moves posteriorly out of the acetabulum, thus indicating instability.

Ortolani test

The hip is held in flexion with the leg abduction. In this position anterior pressure (pull) is applied to the hip. Movement of the hip over the acetabulum indicates a dislocated hip and assesses reducibility.

Ultrasound examination of the infant hip

In infants under 6 months of age a high-frequency linear array transducer should be used. This is often a broadband frequency such as 12 MHz.

Graf technique

This requires a practised technique and is not to be undertaken sporadically by untrained operators.

Graf assessed acetabular morphology and devised a classification system based on the angles of inclination of the bony and

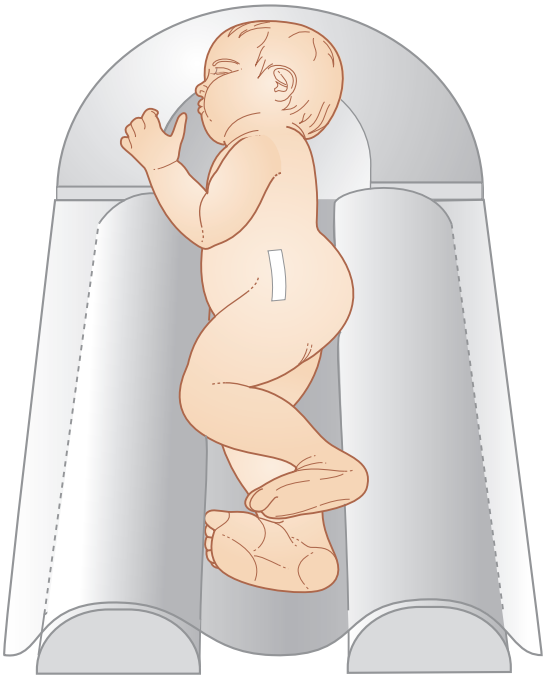

Figure 73.3 The Graf cradle used to support a baby in the lateral decubitus position for ultrasound of the hip.

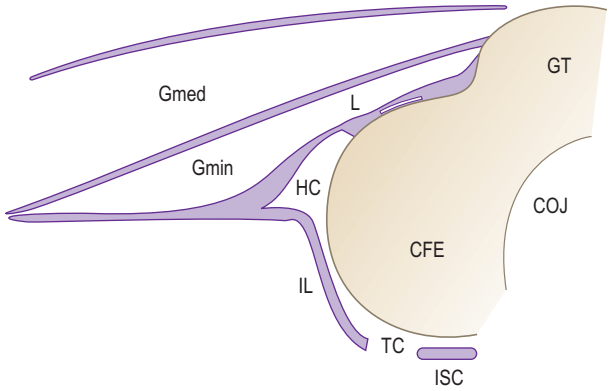

Figure 73.4 A coronal neutral diagram of a developmentally mature hip (Graf type I) showing the cardinal landmarks that define the standard plane. Gmed, gluteus medius; Gmin, gluteus minimus; L, labrum; HC, hyaline cartilage; IL, ilium; TC, triangular cartilage; ISC, ischium; GT, greater trochanter; CFE, capital femoral epiphysis; COJ, chondro-osseous junction.

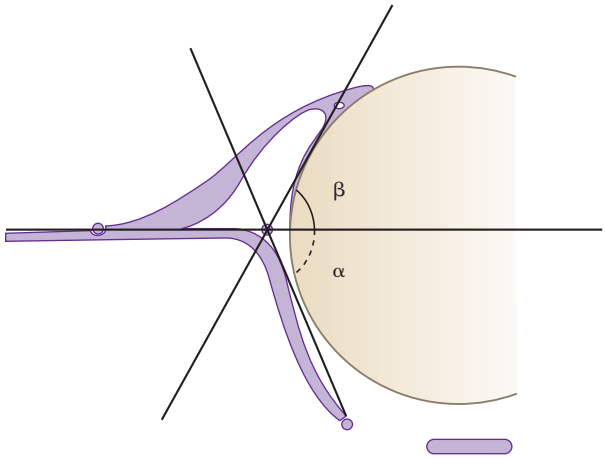

Figure 73.5 Graf's alpha and beta angles. Diagram showing lines drawn on a coronal neutral image of a developmentally mature hip to define Graf's alpha and beta angles.

Table 73.2 Ultrasound assessment of the infant hip

Technique	Assessment	Classification
Graf	Static	Bony/cartilaginous roofs
Modified Graf	Static	Bony/cartilaginous roofs Femoral head is centred within the acetabulum
Harcke	Dynamic	Position and stability of femoral head
Terjesen	Dynamic	Femoral head coverage

cartilaginous roofs.[5,9,10] Graf recommends that the baby is supported in a lateral decubitus position using a special cradle. The hip is positioned in approximately 20° of flexion and slight internal rotation: this represents the neutral position for an infant and brings the femoral head, neck, greater trochanter and acetabulum into the same plane (Fig. 73.3). The transducer is positioned over the greater trochanter and held parallel to the cradle and long axis of the body to obtain a coronal image of the acetabulum showing its maximum depth (Fig. 73.3).

Precise positioning is essential to acquire the standard image for interpretation.

The cardinal landmarks are:

- the inferior edge of the ilium
- the lateral margin of the ilium projected as a horizontal line
- the acetabular labrum.

The chondro-osseous junction should also be visible as a linear echo below the femoral head (Fig. 73.4).

The alpha angle (Fig. 73.5)

This measures the depth of the acetabulum.

The baseline is drawn along the straight lateral margin of the ilium from the point where the perichondrium meets the ilium and a second line is drawn from the inferior point of the iliac bone tangential to the bony acetabulum (the bony roof line).

The alpha angle is the angle between these two lines. A small alpha angle indicates a shallow acetabulum.

Graf also describes a beta angle between the baseline and the cartilaginous roof line, to assess the degree of superior displacement of the femoral head, but this is not commonly measured or reported.

The beta angle cannot be measured in a dislocated hip.

Graf type I (Fig. 73.6)

The hip is developmentally mature.

The acetabulum is deep with a steeply inclined bony acetabular roof.

The bony roof is well developed with a sharp ossific rim. The cartilage roof is long and narrow and extends over the femoral head.

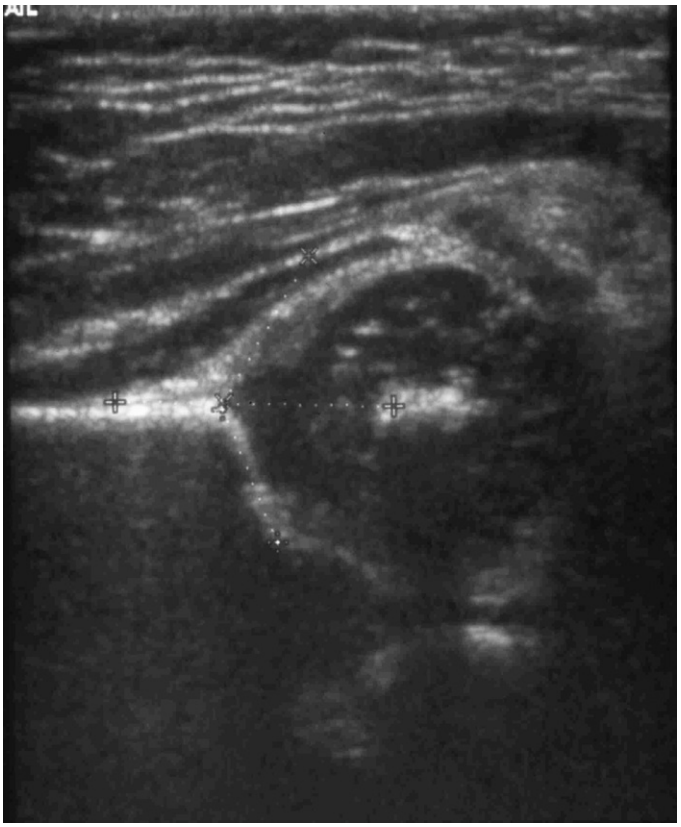

Figure 73.6 Graf type I. The alpha angle is >60° and the hip is developmentally mature.

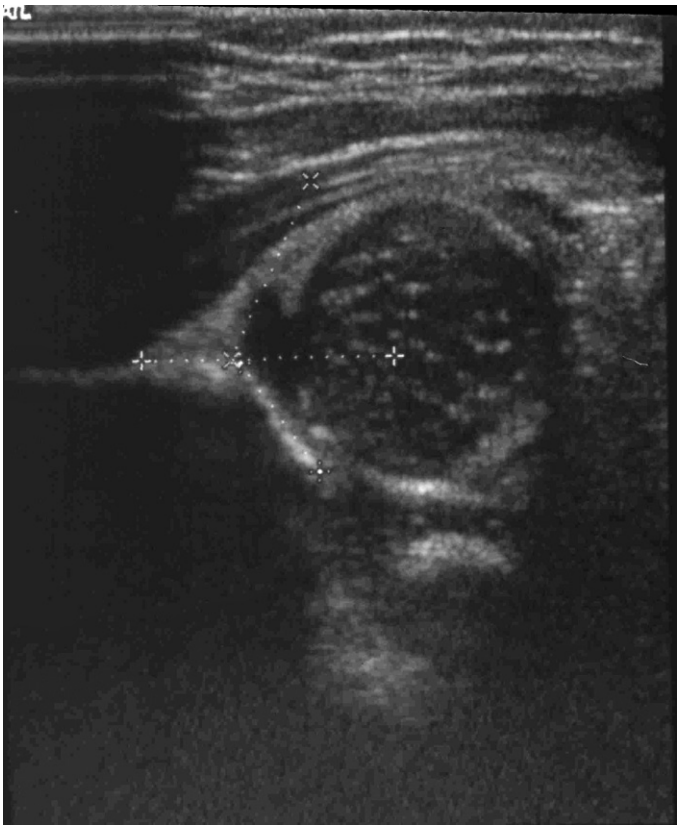

Figure 73.7 Graf type IIa/IIb. The alpha angle is 50–59°. The classification is determined by the age of the patient.

The alpha angle is >60°.

These patients have a described risk of developing dysplasia in later infancy, but coexisting hip instability does not appear to be a predictive indicator.[11]

Graf type IIa (Fig. 73.7)

A shallow acetabulum in an infant under 3 months of age may simply reflect physiological immaturity.

The bony roof is deficient due to delayed ossification and the ossific rim is rounded. The cartilage roof covers the femoral head.

The alpha angle is 50–59°.

A recent meta-analysis revealed that between 84% and 95% of these will develop normally without treatment[11] within 3 months.

Graf type IIb

Appearances are equivalent to those in Graf IIa in a patient of greater than 3 months of age.

A shallow acetabulum in an infant over 3 months of age is considered to be dysplastic, but stable.

The alpha angle is 50–59°.

This requires referral to the orthopaedic surgeons for treatment.

The appearance is equivalent to Graf type IIa and the age of the patient differentiates the types.

Graf type IIc (Fig. 73.8)

The bony roof is deficient with a rounded/flat ossific rim. The cartilage roof covers the femoral head.

A shallow acetabulum in an infant of any age where the alpha angle is 43–49° requires assessment of stability and immediate treatment.

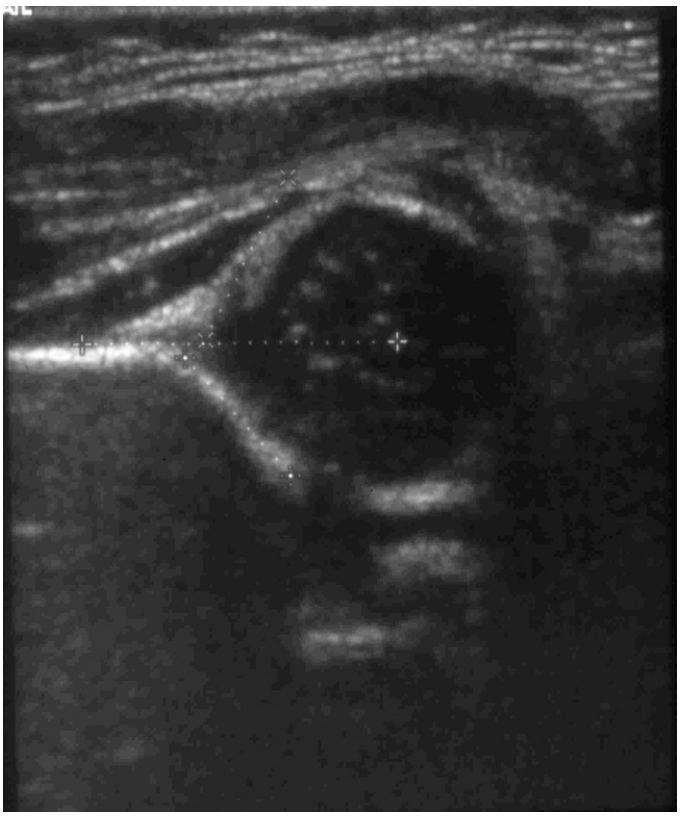

Figure 73.8 Graf type IIc. Deficient bony roof. The alpha angle is 43–49°.

Graf type D

The bony roof is severely deficient with a rounded/flat ossific rim. The cartilage roof is compressed and the hip is at risk of dislocation.

There is a shallow acetabulum with an alpha angle of between 43° and 49° that is inherently unstable.

Graf types IIIa, IIIb, IV (Fig. 73.9)

The hip is dislocated.

The alpha angle is less than 43°.

The bony roof is deficient with a flat ossific rim. The types are differentiated by the position of the cartilaginous roof.

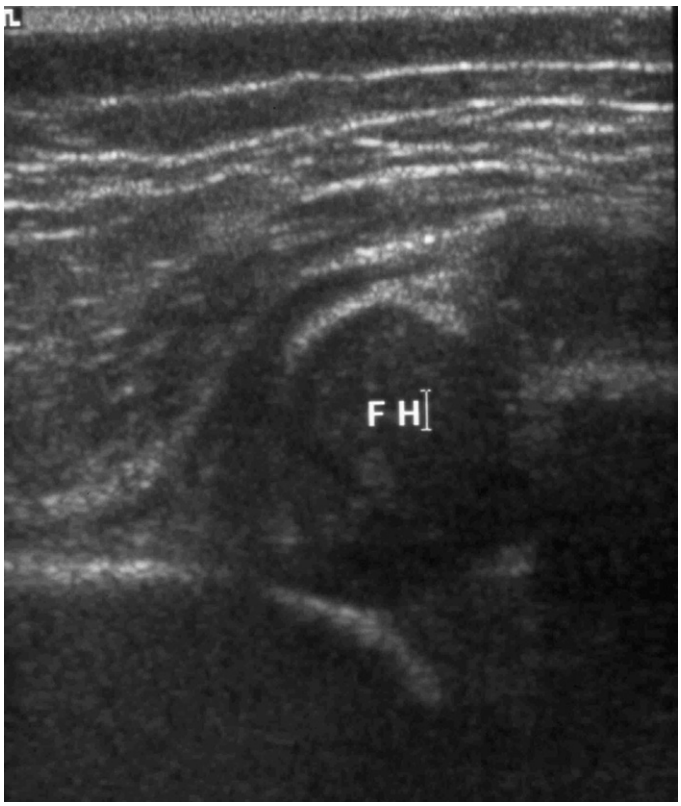

Figure 73.9 Graf type III. The hip is dislocated. The alpha angle is <43°. FH, femoral head.

Pitfalls

There are several technical pitfalls to be aware of:

- Slight flexibility of the acetabular labrum occurs in normal hips when the femoral head is manipulated and should not be mistaken for instability.[12]
- Anterior angulation of the transducer results in an apparent reduction in femoral head coverage.
- Posterior angulation of the transducer results in an apparent increase in femoral head coverage.
- Caudocranial angulation of the transducer can make a normal hip appear dysplastic.
- Dorsoventral angulation of the transducer results in a concave contour of the ilium representing the gluteal fossa.
- It is important to note that although it is possible to make a normal hip appear abnormal on ultrasound, it is not possible to make an abnormal hip appear sonographically normal.

Modified Graf technique

Rosendahl et al. described a technique where the femoral head is centred within the acetabulum on the ultrasound image.[11]

The Harcke technique

This is a dynamic assessment of the hip with application of stress manoeuvres similar to the techniques used during clinical examination.[6,13]

The hip is scanned in the coronal and transverse planes with the baby supine.

There are four steps.

Step 1: coronal neutral

This view is equal to the coronal view advocated by Graf but Harcke and colleagues advocate a visual subjective assessment without the use of specific measurements.[6]

Step 2: coronal flexion (Figs 73.10 and 73.11)

This view is similar to the coronal neutral view except that the hip is flexed to 90°.

The transducer is moved anteriorly and posteriorly relative to the standard mid-acetabular plane in order to evaluate the entire hip.

An image is obtained over the posterior lip of the triradiate cartilage in which a normally located femoral head is not visible; visualisation of the femoral head implies posterior dislocation.

Table 73.3 Graf classification of hip dysplasia

Graf type	Acetabulum	Alpha angle	Patient age	Stability	Other
Ia	Deep	>60°	Any	Stable	Developmentally mature
IIa	Shallow	50–59°	<3 months	Stable	Physiological immaturity
IIb	Shallow	50–59°	>3 months	Stable	Dysplastic
IIc	Shallow	43–49°	Any	May be unstable	
D	Shallow	43–49°	Any	Unstable	
TYPES IIIA, IIIB AND IV ARE DISTINGUISHED BY THE APPEARANCE OF THE CARTILAGE ROOF					
Graf type	**Acetabulum**	**Alpha angle**	**Patient age**	**Stability**	**Cartilage roof**
IIIa	Shallow	<43°	Any	Dislocated	Displaced up Echo-poor
IIIb	Shallow	<43°	Any	Dislocated	Displaced up More reflective than femoral head
IV	Shallow	<43°	Any	Dislocated	Interposed

Figure 73.10 Normal hip. Normal image obtained over the posterior lip of the triradiate cartilage in a coronal flexion view of a neonatal hip. The femoral head should not be visible. IL, ilium; TC, triangular cartilage; ISC, ischium.

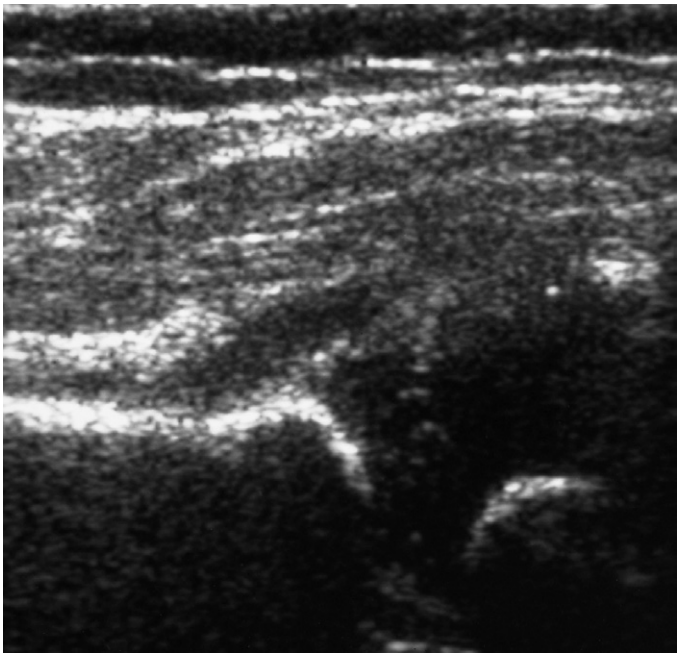

Figure 73.11 Normal hip, coronal flexion view. Normal image obtained over the posterior lip of the triradiate cartilage in a coronal flexion view.

With the infant relaxed and the transducer held over the posterior lip of the triradiate cartilage, firm but gentle pressure is applied to the knee in both an anterior and posterior direction, i.e. a push–pull movement.

In an unstable hip the femoral head will appear over the posterior lip of the triradiate cartilage with the application of posterior pressure (push).

Step 3: transverse flexion (Figs 73.12 and 73.13)

The baby is moved into a supine oblique position with the hip flexed to 90°.

The transducer is held in a transverse plane posterolaterally over the hip.

The normal appearance is a 'U' configuration with the femoral capital epiphysis central to the femoral metaphysis and the ischium.

When dislocated the femoral capital epiphysis cannot be seen within the 'U'.

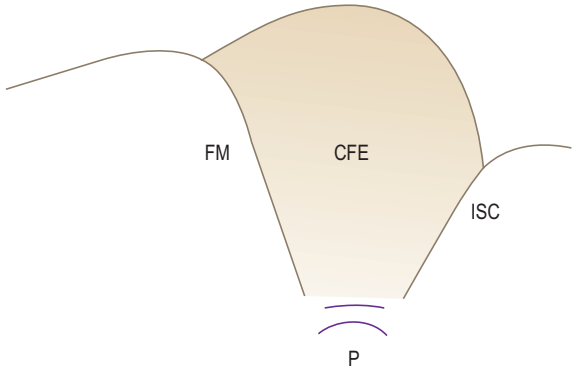

Figure 73.12 Normal hip, transverse flexion view. 'U' configuration of normal transverse flexion view of a neonatal hip. FM, femoral metaphysis; CFE, capital femoral epiphysis; P, pubis; ISC, ischium.

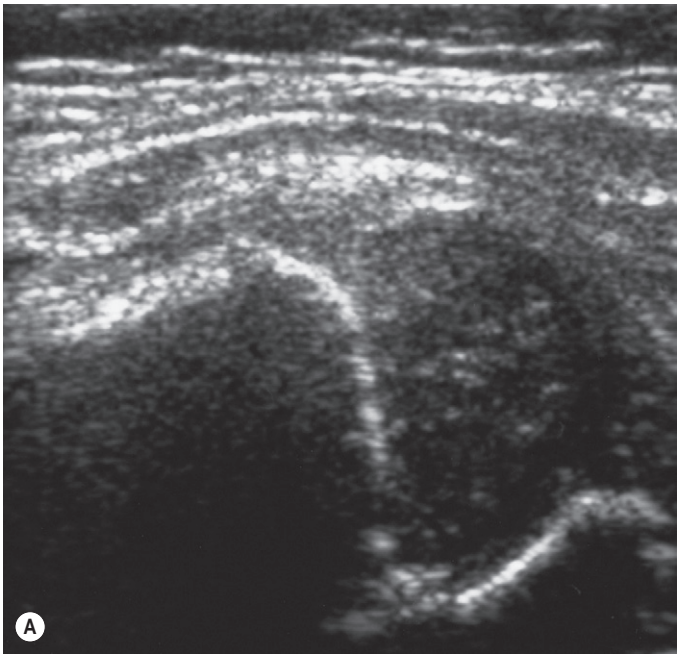

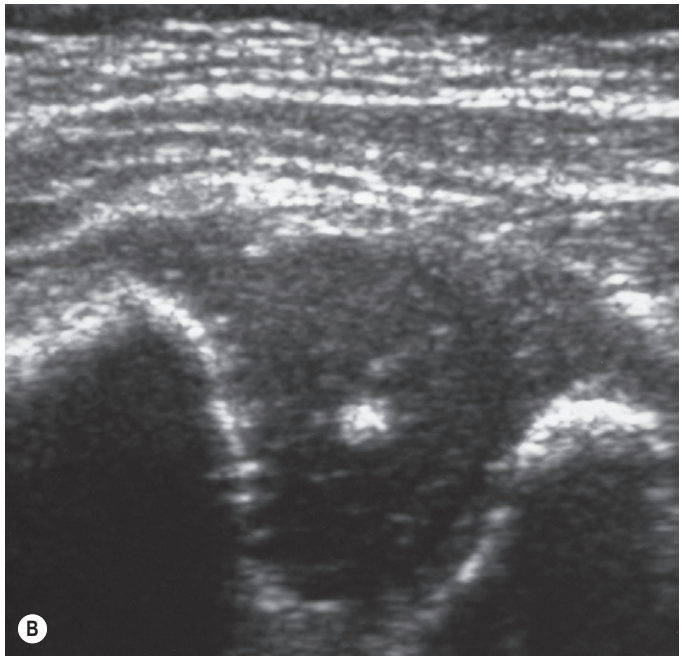

Figure 73.13 Normal hip, transverse flexion view. A: Transverse flexion view of a normal hip showing 'U' configuration. **B:** Similar view in an older baby with visible ossification centre of the capital femoral epiphysis.

Posterior stress on the adducted hip during examination can cause an increase in the gap between the femoral head and acetabulum, indicating instability/subluxation.

Anterior stress on the abducted hip, as in the Ortolani test, allows visualisation of relocation of the hip.

Step 4: transverse neutral (Figs 73.14 and 73.15)

The hip is in the neutral position and the hip is scanned transversely.

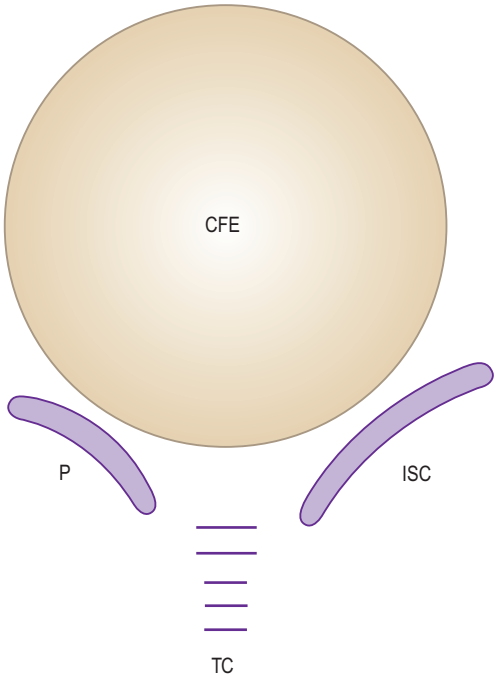

Figure 73.14 Normal hip, transverse neutral view. Normal transverse neutral view of a neonatal hip. CFE, capital femoral epiphysis; P, pubis; TC, triangular cartilage; ISC, ischium.

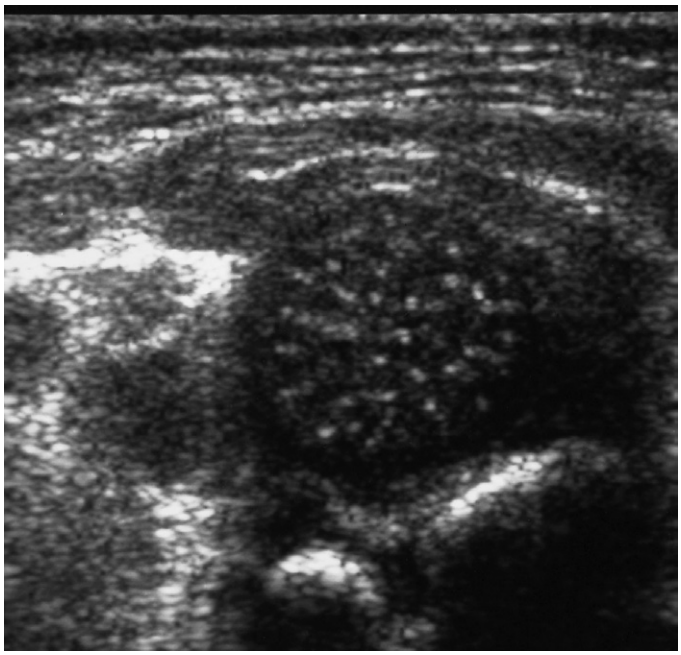

Figure 73.15 Normal hip, transverse neutral view.

The image acquired is of the acetabulum at the centre of the triradiate cartilage.

The bony acetabulum consists of the larger ischial portion posteriorly and the anterior pubic portion, with the two portions connected by the echo-poor triradiate cartilage. The femoral head is normally positioned centrally within the acetabulum with its midpoint approximately over the triradiate cartilage. There should be no echoes between the femoral head and the bony acetabulum.

As with the Graf method, this technique requires skilled, practised operators.

Terjesen technique

Terjesen describes a dynamic technique that assesses femoral head coverage.

The infant lies supine with the leg in the neutral position and the hip slightly flexed.

The transducer is positioned over the lateral aspect of the hip and images are acquired in the longitudinal and transverse planes.

As with the Graf technique, a baseline is drawn. Further lines are drawn tangential to the medial junction of the femoral head with the acetabular fossa and through the lateral margin of the acetabulum parallel to the long axis of the transducer. Femoral head coverage is defined as the distance between the baseline and the medial line divided by the distance between the medial and lateral lines multiplied by 100.

The lower limits of normal are defined as 46% in boys and 44% in girls.[11]

The irritable hip

The commonest cause of an irritable hip is transient synovitis, but the differential diagnosis includes septic arthritis, Perthes disease and slipped capital femoral epiphysis.

Ultrasound is a useful first-line investigation in the assessment of a limping child.

If a joint effusion is identified it is the clinician's role to narrow the differential diagnosis. Transient synovitis can be treated conservatively, whereas septic arthritis requires prompt intervention and treatment.

The patient lies supine with both legs straight and in the neutral position. The transducer is placed anteriorly in a parasagittal oblique orientation along the femoral neck.[14,15] It is important to ensure that the proximal femoral shaft is visible in the scan plane, to avoid a false negative scan (Fig. 73.16).

Both hips should be scanned during the same examination.

Dual imaging is useful in demonstrating both hips side by side for comparison.

Transient synovitis

In transient synovitis there is inflammation of the synovial lining of the hip joint, often with a joint effusion.

Transient synovitis typically affects children of between 2 and 10 years of age. The aetiology is unknown but there is sometimes a history of recent upper respiratory tract infection. The pain is decreased at rest and usually resolves within a few days, but the effusion may persist, generally resolving within 4–11 days.[16]

Ultrasound is extremely sensitive for the detection of a hip joint effusion, and relies on visible displacement of the hip joint capsule (Fig. 73.17). The normal hip joint capsule is seen as a continuous concave reflective line paralleling the anterior aspect of the femoral neck and capital femoral epiphysis. Synovial thickening or an effusion causes the joint capsule to become convex and bulge anteriorly. Synovial thickening is often seen both anterior to the fluid collection and in the synovial reflection along the femoral neck.

The anteroposterior diameter (anterior capsular distance) of the effusion can be measured and provides a reproducible objective assessment.

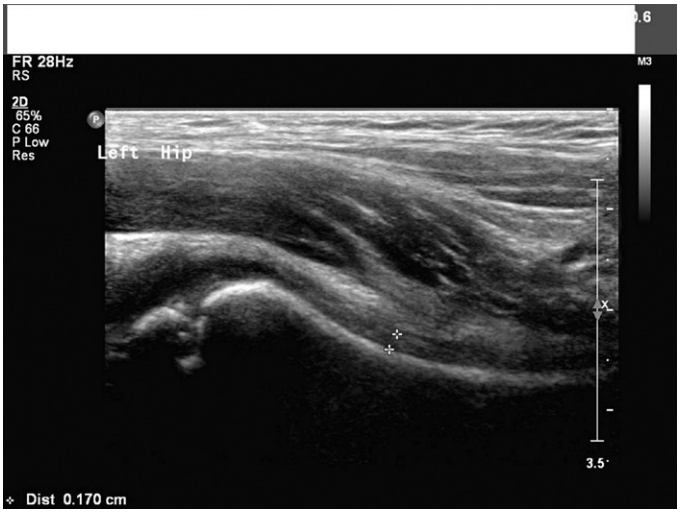

Figure 73.16 Ultrasound of the normal hip including the proximal femoral shaft.

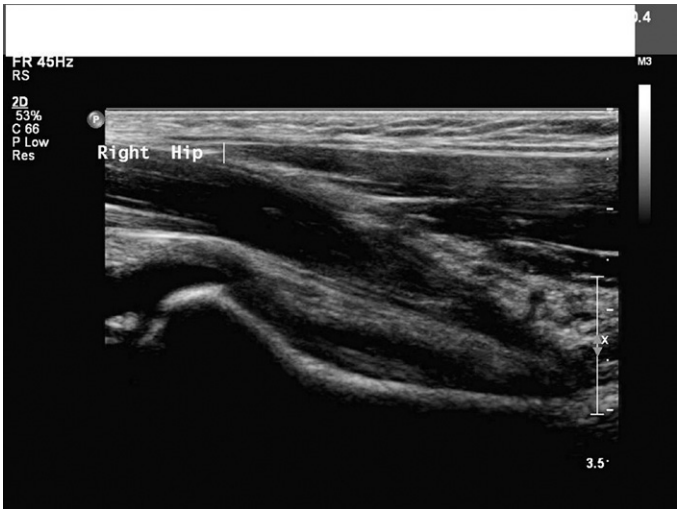

Figure 73.17 In the presence of a joint effusion at the hip the joint capsule is distended and the capsule is lifted away from the proximal femoral shaft.

Table 73.4 Anterior capsular distance (ACD)

Age	ACD: upper limit of normal
<4 years	5 mm
4–7 years	6 mm
8 years	7 mm

Source: Graf and Wilson.[12]

A difference of greater than or equal to 2 mm between the left and right hips can also indicate a joint effusion, but it should be considered that joint effusions can be bilateral.

The interface sign is where an additional line is seen anterior to the echo-poor cartilage of the femoral head, corresponding to the junction between the cartilage of ossification and the articular cartilage (Fig. 73.18). The interface sign is absent in the presence of a joint effusion.

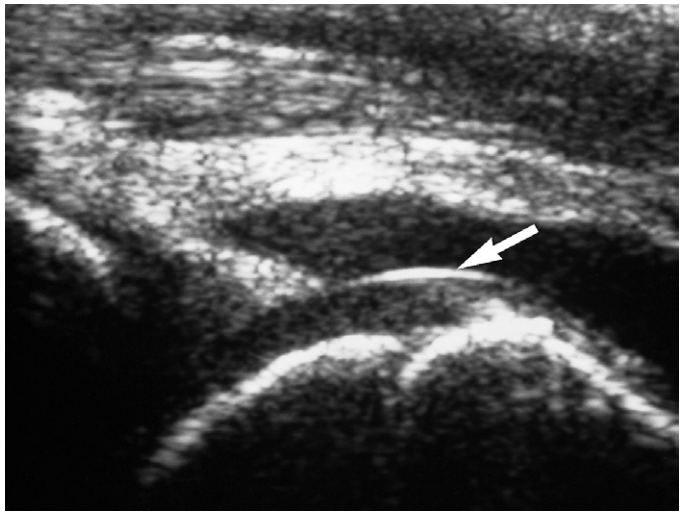

Figure 73.18 Joint fluid. Image showing the interface sign representing the extra interface (arrow) between articular cartilage and joint fluid.

Joint effusion fluid is usually anechoic, but may contain fine echoes depending on the cellular content of the fluid. The appearance of the fluid is not a reliable indicator for distinguishing between transient synovitis and septic arthritis. If there are clinical concerns the joint fluid should be aspirated for culture.

Legg–Calvé–Perthes disease

This condition usually affects children between 3 and 12 years of age with a peak incidence of 5–8 years and a slight male preponderance. Around 15% of cases are bilateral.[17]

Although ultrasound has a theoretical role in the diagnosis and follow-up of Legg–Calvé–Perthes disease, in practice plain radiography, magnetic resonance imaging (MRI) and nuclear medicine studies are more sensitive and specific.

The initial diagnosis is made clinically and with plain X-rays, but ultrasound may be the initial investigation of a child with hip pain or a limp. It is therefore imperative that the hip is examined in its entirety, including the femoral capital epiphysis (Fig. 73.19).

The earliest sonographic sign is that of a joint effusion.

The features that help to differentiate Legg–Calvé–Perthes disease from transient synovitis are:

1. thickening of the joint capsule
2. mild contralateral capsular distension
3. a joint effusion that persists for more than 2 weeks.

On ultrasound the unossified cartilage of the femoral head is hypoechoic, whereas the ossification centre is seen as a band of high echogenicity with posterior acoustic shadowing.

The margin of the femoral ossification centre can be defined with ultrasound and ultrasound can be used to identify irregularity, flattening or fragmentation. In the more chronic phases of the disease ultrasound can identify new bone formation earlier than the plain radiograph and may also identify recalcification.

In this instance the strong echoes of the necrotic bone disappear and are replaced by less reflective material that extends over the epiphysis and shows gradual increase in ossification.

In the more acute stage of the condition the articular cartilage becomes thickened and this increases with progressive collapse of the femoral head.

Slipped femoral capital epiphysis

Conventional radiography remains the first-line investigation for suspected slipped upper femoral epiphysis (SUFE) and any child

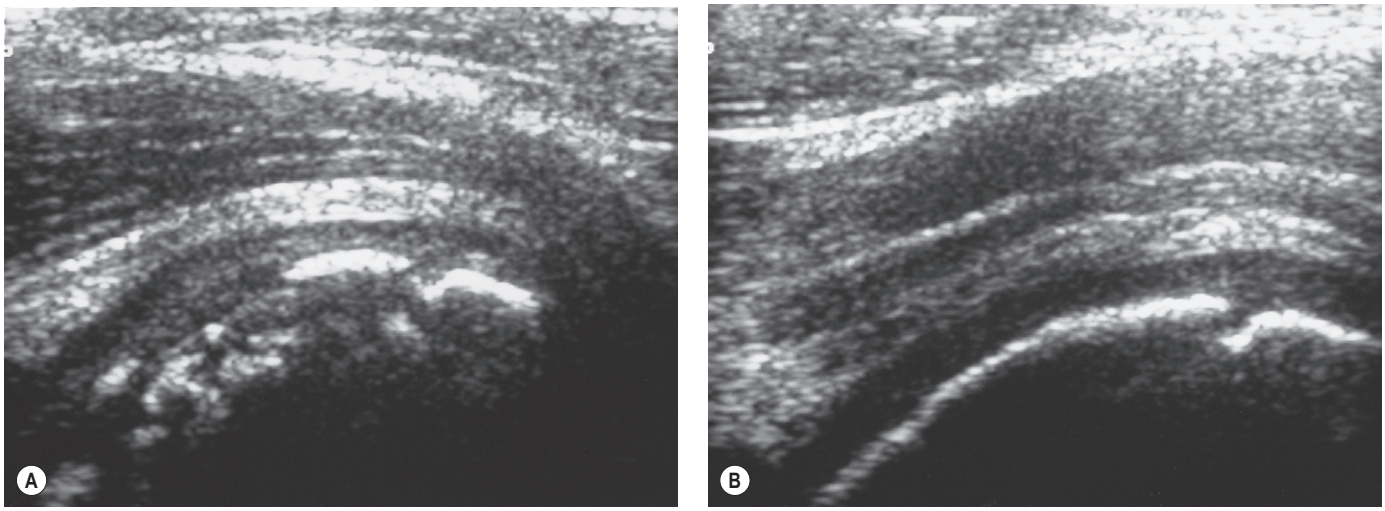

Figure 73.19 Legg–Calvé–Perthes disease. A: Image showing irregular, flattened and fragmented capital femoral epiphysis compared to **B:** the normal contralateral side.

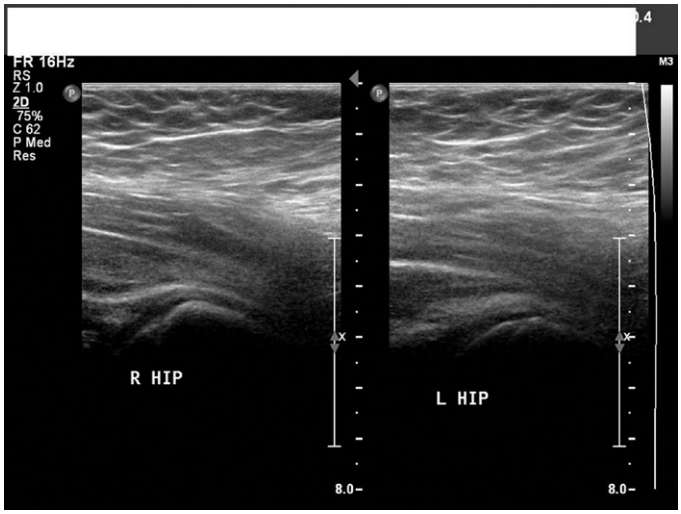

Figure 73.20 Slipped capital femoral epiphysis. On the left the epiphysis is normally aligned with the femoral metaphysis. On the right the epiphysis is stepped posteriorly in relation to the metaphysis.

Hip ultrasound	
Use a linear probe	
CDH: Graf technique:	Position the hip in flexion and internal rotation
	Align the transducer parallel to the body
	Identify the landmarks
	Measure the depth of the acetabulum with the alpha angle
Hip effusion	Align the probe with the femoral neck
	Include the proximal femoral shaft in the field of view
	Examine both hips
Perthes	The femoral head becomes irregular/flattened/fragmented
	The joint capsule becomes thickened
SUFE	Malalignment of the proximal femoral epiphysis with the proximal femoral metaphysis

over 8 years of age presenting with hip pain should have anteroposterior and frog lateral views of the pelvis in the first instance.

SUFE can occur in younger children who present with hip pain and have ultrasound as the initial investigation. It is therefore important to assess the alignment of the femoral capital epiphysis relative to the femoral metaphysis during routine ultrasound examination of the hip[18] (Fig. 73.20).

If there is suspicion on ultrasound, anteroposterior and frog lateral X-rays should be acquired. Prompt diagnosis is essential to allow prompt orthopaedic intervention and avoid long-term complications such as avascular necrosis.

PAEDIATRIC TRAUMA

Conventional radiography remains the best initial investigation for suspected bony injury. Ultrasound should, however, be the initial investigation for most suspected soft tissue injuries in children. This may be subsequently supplemented by MRI.

Ultrasound is also useful in instances where there may be trauma to non-ossified cartilage.

Acute trauma

Conventional radiographs may not demonstrate physeal fractures in young children with non-ossified epiphyses or apophyses.

Ultrasound can show extension of the fracture line through the epiphysis or show epiphyseal displacement with transphyseal fractures.

The apophysis is a focal area of ossification at the periphery of the bone. It ossifies in cartilage and has a cartilaginous connection to the adjacent bone. In the immature skeleton the apophyseal growth plate is a point of particular weakness. Apophyseal avulsion injuries typically occur at a bony prominence that serves as a tendon or ligament attachment site, for example at the anterior inferior iliac crest, with a peak incidence for injury between 10 and 20 years of age, i.e. when the apophyseal growth plate is just closing or just after radiographic closure.

In these cases the radiograph may be normal and ultrasound may be helpful in identifying apophyseal displacement or associated intramuscular injury.

Sonography may also be useful in diagnosing fracture complications. An avulsed ischial tuberosity may lead to long-term

Trauma	
Muscle tear	Disruption of the normal alignment of the muscle fibres with a focal area of echogenicity
Haematoma	Mixed echogenicity lesion with disruption of the muscle fibres
	No abnormal vascularity within the lesion
Foreign bodies	Highly reflective focus with posterior acoustic shadowing

morbidity due to sciatic nerve entrapment and in these circumstances ultrasound may show the precise relationship of the fracture callus to the sciatic nerve. Infection of fracture haematomas is a recognised complication following muscle and tendon avulsion injuries and can be diagnosed with ultrasound.

Accessory ossification centres can cause confusion on a radiograph. Ultrasound can be used to differentiate them from fractures. An accessory ossification centre will be seen as a small, highly reflective focus within the cartilage of the adjacent bone, without disruption of this cartilage.

A fracture will be associated with disruption of the cartilage and in the acute phase is also associated with soft tissue swelling or a haematoma.

Non-accidental injury

The Standards for Radiological Investigations of Suspected Non-accidental Injury issued jointly by the Royal College of Radiologists and the Royal College of Paediatrics and Child Health in March 2008 state that there are case reports of the use of ultrasound in the identification of subperiosteal haematomas in occult rib fractures and around fractures prior to any radiographically visible signs of healing.

The guidance also states that the use of ultrasound in the investigation of bony injury has not been validated in suspected non-accidental injury and cannot be advocated as a primary tool for the investigation of bone injury.[19]

Overuse injuries

Repetitive microtrauma in children can lead to conditions affecting bone, cartilage and soft tissues that are specific to the immature skeleton, but affect children of different ages differently. Repetitive trauma that causes apophysitis at a tendon insertion site in a young child will often cause tendinitis in an older child.

Osgood–Schlatter disease is a clinical diagnosis, based on anterior knee pain localised to the tibial tuberosity, assumed to occur following repetitive traction trauma. Affected children are typically very active and aged between 10 and 15 years, with a peak incidence at 13–14 years.

Ultrasound can be useful in atypical cases, where it can identify fragmentation of the tibial tuberosity apophysis, swelling of the overlying cartilage and focal thickening and heterogeneity of the patellar tendon. In some cases there may be a fluid collection deep to the inferior aspect of the patellar tendon representing pretibial bursitis.[20]

The cartilage changes usually occur first and are followed by tendon or bursal abnormalities, and if detected, changes in the latter structures are an indication of more severe or well-established disease.

The tibial apophysitis and associated swelling has a compressive effect on the distal tendon, elevating it towards the anterior tibial plateau. The pretibial bursa acts as a shock absorber and the repeated injury with movement causes inflammation of the tendon and bursa. Rarely, a true avulsion of the tibial tuberosity epiphysis can be demonstrated with ultrasound.

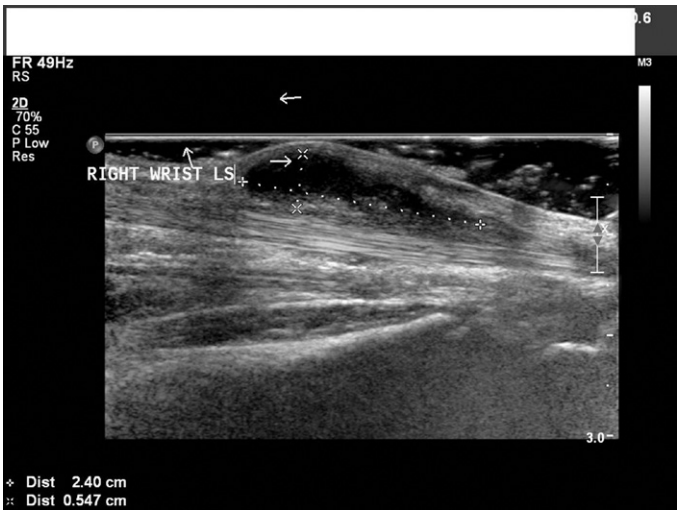

Figure 73.21 An anechoic fluid collection adjacent to the tendon fibres, with associated synovial thickening.

Sinding-Larsen and Johansson independently described the disease of apophysitis at the inferior pole of the patella with abnormality within the proximal third of the patellar tendon. This usually occurs in children aged 10–14 years who are involved with jumping sports.

Ultrasound shows fragmentation of the inferior pole of the patella and focal thickening and heterogeneity within the proximal patellar tendon.[20] Small focal echoes may be seen consistent with calcification within the tendon.

A sleeve fracture can occur with avulsion of the extension mechanism at the inferior pole of the patella. This is usually visible on a plain radiograph, but can also be detected sonographically.

Ultrasound is particularly useful in assessing overuse injuries to the soft tissues.

The unfused growth plate is a particular weak point in the skeleton and will often fracture before the soft tissues are damaged.

Children and young adults involved in sports can, however, present with superficial tendon pathology. The tendon at the point of insertion is most commonly affected. Sonographic findings include fluid around the tendon/within the tendon sheath, thickening of the tendon and loss of the normal homogeneous signal (Fig. 73.21).

In young people involved in running or jumping activities the tendons around the ankle joint are commonly affected, whilst the Achilles and popliteal tendons are less often involved.

Throwing sports such as cricket or racquet sports can cause injury to the tendons and soft tissues of the glenohumeral joint. Rotator cuff tears are uncommon in paediatrics, and when present are often associated with os acromiale or joint instability.

Muscle injury

Ultrasound is particularly useful in assessing muscle injuries in children. Unlike MRI, ultrasound is readily available, can be used in the acute setting and does not require sedation or anaesthesia.

Young children may present with a soft tissue lump without a history of specific trauma. Ultrasound is not only useful for the diagnosis of haematomas or muscle tears but also in identifying the subsequent complications, including infection and myositis ossificans.

Muscle tears

In the presence of a tear the normal architecture of the muscle is disrupted by an area of increased echogenicity. This is seen as a

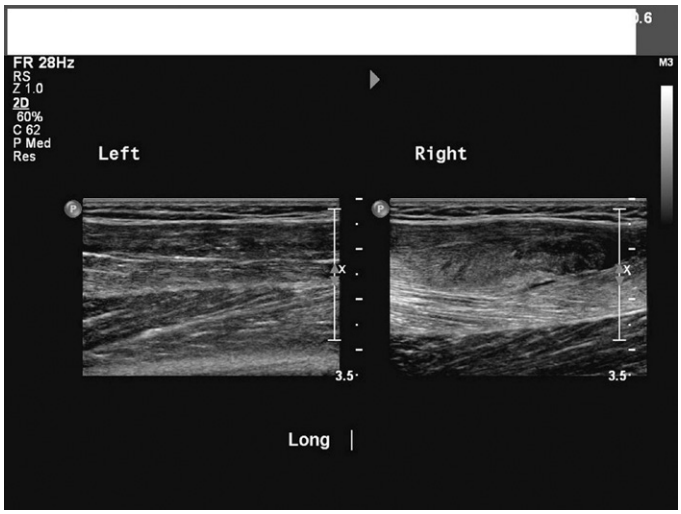

Figure 73.22 Muscle tear. The normal muscle architecture on the left and disruption of the fibres on the right due to a muscle tear.

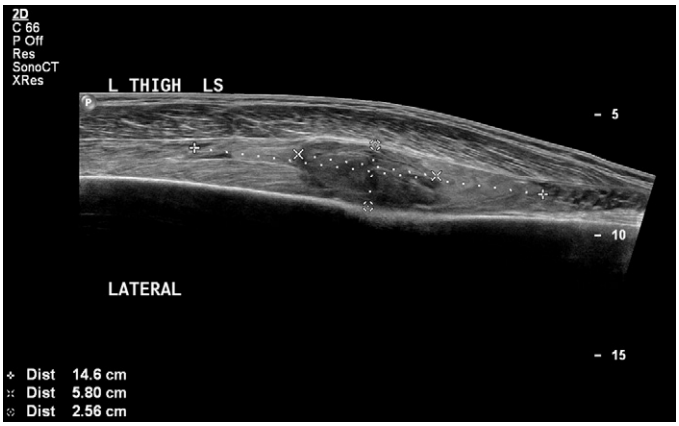

Figure 73.24 A large haematoma in the triceps muscle.

Figure 73.23 Extended field-of-view technique to demonstrate the tear.

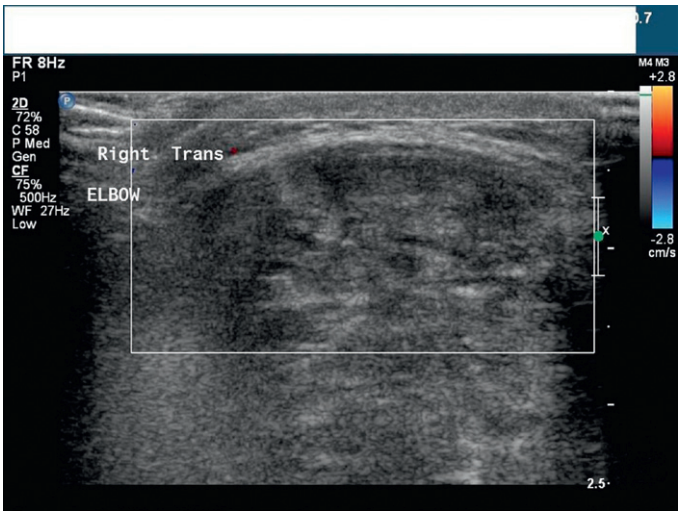

Figure 73.25 Colour flow imaging is useful in identifying vascularity within the lesion. This helps to distinguish between haematoma and tumour, but is not definitive.

diffuse area of abnormality without mass effect, with or without associated soft tissue swelling (Figs 73.22 and 73.23).

Interval scanning reveals gradual resolution of the changes.

If there is concern, cross-sectional imaging with MRI is helpful but biopsy of the abnormal area may be the only definitive way of excluding a malignancy.

Haematoma (Figs 73.24 and 73.25)

A haematoma will appear as a mixed echogenicity mass within the muscle, causing distortion of the muscle fibres. The adjacent tissues may be oedematous or show signs of reactive inflammation.

There should be no evidence of increased vascularity within a haematoma on colour Doppler imaging. This helps to distinguish it from other more sinister soft tissue lesions, but is not conclusive. The mass may show central anechoic areas consistent with areas of fluid as well as more echogenic foci consistent with localised haemorrhage.

The lesion will change in appearance and morphology over time, but should not progress unless there has been repeated trauma or there is an underlying bleeding disorder. Large, unresolving lesions should be carefully examined to exclude an underlying vascular malformation.

Foreign bodies

Imaging in trauma is a large part of paediatric radiology and identification and location of foreign bodies is a frequently requested investigation.

Large, radio-opaque foreign bodies are easily detected on plain radiographs.

Ultrasound is particularly useful in locating small, non radio-opaque foreign bodies, such as wood, thorns and other vegetable matter and even in visualising small fragments of glass.[21] Wooden foreign bodies as small as 2 mm in the soft tissues of the hand or foot can be located with a sensitivity of 90–100% and a specificity of 97–100%.[22–24]

Ultrasound can be used to more specifically locate large radio-opaque foreign bodies and position them in relation to adjacent structures, such as blood vessels. Sonography can also provide intra-operative guidance to surgeons, but caution should be applied not to mistake air within the soft tissues for a removable foreign body.

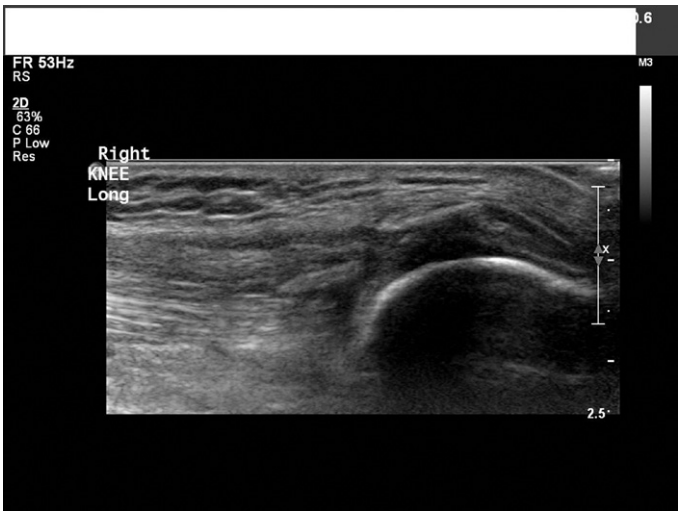

Figure 73.26 **With foreign bodies** it is important to assess the whole area. There are two foreign bodies within the soft tissues of the knee on this scan.

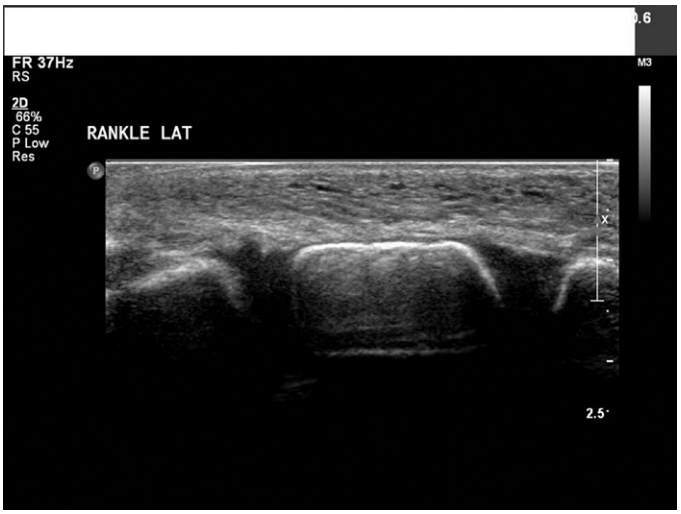

Figure 73.28 **Diffuse thickening of the subcutaneous fat** with multiple small areas of low echogenicity throughout the tissue consistent with oedema.

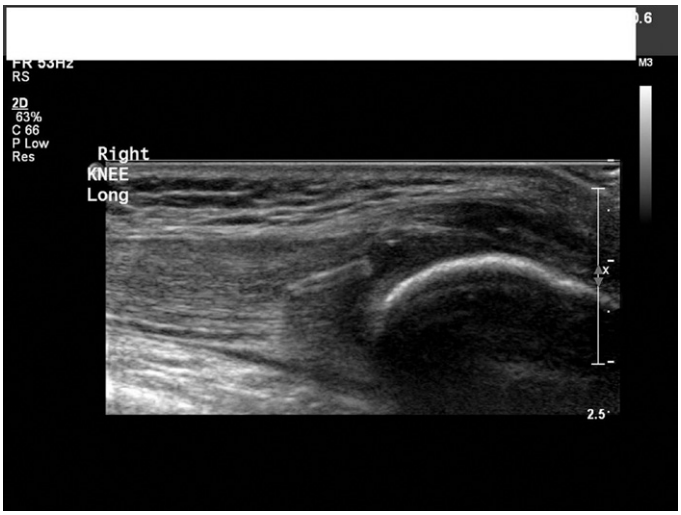

Figure 73.27 **A wooden splinter within the soft tissues,** seen as a linear area of focal echogenicity with posterior acoustic shadowing.

Foreign bodies appear on ultrasound as highly reflective foci. They typically demonstrate posterior acoustic shadowing, most notable when the foreign body is orientated perpendicular to the ultrasound beam (Figs 73.26 and 73.27).

Oedema or granulation tissue may develop around the foreign object, particularly around vegetable matter and chronic foreign bodies, and can cause a reflective halo that increases the visibility of the foreign body. These appearances will change over time and the foreign body will become less reflective as the inflammatory mass increases.

Myositis ossificans

The commonest site for myositis ossificans is the quadriceps femoris muscle. The radiographic appearances become definitive at 3–4 weeks after an injury when a characteristic cleavage plane can be seen between the area of calcification or ossification and the adjacent bone.

The typical centrifugal calcification or circumscripta pattern can be seen on computed tomography at about 2–3 weeks following injury, but clinical concern regarding an evolving soft tissue mass makes exclusion of a sinister lesion at an early stage very valuable. Ultrasound can identify calcification as early as 7 days post injury and can provide the necessary reassurance.

INFECTION

Superficial soft tissues

Infection of the superficial soft tissues causes disruption of the normal planes between the skin and the subcutaneous fat. In cellulitis the subcutaneous fat becomes thickened and echogenic (Fig. 73.28).

Ultrasound can be used to identify focal fluid collections within the soft tissues. These are typically anechoic or hypoechoic and may have poorly defined margins. The collection may extend across the planes between fat, skin and muscle.

Pyomyositis

Pyomyositis may develop following trauma or as a result of haematogenous spread of infection and should be considered in immunocompromised patients with unexplained pyrexia and limb pain.

Differentiation between haematoma and intramuscular infection can be difficult as the appearances are similar and range from focal thickening with disruption of the normal muscle architecture to a discrete anechoic or hypoechoic collection. Once identified, the true extent of the infection is best assessed by MRI, but sonographic follow-up is useful where MRI availability is limited.

Osteomyelitis

A subperiosteal collection may be the first indicator of osteomyelitis in a child (Fig. 73.29) and can precede radiographic features of osteomyelitis by several days.[24] This appears as a thin margin of fluid below the dark periosteal layer overlying the bone, and is not usually seen in older patients or adults where the periosteum is more strongly adherent to the bone. The typical sites affected are proximal femur, distal tibia, proximal humerus and distal radius/ulna.[17]

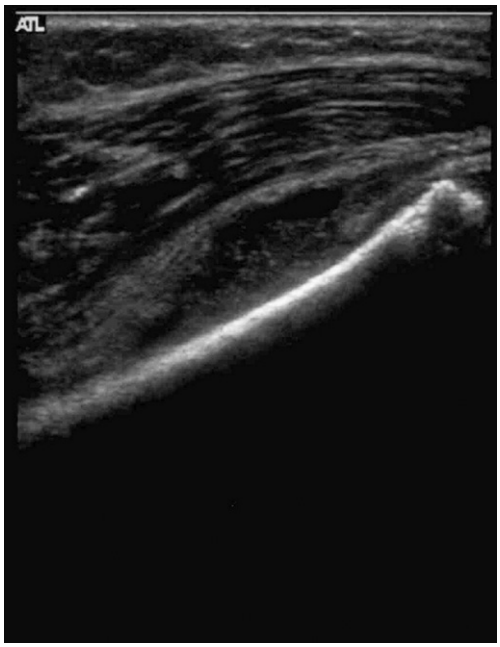

Figure 73.29 In osteomyelitis a subperiosteal collection may be the first radiological sign.

Infection	
Superficial infection	Disruption of the distinct planes between the tissues
Pyomyositis	Mixed echogenicity mass within the muscle with a focal area of low echogenicity
Osteomyelitis	Subperiosteal collection below the anechoic periosteum layer
Septic arthritis	Fluid within the joint Distension of the joint capsule

In more established infection ultrasound may show cortical breech or an associated pyomyositis or septic arthritis.

Doppler ultrasound can be used to assess disease progression. It has been reported that persistently increased vascularity around the periosteum, despite antibiotic therapy, is an indication for surgical intervention.

MONITORING LEG LENGTHENING PROCEDURES

Leg lengthening involves surgical resection of a portion of the diaphysis with progressive distraction of the opposing ends until a satisfactory length has been achieved.

Imaging is required to evaluate the intervening new bone formation and to help determine the rate of distraction. If distraction is too slow premature fusion may occur, whereas if distraction is too rapid new bone formation may be inadequate.

In order to avoid significant radiation doses ultrasound can be used in place of serial radiographs to assess new bone formation in leg lengthening procedures.

The external fixation device often makes radiography technically difficult and can obscure the area of interest; this is less of a problem for sonography, especially if a small footprint probe is used.

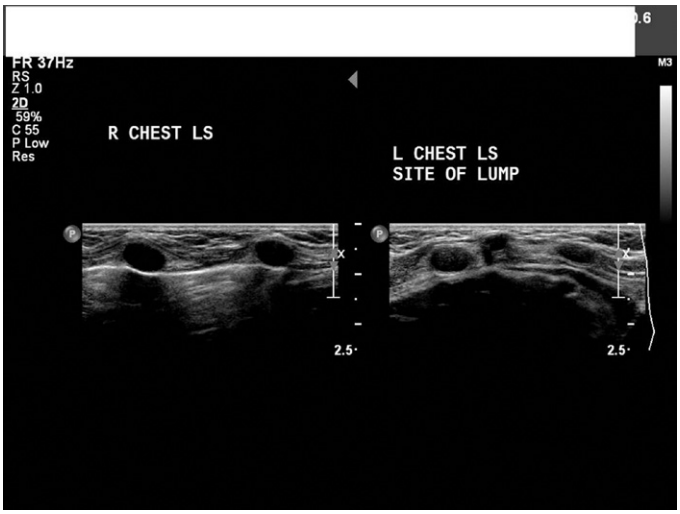

Figure 73.30 Bifid rib. A transverse section through an area of chest asymmetry due to a bifid rib on the left. Note the visualised structures are intact and undistorted.

Intervening bone within the distraction gap is visible on plain radiographs at approximately 8 weeks, whereas on ultrasound reflective foci appear by approximately 2 weeks. These foci are initially disorganised within the developing matrix, but start to align longitudinally by 4 weeks, developing into reflective bone continuous with the cortex at the bone ends and with a characteristic concave contour by 8 weeks.[25] This intervening new bone progresses to form a dense cortical line with posterior acoustic shadowing. Cystic spaces may develop within the distraction gap and interrupt new bone formation. These can be identified and even aspirated under ultrasound guidance.[26]

During the early stages of distraction when the edges are still well defined, ultrasound can provide accurate measurement of the distraction gap without the magnification created by conventional radiographs. Subsequently, new bone formation obscures the margins of the osteotomy.[27] Unfortunately, because of its limited field of view, ultrasound is less sensitive than radiography for the assessment of alignment.[28] Ultrasound can thus reduce the need for conventional radiographs in lower limb lengthening patients but cannot replace radiography entirely.

MASSES

Children frequently present with soft tissue 'lumps' that are not associated with trauma or other signs or symptoms.

Assessment of these with ultrasound is quick, simple and can be very reassuring. Equally ultrasound can be used to differentiate between those that need further imaging and those that do not.

Prior to examination with ultrasound it is pertinent to ask the patient or parent to localise the area of pathology. If appropriate, clinical examination prior to sonographic evaluation can be invaluable.

Normal anatomical variation

Chest wall asymmetry or intermittent soft tissue swelling of a periphery can easily be assessed with ultrasound.

Prominent or bifid ribs can be defined and compared with the contralateral side and reassurances given regarding the absence of a soft tissue mass or sinister lesion. In these cases it is important to ensure that the echogenic cortex of the rib is intact and that the overlying soft tissues are not swollen or distorted (Figs 73.30 and 73.31).

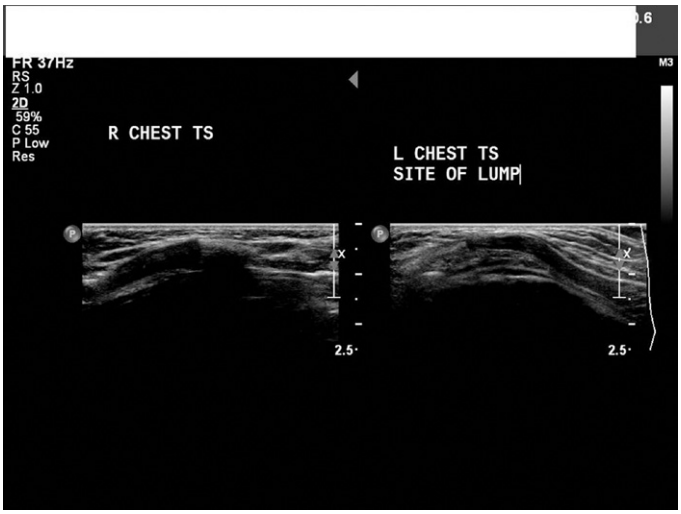

Figure 73.31 A longitudinal view of the left-sided bifid rib. There is no evidence of a soft tissue mass.

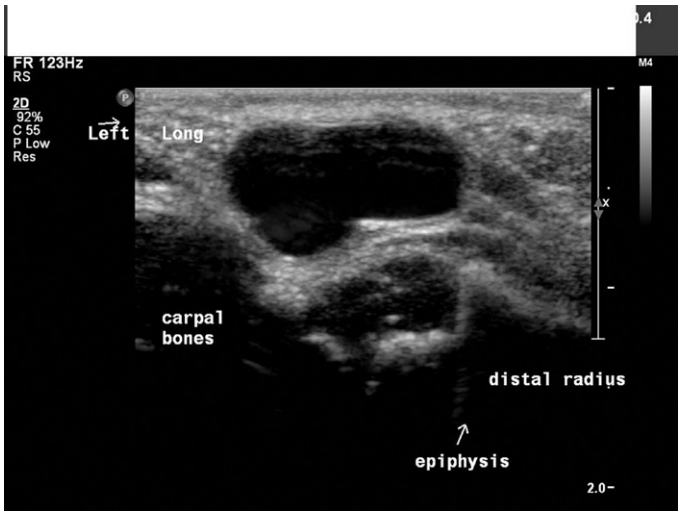

Figure 73.32 A thin-walled multiloculated synovial cyst (ganglion) arising from the midcarpal joint.

Doppler assessment of the area is useful in excluding a vascular malformation.

Intermittent swelling can be difficult to assess if the child presents for ultrasound during a quiescent episode. At this point it is helpful to exclude an underlying mass or vascular lesion and to ensure normal architecture of the tissues at the site of the swelling.

Colour Doppler should be applied to the area to exclude abnormal vascularity or signs of inflammation.

If further reassurance is required a repeat scan at the time of swelling is indicated.

Ultrasound is relatively non-invasive and requires no radiation exposure. It is almost always appropriate to examine the contralateral limb or adjacent structures for comparison, but it should be noted that pathology can be bilateral and that both sides may be abnormal.

Cysts

These can often be defined by their size and location.

Ganglions are small, well-defined synovial cysts that are most commonly associated with the small joints of the wrist and hand. They are usually less than 2 cm in diameter and are seen as well-demarcated anechoic cysts with posterior acoustic enhancement. The cyst may be unilocular or septated, but does not typically contain debris or echogenic material (Fig. 73.32).

Ganglions are very common in adults, but as many as 15% are seen in patients under 21 years of age.

Baker's cysts are synovial cysts arising from the posteromedial aspect of the knee joint, that typically present as a painless swelling in the popliteal fossa. They can occur in isolation or following trauma, but may be associated with inflammatory arthropathy in the knee joint. As with ganglions of the hand, popliteal cysts are typically thin-walled, anechoic and may be uni- or multilocular (Fig. 73.33). They arise between the semitendinosus and medial head of gastrocnemius and there may be a visible communication with the joint.

Baker's cysts can rupture and present with acute pain behind the knee. Ultrasound may show a fluid collection tracking between the muscle bundles, with associated diffuse soft tissue swelling and loss of definition of the muscle planes on the symptomatic side.

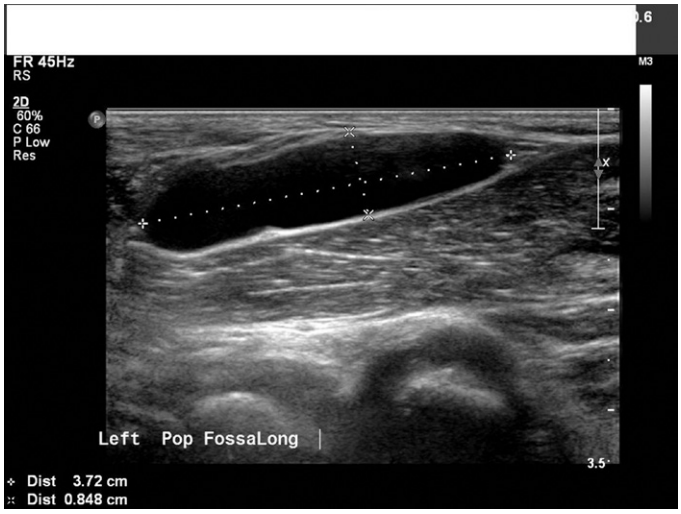

Figure 73.33 Baker's cyst. A thin-walled unilocular cyst in the popliteal fossa with no visible communication with the joint on this scan.

Vascular/Lymphatic malformations

Vascular lesions may have the classical clinical appearance of a superficial soft tissue swelling with a bluish hue and an audible bruit, but may present as an unexplained mass without specific clinical features.

Ultrasound, with Doppler imaging, is particularly useful in assessing these lesions.

These lesions may be predominantly vascular or lymphatic, but may be mixed. The vascular lesions appear as serpiginous, compressible, low-echogenicity masses with variable colour flow seen within the low-echogenicity areas (Figs 73.34 and 73.35). The lymphatic portions of the mass will not show colour flow, but will appear as anechoic cysts. Sometimes the loculi may be reflective or show fluid or debris levels due to haemorrhage or infection.

Vascular/lymphatic malformations may be superficial, but may be deep within the soft tissues. Usually their extent can be defined with ultrasound, particularly with the use of panoramic imaging, but occasionally these are extensive malformations requiring MRI to determine their complexity.

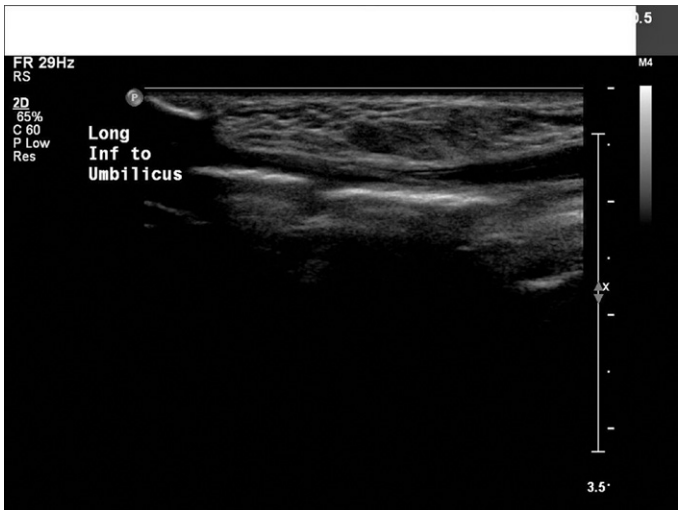

Figure 73.34 A relatively low-echogenicity lesion within the subcutaneous tissues of the abdominal wall.

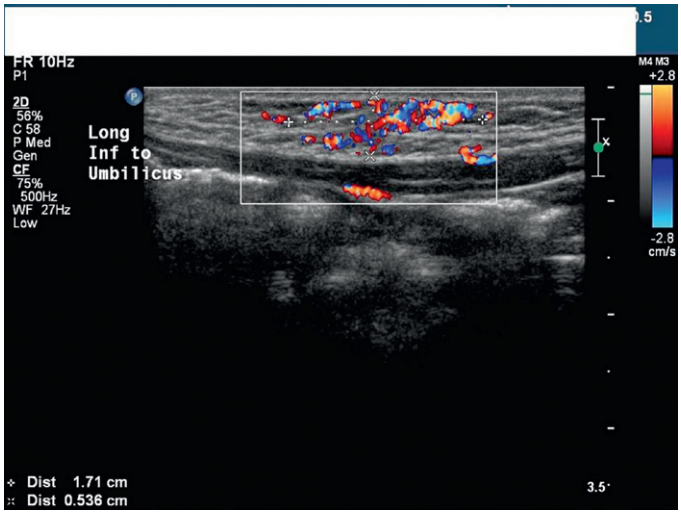

Figure 73.35 Colour Doppler scan of a soft tissue lump. The marked vascularity is characteristic of a vascular malformation.

Sternocleidomastoid tumour[29]

This is a lesion of uncertain aetiology also known as fibromatosis colli. It may be related to birth trauma and typically presents in infants at about 2–3 weeks of age as a firm swelling in the neck, with or without torticollis.

On ultrasound a localised swelling of the sternocleidomastoid muscle can be seen at the site of the palpable mass. There is distortion of the alignment of the muscle fibres but the structure of the muscle is usually maintained. These appearances represent fibrosis of the muscle (Fig. 73.36). This is usually unilateral and comparison with the normal, contralateral side can be useful.

These lesions typically regress spontaneously within a few months.

Lipoma

Lipomas are uncommon in children, but do occur and show the same appearances as in adulthood.

The mass is of relatively high echogenicity with posterior acoustic shadowing, it is well defined and located within the subcutaneous fat. There is absence of abnormal colour flow and the adjacent structures are normal (Figs 73.37 and 73.38).

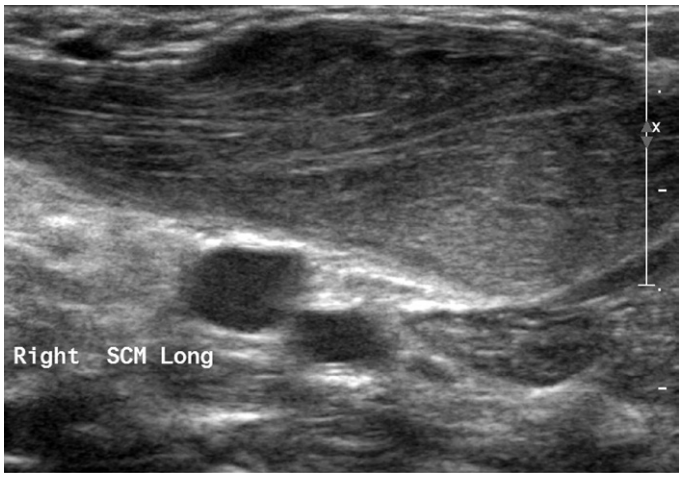

Figure 73.36 Diffuse swelling and increased echogenicity within the sternocleidomastoid tumour, without loss of the normal fibrous architecture.

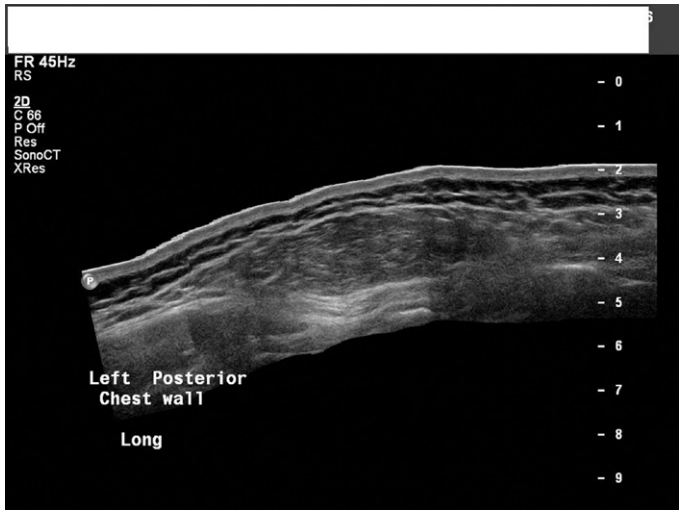

Figure 73.37 A well-defined chest wall lipoma.

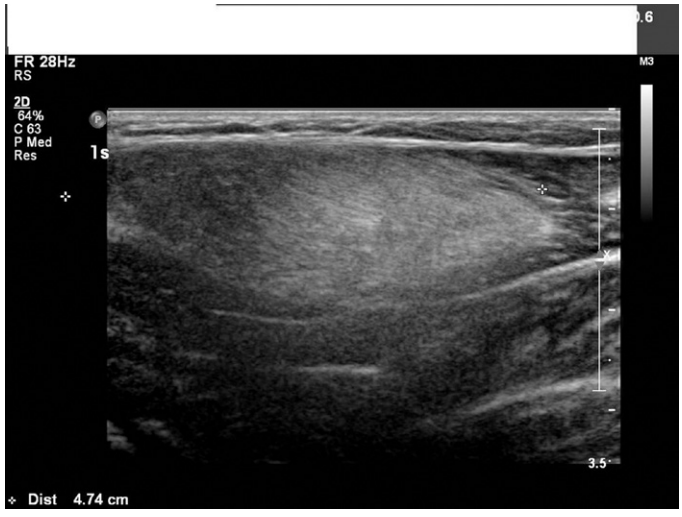

Figure 73.38 A more diffuse lipoma within the fibres of the gastrocnemius muscle.

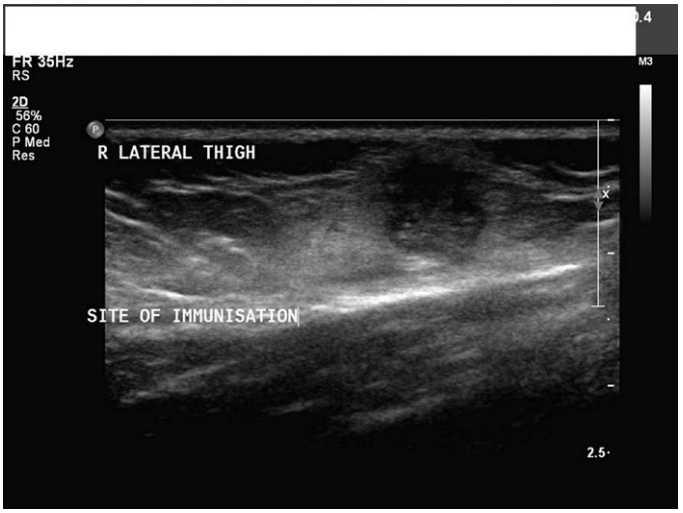

Figure 73.39 **There is disruption of the superfield fat** at the site of a recent immunisation in keeping with localised fat necrosis.

Masses	
Normal anatomical variants	Normal echogenicity of the soft tissues with no focal pathology
Synovial cyst	Well-defined, anechoic structures associated with a joint
Vascular malformation	Multiloculated, serpiginous anechoic structure with increased vascularity
Lipoma	Focal area of increased echogenicity within the subcutaneous fat or muscles
Sarcoma	Mixed echogenicity mass with irregular margins that extends across the tissue planes
	Abnormal vascularity within the lesion

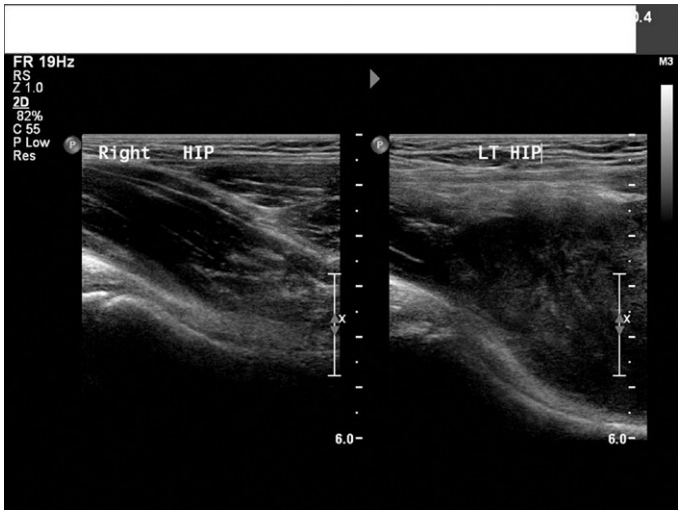

Figure 73.40 **Soft tissue mass.** Normal appearances on the right, with a large soft tissue mass disrupting the soft tissue planes on the left.

Fat necrosis can be seen following immunisation and may present with a palpable lump or with a focal indentation of the skin.

On ultrasound the area will appear as a superficial area of irregular low echogenicity within the subcutaneous fat. There should be no abnormal colour flow and no extension into the deeper tissues (Fig. 73.39).

Any superficial mass that extends into the muscle layer should be diagnosed with caution. Follow-up ultrasound is certainly warranted to assess any change and if there are concerns MRI is justified.

Sinister lesions

Soft tissue sarcomas or even bony sarcomas may present as a palpable lump and ultrasound may be the primary investigation.

Any lesion that has ill-defined margins, extends across the different tissue planes and has abnormal vascularity should raise concerns and be investigated further and without delay (Fig. 73.40).

The presence or absence of calcification should be noted and the adjacent bony cortex should be examined to define any cortical breech or associated periosteal reaction.

REFERENCES

1. Wynne-Davies R. Acetabular dysplasia and familial joint laxity: 2 etiological factors in congenital dislocation of the hip. A review of 589 patients and their families. J Bone Joint Surg Br 1970;52B:704–716.
2. Cooperman DR, Wallensten R, Stulberg SD. Acetabular dysplasia in the adult. Clin Orthop 1983;175:79–85.
3. Place MJ, Parkin DM, Fitton JM. Effectiveness of neonatal screening for congenital dislocation of the hip. Lancet 1978;ii:249–251.
4. Standing Medical Advisory Committee. Screening for the detection of congenital dislocation of the hip in infants. London: Department of Health and Social Services; 1969.
5. Graf R. The diagnosis of congenital hip-joint dislocation by the ultrasonic-Combound treatment. Arch Orthop Trauma Surg 1980;97:117–133.
6. Harcke HT, Grissom LE. Performing dynamic sonography of the infant hip. AJR Am J Roentgenol 1990;155:837–844.
7. Yousefzadeh DH, Ramillo JL. Normal hip in children: correlation of ultrasound with anatomic and cryomicrotome sections. Radiology 1987;165:647–655.
8. Harcke HT. Hip in infants and children. Clin Diagn Ultrasound 1995;30:179–199.
9. Graf R. Classification of hip joint dysplasia by means of sonography. Arch Orthop Trauma Surg 1984;102:248–255.
10. Graf R. Hip sonography. Diagnosis and management of infant hip dysplasia. 2nd ed. Berlin: Springer; 2006.
11. Rosendahl R, Toma P. Ultrasound in the diagnosis of developmental dysplasia of the hip in newborns. The European approach. A review of methods, accuracy and clinical validity. Eur Radiol 2007;17:1960–1967.
12. Graf R, Wilson B. Sonography of the infant hip and its therapeutic implications. Weinheim: Chapman and Hall; 1995.
13. Harcke HT, Clark NMP, Lee MS, et al. Examination of the hip with real time ultrasound. J Ultrasound Med 1984;3:131–139.
14. Boal DKB, Schwentker EP. Assessment of congenital hip dislocation with real time ultrasound. A pictorial essay. Clin Imaging 1991;15:77–90.
15. Terjesen T, Osthus P. Ultrasound in the diagnosis of and follow up of transient synovitis of the hip. J Paediatr Orthop 1991;11:608–613.
16. Marchal GJ, Van Holsbeeck MT, Raes M, et al. Transient synovitis of the hip in children: role of ultrasound screening. Radiology 1987;162:825–828.
17. Bryn R. Paediatric ultrasound. How, why and when. London: Elsevier; 2005. p. 301–319.
18. Bellah R. Ultrasound in pediatric musculoskeletal disease. Techniques and applications. Radiol Clin North Am 2001;39(4):597–618.
19. Standards for imaging in suspected non accidental injury. Royal College of Radiologists/Royal College of Paediatrics and Child Health; March 2008.

20. De Flavius L, Nessi R, Scaglione P, et al. Ultrasonic diagnosis of Osgood-Schlatter and Sinding-Larsen-Johansson diseases of the knee. Skeletal Radiol 1989;18:193–197.
21. Banerjee B, Das RK. Sonographic detection of foreign bodies of the extremeties. Br J Radiol 1991;64:107–112.
22. Bray PW, Mahoney JL, Campbell JP. Sensitivity and specificity of ultrasound in the diagnosis of foreign body in the hand. J Hand Surg (Am) 1995;20A:661–666.
23. Rockett MS, Gentile SC, Gudas CJ, et al. The use of ultrasonography for the detection of retained wood foreign bodies of the foot. J Foot Ankle Surg 1995;34:478–484.
24. Riebel E, Nash R, Nazarenko O. The value of sonography in the detection of osteomyelitis. Paediatr Radiol 1996;26:291–297.
25. Young JWR, Kovelman H, Resnik CS, Paley D. Radiological assessment of bones after Ilizarov procedures. Radiology 1990;177:89–93.
26. Young JWR, Kostrubiak IS, Resnik CS, Paley D. Sonographic assessment of bone production in the distraction site for Ilizarov limb lengthening procedures. AJR Am J Roentgenol 1990;154:125–128.
27. Eyres KS, Hughes T, Fixsen JA. Methods for assessing new bone formation during limb lengthening – ultrasonography, dual energy X-ray absorptiometry and radiography compared. J Bone Joint Surg Br 1993;75B:358–364.
28. Maffulli. N, Hughes T, Fixsen JA. Ultrasonographic monitoring of limb lengthening. J Bone Joint Surg Br 1992;74B:130–132.
29. Dahnert W. Radiology review manual. 5th edn. Philadelphia: Lippincott Williams and Wilkins; 2003. p. 379.

INDEX

Note: Page numbers followed by b indicate boxes, f indicate figures and t indicate tables.

A

B

C

D

E

F

G

H

I

J

K

L

M

N

O

P

Q

R

S

T

U

V

W

X

Y

Z